(昭和30年6月23日 第三種郵便物認可 J. Phys. Soc. Japan, Vol. 15, No. 7 昭和35年7月5日発行 毎月1回5日発行)

5/Jl-Dec

1960

JOURNAL
OF THE
PHYSICAL SOCIETY
OF JAPAN

PT 2

Volume 15 Number 7

July 1960

Published by the
PHYSICAL SOCIETY OF JAPAN

Journal of the Physical Society of Japan

Published monthly by the Physical Society of Japan and devoted to original papers in physics and related fields which materially contribute to the progress of physics

BOARD OF EDITORS (1959-1960)

T. Kato (Chief Editor), S. Asaka, M. Hatoyama, H. Horie, I. Imai, T. Inui, E. Ishiguro, K. Ishiguro, K. Kinosita, G. Kuwabara, S. Miyahara, T. Nagamiya, S. Ono, S. Ogawa, K. Senda, T. Suzuki, S. Suwa, H. Takahasi, T. Tanaka, E. Tatsumoto, M. Toda, Y. Tomono, S. Tomotika, R. Uyeda.

SUGGESTIONS TO OVERSEAS CONTRIBUTORS

Manuscript should be addressed to the Office of the Physical Society of Japan, Room No. 342, Physics Building, Faculty of Science, University of Tokyo, Bunkyo-ku, Tokyo.

Each manuscript should be prepared as concisely as possible. Its organization should conform to the following: title, author's name, name and address of the author's institution, synopsis of about 100 words, body of the paper, list of references, tables and figures. The textual material should be typewritten, double-spaced on white bond paper of letter size. The original copy is required. Literature reference should be numbered consecutively. Figures and photographs will be printed in any of the following sizes (at the choice of the author): 3 cm, 6 cm, 12 cm in breadth, less than 18 cm in height. The original should be 2.5 to 3 times as large as the size in print. The drawing should be a very neatly prepared original with lettering, in Indian ink. Self-explanatory titles to figures and photographs are essential.

Short Note Section is provided for brief reports which need prompt publication. The manuscript of a Short Note should follow the same style and form as that required for a full paper with the exception that it needs no synopsis. The available space for a Short Note is one page of the Journal (about 800 words).

Galley proof only will be sent to the author. Proof should be carefully corrected and returned as soon as possible to the Office of the Society. For prompt publication, proof of the Short Note will sometimes be read by the Editor in place of the author.

Reprints may be ordered in lots of 50. The author or the author's institution is requested to pay charges according to the following formulae:

$\$\,(2.00+0.10p^2+(1.50+0.01x)p+3A)$ for full paper, $\$\,(3.00+0.01x)$ for Short Note.
Here p stands for the number of printed pages of the paper, x for the number of copies required, and A for the number of sheets of art paper if any.

SUBSCRIPTION

Subscription orders as well as related inquiries should be addressed to the Office of the Society or to one of the following agents:

Maruzen Co. Ltd.: P. O. Box 605, Central, Tokyo
Nauka Ltd.: 2-chome, Jinbocho, Kanda, Tokyo
Charles E. Tuttle Co.: 15 Edogawa-cho, Bunkyo-ku, Tokyo
Charles E. Tuttle Co.: Rutland, Vermont, U.S.A.
Parkins Oriental Books: 5011, York Blvd., Los Angeles 42, Calif., U.S.A.

Subscription rate (for non-members, postage covered)

Annual..................$ 10.00 Single issue ....$ 1.00

Back numbers (postage covered)

	Yearly	Single copies, each
Vol. 1 (1946)	$ 1.00	
Vol. 2 (1947) -6(1951)	$ 5.00	$ 1.00
Vol. 7 (1952) -9(1954)	$ 6.00	$ 1.20
Vol. 10 (1955)-12(1957)	$ 8.00	$ 1.00
Vol. 13 (1958)-14(1959)	$12.00	$ 1.20

—投稿規定は 1959 年発行の会員名簿に掲載してあります—

JOURNAL OF THE PHYSICAL SOCIETY OF JAPAN, Vol 15, No. 7, JULY, 1960

Gamma Rays from Several Elements Bombarded by 10 and 14 MeV Protons.

By Tetsuo WAKATSUKI, Yasuo HIRAO, Eiji OKADA, Iwao MIURA,
Kenzo SUGIMOTO and Akira MIZOBUCHI

Department of Physics and the Laboratory of Nuclear Studies,
Faculty of Science, Osaka University, Osaka

(Received December 14, 1959)

Gamma ray spectra and intensities from C, O, Mg, Al, Si, Ca, Ti, Cr, Fe, Ni, Cu, Ag, Cd, Sn, Pt, Au and Pb bombarded by 10 and 14 MeV protons have been studied.

For C, O, Mg, Si and Ca, most of the gamma rays could be attributed to the inelastic scattering. New levels at 7.08 and 8.13 MeV are suggested in ^{40}Ca.

§ 1. Introduction

The analysis of gamma rays from the excited states of nuclei gives valuable informations on the properties of nuclei. Detailed investigations have been carried out for many nuclear levels following the decays of radioactive nuclides and for nuclear levels of nuclides formed by proton or neutron capture. Compared to these investigations, excitations of nuclear levels by the inelastic scattering of protons has the advantage that it can be applied for most of the nuclei and is especially suitable for studying relatively lower levels. Gamma rays resulting from inelastic scattering of protons have been studied only for few elements at relatively low proton energies. We have investigated the gamma rays due to inelastic scattering of protons using proton energies up to 5.7 MeV for some light elements[1]. In this paper, we shall report the results of similar investigations in which we employ 10 and 14 MeV protons in an attempt to observe gamma rays from higher excited states. In this case, however, due to higher proton energies, gamma rays following (p, n), $(p, \alpha)\cdots$ reactions pile up upon those due to inelastic scattering for most elements.

For C, O, Mg, Si and Ca, the gamma ray spectra could be resolved and identified for the most part as coming from various levels excited by the inelastic scattering of protons. For the other elements investigated (Al, Ti, Cr, Fe, Ni, Cu, Ag, Cd, Sn, Pt, Au and Pb) the spectra could not be fully resolved. In these cases, a survey on the energy spectra was made including higher energy spectra following capture of protons.

§ 2. Experimental Arrangements

The proton beam from 63 in. variable energy cyclotron of the Institute for Nuclear Study of the University of Tokyo was used. The general arrangements are shown in Fig. 1.

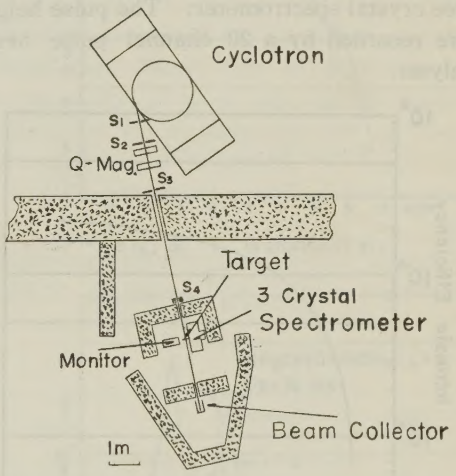

Fig. 1. T. Wakatsuki etc.

To avoid background due to neutrons, the protons were collimated to a narrow beam by slits S_1 (6 mm × 6 mm), S_2 (7 mm width) and S_3 (7 mm height) in the cyclotoron room so that no proton hit the wall of the beam duct. S_4 is a slit 6 mm wide and 10 mm high in front of the target. All those slits were made of graphite and a lead block of 10 cm thickness with a hole of size 8 mm × 12 mm was placed just behind the slit S_4 to absorb the gamma rays emitted from graphite along the beam duct. The targets used were all thin foils and protons after traversing the target were collected in a Faraday cup placed 2.7 m

1155'' 63 / 10

away from the target and measured by a current integrater. The size of the beam, as measured by colouration of a glass plate at the position of the target, was 2 mm in width and 14 mm in height. The target, detecter and Faraday cup were shielded by surrounding with concrete blocks as shown in Fig. 1.

The detectors for gamma rays were single crystal spectrometer with NaI (Tl) 3 in. in diameter and length, and a three crystal scintillation pair spectrometer with a center crystal of 1½ in. diameter and 4 in. long. The side crystals were 3 in. in diameter and length. The gamma ray to the three crystal pair spectrometer was collimated by a lead block with a hole 2.5 cm in diameter and 10 cm in length. Scintillation crystals were shielded by 10 cm thick lead blocks. The distance from the target to the surface of the scintillation crystal was 12 cm for the single crystal spectrometer and 18 cm for the center crystal of three crystal spectrometer. The pulse heights were recorded by a 20 channel pulse height analyzer.

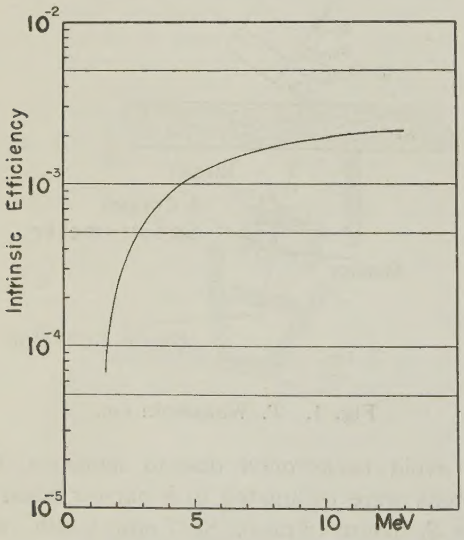

Fig. 2. Calculated efficiency of the three crystal spectrometer for the gamma ray incident on the center crystal surface.

To determine the cross sections we used a calculated efficiency curve for our three crystal spectrometer shown in Fig. 2. The absolute value was normalized at 4.43 MeV gamma rays produced by $^{12}C(p, p'\gamma)$ reaction at proton energy of 14 MeV for which inelastic cross section has been determined by Peelle at 14.0 MeV[2]. For a single crystal spectrometer, efficiency curves obtained by Lazer et al. were utilized[3]. The spectrometer was calibrated for gamma ray energies by ^{60}Co(1.17 and 1.33 MeV), ThC″(2.62 MeV) and $^{12}C(p, p'\gamma)$ (4.43 MeV). The energy resolution of our three crystal spectrometer was 13.8% at 2.62 MeV and 9.7% at 4.43 MeV. The resolution of the single crystal spectrometer was 6.3% at 2.62 MeV.

§ 3. Results and Discussions

1) C

Three crystal pair spectra of gamma rays from polyethylene target 4.3 mg/cm² thick bombarded by 14 and 10 MeV protons are shown in Fig. 3 and Fig. 4, respectively. Besides the intense 4.43 MeV gamma ray from the first excited state of ^{12}C, there appear weaker gamma rays of energy between 6 and 8 MeV. The ratio of the intensity to that of 4.43 MeV is about 1/300 for both 14 and 10 MeV protons considering the detector efficiency. The second excited state of ^{12}C at 7.66 MeV has been investigated by authors[4] and its spin is assigned as 0^+, which decays to ^{8}Be and α particle and no ground state gamma transition can be expected. From the above value of the ratio of gamma rays we may calculate the upper limit of Γ_γ/Γ for

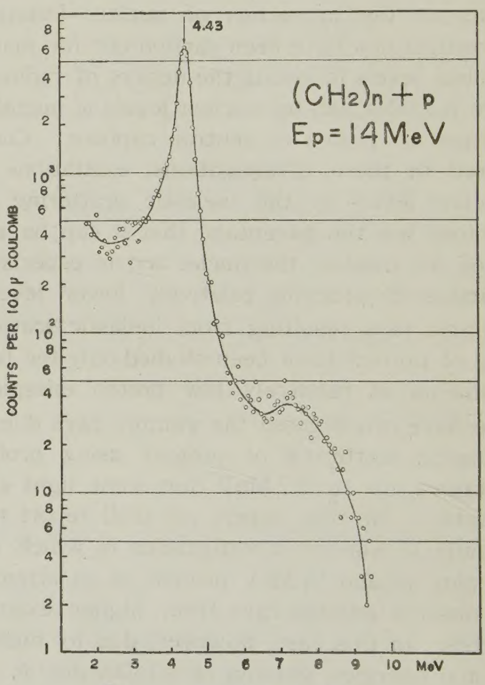

Fig. 3. T. Wakatsuki etc.

7.66 MeV level if the ratio of cross sections for inelastic scattering leading to 7.66 and 4.43 MeV level is known. As the cross sections for 14.0 MeV protons are not available, we used the cross sections at 16.7 MeV[2] and obtained the result $\Gamma_\gamma/\Gamma<10\%$. The value of upper limit 10% is consistent 1.4% obtained by Moak et al.[5]

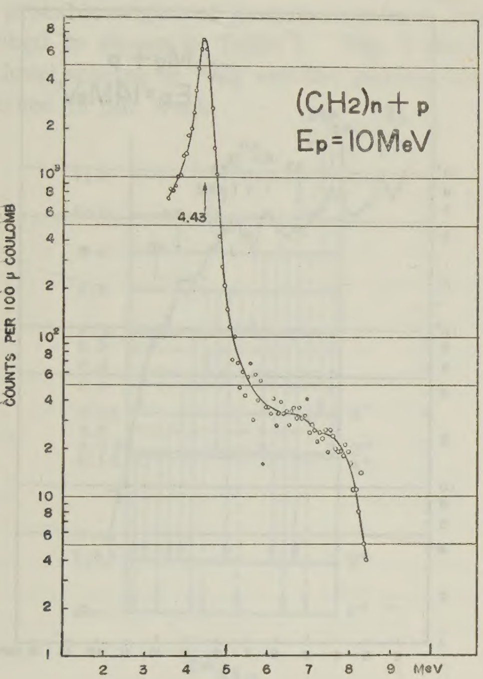

Fig. 4. T. Wakatsuki etc.

To see if the gamma rays between 6 and 8 MeV comes from the capture of protons by ^{12}C, we measured the gamma ray spectra under similar conditions using 5.5 MeV protons from 44 in. cyclotron at Osaka University. Though the capture gamma rays are expected to increase compared to 4.43 MeV inelastic gamma rays at lower bombarding energies, the intensity of higher energy gamma ray was observed not to exceed the intensity (compared to 4.43 MeV gamma rays) at proton energy of 14 MeV. Therefore, the origins of the higher energy gamma rays at 6∼8 MeV observed in the present experiment are perhaps ^{13}C$(p, p'\gamma)$ reaction but some part may be the results of ^{13}C$(p, n\gamma)$ reaction and pile up of 4.43 MeV gamma rays.

2) O

Self supporting film of polyvinylacetate $-CH_2CH(O\cdot CO\cdot DH_3)-$ 2.8 mg/cm² thick was bombarded by 14 and 10 MeV protons. Three crystal pair spectra are shown in Fig. 5 and Fig. 6. Besides 4.43 MeV gamma rays from ^{12}C, intense gamma rays from the excited states of ^{16}O at 6.13, 6.19 and 7.10 MeV were observed for both proton energies. Moreover, for proton energy of 14 MeV, 8.87 and 5.65

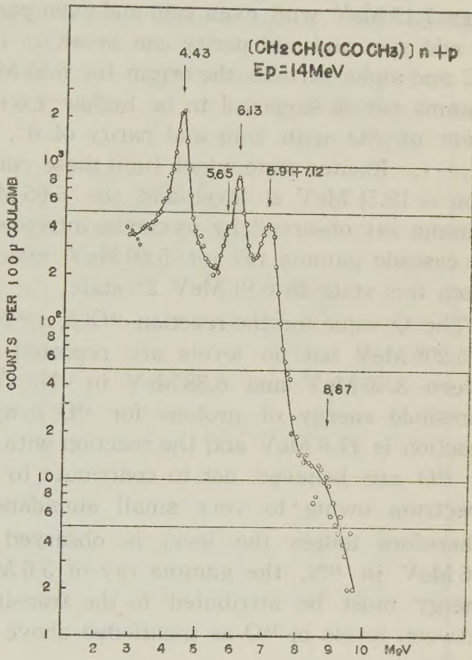

Fig. 5. T. Wakatsuki etc.

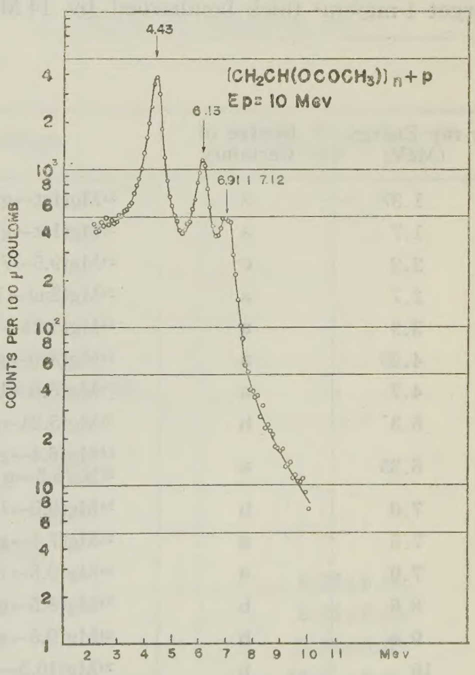

Fig. 6. T. Wakatsuki etc.

MeV gamma rays were observed. The former comes from 8.87 MeV state of ^{16}O and the latter, not observed for proton energy of 10 MeV and observed also from SiO_2 bombarded by 14 MeV protons (Fig. 9) can be interpreted as cascade gamma ray from higher excited state of ^{16}O. As the excited state of ^{16}O higher than 7.15 MeV with even spin and even parity or odd spin and odd parity can break up into ^{12}C and alpha particle, the origin for 5.65 MeV gamma ray is supposed to be higher excited state of ^{16}O with spin and parity of 0^-, 1^+, 2^-, $\cdots$. Excited state which fulfil these condition is 12.51 MeV 2^- level and the 5.65 MeV gamma ray observed by us can be interpreted as cascade gamma ray (of 5.60 MeV energy) from this state to 6.91 MeV 2^+ state.

The Q value for the reaction $^{16}O(p, \alpha)^{13}N$ is -5.208 MeV but no levels are reported between 3.56 MeV and 6.38 MeV in ^{13}N. The threshold energy of protons for $^{16}O(p, n)^{16}F$ reaction is 17.8 MeV and the reaction with ^{17}O or ^{18}O are believed not to contribute to the spectrum owing to very small abundances. Therefore unless the level is observed at 5.6 MeV in ^{13}N, the gamma ray of 5.6 MeV energy must be attributed to the transition between levels in ^{16}O as mentioned above.

3) Mg

A gamma ray spectrum from magnesium target 1 mg/cm² thick bombarded by 14 MeV protons is shown in Fig. 7. Q values for $^{24}Mg(p, n)^{24}Al$, $^{25}Mg(p, n)^{25}Al$ and $^{26}Mg(p, n)^{26}Al$ are -14.8, -5.02 and -4.5 MeV, respectively. Q values for $^{24}Mg(p, \alpha)^{21}Na$, $^{25}Mg(p, \alpha)^{22}Na$ and $^{26}Mg(p, \alpha)^{23}Na$ are -6.880, -3.161, -1.848 MeV, respectively. Q values for $^{24}Mg(p, \alpha)^{21}Na$, $^{25}Mg(p, \alpha)^{22}Na$ and $^{26}Mg(p, \alpha)^{23}Na$ are -6.880, -3.161 and -1.848 MeV,

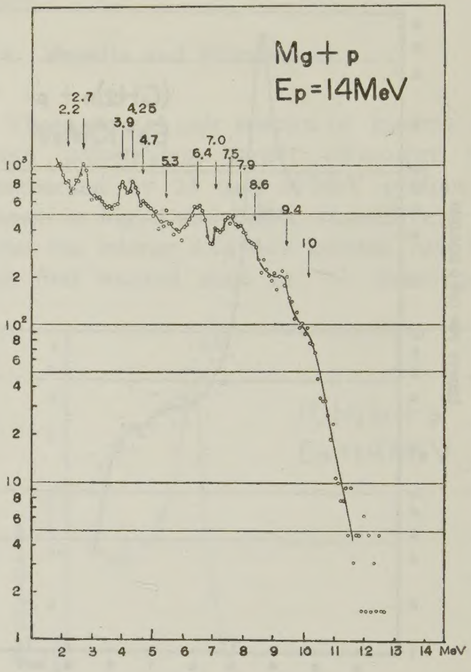

Fig. 7. T. Wakatsuki etc.

Table I.

γ-ray Energy (MeV)	Degree of Certainty	Possible Origin
1.37	a	^{24}Mg(1st→g)
1.7	a	^{26}Mg(1st→g), ^{25}Mg(3rd→g)
2.2	c	^{24}Mg(9.5→7.4), ^{24}Mg(8.5→6.4), ^{22}Na(2.22→g), ^{23}Na(2.64→0.44)
2.7	a	^{24}Mg(2nd→1st), ^{23}Na(2.71→g)
3.9	a	^{24}Mg(5.24→1st), ^{25}Al(3.85→g)
4.25	a	^{24}Mg(3rd→g), ^{24}Mg(9.5→5.25; 8.5→4.24), ^{25}Al(4.22→g)
4.7	a	^{24}Mg(6.0→1.37), ^{24}Mg(9.5→4.8; 11.5→6.9; 10.5→6.0), ^{23}Na(4.78→g)
5.3	b	^{24}Mg(5.24→g; 9.5→4.12), ^{25}Al(5.30→g)
6.35	a	^{24}Mg(6.4→g; 10.5→4.12 or 4.24; 11.5→5.25), ^{26}Al(6.80→0.418) ^{23}Na(6.3→g)
7.0	b	^{24}Mg(9.5→1.37), ^{26}Al(7.20→0.228), ^{23}Na(7.2→g)
7.5	a	^{24}Mg(7.4→g)
7.9	a	^{24}Mg(9.5→1.37)
8.6	b	^{24}Mg(8.5→g)
9.4	b	^{24}Mg(9.5→g)
10	b	^{24}Mg(10.5→g; 11.5→1.37)

respectively. Matsuda, Oda and others measured energy spectra of scattered protons from magnesium using 14 MeV protons[7]. They have found scattered protons from 1.37, 4.2 (4.12, 4.24), 5.24, 6.0, 7.4, 8.5 and 9.5 MeV levels of ^{24}Mg. Considering these results and Q values for (p, n) and (p, α) reactions as well as the previous works with magnesium[1),6)] the probable origins of gamma rays have been ascribed as shown in Table I. Fig. 8 shows the level scheme of ^{24}Mg and the gamma rays observed in our work.

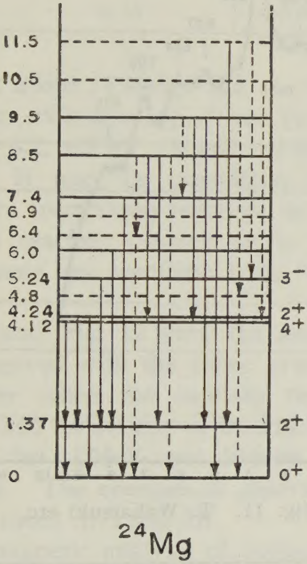

Fig. 8. T. Wakatsuki etc.

4) Si

A thin target of SiO$_2$ of 1.5 mg/cm^2 in thickness was used. The Q values of (p, n) and (p, d) reactions for ^{28}Si and ^{16}O are negative and larger than about 14 MeV. For (p, α) reactions, these values are −7.71 and −5.20 MeV for ^{28}Si and ^{16}O, respectively. But considering barrier penetrabilities, high energy

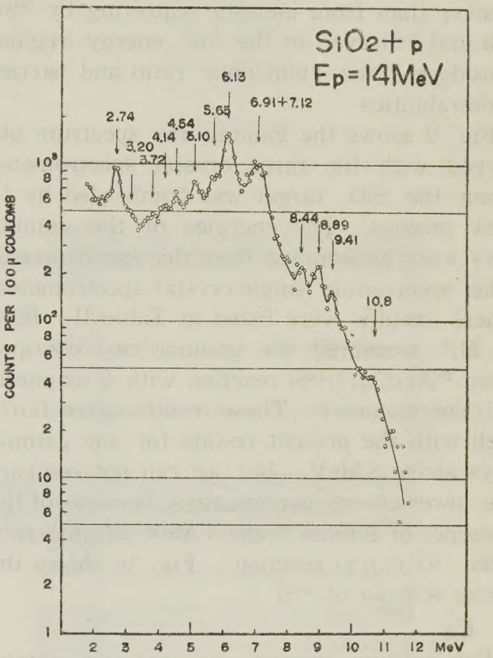

Fig. 9. T. Wakatsuki etc.

Table II.

γ-ray Energy (MeV)	Degree of Certainty	Possible Origin	Results from the work of Bent et al[8)]
1.72	a	^{28}Si(1st→g)	
1.96	c	^{29}Si(2nd→g)	
2.29	c	^{30}Si(1st→g)	
2.74	a	^{28}Si(2nd→1st)	
3.20	b	^{28}Si(3rd→1st)	
3.72	b	^{30}Si(3rd→g), ^{28}Si(8.3→4.6)	
4.14	b	^{28}Si(8.6→4.6), ^{29}Si(6.10→2.03)	
4.54	a	^{28}Si(2nd→g)	
5.10	a	^{28}Si(3rd→g)	
5.65	a	^{16}O(12.51→6.91)	
6.13	a	^{16}O(2nd→g)	
7.0	a	^{16}O(3rd→g), (4th→g)	
8.44	a	^{28}Si(8.3→g)	8.28±0.04
8.89	b	^{28}Si(8.6→g)	8.75±0.04
9.41	c	^{28}Si(9.3→g)	9.45±0.08
10.8	b	^{28}Si(10.03(10.7)→g)	10.7 ±0.2

gamma rays from these reactions are considered to be less intense than from the (p, p') reactions.

The Q values for $^{29}Si(p, n)$, (p, d) and (p, α) reactions are −5.75, −6.25 and −4.82 MeV, respectively. These values for ^{30}Si are −5.05, −8.3 and −2.38 MeV, respectively. These reactions may occur, but the gamma ray intensities from these reactions may be also weaker than from inelastic scattering by ^{28}Si, ^{29}Si and ^{30}Si even in the low energy region, considering the abundance ratio and barrier penetrabilities.

Fig. 9 shows the gamma ray spectrum observed with the three crystal spectrometer when the SiO_2 target was bombarded by 14 MeV protons. The energies of the gamma rays were determined from this spectrum and other spectrum of single crystal spectrometer. These results were listed in Table II. Bent et al.[8] measured the gamma ray energies from $^{27}Al(d, n\gamma)$ ^{28}Si reaction with a magnetic pair spectrometer. These results agree fairly well with the present results for the gamma rays above 8 MeV. But we can not compare the lower energy gamma rays, because of the presence of intense 6 and 7 MeV gamma rays from $^{16}O(p, p'\gamma)$ reaction. Fig. 10 shows the decay scheme of ^{28}Si.

5) Ca

For calcium targets, we used two metalic calcium foil targets of different thickness, one of which was 0.8 mg/cm² and the other was 2.0 mg/cm² in thickness, in order to estimate the effect of oxygen impurity on the surface of the foil. This effect could not be observed. The isotopic abundance of ^{40}Ca is 97% and that of ^{44}Ca is 2%. The Q values of $^{40}Ca(p, n)$ and (p, d) reactions are also negative and

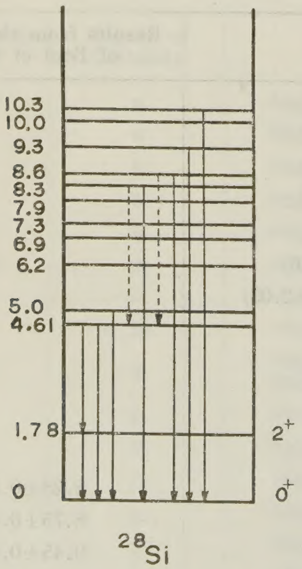

Fig. 10. T. Wakatsuki etc.

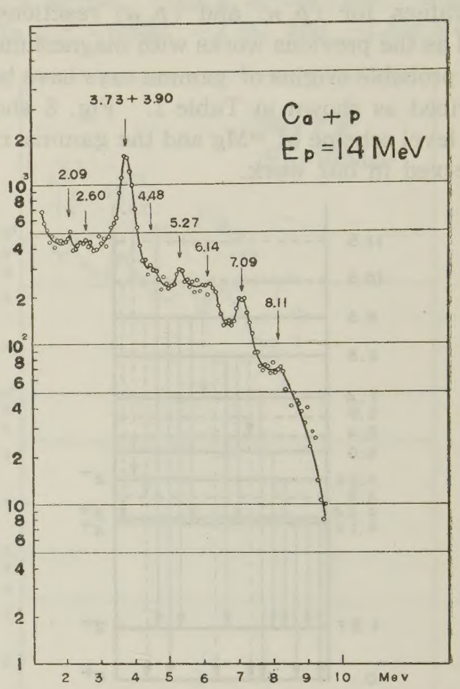

Fig. 11. T. Wakatsuki etc.

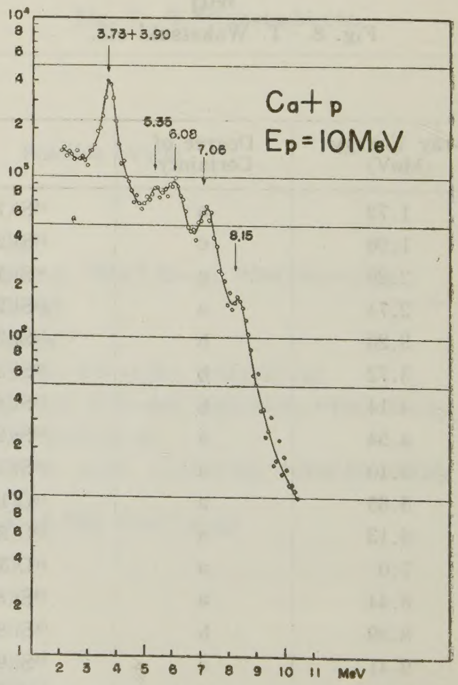

Fig. 12. T. Wakatsuki etc.

Table III.

γ-ray Energy (MeV)			Degree of Certainty	Possible Origin
E_p=10 MeV	E_p=14 MeV	Mean Value		
—	2.09	2.09	b	^{40}Ca(6.03→3.90)
2.57	2.60	2.59	b	^{40}Ca(6.03→3.35; 7.09→4.48)
3.73	3.73	3.73	a	^{40}Ca(3.73→g)
3.90	3.90	3.90	(not resolved)	^{40}Ca(3.90→g)
4.90	4.48	4.70	b	^{40}Ca(4.48→g)
5.35	5.27	5.31	a	^{40}Ca(5.27→g)
6.08	6.14	6.11	a	^{40}Ca(6.03→g)
7.06	7.09	7.08	a	^{40}Ca(7.08→g)
8.15	8.11	8.13	a	^{40}Ca(8.13→g)

larger than about 14 MeV. But the Q values of ^{40}Ca(p, α), ^{44}Ca(p, n), (p, d) and (p, α) reactions are −5.2, −3.65, −9 and −1 MeV, respectively. It may be considered that the gamma rays from these reactions as well as ^{44}Ca($p, p'\gamma$) reaction overlap on to the low energy gamma ray spectrum from ^{40}Ca(p, p') reaction.

Fig. 11 and Fig. 12 show the gamma ray spectra observed with the three crystal pair spectrometer when the calcium targets of 0.8 mg/cm^2 and 2.0 mg/cm^2 in thicknesses were bombarded by 14 MeV and 10 MeV protons, respectively. The energies of observed gamrays were listed in Table III.

By the magnetic analysis of inelastic scattering of 6 to 8 MeV protons by ^{40}Ca, the level energies have been determined up to 6 MeV. The levels above 9 MeV have been studied by ^{39}K(p, γ) reaction[6]. But any information for levels in the region from 6 to 9 MeV have not been reported. The gamma rays observed in the present work in the energy range from 2.09 to 6.11 MeV can be expected from the results of the magnetic analysis of the inelastic scattering. But two gamma rays of 7.08 and 8.13 MeV are both newly found gamma rays and can not be explained as cascade gamma rays between well established states. It is also impossible to consider that these gamma rays result from other reactions or ^{44}Ca, considering the intensites of both gamma ray spectra by 14 and 10 MeV protons, Q values, barrier penetrabilities and abundance. We concluded, therefore, that ^{40}Ca have the levels at 7.08 and these two gamma rays are of the direct ground state trasitions. Shook[9] reports a 8.4 MeV level in ^{40}Ca by the observation of α particle groups from the inelastic scattering of 43 MeV α particles. This level may be the same one as the 8.13 MeV level above mentioned. Fig. 13 shows the levels and gamma rays in ^{40}Ca.

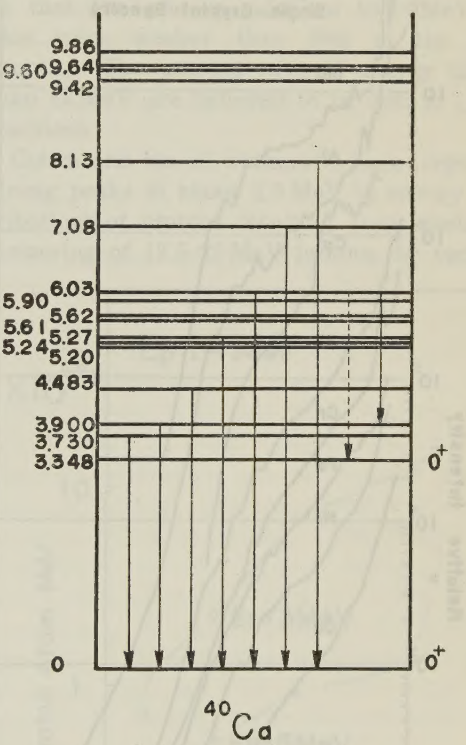

Fig. 13. T. Wakatsuki etc.

6) Other elements

A survey was made on the energy spectra of gamma rays from natural Al, Ti, Cr, Fe, Ni, Cu, Ag, Cd, Sn, Pt, Au and Pb bombarded by 14 MeV protons. The targets used were thin metal foils and most measurements were made with the single crystal spectrometer. In the cases of Al, Cu, Sn, Pt and Pb, these gamma ray energy spectra were also measured with the three crystal spectrometer.

The proton energy of 14 MeV is larger than the threshold energy for (*p*, *n*) reactions of these targets. (*p*, *pn*), (*p*, 2*n*) and (*p*, *α*) reactions are also possible for some nuclei, but proton energy of 14 MeV is not sufficiently higher than the threshold of (*p*, *pn*) and (*p*, 2*n*) reactions for most of these elements. Therefore the gamma rays following (*p*, *pn*), (*p*, 2*n*) and (*p*, *α*) reactions may be weaker than the gamma rays following (*p*, *p′*) and (*p*, *n*) reactions for most of these elements.

Neutrons arising from (*p*, *n*), (*p*, *pn*) and (*p*, 2*n*) reactions in the targets pass through the NaI (T1) scintillation crystal, and gamma rays following neutron nonelastic scattering in scintillation crystal and neighboring matters overlap on the gamma ray spectra. But the intensities of gamma rays following neutron scattering are estimated to be weaker than

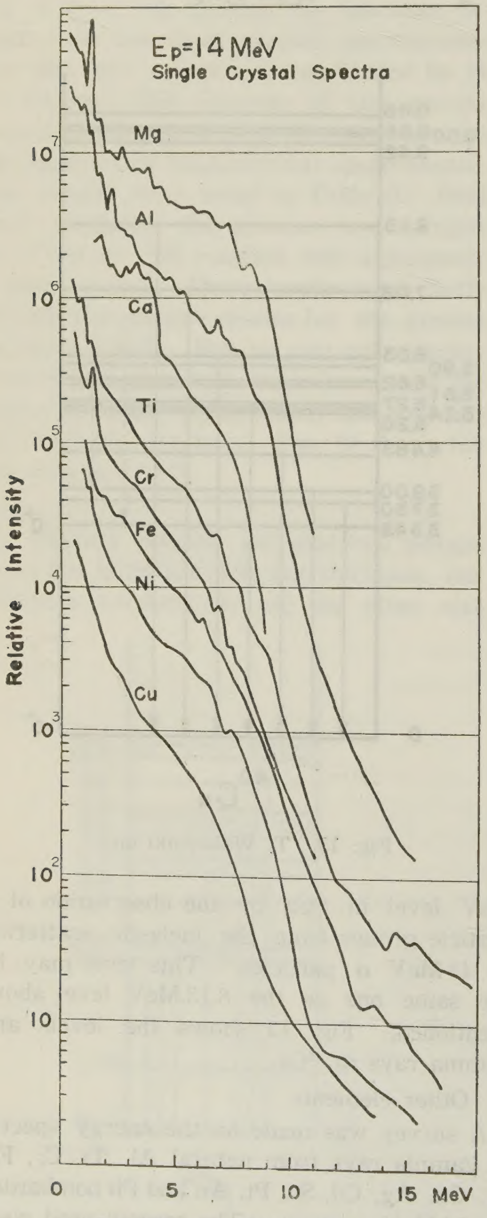

Fig. 14. T. Wakatsuki etc.

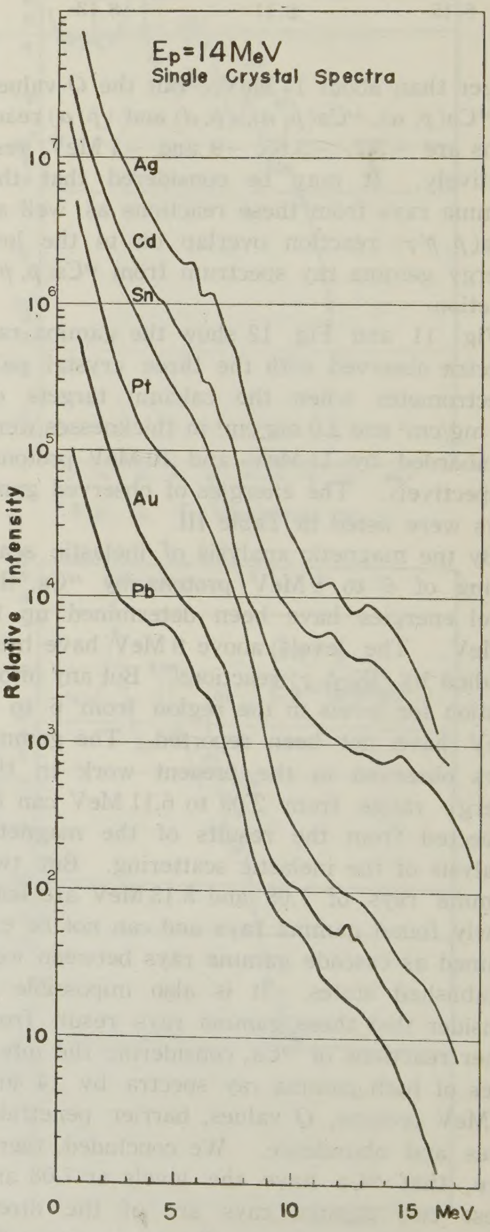

Fig. 15. T. Wakatsuki etc.

10% of the gamma rays from the targets.

The single crystal spectra and the three crystal spectra of the gamma rays from 14 MeV proton bombardments of several targets are shown in Fig. 14, 15 and 16, respectively.

For the gamma ray spectra of Al, many peaks were observed and the origin of 1.37 MeV, 2.21 MeV and 3.0 MeV gamma ray may be assigned to (3rd→1st), (3rd→gnd) and (5th or 6th→gnd) transitions, respectively.

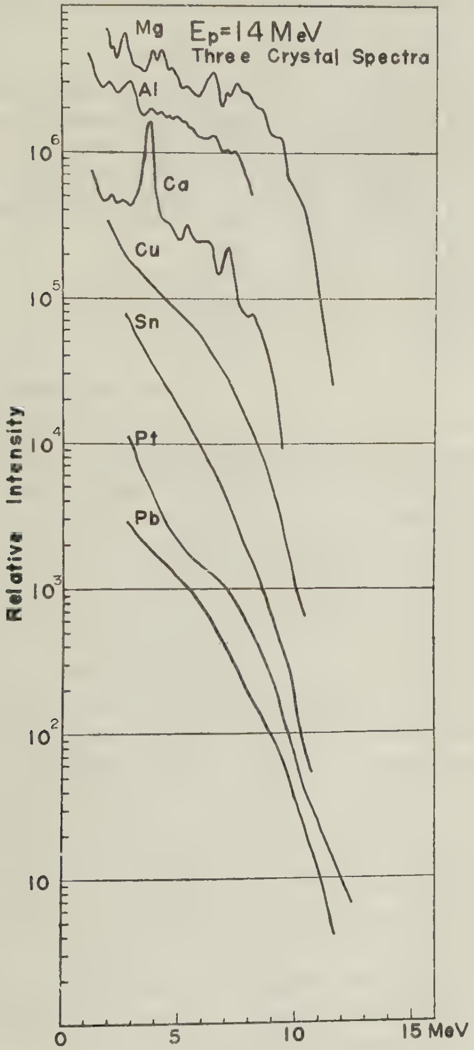

Fig. 16. T. Wakatsuki etc.

For Ti, Cr, Fe, Ni, Cu, Ag, Cd, Sn, Pt, Au and Pb, gamma ray spectra are almost continuous, but gamma rays from the 1st excited states of ^{48}Ti, ^{52}Cr, and ^{58}Ni could be resolved and broad peaks were observed at about 7 MeV and 13 MeV for some elements.

Almost all the intense gamma rays up to about 8 MeV may be the gamma rays following (p, p') and (p, n) reactions for most elements. As shown in Fig. 14, 15 and 16, the declivity of the gamma ray spectra up to about 8 MeV increases with atomic number. This behavior of gamma ray spectra is reasonable since the level densities of the residual states for gamma ray emissions increase with the atomic numbers.

The gamma ray intensities decrease suddenly at about 8 MeV, and the intensity ratios of about 1 MeV and about 12 MeV gamma rays are about 10^3: 1, correcting for the detector efficiency. The counting rates were kept low, so that the pile up pulses of 10–14 MeV region were weaker than 10% of the true counts. The gamma rays of energy larger than 12 MeV are believed to be due to (p, γ) reactions.

Cohen and his co-workers[10] have reported strong peaks at about 2.5 MeV in energy distributions of protons resulting from inelastic scattering of 12.5–23 MeV protons by various

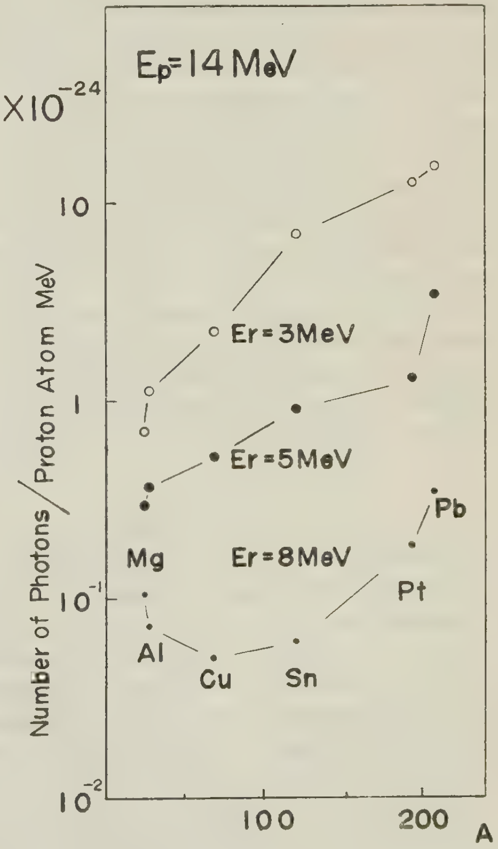

Fig. 17. T. Wakatsuki etc.

medium weignt and heavy nuclei. In this experiments, no peaks were observed at about 2.5 MeV on the gamma ray spectra for 14 MeV proton bombardments of various nuclei.

The yields of 3 MeV, 5 MeV and 8 MeV gamma rays for 14 MeV proton bombardments of Mg, Al, Cu, Sn, Pt and Pb are calculated from the three crystal spectra and are shown in Fig. 17.

The yields of 3 MeV and 5 MeV gamma rays and yield ratios of 3 MeV gamma rays to 5 MeV and to 8 MeV gamma rays increase with the atomic numbers. These behaviors of the gamma ray yields are also reasonable considering the increase of level densities with atomic numbers and excitation energies.

The authors wish to thanks cyclotron crew of the Institute for Nuclear Study for the operation of the cyclotron and for kind assistances throughout the work.

References

1) T. Wakatsuki, Y. Hirao, E. Okada and I. Miura: J. Phys. Soc. Japan **13** (1958) 233, 541; **14** (1959) 239.
2) R. W. Peelle: Phys. Rev. **105** (1957) 1311.
3) Handb. d. Physik Band XLV. 128.
4) F. Ajzenberg-Selove and T. Lauritsen: Nucl. Phys. **11** (1959) 1.
5) C. D. Moak, A. Galonsky, R. L. Traughber and C. M. Jones: Phys. Rev. **110** (1958) 1369.
6) P. M. Endt and C. M. Braams: Rev. Mod. Phys. **29** (1957) 683.
7) To be published.
8) R. D. Bent, T. W. Bonner, J. H. McCrary and W. A. Ranken: Phys. Rev. **100** (1955) 774.
9) G. B. Shook: Phys. Rev. **114** (1959) 310.
10) B. L. Cohen: Phys. Rev. **105** (1957) 1549.
B. L. Cohen and A. G. Rubin: Phys. Rev. **111** (1958) 1568.

Journal of the Physical Society of Japan, Vol. 16, No. 7, July, 1960

Elastic and Inelastic Scattering of Protons from Nickel Isotopes; Ni^{58} and Ni^{60}, in the Energy Range from 7.0 MeV to 15.3 MeV

By Shinsaku Kobayashi*, Kazuhisa Matsuda*,
Yukio Nagahara**, Yukiyasu Oda*** and
Nobuhiro Yamamuro***

Institute for Nuclear Study, University of Tokyo,
Tanashi-machi, Kitatama-gun, Tokyo

(Received February 4, 1960)

Angular and energy dependence of the elastic and the inelastic scattering of protons from nickel isotopes, Ni^{58} and Ni^{60}, were investigated in the energy range from 7.0 MeV to 15.3 MeV. Angular distributions in the high energy region ($E_p \geq 10$ MeV) showed small difference between both isotopes. Energy dependence of the differential cross sections in the low energy region (7 MeV $< E_p <$ 9 MeV) showed some fluctuations both for the elastic and the inelastic scattering. The inelastic yield for Ni^{58} was larger than that for Ni^{60} in the low energy region ($E_p \leq 9$ MeV). These yields decreased gradually as the incident energy increased. The results of present work are compared with our previous one and with the investigations of Thirion et al., Greenlees et al., and Seward.

§1. Introduction

The angular distribution for inelastic scattering of protons leaving the target nucleus to a definite excited state of medium weight nuclei ($A>40$) was investigated by Schrank, Gugelot and Dayton1), who bombarded the natural iron target by protons of 17 MeV. Sherr2) also reported the result of the angular correlation measurements for Fe. These results obtained at Princeton suggested the so-called "direct process" for the mechanism of inelastic scattering of protons leaving the target nucleus to the lowlying excited state. Experiments with separated isotopes have been done by several authors at proton energies of about 10 MeV. Hintz et al.3) used Fe^{54}, Fe^{56}, Cu^{65}, Ni^{58} and Zn^{66}, Thirion et al.4) used Zn^{64}, Zn^{66} and Zn^{68}, Greenlees and Rolph5) used Ni^{58} as targets.**** At lower incident energies, Seward6) investigated the angular distribution of inelastic protons from Ti and Cr, the angular correlation between protons and de-exitation gamma rays from Cr, and the energy dependence of the cross section of inelastic scattering at 90° from Ti, Cr and Fe. We9),10) investigated the angular dependence of elastic and the inelastic scattering for the medium weight nuclei (Ti, Cr, Fe, Ni and Zn) with their natural isotopic abundances at several incident energies of protons from 8 MeV to 14 MeV. The results of our previous work led us to a similar investigation with separated isotropes. The work reported here is very similar to the recent measurement done by Greenlees and Rolph. Both nuclei, Ni^{58} and Ni^{60}, however, were investigated in a wider energy range of incident protons.

§2. Experimental

Proton beam was obtained from the INS (Tokyo) variable energy cyclotron.11) The beam focusing system and the scattering chamber used in this experiment were described elsewhere.9),11),12) However, the experimental procedure was different from the previous works in the following point. We used fifteen scintilation counters at the same time, which were attached to the side windows of the large scattering chamber. Seventeen windows open at each ten degrees from

---

* Institute for Nuclear Study, University of Tokyo.

** Department of Physics, Yokohama National University.

*** Department of Physics, Tokyo Institute of Technology.

**** We must also mention the works of B. L. Cohen and his colaborators,7) and experiments of the inelastic scattering of alpha particles.8)

10° to 170° on one half of the side wall of the chamber, and sixteen from −15° to −165° on the other half of the wall.

The foil targets of separated nickel isotope which were obtained from A.E.R.E. (Harwell), were set at the centre of the scattering chamber making an angle of 45° to the incident beam. The angles of detection in the laboratory system were 25°, 30°, 40°, 50°, 60°, 70°, 80°, 90°, 105°, 115°, 125°, 135°, 145°, 155° and 165°. High voltage was fed always to each counter and the signals from each counter were always sent to the measuring room through a cathode follower and coaxial cable. We used five sets of linear amplifiers and multi-channel pulse height analysers; thus we could measure the yields at five angles simultaneously. When we introduced the signal from another five counters to the five sets of electronics, we could measure the yields at the next five angles. For the investigation of energy dependence we could measured the yields at 30°, 60°, 90° 125° and 165°, at the same time. For the investigation of the angular dependence, we always measured the yield at 90° as the monitor of the system. Only four sets of such measurements gave us the angular dependence at one incident energy. This method gave us very reliable data on the angular distribution especially at the region region where the yields change remarkably with the incident energy. The solid angles subtended by the detectors at the forward angles were made smaller than those by other counters, as the diameters of the defining apertures, which were 505 mm apart from the centre, were 3 mm, 5 mm, and 10 mm at 25°, 30°–50° and 60°–165° respectively. These different solid angles made the counts from each counter to be of the same order. The slit edge effect and the correction for the multiple scattering, however, were neglected in the analysis of the data.

The thicknesses of the foils of Ni^{58} and Ni^{60} were informed by A.E.R.E. to be 2.62 mg/cm^2 and 2.42 mg/cm^2, respectively. We used these values for the determination of the absolute cross sections. From the observed cross sections at 14.3 MeV for both isotopes, we calculated the average cross sections of the elastic scattering and the inelastic scattering, corresponding to the natural nickel element; $1/4\cdot\{3(d\sigma/d\Omega)_{Ni^{58}}+(d\sigma/d\Omega)_{Ni^{60}}\}$, and compared these values with our previous data.[9] The agreement was fairly good as shown in Fig. 1(a) and (b), the errors being about ±5%.

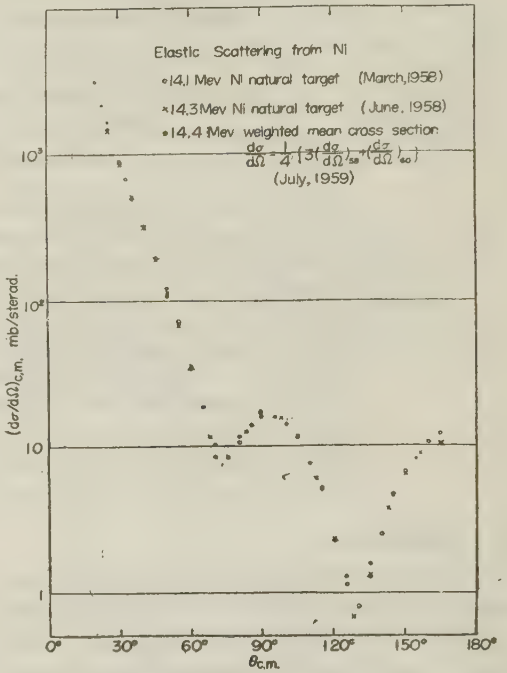

Fig. 1(a). Comparison among the results of the elastic scattering from Ni in our laboratory.

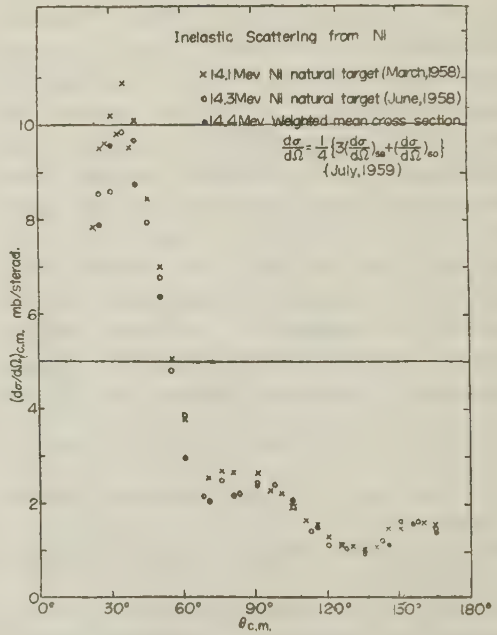

Fig. 1(b). Comparison among the results of the inelastic scattering from Ni in our laboratory.

The energy spread of the cyclotron beam cannot be precisely determined. This spread was not always constant during a long run, and in some cases it would be about 0.5% but in other cases it would be near 1%.

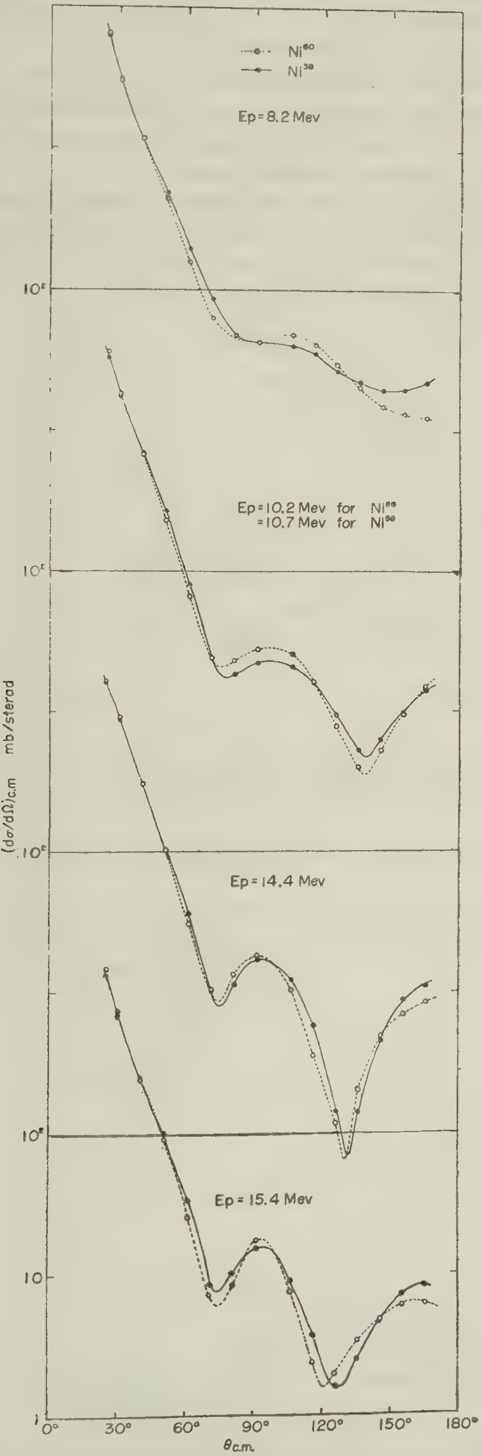

Fig. 2. Angular distributions of the elastic scattering from Ni^{58} and Ni^{60}.

§ 3. Results

Fig. 2 shows the angular distribution of

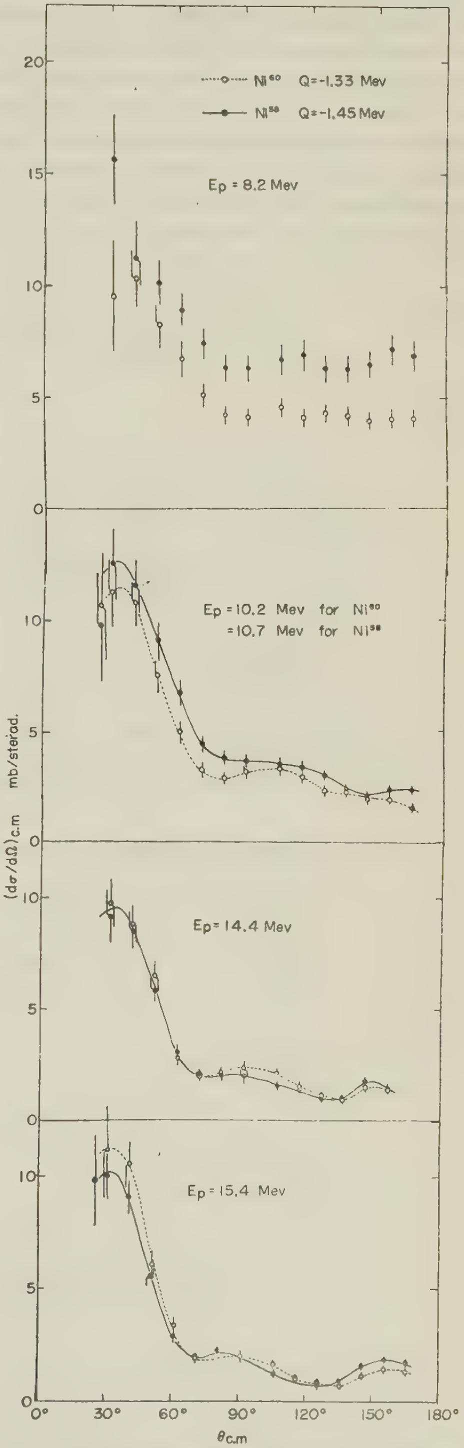

Fig. 3. Angular distributions of the inelastic scattering from Ni^{58} and Ni^{60}.

the elastic scattering at 15.3 MeV, 14.3 MeV, 10 MeV and 8.1 MeV. The angular distributions from these two isotopes are similar. Especially at forward angles, the cross sections agree with each other within the experimental errors at four incident energies. The cross sections for both isotopes at large angles ($\geq 60°$) differ a little from each other over the whole range of the incident energy. Errors of the absolute values of elastic cross sections appear to be less than 10% as mentioned above.

Fig. 3 shows the angular distribution of the inelastic scattering. In some cases, the angular distribution of inelastic scattering differ between Ni^{58} and Ni^{60} as follows:

1) the larger cross sections for Ni^{58} than for Ni^{60} at 8.1 MeV;

2) the presence of small differences of the angular distribution at high incident energies. As indicated in the figure, the errors were not small at forward angles.

Fig. 4 and Fig. 5 show the energy dependences of the cross sections for Ni^{58} and Ni^{60}

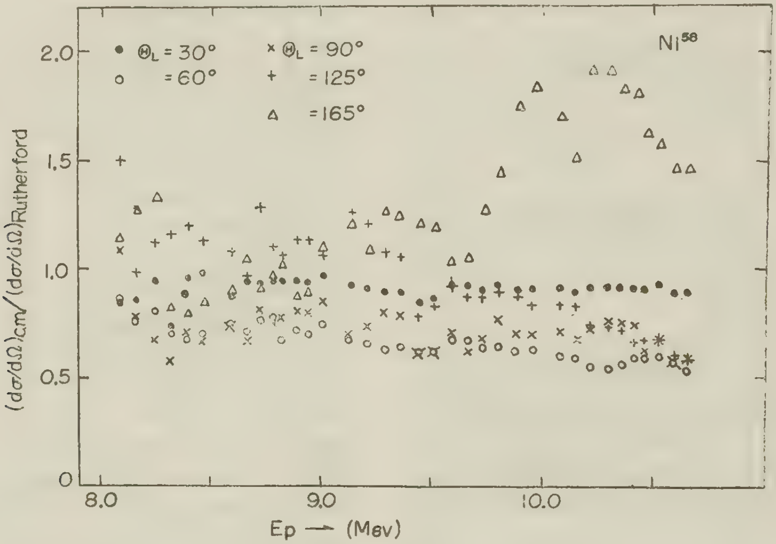

Fig. 4(a). Energy dependence of differential cross sections of the elastic scattering from Ni^{58}.

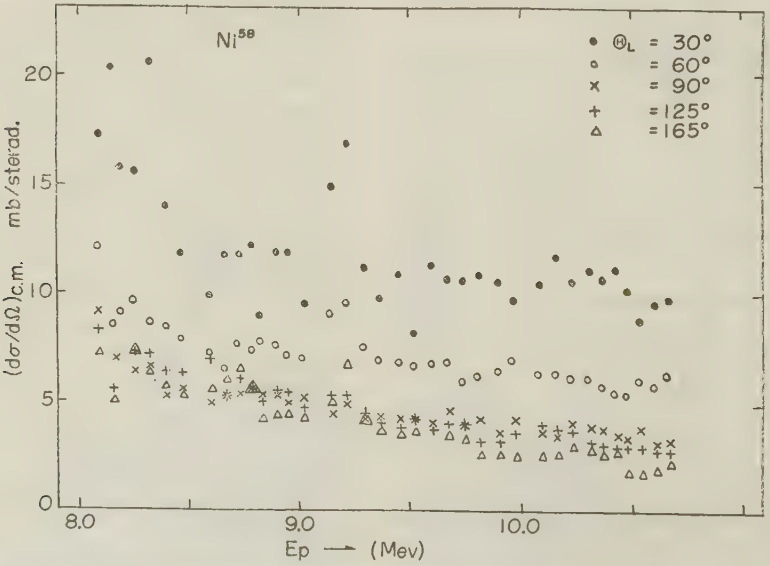

Fig. 4(b). Energy dependence of differential cross sections of the inelastic scattering ($Q = -1.45$MeV) from Ni^{58}.

respectively. For the elastic scattering, the ratio of $(d\sigma/d\Omega)_{cm}$ to the cross section of the Rutherford scattering is represented on the figures. The energy dependence of the inelastic scattering at $\theta_L=30°$ for Ni^{60} was also measured but the experimental errors seemed too large for the energy dependence to be precisely discussed; so we omitted the details and showed only the average behavior of the 30° cross section in the energy range. There exist some energy-dependent fluctuations both in the elastic and in the inelastic cross sections. In some cases, for example, at 9.2 MeV for Ni^{58}, the energy dependence in inelastic scattering shows a resonance-like behaviour, which is believed to correspond to the anomaly found at 9.3 MeV our previous work.[7]* Such an anomaly in the differential cross section does not necessarily occur at the same incident energy in elastic and inelastic scattering. The energy dependence of the inelastic cross section is remarkable at forward and at backward angles, while that of the elastic cross section is not so remarkable at forward angles as at backward angles. The energy dependence of the elastic cross section is not so remarkable at forward an-

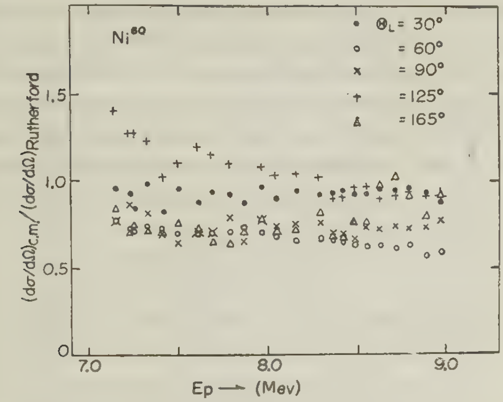

Fig. 5(a). Energy dependence of differential cross sections of the elastic scattering from Ni^{60}.

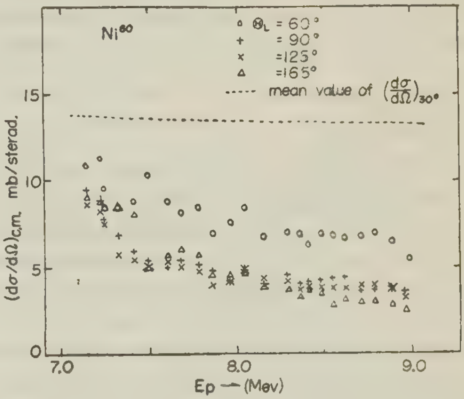

Fig. 5(b). Energy dependence of the differential cross sections of the inelastic scattering ($Q=-1.33$ MeV) from Ni^{60}.

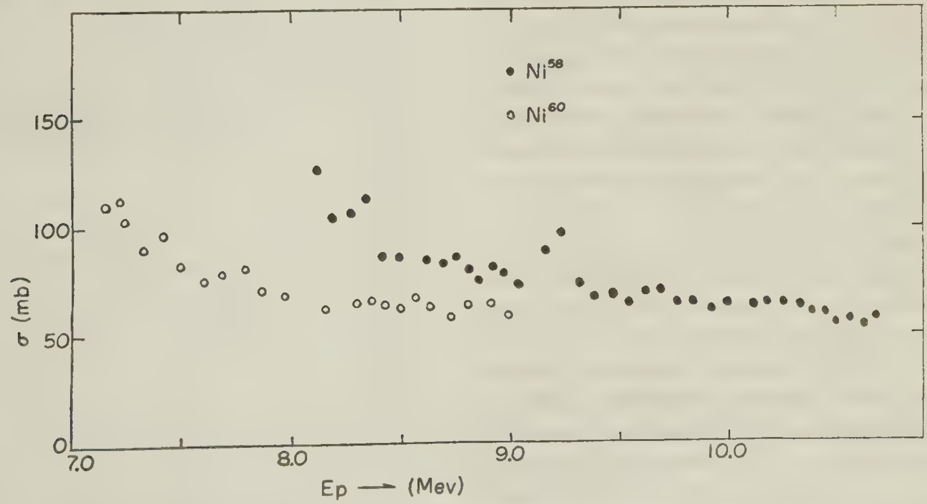

Fig. 6. Energy dependence of inelastic total cross section for the inelastic scattering (to the first excited states).

---

* The discrepancy of resonance energy between the two experiments is due to the difference of the range-energy relations used. We used that of reference 13 previously and used that of reference 14 in the present work.

gles as at backward angles. The energy dependence of the elastic cross section at 165° for N^{58} shows gross structure at a energy region larger than 9.6 MeV. The inelastic cross sections at more than 60° increase gradually as the incident energy decreases. The cross section for Ni^{60} fluctuates less than that for Ni^{58} and the absolute yields of inelastic scattering for Ni^{60} are less than those for Ni^{58} at the same energy region of incident protons. Total inelastic cross sections for the first excited state, estimated roughly from these values of differential cross sections at five angles, are showe in Fig. 6. It is to be noted that the energy dependence curve is more smooth in the total cross section.

§ 4. Discussion

1) No analysis by the optical model has yet been attempted to fit the present data of elastic scattering. The positions of the minima and maxima of the diffraction pattern seem to change regularly with atomic mass. The only exception is in the case of the first minimum at 15.3 MeV, where the present data do not give any definite conclusion, because the angular intervals of the observation were rather large.

2) The larger inelastic cross section for Ni^{58}, found in the energy region from 8 MeV, in comparison with that for Ni^{60}, may be caused by the high threshold energy of the $Ni^{58}(p, n)Cu^{58}$ reaction, or by the smaller level density of Ni^{58}. The last two factors diminish the number of the open channels and might make the contribution of the compound process to the inelastic scattering for Ni^{58} (for the first excited state) more predominant than for Ni^{60}.

3) Thirion et al. found rather large differences among the inelastic yields for zinc isotopes at 11 MeV. The results of our previous work with natural elements showed that there exist marked differences in the inelastic yield from different nuclide especially at forward angles. The results of the present work show that at the high incident energy these two particular isotopes of nickel give similar yields. We are now attempting to measure the cross section at forward angles more accurately by magnetic analysis. Present data cover the region investigated by Greenlees. Our results agree with his conclusion but the values of the cross sections do not agree with his within the estimated experimental errors.

4) The differential cross section of inelastic scattering at 90° increases as the incident energy decreases, and that for Ni^{60} reaches about 8 or 10 mb/sterad. near 7 MeV. These values can be compared to the results obtained by Seward, who measured the differential cross sections of the similar inelastic scattering for Ti, Cr and Fe in energy range from 3 MeV to 7 MeV. The cross sections measured by him at 7.0 MeV were about 9 or 10 mb /sterad. for these medium weight nuclei. Moreover, the cross sections obtained at five angles in the present work indicate that the angular dependence becomes more isotropic as the incident energy decreases. So, Seward's results that the angular distributions for nuclei of these atomic weights are nearly

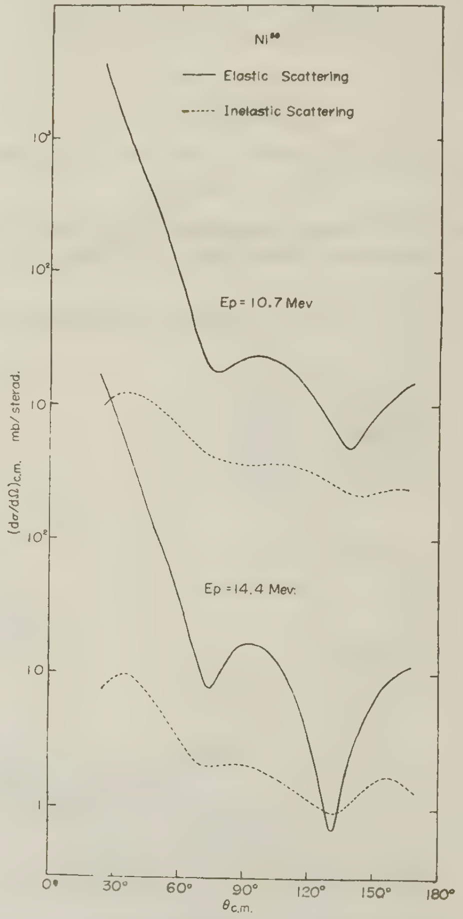

Fig. 7. In-phase relation between the elastic and the inelastic scattering.

isotropic below 7.0 MeV, can be smoothly connected to our results.

5) The total cross sections depend less on the incident energy than the differential cross sections do. The decrease of the total cross section with increasing energy is more gradual than that predicted by the theory of compound process and statistical level density. We can find some anomalies in the excitation curves of the total cross section. Those at E_p=8.2 MeV and at E_p=9.1 MeV for Ni^{58} are evident, which correspond to the excitation energies of 11.7 MeV and 12.5 MeV for Cu^{59}, respectively.

6) Fig. 7 shows the angular distributions of elastic and inelastic scattering from Ni^{58}. We can see from this figure that there exists an "in-phase" relation between them. This in-phase relation does not agree with the calculation proposed by Blair[15] for the scattering of alpha particles. This inphase relation which is found in inelastic scattering leaving the target nucleus to the first excited state at such a mass number region generally,[9] may be accidentally due to the distortion of the proton wave; nevertheless the fact, that the angular frequencies of the diffraction patterns are similar for the elastic and the inelastic scattering, seems to suggest us some under-lying similarity between these two phenomena.

The authors thank to Professor S. Kikuchi, who encouraged them through-out their experiments and gave them many valuable suggestions during his presidency of our laboratory. Particularly, the design of the scattering chamber with many side windows was suggested by him, and they used many counter systems according to his recommendation. They also with to thank Professor I. Nonaka for his kind encouragement. They are to say thanks to Messrs. T. Karasawa, A. Suzuki, H. Ogawa and other numbers of the cyclotron crew.

References

1) G. Schrank, P. C. Gugelot and I. E. Dayton Phys. Rev. **96** (1954) 1156.
2) Sherr: Proceedings of the University Pittsburg Conference on Nuclear Structure, (1957) 361.
3) Univ. Minnesota, Ann. Progr. Rep. March 1958, p. 39.
4) J. Thirion et al. (Private communication).
5) G. W. Greenlees and P. M. Rolph (Private communication).
6) F. D. Seward: NYO-2267 (1958) Phys. Rev. **114** (1959) 514.
7) B. L. Cohen: Phys. Rev. **105** (1957) 1549. B. L. Cohen and A. G. Rubin: Phys. Rev. **111** (1958) 1568.
8) D. K. McDaniels, J. S. Blair, S. W. Chen and G. W. Farwell (to be published).
9) K. Kikuchi, S. Kobayashi and K. Matsuda: J. Phys. Soc. Japan **14** (1959) 121.
10) C. Hu et al.: J. Phys. Soc. Japan **14** (1959) 861.
11) S. Kikuchi et al.: J. Phys. Soc. Japan **15** (1960) No. 1.
12) K. Matsuda et al.: INSJ-14 (1959).
13) W. A. Aron, B. G. Hoffman and F. C. Williams: AECU-663 (1949).
14) H. Bichsel, R. F. Mozley and W. A. Aron: Phys. Rev. **105** (1957) 1788.
15) J. Blair: Phys. Rev. **115** (1959) 928.

JOURNAL OF THE PHYSICAL SOCIETY OF JAPAN, Vol. 15, No. 7, JULY, 1960

Elastic and Inelastic Scattering of Alpha Particles by Carbon

By Takashi MIKUMO, Hisashi YAMAGUCHI, Itaru NONAKA,
Masatoshi ODERA*, Yoshio HASHIMOTO**,
Motoo KONDO* and Takashi MAKI***

Institute for Nuclear Study, University of Tokyo,
Tanashi-machi, Kitatama-gun, Tokyo,

(Received February 5, 1960)

Angular distributions of alpha particles scattered elastically and inelastically ($Q=-4.43$ MeV) by carbon nucleus were measured with incident alpha energies of 28.4, 31.0 and 33.6 MeV.

Angular distributions of inelastic alpha groups corresponding to $Q=-7.66$ and -9.63 MeV and a broad alpha group with $Q\simeq 12.7$ MeV were also obtained at $E_\alpha=28.4$ MeV. The data were compared with Blair's diffraction scattering model and fairly good agreements were obtained for both elastic and inelastic ($Q=-4.43$ MeV) angular distributions for forward angles for three energies. The rises of cross sections at back angles, however, seem to occur from other mechanisms. Spin and parity assignments were tried for 7.66 and 9.63 MeV levels of carbon.

§ 1. Introduction

Angular distributions of elastic scattering of alpha particles in the energy range of 20- to 50-MeV were widely investigated in recent years. Some of the data were analyzed in the light of the optical model[1),2)] especially for heavy and intermediate nuclei.

Elastic scattering by heavy nuclei were fairly well fitted also with the semi-classical model proposed by J. S. Blair[3),4)]. This simple model, however, does not apply well to the data obtained with light nuclei as does to heavy nuclei.

On account of short mean free paths of alpha particles in the nucleus, several attempts[5)–8)] were made to fit the data with conventional diffraction model taking the nucleus to be black.

These theories described above were all based on the assumption that the nuclear matter was opaque or black against the alpha particles. But this is in contrast with the success in fitting the data of inelastic alpha scattering with simple direct interaction model, in which the incident and final unbound particles were assumed to be well represented by plane waves[9)–11)].

Recently J. S. Blair[12)] suggested a diffraction model to overcome the paradox mentioned above. He extended the diffraction theory introduced by S. I. Drozdov[13)] and E. V. Inopin[14)] to scattering of alpha particles or deuterons by "black" nuclei. These theories discussed inelastic scattering through either excitation of rotational states of ellipsoidally deformed nuclei or excitation of quadrupole vibrational states introducing either deformation parameter β_l or surface tension C_l defined by A. Bohr et al.[15)].

In the present situation, however, it is desirable to obtain more experimental facts which cover wide range of atomic numbers of target nuclei and energies of incident alpha particles to have a correct understanding of the mechanism of elastic and inelastic scattering of alpha particles by nuclei. Especially, the variations of angular distributions with the energies of incident alpha particles are considered to be the most important factor to be investigated. We planned, therefore, to measure the angular distributions of elastic and inelastic scattering as a function of the energy of incident alpha particle around 30 MeV.

As the first step of this plan we selected carbon as the target because the low lying levels of this nucleus are widely spaced and it is easy to separate experimentally the elastic and inelastic groups one another. Angular distributions of elastic and inelastic scattering of alpha particles by C^{12} were measured by F. J. Vaughn[16] at 48 MeV, by Igo, Wegner and Eisberg[17] at 40 MeV, by H. J. Watters[6] at 31.5 MeV, by Hu, Kato, Oda and Takeda[7] at 22 MeV, and by A. I. Yavin and G. W. Farwell[8] at 40 and 41 MeV. All of these data show more or less sharp diffraction patterns for both elastic and inelastic scatterings, but the patterns are quite different in shape and in size as the bombarding energy changes.

---

* Tokyo Institute of Technology.

** Faculty of Science, University of Tokyo.

*** Faculty of Science, Kyushu University.

In the present experiment, angular distributions were measured at three values of energies of incident alpha particles, 28.4, 31.0 and 33.6 MeV respectively, but more data will be taken at many other energies in near future.

§ 2. Experimental Procedure

We have made measurements of elastic and inelastic scattering of alpha particles by carbon with the 160 cm INS (Tokyo) variable energy cyclotron, from which alpha particles of energy from 27 to 43 MeV are obtained. Details of the cyclotron and the scattering chamber system are reported previously[18]. At the centre of the 100 cm scattering chamber was placed a self-supporting carbon foil of 2.38 mg/cm² in thickness, making an angle of 45° to the alpha particle beam. The target was prepared by the same method as that used in the course of $C^{12}(\alpha, p)N^{15}$ experiment[17]. Two proportional counter-CsI(Tl) scintillation counter telescopes 180° apart were placed on a turn table in the scattering chamber. Linearly amplified pulses from scintillation counters were gated by those from proportional counters which were biased at adequate voltages. By this procedure the discrimination of alpha particles against singly charged particles were performed without difficulty. The energies of alpha particles incident to the target were measured at the end of each energy run using aluminium absorbers and an ionization chamber, and were known to be 28.7_5, 31.3_0 and 33.9_0 MeV respectively. The average energies in the target were $E_\alpha=28.4$, 31.0 and 33.6 MeV, respectively.

Fig. 1 shows a typical histogram obtained at 30° at $E_\alpha=28.4$ MeV using three 20 channel and two 10 channel pulse height analyzers. Widths of elastic peaks at half-maximum were 3 to 4 per cent for "forward" counter, but they were as broad as 20 to 30 per cent for "backward" counter which caught reflected particles.

Elastic angular distributions and inelastic angular distributions corresponding to $Q=-4.43$ MeV were measured at all these three energies, at angular interval of 1° to 2.5°. Angular distributions of inelastic groups corresponding to $Q=-7.66$ and -9.63 and a broad peak around $Q\cong-12.7$ MeV were measured only at $E_\alpha=28.4$ MeV (owing to the limitation of machine time).

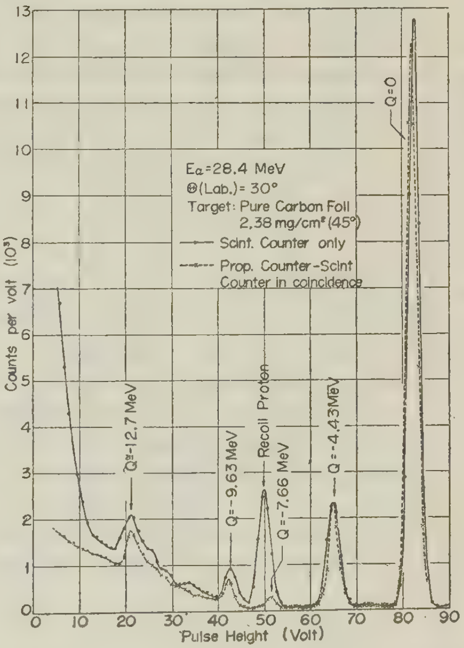

Fig. 1. Typical pulse height distribution obtained at $\Theta_{lab}=30°$ and $E_\alpha=28.4$ MeV with and without proportional counter.

The errors are considered to arise from the following sources; i) Inhomogeneity of target foil <20%; ii) Beam energy fluctuation <1%; But owing to the steepness of diffraction pattern in angular distributions and to the remarkable changes of cross sections with energy, a small energy change might influence the magnitude of cross sections considerably; iii) Errors in values of scattering angles: <0.15°; iv) Counting loss: at $\Theta_{lab}\leq 30°$ it was necessary to make the beam intensity as small as possible, otherwise the loss reached as high as 30%. The data shown in the figures are expected to have losses of less than 5%; v) Statistical errors: concerning the elastic group and inelastic group for $Q=-4.43$ MeV, these errors are very small except for several angles at which angular distributions show steep minima; vi) Background subtraction: This source of errors is the most serious one in particular at large angles and for inelastic groups corresponding to $Q=-7.66$, -9.63 and $\cong -12.7$ MeV. Errors from this source were estimated to be 10% at most.

§ 3. Results and Discussions

Angular distributions of elastic scattering as well as those of inelastic scattering to the 4.43 MeV state of C^{12} were obtained at $E_\alpha=28.4$, 31.0 and 33.6 MeV. Because of the energy losses of scattered alpha particles in the target and in the counter foils, the measurements were limited for backward angles to 110° to 130°.

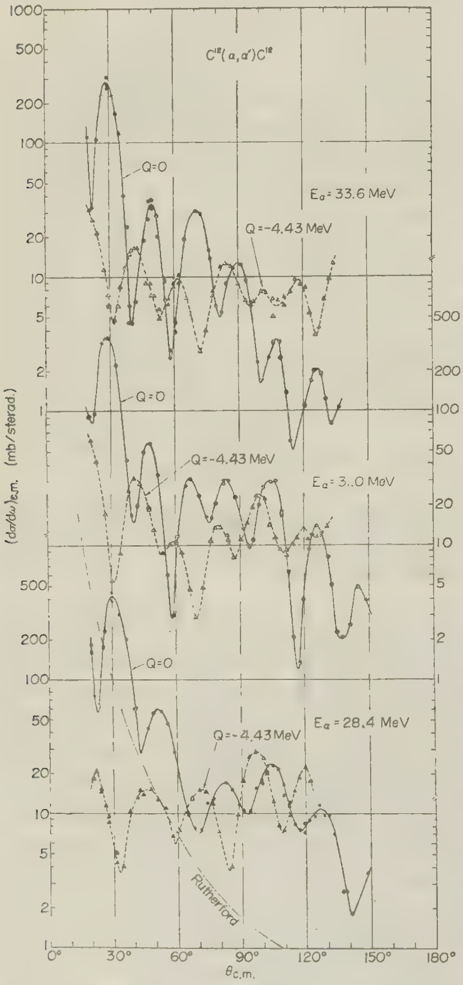

Fig. 2. Angular distributions of elastic scattering and inelastic scattering ($Q=-4.43$ MeV) obtained at three alpha particle energies.

Fig. 2 shows the angular distributions for both groups at these three energies.

Fig. 3 shows the results obtained for the groups corresponding to $Q=-7.65$, -9.76 and a broad peak at $Q\cong -12.7$ MeV at $E_\alpha=28.4$ MeV together with the elastic group.

We now discuss each group separately.

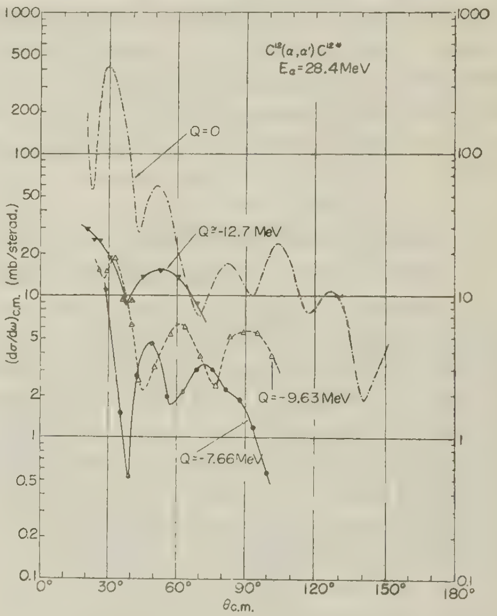

Fig. 3. Inelastic angular distributions at $E_\alpha=28.4$ MeV leaving the residual nucleus at higher excitations. For comparison, elastic angular distribution is also shown.

i) $C^{12}(\alpha, \alpha)C^{12}$, $Q=0$

As shown in Fig. 2, angular distributions of elastic groups at three different energies show pronounced diffraction patterns. Rutherford cross section for $E_\alpha=28.4$ MeV is also shown in Fig. 2. The observed cross sections are higher than the Rutherford cross sections except at very forward angles, and the ratios $\sigma(\theta)_{obs}/\sigma(\theta)_{Ruth}$ are especially high at backward angles. This behaviour is in contrast with the case of heavy elements and in agreement with the general trend found by Igo et al[1),17)]. There appears no systematic shift in diffraction patterns with energy, except at extremely forward angles ($\theta<40°$). At 31.0 MeV we have not observed the plateau around $60°\lesssim\theta\lesssim 75°$ reported by Watters[6)] at 31.5 MeV. His average energy at the target centre is not known because of the uncertainty of the target thickness, and it was probably somewhat less than our 31.0 MeV. The positions of maxima and minima of the angular distributions are nearly equidistant in θ rather than in $\sin(\theta/2)$, except for $E_\alpha=28.4$ MeV, where equidistance relation is largely violated for $\theta>60°$. These angular distributions were analyzed in terms of diffraction scattering formula. For small θ, absolute differential cross sections of elastic scattering are expressed by the formula

$$\frac{d\sigma(\theta)}{d\omega}=k^2R_0^4\left(\frac{J_1(kR_0\theta)}{kR_0\theta}\right)^2$$

where $k=k_i$ is the c.m. wave number of the incident particle, R_0 is the interaction radius between the target nucleus and the incident alpha particle, $J_1(x)$ is the first order Bessel function. We took the argument of $J_1(x)$ as $x=kR_0\theta$ instead of $x=2kR_0\sin(\theta/2)$ because of simplicity and of equidistancy in θ of the experimental results as mentioned above. Fig. 4 shows the results of the analyses. The values of R_0 were adjusted so that the best fits were obtained with the experimental data, at least for the positions of the first and the second maxima and minima. Values of R_0 thus obtained were

$(5.4\pm0.1)\times10^{-13}$ cm	for	$E_\alpha=28.4$ MeV
(5.5 ± 0.1)		$E_\alpha=31.0$
(5.2 ± 0.1)		$E_\alpha=33.6$

For $E_\alpha=31.0$ MeV the positions of maxima and minima were very well fitted even for the fourth maximum. As regards absolute values, the observed cross sections were twice or three times larger than the calculated ones, except at the second maximum for $E_\alpha=33.6$ MeV, where they were nearly equal. The origin of these discrepancies in absolute values are not yet very clear; Coulomb correction does not change the situation very much except at extreme forward angles*. It is interesting to compare the values of R_0 with those obtained by other authors**. In Fig. 5 values of R_0 are plotted against E_α between 22 and 48 MeV. As can be readily seen R_0 decreases as E_α increases. The reason of this fact is not clear at present.

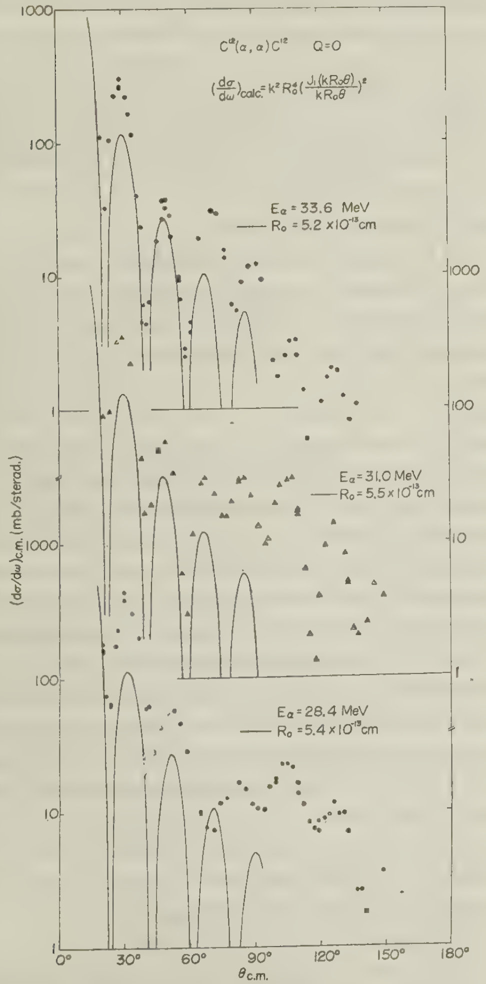

Fig. 4. Comparison of calculated elastic angular distributions based on diffraction model with observed ones.

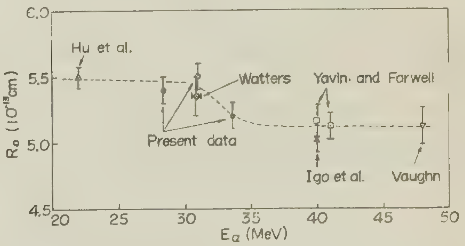

Fig. 5. Relations between R_0 and E_α for elastic scattering of alpha particles by carbon, obtained by the diffraction model. Values of R_0 are recalculated by the present authors so as to fit the positions of experimental first or/and second maxima.

---

* According to Blair, diffraction scattering and Coulomb scattering (with finite nuclear size) are out of phase, and both cross sections can be added to give differential cross section at each angle.

** The values of R_0 were recalculated by the present authors so as to fit the experimental data for the first and/or second maxima.

ii) $C^{12}(\alpha, \alpha')C^{12*}$, $Q=-4.43$ MeV

As are readily seen in Fig. 2 these angular distributions also show pronounced diffraction patterns, and they are "out of phase" with those of corresponding elastic alphas. This indicates, according to Blair's diffraction theory, that the parity of 4.43 MeV state is the same as that of the ground state. Really the 4.43 MeV state of C^{12} is known to be 2+. Blair predicts the differential cross section for (0+→2+) transition for $k_f \simeq k_i \simeq k$ to be

$$\frac{d\sigma(\theta)}{d\omega}(0\rightarrow 2)=(kR_0)^2\frac{5}{4\pi}\frac{\hbar\omega_2}{2C_2}\times\left[\frac{1}{4}\{J_0(kR_0\theta)\}^2+\frac{3}{4}\{J_2(kR_0\theta)\}^2\right]$$

where R_0 is the interaction radius which gives the best fit with observed elastic angular distribution, $\hbar\omega_2=4.43$ MeV is excitation energy of the final nucleus and C_2 is a quantity corresponding to the surface tension, when C^{12} is assumed to be a spherical vibrational nucleus and 4.43 MeV states be excited through collective quadrupole vibration.

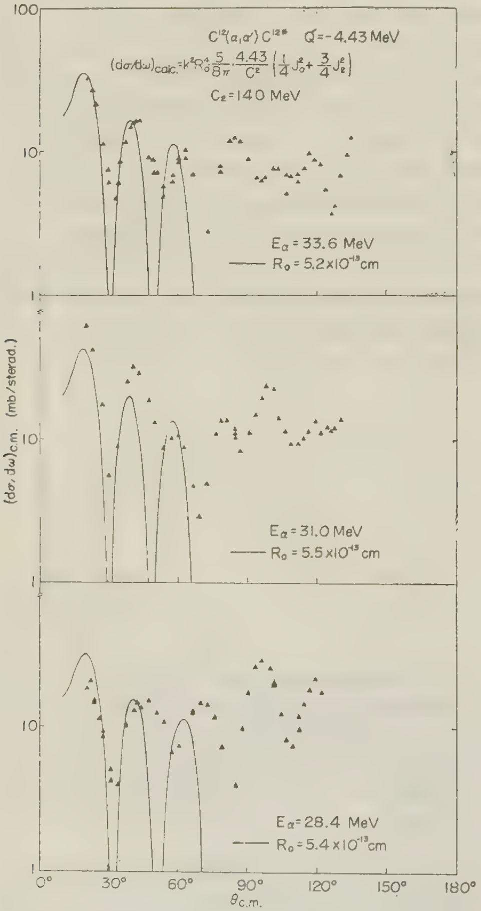

Fig. 6. Comparison of calculated inelastic angular distributions ($Q=-4.43$ MeV) based on diffraction model with observed ones. Values of R_0 are those which give the best fits with observed elastic angular distributions.

In Fig. 6 are shown comparisons between observed and calculated cross sections. Absolute values around the second maximum are only fitted by taking the values of C_2 to be around 140 MeV which is a value ten times larger than that given by Alder et al.[15], except for $E_\alpha=31.0$ MeV where a good fiit is obtained as to the positions of maxima but a value of about 90 MeV for C_2 must be taken to obtain a fit with the absolute values of cross sections. As is seen from Fig. 2, experimental cross sections do not decrease so remarkably as the theory predicts at large angles, showing even some rise at backward angles. It must be very interesting to get more data at large angles and compare them with the theory in order to elucidate scattering mechanism more clearly. Any theories are hoped for which could handle the angular distributions at large angles.

iii) $C^{12}(\alpha, \alpha')C^{12*}$, $Q=-7.66$ MeV

Fig. 3 shows inelastic angular distribution data obtained at $E_\alpha=28.4$ MeV leaving the residual nucleus in excitations of 7.66, 9.63 and about 12.7 MeV. For comparison, the angular distribution of the elastic scattering was shown together. For these data of inelastic scattering, no numerical analysis was made, because the conditions $\hbar\omega_i \ll E$, $k_f \simeq k_i$ are not satisfied in these cases. It seems, however, that the angular distribution corresponding to $Q=-7.66$ MeV is rather out of phase with the elastic angular distribution. This is in agreement with the current assignment of 0+ to this level. Unfortunately, it was not possible to take data at backward angles to obtain the ratio of the cross section for 7.66 MeV level to that for 4.43 MeV level $(\sigma(0+\rightarrow 0+)/\sigma(0+\rightarrow 2+))$. More extensive investigation of the inelastic scattering to this state at $E_\alpha=42$ MeV has recently been reported by Eccles and Bodansky[19].

iv) $C^{12}(\alpha, \alpha')C^{12*}$, $Q=-9.63$ MeV

As is seen from Fig. 3 the inelastic angular distribution corresponding to this state is rather out of phase with that to 7.66 MeV state, so that the former is in phase with the elastic scattering angular distribution. Therefore, though the excitation energy is too high to be compared with the theory, it seems probable that this state have odd parity. This is in contrast to the assignment of 0+ or 2+ to this state given by Yavin and Farwell[8], and in favor to 1− assignment as given in the table by Ajzenberg-Selove and Lauritsen[20].

v) $C^{12}(\alpha, \alpha')C^{12*}$, $Q \simeq 12.7$ MeV

This group consists of excitations to at least unresolved two states (12.73 and 13.30 MeV states[20]). The angular distribution obtained at $E_\alpha = 28.4$ MeV is given in Fig. 3. No analysis was yet made, but at $E_\alpha = 31.0$ MeV and 33.4 MeV this group seems to be excited much less strongly. It will be of interest to investigate the energy variation of cross sections with better resolution to elucidate the excitation mechanism of this group.

We are now intending to investigate the behaviour of the change of elastic and inelastic angular distributions with energies for C, in detail, and also for O, Ne, Mg, etc.

The authors are indebted to Dr. J. S. Blair for sending them his article before publication and to Dr. M. Sano for valuable discussions. They are very much grateful to the cyclotron technical staff of the Institute for Nuclear Study.

Note Added in Proof:

We have just made additional measurements of angular distributions of elastic and inelastic scattering ($Q = -4.43$ MeV) at eight more energies. We have reproduced Watters' plateau in the elastic angular distribution at $E_\alpha \cong 30.0$ MeV. There is a kind of very sharp resonance near this energy. Inelastic angular distributions are closely correlated to those of elastic scattering of the same energies even near this resonance. These results will be reported in near future.

References

1) G. Igo and R. M. Thaler: Phys. Rev. **106** (1957) 126. G. Igo: Phys. Rev. Letters **1** (1958) 72.
2) W. B. Cheston and A. E. Glassgold: Phys. Rev. **106** (1957) 1215.
3) J. S. Blair: Phys. Rev. **95** (1954) 1218.
4) D. D. Kerlee, J. S. Blair and G. W. Farwell: Phys. Rev. **107** (1957) 1343.
5) P. C. Gugelot and M. Rickey: Phys. Rev. **101** (1956) 1613.
6) H. J. Watters: Phys. Rev. **103** (1956) 1763.
7) C. Hu, S. Kato, Y. Oda and M. Takeda: J. Phys. Soc. Japan **14** (1959) 549.
8) A. I. Yavin and G. W. Farwell: Nucl. Phys. **12** (1959) 1.
9) N. Austern, S. T. Butler and H. McManus: Phys. Rev. **107** (1953) 350.
10) S. Hayakawa and S. Yoshida: Progr. Theor. Phys. **14** (1955) 1; Proc. Phys. Soc. A, **68** (1955) 656.
11) J. S. Blair and E. M. Henley: Phys. Rev. **112** (1958) 2029.
12) J. S. Blair: Private comm. and Phys. Rev. **115** (1959) 928.
13) S. I. Drozdov: J. Exp. Theor. Phys. **28** (1955) 588, 591; **34** (1957) 1288.
14) E. V. Inopin: J. Exp. Theor. Phys. **31** (1956) 901.
15) K. Alder, A. Bohr, T. Huus, B. Mottelson and A. Winter: Rev. Mod. Phys. **28** (1956) 432.
16) F. J. Vaughn: UCRL 3174 (1955) unpublished, private comm.
17) G. Igo, H. E. Wegner and R. Eisberg: Phys. Rev. **101** (1956) 1508.
18) I. Nonaka, H. Yamaguchi, T. Mikumo, I. Umeda, T. Tabata and S. Hitaka: J. Phys. Soc. Japan **14** (1959) 1260.
19) S. F. Eccles and D. Bodansky: Phys. Rev. **113** (1959) 608. see also Cook, W. A. Fowler, C. C. Lauritsen and T. Lauritsen: Phys. Rev. **107** (1957) 975.
20) H. Ajzenberg-Selove and T. Lauritsen: Nucl. Phys. **11** (1959) 1.
21) E. Almqvist, D. A. Bromley, A. J. Ferguson, H. E. Gove and A. E. Litherland: Phys. Rev. **114** (1959) 1040.

JOURNAL OF THE PHYSICAL SOCIETY OF JAPAN, Vol. 15, No. 7, JULY, 1960

Elastic and Inelastic Scattering of Protons by Oxygen in the Energy Region of 6.9 MeV to 15.6 MeV

By Shinsaku KOBAYASHI

Institute for Nuclear Study, University of Tokyo
Tanashi-machi, Kitatama-gun, Tokyo

(Received April 11, 1960)

Extensive experimental results are presented, showing the variation with energy of the absolute angular distributions for the elastic and inelastic scattering of medium energy protons on oxygen.

For the elastic scattering, angular distributions between 20 deg and 160 deg were obtained for twenty incident proton energies spaced between 6.87 MeV and 15.6 MeV. The absolute angular distributions for the inelastic proton groups, leading to the excitation of about 6 MeV (6.06 and 6.14 MeV) and 7 MeV (6.92 and 7.12 MeV) states of O^{16}, were measured at five energies from 11.9 MeV to 15.6 MeV. Although angular distributions vary remarkably with the incident energy, integrated cross section decreases monotonically as incident energy increases. In particular, at $E_p=15.6$ MeV the total inelastic scattering cross section was roughly measured to be 240±40 mb. From this result and the reported results for other reaction cross sections, we may deduce that O^{16} nucleus is considerably transparent even for this rather high incident energy, where the mean free path of nucleon in nuclear matter has nearly the minimum value in usual nuclei.

The excitation function for the elastic scattering shows appreciably sharp resonances at energies, 7.2, 10.6 and 14.7 MeV, and its gross structure has a large scale resonance of a width about 4 MeV, at incident energy of about 13 MeV. It appears that this resonance is the f-wave giant resonance expected from the shell model.

§ 1. Introduction

The elastic scattering of protons by oxygen has been investigated by many researchers[1)-10)], and some of their studies have thrown light on the low-lying levels of F^{17}. O^{16} contains 8 neutrons and 8 protons, and can be considered as a closed shell neucleus both in neutrons and protons. If this shell model of the nucleus is correct, the compound nucleus F^{17}, formed under bombardment of O^{16} by protons, will consist of one proton outside a closed shell. Therefore F^{17} is a single particle nucleus in the sense that it should show the states of a single particle moving in a central field. Of course levels due to the excitation of the O^{16} core should also appear. F^{17} should be constructed by the addition of an $s_{1/2}$, $d_{5/2}$ or $d_{3/2}$ proton to the O^{16} core and the states corresponding to these protons are expected. In fact, the ground state, the first excited state (at 0.500 MeV), and the state at about 4.7 MeV of F^{17} are believed to be single particle states and the spins and parities of these states are 5/2 +, 1/2+, and 3/2+ respectively. Possibly the level 7/2− (at 3.86 MeV) is not a single particle state of $f_{7/2}$, because this state has a small nucleon reduced width.

The energy region presented in this paper begins just above those of other works[1)-5)] and includes the bombarding energy in the work of Burcham et al.[6)]. The result of Burcham et al. was analyzed in terms of the optical model by Fujimoto et al.[11)], using complex square well potentials. They showed that the potential with small imaginary part ($V=36+2i$ MeV, $R=1.45\times10^{-13}A^{1/3}$ cm) gave the best fit to the experimental result. We may deduce from this fact[26)] that the deviations from the prediction of shell model are appreciably small at this somewhat high excitation energy ($E_p=9.5$ MeV). Therefore there is a possibility that a large scale resonance due to the f-state is detectable at energies higher than 10 MeV. This means that the states of F^{17} in this energy region are predominantly *f*-states and hence have a spin of 5/2 or 7/2, thereby showing that the intermediate coupling model due to Lane, Thomas and Wigner[26] should be in this case a sufficiently good approximation for explaining the energy states concerned.

Previously we measured the elastic scattering of protons by oxygen at energies 7.72, 9.64, 11.7 and 14.1 MeV, and showed that the angular distributions varied irregularly with the incident energy, contrary to the variations in the elastic scattering on medium weight nuclei[12]. More detailed investigation of variations is the aim of the present work.

§ 2. Apparatus

A. *Production of the Focused Proton Beam*

The proton beam is deflected by an A.C. deflector from the variable energy INS (Tokyo) cyclotron[13] and passing through a magnetic shielding channel, leaves the cyclotron chamber. Then it is focused by a pair of quadrupole magnets and is deflected by a sector magnet. The combined lens action of the quadrupole magnets and the sector magnet[14] produces a beam spot about 5 mm wide and 10 mm high, whose intensity can be changed stably from a few μA to 0.01 μA or less, before the collimator slits. The beam then passes through the collimator which has two defining apertures of graphite, 5 mm in diameter, spaced 80 cm apart. To remove slit-scattered protons from the beam, five graphite baffles, each 7.5 mm in diameter, are used.[15]

B. *Scattering chamber and gas target chamber*

Details of the scattering chamber were described elsewhere.[13],[15] It consists of a turn table, a target assembly and a vacuum can containing them. The vacuum can has an inner diameter of nearly 100 cm and a height of 40 cm, whose side wall has 32 windows. The side windows open at each ten degrees from 10° to 170° on one half of the side wall of the chamber and from $-15°$ to $-165°$ on the other half of the wall. These windows allow us each 5 degree observations, but in this work we used the windows of one half of the side wall.

Commercial tank oxygen was used as the target gas. Volumetric analysis showed that this gas consisted of 99.85% O_2 and 0.15% N_2, other impurities being negligible. The isotopic content of O^{16} is 99.76%. The gas was filled in a container, which was made of a brass cylinder of 9 cm in diameter and of 6 cm in height and had a window extending along an angle of more than 180° including the beam entrance and the beam exit. This window was sealed with a sheet of alminum foil 20 μ in thickness. The gas target chamber was located at the center of the scattering chamber. The pressure of the target gas was 40.6 cm Hg (at 27°C) which was measured with a mercury manometer.

The unscattered beam was collected in a Faraday cup. In order to reduce the effect of secondary electrons, the collector cup was equipped with a couple of magnets which produce magnetic fields of about 300 gausses. The collected charge was measured electronically by using 100% feed back type beam current integrator. At the bottom of the cup, an aperture of 3 mm in diameter was equipped, through which a part of the unscattered beam could be extracted from the vacuum and led into an ionization chamber for the beam energy measurement which was placed behind the cup. This aperture was closed with a small piece of permanent magnet during the cross section measurement and could be opened by changing the polarity of the Faraday cup magnet.

C. *Beam energy measurement*

The INS (Tokyo) cyclotron, with its wide range magnet and variable frequency oscillator system, can offer proton beams of energies from 7 MeV up to 16 MeV to the scattering chamber without appreciable change in intensity. In this work, proton beams of various energy were obtained mainly changing the cyclotron parameters, but the small energy changes ($\leq$200 kev) were performed by inserting Al absorbers before the beam collimator. At each energy studied, the energy of the incident beam was determined as follows. The unscattered proton beam entered into an argon-filled shallow parallel-plate ionization chamber, after passing through the small aperture prepared at the bottom of the Faraday cup. By changing the thickness of aluminum absorbers placed in front of the ionization chamber, one could obtain the Bragg curve, which determined the mean range of the incident beam.[16] Thus, using the range energy relation obtained by Bichsel, Mozley, and Aron,[17] the absolute value of the beam energy was determined. The energy spread of the incident proton was estimated to be about ±0.5%.

D. *Detector system*

We used sixteen scintillation counters in each measurement. Fifteen counters were attached to the side windows of the scattering chamber. A spare counter was set up on the turn table in the scattering chamber, and could be placed at any desired scattering angle. The side window counters were equipped at each ten degree from 20° to 160° on one half of the side wall of the chamber. (Fig. 1) Scintillation counters were similar to that used in our previous work.[15] Each consisted of a thallium-activated NaI scintillation crystal of about $20\times20\times1.5$ mm and a photomultiplier tube (mostly RCA 5819 and the remainder RCA 6342, 6655 and DuMont 6292). The energy resolution of these counters was about 2.3% at $E_p=15.6$ MeV. Each counter equipped with a defining slit system, which consisted of a vertical front slit and a circular rear aperture. The G-fractors of these counters were estimated using the equation of Silverstein,[18] including the correction for finite beam size. We found the higher order terms of the equation, including 1st order, negligible compared with the accuracy of the defining slit dimension (about ±0.5%).

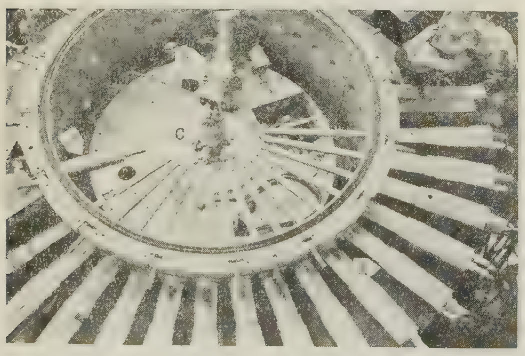

Fig. 1. A perspective view of the experimental apparatus. A: Scintilllation counters attached to the side windows of the scattering chamber. B: Spare counter set up on the turn table in the scattering chamber. C: Target chamber. D: Beam collimator. E: Defining slit system of detector. F: Faraday cup. G: Al absorbers for the beam energy measurement.

The G-factors of these counters were on the average as follows; for the side window counter, 2.26×10^{-4} cm (from 60° to 160°), 0.566×10^{-4} cm (from 30° to 50°), 0.204×10^{-4} cm (20°), and for the turn table counter, 6.06×10^{-4} cm.

The signal pulses, after passing through a cathode follower (White type), were sent to the counting room about 50 meters apart from the measuring room, through a coaxial cable (RG63U). And after amplified by a linear amplifier (Bell-Jordan type), the pulses were fed to a multi-channel pulse height analyzer (Joenstone type). We used five sets of linear amplifiers and multi-channel pulse height analyzers simultaneously. All the electronic equipments were constructed in the electronics division of our laboratory.

§ 3. Experimental Procedure

The angles of detection in the laboratory system range from 20° to 160° at intervals of ten degrees. In addition, a spare counter was set at 55° or 65° according to the incident proton energy. High voltages were supplied always to each counter and the signals from each one were always sent to the counting room. As described in § 2. D, we used simultaniously five sets of electric equipments, each of which includes a multichannel pulse height analyzer. When we connected the cables from the counters at five other scattering angles to the inputs of the five sets of electronic equipments, we could measure the yields at next new five scattering angles. The observation of the angular dependence at a given incident proton energy, needed only four times of such measurement. In a series of measurements at a given energy, we always measured the yield at 90° as the monitor of the system, to obtain important checks upon the operation of the current integrator and upon the conditions of target gas.

This method gave us more reliable data on the angular distribution especially at the region, where the yields change remarkably with the incident energy. The G-factors of the detector at forward angles were made smaller than at other angles, so that the statistical errors in the number of counts did not change markedly with the detection angle. The counting rate was so adjusted by controlling the beam intensity that the counting loss may be much less than 1%.

§ 4. Analysis of the Data

A. *Subtraction of background*

A typical pulse height distribution is shown in Fig. 2. The elastic peak was found to be always accompanied by a uniformly distributed low-pulse-height tail. The greater part of the tail seems to be due not to the low energy component of the incident beam, but due to the multiple scattering by the detector slit edges.[21] Therefore on determining the number of protons elastically scattered by the target gas we set the cutoff threshold just below the elastic peak and discarded all counts falling in the tail. The resolution of the detector being takes into account, this procedure is justified by Courant's calculation,[19] and eliminates the effect due to the slit edge penetration and scattering. The low-energy components of the incident beam were estimated to be less than 0.5%. Therefore we neglected this effect.

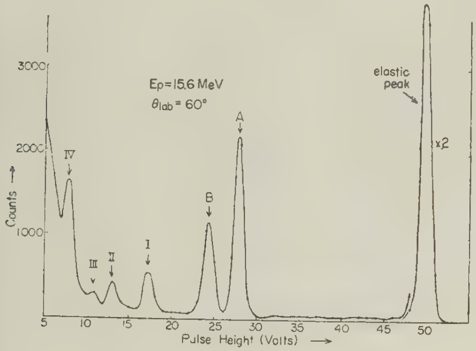

Fig. 2. Typical pulse height spectrum obtained with an NaI(Tl) detector for protons of 15.6 MeV incident energy scattered by oxygen gas at angle of 60°.

In the inelastic groups, ($Q \simeq -6.1$ MeV and -7.0 MeV), there is another background source due to γ rays, especially for the lower energy side, in addition to the above-mentioned origin. This fact made us to give up the measurement of the inelastic groups at the lower incident proton energies ($E_p \leq 10$ MeV). We followed the procedure for the background subtraction, described in our previous papers.[15] In each individual case, an estimated probable error is assigned to this background, commensurate with the extent to

Table I (i). Differential cross sections for the elastic scattering of protons on oxygen.

$\left(\frac{d\sigma}{d\Omega}\right)_{c.m.}$ (mb/sterad)

E_p (MeV) / $\theta_{c.m.}$ (degrees)	6.87	7.13	7.53	8.04	8.44
21.2	989 (10.2)	944 (10.2)	1567 (9.3)	1533 (8.3)	1583 (7.3)
31.8	162 (3.7)	257 (3.4)	536 (3.4)	504 (3.4)	465 (3.0)
42.3	84.1 (2.9)	145 (2.6)	260 (2.6)	214 (2.6)	168 (2.6)
52.7	61.9 (3.1)	92.2 (2.7)	133 (2.6)	84.1 (2.7)	52.8 (2.9)
57.9	—	—	—	50.0 (2.5)	27.8 (2.6)
63.1	41.2 (2.8)	68.7 (2.6)	78.3 (2.6)	33.9 (2.7)	18.4 (2.8)
68.2	32.7 (2.6)	64.8 (2.5)	71.2 (2.5)	—	—
73.4	26.9 (2.9)	65.0 (2.6)	69.8 (2.6)	30.6 (2.7)	27.0 (2.7)
83.5	19.5 (3.1)	68.1 (2.6)	72.4 (2.6)	50.9 (2.6)	51.9 (2.6)
93.6	23.3 (2.6)	71.1 (2.5)	83.2 (2.5)	73.1 (2.5)	74.7 (2.5)
103.5	39.3 (2.8)	74.2 (2.6)	90.4 (2.6)	86.5 (2.6)	87.2 (2.6)
113.4	62.9 (2.7)	76.7 (2.6)	95.8 (2.6)	82.9 (2.6)	81.1 (2.6)
123.1	87.6 (2.6)	83.2 (2.6)	96.7 (2.6)	67.5 (2.6)	61.5 (2.6)
132.7	111 (2.6)	99.5 (2.6)	93.9 (2.6)	48.0 (2.6)	35.9 (2.7)
142.3	123 (2.6)	123 (2.5)	89.3 (2.6)	29.3 (2.7)	17.9 (2.8)
151.8	120 (2.6)	150 (2.5)	76.5 (2.6)	17.2 (2.7)	10.4 (2.9)
161.2	115 (2.5)	183 (2.5)	66.8 (2.5)	12.4 (2.7)	13.5 (2.7)

E_p=mean incident proton energy at the center of target, in lab. system. (MeV) In the bracket, the probable error (§ 4) is given. (%)

Table I (ii).

E_p (MeV) $\theta_{c.m.}$ (degrees)	8.66	9.42	10.2	10.5	10.8
21.2	1137 (7.3)	1131 (6.4)	1093 (5.5)	950 (5.5)	803 (5.5)
31.8	309 (3.0)	362 (3.0)	327 (2.7)	291 (2.8)	253 (2.8)
42.3	113 (2.6)	134 (2.6)	107 (2.7)	88.7 (2.6)	88.7 (2.7)
52.7	34.2 (3.0)	36.4 (3.0)	23.2 (3.3)	17.8 (2.9)	20.8 (3.4)
57.9	17.2 (2.6)	16.0 (2.6)	9.84(2.7)	9.86(2.9)	11.2 (2.7)
63.1	12.2 (2.9)	7.13(3.2)	7.76(3.2)	11.3 (3.4)	9.98(3.0)
68.2	—	—	—	—	—
73.4	17.7 (2.8)	17.0 (2.9)	19.5 (2.8)	29.7 (2.9)	25.9 (2.7)
83.5	37.2 (2.7)	45.6 (2.7)	38.6 (2.7)	48.2 (2.8)	46.6 (2.6)
93.6	55.4 (2.5)	69.4 (2.5)	52.0 (2.5)	59.1 (2.6(	60.3 (2.5)
103.5	66.5 (2.6)	79.7 (2.6)	58.6 (2.6)	64.7 (2.7)	60.1 (2.6)
113.4	65.2 (2.6)	74.8 (2.6)	54.2 (2.6)	61.0 (2.7)	48.2 (2.6)
123.1	52.7 (2.6)	53.9 (2.6)	41.7 (2.7)	52.6 (2.8)	30.4 (2.7)
132.7	36.8 (2.7)	35.0 (2.7)	26.5 (2.7)	44.1 (2.8)	16.4 (2.9)
142.3	22.2 (2.7)	19.8 (2.7)	16.2 (2.8)	37.9 (2.8)	14.0 (2.9)
151.8	15.5 (2.7)	11.5 (2.8)	11.2 (2.8)	34.7 (2.7)	21.6 (2.7)
161.2	12.5 (2.7)	11.1 (2.7)	13.3 (2.7)	33.7 (2.7)	37.4 (2.6)

Table I (iii).

E_p (MeV) $\theta_{c.m.}$ (degrees)	11.1	11.4	11.9	12.9	13.9
21.2	907 (4.6)	899 (4.6)	867 (4.6)	706 (3.8)	719 (3.8)
31.8	304 (2.8)	311 (2.8)	257 (2.6)	260 (2.6)	271 (2.6)
42.3	108 (2.8)	108 (2.8)	77.3 (2.7)	85.1 (2.7)	80.2 (2.7)
52.7	29.2 (3.7)	31.7 (3.6)	19.6 (3.4)	24.0 (3.3)	20.1 (3.4)
57.9	21.0 (2.7)	20.1 (2.7)	15.5 (2.6)	18.2 (2.7)	18.3 (2.6)
63.1	21.5 (3.0)	18.8 (3.0)	20.5 (2.8)	20.2 (2.8)	23.5 (2.7)
68.2	—	—	—	—	—
73.4	35.8 (2.9)	35.8 (2.9)	41.7 (2.7)	34.1 (2.7)	42.4 (2.7)
83.5	52.9 (2.8)	54.2 (2.8)	56.5 (2.6)	44.8 (2.7)	52.2 (2.6)
93.6	62.4 (2.6)	63.8 (2.6)	57.6 (2.5)	47.3 (2.5)	49.4 (2.5)
103.5	63.8 (2.7)	64.2 (2.7)	54.9 (2.6)	44.3 (2.7)	42.4 (2.7)
113.4	46.5 (2.8)	52.4 (2.8)	39.7 (2.7)	35.5 (2.7)	30.3 (2.7)
123.1	27.1 (3.0)	34.7 (2.9)	27.9 (2.7)	24.5 (2.8)	21.9 (2.8)
132.7	12.2 (3.4)	21.3 (3.0)	21.4 (2.8)	17.7 (2.8)	17.2 (2.8)
142.3	7.71(3.6)	15.6 (3.1)	19.0 (2.8)	16.1 (2.8)	17.2 (2.8)
151.8	15.2 (3.0)	19.5 (2.9)	21.6 (2.7)	18.4 (2.7)	20.7 (2.7)
161.2	31.0 (2.7)	31.9 (2.7)	27.9 (2.6)	24.6 (2.6)	24.9 (2.6)

which its value appeard uncertain.

B. *Discussion of errors*

(i) *Uncertainly in the cross sections*

The error in the collected charge, consisting of errors in calibration of the integrator including its zero drift, was ±1.5%.

The error coming from the target gas, such as the amounts of impurity and that in the measurement of density (pressure and temperature), was estimated to be ±1.0% or less.

Insufficient accuracy of the exact scattering geometry and the method of background subtraction were already described in § 2. D and

Table I (iv).

E_p (MeV) / $\theta_{c.m.}$ (degrees)	14.3	14.5	14.7	15.2	15.6
21.2	685 (3.8)	642 (3.8)	656 (3.8)	774 (3.8)	776 (3.8)
31.8	265 (2.6)	260 (2.6)	259 (2.6)	297 (2.6)	287 (2.5)
42.3	86.6 (2.9)	87.6 (2.9)	74.2 (2.7)	75.5 (2.9)	67.4 (2.7)
52.7	20.7 (4.1)	25.7 (3.8)	22.8 (3·3)	22.2 (4.0)	18.4 (3.5)
57.9	—	—	25.0 (2.7)	27.6 (2.7)	—
63.1	19.7 (3.1)	21.4 (3.0)	31.7 (2.7)	35.1 (2.8)	39.6 (2.7)
68.2	28.2 (2.7)	28.5 (2.7)	—	—	—
73.4	35.5 (2.9)	35.4 (2.9)	45.9 (2.6)	50.8 (2.8)	61.4 (2.6)
83.5	43.8 (2.8)	43.2 (2.8)	46.0 (2.7)	46.2 (2.8)	56.2 (2.6)
93.6	42.5 (2.5)	43.9 (2.5)	41.2 (2.5)	33.4 (2.5)	36.4 (2.6)
103.5	34.4 (2.9)	39.2 (2.9)	37.5 (2.7)	22.2 (3.1)	17.7 (2.9)
113.4	24.6 (3.0)	30.4 (2.9)	31.9 (2.7)	14.0 (3.4)	8.30 (3.3)
123.1	16.4 (3.2)	18.7 (3.2)	24.7 (2.8)	11.8 (3.5)	9.19(3.2)
132.7	12.5 (3.4)	13.8 (3.3)	19.8 (2.8)	14.3 (3.3)	16.1 (2.9)
142.3	15.4 (3.1)	15.6 (3.1)	23.0 (2.7)	20.1 (3.0)	22.2 (2.7)
151.8	23.8 (2.8)	26.5 (2.8)	36.5 (2.6)	27.4 (2.8)	22.9 (2.7)
161.2	30.6 (2.7)	44.3 (2.6)	59.3 (2.5)	37.1 (2.7)	23.1 (2.6)

§4. A, respectively.

In addition, the loss in beam charge collection due to multiple scattering in the target gas and in the foils of the target chamber, should be allowed for. This was estimated, according to the treatment of Bethe for multiple scattering[20] and was corrected. The error after this correction is believed to be appreciably small. The effect of multiple scattering by Al foil and O_2 gas on the scattered particles to be detected was also estimated. It is considerably reduced by mutual compensation of the scattered-in and -out.[21] The deviation in this compensation was appreciably small (<1%) at over all detection angles in this work except at $\vartheta_{\rm lab}=20^\circ$ and 30°.

The various errors considered above, together with that due to the counting statistics, have been combined quadratically, although they are not all truly random, and are given in the bracket of Table I as estimated probable errors.

The largest parts of errors of the inelastic cross section come from the background subtraction, described in §4. A already.

The statistical error in the number of pulses counted was mostly of the order of 1%.

(ii) *Uncertainty in the scattering angle*

Uncertainty in the scattering angles (±0.15°) was mainly compounded from the following sources: the uncertainty in the zero-angle correction (±0.01° or less) and the error in the alignment of the defining slit in front of the scintillation detector.

(iii) *Uncertainty in the incident energy*

As is described in §2. C., uncertainty in the determination of incident energy is due to the error, in the measurement of Bragg curve and in the determination of the absolute thickness of Al absorber. The uncertainty in the beam energy at the target center was estimated to be ±0.5%. Of course, this depends on the range-energy relation based on the work of Bichsel, Mozly and Aron.[17]

§5. Results and Discussion

A. *Elastic scattering*

Table I gives the data obtained for elastic scattering at the twenty incident energies used. The differential cross sections for elastic scattering expressed as ratios to Rutherford cross sections, are shown in Fig. 3. The excitation function is given, as a function of incident energies at $\vartheta_{\rm lab}=140^\circ$, 150° and 160°, in Fig. 4, which also contains our pre-

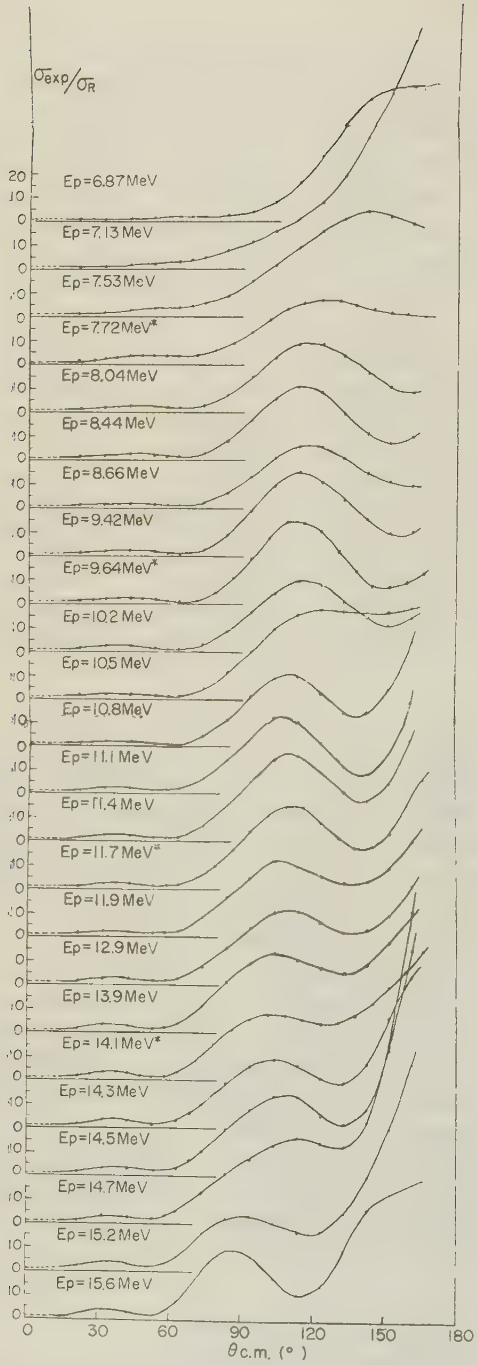

Fig. 3. Differential cross sections for the elastic scattering of protons by oxygen, in units of the Rutherford cross section. * our previous results (2).

vious data[12] and Burcham's data.[6]* The excitation function shows appreciable sharp resonances at energies 7.2, 10.6 and 14.7 MeV. The lowest resonance at 7.2 MeV continues to the Zürich data[3] qualitatively.

The excited states higher than 7 MeV, in F^{17} nucleus, have not been investigated. On the other hand, we know considerably well of the higher excited states in O^{17} nucleus,[22] which is the mirror nucleus of F^{17}, and the correspondence is appreciably good in lower excited states. The formula

$$\omega(E)=0.2\exp[2(0.5E)^{1/2}]/\mathrm{MeV}$$

agrees fairly well with the experimentally determined average level densities for O^{17} at 6.0 MeV and 8.0 MeV excitation,[22], and therefore it is used to estimate the average level densities for F^{17} nucleus. This formula gives $\omega\simeq 20$, and 50 levels per MeV at excitations 10 MeV and 15 MeV, respectively.** There-

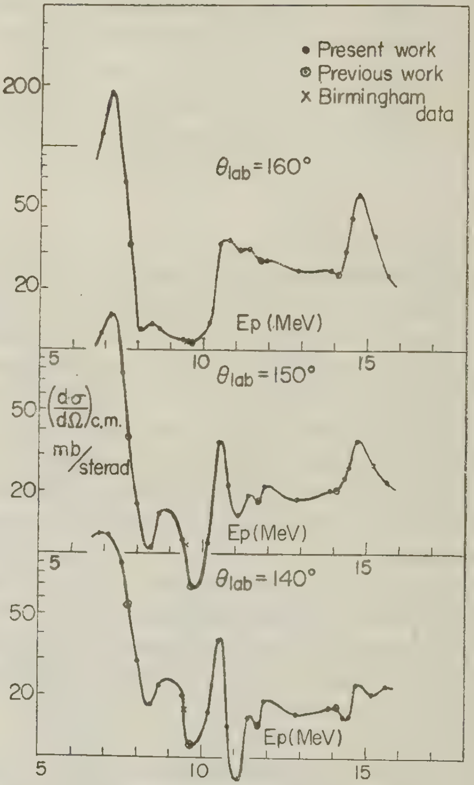

Fig. 4. Excitation curves of the elastic scattering on oxygen.

---

* Although a part of incident energy used by Kinsey and Stone[7] was included in our energy region, unfortunately they did not reported the data at backward scattering angles ($\vartheta \geq 130°$). Any comparison with their result has not been done.

** Excitation energy in F^{17} nucleus is given by $(16/17\cdot E_p+0.596)$ (MeV), where E_p is mean incident proton energy at the center of target in lab. system.

fore allowing for the beam energy spread used, we should not discuss the one level problem, but the gross structure problem or the average problem, at an incident energy higher than 10 MeV. The result of Burcham et al. at $E_p=9.5$ MeV[6] was analyzed in terms of the optical model by Fujimoto et al.[11] as was described in § 1. Following their procedure, we fitted our experimental result at $E_p=12.9$ MeV, using complex square well potentials. The result analyzed by the potential $V=35+2i$ MeV ($R=1.45\times10^{-13}A^{1/3}$ cm), agrees with the angular position of the first minimum and the value of the first maximum, of the experimental differential cross section, and is shown in Fig. 5.* In our energy region, the wavelength of the incident proton is of the same order as the radius of the nucleus and therefore the effect of the edge is not so serious as it is for higher energies. It should be noted that W_0 is considerably small. This fact means that the mean free path of the incident protons in nuclear matter is 16.1×10^{-13} cm, which is much larger than the radius of the target nucleus. This value is calculated from the relation[24]

$$1/\Lambda^2=2\left[\left\{\left(\frac{W_0}{E+V_0}\right)^2+1\right\}^{1/2}-1\right]K^2,$$

using the best value of V_0 and W_0. From the following reasons, we may understand such a small imaginary part of the optical model. The first is due to the high threshold of $(p,\ n)$ reaction (Eth$=17.3$ MeV), and so open channels except $(p,\ p')$ scattering are mainly $(p,\ \alpha)$ (Eth$=5.53$ MeV), $(p,\ \gamma)$ and $(p,\ d)$ reactions (Eth$=14.2$ MeV). The largest contribution except $(p,\ p')$ scattering is perhaps based on $(p,\ \alpha)$ reaction, the cross section of which is at most 50 mb.[28] Therefore the main part of proton induced reaction comes from inelastic scattering. This inelastic scattering does not open at $E_p\leq 6$ MeV in oxygen. So the level density of the lowlying level of O^{16} is relatively small. In our measurements, total cross section of $(p,\ p')$ scattering is roughly estimated to be 240 ± 40 mb at $E_p=15.6$ MeV. (See, Table II) The compound nucleus formation cross section σ_c was estimated from the continium theory[25] to be about 630 mb. Thus, $(p,\ p')+(p,\ \alpha)$ cross section is smaller than a half of σ_c, and this is consistent with the small imaginary part W_0. We cannot exclude, however, the contribution of the compound elastic scattering to σ_c to a considerable extent.

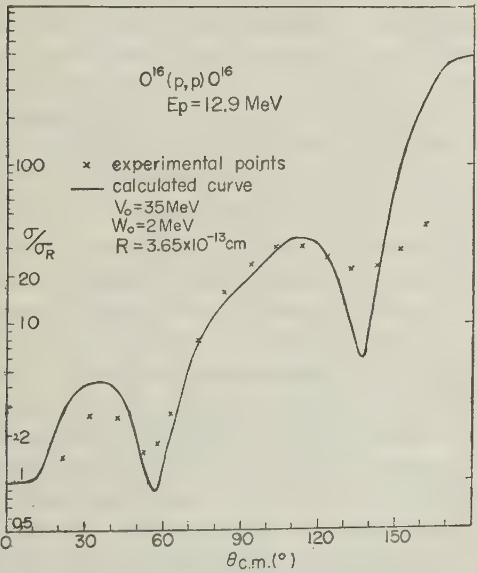

Fig. 5. Angular distribution of elastically scattered protons from Oxygen, with the calculated curve based upon the optical model. Ordinates are ratios to Rutherford cross-section.

Table II. Total integrated cross sections.

Group	$-Q$ (MeV)	σ_t (mb)	
		$E_p=15.6$ MeV	$E_p=19.0$ MeV
A	6.14	94 ± 10	59 ± 7
B	7.02	57 ± 6	34 ± 4
I	8.87	28 ± 5	28 ± 3
II	9.85	18 ± 4	8 ± 2
III	10.34	8 ± 2	8 ± 2
IV	11.08	30 ± 10	19 ± 3
V	11.51	—	11 ± 2
VI	12.02	—	6 ± 2
VII	12.53	—	11 ± 2

$E_p=15.6$ MeV (Present work)
$E_p=19.0$ MeV (Princeton dada).

The smallness of imaginary part W_0 leads us to the conclusion that the departure from the shell model is small at somewhat high energy, and thereby the sharp appearance of the large-scale resonance is predicted. From the above-mentioned analysis based on the optical model, it is seen that the maximum contribution to the scattering comes from proton waves of angular momentum $l=3$*. Namely, using the potential $V=35+2i$ MeV, we find an f-wave characteristic resonance ($N_3=-\Delta_3+\mathrm{Re}\,f_3=0$)[27] at energy about 13.5 MeV. The width of this resonance should be related to twice of the imaginary part.[26] Thus this width is expected to be about 4 MeV. In other usual nuclei, the imaginary part of optical potentical is much larger than that in O^{16} at $E_p \gtrsim 10$ MeV. Consequently the width of the giant resonance will appear to be broadened. Thus possibly, O^{16} appears to be one of the examples of such unusual nuclei, in which the giant resonance is clearly observed at $E_p \gtrsim 10$ MeV.

---

* Without an electronic computer, it is impracticable to study these results fully, and we have merely attempted to obtain approximate agreement.

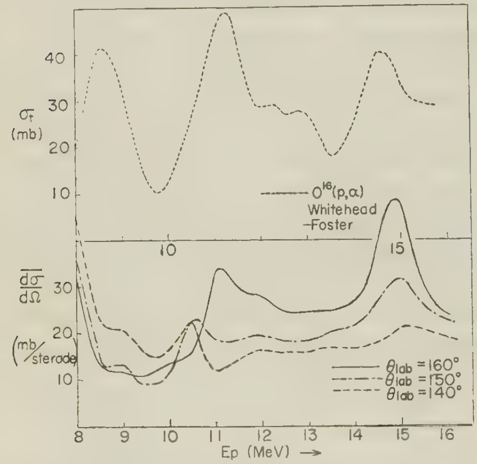

Fig. 6. The averaged excitation curves of the elastic scattering on Oxygen. The excitation function for $O^{16}(p, \alpha)$ reaction measured by Whitehead and Foster is also included.

In view of the gross structure problem, which we concern, we will average the experimental differential cross sections at energy interval ±500 kev. This magnitude of energy interval includes, on an average, about three measuring points. The average cross section is plotted in Fig. 6 as a function of the incident energy. Particularly the average excitation function of differential cross section at $\vartheta_{\mathrm{lab}}=160°$, has an apparent gross structure. In Fig. 6, the excitation function for O^{16} (p, α) reaction, which was measured by Whitehead et al.,[23] is also included, and the positions of this large scale resonance agree fairly well with each other. This seems to be the above-mentioned f-wave giant resonance from the following reasons. In the approximation based on the optical model, neglecting a spin-orbit coupling term, we expect that the f-wave resonance does not appear near $\vartheta_{\mathrm{lab}}=140°$, which is the zero point of the third order Legendre function. In fact, in Fig. 6, we cannot find the occurrence of the large-scale resonance in the excitation function at $\vartheta_{\mathrm{lab}}=140°$. This statement is also verified qualitatively by comparing our analysis based on the optical model with that of Fujimoto et al.; that is, at $\vartheta_{\mathrm{lab}} \cong 140°$ our result nearly equals to that of Fujimoto et al., while at $\vartheta_{\mathrm{lab}} \cong 160°$ our calculated result at $E_p=12.9$ MeV is much larger than theirs at $E_p=9.5$ MeV.

Therefore this suggests that the states of F^{17} in this characteristic resonance region are predominantly f states and hence have spins of 5/2 or 7/2, thereby showing that the intermediate coupling model due to Lane, Thomas and Wigner,[26] is in this case a sufficiently good approximation for explaining the energy states concerned. The result of the above-mentioned O^{16} (p, α) reaction[23] may also be explained as an f-wave resonance.

B. *Inelastic scattering*

The inelastic proton grouds, leading to the excitation of about 6 MeV (group A) and 7 MeV (group B) states of O^{16}, were observed at five energies from 11.9 MeV to 15.6 MeV together with the elastic proton group. Group A gives an energy excitation of the 3− level at 6.14 MeV in O^{16}. The group B corresponds to an energy of about 7.0 MeV states in O^{16} and appears to be the unresolved 6.91 and 7.12 MeV states. The resulting differential cross sections are shown in Fig. 7; a part of the angular distribution curves could not be measured because of the background and is excluded from Fig. 7. Although angular distributions vary remarkably with the incident energy, the integrated cross section decreases monotonically as incident energy increases. This is shown in Fig. 8, including the work of Hornyak and Sherr.[8] There appears a

---

* The calculated cross section for the formation of the compound nucleus (optical model) at energy 12.9 MeV was as follows. $\sigma_c = \sum_{l=0}^{4} \sigma_c^{(l)} \simeq 460$ mb.

	$l=0$	$l=1$	$l=2$	$l=3$	$l=4$	
$\sigma_c^{(l)}$	22	38	42	354	2	(mb)

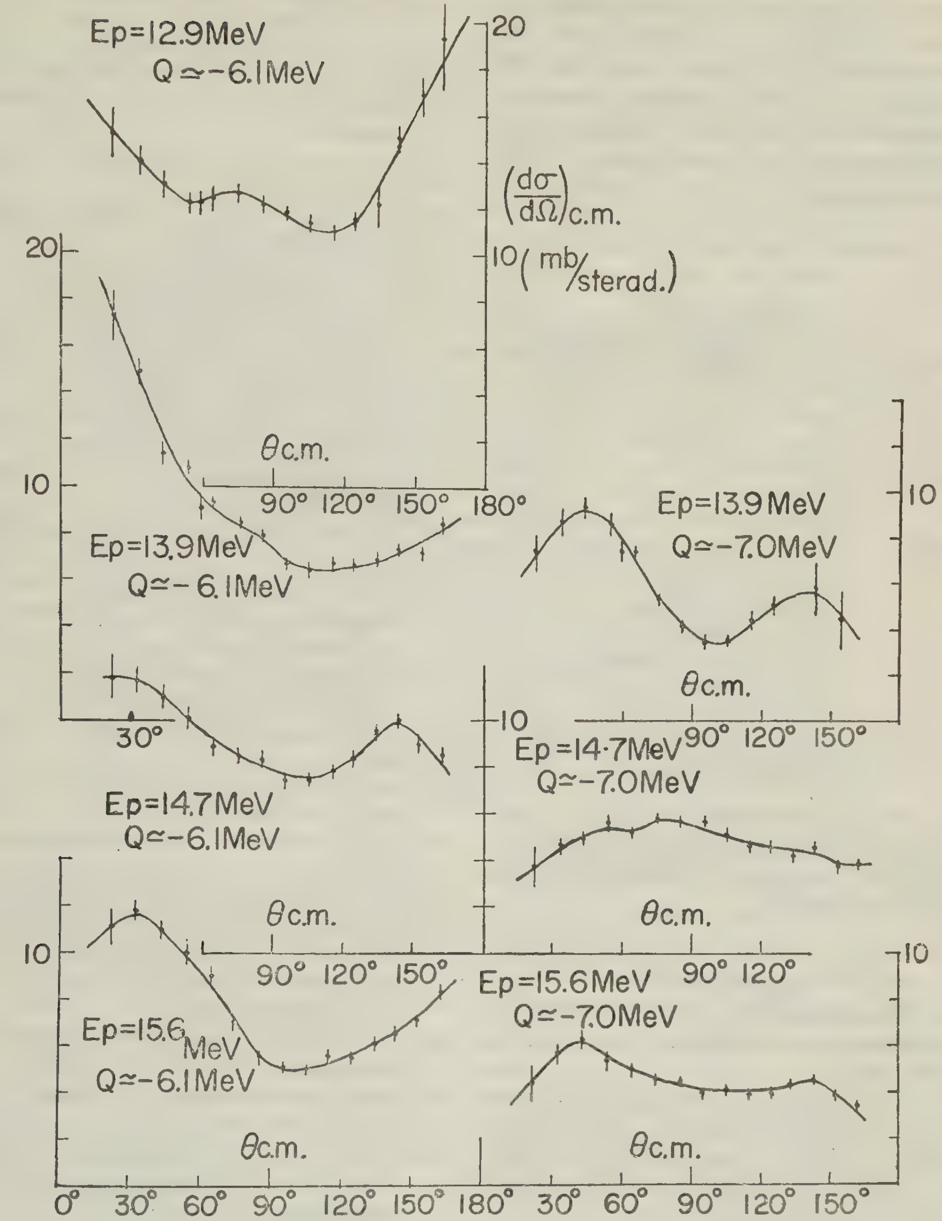

Fig. 7. Differential cross sections for $O^{16}(p, p')O^{16*}$. The smooth curves are drawn primarily to connected points; the estimated probable errors are shown.

shoulder at $E_p \simeq 14.7$ MeV for group A. Table II gives the total integrated cross section and was compared with Princeton data.[8] Any comparison with the theory of inelastic scattering has not been done.

The author is particulary indebted to Professors S. Kikuchi and I. Nonaka for their guidance and encouragement, and to Professor Y. Oda for helpful discussions held throughout the course of the work. The author wishes to express his deepest appreciation to Professor K. Matsuda. Without his active guidance and severe criticism, the present work, doubtlessly, would not have been completed. It is a distinct pleasure to thank Messrs N. Yamamuro and Y. Nagahara for their active participation in obtaining the data, Professor S. Suwa for his invaluable suggestion in the data analysis, Messrs T. Karasawa, A. Suzuki, H. Ogawa and the members of the INS (Tokyo) cyclotron crew for providing excellent cyclotron operation and Messrs M. Otsuka and N. Yoshimura for their maintenance and construction of the electronic equipments.

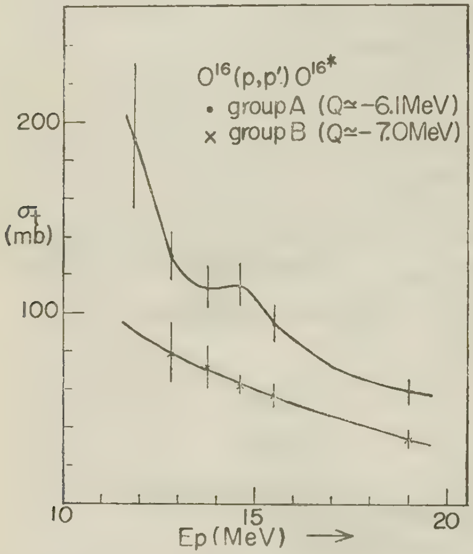

Fig. 8. Excitation functions for group A ($Q\simeq -6.1$ MeV) and group B ($Q\simeq -7.0$ MeV) in $O^{16}(p,p')O^{16*}$ scattering. Ordinates are integrated cross sections.

References

1) R. A. Laubenstein, M. J. W. Laubenstein, L. J. Koester and C. Mobley: Phys. Rev. **84** (1951) 12.
2) F. J. Eppling, J. R. Cameron, R. H. Davis, A. S. Divatia, A. J. Galonsky, E. S. Goldberg and R. W. Hill: Phys. Rev. **91** (1953) 438A.
3) M. Sempert, H. Schneider and M. Martin: Helv. Phys. Acta **27** (1954) 313.
4) R. R. Henry, G. C. Phillips, C. W. Reich and J. L. Russel: Bull. Amer. Phys. Soc. **1** (1956) 96.
5) P. V. Sorokin, A. K. Val'ter, B. V. Gavrilovski, K. V. Karadzhev, V. I. Man'ko and A. I. A. Taranov: Soviet Physics (JETP) **1** (1958) 466.
6) W. E. Burcham, W. M. Gibson, A. Hossain and J. Rotblat: Phys. Rev. **92** (1953) 1266. W. M. Gibson, D. J. Prowse and J. Rotblat: Proc. Roy. Soc. **243** (1957) 237.
7) B. B.Kinsey: Phys. Rev. **99** (1955) 332. B. B. Kinsey and T. Stone: Phys. Rev. **103** (1956) 975.
8) W. F. Hornyak and R. Sherr: Phys. Rev. **100** (1955) 1409.
9) R. H. Chow and B. T. Wright: Canadian J. Phys. **35** (1957) 184.
10) R. A. Vanetsian and E. D. Fedchenko: Soviet J. of Atomic Energy **2** (1957) 141.
11) Y. Fujimoto and A. Hossain: Phil. Mag. **46** (1955) 542. Burge, Y. Fujimoto and A. Hossain: Phil. Mag. **1** (1956) 19.
12) C. Hu, K. Kikuchi, S. Kobayashi, K. Matsuda, Y. Nagahara, Y. Oda, N. Takano, M. Takeda and T. Yamazaki: J. Phys. Soc. Japan **14** (1959) 861.
13) S. Kikuchi et al.: J. Phys. Soc. Japan **15** (1960) 41.
14) K. Matsuda, T. Mikumo, K. Nisimura, S. Kobayashi, H. Ogawa and H. Adachi: INSJ-14, January 15, 1959.
15) K. Kikuchi, S. Kobayashi and K. Matsuda: J. Phys. Soc. Japan **14** (1959) 121.
16) R. Mather and E. Segre: Phys. Rev. **84** (1951) 191.
17) H. Bichsel, R. F. Mozley and W. A. Aron: Phys. Rev. **105** (1957) 1788.
18) E. A. Silverstein: Nuc. Instr. and Meth. **4** (1959) 53.
19) E. D. Courant: Rev. Sci. Instr. **22** (1951) 1003.
20) H. Bethe: Phys. Rev. **89** (1953) 1256.
21) S. Kikuchi, J. Sanada, S. Suwa, I. Hayashi, K. Nishimura and K. Fukunaga: J. Phys. Soc. Japan **15** (1960) 9.
22) F. Ajzenberg-Selove and T. Lauritsen: Nucl. Phys. **11** (1959) 1.
23) A. B. Whitehead and J. S. Foster: Canadian J. Phys. **36** (1958) 1276.
24) P. M. Endt and M. Demeur: *Nuclear Reactions* **1** (North-Holland pub. co., Amsterdam, 1959) Gugelot's eq. (11) P. 402.
25) J. M. Blatt and V. F. Weisskopf: *Theoretical Nuclear Physics* (John Willey and Sons, Inc., New York, 1952) 350.
26) A. M. Lane, R. G. Thomas and E. P. Wigner: Phys. Rev. **98** (1955) 693.
27) H. Feshbach, C. E. Porter and V. F. Weisskopf: Phys. Rev. **96** (1954) 448.

JOURNAL OF THE PHYSICAL SOCIETY OF JAPAN, Vol. 15, No. 7, JULY, 1960

On the High Energy Soft Component Near Sea Level

By Tadashi KAMEDA

Department of Physics, Kobe University, Kobe

(Received February 9, 1960)

As the features of the high energy soft components of cosmic rays have not yet been thoroughly investigated, it is of great interest to study them at present day, especially in very high energy region (above BeV). To obtain the energy of such high energy electron or photon, the electromagnetic shower theory can be applied.

Using an experimental arrangement consisting of GM-counter hodoscopes and an ionization chamber with large area, the pulse height distribution of cosmic-ray showers produced by electrons or photons in lead and iron absorbers of different thickness was measured. The number of shower particles was estimated from the pulse height considering the angular spread of shower particles, and the energy of electrons or photons was obtained from the results of shower theory. The results of the present experiment show that, i) the differential energy spectra can be represented by a power law of the form $E^{-\gamma}$, with γ of 2.90 and 2.80 for electrons and photons of 2–20 BeV, respectively, ii) the zenith angle distribution of electrons is expressed by $\cos^2\theta$, and iii) upper limit of the ratio of the number of electrons to that of photons is 1.1. It is also found that the calculated results by Ivanenko are favorable to explain the observed results for lead and iron absorbers. The essential part of this investigation is to provide a classification of the incident electrons or photons by the GM-counter hodoscopes, that is, single incident particles, multiple incident ones, and those associated with EAS are separated in order to minimize the ambiguity involved in the results.

§1. Introduction

According to the generally accepted interpretation, cosmic-ray electrons and photons in the lower atmosphere are produced by decay and collision processes of μ-mesons, and by decay process of π^0-mesons resulting from nuclear interactions. It is of importance to obtain detailed information concerning the origin of the soft components, comparing the results of the observations at different altitudes with the suppositions based on the above-mentioned processes.

Experiments on the soft components have been performed hitherto by means of various methods, through which we have fairly accurate knowledge concerning the soft component of relatively low energy ($\leqslant$500 MeV),[1)–4)] but the observation in high energy region ($\geqslant$1 BeV) is not sufficient[2),4)].

The present experiment was planned to obtain energy spectra, absolute intensities, and zenith angle dependence of electrons and photons of very high energy. For this purpose, an ionization chamber of large area and counter hodoscopes were used. The ionization chamber is useful in the study of high energy electrons and photons as compared to the cloud chamber, because they produce so dense showers that individual tracks can not be identified separately in the latter case. Results obtained by experiments with ionization chambers, however, are apt to contain considerable uncertainties because of the variety of events giving rise to bursts. The uncertainties will be minimized under due caution, that is, if individual events associated with ionization bursts are identified by some auxiliary means. GM-counter hodoscopes in our experiment serve to select the events caused by electrons and photons. The events associated with extensive air showers are distinguished from unassociated ones by means of air shower trays. It is necessary to distinguish the events associated with EAS, because, if electrons and photons are associated with them, not only the particles initiating the cascade showers in absorber are not identified, but also the number of shower particles becomes uncertain because of large area of the ionization chamber. Further it is generally accepted that high energy electrons and photons in EAS have different energy spectra from those of single incoming particles[5].

In this paper we describe the method of experiments and the results otained near sea level. The observation at mountain altitude and the related discussion will be reported in the succeeding paper.

§ 2. Apparatus

Fig. 1 a and b show the experimental apparatus used in this experiment. The number of GM-counters in each tray and the effective area of each counters are listed in Table I.

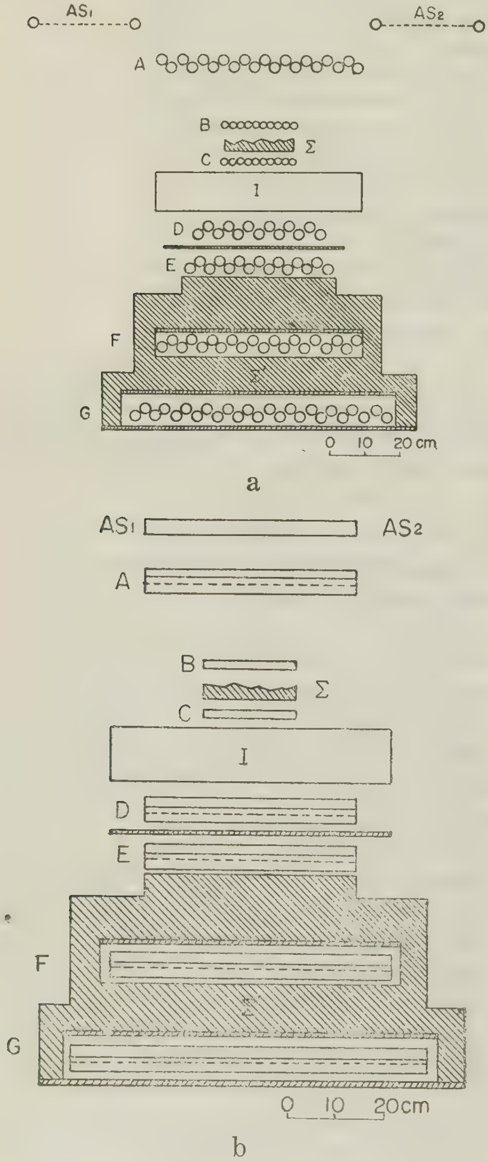

a

b

Fig. 1. Arrangement of the apparatus.

Trays AS_1 and AS_2 are located 230 cm and 170 cm apart from the centre of Tray A respectively, lying immediately under the roof of the laboratory. All counters of the above trays are connected to neon lamps of the hodoscopes.

Table I.

Tray No.	Number of GM-counter	Effective Area of Each Counter	
A	20	2.8 cm	43.5 cm
B	10	2.0 cm	18.5 cm
C	10	〃	
D	13	2.8 cm	43.5 cm
E	15	〃	
F	20	2.8 cm	58.5 cm
G	25	2.8 cm	70.0 cm
AS_1	20	2.8 cm	43.5 cm
AS_2	20	〃	

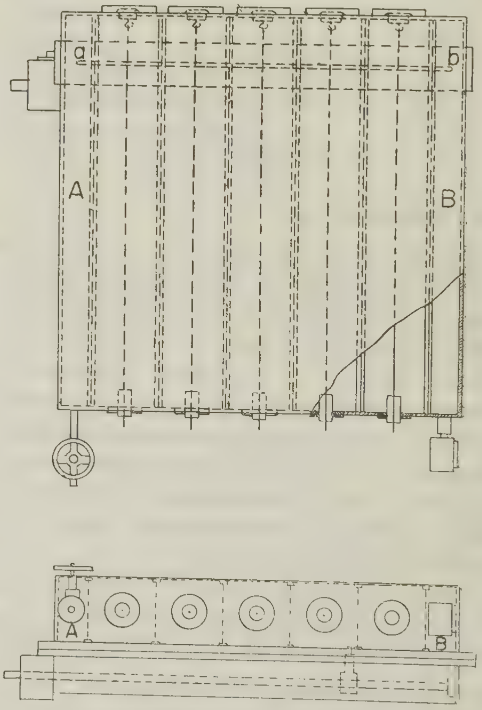

Fig. 2. Ionization chamber.

I in the Fig. 1 is the ionization chamber which was constructed in the form of rectangular parallelepiped of 10 cm height, 50 cm width and 50 cm length, and was filled with commercial argon of 99.9% purity at a pressure of 5.0 atmosphere (at 0°C). The top plate of the chamber is made of 3 mm thick iron, and the bottom and the sides are 5 mm thick iron plates. The chamber is divided into five compartments of 10 cm width by brass meshes as shown in Fig. 2, and dummy spaces of both sides (A and B in the Fig. 2) are provided against the effect of side walls. Each compartment has an effec tive volume of 10 cm × 10 cm × 50 cm, and a molybdenum wire of 1 mm diameter is stretched at the centre along the long axis. A polonium α source for calibration can be moved along the slit (ab in Fig. 2) of the bottom plate by the gear system, and in normal operation the source is placed within the dummary compartment.

Σ in Fig. 1 is a shower producer of lead or iron of 20 cm × 20 cm area, in which the electromagnetic showers, initiated by incident electron or photon, develop, and of different thickness, 0, 1, 2, 3, and 4 cm of lead, and 4 8 cm of iron.

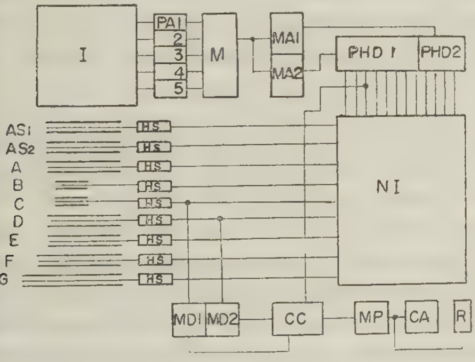

Fig. 3.
Block diagram

PA: preamplifier
M: mixer
MA: main amplifier
PHD: pulse height discriminator
HS: holdoscope circuits
NI: neon indicator
MD: mixing discrimimator
CC: coincidence circuits
MP: master pulse generator
CA: camera driver
R: register

The block diagram of the circuit is shown in Fig. 3. The amplifier for the ionization chamber is that of Jordan-Bell⁶⁾, and the output pulses of the amplifier are fed into a pulse height analyser of 12 channels, each channel being connected to a neon lamp. These neon indicators of pulse height and the GM-counter hodoscopes are photographed on the same film of 16 mm cine-camera.

The hodoscopes are triggered by a master pulse generated when an ionization pulse higher than the predetermined pulse height occured simultaneously with the discharges of any GM-counters in tray C, and the discharges of three or more GM-counters in tray D (hereafter we designate it for abbreviation as $C^{\geq 1}\ D^{\geq 3}\ I^{\geq x}$, where x is expressed by a pulse height of ionization measured in terms of unit of Po$-\alpha$).

Experiments were performed from spring to summer in 1956 in the hut on the university building (30 m a.s.l.), the roof of which has 0.7 g/cm² thickness of wood and zinc. counters and all circuits were checked daily, and if there was something wrong, the data after the previous check were omitted from the analysis*.

§ 3. Analysis of the Data

A) *Classification of events*

The photographic records were reproduced on drawings of the apparatus on a reduced scale of 0.1. These records were classified on the basis of the following criteria:

a) Association and non-association with EAS of density $\Delta \geqslant 4/\mathrm{m}^2$.

For this purpose, events were classified into two groups by the number of discharged GM-counters of trays AS_1 and AS_2. We designate the events in which none of trays AS_1 and AS_2 discharged as non associated events with EAS of $\Delta \geqslant 4/\mathrm{m}^2$, and the one in which the discharge of one or more counters in tray AS_1 and AS_2 occurred as associated events with EAS.

b) Electron (or photon) initiated showers and penetrating showers.

The showers in which none of the GM-counters in trays F and/or G discharged are regarded as electron (or photon) initiated showers, and those in which any GM-counters in trays F and/or G discharged as penetrating showers.

c) Single incident particle and multiple incident particles.

This classification was made by the number of discharged GM-counters in trays A and B. We regard the showers as those initiated by single incident particle, when one or two (adjoining) GM-counters in each of trays A and B discharged, and as showers initiated by multiple incident particles when three or more GM-counters in close proximity in trays A and B discharged. However, in the cases where 4 or less GM-counters in tray A discharged scatteringly and one or two (adjoining) GM-counters in tray B discharged, we regard these events also those initiated by single incident particles.

---

* Such cases were found five times during the experiments running for four months.

d) Electron initiated showers and photon initiated showers

When none of the GM-counters in tray A and B discharged and the first criterion in (b) is fulfilled, the shower is regarded as photon initiated showers. If the first criterion in (b) and in (c) are fulfilled respectively, we regard the showers as electron initiated showers.

e) Uncertain events

There were many pictures which satisfied the criteria a), b), and c), but not d); for example, pictures in which none of tray A but one or more GM-counters in tray B discharged or vice versa. There were also some pictures in which an electron (or photon) was incident with some penetrating particles in parallel, and these might be classified as penetrating showers according to b). We omitted these indistinct records when the energy spectra were concidered, but a part of them were adopted under due correction when intensities of electrons and photons were the subject of interest.

Some remarks are necessary for trays D and E. Appearance of the discharge plots of GM-counters in these trays was utilized to distinguish electron (or photon) initiated showers from nuclear disruptions which were initiated in gases or walls of the ionization chamber and produced some heavily ionizing particles and grey particles.

B) *Estimate of the number of shower particles*

The average number of shower particles traversing the ionization chamber is estimated by the following procedures:

a) The number of particles N_{10} corresponding to pulse height of 1 Po$-\alpha$, which traverse the ionization chamber vertically to the axis is obtained as usual by the equation

$$N_{10}=\frac{5.3\times10^6}{j\,W_0\delta lf}\,, \qquad (1)$$

where j is an average specific ionization in terms of ion-pairs per gram per square centimeter, W_0 an average energy to produce an ion pair, δ the density of gas, l the length of path in the chamber, and f the geometrical factor which is characteristic for the size of the ionization chamber. In our chamber, $f=0.93$ (obtained by a graphical calculation), $l=10$ cm, and for $j\,W$ we use $2.1\times10^6\,eV/g\,\text{cm}^2$. Thus we obtain for N_{10} the value 30.7.

b) If we measure the pulse height distribution of the ionization bursts caused by EAS at certain places where the density distribution of EAS is known by some other methods, N_{10} will be deduced comparing the pulse height and density distribution. Thus, the pulse height distribution of ionization bursts were measured at Mt. Norikura (2770 m a.s.l.) by triggering the ionization chamber with the simultaneous discharge of 5 or more GM-counters of trays AS$_1$ and AS$_2$. The frequency of EAS corresponding to pulse height more than 1.4 Po$-\alpha$ was 3.8±0.2/hr. Representing the integral density distribution at 2770 m[7] by

$$S(\geqslant\Delta)=5.0\times10^3\Delta^{-1.46}/\text{hr}\,,$$

and substituting the above mentioned value for S, we obtained for N_{10} the value 30.3.

c) Actual number of shower particles, corresponding to 1 Po$-\alpha$, should be less than N_{10} on account of the scattering of particles in Σ. The angular distribution of the cascade electrons may depend on the thickness of the absorber used, and on the energy of primary electron (or photon). However, for simplicity, we assume for it the result obtained by Franchetti et al.[8] below lead absorber in a cloud chamber, and as well assume that rms angle of the particles under lead and iron is expressed by the relation

$$\sqrt{\overline{\theta^2}}=a+\frac{b}{n}\,, \qquad (2)$$

where n is the number of particles, a and b are constants depending on the materials and their thickness. According to ref. (8), $a=30°$, $b=50°$ for 2, 3 and 4 cm thickness of lead. These values were obtained immediately below the lead plate. But it may not be correct to adopt these values in our case, where there are aluminum wall of the GM-counters and iron wall of the ionization chamber between Σ and the gaseous volume of the chamber. We, nevertheless, assume that $a=30°$, neglecting the second term of the right side of the equation (2) because of large n in our case, and that the same angular distribution holds for lead and iron. Thus, the average shower particles initiated by a vertically incident electron (or photon) N_1, corresponding to the pulse height of 1 Po$-\alpha$, is calculated numerically, namely,

$$N_1 = gN_{10} = 24.0\ , \tag{3a}$$

where $g=0.79$, and $N_{10}=30.5$. The number of shower particles corresponding to the pulse height of x Po$-\alpha$, N_x, is

$$N_x = 24.0\ x\ . \tag{3b}$$

C) When there was no material at Σ, electron (or photon) initiated showers were observed at low frequency. These background events seem to initiate from the surrounding materials and from the walls of GM-counters and of the ionization chamber, and these rates were subtracted from the data obtained with material at Σ.

D) *For the analysis of the observations, following assumptions were made*:

a) Total number of electrons obtained from the shower theory $\Pi_{th}(E_0, 0, t)$, initiated by primary electron (or photon) of energy E_0 at depth t, is represented by

$$\Pi_{th}(E_0, 0, t) = \eta \Pi(E_0, 0, t)\ , \tag{4}$$

where $\Pi(E_0, 0, t)$ is number of electrons actually observed below the absorber of thickness t, and η is a constant. We assume that η is independent on E_0.

b) The differential energy spectra of electrons and photons are expressed by

$$G(E)dE = cE^{-\gamma}dE\ , \tag{5}$$

where c and γ are constants.

c) Fluctuation of the number of shower particles obeys Poisson's distribution. Accordingly, probability P that N particles emerge in the shower initiated by primary electron (or photon) of energy E_0 is

$$P(E_0, N) = e^{-\pi}\Pi^N / N!\ , \tag{6}$$

where Π is the abbreviation of $\Pi(E_0, 0, t)$.

d) At a certain depth t, the following relation between E_0 and Π_{th} exists in some range of E_0,

$$E_0 = k\Pi_{th}^{\alpha} = k\eta^{\alpha}\Pi^{\alpha}\ , \tag{7}$$

where k and α are constants depending on t. Moreover, we neglect the variation of Π_{th} with small variation of t, and this is validated near the shower maximum.

e) Zenith angle distribution of primary electrons or photons is represented by the form of $\cos^n\theta$, where n does not depend on their energy.

f) The mean path length, in the ionization chamber, of the shower particles initiated by a primary electron (or photon) of zenith angle θ, is longer than that initiated by vertically incident one roughly by a factor of $1/\cos\theta$. This simplification is approximalely valid, even if the angular spread of the shower particles is taken into consideration.

Under the above mentioned assumptions, the counting rates of the electrons (or photons) producing cascade showers of pulse height of more than x are represented by

$$\begin{aligned} F(\geqslant N_x) &= \int_S \int_\omega \cos^n\theta dS' d\omega' \int_{N_x\cos\theta}^{\infty} G(E)dE \frac{e^{-\pi}\Pi^N}{N!} \\ &= A\int_S \int_\omega \cos^n\theta dS' d\omega' \int_{N_x\cos\theta}^{\infty} dN \frac{\Gamma(N-\alpha\gamma-\alpha)}{N!}\ , \end{aligned} \tag{8}$$

where $A=c(k\eta^{\alpha})^{-\gamma+1}$, S is the area of Σ, and ω is the solid angle which is subtended by tray A on each elements of area of Σ and in which the effective area of tray D is contained. For large N, we may obtain

$$\begin{aligned} F(\geqslant N_x) &= A\int_S \int_\omega \cos^n\theta dS' d\omega' \int_{N_x\cos\theta}^{\infty} dN \cdot N^{-(\alpha\gamma-\alpha+1)} \\ &= A' N_x^{-(\alpha\gamma-\alpha)} \int_S \int_\omega \cos^m\theta d\omega' dS'\ , \end{aligned} \tag{9}$$

where

$$A' = \frac{c(k\eta^{\alpha})^{-\gamma+1}}{\gamma-1}\ ,$$

and

$$m = n - \alpha(\gamma-1)\ . \tag{9a}$$

From the equation (7), the integral number spectra are represented by

$$F(\geqslant N_x)=BN_x^{-\nu}\ , \tag{10}$$

and

$$\nu=\alpha\gamma-\alpha\ . \tag{10a}$$

As seen in (9) the zenith angle distribution of the primary particles giving pulse height more than x is represented by $\cos^m\theta$, the relation between m and n being expressed by (9a). Thus from observed ν and m, we are able to obtain γ and n by (9a) and (10a).

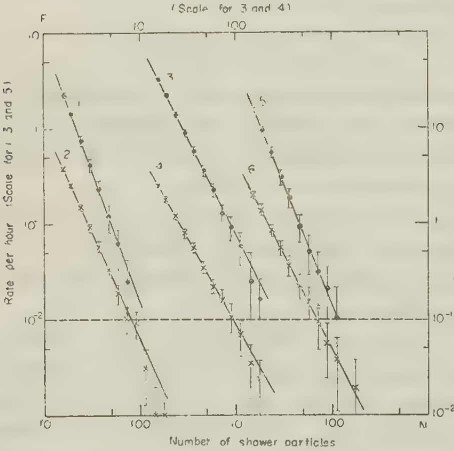

a

Fig. 4 (a). Number spectra of shower particles initiated by single incident electron 1: 1 cm Pb, 2: 2 cm Pb, 3: 3 cm Pb, 4: 4 cm Pb, 5: 4 cm Fe, 6: 8 cm Fe.

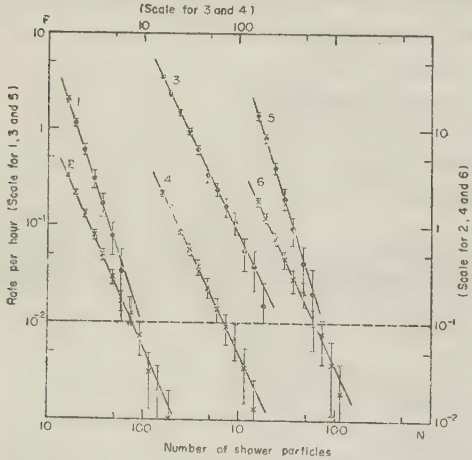

b

Fig. 4 (b). Number spectra of shower particles initiated by single incident photon 1: 1 cm Pb, 2: 2 cm Pb, 3: 3 cm Pb, 4: 4 cm Pb, 5: 4 cm Fe, 6: 8 cm Fe.

§ 4. Results and Discussion

(A) *Energy spectra of primary electrons and photons.*

Integral number spectra obtained by converting mere the pulse height into the number of shower particles using (3b), are shown in Fig. 4 (a) and (b).

The former gives the spectra for the electron initiated showers, and the latter those for the photon initiated showers. The errors indicated are the statistical ones. As shown in the Figs, the integral number spectra are well represented by the power law of the form

$$F(\geqslant N)=aN^{-\nu}\ , \tag{11}$$

where ν's are listed in Table II.

In order to find γ from these ν's, we must know the values of α's. However, as α's are slowly varying functions of energy, it is necessary to find the energy interval of the primary electrons (or photons) measured in our experiment. For this purpose, we proceed as follows:

i) Barker[3] obtained an energy spectrum of of electrons of 10 MeV–400 MeV near sea level, and he also gives the absolute vertical intensities of electrons with energy higher than 10 MeV. As to $E\geqslant 300$ MeV, Chou[2] obtained energy spectra of electrons and photons near sea level up to 2 BeV. Since he did not give the absolute intensities, ordinate of the Chou's curve was normalized at 300 MeV. Our results for electrons may be diretly compared with theirs, because the above mentioned authors measured the single incident electrons. Thus it is found that the absolute intensity is represented by

$$G(E)dE$$
$$=2.2\times(\gamma-1)10^{-5}EdE/\mathrm{cm}^2\cdot\mathrm{sec}\cdot\mathrm{sterad}\cdot\mathrm{BeV}\ , \tag{12}$$

where E is energy measured in terms of BeV.

ii) As first approximation, we assume that $\alpha=1$, and $\gamma=3$, then $n=2$ by putting $m=0$ in (9a), and that the number of shower particles does not fluctuate, i.e., a certain pulse height corresponds to a certain value of energy of a primary electron. From the counting rates observed, the energy interval of the vertically incident primary electrons measured by our apparatus is estimated to be 3–20 BeV, thereby a small correction is applied to the counting rates for the particles passing through the

Table II.

Absorber Material			Pb				Fe	
Absorber Thickness			1 cm	2 cm	3 cm	4 cm	4 cm	8 cm
α	electron	Serber & Snyder	1.92	1.32	1.03	0.82	1.78	1.15
		Ivanenko	1.48	1.15	1.04	0.96	1.51	1.07
	photon	Serber & Snyder	2.44	1.41	1.13	0.90	2.35	1.27
		Ivanenko	1.60	1.24	1.16	1.12	1.66	1.20
ν	electron		2.82±0.25	2.23±0.12	2.03±0.10	1.82±0.10	2.82±0.25	2.00±0.15
	photon		2.92±0.25	2.23±0.12	2.03±0.10	2.07±0.10	3.10±0.25	2.10±0.12
γ	electron	S.S	2.47±0.13	2.67±0.09	2.97±0.10	3.22±0.12	2.58±0.14	2.74±0.13
		I	2.91±0.17	2.94±0.10	2.95±0.10	2.90±0.11	2.87±0.17	2.87±0.14
	photon	S.S	2.20±0.10	2.58±0.09	2.80±0.90	3.30±0.11	2.32±0.09	2.65±0.12
		I	2.83±0.16	2.80±0.10	2.75±0.09	2.85±0.09	2.87±0.15	2.75±0.13

ineffective spaces between GM-counters of trays A and B (i.e. a part of the uncertain events mentioned in § 3, A). Therefore, we use as the values of α's those between 2 BeV and 20 BeV, taking into account the obliquely incident particles.

The values of α's are obtained graphically from the calculated results by Sneider and Serber[9], and from those by Ivanenko[10),13)]. The results are listed with the values of ν's in Table II. As the values of $\Pi_{th}(E_0, 0, t)$ for photon initiated shower are not described in Ref. (10), we calculate them by the approximation formula indicated in it.

As shown in the Table, using Ivanenko's calculated results the almost constant value of γ is obtained for various thickness of lead and iron absorbers.

Thus, the values of γ's are obtained as follows:

$$\left.\begin{aligned} \gamma_e &= 2.90 \pm 0.05 \quad \text{for electrons} \\ \gamma_p &= 2.80 \pm 0.05 \quad \text{for photons}\,, \end{aligned}\right\} \qquad (13)$$

where the suffix e and p express the quantities for electrons and photons respectively.

(B) *Zenith angle distribution of primary electrons.*

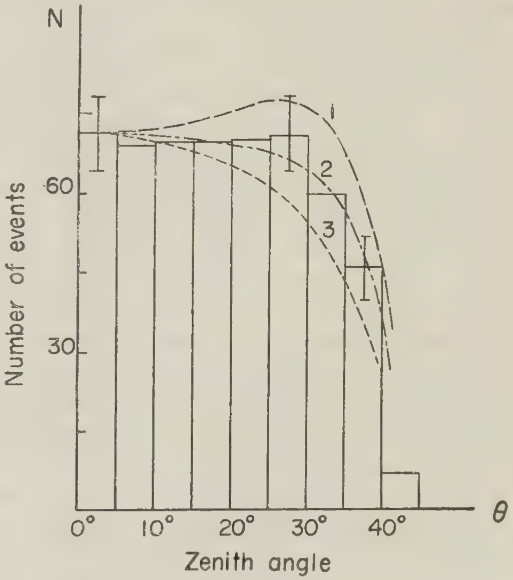

Fig. 5. Zenith angle distribution.
1: $m=-1$; 2: $m=0$; 3: $m=1$.

Concerning the electrons which produced pulse height of more than 2/3 Po$-\alpha$, we plotted the projected zenith angle distribution obtained by the discharged GM-counters in trays A and B. Fig. 5 is an example for 2 cm thickness of lead, and the curves in the Fig. are the calculated distributions for our geometry obtained by assuming $\cos^m \theta$ distribution. In the case of other thicknesses, similar results were obtained. The mean value of m thus obtained is

$$m = 0.0 \pm 0.5 \quad \text{2 cm, 3 cm and 4 cm lead and 8 cm iron}\,. \qquad (14)$$

According to (9a), these figures give $n=2\pm0.5$.

(C) *The ratio of the number of electrons and photons*

Substituting in (9) the values of γ's, m and

α's, and assuming the relation (5), the values of η's are determined for various thickness of absorbers. The results thus obtained are as follows;

$$\left.\begin{array}{ll} \eta_{\mathrm{Pb}}=2.2 & \text{for 1 cm thickness of lead,} \\ \eta_{\mathrm{Pb}}=3.0 & \text{for 2, 3 and 4 cm thickness of lead,} \\ \eta_{\mathrm{Fe}}=1.7 & \text{for 8 cm thickness of iron*.} \end{array}\right\} \quad (15)$$

It would be noted that the value of η_{Pb} is same for every thickness of lead thicker than 2 cm. (cf. (E)).

Assuming the same angular distribution for photons as that of electrons, the following value for c_e/c_p is obtained,

$$c_e/c_p=1.10\pm1.10 \ .$$

Of course, this value is the upper limit of the ratio, because we cannot separate individually the particles consisting of a narrow bundle of electrons and photons, which may likely occur in the case of high energy soft component.

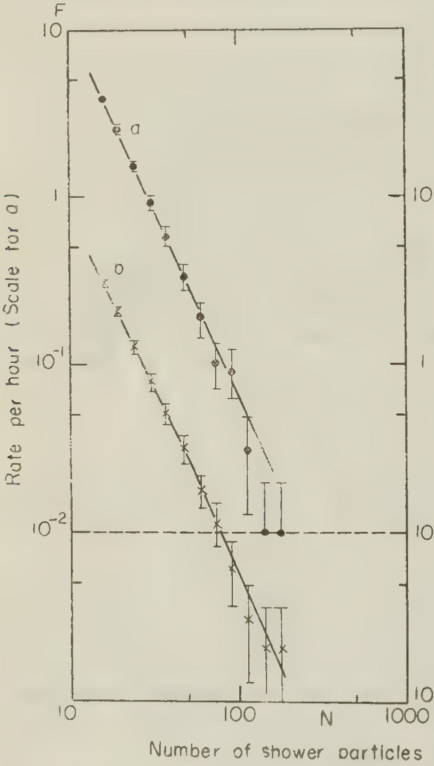

Fig. 6. Number spectra of shower particles.
a: single incident electron
b: multiple incident electrons and photons absorber thickness: 2 cm Pb.

(C) *Multiple incident electrons and photons.*

The integral number spectrum of the shower particles, initiated by multiple incident electrons and photons under 2 cm thickness of lead, is shown in Fig. 6, and that of single incident electrons under the same absorber is also shown in the same figure for comparison. Though, as seen from the Fig., the exponent of the multiple events is a little lower than that of single incident events for smaller N, we can say little about the composition of the particles and the energy of each particles in multiple events. Hewever from the ratio of multiple events to single events tabulated in Table III, we may conclude that the major part of the particles in multiple events has not so high energy that it is considerably absorbed between 2 cm and 3 cm thickness of lead.

(D) *High energy electrons and photons associated with EAS.*

The number of the events which are associated with EAS of $\Delta \geqslant 4/m^2$ and do not contain any penentrating particle is within 2% of the total single events for the pulse height of $\geqslant 2/3\,\mathrm{Po}-\alpha$ and for various thickness of absorbers. If all the events associated with EAS of $\Delta \geqslant 4/m^2$ and containing some penetrating particles are interpreted as the events produced by high energy electrons or photons incoming simultaneously with some penetrating particles, the above percentage value is raised to 11% of the total single events. This is the upper limit of the number of high energy electrons and photons associated with EAS of $\Delta \geqslant 4m^{-2}$.

In Table III, we summarized the rate of occurrence of each kind of event obtained in our measurements.

(E) *Errors involved in the data.*

a) Nuclear interactions.

Nuclear interactions in the absorber which give rise to some π^0-mesons of high energy only, or these π^0-mesons and some charged π-mesons of energy $\leqslant 380$ MeV, are classified in our criterion as the multiplicative showers initiated by primary electrons and photons. The amount of these interactions was estimated by comparison of the results

---

* According to the calculated results of Ivanenko[13]. $\eta_{\mathrm{Fe}}=1.0$ for 4 cm thickness of iron, and $\eta_{\mathrm{Fe}}=1.4$ for 8 cm iron.

Table III. No. of Events $\geq 2/3\ P_0-\alpha$ (/hr).

Absorber Material	Pb				Fe	
Absorber Thickness	1 cm	2 cm	3 cm	4 cm	4 cm	8 cm
Electron shower	2.28±0.17	3.87±0.20	3.30±0.16	2.57±0.17	1.58±0.13	2.02±0.20
Photon shower	1.96±0.16	3.14±0.18	3.42±0.16	2.21±0.16	1.40±0.12	1.82±0.19
Multiple events	1.88±0.15	3.09±0.18	1.34±0110	1.06±0.11	0.14±0.04	0.25±0.07
E.A.S. associated shower	0.04±0.02	0.10±0.03	0.05±0.02	0.04±0.01	0.03±0.01	0.04±0.02
Penetrating shower	0.85±0.10	0.92±0.10	1.05±0.09	1.10±0.11	0.35±0.06	0.83±0.13
〃 (E.A.S. associated)	0.40±0.06	0.45±0.07	0.61±0.07	0.88±0.09	0.27±0.55	0.22±0.13
Uncertain events	0.73±0.09	0.90±0.10	0.82±0.08	0.70±0.09	0.65±0.08	0.72±0.12

obtained for the electron (or photon) initiated showers under 2 cm Pb and 8 cm Fe at sea level with those at mountain altitude (2770 m a.s.l.), as will be mentioned in the succeeding paper. According to it, errors due to the nuclear interactions are at most 3% of the total electron (or photon) initiated showers at all energy even for 4 cm thickness of lead and ~10% for 8 cm thickness of iron absorber.

b) Penetrating showers.

As mentioned in §3, we classified the events, in which one or more GM-counters in tray F discharged, as the penetrating showers. There is, however, some probability that low energy cascade photons discharge them under 15 cm thickness of lead. This probability is small for $E \leqslant 10$ BeV, but increases rapidly with the increasing primary energy.[10),11)] Therefore, the deviation of the observed frequency from the power spectrum with constant exponent for large N, as seen in the Fig. 4, does not necessarily mean that the value of γ increases with increasing N, and it is rather reasonable to consider that the power law with constant γ is valid for the energy range measured.

Further, among the penetrating showers defined by §3, there will be some events in which high energy electrons (or photon) are incident on the absorber associated with the penetrating particles, and by appearance they seem to be the penetrating showers. Indeed, there are some pictures in which an electron (or photon) and a penetrating particles are incident in parallel. Though accurate probability of these events cannot be obtained, we estimate from the parallel events that it is smaller than 5% of the total number of the penetrating showers of our classification.

The accidental coincidence of electron (or photon) showers with penetrating particles, resulting from the resolving time of the hodoscopes (30 μsec) is less than 0.2% of the total number of the penetrating showers.

c) Criticism of the assumptions

We assumed Poisson's distribution for the number of shower particles emerging beneath the absorber. This assumption may be approximately valid for large N and near the shower maximum, except at small t. In our experiment where the energy range measured is 2–20 BeV, the above mentioned conditions may be fulfilled for $t=3\sim 8$. The assumption that g is a constant for various thickness and for E_0, and η a constant for E_0, may not be valid, nevertheless, we obtained a constant value of η for various thickness of lead, except at small t. This may be interpreted as the product $g\eta$ is nearly constant for various thickness and for E_0, because at higer energy g becomes larger owing to smaller spread of shower particles, and η becomes smaller owing to the shower particles of higher energy. The value of $g\eta$ is 2.36 and 1.32* for lead and iron absorber respectively.[12)] Further, it will be noted that the iron plate of the ionization chamber and the alminum wall of GM-counter in tray C absorb electrons of energy lower than 5.5 MeV, and so, in the case of lead absorber η involves this effect.[13)]

(F) *Comparison with others.*

Energy spectrum up to 100 BeV of the soft component at sea level was reported by Carmichael.[4)] According to his result, integral energy spectrum beyond 1.6 BeV is represented by a power law of slope −2.00. This result is not inconsistent with ours, taking into consideration that, though he measured electrons, photons, and multiple events in our classification as a whole, they have the nearly same exponents. Concerning to the zenith angle distribution, Barker[3)] obtains $\cos^3\theta$ distribution for electrons of lower energy. The value of the power for electrons of higher energy is less by one, and it will be discussed in relation to the origin of the high energy soft component in the succeeding paper. Chou[2)] reported that the ratio of the number of electrons is about one, and our results are in accord with his results too.

---

* Referring to (13), this value is 1.11.

§ 5. Conclusion

Concerning the electrons and photons 2–20 BeV, the following points are concluded:

(1) The differential energy spectra of electrons and photons are represented by the power law, the values of power are 2.90±0.05 and 2.80± 0.05 for electrons and photons, respectively.

(2) Vertical intensities of single incident electrons and photons of the above-mentioned energy interval are

$$G_e(E)dE=(4.1\pm0.4)\times10^{-5}E^{-2.90}dE/\mathrm{cm}^2\ \mathrm{sec.\ sterad.\ BeV}\quad \text{for electrons}$$

$$G_p(E)dE=(3.7\pm0.4)\times10^{-5}E^{-2.80}dE/cm^2\ \mathrm{sec.\ sterad.\ BeV}\quad \text{for photons,}$$

Multiple events and the soft component in EAS will increase these figures by a factor of 1.15 at most for the intensities of the total electrons and photons. In Fig. 7 the above mentioned results are summarized and illustrated.

(3) Zenith angle dependence of a single electrons is expressed by $\cos^n\theta$ where n is 2.0±0.5.

(4) The upper limit of the ratio of single electrons and photons is 1.1±0.1 at 1 BeV.

(5) The number of shower particles under the absorber is reduced by a factor of 1/3 and 1/1.4 for lead and iron respectively, comparing with the theoretically expected number.

(6) The total number of shower particles under lead absorber calculated by Ivanenko gives consistent results for our experimental data.

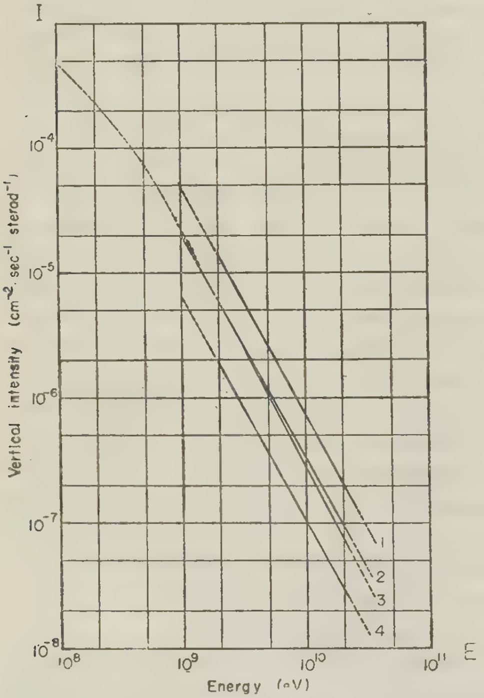

Fig. 7. Integral energy spectra of soft component.
1: total electronic component
2: single incident photon
3: single incident electron
4: multiple incident and EAS associated electronic component

The author wishes to express their appreciation to Prof. O. Minakawa for encouraging him for this work and for valuable advice. He also wishes to thank Mr. Maeda and Mr. Watanabe for assistance in carrying out this work and analysing the data.

References

1) E. D. Palmatier: Phys. Rev. **88** (1952) 761.
2) C. N. Chou: Phys. Rev. **90** (1953) 473.
3) P. R. Barker: Phys. Rev. **100** (1955) 860.
4) H. Carmichel: Phys. Rev. **107** (1957) 1407.
5) S. Miyake et al.: J. Phys. Soc. Japan **13** (1958) 782. N. Doblotin et al.: Private communication to Dr. Kamata.
6) W. H. Jordan and P. R. Bell: Rev. Sci. Instr. **18** (1947) 703.
7) T. Kameda, T. Maeda and Y. Toyoda: To be published.
8) S. Franchetti: Nuovo Cimento **10** (1953) 551. G. Di Caporiacco and M. Giovannozzi: Nuovo Cimento **3** (1956).
9) B. Rossi: High Energy Particles.
10) I. P. Ivanenko: Dokl. Akad. Nauk SSSR **107** (1956) 819.
11) K. Greisen: Phys. Rev. **75** (1949) 1071.
12) The reduction of the cascade electrons below absorber of heavy material are discussed by many authors on their viewpoints. R. R. Wilson: Phys. Rev. **86** (1952) 261. W. E. Hazen: Phys. Rev. **99** (1955) 911. P. A.

Bender: Nuovo Cimento **2** (1955) 980. H. Carmichel: op. cit. M. R. Gupta: Nuovo Cimento **7** (1958) 39. Belenky: Rossi's High Energy Particle.

13) I. P. Ivanenko and B. E. Samosdov: Sov. Phys. JETP **35**(**8**) (1959) 884.

14) V. A. Dmitriev: Sov. Phys. JETP **35**, **8** (1959) 382.

JOURNAL OF THE PHYSICAL SOCIETY OF JAPAN, Vol. 15, No. 7, JULY, 1960

Ferroelectricity in Potassium Ferrocyanide Trihydrate and its Isomorphous Substances

By Shigeru WAKU, Kunio MASUNO, Toshisuke TANAKA
and Hiroshi IWASAKI

Electric Communication Laboratory, Nippon Telegraph and Telephone Public Corporation

(Received January 14, 1960)

Several $A_4[M(CN)_6]\cdot 3H_2O$ type cyano-complexes belonging to the crystal class C_{2h} were studied to examine ferroelectricity. Isomorphous substances obtained through replacing the Fe^{++} ion by Ru^{++}, Os^{++} and Mn^{++} ions show ferroelectric behavior below −14°C, −2.4°C and −40°C respectively. Ferroelectric behavior of these compounds are very similar to that of the potassium ferrocyanide trihydrate, reported before. The potassium ferrocyanide group ferroelectrics has ferroelectric axis parallel to $[10\bar{1}]$ direction. Ferroelectric transition of these substances is probably of the second order.

§1. Introduction

In the previous paper,[1] we reported the ferroelectric behavior in potassium ferrocyanide trihydrate, $K_4[Fe(CN)_6]\cdot 3H_2O$ of which crystal class is monoclinic C_{2h} and space group is $C_{2/c}$ at room temperature. The ferroelectric hysteresis loop was observed under the application of electric field parallel to [101] and $[10\bar{1}]$ direction. We could not, however, determine the direction of ferroelectric axis, and the reason why the multiple peaks appear in the dielectric constant versus temperature curve was not understood.

Some problems in the ferroelectric properties of potassium ferrocyanide trihydrate were reexamined, in parallel with the attempt to search new ferroelectric substances in its isomorphous cyano-complexes.

§2. Specimens

We growed single crystals of the cyano-complex substances, which have $A_4[M(CN)_6]\cdot 3H_2O$ type chemical composition and belong to the crystal class C_{2h}. In this paper, we will report the ferroelectric behavior in potassium ferrocyanide trihydrate and its isomorphous substances obtained through replacing the Fe^{++} ion by Ru^{++}, Os^{++} and Mn^{++}. Method of preparation of these compounds, solubility and dehydration versus temperature curves will be reported in another paper.[2] The crystals were cut perpendicular to the cleavage plane (010) and silver-painted to measure the dielectric properties.

The evaporated metal electrode was not used, as the evacuation brought about some dehydration of the crystals. Dielectric constant was measured by tuning method in 1 MC. Hysteresis loop in 50 cps was measured by ordinary Sawyer and Tower's circuit. Ferroelectric behavior of the isomorphous substances obtained through replacing some part of the potassium ions by other mono-valent ions will be reported subsequently.

Table I. Axial ratio and optical constants of $A_4[M(CN)_6]\cdot 3H_2O$ type cyano-complexes belonging to the crystal Class of C_{2h}

substance	$a:b:c$	β	$2V$	θ
$K_4[Fe(CN)_6]\cdot 3H_2O$	0.3936:1:0.3943	90°2′	78°10′	31°50′
$K_4[Ru(CN)_6]\cdot 3H_2O$	0.3936:1:0.3948	90°6′	54° 0′	32°10′
$K_4[Os(CN)_6]\cdot 3H_2O$	0.3929:1:0.3941	90°6′	47° 0′	30°10′

§ 3. Experimental Results

(1) *Optical anomaly*

Fig. 1 illustrates the external form of the crystal, crystal axes a, b, c, and optic elasticity axes X, Y, Z for complexes listed in Table I. The optical angle 2V, and the angle between $[10\bar{1}]$ and X axis, θ, in the table, are quoted from a literature.[3)]

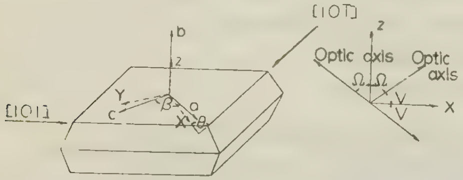

Fig. 1. Crystallographic axes *a*, *b*, *c*, optic elasticity axes *X*, *Y*, *Z* and optic axes of potassium ferrocyanide trihydrate and its isomorphous substances.

Optical anomaly is frequently observed in these crystals. From the Table I, potassium ferrocyanide single crystals are supposed to give a value of 101°50 for the optic axial angle $2\Omega=\pi-2V$. In some small crystals 2Ω is approximatly equal to this expected value, but all the large crystals give smaller angles than this, and in the extreme case, the crystals seem as if they are uniaxial. Hereafter, we will denote the former class as "normal" crystals and the latter two classes as "abnormal" crystals.

(2) *Ferroelectric Behavior in Potassium Ferrocyanide*

In the previous paper, we reported the small signal dielectric constant, spontaneous polarization and coercive field versus temperature in potassium ferrocyanide trihydrate crystal. In the curve of the dielectric constant, three conspicuous peaks at −22°C, −26°C and −33°C and two smaller peakes at −43°C and −80°C, were shown. The specimen used in the previous work was found to be an abnormal crystal with very small optic axial angle.

For a selected normal single crystal, the multiple peaks vanish except only one peak which turned out to correspond to the Curie point, as shown in Fig. 2. The figure in-

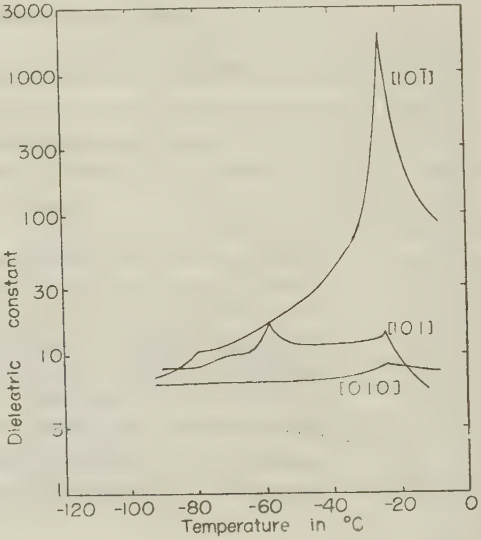

Fig. 2. Dierectric constant of $K_4[Fe(CN)_6]\cdot 3H_2O$ as a function of temperature.

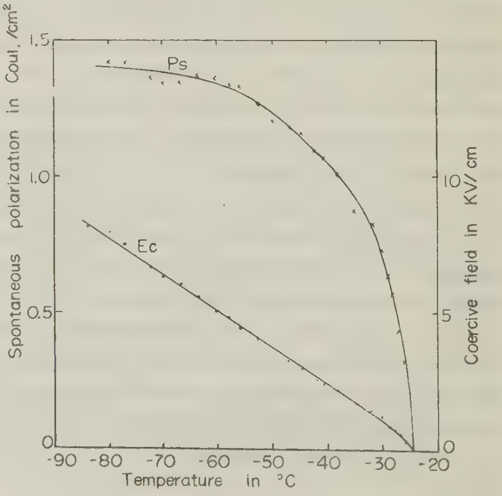

Fig. 3. Spontaneous polarization and coercive field along $[10\bar{1}]$ direction of $K_4[Fe(CN)_6]\cdot 3H_2O$ as a function of temperature.

cludes the measurements along three directions, [010], [101] and $[10\bar{1}]$. A remarkable anomaly in $[10\bar{1}]$ direction is observed at −24.5°C, but we can see no more than very weak anomaly in two other directions.

In the abnormal crystals, ferroelectric hysteresis loop appears in [101] as well as in $[10\bar{1}]$ direction, while in normal crystals it can be observed only in $[10\bar{1}]$ direction. Fig. 3 shows the curves of spontaneous polarization and coercive field strength of the normal crystal, as a function of the temperature. An abrupt increase of the spontaneous polarization, as seen at −33°C in the abnormal crystal, disappears. The spontaneous polarization of the normal crystal is two or three times as large as that of the abnormal crystal, and the coercive field of the former crystal is about a quater of that of the latter one.

(3) *Ferroelectricity in potassium ruthenoanc osmo-cyanide trihydrate complexes*

Fig. 4 and 5 show the temperature dependence of the small signal dielectric constant observed in the normal crystals of potassium

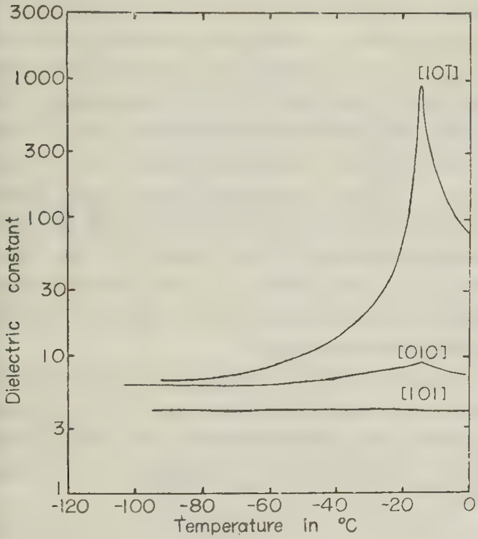

Fig. 4. Dielectric constant of $K_4[Ru(CN)_6]\cdot 3H_2O$ as a function of temperature.

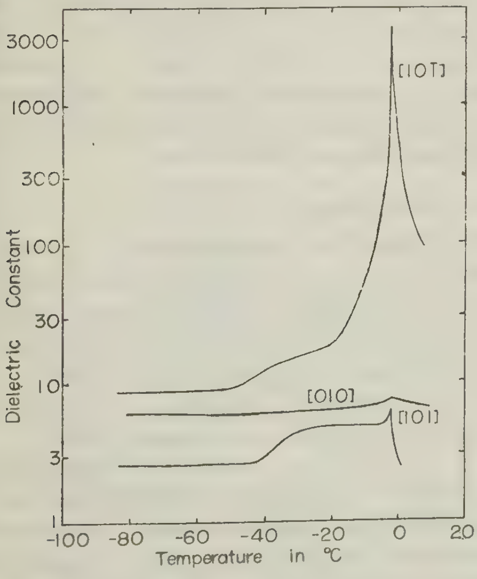

Fig. 5. Dielectric constant of $K_4[Os(CN)_6]\cdot 3H_2O$ as a function of temperature.

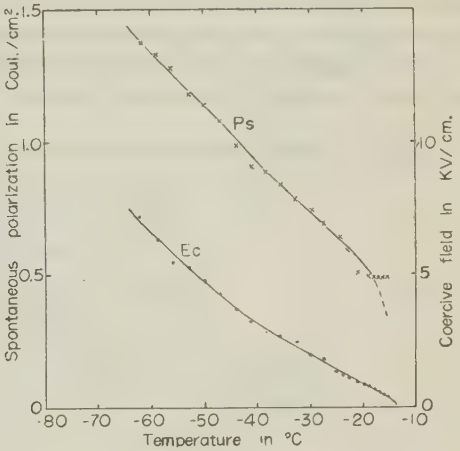

Fig. 6. Spontaneous polarization and coercive field along $[10\bar{1}]$ direction of $K_4[Ru(CN)_6]\cdot 3H_2O$ as a function of temperature.

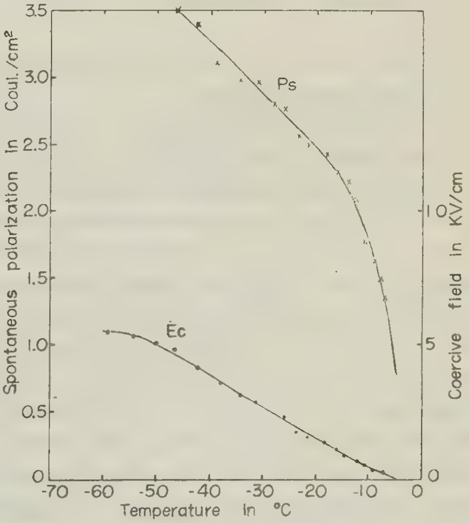

Fig. 7. Spontaneous polarization and coercive field along $[10\bar{1}]$ direction of $K_4[Os(CN)_6]\cdot 3H_2O$ as a function of temperature.

rutheno- cyanide trihydrate, $K_4[Ru(CN)_6]\cdot 3H_2O$ and potassium osmo-cyanide trihydrate, $K_4[Os(CN)_6]\cdot 3H_2O$, respectively. In the curve measured along [10$\bar{1}$] direction, remarkable peaks appear at −14°C for the ruthenocyanide and −2.4°C for the osmocyanide. These peaks correspond to the one observed at −24.5°C for potassium ferrocyanide.

Spontaneous polarization and coercive field along [10$\bar{1}$] direction are shown in Fig. 6 for the ruthenocyanide and in Fig. 7 for the osmocyanide. In the [101] and [010] directions, the hysteresis loop does not appear in the whole temperature range of measurement for two substances. By and large, the properties of these crystals are very similar to those of the normal crystal of potassium ferrocyanide.

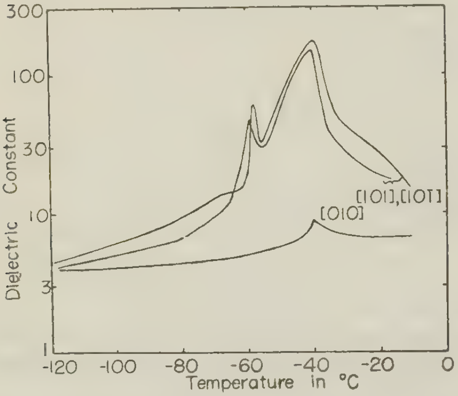

Fig. 8. Dielectric constant of $K_4[Mn(CN)_6]\cdot 3H_2O$ as a function of temperature.

(4) *Ferroelectricity in potassium manganocyanide trihydrate complex*

Fig. 8 shows the temperature dependence of the small signal dielectric constant of potassium manganocyanide trihydrate, $K_4[Mn\cdot(CN)_6]\cdot 3H_2O$. There are two peaks at about −40°C and −58°C in the curves measured along [101] and [10$\bar{1}$] directions. Ferroelectric hysteresis loop appears in both directions below −40°C. The existence of conspicuous peak of dielectric constant at other temperatures than Curie point and the existence of the ferroelectric hysteresis phenomenon in both [101] and [10$\bar{1}$] directions are quite similar to the dielectric behavior of abnormal potassium ferrocyanide crystal having small optic axial angle 2Ω. This crystal is supposed to be also an abnormal one having small optic axial angle. Since the color of this crystal is dark violet, conoscopic observation of the interference figure was unsuccessful.

Spontaneous polarization of this crystal is very small and coercive field is very large.

§4. Discussions

In the preceding sections, we see that the normal single crystals of three isomorphous cyano-complexes exhibit remarkable dielectric anomaly and hysteresis loop only in the [10$\bar{1}$] direction. The fact shows that the ferroelectric axis lies along [10$\bar{1}$] direction. On the other hand, when the crystals have optical anomaly, dielectric anomaly and hysteresis loops are observable in two independent directions, and furthermore peculiar peaks appear in the dielectric constant versus temperature curve. These discrepancies, which makes the situations complicated, will be explained in connection with the cause of the optical anomaly. Discussions on the optical anomaly related to the X-ray study will be reported in a subsequent paper.

Change of the spontaneous polarization near the Curie point as seen in Fig. 3, 6 and 7 suggests that the transition in these isomorphous substances is probably of a second order.

Covalent radii of Fe^{++}, Ru^{++}, Os^{++} and Mn^{++} having octahedral coordination are 1.23, 1.33, 1.33 and 1.12Å respectively, while the Curie points of these four ferroelectric complexes are −24.5°, −14°, −2.4°, and −40°C respectively. Hence, it may be concluded that the ferroelectric transition temperature increases with increasing the ionic radius of the complex ion $M(CN)_6^{----}$.

§5. Conclusions

1. Potassium rutenocyanide, potassium osmocyanide and potassium manganocyanide show ferroelectric behavior below −14.5°C, −2.4°C and −40°C respectively similar to that obtained for potassium ferrocyanide.

2. Ferroelectric transition of these substances is probably of a second order.

3. As the ionic radious of complex ion $M(CN)_6^{----}$ of potassium ferrocyanide group ferroelectrics becomes larger, ferroelectric transition temperature shifts toward the higher side.

4. There are remarkable differences in

ferroelectric behavior between normal crystals having the normal optic axial angle and abnormal crystals having smaller optic axial angles. Only in [10$\bar{1}$] direction, normal crystals show dielectric anomaly and hysteresis loop.

5. Ferroelectric axis of these substances is parallel to [10$\bar{1}$] direction.

The authors are very grateful to Dr. H. Hirabayashi, Dr. R. Kiriyama, Mr. H. Toyoda and Dr. N. Niizeki for their helpful discussions.

References

1) S. Waku, H. Hirabayashi, H. Toyoda, H. Iwasaki and R. Kiriyama: J. Phys. Soc. Japan **14** (1959) 973.
2) S. Waku, K. Masuno, H. Watanabe: to be published in J. Ind. Chem. Japan.
3) M. W. Porter, R. C. Spiller: *The Barker Index of Crystals* (W. Heffer and Sons Ltd., Cambridge, 1956) M. 105, 106, 107.

JOURNAL OF THE PHYSICAL SOCIETY OF JAPAN, Vol. 15, No. 7, JULY, 1960

Interaction of Conduction Electrons with Acoustic Waves in Many-Valley Semiconductors

By Nobuo MIKOSHIBA
Electrotechnical Laboratory, Nagatacho, Tokyo

(Received February 6, 1960)

A semi-classical theory is given for explaining the characteristics of the interaction of conduction electrons with acoustic waves in many-valley semiconductors such as n-Ge. In general, the ultrasonic absorption coefficient can be written as

$$\Lambda=\Lambda_P+\Lambda_K\ ,$$

where Λ_P is due to the change of the deformation potential energy of electrons caused by net intervalley transitions, Λ_K due to the change of the kinetic energy caused by intravalley transitions. The acousto-electromotive force can be also written as

$$F=F_P+F_K\ .$$

In the low frequency range the dominant terms are Λ_P and F_P, but Λ_K and F_K predominate in sufficiently high frequency range. For longitudinal waves propagating in the ⟨110⟩ direction and transverse waves propagating in the ⟨100⟩ direction and polarized in the ⟨010⟩ direction, F is identical with the formula of Weinreich-Sanders-White in the low frequency range. But in contrast to their formula, F does not decrease in the high frequency range owing to the increase of F_K and has the same order of magnitude as that for longitudinal waves in simple semiconductors. In special cases such as for longitudinal waves propagating in the ⟨100⟩ direction and transverse waves propagating in the ⟨110⟩ direction and polarized in the ⟨1$\bar{1}$0⟩ direction, $\Lambda_P=F_P=0$ and then the interaction becomes essentially identical with that in simple semiconductors.

§1. Introduction

Recently, Weinreich-Sanders-White[1] have derived a correct formula for the acousto-electric effect by transverse waves in n-Ge using so-called phenomenological approach, which is in good agreement with their experiments. There remain some questions, however, about the applicability of their phenomenological approach, because (a) it ignores the effect of the motion of the impurity charge and (b) it may be applicable only to the low frequency range i.e. $ql \ll 1$, where q is the wave number of acoustic waves and l the mean free path of conduction electrons. In fact, as has been shown in the previous paper[2], Weinreich-Holstein's phenomenological approach[3] for longitudinal waves in simple semiconductors was applicable only under two conditions; (a) $C \gg m\omega_P^2/q^2$ and (b) $ql \ll 1$, where C is the deformation potential constant, m the effective mass, ω_P the plasma frequency of conduction electrons.

The object of this paper is to apply a self-consistent semiclassical method to many-valley semiconductors such as n-Ge and to clarify the characteristic features of the interaction of conduction electrons with acoustic waves. The Brillouin zone of Ge is a truncated octahedron and the minima of conduction band lie on the edges in the ⟨111⟩ direction. Then n-Ge has eight half-valleys, i.e., four valleys, the deformation potential of which is given by[4]

$$U^{(\alpha)}=[\Xi_d\delta_{ij}+\Xi_u K_i^{(\alpha)}K_j^{(\alpha)}]u_{ij}\ , \tag{1.1}$$

where Ξ_d and Ξ_u are the deformation potential constants for the dilatation and the uniaxial shear respectively, $K_i^{(\alpha)}$ the i-component of the unit vector pointing from the center of the Brillouin zone to the (α)-valley, u_{ij} the (i, j)-component of the strain tensor. It will be sufficient for the object of this paper to consider following four cases.

(A) Longitudinal Waves:

(A1) Asymmetrical two class case. For longitudinal waves propagating in the ⟨110⟩ direction, for example, four valleys are classified into (+) and (−)-classes, the deformation potentials of which are

$$\left.\begin{aligned} U^{(+)}&=(\Xi_d+\tfrac{1}{3}\Xi_u+\tfrac{1}{3}\Xi_u)u_{ll}=(\Xi_d+\tfrac{2}{3}\Xi_u)u_{ll}\ , \\ U^{(-)}&=(\Xi_d+\tfrac{1}{3}\Xi_u-\tfrac{1}{3}\Xi_u)u_{ll}=\Xi_d u_{ll}\ , \end{aligned}\right\} \tag{1.2}$$

respectively. Then net interclass transitions may take place between two classes, similarly to (B1)-case.

(A2) Simple case. For longitudinal waves propagating in the ⟨100⟩ direction, for example, the deformation potentials are the same for four valleys and are given by

$$U=(\Xi_d+\tfrac{1}{3}\Xi_u)u_{ll}\ . \tag{1.3}$$

Therefore, if we take the *directionally averaged* effective mass and intravalley relaxation time, the interaction in this case is essentially identical with that in simple semiconductors discussed in the previous paper[2].

(B) Transverse Waves:

(B1) Symmetrical two class case. For transverse waves propagating in the ⟨100⟩ direction and polarized in the ⟨010⟩ direction, four valleys are classified into (+) and (−)-classes, the deformation potentials of which are

$$U^{(\pm)}=\pm\tfrac{1}{3}\Xi_u u_{ij}\ , \tag{1.4}$$

respectively. This case was studied by Weinreich et al.[1] from a phenomenological point of view.

(B2) Simple case. For transverse waves propagating in the ⟨110⟩ direction and polarized in the ⟨$1\bar{1}0$⟩ direction, the deformation potentials of valleys are all equal to zero. Therefore, if we take the *suitably averaged* effective mass and intravalley relaxation time, the interaction is essentially identical with that in simple semiconductors. We shall study the characteristic features of many-valley semiconductors i.e. (A1) and (B1)-cases in this paper.

In § 2, the basic equations of the semiclassical approach are solved for these cases. The numerical estimations and the approximate expressions for physical quantities involved in the basic equations are tabulated in § 3. In § 4, we shall calculate the ultrasonic absorption and the acoustoelectric effect for various frequency ranges. Some physical discussions of the results obtained will be given in the last section.

§ 2. Basic Equations

We make the following assumptions throughout this paper.

(a) We consider only the case of one carrier. Then the recombination of electrons and holes is neglected.

(b) Following effects induced by acoustic waves are ignored; (b1) ionization of electrons from impurities and (b2) recombination of electrons with charged impurities.

(c) The anisotropy of the effective mass and the relaxation time in each valley is taken into account, by using the directionally averaged quantities of them.

(d) The relaxation time of the distribution of electrons in each valley, τ_0, is written as[4]

$$1/\tau_0=1/\tau_1+1/\tau'\ , \tag{2.1}$$

where τ_1 is the intravalley transition time and τ' the intervalley transition time. The velocity dependence of τ_1 and τ' are neglected.

(e) We classified the loss mechanism of the acoustic energy into two parts. One is due to the change of the deformation potential energy of electrons caused by the interclass transition. When the local fluctuation of the number density of electrons in (+) or (−)-class, $n^{(+)}$ or $n^{(-)}$, deviates from the local equilibrium fluctuation, $n_{eq}^{(+)}$ or $n_{eq}^{(-)}$, $n^{(\pm)}$ relaxes to $n_{eq}^{(\pm)}$ in the interclass relaxation time τ, being accompanied with the energy transfer from acoustic to lattice systems. The other is due to the change of the kinetic energy caused by the intravalley transition. When the distribution function f of electrons in each valley deviates from the local equilibrium distribution f_0, f relaxes to f_0 in the intravalley relaxation time τ_0, being accompanied with the kinetic energy transfer. Two loss mechanisms are assumed to be *independent* and then total losses are given by the sum of two terms.

(f) The local equilibrium fluctuations, $n_{eq}^{(+)}$ and $n_{eq}^{(-)}$, associated with net interclass relaxation are determined by two assumptions.

(f1) The ratio of $n_{eq}^{(+)}$ and $n_{eq}^{(-)}$ is determined by the Boltzmann factor of the difference of the deformation potentials between two classes. This assumption does not hold for a degenerate electron gas.

(f2) It is assumed that intervalley transition has no influence on the distribution of electrons in $\boldsymbol{r}$-space in the first approximation. Then the sum of $n_{eq}^{(+)}$ and $n_{eq}^{(-)}$ can be put nearly equal to $(n^{(+)}+n^{(-)})$. The assumptions (e) and (f2) may be verified from the fact that $\tau \gg \tau_0$.

Making use of these assumptions, we shall solve Maxwell's equation, the equation of continuity and the Boltzmann equation, for the self-consistent determinations of $n^{(\pm)}$ (local fluctuation of the number density of electrons), $\boldsymbol{E}$ (internal electric field) and $\boldsymbol{J}^{(\pm)}$ (internal current density). Maxwell's equation is written as

$$\frac{\partial}{\partial t}\left(\boldsymbol{J}-N_0e\boldsymbol{u}+\frac{\varepsilon}{4\pi}\cdot\frac{\partial \boldsymbol{E}}{\partial t}\right)=-\frac{c^2}{4\pi}\cdot \mathrm{curl\,curl}\,\boldsymbol{E}\,, \tag{2.2}$$

where N_0 is the number density of ionized impurities and equal to the density of electrons in equilibrium, ε the dielectric constant, c the light velocity, e the charge of an electron. Since the local velocity of ionized impurities varies as $\boldsymbol{u}\propto \exp[i(\omega t-\boldsymbol{qr})]$, we get from (2.2)

$$E_{\parallel}=\frac{i\omega_P{}^2m_{\parallel}}{\omega e}\left(\frac{J_{\parallel}{}^{(+)}+J_{\parallel}{}^{(-)}}{N_0e}-u_{\parallel}\right), \tag{2.3a}$$

$$E_{\perp}=-\frac{m_{\perp}k_0{}^2}{q^2e\tau_0}\left(\frac{J_{\perp}{}^{(+)}+J_{\perp}{}^{(-)}}{N_0e}-u_{\perp}\right), \tag{2.3b}$$

where the subscripts $\parallel$ and $\perp$ refer to components parallel and perpendicular to $\boldsymbol{q}$ taken in z-direction, respectively, and we put

$$\left.\begin{aligned}\omega_P{}^2&=4\pi N_0\, e^2/m_{\parallel}\varepsilon\,,\\ k_0{}^2&\equiv i4\pi N_0\, e^2\omega\tau_0/m_{\perp}c^2\,.\end{aligned}\right\} \tag{2.4}$$

In (2.3b) we neglect the displacement current.

The equation of continuity in each class is given by

$$\frac{\partial}{\partial t}[n^{(\pm)}e]+\frac{\partial J_{\parallel}{}^{(\pm)}}{\partial z}=R(\mp\to\pm)\,, \tag{2.5}$$

where $R(\mp\to\pm)$ means the rate of net interclass relaxation.[1] From the assumption (f), the local equilibrium fluctuation associated with the interclass transition is determined by

$$\left.\begin{aligned}&(N_0/2+n_{eq}^{(+)})/(N_0/2+n_{eq}^{(-)})=\exp[-(U^{(+)}-U^{(-)})/kT]\,,\\ &n_{eq}^{(+)}+n_{eq}^{(-)}=n^{(+)}+n^{(-)}\,,\end{aligned}\right\} \tag{2.6}$$

i.e.,

$$n_{eq}^{(\pm)}=\frac{n^{(+)}+n^{(-)}}{2}\pm\frac{N_0\Delta qu}{4kT\omega}, \tag{2.7}$$

where k is the Boltzmann constant, T the absolute temperature and we make use of the relations,

$$U^{(\pm)}\equiv C^{(\pm)}u_{ij}=-C^{(\pm)}qu/\omega, \qquad \Delta\equiv C^{(+)}-C^{(-)}.$$

In (2.7) and hereafter, u means $u_{\parallel}$ or $u_{\perp}$ according as it is concerned with longitudinal or transverse waves. Then

$$R(\mp\to\pm)=-\left(\frac{2e}{\tau_c}\right)\left[n^{(\pm)}-\frac{n^{(+)}+n^{(-)}}{2}\mp\frac{N_0\Delta qu}{4kT\omega}\right], \tag{2.8}$$

where it is taken into account that only *two* or *three* intervalley transitions belong to the interclass transition, i.e. the interclass transition time $\tau_c=3\tau'/2$. The factor 2 in a numerator in the right hand side of (2.8) is due to the fact that one interclass transition gives rise to a decrease of $(n^{(+)}-n^{(-)})$ by 2. Defining the interclass relaxation time as $\tau\equiv\tau_c/2$, we obtain from (2.5) and (2.8),

$$n^{(\pm)}=\frac{q}{2\omega e}(J_{\parallel}^{(+)}+J_{\parallel}^{(-)})\pm\frac{1}{(1+i\omega\tau)}\left[\frac{iq\tau}{2e}(J_{\parallel}^{(+)}-J_{\parallel}^{(-)})+\frac{N_0\Delta qu}{4kT\omega}\right]. \tag{2.9}$$

For the electrons in each valley, whose equilibrium concentration is $N\equiv N_0/4$, the Boltzmann equation is written as

$$\frac{\partial f}{\partial t}+(\boldsymbol{v}\cdot\nabla_r)f+\frac{e}{m}(\boldsymbol{E}'\cdot\nabla_v)f=-\frac{f-f_0(|\boldsymbol{v}-\boldsymbol{u}|)}{\tau_0}, \tag{2.10}$$

where

$$E_{\parallel}'\equiv E_{\parallel}-iCq^2u/\omega e, \qquad E_{\perp}'\equiv E_{\perp}. \tag{2.11}$$

The distribution function is solved as

$$\left.\begin{aligned}
&f=f_0(|\boldsymbol{v}-\boldsymbol{u}|)-\boldsymbol{\Psi}(\boldsymbol{v})\cdot\partial f_0/\partial v,\\
&f_0(\boldsymbol{v})=\exp\left[\tfrac{1}{2}m(v_1^2-v^2)/kT\right],\\
&v_1^2=\left(\frac{2kT}{m}\right)\ln\left\{2^{1/2}\pi^{3/2}\left(\frac{h^2}{mkT}\right)^{3/2}(N+n)\right\},
\end{aligned}\right\} \tag{2.12}$$

where

$$\left.\begin{aligned}
&\boldsymbol{\Psi}(\boldsymbol{v})=\frac{[(e\boldsymbol{E}'\tau_0/m)+\boldsymbol{u}](\boldsymbol{v}/v)+(nv_0^2/3Nv)}{1+i\omega\tau_0-iq\tau_0v_z}-\left(\frac{\boldsymbol{u}\boldsymbol{v}}{v}+\frac{nv_0^2}{3Nv}\right),\\
&v_0^2=3kT/m_{\parallel},
\end{aligned}\right\} \tag{2.13}$$

and h is the Planck constant. For longitudinal waves in (A1)-case, we get

$$\Psi(v)=\frac{aA}{ql}\cdot\frac{x}{1-iax}+\frac{aB}{ql}\cdot\frac{v_0}{v}\cdot\frac{1}{1-iax}-u_{\parallel}x-B\frac{v_0}{v}, \tag{2.14}$$

where we put for brevity

$$A\equiv\frac{eE_{\parallel}\tau_0}{m_{\parallel}}-i\frac{C\tau_0q^2u_{\parallel}}{m_{\parallel}\omega}+u_{\parallel}, \qquad B\equiv\frac{nv_0}{3N} \tag{2.15}$$

and

$$a\equiv ql/(1+i\omega\tau_0), \qquad l\equiv\tau_0v, \qquad x\equiv\cos\theta.$$

For transverse waves in (B1)-case,

$$\Psi(\boldsymbol{v})=\frac{aA_1}{ql}\cdot\frac{\sqrt{1-x^2}}{1-iax}\cos\phi-u_\perp\sqrt{1-x^2}\cos\phi$$
$$+\frac{aA_2}{ql}\cdot\frac{x}{1-iax}+\frac{aB}{ql}\cdot\frac{v_0}{v}\cdot\frac{1}{1-iax}-B\,\frac{v_0}{v}\,, \tag{2.16}$$

where

$$A_1\equiv\frac{eE_\perp\tau_0}{m_\perp}+u_\perp\,,\qquad A_2\equiv\frac{eE_\parallel\tau_0}{m_\parallel}-i\,\frac{C\tau_0q^2u_\perp}{m_\parallel\omega}\,. \tag{2.17}$$

The local current density is calculated from (2.14), (2.16) and the current expression,

$$\boldsymbol{J}=Ne\boldsymbol{u}-\frac{2em^3}{h^3}\int\boldsymbol{v}\Psi(\boldsymbol{v})\frac{\partial f_0}{\partial v}\,d^3v\,, \tag{2.18}$$

as follows;

$$J_\parallel=\frac{3Nep_0}{ql_0}\left(\frac{A}{a_0}+iB\right),\qquad J_\perp=0 \tag{2.19}$$

for longitudinal waves and

$$J_\parallel=\frac{3Nep_0}{ql_0}\left(\frac{A_2}{a_0}+iB\right),\qquad J_\perp=\frac{Nea_0g_0A_1}{ql_0} \tag{2.20}$$

for transverse waves. In (2.19) and (2.20), modified Pippard's functions[5] p_0 and g_0 are used, and their approximate expressions for various frequency ranges are given by

$$\left.\begin{aligned}p_0&\cong\frac{1}{3}(ql_0)^2-\frac{1}{3}(ql_0)^4 &&(ql_0\ll1)\,,\\ &\cong1-\left(\frac{3\pi}{2}\right)^{1/2}(ql_0)^{-1} &&(ql_0\gg1)\,,\\ &\cong1-3(\omega\tau_0/ql_0)^2 &&(\omega\tau_0\gg1)\end{aligned}\right\} \tag{2.21}$$

and

$$\left.\begin{aligned}g_0&\cong1-\frac{1}{3}(ql_0)^2 &&(ql_0\ll1)\,,\\ &\cong\left(\frac{3\pi}{2}\right)^{1/2}(ql_0)^{-1} &&(ql_0\gg1)\,,\\ &\cong3(\omega\tau_0/ql_0)^2 &&(\omega\tau_0\gg1)\,,\end{aligned}\right\} \tag{2.22}$$

where

$$l_0\equiv\tau_0v_0\,,\qquad a_0\equiv ql_0/(1+i\omega\tau_0)\,.$$

The self-consistent solutions for $n^{(\pm)}$, $\boldsymbol{E}$, $\boldsymbol{J}^{(\pm)}$ can be obtained from (2.3a), (2.3b), (2.9), (2.19) and (2.20). They are arranged as follows:

(A) Longitudinal Waves;

$$J_\parallel{}^{(\pm)}=\frac{N_0eu_\parallel}{2}(Q_1\mp Q_2)\,, \tag{2.23}$$

$$n^{(\pm)}=\frac{qN_0u_\parallel}{2\omega}\left(Q_1\pm\frac{\Delta}{2kT}G\right), \tag{2.24}$$

$$E_\parallel=\frac{i\omega_P{}^2m_\parallel u_\parallel}{\omega e}(Q_1-1)\,, \tag{2.25}$$

where we put for brevity as

$$\left.\begin{aligned} Q_1 &\equiv \frac{1+i\dfrac{\omega\tau_0}{(\omega_P\tau_0)^2}+\dfrac{1}{2}\cdot\dfrac{C^{(+)}+C^{(-)}}{m_{\|}v_0^2}\cdot\dfrac{(ql_0)^2}{(\omega_P\tau_0)^2}}{1+i\dfrac{ql_0a_0(\omega\tau_0)}{3(\omega_P\tau_0)^2p_0}\left(1-i\dfrac{p_0}{\omega\tau_0}\right)}\ , \\ Q_2 &\equiv i\frac{\Delta p_0}{2kT\omega}\{(1+i\omega\tau_0)-(1+i\omega\tau)^{-1}\}/\{\tau_0+p_0\tau(1+i\omega\tau)^{-1}\}\ , \\ G &\equiv \left\{\frac{1}{\tau}+\frac{p_0}{\tau_0}(1+i\omega\tau_0)\right\}\Big/\left\{\frac{1}{\tau}(1+i\omega\tau)+\frac{p_0}{\tau_0}\right\}\ . \end{aligned}\right\} \tag{2.26}$$

(B) Transverse Waves;

$$J_{\|}^{(\pm)}=\mp\frac{N_0eu_\perp}{2}Q_2\ , \tag{2.27}$$

$$n^{(\pm)}=\pm\frac{qN_0u_\perp}{2\omega}\cdot\frac{\Delta}{2kT}G\ , \tag{2.28}$$

$$E_{\|}=0 \tag{2.29}$$

and

$$J_\perp=2J_\perp^{(+)}=2J_\perp^{(-)}=N_0eu_\perp P\ , \tag{2.30}$$

$$E_\perp=\frac{m_\perp k_0^2u_\perp}{eq^2\tau_0}(1-P)\ , \tag{2.31}$$

where

$$P\equiv g_0'(q^2+k_0^2)/(q^2+g_0'k_0^2)\ , \qquad g_0'\equiv a_0g_0/ql_0\ . \tag{2.32}$$

In the limit of $\Delta\to0$, these basic equations are reduced to those in simple semiconductors.[2]

§ 3. Numerical Estimations

In this section, we take tentatively a sample of n-Ge for the numerical estimations of physical quantities involved in the basic equations. The values of physical parameters are taken as $\rho=5.4\ \mathrm{g\ cm^{-3}}$, $\mathcal{E}=16$, $m=0.1m_0$ (m_0: electronic mass), $V=5\times10^5\ \mathrm{cm\ sec^{-1}}$, $\Xi_d=-3.7$ ev, $\Xi_u=16$ ev, $\tau_0=5\times10^{-13}$ sec, $\tau=10^{-10}$ sec, $T=10^2$ °K, $N_0=10^{16}\ \mathrm{cm^{-3}}$. For later uses the approximate expressions of A and B will be given for various frequency ranges, the critical frequencies of which are given as follows:

$\omega_1=5\times10^{10}$ (the frequency at which $ql_0=1$) ,

$\omega_2=2\times10^{12}$ (the frequency at which $\omega\tau_0=1$) ,

$\omega_3=10^{10}$ (the frequency at which $\omega\tau=1$) ,

$\omega_4=2.6\times10^4$ (the frequency at which $q^2=|k_0^2|$) ,

$\omega_5=1.1\times10^{10}$ (the frequency at which $|C^{(+)}+C^{(-)}|/2=m_{\|}^*\omega_P^2/q^2$ for longitudinal waves) ,

$\omega_6=1.6\times10^{11}$ (the frequency at which $v_0^2=3\omega_P^2/q^2$) .

First we shall give the approximate expression of the function G in (2.26). If $ql_0\ll1$ and $\omega\tau\ll1$, we can put

$$G\cong(1+i\omega\tau_R)^{-1}\cong1-i\omega\tau_R\ , \tag{3.1}$$

where

$$1/\tau_R=1/\tau+p_0/\tau_0\cong 1/\tau+q^2D \tag{3.2}$$

and D is the diffusion constant[1]. If $ql_0\gg 1$, $\omega\tau\gg 1$ and $\omega\tau_0<1$, G becomes

$$G\cong\frac{ql_0}{a_0}\left(1-i\frac{\omega\tau_0}{p_0}\right). \tag{3.3}$$

Under the condition $\omega\tau_0\gg 1$, G approaches p_0.

For longitudinal waves, we consider three frequency ranges in which the approximate expressions for A and B are given as follows:

(1) $ql_0\ll 1$, $\omega\tau\ll 1$, $|C^{(+)}+C^{(-)}|/2\ll m_{\|}\omega_P^2/q^2$, $v_0^2\ll 3\omega_P^2/q^2$;

$$A^{(\pm)}\cong\frac{ql_0a_0}{3p_0}\left(1-i\frac{p_0}{\omega\tau_0}\right)u_{\|}\mp\frac{i}{3}\cdot\frac{(ql_0)^2}{\omega\tau_0}\cdot\frac{\Delta}{2kT}u_{\|}\,, \tag{3.4a}$$

$$B^{(\pm)}\cong\frac{1}{3}\cdot\frac{ql_0}{\omega\tau_0}u_{\|}\pm\frac{1}{3}\cdot\frac{ql_0}{\omega\tau_0}\cdot\frac{\Delta}{2kT}(1-i\omega\tau_R)u_{\|}\,. \tag{3.4b}$$

(2) $ql_0\gg 1$, $\omega\tau\gg 1$, $|C^{(+)}+C^{(-)}|/2\gg m_{\|}\omega_P^2/q^2$, $v_0^2\ll 3\omega_P^2/q^2$;

$$A^{(\pm)}\cong\mp\frac{i}{3}\,\frac{(ql_0)^2}{\omega\tau_0}\cdot\frac{\Delta}{2kT}u_{\|}+\frac{1}{3}\cdot\frac{C^{(+)}+C^{(-)}}{2kT}\cdot\frac{(ql_0)^3a_0}{3(\omega_P\tau_0)^2p_0}\left(1-i\frac{p_0}{\omega\tau_0}\right)u_{\|}\,, \tag{3.5a}$$

$$B^{(\pm)}\cong\pm\frac{1}{3}\cdot\frac{(ql_0)^2}{\omega\tau_0a_0}\cdot\frac{\Delta}{2kT}\left(1-i\frac{\omega\tau_0}{p_0}\right)u_{\|}+\frac{1}{3}\cdot\frac{C^{(+)}+C^{(-)}}{2kT}\cdot\frac{(ql_0)^3}{3(\omega_P\tau_0)^2(\omega\tau_0)}u_{\|}\,. \tag{3.5b}$$

(3) $ql_0\gg 1$, $\omega\tau\gg 1$, $|C^{(+)}+C^{(-)}|/2\gg m_{\|}\omega_P^2/q^2$, $v_0^2\gg 3\omega_P^2/q^2$;

$$A^{(\pm)}\cong-\frac{i}{3}\cdot\frac{C^{(\pm)}}{kT}\cdot\frac{(ql_0)^2}{\omega\tau_0}u_{\|}\,, \tag{3.6a}$$

$$B^{(\pm)}\cong\frac{1}{3}\cdot\frac{(ql_0)^2}{\omega\tau_0a_0}\cdot\frac{C^{(\pm)}}{kT}\left(1-i\frac{\omega\tau_0}{p_0}\right)u_{\|}\,. \tag{3.6b}$$

The expressions of A_2 and B in transverse waves are given in two frequency ranges:

(1) $ql_0\ll 1$, $\omega\tau\ll 1$;

$$A_2^{(\pm)}\cong-\frac{i}{3}\cdot\frac{\Delta}{2kT}\cdot\frac{(ql_0)^2}{\omega\tau_0}u_{\perp}\,, \tag{3.7a}$$

$$B^{(\pm)}\cong\pm\frac{1}{3}\cdot\frac{ql_0}{\omega\tau_0}\cdot\frac{\Delta}{2kT}(1-i\omega\tau_R)u_{\perp}\,. \tag{3.7b}$$

(2) $ql_0\gg 1$, $\omega\tau\gg 1$;

$$A_2^{(\pm)}\cong-\frac{i}{3}\cdot\frac{C^{(\pm)}}{kT}\cdot\frac{(ql_0)^2}{\omega\tau_0}u_{\perp}\,, \tag{3.8a}$$

$$B^{(\pm)}\cong\frac{1}{3}\cdot\frac{(ql_0)^2}{\omega\tau_0a_0}\cdot\frac{C^{(\pm)}}{kT}\left(1-i\frac{\omega\tau_0}{p_0}\right)u_{\perp}\,. \tag{3.8b}$$

Finally we can put

$$A_1^{(\pm)}\cong u_{\perp}/g_0' \tag{3.9}$$

for $q^2\ll|k_0^2|$ and

$$A_1^{(\pm)}\cong u_{\perp} \tag{3.10}$$

for $q^2 \gg |k_0^2|$.

In the next section, we shall calculate the ultrasonic absorption and the acoustoelectric effect using these approximate expressions for A and B.

§ 4. Ultrasonic Absorption and Acoustoelectric Effect

As has been mentioned previously in § 2, the absorption coefficient by conduction electrons is given by the sum of two terms, one due to the change of the kinetic energy and the other due to the change of the deformation potential energy of electrons. The coefficient Λ_P due to the deformation potential can be calculated as follows. When the local fluctuation $n^{(\pm)}$ deviates from $n_{eq}^{(\pm)}$, the potential energy $(U^{(\pm)}-U^{(\mp)})$ is transferred to lattice system in the interclass transition time τ_c owing to one transition. Therefore, the energy absorbed per unit volume and unit time $W_{P^{(\pm)}}$ becomes

$$W_{P^{(\pm)}}=\frac{1}{2}\,\mathrm{Re}\left[\left(\frac{U^{(\pm)}-U^{(\mp)}}{2\tau}\right)^*(n^{(\pm)}-n_{eq}^{(\pm)})\right]. \tag{4.1}$$

Then,

$$\begin{aligned}\Lambda_P&=2(W_{P^{(+)}}+W_{P^{(-)}})/\rho|u|^2V\\&=\frac{N_0\Delta^2}{4\rho V^3kT\tau}\cdot\mathrm{Re}\,(H+I)\,,\end{aligned} \tag{4.2}$$

where we put

$$H=\left(\frac{p_0}{\tau_0}\right)\cdot\frac{(1+i\omega\tau)^{-1}-(1+i\omega\tau_0)}{(1+i\omega\tau)/\tau+p_0/\tau_0}\,, \tag{4-3}$$

$$I=i\omega\tau/(1+i\omega\tau)\,. \tag{4.4}$$

The formula (4.2) can be applied to both longitudinal and transverse waves.

The coefficient Λ_K due to the kinetic energy can be calculated by a similar formula for monovalent metals[6] and simple semiconductors[2];

$$\Lambda_K=\Lambda_{K^{(+)}}+\Lambda_{K^{(-)}}\,, \tag{4.5a}$$

$$\Lambda_{K^{(\pm)}}=-\frac{2m^4}{\rho|u|^2V\tau_0h^3}\int_0^\infty\frac{\partial f_0}{\partial v}\,v^3\,dv\int_{-1}^1dx\int_0^{2\pi}d\phi|\Psi^{(\pm)}(\boldsymbol{v})|^2\,. \tag{4.5b}$$

Total losses are given by $\Lambda=\Lambda_P+\Lambda_K$.

The acoustoelectric effect can be defined as the average dc force exerted by acoustic waves on an electron[1]. Effective forces responsible for the effect have two components, one associated with the intravalley transition in each valley and the other associated with the interclass transition. Owing to the interclass transition, the acoustic energy density suffers an energy loss $(U^{(\pm)}-U^{(\mp)})$ from each of $(n^{(\pm)}-n_{eq}^{(\pm)})$ electrons in a distance $V\tau_c$. This means that each electron exerts an effective force $-(U^{(\pm)}-U^{(\mp)})/V\tau_c$ on acoustic vibrations. From the principle of reaction, each electron is exerted the effective force

$$X^{(\pm)}=\{U^{(\pm)}-U^{(\mp)}\}/2V\tau \tag{4.6}$$

by acoustic waves. As has been shown in the previous papers,[2],[6] the acoustic energy density suffers also an energy loss $mv\Psi^{(\pm)}(v)$ from an electron with the velocity $\boldsymbol{v}$ in a distance $V\tau_0$. Then in a similar way to (4.6), the effective force associated with the intravalley transition is given by

$$Y^{(\pm)}(\boldsymbol{v})=mv\Psi^{(\pm)}(\boldsymbol{v})/V\tau_0\,. \tag{4.7}$$

Thus, the acousto-electromotive force can be written as

$$F=\frac{1}{2N_0e}\,\mathrm{Re}\Big[X^{(+)*}(n^{(+)}-n_{eq}^{(+)})+X^{(-)*}(n^{(-)}-n_{eq}^{(-)})$$
$$+\sum_{\boldsymbol{v}} Y^{(+)*}(\boldsymbol{v})\Big\{-\Psi^{(+)}(\boldsymbol{v})\frac{\partial f_0}{\partial v}\Big\}+\sum_{\boldsymbol{v}} Y^{(-)*}(\boldsymbol{v})\Big\{-\Psi^{(-)}(\boldsymbol{v})\frac{\partial f_0}{\partial v}\Big\}\Big], \tag{4.8}$$

which satisfies a well-known relation

$$F=\Lambda\gamma/N_0eV \tag{4.9}$$

($\gamma\equiv\rho|u|^2V/2$: acoustic energy flow density). In the same manner as Λ, we can write $F=F_P+F_K$.

First we calculate Λ_P and F_P from (4.2), (4.3), (4.4) and (4.8). The formulae for various frequency ranges are tabulated as follows:

(a) $ql_0\ll1,\ \omega\tau\ll1,\ \omega\tau_0\ll1$;

$$\Lambda_P\cong\frac{N_0\Delta^2}{4\rho V^3kT}\cdot\omega^2\tau\Big(1-\frac{2}{3}q^2v_0^2\tau\tau_0\Big), \tag{4.10a}$$

$$F_P\cong\frac{\Delta^2\gamma}{4\rho eV^4kT}\cdot\omega^2\tau\Big(1-\frac{2}{3}q^2v_0^2\tau\tau_0\Big). \tag{4.10b}$$

(b) $ql_0\gg1,\ \omega\tau\gg1,\ \omega\tau_0<1$;

$$\Lambda_P\cong\frac{N_0\Delta^2}{4\rho V^3kT}\Big(\frac{3\pi}{2}\Big)^{1/2}\Big(\frac{V\tau_0}{v_0\tau}\Big)\omega, \tag{4.11a}$$

$$F_P\cong\frac{\Delta^2\gamma}{4\rho eV^4kT}\Big(\frac{3\pi}{2}\Big)^{1/2}\Big(\frac{V\tau_0}{v_0\tau}\Big)\omega. \tag{4.11b}$$

(c) $ql_0\gg1,\ \omega\tau\gg1,\ \omega\tau_0\gg1$;

$$\Lambda_P\to\frac{3N_0\Delta^2}{4\rho V^3kT\tau}\Big(\frac{V}{v_0}\Big)^2, \tag{4.12a}$$

$$F_P\to\frac{3\Delta^2\gamma}{4\rho eV^4kT\tau}\Big(\frac{V}{v_0}\Big)^2, \tag{4.12b}$$

which hold for both longitudinal and transverse waves. We can see that the interclass transition rapidly decreases as the frequency of waves exceeds $1/\tau$.

The formulae for Λ_K and F_K in longitudinal waves are calculated from (4.5), (4.8), (2.14), (3.4)–(3.6) as follows:

(1) $ql_0\ll1,\ \omega\tau\ll1,\ |C^{(+)}+C^{(-)}|/2\ll m_{\parallel}\omega_P^2/q^2,\ v_0^2\ll3\omega_P^2/q^2$;

$$\Lambda_K=\frac{N_0\Delta^2\omega^2\tau_0}{4\rho V^3kT}\Big(1+\frac{1}{3}q^2v_0^2\tau_R^2\Big), \tag{4.13a}$$

$$F_K=\frac{\Delta^2\gamma\omega^2\tau_0}{4\rho eV^4kT}\Big(1+\frac{1}{3}q^2v_0^2\tau_R^2\Big). \tag{4.13b}$$

(2) $ql_0\gg1,\ \omega\tau\gg1,\ \Delta/2kT\gg|C^{(+)}+C^{(-)}|q^2/2m_{\parallel}\omega_P^2\gg1,\ v_0^2\ll3\omega_P^2/q^2$;

$$\Lambda_K=\frac{N_0\Delta^2\omega}{4\rho V^3kT}\Big(\frac{3\pi}{2}\Big)^{1/2}\Big(\frac{V}{v_0}\Big), \tag{4.14a}$$

$$F_K=\frac{\Delta^2\gamma\omega}{4\rho eV^4kT}\Big(\frac{3\pi}{2}\Big)^{1/2}\Big(\frac{V}{v_0}\Big). \tag{4.14b}$$

(3) $ql_0 \gg 1,\ \omega\tau \gg 1,\ |C^{(+)}+C^{(-)}|q^2/2m_{\parallel}\omega_P{}^2 \gg \Delta/2kT,\ v_0{}^2 \ll 3\omega_P{}^2/q^2$;

$$\Lambda_K = \frac{1}{3}\left(\frac{3\pi}{2}\right)^{1/2}\left(\frac{C^{(+)}+C^{(-)}}{2}\cdot\frac{q^2}{m_{\parallel}\omega_P{}^2}\right)^2\cdot\frac{N_0 m_{\parallel} v_0\omega}{\rho V^2}, \tag{4.15a}$$

$$F_K = \frac{1}{3}\left(\frac{3\pi}{2}\right)^{1/2}\left(\frac{C^{(+)}+C^{(-)}}{2}\cdot\frac{q^2}{m_{\parallel}\omega_P{}^2}\right)^2\cdot\frac{m_{\parallel} v_0\omega\gamma}{\rho e V^3}. \tag{4.15b}$$

(4) $ql_0 \gg 1,\ \omega\tau \gg 1,\ v_0{}^2 \gg 3\omega_P{}^2/q^2$;

$$\Lambda_K = \left(\frac{3\pi}{2}\right)^{1/2}\left\{\frac{|C^{(+)}|^2+|C^{(-)}|^2}{2}\right\}\frac{N_0\omega}{\rho V^2 kTv_0}, \tag{4.16a}$$

$$F_K = \left(\frac{3\pi}{2}\right)^{1/2}\left\{\frac{|C^{(+)}|^2+|C^{(-)}|^2}{2}\right\}\frac{\omega\gamma}{\rho e V^3 kTv_0}. \tag{4.16b}$$

It should be remarked that in the low frequency range a term due to the electronic viscosity,

$$\Lambda_{K,vis} \cong \frac{2N_0kT\omega^2\tau_0}{\rho V^3} \tag{4.17a}$$

or

$$F_{K,vis} \cong \frac{2kT\omega^2\tau_0\gamma}{\rho e V^4} \tag{4.17b}$$

must be added to (4.13). But this term can be neglected in comparison with the main term in (4.13).

The formulae for Λ_K and F_K in transverse waves are calculated from (4.5), (4.8), (2.16), (3.7) and (3.8). As is easily seen, Λ_K or F_K can be divided into two independent terms, one associated with $J_{\parallel}$ and the other associated with $J_{\perp}$; i.e.

$$\left.\begin{aligned}\Lambda_K &= \Lambda_{K\parallel}+\Lambda_{K\perp},\\ F_K &= F_{K\parallel}+F_{K\perp}.\end{aligned}\right\} \tag{4.18}$$

The formula for each term in (4.18) are calculated as follows:

(A) $\Lambda_{K\parallel}$ and $F_{K\parallel}$.

(1) $ql_0 \ll 1,\ \omega\tau \ll 1$;

$$\Lambda_{K\parallel} \cong \frac{N_0\Delta^2\omega^2\tau_0}{4\rho V^3 kT}\left(1+\frac{1}{3}q^2v_0{}^2\tau_R{}^2\right), \tag{4.19a}$$

$$F_{K\parallel} \cong \frac{\Delta^2\gamma\omega^2\tau_0}{4\rho e V^4 kT}\left(1+\frac{1}{3}q^2v_0{}^2\tau_R{}^2\right). \tag{4.19b}$$

(2) $ql_0 \gg 1,\ \omega\tau \gg 1$;

$$\Lambda_{K\parallel} \cong \left(\frac{3\pi}{2}\right)^{1/2}\frac{C^2N_0\omega}{\rho V^2 kTv_0}, \tag{4.20a}$$

$$F_{K\parallel} \cong \left(\frac{3\pi}{2}\right)^{1/2}\frac{C^2\omega\gamma}{\rho e V^3 kTv_0}, \tag{4.20b}$$

where $|C| \equiv |C^{(+)}| = |C^{(-)}|$.

(B) $\Lambda_{K\perp}$ and $F_{K\perp}$.

(1) $ql_0 \ll 1,\ q^2 \lesssim |k_0{}^2|$;

$$\Lambda_{K\perp} \cong \frac{N_0kT\omega^2\tau_0}{\rho V^3}, \tag{4.21a}$$

$$F_{K\perp} \cong \frac{kT\omega^2\tau_0\gamma}{\rho e V^4}. \tag{4.21b}$$

(2) $ql_0 \gg 1,\ q^2 \gg |k_0{}^2|$;

$$\Lambda_{K\perp} \to N_0 m_{\perp}/\rho V\tau_0, \tag{4.22a}$$

$$F_{K\perp} \to m_{\perp}\gamma/\rho e V^2\tau_0. \tag{4.22b}$$

The results obtained in this section will be discussed in the next section.

§ 5. Discussions

(A) Low frequency range ($ql_0 \ll 1,\ \omega\tau \ll 1$).

The terms due to the electronic viscosity, (4.17) for longitudinal and (4.21) for transverse waves, can be neglected in general. Because of the fact,

$$\Lambda_P/\Lambda_K = F_P/F_K \cong \tau/\tau_0 \tag{5.1}$$

from (4.10), (4.13) and (4.19), the terms due to the change of the deformation potential energy predominate in the low frequency range. The complete formulae can be rewritten as

$$\Lambda \cong \frac{N_0\Delta^2}{4\rho V^3 kT}\cdot\omega^2(\tau_R+\tau_0), \tag{5.2a}$$

$$F \cong \frac{\Delta^2\gamma}{4\rho e V^4 kT}\cdot\omega^2(\tau_R+\tau_0), \tag{5.2b}$$

using the definition of τ_R in (3.2). This formula, (5.2b), is nearly identical with Weinreich-Sanders-White's[1)],

$$F = \frac{\Delta^2\gamma}{4\rho e V^4 kT}\cdot\frac{\omega^2\tau_R}{1+(\omega\tau_R)^2}, \tag{5.3}$$

which is in good agreement with the experiment by transverse waves in the low frequency range.

(B) High frequency range ($ql_0 \gg 1$, $\omega\tau \gg 1$).

From (4.11), (4.14) or (4.16) and (4.20), we get

$$A_P/A_K = F_P/F_K \simeq \tau_0/\tau \tag{5.4}$$

i.e., the terms due to the change of the kinetic energy predominate in the high frequency range. As the frequency increases, A and F do not decrease, in contrast to Weinreich-Sanders-White's formula, owing to the increase of A_K and F_K. In the sufficiently high frequency range, we can see that each valley has *independent contributions* to A and F by the amount of the same order as that of longitudinal waves in simple semiconductors[2] (see (4.16) and (4.20)). The experimental check of our theory may be expected in future.

The author should express his thanks to M. Shibuya and W. Sasaki for the valuable discussions.

References

1) G. Weinreich, T. M. Sanders and H. G. White: Phys. Rev. **114** (1959) 33.
2) N. Mikoshiba: J. Phys. Soc. Japan **15** (1960) 982.
3) G. Weinreich: Phys. Rev. **104** (1956) 321. T. Holstein: Westinghause Research Memo 60-94698-3-M15 (1956).
4) C. Herring: Bell System Tech. Jour. **34** (1955) 237.
5) A. B. Pippard: Phil. Mag. **46** (1955) 1104.
6) N. Mikoshiba: J. Phys. Soc. Japan **14** (1959) 1691.

JOURNAL OF THE PHYSICAL SOCIETY OF JAPAN, Vol. 15, No. 7, JULY, 1960

Filamentary Crystals grown from the Solid Metal

By George SINES

University of California, Los Angeles 24, California, U.S.A.

(Received February 13, 1960)

A theoretical analysis and experimental evidence show that a source of energy for spontaneous whisker growth is the elastic strain energy arising from the anisotropy of thermal expansion. Observation of whisker growth on a Bragg bubble raft suggests that the growth mechanism could be by cooperative repetitive movement of dislocations. The conditions for whisker growth from the solid are presented and by fulfilling them growths were produced on gold, silver, bismuth, lead, indium, and lead-indium alloys. The crystallographic orientations of a number of tin whiskers are reported, one of which had a transition between two orientations although it was straight. The tensile strengths of several tin whiskers were measured and observed to be lower than calculated from bending tests. The high elastic strain of 5% in bending was observed for an indium one.

§ 1. Introduction

Although filamentary crystals have been recognized as an interesting phenomenon for over a hundred years,[1] it is only recently that appreciable attention has been focused on them by chance observations of new forms.[2],[3] Also, only recently has the knowledge of crystal imperfections become sufficient to propose possible mechanisms for their growth.

Filamentary crystals, commonly called whiskers, are characterized by (1) their high ratio of length to thickness, (2) the presence of some with straight sections, (3) constancy in cross-section over considerable portions of their length, (4) many them being single crystals, (5) straight sections which have major crystallographic directions as their axes, (6) their thickness which is usually within the range of 0.01 to 10 microns, (7) and that some are hundreds of times stronger than the metal from which they grew.[4–7,20]

Some of the processes by which filamentary crystals have been grown are the controlled supersaturation of vapor over a suitable surface,[8–10] the reduction of metal halides on a suitable substrate,[5,11,12] the chemical reaction on a solid,[13,14] the precipitation from a solution,[15–17,20] the heating of metals,[18,19] and a spontaneous action on solid metal.[21] This paper is concerned with the properties and conditions for growth of filamentary crystals of the last process. Filamentary crystals grown by several different processes are unusually strong,[4–7,20] but it was crystals of this type that were first shown by Herring and Galt[4] to have unusual strength: they bent tin ones to cause an elastic strain of 2 or 3% at the outer fiber.

Two recent papers review the various types of filamentary growths.[22,23]

§ 2. Sources of Energy for Growth

Several sources of energy for the creation of the free surface of the filament which grows spontaneously from the solid should be considered:

(1) The surface may oxidize to a depth sufficient to make the net surface free energy negative has been proposed by Frank[24]. Thus an initial microscopic protrusion would tend to grow in order to expose more surface for oxidation.

(2) If the filament is free, or almost free, of dislocations and if the bulk material is filled with dislocations, the energy of distortion of the crystal lattice by the dislocations becomes available as the whisker grows. However, a mechanism for unsnarling the many interlocked dislocations to release their energy is difficult to imagine.

(3) The author suggests that a probable source of energy is the release of elastic strain energy on a scale more gross than that of the crystal imperfections, such as dislocations. The energy could be from micro-residual stresses or from externally applied forces. All of the metals which have been shown to grow whiskers spontaneously from the solid, i.e. tin, cadmium, zinc,[21] and antimony[25] have a common characteristic: They all have a high degree of anisotropy in their coefficients of thermal expansion as is shown in Table I. Such great anisotropy of thermal expansion causes residual stresses in a polycrystalline medium if the temperature is changed from that at which it solidified or was deposited.

Table I. (Ref. 26)

Metal	Temperature	Coefficients of thermal expansion ($\times 10^{-6}$/°C	
		parallel to principal axis	perpendicular to
zinc	20–100°C	63.9	14.1
cadmium	20	52.6	21.4
beta tin	20	30.5	15.5
antimony	20	15.6	8.0

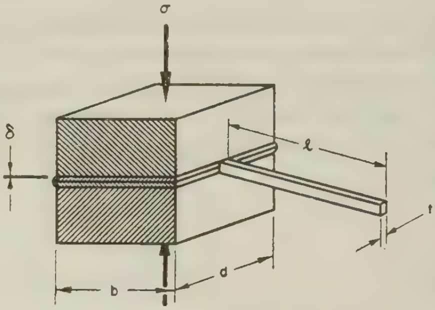

Fig. 1. Compression-induced growth of filaments from between plated blocks.

The following analysis shows that a moderate stress can provide sufficient energy for a whisker to grow. Figure 1 shows a whisker growing out from the edge of the plating between two plated blocks which are being compressed by a stress σ. The length of the whisker is l and it has a square cross-section t thick. As the plating metal moves out from between the blocks to form the whisker, the separation between the backing surfaces will decrease by an amount δ. Assuming the plating decreases uniformly in thickness over the region under consideration which is b wide by d long, the volume of the metal extruded is $bd\,\delta$. The volume of the metal extruded must equal the volume of the whisker

$$bd\,\delta = lt^2 \qquad \text{so} \qquad \delta = lt^2/bd\,. \tag{1}$$

For the free surface which is created, $4tlS$ units of energy must be provided, where S is the surface energy per unit area. The work done by the stress in moving through the distance σ is $\sigma\, bd\,\delta$. This provides the energy for the surface. An additional source f energy is the elastic energy which the vhisker material had while it was under tress between the plates.

$$\sigma\, bd\,\delta+\frac{\sigma^2}{2E}lt^2=4tlS\,. \qquad (2)$$

The term $(\sigma^2/2E)lt^2$ is much smaller than $bd\,\delta$ and can be neglected. Inserting δ from Eq. (1)

$$\sigma=4S/t\,. \qquad (3)$$

Assuming a common value for the surface energy of a metal of 10^3 ergs/cm² and a whisker of a thickness of 10^{-4} cm, $\sigma=4\times10^7$ dynes/cm² or about 600 psi. This shows that he relief of a very moderate stress can provide the surface energy needed.

The applied stress σ could be caused by external forces or it could be a residual stress caused by interaction with adjacent grains. Consider a metal oriented so that its direction of maximum coefficient of thermal expansion s parallel to the minimum of the adjacent grains. For a change of temperature ΔT, his would cause a stress of approximately

$$\sigma=\Delta T(\alpha_{\max}-\alpha_{\min})E$$

where E is the modulus of elasticity. A change in temperature of only 10°C would cause a stress in tin of $10(1.5\times10^{-4})7\times10^6=1000$ psi. For this order of magnitude calculation, an average value of E was used.

The above calculation demonstrates that he energy can be easily supplied by residual tresses arising from the anisotropy of the he coefficient of thermal expansion in a polycrystalline sample. Further evidence that oxidation may not be essential to the growth f filamentary crystals from the solid has been found at Bell Laboratories,[25] where they grew tin whiskers in a highly gettered vacuum of better than 10^{-8} mm of oxygen. A ough calculation shows that there was not nough oxygen to form a monomolecular layer on a one micron-size whisker a millimeter long, thus, it is likely that the source f energy was from the release of residual tresses.

A demonstration that a source of energy or whisker growth exists other than that of oxidation would be to grow them on a metal hat does not oxidize. In Experiment E9-1, See Sec. F) gold whiskers grew under an externally applied compressive stress from old plated on stainless steel. These whiskers were thin and straight as can be seen in Fig. 2. Gold does not oxidize although it may have an adsorbed monomolecular layer of oxygen. Even with an adsorbed layer, the net surface free energy is not negative. In Exp. E9-2, whiskers also grew from silver in pressure clamps at 400°C, which is above the temperature for dissociation of silver oxide.

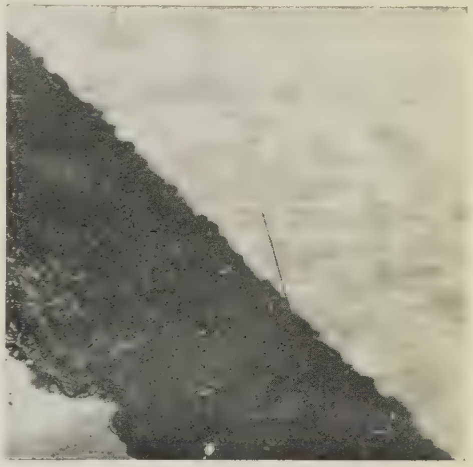

Fig. 2. Compression-induced gold filamentary crystals. Magnification: ×450 with ×1/2 in reproduction. See Summary of Experiments, Exp. E9-1.

Some metals which readily oxidize, lead, indium,[21),25)] and lead-indium alloys have not been observed to grow whiskers spontaneously,* but grew them when placed in pressure clamps. (Exp. E10-1, E10-2, and E10-3)

A compressive stress applied to the plated surfaces as shown in Fig. 1 greatly accelerates the rate of growth of whiskers on metals on which they also grow spontaneously. This was shown by Fisher, Darken, and Carroll[27)] for tin. Appreciable crops of whiskers grew within a day instead of the weeks or months required for spontaneous growth. Exp. E11-1 and E11-2 show that the growth of whiskers can also be accelerated on zinc and cadmium plate.

This acceleration of growth by the compressive stress has been explained as the effect of the stress gradient in accelerating the diffusion of the metal in the bulk to the base of the whisker.[27),28)] An additional effect which could hasten the growth is the reduction of the activation energy of the atom when it moves from the bulk into the whisker. Although it has been shown here that a moderate stress can provide sufficient energy for the formation of the free surface, it says nothing about the rate at which growth proceeds. Both oxidation and stress could reduce the height of the activation barrier which the atom must cross to become part of the whisker.

---

* Whiskers grew on bismuth under pressure, Exp. E10-4, but no reports of long-term observations for spontaneous growth are published. It is likely that spontaneous growth would occur at room temperature because its diffusivity and anisotropy of thermal expansion is comparable to those of the metals which do.

An additional cooperative action could occur with stress and oxidation. A whisker could start by the release of elastic strain energy, thereby creating the surface geometry required by Frank's[24)] analysis and then proceed to grow from energy of oxidation. This could partially explain the transition from a high initial growth rate to the much slower final growth rate observed by Fisher et al.[27)]

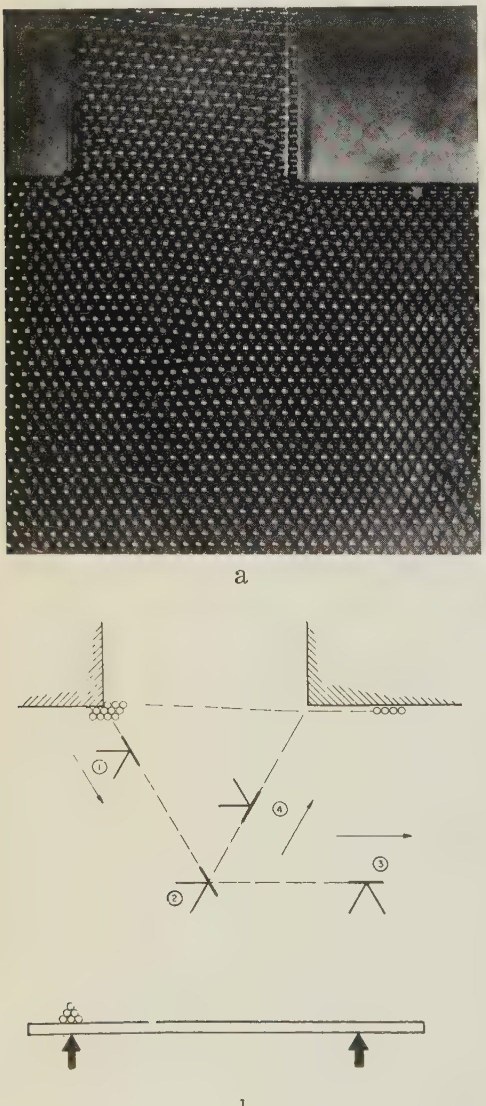

a

b

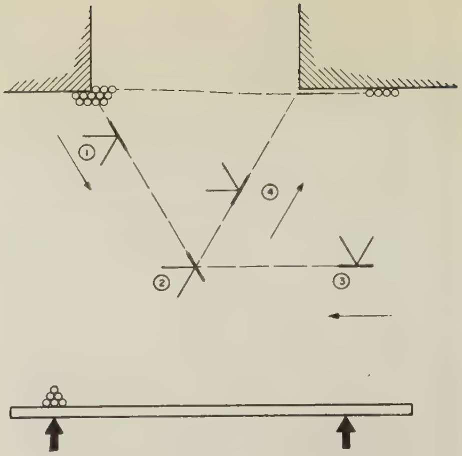

c

Fig. 3. The extrusion of a "filamentary crystal" with a Bragg bubble model. Fig. 3a shows the bubbles being forced between two square-cornered barriers in the upper left and upper right corners by a pusher out of view at the bottom. Often the movement shown in Fig. 3b occurs: A dislocation is created at the left corner and moves to the apex position (2) where it aids in the formation of another dislocation which moves off to the right (3), and then the remaining dislocation moves up to the right (4), thereby depositing another row of atoms to the base of the filament. Then the procedure repeats from left to right as in a mirror image to add the next row. Readjustments occur in the parent crystal by additional movements of dislocations to its boundaries. Fig. 3c illustrates an alternate action which is often observed. A dislocation moves from the crystal boundary (3) to join the one already at the apex (2), combines with it and then the resultant moves up and to the right (4) as before. Several other repetitive processes also have been observed. In the photograph of the bubble model, Fig. 3a, a dislocation is at position 2 and another at position 4 as identified in both Figs. 3b and 3c

§ 3. The Mechanism for Growth of Filamentary Crystals from the Solid

The continuing movement of a dislocation or the repetitive generation and movement of

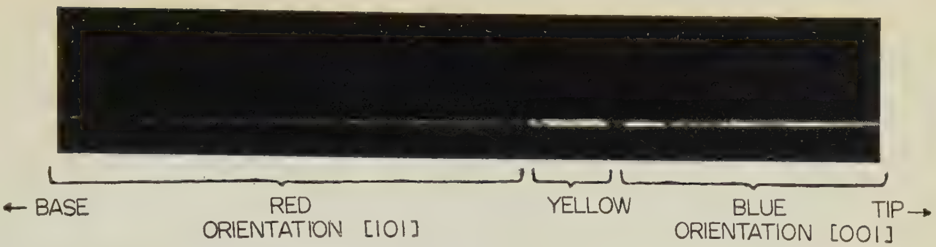

Fig. 4. Transition in crystallographic orientation revealed by polarized light. (Color photograph copied through medium filter. Magnification: ×500 with ×2 in printing and ×1/2 in reproduction.)

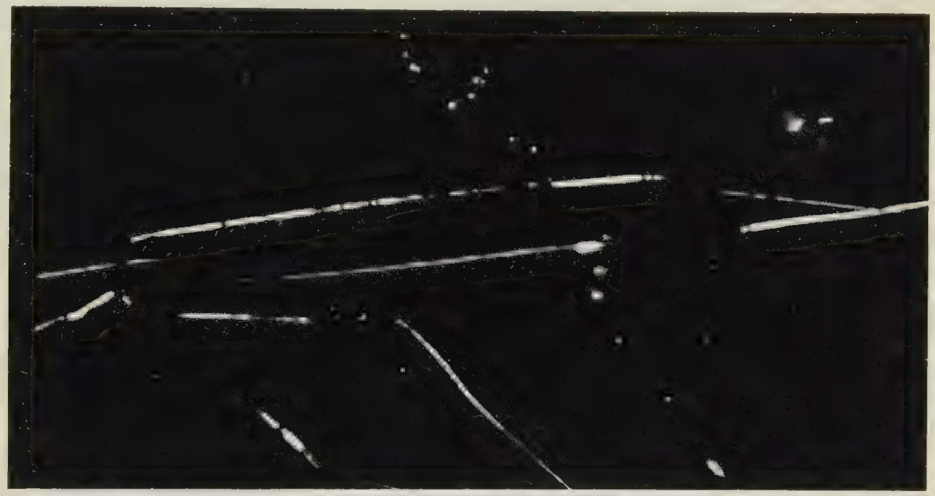

Fig. 5. Compression-induced tin filaments: polarized light, color photograph copied through medium green filter. Magnification: ×200 with ×2.7 in printing and ×3/5 in reproduction.

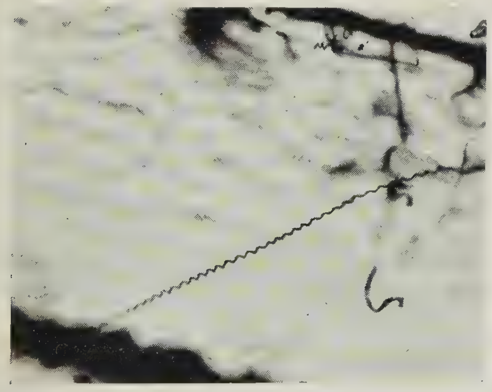

Fig. 6. Helical tin whisker, compression-induced growth. (Magnification: ×300 with ×1/2 in reproduction.

dislocations have been advanced by Frank[24] and by Eshelby[29], respectively, as mechanisms by which atoms could move from the bulk into the regular crystalline structure of the filament. This is compatible with the observation of Arnold[30] that growth occurs from the base. It may be possible that a cooperative movement of dislocations exists which would result in their growth but with less dislocation climb. In Fig. 3 a two dimensional cooperative movement of dislocations is shown to result in the deposition of an additional layer of bubbles to the “filamentary crystal”. It should be possible to conceive repetitive, three-dimensional cooperative movements of dislocations which could add layer after layer to a filament.

Filaments have been known to grow on metals having only one or only a few planes of easy slip: tin is tetragonal, and cadmium and zinc are hexagonal; therefore, it incorrectly might be supposed that growth can occur only on metals having a few slip systems. However, Exp. E9–1 and E10–1 show that gold and lead, which are face-centered cubic metals having many slip systems, grow whiskers.

For those metals which grow whiskers spontaneously at room temperature, Zn, Cd, Sn, and Sb, the room temperature was be-

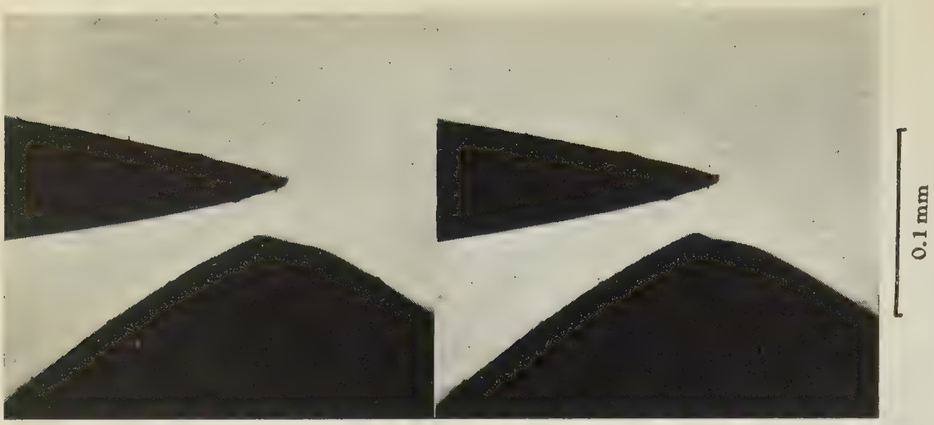

Fig. 7 (a). An indium whisker of 0.8μ diameter elastically bent to a radius of curvature of 8μ. See the Summary of Experiments, Exp. S-3b. (b) The indium whisker after failing by sudden plastic deformation at two localized places.

tween 0.4 and 0.6 of their melting temperatures expressed in degrees absolute. Metals on which compression-induced growth occurred, indium, lead, lead-indium alloys, and bismuth, are in this same range except for indium which is even nearer to its melting point at room temperature. A rough direct correlation can be made between the melting points and the activation energies for both the rates of diffusion and of creep for metals, the interrelated phenomena which cause mass transport in solids. Thus, to get sufficient mass transport in metals having higher melting temperatures, silver and gold, it was necessary to use elevated temperatures to obtain compression-induced growth. (Exp. E9-1, E9-2)

In compression-induced growth, some consideration has been given to the effect of the pressure gradient in aiding the transport of metal to the base.27),28) The applied compression, probably greatly intensified by the stress concentration of the contacting surface disparities of the plate, is reduced to zero on the free filament. The theory of plasticity shows that the change in stress occurs in a distance roughly equal to the thickness of the plate. The effect of this severe pressure gradient in compression-induced growth is necessary in order to explain the unusual rapidity of mass transport. A crude analysis of soft plating being squeezed between steel plates shows that the gradient is inversely proportional to the thickness of the plating. If the growth rate is limited by the rate of mass transport under a pressure gradient, the thicker layers of plating would grow whiskers more slowly. (also gross extrusion of the plating occurs when it is thick.) In the experiments by the author, it was generally observed that thin plating does grow filaments faster but that there is a limit to the thinness of the plating on which abundant growth occurs. Reasons for this limit may be (1) the thickness of the plating tends to limit the thickness of the filament and the dislocation mechanism may have to be a certain critical size to operate, (2) the supply of metal available for the growth is more limited and also (3) the ratio of surface energy needed, to the elastic energy released, is less for thin whiskers. (however, if oxidation is the source of energy, one would expect thinner filaments to grow more rapidly because they expose more surface to oxidation) Many observations by the author indicated that when the plating is thinner than 0.00005″ few whiskers grew.

In Exp. E10-3, compression-induced whiskers grew on 64%Pb-36%In and 84%In-16%Pb alloys. (weight) Growths on alloys have also been obtained by Baker13) on 95%Sn-5%Sb, 95%Sn-5%Pb, 95%Sn-5%Zn, and 90%-Sn-10%Zn. All of his alloys have very little solid solubility at room temperature, except antimony which has about 3%. Whiskers failed to grow on terne plate, 25%Sn-75%Pb, by compression-induction in Exp. E11-4. These results indicate that when the extent of two phases are of the same magnitude that filaments may not grow, that when the primary constituent is continuous they do, and that alloy whiskers can grow from solid solutions.

An essential feature of the growth of a filamentary crystal from the solid is the mechanism of mass transport to its root. Growths on alloys may reveal something of the mechanism because, if simple diffusion is the means of transport, enrichment of one of the species of the alloy would be expected in the filament because there is usually a large difference in the rate of diffusion of the species. In Exp. E10–3 on 84%In–16%Pb alloy, the whisker examined had the same composition as the parent metal. This indicates that the transport mechanism may not be simple diffusion but by some mechanism more akin to creep in that the transport of metal may be by the movement of dislocations throughout the bulk of the metal which would cause little or no enrichment.

Several metals were cast as single crystals, bi-crystals, and large-grained poly-crystals and then were set aside to see if they would spontaneously grow whiskers. According to the analysis on the effect of micro-residual stress, none would be expected to grow on the single crystals but should on the others. Exp. P–1 showed that only a few grew and that one of the few groups, three whiskers, occurred on a small sliver crystal in a specimen which consisted of a very large crystal of tin and that the whiskers grew near to their interface. Also there was evidence that the sample had been plastically deformed in handling. While these tests are not conclusive for the original purpose, they do reveal an unusual sparseness of growth. This may indicate that the dislocations which form during solidification may not be adequate to provide a proper array of dislocations for the growth mechanism and thus plastic deformation may be a pre-requisite to abundant growth. Growth on a sample consisting of a few grains might be expected to occur near a grain boundary because the larger thermal stresses and the greater diffusivity there would supply energy for the growth and aid the transport of metal to the root.

§ 4. The Structure of Filamentary Crystals

X-ray studies on whiskers grown from the solid metal have shown that a major crystallographic direction is along the fiber axis: Zinc and cadmium ones have their hexagonal *c*-axes in the fiber direction.[25)] Tin has been observed to have the [001] and [111] directions along the axis; the author in Exp. 0–1 found these two orientations and also the [101] and [100] directions, and for a Pb–In alloy [111] (Exp. E10–3c).

It has been postulated by Levy[31)] and by Baker[18)] and reasonably substantiated that the "kink" angles between straight segments of whiskers can be correlated with their probable crystallographic axes. However, Fig. 4, presents a tin whisker which showed no discontinuity of surface texture, cross-section, or direction, although it showed both the [101] and [001] orientations on the X-ray film. More careful study showed that the base had the [101] and the tip the [001] orientation. Only when viewed under polarized light could the transition be detected by the colors. This may be a rather common occurrence because the tin whiskers shown in Fig. 5 show many discontinuities in color when viewed under polarized light at places where no physical discontinuity can be observed. This does not contradict the observations of Levy and of Baker for if a change in direction occurs the angle may be related to the orientations of the adjacent segments.

Three whiskers out of six when subjected to a lateral compression split longitudinally as a reed might when stepped upon. This was interpreted to indicate that the whiskers were either hollow or had some type of a longitudinal imperfection. Later direct examination of cross-sections showed that some were indeed hollow.[32),33)]

The structure of the curled and twisted crystals must be very interesting but no one has studied it. Although not common, a uniform helical whisker as shown in Fig. 6 is sometimes observed.

§ 5. Strength of Filamentary Crystals grown from the Solid

It was noticed that among the whiskers grown from the many metals, that many of each metal had strengths comparable to those measured previously for tin[4)] (except silver for which the growth was too sparse for a determination). More quantitative bend tests on lead, an indium-lead alloy, indium, and tin are presented in Exp. S–1, S–2, S–3, and S–4.

One indium whiskers was very strong: Fig. 7 shows it bent to a strain of 5% in the outer fibers. This is within the range predicted for the theoretical strength for metals by Orowan[34] who states that it seems reasonable for the theoretical shear strength to be between 1/10 and 1/50 of the shear modulus, which corresponds to elastic tensile strains between 7.5 and 1.5%.

The great increase of the strength of filamentary crystals over the strength of larger specimens can not be attributed to just their smallness, because the author and others[13] have handled many which had no appreciable strength. Moreover, Baker[35] has drawn wires down to the thinness of whiskers by the "Taylor Process". These wires did not have unusual strength; therefore, it is presumed that the filamentary crystals exhibit such high strengths because they are perfect[4] or nearly perfect.[36]

Note the catastrophic nature of the failure of the indium whisker shown in Fig. 7b. Severe local plastic deformation occurred suddenly at the two places when the stress was only slightly increased (as can be seen by the slight change in spacing of the probes when compared to Fig. 7a). The sharp bends are probably not fractured because the bottom segment is smoothly curved which indicates that stress is still being transmitted to the next segment.

In Exp. S–5a a successful tensile test was made on a tin whisker 1.5 microns thick. It withstood a tensile stress of 10,600 psi (7.3×10^8 dyne/cm^2) which corresponds to an estimated elastic strain of 0.16% before fracturing. No necking at the fracture could be observed at the magnification of ×500. Another tin whisker broke near to the point of attachment in Exp. S–5b, but it did withstand a stress of 3,500 psi (2.4×10^8 dyne/cm^2).

Some reasons why tensile tests may show lower strength than bending tests are (1) the danger of damage is greater because more handling is needed in tensile tests, (2) the comparatively few tensile tests which have been performed may not have been sufficient to discover unusually strong one, and (3) the possible existence of a "size effect", i.e. the volume of material subjected to high stress is much greater in the tensile test so there is a greater probability of having an imperfection highly stressed. Although the tensile strength of whiskers may be lower than the bending strength, nevertheless it is usually much higher than a large single crystal of the same material.

§ 6. Summary of Experiments

For compression induced growth, ring clamps similar to Fisher's[27] were used. The outer diameter was 1-1/2 in., the inner diameter 7/8 in. and 3/8 in. in thickness. The compression was applied by a 1/4 in. Nat. Fine screw. For high temperature use, all parts were made of stainless steel.

The plated steel was cut into 3/8 in. squares, stacked between 1/4 in. thick backing plates, placed in the clamp and the screw lightly tightened. The thickness of the steel plate was in the range of 0.006 and 0.020 in.. Usually the stack consisted of about eight pieces of varying thickness of plating, from the thinnest flash plating of less than 0.0001 to about 0.002 in.. One side of the laminated stack was filed flat, given a metallographic polish, and then the screw was tightened. Quantitative measurement of the clamping force was not meaningful because the disparities of the plate and plating must cause the stress to be very non-uniform, thus making it impossible to know the local stress at the point where the individual growths occurred. It was common to have some gross extrusion of the plating at the lamina thicker than 0.0005 in., and sometimes local plastic deformation could be seen at some places on the steel plate.

Exp. E9–1

Sample: gold electroplated on stainless steel sheet. Environment: dry hydrogen. Test: 11 days at 250°C—no whiskers, +11 days at 300°C—possibly two very fine short whiskers, +14 days at 325°C—whiskers appeared, +16 days at 325°C—more whiskers appeared. Whisker growths occurred at the interfaces between 0.0001–0.0001, 0.0001–0.0003, and 0.0003–0.0003 in. plating. See Fig. 2.

Exp. E9–2a

Sample: silver electroplated on mild steel. Environment: nitrogen at 5 psi above atmospheric, not very pure because blue oxide formed on the clamp. Test: 48 hrs. at 400°C two whiskers appeared, one straight, 1μ thick $\times 80\mu$ long; the other a segmented 4 piece iral polygon of total length of 100μ, thick-ess 1μ. The spiral polygon was very similar the tin ones grown by Levy.[31] The plating the interface was 0.005 in..

xp. E9–2b

ample: silver electroplated on stainless steel. nvironment: nitrogen. Test: 11 days at 50°C—very short whiskers appeared on the innest lamina which was less than 0.0001 ., +11 days at 550°C—no appreciable ngthening. (suspect sublimation rate is equal their growth rate.)

xp. E9–2c

ample: silver electroplated on mild steel. nvironment: nitrogen. Test: 18 hours at 00°C. Very fine, 0.2μ, short, 5μ, dense rowth appeared on the thickest lamina 0.003 ..

xp. E10–1

ample: lead electroplated <0.0001, 0.0003, .0005, and 0.0008 in. thick on mild steel. nvironment: room temperature and atmo-phere. Test: whiskers appeared in less than ne minute after tightening the clamp. rowths appeared only on the interfaces be-ween the bare steel—0.0001 and 0.0001—.0003 in. plating. Most growths curled and inked, but some were straight.

xp. E10–2a

ample: indium electroplated ≪0.0001, <.0001, and 0.0001 in. thick on mild steel. nvironment: room temperature and air. est: whiskers appeared in about 10 seconds n the interface between the thinnest and ext thinnest plating.

xp. E10–2b

ample: indium hot-dipped on steel, scraped about 0.0001 in. and then remelted. En-ironment: room temperature and air. Test: hiskers appeared in about an hour.

xp. E10–3a

ample: indium-lead alloy, 84% indium by eight, hot-dipped on steel, scraped to about .0001 in. thickness, and remelted. Environ-nent: room temperature and air. Test: hiskers appeared in about one minute.

xp. E10–3b

ample: lead-indium alloy, 64% lead by weight, ot-dipped on steel, scraped to about 0.0001 . thickness, and remelted. Environment: oom temperature and air. Test: whiskers ppeared in several minutes.

Exp. E10–3c

Purpose: Compare the composition of an alloy whisker with that of the metal from which it grew.

Sample: (1) a whiskers grown by pressure induction from indium-lead alloy. See Exp. E10-3a. Approximate size 1μ×1μ×0.3 mm. (2) fine filings from the parent plating, extruded with gum tragacanth into a filament shaped specimen 0.5 mm. dia..

Apparatus: X-ray diffraction Cu K_α 50 kV, 15 ma. beam collimated to 0.5 mm. diameter. Single crystal rotation camera of 60 mm. dia. called " Unicam ".

Test: The diffraction pattern from the whisker rotating about its fiber axis was superimposed upon the same film with that of the filing sample rotating about its axis. Exposure time for the whisker was 90 hrs; the filings 8 hrs. Comparison of the powder line and the layer line spots at about $\theta=45°$ for the (123) line showed the spots and the line superimposed within the accuracy of observation using a strong magnifying glass. The estimated accuracy of the film reading was ±0.03 mm. The values for the change of lattice parameter with composition for indium-lead alloys as measured by Tyzack and Raynor[37] show this accuracy of measurement corresponds to ±0.8 atom % lead. The alloy's composition as measured by chemical analysis was 9.57 atom % lead. From the layer line spacing and the identification of all the single crystal diffraction spots, the axis of the whisker was determined to be the [111] direction using the body-centered tetragonal lattice.

Exp. E10–4

Sample: Bismuth electroplated on steel. Plating was 0.002 in. thick. Environment: Room temperature and air. Test: The sample was inspected at approximately two month intervals. No growth was noticed until 11 months. Profuse growth with many whiskers 100μ long.

Exp. E11–1

Sample: Zinc electroplated on steel. Plating was <0.0001, 0.0003, 0.0005, 0.0014 in. in thickness. Environment: Room temperature and air. Test: The sample was inspected every two days and whiskers were observed after eight days. Most of the growth was on the 0.0001—0.0003 interface and the 0.0003—0.0003 interfaces. No growth on the thicker interfaces at that time. The longest whisker was about 25μ at the eighth day.

Exp. E11-2

Sample: Cadmium electroplated on steel. The plating had a rough appearance with protruding crystals against a finer crystalline background 0.007 in. thick as measured with a micrometer. Environment: Room temperature and air. Test: No growth in the first 6 hrs. At 24 hrs. there were 7 whiskers 4 to 30μ long. At 4 days no additional lengthening of existent whiskers could be seen. There was one additional whisker noted but it could have been missed in previous examinations.

Exp. E11-3

Sample: Terne plate of nominal composition 85% lead and 15% tin (by weight), hot-dipped. 4 lb/single base box and also 1 lb/single base box of nominal thickness 0.00017 and 0.00004 in. respectively. Environment: Room temperature and air. Test: In first day small knobby protrusions appeared which were about 5μ long. After 3 years no whiskers or other growth appeared.

Exp. 0-1 Crystallographic orientation of whiskers (See also Exp. E10-c.)

Samples: Compression-induced tin whiskers, 10 samples from 1 to 2μ thick and longer than 0.5 mm.

Apparatus: X-ray diffraction using a Cu K_α 50 kV, 15 ma. beam collimated to 0.5 mm. diameter. Single crystal rotation camera of 60 mm. dia. called "Unicam." Exposures were from 10 to 24 hrs.

Test: Crystallographic direction of the whisker axes were (1) [100], (2) [100], (3) [101], (4) [100], (5) [001], (6) [100], (7) [101], (8) straight but consists of two crystals, tip segment [001] and base segment [101], (9) [001], and (10) consists of two crystals at a small angle to each other, tip segment [100] and the base segment [101]. Summary: 5 segments [100], 4 segments [101] and 3 segments [001].

Exp. P-1 Spontaneous growth

Zinc, tin, and cadmium samples were cast in bars 1/8 in. dia. and 3 in. long. The casting process was varied so that some samples had fine grain while others had larger grain up to where some consisted of a single crystal. They were stored in plastic boxes and examined after a 4 year period. Because of the danger of destroying growths by handling, only the upper half surface was examined. 25 samples were examined. On a zinc sample of three grains, a cadmium sample of 10 grains, and a tin sample of 2 grains, groups of straight fibers, 4 to 10 per sample, grew close together and they were definitely not stray particles. The most interesting aspect is the small number of growths which appeared on such a large total surface that clearly recognizable as whiskers.

Bending strengths of whiskers

The whiskers were loaded as buckled columns by micromanipulators. The curvature of the bends were measured from microphotographs. The thicknesses were estimated at × 500 magnification by using a scale in the ocular of the microscope. All whiskers were compression-induced growths from plated steel.

Experiment	Material	Thickness (μ) t	Radius (μ) r	Strain (%) $e=t/2r$
S-1a	Pb	1.7	28	3.0
S-1b	Pb	1.7	52	1.6
S-2	Pb-In, 84% In	3.0	50	3.0
S-3a	In	1.8	20	4.5*
S-3b	In	1.8		3.4**
S-3c	In	0.8	8	5.0
S-4	Sn	1.5	190	0.4

* possibly some plastic bending

** bent from an initial curvature of $r_1=45$ to $r_2=25$

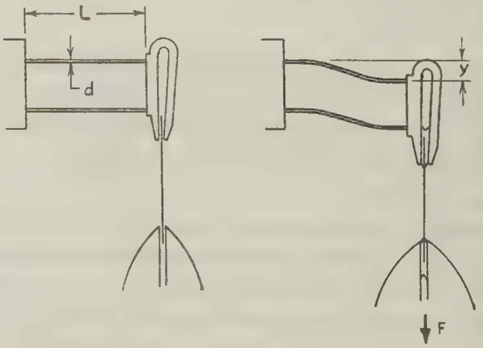

Fig. 8. Force measuring device for tensile tests of fine filaments.

Tensile tests on tin whiskers

A schematic drawing of the tensile testing apparatus is shown in Fig. 8. The force measuring device consists of two parallel ixed-end flexure beams which avoid rotation f the crosshead. The force F to cause the leflection y of this system is calculated to be $=(FL^3/24EI)$ where $I=(\pi d^4/64)$. The length f the weighing beams was 0.50 in.. The eam set No. 1 was made of tungsten wire .003 in. dia. and a more sensitive set, No. 2, vas made of molybdenum wire 0.002 in. dia.

The whisker was detached from its growth ite and inserted in the 10μ-slot in the crosshead. Cellulose cement, greatly thinned with cetone, was applied, it flowed into the slot y capillary attraction and quickly hardened, hereby fastening the whisker. The other nd of the whisker was similarly fastened nto a slot on a bar held by a micro-manipuator. The micro-manipulator pulled the whisker and the deflection of the weighing beams was measured by a scale in the ocular of the microscope.

Attachment by cellulose cement minimizes the stress concentration at the point of attachment because its modulus of elasticity is much lower than that of the metal.

The calculated force-deflection characteristics for the weighing beams were used instead of an experimentally calibrated values because this error was small compared to that in estimating the size and shape of the specimens' cross-section.

Exp. S–5a was performed on a tin whisker from compression induced growth. The measured thickness was 1.5μ and the cross-section was assumed to be square.

	Test	Metal	Thickness (microns)	Length (microns)	Weigh Beam	Deflection of weigh Beam (microns)	Stress (psi)	(10^8 dyne/cm^2)	Fracture location
Exp. S–5a,	*1	Sn	1.5	240	#1	25	10,600±1200	7.3	Center
	2			120	#1	18	8,000±1000	5.5	At attachment
	3			25	#1	25	10,600±1200	7.3	Near 〃
Exp. S–5b,		Sn	1.3	—	#2	34	3,500± 500	2.4	

* All three tests were performed on the same whisker which was progressively shorter after repeated fractures.

§ 7. Conclusions

The success of growing whiskers from a number of solid metals by providing the necessary conditions for their growth leads the author to believe that they can be grown on many other metals and alloys. An opportunity to study the material transport mechanism operative at the root of the whisker is presented by the discovery of alloy whiskers; enrichment (or the absence of enrichment) of one species of metal in the whisker should distinguish between pure diffusion and dislocation movement. The author intends to xploit this opportunity provided by alloy whiskers in future studies.

The author wishes to thank the many sponsors of the Institute for the Study of Metals, niversity of Chicago, for their support of his research and to thank his colleagues here for their helpful interest. Mrs. Betty ealson and Mr. K. Ikeuye greatly helped in he preparation and examination of the specimens. Dr. W. Hu made the X-ray determinations of the whisker orientations.

The author wishes to thank the Fulbright Commission which made it possible for him to prepare this manuscript at the Tokyo Institute of Technology and to thank Profs. Y. Takagi and H. Maniwa, of that Institute, for their aid and advice.

References

1) G. Bischof: Ann. Physik (*Poggendorff*) **60** (1843) 285.
2) H. L. Cobb: *Monthly Review* (American Electroplaters Soc.) **33** (1946) 28, 95.
3) G. Pfefferkorn: Naturwiss. **40, 21** (1953) 551–552.
4) C. Herring, and J. K. Galt: Phys. Rev. **85** (1952) 1060.
5) A. W. Cochardt and H. Wiedersich: Naturwiss. **11** (1955) 342.
6) G. W. Sears, A. Gatti and R. L. Fullman: Acta Metallurgica **2** (1954) 727.
7) W. W. Webb and W. D. Forgeng: J. Appl. Phys. **28** (1957) 1449.
8) W. Piper, and W. L. Roth: Phys. Rev. **92** (1953) 505.

9) G. W. Sears: Acta Metallurgica **1** (1953) 457.

10) J. H. Howey: Phys. Rev. **55** (1939) 578.

11) E. R. Johnson and J. A. Amick: J. Appl. Phys. **25** (1954) 1204.

12) H. W. Kohlschuetter: Z. Electrochem. **38** (1932) 345.

13) G. S. Baker: *Technical Report No. 6*, (University of Illinois Contract DA-11-022-ORD-1212, October, 1954).

14) W. Fink: *Aluminum Company of America*, (New Kensington, Pennsylvania, Private Communication, 1954).

15) Z. Gyulai: Z. Phys. **138** (1954) 317.

16) J. B. Newkirk and G. W. Sears: Bcta Metallurgica **3** (1955) 110.

17) H. D. Keith and J. W. Mitchell: Phil. Mag. **44** (1953) 877.

18) G. Pfefferkorn: Umschau. Wiss. u. Tech. **21** (1954) 654.

19) S. M. Arnold and S. Eloise Koonce: J. Appl. Phys. **27** (1956) 964.

20) J. E. Gordan: Nature **179** (1957) 1270.

21) K. G. Compton, A. Mendizza and S. M. Arnold: Corrosion **7** (1951) 327.

22) H. K. Hardy: Progr. Met. Phys. **6** (1956) 45.

23) F. R. N. Nabarro: *International Conference on Crystal Growth* (Cooperstown, New York, August, 1958) (published by John Wiley & Sons, Inc., New York, Editor: B. W. Roberts).

24) F. C. Frank: Phil. Mag. **44** (1953) 854.

25) S. M. Arnold: Proceedings of the 1954 Electronic Components Symposium, pp. 38-44; also Bell Tel. Syst. Tech. Pub., Monograph 2338, Nov., 1954.

26) E. Schmid and W. Boas: *Plasticity of Crystals* (F. A. Hughes & Co., London, 1950) 195; also *Kristallplastizitaet* (Springer, Berlin, 1935, republished Edward Bros., Ann Arbor, Michigan, 1945) 203. (In German).

27) R. M. Fisher, L. S. Darken and K. G. Carroll: Acta Metallurgica **2** (1954) 368.

28) R. R. Hasiguti: Acta Metallurgica **3** (1955) 200.

29) J. D. Eshelby: Phys. Rev. **91**, No. 3, 755, Aug. 1953.

30) S. M. Arnold: Bell Telephone Record 417, November, 1954).

31) W. P. Levy and Otto F. Kammerer: J. Appl. Phys. **26** (1955) 1182.

32) E. E. Thomas: Acta Metallurgica **4** (1956) 94.

33) P. W. Marshall and A. G. Lee: United States Steel Corp. Applied Research Lab.: Private communication. 1957.

34) E. Orowan: *Dislocations in Metals—Mechanical Properties* (AIME, New York, 1954), 75.

35) G. S. Baker: Physics Dept. University of Illinois: Private Communication. 1954.

36) J. D. Eshelby: J. Appl. Phys. **24** (1953) 176.

37) C. Tyzack and G. V. Raynor: Trans. Faraday Soc. **50** (1954) 675.

JOURNAL OF THE PHYSICAL SOCIETY OF JAPAN, Vol. 15, No. 7, JULY, 1960

Heitler-London Approach to Electrical Conductivity, II. A Proof of the Hopping Motion

By Tatsumi KUROSAWA

Institute for Solid State Physics, University of Tokyo, Tokyo, Japan

(Received March 1, 1960)

A foundation of the Heitler-London approach to electrical conductivity is given, which has been left unproved in the previous paper (J. Phys. Soc. Japan **15** (1960) 802), applying Van Hove's method. The hopping motion of electron is realized under the conditions: large effective mass, strong interaction with lattice and the presence of a potential fluctuation through lattice.

§ 1. Introduction

As discussed in detail in the previous paper[1], the Heitler-London approach is more adequate than the usual Bloch approach to treat the conduction problem in the case that the effective mass of electrons (or holes) is very large and the electron-lattice interaction is also very strong. In that paper, we also discussed some characteristic features expected on the basis of the Heitler-London approach and applied the theory to several examples for which this approach seems to be adequate. However, we considered the motion of the electron in the crystal to be represented by the hopping motion, that is, a sort of random flight motion from an ion to an adjacent ion with certain transition probabilities, without any proof. In other words, we regarded the motion of the electron as characterized by the transport equation

$$\frac{dP_n(t)}{dt}=\sum_{n'}\{W_{nn'}P_{n'}(t)-W_{n'n}P_n(t)\}\,, \qquad (1)$$

where $P_n(t)$ is the probability that the electron is localized around an ion n at a time t, and $W_{n'n}$ is the transition probability of the electron from the ion n to n'.

In this paper, we shall prove this equation under two conditions. The two conditions are as follows. (I) The interaction energy between two states, one of which corresponds to the state where the electron is localized around an ion and another corresponding to that around the other ion, is very small. In other words, the effective mass of the electron is very large. (II) There exists some amount of potential fluctuation from ion to ion due to impurities and other wandering electrons; more exactly speaking, the electron finds no place of the equal potential energy among the nearest neighbouring and the second nearest neighbouring ions. These conditions are rather formal and abstract, and physically more useful but mathematically less exact expression of these conditions may be

$$\hbar\times(\text{transition probability}) < (\text{mean potential fluctuation})\,. \qquad (2)$$

In his two papers of 1955[2] and 1957[3], which we shall refer as A and B in the following, Van Hove has proved that the statistical behaviour of a sufficiently large system started from an appropriate initial state obeys such equations as Eq. (1), if the perturbing Hamiltonian is sufficiently small and has characteristic singularity properties. In our case, however, the perturbing Hamiltonian, which causes the jumping motion of the electron from an ion to another, has extra singularities in addition to those required by Van Hove. These extra singularities work to maintain the wave-like motion of the electron as a usual polaron. If the conditions mentioned before are not satisfied, the motion of the electron becomes more or less wave-like in virtue of the extra singularities. Thus, Eq. (1) is not exact in this case. If the conditions are satisfied, however, we can prove that the extra singularities do not cause any wave-like motion, though this is to be said rather self-evident, because the jumping motion of the electron must be accompanied with emission or absorption of phonons to conserve the energy.

§ 2. A Proof of the Hopping Motion

Let us imagine an electron (or a hole) with large effective mass and interacting strongly with lattice. As discussed in the previous paper, the electron is bound around a certain ion by its deep potential and induced lattice deformation, for a considerably long time. We express such a state as $|n, \{N(n)\}\rangle$. By the notation n we denote the position of the ion which captures the electron, and by $\{N(n)\}$* a set of quantum numbers of the lattice vibration. Further, by use of the notation (n), we understand that the lattice makes a vibration deforming around the ion n. We denote the total Hamiltonian of the system as $H+\lambda V$. The states $|n, N(n)\rangle$'s are the eigenstates of H. So that,

$$H|n, N(n)\rangle=\{E(N)+\Delta V(n)\}|n, N(n)\rangle\ , \qquad (3)$$

where $E(N)$ means the energy of the phonon system:

$$E(N)=\sum_i N_i\hbar\omega_i\ , \qquad (4)$$

and $\Delta V(n)$ is the potential energy of the electron which comes from the fluctuation of the lattice potential.** The second term of the Hamiltonian λV is the perturbation which connects the states with different n's, and λ is a dimensionless parameter characterizing the size of the perturbation. We assume that the perturbation has a finite matrix element only when the ions n and n' are nearest neighbouring.*** Moreover, we assume that

$$\langle n, N(n)\,|\,n', N'(n')\rangle=\delta_{nn'}\cdot\delta_{NN'}\ . \qquad (5)$$

As is well-known, Van Hove2),3)**** has proved that the statisticalbehaviours of a system follow the transport equation of the Markoff type in the limit of $\lambda\rightarrow 0$, if the size of the system is sufficiently large and the perturbation satisfies certain conditions. Therefore, we see that, if these conditions are satisfied in the present case, we have Eq. (1). The perturbation λV which we consider, however, does not satisfy Van Hove's condition (see Section 2 of A) in the following two points.***** (1) When $N\neq N'$, the matrix element $\langle n, N(n)|V|n', N'(n')\rangle$ is a quantity of the order of magnitude $\Omega^{-s/2}$ ($s=1, 2, 3, \cdots$; Ω is the total volume of the system). However, it may be a finite quantity even when $n\neq n'$, if N happens to be equal to N'; the presence of the singularity of the type $\delta_{NN'}$. (2) The matrix element

$$\langle n, N(n)|\,VA_1VA_2V\cdots A_mV\,|n', N'(n')\rangle$$

has a singularity of the type $\delta_{NN'}$ besides the type $\delta_{nn'}\cdot\delta_{NN'}$ in Van Hove's papers. The operators A_k's represent some diagonal operators with respect to $|n, N(n)\rangle$. The physical meaning of these singularities is very important. They work to maintain the wave-like motion of the electron as a polaron. If the effective mass of the electron is small and the electron-lattice interaction is weak, the matrix element $\langle n, N(n)|V|n', N(n')\rangle$ is large and the effect of these singularities is so predominant, that the Heitler-London picture of the current breaks down. If, however, the effective mass is large and the interaction is strong, the effect of the singularities to the motion of the electron will be small as compared with that of the other transition matrix elements. Hence we may be allowed to use Eq. (1) as an approximate equation. We shall, however, assume that the potential energy of the electron is slightly different from ion to ion because of a random distribution of impurity ions and other wandering electrons. Then, we shall see that Eq. (1) is valid so long as the conditions (I) and (II) are satisfied. By following closely to Van Hove's procedure we shall derive Eq. (1) for the hopping motion of the electron in a lattice with a fluctuating potential.

We assign the initial state of the system as:

$$\psi(0)=\sum_n\sum_N c(n, N)\,|\,n, N(n)\rangle\ . \qquad (6)$$

The nature of the coefficients $c(n, N)$ has been discussed in A and B. The time variation of ψ is determined by:

$$\begin{aligned}\psi(t)&=\exp\left[-\frac{i}{\hbar}(H+\lambda V)t\right]\psi(0)\\ &=U(t)\psi(0)=\sum_\mu U_\mu(t)\psi(0)\ ,\end{aligned} \qquad (7)$$

where $U_\mu(t)$ is

---

* Hereafter, we abbreviate $\{N(n)\}$ to $N(n)$.

** Here we take the electron energy in the average lattice potential as the energy standard.

*** This assumption is not essential but introduced for the sake of convenience.

**** Hereafter we shall refer to these papers as A and B.

***** The following discussions are similar to Van Hove's in many points. In such cases, we shall only refer to the relevant places in Van Hove's papers, for the sake of simplicity.

$$U_\mu(t)=\left(-\frac{i\lambda}{\hbar}\right)^\mu\int_{t\geq t_\mu\geq t_{\mu-1}\geq\cdots\geq t_1\geq0}dt_1\,dt_2\cdots dt_\mu\sum_{n_\mu}\cdots\sum_{n_0}$$
$$\times\sum_{N_\mu}\cdots\sum_{N_0}|n_\mu,N_\mu(n_\mu)\rangle\cdot\exp\Big[-\frac{i}{\hbar}\{\mathcal{E}_\mu(t-t_\mu)+\mathcal{E}_{\mu-1}(t_\mu-t_{\mu-1})$$
$$+\cdots+\mathcal{E}_1(t_2-t_1)+\mathcal{E}_0t_1\}\Big]\cdot\langle n_\mu,N_\mu(n_\mu)|V|n_{\mu-1},N_{\mu-1}(n_{\mu-1})\rangle$$
$$\times\cdots\langle n_1,N_1(n_1)|V|n_0,N_0(n_0)\rangle\cdot\langle n_0,N_0(n_0)|\,, \tag{8}$$

nd

$$\mathcal{E}_i=E(N_i)+\Delta V(n_i)\,. \tag{9}$$

First, we can prove that the effect of the extra singularities mentioned before on $U_\mu(t)$ is nly an energy shift of the states $|n,N(n)\rangle$. For this purpose, it is convenient to decompose $U_\mu(t)$ into components each of which corresponds to a definite spatial path $n_0\to n_1\to\cdots\to n_\mu$:

$$U_\mu(t)=\sum_{n_0}\cdots\sum_{n_\mu}U_\mu(t;[n_0,n_1,\cdots,n_\mu])=\sum_j U_\mu(t;[j])\,. \tag{10}$$

$U_\mu(t;[j])$ contains only summations over the states of the lattice vibration N, therefore it esembles Van Hove's $U_\mu(t)$ in its singularity properties* except that $\langle N|V|N'\rangle$ has the ingularity $\delta_{NN'}$ in the present case. Thus, as Van Hove has shown, we can disregard the o-called interlocked pairs.

At first, we consider the case $N_0=N_\mu$. It corresponds to the diagonal transition schemes of A. From the same reason as in A, we can neglect the transition schemes containing higher order processes like $N_0\to N'\to N''\to N'\to N_0$ or $N_0\to N'\to N''\to N_0$, in the limit of $\lambda\to0$. Thus, we know that $U_\mu(t;[j])$ consists of only three kinds of successive transitions: $N_0\to N_0$, $N_0\to N'\to N_0$ and $N_0\to N'\to N'\to N_0$.

The corresponding part of these processes in Eq. (8) is, for $N_0\to N_0$,

$$\langle n_i,N_0(n_i)|V|n_{i-1},N_0(n_{i-1})\rangle\exp\left[-\frac{i}{\hbar}\{\mathcal{E}_i(t_{i+1}-t_i)+\mathcal{E}_{i-1}(t_i-t_{i-1})\}\right], \tag{11}$$

for $N_0\to N'\to N_0$,

$$\sum\nolimits_{N'}\langle n_{i+1},N_0(n_{i+1})|V|n_i,N'(n_i)\rangle\langle n_i,N'(n_i)|V|n_{i-1},N_0(n_{i-1})\rangle$$
$$\times\exp\left[-\frac{i}{\hbar}\{\mathcal{E}_{i+1}(t_{i+2}-t_{i+1})+\mathcal{E}_i(t_{i+1}-t_i)+\mathcal{E}_{i-1}(t_i-t_{i-1})\}\right], \tag{12}$$

and for $N_0\to N'\to N'\to N_0$, a similar but somewhat lengthy formula. If we integrate (11) with respect to the intermediate time t_i, it becomes

$$\frac{\hbar}{i}\frac{1}{(\mathcal{E}_i-\mathcal{E}_{i-1})}\langle n_i,N_0(n_i)|V|n_{i-1},N_0(n_{i-1})\rangle\Big[\exp\left\{-\frac{i}{\hbar}\mathcal{E}_{i-1}(t_{i+1}-t_{i-1})\right\}$$
$$-\exp\left\{-\frac{i}{\hbar}\mathcal{E}_i(t_{i+1}-t_{i-1})\right\}\Big], \tag{11$'$}$$

when $\mathcal{E}_i\neq\mathcal{E}_{i-1}$, and

$$\langle n_i,N_0(n_i)|V|n_{i-1},N_0(n_{i-1})\rangle(t_{i+1}-t_{i-1})\exp\left\{-\frac{i}{\hbar}\mathcal{E}_i(t_{i+1}-t_{i-1})\right\}, \tag{11$''$}$$

when $\mathcal{E}_i=\mathcal{E}_{i-1}$, although this case can not happen because of the condition (II) in §1. Similarly, we can integrate the other two processes with respect to the intermediate times. The results are summarized illustratively in Figs. 1, 2, 3, where only the order of magnitude** and the frequency of time variation are shown, for only these two factors are important to the present discussion. The meaning of these figures may be self-explanatory, for instance, Fig. 1 means that the integration of (11) gives

---

* This fact may be easily seen, if we disregard the fixed quantum numbers $n_0, n_1, \cdots, n_\mu$ and identify our N with Van Hove's α.

** Note that $O(t_{i+1}-t_{i-1})$'s are $O(\lambda^{-2})$.

$$O(1)\times\exp\left\{-\frac{i}{\hbar}\mathcal{E}_{l-1}(t_{l+1}-t_{l-1})\right\}+O(1)\times\exp\left\{-\frac{i}{\hbar}\mathcal{E}_{l}(t_{l+1}-t_{l-1})\right\}\qquad(\mathcal{E}_l\neq\mathcal{E}_{l-1}),$$

and

$$O(t_{l+1}-t_{l-1})\times\exp\left\{-\frac{i}{\hbar}\mathcal{E}_{l}(t_{l+1}-t_{l-1})\right\}\qquad(\mathcal{E}_l=\mathcal{E}_{l-1})$$

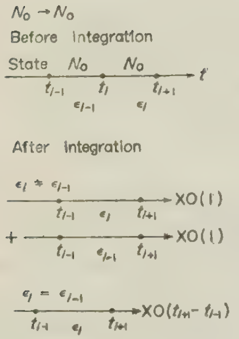
$N_0\to N_0$
Before Integration
State N_0 N_0
t
t_{l-1} t_l t_{l+1}
ϵ_{l-1} ϵ_l
After Integration
$\epsilon_l\neq\epsilon_{l-1}$
t_{l-1} ϵ_l t_{l+1}
×O(1)
+
t_{l-1} ϵ_{l-1} t_{l+1}
×O(1)
$\epsilon_l=\epsilon_{l-1}$
t_{l-1} ϵ_l t_{l+1}
$\times O(t_{l+1}-t_{l-1})$

Fig. 1.

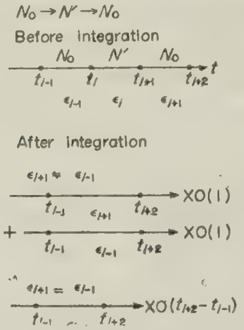
$N_0\to N'\to N_0$
Before Integration
N_0 N' N_0
t
t_{l-1} t_l t_{l+1} t_{l+2}
ϵ_{l-1} ϵ_l ϵ_{l+1}
After Integration
$\epsilon_{l+1}\neq\epsilon_{l-1}$
t_{l-1} ϵ_{l+1} t_{l+2}
×O(1)
+
t_{l-1} ϵ_{l-1} t_{l+2}
×O(1)
$\epsilon_{l+1}=\epsilon_{l-1}$
t_{l-1} t_{l+2}
$\times O(t_{l+2}-t_{l-1})$

Fig. 2.

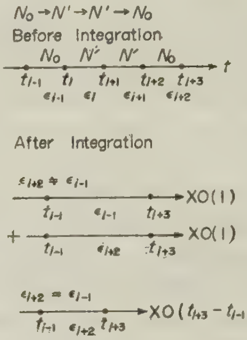
$N_0\to N'\to N'\to N_0$
Before Integration
N_0 N' N' N_0
t
t_{l-1} t_l t_{l+1} t_{l+2} t_{l+3}
ϵ_{l-1} ϵ_l ϵ_{l+1} ϵ_{l+2}
After Integration
$\epsilon_{l+2}\neq\epsilon_{l-1}$
t_{l-1} ϵ_{l-1} t_{l+3}
×O(1)
+
t_{l-1} ϵ_{l+2} t_{l+3}
×O(1)
$\epsilon_{l+2}=\epsilon_{l-1}$
t_{l-1} ϵ_{l+2} t_{l+3}
$\times O(t_{l+3}-t_{l-1})$

Fig. 3.

respectively.

The further integration with respect to the end times of each process can be performed by applying the results of Fig. 1 and by substituting $O(t)$ for the factors like $O(t_{l+1}-t_{l-1})$. This substitution is permissible so long as we are interested in only the order of magnitude, because $O(t_{l+1}-t_{l-1})$'s are slowly varying functions of t_{l+1} and t_{l-1} compared with $\exp\{-i\mathcal{E}_l(t_{l+1}-t_{l-1})/\hbar\}$'s.

Thus, we can examine the contribution to $U_\mu(t;[j])$ with $N_0=N_\mu$ from an arbitrary transition scheme $|n_0, N_0(n_0)\rangle\to|n_1, N_1(n_1)\rangle\to\cdots\to|n_\mu, N_0(n_\mu)\rangle$. The results can be summarized as follows. If there are n_α states with energy $\mathcal{E}_\alpha$, n_β states with energy $\mathcal{E}_\beta$ and so on, among the states with the phonon state N_0 in a transition scheme, this transition scheme contributes to $U_\mu(t;[j])$ the following order of magnitude,

$$\lambda^\mu\left\{O(t^{n_\alpha-1})\exp\left(-\frac{i}{\hbar}\mathcal{E}_\alpha t\right)+O(t^{n_\beta-1})\exp\left(-\frac{i}{\hbar}\mathcal{E}_\beta t\right)+\cdots\right\}. \tag{13}$$

Thus, remembering the condition (II) in §1, we may conclude that the $U_\mu(t)$ with $N_0=N_\mu$ consists of the repetitions of only two types of the processes $|n_0, N_0(n_0)\rangle\to|n', N'(n')\rangle\to|n_0, N_0(n_0)\rangle$ and $|n_0, N_0(n_0)\rangle\to|n', N_0(n')\rangle\to|n_0, N_0(n_0)\rangle$, in the limit of $\lambda\to0$. These processes only contribute to the energy shift of the unperturbed state $|n_0, N_0(n_0)\rangle$.

After the same manipulations as in A (Section 5), we know that $U^W(t)$, the sum over all $U_\mu(t)$'s with $N_0=N_\mu$, is given by a simple formula

$$\langle n, N(n)|U^W(t)|n', N'(n')\rangle=\delta_{nn'}\cdot\delta_{NN'}u^W(t;n,N), \tag{14}$$

and

$$u^W(t;n,N)=\exp\left[-\frac{i}{\hbar}\{E(N)+\Delta V(n)+\lambda^2\Delta(n,N)\}t-\frac{\lambda^2}{\hbar}\Gamma(n,N)t\right]. \tag{15}$$

Here $\lambda^2\Delta(n,N)$ and $\lambda^2\Gamma(n,N)$ are the energy shift and the width of the state $|n, N(n)\rangle$.

Moreover, we have

$$u(t)=U^W(t)+\sum_{\mu=1}^{\infty}\tilde{U}_\mu(t)\ , \tag{16}$$

here

$$\tilde{U}_\mu(t)=\left(-\frac{i\lambda}{\hbar}\right)^\mu\int dt_1\cdots dt_\mu\{U^W(t-t_\mu)VU^W(t_\mu-t_{\mu-1})\cdots VU^W(t_1)\}_{nd}\ . \tag{17}$$

he notation $\{\ \ \}_{nd}$ means that the states connected by V in $\{\ \ \}_{nd}$ are to have mutually fferent N, hence we have Eqs. (16) and (17) without special concern for the extra singular-ies. Thus, the extra singularities make a finite contribution to $U(t)$ only through the above vo types of processes and cause only the energy shift.

Next, let us consider the probability that the electron is found at a time t on an ion n:

$$\begin{aligned}P_n(t)&=\sum_N\langle U(t)\psi(0)|n,N(n)\rangle\langle n,N(n)|U(t)\psi(0)\rangle\\&=\langle U(t)\psi(0)|\,p_{[n]}|U(t)\psi(0)\rangle\ .\end{aligned} \tag{18}$$

the process of reduction, we insert (16) into (18), and the following matrix element appears,

$$\langle\psi(0)|\{U^{W*}(t_1')V^*\cdots V^*U^{W*}(t-t_{\mu'}')\}_{nd}\,p_{[n]}\{U^W(t-t_\mu)V\cdots VU^W(t_1)\}_{nd}|\psi(0)\rangle\ .$$

Vhen we write it explicitly by the $|n,N(n)\rangle$ representation, we see that it contains the ingularity of the type (2):

$$\sum_N\langle n',N'(n')|\{\ \ \}_{nd}|n,N(n)\rangle\langle n,N(n)|\{\ \ \}_{nd}|n'',N'(n'')\rangle\ ,\qquad(n'\neq n'')\ .$$

he physical meaning of this singularity is the interference between the partial wave which omes from $|n',N'(n')\rangle$ to $|n,N(n)\rangle$ and that from $|n'',N'(n'')\rangle$ to $|n,N(n)\rangle$ $(n'\neq n'')$. In rder to investigate this interference we imagine two definite paths $[j]$ and $[j']$, and consider he matrix element

$$\begin{aligned}&\langle\tilde{U}_\mu(t;[j'])\psi(0)|\,p_{[n]}|\tilde{U}_\mu(t;[j])\psi(0)\rangle\\&=\left(\frac{\lambda}{\hbar}\right)^{2\mu}\int_{t\geq t_\mu'\geq\cdots\geq t_1'\geq0,\ t\geq t_\mu\geq\cdots\geq t_1\geq0}dt_1'\cdots dt_\mu'dt_1\cdots dt_\mu\cdot\sum_{N_\mu'}\cdots\sum_{N_0'}\sum_{N_\mu}\cdots\sum_{N_0}\\&\qquad c^*(n_0',N_0')c(n_0,N_0)\{\langle n_0',N_0'(n_0')|V|n_1',N_1'(n_1')\rangle\\&\qquad\times\cdots\langle n_{\mu-1}',N_{\mu-1}'(n_{\mu-1}')|V|n_\mu',N_\mu'(n_\mu')\rangle\}_{nd}\\&\qquad\times\langle n_\mu',N_\mu'(n_\mu')|\,p_{[n]}|n_\mu,N_\mu(n_\mu)\rangle\{\langle n_\mu,N_\mu(n_\mu)|V|n_{\mu-1},N_{\mu-1}(n_{\mu-1})\rangle\\&\qquad\times\cdots\langle n_1,N_1(n_1)|V|n_0,N_0(n_0)\rangle\}_{nd}\\&\qquad\times u^{W*}(t-t_\mu';n_\mu',N_\mu')u^W(t-t_\mu;n_\mu,N_\mu)\\&\qquad\times\cdots u^{W*}(t_1';n_0',N_0')u^W(t_1;n_0,N_0)\ ,\end{aligned} \tag{19}$$

here the summation is taken over all phonon states. This matrix element has a similar tructure as (6–9) in A: $\langle U(t)\varphi|A|U(t)\varphi'\rangle$. In Van Hove's case, the finite contribution comes nly from the following procedure. Take the sum concerning $N_\mu(N_\mu=N_\mu')$ under the con-ition $N_{\mu-1}=N_{\mu-1}'$, and then take the sum concerning $N_{\mu-1}$ $(=N_{\mu-1}')$ under the condition $_{\mu-2}=N_{\mu-2}'$, and so on. We easily see that the situation is the same in the present case. y performing such summation we have the expression:

$$\begin{aligned}&\left(\frac{\lambda}{\hbar}\right)^{2\mu}\int dt_1'\cdots dt_\mu'dt_1\cdots dt_\mu\sum_{N_0}\cdots\sum_{N_\mu}c^*(n_0',N_0)c(n_0,N_0)\\&\quad\times\langle n_\mu',N_\mu(n_\mu')|\,p_{[n]}|n_\mu,N_\mu(n_\mu)\rangle\{\langle n_\mu,N_\mu(n_\mu)|V|n_{\mu-1},N_{\mu-1}(n_{\mu-1})\rangle\\&\quad\times\langle n_{\mu-1}',N_{\mu-1}(n_{\mu-1}')|V|n_\mu',N_\mu(n_\mu')\rangle\cdots\langle n_1,N_1(n_1)|V|n_0,N_0(n_0)\rangle\\&\quad\times\langle n_0',N_0(n_0')|V|n_1',N_1(n_1')\rangle\}_{nd}u^{W*}(t-t_\mu';n_\mu',N_\mu)u^W(t-t_\mu;n_\mu,N_\mu)\\&\quad\times\cdots u^{W*}(t_1';n_0',N_0)u^W(t_1;n_0,N_0)\ .\end{aligned} \tag{20}$$

In order to perform the time integrals, we introduce new variables

$$\tau_j=\frac{1}{2}(t_j+t_j')\,,\qquad \tau_j'=t_j-t_j' \tag{21}$$

and insert (15) into (20). After a simple calculation we reduce the time dependent part of (20) to a product of the following factors:

$$\begin{aligned}&\exp\Big[-\frac{i}{\hbar}\{(V_j'+\lambda^2\varDelta_j')-(V_j+\lambda^2\varDelta_j)-(V_{j-1}'+\lambda^2\varDelta_{j-1}')+(V_{j-1}+\lambda^2\varDelta_{j-1})\}\tau_j\\&\qquad+\frac{\lambda^2}{\hbar}\{(\varGamma_j+\varGamma_j')-(\varGamma_{j-1}+\varGamma_{j-1}')\}\tau_j\Big]\\&\times\exp\Big[-\frac{i}{\hbar}\{E(N_{j-1})+(V_{j-1}'+\lambda^2\varDelta_{j-1}'+V_{j-1}+\lambda^2\varDelta_{j-1})/2\}\tau_j'\\&\qquad+\frac{i}{\hbar}\{E(N_j)+(V_j'+\lambda^2\varDelta_j'+V_j+\lambda^2\varDelta_j)/2\}\tau_j'\\&\qquad+\frac{\lambda^2}{\hbar}\{(\varGamma_j-\varGamma_j')/2-(\varGamma_{j-1}-\varGamma_{j-1}')/2\}\tau_j'\Big]\,,\qquad (j=1,2,\cdots,\mu)\end{aligned} \tag{22}$$

where $V_j=\varDelta V(n_j)$ and $\varDelta_j=\varDelta(n_j, N_j)$. According to Van Hove, we perform the integrations concerning τ_j'. When the path $[j]$ is identical to the path $[j']$, each n_j is equal to n_j' and we have in the limit $\lambda\to 0$:

$$2\pi\exp\left\{\frac{2\lambda^2}{\hbar}(\varGamma_j-\varGamma_{j-1})\tau_j\right\}\cdot\delta(E(N_{j-1})+\varDelta V(n_{j-1})-E(N_j)-\varDelta V(n_j))\,.$$

If we perform the integration with respect to τ_j's, we obtain the result of the order of magnitude $\lambda^{2\mu}\times O(t^\mu)=O(1)$. On the other hand, when the path $[j]$ is different from the path $[j']$, there appears at least one factor of the following type:

$$\exp\left\{-\frac{i}{\hbar}(\varDelta V(n_j)-\varDelta V(n_j'))(\tau_{j+1}-\tau_j)\right\}\,,\qquad \varDelta V(n_j)\neq\varDelta V(n_j')\,.$$

Thus, we see that the matrix element,

$$\langle\tilde{U}_\mu(t;\,[j'])\psi(0)|p_{[n]}|\tilde{U}_\mu(t;\,[j])\psi(0)\rangle\qquad([j]\neq[j'])\,,$$

has the order of magnitude of $\leq\lambda^{2\mu}\times O(t^{\mu-1})=O(\lambda^2)$. By a similar argument, we see that the matrix element,

$$\langle\tilde{U}_{\mu'}(t;\,[j'])\psi(0)|p_{[n]}|\tilde{U}_\mu(t;\,[j])\psi(0)\rangle\qquad(\mu'\neq\mu)\,,$$

has the order of magnitude of $\leq O(\lambda^{|\mu'-\mu|})$. Therefore, we find that the interference between the different paths does not contribute in the limit of $\lambda\to 0$. Thus, the extra singularities have no effect, and we can conclude that the time evolution of $P_n(t)$ follows the transport equation (1).

Thus the Eq. (1) is derived under the condition $\lambda\to 0$. Although the neglected higher order terms with respect to λ are very complicated and have not a simple physical meaning, by examining them we may imagine that a rough condition for the hopping motion will be given by (2).

References

1) T. Kurosawa and J. Yamashita: J. Phys. Soc. Japan **15** (1960) 802.
2) L. Van Hove: Physica **21** (1955) 517.
3) L. Van Hove: Physica **23** (1957) 441.

JOURNAL OF THE PHYSICAL SOCIETY OF JAPAN, Vol. 15, No. 7, JULY, 1960

Exchange Interaction and Cubic Crystal Field Splitting Parameter of Fe^{3+} in Spinel Structure

By Yoshikazu SUGIURA

Electrotechnical Laboratory, Nagata-cho, Tokyo, Japan

(Received March 5, 1960)

The line widths of paramagnetic resonance absorption of Fe^{3+} ions in $MgAl_2O_4$ and $ZnAl_2O_4$ polycrystals and of Mn^{2+} ions in $ZnAl_2O_4$, having the same spinel crystal structure as ferrite, are measured as a function of concentration.

The cubic crystal field splitting parameters a of Fe^{3+} ion at A- and B-sites are determined from the line widths extrapolated to zero concentration: $a_A=1.0\times10^{-2}\,\mathrm{cm}^{-1}$ and $a_B=3.1\times10^{-2}\,\mathrm{cm}^{-1}$. $a_B/a_A=3.1$.

On the other hand, the magnitudes of exchange integral between Fe^{3+} ions in A- and B-sites or in B- and B-sites are estimated from the decrease of line width due to exchange narrowing as the concentration increases, namely, $J_{AB}/g\beta=1.32\times10^5$ Oe and $J_{BB}/g\beta=1.90\times10^3$ Oe. The Curie temperatures obtained from the exchange integral are in agreement with the Curie temperatures of Mg-ferrite and Zn-ferrite measured experimentally.

§1. Introduction

Since the mechanism of magnetization in ferrites was cleared by Néel[1] and was called "Ferrimagnetism", the development on basic understanding of ferrite has been very great.

Ferrites are oxides constructed with divalent ions (Mn^{2+}, Fe^{2+}, Ni^{2+} and Co^{2+} etc.) and trivalent iron ions. The crystal structure is similar to that of $MgAl_2O_4$ and hence is called "Spinel" structure. A unit cell is constructed of 8 A-sites (metal ions surrounded by 4 oxygen ions forming a regular tetrahedron) and 16 B-sites (metal ions surrounded by 6 oxygen ions forming a regular octahedron). The total number of oxygen ions in the unit cell is 32.

It is well known that, in ferrimagnetic crystals, the magnetic ions in A- and B-sites have a strong tendency to have their spin oriented antiparallel to each other, and the interactions between magnetic ions in A- and A-sites or in B- and A-sites are weak, so the total magnetization is given by the difference of magnetization between ions in A-sites and B-sites. The magnitudes of such exchange interaction are estimated from the Curie temperatures and the curves of magnetization *vs* temperature.

On the other hand, it is very interesting to see what the origin of magnetic anisotropy in ferrites are. It is suggested by Yoshida and Tachiki[2], using one-ion model, that the magnetic anisotropy of Ni- and Mn-ferrites arises from the anisotropy of the crystalline field acting on Fe^{3+} ion. They estimate the cubic crystal field splitting parameter a in the cubic term of the ground-state spin Hamiltonian, $a/6x(S_x^4+S_y^4+S_z^4)$, at A- and B-sites, respectively, by analyzing the experimental anisotropy constant *vs* temperature in Mn-ferrite

In order to examine the validity of the theory, it is needed to measure directly the values and signs of cubic crystal splitting parameter of Fe^{3+} ion in A- and B-sites of ferrite.

The values and signs of a were estimated by Rado *et al*[3] and Kriessman *et al*[4] by analyzing the magnetic anisotropy of Mg-ferrite, where the population of Fe^{3+} ions in A- and B-sites depended on the initial temperature whence the samples were cooled rapidly to room temperature, and the magnetic anisotropy varied with the population.

Watanabe[5] calculated a of Mn^{2+} ion and Fe^{3+} ion in nearly cubic crystalline field by the higher-order perturbation method. From his result the sign of a is concluded to be always positive in both sites, but this conclusion is in conflict with the negative sign of a obtained in Mg-ferrite by Rado *et al.*

In relation to this problem, Geschwind[6] determined the values and signs of a in Fe^{3+} ion surrounded by oxygen ions forming octahedron and tetrahedron in yttrium gallium garnet, $3Y_2O_3\cdot5Ga_2O_3$, having a crystal struc ture different from ferrite, and showed that the signs of a in both sites are positive and $a_{oct.}/a_{tet.}=3.0$.

Our purposes are to show how the line widths of paramagnetic resonance absorption of Fe^{3+} and Mn^{2+} ions in $MgAl_2O_4$ and $ZnAl_2O_4$ polycrystals depend on the concentration and how this behaviour is explained by the dipole-dipole interactions and the exchange narrowing.

The magnitudes of cubic crystal field splitting parameter a of Fe^{3+} ion in A- and B-sites and the values of exchange integral between Fe^{3+} ions in A- and B-sites or in B- and B-sites are also estimated by analyzing the experimental results.

§ 2. Experiment

$MgAl_2O_4$ and $ZnAl_2O_4$ were selected for the material from the following reasons.

They have the crystal structure of spinel type, isomorphous with ferrite. Moreover, in regard to the positions of Fe^{3+} and Mn^{2+} ions it is allowable to take the next assumptions.

$ZnFe_2O_4$ and $ZnAl_2O_4$ are both known to be of normal spinel structure, namely, all the Fe^{3+} and Al^{3+} ions occupy B-sites in these crystals. So it is quite natural to assume that Fe^{3+} ions occupy B-sites in place of Al^{3+} ions in $ZnAl_2O_4$.

On the other hand, Fe^{3+} ions in $MgFe_2O_4$ take either A- or B-site according to the initial temperature where rapid cooling treatment begins, hence it is supposed that they can occupy both of the two sites also in $MgAl_2O_4$.

Thus by observing the behaviour of Fe^{3+} ions in $ZnAl_2O_4$ and $MgAl_2O_4$ we can get information about the interaction between Fe^{3+} ions in B- and B-sites and A- and B-sites. Moreover, it has been revealed during the experiment that for very low concentration, Fe^{3+} ions occupy A-site in $MgAl_2O_4$.

Mn^{2+} ions in $ZnAl_2O_4$ are used for the purpose of investigating the interaction of ions in A- and A-sites.

It should be desirable to use single crystals for such an experiment, but single crystals of $MgAl_2O_4$ prepared by flame fusion technique proved to be unsatisfactory for the present experiment because of the broadness of the resonance line, and single crystals of $ZnAl_2O_4$ could not be obtained at all. So polycrystalline samples were used throughout the experiment.

Al_2O_3, Fe_2O_3, MgO, ZnO and $MnCO_3$, all of chemical pure grade, are used for preparing the sample. Proper amounts of components are mixed in a mill, and after having been pressed into a small circular disc, they are sintered in air at 1200°C. Higher sintering temperature would lead to a production of Fe^{2+} ions.

The X-ray patterns show that $Zn(Al, Fe)_2O_4$ have perfectly spinel structure for the whole range of concentration, but, for $Mg(Al, Fe)_2O_4$, pure spinel structure is only observed when the concentration of Fe^{3+} ions is high (>1%), while for lower concentration an evidence for the existence of a second phase of unknown structure is also found in the patterns.

The measurements of paramagnetic resonance absorption are performed with the ordinary microwave transmission method, using a rectangular resonant cavity of TE_{103} mode, at a frequency of about 24.5 KMc. The magnetic field is modulated with a frequency of about 1 Kc.

As the modulation of magnetic field is used, the result obtained is the differential of the absorption curves. So the width between maximum slope of absorption curve is measured in various samples and it is simply described as line width in the following.

Fig. 1 indicates the variation of line width with the concentration* of $MgFe_2O_4$ in

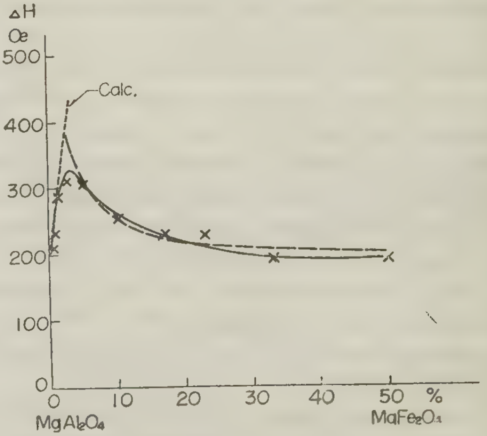

Fig. 1.

---

* The percentage indicated means the atomic percentage of Fe^{3+} measured from the composition ratio before sintering.

gAl$_2$O$_4$. In the range of small concentration f MgFe$_2$O$_4$ the line width increases rapidly, nd beyond about 4% of MgFe$_2$O$_4$ it decreases lown to a value nearly equal to the one exrapolated to pure MgAl$_2$O$_4$. The results will e discussed in the next section, considering he cubic crystal field splitting parameter and he exchange interaction.

In Fig. 2 the variation of line width with he concentration of ZnFe$_2$O$_4$ in ZnAl$_2$O$_4$ is hown. The tendency of the curve is similar o the one shown in Fig. 1, but the value exrapolated to zero concentration is about three imes as large as in Fig. 1 and the composition orresponding to the maximum of line width s about 30% of ZnFe$_2$O$_4$. The difference will e explained with the different crystal field cting on the magnetic ions situated at *A*-ite and *B*-site, as discussed in the next ection.

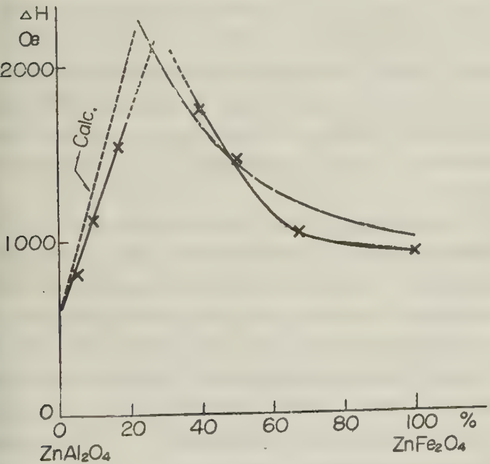

Fig. 2.

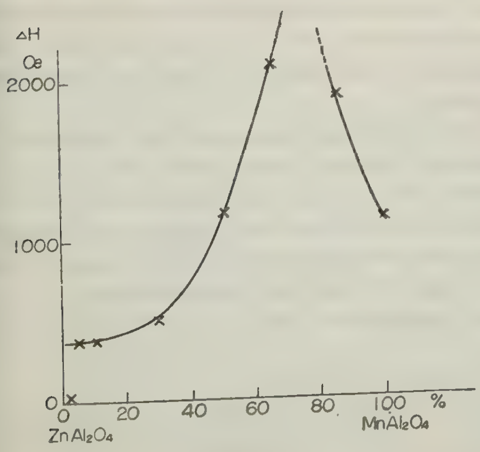

Fig. 3.

Fig. 3 indicates the same behaviour of line width in the case of MnAl$_2$O$_4$ mixed in ZnAl$_2$O$_4$. As Mn^{2+} ions have nuclear moments, hyperfine structure consisting of six lines is observed in the range below 1% of MnAl$_2$O$_4$. The distances between absorption lines are nearly equal, giving a numerical value of 86±2 oersteds, in agreement with the hyperfine splitting of other oxides[7]. The line width of each single line is 23 oersteds at 1% of MnAl$_2$O$_4$. For Mn^{2+} concentration >5%, the lines overlap with one another to give a single broad line, and the overall width of this broad line is the only observable quantity, which is shown in Fig. 3. The result that the apparent width of the line is nearly constant for concentrations less than 30% will be due to the line splitting.

§ 3. Results and Discussions

(A) *Cubic crystal field splitting parameter*

When the concentration of Fe^{3+} ion approaches zero, the line width tends to a finite value in each case of MgAl$_2$O$_4$ and ZnAl$_2$O$_4$, namely 190 oersteds and 580 oersteds, respectively.

It is likely that the line width is due to the crystalline field of Fe^{3+} ions directed at random in polycrystal, because the dipole-dipole interaction does not contribute to line width in very low concentration. Therefore, the difference of the extrapolated width in the two cases seems to show the different crystalline field of Fe^{3+} ion in MgAl$_2$O$_4$ and ZnAl$_2$O$_4$. Considering that Fe^{3+} ions in MgAl$_2$O$_4$ can take the position of *A*-site and Fe^{3+} ion in ZnAl$_2$O$_4$ prefer to occupy *B*-site, it may be concluded that the difference corresponds to the different crystalline field in *A*- and *B*-sites.

It is well known that Mn^{2+} and Fe^{3+} ions have a ground state of $^6S_{5/2}$ and a cubic field splits the sixfold degeneracy of the free ion into a twofold and fourfold degenerate level. Using the cubic crystal field splitting parameter a, the magnetic fields necessary for the transition of five fine structure lines in the very strong field range are given to the first order by[8]

$$M=\frac{1}{2}\longrightarrow-\frac{1}{2}\qquad H=H_0\,,$$

$$M=\pm\frac{3}{2}\longrightarrow\pm\frac{1}{2}\qquad H=H_0\pm\left(\frac{5}{2}\right)pa\,,$$

$$M=\pm\frac{5}{2}\longrightarrow\pm\frac{3}{2}\qquad H=H_0\mp 2pa\ ,$$

where $3a$ is the splitting between the twofold and fourfold levels, $p=1-5\phi$, $\phi=l^2m^2+m^2n^2+n^2l^2$ and l, m, n are the direction cosines of the magnetic field with respect to the cubic axes of the crystals.

In the case of polycrystal the five lines are brought together to be observed as a single line. The second moment of such an absorption line is given by

$$\langle \Delta H^2\rangle=\frac{16}{21}\frac{a^2}{(g\beta)^2}\ ,$$

where the line width of an individual absorption line is neglected in comparison with the splitting. g is the g-factor of the magnetic ion and β is the Bohr magneton.

From this relation the splitting parameter a will be obtained from the second moment of experimental resonance absorption line. As it is very difficult to determine the second moment from the experimental curves directly, it is calculated using its relation with the width of the absorption line, assuming the latter to be gaussian, although the assumption is not a very good approximation.

The magnitude of a in each site are obtained from the line width extrapolated to zero concentration as follows.

$$|a_A|=1.0\times10^{-2}\,\mathrm{cm}^{-1}\ ,$$

$$|a_B|=3.1\times10^{-2}\,\mathrm{cm}^{-1}\ .$$

The ratio a_B/a_A is 3.1, but the sign cannot be estimated.

These values are to be compared with the a-value of Fe^{3+} in MgO[9], surrounded by oxygen ions forming octahedron, namely, $+2.05\times10^{-2}\,\mathrm{cm}^{-1}$, and with the values obtained in yttrium gallium garnet, namely, $+0.616\times10^{-2}\,\mathrm{cm}^{-1}$ and $+1.850\times10^{-2}\,\mathrm{cm}^{-1}$ for Fe^{3+} ions in tetrahedral and octahedral sites, respectively. Although the estimations given here is very rough, the agreement seems to be rather satisfactory, indicating that the assumptions made on the positions of Fe^{3+} ions in the present experiment are appropriate ones.

The ratio of the values of a for A- and B-sites given above is more reliable than the individual a-values, because the difficulty arising from the line shape is cancelled out.

This ratio will be used in the next place to calculate the position of oxygen ions in the crystal according to the method used by Geschwind[6].

Watanabe[5] has shown that a splitting arising from perturbations by excited state involve the cubic crystalline potential, $V=C(x^4+y^4+z^4-3/5\,r^3)$, to even powers only and will first appear as V^2. Consequently, the sign of a should be independent of the sign of V. The constant C appearing in the cubic potential V is $-35q/9d^5$ and $+35q/4d^5$ for tetrahedral and octahedral sites, respectively, where d is the distance from the center of the site to the charges q located at the corners. If $a\propto V^2$, then $a_B/a_A=(9/4)^2\times(d_A/d_B)^{10}$.

In spinels d is given as[10]

$$d_A=a(1/8+\delta)\sqrt{3}\ ,$$

$$d_B=a\sqrt{1/16-1/2\,\delta+3\delta^2}\ ,$$

where $\delta=u-3/8$. Parameter u indicates the positions of the oxygen ions in the spinel structure and is in the neighbourhood of 3/8. If u is exactly 3/8, the oxygen ions from a cubic close-packed array. A value of u greater than this implies a contraction of the oxygen lattice about the octahedrally coordinated metal ions and a corresponding expansion about the tetrahedrally coordinated ones.

Taking $u=0.383$, we can obtain $a_B/a_A=3.06$ almost equal to the experimentally obtained value, 3.1. This value of u is considered to be fairly well defined, as the value of a is very sensitive to a slight change in the u-value, (2.74 for $u=0.382$ and 3.38 for $u=0.384$). Hasting and Corliss[11] determined u by the neutron diffraction as 0.385 in $ZnFe_2O_4$ and 0.381 in $NiFe_2O_4$.

From the agreement between their values and the present value it is concluded that the assumption of $a\propto V^2$ is valid, provided it is allowed to calculate V with the point charge model.

Geschwind[6] obtained $a_{oct.}/a_{tet.}=3.00\pm0.1$ in yttrium gallium garnet, which is of different crystal structure from spinel structure, and the signs of a are always positive. He showed also by reexamination that the negative sign of a reported before was a mistake.

In Mg-ferrite Rado[3] and Kriessman[4] reported the values of a_A and a_B together with their signs. According to their results, the sign is positive at B-site and negative at A-site. This is in conflict with both Watanabe's theory and our conclusion.

We also measured the magnetic anisotropy of Mg-ferrite at 4.2°K, 90°K and room temperature. Diverse results were obtained according to the thermal history of the sample. No definite conclusions about the sign of a_A nor a_B can be given at present.

In the case of 1% Mn^{2+} ions in $ZnAl_2O_4$, the line width of 23 Oe is observed. From this value, a of Mn^{2+} ion at A-site is estimated to be $1.2\times10^{-3}\,cm^{-1}$, in agreement with the values already reported for Mn^{2+} ions in various crystals.

B) *Interaction between magnetic ions*

It is found in Figs. 1 and 2 that, as the concentration of Fe^{3+} ions increases, the line width increases rapidly and when it reaches a certain value, the line width begins to decrease down to a finite value.

This behaviour can be explained by the dipole-dipole interaction and the exchange nteraction as shown in the following.

Dipole interactions are long range forces, so their contribution to the line width is large n the low concentration of magnetic ions. They are described in the simple cubic lattice structure on an isotropic average[12] as

$$\Delta H_d^{M.sl.}=2\sqrt{5.1}\quad g\beta n\sqrt{S(S+1)}\ ,$$

where n is the density of spins per cubic centimeter and S is spin quantum number. The line shape is assumed to be gaussian. The values calculated with the lattice constant of 8.09Å for $MgAl_2O_4$ and $ZnAl_2O_4$ are plotted n Figs. 1 and 2 with the dotted lines. In spite of rough estimation, the curves coincide satisfactorily with experimental results. So he increase of line width in the low-concentration region may be attributed to the dipole-dipole interactions between magnetic ons.

When the exchange interactions are strong between the same kind of magnetic ions, the ine width by dipole interactions are narrowed s explained by Van Vleck[13] and Anderson *t al*[12]. The decrease of line width observed n the present experiment seems to be due to his exchange narrowing. In the following ve shall try to explain this decrease on this point of view and estimate the magnitude of xchange integral.

Now, we assume that the effective exchange nteractions exist between magnetic ions. 'ollowing the method by Anderson and Weiss[12], the line width in simple cubic crystal on an isotropic average is given as

$$\Delta H^{M.sl.}=2\frac{H_d^2}{H_e^{eff}}\ ,$$

$$H_d^2=5.1\ (g\beta n)^2\ S(S+1)\ ,$$

$$H_e^{eff}=\sqrt{2.83}\quad\frac{J^{eff}}{g\beta}\quad\sqrt{S(S+1)}\ ,$$

where the line shape is again assumed to be gaussian. H_d means the field of the dipole interaction, H_e^{eff} means the field of the effective exchange interaction and J^{eff} is an effective exchange integral to be discussed below.

The density of spins n is translated to mole percent of $MgFe_2O_4$ or $ZnFe_2O_4$, x, by

$$n=\frac{16x}{a^3}\ ,$$

where a is the lattice constant.

It is found in this experiment that H_d increases in proportion to x and after the exchange narrowing begins at $H_d\approx H_e^{ff}$, H_d^2/H_e^{ff} decreases as x increases. So H_e^{eff} must be a function of the third or higher power of x.

Now, we assume

$$J^{eff}=\alpha Jx^3\ ,$$

where α is a proportional constant and J is an exchange integral between valence electrons of adjacent magnetic ions. In accordance with the kind of sites occupied by magnetic ions, J means J_{AA}, J_{AB} and J_{BB}, and corresponds to the exchange integral used in pure ferrites.

The values of $\Delta H^{M.sl}$ calculated according to this assumption are also given in Figs. 1 and 2 in broken lines, taking 9.45×10^5 oersteds and 1.36×10^4 oersteds as $\alpha\frac{J}{g\beta}$ for Mg(Al, Fe)$_2$O$_4$ and Zn(Al, Fe)$_2$O$_4$, respectively. In spite of rough assumptions used of the simple cubic crystal, the calculated curves show considerable agreements with the experimental curves.

The meaning of J^{eff} will be considered next and the value of α will be estimated. Then, the Curie temperatures estimated from the J values obtained in such a way shall be compared with the experimental Curie temperatures of Mg- and Zn-ferrites.

The number of pairs between magnetic ions is $n(n/N)^2z$, where n is the number of magnetic ions, N is the total number of sites which can be occupied by the magnetic ions, and z is the number of the nearest neighbours. It is assumed that a magnetic ion occupies a lattice point independently and the probability is n/N. As the energy of exchange interaction per pair is $2JS(S+1)$, the total energy of a magnetic system is given by

$$2JS(S+1)n(n/N)^2z$$

Then, a single lattice point has the energy of $2JS(S+1)(n/N)^3z$ on an average.

In order to compare the case of dilluted magnetic ions with the case of undiluted ions treated by Anderson *et al*, the following concept is introduced. All lattice points are occupied by magnetic ions with quantum number S, and are placed in the effective field of exchange interaction H_e^{eff}, so the energy per one lattice point is $g\beta H_e^{eff}\sqrt{S(S+1)}$. If this energy is assumed to be the same as the energy obtained in the case of diluted magnetic ions, the effective exchange integral is given by J as follows, using H_e^{eff} by Anderson.

$$J^{eff}=\frac{2}{\sqrt{2.83}}zJ\left(\frac{n}{N}\right)^3=\frac{2}{\sqrt{2.83}}zJx^3 .$$

If we set z equal to six for consistency with our previous assumption of simple cubic lattices, α is calculated as 7.15. Using this value of α, $J/g\beta$ are calculated to be 1.32×10^5 and 1.90×10^3 oersteds in $MgAl_2O_4$ and $ZnAl_2O_4$, respectively. These values of J seem to correspond to the exchange integrals between A- and B-sites and between B- and B-sites, respectively.

Using the relation between the Curie temperature and the exchange integral in simple cubic lattices, $k\theta=\frac{2}{3}JzS(S+1)$, the Curie temperature of Mg- and Zn-ferrites can be estimated at 620°K and 9°K from the value of J obtained above.

The Curie temperature of Mg-ferrite was reported as 713°K by Gorter[10] and the Néel point of Zn-ferrite as 9°K by Corliss[14]. In spite of the rough assumption of exchange narrowing, our values show surprising agreements with these obtained by Gorter and Corliss. So the values of exchange integral estimated above are thought to be satisfactory.

Using the same methods, the value of exchange integral of Mn^{2+} ions in A- and A-sites is estimated to be 1.90×10^2 oersteds and the Curie temperature is expected to be 0.9°K in $MnAl_2O_4$.

§4. Summary

The variation of line widths of paramagnetic resonance absorption with the concentration of Fe^{3+} ions in $MgAl_2O_4$ and $ZnAl_2O_4$ are observed and explained by the dipole-dipole and exchange interactions.

The cubic crystal field splitting parameter a of Fe^{3+} ion are estimated to be 1.0×10^{-2} cm^{-1} and 3.1×10^{-2} cm^{-1} at the A- and B-sites, respectively. The ratio a_B/a_A is 3.1 and is explained by the potential due to point charge according to Geschwind, considering u-parameter of oxygen position. The value of $u=0.383$ gives the best fit for the ratio obtained in experiment.

The exchange integral between A- and B-sites and B- and B-sites are obtained. The values are $J_{AB}/g\beta=1.32\times10^5$ Oe and $J_{BB}/g\beta=1.90\times10^3$ Oe, and the Curie temperature of Mg-ferrite and the Nèel point of Zn-ferrite estimated from the values of J are in good agreement with the experimental ones.

On Mn^{2+} ions in $ZnAl_2O_4$ the values of a and $J_{AA}/g\beta$ are obtained to be 1.2×10^{-3} cm^{-1} and 1.90×10^2 Oe. The Curie point of $MnAl_2O_4$ is estimated to be 0.9°K.

The author would like to express his gratitude to Dr. G. M. Hatoyama for his kind encouragement. I am also indebted to Dr. K. Yoshida and T. Mitsuma for the many helpful discussions and Mr. A. Nakamura for the measurement.

References

1) L. Néel: Ann. physique **3** (1948) 137.
2) K. Yoshida and M. Tachiki: Progr. Theor. Phys. **17** (1957) 331.
3) V. J. Folen and G. T. Rado: J. Appl. Phys. **29** (1958) 438.
4) H. S. Belson and C. J. Kriessman: J. Appl. Phys. **30** (1959) 170 s.
5) H. Watanabe: Progr. Theor. Phys **18** (1957) 405.
6) G. Geschwind: Phys. Rev Letters **3** (1959) 207.
7) J. S. Wieringen: Faraday Soc. Dis. **19** (1955) 118.
8) B. Bleaney and D. J. E. Ingram: Proc. Roy. Soc. **A, 205** (1951) 336.
9) W. Low: Phys. Rev. **105** (1957) 792.
10) E. W. Gorter: Philips Research Reports **9** (1954) 295, 403.
11) J. M. Hastings and L. M. Corliss: Rev. Mod. Phys. **25** (1953) 114.
12) P. W. Anderson and P. R. Weiss: Rev. Mod. Phys. **25** (1953) 269.
13) J. H. Van Vleck: Phys. Rev. **74** (1948) 1168.
14) L. M. Corliss and J. M. Hastings: Third Intern. Congr. Cryst. Paris (1954).

JOURNAL OF THE PHYSICAL SOCIETY OF JAPAN, Vol. 15, No. 7, JULY, 1960

Characteristics of Germanium *p-n* Junction with Irregular Structure

By Masami TOMONO

Central Research Laboratory, Hitachi, Ltd.
Kokubunji, Tokyo, Japan

(Received March 9, 1960)

A transistor was made with an imperfect emitter junction having an irregular structure made by applying a very thin indium layer on an *n* type germanium pellet and a comparatively perfect collector junction having regular structure. The current flowing into the imperfect emitter was divided into various components, and the voltage-current characteristics of each component was studied. Among these, a particular attention was paid on the electron current component which flows through the minute area of the *m–n* junction existing at the irregular part of the *p–n* junction. From these studies the phenomena of the voltage-current characteristics of the emitter differing greatly from the Shockly Equation, the abnormally strong current dependency of the current amplification factor of the transistor, and the floating-potential of the emitter are explained.

1. Introduction

Considerable research has been carried out eretofore concerning the electrical properties f the comparatively perfect *p-n* junction made y alloying indium on *n* type germanium. And it is well known that its electrical properties follow the Shockley Equation quite losely(1)(2). However, it is also known that, n the case of an actual *p-n* junction, there re many defects around the edge and a large everse current flows through these area(3). is known from experience that, even when e edges are removed by careful electrolytic ching process(4)(5), a large reverse current ill persists in some cases and thus the elerical properties do not conform with the ockley Equation. This is probably due to regular structure at parts other than the dge of the *p-n* junction. There have been any reports dealing with such irregular structure, but the direct relation between such ructure and the rectifying characteristics has ot been explained very clearly. In order to arify the electrical properties of a *p-n* juncon having such an irregular structure, the thor made a transistor with a very imperct *p-n* junction by alloying a very thin indin layer on the surface of an *n* type geruma- um pellet to serve as the emitter and a perct *p-n* junction by alloying a sufficiently ick layer of indium on the other surface of the pellet to serve as the collector. The forward and reverse characteristics of the transistor were then measured. The current flowing through the imperfect emitter junction was divided into many components in an attempt to examine the phenomenon of the great deviation of the voltage current-characteristics from the Shockley Equation.

§ 2. Method of Experiment

p-n junctions were made by alloying indium layers of $15\,\mu\sim200\,\mu$ in thickness and diameter of approximately 0.8 mm on *n* type germanium having a $2.55\,\Omega$cm resistivity. Thin indium layers of $20\,\mu$ or less were applied on the germanium by vacuum evaporation. A spacer and weight were used in order to prevent spherical coagulation due to surface tension and to insure the uniform alloying of the indium over the prescribed area when the indium layer is thin. The maximum temperature of alloying is 515°C. In the first experiment, after alloying indium on only one surface of the germanium pellet, the indium was amalgamated by the ordinary method using mercury and this amalgam was removed by using nitric acid. The recrystallized layer of *p* type germanium thus exposed was observed with a microscope. On the other hand, the cross section of the germanium pellet was made and polished to study the structure of the *p-n* junction. The relationships between the thickness of the indium layer and the electrical properties of the rectifiers of the *p-n* junctions made in this manner were investigated. Next, in order to investigate the cause and characteristic of the excess current of an imperfect *p-n* junction having a thin indium layer, thansistors of the type shown in Fig. 1 were made with various alloyed indium thickness for the emitter and sufficient indium thickness for the collector.

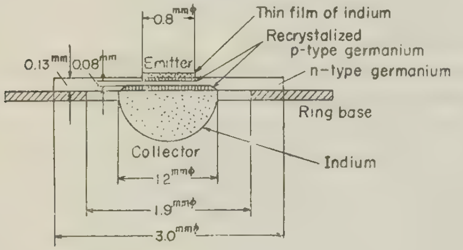

Fig. 1. Dimensions of the transistors used in the experiment.

The measurements were made after removing the imperfect *p-n* junction around the edge of the collector dot by ordinary electolytic etching(4)(5). The forward and reverse currents flowing through the emitter, collector and base electrodes as well as the emitter's floating potential when reverse bias is applied on the collector and the current amplification factor of the transistor were measured.

§ 3. Experimental Results

3.1 *Microscopic observation*

The results of observation of the surface of the recrystalized *p* type germanium layer exposed after the removal of the indium through amalgamation with mercury, are shown in Fig. 2.

It can be seen that the *p* type germanium and *n* type germanium exist in mossaic form when the indium layer is thin. In order to ascertain this finding, a heated tungsten needle was applied along the diameter of the recystallized germanium layer part of a specimen with indium thickness of 20 μ, and the polarity (+) (−) of the thermo-electromotive force was determined. The polarity of the electormotive force would be different depending whether the part with which the needle is in contact is *p* type or *n* type. The results are shown in Fig. 3. From this results, it can be seen that *n* type germanium remained unchanged at the parts of the plaits of figure 2 (A) sample.

Next, Fig. 4. shows the results of observation of the cross section of the *p-n* junction obtained by polishing the pellet at an angle of about 10° to the surface. As shown in Fig. 4 (A) when the thickness of indium is 30 μ, the *p* layer is very irregular and there are some parts where the *p* layer has not been formed. When the indium layer is 60 μ, Fig. 4 (B), the *p* layer becomes more regular, but the *p-n* boundary shape is still irregular. In constrast, when the indium layer is 200 μ, Fig. 4 (C), the *p-n* boundary is formed completely but there are some irregular parts along its edge.

Next, a specimen was made by alloying a thick indium layer on *n* type germanium. When the irregular part around the edge of this specimen's *p* layer was examined, it was found that fine line shaped and dot shaped indium was left in the *p* type germanium layer and that these indium streaks and dots were in direct contact with the *n* type germanium base. One such example is shown in Fig. 5. The size of the remaining indium streaks

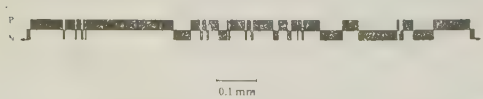

Fig. 3. Distribution of *p*-and *n*-regions on the recrystalized surface
(indium thickness 20μ)

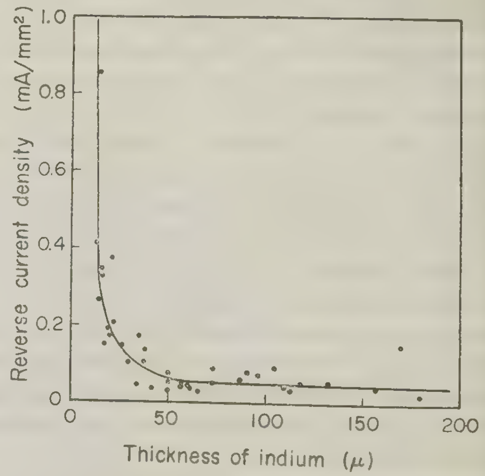

Fig. 6. Reverse current density of alloyed type junctions using indium layers of various thickness
(reverse bias, −6V)

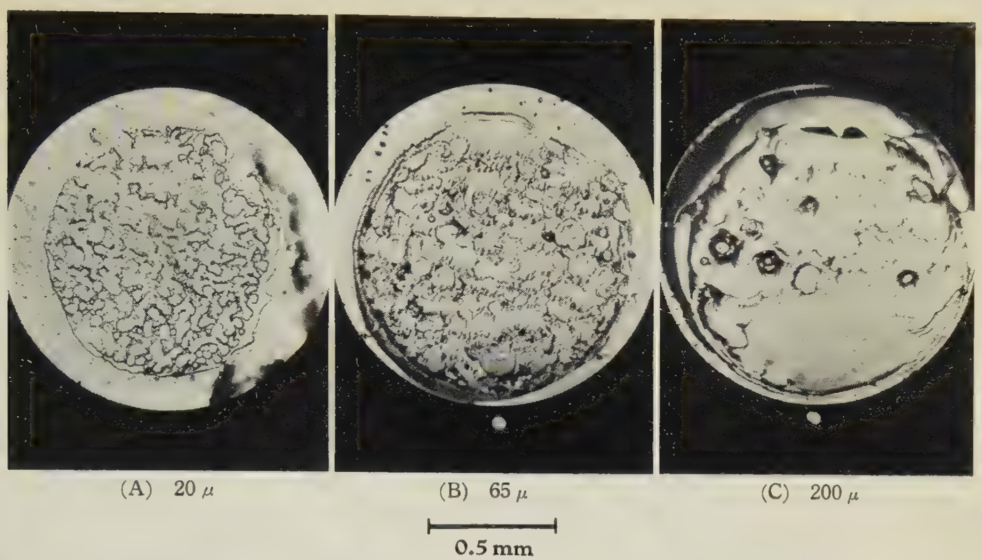

Fig. 2. Microscopic photographs of p type germanium produced by alloying

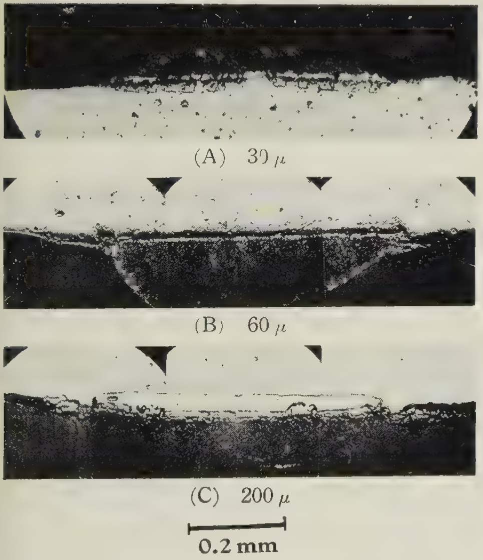

Fig. 4. Cross sections of p–n junctions

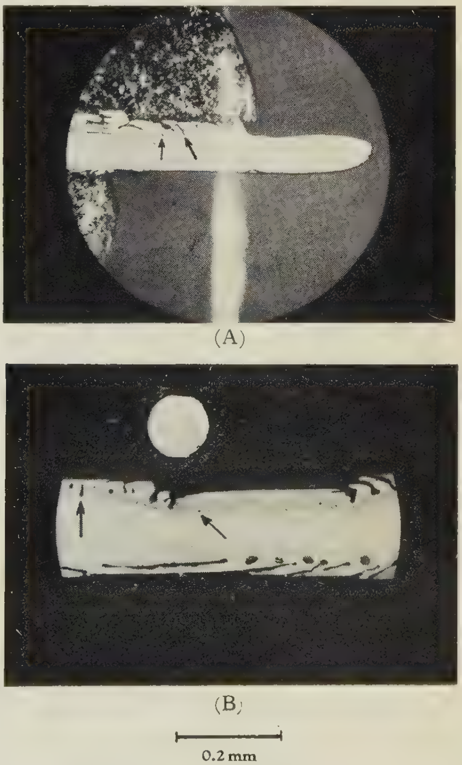

Fig. 5. Minute indium parts (indicated by arrows) left in p type germanium and directly contacting n type germanium

ndicated by the arrow marks in the Figure re about 10 μ, but the tip of the streaks hich are in dierect contact with the n type ermanium base are about 1 μ in diameter. he Figure also shows indium left in dot orm which directly contacts the germaniun ase.

2 *Relation between indium layer thickness and p-n junction characteristics*

Voltage-current characteristics were measu- ed for p-n junctions made by varying the ickness of the indium layer over the range of 15 μ~200 μ. Fig. 6 shows the relation between the current density and the thickness of the indium layer obtained for many specimens by applying a reverse voltage of

-6 V. It can be seen that, when the indium layer thickness becomes less than 30 μ, the reverse current flowing through the junction increases quite rapidly.

3.3 *Forward characteristics of transistor's emitter, collector and base*

The transistors used for these measurements were constructed with collector having the alloyed indium layer of sufficient thickness, and the emitter having the indium layer of various thickness. The voltage-current relations of the transistor's collector and base were measured while the bias of -6 V was applied on the collector and the emitter was variously biased in forward direction.

Table I. Indium layer thickness of emitter of specimens

Specimen	Thickness of indium larger
No. 1	200 μ
No. 2	60
No. 3	20
No. 4	30
No. 5	15

The thicknesses of the indium layers of the specimens used in this experiment are given in Table I. Fig. 7 shows the realtion between the emitter voltage and emitter current.

The relation between voltage V and current I can generally be expressed by the following equation.

$$I=I_0\{\exp(\beta V)-1\} \quad (1)$$

When the value of β in the above equation is obtained directly from the incline of the curve in the 100~150 mV range, it is near 40 Volt^{-1} for the specimens No. 1 and No. 2. This value is near $8/kT$ at normal temperature. Here q is the electron charge, k is Boltzmann's constant and T is the absolute temperature. But, in the cases of No. 4 and No. 5, the value is somewhat smaller. All these values are listed in Table II.

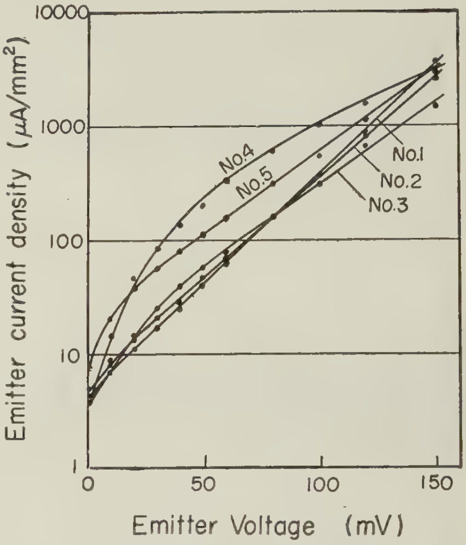

Fig. 7. Relation between emitter voltage and emitter current when emitter bias is positive and collector bias is negative (collector bias, -6V)

It is noted that for the specimens No. 4 and No. 5 the absolute values of the current in the relatively low voltage range (below 0.1 volt) is much larger than those obtained for No. 1, No. 2 and No. 3 The collector currents under the same bias

Table II. Constants for the emitter, collector and base when emitter bias is positive and collector bias is negative (collector bias, -6V)

Constants / Specimen	Currents when $V_E=100$ mV			β		
	emitter	collector	base	emitter	collector	base
No. 1	μA/mm² 317	μA/mm² 306	μA/mm² 14	Volt^{-1} 42.7	Volt^{-1} 42.7	Volt^{-1} 43.1
No. 2	369	316	58	40.8	41.4	34.2
No. 3	312	221	96	36.0	36.0	32.5
No. 4	964	188	783	*——	32.3	*——
No. 5	557	415	186	32.5	44.8	22.4

* β was not determined because V~log I curve had no linear part.

nditions are given in Fig. 8. Comparison Fig. 8 with Fig. 7 shows that, in case of). 1, No. 2 and No. 3, the general trend of e collector current is quite similar to that the emitter current. In the cases of No. and No. 5, the values of β obtained in the nge of 100~150 mV are somewhat smaller an these of the former three. These values e given in Table II. For the case of No. 5 e amount of the current in the low voltage nge is about twice as large as those of No. No. 2, No. 3 and No. 4.

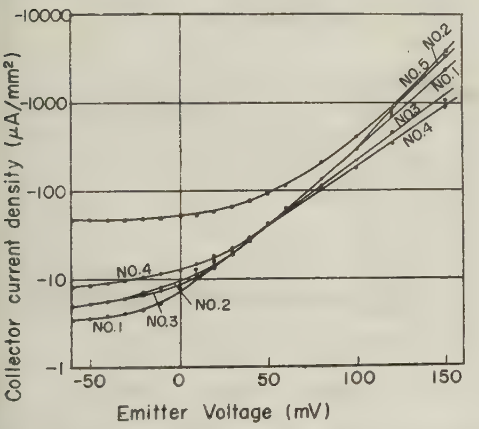

ig. 8. Relation between forward emitter voltage and rollector current when emitter bias is positive and collector bias is negative (collector bias, -6V)

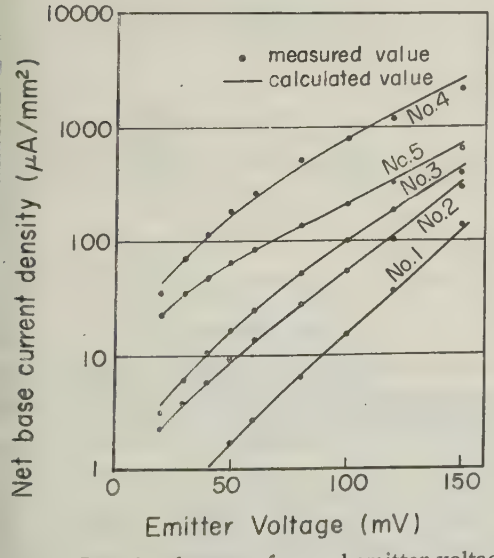

ig. 9. Relation between forward emitter voltage and net base current when emitter bias is positive and collector bias is negative (1) (collector bias, -6V)

Fig. 9 shows the relation between the forward emitter voltage and the net base current I_B+I_{CSO}, where I_B is the base current under the same condition and I_{CSO} is the collector cut-off current. In this case, contrary to the results shown in Fig. 7 and Fig. 8, the absolute value of the current changes greatly from one transistor to another. The base current of No. 1 is very small but those of No. 4 and No. 5 are about 10 times as large. As for the value of β, it is difficult to obtain for No. 4 because there is no linear part in the curve, and in case of No. 5, the value is very small. These results are given in Table II.

Furthermore, in order to examine the base current, the $V_B\sim(I_B+I_{CSO})$ relation is given by linear scale in Fig. 10. (V_E is the emitter voltage.) A distinctive feature is that the low voltage parts of the curves are straight lines.

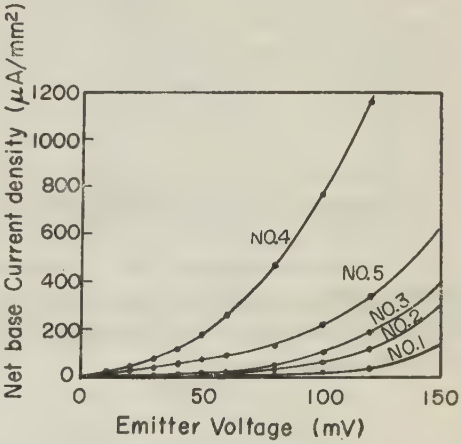

Fig. 10. Relation between forward emitter voltage and net base current when emitter bias is positive and collector bias is negative (2) (collector bias, -6V)

3.4 *Reverse characteristics of emitter and collector*

Fig. 11 shows the voltage-current characteristics obtained when the collector was biased at -6 V and reverse various voltage was applied on the emitter. In the cases of specimens No. 1 and No. 2, the absolute value of the current is small and the current saturates when the voltage becomes high, while, in the case of No. 3, the current shows no saturation characteristics. In cases of No. 4 and No. 5, the absolute value of the current is extremely large and it increases gradually with the increase of the applied voltage.

Fig. 12 shows the relation between the collector voltage and collector current when a negative bias of -6 V was applied on the emitter and the collector was variously biased in the reverse direction. The reverse currents of No. 1, No. 2 and No. 3 are small as in the case of Fig. 11, but the reverse current of No. 4 is 2~3 times larger and that of No. 5 is much greater. In contrast to the aforementioned case of the emitter, all specimens showed current saturation characteristics.

Fig. 13 shows the characteristics when the emitter voltage is low in Fig. 11. In this case, the currents of specimens No. 1, No. 2, No. 3 and No. 4 show saturation characteristics, but the rise of the curve of No. 5 is very slow and shows no saturation characteristics.

Fig. 14 shows the characteristics when the collector voltage of Fig. 12 is low. In comparison to Fig. 13, the absolute value of the current is small but the general tendency is the same.

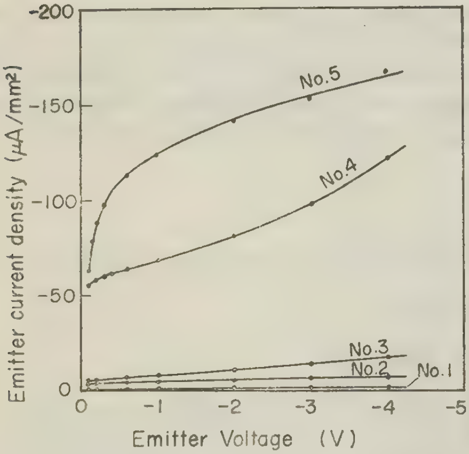

Fig. 11. Reverse characteristics of emitter when collector bias is negative and sufficiently large (1) (collector bias, -6V)

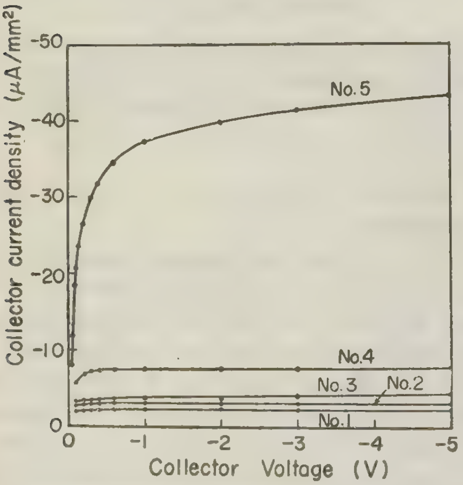

Fig. 12. Reverse characteristics of collector when emitter bias in negative and sufficiently large (1) (collector bias, -6V)

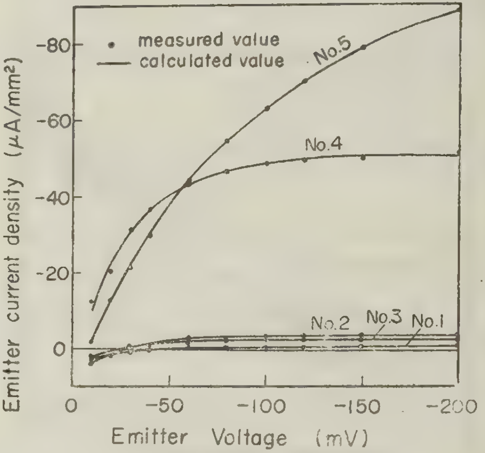

Fig. 13. Reverse characteristics of emitter when collector bias is negative and sufficiently large (2) (collector bias, -6V)

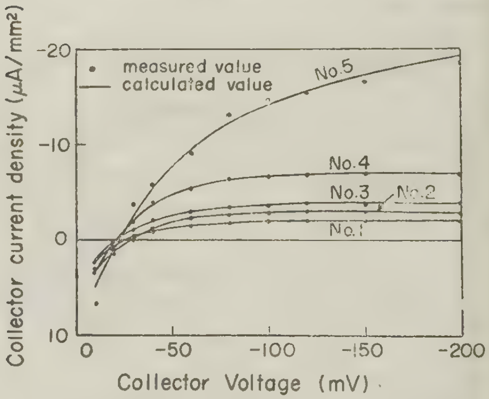

Fig. 14. Reverse characteristics of collector when emitter bias is negative and sufficiently large (2) (collector bias, -6V)

3.5 *Current amplification factor*

Fig. 15 shows the relation between the emitter current and current amplification factor α_{oe} when the collectors of these transistors are biased at -6 V. In case of No. 1 which has a complete emitter, the current mplification factor α_{ce} is practically constant, respective of the emitter current. But, in e cases of No. 4 and No. 5 whose emitters re incomplete, the absolute value of α_{ce} is mall and depends quite heavily upon the mitter current. It has been known that the $_{ce}$ of silicon transistors is highly dependent n the emitter current(7)(8), and the compara-vely smaller dependency of α_{ce} of germa-ium transistors in the range of low emitter urrents has also been known(9). However, uch a strong current dependency of α_{ce} of ermanium transistors was little known eretofore.

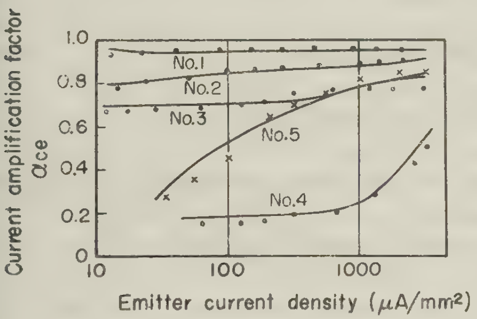

Fig. 15. Relation between emitter current and amplification factor
(●, × measured value, ——computed value)

Table III. Measured value and computed value of floating potential

Speci-men	Measured value of α_{ce}	Calculated V_f value from Eq. (25)	Calculated V_f value from Eq. (20)	Measured V_f value
No. 1	0.928	−66.9mV	−68.3mV	−67.0mV
No. 2	0.719	−32.3	−23.4	−28.1
No. 3	0.646	−26.4	−17.8	−21.2
No. 4	0.139	− 3.81	− 2.41	− 2.86
No. 5	0.171	− 4.77	− 5.19	− 7.43

.6 *Floating potential of emitter*

Table III shows the results obtained by mea uring the floating potentials which were in uced between the emitter and base when he collector was biased at −6 V. The magni udes of the floating potentials are in the ame order as the α_{ce} values in Fig. 15. A oteworthy point is that the floating potantials f No. 4 and No. 5 are very small.

§ 4. Discussion

The results of the foregoing experiments clarified that *p-n* junctions made by alloying a thin indium layer on *n* type germanium have irregular structure whereby the rectifying characteristics and transistor characteristics are abnormal. The relation between the structure and abnomal electrical properties of such *p-n* junctions shall be discussed in the following.

4.1 *Irregular structure of p-n junctions*

As seen in Fig. 2, Fig. 3 and Fig. 4, *p-n* junctions made by alloying a thin layer of indium on germanium have locally well grown and undergrown *p* type germanium parts mosaically on the lower side of the indium layer. This condition is believed to be caused by the different conditions, in which the indium wets the germanium during the initial period of alloying, probably due to the difference in the states of germanium oxide layer existing from the begining on the surface. Such phenomenon will not occur if sufficiently thick indium is alloyed. But, even in this case, a minute portion of indium may be left in the *p* type germanium and this may directly contact the *n* type germanium of the base as shown in Fig. 5. The model of the structure of a *p-n* junction having such an irregular structure is shown in Fig. 16. It may be supposed that such irregular structures will appear in the various forms listed below.

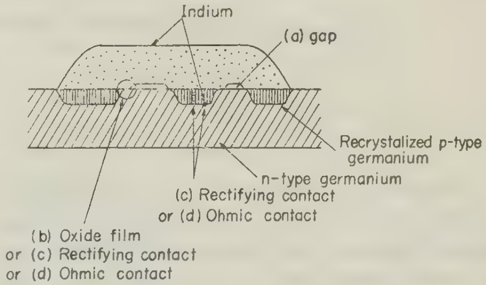

Fig. 16. Model diagram of the cross section of imperfect *p–n* junction

a. There is a gap between the indium and *n* type germanium base.

b. The indium and *n* type germanium are contacting via an insulating oxide film.

c. The indium and *n* type germanium base have a rectifying contact (called *m–n* junction hereafter).

d. The indium and n type germanium base have an ohmic contact.

e. An area having a large surface recombination velocity exists around the edge of any of the above irregular structures.

4.2 *Equations of the voltage-current characteristics of an irregular p-n junction*

By combining all the aforementioned results, the following equations can be given for the electrical characteristics of irregular p-n junctions. In these equations, both the voltage and current of the emitter and collector are expressed, respectively, as positive when they are in the direction going into the transistor from the electrode. In regard to the base electrode, the direction coming from the interior of the transistor towards the base electrode is expressed as positive.

The following equation can be obtained for the emitter current.

$$I_E = I_{Eo}\left\{\exp\left(\frac{qV_E}{kT}\right)-1\right\}+(I_{ESo}+I_{EMo})\left[\exp\left\{\frac{q(V_E-V_B)}{kT}\right\}-1\right]+I'_{EMo}\left[\exp\left\{\frac{q(V_E-V'_B)}{kT}\right\}-1\right]$$
$$-I_{Eo}\left\{\exp\left(\frac{qV_C}{kT}\right)-1\right\}+g_l V_E \qquad (2)$$

The following equation can be obtained for the collector current.

$$-I_C = I_{Eo}\left\{\exp\left(\frac{qV_E}{kT}\right)-1\right\}-I_{Eo}\left\{\exp\left(\frac{qV_C}{kT}\right)-1\right\}-I_{CSo}\left\{\exp\left(\frac{qV_C}{kT}\right)-1\right\} \qquad (3)$$

From equations (2) and (3), the following equation can be derived for the base current.

$$I_B = I_E + I_C = (I_{ESo}+I_{EMo})\left[\exp\left\{\frac{q(V_E-V_B)}{kT}\right\}-1\right]+I'_{EMo}\left[\exp\left\{\frac{q(V_E-V'_B)}{kT}\right\}-1\right]$$
$$+I_{CSo}\left\{\exp\left(\frac{qV_C}{kT}\right)-1\right\}+g_l V_E \qquad (4)$$

where:

$$I_{Eo} = A_E q\frac{D_p p_o}{W} \qquad (5)$$

$$I_{ESo} = A_s q S p_o \qquad (6)$$

$$I_{EMo} = A_M q \mu_n n_o \left\{\frac{q(V_{Mo}-V_E)q\pi n_o}{K}\right\}^{\frac{1}{2}} \exp\left(-\frac{qV_{Mo}}{kT}\right) \qquad (7)$$

$$I'_{EMo} = A_M' q \mu_n n_o \left\{\frac{q(V_{Mo}-V_E)q\pi n_o}{K}\right\}^{\frac{1}{2}} \exp\left(-\frac{qV_{Mo}}{kT}\right) \qquad (8)$$

$$I_{CSo} = A_C q\frac{D_p p_o}{W'} \qquad (9)$$

In the above equations, V_E is the voltage between the emitter and base, V_C is the voltage between the collector and base, and g_l is the conductance corresponding to the emitter's leak current. I_{Eo} in the first term on the right side of equation (2) is the saturation current through the regular parts of p-n junction of the emitter. Equation (5) is the well known Shockley Equation(1). A_E is the area of the emitter junction. I_{ESO} in the second term on the right side of equation (2) is the saturation current due to the surface recombination around the emitter, and equation (6) is well known(1). A_S is the surface area at which the positive holes injected from the emitter recombine. The equation for A_S can be obtained by slightly modifying Webster's treatment(10) of a diode with a p-n junction having a diameter of a.

$$A_s = \pi\sqrt{\frac{WD_p}{2S}}\left(2a+\sqrt{\frac{WD_p}{2S}}\right) \qquad (10)$$

In regard to surface recombination at inperfact p-n junctions, it is necessary to consider not only around the edge but also around inperfect parts inside. Also, if area of high surface recombination velocity exist locally as in 4.1 (e), the effective value of A_S may ecome still larger.

I_{EMo} in the second term of equation (2) is he saturation current of the *m-n* junctions f compartively large area (diameter of larger han 1 μ) explained in 4.1 (c), and equation 7) is given by Schottky(11), where A_M is the otal area of such *m-n* junctions. In the same nanner, I_{EMo}' in the third term of equation 2) is the saturation current of the *m-n* juncions of small area (diameter of about 1 μ or ess) which have been explained in 4.1 (c). A_M' in equation (8) is the total area of such *n-n* junctions. The fourth term on the right ide of equation (2) is the current component lue to the extraction(2)(12) at the collector unction. The fifth term expresses the leak urrent due to the ohmic contact explained n 4.1 (d). I_{CSO} in the third term on the right ide of equation (3) is the collector's saturaion current. In the present case, the colector is considered to be a complete junction nd no excess current components are assumd. A_C in equation (9) is the area of the colector junction. V_B is the voltage drop due o internal resistance r_{bb}' of the germanium ase. V_B' is the voltage drop due to the spreading resistance through a small area. q is the electron charge, D_P is the diffusion oefficient of the positive holes in the *n* type ermanium, and p_o is density of the positive oles which are in the thermal equilibrium n the *n* type germanium. W is the base vidth between the emitter and collector, vhile W' is the effective base width consilered for the collector junction and generaly differs from W. S is the surface recombiation velocity of the positive holes. μ_n is he mobility of the electrons in the *n* type ermanium. n_o is the density of the electrons vhich are in the thermal equilibrium in the *n* type germanium. K is the dielectric consant of germanium, k is Boltzmann's constant, nd T is the absolute temperature. V_{Mo} is he so-called diffusion potential of the *m-n* unction. The irregular structure described n 4.1 (a) presents no problem because no urrent flows. The irregular structure descried in 4.1 (b) has not been taken into consileration in the foregoing treatment, but there s a possibility that reverse current may flow lue to tunnel effect or breakdown when the everse voltage becomes high.

4.3 *Equation for voltage-current characteristics of actual transistors*

For the actual cases undertaken by the author, the equations (2), (3) and (4) can be simplified further. We shall now consider the case where a sufficiently large negative bias is applied on the collector and a positive bias is applied on the emitter. Let us first consider the equation (2). The voltage V_B in the second term on the right side can be expressed as follows

$$V_B=(I_B+I_{CSO})r_{bb'} \tag{11}$$

r_{bb}' is the internal resistance of the transistor. As for the third term on the right side of equation (2), the voltage drop of the junction is comparatively small, while in comparison, the voltage drop due to the spreading resistance in the base germanium through the small *m-n* junctions, r_s, would be large. Therefore, it can be expressed as follows.

$$I'_{EMO}\left[\exp\left\{\frac{q(V_E-V_B')}{k\mathrm{T}}\right\}-1\right]$$
$$=\frac{V_B'}{r_s}\fallingdotseq\frac{V_E}{r_s} \tag{12}$$

The fifth term can be neglected. This is clearly seen by the fact that no leak current component is detected as shown in Fig. 11 and 13. In order to get the expression for the forward characteristics of the emitter, the above results are combined and equation (2) is replaced by the following.

$$I_E=I_{EO}\exp(\beta_E V_E)+(I_{ESo}+I_{EMo})$$
$$[\exp\{\beta_{ESM}(V_E-V_B)\}-1]+\frac{V_E}{r_s} \tag{13}$$

In this case, q/kT in the first term and second term on the right side of equation (2) are replaced by β_E and β_{ESM} respectively.

Next, in considering the collector current, if we assume V_C is negative and sufficiently large, equation (3) can be simplified as follows.

$$-I_c=I_{EO}\exp(\beta_E V_E)+I_{CSO} \tag{14}$$

As for the base current, equation (4) can be simplified as follows.

$$I_B=(I_{ESo}+I_{EMo})[\exp\{\beta_{ESM}(V_E-V_B)-1]$$
$$+\frac{V_E}{r_s}-I_{CSO} \tag{15}$$

When we consider the emitter's reverse characteristics applying a sufficiently negative bias upon the collector, V_B and V_B' can be neglected. In this case equation (2) can be expressed as follows.

$$I_E = I_{Eo}\exp(\beta_E V_E) + (I_{ESo} + I_{EMo} + I'_{EMo})\{\exp(\beta'_{ESM} V_E) - 1\} \quad (16)$$

In this case, q/kT in the second term and third term on the right side of equation (2) are replaced by mean value β'_{ESM}.

Next the collector's reverse characteristics, when a sufficiently large negative bias is applied, can be expressed as follows by simplifying equation (3).

$$-I_C = -I_{Eo}\exp(\beta_C V_C) - I_{CSo}\{\exp(\beta_{CS} V_C) - 1\} \quad (17)$$

q/kT in the second term and third term on the right side of equation (3) are replaced by β_C and β_{CS} respectively.

Current amplification factor α_{ce} can be expressed as follows from equations (13), (14), (15) and (11).

$$\alpha_{ce} = \frac{\partial I_c}{\partial I_E} = \frac{\beta_E I_{Eo}\exp(\beta_E V_E)}{\beta_E I_{Eo}\exp(\beta_E V_E) + \beta_{ESM}(I_{ESo} + I_{EMo})\exp\{\beta_{ESM}(V_E - V_B)\}\left(1 - r_{bb'}\dfrac{\partial I_B}{\partial V_E}\right) + \dfrac{1}{r_s}} \quad (18)$$

where:

$$\frac{\partial I_B}{\partial V_B} = \frac{\beta_{ESM}(I_{ESo} + I_{EMo})\exp\{\beta_{ESM}(V_E - V_B)\} + \dfrac{1}{r_s}}{1 + r_{bb'}\,\beta_{ESM}(I_{ESo} + I_{EMo})\exp\{\beta_{ESM}(V_E - V_B\})} \quad (19)$$

For the floating potential V_f, the value of V_E for $I_E = 0$ in equation (13) is equal to V_f. In this case β_E and β_{ESM} are expressed in the original form as q/kT respectively. This is permissible because β_E and β_{ESM} are almost equal to q/kT in all cases as will be explained later.

$$\exp\left(\frac{qV_f}{kT}\right) = \frac{I_{ESo} + I_{EMo}}{I_{Eo} + I_{ESo} + I_{EMo}} - \frac{V_f}{(I_{Eo} + I_{ESo} + I_{EMo})r_s} \quad (20)$$

4.4 *Analysis of the voltage-current characteristics*

In order to analyze the characteristics for the case where a sufficient large negative bias is applied upon the collector and a suitable positive bias is applied upon the emitter, Fig. 8 and Fig. 9 shall be compared respectively with equation (14) and equation (15). It should be possible to analyze I_E by using the relation $I_E = I_B - I_C$. From equation (14) we obtain the following.

$$-I_c - I_{CSo} = |I_c| - I_{CSo} = I_{Eo}\exp(\beta_E V_E) \quad (14)'$$

The values of $|I_C| - I_{CSo}$ are obtained from the results of Fig. 8 and the measured values of I_{CSo}. Fig. 17 shows the relation between V_E and these values of $|I_C| - I_{CSo}$. Differing from the relation of V_E and I_C in Fig. 8, each curve is nearly a straight line even into the region of negative V_E and their slopes are almost equal, satisfying equation (14)′ quite well.

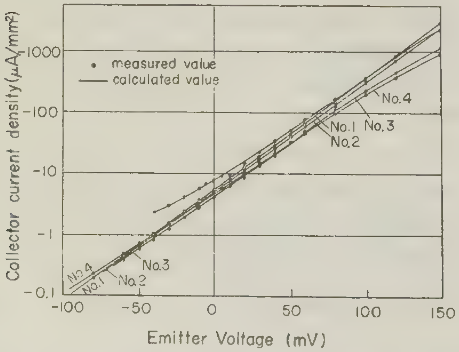

Fig. 17. Relation between V_E and $|I_C| - I_{CSO}$ when collector bias is negative and sufficiently large (collector bias, -6V)

Table IV. Various constants of equation (14)

Specimen	I_{CSO}	I_{EO}	β_E
	μA/mm²	μA/mm²	Volt⁻¹
No. 1	2.96	5.12	41.3
No. 2	4.67	4.94	40.5
No. 3	4.75	4.40	40.2
No. 4	8.02	4.86	36.6
No. 5	44.3	7.02	39.2

The measured values of I_{CSo}, and the I_{Eo} and β_E values obtained from Fig. 17 are shown in Table IV. The I_{Eo} value is reasonable nce it corresponds to the value where W in quation (5) is 0.1~0.07 mm. Since $q/kT=39.19$ olt^{-1} at 23°C, it can be seen that the values f β_E are very close to the theoretical one. $_E$ of No. 3, No. 4 and No. 5 are quite diffeent from those in Table II. Next, we shall onsider Fig. 9 in terms of equation (15). ccording to equation (15), it should be posible to obtain an approximate value of r_S rom the characteristics of the small current egion of the net base current I_B+I_{CSO} which ould be obtained when the collector cut-off urrent is added to the observed base current. he approximate values of r_S obtained from he slopes of the small current region in Fig. 0 are given in Table V.

Table V. Approximate r_s value obtained from minute current part of I_B+I_{CSO}.

Specimen	r_s
No. 1	~
No. 2	10.0 KΩ
No. 3	8.4
No. 4	0.61
No. 5	0.88

Table VI. Various constants of equation (15) determined from experimental results

Specimen	$I_{ESO}+I_{EMO}$	β_{ESM}	r_s	$r_{bb'}$
	μA/mm^2	Volt^{-1}	KΩ	Ω
No. 1	0.225	42.4	714	17.5
No. 2	1.00	39.5	17.5	18.5
No. 3	2.60	36.2	20.0	9.0
No. 4	23.2	37.9	1.11	10.5
No. 5	2.45	38.6	0.987	12.4

Table VI shows the values of the three onstants, $(I_{ESo}+I_{EMO})$, β_{ESM} and r_S determined to best fit equation (15) to the curves in ig. 9. In this case, the values of V_B were btained from equation (11) using the experimental values of $r_{bb'}$. Fig. 9 also shows the esults obtained by computing the relation etween V_B and I_B+I_{CSO} using equation (15) ogether with these constants. As can be een the values thus calculated agree quite ell with the experimental results. It can also be seen that the r_S values in Table 5 are approximately equal to those given in Table VI. It is seen that the saturation current $I_{ESo}+I_{EMO}$ differs to quite a degree among these specimenns.

Next, we shall estimate the value of I_{ESo} using equations (6) and (10) When following values are assumed,

$W=0.008$ cm, $D_p=48.5$ cm^2/sec., $S=100$ cm/sec. and $a=0.056$ cm

we obtain the following from equations (6) and (10)

$$I_{ESo}=0.22\mu A \tag{21}$$

Consequently, the value of $I_{ESo}+I_{EMO}$ of specimen No. 1 in Table 6 can be considered as one in which the contribution from I_{ESO} predominates. In the cases of other specimens, when the indium becomes thinner I_{ESO} can be also supposed to become somewhat larger because of the increase in the effective values of A_S in equation (6) as seen from Fig. 2 and Fig. 4. Although the value of No. 4 is extremely large, it is probably due to the fact that the I_{EMO} value became large owing to formation of a relatively large *m*-*n* junction.

Next, we shall examine an *m*-*n* junction of small area. As explained in regard to Fig. 5 and Fig. 16, the diameter $\varDelta$ of a small area junction may be considered to be about 1 μ. If it is assumed that the existing number of such junctions is n/mm^2, r_S of equation (12) will be as follows.

$$r_S=\frac{M\rho}{2n\varDelta} \tag{22}$$

The current flowing in the base germanium from the emitter towards the base tab does not spread semi-infinitely but spreads only in the comparatively small solid angle which glances the base tab from the emitter. M is the compensating factor for this difference in spreading condition. For the present case, the ratio of this solid angle to the semi-infinitely spreading one is about 0.04. Assuming that the current flow will spread somewhat more than this, we shall approximate the value as $M=10$. When we consider specimens No. 4 and No. 5 as examples, the experimental values of their r_S are about 1000Ω. If $\rho=2.55\Omega$ cm and $\varDelta=1\,\mu$ in equation (22), we get; $n=130$. When the value of A_M' is computed using these values of n and $\varDelta$, and is substituted into equation (8) together with the following figures,

$n_o=6{,}28\times 10^{14}\mathrm{cm}^{-3}$(13) $T=295°K$, $\mu_n=3900\mathrm{cm}^2/\mathrm{sec.\,volt}$ $V_{Mo}=0.05$ volt, $K=16$,

$$\text{we get } I_{EMO}'=178\,\mu\mathrm{A/mm}^2 \tag{23}$$

And if we examine the case where $V_E=20$ mV;

$$V_E-V_B'=2.40\,\mathrm{mV}$$

Therefore

$$\frac{V_E-V_B'}{V_E}=0.120 \tag{24}$$

When V_E becomes larger than 20 mV, the above ratio will become still smaller, showing that the aproximate equation (12) is nearly correct. In the case of No. 4, although the value of $I_{ESo}+I_{EMO}$ is much greater than those of other specimens, the r_S Value is almost equal to that of No. 5. This is believed to be due to the fact that $I_{ESo}+I_{EMO}$ contains a current component which flows through a *m-n* junction of rather large area. In the cases of specimens No. 2 and No. 3, it can be assumed that n is several/mm². In the case of specimen No. 1, it may be considered that, practically there exist no such defect.

Next, the emitter's reverse characteristics when a sufficiently negative bias is applied on the collector and the collector's reverse characteristics when a sufficiently negative bias is applied on the emitter can be analyzed by comparison of Fig. 13 and 14 with equations (16) and (17) respectively. The values given in Table IV were used for β_E of the first term on the right side of equation (16). The value of I_{Eo} was determined for the range where V_E is small, and $(I_{ESo}+I_{EMO}+I_{EMO}')$ and β_{ESM}' were determined for the other range. The various constants obtained in this manner are listed in Table VII.

Table VII. Various constants obtained from the reverse characteristics of the emitter

Specimen	I_{EO}	$I_{ESO}+I_{EMO}$ $+I'_{EMO}$	β'_{ESM}
	μA/mm²	μA/mm²	Volt^{-1}
No. 1	5.12	0.45	42.4
No. 2	6.09	3.52	28.1
No. 3	4.54	2.44	38.4
No. 4	7.86	49.5	36.8
No. 5	10.0	105	9.12

Fig. 13 also shows the results obtained by computing the relation between V_E and I_E by using these constants. The computed values match the experimental results very well. Next, the collector's reverse characteristics can be analyzed by comparison of equation (17) and Fig. 14. The value given in Table 7 was used for the constant I_{Eo} in the first term on the right side of equation (17). The average of β_E and β_{ESM} in equation (13) was used for β_C. The other constants I_{CSO} and β_{CS} in equation (17) can also be determined. The values of these constants are listed in Table VIII.

Table VIII. Various constants obtained from the reverse characteristics of the collector

Specimen	I_{CSO}	β_C	β_{CS}
	μA/mm²	Volt^{-1}	Volt^{-1}
No. 1	2.17	41.9	42.8
No. 2	3.00	40.0	40.0
No. 3	3.95	38.2	36.5
No. 4	7.03	37.3	38.1
No. 5	21.5	38.9	10.7

Fig. 14 shows the results of the voltage-current characteristics computed by using these constants. They agree with the experimental results very well. These results shall now be discussed. In the cases of No. 1, No. 2 and No. 3, the I_{Eo} values in Table VII obtained for the reverse characteristics of emitters are about equal to those in Table IV obtained for the forward characteristics, but in the cases of No. 4 and No. 5, the formers are about 40~50% larger than the latters. This, as will be explained below, is believed to be the results of a condition in which a portion of the positive holes produced near the imperfect junction flow into the emitter instead of flowing as the collector's cut-off current, (I_{CSO} in equation (17)), when the sufficiently large negative bias is applied on the collector and suitable smaller negative bias is applied on the emitter. As the collector junction can be considered to be complete, I_{CSO} in Table VIII which is the saturation current of the collector junction may be mainly a positive hole current through the collector junction owing to the generation of hole-electron pairs at the germanium surface and the ohmic contact etween the base tab and germanium. In he case of specimens No. 4 and No. 5 whose mitter junctions are much more irregular, his value is quite high. As mentioned above ı respect to I_{EO}, this high value is believed ɔ be the result of a condition where the ositive holes appearing near the emitter unction are not all collected into the emitter, ut some of them flow into the collector vhen the sufficiently large negative bias is pplied on the emitter and a suitable smaller egative bias is applied on the collector. uch mutual effect of the emitter and collector as been known heretofore, to a certain exent(10)(11).

The value of I_{EMO}' can be obtained by comaring the values of $I_{ESo}+I_{EMO}+{}_{EMO}'$ in Table II with the value of $I_{ESo}+I_{EMO}$ in Table VI. he values of I_{EMO}' obtained by this method re given in Table 9.

Table IX. I_{EMO}' values

Specimen	I'_{EMO} μA/mm^2
No. 1	0.22
No. 2	2.52
No. 3	−0.16
No. 4	26.3
No. 5	103

$_{EMO}'$ of specimen No. 5 nearly matches the he value 178 μA/mm^2 of equation (23). As or specimen No. 4 I_{EMO}' less matches equaion (23) but when we consider that equation 23) is only an order estimation, the agreenent of this degree is what one can hope for. ince the measurements for Table VI and Table were made on different days, some change ı the surface conditions resulting in the uctuation of I_{ESo} could not be avoided. This probably the reason why I_{EMO}' of No, 3 ecame slightly negative. The same can be aid for No. 2, but the value of 2.52 μA/mm^2 iven for I_{EMO}' can be believed to be correct ithin an order. According to equations (22) nd (8), r_S is inversely proportional to n, the umber of the m-n junctions of small area, ut I_{EMO}' should be proportional to n. It can e seen from Table VI and Table IX that r_S nd I_{EMO}' of specimens No. 1, No. 2, No. 4 nd No. 5 are roughly inversely proportional each other. As it can be assumed that the collector junctions of all specimens are complete, β_C of equation (17) is expected to be near the value of q/kT and in this respect the values in Table VIII are reasonable. β_{ESM}' in Table VII seems smaller than q/kT when $I_{EMO}'/(I_{ESo}+I_{EMO}+I_{EMO}')$ is large, i. e. when there is a large percentage of reverse current passing through the m-n junctions of small area in the second term of the right side of equation (16). The values of $I_{EMO}'/(I_{ESo}+I_{EMO}+I_{EMO}')$ are given in Table X.

Table X. Values of $I'_{EMO}/(I_{ESO}+I_{EMO}+I'_{EMO})$

Specimen	$I'_{EMO}/(I_{ESO}+I_{EMO}+I'_{EMO})$
No. 1	0.49
No. 2	0.72
No. 3	——
No. 4	0.53
No. 5	0.93

In respect to No. 5 for which this ratio is very near 1 in Table X, the β_{ESM}' in Table VII has a very small value of 9.12 Volt^{-1}. In respect to specimen No. 2 for which this ratio is 0.72, the β_{ESM}' value in Table VII is 28.1 Volt^{-1}. These values are much smaller than q/kT. The above results show that the rectifying effect of small area m-n junction is very incomplete and the value of β becomes much smaller than q/kT. It has been known that, if the contact between n type germanium and indium metal is complete, β will be near the value of q/kT(15). Since a rather large m-n junction probably corresponds to this case being discussed, the β_{ESM} of all specimens in Table VI may have approximately q/kT value whereas the small area m-n junctions, possessing imperfect contact, probably have smaller β values as stated before. In respect to β_{CS} in Table VIII, the positive holes generated near the imperfect structure part of the emitter junction can be considered to have a large effect for those specimens having a large I_{CSO} value, as explained previously concerning I_{CSO} in reference to equation (17). Then if we assume that most of such positive holes are drawn to the emitter due to the sufficiently large reverse bias of the emitter and only a small portion flows as the collector's reverse current and that it does not increase much with the increase of the collector's reverse voltage, it can be understood why the β_{cs} value of specimen No. 5 is very small.

Lastly Fig. 11 shows that with the increase of the emitter's reverse voltage, the current of the specimens No. 1 and No. 2 is approximately saturated but that of No. 3 gradually increases despite of the fact that the comparison of the characteristics of the specimens No. 1, No. 2 and No. 3 in Table VII shows little difference. Also in the cases of No. 4 and No. 5, the current increases with the increase of emitter voltage. Such increase of current is believed to be caused, not by the aforementioned surface recombination or *m-n* junctions, but by the irregular structure of the *p-n* junction due to the thinness of the indium layer as indicated in Fig. 4. This reasoning is certified by the fact that the reverse current increases rapidly when the indium layer becomes less than 30 μ in Fig. 6. This condition is believed to occur when the indium and *n* type germanium are contacting via an insulation film of oxide, etc. and the increase in the voltage results in the increase of the current flow through this part due to tunnel effect or local breakdown. On the other hand, because of the absence of such irregular structure of the collector junction, the reverse currents of all specimens are saturated with the increase of collector voltage in Fig. 12.

4.5 *Current amplification factor*

Fig. 15 shows the computed results of the dependency of the current amplification factor, α_{ce}, upon the emitter current by using the constants given in Tables IV and VI for equation (18). The results show that the measured values and computed values agree relatively well. In the cases of such transistors as No. 4 and No. 5 whose emitters are incomplete and r_S values in Table VI are small; α_{ce} has a very small value when the emitter's forward voltage is low and the emitter current is small, because the current flowing through r_S is comparatively larger than the current flowing through a normal *p-n* junction. However, when the emitter voltage becomes comparatively high the positive hole current through the emitter's *p-n* junction increases as an exponential function of the voltage while the current due to r_S is of a linear function and consequently the ratio of the current through r_S to that of the positive holes becomes gradually small and α_{ce} approaches to unity. In the case of specimen No. 1 which has a practically perfect emitter junction, α_{ce} has a constant value.

4.6 *Floating potential*

The floating potential of the emitter, when a sufficiently large reverse bias is applied on the collector, has been known to satisfy the following relation⁽²⁾.

$$V_f=-\frac{kT}{q}\log(1-\alpha_{ce})$$ (25

The value of α_{ce} when $I_B \to 0$ should be used for equation (25). Table III gives the α_{ce} values measured when $I_B=1\ \mu$A and the floating potentials computed from equation (25) by using these values. The table also gives the V_f values derived from equation (20) and the V_f values obtained by measurement. When we compare the V_f obtained by equation (20 and the V_f obtained from equation (25) in the Table, the former is closer to the measured value in the case of specimens No. 4 and No 5 whose r_S are small.

The author wishes to thank Mr. T. Tokuyama and Mr. K. Uehara for their aid in the experiments.

References

1) W. Shockley: *Electrons and Holes in Semiconductors* (Van Nostrand Co., New York, 1950)
2) W. Shockley, M. Sparks and G. K. Teal: Phys. Rev. **83** (1951) 151
3) M. Kikuchi: J. Phys. Soc. Japan **12** (1957) 133
4) H. P. Burcham et al: Transistor Technology Vol. **3** (1958) 175
5) J. S. Hanson: IBM Journal **1** (1959) 279
6) A. S. Rose: RCA Rev. **29** (1958) 423
7) M. Tanenbaum and D. C. Thomas: B.S.T.J. **35** (1956) 1
8) J. L. Mool et al: Proc. Inst. Radio. Eng. **44** (1956) 1174
9) W. M. Webster: Proc. Inst. Radio. Eng. **42** (1954) 914
N. H. Fletcher: Proc. Inst. Radio. Eng. **44** (1956) 1475
10) W. M. Webster: Proc. Inst. Radio. Eng. **43** (1955) 2.7
11) W. Shottky: Zeits f. Phys. **118** (1942) 539
12) J. J. Ebers and J. L. Moll: Proc. Inst. Radio. Eng. **42** (1954) 1761
13) E. M. Conwell: Proc. Inst. Radio. Eng. **45** (1958) 1281
14) M. Kikuchi: J. Phys. Soc. Japan **13** (1958) 350
15) R. F. Schwarz and J. F. Walsh: Proc. Inst. Radio. Eng. **40** (1953) 1715

JOURNAL OF THE PHYSICAL SOCIETY OF JAPAN, Vol. 15, No. 7, JULY, 1960

Note on the Field Dependence of the Mobility in Semiconductors

By Masumi HATTORI
Department of Physics, University of Nagoya
and Hisanao SATO
Research Department, Wireless Division, Matsushita
Electric Industrial Co. Ltd., Kadoma, Osaka

(Received March 19, 1960)

By assuming that the mobility μ can be expanded in powers of the field strength F as $\mu=\mu_0(1-\nu F^2)$, ν is calculated for non-polar and polar semiconductors. The electron-electron interactions are neglected completely and the Boltzmann equation is solved by means of the variation method. It is shown that ν calculated in this way differs significantly from that calculated in the previous paper and in Stratton's particularly at low temperatures. The electric field dependence of the Hall coefficient is also estimated.

1. Introduction

One of the authors investigated the electric
eld dependence of the electron mobility in
-Ge in the preceding paper(1), which we shall
all I in this paper. There was assumed the
oltzmann distribution which was displaced a
onstant magnitude in the direction of the
lectric field in momentum space. But in low
lectron density, the electron-electron interac-
ion may be so weak that the above assump-
ion seems to be wrong. In this paper we
alculate the mobility of electrons in semi-
onductors neglecting the collisions between
lectrons. The Boltzmann equation will be
olved by means of the variation method(2),
hich is shown to be useful at high electric
eld even in the presence of the static magne-
c field. The variational approach to the
igh field problem is also proposed by
dawi(3).

At relatively low field, the mobility μ can
e expanded in powers of the field strength
as follows:

$$\mu=\mu_0(1-\nu F^2). \tag{1}$$

In this paper we evaluate the coefficient ν,
ough the method is applicable to cases of
arbitrary field strength. In §2 the value
ν for n-Ge is compared with that calcula-
d in I. The mobility for non-polar semi-
nductors was investigated by Yamashita(4)
a different way. It is shown in §3 that
e Hall coefficient of n-Ge, where the spheri-
l energy surface is assumed, decreases sli-
ghtly with the electric field strength. The field dependence of the Hall coefficient is found to be sensitive to the scattering mechanism(5). In §4 the mobility in polar semiconductors is computed and compared with the calculation of Stratton(6).

§2. Non-Polar Semiconductors

In I the rate of the change of the electron distribution due to electron-phonon interactions in n-Ge was investigated. Letting the electric field be directed in x axis, we assume here that the electron distribution function $f(\boldsymbol{k})$ in the following from:

$$f(\boldsymbol{k})=f_0(w)+k_x\chi(w), \tag{2}$$

where w is the energy of an electron E divided by k_0T (k_0, the Boltzmann constant). As shown in Appendix A, the Boltzmann equation is separated into two equations, (3) and (4),

$$-w^{3/2}\frac{d}{dw}(e^{-w}g)=e^{-w}w^{3/2+n}c(w), \tag{3}$$

$$-M\frac{d}{dw}(w^{3/2}e^{-w}c)=e^{-w}L_N[g], \tag{4}$$

$$f_0(w)=e^{-w}g(w), \tag{5}$$

$$\chi(w)=-\frac{e\hbar F}{mk_0T\xi q}e^{-w}c(w), \tag{6}$$

where M and $L_N[g]$ are defined by (A11) and (A10) respectively, and n, ξ, and q the constants which may depend on temperature. Changing the sum over $\boldsymbol{k}$ to an integral

$$\sum_k \to A\int w^{1/2}dw,$$

the electric current density j is given by, using (2) and (6),

$$j=\frac{2e^2FA}{3m\xi q}\int_0^\infty w^{3/2}e^{-w}c(w)dw. \tag{7}$$

Let N be the number of electrons per unit volume, and it follows that

$$N=A\int w^{1/2}e^{-w}g(w)dw. \tag{8}$$

We expand $g(w)$ and $c(w)$ in terms of electric field F up to the second order

$$g(w)=g_0\{1+g_1(w)\}, \tag{9}$$

$$c(w)=c_0(w)+c_1(w), \tag{10}$$

where g_0 and c_0 are independent of F, and g_1 and c_1 are propotional to F^2. In the first approximation, $g=g_0$ and $c=c_0$, we have from (8)

$$Ag_0=N/\Gamma(3/2), \tag{11}$$

where $\Gamma(n)$ is the gamma function.

From (3) we get

$$c_0(w)=g_0w^{-n} \tag{12}$$

so that, corresponding to c_0, j_0 is given by, using (7) and (11),

$$j_0=\frac{Ne^2F}{m\xi q}\cdot\frac{\Gamma(5/2-n)}{\Gamma(5/2)q}, \tag{13}$$

and the zero-field mobility μ_0 becomes

$$\mu_0=\frac{e}{m\xi q}\cdot\frac{\Gamma(5/2-n)}{\Gamma(5/2)}, \tag{14}$$

In the next approximation g_1 is obtained by replacing c by c_0 in (4), namely

$$e^{-w}L_N[g_1]=-M\frac{d}{dw}(e^{-w}w^{3/2-n}). \tag{15}$$

As to the properties of L_N, the symmetry relation

$$\int e^{-w}h(w)L_N[g(w)]dw=\int e^{-w}g(w)L_N[h(w)]dw$$

and the inequality

$$\int e^{-w}gL_N[g]dw\geq 0$$

are easily proved, so we can apply the variation method to solve the equation (15). Expanding g_1 in powers of w

$$g_1=\sum_{r=0}^{\infty}b_rw^r, \tag{16}$$

it can be shown that the coefficients b_r ($r\geq 1$) satisfy the infinite set of linear equations(2)

$$\sum_{s=1}^{\infty}l_{rs}b_s=\alpha_r,\quad (r=1,2,\cdots) \tag{17}$$

where

$$l_{rs}=\int e^{-w}w^rL_N[w^s]dw,$$

$$\alpha_r=-M\int w^r\frac{d}{dw}(e^{-w}w^{3/2-n})dw. \tag{18}$$

b_0 is determined by the condition

$$\sum_{\mathbf{k}}e^{-w}g_1(w)=0, \tag{19}$$

which follows from the definition of g_0, (11).

From Eqs. (3), (9), (10) and (12) we have

$$w^{3/2}e^{-w}c_1(w)=-g_0w^{3/2-n}\frac{d}{dw}(e^{-w}g_1) \tag{20}$$

Let j_1 be the current density due to c_1, then we get from (7) and (20)

$$j_1=\frac{Ne^2F}{m\xi q\Gamma(5/2)}\left(\frac{3}{2}-n\right)\left\{\sum_{r=0}^{\infty}b_r\Gamma\left(\frac{3}{2}-n+r\right)\right\}, \tag{21}$$

where the coefficients b_r are not all independent, but is there a relation

$$\sum_{r=0}^{\infty}b_r\Gamma\left(\frac{3}{2}+r\right)=0, \tag{22}$$

which is derived from (19) and (16). Then from (21), (22), and (14) we have the mobility μ:

$$\mu=\mu_0\left[1-n\left\{b_1+(4-n)b_2+\left(\frac{71}{4}-\frac{15}{2}n+n^2\right)b_3+\cdots\right\}\right] \tag{23}$$

We shall evaluate ν in the following approximations.

(i) As the simplest assumption we put

$$g_1=b_0+b_1w. \tag{24}$$

Then from (23)

$$\mu=\mu_0(1-nb_1), \tag{25}$$

where

$$b_1=\alpha_1/l_{11}$$

Accordingly we have

$$\nu=\frac{n\alpha_1}{l_{11}F^2}=\frac{4nq\left[\Gamma\left(\frac{5}{2}\right)\right]^2}{3\Gamma\left(\frac{5}{2}-n\right)l_{11}}\left(\frac{\mu_0}{v_T}\right) \tag{26}$$

where $v_T^2=2k_0T/m$ and ξ is replaced in terms of μ_0.

We write ν_B as the value of ν calculated in I, which is given in Appendix B. Comparing (26) with (B11), we find

$$-\frac{\nu}{\nu_B}=\frac{[\Gamma(5/2)]^2}{\Gamma(5/2-n)\Gamma(5/2+n)}=\frac{9\pi}{32}, \qquad (27)$$

here we put $n=1/2$ and equated μ_0 in (26) that of (B11) as being replaced by the ex- rimental value, although two have the di- erent meanings from each other.

) In the next approximation we assume

$$g_1=b_0+b_1\,w+b_2\,w^2$$

The numerical results are given in Table I the case of $n=1/2$ and $a=0.2$, where ν_1 d ν_2 are the values of approximations (i) d (ii), respectively. For the numerical lues of other parameters, the same values in I are used.

As shown in Table I, at high temperatures e result of (ii) is not so different from that (i), but at low temperatures it is rather fferent, so that it may be said that the ap- oximation (i), and ν_B also, becomes not good relatively low temperatures: the tempera- res at which $u\gg1$.

Table I.

$=(\hbar\omega/k_0T)$	ν_1/ν_2	b_2/b_1
1	0.92	−0.058
2	0.74	−0.094
3	0.51	−0.106

Hall Coefficient for Non-Polar Semiconductors

Let us assume that the uniform magnetic ld H is directed in z axis and the electric ld F is in xy plane. To obtain the Hall efficient in the limit $H\rightarrow0$, it is sufficient to iow the distribution function up to the linear rms in H.

We assume the followings similar to (2)

$$f=f_0(w)+k_x\,\chi_x(w)+k_y\chi_y(w), \qquad (28)$$

$$\chi_x=\chi_x^0+\chi_x^1, \qquad (29)$$

$$\chi_y=\chi_y^0+\chi_y^1,$$

iere $\chi^0{}_{x,y}$ and $\chi^1{}_{x,y}$ are zero and first order H, respectively. Since $f_0(w)$ should not ve the linear term in H, we obtain from e linear terms in the Boltzmann equation

$$\omega_H\,\chi_y^0=-\xi q\,w^n\,\chi_x^1, \qquad (30)$$

$$-\omega_H\,\chi_x^0=-\xi q\,w^n\,\chi_y^1,$$

here $\omega_H=(eH/mc)$ and χ_x^0 or χ_y^0 is given by), in which F is to be replaced by F_x or F_y.

If we define $s(w)$ by the following equations

$$\chi^1{}_x=\left(\frac{e\hbar F_y}{mk_0T\xi q}\right)\left(\frac{\omega_H}{\xi q}\right)e^{-w}s(w), \qquad (31)$$

$$\chi^1{}_y=-\left(\frac{e\hbar F_x}{mk_0T\xi q}\right)\left(\frac{\omega_H}{\xi q}\right)e^{-w}s(w)$$

(30) is reduced to

$$s(w)=w^{-n}\,c(w) \qquad (32)$$

The Hall coefficient R becomes after some elementary calculations

$$|RNec|=g_0\,\Gamma(5/2)\,p_1/p_0^2 \qquad (33)$$

where

$$p_0=\int e^{-w}w^{3/2}c(w)dw,$$

$$p_1=\int e^{-w}w^{3/2-n}c(w)dw, \qquad (34)$$

which become from (12) and (20)

$$p_0=g_0\Gamma\left(\frac{5}{2}-n\right)[1-n\{b_1+(4-n)b_2+\cdots\}], \qquad (35)$$

$$p_1=g_0\Gamma\left(\frac{5}{2}-2n\right)[1-2n\{b_1+(4-2n)b_2+\cdots\}] \qquad (36)$$

As b_1, b_2, $\cdots$ are of order of F^2, we can expand (33) with regard to them:

$$|RNec|=\frac{\Gamma(5/2)\Gamma(5/2-2n)}{[\Gamma(5/2-n)]^2}(1+2n^2b_2+\cdots\cdot) \qquad (37)$$

Comparing (37) with (23), we find that the field dependence of the mobility is determined almost by b_1, while that of the Hall coefficient is determined by b_2, which is far smaller than b_1 as shown in Table I. For n-Ge b_2 is negative so that the Hall coefficient decreases as the field increases, but its magnitude is far less than that of the mobility. Besides, including both optical and acoustical mode scatterings, b_2 becomes very much small in magnitude compared with the case including only acoustical mode scattering. It should be noted, however, that we have assumed the spherical energy surface.

§ 4. Polar Semiconductors

The interaction between a free electron and the optical vibration in ionic crystals was investigated in detail by Fröhlich(7) and the mobility was calculated by means of the variation method by Howarth and Sondheimer(8). Stratton(6) calculated the mobility in strong electric field, assuming the distribution function to be $\exp\{-(\boldsymbol{p}-\boldsymbol{p}_0)^2/2mk_0T_e\}$, where T_e is the electron temperature.

As shown in Appendix *C*, the equation corresponding to (3) and (4) become in this case

$$-w^{3/2}\frac{d}{dw}(e^{-w}g)=e^{-w}L[c], \tag{38}$$

$$-M'\frac{d}{dw}(w^{3/2}e^{-w}c)=e^{-w}L_p[g]. \tag{39}$$

Since L and L_P both satisfy the symmetry relation and the inequality as L_N, we can apply the variation method to solve (38) and (39).

We assume that g and c are expanded in powers of w:

$$g(w)=\sum_{r=0}^{\infty} g_r w^r, \tag{40}$$

$$c(w)=\sum_{r=0}^{\infty} c_r w^r \tag{41}$$

To evaluate ν, it will be sufficient to take first few terms. The more terms consider we, in the stronger field will it be valid.

Substituting (40) and (41) into (38) and (39), multiplying both sides of them by w^r, and integrating over w, we have the two sets of linear equations, from which g_r $(r\geq 0)$ and c_r $(r\geq 0)$ can be determined:

$$\sum_{s=0}^{\infty} d_{rs}c_s=\alpha'_r, \quad (r=0,1,2,\cdots) \tag{42}$$

$$\sum_{s=1}^{\infty} l'_{rs}g_s=\beta_r \quad (r=1,2,\cdots) \tag{43}$$

where

$$d_{rs}=\int w^r L[w^s]e^{-w}dw, \tag{44}$$

$$\alpha'_r=-\int w^{3/2+r}\frac{d}{dw}(e^{-w}g)dw, \tag{45}$$

$$l'_{rs}=\int w^r L_p[w^s]e^{-w}dw, \tag{46}$$

$$\beta_r=-M'\int w^r\frac{d}{dw}(w^{3/2}e^{-w}c)dw. \tag{47}$$

and g_o is related to g_r by the total number N,

$$\sum_{\mathbf{k}} e^{-w}g(w)=N \tag{48}$$

Setting the mobility $\mu=\mu_o[1-\delta_n(\mu_o F/v_T)^2]$, numerical values of δ_n is given in Table 2, where δ_n means that first n terms are taken into account as the variation parameters:

$$g=g_0+\sum_{r=1}^{n} g_r w^r,$$

$$c=\sum_{r=0}^{n-1} c_r w^r.$$

δ_s is the value calculated by Stratton's method which is explained in Appendix *D*, since Eq. (2.24) in his paper is mistaken.

As we can see from Table II, the difference between δ_s and δ_n is significant at low temperatures. Moreover, we must take more parameters at $u=3$, since the difference between δ_2 and δ_3 is serious.

Table II.

$u=(\hbar\omega/k_0T)$	δ_s	δ_2	δ_3
1	0.139	0.179	
2	1.71	0.405	0.49
3	3 14	0.186	0.43

In conclusion, we can estimate in some cases the difference of the two approximations: one assumes that the electron-electron interaction plays the dominant role and the other neglects it completely. In order to analyse the recent experiment on InSb of Kanai(9), we must know the Hall coefficient of polar semiconductors, the calculation of which requires more parameters to be considered than in this section as seen from the discussion of § 3. Moreover, it seems desirable to take the electron-electron interaction into consideration more accurately.

Appendix A

When the static electric field F is directed in x axis, the Boltzmann equation is

$$\frac{eF}{\hbar}\frac{\partial f}{\partial k_x}+\left(\frac{\partial f}{\partial t}\right)_L=0 \tag{A1}$$

where $(\partial f/\partial t)_L$ means the change of the distribution function per unit time due to electron-phonon collisions.

We expand $f(\boldsymbol{k})$ in terms of spherical harmonics and take the first two terms:

$$f=f_0+f_1, \tag{A2}$$

$$f_0=f_0(w), \quad f_1=k_x\chi(w), \tag{A3}$$

where $w=(E/k_0T)$ and k_0 is the Boltzmann constant.

From Eqs. (42), (A17), (A13), and (A19) in I, we can easily show that

$$\begin{aligned}\left(\frac{\partial f_0}{\partial t}\right)_L=\xi\,[\lambda w^{1/2}\Big\{2\left(f_0+\frac{df_0}{dw}\right)\\ +w\left(\frac{df_0}{dw}+\frac{d^2f_0}{dw^2}\right)\Big\}+\eta\{[f_0(w+n)e^u\\ -f_0(w)](w+u)^{1/2}+\Delta(w)[f_0(w-u)\\ -f_0(w)e^u](w-u)^{1/2}\}],\end{aligned} \tag{A4}$$

$$\left(\frac{\partial f_1}{\partial t}\right)_L = -\xi[w^{1/2}+\eta\{(w+u)^{1/2} + \Delta(w)e^u(w-u)^{1/2}\}]k_x\chi(w), \quad \text{(A5)}$$

here ξ is a product of Γ of I and $(k_0T)^{1/2}$ nd therforefore has the inverse dimention of me. Besides we used the following notaons:

$$\lambda=(2ms^2/k_0T), \qquad \Delta(w)=\begin{cases}1; w\geq u\\ 0; w<u\end{cases}$$

$$u=(\hbar\omega/k_0T)$$

$$n_0=(e^u-1)^{-1}$$

$$\eta=n_0au$$

here s is the sound velocity, $\hbar\omega$ is the nergy of an optical phonon and a is a consnt which represents the ratio of magnitudes optical-mode scattering to that of acousticalode scattering. In order to simplify the lculation, we replace (A5) by the approxiate equation

$$\left(\frac{\partial f_1}{\partial t}\right)_L = -\xi q w^n k_x\chi(w). \quad \text{(A5')}$$

n-Ge a being small (~ 0.2), η becomes egligible at low temperatures and we may it $n=1/2$ and $q=1$. At high temperatures $>u$, $n\sim 1/2$ and q becomes a constant also. ut in cases $u\sim 1$, the approximation (A5) ay not be good.

Expanding the drift term in (A1) in terms spherical harmonics we get

$$-w^{3/2}\frac{d}{dw}(e^{-w}g)=e^{-}w^{3/2+n}c(w), \quad \text{(A6)}$$

$$-M\frac{d}{dw}(w^{3/2}e^{-w}c)=e^{-w}L_N[g], \quad \text{(A7)}$$

here

$$f_0(w)=e^{-w}g(w), \quad \text{(A8)}$$

$$\chi(w)=-\left(\frac{e\hbar F}{mk_0T\xi q}\right)e^{-w}L_N[g], \quad \text{(A9)}$$

$$L_N[g]=\lambda w(-2g'+wg'-wg'')$$
$$+\eta[\{g(w)-g(w+u)\sqrt{w(w+u)}$$
$$+\Delta(w)e^u\{g(w)-g(w-u)\}\sqrt{w(w-u)}] \quad \text{(A10)}$$

$$M=(2e^2F^2/3mk_0T\xi^2q) \quad \text{(A11)}$$

ppendix B

Let the electron temperature and the drift locity be $T+\Delta T$ and p_0/m, respectively, and e distribution function is written as

$$f=B\exp\left\{\frac{-|\boldsymbol{p}+\boldsymbol{p}_0|^2}{(mk_0(T+\Delta T)}\right\}. \quad \text{(B1)}$$

Expanding this in terms of p_0 and $(\Delta T/T)=\gamma$, we can obtain⁽¹⁾

$$f_0(w)=B_0e^{-w}\left(1-\frac{3}{2}\gamma+\gamma w\right), \quad \text{(B2)}$$

$$k_x\chi(w)=\frac{p_xp_0}{m}\frac{\partial f_0}{\partial E}=$$
$$-\left(\frac{\hbar k_xp_0}{mk_0T}\right)B_0e^{-w}\left(1-\frac{5}{2}\gamma+\gamma w\right). \quad \text{(B3)}$$

Comparing (B2) with (5) and (B3) with (6), we have

$$g(w)=B_0\left(1-\frac{3}{2}\gamma+\gamma w\right), \quad \text{(B4)}$$

$$c(w)=(p_0\xi q/eF)B_0\left(1-\frac{5}{2}\gamma+\gamma w\right). \quad \text{(B5)}$$

Substituting (B4) and (B5) in (3), integrating over w, the following equation results

$$\Gamma\left(\frac{5}{2}\right)=(p_0\xi q/eF)\Gamma\left(\frac{5}{2}+n\right)(1+n\gamma). \quad \text{(B6)}$$

Setting $p_0=m\mu F$, we obtain for the mobility μ

$$\mu=(e/m\xi q)\left(\Gamma\left(\frac{5}{2}\right)\Big/\Gamma\left(\frac{5}{2}+n\right)\right)(1-n\gamma) \quad \text{(B7)}$$

Therefore we have the zero-field mobility μ_0 in this case as

$$\mu_0=(e/m\xi q)\left(\Gamma\left(\frac{5}{2}\right)\Big/\Gamma\left(\frac{5}{2}+n\right)\right), \quad \text{(B8)}$$

which is of course different from (14).

The electron temperature, γ, is determined in the same way as b_1. Multiplying (4) by w and integrating, we obtain

$$M(p_0\xi q/eF)\Gamma\left(\frac{5}{2}\right)=\gamma l_{11} \quad \text{(B9)}$$

We can put $p_0=m\mu_0F$ in (B9), where μ_0 is given by (B8), then

$$\gamma=\frac{\left(\Gamma\left(\frac{5}{2}\right)\right)^2}{\Gamma\left(\frac{5}{2}+n\right)}\cdot\frac{M}{l_{11}}. \quad \text{(B10)}$$

ν_B, which means ν in this aprroximation, is given by

$$\nu_B=\frac{4nq\Gamma\left(\frac{5}{2}+n\right)}{3l_{11}}\left(\frac{\mu_0}{v_T}\right)^2 \quad \text{(B11)}$$

where

$$v_T^2=(2k_0T/m).$$

Appendix C

Since $(\partial f/\partial t)_L$ in polar semiconductors due to optical-mode scattering is given by Stratton(6) (Eqs. (2.2), (2.3), and (2.4) in his paper), we can immediately obtain the following equations

$$-w^{3/2}\frac{d}{dw}(e^{-w}g)={}^{-w}L[c], \tag{C1}$$

$$-M'\frac{d}{dw}(w^{2/2}e^{-w}c)=e^{-w}L_p[g], \tag{C2}$$

where

$$f_0=e^{-w}g(w), \tag{C3}$$

$$\chi(w)=-(e\hbar t_0F/mk_0T)e^{-w}c(w),$$

$$L[c]=w\phi(w)c(w)-c(w+u)\left\{\left(w+\frac{u}{2}\right)\phi(w)-\sqrt{w(w+u)}\right\}+\Delta(w)e^u\left[w\phi(w-u)c(w)-c(w-u\left\{\left(w-\frac{u}{2}\right)\phi(w-u)-\sqrt{w(w-u)}\right\}\right], \tag{C4}$$

$$L_p[g]=\{g(w)-g(w+u)\}\phi(w)+\Delta(w)e^u\{g(w)-g(w-u)\}\phi(w-u), \tag{C5}$$

$$\phi(w)=ln\frac{\sqrt{w+u}+\sqrt{w}}{\sqrt{w+u}-\sqrt{w}}, \tag{C6}$$

$$M'=\frac{2(eFt_0)^2}{3mk_0T}, \tag{C7}$$

and t_0 is equal to $(2mk_0T)^{1/2}/(eF_0N_0)$ in Stratton's notation.

Appendix D

g and c are defined in Appendix B. Let ξq be equal to t_0^{-1}, (B4) and (B5) become

$$g(w)=B_0\left(1-\frac{3}{2}\gamma+\gamma w\right), \tag{D1}$$

$$c(w)=(p_0/eFt_0)B_0\left(1-\frac{5}{2}\gamma+\gamma w\right), \tag{D2}$$

By using the above two equations and integrating both sides of (38) over w, the following results

$$\Gamma\left(\frac{5}{2}\right)=(p_0/eFt_0)\left\{\left(1-\frac{5}{2}\gamma\right)d_{00}+d_{10}\gamma\right\}. \tag{D3}$$

Putting $p_0=m\mu F$, we obtain

$$\mu=\left(\frac{et_0}{m}\right)\frac{\Gamma\left(\frac{5}{2}\right)}{d_{00}}\left[1-\gamma\left\{\frac{d_{10}}{d_{00}}-\frac{5}{2}\right\}\right], \tag{D4}$$

so that

$$\mu_0=\frac{et_0}{m}\cdot\frac{\Gamma\left(\frac{5}{2}\right)}{d_{00}} \tag{D5}$$

Next, by multiplying both sides of (39) by w and integrating, we have

$$M'(p_0/eFt_0)\Gamma\left(\frac{5}{2}\right)=\gamma l_{11}$$

Setting $p_0=m\mu_0F$ and rewriting t_0 in terms of μ_0, we obtain

$$\gamma=(4d_{00}/3l_{11})(\mu_0F/v_T)^2, \tag{D6}$$

$$\mu=\mu_0\left\{1-\frac{4}{3l_{11}}\left(d_{01}-\frac{5}{2}d_{00}\right)(\mu_0F/v_T)^2\right\}, \tag{D7}$$

$$\delta_s=(4/3l_{11})\left(d_{01}-\frac{5}{2}d_{00}\right), \tag{D8}$$

References

1) H. Sato: J. Phys. Soc. Japan **14** (1959) 1275
2) A. H. Wilson: *The theory of metals.* (Cambridge Univ. Press, 1953) 300
3) I. Adawi: Phys. Rev. **115** (1959) 1152
4) J. Yamashita: Phys. Rev. **111** (1958) 1529
5) M. S. Sodha and P. C. Eastman: Phys. Rev. **110** (1958) 1314
6) R. Stratton: Proc. Roy. Soc. A, **246** (1958) 406
7) H. Frohlich: Adv. Phys. **3** (1954) 325
8) D. J. Howarth and E. H. Sondheimer: Proc. Roy. Soc. A, **219** (1953) 53
9) Y. Kanai: J. Phys. Soc. Japan **14** (1959) 1302

JOURNAL OF THE PHYSICAL SOCIETY OF JAPAN, Vol. 15, No. 7, JULY, 1960

Dynamic Behaviour of Twinning in Tin Crystals at Various Temperatures and Strain Rates

By Saiyu MARUYAMA

Department of Physics, Osaka Women's University

(Received April 6, 1960)

Twinning behaviour of tin was investigated as a function of temperature and strain rate. The resolved shear stress for twin became large and the scatter of individual values was pronounced, as the temperature was lowered and strain rate was increased. The observed twinning stress was not so large as to expand the stacking-fault across the crystal, but it was sufficient to trigger twin nucleus if local stress concentration was produced, say, by dislocation pile-ups. As the temperature was raised and strain rate was decreased, deformation by slip preceding twin became dominant, and twin formation was finally prohibited. The activation energy derived from the ductile-brittle transition temperatures is approximately that of self diffusion, suggesting that recovery due to dislocation climb releases local stress and prohibits twin nucleation. Hardening of twin boundary migration was found at low temperatures or at high strain rates, while the initial migration stress was not raised by these factors but raised by prestrain. It was about one order of magnitude smaller than that for twin initiation, and too small for the creation of twin dislocation ring on the existing twin layer. A mechanism of sweeping and climbing of the twin dislocation around a pole dislocation is necessary to explain the observedvalue.

§ 1. Introduction

Although the crystallography of mechanical twinning has considerably been investigated, he dynamic behaviour of twinning has very ittle been examined. Even the critical shear stress criterion for mechanical twinning has ot yet been established well, at least in h. c. p. metals. In the earlier experiments, as was shown by Cahn1),2), the values of 'critical hear stress' obtained by different investigaors for material of similar purity were quite different, and the values in any one series of xperiments usually had a large scatter.

As for f.c.c. metals, however, it has been eported3) that the critical shear stress crierion holds in the initiation of the twins, he value of the stress depending closely on he energy of the stacking fault.

Later, Bell and Cahn4) measured a resolved hear stress for twin initiation (r.s.s.t.) by arefully handling the zinc specimen and by eeping away from using pin chucks, in order o prevent the specimen from containing any win nucleus and local stress concentration rior to the test. The value thus obtained was about one order of magnitude larger than that obtained by the earlier investigators. They concluded that the earlier investigators had measured not the stress to start twinning but the stress to spread the already existing twins. Further, they found that the value of their r.s.s.t. was altered noticeably by changing the specimen orientation slightly or by changing the specimen length, and concluded that r.s.s.t. is determined simply by the tensile stress required to bring the specimen to the point of double slip, which would raise the local stress.

The necessity for local stress concentration, which would not be consistent with a critical shear stress criterion at the onset of twinning, is supported by the following experimental facts: burst of twinning by the indentation under the applied tensile stress4), lowering of the r.s.s.t. of the indented crystals5), twin initiation at the bending plane6) or by double slip4), delayed twinning with the aid of residual high strain of a surface layer produced in the crystal growth7), initiation of the secondary twin at the twin intersection8), etc. The precise picture of this stress concentration presented by Bilby and Entwisle[9] on the basis of semi-quantitative calculations is that dislocations piled up against a barrier generate a high local stress, large enough to trigger the twin nucleation, on one or more of the twinning planes.

The mechanism of twin nucleation by the local stress concentration might be assured by the aid of recovery phenomena. In the circumstances where either static or dynamic recovery in Zeeger's sense[10] is substantial in the process of deformation, the local stress will not be enhanced high enough for twin nucleation, slip and other mode of ductile deformation will then be preferred, and *vice versa* when the recovery is insignificant. The well known preference to mechanical twinning under impact loading at low temperature may be the latter case.

In this work, tin crystals were used. White tin shows significant recovery even at room temperature and at moderate strain rate[11]. It is considered to be static recovery by dislocation climb, because tin has low activation energy for self diffusion. The crystals were tested under the various temperatures and strain rates, to confirm the influence of recovery phenomena upon the twin nucleation and to discern the modes of stress concentration and of associated recovery phenomena.

§ 2. Experimental Details

In order to avoid the activation of any other twin plane except the one which has the greatest resolved shear stress (this may also be necessary for the migration stress measurements of the twin boundary) the author ought to use the compression test, although it is less desirable than the tension test. The specimens were grown from the seed crystal and their axes made angles 15°～20.5° with [100] on the [010] great circle. The r.s.s.t. on the most highly stressed twin plane (301) (the angle χ between the specimen axis and the twinning plane is 43.5°～38°) is at least two times higher than that on any other twin planes, and the latter was kept inoperative until the former covered almost entire length of the crystals.

The crystals were grown from the melt of tin containing impurities less than 0.01%, in pyrex glass tubes with inner diameter 4.2 mm. To prevent any slightest deformation in the course of specimen preparation, the pyrex glass tube was dissolved in hydrofluoric acid, and the specimen was acid cut in pieces of length 35 mm. After about 30 hours annealing at 180°C, oxides were removed off chemically. Cooling down after crystal growth and after annealing was slow enough to avoid any thermal stress.

In the earlier stage of the present experiment, the ends of the specimen were ground flat and parallel by emery paper before annealing, and were lubricated with glease before testing the specimen. The mechanical twin started always at the ends and at a lower stress than that found in the later experiment as described below, indicating that fine grains scarcely greater than 1 mm recrystallized at the ends raised local stress to trigger twin nucleation with ease, although the effect was negligible when slip preceding the twin was dominant.

In the later experiment, iron caps were used instead of pin chucks or soldering which might act as local stress raiser. Holding the space between cap wall and specimen closer than 0.1 mm, they were cemented with 'Araldite' which was found more stiff than the tin crystal for the deformation. Special device was made to hold the top surfaces of the caps at right angle with the crystal axis. In this case, twin started at any point excluding the cemented parts at higher stresses than the earlier case.

The compression container in which the specimen was compressed at low temperature was such as used by Kraft *et al*[12]. To record the load-extension curve and vary the strain rate, 'Instron Testing Machine for Textile' with load cell of 500 kg was utilized.

For the measurement of the stress of twin initiation, load was relaxed as soon as the load dropped with a loud twinning click, and the twin lamella just formed was observed. On the other hand, for the measurement of the migration stress of the twin boundary, the compression was continued until the specimen was covered wholly with twinned part, leaving only the gripped ends. In this case, only poor information about twin initiation was obtained because the starting point of the twin formation was uncertain.

Experimental Results

1) *Effects of changing temperature and strain rate upon twin initiation*

xperiments were mainly restricted to the
cimens with $\chi=43.5^\circ\sim38^\circ$. The range of
perature tested was between −80°C∼20°C,
the rate of deformation was between
∼5 cm/min. (Strain rate of 2.5∼
%/min.) The gauge length of the speci-
n was about 20 mm.

xperiments at the temperature lower than
room temperature (20°C) was carried out
dipping the specimens into the mixture of
thyl alcohol and solid carbon dioxide. The
thyl alcohol atmosphere was used even at
room temperature in order to avoid, if
, secondary contributions of the surround-
atmosphere.

he rate of deformation was controlled by changing the head speed and the chart speed of the Instron machine proportionally. The rate of deformation higher than 5 cm/min. was not applied because the speed of the recording pen did not follow the deformation.

The typical load-extension curves in the various circumstances are shown in Fig. 1a∼1e.

The effect of changing temperature and strain rate upon the stresses at which twinning starts (solid circle), and the magnitude of deformation before twinning plane operates (horizontal line) are illustrated in Fig. 2a,b,c. The cross mark indicates that the twinning did not start within the magnitude of deformation here illustrated.

To summarize briefly the general features:

i) As the temperature is raised and the strain rate is diminished, the magnitude of the deformation necessary to start twinning increases, and the mechanical twinning becomes hard to realize.

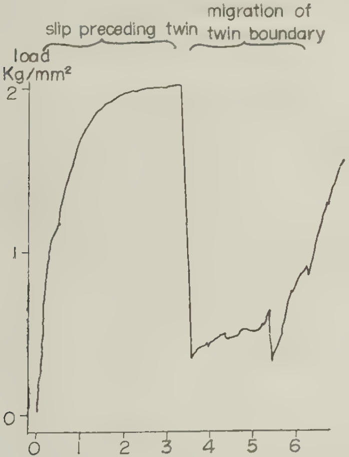

Fig. 1a. Temperature: −30°C
Strain rate: 25%/min.

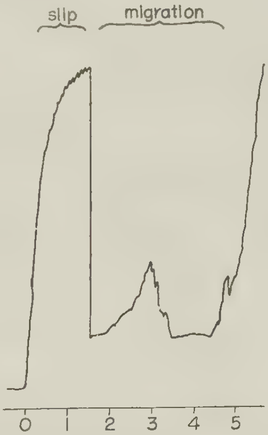

Fig. 1b. Temperature: −60°C
Strain rate: 2.5%/min.

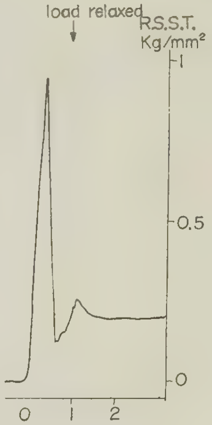

Fig. 1c. Temperature: −80°C
Strain rate: 25%/min.

ii) In the range of twin formed under a dominant slip, the twinning shear stress gives a constant value and it becomes higher as the temperature is lowered or the strain rate is increased. Whereas in the case of the twin formed under an insignificant slip, a large scatter of the value of the twinning stress is found.

(2) *Effect of changing specimen orientation*

As for the slip system in tin, there is very little literature. According to the old litera-

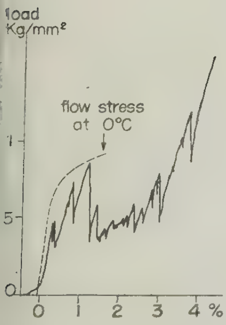

1d. Temperature: −195°C
ain rate: 2.5%/min.

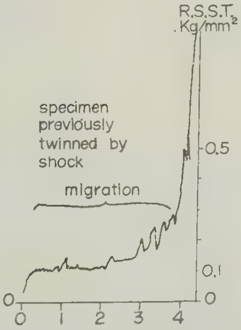

Fig. 1e. Temperature: 20°C
Strain rate: 2.5%/min.

ture, written by Obinata and Schmid[11], the main slip system in white tin is $t=[001]$ $T=\{100\}$ or $\{110\}$ at room temperature. Occasionally, the system $t=[10\bar{1}]$, $T=\{101\}$ or $\{121\}$ was observed. The critical shear stresses for these four systems were 189, 133, 160 and 170 gm/mm², respectively. As the glide strain increases, the flow stress of the main slip system increases only slightly, becaus tin crystals show substantial recovery ever at room temperature. On the other hand the hardening of the system $t=[101]$ is rapid This is the reason why the system operates only in exceptionally rare cases.

In the present experiment, to see the effe of changing specimen orientation upon tw nucleation, the specimens with $\chi=53.5°$ were prepared. (The specimen is noted as B hereafter, whereas the other specimen with $\chi=43.5°\sim38°$ is noted as A.) The axis of these specimens made an angle of 85° with the main silp direction [001]. The resolved shear stress for main slip [001]/(100) is about three or four times higher than that in the specimen A, but the resolved shear stress for twin is nearly equal in the magnitude. The load-extension curve in crystal B was raised, however, only about 25% than in crystal A, suggesting that the secondary slip system was operative in either case, although the temperature range and strain rate was not the same as in the case of Obinata and Schmid.

The stress for the twin initiation in speci-

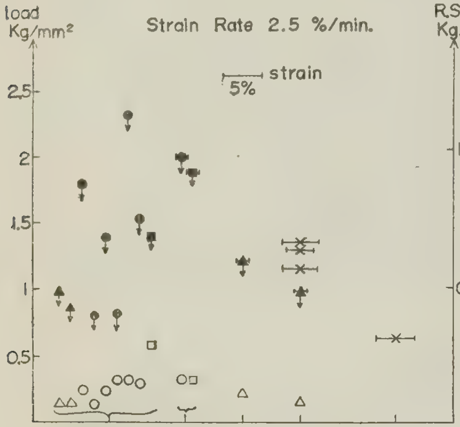

Fig. 2a.

Solid mark: stress for twin initiation
Open mark: initial stress for twin bounda migration
Circle: crystal A with $\chi=43.5°\sim38°$
Square: crystal B wite $\chi=53.5°$
Triangle: specimen with orientation A, used i the earlier stage
Horizontal line: deformation preceding twin
Cross: lack of twinning under the illustrat magnitude of deformation

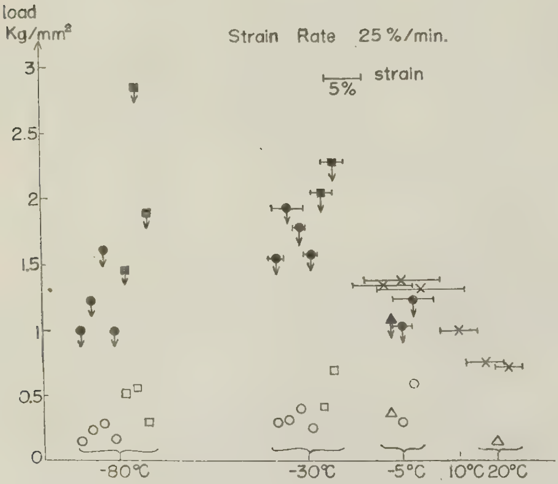

Fig. 2b.

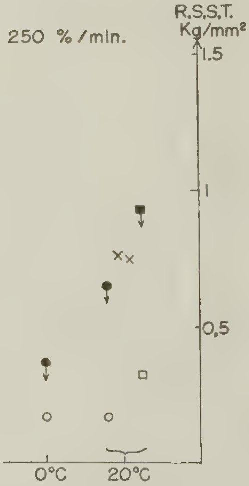

Fig. 2c. (Deformation prior to twin is not recorded.

n B was always somewhat higher than t in A. This is in accord with the Bell l Cahn's hypothesis. Because in the speci-n B, the r.s.s. for [001]/(100) main slip is ıch larger than that in A, and the point double slip which is supposed to begin h the secondary slip [10$\bar{1}$]/(101), followed the main slip [001]/(100), may be delayed ın the case in A. This results in the raise twinning stress.

The precise discussion must, of course, be sed on the observations of slip traces by metallographic treatment of the specimen face, but they failed chiefly because of the ıallness of the strain preceding twin.

3) *Migration of the twin boundary*

Bell and Cahn[4] measured the resolved shear ess of the twin boundary migration (r.s.s.) in zinc about one order of magnitude ıaller than the r.s.s.t., the magnitude of ıt stress being comparable with that served by the earlier investigators as twinn-g stress.

In the present work, the initial r.s.s.m. is own by open mark in Fig. 2, and again rresponds to about one order of magnitude ıaller than that of the r.s.s.t.

Effect of changing temperature and strain te upon migration stress is not substantial. is not the temperature or the strain rate elf, but the magnitude of deformation eceding twin, which affects the migration ess.

At a low temperature, -80°C, prestrain is small that the r.s.s.m. shows the lowest lue 70 gm/mm^2. As the temperature is ised and the strain rate is decreased, pre-rain becomes considerable magnitude, r.s.s. . then increases. When a kink band was rmed at the strain rate of 25%/min. and at e temperature -30°C or -5°C, the r.s.s.m. as raised about four times higher than the west value. Further, even at room tem-rature, when the crystal had been twinned advance by impact shock, the prestrain in is case being very small[5], the r.s.s.m. ıowed then the lowest value 70 gm/mm^2 ig. 1e).

On the other hand, the hardening in the undary migration process is affected by mperature and probably by strain rate. At om temperature, the specimen twinned in advance by impact does not show hardening through the whole process of twinning. In the liquid nitrogen experiment, however, a serrated curve was recorded (Fig. 1d). Loud twinning crick was heard at every moment of the fall of stress. At this temperature, the migration stress in the true sense is not recorded, but rapid hardening of the twin boundary movement and twin nucleation assisted by the local stress of the operating twin itself appears alternately. These results show that the recovery process in the tin crystals is operative at room temperature even in the twin boundary movement.

§ 4. Considerations and Discussions

It is supported by this experiment that the mechanism of twin nucleation by the local stress concentration in zinc holds in tin crystals as well, and the criterion for the critical shear stress for the initiation of twin does not hold in both metals. The twinning process is therefore excluded, under the condition in which crystal recovery is dominant and the local stress is insignificant. The results of the experiments which support these hypotheses are as follows:

i) As the temperature is raised and the strain rate is decreased, the deformation by slip should be large before the twin initiation.

ii) At low temperature, -80°C, the twinning stress is very sensitive to the crystal imperfection. Even under the constant temperature and constant strain rate and for the same crystal orientation, the observed twinning stress is not regarded as constant.

iii) The r.s.s.t. varies appreciably by changing specimen orientation. It is affected by the operating slip systems.

The theory for the twin formation to explain these results will be discussed somewhat quantitatively below:

1) *Model of spreading a stacking fault*

The critical shear stress for the twin initiation is, following Friedel[13], the applied shear stress to develope a stacking fault across a crystal. This model is applicable in the case where the energy of stacking fault is low and the applied stress is high. For example, in the case of f.c.c. metals, Suzuki and Barrett[3] expressed the critical shear stress for twin initiation,

$$\sigma=\frac{\gamma}{2b}+\frac{2T}{lb}$$

using double stacking fault model. Here γ is the stacking fault energy, b is the Burgers vector of a half-dislocation, T is the tension of the half-dislocation line, and l is the mean distance between the intersecting dislocations. The equation was in accord with their observed values.

But in our case on tin crystals, taking

$$\gamma=20 \text{ ergs/cm}^2,\ b=0.2\times10^{-8} \text{ cm},$$

and neglecting the resisting force due to the intersecting dislocations

$$\sigma=50 \text{ Kg/mm}^2$$

In other words, the applied shear stress of about 50 times larger than that observed in this experiment is expected by this model. The model is obviously not adequate in the case of tin.

2) *Model of twin nucleation by the aid of local stress*

The other model for twin initiation was proposed by Orowan[14)], and somewhat modified and applied by Bell and Cah[4)] in zinc crystals. If the applied stress is in some way magnified 'locally' to the theoretical twinning stress, a twin nucleus of the critical diameter will be triggered. This nucleus will be able to grow further by the applied stress of the order of the observed value[5)]. Because the local stress at the top of the nucleus will be enhanced to the twinning stress by its own twin dislocation array along the periphery of the twin nucleus.

Now, the mechanism of the local magnification of the applied stress is uuknown. But the most probable mechanism which might occur in such an early stage of deformation is the piling up of the slip dislocations against a barrier, as in the case of brittle fracture. The number of pile-ups necessary for the twin nucleation is that which magnifies the applied shear stress on the piled up slip plane to the theoretical twinning shear stress throughout the twin nucleus of the critical diameter. The calculation is made by Bell and Cahn[4)] in zinc, in which the twin nucleus is calculated by the method of Orowan, and the magnification of the applied stress is estimated by the expressions derived by Frank, Eshelby and Nabarro[15)]. In the present case, we take the self energy of twinning dislocation $\Gamma=Gb_t$ where G is appropriate shear modulus and b_t is Burgers vector of the twinning dislocation, applied shear stress on the slip plane 4.4×10^7 dynes/cm², and the theoretical twinning stress $(G/2\pi)\gamma$ following Orowan where γ is the twinning shear. The estimated number of the pile-ups of the slip dislocations is then approximately one hundred, which is not unreasonable value. Here, of course, the estimation is very approximate. For example, the theoretical twinning stress will be smaller if the atomic force is considered more precisely[16)]. The stress distribution function should be used along the dimensions of twin nucleus. These abbreviations make the number of the pile-ups too overestimated. Whereas, the interaction energy of the twin dislocations is neglected. This makes the number of the pile-ups too underestimated.

3) *Twin prohibition by recovery*

These piling-ups of the slip dislocations may be released with the aid of thermal activation, and the twin nucleation will be prohibited, if the temperature is raised and the strain rate is decreased. On the contrary, under the reversed condition, the probability for the release will diminish and twin nucleation will be operative.

The situation is analogous to the case of the ductile-brittle transition in iron polycrystals. The following treatment is essentially that of Stroh[17)] except that the release occurs by recovery process instead of the operation of Frank-Read source in the neighbouring grain, and the activation energy U for the stress release is then the energy corresponding to the recovery process, not to the breaking up of Cottrell locking.

The mean time for stress release is, in the atmic scale,

$$\tau=\frac{1}{\nu}\exp\{U/k\mathrm{T}\}.$$

The probability that the release does not occur in a time interval t will be

$$\begin{aligned}p&=\exp\{-t/\tau\}\\&=\exp[-\nu t\exp\{-U/k\mathrm{T}\}].\end{aligned}$$

Owing to the form of double exponential, p falls abruptly from 1 to 0 as the temperature is raised. The transition temperature is, taking $p=1/e$,

$$T_c = U/k \log \nu t\ .$$

he effect of strain rate is introduced through t is the order of time elapsed before the train reaches $\mathcal{E}_t$ necessary for the twin initia-on. Apart from numerical factor, we expect

$$t = \mathcal{E}_t/\dot{\mathcal{E}}$$

lere, being different from the case of fra-ture both $\mathcal{E}_t$ and $\dot{\mathcal{E}}$ are the values beyond he elastic region. The transition tempera-ure is related to the strain rate in the from

$$1/T_c = -(k/U)\log\dot{\mathcal{E}} + (k/U)\log \nu\mathcal{E}_t$$

og $\dot{\mathcal{E}}$ is plotted against $1/T_c$ in Fig. 3. The ark △ shows the transition point, and lines p with the inclination giving an activation nergy of about 0.58 eV (13 kcal). This is ompared with the activation energy for the elf diffusion in tin, 10.5 kcal in c direction[18], uggesting that twinning is prohibited by the islocation climb. Here, the self diffusion in direction is rejected, for it involves ring echanism[19]. According to Mott's theory[20], e rate of climbing is

$$\nu \exp\{-(E-\gamma n b^3\sigma)/kT\}$$

here ν is atomic frequency, γ is a numeri-al constant of order of unity, σ is the flow tress and n is the number of pile-ups. E is e activation energy for a free dislocation nd of the order of that for the self diffusion. ut if the jogs is not supplied enough, it in-olves the formation energy of jogs which is qual to about one half of the energy for the elf diffusion. Taking into account the formation energy of the jogs, the obtained activation energy U corresponds to that for climbing, *i. e.*, $E-\gamma n b^3\sigma$, which is weakly dependent on stress for $n \simeq 100$. U will also correspond to the activation energy for creep in tin, 11 kcal[19], interpreted by the climb mechanism.

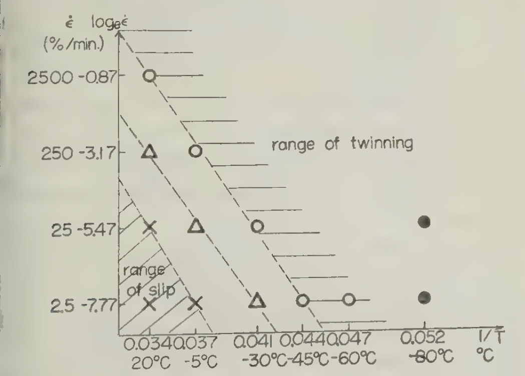

Fig. 3. Probability for twinning under varied temp. and strain rate.
- ●: twin formed under insignificant slip
- ○: twin formed after flow stress reach a constant value
- △: transition point
- ×: twin inhibited

As for the other mode for the release, for example, the operation of *F-R* source from Cottrell locking or cross slip by the breaking up of Lomer-Cottrell barrier, nothing decisive can be said, because the activation energy for them can hardly be estimated. But the former is hard to conceive because the transition point illustrated is well beyond the elastic region, and the latter is also put aside because the cross slip in tin has not been reported.

4) *The nature of barriers*

The nature of barriers dumming up the dislocation array is left to be discussed. At an elevated temperature and a decreased strain rate, it is expected that double slip generates barriers resulting the pile-ups of dislocations, as was shown by Bell and Cahn. This is because, in the present experiment, twins start simultaneously at many points along the gauge length of the specimen under such conditions.

While, at low temperature and at high strain rate, the above model is not reasonable. Because twin operates under the applied stress not far from elastic limit, with insignificant lattice rotation. Instead, other types of stress concentrators are expected. For xeample, Frank partial sessile dislocations[21], dislocation arrays of opposite sign on neighbouring slip planes[22], segregation of impurity atoms during annealing, etc. Even the constraint at the cemented part seems to act as stress raiser. Here, we put aside nucleation by thermal stress or phase transformation at -80°C, because nucleation click was not heard, and the specimen kept -80°C for 2.5 hrs did not show any traces of phase transformation by *X*-ray examination.

5) *The stress values for twin initiation*

If we admit the nature of stress concentrators as described above, the variation of the stress for twin initiation is understood as follows. Under the condition of dominant slip, the stress for twin initiation, if it occurs, is determined simply by the magnitude of the flow stress at the point of double slip forming barriers. The raise of the twinning stress by the lowering of temperature and by increasing strain rate as well as the marked change of the r.s.s.t. with crystal orientation is a natural consequence. Whereas, in cases with insignificant slip, twin initiates in the course of rapid hardening of the flow stress. Thus the large scatter of the twinning stress results. The scatter of the r.s.s.t. in the orientation of insignificant slip was also observed under impact test[5]), which would correspond to the low temperature experiment.

6) *The resolved shear stress for boundary migration*

Last of all, the magnitude of the r.s.s.m. is referred to. Let us estimate the r.s.s.m. necessary for successive nucleation of a twin dislocation ring on the twin surface. Here, a new stacking fault energy or twin boundary energy is not required. The shearing stress necessary to form a hill of one atomic height on a coherent twin boundary is therefore calculated like that required to form a slip dislocation ring in a perfect crystal[23]). The critical radius of the hill under the observed minimum r.s.s.m., 70 gm/mm^2, is 3400 Å, the activation energy of 25.5 eV is then required. If the creation is allowed under the activation energy of the order of 0.4 eV, the r.s.s.m. required is 1.6 Kg/mm^2, much larger than the stress for the 'twin initiation'. The nucleation of this ring by the piling up of slip dislocations against the twin boundary is also rejected. Because the applied stress giving the minimum migration stress is far from giving a critical shear stress for any slip, and the constancy of minimum r.s.s.m. at various temperatures and strain rates refuses the process which requires the thermal activation.

The most probable model for the migration of twin boundary is the continuous growth on an atomic scale by the sweeping twin dislocation around a pole dislocation, such as presented by Cottrell and Bilby[24]). The migration stress is then the resisting force to the moving twin dislocation. The resisting force will be dependent on the crystal perfection. In crystals prepared by recrystallization, the minimun r.s.s.m. was reported[25]) to be 50 gm/mm^2, somewhat lower than the present experiment. The raise of of the stress by the deformation preceding twin is a natural consequence. But the resisting force will be only weakly dependent on temperature and strain rate, because a jog in the twin dislocation does not necessarily drag vacancies. Of course, accomodation process accompanying incoherent twin boundary movement will be necessary in the later stage of migration, this will result in the hardening of the migration stress at low temperature.

In conclusion, the author wishes to express his cordial thanks to Prof. K. Tanaka, Kyoto Univ., for his cotinuous encouragement and criticism on this subject. He also wishes to thank to Prof. J. Takamura, Kyoto Univ. for his instructive suggestion, and to Prof. T. Sugeno, Tokyo Univ., for his criticism. His thanks are especially due to Dr. H. Kiho, Kyoto Univ., for his stimulating discussions throughout this work. He is much indebted to Master T. Kishimoto and Mr. H. Ito, Japan Synthetic Textile Inspection Institute Foundation, for kindly utilizing Instron Machine.

References

1) R. W. Cahn: Adv. Phys. **3** (1954) 423.
2) R. L. Bell. and R. W. Cahn: Acta Metallurgica **1** (1953) 752.
3) H. Suzuki and C. S. Barrett: Acta Metallurgica **6** (1958) 156.
4) R. L. Bell and R. W. Cahn: Proc. Roy. Soc. **A, 239** (1957) 494.
5) K. Ishii: J. Phys. Soc. Japan **14** (1959) 1315.
6) E. C. Burke and Hibbard, Jr.: Trans. Amer. Inst. Mech. Engrs. **194** (1952) 295.
7) B. Ancker: Ann. Physik **12** (1953) 121, 145.
8) S. Maruyama and H. Kiho: J. Phys. Soc. Japan **11** (1956) 516.
9) B. A. Bilby and A. R. Entwisle: Acta Metallurgica **2** (1954) 15
10) A. Zeeger: Z. Naturforsch. **9a** (1956) 985.
11) J. Obinata und E. Schmid: Z. Phys. **82** (1933) 224.
12) J. M. Kraft, A. M. Sullivan and C. F. Tipper: Proc. Roy. Soc. **A, 221** (1953) 114.
13) J. Friedel: Phil. Mag. **46** (1955) 1169.
14) E. Orowan: *Dislocations in Metals* (Amer. Inst. Min. Metall. Engrs., New York, 1954) 116.
15) J. D. Eshelby, F. C. Frank and F. R. N. Nabarro: Phil. Mag. **42** (1951) 351.
16) A. H. Cottrell: *Dislocations and Plastic Flow in Crystals* (Oxford 1953) 9.
17) A. N. Stroh: Adv. Phys. **6** (1957) 418.
18) P. J. Fensham: Australian J. Sci. Research **3** (1950) 91.

19) J. Weertman and J. E. Breen: J. Appl. Phys. **27** (1956) 1189.
20) N. F. Mott: Phil. Mag. **44** (1953) 742.
21) F. C. Frank: Proc. Phys. Soc. London. **A**, **62** (1949) 202.
22) N. F. Mott: Nature **175** (1955) 365.
23) A. H. Cottrell: *Dislocations and Plastic Flow in Crystals* (Oxford. Clarendon press, 1953).
24) A. H. Cottrell and B. A. Bilby: Phil. Mag. **42** (1951) 573.
25) T. Hirokawa: Read at the Annual Meeting of Phys. Soc. of Japan, Hiroshima (1959).

JOURNAL OF THE PHYSICAL SOCIETY OF JAPAN, Vol. 15, No. 7, JULY, 1960

Study on the Ordered Alloys of Gold-Manganese System by Electron Diffraction, II. Au_4Mn*

By Denjiro WATANABE

The Research Institute for Iron, Steel and Other Metals,
Tohoku University, Sendai, Japan

(Received February 23, 1960)

The ordered Au_4Mn alloy has been investigated by electron diffraction, using oriented, evaporated films. This ordered alloy has been found below about 400°C to have the body-centred tetragonal unit cell which is 2.5 times as large as the fundamental cell in volume. The structure is isomorphous to that of Ni_4Mo and belongs to the space group $I4/m-C_{4h}^5$. This structure is not the so-called anti-phase domain structure. Some qualitative discussions have been given of the structural transition between the ordered Au_4Mn and Au_3Mn and of the origin of ferromagnetism in Au_4Mn, on the basis of the proposed structure model.

§1. Introduction

In Part I of the present study[1], the structure f the ordered Au_3Mn alloy was investigated y electron diffraction, using thin single-rystalline films prepared by evaporation, and t was shown that this alloy possesses a two-limensional anti-phase domain structure of a ew kind, whose fundamental lattice consists f a face-centred orthorhombic cell with the tomic arrangement similar to Cu_3Au. On he other hand, it was found by Kussmann nd Raub[2] that the alloy Au_4Mn has an rdered face-centred tetragonal lattice ($c/a<1$) elow about 420°C, but its atomic arrangenent has as yet been unknown. According o the said authors and Meyer[3], the ordered u_4Mn alloy is ferromagnetic below about 8°C. The structure determination of this rdered alloy, therefore, seemed to be necesary from the crystallographic as well as from the magnetic points of view. The present author studied the superlattice of Au_4Mn by electron diffraction, using thin single-crystalline films, and was able to determine its complex ordered structure.

In the present paper, it will be shown that the ordered Au_4Mn phase has not the so-called anti-phase domain structure but a body-centred tetragonal lattice with a unit cell of Ni_4Mo-type which is 2.5 times as large as the disordered unit cell in volume.

§ 2. Experimental Results

In the present study, the experimental procedures involving preparation of specimens, heat treatment and electron diffraction technique were quite the same as those in Part I.

The alloy films containing manganese less than 25 per cent** showed diffraction patterns of Au_3Mn-type superlattice after quenching from temperatures above 400°C. When they were annealed for a long period below 400°C, however, the patterns changed their aspects as follows: The specimen giving the pattern as shown in Photo. 1 (a) ($a_1=4.09$, $a_2=4.06$, $a_3=4.04\pm0.01$ Å, $M_1=1.18$, $M_2=2.23$*) after quenching from about 400°C showed the pattern as shown in Photo. 1 (b) after annealing at 360°C for 24 hrs. In this pattern, we can see a new kind of superlattice spots besides those of Au_3Mn-type. The longer the annealing time, the stronger the intensity of new spots became, and the superlattice spots consisted of those of a new kind alone after further annealing at 350°C for 40 hrs., as shown in Photo. 1 (c). Photo. 1 (d) shows the pattern of the same film as in Photo. 1 (c) taken at oblique incidence, the angle between the incident electron beam and the film normal being several degrees. The further annealing below 350°C did not change the aspect of the pattern any more. The pattern changed almost reversibly when the specimen was again heated at higher temperatures, and the spots of Au_3Mn-type structure entirely recovered their intensity at about 400°C.

---

* A short note concerning this work has been ublished in Acta Cryst. **10** (1957) 483.

** In the present paper, all percentages refer to atomic per cent.

The above observation enables us to suggest that the alloys containing manganese less than 25 per cent possess below 400°C an ordered structure different from that of Au_3Mn-type. Moreover, it was found by Kussmann and Raub that the alloy Au_4Mn has an ordered lattice below 420°C which is different from the Au_3Mn-type lattice, as already mentioned, and therefore it seems that the ordered structure observed in the present experiment is identical with that of Au_4Mn. In fact, the lattice spacings measured from all the diffraction spots agree well with those obtained from an X-ray Debye photograph by Kussmann and Raub, as shown in Table I, and so it is sure that such patterns as shown in

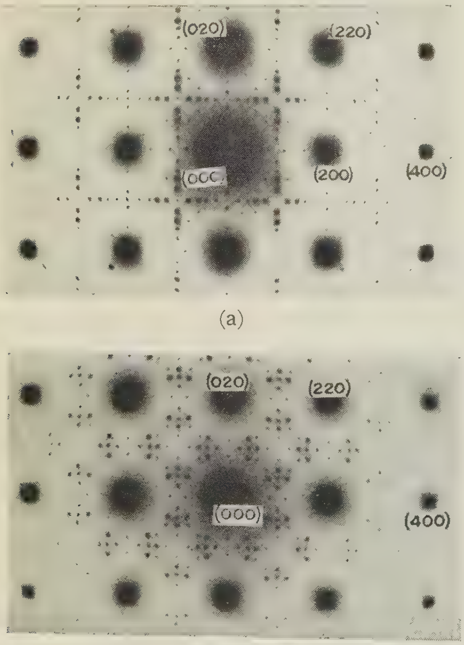

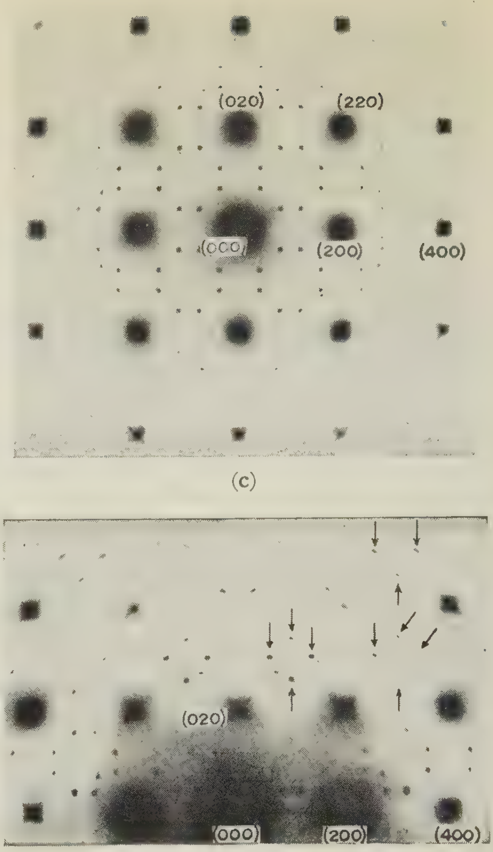

Photo 1. Electron diffraction patterns obtained after annealing at various temperatures from thin alloy films containing about 20% Mn. Indices assigned to main reflections are referred to the disordered cubic system.

(a) Annealed at 400°C; normal incidence.

(b) Annealed at 360°C for 24 hr.; normal incidence.

(c) Further annealed at 350°C for 40 hr.; normal incidence.

(d) Diffraction pattern of the same film as in (c); oblique incidence.

---

* M_1 and M_2 have the same significance as in Part I.

Table I. Lattice spacings and intensities of reflections for the ordered Au_4Mn.

Index		$d_{obs.}$ (Å)	$I_{obs.}$	$I_{cal.}$	$d_{x\text{-}ray}$ (Å)*	$I_{x\text{-}ray}$*
H_1, H_2, H_3	H_1', H_2', H_3'					
4, 2, 0	1, 1, 0	4.55	w.	2.5	4.609	v.w.
1, 3, 1	0, 1, 1	3.42	w.	2.3	3.442	m.w.
2, 6, 0	0, 2, 0	3.22	w.	2.2	3.246	w.
5, 5, 1	1, 2, 1	2.345	v.v.st.	127	2.349	v.v.st.
7, 1, 1	2, 1, 1		w.	1.7		
8, 4, 0	2, 2, 0	2.281	w.	1.7	—	—
10, 0, 0	3, 1, 0	2.038	v.v.st.	100	2.043	st.
6, 8, 0	1, 3, 0		w.	1.4		
0, 0, 2	0, 0, 2	2.015	v.v.st.	98	2.017	m.st.
3, 9, 1	0, 3, 1	1.897	w.	1.3	1.890	v.w.
4, 2, 2	1, 1, 2	1.843	w.	1.2	1.839	v.w.
2, 6, 2	0, 2, 2	1·710	v.w.	1.0	1.705	v.w.
9, 7, 1	2, 3, 1	1.635	v.w.	1.0	1.637	v.v.w.
4, 12, 0	0, 4, 0	1.611	v.w.	0.9	—	—
12, 6, 0	3, 3, 0	1.519	v.w.	0.9	1.515	v.v.w.
8, 4, 2	2, 2, 2	1.510	v.w.	0.9		
13, $\bar{1}$, 1	4, 1, 1	1.457	v.w.	0.8	1.459	v.v.w.
7, 11, 1	1, 4, 1		v.w.	0.8		
10, 10, 0	2, 4, 0	1.440	v.st.	51	1.435	m.st.
14, 2, 0	4, 2, 0		v.w.	0.8		
6, 8, 2	1, 3, 2	1.433	v.w.	0.8	1.427	st.
10, 0, 2	3, 1, 2		v.st.	50		
1, 3, 3	0, 1, 3	1.316	v.w.	0.7	1.308	v.v.w.
8, 14, 0	1, 5, 0	1.264	v.w.	0.6	1.260	v.w.
4, 12, 2	0, 4, 2	1.259	v.w.	0.6		
5, 15, 1	0, 5, 1	1.229	st.	35	1.224	v.v.st.
15, 5, 1	4, 3, 1		st.	35		
13, 9, 1	3, 4, 1		v.w.	0.6		
7, 1, 3	2, 1, 3	1.218	v.w.	0.6	1.214	m.st.
5, 5, 3	1, 2, 3		st.	35		
12, 6, 2	3, 3, 2	1.214	v.w.	0.6		
10, 10, 2	2, 4, 2	1.173	st.	32	1.169	st.

* $d_{x\text{-}ray}$ and $I_{x\text{-}ray}$ are the data obtained from an X-ray Debye photograph by Kussmann and Raub2).

hoto. 1 (c) and (d) are obtained from the rdered structure of Au_4Mn. The fundamental ell of the alloy referring to the original disrdered unit cell is face-centred tetragonal, ith the lattice constants

$${}_1=a_2=4.08, \quad a_3=4.03\pm0.01\,\text{Å}, \quad a_3/a_1=0.988.$$

he pattern in Photo. 1 (b) is considered to eveal the transition state from the ordered u_3Mn-type structure to the ordered Au_4Mn-ype structure.

3. Determination of the Ordered Structure

The superlattice reflections in the patterns hown in Photo. 1 (c) and (d) appear as if ey are formed as a result of the splitting f the reciprocal lattice points with mixed ntegers, h_1, h_2 and h_3†, and it may be susected that the alloy Au_4Mn possesses some ind of anti-phase domain structure. Figs. (a) and (b) are illustrations of the patterns in Photo. 1 (c) and (d) respectively. It was found from the fine splits of main reflections as well as from the positions of the superlattice reflections in Figs. 1 (a) and (b) that the patterns correspond to a superposition of such three orientations that the tetragonal axis of the ordered lattice distributes into three directions of the original disordered cubic axes. After a careful examination the intensity distribution in reciprocal space which corresponds to one orientation can be induced, as shown in Fig. 2 (a). Since a set of four spots which are considered to be split from (100) or (101) is superposed on a set split from (010) or (011), respectively, when the reciprocal lattice is rotated by 90° around the h_3-axis, some of the superlattice spots depicted in Fig. 2 (a) may not be necessary in the fundamental intensity distribution. But, as this is unknown from the observation, we cannot help utilizing Fig. 2 (a) in order to proceed the analysis. There are two values of separation, "m_1" and "m_2", in the split, as shown in Figs. 1

---

† h_1, h_2 and h_3 are used in terms of the fundaental lattice.

and 2 (a), and they satisfy the following relations,

$$m_1/2=a_1^*/2.5\,,\qquad m_2/2=a_1^*/5\,,$$

where a_1^* is a reciprocal lattice constant corresponding to $\boldsymbol{a}_1$. If the split is formed as a result of the formation of anti-phase domains, the alloy $\mathrm{Au_4Mn}$ is likely to possess a two-dimensional anti-phase domain structure because of the appearance of two values of separation in the split, and the sizes of the domains have to be $1.25a_1$ and $2.50a_1$, respectively. But these values in the present alloy never changed with a change of the composition, unlike the ordered alloys with anti-phase domains, CuAu(II)[4], $\mathrm{Cu_3Pd}$[5], $\mathrm{Ag_3Mg}$[6] and $\mathrm{Au_3Mn}$[1], and moreover, we cannot explain the intensity distribution by any kind of anti-phase domain structure based upon the $\mathrm{Cu_3Au}$-type atomic arrangement.

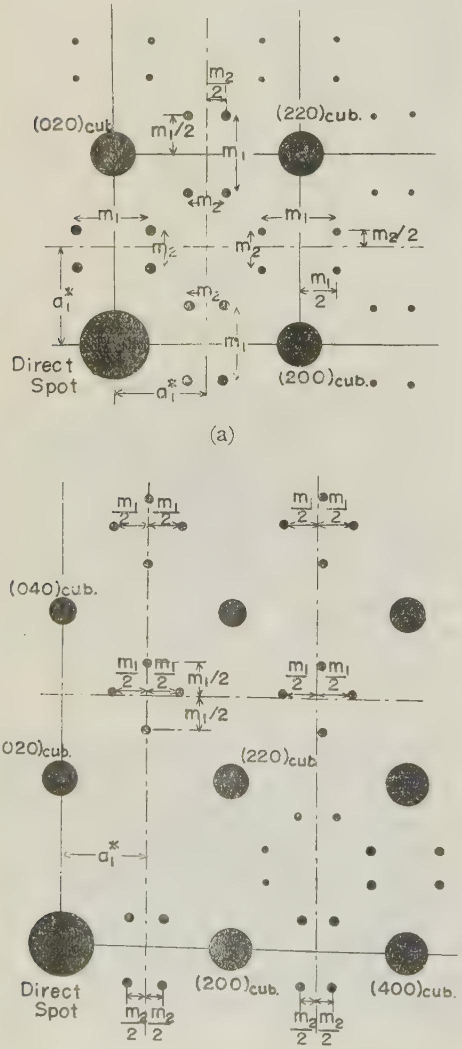

(a)

(b)

Fig. 1 (a). Illustration of Photo. 1 (c).
(b). Illustration of Photo. 1 (d).

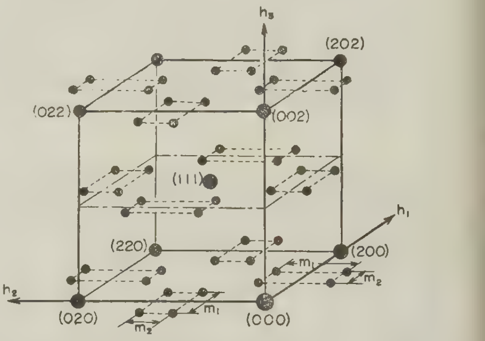

Fig. 2 (a). Intensity distribution in reciprocal space induced from diffraction patterns of $\mathrm{Au_4Mn}$ film.

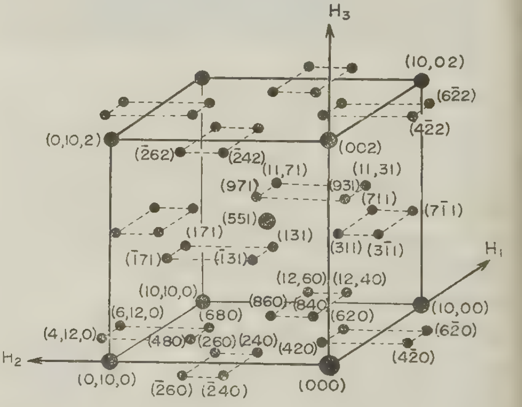

Fig. 2 (b). Indexing of the reciprocal lattice points in Fig. 2 (a).

We shall carry out the structure analysis on the basis of the space group. In order that all the reflections may be indexed with integers, a large unit cell must be taken, the size being $5a_1\times5a_2\times a_3$, and the indexing of the reciprocal lattice points corresponding to this unit cell is shown in Fig. 2 (b)†. The possible space group satisfying the extinction rule is C_{4h}^4-$P4_2/n$. The large unit cell is 25 times as large as the fundamental cell and there are 100 atoms in the unit cell, i.e. 20 manganese and 80 gold atoms. Since the fundamental lattice of this ordered alloy is face-centred as in the case of $\mathrm{Au_3Mn}$, we can easily determine the positions of atoms as follows: 4 atoms must be situated on 4 (c) ositions (000; $\frac{1}{2}\frac{1}{2}0$; $0\frac{1}{2}\frac{1}{2}$; $\frac{1}{2}0\frac{1}{2}$) and the remaining 6 atoms on twelve kinds of 8 (g) positions

---

† In Fig. 2 (b), indices, $(H_1H_2H_3)$, are used in order to distinguish from $(h_1h_2h_3)$ in Fig. 2 (a).

$$(x_i, y_i, z_i:\ \tfrac{1}{2}-x_i, \tfrac{1}{2}-y_i, z_i:\ \bar{y}_i, \tfrac{1}{2}+x_i, \tfrac{1}{2}+z_i:$$
$$\tfrac{1}{2}+y_i, \bar{x}_i, \tfrac{1}{2}+z_i:\ \bar{x}_i, \bar{y}_i, \bar{z}_i:\ \tfrac{1}{2}+x_i, \tfrac{1}{2}+y_i, \bar{z}_i:$$
$$y_i, \tfrac{1}{2}-x_i, \tfrac{1}{2}-z_i:\ \tfrac{1}{2}-y_i, x_i, \tfrac{1}{2}-z_i)$$

ith $z_i=0$. Twelve kinds of parameters, x_i nd y_i, are given by

$$\begin{array}{ll} x_1=0.1,\ y_1=0.1\ ; & x_7=0,\ \ y_7=0.4 \\ x_2=0.2,\ y_2=0\ \ ; & x_8=0.6,\ y_8=0.2 \\ x_3=0.2,\ y_3=0.2\ ; & x_9=0.2,\ y_9=0.6 \\ x_4=0.1,\ y_4=0.3\ ; & x_{10}=0.6,\ y_{10}=0.4 \\ x_5=0.3,\ y_5=0.1\ ; & x_{11}=0.8,\ y_{11}=0.2 \\ x_6=0.4,\ y_6=0\ \ ; & x_{12}=0,\ \ y_{12}=0.2 \end{array}$$

: is most reasonable to arrange 4 and 16 anganese atoms on 4 (c) positions and two inds of 8 (g) positions, respectively. The tructure amplitudes are given by

$$\text{(i)}\quad F=4E_{\mathrm{Mn}}+8\sum_{i=1}^{12}E_i \cdot\cos\pi[(H_1-H_2)x_i+(H_1+H_2)y_i] \cdot\cos\pi[(H_1+H_2)x_i-(H_1-H_2)y_i]\ ,$$

or $H_1+H_2=2n$, $H_2+H_3=2n$;

$$\text{(ii)}\quad F=-8\sum_{i=1}^{12}E_i \cdot\sin\pi[(H_1-H_2)x_i+(H_1+H_2)y_i] \cdot\sin\pi[(H_1+H_2)x_i-(H_1-H_2)y_i]\ ,$$

or $H_1+H_2=2n$, $H_2+H_3=2n+1$;

$$\text{(iii)}\quad F=0,$$

or $H_1+H_2=2n+1$, $H_2+H_3=2n$, and $H_1+H_2=2n+1$, $H_2+H_3=2n+1$,

here E_i is the atomic scattering factor for lectrons of i-th atom. After a detailed trial, it was found that there is no atomic arrangement which can completely explain the intensity distribution in Fig. 2 (b) by itself. But kinds of we consider the following two kinds of positions of manganese: (A), $(x_4, y_4, 0)$ and $(x_9, y_9, 0)$, (B), $(x_5, y_5, 0)$ and $(x_8, y_8, 0)$. The former arrangement can explain only one half of the superlattice spots and the latter only the remaining superlattice spots. Fig. 3 shows the atomic arrangement corresponding to (A). It is readily understood that the arrangement corresponding to (B) is crystallographically identical with that in Fig. 3, that is to say, we can produce the former, (B), by rotating clockwise the latter, (A), about the a_3 axis by ~53°. Here, we shall call these two types of lattice "A-lattice" and "B-lattice", respectively. The intensity distribution in reciprocal space corresponding to the model in Fig. 3 (A-lattice) is derived as shown in Fig. 4. It should be noted that the reciprocal lattice shown in Fig. 2 corresponds not to a true single crystal lattice of Au_4Mn but to a superposition of the A- and B-lattices.

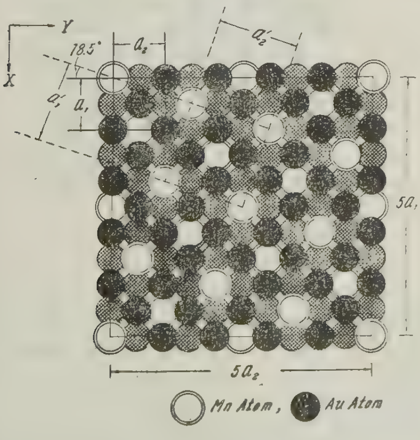

Fig. 3. The Au_4Mn structure corresponding to (A)-lattice, viewed along [001].

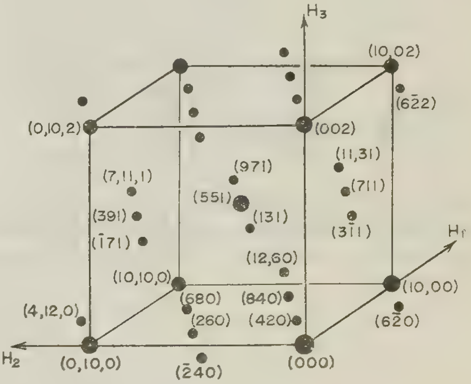

Fig. 4. Intensity distribution in reciprocal space corresponding to Fig. 3.

Although the unit cell with the size of $5a_1\times 5a_2\times a_3$ was adopted in the above analysis, it is known from Fig. 3 that a true unit cell of the ordered lattice is represented by the small cell indicated by the broaken lines in Fig. 3. It is body-centred tetragonal and 2.5 times as large as the fundamental cell in volume, the lattice constants being

$$a_1'=a_2'=\sqrt{5/2}\ a_1=6.45\text{Å}\ ,\quad a_3'=a_3=4.03\text{Å}\ ,$$
$$a_3'/a_1'=0.625\ .$$

Atoms included in the cell are ten, i.e. eight gold and two manganese atoms. The space group for this cell is $I4/m-C_{4h}^5$, and two manganese atoms are placed in 2 (*a*) at 0, 0, 0 and $\frac{1}{2}, \frac{1}{2}, \frac{1}{2}$ and eight gold atoms in 8 (*h*) $\{(0, 0, 0;\ \frac{1}{2}, \frac{1}{2}, \frac{1}{2}) + x', y', 0;\ \bar{x}', \bar{y}', 0;\ \bar{y}', x', 0;\ y', \bar{x}', 0\}$ with parameters $x'=0.2$, $y'=0.4$. The structure amplitudes are given by

$$F'=2E_{\mathrm{Mn}}+4E_{\mathrm{Au}}\{\cos 2\pi(H_1'x'+H_2'y') + \cos 2\pi(H_1'y'-H_2'x')\}\ . \qquad (2)$$

The relation between the reciprocal lattice corresponding to the new cell and that in Fig. 4 is shown in Fig. 5, where indices refer to the true cell. The calculated intensities, using Eq. (2), are tabulated in Table I and agree satisfactorily with the present observation and also with the X-ray result obtained by Kussmann and Raub[2].

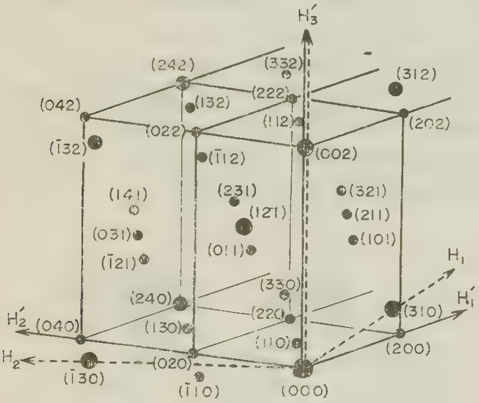

Fig. 5. The relation between the reciprocal lattice corresponding to the body-centred tetragonal cell and that in Fig. 4. Indices refer to the b.c.t. cell.

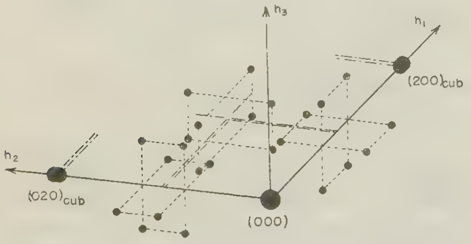

Fig. 6. Sixfold superposition of the intensity distribution in reciprocal space.

While Fig. 4 or 5 represents the intensity distribution in reciprocal space corresponding to one orientation of the lattice, there are six possible orientations in an actual ordered alloy, because, first, the a_1' axis in Fig. 3 can take either position making a positive or negative angle of 18.5° to one of the original cubic axes, corresponding to the above-mentioned *A*- or *B*-lattice and, secondly, the tetragonal axis can lie along any of the three original cubic axes, as already considered in the introduction of Fig. 2 (a). In Fig. 6, the sixfold superposition of intensity distribution is given. Photo. 1 (c) corresponds to the intensity distribution in the plane of coordinates of Fig. 6, while the arrows in Photo. 1 (d) indicate the intensities not lying in this plane.

§ 4. Discussion

In the present electron diffraction study it was elucidated that the ordered Au_4Mn alloy has not the so-called anti-phase domain structure in spite of the resemblance between the diffraction patterns of the present alloy and those of the ordered alloys CuAu (II)[4], Cu_3Pd[5] and Au_3Mn[1] but a body-centred tetragonal lattice belonging to the space group $I4/m-C_{4h}^5$, as described in the preceding chapter. This type of ordered structure has already been found by Harker[7] in the alloy Ni_4Mo.

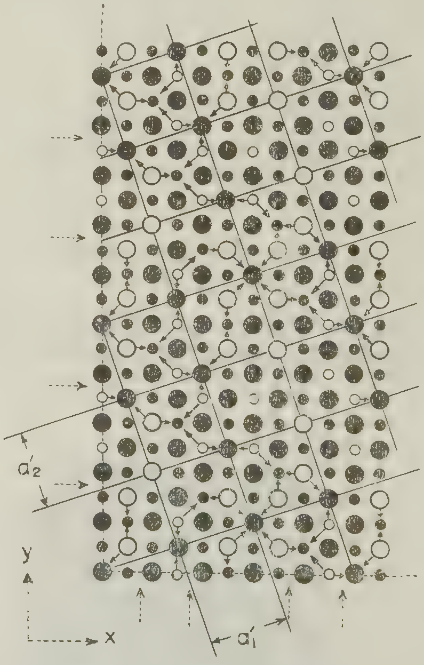

Fig. 7. The relation between the ordered Au_3Mn-type structure and the ordered Au_4Mn-type structure. The open and closed circles represent Mn and Au atoms, respectively. Out-of-steps in the Au_3Mn structure occur at places indicated by dotted arrows. The full arrows show the possibility of interchange between nearest neighbor atoms.

He determined this structure, analyzing X-ray Debye patterns, and called the fifth ordered structure of the face-centred cubic lattice. Subsequently, Epremian and Harker[8] found the same type of structure also in the alloy Ni$_4$W. It seems noticeable that the Ni$_4$Mo-type ordered structure was confirmed in the present case, using single-crystalline patterns of evaporated films.

As seen from the patterns in Photo. 1, the Au$_4$Mn alloy possesses the ordered Au$_3$Mn-type structure above about 400°C. Here, we shall consider the mechanism of the structural transition between the ordered Au$_4$Mn and Au$_3$Mn in terms of both the present model and the atomic arrangement elucidated in Part I. One of examples of the atomic arrangement of Au$_3$Mn-type corresponding to the pattern in Photo. 1 (a) is shown in Fig. 7, where M_1 and M_2 are assumed to be 1.2 and 2.2 respectively, the dotted lines represent the line-up directions of anti-phase domains and the full lines correspond to the directions parallel to a_1' and a_2' axes of Au$_4$Mn lattice. It is readily known that the transformation can be done only by the interchange of nearest neighbor atoms, as shown by full arrows in Fig. 7. While the above model corresponds to the 25 per cent manganese alloy, the circumstances seem to be much the same for 20 per cent manganese alloy.

Manganese atoms are farther distant from one another in the present ordered structure than in the ordered Au$_3$Mn: all the twelve first nearest neighbors* of a manganese atom are gold atoms, and among the second and third nearest neighbors there are only two and eight manganese atoms, respectively, manganese-manganese distance being 4.03 and 4.99 Å, which are far larger than in metallic manganese. These circumstances may be responsible for the occurrence of ferromagnetism in the ordered Au$_4$Mn alloy.

The present author wishes to express his sincere thanks to Professor S. Ogawa for the kind guidance and encouragement. His thanks are also due to Dr. M. Hirabayashi whose discussion was very useful.

The present investigation has partly been supported by the fund of the Ministry of Education in Aid of Scientific Researches.

References

1) D. Watanabe: J. Phys. Soc. Japan **15** (1960) 1030.
2) A. Kussmann and E. Raub: Z. Metallkde. **47** (1956) 9.
3) A. J. P. Meyer: Compt. rend. **242** (1956) 2315.
4) S. Ogawa and D. Watanabe: J. Phys. Soc. Japan **9** (1954) 475.
5) D. Watanabe and S. Ogawa: J. Phys. Soc. Japan **11** (1956) 226.
6) K. Fujiwara, M. Hirabayashi, D. Watanabe and S. Ogawa: J. Phys. Soc. Japan **13** (1958) 167.
7) D. Harker: J. Chem. Phys. **12** (1944) 315.
8) E. Epremian and D. Harker: Trans. Amer. Inst. Mech. Engrs. **185** (1949) 267; J. Metals **1**. April.

---

* In considering the nearest neighbors, the slight tetragonality is neglected.

JOURNAL OF THE PHYSICAL SOCIETY OF JAPAN, Vol. 15, No. 7, JULY, 1960

The Binding Energy of the σ Bond, II. Application to the Diamond Crystal.

By Kiyosi O-OHATA

Physics Department, Tokyo Institute of Technology
O-okayama, Meguro-ku, Tokyo

(Received November 17, 1959)

A calculation of the cohesive energy of the diamond crystal has been carried out by using the general scheme which is derived by the Heitler-London approximation in the preceding article. It has been found that the value of the binding energy is about 3.26 eV per a bond in rather good agreement with the observed one.

§ 1. Introduction

In the preceding article[1] we have derived the general scheme for calculating the binding energy of the σ bond. The aim of this article is to apply this scheme to the calculation of the binding energy of the C–C bond in the diamond crystal.

§ 2. Atomic Wave Functions and Energy Leaves

We will use the following atomic orbitals of the Slater type:

$$\left.\begin{aligned} (1s)&=\sqrt{\frac{\delta_0^3}{\pi}}\exp(-\delta_0 r)\,,\\ (2s^\circ)&=a\sqrt{\frac{\delta^5}{3\pi}}\,r\exp(-\delta r)+b(1s)\,,\\ (2px)&=\sqrt{\frac{\delta^5}{\pi}}\,x\exp(-\delta r),\ \text{etc.}\end{aligned}\right\} \qquad (2.1)$$

where δ_0 and δ are parameters of which values are here taken to be 5.70 and 1.60, respectively. These values are chosen so as to be approximately equal to the corresponding ones given by Slater and Zener.[2] The small difference of these values may not yield any serious change to the following results. a and b are parameters determined by the condition of the orthogonalization between $1s$ and $2s$ functions. The total energy of the ground state and the energies of the excited states relative to that of the ground state are calculated, of the carbon atom, by the use of the atomic orbitals (2.1). The results are given in Table I, where the comparison is made with the corresponding experimental ones.

As a whole, the agreement between the calculated values and the observed ones is satisfactory in spite of the somewhat arbitrary choice of the parameters. The calculated value of the total energy of the ground state is 6.4 eV larger than the experimental one.

Table I. The total energy of the ground state and the energies of the excited states relative to the ground state of the carbon atom.

Electron configurations	States	Calc. values (in eV)*	Exp. values[3] (in eV)
	^3P	0.00 (−1023.4)**	0.00 (−1029.8)**
s^2p^2	^1D	1.84	1.26
	^1S	4.59	2.68
	^5S	2.70	4.16
	^3D	8.83	7.94
sp^3	^3P	10.66	9.33
	^3S	15.58	—
	^1D	16.20	13.12
	^1P	17.41	—

* We take 1 a.u. as 27.204 eV.

** The values in brackets are the total energy of the ground state.

This state of affairs does not change appreciably, even if we use the Hartree wave functions.[4] As seen from Table I the calculated excitation energy to the ^5S state is smaller than the experimental one by about 1.5 eV. This can be expected from the fact that the correlational energy in the ^5S states is smaller than that in the ^3P state. Thus we take the ^5S state as a reference level in the calculated atomic energies, and assume that the ground state ^3P lies by 4.16 eV below the ^5S state, taking into account the exerimental value for the energy separation between these states. The energy of the ground state determined in such a way is also about 5 eV larger than the experimental one. This difference is mainly due to the correlational energy between the two electrons in the 1*s* orbital. The detail discussion on this problem was reported by Arai and Onishi.[5] The discrepancy between the calculated and experimental values above mentioned may not give rise any any serious error in the calculation of the binding energy, since it might be legitimate to treat the two electrons in the 1*s* orbital as the core electrons and to assume the same correlational energy in both of the free and bound atoms. The tetrahedral valence state V_{4t} of the carbon atom is calculated to be 4.15 eV above the ^5S state. Thus we assume 8.31 eV for the excitation energy of V_{4t} state from the ground state. This value corresponds to the promotional energy for the infinitely separated atom in diamond in the Heitler-London approximation.

Table II. The ionization potentials and electron affinities in the valence state of the carbon atom.

		Calc. values	Estimated values
Ionization potentials	$E(C^+,\ p^3,\ V_3)-E(C,\ sp^3,\ V_4)$	19.74 eV	21.06 eV
	$E(C^+,\ sp^2,\ V_3)-E(C,\ sp^3,\ V_4)$	9.54	11.17
Electron affinities	$E(C,\ sp^3,\ V_4)-E(C^-,\ sp^4,\ V_3)$	−7.50	0.69
	$E(C,\ sp^3,\ V_4)-E(C^-,\ s^2p^3,\ V_3)$	4.31	8.79

We have also calculated the ionization potential and the electron affinity for the valence state $V_4(sp^3)$ of the carbon atom. These correspond to the case where one electron is subtracted from or added to the electron configuration $1s)^2 2s)^1 2px)^1 2py)^1 2pz)^1$. The result is listed in Table II, where the values estimated by Mulliken[6] are given for comparison. As seen from this table, our atomic orbitals are suitable to compute the ionization potential, but not to the electron affinity. This is familiar fact suggested by Moffitt,[7] but we do not adopt any particular treatment to avoid this defect. For necessity in the calculation of the later section, we have also computed the ionization potential for the tetravalent state $V_{4t}(sp^3)$ to be 13.24 eV.

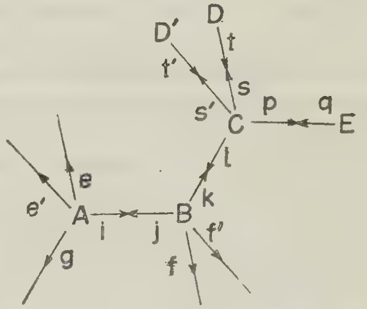

Fig. 1. Structural Diagram of the Diamond lattice. Capital letters show the constituent atoms and small letters denote the directional valence orbitals.

§ 3. The Binding Energy of Diamond Crystal

Diamond consists of the equivalent carbon atoms liked together by the equivalent C–C σ bonds and can be considered as a saturated giant molecule. The spatial arrangement of the atoms in the diamond crystal is shown in Fig. 1. We assume the nuclear distance between the nearest neighbour atoms to be 1.54 A. The method for the calculation of the binding energy of the σ bond with the Heitler-London method was given in I. The binding energy $D(AB)$ of a bond A–B in a saturated molecule was given by Eq. (6.1) in I, that is,

$$
\begin{aligned}
D(AB)=Q(AB)&+\sum_{C}\frac{1}{n_A+n_C}Q(AC)\\
&+\sum_{D}\frac{1}{n_B+n_D}Q(BD)+J(ij)\\
&-\frac{1}{4}\sum_{(kl)\neq(ij)}J(ij,\ kl)\\
&+\left\{\frac{1}{n_A}(E_A{}^*-E_A)+\frac{1}{n_B}(E_B{}^*-E_B)\right\},
\end{aligned}
\tag{3.1}
$$

where n_A, n_B, n_C and n_D are the total numbers of the valence orbitals of the atoms A, B, C and D, respectively, and all of them are equal to 4 in the diamond. $E_A{}^*-E_A$ and $E_B{}^*-E_B$, being the promotional energy from the ground state to the tetravalent state in the carbon atom, are taken, from the preceding paragraph, as

$$E_A{}^*-E_A=E_B{}^*-E_B=8.31\ \text{eV}. \tag{3.2}$$

The expressions of $Q(AB)$, $Q(AC)$, $Q(BD)$, $J(ij)$ and $J(ij,\ kl)$ are given in I in terms of the overlap and molecular energy integrals, of which values can be obtained by using the tables given by Kotani et al..[8] After a tedious calculation we get

$$D(AB)=-3.54\ \text{eV} \tag{3.3}$$

as the binding energy of a C–C bond in the diamond crystal. To obtain the value (3.3) from Eq. (3.1), we took the summations $\sum_{C}$ and $\sum_{D}$ in Eq. (3.1) only over the second neighbour atoms from the atoms A and B, respectively, since the total contribution from the third neighbours is very small ($\simeq -0.005$ eV). We also took the summation $\sum'_{(kl)}$ in Eq. (3.1) over the nearest and second nearest neighbour bonds with respect to the bond (ij), since the value of $\Delta(ij,\ kl)$, which is found in the expression of $J(ij,\ kl)$ and manifests the effect of the non-orthogonality between the two bonds (ij) and (kl), may be exceedingly small in the case that the two bonds (ij) and (kl) are the third or more remote neighbours. The values of $\Delta(ij,\ kl)$ are listed in Table III for the first and second neighbour bonds, and the values of the corresponding $J(ij,\ kl)$ are listed in Table IV. The values of the other terms in Eq. (3.1) are

$$Q(AB)=-5.773\ \text{eV},\quad J(ij)=-4.50\ \text{eV}$$

and

$$\frac{1}{8}\left\{\sum_{C}Q(AC)+\sum_{D}Q(BD)\right\}=-0.317\ \text{eV}.$$

In the evaluation of the value of $J(ij,\ kl)$, we assumed that the values of the many center energy integrals can be estimated by the Mulliken approximation analogous to Eq. (5.6) in I, and further $J(ij,\ kl)$ involves the operator depending only on the potential of the atoms to which the orbitals ϕ_i, ϕ_j, ϕ_k and ϕ_l belong. The latter assumption is approximately warranted by the former assumption. This is explained in the following.

The original form of $J(ij,\ kl)$ can be written so as to involve the potential of the whole molecule, that is, it is seen from Eq. (4.6) in I that the terms of the following two types

Table III. The values of Δ's.

	Nearest neighbour	Second neighbours*	
		gauche	trans
$\Delta(ij,\ kl)$	0.05555 34	0.01248 76	0.01407 17

* There are two kinds of the second neighbour bonds with respect to a bond (ij), as seen from Fig. 1. The first locates at the gauche position and the second at the trans position for the bond (ij).

Table IV. The values of $J(ij,\ kl)$. (in eV)

	Nearest neighbour	Second neighbours	
		gauche	trans
$J(ij,\ kl)$	−1.543	−0.161	−0.066

$$\alpha_i = I_{ii} + \sum_{(pq)}'' \frac{1}{1+S_{pq}^2}(C_{ip}+C_{iq}+2S_{pq}D_{i,pq}) \tag{3.4}$$

and

$$\beta_{ij} = I_{ij} + \sum_{(pq)}'' \frac{1}{1+S_{pq}^2}(D_{p,ij}+D_{q,ij} + 2S_{pq}N_{pq,ij}) \tag{3.5}$$

are involved in $J(ij, kl)$, where $I_{ij}=(\phi_i|h|\phi_j)$, h is the part of the total Hamiltonian depending only on one electron, $C_{ip}=(\phi_i\phi_i;\ \phi_p\phi_p)$, $D_{i,pq}=(\phi_i\phi_i;\ \phi_p\phi_q)$, $N_{pq,ij}=(\phi_p\phi_q;\ \phi_i\phi_j)$, and the summation extends over all the orbital pairs other than the two pairs (ij) and (kl). Using the Mulliken approximation, we can estimate the above two terms as

$$\left.\begin{aligned} \alpha_i &= I_{ii} + \sum_{(pq)}'' (C_{ip}+C_{iq})\ , \\ \beta_{ij} &= I_{ij} + \sum_{(pq)}'' (D_{p,ij}+D_{q,ij})\ . \end{aligned}\right\} \tag{3.6}$$

These involve the potential $\mathscr{V}^X$ of the atom X which is expressed as

$$\mathscr{V}^X = V^X + \sum_x C_x\ , \tag{3.7}$$

where V^X denotes the core potential of the atom X, C_x represents the Coulomb potential due to the electron in the orbital ϕ_x, ϕ_x is a valence orbital of the atom X. This potential is the one due to the neutral atom X, and its expectation value will, of course, be small. In terms of $\mathscr{V}^X$ Eq. (3.6) are rewritten as

$$\left.\begin{aligned} \alpha_i &= \mathscr{K}_{ii} + \sum_X \mathscr{V}_{ii}^X - (C_{ii}+C_{ij}+C_{ik}+C_{il})\ , \\ \beta_{ij} &= \mathscr{K}_{ij} + \sum_X \mathscr{V}_{ij}^X - (D_{i,ij}+D_{j,ij}+D_{k,ij}+D_{l,ij}), \end{aligned}\right\} \tag{3.8}$$

where

$$\mathscr{K}_{ij} = \left(\phi_i \left| -\frac{1}{2}\varDelta \right| \phi_j\right),$$

and the summation $\sum_X$ extends over all the atoms of the molecule. Furthermore, we use the Mulliken approximation for the many center energy integrals involved in β_{ij}:

$$\mathscr{V}_{ij}^X = \frac{1}{2}S_{ij}(\mathscr{V}_{ii}^X + \mathscr{V}_{jj}^X)\ , \tag{3.9}$$

if the atom X is the one other than the atoms to which ϕ_i and ϕ_j belong. If we apply the above treatment to the other α's and β's appearing in the expression of $J(ij, kl)$, it is easily seen that the potential of the atoms to which the orbitals ϕ_i, ϕ_j, ϕ_k and ϕ_l do not belong drops out from the expresssion of $J(ij, kl)$. If $J(ij, kl)$ is the exchange term between adjacent bonds and ϕ_j and ϕ_k are the different orbitals of the same atom, we cannot use the Mulliken approximation in the second step. In this case, it may be plausible to assume that the value of $\mathscr{V}_{jk}^X$ is small enough to be neglected because of the orthogonality between ϕ_j and ϕ_k. If we adopt the notations for the atoms and orbitals as shown in Fig. 1, we must take into account, for the computation of $J(ij, kl)$, only the atoms A, B, and C, and the orbitals belonging to these atoms, for that of $J(ij, st)$, only the atoms A, B, C and D and the atomic orbitals belonging to these atoms, and so on.

As the result of the above calculation, we have found that the value of the binding energy depends considerably on the exchange terms between the nearest neighbour bonds, but not appreciably on those between the second neighbour bonds. We note here that hitherto we followed the definition (5.6) in I for $J(ij)$. If, however, we assume that the valence orbitals fulfil Eq. (5.8) in I and adopt the definition (5.9) in I for $J(ij)$, we obtain the value of the exchange terms between adjacent bonds to be -0.124 eV. This value is very small compared with the one listed in Table IV. This apparent discrepancy comes mainly from the difference of the subtraction of the exchange integrals from $J(ij, kl)$ in the above two treatments. In the latter treatment, we obtain -4.38 eV as the value of $D(AB)$, by neglecting the contribution of the second or more remote neighbour bonds, as it may be much smaller than that of $J(ij, kl)$. This value of $D(AB)$ is somewhat different from that in (3.3), but this discrepancy seems not be so serious as that of $J(ij, kl)$. Although it must be kept in mind that the atomic wave function used here is not a good approximation for the eigenfunction of the Hartree-Fock type equation (5.8) in I, particularly at the region distent from the atomic nucleus, the above fact suggests that the effect of the exchange terms can be reduced if the appropriate atomic orbitals are used and the intra-atomic exchange integrals are taken into account adequately.

§ 4. Discussion

In the estimation of the molecular energy integrals in the preceding section, we assumed that the core potential of an atom can be replaced by the nuclear potential with an effective nuclear charge, that is,

$$V_{ij}{}^{A}=\int \phi_i(1)\,\frac{4}{r_{A1}}\,\phi_j(1)dv_l\ . \tag{4.1}$$

The effect of the extension of the 1s orbital was discussed by Nagahara,[9] who suggested that the contribution from this effect to the binding energy is by no means unimportant even at the equilibrium nuclear distance. There are two reasons which affect the value of the binding energy from this effect. The one comes from the fact that we must orthogonalize the valence orbital to 1s orbital of the other atoms. The second comes from we must consider the exchange terms between the two orbitals mentioned above. To study the first point, though it is preferable that we orthogonalize each valence orbital to the core orbitals of all the other atoms, it may be sufficient, as discussed in § 3 of I, that we orthogonalize the valence orbital only to the core orbitals of the atom bonded with the considering valence orbital, because of the smallness of the other overlap integrals in our case. For the bond A–B between the atoms A and B the revised valence orbitals are

$$\left.\begin{aligned}\tilde{\phi}_i{}^{A}&=\frac{1}{\sqrt{1-T_{i\nu}{}^2}}\,(\phi_i{}^{A}-T_{i\nu}\phi_\nu{}^{B})\ ,\\ \tilde{\phi}_j{}^{B}&=\frac{1}{\sqrt{1-T_{j\mu}{}^2}}(\phi_j{}^{B}-T_{j\mu}\phi_\mu{}^{A})\ ,\end{aligned}\right\} \tag{4.2}$$

where $\phi_i{}^{A}$ and $\phi_j{}^{B}$ are the valence orbitals of the atoms A and B, respectively, and are responsible for the construction of the bond A–B, $\phi_\mu{}^{A}$ and $\phi_\nu{}^{B}$ are the 1s orbitals of the atoms A and B, respectively, and $T_{i\nu}$ is the overlap integral between $\phi_i{}^{A}$ and $\phi_\nu{}^{B}$. In the molecular integrals involving these modified valence orbitals (4.2), can be calculated by expanding the integrals as a power series of $T_{i\nu}$. We neglected the third and higher order terms of this series due to the smallness of the value of $T_{i\nu}$. Following the above treatment, it is found that the effect of the overlap reduces the binding energy by about 0.67 eV per a bond. To study the second point, we calculated $-K_{i\nu}-K_{j\mu}$, where $K_{i\nu}$ and $K_{j\mu}$ are the exchange integrals between the valence orbital of one atom and the core orbital of another in the bond (ij). The method of calculation is the same as that in Kotani's Table.[8] The values of the auxiliary functions are found by interpolating the ones given by this table. The result is found to be -0.39 eV per a bond. Thus the total effect of the extension of the 1s orbitals on the binding energy is about 0.28 eV per a bond. This result seems to be somewhat different from Nagahara's result. With the value (3.3), the resultant binding energy of the C–C bond in the diamond crystal is found to be 3.26 eV, while the experimental one is 3.712 eV, although several different experimental values are reported.[10]

Nagahara also calculated the binding energy of the C–C bond in the investigation of the electronic state of a C–C radical. The fundamental equation (30) in his articale shows that the normalization factor of the total wave function is $(1+k-ks^2)^{-1/2}$, where k is the square of the overlap integral between bonded orbitals and s^2 is the sum of the square of the overlap integrals between unpaired orbitals. It seems to be rather strange that the normalization factor does not involve the term which depends on s^2 alone. Schmid[10] also calculated the binding energy of the diamond crystal with the use of the orthogonalized atomic orbitals, where the effect of non-orthogonality was considered up to the second order of all the overlap integrals. Such treatment seems not to be legitimate as there are some large overlap integrals, of which third order terms are unable to be neglected. On the other hand, in our treatment the overlap integrals are classified into two classes by utilizing the directional character of the valence orbitals. The overlap integral between paired orbitals is very large: $S\simeq 0.7$, and that between unpaired orbitals is very small: $T\simeq 0.1$. Then, S should be throughly taken into account, while T^3 and higher order terms can be neglected. Through this treatment, Eq. (3.1) was derived in I. From the actual calculation in the preceding section, we found that we can obtain a good approximate value for the binding energy of the σ bond, if we take the Coulomb and exchange terms between bonded orbitals and the exchange terms between the nearest neighbour bonds, since the contribution of the exchange terms between the second neighbour bonds is not appreciable. It, then, seems to be plausible that we neglect the exchange terms between the third or more remote neighbour bonds. As to the Mulliken approximation (5.6) in I we already discussed in § 6 of I. Furthermore, as seen from the discussion in the preceding section, the use of the Mulliken approximation served to show that the potential of the effectively neutralized atoms cancel out in the expression of $J(ij, kl)$. Then in our calculation a significant error may not arise from the use of the Mulliken approximation for the estimation of the values of the many center energy integrals. Furthermore we assumed that the orthogonalized $2s$ atomic orbital can be replaced by the non-orthogonal one in the calculation of the two electron molecular integrals other than some of Coulomb integrals. This may be serious but the order of magnitude of each term discussed in the preceding section seems not to vary radically by this approximation.

It will be reported in the next article of this series to revise the calculated value of the binding energy with the inclusion of the ionic terms of the bond.

The author wishes to express his sincere thanks to Professor K. Niira for his incessant encouragement and also for his kind reading of the manuscript, and to Professor E. Ishiguro for his valuable suggestions. The author is indebted to the Ministry of Education for the research grant.

References

1) K. O-ohata: J. Phys. Soc. Japan **15** (1960) 1048. This paper will be refered to as I.
2) J. C. Slater: Phys. Rev. **36** (1930) 57. C. Zener: Phys. Rev. **36** (1930) 51.
3) W. Moffitt: Proc. Roy Soc. **A, 220** (1950) 534.
4) C. W. Ufford: Phys. Rev. **53** (1938) 568.
5) T. Arai and T. Onishi: J. Chem. Phys. **26** (1957) 70.
6) R. S. Mulliken: J. Chem. Phys. **2** (1934) 782.
7) W. Moffitt: Proc. Roy. Soc. **A, 215** (1951) 245.
8) M. Kotani, A. Amemiya, E. Ishiguro and T. Kimura: *Table of Molecular Integrals* (Maruzen Co., 1955). M. Kotani, E. Ishiguro, K. Hijikata, T. Nakamura and A. Amemiya: J. Phys. Soc. Japan **8** (1953) 463. M. Kotani, E. Ishiguro and K. Hijikata: J. Phys. Soc. Japan **8** (1954) 553.
9) S. Nagahara: J. Phys. Soc. Japan **14** (1959) 331.
10) L. A. Schmid: Phys. Rev. **92** (1953) 1373.

JOURNAL OF THE PHYSICAL SOCIETY OF JAPAN, Vol. 15, No. 7 JULY, 1960

Magnetic Properties of the Pd and Pt Group Transition Metal Complexes

By Hiroshi KAMIMURA,
Department of Physics, Faculty of Science, University of Tokyo
Shoichiro KOIDE,
Institute of Physics, College of General Education, University of Tokyo
Hisao SEKIYAMA,
Faculty of Engineering, Kanagawa University
and Satoru SUGANO*
Department of Physics, Faculty of Science, University of Tokyo

(Received March 26, 1960)

The magnetic susceptibilities and the g-values of the Pd and Pt group transition metal complexes are calculated by means of the intermediate coupling scheme. Crystalline field with cubic symmetry is assumed to be strong, so that the effect of $d\gamma$ orbitals is neglected. The effect of Coulomb repulsion is considered to be comparable with that of the spin-orbit interaction. The results are expressed by functions of parameters $\eta=\zeta_d/(3B+C)$ and kT/ζ_d, where B and C are Racah's parameters and ζ_d the coefficient of spin-orbit coupling of a d-electron. Comparison with available experimental data is also made.

§ 1. Introduction

As the result of growing interest in the magnetic properties of the Pd($4d$) and Pt($5d$) group transition metal compounds, several experimental works have recently been carried through concerning the electron spin resonance and the susceptibility on these salts. It is well known that the general aspect of the magnetic moments (some are very near to the free ion values but some are much lower than those) are well accounted for by the Van Vleck and the Pauling models. Kotani[1] explained the behaviour of the low magnetic moments and their temperature variations quantitatively by taking the spin-orbit coupling of the d-electrons into account. He obtained good agreements with experiments as far as the first ($3d$) transition metal complexes are concerned.

Quite recently, Figgis et al[2] have applied the Kotani theory to the magnetic susceptibility of the Pd and Pt group transition metal complexes and found remarkable discrepancies between their experimental values and those obtained by the Kotani theory. For example, the ions with $(5d\varepsilon)^3$ configuration have the effective Bohr magneton numbers fairly smaller than the values expected from the theory. According to the theory all the octahedral complex ions with $d\varepsilon^3$ configuration should have the temperature independent value 3.88 of the effective Bohr magneton number, which is fairly large compared with the experimental values mentioned in Table I. For comparison, those of the iron group complexes, which agree very well with the Kotani theory, are also listed in the table.

Table I.

Iron Group	$n_{300°K}$	Platinum Group	$n_{300°K}$	n'_{eff}	ϑ(°K)
$K_3[Cr(CN)_6]$	3.74β	K_2ReF_6	3.32β	3.50β	40
$[Cr(NH_3)_6]I_3$	3.80β	K_2ReCl_6	3.25β	3.70β	86
$[Cr(NH_3)_6]Br_3$	3.77β	K_2ReBr_6	3.19β	3.70β	105
$[Cr(OC(NH_2)_2)_6]Cl_3$	3.64β	K_2ReI_6	3.32β	3.70β	100
$[Cr(OH_2)_6]Cl_3$	3.78β	K_2OsF_6	3.2 β		

In order to clarify the reason of the discrepancies, let us mention the basic assumptions of the Kotani theory:

(i) the effects of the ligand field are much greater than those of the Coulomb repulsion between the d-electrons;

---

* Present address: Bell Telephone Laboratory, Murray Hill, N.J., U.S.A.

(ii) the Coulomb repulsion is much stronger than the spin-orbit coupling;

(iii) the ligand field is of perfectly cubic symmetry; and

(iv) the magnetic interaction between ions is negligible.

Recent experiments on the electron spin resonance yield the evidence that the charge clouds of the $4d$- and $5d$-electrons spread much more widely than the $3d$-electrons. The assumption (iv) is, therefore, not correct in the former case.

The spin-orbit coupling is also very strong for the $4d$- and $5d$-electrons, and has the strength comparable to the Coulomb repulsion. Therefore, the assumption (ii) is also invalid for these electrons. Thus we may conclude that the discrepancies arise from the assumptions (ii) and (iv) which are not satisfied by the $4d$- and $5d$-electrons.

In fact, Figgis et al have measured the susceptibilities of the salts mentioned in Table I over the temperature region 80° to 300°K and found that the observed values of the susceptibilities obey the Curie-Weiss law $\chi = C/(T+\vartheta)$. Thus they attribute a part of the enormous lowering of the magnetic moments to the anti-ferromagnetic interaction between ions. If one considers, after Figgis et al, that the effects of such interaction are all involved in the Weiss constant ϑ, then the effective Bohr magneton number will be given by the expression $n'_{eff} = 2.84\sqrt{\chi(T+\vartheta)}$. The values of n'_{eff} obtained in this manner are listed in Table I. These may be regarded as the magnitudes of the magnetic moments of the individual ions, and the deviation of their values from those predicted by the Kotani theory may be due to the break-down of the assumption (ii). From this standpoint we will pay attention only to the values of n'_{eff} and examine the interplay between the Coulomb interaction and the spin-orbit coupling.

In the present work, therefore, we shall calculate the energy eigenvalues and the magnetic susceptibilities for each of the electron configurations $d\varepsilon^n$ ($n=1, 2, \cdots, 5$) assuming only (i) and (iii).

Since the effect of the spin-orbit interaction is comparable to that of the Coulomb repulsion for the $4d$ and $5d$ transition group complexes, the intermediate coupling scheme has to be adopted for our purpose. For the configuration $d\varepsilon^1$, however, there is no Coulomb repulsion. Hence we need not consider the effect of the Coulomb interaction in this case. Since $d\varepsilon^5$ is regarded as the configuration in which there remains one hole in the closed shell $d\varepsilon^6$, the level scheme is the same as that of the $d\varepsilon^1$ configuration. The Kotani theory can, therefore, be applied to $d\varepsilon^1$ and $d\varepsilon^5$ even in the case of very strong spin-orbit coupling. The configuration $d\varepsilon^4$ can also be treated in the same scheme as $d\varepsilon^2$ except for changing the sign of the spin-orbit coupling parameter. After all, we have only to calculate the energy eigenvalues for the configurations $d\varepsilon^2$ and $d\varepsilon^3$.

§ 2. Energy Levels

The Hamiltonian of a transition metal ion in an external magnetic field is given by

$$\mathscr{H} = \mathscr{H}_0 + V_{\text{cubic}} + \sum_{i>j} \frac{e^2}{r_{ij}} + \zeta_d \sum_i \boldsymbol{l}_i \cdot \boldsymbol{s}_i + \beta \boldsymbol{H} \cdot \sum_i (\boldsymbol{l}_i + 2\boldsymbol{s}_i) \quad (1)$$

where $\mathscr{H}_0$ stands for the sum of the kinetic- and the potential energy of d-electrons moving in the field due to the atomic core of the ion. The third term denotes the Coulomb repulsion between the d-electrons, and the fourth term is their spin-orbit interaction. The last term expresses the Zeeman energy due to the external magnetic field. As is emphasized in § 1, the purpose of the present paper is to show the joint effects of the spin-orbit interaction and of the Coulomb repulsion on the magnetic properties of the complex ion. Hence, for simplicity, the ligand field expressed by the second term of (1) is assumed to be completely cubic and the field components with lower symmetry will be neglected. Besides we assume that all the effects of the magnetic interaction between ions are included in the Weiss constant ϑ.

According to the assumption (i), the ligand field is so strong that the splitting between $d\varepsilon$ and $d\gamma$ levels is sufficiently large and we shall disregard the effect of the latter orbitals. In the following, therefore, the effect of the ligand field will be implicitly involved in that we merely consider the configurations $d\varepsilon^n$ ($u=2$, 3 and 4). Thus the contribution of $\mathscr{H}_0 + V_{\text{cubic}}$ will not appear explicitly in the calculation because it only gives a constant term common to all the diagonal elements of the energy matrix.

For the configurations $d\varepsilon^2$ and $d\varepsilon^4$, the Coulomb repulsion between d-electrons gives rise to four levels ${}^3\mathrm{T}_1$, ${}^1\mathrm{E}$, ${}^1\mathrm{T}_2$ and ${}^1\mathrm{A}_1$. After Tanabe and Sugano[3], the eigenfunctions of these states will be denoted by the following:

$$\begin{array}{llll} {}^3\mathrm{T}_1: & |\alpha(M_s)\rangle, & |\beta(M_s)\rangle, & |\gamma(M_s)\rangle \qquad (M_s=1,0,-1)\,. \\ {}^1\mathrm{E}: & |u\rangle, & |v\rangle, & \\ {}^1\mathrm{T}_2: & |\xi\rangle, & |\eta\rangle, & |\zeta\rangle \\ {}^1\mathrm{A}_1: & |e\rangle\,. & & \end{array}$$

$d\varepsilon^2$: The matrix elements of the spin-orbit interaction with respect to the eigenfunctions mentioned above are given in Appendix I. We shall first omit the Zeeman energy term and diagonalize the Coulomb repulsion plus the spin-orbit interaction. The eigenvalues and the eigenfunctions thus obtained are the following:

$$W_1=\zeta_d/2 \qquad \text{(Triply degenerate)}$$

$$\psi_{10}=\frac{1}{2}[i\{|\alpha(1)\rangle+|\alpha(-1)\rangle\}+|\beta(1)\rangle-|\beta(-1)\rangle]$$

$$\psi_{1\pm1}=\frac{1}{2}\{i|\alpha(0)\rangle\mp|\beta(0)\rangle\}-\frac{i}{\sqrt{2}}|\gamma(\pm1)\rangle$$

$$\left.\begin{matrix}W_2\\W_3\end{matrix}\right\}=\frac{\zeta_d+Q}{2}\pm\frac{1}{2}\sqrt{(\zeta_d-Q)^2+8\zeta_d^2} \qquad \text{(the upper and lower signs correspond to } W_2 \text{ and } W_3 \text{ respectively)}$$

$$\left.\begin{matrix}\psi_2\\\psi_3\end{matrix}\right\}=\frac{1}{\sqrt{2\zeta_d^2+(Q-W_{2,3})^2}}\{\sqrt{2}\,\zeta_d|e(1)\rangle+(Q-W_{2,3})|\varphi_0\rangle\}$$

$$\left.\begin{matrix}W_4\\W_5\end{matrix}\right\}=\frac{P}{2}-\frac{\zeta_d}{4}\pm\frac{1}{2}\sqrt{\left(\frac{\zeta_d}{2}+P\right)^2+2\zeta_d^2} \qquad \text{(each has five-fold degeneracy specified by } \gamma_J)$$

$$\left.\begin{matrix}\psi_4(\gamma_J)\\\psi_5(\gamma_J)\end{matrix}\right\}=\frac{1}{\sqrt{\frac{\zeta_d^2}{2}+\left(\frac{\zeta_d}{2}+W_{4,5}\right)^2}}\left\{-\frac{\zeta_d}{\sqrt{2}}|\varphi_1(\gamma_J)\rangle+\left(\frac{\zeta_d}{2}+W_{4,5}\right)|\varphi_2(\gamma_J)\rangle\right\}$$

$$(\gamma_J=2,1,0,-1,-2)\,.$$

Here

$$P=2(3B+C) \quad \text{and} \quad Q=5(3B+C)\,,$$

B and C being the Racah parameters, and

$$|\varphi_0\rangle=\frac{1}{\sqrt{6}}\{i|\alpha(1)\rangle-i|\alpha(-1)\rangle+|\beta(1)\rangle+|\beta(-1)\rangle\}-\frac{i}{\sqrt{3}}|\gamma(0)\rangle$$

$$|\varphi_1(0)\rangle=\frac{1}{2\sqrt{3}}[i\{|\alpha(1)\rangle-|\alpha(-1)\rangle\}+\{|\beta(1)\rangle+|\beta(-1)\rangle\}]+\sqrt{\frac{2}{3}}\,i\,|\gamma(0)\rangle$$

$$|\varphi_1(\pm2)\rangle=\frac{1}{\sqrt{2}}\{i|\alpha(-1)\rangle\pm|\beta(-1)\rangle\}$$

$$|\varphi_1(\pm1)\rangle=\frac{1}{2}\{i|\alpha(0)\rangle\pm|\beta(0)\rangle\}+\frac{1}{\sqrt{2}}|\gamma(\mp1)\rangle$$

$$|\varphi_2(0)\rangle=|u\rangle$$

$$|\varphi_2(\pm 2)\rangle = \frac{1}{\sqrt{2}}\{|\zeta\rangle \pm i|v\rangle\}$$

$$|\varphi_2(\pm 1)\rangle = \frac{1}{\sqrt{2}}\{|\xi\rangle \pm i|\eta\rangle\}$$

$d\mathcal{E}^4$: All the expressions can be derived from those of $d\mathcal{E}^2$ by changing the sign of the spin-orbit interaction parameter ζ_d, i.e. $\zeta_d \to -\zeta_d$. The energy levels are shown in Fig. 1.
$d\mathcal{E}^3$: The Coulomb repulsion gives rise to four levels $^4A_2$, ^2E, $^2T_1$ and $^2T_2$ in this case. The eigenfunctions of these levels will be denoted by the following:

$$^4A_2: \quad |e^{++}\rangle, \quad |e^{+}\rangle, \quad |e^{-}\rangle, \quad |e^{--}\rangle$$

$$^2E\ : \quad |u^{+}\rangle, \quad |u^{-}\rangle, \quad |v^{+}\rangle, \quad |v^{-}\rangle$$

$$^2T_1: \quad |\alpha^{+}\rangle, \quad |\alpha^{-}\rangle, \quad |\beta^{+}\rangle, \quad |\beta\rangle, \quad |\gamma^{+}\rangle, \quad |\gamma^{-}\rangle$$

$$^2T_2: \quad |\xi^{+}\rangle, \quad |\xi^{-}\rangle, \quad |\eta^{+}\rangle, \quad |\eta^{-}\rangle, \quad |\zeta^{+}\rangle, \quad |\zeta^{-}\rangle$$

Here the plus and the minus signs correspond to the M_z values 1/2 and $-1/2$ respectively, and the double signs to those of 3/2 and $-3/2$ respectively.

The non-vanishing matrix elements of the spin-orbit interaction with respect to the above functions are given in Appendix II. By reducing the energy matrix without the Zeeman term, we can immediately determine eight of the eigenstates as:

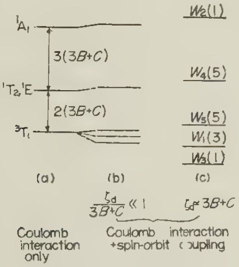

Fig. 1. A schematic energy-level diagram for $(d\varepsilon)^4$. Figures in parentheses represent degeneracy of each energy level.

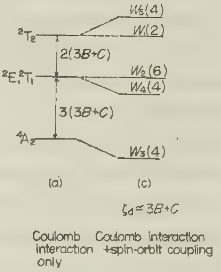

Fig. 2. A schematic energy-level diagram for $(d\varepsilon)^3$.

$W_1 = 15B + 5C$:

$$\frac{1}{\sqrt{3}}\{\pm i|\xi^{\pm}\rangle + |\eta^{\pm}\rangle - i|\zeta^{\mp}\rangle\}$$

$W_2 = 9B + 3C$

$$\frac{1}{\sqrt{5}}\{3|u^{\pm}\rangle - i|\alpha^{\mp}\rangle \mp |\beta^{\mp}\rangle\}$$

$$\frac{1}{\sqrt{2}}\{|v^{\pm}\rangle \pm i|\gamma^{\pm}\rangle\}$$

$$\frac{1}{\sqrt{10}}\{|v^{\pm}\rangle \mp i|\gamma^{\pm}\rangle - 2i|\alpha^{\mp}\rangle + 2|\beta^{\mp}\rangle\}.$$

In order to determine the remaining twelve states, we have to diagonalize the following three-dimensional matrix. The eigenvalues and the eigenfunctions are obtained numerically. Each of the three eigenvalues is of four-fold degeneracy. Energy levels are (schematically) given in Fig. 2.

$\pm\frac{1}{\sqrt{2}}\{i\|\xi^{\pm}\rangle\mp\|\eta^{\pm}\rangle\}$	$\frac{1}{\sqrt{10}}\{\pm 2\|v^{\mp}\rangle+2i\|\gamma^{\mp}\rangle\pm i\|\alpha^{\pm}\rangle+\|\beta^{\pm}\rangle\}$	$\|e^{\pm\pm}\rangle$
$\mp\frac{1}{\sqrt{6}}\{i\|\xi^{\pm}\rangle\pm\|\eta^{\pm}\rangle\pm 2i\|\zeta^{\mp}\rangle\}$	$\pm\frac{1}{\sqrt{10}}\{2\|u^{\mp}\rangle+\sqrt{3}\,i\|\alpha^{\pm}\rangle\mp\sqrt{3}\,\|\beta^{\pm}\rangle\}$	$\|e^{\mp}\rangle$
$15B+5C$	$\sqrt{5}\,\zeta_d/2$	ζ_d
	$9B+3C$	0
		0

§ 3. Magnetic Susceptibilities and g-values

Matrix elements of the Zeeman term can be easily obtained by means of Tanabe-Kamimura's tables[4]. Then the calculation of magnetic susceptibilities is carried out by using the well-known formula based on the perturbational treatment of the Zeeman energy. As easily seen from Figs. 1 and 2, the g-values and the susceptibilities can respectively be expressed in terms of functions of $\eta=\zeta_d/(3B+C)$ and of functions of η and kT/ζ_d. The limiting case of $\eta\rightarrow 0$ is the one given by the Kotani theory.

$d\varepsilon^2$: The result of calculation for the effective Bohr magneton number $n_{eff}=\sqrt{3kT\chi/N\beta^2}$ is plotted as a function of η and kT/ζ_d in Fig. 3. So far there is no experimental data for this configuration. The result shown in Fig. 3 may be used for the future analysis.

$d\varepsilon^3$: Our results for the g-value and n_{eff} are plotted in Fig. 4 and Fig. 5 respectively. As seen in Fig. 4, the g-value decreases with increasing η and becomes smaller than 2. The value of n_{eff} also decreases with increasing η and shows a slight temperature dependence.

$d\varepsilon^4$: The ground level is a singlet in this

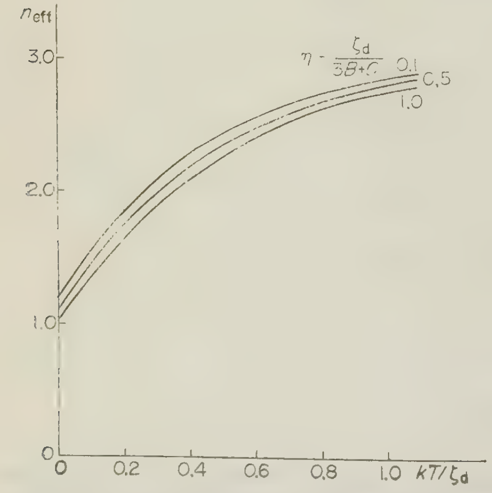

Fig. 3. The effective Bohn magneton number n_{eff} as a function of $\eta=\frac{\zeta_d}{3B+C}$ and $\frac{kT}{\zeta_d}$ for $(d\varepsilon)^2$.

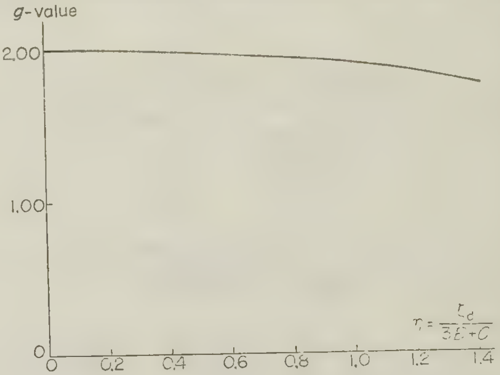

Fig. 4. The g-value as a function of η for $(d\varepsilon)^3$.

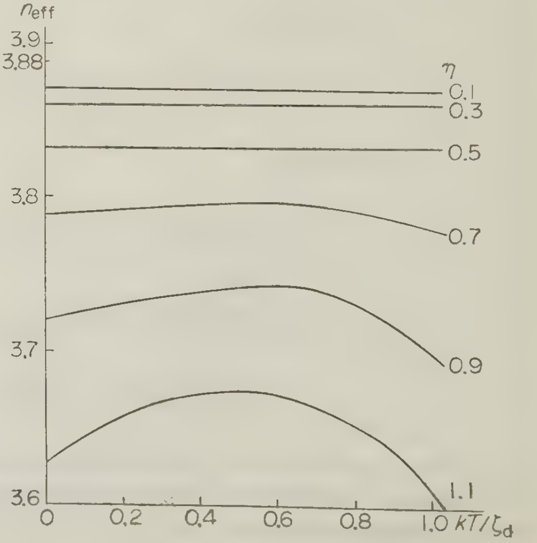

Fig. 5. n_{eff} for $(d\varepsilon)^3$.

case. Hence $g=0$. The behaviour of n_{eff} as a function of η and kT/ζ_d is illustrated graphically in Fig. 6.

§ 4. Comparison with Experiments and Discussions

In comparing the calculated Bohr magneton numbers with experiments, we have to separate the contribution of the interaction between ions from the observed susceptibilities which obey the Curie-Weiss law $\chi=C/(T+\vartheta)$. If the constants C and ϑ are determined so as to get the best fit with experimental values, we may consider the effect of the interaction to be involved in the Weiss constant ϑ. Then the effective Bohr magneton number given by the expression $n'_{eff}=2.84\sqrt{C}$ is regarded as the magnetic moment of a single ion.

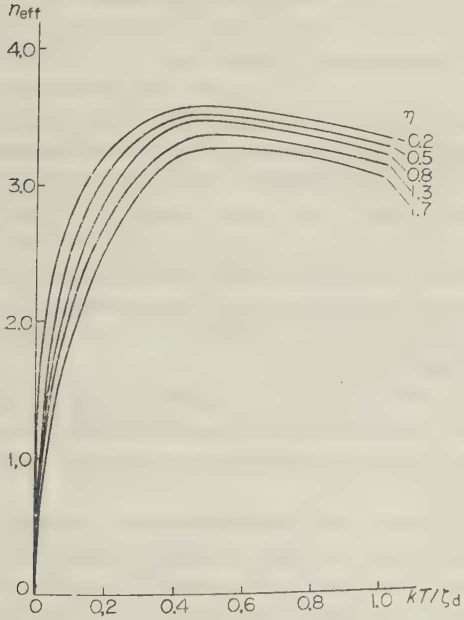

Fig. 6. n_{eff} for $(d\varepsilon)^4$.

$d\mathcal{E}^3$: It is seen in Table I that the effective Bohr magneton numbers of K_2ReX_6, thus obtained (X being halogen atom) have the common value for Cl, Br and I of X. According to our assumption, the effect of the ligands is involved in the cubic field and so is taken care of in considering only the configulation $d\mathcal{E}^n$.

Consequently, there is no room in our treatment for the ligands to exhibit their differences. The above-mentioned experimental result seems to justify our basic assumptions in the case of K_2ReX_6. We cannot, however, determine the values of the parameters η and ζ_d by comparing our theory with the experiments of susceptibilities, because the temperature dependence of n'_{eff} has not been reported yet. However, experimental data of the electron spin resonance are available for K_2ReCl_6 [5] and gives a provisional value of $g=1.8$, from which we can determine the value of η as 1.3. Using this value and the value 3.70 of n'_{eff} at room temperature, we obtain $\zeta_d=2600\,\text{cm}^{-1}$ and $3B+C=2000\,\text{cm}^{-1}$.

Using the intermediate coupling scheme, Jørgensen[6] estimated the values of these parameters from the splitting of the optical absorption peak due to the spin-orbit interaction. His results, $\zeta_d=2250\,\text{cm}^{-1}$ and $3B+C=2800\,\text{cm}^{-1}$, have the same order of magnitude as those obtained above.

If we adopt the same procedure as the Kotani theory and take account of the effect of the spin-orbit coupling on the ground state ^4A by perturbation method, then we get the expression for n'_{eff} as

$$n'_{eff}=n_{\text{spin only}}\left(1-\frac{4\zeta_d}{30Dq}\right),$$

where $10Dq$ stands for the energy difference between $d\mathcal{E}$ and $d\gamma$ orbits. If we use the value of $10Dq=27000\,\text{cm}^{-1}$, which is determined from the optical absorption data, and adjust the value of ζ_d so as to get a good fit of n'_{eff} to experiment, then we obtain $\zeta_d=1350$

Table II.

	ζ_d (cm^{-1})			$3B+C$ (cm^{-1})	
	Present calculation	Jørgensen	Kotani	Present calculation	Jørgensen
K_2RuCl_6	1400	—	1610	3500	—
K_2OsCl_6	3600	3600	6700	2770	2100

cm^{-1}. As is seen in Fig. 5, temperature variation of n'_{eff} is expected to some extent from our calculation.

$d\varepsilon^4$: Temperature variation of the magnetic susceptibilities has been observed for K_2RuCl_6 and K_2OsCl_6.[7] In Table II the values of the parameters determined so as to get the best fit of the calculated temperature variation with the experiments are set out in the second and fifth column. In Fig. 7 it may be seen that the magnitude and temperature dependence of the magnetic susceptibilities of these complex ions are fairly well reproduced by our theoretical results with parameters shown in Table II. The values determined by Jørgensen from the optical absorption data are also listed. The figures in the fourth column show the values of ζ_d which we obtain by fitting the limiting value of the susceptibility at 0°K to the one calculated by means of the Kotani theory; $\chi_0=24N\beta^2/\zeta_d$, where N is Avogadro's number and β is the Bohr magneton.

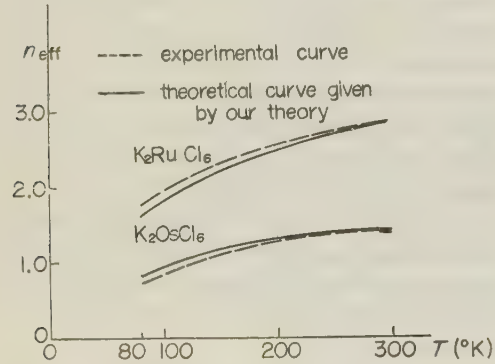

Fig. 7. Variation with temperature of n_{eff} for K_2RuCl_6 and K_2OsCl_6.

As seen in this table, our results agree quite well with those obtained by Jørgensen from the optical absorption data. The values of ζ_d obtained by the Kotani theory are larger than ours. In particular the value for K_2OsCl_6 is twice as large as those given by Jørgensen and by the present calculation. As is pointed out by Figgis et al, the jj-coupling scheme yields the expression of the magnetic susceptibility at 0°K as $\chi_0=8N\beta^2/\zeta_d$. Hence, if we determine ζ_d by comparing the observed χ at 0°K with the expression derived by means of the intermediate coupling scheme, its value is one-third of that by the Kotani theory. According to the results by Figgis et al, the values of ζ_d obtained in this way are 2500 cm^{-1} for Os^{4+} and 2900 cm^{-1} for Ir^{5+}. The Kotani theory gives 8700 cm^{-1} for the latter. Recent numerical calculation on the value of ζ_d for the Ir^{4+} ion by one of the present authors[8] gives $\zeta_d(Ir^{4+})=2400\,\mathrm{cm}^{-1}$. Cooke et al[9] also determined $\zeta_d\simeq 2000\,\mathrm{cm}^{-1}$ from the temperature dependence of the susceptibility of the complexes ion $[IrCl_6]^{2-}$.

It is seen from these values that the Kotani theory is not applied to the $4d$- and $5d$ group ions and that the spin-orbit interaction is as important as the Coulomb repulsion between the d-electrons in these ions.

As seen in the above, the comparison of our results with experiments gives reasonable values of the parameters and our assumptions seem to be justified as far as the available experimental data are concerned. The observed data are, however, still too few to confirm the validity of our basic assumptions in more general cases. Improvement might be required with respect to the following points:

(1) We have assumed perfectly cubic ligand field. The field with lower symmetry should be taken into consideration for more detailed analysis.

(2) There are some evidences showing the importance of the covalency effect in the cases of $4d$- and $5d$-electrons. It would therefore be necessary to introduce another parameter which represents the amount of this effect.

(3) We have neglected the effect of the $d\gamma$ orbitals. This is also one of the assumptions to be examined in the future investigations.

We expect, however, that the present work would give an important clue in more detailed analyses of the future experiments.

The authors wish to express their sincere thanks to Professor Masao Kotani for his much instructive advice and continual encouragement during the course of this work. They would like also to thank Miss H. Takeda and Miss S. Kosugi for their assistance in the numerical work.

References

1) M. Kotani: J. Phys. Soc. Japan **4** (1949) 293.
2) B. N. Figgis, J. Lewis, R. S. Nyholm and R. D. Peacock: Disc. Farad. Soc.
B. N. Figgis: *International Series of Mono-*

Appendix I.

			S'	0	1			1			1			0		0		
			M_s'	0	1			0			-1			0		0		
			Γ'	A_1	F_1			F_1			F_1			E		F_2		
S	M_s	Γ	$\gamma \backslash \gamma'$	e_1	α	β	γ	α	β	γ	α	β	γ	u	v	ξ	η	ζ
0	0	A_1	e_1		$\frac{i\zeta_d}{\sqrt{3}}$	$-\frac{\zeta_d}{\sqrt{3}}$				$-\sqrt{\frac{2}{3}}i\zeta_d$	$-\frac{i\zeta_d}{\sqrt{3}}$	$-\frac{\zeta_d}{\sqrt{3}}$						
1	1	F_1	α			$\frac{i\zeta_d}{2}$				$-\frac{\zeta_d}{2\sqrt{2}}$				$-\frac{i\zeta_d}{2\sqrt{6}}$	$\frac{i\zeta_d}{2\sqrt{2}}$			$\frac{\zeta_d}{2\sqrt{2}}$
			β							$\frac{i\zeta_d}{2\sqrt{2}}$				$-\frac{\zeta_d}{2\sqrt{6}}$	$-\frac{\zeta_d}{2\sqrt{2}}$			$\frac{i\zeta_d}{2\sqrt{2}}$
			γ					$\frac{\zeta_d}{2\sqrt{2}}$	$-\frac{i\zeta_d}{2\sqrt{2}}$							$\frac{\zeta_d}{2\sqrt{2}}$	$\frac{i\zeta_d}{2\sqrt{2}}$	
1	0	F_1	α										$-\frac{\zeta_d}{2\sqrt{2}}$				$-\frac{i\zeta_d}{2}$	
			β										$\frac{i\zeta_d}{2\sqrt{2}}$			$-\frac{i\zeta_d}{2}$		
			γ								$\frac{\zeta_d}{2\sqrt{2}}$	$-\frac{i\zeta_d}{2\sqrt{2}}$		$-\frac{i\zeta_d}{\sqrt{3}}$				
1	-1	F_1	α									$-\frac{i\zeta_d}{2}$		$\frac{i\zeta_d}{2\sqrt{6}}$	$-\frac{i\zeta_d}{2\sqrt{2}}$			$\frac{\zeta_d}{2\sqrt{2}}$
			β											$-\frac{\zeta_d}{2\sqrt{6}}$	$-\frac{\zeta_d}{2\sqrt{2}}$			$-\frac{i\zeta_d}{2\sqrt{2}}$
			γ													$\frac{\zeta_d}{2\sqrt{2}}$	$-\frac{i\zeta_d}{2\sqrt{2}}$	

The matrix elements of the spin-orbit interaction in $|SM_s\Gamma\gamma\rangle$ scheme for the configuration $(d\varepsilon)^2$, where S and M_s's are spin quantum numbers, and Γ and γ's are the symbols for the irreducible representation of the octahedral group.

graphs on Inorganic Chemistry (Pergamon Press, 1958) 476.

3) Y. Tanabe and S. Sugano: J. Phys. Soc. Japan **9** (1954) 753.

4) Y. Tanabe and H. Kamimura: J. Phys. Soc. Japan **13** (1958) 394.

5) K. D. Bowers and J. Owen: Rep. Progr. Phys. **18** (1955) 304.

6) C. K. Jørgensen: *Final Technical Report on Absorption Spectra of Complexes of Heavy Metals*, No. 1 (1958).

7) A. Earnshaw, B. N. Figgis, J. Lewis and R. S. Nyholm: Nature **179** (1957) 1121.

8) H. Kamimura: to be published.

9) A. H. Cooke, R. Lazenby, F. R. McKim, J. Owen and W. P. Wolf: Proc. Roy. Soc. **A**, **250** (1959) 97.

Appendix II.

			S'	$\frac{1}{2}$			$\frac{1}{2}$		
			M_s'	$\frac{1}{2}$			$-\frac{1}{2}$		
			Γ'	F_2			F_2		
S	M_s	Γ	γ \ γ'	ξ	η	ζ	ξ	η	ζ
$\frac{3}{2}$	$\frac{3}{2}$	A_2	e	$-\frac{\sqrt{2}}{2}i\zeta_d$	$-\frac{\sqrt{2}}{2}\zeta_d$				
	$\frac{1}{2}$	A_2	e			$\frac{\sqrt{6}}{3}i\zeta_d$	$-\frac{\sqrt{6}}{6}i\zeta_d$	$-\frac{\sqrt{6}}{6}\zeta_d$	
	$-\frac{1}{2}$	A_2	e	$\frac{\sqrt{6}}{6}i\zeta_d$	$-\frac{\sqrt{6}}{6}\zeta_d$				$\frac{\sqrt{6}}{3}i\zeta_d$
	$-\frac{3}{2}$	A_2	e				$\frac{\sqrt{2}}{2}i\zeta_d$	$-\frac{\sqrt{2}}{2}\zeta_d$	
$\frac{1}{2}$	$\frac{1}{2}$	E	u			$-\frac{\sqrt{3}}{3}i\zeta_d$	$\frac{\sqrt{3}}{6}i\zeta_d$	$\frac{\sqrt{6}}{6}\zeta_d$	
			v				$-\frac{i}{2}\zeta_d$	$\frac{1}{2}\zeta_d$	
$\frac{1}{2}$	$-\frac{1}{2}$	E	u	$\frac{\sqrt{3}}{6}i\zeta_d$	$-\frac{\sqrt{3}}{6}\zeta_d$				$\frac{\sqrt{3}}{3}i\zeta_d$
			v	$-\frac{i}{2}\zeta_d$	$-\frac{1}{2}\zeta_d$				
$\frac{1}{2}$	$\frac{1}{2}$	F_1	α		$-\frac{i}{2}\zeta_d$				$-\frac{1}{2}\zeta_d$
			β	$-\frac{i}{2}\zeta_d$					$-\frac{i}{2}\zeta_d$
			γ				$-\frac{1}{2}\zeta_d$	$-\frac{i}{2}\zeta_d$	
$\frac{1}{2}$	$-\frac{1}{2}$	F_1	α			$\frac{1}{2}\zeta_d$		$\frac{i}{2}\zeta_d$	
			β			$-\frac{i}{2}\zeta_d$	$\frac{i}{2}\zeta_d$		
			γ	$\frac{1}{2}\zeta_d$	$-\frac{i}{2}\zeta_d$				

The matrix elements of the spin-orbit interaction for the configuration $(d\varepsilon)^3$.

JOURNAL OF THE PHYSICAL SOCIETY OF JAPAN, Vol. 15, No. 7, JULY, 1960

Microwave Spectrum of Ethyl Iodide, II.

By Takahiro KASUYA

Departmeut of Physics, Faculty of Science,
University of Tokyo, Tokyo

(Reveived, March 26, 1960)

The potential barrier which hinders the internal rotation in ethyl iodide molecule was studied. If the potential energy is assumed to be of the sinusoidal form $\frac{H}{2}$ (1−cos 3x), the barrier height is determined as $H=3.22\pm0.5$ kcal/mole from the Q^b-type transition in the first excited torsional state. The torsional frequency is about 230 cm^{-1}. The effect of internal rotation on the quadrupole hyperfine structure of $K=1$ levels was analyzed.

§ 1. Introduction

In the previous paper[1)*], the microwave spectrum of ethyl iodide molecule in the ground vibrational state was studied by the rigid rotor treatment. The analysis of the quadrupole hyperfine structure of the spectrum due to the quadrupole moment of iodine nucleus was described there. The object of the present paper is to discuss the hindered rotation about the *C-C* bond, and to determine the precise magnitude of the hindering barrier height.

§ 2. Experimental Results

Since the barriers to the internal rotation in ethyl halide molecules are very high, the microwave spectrum of the transitions for the ground vibrational state is essentially the

Table I. Frequeucies of Q^b-type Transitions.

transition	observed frequencies (in Mc/sec)		splitting (″)		barrier height (in kcal/mole)
	ground state	excited state	$\varDelta\nu$	$\varDelta\nu$ (corrected)	
$6_{15}\leftarrow6_{06}$					
17/2←17/2	28291.66	28188.82 (E) 28186.94 (A)	1.88	1.81	3.20
15/2←15/2	28339.12	28237.20 (E) 28235.42 (A)	1.78	1.72	3.23
13/2←13/2	28347.34	28246.1 (?) a			
11/2←11/2	28324.08	28221.33 (E) 28219.44 (A)	1.89	1.79	3.21
9/2← 9/2	28275.88	28173.18 (E) 28171.66 (A)	1.42	1.63	3.25
7/2← 7/2	28264.34	28154.7 (?) a			
$5_{14}\leftarrow5_{05}$					
15/2←15/2	27597.48	b			
13/2←13/2	27639.18	27502. (E) 27501. (A)	1.	1.	3.
11/2←11/2	27664.54	27529.56 (E) 27528.10 (A)	1.46	1.63	3.23
9/2← 9/2	27593.5	b			
7/2← 7/2	27596.	b			
5/2← 5/2	27562.46	27432.46 (E) 27430.70 (A)	1.76	1.75	3.20

a: Accuracy of measurement is ±0.5 Mc/sec.
b: Several lines measured at about 27458 Mc/sec could not be assigned.
A: Nondegenerate torsional sublevel, E: Degenerate torsional sublevel.

---

*) hereafter referred to as (I) in this paper.

same as normal rigid rotor pattern. It is well known that even in the molecules with very high barrier the effect of internal rotation can be expected to exert a detectable influence on the energy levels in the excited torsional state. For example, R^a-type transitions involving nearly degenerate $K=2$ levels in the first excited torsional state were adopted for the determination of barriers in C_2H_5Br, C_2H_5Cl and C_2H_5CN[2),3)].

In the case of ethyl iodide, however, the analysis of the torsional satellite lines had to be given up, because the spectral lines of transitions involving levels with $K \geqq 2$ overlapped with each other, and the spectral pattern was found to be quite complicated by the quadrupole hyperfine structure due to the large coupling constant along the C-I bond. On the other hand, if the torsional satellites of Q^b-type transitions are observed the larger

Table II. Frequencies of R^a-type transitions.

transition	observed frequencies	second order quadrupole effect	calculated frequencies	$\varDelta$	$\varDelta$ (corrected)	center frequencies
$3_{13}\leftarrow 2_{12}$						17054.25
11/2← 9/2	17096.08	0.69	17096.84	−0.24	−0.61	
9/7← 7/2	17034.84	−0.47	17035.30	0.46	0.05	
	17033.75	−0.47		1.55	0.05	
5/2← 3/2	16976.8	−3.89	16776.6	−0.2	0.1	
3/2← 1/2	17007.76	0.56	17013.52	5.76	0.62	
5/2← 5/2	17110.23	0.09	17109.62	−0.61	0.38	
$3_{12}\leftarrow 2_{11}$						17601.08
11/2← 9/2	17643.66	3.91	17643.38	−0.28	0.10	
9/2← 7/2	17575.24	−1.15	17575.84	0.60	−0.10	
	17574.5	−1.15		1.3	−0.1	
7/2← 5/2	17549.70	1.31	17549.38	−0.36	0.56	
3/2← 3/2	17662.8	−2.18	17661.9	−0.9	0.0	
1/2← 1/2	17676.2	0.25	17676.1	−0.1	0.1	
$4_{14}\leftarrow 3_{13}$						22736.41
13/2←11/2	22759.50	0.63	22759.80	0.30	0.41	
11/2← 9/2	22740.73	−1.41	22739.13	−1.60	−0.64	
9/2← 7/2	22709.40	−0.72	22709.32	−0.08	0.33	
7/2← 5/2	22690.03	−0.30	22690.60	0.57	−0.18	
3/2← 1/2	22734.40	−0.07	22735.18	0.78	0.41	
$4_{13}\leftarrow 3_{12}$						23439.50
13/2←11/2	23467.01	5.17	23466.00	−1.01	0.90	
11/2← 9/2	23438.13	−1.40	23439.33	1.20	0.53	
9/2← 7/2	23414.58	0.16	23415.63	1.05	−0.69	
5/2← 3/2	23474.88	−1.00	23473.80	−1.08	0.21	
$5_{15}\leftarrow 4_{14}$						28417.68
15/2←13/2	28433.50	0.55	28433.23	−0.27	0.11	
13/2←11/2	28425.40	−0.05	28426.19	0.79	0.30	
11/2← 9/2	28405.78	0.19	28405.00	−0.78	−0.47	
9/2← 7/2	28390.42	−1.14	28391.58	1.16	−0.83	
7/2← 5/2	28389.12	0.35	28388.07	−1.05	0.28	
5/2← 3/2	28413.20	−0.10	28414.20	−1.00	−0.55	
$5_{14}\leftarrow 4_{13}$						29331.45
15/2←13/2	29357.16	4.55	29357.46	0.03	−0.17	
13/2←11/2	29337.28	0.09	29338.41	1.13	−0.91	
11/2← 9/2	29324.64	0.50	29322.89	−1.76	0.59	
9/2← 7/2	29319.70	2.15	29319.08	−0.66	−0.38	
7/2← 5/2	29320.60	2.70	29320.10	−0.50	0.19	
5/2← 3/2	29332.26	−0.05	29332.53	0.27	0.37	

Here, $\varDelta$ indicates the discrepancies between the observed and the calculated frequencies carried out without the consideration of the effects of internal rotation.

effect of internal rotation can be found than in the case of R^a-type transitions. A rough estimation[*] shows that each hyperfine component of Q^b-type transition split into doublet of about 1 Mc/sec.

The spectrometer and the sample used were the same as were reported in (I). The observed frequencies are listed in Table I. The intensity of these Q^b-type lines are weak as the electric dipole moment is nearly along the a-axis.

Some additional observed frequencies of R^a-type transitions involving $K=1$ levels, omitted in (I), are listed in Table II.

§ 3. Discussions

The magnitude of splittings $\Delta\nu$ listed in Table I averages 1.74 Mc/sec for $J=6$ transitions and 1.61 Mc/sec for $J=5$ transitions. These values give the barrier height of about 3.25 kcal/mole. The theoretical treatment used in the interpretation of the observed splitting was that of Hecht and Dennison[6].

Table III. Molecular constants used in calculation.

A	180.91 amu. A^2	$(C_2/C)^*$	0.141
B	91.23 〃	$\frac{2\pi}{3}(C_1/C)^*$	1.797 rad.
C	86.27 〃	$\frac{\hbar^2}{2}(C/C_1C_2)^*$	5.770 cm^{-1}
D	75.99 〃		
C_2	3.28 〃	β	0.0923

The data was also interpreted by another approach according to Herschbach[5], and the same results were obtained. The molecular constants necessary in the analysis of internal rotation problem were derived from those reported in (I) and they are shown in Table III.

It can be seen in Table I that the magnitude of splitting corresponding to each quadrupole hyperfine component varies considerably with each other. Hence, the effects of internal rotation on the quadrupole interaction must be taken into account. The matrix elements of S of reference (6), which transforms the coordinate axis to the principal axis system, and performs the Wang's transformation to the rigid rotor part of the Hamiltonian referred to the principal axis, can be expanded in power series of geometrical parameter β[8]. The expansion accurate to the order of β^2 is:

$$<K|K>=<K|-K>=<-K|K>$$

$$=-<-K|-K>=[1-\beta^2(J^2+J-K^2)/4]/\sqrt{2}$$

$$\text{(for } K>1)$$

$$<\pm K|\pm(K+1)=-<\pm(K+1)|\pm K>$$

$$=\mp<\mp K|\pm(K+1)>=\pm<\pm(K+1)|\mp K>$$

$$=-\beta\sqrt{(J-K)(J+K+1)}/2\sqrt{2} \quad \text{(for } K>1)$$

$$<0|\pm 1>=\mp\beta\sqrt{J(J+1)}/2, \quad <-1|0>=0,$$

$$<-1|0>=\beta\sqrt{J(J+1)/2},$$

$$<0|0>=1-\beta^2 J(J+1)/4,$$

$$<1|\pm 1>=[1-\beta^2(J-1)(J+2)/8]/\sqrt{2}$$

$$<-1|\pm 1>=\pm[1-\beta^2(3J^2+3J-2)/8]\sqrt{2}.$$

The wave function in the rigit rotor limit can be written by symmetric rotor basis $S_K{}^{\pm}$ as,

$$\begin{aligned}\Phi_K{}^{\pm}=&[1-\beta^2(J^2+J-K^2)/4]S_K{}^{\pm}\\&\pm\beta g_{\mp K}S^{\pm}{}_{K\mp 1}\mp\beta g_{\pm K}S^{\mp}{}_{K\pm 1}\end{aligned} \qquad (2)$$

and

$$\Phi^+{}_1=[1-\beta^2(J^2+J-2)/8]S^+{}_1-\beta g_1 S^-{}_2$$

$$\Phi^-{}_1=[1-\beta^2(3J^2+3J-2)/8]S^-{}_1+\beta g_1 S^+{}_2+\beta g_0\Psi_0$$

$$\Phi_0=[1-\beta^2 J(J+1)/4]\Psi_\theta-\beta g_0 S^-{}_1,$$

where $g_K=\sqrt{(J-K)(J+K+1)}/2,$

$$S_K{}^{\pm}=(\Psi_K\pm\Psi_{-K})/\sqrt{2}.$$

Then the quadrupole interaction term for symmetric top limit is given as[**],

$$\frac{eq'Q}{(J+1)(2J+3)}\Big[\{3_K{}^2-J(J+1)\}(1+2\xi'\beta)$$

$$-\Big\{\frac{J^2(J+1)^2+J(J+1)(4K^2+3)}{2}$$

$$+f(J,K)\eta'\Big\}\beta^2+\cdots\Big] \qquad (K>1)$$

---

[*] According to Kilb, Lin, Wilson[4] and Herschbach's[5] notation, the rotational energy deviates from that of rigid rotor as

$$\Delta W=\partial_A W\Delta+\partial_B W\Delta B+0(\gamma^4) \qquad (1)$$

where $\partial_A W=K^2-\sum_{n=2}(n-1)C_n b^n$

$$\partial_B W=J(J+1)(1-\delta_{K,1}/2)/2-K^2/2+\sum_{n=2}nC_n b^{n-1}.$$

For the expected magnitude of barrier height ($H\sim 3$ kcal/mole),

$\Delta A=F\alpha^2\Delta\eta$ and $\Delta B=F\beta^2\Delta\eta$ are about 2.4 and 0.03 Mc/sec, respectively.

[**] For C_2H_5I, $\beta\sim 0.1$ and $b_p\sim -0.003$, the correction to quadrupole interaction coming from the molecular asymmetry is negligible as far as the effects of internal rotation is considered.

and

$$\frac{eq'Q}{(J+1)(2J+3)}\Big[3-J(J+1)+\frac{J(J+1)}{2}\eta' -3(J-1)(J+1)\xi'\beta+\frac{(J+1)(J+2)}{4}\left(9-\frac{J(J+1)}{2}\eta'\right)\beta^2+\cdots\Big]$$

$$(K=1,\ \text{even } J+K+\gamma), \qquad (3)$$

$$\frac{eq'Q}{(J+1)(2J+3)}\Big[-J(J+1)(3+\xi'\beta)+\frac{J(J+1)}{2}\left(3-\frac{J(J+1)}{2}\eta'\right)\beta^2+\cdots\Big] \qquad (K=0)$$

Here, quantities q, ξ, and η referring to the "internal axis" coordinate system are denoted by prime. They are written in terms of the diagonalized form of tensor $\boldsymbol{q}$ (q_x, q_y q_z) given in (I):

$$\boldsymbol{q}'=\boldsymbol{R}\boldsymbol{q}\boldsymbol{R}^{-1},\ \boldsymbol{R}=\boldsymbol{R}_z(\rho x)\boldsymbol{R}_x(\alpha).$$

That is,

$$\begin{aligned} q'&=\cos^2\alpha q_z+\sin^2\alpha q_y\\ \xi'&=\sin\alpha\cos\alpha(q_y-q_z)(1-\delta^{(1)})/q' \qquad (4)\\ \eta'&=(q_x-\cos^2\alpha q_y-\sin^2\alpha q_z)(1-\delta^{(2)})/q'. \end{aligned}$$

$\boldsymbol{R}_x(\alpha)$ is the rotation of angle $\alpha=<\mathrm{CCI}+\tan^{-1}D/B$ in the y_z plane, $\boldsymbol{R}_z(\rho x)$ the subsequent rotation about z axis (ρ being $(C_2/C)^*$ in Table III, and x the internal rotation angle), $\delta^{(1)}$ and $\delta^{(2)}$ the barrier dependent small quantities*).

When the K-type splitting of the K level d_K competes with the off diagonal element of Hamiltonian $(S^{-1}HS)_{K,-K}=\delta_K$ which comes from internal rotation, Wang's symmetric limit wave function $S^{\pm}{}_{J,K}$ must be replaced by the mixed form $mS^{\gamma}+nS^{\gamma'}$ ($m^2+n^2\simeq1$). Hence, η' is multiplied by a factor $\mathcal{E}=m^2-n^2$.[7] This effect is not negligible in the particular term $J\eta'/2(2J+3)$ in Eq. (3) which comes from the $K=1\leftrightarrow-1$ interaction of the quadrupole energy and is of zeroth order of magnitude in β. For A state of internal rotation $|\mathcal{E}|=1$, while for E state $|\mathcal{E}|$ takes the value less than unity sensitivively dependent on the barrier height. An approximate form of $\mathcal{E}$ is

$$\mathcal{E}\simeq\delta_1/(d_1{}^2+\delta_1{}^2)^{1/2},$$

$$\delta_1\simeq\frac{1}{\sqrt{3}}\Delta_0{}^{(1)}\sin\frac{2\pi}{3}\left(\frac{C_2}{C}\right)^{*}.^{[8]**} \qquad (6)$$

Though the hindering barrier is very high in C_2H_5I, the molecular asymmetry is sufficiently small ($b_p\simeq-0.003$) and the quadrupole coupling constant along the C-I bond is enormously large (eq$Q\simeq-1770$ Mc/sec), so that the above competition must be considered for each hyperfine component. First, contribution of the above mentioned effect to the splitting of spectrum was evaluated for each hyperfine component using a crude value of barrier height ($H\simeq3.25$ kcal/mole), and was subtracted from the observed splitting. The remaining splitting was then attributed to the coupling between the overall and internal rotation, which permits the determination of barrier height in an improved accuracy. This procedure was successively repeated until the average barrier height converges to a constant value.

The splitting $\Delta\nu$ (corrected) in Table I are those ultimately obtained by this analysis purely corresponding to the coupling between overall and internal rotation. From this, the barrier height in C_2H_5I was determined as

$$H=3220\pm100\ \text{cal/mole}=1130\pm30\ \text{cm}^{-1}.$$

This implies the torsional frequency of methyl group of about 230 cm^{-1}.

The spectrum of R^a-type transitions involving levels with $K=1$ which was omitted in the report on C_2H_5Cl[9] and C_2H_5Br[10] were also analyzed for C_2H_5I by taking into account of the internal rotation (Table II). Since in R^a-type transition this effect is too small to be observed except for a few cases with the resolution available in a conventional microwave spectrometer, the average frequencies calculated for two species of torsional sublevels were compared with the observations. Then the calculated spectrum showed better agreement with the observed spectrum (Table II). The splitting into doublet observed in a

---

*) For the first excited torsional state, $\delta^{(1)}$ and $\delta^{(2)}$ can be expanded in power series of $\chi=(C_2/C)^*H'$, $H'=H/\frac{\hbar^2}{2}(C/C_1C_2)^*$ as $\delta^{(1)}=2\chi-1.11\chi^2+\cdots$, $\delta^{(2)}=0.5\chi-0.07\chi^2+\cdots$. (5)

**) As is well known, Δ_0 is the very sensitive function of barrier height, the functional dependence of which is given for the first excited torsional state in good approximation as,

$$\Delta^{(1)\prime}{}_0=23.93H'^{1.25}\exp-1.307\sqrt{H'},$$

$$\left(\Delta^{(1)\prime}{}_0=\Delta^{(1)}{}_0/\frac{\hbar^2}{2}(C/C_1C_2)^*\right). \qquad (7)$$

few cases (marked * in Table II) could be interpreted fairly well by the consideration of the effect given in Eq. (6).

Though Eq. (7) is expected to be accurate to within ± 2% in the range of $100 \leq H' \leq 250$, the assumption of structural parameters of methyl group introduces another error of about 5% in the determination of barrier height. In conclusion, it can be said that the magnitude of the barrier height to the internal rotation in ethyl iodide is nearly the same as those of the other ethyl halide molecules, 3306 cal/mole for $C_2H_5F^{11)}$, 2560 cal/mole for $C_2H_5Cl^{2)}$ and 3567 cal/mole in $C_2H_5Br^{2)}$.

The author is indebted to Professor Koichi Shimoda for his kind guidance and encouragement throughout the course of this investigation. He is also grateful to Mr. Takeshi Oka for his helpful discussions.

Referencee

1) T. Kasuya and T. Oka: J. Phys. Soc. Japan **15** (1960) 296.
2) D. R. Lide, Jr.: J. Chem. Phys. **30** (1959) 37.
3) V. W. Laurie: J. Chem. Phys. **31** (1959) 1500.
4) R. W. Kilb, C. C. Lin and E. B. Wilson, Jr.: J. Chem. Phys. **26** (1957) 1650.
5) D. R. Herschbach: J. Chem. Phys. **31** (1959) 91.
6) K. T. Hecht and D. M. Dennison: J. Chem. Phys. **26** (1957) 31.
7) D. R. Lide, Jr.: J. Chem. Phys. **27** (1957) 343.
8) D. R. Lide, Jr. and D. E. Mann: J. Chem. Phys. **27** (1957) 868.
9) R. S. Wagner and B. P. Dailey: J. Chem. Phys. **26** (1957) 1588.
10) R. S. Wagner, B. P. Daily and N. Solimene: J. Chem. Phys. **26** (1957) 1593.
11) D. R. Herschbach: J. Chem. Phys. **25** (1956) 358.

JOURNAL OF THE PHYSICAL SOCIETY OF JAPAN, Vol. 15, No. 7, JULY, 1960

Proton Magnetic Resonance in Hydrogen Bonded Dimers in Solids

By Kiyoshi KUME and Yoshinobu KAKIUCHI

The Institute for Solid State Physics, University of Tokyo

(Received March 29, 1960)

It is concluded through proton magnetic resonance that the positions of protons in boric acid crystals lie considerably away from the lines connecting two hydrogen bonded oxygens, in contrast to the case in potassium bicarbonate crystals, where protons are approximately on the oxygen-oxygen lines. The result is discussed in connection with the difference in strength of the hydrogen bond both cases.

§ 1. Introduction

The determination of the positions of protons in hydrogen bonds are now being widely discussed in various cases$^{(1-7)}$, because of their basic significance in the study of the properties of hydrogen bonds. We have attempted to attack this problem through the proton magnetic resonance of hydrogen bonded dimers in certain crystals. In a hydrogen bonded dimer, protons approximately form, a two proton system and can favorably be treated by this technique, as far as the effect of neighboring dimers is successfully taken into consideration. We have selected two kinds of crystal, namely potassium bicarbonate and boric acid crystals. In the former, the hydrogen bond is relatively short (2.61 Å)$^{(13)}$ among O–H....O bonds and consequently rather strong, whereas in the latter it is relatively long (2.72 Å)$^{(11-12)}$ and weak. We shall discuss the results of the experiment in connection with these features. The fundamental difficulties in experimental technique lies in the fact that these crystals have in general longer T_1, hence is required the extremely high sensitivity of the spectrometer, which has been successfully attained throughout the present investigation.

§ 2. Resonance Technique

In order to determine the shape of the resonance absorption line in these crystals accurately, the r.f. power level H_1 within the sample coil, should be reduced as low as about 50 microgauss, because of their longer T_1 of the order of 10 minutes, otherwise the observed derivative of the absorption curve would become asymmetric. The conventional Pound-Watkins, detector, which cannot maintain sufficiently a low value of H_1 is, therefore, undesirable in our case, and the bridge type detecter is much more preferable. The second problem is to measure the absorption successfully under such a low r.f. level, especially in the case of broad line, and considerable attention should be paid to improve the signal to noise ratio. For example, in boric acid crystals, the calculated signal voltage across the sample coil amounts only to 4.4×10^{-7} volts, at room temperature corresponding to the sample volume of roughly 2 cc, the Q value of the sample coil of about 200, the amplitude of field modulation of 3 Gauss, and the r.f. level of 50 microgauss. The Twin-T bridge(17) is used under the minimum noise figure conditions(18), comined with a low noise preamplifier. The overall noise figure of the whole detecting system is found to be about three, under practical operating conditions(18). Moreover, the overall bandwidth of the detecting system is as narrow as 0.16 cps. The maximum equivalent noise voltage amplitude across the sample coil can thus be reduced to 2×10^{-8} volts. The estimated signal to noise ratio of $4.4 \times 10^{-7}/2 \times 10^{-8}$ is nearly equal to the observed one. (Fig. 7)

The electromagnet built by the Japan Electron Optics Company is operated at about 7060 Gauss (the proton magnetic resonance frequency being 30.00 Mc). The inhomogeneity of the magnetic field over the sample of 2 cc in volume, is less than 100 milligauss, which gives negligible influence on the results. Details of the measuring equipment used is given elsewhere(19).

§ 3. Specimens

The specimens used are either of "guaranteed grade" (boric acid) or of "chemically pure" grade (potassium bicarbonate), available from the Wako Pure Chemical Company. In order to gain as high a signal to noise ratio as possible, samples are pressed into a lozenge under 3 ton/cm^2 pressure. In this case, no evidence for the lattice distortion is detectable through an X-ray powder photograph. The single crystal of potassium bicarbonate is grown from its aqueous solution by lowering its temperature by 10 degrees, at a rate of 0.5 degree per day in the initial stage, and 1 degree per day in the later stage. The crystal thus obtained is about $20 \times 20 \times 8$ cm^3 in size. Although there are several discontinuities, which look like annual rings, it nevertheless forms a perfect single crystal. The X-ray Laue pattern shows orientational distributions of 10 degrees around the "b" axis, but this is fortunately relatively unimportant to our measurements. In order to make size and shape convenient to our measurements, three single crystals having the same crystallographic orientations are cemented together and shaped into a suitable form. All samples used here are 12 mm in diameter and about 20 mm in height.

§ 4. Results

(a) *Potassium bicarbonate powder*

The recorded derivative of the saturation free proton magnetic resonance curve in potassium bicarbonate crystal powder at room temperature is reproduced in Fig. 1. The sharp central peak having a width equal to the full amplitude of field modulation which disappears at low temperatures may safely be attributed to a signal from contaminating free-water. Subtracting graphically the contributions from this contaminating water, we obtain the powder line, characteristic to a two proton system. The second moment of the curve is 3.4±0.1 Gauss^2, which is the average of six independent data, ± indicating standard deviation. Althrough we have made only a qualitative experiment at low temperatures, the absorption seems to have no temperature dependence from −180°C up to the room temperature.

According to the crystal structure of potassium bicarbonate determined through X-ray diffraction studes(13), four carbonate radicals form two dimers in the unit cell. These two dimers are coplaner, and are, roughly speaking, parallel with each other (Fig. 2). Thus far, nothing is known about the positions of protons.

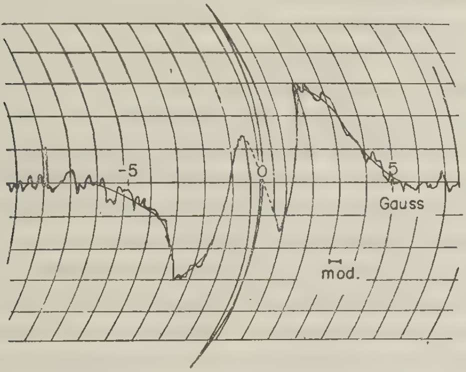

Fig. 1. Derivative of the absorption curve for potassium bicarbonate powder
Sample: Chemically pure grade specimen of Wako Pure Chemical Company. Compressed powder 12 mm$\phi \times$20 mm
Field: 7060 Gauss
Field sweep: 0.51 Gauss/min
Frequency: 30.0 MC
R.f. field within sample coil: 70 microgauss
Time constant: 12 sec
Temperature: 25°C

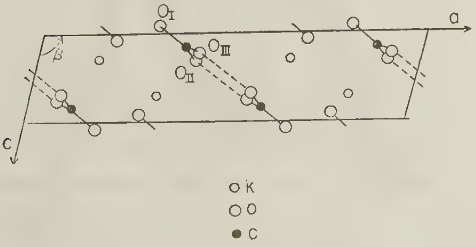

Fig. 2 Crystal structure of potassium bicarbonate

If we make the plausible assumption that configuration of protons also follows the same crystallographic symmetry with that of other kinds of atoms determined by X-ray diffraction, the center of the interproton vector of a pair of protons in each dimer, should coincide with that of the dimer. Further, we shall make another assumption that protons, and consequently the interproton vector, are contained in the plane of the dimer. Then, the results from the powder experiment on the second moment of the absorption curve given above, is quite sufficient in determining the length of the vector. Strictly speaking, the contribution from inter-dimer interactions, which should be subtracted from the total second moment in order to obtain the intra-dimer contribution, will depend upon the orientation of the inter-proton vector. Actually, however, a simple estimation shows that, the resulting ambiguity in inter-proton length amounts only to 0.01 Å, which is indicated by the solid arcs in Fig. 3. Taking also the error involved in the determination of the total second moment into account, the length is finally determined to be 2.27±0.03 Å.

(b) *Potassium bicarbonate single crystal*

Next, we shall proceed to the single crystal measurement, and determine the orientation of the interproton vector, whose length is already fixed by the preceeding powder experiment. It is obvious from the crystal structure shown in Fig. 2, that there are two independent interproton vectors in a unit cell. The resonance line, therefore in general, consists of four lines which can not be well separated, because of rather weak dipole interactions. It is, however, possible to fix the orientation of these two inter-proton vectors relative to the crystal axis, so as to obtain the best fit between calculated and observed line shapes, assuming the inter-proton length obtained above, and taking the crystallographic symmetry into consideration. As is readily seen from Fig. 3, both the OH bond length and the COH bond angle, will be obtained as soon as the orientation of the interproton vector is thus fixed

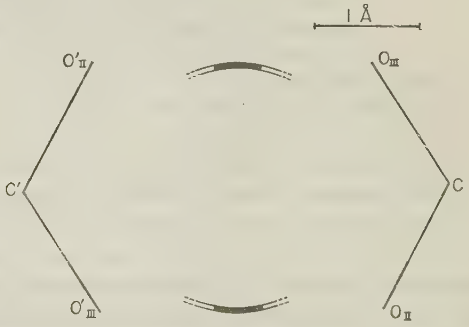

Fig. 3. Experimentally determined positions of protons in potassium bicarbonate. The powder experiment left the arc-shape region as the possible positions for protons, and single crystal experiment reduced it into the shaded portion.

The external magnetic field is applied in a direction making an angle Φ to the "b" axis, and in a plane containing the "b" axis, which is at the same time perpendicular to the "a" plane described in the literature(13). The recorded derivative of the saturation free resonance absorption curve at $\Phi=25$ degrees is reproduced in Fig. 4. The origin for the angle Φ is checked by confirming that the line shape at $\Phi=-25$ degrees coincides with that of $\Phi=25$ degrees within the experimental error. The sharp extra central peak is again subtracted graphically as shown by the broken line. In Fig. 5 is shown by open circles, the absorption obtained by numerical integration of the observed derivative together with the calculated lines, assuming various OH distances ranging from 1.0 Å to 1.3 Å. Owing to the fact that the $C' O'_{II} O_{III} CO_{II} C'_{III} C'$ hexagon is somewhat distorted, the angle between the interproton vector and the crystallographic axes differs a little, according to whether the proton is on the side of O_{II} or of O_{III}, even if we assume the same OH distance; and as a result, the calculated line profile will also be different either for $O_{II}H$ or $O_{III}H$ configurations. In the above calculation, the component lines are assumed to have Gaussian shape, whose second moments are estimated from well-known Van Vleck's formula(8), the normalization being made so as to obtain the best fit between the calculated and observed total intensities. As for the interproton distance we assumed the value 2.27 Å, obtained from the powder measurement, and the possible error of one percent involved in it, will result in an error of about three percents in the calculated width of the line. The figure shows that the OH bond length should approximately be 1.2 Å, the corresponding COH bond angle being 121 degrees when the protons lie on the side of O_{II}, or 116 degrees when on the side of O_{III}. The possibility that the protons exist at the center of the two oxygens, however, cannot entirely be ruled out from this experiment.

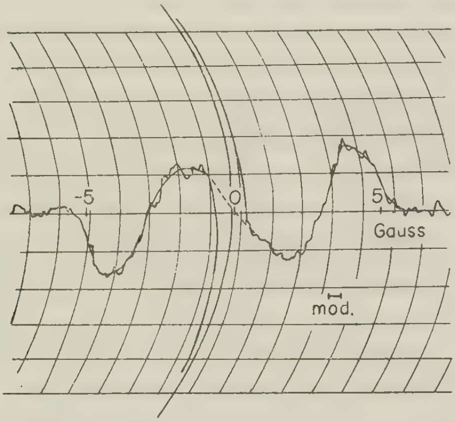

Fig. 4. Derivative of the absorption curve of potassium bicarbonate single crystal at $\Phi=25$ degrees. See the text for the meaning of Φ.

Sample: A single crystal 12 mmφ × 20mm made from the aqueous solution of chemically pure grade specimen of Wako Pure Chemical Company

Field: 7060 Gauss

Field sweep: 0.51 Gauss/min

Frequency: 30.0 MC

R.f. field within sample coil: 70 microgauss

Time constant: 12 sec

Temperature: about 25 degrees

Thus the result of the single crystal measurement restricts the possible proton positions within the range shown by the shaded

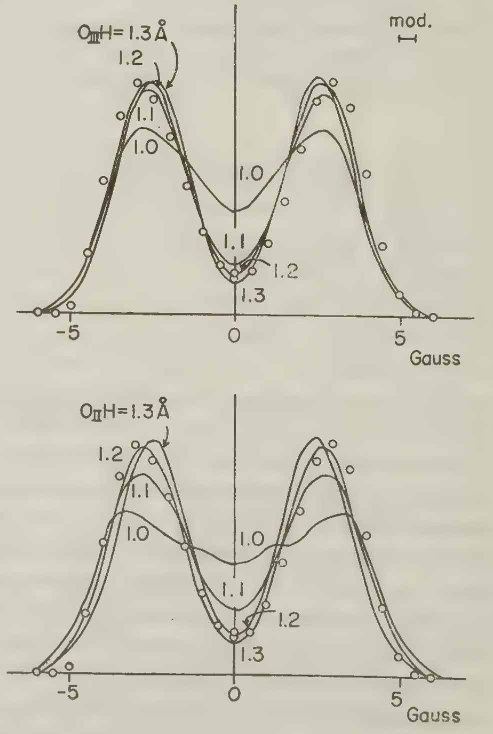

Fig. 5. Absorption line profile of potassium bicarbonate single crystal at $\Phi=25$ degrees. The curves indicate the calculated and the circles indicate the experimental.

area in Fig. 3, and more likely the protons may be located nearer to the side either of of the O_{III} type or of O_{II} type oxygens.

For the purpose of confirmation of the proton configuration obtained above, the comparison between the calculated absorption line positions of a two proton system and general profiles of the experimental curves for various Φ values is made in Fig. 6, the coincidence of which seems quite satisfactory, judging from the accuracies of both measurements and of the method of analysis involved.

(c) *Boric acid powder*

The positions of protons in boric acid crystals have been already inferred, although with somewhat less accuracy, from X-ray(11) as well as electron diffraction studies(12). The X-ray analysis find the protons approximately on the lines connecting oxygens, whereas the electron diffraction studies conclude that they are in much more inward positions. In view of the fact that the X-ray method does not reveal the position of the nuclei, but the distribution of the electrons around them, the accuracy of which is especially poor in the case of the hydrogen atom, the electron diffraction experiment seems to be much more favorable to the situation, although the latter investigation might be handicapped by the assumption involved in processing the data in connection with stacking disorders(12). The authors, however, believe the present investigation will be sufficient to settle this problem.

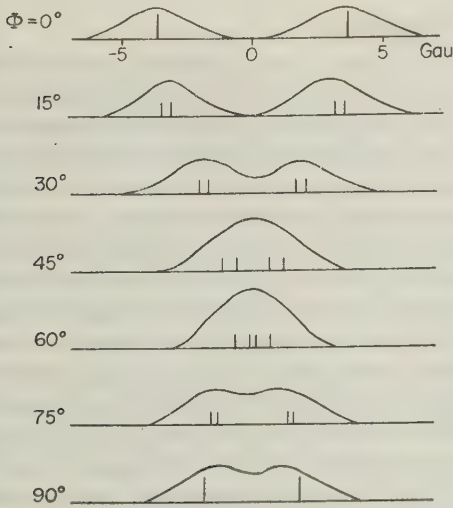

Fig. 6. Line profiles of potassium bicarbonate single crystal for various Φ values. The curves indicate the general behavior of experimental results, and the lines indicate the result of calculation, assuming $r=2.27$ Å and $O_{III}H=1.2$ Å

The recorded derivative of the saturation free proton magnetic resonance curve of the boric acid crystal powder is reproduced in Fig. 7. A somewhat flattened portion is seen at the center. The observed second moment of the curve is found to be 10.6 ± 0.9 Gauss^2, which is again the average of six independent data. The temperature dependence of this value is found to be insignificant, from −180°C up to the room temperature.

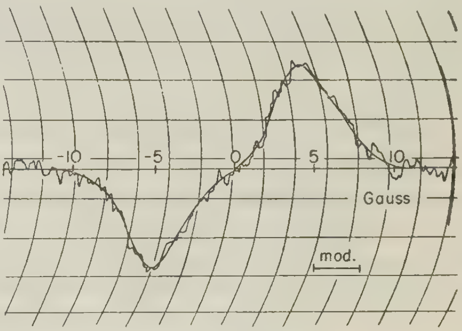

Fig. 7. Derivative of the absorption curve of boric acid powder

Sample: Guaranteed grade specimen from Wako Pure Chemical Company. Compressed powder 12 mmϕ × 20 mm in size
Field: 7060 Gauss
Field sweep: 0.95 Gauss/min
Frequency: 30.0 MC
R.f. field across sample coil: 50 microgauss
Time constant: 12 sec
Temperature: about 30°C

According to the X-ray structure analysis the boric acid crystal is known to have a layer structure. The structure of each layer is reproduced in Fig. 8, all the boron and oxygen atoms being approximately in this plane.

First, we assume the position of the proton as determined by X-ray analysis, in which the protons lie on the lines connecting two oxygens. The resulting second moment amounts only to 7.7 Gauss^2. And even if a somewhat elongated OH distance of 1.02 Å on the average, which has been inferred from the combination of infra-red data(14) and Badgers(9) rule, is assumed, keeping the OH directions as they were, it amounts only to 8.3 Gauss^2. These values are considered to be well outside the range of the experimental error given above. Therefore, the resonance data are not compatible with X-ray results.

Next, we will assume the inward positions of protons as was concluded by electron diffraction studies. When the protons are placed at inward positions, the interaction between the two protons increases, and it would therefore be favorable in explaining the large experimental value. The next problem is to find out the BOH angle compatible with the magnetic resonance experiment, by changing the angle in the layer plane, the OH distance being again 1.02 Å, as was assumed above. The parameters of all atoms beside hydrogen are already given from X-ray data.

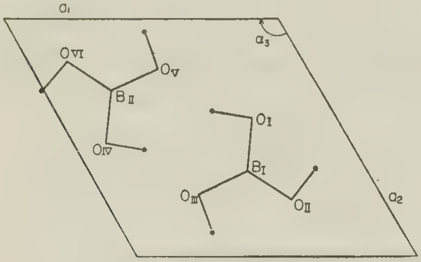

Fig. 8. Crystal structure of boric acid. Proton positions determined through the present work is indicated by the closed circles, their size corresponding roughly to the experimental error.

The summation $\sum_{i>j} 1/r_{ij}^6$ is carried out numerically, for all r_{ij} values shorter than 5 Å. The number of different interproton distances to be considered amounts to as many as about 70 for each BOH angle. The similar calculation is repeated for several BOH angles. The whole process is very long and tedious, and is actually carried out with the parametron computer PC-1 of the University of Tokyo, applying the programming tape originally prepared for calculating interatomic distances r_{ij} in crystal structure analysis$^{(10)}$.

The summation corresponding to r_{ij} longer than 5.0 Å is approximated by integration.

The relation between the BOH angle and the second moment, which is obtained by the above calculation is shown in Fig. 9. When the experimental value of the second moment is assumed, the BOH angle is found to be 96±2 degrees. This could be compared with 95 degrees, obtained from the electron diffraction studies, although there might exist some ambiguities due to the stacking disorder in the sample used for diffraction studies. The result from the present magnetic resonance studies is shown in Fig. 8 by closed circles, whose size represent roughly the experimental error.

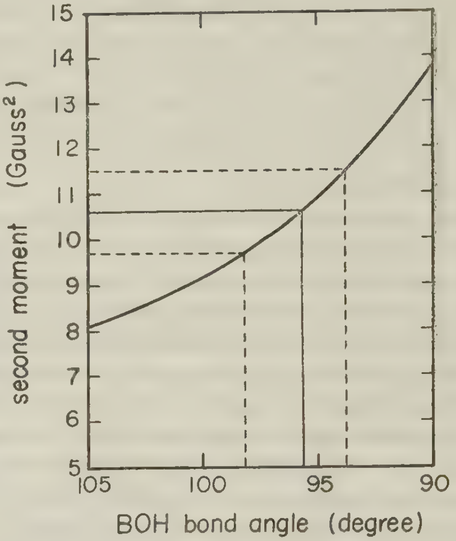

Fig. 9. Relation between BOH bond angle and second moment in boric acid crystal. The solid line indicates the experimental valve for the second moment 10.6 Gauss^2, and the corresponding bond single 95.6°. The broken lines show the allowance due to the experimental error.

§ 5. Discussions

The results of the foregoing experiments may well be summarized schematically in Fig. 10. The striking contrast between boric acid and potassium bicarbonate crystals exists in the fact that in the former the BOH angle is rather small and the OH length is relatively short, whereas in the latter the COH angle is much larger and the OH length is relatively long. This fact suggests that the long (2.72 Å) and weak O–H··O hydrogen bond in boric acid shows only a small deviation from the geometry of the non-hydrogen-bonded radical, whereas in the short (2.61 Å) and strong hydrogen bond in potassium bicarbonate both the XOH angle and the OH bond length are considerably affected by the formation of hydrogen bond. In case of potassium bicarbonate, we should take into consideration another possibility that the double bond character of the bond between C and O-H might tend to increase the COH bond angle. This possibility, however, seems to be largely negated by the fact that in the formic acid monomer(16), which has approximately the same C-O bond length, hence the same order of double bond character with potassium bicarbonate, the COH angle amounts to only 107°48′. The C-O distance is actually 1.31 Å in the former and 1.33 Å in the latter. The above consideration seems to suggest the fact that the COH bond angle in acid dimers largely depends upon the interaction between hydrogen atoms and lone pair electrons of the hydrogen bonded oxygen atoms.

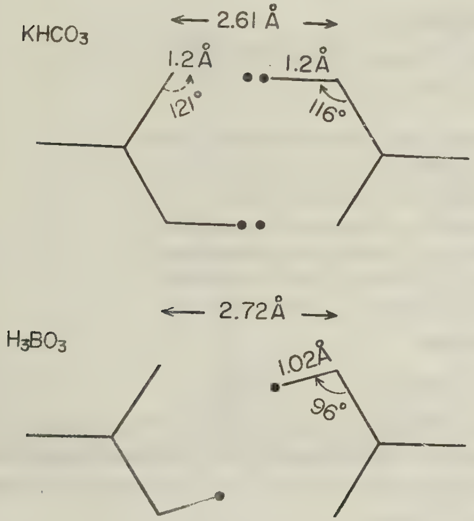

Fig. 10. Summary of our result.

The general tendency that weak hydrogen bonds affect the geometry of the non-hydrogen-bonded radical little, whereas strong ones do considerably, can be seen in other examples. The dependence of OH bond lengths upon interoxygen distances has already been thoroughly studied(15). As for XOH bond angles, they are little affected by weak hydrogen bonds in crystals such as α-resorcinol(3), sodium sesquicarbonate(2) and oxalic acid dihydrate(6), as were studied through neutron diffraction, and also in adipic acid crystal(7) as was found through polarized infra-red spectroscopy. Therefore, protons lie considerably away from the line connecting two oxygens. In cases of strong hydrogen bonds, however, it is difficult to find the case, where protons line considerably away from the lines(1)-(7). Direct confirmation through neutron diffraction studies are also desirable in boric acid and potassium bicarbonate crystals, although the present magnetic resonance method is beleived to have adequate accuracy for our present discussions.

A part of this investigation is a special research program, assisted by the Ministry of Education. The authors express their hearty thanks to Mr. H. Komatsu for his helpful suggestions to our experiments, and also for his giving them detailed informations from his own laboriours preliminary experiments of boric acid under the colaboration of one of the authors (Y. K.), and to Prof. S. Nagakura for his valuable discussions. Their thanks are also due to Mr. T. Sakurai for his X-ray measurements and Mr. R. Shishikura for his courtesy shown during the single crystal development. Their special gratitude is given to Prof. H. Takahashi, who offered them the chance of using the parametron computer PC-1, and to Mr. E. Wada for his preparing the programming tape as well as for his actual operation.

References

1) G. E. Pake: J. Chem. Phys. **16** (1948) 327. and other several works done through the proton magnetic resonance method.
2) G. E. Bacon and N. A. Curry: Acta Cryst. **9** (1956) 82.
3) G. E. Bacon and N. A. Curry: Proc. Roy. Soc. **235** (1956) 552.
4) S. W. Peterson and H. A. Levy: Phys. Rev. **92** (1953) 1082
5) G. E. Bacon and R. S. Pease: Proc. Roy. Soc. **A**, **230** (1955) 359.
H. A. Levy, S. W. Peterson and S. H. Simonson: Phys. Rev. **93** (1954) 1120.
6) B. S. Garett: Oak Redge Natl. Lab. Rep. No. 1745 and other several works done through the neutron diffraction method.
7) E. J. Ambrose, A. Elliot and R. B. Temple: Proc. Roy. Soc. **206** (1951) 192.
8) J. H. Van Vleck: Phys. Rev. **74** (1948) 1168.
9) R. M. Badger: J. Chem. Phys. **2** (1934) 128 ibid **3** (1935) 710.
G. Glocklen, G. E. Evans: J. Chem. Phys. **10** (1942) 606.
10) Y. Iitaka and T. Sakurai: Kôbutsugoku-Zasshi (Japanese) **4** (1960) to be published.
11) W. H. Zachariazen: Z. Kryst. **88** (1934) 150 Acta Cryst. **7** (1954) 305.
12) J. M. Cowley: Acta Cryst. **6** (1953) 522.
13) I. Nitta, Y. Tomiie and C. H. Koo: Acta

Cryst. **5** (1952) 292. ibid **7** (1954) 140.
14) D. E. Bethell and N. Sheppard: Trans. Faraday Soc. **51** (1955) 9.
15) H. K. Welsh: J. Chem. Phys. **26** (1957) 710.
16) R. G. Lermer, J. P. Friend and B. P. Daily: J. Chem. Phys. **23** (1955) 210.
17) H. L. Anderson: Phys. Rev. **76** (1949) 1460
18) K. Kume: to be published in Technical Report of ISSP. B
19) Operation Manual for "the Institute for Solid State Physics NMR-1 Spectrometer" (unpublished)

JOURNAL OF THE PHYSICAL SOCIETY OF JAPAN, Vol. 15, No. 7, JULY, 1960

Microwave Spectrum of Methyl Mercaptan

By Takeshi KOJIMA

Faculty of Literature and Science, Toyama University

(Received April 8, 1960)

Two new series of $\Delta J=0$ transitions in the first excited torsional state as well as one series of the S^{34} isotopic molecule were found in the range up to 37 Gc/sec besides those reported in the previous paper. The two series in the first excited torsional state are discussed, confirming the potential barrier height $V_3=443.9\pm1.0\,\mathrm{cm}^{-1}$ which were determined from $\Delta J=\pm1$, $\Delta K=\mp1$ lines in the ground torsional state. Moreover, the hindering potential is considered to be sinusoidal with an accuracy of better than one percent from those analyses.

§ 1. Introduction

Methyl alcohol, methyl mercaptan and methyl-amine form an interesting class of molecules for the study of hindered internal rotation. They are characterized by the structural similarity and the barrier of intermediate height. The potential barriers of methyl alcohol[1] and methyl-amine[2],[3],[4] have been precisely determined from the analysis of the series of lines which correspond to the transitions $\Delta J=0$, $\Delta K=\pm1$. In a previous paper[5] we have determined the potential barrier of methyl mercaptan to be 444 ± 10 cm^{-1} from the analysis of the $\Delta J=\pm1$, $\Delta K=\mp1$ lines in the ground torsional state, because the series of $\Delta J=0$ lines in the ground torsional state have their origins in the higher frequency region outside the observed range. However, three series in the first excited torsional state and one series in the second excited torsional state have been observed. The validity of the assumption that the potential barrier is expressed in the simple sinusoidal form $\frac{1}{2}V_3(1-\cos 3x)$ is discussed from analysis of the lines in the excited torsional states.

§ 2. Theory

According to the theory[1],[3] developed to interpret the spectra of CH_3OH-type molecules, the rotational energy can be separated into three terms:

$$W=W_{JK}+W_{K\mu n}+W^{(1)} \tag{1}$$

where W_{JK} is the rotational energy of a hypothetic rigid rotor, $W_{K\mu n}$ the energy of internal rotation and $W^{(1)}$ the perturbation energy due to asymmetry. The rotational energy W_{JK} is

$$W_{JK}=\frac{A+B}{2}\{J(J+1)-K^2\}+CK^2 \tag{2}$$

where

$$A=\frac{h^2}{8\pi^2 I_x}\,,\qquad B=\frac{h^2 I_y}{8\pi^2(I_y^2+D^2)}$$

and

$$C=\frac{h^2}{8\pi^2}\left(\frac{I_y+I_z}{I_yI_z-D^2}-\frac{I_y}{I_y^2+D^2}\right)$$

The definitions of the moments of inertia, I_x, I_y, I_z, and the product of inertia, D, were given in the previous papers[6] (also see Fig. 1).

The internal rotation energy, $W_{K\mu n}$, is given by the eigen-value of the wave equation which describes the internal rotation:

$$\frac{h^2}{8\pi^2}\left(\frac{I_z}{I_1 I_2}\right)^*\frac{d^2M}{dx^2}+[W_{K\mu n}-\tfrac{1}{2}V_3(1-\cos 3x)]M=0 \tag{3}$$

where

$$\left(\frac{I_z}{I_1 I_2}\right)^*=\frac{I_y I_z-D^2}{I_2(I_1 I_y-D^2)} .$$

The moment of inertia of the methyl group about its symmetry axis is I_2, and $I_1=I_z-I_2$.

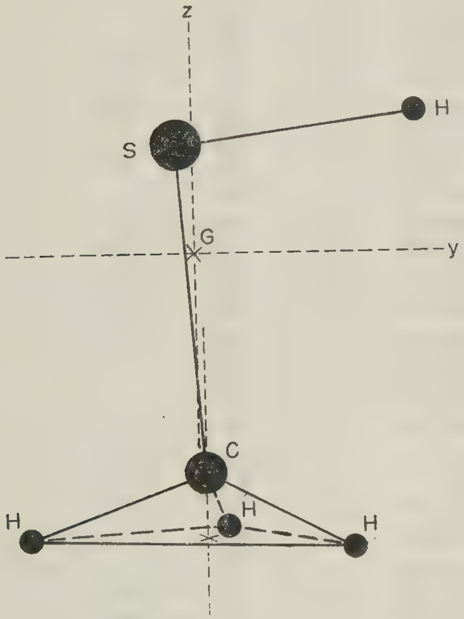

Fig. 1. Structure of methyl mercaptan.

The solution of (3) is expressed by

$$M(x)=\exp\left\{i\left(\frac{I_2}{I_z}\right)^*Kx\right\}\cdot Q(x) \tag{4}$$

where

$$\left(\frac{I_2}{I_z}\right)^*=\frac{I_2\sqrt{I_y^2+D^2}}{I_y I_z-D^2}$$

and $Q(x)$ is expanded in a Fourier series

$$Q(x)=\sum_{m=-\infty}^{\infty}a_m e^{imx} .$$

We have three types of solutions designated by $\mu=0$, 1 and -1:

$$\left.\begin{aligned} Q_{\mu=0}(x)&=\sum_{l=-\infty}^{\infty}a_{3l}e^{i3lx} ,\\ Q_{\mu=1}(x)&=\sum_{l=-\infty}^{\infty}a_{3l+1}e^{i(3l+1)x} ,\\ Q_{\mu=-1}(x)&=\sum_{l=-\infty}^{\infty}a_{3l-1}e^{i(3l-1)x} .\end{aligned}\right\} \tag{5}$$

The selection rule is $\Delta\mu=0$ in this expression.

The equations, (4) and (5), are expressed in a compressed form:

$$M(x)=\exp\left[i\left\{\left(\frac{I_2}{I_z}\right)^*K+\mu\right\}x\right]\cdot\sum_{l=-\infty}^{\infty}a_{3l+\mu}e^{i3lx} .$$

Then the internal rotation energy, $W_{K\mu n}$, is easily seen to be periodic in $(I_2/I_z)^*K+\mu$ with period 3.

When the barrier is relatively high, $W_{K\mu n}$ can be expressed in the first order approximation by[3),7)]

$$W_{K\mu n}=\alpha_n-\beta_n\cos\frac{2\pi}{3}\left\{\left(\frac{I_2}{I_z}\right)^*K+\mu\right\} \tag{6}$$

where α_n is the n-th torsional vibration energy in the high barrier limit.

The perturbation energy $W^{(1)}$ arises from the off-diagonal elements of the Hamiltonian, which were given in the previous papers[3),7)].

If a small sixfold term is allowed in the barrier such that

$$V=\frac{V_3}{2}(1-\cos 3x)+\frac{V_6}{2}(1-\cos 6x) , \tag{7}$$

then the rotational energy is expressed by

$$W=W_{JK}+W_{K\mu n}+W^{(1)}+W^{(6x)}_{K\mu n} , \tag{8}$$

where $W^{(6x)}_{K\mu n}$ is the perturbation term which arise from the sixfold term in the barrier and is given by the following equation:

$$\begin{aligned} Q^{(6x)}_{K\mu n}&=\int Q^*_{K\mu n}(x)\frac{V_6}{2}(1-\cos 6x)Q_{K\mu n}(x)dx\\ &=\frac{V_6}{2}\left(1-\sum_{m=-\infty}^{\infty}a_m a_{m+6}\right) . \end{aligned} \tag{9}$$

Since $W^{(6x)}_{K\mu n}$ is also periodic in $(I_2/I_z)^*K+\mu$ and can be expressed in the similar form as (6), it is impossible to determine the value of V_6 from the lines in only one torsional state.

§ 3. Experimental Results

The spectrometer used was the conventional Stark modulation type with both visual and recorder display. The observed lines within the range from 14 to 29 Gc/sec were previously reported[5)]. The observed lines in the range up to 37 Gc/sec are listed in Table I. The three series of lines, s, t, u, which show first-order Stark effects have been found in the range. The frequencies of lines of these series are plotted against the rotational quantum number J in Fig. 2, as well as those of the series, p, q, r, which were previously reported. The J values of the lines of the s-

Table I. Microwave Spectrum of Methyl Mercaptan.

Frequency (Mc/sec)	Stark Effect(a)	Intensity	Assignment
29772.81	1(o)	MW	s (30)[b]
30083.34	1(o)	MW	s (29)
30366.66	1(o)	MW	s (28)
30395.6	1	WWW	
30446.3	1	WWW	
30487.4	1	WWW	
30508.62	2(−)	MW	$14_{1,14}\leftarrow13_{2,11}$ $n=0$
30626.50	1(o)	MW	s (27)
30652.31	1(o)	W	
30666.43	1(o)	W	
30741.76	2(+)	MW～M	$12_1\leftarrow11_2$ $n=0$
30859.78	1(o)	MW	s (26)
30874.84	2(+)	MW	r (17)
30972.32	1(i)	MW	
31051.0	2(−)	MW	
31068.24	1(o)	MW	s (25)
31252.87	1(o)	MW	s (24)
31378.7	1	WWW	
31414.80	1(o)	M	s (23)
31450.2	1	WWW	
31476.5[c]	1	WWW	
31479.3	1	WWW	
31489.3	1	WWW	
31496.2	1	WWW	
31500.8	1	WW	
31522.7	1	WWW	
31527.2	1	WWW	
31529.9	1	WWW	
31540.4	1	WWW	
31555.09	1(o)	M	s (22)
31563.8	1	WW	
31567.9	1	WW	
31571.8	1	WW	
31575.4	1	WW	
31675.02	1(o)	M	s (21)
31776.04	1(o)	M	s (20)
31859.54	1(o)	M	s (19)
31880.2	1(i)	W	
31927.27	1(o)	M	s (18)
31980.68	1(o)	M	s (17)
31989.58	1(o)	W	s (1)
31994.74	1(o)	W	s (2)
32002.23	1(o)	W	s (3)
32011.70	1(o)	W	s (4)
32021.14	1(o)	W	s (16)
32022.71	1(o)	W	s (5)
32034.82	1(o)	W	s (6)
32047.20	1(o)	W	s (7)
32050.46	1(o)	MW	s (15)
32059.35	1(o)	W	s (8)
32070.04	1(o)	MW	s (14)
32070.15	1(o)	MW	s (9)
32078.93	1(o)	MW	s (10)
32081.32	1(o)	MW	s (13)
32084.51	1(o)	MW	s (11)
32085.74	1(o)	MW	s (12)
32278.04	1(i)	W	
32819.24	1(o)	W	t (3)
32820.71	1(o)	W	t (4)
32827.91	1(o)	W	t (5)
32844.33	1(o)	MW	t (6)
32874.34	1(o)	MW	t (7)
32880.05	1(o)	W	
32922.31	1(o)	MW	t (8)
32994.15	1(o)	MW	t (9)
33077.91	2(+)	MW	$10_{2,8}\leftarrow11_{1,11}$ $n=0$
33095.66	1(o)	M	t (10)
33096.66	2(−)	MW	
33233.51	1(o)	M	t (11)
33277.30	2(+)	WW	
33414.78	1(o)	MS	t (12)
33416.85	2(−)	W	
33647.20	1(o)	M	t (13)
33658.81	2(+)	MW	r (30)
33738.45	2(−)	MW	
33838.93	1(i)	W	
33858.74	1(i)	MW	
33938.69	1(o)	M	t (14)
34013.70	1(i)	W	
34193.09	2(+)	M	r (16)
34237.2	1(o)	WW	
34298.00	1(o)	MS	t (15)
34488.25	2(+)	MW	
34527.38	2(−)	MW	
34616.85	2(i)	MW	
34733.89	1(o)	MS	t (16)
34942.56	1(o)	W	
35255.73	1(o)	M	t (17)
35373.8	2(+)	WW	
35521.54	1(o)	W	
35543.34	1(i)	M	
35547.33	1	WW	
35552.2	1(o)	W	
35597.59	1(i)	MW	
35731.0	1(o)	WWW	u (3)
35754.19	1(o)	WW	u (4)
35791.03	1(o)	WW	u (5)
35792.1	2(+)	WW	
35846.05	1(o)	WW	u (6)
35857.35	1(i)	M	$4_0\leftarrow3_1$ $n=0$
35873.42	1(o)	MS	t (18)
35913.50	1(i)	M	$11_1\leftarrow10_2$ $n=0$
35924.22	1(o)	WW	u (7)
36026.20	1(o)	W	
36030.87	1(o)	WW	u (8)
36172.20	1(o)	WW	u ( )
36216.46	1	WW	
36281.75	1(o)	WW	
36354.69	1(o)	WW	u (10)
36585.17	1(o)	WW	u (11)
36597.09	1(o)	MS	t (19)
36822.40	1(o)	W	
36824.83	1(i)	MW	
36871.10	1(o)	WW	u (12)
37220.42	1(o)	WW	u (13)
37437.33	1(o)	M	t (20)

(a) The Stark effects are designated by 1(o) for the first order Stark effect with the strongest outer components, 1(i) for the first-order Stark effect with the strongest inner components, 2(+) for the second-order Stark effect with positive Stark displacement and 2(−) for the second-order Stark effect with negative Stark displacement.

(b) The number in parenthesis shows the J value of the line.

(c) Many very weak lines from 31476 to 31575 Mc/sec are expected to be the series lines which arise from the isotopic molecule, $C^{12}H_3S^{34}H$.

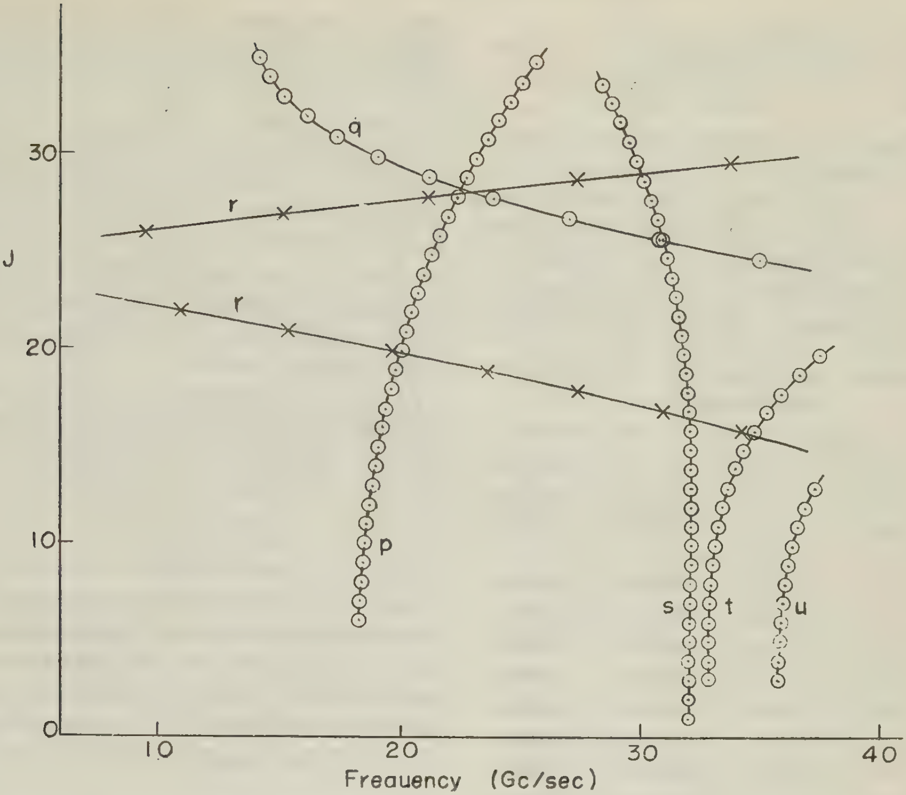

Fig. 2. ν−J diagram of the series lines.

Table II.

Series	ν_0	a	b	c	d	A	B
s	31986.96	1.319	−0.00321	-6.1×10^{-5}	9.1×10^{-7}	...	...
t	32824.40	0.809	0.03222	-5.89×10^{-5}	4.6×10^{-7}	0.646	0.0054

and t-series are determined from the Stark effects, while the J values of the lines of the other series are the estimated values.

The frequencies of the individual lines in the series can be expressed as a power series expansion in J^2+J as follows:

$$\nu=\nu_0+a(J^2+J)+b(J^2+J)^2 +c(J^2+J)^3+d(J^2+J)^4+\cdots$$

The values of these coefficients for s- and t-series were determined from the first five members of each series. They are listed in Table II.

The Stark effects of the lines of t-series were measured. The Stark displacement is expressed by $M\mathcal{E}[(A/J^2+J)+B]$, where $\mathcal{E}$ is the electric field and M the component of J along the field. The experimental values of A and B in (Mc/sec)/(V/cm) are listed in the last two columns of Table II.

§ 4. Analysis of the Ground Torsional State

(a) $\Delta J=\pm1$, $\Delta K=\mp1$ *lines*

Since the origins of the series corresponding to the transitions $\Delta J=0$, $\Delta K=\pm1$, $n=0\leftarrow0$ for methyl mercaptan are expected to lie far outside the observed range, the $\Delta J=\pm1$, $\Delta K=\mp1$ lines have been used in determining the potential barrier and the molecular structure as before[5].

The first six lines in Table III were identified from their Stark effects. The assignments of these lines were confirmed by the combination rule.

The frequencies of the lines corresponding to the transitions $(2_{1,2}\leftarrow3_{0,3}$, $\mu=0$, $n=0)$, $(2_1\leftarrow3_0$, $\mu=1$, $n=0)$ and $(1_1\leftarrow2_0$, $\mu=-1$, $n=0)$, are given by the following equations:

$$\left.\begin{aligned} 29091.9&=(W_{100}-W_{000})/h-3\nu_1+\varepsilon_1\,, \\ 23339.2&=(W_{110}-W_{010})/h-3\nu_1+\varepsilon_2\,, \\ 14764.5&=(W_{1-10}-W_{0-10})/h-2\nu_1+\varepsilon_3\,, \end{aligned}\right\}$$

where $W_{K\mu n}$ is the internal rotation energy and $\nu_1=25291$ Mc/sec is the frequency of the $J=1\leftarrow 0$, $K=0\leftarrow 0$ line. The perturbation terms, ε_1, ε_2, ε_3, are the contributions from the off-diagonal elements of the Hamiltonian, and are estimated to be -774.2, 20.2 and 0.4 Mc/sec, respectively. From these equations, the moments of inertia and the barrier height were determined by use of the D value obtained in § 5 (c). They are listed in Table IV.

Table III. $\Delta J=\pm 1$, $\Delta K=\mp 1$ lines in the $n=0$ state.

Assignment		Observed frequency in Mc/sec	Calculated frequency in Mc/sec
$J'_{K'}\leftarrow J_K$ or $J'_{K'_{-1}K'_{+1}}\leftarrow J_{K_{-1}K_{+1}}$	μ		
$2_{1,2}\leftarrow 3_{0,3}$	0	29091.9	(29092)
$5_{0,5}\leftarrow 4_{1,4}$	0	23256.9	23258
$2_1\leftarrow 3_0$	1	23339.2	(23339)
$5_0\leftarrow 4_1$	1	26994.2	26994
$1_1\leftarrow 2_0$	−1	14764.5	(14765)
$4_0\leftarrow 3_1$	−1	35857.4	35858
$9_{2,8}\leftarrow 10_{1,9}$	0	25659.7	25602
$10_{2,8}\leftarrow 11_{1,11}$	0	33077.9	32998
$12_{1,11}\leftarrow 11_{2,10}$	0	30741.8	30841
$14_{1,14}\leftarrow 13_{2,11}$	0	30508.6	30642
$8_2\leftarrow 9_1$	1	18039.5	18205
$11_1\leftarrow 10_2$	1	35913.5	35746
$9_2\leftarrow 10_1$	−1	21973.2	21938
$12_1\leftarrow 11_2$	−1	23801.8	23747

Table IV. Moments of inertia and the barrier height.

$$\left(\frac{I_2}{I_z}\right)^*=0.6522$$

$$\frac{A+B}{2}=25291\ \text{Mc/sec}$$

$$C=102733\ \text{Mc/sec}$$

$$I_1=1.7107\ \text{amuA}^2$$

$$I_2=3.2137\ \text{amuA}^2$$

$$I_z=4.9244\ \text{amuA}^2$$

$$D=-0.35\ \text{amuA}^2$$

$$V_3=443.9\pm 1.0\ \text{cm}^{-1}$$

From the moments of inertia and the barrier height determined above, the frequencies of other lines in the $n=0$ state were calculated. They agree with the observed values within the error of few hundred megacycles as shown in Table III.

(b) *Dipole moment*

The Stark energy for the $\mu=0$ transition is expressed by the sum of the second order perturbation terms which arise from the off-diagonal elements and the interaction terms between K-type doublet levels as in the case of slightly asymmetric rigid molecules, subject to modification of the energy values due to the internal rotation.

From the Stark effect of the $2_{1,2}\leftarrow 3_{0,3}$ line at 29091.9 Mc/sec, the components of the dipole moment parallel and perpendicular to the molecular axis were determined as

$$\mu_{\parallel}=1.33\pm 0.03\ \text{D}\,,$$

$$\mu_{\perp}=0.73\pm 0.03\ \text{D}\,.$$

The dipole moment of the molecule can be estimated from the bond dipole moments. By use of the values $\text{H}^+\rightarrow\text{S}^-=0.68$ D, $\text{C}^+\rightarrow\text{S}^-=1.00$ D and $\text{H}^+\rightarrow\text{C}^-=0.40$ D, one obtains $\mu_{\parallel}=1.30$ D and $\mu_{\perp}=0.71$ D, which agree well with the experimental values.

§ 5. Analysis of the Excited Torsional States

Since the frequency of the torsional vibration is about 200 cm^{-1}, some of the observed weak lines are ascribed to the molecules in the excited torsional states. In Table V the observed frequencies are compared with those

Table V. Lines in the excited torsional states.

(a) $\Delta J=\pm 1$, $\Delta K=\pm 1$ lines.

Assignment			Observed frequency in Mc/sec	Calculated frequency in Mc/sec
$J'_{K'}\leftarrow J_K$ or $J'_{K'_{-1}K'_{+1}}\leftarrow J_{K_{-1}K_{+1}}$	μ	n		
$3_{2,2}\leftarrow 2_{1,1}$	0	1	14320.2	12100
$3_{2,1}\leftarrow 2_{1,2}$	0	1	15339.0	13120
$2_1\leftarrow 1_0$	1	1	18417.6	17690

(b) Series lines ($\Delta J=0$).

Series	Assignment			Frequency of origin in Mc/sec	
	$K'-K$	μ	n	Observed	Calculated
r	$1\leftarrow 2$	0	1	(60800)	63020
s	$0\leftarrow 1$	1	1	31987	32730
t	$3\leftarrow 2$	−1	1	32824	28980
p	$5\leftarrow 6$	−1	2	18300	21780

calculated by using the molecular contants which have been determined in the previous section.

The difference between the internal rotation energies of the two levels with which the transition concerns, $W_{K'\mu n}-W_{K\mu n}$, is sometimes larger than several cm^{-1} in the excited torsional states. Therefore, the spectrum for the excited torsional states is quite different from the spectrum for the ground torsional state as shown in the following subsections.

(a) *Pair lines.*

The lines at 14320.2 Mc/sec and 15339.0 Mc/sec which show the second-order Stark effect are assigned as the transition $J=3\leftarrow2$, $K=2\leftarrow1$, $\mu=0\leftarrow0$, $n=1\leftarrow1$. The Stark components of the lower frequency line move towards higher frequencies and those of the higher frequency move towards lower, so that the lines appear to be mirror images. The directions of the Stark displacements, however, are reversed to those of the "mirror lines" observed in the spectrum of methyl alcohol by Hughes, Good and Coles[8].

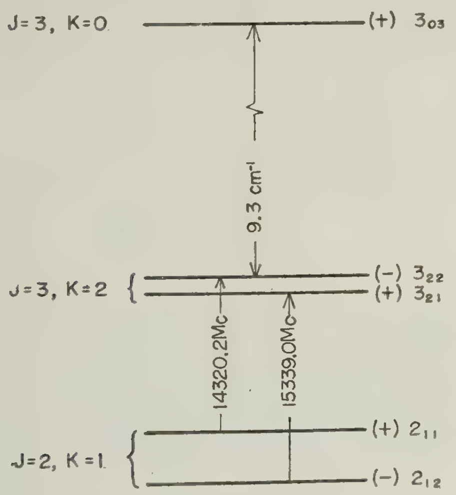

Fig. 3. Pair lines in the $n=1$ state.

Each energy level of $\mu=0$ ($K\neq0$) splits into doublet due to asymmetry (K-type doubling). The wave function for a K-type doublet level of $J=3$, $K=2$ has one of the two following forms:

$$\Psi^{(+)}_{K=2}=a_0\psi_0+a_2(\psi_{-2}+\psi_2) \qquad a_0<a_2 \tag{10a}$$

and

$$\Psi^{(-)}_{K=2}=b_2(\psi_{-2}-\psi_2) \tag{10b}$$

where the ψ_K are the symmetric hindered rotor wave functions. The shift from the symmetric hindered rotor energy*, $W^{(0)}_{J=3,K=2}$ is

$$\Delta^{J=3}_{K=2}=2\frac{\left(\int\psi_2{}^*H^{J=3,K=2}_{J=3,K=0}\psi_0dv\right)^2}{W^{(0)}_{J=3,K=2}-W^{(0)}_{J=3,K=0}} \tag{11}$$

for the $\Psi^{(+)}_{K=2}$ level, while the $\Psi^{(-)}_{K=2}$ level remains unperturbed. As shown in the energy level diagram for the $n=1$ state (Fig. 3), $W^{(0)}_{J=3,K=0}$ is higher than $W^{(0)}_{J=3,K=2}$ by 9.3 cm^{-1} because of the large internal rotation energy of the $J=3$, $K=0$ level. Thus the $\Psi^{(+)}_{K=2}$ level is shifted down by $\Delta^{J=3}_{K=2}$, so that the K-type doublet levels of $J=3$, $K=2$, $\mu=0$, $n=1$ are inverted to those of a rigid asymmetric rotor. In Fig. 3 the notation of energy level, $J_{K_{-1}K_{+1}}$, defined for asymmetric rigid rotor is also used for convenience.

Since the Stark effects of the pair lines are mainly due to the interaction between the near-by levels $3_{2,2}$ and $3_{2,1}$, the Stark components of the $3_{2,2}\leftarrow2_{1,1}$ line at 14320.2 Mc/sec move towards higher frequencies while those of the $3_{2,1}\leftarrow2_{1,2}$ line at 15339.0 Mc/sec towards lower.

Since the splitting of the $J=3$, $K=2$ level is calculated to be 9.3 Mc/sec from (11), the K-type splitting of $J=2$, $K=1$ level, $\Delta^{J=2}_{K=1}$ is obtained as 1028.6 Mc/sec. $\Delta^{J}_{K=1}$ is given by

$$\Delta^{J}_{K=1,n=1}=\frac{A-B}{2}I^{-101}_{101}J(J+1) \tag{12}$$

where

$$I^{-101}_{101}=\int Q^*_{101}Q_{-101}dx \tag{13}$$

The value of I^{-101}_{101} is calculated to be 0.640 by using the moments of inertia and the potential barrier given above. Then $(A-B)/2$ $=267.8$ Mc/sec is obtained. This value can be compared with the value 276.6 Mc/sec which is determined from the lines of K-type transition in the ground state.

(b) *Stark effect of the $J=1\leftarrow0$, $K=0\leftarrow0$ lines.*

The Stark effects of the $J=1\leftarrow0$, $K=0\leftarrow0$ lines are listed in Table VI. It is noticeable that the $\mu=\pm1$, $n=1$ line has small Stark coefficient in comparison with others. The Stark displacement of these lines is theoretically expressed by $\Delta\nu=(A\mu_{\|}{}^2+B\mu_{\perp}{}^2)\mathcal{E}^2$ where $A\mu_{\|}{}^2\mathcal{E}^2$ is the same as in the case of sym-

---

* The symmetric hindered rotor energy, $W^{(0)}_{JK}$ is $(W_{JK}+W_{K\mu n})$ in Eq. (1).

Table VI. Stark displacement of the $J=1\leftarrow 0$, $K=0\leftarrow 0$ lines: $\Delta\nu = C\varepsilon^2$.

Assignment		Frequency in Mc/sec	C in (Mc/sec)/(V²/cm²)
n	μ		
0	0	25290.9	0.994×10^{-5}
0	±1	25291.9	0.994
1	0	25219.5	0.998
1	±1	25206.9	0.576
2	0	25143.6	1.026
2	+1	25154.9	1.011

metric rotor and $B\mu_{\perp}{}^2\mathcal{E}^2$ in the contribution from the $H_{J,K}^{J-1,K-1}$ element of the Hamiltonian. Since the energy differences between the J, K and $J-1$, $K-1$ levels are estimated from the observed lines in the $n=1$ state, the dipole moment can be determined from the coefficients of the $n=1$ lines. The values obtained are

$$\mu_{\parallel}=1.36\ \mathrm{D}$$

and

$$\mu_{\perp}=0.76\ \mathrm{D}\ .$$

They coincide with the values obtained from the $2_{1,2}\leftarrow 3_{0,3}$ line in the $n=0$ state within the estimated accuracy.

(c) *Analysis of the series lines* ($\Delta J=0$)

The Stark effect for the series lines of $\mu=\pm1$ is predominantly of first-order with a small admixture of second-order. The Stark displacement for the t-series lines is given in the first-order expression by

$$\Delta\nu=0.5032\left\{-\frac{\mu_{\parallel}+21.57\mu_{\perp}G}{J^2+J}+3.722\mu_{\perp}G\right\}\mathcal{E}M \tag{14}$$

where $G=(h/8\pi^2)(D/I_y{}^2)$ is in cm^{-1}, ν in Mc/sec, μ in Debye unit and $\mathcal{E}$ in V/cm. By use of the experimental values listed in Table II, the value of D can be determined as -0.35 amuA².

The quantities a and b appearing in Table II are the coefficients of the J^2+J and $(J^2+J)^2$ terms, respectively, in the expansion form of the frequencies for the s- and t-series. The coefficient b is due principally to the off-diagonal elements, $H_{J,K}^{J,K+2}$. The calculated values of b for these series are in good agreement with the experimental values as shown in Table VII. The coefficient a is due to not only the off-diagonal elements $H_{J,K}^{J,K+1}$ and $H_{J,K}^{J,K+2}$, but also the centrifugal stretching of the molecule. The contributions from the off-diagonal elements can easily be calculated, but it is difficult to evaluate the centrifugal effect with any exactness. By modifying the theory which was developed by Kivelson⁹⁾ to interpret the fine structure of the $J=1\leftarrow 0$, $K=0\leftarrow 0$ line of methyl silane and was also successfully applied to methyl alcohol¹⁰⁾ and methyl mercaptan⁵⁾, the displacement of each line of the series from its origin due to the centrifugal effect can be expressed in a rough approximation by

Table VII. Coefficients of the s- and t-series in the expansion form.

Series	b_{cal}	b_{exp}	$a_{\mathrm{centrifugal}}$	$a_{K+1\leftrightarrow K}$	$a_{K+2\leftrightarrow K}$	a_{cal}	a_{exp}
s	−0.0039	−0.00321	1.00	0.236	0.007	1.24	1.319
t	0.03223	0.03222	−4.66	4.06	−0.393	−0.99	−0.809

$$\Delta\nu=(J^2+J)\Big[F_v\{\langle K'|1-\cos 3x|K'\rangle-\langle K|1-\cos 3x|K\rangle\}+\frac{4\pi^2}{h^2}G_v\{\langle K'|p_x{}^2|K'\rangle-\langle K|p_x{}^2|K\rangle\}\Big] \tag{15}$$

where $p_x=(h/2\pi i)(\partial/\partial x)$ and K represents the initial state and K' the final state. Since the coefficients F_v and G_v have been obtained in the previous paper the centrifugal effect can be estimated. The resulting value of a is compared with the experimental value as shown in the last two columns of Table VII.

The r-series has its origin outside the observed range and extends towards lower frequencies. It goes to zero frequency and come again towards higher frequencies. The position of each line of the series is mainly due to the K-type doubling of the levels with which the transition concerns. When the K-type doubling becomes large with high J, the involved levels are reversed. Since the Stark energy for the high J lines of the series is mainly due to the J, $K\leftrightarrow J$, $K-1$ interaction, the Stark components of the observed lines (containing the lines which arise from the transition between the reversed levels) move towards higher frequencies with increasing field. The frequency of the origin of the r-series is estimated to be 60800 Mc/sec by using the frequencies of the pair lines mentioned above which arise from the same transition of internal rotation.

The p-series has its origin at about 18300 Mc/sec and extends towards higher frequencies. Though the J values of the individual lines of the series can not be definitely determined, the dependence of the frequencies on the estimated J values is not inconsistent with the consideration of the centrifugal effect.

The u-series is considered to arise from the isotopic molecule $C^{12}H_3S^{34}$ from its intensity.

§ 6. Discussion of Potential Barrier

In Table V the observed frequencies of the $n=1$ lines are compared with those which are calculated from the moments of inertia determined by the analysis of the ground torsional state. The differences between the observed and calculated frequencies are considered as due to the effects of the deformation of the potential barrier from the sinusoidal form and the nonrigidity of the molecule. The value of V_6 in Eq. (7) is determined as $V_6=-2.0\,\mathrm{cm}^{-1}$ in order to make the best fit between the observed and calculated frequencies of both the $n=0$ lines and the $n=1$ lines. Though this value of V_6 is not significant because of the assumption of the rigid rotor, it may be concluded that the potential barrier of methyl mercaptan is sinusoidal in form with an accuracy of better than one percent. Recently, Burkhard and Dennison[11] obtained a similar result in the case of methyl alcohol.

§ 7. Molecular Structure

The method used to determine the molecular structure is the same as used before[5]. In addition to the values of I_1, I_2 and D obtained in the previous sections, we have the following equation for each of the isotopic molecules:

$$\frac{h}{16\pi^2}\left(\frac{1}{I_x}+\frac{I_y}{I_y^2+D^2}\right)=2B_v \qquad (16)$$

In above equation B_v is the rotational constant corresponding to the equilibrium position of the SH-bond, which is defined by

$$\nu=2B_v+2G_v\frac{4\pi^2}{h^2}\langle 0\mu n|p_x^2|0\mu n\rangle + 2F_v\langle 0\mu n|1-\cos 3x|0\mu n\rangle+\varepsilon \qquad (17)$$

where ν is the frequency of the $J=1\leftarrow0$, $K=0\leftarrow0$, line and ε the contribution from the off-diagonal elements of the Hamiltonian due to asymmetry. By using the values of B_v for CH_3SH, CH_3SD and CD_3SH which were obtained before[5], the molecular dimensions are determined as shown in Table VIII.

Table VIII. Molecular structure of methyl mercaptan.

$d_{SH}=1.335\pm0.010$ A	
$d_{CS}=1.819\pm0.005$ A	$\angle$CSH$=96°30'\pm30'$
$d_{CH}=1.092\pm0.010$ A	$\angle$HCH$=109°45'\pm30'$

The angle between the CS-bond and the symmetry axis of the methyl group is 2°10′±30′.

The author expresses his hearty thanks to Professor Koichi Shimoda for his encouragement and advice throughout this work. Thanks are also due to Dr. Tetsuji Nishikawa for his valuable discussions.

References

1) J. S. Koehler and D. M. Dennison: Phys. Rev. **57** (1940) 1006. D. G. Burkhard and D. M. Dennison: Phys. Rev. **84** (1951) 408. E. V. Ivash and D. M. Dennison: J. Chem. Phys. **21** (1953) 1064.
2) K. Shimoda, T. Nishikawa and T. Itoh: J. Phys. Soc. Japan **9** (1954) 974. T. Nishikawa: J. Phys. Soc. Japan **12** (1957) 668.
3) T. Itoh: J. Phys. Soc. Japan **11** (1956) 264.
4) D. R. Lide, Jr: J. Chem. Phys. **27** (1957) 343. D. Kivelson and D. R. Lide, Jr: J. Chem. Phys. **27** (1957) 353.
5) T. Kojima and T. Nishikawa: J. Phys. Soc. Japan **12** (1957) 680.
6) See for example, C. H. Townes and A. L. Schawlow: *Microwave Spectroscopy* (McGraw-Hill, 1955) 324.
7) K. T. Hecht and D. M. Dennison: J. Chem. Phys. **26** (1957) 31.
8) R. H. Hughes, W. E. Good and D. K. Coles: Phys. Rev. **84** (1955) 1195.
9) D. Kivelson: J. Chem. Phys. **22** (1954) 1733.
10) K. J. Hecht and D. M. Dennison: J. Chem. Phys. **26** (1957) 48. T. Nishikawa: J. Phys. Soc. Japan **11** (1956) 781.
11) D. G. Burkhard and D. M. Dennison: to be published.

Journal of the Physical Society of Japan, Vol. 15, No. 7, July, 1960

Heating of a Plasma by Acoustic Waves

By Tarô Dodo

Hitachi Central Research Laboratory, Kokubunji, Tokyo

(Received March 16, 1960)

Generation of an acoustic wave and transformation of its energy into thermal energy are considered. We generate an acoustic wave, imposing an oscillating magnetic field to a cylindrical plasma in a static magnetic field. When the suitable frequency of oscillating field is chosen, an acoustic wave is excited at an intermediate state between adiabatic and isothermal states. In this situation acoustic energies are transformed into thermal energies through the irreversible flow of heat due to stress relaxation.

In this method, the efficiency of heating is very high. The calculation shows that this method should be suitable to heat a plasma of moderate temperature ($10^5 \sim 10^6$ °K) and of high density ($10^{14} \sim 10^{16}$ particles/cm^3).

§ 1. Introduction

For the creation of a thermonuclear plasma, the heating of plasma through an application of oscillating electromagnetic field[1),2)] is a very important means. When an oscillating field is applied to a plasma, an organized motion will be generated. However, unless the energy of organized motion is transformed rapidly to the random energy, the motion of large amplitude may cause an instability and this method will be inadequate for heating plasma.

Here, it is proposed to heat a plasma through a generation of acoustic wave. As for the thermalization of acoustic energy, we call attention to that a plasma is a dispersive medium with respect to acoustic waves. In ordinary gases and solids, only above ultra high frequencies, 10^9 cycles/sec or more, acoustic waves are generated at isothermal state. But in a high temperature plasma, the thermal conductivity is very high. So acoustic waves are mostly generated at isothermal state. Of course, there is no dissipation of acoustic energy in either the isothermal or the adiabatic state. If the time τ, in which the heat flows from the compressed portion to the dilated portion of acoustic wave, is the same order of magnitude as the period of sound, the heat flows irreversibly. Then the acoustic energy is transformed to the thermal energy. This dispersive absorption is similar to the absorption of the electromagnetic wave in dielectric media or the elastic wave in visco-elastic high polymers.

§ 2. Generation of an Acoustic Wave

We shall consider the generation of acoustic wave in an infinitely long cylindrical plasma confined by static magnetic field $\boldsymbol{B}_0$ directed to z-axis. The radius of the plasma is r_0. When an oscillating field $\boldsymbol{B}_1=\varepsilon\boldsymbol{B}_0\sin kz\exp(i\omega t)$ is superposed to this static field, the radius of plasma cylinder oscillates according to

$$r=r_0[1-(1/2)\varepsilon\sin kz\exp(i\omega t)]\,, \tag{1}$$

because of the relation $r^2B=$constant. If the mean free path of particles is sufficiently shorter than r_0 and $2\pi/k$, an acoustic wave will be generated as shown in the following*.

Let ξ be the axial displacement of the centre of masses, ρ be the mass density and p be the pressure. The equations of motion and of conservation of mass are

$$\rho\frac{\partial^2\xi}{\partial t^2}=-\frac{\partial p}{\partial z}=-\frac{\partial p}{\partial\rho}\frac{\partial\rho}{\partial z}\,, \tag{2}$$

$$\rho_0 r_0^2=\rho r^2\left(1+\frac{\partial\xi}{\partial z}\right). \tag{3}$$

With these equations and Eq. (1), we obtain an equation of forced oscillation

$$\frac{\partial^2\xi}{\partial t^2}=c^2\left(\frac{\partial^2\xi}{\partial z^2}-\varepsilon k\cos kz e^{i\omega t}\right), \tag{4}$$

$$c^2=\frac{dp}{d\rho}\,. \tag{5}$$

Eq. (4) shows that a longitudinal oscillation is generated as a result of the radial oscillation given in Eq. (1).

§ 3. Thermalization of Acoustic Energy

The thermal conduction being taken into

---

* The compatibility of the condition $r^2B=$const. and the condition of excitation of acoustic wave is not discussed here.

account, the sound velocity $c^2=dp/d\rho$ is determined by the equations of state[3]

$$\Delta\rho=(c_T^2)^{-1}\Delta p-\mu\Delta T\,, \tag{6}$$

$$C\frac{\partial}{\partial t}(\Delta T)=K\nabla^2(\Delta T)+\alpha\frac{\partial}{\partial t}(\Delta\rho)\,, \tag{7}$$

where

$$c_T=(\partial p/\partial\rho)_{T=\mathrm{const.}}^{1/2}=(p_0/\rho_0)^{1/2}\,,$$
$$\mu=-(\partial\rho/\partial T)_{p=\mathrm{const.}}=\rho_0/T_0\,,$$
$$\alpha=C(\partial T/\partial\rho)_{\mathrm{adiabatic}}\,,$$

K is the thermal conductivity, C=heat capacity per unit volume, $\Delta\rho$, Δp and ΔT are the deviations from the equilibrium values ρ_0, p_0 and T_0, respectively. Eliminating ΔT from Eqs. (6) and (7), we obtain

$$c_T^2[\tau_A(\Delta\dot{\rho})+\Delta\rho]=\tau_T(\Delta\dot{p})+\Delta p\,, \tag{8}$$

where

$$\tau_A=(c_A^2/c_T^2)\tau_T\,,\quad c_A^2=(1+\mu\alpha/C)c_T^2\,,$$

and τ_T is determined by the equation of heat conduction

$$(K/C)\nabla^2(\Delta T)+\tau_T^{-1}(\Delta T)=0\,.$$

τ_T is the stress relaxation time in which heat flows from the compressed portion to the dilated portion. From the above equation, we get

$$\tau_T^{-1}=(K/C)(2\pi/\lambda)^2\,, \tag{9}$$

where λ is the wave length of sound.

Now we obtain the expression of sound velocity from the equation of state (8). If $\Delta\rho$ and Δp vary as

$$\Delta\rho,\ \Delta p\propto\exp(i\omega t)\,,$$

we obtain the sound velocity

$$\frac{dp}{d\rho}=c^2=\frac{i\omega\tau_A+1}{i\omega\tau_T+1}c_T^2$$
$$=\frac{\omega^2(\tau_A\tau_T)+1+i\omega(\tau_A-\tau_T)}{(\omega\tau_T)^2+1}c_T^2\,. \tag{10}$$

In limiting cases, this expression becomes the adiabatic or the isothermal sound velocity:

$$\frac{dp}{d\rho}=\frac{\tau_A}{\tau_T}c_T^2=c_A^2\quad\text{for}\quad\omega\tau_T\gg1\,,$$

$$\frac{dp}{d\rho}=c_T^2\qquad\text{for}\quad\omega\tau_T\ll1\,.$$

The dispersion relation (10) is well-known for the case of the absorption of electromagnetic wave in dielectric media*.

The phase angle δ between $\Delta\rho$ and Δp is given by

$$\tan\delta=\frac{\text{imaginary part of }c^2}{\text{real part of }c^2}$$
$$=\frac{\omega(\tau_A-\tau_T)}{1+(\omega\tau)^2}=\frac{c_A^2-c_T^2}{\bar{c}^2}\frac{\omega\bar{\tau}}{1+(\omega\bar{\tau})^2}\,, \tag{11}$$

where

$$\bar{\tau}^2=\tau_A\tau_T\quad\text{and}\quad\bar{c}^2=c_Ac_T\,. \tag{12}$$

When δ is not so large, the relation between δ and the fractional decrease of sound energy per cycle $\Delta W/W$ is as follows:

$$2\pi\tan\delta=\Delta W/W\,. \tag{13}$$

The relaxation strength $(c_A^2-c_T^2)/\bar{c}^2$ in this case is very large. So a large fraction of the energy of organized motion is transformed to the thermal energy.

§ 4. Examples

Two cases are considered for the acoustic heating, one is the heating by standing wave and the other is by travelling wave.

We shall first discuss the heating by standing wave. The solution of Eq. (4) is

$$\xi=\xi_0\cos kz\exp(i\omega t)\,,\qquad \xi_0=\frac{\mathcal{E}kc^2}{\omega^2-c^2k^2}\gtrsim\frac{\mathcal{E}}{k}\,. \tag{14}$$

If the frequency of external field is not equal to the natural frequency of plasma, ξ_0 is the order of $\mathcal{E}/k$. The acoustic energy is $(1/2)\rho\cdot(\omega\xi_0)^2\simeq(1/2)\rho c^2\mathcal{E}^2\simeq(1/2)p\mathcal{E}^2$. In usual cases, $p\simeq(1\sim10^{-1})\times$(magnetic energy for confinement), so the acoustic energy is $(1\sim10^{-1})\times$(energy of osillating magnetic field). Therefore, the thermal energy supplied to the plasma through acoustic energy is $(10^{-1}\sim10^{-2})\times$(magnetic energy of oscillating magnetic field), because $\tan\delta\simeq10^{-1}$.

On the other hand, the Q-value of coil system, the ratio of the energy of oscillating magnetic field multiplied by the angular frequency to the ohmic power loss in the coil, is order of 10^2. Therefore, the thermal energy supplied to the plasma is $(10\sim1)\times$(energy dissipated in the coil). Thus we get the efficiency of suppling energy to plasma through standing wave of suitable frequency as 50% or more.

For the particular case of deuterium plasma, the sound velocities and the thermal diffusion coefficient are

---

* ρ, p and c^2 correspond to the electric field $\boldsymbol{E}$, displacement $\boldsymbol{D}$ and dielectric constant ε, respectively.

$$\left.\begin{aligned} c_A&=\sqrt{\gamma p/\rho}=\sqrt{\gamma(Z+1)n_i\kappa T/n_i m_i}\\ &=1.17\times10^4 T^{1/2} \quad \text{cm/sec deg}^{1/2}\,,\\ c_T&=\sqrt{p/\rho}=9.1\times10^3 T^{1/2} \quad \text{cm/sec deg}^{1/2}\,,\\ \bar{c}&=\gamma^{1/4}(p/\rho)^{1/2}=1.03\times10^4 T^{1/2} \quad \text{cm/sec deg}^{1/2}\,, \end{aligned}\right\} \tag{15}$$

$$\left.\begin{aligned} K/C=D&=\alpha(\kappa T)^{5/2}/m_e^{1/2}e^4 Z n_i=5.7\\ &\times10^9 T^{5/2} n_i^{-1} \quad \text{cm}^{-1}\,\text{sec}^{-1}\,\text{deg}^{-5/2}\,, \end{aligned}\right\} \tag{16}$$

where γ is the ratio of specific heats, C_p/C_v, κ is the Boltzman constant and α has the magnitude[4] around 10. For a cylindrical deuterium plasma of radius 5 cm, density 10^{15} ions/cm³ and 10^5 °K, numerical values of the above expressions are

$$\left.\begin{aligned} c_A&=3.7\times10^6\ \text{cm/sec}\,, \quad c_T=2.88\times10^6\ \text{cm/sec}\,,\\ \bar{c}&=3.25\times10^6\ \text{cm/sec}\,, \quad D=1.8\times10^7\ \text{cm}^2/\text{sec}\,, \end{aligned}\right\} \tag{17}$$

and a suitable wave length λ to generate an acoustic wave will be

$$\lambda\simeq20\ \text{cm}\,. \tag{18}$$

For the most efficient frequency $f=(2\pi\bar{\tau})^{-1}$, we get from Eqs. (9), (12), (17) and (18)

$$\begin{aligned} f&=(2\pi\bar{\tau})^{-1}=D(2\pi/\lambda^2)/2\pi(\gamma)^{1/2}\\ &=2.2\times10^5\ \text{cycles/sec}\,. \end{aligned} \tag{19}$$

In this case, using the above numerical values, we get the acoustic energy $(1/2)\rho(\omega\xi_0)^2$ as

$$(1/2)\rho(\omega\xi_0)^2\simeq(3/2)p\mathcal{E}^2\,. \tag{20}$$

When $\tan\delta$ is not so small, $\varDelta W/W$ should be given by, instead of Eq. (14),

$$\varDelta W/W=[1-\exp\{-4\pi\tan(\delta/2)\}]\,. \tag{21}$$

In our case, from Eq. (11)

$$\tan\delta=\frac{\gamma-1}{\gamma^{1/2}}\frac{1}{2}=\frac{1}{\sqrt{15}}\,, \tag{22}$$

and we get

$$\varDelta W/W\simeq0.8\,.$$

If the gas pressure p is one tenth of the magnetic energy for confinement, the thermal energy supplied by the oscillating magnetic field is

$$\varDelta W\simeq(0.8)\times(3/2)\times(1/10)\times(\text{energy of oscillating magnetic field})\,.$$

When the Q-value of coil system is 100, the effeciency η is in this example

$$\begin{aligned} \eta&=\frac{\varDelta W}{\varDelta W+\text{ohmic loss}}=\frac{10^{-1}}{[10^{-1}+2\pi(100)^{-1}]}\\ &\simeq60\%\,. \end{aligned} \tag{23}$$

We shall next discuss the heating by travelling wave. If we generate a travelling acoustic wave by imposing an oscillating magnetic field on a small longitudinal section (heating section) of a cylindrical plasma, the wave length λ is determined automatically by the frequency of oscillating field and the temperature of plasma. In this case, the most suitable frequency is determined by the following simultaneous equations:

$$\left.\begin{aligned} f&=(2\pi\bar{\tau})^{-1}=D(2\pi/\lambda)^2/2\pi(\gamma)^{1/2}\,,\\ f&\simeq\bar{c}/\lambda\,. \end{aligned}\right\} \tag{24}$$

For the deuterium plasma employed in the above example, $n_i=10^{15}$ and $T_i=T_e=10^5$ °K, the frequency and the wave length determined by the above equations are

$$f=1.2\times10^5\ \text{cycles/sec} \quad \text{and} \quad \lambda=27\ \text{cm}\,. \tag{25}$$

The logarithmic decrement of the wave amplitude is

$$\text{log. dec.}=2\pi\tan(\delta/2)\simeq\pi\tan\delta=0.8\,,$$

using the numerical value in Eq. (22). The eighty per cents of acoustic energy are transformed to the thermal energy after travelling one wave length (=27 cm).

Appendix.

The Physical Meaning of τ_T and τ_A

If we decrease rapidly the volume of the container of gases, the gas pressure increases by the amount $\varDelta p=c_A^2\varDelta\rho$. As the time elaspses, heat flows from the gases to the surrounding walls and the increment $\varDelta p$ approaches to $\varDelta p=c_T^2\varDelta\rho$. The decay constant τ_T of $\varDelta p$ is called the stress relaxation time. (See Fig. 1 (a))

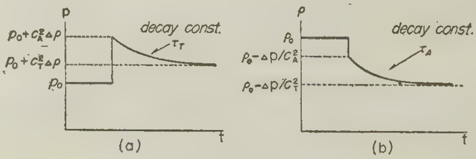

Fig. 1. (a) The stress $c_A^2\varDelta\rho$ relaxes with the time constant τ_T. (b) The strain $\varDelta p/c_A^2$ relaxes with the time constant τ_A.

In the similar way, when we increase the pressure applied to the container of gases, decrement $\varDelta\rho$ approaches to $\varDelta\rho=\varDelta p/c_T^2$ with the decay time τ_A. (See Fig. 1 (b))

References

1) J. M. Berger, W. A. Newcomb, J. M. Dawson,

E. A. Frieman, R. M. Kulsrud and A. Leneard: Phys. Fluids **1** (1958) 301.
2) T. H. Stix: Phys. Fluids **1** (1958) 308.
3) C. Zener: *Elasticity and Anelasticity of Metals.* (University of Chicago press, 1948).
4) L. Spitzer, Jr.: *Physics of Fully Ionized Gases.* (Academic press, 1955) 87.

JOURNAL OF THE PHYSICAL SOCIETY OF JAPAN, Vol. 15, No. 7, JULY, 1960

Exciton-Induced Luminescence in KI/Tl.*

Masao TOMURA and Yozo KAIFU
Department of Applied Physics, Osaka City University, Osaka

(Received on February 17, 1960)

In a single crystal of KI/Tl, emissions from Tl^+ ion and a certain impurity were observed under excitation of light in the first characteristic absorption band of KI. These exciton-induced luminescences were measured at various temperatures for specimens of several concentrations of Tl^+ ion. The intensities of the exciton-induced luminescences attained saturated values at about liquid oxygen temperature. In consideration of the amount of energy transferred to the impurity, the saturated intensities of the exciton-induced luminescence from Tl^+ ion are almost independent of the concentration of Tl^+ ion in the range of $10^{15} \sim 10^{19}/cm^3$ and showed a quantum efficiency as high as 30%. Therefore the migration of an exciton through the crystal was confirmed.

§ 1. Introduction

A possibility of migration of an exciton in alkali halide crystals has been discussed theoretically[1], and an explanation[2] for no appearance of the edge luminescence of alkali halides was based on the nature of migration of an exciton through the crystals.

Apker and Taft[3] have observed that the excitons in alkali halides interacted with F centers and transferred their energy to the latter, ejecting electrons out of these centers. They adopted the external photoelectric effect as the detecting method and obtained the value of quantum yield as small as 1×10^{-3} for the exciton-induced photoelectric effect. Although the real quantum yield for ejecting an electron out of the F center was not determined, they estimated the yield of 10^{-2} in the order of magnitude by considering the lost part of ejected electrons in the erystal. Because of the very small quantum yield, they could not deny a possibility of energy-transfer from the exciton to the F center through the so-called dipole-dipole interaction proposed by Dexter[4]. On the other hand Dexter and Heller[5] have calculated the interaction between the exciton and the F center, obtaining 10^{12} sec^{-1} as the probability of ionization of the F center. Then in the case of Apker and Taft's experiment where the concentration of the F center was estimated as high as $10^{18}\sim10^{19}/cm^3$, the exciton-induced yield of the ionization should be unity in the order of magnitude on the stand point of the migration of the exciton.

In the next place, Inchauspé[6] has carried out a similar experiment as that by Apker and Taft, using a method of detecting photoconductivity. His results showed that the exciton-induced photocurrent was independent of the F center concentration, and seemed to show the migration of the exciton. The exciton-induced photocurrent, however, could be observed only in the region of the long wavelength tail of the exciton absorption band, and then it is ambiguous that the photoelectron he caught came from the F center alone. In his experiment, a value of about twenty can be obtained as the real quantum yield of the exciton-induced photoconductivity, if we assume that the same process takes place as in the case of ionization of the F center under irradiation of F band light. Furthermore, his results were obtained through D. C. method, so the real magnitude of photocurrent might be hardly obtained in these insulators because of the space charge formation. It is necessary to clarify the process of interaction between the exciton and the F center in order to interpretate his results.

---

* Reported at the meetings of the Physical Society of Japan. Oct. (1958) & Apr. (1959).

Ueta and co-workers7) have also studied on the interaction between the exciton and the F center through detecting F center bleaching. In their experiments only light in the tail of the characteristic absorption band was used. The quantum yield of the bleaching effect by excitons was about 15, and they proposed a model that the thermal spike due to excitons took place and eventually F centers were thermally bleached, being converted to metallic colloids. In their experiments, however, the problem of exciton-migration was not touched.

Although the interaction of the exciton with the F center in alkali halide crystals was confirmed as mentioned above, the nature of exciton-migration has not been clarified. In the present work, measurements were carried out to make ascertain the existence of the moving exciton in KI by detecting the exciton-induced luminescence which is the most suitable for the present purpose.

§ 2. Luminescence of KI/Tl

It is well known about natures of luminescence of alkali halides containing Tl$^+$ ion as an activator8). A few characteristic properties of the luminescent material are as follows. Tl$^+$ ion occupies substitutionally some of the sites of alkali metal ion, distributing randomly in the crystal. The quantum yield of luminescence is nearly unity. The luminescence has no nature of thermal quenching below room temperature and also concentration quenching even in the case of rather high concentration of the activator. Then the luminescent material is very useful for studying the interaction between excitons and Tl$^+$ ion. For instance, in measuring of temperature-and concentration-dependence of the interaction, the above mentioned properties of the direct luminescence from Tl$^+$ ion itself will not confuse results.

KI/Tl single crystals were prepared by the Kylopoulos method. The concentration of Tl$^+$ ion was determined by measuring the optical density of the absorption band peaked at 283 mμ at room temperature. As the oscillator strength of the absorption band, the data given by Yuster and Delbecq9) were adopted. The oscillator strength at room temperature was assumed to be equal to the one at liquid nitrogen temperature which was obtained by the above authors. In case of very high concentration of Tl$^+$ ion, the amount of Tl$^+$ ion was obtained by the chemical analysis.

All the intensities of emissions observed varied proportionally with the intensity of incident light, therefore measurements of luminescence were carried out as reported before10). Absolute values of quantum yield of luminescence were not determined, however, yields were obtained through refering to the intensity of the direct emission due to Tl$^+$ ion itself in the case of high concentration of Tl$^+$ ion such as 10^{18}/cm^3 where the almost all of the incident light was absorbed in the specimen. The quantum yield of the direct emission from Tl$^+$ ion is about 80%.

The optical absorption curve of KI/Tl at liquid nitrogen temperature9) is shown in Fig. 1. The dominant absorption bands appear at 224, 233, 244 and 282 mμ. The first band is

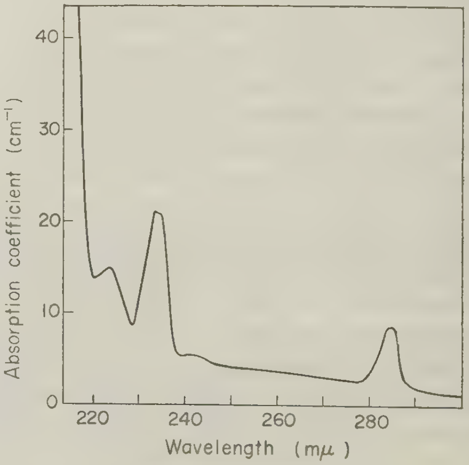

Fig. 1. The absorption curve of KI/Tl at liquid nitrogen temperature. Tl$^+$ ion concentration is 1.2×10^{-6} mol. (after Yuster and Delbecq).

known as the Greek band due to Tl^+ ion, that is the adsorption band of the localized exciton around Tl^+ ion. In cases of very high concentration of Tl^+ ion, absorption bands at 250 and 290 mμ appear. They are due to double Tl^+ ions center.

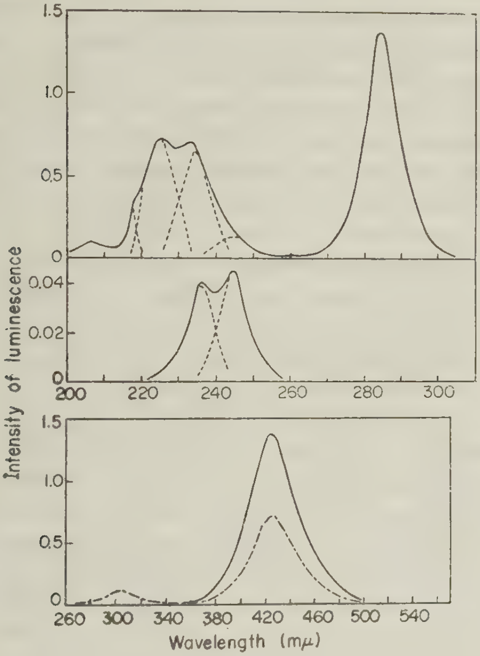

Fig. 2. The emission and excitation spectra for KI/Tl at liquid oxygen temperature. Tl^+ ion concentration is $3\times10^{17}/cm^3$.
Upper: The excitation spectra for the emission at 440 mμ.
Middle: The excitation spectra for the emission at 305 mμ.
Lower: The emission bands under excitation of 283 mμ (solid line) and 250 mμ (chained line) lights.

There are little data on the luminescence of KI/Tl, so we have attempted to study detailed properties of the above luminescence. In Fig. 2* one example of the luminescence of KI/Tl at liquid oxygen temperature is shown. As in the following, intensities of emission are shown for constnt energy of incident light through out all of the wavelength region. At liquid oxygen temperature, an emission band lying at 425 mμ is observed under excitation of 224, 233 and 282 mμ lights and an emission at 305 mμ appears under excitaion of only 233 and 244 mμ lights. The latter emission quenches thermally at room temperature against the former. In cases of very high concentration of Tl^+ ion, a new emission at 320 mμ appears under excitation of 250 and 290 mμ lights. It may be attributed to the double Tl^+ ion center.

§3. Exciton-induced Luminescence of KI/Tl

At liquid oxygen temperature, under excitation by exciton light, two kinds of emission are observed. As Fig. 3 shows, one lies at 425 mμ and the other at 360∼380 mμ.** The former is coincident with the direct emission from Tl^+ ion itself and the latter is the same

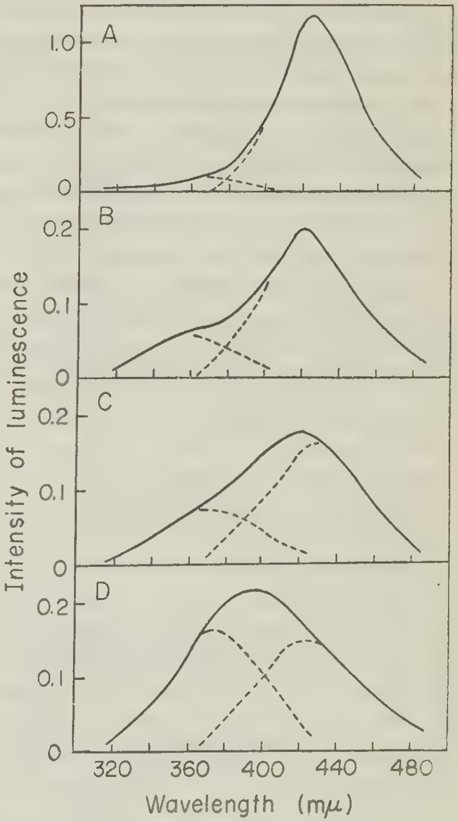

Fig. 3. The emission spectra under excitation of the exciton energy (216 mμ) at liquid oxygen temperature. Tl^+ ion concentrations are; A: $6\times10^{18}/cm^3$, B: $3\times10^{17}/cm^3$, C: $1\times10^{17}/cm^3$ and D: $5\times10^{15}/cm^3$.

---

* The intensity scale of luminescences shown in Fig. 2 and 3 is different from that shown in the following figures. The band pass of the incident light was 4 mμ at 220 mμ through out the present measurements.

** The crystal used in this measurement is obtained from another reagent than that used for the crystals in the following measurements.

one as that appeared in pure KI crystal[10)11)]. The emission at 305 mμ from Tl^+ ion mentioned before cannot be found in this case. Therefore we have confirmed actually the exciton-induced luminescences from Tl^+ ion and a certain impurity involvod in the host crystal. In the other words, the exciton transfers its energy to Tl^+ ion and the unknown impurity, whose excitations lead eventually to emit their own luminescences. The figure shows that the higher is the concentration of Tl^+ ion, the more intense is the emission lying at 425 mμ against the emission band at 360∼380 mμ.

In the next place, temperature-dependences of the exciton-induced luminescences were measured for specimens of various concentrations of Tl^+ ion. In these measurements, two sets of glass filters (Toshiba Electric co.) were adopted to separate the above two kinds of emission in place of the monochromator used for measurement of the emission spectrum. A set of V-Y3C and V-CIA filters was used for the emission from Tl^+ ion, and a set of UV-DI and UV-DII filters for the emission at 360∼380 mμ which came from the unknown impurity. (In the following, we call this impurity D impurity.) The transmission curves of these filters are shown in Fig. 4. As both emissions hardly alter their positions over all the temperature region in the present measurement, these filters are sufficient for separation of the two emissions.

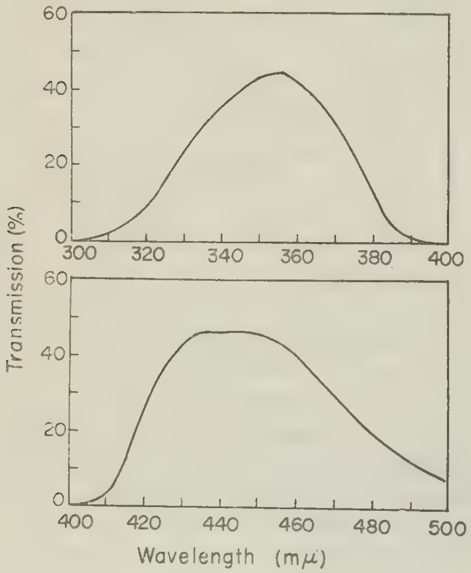

Fig. 4. Transmission curves of optical filters. Upper: UV–DI+UV–DII. Lower: V–Y3C+V–CIA.

Fig. 5 shows one example of excitation spectra of the exciton-induced luminescences from Tl^+ ion and D impurity at various temperatures. The excitation bands due to the direct absorption by Tl^+ ion in the longer wavelength region than the exciton absorption band are omitted for the moment in the figure. The excitation curve for the exciton-induced luminescence from Tl^+ ion overlaps with the excitation curve due to Tl^+ ion itself, so they are designated roughly separately with dotted curves in the figure.

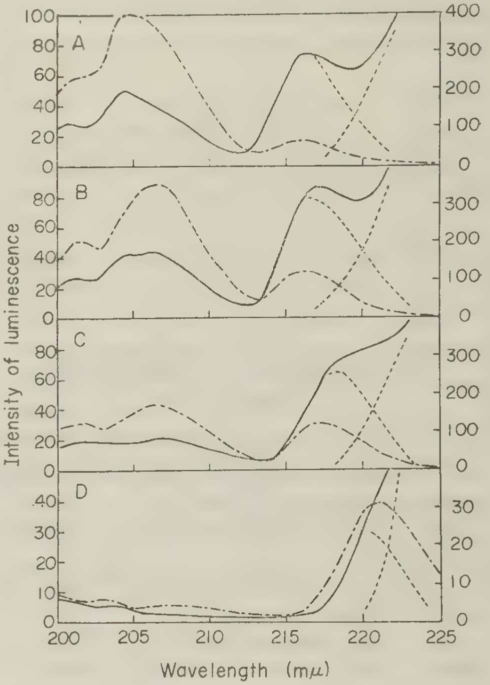

Fig. 5. The excitation spectra for the exciton-induced luminescences from Tl^+ ion (solid line) and D impurity (chained line) at several temperatures. Tl^+ ion concentration is $4.2\times10^{16}/cm^3$. A: −211°C, B: −202.5°C, C: −174°C and D: −138.5°C. The left and right ordinate scales correspond to the solid and chained lines respectively.

The peak of the exciton absorption band of KI lies at 214 mμ at liquid nitrogen temperature and 220 mμ at room temperature. As the figure shows, the exciton-induced responses are found in these wavelength region. At low temperatures the shape of excitation spectrum for the exciton-induced luminescence is similar to that for the exciton-induced photoelectric effect observed by Apker and Taft[3]. At higher temperatures, however, the exciton-induced luminescence decreases and the shape of the excitation spectrum becomes flat as in the case of the above authors.

The yield of the exciton-induced luminescence at lower temperatures shows a minimum just at the peak of exciton absorption band. Because of very high absorption coefficient at this peak the exciton may decomposes near the surface of the crystal and the yield may diminish markedly. Thus the shape of excitation spectrum is not so simple to define the intensity of the exciton-induced luminescence. We shall tentatively take the maximum height of the excitation spectrum which lies at above 216 mμ in the case of lowest temperature as the intensity of the exciton-induced luminescence from Tl^+ ion. As will be discussed in the following paper, at the wavelengh region of this maximum the absorption coefficient seems to be so small that excitons are created deep in the interior of the crystal under irradiation of light at this wavelength. Therefore this induced luminescence will not suffer from the influence of the surface of the crystal. It can be seen in Fig. 1 that the absorption coefficient of a single crystal at 216 mμ is so small as $10^2\,cm^{-1}$ in contrast with the one of evaporated polycrystalline film which is about $10^5\,cm^{-1}$.

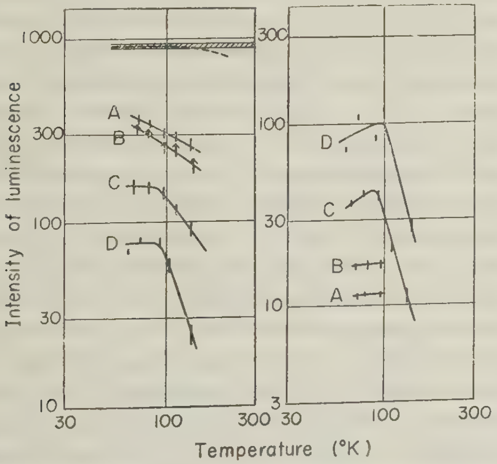

Fig. 6. The temperature-dependence of the exciton-induced luminescences from Tl^+ ion and D impurity for specimens of several concentrations. Tl^+ ion concentrations are A: $2.7\times10^{19}/cm^3$, B: $5.7\times10^{18}/cm^3$, C: $7\times10^{17}/cm^3$ and D: $4.4\times10^{16}/cm^3$. Left is for Tl^+ ion and right for D impurity. In the left figure the hatched line shows the maximum intensity of the direct emission from Tl^+ ion and the broken line shows the maximum intensity of emission in the Greek band due to Tl^+ ion.

Since the excitation spectrum of the exciton-induced luminescence overlaps with that of the direct emission in the Greek band of Tl^+ ion, rather large errors come into the procedure of separation of both excitation spectra, especially at higher temperatures and for specimens of higher concentration of Tl^+ ion. As for the exciton-induced luminescence from the D impurity, its intensity at the wavelength where the excitation spectrum for Tl^+ ion emission shows maximum was taken instead of the maximum value of the excitation spectrum for the D emission. Thus we obtained the intensities of the exciton-induced luminescence at various temperatures for specimens of several concentrations of Tl^+ ion. The results are shown in Fig. 6.

The yield of the exciton-induced luminescence increases with decrease of temperature and attains a saturated value at about liquid oxygen temperature.

§ 4. Migration of Exciton

We have obtained already an evidence that the exciton transfers its energy to both Tl^+ ion and D impurity. Therefore, if we want to discuss the real yield of the exciton-induced luminescence from Tl^+ ion only, we must correct the obtained intensity by the amount of the energy transferred to D impurity other than Tl^+ ion. If the host crystal contained no D impurity, the energy transferred to D impurity should be also transferred to Tl^+ ion.

The exciton will loses its energy also through creating and ionizing F centers. At present we have no quantitative knowledge of these effects, however, the amount of dissipating energy might not overcome the one transferred to D impurity. Furthermore, there may be many defects such as dislocation and vacancy in the crystal, and the exciton may decompose at these imperfections. In order to detect such effects, the surface of the annealed crystals were polished and the influence of polishing was observed. By polishing the exciton-induced yield decreases at the wavelength regions of maxima of the excitation spectra as shown in Fig. 7. In viewing of these results, it is known that some defects which are perhaps dislocations hinder the energy-transfer of the exciton to Tl⁺ ion and D impurity.

Then if we correct the intensity of the exciton-induced luminescence from Tl⁺ ion by the amount of the exciton energy lost to the D impurity and imperfections, it seems to become nearly independent of the concentration of Tl⁺ ion in the range of $10^{15}\sim10^{19}/\text{cm}^3$. The curve A in Fig. 8 shows the concentration-dependence of the exciton-induced luminescence at liquid oxygen temperature at which the yields have the saturated values. The dependence seems rather weak. Correcting it by the lost part of exciton energy to D impurity which is shown with the curve B, the curve C is obtained.

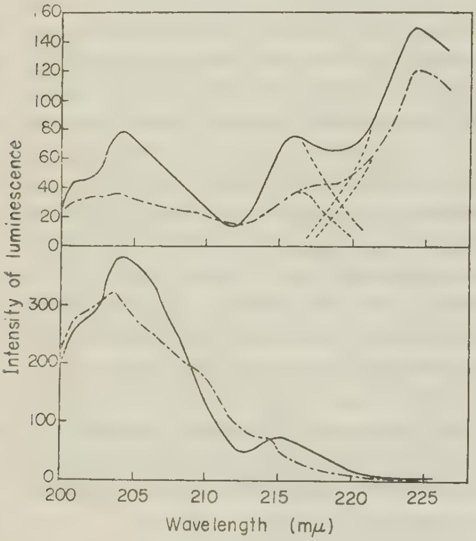

Fig. 7. The influence of polishing on the exciton-induced luminescences. Tl⁺ ion concentration is $4.2\times10^{16}/\text{cm}^3$. Upper: excitation spectra for Tl⁺ emission. Lower: excitation spectra for D emission. The solid and chained lines correspond to the annealed crystal (−207°C) and polished crystal (−209°C) respectively.

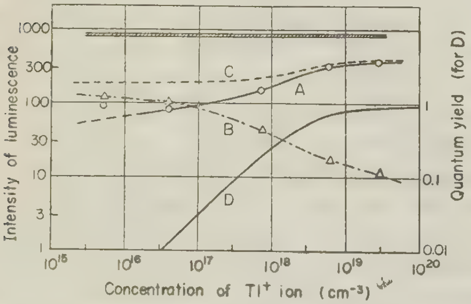

Fig. 8. The relations between the saturated intensities of the exciton-induced luminescences and the concentrations of Tl⁺ ion. A: for Tl⁺ ion emission and B: for D emission. C: the sum of the intensities of emissions from Tl⁺ ion and D impurity. D: the quantum yield calculated by Dexter for the case of energy transfer through dipole-dipole interaction. The hatched line shows the maximum intensity of the direct emission from Tl⁺ ion.

As for the absolute quantum efficiency of the exciton-induced luminescence, the curve C should be compared to the hatched line in the figure. The latter shows the maximum intensity of the luminescence due to the absorption by Tl⁺ ion itself as mentioned in § 2. The efficiency attains about 40% of the above reference intensity.

In the process of energy-transfer, there are two mechanisms to be considered. One is the so-called dipole-dipole interaction proposed by Dexter[4] and the other is the migration of the exciton through the crystal[1]. According to the former theory, the exciton transfers its energy to Tl⁺ ion over some distances and the probability of transfer-process decreases rapidly at lower concentrations of Tl⁺ ion. The curve D in Fig. 8 shows the concentration-dependence of energy-transfer calculated for NaCl at an appropriate condition by Dexter[4]. Since the present experiment shows already the intensity of the exciton-induced luminecence from Tl⁺ ion nearly independent of Tl⁺ ion concentration in the range of $10^{15}\sim10^{19}/\text{cm}^3$, the migration mechanism of exciton through the crystal is found to play a dominant role. The exciton collides with a Tl⁺ ion after wandering to a more or less distance through the crystal, transferring its energy to Tl⁺ ion, of which excitation leads eventually to its own luminescence. The high quantum efficiency of the exciton-induced luminescence such as 40% of the efficiency of direct emission from Tl⁺ ion itself also seems to support the above process.

The emission band at 305 mμ from Tl⁺ ion can be observed only under excitation of lights in 233 and 244 mμ absorption bands at low temperatures, and does not appear under excitation of lights in the exciton absorption band as well as the Greek band 224 mμ due to Tl⁺ ion. In view of the fact that irradiation of light in the exciton absorption band which has higher energy than lights in the absorption bands 233 and 244 mμ cannot give rise to the emission at 305 mμ in contrast to the latter lights, the following model will be proposed. After an exciton meets a Tl$^+$ ion, it may be trapped around the ion with dissipating a small part of its energy to the lattice and then only the emission at 425 mμ takes place in a similar way as in the Greek band due to Tl$^+$ ion around which an exciton localizes.

As mentioned before, the direct emission of Tl$^+$ ion below room temperature is found to be nearly temperature-independent. On the other hand, the emission in the Greek band seems to show a weak temperature-dependence in the case of high Tl$^+$ ion concentration as shown in Fig. 6. This phenomenon may be caused by broadening effect of the tail of exciton absorption band with increase of temperature, that is by resulting decrease of the amount of absorption in the Greek band itself. As the intensity of the emission in the Greek band increases with annealing of the specimen (See Fig. 7), it seems that the absorption coefficient at the tail of the exciton absorption band decreases with annealing and eventually the amount of absorption in the Greek band increases, resulting the increases of the emission in the Greek band. Accordingly, it is natural to consider that the above emission in the Greek band is temperature-independent below room temperature.

On the other hand, the exciton-induced luminescence shows clearly temperature-dependence as seen in Fig. 6. Also in Apker and Taft's experiment, the yield of the exciton-induced photoelectric effect at room temperature is so small as few tenths of that at liquid nitrogen temperature. As the emission due to direct absorpton by Tl$^+$ ion shows no temperature-dependence, the cause of temperature-dependence of the exciton induced luminescence may be attributed to the process of interaction between the exciton and Tl$^+$ ion or the nature of the exciton itself.

§5. Exciton-induced Luminescence from D Impurity.

Under irradiation of light in the first characteristic absorption band the emission at 360~380 mμ as well as the emission from Tl$^+$ ion was found as mentioned in §3. The peak of the former emission changes its position a little from specimen to specimen even in pure KI crystal. Because the original reagent of KI involves a little amount of Tl$^+$ ion, the exciton-induced emission from Tl$^+$ ion deforms the shape of D emission at the longer wavelength side a little. As shown in Fig. 5 the excitation spectrum for D emission has a different shape from that for Tl$^+$ ion emission. At lower temperatures the height of maximum at the shorter wavelength (about 206 mμ) is higher than that at the longer wavelength (about 216 mμ) in contrast with the case for Tl$^+$ ion emission. The height of the latter maximum depends on Tl$^+$ ion concentration, and in the case of very high concentration the maximum disappears, being converted to a step.

Considering these results, the distribution of D impurity may be different from that of Tl$^+$ ion which should be uniform in the crystal. The difference between relative intensities of D emission to Tl$^+$ ion emission in the wavelength regions of larger and smaller absorption coefficients may mean that D impurity localizes especially in the vicinity of of the surface of the crystal. The intensity of D emission shown in Fig. 3 indicates that the effective concentration of this impurity in the deep interior of the crystal is $10^{16}/\mathrm{cm}^3$ in the order of magnitude with reference to the intensity of the exciton-induced emission from Tl$^+$ ion. Therefore, we can hardly suppose the emission in question to be the emission of intrinsic type from the host KI crystal against the opinion by Teegarden[11]. Furthermore, it is difficult in the usual theory of exciton to assume that the exciton gives rise to the emission suffered with such a large Stokes shift.

The exciton-induced luminescence from D impurity is thermally quenched thoroughly at room temperature against that from Tl$^+$ ion and the activation energy in this process is about 0.08 eV. Thus the temperature-dependence of exciton-induced luminescence from D impurity is stronger than that from Tl$^+$ ion.

§6. Conclusion.

In order to confirm the nature of migration of exciton in a KI single crystal, details of luminescences from KI/Tl under excitation of light in the first characteristic absorption band were measured. The exciton-induced luminescences from Tl^+ ion and a certain impurity localized in the vicinity of the surface of the crystal were found. At liquid oxygen temperature, the intensity of the exciton-induced luminescence from Tl^+ ion was found to be independent of the concentration of Tl^+ ion in the range of $10^{15}\sim10^{19}/cm^3$. Accordingly, the migration of the exciton through the crystal was conculuded. The exciton-induced effect, however, was found to decrease at higher temperatures.

Details of the interpretation on the exciton-induced luminescence will be reported in the following paper[12].

We wish to thank Messrs. H. Hosaka and M. Yamakawa for their active supports in the measurement.

References

1) e. g. W. R. Heller and A. Marcus: Phys. Rev. **84**. (1951) 809.
2) F. Seitz: Rev. Mod. Rhys. **26** (1954) 29.
3) L. Apker and E. A. Taft: Phys. Rev. **79** (1950) 964; **81** (1951) 698; **82** (1951) 814. H. R. Philipp and E. A. Taft: Phys. Rev. **106** (1957) 671.
4) D. L. Dexter: J. Chem. Phys. **21** (1953) 836.
5) D. L. Dexter and W. R. Heller: Phys. Rev. **84** (1951) 377.
6) N. Inchauspé: Phys. Rev. **106** (1957) 898.
7) M. Ueta, M. Hirai and H. Watanabe: J. Phys. Soc. Japan **14** (1959) 253.
8) e. g. F. D. Johnson and F. E. William: J. Chem. Phys. **18** (1950) 1477.
9) P. H. Yuster and C. J. Delbecq: J. Chem. Phys. **21** (1953) 892.
10) M. Tomura and Y. Kaifu: J. Phys. Soc. Japan **15** (1960) 314.
11) K. J. Teegarden: Phys. Rev. **105** (1957) 1222.
12) M. Tomura: J. Phys. Soc. Japan **15** (1960) in press.

JOURNAL OF THE PHYSICAL SOCIETY OF JAPAN Vol. 15, No. 7, JULY, 1960

Dichroism of Z Bands

By Masakazu ISHIGURO, Etsu SUGIOKA and Nozomu TAKEUCHI

Institute of Scientific and Industrial Research,
Osaka University, Kitahanada, Sakai

Received March 14, 1960)

The dichroic properties of Z bands and their correlation to that of the F band have been studied on NaCl:Sr and KCl:Sr single crystals.

From the experiment on the anisotropic bleaching, the Z_1 center was found to be a center of high symmetry in agreement with the result of paramagnetic resonance experiment. The Z_2 band showed dichroism when irradiated with [010] polarized light in the Z_2 or F band at room temperature, accompanying the dichroism of opposite sign in the F band. This is another example of the correlation in dichroism between two absorption bands as shown in the F-M system which has been found by Van Doorn and Haven. It is, however, questionable to simply decide the symmetry of the Z_2 center from the dichroism mentioned above, because in the case of KCl:Sr its peak position is shifted to shorter wavelength than the normal Z_2 band.

§1. Introduction

Z bands in KCl and NaCl crystals containing divalent cation impurities have been studied by many authors. Pick[1] and Seitz[2] proposed different models for the centers responsible for the Z_1, Z_2 and Z_3, and Cole and Friauf[3] for the Z_4 band (Fig. 1). The work of Kawamura[4] et al on the electron spin resonance of the Z_1 center suggested the high symmetry of this center and provided a powerful support for the Seitz's model which is an electron trapped at a divalent cation at a normal cation site. On the other hand, Pick's models of the Z_1 center should give some dichroism in [011] direction, for it is an electron trapped at a divalent cation with a positive ion vacancy in the nearest cation site. West and Compton[5] have measured the degree of polarization of the emission induced by the polarized Z_2 light excitation at 77°K in KCl : Sr crystal and concluded that the Z_2 center is of high symmetry. Thus, they supported the high symmetry model of Z_2 center proposed by Pick which is an electron trapped at a divalent cation. G. Chiarotti et al[6] tried the anisotropic bleaching with [010] polarized Z_2 light irradiation at dry ice temperature, but failed to find any dichroism after 25% bleaching of Z_2 band. Recently, however, Remaut et al[7] found small dichroism in the initial stage of the bleaching with [010] polarized Z_2 light in NaCl : Sr. Thus, the experimental results for the Z_2 band are very much complicated, moreover, Seitz's model which is an electron trapped at a divalent cation next to a paired vacancy gives an ambiguity for its symmetry.

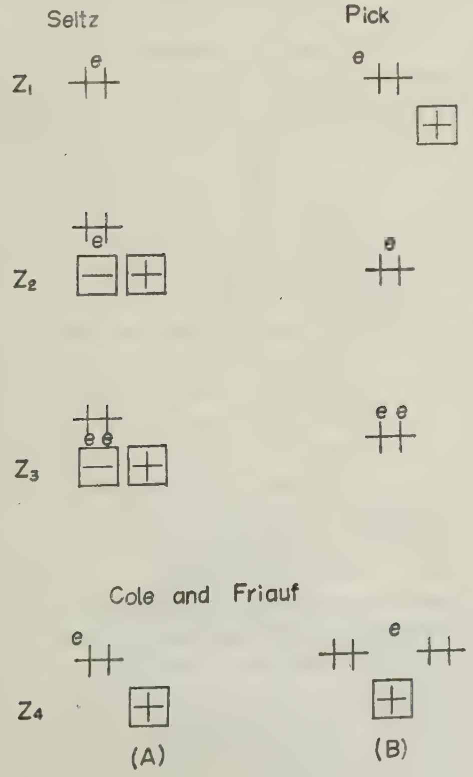

Fig. 1. Models for Z centers.

The present authors tried some experiments on the dichroic properties of the Z_1 and Z_2 bands in more involving way to obtain a little more clear knowledge to the model of these centers and also to see whether or not any correlation in dichroism presents between these bands and the F band.

§2. Experimental Procedure

Single crystals of KCl : Sr were grown by the Kyropoulos method from the melt of KCl containing 0.1 mole% $SrCl_2$. The rate of withdrawal from the melt was about 1 cm per hour, so the crystals are supposed to contain about 0.01 mole% $SrCl_2$. The additive coloration was achieved by heating in potassium vapour at about 500°C for 3 hours in a Pylex envelope and cooling slowly to room temperature. Immediately prior to an experiment a sample of about 0.1 cm thick cleaved from a colored block was wrapped in aluminium foil to prevent optical bleaching and heated at 400°C for 3 minutes, with subsequent quenching to room temperature. The crystal thus prepared showed the F band only. The Z_1 band was formed by irradiating it with the light in the F band at room temperature. Besides, there appeared another band called Z_4 after prolonged F light irradiation. When the crystal containing F and Z_1 bands was heated to 110°C and then cooled slowly to room temperature, comparable amount of F and Z_2 bands were formed. The Z_2 band can also be formed by slow cooling from the temperature of additive coloration. We used here the Z_2 band formed in either way and got the same results.

NaCl : Sr crystal was also grown from the melt of NaCl containing $SrCl_2$ of 0.1~0.03 mole% to give the various concentrations of Z_2 center. When such crystals were heated in sodium vapour at 600°C for 2 hours and quenched to room temperature in the dark, Z_2 and F bands appeared. The ratio of these bands can be controlled from the major F to the major Z_2 by the concentration of strontium in the virgin crystal.

The optical absorption was measured as a function of wavelength with a recording spectrometer modified for the measurements at low temperature. In the irradiation of the crystal, light from a tungsten lamp or a super high pressure mercury lamp through glass filters or a monochromator were used. In the experiment with polarized light, a polarized film and a nicol prism were used, and all the anisotropic optical bleaching was made at room temperrture unless otherwise stated.

§ 3. Results

F and Z_1 bands in KCl : Sr crystal convert to each other by the irradiation in the F or Z_1 band. The anisotropic bleaching with [010] or [011] polarized Z_1 band light in KCl : Sr crystal containing both F and Z_1 bands gives no dichroism at all in any band regions, and similar result is given in the bleaching with F band light, indicating either of F and Z_1 centers cannot be an origin of dichroism (see Fig. 2). On the other hand, in the crystal containing the F and Z_2 bands, the situation is striking; when such crystals are exposed to the irradiation of [010] polarized Z_2 light, the Z_2 and F bands show dichroism whose signs at the peak positions are opposite with each other (Fig. 3A). This time, the Z_2 band increases at the expense of the F band even under Z_2 light irradiation; in the irradiation with [010] polarized Z_2 light, the increase of Z_2 and the decrease of F in the absorption measured with the light polarized parallel to the irradiation light are less than those measured with the light perpendicular to the irradiation light. A Similar experiment with [010] polarized F light shows the dichroism in the F band and that of opposite sign in the Z_2 band, as shown in Fig. 3B. In Fig's 3A and 3B, the upper curves, which are termed the dichoroic spectrum, are the differences between absorptions measured with the polarized light parallel and perpendicular to the irradiation light. There is some discrepancies between the peak positions of the dichroic spectra and those of the absorption bands; the peak position of the F band region in the dichroic spectra is nearly equal to that of the F band, but the peak of the Z_2 band region seems to be considerably shorter than that of the Z_2 absorption band rather close to the Z_1 band.

After prolonged irradiation of [010] polarized Z_2 light, the Z_2 band reaches its saturation value, and the dichroism in the F and Z_2

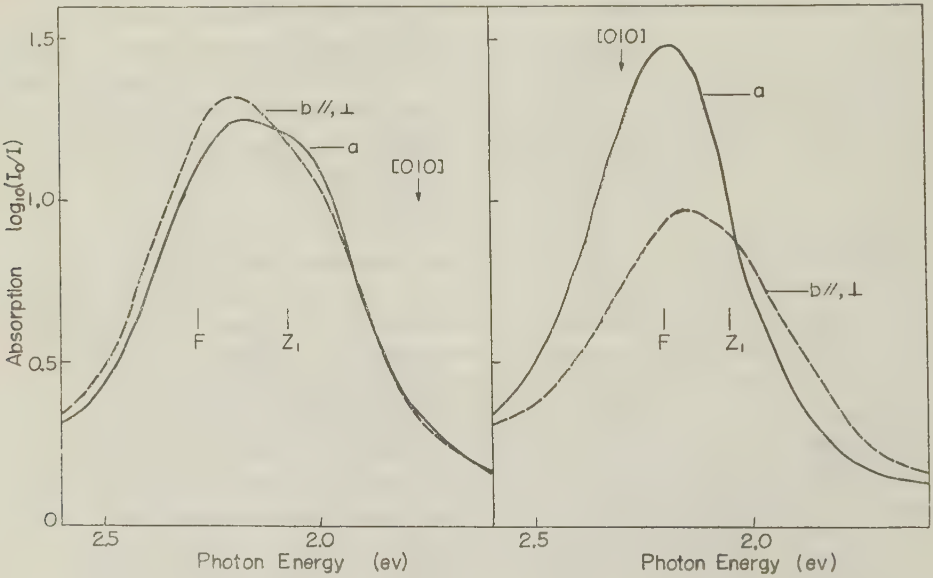

Fig. 2A) Anisotropic irradiation of Z_1 band in KCl:Sr crystal containing Z_1 and F. Curve a—before irradiation, measured with [010] and [001] polarized light. Curve b—after [010] polarized Z_1 light irradiation at room temperature, measured with [010] and [001] polarized light. Measured at -150°C.

Fig. 2B) Anisotropic irradiation of the F band in KCl:Sr crystal containing Z_1 and F. Curve a—before irradiation, measured with [010] and [001] polarized light. Curve b—after [010] polarized F light irradiation at room temperature, measured with [010] and [001] polarized light. Measured at room temperature.

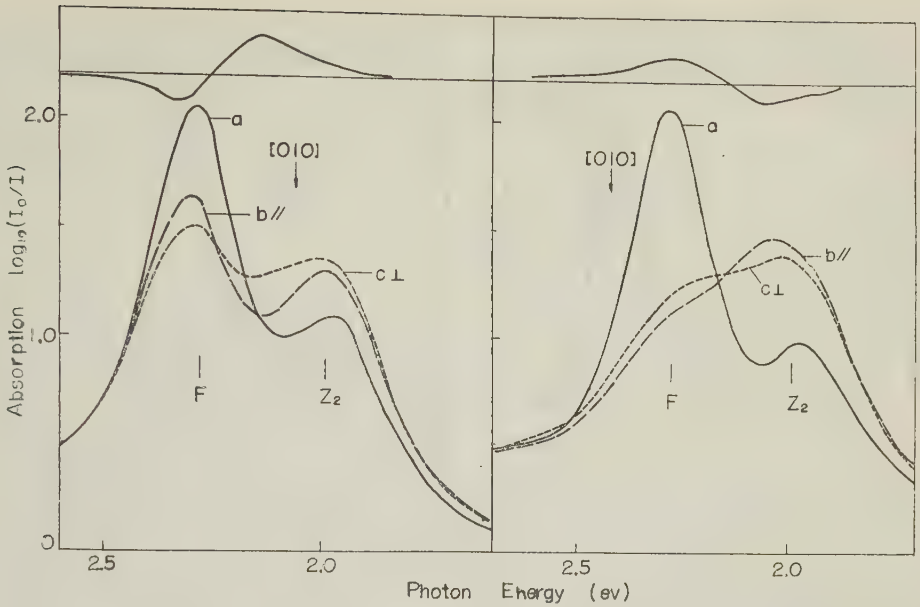

Fig. 3A) Anisotropic irradiation of the Z_2 band in KCl:Sr crystal containing Z_2 and F. Curve a—before irradition, measured with [010] and [001] polarized light. After [010] polarized Z_2 light irradiation at room temperature, curve b—measured with [010] polarized light, curve c—measured with [001] polarized light. Measured at −150°C.

Fig. 3B) Anisotropic irradiation of the F band in KCl:Sr crystal containing Z_2 and F. Curve a—before irradiation, measured with [010] and [001] polarized light. After [010] polarized F light irradiation at room temperature curve b—measured with [010] polarized light, curve c—measured with [001] polarized light. Measured at −150°C.

band regions disappears. When [011] polarized light is used in place of [010] light as the bleaching light, to confirm the symmetry of the centers, there is no dichroism found in either of the Z_2 or F band.

Our present results in KCl : Sr crystal seems to contradict with the experimental data concerning its symmetry reported up to the present, but these investigators carried out the bleaching and excitation of the samples at low temperatures. Thus the temperature effect on the dichroic properties has been confirmed. In the bleaching with Z_2 light at −150°C, the Z_2 band is bleached at first as well as the F band, accompanying formation of the F′ and Z_3 bands, then it shows very rapid recovery to the initial curve even under continuous Z_2 light irradiation, thus the observation of dichroism becomes impossible. At dry ice temperature, though it is also difficult to measure because of its rapid recovery to the initial sbsorption curve. there is the same dichroism observed as at room temperature.

NaCl : Sr crystal containing Z_2 and F bands shows the similar dichroic behaviour to that in KCl : Sr crystal for the irradiation with [010] polarized Z_2 light as shown in Fig. 4A. This time, both F and Z_2 bands bleach in the initial stage, then the F band appears to rise while the Z_2 band continues to decrease slowly. As the position of the Z_2 band is very close to the Z_1 band which is supposed to be formed after intense irradiation with Z_2 light, it is difficult to analyse the resultant absorption curve into these two bands even in the low temperature measurement. Prolonged irradiation with this light removes the dichroism, producing new bands at the longer wavelength side of the Z_2 band and at the shorter wavelength side of the F band. The dichroism mentioned above is lost whithin several hours in the dark at room temperature. A Similar experiment with [010] polarized F light also shows the dichroism in the F band and that of opposite sign in the Z_2 band as shown in Fig. 4B. This case, however, the F band bleaches rapidly while the Z_2 band seems to bleach a little and the newly formed bands are the same as in the

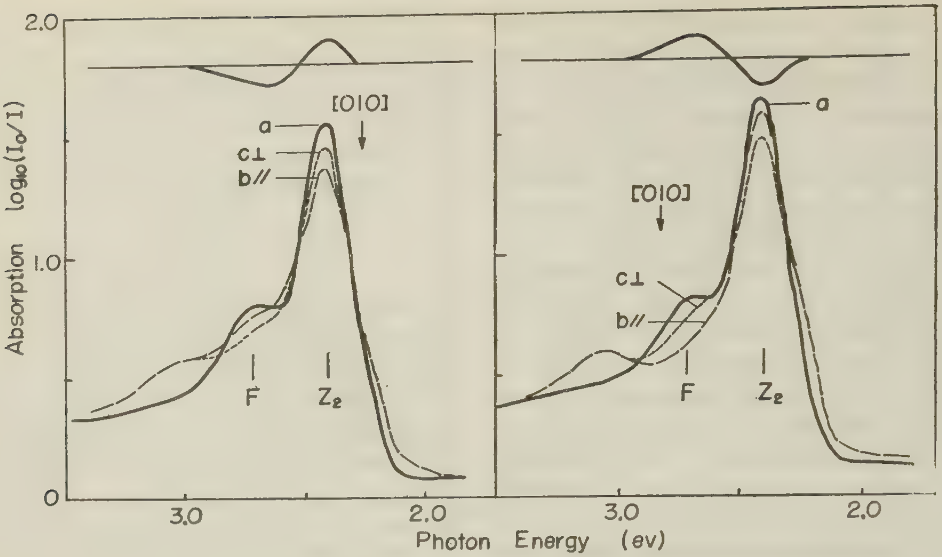

Fig. 4A) Anisotropic irradiation of the Z_2 band in NaCl:Sr crystal containing Z_2 and F. Curve a—before irradiation, measured with [010] and [001] polarized light. After [010] polarized Z_2 light irradiation at room temperature, curve b—measured with [010] polarized light, curve c—measured with [001] polarized light. Measured at -150°C.

Fiff. 4B) Anisotropic irradiation of F band in NaCl:Sr crystal containing Z_2 and F. Curve a - before irradition, measured with [010] and [001] polarized light. After [010] polarized F light irradiation at room temperature, curve b—measured with [010] polarized light, curve c—measured with [001] polarized light. Measured at -150°C.

case of the bleaching with Z_2 light. The peak positions of the dichroic spectrum in either case are not definitely determined because of their small amount and overlapping due to the proximity of their wavelength, but the peak in the F band region lies at about the same wavelength as the F absorption band and the peak in the Z_2 band region is nearly equal to that of the Z_2 absorption band.

In this system [011] polarized light in the Z_2 or F band dose not produce any dichroism in either band. Thus, these dichroic behaviours are very much alike to those in KCl : Sr system described above.

The correlation in dichroism between the F and Z_2 bands is similar to that between the F and M bands which has been reported by Van Doorn[8]. Thus, we tried some experiments to examine the present phenomena from the view point of " overlapping " proposed by Van Doorn; if this hypothesis " overlapping " is realized, the ratio of the amount of dichroism in the F and Z_2 band regions should be constant irrespective of the amount, and even of the methods of induc-

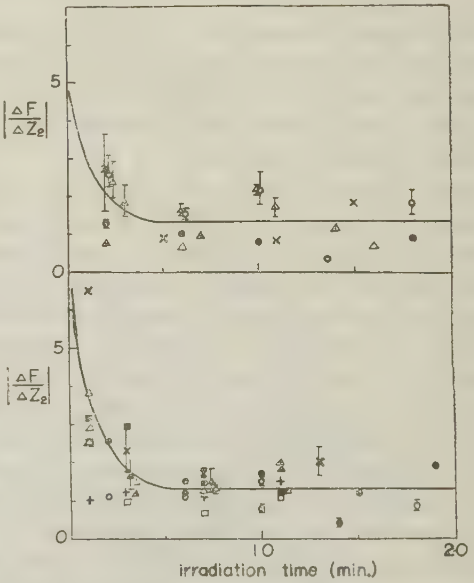

Fig. 5A) The ratio of the amount of dichroism in the F band to that in the Z_2 band in NaCl:Sr crystal as a function of the [010] polarized Z_2 light irradiation time.

Fig. 5B) The ratio of the amount of dichroism in the F band to that in the Z_2 band in NaCl:Sr crystal as a function of the [010] polarized F light irradiation time.

ing dichroism in the center whose symmetry axis is along the [010] direction. Fig. 5 shows this situation; at the initial part of bleaching, the ratio is larger than unity, but as the bleaching proceeds, it approaches to unity for the polarized F or Z_2 light irradiation.

§ 4. Discussion

That no dichroism was found in the crystal containing Z_1 and F bands, seems to be a nice agreement with the result obtained by the paramagnetic resonance experiment, supporting the high symmetry of Seitz's model for this center. On the other hand, Pick's model of Z_1 center should show some dichroism in the bleaching with [011] and also [010] polarized light, but the absence of it decreases the reliability of this model*.

The model of the Z_2 center will be supposed to be the one whose symetry axis is along ⟨100⟩ direction from the dichroism of this band described in the previous section, but the details of the dichroism obtained in the present experiment seem to be so complicated in KCl : Sr crystal that the symmetry of this center cannot be simply decided from it: (1) Z_2 light irradiation on the sample containing Z_2 band shows an increase in the Z_2 band and a decrease of the F band, with a shift of both peaks to shorter wavelength side. (2) The peak of the dichroic spectrum in the Z_2 band region shifts to shorter wavelength than the normal Z_2 band peak or rather to the Z_1 band peak. (3) The F light irradiation on the same sample also shows an increase in the Z_2 band with the same shifts of the peak as in the above case. The peak of the dichroism in the Z_2 band region induced by polarized F light irradiation also lies at the shorter wavelength side as shown in Fig. 3B. (4) The prolonged irradiation with polarized Z_2 or F light causes decrease of the dichroism in the Z_2 and F band regions and finally disappearance in the both regions, still leaving considerable amount of absorption. From the fact described above, it appears that the dichroism in the Z_2 band region is not due to the symmetry of the Z_2 center itself, but may be caused by some center which appears in the optical process under the irradiation of Z_2 or F light.

In connection with the above speculation, it is interesting to note that there are several configurations similar to the Seitz's model of the Z_2 center, one of which has optical dipole or dipoles oriented along the cubic axis.

Thus in the present stages, we cannot conclude any decisive model for the Z_2 center, but the Seitz's model of this center seems to be the one which should be preserved for the present.

It is serious that there is the same correlation in dichroism between the F and Z_2 band regions as that between the F and M bands. Though, it is difficult to proceed analysis quantitatively about this phenomena because of the very close position of the Z_2 band to the F band, we tried some experiments along the Van Doorn's hypothesis "overlapping" as mentioned in the previous section. The fact that, as the anisotropic irradiation proceeds, the ratio of the dichroism in F and Z_2 band regions approaches to unity irrespective of the amounts or the methods of inducing dichroism gives a support to the "overlapping" hypothesis, but the anomalous large values at the initial stages of the irradiation leave room for considerable doubt to it.

References

1) H. Pick: Z. Phys. **114** (1939) 127, Ann. Physik **35** (1939) 73
2) F. Seitz: Phys. Rev. **83** (1951) 134
3) G. R. Cole, R. J. Friauf: Phys. Rev. **107** (1957) 387
4) H. Kawamura and K. Ishiwatari: J. Phys. Soc. Japan **13** (1958) 574
5) E. J. West and W. D. Compton: Phys. Rev. **108** (1957) 576
6) G. Chiarotti, F. G. Fumi and L. Guilotto: *Defects in Crystalline Solids*, (*Bristol Conference.*, 1954) 317
7) G. Remaut and W. Dekayser: Physica **24** (1958) 20
8) Van Doorn and Y. Haven: Phys. Rev. **100** (1955) 753
9) M. Ishiguro and N. Takeuchi: Mem. Inst. Sci. Ind. Res. Osaka Univ. **17** (1960)

---

* Recently, the present authors[9] found that the symmetry of Z_4 center corresponds to the Pick's model for Z_1 center.

JOURNAL OF THE PHYSICAL SOCIETY OF JAPAN, Vol. 15, No. 7, JULY, 1960

Thermal Bleaching of Color Centers in KCl Crystals Containing *U* Centers

By Masamitsu HIRAI

Department of Physics, The Faculty of Science,
University of Tohoku, Sendai

(Received April 6, 1960)

From the study of thermal bleaching of the *F*, *M* and R_2 bands in KCl crystals containing *U* centers, the behavior of the hydrogen molecules produced from *U* centers was examined. The hydrogen molecules do not react with *F* centers but with *M* centers by bimolecular reaction and make *M* centers convert to *U* centers.

Furthermore, thermal bleaching of the Z_1 and Z_2 bands in KCl crystals containing divalent cations was also investigated. The Z_1 and Z_2 bands are thermally unstable at temperature above 80°C, while they are stable up to 110°C and 250°C, respectively, in the crystal containing no *U* centers. From these results, in KCl:Sr crystals it is supposed that Z_1 centers do not return to *U* centers but form unknown centers by combining with the hydrogen molecules.

§ 1. Introduction

The alkali halide crystals are colored with the introduction of the *F* band by the addition of a stoichiometric excess of alkali metal, and the following phenomena have been well known. When KCl crystals containing *F* centers are illuminated at room temperature, with light absorbed in the *F* band (*F* light), the *F* band bleaches partially, while the *M*, R_1, R_2 and *N* bands appear on the longer wavelength side of the *F* band. These bands are stable in dark at room temperature.

The model of the *F* center given by de Boer[1] as shown in Fig. 1 has been confirmed by many optical and paramagnetic resonance experiments[2]. While, investigations on the dichroic property[3] of the *M* band suggest that it has a structure of non-cubic symmetry as shown in Fig. 1[4]. Furthermore, it is inferred that if the *M* band grows, its second absorption band becomes to overlap the *F* band[5]. Models of the other centers were given by Seitz as shown in Fig. 1, but they have not yet been confirmed exactly[4].

On the other hand, it was previously found[6] that the *F* band converted from the *U* band is thermally stable at room temperature and it bleaches by the *F* light illumination, and the *M*, R_1, R_2 and *N* bands appear as in the case of the additively colored pure crystal. However, the *M* band thus produced is thermally unstable at room temperature and bleaches completely. The *F* band bleaches partially too and its decrement in the optical density is nearly equal with that of the *M* band.

The so-called *U* band appears in the ultraviolet region when the additively colored crystal is heated in the atomosphere of the hydrogen gas. Its absorption maximum lies at λ 216 mμ in KCl crystals at room temperature. The model of the *U* center is tentatively considered by Hilsch and Pohl[7] to be an H^- ion occupying substitutionally the negative ion site. When the crystals containing *U* centers (KCl+*U* crystals) are illuminated with light in the *U* band (*U* light) at room temperature, the *U* band bleaches partially and only the F band appears again photochemically. The other bands such as *M*, R_1, R_2 and *N* bands do not appear in the process of $U \rightarrow F$ conversion. The conversion mechanism was explained by Mott and Gurney[8] as follows. The excited state of the *U* center is metastable as a result of crossing of the crystalline Franck-Condon levels, and a hydrogen atom may escape from the center in the metastable state, leaving an *F* center. The hydrogen atoms migrate through the crystal and combine immediately with each other to form the molecules, as indicated by the disappearance of the paramagnetic absorption[9]. However, there is no information concerning the migration of the hydrogen molecules through the crystal.

In the present paper, from the observation on thermal bleaching of the M band in KCl+U crystals and its dependence on the concentration of the hydrogen molecules, it will be discussed how the hydrogen molecules behave in the crystal and how they interact with M centers.

Furthermore, thermal bleaching of the Z_1 and Z_2 bands in KCl crystals containing divalent ions was also investigated. These bands lying on the longer wavelength side of the F band were discovered by Pick[10] in the additively colored crystals containing divalent ions. Models of the centers corresponding to these bands were proposed independently by Seitz and Pick as shown in Fig. 1. From the fact that the behavior of the Z_1 and Z_2 bands in the crystals containing U centers differ from that in the crystals containing no U centers, it will also be discussed how the hydrogen molecules react with Z_1 centers.

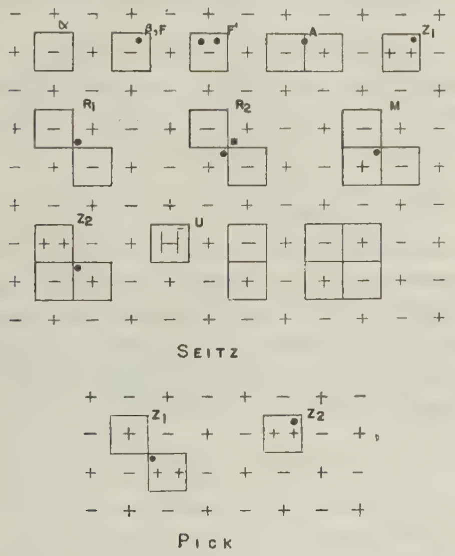

Fig. 1. The model of various color centers and vacancy clusters.

§ 2. Experimental Procedures.

KCl crystals obtained from Harshaw Chemical Co. were additively colored with F centers by the conventional method. The concentration of F centers was about 3×10^{18}/c. c., which was determined optically by using well known Smakula's equation,

$$n_F\cdot f_F=1.31\times10^{17}\times\frac{n'}{(n'^2+2)^2}\times\alpha_M\times H_F. \quad (1)$$

Putting $f_F=0.81$, $n'=1.49$ and $H_F=0.35$ ev. for KCl crystals, Eq. (1) is simplified as follows:

$$n_F=1.09\times10^{16}\times(\log I_0/I)_F/d, \quad (2)$$

where $(\log I_0/I)_F$ is the optical density at the F band peak, and d is the thickness of the crystal in centimeter.

The crystals colored with F centers were heated again at 500°C for 3 hours in a hydrogen atmosphere of about 90 atmospheric pressure in a stainless steel tube of 1 cm in thickness. F centers in the crystals disappeared completely by this treatment and were converted to U centers. The number of U centers was calculated by the equation

$$n_U=1.27\times10^{16}\times(\log I_0/I)_U/d, \quad (3)$$

which was determined from the present work as described in the later section. $(\log I_0/I)_U$ is the optical density at the U band peak.

The hydrogen discharge tube, of which operation voltage and current were A.C. 2000 volt and 1.6 ampere, respectively, was used for the illumination to generate F centers from U centers. The crystals were illuminated through the crystalline quartz window and through the air layer of about 1 cm in thickness, so that the wavelengths of light actually incident on the crystal were longer than 185 mμ. "The full light" used hereinafter means light in this spectral region. Spectral absorption measurements between λ 200 mμ and λ 1200 mμ were made with a Hitachi-spectrophotometer (Model EPU-2). The F light illuminations were made with the full light in the spectral region from 540 mμ to 580 mμ.

§ 3. Experimental Results.

3–1. *Absorption spectra.*

Fig. 2 shows a sequence of absorption measurements performed on a specimen of KCl+U crystals at room temperature. Curve (A) shows the initial state of the crystal showing only the U band. Curve (B) shows the state after about 30 minutes' illumination with "the full light". In this process only the F band appeared and it was thermally stable at room temperature. The crystal showing such absorption spectra is hereinafter referred to as "the crystal showing the U, F bands". U centers were not completely converted to F centers by the further illumination. This may be due to the fact that F centers return to U centers by the back reaction caused by the illumination with the visible light of the hydrogen discharge tube or by the destructive action of *F* centers due to the exciton[11] created by light near λ 185 mμ. By the *F* light illumination on "the crystal showing the *U*, *F* bands" the *F* band bleached partially and the *M* band appeared as shown by curve (C). ("The crystal showing the *U*, *F*, *M* bands"). By a prolong illumination the *F* band bleached further, and the *M* band did also after reaching its maximum value and the R_1 and R_2 bands appeared as shown by curve (D). ("The crystal showing the *U*, *F*, *M*, *R* bands"). These bands in the visible region were thermally unstable at room temperature and bleached completely for a long period of the *F* light illumination and returned to the *U* band.

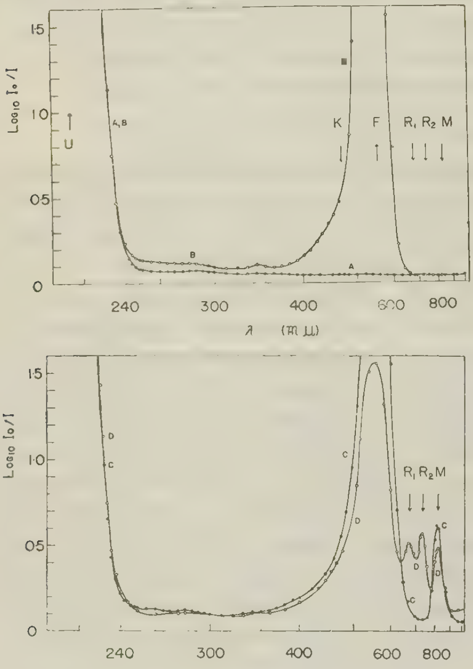

Fig. 2 A sequence of the absorption measurements on a specimen of KCl+*U* crystals subject to the illumination with *U* or *F* light at room temperature.

Curve (A) The initial state showing only the *U* band.

Curve (B) The state after 30 minutes' illumination with "the full light". In this process only the *F* band appeared.

Curve (C) and (D) Successive states of the illumination with *F* light at room temperature. The *M*, R_1 and R_2 bands appeared and they bleached completely with a prolong illumination.

3-2. *The Oscillator strength of the U center in KCl crystals.*

The oscillator strength of the *U* center in KCl crystals was determined as follows. As mentioned in section 3 1, during the process of *U*→*F* conversion at room temperature, only the *F* band appears. Assuming, therefore, that an *F* center is created from a *U* center we can put as follows,

$$-\Delta n_U = \Delta n_F, \tag{4}$$

where $-\Delta n_U$ and Δn_F are the number of destroyed *U* centers and that of created *F* centers, respectively. If we use Smakula's equation for the calculation of the number of *U* centers, it may be expressed by Eq. (1), with putting $n'=1.66$ and $H_U=0.54$ eV. in KCl crystals at room temperature. Namely,

$$n_U f_U = 1.19\times 10^{16}\times(\log I_0/I)_U/d, \tag{5}$$

where f_U is the osillator strength of the *U* center. By using Eqs. (2), (4) and (5), f_U can be determined by the equation:

$$f_U = 1.19\times\frac{\Delta(\log I_0/I)_U}{\Delta(\log I_0/I)_F}, \tag{6}$$

where Δ (log $I_0/I)_U$ and Δ (log $I_0/I)_F$ are the quantities of the changes of the optical density at the *U* and *F* band peaks, respectively. Fig. 3 shows the relation between the increment of the *F* and the decrement of the *U* band peaks in the processes of *U*→*F* con-

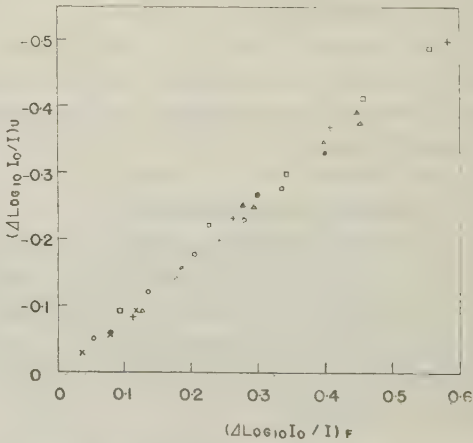

Fig. 3. The increment of the *F* and the decrement of the *U* band peaks in the process of *U*→*F* conversion by the illumination with "the full light" at room temperature.

version in several crystals containing different concentrations of U centers. Using this relation f_U was determined as 0.94 ± 0.01. Terefore, the formula to determine the number of U centers can be written as Eq. (3).

3-3. *Optical bleaching of the F band in KCl+U crystals at −70°C.*

In order to examine wherther or not free electrons released from F centers react with the hydrogen molecules, the following experiment was carried out. When "the crystal showing the U, F bands" (curve A in Fig. 4) was cooled to −70°C and illuminated with F light, the F band bleached rapidly and the F' band was formed. (Curve C). This fact is analogous to the case of the crystal containing no U centers[12]. However, the height of the U band did not increase. Furthermore, when the crystal was warmed to room temparature after the attainment of this state, its absorption spectra (curve D) coincided with that (curve A) at the initial state. This fact shows that the change of the number of U and F centers in the crystal was not caused by the F light illumination at −70°C.

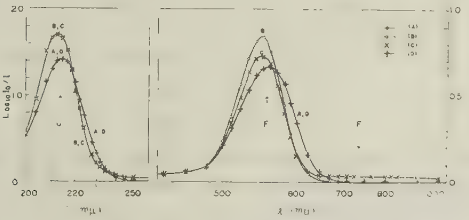

Fig. 4. Optical bleaching of the F band (at −70°C) converted from the U band in KCl crystals.

Curve (A) The initial state after $U\rightarrow F$ conversion by the illumination with "the full light" measured at room temperature.

Curve (B) The state after cooling the crystal of curve (A) to -70°C.

Curve (C) The state after the illumination with F light at -70°C. Measurements were made at the same temperature.

Curve (D) The state after warming the crystal of curve (C) to room temperature. Measurements were made at room temperature.

3-4. *Thermal bleaching of the F, M and R_2 bands.*

As mentioned before, when "the crystal showing the U, F, M bands" was kept in dark at room temperature, the F and M bands bleached thermally by nearly equal amount in the optical density. Curves (F) and (M) in Fig. 5 show the decrement of the optical density at the F and M band peaks of the crystal kept in dark at room temperature, and curve (U) shows the increment of the U band as a function of time. From the fact that the optical density changes are nearly equal in all bands, it may be considered that the hydrogen molecules react with F or M centers and make them convert to U centers. However, as mentioned in section 3-1, the F band in "the crystal showing the U, F bands" is stable, so that it is supposed that the hydrogen molecules do not react with F centers. On the other hand, we considered previously[6] that the process might be explained as follows, using the C_{2V} model for M center.

$$(1)\quad H_2+M\rightarrow H_2^{-}+V_-+V_+V_-$$
$$\rightarrow U\ \text{center}+H+\text{vacancy pair},$$
$$(2)\quad H+F\rightarrow U\ \text{center},$$

where V_- and V_+ are the negative and the positive ion vacancy, respectively. On that occasion, we did not consider the possibility of the existence of the second absorption band of the M center superposed on the F band and there was no information on the oscillator strength of the M band.

Now, from the determination of the oscillator strength[13], it is possible to calculate the absolute number of destroyed M centers. The absolute number of increased U centers is also calculated by Eq. (3). From these calculations, it was confirmed that both numbers are nearly equal in the present case. Therefore, it is reasonable to consider that the hydrogen molecules react with M centers and make them convert to U centers and the partial bleaching of the F band is due to the disappearance of the second absorption band of the M center. From these considerations, it is inferred that the height and the half height width of the second absorption band of the M center are nearly equal to that of the first M band (820 mμ) and to that of the F band, respectively. However, for the definite conclusion, mcre detailed experiments will be necessary.

When "the crystal showing the U, F, M, R bands" was kept in dark at room temperature, the M, R_1 and R_2 bands bleached completely and the F band did partially, and the U band recovered too, as shown in the lower figure of Fig. 5. From this result it is supposed that the hydrogen molecules migrate and react with R_2 centers too. However, in this case the transformation of R_2 to M centers might partially cause the bleaching of the R_2 band, because the increment of the U band was much larger than the decrement of the M band.

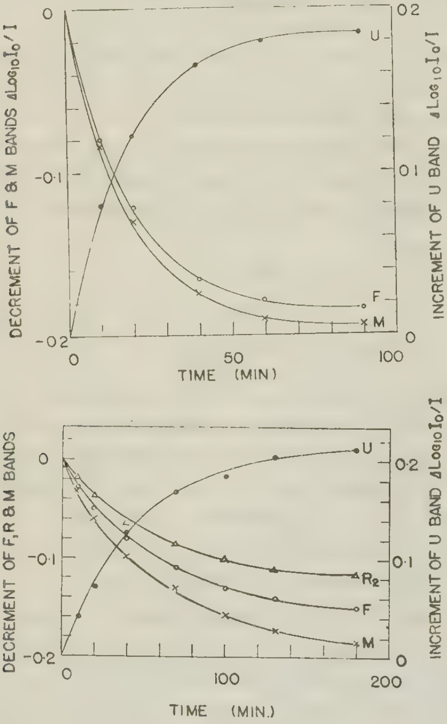

Fig. 5. Thermal bleaching of the F and M bands and recovering of the U band in KCl+U crystals kept in dark at room temperature. The lower figure shows the case in which the R_2 band exists together with the above bands.

If the hydrogen molecules migrate through the crystal, as mentioned above, it is expected that the bleaching rate of the M band will depend on the concentration of the hydrogen molecules. The following experiment was made in this consideration. A numbers of F centers were converted from U centers at 23°C in a specimen of KCl+U crystals, of which thickness was 1.08 mm. Then, by illuminating the crystal with F light, the M band was grown with the optical density of 0.2. The crystal was kept in dark and thermal bleaching of the M band was measured. Curve (1) in Fig. 6 shows the bleaching curve of the M band (first stage). After the complete bleaching of the M band, the crystal was again illuminated with F light so as to produce the M band under the same condition and with the same optical density as in the first stage. The crystal was then kept again in dark and thermal bleaching of the M band was measured (second stage) as shown by curve (2). Such treatments of the crystal for the third and fourth stages were repeated as shown by curves (3) and (4), respectively.

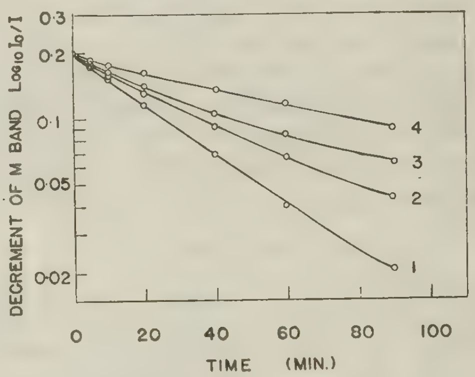

Fig. 6. The dependence of the thermal bleaching of the M band on the concentration of the hydrogen molecules in a specimen of KCl+U crystals.

The fact that the bleaching rates of the M band are smaller at the later stages is due to the smaller concentrations of the hydrogen molecules ($N(O)_t$) at the later stages as tabulated in Table I. The hydrogen molecules return to U centers during successive F light illumination, therefore, the concentrations of them are smaller at the later stages. Determination of the concentration of the hydrogen molecules will be described in section § 4.

3–5. *Thermal bleaching of the Z_1 and Z_2 bands.*

As mentioned above, the M and R_2 bands in KCl+U crystals bleach thermally. In connection with this, thermal bleaching of the Z_1 and Z_2 bands in KCl:Sr, KCl:$\mathrm{C_a}$ and KCl : Ba crystals containing U centers (KCl:Sr+U, KCl:Ca+U and KCl:Ba+U crystals) was also investigated. KCl:Sr, KCl:Ca and KCl:Ba crystals mean the KCl crystals containing halides of Sr, Ca and Ba of about one mol. percent. In these crystals the U band was introduced by the same manner as in the case of the pure crystal. The peak position and the half height width of the U band in these crystals were identical with those of the pure crystal. Fig. 7 (A), (B) and (C) show the absorption measurements on KCl:Sr+U, KCl:Ca+U and KCl:Ba+U crystals, respectively. All measurements were made at liquid air temperature. Curves (a) in the figures show the absorption spectra of the crystals showing only the U band. By the illumination with "the full light", the U band bleached partially, and two or three absorption bands appeared in the visible region. (Curves b). They are ascribed to the F, Z_1 and Z_2 bands. When KCl:Sr+U crystals were warmed up to 80°C and kept in dark for 30 minutes at 80°C, the Z_1 band almost disappeared and the F band slightly did as shown by curve (c) in Fig. 7 (A). In the case of KCl : Ca+U crystals the Z_1 band almost disappeared too, but the F band was enhanced a little. (Curve c in Fig. 7 (B)). However, in both cases the U band did not recover so much in spite of much decreasing of the absorption area in the visible region. In the case of KCl:Ba+U crystals, on the other hand, the Z_1 and Z_2 bands were converted to the F band, but the U band did not recover as shown in Fig. 7 (C).

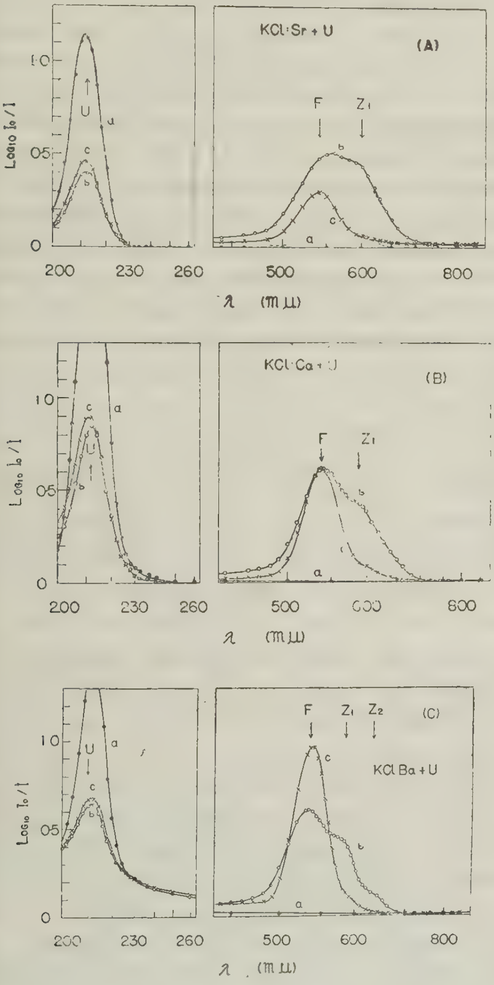

Fig. 7. Thermal bleaching of the Z_1 and Z_2 bands in KCl:Sr, KCl:Ca and KCl:Ba crystals containing U centers. All measurements were made at -193°C.

Curves (a) The initial state showing only the U band.

Curves (b) The state after the illumination with "the full light" at room temperature.

Curves (c) The state after warming the crystals to 80°C for 30 minutes in dark, following curves (b).

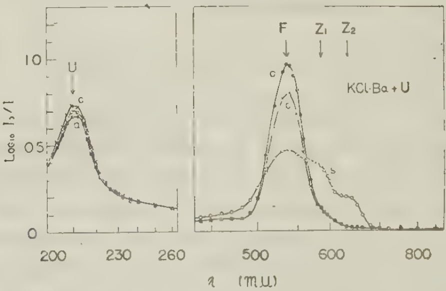

Fig. 8. The growth and the thermal bleaching of the Z_1 and Z_2 bands in KCl:Ba crystals containing U centers.

Curve (a) The same state as in curve (c) in Fig. 7 (C).

Curve (b) The state after the F light illumination at room temperature.

Curve (c) The state after warming the crystals of curve (c) up to 80°C.

Furthermore, when KCl:Ba+U crystals were illuminated with F light at room temperature after the attainment of the state corresponding to curve (c) in Fig. 7 (C), the Z_1 and Z_2 bands appeared again as shown by curve (b) in Fig. 8. By warming the crystals up to 80°C these bands bleached and returned again to the F band as shown by curve (c) in Fig. 8. The behavior of the Z_1 and Z_2 bands differs from that of the crystals containing no U centers[10]. Namely, when the latter crystlas are illuminated with F light at room temperature, only the Z_1 band appears, and the Z_2

band appears by warming the crystals at temperature near 110°C. Furthermore, the Z_1 and Z_2 bands are thermally stable at temperatures up to 110°C and 250°C, respectively.

§ 4. Discussion and Conclusion.

It is generally considered that when KCl+U crystals are illuminated with U light at room temperature, the hydrogen atoms released from U centers combine immediately with each other to form the molecules. From the present results concerning thermal bleaching of the M and Z_1 bands it is concluded that the hydrogen molecules migrate through the crystal, because these bands in the crystal containing no U centers are stable.

From the result shown in Fig. 6 it will be considered how the hydrogen molecules react with M centers. If a hydrogen molecule reacts with an M center as soon as the former collides with the latter, the reaction rate may be given by the equation,

$$-\frac{dn(t)_i}{dt}=\alpha\cdot n(t)_i\cdot N(t)_i=\alpha\cdot n(t)_i\cdot(n(t)_i+a_i), \quad (7)$$

where α is the reaction constant, and $n(t)_i$ and $N(t)_i$, (i=1, 2, 3, 4) are the concentrations of M centers and the hydrogen molecules after t sec's reaction at *i-th* stage of the M band bleaching, respectively. a_i is the concentration of the hydrogen molecules remaining after the finish of all reactions at *i-th* stage. From Eq. (7), $n(t)_i$ is given by the equation

$$n(t)_i=\frac{N(t)_i n(O)_i}{N(O)_i}e^{-\alpha(N(O)_i-n(O)_i)t}, \quad (8)$$

where $n(O)_i$ and $N(O)_i$ are the initial concentrations of M centers and the hydrogen molecules at *i-th* stage, respectively. In the present case it may be put as $N(O)_i \gg n(O)_i$ and $N(t)_i \approx N(O)_i$, because the concentration of the hydrogen molecules is much larger than that of M centers. Therefore, Eq. (8) may be expressed as follows,

$$n(t)_i=n(O)_i e^{-\alpha N(O)_i t},$$

$$\log n(t)_i=\log n(O)_i-\frac{1}{2.3}\alpha\cdot N(O)_i\cdot t. \quad (9)$$

Therefore, if the bleaching curves of the M band plotted on logarithmic scale are the straight lines and the slopes (α_i) are expressed by $-\frac{1}{2.3}\cdot\alpha\cdot N(O)_i$, in other words, if the reaction constant (α) is the same in all curves, it may be supposed that the hydrogen molecules react with M centers by the bimolecular reaction expressed by Eq. (9).

As shown in Fig. 6, the bleaching curves of the M band are expressed by nearly straight lines in all cases. Then, in the next place it is shown that the reaction constant (α) obtained by normalizing α_i by $N(O)_i$ is nearly equall in all curves.

The slope (α_i) of each curve in Fig. 6 is represented by the equation

$$\alpha_i=\frac{\log(n(O)_i/n(t)_i)}{t}$$

$$=\frac{1}{t}\log\frac{(\log I_0/I)_M(O)_i}{(\log I_0/I)_M(t)_i}, \quad (10)$$

where $(\log I_0/I)_M(O)_i$ and $(\log I_0/I)_M(t)_i$ are the optical densities at the M band peak at the initial and after t sec's bleaching of the M band at each curve, respectively. By using the values of $(\log I_0/I)_M(O)_i$, which are 0.200±0.005 in all curves, and the values of $(\log I_0/I)_M(t)_i$ at each *i-th* stage shown in Fig. 6, α_i's were obtained as tabulated in Table I.

Table I.

i	1	2	3	4
$2.3\times\alpha_i$	4.40	3.04	2.41	1.51×10^{-4}/sec.
$N(O)_i$	1.35	0.91	0.77	0.53×10^{-17}/c.c.
α	3.25	3.34	3.13	2.85×10^{-21}/sec.
mean value of α	$(3.15\pm0.20)\times10^{-21}$/sec.			

On the other hand, it may be reasonable to consider that the concentration of the hydrogen molecules $N(O)_i$ is a half of that of F centers at the initial state in each stage, because a hydrogen molecule is created by the destruction of two U centers and the creation of two corresponding F centers. Then, by measuring the height of the F band, $N(O)_i$'s were obtained as tabulated in Table 1. From the values of α_i's and $N(O)_i$'s in Table 1, α was obtained as $(3.15\pm0.20)\times10^{-21}$/sec., as the mean value. The values of α are nearly equal in all cases within the experimental error of about 5%. Namely, as mentioned above, it may be concluded that the hydrogen molecules react with M centers by the bimolecular reaction expressed by Eq. (9).

The hydrogen molecules might exist much near the crystal surface illuminated with "the full light". However, in the present case it is assumed that they are uniformly distributed over the crystal, by the following reason. "The full light" contains light near λ 185 mμ. While the absorption coefficients of KCl+U crystals are comparatively small in the spectral region near λ185 mμ. Therefore, the light can well penetrate into the crystal, and moreover, it makes the conversion of U to F centers with quantum yield of nearly unity[14]. Therefore, it may be considered that the hydrogen molecules are uniformly distributed.

According to Pick[10], the Z_1 and Z_2 bands in KCl:Sr crystals are stable at temperatures above near 110°C and 250°C, respectively. However, the behavior of these bands in the crystals containing U centers differs from that in the above crystals on the following points.

(1) The Z_1 band in KCl:Sr+U and KCl:Ca+U crystals was unstable at 80°C, and in spite of the bleaching of the Z_1 band, the U, F and Z_2 bands were not enhanced.

(2) The Z_2 band appeared by the F light illumination upon KCl:Ba+U crystals showing the U and F bands and it was unstable at temperature even near 80°C. In the present case the Z_1 and Z_2 bands were converted to the F band, but the U band did not recover.

From the fact (1), it is supposed that Z_1 centers do not return to U or F centers but form unknown centers, because the absorption intensity on the shorter wavelength side of the U band was slightly enhanced. This fact may be explained by the character of the model of the Z_1 center shown in Fig. 1, which can not form the U center even if it traps a hydrogen molecule.

From the results concerning optical bleaching of the F band at −70°C, it will be supposed that the free electrons released from F centers do not play any role in the conversion of the hydrogen molecules to U centers.

From the results mentioned above it may be concluded that the hydrogen molecules interact only with complex centers such as M, R_2 or Z_1 centers, but they can not interact with F centers at least near room temperature. These centers except for the Z_1 center consist of the electron and the vacancy cluster, and form comparatively large holes in the crystal. Therefore, it will be supposed that the hydrogen molecules may easily be trapped by these large holes.

The hydrogen molecules may be trapped more stably at the vacancy cluster such as vacancy pair or quartet, which form large holes in the crystal too. However, any absorption band corresponding to such trapping was not observed even in the crystals which were considered to contain a large number of vacancies.

The author wishes to express his cordial thanks to Prof. Masayasu Ueta for constant encouragement and valuable advice throughout the present work.

References

1) J. H. de Boer: Rec. Trav. Chim. Pays-Bas **56** (1937) 301.

2) C. A. Hutchison: Phys. Rev. **75** (1949) 1769. Kip. Kittel, Levy and Portis: Phys. Rev. **91** (1953) 1066. G. Feher: Phys. Rev. **105** (1957) 1122.

3) M. Ueta: J. Phys. Soc. Japan **7** (1952) 107.

4) F. Seitz: Rev. Mod. Phys. **18** (1946) 384.

5) C. Z. van Doorn & Y. Haven: Phys. Rev. **100** (1955) 753.

6) M. Ueta & M. Hirai: J. Phys. Chem. Solids **2** (1957) 83.

7) R. Hilsch & R. W. Pohl: Trans. Faraday Soc. **34** (1938) 883.

8) N. F. Mott. & R. W. Gurney: *Electronic Processes in Ionic Crystals*, 2nd ed. (Oxford, 1948) *chap.* 4.

9) C. J. Delbecq, B. Smaller & P. H. Yuster: Phys Rev. **104** (1956) 599.

10) H. Pick: Ann. Physik. **35** (1939) 73., Z. Phys. **114** (1939) 127. F. Seitz: Phys. Rev. **83** (1951) 83. P. Camagni and G. Chiarotti: Il Nuovo Cimento **11** (1954) 1. G. Chiarotti, F. G. Fumi and L. Giulotto: Bristol Conference on Defects in Crystalline Solids.

11) L. Apker and E. Taft: Phys. Rev. **79** (1950) 914; **81** (1951) 698; **82** (1951) 814. N. Inchauspé: Phys. Rev. **106** (1957) 898. M. Ueta, M. Hirai and H. Watanabe: J. Phys. Soc. Japan **14** (1959) 253.

12) H. Pick: Ann. Physik: **31** (1938) 365. R. W. Phol: Proc. Phys. Soc. **49** (1937) 11.

13) M. Hirai: J. Phys. Soc. Japan **14** (1959) 1400. T. Tomiki: J. Phys Soc. Japan **15** (1960) 488.

14) M. Ueta, M. Hirai and H. Watanabe: J. Phys. Soc. Japan **15** (1960) 593.

JOURNAL OF THE PHYSICAL SOCIETY OF JAPAN, Vol. 15, No. 7, JULY, 1960

Effect of Transverse Magnetic Field on the Flow due to an Oscillating Flat Plate, II.

By Tsunehiko KAKUTANI

Department of Physics, Faculty of Science, Kyoto University

(Received March 3, 1960)

This paper deals with the hydromagnetic flow of an electrically conducting fluid due to an oscillating flat plate of *perfect conductor* in the presence of transverse magnetic field. Exact solutions for arbitrary values of R (the Reynolds number), R_m (the magnetic Reynolds number) and S (the magnetic pressure number) are first derived and then some special cases are discussed corresponding to limiting values of the parameters S and R_m in order to clarify the hydromagnetic effect, and especially an interesting special case corresponding to the 'magnetic Stokes approximation' is discussed in some detail.

Next, the drag on the plate is calculated for both cases of *non-conducting* plate and *perfectly conducting* plate. It is found that, in both cases, the amplitudes of the total drag (shear-stress+Maxwell's stress) always *increase* and the initial phases of the total drag are always *retarded* for any values of R, R_m and S compared with those of the well-known classical case, i.e., the case of no magnetic field and/or electrical conductivity of the fluid being zero.

§1. Introduction

In a previous paper[1)], the present writer investigated the effect of magnetic field upon the flow of a conducting fluid due to an oscillating flat plate of *non-conductor*, and obtained exact solutions for the modified Navier-Stokes and Maxwell's equations.

In this paper, we attempt to extend the problem to the case of the flow due to an oscillating plate of *perfect conductor*. It is found that exact solutions of magnetohydrodynamical equations can also be obtained in this case. A principal difference between the results obtained in the previous and the present work is that in the latter case the 'sheet current' flows at the boundary between the fluid and the plate, and H_x, the component of the induced magnetic field along the plate, jumps discontinuously from a finite value in the fluid to zero in the plate, whereas in the former no sheet current flows and there occurs no abrupt change in the magnetic field at the boundary.

These solutions, obtained in the previous and the present papers, may give a bright prospect for studies of the boundary-layer flow. The problems of the boundary-layer flow are generally much complicated even if the 'boundary-layer approximation' is introduced, and exact solutions cannot be obtained except a few fortunate cases. Moreover, there is a clear *dualism* of the viscous boundary-layer and the magnetic boundary-layer characterized respectively by the parameters R and R_m, so that the ordinary boundary-layer approximation used in classical hydrodynamics is not generally applicable to the magnetohydrodynamical cases unless some modifications are made. Fundamental questions in the problem of magnetohydrodynamical boundary-layer flow such as this dualism may be clarified in these simple but *exact* solutions obtained in the previous and the present papers.

The general solutions for arbitrary values of S, R and R_m are first derived and then some special cases are discussed corresponding to limiting values of the parameters S and R_m in order to clarify the hydromagnetic effect.

Next, the drag experienced by the plate is calculated in some detail for both cases of *non-conducting* plate and *perfectly conducting* plate. It is found that, in both cases, the amplitudes of the total drag (shear-stress+Maxwell's stress) always *increase* for any values of S, R and R_m by the hydromagnetic effect compared with that of the well-known classical case. For non-conducting plate, the shear-stress itself increases and Maxwell's stress is identically zero, whereas in the case of *perfectly conducting* plate, the shear-stress decreases compared with that of the classical case but there appears Maxwell's stress exceeding this reduction in shear-stress, so that the net increase in total drag also results. In this context, it is also found that, in both cases, the initial phases of the total drag are always *retarded* for any values of S, R and R_m compared with that of the classical case.

Finally, we discuss an interesting special case corresponding to the 'magnetic Stokes approximation ($R_m \ll 1$, $SR_m = O(1)$)', which is frequently used in magnetohydrodynamics. It is shown that the approximate velocity distributions of the same problem obtained by Ong and Nicholls[2] on the basis of Rossow's assumption[3] (neglect of the induced magnetic field) can be derived as a limiting case of our solutions by putting $R_m \to 0$ and $SR_m = O(1)$. The case of 'the magnetic field being fixed *to the fluid*' corresponds to the case of our *non-conducting* plate, and the case of 'the magnetic field being fixed *to the plate*' corresponds to the case of our *perfectly conducting* plate. Thus we may assert that Rossow's assumption is permissible only for the cases of small magnetic Reynolds number with large magnetic pressure number. Furthermore, it is also found that their respective considerations of the fundamental equations for the cases of the magnetic field being fixed 'to the fluid' or 'to the plate' may become unnecessary by including the electric field E in the analysis as in our paper, and the difference between their respective fundamental equations may be replaced simply by the difference of the boundary conditions expressing the physical properties of the plate.

§ 2. Analysis and Solutions for Perfect Conducting Plate

The fundamental equations for the velocity of the fluid, $\boldsymbol{v}$, and the intensity of the magnetic field, $\boldsymbol{H}$, are derived from the modified Navier-Stokes equations of motion and Maxwell's electromagnetic equations. As usual, assuming Ohm's law to be valid, we have the following dynamical equation and induction equation for $\boldsymbol{v}$ and $\boldsymbol{H}$:

$$\frac{\partial \boldsymbol{v}}{\partial t} + (\boldsymbol{v}\cdot\mathrm{grad})\boldsymbol{v}$$

$$= -\frac{1}{\rho}\,\mathrm{grad}\,p + \nu\nabla^2\boldsymbol{v} + \frac{\mu}{4\pi\rho}(\mathrm{curl}\,\boldsymbol{H}\times\boldsymbol{H})\,, \quad (2.1)$$

$$\frac{\partial \boldsymbol{H}}{\partial t} = \mathrm{curl}\,(\boldsymbol{v}\times\boldsymbol{H}) + \eta\nabla^2\boldsymbol{H}\,, \quad (2.2)^\dagger$$

with the equations of continuity for the velocity and the magnetic fields:

$$\mathrm{div}\,\boldsymbol{v} = 0\,, \quad (2.3)$$

$$\mathrm{div}\,\boldsymbol{H} = 0\,, \quad (2.4)$$

where p is the pressure, ρ the density of the fluid, ν and η $(=1/(4\pi\mu\sigma))$ the kinematic and the magnetic viscosity of the fluid respectively, and μ and σ are the permeability and the electrical conductivity of the fluid respectively. The electromagnetic units of system have been used throughout the present paper.

In the present problem, we take the coordinate origin O at an arbitrary point on the oscillating plate, which is assumed here to be a perfect conductor and to have the same permeability as that of the fluid, and use Cartesian coordinates x, y and z with the axes Ox and Oy along and perpendicular to the plate respectively, and assume that

(1) the flow is parallel to the plate, that is, $\boldsymbol{v} = \boldsymbol{v}(u, 0, 0)$;

(2) the magnetic field imposed is uniform and perpendicular to the plate, so that in the region considered, $\boldsymbol{H} = \boldsymbol{H}(H_x, H_y, 0)$;

(3) all quantities are functions of the space coordinate y and time t only.

The fundamental equations of our problem then become

$$\frac{\partial u}{\partial t} = \nu\frac{\partial^2 u}{\partial y^2} + \frac{\mu}{4\pi\rho}H_y\frac{\partial H_x}{\partial y}\,, \quad (2.5)$$

$$\frac{\partial}{\partial y}\left(\frac{p}{\rho} + \frac{\mu}{8\pi\rho}H_x^2\right) = 0\,, \quad (2.6)$$

$$\frac{\partial H_x}{\partial t} = H_y\frac{\partial u}{\partial y} + \eta\frac{\partial^2 H_x}{\partial y^2}\,, \quad (2.7)$$

$$\frac{\partial H_y}{\partial t} = \eta\frac{\partial^2 H_y}{\partial y^2}\,, \quad (2.8)$$

while the equation of continuity for the velocity field (2.3) is automatically satisfied by the above assumptions.

The boundary donditions for the velocity field are exactly the same as those in classical hydrodynamics, that is, on the oscillating plate the velocity of the fluid coincides with that of the plate, and at far distances from the plate u tends to zero asymptotically. Thus we have

---

† Details for the derivation of Eqs. (2.1) and (2.2) are given in Reference 1.

$$y=0: \quad u=Ue^{i\omega t}; \qquad y\to\infty: \quad u\to 0, \tag{2.9}$$

where U and ω denote respectively the velocity amplitude and the angular frequency of the oscillating plate.

The boundary conditions for the magnetic field may be obtained as follows. Since the velocity tends to zero asymptotically at a great distance from the plate, no interaction exists there. Hence the magnetic field tends to the applied field H_0 as $y\to\infty$. Thus we have the following conditions for large y:

$$y\to\infty: \quad H_y\to H_0; \qquad H_x\to 0. \tag{2.10}$$

At the plate, on the other hand, the normal component of the magnetic field[†] and the tangential component of the electric field $\boldsymbol{E}$ should be continuous. Hence we have

$$y=0: \quad H_y=H_0; \qquad \frac{\partial H_x}{\partial y}=0. \tag{2.11}$$

The former implies that the normal component of the magnetic field is continuous to the applied field H_0, while the latter is derived by requesting the continuity of the tangential component of the electric field. Because, if $\boldsymbol{j}$ denotes the electric current density, we have

$$\boldsymbol{j}=\frac{1}{4\pi}\operatorname{curl}\boldsymbol{H}=\sigma(\boldsymbol{E}+\mu\boldsymbol{v}\times\boldsymbol{H}), \tag{2.12}$$

from which we obtain

$$E_z=-\frac{1}{4\pi\sigma}\frac{\partial H_x}{\partial y}-\mu u H_0.$$

Applying this equation to $y=\pm 0$, and remembering that the conductivity of the plate is infinite, we have

$$E_z\Big|_{y=-0}=-\frac{1}{4\pi\sigma}\frac{\partial H_x}{\partial y}\Big|_{y=+0}-\mu H_0 u_{\text{plate}},$$

and

$$E_z\Big|_{y=-0}=-\mu H_0 u_{\text{plate}}.$$

Equating the left-hand sides of the above two equations, we arrive at the conclusion:

$$\frac{\partial H_x}{\partial y}=0 \quad \text{at} \quad y=0.$$

Our problem is now to determine the four unknowns u, H_x, H_y and p from Eqs. (2.5)∼(2.8) subject to the boundary conditions (2.9), (2.10) and (2.11).

Now, remembering the boundary conditions for H_y, we can easily solve Eq. (2.8) and obtain

$$H_y\equiv H_0, \tag{2.13}$$

which can also be derived from Eq. (2.4) together with the assumption (3). If the pressure at infinity is p_∞, it follows immediately from Eq. (2.6) that

$$p+\frac{\mu}{8\pi}H_x^2=p_\infty, \tag{2.14}$$

which shows the balance between the fluid pressure and the 'magnetic pressure' in the flow field, since H_y is uniform throughout the whole flow field as has been just shown above. Introducing (2.13) into (2.5) and (2.7) and eliminating H_x between them we have

$$\left[\left(\nu\frac{\partial^2}{\partial y^2}-\frac{\partial}{\partial t}\right)\left(\eta\frac{\partial^2}{\partial y^2}-\frac{\partial}{\partial t}\right)-k\frac{\partial^2}{\partial y^2}\right]u=0, \tag{2.15}$$

where $k=\mu H_0^2/(4\pi\rho)$, which represents the square of the characteristic velocity of 'Alfvén's magnetohydrodynamic wave.' If we eliminate u instead of H_x we have an equation for H_x similar to (2.15). Eq. (2.15) and the similar equation for H_x may be interpreted as generalized equations for 'Alfvén's magnetohydrodynamic wave' with finite diffusivities ν and η.

A formal solution of Eq. (2.15) is given as follows:

$$u=\mathop{\mathsf{S}}_{\kappa} e^{\kappa t}[Ae^{\lambda_1 y}+Be^{-\lambda_1 y}+Ce^{\lambda_2 y}+De^{-\lambda_2 y}], \tag{2.16}$$

where A, B, C and D are constants of integration, which depend on the parameter κ, and symbol S denotes the summation or integration over all possible values of κ. The complex decaying factors λ_1 and λ_2 are given as

$$\lambda_{1,2}=\left[\frac{(k+\kappa\nu+\kappa\eta)\pm\{(k+\kappa\nu+\kappa\eta)^2-4\nu\eta\kappa^2\}^{1/2}}{2\nu\eta}\right]^{1/2}, \qquad \operatorname{Re}(\lambda_{1,2})>0, \tag{2.17}$$

[†] Strictly speaking, we should request the continuity of the normal component of the *magnetic induction* instead of the magnetic field itself, but we have assumed that the permeability of the plate is effectively the same as that of the fluid, that is, both of the fluid and the plate are assumed to be non-magnetic. This assumption is not very restrictive and may be easily removed if necessary.

plus and minus signs corresponding to λ_1 and λ_2 respectively. This convention will also be used hereafter.

By virtue of the boundary condition at infinity for u, we have $A=C=0$. On the other hand, the boundary condition on the plate for u requires that

$$\kappa=i\omega \quad \text{and} \quad B+D=U\,. \tag{2.18}$$

Thus we have

$$u(y,t)=e^{i\omega t}[Be^{-\lambda_1 y}+De^{-\lambda_2 y}]\,, \tag{2.19}$$

with

$$\lambda_{1,2}=\left[\frac{(k+i\omega(\nu+\eta))\pm\{(k+i\omega(\nu+\eta))^2+4\nu\eta\omega^2\}^{1/2}}{2\nu\eta}\right]^{1/2}. \tag{2.20}$$

Inserting (2.19) into (2.5) we have

$$\frac{\partial H_x}{\partial y}=\frac{H_0}{k}e^{i\omega t}[(i\omega-\nu\lambda_1^2)Be^{-\lambda_1 y}+(i\omega-\nu\lambda_2^2)De^{-\lambda_2 y}]\,. \tag{2.21}$$

Integrating (2.21) with respect to y and remembering that $H_x\to 0$ as $y\to\infty$, we have

$$H_x(y,t)=-\frac{H_0}{k}e^{i\omega t}\left[\left(\frac{i\omega}{\lambda_1}-\nu\lambda_1\right)Be^{-\lambda_1 y}+\left(\frac{i\omega}{\lambda_2}-\nu\lambda_2\right)De^{-\lambda_2 y}\right]. \tag{2.22}$$

The boundary condition on the plate for H_x requires that

$$(i\omega-\nu\lambda_1^2)B+(i\omega-\nu\lambda_2^2)D=0\,. \tag{2.23}$$

Solving (2.18) and (2.23) for B and D, we obtain

$$B=\frac{i\omega-\nu\lambda_2^2}{\nu(\lambda_1^2-\lambda_2^2)}U\,, \qquad D=-\frac{i\omega-\nu\lambda_1^2}{\nu(\lambda_1^2-\lambda_2^2)}U\,. \tag{2.24}$$

Insertion of B and D thus determined into (2.19) and (2.22) yields the solutions for u and H_x:

$$u(y,t)=-\frac{(\nu\lambda_1^2-i\omega)(\nu\lambda_2^2-i\omega)}{\nu(\lambda_1^2-\lambda_2^2)}Ue^{i\omega t}\left[\frac{1}{\nu\lambda_1^2-i\omega}e^{-\lambda_1 y}-\frac{1}{\nu\lambda_2^2-i\omega}e^{-\lambda_2 y}\right], \tag{2.25}$$

and

$$H_x(y,t)=-\frac{(\nu\lambda_1^2-i\omega)(\nu\lambda_2^2-i\omega)}{k\nu(\lambda_1^2-\lambda_2^2)}H_0Ue^{i\omega t}\left[\frac{1}{\lambda_1}e^{-\lambda_1 y}-\frac{1}{\lambda_2}e^{-\lambda_2 y}\right]. \tag{2.26}$$

Since $\operatorname{curl}\boldsymbol{H}=4\pi\boldsymbol{j}$, we have

$$\left.\begin{aligned} &j_x=0\,, \qquad j_y=0\,, \\ &j_z(y,t)=-\frac{(\nu\lambda_1^2-i\omega)(\nu\lambda_2^2-i\omega)}{4\pi k\nu(\lambda_1^2-\lambda_2^2)}H_0Ue^{i\omega t}[e^{-\lambda_1 y}-e^{-\lambda_2 y}]\,. \end{aligned}\right\} \tag{2.27}$$

With the aid of Ohm's law: $\boldsymbol{j}=\sigma(\boldsymbol{E}+\mu\boldsymbol{v}\times\boldsymbol{H})$, we have

$$\left.\begin{aligned} &E_x=0\,, \qquad E_y=0\,, \\ &E_z(y,t)=-\frac{i\omega(\nu\lambda_1^2-i\omega)(\nu\lambda_2^2-i\omega)}{k\nu(\lambda_1^2-\lambda_2^2)}\mu H_0Ue^{i\omega t}\left[\frac{1}{\lambda_1^2}e^{-\lambda_1 y}-\frac{1}{\lambda_2^2}e^{-\lambda_2 y}\right]. \end{aligned}\right\} \tag{2.28}$$

The above (2.25)~(2.28) together with (2.13) and (2.14) are the general solutions of the present problem, which should be compared with those of the case of non-conducting plate (see (3.11)~(3.14) of Reference 1) and with that of the classical case: $u=Ue^{i\omega t-\sqrt{i\omega/\nu}\cdot y}$.

It will be seen that all quantities consist of two different oscillations whose complex decaying factors are λ_1, λ_2; $\mathrm{Re}\,(\lambda_{1,2})$ and $\mathrm{Im}\,(\lambda_{1,2})$ respectively representing the decaying factors and the wave numbers of the oscillations. Since $H_y = H_0$, the fundamental equations (2.5) $\sim$(2.8) are all linear, so that we can make up more general solutions by superimposing several oscillations of different amplitudes and different angular frequencies.

It should be noted here that H_x jumps discontinuously at $y = \pm 0$. This is the very different point from the case of non-conducting plate. This discontinuity of H_x implies that there flows the sheet current J_s at the boundary. J_s may be evaluated by integrating $\boldsymbol{j} = \mathrm{curl}\,\boldsymbol{H}/(4\pi)$ in the domain of a thin rectangle with unit width and thickness Δl spanning over the boundary between the fluid and the plate (see Fig. 1), and by letting Δl tend to infinitesimal after integration, that is,

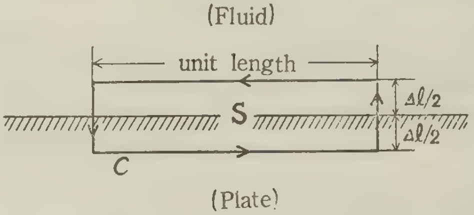

Fig. 1. Sketch of domain to evaluate sheet current.

$$
\begin{aligned}
J_s &= \lim_{\Delta l \to 0} \iint_S (\boldsymbol{j} \cdot d\boldsymbol{S}) \\
&= \lim_{\Delta l \to 0} \frac{1}{4\pi} \iint_S (\mathrm{curl}\,\boldsymbol{H} \cdot d\boldsymbol{S}) \\
&= \frac{1}{4\pi} \lim_{\Delta l \to 0} \oint_c (\boldsymbol{H} \cdot d\boldsymbol{c}) \qquad \text{(by the use of Stokes' theorem)} \\
&= \frac{1}{4\pi} \lim_{\Delta l \to 0} \left[H_x\!\left(-\frac{\Delta l}{2}\right) + H_0 \Delta l - H_x\!\left(\frac{\Delta l}{2}\right) - H_0 \Delta l \right] \\
&= \frac{1}{4\pi} [H_x(-0) - H_x(+0)] \\
&= -\frac{1}{4\pi} H_x(+0) \\
&= -\frac{(\nu\lambda_1^2 - i\omega)(\nu\lambda_2^2 - i\omega)}{4\pi k \nu \lambda_1 \lambda_2 (\lambda_1 + \lambda_2)} H_0 U e^{i\omega t} \, . \qquad (2.29)
\end{aligned}
$$

§ 3. Non-dimensional Forms of the Solutions and their Behaviours in Some Special Cases

Now we proceed to discuss the solutions in non-dimensional forms, and in order to clarify the hydromagnetic effect we shall discuss the behaviours of the solutions in some special cases corresponding to various limiting values of the parameters S and R_m.

We define the following three characteristic parameters:

$$
\left.
\begin{array}{ll}
\text{the Reynolds number:} & R = U^2/(\nu\omega)\,, \\
\text{the magnetic Reynolds number:} & R_m = U^2/(\eta\omega)\,, \\
\text{the magnetic pressure number:} & S = \mu H_0^2/(4\pi\rho U^2)\,,
\end{array}
\right\} \qquad (3.1)
$$

by introducing non-dimensional quantities with asterisk as follows:

$$
\left.
\begin{array}{lll}
u = U u^*\,, & p = \dfrac{1}{2}\rho U^2 p^*\,, & \\
y = \dfrac{U}{\omega} y^*\,, & \boldsymbol{H} = H_0 \boldsymbol{H}^*\,, & \boldsymbol{E} = \mu H_0 U \boldsymbol{E}^*\,, \\
t = \dfrac{1}{\omega} t^*\,, & j = \sigma\mu H_0 U j^*\,, & \\
\lambda_{1,2} = \dfrac{\omega}{U} \lambda_{1,2}^*\,, & J_s = H_0 J_s^*\,. &
\end{array}
\right\} \qquad (3.2)
$$

It is to be noted here that the Hartmann number M frequently used in the analysis of problems in magnetohydrodynamics is equal to $\sqrt{SRR_m}$ in our notations.

Using the non-dimensional quantities defined above, we have the solutions in non-dimensional forms as follows:

$$\left.\begin{aligned}
u^* &= -\frac{(\lambda_1^{*2}-iR)(\lambda_2^{*2}-iR)}{\lambda_1^{*2}-\lambda_2^{*2}}\,e^{it^*}\left[\frac{1}{\lambda_1^{*2}-iR}\,e^{-\lambda_1^* y^*}-\frac{1}{\lambda_2^{*2}-iR}\,e^{-\lambda_2^* y^*}\right],\\
H_x^* &= -\frac{(\lambda_1^{*2}-iR)(\lambda_2^{*2}-iR)}{SR(\lambda_1^{*2}-\lambda_2^{*2})}\,e^{it^*}\left[\frac{1}{\lambda_1^*}\,e^{-\lambda_1^* y^*}-\frac{1}{\lambda_2^*}\,e^{-\lambda_2^* y^*}\right],\\
H_y^* &= 1\,,\\
j_z^* &= -\frac{(\lambda_1^{*2}-iR)(\lambda_2^{*2}-iR)}{SRR_m(\lambda_1^{*2}-\lambda_2^{*2})}\,e^{it^*}[e^{-\lambda_1^* y^*}-e^{-\lambda_2^* y^*}]\,,\\
E_z^* &= -\frac{i(\lambda_1^{*2}-iR)(\lambda_2^{*2}-iR)}{SR(\lambda_1^{*2}-\lambda_2^{*2})}\,e^{it^*}\left[\frac{1}{\lambda_1^{*2}}\,e^{-\lambda_1^* y^*}-\frac{1}{\lambda_2^{*2}}\,e^{-\lambda_2^* y^*}\right],\\
p^* &= -SH_x^{*2}+p_\infty^*\,,\\
J_s^* &= -\frac{(\lambda_1^{*2}-iR)(\lambda_2^{*2}-iR)}{4\pi SR\lambda_1^*\lambda_2^*(\lambda_1^*+\lambda_2^*)}\,e^{it^*}\,,
\end{aligned}\right\} \tag{3.3}$$

with

$$\lambda_{1,2}^* = \left[\frac{SRR_m+i(R+R_m)\pm\{(SRR_m+i(R+R_m))^2+4RR_m\}^{1/2}}{2}\right]^{1/2}. \tag{3.4}$$

It is worthwhile to notice that R and R_m are contained symmetrically in the complex decaying factors $\lambda_{1,2}^*$. This shows that the dualism of the viscous and the magnetic boundary-layers is exactly symmetric with respect to R and R_m in this problem.

Now we consider the behaviours of the solutions corresponding to limiting values of the parameters S and R_m. Since R and R_m are contained symmetrically in $\lambda_{1,2}^*$, we discuss the cases of limiting values of S and R_m instead of those of S, R and R_m. In the following discussions only the first dominant terms are retained in each case.

(1) $S \ll 1$, $R=O(1)$, $R_m=O(1)$.

In this case, if $R>R_m$,

$$\lambda_1^* \sim \sqrt{iR}\left(1-\frac{SRR_m}{2(R-R_m)}i\right), \qquad \lambda_2^* \sim \sqrt{iR_m}\left(1+\frac{SRR_m}{2(R-R_m)}i\right). \tag{3.5}$$

Hence $\dfrac{(\lambda_1^{*2}-iR)(\lambda_2^{*2}-iR)}{\lambda_1^{*2}-\lambda_2^{*2}} \sim -\dfrac{SR^2R_m}{R-R_m}$, so that

$$\left.\begin{aligned}
u^* &\sim \frac{SR^2R_m}{R-R_m}\,e^{it^*}\left[\frac{R-R_m}{SR^2R_m}\,e^{-\sqrt{iR}\,y^*}-\frac{i}{R-R_m}\,e^{-\sqrt{iR_m}\,y^*}\right],\\
H_x^* &\sim \frac{RR_m}{R-R_m}\,e^{it^*}\left[\frac{1}{\sqrt{iR}}\,e^{-\sqrt{iR}\,y^*}-\frac{1}{\sqrt{iR_m}}\,e^{-\sqrt{iR_m}\,y^*}\right],\\
j_z^* &\sim \frac{R}{R-R_m}\,e^{it^*}[e^{-\sqrt{iR}\,y^*}-e^{-\sqrt{iR_m}\,y^*}]\,,\\
E_z^* &\sim \frac{RR_m}{R-R_m}\,e^{it^*}\left[\frac{1}{R}\,e^{-\sqrt{iR}\,y^*}-\frac{1}{R_m}\,e^{-\sqrt{iR_m}\,y^*}\right],\\
J_s^* &\sim \frac{(1-i)\sqrt{RR_m}}{4\sqrt{2}\,\pi(\sqrt{R}+\sqrt{R_m})}\,e^{it^*}\,.
\end{aligned}\right\} \tag{3.6}$$

In the limit of $S\to 0$, u^* reverts to the classical results: $u^*=e^{it^*-\sqrt{iR}\,y^*}$ as expected. The first terms of each quantity (excepting J_s^*) would be appreciable in the domain of

$y^* \lesssim O(1/\sqrt{R})$, which shows a similar character to the viscous boundary-layer, whereas the second terms would be appreciable in the domain of $y^* \lesssim O(1/\sqrt{R_m})$, which shows a similar character to the magnetic boundary-layer, although the domain of $O(1/\sqrt{R})$ or of $O(1/\sqrt{R_m})$ is not necessarily so small as to be called 'boundary-layer,' since we here consider the case of $R=O(1)$ and $R_m=O(1)$.

If $R<R_m$, λ_1^* takes the place of λ_2^* in (3.5) and *vice versa*. Since, however, λ_1^* and λ_2^* are contained symmetrically in u^*, H_x^*, j_z^*, E_z^* and J_s^*, the final expressions of (3.6) remain unaltered.

(2) $S \gg 1$, $R=O(1)$, $R_m=O(1)$.

In this case,

$$\lambda_1^* \sim \sqrt{SRR_m}\left(1+\frac{R+R_m}{2SRR_m}i\right), \quad \lambda_2^* \sim \frac{i}{\sqrt{S}}\left(1-\frac{R+R_m}{2SRR_m}i\right),$$

so that $\dfrac{(\lambda_1^{*2}-iR)(\lambda_2^{*2}-iR)}{\lambda_1^{*2}-\lambda_2^{*2}} \sim -iR$. Hence we have

$$\left.\begin{aligned}
u^* &\sim iRe^{it^*}\left[\frac{1}{SRR_m}e^{-\sqrt{SRR_m}\,y^*}-\frac{i}{R}e^{-i/\sqrt{S}\cdot y^*}\right],\\
H_x^* &\sim \frac{i}{S}e^{it^*}\left[\frac{1}{\sqrt{SRR_m}}e^{-\sqrt{SRR_m}\,y^*}+i\sqrt{S}\,e^{-i/\sqrt{S}\cdot y^*}\right],\\
j_z^* &\sim \frac{i}{SR_m}e^{it^*}\left[e^{-\sqrt{SRR_m}\,y^*}-e^{-i/\sqrt{S}\cdot y^*}\right],\\
E_z^* &\sim -\frac{1}{S}e^{it^*}\left[\frac{1}{SRR_m}e^{-\sqrt{SRR_m}\,y^*}+Se^{-i/\sqrt{S}\cdot y^*}\right],\\
J_s^* &\sim \frac{1}{4\pi\sqrt{S}}e^{it^*}.
\end{aligned}\right\} \tag{3.7}$$

Thus the first terms of each quantity (excepting J_s^*) decay rapidly with increasing y^* and are vanishingly small except the vicinity of the plate. The thickness of this thin layer is of $O(1/\sqrt{SRR_m})$ which depends on both of R and R_m, so that we may interpret this layer as a 'mixed boundary-layer.' Outside this layer become dominant the second terms which represent the oscillations whose phase velocity is the same as that of Alfvén's magnetohydrodynamic wave. Since the most dominant term of the decaying factor of the second terms is purely imaginary, the second terms decay very slowly.

(3) $R_m \ll 1$, $S=O(1)$, $R=O(1)$.

Since

$$\lambda_1^* \sim \sqrt{iR}\left(1-\frac{1}{2}SR_m i\right) \quad \text{and} \quad \lambda_2^* \sim \sqrt{iR_m}\left(1+\frac{1}{2}SR_m i\right),$$

$\dfrac{(\lambda_1^{*2}-iR)(\lambda_2^{*2}-iR)}{\lambda_1^{*2}-\lambda_2^{*2}} \sim -SRR_m$. Hence we have in this case

$$\left.\begin{aligned}
u^* &\sim SRR_m e^{it^*}\left[\frac{1}{SRR_m}e^{-\sqrt{iR}\,y^*}-\frac{i}{R}e^{-\sqrt{iR_m}\,y^*}\right],\\
H_x^* &\sim R_m e^{it^*}\left[\frac{1}{\sqrt{iR}}e^{-\sqrt{iR}\,y^*}-\frac{1}{\sqrt{iR_m}}e^{-\sqrt{iR_m}\,y^*}\right],\\
j_z^* &\sim e^{it^*}\left[e^{-\sqrt{iR}\,y^*}-e^{-\sqrt{iR_m}\,y^*}\right],\\
E_z^* &\sim R_m e^{it^*}\left[\frac{1}{R}e^{-\sqrt{iR}\,y^*}-\frac{1}{R_m}e^{-\sqrt{iR_m}\,y^*}\right],\\
J_s^* &\sim \frac{(1-i)\sqrt{R_m}}{4\sqrt{2}\,\pi}e^{it^*}.
\end{aligned}\right\} \tag{3.8}$$

General character of the solutions is similar to that in case (1), and in the limit of $R_m \to 0$, u^* reverts to the classical result. A different point from the case (1) is that the second terms of each quantity (excepting J_s^*) decrease more slowly than the first terms. This may imply that the thickness of the 'magnetic boundary-layer' becomes too large to say 'boundary-layer' owing to the smallness of R_m.

(4) $R_m \gg 1$, $S=O(1)$, $R=O(1)$.

In this case

$$\lambda_1^* \sim \sqrt{R_m(SR+i)}\left(1+\frac{SR^2 i}{2R_m(SR+i)^2}\right) \quad \text{and} \quad \lambda_2^* \sim i\sqrt{\frac{R}{SR+i}}\left(1-\frac{SR^2 i}{2R_m(SR+i)^2}\right),$$

so that $\dfrac{(\lambda_1^{*2}-iR)(\lambda_2^{*2}-iR)}{\lambda_1^{*2}-\lambda_2^{*2}} \sim -\dfrac{SR^2 i}{SR+i}$. Hence we have

$$\left.\begin{aligned}
u^* &\sim \frac{SR^2 i}{SR+i} e^{it^*}\left[\frac{1}{R_m(SR+i)} e^{-\sqrt{R_m(SR+i)}\,y^*} - \frac{i(SR+i)}{SR^2} e^{-i\sqrt{R/(SR+i)}\,y^*}\right],\\
H_x^* &\sim \frac{iR}{SR+i} e^{it^*}\left[\frac{1}{\sqrt{R_m(SR+i)}} e^{-\sqrt{R_m(SR+i)}\,y^*} + i\sqrt{\frac{SR+i}{R}}\, e^{-i\sqrt{R/(SR+i)}\,y^*}\right],\\
j_z^* &\sim \frac{iR}{R_m(SR+i)} e^{it^*}\left[e^{-\sqrt{R_m(SR+i)}\,y^*} - e^{-i\sqrt{R/(SR+i)}\,y^*}\right],\\
E_z^* &\sim -\frac{R}{SR+i} e^{it^*}\left[\frac{1}{R_m(SR+i)} e^{-\sqrt{R_m(SR+i)}\,y^*} + \frac{SR+i}{R} e^{-i\sqrt{R/(SR+i)}\,y^*}\right],\\
J_s^* &\sim \frac{\sqrt{R}}{4\sqrt{2}\,\pi\sqrt{1+S^2R^2}}\left[\sqrt{\sqrt{1+S^2R^2}+SR} - i\sqrt{\sqrt{1+S^2R^2}-SR}\right] e^{it^*}.
\end{aligned}\right\} \tag{3.9}$$

As in the case (2), the first terms of each quantity (excepting J_s^*) decrease rapidly and the second terms become dominant in the region of $y^* \gtrsim O(1/\sqrt{R_m})$. The thin layer of $O(1/\sqrt{R_m})$ may be regarded as the magnetic boundary-layer. Because this layer is principally characterized by R_m ($\gg 1$) although the decaying factor of the first terms, $\sqrt{R_m(SR+i)}$, contains both R and R_m. In the limit of $R_m \to \infty$, both of the first terms of u^* and H_x^* vanish and hence $u^* \propto H_x^*$, which is a reflection of the so-called 'frozen' effect.

§4. Drag Experienced by the Plate

In this section we shall calculate the drags experienced by the plate for both cases of *non-conducting* plate and *perfectly conducting* plate, and compare them with that of the classical case.

The total drag on the plate generally consists of the shear-stress, τ_f, and Maxwell's stress, τ_m, which are given respectively by the following formulae:

$$\left.\begin{aligned}
\tau_f &= \mathrm{Re}\left(\rho\nu\frac{\partial u}{\partial y}\right)_{y=0},\\
\text{and}\qquad\\
\tau_m &= \mathrm{Re}\left(\frac{1}{4\pi}\mu H_0 H_x\right)_{y=0}.
\end{aligned}\right\} \tag{4.1}$$

For proceeding calculations, it is convenient to define the drag coefficients with reference to $\rho\nu\omega$, that is

$$\tau_f^* = \tau_f/(\rho\nu\omega), \qquad \tau_m^* = \tau_m/(\rho\nu\omega). \tag{4.2}$$

Now we consider the following three cases, (1) the classical case, (2) the case of non-conducting plate, and (3) the case of perfectly conducting plate.

(1) The classical case.

As is well known, there is, of course, no Maxwell's stress in this case, so that the total drag is identical with the shear-stress, $\tau_{f_0}^*$, itself. Thus we have

$$\begin{aligned} \tau_{f_0}^* &= -\mathrm{Re}\,(\sqrt{iR}\,e^{it^*} \\ &= T_0 \sin(t^*+\theta_0)\,, \end{aligned} \tag{4.3}$$

where

$$T_0 = \sqrt{R}\,, \tag{4.4}$$

$$\tan\theta_0 = -1 \qquad (\theta_0 = -\pi/4)\,. \tag{4.5}$$

(2) The case of non-conducting plate.

As shown in Reference 1), Maxwell's stress is identically zero in this case. Therefore, the only contribution to the total drag is the shear stress, $\tau_{f_1}^*$, which is given by[†]

$$\begin{aligned} \tau_{f_1}^* &= -\mathrm{Re}\left[\frac{\sqrt{R}}{\sqrt{R}+\sqrt{R_m}}(\lambda_1^*+\lambda_2^*)e^{it^*}\right] \\ &= T_1 \sin(t^*+\theta_1)\,, \end{aligned} \tag{4.6}$$

with

$$T_1 = \frac{\sqrt{R}}{\sqrt{R}+\sqrt{R_m}}[(a+c)^2+(b+d)^2]^{1/2}\,, \tag{4.7}$$

$$\tan\theta_1 = -\frac{a+c}{b+d} \qquad (-\pi/2 < \theta_1 < 0)\,, \tag{4.8}$$

and

$$a = \mathrm{Re}\,(\lambda_1^*)\,, \qquad b = \mathrm{Im}\,(\lambda_1^*)\,, \qquad c = \mathrm{Re}\,(\lambda_2^*)\,, \qquad d = \mathrm{Im}\,(\lambda_2^*)\,.^{\dagger\dagger} \tag{4.9}$$

(3) The case of perfectly conducting plate.

In this case, both of the shear-stress, $\tau_{f_2}^*$, and Maxwell's stress, τ_m^*, contribute to the total drag. They are given by

$$\begin{aligned} \tau_{f_2}^* &= -\mathrm{Re}\left[\frac{i\sqrt{R}\,(\sqrt{R}+\sqrt{R_m})}{\lambda_1^*+\lambda_2^*}\,e^{it^*}\right] \\ &= T_2 \sin(t^*+\theta_2)\,, \end{aligned} \tag{4.10}$$

with

$$T_2 = \sqrt{R}\,(\sqrt{R}+\sqrt{R_m})[(a+c)^2+(b+d)^2]^{-1/2}\,, \tag{4.11}$$

$$\tan\theta_2 = -\frac{b+d}{a+c} \qquad (-\pi/2 < \theta_2 < 0)\,, \tag{4.12}$$

and

[†] In Reference 1), the shear-stress, τ_{f_1}, is given in dimensional form as

$$\tau_{f_1} = \mathrm{Re}\left[-\rho\nu U e^{i\omega t}\left\{\frac{i\omega(\lambda_1+\lambda_2)}{\lambda_1\lambda_2\nu+i\omega}\right\}\right].$$

[††] Explicit expressions for a, b, c and d are given as follows:

$$\left.\begin{matrix} a \\ b \end{matrix}\right\} = \frac{1}{2}[\{(SRR_m+\alpha)^2+(R+R_m+\beta)^2\}^{1/2} \pm (SRR_m+\alpha)]^{1/2}\,,$$

$$\left.\begin{matrix} c \\ d \end{matrix}\right\} = \frac{1}{2}[\{(SRR_m-\alpha)^2+(R+R_m-\beta)^2\}^{1/2} \pm (SRR_m-\alpha)]^{1/2}\,,$$

where

$$\left.\begin{matrix} \alpha \\ \beta \end{matrix}\right\} = \left[\frac{1}{2}\{[(S^2R^2R_m{}^2-(R-R_m)^2)^2+4S^2R^2R_m{}^2(R+R_m)^2]^{1/2} \pm (S^2R^2R_m{}^2-(R-R_m)^2)\}\right]^{1/2}.$$

$$\tau_m^* = -\mathrm{Re}\left[\frac{SR\sqrt{RR_m}}{\lambda_1^* + \lambda_2^*} e^{it^*}\right]$$
$$= T_m \sin(t^* + \theta_m) , \tag{4.13}$$

with

$$T_m = SR\sqrt{RR_m}\,[(a+c)^2 + (b+d)^2]^{-1/2} , \tag{4.14}$$

$$\tan\theta_m = \frac{a+c}{b+d} \qquad (-\pi < \theta_m < -\pi/2) . \tag{4.15}$$

The total drag is then given by

$$\tau_{2+m}^* = \tau_{f_2}^* + \tau_m^*$$
$$= T_{2+m} \sin(t^* + \theta_{2+m}) , \tag{4.16}$$

where

$$T_{2+m} = \sqrt{R}\left[\frac{S^2R^2R_m + (\sqrt{R} + \sqrt{R_m})^2}{(a+c)^2 + (b+d)^2}\right]^{1/2} , \tag{4.17}$$

$$\tan\theta_{2+m} = -\frac{(a+c)SR\sqrt{R_m} + (b+d)(\sqrt{R} + \sqrt{R_m})}{(a+c)(\sqrt{R} + \sqrt{R_m}) - (b+d)SR\sqrt{R_m}} \qquad (-\pi < \theta_{2+m} < 0) . \tag{4.18}$$

Table I. Amplitudes of drags *versus* magnetic pressure numbers.

I. $R=1$, $R_m=1$

S	T_1	T_2	T_m	T_{2+m}
0	1	1	0	1
0.1	1.0002	0.9998	0.04999	1.0011
0.5	1.0039	0.9961	0.2490	1.0268
1	1.0153	0.9850	0.4925	1.1012
2	1.0574	0.9457	0.9457	1.3375
5	1.2652	0.7904	1.9759	2.1282
10	1.6409	0.6094	3.0471	3.1074
20	2.2581	0.4429	4.4285	4.4506
100	5.0015	0.1999	9.9970	9.9990
∞	∞	0	∞	∞

II. $R=1$, $R_m=0.5$

S	T_1	T_2	T_m	T_{2+m}
0	1	1	0	1
0.1	1.0001	0.9999	0.04142	1.0008
0.5	1.0018	0.9982	0.2067	1.0194
1	1.0073	0.9928	0.4112	1.0746
2	1.0282	0.9726	0.8057	1.2629
5	1.1478	0.8712	1.8043	2.0036
10	1.4092	0.7096	2.9393	3.0238
20	1.8906	0.5289	4.3819	4.4137
100	4.1456	0.2412	9.9915	9.9944
∞	∞	0	∞	∞

III. $R=1$, $R_m=2$

S	T_1	T_2	T_m	T_{2+m}
0	1	1	0	1
0.1	1.0003	0.9997	0.05856	1.0014
0.5	1.0073	0.9928	0.2908	1.0345
1	1.0282	0.9726	0.5697	1.1271
2	1.1013	0.9080	1.0638	1.3986
5	1.4092	0.7096	2.0784	2.1962
10	1.8906	0.5289	3.0985	3.1433
20	2.6335	0.3797	4.4487	4.4649
100	5.8591	0.1707	9.9979	9.9993
∞	∞	0	∞	∞

Now, by tedious but elementary calculations it is shown for any values of the parameters S, R and R_m[†] that

$$T_1 \geqq T_0$$
$$\text{(equal sign holds when } SR_m = 0) , \tag{4.19}$$

which shows that the drag amplitude in the case of non-conducting plate always *increases* in comparison with that of the classical case. Comparing (4.7) with (4.11), we can see immediately that T_2 is exactly inverse to T_1 except the classical factor $\sqrt{R}$. Thus we may conclude that

---

[†] Here and hereafter we exclude the trivial case of $R=0$.

$$T_2 \leqq T_0$$
(equal sign holds when $SR_m=0$) , (4.20)

which shows that the amplitude of the shear-stress in the case of perfectly conducting plate always *decreases* in comparison with that of the classical case.

By elementary calculations similar to those for obtaining (4.19), we can easily show for any values of S, R and R_m that

$$T_{2+m} \geqq T_1 \geqq T_0$$
(equal signs hold when $SR_m=0$) , (4.21)

which shows that the amplitude of the total drag in the case of perfectly conducting plate is always greater than that of the case of non-conducting plate, and hence we may conclude that irrespective of whether the plate is non-conductor or perfect conductor, the amplitude of the total drag experienced by the plate always *increases* compared with that of the classical case. Numerical values of the drag for various values of S are tabulated in Table I and are shown graphically inF ig. 2.

On the other hand, it is easily shown for any values of S, R and R_m that

$$\left|\frac{(a+c)SR\sqrt{R_m}+(b+d)(\sqrt{R}+\sqrt{R_m})}{(a+c)(\sqrt{R}+\sqrt{R_m})-(b+d)SR\sqrt{R_m}}\right| \geqq \frac{a+c}{b+d} \geqq 1, \quad \text{(equal signs hold when } SR_m=0\text{)}, \tag{4.22}$$

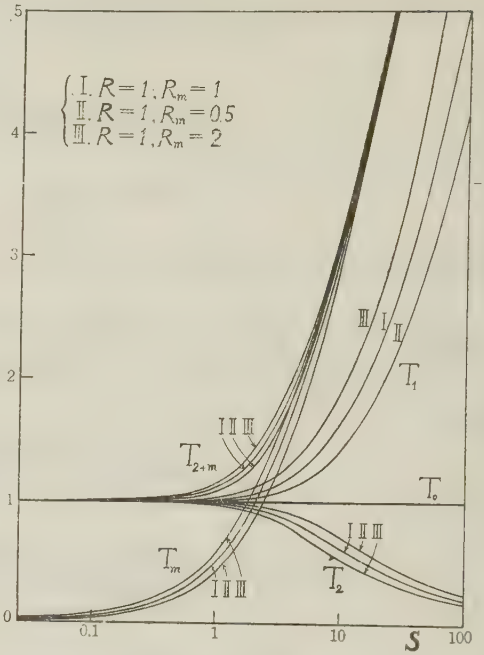

Fig. 2. Amplitudes of drags *versus* magnetic pressure number.

so that we have

$$\left.\begin{aligned} &-\pi/2<\theta_1 \leqq -\pi/4\ , \\ &-\pi/4 \leqq \theta_2 < 0\ , \\ &-3\pi/4 \leqq \theta_m < -\pi/2\ , \\ &-3\pi/4 < \theta_{2+m} \leqq -\pi/4\ , \\ &\theta_{2+m} \leqq \theta_1 \leqq \theta_0(=-\pi/4) \leqq \theta_2\ , \end{aligned}\right\}$$
(equal signs hold when $SR_m=0$) , (4.23)

which imply that the initial phases of the total drags, θ_1 (non-conducting plate) and θ_{2+m} (perfectly conducting plate), are always *retarded* in comparison with that of the classical case. It is to be noted, however, that the initial phase of the shear-stress in the case of perfectly conducting plate, θ_2, always *proceeds* compared with that of the classical case. Noting that $\tan\theta_1=\cot\theta_2=-\tan\theta_m$ and remembering (4.23), we have

$$\left.\begin{aligned} &\theta_1+\theta_2=-\pi/2\ , \\ &\theta_1+\theta_m=-\pi\ , \\ &\theta_2-\theta_m=\pi/2\ . \end{aligned}\right\} \tag{4.24}$$

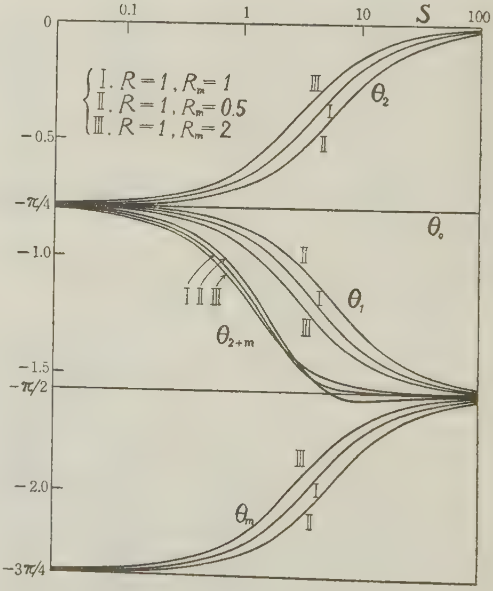

Fig. 3. Initial phases of drags *versus* magnetic pressure number.

Several numerical values of the initial phases *versus* S are tabulated in Table II and are shown graphically in Fig. 3. It is found from Fig. 3 that when $R=1$ and $R_m=0.5$, θ_{2+m} becomes $-\pi/2$ at about $S=6.2$ and makes shallow minimum at about $S=10$ then tends again to $-\pi/2$ as S becomes larger. This is due to the fact that

$$(a+c)(\sqrt{R}+\sqrt{R_m})-(b+d)SR\sqrt{R_m}$$

becomes zero for $R=1$, $R_m=0.5$ and $S \fallingdotseq 6.2$.†

In the special cases corresponding to limiting values of S and R_m, the amplitudes and the initial phases of the drags become as follows.

Table II. Initial phases of drags *versus* magnetic pressure numbers.

I. $R=1$, $R_m=1$

S	θ_1	θ_2	θ_m	θ_{2+m}
0	−0.7854 (−π/4)	−0.7854 (−π/4)	−2.3562 (−3π/4)	−0.7854 (−π/4)
0.1	−0.798	−0.773	−2.344	−0.823
0.5	−0.848	−0.723	−2.294	−0.968
1	−0.908	−0.663	−2.234	−1.127
2	−1.017	−0.554	−2.125	−1.339
5	−1.234	−0.337	−1.908	−1.534
10	−1.381	−0.190	−1.761	−1.564
20	−1.471	−0.0987	−1.671	−1.570
100	−1.551	−0.0200	−1.591	−1.5706
∞	−1.571 (−π/2)	−0	−1.571 (−π/2)	−1.571 (−π/2)

II. $R=1$, $R_m=0.5$

S	θ_1	θ_2	θ_m	θ_{2+m}
0	−0.7854 (−π/4)	−0.7854 (−π/4)	−2.3562 (−3π/4)	−0.7854 (−π/4)
0.1	−0.794	−0.777	−2.348	−0.818
0.5	−0.828	−0.743	−2.314	−0.947
1	−0.871	−0.700	−2.272	−1.093
2	−0.951	−0.620	−2.191	−1.312
5	−1.140	−0.431	−2.002	−1.552
(6.3	−1.198	−0.373	−1.945	−1.579)
10	−1.307	−0.264	−1.835	−1.598
20	−1.429	−0.141	−1.713	−1.593
100	−1.542	−0.0291	−1.601	−1.576
∞	−1.571 (−π/2)	−0	−1.571 (−π/2)	−1.571 (−π/2)

III. $R=1$, $R_m=2$

S	θ_1	θ_2	θ_m	θ_{2+m}
0	−0.7854 (−π/4)	−0.7854 (−π/4)	−2.3562 (−3π/4)	−0.7854 (−π/4)
0.1	−0.803	−0.768	−2.339	−0.827
0.5	−0.871	−0.700	−2.272	−0.985
1	−0.951	−0.620	−2.191	−1.150
2	−1.086	−0.485	−2.056	−1.349
5	−1.307	−0.264	−1.835	−1.506
10	−1.429	−0.142	−1.713	−1.544
20	−1.498	−0.0723	−1.644	−1.558
100	−1.556	−0.0146	−1.586	−1.569
∞	−1.571 (−π/2)	−0	−1.571 (−π/2)	−1.571 (−π/2)

(1) $S \ll 1$, $R=O(1)$, $R_m=O(1)$.

$$\left.\begin{aligned}
&T_1 \sim \sqrt{R}\left[1+\frac{S^2R^2R_m^2}{4(\sqrt{R}+\sqrt{R_m})^4}\right], &&\tan\theta_1 \sim -\left[1+\frac{SRR_m}{(\sqrt{R}+\sqrt{R_m})^2}\right],\\
&T_2 \sim \sqrt{R}\left[1-\frac{S^2R^2R_m^2}{4(\sqrt{R}+\sqrt{R_m})^4}\right], &&\tan\theta_2 \sim -\left[1-\frac{SRR_m}{(\sqrt{R}+\sqrt{R_m})^2}\right],\\
&T_m \sim \frac{SR\sqrt{RR_m}}{\sqrt{R}+\sqrt{R_m}}, &&\tan\theta_m \sim \left[1+\frac{SRR_m}{(\sqrt{R}+\sqrt{R_m})^2}\right],\\
&T_{2+m} \sim \sqrt{R}\left[1+\frac{S^2R^2R_m^2}{4(\sqrt{R}+\sqrt{R_m})^4}\left(1+\frac{2R}{R_m}+\frac{4\sqrt{R}}{\sqrt{R_m}}\right)\right],\\
&&&\tan\theta_{2+m} \sim -\left[1+\frac{SRR_m}{(\sqrt{R}+\sqrt{R_m})^2}\left(1+\frac{2\sqrt{R}}{\sqrt{R_m}}\right)\right].
\end{aligned}\right\} \tag{4.25}$$

(2) $S \gg 1$, $R=O(1)$, $R_m=O(1)$.

---

† General relationship between S, R and R_m which makes $(a+c)(\sqrt{R}+\sqrt{R_m})-(b+d)SR\sqrt{R_m}$ zero is rather complicated to write down explicitly.

$$\left.\begin{aligned}
&T_1\sim R\sqrt{S}\left[\frac{\sqrt{R_m}}{\sqrt{R}+\sqrt{R_m}}\right], && \tan\theta_1\sim-\frac{2SRR_m}{(\sqrt{R}+\sqrt{R_m})^2}\,,\\
&T_2\sim\frac{1}{\sqrt{S}}\left[\frac{\sqrt{R}+\sqrt{R_m}}{\sqrt{R_m}}\right], && \tan\theta_2\sim-\frac{(\sqrt{R}+\sqrt{R_m})^2}{2SRR_m}\,,\\
&T_m\sim R\sqrt{S}\,, && \tan\theta_m\sim\frac{2SRR_m}{(\sqrt{R}+\sqrt{R_m})^2}\,,\\
&T_{2+m}\sim R\sqrt{S}\,, \quad \tan\theta_{2+m}\sim && \begin{cases}-\dfrac{2SRR_m}{R_m-R} & (R-R_m\neq 0 \ \text{ or } \ R-R_m\gg O(S^{-2}))\\[2mm] -\dfrac{2S^3R^3}{16+S^2R(R_m-R)} & (R-R_m\approx O(S^{-2}))\\[2mm] -S^3R^3/8 & (R-R_m=0 \ \text{ or } \ R-R_m\ll O(S^{-2}))\end{cases}
\end{aligned}\right\} \quad (4.26)$$

It will be seen that the amplitude of the total drag in the case of perfectly conducting plate, T_{2+m}, is essentially equal to that of Maxwell's stress, T_m, and that the initial phases θ_1, θ_m and θ_{2-m} are nearly equal to $-\pi/2$ and θ_2 is nearly equal to zero. When $R\doteqdot R_m$, $\tan\theta_{2+m}=O(S^3)$ so that θ_{2+m} tends to $-\pi/2$ more rapidly with increasing S for $R\doteqdot R_m$ than otherwise and when $R>R_m$, $\tan\theta_{2+m}>0$ so that θ_{2+m} tends to $-\pi/2$ from smaller values than $-\pi/2$ with increasing S, while otherwise θ_{2+m} tends to $-\pi/2$ from larger values than $-\pi/2$ (see Fig. 3).

(3) $R_m\ll 1$, $S=O(1)$, $R=O(1)$.

$$\left.\begin{aligned}
&T_1\sim\sqrt{R}\left[1+\frac{1}{4}S^2R_m^2\right], && \tan\theta_1\sim-[1+SR_m]\,,\\
&T_2\sim\sqrt{R}\left[1-\frac{1}{4}S^2R_m^2\right], && \tan\theta_2\sim-[1-SR_m]\,,\\
&T_m\sim SR\sqrt{R_m}\left[1-\sqrt{\frac{R_m}{R}}\right], && \tan\theta_m\sim[1+SR_m]\,,\\
&T_{2+m}\sim\sqrt{R}\left[1+\frac{1}{2}S^2RR_m\right], && \tan\theta_{2+m}\sim-[1+2S\sqrt{RR_m}\,]\,.
\end{aligned}\right\} \quad (4.27)$$

(4) $R_m\gg 1$, $S=O(1)$, $R=O(1)$.

$$\left.\begin{aligned}
&T_1\sim\sqrt{R}\,[1+S^2R^2]^{1/4}\,, && \tan\theta_1\sim-\left[\frac{\sqrt{1+S^2R^2}+SR}{\sqrt{1+S^2R^2}-SR}\right]^{1/2},\\
&T_2\sim\sqrt{R}\,[1+S^2R^2]^{-1/4}\,, && \tan\theta_2\sim-\left[\frac{\sqrt{1+S^2R^2}-SR}{\sqrt{1+S^2R^2}+SR}\right]^{1/2},\\
&T_m\sim SR\sqrt{R}\,[1+S^2R^2]^{-1/4}\,, && \tan\theta_m\sim\left[\frac{\sqrt{1+S^2R^2}+SR}{\sqrt{1+S^2R^2}-SR}\right]^{1/2},\\
&T_{2+m}\sim\sqrt{R}\,[1+S^2R^2]^{1/4}\,, && \tan\theta_{2+m}\sim-\left[\frac{\sqrt{1+S^2R^2}+SR}{\sqrt{1+S^2R^2}-SR}\right]^{1/2}.
\end{aligned}\right\} \quad (4.28)$$

It is to be noted that all of the amplitudes and the corresponding initial phases do not depend on R_m in this limit. It is also interesting to notice that the total drags in both cases of non-conducting plate and perfectly donducting plate are essentially identical with each other in this case.

§ 5. A Special Case Corresponding to 'Magnetic Stokes Approximation'

It may be worthwhile to discuss a special case corresponding to the so-called 'magnetic Stokes approximation' ($R_m\ll 1$, $SR_m=O(1)$) which is frequently used in many investigations of magnetohydrodynamics.

In the limit of $R_m\ll 1$ and $SR_m=O(1)$, we have from (3.4)

$$\left.\begin{aligned} \lambda_1^* &\sim \sqrt{R(SR_m+i)}\left[1+\frac{iSR_m}{2(SR_m+i)^2}\left(\frac{R_m}{R}\right)\right], \\ \lambda_2^* &\sim i\sqrt{R_m/(SR_m+i)}\left[1-\frac{iSR_m}{2(SR_m+i)^2}\left(\frac{R_m}{R}\right)\right]. \end{aligned}\right\} \tag{5.1}$$

We shall consider first the case of non-conducting plate, and next the case of perfectly conducting plate.

(1) The case of non-conducting plate.

From (4.3)∼(4.6) of Reference 1),† we have

$$\left.\begin{aligned} u^* &\sim \frac{SRR_m}{\sqrt{R(SR_m+i)}}e^{it^*}\left[\frac{\sqrt{R(SR_m+i)}}{SRR_m}e^{-\sqrt{R(SR_m+i)}\,y^*}+\frac{\sqrt{R_m/(SR_m+i)}}{R}e^{-i\sqrt{R_m/(SR_m+i)}\,y^*}\right] \\ &\to e^{it^*-\sqrt{R(SR_m+i)}\,y^*} \qquad (\text{as} \quad R_m\to 0)\,, \\ H_x^* &\sim \frac{R_m}{\sqrt{R(SR_m+i)}}e^{it^*}\left[e^{-\sqrt{R(SR_m+i)}\,y^*}-e^{-i\sqrt{R_m/(SR_m+i)}\,y^*}\right]\to \mathrm{O}(R_m)\,, \\ E_z^* &\sim \frac{iR_m}{\sqrt{R(SR_m+i)}}e^{it^*}\left[\frac{1}{\sqrt{R(SR_m+i)}}e^{-\sqrt{R(SR_m+i)}\,y^*}+i\sqrt{\frac{SR_m+i}{R_m}}e^{-i\sqrt{R_m/(SR_m+i)}\,y^*}\right] \\ &\to \mathrm{O}(\sqrt{R_m})\,, \\ j_z^* &\sim \frac{1}{\sqrt{R(SR_m+i)}}e^{it^*}\left[\sqrt{R(SR_m+i)}\,e^{-\sqrt{R(SR_m+i)}\,y^*}-i\sqrt{\frac{R_m}{SR_m+i}}e^{-i\sqrt{R_m/(SR_m+i)}\,y^*}\right] \\ &\to e^{it^*-\sqrt{R(SR_m+i)}\,y^*} \qquad (\text{as} \quad R_m\to 0)\,. \end{aligned}\right\} \tag{5.2}$$

Taking the real part of the expression for u^*, we have

$$\mathrm{Re}\,[u^*]=e^{-ay^*}\cos(t^*-by^*)\,,$$

where

$$\left.\begin{aligned} a&=\mathrm{Re}\,[\sqrt{R(SR_m+i)}\,]=\left[\frac{R}{2}(\sqrt{1+S^2R_m^2}+SR_m)\right]^{1/2}, \\ b&=\mathrm{Im}\,[\sqrt{R(SR_m+i)}\,]=\left[\frac{R}{2}(\sqrt{1+S^2R_m^2}-SR_m)\right]^{1/2}. \end{aligned}\right\} \tag{5.3}$$

This is exactly the same, excepting the notations, as the approximate velocity distribution obtained by Ong and Nicholls[2] on the basis of Rossow's assumption[3] (neglect of the induced magnetic field) for the case of 'the magnetic field being fixed *to the fluid*' (see Eq. (5) of Reference 2)). The other quantities such as H_x^*, E_z^* that are neglected in their analysis vanish in the limit of $R_m\to 0$ as shown in (5.2). Therefore, their approximate solution for the case of the magnetic field being fixed to the fluid may be adequate for the case of non-conducting plate when R_m is very small and $SR_m=\mathrm{O}(1)$.

The drag in this case is given by

---

† From Reference 1)

$$\left\{\begin{aligned} &(4.3) \qquad u^*=-\frac{(\lambda_1^{*2}-iR)(\lambda_2^{*2}-iR)}{(\lambda_1^*-\lambda_2^*)(\lambda_1^*\lambda_2^*+iR)}e^{it^*}\left[\frac{\lambda_1^*}{\lambda_1^{*2}-iR}e^{-\lambda_1^*y^*}-\frac{\lambda_2^*}{\lambda_2^{*2}-iR}e^{-\lambda_2^*y^*}\right], \\ &(4.4) \qquad H_x^*=-\frac{(\lambda_1^{*2}-iR)(\lambda_2^{*2}-iR)}{SR(\lambda_1^*-\lambda_2^*)(\lambda_1^*\lambda_2^*+iR)}e^{it^*}[e^{-\lambda_1^*y^*}-e^{-\lambda_2^*y^*}]\,, \\ &(4.5) \qquad E_z^*=-\frac{i(\lambda_1^{*2}-iR)(\lambda_2^{*2}-iR)}{SR(\lambda_1^*-\lambda_2^*)(\lambda_1^*\lambda_2^*+iR)}e^{it^*}\left[\frac{1}{\lambda_1^*}e^{-\lambda_1^*y^*}-\frac{1}{\lambda_2^*}e^{-\lambda_2^*y^*}\right], \\ &(4.6) \qquad j_z^*=-\frac{(\lambda_1^{*2}-iR)(\lambda_2^{*2}-iR)}{SRR_m(\lambda_1^*-\lambda_2^*)(\lambda_1^*\lambda_2^*+iR)}e^{it^*}[\lambda_1^*e^{-\lambda_1^*y^*}-\lambda_2^*e^{-\lambda_2^*y^*}]\,. \end{aligned}\right.$$

$$\left.\begin{aligned} &\tau_{f_1}^* \sim \sqrt{R}\,(1+S^2R_m^2)^{1/4}\sin(t^*+\theta_1)\,, \\ \text{where}\qquad & \\ &\tan\theta_1 \sim -\left[\frac{\sqrt{1+S^2R_m^2}+SR_m}{\sqrt{1+S^2R_m^2}-SR_m}\right]^{1/2}. \end{aligned}\right\} \tag{5.4}$$

(2) The case of perfectly conducting plate.

In this case, making use of (5.1), we have from (3.6)

$$\left.\begin{aligned} u^* &\sim \frac{iSRR_m}{SR_m+i}e^{it^*}\left[\frac{1}{SRR_m}e^{-\sqrt{R(SR_m+i)}}+\frac{1}{iR}e^{-i\sqrt{R_m/(SR_m+i)}\,y^*}\right], \\ H_x^* &\sim \frac{iR_m}{SR_m+i}e^{it^*}\left[\frac{1}{\sqrt{R(SR_m+i)}}e^{-\sqrt{R(SR_m+i)}\,y^*}+i\sqrt{\frac{SR_m+i}{R_m}}\,e^{-i\sqrt{R_m/(SR_m+i)}\,y_*}\right] \\ &\to O(\sqrt{R_m})\,, \\ E_z^* &\sim -\frac{R_m}{SR_m+i}e^{it^*}\left[\frac{1}{R(SR_m+i)}e^{-\sqrt{R(SR_m+i)}\,y^*}+\frac{SR_m+i}{R_m}e^{-i\sqrt{R_m/(SR_m+i)}\,y^*}\right] \\ &\to -e^{it^*-i\sqrt{R_m/(SR_m+i)}\,y^*} \qquad (\text{as}\quad R_m\to 0)\,, \\ j_z^* &\sim \frac{i}{SR_m+i}e^{it^*}\left[e^{-\sqrt{R(SR_m+i)}\,y^*}-e^{-i\sqrt{R_m/(SR_m+i)}\,y^*}\right], \\ J_s^* &\sim \frac{1}{4\pi}\sqrt{\frac{R_m}{SR_m+i}}\,e^{it^*}\to O(\sqrt{R_m})\,. \end{aligned}\right\} \tag{5.5}$$

If R_m is so small as to make $\sqrt{R_m}\,y_M^* \ll 1$ even for fairly large values of y^*, say y_M^*, we may put $e^{-i\sqrt{R_m/(SR_m+i)}\,y^*}\sim 1$ for the region of $y^* \lesssim y_M^*$. Then the real part of the expression for u^* gives

$$\mathrm{Re}\,[u^*]=\frac{e^{-ay^*}}{1+S^2R_m^2}\left[\cos(t^*-by^*)-SR_m\sin(t^*-by^*)\right]+\frac{SR_m}{1+S^2R_m^2}\left[SR_m\cos t^*+\sin t^*\right], \tag{5.6}$$

which is exactly identical, excepting the notations, with the approximate solution obtained by Ong and Nicholls[2] for the case of 'the magnetic field being fixed *to the plate*' (see Eq. (10) of Reference 2)). It should be noted here that (5.6) is valid only for the region of $y^* \lesssim y_M^*$, and the smaller the magnetic Reyeolds number R_m becomes, the wider becomes the region of the validity of (5.6). Thus the magnetic Stokes approximation may be useful to obtain the velocity field in the region comparatively near the plate in this case. The induced magnetic field H_x^* neglected by Ong and Nicholls[2] tends to zero as the order of $\sqrt{R_m}$, and E_z^* $(\sim -e^{it^*})$ corresponds to the additional term '$-mu_0\cos nt$' in the second term of left-hand side of Eq. (6) of Reference 2).

The drags in this case are given as

$$\left.\begin{aligned} \text{shear-stress:}\qquad & \tau_{f_2}^* \sim \sqrt{R}\,(1+S^2R_m^2)^{-1/4}\sin(t^*+\theta_2)\,, \\ & \tan\theta_2 \sim -\left[\frac{\sqrt{1+S^2R_m^2}-SR_m}{\sqrt{1+S^2R_m^2}+SR_m}\right]^{1/2}, \\ \text{Maxwell's stress:}\qquad & \tau_m^* \sim SR\sqrt{R_m}\,(1+S^2R_m^2)^{-1/4}\sin(t^*+\theta_m)\,, \\ & \tan\theta_m \sim \left[\frac{\sqrt{1+S^2R_m^2}+SR_m}{\sqrt{1+S^2R_m^2}-SR_m}\right]^{1/2}, \\ \text{total drag:}\qquad & \tau_{2+m}^* \sim SR\sqrt{R_m}\,(1+S^2R_m^2)^{-1/4}\sin(t^*+\theta_{2+m})\,, \\ & \tan\theta_{2+m} \sim \left[\frac{\sqrt{1+S^2R_m^2}+SR_m}{\sqrt{1+S^2R_m^2}-SR_m}\right]^{1/2} \end{aligned}\right\} \tag{5.7}$$

As will be seen from (5.7), the total drag is essentially equal to Maxwell's stress, which implies that the contribution from the shear-stress to the total drag is negligible compared with that from Maxwell's stress. Furthermore, noting that $SR_m=O(1)$, we shall find that the amplitudes of Maxwell's stress and the total drag tend to infinity as the order of $O(1/\sqrt{R_m})$. Thus, when the plate is a perfect conductor, the magnetic Stokes approximation is not adequate to obtain the drag on the plate. The state of affairs is quite similar to that in Rossow's solutions[3] for the hydromagnetic boundary-layer flow past a flat plate and the hydromagnetic Rayleigh's problem in the case of 'the magnetic field being fixed to the plate' in which case the drag due to Maxwell's stress does also diverge.

From the above discussions we may assert that Rossow's assumption, i.e., neglect of the induced magnetic field, is valid only for the cases of small magnetic Reynolds number R_m with large magnetic pressure number S, namely, his assumption is permissible only for the cases such that the magnetic Stokes approximation is valid. Moreover, it has been found that the respective considerations of the fundamental equations according as the magnetic field is fixed 'to the fluid' or 'to the plate' are not necessary if the electric field $\boldsymbol{E}$ is included in the analysis as is done in this paper. If one include $\boldsymbol{E}$ in the analysis, the difference between the respective fundamental equations may be replaced simply by that of the boundary conditions expressing the physical properties of the plate, and the physical meaning of 'the magnetic field being fixed *to the fluid* or *to the plate*' may now be clarified.

§ 6. Concluding Remarks

We have obtained the exact solutions for the hydromagnetic flow of an electrically conducting fluid due to an oscillating flat plate under transverse magnetic field for two cases in which the plate is a *non-conductor* (see Reference 1) and a *perfect conductor*. Combining these two kinds of solutions we may infer, at least, qualitative characters of more general cases of the plate having a finite electrical conductivity.

The restriction that the magnetic field is applied *transversely* to the plate may be easily relaxed, and we may extend the problem to the case of the *oblique* magnetic field so far as it has no z-component, because x-component of the applied magnetic field would not interact with the flow field.

The writer wishes to express his cordial thanks to Professor S. Tomotika for his continual encouragement and kind inspection of the manuscript. The writer's thanks are also due to Professor I. Imai for his helpful advices. During the course of this study, the writer has been in receipt of a grant-in-aid for the fundamental scientific research from the Ministry of Education.

References

1) T. Kakutani: J. Phys. Soc. Japan **13** (1958) 1504.
2) R. S. Ong and J. A. Nicholls: J. Aero. Sci. **26** (1959) 314.
3) V. J. Rossow: NACA TN-3971 (1957).

JOURNAL OF THE PHYSICAL SOCIETY OF JAPAN, Vol. 15, No. 7, JULY, 1960

Steady Temperature Field in a Composite Doubly Infinite Strip

By Václav VODIČKA
Plzeň, Czechoslovakia

(Received March 3, 1960)

The present paper extends the classical results on two-dimensional stationary temperature distribution in an infinite plate to the case of a composite strip. General deductions are applied to some special cases leading partly to new results not given in the literature.

§ 1. Statement of the Problem

The doubly infinite strip

$$x_0 \leq x \leq x_n\,, \quad -\infty < y < +\infty\,, \quad -\infty < z < +\infty$$

consists of n homogeneous isotropic layers

$$x_{k-1} \leq x \leq x_k\,, \quad -\infty < y < +\infty\,, \quad -\infty < z < +\infty\,, \quad 1 \leq k \leq n$$

with thermal conductivities λ_k, respectively.

The question is about the steady temperature distribution in the solid provided that its front face $x=x_0$ is maintained at the given temperature $f(y)$ and its back face $x=x_n$ at $g(y)$. Assumed is the continuity both of the temperature and of the flux of heat over the surfaces of separation between several layers of the body.

Mathematically speaking one has to find the solution $u_k=u_k(x, y)$ of the harmonic equations

$$\frac{\partial^2 u_k}{\partial x^2}+\frac{\partial^2 u_k}{\partial y^2}=0\,, \quad x_{k-1}<x<x_k\,, \quad -\infty<y<+\infty\,, \quad 1\leq k\leq n \tag{1.1}$$

with the following conditions:

$$u_1(x_0, y)=f(y)\,, \quad -\infty<y<+\infty \tag{1.2}$$

$$\left.\begin{aligned} &u_{k+1}(x_k, y)=u_k(x_k, y)\,, \quad -\infty<y<+\infty \\ &\frac{\partial u_{k+1}}{\partial x}=\Lambda_k\frac{\partial u_k}{\partial x}\,, \quad x=x_k\,, \quad -\infty<y<+\infty\,, \quad \Lambda_k=\frac{\lambda_k}{\lambda_{k+1}}\,, \quad 1\leq k\leq n-1 \end{aligned}\right\} \tag{1.3}$$

$$u_n(x_n, y)=g(y)\,, \quad -\infty<y<+\infty\,. \tag{1.4}$$

§ 2. The Fourier Transforms of $u_k(x, y)$

Making usual assumptions the familiar transformation

$$\left.\begin{aligned} \bar{h}(\eta)&=F[h(y)]=\frac{1}{\sqrt{2\pi}}\int_{-\infty}^{+\infty} h(y)\, e^{i\eta y}\, dy \\ h(y)&=F^{-1}[\bar{h}(\eta)]=\frac{1}{\sqrt{2\pi}}\int_{-\infty}^{+\infty} \bar{h}(\eta)\, e^{-i\eta y}\, d\eta \end{aligned}\right\} \tag{2.1}$$

changes our problem (1.1)-(1.4) into the following equations for determining the Fourier transforms $\bar{u}_k=\bar{u}_k(x, \eta)$ of the required functions $u_k(x, y)$:

$$\frac{d^2\bar{u}_k}{dx^2}-\eta^2\bar{u}_k=0\,, \quad x_{k-1}<x<x_k\,, \quad 1\leq k\leq n \tag{2.2}$$

$$\bar{u}_1(x_0, \eta)=\bar{f}(\eta) \tag{2.3}$$

$$\left.\begin{aligned}&\bar{u}_{k+1}(x_k,\eta)=\bar{u}_k(x_k,\eta)\\&\frac{d\bar{u}_{k+1}}{dx}=\Lambda_k\frac{d\bar{u}_k}{dx}\,,\qquad x=x_k\,,\qquad 1\le k\le n-1\end{aligned}\right\}\tag{2.4}$$

$$\bar{u}_n(x_n,\eta)=\bar{g}(\eta)\,.\tag{2.5}$$

Integrating (2.2) gives generally

$$\bar{u}_k(x,\eta)=A_k\operatorname{ch}\eta(x-x_{k-1})+B_k\operatorname{sh}\eta(x-x_{k-1})\,,\qquad 1\le k\le n\tag{2.6}$$

whereby the coefficients $A_k=A_k(\eta)$, $B_k=B_k(\eta)$ are to be determined from the conditions (2.3)-(2.5), i.e. from the equations

$$A_1=\bar{f}(\eta)\,,\qquad A_n\operatorname{ch}l_n\eta+B_n\operatorname{sh}l_n\eta=\bar{g}(\eta)\,,\qquad l_n=x_n-x_{n-1}\tag{2.7}$$

$$\left.\begin{aligned}&A_{k+1}=A_k\operatorname{ch}l_k\eta+B_k\operatorname{sh}l_k\eta\\&B_{k+1}=\Lambda_k(A_k\operatorname{sh}l_k\eta+B_k\operatorname{ch}l_k\eta)\,,\qquad l_k=x_k-x_{k-1}\,,\qquad 1\le k\le n-1\,.\end{aligned}\right\}\tag{2.8}$$

Introducing the matrices

$$K_k=\begin{Vmatrix}A_k\\B_k\end{Vmatrix}\,,\qquad 1\le k\le n\,,\qquad M_k(\eta)=\begin{Vmatrix}\operatorname{ch}l_k\eta & \operatorname{sh}l_k\eta\\ \Lambda_k\operatorname{sh}l_k\eta & \Lambda_k\operatorname{ch}l_k\eta\end{Vmatrix}\,,\qquad 1\le k\le n-1\tag{2.9}$$

the Eq. (2.8) can be written in the form

$$K_{k+1}=M_k(\eta)K_k\,,\qquad 1\le k\le n-1$$

which gives, with regard to the first formula (2.7),

$$K_{k+1}=Q_k(\eta)\begin{Vmatrix}\bar{f}(\eta)\\B_1\end{Vmatrix}\,,\qquad Q_k(\eta)=M_k(\eta)M_{k-1}(\eta)\cdots M_1(\eta)\,,\qquad 1\le k\le n-1\,.\tag{2.10}$$

Now the last of the Eq. (2.10) yields

$$A_n=q_{n-1}^{(11)}(\eta)\bar{f}(\eta)+q_{n-1}^{(12)}(\eta)B_1\,,\qquad B_n=q_{n-1}^{(21)}(\eta)\bar{f}(\eta)+q_{n-1}^{(22)}(\eta)B_1\,,$$

$q_{n-1}^{(r,s)}(\eta)$, $r,s=1,2$, being the elements of $Q_{n-1}(\eta)$. Combining this with the second condition (2.7) gives the value of B_1 in terms of η, namely

$$B_1(\eta)=\frac{1}{q_{n-1}^{(12)}(\eta)\operatorname{ch}l_n\eta+q_{n-1}^{(22)}(\eta)\operatorname{sh}l_n\eta}\{\bar{g}(\eta)-\bar{f}(\eta)[q_{n-1}^{(11)}(\eta)\operatorname{ch}l_n\eta+q_{n-1}^{(21)}(\eta)\operatorname{sh}l_n\eta]\}$$

and one comes to the following expressions for the coefficients A_k, B_k:

$$\begin{aligned}&A_1=\bar{f}(\eta)\,,\qquad B_1=\frac{1}{N(\eta)}[-\bar{f}(\eta)Z(\eta)+\bar{g}(\eta)]\,,\\&\begin{Vmatrix}A_{k+1}\\B_{k+1}\end{Vmatrix}=\frac{Q_k(\eta)}{N(\eta)}\left\{\bar{f}(\eta)\begin{Vmatrix}N(\eta)\\-Z(\eta)\end{Vmatrix}+\bar{g}(\eta)\begin{Vmatrix}0\\1\end{Vmatrix}\right\}\,,\qquad 1\le k\le n-1\\&N(\eta)=q_{n-1}^{(12)}(\eta)\operatorname{ch}l_n\eta+q_{n-1}^{(22)}(\eta)\operatorname{sh}l_n\eta\,,\qquad Z(\eta)=q_{n-1}^{(11)}(\eta)\operatorname{ch}l_n\eta+q_{n-1}^{(21)}(\eta)\operatorname{sh}l_n\eta\,;\end{aligned}\tag{2.11}$$

$\bar{f}(\eta)$, $\bar{g}(\eta)$ are the Fourier transforms of the functions $f(y)$, $g(y)$.

§ 3. Solution of the Problem (1.1)-(1.4)

Calculating the coefficients $A_k=A_k(\eta)$, $B_k=B_k(\eta)$ from (2.11) and inserting into (2.6) gives the Fourier transforms $\bar{u}_k(x,\eta)$ of the required functions $u_k(x,y)$. From this one obtains the solution of our problem by (2.1) in the form

$$u_k(x, y)=\frac{1}{\sqrt{2\pi}}\int_{-\infty}^{\infty}[A_k \operatorname{ch}\eta(x-x_{k-1})+B_k \operatorname{sh}\eta(x-x_{k-1})]\, e^{-i\eta y}\, d\eta\,, \qquad 1\leq k\leq n\,. \tag{3.1}$$

Looking at (2.11) shows how the problem in question can be treated as split in two simpler cases letting see the influence of each of the given functions $f(y)$, $g(y)$, separately. The usual difficulty lies in that it is very hard to establish a closed formula for the matrices $Q_k(\eta)$ as defined in (2.10).

§ 4. The First Matrices $Q_k(\eta)$

Intending to prepare the possibility of treating explicitly at least the cases with the smallest values of n, we write down the expressions of the matrices $Q_1(\eta)$, $Q_2(\eta)$ and $Q_3(\eta)$:

$$Q_1(\eta)=\begin{Vmatrix}\operatorname{ch} l_1\eta, & \operatorname{sh} l_1\eta\\ \operatorname{sh} l_1\eta, & \operatorname{ch} l_1\eta\end{Vmatrix}+(A_1-1)\begin{Vmatrix}0\ , & 0\\ \operatorname{sh} l_1\eta, & \operatorname{ch} l_1\eta\end{Vmatrix}$$

$$\begin{aligned}Q_2(\eta)=&\begin{Vmatrix}\operatorname{ch}(l_1+l_2)\eta, & \operatorname{sh}(l_1+l_2)\eta\\ \operatorname{sh}(l_1+l_2)\eta, & \operatorname{ch}(l_1+l_2)\eta\end{Vmatrix}+(A_1-1)\begin{Vmatrix}\operatorname{sh} l_1\eta \operatorname{sh} l_2\eta, & \operatorname{ch} l_1\eta \operatorname{sh} l_2\eta\\ \operatorname{sh} l_1\eta \operatorname{ch} l_2\eta, & \operatorname{ch} l_1\eta \operatorname{ch} l_2\eta\end{Vmatrix}+\\ &+(A_2-1)\begin{Vmatrix}0\ , & 0\\ \operatorname{sh}(l_1+l_2)\eta, & \operatorname{ch}(l_1+l_2)\eta\end{Vmatrix}+(A_1-1)(A_2-1)\operatorname{ch} l_2\eta\begin{Vmatrix}0\ , & 0\\ \operatorname{sh} l_1\eta, & \operatorname{ch} l_1\eta\end{Vmatrix}\end{aligned}$$

$$\begin{aligned}Q_3(\eta)=&\begin{Vmatrix}\operatorname{ch}(l_1+l_2+l_3)\eta, & \operatorname{sh}(l_1+l_2+l_3)\eta\\ \operatorname{sh}(l_1+l_2+l_3)\eta, & \operatorname{ch}(l_1+l_2+l_3)\eta\end{Vmatrix}+\\ &+(A_1-1)\begin{Vmatrix}\operatorname{sh} l_1\eta \operatorname{sh}(l_2+l_3)\eta, & \operatorname{ch} l_1\eta \operatorname{sh}(l_2+l_3)\eta\\ \operatorname{sh} l_1\eta \operatorname{ch}(l_2+l_3)\eta, & \operatorname{ch} l_1\eta \operatorname{ch}(l_2+l_3)\eta\end{Vmatrix}+\\ &+(A_2-1)\begin{Vmatrix}\operatorname{sh}(l_1+l_2)\eta \operatorname{sh} l_3\eta, & \operatorname{ch}(l_1+l_2)\eta \operatorname{sh} l_3\eta\\ \operatorname{sh}(l_1+l_2)\eta \operatorname{ch} l_3\eta, & \operatorname{ch}(l_1+l_2)\eta \operatorname{ch} l_3\eta\end{Vmatrix}+\\ &+(A_3-1)\begin{Vmatrix}0\ , & 0\\ \operatorname{sh}(l_1+l_2+l_3)\eta, & \operatorname{ch}(l_1+l_2+l_3)\eta\end{Vmatrix}+\\ &+(A_1-1)(A_2-1)\operatorname{ch} l_2\eta\begin{Vmatrix}\operatorname{sh} l_1\eta \operatorname{sh} l_3\eta, & \operatorname{ch} l_1\eta \operatorname{sh} l_3\eta\\ \operatorname{sh} l_1\eta \operatorname{ch} l_3\eta, & \operatorname{ch} l_1\eta \operatorname{ch} l_3\eta\end{Vmatrix}+\\ &+(A_2-1)(A_3-1)\operatorname{ch} l_3\eta\begin{Vmatrix}0\ , & 0\\ \operatorname{sh}(l_1+l_2)\eta, & \operatorname{ch}(l_1+l_2)\eta\end{Vmatrix}+\\ &+(A_3-1)(A_1-1)\operatorname{ch}(l_2+l_3)\eta\begin{Vmatrix}0\ , & 0\\ \operatorname{sh} l_1\eta, & \operatorname{ch} l_1\eta\end{Vmatrix}+\\ &+(A_1-1)(A_2-1)(A_3-1)\operatorname{ch} l_2\eta \operatorname{ch} l_3\eta\begin{Vmatrix}0\ , & 0\\ \operatorname{sh} l_1\eta, & \operatorname{ch} l_1\eta\end{Vmatrix}\,.\end{aligned} \tag{4.1}$$

These formulae show clearly the merits of the main difficulties arising at treating problems on composite continua. They give us a much more detailed insight into the inner structure of such questions than has been given in numerous former papers of the author—see ref. 1–3.

§ 5. A Homogeneous Plate

As a first example let us treat the elementary case $A_1=A_2=\cdots=A_{n-1}=1$ corresponding to a homogeneous isotropic strip $x_0\leq x\leq x_n$, $-\infty<y<+\infty$, $-\infty<z<+\infty$.

The matrices $Q_k(\eta)$ can be expressed in closed form

$$Q_k(\eta)=\begin{Vmatrix}\operatorname{ch}(x_k-x_0)\eta, & \operatorname{sh}(x_k-x_0)\eta\\ \operatorname{sh}(x_k-x_0)\eta, & \operatorname{ch}(x_k-x_0)\eta\end{Vmatrix}\,, \qquad 1\leq k\leq n-1 \tag{5.1}$$

and the formulae (2.11) give

$$N(\eta)=\operatorname{sh}(x_n-x_0)\eta\,, \qquad Z(\eta)=\operatorname{ch}(x_n-x_0)\eta$$

$$A_1 \operatorname{ch}(x-x_0)\eta+B_1 \operatorname{sh}(x-x_0)\eta=\bar{f}(\eta)\frac{\operatorname{sh}(x_n-x)\eta}{\operatorname{sh}(x_n-x_0)\eta}+\bar{g}(\eta)\frac{\operatorname{sh}(x-x_0)\eta}{\operatorname{sh}(x_n-x_0)\eta}$$

$$A_{k+1} \operatorname{ch}(x-x_k)\eta+B_{k+1} \operatorname{sh}(x-x_k)\eta=\bar{f}(\eta)\frac{\operatorname{sh}(x_n-x)\eta}{\operatorname{sh}(x_n-x_0)\eta}+\bar{g}(\eta)\frac{\operatorname{sh}(x-x_0)\eta}{\operatorname{sh}(x_n-x_0)\eta}\,, \qquad 1\leq k\leq n-1\,.$$

Introducing this in (3.1) gives the solution in the form

$$u(x, y)=\frac{1}{\sqrt{2\pi}}\int_{-\infty}^{+\infty}\left[\bar{f}(\eta)\frac{\operatorname{sh}(x_n-x)\eta}{\operatorname{sh}(x_n-x_0)\eta}+\bar{g}(\eta)\frac{\operatorname{sh}(x-x_0)\eta}{\operatorname{sh}(x_n-x_0)\eta}\right]e^{-i\eta y}\,d\eta \tag{5.2}$$

which is valid in the whole extent of the body in question.

This result can be expressed in yet another form. For, regarding the well-known relation4)

$$\int_{-\infty}^{+\infty}\frac{\operatorname{sh}\alpha\eta}{\operatorname{sh}\beta\eta}\,e^{i\gamma\eta}\,d\eta=\frac{\pi}{\beta}\cdot\frac{\sin\dfrac{\pi\alpha}{\beta}}{\cos\dfrac{\pi\alpha}{\beta}+\operatorname{ch}\dfrac{\pi\gamma}{\beta}}\,, \qquad |\alpha|<\beta\,,$$

one finds without difficulty

$$\int_{-\infty}^{+\infty}\bar{h}(\eta)\frac{\operatorname{sh}\alpha\eta}{\operatorname{sh}\beta\eta}\,e^{-i\eta y}\,d\eta=\frac{1}{\beta}\sqrt{\frac{\pi}{2}}\,\sin\frac{\pi\alpha}{\beta}\int_{-\infty}^{+\infty}\frac{h(\rho)}{\cos\dfrac{\pi\alpha}{\beta}+\operatorname{ch}\dfrac{\pi(\rho-y)}{\beta}}\,d\rho\,, \qquad |\alpha|<\beta \tag{5.3}$$

and the solution (5.2) appears in its usual form

$$\begin{aligned}u(x, y)=\frac{1}{2(x_n-x_0)}\sin\frac{\pi(x-x_0)}{x_n-x_0}\int_{-\infty}^{+\infty}\Bigg[&\frac{f(\rho)}{\operatorname{ch}\dfrac{\pi(\rho-y)}{x_n-x_0}-\cos\dfrac{\pi(x-x_0)}{x_n-x_0}}+\\&+\frac{g(\rho)}{\operatorname{ch}\dfrac{\pi(\rho-y)}{x_n-x_0}+\cos\dfrac{\pi(x-x_0)}{x_n-x_0}}\Bigg]d\rho\,.\end{aligned} \tag{5.4}$$

Naturally, the integrals entering in the above deductions may be considered in the sense of Cauchy's principal values, as usual in the theory of Fourier transforms.

§ 6. A Two-Layer Plate

In this case we have $n=2$ and the calculations become much more difficult.

One has to do with a single matrix $Q_1(\eta)$, determined by (4.1), and the relations (2.11) give

$$N(\eta)=\operatorname{sh}(l_1+l_2)\eta+(A_1-1)\operatorname{ch}l_1\eta\operatorname{sh}l_2\eta$$

$$Z(\eta)=\operatorname{ch}(l_1+l_2)\eta+(A_1-1)\operatorname{sh}l_1\eta\operatorname{sh}l_2\eta$$

$$\begin{aligned}N(\eta)[A_1\operatorname{ch}(x-x_0)\eta+B_1\operatorname{sh}(x-x_0)\eta]=\bar{f}(\eta)[&\operatorname{sh}(x_2-x)\eta+\\&+(A_1-1)\operatorname{sh}l_2\eta\operatorname{ch}(x_1-x)\eta]+\bar{g}(\eta)\operatorname{sh}(x-x_0)\eta\end{aligned}$$

$$\begin{aligned}N(\eta)[A_2\operatorname{ch}(x-x_1)\eta+B_2\operatorname{sh}(x-x_1)\eta]=A_1\bar{f}(\eta)&\operatorname{sh}(x_2-x)\eta+\\&+\bar{g}(\eta)[\operatorname{sh}(x-x_0)\eta+(A_1-1)\operatorname{ch}l_1\eta\operatorname{sh}(x-x_1)\eta]\,.\end{aligned}$$

Introducing this into (3.1), the solution of the present problem follows in the form

$$\begin{aligned}u_1(x, y)=\frac{1}{\sqrt{2\pi}}\int_{-\infty}^{+\infty}\frac{e^{-i\eta y}}{N(\eta)}\{\bar{f}(\eta)[&\operatorname{sh}(x_2-x)\eta+\\+(A_1-1)\operatorname{sh}l_2\eta\operatorname{ch}(x_1-x)\eta]&+\bar{g}(\eta)\operatorname{sh}(x-x_0)\eta\}\,d\eta\,, \qquad x_0\leq x\leq x_1\end{aligned}$$

$$\left.\begin{aligned} u_2(x, y) &= \frac{1}{\sqrt{2\pi}} \int_{-\infty}^{+\infty} \frac{e^{-i\eta y}}{N(y)} \{ A_1 \bar{f}(\eta) \operatorname{sh} (x_2 - x)\eta + \\ &\quad + \bar{g}(\eta) [\operatorname{sh} (x - x_0)\eta + (A_1 - 1) \operatorname{ch} l_1\eta \operatorname{sh} (x - x_1)\eta] \} \, d\eta \,, \qquad x_1 \leq x \leq x_2 \,; \\ N(\eta) &= \operatorname{sh} (l_1 + l_2)\eta + (A_1 - 1) \operatorname{ch} l_1\eta \operatorname{sh} l_2\eta \,. \end{aligned} \right\} \tag{6.1}$$

Further manipulation with (6.1) depends upon the given functions $f(y)$, $g(y)$. Nevertheless, the integrations required in (6.1) are exceedingly difficult and the author does not know of any closed form for those integrals, even in the case of the simplest functions $f(y)$, $g(y)$.

Apart from the trivial special case $A_1 = 1$ leading to the homogeneous strip, there exists perhaps a single favourable situation where it is possible to get a closed form of the solution (6.1), namely the case characterised by $l_1 = l_2 = l$. Let us examine this state of things.

We have

$$2N(\eta) = (A_1 + 1) \operatorname{sh} 2l\eta$$

and using the above auxiliary relation (5.3) in common with the analogous formula

$$\int_{-\infty}^{+\infty} \bar{h}(\eta) \frac{\operatorname{ch} \alpha\eta}{\operatorname{ch} \beta\eta} e^{-i\eta y} \, d\eta = \frac{\sqrt{2\pi}}{\beta} \cos \frac{\pi\alpha}{2\beta} \int_{-\infty}^{+\infty} h(\rho) \frac{\operatorname{ch} \frac{\pi(\rho - y)}{2\beta}}{\cos \frac{\pi\alpha}{\beta} + \operatorname{ch} \frac{\pi(\rho - y)}{\beta}} \, d\rho \,, \qquad |\alpha| < \beta \,, \tag{6.2}$$

the expressions (6.1) become

$$\left.\begin{aligned} u_1(x, y) &= \frac{1}{2(A_1 + 1)l} \sin \frac{\pi(x - x_0)}{2l} \left\{ \int_{-\infty}^{+\infty} f(\rho) \left[\frac{1}{\operatorname{ch} \frac{\pi(\rho - y)}{2l} - \cos \frac{\pi(x - x_0)}{2l}} + \right.\right. \\ &\quad \left.\left. + \frac{2(A_1 - 1) \operatorname{ch} \frac{\pi(\rho - y)}{2l}}{\operatorname{ch} \frac{\pi(\rho - y)}{l} - \cos \frac{\pi(x - x_0)}{l}} \right] d\rho + \int_{-\infty}^{+\infty} \frac{g(\rho)}{\operatorname{ch} \frac{\pi(\rho - y)}{2l} + \cos \frac{\pi(x - x_0)}{2l}} \, d\rho \right\} \\ u_2(x, y) &= \frac{1}{2(A_1 + 1)l} \sin \frac{\pi(x - x_0)}{2l} \left\{ A_1 \int_{-\infty}^{+\infty} \frac{f(\rho)}{\operatorname{ch} \frac{\pi(\rho - y)}{2l} - \cos \frac{\pi(x - x_0)}{2l}} \, d\rho + \right. \\ &\quad \left. + \int_{-\infty}^{+\infty} g(\rho) \left[\frac{1}{\operatorname{ch} \frac{\pi(\rho - y)}{2l} + \cos \frac{\pi(x - x_0)}{2l}} - \frac{2(A_1 - 1) \cos \frac{\pi(x - x_0)}{2l}}{\operatorname{ch} \frac{\pi(\rho - y)}{l} - \cos \frac{\pi(x - x_0)}{l}} \right] d\rho \right\} . \end{aligned} \right\} \tag{6.3}$$

References

1) V. Vodička: Appl. Sci. Res. **A**, **5** (1955) 108.
2) V. Vodička: Z. angew. Math. Phys. **7** (1956) 345.
3) V. Vodička: Quart. Appl. Math. **16** (1958) 11.
4) I. N. Sneddon: *Fourier Transforms* (New York, 1951).

JOURNAL OF THE PHYSICAL SOCIETY OF JAPAN, Vol. 15, No. 7, JULY, 1960

Circulation Preserving Motions

By A. C. SRIVASTAVA

Department of Mathematics, Indian Institute of Technology, Kharagpur

(Received April 5, 1960)

Two theorems concerning circulation preserving motions have been stated and proved. Two particular examples to illustrate them are also given. It is deduced that two circulation preserving motions in a Newtonian fluid when their sum is circulation preserving are mutually superposable but in a non-Newtonian fluid this proposition is true only if one more condition is satisfied. Similar results have been deduced for self-superposability also.

§ 1. *Circulation preserving motions are defined to be those motions in which the circulation of a reducible circuit does not change.*

The circulation of $\dot{\mathbf{x}}$ round any material circuit is given by $\int_c d\mathbf{x}\cdot\dot{\mathbf{x}}$, where $\mathbf{x}$ is the Eulerian coordinate and the dot denotes the material derivative. For circulation preserving motions

$$\frac{\delta}{\delta t}\int_c d\mathbf{x}\cdot\dot{\mathbf{x}}=0\,, \qquad (1)$$

where $\delta/\delta t$ denotes the material derivative. Truesdell[1] has shown that the condition (1) can be alternatively expressed as

$$\operatorname{curl}\ddot{\mathbf{x}}=0\,. \qquad (2)$$

This condition is known as d'Alembert-Euler conditions. It has been proved that (2) is the necessary and sufficient condition for a motion to be circulation preserving. The conditions (1) and (2) are purely kinematical, valid for arbitrary media.

§ 2. *We state and prove the following two theorems about circulation preserving and superposable fluid motions.*

Theorem 1.

For a fluid whose equations of motion are such that the acceleration is the sum of a linear function of velocity, vorticity and the gradient of a scalar function, the condition that $\mathbf{v}_1+\mathbf{v}_2$ *is circulation preserving provided that* $\mathbf{v}_1$ *and* $\mathbf{v}_2$ *are circulation preserving, is identical with the condition of superposability of* $\mathbf{v}_1$ *and* $\mathbf{v}_2$*; but, if the acceleration is a non-linear function of velocity and its derivatives the above two conditions are quite different.*

Proof:

(a) Let us suppose that the acceleration is a linear function of vorticity, velocity etc. and has the form

$$\ddot{\mathbf{x}}=\Phi_1(\mathbf{v})+\Phi_2(\omega)+\nabla\chi\,, \qquad (3)$$

where Φ_1 and Φ_2 are linear operators $[\Phi(A+B)=\Phi(A)+\Phi(B)]$ and χ is a scalar function. The condition that $\mathbf{v}_1+\mathbf{v}_2$ is circulation preserving, when $\mathbf{v}_1$ and $\mathbf{v}_2$ are circulation preserving, is obtained by Truesdell[1]

$$\operatorname{curl}(\boldsymbol{\omega}_1\times\mathbf{v}_2+\boldsymbol{\omega}_2\times\mathbf{v}_1)=0\,. \qquad (4)$$

This is purely kinematical and does not depend on the form of the equation of motion.

Performing curl operation on (3), we get

$$\operatorname{curl}\ddot{\mathbf{x}}=\operatorname{curl}\Phi_1(\mathbf{v})+\operatorname{curl}\Phi_2(\boldsymbol{\omega})\,. \qquad (5)$$

If $\mathbf{v}_1$, $\mathbf{v}_2$ and $\mathbf{v}_1+\mathbf{v}_2$ satisfy (5), we get

$$\operatorname{curl}\ddot{\mathbf{x}}_1=\operatorname{curl}\Phi_1(\mathbf{v}_1)+\operatorname{curl}\Phi_2(\boldsymbol{\omega}_1)\,, \qquad (6)$$

$$\operatorname{curl}\ddot{\mathbf{x}}_2=\operatorname{curl}\Phi_1(\mathbf{v}_2)+\operatorname{curl}\Phi_2(\boldsymbol{\omega}_2)\,, \qquad (7)$$

$$\begin{aligned}\operatorname{curl}\ddot{\mathbf{x}}_1+\operatorname{curl}\ddot{\mathbf{x}}+\operatorname{curl}(\boldsymbol{\omega}_1\times\mathbf{v}_2+\boldsymbol{\omega}_2\times\mathbf{v}_1)\\=\operatorname{curl}\Phi_1(\mathbf{v}_1+\mathbf{v}_2)+\operatorname{curl}\Phi_2(\boldsymbol{\omega}_1+\boldsymbol{\omega}_2)\,. \qquad (8)\end{aligned}$$

Using (6), (7) and (8), the condition of superposability is

$$\operatorname{curl}(\boldsymbol{\omega}_1\times\mathbf{v}_2+\boldsymbol{\omega}_2\times\mathbf{v}_1)=0\,. \qquad (9)$$

which is same as (4).

This proves the first part of the theorem.

(b) Let us now suppose that acceleration is a non-linear function of velocity and it derivatives and has the form

$$\ddot{\mathbf{x}}=\Phi_1(\mathbf{v})+\Phi_2(\boldsymbol{\omega})+\psi(\mathbf{v})+\nabla\chi\,, \qquad (10)$$

where $\psi(\mathbf{v})$ is a non-linear function of its argument and its derivatives.

The condition of superposability of two motions $\mathbf{v}_1$ and $\mathbf{v}_2$ of a fluid, whose equation of motion is (10), can be derived as in (a). It is

$$\begin{aligned}&\operatorname{curl}(\boldsymbol{\omega}_1\times\mathbf{v}_2+\boldsymbol{\omega}_2\times\mathbf{v})\\&=\operatorname{curl}\psi(\mathbf{v}_1+\mathbf{v}_2)-\operatorname{curl}\psi(\mathbf{v}_1)-\operatorname{curl}\psi(\mathbf{v}_2)\,. \qquad (11)\end{aligned}$$

In general the right-hand member of (11) is not zero, and hence this condition is quite different from (4).

This proves the second part of the theorem.

For $\mathbf{v}_1+\mathbf{v}_2$ to be circulation preserving provided that $\mathbf{v}_1$ and $\mathbf{v}_2$ are circulation preserving, the condition (11) with the help of (4) reduces to

$$\psi(\mathbf{v}_1+\mathbf{v}_2)-\psi(\mathbf{v}_1)-\psi(\mathbf{v}_2)\equiv\operatorname{grad}\Theta\,. \tag{12}$$

Theorem 2.

For a fluid whose equations of motion are such that the accerlation is the sum of a linear function of velocity, vorticity and a gradient of a scalar, a self-superposable motion with steady vorticity is circulation preserving; but, if the acceleration is a non-linear function of velocity and its derivatives, the above statement is not necessarily true.

Proof:

The condition for a motion $\mathbf{v}$ with steady vorticity to be circulation preserving can be deduced from (2) as follows.

$$\ddot{\mathbf{x}}=\operatorname{grad}\left|\frac{1}{2}\dot{\mathbf{x}}\right|^2+(\operatorname{curl}\dot{\mathbf{x}})\times\dot{\mathbf{x}}\,.$$

Taking curl of $\ddot{\mathbf{x}}$, we get

$$\operatorname{curl}(\boldsymbol{\omega}\times\mathbf{v})=0\,. \tag{13}$$

The condition of self-superposability in a fluid, whose equation of motion is (3), can be deduced from (9) by putting $\boldsymbol{\omega}_1=\boldsymbol{\omega}_2=\boldsymbol{\omega}$, $\mathbf{v}_1=\mathbf{v}_2=\mathbf{v}$

$$\operatorname{curl}(\boldsymbol{\omega}\times\mathbf{v})=0\,,$$

which is the same as (13). This proves the first part of the theorem.

In a fluid whose equation of motion is given by (10) the condition of self-superposability is [put $\boldsymbol{\omega}_1=\boldsymbol{\omega}_2=\boldsymbol{\omega}$, $\mathbf{v}_1=\mathbf{v}_2=\mathbf{v}$ in (11)]

$$\operatorname{curl}(\boldsymbol{\omega}\times\mathbf{v})=\operatorname{curl}\psi(2\mathbf{v})-2\operatorname{curl}\psi(\mathbf{v})\,, \tag{14}$$

which is quite different from (13).

If the motion is circulation preserving, (14) gives

$$\psi(2\mathbf{v})-2\psi(\mathbf{v})\equiv\operatorname{grad}\Theta\,. \tag{15}$$

In other words if the condition (15) is satisfied, any self-superposable motion with steady vorticity is circulation preserving, even though the acceleration is a non-linear function of velocity and its derivatives.

§ **3.** *We give two examples to illustrate the theorems 1 and 2.*

Example 1.

The equation of motion for a viscous incompressible Newtonian fluid is

$$\ddot{\mathbf{x}}=-\operatorname{grad}\left(\frac{p}{\rho}\right)-\nu_v\operatorname{curl}\boldsymbol{\omega}\,. \tag{16}$$

Hence we conclude from the first parts of the theorems (1) and (2) that

i) If $\mathbf{v}_1$, $\mathbf{v}_2$ be any two circulation preserving motions in Newtonian incompressible fluids and if $\mathbf{v}_1+\mathbf{v}_2$ is also circulation preserving, then $\mathbf{v}_1$ and $\mathbf{v}_2$ are mutually superposable.

ii) Any circulation preserving motion with steady vorticity is self-superposable.

These conclusions were also drawn by Truesdell1).

Example 2.

The equation of motion for incompressible non-Newtonian fluid [Reiner-Rivlin fluid] is2)

$$\begin{aligned}\ddot{\mathbf{x}}=-\nu_v\operatorname{curl}\boldsymbol{\omega}-2\nu_c\Big[&\frac{\partial\mathbf{v}}{\partial x}\times\frac{\partial\boldsymbol{\omega}}{\partial x}+\frac{\partial\mathbf{v}}{\partial y}\times\frac{\partial\boldsymbol{\omega}}{\partial y}\\&+\frac{\partial\mathbf{v}}{dz}\times\frac{\partial\boldsymbol{\omega}}{\partial z}+(\operatorname{curl}\boldsymbol{\omega}\cdot\nabla)\mathbf{v}+\frac{1}{2}(\boldsymbol{\omega}\cdot\nabla)\boldsymbol{\omega}\Big]\\&-\frac{1}{\rho}\operatorname{grad}\cdot[p+s]\,,\end{aligned} \tag{17}$$

where ν_c is kinematic coefficient of cross- viscosity

$$\frac{s}{\rho}=-2\nu_c\left[\left|\frac{\partial\mathbf{v}}{\partial x}\right|^2+\left|\frac{\partial\mathbf{v}}{\partial y}\right|^2+\left|\frac{\partial\mathbf{v}}{\partial z}\right|^2\right].$$

In this case condition (12) becomes

$$\begin{aligned}&\frac{\partial\mathbf{v}_1}{\partial x}\times\frac{\partial\boldsymbol{\omega}_2}{\partial x}+\frac{\partial\mathbf{v}_2}{\partial x}\times\frac{\partial\boldsymbol{\omega}_1}{\partial x}+\frac{\partial\mathbf{v}_1}{\partial y}\times\frac{\partial\boldsymbol{\omega}_2}{\partial y}+\frac{\partial\mathbf{v}_2}{\partial y}\times\frac{\partial\boldsymbol{\omega}_1}{\partial y}\\&\quad+\frac{\partial\mathbf{v}_1}{\partial z}\times\frac{\partial\boldsymbol{\omega}_2}{\partial z}+\frac{\partial\mathbf{v}_2}{\partial z}\times\frac{\partial\boldsymbol{\omega}_1}{\partial z}+(\operatorname{curl}\boldsymbol{\omega}_1\cdot\nabla)\mathbf{v}_2\\&\quad+(\operatorname{curl}\boldsymbol{\omega}_2\cdot\nabla)\mathbf{v}_1+\frac{1}{2}(\boldsymbol{\omega}_1\cdot\nabla)\boldsymbol{\omega}_2\\&\quad+\frac{1}{2}(\boldsymbol{\omega}_2\cdot\nabla)\boldsymbol{\omega}_1\equiv\operatorname{grad}\Theta\,,\end{aligned} \tag{18}$$

and condition (15) becomes

$$\begin{aligned}&\frac{\partial\mathbf{v}}{\partial x}\times\frac{\partial\boldsymbol{\omega}}{dx}+\frac{\partial\mathbf{v}}{\partial y}\times\frac{\partial\boldsymbol{\omega}}{\partial y}+\frac{\partial\mathbf{v}}{\partial z}\times\frac{\partial\boldsymbol{\omega}}{\partial z}+(\operatorname{curl}\boldsymbol{\omega}\cdot\nabla)\mathbf{v}\\&\quad+\frac{1}{2}(\boldsymbol{\omega}\cdot\nabla)\boldsymbol{\omega}\equiv\operatorname{grad}\Theta\,.\end{aligned} \tag{19}$$

Hence we conclude that

i) The condition that $\mathbf{v}_1+\mathbf{v}_2$ is a circulation preserving motion in non-Newtonian fluid, when $\mathbf{v}_1$, $\mathbf{v}_2$ are circulation preserving, is identical with the condition of superposability of $\mathbf{v}_1$ and $\mathbf{v}_2$ if and only if, (18) is satisfied.

ii) Any circulation preserving motion with steady vorticity is self-superposable in non-Newtonian fluid, if and only if, condition (19) is satisfied.

References

1) C. Truesdell: *Kinematics of vorticity* (Indiana University Press, Bloomington, 1945) 87.

2) A. C. Srivastava: Proc. Second Cong. on Theor. and Appl. Mechanics, India (1956) 187.

Short Notes

This section is intended to secure prompt publication of important discoveries in physics. The reports should not exceed 800 words in length. A figure of size 7 cm × 7 cm will be counted as 150 words.

J. PHYS. SOC. JAPAN **15** (1960) 1339

Thickness-Dependence of Stress in Vacuum Deposited Silver Films

By Koreo KINOSITA and Hideki KONDO*
Department of Physics and Chemistry, Gakushuin University, Mejiro, Tokyo

(Received May 6, 1960)

Recently we carried out measurement of the tensile stress in silver films of 30~2,500 Å thickness vacuum deposited on thin pieces of mica. Fig. 1, reproduced from the previous note[1], shows the magnitude of the stress σ *vs.* the film thickness d.

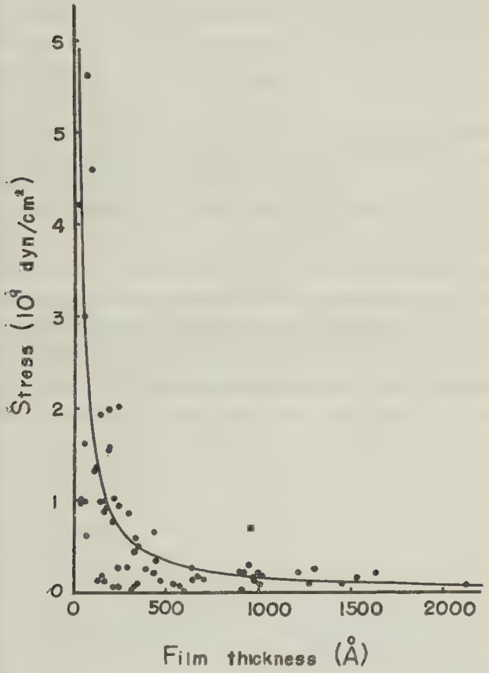

Fig. 1. Stress *vs.* film thickness.

The purpose of the present note is to point out that the relation between σ and d can be very well approximated by an orthogonal hyperbola of the type

$$\sigma d = \text{const}\,. \qquad (1)$$

This will be best illustrated by the curve in Fig. 1, which represents

$$\sigma d = 177 \times 10^9\ (\text{dyn/cm}^2)\ \text{Å}\,. \qquad (2)$$

A tentative explanation of Eq. (1) can be obtained if we admit the following assumptions (refer to Fig. 2):

1° The stress in the film is localized in a very thin *surface layer*.

2° The thickness of this surface layer, d_0, which must be of the order of 10 Å, is constant, irrespective of the total film thickness d.

3° The stress in this layer, σ_0, is constant, irrespective of d.

Obviously it follows that the mean stress in the film, σ, is given by

$$\sigma = \sigma_0 d_0 / d\,, \qquad (3)$$

in accordance with Eq. (1). Eq. (2) will mean that $\sigma_0 d_0 = 177 \times 10^9$ (dyn/cm²) Å. At present separate evaluation of σ_0 and d_0 is not possible.

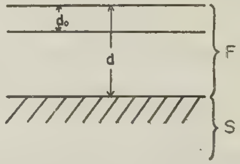

Fig. 2. Model on which Eq. (3) is based. *F* and *S* represent film and substrate respectively.

The *surface layer* mentioned above may be the one adjacent to the free surface of the film, or it may be the one adjacent to the surface of the substrate. If there is tensile stress in either of them, the film as a whole will contract and bend the substrate (mica) as is observed[1]. It is more plausible, however, that the stress is concentrated in a layer adjacent to the free surface, because it has been observed that silver films deposited on the wall of the bell-jar often curl up with the free surface concave.

The reality of the model proposed here will have to be put to severe test because it does not seem to be consistent with the current view that very thin silver films (say $d < 100$ Å) consist of isolated crystallites while thicker ones are continuous. For further discussion the reader is referred to reference 1).

Reference

1) K. Kinosita, H. Kondo and I. Sawamura: J. Phys. Soc. Japan **15** (1960) 942.

---

* Now at Japan Camera Inspection Institute, Tokyo.

J. Phys. Soc. Japan **15** (1960) 1340

Electron Spin Resonance of Mn^{++} in $SrCl_2$, $CdCl_2$ and $CdBr_2$

By Hiroshi KOGA, Kazumi HORAI
and On MATUMURA

Department of Physics, Faculty of Science,
Kyusyu University

(Received March, 22, 1960)

In Connection with the alkali-halide:Mn[1], the electron spin resonance of Mn^{++} ions in the single crystals of $SrCl_2$,$CdCl_2$ and $CdBr_2$ have been measured at room temperature and at the wavelengths of 3 and 0.8 cm.

The crystals were grown from the melt which contained a small amounts of $MnCl_2$ in a closed quartz tube under a vacuum of about 10^{-3} mm Hg.

(1) $SrCl_2$:Mn.

At low Mn concentrations ($<3\times10^{-3}$), the observed spectra are composed of six hyperfine lines. These spectra are interpreted with the usual spin Hamiltonian

$$\mathscr{H}=g\beta\boldsymbol{H}\cdot\boldsymbol{S}+\boldsymbol{A}\cdot\boldsymbol{S}\cdot\boldsymbol{J}+\frac{1}{6}a\Big[S_x{}^4+S_y{}^4+S_z{}^4 -\frac{1}{5}S(S+1)(3S^2+35-1)\Big]$$

with S and $I=5/2, g=2.004$ and $A=82.7\times10^{-4}\,\mathrm{cm}^{-1}$. No significant changes are observed in the spectra for various angular variations of the magnetic field with respect to the crystal axes, and the order of a is estimated as $a<5\times10^{-4}\,\mathrm{cm}^{-1}$. At high Mn concentrations ($>7\times10^{-3}$), only a single line is observed with the apparent g-values are 2.0073 at 3 cm and 2.0015 at 0.8 cm. This difference is supposed to be due to the lower symmetry of the crystalline field and the random distribution of its tetragonal axes orintation. The cause of this lower symmetry is thought to be the difference of ionic radii or depolarzing powers of Mn^{++} and Sr^{++} ions in near sites. From these g-values, the tetragonal field parameter D is estimated as $240\times10^{-4}\,\mathrm{cm}^{-1}$ and the true g-value is 2.000.

(2) $CdCl_2$ and $CdBr_2$:Mn.

Same as $MnCl_2$, these crystals belong to the D^5_{3d} space group and have a layer structure. The spectra have been analysed with the following spin Hamiltonian

$$\mathscr{H}=g\beta\boldsymbol{H}\cdot\boldsymbol{S}+\boldsymbol{A}\cdot\boldsymbol{S}\cdot\boldsymbol{I}+DS_z{}^2+E(S_x{}^2-S_y{}^2)$$

The obtained values of the parameters are listed in the table.

Table I.

Crystal	Mn-concentration	g	A $\times10^{-4}$ cm^{-1}	D $\times10^{-4}$ cm^{-1}	E $\times10^{-4}$ cm^{-1}
$CdCl_2$	1×10^{-3}	2.066	81.6	<15	—
$CdBr_2$	2×10^{-3}	2.014	79.8	202	<10

In the case of $CdCl_2$[2] the spectrum consists of only six hyperfine lines of about 11 gauss width of nearly Lorentzian shape. Thus the upper limit to the value of D has been estimated. In $CdBr_2$, as shown in Fig., the spectrum has 30 lines of about 40 gauss width. This width remains nearly constant for some crystals of the different Mn-concentrations and under various conditions of the crystal growth. The stacking fault in the crystal or the hyperfine interaction between the Mn electrons and the surrounding eight Br nuclei may be the origin of this large line width.

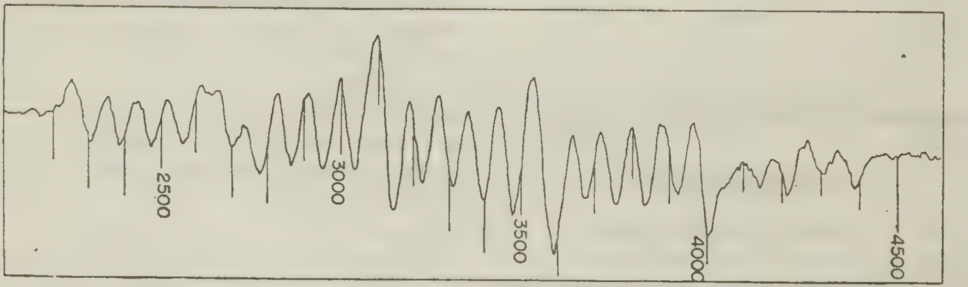

Fig. 1. $CdBr_2$:Mn spectrum. The magnetic field is parallel to |001| axis.

The resonance of $MgBr_2$:Mn and $BaCl_2$:Mn are also measured with the results of $g=2.001$ and $A=82\times10^{-4}\,\mathrm{cm}^{-1}$, and $g=2.003$ (single line) respectively.

The more detailed experiments are being carried out and the full report will be given in the near future. This research is partially supported by the Grant for Promotion of Science from the Ministry of Education.

References

1) K. Morigaki, M. Fujimoto and J. Itoh: J. Phys. Soc. Japan **13** (1958) 1174. G. D. Watkins: Phys. Rev. **113** (1959) 79.
2) J. R. Orton: Rep. Progr. Phys. **22** (1959) 208.

J. PHYS. SOC. JAPAN **15** (1960) 1341

Ultrasonic Measurement of Magnetization in Mn-ferrite Single Crystal

By Kazuo HUSIMI, Katsumi NISHIGUCHI
and Toshimasa SUZUKI

Electrical Communication Laboratory
Musashino-shi Tokyo

(Received May 6, 1960)

The ultrasonic method whicn has been developed as a new measuring technique of ferroelectric polarization without disturbing the domain configuration has several advantages and is shown to be useful for the study of ferroelectrics[1]). It has been pointed out by analogy that the similar means can be available for magnetism by using the dependence of the magnetostriction on the magnetization, and this is applied on the magnetization switching study of Mn-ferrite single crystal grown by the Stockbarger method.

The block diagram of experimenial arrangement is shown in Fig. 1. The sample is always kept in ultrasonic excitation by a quartz crystal. The magnetostrictive output voltage is amplified and displayed on the cathode ray tube CRT-1, and its amplitude is determined by comparing with the signal of a standard attenuator. The direction of magnetization is also detected from the Lissajou figure trajectory on CRT-1. For calibration, double pulses shown in Fig. 1 are applied on the input terminal, and the switching voltage responses are integrated and are displayed on CRT-2 after amplification. From this figure the magnetic flux changes can be measured. The calibration curve of the magnetostrictive output voltages relative to the remanent magnetic flux densities is shown in Fig. 2. In this mesaurement, the magnetic flux density was adjusted by varing the amplitude of the input double pulses.

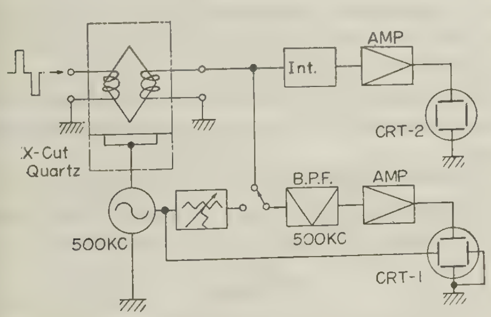

Fig. 1. Block diagram of experimental arrangement.

Differing from the case of ferroelectrics, the ultrasonic output voltage V has no linear relaitonship to the magnetic flux density B, and can be expressed approximately as;

$$V \propto B^{0.7}$$

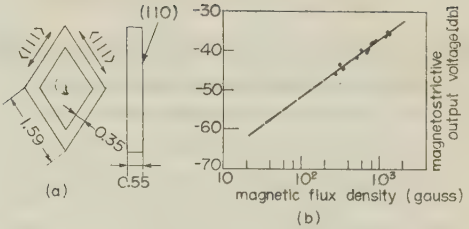

Fig. 2. (a) Dimension of the sample (mm). (b) Calibration curve of magnetostrictive output voltage relative to remanent magnetic flux density.

The magnetization switching processes by single pulses with different amplitudes are shown in Fig. 3. with the pulse width as parameter. In every case, initial negative remanent setting was performed by manual application of the negative field with strength of 2.04 oe for several seconds.

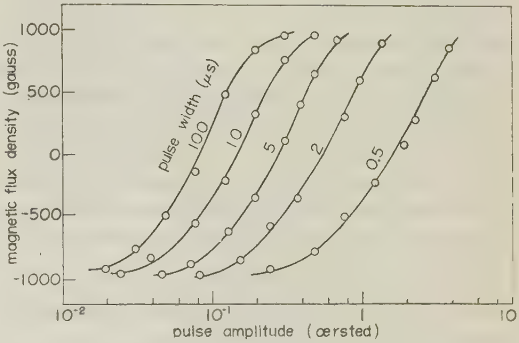

Fig. 3. Magnetization switching processes by single pulses.

The electromechanical transducer, in which the test crystal is mounted, is the same type used for ferroelectrics[1]), and the exciting quartz crystal disk has a fundamental resonant frequency of thickness mode near 500 Kc.

The crystal was finished by the ultrasonic cutter as also shown in Fig. 2[2]) and was annealed.

Unfortunately it was found by x-ray analysis that the legs of the rhombic frame did not precisely lie along <111> direction, therefore we could not carry out farther analysis of domain wall motion of the crystal. But from these experiments, we have made clear that this new method is also adequate for the nondestructive measurement of magnetization, though the magnetostrictive output voltage is small and not proportional to remanent magnetization being different from ferroelectrics.

We wish to thank Dr. M. Hatoyama and Dr. N. Sakamoto of Electrotechnical Laboratory for kind furnish of the single crystal Mn-ferrite, and Dr. Y. Niizeki for x-ray analysis.

References

1) K. Husimi and K. Kataoka: J. Appl. Pnys. **29** (1958) 8.
2) J. K. Galt: Bell Syst. Tech. J. **33** (1954) 5.

J. Phys. Soc. Japan **15** (1960) 1342

The Temperature and Pressure Dependence of the Nuclear Resonance of Co^{59} in Face-Centered-Cubic Cobalt Metal

By Yoshitaka Kōi, Akira Tsujimura and Yoshinori Yukimoto

Faculty of Engineering, Tokushima University, Tokushima

(Received March 2, 1960)

Recently the nuclear resonance of Co^{59} in ferromagnetic f.c.c. cobalt metal was observed by Gossard and Portis[1]. The resonance frequency is 213.1 Mc/sec in zero external magnetic field at room temperature. This indicates an effective magnetic field of 213 400 oersteds at the site of the nucleus, since the nucleus has a magnetic moment of 4.583 nuclear magnetons and a spin number of 7/2. The effective field arises from the hyperfine interaction between the nucleus and both the core and the conduction electrons, as has been discussed by Marshall[2], and can be written as

$$H_{eff}=\lambda AM,$$

where λ is a constant, A represents the hyperfine interaction and M the magnetization.

As in the case of the fluorine resonance in antiferromagnetic MnF_2[3)4)], knowledge of the temperature and the pressure dependence of the resonance frequency will give detailed information about the hyperfine interaction. Therefore, measurements were made in the range from liquid oxygen temperature to 550°C[5] and in the pressure range 1 to 8000 kg/cm². The spectrometer was the one used by one of the authors for the line-width study of pure quadrupole resonance, which has been described elsewhere.[6] It was frequency-modulated, and the resonance was displayed on an oscilloscope. The probable error in the determination of the resonance frequency was ±0.1 Mc/sec.

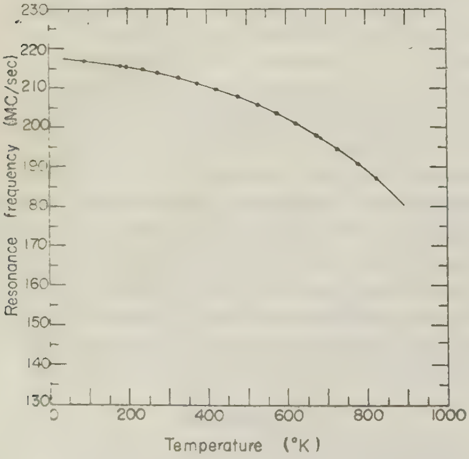

Fig. 1. The temperature dependence of the resonance frequency at atmospheric pressure.

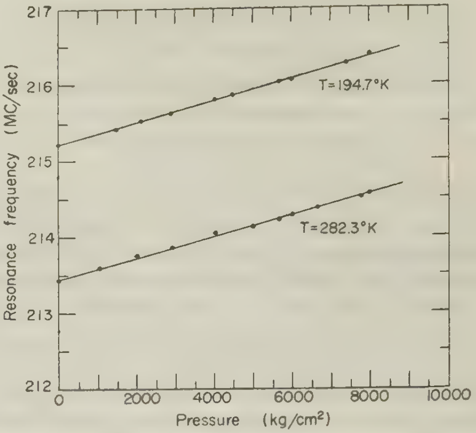

Fig. 2. The pressure dependence of the resonance frequency at 194.7° and 282.3°K.

The results of the measurements are shown in Figs. 1 and 2. The resonance frequency seems to have the same temperature dependence as M, so the temperature dependence would be primarily due to the change in M. However, the change in A would be responsible for the pressure dependence, since M is likely to depend little on pressure[7]. In order to obtain a definite conclusion as to these points, and to know the detailed nature of the interaction, measurements of the temperature and the pressure dependence of M are necessary and now in preparation.

The details of the experimental procedures and the discussions of the results will be published later.

The authors wish to express their sincere thanks to Professor T. Kushida of Hiroshima University for arousing their interest in this problem.

References

1) A. C. Gossard and A. M. Portis: Phys. Rev. Letters **3** (1959) 164. A. C. Gossard and A. M. Portis: Bull. Amer. Phys. Soc. Ser. II **5** (1960) 74.
2) W. Marshall: Phys. Rev. **110** (1958) 1280.
3) V. Jaccarino and R. G. Shulman: Phys. Rev. **167** (1957) 1196.
4) G. B. Benedek and T. Kushida: Technical Report No. 315 (Oct. 30, 1959) Cruft Laboratory, Harvard University.
5) V. Jaccarino: Bull. Amer. Phys. Soc. Ser. II. **4** (1959) 461.
6) Y. Kôi: J. Phys. Soc. Japan **12** (1957) 49.
7) L. Patrick: Phys. Rev. **93** (1954) 384.

J. Phys. Soc. Japan **15** (1960) 1343

The Ferromagnetism of the Compound γ-FeSn

By Mitsuru Asanuma

Department of Physics, Faculty of Science, Hokkaido University

(Received May 21, 1960)

The B8 type structure is frequently formed by alloying the iron group transition elements T with some of the elements B of IIIB, IVB, VB and VIB groups in the periodic table, and is extended in a wide range between the composition T_2B and $T_{1-x}B$ depending on the variety of the components[1,2]. There are a number of ferromagnetic or ferrimagnetic compounds in this structure, and many investigations have been done to the equiatomic structure TB and defect structure $T_{1-x}B$, But excess structure $T_{1+x}B$ has never been sufficiently investigated.

The study was started by taking tin as a B component. According to the phase diagram in the system of iron-tin by Hansen[3], a number of intermediate phases are formed in this system, as shown in Fig. 1. Among them γ-FeSn, having a B8 type structure, is formed peritectically at 940°C in the composion of about 43.5～44 atomic per cent Sn, and decomposes at 780°C. Since the alloy of iron and tin has two immiscible phases in molten state, the specimen was prepared by sintering method. After heating the mixture of iron and tin sealed in evacuated silica tube at 1200°C for a day, it was crushed, baked at 850°C (this is the temperature of formation of B8 structure) for a week, and then quenched in water. The composition of the compound prepared is $Fe_{1.3}Sn$.

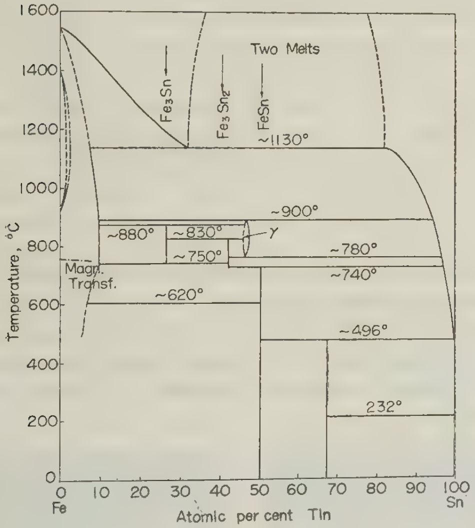

Fig. 1. The phase diagram of the system of iron-tin.

The examination by X-ray diffraction showed that the specimen was mostly constructed of γ-FeSn and contained a few amount of tin. The lattice parameter are $a=4.216$Å, $c=5.244$Å and $c/a=1.243$.

The saturation magnetization was measured by Sucksmith's ring balance, and the result is shown in Fig. 2. The value of the saturation magnetization per mol at absolute zero temperature is estimated as $2.3\mu_B$, i.e. $1.8\mu_B$ per iron atom, and the Curie temperature of this specimen is 676°K. Although the specimen contains a few amount of tin phase and small change of the composition from $Fe_{1.3}Sn$ is expected, there is no doubt that the ferromagnetism shown in Fig. 2 is due to the compound γ-FeSn and not due to the eventual coexistence of α-Fe.

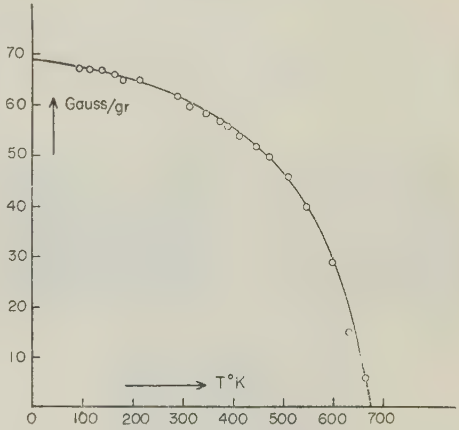

Fig. 2. The depeddence of the saturation magnetization on the temperature.

The magnetic susceptibility above the Curie temperature could not be measured, because γ-FeSn is only stable from 780°C to 940°C and it decomposes by keeping the specimen between the Curie temperature and 780°C for a long time.

In order to explain the measured value of the saturation magnetization, another transition elements-tin systems, i.e. Co-Sn and Ni-Sn systems have been investigated. The results will be published in this Journal.

References

1) L. Castelliz and F. Halla Z. Metallk: **35** (1934) 222.
2) W. Hume-Rothery and G. V. Raynor: *The Structure of Metal and Alloys.* (The Institute of Metals, 1954) 187.
3) M. Hansen: *Constitution of Binary Alloys* (McGarw-Hill Book Comp, 1958).

J. PHYS. SOC. JAPAN **15** (1960) 1344~1345

Optical Absorption of Localized Exciton in KCl:I and NaCl:I Single Crystals

By Kuniya FUKUDA, Riso KATO, Kaizo NAKAMURA and Yoichi UCHIDA

Department of Physics, Faculty of Science, Kyoto University

(Received May 6, 1960)

The first fundamental optical absorption of alkali halides is attributed to the electronic transition from halide ion to neighboring alkali ion[1]. The displacement of the optical absorption due to an impurity halide ion from the first fundamental one of the pure base substance was early found by Hilsch and Pohl on I^- impurity ion in NaCl, KCl and RbCl, but their measurements at room temperature were not made on single crystals[2]. Later, Delbecq *et al.* reported the similar displacement of the absorption of I^- ion substitutionally embedded in NaBr and KBr single crystals[3]. In this case the absorption peak of I^- ion was observed at liquid nitrogen temperature with a definite separation from those of host crystals, and they considered this separation to be due mainly to the difference in electron affinities of Br and I.

In this note, results are given on the absorption band due to I^- impurity in KCl and NaCl single crystals, which may be ascribed to the localized excitation at I^- ion. Single crystals of KCl and NaCl, each containing 0.05 mole % of I^- impurity in melt, were grown up by the Kyropoulos method. Absorption measurements were carried out at room temperature by Seya-Namioka type vacuum ultraviolet monochromator recently constructed in our laboratory[4]. Figure 1 shows the absorption curves of NaCl:I and KCl:I. The absorption peaks of I^- ion are at 188 mμ (189.5 mμ) and 182 mμ (185 mμ) for KCl:I and NaCl:I, respectively, differing slightly from the results of Hilsch and Pohl which are shown above in the brackets. Their results seem to contain some ambiguities concerning peak position and absorption shape because they used quartz spectrophotometer in air. In longer wavelength region, no absorption band was found which might be associated with coaguration of I^- ions.

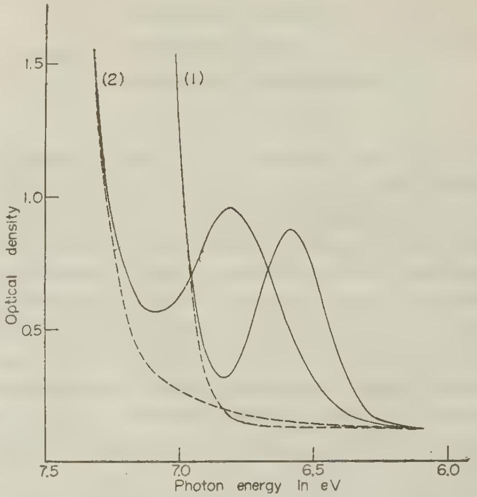

Fig. 1. The optical absorption curves of (1) KCl:I of 0.3 mm in thickness and (2) NaCl:I of 0.5 mm in thickness, at room temperature. Dotted curves show those of pure crystals.

The separation between the I^- band and the first fundamental absorption of host crystal is 1.1 ev for KCl:I and 1.0 eV for NaCl:I. These separations, which are larger than those expected from the difference of 0.6 eV in electron affinities of Cl and I, are considered to contain considerable large contributions from "size-effect" perturbations, that is, the changes of Madelung potential and repulsive energy due to the difference in ionic radii of Cl^- and I^- ions, in comparison with the case of I^- ion in KBr and NaBr . In addition, of course, polarization energy difference in excited state may not be neglected. The band shape of I^- ion absorption, though slightly asymmetric, is approximately Gaussian in both cases of KCl:I and NaCl:I. Obtained results are tabulated in Table I below.

Table I. Energy difference between iodide impurity absorption and fundamental absorption in KCl and NaCl at room temperature.

	(1) first fundamental band of host crystal[5] (eV)	(2) peak of I^- band (eV)	Half-width (eV)	Separation (1)−(2) ΔE (eV)
KCl:I	~7.7 (161 mμ)	6.85 (188 mμ)	~0.27	~1.1
NaCl:I	~7.8 (159 mμ)	6.82 (182 mμ)	~0.35	~1

Similar attempt was made on Br^- impurity in chlorides at room temperature and no separated Br^- band was observed, but the fundamental absorption edge shifted to the longer wavelength side.

The temperature and concentration dependence of I^- band and other phenomena concerning I^- impurity will be reported in a near future.

References

1) K. L. Wolf and K. F. Herzfeld: Handb. d. Phys. **XX** (1928) 632; A. von Hippel: ZS f. Phys. **101** (1936) 680.
2) R. Hilsch and R.W. Pohl: ZS f. Phys. **57** (1929) 145.
3) C. J. Delbecq, J. E. Robinson, and P. H. Yuster: Phys. Rev. **93** (1954) 262.
4) Y. Uchida, K. Fukuda, Y. Nakai, R. Kato and S. Nakazima: J. Appl. Phys. Japan (to be published) (in Japanese).
5) J. E. Eby, K. J. Teegarden, and D. B. Dutton: Phys. Rev. **116** (1959) 1099.

J. PHYS. SOC. JAPAN **15** (1960) 1345

Avalanche Breakdown in CdS Single Crystal

By Sigeru IIZIMA and Makoto KIKUCHI

Electrotechnical Laboratory, Nagatacho, Tokyo, Japan

(Received May 25, 1960)

In the previous note1) we described the avalanche breakdown in CdS single crystal that had an ohmic In contact and a non-ohmic Ag-paste contact, showing that this breakdown was accompanied with the electroluminescence. The construction of CdS cell in the present study is shown in Fig. 1, which is somewhat different from that in the previous note. This construction is convenient to observe through a microscope what part of the crystal luminescens. The feature of the light emission is shown by microphotograph in Fig. 2. The spacing between In and Ag contact is about 0.3 mm, and the light is emitted only when Ag contact is positively biased. 50 cps ac potential of about 200 volts is applied in this case. It should be noted that the light is emitted only at the neighbour of Ag contact. This fact seems to suggest that Ag-paste contact at high positive potential injects positive holes which induce the avalanche breakdown in the neighbourhood of Ag contact.

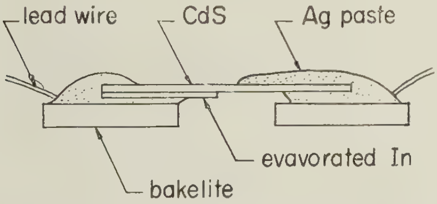

Fig. 1. Construction of the experimental cell.

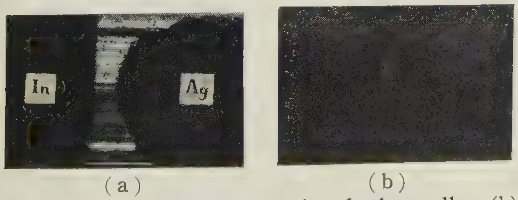

(a) (b)

Fig. 2. (a) Photomicrograph of the cell. (b) Light emission of the cell.

It has been found that this avalanche can be triggered and quenched by illuminating the cell with visible and infrared light, respectively. Fig. 3(a) shows the V-I characteristic on the oscilloscope using 50 cps ac voltage when the cell is in the dark and the avalanche breakdown has not yet occurred. Keeping ac voltage at a proper value so that the avalanche does not occur in the dark, the avalanche breakdown can be triggered on when the cell is illuminated by visible light. The avalanche is maintained even after removing the light. Fig. 3(b) shows the V-I characteristic of such a state after 1 sec exposure to the light of 510 mμ in wavelength. Such a on-(or conducting-) state can be quenched by infrared illumination. Fig. 3(c) shows the V-I characteristic of quenched state after 1 sec exposure to 1350 mμ infrared light.

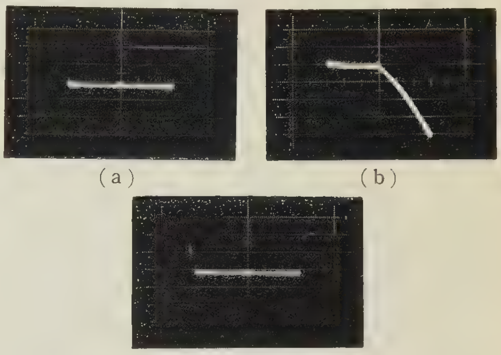

(a) (b)

(c)

Fig. 3. (a) V-I characteristic in the dark. (b) After 1 sec exposure to visible light. (c) After 1 sec exposure to infrared light. (Ordinate: 200μA per division. Abscissa: 50 V per division.)

The triggering effect is induced by increased primary carriers which are generated by the visible light. Once a highly conducting state has been attained, it is maintained by itself even after removing the light, just as in a gas discharge tube which sustains the discharge. Since we observe the conducting or non-conducting state by the V-I characteristics on the oscilloscope using 50 cps ac voltage and the exposure time is 1 sec, it is suggested that the time constant in this phenomenon is at least larger than 20 msec and at most shorter than 1 sec. The quenching effect in the present study is likely concerned with the so-called infrared quenching in the photoconductor, but the detailed mechanism of the present effect is rather ambiguous.

Reference

1) M. Kikuchi and S. Iizima: J. Phys. Soc. Japan **14** (1959) 852.

J. PHYS. SOC. JAPAN **15** (1960) 1346

Pulse Photoconduction and Carrier Lifetime in CdS Single Crystals

By Junji SHIRAFUJI and Yoshio INUISHI

Faculty of Engineering, Osaka University, Osaka

(Received May 5, 1960)

The decay time constants and peak value of photocurrent in CdS single crystals were measured with short duration light pulse (0.5 μ sec) from Xe discharge tube or with chopped light of 5 m sec width. The CdS samples were prepared by the sublimation (S-1 and 2) and by the melt (M-1 and 2) without any impurity added intentionally. With 0.5 μsec light pulse, two components of photocurrent decay were observed on synchroscope figure with time constants of the order of 1 μsec (τ_1) and 30 μsec (τ_2), respectively, at room temperature as shown in Photo. 1. With chopped light pulse (5 msec), two components in photocurrent decay were observed with the decay time constants of 10 msec (τ_3) and 40 msec (τ_4), respectively, at room temperature.

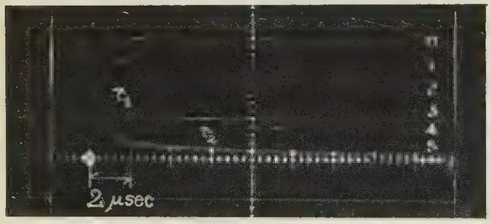

Photo. 1.

Fig. 1 (solid lines) shows the temperature dependence of decay time constants τ_1 and τ_2 in several samples. The temperature dependency of τ_1 was similar in all samples, which shows exponential decrease with decreasing inverse temperature, and τ_2 was rather temperature insensitive in this range. If we assume well known Shockley-Read formula[1)] of recombination in n-type high resistivity sample,

$$\tau = \tau_0 \exp\left[(E_t - E_f)/kT\right],$$

the value of $(E_t - E_f)$, namely the difference between trap level and Fermi level, was estimated from Fig. 1 as 0.052 eV. The dotted line in Fig. 1 shows the temperature dependence of the peak value of photoresponse induced by a 0.5 μsec Xe light pulse of a definite intensity. The photocurrent shows approximately similar temperature dependency to the time constant τ_1. It was proved that τ_1 is sensitive to the surface condition; τ_1 decreases to the half value when exposed to water vapor. The similar phenomena have been reported in CdSe crystals[2)].

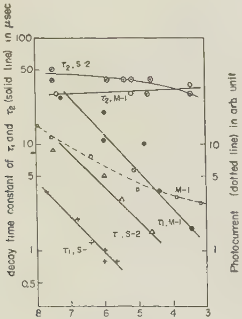

Fig. 1.

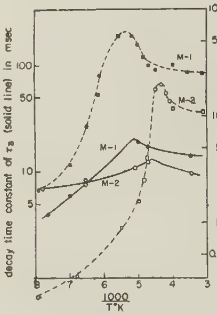

Fig. 2.

Fig. 2 (solid lines) shows the temperature dependence of τ_3 in M-1 and 2 samples, which have a maximum at about 200 °K. The dotted lines in Fig. 2 show the peak value of photocurrent induced by chopped light of 5 msec as a function of temperature, which show remarkable maximum also. We can see that the temperature dependence is similar in both curves.

To clarify the mechanism of the photocurrent decay, we are now proceeding our experiments to the effects of the wavelength, the ambients and the crystal imperfections.

References

1) W. Shockley and W. T. Read: Phys. Rev. **87** (1952) 835.
2) T. Ban et al.: Report at Sectional Meeting of Phys. Soc. of Japan (April, 1959).

J. PHYS. SOC. JAPAN **15** (1960) 1347

Some Observations on Plastic Deformation and Slip Lines of Sodium Chloride Whisker

By Kan-Ichi KAMIYOSHI and Tsutomu YAMAKAMI

Research Institute for Scientific Measurements, Tohoku University, Sendai, Japan

(Received May 6, 1960)

According to the results obtained by Gyulai1), tensile strength of NaCl whisker was strongly dependent on size below 10 μ. Recently, Webb2) found that relatively large NaCl whiskers have low elastic limit but large plastic deformation, whereas whiskers with small cross-sectional area could be expected to show high elastic limit but brittle fracture.

The present authors have made the tensile test of NaCl whiskers which were prepared by the cellophane method following Amelinckx3), and have determined the relation between tensile strength and cross-sectional area (Fig. 1), and the relation between plastic deformation at fracture and cross-sectional area (Fig. 2). Though the experimental values differ considerably from one whisker to another, it may be seen from these results that the tensile strength increases rapidly when the cross-sectional area decreases to below 1×10^{-3} mm². On the contrary, the plastic deformation at first increases with decreasing cross-sectional area, but it decreases sharply to zero when the cross-sectional area decreases further. The point A in Fig. 2 represents the results that the plastic deformation is zero (elastic deformation only) in spite of high tensile strength (11 kg/mm²). Therefore, the property of NaCl whisker may be classified into three groups according to the size:

(1) high yield strength but brittle fracture (whiskers of very small size),

(2) low yield strength but large plastic deformation (whiskers of intermediate size), and

(3) low yield strength and small plastic deformation (whiskers of large size, or normal bulk crystal).

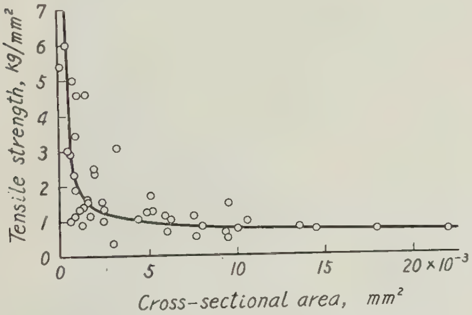

Fig. 1. Dependence of the tensile strength of NaCl whisker on the cross-sectional area.

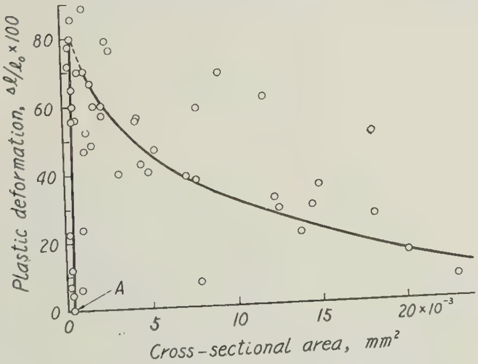

Fig. 2. Dependence of the plastic deformation of NaCl whisker on the cross-sectional area.

Plastic deformation produces the slip lines on the surface. They have been observed by optical microscope and by electron microscope. The slip usually occurs on the single set of (110) slip plane systems. Cross slips are rarely observed. The slip lines are, in some cases, straight and parallel (Fig. 3-b), but in other cases, they are wavy and the branching is observed (Fig. 3-a).

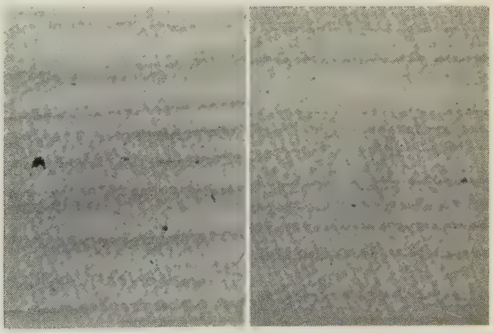

(a) (b)

Fig. 3. Electron micrographs of the slip lines of NaCl whisker. Cr-shadowing. (×2,000)

The authors wish to express their sincere appreciation to Mr. Yada for taking many electron micrographs.

The details of the present results will be published in Sci. Rep. of the Research Institute, Tohoku Univ.

References

1) Z. Gyulai: Z. Phys. **138** (1954) 317.
2) W. W. Webb: J. Appl. Phys. **31** (1960) 194.
3) S. Amelinckx: Physica **24** (1958) 390.

J. Phys. Soc. Japan **15** (1960) 1348~1349

Dislocation Etch Pits on *a*- and *b*-Faces of GASH Crystal

By Terutaro NAKAMURA and Kikuo OHI

Department of Physics, Ochanomizu University, Otsuka, Tokyo

(Received April 26, 1960)

Dislocation etch pits on cleavage surface (that is {0001} face) of ferroelectric GASH crystal has been reported by one of the authors[1]. Present paper reports the observation of etch pits on a surface of *a*- and *b*-plate crystals of GASH. GASH crystal is reported to have the space group $P\text{-}31m$[2] and grow in hexagonal prismatic form.

a- and *b*-plate crystals were cut out from as grown crystals by "thread-and-water-method", and etched by distilled water for about thirty seconds, followed by drying on some kind of blotting paper. Surface of the crystal cut by the thread-and-water-method is rather irregular. By the etching, however, the surface is smoothed out and rectangular etch pits shown in Fig. 1 are observed. Longer sides of the etch pits are of the order of 50μ and shorter sides 20μ. An etch pit has quadrangular pyramidal form, and the depth is of the order of a few microns. The deepest point is displaced by a certain amount from the center of the periphery of the etch pit. This assymmetry of the shape of the etch pit is accompanied by every pit and it can be detected that even the pit, which corresponds to the emergence point of dislocation running perpendicular to the surface of the crystal, is assymmetric. This assymmetry is due to crystal symmetry. *a*-axes of the crystal are defined as normals of edgs of a triangular etch pit on (0001) face, while *b*-axes are defined as normals of edges of a etch pit on $(000\bar{1})$ face, which is related to that on (0001) by two fold axes normals to the *a*-axes, following Wood[2]. The displacement of the deepest point on *a*-face is towards (0001) face and that on *b*-face is towards $(000\bar{1})$ face.

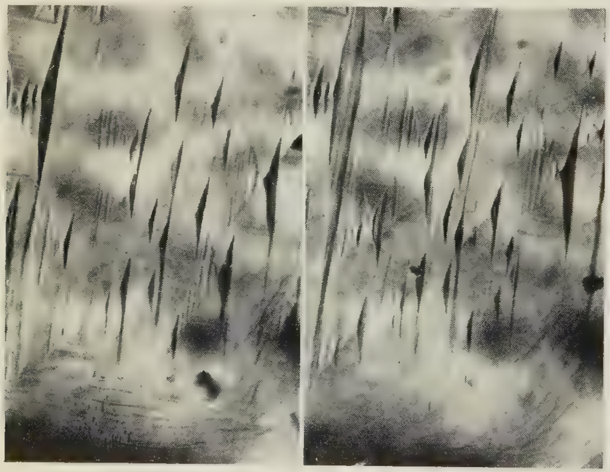
(a) (b)

Fig. 1. Photomicrograph of dislocation etch pits on *a* face. Face shown in (b) is about 50μ below (a), and obtained by continuous dissolution.

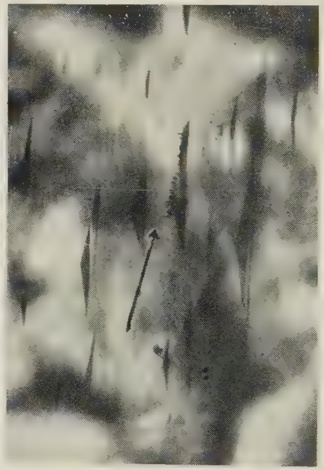
Fig. 3. Photomicrograph of dislocation etch pits produced by mechanical stresses.

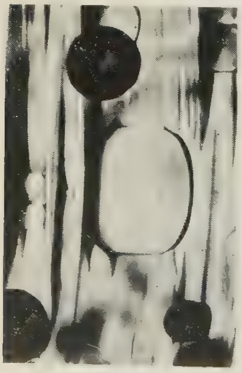
Fig. 2. Penetrating dissolution along the dislocation lines.

By dripping a drop of distilled water on the crystal, continuous change of etched surface is observed. In the dissolution process of the crystal, the etch pits stay at certain sites (Fig. 1. a, b), while shape and size is deformed gradually, untill the water is saturated and the dissolution ceases. In a subsequent addition of water drop, dissolution takes place again, and etch pits are formed at the same sites, as in the previous dissolution process.

By the continuous observation of the dissolution process of *a*- and *b*-cut plate crystals, spacial distribution of the dislocation lines was traced to a certain extent. When the dislocation runs obliquely to the surface of the crystal, it is observed that the pit moves during dissolution process.

When the dissolution process of thin crystal is observed, preferential dissolution takes place at the emergence points of dislocation lines on the top and the bottom surfaces of the crystal, until the “penetrating dissolution” results along the dislocation line (Fig. 2).

a- and *b*-faces of this crystal is mechanically shocked by a contact of point of a needle and etched. An example of this result is illustrated in Fig. 3. This result seems to indicate that dislocations are nucleated by the mechanical shock.

Linear array of etch pits are sometimes observed on *a*- and *b*-faces. It will be likely that some arrays of etch pits correspond to grain boundary.

Above mentioned aspects of the etch pits are quite in parallel with the dislocation etch pits on the cleavage surface of GASH crystal1), and we cannot avoid to conclude that the etch pits on the surface of *a*- and *b*-cut crystals also correspond to emergence points of the dislocation lines.

The pit density or *a*- and *b*-faces is generally of the same order or a little larger than on the cleavage face.

The crystal, in which the distribution of the dislocation lines is highly complex, does not exhibit *P*-*E* hysteresis loop but usual linear *P*-*E* relation. It seems very likely that the dislocation may have very interesting interactions with ferroelectric behavior of GASH crystal.

This work was finantially supported in part by the Grant in Aid from the Ministry of Education.

References

1) T. Nakamura: J. Phys. Soc. Japan **14** (1959) 1022.
2) E. A. Wood: Acta Cryst. **9** (1956) 618.

J. Phys. Soc. Japan **15** (1960) 1349～1350

On A-centers in Colored KCl Crystals

By Hiroshi Ohkura and Katsunobu Awane

Department of Applied Physics, Osaka City University, Osaka Japan

(Received April 27, 1960)

Since the discovery by Petroff1), no further research for *A*-centers has been conducted within the color center research program. Recently, Hirai2) and Tomiki3) noticed the presence of *A*-centers when they carried out the optical absorption measurements at room temperature. We measured the *A*-band absorption at liquid air temperature. To avoid the coagulation of *F*-centers, specimens having low concentrations of *F*-centerswere used.

Single crystals of KCl made by the repetitions of the Kyropoulos method were colored additively. Optical absorption measurements and *F*-light irradiations were made by using the Hitachi EPU-2 type spectrophotometer. The wave-length of *F*-light used to convert *F*-centers to complex conters at room temperature was 530 mμ having band-width of 5 mμ so as not to excite the *A*-band.

At the early stage of *F*-light irradiation, the *A*-band increases exclusively together with a simultaneous rapid decrease of the *F*-band. A typical example of opitical absorption measurements of *F*-bleaching for KCl containing 1.5×10^{16}/cc *F*-centers is shown in Fig. 1, in which the solid curve shows the absorption curve before irradiation and dotted shows that after 30 min. irradiation with *F*-light. The peak of the *A*-band is located at 2.23 eV with half-width of 0.13 ev at liquid air temperature. With the successive irradiation with *F*-light, the *M*- and *R*-band appear and the *A*-band tends to vanish until *F*-bleaching reaction reaches its stationary state. The changes of peak heights of these bands are shown in Fig. 2 against the periods of irradiation with *F*-light.

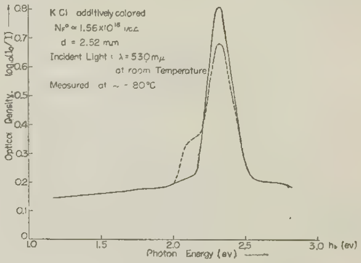

Fig. 1. Optical densities versus photon energies. Solid curve shows before irradiation with *F*-light. Dotted curve shows after 30 min. irradiation with *F*-light at room temperature. All measurements are carried out at liquid air temperature.

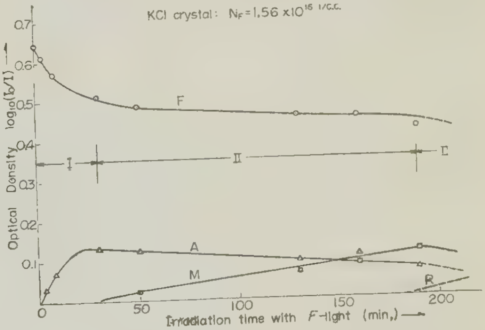

Fig. 2. Changes of peak height of optical density of various color centers versus irradiation periods of *F*-light at room temperature.

At the region I as shown in Fig. 2, products of absorption coefficients and the half-width of the

A-band are plotted against those decrements of the F-band in Fig. 3. If we assume a one to one conversion from F-centers to A-centers and further that the excited states of A-centeas do not overlap with F-band, we obtain a ratio of oscillator strength of the A- and F-band to be 0.62. from the gradient of Fig. 3. Thus we get 0.5C for f_A adopting $f_F=0.81$.

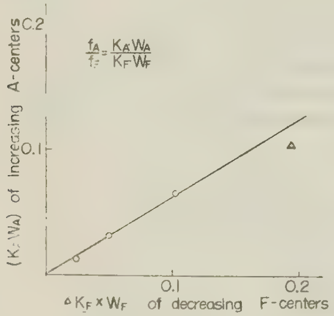

Fig. 3. Products of absorption coefficients and the half-width of A-band versus those decrements for F-band. ⊙: for the same sample as Fig. 1. and 2. △: for the sample having 4.0×10^{16} F-centers per cc. The gradient of this line shows the ratio of the oscillator strength of the A-band to that of the F-band.

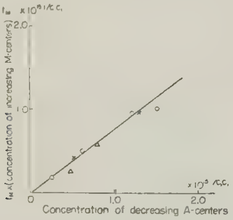

Fig. 4. The concentrations of increasing M-centers versus decreasing A-centers for various concentrations of F-centers. Ordinate is $f_M n_M$ and abscissa is $(N_{A_0}-N_A)$. ⊙; for the same sample as Fig. 1 and 2. △; for the sample having 1.6×10^{16} and ×; for 4.0×10^{16} F-centers per cc.

In the second stage (region II), linear dependence of the concentrations of decreasing A-centers upon those of increasing M-band was held till the R-band is enhanced by further illumination as shown in Fig. 4. Since the variation of the F-band in this region was insignificant, it may be concluded that the M-band appears at the expences of the A-band by F-irradiation.

The studies of the last stage (region III) has been already carried out by several authors[4].

We wish to express our thanks to Professor H. Kawamura for giving us his whole-hearted guidances in the course of this work.

This work was supported by the Scientific Rsesarch Fund of the Ministry of Education.

References

1) S. Petroff: Z. Phys. **127** (1960) 443.
2) M. Hirai: J. Phys. Soc. Japan **14** (1959) 1400.
3) T. Tomiki: J. Phys. Soc. Japan **15** (1960) 488.
4) R. Herman, M. C. Wallis and R. F. Wallis: Phys. Rev. **103** (1956) 87. G. R. Cole and R. J. Friauf: Phys. Rev. **105** (1957) 1464.

J. PHYS. SOC. JAPAN **15** (1960) 1350~1351

Absorption Band due to a Presence of Impurity Bromine in KCl Crystal*

By Koichi KOBAYASHI and Tetsuhiko TOMIKI

Department of Physics,
Tohoku University, Sendai

(Received April 27, 1960)

During the course of our study in preparing pure alkali chloride crystals, we have found an absorption band due to the presence of impurity bromine in KCl at the edge of its fundamental absorption. It is a purpose of this note to report it briefly.

Crystals studied are listed in Table I. These were grown in air by Kyropoulos technique. The crystal, KCl-aK-1, was made from KCl powder prepared from $KHCO_3$ and HCl[1]. KCl-HA-1 is a Harshaw crystal. Others were grown directly from KCl powders of reagent grade obtained from different sources. n/cc is a concentration of electric carriers estimated from low temperature ionic conductivity, which may be a measure of concentration of multivalent metallic ion impurities. The amount of OH ions was estimated optically from the absorption band at 204 mμ[2]. The concentration of bromine in the crystal was determined chemically[3] and is shown in mole fraction.

Table I.

Crystal	n/cc	OH/cc	[Br]
KCl-aK-1	1×10^{15}	2×10^{15}	9×10^{-6}
KCl-HA-1	9×10^{15}	8×10^{15}	7.1×10^{-5}
KCl-bc2K-1	8×10^{15}	2×10^{15}	1.1×10^{-4}
KCl-bK-1	4×10^{15}	2×10^{15}	1.3×10^{-4}
KCl-dK-1	7×10^{15}	2×10^{15}	3.6×10^{-4}
KCl-bc2K-2	1×10^{16}	2×10^{15}	8.1×10^{-4}

Absorption curves at the fundamental absorption edge were measured at 12°C. Those are shown in Fig. 1. The reflection loss was considered for

---

* A part of the present work has been carried out during our temporary stay in Prof. Kanzaki's laboratory of the Institute for Solid State Physics, University ofTokyo.

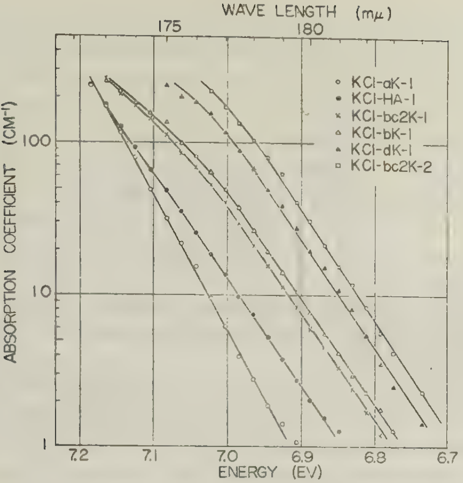

Fig. 1. Absorption curves of KCl crystals.

correcting data. It may be seen from this figure and Table I that the location of the edge does not depend upon the concentration of multivalent metallic ion impurities or hydroxyl ions, but is related to the bromine concentration in such a way that it is shifted to longer wave length side with an increase of bromine concentration.

Results in Fig. 1 suggest a presence of a unique absorption band at the edge. Curves in Fig. 2 were obtained by subtracting the absorption curve for KCl-aK-1, which contains the least bromine, from curves for other crystals. They are bands which grow certainly with an increase of bromine concentration. Therefore, one may conclude that they are due to the presence of bromine in KCl. The half width characteristic of these bands is found to be 0.18 eV if their shape is symmetric. The oscillator strength is estimated roughly as 0.07 assumed that the absorption is due to bromine itself. The long wave length side of this band below one third of its maximum fits nicely to the Urbach rule of constant temperature.

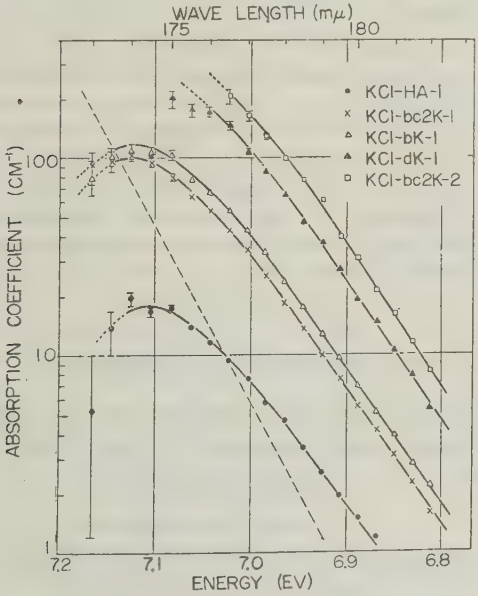

Fig. 2. Absorption bands due to the presence of bromine in KCl. The fundamental absorption edge for KCl-aK-1 is shown as a broken line.

We wish to thank Professor M. Ueta for giving us an opportunity to use his spectrometer and to Professor H. Kanzaki and Mr. S. Tamura for their helpful discussions. A part of this work was supported by the Research Grant from the Ministry of Education.

References

1) K. Kobayashi and T. Tomiki: To be published.
2) H. W. Etzel and D. A. Patterson: Phys. Rev. **112** (1958) 1112.
3) D. F. Boltz: *Colorimetric Determination of Nonmetals* (Intersci. Publ., New York, 1958) 193.

J. Phys. Soc. Japan **15** (1960) 1351～1352

Induced Magnetic Anisotropy of Evaporated Ni–Fe Films

By Minoru TAKAHASHI, Denjiro WATANABE
Tatsuo KŌNO and Shiro OGAWA

The Research Institute for Iron, Steel and Other Metals, Tohoku University, Sendai

(Received May 7, 1960)

The systematic and detailed study on the induced magnetic anisotropy of evaporated films of metals and alloys has recently done by Andrä *et al.*[1], but any quantitative and direct measurement of the anisotropy of Ni–Fe alloys has never been carried out over a wide range of Ni composition. It has been, therefore, desired to study the magnitude and the composition dependence of induced magnetic anisotropy of these evaporated alloy films.

The alloy films were evaporated on a quartz plate under a magnetic field of $H_a=250$ Oe.. The thickness was kept at 600 Å. The apparatus for measuring the torque is the same as reported before[2]. Some examples of torque curves are shown in Fig. 1 for 65% Ni–Fe films. Each torque curve represents an average value of two curves which were measured clockwise and counter-clockwise. The rotational hysteresis loss, $W_r=-\int_0^{2\pi} L d\theta$, is plotted against the measuring field in Fig. 2. As seen from Figs. 1 and 2, the torque curves are considerably deformed at the field strength corres-

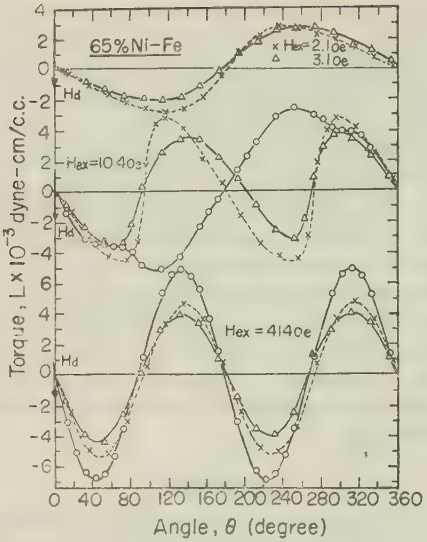

Fig. 1. The torque curves averaged for rotations with decreasing and increasing θ.
⊙; Temperature of substrate is at room temp.
×; Temperature of substrate is at 300°C.
△; The substrate was held at 300°C, heated to 450°C and annealed at this temperature for 2.5 hours in magnetic field.

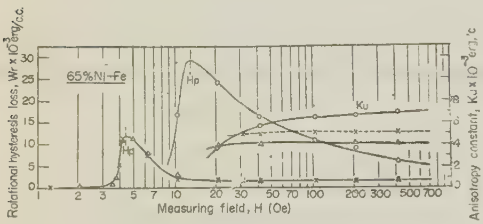

Fig. 2. Rotational hysteresis loss and anisotropy constant as a function of field strength in measurements. Meaning of the marks is the same as in Fig. 1.

ponding nearly to the peak of the rotational loss $(H_p=2K_u/I_s\approx H_c)$. At very low field on the other hand, the curves are almost unidirectional and are expressed in $K_1\sin\theta$. As the field strength increases ($>H_p$), the torque curves begin to be proportional to $\sin 2\theta$. These facts are analogous to the case of small particle permanent magnet[3]. The torque curves corresponding to the field strength more than 20 Oe were analyzed by the Fourier method, and values of the coefficient of $\sin 2\theta$ were shown in Fig. 2. As seen from this figure, K_u is not saturated even at 400 Oe for the films evaporated on the substrate held at room temperature. Therefore the saturated values of K_u were obtained by extraporation to the infinite measuring field. These saturated values are plotted in Fig. 3, where the curve obtained by Chikazumi[4] for bulk specimens is also illustrated. The interesting features are as follows: (i) The anisotropy values are extremely large in thin films and the maximum value exists at 50% Ni-Fe. The

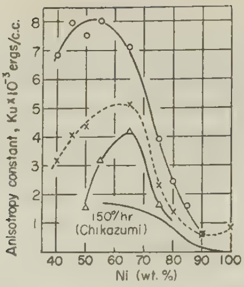

Fig. 3. Uniaxial anisotropy constant against Ni composition. Meaning of the marks is the same as in Fig. 1.

substrate was held at room temperature in this case. (ii) When the substrate was held at 300°C on evaporation and cooled or annealed at 450°C for 2.5 hours after evaporation, the maximum value is displaced to 65% Ni-Fe.

The origin of the extremely large value and large sensibility to heat treatment of the anisotropy may not be explained by the atomic pair orientation theory alone[5]. The detailed report will be published in the near future.

References

1) W. Andrä, Z. Mélek, W. Schüppel und O. Stemme: Naturwiss. **46** (1959) 1; J. Appl. Phys. **31** (1960) 442; Ann. Physik **5** (1960) 174.
2) M. Takahashi, D. Watanabe, T. Sasagawa, H. Saito and S. Ogawa: J. Phys. Soc. Japan **14** (1959) 1459.
3) I. S. Jacobs and F. E. Luborsky: Proc. Conf. on Magnetism and Magnetic Materials (Boston, 1956) 145.
4) S. Chikazumi and T. Oomura: J. Phys. Soc. Japan **10** (1955) 842.
5) L. Néel: Phys. radium **15** (1954) 225. S. Taniguchi: Sci. Rep. Res. Inst. Tohoku Univ. **A7** (1955) 269. S. Chikazumi: J. Phys. Soc. Japan **11** (1956) 551.

J. PHYS. SOC. JAPAN **15** (1960) 1352~1353

Fixing of Magnetic Moment of Ferromagnetic Fine Precipitates in Cu-Co Alloy during Aging

By Kazuo KOBAYASHI

Geophysical Institute, University of Tokyo

(Received May 13, 1960)

Recent investigations[1),4)] have shown that, in the isothermal aging of Cu-Co alloy, the separation of Co-rich ferromagnetic phasme fro the nonmagnetic Cu matrix is completed in the initial stage of precipitation, and with increasing time the average particle size increases in such a way that the total volume of precipitates remains constant. It has been concluded that the particles are first superparamagnetic, then stable single domains and finally become multidomain particles. In the present study this sequence of magnetic behaviours has been examined more explicitly by a successive measurement of both reversible and remanent magnetizations during annealing in various intensities of magnetic field.

The specimen containing ca. 2wt% Co, balance Cu was formed into a rod of about 4 cm in length, 0.8 cm in diameter and was appropriately heat-treated to form a uniform solid solution. Measurements were made with a high temperature ballistic method during the annealing at 750°C in various intensities of magnetic field up to 500 Oe.

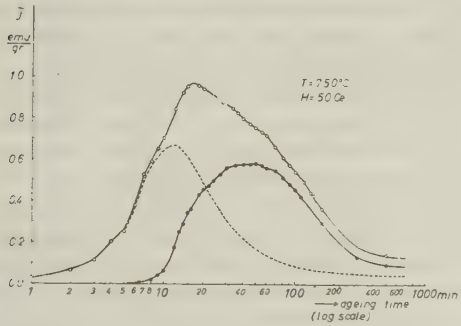

Fig. 1. Change of total, remanent and reversible component of magnetization (hollow and solid circle and broken line, respectively) as a function of aging time.

Fig. 1 shows an example of these measurements. Reversible magnetization due to superparamagnetism (except in later stages of precipitation) is assumed to be equal to the difference between the magnetization with applied field and remanent magnetization. It is noted that the intensities of superparamagnetism and remanent magnetization arrive at their maximum values after constant time of aging, almost independently of the intensity of the applied field. The curves show that the magnetic moments of precipitated particles are fixed along the direction of the magnetic field within a short time interval after the appearance of the maximum superparamagnetism, and the remanent magnetization first increases and then gradually decreases as a result of the formation of magnetic domains.

Fixing of magnetization of the system of superparamagnetic particles may be interpreted in terms of so called "freezing" of magnetization in the similar form as the theory of thermoremanent magnetization given by Néel²⁾, as already suggested by Haigh³⁾. Néel derived the following formula of relaxation time τ for the reversal of spontaneous magnetization of single domain grains due to the thermal Brownian agitation in zero field;

$$\frac{1}{\tau}=f_0\exp\left(-\frac{Kv}{kT}\right).$$

In this expression, v is the volume of the particle, K the anisotropy per volume, f a frequency factor of the order of $10^{-9}\,\mathrm{sec}^{-1}$. Because of the exponential dependence of τ on v/T, there is a fairly well defined value of $\alpha_c=(v/T)_c$ at which the transition from $\tau\ll t$ to $\tau\gg t$ occurs (t; time for experiment). When $v/T<\alpha_c$ the magnetization of each grain is aligned statistically along the direction of applied field in a manner analogous to the Langevin paramagnetism of moment-bearing atoms. This state of magnetization is frozen and memorized when v/T exceeds α_c on the account of the decrease in temperature or owing to the growth in the size of the particles. The former is the case treated by Néel, while the latter will be the case of the remanent magnetization observed in the present study.

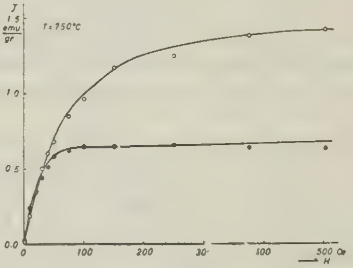

Fig. 2. Field dependence of peak intensities of superparamagnetism (hollow circles) and remanent magnetization (solid circles).

Field dependence of maximum intensities of superparamagnetism and remanent magnetization is shown in Fig. 2. It is remarkable that the intensity of remanent magnetization approaches saturation in an applied field below 100 Oe, which is very weak compared with the coercive force of the alloy in a magnetically-stable stage (several hundreds oersted, by Mitui⁴⁾). This fact also indicates that the remanent magnetization is due to the freezing mechanism.

The analysis of the present study can be extended to the interpretation of some problems in rock-magnetism, especially to that of chemical remanent magnetization of ferromagnetic minerals. Detailed consideration, however, will be discussed elsewhere⁵⁾.

References

1) J. J. Becker: J. Metals **9** (1957) 59, J. Appl. Phys. **29** (1958) 317.
C. P. Bean and J. D. Livingston: J. Appl. Phys. **30** (1959) 120S.
2) L. Néel: Ann. Geophys. **5** (1949) 99; Adv. Phys. **4** (1958) 113.
3) G. Haigh: Phil. Mag. **3** (1958) 267.
4) T. Mitui: J. Phys. Soc. Japan **10** (1955) 1023; **13** (1958) 549.
5) K. Kobayashi: J. Geomag. Geoelec. (to be published).

J. Phys. Soc. Japan **15** (1960) 1354

Ferrimagnetic Resonance in a Single Crystal of Europium-Iron Garnet

Tomonao Miyadai, Hisao Takata
Yūzō Shichijō
Electrical Communication Laboratory, Nippon Telegraph and Telephone Public Corporation, Musashino-shi, Tokyo, Japan
and Noboru Tsuya
Research Institute of Electrical Communication, Tohoku University, Sendai, Japan

(Received May 25, 1960)

It was shown previously by us[1] that the g-value of polycrystalline europium-iron garenet ($Eu_3Fe_5O_{12}$) has an appreciable temperature dependence and the full line width (~1200 Oe at room temperature) increased rapidly at low temperatures. Data are now taken for a single crystal specimen, and these have shown good agreements with the recent theory of Kittel[2][3] on the ferrimagnetic resonance in garnets.

Measurements were made on a single crystal sphere of 0.59 mm in diameter in the temperature range between liquid nitrogen and Curie point (~300°C). The microwave frequency used was 18,320 Mc/sec. The sample was mounted such that it could be rotated about a <110> direction.

g-values and K_1/M_s were calculated from the resonance fields for three principal axes[4] and are shown as functions of temperature in Fig. 1.

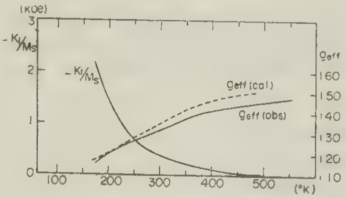

Fig. 1. g_{eff} and $-K_1/M_s$ (cubic anisotropy field) *vs* temperature, dashed curve represents the calculated one by Kittel's formula.

Below room temperature, g-values for the single crystal are slightly smaller than those for polycrystalline sample and show a somewhat stronger temperature dependence; this is a conclusion derived from Schlömann's theory[5] on internal fields for ferromagnetic reasonance in polycrystalline ferrites. K_1/M_s of *EuIG* is negative and an order or more larger than that of YIG. The line width varies with temperature as shown in Fig. 2. Although, in all temperatures investigated, $\Delta H_{<100>}$ seemed to be the narrowest, differences among the line widths for three principal axes are within the experimental errors (~10%) except near −70°C where $\Delta H_{<111>}$ is fairly broader than the others.

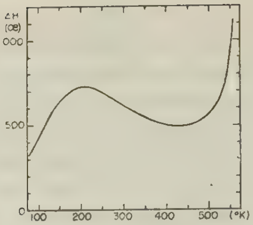

Fig. 2. Line width ($\Delta H_{<111>}$)*vs* temperature.

The line width at room temperature is about 600 Oe and equal to half the one for polycrystalline sample.

Both the g-value and its temperature variation can be explained very well by Kittel's theory which assumes that the spins of rare earth ions are highly damped while ferric ion spins are not. Kittel's theory[2] predicts that the effective g-value for ferrimagnetic resonance in garnets is expressed by $g_{eff}=g(Y)\{M_s(M)/M_s(Y)\}$ where M_s is the saturation moment and Y refers to *YIG* and M to *MIG*. In Fig. 1 is also shown g_{eff} for *EuIG* calculated by the above relation using the data[6] for the saturation moments of *YIG* and *EuIG*. As can be seen, the calculated and the observed curves are in good agreement. Kittel's theory[3] further predicts that the line width increases with increasing temperature at low temperatures, passes through a maximum, then decreases and at last increases rapidly just below the Curie temperature. The observed line width for *EuIG* shows the same temperature dependence as thetheory predicts.

Kittel noted that the theory does not apply to the ions in $L=0$ or $J=0$ states. Since the ground state of Eu^{3+} has $J=0$, the theory would not apply. The theory, however, seems to hold very well in the case of *EuIG* as described above. It may be expected that excited states with $J\neq 0$ are mixed with $J=0$ ground state.

The authors wish to express their thanks to Mr. T. Ito of Nippon Television Company for measurements.

References

1) Y. Shichijo, T. Miyadai and H. Takata: J. Phys. Soc. Japan **15** (1960) 530.
2) C. Kittel: Phys. Rev. **115** (1959) 1587.
3) P. G. de Gennes, C. Kittel and A. M. Portis: Phys. Rev. **116** (1959) 323.
4) J. F. Dillon, Jr., S. Geschwind and V. Jaccarino: Phys. Rev. **100** (1955) 750.
5) E. Schlömann: Conference on Magnetic Materials, Boston 1956 P. 600.
6) R. Pauthenet: Ann. physique **3** (1958) 424.

J. PHYS. SOC. JAPAN **15** (1960) 1355

Electrical Properties of Chromium Sulfides

By Takahiko KAMIGAICHI, Kan-ichi MASUMOTO
Minami Brach, Hiroshima University
and Tadamiki HIHARA
Department of Physics, Hiroshima University

(Received May 17, 1960)

The electrical conductivity and the thermoelectric power of chromium sulfides, CrS_x with $1.00 \leq x \leq 1.20$, were measured between the liquid nitrogen temperature and 600°C in order to clarify the mechanism of conduction in these materials.

The specimens were prepared in the following way. A proper quantity of chromium metal blocks and sulfur powder were put into an evacuated silica tube, and then the tube was heated at 1000°C to make a direct reaction between chromium and sulfur.

The specimens thus obtained were examined by means of X-ray. The specimens with $1.00 \leq x \leq 1.13$ have two phases of the monoclinic and the NiAs structures, and those with $1.14 \leq x \leq 1.20$ a single phase of the NiAs structure. These results are in agreement with those obtained by Jellinek[1]. For all the specimens a superlattice structure was found, the unit cell of which was twenty four times $((2\sqrt{3}\,a)^2 \times 2c)$ as large as that of the pure NiAs structure, a and c being the lattice constant in the hexagonal lattice and given by 3.47 Å and 5.75Å, respectively. This superlattice structure is the same as that previously reported by Haraldsen[2] and Yuzuri et al.[3]

The specimens with $x \leq 1.12$ are p-type semiconductors ($10^{-1} \sim 1$ ohm^{-1} cm^{-1}) at room temperature, but their conductivities increase about 10^3 times between 300°C and 500°C. On the other hand, those with $x \geq 1.13$ are metallic conductors (10^3 ohm^{-1} cm^{-1}) with negative thermoelectric powers. Some results of electrical conductivity and thermoelectric power measurements are shown in Figs. 1 and 2. In order to clarify the nature of the anomalous increase of conductivity with increasing temperature for $x \leq 1.12$, a powder photograph of $x = 1.00$ was taken at 570°C. It showed patterns of pure NiAs structure with $a = 3.44$ Å and $c = 5.63$ Å. This results indicates that the anmalous increase of conductivity is due to the transition from the two phases of the monoclinic and the NiAs structures to the single phase of the pure NiAs structure. Similar X-ray analysis of $x = 1.17$ at 570°C showed that the superlattice structure vanishes and the specimen also has the pure NiAs structure.

The poor conduction in the two-phase region may be ascribed to the monoclinic structure in which the ionic binding might play a predominant role. The metallic conduction in the NiAs structure is due to the increase in the covalent or metallic nature of bonding in this structure.

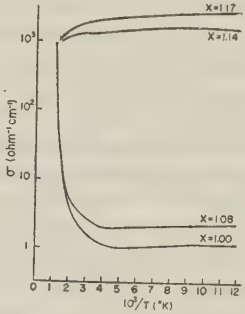

Fig. 1. Electrical conductivity of CrS_x as a function of temperature.

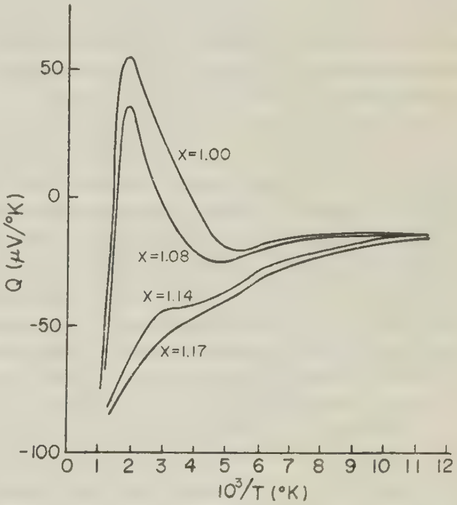

Fig. 2. Thermoelectric power of CrS_x with respect to copper as a function of temperature.

It is to be noted that the conductivity of $x = 1.17$ does not show even slightest anomalies at −120°C where the ferrimagnetism disappears suddenly.

The authors wish to thank Prof. H. Tazaki for his interest and encouragement and Prof. E. Hirahara for the allowance for using the high temperature X-ray camera.

References

1) F. Jellinek: Acta Cryst. **10** (1957) 620.
2) H. Haraldsen: Z. anorg. allgem. Chem. **234** (1937) 372.
3) M. Yuzuri, T. Hirone, H. Watanabe, S. Nagasaki and S. Maeda: J. Phys. Soc. Japan **12** (1957) 385.

J. PHYS. SOC. JAPAN **15** (1960) 1356~1357

Exciton-Induced Photoconductivity of U Centers in KCl Crystal

By Masayasu UETA and Masamitsu HIRAI

Department of Physics, The Faculty of Science, Tohoku University, Sendai

(Received May 25, 1960)

Previously[1] we have reported on the measurement of the quantum efficiency of the exciton-induced photo-chemical conversion of a *U* center to an *F* center, and it was determined to have a value of nearly unity with light of wavelength shorter than 183 mμ and 203 mμ in KCl and KBr crystals, respectively. These wavelengths are in the exciton absorption band of the crystals.

Several mechanisms of the exciton energy-transfer to *U* center are considered; i.e., ionization, excitation or thermal destruction with the thermal spike as proposed by Seitz[2]. Photoconductivity measurements will be valuable to make choice of the most probable mechanism among them.

A KCl crystal (Harshaw Chemical Co.) of $10\times10\times1.4\,\text{mm}^3$ containing *U* centers with a concentration of 4.3×10^{17}/c.c. was clamped between electrodes and an electric field of 1400 volt/cm. was applied to it. Light illuminations were performed along the direction of the electric field through holes drilled in one electrode. The ultra violet light from a hydrogen discharge lamp was monochromated with a vacuum grating monochromator. The purity of the monochromatic light was 1 mμ and the intensity was the order of 10^{11} and 5×10^{11} photons/cm^2. sec. in the region of 170 mμ-200 mμ and 200 mμ-240 mμ, respectively. Photocurrents were measured with a Cary Model 31 vibrating reed electrometer. When the photocurrent was below 5×10^{-14} amp., the polarization effect was negligibly small.

Curve (A) in Fig. 1 is a result showing the photocurrent as a function of photon energy of the illuminating light at the room temperature in a virgin KCl crystal containing *U* centers. Curve A in Fig. 2 shows the spectral distribution of photocurrent obtained from curve A in Fig. 1, with corrections of light intensity and the absorption spectrum of the crystal.

For the comparison, the spectral distribution of the quantum efficiency of $U\rightarrow F$ conversion by light was referred in Fig. 2 curve B, which was reported previously. From these figures, it is seen that the correspondence between the spectral variations of the photoconductivity and the quantum efficiency of the photo-chemical conversion of $U\rightarrow F$ is quite satisfactory. Therefore, the conversion of $U\rightarrow F$ by the exciton will be due to the induced ionization of *U* centers.

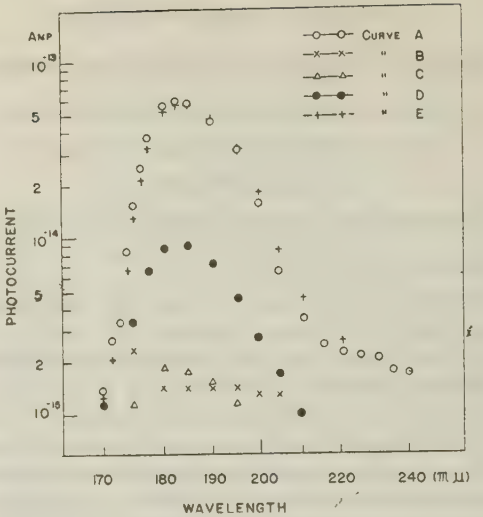

Fig. 1. Photocurrents in KCl crystal containing *U* centers at 20°C.

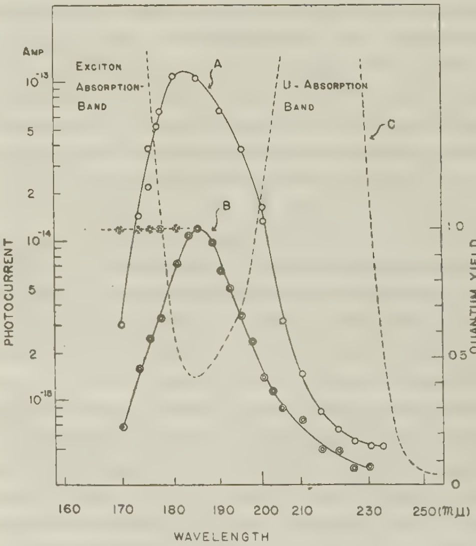

Fig. 2.

Curve A: Spectral distribution of photoconductivity.

Curve B: Spectral distribution of quantum efficiency of the photo-chemical $U\rightarrow F$ conversion.

Curve C: Absorption curve of the KCl crystal containing *U* centers.

When the crystal was suffered from long period illumination of ultra violet lights from the hydrogen lamp through a fused quartz window, more than 50 per cent of *U* centers were converted to *F* centers. In this crystal, the photoconcuctivity was found to decrease to quite a small value as shown in Fig. 1 curve B. If the crystal was successively illuminated by white light, *F* centers disappeared and the concentration of *U* centers recovered to the initial state. In spite of the *U* center recovery, the photoconductivity was still small as shown in curve C. However, after the crystal was annealed at 200°C for one hour, photoconductivity began to recover as shown in curve D, and after the thirty hours' annealing at the same temperature, it was found to have nearly the same photocurrents as the initial virgin crystal as shown by curve E.

In a crystal containing OH ion the photocurrent was not detected.

The results of very small photoconduction in the crystal treated optically in such a manner as $U \rightarrow F \rightarrow U$, and the recovery with annealing, will be attributed to the formation of vacancies and some other imperfections by the irradiation of ultra violet light. These imperfections will be effective to the trapping of electrons released from U centers and will cause the shortening of the Schubweg of electrons.

A full report will be submitted in this journal.

References

1) M. Ueta, M. Hirai and H. Watanabe: J. Phys. Soc. Japan **15** (1960) 593.
2) F. Seitz: Rev. Mod. Phys. **26** (1954) 90.

Errata

Excitation Functions for Alpha-Induced Reactions on Manganese-55

By Sigeo TANAKA, Michiaki FURUKAWA, Takashi MIKUMO, Shiro IWATA
Masuo YAGI and Hiroshi AMANO

J. Phys. Soc. Japan **15** (1960) 545

The measured cross sections for the reactions resulting Mn^{54}, Co^{58}, and Co^{56} (in Figure 3 and Figure 4) should be multiplied by 1.23, 1.23, and 1.67, respectively. The disintegration rates of Mn^{54}, Co^{58} and 1.67, respectively. The disintegration rates of Mn^{54}, Co^{58} and Co^{58} and Co^{56} were calculated from the γ-ray measurement in a poorly defined geometry (in § 3 on p. 548). However, it has become clear from the present authors' subsequent work that the calculated photopeak efficiency (the 26th to the 32nd line from the top on p. 546, right) is not correctly applicable to this experiment. The above corrections are based on the γ-ray measurements calibrated by the various standard sources, the disintegration rates of which have been determined by a γ-γ coincidence counting and a $4\pi\beta$-counting.

PROGRESS OF THEORETICAL PHYSICS

CONTENTS

Progress of Theoretical Physics Vol. 23, No. 4, April 1960

Formulas in the Fermi Theory of Beta Decay. II—*On the Beta-Ray Angular Correlation*— ....Zyun-itiro MATUMOTO..531

A Note on the First Born Approximation in Collisions of Electron with Helium .... Sigeru HUZINAGA..562

On High Energy Limit of Fermion-Fermion Interaction.........Tetz YOSHIMURA..569

Asymptotic Theory of Interacting Fields without Hamiltonian..Tetz YOSHIMURA..576

S-Wave Pion-Σ-Hyperon Scattering.........K. KAWARABAYASHI and T. SAWADA..583

Photodisintegration of the Deuteron in the High Energy Range ....Masahiko MATSUMOTO..597

Spinning Charged Test-Particles in General Relativity...........Anadijiban DAS..610

Some Remarks on the Born-Green-Rodriguez Theory of Condensation .... Kazuyosi IKEDA..616

One-Particle Motions in Many-Particle Systems and the Optical Model in Nuclear Reactions..Mikio NAMIKI..629

Mass Levels of Baryons and Mesons.............S. SAWADA and M. YONEZAWA..662

A Note on the Electromagnetic Response of Normal Metals....Sadao NAKAJIMA..694

On the Meson Mass Differences..............G. W. BUND and P. L. FERREIRA..700

Second Quantization and Lorentz Invariance.......................Shigeo SATO..717

Pion-Pion Interaction and Pion-Nucleon Scattering ....K. ISHIDA, A. TAKAHASHI and Y. UEDA..731

Letters to the Editor:

A Solution of the Combined Gravitational and Mesic Field Equations in General Relativity..........................R. L. BRAHMACHARY..749

The Phase Shift Formula in the Improved WKB Method..H. MORIGUCHI..750

Nucleon Structure and Bev Interactions.........................D. ITŌ..752

A Subjective Generalization of Statistical Mechanics ......K. KAWASAKI..754

An Entropy Concept in Statistical Mechanics ....K. KAWASAKI..755

Price	\$ 1.25 per copy
	\$ 15.00 per year (postage inclusive)

Annual dues for foreign members (individual subscribers)
\$ 12.00 (postage inclusive)
〃 for foreign members of the Physical Society of Japan
\$ 10.00 (postage inclusive)

Application for members, subscriptions and orders for back numbers should be sent, directly or through book-dealers, to

The Publication Office
in
Yukawa Hall, Kyoto University, Kyoto, Japan

. . . .

JOURNAL OF THE PHYSICAL SOCIETY OF JAPAN, Vol. 15, No. 8, AUGUST, 1960

Angular Distribution of n-p Scattering at 14.1 MeV

By Teruo NAKAMURA

Department of Physics, Faculty of Science, Kyoto University

(Received April 18, 1960)

The angular distribution for the scattering of neutrons by protons was obtained at 14.1 MeV by observing the recoil protons by the use of a counter-telescope consisting of a polyethylene target, two proportional counters and a CsI scintillator. The data obtained at scattering angles of 165°, 146°, 118° and 89° in C.M.-system were given with statistical errors of about 1%. The ratio of the cross sections at 180° and 90° in the center-of-mass system was found to be 1.080 ± 0.016 from a least square fit to the form $A+B\cos^2\theta$. Therefore it may be concluded that anisotropy of the angular distribution is confirmed quite clearly.

The absolute values of differential cross sections at various angles were normalized using the total cross section 689 ± 5 mb measured by transmission. The values are in good agreement with the results predicted from the nuclear potentials with "one-pion-exchange-tail" proposed by members of the Nuclear Force Group in Japan.

§ 1. Introduction

Hitherto the angular distributions of fast neutrons scattered by protons were studied by many authors[1] to obtain the information about the nature of the interaction between neutrons and protons. All experimental results in the energy range of less than 10 MeV are consistent with the assumption of spherically symmetric scattering predicted by theories[2]. For neutron energies above 10 MeV appreciable deviation from symmetry is predicted, depending upon the nature of the forces assumed for the neutron-proton interaction, and was confirmed quite clearly by experiments at somewhere above 10 MeV neutron energy. At 17.9 MeV the ratio of the neutron scattering cross sections at 180° and 90° in the center-of-mass system has been reported as 1.08 ± 0.03 by Galonsky and Judisch[3]. The ratio becomes more larger as the neutron energy increases, and has been reported as 3.15 ± 0.10 at 90 MeV by Stahl and Ramsey[4].

At the neutron energies in the region between 10 and 15 MeV, however, it seems that no decisive conclusion has been obtained, although some reports[5] have been presented.

The present work was undertaken to obtain more reliable information about the anisotropy of the angular distribution of neutrons scattered by protons, using a counter-telescope under an improved condition of decreasing systematic and statistical errors. Furthermore, another purpose of the present work is to check the nuclear potential with "one-pion-exchange-tail" proposed by members[6] of the Nuclear Force Group in Japan.

§ 2. Experimental Apparatus and Procedure

The experimental arrangement is shown schematically in Fig. 1. Neutrons were provided by the T-d reaction, employing magnetically analyzed atomic deuteron of 300 keV

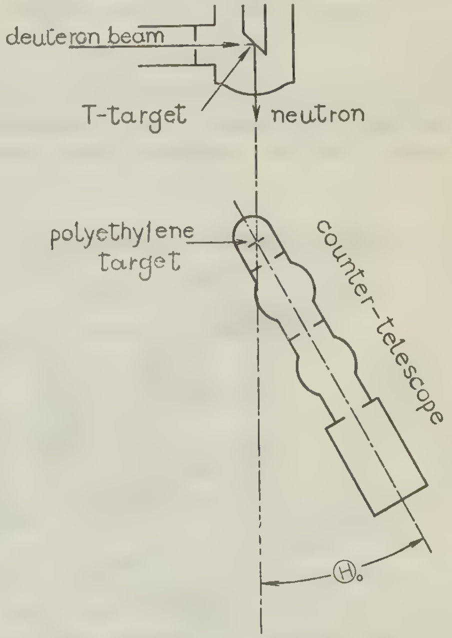

Fig. 1. Experimental arrangement (schematically).

from a Cockcroft-Walton machine. The tritium target consisted of 14 curies absorbed in a 6.6 mg/cm^2 titanium thick foil and was bombarded with a steady beam of several μA. Neutron production was estimated to be about 5×10^8 neutrons/sec. Neutron flux was monitored by counting the recoil alpha particles from the $T(d, n)He^4$ reaction using a proportional counter filled with argon and 5% CO_2 at a pressure of 38 cm Hg. The monitor counter was placed at 150° direction with respect to the deuteron beam. A typical pulse-height distribution of the alpha particles is shown in Fig. 2. During the experiment, all pulses above a certain bias (shown by an arrow in Fig. 2) were counted for monitoring neutron flux.

The interaction of neutrons with protons was studied by observing recoil protons originating in a polyethylene foil in the counter-telescope. The polyethylene target was located at a distance of 14.8 cm from the neutron source, and at 90° direction with respect to the deuteron beam. At this position the incident neutrons were monoenergetic with an energy of 14.10 ± 0.05 MeV. The counter-telescope was mounted on an indexed stand and could be rotated in a horizontal plane about a vertical axis lying in the plane of the polyethylene foil. The foil was 2.45 cm in diameter, and 10.1 mg/cm^2 in thickness. It was backed by a lead sheet (1 mm) to reduce the background. A small bar magnet was mounted on the top of the axle, at the other end of which was the polyethylene target. And the bar magnet allowed the target to be rotated inside the counter-telescope by means of an external magnet in order to expose either the polyethylene foil or the lead blank to the counters and the scintillator of the instrument.

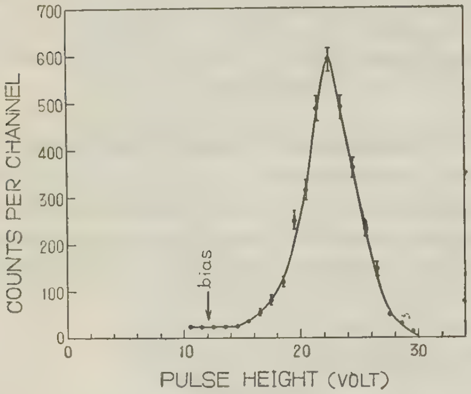

Fig. 2. Pulse-height distribution of alpha particles from the $T(d, n)He^4$ reaction in the monitor counter. Bias limit is indicated by an arrow.

The counter-telescope consisted essentially of two proportional counters and a CsI scintillation crystal with light-pipe coupling to a photomultiplier as shown in Fig. 3. Neutrons impinge on the polyethylene target and recoil protons emitted along the telescope axis travel through the two counters and strike the CsI crystal of the scintillation detector.

The proportional counters were filled with argon and 5% CO_2 at a pressure of 7.6 cm Hg. They were made of brass cylinders, and the inner wall of the first counter was lined with a lead sheet (1 mm) to reduce the background of charged particles produced in the wall.

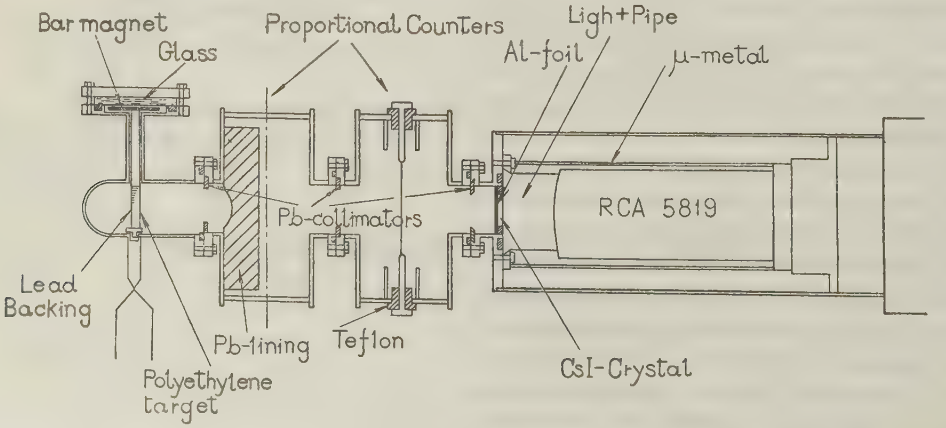

Fig. 3. Counter-telescope.

The CsI crystal was in the form of a disk of 2.5 cm in diameter and 1 mm in thickness. The crystal was pasted with grease on the surface of the lucite light-pipe leading to the photocathode of an RCA type 5819 photomultiplier.

The pulses resulting from the ionization in the two proportional counters and from the scintillation in the CsI crystal were amplified and fed into a triple coincidence circuit. The coincidence output pulses opened the gate of a ten channel pulse-height analyzer in time to receive the delayed pulse-height representations of the scintillation detector. A schematic representation of the counters and the associated electronics are given in Fig. 4. Overall stability of their electronic circuits was found to be sufficiently good and the fluctuation did not exceed 2% a day.

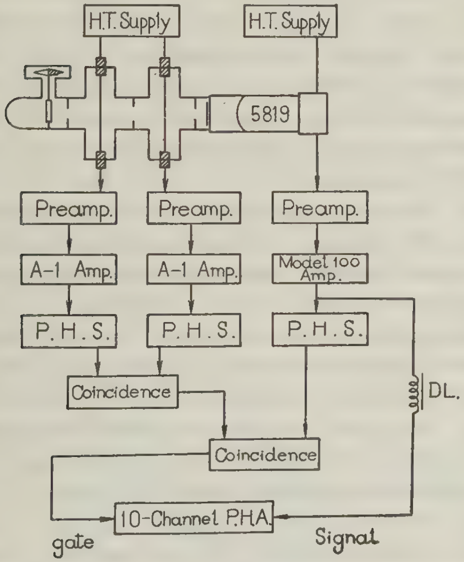

Fig. 4. Schematic representation of the counters and the associated electronics.

In the present work the coincidence counting rate of the counter-telescope was about one count per second, with single counting rates of about 900, 600 and 15 per second in the proportional counters and the scintillation detector, respectively. Therefore, the counting rate of the accidental coincidence was estimated to be less than 10^{-3}/sec from the resolving time of the coincidence circuit. The ratio of the background in the coincidence counts to the true counts of recoil protons from the polyethylene target was measured to be about few per cent from the blank test.

For the test of the proportional counters, the pulse-height distribution of "*dE*/*dx* pulses" of recoil protons in a proportional counter was taken by the ten channel pulse-height analyzer gated by triple coincidence pulses. The pulse-height distribution obtained is in agreement with a Landau curve7) as shown in Fig. 5. During the experiment, all pulses above a certain bias (shown by an arrow in

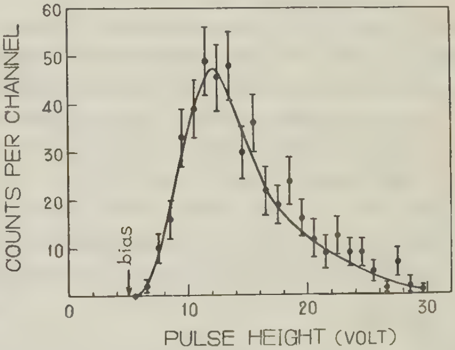

Fig. 5. Pulse-height distribution of "*dE*/*dx* pulses" in a proportional counter. The smooth curve represents the distribution calculated from the Landau and Symon theory.

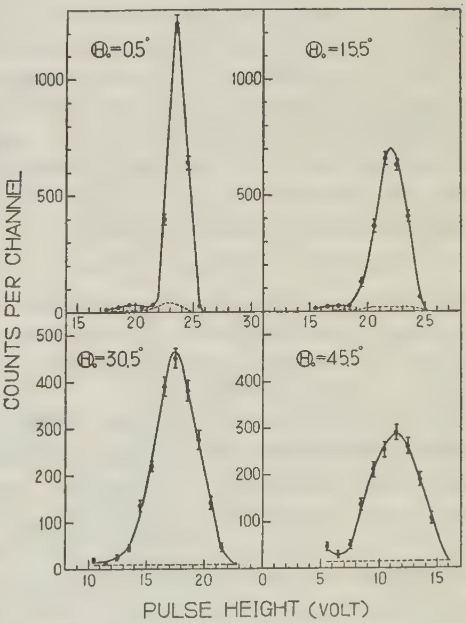

Fig. 6. Typical pulse-height distributions of recoil protons at various angles. Dashed curves represent backgrounds measured by the blank test.

Table I. Total counts of recoil protons at various angles.

Θ_0	0.5°	15.5°	30.5°	45.5°
Total coincident counts	14,563	14,465	13,047	11,035
Monitor counts	5,979,773	6,250,895	6,250,895	6,501,358
Back ground counts	147	137	175	237
Monitor counts	1,310,278	1,360,215	1,361,454	1,361,172
Net counts of recoil protons per monitor 10^4 counts	23.23	22.13	19.12	15.23
Statistical error per monitor 10^4 counts	0.22 (1.0%)	0.21 (1.0%)	0.21 (1.1%)	0.20 (1.3%)

Fig. 5) were fed to the coincidence circuit.

Typical data of the pulse-height distributions of recoil protons are shown in Fig. 6 for various setting angles of the telescope axis. Counts per each channel shown in Fig. 6 are total counts of several runs. In a run the data of all angles were taken for about one hour in order to minimize the relative errors of the differential cross sections.

§ 3. Results

Total counts of recoil protons at various angles are shown in Table I. In order to convert the differential cross sections per unit solid angle in the laboratory system to that in the center-of-mass system, they are roughly divided by $4\cos\Theta_0$, where Θ_0 is the setting angle of the counter-telescope axis with respect to the direction of incident neutrons. For exact conversion, however, the correction for the finite size of the polyethylene target and the aperture of the detector is necessary. Then the differential cross sections in the C.M.-system can be calculated from

$$\sigma_{\mathrm{C.M.}}(\theta)=\sigma_{\mathrm{lab}}(\Theta_0)/4\cos\Theta_0\cdot C(\Theta_0)\,, \qquad (1)$$

where $C(\Theta_0)$ is the correction factor for the finite size of the target and the aperture of the detecting system, and is explicitly formulated in Appendix of this paper.

In the first place, the relative differential cross sections in the C.M.-system at various angles were obtained and the angular distribution could be fitted to $1+(0.080\pm0.015)\cos^2\theta$ from a least square analysis to the form $A+B\cos^2\theta$, where the error of anisotropic term (±0.015) was originated only from statistical errors. Although other errors which affected the relative values of the cross section seemed to be negligible at small angles ($\Theta_0=0.5°$ and 15.5°), at large angles ($\Theta_0=30.5°$ and 45.5°) they were as follows:

(1) Correction factor $C(\Theta_0)$ for the finite solid angle of the counter-telescope. Equation (A-5) in the appendix was derived almost exactly, and the uncertainty of the factor $C(\Theta_0)$ was estimated to be less than 0.1%. The relative errors introduced were negligible.

(2) Setting angle Θ_0 of the counter-telescope axis with respect to the direction of the center line of the neutron source and the polyethylene target. The uncertainty of the direction of the center line was 0.1°. The relative errors introduced were 0.1% and 0.2%, respectively.

(3) The deviation of the center of the polyethylene target from the turning axis of the counter-telescope was measured as 0.35 ± 0.3 mm by a cathetometer. The errors were estimated to be about 0.1% at $\Theta_0=45.5°$ and were negligibly small at other angles, after the corrections of about 0.2%.

(4) Degraded neutrons originated by scattering from the target box surrounding the neutron source contributed by about 1% to the counting rate of recoil protons. This value was estimated from the analysis of the low energy tails of the pulse-height distributions at $\Theta_0=0.5°$ and 15.5° (see Fig. 6). The relative errors arising from these degraded neutrons were estimated to be less than 0.3% at $\Theta_0=45.5°$ and 30.5°.

(5) The other degraded neutrons scattered by other matters such as the floor, walls and ceiling of the laboratory could not be evaluated definitely, but the relative errors arising from these may be thought less than 0.5% at $\Theta_0=$ 45.5° and 30.5°.

Thus, the combined rms errors of the relative differential cross sections at $\Theta_0=30.5°$ and 45.5° were estimated to be 1.2% and 1.4%, respectively. The uncertainty of the anisotropic term of the angular distribution was derived to be 1.6% by a least square analysis where the values with errors estimated above were used. Therefore, the ratio of neutrons scattering cross sections at 180° and 90° was calculated to be 1.080 ± 0.016.

Table II. Differential cross sections per unit solid angle of *n-p* scattering at 14.1 MeV (in C.M.-system) obtained by the normalization to 689 mb of total cross section measured by transmission. The errors indicated in this table do not include the uncertainty due to the error of the total cross section 689 ± 5 mb of *n-p* scattering.

θ	165°	146°	118°	89°
$\sigma(\theta)$ (mb/sterad.)	59.1 ± 0.6	58.3 ± 0.6	56.2 ± 0.6	55.0 ± 0.7

Final results of the differential cross sections in the C.M.-system are shown in Table II and Fig. 7. The absolute values of differential cross sections were normalized using the total cross section 689 ± 5 mb measured by transmission[8]. At the normalization the angular distribution of scattered neutrons was assumed to be of the form resulted from the pion theory (see § 4 below) rather than the form $A + B\cos^2\theta$. The errors indicated in Table II and Fig. 7 do not include the uncertainty arising from the error of the total cross section, but they were statistical errors only.

§ 4. Discussion

In Table III, the ratio of the cross sections at 180° and 90° obtained by the present writer was compared with the results obtained by other workers. It will be seen that the present results are in good agreement with the other results within probable errors. It may be concluded that anisotropy is confirmed quite clearly by the precise data obtained in the present experiment.

Table III. Anisotropy of *n-p* scattering at 14.1 MeV obtained by various authors.

Author	$\sigma(180°)/\sigma(90°)$
Barschall *et al.*	1.06 ± 0.06
Allred *et al.*	1.04 ± 0.05
Seagrave	1.06 ± 0.023
Present	1.080 ± 0.016

Now, the present results of the differential cross section will be compared with the results expected from the meson theory. The pion theory of nuclear forces has been verified by analysis of almost all low energy two-nucleon phenomena below about 20 MeV[6], taking properly into account the reliability of the theory in accordance with the Taketani theory[9]. Therefore, let us compare the present results with those calculated from the two-nucleon potential with the "one-pion-exchange tail" proposed by Iwadare *et al.*[6],[10], rather than from phenomenological potential usually used. The potentials proposed by them are as follows:

$$
\begin{aligned}
V(x) &= V^{(1)}(x) \quad \text{(the one-pion-exchange potential)} && \text{for } x \geq x^{(1)} \\
&= V_{0c} + S_{12} V_{0T} && \text{for } x^{(1)} \geq x \geq 0.7 \\
&= V_{0c}' + S_{12} V_{0T}' && \text{for } 0.7 \geq x \geq x_0 \\
&= \infty && \text{for } x_0 \geq x\,,
\end{aligned}
$$

where x is the inter-nucleon distance in the units of the pion compton wavelength and V_{0c}, V_{0T}, V_{0c}' and V_{0T}' are constants. In the triplet even state, the one-pion-exchange potential is written as

$$
V^{(1)}(x) = -(g_e^2/4\pi\hbar c)\mu c^2[1 + S_{12}(1 + 3/x + 3/x^2)]\, e^{-x}/x\,,
$$

and this potential is applied in the outer region of the hard core ($x_0 = 0.34$), and in the triplet odd state

$$
V^{(1)}(x) = (1/3)(g_e^2/4\pi\hbar c)\mu c^2[1 + S_{12}(1 + 3/x + 3/x^2)]\, e^{-x}/x\,,
$$

$$
x^{(1)} = 1.0\,, \qquad x_0 = 0.32\,,
$$

$$
V_{0c} = -20\ \text{MeV}\,, \qquad V_{0c}' = -100\ \text{MeV}\,,
$$

$$V_{0T}=V_T{}^{(1)}(x=1)\,,\qquad V_{0T}'=0\,.$$

In the singlet even state

$$V^{(1)}(x)=-(g_e{}^2/4\pi\hbar c)\mu c^2\,e^{-x}/x\,,$$
$$x^{(1)}=1.6\,,\qquad x_0=0.45\,,$$
$$V_{0c}=-20\text{ MeV}\,,\qquad V_{0c}'=-5\times10^2\text{ MeV}\,,$$

and in the singlet odd state

$$V^{(1)}(x)=3(g_e{}^2/4\pi\hbar c)\mu c^2\,e^{-x}/x\qquad\text{for}\quad x\geq0.34\,,$$

Table IV. Phase shifts at 14.1 MeV.

State		Phase shift and mixing parameter (radian)		
^3E	$^3S_1+{}^3D_1$	$^3\delta_1{}^\alpha=1.670$	$^3\delta_1{}^\gamma=-0.021$	$\varepsilon_1=0.250$
	$^3D_2$	$^3\delta_2{}^\beta=0.027$		
	$^3D_3+{}^3G_3$	$^3\delta_3{}^\alpha=-0.004$	$^3\delta_3{}^\gamma=0.003$	$\varepsilon_3=-0.794$
	$^3G_4$	$^3\delta_4{}^\beta=0.001$		
	$^3G_5+{}^3I_5$	$^3\delta_5{}^\alpha=0.000$	$^3\delta_5{}^\gamma=0.000$	$\varepsilon_5=$——
^3O	$^3P_0$	$^3\delta_0{}^\gamma=0.138$		
	$^3P_1$	$^3\delta_1{}^\beta=-0.056$		
	$^3P_2+{}^3F_2$	$^3\delta_2{}^\alpha=0.013$	$^3\delta_2{}^\gamma=-0.002$	$\varepsilon_2=-0.472$
	$^3F_3$	$^3\delta_3{}^\beta=0.003$		
	$^3F_4+{}^3H_4$	$^3\delta_4{}^\alpha=0.000$	$^3\delta_4{}^\gamma=0.000$	$\varepsilon_4=$——
^1E	$^1S_0$	$^1\delta_0=0.951$		
	$^1D_2$	$^1\delta_2=0.004$		
	$^1G_4$	$^1\delta_4=0.000$		
^1O	$^1P_1$	$^1\delta_1=-0.080$		
	$^1F_3$	$^1\delta_3=-0.001$		
	$^1H_5$	$^1\delta_5=-0.000$		

with $g_e{}^2/4\pi\hbar c=0.08$. Of course the tensor potentials $S_{12}V_{0T}$ and $S_{12}V_{0T}'$ are absent in the singlet states. The various phase shifts[11] at 14.1 MeV derived from the above potentials are listed in Table IV.

For the unpolarized n-p scattering, the differential cross section was given in the appendix of Ref. 6 and the explicit form of the first several terms of that equation was given by Matsumoto[12] or by Rohrlich and Eisenstein[13]. The equations of the differential cross section per unit solid angle are

$$\sigma(\theta)=\frac{3}{4}\,({}^3\sigma(\theta))+\frac{1}{4}\,({}^1\sigma(\theta))$$
$$^3\sigma(\theta)=\frac{1}{k^2}\sum_{n=0}^{4}{}^3C_n\cos^n\theta$$
$$^1\sigma(\theta)=\frac{1}{k^2}\sum_{n=0}^{4}{}^1C_n\cos^n\theta\,,$$

where $k^2=1.21E_{\text{lab}}\times10^{24}\text{ cm}^{-2}$ and ^3C_n is obtained from the table of Matsumoto's paper (but $^3P_2$ and $^3F_2$ must be interchanged in his table).

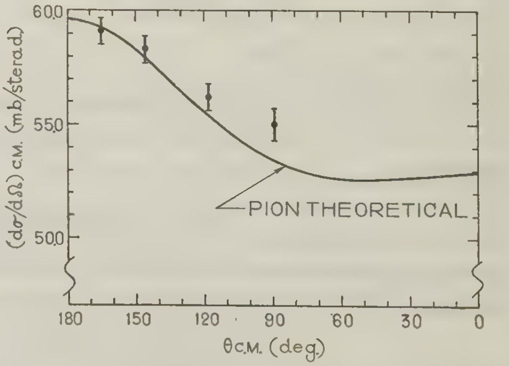

Fig. 7. Differential cross section of n-p scattering at 14.1 MeV. The solid curve represents the cross section calculated from the poin theory.

The numerical equation of the differential cross section at 14.1 MeV is

$$\sigma(\theta)=53.4(1-0.0535\cos\theta+0.0468\cos^2\theta$$
$$-0.0102\cos^3\theta+0.00526\cos^4\theta)\ \text{mb/sterad.},$$

and is shown by a solid-line curve in Fig. 7. The present experimental values are in good agreement with the pion theoretical results. Therefore it can be concluded that these proposed nuclear potentials are verified also for *n-p* scattering at 14.1 MeV.

The author wishes to thank Prof. K. Kimura and Prof. S. Yasumi for their interest and encouragement during the course of this work. He expresses his sincere thanks to Dr. I. Kumabe and Dr. H. Ogata for their valuable suggestions, many discussions and co-operative contributions to this work. His thanks are also due to Dr. W. Watari for valuable theoretical discussions. This work has been supported by the Scientific Research Expenditure of the Ministry of Education.

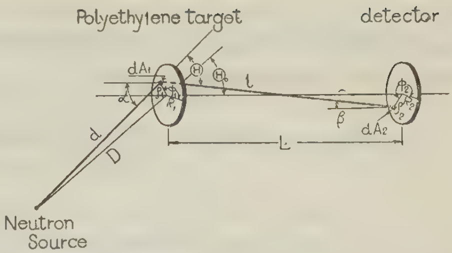

Fig. 8. Geometry of the counter-telescope. R_1 is the radius of the polyethylene target, R_2 is the radius of the aperture of the detector, D is the distance between the neutron source and the polyethylene target, d is the travelling distance of neutrons from the neutron source to the area element dA_1, L is the distance between the target and the aperture of the detector, l is the travelling distance of recoil protons from dA_1 to dA_2, Θ_0 is the setting angle of the counter-telescope axis, Θ is the angle between the travelling lines of the neutron and the recoil proton, α is the angle between d and a line drawn perpendicular to dA_1, and β is the angle between l and a line drawn perpendicular to dA_2.

Appendix

Derivation of the correction factor $C(\Theta_0)$ to the finite solid angle will be described. The geometry and coordinate systems used in the calculation for the derivation of the correction factor $C(\Theta_0)$ are shown in Fig. 8. The number of neutrons which pass through the differential solid angle defined by the area element on the polyethylene target dA_1 is $N_n dA_1\cos\alpha/d^2$ where N_n is the neutron flux per steradian from the source, and α and d are defined in Fig. 8. Hence, the number of proton recoils from dA_1 in the differential solid angle defined by the area element on the detector dA_2 is

$$N_n\left(\frac{dA_1\cos\alpha}{d^2}\right)\left(\frac{P}{\cos\alpha}\right)\sigma_{\text{lab}}(\Theta)\left(\frac{dA_2\cos\beta}{l^2}\right),$$

where P is the number of hydrogen atoms per unit area, $\sigma_{\text{lab}}(\Theta)$ is the differential cross section in the laboratory-system of *n-p* scattering, and β and l are defined in Fig. 8. This equation, when integrated over the planes of the polyethylene target and the aperture of the detector, gives the equation of the counter-telescope counting rate as:

$$n(\Theta_0)=N_n\int^{A_1}\int^{A_2}\frac{dA_1\cos\alpha}{d^2}\,\frac{P}{\cos\alpha}\cdot 4\cos\Theta\cdot\sigma_{\text{C.M.}}(\theta)\,\frac{dA_2\cos\beta}{l^2}, \qquad \text{(A-1)}$$

where $n(\Theta_0)$ is the counting rate at setting angle Θ_0 of the counter-telescope axis, and the differential cross section in the C.M.-system $\sigma_{\text{C.M.}}(\theta)$ is inserted into $\sigma_{\text{lab}}(\Theta)$ using the relation of $\sigma_{\text{lab}}(\Theta)=4\cos\Theta\sigma_{\text{C.M.}}(\theta)$.

In order to evaluate Eq. (A-1), polar coordinate systems (ρ_1, ϕ_1) and (ρ_2, ϕ_2) are taken on the planes of the polyethylene target and the aperture of the detector, respectively. Then, Eq. (A-1) is rewritten as:

$$\begin{aligned} n(\Theta_0)=4N_nP\iiiint &\sigma_{\text{C.M.}}(\theta)\cdot L[(DL\cos\Theta_0-\rho_1{}^2+D\sin\Theta_0\rho_1\ \text{cps}\ \phi_1\\ &+\rho_1\rho_2\cos(\phi_1-\phi_2)-D\sin\Theta_0\rho_2\cos\phi_2)/\\ &(D^2+\rho_1{}^2-2D\sin\Theta_0\rho_1\cos\phi_1)^{3/2}\cdot(L^2+\rho_1{}^2+\rho_2{}^2-2\rho_1\rho_2\cos(\phi_1-\phi_2))^2]\\ &\times\rho_1\rho_2\,d\rho_1\,d\rho_2\,d\phi_1\,d\phi_2, \end{aligned} \qquad \text{(A-2)}$$

where D, L and Θ_0 are constants defined in Fig. 8.

This Eq. (A-2) can be integrated analytically, if $\sigma_{\text{C.M.}}(\theta)$ can be assumed to be constant in the region of the integration, giving

$$n(\Theta_0)=4N_nP\sigma_{\text{C.M.}}(\theta)\frac{\pi^2R_1{}^2R_2{}^2}{D^2L^2}\left[\cos\Theta_0\left\{1-\frac{R_1{}^2+R_2{}^2}{L^2}-\frac{R_1{}^2}{D^2}\left(\frac{3}{4}-2\sin^2\Theta_0\right)\right\}-\frac{R_1{}^2}{2DL}\left(1-\frac{3}{2}\sin^2\Theta_0\right)\right], \tag{A-3}$$

where θ is the mean angle (in the C.M.-system) of scattered neutrons in the region of the integration, and R_1 and R_2 are the radii of the polyethylene target and the aperture of the detector, respectively. (Terms of higher order than $(R_1/D)^4$ or $(R_2/L)^4$ have been neglected, since they are negligibly small in the present experimental geometry.) From the counting rate equation, the differential cross section per unit solid angle in the C.M.-system is rewritten as

$$\sigma_{\text{C.M.}}(\theta)=\frac{n(\Theta_0)}{G}\Big/4\cos\Theta_0\cdot C(\Theta_0)\ , \tag{A-4}$$

where $G\equiv N_nP(\pi^2R_1{}^2R_2{}^2/D^2L^2)$ and $C(\Theta_0)$ is the correction factor to the finite solid angle, which is given by

$$C(\Theta_0)=1-\left[\frac{R_1{}^2+R_2{}^2}{L^2}+\frac{R_1{}^2}{D^2}\left(\frac{3}{4}-2\sin^2\Theta_0\right)+\frac{R_1{}^2}{2DL\cos\Theta_0}\left(1-\frac{3}{2}\sin^2\Theta_0\right)\right]. \tag{A-5}$$

Numerical values of $C(\Theta_0)$ calculated by this Eq. (A-5) are shown in Table V.

Table V. Correction factors to the finite solid angle at various setting angles.

Θ_0	0.5°	15.5°	30.5°	45.5°
$C(\Theta_0)$	0.9893	0.9900	0.9921	0.9950

References

1) For a review of the angular distribution of *n-p* scattering, see J. L. Fowler and J. E. Brolley: Rev. Mod. Phys. **28** (1956) 103.
2) W. Pauli: *Meson Theory of Nuclear Forces* (Interscience Publishers, Inc., New York, 1946), 55.
3) A. Galonsky and J. Judish: Phys. Rev. **98** (1955) 1168.
4) R. H. Stahl and N. F. Ramsey: Phys. Rev. **96** (1954) 1310.
5) H. H. Barschall and R. F. Taschek: Phys. Rev. **75** (1949) 1819. J. C. Allred, A. H. Armstrong and L. Rosen: Phys. Rev. **91** (1953) 90. J. D. Seagrave: Phys. Rev. **97** (1955) 757.
6) J. Iwadare, S. Otsuki, R. Tamagaki and W. Watari: Supp. Progr. Theor. Phys. **3** (1956) 32 (Part II).
7) For example, B. Rossi: *High-Energy Particles* (Prentice-Hall, Inc., New York, 1952) 29.
8) H. L. Poss, E. O. Salant, G. A. Snow and Luke C. L. Yuan: Phys. Rev. **87** (1952) 11.
9) M. Taketani, S. Nakamura and M. Sasaki: Progr. Theor. Phys. **6** (1951) 581. M. Taketani: Supp. Progr. Theor. Phys. **3** (1956) 1.
10) T. Hamada, J. Iwadare, S. Otsuki, R. Tamagaki and W. Watari: Progr. Theor. Phys. **22** (1959) 566.
11) W. Watari: Private communication.
12) M. Matsumoto: Progr. Theor. Phys. **13** (1955) 329.
13) F. Rohrlich and J. Eisenstein: Phys. Rev. **75** (1949) 705.

JOURNAL OF THE PHYSICAL SOCIETY OF JAPAN, Vol. 15, No. 8, AUGUST, 1960

On the High Energy Soft Components at 2770 m Altitude

By Tadashi KAMEDA and Toshio MAEDA

Department of Physics, Kobe University, Kobe

(Received Feburary 9, 1960)

An apparatus consisting of GM-counter hodoscopes and an ionization chamber with large area was used to measure cascade showers initiated by electrons and photons at 2770 m altitude (Mt. Norikura). The number of shower particles deduced from the pulse height of the ionization chamber was converted into energy of the electron (or photon) initiating the shower.

The results show that, in the energy range of 2-20 Bev, i) the zenith angle distribution of electrons is represented by $\cos^5\theta$, ii) the differential energy spectra can be represented by a power law of the form $E^{-\gamma}$ with γ of 2.90 ± 0.05 and 2.83 ± 0.05 for electrons and photons respectively, and iii) upper limit of the ratio of the number of electrons to that of photons is 1.1 ± 0.1.

The present results were compared with those obtained near sea level and the origin of the soft component was also discussed.

§ 1. Introduction

To study the origin of the soft component at low altitude, it is desirable to compare the results obtained at different altitude. Hitherto, measurements concerning the soft component of energy higher than 1 Bev have been reported by Schein et al. and by Daion[1]. However, the results reported by Schein et al. can not be compared directly with those obtained by Chou[2] near the sea level, because their apparatus used at sea level and at mountain altitude were different in their arrangement, and the latter did not report the absolute intensities of electrons and photons near sea level. In order to compare the results at different altitude and to deduce some reliable conclusions from them, it is necessary to use the same apparatus and the same arrangement in both measurements.

In the previous paper[3] (hereafter referred to as I) we reported some results concerning the soft component of high energy near sea level. The same apparatus was used at Mt. Norikura (2770 m a.s.l.) to measure the soft component at mountain altitude. In the present paper, the results obtained there and discussions comparing them with those obtained near sea level are reported.

§ 2. Apparatus

The apparatus used to measure the soft component is the same as reported in I, except that GM-counters composing tray B and C have effective length of 18.5 cm and diameter of 2.8 cm (instead of diameter of 2.0 cm and of the same length), and the lead absorber between tray F and G has thickness of 15 cm (instead of 10 cm in I). Centers of the tray AS_1 and AS_2 are apart from the center of the tray A by 170 cm and 240 cm respectively, and are placed immediately under the roof whose thickness is 1.5 g/cm² wood and 0.2 g/cm² copper. Experiments were carried out in the wooden hut at Mt. Norikura in the autumn of 1955.

The hodoscopes are triggered by the master pulse of $C^{\geq 1}D^{\geq 3}I^{\geq x}$, where x is the pulse height in terms of unit of Po$-\alpha$, and the pulse height is indicated by the neon lamps connected to 12 channel discriminator.

§ 3. Analysis of the Data and Results

Method of analysing the data is quite similar to that described in I § 3, that is, by inspecting the photographs of the hodoscopes, and by following the criteria mentioned in I § 3A, we select, a) single incident electrons and photons which do not associate with the extensive air shower (EAS) of density $\Delta\geq 4/\text{m}^2$, b) multiple incident electrons and photons, and c) electrons and photons which associate with EAS of density $\Delta\geq 4/\text{m}^2$. The ionization chamber was filled with argon of 99.9% purity and of 4.0 atm. pressure (at 0°C), alike in the sea level experiments. Therefore, the number of shower particles

N_1 corresponding to the pulse height of unit Po$-\alpha$ is 24.0, if the primary electrons (or photons) are incident vertically to the absorber.

(I) *Single incident electrons and photons*

a) Energy spectra of the electrons and photons

Integral number spectra obtained by changing the pulse height to the number of shower particles initiated by the vertically incident primaries, are shown in Fig. 1a and 1b, the former is those of electrons and the latter those of photons for various thickness of absorber.

These spectra are well represented by the form of

$$F(\geq N_x) \propto N_x^{-\nu} \qquad (1)$$

and the values of ν's are listed in Table I.

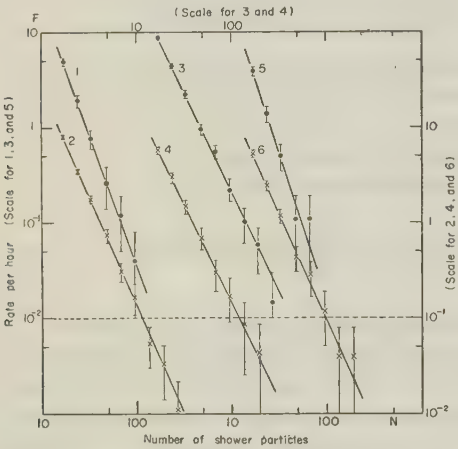

Fig. 1a. Number spectra of shower particles initiated by single incident electron.
1: 1 cm Pb, 2: 2 cm Pb, 3: 3 cm Pb, 4: 4 cm Pb, 5: 4 cm Fe, 6: 8 cm Fe.

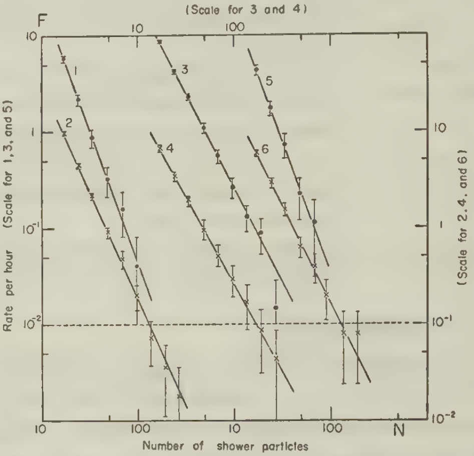

Fig. 1b. Number spectra of shower particles initiated by single incident photon.
1: 1 cm Pb, 2: 2 cm Pb, 3: 3 cm Pb, 4: 4 cm Pb, 5: 4 cm Fe, 6: 8 cm Fe.

Table I.

Absorber material		Pb				Fe	
Absorber thickness		1 cm	2 cm	3 cm	4 cm	4 cm	8 cm
ν	electron	2.70±0.25	2.25±0.14	1.98±0.10	1.86±0.12	2.80±0.28	2.05±0.15
	photon	2.90±0.25	2.28±0.14	2.10±0.10	2.07±0.12	3.08±0.30	2.24±0.15
γ	electron	2.82±0.17	2.95±0.12	2.90±0.10	2.94±0.12	2.57±0.16 (2.86±0·19)*	2.78±0.13 (2.91±0.14)*
	photon	2.81±0.16	2.80±0.11	2.81±0.09	2.85±0.11	2.31±0.13 (2.85±0.18)*	2.84±0.12 (2.87±0.13)*

* These values were calculated by α's obtained from the recent paper of Ivanenko.[13]

As stated in I, assuming that the differential energy spectrum has the form of $E^{-\gamma}dE$, ν is related with γ by the relation

$$\nu = \alpha(\gamma - 1) \qquad (2)$$

where α is a constant appearing in the relation I (7).

For the values of α's for lead, we cited those obtained from the calculated results given by Ivanenko,[4] and for iron those given be Snei der and Serber.[5] The results thus obtained are listed in Table I.

From these figures, the following values of γ are obtained

$$\left.\begin{array}{ll} \gamma_e = 2.90 \pm 0.05 & \text{for electrons,} \\ \gamma_p = 2.83 \pm 0.05 & \text{for photons.} \end{array}\right\} \qquad (3)$$

where the suffix e and p represent the quantity for electron and photon respectively.

(b) Zenith angle distribution of electrons

An example of the projected zenith angle distribution, which is obtained by the discharged GM-counters in tray A and tray B, is illustrated in Fig. 2, which shows the distribution of electrons which initiate the cascade showers giving pulse height of 0.7 Po$-\alpha$ under 2 cm thickness of lead.

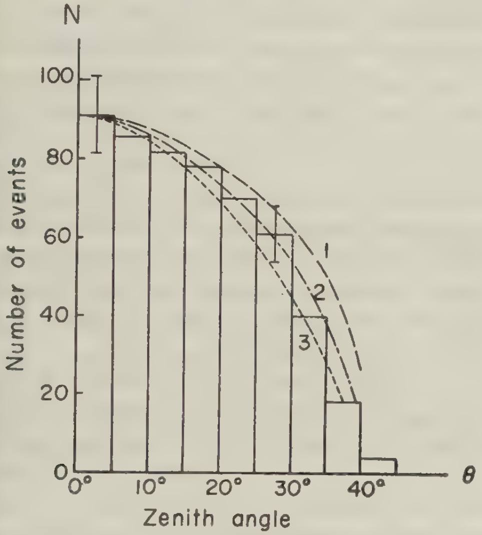

Fig. 2. Zenith angle distribution.
1: m=2,
2: m=3,
3: m=4.

As mentioned in I § 3, if the primary electrons have the zenith angle distribution of the form $\cos^n\theta$, that of the electrons giving rise to pulse heigher than a certain pulse height is represented by the form of $\cos^m\theta$ in our apparatus, where

$$m=n-\alpha(\gamma-1) \qquad (4)$$

The curves in Fig. 2 are the projected zenith angle distribution calculated for the geometry of our apparatus, assuming m=2, 3, and 4. The curve for m=3 appears to fit well with the measured distribution. Therefore, in this case we obtain by (4) n=5, putting $\alpha=1.15$ and $\gamma=2.90$.

Other examples of projected zenith angle distributions obtained for several thicknesses of lead and for 8 cm thickness of iron give the similar results, and from them we conclude that n=5±1.

(c) Absolute intensity of electrons

Absolute intensity of single incident electrons, is obtained by the relation I (9). Assuming the differential energy spectrum of

$$G(E)dE=cE^{-\gamma}dE \qquad (5)$$

and calculating numerically the integral in I (9) for our geometry, we obtained the following value for c_e;

$$c_e \begin{cases} =1.50\times10^{-4}/\text{cm}^2\cdot\text{sec. sterad. BeV for 1 cm and 2 cm thickness of lead} \\ =1.55\times10^{-4}/\text{cm}^2\cdot\text{sec. sterad. BeV for 3 cm thickness of lead} \\ =1.60\times10^{-4}/\text{cm}^2\cdot\text{sec. sterad. BeV for 4 cm thickness of lead} \end{cases} \qquad (6)$$

$$c_e \begin{cases} =1.62\times10^{-4}/\text{cm}^2\cdot\text{sec. sterad. BeV for 4 cm thickness of iron}^{*)} \\ =1.89\times10^{-4}/\text{cm}^2\cdot\text{sec. sterad. BeV for 8 cm thickness of iron}^{*)} \end{cases}$$

The increasing values of c_e for increasing thickness of lead, and the larger value for iron can be consistently explained assuming that the events classified as single incident electron by the criteria I § 3 contain some nuclear events (§ 4 (i)). Correcting these, we obtain

$$c_e=(1.45\pm0.10)\times10^{-4}/\text{cm}^2\cdot\text{sterad. sec. BeV}. \qquad (7)$$

(d) Ratio of the number of electrons and photons

If we assume that the angular distribution for photons is the same as that for electrons, and that the rate of containing the nuclear events is quite similar to the case of electrons, we obtain for various thickness of lead and iron

$$c_e/c_p=1.10\pm0.10\,. \qquad (8)$$

It will be noted that this value is the upper limit of the ratio, because we can not separate individually the particles which are incident close together. Moreover, taking into consideration of the conversion of photons by the roof and upper walls of GM-counters in tray A, the above mentioned value may be lowered to 1.0.

(II) *Multiple incident electrons and photons, and high energy electrons and photons associated with EAS*

---

*) This is calculated by Ivanenko's results.

Table II. No. of Events≥ 0.7 Po-α (/hr).

Absorber material	Pb					
Absorber thickness	1 cm	2 cm	3 cm	4 cm	4 cm	8 cm
Electron shower	5.80±0.40	9.87±0.43	8.58±0.35	6.85±0.55	4.35±0.49	6.02±0.49
Photon shower	4.88±0.37	8.04±0.39	8.80±0.36	5.80±0.50	3.85±0.46	5.37±0.45
Multiple soft shower	4.76±0.44	6.65±0.35	3.15±0.21	2.23±0.31	0.32±0.13	0.54±0.15
E.A.S. associated shower	4.50±0.42	6.07±0.33	2.62±0.22	1.79±0.28	0.32±0.13	0.44±0.12
Penetrating shower	0.82±0.16	1.04±0.08	2.18±0.32	2.67±0.28	1.12±0.25	2.48±0.32
〃 (E.A.S. associated)	2.21±0.30	1.37±0.10	2.73±0.45	3.82±0.33	2.43±0.37	2.25±0.30
Uncertain events	1.92±0.28	2.48±0.21	2.25±0.18	2.05±0.30	1.44±0.28	1.85±0.27

Counting rates of single incident electrons and photons, of multiple incident electrons and photons, and of high energy soft components associated with EAS ($\Delta \geq 4/\mathrm{m}^2$) are listed in Table II. and the number spectrum of multiple incident electrons and photons for 2 cm thickness of lead is illustrated in Fig. 3, as an example. From the table and the figure, the followings are found;

(a) Ratio of the multiple incident electrons and photons to the single incident electrons (or photons) decreases rapidly for 3 cm thickness of lead comparing with that for 2 cm thickness of lead. This fact shows that most of the particles contained in the multiple events are not of high energy but only a few part are of high energy.

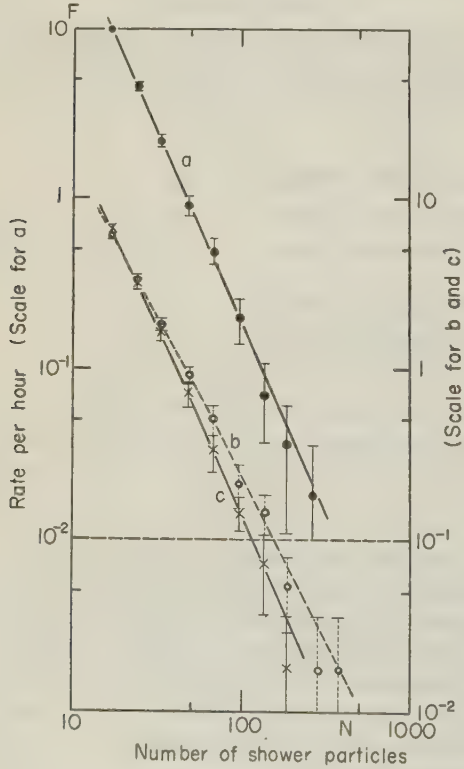

Fig. 3. Number spectra of shower particles.
a: single incident electron
b: EAS associated electrons and photons
c: multiple incident electrons

(b) The number spectrum, as shown in Fig. 3, is less steep than those of single incident electron (or photons) at $N \leq 60$, but approaches to $\nu = 2.25$ for large N. The difference of the values of exponent at $N \leq 60$ is 0.15. The same facts are observed for various thickness of absorber material.

(c) High energy electrons and photons are scarcely found in EAS of small density, and the rate of existence increases slightly in EAS of large density. The same result as stated in (a) is also found in them. The value of ν is less steep than that of multiple events, and at large N (≥ 60) it tends to 1.95 ±0.15.

§ 4. Discussion

i) *Errors involved in the data*

The rate of occurrence of nuclear interactions involved in the data, which is classified as single incident electron (or photon), will be known by comparing the results obtained near sea level with those at mountain altitude. c_e at mountain altitude (c_{em}) to c_e near sea level (c_{es}) is 3.7 for 2 cm thickness of lead (1/8 nuclear interactian length), and is 4.6 for 8 cm thickness of iron (1/2 nuclear interaction length). From these figures, neglecting the nuclear interaction at sea level, we may conclude that the data at mountain altitude classified as the single incident electrons (or photons) contain nuclear interaction of 20% of them for 8 cm iron, and those of 5% for 2cm thickness of lead. This will reasonably explain the difference of the values of c_e for different thickness of lead. Thus, correcting for the nuclear interaction, we obtain for c_{em}/c_{es},

$$c_{em}/c_{es}=3.52\pm0.10\ .$$

ii) *Penetrating showers*

The same facts as mentioned in I (§4, E (b)) are also observed in this measurements. Referring to the discussion stated there, we may conclude that the power law with constant exponent holds for the energy range measured and the electron and photon intensities should be increased by 5% (as the upper limit) taking into account the parallel events, in which the electronic components and penetrating components are incident on the apparatus simultaneously.

The integral energy spectra of soft components, including the events stated in §3 (II) and the above mentioned, are illustrated in Fig. 4. The errors of the total intensity in the figure may be nearly 15%, because of the inaccuracy of the energy of electrons and photons contained in the multiple events and in EAS.

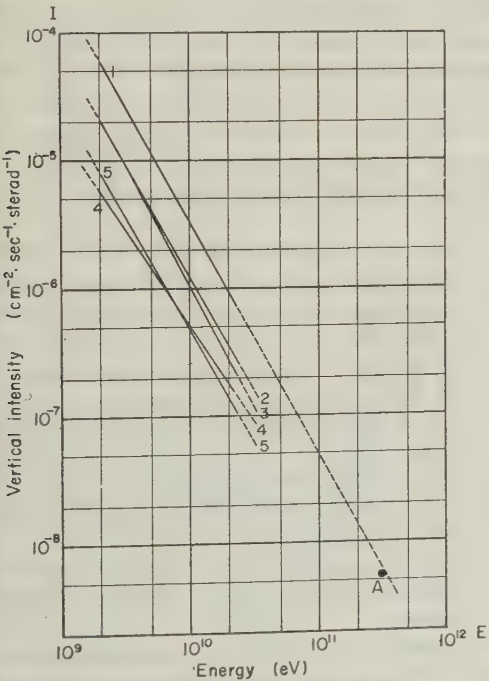

Fig. 4. Integral energy spectra of soft component.

1: total electronic component
2: single incident
3: single incident electron
4: EAS associated electrons and photons
5: Multiple incident electrons and photons
A: I.N.S. emulsion group

iii) *Origin of electrons and photons*

Assuming that the absorption mean free path of nucleons is 120 g/cm² in air, we conclude from the value of ratio c_m/c_s that 70% of the soft components of energy ≥ 2 BeV originate from μ-mesons and 30% from N-components at sea level, and these figures are altered to 20% and 80% at mountain altitude. This explains also the difference of the zenith angle distribution between the two altitudes. The zenith angle distribution of μ-mesons which are the primaries of the soft component of the measured energy interval at sea level and at mountain altitude is expressed by $\cos^{0.5}\theta$, referring to the intensities and zenith angle distribution underground[6] and the momentum spectrum of μ-mesons of vertical and inclined direction.[7] Thus, the zenith angle distributions of the soft components at sea level and at mountain altitude are expressed by $0.3\cos^{8}\theta+0.7\cos^{0.5}\theta$ and $0.8\cdot\cos^{6}\theta+0.2\cos^{0.5}\theta$ respectively, and they may be represented roughly by $\cos^{2}\theta$ and $\cos^{5}\theta$ in the interval of measured zenith angle (0°–40°).

iv) *Comparison with other measurement*

According to Daion,[1] electrons and photons of energy 0.4–2 BeV have the integral energy spectra of the form $E^{-(\gamma+1)}$, where $\gamma=2.5\pm0.2$, and at higher energies the value of γ increases at 3200 m altitude. We believe that the value of γ increases gradually between 1 BeV–3 BeV and reaches to 2.9. Schein and Chou[1] reported that $\gamma=2.6$ between 1 and 30 BeV for the single incident electrons and photons, and $\gamma=2.4$ for the electrons and photons corresponding to the multiple incident ones in our classification. Though their values seem to be less than ours by 0.2–0.3, one of the causes of the difference lies in taking account of the angular spread of the shower particles and the zenith angle distribution of primary particles in our case. We confirmed that the energy spectra obtained neglecting the above accounts had the nearly same form as reported by them. As another reason, the difference of height of the places where the measurements were performed may be also considered.

Recently, the intensity of the electronic component of $\geq$300 BeV is measured at Mt. Norikura by I.N.S. emulsion group.[8] According to their preliminary results, intensity at 300 BeV is $5.4 \times 10^{-9}/\mathrm{cm}^2 \cdot$sec. sterad., and it lies on the line extraporated to 300 BeV in Fig. 4. Thus, the energy spectrum obtained by us seems to hold up to ~300 BeV.

v) *Comparison with the calculated results*

Intensities of electronic components are calculated by Hayakawa[9] and by Tachibana,[10] who calculated the contribution from the μ-meson decay, the collision process of μ-mesons, and π°-meson decay to the electronic component. Contribution from the μ-meson decay and collision, and that from the π°-meson decay are also calculated by Stroffolini[11] and by Cadorin,[12] respectively.

Comparing our results to the calculated ones, the followings are clarified qualitatively:

a) Values of exponents in the energy spectra coincide with the calculated ones within the experimental errors at both altitude.

(b) The calculated ratio of the electronic components from μ-mesons to those from π°-mesons fits well with ours.

c) The calculated absolute intensities fit well with ours in Ref. (9), but in Ref. (10) the difference amounts to factor 3 in both altitudes.

d) The ratio c_e/c_p agrees with ours at sea level but it departs from ours at mountain altitude (calculated $c_e/c_p=0.7$, ours 1.1 ± 0.1).

Though there are some discrepancies between the observed results and the calculated ones, it appears to be verified that the origin of the soft component at the low altitude is explained by the well known processes qualitatively, but there remains some ambiguities quantitatively.

§ 5. Concluding Remarks

The results obtained by the present experiments show that in 2–20 BeV,

i) the zenith angle distribution of single incident electrons is represented by $\cos^5\theta$ at mountain altitude,

ii) vertical flux of single incident electrons and photons is represented by

$$G_e(E)dE = (1.45 \pm 0.10) \times 10^{-4} E^{-2.90} dE/\mathrm{cm}^2 \cdot \mathrm{sec.\ sterad.\ BeV} \text{ for electron}$$

$$G_\nu(E)dE = (1.32 \pm 0.10) \times 10^{-4} E^{-2.83} dE/\mathrm{cm}^2 \cdot \mathrm{sec.\ sterad.\ BeV} \text{ for photon}$$

iii) vertical flux of the total electronic component is obtained taking into consideration the electronic component accompanied by multiple events and EAS, and is represented by

$$G(E)dE = (3.8 \pm 0.5) \times 10^{-4} E^{-(2.82 \pm 0.05)} dE/\mathrm{cm}^2 \cdot \mathrm{sec.\ sterad.\ BeV}$$

iv) ratio of electrons to photons, c_e/c_p, is 1.1 ± 0.1,

v) at mountain altitude, 20% of the electrons and photons originate from μ-mesons and 80% from π°-meson decay, and near sea level their rates are 70% and 30% respectively,

vi) origin of the electronic component at the low altitude appears to be explained by the well known processes.

The authors want to express their deep gratitude to Prof. O. Minakawa for his advice and encouragement for this work. They also wish to thank Mr. Watanabe for his assistance in carring out the experiment. The authors are greatly indebted to Prof. S. Kikuchi, Director of the Cosmic Ray Observatory of Mt. Norikura, and to Prof. Hirata, the former Director of it, for their permission to use the facilities of the observatory.

References

1) M. Schein and C. N. Chou: Phys. Rev. **98** (1955) 162. M. I. Daion: Sov. Phys. JETP **6** (1958) 897.
2) C. N. Chou: Phys. Rev. **90** (1953) 473.
3) T. Kameda: To be published.
4) I. P. Ivanenko: Dokl. Akad. Nauk SSSR **107** (1956) 819.
5) Rossi: High Energy Particles.
6) E. P. George and G. S. Shrinkantia: Nucl. Phys. **1** (1956) 55.
7) B. P. Roe and S. Ozaki: Bull. Americ. Soc. June 28, 1959. S. Ozaki: Private communication.
8) J. Nishimura: Private communication.
9) S. Hayakawa: Cosmic Rays (in Japanese).
10) A. Tachibana: Soryushiron Kenkyu **6** (1954) 635.
11) R. Strofforini: Nuovo Cimento **10** (1953) 300.
12) D. Cadorin: Nuovo Cimento **10** (1953) 364.
13) I. P. Ivanenko and B. E. Samosdov: Sov. Phys. JETP **8** (1959) 884.

JOURNAL OF THE PHYSICAL SOCIETY OF JAPAN, Vol. 15, No. 8. AUGUST, 1960

Graphitization Stress in Polycrystalline Carbon as An Origin of Dislocations

By Takuro TSUZUKU

College of Science and Engineering, Nihon University
Kanda-Surugadai, Chiyoda-ku, Tokyo, Japan

(Received January 23, 1960)

When a polycrystalline carbon is heat-treated for graphitization, large thermal stress is produced owing to the interference of the extremely anisotropic expansion of each crystallite. The stress of this kind is expected to promote the rearrangement of the crystallites, directly or indirectly, from the so-called turbostratic structure to the tri-dimensional graphite lattice, and so it may be adequately called "graphitization stress". The stress analysis has been made on each of the spherical and the cylindrical (filamentarily textured) polycrystals in which the carbon crystallites are aligned with the basal planes parallel to the external surface. These two models accommodate to the structure of pyrolytic carbon particle and to that of fibrous soft coke respectively. It is shown that in either of these two cases about 3×10^{10} dynes/cm^2 tension in a-direction and about 0.9×10^{10} dynes/cm^2 compression in c-direction can be produced by heat treatment at 2500°C, which are enough to buckle the crystal lattice at the stress concentrations of 5～20 times and may lead to the generation of dislocations. From the corresponding strain distribution curves, the criterion on the stress relaxation by these dislocations has been determined in connection with the crystallite size, which may give a measure of distinction between the so-called soft and hard carbons.

§ 1. Introduction

Previously, by means of electron microscope and diffraction, this author[1] has revealed some structural aspects of graphite connected with the dislocations; *e.g.*, pyramidal layer growth, conicla crystal habit, laminar cleavage, polygonization, net work of etch pits *et al.* Using modern high-resolution electron microscopes (operated at large magnification above ×10,000), Grenall[2] and Fujita-Izui[3] have independently succeeded in direct observation of individual dislocations, alignment and motion consistent with theoretical prediction, lying inside of some natural and artificial graphite flakes. These experimental results are accepted to corroborate the presence of dislocations in the graphite structure. Now, it may be significant to investigate how the initial dislocations are introduced, during the so-called graphitization process of pyrolytic carbons. On the origin of dislocations in crystals, though the definitive analysis is not established at present, some probable mechanisms have been suggested hitherto by several authors[4]; *e.g.*, (*a*) misfit of adjacent nuclei generated at local high super-saturation, (*b*) one-dimensional dislocations in the edge row of the growing terrace, (*c*) curvature of the growing crystal which has met with impurities, (*d*) collapse of flat-condensed vacancies, (*e*) mechanical buckling of crystal lattice caused by stress concentration *et al.* Among these proposals, the mechanisms (*d*) and (*e*) attract our attention in the respect that they are considered to accommodate especially to graphite as to be described in the following paragraphs.

In the most cases, graphite crystals are prepared by the heat treatment of polycrystalline carbons at extremely elevated temperature up to 2500～3000°C. Hence, the interference of extremely anisotropic thermal expansion of each crystallite may arise large internal stresses enough to buckle the crystal lattice at the stress concentrations of really possible magnitude, and may lead to the spontaneous formation of dislocations. On the other hand, as pointed out by Mrozowski[5], the stress of this kind is expected to promote the rearrangement of the crystallites from the so-called turbostratic structure to the tridimensional graphite lattice, *i.e.* the growth of the crystallite, and so may be called "graphitization stress" hereafter. This may suggest that the mechanism of graphitization is in close connection with the presence of dislocations.

The collapse of condensed vacancies which may develop to the dislocation ring is presumed to easily take place in graphite because of the characteristic stacking layer structure and of the high temperature treatment, and will be discussed in detail separately.

§ 2. Basic Models and Equations

2A. *Carbon Spherulite*

Firstly, let suppose a spherical carbon particle as schematically illustrated in Fig. 1, in which the turbostratic carbon crystallite are aligned with the basal planes tangential to the external surface, so that the c-axes are radially oriented arround the centre. By means of electron shadow-microscope and diffraction, Grisdale[6] has shown that the structure of black carbons resulting from the pyrolysis of gaseous hydrocarbons is well represented by such a model, which is caused by the intermediate formation of droplets of complex hydrocarbons prior to the solidification. According to him, moreover, the morphology of carbon products obtained from highly cross-linked organic polymers is wholly analogous to those for the pyrolytic black carbons. Therefore, this model is taken to be appropriate, in general, for the structure of hard (non-graphitizing) components which are left over the organic solvent extraction as the so-called free carbons. Hereafter, the structure of this kind may be called "*carbon spherulite*".

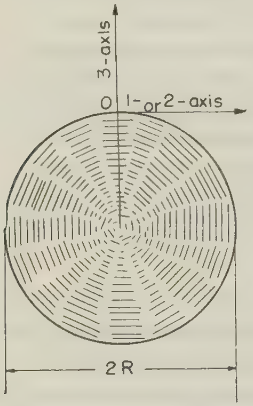

Fig. 1. Structure model of carbon spherulite.

It has been widely accepted that, in polycrystalline carbons, especially the so-called hard one, peripheries of the turbostratic crystallites are tightly hooked by the complicated system of criss-cross valence bonds with one another. Therefore, in discussing the graphitization stresses in a carbon spherulite, we can regard the the aromatic net planes surrounding the centre as to be two-dimensionally continuous and isotropic in approximation. Besides, the strength of the interlayer van der Waals bonds oriented along the radius is supposed to be nearly even all over the particle. Then, if such a spherical elastic continuum is heated uniformly, symmetrical stress distribution with respect to the centre may be obtained, owing to the anisotropy in thermal expansion, and so, the condition of stress equilibrium of a volume element as shown in Fig. 2 is given by the following expression

$$\frac{d\sigma_r}{dr}+\frac{2}{r}(\sigma_r-\sigma_\theta)=0\ , \tag{1}$$

where σ_r and σ_θ denote the normal stresses in radial and tangential directions respectively (shearing components=0). Next, using a rectangular coordinate, 1-, 2-axes in tangential and 3-axis in radial, we obtain the following stress-strain relations;

$$\varepsilon_r-\alpha_r T=s_{33}\sigma_r+2s_{13}\sigma_\theta \tag{2}$$

$$\varepsilon_\theta-\alpha_\theta T=(s_{11}+s_{12})\sigma_\theta+s_{13}\sigma_r\ , \tag{3}$$

where T denotes the temperature variation from the unstressed state, and ε_r, ε_θ, α_r, α_θ and s_{ij} ($i, j=1, 2, 3$) severally represent the strains, the thermal expansivities and the elastic coefficients in the directions indicated by the suffixes.

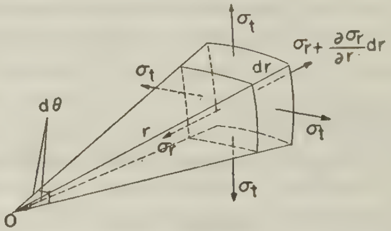

Fig. 2. Volume element in carbon spherulite.

According to Nelson and Riley[7], the thermal expansivity of graphite unit-cell in a-direction has been known very small, even negative below 400°C, as expected for the valence bonding. Since the co-planar bond of ungraphitized carbon is rather stronger than that of graphite, this result may be applicable in the present case; *i.e.*, the second term on the left-hand side of Eq. (3), $\alpha_\theta T$, is neglected in approximation. On the other hand, representing the displacement in the radial direction by u, the strain components are expressed by $\varepsilon_r = du/dr$ and $\varepsilon_\theta = u/r$.

Thus, substituting these relations into the equilibrium equation (1), we can obtain an Euler's differential equation as follows;

$$r^2\frac{d^2u}{dr^2} + 2r\frac{du}{dr} - \frac{2(s_{33}+s_{13})}{s_{11}+s_{12}}u = \frac{2(s_{11}+s_{12}+s_{13})}{s_{11}+s_{12}}\alpha_r T\cdot r\,. \tag{4}$$

According to the present model, α_r is taken to be the expansivity of graphite unit-cell in the *c*-direction determined by Nelson and Riley[7], 28.3×10^{-6}°C^{-1} at room temperature. Similarly, the elastic coefficients of graphite lattice evaluated by Riley[8] are used; *i.e.*,

$$\begin{aligned} s_{11}+s_{12} &= 1.8\times10^{-13}\ \text{cm}^2/\text{dyne}\,,\\ s_{13} &= -4.3\times10^{-13}\quad \text{〃}\,,\\ s_{33} &= 58.5\times10^{-13}\quad \text{〃}\,. \end{aligned}$$

By solving Eq. (4) under the boundary conditions $u=0$ at the centre $(r=0)$ and $\sigma_r(u)=0$ at the external surface $(r=R)$, the stresses and the strains are expressed as the functions of r/R in the following forms;

$$\sigma_r = \left\{5.4\left(\frac{r}{R}\right)^{6.3} - 5.4\right\}T\times10^6\ \text{dynes/cm}^2\,, \tag{5}$$

$$\sigma_\theta = \left\{22.6\left(\frac{r}{R}\right)^{6.3} - 5.4\right\}T\times10^6\quad \text{〃}\,, \tag{6}$$

and

$$\varepsilon_r = \left\{12.5\left(\frac{r}{R}\right)^{6.3} - 1.34\right\}T\times10^{-6}\,, \tag{7}$$

$$\varepsilon_\theta = \left\{1.72\left(\frac{r}{R}\right)^{6.3} - 1.34\right\}T\times10^{-6}\,. \tag{8}$$

2B. *Filamentarily Textured Polycrystal*

The second model is cylindrical one in which the basal planes of the crystallites are parallel to the external surface, surrounding the central axis. In this case, Fig. 1 may be taken to represent the cross section perpendicular to the central axis. This model is appropriate for the filamentary texture of the so-called soft (graphitizing) cokes which is caused by a frozen-in flow pattern, as pointed out by Mrozowski[5], in the viscous fluid at the time of solidification.

The stress analysis may be proceeded in nearly the same way as that for the carbon spherulite, taking into account the contributions of the axial (z) components. The equation of stress equilibrium is given by

$$\frac{d\sigma_r}{dr} + \frac{1}{r}(\sigma_r - \sigma_\theta) = 0\,, \tag{9}$$

similar to the condition in two-dimensional problem. The stress-strain relations are

$$\varepsilon_r - \alpha_r T = s_{33}\sigma_r + s_{13}(\sigma_\theta + \sigma_z) \tag{10}$$

$$\varepsilon_\theta = s_{11}\sigma_\theta + s_{13}\sigma_r + s_{12}\sigma_z\,, \tag{11}$$

$$\varepsilon_z = s_{11}\sigma_z + s_{13}\sigma_r + s_{12}\sigma_\theta\,, \tag{12}$$

where the expansivity of aromatic net-plane surrounding the central axis is neglected (; $\alpha_\theta=0$, $\alpha_z=0$).

Supposing a infinitely long filament, the axial strain ε_z is taken to be zero, and, the radial displacement u is again used as a stress function. Thus, we can obtain another Euler's equation as follows,

$$r^2\frac{d^2u}{dr^2} + r\frac{du}{dr} - \frac{s_{11}s_{33}-s_{12}^2}{s_{11}^2-s_{12}^2}u = \left(1 - \frac{s_{13}}{s_{11}+s_{12}}\right)\alpha_r T\cdot r\,. \tag{13}$$

In the present case, however, the elastic coefficients s_{11} and s_{12} should be separately evaluated for the numerical expression. The aforesaid Riley's treatise[8] on the thermal anisotropy of graphite gives only $s_{11}+s_{12}=1.8\times10^{-13}$ cm²/dyne. Hereupon, by assuming the Poisson ratio of the aromatic plane s_{12}/s_{11} to be 0.3, which is proper value for most isotropic solids, they are computed at $s_{11}=2.57\times10^{-13}$ and $s_{12}=-0.77\times10^{-13}$cm²/dyne.

Thus, the final expressions are as follows;

$$\sigma_r = \left\{5.85\left(\frac{r}{R}\right)^{3.7} - 5.85\right\}T\times10^6\ \text{dynes/cm}^2\,, \tag{14}$$

$$\sigma_\theta = \left\{27.4\left(\frac{r}{R}\right)^{3.7} - 5.85\right\}T\times10^6\quad \text{〃}\,, \tag{15}$$

$$\sigma_z = \left\{18.0\left(\frac{r}{R}\right)^{3.7} - 11.5\right\}T\times10^6\quad \text{〃}\,, \tag{16}$$

and

$$\varepsilon_r = \left\{ 14.6 \left(\frac{r}{R} \right)^{3.7} + 1.87 \right\} T \times 10^{-6} , \qquad (17)$$

$$\varepsilon_\theta = \left\{ 3.13 \left(\frac{r}{R} \right)^{3.7} + 1.87 \right\} T \times 10^{-6} . \qquad (18)$$

§ 3. Numerical Results and Discussions

3A. *Evaluation of Stress*

In order to numerate the graphitization stresses, the temperature variation T should be measured from the point at which the solidifications of carbon material just completes and the stresses are about to arsie. Because of the complex composition of the raw materials, such a point can not be uniquely determined in general, but it would be safe to roughly estimate that at about 1000°C (temperature of industrial baking furnace) the volatilization of the organic components mostly treminates and the high-polymeric plasticity may be replaced by the brittleness of the coke structure. In other words, the constraint on the expansion of each carbon platelets is abruptly strengthened by the increase of the peripheral criss-cross valence bonds, which is coincidently related with the transition from the so-called organic semi-conductor to the carbon semi-conductor in the electron band structure. This estimation is in fairly good agreement with the experimental results concerning the dependence of dimensional change[9], thermal expansion[10] and electronic properties[11] on the heat treatment.

The stresses in the carbon spherulite and the filamentarily textured polycrystal at 2500°C (lowest graphitization temperature) computed by putting $T = 2500 - 1000 = 1500$(°C) are plotted against r/R in Fig. 3. As seen there, the crystallites lying nearby the external surfaces are severally subject to the maximum tension in a-direction, and those in the central parts to the compression in all directions. The maximum values and the ratios to the corresponding Young's modulei of graphite lattice, $1/s_{11} = 39 \times 10^{11}$ dynes/cm^2 in a-direction and $1/s_{33} = 1.7 \times 10^{11}$ dynes/cm^2 in c-direction (see § 2), are tabulated as follows:

(1) Spherulite

Surface $\sigma_\theta = 2.6 \times 10^{10}$ dynes/cm$^2 \approx (150 s_{11})^{-1}$

Centre $\sigma_r = 0.81 \times 10^{10}$ dynes/cm$^2 \approx (21 s_{33})^{-1}$

(2) Filament

Surface $\sigma_\theta = 3.2 \times 10^{10}$ dynes/cm$^2 \approx (120 s_{11})^{-1}$

$\sigma_z = 0.98 \times 10^{10}$ dynes/cm$^2 \approx (395 s_{11})^{-1}$

Centre $\sigma_r = (= \sigma_\theta) = -0.88 \times 10^{10}$ dynes/cm$^2 \approx (19 s_{33})^{-1}$

$\sigma_z = -1.7 \times 10^{10}$ dynes/cm$^2 \approx (230 s_{11})^{-1}$.

In the actual cases, owing to the inevitable assymmetry and heterogenity in the configuration of crystallites, the graphitization stresses may be accompanied by some shearing components other than the normals itemized above. Basing on the assumption that the shearing stress is a sinusoidal function of the displacement with period of the interatomic spacing along the slip plane, the theoretical shearing stress τ_m is expressed by

$$\tau_m = \frac{b}{c} \frac{G}{2\pi} , \qquad (19)$$

where G, b and c denote the seear modulus, the lattice periods parallel and perpendicular

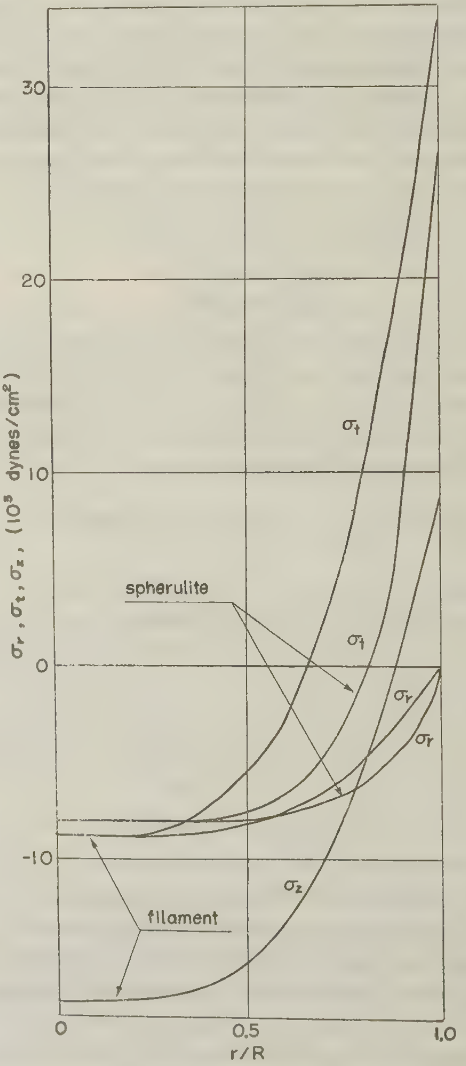

Fig. 3. Stress distribution curves.

to the slip plane respectively[12]. Then, supposing that the abovemensioned ratios in the case of normal stresses are crudely equal to those of the shearing components against the corresponding moduli, one can expect that the graphitization stresses give rise to the local slip at the stress concentrations of about 5∼20 times, breaking the crystal lattice; *i.e.* the spontaneous formation of dislocations. These concentrations may be attained by the presence of the microscopic deffects lying in the graphite structure *a'priori*; *e.g.*, cavities produced by the evaporation of impurities, irregularities nearby the intercrystallite boundaries *et al.*

3B. *Stress Relaxation by Dislocations*

The strain distribution curves at 2500°C are plotted in Fig. 4, corresponding to the stress distribution curves in Fig. 3.

Now, let suppose a crystallite of tangential length x and of thickness δr, lying nearby the external surface. It is easily understood that the crystallite is strained as if a bending deformation is given, and the corresponding curvature is expressed by $1/\rho=(1/x)(\delta x/\delta r)=d\mathcal{E}_\theta/dr$, where ρ and δx represent the curvature radius and the tangential elongation severally. Since the stress is expected to buckle the crystal lattice, as mentioned in the last sub-section, the bending may be taken by plastic flow, and a number of edge dislocations of same sign which have the extra half-planes on the outer side are produced in the way as schematically illustrated in Fig. 5. That is to say, the graphitization stress is released by the formation of dislocations. As well known, the density of such dislocations (n) is determined by the curvature, *i.e.*

$$n=\frac{1}{\rho b}=\frac{1}{b}\,\frac{d\mathcal{E}_\theta}{dr}\,, \tag{20}$$

where b is the magnitude of the Burgers vector.

At the same time, these edge dislocations are expected to cause the so-called polygonization of crystals, through the migration from dispersed distribution to vertical alignment. The polyhedral form of graphitized particles of carbon black *Thermax*, which has been observed by Kmetko[13] and Kuroda-Akamatsu[14], would be explained by this mechanism. While, it is worthy to note that the polygonization has been observed only for the large-particle grade black above 3000 A in diameter. Kuroda ond Akamatsu have shown, in the same experiment, that small-particle grade blacks of 300∼500 A diameter belonging to the typical hard carbon are not polygonized by heat treatment, and some of them ultimately break up into finer fragment at 3000°C. In a ward, the graphitization stress in small particles can not be relaxed by the introduction of dislocations but leads directly to the brittle fracture.

In order to explain this anomaly, our attention should be focussed on the distribution of dislocations. In Fig. 4, one can see that

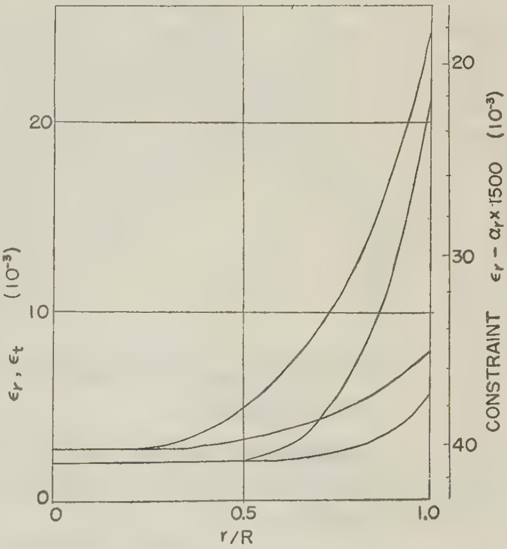

Fig. 4. Strain distribution curves.

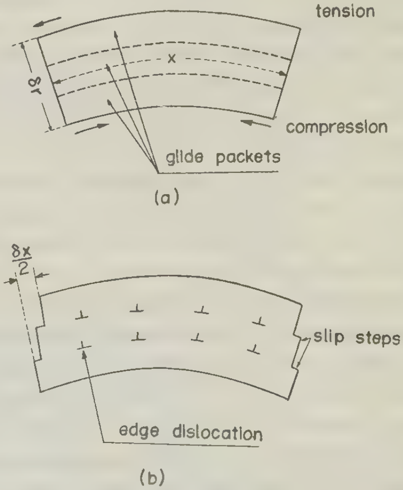

Fig. 5. Formation of edge dislocations by plastic bending of crystal lattice.

the radial gradient of $\mathcal{E}_\theta$ steeply increases toward the external surface, especially in the part between $r/R=0.8\sim1.0$. Therefore, most of the dislocations which contribute to the stress relaxation are concentrated nearby the external surface. Substituting $b=1.42$ A and $\mathcal{E}_\theta$ between $r=0.8R\sim R$ into Eq. (20), the local density n of dislocations in the carbon spherulite and the corresponding average spacing $1/\sqrt{n}$ are plotted against R in Fig. 6 (curves (1) and (2)).

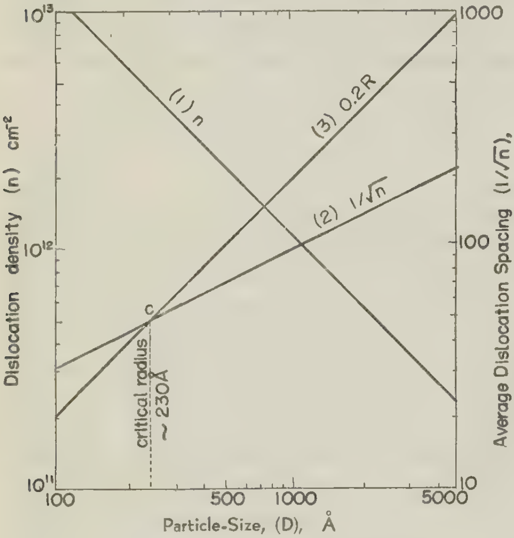

Fig. 6. Dedendence of dislocation density (n) and average dislocation spacing ($1/n$) on particle-size for carbon spherulite.

On the other hand, it is known that on the graphitization of carbon black the limiting size to which the crystallites can grow up is roughly proportional to the particle size; *i.e.* about $1/5\sim1/10$ of the diameter from the X-ray data[15]. Then, it may be appropriate to assume that $0.2R$ $(=R-0.8R)$ just gives the crystallite size itself consisting the spherulite, which is also plotted in Fig. 6 (curve (3)). Now, in the small particles ($R<230$ A) found on the left-hand side of point C in Fig. 6, the crystallite size is smaller than the dislocation spacing, so that some crystallites can not contain the dislocations by which the graphitization stress is released and are inevitably led to fracture by the residual stress.

This explanation implies an assumption that the intercrystallite boundary dividing the spherulite let pass the thermal stress but intercept the stress field arround the dislocations. Such an expectation is seen somewhat arbitrary at the present stage. However, it is possible to say that the stress field of dislocation is less transmissive to the adjacent crystallite as compared with that of thermal stress, since stretching the bond at the boundary is supposed to be fairly anisotropic. In large particles, dislocations are so uniformly dispersed as to form one kind of self-consistent stress field in each crystallite, by which the graphitization stress may be relaxed independently. Conclusively, the basic model assuming the elastic continium can be generally used in the calculation of the graphitization stress, but, in discussing the stress relaxation process it is not applicable for the small particles.

The dependence of n and $1/\sqrt{n}$ on R for the filamentarily textured polycrystal can be similarly computed, and the criterion on the stress relaxation may be formally determined. However, as mensioned before, the filamentary carbons which have been frequently observed in soft cokes are caused by the macroscopic flow pattern in the viscous hydrocarbon fluid, and hence the diameters are by far larger than those of pyrolytic black carbons, ranging from several microns upto about 1/10 mm. Accordingly, the aforesaid criterion is no meaning, and the graphitization stress is easily released by the formation of dislocations and the following motion for redistribution in each crystallite.

§ 4. Concluding Remarks

The principal conclusions obtained in the preceding theoretical investigation are summerized as follows: (1) Heat treatment of polycrystalline carbon for graphitization gives rise to large thermal stress, due to the interference of extremely anisotropic thermal expansion of each crystallite. (2) Evaluation of this so-called graphitization stress made on two representative models (spherical and cylindrical ones) suggests that the stress is enough to produce the dislocations through the direct mechanical buckling of crystal lattice. (3) Stress relaxation process in connection with the formation of dislocation has been discussed, and a criterion is given in order to distinguish the soft and hard carbons. (4) Consequently, the graphitization process of polycrystalline carbon can be thought of a process in which the aforesaid internal stress and the corresponding elastic strain is gradually released, and the generation of dislocations followed by the movement for redistribution may surely play a most important role in it.

In the next stage of the theory, it is required to establish more general treatment of the graphitization mechanism, taking into account the behaviors of the boundary dislocations and other imperfections connected with the crystallite growth.

References

1) T. Tsuzuku: J. Phys. Soc. Japan **12** (1957) 778; Proc. 3rd Carbon Conf., Pergamon Press, London (1959), p. 433.
2) A. Grenall: Nature **182** (1958) 448, and private communication.
3) E. Fujita and K. Izui: Orally published in the Conference on Lattice Defects held at Sendai in Aug. 1959, and private communication.
4) For example, F. C. Frank: Disc. Faraday Soc., Vol. 5 (1948) p. 48.
5) S. Mrozowski: Proc. 1st and 2nd Carbon Conf., University of Buffalo (1959), p. 31.
6) R. O. Grisdale: J. App. Phys. **24** (1953) 1082.
7) J. B. Nelson and D. P. Riley: Proc. Phys. Soc. **57** (1945) 477.
8) D. P. Riley: Proc. Phys. Soc. **57** (1945) 486.
9) F. M. Collins: Proc. 1st and 2nd Carbon Conf., (1955), p. 177.
10) F. M. Collins: Proc. 3rd Carbon Conf., Pergamon Press, London (1959), p. 659.
11) S. Mrozowski: Phys. Rev. **85** (1952) 609, and Errata, Phys. Rev. **86** (1952) 1052.
12) A. H. Cottrell: Dislocations and Plastic Flow in Crystals, Clarendon Press, Oxford (1953), p. 9.
13) E. A. Kmetko: Proc. 1st. and 2nd Carbon Conf. (1955), p. 21.
14) H. Kuroda and H. Akamatsu: Bull. Chem. Soc. Japan **32** (1959) 142.
15) B. E. Warren: Proc. 1st and 2nd Carbon Conf. (1955), p. 49.

JOURNAL OF THE PHYSICAL SOCIETY OF JAPAN, Vol. 15, No. 8, AUGUST, 1960

Kinematic Theory of Ferroelectric Domain Growth

By Terutaro NAKAMURA

Department of Physics, Faculty of Science,
Ochanomizu University, Otsuka, Tokyo

(Received February 6, 1960)

Sidewise motion of 180° wall in ferroelectric barium titanate is described, applying the kinematic wave theory developed by Lighthill-Witham. The rather peculiar shapes of the domain in growing and in shrinking processes, observed by Miller and Husimi, can be derived purely kinematically.

180° wall is described as an assembly of steps. Orientation of the wall is described by step density. There is a part of constant orientation that moves with a constant velocity, which is shown to be identical to the kinematic wave velocity.

Round squares observed in the growing process and straight domain fronts in the shrinking process are fairly well explained as a result of propagation of kinematic waves, assuming a suitable functional relationship between the velocity and the density of the progressing steps. Discontinuity of wall orientation is interpreted as " kinematic shock wave."

§ 1. Introduction

Recently it has been found by Miller[1),2),3)] that the polarization reversal in $BaTiO_3$ single crystal with electrolyte electrodes[9)] is brought about by sidewise motion of 180° wall under application of lower and higher electric fields, in contrast to Merz's[4)] observation that the polarization reversal of crystal with electrodes of evaporated noble metal takes place by nucleation of a good many domains, which appear to grow only in the forward direction under application of higher pulse fields. Very recently, Husimi[5] also observed the sidewise motion of domain walls in crystals with silver-plated electrodes prepared by a chemical process, obtaining essentially similar results as Miller. These authors observed that the smallest switched domains are probably circular in cross sections but grow through sidewide motion of 180° walls into large ones approximately square in cross sections, with sides at 45° to *a*-axis under lower fields, but with sides parallel to *a*-axis under higher fields.

In this paper we discuss the growth and shrinkage of domains in a $BaTiO_3$ single crystal from kinematical point of view, applying the kinematic wave theory developed by Lighthill-Witham[6]. We consider principally the growth and not the nucleation of the domains. The treatment is on the same line as the theory of growth and dissolution of crystals by Cabrera-Vermilyea[7] and Frank[8].

Our treatment indicates that the transient shape of growing domains can be derived by assuming that the rate of motion of steps, that may exist on the domain boundary surface, is a function of the orientation of the surface. Under this assumption, the experimental results by Miller and Husimi will give informations on the progression of steps on the domain boundary surface during domain growth.

§ 2. Kinematic Wave Theory

Consider a one-dimensional flow of a compressible substance in x-direction. Let the particle velocity be $s(x, t)$ and the linear density of the particle be k. The particles must conserve, or we have the equation of continuity:

$$\frac{\partial(ks)}{\partial x}+\frac{\partial k}{\partial t}=\frac{\partial q}{\partial x}+\frac{\partial k}{\partial t}=0 \tag{2.1}$$

where $q=ks$ is the flux, that is, the number of particles passing a particular point in unit time.

Now we shall postulate that the particle velocity s, with which the particles move, is completely determined by proximity of other particles, that is, that the particle velocity s is a function of the linear density:

$$s=s(k) \tag{2.2}$$

and accordingly

$$q=q(k)\ . \tag{2.3}$$

Under this postulate the equation of continuity (2.1) can be rewritten as

$$\frac{dq}{dk}\frac{\partial k}{\partial x}+\frac{\partial k}{\partial t}=0\ . \tag{2.4}$$

If we put

$$dk=\frac{\partial k}{\partial x}dx+\frac{\partial k}{\partial t}dt=0$$

we obtain

$$\frac{dq}{dk}=c(k)=\frac{dx}{dt}\ . \tag{2.5}$$

This means that, if we identify the parts of the substance by the value of k and accordingly of q, then there is a part which moves with a constant velocity $c(x)=dx/dt$. The velocity $c(k)$ is what is called by Lighthill-Witham[6] the "kinematic wave velocity". In $x-t$ space, k and accordingly q are constant along a straight line of slope $c(k)$. This is what is called "characteristic" in the theory of partial differential equations.

Hence we have two important velocities:

$$\left.\begin{array}{l}\text{(1) particle velocity } s(k)=q/k\ ,\\ \text{(2) kinematic wave velocity } c(k)=dq/dk\ .\end{array}\right\} \tag{2.6}$$

If the relation $q=q(k)$ is non-linear, kinematic wave velocity $c(k)$ depends on k, and overtaking of slower waves by faster ones may occur. This is what is called "kinematic shock wave". The shock wave is always accompanied by a discontinuity of k and q. The velocity of the shock wave is given by

$$U=(q_2-q_1)/(k_2-k_1) \tag{2.7}$$

where q_1 and k_1 are the flux and the density on the one side of the shock wave, and q_2 and k_2 are those on the other side.

§ 3. Application of Kinematic Wave Theory to Ferroelectric Domain Growth

The analysis in the foregoing section will be adapted to the two-dimensional growth of domains of barium titanate crystal in $x-y$ plane or the plane perpendicular to c-axis.

For this purpose the domain growth or shrinkage process is conceived of as a progression of steps of lattice planes, as shown in Fig. 1. Let the x-direction be [100] crystallographic axis. The linear density of steps along x-direction is denoted as k, and the height of each step is denoted as h, which is supposed to be an atomic lattice spacing.

It seems not unreasonable to adopt this model, since the domain will have no thickness, change of polarization at the boundary being abrupt, and since the ferroelectric domain boundary is identical to crystallographic twin boundary.

We shall assume that the velocity s of the progression of each step is only the linear density k in x-direction,

$$s=s(k)\,, \tag{3.1}$$

and hence the "step flux" q, that is, the number of steps passing a particular line $x=x_0$ in unit time, is dependent on the step density k alone:

$$q=q(k)\,. \tag{3.2}$$

Then, the method described in § 2 will be applied to a two-dimensional growth of 180° domains in barium titanate.

The density k is taken to be positive for the case shown in Fig. 1a, negative for Fig. 1b. The flux q is taken to be positive, if the steps move in the positive direction of x in Fig. 1a, and positive, if they move in the negative direction of x in Fig. 1b.

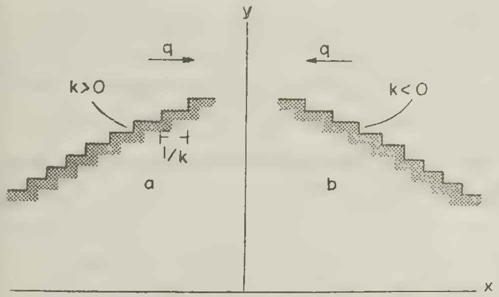

Fig. 1. Description of domain boundary movement by progression of steps.

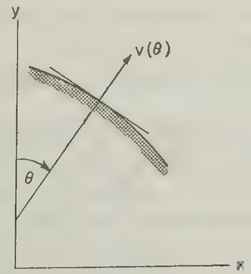

Fig. 2. Orientation of domain boundary surface. θ is the parameter in the couple of Eq. (3.6).

According to our step model, a domain boundary making an angle θ with the (100) plane will be characterised by the density k expressed by:

$$\frac{1}{kh}=\frac{\partial x}{\partial y}=-\frac{1}{\tan\theta}\,. \tag{3.3}$$

The velocity of domain boundary motion along the y-axis is

$$\left(\frac{dy}{dt}\right)_{x=\mathrm{const}}=-\frac{\partial x/\partial t}{\partial x/\partial y}=-qh\,. \tag{3.4}$$

The normal velocity of domain wall is given by

$$v=-qh\cos\theta\,. \tag{3.5}$$

Owing to the functional relationship between q and k on the one hand, and between k and θ on the other hand, we can find a definite functional dependence of v on the angle θ:

$$v=v(\theta)\,.$$

Conversely, if we know the functional form of $v(\theta)$, we have

$$\begin{cases} v(\theta)=-qh\cos\theta\,, \\ \tan\theta=-kh\,, \end{cases} \tag{3.6}$$

which is considered to be an expression of the relation $q=q(k)$ using a parameter θ.

The kinematic wave velocity dq/dk can be brought to a form using $v(\theta)$ as

$$\begin{aligned} c_x(\theta)=\frac{dq}{dk}&=\frac{(d/d\theta)(v(\theta)/\cos\theta)}{(d/d\theta)\tan\theta} \\ &=v(\theta)\sin\theta+v'(\theta)\cos\theta\,. \end{aligned} \tag{3.7}$$

The kinematic wave velocity, $c_x(\theta)$, which is constant for a constant value of θ, is physically interpreted as the x-component of the velocity, with which a point of constant orientation θ on the domain boundary surface moves.

The velocity with which steps actually move in the x-direction (Fig. 1) is

$$s(k)=q/k$$

or

$$s(\theta)=v(\theta)/\sin\theta\,. \tag{3.8}$$

The kinematic shock wave corresponds, in our model, to a discontinuous change of surface orientation and the velocity of the shock wave in x-direction is

$$\begin{aligned} U_x=\frac{q_2-q_1}{k_2-k_1}&=\frac{(v(\theta_1)/\cos\theta_1)-(v(\theta_2)/\cos\theta_2)}{\tan\theta_1-\tan\theta_2} \\ &=\frac{v(\theta_1)\cos\theta_2-v(\theta_2)\cos\theta_1}{\sin\theta_1\cos\theta_2-\cos\theta_1\sin\theta_2}\,. \end{aligned} \tag{3.9}$$

§ 4. Alternative Expression of the Theory

The physical meaning of the kinematic wave will be more intuitively understood as follows. It will be assumed that every point on the domain boundary surface at $t=t_0$ sends out "elementary plane wave," with normal velocity (velocity normal to the boundary surface) $v(\theta)$ which is dependent on the orientation of the boundary surface. After a time interval δt, each "plane wave" will reach a certain position. An envelope of these "elementary plane waves" should give the transient shape of domain boundary at the time $t_0+\delta t$. This procedure may be similar to that used to obtain the wave front of light using Huygens' principle. (Fig. 3)

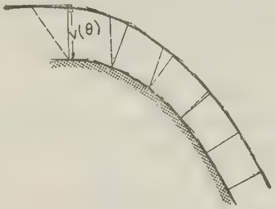

Fig. 3. Movement of a curved domain wall. Note the relation between the normal of domain wall and the trajectory of faces with constant orientation.

Let us take an initial shape of domain boundary given by $F(x, y)=0$. The equation of the tangent to this curve at a point (x, y) on the wall is expressed as

$$x \cdot \sin\theta + y \cdot \cos\theta = p\ , \tag{4.1}$$

where

$$\sin\theta = \frac{F_x(x_0, y_0)}{\pm\sqrt{F_x^2(x_0, y_0)+F_y^2(x_0, y_0)}}\ ,$$

$$\cos\theta = \frac{F_y(x_0, y_0)}{\pm\sqrt{F_x^2(x_0, y_0)+F_y^2(x_0, y_0)}}\ ,$$

$$p = \frac{F_x(x_0, y_0)x_0+F_y(x_0, y_0)y_0}{\pm\sqrt{F_x^2(x_0, y_0)+F_y^2(x_0, y_0)}}\ . \tag{4.2}$$

Note that the envelope of planes (4.1) for various values of θ is identical to the boundary $F(x, y)=0$. The equation of the envelope of the "plane waves" at $t_0+\delta t$ is obtained by eliminating θ from a pair of equations

$$\left\{\begin{array}{l} x \cdot \sin\theta + y \cdot \cos\theta = p + v(\theta)\delta t\ , \\ x \cdot \cos\theta - y \cdot \sin\theta = \qquad v'(\theta)\delta t\ , \end{array}\right. \tag{4.3}$$

and is represented by parameter θ as

$$\left\{\begin{array}{l} x = p \cdot \sin\theta + (v(\theta)\sin\theta + v'(\theta)\cos\theta)\delta t\ , \\ y = p\cos\theta + (v(\theta)\cos\theta - v'(\theta)\sin\theta)\delta t\ . \end{array}\right. \tag{4.4}$$

From the couple of Eq. (4.4) it is obvious that a point of constant orientation θ on the boundary moves with a constant velocity, whose x- and y-components are

$$c_x(\theta) = v(\theta)\sin\theta + v'(\theta)\cos\theta \tag{4.5}$$

and

$$c_y(\theta) = v(\theta)\cos\theta - v'(\theta)\sin\theta \tag{4.6}$$

along a straight line. Note here that $c_x(\theta)$ of (4.5) is the kinematic wave velocity that propagates in the x-direction,

$$c_x(\theta) = dq/dk\ ,$$

and similarly $c_y(\theta)$ of (4.6) is that in the y-direction.

Now, let us consider a functional form, for example,

$$v(\theta) = v_0(1 + A\cos 4\theta) \tag{4.7}$$

which is a continuous function of θ. In Fig. 4 this functional form is represented as a curve

$$r = 1/v(\theta)\ , \tag{4.8}$$

which may be called the polar diagram of reciprocal rate of domain growth.*

First, we consider domain growth from a

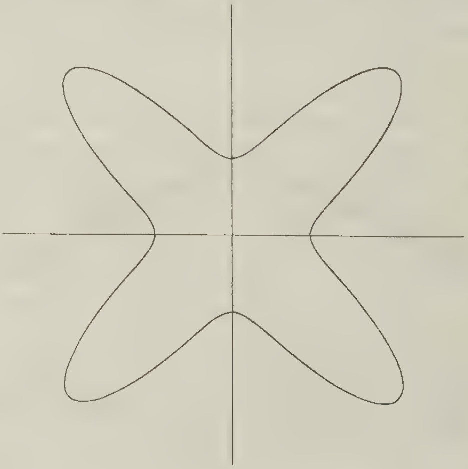

Fig. 4. Polar diagram of reciprocal rate of domain growth

$$r = 1/v_0(1 + A\cos 4\theta). \qquad [A=0.5]$$

---

* Advantage of adopting this curve, instead of $r=v(\theta)$, consists in that the direction of the normal to the curve (4.8) at the point (r, θ) gives the direction of the trajectory of the point of orientation θ on the domain boundary surface. This is easily seen, because the normal to (4.8) has the orientation

$$\frac{c_y(\theta)}{c_x(\theta)} = \frac{v(\theta)\cos\theta - v'(\theta)\sin\theta}{v(\theta)\sin\theta + v'(\theta)\cos\theta}\ .$$

nucleus of circular form. In Fig. 5 are shown trajectories of points with various orientations. For θ smaller than γ, which corresponds to the inflection point of the curve (4.8), trajectories are convergent. In general, however, these trajectories do not focus sharply upon one point, but form an envelope shown in Fig. 5. This situation may be similar to the formation of caustic surface in optical systems.

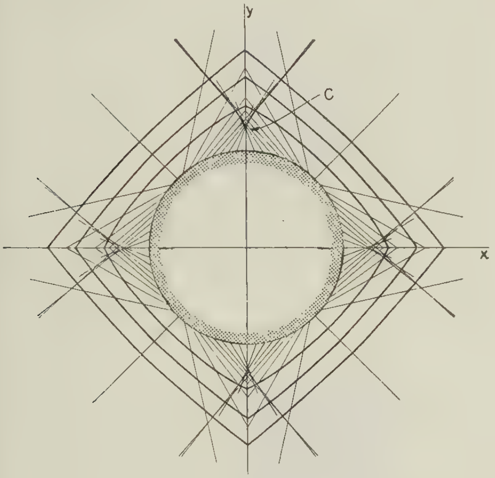

Fig. 5. Theoretical shapes of growing domain, derived from (4.7), trajectories of points with various orientations, and "caustic surface".

Since the equation of a trajectory starting from a point (x, y) on the boundary surface of the circular nucleus domain $x^2+y^2=a^2$ is

$$(x-a\cdot\sin\theta)c_y(\theta)=(y-a\cdot\cos\theta)c_x(\theta)\ , \qquad (4.9)$$

the equation of the envelope of the "caustic surface" is obtained by eliminating θ from (4.9) and

$$-a\cdot\cos\theta c_y(\theta)+(x-a\cdot\sin\theta)c_y'(\theta)$$
$$=a\cdot\sin\theta c_x(\theta)+(y-a\cdot\cos\theta)c_x'(\theta)\ . \qquad (4.9')$$

The equation of the "caustic surface" is

$$\left\{\begin{aligned} x&=-a\frac{v'(\theta)\cos\theta-v''(\theta)\sin\theta}{v(\theta)+v''(\theta)}\ ,\\ y&=a\frac{v'(\theta)\sin\theta+v''(\theta)\cos\theta}{v(\theta)+v''(\theta)}\ , \end{aligned}\right. \qquad (4.10)$$

being represented by parameter θ. The "caustic surface", as shown in Fig. 5, exhibits a cusp at the point C on ⟨010⟩ axis.

Starting from the circular nucleus, the shape of the domain in each stage of its growth will be given by the envelope of the "elementary plane waves", that is, by Eq. (4.4). Since the growth is faster in the direction of the coordinate axis, the shape becomes more and more like a round-sided square. Until the domain boundary reaches the cusp of the "caustic surface", however, the corner is rounded with a finite curuature.

If the domain boundary moves beyond the point C, the discontinuity of the surface orientation of the boundary takes place along ⟨010⟩ axis. That is, trajectories of the point of orientation θ_1 and $-\theta_1$, that statisfy $0<\theta_1<\alpha$, encounter each other on the (100) plane, where α denotes "critical orientation", whose trajectory is parallel to [010] axis, or for which $c_x(\alpha)=0$.* It will be emphasized here that this discontinuity takes place even when we take a continuous function $v=v(\theta)$ as (4.7). This discontinuity or "bunching" corresponds to the kinematic shock wave in the model of the progressing steps. The amount of the discontinuity increases with growing domain, until it reaches an asymptotic value 2α. In the progressing step model the velocity of the kinematic shock wave along x-direction is given by

$$U_x=\frac{v(\alpha)\cos(-\alpha)-v(-\alpha)\cos\alpha}{\sin\alpha\cos\alpha-\sin(-\alpha)\cos\alpha}$$
$$=\frac{v(\alpha)(\cos\alpha-\cos\alpha)}{\sin 2\alpha}=0 \qquad (4.11)$$

in accordance with the fact that the discontinuity moves on the y-axis.

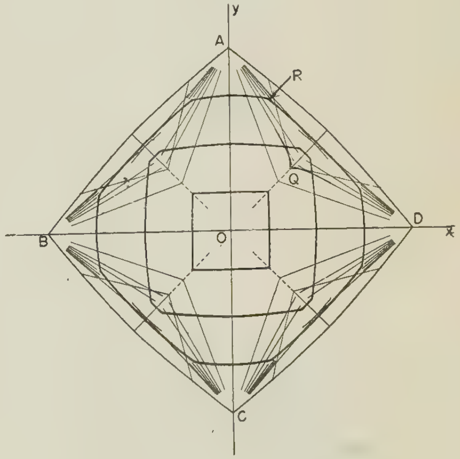

Fig. 6. Theoretical shapes of shrinking domain, derived from (4.7), trajectories of points with various orientations, and "caustic surface".

---

* In the polar diagram representation, ±α correspond to the points at which the outside common tangent contacts with the curve.

Secondly, we consider the process of domain shrinkage that takes place when the field is reversed at a stage in which the domain has grown sufficiently large, as shown by ABCD in Fig. 6. It may be supposed that, in a very narrow region near A, faces of orientations between α and $-\alpha$ are potentially present, and send out the "elementary plane waves". Trajectories for the faces $\theta<\gamma$ starting from the corner are divergent, while ones for faces $\theta>\gamma$ are convergent. In a quite similar manner as in the growing process we may have "caustic surface" formed by the rays of kinematic waves for the faces $\theta>\alpha$, which has a cusp as shown in Fig. 6. Accordingly, when the domain wall reaches the cusp Q while shrinking, a discontinuity of orientation occurs and will move on the line Q_0 in Fig. 6, which is parallel to [110] axis. It must be noted here that, in the shrinking process, another discontinuity R takes place. The latter discontinuity occurs only when the trajectory of the point of orientation $\theta=\gamma$ starts from the corner of the initial domain.

§ 5. Comparison with Experimental Results

From the experimental results obtained by Miller[1], Miller-Savage[2] and Husimi[5], we can summarize the following characteristic aspects of domain growth under lower fields:

(1) On photographs including sequence of domain boundary in a crystal which has been partially switched and successively etched (Photos. 2 and 4) points of given orientation are on a straight line, that is, the trajectory of a point of a given orientation is a straight line.

(2) The normal velocity $v(\pi/4)$ for a surface of $\theta=\pi/4$ is independent of time t.

(3) In the process of domain growth, discontinuity of orientation of domain boundary surface is formed along ⟨100⟩ direction (Photos. 1, 2, 3 and 4), that is, regions of orientation θ which satisfy

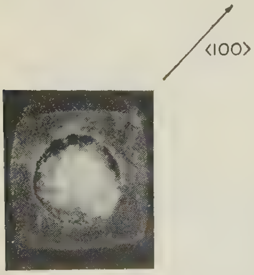

Photo. 1. Photomicrograph of the single switched domain under a lower field, observed on a dimpled sample of $BaTiO_3$. By courtesy of Dr. R. C. Miller.

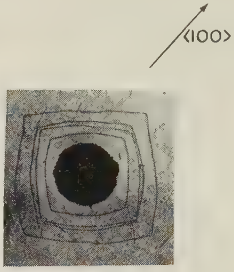

Photo. 2. Photomicrograph of a dimpled $BaTiO_3$ sample which has been partially switched and etched, four times. The transient shape of the growing domain in a stable form is observed. By courtesy of Dr. R. C. Miller.

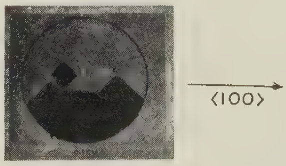

Photo. 3. Photomicrograph of an example of the domain pattern on a $BaTiO_3$ switched at the field 300 v·cm^{-1}. The electrode periphery is shown. By courtesy of Dr. R. C. Miller.

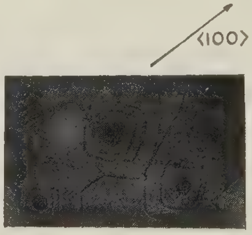

Photo. 4. Photomicrograph showing shape of growing domains, switched under a low field. By courtesy of Dr. K. Husimi.

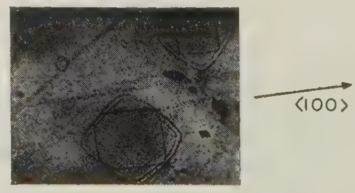

Photo. 5. Photomicrograph showing shape of shrinking domains. Note that the wave front in shrinking process is sharply straight. By courtesy of Dr. K. Husimi.

$$-\alpha \leq \theta \leq \alpha$$

are not realized, where α is found to be about 33°.

(4) In the process of domain shrinkage, a discontinuity is formed along ⟨110⟩ direction. Walls are in this case scarcely curved. There occurs another discontinuity, where the straight wall front meets the round wall that has started from the edge. (Photo. 5)

It will be seen that all the above features are what we have expected from our theory. That is, the domain wall motion can be described as the propagation of kinematic waves. From the observed angle of discontinuity in the growing process, we obtain the polar diagram of reciprocal domain growth rate as shown in Fig. 8, where the normal becomes parallel to [010] axis at $\theta \fallingdotseq \pm 33°$. To interpret the form of the domain wall with the nearly straight sides observed in the shrinking process, the part near P of polar diagram in Fig. 8 would be rather sharp. The velocity $v(0)$ for $\theta=0$ may be about ten times as large as $v(\pi/4)$. (after Husimi[5])

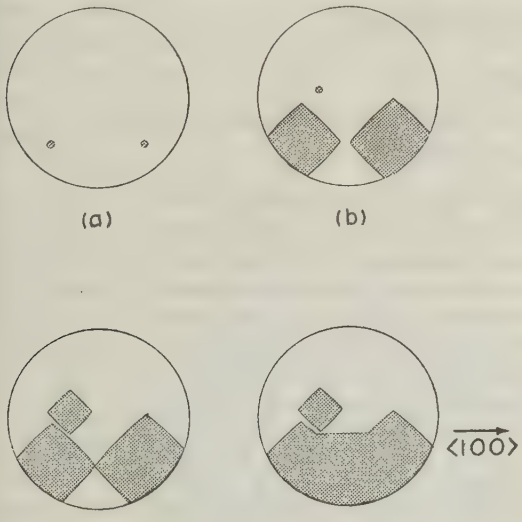

Fig. 7. Successive stages of growth process of the domains shown in Photo. 3.

It is interesting to note that, by applying our theory, we can tell to a certain extent the history that a domain configuration has gone through. For example, let us look at Photo. 3. This domain configuration will be supposed to have been realized by a process as follows. 1) Two nuclei are first formed (Fig. 7a). 2) They grow in a form as shown in Fig. 7b, while a third nucleus is born. 3) Previous two domains coalesce (Fig. 7c). 4) From the concave part of the boundary starts the propagation of a straight wall, which is quite similar as that in the shrinking domain (Fig. 7d).

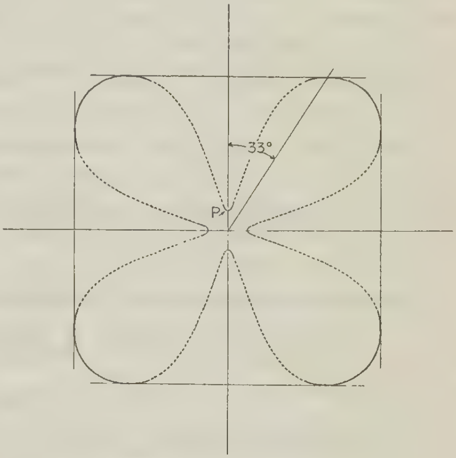

Fig. 8. Polar diagram of reciprocal rate of domain growth, which explains experimental results.

§ 6. Concluding Remark

Present theory indicates that the rather peculiar behavior of domain shape can be derived purely kinematically, only by assuming a suitable functional relation between the velocity and the density of the moving steps in the growing as well as in the shrinking process.

It must be admitted that the present theory is purely phenomenological and the mechanism of step nucleation as well as the factors that determine the elementary processes of step progression under applied fields remain unanswered.

The author wishes to express his sincere gratitude to Professor H. Takahasi of University of Tokyo for his invaluable discussions and encouragement. He is also thankful to Dr. R. C. Miller of Bell Telephone Laboratories and the Physical Review and to Dr. K. Husimi of Electrical Communication Laboratory and the Journal of Physical Society of Japan, for their kind permissions to reproduce photographs. This work was finantially supported by the Grant in Aid for Scientific Research from the Ministry of Education.

References

1) R. C. Miller: Phys. Rev. **111** (1958) 736.
2) R. C. Miller and A. Savage: Phys. Rev. **112** (1958) 755.
3) R. C. Miller and A. Savage: Phys. Rev. Letters **3** (1959) 301; Phys. Rev. **115** (1959) 1176.
4) W. J. Merz: Phys. Rev. **95** (1954) 690.
5) K. Husimi: J. Phys. Soc. Japan **15** (1960) 731.
6) M. J. Lighthill and G. B. Witham: Proc. Roy. Soc. London **229** (1955) 281.
7) N. Cabrera and D. A. Vermilyea: Growth and Perfection of Crystals (Int. Conf. Reports) John Wiley & Son Inc. New York, 1958, p. 398.
8) F. C. Frank: ibid p. 411.
9) *Note added in Proof*
Recently it has been shown by Miller and Savage that aspects of domain growth in metal electroded $BaTiO_3$ crystals are essentially similar to those found with liquid electroded samples. Extensive sidewise motion occurs in both liquid and metal electroded crystals.
R. C. Miller and A. Savage: Phys. Rev. Letters **2** (1959) 294, J. Appl. Phys. **31** (1960) 662.

JOURNAL OF THE PHYSICAL SOCIETY OF JAPAN Vol. 15, No. 8, AUGUST, 1960

Change in Modulus of Rigidity of Brass Wires by Cold-Working and Subsequent Annealing

By Jun KUROYANAGI

Department of Physics, Faculty of Liberal Arts and Science, Yamagata University

(Received March 29, 1960)

The change in the modulus of rigidity caused by cold-working and subsequent annealing was measured on brass wires containing 10.14, 30.15 and 40.24 per cent zinc and a commercial brass wire (32.66 per cent zinc), and compared with that of pure copper wire. The results showed that; (1) in well annealed state, the modulus of rigidity of brass wires decreases quasi linearly with the increase of zinc content, (2) the modulus of rigidity of a brass wire always decreases with the increase of the degree of cold-working, but the relative decrease of the modulus of rigidity compared with the decrease of a pure copper wire equally cold-worked different according to the zinc content and (3) the variations in the temperature coefficient of the modulus of rigidity with the method of cold-working and with the degree of cold-working have a characteristics according to the zinc content.

§ 1. Introduction

Previously[1], the present author measured the change in the rigidities of wires of pure copper and also of 70/30 brass which had been subjected to a cold-working and subsequent annealing, and found that the existence of 30 per cent zinc gives a conspicuous influence on the effect of the above mentioned treating. Now, as it seems to him interesting to elucidate this phenomenon in detail, this investigation was undertaken.

§ 2. Specimens and method of measurement

The materials used were the three kinds of alloys containing 10.14, 30.15 and 40.24 per cent zinc in copper, and also a commercial brass was added. The X-ray diffraction patterns obtained in a Debye-Scherrer camera from these alloys were essentially the same as that of copper. The existence of β phase could not be found even in the brass containing 40.24 per cent zinc. Nevertheless, according to the phase diagram, β phase should coexist with α phase in this brass which may exert some influence on the rigidity of this specimen. The chemical composition of these materials are shown in Table 1. They were drawn into wires, about 1 mm in diameter, from which proper lengths were taken for the specimens. The specimens were first annealed at 600°C for 2 hours in nitrogen atmosphere, and then subjected to cold-working in the manner of

Table 1. Composition of materials used (wt. %)

Materials	Zn	Fe	As	Sb	Bi	Pb
Copper		0.0007	0.00003	0.00001	0.0004	0.0002
Brass 1	10.14	0.004	0.00006	0.00003	0.0004	0.0096
Brass 2	30.15	0.0037	0.00006	0.00003	0.0004	0.0046
Brass 3	40.24	0.0028	0.00006	0.00003	0.0006	0.0024
Brass 4 (Commercial)	32.66	0.0039	0.010	0.001	0.0004	0.15

rolling and twisting. As the degree of rolling was defined by the reduction of area $(A-a)/A$, where A and a denote the cross-sectional area of a wire before and after the rolling, respectively. As the degree of twisting was defined by nd/l, where n is the number of turns, d is the diameter and l is the gauge length. The used technique of the measurement and apparatus were the same as that have been described in the previous paper. The measurements were always made after the specimens had been aged at room temperature for one month.

The specimen set in the apparatus was heated at the constant rate of 1.7°C/min from room temperature to 400°C and the time of 100 rotating oscillations of the pendulum was measured with a stopwatch at every temperatures of 20°C interval during heating.

In addition, the behaviour of the hardness was traced for varying degree of cold-working in correspondence to the rigidity, by means of a micro Vickers hardness tester. To eliminate the error due to the influence of the amount of the loads applied to the indentor on the hardness number, the load was fixed to 500 g and the time of indentation to 1 min.

§ 3. Results

The relations between the square of the frequency f of torsional oscillation, which is approximately proportional to the modulus of rigidity, and the degree of cold-working or temperature of measurement were obtained but not the absolute value of the modulus of rigidity, because the present purpose was to see the relative change in modulus of rigidity.

(1) *Influence of the change of zinc content*

To see the variation of the modulus of rigidity of brass wires with the change of zinc content, the relations between $(f^2_{\mathrm{Brass}}-f^2_{\mathrm{Cu}})/f^2_{\mathrm{Cu}}$ and zinc content were obtained for annealed and cold-rolled specimens at room temperature, where f_{Brass} and f_{Cu} are the frequencies of torsional oscillation, respectively, of brass wire and copper wire equally cold-rolled. Figs. 1 and 2 show the above relations which were obtained for cold-rolled specimens, the degree of cold-rolling of which were 10.5 and 57.5 per cent, before and after they were heated at 400°C for 1 hour and then cooled slowly to room temperature, respectively.

From Fig. 1 it can be seen that the modulus of rigidity of brass wire containing 10 per cent zinc is higher than that of pure copper wire, but that of brass wires containing more than 10 per cent zinc decreases quasi linearly in proportion to the increase of zinc content in the case of 10.5 per cent cold-rolled specimens.

In the case of annealed specimens, before they were heated at 400°C for 1 hour, the modulus of rigidity of pure copper wire is lower than the value which was obtained by the method of extrapolation from the quasi linear relationship, which holds to the modulus of rigidity of brass wires containing more than 10 per cent zinc, as can be seen from Fig. 1. On the other hand, after the specimens were heated at 400°C for I hour, as can be seen

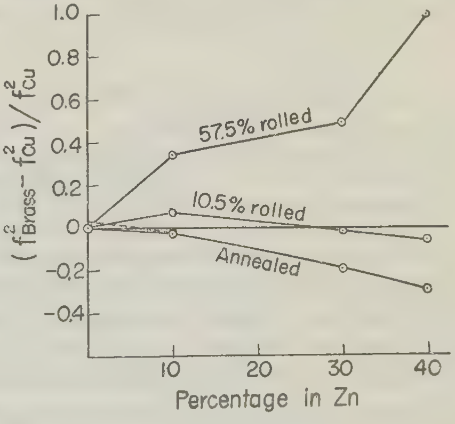

Fig. 1. Modulus of rigidity *vs* percentage of zinc content for cold-rolled brass wires.

from Fig. 2, the modulus of rigidity of the specimens which were either annealed or cold-rolled 10.5 per cent decreases quasi linearly through the whole extent of zinc content.

In the case of the specimens which were cold-rolled 57.5 per cent, regardless of the heating at 400°C for 1 hour, the modulus of rigidity does not change quasi linearly with the increase of zinc content and the specific ratio of the modulus against to that of pure copper increases with the increase of zinc content on the contrary to the case of the specimens which were cold-rolled 10.5 per cent.

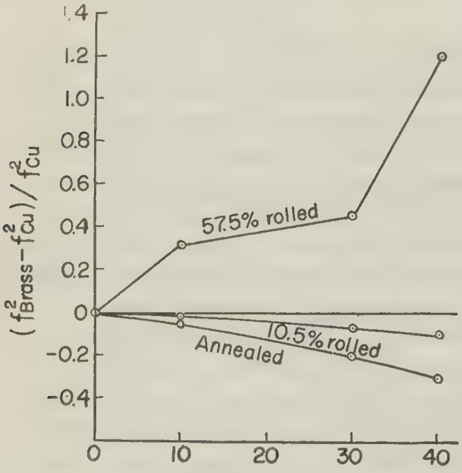

Fig. 2. Modulus of rigidity *vs* percentage of zinc content for cold-rolled brass wires, after annealed400$_0$C, 1 hr.

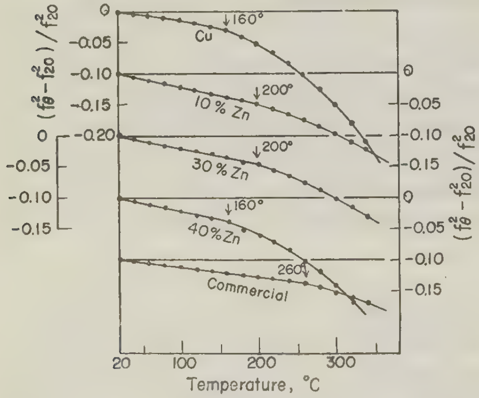

Fig. 3. Change in modulus of rigidity for annealed specimens due to the rising temperature of annealing with constant rate of 1.7°C/min.

(2) *Influence of the rise of temperature at annealed state*

The variation of the rigidity with the rise of temperature was measured with annealed specimens, results being obtained as shown in Fig. 3. In this figure f_θ and f_{20} represents the frequencies of torsional oscillation at a temperature θ and at room temperature (20°C), respectively. Through a set of measurement the observed values in the heating stage almost coincided with that in the following cooling stage at the corresponding temperature respectively. From this figure it can be seen that the rigidity of the normalised specimen decreases slowly in an approximately way with rising temperature, and then remarkably decreases, especially in pure copper and in brass wire containing 40.24 per cent zinc, but in the case of commercial brass wire the temperature range of linearity extends up to a higher point than pure copper and other brass wires.

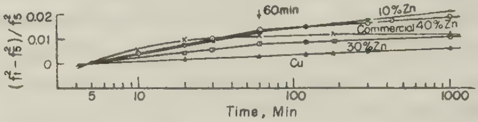

Fig. 4. Relations between $(f_t^2-f_5^2)/f_5^2$ and logarithm of time t at room temperature for cold-rolled specimens, where f_t and f_5 are the frequencies of torsional oscillation at time t and 5 minutes after deformation. Degree of cold-rolling$=$30.5 per cent.

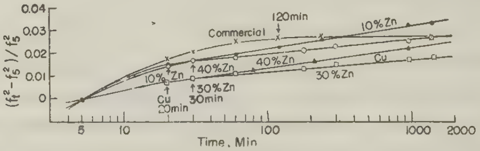

Fig. 5. Relations between $(f_t^2-f_5^2)/f_5^2$ and logarithm of time t at room temperature for cold-twisted specimens, where f_t and f_5 are the frequencies of torsional oscillation at time t and 5 minutes after deformation. Degree of cold-twisting $nd/l=0.10$.

(3) *Recovery of rigidity at room temperature*

The early recovery of the rigidity of a cold-worked specimen is clearly seen from isothermal data. Figs. 4 and 5 show the relations between $(f_t^2-f_5^2)/f_5^2$ and logarithm of the time at room temperature after the cold-work, where f_t and f_5 are the frequencies of torsional oscillation at a time t and 5 minutes after deformation, respectively. From these figures it can be seen that a freshly deformed metal has a relatively low value rigidity, which increases very rapidly in a short time with deformation and then increases almost exponentially from about one hour after deformation, even at room temperature.

(4) *Recovery of rigidity with the rise of temperature in cold-rolling specimens*

Figs. 6–8 show the observed values of $(f^2_{A,\theta}-f^2_{A,20})/f^2_{A,20}$ with relations to temperature for brass wires of various compositions as well as for pure copper wire at various cold-rolled states, where $f_{A,\theta}$ and $f_{A,20}$ are the frequencies of torsional oscillation of the cold-rolled specimens at a temperature θ and 20°C, respectively. It is interesting that the change in the temperature coefficient of the modulus of rigidity with the temperature and with the degree of cold-rolling have a characteristic aspects according to the amount of zinc and impurities contained. Although a definite information cannot be given of the relation between the temperature coefficient of the modulus of rigidity and zinc content, the temperature coefficient in the brass wires containing 10.14 and 30.15 per cent zinc show a great difference from that of the brass wires containing 40.24 per cent zinc and from that of the commercial brass wire. From these figures it can also be seen that the variation of the rigidity with the rise of temperature in copper wire and brass wire subjected to low degree of cold-rolling (10.5 and 30.5 per cent reduction) differs substantially from that subjected to high degree of cold-rolling (57.5 per cent reduction) with an exception of commercial brass wire.

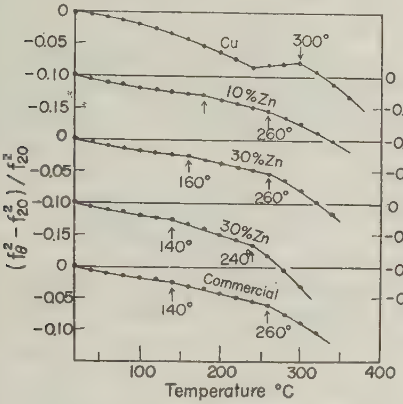

Fig. 6. Relations between $(f_\theta^2-f_{20}^2)/f_{20}^2$ and temperature for cold-rolled various brass wires, where f_θ and f_{20} are the frequencies of torsional oscillation at a certain temperature θ and room temperature, respectively. Degree of cold-rolling was 10.5 per cent for all specimens.

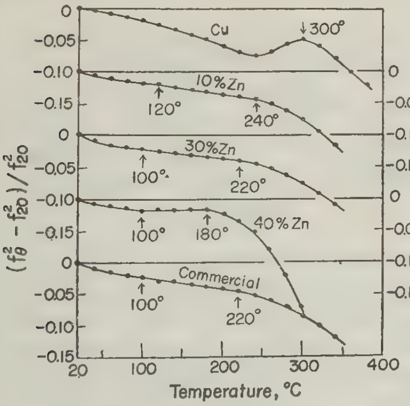

Fig. 7. Relations between $(f_\theta^2-f_{20}^2)/f_{20}^2$ and temperature for cold-rolled various brass wires, where f_θ and f_{20} are the frequencies of torsional oscillation at a certain temperature θ and room temperature, respectively. Degree of cold-rolling was 30.5 per cent for all specimens.

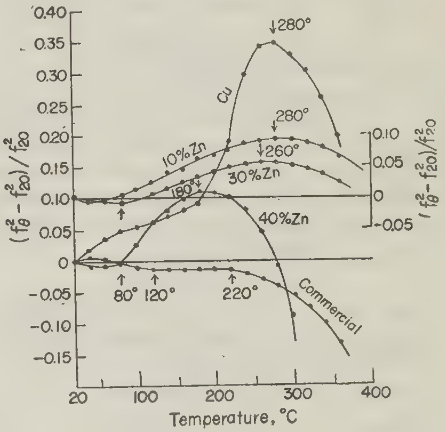

Fig. 8. Relations between $(f_\theta^2-f_{20}^2)/f_{20}^2$ and temperature for cold-rolled various brass wires, where f_θ and f_{20} are the frequencies of torsional oscillation at a certain temperature θ and room temperature, respectively. Degree of cold-rolling was 57.5 per cent for all specimens.

(5) *Recovery of rigidity with the rise of temperature in cold-twisted specimens*

The same observations as above were carried out with cold-twisted wires, the results obtained being shown in Fig. 9. In this case, the temperature coefficient of the modulus of rigidity also varied with temperature and with degree of cold-twisting, showing a characteristic aspect according to the amount of zinc and impurities contained in brass wires. But, this characteristic is not so obvious as that in cold-rolled specimens.

(6) *Change in rigidity due to the removal of internal stress*

Fig. 10 shows the variation of rigidity with the rise of temperature in the brass wire, containing 40.24 per cent zinc, subjected to the cold-rolling of 57.5 per cent. Curve *A* was obtained during first heating, and curve *B* during reheating this specimen after the first heating. Curve *B* was almost reproducible; hence, it may be considered to show the variation of the rigidity with rising temperature of the well annealed specimen. Accordingly, the variation of $(f^2_{A,\theta}-f^2_{B,\theta})/f^2_{B,\theta}$ with temperature θ, where $f_{A,\theta}$ and $f_{B,\theta}$ are the values respectively of the curve A and B at a temperature θ, may be said to show the recovery of the modulus of rigidity by the removal of internal stress due to the rise of temperature.

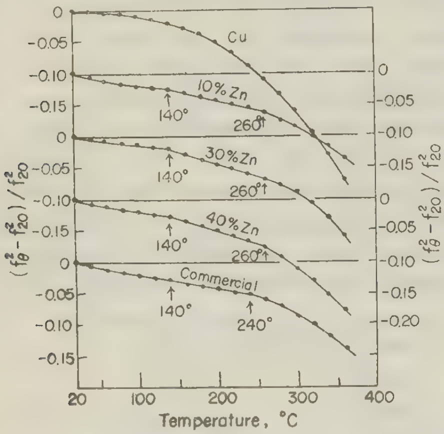

Fig. 9. Relations between $(f_\theta{}^2-f_{20}{}^2)/f_{20}{}^2$ and temperature for cold-twisted various brass wires, where f_θ and f_{20} are the frequencies of torsional oscillation at a certain temperature θ and room temperature, respectively. Degree of cold-twisting was 0.10 for all specimens.

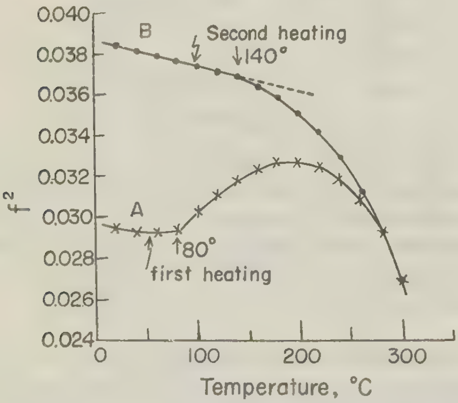

Fig. 10. Change in the modulus of rigidity of the cold-rolled brass wire containing 40.24 per cent zinc, degree of cold-rolling of which was 57.5 per cent, due to the rising temperature of annealing with constant rate of 1.7°C/min.

(a) *Cold-rolled specimens*

To see the effect of zinc on the recovery of rigidity due to the removal of internal stress in cold-rolled specimens, the variation of $(f^2_{A,\theta}-f^2_{B,\theta})/f^2_{B,\theta}$ with temperature θ was measured for various brass wires cold-rolled at almost the same degree (57.5 per cent). The results are shown in Fig. 11. In copper wire the recovery occurs mainly in one stage of the temperature range 180°–320°C as shown in the previous paper[1]. In brass wires containing 10.14 and 30.15 per cent zinc the recovery occurs gradually over the wide range of temperature 80°–360°C, which can be divided into three stages, i. e. 80°–200°C, 200°–

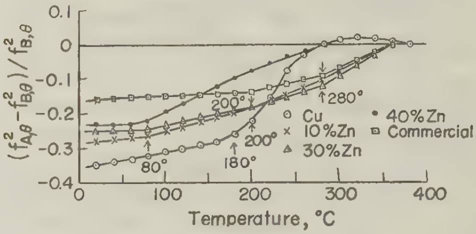

Fig. 11. Relations between $(f^2_{A,\theta}-f^2_{B,\theta})/f^2_{B,\theta}$ and temperature for cold-rolled various brass wires, where $f_{A,\theta}$ and $f_{B,\theta}$ are the frequencies of torsional oscillation at a certain temperature θ for cold-rolled and annealed specimens, respectively. The degree of cold-rolling was 57.5 per cent for all specimens.

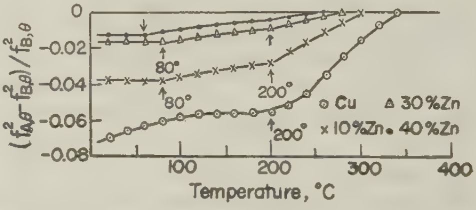

Fig. 12. Relations between $(f^2_{A,\theta}-f^2_{B,\theta})/f^2_{B,\theta}$ and temperature for cold-twisted various brass wires, where $f_{A,\theta}$ and $f_{B,\theta}$ are the frequencies of torsional oscillation at a certain temperature θ for cold-twisted and annealed specimens, respectively. The degree of cold-twisting was 0.10 for all specimens.

280°C and 280°–360°C. In commercial brass wire the recovery occurs mainly in the range of temperature 200°–360°C, which can be divided into the two stages, i. e. 200°–280°C and 280°–360°C. In all cases the recovery takes the greatest rate at the last stage. In brass wire containing 40.24 per cent zinc the recovery occurs rapidly in one stage of the temperature range 80°–280°C.

(b) *Cold-twisted specimens*

Fig. 12 shows the relations between $(f^2_{A,\theta}-f^2_{B,\theta})/f^2_{B,\theta}$ and temperature θ for various brass wires cold-twisted at almost the same degree $(nd/l=0.125)$. In this case, the rigidity of all brass wires recovers over the temperature ranges 80°–200°C and 200°–300°C, and the rate of recovery at latter srage is greater than that at the former stage. These two stages of recovery may by correspond to the former two stages of recovery in the cold-rolled specimens as mentioned in the previous paper¹⁾.

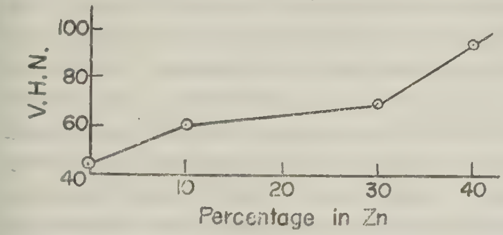

Fig. 13. Relation between Vickers hardness and percentage in zinc content for annealed various brass wires.

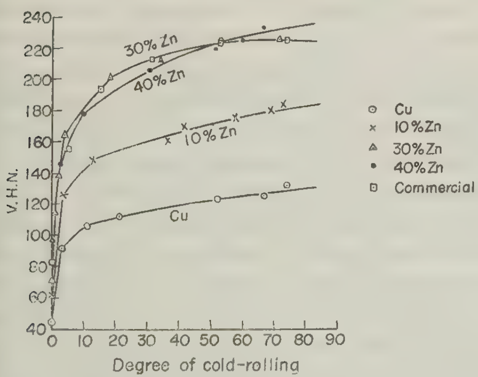

Fig. 14. Relations between Vickers hardness and degree of cold-rolling for cold-rolled various brass wires.

(7) *Change in hardness caused by cold-working*

In Fig. 13 the variation of the Vickers hardness of the annealed brass wires is plotted against the change of zinc content. From this figure it can be seen that the hardness of the annealed brass increases quasi linearly with the increase of zinc content on the contrary to the change of the modulus of rigidity. The change in hardness with the increasing degree of cold-rolling is plotted in Fig. 14. From this figure it can be seen that the curves showing the change in hardness with the increasing degree of cold-rolling are similar to the stress-strain curves which obtained by many workers with brass. It can also be seen that the slopes of these curves increase in proportion to the increase of zinc content.

§ 4. Discussion

(1) *Variation of rigidity of brass wires with the change of zinc content*

The relation between the rigidity and composition in metal alloy is very complicated and it has not yet been satisfactory established.

(a) *Well annealed specimens*

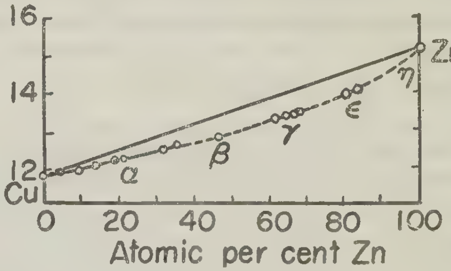

Fig. 15. Volume per atom in Cu-Zn alloy. (Westgren and Almin).

The variation of rigidity of thoroughly annealed and then slowly cooled solid solution alloys of copper can be described in terms of three effects.

(i) *Lattice strain caused by the difference in the atomic radii of the copper and zinc atoms.* It was thought at one time that the variation of lattice parameter in a single phase alloy was an exact linear function of the composition, which is known as Vergard's law. Generally speaking, however, all systems show a greater or less deviation from this law and, when intermediate phases are formed, they are often accompanied by a marked contraction in atomic volume. It appears to be desirable, therefore, to determine the change in lattice constant for the alloys under investigation, in order to measure the lattice strains which they induce. The volume per atom in Cu–Zn alloy is illustrated in Fig. 15, the results being taken from the work of Westgren and Almin[2]. From this figure, it can be seen that the lattice parameter in Cu–Zn alloy increases quasi linearly in the range of α-phase. Zener[3] has studied this problem and found a good correlation between the lowering of the rigidity upon solute addition and the residual strain energy resulting from atomic size disparity.

(ii) *Difference in valence between the solute and solvent metals.* Rigidity of solid solution alloys should be varied with the change in the average number of electrons per atom upon the addition of solute elements. Elliot and Axon[4] showed that the rigidity decreases as the valence of the solute element increase in the case of copper base alloys.

(iii) *Difference in rigidity between the solute and solvent metals.* The fact that the rigidity of pure copper is greater than that of pure zinc should be considered as one of the cause of the decrease of the rigidity of brass wire with the increase of zinc content. Swalinin[5] showed theoretically that the rigidity vary linearly with mole fraction of solute metal for germanium-silicon alloys from this point of view.

(b) *Specimens cold-rolled 10.5 per cent*

In this case, the rigidity of pure copper wire is less than that of brass wire containing 10.14 per cent zinc and deviates from the quasi linear relationship which holds for the modulus of rigidity of the brass wires containing more than 10 per cent zinc. Moreover, the slope of this quasi linear curve is slower than that of well annealed specimens. These facts indicate that the decrease of rigidity in pure copper wire due to the small amount of cold-rolling is very large as compared with that of the brass wire containing 10 per cent zinc and the decrease of rigidity in brass wires containing more than 10 per cent zinc dwindles as the zinc content increase.

The decrease of the modulus of rigidity in the strained pure metal and the associate deviation from the quasi linear relationship in very dilute solution alloys has been observed by Bradfield and Pursey[6] for copper alloys, who observed that after the initial rise of modulus at low concentrations the modulus/concentration curve becomes quasi linear and fall with a slope which may be related to the solidus variations of the particular system, or, perhaps more profitably, to such conventionally accepted alloying factor as atomic size and valence[7]. Furthermore, these phenomena have been discussed by Friedel[8] and by Elliot and Axon[4] in detail, who visualized the effects as being due to the generation of mobile dislocations by small amount of plastic strain and as due to the progressive locking of mobile dislocations with the increase of solute elements. In the present experiment, studied by means of X-ray and metallographic examination, any significant change in structure that account for the change in modulus of rigidity was observed neither before nor after cold-rolling in 10.5 per cent cold-rolled specimens. Consequently, the decrease of rigidity of pure copper wire produced by 10.5 per cent cold-rolling should be due entirely to the lattice distortion and structural defects, without the complicating influence of preferred orientation. In other words, we can visualize this effect as being due to the generation of mobile dislocations by cold-rolling. Mobile dislocations in the crystal tend to decrease the rigidity from the value it would reach in their absence. Any alternation in the number of mobile dislocations, which may arise from cold-working (or the annealing out of cold-working effects), or in the mobility of mobile dislocations, which may result from the locking of dislocations at impurity atoms, will produce an additional contribution to the alternation of rigidity over and above any changes to be expected of conventional alloy theory. In the dilute solid-solution range, increasing concentration of solute atoms will increase the probability of locking, and hence, will increase the rigidity even without special annealing treatment, but on the other hand, at high solute concentration the dislocations are saturated with solute atoms, and the dislocation contribution to the rigidity swamped. The fact that the rigidity of brass wire containing 10.14 per cent zinc is larger than that of pure copper wire can be explained by locking of dislocations at solute atoms.

(c) *Specimens cold-rolled 57.5 per cent*

The fact that the rigidity of brass wires is greater than that of pure copper wire and increases with the increase of zinc content may be correlated with the preferred orientations which were developed by the heavily cold-rolling.

Cook and Richards[9] found the following facts from X-ray studies; (1) when polycrystalline copper and brass strips are cold-rolled, the deformation proceeds by a slip mechanism up to about 33 per cent reduction in thickness for copper and slightly more for brass, and beyond this stage it proceeds by a breakdown of the crystals into minute blocks with glide over flow layer, (2) marked preferred orientation develops during this second stage of deformation and the degree of preferred orientation increases progressively with the increase of cold-rolling.

Merlini and Beck[10] showed that three preferred orientations of the following types are present in rolled copper and brass strips; $(011)[2\bar{1}1]$, $(112)[11\bar{1}]$ and $(011)[100]$. The orientation represented by $(011)[2\bar{1}1]$ is present in large amount for any zinc content between 0 and 30 per cent. The orientation represented by $(112)[11\bar{1}]$ is typical of copper and decreases in intensity with increasing zinc content[11]. The orientation represented by $(011)[100]$ is typical of 70–30 brass and decreases in intensity with decreasing zinc content.

It is well known that the rigidity G depends on the orientation according to the formula[12]

$$\frac{1}{G}=\frac{1}{G_{\max}}+3\left(\frac{1}{G_{\min}}-\frac{1}{G_{\max}}\right)\cdot F \qquad (1)$$

$$F=\gamma_1^2\gamma_2^2+\gamma_2^2\gamma_3^2+\gamma_3^2\gamma_1^2=\frac{h^2k^2+k^2l^2+l^2h^2}{(h^2+k^2+l^2)^2} \qquad (2)$$

where γ_1, γ_2, γ_3 are the direction cosine of the direction under consideration with respect to the cubic axis and h, k, l are the Miller indices. As $F_{\min}=0$ for $[100]$ and $F_{\max}=1/3$ for $[111]$, it follows that the rigidity is largest in the direction $[100]$ and smallest in the direction $[111]$.

Consequently, if the Merlini and Beck's results are tentatively accepted, the increase of the modulus of rigidity with the increase of zinc content of the 57.5 per cent cold-rolled specimens may by explained by the increase of the intensity of preferred orientation represented by $(011)[100]$, for which the value of the modulus of rigidity is largest, and the decrease of the intensity of preferred orientation represented by $(112)[111]$, for which the value of the modulus of rigidity is smallest, with the increase of zinc content.

(2) *Variation of hardness with the change of zinc content*

The hardening of an metal by the addition of solute metal has been explained by Mott and Nabarro[13] and by Cottrell[14] on the basis of interaction between dislocations and solute atoms. In addition, Dorn, Pietrokowsky and Tietz[15] found on some aluminium alloys that part of the solid solution hardening should be attributed to (1) the difference in valence between the solute and solvent metals, (2) lattice strain caused by the difference in the atomic radii of the host and solute atoms. The experimental results mentioned above seems to be due to the combined effect of these factors.

(a) *In the case of annealed specimens*, the increase of hardness with the increase of zinc content may be due to the effect of the lattice strain and the change in the number of electrons per atom with the addition of zinc. The fact that the hardness of the specimen containing 40 per cent zinc is especially large can be explained by the coexistence of β phase.

(b) *The rapid increase in hardness at early stage of cold-rolling* should be due to the rapid increase of the density of free dislocations, and the gradual increase in hardness at high stage of cold-rolling seems to show the density of dislocations is getting near to a saturated state as the degree of cold-rolling steadily increases.

(c) *The fact that the variation in hardness with zinc content of the cold-rolled specimens, the degree of cold-rolling of which being the same in all cases, is larger than that of annealed specimens* can be explained as the additional effect of the interaction between dislocations and solute atoms to the lattice strain and change in valence. This interaction may increase with increasing concentration of solute atoms when the degree of cold-rolling being the same.

(3) *Room temperature recovery of rigidity*

It is well known that a crystal contains a three dimensional network of dislocation loops or segments and that the presence of such a dislocation network will act to reduce the rigidity of the material. If N is the dislocation density, viz, the total length of dislocation lines per cm³ and L is the effective loop length of the dislocation segments, the decrease in modulus of rigidity G is represented by[16]

$$\Delta G/G\sim N\cdot L^2 \qquad (3)$$

It is suggested that the modulus defect which recovers rapidly even at room temperature is attributed to the existence of relatively free dislocations within the subgrain structure, and is regarded as not influenced by dislocations that form the subgrain boundaries. In view of this model, the question next arises: what is happening to the interior dislocations in the early stage of recovery, i. e., when the rigidity are changing so rapidly? Two general mechanism have been suggested as to this problem.

(a) *The first theory*(17) assums that point defects created by the deformation pin the dislocation segments to produce recovery. According to this theory, the modulus defect can be eliminated through the shortening of the dislocation loops due to defect pinning, before any dislocation migration or rearrangement takes place. Dislocations may be pinned by point defects, impurities and solute atoms along the straight portions. If the concentration of the solute element is large enough, a dislocation segment (L) meets solute atoms on the average at a distance (L_0) which decreases when the concentration of solute atoms increases, so that the rate of recovery of the rigidity should increase with the increase of the concentration of solute atoms. The rigidity of the cold-worked commercial brass wire, in which large amount of impurities are contained than in the other specimens, recovers much faster than the other specimens in a short time after deformation and thereafter it recovers with a slower rate than the other specimens in both cases of rolling and twisting, as was expected. But, in regard to the other specimens this fact is not obvious. In the case of cold-rolled specimens, the rate of recovery in a short time after deformation is slowest in pure copper wire and increases with the increase of zinc content, except the brass wire containing 10.14 per cent. Nevertheless, in the case of cold-twisted specimens the relation between the rate of recovery and zinc content is complicated and can not be explained with the above theory.

(b) *The second theory*(17) considers that dislocation rearrangement is responsible for the recovery of this stage. According to this theory, it is assumed that dislocations in the interior of the subgrains undergo rearrangement which serves to reduce either their effective length or their loop length L. The concept that the rapid rearrangement is taking place immediately after plastic deformation to produce the recovery of rigidity was suggested by Nowick(17). According to this theory, the rate of rearrangement of dislocations, or consequently, the rate of recovery should decrease rapidly by the pinning of dislocations with solute atoms, viz, be the formation of Cottrell atmosphere and the time necessary to cease the recovery practically should become shorter with the increase of the concentration of solute atoms and impurities. Our experimental results show that the rate of recovery decreases with the increase of zinc and impurity content at a certain time after deformation on the whole as can be seen from Figs. 5 and 6.

It is impossible to conclude which one of these two theories is correct only by these experimental results.

(4) *Recovery of rigidity at the elevated temperature*

The recovery occurring between room temperature and recrystallization temperature is concerned with both point defects and dislocations, and their combination varies with the method and degree of cold-working, kind of metal and alloy, and impurities content, etc. as mentioned in the previous paper(1).

For the pure copper wire used in this experiment practically no recovery of rigidity occurs before recrystallization, suggesting that almost all recovery processes occur during the deformation and during the period of aging at room temperature. However, for the brass wires the manner of the recovery of rigidity differs from that of pure copper wire and begins to occur at about 80°C as shown in Figs. 12 and 13. This may be due to the formation of atomosphers of zinc atoms around the dislocations during and after deformation at room temperature. Thus the movement of the dislocations involved in recovery would occur either by the breaking away of dislocations from their atmosphers of solute atoms or by the disappearance of atmosphers moving with the dislocations. Both of these processes would require higher temperature than would be necessary in pure copper.

The author wishes to express his sincere thanks to Professor Tokutaro Hirone of Tohoku University for the kind guidance and to Mr. Toyojiro Isano for his assistance.

References

1) J. Kuroyanagi: Sci. Rep. RITU A, **11** (1959) 30.
2) A. Westgren and A. Almin: Z. Physik. Chem. **B, 5** (1929) 14.
3) C. Zener: Acta Cryst. **2** (1949) 163.
4) B. J. Elliot and H. J. Axon: J. Inst. Metals **86** (1956-57) 24.
5) R. A. Swalinin: Acta Met. **6** (1958) 129.
6) G. Bradfield and H. Pursey: Phil. Mag. **44** (1953) 437.
7) A. D. N. Smith: J. Inst. Metals **80** (1951-52) 477.
8) J. Friedel: Phil. Mag. **44** (1958) 444.
9) M. Cook and T. L. Richards: J. Inst. Metals **66** (1940) 1.
0) A. Merlini and P. A. Beck: J. Metals **7** (1955) 385.
11) According to W. Iweronow and G. Schdanow (Tech. Phys. U. S. S. R., **1** (1934) 64) the preferred orientation (112) [111] is absent in α-brass containing 5 per cent or more of zinc.
12) W. Boas: *An Introduction to the Physics of Metals and Alloys*, Mellborne (1947) 49.
13) N. F. Mott and F. R. N. Nabarro: *Report on the Strength of Solids, Physical Society, London* (1948).
14) A. H. Cottrell: *Report on the Strength of Solids, Physical Society, London* (1948)
15) J. E. Dorn, P. Pietrokowsky and T. E. Tietz: Trans. A. I. M. E. **188** (1950) 933.
16) A. S. Nowick: *Creep and Recovery, American Society for Metals* (1957) 167.
17) A. S. Nowick: Acta Met. **3** (1955) 312.
18) A. H. Cottrell: Phil. Mag. **44** (1953) 829.

JOURNAL OF THE PHYSICAL SOCIETY OF JAPAN, Vol. 15, No. 8, AUGUST, 1960

Study on Some Tl Base Alloys, with Reference to their Electronic Structure

By Ryōji SUGANUMA

Physical Institute, Kyoto Prefectural University of Medicine

(Received February 27, 1960)

Kinds and boundaries of phases at room temperature in Tl-rich sides of the alloy systems of Tl-Cd, Tl-Sn and Tl-Sb were determined by X-ray and electron diffraction. From the consideration of experimental results obtained in the present work as well as in previous works by other workers, it was deduced that phase boundaries of a particular structure in some Tl base alloys appeared to correspond to the same electron atom ratio and to be affected mainly by the electronic factor. The results obtained from the lattice constant and density measurements in the f.c.c. region of Tl-Sn system, which was confirmed to be stable, were interpreted in terms of the Brillouin zone concept. Considering Matyas' result for trivalent Al, a suggestion for the high energy portion of $N(E)$ curve for the f.c.c. structure was proposed.

1. Introduction

The electronic structures of the metals and lloys which involve the overlap of electrons rom the first Brillouin zone are complicated nd still uncertain. The first calculation of $V(E)$ curve for the f.c.c. structure was made y Mott and Jones[1] in 1937, but its high nergy portion was highly speculative and the se of this curve was a very approximate rocedure for the cases where the electron oncentration was nearly 3 and involved the overlaps. Recent results for trivalent Al calculated by Matyas[2,3] differ from that of Mott and Jones, and the overlap across the {200} planes from the first Brillouin zone into the second one does not occur. His explanations are supported to some extent by the shape of the soft X-ray emission bands of Al obtained by Skinner,[4] and also by the magnetic susceptibility measurement for Al made by Lingelbach *et al.*[5] There is, however, evidence that the electronic structure of Al is somewhat different from that of Matyas. Leigh,[6] in a discussion on the elastic constants of Al, has shown that it is necessary also to take account of a small overlap across the {200} faces of the first zone.

On the other hand, the experimental informations have not yet been obtained sufficiently, especially for the cases in which the electron concentration is considerably higher than 3, because the f.c.c. phases having such an electron concentration seem to be restricted to the solid solutions of Al and some Tl base alloys. However, the elements of higher or lower valency than Al have not appreciable solubilities in Al. For example, Si and Ge have the solubilities of only one or two atomic percentages in Al. Whereas, the Tl base alloys have not yet been investigated. From these points of view, the f.c.c. phases in Tl base alloys are particularly of interest.

According to Hansen,[7] the Tl base alloys seem to be restricted to the case where the solute elements are situated in the vicinity of Tl in the Periodic Table. Tl forms a simple eutectic with Ag or Au (Group I_B) and the solid solubility ranges exist in Ag- or Au-rich side but not in Tl-rich side. Tl-Cd (Group II_B) and Tl-Hg (Group II_B) are also eutectic*, and contrary to the case where Ag or Au is a solute, the terminal solid solutions exist in Tl-rich sides, although it has not yet been determined in the Tl-Cd case. Tl and In which have the same group valencies tend to form a continuous series of solid solutions. Tl-Pb (Group IV_B) resembles Tl-Bi (Group V_B) in its Tl-rich side and has the f.c.c. phase following a small range of α terminal solid solution, and in addition, the latter has another compound in Bi-rich side. However, Tl-Sn (Group IV_B) and Tl-Sb (Group V_B) seem to be quite different from Tl-Pb and Tl-Bi, respectively, and are reported to have the wide ranges of α solid solutions but not the f.c.c. phases. As to the systems of Tl-Cd, Tl-Sn and Tl-Sb, however, there is some uncertainty in their phase diagrams which will be discussed briefly in the next paragraph, and hence the reexaminations are necessary. If the systematic changes in the homogeneity ranges of the terminal solid solutions in α-Tl or the f.c.c. phases with solute valency were observed, some information concerning the electronic effect upon the phase boundaries in Tl base alloys would be available. Therefore, the writer intended to investigate the three Tl-rich alloys mentioned above by X-ray and electron diffraction methods. Kinds and boundaries of phases at room temperature were determined in connection with the effect of their electron concentrations, and then some detailed investigations for the f.c.c. phase in Tl-Sn system, which was confirmed to be stable by the present investigations, were performed in relation to its electronic structure and a possible high energy portion of $N(E)$ curve consistent with the experimental observations was proposed.

§ 2. Previous Work on the Pase Diagrams

2-1. *Case of Tl-Sn*

The phase diagram due to Hansen[7] is shown in Fig. 1(a). The liquidus curve was drawn on the basis of thermal analysis. The solid solubility of Sn in Tl up to 140°C was determined by measuring the electrical resistivity. Fuchs[8] showed by thermal analysis that the phase transformation temperature of Tl was lowered by addition of Sn, as shown in Fig.

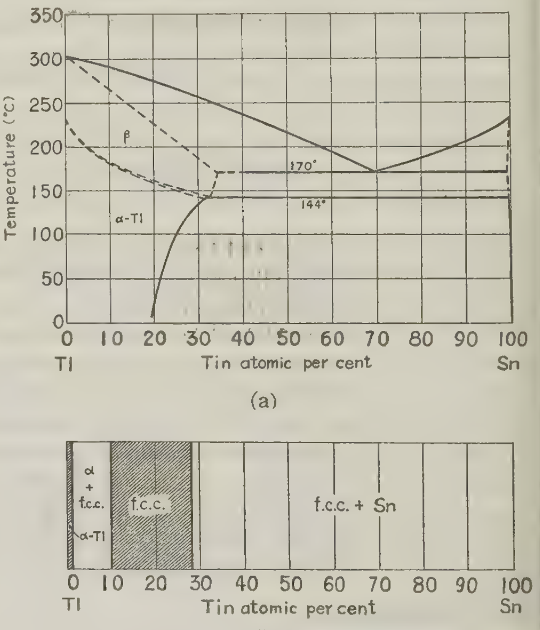

(a)

(b)

Fig. 1. (a) Phase diagram of Tl-Sn after Hansen.
(b) Kinds of phases at room temperature after the present work.

---

* The system of Tl-Hg has a f.c.c. phase at about 25 at. % Hg below 14.5°C, but not in Tl-rich side.

1(a). Sekito[9)] reported that the alloys containing 16 and 30 at. % Sn which were quenched into ice water from the melt possess the f.c.c. lattice. The result of this X-ray work, however, seems to be curious, because it has been established afterwards that β-Tl has a b.c.c. structure.[10)] Therefore, Sekito's f.c.c. structure has been considered to be a metastable one resulting from the β → α transformation of the solid solution in β-Tl. No other reliable X-ray work has yet been carried out.

2–2. *Case of Tl-Sb*

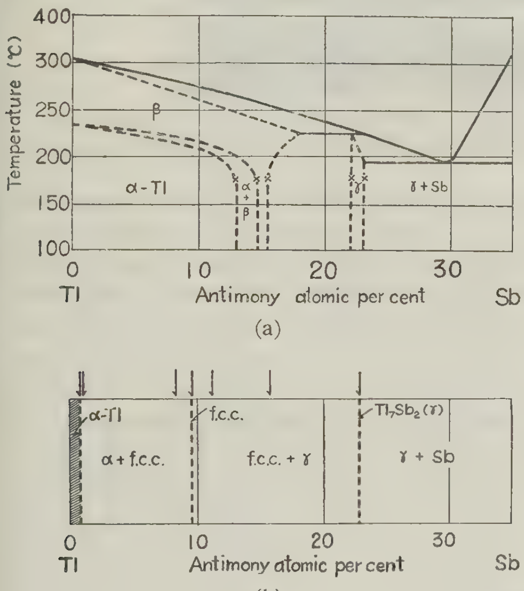

(a)

(b)

Fig. 2. (a) Phase diagram of Tl-Sb after Hanson.
(b) Kinds of phases at room temperature after the present work.

The phase diagram appearing in Hansen[7)] is shown in Fig. 2(a). The liquidus and solidus curves indicated by solid line were based on the thermal data. The existence of intermediate phase γ was confirmed by Barth[11)] and Persson[12)] *et al.* by the metallographic and X-ray studies. The phase boundaries of α-Tl, β-Tl and γ-phase at 180°C as indicated by crosses in Fig. 2(a). were fixed by Kurzyniec[13)] on the basis of resistivity measurements. While, it was reported by Persson *et al.* that β-Tl was apparently stabilized down to room temperature at about 10∼11 at. % Sb, although the composition of γ-phase agreed closely with the result of Kurzyniec. It should be noted, however, that β-Tl is believed to be f.c.c. rather than b.c.c.. Therefore, the kinds of phases in the Tl-rich alloys are not yet fully established and should be examined.

2–3. *Case of Tl-Cd*

Tl and Cd form a eutectic and no intermediate phases are known.[7)] The solubility of Cd in Tl was estimated to be about 4.3 at. % Cd at 203°C from the thermal data,[14)] but not determined at room temperature. No X-ray work on this system can be found in existing literatures.

§ 3. Determinations of Kinds and Boundaries of Phases in Tl Base Alloys

3-1. *Case of Tl-Sn*

(a) *Kinds and boundaries of phases at room temperature*

Accurately weighed quantities of the component metals (99.9+% Tl and 99.999% Sn), whose total amount was approximately 2 g, were melted in sealed Pyrex tube of about 8 mm in diameter. After air-cooling to room temperature, needle-like specimens of about 0.3 mm in diameter were cut from the ingots and then annealed for 30∼50 hours at about 100°C in glycerin, and after the room temperature aging for 2∼3 days they were examined by X-rays. Cu K_α radiation was used with Ni filter. The applied voltage was about 40kV and the tube current for the rotating target X-ray tube was about 50 mA. The exposure time required was 40∼50 minutes. Among the specimens listed in Table I, those designated by symbol A in the last column were prepared and heat-treated as mentioned above. Another kind of specimens containing 8∼30 at. % Sn was prepared in quantity of approximately 10 g using the same conditions of preparation and heat-treatments. These specimens, designated by symbol B in Table I, were subjected to density measurements at first and then examined by X-rays.

Kinds of phases at room temperature obtained by X-ray diffraction method with the annealed specimens is shown in Fig. 3 and Table I. The lattice constant measured for each specimen attained a constant value within the limit of experimental error after the annealing for about 20 hours at about 100°C, and the lattice constants for two specimens of the same composition prepared by different two methods (see the last column of Table I)

Table I.

At. % Sn	Phase	a (Å)	c (Å)	c/a	ρ_c (g cm^{-3})	ρ_m (g cm^{-3})	Percentage of filled sites (%)	Number of electrons per site	Number of electrons per atom	Method of specimen preparation
0	α	3.4585	5.5270	1.5980	11.854				3.00_0	A, C
0.8_6	α	3.4629	5.5325	1.5976	11.768				3.00_9	A
1.7_1	α	3.4651	5.5384	1.5983	11.696				3.01_9	A, C
2.5_5	α+f.c.c.	3.4650	5.5428	1.5997	11.648				3.02_6	A
3.3_9	α+f.c.c.	3.4650	5.5456	1.6005	11.601				3.03_4	A, C
8.3	f.c.c.+α	4.8490			11.491	11.51_6	100.2	3.08_9	3.08_3	B, C
9.9	f.c.c.	4.8479			11.419	11.41_0	99.9_2	3.09_7	3.09_9	B
11.5	f.c.c.	4.8440			11.366	11.34_8	99.8_4	3.11_0	3.11_5	B
13.8	f.c.c.	4.8435			11.255	11.22_8	99.7_6	3.13_0	3.13_8	B
16.1	f.c.c.	4.8422			11.148	11.09_2	99.4_9	3.14_5	3.16_1	B, C
17.6	f.c.c.	4.8420			11.080	11.03_7	99.6_1	3.16_4	3.17_6	B
19.0	f.c.c.	4.8423			11.003	10.96_7	99.6_7	3.17_9	3.19_0	B
20.5	f.c.c.	4.8418			10.931	10.90_9	99.7_9	3.19_8	3.20_5	B
21.9	f.c.c.	4.8421			10.859	10.83_9	99.8_1	3.21_3	3.21_9	B
23.3	f.c.c.	4.8424			10.786				3.23_3	A
24.7	f.c.c.	4.8425			10.716	10.72_4	100.1	3.25_0	3.24_7	B
25.4	f.c.c.	4.8416			10.686				3.25_4	A
27.4	f.c.c.	4.8436			10.573	10.59_1	100.1	3.27_7	3.27_4	B
28.1	f.c.c.	4.8454			10.526				3.28_1	A
30.1	f.c.c.+Sn	4.8457			10.425	10.44_8	100.2	3.30_8	3.30_1	B, C

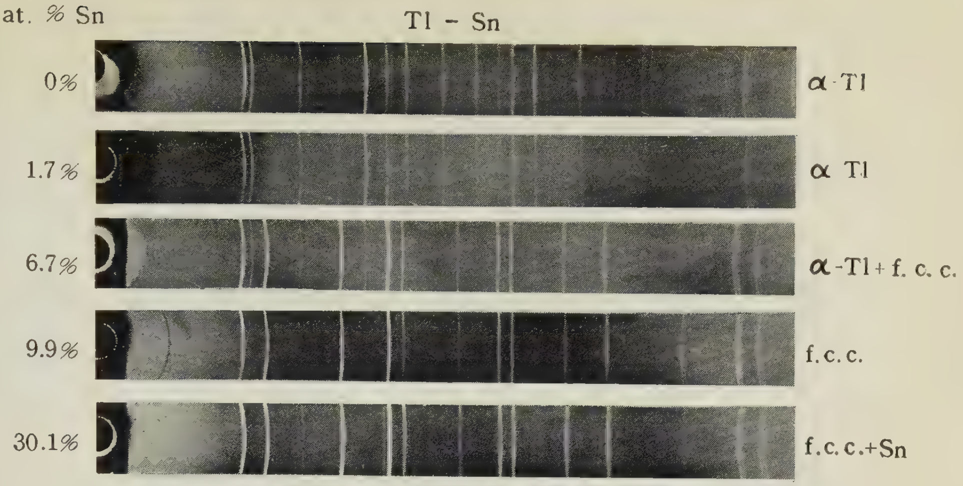

Fig. 3. Kinds of phases at room temperature obtained by X-ray diffraction.

also agreed with each other after the same heat-treatment. As seen from Fig. 3 and Table I, the Tl-rich side of Tl-Sn system differs considerably from that of Fig. 1. The solid solubility of Sn in α-Tl at room temperature was reduced to about 1.7 at. % Sn and the disordered f.c.c. lattice was observed between about 9 and about 28 at. % Sn. No changes in diffraction pattern were detected after the annealing for more than about 50 hours at 100°C. For comparison with Sekito's results obtained by quenching from the melt, specimens prepared in quantity of about 2 g were melted in Pyrex tube and poured into ice water or diffusion pump oil of about −30°C cooled by dry ice. The X-ray examination of these specimens were finished within about one hour after quenching, but showed the same kinds of phases as the annealed ones. These specimens are designated by symbol C in Table I.

The lattice constants of pure Tl are also shown in Table I. For comparison, the results of other workers are summarized as follows:

a	*c*	*c/a*	ref.
3.456 ±5Å	5.530 ±6Å	1.60	(**10**)
3.4566±2	5.5248±4	1.5983	(**15**)

(b) *Kinds and boundaries of phases at high temperature*

Kinds of phases at high temperature was investigated by electron diffraction with thin films containing about 78, 23 and 7 at. % Sn, which were prepared in vacuum (about 10^{-5} mmHg) by successive evaporation of Sn and Tl on Formver films at room temperature. Film thickness was of the order of 35 mμ. Specimens were set in camera with heating device and diffraction pattern were taken at various temperatures. The composition of the film was estimated approximately from the evaporated quantities of component metals.

The alloy formation by successive deposition of constituent metals was observed as seen in some other systems.[16] The kinds of phases at room temperature after suitable heat-treatment was in accordance with the results obtained by X-ray diffraction.

The alloys containing about 78 at. % Sn (Fig. 4(a)), which show the mixed patterns of disordered f.c.c. and Sn at room temperature, exhibit halos superposed on the crystalline pattern of Sn at about 164∼170°C and, after cooling to room temperature, show the same patterns as those obtained before heating. These alloys were annealed for about 2 hours at about 130°C and for about 1.5 hours at about 156°C respectively, but no changes in the diffraction patterns were observed. Therefore, the thermal effect at 144°C shown in Hansen's diagram (Fig. 1(a)) could not be confirmed in the present examination.

The films containing about 23 at. % Sn (Fig. 4(b)) gave the pattern of disordered f.c.c. phase only. By heating these specimens, the pattern completely changes to halos at about 256°C without any other change during heating. After subsequent cooling to room

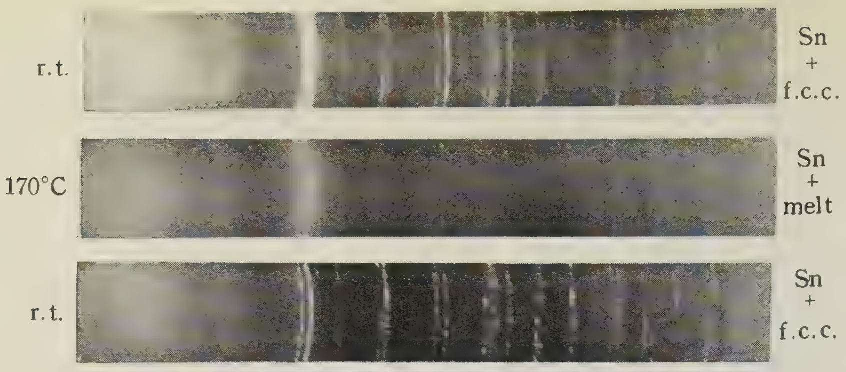

Fig. 4 (a). Electron diffraction pattern from thin film of Tl-Sn containing about 78 at. % Sn.

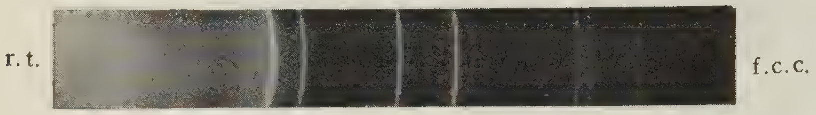

Fig. 4 (b). Electron diffraction pattern from thin film of Tl-Sn containing about 23 at. % Sn.

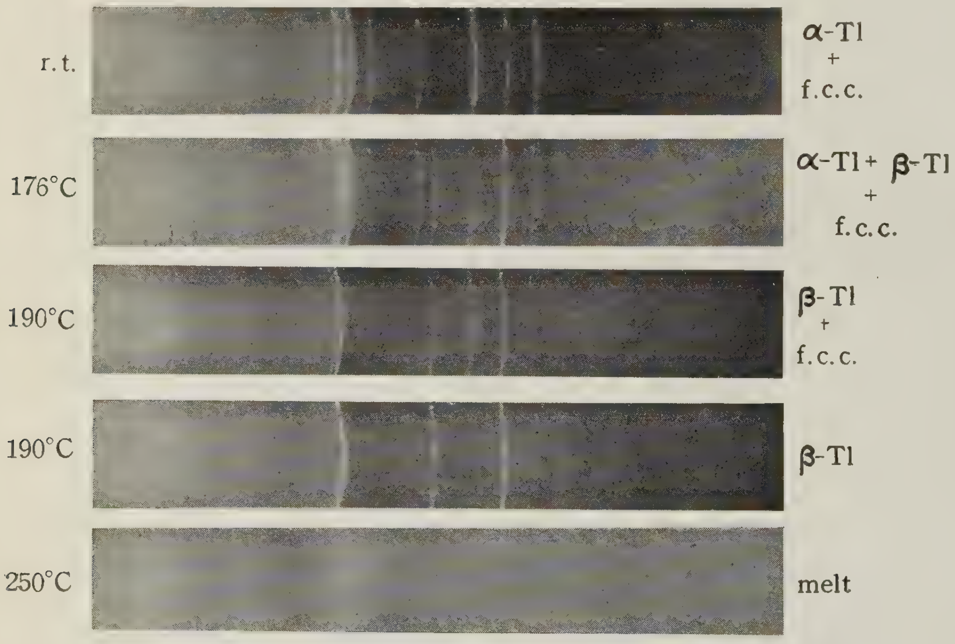

Fig. 4 (c). Electron diffraction pattern from thin film of Tl-Sn containing about 7 at. % Sn.

temperature, these films show again the pattern of f.c.c. phase only. With the specimens of this composition various heat-treatments were carried out: They were (i) aged for about a week at room temperature, (ii) annealed for about one day at about 100°C, (iii) after homogenizing for one hour at 160~170°C, cooled to 86°C at the rate of about 0.3°C per minute and then annealed for 5 hours at 86~80°C. In all cases, no extra lines and no changes in the relative intensities of the disordered f.c.c. lines were observed. The diffraction pattern at room temperature after the heat-treatment (iii) is given in Fig. 4(b). Deducing from their lattice constant measurements, Tang and Pauling[17] reported that an ordered structure exists in f.c.c. region of Pb-Tl system, but the direct evidences could not be obtained, because the scattering power of Tl is close to that of Pb.

If any superlattice were formed in f.c.c. region of Tl-Sn system, it should be detected, since the scattering powers of component elements are considerably different.

The specimens containing about 7 at. % Sn (Fig. 4 (c)) show the diffraction rings of α-Tl and f.c.c. between room temperature and about 150°C. No changes were observed after annealing for about one hour at about 155°C, but the rings of β-Tl began to be superposed on those of α-Tl and f.c.c. phase after annealing for about 30 minutes at about 176°C. After annealing for one hour at about 190°C, these specimens exhibited the rings of β-Tl and f.c.c. only, and these two phases changed into the halo pattern at 245~250°C by further heating. In some cases, a part of the film which showed α-Tl and f.c.c. below 170°C indicated β-Tl only at about 190°C. The transformation from (α-Tl+f.c.c.) to (β-Tl+f.c.c.) is supposed to be very drastic and the accurate transformation temperature cannot be determined from the present experiment, but it is estimated to lie between 155 and 176°C.

The experimental informations about the phase diagram of Tl-Sn system obtained by the present investigation may be summarized

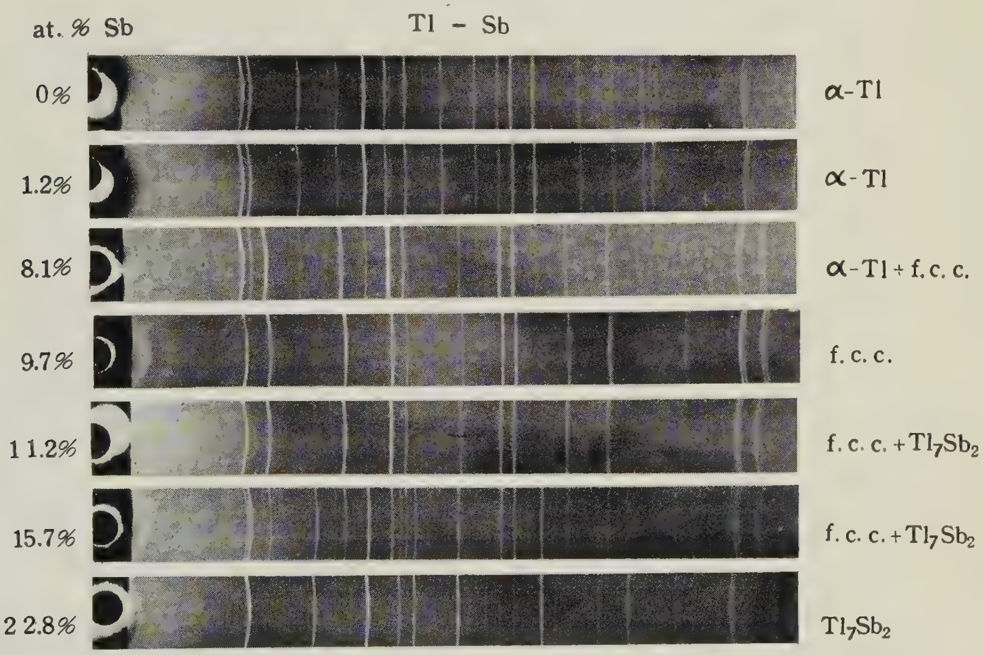

Fig. 5. Kinds of phases at room temperature obtained by X-ray diffraction.

Table II.

At. % Sb	Phases	a (Å)	c (Å)	c/a	Number of electrons per atom
1.2	α	3.4622	5.5408	1.6003	3.02_4
1.6	α+f.c.c.				3.03_2
8.1	f.c.c.+α	4.8592			3.16_2
9.7	f.c.c.	4.8602			3.19_4
11.2	f.c.c.+Tl_7Sb_2	4.8597			3.22_4
15.7	Tl_7Sb_2+f.c.c.				
22.8	Tl_7Sb_2				

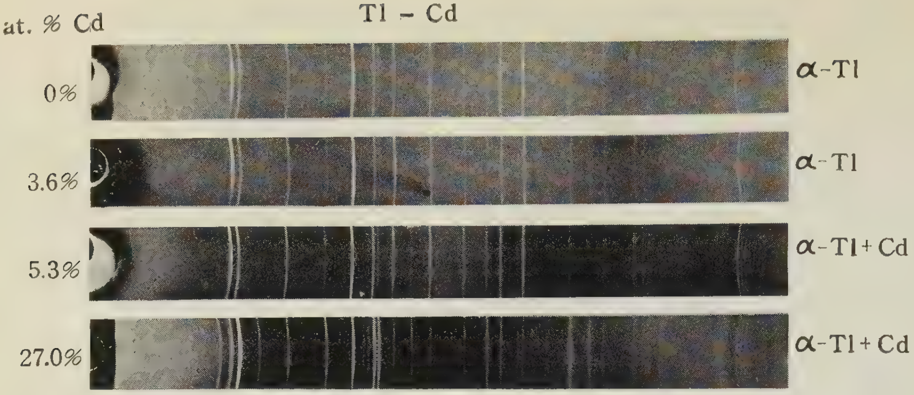

Fig. 6. Kinds of phases at room temperature obtained by X-ray diffraction.

Table III.

At. % Cd	Phases	a (Å)	c (Å)	c/a	Number of electrons per atom
1.8	α	3.4591	5.5230	1.5966	2.98_2
3.6	α	3.4672	5.5343	1.5962	2.96_4
5.3	α+Cd	3.4730	5.5449	1.5966	2.94_7
7.0	α+Cd				
27.0	α+Cd				

as follows. The kinds and boundaries of phases at room temperature may be confirmative, and is shown in Fig. 1(b) diagramatically. Although further extensive evidences will be required for the accurate determination of phase boundaries, the solid solubility of Sn in α-Tl at room temperature was determined to be about 2 at. % Sn and the f.c.c. phase was found to be stable between about 10 and 28 at. % Sn. The high temperature portion of this system, deduced mainly from the results obtained by electron diffraction with thin films, may be somewhat speculative. From the consideration of the facts mentioned above, however, the Tl-rich side of the present system seems to be quite different from that which appeared in Hansen's diagram, but it is suggested that the high temperature portion of Tl-rich side of the present system is quite analogous to those of Tl-Pb and Tl-Bi systems. As for the region of f.c.c. phase, the lattice constants and density will be described in detail in the next paragraph.

3-2. *Case of Tl-Sb*

Materials used were 99.9+% Tl and 99.999% Sb. The specimens were prepared and heat-treated under the same conditions as those described in Tl-Sn system (total amount was about 2 g). All measurements were made by X-ray diffraction at room temperature. The experimental results are shown in Fig. 5 and Table II. The diagramatical expression is made in Fig. 2(b), in which the arrows indicate the compositions at which the X-ray diffractions were carried out.

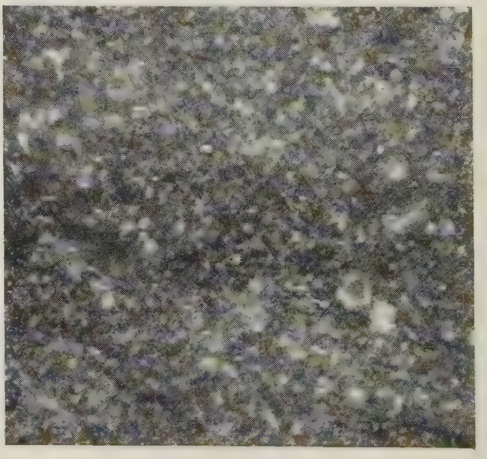

Fig. 7. Micrograph of the f.c.c. phase in Tl-Sn containing 20.5 at. % Sn.

The solid solubility of Sb in α-Tl at room temperature is of the order of one at. % Sb and the f.c.c. phase is stable as in the case of Tl-Sn system at about 10 at. % Sb. Whether this phase possesses a small homogeneity range or not could not be decided from the present experiment. Tl_7Sb_2 was also observed at about 22 at. % Sb which agreed well with that of Fig. 2(a). The kinds and boundaries of other phases at room temperature differ from those of Fig. 2(a), but show practical agreement with the results reported by Persson and Westgren.[12] They detected the f.c.c. lattice at about 10 at. % Sb, and considered it to be β-Tl stabilized down to room temperature, because it was believed in those days that β-Tl had the f.c.c. structure. They also reported that alloys containing 8.1 at. % Sb consisted of α-Tl and f.c.c. at room temperature, and again this agrees well with the present results. Although they did not say anything about the solubility limit of Sb in α-Tl, this limit is estimated to be of the order of one at. % Sb in the present work. If the phase boundaries of α-Tl and f.c.c. at room temperature obtained from the present study are compared with those at 180°C reported by Kurzyniec[13] (indicated by crosses in Fig. 2 (a)), the solid solubility of Sb in α-Tl at high temperatures should be considerably increased and marked curvature of α-Tl/(α-Tl+f.c.c.) boundary should be observed. A systematic study at high temperature will be required.

3–3. *Case of Tl-Cd*

Materials used were 99.9+% Tl and Merk's Cd. The specimen preparation and heat-treatments were the same as those in Tl-Sb system. The experimental results obtained by X-ray diffraction at room temperature are shown in Fig. 6 and Table III. It was confirmed that Tl and Cd form the simple eutectic and no intermediate phases exist at room temperature, as shown in Hansen's diagram. The solid solubility of Cd in α-Tl obtained at room temperature was of the order of 4 at. % Cd which seems to be reasonable as compared with diCapua's value,[14] 4.3 at. % Cd, at the eutectic temperature.

§4. The f.c.c. Phase in Tl-Sn Alloy

As mentioned in §1, the f.c.c. phase in Tl base alloys is of interest in connection with its electronic structure. Therefore, the lattice constant and density of the f.c.c. phase in Tl-Sn system were measured for the same specimens, which were prepared as mentioned in §3–1, in relation to the electronic structure of the f.c.c. phase.

The X-ray diffraction patterns were photographed by Debye-Scherrer camera of the usual type whose diameter was 9 cm, calibrated against the lattice constant of 99.99% Al. The calculated lattice spacings were corrected for systematic errors by the extrapolation method of Nelson and Riley.[18] The effect of film shrinkage was considered, but no correction for refractivity was made. The experimental error was estimated to be about 0.02% and all measurements were performed at 32±2°C.

The displacement liquid was glycerin which was a very good protective liquid for the Tl base alloys and whose density was determined to be $1.254_5\ \mathrm{g\,cm^{-3}}$ at 32°C. Specimens were microscopically examined and confirmed to be free from porosities (Fig. 7). The accuracy of about 0.1% could easily be obtained for the specimens of about 10 g in the present case. All measurements were carried out at 32°C.

The lattice constant a and density ρ_m measured in the present experiment are summarized in Table I and plotted in Fig. 8. Table I also includes the calculated density ρ_c, which was calculated from the measured lattice constant using the expression $\rho_c = mMN/a^3$, where M was the mean atomic weight, N the number of atoms in the unit cell, m the atomic unit of mass (1.66035×10^{-24} g), and a the lattice constant in cm. The percentage of filled sites for each composition calculated from ρ_m and ρ_c is listed in Table I, and using these values, the number of electrons per lattice site was calculated. These values are also shown in Table I with those of the number of electrons per atom, calculated on the basis that each unit cell contains four atoms. These results of lattice constant and density measurements will be discussed in §5–2.

§5. Discussions

5–1. *Kinds of phases at room temperature of some Tl base alloys*

From the considerations of the present results with the systems of Tl-Cd, Tl-Sn and

Tl-Sb, and of the previous results with those of Tl-Ag, Tl-Au, Tl-Hg, Tl-In, Tl-Pb and Tl-Bi obtained by other workers, some regularity in the constitutional diagrams of these systems may be deduced. Remarks on these diagrams and the solute percentage at phase boundaries are summarized in Table IV. Except the elements of Group I_B as solutes, all other elements can be dissolved in α-Tl, and solid solubility is most marked for the system of Tl-In, both components of which belong to the same group, and becomes less marked for other systems with increasing solute valency. The f.c.c. phase is found in the systems of Tl-Sn, Tl-Pb, Tl-Sb and Tl-Bi in which the solute elements have higher valen-

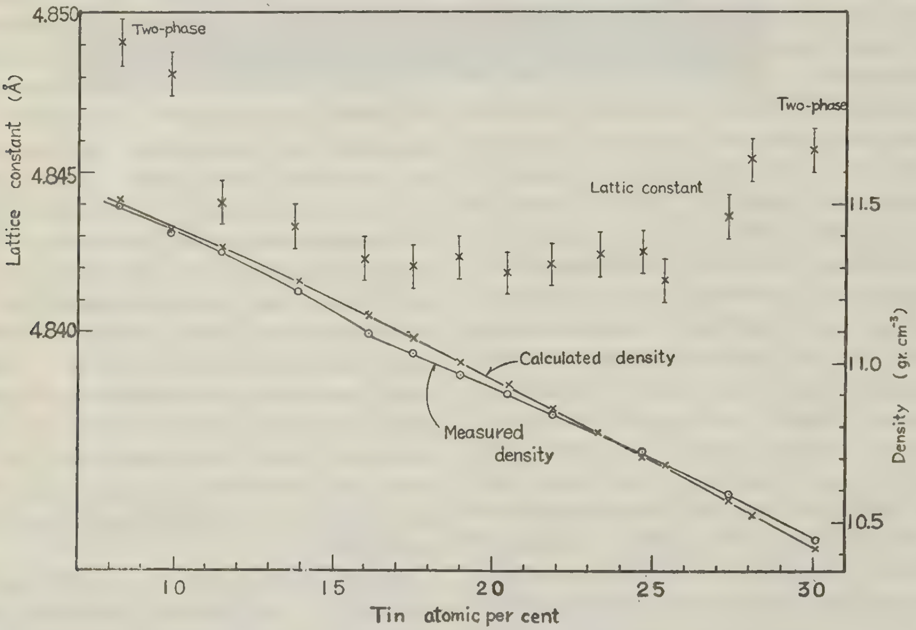

Fig. 8. The changes of lattice constant and density with atomic percentage of Sn.

Table IV.

Group	Solute	Remarks on phase diagram	At. % of solute at the solubility limit		Ref.
			Solid solution in α-Tl	Tl rich side of f.c.c. phase	
I_B	Ag	eutectic	—	—	(7)
I_B	Au	eutectic	—	—	(7)
II_B	Cd	eutectic	~ 4	—	—
II_B	Hg	eutectic*	~ 4	—	(7)
III_B	In	cont. solid solution**	~10	~40	(7), (25)
IV_B	Sn	f.c.c.	~ 2	~10	—
IV_B	Pb	f.c.c.	~ 3	~12	(7), (17)
V_B	Sb	f.c.c., Tl_7Sb_2	~ 1	~10	—
V_B	Bi	f.c.c., $TlBi_2$	~ 1	~ 5***	(7), (26)***

* A f.c.c. phase exists at about 25 at. % Hg below 14.5°C, but not in Tl rich side.

** Component metals have a tendency to form a continuous solid solution like the systems of Mg-Cd etc., but are prevented from doing so because their crystal structures are different.

*** In Ölander's paper, the specimen containing about 4 at. % Bi is reported to be two phases of α solid solution and f.c.c.. Therefore, the specimen containing about 5.2 at. % Bi was prepared by the present author and confirmed to be a single phase of f.c.c..

cy than Tl, and another intermediate compound ($TlBi_2$ or Tl_7Sb_2) appears in Tl-Bi or Tl-Sb.

The phase boundary of α solid solution and Tl-rich side of the f.c.c. phase for each system are shown diagramatically in Fig. 9, taking the electron atom ratio as abscissa. It was assumed here that Tl, Sn and Pb exhibit their group valencies, although it was often claimed[19] that these metals were incompletely ionized in the state of element. The solute-rich side of the f.c.c. phase will be different in the electron concentration from system to system and is not discussed at present. It is apparent that the phase boundary for each system is closely related to almost the same electron concentration except the case of Sb as a solute. That is, the Tl-rich side of the f.c.c. phase corresponds approximately to 3.10 electrons per atom, and for the hexagonal solid solution, the phase boundary which is rich in the solutes of higher valency than Tl corresponds to about 3.02 electrons per atom, while that which is rich in the solutes of lower valency than Tl corresponds to about 2.96 electrons per atom.

According to Hume-Rothery[3] and Raynor *et al.*,[20] various factors other than valency are responsible for the stabilities of alloy phases. Atomic size factor of the solute elements concerned with the systems shown in Fig. 9 is about 10% and within the favorable zone. That of Ag or Au exceeds 20% and is apparently unfavorable, which may be the reason why these metals cannot be dissolved in α-Tl. Electrochemical difference between Tl and each solute element is small, but in Tl-Sb and probably in Tl-Bi some contribution from this factor may be considered. The effect of ionic radius may be marked only when a relatively large ion of solute is forced into the relatively small ions of solvent and the electron cloud of the former begins to overlap that of the latter, but except the case of Hg as a solute, the ionic radius of solutes is smaller than that of solvent in the present case. As a result, it appears that the phase boundaries of some Tl base alloys concerned in Fig. 9 are affected mainly by electron concentration, suggesting that in every case the homogeneity of a particular structure may be restricted by the appropriate Brillouin zone.

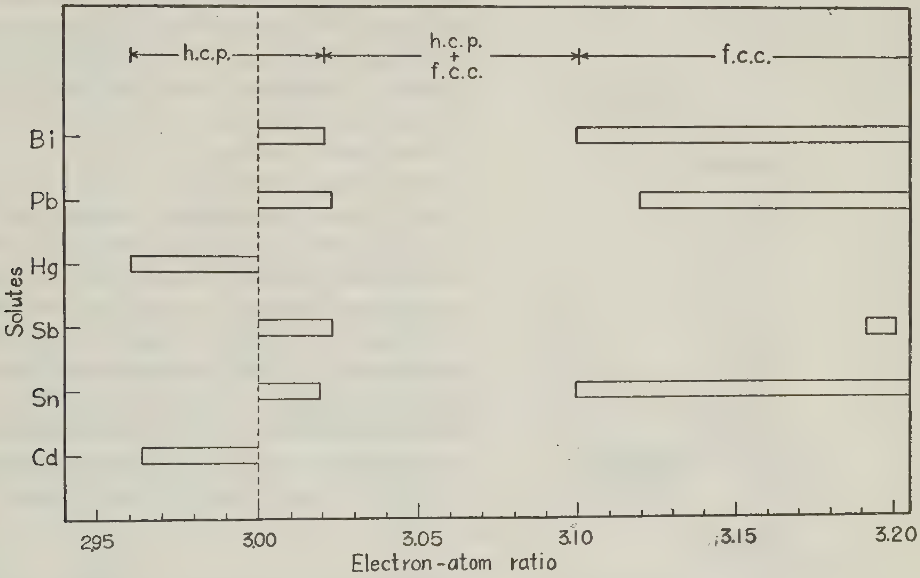

Fig. 9. The ranges of homogeneity in terms of electron concentration.

5-2. *N(E) curve for the f.c.c. phase in Tl-Sn*

As described briefly in § 1, experimental informations about the high energy portion of *N*(*E*) curve for the f.c.c. structure have not completely been obtained. Since the first Billouin zone for f.c.c. can contain only two electrons per atom, it is clear that considerably overlap into the second zone must occur across the {111} faces or across both {111} and {200} faces in the present case. Calculating the $N(E)$ curve for the f.c.c. structure, Mott and Jones[1] assumed that the energy gaps at the surface of the first Brillouin zone were equal to those for copper deduced from its optical properties. Consequently the high energy portion of this curve is highly speculative and seems to be inadequate for the discussion with trivalent metals (Fig. 10(a)). Recent results for Al calculated by Matyas,[2] whose curve[3] is shown in Fig. 10(b), indicate that the first zone is nearly filled with slightly less than two electrons per atom but contains unoccupied states in the form of thin slabs parallel to the {200} faces of the first zone and that slightly more than one electron per atom passes into the second zone. Consequently the overlap into the second zone occurs across the {111} faces but not across the {200} faces at three electrons per atom.

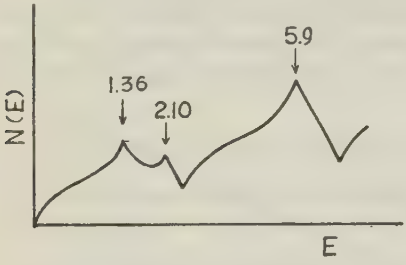

Jones
(a)

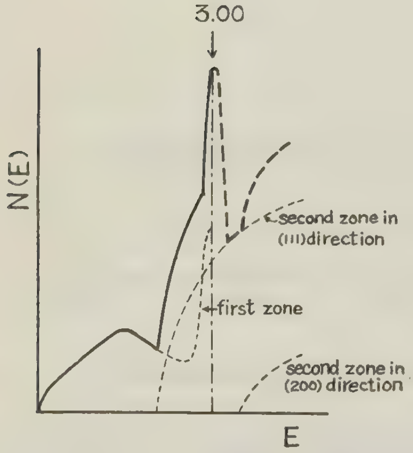

Matyas
(b)

Fig. 10. $N(E)$ curve for f.c.c. structure. Numericals in these figures refer to the corresponding electron atom ratios.
(a) After H. Jones.
(b) After Z. Matyas. The portion of total $N(E)$ curve in broken line is hypothetical, and drawn by the present author.

So far as the Brillouin zone effect is concerned, the lattice expansion may be expected with the increasing electron concentration, and if the change in composition results in the occurrence of the overlap across the faces of an appropriate Brillouin zone, a kink in lattice constant *versus* composition curve will be produced. It may also be supposed that the lattice expansion should be much increased if the {200} overlap is superposed on {111} overlap, compared with the case of {111} overlap only, for the f.c.c. phase concerned in the present work.

The lattice expansion is considered to be due to the simultaneous effects of solute valency and atomic size difference between solute and solvent atoms. In the present experiment, volume per atom was taken as a measure of atomic size, because Tl and Sn have not a cubic symmetry and there may be some uncertainty in the concept of usual atomic diameter. The change of lattice constants due to atomic size difference can be calculated from Vegard's law expressed as

$$a_{\mathrm{S}} = x a_{\mathrm{Sn}} + (1-x) a_{\mathrm{Tl}} ,$$

where a_{Tl} and a_{Sn} are the lattice constants of hypothetical f.c.c. lattices having the same volumes per atom as pure Tl and Sn, respectively, and x is the atomic fraction of Sn. In the present case a_{Sn} is smaller than a_{Tl}, and therefore, linear decrease in a_{S} with increasing atomic percentage of Sn should be expected. The difference Δa between observed lattice constants a and calculated ones a_{S} may be considered as the measure of valency effect only to the first approximation, and is shown in Fig. 11.

The large positive deviation from Vegard's law and a kink at about 16 at. % Sn are evidently observed. A kink of such kind has been detected in c-spacings for Mg-rich alloys and has been explained as a result of the internal stress present in the lattice due to the zone overlap in the direction parallel to the hexagonal axis. Detailed discussions and theoretical treatments were made by Raynor[21] and Jones,[22] respectively.

From Matyas' results and the above discussions, it will be suggested that the kink observed in Fig. 11 (the corresponding electron concentration is 3.16 electrons per atom) may be associated with the onset of overlap across the {200} faces of the first Brillouin zone, although the form of total *N*(*E*) curve for electron concentration higher than three electrons per atom was not given by Matyas. There will also be some ambiguity in discussing the present results from Tl base alloys in relation to the *N*(*E*) curve derived for Al.

Matyas' results suggest the existence of a sharp fall in *N*(*E*) curve before the onset of {200} overlap. The density measurement made in the present work also suggests this

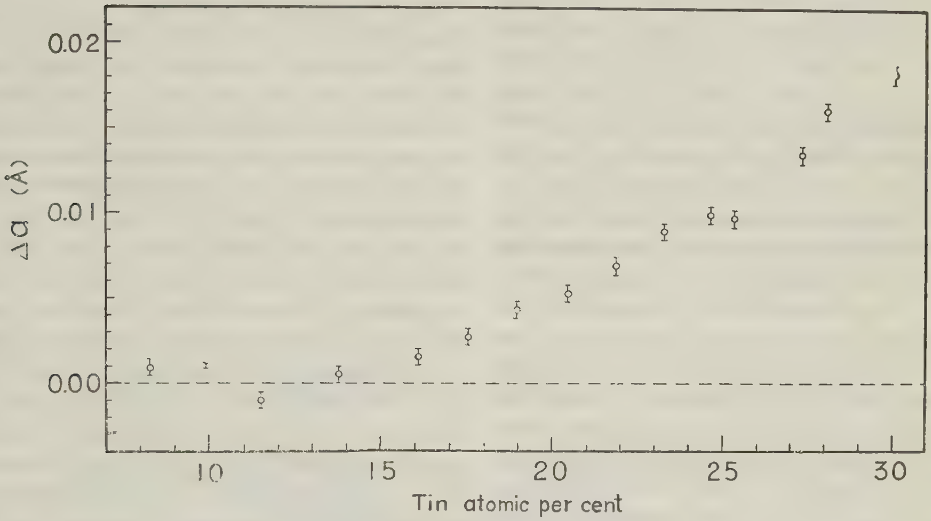

Fig. 11. The change of Δa with atomic percentage of Sn.

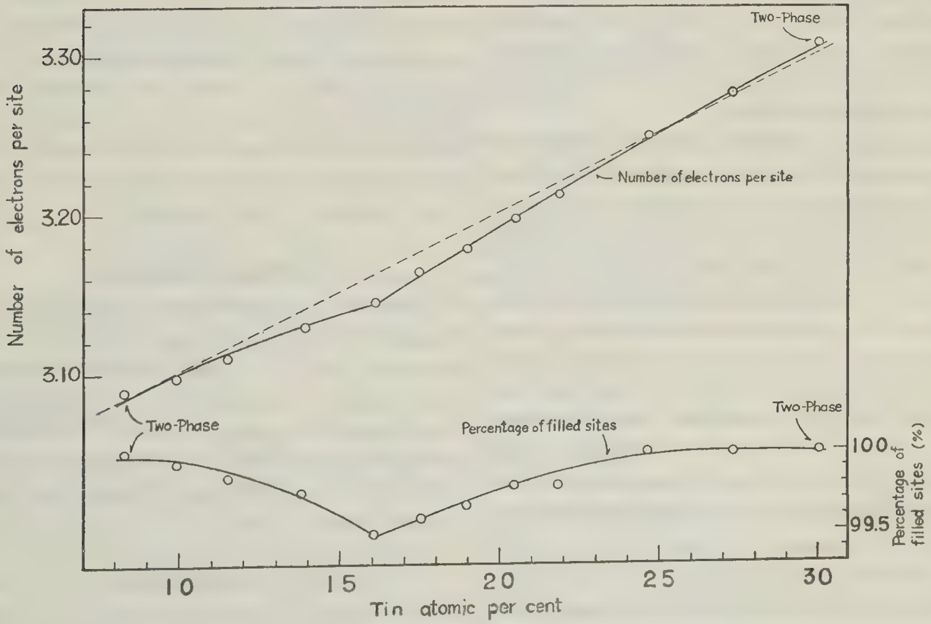

Fig. 12. The changes of the percentage of filled sites and the number of electrons per lattice at site with atomic percentage of Sn.

as follows. Since the discrepancies between the measured and calculated densities (Fig. 8) are much larger than the limit of experimental error and the specimens used for density measurement seem to be free from porosities, these discrepancies may be attributed to the formation of vacant sites. The percentage of filled sites and the corresponding number of electrons per site are shown in Fig. 12.

The vacant sites gradually increase with increasing solute concentration and a maximum is reached at about 16 at. % Sn which agrees with the atomic percentage at which the kink in the lattice constant versus composition curve occurs. After this maximum gradual decrease is observed until lattice sites are completely filled. The number of valence electrons per site (solid line in Fig. 12), therefore, shows less increase with increasing solute concentration than that corresponding to the complete filling of sites (broken line in Fig. 12). The introduction of vacancies into the structure to avoid rapid increase in the number of electrons per site is typical for the case where the $N(E)$ curve has a sharp fall which causes more rapid increase in the total energy of valence electrons with increasing number of electron per site. It is probable, therefore, that the rising portion of $N(E)$ curve corresponds to the range where vacancies are disappearing. Therefore, it may be said that the portion at which the vacancy concentration is maximum would be a trough of $N(E)$ curve and consequently this portion is comparatively unstable.

The occurrence of vacancy with increasing electron concentration, for example, was observed in solute-rich side of γ-phase in Cu-Al or Cu-Ga and is closely related to the sharp fall of $N(E)$ curve for the structure of γ-brass type.[23] Both the occurrence and the disappearance of vacancy were found in some Sn base alloys and interpreted to some extent by the Brillouin zone structure suggested for Sn.[24] In this case, however, the disappearance occurs in the range of falling in the suggested $N(E)$ curve and hence seems to be somewhat different from the present results.

Now, the existence of the rise in $N(E)$ curve, which suggests the onset of {200} overlap, following the sharp fall at about 3.16 electrons per atom is proposed as the result of consistent explanation for both changes of lattice constant and density with composition, and this is to be expected when Matyas' results are taken into account.

§ 6. Summary

Kinds and boundaries of phases in Tl-rich sides of the systems of Tl-Cd, Tl-Sn and Tl-Sb were determined by X-ray and electron diffraction. Considering the experimental results obtained in the present work as well as those obtained by previous workers, it was deduced that phase boundary of a particular structure in Tl base alloys corresponds to the same electron concentration, namely, 3.10 electrons per atom for the Tl-rich side of f.c.c. phase, and in the case of the hexagonal α solid solution, 3.02 electrons per atom for the side which is rich in the solute of higher valency than Tl and 2.96 electrons per atom for the case of lower valency than Tl. The phase boundaries of α solid solution and f.c.c. phase of Tl base alloys, therefore, seem to be mainly affected by the electronic factor.

The changes of lattice constant and density with composition in the f.c.c. region of Tl-Sn system, which was confirmed to be stable, were also measured. The kink observed in Δa, and the formation of vacant sites deduced from the discrepancies between the measured and calculated density were interpreted in terms of the Brillouin zone concept. Considering Matyas' results for trivalent Al, a suggestion for the high enery portion of $N(E)$ curve for the f.c.c. structure, namely, the existence of the sharp fall in $N(E)$ curve at about 3.16 electrons per atom followed by the rising portion, which suggests the onset of {200} overlap, was proposed.

Acknowledgements

The writer would like to express his sincere thanks to Prof. K. Tanaka of Kyōto University and Prof. Y. Fujiki in this Institute for their helpful discussions and encouragement throughout the present work. The writer is also grateful to Mr. T. Yoshida in this Institute for his assistance in carrying out the experiments.

References

1) N. F. Mott and H. Jones: Proc. Roy. Soc. A, **162** (1937) 49.
2) Z. Matyas: Phil. Mag. **39** (1948) 429.

3) H. J. Axon and W. Hume-Rothery: Proc. Roy. Soc. A, **193** (1948) 1.
4) H. W. B. Skinner: Phil. Trans. Roy. Soc. A, **239** (1940) 95.
5) R. Lingelbach and E. Vogt: Acta Met. **7** (1959) 441.
6) R. S. Leigh: Phil: Mag. **42** (1951) 139, 876.
7) M. Hansen: *Constitution of Binary Alloys* (McGraw-Hill, 1958).
8) P. Fuchs: Z. anorg. Chem. **107** (1919) 308.
9) S. Sekito: Z. Krist. **74** (1930) 193.
10) H. Lipson and A. R. Stokes: Nature **148** (1941) 437.
11) T. Barth: Z. Phys. Chem. **127** (1927) 113.
12) E. Persson and A. Westgren: Z. phys. Chem. **136** (1928) 208.
13) E. Kurzyniec: See reference 7).
14) C. diCapua: See reference 7).
15) A. Schneider and G. Heymer: Z. anorg. Chem. **286** (1956) 118.
16) Y. Fujiki: J. Phys. Soc. Japan **14** (1959) 913.
17) Y. Tang and L. Pauling: Acta Cryst. **5** (1952) 39.
18) J. B. Nelson and D. P. Riley: Proc. Phys. Soc. London **57** (1945) 160.
19) W. Hume-Rothery and G. V. Raynor: *The Structure of Metals and Alloys* (Inst. of Metals, London, 1954) 53.
20) C. Tyzack and G. V. Raynor: Acta Cryst. **7** (1954) 505.
21) G. V. Raynor: Proc. Roy. Soc. A, **180** (1942) 107. G. V. Raynor: Proc. Roy. Soc. A, **174** (1940) 457, 471. W. Hume-Rothery and G. V. Raynor: Proc. Roy. Soc. A, **177** (1940) 27.
22) H. Jones: Phil. Mag. **41** (1950) 663. See also, J. Goodenough: Phys. Rev. **89** (1953) 282.
23) W. Hume-Rothery, J. O. Betterton and J. Reynolds: J. Inst. Met. **80** (1951–2) 609.
24) J. A. Lee and G. V. Raynor: Proc. Phys. Soc. London **67** (1954) 737.
25) L. Guttman: J. Met. **2** (1950) 1472.
26) A. Olander: Z. Krist. A, **89** (1934) 89.

JOURNAL OF THE PHYSICAL SOCIETY OF JAPAN, Vol. 15, No. 8, AUGUST, 1960

Observations of Dislocation Networks in an Alloy of Body-Centered Cubic Lattice by Electron Microscopy

By Soji NENNO, Toshio SABURI and Masayoshi TAGAYA
Department of Metallurgy, Faculty of Engineering, Osaka University
Zenji NISHIYAMA
Institute of Scientific and Industrial Research, Osaka University

(Received May 6, 1960)

Electron microscopic observations were made on dislocation networks in thin foils of 55%Cr–Fe alloy annealed at 720°C after cold working. Dislocation cross-grids, hexagonal networks and networks of irregular shape are observed. From the presence of three-fold nodes, it is suggested that Burgers vectors of type [100] may be stable as well as those of type ½[111].

§1. Introduction

Direct observation of dislocation networks in body-centered cubic metal by electron microscopy has not yet been made except the one on α-Fe reported briefly by Hirsch[1]. The present writers have found dislocation networks in 55%Cr–Fe alloy during their studies on the sigma phase formation in body-centered cubic matrix. Some of the experimental results will be described in the following section.

§2. Experimental Procedure and Results

The material used is a forged bar of the alloy with the following compositions: Cr: 55%, C: 0.007%, N: 0.007%, H: 0.00023%, O: 0.078% and Fe: balance. It was again forged to a plate of 0.3 mm thick and pieces taken out from the plate were beaten until crack began to occur, followed by annealing at 720°C for 24 hrs. From these pieces thin foils for the electron microscopic observation were obtained by electro-polishing under the following conditions:

electrolyte perchloric acid 200 cc/l
glacial acetic acid 800 cc/l
current 0.6 amp., voltage 12 volt, 8°C.

The electron microscope was operated at 60 kV, unless otherwise mentioned.

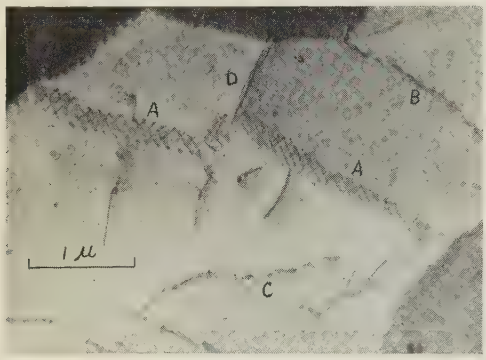

Fig. 1. Dislocation cross-grids constituting slightly misoriented subgrains.

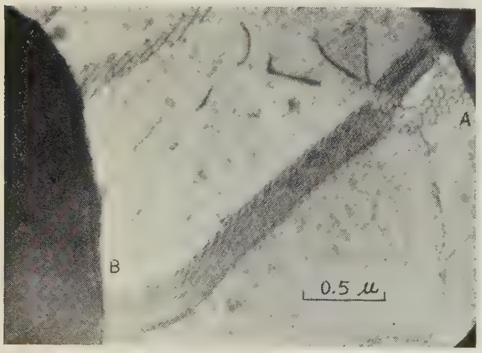

Fig. 2. Hexagonal network of dislocations between two subboundaries A and B.

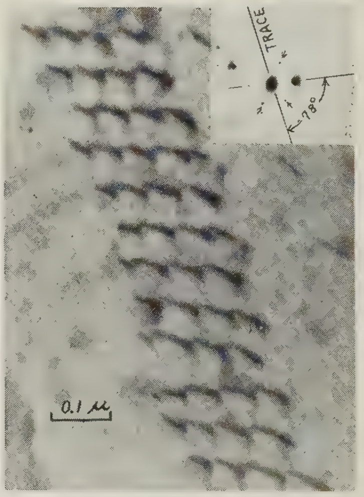

Fig. 3. Network with possibly extended dislocation ribbons and its selected-area diffraction pattern.

Some examples of electron micrographs are given in Fig. 1 to 6. Fig. 1 represents an example of dislocation cross-grids, at A, which constitute the boundaries of slightly misoriented subgrains. In view of the treatment given to the specimen, such a cross-grid seems to be fairly stable in this alloy. At subboundaries B and C, dislocations display double images. Subboundary at D is considered as consisting of dislocations rather than of incoherent precipitates. Fig. 2 indicates a hexagonal network in which segments of the network with a particular direction are absent, probably because Bragg condition is not fulfilled. The network stretches over between two adjacent subboundaries, with two kinks near subboundaries A and B. The size of each net is smaller at the middle region than near subboundaries A and B. In body-centered cubic crystals, it was proposed[2] that the diamond structure of dislocation network is stable. Only when two layers of diamond network are viewed at a particular direction, they look like a hexagonal network. Since, in the present case, hexagonal networks were found in many photographs, it is unlikely to attribute all of them to the two layers of diamond network. Fig. 3 shows a cross-grid or a hexagonal array of dislocations in which one component of dislocation segments is much shorter than the other two. At the nodes the dislocations are broadened to some extent and they may be interpreted as the extended dislocations. In the corner of this figure is inserted the selected-area diffraction pattern* of the dislocation network, in which the trace of the plane of the network is also shown corrected for rotation of the image. The index of the foil plane as derived is (1.31, 1.59, 1.00) and the direction of the trace of the network [−1.16, 0.327, 1.00] or [−5.63, 4.00, 1.00]. Hence the possible index of the plane of the network is (101) or (112). (112) appears more likely if we consider the projected width of the network plane and its inclination to the foil plane, although it is not yet conclusive, at present, which is more probable.

---

* The spots indicated by arrows have been retouched in order to make reproduction possible.

In Fig. 4, dislocations in the direction marked with the arrow look consisting of spots. This may be attributed to the Pendellösung effect. The extinction distance estimated from the photograph is about 300 Å which is of the same order of magnitude as those already calculated for Ni and Cu[3]. In Fig. 5, subboundary A seems to consist of dislocations perpendicular to the foil, and terminates at B where an irregular dislocation network is found. In region C where subboundaries are not yet completed, many of dislocations are distributed in rather random fashion. Dislocation nodes at D are thought to be formed by a reaction of the following type as a result of intersection of dislocations in two families.

$$\tfrac{1}{2}[111]+\tfrac{1}{2}[1\bar{1}\bar{1}]\rightarrow[100]\ .$$

The presence of this type of nodes and hexagonal networks suggests that in body-centered cubic crystal Burgers vectors of [100] type may be stable as well as those of ½[111] type, as pointed out by Hirsch[1].

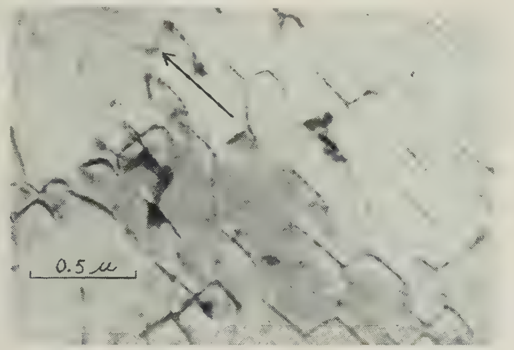

Fig. 4. Dislocation images consisting of spots lined in the direction of arrow.

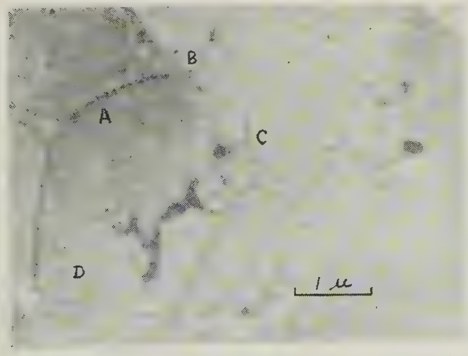

Fig. 5. Irregular dislocation networks and three-fold nodes.

Fig. 6(a)* appears to show a process[4] in which dislocations in two families intersect and form network. This region corresponds to area A in Fig. 6(b)*. In this figure the black broad band running obliquly is a Neumann band formed by hammering at room temperature. The bright area might correspond to the original single grain before hammering. In areas B and C some of subgrains are found. At D, a subboundary is being formed.

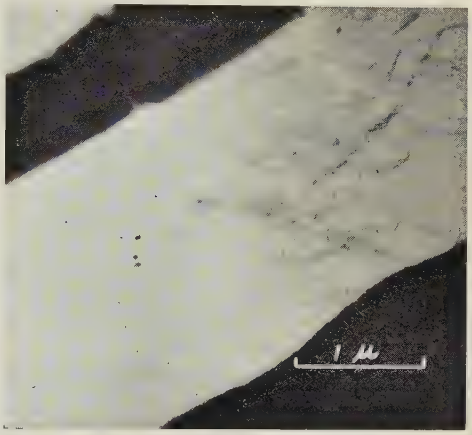

Fig. 6(a).

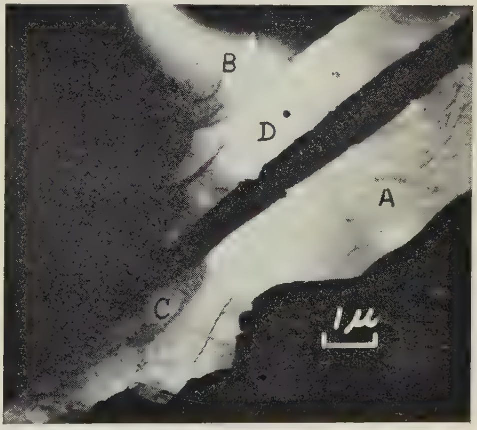

Fig. 6(b).

Fig. 6. (a) Dislocation network being formed from intersection of dislocations. (b) Neighboring region of the area of (a).

The writers wish to thank Messrs. K. Shimizu and H. Fujita for helping to carry out the present work. They are grateful to Professor R. Uyeda, Nagoya University and Dr. H. Suzuki, Japan Atomic Energy Research

---

* This photograph was taken at 50 kV.

Institute for valuable discussions. Thanks are due to Professor T. Terasaki and Dr. K. Shioda, and Mr. A. Kore'eda for helping to take electron micrographs. They would like to thank Mr. W. O. Binder, Electro Metallurgical Company, N. Y., for supplying the high purity alloy used in the present work. This work is partially supported by the grant from the Scientific Research Fund of the Ministry of Education.

References

1) P. B. Hirsch: J. Inst. Metals **87** (1958-59) 406.
2) T. Suzuki and H. Suzuki: Sci. Rep. Tôhoku Univ. **A**, **6** (1954) 573.
3) M. J. Whelan: J. Inst. Metals **87** (1958-59) 392.
4) S. Amelinckx: Phil. Mag. **1** (1956) 269; Acta Met. **6** (1958) 34.

JOURNAL OF THE PHYSICAL SOCIETY OF JAPAN, Vol. 15, No. 8, AUGUST, 1960

An X-ray Study on the Structure of Cobalt Dichloride Hexahydrate

By Jōji MIZUNO

The Research Institute for Iron, Steel and Other Metals,
Tohoku University, Sendai Japan

(Received February 27, 1960)

The crystal structure of $CoCl_2 \cdot 6H_2O$ has been determined by the X-ray single crystal method. The unit cell is monoclinic with $a=10.34$ Å, $b=7.06$ Å, $c=6.67$ Å and $\beta=122°20'$. The space group is C_{2h}^3-C2/m and the unit cell contains two molecules. Two Cl^- ions and four water molecules are octahedrally coordinated to Co^{2+} ion to form the group $[CoCl_2 \cdot 4H_2O]$. These groups are held together parallel to the b axis by O···H-O type hydrogen bonds. The other two water molecules of the formula unit are far from Co^{2+} ion. The crystal has the layer structure parallel to (001), and this causes the perfect cleavage. The structure proposed for this salt by Stroganov *et al.* seems to be incorrect.

§1. Introduction

There has been no report on the crystal structure of cobalt dichloride hexahydrate, $CoCl_2 \cdot 6H_2O$, until 1958. Since several years ago, the structural information has been keenly required in relation with the magnetic behavior of this salt at the liquid helium temperature. Haseda and Kanda[1] measured the magnetic susceptibilities of powdered samples of this salt and found an anomaly at about 3°K. Haseda[2] also found the same magnetic behavior on the single crystal samples. These authors considered this behavior to be caused by the anti-ferromagnetic transition. Since the above transition temperature is higher than that expected when each metallic ion was octahedrally surrounded by six water molecules as in alums or Tutton salts, they inferred that one or two chlorine atoms in $CoCl_2 \cdot 6H_2O$ would occupy the positions of the octahedral coordination around a cobalt atom in the place of water molecules and these octahedrons would be adjacent to one another without insertion of any atom or any molecule. It was considered desirable, therefore, to examine whether Cl^- ions in $CoCl_2 \cdot 6H_2O$ were directly coordinated to Co^{2+} ion or not.

The present work was thus undertaken. Rotation, oscillation and multiple-film equi-inclination Weissenberg photographs have been taken about the a and the b axes with Fe$K\alpha$ and Mo$K\alpha$ radiations. The structure has been determined in the usual way by the Patterson and the Fourier syntheses and has been refined by both the difference Fourier syntheses and the method of least squares.

From the intensities of ($h1l$) and ($1kl$) reflections, the proposed model has been confirmed to be correct. A part of the present work was preliminarily reported[3].

Before the present work was not finished, Stroganov, Kozhina and Andreev[4] proposed in 1958 the crystal structure of this salt, but their structure model reported is entirely different from the result in the present paper. The differences will be discussed in § 6 and it will be concluded that the present structure model is reasonable.

§ 2. Data from the Literature on $CoCl_2 \cdot 6H_2O$

In "*Chemische Kristallographie*, **I** Teil" (Groth, 1906)[5] the following data are given: the crystal is monoclinic prismatic, the axial ratios $a:b:c$ are 1.4788:1:0.9452, β being 122°19′. The crystal shows a perfect cleavage parallel to (001), an imperfect cleavage parallel to (110) and well-developed faces parallel to (100). It is dark red in colour and hygroscopic. The density is 1.924 gr./cm³.

§ 3. Experimental

Dark red single crystals were grown from saturated aqueous solution. They were similar in habit, especially in well-developed faces parallel to (100), as described by Groth. Samples used for the X-ray study were cut out of these crystals and enclosed in thin-walled glass capillaries. They were about $0.3 \times 0.3 \times 2.5\ \mathrm{mm}^3$ in dimension. The rod axis was the a or the b axis.

At first, rotation and oscillation photographs were taken about the a and the b axes using Mn-filtered Fe$K\alpha$ and Zr-filtered Mo$K\alpha$ radiations. Next, multiple-film equi-inclination Weissenberg photographs of zero-, the first-, the second- and the third-layer were taken about the a and the b axes using Zr-filtered Mo$K\alpha$ radiation. These photographs gave the unit cell with the following constants:

$$a = 10.34\ \text{Å}, \quad b = 7.06\ \text{Å}, \quad c = 6.67\ \text{Å}$$

$$a:b:c = 1.47:1:0.945$$

$$\beta = 122°20′\ .$$

The number of molecules contained in the unit cell was calculated, from these lattice constants and the density value, 1.924 gr/cm³, to be 2.02, which means the existence of two molecules per unit cell. From the indexed oscillation and Weissenberg photographs, it was ascertained that general reflections (hkl) are present only if $h+k=2n$ and reflections ($h0l$) and ($0kl$) are present only if $h=2n$ and $k=2n$, respectively. Thus the space group was determined as $C_{2h}^3 - C2/m$.

The diffracted intensities on photographs were estimated by visual comparison with the time-exposure calibrated strips, and also by microphotometry, and were corrected in the usual way for Lorentz and polarization factors. The linear absorption coefficients were calculated to be 174.2 cm⁻¹ and 27.76 cm⁻¹ for Fe$K\alpha$ and Mo$K\alpha$ radiations, respectively. Using these coefficients, the rough absorption correction was made by assuming cylindrical shape of the sample.

§ 4. Determination of the Structure

As a first step, a Patterson projection on the (010) plane of the unit cell was made using ($h0l$) data obtained from oscillation photographs taken about the b axis with Mn-filtered Fe$K\alpha$ radiation. The general position is eightfold in the space group $C_{2h}^3 - C2/m$, and since there are two formula units of [$CoCl_2 \cdot 6H_2O$], in the unit cell, it follows that the cobalt atoms must lie in twofold special positions, one of which may be chosen for the origin. There were three peaks besides those at (0, 0) and ($\frac{1}{2}$, 0) in the projection. Two peaks of the former were at the distances 2.43 Å and 1.50 Å from the origin and were interpreted in terms of the Co–Cl and the Co–O interatomic distances, respectively. The angle between the two lines joining these two peaks with the origin was about 90°. Although the third lowest peak at the distance 2.42 Å from the origin was not clearly interpreted, it suggested the existence of water molecules located far from Co atoms. Thus, a structure model was tentatively derived, in which two Cl atoms and four water molecules are octahedrally coordinated to Co atom to form the group [$CoCl_2 \cdot 4H_2O$] and the other two water molecules of the formula unit are relatively free. The atoms are located at the following positions:

$(0, 0, 0;\ \frac{1}{2}, \frac{1}{2}, 0) +$

2Co at (a) $0, 0, 0$

4Cl at (i) $x, 0, z;\ \bar{x}, 0, \bar{z}$

$8O_{I}$ at (j) $x, y, z;\ x, \bar{y}, z,\ \bar{x}, y, \bar{z};\ \bar{x}, \bar{y}, \bar{z}$

$4O_{II}$ at (i) $x, 0, z;\ \bar{x}, 0, \bar{z}$.

The parameter values for the positions of the atoms could approximately be determined by the trial-and-error method, using the $F(h0l)$'s obtained from oscillation photographs taken about the *b* axis with Zr-filtered Mo$K\alpha$ radiation. They are listed in Table I. The *y* parameter of O_I was estimated, assuming that four water molecules around Co atom are arranged in a square. The reliability factor, $R=\Sigma||F_0|-|F_c||/\Sigma|F_0|$ was 0.19 for the observed spectra of $F(h0l)$'s. No corrections for temperature were made in the calculation of F_c.

Table I. Parameter values of atoms determined by the trial-and-error method.

Atom	*x*	*y*	*z*
Co	0	0	0
Cl	0.270	0	0.160
O_I	0.0325	(±0.224)	0.261
O_{II}	0.283	0	0.717

As the next step, Fourier projections on (010) and (100) were synthesized, based on the above structure model, using the $F(h0l)$'s and $F(0kl)$'s obtained from oscillation photographs taken about the *b* and the *a* axes with Zr-filtered Mo$K\alpha$ radiation. Improved values of atomic parameters were obtained from these Fourier projections. They are given in Table II. The reliability factors calculated only from observed spectra were 0.154 for the $F(h0l)$'s and 0.145 for the $F(0kl)$'s, respectively. *B*, the coefficient in the exponent of the isotropic temperature factor $\exp[-B\cdot\sin^2\theta/\lambda^2]$, was estimated as 1.5 Å^2 for Co^{2+} and 3.0 Å^2 for Cl^- and O^{2-}, respectively, from comparison between F_c and F_0.

Table II. Atomic parameters.

Atom	*x*			*y*			*z*		
	From oscil-lation photo.	From Weis-senberg photo.	From the method of least squares	From oscil-lation photo.	From Weis-senberg photo.	From the method of least squares	From oscil-lation photo.	From Weis-senberg photo.	From the method of least squares
Co	0	0	0	0	0	0	0	0	0
Cl	0.278	0.278	0.274	0	0	0	0.175	0.172	0.171
O_I	0.0288	0.0288	0.0312	±0.221	±0.213	±0.208	0.255	0.252	0.251
O_{II}	0.275	0.275	0.288	0	0	0	0.700	0.707	0.702

O_I: $4H_2O$ coordinated to Co^{2+} ion. O_{II}: $2H_2O$ far from Co^{2+} ion.

As the final step, the Fourier projections and the difference Fourier projections on (010) and on the plane normal to the *a* axis were synthesized, using the $F(h0l)$'s and $F(0kl)$'s obtained from Weissenberg photographs. In these procedures, the *y* and the *z* parameters were improved as given in Table II. The value of *B* for Co^{2+} was also improved to be 1.7 Å^2. The reliability factors were 0.137 and 0.135 for the $F(h0l)$'s and the $F(0kl)$'s of observed spectra, respectively. The method of least squares was finally applied and the atomic parameters were determined. They are listed also in Table II. The Fourier projections finally synthesized are shown in Fig. 1 (a) and (b). The calculations of the method of least squares and the final Fourier syntheses were carried out with PC-1 Parametron Computer of Tokyo Univ..

Table III gives a comparison between observed and calculated structure factors for the present structure model. The agreement is fairly good, and the reliability factors are 0.196 and 0.160 for all $(h0l)$ and $(0kl)$ amplitudes, for which the maximum observed values of $\sin\theta/\lambda$ were 0.8324 and 0.7773, respectively. These amplitudes include those of unobserved reflections. The reliability factors for $F(h0l)$'s and $F(0kl)$'s of observed spectra alone are 0.132 and 0.121, respectively. In the calculation of F_c, the values of the atomic scattering factors were taken from "*Internationale Tabellen zur Bestimmung von Kristallstrukturen* II" (1935). In the calculation by PC-1 computer, they were taken from the paper of Vand, Eiland and Pepinsky[6].

§ 5. Description of the Structure

The schematic representation and the arrangement of atoms projected on (010) plane

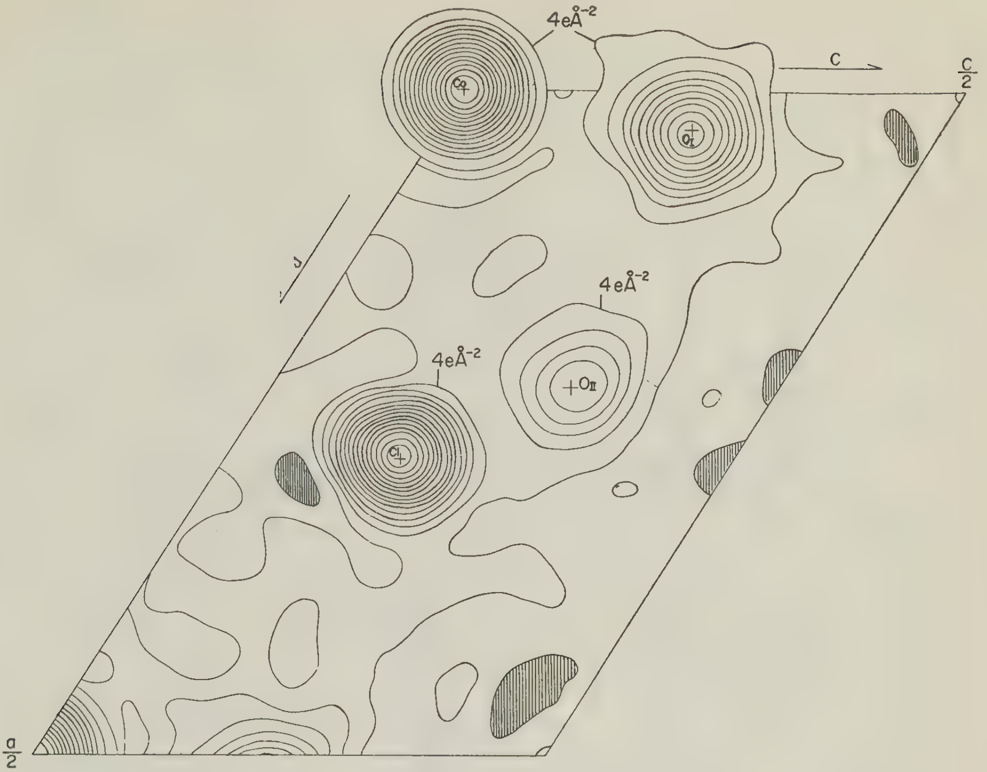

Fig. 1(a).

Fig. 1. The final Fourier projections of electron density on (010), (a) and on a plane normal to the *a* axis, (b). Contours are drawn at intervals of $2e\text{Å}^{-2}$. Co atom is contoured at intervals of $4e\text{Å}^{-2}$. In (b) contours of 15.5 and $15.7e\text{Å}^{-2}$ are drawn at the central region of $O_{I \cdot 1}$ and $O_{I \cdot 2}$. Negative areas are shaded. Crosses show the final atomic positions.

are shown in Fig. 2 and Fig. 3, respectively. As seen from the former figure, two Cl^- ions and four water molecules are octahedrally coordinated to Co^{2+} ion to form the group $[CoCl_2 \cdot 4H_2O]$. These four water molecules are arranged in a square form. The other two water molecules of the formula unit are located far from Co^{2+} ion.

Exactly speaking, the two side lengths of the square of water molecule are not equal but estimated to be 3.05 Å and 2.94 Å, respectively, and hence the form is a rectangle close to a square. The plane of the " square " is perpendicular to (010) and is inclined to the *c* axis by an angle of about 10°. The Cl^-–Co^{2+}–Cl^- bond is perpendicular to the plane of the " square ". Interatomic distances and interbond angles are given in Table IV. From both the distance between O_I and O_{II} and the angle $\angle O_I \cdots O_{II} \cdots O_I$, it is almost certain that the groups $[CoCl_2 \cdot 4H_2O]$ are held together parallel to the *b* axis by $O \cdots H$–O

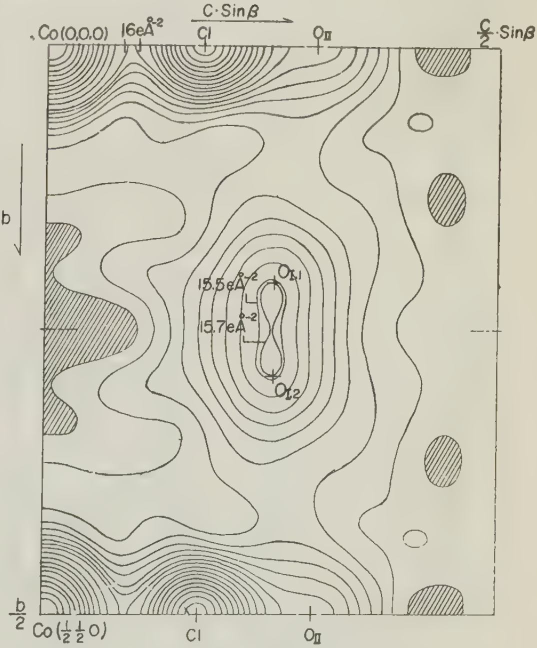

Fig. 1(b).

Table III. Comparison between F_c and $\lvert F_0\rvert$ for the $(0kl)$ and $(h0l)$ reflections.

h	0	l	$\lvert F_0\rvert$	F_c
2	0	0	11.0	8.1
4	0	0	41.3	47.0
6	0	0	7.9	6.6
8	0	0	13.7	10.1
10	0	0	5.2	5.6
12	0	0	0	1.3
* 14	0	0	0	2.8
0	0	1	32.6	32.6
2	0	1	7.6	3.2
4	0	1	7.5	6.4
6	0	1	6.0	4.3
8	0	1	0	0.5
10	0	1	6.7	5.4
* 12	0	1	0	0.5
$\bar{2}$	0	1	20.0	23.7
$\bar{4}$	0	1	36.6	40.7
$\bar{6}$	0	1	16.2	13.7
$\bar{8}$	0	1	24.3	22.6
$\overline{10}$	0	1	4.2	5.3
$\overline{12}$	0	1	8.6	8.5
* $\overline{14}$	0	1	0	2.0
0	0	2	23.2	−25.9
2	0	2	21.0	21.4
4	0	2	10.6	−10.0
6	0	2	18.6	16.1
8	0	2	0	0.5
10	0	2	8.3	6.7
* 12	0	2	0	2.0
$\bar{2}$	0	2	10.4	8.9
$\bar{4}$	0	2	2.9	3.6
$\bar{6}$	0	2	2.6	0.7
$\bar{8}$	0	2	20.5	19.0
$\overline{10}$	0	2	1.0	1.1
$\overline{12}$	0	2	15.2	11.9
* $\overline{14}$	0	2	0	1.5
$\overline{16}$	0	2	5.9	3.5
0	0	3	5.2	2.9
2	0	3	24.7	24.6
4	0	3	7.0	6.1
6	0	3	13.6	14.1
8	0	3	4.0	4.7
10	0	3	4.3	4.0
$\bar{2}$	0	3	19.5	19.9
$\bar{4}$	0	3	1.6	−4.0
$\bar{6}$	0	3	7.9	8.2
$\bar{8}$	0	3	0	−0.7
$\overline{10}$	0	3	2.0	4.6
$\overline{12}$	0	3	4.5	3.7
$\overline{14}$	0	3	1.8	2.4
$\overline{16}$	0	3	4.1	2.9
0	0	4	17.9	16.3
2	0	4	14.4	13.2
4	0	4	14.5	13.1
6	0	4	3.4	2.6
8	0	4	5.4	5.6
10	0	4	1.8	0.6
$\bar{2}$	0	4	32.6	31.7
$\bar{4}$	0	4	7.5	5.2
$\bar{6}$	0	4	32.4	31.4

h	0	l	$\lvert F_0\rvert$	F_c
$\bar{8}$	0	4	3.2	−3.8
$\overline{10}$	0	4	17.0	15.0
$\overline{12}$	0	4	0	−1.0
$\overline{14}$	0	4	4.7	4.3
* $\overline{16}$	0	4	0	1.4
0	0	5	11.1	11.1
2	0	5	1.1	1.6
4	0	5	7.4	7.2
6	0	5	0	−0.3
* 8	0	5	0	3.3
$\bar{2}$	0	5	12.9	11.9
$\bar{4}$	0	5	14.7	13.9
$\bar{6}$	0	5	22.9	19.9
$\bar{8}$	0	5	9.5	10.8
$\overline{10}$	0	5	20.1	15.0
$\overline{12}$	0	5	0	4.3
$\overline{14}$	0	5	9.0	6.8
* $\overline{16}$	0	5	0	1.2
0	0	6	10.6	9.4
2	0	6	1.7	−0.6
4	0	6	4.6	4.4
6	0	6	2.8	1.9
$\bar{2}$	0	6	6.5	−5.8
$\bar{4}$	0	6	14.7	14.6
$\bar{6}$	0	6	1.5	−2.8
$\bar{8}$	0	6	12.6	13.3
$\overline{10}$	0	6	7.0	5.7
$\overline{12}$	0	6	7.9	6.5
$\overline{14}$	0	6	7.8	6.5
* $\overline{16}$	0	6	0	1.9
0	0	7	8.5	7.2
2	0	7	1.8	3.6
4	0	7	4.0	3.0
$\bar{2}$	0	7	0	1.2
$\bar{4}$	0	7	11.1	9.1
$\bar{6}$	0	7	1.7	−1.9
$\bar{8}$	0	7	9.1	7.6
$\overline{10}$	0	7	0	−0.4
$\overline{12}$	0	7	5.0	5.4
$\overline{14}$	0	7	2.9	1.8
* $\overline{16}$	0	7	0	2.9
0	0	8	4.3	2.4
2	0	8	5.7	4.8
$\bar{2}$	0	8	8.8	8.2
$\bar{4}$	0	8	4.9	4.9
$\bar{6}$	0	8	6.3	6.5
$\bar{8}$	0	8	6.2	6.8
$\overline{10}$	0	8	0	1.2
$\overline{12}$	0	8	6.7	6.1
* $\overline{14}$	0	8	0	−0.4
* $\overline{16}$	0	8	0	3.4
* 0	0	9	0	0.7
* $\bar{2}$	0	9	0	5.3

h	0	l	$\lvert F_0\rvert$	F_c
* $\bar{4}$	0	9	0	2.2
$\bar{6}$	0	9	5.6	7.0
$\bar{8}$	0	9	4.2	4.4
$\overline{10}$	0	9	3.7	5.2
$\overline{12}$	0	9	5.2	4.4
* $\overline{14}$	0	9	0	2.3
* $\overline{16}$	0	9	0	2.6
* $\bar{2}$	0	10	0	1.9
* $\bar{4}$	0	10	0	1.0
$\bar{6}$	0	10	4.0	4.0
$\bar{8}$	0	10	2.8	0.7
$\overline{10}$	0	10	4.5	5.2
* $\overline{12}$	0	10	0	1.2
* $\overline{14}$	0	10	0	3.7
* $\bar{8}$	0	11	0	0.9
* $\overline{10}$	0	11	0	2.4

0	k	l	$\lvert F_0\rvert$	F_c
0	2	0	32.8	37.0
0	4	0	43.7	40.3
0	6	0	23.6	21.7
0	8	0	10.6	11.1
0	10	0	9.4	7.7
0	0	1	33.3	32.6
0	2	1	30.9	26.7
0	4	1	21.2	17.9
0	6	1	13.3	12.2
0	8	1	7.8	7.8
0	10	1	5.1	4.4
0	0	2	29.0	−25.9
0	2	2	18.8	12.4
0	4	2	3.7	−4.0
0	6	2	0	1.4
0	8	2	0	3.1
* 0	10	2	0	0.5
0	0	3	5.4	2.9
0	2	3	5.1	2.4
0	4	3	0	2.3
0	6	3	2.1	2.0
0	8	3	0	1.6
* 0	10	3	0	1.2
0	0	4	18.4	16.3
0	2	4	1.8	0.8
0	4	4	7.8	8.7
0	6	4	3.4	4.7
0	8	4	2.1	2.3
0	0	5	10.1	11.1
0	2	5	9.5	10.7
0	4	5	8.2	8.8
0	6	5	5.2	6.5
0	8	5	3.6	4.2
0	0	6	9.4	9.4
0	2	6	13.7	15.0
0	4	6	8.4	8.7
0	6	6	6.0	6.9
0	8	6	5.2	4.6
0	0	7	6.0	7.2
0	2	7	6.0	6.5
0	4	7	4.6	5.4
* 0	6	7	0	3.8
0	0	8	3.1	2.4
* 0	2	8	0	0.3
* 0	4	8	0	1.5

*: Tnobserved Spectra.

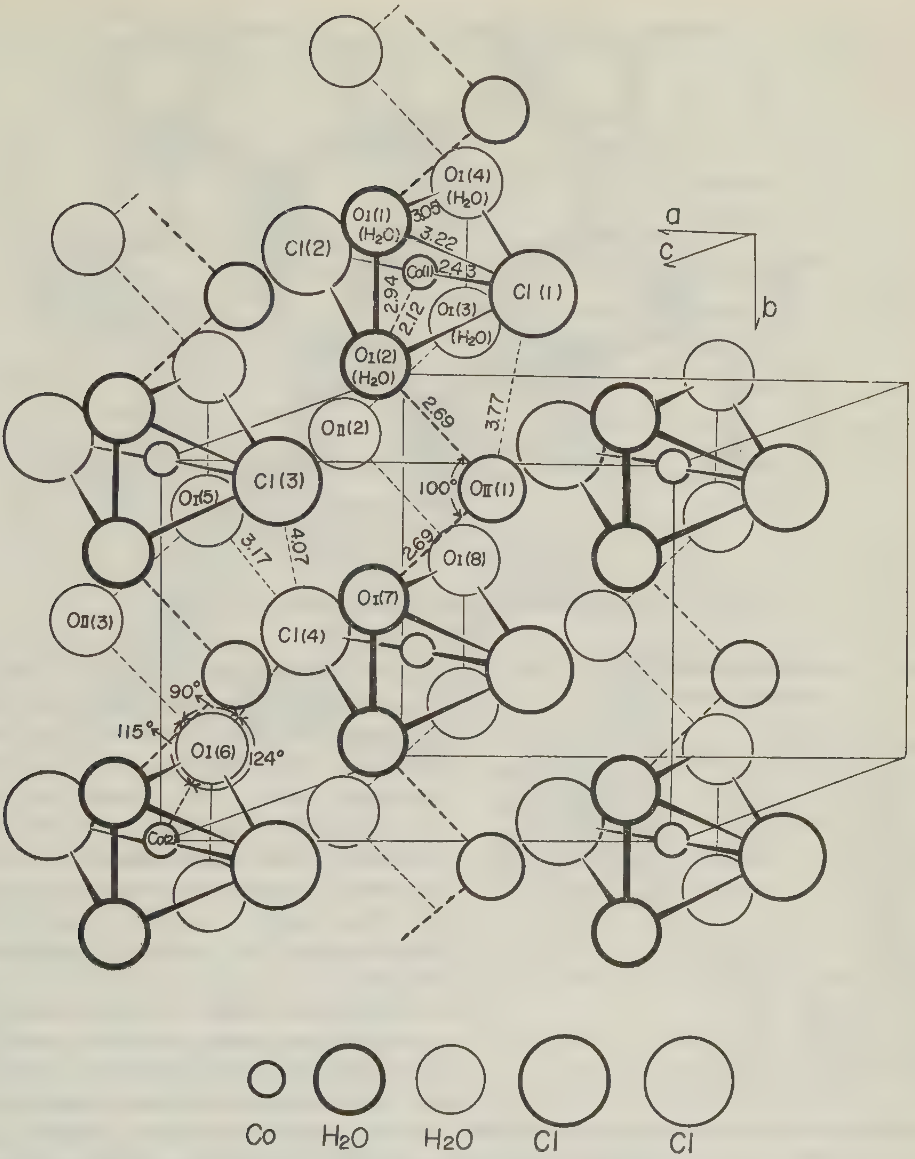

Fig. 2. The schematic representation of the crystal structure of $CoCl_2 \cdot 6H_2O$.

type hydrogen bonds between O_I and O_{II}. As seen from Fig. 3, the structure is also composed of atomic layers parallel to (001). Thus, the perfect cleavage parallel to (001) can reasonably be explained.

§ 6. Discussion

Stroganov *et al.* already reported the crystal structure of $CoCl_2 \cdot 6H_2O$. According to them, important data of the structure are as follows:

i) Space group: $C_{2h}^5 - P2_1/c$

ii) Unit cell dimensions: $a = 6.58$ kX, $b = 7.03$ kX, $c = 11.50$ kX, $\beta = 49°30'$

iii) Four water molecules and two Cl^- ions are coordinated to Co^{2+} ion to form the group $[CoCl_2 \cdot 4H_2O]$, in which four water molecules are arranged in a rectangular form around Co^{2+} ion. The side lengths of the rectangle are 2.6 kX along the *b* axis and 3.3 kX along (010), respectively. The angle between the $Cl^- - Co^{2+} - Cl^-$ bond and the normal to the plane of the rectangle is 19°. The interatomic distances $Co-H_2O$ and $Co-Cl$ in the group are 2.12 kX and 3.10 kX, respectively.

iv) The other two water molecules of the formula unit are located near the group

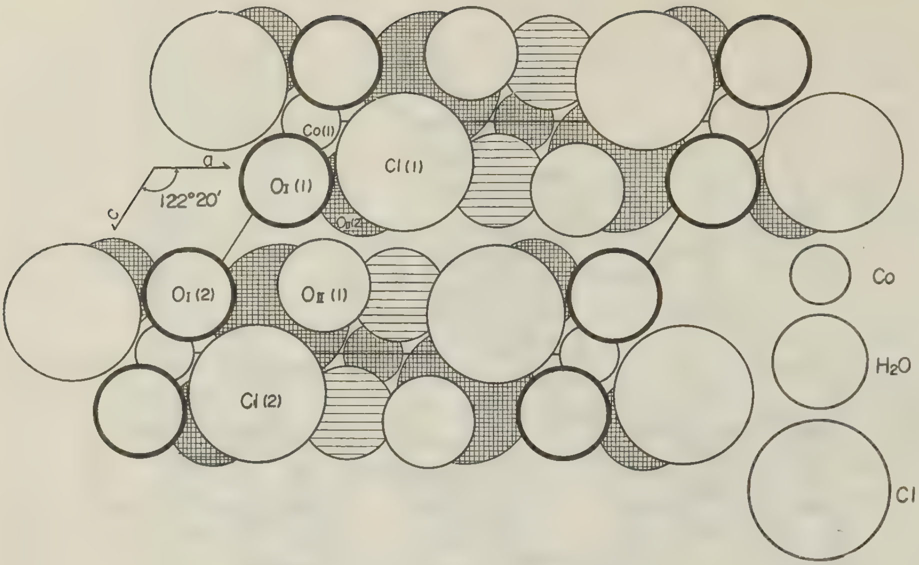

Fig. 3. The arrangement of atoms projected on (010).

Table IV. Interatomic distances (in Å) and interbond angles.

Refer to Fig. 2		Refer to Fig. 3	
Co(1)-O$_I$(1,2,3,4)	2.12	O$_I$(1)-O$_I$(2)	3.69
Co(1)-Cl(1,2)	2.43	O$_I$(1)-O$_{II}$(1)	3.14
O$_I$(1)-O$_I$(4)	3.05	O$_I$(2)-O$_{II}$(1)	3.77
O$_I$(1)-O$_I$(2)	2.94	Cl(1)-O$_{II}$(1)	3.48
Cl(1)-O$_I$(1)	3.22	Cl(2)-O$_{II}$(1)	3.20
O$_I$(2)-O$_{II}$(1)	2.69	O$_{II}$(1)-O$_{II}$(2)	4.26
O$_I$(7)-O$_{II}$(1)		Co(1)-O$_{II}$(2)	4.07
O$_I$(5)-Cl(4)	3.17		
O$_I$(6)-Cl(4)			
Cl(3)-Cl(4)	4.07		
Cl(1)-O$_{II}$(1)	3.77		
O$_I$(2)-O$_{II}$(1)-O$_I$(7)	100°		
O$_{II}$(3)-O$_I$(6)-Co(2)	115°		
Cl(4)-O$_I$(6)-Co(2)	124°		
O$_{II}$(3)-O$_I$(6)-Cl(4)	90°		

[$CoCl_2 \cdot 4H_2O$] and symmetrically to Co^{2+} ion in the plane (010). The interatomic distance Co-H_2O is 3.20 kX, and the angle between O-Co-O line and the normal to the above rectangle is 40°.

v) The cleavage plane is (010).

Compared with their structure model, the data of the present structure are as follows:

i) Space group: C_{2h}^3-C2/m.

ii) Unit cell dimension: $a=10.34$ Å, $b=7.06$ Å, $c=6.67$ Å, $\beta=122°20'$

iii) The group [$CoCl_2 \cdot 4H_2O$] is formed similarly to their structure model, but its detailed structure is different. Four water molecules are arranged in the "square" around Co^{2+} ion and the Cl^--Co^{2+}-Cl^- bond is perpendicular to the plane of this "square". The Co-H_2O and Co-Cl distances are 2.12 Å and 2.43 Å, respectively. The other two water molecules of the formula unit are by 4.07 Å distant from Co^{2+} ion. The fact that two kinds of water molecules exist in the present salt, namely, one is located near Co^{2+} ion and the other far from it, was also deduced in the study of proton magnetic resonance by Sugawara[7].

iv) The structure leads to the perfect cleavage parallel to (001) in accordance with Groth[5].

Sugawara's result and the result (iv) suggest that the present model is more reasonable one than that reported by Stroganov *et al.*. It is noticed, however, the fact that the following four kinds of the atomic arrangement, (I), (II), (III) and (IV) are conceivable so far as the Fourier projections shown in Fig. 1 (a) and (b) are concerned. In the arrangement (I), which was adopted by the present author, Cl and O_{II} in Fig. 1 (a) are located at $(x, 0, z)$ and $x, \frac{1}{2}, z)$, respectively, and the former atom is coordinated to Co at (0, 0, 0), and $O_{I\cdot 1}$ and $O_{I\cdot 2}$ in Fig. 1 (b) are located at (x, y, z) and $(x, \frac{1}{2}-y, z)$ and coordinated to Co at (0, 0, 0) and Co at $(\frac{1}{2}, \frac{1}{2}, 0)$, respectively. In the arrangement (II), Cl and O_{II} in Fig. 1 (a) occupy the positions of the arrangement (I) and $O_{I\cdot 2}$ and $O_{I\cdot 1}$ in Fig. 1 (b) are coordinated to Co at (0, 0, 0) and Co at $(\frac{1}{2}, \frac{1}{2}, 0)$, respectively. Consequently, four water molecules coordinated to Co are ar-

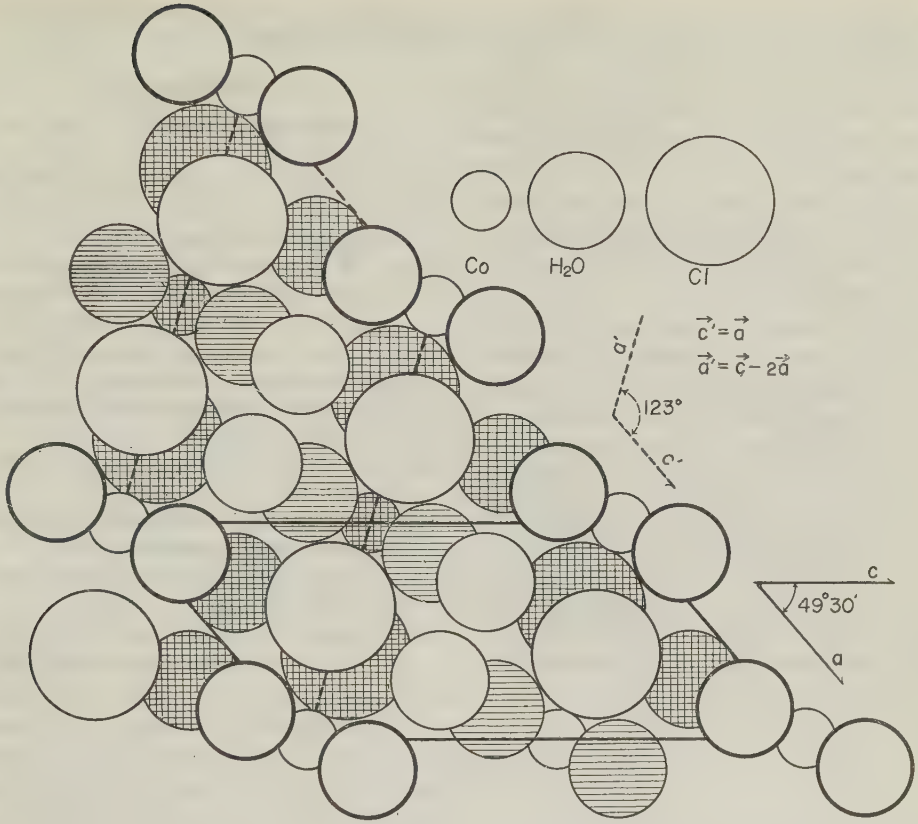

Fig. 4. The arrangement of atoms projected on (010) of the structure determined by Stroganov *et al.*

ranged in a rectangular form. In the arrangement (III), Cl in Fig. 1 (a) is located at $(x, \frac{1}{2}, z)$ and coordinated to Co at $(\frac{1}{2}, \frac{1}{2}, 0)$, and O_{II} is located at $(x, 0, z)$, and $O_{I\cdot1}$ and $O_{I\cdot2}$ in Fig. 1 (b) occupy the positions of the arrangement (I). In the arrangement (IV), Cl and O_{II} in Fig. 1 (a) are located at the positions of the arrangement (III) and $O_{I\cdot1}$ and $O_{I\cdot2}$ in Fig. 1 (b) are located at the positions or the arrangement (II).

It is interesting to note the circumstance that the projections on (010) of the atomic arrangements (III) and (IV) are very similar to the portion surrounded with broken lines in Fig. 4 which represents the atomic arrangement proposed by Stroganov *et al.*. In this figure a' and c' are related to their a and c, respectively by the following vector equations:

$$\vec{c}\,' = \vec{a}$$

$$\vec{a}\,' = \vec{c} - 2\vec{a}$$

The length of a' is 10.4 kX, and $\vec{a}\,'$ makes an angle 123° with $\vec{c}\,'$. As the length of c' is 6.58 kX, the unit cell formed by a', b and c' is nearly equal to that of the present structure.

It is important to determine which one of these four kinds of the atomic arrangement is correct. Because of $F_c = 8\Sigma f \cos 2\pi(hx+lz) \cdot \cos 2\pi ky$, this can not be determined by $(h0l)$ and $(0kl)$ data alone but by $(h1l)$ and $(1kl)$ data. The reliability factors for the above four atomic arrangements were calculated using thirty-one $F(h1l)$'s and seventeen $F(1kl)$'s. They are listed in Table V. These data show

Table V. The reliability factors for four kinds of the atomic arrangement.

Kind of atomic arrangement	Reliability factor	
	for $F(h1l)$'s	for $F(1kl)$'s
(I)	0.11	0.087
(II)	0.25	0.35
(III)	0.91	0.89
(IV)	0.92	0.84

that the structure I is decidedly reliable.

In a single crystal as well as a powdered sample of $NiCl_2 \cdot 6H_2O$ isomorphous to $CoCl_2 \cdot 6H_2O$ the antiferromagnetic transition was found at about 6°K[8),9)]. According to the preliminary study on the structure of the former salt by the author[10)], this salt seems to resemble $CoCl_2 \cdot 6H_2O$ in its atomic arrangement. The structure analysis of $NiCl_2 \cdot 6H_2O$ is now in progress.

The author wishes to express his sincere thanks to Professor S. Ogawa for his continued encouragement throughout the present work. His hearty thanks are also due to Professor T. Sugawara of the Institute for Solid State Physics, Tokyo University and Mr. T. Ukei for their valuable discussions. He is also indebted to Dr. T. Haseda and Mr. T. Satō for preparation of the good single crystals, and to Dr. Y. Takeuchi, Mr. M. Tokonami and the members of Professor R. Sadanaga's laboratory, Tokyo University for their aids in calculations using PC–1 Parametron Computer.

References

1) T. Haseda and E. Kanda: J. Phys. Soc. Japan **12** (1957) 1051.
2) T. Haseda: J. Phys. Soc. Japan **15** (1960) 483.
3) J. Mizuno, K. Ukei and T. Sugawara: J. Phys. Soc. Japan **14** (1959) 383.
4) E. V. Stroganov, I. I. Kozhina and S. N. Andreev: Vestnik Leningrad Univ. **13**, No. 10, Ser. Fiz. i Khim. No. 2 (1958) 109.
5) P. Groth: *Chemische Kristallographie*, **I** Teil (Wilhelm Engelmann, Leipzig, 1906) 248.
6) V. Vand, P. E. Eiland and R. Pepinsky: Acta Cryst. **10** (1957) 303.
7) T. Sugawara: J. Phys. Soc. Japan **14** (1959) 1248.
8) T. Haseda, H. Kobayashi and M. Date: J. Phys. Soc. Japan **14** (1959) 1724.
9) T. Haseda and M. Date: J. Phys. Soc. Japan **13** (1958) 175.
10) J. Mizuno: Read at the Annual Meeting of the Phys. Soc. Japan held in Oct. 1958.

JOURNAL OF THE PHYSICAL SOCIETY OF JAPAN, Vol. 15, No. 8, AUGUST, 1960

Study on the Twin Formation in Evaporated Silver Films

By Akira NAGASAWA* and Shiro OGAWA
The Research Institute for Iron, Steel and Other Metals,
Tohoku University, Sendai

(Received March 15, 1960)

Well oriented silver films have been formed by evaporation onto heated cleavage (001) surfaces of rock-salt in vacuum, the evaporation period having been changed in a wide range in case of the thickness kept at about 400 Å, and the influence of the formation speed on the twinning in the films has been examined by electron diffraction and electron microscopy. The diffraction patterns have shown that the frequency of the twin formation is not seriously decreased by the lowest formation speed, but that imperfections such as bending or twisting of films are largely decreased. The interference fringes caused by the dynamical effect have been observed on the electron micrographs of slowly formed films. This fact means that the slow formation of films decreases also imperfections such as dislocations and vacancies and makes the lattice more perfect. The fringes are believed to be so-called equal thickness fringes originated from wedges due to the twin formation.

§ 1. Introduction

On the transmission electron micrographs of evaporated single-crystal-like films of silver, gold, copper, nickel and palladium, a number of parallel broad striations running along two orthogonal directions were observed, and they were considered to be caused by twin lamellae, the contrast being due to the Bragg reflection[1]. This consideration was later proved by a selected area diffraction[2]. A similar fact was found also in case of nickel films electro-deposited on a single crystal of copper[3]. The twin striations correspond to the twin spots on the electron diffraction patterns.

There is an interesting result obtained by Thirsk[4] that the untwinned single-crystal structure was found by electron diffraction in platinum films very slowly formed on fresh cleavage face of potassium chloride in vacuum by several-hour evaporation. It may be considered that the slowdown of the formation speed increases the perfectness of the crystal lattice because of the removal or the decrease of various kinds of imperfection. Since the growth twinning is caused by a stacking fault which is a kind of crystal imperfection, the decrease of the twin formation might also result from the slow evaporation. It was thought to be interesting to study by electron diffraction and electron microscopy whether such an effect on the twin formation could be observed in cases other than platinum or not, and thus the present work was started.

According to the present results obtained in evaporated silver films, the slowdown of the formation speed does not seriously influence the twin formation but considerably decreases such imperfections as vacancies, dislocations and sub-boundaries. Furthermore, the improvement of perfectness of the lattice gives rise to interference fringes due to the dynamical effect, similar to those observed by Bassett and Pashley[5]. The present report will discuss also the nature of these fringes.

§ 2. Experimental

Many single-crystal-like films of silver were formed on fresh (001) cleavage faces of rock-salt heated at 180°C in vacuum. The mean thickness of each film was always controlled to be about 400 Å, and the formation speed was arranged to range from 400 Å to 0.02 Å per second. For reference, thin films of gold were formed on (001) cleavage surfaces of rock-salt heated at 400°C.

An electron diffraction camera with the camera length of 309 mm and an electron microscope with the resolving power of about 30 Å were used. The applied voltage was 50 kV in both apparatus.

---

* Present address: Department of Physics, Faculty of Science, Osaka City University, Osaka.

§ 3. Results

Photo. 1 shows electron diffraction patterns and electron micrographs, taken from silver films epitaxially grown on rock-salt, in serial order of the formation speed. On the diffraction patterns of the normal incidence the twin spots appear to decrease their intensity with the decreasing formation speed and to vanish on the pattern, (c_1). On the other hand, they do not seriously change their intensity at the [101] incidence. The twin formation in evaporated silver films, therefore, is not largely influenced by the formation speed, against the expectation. The twin spots were found even on the diffraction pattern of the [101] incidence obtained from the specimen formed by seven-hour-evaporation. The rather strong streaks along the ⟨111⟩ direction were observed on all the diffraction patterns of the [101] incidence and also on the patterns of the normal incidence when the formation speed was low. The streaks behave with the change of the formation speed in almost the same way as the twin spots. They are thought of as due to stacking faults. On all the electron micrographs dark striations are seen. They run along two perpendicular directions which are the intersections of the film plane with two (111) planes*. It seems that the lower formation speed gives rise to a little decrease of the number of the striations. The annealing of the films in vacuum at 180°C had very little effect on the striations.

The lower formation speed, however, seems to influence largely the aspect of the striations. This is seen in Photo. 1 (c_3) and Photo. 2 both of which were taken from the four-hour-evaporation film. In these micrographs, the dark striations are often split into fringes consisting of three or four fine lines. It should be noted that the fine lines are regularly spaced, in most cases, at intervals of about 200 Å. The fringes are quite similar in their feature to those observed in an evaporated gold film by Bassett and Pashley. According to the present authors' opinion, however, they are, mostly, not caused by stacking faults against the opinion of Bassett and Pashley, but are so-called equal thickness fringes caused by wedge-shaped parts due to the twin formation. The discussion will be given in the next section.

§ 4. Interpretations and Discussions of the Results

The twin spots and the streaks passing them, seen on the diffraction patterns of the normal incidence obtained from the quickly formed films, make their appearance owing to bending or twisting of films, as they lie on the body diagonals of the reciprocal lattice. The disappearance of them on the diffraction patterns of the normal incidence obtained from the slowly formed films, therefore, means not the decrease of twins or stacking faults but the decrease of bending or twisting of films. As the bending or the twisting is thought of as originated from sub-boundaries, these boundaries are decreased by the lower formation speed. The decrease of the striations on the micrographs of the normal incidence with decreasing formation speed does not correspond to the actual decrease of twins or stacking faults, too. It is not unnatural to suppose that such imperfections as dislocations and vacancies are also decreased in the slowly formed films, and this tendency of the decrease of such imperfections can be deduced from the fringes obtained from the very slowly formed films, because the dynamical interaction will not be strong unless the perfectness of the lattice is considerably high.

Recently, Bassett and Pashley[5] obtained fringes similar to those in the present work from an evaporated gold film and ascribed the origin of them to stacking faults, as Whelan and Hirsch[6],[7] discussed. There seems, however, to be an alternative explanation in the present case, i.e, that which considers the present fringes as the equal thickness fringes due to the twin formation. As illustrated in Fig. 1, there are wedge parts in both the normal crystal and the twin crystal. The equal thickness fringes may be formed in either of the wedge parts, provided that electrons diffracted in one side of the twinning plane behave incoherently in the other side of the plane. The two lattices on both sides of the (111) plane behave coherently

---

* The striations were also observed in (011) films of silver grown epitaxially on the (011) cleavage surfaces of rock-salt. They run along three directions which are the intersections of the film plane with three (111) planes.

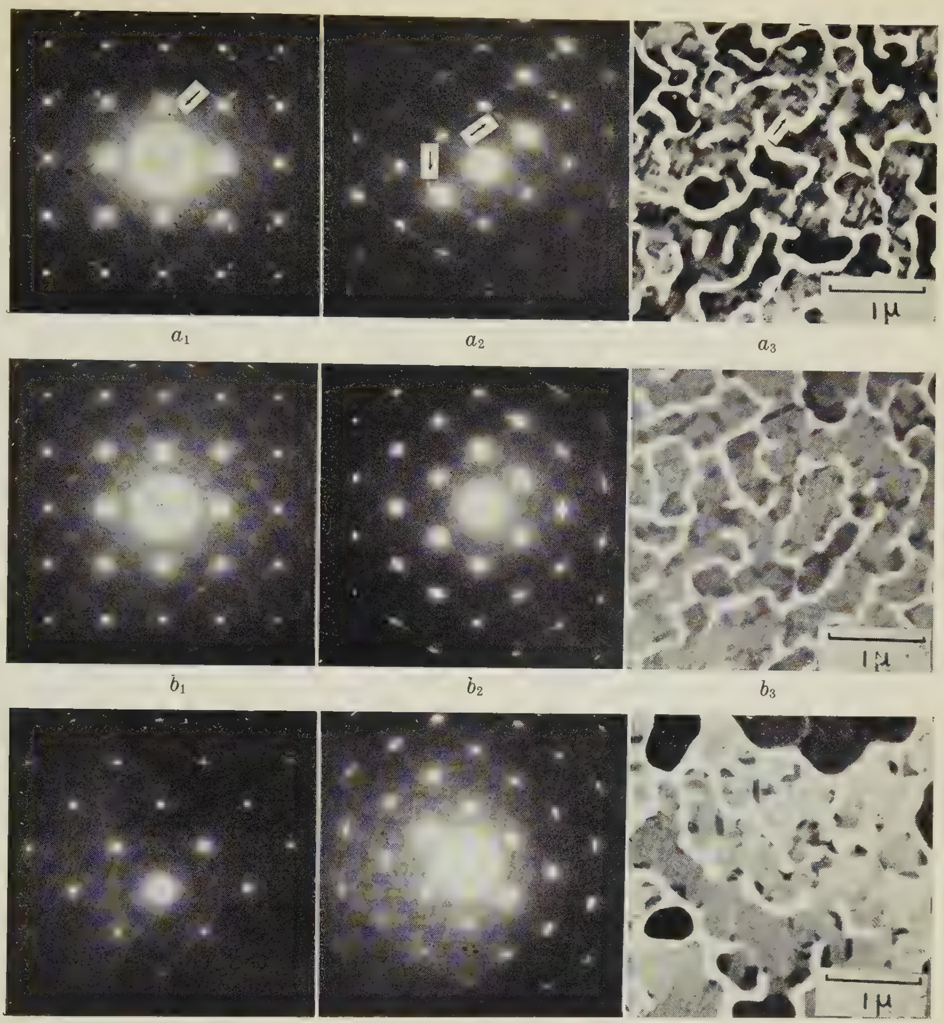

a_1 a_2 a_3

b_1 b_2 b_3

c_1 c_2 c_3

Photo. 1. Electron diffraction patterns and electron micrographs obtained for various formation speeds. (a): 400 Å/1 minute, (b): 400 Å/10 minutes, (c): 400 Å/4 hours. Diffraction patterns were obtained by the normal incidence in (a_1), (b_1) and (c_1) and by the oblique incidence in (a_2), (b_2) and (c_2). The beam is parallel to a face diagonal in the later case. Electron micrographs, (a_3), (b_3) and (c_3), correspond to (a_1), (b_1) and (c_1), respectively. The twin spots and the twin striations are shown by the arrows.

with each other in case of stacking faults.

In order to decide which explanation is adequate in the present case, it is necessary to compare calculated values of the line interval and the whole width of fringes with observed values. MacGillavry's formula[8] for the intensity transmitted through the lattice (Laue case) is approximately expressed as the following equation:

$$I=I_0\left\{\frac{V_{hkl}}{\lambda E}D_0\cos\left(\pi\frac{D}{D_0}\right)\right\}^2. \qquad (1)$$

and

$$D_0=\left\{\left(\frac{V_{hkl}}{\lambda E}\right)^2+\left(\frac{\theta-\theta_0}{d_{hkl}}\right)^2\right\}^{-1/2}, \qquad (2)$$

where I_0 is the intensity of the incident beam, V_{hkl} the Fourier coefficient of the lattice potential for (hkl) reflection, λ the wave length of the incident beam, E the accelerating voltage, D_0 the extinction distance, D the penetration depth along the incident direction, θ the glancing angle of (hkl) plane, θ_0 the Bragg angle of (hkl) plane and d_{hkl} the interplaner spacing of (hkl) plane. In case of the equal thickness fringes arising from such a wedge as shown in Fig. 2(a), the interval of fringes, S_W, on the electron micrograph is given by

$$S_W = D_0 \cot \alpha \,, \tag{3}$$

where α is an angle between the (111) plane and the film surface. In case of a stacking fault, on the other hand, the extinction distance, D_0', is given as the following expression⁷⁾:

$$D_0' = \frac{D_0}{2}(1-x^2)^{-1/2} \,, \tag{4}$$

where x is a parameter indicating the deviation from the Bragg angle. If $(\theta-\theta_0)$ is zero, D_0' is just half of D_0. Thus the interval of fringes due to a stacking fault, S_F, is, at maximum, given by

$$S_F = \frac{D_0}{2} \cot \alpha \,. \tag{5}$$

The circumstances are illustrated in Fig. 2(b).

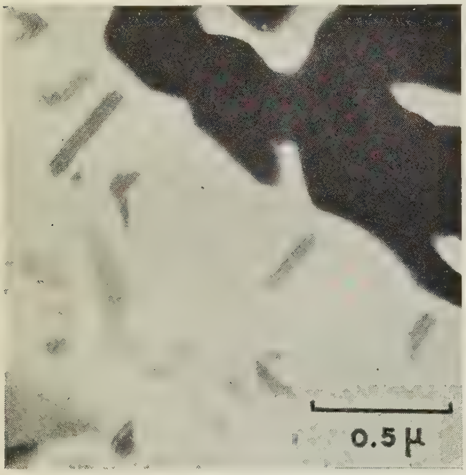

Photo. 2. Electron micrographs of silver film formed by four-hour evaporation.

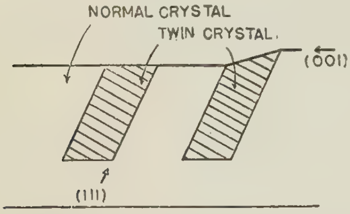

Fig. 1. Schematic picture of (001) film twinned on (111) plane, viewed from <1$\bar{1}$0> direction.

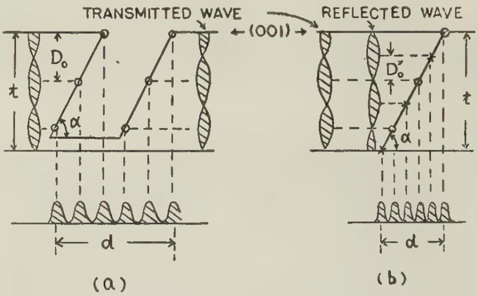

Fig. 2. Formation of fringes due to the twin formation (a) and due to a stacking fault (b). The angle, α, is 54°44′ in both cases.

Table I. Calculated values of extinction distance, D_0, and line intervals of fringes, S_W and S_F, of silver for 50 kV electrons.

Reflection	D_0 (Å)	S_W (Å)	S_F (Å)
(200)	190	134	67
(400)	411	291	145
(600)	723	511	256
(800)	1070	756	378
(220)	273	193	97
(420)	505	357	179
(440)	686	485	243

Under the condition that the incident beam is nearly perpendicular to the [001] film plane, lattice planes parallel to the (001) direction have chances to reflect electrons. They are the planes, (200), (020), (220), (2$\bar{2}$0), (400), (040), (420) etc., of the normal lattice and the planes, (2$\bar{2}$0), (204) etc., of the twin lattice. The line intervals, S_W and S_F, are calculated by using the above mentioned equations and shown in Table I. In the calculated values of S_W, that for (220) reflection, 193 Å, best fits to the observed interval, about 200 Å. In the calculated values of S_F, on the other hand, those for (600), (420) and (440) reflections seem to fit. However, the calculated value of the whole width of the fringe, d, should also be compared with the observation. If the present fringes are caused by a stacking fault, d is calculated by

$$d = t \cot 54°44' \,, \tag{6}$$

as shown in Fig. 2(b). In the present study, the mean thickness of films, t, was always controlled to be about 400 Å, and it gives about 280 Å as the calculated width. This value is far smaller than the observed value, about 600 Å. This discrepancy proves the inadequacy of the explanation by a stacking fault. Though the increase of local thickness due to the patch-like structure may somewhat favour to decrease the discrepancy, it will not change the general trend. According to the explanation by wedges due to the twin formation, on the other hand, the calculated fringe width is possible to be about 600 Å, as shown in Fig. 2(a), if the thickness of a twin layer is moderate. Therefore, there is a considerable possibility that the present fringes are produced by the (220) reflection of the normal lattice in the wedges. This well coincides with the fact that no twin spot is found in the diffraction pattern, (c_1) in Fig. 1. The $(2\bar{2}0)$ reflection can also take place in the twin lattice, but it is a common reflection to both lattices, and hence the equal thickness fringes cannot be produced in that case.

Gold films about 400 Å thick were formed by three-hour-evaporation on cleavage faces of rock-salt at 400°C and examined by electron microscopy. The interference fringes were also observed and the line interval was about 130 Å. The calculated value is 132 Å in the wedge case for the (220) reflection from the normal lattice. This coincidence between calculation and observation strongly supports the present authors' opinion.

The present authors wish to express their sincere thanks to Dr. D. Watanabe and Mr. Y. Fukano for their valuable discussions.

References

1) S. Ogawa, D. Watanabe and F. E. Fujita: J. Phys. Soc. Japan **10** (1955) 429.
2) L. Reimer: Optik **16** (1959) 30.
3) S. Ogawa, J. Mizuno, D. Watanabe and F. E. Fujita: J. Phys. Soc. Japan **12** (1959) 999.
4) H. H. Thirsk: Proc. Phys. Soc. **B, 63** (1950) 833.
5) G. A. Bassett and D. W. Pashley: J. Inst. Metals **87** (1958–59) 449.
6) M. J. Whelan and P. B. Hirsch: Phil. Mag. **2** (1957) 1121.
7) M. J. Whelan and P. B. Hirsch: Phil. Mag. **2** (1957) 1303.
8) C. MacGillavry: Physica **7** (1940) 334.

JOURNAL OF THE PHYSICAL SOCIETY OF JAPAN, Vol. 15, No. 8, AUGUST, 1960

X-ray Line Broadening from the Polished Surfaces of Silver and Gold

By Masao KURIYAMA

The Institute for Solid State Physics, University of Tokyo
Shin-Ryudo-cho, Minato-ku, Tokyo, Japan

(Received March 3, 1960)

The linear relation (Hall's formula) and the quadratic relation between the integral breadth and the scattering angle can be derived from the general formula for intensity distribution by the assumption of the appropriate distribution for both size and strain. The use of these two formulae (line breadth method) can give not only the magnitude but also the plausible distribution for strain and size. The advantage of this method consists in the point that the magnitude and the distribution for size and those for strain can be separately obtained, in contrast with the Fourier analysis of line profile (line profile analysis method). The line breadth method is applied to the polished surfaces of Ag and Au and the results obtained are confirmed to be correct by the line profile analysis. On the other hand, the line profile analysis is required to study the strain variation with the depth in specimens, as far as only one kind of radiation is used. This strain variation can be observed by the line breadth method with the use of different radiations, and the comparison is made between the results from the line breadth method and from the line profile analysis method.

§ 1. Introduction

Fourier analysis of X-ray line broadening (line profile analysis method) has presented a useful information on lattice imperfections since Warren and Averbach[1] first developed this method. The two parts of a Fourier coefficient due to size and strain, however, could not be separated without any assumption. This difficulty was discussed in detail by Williamson and Smallman[2]. On the other hand, Hall[3] had already observed for many cold-worked metals the dependence of line breadth on diffraction angle which he had derived under the simple assumption of additivity of the strain and size effects. Hall's formula is still often used to obtain the magnitude of size and strain in the field of metallurgy, because it is more convenient than the Fourier analysis method.

It has been generally recognized that Hall's formula or another formula (quadratic formula) for the angular dependence of line breadth is simply empirical and cannot give so much information on the distribution of strain and size as the line profile analysis does. As already pointed out in the previous paper[4], these two formulae can be derived simply under the assumption that both the line profile due to size and the one due to strain are either Gaussian or of Gauchy.

In this paper, however, these two formula will be derived with a physical significance from the general formula for the intensity distribution on a diffraction line by the assumption of the appropriate distribution for size and strain. In other words, the plausible distribution and the magnitude for strain and those for size can be obtained separately if any one of these two formulae can well explain the observed angular dependence of line breadth. (This method is, hereafter, called as the line breadth method.) This method seems quite useful because it is not only more convenient than the line profile analysis, but also has the advantage mentioned above.

The line breadth analysis will be applied to the polished surfaces of Au and Ag and the results will be confirmed in § 5 by the line profile analysis. If a specimen gives rise to a dominant strain broadening, the comparison can be easily made between the results from the line breadth method and from the line profile analysis method. Polished surface of metals, as shown in this paper, gives a strain broadening about ten times larger than that due to size and can be considered to be a suitable sample. This is the reason why the polished metals were chosen.

Although the line breadth method gives the same information as the line profile method does, the use of different radiations is required to study the strain variation with the depth in specimens. On the other hand, the line profile analysis method gives enough information to know the strain variation, even if only one kind of radiation is used. This point will be shown in this paper with the comparison between the results from the two methods.

This paper also deals with the study on the distorted structure of the inner part under the Beilby layer by the line breadth method.

§ 2. Experimental Conditions

Some annealed plates of silver and gold (40 mm × 40 mm × 5 mm for Ag and 25 mm × 25 mm × 1 mm for Au) were polished by emery papers and lapped by cloth with carborandum and rouge in order to obtain the flat surface. The surface was etched as heavily as a fresh flat surface appeared, and was finally polished by chamois leather for a considerably long time. During polishing, they were pressed onto a rotating disc with the pressure of 100 g wt./cm². The polishing apparatus has been previously described[4]. The time of polishing is listed in Table I.

After the line profile was recorded, every specimen was annealed for about 40 hours at 400°C, and again recorded. The profile of diffraction lines was observed by the Norelco x-ray diffractometer. A proportional counter operated at 1850 v was covered by a suitable filter. Divergence and scatter slits had 1° openings and a receiving slit 0.006 in. The driving speed of a counter was 1/8° a minute.

As numerous diffraction lines had to be observed, a rate meter and a recorder were used. A reliability of a recorded line profile was confirmed by comparing it with the profile observed by the fixed time counting. The driving speed of a recording chart was half an inch a minute.

The precise intensity distribution of the background scattering was also obtained by counting the intensity at many positions where any diffraction line could be observed. The overlapping of the adjacent lines was estimated by the background scattering curve.

Diffraction lines were observed by using three different radiations (CuKα, FeKα and MoKα), in order to study the change in state with the depth from a surface. In the case of Mo radiation for gold specimens, a nickel filter in addition to a Zr filter was used in front of a counter to eliminate the fluorescent Au L radiation*.

The breadth of lines becomes sharp if more than one day elapses after polishing. This is due to the recovery effect in the polished state. The rapid observation of the line broadening should follow polishing. This is another reason why a rate meter and a recorder were used.

§ 3. Theory of Line Broadening**

The general formula of intensity distribution on a diffraction lines is given by Estabrook and Wilson[5] as

$$I(2\vartheta)=KNF_0^2(2\vartheta)\sum S(R_m)J(H, R_m)\times\exp[2\pi isR_m]\,, \qquad (1)$$

where

$$J(H, R_m)=\int P(e, R_m)\exp[2\pi iHe(R_m)R_m]de(R_m)\,, \qquad (2)$$

and K is dependent upon ϑ but assumed constant in the vicinity of any reflection, N the average number of unit cells in a crystallite, and $s=2(\sin\vartheta-\sin\vartheta_H)/\lambda$, $H=2\sin\vartheta_H/\lambda$.

The range of summation extends to infinity, introducing the shape function $S(R_m)$. $P(e, R_m)$, called the strain distribution function, is a probability of two cells R_m distance apart for which the average strain is $e(R_m)$. Normalization is made respectively for the shape and the strain functions:

$$S(0)=1 \quad\text{and}\quad J(H, 0)=\int P(e, 0)de=1\,. \qquad (3)$$

Let us show below that the typical formulae for the angular dependence of line breadth can be derived from the general formula (1), assuming the appropriate distribution for both strain and size. It will be shown from this calculation that the linear formula (Hall's empirical formula) can be derived from the two different types of distribution for strain and size and the quadratic formula from the Gaussian distribution.

---

* Cu foil is of course the most suitable filter eliminating Au L. As a nickel filter, however, can be readily obtained, it is used here.

** This part and next section have been already read at the meeting of Physical Society of Japan, April, 1959.

I. *Gaussian type*

At first the Gaussian type of distribution function is assumed for both functions:

$$S(R_m)=\exp\left[-(\pi/C^2)R_m{}^2\right] , \quad (4)$$

and

$$P(e,\ R_m)=(1/E)\exp\left[-(\pi/E^2)e^2\right] , \quad (5)$$

where C is the integral breadth of the shape function and E the integral breadth of the strain distribution. E should be in general dependent not only upon R_m but also upon the location of the relevant unit cells. It is, however, assumed here not to depend on these factors for the convenience of calculation. Such an approximation will be discussed in § 6. The root mean square values of size and strain are $C/\sqrt{2\pi}$ and $E/\sqrt{2\pi}$, respectively. Substituting (5) into (2),

$$J(H,\ R_m)=\exp\left[-\pi E^2H^2R_m{}^2\right] \quad (6)$$

is obtained. From (1) the intensity profile is obtained;

$$I(2\vartheta)=KNF_0{}^2\left(\frac{1}{d_H}\right)\left\{\frac{1}{(1/C)^2+E^2H^2}\right\}^{1/2}$$
$$\times\exp\left[-\left\{\frac{\pi s^2}{(1/C)^2+E^2H^2}\right\}\right] . \quad (7)$$

d_H is an interplanar distance for the lowest order. This profile is also of the Gaussian form. The integral breadth in the present case becomes the quadratic formula:

$$(\beta\cos\vartheta/\lambda)^2=(1/C)^2+4E^2(\sin\vartheta/\lambda)^2 . \quad (8)$$

This relation has been so far recognized empirically in some cases.

II. *Cauchy type for the strain distribution*

Shape function is, here, assumed to be of the form

$$S(R_m)=\exp\left[-(2/C)R_m\right] \quad (9)$$

C is the size of a mean crystallite and the physical meaning of this derivation will be discussed in § 6. Strain distribution function is assumed to have another familiar type

$$P(e,\ R_m)=(1/E)\left(\frac{1}{1+(\pi/E^2)e^2}\right) . \quad (10)$$

$(E/2)$ is considered as the magnitude of mean strain, though the Cauchy distribution has not any moments. Then $J(H,\ R_m)$ is given by

$$J(H,\ R_m)=\exp\left[-2EH|R_m|\right] . \quad (11)$$

The line profile, therefore, becomes a Cauchy form:

$$I(2\vartheta)=KNF_0{}^2\left(\frac{1}{d_H}\right)\frac{(1/C)+EH}{\{(1/C)+EH\}^2+\pi^2s^2} \quad (12)$$

The integral breadth is expressed by

$$\beta\cos\vartheta/\lambda=(1/C)+2E(\sin\vartheta/\lambda) . \quad (13)$$

This has been also so far recognized empirically in many cases as Hall's formula[3].

In contrast with case I, the linear formula (13) can also be derived from the different distribution, as shown below.

III. *Exponential type for the strain distribution*

Shape function is a Cauchy type;

$$S(R_m)=\frac{1}{1+(\pi/C)^2R_m{}^2} , \quad (14)$$

and strain distribution is given by

$$P(e,\ R_m)=(1/E)\exp\left[-(2/E)|e|\right] . \quad (15)$$

Then $J(H,\ R_m)$ becomes

$$J(H,\ R_m)=\frac{1}{1+\pi^2E^2H^2R_m{}^2} , \quad (16)$$

The line profile is, therefore, given by

$$I(2\vartheta)=KNF_0{}^2\left(\frac{1}{d_H}\right)\frac{EH}{C\{E^2H^2-(1/C)^2\}}$$
$$\times\left\{Ce^{-(2/EH)|s|}-\frac{1}{EH}e^{-2C|s|}\right\} \quad (17)$$

This profile has a steep decrease around the Bragg angle if either strain or size is dominant or the effects due to strain and size are comparable. Integral breadth thus becomes

$$\beta\cos\vartheta/\lambda=(1/C)+2E(\sin\vartheta/\lambda) . \quad (18)$$

It is noted that this case also gives Hall's formula, but gives the different line profile from case II.

It has been pointed out[4] that (8) in case I and (13)* in case II can be derived simply by the assumption that the line profile due to size and the one due to strain are either Gaussian or of Cauchy.

§ 4. Line Breadths

When the metallic surfaces are highly polished, the Beilby layer covers the surface. The thickness of this layer is considered to be about a few hundred angstroms as Kranert and Raether have estimated[6]. The structure of this layer is heavily distorted with a considerable amount of strain and differs from the crystalline state[7]. It is, therefore, expected that the inner part (more than 1 micron deep from the surface) would have the distorted state with a few percent strain. It is thus worthwhile to obtain from such a specimen the magnitudes of strain and size as well as, if possible, the strain distribution.

---

* Although (13) and (18) have the mathematically same form, (13) means the equation derived under the assumption in II and similarly (18) the equation derived in III.

Line breadths were measured for the spe-

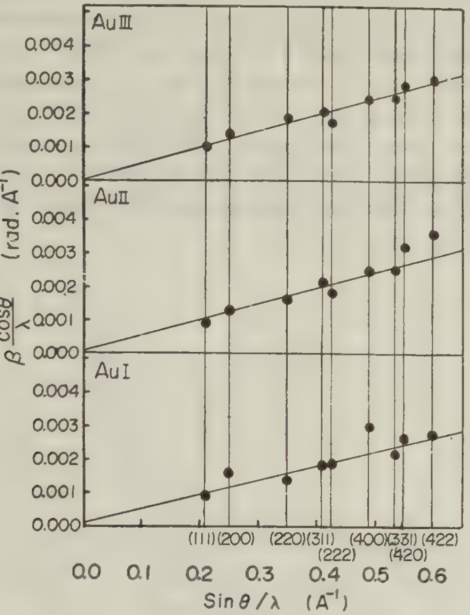

Fig. 1a.

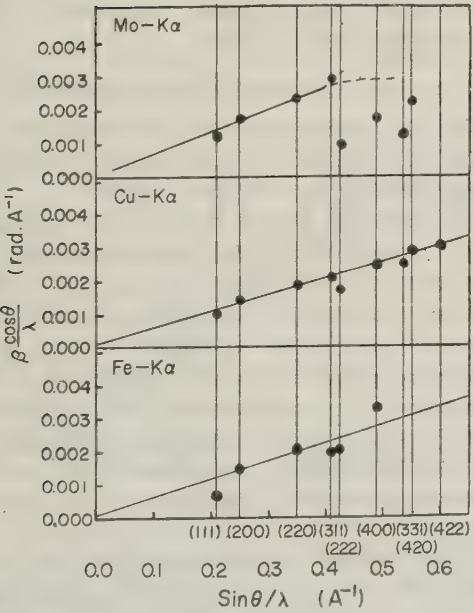

Fig. 1b.

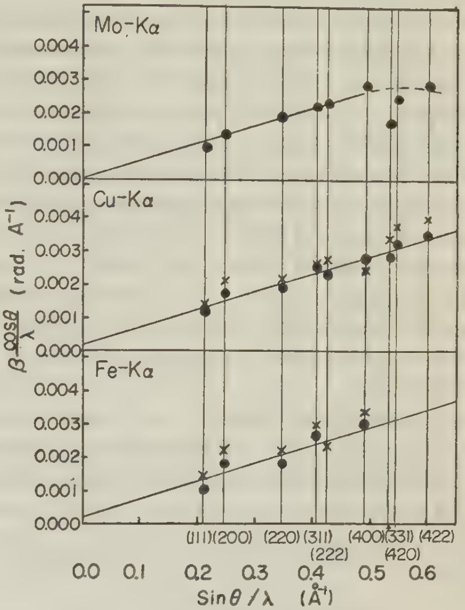

Fig. 1c.

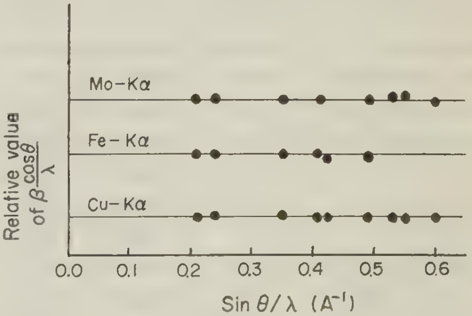

Fig. 1d.

Fig. 1. The angular dependence of line breadth.

a. Specimens, here, of gold polished under different conditions, show different slopes (CuKα).
b. The use of different radiations (FeKα, CuKα and MoKα) makes clear the distinction of slopes even for the same specimen, here Au II.
c. Ag II shows the same slopes for the cases of FeKα and CuKα. Solid circles correspond to breadths obtained by Jones' method and cross marks to breadths from the Fourier coefficients of line profile.
d. A well annealed specimen shows no angular dependence. An example is shown here for Ag II. The different values of $\beta \cos\vartheta/\lambda$ for different radiations shown in this figure has no significance.

cimens listed in Table I. Three different wavelengths were used for Ag II and Au II. The separation of a doublet was made by the Jones method[8], assuming the line breadth from an annealed specimen as an instrumental line breadth. Line breadth thus obtained was attempted to be plotted against both $\sin\vartheta/\lambda$ and $(\sin\vartheta/\lambda)^2$. The former plotting is shown in Fig. 1a, b and c. The angular dependence of line breadth from the annealed specimen is also shown in Fig. 1d with an arbitrary scale for breadth. Figs. 1a, b and c show that the linear relation of (13) or (18) is valid. With the use of (13) or (18) the magnitude of size and strain is obtained and listed in Table I.

It is found from Fig. 1 and Table I that Au II and Ag II show the different properties for strain variation. It is clearly shown for Au II from Fig. 1b and Table I that the observed value of strain decreases in the order of FeKα, CuKα and MoKα, while an effective penetration depth of radiations increases in the above order because of absorption. This implies that the magnitude of strain in Au II decreases with the depth. On the other hand, Fig. 1c and Table I show for Ag II that polishing influences more deeply than in Au and the variation of strain againt depth is much smaller than in Au II, since the uses of FeKα and CuKα show the almost same magnitudes of strain. The latter fact (no strain variation) is necessary for comparing the result from the line profile analysis with that from the line breadth analysis, as described in § 5.

Table I. Polishing conditions and magnitudes of size and strain.
(Line breadth method by (13))

Specimen number	Time of polishing	Mean size	Mean strain
Ag I	15 hrs.	4000 A	0.18%
Ag II (FeKα)	13	5000	0.16
Ag II (CuKα)	13	5000	0.16
Ag II (MoKα)	13	large	(0.13)
Ag III	8	4000	0.11
Ag IV	3	large	0.08
Au I	4	7000	0.11
Au II (FeKα)	8	7000	0.18
Au II (CuKα)	8	7000	0.12
Au II (MoKα)	8	large	(0.10)
Au III	10	7000	0.13

From the fact that line breadths depend linearly on $\sin\vartheta/\lambda$, the strain distribution can be expected to be either of a Cauchy type (case II) or of an exponential type (case III), even if the line profile like (17) corresponding to an exponential strain distribution could hardly be seen. It can be said in the present case without the use of the line profile analysis that the Cauchy distribution of strain is plausible, since the diffraction line profile has no steep decrease around the Bragg position as shown in Fig. 2*.

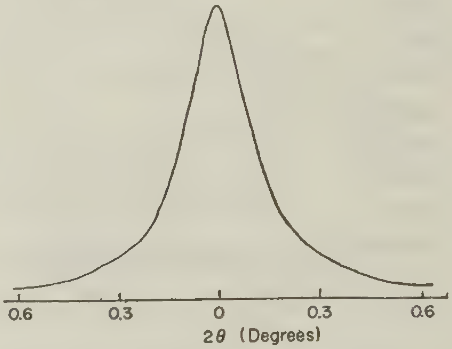

Fig. 2. An example of the pure diffraction profiles without an instrumental broadening. (220)-reflection of Ag II (FeKα).

§ 5. Fourier Analysis of Line Profiles

The line profile analysis is desirable to be made to examine the correctness of the results from the line breadth method.

The observed distribution of x-ray intensity is a convolution of the distribution due to instrumental broadening and that due to diffraction broadening[8]. According to the Stokes method[9], the Fourier coefficient of the pure diffraction profile can be obtained by electronic computer PC-1, assuming the line broadening from a well annealed specimen as an instrumental broadening. Imaginary part of a Fourier coefficient is negligible in the present results.

In the Fourier transformation of the line profile we cannot treat the line profile function as a continuous function extending over the infinite range. Practically we can only treat the Fourier synthesis confined to the definite range with discrete intervals. If $A(k)$ is the coefficient of the Fourier synthesis and $S(R_m)J(H, R_m)$ is abbreviated to $Y(H, R_m)$,

---

* Although Fig. 2 shows the pure diffraction profile without an instrumental broadening, the observed line shape can give the same information on this point, if an instrumental broadening is small.

$$\begin{aligned}A(k)&=\{M\Delta(2\vartheta)\cos\vartheta/\lambda\}^{-1}Y(\lambda k/M\Delta(2\vartheta)\cos\vartheta)\\&=\text{const.}\sum_{t=-\infty}^{+\infty}\sum_{m=-M}^{+M}I(2\vartheta)\exp\left[2\pi it\frac{m\Delta(2\vartheta)}{M\Delta(2\vartheta)}\right]\\&\quad\times\frac{\sin\pi M\Delta(2\vartheta)k-t}{\pi M\Delta(2\vartheta)k-t}\end{aligned}\tag{19}$$

where M is the number of division and $\Delta(2\vartheta)$ is the magnitude of a discrete interval. Here the large value of M is required in order to obtain a precise curve of $A(k)$ against k. M was taken to be 100, 120, 160 or 200. Calculation was performed by the electronic computer PC 1.

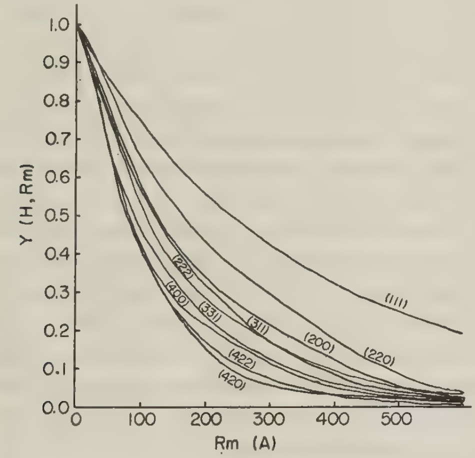

Fig. 3. An example of Fourier coefficients is shown for Ag II (CuKα).

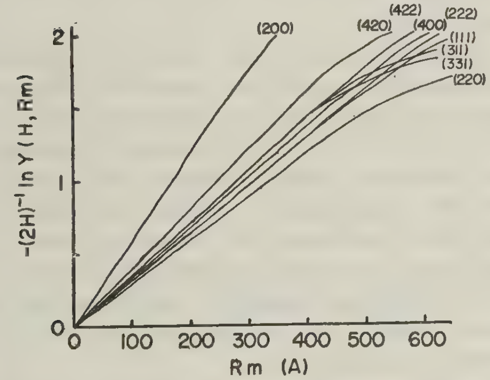

Fig. 4. Logarithmic plotting for Fourier coefficients in Fig. 3. The ordinate corresponds to the value of $-(2H)^{-1}\ln Y(H, R_m)$. (111) and (222) have the same slope, but (200) has the larger slope than (400) does.

In order to examine the correctness of the line breadth analysis, it is desirable that the line profile analysis is performed for the specimen in which strain does not vary to the large extent with the depth. Since Ag II specimen has little gradient of strain against depth as described in § 4, the Fourier coefficients for this specimen were, at first, obtained from line profiles observed by both FeKα and CuKα. Fourier coefficients obtained in the case of CuKα are plotted against R_m in Fig. 3. Moreover, $-(2H)^{-1}\ln Y(H, R_m)$ is plotted against R_m as shown in Fig. 4. The same plottings were performed for the case of FeKα. It is clear in Fig. 4 that a linear relation holds with a good approximation. This fact proves that $Y(H, R_m)$ can be expressed by the product of (9) and (11) and the strain distribution is of the Cauchy form. This result is the one expected from the line breadth analysis alone. In this case the slope of the straight line in Fig. 4 is equal to $(1/CH)+E$. Values for different reflections are listed in Table II. The magnitude of size *i.e.* C can be estimated in both Fig. 1 and Fig. 3. In Fig. 3 the fall-off of Fourier coefficients to zero determines the lower limit of size (a coherent size). This shows that $(1/CH)$ is much smaller than E. Estimated size value is also listed in Table II and shows no great difference from the value obtained by the line breadth analysis. The magnitude of strain $E/2$ is derived from the above values by the assumed C and seen also in Table II. The assumed value of C hardly effects the value of E. It is concluded that E is not seriously dependent on the crystallographic direction in this case. This conclusion also does not contradict the results in § 4.

In contrast with the above case, it is found in Ag IV that, although the Cauchy type distribution of strain is again obtained, the magnitudes of E obtained from the higher order reflections are smaller than those from low order ones, as shown in Table II. It is clear in this case that there is a gradient of strain against depth, because the mean penetrating depth of radiation increases as the scattering angle increases.

Such an effect would be also expected in the case of Au II, since the line breadth analysis in § 4 shows the decrease of the mean strain obtained by CuKα and MoKα com-

Table II. Results from line profile analysis.

Indices of reflection	$\{(1/CH)+E\}/2$			$\langle e\rangle=E/2$		
	Ag II (FeKα)	Ag II (CuKα)	Ag IV	Ag II (Fe)	Ag II (Cu)	Ag IV
(111)	0.19%	0.17%	0.12%	0.15%	0.14%	0.10%
(200)	0.30	0.30	0.15	0.27	0.27	0.13
(220)	0.17	0.15	0.09	0.15	0.13	0.08
(311)	0.20	0.18	0.08	0.18	0.16	0.07
(222)	0.19	0.17	0.08	0.17	0.15	0.07
(400)	0.19	0.18	0.08	0.17	0.16	0.07
(331)		0.18	0.07		0.16	0.06
(420)		0.20	0.07		0.18	0.06
(422)		0.18	0.06		0.16	0.05
Estimated C	5000 A	5000 A	8000 A			

paring with that by FeKα.

Integral breadth can be also obtained from the Fourier coefficients and shown in Fig. 1b by a different mark.

§ 6. Discussions

a. *Size distribution function*

The physical meaning of the size distribution function $S(R_m)$ having the form of (9) is the following one: If the two adjacent cells have a probability $p(01)$ for appearing without regard to their locations, the product of structure factors for the two unit cells R_m distance apart is equal to $p(01)^m F_0^2$. For the crystal with an infinite dimension, $p(01)$ should be equal to 1, and for the crystal with a finite dimension $p(01)$ can be put $1-\alpha$. Then $p(01)^m$ becomes $\exp -\alpha m$ approximately. This is the form of (9).

b. *Strain distribution*

For the calculation in § 3, the assumption that $E(H, R_m)$ is independent on R_m, was adopted. If the magnitude of strain does not vary to a large extent at any positions within a crystallite, $E(H, R_m)$ can be replaced by $E(H, 0)$ within a certain range $R_m=0$ to R. On the other hand, $J(H, R_m)$ rapidly decreases as R_m decreases. It can be, therefore, said that this assumption is fairly good if $E(H, R_m)$ can be assumed to be constant where $J(H, R_m)$ is not so small. If the strain is taken to be 0.5% and $J(H, R)$ is 1/100, R is 120 spacings for the Gauss distribution of strain and 230 spacings for the Cauchy one. Since the above assumption is satisfied in the present case as shown in § 5, Hall's formula can be used for the line breadth.

c. *Linear relation of line breadth*

In the present experiment, every specimen of Au and Ag except the case of Mo radiation shows the validity of the linear relation for the line breadth. Judging only from this relation, there might be two possible strain distributions (case (II) and case (III)). The present line shape, however, has not a steep decrease around the scattering angle of $2\vartheta_H$. It thus can be found that the strain distribution is of a Cauchy type.

In the case of Mo radiation, the linear relation does not hold. This is attributed to the variation of the strain with the depth from a surface.

Results obtained from the line breadth analysis in § 4 were also assured by the line profile analysis in § 5 and have no room to be improved. It can be, therefore, concluded that the line breadth analysis can give not only the magnitudes of strain and size but also the distributions of strain and size. It might be, however, necessary to take into account the line shape if Hall's formula is valid, although the line profile like (17) could hardly be seen.

In the present case, the strain is nearly isotropic. If the strain is not isotropically uniform and Young's modulus in any direction is known, Hall's formula is also available, substituting [E/Young's modulus] in place of E.

On the other hand, it is noted that the line profile analysis method can give the information on the strain variation without the use of different radiations.

d. *Discussions for the polished state*

The results obtained in §4 and 5 shows that polishing gives the distortion not only in the shallow part but also in the deep part, and the magnitude of strain decreases slowly with the depth. Heavy polishing influences to the deeper part than light polishing does, as shown in Fig. 1a. These results support the view of the highly distorted state in the Beilly layer reported previously⁷⁾.

The author wishes to express his sincere thanks to Profs. H. Takahashi and E. Goto for allowing him to use the electronic computer PC-1 and to Mr. T. Sakurai for the use of programme. He is also grateful to Profs. S. Takagi, S. Hosoya and Mr. T. Suzuki for their kind discussion. This work was partly supported by a research grant of the Ministry of Education.

References

1) B. E. Warren and B. L. Averbach: J. Appl. Phys. **21** (1950) 595.
2) G. K. Williamson and R. E. Smallman: Acta Cryst. **7** (1954) 574.
3) W. H. Hall: Proc. Phys. Soc. **A, 62** (1949) 741.
4) M. Kuriyama, K. Kohra and S. Takagi: J. Phys. Soc. Japan **12** (1957) 151.
5) J. N. Estabrook and A. J. C. Wilson: Proc. Phys. Soc. **B, 65** (1952) 67.
6) W. Kranert and H. Raether: Ann. Physik **43** (1943) 520.
7) M. Kuriyama: J. Phys. Soc. Japan **14** (1959) 487.
8) F. W. Jones: Proc. Roy. Soc. **A, 166** (1938) 16.
9) A. R. Stokes: Proc. Phys. Soc. **61** (1948) 382.

JOURNAL OF THE PHYSICAL SOCIETY OF JAPAN, Vol. 15, No. 8, AUGUST, 1960

X-ray Measurement of the Scattering Factor of Iron in Ordered Fe$_3$Al

By Yukitomo KOMURA

Institute of Polytechnics, Osaka City University,
Kita-ku, Osaka Japan

Yujiro TOMIIE and Robert NATHANS*

Faculty of Science, Osaka University,
Nakanoshima, Osaka, Japan

(Received April 26, 1960)

X-ray measurements on the absolute integrated intensities of several superlattice reflections on an ordered Fe$_3$Al single crystal were made to obtain an estimate of the number of localized 3*d* electrons in iron. The experiments were made with MoK_α radiation with a thin single crystal cut for transmission geometry, so as to avoid surface roughness effects. Extinction effects, minimized by restricting the measurements to the comparatively weak superlattice reflections, were estimated from a wavelength analysis of the integrated intensities. Finally, neutron analysis was used for obtaining a knowledge of the state of atomic ordering in the particular sample and for establishing the temperature factors of the iron and aluminum atoms. Calculations of the iron scattering factor from the final results show it to be in substantial agreement with that of the free iron atom (6 3*d* electrons). This is in agreement with the conclusions of Batterman2),3) and contrasts with the low number of 3*d* electrons given by Weiss and DeMarco1).

§1. Introduction

The number of localized 3*d* electrons in metallic iron has recently been the subject of some controversy. Weiss and DeMarco1) originally reported an unexpectedly low value of of (2.3±0.3) 3*d* electrons in iron. The method used by these authors was to determine the atomic scattering factor from the absolute intensities of Bragg reflections in single crystals of iron, suitably corrected for effects of extinction and surface roughness. To obtain an estimate for the number of 3*d* electrons, the calculated contribution of the argon core was subtracted from the measured absolute scattering factor. Following this work Batterman2),3) reported an atomic scattering factor for iron which was in substantial agreement with the free atom calculated by Freeman and Wood4), based on 6 3*d* electrons. This determination was based on an analysis of cold-worked powder samples which were thought free of extinction, surface roughness, and preferred orientation effects. Weiss and DeMarco5) thereupon repeated Batterman's procedure using the samples, but found once again a low number of 3*d* electrons in confirmation of their single crystal measurements.

As this problem is of some importance in the present theoretical discussions on the outer electron configuration in metallic iron, we have made single crystal measurements on ordered Fe$_3$Al, and have found the outer electron configuration of the iron atoms in this alloy to be close to that calculated for the free iron atom. Since the magnetic scattering data6) from the ordered Fe$_3$Al support the notion that no large difference in the 3*d* electron configuration is expected between the iron atoms in this ordered alloy and those in pure iron, our results can be considered to be in contrast with Weiss and DeMarco's conclusion. A preliminary note has already been reported7), and in this paper experimental procedures, measured data, and the results will be presented in detail.

§2. Method

The expression of the integrated reflection by a single crystal of thickness t in a transmission geometry as shown in Fig. 1 for monochromatized X-ray is given by[8)]

---

* Fulbright Lecturer on leave from Pennsylvania State University. Present address: Lincoln Laboratory, Massachusetts Institute of Technology, P. O. Box 73, Lexington 73, Massachusetts, U.S.A.

$$\frac{P}{I}=\left(\frac{Ne^2}{mc^2}\right)^2\frac{\lambda^3}{\mu}\frac{1+\cos^2 2\theta_M\cos^2 2\theta}{\sin 2\theta(1+\cos^2 2\theta_M)}F_{hkl}^2$$
$$\times\frac{\sec(\theta-\phi)}{\sec(\theta-\phi)-\sec(\theta+\phi)}$$
$$\times\{e^{-\mu t\sec(\theta+\phi)}-e^{-\mu t\sec(\theta-\phi)}\}, \qquad (1)$$

where P=total diffracted power (counts/sec.), I=power of the incident beam falling on the sample after reflecting by crystal monochromator, λ=wavelength, N=number of unit cells per unit volume, μ=linear absorption coefficient of the sample, θ=Bragg angle for a plane (hkl), θ_M=Bragg angle for the monochromator, F_{hkl}=structure factor and ϕ=angle between the reflecting plane and the normal to the surface of the sample. In this expression the normal to the surface lies in the plane formed by the incident and reflected beams.

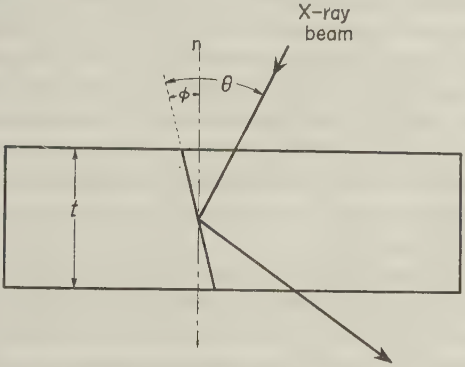

Fig. 1. Transmission geometry used in our measurements. ***n*** is the normal to the surface of the sample.

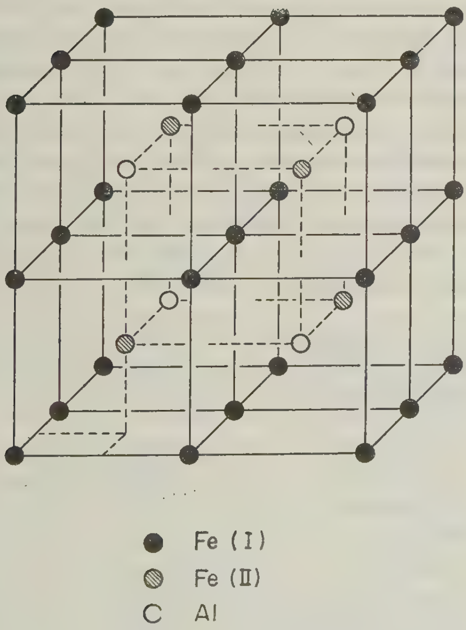

Fig. 2. Ordering arrangement in ordered Fe_3Al.

In the ordered structure of Fe_3Al shown in Fig. 2, F_{hkl}^2 of the superlattice reflections in Eq. (1) is given by

$$F_{hkl}^2=16S_{0,e}^2\left\{(f_{\mathrm{Fe}}^{Ar}+f_{\mathrm{Fe}}^{3d})\exp\left[-B_{\mathrm{Fe}}\left(\frac{\sin\theta}{\lambda}\right)^2\right]\right.$$
$$\left.-f_{\mathrm{Al}}\left[-B_{\mathrm{Al}}\left(\frac{\sin\theta}{\lambda}\right)^2\right]\right\}^2, \qquad (2)$$

where $S_{0,e}^2$=long-range order parameter, for odd and even reflections, f_{Fe}^{Ar}=contribution of the argon core, f_{Fe}^{3d}=contribution of the outer electrons in iron, f_{Al}=atomic scattering factor of alminum and B_{Fe}, B_{Al}=temperature factors of iron and aluminum atoms respectively.

There are two outstanding difficulties in a reflection geometry in estimating the precise absolute scattering factor from single crystal intensities; these are the corrections for extinction effects and surface roughness. In our experimental arrangement, the effect of the surface problem was avoided altogether by using a very thin crystal (t=0.0141 cm) in a transmission geometry. Further the use of superlattice reflections which are of low reflecting power, serves to reduce the extinction effects to the point of insignificance. Intensity measurements of the strongest of the superlattice reflections with two different wavelengths (i.e. MoK_α and its half wavelength) showed the extinction corrections to be negligible within ±3% accuracy of the measurements.

The use of the superlattice reflections has several other advantages over the use of the pure metal: (1) Since the amplitude of superlattice reflection is proportional to the difference between the scattering factor of iron and aluminum, as is seen from Eq. (2), the effect of $3d$ electron contribution on the measured intensities is enhanced. That is, there is a partial cancellation of the argon core contribution by the aluminum. (2) The number of allowed reflections in the Fe_3Al structure is greater in the angular region of interest than that of pure iron as we see in Table

I. Thus, in addition to offering more detailed information on the 3*d* electron distribution, this also permits an intercomparison between different peaks and hence a check on the experimental method.

There are, however, some disadvantages in using an ordered alloy as opposed to the pure iron. It is now necessary to establish the long-range order parameter S^2, as well as to obtain some estimate of the individual temperature factors for the iron and aluminum atoms. Further some assumptions must be made as to the magnitude of f_{Al}. A neutron diffraction study of the same single crystal examined with X-rays has provided this information. The considerations regarding f_{Al} will be discussed in a later section.

Table I. Possible Bragg reflections of Fe and Fe_3Al up to $\sin\theta/\lambda=0.345$.

Fe	Fe_3Al
	(111)
	(200)
(110)	(220)
	(311)
	(222)
(200)	(400)

§ 3. Experimental

(1) *General considerations*

Absolute intensity measurements were made at room temperature on an ordered Fe_3Al sample by utilizing a Bragg-type spectrometer, the ionization chamber being replaced by a NaI-scintillation counter. On a Norelco X-ray unit, monochromatic MoK_α radiation was scattered from a flat lithium fluoride monochromator. The tube voltage for the measurements was 30 kV in order to eliminate the half wavelength. A pulse height analyzer was used to discriminate against unwanted radiation.

The ordered Fe_3Al sample was made available for us by courtesy of Professor Chikazumi at University of Tokyo. The shape of the specimen was a disk, 0.8 cm in diameter with a thickness of 0.0141 cm. The composition of the specimen was 76 at. % Fe and 24 at. % Al. The specimen was annealed at 800°C, cooled down to 650°C in the furnace and slowly cooled to 300°C at a rate of 0.1°C/min., then allowed to cool down to room temperature. The specimen was then treated by electropolishing. Checks were made for the existence of other phases such as Fe_3AlC[9] by taking Laue and Weissenberg photographs. The surface of the specimen was 10.0° off from (110) so that the angle ϕ in Eq. (1) was equal to 10° for the reflecting plane (001). ϕ's for other planes can be calculated easily by a simple geometry.

Linear absorption coefficient μ of the sample was determined from the attenuation of the incident beam passing through the sample, since tabulated values were found to be unsatisfactory. The uniformity of the thickness of the sample was checked at the same time. The power of the incident beam was measured directly by placing several absorbers with predetermined transmission factors in the beam to reduce the counting rate to manageable proportions.

In taking data for integrated intensities the specimen was rotated manually through a position of Bragg reflections at increments of of 2.5′ step by step, while counter was rotated at the same increment taking counting rate by a fixed counting method. The area beneath the rocking curve thus obtained gave the total diffracted power P after subtracting of the background. This was estimated at points beyond the tails of the peak. For the above condition, the window of the scintillation counter was wide enough so as to detect the entire diffracted beam. The Hönl corrections were taken from the tabulation given by James[10] and that of Dauben and Templeton[11], both values giving no significant difference at least for the lower order reflections. The

Table II. Experimental and calculated parameters used in Eqs. (1) and (2) to evaluate atomic scattering factors.

N (cm^{-3})	0.0051471×10^{24}
λ (cm)	0.7107×10^{-8}
μ (cm^{-1})	217.80
θ_M	10°11′
t (cm)	0.0141
$\Delta f'$ for Fe $\Delta f''$ for Fe	0.31 0.78
$\Delta f'$ for Al $\Delta f''$ for Al	0.07 0.05
S^2	0.75
B_{Fe}	0.35
B_{Al}	0.45

parameters used to calculate the atomic scattering factor from the intensity data are given in Table II.

(2) *Determination of the order parameter and the temperature factors*

As we mentioned earlier, the long-range order parameter S^2 and the temperature factors B_{Fe} and B_{Al} (cf. Eq. (2)), must be known in order to obtain atomic scattering factors from observed intensities.

Structure factors of ordered $\mathrm{Fe_3Al}$ structure for unpolarized neutron beam are given as follows:

$$^{N}F^2_{hkl}(f)=16\left\{3b_{\mathrm{Fe}}\exp\left[-B_{\mathrm{Fe}}\left(\frac{\sin\theta}{\lambda}\right)^2\right]+b_{\mathrm{Al}}\exp\left[-B_{\mathrm{Al}}\left(\frac{\sin\theta}{\lambda}\right)^2\right]\right\}^2 \quad (3)$$

for fundamental reflections (such as (220), (400), (440), (800)), and

$$^{N}F^2_{hkl}(s)=16S^2_{0,e}\left\{b_{\mathrm{Fe}}\exp\left[-B_{\mathrm{Fe}}\left(\frac{\sin\theta}{\lambda}\right)^2\right]-b_{\mathrm{Al}}\exp\left[-B_{\mathrm{Al}}\left(\frac{\sin\theta}{\lambda}\right)^2\right]\right\}^2 \quad (4)$$

for supperlattice reflections (such as (111), (222), (311), (511)), where b_{Fe} and b_{Al} are the nuclear scattering amplitudes for neutrons for iron and aluminum atoms.

Regarding the temperature factors B_{Fe} and B_{Al}, the values were taken as consistent with the fall off of the neutron-diffraction intensities of the fundamental and superlattice reflections with $(\sin\theta/\lambda)^2$. The value of B_{Fe} can be obtained by the ratio of the fundamental lines, assuming the difference between two temperature factors being small as a first approximation. The ratios I_{440}/I_{220} and I_{400}/I_{800} gave the value $B_{\mathrm{Fe}}=0.35$. The above assumption was supported by a fact that I_{511}/I_{400} gave a value of S^2 which was not much different from that obtained from I_{111}/I_{400} using same temperature factor for iron and aluminum. The value of B_{Al} was then estimated based on the ratio of the superlattice reflections, such as I_{511}/I_{111}, and came out to be approximately 0.45 which was nearly half of that in metallic aluminum. It should be mentioned that small extinction effects observed for (220) and (400) were corrected using a polarized neutron beam technique.

Knowing the nuclear scattering amplitudes and the temperature factors for iron and aluminum, the ratio of superlattice reflection to fundamental reflection (Eq. (4) to (3)) gives directly the order parameter S^2. Since there are two sets of order parameters for odd and even superlattice reflections, they were evaluated by the ratios I_{111}/I_{220}, I_{111}/I_{400}, I_{511}/I_{220}, I_{511}/I_{400} and I_{200}/I_{220}, I_{200}/I_{400}, I_{222}/I_{220}, I_{222}/I_{400}. The values of S^2 calculated from these ratios were approximately consistent with each other. There was no evidence within the experimental accuracy to suggest that S^2 from the (200) reflections was significantly different from the (111) reflections, therefore we have used the same value of $S^2=0.75\pm0.03$ for both even and odd reflections.

(3) *Results*

A list of the observed F^2_{obs} values for the first five superlattice reflections is given in Table III. These F^2_{obs} are determined in such a way that the values of F^2 obtained from Eq. (1) by X-ray measurements are divided by $S^2=0.75$, so that F^2_{obs} are independent of the order parameter S^2 (cf. Eq. (2)). The uncertainties given for the F^2_{obs} in Table III represent the overall standard deviations in X-ray and neutron measurements. Also given are the F^2_{calc} values calculated from Freeman and Wood's free-atom scattering factor (six 3*d* electrons) and those based on Weiss and DeMarco's results (2.3 3*d* electrons). The calculated values have been corrected for temperature effects using $B_{\mathrm{Fe}}=0.35$, $B_{\mathrm{Al}}=0.45$ and assuming that the argon core contribution is the same as in the free atom. Because of the lack of the precise knowledge for the electronic states of aluminum in this alloy, we have used calculated atomic scattering factors for aluminum with different ionized states[12] for the calculated F^2_{calc} value of (111) and (200). At the (311) reflection and beyond no practical differences of F^2_{calc} are found for the different states of ionization of aluminum.

The results of Table III show that the scattering factor of iron in ordered $\mathrm{Fe_3Al}$ agrees closely with that for the free atom calculated by the self-consistent field wave functions. We have calculated the number of effective 3*d* electrons of iron using Eq. (2), which came out to be 5.0 ± 1.0 electrons.

In Fig. 3, theoretical curve for five 3*d* electrons (solid curve) and for 2.3 3*d* electrons (dotted curve) are shown. The observed

Table III. Comparison of the observed and calculated F^2 values.

hkl	$\sin\theta/\lambda$	$F^2_{obs.}$	$F^2_{calc.}$ six $3d$ electrons	$F^2_{calc.}$ 2.3 $3d$ electrons
111	0.1495	2060±100	Al 2397 Al+ 2425 Al++ 2516 Al+++ 2658	1267 1287 1354 1459
200	0.1726	2000±100	Al 2235 Al+ 2243 Al++ 2292 Al+++ 2389	1259 1264 1302 1375
311	0.2863	1270±60	1425	955
222	0.2990	1220±60	1348	917
511	0.4486	609±30	692	536

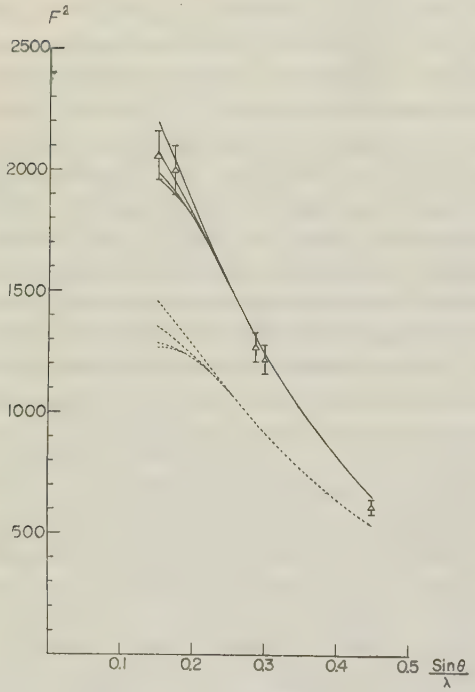

Fig. 3. The structure factors observed (Δ) and calculated for Fe:5 $3d$ (——) and Fe:2.3 $3d$ (- - - -). Four branches of each curve denote the calculated F^2 for Al, Al^+, Al^{++} and Al^{+++} from bottom to top respectively.

values are indicated along with the estimated experimental errors.

§ 4. Discussions

Since F^2_{calc} for (111) and (200) have uncertainties with respect to the electronic state of aluminum, the (311) and (222) reflections are the critical ones to compare with the calculated values. These two reflections have values of $\sin\theta/\lambda$ near the (110) reflection of pure iron (0.247) which was the essential reflection of Weiss and DeMarco's experiments. Correction of temperature effect for these reflections is small, as these are reflections at such a low Bragg angle. Therefore the calculated F^2 values are not very sensitive to the errors introduced in B_{Fe} and B_{Al} obtained from the neutron analysis.

The difference between the number of $3d$ electrons obtained by us and that calculated for the free iron atom lies within the experimental errors, while the discrepancy between our results and those calculated from the Weiss and DeMarco's estimate of 2.3 $3d$ electrons (more than 25%) is quite evident. It appears unlikely that any combination of errors would make such a large deviation.

There is a question in making a measurement on ordered Fe_3Al as to whether the scattering factor of iron in this alloy differs from that of pure iron. In the ordered state of Fe_3Al two types of iron atoms are present with respect to the nearest neighbor environment (cf. Fig. 2). A neutron diffraction study by Nathans, Pigott and Shull[6] showed that the average magnetic moment per atom at room temperature was 1.46 μ_B for the iron atoms (Fe(I) in Fig. 2) having 4 Fe and 4 Al as nearest neighbors. For the other type of iron atoms (Fe(II) in Fig. 2) surrounded by 8 Fe atoms, the observed average moment was 2.14 μ_B which was close to the value, 2.2 μ_B, observed in metallic iron. The interpretation of these results can proceed along three directions: (1) According to the suggestion of Sato and Arrott[13], the two iron sublattices can be considered as in different states of magnetic saturation at room temperature. In this case, no large difference in the $3d$ electron configuration is expected, at least in the number of localized $3d$ electrons. (2) We may invoke the recent theoretical arguments of Goodenough[14] in which the low moment of the one iron sublattice is explained by putting a fraction of the iron atoms on this sublattice antiparallel to the majority of atoms—a sort of ferrimagnetism. Again since no intrinsic change in the moment of the iron atoms is assumed, $3d$ electron configuration is not expected to be different. (3) We may assume that there is an electron transfer between the iron and aluminum atoms which lowers the intrinsic moment per iron atom. If this is true then a difference in the number of $3d$ electrons in pure iron and in the iron atoms in Fe_3Al would be possible. However, the accurate measurement of the shape of the magnetic form factor in ordered Fe_3Al and in metallic iron showed no large difference between the form factors for two iron sites in ordered Fe_3Al and that found in the pure iron metal was observed.

The authors wish to thank Professor S. Chikazumi of University of Tokyo for providing us with the Fe_3Al single crystal. We would also like to acknowledge the Rigaku-Denki Co., Ltd. for the courtesy to accomodate us with counter instruments. We are particularly indebted to Professors I. Nitta, T. Watanabé, T. Nagamiya of Osaka University and J. Kakinoki of Osaka City University for their stimulating discussions and encouragement on these experiments. Two of the authors (Y.K. and Y.T.) wish to thank the Ministry of Education for the Research Grant.

References

1) R. J. Weiss and J. J. DeMarco: Rev. Mod. Phys. **30** (1958) 59.
2) B. W. Batterman: Phys. Rev. Letters **2** (1959) 47.
3) B. W. Batterman: Phys. Rev. **115** (1959) 81.
4) A. J. Freeman and J. H. Wood: Acta Cryst. **12** (1959) 271.
5) R. J. Weiss and J. J. DeMarco: Phys. Rev. Letters **2** (1959) 148.
6) R. Nathans, M. T. Pigott and C. G. Shull: J. Phys. Chem. Solids **6** (1958) 38.
7) Y. Komura, Y. Tomiie and R. Nathans: Phys. Rev. Letters **3** (1959) 268.
8) The International Union of Crystallography: *International Tables for X-ray Crystallography* (The Kynoch Press, England 1959).
9) A. Taylor and R. M. Jones: J. Phys. Chem. Solids **6** (1958) 16.
10) R. W. James: *The Optical Principles of the Diffraction of X-rays* (G. Bell and Sons, London, 1954).
11) C. H. Dauben and D. H. Templeton: Acta Cryst. **8** (1955) 841.
12) A. J. Freeman: Acta Cryst. **12** (1959) 261.
13) H. Sato and A. Arrott: J. Appl. Phys. **29** (1958) 515.
14) J. B. Goodenough: Private Communication.

JOURNAL OF THE PHYSICAL SOCIETY OF JAPAN, Vol. 15, No. 8, AUGUST, 1960

The Photoionization of H_2 and the Spatial Correlation between Electrons

By Mikio SHIMIZU*

Department of Physics, University of Tokyo

(Received September 23, 1959)

The photoionization of H_2 by photons of sufficiently short wave length produces the molecular ion H_2^+ as well as the atomic ion H^+. The relative yield H^+/H_2^+ has been calculated as the function of energies of photons. The description of the ground state of H_2 is given by the superpositon of two configurations: $\sigma_g^2+\lambda\sigma_u^2$, taking account of the spatial correlation between electrons, while those of H_2^+ by the linear combinations of Wang type atomic orbitals. The results show that the relative yield curve has a plateau in the high-energy range and its height is essentially proportional to λ^2. The various approximations used in our calculation (Franck Condon approximation, Born approximation, dipole velocity approximation, the neglect of possibility of production of H_2^+ and H^+ through autoionization and multiple ionization etc.) have been carefully discussed. The velocity distribution of the ejected protons has also been calculated according to the Franck Condon principle.

§ 1. Introduction

It is well known that the electron bombardment on hydrogen molecules produces the molecular ion H_2^+ as well as the atomic ion H^+. Hence it can be expected that these ions will be produced by the irradiation with photons of sufficiently short wave length as well. Now the production of H_2^+ mostly occurs through the excitation of the molecule from the ground state ${}^1\Sigma_g^+$ to that of molecular ion ${}^2\Sigma_g$, while that of H^+ is made possible through ionization to its repulsive, first excited state, ${}^2\Sigma_u$. The single electrons left in ${}^2\Sigma_g$ and ${}^2\Sigma_u$ have wave functions of σ_g and σ_u type respectively. On the other hand, the ground state ${}^1\Sigma_g^+$ is most simply described as σ_g^2. If this description were exact, ${}^2\Sigma_u$ state could not be reached by single-electron jump from ${}^1\Sigma_g^+$, and the production of H^+ could hardly be expected. A more refined description of ${}^1\Sigma_g^+$ state is given, however, by a superposition of two configurations: $\sigma_g^2+\lambda\sigma_u^2$. Hence the relative yield of H_2^+ and H^+ will give us some information about the magnitude of λ. We shall show later that the curve of the ratio H^+/H_2^+ as a function of photon energies has a plateau in the region of high energies and that its height is essentially proportional to λ^2.

The aspect which has been discussed in the case of the hydrogen molecule will be similarly applicable to the other molecules. The mixing of antibonding orbitals with bonding ones due to the Coulomb repulsion between two bonding electrons may correlate with the composition of ionization products. Hence we can expect that, if the ionization phenomena are investigated experimentally in such a manner described in this paper, we shall be able to obtain further knowledge about the electronic structure of various molecules. Further we may expect that such a calculation gives a fundamental basis to the research for the effects of high energy radiation on the polymers.

In this paper, we are only concerned with the region of high energies of photons, because we find some difficulties in the treatment of the motion of a slow electron in the field of a molecular ion. We shall discuss the effect of the distorsion due to the field of a molecular ion in the photoionization process ${}^1\Sigma_g^+\rightarrow{}^2\Sigma_g$ in the following paper.

The atomic untits have been adopted throughout this paper.

§ 2. Calculation of the Relative Yield

Fig. 1 illustrates the potential-energy curves for some electronic states of the hydrogen molecule and of the hydrogen molecular ion. As can be seen from the figure, the production of the two kinds of ions, H_2^+ and H^+, by irradiation with photons of sufficiently short wave length is possible through many processes. Of these processes concerned, however, the transition to the lowest, ${}^2\Sigma_g$, state of the H_2^+ ion and that to the repulsive, ${}^2\Sigma_u$, state of the same ion are most important. These ions can be produced also through the jumps to the highly excited states of H_2^+. Still another way of their production is through the autoionization from some excited states of H_2 to unstable states of H_2^+. For simplicity, however, we shall neglect these processes except the first two transitions for the time being. Further discussions on this point will be seen in the next section. Under such an assumption, the relative yield H^+/H_2^+ will be determined by the ratio of the transition probability of the process ${}^1\Sigma_g^+ \rightarrow {}^2\Sigma_u$, to that of the process ${}^1\Sigma_g^+ \rightarrow {}^2\Sigma_g$.

---

* Present address: Department of Physics, Ochanomizu University, Tokyo.

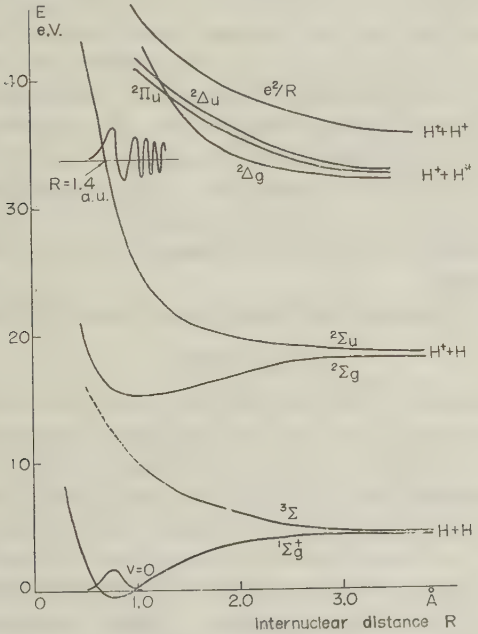

Fig. 1. Potential curves of some states of H_2 and H_2^+.

The states of the total system can be written as

$$\psi = \psi_e(\boldsymbol{r}_1, \boldsymbol{r}_2, \boldsymbol{R}) \frac{\psi_v(R)}{R} , \qquad (1)$$

where ψ_e is the wave function for the electronic state and ψ_v/R is that of the vibrational one, $\boldsymbol{r}_1$ and $\boldsymbol{r}_2$ being the electronic coordinates, $\boldsymbol{R}$ the internuclear distance vector, and R the absolute value of $\boldsymbol{R}$ respectively. Hereafter the excited states will be denoted as ψ_e' etc.. The interaction operator is

$$H' = -\frac{i}{c} \sum_i \boldsymbol{P}_i \cdot \boldsymbol{A}(i) , \qquad (2)$$

where $\boldsymbol{A}(i)$ is the vector potential of the electromagnetic wave, and $\boldsymbol{P}_i$ the momentum operator of each particle. Then the transition probability is given by

$$\frac{1}{2} \sum_v \sum_{v'} N e^{-\varepsilon_v/kT} \sum_j \int d\Omega \int \frac{d\omega}{4\pi} \left| \int \psi_{e'}^* \frac{\psi_{v'}}{R} H' \psi_e \frac{\psi_v}{R} d\tau_e d\tau_R \right|^2 \rho(E) , \qquad (3)$$

where $\sum_v N e^{-\varepsilon_v/kT}$ means the average over the initial vibrational states, $\sum_{v'}$ the sum over the final vibrational states, $1/2 \sum_j$ the average over the polarization of the incident photons, $\int d\Omega$ the sum over the direction of the ejected electron, $1/4\pi \int d\omega$ the average over the direction of the incident photons, and $\rho(E)$ the state density of the ejected electron respectively. In the usual experimental temperatures, we have only to consider the lowest vibrational state $v=0$ for ψ_v, while for $\psi_{v'}$ we must consider various vibrational states.

It is difficult to calculate the transition amplitude

$$\int \psi_{e'}^* \frac{\psi_{v'}^*}{R} H' \psi_e \frac{\psi_v}{R} d\tau_e d\tau_R$$

exactly. So we shall introduce here the following approximations. The integral

$$M = \int \psi_{e'}^* H' \psi_e d\tau_e$$

is a slowly varying function of the internuclear distance R, compared with ψ_v and $\psi_{v'}$. Thus we replace it by the value evaluated at the equilibrium distance R_0 of the ground state of H_2, taking account of the form of ψ_v for $v=0$. Then the transition amplitude becomes

$$4\pi \left(\int \psi_{e'}^* H' \psi_e \, d\tau \right)_{R=R_0} \int \psi_{v'}^* \psi_v dR ,$$

which corresponds to the Franck Condon principle[1]. Further, due to the orthonormality of $\psi_{v'}$, we have

$$\sum_{v'} \left| \int \psi_{v'}^* \psi_v dR \right|^2 = 1 . \qquad (4)$$

Hence only the electronic part of transition amplitude will be taken into account later.

The electronic wave function ψ_e for H_2 is described in the form

$$\frac{\sigma_g^2+\lambda\sigma_u^2}{\sqrt{1+\lambda^2}}\,. \tag{5}$$

This approximation means that we have partly taken account of the spatial correlation between two electrons which cannot be expressed by the simple molecular orbital description σ_g^2. This description is equivalent to that by Coulson and Fischer[2], the semilocalized orbital scheme, and that by Weinbaum[3], the mixing of ionic states in Heitler London treatment.

The importance of the configuration interaction in the calculation of the molecular energies has been stressed by many authors. This is also true for the calculation of the electronic transition probabilities[4]. In our problem, as we have stated in the previous section, the production of atomic ion H^+ can be hardly expected without the use of this description.

Wave functions for the final states, in which the ion is left in ${}^2\Sigma_g$ and ${}^2\Sigma_u$ are

$$\psi_{e'}\propto\begin{cases}\sigma_{g'}(1)f(2)+\sigma_{g'}(2)f(1)\,,\\ \sigma_{u'}(1)f(2)+\sigma_{u'}(2)f(1)\,,\end{cases} \tag{6}$$

respectively without normalization, f denoting the wave functions of the ejected electrons.

The orbitals σ_g and $\sigma_{g'}$ are approximated as linear combinations of ls type atomic orbitals with appropriate effective charges Z and Z', and similarly with Z and Z'' for σ_u and $\sigma_{u'}$ orbitals. Z and λ are obtained from the result of the calculation by Weinbaum[3]:

$$Z=1.193 \quad \text{and} \quad \lambda=-0.113\,.$$

We calculated Z' and Z'' by the variational method, fixing the nuclear distance at $R_0=1.4$, i. e., the equilibrium internuclear distance of H_2, in accord with the Franck Condon principle. The results are

$$Z'=1.386 \quad \text{and} \quad Z''=0.773\,.$$

Comparing Z' with the effective charge $Z=1.288$ determined at the equilibrium internuclear distance of H_2^+,[5] we can see that Z' becomes a little larger, which means the shrinking of the wave function to the central region. Z'', the effective charge of a repulsive state, is far smaller than those of the stable states.

Bates et al. have calculated the transition probabilities between various states of H_2^+ and HeH^{2+} using the exact wave functions and some approximate ones[6]. According to them, the accuracy of a calculation of this type depends rather sensitively on the way of approximations. In respect of this, our approximate functions are not so satisfactory one. But, as no calculation seems to have ever been carried out about the ionization of the hydrogen molecules, we believe that the calculation even in such an approximation has still some meaning.

As the next step of simplification, we shall approximate the wave functions of the ejected electron, $f(r)$, by plane waves (Born approximation). The plane waves for the ${}^2\Sigma_g$ case and that for the ${}^2\Sigma_u$ case differ only in the magnitude of their wave number vectors, which we call hereafter $\boldsymbol{k}_1$ and $\boldsymbol{k}_2$ respectively. In the photoionization, almost all the energy of the absorbed light quantum is consumed for ejecting an electron. Thus this approximation may be fairly reasonable. The state density $\rho(E)$ is also calculated in this approximation.

The exponential factor in the vector potential

$$\boldsymbol{A}=\exp(i\boldsymbol{q}\cdot\boldsymbol{r})\boldsymbol{e}\,,$$

where $\boldsymbol{q}$ is the propagation vector and $\boldsymbol{e}$ the polarization vector, can be approximated by unity (dipole velocity approximation) for the photons with the wave lengths longer than several Å. The dipole length approximation is not suitable for our calculation because of the lack of orthogonality of the initial and the final wave functions. When we used it, the transition amplitude would come to depend on the choice of the origin of coordinates.

Then the calculation of the transition probabilities is made straightforwardly using the spherical wave expansion of the plane waves and the Coulson integrals[7]. By referring to the coordinate system fixed in the molecule, and by taking the molecular axis as z axis, the vector components of transition amplitudes are expressed as proportional to

$$\left.\begin{aligned}&\int\sigma_g P_x f_{k_1}d\tau\int\sigma_g\sigma_{g'}d\tau\,,\\ &\int\sigma_g P_y f_{k_1}d\tau\int\sigma_g\sigma_{g'}d\tau\,,\\ &\int\sigma_g P_z f_{k_1}d\tau\int\sigma_g\sigma_{g'}d\tau+\lambda\int\sigma_u P_z\sigma_{g'}\,d\tau\int\sigma_u f_{k_1}d\tau\,,\end{aligned}\right\} \tag{7}$$

for H_2^+, and

$$\left.\begin{aligned}&\lambda\int\sigma_u P_x f_{k_2} d\tau \int\sigma_u\sigma_{u'} d\tau\ ,\\&\lambda\int\sigma_u P_y f_{k_2} d\tau \int\sigma_u\sigma_{u'} d\tau\ ,\\&\lambda\int\sigma_u P_z f_{k_2} d\tau \int\sigma_u\sigma_{u'} d\tau + \int\sigma_g P_z \sigma_{u'} d\tau \int\sigma_g f_{k_2} d\tau\ ,\end{aligned}\right\} \tag{8}$$

for H^+ respectively. The second terms in each z component represent the indirect transitions through the overlap between f and σ_g or σ_u. The result of the numerical calculation will show that the contribution from these terms is, as can be expected, far smaller than that from the direct transitions explained in the previous section.

After averaging over the polarization and over the direction of the photon, and finally integrating over the direction of the ejected electron, we have obtained the relative yield H^+/H_2^+ as

$$\frac{k_2{}^3\mathrm{I}^2(k_2)\left\{\lambda^2 k_2{}^2\dfrac{\varDelta^2_{uu'}}{1-S}\left(1-\dfrac{\sin k_2R_0}{k_2R_0}\right)+\lambda A+C\right\}}{k_1{}^3\mathrm{I}^2(k_1)\left\{k_1{}^2\dfrac{\varDelta^2_{gg'}}{1+S}\left(1+\dfrac{\sin k_1R_0}{k_1R_0}\right)-\lambda B+\lambda^2 D\right\}}\ , \tag{9}$$

where

$$A=\frac{4Z''J_6(Z'',Z,R_0)k_2\varDelta_{uu'}}{2\pi}j_2(k_2R_0)\sqrt{\frac{Z^3Z''^3}{(1+S)^2(1-S)(1-S'')}}\ , \tag{10}$$

$$B=\frac{4Z'J_6(Z',Z,R_0)k_1\varDelta_{gg'}}{2\pi}j_2(k_1R_0)\sqrt{\frac{Z^3Z'^3}{(1-S)^2(1+S)(1+S')}}\ , \tag{11}$$

$$C=\frac{Z^3Z''^4J_6{}^2(Z'',Z,R_0)}{\pi^2(1+S)^2(1-S'')}\left(1+\frac{\sin k_2R_0}{k_2R_0}\right), \tag{12}$$

and

$$D=\frac{Z^3Z'^4J_6{}^2(Z',Z,R_0)}{\pi^2(1-S)^2(1+S')}\left(1-\frac{\sin k_1R_0}{k_1R_0}\right). \tag{13}$$

The meaning of notations is as follows: S, S' and S'' are the overlap integrals $\int\varphi_a\varphi_b d\tau$ where φ_a is 1s type atomic orbitals around the nucleus, say a, with effective charges Z, Z' and Z'' respectively. $\varDelta_{gg'}$ and $\varDelta_{uu'}$ are $\int\sigma_g\sigma_{g'}d\tau$ and $\int\sigma_u\sigma_{u'}d\tau$ respectively. $\mathrm{I}(k)=\dfrac{2Z}{k(k^2+Z^2)}$, j_2 is the spherical Bessel function of the second order and J_6 is the Coulson integral in his notation.

When the wave length of photons is very short, the dipole approximation becomes bad and the calculation of the indirect transition amplitude becomes difficult. But, taking account of the fact that the contribution from the indirect transitions decreases as $k\to\infty$, we may safely neglect these terms. Then, in the limit of short wave length, we need not use the dipole approximation and the relative yield is essentially represented as follows:

$$\frac{\varDelta^2_{uu'}}{\varDelta^2_{gg'}}\cdot\frac{1+S}{1+S}\lambda^2\ . \tag{14}$$

This conclusion is, however, valid subject to the condition that Compton scattering is negligible, which, in reality, sets in as the wave length gets shorter than about 1Å.

The numerical calculations have been carried out for the wave lengths of photons 60Å, 20Å, 10Å and the short wave limit $\nu/c\to\infty$. The resulting relative yields are

$$\begin{aligned}&4.98\lambda^2 &&\text{for}\quad \nu/c\to\infty\\&\left.\begin{aligned}&\frac{0.156+0.330\lambda+262\lambda^2}{55.9-0.666\lambda+0.149\lambda^2} &&\frac{c}{\nu}=10\text{Å}\ ,\\&\frac{0.185-1.12\lambda+154\lambda^2}{26.5+0.972\lambda+0.147\lambda^2} &&\frac{c}{\nu}=20\text{Å}\ ,\\&\frac{0.212-0.597\lambda+63.8\lambda^2}{6.97-0.653\lambda+0.14\lambda^2} &&\frac{c}{\nu}=60\text{Å}\ ,\end{aligned}\right\}\end{aligned} \tag{15}$$

without inserting the numerical value in λ. Further the numerical values of the relative yields are tabulated in Table 1 for a special

Table 1. The calculated relative yield.

Wave length	$(c/\nu)\to 0$	10Å	20Å	60Å
H^+/H_2^+ (%)	6.37	6.18	7.36	12.96

value of $\lambda=-0.113$.

We can see from the above results that the yield curve has a plateau in the high-energy range and that the height of the plateau depends on the value of λ sensitively, namely, it is essentially proportional to λ^2.

The value of the relative yield for $c/\nu=60$Å is unexpectedly larger than the others. This is partly due to the approximations employed in our calculation, particularly the Born approximation for $f(r)$ and the LCAO approximations for σ_g's and σ_u's. We shall show later that the wave function of the ejected electron is considerably distorted in this energy range by the long range Coulomb force. The invalidity of the LCAO approximations is suggested from the large contribution of the indirect transitions which is expected to be small in the exact treatment.

Finally, we shall investigate how much the relative yield changes when we adopt the linear combinations of s–p hybridized atomic orbitals for σ_g's and σ_u's. The assumed forms for the electronic wave functions are, for ${}^1\Sigma_g{}^+$,

$$\psi_e=\tilde{\sigma}_g(1)\tilde{\sigma}_g(2)+\mu\tilde{\sigma}_u(1)\tilde{\sigma}_u(2)\ , \tag{16}$$

where

$$\tilde{\sigma}_g=(\varphi^a_{1s}+\nu\varphi^a_{2p\sigma})+(\varphi^b_{1s}+\nu\varphi^b_{2p\sigma})\ ,$$

and

$$\tilde{\sigma}_u=(\varphi^a_{1s}+\nu\varphi^a_{2p\sigma})-(\varphi^b_{1s}+\nu\varphi^b_{2p\sigma})\ ,$$

φ^a_{1s} and $\varphi^a_{2p\sigma}$ being $1s$ and $2p\sigma$ atomic functions around one nucleus, say a, with a common effective charge Z. Similar expressions are used for $\sigma_{g'}$ and $\sigma_{u'}$ with ν', Z' and ν'', Z'' respectively. The parameters in ψ_e are obtained by transforming the calculated values by Weinbaum[3)], while those in $\psi_{e'}$ are calculated using the variational method, the internuclear distances being fixed at R_0. Those are

$$Z=1.190\ ,\quad \mu=-0.100\ ,\quad \nu=0.07\ ,$$
$$Z'=1.3979\ ,\qquad \nu'=0.1573\ ,$$
$$Z''=1.0438\ ,\qquad \nu''=-0.3312\ .$$

The calculation has been carried out only for the short wave length limit. The results are $6.64\,\mu^2$ or 6.64%, which is very close to the previous value.

The experimental data with which these theoretical results are to be compared are not yet available. The experiments for photoionization phenomena have been carried out rather for photons of wave lengths more than 500Å. In this energy range, however, some of our approximations may be invalid. The distortion of the wave of an ejected electron must be taken explicitly into account and the higher accuracy will be required in the functional form of the molecular orbitals.

It is interesting to see the experimental results about the ionization of H_2 by electron impact. We, of course, cannot compare the theoretical results for light quanta directly with this experiment. But, as is well known, the electromagnetic field around an electron with high velocity is quite similar to that of light quanta. Thus we may expect that the relative yield curves in these two cases behave in a similar manner in the high-energy range. Bleakney measured the curve up to the electron energy 600 eV by use of a mass-spectrograph[8)], of which the results were reported in detail on the survey by Smyth[9)]. According to his result, the curve has a plateau in the high-energy range, and its height is about 7%. Later Newhall pointed out a defect of this experiment and measured again the relative yield curve up to the electron energy 180 eV by another mass-spectrographic method[10)]. His results are quite different from those by Bleakney; the curve increases throughout the investigated energies and the height at 180 eV is only about 0.5%. Unfortunately his experiment is restricted in too low electron energies. Thus we cannot obtain a decisive conclusion from the electron impact data yet.

§ 3. Discussions on the used Approximations

In the previous section we have calculated the relative yield of two kinds of ions H^+ and H_2^+ which are produced through the ionization of the hydrogen molecules by the irradiation of photons of short wave length, using some approximations. In this section, we shall try to discuss the accuracy of these approximations used and the effects of other ionization processes which we have not taken into account.

3.1. *Franck Condon Approximation*

We have separated the wave function of hydrogen molecule into the electronic and the vibrational parts according to the Franck

Condon principle[1]. Thus the transition amplitude is approximated by

$$\int \psi_{e'}{}^* \frac{\psi_{v'}{}^*}{R} H' \psi_e \frac{\psi_v{}^*}{R} d\tau_e d\tau_R$$
$$\sim 4\pi \left(\int \psi_{e'}{}^* H' \psi_e d\tau_e \right)_{R=R_0} \int \psi_{v'}{}^* \psi_v dR \ . \quad (17)$$

In this approximation, we have only to calculate the overlap integrals to obtain the transition probabilities from the lowest vibrational state in the electronic ground state of H_2 to the vibrational states v' of an upper electronic state. Of course, such an approximation will be admitted when the variation of these electronic integrals with the nuclear distance R is sufficiently small. But it is rather troublesome to show it directly from the calculation. Thus we shall calculate the vibrational transition probabilities under this assumption and derive the velocity distributions of ejected protons and electrons. Then, by comparing them with experimental data when available, a necessary condition for the validity of the approximation will be obtained.

As for the electrons, they will be ejected from ions with the energy $h\nu - E({}^2\Sigma_g \text{ or } {}^2\Sigma_u; v') + E({}^1\Sigma_g{}^+; 0)$, but the measurement of this velocity distribution seems to be difficult. That of protons which are produced through the jump to either continuous states of ${}^2\Sigma_g$ or repulsive ${}^2\Sigma_u$ state are more tractable. On account of the large masses of the ions, their initial velocities may be negligible. Then, the kinetic energies of the ejected protons are half the differences of energies $E_c - E_\infty$, where E_∞ is the energy at $R=\infty$ and E_c the energies of the continuous states.

In order to calculate the transition probabilities, it is necessary to determine the wave functions for ${}^1\Sigma_g{}^+$, ${}^2\Sigma_g$ and ${}^2\Sigma_u$ states. Neglecting the effects of the centrifugal force on the vibrational states, we obtain the equations for the wave functions of the form,

$$\frac{d^2\psi}{dR^2} + \{2\mu(\mathcal{E} - V(R))\}\psi = 0 \ , \quad (18)$$

where $\mathcal{E}$ is the proper energy value, μ the reduced mass.

As the types of the potentials, we shall assume the Morse curve for ${}^1\Sigma_g{}^+$ and ${}^2\Sigma_g$ and the repulsive exponential curve for ${}^2\Sigma_u$.

In the first two cases, numerical values of the parameters are determined from the data given in the book by Herzberg[11]. Then

$$V = \begin{cases} 0.174(1 - e^{-1.03(R-1.4)})^2 & \text{for } H_2({}^1\Sigma_g{}^+) \ , \quad (19) \\ 0.102(1 - e^{-0.704(R-2.0)})^2 & \text{for } H_2{}^+({}^2\Sigma_g) \ . \quad (20) \end{cases}$$

For the above choice of parameter values, the number of bound states are 16 and 18 for H_2 and $H_2{}^+$ respectively. The transition probabilities from the lowest vibrational state of ${}^1\Sigma_g{}^+$ to the various vibrational states of ${}^2\Sigma_g$ have been calculated numerically. The result is tabulated in Table 2. It shows that the transition probabilities have a maximum at $v'=2$, and the sum of the probabilities up to $v'=6$ is already about 95.2%. Thus we may expect that, if the validity of the Franck Condon principle is not very poor in this case, the number of protons produced from the jumps to continuous states of ${}^2\Sigma_g$ should be very small.

Table 2. The ratio of transition for various vibrational states of ${}^2\Sigma_g$.

v'	0	1	2	3	4	5	6	...	total
ratio (%)	10.2	19.0	21.3	17.9	13.3	8.6	4.9	...	100

For the repulsive state ${}^2\Sigma_u$, we put $V = Ae^{-\beta R}$, A and β fitted with the calculated values by Morse and Stückelberg at $R=1$ and $R=3$[12]. Then

$$V = 2.7976 e^{-1.0891R} \quad \text{for} \quad H_2{}^+({}^2\Sigma_u) \ . \quad (21)$$

The wave $\psi(E_c)$ in this potential can be expressed by the Bessel function of imaginary order. But, on account of the practical reason, they have been numerically calculated for some E_c. The integration were carried out from the origin outwards. The wave functions were connected smoothly with the WKB type solutions at the approximate loops of waves, and the asymptotic amplitudes without normalization were determined.

The normalization condition for the continuous state is that

$$\lim_{\tau_0 \to \infty} \int_{\Delta E} dE_c' \int_{\tau_0} \psi^*(E_c')\psi(E_c) d\tau = 1 \ . \quad (22)$$

This condition requires that the asymptotic amplitude of $\psi(E_c)$ is $1/\sqrt{\pi}\sqrt{2\mu(E_c - E_\infty)}$ as shown by Hargreaves[18].

As representatives of $\psi(E_c)$, we have taken five functions of the repulsive states with the total energies which cut the potential curves at $R=1.1$, 1.25, 1.4, 1.55, 1.7 respectively. (see Fig. 1)

Table 3. The transition probabilities for various continuous states of ${}^2\Sigma_u$.

R at the cutting point	$E_{\text{kin.}}$ energy of protons	Pelative transition probabilities		Absolute transition probabilities
		δ function approx.	numerical cal.	numerical cal.
1.1 (a. u.)	11.1 (eV)	9.1	8.0	$.084\times10^{-3}$
1.175	10.2	24.0		
1.25	9.4	49.4	43.2	.454
1.325	8.6	76.8		
1.4	7.9	100.0	100.0	1.045
1.475	7.2	101.0		
1.55	6.6	81.6	82.0	.860
1.7	5.6	34.3	37.0	.389
1.9	4.7	7.8		

In the case of relative transition probabilities, the value at $R=1.4$ is taken as 100.

A rough approximation of $\psi(E_c)$ of repulsive states is to replace the first mountains of $\psi(E_c)$ by δ functions and neglect the other parts of the functions[1),11)]. Because, the contribution from the latters to the overlap integrals will be very small by the cancellation of mountains and valleys. This method gives us the relative transition probabilities and are applied together with the exact one.

The overlap integrals between the ψ_v and $\psi(E_c)$ states were numerically calculated, the results of which are shown in Table 3. Both the solutions from the exact and δ functional methods give a nearly equal energy distribution of ejected protons as can been seen from Table 3. When the experiment of photoionization in the high energy range becomes available in future, it is interesting to compare the experimental energy distribution with this theoretical one.

3.2. *The Born approximation and the dipole approximation*

We have approximated the wave function of the ejected electron as a plane wave (Born approximation). But, to be more accurate, we must take account of the distorsion of the wave caused by the Coulomb force between the ejected electron and the molecular ion left behind. We will show that the distortion is not so large when the wave length of incident light quanta is shorter than 20Å.

The field of hydrogen molecular ion can be approximated by that of two $+\frac{1}{2}e$ charges fixed at a distance R. Then we may expect the degree of the distorsion in the present problem will be estimated by comparing the plane wave with the distorted one in this field. We will not distinguish ${}^2\Sigma_g$ and ${}^2\Sigma_u$, and fix the nuclear distance R at 1.4. Only the partial waves $s\sigma$ will be compared, because the effect of distortion may appear most appreciably in those components.

By adopting the elliptic coordinates ξ, η and ϕ, the wave equation in the above potential can be separated as

$$\Phi=X(\xi)Y(\eta)e^{im\phi} \qquad (m=0,1,\cdots)\,, \tag{23}$$

$$\frac{d}{d\xi}\left[(\xi^2-1)\frac{d}{d\xi}X\right]+\left[c^2\xi^2+R\xi-\lambda_{n,m}-\frac{m^2}{\xi^2-1}\right]X=0\,, \tag{24}$$

$$\frac{d}{d\eta}\left[(\eta^2-1)\frac{d}{d\eta}Y\right]+\left[c^2\eta^2-\lambda_{n,m}-\frac{m^2}{\eta^2-1}\right]Y=0\,, \tag{25}$$

where c is $kR/2$, $\lambda_{n,m}$ the separation constant.

The equation (25) has been investigated by many authors[13)] and the solution which is regular at $\eta=\pm1$ has been obtained in the form of expansion in terms of the associated Legendre functions,

$$Y_n{}^m=\sum A^m_{n,l}Pe_l{}^m(\eta) \qquad (|l-n|\ \text{odd})\,. \tag{26}$$

We can find the formulae for the separation constant $\lambda_{n,m}$ and expansion coefficients $A^m_{n,l}$, for instance, in the text book by Stratton, Morse, Chu and Hunter[13]. On the other hand, the equation (24) is rather difficult to solve analytically. A plausible form suggested from the eigenvalue problem of hydrogen molecular ion is[14]

$$X=Ne^{-(ikR/2)\xi}(\xi^2-1)^{m/2}\left(\frac{1}{\xi+1}\right)^{m+1+(i/k)}\sum_n a_n\left(\frac{\xi-1}{\xi+1}\right)^n , \tag{27}$$

where N is the normalization constant, and the complex coefficients a_n should be determined by a three terms recurrence formula. The logarithmic phase which is characteristic in the Coulomb field comes, of course, from the third factor. Unfortunately the convergence of the series is not so good. Therefore, we have adopted the numerical calculations to obtain the wave functions for some parameters. By writing

$$X=\frac{U}{\sqrt{\xi^2-1}} , \tag{28}$$

the equation (24) has been transformed into the equation

$$\frac{d^2}{d\xi^2}U+\frac{1}{\xi^2-1}\left[c^2\xi^2+R\xi-\lambda_{n,m}-\frac{m^2-1}{\xi^2-1}\right]U=0 . \tag{29}$$

The calculation has been carried out for $c=3$ and 5 which correspond to the photons of wave length 50Å and 17Å respectively. The normalization of the wave has been determined by connecting them with the WKB solutions just in the same way as in (3.1).

The corresponding solutions in the free field can be obtained in the form of expansion in terms of the spherical Bessel functions,

$$X_0{}^0=\kappa_0\sum_{l=0}^{\infty}{}'(-)^{l/2}A^0_{0,l}(c)j_e(c\xi)\xrightarrow{\xi\to\infty}\frac{\sin c\xi}{c\xi} , \tag{30}$$

where $\kappa_0=1/\sum_{l=0}^{\infty}{}'A^0_{0,l}$ and Σ' means the sum over even integers only.

Comparing the partial wave in the Coulomb field with those of the plane wave, we have found that in the case of $c=5$ there is no appreciable distortion, while for $c=3$ the effect of Coulomb field has come to appear. This results will support the assumption that the Born approximation is reasonable for the wave function of the electron which is ejected by the incident light with wave length shorter than about 20Å.

Next we will make a remark about the dipole approximation. In the previous section the vector potential has been replaced by unity. In other words, the electromagnetic field over the molecule has been assumed nearly constant. In order to make sure, we have estimated the magnitude of the next term in the expansion of exponential function. A similar calculation like the previous section has been carried out. The ratio of the magnitude of the electric diole transition elements to the magnetic diole and electric quadrupole ones has been found to be 20 : 1 for the wave length 10Å. Then we may conclude the dipole velocity approximations in the previous section is fairly sufficient.

3.3. *Remarks on the neglected ionization processes*

So far we have been exclusively concerned with the accuracy of our calculations. Now we will discuss some other factors which we have not taken into account. In the previous section we have assumed that the relative yield $H^+/H_2{}^+$ can be determined by the processes ${}^1\Sigma_g{}^+\to{}^2\Sigma_g$ and ${}^1\Sigma_g{}^+\to{}^2\Sigma_u$. But, in general, other processes such as the excitation to the higher states than these two and the autoionization through potential crossings will also contribute to produce these ions. It is difficult to estimate these contributions theoretically because it requires much knowledge about the wave functions of the highly excited states of H_2 and $H_2{}^+$. Hence we will here investigate the experimental data on these phenomena[15] and try to estimate these contributions.

As for the autoionization, each state of hydrogen molecule shown in Table 4 has the

Table 4. The levels which may cause the autoionization.

Levels	$^1\pi_u$	$^3\Delta_g$	$^3\pi_u$	$3'K$	^1N	^1L	^1M	4^1K
r_0 (Å)	~ 1.06	1.8	1.05	~ 1.7	~ 1.38	~ 1.8	1.6	1.33
ω_e (cm^{-1})	2257			2293	1983.3	1835	2176	
a (Å^{-1})				1.32	1.28	1.12	1.34	
D_e (eV)	2.554			2.71	2.28	2.50	2.48	
Configuration	$\left(\begin{array}{l}1s\sigma\\3p\pi\end{array}\right.$	$\left(\begin{array}{l}1s\sigma\\3d\sigma\end{array}\right.$	$\left(\begin{array}{l}1s\sigma\\3p\pi\end{array}\right.$	$\left(\begin{array}{l}2p\sigma\\2p\sigma\end{array}\right.$	$\left(\begin{array}{l}2p\sigma\\3p\sigma\end{array}\right.$	$\left(\begin{array}{l}2p\pi\\2p\pi\end{array}\right.$	$\left(\begin{array}{l}2p\pi\\2p\pi\end{array}\right.$	$\left(\begin{array}{l}2p\sigma\\4p\sigma\end{array}\right.$
Remark	$v'=6$ preionization observed	$v'=3$ $\kappa'=4$	$v'=7, 8, 9$ $\kappa>1$					

possibility of dissociation to H_2^+. For instance, the autoionization through the level $^1\pi_u$ was concluded from the diffuseness of a emission band and this phenomenon was interpreted as the result of radiationless transition from $^1\pi_u$ to $^2\Sigma_g$ of H_2^+[16]. But the number of H_2^+ produced through the processes of this type will be very small, because the number of the diffused bands is rather small and the degree of their diffuseness is usually not so great. Knowledge about the group of doubly excited states 3^1K, ^1N etc. are less little[15]. But, as can be seen from their large internuclear distances, there are some possibilities that these levels cross over $^2\Sigma_g$ or $^2\Sigma_u$. The crossing of levels is also probable in the case of many repulsive potentials of H_2. Though we cannot deny the roles of these levels, we must say, at the same time, that the transition probabilities to these states are probably very small.

Further the transitions to the highly excited states of H_2^+ will produce H_2^{+*}, $H^+ + H^*$ and $H^+ + H^+$. In the experiment of electron impact, only small trace of double ionization has been found[17]. This may be also true in the case of irradiation with light quanta. On the other hand, the transition probabilities to the lower excited states seem to be not so small enough. Unfortunately adequate simple wave functions for these states have not been obtained so that we could not estimate their contribution distinctly.

The author wishes to express his sincere thanks to Prof. M. Kotani for suggesting this problem and for his invaluable advices throughout his work. The author is also very grateful to Dr. K. Takayanagi for reading the manuscript and showing profound interest, and to the members of Kotani Laboratory for their fruitful discussions.

References

1) A. S. Coolidge, H. M. James and R. D. Present: J. Chem. Phys. **4** (1936) 193.
2) C. A. Coulson and I. Fischer: Phil. Mag. **40** (1948) 386.
3) S. Weinbaum: J. Chem. Phys. **1** (1933) 593.
4) R. S. Mulliken: ibid. **7** (1939) 14. C. W. L. Bevan and D. P. Craig: Trans. Farad. Soc. **42** (1951) 564. C. A. Coulson and J. Jacb: Proc. Roy. Soc. A, **206** (1951) 287.
5) B. N. Finkelstein and G. E. Horowitz: Z. S. für Physik **48** (1928) 118.
6) D. R. Bates et al: Phil. Trans. Roy. Soc. A, **246** (1953) 215; Proc. Roy. Soc. A, **234** (1956) 207; Proc. Phys. Soc. A, **67** (1954) 343; ibid. A, **70** (1957) 489, 507.
7) C. A. Coulson and M. P. Barnett: Phil. Trans: Roy. Soc. A, **243** (1951) 221.
8) W. Bleakney: Phys. Rev. **35** (1930) 139, 1180.
9) H. D. Smyth: Rev. Mod. Phys. **3** (1931) 347.
10) H. F. Newhall: Phys. Rev. **61** (1942) 737.
11) G. Herzberg: Spectra of Diatomic Molecules, D. van Norstrand Company, Inc. (1952).
12) P. M. Morse and E. C. G. Stückelberg: Phys. Rev. **33** (1929) 932.
13) F. Möglich: Ann. Physik. **83** (1927) 609. M. Kotani: Proc. Phys. Math. Soc. Japan **14** (1933) 30. J. A. Stratton, P. M. Morse, L. J. Chu and R. A. Hunter: Elliptic Cylinder and Spheroidal wave functions, Technology Press of M. I. T. (1941).
14) G. Jaffe: Z. S. für Physik **87** (1933) 535. S. K. Chakraverty: Phil. Mag. **28** (1939) 423.
15) G. Herzberg: loc. cit. D. W. Richardson: Molecular Hydrogen and its spectra, Yale Univ. Press (1934).
16) G. Herzberg: loc. cit. H. Beutler and H. O. Junger: Z. S. für Physik **100** (1936) 80, **101** (1936) 285.
17) H. S. W. Massey and E. H. S. Burhop: Electronic and Ionic Impact Phenomena, Oxford Press. (1952).
18) J. Hargreaves: Proc. Cambr. Phil. Soc. **25** (1929) 75.

JOURNAL OF THE PHYSICAL SOCIETY OF JAPAN, Vol. 15, No. 8, AUGUST, 1960

The Binding Energy of the σ Bond, III. Discussion on the Ionic Structures

By Kiyoshi O-OHATA

Physics Department, Tokyo Institute of Technology,
O-okayama, Meguro-ku, Tokyo

(Received December 2, 1959)

The ionic terms of the σ bonds are explicitly considered by the use of the semi-localized orbitals and their contribution to the binding energy of the bond is discussed. A theoretical basis for the relation between Pauling's scale of electronegativity and Mulliken's one is given under some assumptions. The value of the binding energy of the C-C bond in the diamond crystal is computed to be 3.64 eV per bond, if the ionic terms of the bond are included. It is shown that the value of the binding energy of the diamond crystal in the Heitler-London approximation is almost equal to that in the molecular orbital method and less than the above value by about 0.4 eV per bond. The resultant state, however, is found to be rather well expressed by the Heitler-London approximation.

§1. Introduction

In the preceding papers I and II[1], we discussed mainly the binding energy of the σ bond by the use of the Heitler-London approximation, where the ionic structures were neglected. This is not adequate when we discuss the heteropolar bond. Even in the case of the homopolar bond like the C-C bond in the diamond crystal this is by no means a good approximation. Mueller and Eyring[2] proposed the semi-localized orbital method to discuss the electronic states of diatomic molecules. We shall also use this method in order to take the ionic structures of a chemical bond into account, because this method has several advantages as follows. According to this method we can describe the heteropolar bond by using the wave function involving the ionic structures adequately, can take into consideration the correlational interaction between the two electrons which are responsible for a chemical bond, and can obtain a simple formula to give the total energy.

We consider a bond A-B between the atoms A and B in a saturated molecule (we use this term to express a molecule contructed only by σ bonds) and denote the directional atomic valence orbitals of the atoms A and B as ϕ_i and ϕ_j, respectively. The orbital ϕ_i proects out from A to B and the orbital ϕ_j from B to A. The pair of orbitals (ϕ_i, ϕ_j) is n charge of the formation of the bond A-B in the Heitler-London approximation. In the semi-localized orbital method we replace the paired orbitals (ϕ_i, ϕ_j) by a pair of semi-localized orbitals (ψ_i, ψ_j). (We shall use the notation (ij) for the pair of orbitals (ψ_i, ψ_j) and it will be also used to express the corresponding bond.)

Following Eq. (2.2) in I, we get the semi-localized orbitals ψ_i and ψ_j:

$$\left.\begin{aligned}\psi_i&=\frac{1}{\sqrt{N_i}}(\phi_i+\lambda\phi_j)\,,\\ \psi_j&=\frac{1}{\sqrt{N_j}}(\phi_j+\mu\phi_i)\,,\end{aligned}\right\}\tag{1.1}$$

where $N_i=1+2\lambda S_{ij}+\lambda^2$, $N_j=1+2\mu S_{ij}+\mu^2$, S_{ij} is the overlap integral between the directional atomic valence orbitals ϕ_i and ϕ_j, and λ and μ are the parameters which are related to the inclusion of the ionic structures. The total electronic wave function Ψ of the molecule can be expressed by the use of an assembly of the pairs of the orbitals, that is,

$$\Psi:\ (ij)(kl)(pq)(st)\cdots\,,\tag{1.2}$$

where we can include not only the pairs of the valence orbitals but also the lone pairs and the pairs of the core orbitals. The parameters λ and μ may take the different values in the individual orbital pairs and their values should be determined by the minimization of the total energy. The expression for the total energy of the saturated molecule was given in I, where the total energy was expanded as a power series of the overlap integrals between the unpaired orbitals. (We have used the notation T for these overlap integrals in order to distinguish them from those between paired orbitals S.) As the exchange integrals between the unpaired orbitals are considered to be of the order of T^2, we can express the total energy of the molecule as

$$E=\frac{H_0}{\Delta_0}+\frac{H_2}{\Delta_0}-\frac{H_0\Delta_2}{\Delta_0^2}\,, \tag{1.3}$$

taking terms up to the order of T^2 into account. This equation is the same as Eq. (3.10) of I. The term H_0/Δ_0 is the zeroth order term in T and its explicit form was given by Eqs. (4.2)-(4.4) of I. The second and third terms in Eq. (1.3), which are the second order terms in T, were given by Eqs. (4.5)-(4.8) of I. The only difference from the previous case is that the orbitals involved in the molecular integrals in Eqs. (4.2)-(4.8) of I are $\psi_i, \psi_j, \cdots$ instead of $\phi_i, \phi_j, \cdots$. The formulae in § 5 of I are unable to be used, as they were deduced under the Heitler-London approximation. In the next section we shall discuss the results due to the mixing of the ionic structures of the bond. In § 3 we shall give some qualitative discussion on the heteropolar bonds. In § 4 we shall give the result of the calculation of the binding energy of the C-C bond in the diamond crystal with the inclusion of the ionic structures of the bonds. The maximum value of its binding energy has been computed to be 3.64 eV per bond at $\lambda=\mu=0.16$.

§ 2. Details of the Energy Expression

As mentioned above it is sufficient, for obtaining the binding energy of a bond by the semi-localized orbital method, to find the values of the molecular integrals in Eqs. (4.2)-(4.8) of I which involve the orbitals (1.1). We will express the energy formulae in terms of the parameters and the molecular integrals involving ϕ_i, ϕ_j, $\cdots$, to find out the effect of the ionic structures on the binding energy of a bond. Thus we express the zeroth order term H_0/Δ_0 in the total energy as follows:

$$\frac{H_0}{\Delta_0}=\sum_{(ij)}H(ij)+\sum_{\{(ij)(kl)\}}A(ij,\,kl)+\sum_{(XY)}\frac{Z_XZ_Y}{R_{XY}}, \tag{2.1}$$

with

$$\begin{aligned}H(ij)=&\frac{1}{N_{ij}}[A_iI_{ii}+A_jI_{jj}+2B_{ij}I_{ij}+(1+\lambda\mu)^2C_{ij}\\&+\{(1+\lambda\mu)^2+4\lambda\mu\}K_{ij}+2\lambda^2C_{jj}+2\mu^2C_{ii}+4(1+\lambda\mu)(\lambda D_{j,ij}+\mu D_{i,ij})\,,\\A(ij,\,kl)=&\frac{1}{N_{ij}N_{kl}}[A_iA_kC_{ik}+A_jA_kC_{jk}+A_iA_lC_{il}+A_jA_lC_{jl}\\&+2B_{ij}(A_kD_{k,ij}+A_lD_{l,ij})+2B_{kl}(A_iD_{i,kl}+A_jD_{j,kl})\\&+4B_{ij}B_{kl}N_{ij,kl}]\,,\end{aligned} \tag{2.2}$$

where

$$\left.\begin{aligned}&N_{ij}=N_iN_j+R_{ij}^2,\quad A_i=N_i\mu^2+2R_{ij}\mu+N_j\,,\\&A_j=N_j\lambda^2+2R_{ij}\lambda+N_i,\quad B_{ij}=N_i\mu+N_j\lambda+R_{ij}(1+\lambda\mu)\,,\end{aligned}\right\}$$

and

$$R_{ij}=\lambda+\mu+(1+\lambda\mu)S_{ij}\,, \tag{2.3}$$

The other notations represent the molecular integrals with respect to the atomic orbitals and were already defined by Eq. (4.4) of I. With Mulliken's notation they are expressed as

$$\left.\begin{aligned}&I_{ij}=(\phi_i|h|\phi_j)\,,\quad C_{ij}=(\phi_i\phi_i;\ \phi_j\phi_j)\,,\quad K_{ij}=(\phi_i\phi_j;\ \phi_i\phi_j)\,,\\&D_{k,ij}=(\phi_k\phi_k;\ \phi_i\phi_j)\,,\quad N_{ij,kl}=(\phi_i\phi_j;\ \phi_k\phi_l)\,,\quad S_{ij}=(\phi_i|\phi_j)\,,\end{aligned}\right\} \tag{2.4}$$

where h denotes the part of the total Hamiltonian depending on only one electron. The summations $\sum\limits_{(ij)}$ and $\sum\limits_{\{(ij),(kl)\}}$ in Eq. (2.1) extend over all the orbital pairs and all the pairs of orbital pairs, respectively. The last term in Eq. (2.1) represents the repulsive potentials between the constituent nuclei.

There is a relation among the coefficient (2.3) as follows:

$$2N_{ij}=A_i+A_j+2S_{ij}B_{ij}\,, \tag{2.5}$$

Using this relation and assuming the Mulliken approximation (5.6) of I for the estimation of the values of the many center energy integrals, we obtain from Eq. (2.1)

$$\frac{H_0}{\varDelta_0}=\sum E_A{}^*+\sum_{(ij)}F_{ij}(AB)+\sum_{(ij)}P(ij)+\sum_{\{(ij)(kl)\}}R(ij,\,kl)+G \tag{2.6}$$

with

$$\begin{aligned}F_{ij}(AB)=&\frac{1}{2}\,\frac{A_i+A_j}{N_{ij}}\,(V_{ii}{}^B+\sum_{b\neq j}{}' C_{ib}+V_{jj}{}^A+\sum_{a\neq i}{}' C_{ja})\\&+\frac{1}{N_{ij}}\,[(1+\lambda\mu)^2C_{ij}+\{(1+\lambda\mu)^2+4\lambda\mu\}K_{ij}\\&+(\lambda^2+\mu^2)(C_{ii}+C_{jj})+2(\lambda+\mu)(1+\lambda\mu)(D_{i,ij}+D_{j,ij})]\\&+\frac{2B_{ij}}{N_{ij}}\{I_{ij}{}^{AB}+\sum_{a\neq i}{}' D_{a,ij}+\sum_{b\neq j}{}' D_{b,ij}\}+\sum_{a\neq i}{}' V_{aa}{}^B+\sum_{b\neq j}{}' V_{bb}{}^A\\&+\frac{1}{2}\sum_{a\neq i}{}'\sum_{c\neq j}{}' C_{ab}+V_{AB}-\frac{S_{ij}B_{ij}}{N_{ij}}(\varepsilon_i{}^A+\varepsilon_j{}^B)\,,\end{aligned} \tag{2.7}$$

$$P(ij)=\frac{1}{2}\,\frac{A_i-A_j}{N_{ij}}\,(\chi_i-\chi_j)\,, \tag{2.8}$$

$$R(ij,\,kl)=\frac{1}{4}\,\frac{A_i-A_j}{N_{ij}}\,\frac{A_k-A_l}{N_{kl}}(C_{ik}-C_{jk}-C_{il}+C_{jl})\,, \tag{2.9}$$

and

$$G=\sum_{(AC)}Q(AC)\,, \tag{2.10}$$

where the notations are almost the same as those defined in I, that is, $V_{ij}{}^B=(\phi_i|\,V^B|\phi_j)$, $I_{ij}{}^{AB}=(\phi_i|-\frac{1}{2}\varDelta+V^A+V^B|\phi_j)$, V^A and V^B are the core potentials of the atoms A and B, respectively, the subscripts a and b denote the atomic orbitals of the atoms A and B, respectively, the summations $\sum\limits_a{}'$ and $\sum\limits_b{}'$ extend over all the valence orbitals of the atoms A and B other than the orbitals ϕ_i and ϕ_j, respectively, and V_{AB} represents the interaction energy between the atomic cores A and B. The intra-atomic exchange integrals are involved in Eq. (2.6), since these integrals are considered to be the zeroth order terms in T. Then the quantity $E_A{}^*$ represents the total energy of the valence state of the atom A, and the quantity $-\varepsilon_i{}^A$ denotes the ionization potential for the orbital ϕ_i of the atom A. The quantity χ_i is expressed as

$$\chi_i=\varepsilon_i{}^A+\frac{1}{2}\,C_{ii}+\sum_X{}'\,\{V_{ii}{}^X+\sum_x C_{ix}\}\,, \tag{2.11}$$

where the summation $\sum\limits_X{}'$ extends over all the constituent atoms of the molecule other than the atom A and the summation $\sum\limits_x$ extends over all the valence orbitals of the atom X. We have assumed the approximate relations $D_{j,ij}=\frac{1}{2}S_{ij}(C_{ii}+C_{ij})$ and $D_{j,ij}=\frac{1}{2}S_{ij}(C_{ij}+C_{jj})$ in order to derive Eq. (2.11). As we may assume that the term $\sum\limits_X{}'\,\{V_{ii}{}^X+\sum\limits_x C_{ix}\}$ in Eq. (2.11), which represents the contribution from the neutral atoms, is small enough to be neglected, we consider that the quantity $-\chi_i$ represents the electronegativity with respect to ϕ_i of the atom A in Mulliken's scale. The term $Q(AC)$ which represents the interaction energy between the atoms A and C is defined by

$$Q(AC)=\sum_a V_{aa}{}^C+\sum_b V_{cc}{}^A+\frac{1}{2}\sum_a\sum_c C_{ac}+V_{AC}\ , \tag{2.12}$$

where the summations $\sum\limits_a$ and $\sum\limits_c$ extend over all the valence orbitals of the atoms A and C, respectively, and the summation $\sum\limits_{(AC)}$ in Eq. (2.10) is taken over all the pairs of the second or more remote neighbours.

According to Eq. (2.6), we can define the binding energy $D_0(AB)$ of the bond A-B in the zeroth order approximation as

$$D_0(AB)=F_{ij}(AB)+P(ij)+\frac{1}{2}\sum_{(kl)\neq(ij)}{}' R(ij,\ kl)+G'+U\ , \tag{2.13}$$

with

$$G'=\sum_C\frac{1}{n_A+n_C}Q(AC)+\sum_D\frac{1}{n_B+n_D}Q(BD)\ ,$$

$$U=\frac{1}{n_A}(E_A{}^*-E_A)+\frac{1}{n_B}(E_B{}^*-E_B)\ ,$$

where the terms G' and U are the same as those defined in §6 of I, n_A is the total number of the valence orbitals of the atom A, the summation $\sum\limits_C$ extends over the atoms which are not directly bonded to the atom A, E_A is the atomic energy of the ground state of the atom A, $E_A{}^*-E_A$ is the promotional energy from the ground state to the valence state in the atom A, and so on.

Next, we shall discuss the energy terms in the second order approximation. They are $H_2/\varDelta_0-H_0\varDelta_2/\varDelta_0{}^2$ in Eq. (1.3) and expressed as

$$H_2/\varDelta_0-H_0\varDelta_2/\varDelta_0{}^2=-\frac{1}{2}\sum_{[(ij)(kl)]}J(ij,\ kl) \tag{2.14}$$

with

$$\begin{aligned}J(ij,\ kl)=B(ij,\ kl)-\varDelta(ij,\ kl)[&H(ij)+H(kl)\\&+A(ij,\ kl)+\sum_{(pq)}{}''\{A(ij,\ kl)+A(kl,\ pq\}]\ ,\end{aligned} \tag{2.15}$$

where $B(ij,\ kl)$ has a rather complicated expression as shown by Eq. (4.6) of I and will not be written here again. The summation $\sum\limits_{(pq)}{}''$ in Eq. (2.15) is taken over all the bonds other than the bonds (ij) and (kl). $\varDelta(ij,\ kl)$ which represents the effect of the non-orthogonality between the bonds (ij) and (kl) is expressed as

$$\begin{aligned}\varDelta(ij,\ kl)=\frac{1}{N_{ij}N_{kl}}\{&A_iA_kT_{ik}{}^2+A_jA_kT_{jk}{}^2+A_iA_lT_{il}{}^2+A_jA_lT_{jl}{}^2\\&+2B_{ij}(A_kT_{ik}T_{jk}+A_lT_{il}T_{jl})+2B_{kl}(A_iT_{ik}T_{il}+A_jT_{jk}T_{jl})\\&+2B_{ij}B_{kl}(T_{ik}T_{jl}+T_{il}T_{jk})\}\ ,\end{aligned}$$

where T_{ik} is the overlap integral between the atomic orbitals ϕ_i and ϕ_k and so on. We can easily rewrite the expression of $\varDelta(ij,\ kl)$, deviding it into the terms with the even or odd symmetry with respect to the interchange of λ and μ:

$$\begin{aligned}\varDelta(ij,\ kl)=&q_{ij}q_{kl}(T_{ik}{}^2+T_{jk}{}^2+T_{il}{}^2+T_{jl}{}^2)+2B_{ij}q_{kl}(T_{ik}T_{jk}+T_{il}T_{jl})\\&+2B_{kl}q_{ij}(T_{ik}T_{il}+T_{jk}T_{jl})+2B_{ij}B_{kl}(T_{ik}T_{jl}+T_{il}T_{jk})\\&+p_{ij}p_{kl}(T_{ik}{}^2-T_{jk}{}^2-T_{il}{}^2+T_{jl}{}^2)+2B_{ij}p_{kl}(T_{ik}T_{jk}-T_{il}T_{jl})\\&+2B_{kl}p_{ij}(T_{ik}T_{il}-T_{jk}T_{jl})\ ,\end{aligned}$$

where $q_{ij}=(A_i+A_j)/2N_{ij}$, $p_{ij}=(A_i-A_j)/2N_{ij}$, and so on. The quantities q_{ij} and p_{ij} have the even and odd symmetry with respect to the interchange of λ and μ, respectively. The term $B(ij, kl)$ in Eq. (2.15) can be shown to have the similar expression as $\Delta(ij, kl)$, as that term comes mainly from the overlap between unpaired orbitals. As seen from Eq. (2.17), we can expect that the odd part of $B(ij, kl)$ and $\Delta(ij, kl)$ gives a rather small contribution to the binding energy, since the terms appearing in this part cancel each other.

The contribution of the second order terms, $-\frac{1}{4}\sum_{\{(ij)(kl)\}} J(ij, kl)$, to the binding energy of a bond should be added to Eq. (2.13), if we take terms up to the second order in T into account. We here note, however, that we must subtract the terms of the intra-atomic exchange integral,

$$\left(1-\frac{S_{ij}B_{ij}}{N_{ij}}-\frac{S_{kl}B_{kl}}{N_{kl}}+p_{ij}+p_{kl}\right)K_{jk}$$

from $J(ij, kl)$, if the two bonds (ij) and (kl) are adjacent and ϕ_j and ϕ_k are the atomic orbitals of the same atom.

§ 3. Consideration about the Pauling Scale of Electronegativity

Considering the relation (2.5) among the coefficients (2.3), we may interpret that the quantities A_i/N_{ij} and A_j/N_{ij} are the charge densities of the atoms A and B, respectively, and the quantity $2S_{ij}B_{ij}/N_{ij}$ is the charge density in the overlap region due to the bond (ij). Then, the quantity p_{ij} represents the amount of charges in the bond (ij) which are transferred from the atom B to the atom A. In the expression of the binding energy of a bond, the terms involving the coefficient p_{ij} are $P(ij)$, $R(ij, kl)$ and a part of $J(ij, kl)$. If we assume that the contribution from $R(ij, kl)$ is small enough to be neglected, we can interpret that $P(ij)$ is the extra binding energy for the bond (ij) due to the polarity of the bond. As shown later, the assumption holds at a large inter-bond separation. If we assume that the homopolar part of the binding energy of the bond A-B is replaced by the additive mean of the binding energies of the bond A-A and B-B, we may assume that $-P(ij)$ is the "extra ionic resonance energy" given by Pauling.[3] Then we get the expression

$$-P(ij)=(x_A-x_B)^2\ , \qquad (3.1)$$

where x_A and x_B are the electronegativities of the atoms A and B in the Pauling scale, respectively. On the other hand, $-\chi_i$ is approximately equal to the electronegativity of the atom A in the Mulliken scale, as mentioned in the preceding section. According to Mulliken's discussion,[4] $-\chi_i$ may be a little smaller than the electronegativity X_A of the atom A in the Mulliken scale, that is, $-\chi_i=cX_A$, where $c\simeq 0.7$. According to the physical meaning of the Mulliken scale of electronegativity, it may be reasonable to assume p_{ij} proportional to (X_A-X_B). From Eq. (2.8), we get the relation

$$-P(ij)=-p_{ij}(\chi_i-\chi_j)=c\gamma(X_A-X_B)^2\ , \qquad (3.2)$$

where γ is the proportionality factor between p_{ij} and (X_A-X_B). From Eqs. (3.1) and (3.2), we obtain the linear relation between the two scales of electronegativity which are given by Pauling and Mulliken independently:

$$x_A-x_B=\sqrt{c\gamma}(X_A-X_B)\ . \qquad (3.3)$$

From the results of the measurement of eQq, Gordy[5] gave an empirical relation

$$p_{ij}=\frac{1}{2}(x_A-x_B)\ ,$$

from which we get $\gamma=c/4$. Thus, we have the relation

$$x_A-x_B=\frac{c}{2}(X_A-X_B)\simeq 0.35(X_A-X_B)\ .$$

This agrees excellently well with the empirical rule:

$$x_A-x_B=0.36(X_A-X_B)\ .$$

Similar discussion was given by Mulliken[4] with the use of the molecular orbital method. His theory is, however, applicable only when the atoms A and B are rather similar atoms, since the energies of the molecular orbitals are given as a power series of the ratio of the difference of the Coulomb integral for the atomic orbital ϕ_i from that of ϕ_j to the resonance integral between them.

The term $R(ij, kl)$ which represents the interaction energy between the polar bonds may give the so called inductive effect. This term will decrease rather rapidly with increase of the separation between the bonds (ij) and (kl), because the Coulomb integrals appearing in the expression (2.9) of $R(ij, kl)$ cancel each other. There are, of course, the terms depending on both of the coefficients p_{ij} and p_{kl} in the second order term $J(ij, kl)$, but the magnitudes of these terms will also decrease rapidly with increase of the separation between the bonds (ij) and (kl). This may be seen from the corresponding terms in $\Delta(ij, kl)$ of Eq. (2.17).

§ 4. Application to the C-C Bond in the Diamond Crystal

We here consider the application of the present method to the C-C bond of the diamond crystal, in which the individual bonds are homopolar and equivalent. Then, we can put $\lambda=\mu$ in the wave functions (1.1). Each carbon atom in the diamond crystal has four equivalent valence orbitals. Each bond has six nearest neighbour bonds and eighteen second nearest neighbour bonds in which twelve bonds locate at the gauche positions and other six bonds at the trans positions. Considering the above facts, the expression for the binding energy of a bond is derived from Eq. (2.13) with including the second order term as

$$\begin{aligned} D(AB)=F_{ij}(AB)+\frac{1}{8}\{\sum_C Q(AC)+\sum_D Q(BD)\} \\ -\frac{3}{2}J(ij,\ kl)-3J(ij,\ st) \\ -\frac{3}{2}J(ij,\ pq) \\ +\frac{1}{4}\{E_A{}^*-E_A)+(E_B{}^*-E_B)\}\ , \end{aligned}$$

where the summations $\sum_C$ and $\sum_D$ are taken only over the second nearest neighbour atoms from the atoms A and B, respectively, because of smallness of the contribution from the more remote neighbours, (kl) is an adjacent bond of the bond (ij), (st) is the second nearest neighbour bond at gauche position for the bond (ij), and (pq) is the one at the trans position. In Eq. (4.1), we neglected the second order terms owing to the third nearest or more remote neighbour bonds, since their effect will be small enough to be neglected. Following the scheme of calculation as in II, the value of $D(AB)$ is obtained as a function of the parameter λ. The result is shown in Fig. 1. From this figure we find 3.92 eV as the binding energy of the C-C bond in the diamond crystal and the optimum value of λ is 0.16. It is also shown in this figure that the value of the binding energy of the bond in the Heitler-London approximation ($\lambda=0$) is almost equal to that in the molecular orbital one ($\lambda=1$), and they are less than the resultant value of the binding energy by about 0.4 eV per bond. This value can be interpreted as the ionic effect from the point of view in the Heitler-London scheme and as the correlational effect from that in the molecular orbital scheme. Furthermore, in our calculation we found that the second order terms are scarcely influenced by the inclusion of the ionic terms and the minimum point in Fig. 1 is almost determined by the zeroth order terms. The effect of the non-orthogonality between a valence orbital of one atom and a core orbital of another atom in the semi-localized orbital method, which is almost equal to that in the Heitler-London approximation, reduces the binding energy by about 0.28 eV per bond. Finally we obtain 3.64 eV per bond as the approximate binding energy of the C-C bond in the diamond crystal.

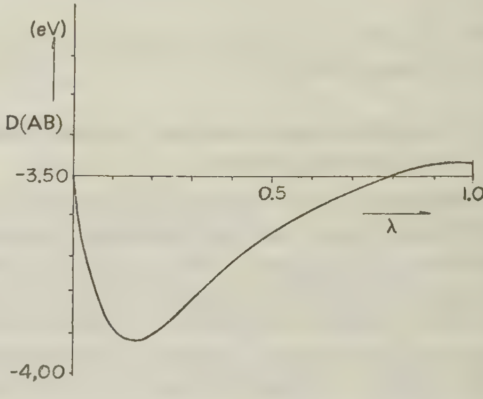

Fig. 1. The variation of the value of $D(AB)$ with λ for the C–C bond in the diamond crystal.

§ 5. Conclusion

We discussed the ionic structure of the σ bond with the use of the semi-localized orbital method, for this method has several advantages as mentioned in § 1, and so can extract the contribution of the ionic structures on the binding energy in a simple manner. We, hen, found an interesting fact that the difference between the electronegativities of he atoms A and B in the Mulliken scale is found in the expression of the binding energy of the bond A-B in connection with the polarity of this bond. Under the assumptions mentioned in § 3, it was shown that we can find theoretically the relation between the scale of electronegativity given by Pauling and that given by Mulliken. We also obtained a qualitative interpretation for the rapid decreasing of the inductive effect with increasing the separation between the bonds. We, however, postpone the quantitative discussion on the heteropolar bonds.

We calculated the binding energy of the C-C bond in the diamond crystal with including the ionic structures of the bonds. We found that the maximum value of the binding energy of the bond was 3.64 eV per a bond and the corresponding value of λ was 0.16. The calculated value of the binding energy of the C-C bond is in good agreement with the experimental one 3.716 eV per bond.$^{6)}$ From the best value of λ it is found that the resultant wave function is rather well expressed by the Heitler-London approximation. This result is different from that given by Schmid$^{6)}$ who concluded the molecular orbital approximation to be almost near to the best. Our criticism against Schmid's calculation was already cited in § 4 of II. Our calculation shows that the correlational effect on the binding energy neglected in the molecular orbital scheme is about 0.4 eV per bond, that is, 0.8 eV per atom in the diamond crystal.

The author wishes to express his sincere thanks to Professor K. Niira for his incessant encouragement and for his kind reading of the article. The author is indebted to the Ministry of Education for the research grant.

References

1) K. O-ohata: J. Phys. Soc. Japan, 15 (1960), 1048.
2) C. R. Mueller and H. Eyring: J. Chem. Phys. **19** (1951), 1495.
3) H. O. Pritchard and H. A. Skinner: Chem. Rev. **55** (1955), 745.
4) R. S. Mulliken: J. de Chim. Phys. **46** (1946), 497, 675.
5) W. Gordy, W. V. Smith and R. F. Trambarulo: *Microwave Spectroscopy*, (John Wiley and Sons, Inc., 1953), p. 284.
6) L. A. Schmid: Phys. Rev. **92** (1953), 1373.

Journal of the Physical Society of Japan, Vol. 15, No. 7, August, 1960

On the Effect of Heat Treatment in a Magnetic Field on Magnetic Properties of Iron-Aluminium Alloys

By Makoto Sugihara

The Electrical Communication Laboratory, Nippon Telegraph and Telephone Public Corporation, Tokyo, Japan

(Received December 14, 1959)

When the specimens of iron-aluminium alloys were cooled in a magnetic field from high temperatures, the percent increase of initial permeability is generally not large, but that of maximum permeability is considerably large and it has a maximum at the concentration of 10.20 percent aluminium. The effect of heat treatment in a magnetic field is small for the concentration of more than 11.5 percent aluminium. When the quenched specimen of 10.20 percent aluminium was annealed again at various temperatures in a magnetic field and cooled in the field, the lowest effective temperature of heat treatment in a field becomes about 225~250°C. This temperature is 100°C lower than the usual lowest effective temperature for the specimen without quenching. Maximum permeability of the specimen which was quenched at first and heat treated at about 250°C in a magnetic field reaches to the highest value of about 30,000.

1. Introduction

Masumoto and Saitō[1] studied the effect of heat treatment on alloys containing up to 17 percent aluminium and found the maximum and initial permeabilities, the coercive force, and the residual induction are sensitive to cooling rate, especially in the neighbourhood of 14 16 percent aluminium. The highest permeabilities were obtained with the alloys containing about 16 percent aluminium that were quenched from 600°C. These alloys were named Alperm. The alloy containing about 13 percent aluminium that has high magnetostriction, was named Alfer. Alperm was noticeable as a new magnetic material at that time, since its specific resistance was 140 $\mu\Omega$–cm and it did not contain the expensive material, such as nickel or cobalt. The questions of manufacturing, however, could not be settled at that time. Afterwards, Nachman and Buehler[2] reported that the alloy containing about 16 percent aluminium can be rolled to 0.01 mm in thickness at room temperature after it has been rolled to about 0.1 mm at about 575°C.

In the range of solid solubility, 0–32 percent aluminium, two types of superstructure are formed. They are designated Fe_3Al and FeAl corresponding to 13.9 and 32.6 percent aluminium by weight. Saitō[3] reported that an other phase than the two phases mentioned above should exist in the alloy containing about 10 percent aluminium, considering from the variation of electrical resistance and specific heat with temperature. Saitō supposed that this phase is a superlattice $Fe_{13}Al_3$ (10.03 percent aluminium). Recently, Taylor and Jones[4] reported that this phase exists, as a result of X-ray analysis.

Arrott and Sato[5] reported the alloys above 19.2 percent (33 atomic percent) aluminium exhibit antiferromagnetism and those below 15.8 percent (28 atomic percent) aluminium are ferromagnetic. They also found that between 15.8 and 19.2 percent aluminium, the behaviour is ferromagnetic at room temperature but shows a transition to Antiferromagnetism on lowering the temperature, and the antiferromagnetism exists only in the ordered structures.

These investigations make our attention again direct to this alloy. Recently, Nachman and Buehler[6], and the author[7] found that the initial and maximum permeabilities of the alloys containing about 12 percent aluminium are very high in an annealed state. The present paper reports the result of the further study on these alloys especially on the effect of heat treatment in a magnetic field on the permeability and hysteresis loop of the alloys.

§ 2. Specimens and Experimental Methods

Specimens were prepared by induction melting in vacuum from electrolytic iron (99.9%) and pure aluminium (99.99%) were used for the preparation of the alloys. One part of each cast was hot roll-forged to prepare a square-rod specimen (about 2 mm square and 50 cm in length), and the other part was hot rolled to about 0.8 mm in thickness in order to prepare a ring-shape specimen (27 mm in outer diameter, 19 mm in inner diameter).

All the specimens were first annealed at 1000°C for 1 hour and then furnace cooled in vacuum. Subsequent various heat treatments were applied thereafter.

The measurement of magnetization was made at room temperature by a usual ballistic method for the rod specimens and by a recording flux meter for the ring-shape specimens. Before each measurements, the specimens were always demagnetized with a.c. field.

§ 3. Experimental Results

The rod specimens were heated in vacuum in a non inductive electric furnace at 800°C for 30 minutes, cooled to 120°C at the rate of 150°C per hour without a magnetic field or under an application of longitudinal magnetic field with the strength of 12.5 Oe and then furnace cooled to room temperature. The results of measurement on the initial and maximum permeabilities of these specimens are given in Fig. 1 together with those of the specimens quenched in water from 600°C. As is shown in the figure, in a case of initial permeability, the values are not so different between the two slow cooled specimens with and without a magnetic field, whereas, in the case of maximum permeability, the values are quite different and the values with a magnetic field have a maximum in the vicinity of 10 percent aluminium as already reported by the author[7].

Fig. 2 shows the magnetization curves and the hysteresis loops of the ring-shape specimens of seven alloys containing about 5–12 percent aluminium. Curve (a) indicates the case that each specimen was heated at 800°C in vacuum in a non inductive electric furnace for 30 minutes and cooled without a field. Curve (b) indicates the case that each specimen heat treated as mentioned above was reheated to 550°C and furnace cooled in a circular magnetic field with the strength of 12 Oe. It had been known from the other preliminary experiment, that such a strength of magnetic field is sufficient for the effect. Fig. 3 shows the variation of initial and maximum permeabilities with composition. In this case also, the permeability of the alloy containing 10.20 percent aluminium was increased most remarkably by heat treatment in a field. The minimum of coercive force is also obtained with the alloy containing 10.20 percent aluminium. In this case, we found that the maximum permeability of the alloy of 12.12 percent aluminium decreases extremely after the second heat treatment in a magnetic field.

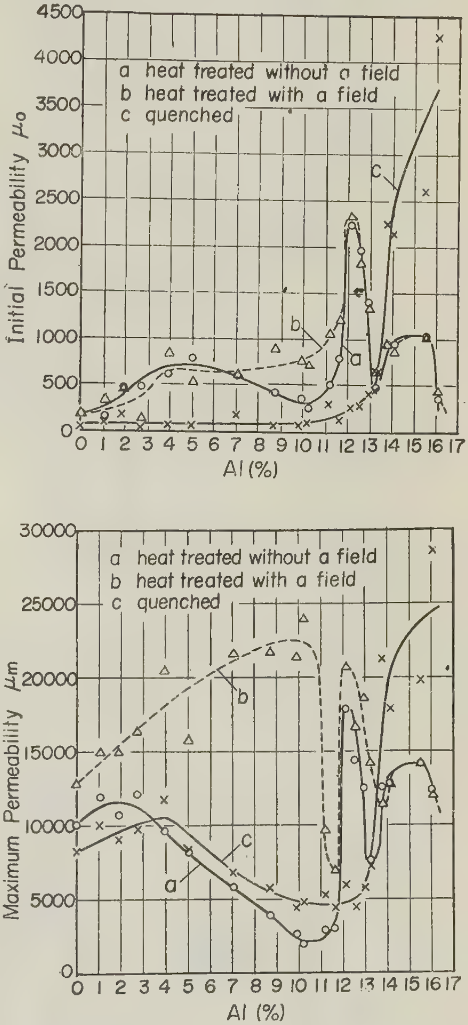

Fig. 1. Initial and maximum permeabilities of the rod specimens of iron-aluminium alloys with different heat treatment.

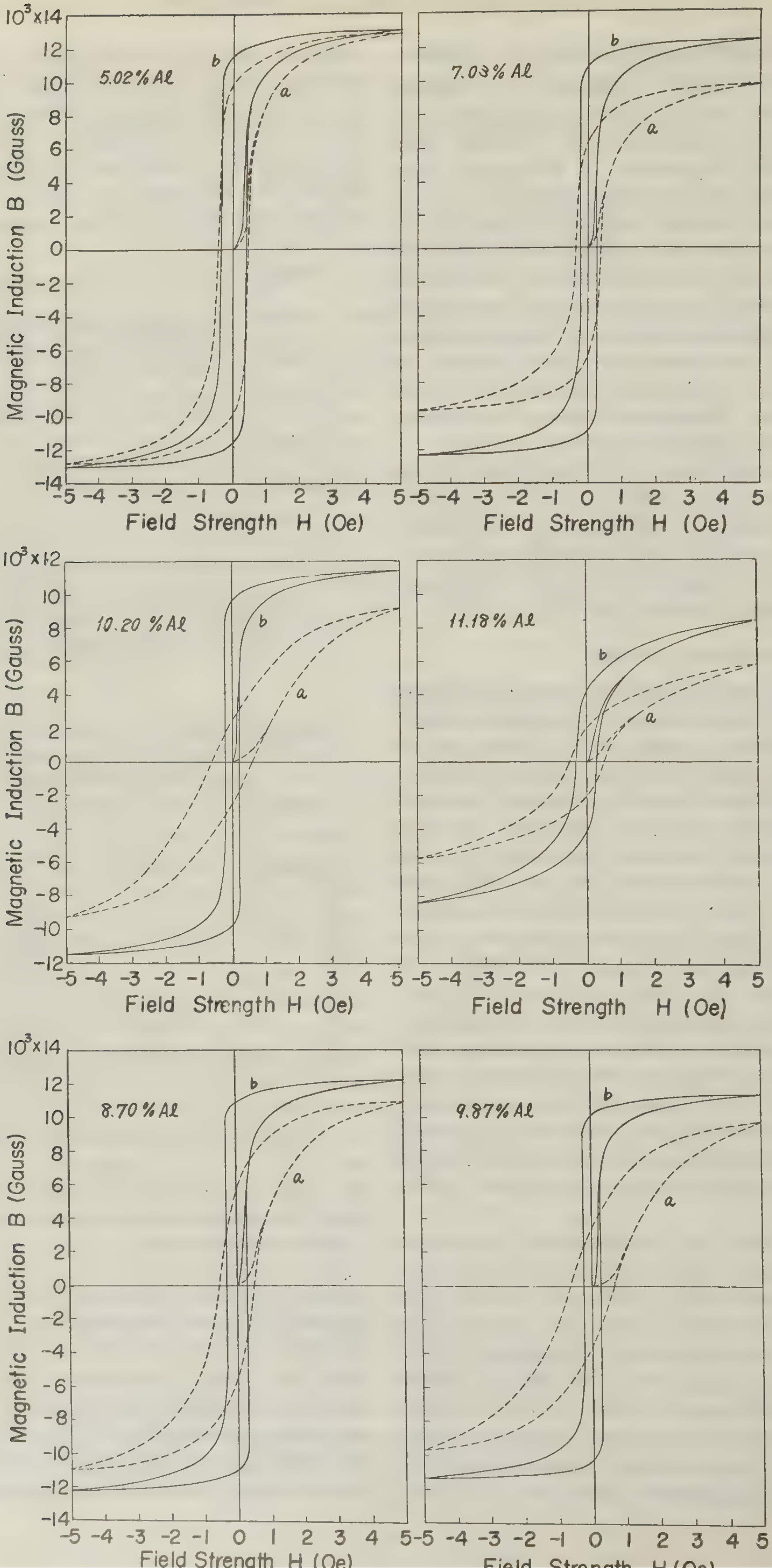
5.02% Al
7.03% Al
10.20 % Al
11.18% Al
8.70 % Al
9.87% Al
a
b
10³×14
10³×12
Magnetic Induction B (Gauss)
Field Strength H (Oe)
-5 -4 -3 -2 -1 0 1 2 3 4 5

From Figs. 1~3, it is concluded that the change of permeability and hysteresis loop by heat treatment in a field is most remarkable at the concentration of about 10 percent of aluminium. The following experiment was made mainly on the rod specimen of containing 10.20 percent aluminium. The relation between the permeability at room temperature and the temperature at which the magnetic field was first applied was observed for three different procedures. At first the specimen was cooled from 800°C at the rate of 150°C per hour and the magnetic field of 12.5 Oe was applied from various temperatures of the cooling. Curves (a) in Figs. 4 and 5 show the result.

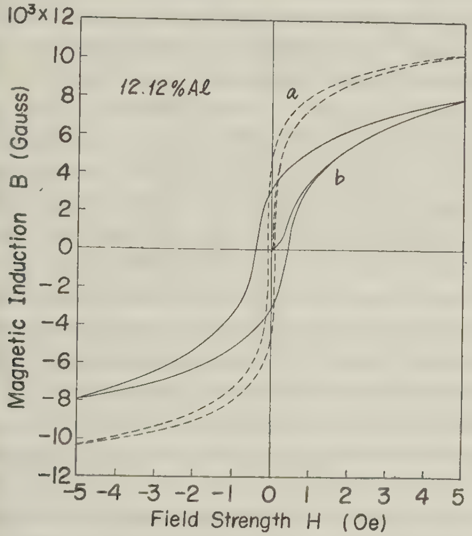

Fig. 2. Magnetization curves and hysteresis loops of the ring-shape specimens of several iron-aluminium alloys heat treated without or with a field.

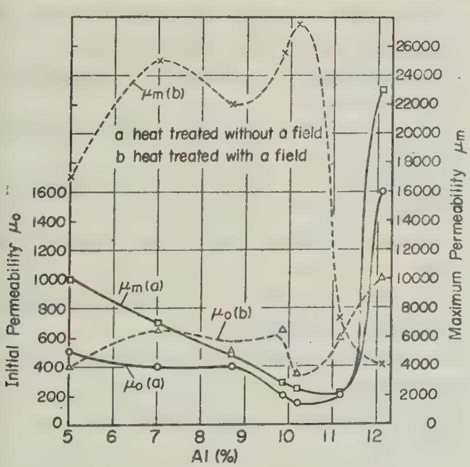

Fig. 3. Initial and maximum permeabilities of the ring-shape specimens of seven iron-aluminium alloys heat treated without or with a field.

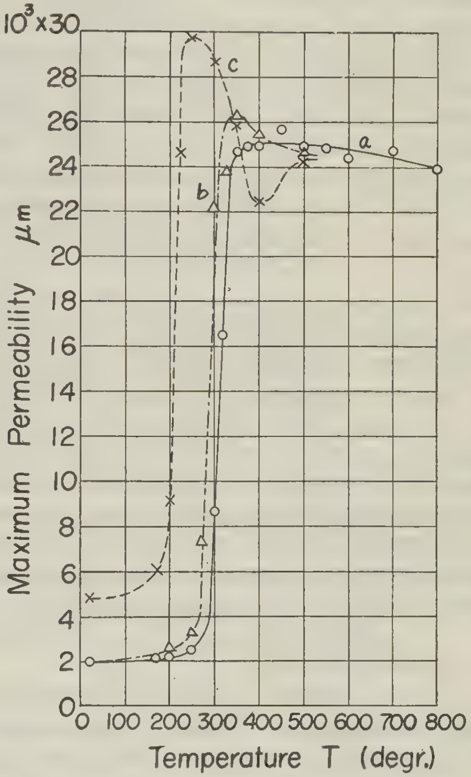

Fig. 4. Relation of maximum permeability (μ_m) of the specimen containing 10.20 percent aluminium to the temperature (T) from which a magnetic field was applied.

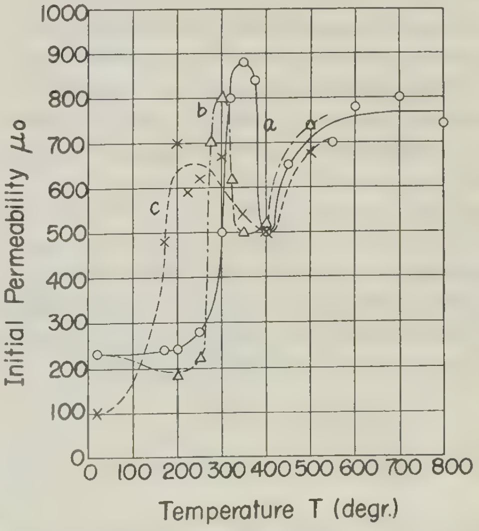

Fig. 5. Relation of initial permeability (μ_0) of the specimen containing 10.20 percent aluminium to the temperature (T) from which a magnetic field was applied.

Next the specimen which was first cooled from 800°C at the rate of 150°C per hour without a magnetic field was again inserted into the furnace at various temperatures and with a magnetic field, kept 30 minutes and cooled with the field at the rate of 150°C per hour. Curves (b) in Figs. 4 and 5 show the result. Lastly the specimen was first quenched from 600°C during cooling from 800°C, and the procedure identical to the case (b) followed. The result is shown by curves (c) in Figs. 4 and 5.

In Fig. 4, remarkable decreases in the maximum permeability μ_m are seen in the temperature range from 200°C to 320°C and the critical temperature is appreciably lower for curve (c). The maximum value of about 30,000 for curve (c) at $T=250$°C is the largest value of the maximum permeability in this study. In Fig. 5, considerably sharp maxima are observed in curves (a) and (b), and the corresponding temperatures are 350°C and 300°C for curves (a) and (b) respectively.

§ 4. Short Discussion

It is first pointed out in Fig. 4 that the effective temperature range of the magnetic field annealing is extended to 250∼225°C for the quenched specimen and the maximum permeability reaches its maximum value at this temperature range. This result will show that the most available effect of heat treatment in a magnetic field is present when the magnetic field is applied to the alloy that is recovering slowly from the quenched state. It is remarkable that such an large effect of heat treatment in a magnetic field is present at a comparatively low temperature range, ∼250°C.

In both curves (a) and (b) in Fig. 5, maximum values of initial permeability μ_0 are obtained by critical heat treatments in a magnetic field. This phenomenon is analogous to the one that was found in 65 permalloy and 45 25 perminvar by the author[8]. It is also interesting that a maximum value of μ_0 of iron-aluminium alloys was obtained when the heat treatment in a magnetic field was set up from the temperature at which the effect of this treatment on μ_m decreases rapidly.

§ 5. Summary

The permeabilities of vacuum melted ferromagnetic iron-aluminium alloys were measured and the relation of permeabilities to concentration of aluminium was also investigated for specimens heat treated with and without a magnetic field. In the concentration range of about 5 to 11 percent aluminium, the maximum permeability was increased and the hysteresis loop became rectangular after the heat treatment in a magnetic field. The change in these properties by heat treatment in a field was most remarkable at the concentration of about 10 percent aluminium, and the maximum permeability increased to 10–11 times as large as in the annealed state.

In conclusion the author wishes to express his hearty thanks to Dr. Y. Shichijō, the chief of the magnetic material research section of the Electrical Communication Laboratory, for encouragement.

References

1) H. Masumoto, H. Saitô, Sci. Rep. RITU **A 3** (1951), 523; **A 4** (1952), 321; 338.
2) J. F. Nachman, W. J. Buehler, J. Appl. Phys. **25** (1954), 307.
3) H. Saitō, Nippon Kinzoku Gakkai-Shi **B 14** (1950), No. 5, 6.
4) A. Taylor, R. M. Jones, J. Phys. Chem. Solids **6** (1958), 16.
5) A. Arrott, H. Sato, Phys. Rev. **114** (1959), 1420.
6) J. F. Nachman, W. J. Buehler, NAVORD Report 4130, (1955).
7) M. Sugihara, Reports of the E.C.L. NTT **7** (1959), 333.
8) M. Sugihara, Sci. Rep. Tôhoku Univ. (1) **41** (1958), 221.

JOURNAL OF THE PHYSICAL SOCIETY OF JAPAN, Vol. 15, No. 8, AUGUST, 1960

Magnetic Anisotropy of Iron-Cobalt Ferrite measured by Ferromagnetic Resonance

By Yoshikazu SUGIURA

Electrotechnical Laboratory, Nagata-cho, Tokyo, Japan

(Received February 6, 1960)

The magnetic anisotropy of iron-cobalt ferrite is studied by means of ferromagnetic resonance. The cubic magnetic anisotropy K_1/M and the uniaxial magnetic anisotropy K_T/M induced by heat treatment in magnetic field are measured in the temperature range between 70°C and 250°C.

The secondary peak observed in the ferromagnetic resonance of iron-cobalt ferrite are explained by the domains having different orientation of uniaxial magnetic axis. From the experimental results g-factor of iron-cobalt ferrite is determined to be 2.86. The temperature dependence of g-factor has not been observed within limits of errors.

§ 1. Introduction

Numerous investigations have recently been made on single crystals of cobalt ferrite. It is well known that cobalt ferrite has a positive cubic magnetic anisotropy of large magnitude and exhibits a uniaxial magnetic anisotropy by heat treatment in magnetic field(1),(2),(3),.

The magnetic anisotropy of cobalt-substituted magnetite single crystals was measured by Bickford *et al*(4) and the origin of its magnetic anisotropy was explained by Slonczewski(5), considering the spin-orbit coupling energy of divalent cobalt ions placed in the crystal electric field of trigonal symmetry.

However, up to date, there have not been enough experiments for the mechanism of magnetic anisotropy of cobalt ferrite to be cleared. Especially, the temperature dependence of the uniaxial magnetic anisotropy constant has not been measured.

The ferromagnetic resonance of cobalt ferrite cannot be observed at room temperature by an ordinary method because of its large anisotropy energy, and its observations have been made only at elevated temperature at 24 KMc or higher frequencies(6). The resonance line is not simple, but secondary peaks are observed. Artman(7) suggested that the secondary peaks could be explained by the effect of unsaturated magnetization.

Our purposes are to show (1) how uniaxial magnetic anisotropy induced by magnetic annealing and cubic magnetic anisotropy of $Co_{0.8}Fe_{2.2}O_4$ depend on temperature and (2) whether secondary peaks of resonance lines can be explained by the domains having different orientations of uniaxial magnetic anisotropy, with results of ferromagnetic resonance observed at temperatures between 70°C and 250°C, using single crystals of the material with or without magnetic annealing.

§ 2. Experiment

The single crystals of iron-cobalt ferrite used for the measurement of ferromagnetic resonance are the same one reported by Sawaguchi *et al*(8), which are grown from the melt in a platinum crucible in air, using borax as flux. The composition was determined by chemical analysis as $Co_{0.8}Fe_{2.2}O_4$. The single crystals having regular shapes of octahedron of about 0.5 mm in side were selected.

A typical microwave transmission technique at 24.4 KMc is applied to measure the ferromagnetic resonance. The cavity used is that of TE_{109} mode, constructed of rectangular waveguide. As shown in Fig. 1, a mica plate is inserted in the middle point of the cavity to insulate thermally the lower part of the cavity from the upper. Chromel wires insulated with mica plates and glass ribbons are wound around the cavity to act as a furnace. In this way the temperature of the specimen is changed from room temperature to about 250°C. The loaded Q of the cavity is about 1000.

The electromagnet has pole pieces of 12 cm diameter with 2.95 cm gap between them. The maximum value of magnetic field is about 11300 oersteds at 10 amperes.

The specimen is rotated in such a way that the magnetic field is in the (010) plane.

The measurements are performed using the same specimen, under the three conditions as follows: (1) The specimen is fresh and magnetic annealing is not performed on it. (2) The specimen is annealed in the magnetic field parallel to its ⟨001⟩-axis. (3) The specimen is annealed in the magnetic field parallel to ⟨101⟩.

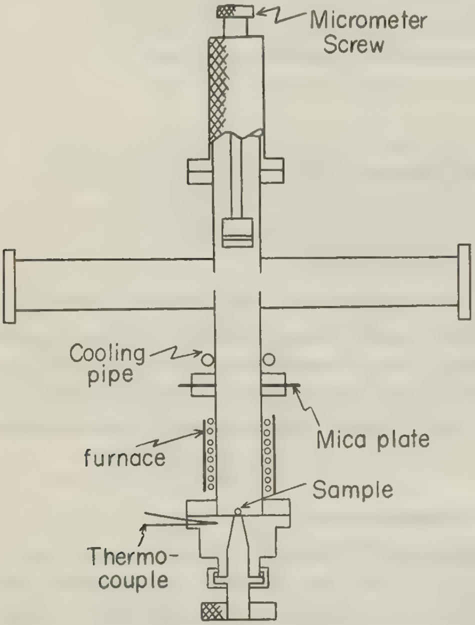

Fig. 1. Resonant cavity

The results obtained in each case will be described successively.

(1) *No magnetic annealing*

Magnetic resonance absorption cannot be observed at room temperature, but broad lines are found above about 70°C. In Fig. 2, the absorption lines at 148°C are shown as examples for various angles between the crystallographic axis and the external magnetic field. The angle zero means that the external magnetic field is parallel to ⟨001⟩.

Two peaks are observed in the resonance curve for each case and values of magnetic field at peaks depend on the angle and the temperature. This behaviour is shown in Fig. 3 at 82°C and 148°C. At 82°C the secondary peaks are not observed; from the curve given later in Fig. 4, which shows the temperature dependence of the secondary peaks, it is seen that the value of H where the secondary peaks appear decreases as the temperature is decreased, and will become zero for a certain temperature between 82°C and 148°C.

Taking the temperature of the specimen as absissa, the values of magnetic field at resonance are plotted in Fig. 4 at directions of ⟨001⟩, ⟨101⟩ and 23° from ⟨001⟩ in (010) plane.

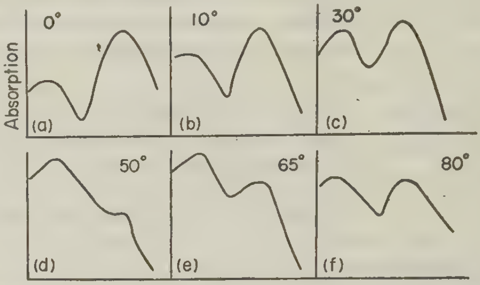

Fig. 2. Absorption *vs.* magnetic field at 148°C and 24.4 KMc.

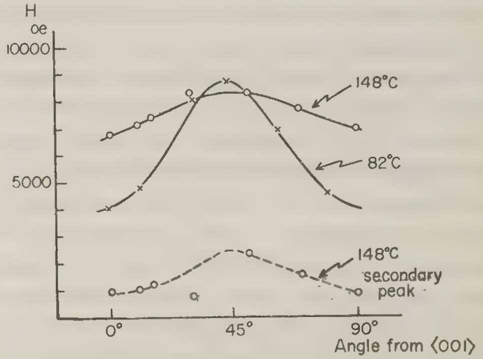

Fig. 3. Magnetic field at resonance *vs.* angle in (010) plane.

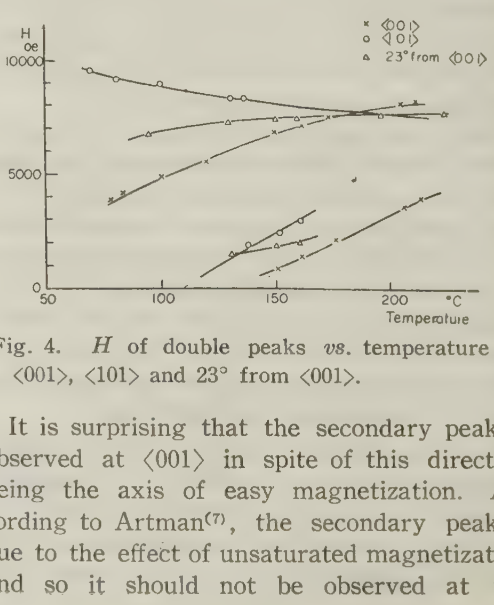

Fig. 4. H of double peaks *vs.* temperature at ⟨001⟩, ⟨101⟩ and 23° from ⟨001⟩.

It is surprising that the secondary peak is observed at ⟨001⟩ in spite of this direction being the axis of easy magnetization. According to Artman⁽⁷⁾, the secondary peak is due to the effect of unsaturated magnetization and so it should not be observed at the direction of easy magnetization. It should be concluded that these secondary peaks appear from another causes; this problem will be discussed in the next section.

Above 170°C the secondary peaks at ⟨101⟩ and 23° from ⟨001⟩ are not distinguished from the primary peaks. The broad primary peak seems to have masked the secondary one. Therefore, the values of magnetic field at resonance in this temperature region are not reliable. So it may not be concluded whether the magnetic anisotropy changes its sign at higher temperatures, although the upper curves in Fig. 4 cross one another at ca. 200°C.

(2) *Magnetic annealing parallel to* ⟨001⟩

The cobalt ferrite single crystal was cooled in air from 580°C to 200°C in one hour in a magnetic field of 10,000 oersteds parallel to ⟨001⟩. Then it was cooled down to room temperature in the same magnetic field within about half an hour.

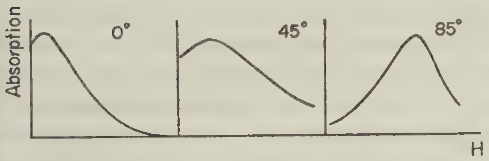

Fig. 5. Absorption *vs*. magnetic field at 115°C and 24.4 KMc, magnetic annealing parallel to ⟨001⟩. 0° shows the direction of ⟨001⟩.

Fig. 5 shows examples of the results obtained with the sample treated in this way, for various angles between the external magnetic field and ⟨001⟩ axis at 115°C. As shown in the figure, the line shape is simple and the secondary peak observed in the case of no magnetic annealing disappears. In Fig. 6 the magnitude of magnetic field at resonance is plotted against the angle. The measurements were performed at 66°C, 115°C and 165°C. The values of the external magnetic field at ⟨001⟩ and ⟨100⟩ are different from each other. This fact shows that the uniaxial magnetic anisotropy has been induced in the direction of ⟨001⟩ by heat treatment. The uniaxial anisotropy constant can be determined from the difference of these values. Its magnitude will be given in the following section.

Fig. 7 indicates the temperature dependence of resonance magnetic field strength for three different directions of the magnetic field relative to the crystal axes, namely ⟨001⟩, ⟨100⟩ and ⟨101⟩, of which ⟨001⟩ is parallel to the direction of the field at magnetic cooling.

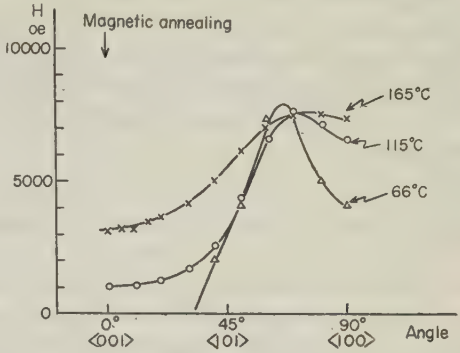

Fig. 6. Magnetic field at resonance *vs*. angle in (010) plane, magnetic annealing paralell to ⟨001⟩.

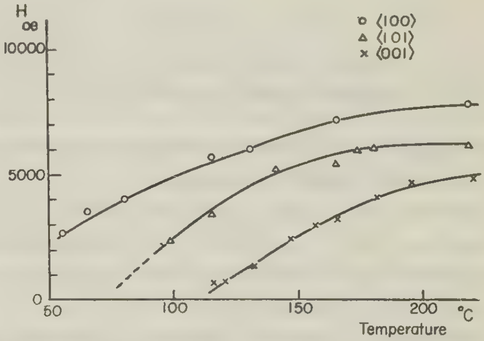

Fig. 7. Magnetic field at resonance *vs*. temperature, magnetic annealing parallel to ⟨001⟩.

(3) *Magnetic annealing parallel to* ⟨101⟩

In this case the line shapes are similar to those of ⟨001⟩ magnetic annealing given above. The resonance magnetic field strength is plotted in Fig. 8 against the direction of the magnetic field for three temperatures,

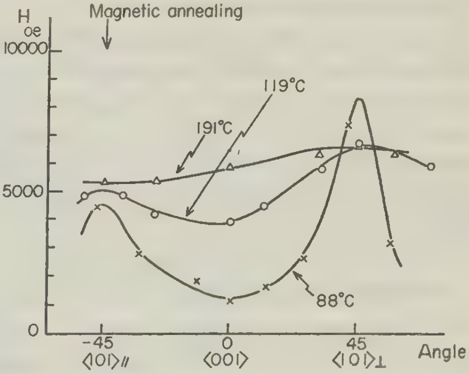

Fig. 8. Magnetic field at resonance *vs*. angle in (010) plane, magnetic annealing parallel to ⟨101⟩.

88°, 119° and 191°C. The same is plotted in Fig. 9 against temperature for the direction of the magnetic field at ⟨001⟩ and ⟨101⟩.

From these results it is found that the uniaxial magnetic anisotropy is induced in ⟨101⟩ by heat treatment in magnetic field.

The values of anisotropy constant will be given later.

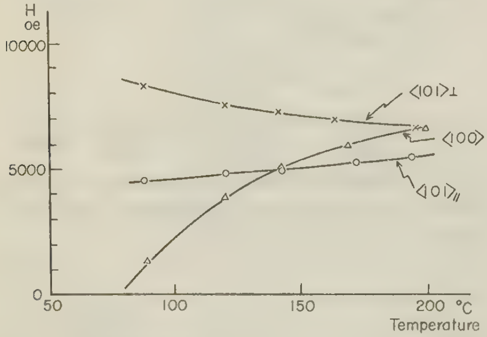

Fig. 9. Magnetic field at resonance *vs.* temperature, magnetic annealing parallel to ⟨101⟩.

§ 3. Relations between frequency and magnetic field at resonance

At first we shall consider the relations between the frequency and the external magnetic field at resonance in order to analyse the results of experiment.

It has been known from the observations that iron-cobalt ferrites have uniaxial magnetic anisotropy besides the ordinary cubic one. As there have been no quantitative studies on such a case, we shall calculate the conditions for the resonance according to the method used by Smit *et al*(9) and Suhl(10). We describe cubic and uniaxial magnetic anisotropy as K_1 and K_T, respectively. The higher terms of magnetic anisotropy are neglected in the following calculations.

Taking the cubic crystallographic axes as coordinates, we shall denote with α_1, α_2 and α_3 the direction cosines of the direction of magnetization M and β_1, β_2 and β_3 those of external magnetic field H. For a magnetic system the free energy can be written as follows.

$$\begin{aligned}F=&K_T\sin^2\theta+K_1(\alpha_1{}^2\alpha_2{}^2+\alpha_2{}^2\alpha_3{}^2+\alpha_3{}^2\alpha_1{}^2)\\&-MH(\alpha_1\beta_1+\alpha_2\beta_2+\alpha_3\beta_3)\\&+\frac{M}{2}(N_x\alpha_1{}^2+N_y\alpha_2{}^2+N_z\alpha_3{}^2),\end{aligned}$$

where θ is the angle between the uniaxial axis induced by magnetic annealing and M; N_x, N_y and N_z are the geometrical demagnetization factors.

The first term on the right-hand side is the uniaxial magnetic anisotropy energy and the second term is the cubic one. The third term is the magnetic interaction with the external magnetic field. The last term is the energy of demagnetization. The term of magnetostrictive energy is neglected.

The direction, in which this free energy has minimum value, is that of magnetization at equilibrium. Using this free energy, F, the resonance frequency is in general as follows.

$$\frac{\omega}{\gamma}=\frac{1}{M\sin\theta}\left[\frac{\partial^2F}{\partial\theta^2}\frac{\partial^2F}{\partial\varphi^2}-\frac{\partial^2F}{\partial\theta\partial\varphi}\right]^{1/2}.$$

θ and φ are the angles of magnetization in the spherical coordinate. γ is the gyromagnetic ratio. For simplicity, we assume henceforth that the sample is a shpere and $N_x=N_y=N_z=\frac{4\pi}{3}$ and external magnetic field is large enough that the magnetization can be considered homogeneous in the specimen.

The detail of calculations of resonance condition in various cases are not shown here, but it has been preformed according to the method by Artman(7). The relations between frequency and the magnetic field at resonance are summarized in the following.

Case I: H and uniaxial axis are always in (010) plane. The frequency at resonance is

$$\begin{aligned}\left(\frac{\omega}{\gamma}\right)^2=&\left[\frac{K_T}{M}\{1+\cos 2(\theta^1-\theta_0)\}\right.\\&\left.+\frac{K_1}{2M}\{3+\cos 4\theta_0\}+H\right]\\&\times\left[\frac{2K_T}{M}\cos 2(\theta^1-\theta_0)+\frac{2K_1}{M}\cos 4\theta_0+H\right].\end{aligned}$$

θ_0 is the angle between H and ⟨001⟩, and θ^1 is the angle between uniaxial axis and ⟨001⟩.

In this case the angle between H and M is given as

$$\varepsilon=\theta_0-\theta=-\frac{K_T}{MH}\sin 2(\theta^1-\theta)+\frac{K_1}{2MH}\sin 4\theta.$$

If cubic magnetic anisotropy only exists, it is seen from this equation that M coincides with H at $\theta=0$, $\frac{\pi}{4}$ and $\frac{\pi}{2}$. But if there is uniaxial magnetic anisotropy parallel te ⟨001⟩, $\varepsilon=0$ at $\theta=0$ and $\frac{\pi}{2}$. In general, except in the case where H is large enough compared with K/M, M dose not coincide with H at any direction. When this departure is large, the magnetic field at resonance differ considerably from the one obtained by putting $\varepsilon=0$. So when K/M is large, the magnetic fields at resonance cannot be used to estimate the anisotropy energy except the point of $\varepsilon=0$.

Case II: Uniaxial axis coincides with z-axis, but H is rotated in the (001) plane perpendicular to uniaxial axis.

In this case the frequency at resonance is given as follows.

$$\left(\frac{\omega}{\gamma}\right)^2=\left[\frac{2K_1}{M}\cos 4\varphi_0+H\right]$$
$$\times\left[-\frac{2K_T}{M}+\frac{K_1}{2M}\{3+\cos 4\varphi_0\}+H\right].$$

φ_0 is the angle between H and x-axis. Coincidence of M and H happens at $\varphi=0$, $\frac{\pi}{4}$ and $\frac{\pi}{2}$.

In the case of H and uniaxial axis being in the (110) plane the resonance frequency is given as follows, which we need not use for the present experiment.

$$\left(\frac{\omega}{\gamma}\right)^2=\left[\frac{K_T}{M}\{1+\cos 2(\theta^1-\theta_0)\}\right.$$
$$\left.+\frac{K_1}{8M}\{3\cos 4\theta_0+16\cos 2\theta_0-3\}+H\right]$$
$$\times\left[\frac{2K_T}{M}\cos 2(\theta^1-\theta_0)\right.$$
$$\left.+\frac{K_1}{2M}\{3\cos 4\theta_0+\cos 2\theta_0\}+H\right].$$

Although K_1/M and K_T/M can be obtained from the equations of resonance frequency mentioned above, the result is very complicated. But if K_1/M, $K_T/M \ll \boldsymbol{H}$, these equations are simplified in a good approximation as follows.

$$\text{Case I:}\quad H=\frac{\omega}{\gamma}-\frac{K_T}{2M}\{1+3\cos 2(\theta^1-\theta_0)\}$$
$$-\frac{K_1}{4M}\{3+5\cos 4\theta_0\},$$

$$\text{Case II:}\quad H=\frac{\omega}{\gamma}+\frac{K_T}{M}-\frac{K_1}{4M}\{3+5\cos 4\varphi_0\}.$$

In this case these simplified relations may be used to estimate magnetic anisotropy constant.

§ 4. Results

(A) K_1/M, K_T/M and g factor

We shall first discuss the case of magnetic annealing. The K_1/M and K_T/M values of the samples annealed in magnetic fields parallel to ⟨001⟩ and ⟨101⟩ are plotted in Fig. 10 against temperature.

(1) It can be known from this figure that K_1/M are nearly equal in both cases. These values are somewhat smaller than the one obtained for cobalt ferrite by Tannenwald(6), which are shown in the same figure by crosses. However, the temperature dependence of K_1/M obtained by him seems to agree with our results, as shown with dotted line. The discrepancy in K_1/M is likely to be due to the difference in the composition of cobalt ferrite used.

It might seem from Fig. 10 that K_1/M changes its sign at 200°C in the case of ⟨001⟩ magnetic annealing, but too much emphasis should not be put on this point, since there should be some error coming from the neglect of the effect of demagnetization in calculating such a small magnitude of K_1/M from the experimental results.

(2) The values of K_T/M depend on the direction of magnetic annealing. K_T/M in ⟨001⟩ magnetic annealing are twice as large as the one in ⟨101⟩.

According to the experimental results by Bozorth *et al*(1), the magnitudes of uniaxial magnetic anisotropy induced by magnetic annealing should be equal in all directions. In conflict with this conclusion, Iida *et al*(3) and Bickford *et al*(4) showed that ⟨100⟩ is the most effective direction for the magnetic annealing, while ⟨110⟩ is the least effective one in (001) plane. Our results lead to the same conclusion as the one obtained by Iida and Bickford. According to Iida's results using the sample $\frac{Co}{Co+Fe}=0.253$, $K_T=3.0\times10^5$ erg/g for ⟨100⟩ magnetic annealing and 1.6×10^5 erg/g for ⟨101⟩ at room temperature. In our experiment K_T are only measured above 100°C, and the composition of the sample, $\frac{Co}{Co+Fe}=0.267$, is different from Iida's. So our results are not directly compared to the one obtained by Iida. However, it should be noted that both results lead to the same conclusion that the ratio of K_T in ⟨001⟩ and ⟨101⟩

magnetic annealing is about two and ⟨001⟩ is the most effective direction for heat treatment in magnetic field.

(3) The temperature dependence of K_1/M and K_T/M are shown in Fig. 10. It is known from these curve that K_T/M in ⟨001⟩ and ⟨101⟩ magnetic annealing vary similarly with temperature, and that while K_1/M decreases rapidly with temperature and almost disappears at about 200°C, K_T/M values slowly and takes finite value 200°C.

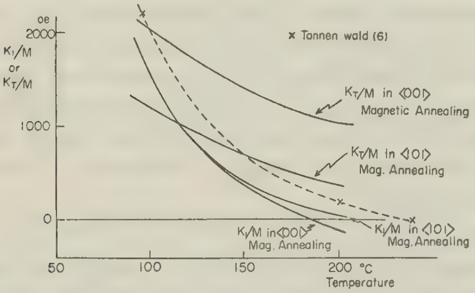

Fig. 10. K_1/M and K_T/M in magnetic annealing *vs.* temperature.

As a matter of course, these phenomena relate to the origin of induced uniaxial magnetic anisotropy and shall be discussed in section 5.

(4) *g* factor of iron-cobalt ferrite

The *g* factor of $Co_{0.8}Fe_{2.2}O_4$ is estimated from these experimental results as 2.86±0.06 in all range of temperature measured. The *g* factors reported by Tannenwald(6) are 2.7±0.3 at 90°C and 2.27±0.05 at 200°C. The reason for the discrepancy is not distinct, but it seems to be owing to the method of analysis.

(B) Secondary peaks

We consider the case of no magnetic annealing.

As shown in Fig. 2, resonance lines are broad and have secondary peaks. In crystals having large magnetic anisotropy the secondary peaks have previously been explained as follows(7). The external magnetic field is comparable with the magnetic anisotropy and hence magnetization cannot be aligned. Therefore, there exist domains with various direction of magnetization and the effect of domain walls produce the secondary peaks. According to this explanation, secondary peaks are not expected to be observed in the direction of easy axis.

We shall try the explanation from another point of view. Iron-cobalt ferrites, being cooled in zero magnetic field, have many domains. When they pass the Curie point and cool down, they are under the influence of a magnetic field parallel to their spontaneous magnetization. So in this specimen there are three kinds of domains having induced uniaxial anisotropy parallel to ⟨100⟩, ⟨010⟩ and ⟨001⟩, respectively. These domains cannot be brought to resonance for the same value of external magnetic field. When the magnetic field strength satisfies the conditions necessary for resonance for each domain, absorption takes place at different field strengths and secondary peaks are observed.

The experimental results shall be analized on this standpoint, with the assumption that each domain has the same volume.

When *H* is parallel to ⟨001⟩, the resonance condition is satisfied at two points of magnetic field by two parts of domains. The one has easy axis parallel and the other perpendicular to *H*. The volume of the latter is twice that of the former and is expected to show stronger resonance absorption, which is actually the case shown in Fig. 2 (a).

When *H* is parallel to ⟨101⟩, it makes 45° with the easy axis in the domains having uniaxial axis parallel to ⟨100⟩ and ⟨001⟩, but is perpendicular to easy axis in the domain having uniaxial axis parallel to ⟨010⟩. So the resonance absorption lines observed at lower and higher magnetic field and the former is twice as strong as the latter, as shown in Fig. 2 (d).

In the general case of *H* rotated in (010) plane, the domain having uniaxial axis parallel to ⟨010⟩ always satisfies the same condition of *H* being perpendicular to each axis, but the other domains satisfy different conditions depending upon angles, so three lines must exist, but they are not distinguished because of their broadness.

In calculating the value of K_1/M and K_T/M from Fig. 4, only the results with *H* in the ⟨001⟩-direction should be used, since the direction of *H* and *M* is not expected to be the same unless *H* is either parallel or perpendicular to uniaxial axis.

The results of the calculations for temperatures 100°, 150°, and 200°C are tabulated in Table I in comparison with these for magneti-

Table I.

	No magnetic annealing		<001> Magnetic Annealing		<101> Magnetic Annealing	
Temperature	K_1/M oe	K_T/M oe	K_1/M oe	K_T/M oe	K_1/M oe	K_T/M oe
100	1750	2180	1540	2030	1590	1670
150	640	1960	360	1420	400	700
200	−140?	1620	−100?	1050	50	370

cally annealed samples. The same g factor as obtained in the magnetic annealing has been used.

The values of K_1/M and K_T/M obtained from non-magnetically annealed samples are somewhat larger than these obtained from magnetically annealed samples, but considering the uncertainty due to the broadness and the different heat treatment, they seem to be rather in a good agreement.

It seems to be clear from these results that secondary peaks observed in cobalt ferrite are due to the domains having different uniaxial axis induced by the magnetic annealing owing to spontaneous magnetization.

§ 5. **Discussions**

(1) Cubic magnetic anisotropy K_1/M

The origin of magnetic anisotropy of ferrite has been recently discussed from many points of view. Among these theories, the assumption that the anisotropy is due to that of the crystalline field acting on the ions under question seems to be the most important in Mn- and Ni-ferrite. However, magnetic anisotropy of Co-ferrite has not been explained sufficiently.

K_1 of cobalt-substitued magnetite was measured by Bickford *et al*(4) between 120°K and 450°K. It was found that the total anisotropy of the cobalt-substituted magnetite is the additive effect of a contribution of the divalent cobalt ions superimposed on the anisotropy of magnetite itself and the contribution of the cobalt ions appears to be a linear function of concentration as long as the concentration is small.

Slonczewski(5) gave one-ion model. According to this model, cobalt ions occupying the octahedral sites of ferrite suffer from crystal electric field with trigonal symmetry and their spin couples to the axis through the spin-orbit coupling, so cubic anisotropy is produced on an average.

Slonczewski succeeded in explaining Bickford's results with his model. But his theory cannot be applied to the present cases, as the cobalt concentration is high in our experiment. Indeed, a formal calculation after Slonczewski's model gives about 10 times larger anisotropy value than our experimental anisotropy at 100°C.

Tachiki(11) has suggested that for a high concentration of cobalt ions the effects of Fe^{2+}, Fe^{3+}, and Co^{2+} ions should be taken into account. Our results may be explained with one-ion model in his regard. The temperature dependence of anisotropy will give a useful aid for the validity of the theory.

(2) Uniaxial magnetic anisotropy K_T/M

On the origin of uniaxial magnetic anisotropy induced by magnetic annealing, many theories based on following mechanisms has been presented. (1) Néel-type directional order between cobalt and iron ions(12), (2) The directional order between cobalt ion and cation vacancy(3), (3) Interaction between cobalt ion and the nearest cation through spin-orbit coupling(4), (4) The preferential growth of micro-precipitates of a second phase(13).

Iida and Bickfard discussed these mechanisms in detail and pointed out certain difficulties involved in them. However, it has not been understood which of the second and the third mechanisms is likely to be correct. No decisive conclusion can be obtained from our results.

From the facts obtained from the present experiment we shall consider the mechanism producing the uniaxial anisotropy. In magnetic field at higher temperature cations and cation vacancies in iron-cobalt ferrite line up in such a way that the interaction energy of cobalt ions with surrounding ions through spin-orbit coupling becomes minimum. While the sample is being cooled the alignment of cations and vacancies are left as it was, so cobalt ion will be placed in a crystalline field whose symmetry is different from trigonal one due to averaged cations in octahedron site, which gives cubic anisotropy on an average, and will have uniaxial anisotropy parallel to magnetic field.

(3) *g* factor

It is assumed generally that *g* factor is insensitive to temperature. Indeed, almost all ferrites have *g* factor independent or slightly dependent on temperature and our result shows the same behaviour within limits of errors. However, *g* factor of cobalt ferrite obtained by Tannenwald shows large temperature dependence. It seems reasonable that uniaxial magnetic anisotropy gives rise to an error for *g* factor, if only cubic anisotropy is taken into consideration.

(4) Secondary peaks

The secondary peaks observed in resonance absorption lines of iron-cobalt ferrite are discussed in the above section. It is worth while describing that if specimen has a large uniaxial anisotropy and has various domains even in an external magnetic field, subsidiary peaks owing to these domains must be considered. Indeed the secondary peaks suggested by Artman would also exist in this case.

The author would like to express their gratitude to Dr. G. M. Hatoyama for his kind encouragement. He is also indebted to Mr. E. Sawaguchi and Mr. N. Sakamoto for disucussions and preparations of specimen and to Mr, K. Matuura for measurements.

References

1) R. M. Bozorth, E. F. Tilden and A. J Williams: Phys. Rev. **99** (1955) 1788.
2) H. Shenker: Phys. Rev. **107** (1957) 1246.
3) S. Iida, H. Sekizawa and Y. Aiyama: J. Phys. Soc. Japan **13** (1958) 58.
4) L. R. Bickford, J. M. Brownlow and R. F. Penoyer: Proc. I.E.E, **104** B Supl. (1957) 238 R. F. Penoyer and L. R. Bickford: Phys. Rev. **108** (1957) 271.
5) J. C. Slonczewski: Phys. Rev. **110** (1958) 1341.
6) P. E. Tannenwald: Phys. Rev. **99** (1955) 463.
7) J. O. Artman; Phys. Rev. **105** (1957) 62, Proc I.R.E. **44** (1956) 1284.
8) E. Sawaguchi and Z. Ishii: Bull. Electrotech. Lab. **20** (1956) 1 (in Japanese .
9) J, Smit and H. G. Beljers: Philips Res. Rep. **10** (1955) 113.
10) H. Suhl: Phys. Rev. **97** (1955) 555.
11) M. Tachiki: Spoken at Ann. Meeting of Phys. Soc. Japan, March 31 and Oct. 11 (1959).
12) L. Neel: J. Phys. Radium **15** (1954) 225,
13) Williams, Heidenrich and Nesbitt: J. Appl. Phys. **27** (1956) 85.

JOURNAL OF THE PHYSICAL SOCIETY OF JAPAN, Vol. 15, No. 8, AUGUST, 1960

The Recovery of Initial Magnetic Susceptibility in Pure Nickel

By Mitsuru ASANUMA

Department of Physics, Faculty of Science, Hokkaido University

(Received February 18, 1960)

The process of recovery in cold-worked pure nickel was investigated by means of the initial magnetic susceptibility and the electrical resistance measurements. In our specimens, which were elongated by about 5 percent, the recovery of the initial magnetic susceptibility was observed above 450°C, and could not be observed below that temperature. The recovery in the temperature range of our investigation was expressed by logarithmic law, and analysed by Kuhlmann's formulation, its activation energy being 3.0 ev. This value is in good agreement with the activation energy of self-diffusion in pure nickel. Therefore, it is considered that the recovery of the initial magnetic susceptibility is due to the disappearance of dislocation in the stage of recrystallization

On the other hand, the recovery below 450°C in which the change of initial magnetic susceptibility could not be observed was investigated by measuring the electrical resistance and the activation energy 0.91 ev was obtained. This value is in good agreement with the activation energy of vacancy migration. Therefore, it must be assumed that the disappearance of vacancy does not affect the initial magnetic susceptibility.

1. Introduction

Since the cold-worked condition is themoynamically more unstable than the unstrained ne, cold-worked metal undergoes spontaneous hanges to reduce the extra free energy which as gained from the work done on metal. he processes which reduce the extra free nergy, that is, recovery, primary recrystalization, secondary recrystallization and grain rowth are distinguished one another in etallographic observation. Recovery is the henomenon in which cold-worked metal is oftened without recrystallization, and can not e detected by conventional metallographic ethod, but detected by means of measureents of specific heat, mechanical hardness, ield stress, electrical resistance and the line idth of X-ray Debye-Scherrer line. In addiion to the above mentioned annealing process he phenomena which is called polygonization s found by Orowan and Chan¹⁾. It seems referable to regard this phenomenon as one f the process of recovery, but this is not the hole of recovery. This is shown by the fact hat the recovery occurs after laminar plastic ow in hexagonal crystals where there is no attice bending to provide the excess edge islocations of one sign needed for polygonizaion. Thus the mechanism in recovery is omplicated. In the past, many investigators attempted to explain the basic process in recovery. Burgers²⁾ suggested that this process was the annihilation of two dislocations of opposite signs in the same slip system, but he did not discuss how they annihilate one another when they are on different planes.

Kuhlmann³⁾ considered that the recovery occurs by dislocations gliding in their slip planes over barriers with aid of thermal activation, and developed a formal theory under the idea that the activation energy for recovery is a decreasing function of mean internal stress in the material, and explained the logarithmic law of softening during recovery in the experiments of Kuhlmann, Masing and Raffelsieper⁴⁾, Cottrell and Aytekin⁵⁾ and Borelius⁶⁾.

On the other hand, Mott⁷⁾ believed that the basic process is the climbing of dislocations out of their slip planes by the migration of vacancies, and formulated an expression of recovery.

Thus, the details of recovery has not yet been clarified. In such an investigation it is needed to investigate by using the sensitive quantities to structural changes in material due to recovery.

In ferromagnetic metals, a typical one of the structure-sensitive quantities in the initial magnetic susceptibility or the coercive force, and these quantities can more precisely be measured than the mechanical hardness or the yield stress. Moreover it was qualitatively shown that the initial magnetic susceptibility and the coercive force were connected with the internal stress in materials by Becker and Kersten[8], and these quantities were recently discussed in association with dislocation which was the origin of internal stress by Kersten[9], Kneller[10] and Vicena[11]. Then, in order to investigate the annealing process of metals, the initial magnetic susceptibility was used.

§ 2. Specimen and Experimental Procedures

The specimen in which the internal stress has predominant effect on the initial magnetic susceptibility must be selected for the purpose of the present investigation. The internal stress affects the initial magnetic susceptibility through the magnetostriction. Thus a metal whose magnetostriction constant is large must be selected. Among the pure metal nickel is adapted for the above conditions.

Nickel wires which were of 1.2 mm in diameter and 180 mm in length were prepared, and at first they were annealed in vacuum at 1100°C during two hours. Then they were streched by 5 percent as uniformly as possible, and tempered at an appropriate temperature. And the changes of the initial magnetic susceptibility or the electrical resistance were measured as a function of tempering time.

The initial magnetic susceptibilities were measured by means of ballistic galvanometer method, and the values of the initial magnetic susceptibilities were about 30 *emu* in annealed state and about 2 *emu* in cold-worked state, respectively.

§ 3. Experimental Results and Analysis

Tempering temperatures were chosen at 50°C interval from 300°C to 700°C, and at each temperature the relation of the initial magnetic susceptibility to the tempering time was shown in Fig. 1. The changes of the initial magnetic susceptibilities were not recognized at temperatures below 450°C, but clearly detected in tempering above 500°C. The time dependences of the initial magnetic susceptibilities were followed by logarithmic law for all temperature. Therefore, the author attempted to analyse this experimental result according to Kuhlmann's formulation[3]

The apparent activation energy for recovery is assumed to decrease linearly to internal stress as far as it is small:

$$U(\sigma)=U_0-\beta\sigma$$

where U_0 is the intrinsic activation energy, U is the apparent activation energy, β is a constant for the range of stress chosen and σ is internal stress. The rate of recovery of internal stress is

$$\frac{d\sigma}{dt}=-C\exp\left\{-\frac{U_0-\beta\sigma}{kT}\right\}. \qquad (1)$$

On the other hand, the internal stress is related approximately by the initial magnetic susceptibility χ as follows;

$$\sigma=\frac{D}{\chi}, \qquad (2)$$

where D is a function of the saturation magnetization and the magnetostriction constant, and depends upon the mechanism that the magnetization proceeds, or magnetic domain distribution. As the saturation magnetization I_s and the magnetostriction constant do not sensitively depend on cold-working, D is approximately regarded as a constant which depends on ferromagnetic materials.

From equation (1) and (2)

$$t=\frac{kT}{C\beta}\exp\left(\frac{U_0}{kT}\right)$$

$$\left\{\exp\left(-\frac{\beta D}{kT}\frac{1}{\chi}\right)-\exp\left(-\frac{\beta D}{kT}\cdot\frac{1}{\chi_0}\right)\right\},$$

where χ_0 is the value of χ in $t=0$, i.e. just after cold-working. When one takes to

$$t_0=\frac{kT}{C\beta}\exp\left\{\frac{U_0-\beta D\frac{1}{\chi_0}}{kT}\right\}, \qquad (3)$$

and reduces by $1/\chi$ values in $t=0$,

$$\frac{1}{\chi}\bigg/\frac{1}{\chi_0}=\mathrm{B}-A\ln(t+t_0), \qquad (4)$$

$$\text{where}\quad \left.\begin{aligned}A&=\frac{kT}{\beta D}\\ B&=\frac{kT\chi_0}{\beta D}\ln\frac{kT}{C\beta}+\frac{U_0\chi_0}{\beta D}\end{aligned}\right\} \qquad (5)$$

Therefore, the recovery of the initial magnetic susceptibility is expressed by the logarithmic law, when $t_0 \ll t$, that is,

$$\frac{1}{\chi}\bigg/\frac{1}{\chi_0}=B-A\ln t. \qquad (6)$$

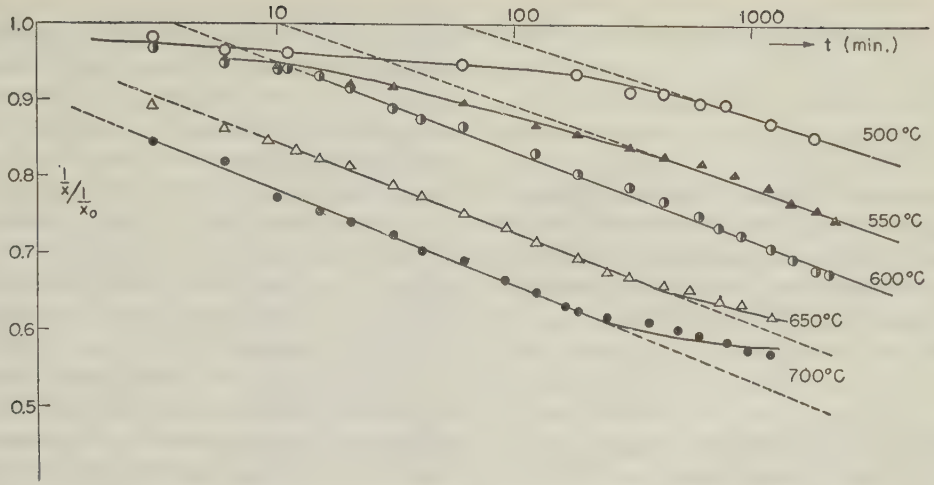

Fig. 1. Isothermal recovery of the initial magnetic susceptibility of pure nickel.

Now, from the inclinations of linear parts of he curves in Fig. 1 the values of A correspon-ing to each temperature are obtained. When the values of A are plotted against bsolute temperature T, Fig. 2 is obtained, nd the curve is represented as the straight ine through the origin as follows:

$$A=6.26\times10^{-5}T. \qquad (7)$$

From the equations (5) and (7)

$$\frac{\beta D}{\chi_0}=\frac{k}{6.29}\times10^5=1.37\text{ ev}. \qquad (8)$$

Further, considering B in equation (5), logari-hmic factor in the expression of B changes nly about 2% in the present temperature ange, so that it is approximately regarded s that first term of B is proportional to bsolute temperature T. The values of B vere determined by extrapolating the parts f the straight lines in Fig. 1, and finding the ntersecting points with longitudinal axis. And vhen these values are plotted against the bsolute temperature, B curve in Fig. 2 is btained and this curve is represented as ollowing straight line:

$$B=2.19-1.32\times10^{-3}T \qquad (9)$$

ombining equations (5) and (9)

$$\frac{U_0\chi_0}{\beta D}=2.19. \qquad (10)$$

rom equations (8) and (10)

$$U_0=3.0\text{ eV}.$$

hus the activation energy for recovery of e initial magnetic susceptibility is 3.0 ev.

On the other hand, the recovery in the temperature range below 450°C which does not affect the initial magnetic susceptibility can be detected by measuring the change of the electrical resistance followed by isothermal tempering. If the change of the electrical resistance is expressed by the following relation;

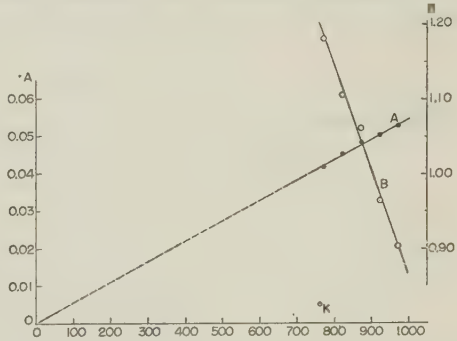

Fig. 2. The dependence of parameter A and B on temperature.

$$\frac{R_0-R_t}{R_0-R_\infty}=1-\exp\left(-\frac{t}{\tau}\right),$$

or

$$\ln\frac{R_t-R_\infty}{R_0-R_\infty}=-\frac{t}{\tau}, \qquad (11)$$

where R_0, R_∞ and R_t are the values of the electrical resistance in $t=0$, $t=\infty$ and $t=t$, respectively, and t is an annealing time and τ is the relaxation time.

Plotting the experimental values according to the equation (11), Fig. 3 is obtained. The relation between the relaxation time τ and the activation energy U' is expressed as follows:

$$\tau=\tau_0\exp\left(\frac{U'}{kT}\right). \tag{12}$$

Therefore

$$\ln\tau=\ln\tau_0+\frac{U'}{kT} \tag{13}$$

The relaxation times are determined from the inclinations of the straight lines in Fig. 3 at various temperatures, and plotted against the inverse temperature. Fig. 4 shows this result. From Fig. 4 it is determined that

$$U'=0.91\text{ eV}.$$

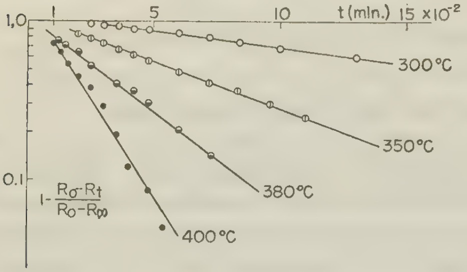

Fig. 3. Isothermal recovery of electrical resistivity.

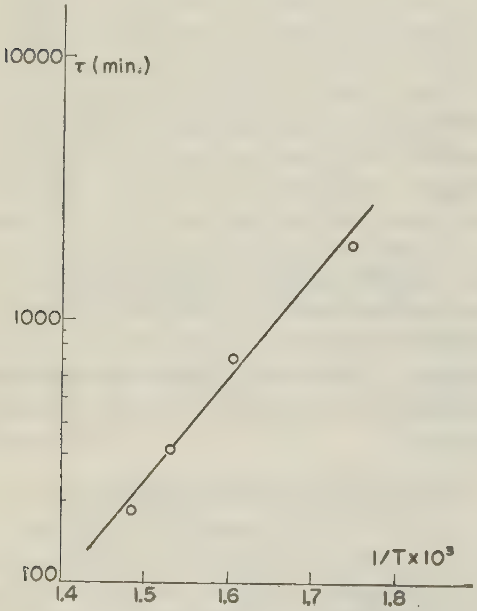

Fig. 4. The dependence of the relaxation time of recovery in electrical resistance on temperature.

§ 4. Discussion

In order to investigate the annealing kinetics. Boas[12] measured the changes in internal energy, electrical resistivity, density and hardness which occur during the annealing of nickel deformed at room temperature. According to his result, the energy stored during deformation is released in three stages and the change in internal energy has two distinct peaks. The first stage is accompanied with the decrease in electrical resistivity, but any reduction in hardness does not occur. The second stage occurs over a temperature range where there are only a slight decrease in hardness and electrical resistivity. The third stage is associated with a large and sudden decreases in hardness and electrical resistivity.

He has explained the origins of the first, the second and the third stages as being due to the disappearance of vacancies, the rearrangement of dislocations into configurations with lower energy and the disappearance of dislocations during recrystallization, respectively. His experiment shows that the activation energy for the first stage is 1.0 eV and it is in good agreement in order of magnitude with the results of the experiments in quenched or neutron irradiated pure nickel.

The results obtained in the present work at the temperature range below 400°C show that the activation energy for recovery in this range is about 0.9 eV, and the change of the initial magnetic susceptibility has not been recognized. Since the magnetic properties are of volume-effect, and the internal strain caused by the vacancy in material is considered as of short-range, it is not unreasonable to assume that the disappearance of vacancies shows no effect on the initial magnetic susceptibility. Furthermore, this activation energy, 0.9 eV, agrees with the result by Boas[12] and it is concluded that the origin of recovery at the temperature range below 400°C is the disappearance of excess vacancies created into material by cold-working. While it seems that the change of the electrical resistance is described at least in one simple vacancy mechanism below 400°C, the critical temperature in which the another mechanism is superposed on it is not clearly determined.

Recently, the effect of quenching vacancy on the magnetization in earth magnetic field was studied by Takamura and Nakamura[13], and they explained that the climbing of dislocations following the vacancy migration to dislocations affects the magnetization in earth magnetic field. However, the defects which are created on quenching are a large number of vacancies and small amounts of dislocations, and if these vacancies diffuse towards the dislocations and the dislocations climb out of their slip planes at room temperature, a sufficient number of jogs must be always present. The climbing of the dislocation without jog needs a large activation energy in nickel having half-dislocation and will hardly occur. A sufficient number of jogs will be created only by the motion of dislocations through the forest of screw dislocations. In their quenching experiments, therefore, the number of jogs will not be sufficiently much, and the rate of climbing of the dislocation should be greatly reduced as compared with the case in which a sufficient number of jogs is present, and the activation energy of climbing should be equal to that of self-diffusion. From these view points, it seems that their explanations of the results in their experiments which were done in room temperature are not appropriate. However, as the diffusion of vacancy and the climbing of dislocation depend on the purity of specimen, in order to conclude the problem, more detail experiments on the specimens having various purities are desirable to be attempted.

On the other hand, the result at the temperature range above 450°C shows the remarkable increases of the initial magnetic susceptibility which depends on internal stress in material according to the equation (2). The decrease of internal stress following annealing will be caused by the disappearance or the rearrangement of dislocations which were created by cold-working. The activation energy obtained in the present work at high temperature is 3.0 eV, and this is in good agreement with the activation energy of self-diffusion in pure nickel which Seeger[14] has obtained. This energy is also nearly equal to the activation energy for the steady-state creep at high temperature which is explained by the climbing of dislocations, wnich is promoted by self-diffusion. According to Kersten[9], the initial magnetic susceptibility is inversely proportional to square root of dislocation density and Vicena[11] has been suggested that the coercive force of pure bulk ferromagnetics is proportional to square root of dislocation density. In the former regular arrangement of dislocations, in the latter statistical distribution of dislocations were assumed, respectively. Moreover, according to Seeger[15] the flow stress in the case in which the dislocations are distributed at random is given by the equation, $\sigma = \alpha b G\sqrt{n}$, where n, b, G and α are the number of dislocations in unit area, Burger's vector, shear modulus and constant which depens on the arrangement of dislocations, respectively. From the above mentioned results, it is concluded that the decrease of the number of dislocations which is caused by self-diffusion plays an important role in the increase of the initial magnetic susceptibility. The dependence of the initial magnetic susceptibility on the rearrangement of dislocations is not clear.

The apparent activation energy of recovery of the initial magnetic susceptibility at high temperature, $U_0 - \beta\sigma_0$, depends on the degree of cold-working. In the present work, this activation energy is evaluated from Fig. 5, which is drawn according to the equation (3), and

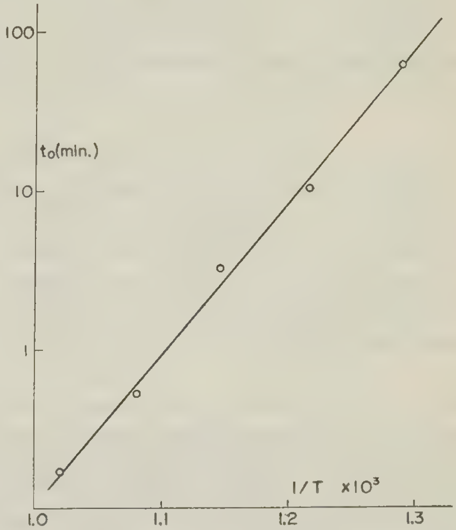

Fig. 5. The dependence of t_0 on temperature.

$$U_0 - \beta\sigma_0 = 43.6\ \text{kcal/mol}. \qquad (14)$$

Hence, $\beta\sigma_0 = 25.4$ kcal/mol. The apparent activation energy which is shown in equation (14) must be distiguished from the activation energy of recovery of the electrical resistance at low temperature, since in the present degree of cold-working $\beta\sigma_0$ is 25.4 kcal/mol and the apparent activation energy at $t=0$ is 43.6 kcal/mol and is greater than the activation energy of vacancy migration. If the degree of cold-working is more high, in other words, if $\beta\sigma_0$ is more large, the apparent activation energy become less and the recovery of the initial magnetic susceptibility will be found at lower temperature than the present case.

The change of the electrical resistance in high temperature region was not measured. But it is expected that both mechanism of the disappearance of dislocations and vacancies will be superposed.

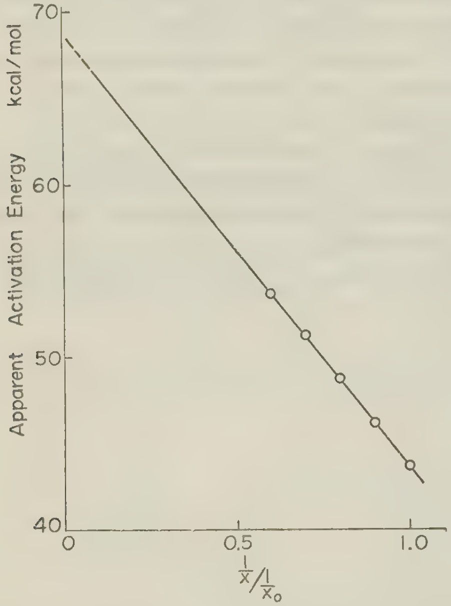

Fig. 6. The dependence of the apparent activation energy on $\frac{1}{\chi}\Big/\frac{1}{\chi_0}$.

When the apparent activation energy, $U_0-\beta\sigma=U_0-\frac{\beta D}{\chi}$, is plotted against $\frac{1}{\chi}\Big/\frac{1}{\chi_0}$, fig, 6 is obtained. This result shows that β is a constant for the range of stress chosen, as one assumed in equation (1). The evaluation of β is difficult, unless σ is measured directly, because D depends on the magnetic domain distribution and the mechanism of magnetization in weak magnetic field and can not be precisely determined.

§ 5. Conclusions

The recovery of the initial magnetic susceptibility was followed by logarithmic law at all temperatures, and it was analysed by Kuhlmann's formulation. Its activation energy was 3.0 eV and agreed with that of self-diffusion in pure nickel. It is concluded that the mechanism of recovery of the initial magnetic susceptibility is disappearance of dislocations followed by climbing of dislocations through the self-diffusion and it corresponds to the stage of recrystallization.

The recovery in the region where the change of the initial magnetic susceptibility could not be found was investigated by the measurement of electrical resistance, and the activation energy was estimated to be 0.9 ev. This activation energy agrees with that of vacancy migration. Hence, it is concluded that the recovery at low temperature is caused by the disappearance of excess vacancies. It is noted that the structure-sensitive magnetic properties are successfully adopted for the investigation of the recovery.

The author wishes to express his sincere thanks to Professor S. Miyahara and Professor S. Kôda for valuable advice and discussion throughout the course of the present study.

Reference

1) R. W. Cahn: *Progress in Metal Physics*, II (Pergamon Press 1950) 151 P.
2) W. G. Burgers: Proc. Roy. Acad. Sci. Amsterdam **50** (1947) 452, 595, 719, 858.
3) D. Kuhlmann: Z. Phys. **124** (1947) 468.
4) D. Kuhlmann, G. Masing, and J. Raffelsieper: Z. Metallk. **40** (1949) 241.
5) A H. Cottrell and V. Aytekin: J. Inst. Met. **77** (1950) 389.
6) G. Borelius: Rep. of 9th. Solvay Conf. (1952) 427.
7) N. F. Mott: Phil. Mag. **44** (1953) 742.
8) R. Becker and M. Kersten: Z. Phys. **64** (1930) 660.
9) M. Kersten: Ann. Physik **20** (1957) 237.
10) E. Kneller and H. Dietrich: Z. Metallk. **47** (1956) 716.
11) F. Vicena: Czechosl. J. Phys. **5** (1955) 480.
12) W. Boas: *Defects in Crystalline Solids* (Rep. Bristol conference, 1955) 212 P.
13) J. Takamura and Y. Nakamura: J. Phys. Soc. Japan **13** (1958) 316.
14) A. Seeger: *Defects in Crystalline Solids* (Rep. Bristol Conference 1955) 319 P.
15) A. Seeger: *Dislocations and Mechanical Properties of Crystals.* (1956) 243. (International Conference held at Lake Placid.

Journal of the Physical Society of Japan, Vol. 15, No. 8, August, 1960

The Electron Paramagnetic Resonance of Mn^{2+} Ions Surrounded by an Octahedron of Fluorine Ions

By Shinji Ogawa

Research Institute of Applied Electricity,
Hokkaido University, Sapporo

(Received March 3, 1960)

The measurements of the EPR of Mn^{2+} ions as dilute, substitutional impurities in the single crystals of $KMgF_3$, $KCdF_3$, $KCaF_3$, K_2MgF_4 and $NaMgF_3$ were made. An X-ray examination revealed that divalent metal ions in these crystals were surrounded by an octahedron of six fluorine ions. The F^{19} "super-hfs" superimposed on the usual hfs of Mn^{55} has been observed. The dependence of the F^{19} hf interaction constant (A_s) upon the Mn^{2+}–F^- distance has been noticed and discussed. The A_s in $KMnF_3$ has been estimated to be somewhat smaller than $16.7\times10^{-4}\,cm^{-1}$.

1. Introduction

Since Griffiths and Owen[1] observed the yper fine structure (hfs) due to the nuclear pins of neighboring anions in the electron aramagnetic resonance (EPR) of Ir ions in he alkali chloroplatinates, the so-called "super-fs" has been observed in a few fluorides[2–5] nd found to be very powerful tool, together vith the shift in the NMR[6], in investigating he electronic state of magnetic electrons in rimarily ionic crystals.

On the other hand, the strong magnetic iteraction in an antiferromagnetic or ferri-iagnetic compound of ionic nature has been xplained by the superexchange interaction[7] vhich result from a departure from a purely onic state, due to partial covalency and overapping with neighboring ions. Therefore, ie observation of the super-hfs will also offer n important information to understand the uperexchange interaction.

In the EPR experiment of Mn:ZnF_2, Tinkam[2] found a rather large difference in two ^{19} hf interaction constants which correspond) two types of Mn–F pairs with slightly diferent separations. Although a recent rexamination[3] has diminished the difference, ie dependence of the F^{19} hfs upon the Mn– distance should be studied in order to know ie F^{19} hf interaction constant in a dense, iagnetic crystal and compare the EPR data vith the NMR data.

In connection with the antiferromagnetism bserved in $KMnF_3$[8], an EPR experiment of ie Mn^{2+} ions diluted in many compounds as ossible which have a similar anion environment to $KMnF_3$ was intended. The present paper reports the EPR experiment of Mn^{2+} ions in the single crystals of $KMgF_3$, $KCdF_3$, $KCaF_3$, K_2MgF_4 and $NaMgF_3$. Although the result of Mn^{2+}:$KMgF_3$ has been reported briefly[9], it is included in this paper for the detailed account and a slight correction.

§ 2. Preparation of Crystals

The compounds such as $KMgF_3$, K_2MgF_4, $KCdF_3$, $KCaF_3$ and $NaMgF_3$ have been hitherto prepared by several ways; by precipitating from aqueous solutions, by a direct fusion of RF and MF_2, or by the reaction $MO+3RF\rightarrow RMF_3+R_2O$ (where R is K or Na and M is Mg, Cd or Ca).

In the present study, a flux method was tried and found to be suitable to get the single crystals being sufficiently large for our purpose. To prepare the KMF_3, anhydrous MCl_2 and $3KHF_2$ were heated up to melt in a platinum crucible in the air and cooled slowly at the rate of about 50°~20°C per hour. They melted above ca. 850°C and the reaction $MCl_2+3KHF_2\rightarrow KMF_3+2KCl+3HF\uparrow$ occurred. On cooling, the compound KMF_3 precipitated in the flux KCl. After the flux was washed out by water, single crystals of cubic shape with surfaces parallel to {100} planes were obtained. The crystal K_2MgF_4 was prepared from $MgCl_2$ and $4KHF_2$ at first. After a few trials, an addition of excess KHF_2 was found to be useful to prevent a growing of the mixed crystal of $KMgF_3$ and K_2MgF_4 which had grown frequently when the exact 1 to 4 ratio of mixing had been used. The single crystal of $NaMgF_3$ was obtained in a similar way using $NaHF_2$ instead of KHF_2. The largest single crystal obtained was that of $KMgF_3$ with a dimension $12 \times 10 \times 7\ mm^3$. It was rather difficult to grow up the single crystals of $KCdF_3$ and $KCaF_3$. A long time and a slow cooling rate of about 20°C per hour were necessary to get a single crystal of $3 \times 3 \times 2\ mm^3$.

For the purpose of EPR study, manganese ions were solved in the above crystals by adding the anhydrous $MnCl_2$ in about 0.1% molar concentration to the starting mixture, but the intensity of EPR spectrum suggested that about one tenth of added manganese ions had solved into the single crystals. The pink color of the KCl flux showed that the rest of manganese ions remained as solved in KCl.

§ 3. X-ray Examination

There have been many studies of the crystal structure of the above mentioned compounds, but some are contradictory to others. For example, cubic perovskite and monoclinic structures are reported for $KMgF_3$. Because of this confusion, all crystals used in the EPR experiment were examined by X-ray measurements through Debye-Scherrer and rotating crystal methods. In contrary to the lower symmetry reported earlier, our specimens of $KMgF_3$, $KCdF_3$ and $KCaF_3$ had a perfectly cubic symmetry. The width of diffraction lines was very narrow, less than 0.15 degree in 2θ. The discrepancy in crystal symmetry is possibly due not to the error in measurement but to the crystals themselves prepared in different ways. The data of our examination are listed in Table I.

Table I.

Compound	Crystal structure and lattice constant	M^{2+}–F^- distance	Structures reported hitherto
$KMgF_3$	Cubic (perovskite-like) $a=3.987 \pm .001$Å	1.994Å	Cubic[a,b,c,d,e], monoclinic[f,g]
$KCdF_3$	〃 〃 $a=4.334 \pm .001$Å	2.167Å	Cubic[h], pseudo-cubic[i]
$KCaF_3$	〃 〃 $a=4.375 \pm .001$Å	2.188Å	Pseudo-cubic[a], monoclinic[h]
K_2MgF_4	Tetragonal, D_{4h}–17 $a=3.982 \pm .002$Å $c=13.145 \pm .005$Å	1.991Å	Tetragonal[e], D_{4h}–17[j]
$NaMgF_3$	Orthorhombic $a=5.485$Å, $b=7.678$Å $c=5.356$Å all in ± 0.005Å	——	Tetragonal[j]

a) H. A. Klassens, P. Zalm and F. O. Huysman: Philips Res. Rep. **8** (1953) 441.
b) R. C. DeVries and R. Roy: J. Amer. Chem. Soc. **75** (1953) 2479.
c) H. Remy and W. Seeman: Rec. trav. Chim. Pays-Bas **59** (1940) 516.
d) A. E. Van Arkel: Physica **5** (1925) 162.
e) H. Remy and F. Hansen: Z. anorg. allg. Chem. **283** (1956) 277.
f) W. L. W. Ludekens and A. J. E. Welch: Acta Cryst. **5** (1952) 841.
g) St. v. Naray-Szabo: Publ. Univ. Tech. Sci. Bp. **1** (1947) 36.
h) C. Brici: Ann. Chim. (Rome) **42** (1952) 356.
i) R. L. Martin, R. S. Nyholm and N. C. Stephenson: Chemistry and Industry (1956) 83.
j) B. Brehler and H. G. F. Winkler: Heidelberger Beitr. Mineral. u. Petrog. **4** (1956) 6.

The rotating crystal photograph revealed that the most probable space group of $NaMgF_3$ was D_{2h}–16, though the lower symmetry was not impossible. This orthorhombic lattice can be regarded as a distorted perovskite-like structure. The relation is shown in Fig. 1 together with the crystal structure of K_2MgF_4.

§ 4. EPR Experiment

The EPR experiment was carried out by a standard X-band ($\sim 0.3\ cm^{-1}$) spectrometer with a cavity of reflection type. A technique of magnetic modulation of small field (about 2∼3 Oe.) and phase sensitive detection was used. A derivative of absorption was therefore recorded. The measurement was made at room temperature and at 77°K.

Divalent metal ions in the compounds KMF_3 having a cubic perovskite structure occupy only one crystallographic site (1b) which is surrounded by six fluorine ions at the corners of an octahedron. All manganese ions which were substituted for the divalent metal ions are therefore expected to show an equivalent spectrum.

The ground state of the Mn^{2+} ion, $3d^5\ {}^6S$,

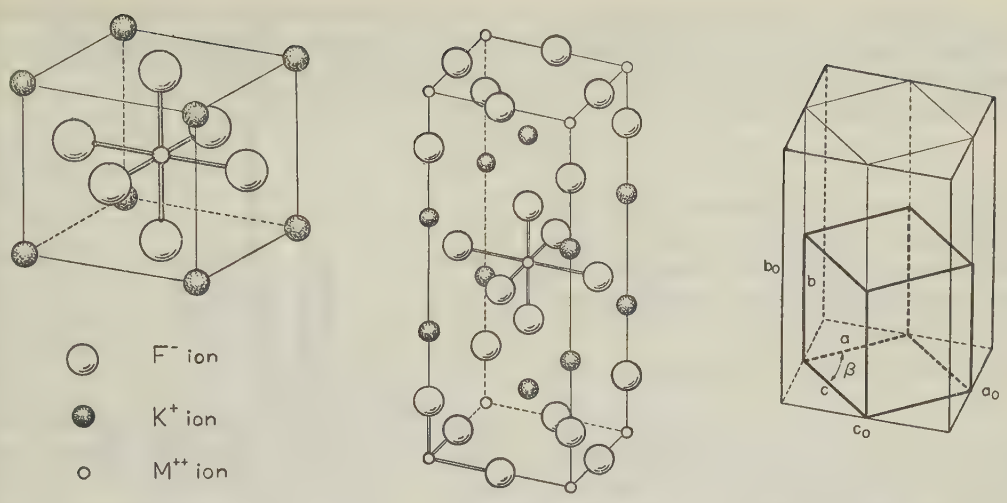

(a) (b) (c)

Fig. 1(a). A cubic perovskite structure. (b) The crystal structure of K_2MgF_4, D_{4h}-16. (c) The relation between an orthorhombic unit cell (a_0, b_0, c_0) and a distorted perovskite-like (monoclinic) pseuao-cell ($a=c, b, \beta$).

in a crystalline field of cubic symmetry is described in a good approximation by the spin Hamiltonian:

$$\mathscr{H}=g\beta\boldsymbol{S}\cdot\boldsymbol{H}+A^{55}\boldsymbol{S}\cdot\boldsymbol{I}+(a/6)[S_x^4+S_y^4+S_z^4-(1/5)S(S+1)(3S^2+3S-1)]\,, \tag{1}$$

where S and I are both 5/2, A^{55} is the hf interaction constant of a divalent Mn^{55} ion, a the cubic crystalline field splitting parameter, and g and A^{55} are assumed to be isotropic. The resonance field, H_r, can be deduced[10] from (1) in an approximation in first order of a and second order of A^{55};

$$g\beta H_r=h\nu_0-A^{55}m_I-[(A^{55})^2/2h\nu_0][I(I+1)-m_I^2+m_I(2M-1)]+F(a)\,, \tag{2}$$

where

$$F(a)=\begin{cases}0 & (\text{for } M=+1/2\leftrightarrow-1/2 \text{ transition})\\ \pm(5/2)pa & (\text{for } M=\pm3/2\leftrightarrow\pm1/2 \text{ transitions})\\ \mp2pa & (\text{for } M=\pm5/2\leftrightarrow\pm3/2 \text{ transitions})\,,\end{cases}$$

$$p=1-5(l^2m^2+m^2n^2+n^2l^2)\,,$$

and l, m and n are direction cosines of the external magnetic field with respect to the cubic axes of crystal.

In addition, there will be an interaction between an electron spin of a manganese ion and nuclear spins of six fluorine ions in its neighboring lattice sites. A theory of this interaction has been given by Tinkham[11] and its modification by Clogston *et al.*[3] for $Mn{:}ZnF_2$.

The interaction Hamiltonian is,

$$\mathscr{H}'=g\beta\gamma\beta_N\sum_{i,j}\left[-\frac{\boldsymbol{S}_i\cdot\boldsymbol{I}_j}{r_{ij}^3}+\frac{3(\boldsymbol{r}_{ij}\cdot\boldsymbol{S}_i)(\boldsymbol{r}_{ij}\cdot\boldsymbol{I}_j)}{r_{ij}^5}+\frac{8\pi}{3}\delta(\boldsymbol{r}_{ij})\boldsymbol{S}_i\cdot\boldsymbol{I}_j\right] \tag{3}$$

where r_{ij} is the electron-nucleus distance and i is summed over electrons and j over neighboring six fluorine nuclei.

By taking an expectation value with the orbital wave function of magnetic electron, one can get an effective spin Hamiltonian. Tinkham[11] has chosen the molecular orbitals used by Stevens and Owen[12] for the wave function of magnetic electron, and Clogston *et al.*[3] have moreover taken into account of the electron transfer effect. The spin Hamiltonian can be written in the from,

$$\mathscr{H}'=\sum_j \boldsymbol{S}\cdot A_j^{19}\cdot \boldsymbol{I}_j\,. \qquad (4)$$

The above theories were originally given for an orthorhombic symmetry. In our case of a cubic symmetry, the treatment can be simplified and the shift of the resonance field due to (4) is given by

$$\delta H=A_s\sum_j m_j+(A_p+A_D)\sum_j m_j(3\cos^2\theta_j-1)\,, \qquad (5)$$

where $m_j=+(1/2)$ or $-(1/2)$, θ_j is the angle between the external magnetic field and the σ-bonding axis to the j-th fluorine ion, A_s is a contribution from the admixed fluorine $2s$ orbital, A_D a dipole contribution from the original $3d$ electrons, and A_p a contribution from the admixed fluorine $2p$ orbital and is equal to $(A_{p\sigma}-A_{p\pi})$. Since the two $p\pi$ orbitals are equivalent to each other in the case of cubic symmetry, the term $(A_{p\pi'}-A_{p\pi})$ vanishes. Clogston *et al.* have pointed out the possibility of the $\Delta m=\pm1$ transition, but this anomalous transition has not been found in our spectra.

a) Mn:$KMgF_3$

All observed spectra consisted of six groups, each corresponding to a hfs component of Mn^{55}. Thus, hf interaction constant A^{55} was immediately determined using (2). However, the observed spectra were resolved not completely into the expected components. This is because a and A^{19}'s are comparable in magnitude and so F^{19} hfs components of neighboring fs components overlap each other.

When $H\|[111]$, the splittings due to F^{19} hf interaction should be simplest, but the resolution was not complete. Analysis was therefore made by trial and error. In spite of the incomplete resolution of each component, overall pattern of the spectrum was sensitive to a and A_s. The calculated spectra with $a=8\sim9.5$ Gauss and $A_s=19\sim20$ Gauss resembled closely to the observed spectrum. After the approximate values of parameters had thus been known, the more accurate values could be determined by some particular components. For example, the $m_I=-3/2$ hfs component in the $H\|[110]$ spectrum was expected to have a very small splittings due to fs. The best resolution of F^{19} hfs was therefore expected in this spectrum and really observed as shown in Fig. 2.

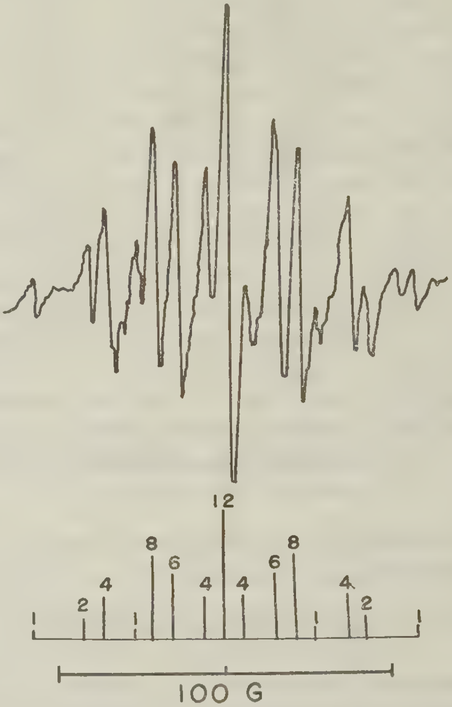

Fig. 2. The observed and calculated F^{19} hfs' in the $m_I=-2/3$ hfs component in the EPR of Mn^{2+}:$KMgF_3$ with $H\|[110]$.

b) Mn:$KCdF_3$ and Mn:$KCaF_3$

In contrast to Mn:$KMgF_3$, the spectra of Mn^{2+} in $KCdF_3$ and $KCaF_3$ has somewhat simpler patterns which were expected from (2) and (5) neglecting the crystalline field term in (2). The resolved spectral lines were however broader than those of Mn:$KMgF_3$; their width being 5∼10 Gauss. This is probably because a is so small that the fs components are not resolved. The upper bound of a was estimated from the width. The parameters other than a could be determined directly from the separations.

c) Mn:K_2MgF_4

As shown in Fig. 1, Mg ions in K_2MgF_4 have very similar environment and nearly the same Mg-F separation to that of $KMgF_3$. The observed spectrum was also very similar.

d) Mn:$NaMgF_3$

The crystal $NaMgF_3$ contains four molecules in unit cell, so four sets of spectra may be in general expected. However, the observed spectra had simple patterns just as seen in

Table II. g-factors, hf interaction constant A^{55}'s, cubic crystalline field splitting parameter a's and F^{19} hf interaction constants A_s's and (A_p+A_D)'s of Mn^{2+} ions in $KMgF_3$, $KCdF_3$, $KCaF_3$, K_2MgF_4 and $NaMgF_3$. The unit of all parameters other than g is 10^{-4} cm^{-1}. Experimentally, only the relative signs were determined; $A^{55}/a<0$ and $(A_p+A_D)/A_s>0$. The negative A^{55} and positive a are now commonly accepted.

Compound	g	A^{55}	a	$\lvert A_s\rvert$	$\lvert A_p+A_D\rvert$
$KMgF_3$	2.000±.002	−91.2±0.9	8.0±1.0	18.1±0.7	4.2±0.5
$KCdF_3$	2.002±.002	−92.6±0.9	$\leqq$4.0	15.8±0.5	2.9±0.5
$KCaF_3$	2.002±.002	−93.1±0.9	$\leqq$4.0	15.5±0.5	2.8±0.5
K_2MgF_4	2.000±.002	−91.5±0.9	8.0±1.0	18.2±0.7	4.2±0.5
$NaMgF_3$	2.001±.002	−92.5±1.5	——	18.1±1.0	3.0±1.5

the cases of $Mn:KCdF_3$ and $KCaF_3$, although the broader line suggested the unresolved splitting due to the four inequivalent Mn^{2+} ions. Since the resolution was poor and the exact atomic arrangement had not been known, the spectrum was analysed for convenience by assuming a pseudo-cubic structure. The values of parameters are therefore less reliable.

All of the parameters thus determined are summarized in Table II.

§ 5. Discussion

a) g and A^{55}

It has been known that g-factor and hf interaction constant are somewhat sensitive to the electronic state of the magnetic electron. When there is some covalency, magnetic electron moves in a somewhat extended orbital. This reduces the electron density near its nucleus and so the magnitude of hf interaction constant. The g-factor is also affected by the change of orbital state. However, if there is no orbital contribution to the total angular momentum as is the case for the ground state of Mn^{2+}, $3d^5\ {}^6S$, g-factor will not change as far as the covalency does not disturb the ${}^6S$ state.

In the crystals studied in our experiment, divalent metal ions have environments of the same symmetry but different separations, except $NaMgF_3$. At larger separation, the electronic state of metal ion should be closer to the state of a free ion and so the A^{55} will increase in magnitude. On the other hand, no change of the multiplicity ${}^6S$ may be expected for the ions with environments of the same symmetry. Therefore, the g-factor will be expected to be constant. Except the case of $Mn:NaMgF_3$ where the atomic arrangement and interatomic distances have not been known, the observed g's and A^{55}'s are in good accordance with the expected tendency, though a slight difference in g's is found within the experimental error. The electron transfer effect[3),13)] which mixes an excited non-${}^6S$ state into the ground state, may possibly account for this difference.

b) Cubic crystalline field splitting parameter a

A cubic crystalline field parameter Dq is proportional to the inverse fifth power of the interatomic distance R. According to the Watanabe's theory[14)], a cubic crystalline field splitting parameter a depends upon Dq as

$$a=(Dq)^2(8.526+0.102(Dq)^2\times10^{-6})\times10^{-10}\ \mathrm{cm}^{-1}.$$

If the small second term is neglected, a is proportional to R^{-10}. Using the values of R listed in Table I, one finds that $a(KCdF_3)/a(KMgF_3)=0.45$ and $a(KCaF_3)/a(KMgF_3)=0.41$. This is consistent with the observed ratios; $a(KCdF_3)/a(KMgF_3)\leqq0.50$ and $a(KCaF_3)/a(KMgF_3)\leqq0.50$.

c) F^{19} hf interaction constants

To separate the p-electron contribution A_p from the observed (A_p+A_D), the contribution from direct dipole-dipole interaction A_D must be subtracted. For that purpose, certain assumptions concerning the inter-ion separation and the distribution of magnetization must be made. If one assumes that the bond length for Mn^{2+} ion is equal to the metal-fluorine distance, R, of the host lattice and that all the Mn^{2+} spin magnetization is contained in a sphere of radius $r<R$, then $A_D=$ 3.2, 2.5 and 2.4×10^{-4} cm^{-1} for Mn^{2+} ions in $KMgF_3$, $KCdF_3$ and $KCaF_3$ respectively. Thus obtained A_p's (1.0, 0.4 and 0.4×10^{-4} cm^{-1}) show a large dependence upon the inter-ion separation, but their accuracy is not so high

that we shall not discuss them and confine ourselves to the *s*-electron contribution A_s.

To see the dependence of A_s upon the Mn^{2+}–F^- distance, the experimental values in this work are plotted against R in Fig. 3 together with the EPR datum of Mn:ZnF_2[3] and the NMR data of MnF_2[6] and $KMnF_3$[15].

Here, it must be emphasized that R in Fig. 3 is the metal-fluorine distance of the host lattice. In the EPR experiment, Mn^{2+} ion is diluted in the host lattice as a substitutional impurity. The true Mn^{2+}–F^- distance is therefore possible to be different from R. Although the same valency and close ionic radius hardly suggest a large distortion of the surrounding fluorine ions, the exact Mn^{2+}–F^- distance cannot be known at present.

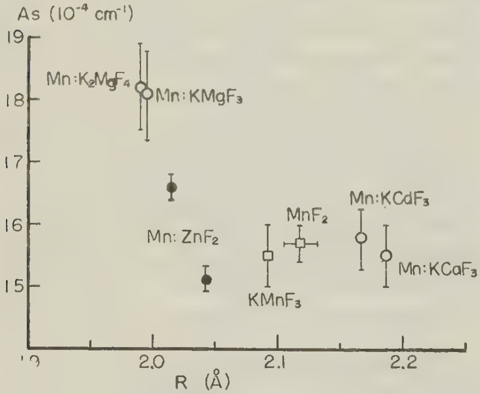

Fig. 3. A_s's plotted against R. The R's for ZnF_2 and MnF_2 are taken from Bauer[16].

Apart from this question, an appreciable variation of the A_s's is seen in Fig. 3. It is interesting that the experimental points can be fitted on a curve which concaves to the R axis rather than a linear line. As Keffer *et al.*[13] and Clogston *et al.*[3] have discussed, the A_s is proportional to $(S_s+\lambda_s)^2$ where S_s is the overlap integral between a manganese 3*d* wave function and a fluorine 2*s* wave function and λ_s is the fraction of the transferred electron from the fluorine 2*s* orbital to the manganese orbital. The wave functions may be expressed by the exponential functions at an outer part of orbital. The S_s may also have an exponential-like dependence upon R. Though it is difficult to know the dependence and the magnitude of λ_s, Keffer *et al.* have estimated S_s and λ_s to be 0.05 and 0.01 respectively for MnF_2. Because of the relative smallness of λ_s, A_s may be supposed to have an exponential-like dependence. This situation explains qualitatively the observed behavior of A_s. It is desired that the "first-principles" calculation as have been done by Mukherji and Das[17] will be carried out at more wide range of interionic separation.

Shulman *et al.*[15] have made the NMR measurement of F^{19} in $KMnF_3$ and determined A_s to be 15.5×10^{-4} cm^{-1}. The Mn^{2+}–F^- distance in $KMnF_3$ is a half of the lattice constant, $a_0=4.186$ Å[8], and lies among the metal-fluorine distances in the crystals studied in the present experiment. Therefore, in spite of the ambiguity of the Mn^{2+}–F^- distances in the host lattices, it can be safely said from our EPR data that the A_s in the dense, magnetic crystal $KMnF_3$ lies between 15.5 and 18.2×10^{-4} cm^{-1}. If a linear interpolation is made, the A_s is 16.7×10^{-4} cm^{-1}, but it will be somewhat close to 15.5×10^{-4} cm^{-1} by reason of the above discussed dependence of A_s upon R, in agreement with the value obtained from NMR with in the the experimental error.

In conclusion, magnetic electrons of the Mn^{2+} ion surrounded by a complete octahedron of fluorine ions with the bond length of 1.99 ∼2.19 Å have 0.58∼0.49% 2*s* character at each Mn^{2+}–F^- bond, or $(S_s+\lambda_s)^2$ in Keffer's notation is $0.58\sim0.49\times10^{-2}$.

§ 6. Summary

1) The Mn^{2+} ions as dilute, substitutional impurities in $KMgF_3$, $KCdF_3$, $KCaF_3$ and K_2MgF_4 surrounded by a complete octahedron of six fluorine ions and that in $NaMgF_3$ by a nearly complete octahedron.

2) The *g*-factors are constant and A^{55}'s increase slightly in magnitude with increasing Mn^{2+}–F^- distance, in accordance with the theoretically expected tendency.

3) The F^{19} hf interaction constant A_s has shown an appreciable dependence upon Mn^{2+}–F^- distance. It should be taken care of this dependence when one deduces the value of F^{19} hf interaction constant in a dense, magnetic crystal from the EPR data of the paramagnetic ion diluted in the host isomorphic diamagnetic crystal. When the dependence is taken into account, both the A_s's obtained from EPR and NMR measurements are in rather good agreement with each other.

Acknowledgements

The author wishes to express his sincere thanks to Professor Y. Yokozawa for his kind encouragement throughout the course of this work, and to Drs. H. Watanabe and T. Asahi for their helpful and stimulating discussions. He is also indebted to Dr. V. Jaccarino for a reprint of his work.

References

1) J. H. E. Griffiths and J. Owen: Proc. Roy. Soc. A, **226** (1954) 96.
2) M. Tinkham: Proc. Roy. Soc. A, **236** (1956) 535.
3) A. M. Clogston, J. P. Gordon, V. Jaccarino, M. Peter and L. R. Walker: Phys. Rev. (to **117** (1960) 1222.
4) J. M. Baker, B. Bleaney and W. Hayes: Proc. Roy. Soc. A, **247** (1958) 141.
5) W. Hayes and D. A. Jones: Proc. Phys. Soc. London **71** (1958) 503.
6) R. G. Shulman and V. Jaccarino: Phys. Rev. **108** (1957) 1219.
7) P. W. Anderson: Phys. Rev. **79** (1950) 350.
8) S. Ogawa: J. Phys. Soc. Japan **14** (1959) 1115.
9) S. Ogawa and Y. Yokozawa: J. Phys. Soc. Japan **14** (1959) 1116.
10) See for example, W. Low: Phys. Rev. **105** (1957) 793.
11) M. Tinkham: Proc. Roy. Soc. A, **236** (1956) 549.
12) K. W. H. Stevens: Proc. Roy. Soc. A, **219** (1953) 542, and J. Owen: *ibid.* A, **227** (1955) 183.
13) F. Keffer, T. Oguchi, W. O'Sullivan and J. Yamashita: Phys. Rev. **115** (1959) 1553.
14) H. Watanabe: Progr. Theor. Phys. **18** (1957) 405.
15) R. G. Shulman, K. Knox and B. J. Wyluda: Bull. Amer. Phys. Soc. **4** (1959) 166.
16) W. H. Bauer: Acta Cryst. **11** (1958) 488.
17) A. Mukherji and T. P. Das: Phys. Rev. **111** (1958) 1479.

Note added in proof: (1) In a recent paper (Phys. Rev. Letters 4 (1960) 603), Shulman and Knox have reported new value of the A_s in $KMnF_3$ as $(16.26\pm0.5)\times10^{-4}\,cm^{-1}$. The A_s estimated from EPR in the text is now in satisfactory agreement with the NMR result.

(2) Benedek and Kushida (Phys. Rev. **118** (1960) 46) have recently shown the dependence of A_s upon Mn-F distance in MnF_2 by applying hydrostatic pressure while measuring the F^{19} resonance frequency at the antiferromagnetic state of MnF_2. They have shown a satisfactory agreement of their experimental results with those calculated by Marshall and Stuart (quoted in the paper by Benedek and Kushida). Marshall and stuart calculated f_{2s}, the degree of unpairing of the $2s$ fluorine orbital, for the Mn-F distances of 2.10 to 2.14Å at intervals of 0.01Å. If we assume that these calculated values can be applied to Mn^{2+} ions in the crystals studied in our experiment and assume a linear extrapolation to be hold, we can determiee the Mn-F distances in the host crystals of $KMgF_3$, $KCdF_3$, and $KCaF_3$ to be 2.080 2.119, and 2.124Å respectively. The more accurate values of A_s in more wide range of Mn-F distance are desired to be established by theoretical calculations and NMR study of F^{19} in $KMnF_3$ with application of hydrostatic pressure. Then, the A_s obtained from EPR measurement will give us an accurate knowledge of the local distortion arround impurity ion.

Journal of the Physical Society of Japan, Vol. 15, No. 8, August, 1960

The Dipole Moment and End-to-end Length of the Isotactic Vinyl Polymer, I. Mutual Dependence between Dipole Moment and End-to-end Length

By Tsugio Mori

Ôtsu Senior High School, Ôtsu, Shiga-ken, Japan

(Received March 28, 1960)

The formulas for the mean-squared dipole moment and end-to-end length of the isotactic vinyl polymer are derived. The polymer model used in these derivations is similar to Lifson's one[1], but the dependence of these mean-squared quantities on molecular weight of the polymer is considered in the present calculations. The two mean-squared quantities, dipole moment and end-to-end length, are not independent of each other, and it is pointed out that they are connected by a simple expression. On the other hand, the present treatment is useful to see the corrected Staudinger's viscosity rule from a new point of view.

§ 1. Fundamental Notations

The linear polymer discussed in this paper is the polar isotactic vinyl-type one, and is treated in state of an infinitely diluted solution. The molecular formula of this polymer is $(CH_2-CHR)_nCH_2$, where R is a dipolar substituent. The number of skeletal carbon atoms is

$$N=2n+1\,, \tag{1}$$

and we designate these carbon atoms by

$$C_1,\ C_2,\ \cdots,\ C_{2n+1}$$

successively from one end of the skeletal chain. The bond vector from C_k to C_{k+1} is denoted by $\boldsymbol{b}_k$, and lengths of vectors

$$\boldsymbol{b}_1,\ \boldsymbol{b}_2,\ \cdots,\ \boldsymbol{b}_{2n}$$

are assumed to be all equal to b_0. The electric dipole moment vector of the side chain $C_{2i}-R_i$ is denoted by $\boldsymbol{\mu}_i$, and lengths of vectors

$$\boldsymbol{\mu}_1,\ \boldsymbol{\mu}_2,\ \cdots,\ \boldsymbol{\mu}_n$$

are assumed to be all equal to μ_0. The above polymer model and notations are shown in Fig. 1.

Four bonds meeting at a skeletal carbon atom construct a set of tetrahedral angles, which are assumed to undergo no change through internal rotation of the chain.

Then we discuss the internal rotation of the skeletal chain. The angle of two adjoining bond vectors is denoted by γ, which is a constant and equal to the supplement of the bond angle. The vector $\boldsymbol{b}_{j-1}$ may be considered to rotate regarding $\boldsymbol{b}_{j-2}$ as a fixed axis. Here we denote the rotation angle of $\boldsymbol{b}_{j-1}$ by φ_j, and put $\varphi_j=0$ when $\boldsymbol{b}_{j-3}$ and $\boldsymbol{b}_{j-1}$ form the trans type connection holding $\boldsymbol{b}_{j-2}$ between them. Next we define the system of unit vectors $\boldsymbol{i}_j$, $\boldsymbol{j}_j$, $\boldsymbol{k}_j$ attached to the carbon atom C_j according to the following scheme. In the first place, we set $\boldsymbol{k}_j$ in the

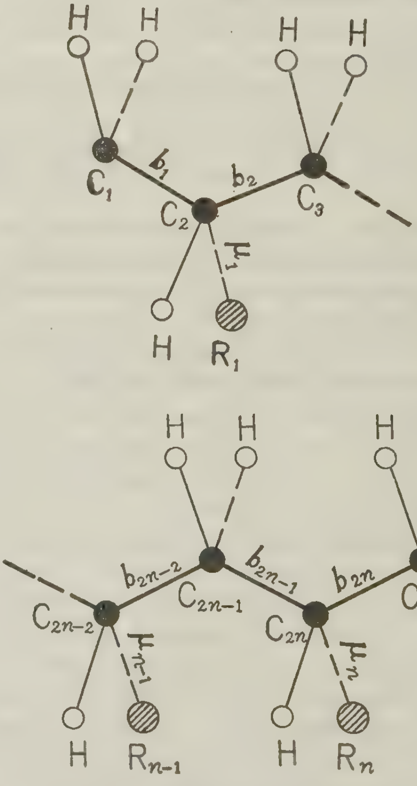

Fig. 1. Isotactic vinyl polymer.

same direction as $\boldsymbol{b}_{j-1}$. Next, let us consider two projected lines both of which start from C_j on the plane determined by three points C_{j-2}, C_{j-1}, C_j and are prependicular to $\boldsymbol{k}_j$. The one of those two projected lines should ntersect the vector $\boldsymbol{b}_{j-2}$ or its extension, and this projection defines the direction of $\boldsymbol{i}_j$. Last of all, $\boldsymbol{j}_j$ is introduced in order to obtain the right-handed orthogonal system formed by $\boldsymbol{i}_j$, $\boldsymbol{j}_j$, $\boldsymbol{k}_j$. These notations are illustrated n Fig. 2.

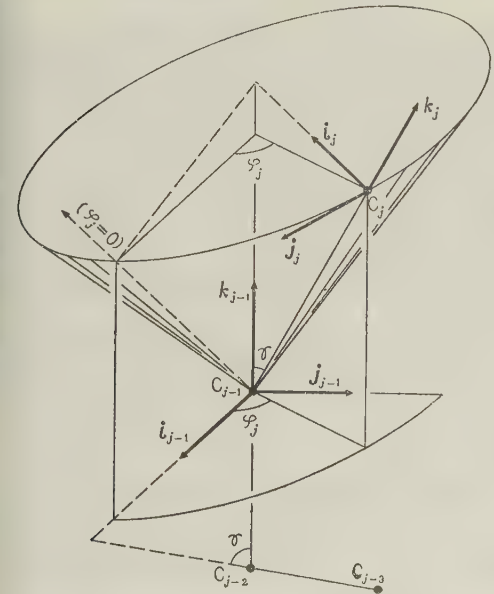

Fig. 2. Internal rotation of skeletal chain.

According to the above discussion, we may consider two sets of components of a vector, namely, components x_j, y_j, z_j in the directions of $\boldsymbol{i}_j$, $\boldsymbol{j}_j$, $\boldsymbol{k}_j$ respectively, and x_{j-1}, y_{j-1}, z_{j-1} n the directions of $\boldsymbol{i}_{j-1}$, $\boldsymbol{j}_{j-1}$, $\boldsymbol{k}_{j-1}$ respectively. Then we have

$$x_j\boldsymbol{i}_j+y_j\boldsymbol{j}_j+z_j\boldsymbol{k}_j=x_{j-1}\boldsymbol{i}_{j-1}+y_{j-1}\boldsymbol{j}_{j-1}+z_{j-1}\boldsymbol{k}_{j-1}\ . \tag{2}$$

We denote the matrix which transforms x_j, y_j, z_j into x_{j-1}, y_{j-1}, z_{j-1} by $\mathbf{D}_j$:

$$\begin{pmatrix} x_{j-1} \\ y_{j-1} \\ z_{j-1} \end{pmatrix}=\mathbf{D}_j\begin{pmatrix} x_j \\ y_j \\ z_j \end{pmatrix}. \tag{3}$$

Let us put, for convenience' sake,

$$\alpha=\cos\gamma\ , \qquad \beta=\sin\gamma\ , \tag{4}$$

and define the matrix $\mathbf{D}$ or $\mathbf{D}(\varphi)$ by

$$\mathbf{D}=\mathbf{D}(\varphi)=\begin{pmatrix} -\alpha\cos\varphi & \sin\varphi & \beta\cos\varphi \\ -\alpha\sin\varphi & -\cos\varphi & \beta\sin\varphi \\ \beta & 0 & \alpha \end{pmatrix}, \tag{5}$$

then the matrix $\mathbf{D}_j$ in Equation (3) is given by

$$\mathbf{D}_j=\mathbf{D}(\varphi_j)\ . \tag{6}$$

The matrix $\mathbf{D}$ has the following natures:

(i) $\mathbf{D}$ is an orthogonal transformation, namely

$$\mathbf{D}^T(\varphi)\mathbf{D}(\varphi)=\mathbf{1}\ , \tag{7}$$

where $\mathbf{D}^T(\varphi)$ is the transposed matrix of $\mathbf{D}(\varphi)$, and $\mathbf{1}$ is the unit matrix.

(ii) The skeletal chain extended to the zig-zag style on a plane is considered as the repetition of trans type connections, namely, parallel bond vectors repeate every two ones is such planar chain. Accordingly we have

$$[\mathbf{D}(0)]^2=\mathbf{1}\ . \tag{8}$$

(iii) In the crystalline state, the skeletal chain is composed of the alternating trans and gauche type connections. Let us consider the unit chain CH_2-CHR being a segment, then three segments complete one period of the chain. Then we have

$$[\mathbf{D}(2\pi/3)\mathbf{D}(0)]^3=\mathbf{1}\ . \tag{9}$$

It is remarked that Eq. (9) is a special case of

$$[\mathbf{D}(2\pi/k)\mathbf{D}(0)]^k=\mathbf{1}\ , \tag{10}$$

where k is an integer.

Although the above natures (i)~(iii) of the matrix $\mathbf{D}$ are self-evident, some authors have given no care upon the confermation test of Eqs. (7)~(9), and used incorrect matrices.

§2. General Formulas for Mean Square of Electric Dipole Moment

The electric dipole moment vector of the polymer, denoted by μ, is given by

$$\mu=\mu_1+\mu_2+\cdots+\mu_n\ . \tag{11}$$

Then the square of the absolute value of μ is given by

$$\mu^2=\left(1+\frac{2}{n}\sum_{i<i}^{n}\sum\cos\omega_{ij}\right)n\mu_0^2\ , \tag{12}$$

where ω_{ij} signifies the angle between μ_i and μ_j, and the double summation is taken for i- and j-values given by

$$i=1,\ 2,\ \cdots,\ n$$

and

$$j=2,\ 3,\ \cdots,\ n$$

but $i<j$. If we take the mean of μ^2, Eq. (12) is replaced by

$$\langle\mu^2\rangle=\left(1+\frac{2}{n}\sum_{i<j}^{n}\sum\langle\cos\omega_{ij}\rangle\right)n\mu_0^2\,, \tag{13}$$

where the notation $\langle\cos\omega_{ij}\rangle$ signifies the mean of $\cos\omega_{ij}$ for all configurations of the polymer chain in an infinitely diluted solution.

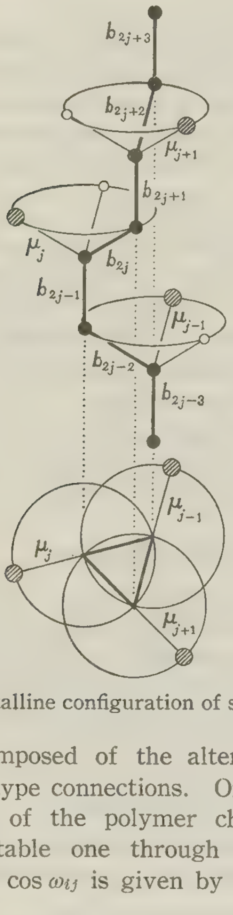

Fig. 3. Crystalline configuration of skeletal chain.

In order to estimate $\langle\cos\omega_{ij}\rangle$, we assume that our polymer chain is most stable in the crystalline configuration illustrated in Fig. 3 which is composed of the alternating trans and gauche type connections. Of course, the configuration of the polymer chain deviates from this stable one through the internal rotation, and $\cos\omega_{ij}$ is given by

$$\cos\omega_{ij}=(001)\mathbf{D}^T\left(\varphi_{2i+1}-\frac{2\pi}{3}\right)\mathbf{D}_{2i+1}\mathbf{D}_{2i+2}\cdots$$
$$\cdots\mathbf{D}_{2j-1}\mathbf{D}_{2j}\mathbf{D}\left(\varphi_{2j+1}-\frac{2\pi}{3}\right)\begin{pmatrix}0\\0\\1\end{pmatrix}, \tag{14}$$

where the notations $\mathbf{D}(\varphi_{2j+1}-2\pi/3)$ and $\mathbf{D}_{2j}$ designate respectively the substitutions of $\varphi=\varphi_{2j+1}-2\pi/3$ and $\varphi=\varphi_{2j}$ in $\mathbf{D}(\varphi)$ defined by (5), and other notations in (14) may also be understood in the similar way. In order to take the mean of (14), we put the second assumption that the rotations of segments as a whole are independent of each other, but in a segment there is a correlation between rotations of two bond vectors. A similar as- sumption has been attempted by Lifson[1]. We devide φ-variables into the following scheme:

$$|\varphi_3\varphi_4|\varphi_5\varphi_6|\cdots|\varphi_{2j-1}\varphi_{2j}|\cdots|\varphi_{2n-1}\varphi_{2n}|\,,$$

and consider that, φ_{2j-1} and φ_{2j} are correlate to each other, but other φ-variables have n correlation to these two variables. In this way, we assume

$$\varphi'=\varphi'(\varphi)\,,\qquad \varphi'(0)=2\pi/3\,, \tag{15}$$

where φ' and φ are abbreviations of φ_{2j-1} and φ_{2j}, respectively. We assume the relations (15) for all φ-pairs commonly. For example, if φ' denotes φ_3, then φ denotes φ_4. The second relation of (15) is concerned with the first assumption which states that the most stable configuration may be realized for $\varphi'=2\pi/3$ and $\varphi=0$.

According to these assumptions we can write

$$\langle\cos\omega_{ij}\rangle=(001)\mathbf{Y}^T\mathbf{X}^{|j-i|}\mathbf{Y}\begin{pmatrix}0\\0\\1\end{pmatrix}, \tag{16}$$

where we put

$$\langle\mathbf{D}_3\mathbf{D}_4\rangle=\langle\mathbf{D}_5\mathbf{D}_6\rangle=\cdots=\langle\mathbf{D}_{2n-1}\mathbf{D}_{2n}\rangle$$
$$=\langle\mathbf{D}(\varphi')\mathbf{D}(\varphi)\rangle=\mathbf{X} \tag{17}$$

and

$$\mathbf{D}\left(\varphi_3-\frac{2\pi}{3}\right)=\cdots=\mathbf{D}\left(\varphi_{2n+1}-\frac{2\pi}{3}\right)$$
$$=\mathbf{D}\left(\varphi'-\frac{2\pi}{3}\right)=\mathbf{Y}\,. \tag{18}$$

Substitution of (16) in Eq. (13) yields

$$\langle\mu^2\rangle=\left\{1+2(001)\mathbf{Y}^T\mathbf{X}\right.$$
$$\left.\times\left(\frac{1}{n}\sum_{i<j}^{n}\sum\mathbf{X}^{j-i-1}\right)\mathbf{Y}\begin{pmatrix}0\\0\\1\end{pmatrix}\right\}n\mu_0^2\,. \tag{19}$$

The summation in this expression should be read

$$\frac{1}{n}\sum_{i<j}^{n}\sum\mathbf{X}^{j-i-1}$$
$$=(\mathbf{1}-\mathbf{X})^{-1}\left\{\mathbf{1}+\frac{1}{n}(\mathbf{1}-\mathbf{X})^{-1}(\mathbf{X}^n-\mathbf{1})\right\}. \tag{20}$$

Let us denote the null matrix by $\mathbf{0}$, then it is evident that

$$\lim_{n\to\infty}\frac{1}{n}[\mathbf{D}(\varphi')\mathbf{D}(\varphi)]^n=\mathbf{0}\,, \tag{21}$$

for the product $\mathbf{D}(\varphi')\mathbf{D}(\varphi)$ is orthogonal*, so is $[\mathbf{D}(\varphi')\mathbf{D}(\varphi)]^n$. However, the formula

$$\lim_{n\to\infty}\frac{1}{n}[\langle\mathbf{D}(\varphi')\mathbf{D}(\varphi)\rangle]^n=\mathbf{0} \quad \text{or} \quad \lim_{n\to\infty}\frac{1}{n}\mathbf{X}^n=0 \tag{22}$$

is not evident, for $\mathbf{X}$ is not orthogonol. Some authors have assumed the formula (22), or treated only the case satisfying (22), and they have reduced (20) to

$$\frac{1}{n}\sum_{i<j}^{n}\sum \mathbf{X}^{j-i-1}\rightarrow(\mathbf{1}-\mathbf{X})^{-1}$$

as $n\rightarrow\infty$, with no study of conditions for the convergence. In this paper, however, we consider that the formula (22) is not satisfied in general, and approximate the formula (20) to

$$\frac{1}{n}\sum_{i<j}^{n}\sum \mathbf{X}^{j-i-1}=\{1+g(n)\}(\mathbf{1}-\mathbf{X})^{-1}\,, \tag{23}$$

where $g(n)$ is a function of n, and it is expected that

$$\lim_{n\to\infty} g(n)\left\{\begin{aligned} &=\infty \text{ (for most chain configurations).}\\ &=\text{a const. (for the random coil).}\end{aligned}\right\} \tag{24}$$

Substitution of (23) in (19) yields

$$\langle\mu^2\rangle=\left[1+\{1+g(n)\}\left(\frac{\langle\mu^2\rangle_0}{n\mu_0^2}-1\right)\right]n\mu_0^2\,, \tag{25}$$

where $\langle\mu^2\rangle_0$ signifies the value of $\langle\mu^2\rangle$ when $g(n)$ is neglected, namely,

$$\langle\mu^2\rangle_0=\left\{1+2(001)\mathbf{Y}^T\mathbf{X}(\mathbf{1}-\mathbf{X})^{-1}\mathbf{Y}\begin{pmatrix}0\\0\\1\end{pmatrix}\right\}n\mu_0^2\,. \tag{26}$$

The details of the function $g(n)$ may be explained later in concerning with the treatment of the mean square end-to-end length of the polymer.

§ 3. General Formulas for Mean Square of End-to-end Length

The vector from C_1 to C_{2n+1}, denoted by R, is given by

$$\boldsymbol{R}=\boldsymbol{b}_1+\boldsymbol{b}_2+\cdots+\boldsymbol{b}_{2n}\,. \tag{27}$$

Then the mean square of the absolute value of R is

$$\langle R^2\rangle=\left(1+\frac{1}{n}\sum_{i<j}^{2n}\sum\langle\cos\theta_{ij}\rangle\right)2nb_0^2\,, \tag{28}$$

where θ_{ij} signifies the angle between two vectors b_i and b_j, and the meaning of $\langle\cos\theta_{ij}\rangle$ is similar to that of $\langle\cos\omega_{ij}\rangle$ in the preceding section. Some differences between (13) and (28) are due to the fact that the double summations extend to $j=n$ and $j=2n$, respectively, in (13) and (28). The formula for $\cos\theta_{ij}$ is given by

$$\cos\theta_{ij}=(001)\mathbf{D}_{i+2}\mathbf{D}_{i+3}\cdots\mathbf{D}_{j+1}\begin{pmatrix}0\\0\\1\end{pmatrix} \tag{29}$$

which differs from $\cos\omega_{ij}$. It is remembered that the number of matrices in (14) is even and there are naturally the division

$$|\mathbf{D}_3\mathbf{D}_4|\mathbf{D}_5\mathbf{D}_6|\cdots|\mathbf{D}_{2n-1}\mathbf{D}_{2n}|\,.$$

Thus $\langle\cos\omega_{ij}\rangle$ is able to reduce to the form as (16). However, the formula (29) has not such regularity, and we need another method in order to estimate $\sum\sum\langle\cos\theta_{ij}\rangle$.

If we put

$$\langle\mathbf{D}_4\rangle=\langle\mathbf{D}_6\rangle=\cdots=\langle\mathbf{D}_{2n}\rangle=\langle\mathbf{D}(\varphi)\rangle=\mathbf{Z} \tag{30}$$

and

$$\langle\mathbf{D}_3\rangle=\langle\mathbf{D}_5\rangle=\cdots=\langle\mathbf{D}_{2n+1}\rangle=\langle\mathbf{D}(\varphi')\rangle=\mathbf{Z}' \tag{31}$$

and use $\mathbf{X}$ defined by (17), we find five kinds of expressions of the mean $\langle\mathbf{D}_{i+2}\mathbf{D}_{i+3}\cdots\mathbf{D}_{j+1}\rangle$ for the combinations of even and odd values of j and i. These expressions are shown in Table I.

Table I.

j	i	$\langle\mathbf{D}_{i+2}\mathbf{D}_{i+3}\cdots\mathbf{D}_{j+1}\rangle$
$2l-1$ (odd)	$2k$ (even)	$\mathbf{Z}\mathbf{X}^{l-k-1}$
$2l-1$ (odd)	$2k-1$ (odd)	$\mathbf{X}^{l-k}$
$2l$ (even)	$2k$ (even)	$\mathbf{Z}\mathbf{X}^{l-k-1}\mathbf{Z}'$
$2l$ (even)	$2k-1$ (odd)	$\mathbf{X}^{l-k}\mathbf{Z}'$
$2l$	$2l-1$	$\mathbf{Z}'$

(for $l>k$)

Accordingly we have

$$\begin{aligned}\sum_{i<j}^{2n}\sum\langle\cos\theta_{ij}\rangle&=(001)\left\{\sum_{k<l}^{n}\sum(\mathbf{Z}\mathbf{X}^{l-k-1}+\mathbf{X}^{l-k}+\mathbf{Z}\mathbf{X}^{l-k-1}\mathbf{Z}'+\mathbf{X}^{l-k}\mathbf{Z}')+n\mathbf{Z}'\right\}\begin{pmatrix}0\\0\\1\end{pmatrix}\\ &=(001)\left\{(\mathbf{Z}+\mathbf{X})\left(\sum_{k<l}^{n}\sum\mathbf{X}^{l-k-1}\right)(\mathbf{1}+\mathbf{Z}')+n\mathbf{Z}'\right\}\begin{pmatrix}0\\0\\1\end{pmatrix};\end{aligned} \tag{32}$$

---

* Eq. (7) yields the relation $[\mathbf{D}(\varphi')\mathbf{D}(\varphi)]^T[\mathbf{D}(\varphi')\mathbf{D}(\varphi)]=\mathbf{D}^T(\varphi)\mathbf{D}^T(\varphi')\mathbf{D}(\varphi')\mathbf{D}(\varphi)=\mathbf{D}^T(\varphi)\mathbf{D}(\varphi)=\mathbf{1}$. Therefore $\mathbf{D}(\varphi')\mathbf{D}(\varphi)$ is orthogonal.

remarking that j and l in double summations run to $2n$ and n, respectively. For further reductions of (32), let us remember the assumption that

$$\frac{1}{n}\sum\sum_{k<l}^{n}\mathbf{X}^{l-k-1}=\{1+g(n)\}(\mathbf{1}-\mathbf{X})^{-1}\,,$$

and replace $\mathbf{Z}+\mathbf{X}$ by $(\mathbf{1}+\mathbf{Z})-(\mathbf{1}-\mathbf{X})$. Then we have

$$\frac{1}{n}\sum\sum_{i<j}^{2n}\langle\cos\theta_{ij}\rangle=\{1+g(n)\}(001)(\mathbf{1}+\mathbf{Z})(\mathbf{1}-\mathbf{X})^{-1}(\mathbf{1}+\mathbf{Z}')\begin{pmatrix}0\\0\\1\end{pmatrix}-g(n)(1+\alpha)-1\,. \tag{33}$$

Substitution of (33) in Eq. (28) yields

$$\langle R^2\rangle=\{1+(1-P)g(n)\}\langle R^2\rangle_0\,, \tag{34}$$

where

$$P=\frac{1+\alpha}{(001)(\mathbf{1}+\mathbf{Z})(\mathbf{1}-\mathbf{X})^{-1}(\mathbf{1}+\mathbf{Z}')\begin{pmatrix}0\\0\\1\end{pmatrix}} \tag{35}$$

and

$$\langle R^2\rangle_0=(001)(\mathbf{1}+\mathbf{Z})(\mathbf{1}-\mathbf{X})^{-1}(\mathbf{1}+\mathbf{Z}')\begin{pmatrix}0\\0\\1\end{pmatrix}2nb_0^2\,. \tag{36}$$

In this way, $\langle R^2\rangle_0$ signifies the value of $\langle R^2\rangle$ when $g(n)$ is neglected.

§ 4. Discussion of $g(n)$ Term

The formula (36) agrees with Lifson's result[1], and the so-called mean square end-to-end lengths treated customarily are mostly of such type, of which the character is to neglect the $g(n)$ term.

In this paper, however, the $g(n)$ term is not negligible, but infinitely large as $n\to\infty$. Now we should estimate the order of infinity of $g(n)$. Let us consider, in the first place, the limit in which the polymer is extended as a rigid straight rod, then $\langle R^2\rangle$ is equal to $(2nb_0)^2$ and is infinity of the order of n^2 while $\langle R^2\rangle_0$ is infinity of the order of n. Therefore we conclude that $g(n)$ is infinity of the order of n from Eq. (34) in the limit of ridid straight polymer. Let us consider, next, another limit that the polymer is in the so-called unperturbed configuration and $\langle R^2\rangle=\langle R^2\rangle_0$. In this limit, $g(n)$ must vanish. According to these considerations, we assume

$$g(n)=K(n^\nu-1)\,, \tag{37}$$

where K and ν are both constants independent of n. In special, ν is limited within the interval

$$0\leqq\nu\leqq1\,. \tag{38}$$

Of course, $\nu=1$ and $\nu=0$ correspond to the ridid straight configuration and the unperturbed one respectively. In principle, the values of K and ν should be estimated through the potential of the internal rotation of the polymer chain. However, the assumption (37) is needed in this stage to avoid difficulties of theoretical treatment of $g(n)$. Then it should be an immediate problem for us, whether we can find the value of ν within the interval (38) or not, through comparison of the assumption (37) with experiments.

If we put

$$\rho=(\langle R^2\rangle/\langle R^2\rangle_0)^{1/2}\,, \tag{39}$$

the parameter ρ is the same as Flory's one introduced in his theory of the effect of excluded volume, namely, the linear expansion ratio of the polymer through that effect. From (34), (39) and (37), we have

$$\rho^2-1=K(1-P)(n^\nu-1)\,, \tag{40}$$

accordingly ρ is an increasing function of n. Therefore we should have a straight line, of which the slope is one, in the plot of $\log(\rho^2-1)$ against $\log(n^\nu-1)$ under suitable choice of ν. It is unavoidable to use experimental values of atactic polymers in place of that values of isotactic ones, because the lack of data of isotactic ones.

Some data of molecular weights and cubes of ρ are shown in Tables II and III, in which the former Table concerns with polyisobutylen-

Table II. Polyisobutylen-cyclohexane (30°C), $M_0=56.104$

M	ρ^3	$n^{0.25}-1$	ρ^2-1
9.5×10^3	1.39	2.61	0.245
5.02×10^4	1.96	4.47	0.565
5.58×10^5	3.10	8.99	1.126
2.72×10^6	4.46	13.8	1.71

Table III. Polystyrene-benzene (20°C), $M_0=104.144$.

M	ρ^3	$n^{0.25}-1$	ρ^2-1
4.45×10^4	1.55	3.55	0.339
6.55×10^4	1.70	4.01	0.423
2.62×10^5	2.54	6.08	0.860
6.94×10^5	3.03	8.03	1.094
2.55×10^6	4.22	11.51	1.61
6.27×10^6	5.73	14.7	2.20

cyclohexane solution, and the latter with polystyrene-benzene solution. These values are taken from Flory's text book[2].

In these Tables, M and M_0 denotes the molecular (or submolecular) weights of the polymer and segment, respectively, and the relation

$$n=M/M_0 \tag{41}$$

is self-evident. The values of $n^\nu-1$ and ρ^2-1 are also shown in these tables, where the value $\nu=0.25$ is chosen. The plots of $\log(\rho^2-1)$ against $\log(n^\nu-1)$ due to Tables II and III are illustrated in Fig. 4.

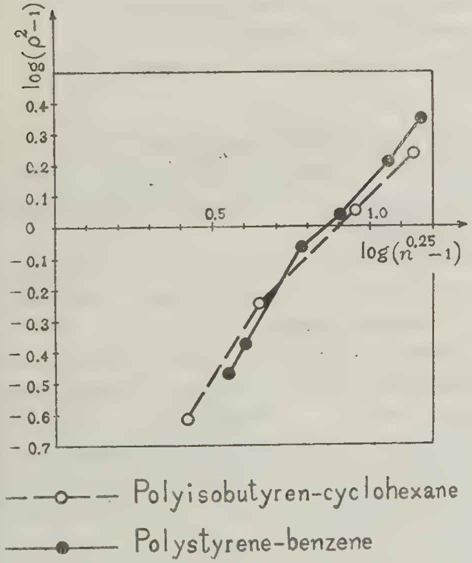

Fig. 4. log-log plots of (ρ^2-1) against $(n^\nu-1)$.

The plots seem nearly straight lines of which each slope is one. Thus the relation (40) is satisfactory beyond such a rough treatment, namely, an experimental foundation has been given to the assumptions (37) and (23).

There is another interest in discussion of the constant ν with the viscosity of solution. If we denote the intrinsic viscosity by $[\eta]$, the Staudinger's rule is written as

$$[\eta]=(\text{const.})M\,.$$

But this rule agrees not always with experiment, and it is corrected to the form

$$[\eta]=(\text{const.})M^{\zeta}\,, \tag{42}$$

where $\zeta=0.5\sim1$ for almost polymers, and $\zeta=2$ for straight rod polymers. Till now, there are two kinds of independent theories, the one of which explains Eq. (42) for $\zeta=2$, although unfortunately the author has no convenience to seek for which paper describes that theory. Another kind of theories[2,3,4] explains Eq. (42) for $\zeta=0.5\sim1$. However, we have an unified treatment that explains Eq. (42) for $\varepsilon=0.5\sim2$ if we combine the relation (40) with Elory's method[2]. According to Flory, we use the relation

$$[\eta]=(\text{const.})M^{1/2}\rho^3\,. \tag{43}$$

From (40) and (41), we write

$$\rho=(\text{const.})n^{\nu/2}=(\text{const.})M^{\nu/2} \tag{44}$$

for large n and ρ. Let us substitute (44) in (43), and compare with (42). Then we have

$$\zeta=(3\nu+1)/2\,. \tag{45}$$

Remembering the interval (38) of ν, we have $\zeta=0.5$ for unperturbed polymer chain, and $\zeta=2$ for straight polymer chain. Thus we have a simple treatment that explains (42) within the interval

$$0.5\leqq\zeta\leqq2\,.$$

§ 5. Mutual Dependence between Electric Dipole Moment and End-to-end Length

In general $g(n)$ relates to $\langle R^2\rangle$ and $\langle R^2\rangle_0$ according to the relation

$$1+g(n)=\frac{\rho^2-P}{1-P}=\frac{\langle R^2\rangle-(1+\alpha)Nb_0^2}{\langle R^2\rangle_0-(1+\alpha)Nb_0^2} \tag{46}$$

which is derived from (34), (35), (36) and $N=2n+1\simeq2n$. Substitution of (46) in (25) yields

$$\frac{\langle\mu^2\rangle}{n\mu_0^2}=1+\frac{\rho^2-P}{1-P}\left(\frac{\langle\mu^2\rangle_0}{n\mu_0^2}-1\right), \tag{47}$$

or

$$\frac{\langle\mu^2\rangle-n\mu_0^2}{\langle\mu^2\rangle_0-n\mu_0^2}=\frac{\langle R^2\rangle-(1+\alpha)Nb_0^2}{\langle R^2\rangle_0-(1+\alpha)Nb_0^2}\,. \tag{48}$$

Therefore $\langle\mu^2\rangle$ and $\langle R^2\rangle$ are dependent on each other through Eq. (48). Numerical calculations of $\langle\mu^2\rangle_0/n\mu_0^2$ and $\langle R^2\rangle_0/Nb_0^2$ may be carried out independently. However, three kinds of values, $\langle\mu^2\rangle_0/n\mu_0^2$, $\langle R^2\rangle_0/Nb_0^2$ and ρ, are needed when we wish to calculate the numerical values of $\langle\mu^2\rangle/n\mu_0^2$. These calculations may be performed in the succeeding paper[5] for a special type of internal rotation.

References

1) S. Lifson: J. Chem. Phys. **29** (1958) 80.
2) P. J. Flory: *Principles of Polymer Chemistry*, Chap. 14, Cornell University Press, New York (1953).
3) P. Debye and A. M. Bueche: J. Chem. Phys. **16** (1948) 573.
4) J. G. Kirkwood and J. Riseman: J. Chem. Phys. **16** (1948) 565.
5) T. Mori: J. Phys. Soc. Japan **15** (1960) No. 9, in the press.

JOURNAL OF THE PHYSICAL SOCIETY OF JAPAN, Vol. 15, No. 8, AUGUST, 1960

Magneto-plasma Resonance in Semiconductors (I)

Muneyuki DATE
Department of Physics, Faculty of Science,
Osaka University, Osaka

(Received April 1, 1960)

Theory of the magneto-plasma resonance in semiconductors is developed for the general case where several kinds of free carriers are moving under a static magnetic field. The absorption and dispersion relations are obtained which are applicable to the usual semiconductors such as Si and Ge. It is shown that, under favorable conditions, the resultant plasma frequency can be determined in a way as if there were only one kind of carrier which has the reduced mass of all the carriers concerned. The experimental method to determine the parameter of the magneto-plasma resonance is also discussed.

§ 1. Introduction

As is well known, there have been two important discoveries in the study of the resonance phenomena in semiconductors at microwave frequencies. One is the electron spin resonance of the free carriers or the trapped electrons; the other is the cyclotron resonance. In connection with the experiment of the cyclotron resonance, however, Dresselhaus, Kip and Kittel have pointed out that the magneto-plasma resonance of the free carriers becomes also important when the number of the free carriers is increased.[1] This problem was further discussed by the same authors[2]* for the simplest case in which the effective mass is cubic and when minority carries are concerned. They also observed the magneto-plasma resonance in InSb in the microwave region.

Since then, this problem has not been considered until Wolf came again to discuss the plasma resonance.[3] He considered the possibility of exciting the multi-mode resonance under simple conditions such as those discussed by *DKK*.

In actual semiconductors such as Si and Ge, however, the problem is more complicated. The effective mass has a tensor character and there are several kinds of free carriers which have different effective masses and relaxation times. Accordingly, it is desirable to make a more general treatment of the free carriers for the magneto-plasma resonance. Moreover, this may be necessary for the study of the spin resonance and cyclotron resonance of such substances as Si and Ge in which the magneto-plasma resonance may have an appreciable influence on these resonances. As an example, let us consider the following case. When there are about 10^{14} donors/cc with an excitation energy of 0.01 eV to the conduction band in Ge, the plasma frequency in the spherical specimen will be about 10^{10}/sec at 20°K, namely it comes into the microwave region. Then, it is quite conceivable that the magneto-plasma resonance, whose frequency is of the same order of magnitude as that of the ordinary plasma frequency, is necessarily associated with the observation of the electron spin and cyclotron resonances.

---

* Hereafter we shall call this paper as *DKK*.

Now let us consider the experimental method of studing the magnetoplasma resonance. To investigate the properties of the free carriers at rf-frequencies, it will be convenient to use the device developed by Okamura, Fujimura and the present author4)* for measuring the dielectric constant, permeability and conductivity of ferrites at microwave frequencies. Later, this method was applied to the study of the same sort of measurements on semiconductors.5),6) In this *OFD* method, the resonance shift and the loss of the resonant cavity containing the specimen are measured, and from these quantities the high frequency properties of the free carriers, represented by a complex susceptibility and a complex conductivity are deduced. The loss and shift are related to these quantities in the following way:

$$\frac{1}{Q}=\left(\mathcal{E}''+\frac{\sigma'}{\mathcal{E}_0\omega}\right)\int_{\Delta V}E^2dv\,,$$

$$-2\frac{\Delta\omega}{\omega}=\left(\mathcal{E}'-1-\frac{\sigma''}{\mathcal{E}_0\omega}\right)\int_{\Delta V}E^2dv\,.$$

The first equation represents the loss factor of the cavity and the second is the relation for the resonance shift. In these equations, the dielectric constant and conductivity are defined as

$$\mathcal{E}=\mathcal{E}_0(\mathcal{E}'-i\mathcal{E}'')\,,$$

$$\sigma=\sigma'-i\sigma''\,.$$

The integral $\int_{\Delta V}E^2dv$ over the volume of the specimen must be evaluated, and if the sample is at the place where the microwave electric field is the greatest, its volume becomes $4\cdot\Delta V/V$, where $\Delta V/V$ is the ratio of the volume of the sample to that of the resonant cavity. Thus, if the magneto-plasma resonance of the semiconductor could satisfactorily be represented by an anomaly in the complex conductivity, we can study it experimentally using the *OFD* method. Usually, $\mathcal{E}'$ is known and $\mathcal{E}''$ can be considered as zero.

In the next section, the *DKK* method will be modified in such a way that the magneto-plasma resonance of the simple system is represented by a complex conductivity. In the third section, a similar calculation for the general case where several species of carriers exist in the semiconductor will be made assuming that the carrier density is not very high and the motion of each carrier is determined by the rf-electric field, long range depolarization field and external magnetic field.* Conclusions of these discussions will briefly be described in the last section.

§ 2. The Complex Conductivity in the one-carrier Problem

There are several differences between the plasma oscillations in metals and those in semiconductors. One of the important differences is seen in the boundary conditions. In metals, the plasma wave length is much smaller than the size of the specimen. Accordingly, the boundary effect is unimportant in metals. On the contrary, it is important in semiconductors in which the plasma wavelength is larger than the size of the sample. As was described in the preceding section, Wolf pointed out the possibility of the multi-plasma resonance in semiconductors. But the occurrence of this mode is limitted by severe conditions which are rather exceptional in semiconductors. Accordingly we omit to discuss the magneto-plasma resonance of multi-mode.

The semi-classical equation of motion for the carriers was first proposed by *DKK* and it is as follows:

$$m^*\left(\frac{d\vec{V}}{dt}+\rho\vec{V}\right)=e(\vec{E}-L\vec{P})+\left(\frac{e}{c}\right)\vec{V}\times\vec{H}\,, \qquad (1)$$

where $\vec{V}$ is the velocity of the conduction electrons, m^* their effective mass, $\vec{E}$ the external electric field, L the depolarization factor, $\vec{H}$ the external magnetic fiedld, P the dielectric polarization and ρ the relaxation frequency ($\rho=\tau^{-1}$ where τ is the relaxation time). Starting from Eq. (1), the complex conductivity can be calculated in the following way. Assuming $E\propto e^{i\omega t}$, we obtain from Eq. (1):

---

* Hereafter we shall call this the *OFD* method.

* This case will be called hereafter the n-carrier problem. The case where only one kind of carrier is present, as was discussed by *DKK*, may thus be called the one-carrier problem.

$$(i\omega'+\rho)\vec{V}=\left(\frac{e}{m^*}\right)\vec{E}_i+\vec{V}\times\vec{\omega}_c\,, \tag{2}$$

where $\vec{E_i}$ is the reduced field and was defined by *DKK* as

$$\vec{E}_i=\vec{E}\Big/\left\{1+\frac{L(\mathcal{E}'-1)}{4\pi}\right\}.$$

The definition of the various frequencies is as follows:

ω: external frequency,

$\omega_c=\dfrac{eH}{m^*c}$: cyclotron frequency,

$\omega_p=\sqrt{\dfrac{L_iNe^2}{m^*}}$: plasma frequency,

$\omega'=\omega-\dfrac{\omega_p{}^2}{\omega}$: reduced frequency.

L_i is the reduced depolarization factor defined by *DKK* as

$$L_i=L\Big/\left\{1+\frac{L(\mathcal{E}'-1)}{4\pi}\right\}.$$

Assuming that $\vec{E}_i$ is along the x-axis and $\vec{H}$ along a direction perpendicular to it, the comple conductivity is obtained from Eq. (2) as

$$\sigma=\frac{I_x}{E_{ix}}=\frac{Ne^2}{m^*}\frac{1}{(i\omega'+\rho)+\dfrac{\omega_c{}^2}{(i\omega'+\rho)}}\,. \tag{3}$$

From this equation, the real and imaginary parts of the conductivity can be calculated as follows:

$$\sigma'=\frac{\sigma_0(1+\omega_c{}^2\tau^2+\omega'^2\tau^2)}{(1+\omega_c{}^2\tau^2-\omega'^2\tau^2)^2+4\omega'^2\tau^2}\,, \tag{4}$$

$$\sigma''=\frac{\sigma_0\omega'\tau(1+\omega'^2\tau^2-\omega_c{}^2\tau^2)}{(1+\omega_c{}^2\tau^2-\omega'^2\tau^2)^2+4\omega'^2\tau^2}\,, \tag{5}$$

where $\sigma_0=Ne^2\tau/m^*$. When no magnetic field is present, Eqs. (4) and (5) reduce to

$$\sigma_0'=\frac{\sigma_0}{1+\omega'^2\tau^2}\,, \tag{6}$$

$$\sigma_0''=\frac{\sigma_0\omega'\tau}{1+\omega'^2\tau^2}\,. \tag{7}$$

Eqs. (4) and (6) were first obtained by *DKK*. Eqs. (5) and (7) are our additional results.

Now it will be interesting to see in what way the sign of the imaginary part of the conductivity, σ'', changes with frequency and magnetic field strength. From (5), we see that when $\omega>\omega_p$ (high frequency or low temperature) σ'' is negative for $\omega_c{}^2<\omega'^2+1/\tau^2$ and positive for $\omega_c{}^2>\omega'^2+1/\tau^2$, while the reverse is true when $\omega<\omega_p$ (low frequency or high temperature). Since σ'' appears in the reactance of the sample and behaves as if it were an effective dielectric constant, this change of sign is a convenient measure in the characteric quantities of the semiconductor.

Now it must be noted that by measuring the complex conductivity at $H=0$ and the magnetic fied H_0 at which the sign of σ'' changes, N, τ and m^* can be obtained from the following calculations. Assuming $\omega'\neq0$ in Eq. (5), H_0 must satisfy the following relation:

$$1+\omega'^2\tau^2-\omega_c{}^2\tau^2=0\,. \tag{8}$$

Using Eqs. (6), (7) and the definition of ω_c, τ/m^* can be obtained from Eq. (8) as follows:

$$1+\left(\frac{\sigma_0''}{\sigma_0'}\right)^2=\left(\frac{eH_0}{c}\right)^2\left(\frac{\tau}{m^*}\right)^2. \tag{9}$$

On the other hand, the following relation is obtained from Eqs. (6) and (7):

$$\sigma_0=\frac{Ne^2\tau}{m^*}=\frac{\sigma_0'^2+\sigma_0''^2}{\sigma_0'}\,. \tag{10}$$

Utilizing Eqs. (9) and (10), N can be obtained as

$$N=\frac{H_0}{ec}\sqrt{\sigma_0'^2+\sigma_0''^2}\,. \tag{11}$$

τ and m^* are obtained in the following way. Using Eqs. (6), (7) and the definition of ω_p, we obtain

$$\frac{\sigma_0''}{\sigma_0'}=\tau\left(\omega-\frac{L_iNe^2}{m^*\omega}\right). \tag{12}$$

Then, using Eqs. (9) and (12), τ and m^* can be obtained separately as

$$\tau=\frac{1}{\omega}\left\{\frac{\sigma_0''}{\sigma_0'}+\frac{L_i}{\omega}\,\frac{\sigma_0'^2+\sigma_0''^2}{\sigma_0'}\right\}, \tag{13}$$

$$m^*=\frac{H_0e}{c\omega}\left\{\frac{\sigma_0''}{\sqrt{\sigma_0'^2+\sigma_0''^2}}+\frac{L_i}{\omega}\sqrt{\sigma_0'^2+\sigma_0''^2}\right\}. \tag{14}$$

§ 3. The Complex Conductivity in the *n*-carrier Problem

As was mentioned before, there are several kinds of free carriers in usual semiconductors. In such cases the problem is very difficult to solve rigorously. But when the densities of the carriers are so small that their interaction can be represented by a common long range depolarization force acting on each of them, the problem can be solved as follows. Let us assume that the carrier are all electrons. This is no essential restriction to the theory and if desired, holes can also be included without much altering the treatment. The equation of motion can be written as follows:

$$\begin{aligned}
&(i\omega+\rho_1)V_{1x}-i\alpha\frac{1}{m_1{}^*}\sum_{j=1}^{n}N_jV_{ix}=\frac{e}{m_1{}^*}E_i+V_{1y}\omega_c\ ,\\
&(i\omega+\rho_1)V_{1y}-i\alpha\frac{1}{m_1{}^*}\sum_{j=1}^{n}N_jV_{jy}=-V_{1x}\omega_{c1}\ ,\\
&\cdots\cdots\cdots\cdots\\
&(i\omega+\rho_n)V_{nx}-i\alpha\frac{1}{m_n{}^*}\sum_{j=1}^{n}N_jV_{jx}=\frac{e}{m_n{}^*}E_i+V_{ny}\omega_{cn}\ ,\\
&(i\omega+\rho_n)V_{ny}-i\alpha\frac{1}{m_n{}^*}\sum_{j=1}^{n}N_jV_{jy}=-V_{nx}\omega_{cn}\ ,
\end{aligned}\tag{15}$$

where $\alpha=L_ie^2/\omega$. The second terms in the left-hands of these equations represent the average effect of the other electrons producing a long range polarizing field. The equations reduce to Eq. (2) if we put $N=1$. As before, the magnetic field is along the z-direction and the rf-electric field is along the x-direction. From these equations, we obtain the following relations:

$$V_{jx}=\frac{(i\omega+\rho_j)\dfrac{e}{m_j{}^*}E_i+i(i\omega+\rho_j)\dfrac{\alpha}{m_j{}^*}X+i\dfrac{\alpha}{m_j{}^*}\omega_jY}{(i\omega+\rho_j)^2+\omega_{cj}{}^2}\ ,\tag{16}$$

$$V_{jy}=\frac{-\dfrac{e}{m_j{}^*}\omega_{cj}E_i-i\dfrac{\alpha\omega_{cj}}{m_j{}^*}X+i(i\omega+\rho_j)\dfrac{\alpha}{m_j{}^*}Y}{(i\omega+\rho_j)^2+\omega_{cj}{}^2}\ ,\qquad (j=1,\ 2,\ \cdots,\ m)\tag{17}$$

where X and Y are

$$\left.\begin{aligned}
X&=\sum_{j=1}^{n}N_jV_{jx}\ ,\\
Y&=\sum_{j=1}^{n}N_jV_{jy}\ .
\end{aligned}\right\}\tag{18}$$

Now we obtain the following relations by multiplying Eqs. (16) and (17) by N_j and summing over j:

$$X=\sum_{k=1}^{n}\frac{e\dfrac{N_k}{m_k{}^*}(i\omega+\rho_k)}{(i\omega+\rho_k)^2+\omega_{ck}{}^2}E_i+\sum_{k=1}^{n}\frac{i\alpha\dfrac{N_n}{m_n{}^*}(i\omega+\rho_k)}{(i\omega+\rho_k)^2+\omega_{ck}{}^2}X+\sum_{k=1}^{n}\frac{i\alpha\dfrac{N_k}{m_k{}^*}\omega_{ck}}{(i\omega+\rho_k)^2+\omega_{ck}{}^2}X\ ,\tag{19}$$

$$Y=\sum_{k=1}^{n}\frac{-e\dfrac{N_k}{m_k{}^*}\omega_{ck}}{(i\omega+\rho_k)^2+\omega_{ck}{}^2}E_i-\sum_{k=1}^{n}\frac{i\alpha\dfrac{N_k}{m_k{}^*}\omega_{ck}}{(i\omega+\rho_k)^2+\omega_{ck}{}^2}X+\sum_{k=1}^{n}\frac{i\alpha\dfrac{N_k}{m_k{}^*}(i\omega+\rho_k)}{(i\omega+\rho_k)^2+\omega_{ck}{}^2}Y\ .\tag{20}$$

Solving these Eqs. (19) and (20), one obtains X and Y.

On the other hand, the resultant conductivity is defined by

$$\left.\begin{aligned}
\sigma_x&=\frac{eX}{E_{ix}},\\
\sigma_y&=\frac{eY}{E_{ix}},
\end{aligned}\right\}\tag{21}$$

where σ_x represents the drift conductivity and σ_y the Hall conductivity. With the use of Eqs. (19) and (20), conductivities can be written in another way as

$$\sigma_x=\frac{ie^2}{\alpha}\left(1-\frac{P}{P^2-Q^2}\right),\tag{22}$$

$$\sigma_y=\frac{e^2}{\alpha}\frac{Q}{P^2-Q^2}\ ,\tag{23}$$

where P and Q are defined by

$$P=1-i\sum_{k=1}^{n}\frac{\dfrac{\omega_{pk}{}^2}{\omega}(i\omega+\rho_k)}{(i\omega+\rho_k)^2+\omega_{ck}{}^2}\ ,\tag{24}$$

$$Q=\sum_{k=1}^{n}\frac{\frac{\omega_{pk}^2}{\omega}\omega_{ck}}{(i\omega+\rho_k)^2+\omega_{ck}^2}\,, \tag{25}$$

In this way we obtained the solution. Since it is not easy to obtain from this result separate formulae for σ' and σ'' in the general case, we shall discuss only special but important cases.

(1) $\omega_{ck}=0$ and $\rho_k=0$ (vanishing magnetic field neglecting relation effects).

This is the simplest case, σ_y and σ_x' are zero and σ_x'' is given by

$$\sigma_x''=\frac{e^2\sum_{k=1}^{n}\frac{N_k}{m_k^*}}{\omega_n'}\,, \tag{26}$$

where $\omega_n'=\omega-\sum_{k=1}^{n}\omega_{pk}^2/\omega$ is introduced as the generalized reduced frequency. It is interesting to note that the resonance frequency of this system is determined by the vanishing of the generalized reduced frequency, i.e., $\omega_n'=0$. Furthermore, the resultant reduced mass, μ, defined by

$$\frac{N}{\mu}=\sum_{k=1}^{n}\frac{N_k}{m_k^*}\quad\left(N=\sum_{k=1}^{n}N_k\right), \tag{27}$$

can be used.

(2) $\omega_{ck}=0$ and $\rho_k=\rho$ (vanishing magnetic field with a common relaxation time).

The complex conductivity can be written as

$$\begin{aligned}\sigma_x'&=e^2\sum_{k=1}^{n}\left(\frac{N_k}{m_k^*}\right)\frac{\rho}{\omega_k'^2+\rho^2}\,,\\ \sigma_n''&=e^2\sum_{k=1}^{n}\left(\frac{N_k}{m_k^*}\right)\frac{\omega_k'}{\omega_k'^2+\rho^2}\,,\\ \sigma_y&=0\,.\end{aligned} \tag{28}$$

For other cases, such as the case of $\omega_{ck}=0$ and $\rho_k\neq\rho_{k'}$ (vanishing magnetic field with different relaxation times), where the coherency of the motions of different carriers is spoiled by the difference of their relaxation times, or $\omega_{ck}\neq\omega_{ck'}$ and $\rho_k=0$ (different cyclotron frequencies and neglecting relaxation effect), where the different carriers move with different cyclotron frequencies, no simple expression can be obtained for σ_x', σ_x'', σ_y' and σ_y''.

For Si and *Ge*, the cases (1) and (2) may be realized at liquid helium temperatures in mm wave region. The dynamical motion of the various free carriers can be analyzed by varying the impurity concentration, the measuring temperature and the shape of the sample. It may be interesting to investigate the temperature range where the impurity band conduction begins. Because the accuracy of the α'' measurements can be reduced to the accuracy of the frequency measurement of the resonant cavity, we may be able to detect the fine variation of the phenomena which is not easily observable by *DC*-method.

§ 4. Conclusion

Using this theory of the magneto-plasma resonance of the *n*-carrier problem, we can obtain the following practical informations of the dynamical properties of the free carriers in semiconductors:

(1) The pure magneto-plasma resonance frequency and the relaxation time in Si and Ge etc. using Eqs. (26), (27) and (28).

(2) The carrier density, the effective mass and the relaxation time at microwave frequencies by measuring the loss and shift of the resonant cavity as are shown in Eqs. (11), (13) and (14). The resonance is observed as an anomaly of the complex conductivity.

(3) The resonance phenomena which are observed in association with the cyclotron and spin resonance can be discussed quantitatively as the magneto-plasma resonance.

References

1) G. Dresselhaus, A. F. Kip and C. Kittel: Phys. Rev. **98** (1955) 368.
2) G. Dresselhaus, A. F. Kip and C. Kittel: Phys. Rev. **100** (1955) 618.
3) P. A. Wolf: Phys. Rev. **112** (1958) 66.
4) T. Okamura, T. Fujimura and M. Date: Sci. Rep. RITU, **A-4** (1952) 191.
5) T. Fukuroi and M. Date: Sci. Rep. RITU, **A-9** (1957) 190.
6) T. Fukuroi and K. Yamagata: Sci. Rep. RITU, **A-11** (1959) 285.

JOURNAL OF THE PHYSICAL SOCIETY OF JAPAN, Vol. 15, No. 8, AUGUST, 1960

Proton Magnetic Resonance in Pure and Doped Ice

By Kiyoshi KUME

The Institute for Solid State Physics, University of Tokyo, Tokyo

(Received April 14, 1960)

Basing upon a carefully designed method of measurement in samples showing long T_1, a complete proton magnetic resonance experiment of ice is attempted. First, on a second moment argument in rigid lattice state, the possibility that protons do not lie on the inter-oxygen lines is pointed out, in connection with the neutron diffraction studies. Secondly, from the relaxation time and line-narrowing measurements, the difference between the behaviors of protons in pure and doped ice is discussed, the results of the dielectric and the direct current conductivity measurements by Zürich group being taken into consideration.

§ 1. Introduction

It was established through X-ray analysis(1), that ice crystal belongs to the hexagonal space group D^4_{6h}-$C6/mmm$ under ordinary pressures and temperatures, the oxygen atoms occupying regular lattice points ± (1/3, 2/3, 1/16) and ± (1/3, 2/3, 7/16) as is shown in Fig. 1, each surrounded by the neighboring four atoms approximately tetrahedrally. But as for the positions of hydrogens, the X-ray analysis can tell hardly anything, and the problem has been left for later investigations.

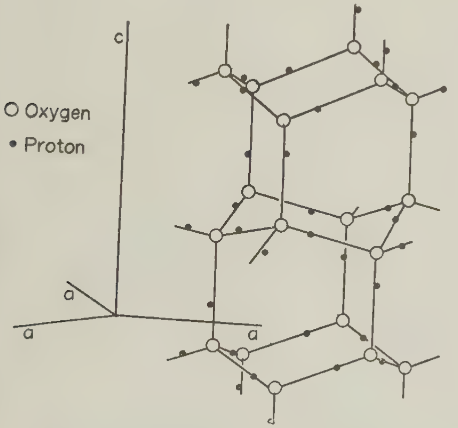

Fig. 1. Crystal structure of ice.

On the other hand, several properties of ice have been discovered, which are considered to have some connection with the arrangement or the rearrangement of protons. First, by specific heat measurement, the residual entropy of 0.82 ± 0.05 cal/deg mole was concluded by Giauque et al at 10°K(2)(3), and this fact was explained by Pauling(4), assuming a disordered arrangement of protons in the ice crystal. According to his model, protons are assumed to obey the following three rules. Namely, first, two protons exist among the four possible positions surrounding each oxygen, secondly, protons lie on the lines connecting two oxygens, and thirdly, no two protons can exist on any one such oxygen-oxygen line. Moreover, as far as these three rules can admit, protons can take any of the possible arrangements at random. The calculated value of residual entropy upon this model is $k \ln (3/2)^N = 0.806$ cal/mol degree, and is considered to agree well with the observed. Next, the dielectric behavior was rather thouroughly examined by Smith-Hitchcock(5), Auty-Cole(6) and other authors(7), and shown to exhibit Debye-type dispersion at rather low frequencies and at relatively high temperatures. The dispersion has naturally been attributed to the reorientation of dipoles associated with water molecules

Recent neutron diffraction studies by Peterson-Levy(8) revealed the positions of protons (actually deuterons) to be consistent with the Pauling model. As for the dynamical behavior of protons, some effort was made to study it by measuring the dielectric behavior, not only of a pure sample but also of a doped one(9)(10). The most systematic attempt of this kind made recently seems to be the dielectric as well as the direct current conductivity measurements on HF doped ice by the school in Zürich(9).

Under these circumstances, we attempted rather complete proton magnetic resonance studies to shed some light on these problems from a somewhat different point of view. The characteristic features of the method exist in that, first, protons are concerned exclusively with it, and secondly, the method is rather microscopic in the sence that only very short range interactions are concerned, and both of these two features are essentially favorable to our studies on ice. In section 2, the quantitative line shape measurements on a rigid lattice at sufficiently low temperatures will be discussed in connection with the positions of protons, at the same time, taking into account the result of the neutron diffraction studies. In sections 3, the experimental result on the temperature dependence of the length of the relaxation time T_1 and of the narrowing of the absortion line in pure as well as in doped specimens, will be interpreted from the standpoint of the dynamical behavior of protons. The arguments should mainly be compared with the results of dielectric measurements(9), which might, however, not entirely be free from the influence of some macroscopic effects like electrode polarization.

The proton magnetic resonance experiment on ice crystals, is not entirely novel. Following the pioneer work by B.B.P.(11), some attempts of refining or extending it were made by the group in Osaka University(12) from the angle of line shape measurements, and by T.E. Turner(13) and others(14) from the angle of relaxation time measurement. Nevertheless, their results were not necessarily satisfactory, as will be mentioned in the following sections, because the proton system in an ice crystal has a longer relaxation time, especially at low temperatures, and consequently the accurate measurements of absorption line shapes as well as of relaxation time is rather difficult; therefore, thus far, no satisfactory result has even been attained. The author has made some effort in improving the measuring technique in case of longer T_1, with much success as is given below. As for specimens, the author used a carefully purified one, as well as one specifically doped with non-paramagnetic ions in order to clarify the mechanism of relaxation.

§ 2. Line Shape of a Polycrystalline Sample in Rigid Lattice State

Although the specimen used in this case is of not so high purity, it has a long T_1 of the order of ten minutes, special precaution being to thus necessary to cut down the r.f. level as low as 40 microgauss to prevent saturation. The detecting system used, is of a bridge type, having sufficiently low noise figure.(23)(24

A recorded derivative of the saturation free absorption line in polycrystalline ice at –180°C is reproduced in Fig. 2. There is seen

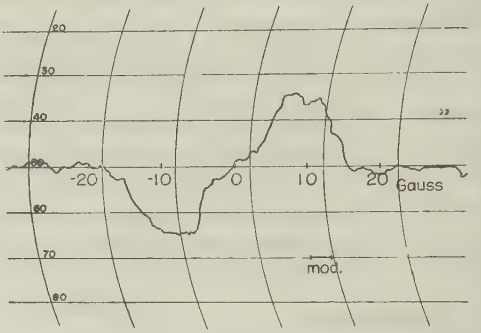

Fig. 2. Derivative of absorption curve of polycrystalline ice.
Sample: Ice polycrystal of not so high purity. See the text for details.
Field: 7060 Gauss.
Field sweep: 2.6 Gauss/min.
Frequency: 30.0 MC.
R. f. field within sample coil: 40 microgauss.
Time constant: 12 sec.
Temperature: 90°K.

somewhat flattened portion at the center, which may be considered to show the two spin character of the proton system, which is much more pronounced in the single crystal experiment(25). It has a maximum-slope-linewidthof $16._0$ Gauss, which is compatible with the data of B.P.P.(11) as well as with that of Osaka Group(12) at higher temperatures. The second moment of the absorption line is found to be 36.7±1.7 Gauss(2), the modulation correction being made after Andrew(16). The second moment shown above is the average of six independent data, together with the standard deviation.

The above measurements are made on a specimen, frozen at a temperature near the melting point at rather a high rate of about one minute, and then cooled to –180°C within 150 minutes and then kept there for about 120 minutes. An independent measurement is made on a specimen at –180°C, after being kept at about –5°C for a few weeks. The latter showed almost the same line shape as above, within the experimental error, although it has a longer T_1 of about 40 minutes. In the line shape measurement in this case, the r. f. field is cut to zero except during short periods for measurements to escape from saturation and the result is rather qualitative in character(27).

Through the second moment arguments in case of the rigid lattice, we shall discuss the stable positions of protons in the crystal lattice as follows. We assume the so-called Pauling rules, which are already mentioned in section 1. Although these rules lay certain restrictions on the arrangement of protons, there still remain some possibilities. According to the orientation of the central water molecule, the protons "0", "1" and "2" are fixed as shown in Fig. 3 through above mentioned rules. The remaining protons of the molecules I, II, III, which are not shown in the figure, as well as the protons of the molecule other than the nearest, cannot be uniquely fixed. In Pauling's disordered model(4), such protons are placed at random, and in other kinds of proposed ordered structures(17), they are fixed with certain regularities. As far as the second moment argument is concerned, however, we cannot discriminate the former from the latter, because the contributions to the proton "0" from protons attatched to molecule I is the same, on whichever O—O line among the possible three they are situated, and furthermore the difference in the contributions from those of II, III or those of the protons of the molecules other than the nearest is too small to influence the total second moment. Actually, the contribution from the molecule II is 0.37 Gauss^2 in case of Pauling model, compared with 0.35 Gauss^2 in case of Bjerrum's ordered structure(17), and that from the molecules III is 0.31 Gauss^2 in the former, compared with 0.29 Gauss^2 in the latter. And in total, the difference between the two models is found to be 0.06 Gauss(2), which value is not so sensitive to the assumed parameters concerning the shape of the water molecule.

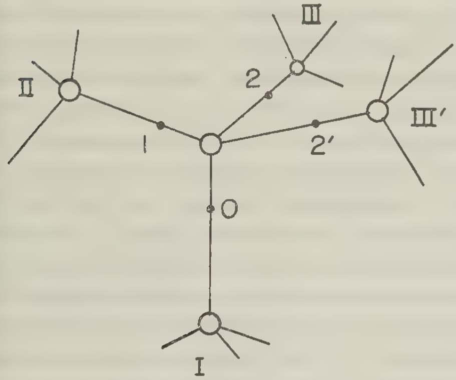

Fig. 3.

The main contribution to the total second moment is determined by the shape of the water molecule, namely the OH length and the HOH angle. Actually, in the powder experiment, only the second moment is available, and this gives a relation between these two unknown parameters. The result is shown graphically in Fig. 4 by the shaded area, the width of which corresponds to the experimental error given above.

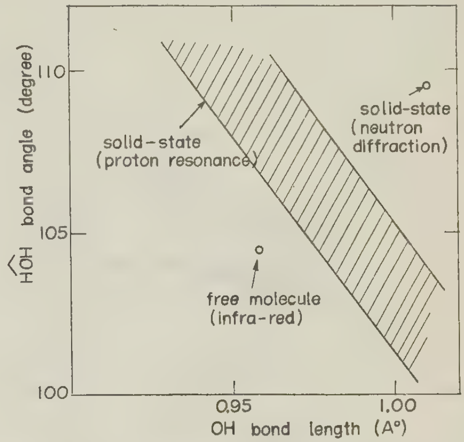

Fig. 4. Shapes of water molecules determined through various methods in free- as well as in solid-state.

First, if we assume the shape of the water molecule to be the same as that of the free molecule(18) (OH = 0.958_4 Å, HOH angle = 104°27′), the calculated second moment is obviously outside of the experimental error (Fig. 4). This suggests that, in a crystalline state, the OH bond is lengthened or/and the HOH angle is more opened, through the influence of the hydrogen bonding between molecules.

On the other hand, the neutron diffraction(8) gives an OH bond length of 1.01 Å as well as the tetrahedral bond angle HOH of 109.5°, the resulting second moment is again outside the experimental error, whereas this bond length is required to have the value of 0.95_5 ±0.01 Å in order to be consistent with the observed second moment, keeping the tetrahedral bond angle. On the contrary, if we assume the OH distance of 1.01 Å, and adjust the bond angle HOH so as to obtain the best fit with the observed second moment, the resulting bond angle will be 102±2 degrees, which is rather close to the bond angle of 104.5 degrees in a free molecule. At first sight, the discrepancy between neutron and resonance studies might seem to be serious, judging from the higher accuracy of the neutron diffraction studies. In Pauling model, however, it is natural to ascribe equal probability to the possible three alternatives as shown in Fig. 5. Because of the restriction imposed upon the arrangement of the protons, this does not violate the validity of Pauling's entropy arguments. According to the neutron diffraction, the contour of the hydrogen is much more elongated in the direction perpendicular to, rather than in the direction parallel to the O—O line. Although we have only a single proton among points H_1, H_2 or H_3 a random spacial configuration results in the contour diagram such as the one observed, as a result of the superposition of the off O—O line positions of hydrogen atoms. The above anisotropy reported by neutron diffraction studies is of the order of magnitude consistent with resonance data, assuming the HOH angle of 104.5 degrees, and hence the bond length of 1.01 Å.

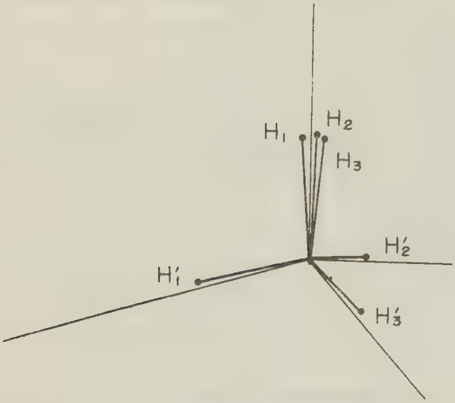

Fig. 5.

Thus the present second moment argument suggests that although the effect of hydrogen bonding distorts molecules appreciably, it is not large enough to pull out the hydrogen, so as to come on the O—O line. This conclusion is compatible with the existing neutron diffraction data on weak O-H---O hydrogen bonds such as in the case of the water of crystallization in sodium sesquicarbonate(19) (O—O length 2.78 Å), and oxalic acid dihydrate (O—O length 2.86 Å)(20), as well as our nuclear resonance data on boric acid (O—O length 2.72 Å)(26).

§ 3. Temperature Dependence of Relaxation Time and Line Width

(a) *Specimen*

For the purpose of T_1 measurements, a highly purified specimen is necessary, because, in the first place, as is well known(21), even the slightest contamination by paramagnetic impurities drastically affects the T_1 value, and at the same time, in connection with the dielectric measurements,(9)(10) even non-paramagnetic impurities may become a cause of certain types of lattice defects, which will also affect the T_1 value appreciably.

The water distilled with an ordinary type metal distillater is further purified through a distillation column of about 1 meter in height, which is filled with a mixture of two kinds of ordinary ion exchange resin, AG Amberlite IR-120 and IRA-400 from the Japan Organo Co. LTD. The water thus purified is shown to have a specific electric conductivity of 1.0~1.5 μ℧/cm, and is sealed in fused-silica ampoules under a nitrogen atmosphere, after being bubbled with nitrogen to get rid of the oxygen gas dissolved in the water, which might affect the value of T_1 owing to its paramagnetic character. The water thus prepared is frozen at about -5°C in the refrigerator. According to Turner's experiment(13), a gradual rise in T_1 value is observed as time elapses after freezing, and finally reaches the stationary value. A similar phenomena has been observed in our preliminary experiment. Therefore, the sample used in the present measurement has all been annealed at -5°C over six months. The specimen thus prepared is considered to be free from alkaline substances, for the operations were made in polyethylene or silica containers, and not in the glass.

Besides the 'pure' specimen, thus prepared, we also measured the T_1 in a "doped" one. 1/1000 N of KOH is added to the pure liquid water, and the liquid is frozen at -10°C and then annealed. If it were assumed that all of the KOH molecules remained in ice, there would exist one KOH molecule per five thousand water molecules. And we also measured the T_1 in two kinds of "pure" specimens, which are supposed to have a different purity from each other.

(b) *Method of measuring longer T_1*

In case of longer T_1 of several hours, it is practically impossible to observe "steady-state" signals. In this case, however, T_1 can be determined by combining the following two informations. One is the height of the "transient" absorption signal, which is given after the appropriate time from the time, at which the magnetization starts to recover from the state of complete saturation. The other is the saturation-free signal, which is, in principle, can be obtained from the measurement, made after the elapse of sufficiently a long time compared with T_1 of the sample to be measured, since the foregoing irradiation of high frequency magnetic field is cut off. This is practically impossible in case of longer T_1. A specimen of ice, which has sufficiently a short T_1 due to added parramagnetic impurities, is therefore made use of, to determine the saturation-free value. The calibrator signals are used for determining the scale, throughout the measurement. The long range stabilities of the magnetic field and the whole detecting system are checked by a field monitor, and a calibrator, respectively, and the balance of the bridge is readjusted just before the transient signal is given. For details of the procedure adopted here, see the separated paper(27). Fig. 6 shows an example of the transient signal.

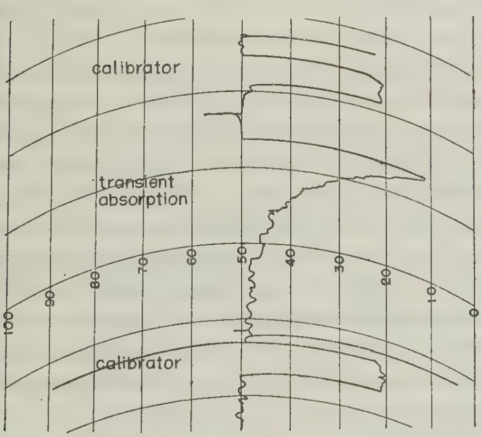

Fig. 6. An example of the transient signal.
Sample: Ice pure "1", see the text for details.
Field: 7060 Gauss.
Field sweep: fixed.
Frequency: 30.0 MC.
R. f. field within sample coil: 1 milligauss.
Time constant: 0.7 sec.
Temperature: 193° K.
Flow rate of the chart: 1 cm/30 sec.

(c) *Results*

In Fig. 7 is shown the temperature dependence of relaxation time T_1. The T_1 shorter than twenty seconds is measured by the saturation method, and the one between ten minutes and twenty seconds is measured by the ordinary direct method. The measurement of a T_1 longer than five minutes is done by the method described in the preceding paragraph. Before each measurement at a certain temperature, the specimen is kept at that temperature for more than 40 minutes in order to obtain thermal equilibrium. In a preliminary experiment, we confirmed that T_1 did not change over 10% during 8 hours at -85°C. Therefore, equilibrium would sufficiently be attained after 40 minutes. It is obvious from Fig. 7 that the curve of the

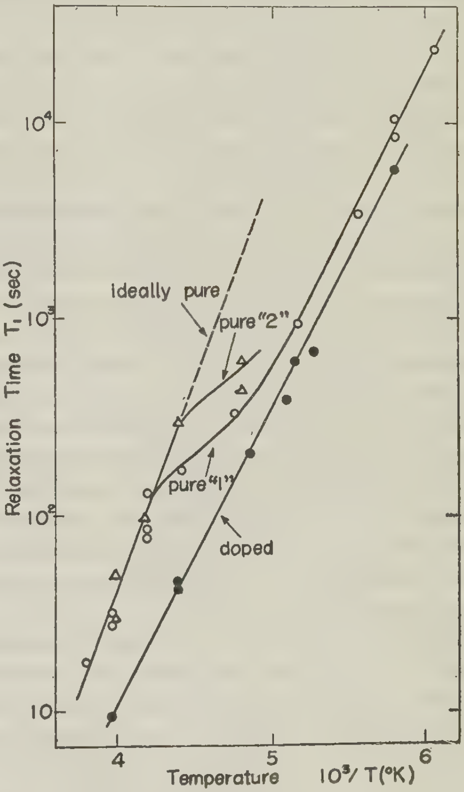

Fig. 7. Temperature depencence of relaxation time T_1 in pure as well as in doped polycrystalline ice.

sample numbered "pure 1" consists of three regions. The first region above -40°C has a maximum slope, which corresponds to the activation energy of 0.44 eV, and the second region between -40°C and -80°C has a minimum slope of about 0.17 eV, and finally the third and the lowest temperature region has a medium slope of 0.30 eV. T_1 versus temperature curve for the "pure 2" has the first region in common with that of "pure 1" at higher temperatures. The second region, however, is different in absolute value, but still has the same slope with that of "pure 1". Compared with these pure samples, the "doped" one has a straight line, whose slope is the same as that of the third region of "pure 1". At first sight, it might appear strange that the "doped" one has a straight line, and the "pure" has a crooked one. The explanation might be as follows. Suppose that the perfectly pure specimen shows a straight line as shown in Fig. 7 with an extrapolated broken line. By adding a small amount of impurities, the curve is bent into three as in the case of "pure", and the second region gradually shifts to the higher temperature side by the further addition of impurities, and then finally in sufficiently doped samples, the curve has only a slope which corresponds to the third region of the "pure" specimen.

The difference between the "pure" and the "doped" ice is also seen in the temperature dependency of the line width (Fig. 8). As the temperature is raised, the absorption line of the "doped" ice becomes narrower more rapidly than that of the "pure" ice. This behavior can be correlated with the difference between the T_1's of the pure and doped ice, in the corresponding regions shorter than one minute. In the corresponding regions longer than one minute, however, the correlation time τ_c, which is related to the observed T_1 through the well-known formula $\tau_c=\frac{<\Delta\nu^2>_{AV}}{\nu^2}T_1$, where $<\Delta\nu^2>_{AV}$ and ν mean the second moment of the absorption line width, and the resonance frequency, respectively, is longer than the reciprocal of the line width in frequency scale, and consequently the line width saturates at a value of so-called "rigid lattice case" and difference between the "pure" and the "doped" also disapears.

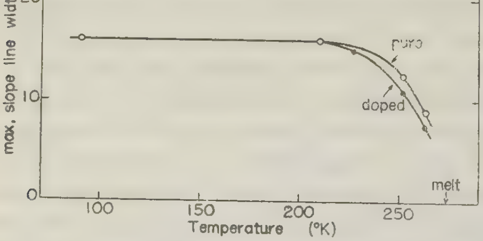

Fig. 8. Narrowing of absorption line in pure as well as in doped polycrystalline ice.

(d) *Discussion*

First, we will comment on the comparison with the previously reported value of T_1 by B.P.P.(11) and Turner(13). B.P.P. measured T_1 only in the higher temperature region above -35°C. Compared with the present results, their results are about three times as short, although the difference in temperature dependency is insignificant. The difference might be attributed to either the difference in purity, of which effect is already obvious from the present work, or perhaps in the difference in thermal treatment. Turner extended B.P.P.'s measurements to lower temperatures. Comparing this again with the present work, his T_1 curve has approximately the same slope as ours in the second region mentioned above, although his results are about twice as long as that of our specimen "pure 2" in absolute value. In the third region, however, his curve deviates gradually from ours to the shorter T_1-side, and finally reaches a constant value of 10^4 seconds. The latter behavior might naturally be considered to be due to the effect of paramagnetic impurities existed in Turner's samples, which are considered to provide a temperature-independent relaxation mechanism(21). Throughout the above comparison, we have ignored the difference in T_1 due to a different external magnetic field.

Secondly, the correlation time τ_c, which is obtained from the observed T_1 through the above-mentioned formula, is compared with the dielectric relaxation time τ reported by the Zürich group(9). The Zürich group has measured the dielectric relaxation time τ as the function of the impurity (HF) content at three fixed temperatures -36°C, -10°C, -3°C. They have found that as the impurity increases, the activation energy decreases from the initial value of 0.58 eV to a minimum value of 0.23 eV, and then increases again to reach the final value of 0.32 eV. This behavior is quite similar to what we have found. If we cut a group of T_1 versus $1/T$ curves in Fig. 7 by a straight line corresponding to a fixed temperature, for example at −60°C, it is readily seen that the activation energy first gets the highest value, then drops to the lowest, and then reaches to a final medium value as the amount of impurities added increases. The comparison between the activation energies in both cases are shown in Table 1. The activation for the dielectric relaxation differs a little from that for the resonance, according to their definitions. Taking this difference into account, the coincidence between the correlation time in proton magnetic resonance and the dielectric relaxation time is considered to be satisfactory. Judging from the experimental results, the difference between species of ionic impurities in their effects on the activation energies is insignificant, as far as they are diamagnetic, because KOH and probably H_2CO_3 too in our work give similar results with the HF impurities in Zürich's experiment. The corresponding behaviors between the proton magnetic and the dielectric relaxation, ensures the fact that the phenomena is based actually upon the microscopic relative motion of protons. If the change in the relaxation time were due to the effect of paramagnetic impurities, it should not be observed in the dielectric measurement. On the other hand, if the change in relaxation were due to any ions other than protons or due to any macroscopic phenomena like the electrode polarization effect, it should not be observed in the proton magnetic resonance experiment.

Table 1. Comparison between various activation energies

	"pure"		"sufficiently doped"
	1st	2nd	3rd
proton magnetic resonance (present work)	0.44	0.17	0.30 eV
dielectric constant (Zürich group)			
Auty-Cole definition	0.58	0.23	0.32
Debye definition	0.51		
Direct current conductivity (Zürich group)			
Au-electrode	0.6		
sandwitch-electrode			0.33

The experimental result shows that, by the addition of small amount of ionic impurities, a new state appears. The state, which is called "third region" in the above description, is considered to be of rather well-defined one. Bacause, once the state has been realized by the addition of a certain small amount of impurities, not only the activation energy, but also the absolute values can be changed little, by further addition of the impurities. This fact is seen by comparing the above data for doped sample which has a considerable amount of impurities with those for "pure", which has only a trace of such impurities. As is obvious from Fig. 7, the T_1 value of pure specimen in the first region is determined by the different mechainsm corresponding to higher activation energy, whereas T_1 in the third region is due to the same mechainsm as is seen in the doped sample, because there is a justice to believe the existence of a trace of impurities in the so-called "pure" specimen. In the following, we shall call the third region as "sufficiently doped" state and the first region, as "pure" state, and give a discussion concerning the difference between the two states, in connction with the Zürich(9) and other(22) results of direct current conductivity. In contrast to the "third region", "the second region" is structure-sensitive, as is readily seen in the above description.

As is well known, the microscopic diffusion constant of protons is deduced through the well-known formula $D_{\mathrm{n.m.r.}}=\frac{<r^2>}{\tau_c}$, where the correlation time τ_c is known from the proton magnetic resonance experiment, and the mean flight distance r is assumed so as to be consistent with the crystal structure. If the diffusion is not localized, it would result in macroscopic conductivity under an applied electric field, and the specific conductitify is related with the diffusion constant through the so-called Einstein relation $D_{\mathrm{n.m.r.}}=\sigma\frac{kT}{Nq^2}$, where N and q mean the number in unit volume and the charge of carriers, respectively.

Actually, the equation does not hold in "pure" state; as is already pointed out by Bradley[(22)]. If we tacitly adhere to the above equation, we are forced to assume too small a value of 0.02 Å for r. In the "sufficiently doped" state, however, the equation is found to hold fairly well, in contrast to the "pure" state, the left and right hand sides of the equation amounting to 2×10^{-12} cm/sec and $2\sim3\times10^{-12}$ cm/sec at 250°K, respectively, under a reasonably assumed value of 1 Å for r. The data of the conductivity in the "sufficiently doped" state which are used in the above discussions, are actually those in "pure ice" with sandwitch-electrodes of HF-doped ice. However, as is reported, the specimen is naturally considered to be a doped one, because the lattice deffects from the electrode flow into the specimen. According to their discussion the conduction is believed to be due to neither electrons nor ions of any kind other than protons.

In general, two kinds of motion of protons are thought to be possible in ice crystals[(17)]. One of them is the motion of protons accompanied by the rotational motion of the water molecule, leaving one of the hydrogen bonds as it is, and only breaking the other. The other is the so-called "proton transfer" along the hydrogen bond without any rotation. As is readily seen from the crystal structure of ice (Fig. 1), these two kinds of proton motion give approximately the same order of magnitude of local magnetic field fluctuations; consequently the arguments on the order of magnitude such as given above, cannot discriminate, which of them is actually resposible for the phenomena observed in the present investigation. Nevertheless, from the facts given above, that the Einstein equation holds in the "sufficiently doped" ice and does not hold in the "pure" ice, we might safely say as follows: In the case of "sufficiently doped" ice, protons move smoothly in the crystal of ice through both of the two kinds of motions. On the contrary, in pure ice, it is rather difficult for protons to move because of the fact, that the motion is of a localized, or that the number of carriers is much smaller. A small number of lattice defects such as hydroxyl ions or oxionium ions produced by the addition of alkaline or acidic impurities would facilitate the motion of protons. The activation energy is expected to be lowered by the presence of the added impurity. This is in agreement with the observation descibed above.

Zürich group attempted interpretations of the two states through dielectric and conductivity measurements, especially through discussions of the static dielectric constant. They attributed the activation energy of 0.58 eV in the pure state to the thermal production of the imperfection as well as the rotation of the water molecule, and that of 0.32 eV in the "sufficiently doped" state to the production of the ion, accompanied by the proton conduction due to the addition of HF. These conclusions seem to be consistent with our results.

The author wishes to express his hearty thanks to Prof. Y. Kakiuchi for suggesting the subject, and also for his kind guidance with deep insight.

References

1) W. H. Bragg: Proc. Phys. Soc. London **34** (1922) 98.
W. H. Barnes: Proc. Roy. Soc. **A 125** (1929) 670.
H. D. Megaw: Nature, **134** (1934) 900.
2) W. F. Giauque and M. F. Ashley: Phys. Rev. **43** (1933) 81.
3) E. A. Long and J. D. Kemp: ibid. **58** (1936) 1829.
4) L. Pauling: J. Amer. Chem. Soc. **57** (1935) 2680.
5) C. P. Smith and C. S. Hitchcock: J. Amer. Chem. Soc. **54** (1932) 4631.
6) R. P. Auty and R. H. Cole: J. Chem. Phys. **20** (1952) 1309.
7) J. Errera: J. Phys. USSR **5** (1924) 304.
J. Granier: Compt. rend. **179** (1824) 1314.
H. Wintsch: Helv. Phys. Acta **5** (1932) 126.
E. J. Murphy: Trans. Electroch. Soc. **65** (1934) 133.
F. Humbel, F. Jona and P. Scherrer: Helv. Phys. Acta **26** (1953) 17.
Ad. Steinemann and H. Gränicher: Z. Krist **110** (1958) 432. Helv. Phys. Acta. **30** (1957) 553.
8) S. W. Peterson and H. A. Levy: Acta Cryst. **10** (1957) 70.
9) Ad. Steinemann and H. Gränicher: Helv. Phys Acta **30** (1957) 553.
Ad. Steinemann: ibid **30** (1957) 581.
10) S. Zaromb and R. F. Brill: J. Chem. Phys. **24** (1956) 895.

S. Zaromb: ibid **24** (1956) 1110, **25** (1956) 350.
R. F. Brill, H. Ender and A. Feuersanger: Z. Electro. **61** (1957) 1071.
11) N. Bloembergen, E. M. Purcell and R. V. Pound: Phys. Rev. **73** (1948) 679.
12) J. Itoh, et. al. unpublished.
13) T. E. Turner: Ph. D. thesis (Harvard Univ.).
14) G. E. Pake and H. S. Gutowsky: Phys. Rev. **74** (1948) 979.
15) R. Hoshino: unpublished.
16) E. R. Andrew: Phys. Rev. **91** (1953) 425.
17) N. Bjerrum: Kgl. Danskab. Selskab. Math-fys Medd. **27** (1951) 1. Science **115** (1952) 385.
P. G. Owston: J. Chim. Phys. **50** (1953) C 13.
R. E. Rundle: J. Chem. Phys. **21** (1953) 1311, ibid **22** (1954) 344, J. Phys. Chem. **59** (1955) 680.
K. S. Pitzer and J. Polissar: J. Phys. Chem. **60** (1956) 1140.
18) Herzberg: *Infra-red and Raman Spectra* P 489
19) G. E. Bacon and N. A. Curry: Acta Cryst **9** (1956) 82.
20) B. S. Garrett: Oak Ridge Natl. Labl. Rep. No. 1745.
21) N. Bloembergen: Physica **15** (1949) 386.
22) R. S. Bradley: Trans. Faraday Soc. **53** (1957) 687.
23) *Operation Manual of the Institute for Solid State Physics NMR-1 Spectrometer*, unpublished.
24) K. Kume: Technical Report of ISSP Series B No. 1 (1960) 1.
25) K. Kume and R. Hoshino: to be published in J. Phys. Soc. Japan.
26) K. Kume and Y. Kakiuchi: J. Phys. Soc. Japan **15** (1960) 1277.
27) K. Kume: Technical Report of ISSP Series B No. 1 (1960) 7.

JOURNAL OF THE PHYSICAL SOCIETY OF JAPAN, Vol. 15, No. 8, AUGUST, 1960

Radiation Effects on Dimethyl-diphenyl Siloxane Copolymer. I. Protective Effect of Phenyl Radical on the Cross-linking.

By Mitsuru KOIKE and Akibumi DANNO
Japan Atomic Energy Research Institute, Tokai-mura, Naka-gun, Ibaraki-ken, Japan

(Received March 19, 1960)

The radiation effects both of polydimethyl siloxane and dimetyl-diphenyl siloxane copolymers were studied by the use of gamma rays of cobalt-60 in order to estimate the protective effect due to phenyl radical against the radiation-induced cross-linking. The viscosity of irradiated sample increased with the absorbed dose and finally the sample became gel. The efficiency of cross-linking of copolymers is remarkably reduced with increasing concentration of diphenyl siloxane. The minimum absorbed dose for gel formation, the efficiencies of cross-linking per monomer unit were obtained as a function of the concentration of phenyl radical. It is estimated that the protective effect of diphenyl siloxane may extend over five or six neighbouring monomers of dimethyl siloxane.

§ 1. Introduction.

The effects of ionizing radiation on high polymers have been studied by many workers, and it is well known that polystyrene is the most stable polymer against radiations[1)-6)]. An ordinally polymer needs the absorbed energy of about 20 eV for one cross-linking, whereas polystyrene requires much higher value of about 3,000 eV[1)]. The stability of polystyrene is due to the presence of phenyl radical within the polymer molecule.

In order to obtain polymers of higher radiation stability, several studies on the copolymers containing phenyl group were carried out. For examples, Sisman and Bopp[2)] studied the radiation effect of styrene-butadiene and styrene-acrilonitrile copolymers irradiated in a nuclear reactor. They observed that the change in hardness of the copolymers was much less than that of pure polybutadiene and polyacrilonitrile. Alexander and Charlesby[7] studied the irradiation behavior of copolymer containing various proportions of styrene and isobutyrene, and found that the degradation of isobutyrene was greatly suppressed with increasing content of styrene. They also calculated the degree of protection due to phenyl group assuming a random distribution of styrene and isobutyrene units throughout the copolymer molecule, and came to a conclusion that phenyl group in styrene monomer unit protects about four neighbouring carbon atoms in the main-chain.

The irradiation behavior of polydimethyl siloxane also has been studied by may investigators.[2,3,8-10] They concluded that the cross-linking is formed in the polymer by the irradiation[11-15]. The stabilizing effect of phenyl group, in dimethyl-diphenyl siloxane copolymer, was observed by Warrick[13]. He found that in this copolymer the energy required, for the same order of cross linking formation, was 20 times as that of polydimethyl siloxane. However, his result has not been reported in detail.

In the present work, measurement were carried out on the change of viscosity caused by the irradiation on dimethyl-diphenyl siloxane copolymer, for various concentrations of diphenyl siloxane and also for different initial molecular weight of the copolymers, in order to study the protective effect of phenyl group against the radiation-induced cross-linking of siloxane copolymer. From the experimental results obtained some informations on the protective effect of phenyl group against cross-linking was obtained.

§2. Experimental.

The polydimethyl siloxane and the copolymer of dimethyl siloxane and diphenyl siloxane used in this experiment are transparent and viscous liquid*. The concentration of phenyl group in the copolymer were selected to be 5 and 25 mol%, respectively.

Molecular weight of the polymer was obtained from viscosity measurement using the Stauding's law,

$$\eta = KM^{\alpha}, \tag{1}$$

where η is viscosity, M the molecular weight, K and α constants for a given polymer. In the case of polydimethyl siloxane[11], Eq. (1) applies with bulk viscosity, η, in cs at 25°C; $K=5.3\times10^{-4}$, $\alpha=1.39$ when $M<30{,}000$; and $K=2.7\times10^{-14}$, $\alpha=3.7$ above this molecular weight. The value of M thus obtained should be the weight average[12]. In order to determine the molecular weight of copolymer, the same value as for polydimethyl siloxane were tentatively applied for K and α in Eq. (1), since the value of K and α for the copolymer have not been published. For the calculation of the degree of polymerization of the copolymer, the molar average molecular weight was used as the molecular weight of apparent monomer, assuming that the copolymer consisted hypothetically of one kind of monomers. Data thus obtained are shown in Table I.

Table I. Phenyl radical content, initial bulk viscosity, η_0, initial molecular weight (weight average), M, and initial degree of polymerization, P, of the samples.

content of phenyl radical (mol %)	η_0 (cs)		M	P
	normal	observed (at 25°C)		
0	0.65	——	1.62×10^2	2
	100	1.04×10^2	6.42×10^3	87
	1,000	1.00×10^3	3.01×10^4	407
	10,000	9.55 〃	5.53 〃	748
5	100	1.12×10^2	6.78×10^3	88
	1,000	1.01×10^3	3.01×10^4	391
	3,000	3.17 〃	4.10 〃	532
25	450	4.42×10^2	1.82 〃	194

Irradiation was carried out with the cylindrical 10 kilo-curie cobalt-60 source[16]. The maximum field strength of 2×10^6 rad/hr was available at the center of the source cylinder. Dose rate of about 2.0×10^6 rad/hr was usually used for irradiation, but sometimes about 5×10^5 rad/hr was also used. The upper limit of absorbed dose for the experiment was 1.4×10^9 rad. A test tube of hard glass of 20 cm in height and 1.8 cm in diameter was filled with sample liquid and plugged with a glass stopper leaving air column of about 2 cm high above the liquid surface. Samples thus prepared were placed inside or outside of the source cylinder and irradiated at room temperature.

---

* The samples were supplied by Shin-etsu Chemical Industry Co., Ltd.

The change in bulk viscosity of irradiated samples was measured by a rotation viscometer of concentric cylinder type at 25°C. This viscometer consists of inner and outer cylinders; the outer cylinder rotates at constant speed and the inner cylinder is suspended vertically by a torsion wire. A sample to be measured is filled in the gap between the inner and the outer cylinders. The bulk viscosity of liquid can be measured from the angular deflection of the torsion wire. Varying the dimensions of the torsion wire and the inner cylinder, it is possible to measure a viscosity change in a wide range.

§ 3. Results of experiment.

The viscosity of copolymers increases more slowly with increasing radiation dose than that of polydimethyl siloxane. The change in viscosity of these polymers by the irradiation depends both on the initial molecular weight and on the concentration of phenyl group. Fig. 1 shows the relationship between these changes in viscosity and the absorbed dose. The initial viscosity of the low molecular sample of polydimethyl siloxane is 0.65 cs. The viscosity change of this low molecular sample was very small even after the irradiation of 1.4×10^9 rad. In other samples, the viscosities increased with increasing absorbed dose and finally samples appeared gel-like. Between the samples having the same phenyl group content, but of different molecular weight, the higher molecular samples required larger absorbed dose than that of the lower molecular weight, for the same amount of viscosity change. On the other hand, between the samples having the same initial molecular weight but containing different amount of phenyl groups. Samples of the higher phenyl group content required larger absorbed dose for the same amount of viscosity change. Further, a similar relation is observed on the minimum absorbed dose for gel formation as mentioned below.

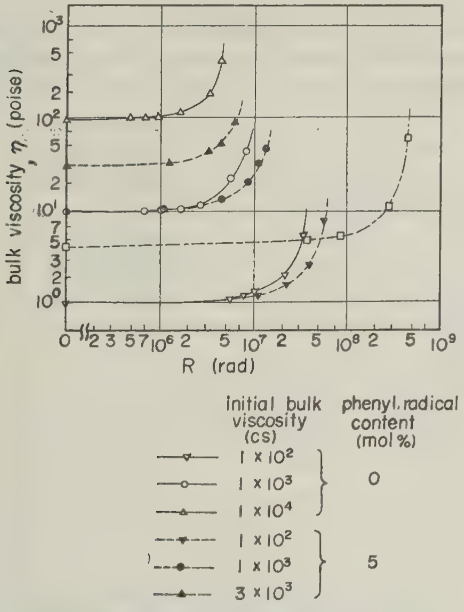

Fig. 1. The change in bulk viscosity by gamma irradiation.

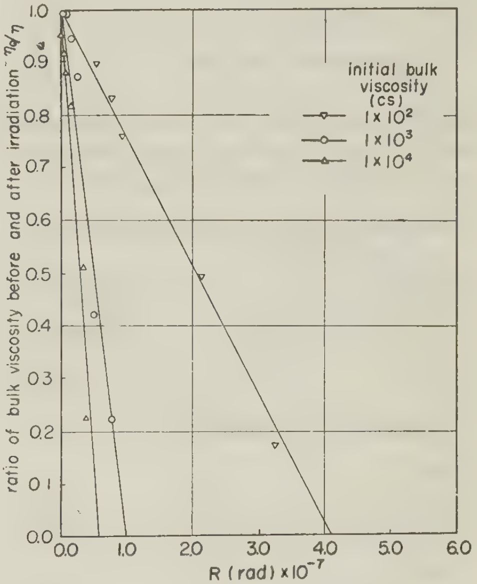

Fig. 2. The relationship between the absorbed dose and the ratio of bulk viscosity before and after irradiation for polydimethyl siloxane.

Figs. 2, 3, and 4 show the relationship between the absorbed dose, R, and the ratio of viscosities, η_0/η, for 0.5 and 25 mol% copolymers, respectively. Setting aside the beginning range where R is small, the linear relationship between η_0/η and R are found both for polydimethyl siloxane and for copolymers. Accordingly, it may be assumed that η_0/η is proportional to R, then the relationship between η_0/η and R can be written, as

$$\eta_0/\eta = 1 - AR \,. \qquad (2)$$

In Eq. (2), A, slope of straight lines in Figs.

2, 3 and 4, is the function of initial molecular weight and the concentration of phenyl radical.

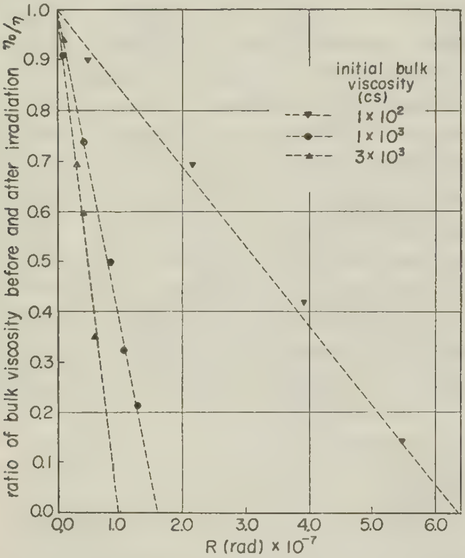

Fig. 3. The relationship between the absorbed dose and the ratio of bulk viscosity before and after irradiation for 5 mol % copolymer.

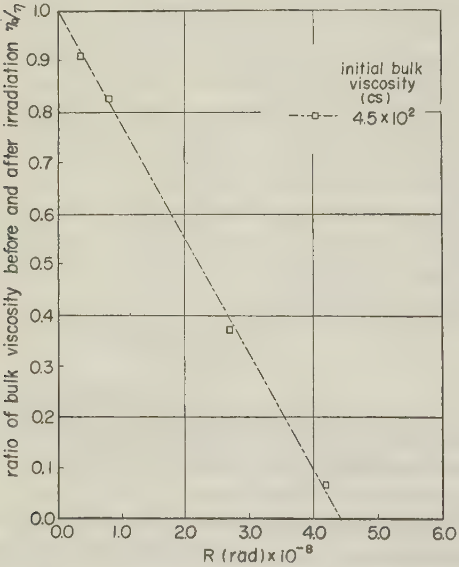

Fig. 4. The relationship btween the absorbed dose and the ratio of bulk viscosity before and after irradiation for 25 mol % copolymer.

The increase in viscosity of irradiated sample is due to the formation of cross-links. When the cross-linked monomer in the molecule is formed to some extent, sample becomes gel. Theoretically, the first gel formation occurs at an absorbed dose of R_g which is needed to produce one cross-linked monomer unit per weight average molecule[17]. Experimentally R_g can be obtained as the dose corresponding to $\eta \to \infty$[18],[19], or $\eta_0/\eta=0$ in Figs. 2, 3 and 4, because η_0/η decreases linearly with the absorbed dose, R, as shown in Eq. (2). The values of R_g obtained in this way are shown in Table II.

Table II. Minimum absorbed dose needed for gel formation, R_g, and the product of R_g and initial molecular weight, M.

content of phenyl radical (mol %)	η_0 normal (cs)	R_g (rad)	$R_g \times$ M (rad)	
0	100	4.1×10^7	2.7×10^{11}	$3\ 0\times10^{11}$
	1,000	9.8×10^6	3.0 〃	
	10,000	5.9 〃	3.3 〃	
5	100	6.3×10^7	4.3 〃	4.3×10^{11}
	1,000	1.6 〃	4.7 〃	
	3 000	9.8×10^5	4.0 〃	
25	450	4.4×10^8	8.0×10^{2}	

Fig. 5 shows the relation between η_0/η and *PR*. In this figure, it is seen that the plots for samples containing the same amount of phenyl groups fall on a straight line independently of the initial molecular weights. Therefore, the relation between η_0/η and *PR* can be expressed as follows;

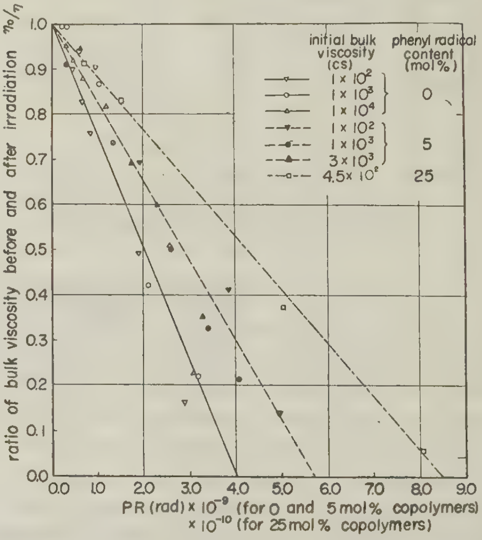

Fig 5. The relationship between η_0/η and *PR*.

$$\eta_0/\eta = 1 - \varepsilon_p PR\ , \tag{3}$$

where ε_p denotes the slope of each line shown in Fig. 5. Suffix p represents the concentration of phenyl group. $\mathcal{E}_p$ signifies the efficiency of cross-linking of any given monomer unit in the molecule per unit absorbed dose in rad. It depends not on the initial molecular weight but only on the concentration of phenyl group.

Eq. (3) may be extended to gel point. As η_0/η is zero and R is R_g at the gel point, Eq. (3) gives ;

$$\mathcal{E}_p=1/(PR_g) \qquad (4).$$

So far as Eq. (4) is satisfied at the gel point, the product PR_g, and hence the product MR_g must be constant for the copolymer containing the same amount of phenyl group. Fig. 6 shows the relationships $\log R_g$ *vs* $\log M$ for each phenyl radical content as a parameter. A linearity is seen between $\log R_g$ and $\log M$, and the slope of this line is nearly one. Furthermore, the line for polydimethyl siloxane was parallel to the line for 5 mol% copolymer. Accordingly, a relationship of $R_g \times M$=constant is obtained and this relation agrees with Charlesby's result for a pure silicone oil[11]. As shown in Table II, the mean values of product $R_g \times M$ for 0, 5 and 25 mol% copolymers are 3.0×10^{11}, 4.3×10^{11} and 8.0×10^{12} rad, respectively.

In general, the efficiency of cross-linking of a given monomer unit, $\mathcal{E}$, for each copolymer can be obtained as $1/(PR_g)$ using Eq. (4). The values of $\mathcal{E}$ obtained in this way are shown in Table III. The energy absorbed per cross-linked unit is defined by reciprocal of $\mathcal{E}$. Since the value of energy absorption to produce one ion pair in air, W, is 34 eV and the electron density of silicone is very similar to that of water, the absorbed energy in eV per cross-linked unit is

$$\frac{6.1\times10^{13}\,\text{eV}\times\text{molecular weight of monomer}}{6.0\times10^{23}\times\mathcal{E}}.$$

The energy absorbed per cross-linking (corresponding to two cross-linked units), E, is twice the above value, and the G-value of cross-link formation becomes $100\,\text{eV}/E$. The values of E and G for each irradiated sample are also shown in Table III.

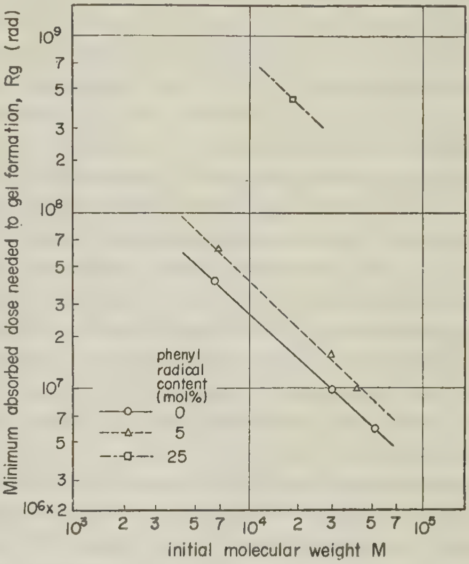

Fig. 6. The relationship between the minimum absorbed dose for gel formation, R_g, and the initial molecular weight, M, for each phenyl radical content as a parameter.

Table III. Efficiency of cross-linking of monomer per one rad, $\mathcal{E}$, absorbed energy per cross-linking, E, and G-value of cross-linking.

content of phenyl radical (mol %)	η_0 normal (cs)	$\mathcal{E}$ (rad^{-1})		E (eV)		G-value	
0	100	2.74×10^{-10}	2.45×10^{-10}	56	62	1.79	1.60
	1,000	2.46 〃		62		1.61	
	10,000	2.25 〃		68		1.47	
5	100	1.79 〃	1.82×10^{-10}	89	90	1.12	1.12
	1,000	1.64 〃		97		1.03	
	3.000	1.92 〃		83		1.21	
25	450	1.17×10^{-11}		1.6×10^3		0.06	

§ 4. Discussion of the result.

The efficiency of formation of cross-links in dimethyl-diphenyl siloxane copolymers by the irradiation of gamma rays depends not on the initial molecular weight but on the concentration of phenyl group in the copolymer as stated above. Recently, Watanabe[19] pointed out from the theoretical consideration that the relationship η_0/η *vs* R was represented not always by a linear function but by a function involving the parameter α appeared in Eq. (1). The theoretical curve is shaped S. Our observed curve is considered to be a straight line within the experimental error for samples of low molecular weight and approaches the theoretical curve of $\alpha=3.7$ for high molecular weight samples. Therefore, the slight deviation from straight line in our observed curves may be explained by his theory. However, we treated the observed curve as a straight line in first apploximation.

As shown in Table III, E for polydimethyl siloxane is 62 eV. This value is considerably larger than the value of 32 eV given by Charlesby[12] for the same polymer irradiated in a nuclear reactor. When Charlesby calculated the absorbed energy, however, the value adopted for W was 29 eV. The latest value of W is 34 eV, and his value of E, 32 eV, should be modified to 38 eV. His experiment of gamma irradiation gave 40 eV as the value of E to the same polymer. The discrepancy between the value of present authors and that of Charlesby may be attributed to three factors; (1) the presence of air, (2) different dose rate and (3) the different ways of the determination for R_g. Concerning the third, it may be considered that the values of R_g, or E, determined from a straight line between η_0/η and R will be somewhat larger than that could be determined from the theoretical curve shaped S.

Moreover, in 5 and 25 mol% copolymers the values of E are 9.0×10 and 1.6×10^3 eV, respectively. The increase of E with the increasing concentration of phenyl group, is due to the increment of a ratio of dimethyl siloxane monomer units which is protected by phenyl group to the total number of its monomers. Even in 25 mol% copolymer, however, the protective effect by phenyl group is not sufficient compared with that in the case of polystyrene in which E is 3,000–5,000 eV[1]. On the other hand, even after the absorotion of 1.4×10^9 rad, the low molecular sample of 0.65 cs initial bulk viscosity did not show any appreciable change in viscosity as far as we have explored.

Based on the assumption of random distribution of dimethyl siloxane and diphenyl siloxane units throughout the copolymer molecule, a calculation was carried out on the range of protection of phenyl group according to the reasoning of Alexander and Charlesby[7]. They deduced the range of protection from the reduced degradation rate, but the present authors from the reduced cross-linking efficiency. For this purpose let M represent a dimethyl siloxane and P a diphenyl siloxane unit. Let f denote the probability that any given monomer unit is M. The numerical values of f are given in Table IV for 5 and 25 mol% of phenyl group.

Let us now assume that any given dimethyl siloxane unit **M** is only protected by P unit against cross-linking, if its nearest neighbour unit is a diphenyl siloxane unit P. The probability of such an arrangement as M**M**M, of which only such **M** unit is able to cross-link, is given by f^2. Therefore the ratio of such **M** units to the total number of units in the specimen is given by f^3. In general, it is assumed that P unit protects n-units of M successibly arranged in the nearest neighbour of P unit. Then the ratio of M units possible to cross-link to the total number of units is given by f^{2n+1}. Now, the ratio of cross-linked monomer units to the total number of units under the protection of phenyl group is defined as the degree of protection. The numerical values of f^{2n+1} for given f and n are shown in Table IV.

Table IV. Comparison of theoretical and observed values of the degree of protection.

		degree of protection	
content of phenyl radical		5 mol %	25 mol %
probability of dimethyl siloxane, f		0.975	0.875
theoretical values			
f^{2n+1}	$n=1$	0.93	0.67
	4	0.80	0.30
	5	0.76	0.23
	6	0.72	0.18
	7	0.68	0.13
observed values			
$\mathcal{E}_p/\mathcal{E}_0$		0.74	0.05

On the other hand, the observed degree of protection is obtained as the ratio of cross-linking efficiency of copolymer, $\mathcal{E}_p$, and that of polydimethyl siloxane, $\mathcal{E}_0$. It was calculated as follows,

$\mathcal{E}_p/\mathcal{E}_0=1.82\times10^{-10}/2.45\times10^{-10}=0.74$ for 5 mol%

$\mathcal{E}_p/\mathcal{E}_0=1.17\times10^{-11}/2.45\times10^{-10}=0.05$ for 25 mol%

These ratios are also summarized in Table IV.

The degree of protection observed is 0.74 for 5 mol% copolymer and 0.05 for 25 mol% copolymer, respectively. Comparison of the degree of protection observed with f^{2n+1} calculated, makes clear that in the case of 5 mol% copolymer the observed value, 0.74, is placed between the calculated, 0.76 for $n=5$ and 0.72 for $n=6$. In the case of 25 mol%, however, the observed value, 0.05, is smaller than the value of 0.18 calculated using $n=6$. The value of $\mathcal{E}_p$ for 5 mol% copolymer is the mean value for three samples having different molecular weight and it is more reliable than that for 25 mol% copolymer. Therefore, it may be considered that the protection by single diphenyl siloxane unit extended over five or six monomer units of dimethyl siloxane on the average.

For the vinyl polymer, copolymer of isobutylene and styrene, Alexander and Charlesby reported that the range of protection by phenyl group extends over four main-chain carbon atoms[7]. However, there is a considerable difference in the range of protection by phenyl group between vinyl copolymer and siloxane copolymer. This difference of the range of protection between two kinds of the copolymers may be regarded as due to the difference in the number of phenyl radicals in monomer unit, and the difference in the main-chain structure. The copolymer used by Alexander and Charlesby has only one phenyl group in one styrene monomer unit. However, the copolymer used in the present work has two phenyl groups in one diphenyl siloxane monomer unit.

Provided that the excitation or ionization of π electron in phenyl group has no chemical effects on cross-linking or degradation, diphenyl siloxane monomer unit will be able to dissipate more energy by the existence of two phenyl groups than styrene monomer unit will. Secondary, we may consider the difference in main-chain structure between vinyl copolymer and siloxane copolymer. Vinyl copolymer consists of *–C–C–* and siloxane copolymer of *–Si–O–*. In the latter, silicon and oxygen atoms have more electrons content than carbon atom has. Moreover, oxygen atom has movable lone pair electrons in its $2p$ orbit. Therefore electron may be more easily movable in *–Si–O–* chain than in *–C–C–* chain. It is assumed that electron in molecule is excited or ionized by radiation and the transition of its excited or ionized state can occur by electron migration through the main-chain into phenyl groups and its energy is dissipated by the resonance strcture of phenyl radical. The mechanism of protective effect in the copolymer under consideration may be explained by above mentioned assumption. It may be reasonable that the siloxane copolymer in which the electron migrates easily through the main-chain *–Si–O–* is protected more notably by phenyl groups than the vinyl copolymer is protected.

Therefore, it may be reasonably concluded that the range of protection by phenyl radical in the diphenyl siloxane can extend over five or six monomer units of dimethyl siloxane.

Acknowledgements

Authors wish to acknowledge to Dr. K. Kimura, a director of the Institute, for his kind encouragement throughout the entire course of this study, and to Dr. T. Watanabe for his valuable discussions. They also wish to express their thanks to Shin-etsu Chemical Industry Co., Ltd, for their kind offer of the samples and to Mr. M. Yamamoto, member of the Central Reserch Institute, above firm, for his useful advices.

References

1) A. Charlesby: J. Polymer Sci. **11** (1953) 521.
2) C. D. Bopp and O. Sisman: ORNL–1373 (1953).
3) A. Charlesby: Nucleonics **12** No. 6 (1954) 18.
4) P. Y. Ferry and J. W. Kennedy: J. Amer. Chem. Soc. **77** (1954) 847.
5) C. D. Bopp and O. Sisman: Nucleonics **13** No. 10 (1955) 51.
6) O. Sisman and C. D. Bopp: ON ≀ Symp. Report ACR–2 (1954).
7) P. Alexander and A. Charlesby: Proc. Roy. Soc. **A 230** (1955) 136.
8) E. J. Lawton, A. M. Bueche and J. S. Balvit: Nature **172** (1953) 76.
9) A. Charlesby: ibid. **173** (1954) 679.

10) R. Harrington: Nucleonics **14** No. 9 (1956) 70.
11) A. Charlesby: J. Polymer Sci. **17** (1955) 379.
12) A. Charlesby: Proc Roy. Soc. **A 230** (1955) 120.
13) E. L. Warrick: Ind. Eng. Chem. **47** (1955) 2388.
14) A. M. Bueche: J. Polymer Sci. **19** (1956) 297.
15) A. A. Muller: Symp. on Chem. Effect of High Energy Radiation No. 9 (Des. 28, 1958), (at Notre Dame Univ.).
16) A. Danno et al: 2nd Intern. Conf. of Peaceful Use of Atomic Energy P/1328 Geneva, (1958),
17) A. Charlesby: Proc Roy. Soc. **A222** (1954) 542.
18) O. Saito: J. Phys. Soc. Japan **13** (1958) 1465.
19) T. Watanabe: private communication. (to be published elsewhere).

JOURNAL OF THE PHYSICAL SOCIETY OF JAPAN, Vol. 15, No. 8, AUGUST, 1960

Interpretation of Exciton Induced Luminescence in KI/Tl

By Masao TOMURA

Department of Applied Physics, Osaka City University, Osaka

(Received April 23, 1960)

Details of the exciton induced luminescence in KI/Tl1) are discussed. It is pointed out that the absorption coefficient at the long wavelength tail of the first characteristic absorption band of a single crystal of KI is much smaller than that of an evaporated polycrystalline film of KI, and then the complex shapes of excitation spectra of the exciton induced luminescences from Tl^+ ion and a certain impurity are explained. Furthermore, a new weak absorption band is found in the long wavelength tail of the first exciton absorption band, which is infered to be due to the triplet-like state of the exciton.

Some discussions are given on the problem of migration of excitons and the life time of the exciton is estimated to be much longer than 10^{-8} sec.

§1. Introduction

In the preceding work1) the exciton induced luminescences (being denoted as E.I.L. in the following) from single crystals of KI/Tl have been measured at various temperatures for specimens of several concentrations of Tl^+ ion. It was concluded that excitons migrate through the crystal and transfer their energies to Tl^+ ions as well as to certain impurities, giving rise to their own luminescences. The excitation spectra for both E.I.L. were not simple and different from each other in shape. The absorption coefficient of the exciton absorption band is so large ($\sim 10^6\,cm^{-1}$) that almost all of excitons are created just near the surface of the crystal and may decompose under the influence of the surface in some ways. Then the shapes of the excitation spectra should be analysed in connection with the absorption coefficient of the exciton absorption band.

In the next place, concerning the life time of the exciton, it has been believed that the exciton should have the life time corresponding to dipole radiation, that is, 10^{-8} sec in the order of magnitude2). On the other hand, Takeuti3) has shown from his theoretical calculation that there are singlet and triplet states of the exciton band. Then if the singlet exciton which can be created with irradiation of ultra-violet light would drop into the triplet state in the course of migration through the crystal, it might obtain a rather longer life time because of its forbidden nature in transition to the original ground state.

In the present paper, some discussions will be given on the above two problems as well as on the temperature-dependence of E.I.L which was observed in the preceding work1).

§ 2. Exciton absorption band of KI

The absorption coefficient of the first characteristic absorption band of KI has been measured by several authors[4]. At liquid nitrogen temperature, it has values of about $1\times10^5\,\text{cm}^{-1}$ at the peak of the band, that is, 214 mμ, and about $1\times10^5\,\text{cm}^{-1}$ at 216 mμ, and the shape of the absorption band seems to be symmetric at least in the middle region of the band. However, these measurements were carried out for thin polycrystalline films which were evaporated on appropriate substrates.

On the other hand, a few measurements have been carried out for single crystals only in the region of the long wavelength tail of the absorption band[5]. Although the values of absorption coefficient in this region differ from specimen to specimen, they do not seem to exceed $10^2\,\text{cm}^{-1}$ in the order of magnitude at about 216 mμ. Some examples of the absorption coefficients are shown in Fig. 1.

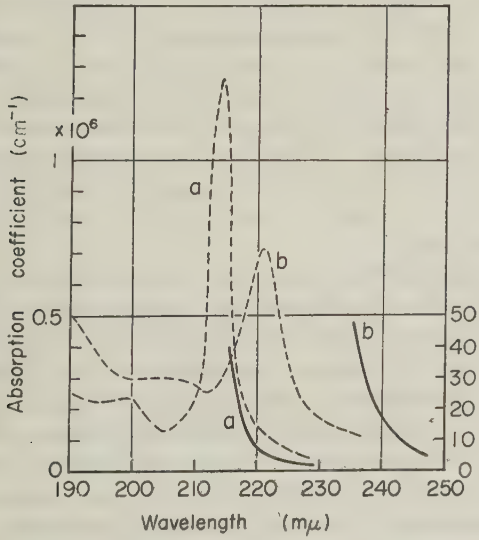

Fig. 1. The absorption coefficients of a single crystal (solid line) and thin polycrystalline film (broken line) of KI. a : at liquid nitrogen temperature and b: at room temperature. The left and right ordinate scales are for the broken and solid lines respectively. The magnitude of the left one was estimated roughly.

It is remarkable that the absorption coefficient of a single crystal in the long wavelength tail is smaller than that of a thin polycrystalline film by the order of 10^3 or so. In the wavelength region shorter than the peak of exciton absorption band, the absorption coefficient of a single crystal was so high* that it could not be measured. Perhaps its value might be larger than $10^3\,\text{cm}^{-1}$ at least.

The absorption coefficients of alkali halides have been usually obtained for thin polycrystalline films of 100∼1000 Å in thickness. Heller and Marcus[6] have pointed out that the dipole-dipole interaction which is the most important in the configuration-interaction of excitons in alkali halides is very sensitive to the size of the crystal. If the crystal has dimensions smaller than the spread of the exciton wave packet, the exciton may alter its nature, making the position and shape of the exciton absorption band to be changed. In the case of KI, the position of the exciton absorption band actually varies with the thickness of the specimen[7].

In view of these facts, the shape of the excitation spectra of E.I.L. which were measured in a single crystal shall be analysed on the stand point of very small absorption coefficients in the long wavelength tail of the exciton absorption band.

§ 3. Excitation spectra of E.I.L.

Examples of the excitation spectra of E.I.L. are shown in Fig. 5 in the preceding paper[1]. In the present paper, the excitation spectra of E.I.L. near the peak of the exciton absorption band which were measured with a fine

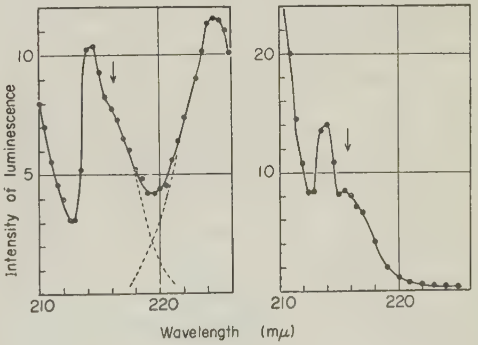

Fig. 2. The excitation spectra of E.I.L. from Tl^+ ion (left figure) and a certain impurity (right figure) at -210°C. Tl^+ ion concentration is $1\times10^{16}/\text{cm}^3$. Band pass is 6 Å at 220 mμ. The step pointed by an arrow corresponds to the weak absorption band discussed in §7. The maximum at 224 mμ in the left figure is due to the localized exciton around a Tl^+ ion.

---

* The present author is indebted to Dr. T. Onaka for this measurement.

band pass of 6 Å at 220 mμ are shown in Fig. 2.

The dominant properties of the excitation spectra are as follows. There is a minimum at the position of the peak of the exciton absorption band, that is 214 mμ* at liquid oxygen temperature. With increase of temperature, the position of the minimum moves to the longer wavelength side along with the peak of the absorption band. Further, a step is seen at about 202 mμ which may correspond to the second weak absorption band at 200 mμ in Fesefeldt's measurement[4]. The position of the first maximum, that is about 216 mμ*, lies in the region of the long wavelength tail of the exciton absorption band where the absorption coefficient is as small as 10^2 cm^{-1} as mentioned in § 2. As for the second maximum in the excitation spectra, its position corresponds to the region of the minimum in the exciton absorption bands, that is about 206 mμ. (See Fig. 1.)

In the present measurement the thickness of the specimen is about 2 mm, so that almost all of the incident light is absorbed in the crystal when the absorption coefficient exceeds about 30 cm^{-1}. Then if the quantum yield of E.I.L. is constant the shape of excitation spectrum should be flat in the middle region of the exciton absorption band. However, the higher is the absorption coefficient, the smaller is the intensity of E.I.L.; so it is inferable that the exciton decomposes preferentially in the vicinity of the surface of the crystal just as in the case of Apker and Taft's experiment[8]. In the region of the long wavelength tail where the absorption coefficient is smaller than 10^2 cm^{-1}, the intensity of E.I.L. may be proportional to the absorption coefficient, resulting a maximum in the excitation spectrum between the regions of very small and large absorption coefficients. The first maximum in the excitation spectrum which lies at about 216 mμ corresponds to the above maximum.

As shown in Fig. 2 a flatted top is seen at the above maximum point. Therefore, almost all of the incident light is absorbed at this wavelength, and the exciton is created deep in the interior of the crystal, being freed from decomposition under the influence of the surface of the crystal. In the preceding paper we have employed the intensity of luminescence at this wavelength as the intensity of E.I.L. This choice seems to be right in order to obtain the proper yield for E.I.L.

As for the excitation spectrum for E.I.L. from the unknown impurity (being denoted as *D* impurity in the following), it is different from that from Tl$^+$ ion in shape. The position of its first maximum lies at a little shorter wavelength than that for the latter and the intensity at its second maximum is higher than that at the first maximum in contrast to the case of E.I.L. from Tl$^+$ ion. On the stand point that the exciton migrates through the crystal, eventually meeting both Tl$^+$ ion as well as *D* impurity, the above facts are only understood by assuming that *D* impurities exist preferentially near the surface of the crystal in constrast with Tl$^+$ ion which distributes uniformly in the crystal. If the absorption coefficient is large, the exciton is created for the most part near the surface of the crystal, while in the case of smaller absorption the exciton is created deep in the interior of the crystal. Therefore, the relative probability of the exciton to meet a Tl$^+$ ion and *D* impurity differs according to the absorption coefficient.

In Fig. 3* the ratios of the intensities of E.I.L. from Tl$^+$ ion to that from *D* impurity are shown. In the larger absorption region, that is, the shorter wavelength region than the peak of the exciton absorption band, the ratio is rather weakly dependent of wavelength. Accordingly, we may infer that the absorption coefficients in this region are roughly unchanged in the order of one or two, coinciding with the results of measurements on thin polycrystalline films mentioned in § 2.

In the case of 2.7×10^{19}/cm^3 Tl$^+$ ion concentration the ratio is nearly unity at the wavelength of 212.5 mμ where the absorption coefficient is about 1×10^6 cm^{-1}, so the mean concentration of *D* impurity in the depth of 10^{-6} cm from the surface of the crystal may be equal as the concentration of Tl$^+$ ion, that is 10^{19}/cm^3 in the order of magnitude. With decrease of the absorption coefficient the value of the ratio increases and then the concentration of D impurity decreases towards the interior of the crystal. As mentioned in the preceding paper, at the wavelength of the first maximum in the excitation spectrum the intensity of D emission is roughly equal to that of Tl^+ emission in the specimen of $10^{16}/cm^3$ Tl^+ ion concentration. In the other words, the apparent concentration of D impurity is $10^{16}/cm^3$ in the order of magnitude in the deep interior of the present crystal.

---

* At about 60°K, the position of the exciton absorption peak moves to about 212.5 mμ and that of the first maximum in the excitation spectrum to about 214 mμ.

* Fig. 3, 4 and 5 are obtained from the measurements reported in the preceding paper.

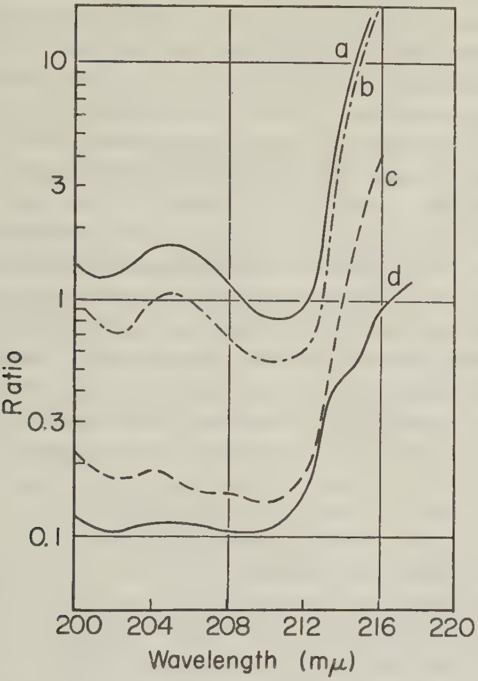

Fig. 3. The ratios of the intensities of E.I.L. from Tl^+ ion to that from D impurity at about −215°C. Tl^+ ion concentrations are a: $2.7\times 10^{19}/cm^3$, b: $5.7\times 10^{18}/cm^3$, c: $7\times 10^{17}/cm^3$ and d: $4.2\times 10^{16}/cm^3$.

Recently Teegarden and Weeks[9] have reported that D impurities are to be attributed to F centers which are created by the exciton from negative ion vacancies near the surface of the crystal. Their conclusion is just coincident with the present result.

Furthermore, the step in the excitation spectrum for E.I.L. at 202 mμ may be perhaps attributed to a kind of the exciton absorption band and not to an absorption band due to band to band transition. The induced luminescence at this wavelength shows no distinct properties other than those of E.I.L. at the longer wavelength region.

§ 4. Further discussions on the shape of the exciton absorption band

The ratio of both intensities of E.I.L. mentioned in § 3 increases abruptly towards the long wavelength region. (See Fig. 3.) In view of the difference between the distributions of Tl^+ ion and D impurity, we can infer from the above result that the absorption coefficient at low temperatures varies from $10^6\,cm^{-1}$ to $10^2\,cm^{-1}$ corresponding to just a little change of wavelength from 212.5 mμ to 214 mμ. This conclusion is coincident with the new information concerning the absorption coefficient of the exciton absorption band obtained in § 2. Thus the shape of the exciton absorption band of a single crystal seems to be completely asymmetric. Although measurements of absorption coefficients are rather difficult when the crystal is luminescent, the small absorption coefficient in the tail of the exciton absorption band observed by Teegarden and other authors[5] is confirmed by the above measurements of E.I.L. The asymmetry of the shape of the excitation spectrum near the region of its minimum shown in Fig. 2 also supports this conclusion, because the magnitude of the absorption coefficient corresponds to the intensity of E.I.L. in the opposite direction.

Toyozawa[10] has analysed the shape of the exciton absorption band of KI by using the data for thin polycrystalline films obtained by Fischer[4] and concluded that the lowest exciton band had its minimum at $K \neq 0$. (K is the wave number vector of the exciton.) From the present analysis, however, the minimum of the exciton band should lie at $K=0$ or $K\approx 0$. Then the absorption in the shorter wavelength region than the peak of the exciton absorption band may be caused by indirect transition.

In the next place, the influence of polishing the surface of the crystal was examined. Fig. 4 shows the ratio of the intensity of E.I.L. in a crystal of which surface is polished with a sand paper to that in a annealed crystal. The value of the ratio increases at the positions of the maxima of the exciton absorption band, that is, 212.5 and 202 mμ; while it decreases at about 206 mμ where the absorption coefficient is rather small. As before mentioned, E.I.L. in the high absorption region has the smaller yield for the higher absorption coefficient, so these results may mean that by the procedure of polishing the magnitudes of the absorption coefficients at the maxima decrease and that at the minimum increases with eventual increasing and decreasing of the intensity of E.I.L. respectively.

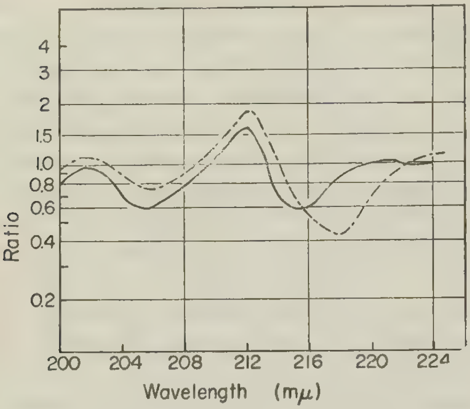

Fig. 4. The ratios of the intensities of E.I.L. in a crystal of which surface is polished with a sand paper to that in a annealed crystal for one hour at 400°C. Tl$^+$ ion concentration is $4.2 \times 10^{16}/\mathrm{cm}^3$ and temperature is -208°C. The solid and chained lines ane for E.I.L. from Tl$^+$ ion and D impurity respectively.

Blackney and Dexter[11)] have calculated increase of the edge absorption of alkali halides due to dislocations on the stand point that the deformation potential due to dislocations alters the energy of the exciton state to larger and smaller values, resulting increase and decease of absorption coefficients at the tails and the peak of the absorption band respectively.

In view of the above facts, in a perfect crystal which has no dislocations the absorption coefficient at the peak of exciton absorption band may be much larger than in an evaporated polycrystalline film. Differences between the shapes of the exciton absorption band of a single crystal and thin polycrystalline film are very interesting. The long range interaction such as dipole-dipole interaction may have a dominant role in the configurational interaction of excitons in alkali halides and then the surface of the crystal will have influences on tne electronic structure of the exciton.

§ 5. Temperature-dependence of E.I.L.

The temperature-dependence of E.I.L. has been described already in the preceding report. In the region of strong absorption, the larger is the absorption coefficient, the smaller is the intensity of E.I.L. as mentioned in § 3, therefore real properties of the temperature-dependence of E.I.L. can not be obtained from the intensities of E.I.L. at the positions of the minimum and second maximum of the excitation spsctrum. Thus the intensity of E.I.L. at the first maximum should be taken in order to discuss its temperature-dependence. Although both E.I.L. from Tl$^+$ ion and *D* impurity must be considered simultaneously in the discussion on the temperature-dependence of E.I.L. because of energy-transfer of the exciton to both centers, only E.I.L. from Tl$^+$ ion will be analysed easily, because Tl$^+$ ion distributes uniformly in the crystal.

According to Teegarden and Weeks[9)] the the origin of *D* impurities may be attributed to incipient negative ion vacancies in the host crystal. Therefore, though E.I.L. from *D* impurity quenches thoroughly at room temperature, the exciton itself may collide with the impurity, dissipating its energy even at higher temperatures. Then in the discussion of the temperature-dependence of E.I.L. from Tl$^+$ ion, the amount of energy which is dissipated to *D* impurities should be considered even at higher temperatures.

The E.I.L. from Tl$^+$ ion decreases with temperature especially in cases of lower Tl$^+$ ion concentrations, while that from *D* impurity seems to increase with temperature, if the nature of thermal quenching is subtracted. (See Fig. 6 in the preceding report.) Concidering these results, the sum of energies which are transfered to Tl$^+$ ion and *D* impurity seems to show no temperature-dependence even in the case of lower concentration of Tl$^+$ ion. In other words, the total amount of energy of the exciton which should be transfered to imperfections does not depend on temperature, though the intensity of E.I.L. from Tl$^+$ ion appears to depend on temperature.

In the case of higher concentration of Tl$^+$ ion such as $10^{19}/\mathrm{cm}^3$ where *D* impurities have no role because of smaller density, E.I.L. from Tl$^+$ ion shows actually a weak temperature-dependence. At the wavelength of the first maximum of the excitation spectrum, the absorption band due to the exciton and that due to the localized exciton around Tl$^+$ ion overlap a little with each other and the amount of overlapping becomes greater with increase of temperature, because both absorption bands show broadening with increase of temperature. Then the intensity of E.I.L. from Tl^+ ion decreases with increase of temperature through decreasing of absorption due to the exciton.

On the other hand, the above overlapping of both absorption bands is negligible in the case of lower concentration of Tl^+ ion, so the temperature-dependence of E.I.L. from Tl^+ ion must be explained by other reason.

As the migration of the exciton in the crystal of KI has been concluded in the preceding work, the exciton may be considered to become thermalized in the course of wandering through the crystal. The yield of E.I.L. from Tl^+ ion η may be shown as

$$\eta=\frac{f_{Tl}}{t_{Tl}+f_D+f_I}.$$

Here, f_{Tl}, f_D and f_I are frequencies of collision of the exciton with Tl^+ ion, D impurity and other imperfections such as dislocation, the surface of the crystal and etc. These frquencies should be represented as $v\sigma n$ where v is the velocity of the thermalized exciton, σ the cross section of collision between the exciton and the above defects at which the exciton dissipates its energy and n the densities of these defects.

when an exciton comes to an I^- ion next to a Tl^+ ion, it may be trapped around the Tl^+ ion after emitting some phonons* or move to the next I^- ion. The former process will need a duration of about 10^{-13}** sec and the latter 10^{-14} sec. Therefore, the probability of trapping of the exciton around a Tl^+ ion may be about one tenth of that of moving to the next I^- ion. The trapped exciton will transfer its energy to the Tl^+ ion through two center Auger transition of which the probability is about 10^{12}/sec after calculation by Dexter and Heller[12].

On the other hand, the trapped exciton around a Tl^+ ion might become a moving one through a kind of activation process of which the probability will be represented as $pe^{-E/kT}$. Here p is frequency factor of 3×10^{12}/sec* and E is the difference of energy between the states of the moving exciton and the trapped exciton around the Tl^+ ion. Thus σ_{Tl}, the cross section of excitation of Tl^+ ion by the moving exciton, is

$$\sigma_{Tl}=\sigma_0\frac{\nu_{Tl}}{\nu_{Tl}+pe^{-E/kT}}$$

where σ_0 is the product of trapping probability of the exciton around a Tl^+ ion mentioned before and the area covering the lattice spacing, that is, about $10^{-16}\,\mathrm{cm}^2$; and ν_{Tl} the probability of the above two center Auger transition.

Accordingly, η may be shown as

$$\eta=\frac{1}{1+\frac{n'\sigma'+n''\sigma''}{n\sigma_0}+\frac{n'\sigma'+n''\sigma''}{n\sigma_0}\cdot\frac{p}{\nu_{Tl}}e^{-E/kT}}.$$

The singly and doubly primed notations are for D impurity and the other imperfections respectively. Thus the yield of E.I.L. from Tl^+ ion has a similar nature to that of thermal quenching of normal luminescent materials. As $n'\sigma'$, $n''\sigma''$ and $n\sigma_0$ are all equal in the order of magnitude and E is estimated as 0.04 eV from the measurement in the case of $10^{16}/\mathrm{cm}^3$ Tl^+ ion concentration, η may show the temperature-dependence in the range of temperature in the present experiments. (See Fig. 5)

The Greek bands due to Tl^+ ion and F center lie at 224 and 238 mμ respectively, so the difference of energy between the exciton and these localized excitons are 0.25 and 0.58 eV respectively. As will be mentioned in the next section, considering the triplet-like exciton band through which the exciton migrates, the energy-differences between the electronic states of the moving exciton and the localized ones become much smaller. Further, the optical energy difference might be large than the thermal one, so the activation energy of 0.04 eV might be assumed to be the thermal energy difference. The electronic state of the localized exciton around a *F* center (being denoted as *D* impurity in this paper) is deeper than that around a Tl^+ ion, so σ' may be considered to be insensitive to temperature in the region of the present measurement.

---

* In the preceding work, it was shown that the spectral distribution of E.I.L. from Tl^+ ion is the same as that of the emission in the Greek band due to Tl^+ ion and is different from that of emission in the absorption bands at 233 and 244 mμ due to Tl^+ ion itself. Then the moving exciton may be assumed to become trapped around a Tl^+ ion before it transfers its energy to the Tl^+ ion.

** The broadening of the exciton absorption band, that is 0.1 eV, at liquid nitrogen temperature, was assumed to be caused by the interaction of the exciton with phonons.

* The residual absorption of KI lies at 102 μ.

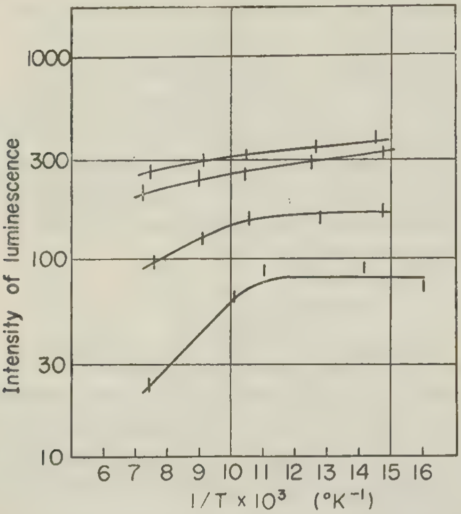

Fig. 5. The temperature dependence of the intensity of E.I.L. from Tl^+ ion. Tl^+ ion concentrations are $2.7\times10^{19}/cm^3$, $5.7\times10^{18}/cm^3$, $7\times10^{17}/cm^3$ and $4.2\times10^{16}/cm^3$ in order from the upper side.

If the yield of E.I.L. from Tl^+ ion decreases with increase of temperature, the yield of E.I.L. from *D* impurity may show the reverse temperature-dependence, because the total energy of the exciton to be transfered to imperfections is independent of temperature as mentioned before. However, the latter yield also decreases at higher temperature because of its nature of thermal quenching.

§6. Quantum yield of E.I.L. and life time of a moving exciton

As shown in Fig. 5 in the preceding report, in the case of lower concentrations of Tl^+ ion such as $10^{16}\sim10^{17}/cm^3$, the sum of the intensities of E.I.L. from Tl^+ ion and *D* impurity at the second maximum of the excitation spectrum attains quantum yield of nearly unity, while that at the first maximum is smaller about two or three times than the former. Although the exciton is created deep in the interior of the crystal under irradiation at the wavelength of the first maximum, there may exist some impurities at which the exciton dissipates its energy, the amount of which is estimated to be about $10^{16}/cm^3$ in the order of magnitude in refering to the concentration of Tl^+ ion. The fact that the yield at the second maximum is very high inspite of the possibility of destruction of the exciton near the surface of the crystal should be attributed to the localization of *D* impurities near the surface of the crystal.

Thus the intensity of E.I.L. from Tl^+ ion is reduced by the overlapping of the exciton absorption band with the absorption band at 224 mμ in the case of very high concentration of Tl^+ ion and by the presence of the other imperfections in the case of lower concentration of Tl^+ ion, so the observed value of the yield of E.I.L. from Tl^+ ion, that is 40%, seems to be apropriate for the migration of the exciton.

As the original reagent of KI involves a little amount of Tl^+ ion, the present single crystal of KI contains already $5\times10^{14}/cm^3$ of Tl^+ ion without intentional adding of TlI. The E.I.L. from Tl^+ ion can be observed even in these crystals. Then the frequency of the interaction between the exciton and Tl^+ ion $v\sigma n$ can be estimated to be of the order of 10^5/sec by assuming the effective mass of the moving exciton to be the free electron mass and σ to be $10^{-16}/cm^2$. The corresponding life time of the thermalised exciton, that is 10^{-5} sec, is much longer than the one which has been convinced to be 10^{-8} sec for the exciton[2].

It has not been found that the exciton in KI does emit its own edge luminescence after annihilation. The above conclusion may well explain this fact. After creation of an exciton, it may drop into the triplet like state which has a very small transition probability to go back to the original ground state.

On the other hand, it has been known that the exciton in CdS does emit its edge luminescence[13]. The exciton in this case is of hydrogen like type, so the energy difference between the singlet and triplet states may be very small against the case of KI, because of a rather small exchange energy. Then the population of the exciton in the singlet state may be large, eventually leading a large transition probability to go back to the ground state through emitting normal dipole radiation. These explanation may be the reason for the exciton whether it emits own edge luminescence or not.

§ 7. A new exciton absorption band of KI.

In Fig. 2 steps at about 216 mμ are found in the excitation spectra for E.I.L. from Tl$^+$ ion and *D* impurity. As they appeare in the tail of the exciton absorption band where the absorption coefficient is small, they might be due to an impurity of some kind. The step, however, is observed in both excitation spectra, so the excitation at the step seems to show transfer of excitation energy to Tl$^+$ ion as well as to *D* impurity. Furthermore, the spectral distribution of the emission at the step is the sames as the one at the first maximum of the excitation spectrum of E.I.L. as shown in Fig. 6.

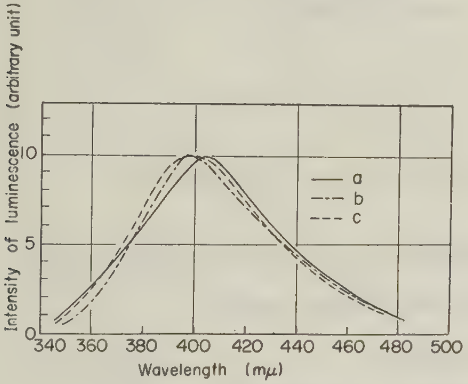

Fig. 6. The spectral distributions of emission bands under irradiation of lights 218 (a), 216 (b) and 214 mμ (c) at −204°C. Tl$^+$ ion concentration is 5×10^{15}/cm^3. These emission bands are composed of E.I.L. from Tl$^+$ ion as well as D impurity.

Accordingly, the step should not be attributed to an particular impurity. However, the most probable kind of impurities in KI such as Na$^+$ ion might be the cause of this weak absorption band, because the localized exciton around Na$^+$ ion might become the moving one in some cases. Fig. 7 shows the excitation spectra for E.I.L. from *D* impurity in pure KI and KI/NaI single crystals. In the case of 2×10^{-2}mol NaI concentration, another minimum appeares in the excitation spectrum at 215.5 mμ in addition to the minimum which corresponds to the peak of the exciton absorption band lying at 212.5 mμ. The former minimum corresponds to the absorption due to the localized exciton around Na$^+$ ion. On the other hand, the peak of the exciton aborption band of pure NaI lies at 222 mμ[4]. Accordingly, in the case of the present KI single crystal which may contain Na$^+$ ion by the amount of $10^{17}\sim10^{18}$/cm^3 the absorption due to Na$^+$ ion will not lie at the region of 216 mμ where the new weak absorption has appeared, but may lie at a shorter wavelength. Therefore, the new weak absorption band might correspond to a transition to a kind of exciton bands. As seen in Fig. 2, the intensity of E.I.L. at the step is a fraction of the intensity at the first maximum of excitation spectrum, so the order of the value of absorption coefficient of the new absorption band is estimated to be 10^2 cm^{-1}. In viewing of such a small absorption coefficient, the new absorption band might be attributed to a transition to the triplet like exciton band.

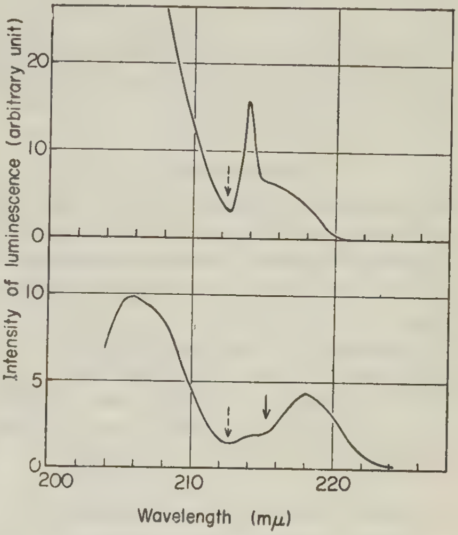

Fig. 7. The excitation spectra for E.I.L. from D impurity in KI (upper figure) and KI/NaI of 2×10^{-2} mol Na$^+$ ion (lower figure) at −205°C. The dotted and solid arrows point the wavelengths corresponding to the peak of the exciton absorption band of KI and that of the absorption band due to the localized exciton around a Na$^+$ ion respectively. Band pass is 6 Å at 220 mμ.

Considering the spin-orbit coupling in the calculation of exciton bands in KI, singlet and triplet states will not be obtained as good quantum states. However, singlet like and triplet like states might be obtained. Goodman and Oen[14] has calculated the electronic states of excitons in alkali halides considering the spin-orbit coupling, and obtained an absorption band of very small absorption coefficient at a wavelength a little longer than the familiar strong absorption band. The new weak absorption band might correspond to the above absorption band calculated by Goodman and Oen.

The author thanks Prof. T. Muto for his interests in this work and Dr. Y. Toyozawa for his discussions, and is also indebted to Messrs. Y. Kaifu and M. Yamakawa for their helps in the measurements.

References

1) M. Tomura & Y. Kaifu: J. Phys. Soc. Japan **15** (1960) 1295
2) F. Seitz: Rev. Mod. Phys. **23** (1951) 328
3) Y. Takeuti: Prog. Theoret. Phys. **18** (1957) 421
4) H. Fesefeldt: Z. Phys. **64** (1930) 680
F. Fischer: Z. Phys. **139** (1954) 328
K. J. Teegarden: Phys. Rev. **108** (1957) 660
W. Martienssen: J. Phys. Chem. Solids **8** (1959) 294
5) P. H. Yuster & C. J. Delbecq; J. Chem. Phys. **21** (1953) 892
K. J. Teegarden: Phys. Rev. **105** (1957) 1222
6) W. R. Heller & A. Marcus: Phys. Rev. **84** (1951) 809
7) F. Fischer: Z. Phys. **139** (1954) 328
8) M. H. Hebb: Phys. Rev. **81** (1951) 702
9) K. J. Teegarden & R. Weeks: J. Phys. Chem. Solids **10** (1959) 211
10) Y. Toyozawa: Prog. Theoret. Phys. **20** (1958) 53
11) R. M. Blakney & D. L. Dexter: Rep. Conf. on Defects in Crystalline Solids (Bristol) (1954) 108
12) D. L. Dexter & W. R. Heller: Phys. Rev. **84** (1951) 377
13) E. Grillot & M. Bancie-Grillot: J. Phys. Chem. Solids **8** (1959) 187
14) B. Goodman & O.S. Oen: J. Phys. Chem. Solids **8** (1959) 291

JOURNAL OF THE PHYSICAL SOCIETY OF JAPAN, Vol. 15, No. 8, AUGUST, 1960

Jets of a Perfectly Conducting Inviscid Gas in the Presence of a Magnetic Field parallel to the Stream

By Shigeki MORIOKA

Department of Aeronautics, Faculty of Engineering,
Kyoto University

(Received March 14, 1960)

The two-dimensional and the axially symmetrical jets of a perfectly conducting inviscid gas in the presence of a magnetic field parallel to the stream are investigated on the basis of the linearized theory, when the jets are governed by the supersonic hyperbolic equation. To this approximation, the fundamental equations and the boundary conditions are found to agree in their forms with those in the ordinary gasdynamic case, except for some parameters. Therefore, it is possible to obtain the solutions at once by making suitable substitution of the parameters in the well-known solutions for the gasdynamic case.

However, when the surrounding flow is governed by the subsonic hyperbolic equation, the circumstance is somewhat different from the gasdynamic case because disturbances in the surrounding flow propagate along the upstream characteristics. The structure of such a jet in the two-dimensional case is re-examined from the view point of reflection and refraction of a weak plane shock wave incident upon an interface between two streams.

§1. Introduction

Let a jet issue as a uniform, parallel stream from a nozzle of a semi-width (or radius in axially symmetrical jet) Y with Mach number M_1, velocity U_1, density ρ_1, and pressure p_1; let it issue into a fluid at rest or into a uniform stream in the same direction as the jet, with Mach number M_2, velocity U_2, density ρ_2, and pressure p_2. (see Fig. 1) In this paper, we shall only be concerned with the case in which the governing equation is of supersonic hyperbolic type in the domain of the jet, so that the external disturbance does not propagate upstream into the nozzle. The motion is supposed to be steady, and heat conduction as well as viscosity are neglected. The jet and the surrounding fluid are assumed to be an ideal gas with the ratio of the specific heats γ, permeability μ, and infinite conductivity. In the following, we consider two cases; (1) a magnetic field parallel to the stream is imposed on the jet only and (2) a magnetic field parallel to the stream is imposed on both the jet and the surrounding fluid. The difference of the total pressures in the uniform streams q_1-q_2 is assumed to be small compared with q_1, where $q=p+(\mu H^2/8\pi)$, p and H denote respectively the gasdynamic pressure and the intensity of the magnetic field. (Suffices 1 and 2 refer respectively to the jet and to the surrounding fluid.)

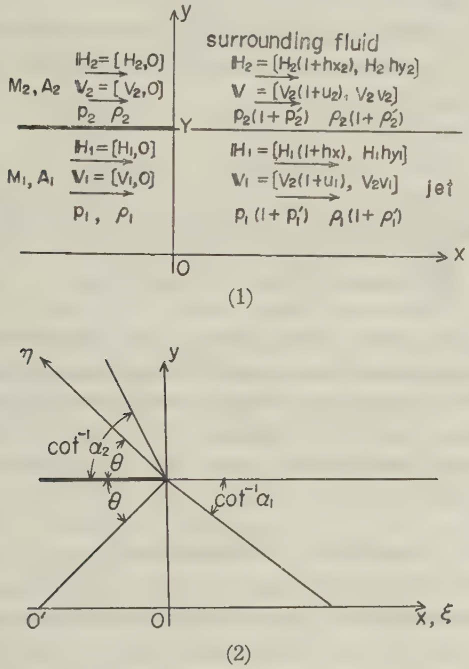

(1)

(2)

Fig. 1.

In addition, we assume that the flow and the magnetic field are nearly uniform, so that we may linearize the fundamental equation as well as the boundary conditions on account of small perturbations. The resulting equations are found to have the same forms as those for the gasdynamic case (with no magnetic field), except for some constant parameters. Since the corresponding gasdynamic problems have already been investigated by several writers,[2),3)] we can obtain the solution of the present problem at once by making suitable substitution (or interpretation) of the parameters in the previous investigations.

However, when the surrounding flow is governed by the subsonic but hyperbolic equation, the circumstance is different from the ordinary gasdynamic case in that the disturbance there propagates along the upstream characteristics. In order to clarify the character of such a jet in the two-dimensional case, the reflection and refraction of the magneto-gasdynamic shock wave incident upon the interface of two streams are also investigated.

§ 2. Fundamental Equations and Boundary Conditions

The fundamental equations for the present problem may be written in the forms:

$$\left.\begin{aligned}
&\operatorname{div}(\bar\rho\boldsymbol{v})=0\\
&\operatorname{div}\boldsymbol{H}=0\\
&\operatorname{rot}(\boldsymbol{v}\times\boldsymbol{H})=0\\
&(\boldsymbol{v}\operatorname{grad})\boldsymbol{v}=-\frac{1}{\bar\rho}\operatorname{grad}\bar p+\frac{\mu}{4\pi\bar\rho}\operatorname{rot}\boldsymbol{H}\times\boldsymbol{H}\\
&\frac{d\bar p}{d\bar\rho}=\frac{\gamma\bar p}{\bar\rho}
\end{aligned}\right\}\tag{1}$$

where $\boldsymbol{v}$, $\boldsymbol{IH}$, $\bar p$ and $\bar\rho$ are velocity, intensity of magnetic field, pressure, and density, respectively.

In Eqs. (1), writing $\boldsymbol{v}=[U(1+u), Uv]$, $\boldsymbol{IH}=[H(1+h_x), Hh_y]$, $\bar\rho=\rho(1+\rho')$, $\bar p=p(1+p')$, and $x/Y\to x$, $y/Y\to y$, we assume that u, v, h_x, h_y, p', and ρ' are all small compared with unity, and we neglect squares and products of these quantities, thus obtaining the equations:

$$\left.\begin{aligned}
&h_x=(1-M^2)u \qquad h_y=v\\
&\rho'=-M^2u \qquad p'=\gamma\rho'
\end{aligned}\right\}\tag{2}$$

$$\left.\begin{aligned}
&\frac{A^2-1}{M^2+A^2-1}\frac{\partial v}{\partial x}-\frac{\partial u}{\partial y}=0\\
&(M^2-1)\frac{\partial u}{\partial x}-\frac{\partial v}{\partial y}=\frac{\sigma v}{y}
\end{aligned}\right\}\tag{3}$$

where $A=U(\mu H^2/4\pi\rho)^{-1/2}$ denotes Alfvén number and the index σ takes the values 0 or 1 according as the jet is two-dimensional or axially symmetrical. The relations (2) show that the magnetic field is frozen in the fluid, Introducing the potential ϕ of the disturbance velocity, defined as

$$u=\frac{A^2-1}{M^2+A^2-1}\frac{\partial\phi}{\partial x}\,,\qquad v=\frac{\partial\phi}{\partial y} \tag{4}$$

we obtain from (3) the fundamental equation for the present problem:

$$\frac{(M^2-1)(A^2-1)}{M^2+A^2-1}\frac{\partial^2\phi}{\partial x^2}-\frac{\partial^2\phi}{\partial y^2}=\frac{\sigma}{y}\frac{\partial\phi}{\partial y}\,. \tag{5}$$

This is nothing but the Sears-Resler equation[1]. The field of flow is of elliptic or of hyperbolic character according as $(M^2-1)(A^2-1)/(M^2+A^2-1)$ is negative or positive. Change of the type of the flow field is shown in Fig. 2.

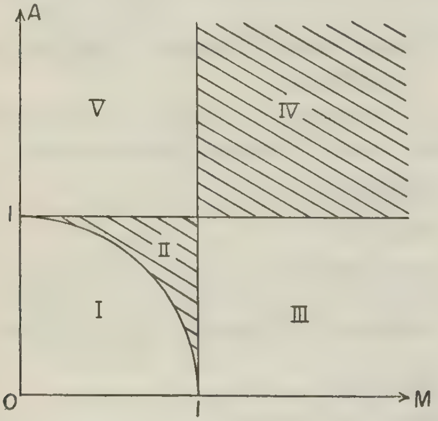

Fig. 2. Change of the type of Eq. (5). Blank and shaded areas are respectively elliptic and hyperbolic.

Since the flow is symmetrical about the axis of the jet, it is sufficient to consider only the upper half of the flow and magnetic fields.

The boundary conditions for the present problem then are expressed as follows.

1) The y-component of the velocity vanishes on the axis of the jet:

$$\frac{\partial\phi_1}{\partial x}=0 \qquad \text{for} \quad y=0\,. \tag{6}$$

2) The total pressure is continuous across the boundary of the jet:

$$q_1-\rho_1U_1^2u_1+\frac{\mu H_1^2}{4\pi}h_{x1}=q_2-\rho_2U_2^2u_2+\frac{\mu H_2^2}{4\pi}h_{x2}$$
$$\text{for} \quad x>0,\ y=1 \tag{7}$$

where q_1 and q_2 are the total pressures in the uniform streams. Since $q_1\simeq q_2$, we may obtain

$$\frac{\rho_2U_2^2}{\rho_1U_1^2}\simeq\frac{M_2^2A_2^2(\gamma M_1^2+2A_1^2)}{M_1^2A_1^2(\gamma M_2^2+2A_2^2)}\,.$$

Inserting this relation together with (2), (4) into Eq. (7), we get

$$\frac{\partial\phi_1}{\partial x}-\frac{M_2^2(A_2^2-1)(\gamma M_1^2+2A_1^2)}{M_1^2(A_1^2-1)(\gamma M_2^2+2A_2^2)}\frac{\partial\phi_2}{\partial x}$$
$$=\frac{A_1^2}{A_1^2-1}\frac{q_1-q_2}{q_1U_1^2} \qquad \text{for} \quad x>0,\ y=1\,. \tag{7'}$$

3) The direction of the flow is continuous across the boundary of the jet:

$$\frac{\partial\phi_1}{\partial y}=\frac{\partial\phi_2}{\partial y} \qquad \text{for} \quad x>0,\ y=1\,. \tag{8}$$

4) As the condition at the exit of the nozzle, we assume undisturbed, uniform flow:

$$\frac{\partial\phi_1}{\partial x}=\frac{\partial\phi_1}{\partial y}=0 \qquad \text{for} \quad x=0,\ 0\leq y<1\,. \tag{9}$$

5) For the conditions at infinity, if the surrounding stream obeys an elliptic type equation, the disturbance should vanish there:

$$\frac{\partial\phi_2}{\partial x} \quad \text{and} \quad \frac{\partial\phi_2}{\partial y}\to 0 \qquad \text{for} \quad y\to\infty\,. \tag{10}$$

On the other hand, if it obeys a hyperbolic type equation, any small disturbance propagates along the characteristics and there should be no disturbance in front of the leading characteristic starting at the edge of the nozzle wall.

§ 3. Formulae of the Substitution

The results obtained in the preceding section differ from the ordinary gasdynamic case in three points: the definition of the velocity potential (4), the equation of flow (5), and the condition (7′) for the continuity of the total pressure across the boundary of the jet.

In order to contrast the magneto-hydrodynamic and gasdynamic cases, we shall adopt the following abbreviations:
for the jet,

$$\alpha_1^2\frac{\partial^2\phi_1}{\partial x^2}-\frac{\partial^2\phi_1}{\partial y^2}=\frac{\sigma}{y}\frac{\partial\phi_1}{\partial y}$$
$$\alpha_1^2=\frac{(M_1^2-1)(A_1^2-1)}{M_1^2+A_1^2-1} \tag{11}$$

for the surrounding fluid,

$$\pm\alpha_2^2\frac{\partial^2\phi_2}{\partial x^2}-\frac{\partial^2\phi_2}{\partial y^2}=\frac{\sigma}{y}\frac{\partial\phi_2}{\partial y}$$
$$\alpha_2^2=\left|\frac{(M_2^2-1)(A_2^2-1)}{M_2^2+A_2^2-1}\right| \tag{12}$$

(where signs ± are taken according as

$(M_2^2-1)(A_2^2-1)/(M_2^2+A_2^2-1)\gtrless 0)$, and for the condition of continuity of total pressure across the boundary of the jet,

$$
\begin{aligned}
&\frac{\partial\phi_1}{\partial x}-\beta\frac{\partial\phi_2}{\partial x}=\varepsilon\\
&\beta=\frac{M_2^2(A_2^2-1)(\gamma M_1^2+2A_1^2)}{M_1^2(A_1^2-1)(\gamma M_2^2+2A_2^2)} \qquad (13)\\
&\varepsilon=\frac{A_1^2}{A_1^2-1}\frac{q_1-q_2}{\rho_1U_1^2}\,. \qquad (14)
\end{aligned}
$$

All these reduce of course to the expressions in the ordinary gasdynamic case by taking the limit $A\rightarrow\infty$ $(H\rightarrow 0)$. Namely, in the gasdynamic case,

$$
\left.\begin{aligned}
&\alpha_1^2=M_1^2-1\,\cdot \qquad && \pm\alpha_2^2=M_2^2-1\\
&\beta=\frac{M_2^2}{M_1^2}\,, && \varepsilon=\frac{p_1-p_2}{\rho_1U_1^2}\,.
\end{aligned}\right\} \qquad (15)
$$

Then, it will be seen that we can obtain at once the solution for the present problem by substituting the generalized expressions (11) ~(14) for the corresponding parameters (15) in the ordinary gasdynamic solution. Since α_1^2 as given by (11) is assumed to be positive in the present paper, various values of M_2^2-1 and $(p_1-p_2)/\rho_1U_1^2$ considered in the gasdynamics may cover the possible values of $\pm\alpha_2^2$ and ε in the present problem. As to β, on the other hand, there occurs only the case $\beta>0$ in the gasdynamics. In the present problem, however, the case $\beta<0$ may also occur. This is peculiar to the magneto-gasdynamic jet.

§ 4. Main Results

In this section, we summarize the main results obtained by making use of the formulae for the substitution stated in the preceding section. To do this, we shall designate, for shortness, as "Case I" the case in which the magnetic field is imposed only on the jet: and as "Case II" the case in which the magnetic field is imposed on both the jet and the surrounding fluid. We also designate as E_{sub}, H_{sub}, E_{sup}, and H_{sup} respectively the subsonic elliptic regions (I) and (V), the subsonic hyperbolic region (II), the supersonic elliptic region (III), and the supersonic hyperbolic region (IV) in Fig. 2.

Two-dimensional jet

1) *Jet issuing into a fluid at rest*

Case I The jet has a periodic structure. If we express the boundary of the jet by $y=Y[1+F(x)]$ ($F(x)$ has the same meaning in the following)

$$F(x)=\alpha_1^2\varepsilon H(x;\,4\alpha_1) \qquad (16)$$

where $H(x;\,2T)=\begin{cases}x & (0\leq x\leq T)\\ 2T-x & (T\leq x\leq 2T)\end{cases}$ is a triangular wave function. The amplitude a and the wave length λ are given by

$$
\left.\begin{aligned}
&a=\alpha_1^2\varepsilon=\frac{(M_1^2-1)A_1^2}{M_1^2+A_1^2-1}\frac{q_1-q_2}{\rho_1U_1^2}\,,\\
&\lambda=4\alpha_1=4\sqrt{\frac{(M_1^2-1)(A_1^2-1)}{M_1^2+A_1^2-1}}\,.
\end{aligned}\right\} \qquad (17)
$$

Case II The boundary of the jet is given by

$$F(x)=\alpha_1^2\varepsilon\left\{1-\sum_{n=0}^{\infty}(-1)^nC_n\sin\delta\cdot\cos\frac{\delta+n\pi}{\alpha_1}x\right\} \qquad (18)$$

where C_n must satisfy the equation

$$\sum_{n=0}^{\infty}C_n(\delta+n\pi)\cos(\delta+n\pi)y=1$$

and $\delta=\tan^{-1}\alpha_1/\beta$. In this case the jet has almost periodic structure, which is similar to a supersonic jet issuing into a uniform subsonic stream in the ordinary gasdynamics.[2] As a first approximation, the wave length of this (almost periodic) jet is given by

$$\lambda\simeq\frac{2\pi\alpha_1}{\delta}\,. \qquad (19)$$

2) *Jet issuing into a uniform subsonic stream*

Case I The jet has almost periodic structure.

Case II When (M_2, A_2) is a point in E_{sub}, the jet has almost periodic structure.

When (M_2, A_2) is a point in H_{sub}, the circumstance is somewhat different from the ordinary gasdynamic case. Namely, the disturbance in the surrounding stream propagates in this case along the upstream characteristics. (The reason for this phenomenon is described in § 5.) However, we may adopt the method of solution similar to that given in Ref. 3 (a supersonic jet in a uniform supersonic stream in the ordinary gasdynamics) by using the new coordinate system (see Fig. 1-(2));

$$
\left.\begin{aligned}
&\xi=x-\cot\theta\cdot(y-1)\,, && \eta=\operatorname{cosec}\theta\cdot y\\
& && \text{for}\quad 0\leq y\leq 1\\
&\xi=x+\cot\theta\cdot(y-1)\,, && \eta=\operatorname{cosec}\theta\cdot y\\
& && \text{for}\quad y\geq 1
\end{aligned}\right\} \qquad (20)
$$

where we must take θ as $\cot\theta>\alpha_2$. In this case, we may define the reflection factor R as the ratio of the amplitude of the reflected wave (the coefficient of the third term in ϕ_1) to that of the incident wave (the coefficient of the first term in ϕ_1), and the transmission factor T as the ratio of the amplitude of the transmitted wave (the coefficient of the second term in ϕ_2) to that of the incident wave. These factors are calculated to be

$$R=\frac{\beta+(\alpha_2/\alpha_1)}{\beta-(\alpha_2/\alpha_1)}\,,\qquad T=\frac{2}{\beta-(\alpha_2/\alpha_1)}\,. \tag{21}$$

Here, we may notice that $\beta<0$ and hence $|R|<1$. Putting $t=x/\alpha_1$, the boundary of the jet is given by

$$F(x)=\frac{\alpha_1\alpha_2\mathcal{E}}{(\alpha_2/\alpha_1)-\beta}\times\left\{t-(1-R)\sum_{n=1}^{\infty}R^{n-1}(t-2n)\cdot u(t-2n)\right\} \tag{22}$$

where $u(t-t_0)=\begin{cases}0 & (t<t_0)\\ 1 & (t>t_0)\end{cases}$ is the unit step function. Thus, for $R>0$ the jet experiences monotonous expansion or contraction, attaining asymptotically another uniform state in the downstream passage; and for $R<0$ it experiences a damped oscillation.

3) *Jet issuing into a uniform supersonic stream*

Case I The structure of the jet is similar to that of a supersonic jet in a uniform supersonic stream in the ordinary gasdynamics. The reflection factor R and the transmission factor T are given as follows:

$$R=\frac{\beta-(\alpha_2/\alpha_1)}{\beta+(\alpha_2/\alpha_1)}\,,\qquad T=\frac{2}{\beta+(\alpha_2/\alpha_1)}\,. \tag{23}$$

Here, it may be noted that $\beta>0$ and $|R|<1$. The boundary of the jet is given by

$$F(x)=\frac{\alpha_1\alpha_2\mathcal{E}}{(\alpha_2/\alpha_1)+\beta}\times\left\{t-(1-R)\sum_{n=0}^{\infty}R^{n-1}(t-2n)\cdot u(t-2n)\right\} \tag{24}$$

Thus, the jet experiences expansion or contraction, which damps out steadily or in oscillation according as $R>0$ or $R<0$.

Case II If (M_2, A_2) belongs to E_{sup}, the jet has the almost periodic structure. If (M_2, A_2) belongs to H_{sup}, it experiences expansion or contraction damping steadily or in oscillation.

Axially symmetrical jet

1) *Jet issuing into a fluid at rest*

The boundary of the jet, interpreting the gasdynamic case[2)], is expressed as

$$F(x)=\frac{\alpha_1{}^2\mathcal{E}}{2}\left\{1-4\sum_{n=0}^{\infty}\frac{1}{(\alpha_1k_n)^2}\cos k_nx\right\} \tag{25}$$

where k_n is the root of the following equation:

$$\alpha_1K_1(\alpha_2k_n)J_0(\alpha_1k_n)-\alpha_2\beta K_0(\alpha_1k_n)J_1(\alpha_1k_n)=0\,. \tag{26}$$

2) *Jet issuing into a uniform subsonic stream*

In *Case I* always and in *Case II*, if (M_2, A_2) belongs to E_{sub}, the jet has similar structure as 1).

In *Case II*, if (M_2, A_2) belongs to H_{sub}, using the coordinate system given by Eq. (20), we can follow the procedure given in Ref. 3 for treating the jet surrounded by a uniform supersonic stream (in the ordinary gasdynamics). Thus, putting $x/\alpha_1=t$, $\alpha_2/\alpha_1=\alpha$, and $\alpha/\beta=k$, the asymptotic form of the boundary may be expressed as

$$\left.\begin{aligned}F(x)&=\frac{\alpha_1{}^2\mathcal{E}}{2}\left\{1+\frac{\alpha}{2kt^2}-\frac{3\alpha^2}{k^2}(1-k\alpha)\frac{\ln t}{t^4}+\cdots\right\}\quad\text{for}\quad t\to\infty\\ F(x)&=\alpha_1{}^2\mathcal{E}k\left\{\frac{1}{1+k}\,t+\frac{1-k\alpha}{4\alpha(1+k)^2}t^2-\frac{(1-k\alpha)^2+3k(1+\alpha)^2}{48\alpha^2(1+k)^3}t^3+\cdots\right\}\quad\text{for}\quad t\to0\,.\end{aligned}\right\} \tag{27}$$

Here, it may be noted that $\beta<0$ and $k<0$.

3) *Jet issuing into a uniform supersonic stream*

In *Case I* always and in *Case II*, if (M_2, A_2) belongs to H_{sup}, the jet is similar to the supersonic jet surrounded by a uniform supersonic stream in the ordinary gasdynamics[3)]. The asymptotic form of the boundary may be given by Eq. (27), with $k>0$.

In *Case II*, if (M_2, A_2) belongs to E_{sub}, the jet will have similar structure to 1).

§ 5. Reflection and Refraction of a Weak Plane Shock Wave at the Interface between Two Streams, and the Structure of the Two-Dimensional Jet of a New Type

In order to obtain deeper understanding of the structure of the new type jet which appears when the field is two-dimensional and the surrounding flow is governed by the subsonic hyperbolic equation, we shall study the problem of reflection and refraction of a weak plane shock wave incident upon the interface between two streams. For this purpose, we first solve the magneto-gasdynamic shock relations on the basis of a weak shock approximation.

The conditions for an oblique shock wave in a perfectly conducting gas in the presence of a magnetic field are given, with the system of reference in which the shock is at rest and the streamlines are parallel to the lines of force, as follows:[4)]

$$\left.\begin{aligned}
&H\sin\alpha=H'\sin\beta\\
&\rho v\sin\alpha=\rho' v'\sin\beta\\
&p+\rho v^2\sin^2\alpha+\frac{\mu H^2}{8\pi}\cos^2\alpha\\
&\qquad=p'+\rho' v'\sin^2\beta+\frac{\mu H^2}{8\pi}\cos^2\beta\\
&\left(\rho v-\frac{\mu H^2}{4\pi}\right)\sin\alpha\cos\alpha\\
&\qquad=\left(\rho' v'-\frac{\mu H^2}{4\pi}\right)\sin\beta\cos\beta\\
&\frac{\gamma}{\gamma-1}\frac{p}{\rho}+\frac{1}{2}v^2=\frac{\gamma}{\gamma-1}\frac{p'}{\rho'}+\frac{1}{2}v'^2
\end{aligned}\right\}\qquad(28)$$

where α is the angle between the shock and the stream toward the shock and β is the angle between the shock and the stream behind the shock, and the quantities behind the shock are denoted by primes. If we put

$$x\equiv\frac{\tan\beta}{\tan\alpha}\qquad(29)$$

we obtain, after some calculation, the following equation for x:

$$\begin{aligned}
&(\gamma+1)(A^2-1)^2M^2x^3+(A^2-1)\{(\gamma+1)M^2\\
&\quad-2A^2-(\gamma-1)M^2A^2-(\gamma M^2+2A^2)\cot^2\alpha\}x^2\\
&\quad-\{(\gamma-1)+(2-\gamma)A^2\}M^2\cot^2\alpha x\\
&\qquad\qquad-M^2\cot^2\alpha=0\,.
\end{aligned}\qquad(30)$$

Once x is found, the other quantities may easily be determined by the following relations:

$$\left.\begin{aligned}
&\frac{H'^2}{H^2}=\frac{\sin^2\alpha}{\sin^2\beta}=\frac{x^2+\cot^2\alpha}{(1+\cot^2\alpha)x^2}\\
&\frac{A'^2}{A^2}=\frac{1}{A^2}+\frac{A^2-1}{A^2}x\\
&\frac{M^2}{M'^2}=\left(1+\frac{\gamma-1}{2}M^2\right)\frac{A^4}{A'^4}\frac{\sin^2\beta}{\sin^2\alpha}-\frac{\gamma-1}{2}M^2\\
&\frac{p'}{p}=\frac{M^2}{M'^2}\frac{A'^2}{A^2}\frac{\sin^2\alpha}{\sin^2\beta}\\
&\frac{\rho'}{\rho}=\frac{A^2}{A'^2}\,.
\end{aligned}\right\}\qquad(31)$$

In addition to the above we must consider the condition that the entropy of the fluid must increase in passing through the shock; $s'-s=\{R/(\gamma-1)\}\cdot\ln\{(p_2/p_1)(\rho_1/\rho_2)^\gamma\}>0$. It is found from this condition that the shock originated at a concave corner must be inclined to the upstream direction in case when the flow is governed by the subsonic hyperbolic equation (Fig. 3). This suggests that any small disturbance propagates into fluid along the upstream characteristic in this circumstance. Moreover, K. Tamada pointed out[5)] that the stationary wave front in the subsonic hyperbolic flow may be interpreted as an envelope of the unsteady wavefronts of the so-called magneto-gasdynamic slow wave emanated from a point source at successive time intervals and this envelope is nothing other than an upstream characteristic. This peculiar property of the wave field in subsonic hyperbolic flow may yield new types of jet in the present problem.

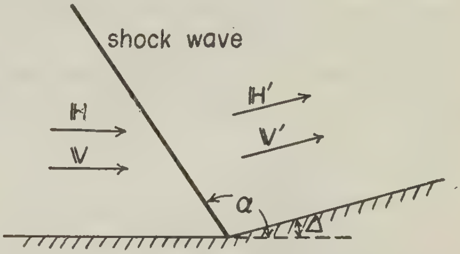

Fig. 3. Oblique shock at concave corner.

Now, in Eq. (30), $x=1$ is seen to be a root for $\cot^2\alpha=(M^2-1)(A^2-1)/(M^2+A^2-1)$. Also, let $x=1+\delta$ be the root corresponding to $\cot^2\alpha=(M^2-1)(A^2-1)(1-\varepsilon)/(M^2+A^2-1)$, where δ, ε are supposed to be sufficiently small. Then, with such a weak shock approximation, Eq. (30) reduces to

$$\delta=\frac{2(M^2-1)(M^2+A^2-1)}{M^2\{3(M^2-1)+(\gamma+1)(A^2-1)\}}\varepsilon\qquad(32)$$

and Eqs. (31) reduce to

$$\left.\begin{aligned}
&\frac{H'^2}{H^2}=\frac{\sin^2\alpha}{\sin^2\beta}=1+\frac{2(M^2-1)(A^2-1)}{M^2A^2}\delta\\
&\frac{A'^2}{A^2}=1-\frac{A^2-1}{A^2}\delta\\
&\frac{M'^2}{M^2}=1-\frac{(A^2-1)\{2+(\gamma-1)M^2\}}{M^2A^2}\delta\\
&\frac{p'}{p}=1+\frac{\gamma(A^2-1)}{A^2}\delta
\end{aligned}\right\}\qquad(33)$$

$$\left.\begin{aligned}\frac{\rho'}{\rho}&=1+\frac{A^2-1}{A^2}\delta\\ \frac{q'}{q}&=1+\frac{2\gamma(A^2-1)(M^2+A^2-1)}{A^2(\gamma M^2+2A^2)}\delta\,.\end{aligned}\right|$$

Using these results, we can examine how a weak plane shock wave reflects and refracts at the interface between two streams. Since the shock is assumed to be so weak that the entropy change across it can be neglected, we need not distinguish the transitions by shock and by expansion waves.

Let us consider a shock configuration as shown in Fig. 4. The conditions on the interface are that the total pressure as well as the stream deflection are continuous across it. Hence

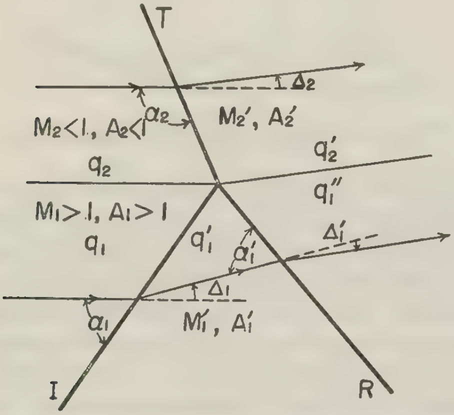

Fig. 4. Shock reflection and refraction at an interface of two streams.

$$\frac{q_2'}{q_2}=\frac{q_1''}{q_1}\,,\qquad \Delta_2=\Delta_1-\Delta'_1\,. \tag{34}$$

Using Eq. (33) and $\Delta=\delta/(\cot\alpha+\tan\alpha)$, these become as follows

$$F_2\delta_2-F_1\delta_1'=F_1\delta_1\,,\quad -G_1\delta_2+G_2\delta_1'=G_2\delta_1 \tag{35}$$

where $F\equiv(M^2-1)(M^2+A^2-1)/A^2(\gamma M^2+2A^2)$ and $G\equiv M^2A^2/\{(M^2-1)(A^2-1)(M^2+A^2-1)\}^{1/2}$. Hence, putting $(F_2G_2+F_1G_1)/(F_2G_2-F_1G_1)\equiv R'$ and $2F_1G_2/(F_2G_2-F_1G_1)\equiv T'$, we get

$$\delta_1'=R'\delta_1\,,\qquad \delta_2=T'\delta_1\,. \tag{36}$$

Thus, we are able to distinguish the four different shock configurations for various values of $M_1>1$, $A_1>1$; $M_2<1$, $A_2<1$ (c.f. Fig. 5).

The reflection factor R and transmission factor T, given by Eqs. (21), are related to the factors R' and T' in Eqs. (36) as follows:

$$R\equiv R'\,,\qquad T\equiv\frac{M_1{}^2A_1{}^2(M_2{}^2+A_2{}^2-1)}{M_2{}^2A_2{}^2(M_1{}^2+A_1{}^2-1)}T'\,. \tag{37}$$

As expected, R is equal to R', while T has the same sign as T' since (M^2+A^2-1) is positive for the present case (subsonic hyperbolic). Thus, when M_1, A_1 (>1), M_2, A_2 (<1) and hence R are given, we can find the structures of the two-dimensional jet of new type according to the considerations on the shock configuration stated above. They are shown schematically in Fig. 5.

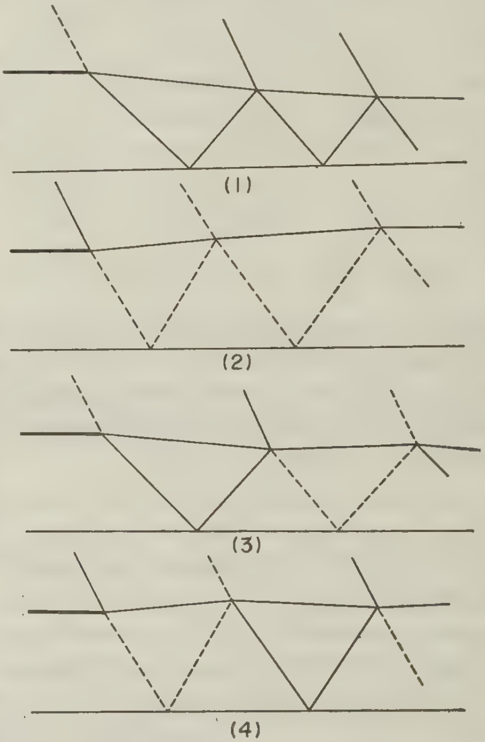

Fig. 5. Structure of the two-dimensional jet of new type. (1) and (2) for $R>0$, (3) and (4) for $R>0$. Full and broken lines represent respectively shocks and expansion waves.

The writer wishes to express his hearty thanks to Prof. K. Tamada for valuable discussion and kind inspection of the manuscript, and to Dr. T. Sakurai for valuable discussion.

References

1) I. Imai: *Magneto-hydrodynamics* (Iwanami Shoten Publ., 1959) 54 (in Japanese).
2) S. I. Pai: *Fluid dynamics of jet* (D. Van Nostrand, 1954) 46.
3) D. C. Pack: J. Aero. Sci. **23** (1956) 747.
4) H. L. Helfer: Astro. Phys. **117** (1953) 177.
5) K. Tamada: unpublished.

JOURNAL OF THE PHYSICAL SOCIETY OF JAPAN, Vol. 15, No. 8, AUGUST, 1960

Some Remarks on the Magnetogasdynamic Linearized Theory

By Shigenori ANDO

Engineering Division, Gifu Seisakusho, Kawasaki Aircraft Co.

(Received March 29, 1960)

The general theory of magnetogasdynamic linearized flow is extended to cover the case of unsteady flow in an arbitrary direction with respect to the magnetic field. This theory is also valid in the case when the frame is "body axes" slightly inclined against the free stream direction. For the case of steady flow, quadratic expression for the pressure disturbance is derived. Some problems when weak electromagnetic interaction exists are solved for illustration of the application.

§ 1. Introduction

In a previous paper[1] the author presented the magnetogasdynamic linearized theory for steady flow. Resler and McCune[2] derived the linearized equations written in terms of electric current for unsteady flow. As pointed out by them the unsteady flow equations are very useful, because, the stability of the flow can also be investigated. Although Resler and McCune did not explicitly show the procedure of appliation of their equations, their method seems to be more complicated than the present author's method. First, they give an equation for the electric current. When the current has been obtained, then other variables must be found by *integration of the differential equations* for them. Second, their equation for the three-dimensional case is written in a vector form, which adds many inconveniences in solving problems. On the other hand, the present author's equation is written in a scalar form even for the three-dimensional case. Once only one parametric function is obtained, the other quantities can be obtained by *differentiation* only.

As illustration of the present author's technique, some problems when weak electromagnetic interaction exists are solved, namely for a two-dimensional thin wing and for an axisymmetric body. These problems have been solved by previous authors, Sakuai[3] and Kusukawa[4] in their own ways.

Kusukawa has given a quadratic expression for the pressure disturbance on the surface of a slender body[4]. In this paper the more general formula will be derived.

§ 2. Symbols

The symbols used in the present paper are the conventional ones and almost the same as those in reference[1] unless otherwise stated.

§ 3. Extension of the Linearized Theory

3.1 *Extension of the theory*

In the present paper the general theory of magnetogasdynamic linearized flow will be established under the following assumptions.

1) The usual magnetohydrodynamic assumptions are valid.
2) The flow is inviscid and thermally non-conducting.
3) The fluid is a perfect gas.
4) The electrical conductivity or the magnetic Reynolds number is arbitrary.
5) The body which is either two- or three-dimensional makes small disturbance in the flow-and the electromagnetic-field. The undisturbed fields are uniform, where no electric current exists.
6) The applied magnetic field may have all three components $(\bar{B}_{\infty x}, \bar{B}_{\infty y}, \bar{B}_{\infty z})$.
7) Slightly unsteady motion with small angle of attack may be involved. The reference frame $S(0\text{-}\ \bar{x}, \bar{y}, \bar{z})$ is considered as the "body axes" moving with the average velocity (nearly constant) of the body.

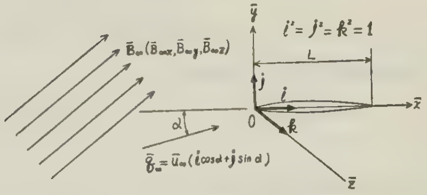
$\bar{y}$
$i^2=j^2=k^2=1$
$\bar{B}_\infty(\bar{B}_{\infty x}, \bar{B}_{\infty y}, \bar{B}_{\infty z})$
L
j
i
$\bar{x}$
α
0
k
$\bar{q}_\infty = \bar{u}_\infty(i\cos\alpha + j\sin\alpha)$
$\bar{z}$

Fig. 1. Configuration and Symbols.

It is noted that the last two assumptions differ from the ones used in the previous work[1].

The basic equations are written in dimensionless form as follows:

$$\operatorname{rot} \boldsymbol{E}_* = -\partial \boldsymbol{B}_*/\partial t \tag{1}$$

$$\operatorname{div} \boldsymbol{E}_* = \rho_{e*} \tag{2}$$

$$\operatorname{rot} \boldsymbol{B}_* = R_m \boldsymbol{J}_* \tag{3}$$

$$\operatorname{div} \boldsymbol{B}_* = 0 \tag{4}$$

$$\boldsymbol{J}_* = \boldsymbol{E}_* + \boldsymbol{q}_* \times \boldsymbol{B}_* \tag{5}$$

$$\frac{\partial \rho_*}{\partial t} + \operatorname{div}(\rho_* \boldsymbol{q}_*) = 0 \tag{6}$$

$$\rho_* \left[\frac{\partial}{\partial t} + (\boldsymbol{q}_* . \nabla)\right] \boldsymbol{q}_* = -\nabla p_* + R_m S(\boldsymbol{J}_* \times \boldsymbol{B}_*) \tag{7}$$

$$(\gamma-1)^{-1} \rho_* \left[\frac{\partial}{\partial t} + (\boldsymbol{q}_* . \nabla)\right] T_* = -p_* \nabla . \boldsymbol{q}_* + R_m S \boldsymbol{J}_*^2 \tag{8}$$

$$p_* = \rho_* T_* \tag{9}$$

where $t_* \equiv t = \bar{t}/(L\bar{u}_\infty^{-1})$, $R_m \equiv \mu_e \sigma \bar{u}_\infty L$ and $S \equiv \bar{B}_\infty^2/\mu_e \bar{\rho}_\infty \bar{u}_\infty^2$. All the other quantities marked with asterisk are dimensionless. On the other hand, the ones marked with bar are physical quantities having dimensions. The reference speed $\bar{u}_\infty$ used in the present paper is the average speed (nearly constant) of the body. R_m is called magnetic Reynolds number and S is pressure number. As the electromagnetic unit, MKS rationalized system is used.

All the quantities marked with asterisk are divided into two parts as follows.

$$\left.\begin{array}{l}
\text{Flow velocity:} \quad \bar{\boldsymbol{q}}/\bar{u}_\infty = \boldsymbol{q}_* = \boldsymbol{i} \cos\alpha + \boldsymbol{j} \sin\alpha + \boldsymbol{v} \doteqdot \boldsymbol{i} + \alpha \boldsymbol{j} + \boldsymbol{v}\,, \qquad \boldsymbol{v}(u, v, w) \\
\text{Magnetic flux density:} \quad \bar{\boldsymbol{B}}/\bar{B}_\infty = \boldsymbol{B}_* = \boldsymbol{B}_\infty + \boldsymbol{b}\,, \qquad \boldsymbol{B}_\infty(B_{\infty x}, B_{\infty y}, B_{\infty z}), \quad \boldsymbol{b}(b_x, b_y, b_z) \\
\text{Pressure:} \quad \bar{p}/\bar{\rho}\bar{u}_\infty^2 = p_* = p_\infty + p \quad (\text{The pressure coefficient } C_p \equiv 2p) \\
\text{Density:} \quad \bar{\rho}/\bar{\rho}_\infty = \rho_* = 1 + \rho \\
\text{Temperature:} \quad R\bar{T}/\bar{u}_\infty^2 = T_* = T_\infty + T \\
\text{Current density:} \quad \bar{\boldsymbol{J}}/\sigma \bar{u}_\infty \bar{B}_\infty = \boldsymbol{J}_* = 0 + \boldsymbol{J}\,, \qquad \boldsymbol{J}(J_x, J_y, J_z) \\
\text{Electric field:} \quad \bar{\boldsymbol{E}}/\bar{u}_\infty \bar{B}_\infty = \boldsymbol{E}_* = -(\boldsymbol{i} + \alpha \boldsymbol{j}) \times \boldsymbol{B}_\infty + \boldsymbol{E}\,, \qquad \boldsymbol{E}(E_x, E_y, E_z) \\
\quad \alpha;\ u, v, w;\ b_x, b_y, b_z;\ p, \rho, T;\ J_x, J_y, J_z;\ E_x, E_y, E_z \approx 0(\varPhi)
\end{array}\right\} \tag{10}$$

where $\varPhi$ is a parametric function of very small magnitude to be difined later. α is the angle between the free stream direction and the x-direction. Our assumptions give

$$(\boldsymbol{q}_* . \nabla) = \partial/\partial x + \alpha(\partial/\partial y) + \boldsymbol{v} . \nabla \approx \partial/\partial x$$

In what follows D/Dt stands for $\partial/\partial t + \partial/\partial x$. Linearization reduces Eq. (1)–(9) to the following forms.

The induction equation:

$$R_m \left\{ -\frac{D\boldsymbol{b}}{Dt} + (\boldsymbol{B}_\infty . \nabla)\boldsymbol{v} - \boldsymbol{B}_\infty \operatorname{div} \boldsymbol{v} \right\} + \nabla^2 \boldsymbol{b} = 0 \tag{11}$$

The momentum equation:

$$\frac{D\boldsymbol{v}}{Dt} = -\nabla p - S\boldsymbol{B}_\infty \times \operatorname{rot} \boldsymbol{b} \tag{12}$$

The continuity equation:

$$\frac{D\rho}{Dt} + \nabla . \boldsymbol{v} = 0 \tag{13}$$

The isentropic relations:

$$p = \gamma(\gamma-1)^{-1} T\,, \qquad \rho = (\gamma-1)^{-1} \frac{T}{T_\infty}\,, \qquad p = \gamma p_\infty \rho = \frac{\rho}{M^2} \tag{14}$$

where M represents the free stream Mach number.

From Eqs. (11)-(14), we can derive the fundamental equations in rather refined way than in reference[1]. By elimination of p in Eq. (12) using (13) and (14), we have the generalized continuity equation:

$$\left(\nabla^2 - M^2\frac{D^2}{Dt^2}\right)\operatorname{div}\boldsymbol{v} = SM^2\nabla^2\frac{D}{Dt}(\boldsymbol{B}_\infty.\boldsymbol{b}) \tag{15}$$

From Eq. (12) we have

$$\frac{D}{Dt}\operatorname{rot}\boldsymbol{v} = S(\boldsymbol{B}_\infty.\nabla)\operatorname{rot}\boldsymbol{b} \tag{16}$$

Let us introduce a scalar function φ defined by

$$\frac{D\boldsymbol{v}}{Dt} = S(\boldsymbol{B}_\infty.\nabla)\boldsymbol{b} + \frac{D}{Dt}\nabla\varphi$$

to represent $\boldsymbol{v}$ in terms of φ and $\boldsymbol{b}$. Then we can write down Eqs. (11) and (15) in terms of φ and $\boldsymbol{b}$ only. Now introduce another scalar function Φ in order for Eq. (11) to be satisfied automatically:

$$\left.\begin{aligned} \varphi &= \left(\nabla^2\frac{D}{Dt} - R_m\frac{D^2}{Dt^2} + R_mS\frac{\partial^2}{\partial\eta^2}\right)\Phi \\ \boldsymbol{b} &= -R_m\frac{D}{Dt}\left(\frac{\partial}{\partial\eta}\nabla - \boldsymbol{B}_\infty\nabla^2\right)\Phi \end{aligned}\right\}, \tag{17}$$

Then Eq. (15) gives the fundamental equation for Φ as follows:

$$\left[\left(\nabla^2 - M^2\frac{D^2}{Dt^2}\right)\left(R_m\frac{D^2}{Dt^2} - \nabla^2\frac{D}{Dt}\right) + R_mS\left(M^2\frac{D^2}{Dt^2} - \frac{\partial^2}{\partial\eta^2}\right)\nabla^2\right]\Phi = 0 \tag{18}$$

or

$$\mathscr{L}_F[\Phi] = 0 \tag{18$'$}$$

where

$$\frac{\partial}{\partial\eta} \equiv (\boldsymbol{B}_\infty.\nabla) \equiv B_{\infty x}\frac{\partial}{\partial x} + B_{\infty y}\frac{\partial}{\partial y} + B_{\infty z}\frac{\partial}{\partial z}$$

$\boldsymbol{b}$ and $\boldsymbol{v}$ are expressed in terms of Φ:

$$\boldsymbol{b} = -R_m\left(\frac{\partial}{\partial\eta}\nabla - \boldsymbol{B}_\infty\nabla^2\right)\frac{D\Phi}{Dt} \equiv \mathscr{L}_b[\Phi] \tag{19a}$$

$$\boldsymbol{v} = \left[\left(\nabla^2\frac{D}{Dt} - R_m\frac{D^2}{Dt^2}\right)\nabla + R_mS\boldsymbol{B}_\infty\nabla^2\frac{\partial}{\partial\eta}\right]\Phi \equiv \mathscr{L}_v[\Phi] \tag{19b}$$

The expression for p can be derived as follows. From Eq. (12), we have

$$\operatorname{grad}\left[p + \frac{D\varphi}{Dt} + S(\boldsymbol{B}_\infty.\boldsymbol{b})\right] = 0$$

and hence

$$p = -\frac{D\varphi}{Dt} - S\boldsymbol{B}_\infty.\boldsymbol{b} = \left(-\nabla^2\frac{D}{Dt} + R_m\frac{D^2}{Dt^2} - R_mS\nabla^2\right)\frac{D\Phi}{Dt} \equiv \mathscr{L}_p[\Phi] \tag{19c}$$

Eqs. (18)-(19) are the fundamental relations.

3.2 *Some remarks on fundamental relations*

Comparison of Eqs. (18)-(19) with Eqs. (31)-(33) in reference[1] shows that $\partial/\partial x$ in the latters is replaced by D/Dt.

Equation (18) contains the four important parameters such as the magnetic Reynolds number R_m, the interaction number R_mS, the free stream Mach number M and the direction of applied magnetic field ($B_{\infty x}$, $B_{\infty y}$, $B_{\infty z}$). Although particular selections of these parameters may reduce Eq. (18) to a simple form, this paper will not be concerned with the reduction procedure in detail except for the two cases $R_m=0$ or $S=0$. When σ or R_m is zero,

$$\mathscr{L}_b=0\,,\qquad \mathscr{L}_v=\nabla\left(\nabla^2\frac{D}{Dt}\right),\qquad \mathscr{L}_p=-\nabla^2\frac{D^2}{Dt^2}$$

and

$$\mathscr{L}_F=\left(M^2\frac{D^2}{Dt^2}-\nabla^2\right)\nabla^2\frac{D}{Dt}\,.$$

Let us put

$$\Phi'\equiv\nabla^2\frac{D\Phi}{Dt}\,.$$

Then the new Φ' is nothing but the velocity potential in pure gasdynamics. In the second case when $\bar{\boldsymbol{B}}_\infty$ or S is zero,

$$\mathscr{L}_b=-R_m\left(\frac{\partial}{\partial\eta}\nabla-\boldsymbol{B}_\infty\nabla^2\right)\frac{D}{Dt}\,,\qquad \mathscr{L}_v=\left(\nabla^2\frac{D}{Dt}-R_m\frac{D^2}{Dt^2}\right)\nabla\,.$$

$$\mathscr{L}_p=-\left(\nabla^2\frac{D}{Dt}-R_m\frac{D^2}{Dt^2}\right)\frac{D}{Dt}$$

and

$$\mathscr{L}_F=-\left(\nabla^2-M^2\frac{D^2}{Dt^2}\right)\left(\nabla^2\frac{D}{Dt}-R_m\frac{D^2}{Dt^2}\right).$$

Put

$$\Phi'\equiv\left(\nabla^2\frac{D}{Dt}-R_m\frac{D^2}{Dt^2}\right)\Phi$$

where

$$\left(\nabla^2-M^2\frac{D^2}{Dt^2}\right)\Phi'=0\,.$$

Then we have $v=\mathrm{grad}\,\Phi'$ and $p=-D\Phi'/Dt$ which are again the well-known relations in pure gasdynamics.

Eqs. (19) give the order of magnitude of various disturbances (in the physical quantities) as follows:

$$\left.\begin{aligned}
&\bar{\boldsymbol{B}}-\bar{\boldsymbol{B}}_\infty=\bar{B}_\infty\cdot O(R_m\Phi)\\
&\bar{\boldsymbol{J}}=\sigma\bar{u}_\infty\bar{B}_\infty\cdot O(\Phi)=\bar{B}_\infty\mu_e^{-1}L^{-1}\cdot O(R_m\Phi)\\
&\bar{\boldsymbol{q}}-\bar{\boldsymbol{q}}_\infty=\bar{u}_\infty\cdot\{O(\Phi)+O(R_m\Phi)+O(R_mS\Phi)\}\\
&\overline{\mathrm{rot}}\,\bar{\boldsymbol{q}}=\bar{u}_\infty L^{-1}\cdot O(R_mS\Phi)\\
&\bar{p}-\bar{p}_\infty=\bar{\rho}_\infty\bar{u}_\infty^2\cdot\{O(\Phi)+O(R_m\Phi)+O(R_mS\Phi)\}
\end{aligned}\right\}\tag{20}$$

When $R_m\leqq O(1)$, in the momentum equation

$$O\left\{\frac{\text{Lorentz force}}{\text{inertia force}}\right\}\sim R_mS\tag{21}$$

that is the reason why R_mS is termed interaction factor[5]. In the energy equation

$$O\left\{\frac{\text{Joule heating}}{\text{convection energy}}\right\}\sim O\left\{\frac{(\bar{B}_\infty\mu_e^{-1}L^{-1}R_m\Phi)^2\sigma^{-1}}{C_v\bar{\rho}_\infty(R^{-1}\bar{u}_\infty^2\Phi)(\bar{u}_\infty L^{-1})}\right\}\sim R_mS\Phi\tag{22}$$

which implies the isentropic relations to be valid. On the other hand, when $R_m \gg 1$, all the operator $\mathscr{L}_F$, $\mathscr{L}_b$, $\mathscr{L}_v$ and $\mathscr{L}_p$ are multiplied by R_m and so we can define new Φ' by the relation $\Phi' = R_m \Phi$. Thus all quantities on the left-hand side of Eq. (20) are of $O(\Phi')$, and so we have

$$O\left\{\frac{\text{Joule heating}}{\text{convection energy}}\right\} \sim S R_m^{-1} \Phi' \tag{23}$$

From above considerations we may think that the isentropic relations and the perturbation theory are valid in the both cases, especially even when $R_m \gg 1$, at least if the body is reasonably thin or slender. Eqs. (20) also suggest that when $R_m \gg 1$ the reasonable reference of electric current would be $\bar{B}_\infty \mu_e^{-1} L^{-1}$ as pointed out by I. Imai[7], although the present method leads to the correct result from another reference $\sigma \bar{u}_\infty \bar{B}_\infty$. The electric current will remain in the same order of magnitude as the other quantities, without becoming infinitely large even when $\sigma \to \infty$.

It is noteworthy that the fundamental equation (18) can be satisfied by many physical quantities. For example, Eq. (19a) gives

$$\operatorname{rot} \boldsymbol{b} = -\frac{D}{Dt} \nabla^2 R_m \boldsymbol{B}_\infty \times \nabla \Phi \equiv \mathscr{L}_{\operatorname{rot} \boldsymbol{b}}(\Phi) .$$

Let us operate $\mathscr{L}_{\operatorname{rot} \boldsymbol{b}}$ on Eq. (18); then

$$\mathscr{L}_{\operatorname{rot} \boldsymbol{b}} \mathscr{L}_F(\Phi) = \mathscr{L}_F \mathscr{L}_{\operatorname{rot} \boldsymbol{b}}(\Phi) = \mathscr{L}_F(\operatorname{rot} \boldsymbol{b}) = 0 .$$

In a similar manner we have also

$$\mathscr{L}_F(\boldsymbol{v}) = 0 , \qquad \mathscr{L}_F(\boldsymbol{b}) = 0 , \qquad \mathscr{L}_F(p) = 0 , \qquad \mathscr{L}_F(\operatorname{rot} \boldsymbol{v}) = 0$$

and so on.

The fact that $\mathscr{L}_F$ is a "scalar" operator with constant coefficients gives such many advantages. Resler and McCune[2] presented the fundamental equation in terms of rot $\boldsymbol{b}$ which contains a vector operator for the three-dimensional case. For the two-dimensional case their equation can be written in a scalar form and agrees with Eq. (18). They also suggested that once the equation for rot $\boldsymbol{b}$ is solved, then it is substituted into the other *differential equations* in order to obtain the remaining quantities. On the other hand, in the present method, we have only to define the parametric function Φ satisfying Eq. (18), since the other quantities can be obtained simply by *differentiation*. (See examples in section 5)

§ 4. The Expression of Pressure Distrubance in Quadratic Form

As is well known in pure gasdynamics, the linearized expression of the pressure disturbance like Eq. (19c) is not satisfactory to give the pressure distribution on the surface of the slender body. Kusukawa[4] derived a quadratic expression for the case of aligned magnetic field. In this section the present author derives the expression for the more general case.

In the case of steady flow Eq. (7) reduces to

$$\nabla p = \rho_* \left[-\nabla\left(\frac{1}{2} q_*^2\right) + \boldsymbol{q}_* \times \operatorname{rot} \boldsymbol{v} \right] - S(\boldsymbol{B}_\infty \times \operatorname{rot} \boldsymbol{b} + \boldsymbol{b} \times \operatorname{rot} \boldsymbol{b})$$

Remenbering $\rho_* = 1 + M^2 p + \cdots$ and $\rho_* \boldsymbol{q}_* = \boldsymbol{i} + \boldsymbol{v} + \alpha \boldsymbol{j} + M^2 p \boldsymbol{i} + \cdots$, we have

$$\nabla p = -\nabla\left(\frac{1}{2} q_*^2\right) - M^2 p \nabla\left(\frac{1}{2} q_*^2\right) + \boldsymbol{i} + \boldsymbol{v} + \alpha \boldsymbol{j} + M^2 p \boldsymbol{i}) \times \operatorname{rot} \boldsymbol{v} - S(\boldsymbol{B}_\infty \times \operatorname{rot} \boldsymbol{b} + \boldsymbol{b} \times \operatorname{rot} \boldsymbol{b}) \tag{24}$$

When the second order small terms are omitted, Eq. (24) is integrated to give

$$p = -u - S(\boldsymbol{i} \times \boldsymbol{B}_\infty) . \int_{-\infty}^{x} \operatorname{rot} \boldsymbol{b} dx \tag{25}$$

Substituting p from Eq. (25) into the right-hand side of Eq. (24) and then integrating, we have the quadratic expression of pressure disturbance as follows (all the terms of $O(u\cdot\Phi)$ have been omitted):

$$p=-u-S(\boldsymbol{i}\times\boldsymbol{B}_\infty).\int_{-\infty}^{x}\operatorname{rot}\boldsymbol{b}dx-\frac{v^2+w^2}{2}+\int_{-\infty}^{x}[(\boldsymbol{i}\times\boldsymbol{v}+\alpha\boldsymbol{k}).\operatorname{rot}\boldsymbol{v}-S(\boldsymbol{i}\times\boldsymbol{b}).\operatorname{rot}\boldsymbol{b}]dx \tag{26}$$

$$=\Big(\underset{O(\Phi)}{-\nabla^2\frac{\partial}{\partial x}}+\underset{O(R_m\Phi)}{R_m\frac{\partial^2}{\partial x^2}}-\underset{O(R_mS\Phi)}{R_mS\nabla^2}\Big)\frac{\partial\Phi}{\partial x}-\underset{O(\cdots\Phi^2)}{\frac{v^2+w^2}{2}}+\int_{-\infty}^{x}[\underset{O(R_mS\Phi^2)}{(\boldsymbol{i}\times\boldsymbol{v}+\alpha\boldsymbol{k}).\operatorname{rot}\boldsymbol{v}}-\underset{O(R_m{}^2S\Phi^2)}{S(\boldsymbol{i}\times\boldsymbol{b}).\operatorname{rot}\boldsymbol{b}}]dx \tag{27}$$

Of course the quadratic expression will be complete when all $\boldsymbol{v}$ and $\boldsymbol{b}$ in Eq. (27) are replaced by $\mathscr{L}_v[\Phi]$ and $\mathscr{L}_b[\Phi]$ respectively.

§ 5. Applications of the General Theory

For illustrative purpose, some problems with parallel magnetic field for the case of weak interaction ($R_m\approx 0$ and $R_mS\equiv K\ll 1$) will be solved for two-dimensional and for axisymmetric flow. It may be mentioned that the former has been solved by Sakurai[3] and the latter by Kusukawa[4] with the aid of their own methods. The assumption $R_m=0$ makes great simplifications, together with another assumption that the permeability of the body is equal to that of the gas μ_e. Eq. (19a) shows $\boldsymbol{b}=0$ for this case, which satisfies all requirements such as

i) the magnetic field, Eq. (19a), in the gas,
ii) the electro-magnetic equations in the body,
iii) the electro-magnetic condition on the interface between the gas and the body (all components of the magnetic field should be continuous.)

Thus we may consider the boundary conditions for the flow field only.

When $R_m\approx 0$, $B_{x\infty}\approx 1$, $B_{y\infty}=\delta\ll 1$ and $B_{\infty z}=0$, the fundamental relations (18)-(19) and (27) reduce to the forms:

$$\left[\frac{\partial^2}{\partial x^2}\pm\frac{1}{|1-M^2|}\left(\frac{\partial^2}{\partial y^2}+\frac{\partial^2}{\partial z^2}\right)+K\frac{\partial}{\partial x}\pm\frac{2K\delta}{|1-M^2|}\frac{\partial}{\partial y}\right]\Phi=0 \qquad \text{for} \quad M\lesseqgtr 1 \tag{28}$$

$$\boldsymbol{v}=\left[\frac{\partial}{\partial x}\nabla+\boldsymbol{i}K\frac{\partial}{\partial x}+K\delta\left(\boldsymbol{j}\frac{\partial}{\partial x}+\boldsymbol{i}\frac{\partial}{\partial y}\right)\right]\Phi \tag{29}$$

$$p=-\left(\frac{\partial}{\partial x}+K\right)\frac{\partial\Phi}{\partial x}-\frac{1}{2}(v^2+w^2) \tag{30}$$

$$\boldsymbol{b}\approx 0$$

5.1 *Steady flow past a two-dimensional symmetric wing with sharp edges.* $\boldsymbol{B}_\infty=\boldsymbol{i}+\delta\boldsymbol{j}$

5.1.1 Subsonic flow

In this case, Eqs. (28)-(30) give the relations:

$$\left.\begin{aligned}
&u=\left[\frac{\partial^2}{\partial X^2}+K\frac{\partial}{\partial X}+K\beta\delta\frac{\partial}{\partial Y}\right]\Phi\\
&v=\frac{\partial}{\partial X}\left[\beta\frac{\partial}{\partial Y}+K\delta\right]\Phi\,, \qquad p=-\left(\frac{\partial}{\partial X}+K\right)\frac{\partial\Phi}{\partial X}\\
&X\equiv x\,, \qquad Y\equiv\beta y\,, \qquad \beta\equiv\sqrt{1-M^2}\\
&\Phi_n\equiv\exp\left[-\frac{K}{2}X-\frac{K\delta}{\beta}Y\right]K_n\left(\frac{c}{2}r\right)e^{in\theta}\\
&\left(\frac{c}{2}\right)^2=\frac{K^2}{4}+\frac{K^2\delta^2}{\beta^2}\,, \qquad r^2=X^2+Y^2\,, \qquad \theta=\tan^{-1}\frac{Y}{X}
\end{aligned}\right\} \tag{31}$$

Φ_n being a particular solution. We try to construct the solution satisfying the boundary condition on the wing surface using Φ_0 only, which is one-valued and converges at infinity. Putting, with approximation

$$K_0\left(\frac{c}{2}r\right) \doteqdot -\ln\frac{c}{4}r - \Gamma$$

for small $(c/2)r$,

$$\Phi(X,\ Y) \equiv \int_0^1 f(\mu) \exp\left[-\frac{K}{2}(X-\mu) - \frac{K\delta}{\beta}Y\right]\left[\ln\frac{c}{4}\sqrt{(X-\mu)^2+Y^2} + \Gamma\right] d\mu \tag{32}$$

($\Gamma = 0.5772\cdots$ being Euler's constant) and substituting it into Eq. (31), we have the boundary condition as follows:

$$v(Y=\pm 0) = \pm\frac{df_B(X)}{dX} = \pm\frac{\partial}{\partial X}\int_0^1 f(\mu)\beta e^{-(K/2)(X-\mu)} \frac{|Y|d\mu}{(X-\mu)^2+Y^2} = \pm\frac{d}{dX}[\pi\beta f(X)]$$

where $y = \pm f_B(x)$ is the contour of the wing. Thus we have

$$f(x) = \frac{1}{\pi\beta} f_B(x) \tag{33}$$

We now substitute $f(x)$ into Φ, and in turn Φ into u; then we have u at $Y \approx \pm 0$ as follows:

$$u = \frac{1}{\pi\beta} C.\int_0^1 \frac{f_B'(\mu)}{X-\mu} d\mu + \frac{K}{2\pi\beta}\int_0^1 f_B'(\mu) \ln|X-\mu| d\mu \pm K\delta f_B(X) \tag{34}$$

where $C.\int$ means Cauchy's principal value. The signs ± are assigned, in accordance with the antisymmetry in δ, for the upper and lower surfaces respectively. Eq. (34) is just the one derived by Sakurai in reference 3).

It is noteworthy that in this method only one function $f(x)$ is used instead of two functions in Sakurai's method. The only one function $f(x)$ may be supplemented by the differential operators $\mathscr{L}_u$ and $\mathscr{L}_v$ having $K\delta$ terms.

5.1.2 Supersonic flow

In this case Eqs. (28)–(30) give the relations:

$$\left.\begin{aligned}
&u = \left[\frac{\partial^2}{\partial X^2} + K\frac{\partial}{\partial X} + KB\delta\frac{\partial}{\partial Y}\right]\Phi \\
&v = \frac{\partial}{\partial X}\left[B\frac{\partial}{\partial Y} + K\delta\right]\Phi, \qquad p = -\left(\frac{\partial}{\partial X} + K\right)\frac{\partial\Phi}{\partial X} \\
&X \equiv x, \qquad Y \equiv By, \qquad B \equiv \sqrt{M^2-1} \\
&\Phi \equiv e^{-(K/2)X-(K\delta/B)Y}\cdot\phi, \qquad \phi_{XX} - \phi_{YY} = \frac{K^2}{4}\left(1-\frac{4\delta^2}{B^2}\right)\phi \equiv \frac{L^2}{4}\phi
\end{aligned}\right\} \tag{35}$$

To solve the telegraph equation in ϕ we use the Laplace transform, which saves labour of calculation in comparison with other (say, Riemann's) method. Assuming $\phi = \partial\phi/\partial X = 0$ for $X \leqq 0$, the Laplace transformation of the above telegraph equation leads to

$$\frac{d^2\bar{\phi}}{d^2y} - \left(s^2 - \frac{L^2}{4}\right)\bar{\phi} = 0, \qquad \bar{\phi} = \int_0^\infty e^{-sX}\phi(X,\ Y,\ Z)dX$$

which is integrated to give

$$\bar{\phi} = A(s)\exp\left(-\sqrt{s^2-\frac{L^2}{4}}|Y|\right)$$

The formula of inverse Laplace transform[6):

$$\mathscr{L}^{-1}[(s^2-\alpha^2)^{-1/2}\exp(-b\sqrt{s^2-\alpha^2})]=u(X-b)I_0(\alpha\sqrt{X^2-b^2})$$

$$b>0\,,\qquad u(X)=\begin{cases}0 & X<0\\ 1 & X>0\end{cases}$$

and the convolution formula give the expression:

$$\phi=\int_0^X f(\mu)u(X-\mu-|Y|)I_0\left(\frac{L}{2}\sqrt{(X-\mu)^2-Y^2}\right)d\mu=\int_0^{X-|Y|}f(\mu)\,I_0\left(\frac{L}{2}\sqrt{(X-\mu)^2-Y^2}\right)d\mu \tag{36a}$$

which is symmetric in Y. The antisymmetric solution in Y can be constructed by differentiation of the symmetric solution with respect to Y. Thus we have for $Y\lesseqgtr 0$,

$$\mp f(X-|Y|)-\frac{LY}{2}\int_0^{X-|Y|}\frac{f(\mu)I_1[(L/2)\sqrt{(X-\mu)^2-Y^2}]}{\sqrt{(X-\mu)^2-Y^2}}d\mu \tag{36b}$$

In general the solution is given as a combination of the symmetric and the antisymmetric ones. Assume that the terms of $O(L^2)$ are negligible and thus $\phi_\pm=f(X-|Y|)\pm g(X-|Y|)$ for $Y\gtrless 0$. The boundary condition on the wing surface can be written as follows:

$$v(Y=\pm 0)=\frac{d}{dX}(f_B{}^c(X)\pm f_B{}^t(X))=\left[\frac{\partial}{\partial X}\left(B\frac{\partial}{\partial Y}+K\delta\right)\Phi\right]_{Y=\pm 0}$$

where $y=f_B{}^\pm(X)=f_B{}^c(X)\pm f_B{}^t(X)$ represent the upper and lower wing surfaces respectively. Necessary substitution for Φ gives

$$f'(X)=-B^{-1}\exp\left(\frac{K}{2}X\right)f_B{}^t(X)$$

and

$$g'(X)=-B^{-1}\exp\left(\frac{K}{2}X\right)f_B{}^c(X)$$

Then we have

$$\Phi=-\frac{1}{B}\exp\left(-\frac{K\delta}{B}Y\right)\left\{\int_0^{X-|Y|}\exp\left[\frac{K}{2}(\mu-X)\right]f_B{}^t(\mu)d\mu\pm\int_0^{X-|Y|}\exp\left[\frac{K}{2}(u-X)\right]f_B{}^c(\mu)\,d\mu\right\}$$

$$u(Y=\pm 0)=\mp\frac{1}{B}\,\frac{df_B{}^\pm(X)}{dX}\pm\frac{K}{2B}f_B{}^\pm(X)+K\delta f_B{}^\pm(X) \tag{37}$$

Alternatively if we treat each half space $Y\gtrless 0$ independently using symmetric ϕ only, then we can obtain the same final expression for u. The expression for the particular case of a symmetric wing agrees with Sakurai's result.[8]

5.2 *Steady flow past a slender axisymmetric body with pointed nose and tail,* $\boldsymbol{B_\infty=i}$.

5.2.1 Subsonic flow

Eqs. (28)–(30) give the relations:

$$\left.\begin{aligned}&u=\left(\frac{\partial}{\partial x}+K\right)\Phi\,,\qquad v_r=\frac{\partial\Phi}{\partial r}\,,\qquad v_\theta=0\\ &p=-u-\frac{1}{2}v_r{}^2\,,\qquad r=\beta\sqrt{y^2+z^2}\\ &\Phi=-e^{-(K/2)x}\int_0^\infty d\lambda\int_{-\infty}^\infty f(\mu)\cos\lambda(x-\mu)K_0\left(r\sqrt{\lambda^2+\frac{K^2}{4}}\right)d\mu\end{aligned}\right\} \tag{38}$$

The boundary condition on the body surface determines the unknown function $f(\mu)$ as follows:

$$\begin{aligned}v_r(r=r_B)&=\frac{dr_B}{dx}=\left.\frac{\partial\Phi}{\partial r}\right|_{r=r_B}\\ &=e^{-(K/2)x}\left[\int_{-\infty}^\infty f(\mu)d\mu\int_0^\infty K_1\left(r\sqrt{\frac{K^2}{4}+\lambda^2}\right)\sqrt{\lambda^2+\frac{K^2}{4}}\cos\lambda(x-\mu)d\lambda\right]_{r=r_B}\end{aligned}$$

Now make use of the formula[6)]

$$\int_0^\infty K_\nu[\alpha(x^2+\beta^2)^{1/2}](x^2+\beta^2)^{(1/2)\nu}\cos(xy)dx$$
$$=2^{-1/2}\pi^{1/2}\alpha^{+\nu}\beta^{(1/2)+\nu}(y^2+\alpha^2)^{-(1/2)\nu-1/4}K_{-\nu-(1/2)}[\beta(y^2+\alpha^2)^{1/2}]$$
$$R\alpha>0\,,\qquad R\beta>0$$

and

$$K_{-3/2}(z)=\sqrt{\frac{\pi}{2z}}\left(1+\frac{1}{z}\right)e^{-z}\approx\sqrt{\frac{\pi}{2}}\,z^{-3/2}\qquad\text{for}\quad z\ll 1$$

Then we have

$$\frac{dr_B}{dx}=\frac{\pi}{2}e^{-(K/2)x}\int_{-\infty}^{\infty}\frac{r_Bf(\mu)d\mu}{[(x-\mu)^2+r_B{}^2]^{3/2}}$$

Noting that for small r_B

$$\int_{-\infty}^{\infty}\frac{f(\mu)r_Bd\mu}{[(x-\mu)^2+r_B{}^2]^{3/2}}\cong\frac{f(x)}{r_B}\int_{-\infty}^{\infty}\frac{d(\mu/r_B)}{\{1+[(\mu-x)/r_B]^2\}^{3/2}}=\frac{2f(x)}{r_B}$$

we obtain

$$f(x)=\frac{1}{2\pi^2}\exp\left(\frac{K}{2}x\right)F'(x)\tag{39}$$

where $F(x)=\pi r_B{}^2$ represents the cross-sectional area of the body. It should be noted that the approximations

$$K_0(z)\approx-\ln\frac{z}{2}-\Gamma\quad\text{and}\quad K_1(z)\approx\frac{1}{z}\qquad\text{for}\quad z\ll 1$$

are not valid under the integral sign $\int_0^\infty\cdots d\lambda$. Substitution from (39) into Φ and thence use of the formula[6)]

$$\int_0^\infty K_0(\alpha\sqrt{x^2+\beta^2})\cos xydx=\frac{\pi}{2}\,\frac{\exp(-\beta\sqrt{y^2+\alpha^2})}{\sqrt{y^2+\alpha^2}}$$
$$R\alpha>0\,,\qquad R\beta>0$$

leads to the expression:

$$\Phi=\frac{1}{4\pi}\left[-\int_0^1F'(\mu)[(x-\mu)^2+r^2]^{-1/2}d\mu+KF(x)\right]+O(K^2)$$
$$=\frac{1}{2\pi}\left[F'(x)\ln\frac{r}{2}+\frac{1}{2}\int_0^1F''(\mu)\frac{\mu-x}{|\mu-x|}\ln|\mu-x|\,d\mu\right]+\frac{K}{4\pi}F(x)\tag{40}$$

In the above derivation we have made use of the relation:

$$\omega(r,\,x;\,\mu)\equiv\frac{\mu-x}{|\mu-x|}\ln\frac{|\mu-x|+\sqrt{(x-\mu)^2+r^2}}{r}\equiv\sinh^{-1}\frac{\mu-x}{r}$$
$$\frac{\partial\omega}{\partial\mu}=[(x-\mu)^2+r^2]^{-1/2}$$

Thus we have

$$u=-\frac{1}{4\pi}\int_0^1\frac{F''(\mu)d\mu}{\sqrt{(x-\mu)^2+r^2}}+\frac{K}{4\pi}\left[F'(x)-\int_0^1\frac{F'(\mu)d\mu}{\sqrt{(x-\mu)^2+r^2}}\right]$$
$$=-\frac{1}{4\pi}\left[F''(1)\ln(1-x)+F''(0)\ln x+2F''(x)\ln\frac{2}{r}-\int_0^1F'''(\mu)\frac{\mu-x}{|\mu-x|}\ln|\mu-x|\,d\mu\right]$$
$$+\frac{K}{4\pi}\left[F'(x)+2F'(x)\ln\frac{r}{2}+\int_0^1F''(\mu)\frac{\mu-x}{|\mu-x|}\ln|\mu-x|\,d\mu\right]\tag{41}$$

Now the drag coefficient is given by

$$C_D=2\int_0^1 F'(x)\left[-u-\frac{1}{2}\left(\frac{dr_B}{dx}\right)^2\right]dx\equiv C_{DO}+C_{DK}$$

where C_{DO} is pure gasdynamic one and C_{DK} represents the magnetogasdynamic effect. Simple calculations show that

$$\left.\begin{aligned} C_{DO}&=2\int_0^1 F'(x)\left[\frac{1}{4\pi}\int_0^1\frac{F''(\mu)d\mu}{\sqrt{(x-\mu)^2+r_B^2}}-\frac{1}{2}\left(\frac{dr_B}{dx}\right)^2\right]dx=0\\ C_{DK}&=\frac{K}{2\pi}\left[\int_0^1\int_0^1\frac{F'(x)F'(\mu)}{\sqrt{(x-\mu)^2+r_B^2}}dxd\mu-\int_0^1[F'(x)]^2dx\right]\\ &=\frac{K}{2\pi}\left[-\int_0^1\int_0^1 F'(x)F''(\mu)\frac{\mu-x}{|\mu-x|}\ln|\mu-x|d\mu dx+\int_0^1\{F'(x)\}^2\left(2\ln\frac{2}{r_B}-1\right)dx\right]\end{aligned}\right\}\tag{42}$$

It seems to be difficult to prove that C_{DK} is positive.

5.2.2 Supersonic flow

In this case we put $\Phi=e^{-(K/2)X}\phi$ and have

$$\phi_{XX}-\phi_{YY}-\phi_{ZZ}-\frac{K^2}{4}\phi=0\tag{43}$$

where

$$X\equiv x\,,\qquad Y\equiv By\,,\qquad Z=Bz\qquad\text{and}\qquad B\equiv\sqrt{M^2-1}$$

With the Laplace transform of ϕ, we obtain for small r,

$$\bar{\phi}=-A(s)K_0\left(r\sqrt{s^2-\frac{K^2}{4}}\right)\doteq A(s)\left(\ln\frac{r}{2}+\Gamma\right)+\frac{A(s)}{2}s\left[\frac{\ln(s-(K/2))}{s}+\frac{\ln(s+(K/2))}{s}\right]$$

where

$$r=\sqrt{Y^2+Z^2}\qquad\text{and}\qquad\bar{\phi}\equiv\int_0^\infty e^{-sX}\phi(X,Y,Z)dx\,.$$

By the inverse transform, we have

$$\phi(X,r)=f(X)\ln\frac{r}{2}-\int_0^X f'(\mu)\ln|X-\mu|d\mu+O(K^2)$$

The unknown function $f(X)$ is determined by the boundary condition as

$$f(X)=\frac{1}{2\pi}\exp\left(\frac{K}{2}X\right)F'(X)$$

Then we have

$$\begin{aligned}\Phi&=\frac{1}{2\pi}\left[F'(X)\ln\frac{r}{2}-\int_0^X F''(\mu)\ln(X-\mu)d\mu+\frac{K}{2}F(X)\right]\\ &=\frac{-1}{2\pi}\int_0^{X-r}\frac{F'(\mu)d\mu}{\sqrt{(X-\mu)^2-r^2}}+\frac{K}{4\pi}F(X)\end{aligned}$$

In the above derivation we have made use of the relations:

$$\bar{\omega}(r,X;\mu)\equiv-\ln\frac{|X-\mu|+\sqrt{(X-\mu)^2-r^2}}{r}\equiv-\cosh^{-1}\frac{X-\mu}{r}$$

$$\frac{\partial\bar{\omega}}{\partial\mu}=[(X-\mu)^2-r^2]^{-1/2}$$

We also have

$$\left.\begin{aligned} u&=\frac{-1}{2\pi}\frac{\partial}{\partial X}\int_0^{X-r}\frac{F'(\mu)d\mu}{\sqrt{(X-\mu)^2-r^2}}+\frac{K}{4\pi}\left[F'(X)-2\int_0^{X-r}\frac{F'(\mu)d\mu}{\sqrt{(X-\mu)^2-r^2}}\right]\\ &=\frac{1}{2\pi}\left[F''(X)\ln\frac{r}{2}-\frac{d}{dX}\int_0^X F''(\mu)\ln(X-\mu)d\mu\right]\\ &\quad+\frac{K}{2\pi}\left[F'(X)\ln\frac{r}{2}-\int_0^X F''(\mu)\ln(X-\mu)d\mu+\frac{1}{2}F'(X)\right] \end{aligned}\right\}\tag{45}$$

$$\left.\begin{aligned} C_D&=C_{DO}+C_{DK}\\ C_{DO}&=-\frac{1}{2\pi}\int_0^1\int_0^1 F''(X)F''(\mu)\ln|X-\mu|dXd\mu>0\\ C_{DK}&=\frac{K}{2\pi}\left\{2\int_0^1 F'(X)\,dX\int_0^{X-r}\frac{F'(\mu)}{\sqrt{(X-\mu)^2-r^2}}d\mu-\int_0^1[F'(X)]^2dX\right\}\\ &=\frac{K}{2\pi}\left\{2\int_0^1 F'(X)\,dX\int_0^X F''(\mu)\ln(X-\mu)d\mu+\int_0^1[F'(X)]^2\left(2\ln\frac{2}{r_B}-1\right)dX\right\} \end{aligned}\right\}\tag{46}$$

It may by difficult to prove that C_{DK} is positive.

§ 6. Conclusion

The general theory of magnetogasdynamic linearized flow is extended and refined. Small unsteadiness and small angle of attack are admitted. The direction of applied magnetic field is completely arbitrary. The fundamental equation derived here is of scalar form even in three-dimensional case. The equation is written in terms of a certain parametric function, and the other quantities are obtained with mere differentiation of the function. All other physical quantities are also governed by the same fundamental equation.

The quadratic expression of pressure disturbance is obtained for steady flow.

For the illustrative purpose some problems with weak magnetic interaction are solved. The general theory saves labour of calculation, and is found to be powerful for the theoretical study of magnetogasdynamic linearized flows.

The author would like to express his gratitude to Dr. T. Sakurai for the guidance and dicussions on the work described in this paper.

References

1) S. Ando: J. Phys. Soc. Japan **15** (1960) 157.
2) E. L. Resler, Jr., and J. E. McCune: *The Magnetodynamics of Conducting Fluids*, ed. by D. Bershader (Stanford Univ. Press, 1959) 120.
3) T. Sakurai: J. Phys. Soc. Japan **15** (1960) 326.
4) K. Kusukawa: Preprint for the 14th Annual Meeting of Phys. Soc. Japan, Oct. 1959, p. 20. (in Japanese).
5) F. Fishman, J. W. Lothrop, R. M. Patrick and H. E. Petschek: *The Magnetodynamics of Conducting Fluids*, ed. by D. Bershader (Stanford Univ. Press, 1959) 90.
6) H. Bateman: Tables of Integral Transforms vol. **1** (McGraw-Hill, 1954).
7) I. Imai: Preprint for the 4th Meeting of Applied Mathematics and Mechanics in Japan, May 1959, p. 30. (in Japanese).
8) T. Sakurai: J. Phys. Soc. Japan **15** (1960) 1135.

Short Notes

This section is intended to secure prompt publication of important discoveries in physics. The reports should not exceed 800 words in length. A figure of size 7 cm × 7 cm will be counted as 150 words.

J. PHYS. SOC. JAPAN **15** (1960) 1534

On the Ferromagnetism in Manganese-Aluminium-Iron System

By Ichiro TSUBOYA and Makoto SUGIHARA

Electrical Communication Laboratory
Nippon Telegraph and Telephone Public Corporation Musashino-shi, Tokyo, Japan

(Received May 27, 1960)

In early days, 1892, Hogg reported the alloy containing 55 wt. % Mn, 25 wt. % Al, and 13 wt. % Fe showed strong ferromagnetic nature.[1] Further studies on the iron-poor Mn-Al-Fe alloys, however, have not yet been made, except for pure Mn-Al system.[2),3)]

In this note, the authors report that there is a new ferromagnetic phase in the iron-poor Mn-Al-Fe alloys at the composition near Hoggl's specimen. The composition range of the ferromagnetic phase is as follows, 35 to 42.5 at. % Mn, 42.5 to 47.5 at. % Al, and 12.5 to 17.5 at. % Fe.

For the preparation of the specimen, electrolytic Mn (99.9%), electrolytic Fe (99.9%), and pure Al (99.99%) were melted in the suitable proportion in air and cast into rods, 10 mm in diameter. These rods were annealed for 1 hour at 900°C in vacuum to remove segregation, then cooled slowly to room temperature.

It was found that the specimens in composition range, 35 to 47.5 at. % Mn, 40 to 47.5 at. % Al and 10 to 17.5 at. % Fe, respectively, have ferromagnetic natures (Fig. 1).

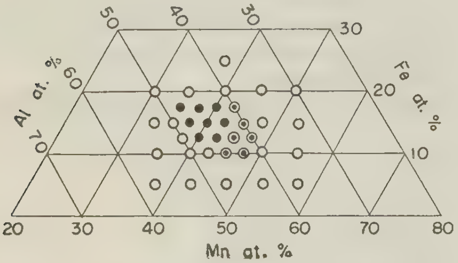

Fig. 1. Results of magnetic examination.
○ non-magnetic,
⊙ week ferromagnetic,
● ferromagnetic.

All specimens were crushed into powder for X ray analysis and the determination of Curie point. According to X-ray analysis, it was found that there is a pure single cubic phase in the composition range of 35 to 42.5 at. % Mn, 42.5 to 47.5 at. % Al, and 12.5 to 17.5 at. % Fe, respectively.

This cubic phase is named "κ phase". (Fig. 2). This composition range coincides with that of the specimens having strong ferromagnetic natures, and weakly ferromagnetic specimens are in the region of the mixture of κ phase and β-Mn phase. The non-magnetic phase have a β-Mn like structure in Mn-rich specimens and an η phase[3)] like in Al-rich ones.

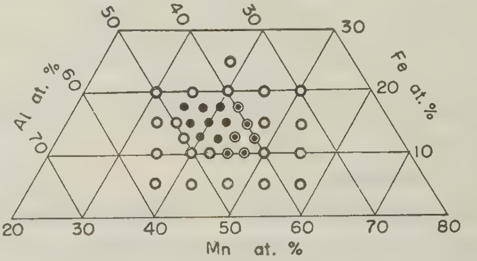

Fig. 2. Results of X-ray diffraction.
● cubic (CsCl type) structure —κ phase,
⊙ mixture of κ phase and β-Mn like phase,
○ β-Mn like phase and/or η phase.

It seems that the structure of κ phase is ordered one of Cs-Cl type, and lattice constant 2.96–2.97Å.

The magnetic properties such as Curie temperature, saturation magnetization, σ-T Curve were also measured. The Curie temperature of the κ phase specimens, measured by the magnetic balance, is from 35°C at the composition of 47.5 at. % Al, 35.0 at. % Mn, and 17.5 at. % Fe to 90°C at 45 at. % Al, 42.5 at. % Mn, and 12.5 at. % Fe. The saturation magnetization of these specimens at liquid nitrogen temperature, at the field strength of 15 K oe, is 380 to 400 Gauss/cc.. As the density of these specimens is 5 to 5.3 gram/cc., the saturation magnetic moment is 75 to 80 Gauss/gram.

It seems that the origin of this ferromagnetism consists in the ferromagnetic exchange interaction between Mn atoms. Further discussion with detailed measurements will be reported later on.

References

1) W. S. Messkin, A. Kussmann: *Die Ferromagnetische Legierungen* (Julius Springer, Berlin, 1932) 143 p.
2) H. Kōno: J. Phys. Soc. Japan **13** (1958) 1444.
3) A. J. J. Koch, P. Hokkeling, M. G. v. d. Steeg, K. J. de Vos: to be published.

J. PHYS. SOC. JAPAN **15** (1960) 1535

The Influence of Oxidation and Reduction on the Parasitic Ferromagnetism of αFe_2O_3

By Akira TASAKI, Kiiti SIRATORI
and Shûichi IIDA

Department of Physics, Faculty of Science, University of Tokyo

(Received June 3, 1960)

A considerable amount of studies has been made in recent years on the parasitic ferromagnetism of αFe_2O_3.[1),2),3),4)] A remarkable progress has been made by Dzyaloshinsky[5)] who has pointed out the presence of a certain lack of crystal symmetry in this rhombohedral antiferromagnet, which should result in a weak ferromagnetism when the spins lie in the basal plane. This idea has been extended by Moriya[6)] to a semiquantitative expression related with spin-orbit and exchange interactions of two neighbouring Fe^{3+} ions.

In spite of the presence of this clear-cut mechanism, however, the experimental results of this crystal are not so sure enough as to ascribe the whole parasitic ferromagnetism to the same mechanism. Here, a new aspect of the parasitic ferromagnetism of αFe_2O_3 is presented which has been found by heat treating the crystal in various pressures of oxygen.

The preparation of specimens was as follows; electrolytic iron was dissolved in nitric acid, dried, pressed and pre-fired at 1000°C for 3 hours. Five different heat treatments were given to these specimens. They are the annealing for 70 hours at 500°C in 100, 20, 5 Kg/cm² pressure of oxygen, and for 3 hours at 1000°C and 700°C in vacuum respectively. Magnetic measurements were made from −40°C to room temperature using a magnetic balance automatically controlled.

Now the magnetization of αFe_2O_3 is expressed by

$$\sigma = \sigma_0 + \chi H .$$

To determine σ_0 and χ, the magnetization was measured at the field strengthes 6.65, 11.8 and 14.3 KOe.

Fig. 1 shows χ and σ_0 vs T curves of these specimens. Here, no systematic change is found for χ both on oxidation and reduction series. While for σ_0, we notice that both oxidation and reduction introduce a residual parasitic ferromagnetism below the transition temperature. This residual parasitic ferromagnetism seems to be temperature independent and superimpose on the intrinsic one predicted by Dzyaloshinsky. This temperature independent parasitic ferromagnetism will be caused by the deviation of the cation-anion ratio from stoichiometry and is probably equal to the isotropic term σ_0 of Néel.[1)] This residual parastic ferromagnetism disappeared by heat treating again these specimens in air (1000°C, 3 hrs.). By this heat treatment, the weight of a oxidized specimen apparently did not change, but a reduced one gained its weight by about 0.2% (about 0.7% of total oxygen content).

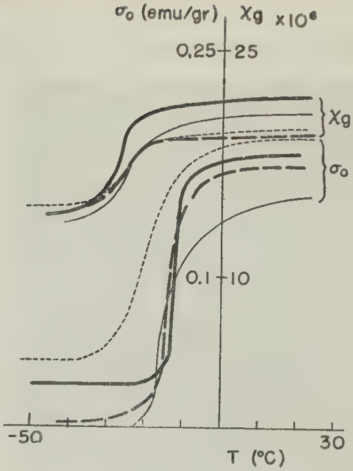

Fig. 1. χ and σ_0 vs T curves of αFe_2O_3. Heat treatments of the samples are as follows:
Oxidized at 500°C, 70 hrs. in 100 (—) and 20 (— —) Kg/cm² oxygen.
Reduced at 1000°C, 3 hrs. in 10^{-3} mmHg (- - -).
Annealed at 1000°C, 3 hrs. in air (—).

From these results, we may conclude that the residual or isotropic part in σ_0 is caused by the deviation from stoichiometry. The relevant ions will be Fe^{2+} in a reduced state and might be Fe^{4+} in an oxidized state. Two mechanisms are possible as the origin of this residual magnetization. One is to assume the presence of another ferromagnetic phase precipitated in the mother matrix of αFe_2O_3 and the other is to ascribe the magnetization to the presence of a certain imperfect structure included substantially in the crystal structure of non-stoichiometric αFe_2O_3. If the former mechanism is true, the relevant phase in a reduced state will probably be a spinel structure like Fe_3O_4 or γFe_2O_3. However, in a oxidized state no ferromagnetic phase is ever known which includes Fe^{4+}.[7)] Further study on this point is going on.

References

1) L. Néel: Rev. Mod. Phys. **25** (1953) 58.
2) Y. Y. Li: Phys. Rev. **101** (1956) 1450.
3) T. Iwata, M. Iwata and M. Yamamoto: J. Phys. Soc. Japan **14** (1959) 855.
4) S. T. Lin: Phys. Rev. **119** (1959) 1447.
5) I. Dzyaloshinsky: J. Phys. Chem. Solids **4** (1958) 241.
6) T. Moriya: Phys. Rev. Let. **4** (1960) 228.
7) H. Watanabe: J. Phys. Soc. Japan **12** (1957) 515.

J. PHYS. SOC. JAPAN **15** (1960) 1536

Emission Spectra from Glow Discharge through Vapors of Aromatic Hydrocarbons and *n*-Hexane

By Masato NISHI, Shiro HAMAMURA
and Hiroshi ARAKI
Department of Physics,
Hiroshima University, Hiroshima

(Received June 13, 1960)

Emission spectra from the positive column in D.C. glow discharge through vapors of aromatic hydrocarbons and *n*-hexane were investigated. Although the experimental method was essentially the same as that in the previous papers[1], the discharge tube itself was modified to avoid effect from the electrodes.

Typical intensity profiles (Fig. 1) show four kinds of spectra which will be temporarily designated as "A", "B", "C", and "D" in this note. "A" represents the spectrum due to π-electron transition of benzene ring and is observable also in the ultraviolet absorption. "B" is a continuous spectrum (300–400 mμ). "C" is another continuum (330–500 mμ). "D" is a band with a structure (445–590 mμ), and was emitted only from vapors of toluene and ethylbenzene. In the case of aromatic hydrocarbons "A", "C" and "D" appeared at lower vapor pressures. With an increase of the vapor pressures, the intensities of "A" and "D" decreased but that of "B" increased overlapping with "C" gradually. In the case of *n*-hexane, a continuum covering "B" and "C" regions was observed at lower vapor pressures, and with an increase of the vapor pressures the continuum faded away gradually but a benzene band ("A") became prominent.

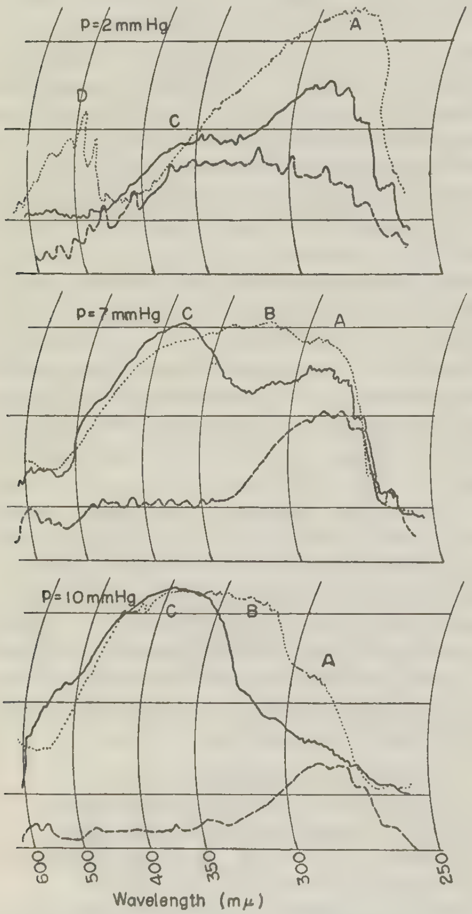

Fig. 1. Typical microphotometric curves corresponding to various pressures with a constant electric current (7 mA). full lines: benzene, dotted lines: toluene, broken lines: *n*-hexane.

H. Schüler et al.[2] found the similar spectra in the discharge through mixtures of aromatic vapors and rare gases. "D" spectrum agrees with the V spectrum named by Schüler et al., and may be attributed to benzyl radicals ($C_6H_5\dot{C}H_2$) as inferred by Schüler et al. Concerning the origin of "B" and "C", Schüler and his coworker inferred benzal radicals ($C_6H_5\dot{C}H$) and $C_6H_5\dot{C}\cdot$ radicals respectively. However, this seems to remain unsolved because of the following observations by the present authors:

(1) Both "B" and "C" were observed in the discharge through benzene vapor.

(2) Concerning the intensity variation of these continua, the pressure dependencies were slightly different with the kinds of molecular species. "B" was more distinct than "C" at higher vapor pressures as a general tendency, and this is reverse to the results by Schüler et al.

A detailed description will be published later.

References

1) M. Nishi: J. Sci. Hiroshima Univ. A, **19** (1955) 407. M. Nishi and S. Hamamura: ibid. A, **23** (1959) 201.
2) H. Schüler and A. Michel: Z. Naturforsch. **10a** (1955) 459.

J. PHYS. SOC. JAPAN **15** (1960) 1537∼1538

Observation of an Anomaly in Transistor Characteristics

By Osamu NAKAHARA

Semiconductor Plant, Sanyo Electric Company, Daito City Osaka Prefecture, Japan

(Received April 26, 1960)

It is found[1] that in the alloy type *pnp* transistor whose base germanium used is of 40 ohm-cm *n*-type, the $V_{ce}-I_c$ curve under the constant forward bias voltage V_{be} applied between the base contact and the emitter shows the dynatron-type negative resistance. This is interpreted as originated from the high base resistance due to the portion held between the emitter side surface and the collector junction, which is easily modulated by the collector voltage. H. Nelson[2] reported the phenomenon of slight negative collector conductance which he attributed to the similar effect in the diffused silicon transistor of particular type.

Here we show the anomaly observed in the transistor whose structure is like shown in Fig. 1.

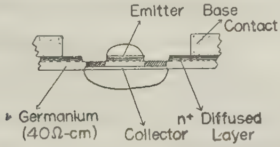

Fig. 1. Cross-sectional view of the transistor. Dimensions except the "neck" part are nearly same with the commercial drift transistor. Geometrical "neck" width was made about 10 microns.

This is just the same with the drift transistor except the high resistivity "neck" in the base formed by the electro-chemical etching. The remaining n^+ diffused surface layer in the base serves only to reduce the unnecessary base resistance for the phenomenon. Impurity gradient under the emitter junction has the effect to be described later besides the accelerating action of minority carriers injected.

In Fig. 2, the photograph of the $V_{ce}-I_c$ characteristics of the transistor is shown with V_{be} as a running parameter. It is seen that the collector current attains to a maximum value within the collector voltage saturation region and further increase in V_{ce} makes it decrease and finally all curves converge into a curve that corresponds to the collector current observed for $V_{be}=0$.

Such negative resistance observed above may be interpreted qualitatively as follows. The base resistance due to the hatched part in Fig. 1 is modulated by the collector voltage so that in the saturation region it is reduced because of the space chage layer shrinking toward the collector junction and the conductivity modulation induced by the injected minority carriers into the base from the collector junction. Thus the emitter action can be set in and the collector current flows easily. As V_{ce} goes to negative direction, however, the base resistance begins to increase because of the space charge layer widening into the base region. This decreases the injected carriers at the emitter under the constant V_{be} by the d.c. voltage drop in the base circuit. If such base resistance modulation feedback effect overcomes the internal feedback effect to increase the collector current, it begins to decrease with increase in V_{ce}, thus the negative collector resistance appears. It is to be noted that the internal feedback effect is much smaller in the case of the graded impurity base than the simple *pnp* structure so that the shape of the negative resistance curve becomes more salient than that observed in the latter structure. Various configurations of the transistor can be considered to realize such a characteristic and an attempt of the optimum design as a negative resistance element may be worthwhile if any its utility is found.

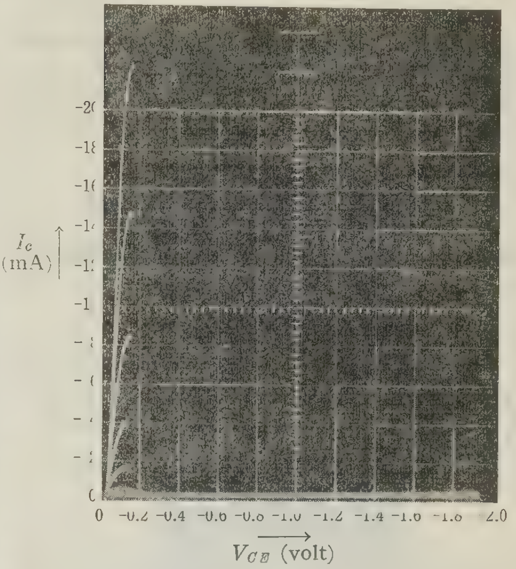

Fig. 2. Photograph of $V_{ce}-I_c$ characteristics of the transistor where V_{be} is taken as a running parameter. Curves are for V_{be} in 0.05 volt step up to 0.45 volt. Collector load resistance is zero.

The author thanks Mr. Endo and Mr. Tomaru, the staffs of the Electrical Communication Laboratory, who have suggested and examined the possible applications of this transistor. He also thanks Dr. Iwase who has guided the work throughout.

References

1) Read at the 15th Annual Meeting of the Physical Society of Japan held at Tokyo on April 3, 1960.
2) H. Nelson: Proc. Inst. Radio Eng. **46** (1958) 1062.

J. PHYS. SOC. JAPAN **15** (1960) 1538

Resonance Transfer of Ionization Energy in Semiconductors

By Shigeharu KOSHINO

Radiation Center of Osaka Prefecture,
Shinke-Cho, Sakai, Osaka

and Toshihiko ANDO

Department of Physics, Kyoto University,
Kyoto

(Received June 1, 1960)

The anomalous thermal conductivity has been observed for several types of simiconductor in the intrinsic range of temperature.[1] Interpretations of this phenomenon have been attempted by several authors.[2] We shall discuss here the resononce transfer of ionization energy of impurity level.

Let us first consider two donors, of which one is occupied by an electron and the other is open. When a conduction electron is trapped by the open donor, the electron which has been trapped by the other donor can be simultaneously excited into the conduction band by the interelectronic interaction. The ionization energy of donor level is then transferred from the former to the latter. If there is the temperature difference between the two donor positions and the distribution of electrons is in the local equilibrium, the netcurrent of ionization energy is produced. When the temperature gradient is present in a sample, the transfer of ionization energy between every two donors produces the net thermal current throughout the sample.

It is first assumed that the interelectronic potential is given by a screened Coulomb type. We neglect then, as the lowest order approximation, the dependence of the matrix elements on the wave number of electron, since the matrix elements cannot in general be calculated analytically. In other words, we replace every matrix element by that of the process in which one electron in transferred from and the other electron transferred to the bottom of the conduction band. Furthermore it is assumed that the distribution of donors in the sample is uniform and the temperature gradient is constant.

Let us now imagine a plane perpendicular to the temperature gradient in the sample. The thermal conductivity may be given by the total net current of energy transferred through the plane divided by the area of the plane and the temperature gradient. The calculated thermal conductivity is

$$\kappa=\frac{2^{10}m_e{}^3e^4N^2kTg_0(1-g_0)}{\hbar^7\alpha^6\beta^3\varepsilon^2}I$$

provided $\alpha\gg\beta$, where

$$I=\int_0^\infty(E_0+kTx)\left\{kx-\frac{1}{T}(E_0+2\eta)+2\frac{\partial\eta}{\partial T}\right\}\cdot f_0(x)\{1-f_0(x)\}xdx\ .$$

In the above equations m_e is the effective mass of electron, α the reciprocal of the modified Bohr radius, β the screening constant, ε the dielectric constant, N the concentration of donor, η the Fermi energy, E_0 the energy difference between the bottom of the conduction band and the donor level, and f_0 and g_0 are the distribution functions of electron in the conduction band and in the donor state, respectively. When the temperature is in the intrinsic range, we obtain

$$\kappa=9\times10^{-14}(m/m_e)^{21/4}(m_h/m_e)^{3/8}\varepsilon^{11/2}N^2T^{-3/4}\cdot\{E_0(E_1-E_0)+2E_1kT+6(kT)^2\}e^{-(E_1-4E_0)/4kT}\ \text{erg/sec-cm °K},$$

where m_h is the effective mass of hole and E_1 is the energy depth of the forbidden band. For InSb, as an example, we obtain

$$\kappa=9\times10^{-33}N^2T^{1/4}\exp(-700/T)\ \text{cal/sec-cm °K}.$$

The magnitude of the obtained conductivity is nearly consistent with Bnsch's experimental one[1] provided the concentration of donor in his sample is of the order of 10^{15}. The essential difference of our mechanism from other ones is the dependence on the concentration of impurity. Finally it is noted that our mechanism is based on the localized model of donor state. It is obvious that the resonance transfer of ionization energy is inefficient when the concentration is so large that the impurity band model is useful.

References

1) G. Busch and M. Schneider, Physica **20** (1954), 1084. A. F. Joffe, Nuovo Cimento Supplement **3** (1956), 702 and Rep. Prog. Phys. **22** (1959).
2) P. J. Price, Phil. Mag. **46** (1955), 1252. A. F. Joffe, Reference 1).

J. PHYS. SOC. JAPAN **15** (1960) 1539

Dislocations in Ferroelectric Glycine Sulfate Single Crystals

By Hiroo TOYODA

Electrical Communication Laboratory, Nippon Telegraph and Telephone Public Corporation, Tokyo

(Received June 10, 1960)

Observations on the dislocations in ferroelectric guanidine aluminium sulfate hexahydrate crystals were reported by Nakamura[1], and the calculation of the effect of dislocation field on the domain structure was presented by him and his co-workers[2]. Dislocation field may give some interesting effects on the other ferrectric properties. There are, however, a few ferroelectric crystals in which the dislocations have been delineated, that is, above-mentioned GASH and potassium ferrocyanide trihydrate crystals[3].

The author observed interesting etch pits on the surfaces of ferroelectric glycine sulfate crystal. A slow etching in alcohol can delineate the domain structure[4] and the effect may be caused by a small amount of water contained in alcohol, while a rapid etching by water gives etch pits quite different from those corresponding to the domain. They are observed on the various crystal faces and show some characteristic features corresponding to the crystal dislocation, as mentioned in followings.

The etch pits have always clear tips. The pits on (010) faces are cone-shaped and those on (001) and (110) faces have trapezoidal bases, the side faces of them being composed of small steps. When a crystal is cleaved away and etched, the position of the pits on two matching (010) faces fit to each other. As a result of observations on the crystals cut by wet thread, it was confirmed that the fits are nearly perfect on (110) and (001) matching faces, respectively. Chemical polishing reveales that the tips go ahead on lines into the crystal. For the pits on (001) face, an actual observation was performed along the length more than 2 mm and the lines lie in the (010) plane. The density of pits varies from parts to parts and ranges over 10^2 to 10^6 per square centimeter on all of the faces. The density is particularly high on the outer faces of the crystal containing much pores, and the etch pits appear on the interfaces of the pores. Mechanical shock applied to the face, such as dropping of or pushing by steel rod, creates new etch pits on (110) and (001) faces. From these observations, it is most probable to consider the pits as showing the locations of the dislocation lines.

In a (010) plate cleaved from the crystal grown in the ferroelectric temperature range, two triangular areas bounded by the lines connecting the seed crystal with the (110) faces include the domains bound by internal electric field[5]. The pits on (010) face are distributed most densely at the areas, and the fact suggests a probable relation to exist between the dislocation and the domain structure. Fig. 1 shows an interferometric picture of of the etched (010) face, and Figs. 2 and 3 exhibit the pits on (001) and (110) faces, respectively. Fig. 2 includes the pits aligned on lines, which may correspond to grain boundaries. Further studies on the dislocation themselves and their effects on the other properties are now in progress.

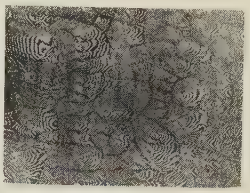

Fig. 1. Interferometric picture of etched b-face, obtained by sodium lamp. Dislocations pass the bright spots. ×35.

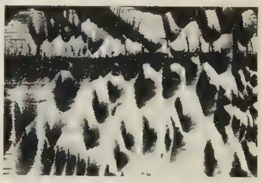

Fig. 2. Etch pits on c-face. b-axis lies vertically in the picture. ×35.

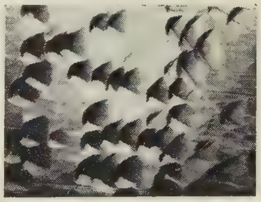

Fig. 3. Etch pits on (110) face. ×35.

References

1) T. Nakamura: J. Phys. Soc. Japan **14** (1959) 1022.
2) H. Takahashi, T. Nakamura and Y. Ishibashi: J. Phys. Soc. Japan **15** (1960) 853.
3) H. Toyoda, N. Niizeki and S. Waku: J. Phys. Soc. Japan; to be published.
4) H. Toyoda, S. Waku and H. Hirabayashi: J. Phys. Soc. Japan **14** (1959) 1003.
5) H. Toyoda and Y. Tanaka: J. Appl. Phys. Papan **28** (1960) No. 8.

J. PHYS. SOC. JAPAN **15** (1960) 1540

A Diffuse Reflexion from a Silicon Carbide Crystal

By Takanori TOMITA

Department of Physics, Saitama University, Urawa

(Received March 29, 1960)

Fig. 1 reproduces the c-axis oscillation photograph showing the diffuse reflexion obtained for a polycrystalline silicon carbide crystal. A small crystallite giving the diffuse reflexion was irradiated with a micro-beam from a fine X-ray source[2]. As shown in Fig. 1, the diffuse reflexion has five intensity maxima corresponding to the reciprocal $(10\bar{1}l)$ period of 6-layer cell and is intense between $(10\bar{1}1)$ and $(10\bar{1}2)$ points and between $(10\bar{1}4)$ and $(10\bar{1}5)$ points.

In order to explain such a feature of diffuse reflexion, we consider a disordered sequence of many ordered ranges having 6-layer structure (ABCACB) and introduce between either two of these ranges the phase relations prepared for the structure analysis of SiC 174 layers[3),4)]. The amplitude of reflexion is

$$\boldsymbol{E}=\boldsymbol{U}\sum_{j=1}^{j_{\max}}\left(\exp 2\pi i\alpha_j\cdot\exp 2\pi i\sum_{n=1}^{j-1}S_nNH_3\right.$$
$$\left.\times\sum_{sN=0}^{S_jN-1}\exp 2\pi isNH_3\right), \qquad (1)$$

where $\boldsymbol{U}$ is the layer form factor for 6-layer cell, the first term in the summation is the phase factor representing translation between two lattices belonging respectively to the first and the j-th ranges ($\alpha_1=0$), H_3 index of 6-layer reciprocal c-axis, N the total number of 6-layer cells along c-axis, and S_jN the number of 6-layer cells in the j-th range; S_nN is not always integer, and the fractional part should be exactly represented as α_n similarly as α_j, but it provides no essential results in the present argument. The intensity can be written as

$$\boldsymbol{I}=|\boldsymbol{E}|^2=|\boldsymbol{U}|^2\left[\sum_j\frac{\sin^2\pi S_jNH_3}{\sin^2\pi H_3}\right.$$
$$+\frac{1}{\sin^2\pi H_3}\sum\sum_{j<k}\left\{\cos 2\pi\left(\alpha_k-\alpha_j+\sum_{n=j+1}^{k-1}S_nNH_3\right)\right.$$
$$\times(\sin^2\pi(S_j+S_k)NH_3-\sin^2\pi S_jNH_3-\sin^2\pi S_kNH_3)$$
$$-2\sin 2\pi(\alpha_k-\alpha_j+\sum S_nNH_3)\cdot\sin\pi S_jNH_3$$
$$\left.\left.\times\sin\pi S_kNH_3\cdot\sin\pi(S_j+S_k)NH_3\right\}\right]. \qquad (2)$$

The first term of Eq. (2) is the sum of contributions from individual range ($j=k$) and gives rise to five maxima corresponding to 6-layer reciprocal period. The second term shows coherency between the reflexions from either two of the ranges ($j\neq k$) and gives on average diffuse reflexion along c-axis. The five maxima are also affected by the phase factors of the second term. The third vanishes on average. The second term is rewritten as

$$\frac{1}{\sin^2\pi H_3}\sum\sum_{j<k}\{\cos 2\pi(\alpha_k-\alpha_j+\delta H_3)\cos 2\pi LH_3$$
$$-\sin 2\pi(\alpha_k-\alpha_j+\delta H_3)\sin 2\pi LH_3\}$$
$$\times\{\sin^2\pi(S_j+S_k)NH_3-\sin^2\pi S_jNH_3$$
$$-\sin^2\pi S_kNH_3\}, \qquad (3)$$

where $L+\delta=\sum_{n=j+1}^{k-1}S_nN$, L and δ being integer and fraction respectively, and the cosine terms in the first parenthesis vanish on average except $L=0$ or at five maxima mentioned above as far as S_nN is considerably large, the sine terms vanishing on average. Finally the intensity becomes

$$\boldsymbol{I}=\frac{|\boldsymbol{U}|^2}{\sin^2\pi H_3}[\sum_j\sin^2\pi S_jNH_3$$
$$-\sum_j\sum_{j+1}\cos 2\pi(\alpha_{j+1}-\alpha_j+\delta H_3)$$
$$\times\{\sin^2\pi S_jNH_3+\sin^2\pi S_{j+1}NH_3$$
$$-\sin^2\pi(S_j+S_{j+1})NH_3\}]. \qquad (4)$$

For $\alpha_{j+1}-\alpha_j+\delta H_3$, 18 phase relations considerable for 6-layer cell (ref. 3) are assumed, and the intensity changes due to these relations are shown in Fig. 2. If all the relations occur at random, the characteristics of the relations are averaged into the intensity given by $|\boldsymbol{U}|^2$ similarly as the photograph presented by Jagodzinski[1]. On the other hand, if some relation occurs dominantly, its characteristic will appear corresponding to the number and size of the ranges having the relation.

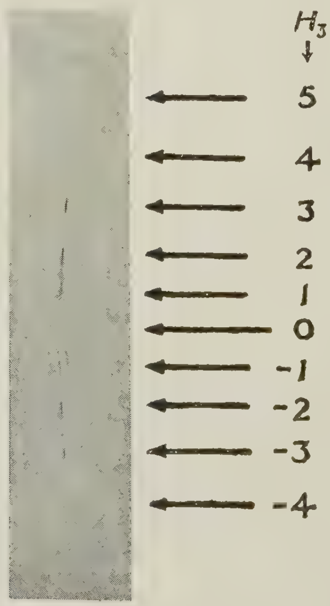

Fig. 1. The diffuse reflexion obtained for 30° c-axis oscillation.

The feature shown in Fig. 1 resembles No. 4 of Fig. 2 corresponding to the phase relation P+2+Q

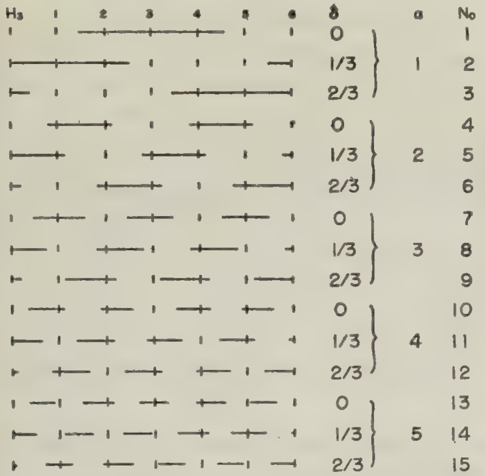

Fig. 2. The intensity change of diffuse reflexion by the phase relation. α and δ are corresponding to those of $P+\alpha+Q(\delta 0)$ of the previous paper (ref. 3). $P+0+Q(00)$, $P+0+Q(+0)$ and $P+0+Q(-0)$ show no changes, and the diffuse reflexions given for them show the intensity of $|U|^2$ own.

(00) (ref. 3) which is also supported by the observation at five maxima as that $(10\bar{1}3)$ peak is strong and sharp compared with $(10\bar{1}1)$ and $(10\bar{1}2)$ peaks (ref. 3 Table II).

The wider interstices between the regular ranges occur, the more intensely the reflexions from the atoms in the interstices appear and prevail over the intensity change introduced here. The coherency between the reflexions from these atoms produces the intensity distribution corresponding to either of Fig. 2, and the total intensity distribution becomes a weighted mean of some of Fig. 2. The point will be discussed in detail in another paper.

References

1) H. Jagodzinski: Acta Cryst. **2** (1949) 298.
2) T. Tomita: Sci. Rep. Saitama Univ. A, **II** (1955) 49; Ibid. **III** (1958) 21.
3) T. Tomita: Sci. Rep. Saitama Univ. A, **III** (1959) 115.
4) T. Tomita: J. Phys. Soc. Jap. **15** (1960) 99.

J. Phys. Soc. Japan **15** (1960) 1541~1542

On the Determination of Diffusion Coefficient of Boron in Silicon

By Jiro Yamaguchi, Shiro Horiuchi,
Koji Matsumura
Department of Electrical Engineering, Faculty of Engineering Osaka University, Osaka
and Yasumasa Ogino
Department of Electrical Engineering, Osaka Institute of Technology, Osaka

(Received March 25, 1960)

Recently, Rohan et al. have suggested an alternate method for the measurement of the diffusion coefficient of Sb-124 in Si by radioassay[1]. The integrated activity in his method may be replaced with the conductivity of the diffused layer under some conditions, because the conductivity results from the total impurity atoms. Then, the same procedure as Rohan's can be applied to the non-radioactive impurities.

We tried to measure the diffusion coefficient of B in Si by the above method. The samples of 20 Ω-cm n type Si slices were pre-coated with B_2O_3 by dipping in the methyl alcohol solution saturated at 20°C, or pre-deposited with B dissociated pyrolytically from BCl_3 mixed in carrier gas[2]. A large amount of diffusant applied to the sample surface in such ways, fixes the surface concentration at the saturated value which correspond to the solid solubility of B in Si, and the diffusion proceeds according to the error function compliment distribution.

In such case, the following relation holds for the conductance of the diffused layer after the removal of the thin layer of thickness x, parallel to the original surface,

$$\sigma(x)=q\int_{x}^{x_j}\mu(C)\left\{C_0\,\mathrm{erfc}\left(\frac{x}{2\sqrt{Dt}}\right)-C_b\right\}dx \qquad (1)$$

where C_0, and C_b are the impurity concentrations at the surface and in the bulk respectively, and x_j is the original junction depth. If x is considerablly smaller than x_j and C_0 large enough to C_b, the equation (1) can be approximated in the following form,

$$\sigma(x)\simeq 2q\mu(C_0)C_0\sqrt{Dt}\int_{u}^{\infty}\mathrm{erfc}\,u\,du \qquad (2)$$

where

$$u=\frac{x}{2\sqrt{Dt}} \qquad (3)$$

Then the following simple relation holds for $\sigma(x)$ and the original surface conductance $\sigma(0)$

$$\frac{\sigma(x)}{\sigma(0)} \simeq \frac{\int_u^\infty \operatorname{erfc} u du}{\int_0^\infty \operatorname{erfc} u du} = \frac{1}{0.565}\int_u^\infty \operatorname{erfc} u du \qquad (4)$$

From the measurement of $\sigma(0)$ and $\sigma(x)$, the value of u corresponding to x is obtained by equation (4) and D can be calculated from the equation (3) independently of the absolute value of the mobility.

This procedure can be applied to the smaller penetration distance than the method employed by Fuller and Ditzenberger. But it is valid only under the condition that the approximate equation (2) can be held, namely $C_b \ll C_0 \leq 10^{20}$ and σ's are almost determined by the contribution from the very high concentration region, in which the concentration dependence of mobility is considerably small.

The results of the diffusion coefficient of B in Si are shown in Fig. 1, and yield the equation

$$D = 17.1 \exp\left(-\frac{84.800}{RT}\right) \text{ cm}^2/\text{sec}$$

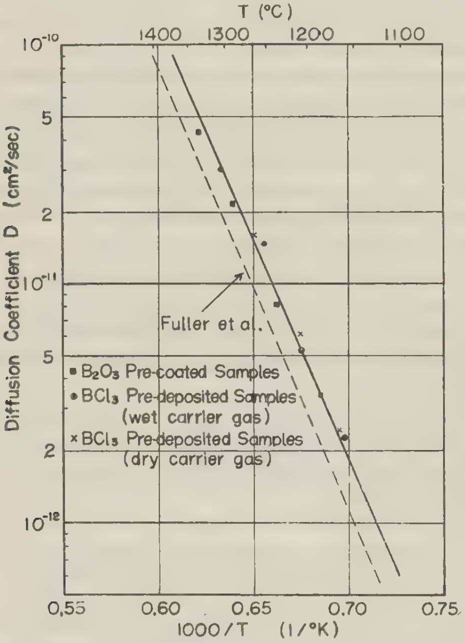

Fig. 1. Temperature Dependence of Diffusion Coefficient of B in Si.

In comparison with the values obtained by Fuller and Ditzenberger[3], the activation energies are in good agreement, while our values of D are about 80% larger over the temperature range studied.

The values of surface concentration C_s obtained from curves of conductivity versus C_s given by Backenstoss[4] are shown in Fig. 2. These values are thought to correspond to the solid solubility of B in Si and shows agreement with the value quoted in the recent paper[5]. On the contrary, C_0's obtained by Fuller and Ditzenberger are so large as to reach the order of 10^{22} atoms/cm³. Although the theoretical value of the solid solubility of B in Si is not yet available, the surface concentrations given by them seem to be unreasonably large and probably result from the underestimation of the diffusion coefficients.

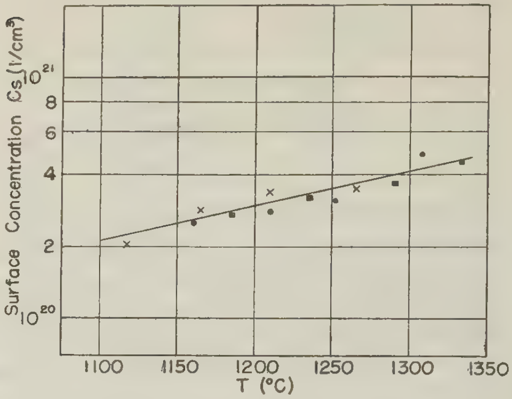

Fig. 2. Temperature Dependence of Surface Concentrations.

References

1) J. J. Rohan, N. E. Pickering and J. Kenneday: J. Electrochem. Soc. **106** (1951) 705.
2) C. J. Frosch: Transistor Technology Vol. 3 ch. 3B, ed. by F. J. Biondi (Van Nostrand, 1958).
3) C. S. Fuller and J. A. Ditzenberger: J. Appl. Phys. **27** (1956) 544.
4) G. Backenstoss: Bell. Syst. Tech. J. **37** (1958) 699.
5) F. A. Trumbore: Bell. Syst. Tech. J. **39** (1960) 205.

J. PHYS. SOC. JAPAN **15** (1960) 1543~1544

On the Weak Interaction of Baryons

By Seitaro NAKAMURA

Department of Physics, University of Tokyo
Tokyo

(Received July 2, 1960)

First, we shall arrange baryons and pions into a triplet and a singlet system with respect to the electric charge[1].

$$p_\mu \equiv \frac{\Xi^- + P}{\sqrt{2}}, \quad \frac{\Xi^- - P}{\sqrt{2}\,i}, \quad \frac{\Xi^0 - n}{\sqrt{2}}, \quad \frac{\Xi^0 + n}{\sqrt{2}}$$

$$q_\mu \equiv \frac{\Sigma^- + \Sigma^+}{\sqrt{2}}, \quad \frac{\Sigma^- - \Sigma^+}{\sqrt{2}\,i}, \quad \Sigma^0, \quad \Lambda$$

$$\pi_\mu \equiv \frac{\pi^- + \pi^+}{\sqrt{2}}, \quad \frac{\pi^- - \pi^+}{\sqrt{2}\,i}, \quad \pi^0, \quad \pi^{0\prime}$$

$$\mu = 1, 2, 3, 0.$$

Since the existence of $\pi^{0\prime}$ is quite doubtful, we omit it in the later discussions.

Next, we describe the Hamiltonian of the weak interaction between baryons and pions in terms of the invariants in this four dimensional isospin space.[2),3)]

$$\begin{aligned} H = a\{&\bar{p}_{[i}\pi_j q_{k]} \\ &+ b\bar{p}_0\pi_j q_j \\ &+ d\{\bar{p}_j\pi_j q_0 + \text{h.c.} \\ &i, j, k = 1, 2, 3 . \end{aligned} \qquad (1)$$

Here a, b and d are the coupling constants. (1) can be written in the usual notation,

$$\begin{aligned} H = \frac{a}{i}\Big\{&(\bar{P}\Sigma^+ - \bar{\Xi}^-\Sigma^-)\pi^0 - (\bar{P}\pi^+ - \bar{\Xi}^-\pi^-)\Sigma^0 \\ &- \frac{1}{\sqrt{2}}\bar{n}(\pi^+\Sigma^- - \pi^-\Sigma^+) - \frac{1}{\sqrt{2}}\bar{\Xi}^0(\pi^-\Sigma^+ - \pi^+\Sigma^-)\Big\} \\ &+ \frac{b}{\sqrt{2}}\Big\{\bar{n}(\pi^+\Sigma^- + \pi^-\Sigma^+) + \bar{\Xi}(\pi^-\Sigma^+ + \pi^+\Sigma^-)\Big\} \\ &+ d\Big\{(\bar{P}\pi^+ + \bar{\Xi}^-\pi^-)\Lambda + \frac{1}{\sqrt{2}}\bar{\Xi}^0\pi^0\Lambda - \frac{1}{\sqrt{2}}\bar{n}\pi^0\Lambda\Big\} . \end{aligned} \qquad (2)$$

Now, let us introduce the assumptions which define the operators of the Minkowski space in the Hamiltonian. Suppose the following charge symmetry transformation (we shall call it S tentatively):

$$\begin{aligned} S:\quad & p_2 \to -p_2, \quad q_2 \to -q_2, \quad \pi_2 \to -\pi_2 \\ & (P \leftrightarrow \Xi^-, \quad \Sigma^+ \leftrightarrow \Sigma^-, \quad \pi^+ \leftrightarrow \pi^-) . \end{aligned} \qquad (3)$$

S will change the sign of the electric charge of charged particles without transforming them into their antiparticle states.

We require that the interaction Hamiltonian must be invariant under the combined transformation of S and X, where $X = \gamma_5$ denotes the chirality transformation proposed by Watanabe.[4)] The chirality was a useful idea which led Marshak and Sudarshan[5)] to determine the $V-A$ type for the universal Fermi interactions.

It will be easily seen that the terms with the coefficient a/i in (2) change sign under the transformation S, while those with the coefficients b and d remain invariant under S. On the other hand, the terms $\bar{\psi}_A\gamma_\mu(1+\gamma_5)\psi_B$ and $\bar{\psi}_A\gamma_\mu(1-\gamma_5)\psi_B$ are chirality invariant and chirality pseudo-invariant,[6)] respectively. Therefore, it is clear that if we take $\Omega_a = \gamma_\mu(1-\gamma_5)$, $\Omega_b = \gamma_\mu(1+\gamma_5)$ and $\Omega_d = \gamma_\mu(1+\gamma_5)$, then we are able to prove the SX invariance in the Hamiltonian (1). Here Ω_a, Ω_b and Ω_d are the Dirac operators to be inserted in the bilinear forms of the two baryon-fields in the terms of (2) with the coefficients a, b and d, respectively. We obtain thus the final expression of (1) with the operators.

$$\begin{aligned} H = ig\{&\bar{P}\gamma_\mu(1-\gamma_5)\Sigma^0\partial_\mu\pi^+ - \bar{P}\gamma_\mu(1-\gamma_5)\Sigma^+\varrho_\mu\pi^0\} \\ &+ ig\sqrt{2}\,\{\bar{n}\gamma_\mu\gamma_5\Sigma^+\partial_\mu\pi^- + \bar{n}\gamma_\mu\Sigma^-\partial_\mu\pi^+\} \\ &+ ig\{-\bar{\Xi}^-\gamma_\mu(1-\gamma_5)\Sigma^0\partial_\mu\pi^- + \bar{\Xi}^-\gamma_\mu(1-\gamma_5)\Sigma^-\partial_\mu\pi^0\} \\ &+ ig\sqrt{2}\,\{\bar{\Xi}^0\gamma_\mu\gamma_5\Sigma^-\varrho_\mu\pi^+ + \bar{\Xi}^0\gamma_\mu\Sigma^+\partial_\mu\pi^-\} \\ &+ ig\Big\{\bar{P}\gamma_\mu(1+\gamma_5)\Lambda\cdot\partial_\mu\pi^+ - \frac{1}{\sqrt{2}}\bar{n}\gamma_\mu(1+\gamma_5)\Lambda\cdot\partial_\mu\pi^0 \\ &\quad + \bar{\Xi}^-\gamma_\mu(1+\gamma_5)\Lambda\cdot\partial_\mu\pi^- \\ &\quad + \frac{1}{\sqrt{2}}\bar{\Xi}^0\gamma_\mu(1+\gamma_5)\Lambda\cdot\partial_\mu\pi^0\Big\} \\ &\quad + \text{h.c.} \end{aligned} \qquad (4)$$

Here we assumed

$$-\frac{a}{i} = b = d \equiv ig . \qquad (5)$$

It is remarkable to note that the present scheme of the weak interaction provides a reasonable explanation on the recent experiments. First, (4) implies that the parity is conserved in the decay processes of $\Sigma^- \to \pi^- + n$ and $\Sigma^+ \to \pi^+ + n$, while it is violated in the processes of $\Sigma^+ \to \pi^0 + P$, $\Lambda \to P + \pi^-$ and $\Lambda \to n + \pi^0$. Cool et al.[7)] have succeeded to measure the angular distribution of the Σ (Λ)-decay in the non-leptonic mode, which seems to support the prediction of the present scheme.[8)] Second, it is quite satisfactory to see that the predicted branching ratios from (5),

$$\begin{aligned} 2:1 \ \text{for}\ & \sigma(\Lambda \to \pi^- + P) : \sigma(\Lambda \to \pi^0 + n) , \\ 1:1:1 \ \text{for}\ & \sigma(\Sigma^+ \to \pi^+ + n) : \sigma(\Sigma^+ \to \pi^0 + P) : \\ & \sigma(\Sigma^- \to \pi^- + n) , \end{aligned}$$

are not at variances with the observed values.[9),10)] The unique prediction of this theory which seems very striking is the sign of the axial vector interaction, A, relative to that of the vector interaction, V.

$$\begin{aligned} V-A:\quad & \Xi^- \to \pi^- + \Lambda , \quad \Xi^0 \to \pi^0 + \Lambda , \\ & \Lambda \to \pi^- + P , \quad \Lambda \to \pi^0 + n ; \\ V+A:\quad & \Sigma^+ \to \pi^0 + P ; \\ A:\quad & \Sigma^+ \to \pi^+ + n ; \qquad V:\quad \Sigma^- \to \pi^- + n . \end{aligned}$$

Experimental check on this problem[11),12)] may come from the studies on the angular distribution of these modes of the hyperon decay.

References

1) S. Nakamura and S. Hatsukade: Nuclear Phys. in press.
2) B. d'Espagnat, J. Prentki and A. Salam: Nuclear Phys, **5** (1958) 447.
3) G. Takeda: Prog. Theor. Phys. **19** (1958) 361.
4) S. Watanabe: Phys. Rev. **106** (1957) 1306. Y. Tanikawa and S. Watanabe: Phys. Rev. **110** (1958) 289.
5) E. C. G. Sudarshan and R. E. Marshak: Phys. Rev. **109** (1958) 1860.
6) M. Morita: Nuclear Phys. **14** (1959) 106.
7) R. Cool, J. W. Cronin, B. Cork, L. Kerth and W. A. Wenzel: Phys. Rev. **114** (1959) 912; New York Meeting 1960.
8) K. Nakagawa: Nuclear Phys. **10** (1959) 20. B. d'Espagnat and J. Prentki: Phys. Rev. **114** (1959) 1367.
9) M. Gell-Mann and A. Rosenfeld: Annual Review of Nuclear Science **7** (1957) 407.
10) S. Okubo, R. E. Marshak and E. C. G. Sudarshan: Phys. Rev. **113** (1959) 944.
11) R. P. Feynman and M. Gell-Mann: Phys. Rev. **109** (1958) 193.
12) R. H. Dalitz: Revs. Mod. Phys. **31** (1959) 823.

Errata

Dynamical Theory of Electron Diffraction in Laue-case

By Fuminori FUJIMOTO

I. General Theory

J. Phys. Soc. Japan **14** (1959) 1558

Page	Column	Line	
1559	Right	5	Eq. (6) should be read Eq. (7)
1560	Lelt	1	of of ζ^i should be read of ζ^i
1561	Eq. (22)	3	$\sum_g' v^*{}_{h-g}{}^* v_h{}^*$ should be read $\sum_g' v^*{}_{h-g} v_g{}^*$
1563	The equation above Eq. (29) should be read $J_h=\cdots=\frac{4}{3k}\left[\left(\frac{D}{2k}\right)^2 v_h{}^2-\cdots\right]^{3/2}\left\{\frac{1}{3}\left(\frac{D}{2k}\right)^4\cdots\right\}^{-1/2}$		
1565	Eq. (33)	5	Numerator $\exp(iz\rho_{g_i})$ should be read $\exp(iz\rho_{g_i})-1$
		12	to the equal to should be read to be equal to
	The first equation in Discussions should be read $V_{12}=v_h-\sum_g'\frac{v_{h-g}v_g}{k^2-k_g{}^2}$		

II. Numerical Calculation of Intensities

J. Phys. Soc. Japan **15** (1960) 859

Page	Column	Line	
862	Eq. (11)	2	$(x^i-x^{g'})$ should be read $(x^i-x^{g'})^2$
866	Fig. 4		G should be removed

III. Forbidden Reflection

J. Phys. Soc. Japan **15** (1960) 1022

Page	Column	Line	
1026, 1027	Eq. (12), (13) and (14)		$(v_{022}^2+12v_{111}^2-2v_{022}b_{100}^2+b_{100}^4)$ should be read $(v_{022}^2+12v_{111}^2+2v_{022}b_{100}^2+b_{100}^4)$
1027	Eq. (15)		$k^2b_{100}^4$ should be read $k^2b_{100}^2$
1028			Fig. 5 should be replaced by the following figure.

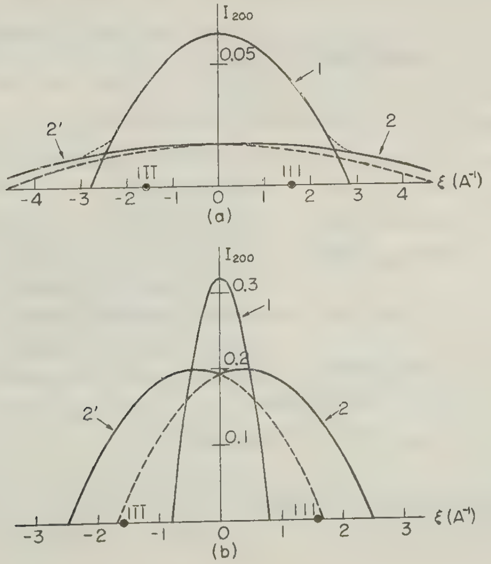

PROGRESS OF THEORETICAL PHYSICS

CONTENTS

Progress of Theoretical Physics Vol. 23, No. 5, May 1960

Energy Loss and Radiation of a Gyrating Charged Particle in a Magnetic Field—*Non-Ionized Medium*— .... Kazuo KITAO..759
On a Non-local Electromagnetic Model for Electron and Muon Masses .... J. L. FERREIRA and Y. KATAYAMA..776
Excitations in a High Density Electron Gas. I .... Tunemaru USUI..787
Excitations in a High Density Electron Gas. II—*Diamagnetism*— .... E. FUJITA and T. USUI..799
Pion-Pion Interaction and Pion Production in Pion-Nucleon Collision .... Tetsuro SAKUMA..810
On Multipole Model of Baryon-Pion Interactions .... K. FUJII and D. ITÔ..815
On the Non-local Boundary Condition in Quantum Field Theory..Haruo Shimazu..821
Theory of Classical Fluids: Hyper-Netted Chain Approximation. III—*A New Integral Equation for the Pair Distribution Function*—..Tohru MORITA..829
K^+-K^0 Mass Difference .... K. DAIYASU and R. SUGANO..846
A Note on the Leptonic Decay of Hyperons .... Ziro MAKI..853
Macroscopic Causality and Analyticity of Scattering Amplitude in Quantum Field Theory .... Kunio YAMAMOTO..859
Inclusion of Hole Motions in Brueckner Theory .... Fumiaki IWAMOTO..871
Classification of Composite Bosons in the Sakata Model ...... Yoshio YAMAGUCHI..882
S-Wave Pion-Nucleon Interaction .... Shigeo MINAMI..887
On Steller Models with Double Energy-Sources .... Minoru NISHIDA..896
Surface Diffuseness and Phenomenological Treatment of O^{17} Nucleus .... Yoshimi AKIYAMA..903
Theory of Relativistic Rotators and Elementary Particles. I .... Takehiko TAKABAYASI..915
Dispersion Relations in Nucleon-Nucleon Scattering..Y. HARA and H. MIYAZAWA..942

Letters to the Editor:

On the Model of Elementary Particles .... Y. MIYATAKE..957
An Example of Nonlocal Interaction .... Y. MIYATAKE..959
Some Considerations on the Parity-Non-conserving Interactions in the Theory of Propagators .... T. YOSHIMURA..960
On the Universality of the Weak Interactions .... D. ITÔ, S. FURUI, K. FUJII and T. SAKUMA..962
Macroscopic Causality and Analyticity of Electromagnetic Form Factor .... K. YAMAMOTO..964
Possible Interconnection between Nucleon-Structure and Multiple Production in Cosmic Ray Energy Regions....H. NAGAI and D. ITÔ..966

Errata:

Cluster Sums and Related Coefficients of the Ising Model (Vol. 20, p. 192) .... S. KATSURA..967
Ground State of a System Consisting of Two Oppositely Charged Particles in Coulomb Field (Vol. 23, p. 186) .... M. INOKUTI, K. KATSUURA and H. MIMURA..967
Contents of Journ. Phys. Soc. of Japan, Vol. 15, No. 3 .... i–ii
Contents of Supplement, Prog. Theor. Phys. No. 13 ii

---

Price $ 1.25 per copy
$ 15.00 per year (postage inclusive)
Annual dues for foreign members (individual subscribers)
$ 12.00 (postage inclusive)
〃 for foreign members of the Physical Society of Japan
$ 10.00 (postage inclusive)

Application for membership, subscriptions and orders for back numbers should be sent, directly or through book-dealers, to

The Publication Office
in
Yukawa Hall, Kyoto University, Kyoto, Japan

. . . .

JOURNAL OF THE PHYSICAL SOCIETY OF JAPAN, Vol. 15, No. 9, SEPTEMBER, 1960

Reactions of Iron-54 with Alpha-Particles

By Shigeo TANAKA, Michiaki FURUKAWA, Shiro IWATA*,
Masuo YAGI**, Hiroshi AMANO*** and Takashi MIKUMO

Institute for Nuclear Study, University of Tokyo,
Tanashi P.O., Tokyo

(Received May 7, 1960)

Excitation functions for the (α, p), (α, n), (α, pn), $(\alpha, 2n)$, $(\alpha, p2n+\alpha, 3n)$, $(\alpha, \alpha n)$, $(\alpha, \alpha pn)$ and $(\alpha, \alpha 2n)$ reactions on Fe^{54} were measured by the activation method using a "stacked-foil" technique, the alpha-particle energies ranging from 10 MeV to 40 MeV. The predominance of proton emission over neutron emission has been observed. The ratios of $\sigma(\alpha, p)/\sigma(\alpha, n)$ and $\sigma(\alpha, pn)/\sigma(\alpha, 2n)$ in the region of maximum yield were found to be 3.4 and 60, respectively. The ratio of $\sigma(\alpha, \alpha pn)/\sigma(\alpha, \alpha 2n)$ at 40 MeV was about 180. A small "knee" was observed at the incident alpha-particle energy of about 20 MeV in the excitation function for the $(\alpha, 2n)$ reaction. The total reaction cross section was found to agree with the value calculated from continuum theory for a nuclear radius constant r_0 of 1.7×10^{-13} cm assuming a nuclear square well potential.

§1. Introduction

In recent years, the experimental data on the competitive modes of decay of medium-weight nuclei bombarded by alpha-particles have been accumulated by several investigators1)–8). The results show a very large variety for the competition between charged-particle and neutron emission. To what extent and in how much detail the competition between various nuclear reactions could be fitted by the statistical theory have been discussed. The recent report by Dostrovsky, Fraenkel and Friedlander9) shows that the experimental excitation functions of nuclear reactions in the mass range Cr^{50}–Se^{74} could be fitted by the evaporation calculation with a unique set of the pairing and shell energy corrections.

As a part of our systematic study in which the cross sections of alpha-induced reactions on medium-weight nuclei at intermediate energies are investigated, we report here the results of the alpha-induced reactions on Fe^{54}. Fe^{54} is a suitable nucleus for measuring the competing reactions between proton and neutron emission. The excitation functions for the (α, p), (α, n), (α, pn), $(\alpha, 2n)$, $(\alpha, p2n+\alpha, 3n)$, $(\alpha, \alpha n)$, $(\alpha, \alpha pn)$ and $(\alpha, \alpha 2n)$ reactions have been measured****.

§2. Experimental

The bombardments were performed with the external alpha-particle beam from the 160 cm INSJ cyclotron by means of a "stacked-foil" technique. The beam was collected in a Faraday cup and the total charge of the beam was measured by a current integrator. A more detailed description of the bombarding system is given in the previous reports10),11). In different experiments, the initial alpha-particle energies were 40.2 and 32.0 MeV, and certain energy region was covered in the different runs. The experiment with 32.0 MeV alpha-particles was duplicated. For the $Fe^{54}(\alpha, \alpha n)Fe^{53}$ and $Fe^{54}(\alpha, \alpha pn)Mn^{52m}$ reactions, the separate bombardments with short irradiation times were performed.

The targets consisted of natural-iron foils (7.7 ± 0.1 mg/cm²) whose impurities were chemically analyzed.

Impurity	C	S	Si	Mn
Content (%)	0.010	0.11	0.011	0.09

---

* Engineering Research Institute, Kyoto University, Kyoto.

** Department of Chemistry, Faculty of Science, Tohoku University, Sendai.

*** Japan Atomic Energy Research Institute, Tokai-Mura, Ibaraki.

**** We knew, after our experiment had already finished, that there were the unpublished data for the (α, p), (α, n), (α, pn), $(\alpha, 2n)$, $(\alpha, p2n+\alpha, 3n)$ and $(\alpha, 2pn)$ reactions on Fe^{54} measured recently by Houck and Miller7).

The contribution of manganese impurity to the $Fe^{54}(\alpha, p)Co^{57}$ cross section was examined from the measured reaction cross sections on Mn^{55} (see ref. 10), and was estimated to be within, 5%.

After the bombardment, the target foil was dissolved in acid and nickel, manganese, cobalt and iron were chemically separated by means of an anion exchange resin.

The disintegration rates of the samples were determined by measuring β-particles with a calibrated GM counter and a 4πβ-counter and γ-rays with an (1-¾ in. dia. ×2 in. high, 1-½ in. dia. ×1 in. high and well type) NaI scintillation counter. The counting techniques and the calibration methods are presented in more detail in the Appendix.

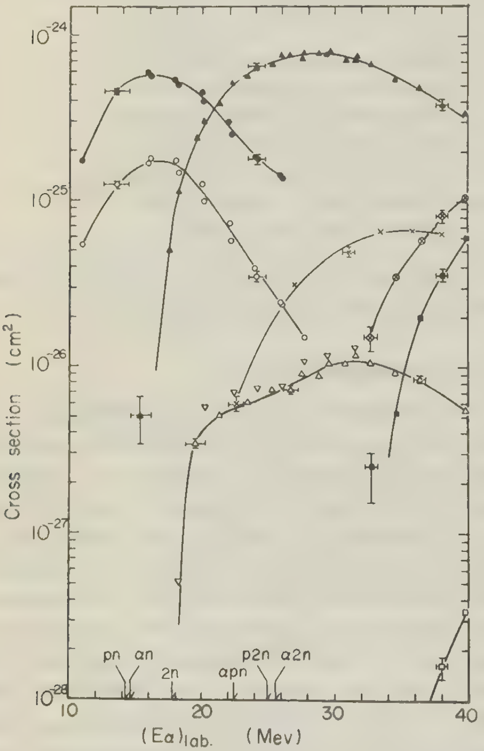

Fig. 1. Excitation functions for the alpha-induced reactions on Fe^{54}.

● $Fe^{54}(\alpha, p)Co^{57}$ ○ $Fe^{54}(\alpha, n)Ni^{57}$

▲ $Fe^{54}(\alpha, pn)Co^{56}$ △ $Fe^{54}(\alpha, 2n)Ni^{56}$

× $Fe^{54}(\alpha, \alpha n)Fe^{53}$

⊗ $Fe^{54}(\alpha, p2n)Co^{55}+Fe^{54}(\alpha, 3n)Ni^{55}$

■ $Fe^{54}(\alpha, \alpha pn)Mn^{52g}$ □ $Fe^{54}(\alpha, \alpha 2n)Fe^{52}$

▽ $Fe^{54}(\alpha, 2n)Ni^{56}$; The ordinary and the inverse triangles represent the data from each separate runs. The systematically high values of ▽ compared with those of △ may be due to the slight contamination of cobalt into nickel fraction.

↓ Calculated threshold for each reaction indicated above the arrow, on Fe^{54}.

The numerical data not shown in this Figure are
$\sigma(\alpha, 2n)$ at ~18 MeV = ~2×10^{-29} cm²
$\sigma(\alpha, \alpha 2n)$ at 36.4 MeV = $(5\pm1)\times10^{-29}$ cm²
$\sigma(\alpha, \alpha 2n)$ at 34.6 MeV = ~1×10^{-29} cm².

§ 3. Results and Discussion

The absolute cross sections are plotted as a function of alpha-particle energy in Fig. 1, together with the energy spread in target foil and with the estimated error of the magnitude of cross section for some experimental points*. The (α, p) and (α, n) excitation functions on Fe^{54} were measured below the thresholds of the (α, p2n) and (α, 3n) reactions on Fe^{56}, respectively.

In obtaining all these cross sections, corrections were made for the "recoil-loss" from target foil. The amounts of "recoil-loss" for each reaction were measured as a function of alpha-particle energy. The amount of "recoil-loss" is abont 7% for the 7.7 mg/cm² iron foil at the incident alpha-particle energy of 40 MeV, and it decreases with decreasing alpha-particle energy.

The present experiment shows quite strikingly the predominance of protron emission over neutron emission. The energy dependences of the ratios of $\sigma(\alpha, p)/\sigma(\alpha, n)$, $\sigma(\alpha, pn)/\sigma(\alpha, 2n)$ and $\sigma(\alpha, \alpha pn)/\sigma(\alpha, \alpha 2n)$ are represented in Fig. 2.

The ratio of $\sigma(\alpha, p)/\sigma(\alpha, n)$ is about 3.5 in this experiment. It is of interest to compare this ratio with the result of Carver and Turchinetz[13] who measured the competing processes in the photo-disintegration of Ni^{58}. The ratio of $\sigma(\gamma, p)/\sigma(\gamma, n)$ is almost constant at the photon energies between 20 and 32 MeV which correspond to the alpha-particle energies of 15–28 MeV, and is about 2.5. In both cases, the proton emission from Ni^{58} appears to be favoured over neutron emission by about the same factor.

It is interesting to note that there is a small "knee" at the incident alpha-particle energy of about 20 MeV in the excitation function for the (α, 2n) reaction on Fe^{54}. This

---

* A part of the present result was reported previously as the Short Note in this Journal[12]. The data in the previous report have been renewed in this paper by some corrections which are mainly due to the determination of counting efficiencies

"knee" was carefully determined by two separate bombardments. The only source of ambiguity may come from the chemical separation of nickel and cobalt. The contamination of cobalt into nickel fraction was reduced below $\sim 1\times 10^{-5}$ by careful procedures. It is thought that this "knee" is beyond the experimental error.

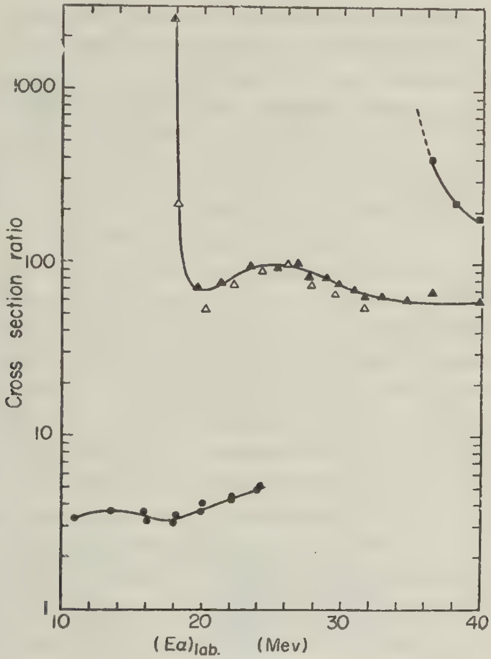

Fig. 2. Ratios for $\sigma(\alpha, p)/\sigma(\alpha, n)$, $\sigma(\alpha, pn)/\sigma(\alpha, 2n)$ and $\sigma(\alpha, \alpha pn)/\sigma(\alpha, \alpha 2n)$.

● $\sigma(\alpha, p)/\sigma(\alpha, n)$ ▲ $\sigma(\alpha, pn)/\sigma(\alpha, 2n)$

■ $\sigma(\alpha, \alpha pn)/\sigma(\alpha, \alpha 2n)$

△ $\sigma(\alpha, pn)/\sigma(\alpha, 2n)$; Derived from the values of ▽ in Fig. 1.

The ratio of $\sigma(\alpha, pn)/\sigma(\alpha, 2n)$ at the incident energy of about 18 MeV shows a large value of about 1000. As the energy of alpha-particles is increased above the threshold for the $(\alpha, 2n)$ reaction this ratio drops rapidly and is observed to have a minimum value of about 70 at $E_\alpha \simeq 20$ MeV, followed by an increase to a maximum of about 100 at 25 MeV, further a gradual decrease with increasing energy. The minimum is a consequence of the "knee" that is observed in the $(\alpha, 2n)$ reaction.

In the compound nucleus picture, the emission probabilities are very sensitive to the binding energies of various particles and to the level densities of residual nuclei. The experimental results in which the (α, pn) reaction competes favourably with the $(\alpha, 2n)$ reaction have been reported in other cases in this mass region; for Ti^{46}, Cr^{50}, Ni^{60}, Zn^{64} and Ge^{70} targets.[1),2),4),5),9)] The residual nuclei of all the $(\alpha, 2n)$ reactions mentioned are even-even, while those of the (α, pn) reactions are odd-odd nuclei and are expected to have a greater density of levels. This differences in the level densities of the residual nuclei may play a role in part to reduce the $(\alpha, 2n)$ reactions, together with the fact that the thresholds of the $(\alpha, 2n)$ reactions are considerably higher than those of the (α, pn) reactions. A support of this view is obtained from the large $(\alpha, 2n)$ cross sections observed for V^{50}, Mn^{55}, Cu^{65}, Ag^{107} and Ag^{109} targets, where the residual nuclei are not even-even.[6),8)-10)] In addition, the effect of closed shell on the level density may be taken into account and this effect further reduces the $(\alpha, 2n)$ reaction on Fe^{54}, since the residual Ni^{56} nucleus is double magic.

The $(\alpha, \alpha pn)$ cross section shown in Fig. 3 is that for ground-state formation. The ratio of the $(\alpha, \alpha pn)$ cross section for isomer formation to that for ground-state formation (σ_m/σ_g) was measured at the incident alpha-particle energy of 40 MeV, and was about 0.05.

The ratio of $\sigma(\alpha, \alpha pn)/\sigma(\alpha, \alpha 2n)$ is about 180 at the highest incident alpha-particle energy attained. As the energy of alpha-particles is increased above the threshold for the $(\alpha, \alpha 2n)$ reaction, this ratio drops rapidly and then probably decreases monotonically to

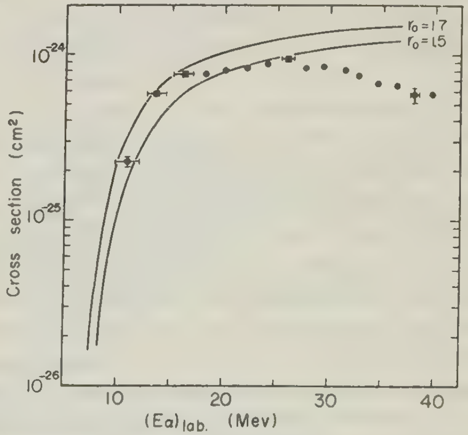

Fig. 3. Sum of the Fe^{54} excitation functions.

— Total reaction cross section calculated from continuum theory.

● Sum of the observed cross sections.

an asymptotic value. Unfortunately, the asymptotic value could not be obtained at the incident alpha-particle energies available in this experiment.

The cross section shown as that of the (α, $p2n+\alpha$, $3n$) reaction is perhaps mainly due to the (α, $p2n$) reaction and of course includes substantial contribution from triton emission. The cross section of the (α, $3n$) reaction may be very small because of the low yield of the (α, $2n$) reaction.

A comparison between the sum of the observed cross sections and the total reaction cross section calculated from continuum theory (according to Shapiro's calculation) is shown in Fig. 3. A value of $r_0=1.7\times10^{-13}$ cm appears to give the reasonable fit to the low energy part of the sum of the observed cross sections. The difference between the calculated total cross section and the sum of the observed cross sections at higher energy part may reflect a substantial contribution of the unobserved reactions. The most probable reactions which are missed in this experiment may be the (α, $2p$), (α, $2pn$), (α, $\alpha\gamma$) and (α, αp) reactions. The threshold of the (α, $2p$) reaction is lower than that of the (α, pn) reaction by about 5.8 MeV, thus the (α, $2p$) reaction may be quite important despite of the Coulomb barrier of proton emission. The (α, αp) reaction may compete favourably with the (α, αn) reaction and contribute substantially to the total reaction cross section, when the enhancement of proton emission and the large ratio of $\sigma(\alpha, \alpha pn)/\sigma(\alpha, \alpha 2n)$ in this study are considered. A rather large value of r_0 has been obtained in other cases in this mass region; 1.7×10^{-13} cm for Mn^{55} and Ni^{58}, 1.6×10^{-13} cm for Zn^{64}.[4),10),14)]

Recently, the total reaction cross section for alpha-particles in the energy range 10–50 MeV has been calculated by Igo[15)] in terms of the optical model using the nuclear potential (exponential at the nuclear surface) derived from the analysis of elastic scattering data. It is interesting to cite that the low energy part of the sum of the observed cross sections in this experiment is found to give a reliable fit to the total reaction cross section predicted from the optical model calculation.

Authors's thanks are due to Prof. I. Nonaka and the other members of staff of Low Energy Division in this Institute for their interest and encouragement. We are grateful to Prof. J. M. Miller and Dr. F. S. Houck (Columbia University and Brookhaven National Laboratory) for making their results available to us prior to publication. The help of Messrs. T. Karasawa, A. Suzuki, H. Ogawa, H. Adachi, Y. Miyazawa and T. Yamada in operating the cyclotron is also gratefully acknowledged.

Table I. Nuclear data necessary for the calculation of disintegration rate.

Nuclide	Half-life	Radiation and Energy	Emission Probability of Beta- and Gamma-Rays (%)	
Ni^{57}	37h	β^+ 0.85 MeV	40	47
		β^+ 0.71 MeV	6	
		β^+ 0.33 MeV	0.9	
Ni^{56}	6d			
Co^{57}	270d	γ 0.122MeV	100	
		γ 0.138MeV		
Co^{56}	77d	β^+ 1.50 MeV	18	
		β^+ 1.00 MeV		
		β^+ 0.44 MeV		
		γ 0.845MeV	100	
Co^{55}	18h	β^+ 1.51 MeV	40	79
		β^+ 1.04 MeV	36	
		β^+ 0.79 MeV	3	
Fe^{53}	8.9m	β^+ 2.86 MeV	98	
		β^+ 2.38 MeV		
		β^+ 1.57 MeV		
Fe^{52}	8.2h	γ 0.165MeV	100	
Mn^{52g}	5.7d	β^+ 0.58 MeV	33	
Mn^{52m}	21m	γ 1.43 MeV	100	

Appendix

Counting and Calibration Procedures

Ni^{57}—The decay of Ni^{57} was followed by a GM counter. The annihilation radiation and the characteristic γ-rays from Ni^{57} were also measured, and these were served for the calculation of relative yields. After Ni^{57} had decayed to Co^{57}, the disintegration rate and the relative yields of Co^{57} were measured by a well-type NaI scintillation counter. The $4\pi\beta$-counting and the measurement of the coincident annihilation radiation (see Co^{56}) of Ni^{57} were also served for the calculation of disintegration rate, and the consistency between the values from these two methods and the value from the measurement as Co^{57} was very good. The relative yields were consistent (within 5%) with each other in several counting procedures.

Ni^{56}—After Ni^{56} was allowed to decay to Co^{56}, the disintegration rate was measured as Co^{56}.

Co^{57}—The 122 and 137 keV γ-ray photopeaks were measured in a well-type NaI scintillation counter. The measurement was performed at about a year after the bombardment in order to reduce the contribution of Co^{56} and Co^{58} from the (α, pn) reactions on Fe^{54} and Fe^{56}. The counting efficiency was taken as 0.85. (see ref. 10)

Co^{56}—The relative yields were obtained by measuring the γ-rays above 1.5 MeV with an NaI scintillation counter. The determination of disintegration rate is as follows. The two 0.51 MeV γ-rays from positron annihilation were detected in coincidence by two NaI scintillation counters positioned 180° from one another with respect to the source. The disintegration rate was obtained by applying the counting efficiency calibrated with an Na^{22} standard source. The absolute activity of the Na^{22} standard source had been determined by a (annihilation γ-1.28 MeVγ) coincidence counting and a $4\pi\beta$-counting within an error of 5%. The Co^{56} was also measured with a calibrated GM counter and a $4\pi\beta$-counter, and the disintegration rates from these two methods were consistent with that from the measurement of the coincident annihilation radiation within 5%. The disintegration rate was also cross-checked by applying the photopeak efficiency to the counting rate of γ-ray measurement. The disintegration rate from the γ-ray measurement is about 28% smaller than that from the measurement of the coincident annihilation radiation. This deviation may be due to the difficulty of estimating the photopeak in the γ-ray spectrum and to the fact that the calculated photopeak efficiency is not correctly applicable to this experiment. The plotted cross sections for the (α, pn) and $(\alpha, 2n)$ reactions are based on the measurement of the coincident annihilation radiation.

Co^{55}—The relative yields were obtained by analyzing the decay curves of the γ-rays above 1.1 MeV. The decay was also followed by the GM counter whose efficiency had been calibrated with various β-emitters of known disintegration rates, and this was served for the calculation of the disintegration rate of Co^{55}.

Fe^{53}—Immediately after the bombardment, without chemical separation, the decay was followed by measuring the coincident annihilation radiation and the disintegration rate was obtained as in the case of Co^{56}.

Fe^{52}—The 165 keV γ-ray photopeak was measured with a well-type NaI crystal. The photopeak efficiency was estimated as 0.80.

Mn^{52g}—The decay was followed with a calibrated GM counter, and a $4\pi\beta$-counting was also performed. The disintegration rates from these two procedures agreed to within 10%.

Mn^{52m}—Immediately after the bombardment, without chemical separation, the decay of the 1.43 MeV γ-ray photopeak was followed with an NaI scintillation counter. The disintegration rate was obtained by applying the photopeak efficiency to the counting rate.

References

1) S. N. Ghoshal: Phys. Rev. **80** (1950) 939.
2) Miller, Friedlander and Markowitz: Phys. Rev. **98** (1955) 1197.
3) K. G. Proges: Phys. Rev. **101** (1956) 225.
4) N. T. Porile: Phys. Rev. **115** (1959) 939.
5) S. Amiel: Phys. Rev. **116** (1959) 415.
6) N. T. Porile and D. L. Morrison: Phys. Rev. **116** (1959) 1193.
7) F. S. Houck: *Atomic Energy Commission Report* NYO-7332, June, 1959 (unpublished). F. S. Houck and J. M. Miller: private communication.
8) Fukushima, Kume, Okamura, Otozai, Sakamoto, Yoshizawa and Hayashi: private communication; (Reactions of Ag^{107} and Ag^{109} with alpha-particles have been investigated.)
9) Dostrovsky, Fraenkel and Friedlander: Phys. Rev. **116** (1959) 683.
10) Tanaka, Furukawa, Mikumo, Iwata, Yaki and Amano: J. Phys. Soc. Japan **15** (1960) 545.
11) S. Kikuchi et al.: J. Phys. Soc. Japan **15** (1960) 41.
12) Tanaka, Furukawa, Yagi, Iwata and Amano: J. Phys. Soc. Japan **14** (1959) 1251.
13) J. H. Carver and W. Turchinetz: Proc. Phys. Soc. **73** (1959) 585.
14) S. Tanaka: to be published (Reactions of nickel with alpha-particles have been investigated.)
15) G. Igo: Phys. Rev. **115** (1959) 1665.

Journal of the Physical Society of Japan, Vol. 15, No. 9, September, 1960

Gamma-rays from the 7.56 MeV Level in O^{15}

By Tatsuo Tabata* and Kotoyuki Okano

Department of Physics, Faculty of Science, Kyoto University

(Received May 12, 1960)

The gamma-rays from the $N^{14}(p, \gamma)O^{15}$ reaction at the $E_p=278$ kev resonance, corresponding to the 7.56 MeV level in O^{15}, were studied with a large crystal scintillation spectrometer. The direct ground state transition gamma-ray of about 3% in intensity of the total decay was found to exist in addition to the three known cascade lines. Angular distributions of these gamma-rays are all isotropic, supporting the $J\pi=\frac{1}{2}+$ assignment to the resonance state. The transition strength (radiation width in units of Weisskopf single particle width) of the direct ground state transition $E1$ gamma-ray is calculated to be $|M|^2=4.15\times10^{-6}$, which is by a factor of 10^{-4} smaller than the normal $E1$ transition strength found in light nuclei. Other transitions in O^{15} are estimated to be of normal strength compared with Wilkinson's estimation.

§ 1. Introduction

The gamma-rays from the $N^{14}(p, \gamma)O^{15}$ reaction at the 278 kev resonance were first studied by Johnson, Robinson and Moak, who found three cascade lines decaying through the levels in O^{15} at about 6.82, 6.18 and 5.23 MeV.[1] Bashkin, Carlson and Nelson studied the high energy gamma-rays with a three crystal scintillation spectrometer, and assigned $J=\frac{5}{2}\pm$ for the resonance state on the basis of the small 0°−90° difference in the ratio of the 6.1 MeV to the 5.2 MeV gamma-ray and also of the absence (<5% of the 6.10 MeV line) of a direct ground state transition gamma-ray.[2]** Overley, Pixley and Whaling, on the other hand, assigned spin and parity $\frac{1}{2}+$ for the resonance state from their elastic scattering measurement of protons.[3] If the $J=\frac{1}{2}+$assignment is correct, the direct ground state transition must be of $E1$ character, with the consequent result that this $E1$ transition is abnormally inhibited compared with the Weisskopf single particle transition rate, and also even with the Wilkinson's estimation for the normal $E1$ transition rate in light nuclei.[4],[5] This point was further investigated in the present work.

§ 2. Experimental Method

Titanium nitride powder, formed by heating and grinding titanium grains in an atmosphere of natural nitrogen,*** was pressed onto a copper backing, and was bombarded with a proton beam up to 100 μA from a Cockcroft-Walton generator. Gamma-rays were detected with a NaI(Tl) crystal, 5 in. in diameter by 4 in. thick, and a 100-channel or a 10-channel pulse height analyzer. The latter was used for gamma-ray energy measurements because of its superior linearity. Energy calibration was carried out by using the radioisotopes, ThC″(2.615 MeV), Sb^{124}(2.088, 1.692 MeV), Na^{22} (1.277, 0.511 MeV), Sc^{46}(1.119, 0.885 MeV), and Cs^{137}(0.662 MeV). Gamma-ray spectra and angular distributions were measured at 0° and 90° directions to the proton beam, with the front face of the crystal usually 150 mm apart from the target. For the purpose of examining the contribution of the sum peak to the 7.56 MeV ground state transition line, various source to crystal distances were employed, as will be mentioned below. Other details of the apparatus and the method of analysis are nearly the same as were described in previous publications.[6],[7]

§ 3. Results and Discussions

Fig. 1 shows the scintillation spectra measured at 0° and 90° directions to the proton beam. Six gamma-rays belonging to the three cascade lines through the levels at 6.80, 6.16 and 5.18 MeV were apparently observed, with the relative branching ratios of (22.3±1.6)%, (57.5±4.0)% and (17.2±1.2)% of the total decay, respectively. In addition, a small peak at the highest energy can be attributed to the direct ground state transition 7.56 MeV gamma-ray, although at the distance of 150 mm between the front face of the crystal and the source as in the case of Fig. 1, about one third of this peak is attributable to the coincident detection of cascade lines.

---

* Present address: Radiation Center of Osaka Prefecture.

** Recently S. Bashkin reported that his latest results showed isotropy,[8] superseding the earlier report of anisotropy.

*** The TiN target was kindly prepared by Prof. T. Nishi of Engineering Research Institute, Kyoto University.

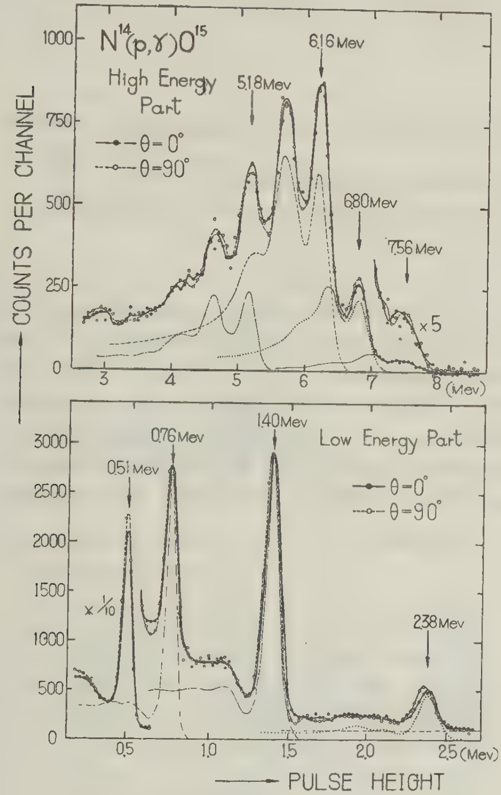

Fig. 1. Scintillation spectra of gamma-rays from the $N^{14}(p,\gamma)O^{15}$ reaction at the 278 kev resonance, taken at zero and 90-degrees to the proton beam. The dotted curves show the decomposed spectra.

To establish the existence of this weak 7.56 MeV gamma-ray, the highest energy part of the spectra was measured at various source to crystal distances between 15 and 280 mm, and the relative counts of the 7.56 MeV peak are plotted as a function of sum peak efficiency in Fig. 2. Least squares fit to the straight line of these points yields (3.03±0.19)% of the total decay as the intensity of the 7.56 MeV gamma-ray. Sum peak contributions in each of these spectra were estimated by using the photopeak efficiencies of the 2.38, 1.40 and 0.76 MeV gamma-rays, taking into account the effect due to the angular correlations of the cascade lines, which were measured recently by Povh and Hebbard.[8] The net relative intensities of the 7.56 MeV gamma-ray thus obtained at each distance are also shown in Fig. 2 (open circles), yieldig (3.03±0.15)% as a mean value, in good agreement with the value cited above. This 7.56 MeV line was checked to be resonant at 278 kev.

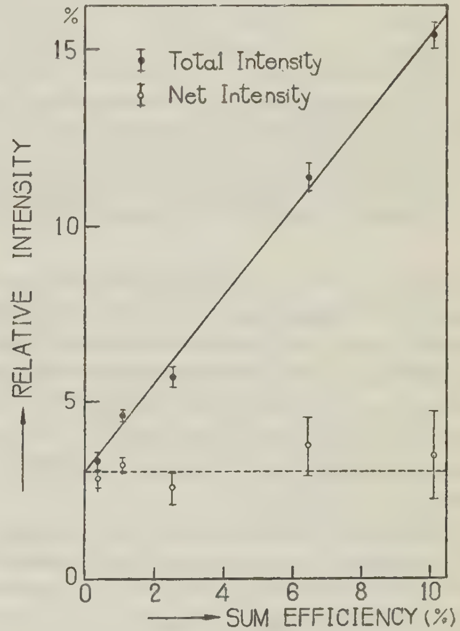

Fig. 2. The relative intensity of the 7.56 MeV peak as a function of sum peak efficiency. The dots represent the total intensity of the 7.56 MeV peak and the circles are the net intensity of the 7.56 MeV gamma-ray after subtracting the sum peak contributions.

Precise energy measurements were carried out for the low energy, primary transitions using the calibration lines already mentioned. Although doublet levels are known to exist in O^{15} at 5.2 MeV (doublet of 5.18 and 5.24 MeV)[9),10)] and 6.8 MeV (doublet of 6.79 and 6.86 MeV),[11)] the inspection of the observed spectral line-shape indicated that the transitions occur mainly to only one member of the doublet. Then, from the measured gamma-ray energies (see Table I), the excitation energies of the feeding levels were estimated as 6.797±0.009, 6.163±0.011 and 5.177±0.016 MeV, using the Q-value of 7.300±0.004 MeV

Table I. Gamma-rays observed at the 278 kev resonance in the reaction $N^{14}(p, \gamma)O^{15}$.

$E\gamma$(MeV)	Transition	Relative intensity**	Anisotropy A_2***	Multipolarity	Transition strength $\|M\|^2$
7.56*	7.56→0	3.0±0.2	0.02±0.10	*E*1	4.15×10^{-6}
6.80*	6.80→0	21.8±10%	−0.02±0.02		
6.16*	6.16→0	57.1 〃	0.00±0.01		
5.18*	5.18→0	18.1 〃	−0.02±0.03		
2.383±0.015	7.56→5.18	16.2±10%	−0.02±0.03	*M*1	2.42×10^{-2}
1.397±0.010	7.56→6.16	57.9 〃	0.00±0.02	*E*1	1.26×10^{-2}
0.763±0.008	7.56→6.80	22.9 〃	−0.01±0.03	*M*1****	9.51×10^{-1}
1.62	6.80→5.18	<1.2			
0.98	6.16→5.18	<1.4			

* These energies were computed using the measured lower gamma-ray energies and the excitation energy of 7.560 MeV for the resonance state.

** High and low energy parts of the spectra were separately normalized.

*** Coefficient of $P_2(\cos\theta)$ term assuming the angular distribution of the form $W'(\theta)=1+G_2A_2P_2(\cos\theta)$.

**** 0.6% *E*2 admixture is present in this transition.[8]

of the $N^{14}(p, \gamma)O^{15}$ reaction[12] and the resonance energy of 278.1±0.4 kev.[12] These excitation energies agree well with those found by other methods within the experimental error, and clearly show that the lower members of the doublets are populated, in agreement with the results of Povh and Hebbard recently reported.

The angular distribution of each gamma-ray component was measured at 0° and 90° relative to the proton beam, which resulted in a complete isotropy, as can be seen in Fig. 1. This eliminates the possibility of $J=\frac{5}{2}\pm$ for the resonance state and supports the $J=\frac{1}{2}+$assignment from the proton elastic scattering experiments,[3] although other assignments such as $\frac{1}{2}-$ or $\frac{3}{2}\pm$ cannot be excluded only on the grounds of the isotropy of capture radiations. This $J=\frac{1}{2}+$assignment to the 7.56 MeV level fixes the character of the weak 7.56 MeV transition as *E*1.

The measured gamma-ray energies, relative intensities and anisotropies are summarized in Table I, together with the assigned transitions and multipolarities and the calculated transition strength $|M|^2$, about which we shall discuss below.

Wilkinson has examined some 70 radiative transitions in light nuclei ($A\leq 20$),[5] and found that the allowed *E*1 transitions have a transition strength of about $|M|^2=0.032$ Weisskopf units with the spread of about a factor of 7 either way. Here transition strength $|M|^2=\Gamma_\gamma/\Gamma_w$ is a radiation width measured in units of Weisskopf single particle width. In particular, transitions with $|M|^2<10^{-4}$ have all been assigned to be isotopic spin forbidden transitions. By using the radiation width of $\Gamma_\gamma=0.040\pm0.009$ ev for the 278 kev resonance reported by Bashkin *et al.* from the radiation

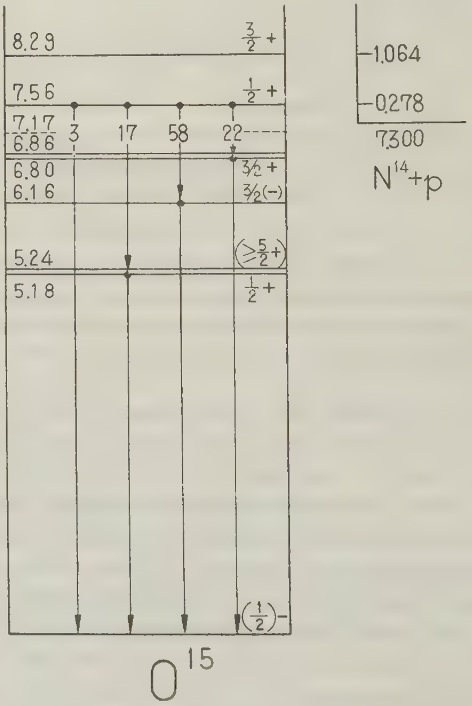

Fig. 3. Level scheme of O^{15} showing the gamma-ray decay of the 7.56 MeV level.

yield measurement,[2] transition strengths of the four primary gamma-rays de-exciting the 7.56 MeV level to the lower levels can be calculated and are listed in Table I. Other known $E1$ transitions in O^{15} are the transitions from the 8.29 MeV $\frac{3}{2}+$ level (corresponding to the 1064 kev resonance) to the ground and 6.16 MeV levels,[13] each having $|M|^2=1.4\times10^{-3}$ and 9.3×10^{-3} respectively. These strengths of $E1$ transitions in O^{15}, which are all of isotopic spin allowed character, are illustrated in the histogram of Fig. 4, together with the other $E1$ transitions compiled by Wilkinson.

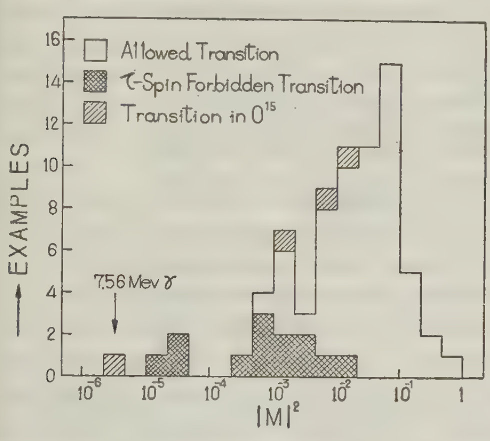

Fig. 4. Distribution of strengths of $E1$ transitions in light nuclei ($A\leq20$).

It is to be added also that the two $M1$ transitions listed in Table I and the 3.05 MeV $M1$ transition from the 8.29 MeV level to the 5.2 MeV level(s) in O^{15}($|M|^2\approx0.55$) all have a normal strength for $M1$ transitions ($|M|^2=0.15$ with the spread of a factor of 20 either way). Only the 7.56 MeV transition is found to have an abnormally small strength compared with all the other known $E1$ transitions in light nuclei, even with the isotopic spin forbidden transitions. This is considered to be due to the very weak fractional parentage overlap of the states concerned, which results in the cancellation of the transition matrix element. Other examples of weak transitions as presented here may also exist, and the distribution of $E1$ or $M1$ transition strengths already known might somewhat have to be modified, since the weak transitions are liable to have escaped detection and are not reported. It would further be necessary to seek for the possible transitions or to set the limits on their strength in order to compare them with model predictions on a firmer basis.

The authors wish to express their gratitude to Prof. K. Kimura, Dr. J. Muto and Dr. S. Yasumi for their encouragements and advices, and to Mr. K. Fukuda for his helpful contributions. This work was supported financially by the Ministry of Education.

References

1) C. H. Johnson, G. P. Robinson and C. D. Moak: Phys. Rev. **85** (1952) 931.
2) S. Bashkin, R. R. Carlson and E. B. Nelson: Phys. Rev. **99** (1955) 107.
3) J. C. Overley, R. E. Pixley and W. Whaling: Bull. Amer. Phys. Soc. **1** (1956) 387.
4) D. H. Wilkinson: Phil. Mag. **1** (1956) 127.
5) D. H. Wilkinson: *Proceedings of the Rehovoth Conference on Nuclear Structure* (North-Holland Publishing Co., Amsterdam, 1958) P. 175.
6) J. Muto: J. Phys. Soc. Japan **15** (1960) 17.
7) K. Okano: J. Phys. Soc. Japan **15** (1960) 28.
8) B. Povh and D. F. Hebbard: Phys. Rev. **115** (1959) 608.
9) B. Povh: Phys. Rev. **114** (1959) 1114.
10) S. Hinds and R. Middleton: Proc. Phys. Soc. **73** (1959) 727.
11) J. B. Marion, R. M. Brugger and T. W. Bonner: Phys. Rev. **100** (1955) 46.
12) F. Ajzenberg-Selove and T. Lauritsen: Nucl. Phys. **11** (1959) 1.
13) D. F. Hebbard and B. Povh: Nucl. Phys. **13** (1959) 642.

JOURNAL OF THE PHYSICAL SOCIETY OF JAPAN, Vol. 15, No. 9, SEPTEMBER, 1960

Lower Excited States in P^{29} from the $Si^{28}(p, \gamma)P^{29}$ Reaction

By Kotoyuki OKANO, Tatsuo TABATA*, Kyue FUKUDA
Department of Physics, Faculty of Science, Kyoto University

and Jiro MUTO
Department of Nuclear Science, Faculty of Science, Kyoto University

(Received May 12, 1960)

The gamma-rays from the $Si^{28}(p,\gamma)P^{29}$ reaction at the $E_p=369$ kev resonance were studied with a large NaI (Tl) crystal scintillation spectrometer. The resonance state, corresponding to the 3.116 ± 0.012 Mev fourth excited state in P^{29}, was found to decay by $(74\pm4)\%$ to the first excited state at 1.384 ± 0.008 Mev and by $(26\pm4)\%$ to the second excited state at 1.961 ± 0.013 Mev which decays predominantly to the ground state.

From the angular distribution measurements of each gamma-ray line, spins and parities of these lower levels in P^{29} were unambiguously assigned as follows: 1.38 Mev(1st), $J=3/2+$; 1.96 Mev(2nd), $J=5/2+$; 3.12 Mev (4th), $J=5/2+$. These assignments are all consistent with the known character of the corresponding levels in the mirror nucleus Si^{29}, and are also in agreement with the theoretical predictions.

From the precise gamma-ray energy measurements, the Q-value of this reaction was estimated as 2.760 ± 0.013 Mev, which is by about 36 kev larger than the published value based on the β-ray end-point energy measurement. The resonance strength $(2J+1)\Gamma_p\Gamma_\gamma/(\Gamma_p+\Gamma_\gamma)$ was found to be $(4.7\pm0.8)\times10^{-3}$ ev.

§ 1. Introduction

The isobaric nuclides Si^{29}–P^{29} are of interest as they possess a single nucleon outside of a closed $d_{5/2}$ sub-shell, and a rather simple theoretical interpretation of their mode of excitation may be possible. Feenberg has applied a weak coupling collective model to the Si^{29}–P^{29} system, assuming the coupling between s and d orbitals through the mediation of surface waves.[1] On the other hand, Bromley, Gove and Litherland have considered the possibility of applying a strong-coupling collective model based on a Nilsson model to explain the level properties of Si^{29}.[2] This model has succeeded in explaining the level sequences of the Mg^{25}–Al^{25} pair, but the extension to the $A=29$ system may not be fully justified on account of decreasing spheroidicity with increasing A in this mass region. Recently Pandya calculated the energy levels and other properties of Si^{29} in some detail, assuming a weak coupling between a single nucleon and the vibrational motion of the core.[3]

The properties of the lower levels in Si^{29} were extensively studied by various reactions, namely, $Si^{28}(d,p)Si^{29}$,[4] $Si^{29}(p,p',\gamma)Si^{29}$ [5] and $Si^{28}(n,\gamma)Si^{29}$,[6] and also by the β-decays of Al^{29} and P^{29}.[5],[7] The low levels of P^{29}, however, have not been so well investigated, but only a study of the $Si^{28}(d,n)P^{29}$ reaction indicated the existence of levels at 1.30 Mev ($l_p=2$), 1.92 Mev ($l_p=2$), 2.5 Mev, 2.9 Mev and 3.5 Mev excitation.[8] Higher excited states in the 4.1–6.4 Mev region in P^{29} ($E_p=1.4$–3.8 Mev) were recently studied through the elastic and inelastic scatterings of protons on Si^{28}, and the spins and parities were assigned.[9] Van Oostrum *et al.* have also established a resonance for the $Si^{28}(p,\gamma)P^{29}$ reaction at 367 ± 2 kev, and the gamma-ray spectra were reported.[10] In the present investigation, more detailed studies of the de-exitation gamma-rays from this reaction were attempted, and some new informations obtained are presented and discussed.

§ 2. Experimental Apparatus

Magnetically analyzed proton beam from a 600 kev Cockcroft-Walton generator was used to bombard a thick metallic silicon target of natural abundance, which was made by grinding pure (99.999%) silicon crystals and pressing onto a 0.5 mm thick copper backing. A rather broad beam spot about 10 mm high and 6 mm wide was used in order to avoid the local melting of the target, and usually a proton beam of about 80μA was safely used.

---

* Present address: Radiation Center of Osaka Prefecture.

Gamma-ray spectra were measured with a large NaI (Tl) crystal, 5 in. in diameter by 4 in. thick, and a Hutchinson-Scarrott type 100-channel or a Johnstone type 10-channel pulse height analyzer. Details of the electronic equipments and the target assembly, together with the method of analysis of gamma-ray spectra, have been described in earlier publications.[11),12)] Special experimental procedures for the present investigation will be described separately in the following sections.

§ 3. Measurements and Results

i) *Gamma-ray Spectra and Decay Scheme*

The excitation curve taken with a thick natural silicon target (Fig. 1) shows resonances for high energy gamma-rays ($E_\gamma > 2.2$ Mev) at about 330 and 415 kev, while for gamma-rays of energies between 0.9 and 2.2 Mev, a sharp step was observed at about 367 kev. These are in complete agreement with the reports for the resonances of the $Si^{29}(p,\gamma)P^{30}$ reaction at 326.4±1.2 and 415.3±1.3 kev, and of the $Si^{28}(p,\gamma)P^{29}$ reaction at 368.9±0.7 kev.[13)] We have measured the gamma-ray spectra above and below the $Si^{28}(p,\gamma)P^{29}$ resonance, namely, at 390±8 kev and at about 340 kev, and the contributions from the $Si^{29}+p$ and the possible contaminant $F^{19}+p$ reactions were subtracted together with various backgrounds. The gamma-ray spectra at the 326 kev resonance of the $Si^{29}(p,\gamma)P^{30}$ reaction have only a weak (5% of the total decay) single 1.45 Mev line in the energy region between 1 and 3 Mev,[14)] which, associated with the small abundance of

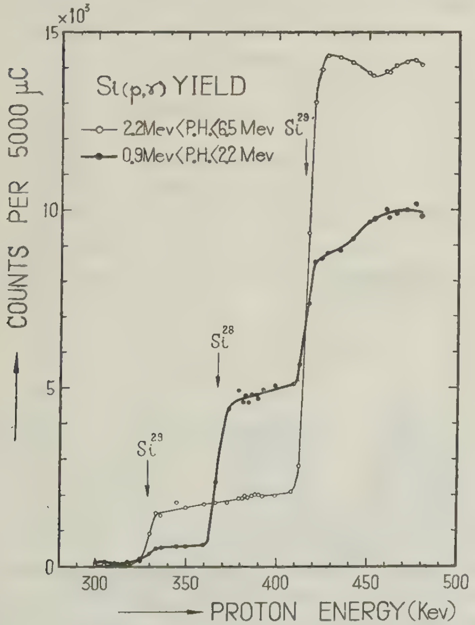

Fig. 1. Gamma-ray yield from proton bombardment of a thick natural silicon target. Slight slopes observed are due to the broad $C^{12}+p$ resonance.

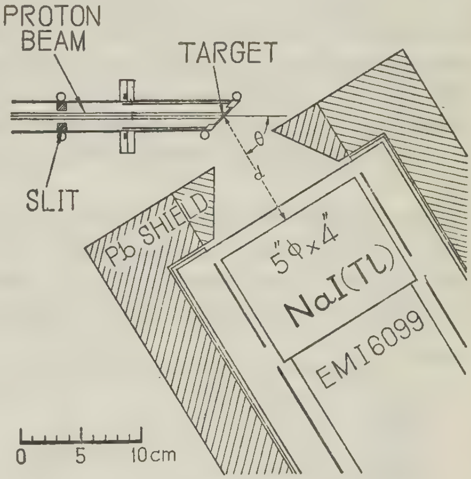

Fig. 2. Target and spectrometer assembly, employed in the measurements at $d=10$ cm. In the case of $d=15$ cm, a cone-shaped lead shield of another type was used.

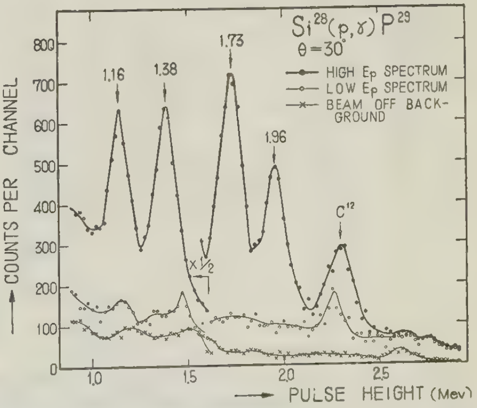

Fig. 3. Gamma-ray spectra taken on the resonance, below the resonance and with no proton beam, at $\theta=30°$ and $d=10$ cm. Background proportion was of nearly the same magnitude in the measurements at $d=15$ cm, on account of increased proton intensity.

Si^{29} (4.68%), made the presence of this lower resonance reaction easily tolerable. At $E_p=390$ kev, 2.30 Mev contaminant gamma-ray from the $C^{12}(p, \gamma)N^{13}$ reaction always appeared. At $E_p=340$ kev, this gamma-ray appeared as 2.25 Mev and much reduced in intensity, so only a part of the low energy side of the peak was subtracted.

Since the radiations from the $Si^{28}(p, \gamma)P^{29}$ reaction were low in energy and weak in intensity, counting rate due to the natural radioactive background was rather appreciable, and a lead shield of cone shape was installed in front of the crystal, as shown in Fig. 2. Examples of the spectra taken on and below the resonance, as well as of the natural background, obtained at θ (direction of the detector to the proton beam) = 30° and at d (distance between the target and the front face of the crystal) = 10 cm, are illustrated in Fig. 3.

The net spectra obtained at $\theta=90°$, 45° and 0°, at $d=15$ cm, with a 100-channel pulse height analyzer, are shown in Fig. 4. Four gamma-rays with energies of 1.96, 1.73, 1.38 and 1.16 Mev were apparently observed, together with the C^{12} contaminant peak. Total spectra were decomposed into these five gamma-rays with the help of the standard line shapes obtained by the interpolation of the line shapes of monochromatic gamma-rays from the $C^{12}(p, \gamma)N^{13}$ reaction (2.37 Mev) and from the radioisotopes Y^{88} (1.85 Mev), Na^{22} (1.28 Mev) and Zn^{65} (1.12 Mev). These standard spectra were taken at $d=10$ and 15 cm respectively, with the standard arrangement, and are shown in Fig. 5 for the case of $d=15$ cm. Each peak in the total spectrum was able to be well fitted to the monochromatic line shape. The relative intensities were calculated using the decomposed spectra and the total detection efficiencies of NaI crystal, tabulated by Wolicki *et al.*, and are listed in Table I. The angular distributions as well as the absorption in the target backing were taken into account.

These relative intensities and the precise determination of gamma-ray energies (see the next section) support the cascade scheme through the 1.38 and 1.96 Mev levels, as had

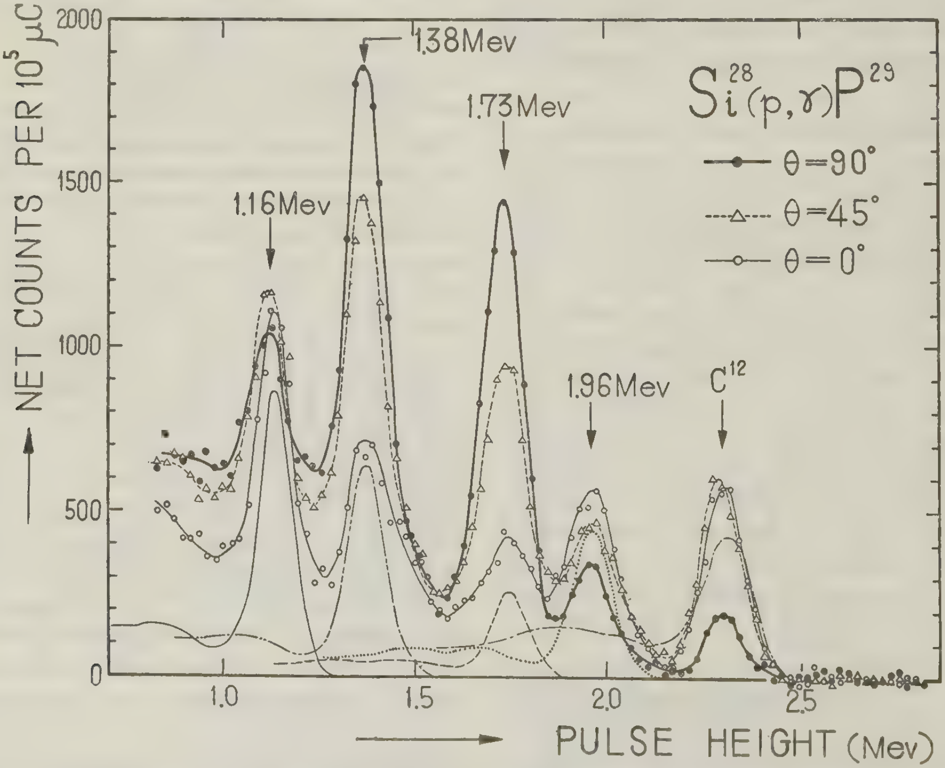

Fig. 4. Scintillation spectra taken at $\theta=90°$, 45° and 0° relative to the proton beam, at $d=15$ cm. Contributions from the lower $Si^{29}+p$ resonance were subtracted. The dotted curves show the individual pulse height spectra into which the zero degree spectrum was decomposed.

been proposed by Van Oostrum *et al.*[10] This was also checked by a coincidence measurement. The branching ratios of these two cascades were calculated to be (74±4)% to (26±4)% from the average of the intensities of cascade lines.

The 3.12 Mev direct ground state transition gamma-ray from the resonance state was estimated to be less than 2.7% of the total decay, after correcting the sum peak contributions due to the coincident detection of cascade lines.

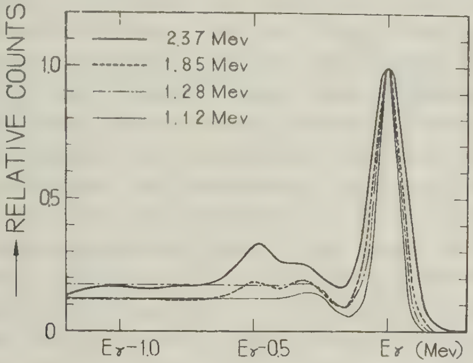

Fig. 5. Line shapes of four monochromatic gamma-rays of energies between 1 and 2.5 Mev, for 5 in. dia.×4 in thick NaI crystal, measured at $d=15$ cm and with no collimation.

Table I. Gamma-rays observed at the 369 kev resonance in the $Si^{28}(p, \gamma)P^{29}$ reaction.

E_γ (Mev)	Transition	Relative intensity per 100 captures	Reaction yield (mev)
1.961±0.015	1.96→0	24.4±10%	
1.731±0.009	3.12→1.38	69.9±10%	0.58±0.10
1.384±0.008	1.38→0	77.6±10%	
1.155±0.006	3.12→1.96	28.1±10%	0.20±0.04
3.12	3.12→0	<2.7	
2.5	2.5 →0	<2.0	
0.58	1.96→1.38	<4	
2.30	C^{12} contamination		
0.511	annih. rad.		

A possible 0.577 Mev gamma-ray as the transition between the 1.96 Mev second and the 1.38 Mev first excited states was not positively observed. An attempt to detect this cascade transition by the coincidence method was unsuccessful because of the very low yield of the gamma-ray and the proximity of the 0.51 Mev annihilation line. Careful examination of the singles spectra indicated the 0.58 Mev cascade line to be at most 15% of the 1.96 Mev direct transition line, if present. This cascade line is expected to be very weak considering the decay mode of the corresponding 2.03 MeV state in Si^{29}, in which case cascade branching ratio of about 1% is reported.[5]

The existence of a level at about 2.5 Mev, known from the $Si^{28}(d, n)P^{29}$ reaction, appears to give rise to a possibility of cascade decays through this level, but from the absence of the 2.5 Mev line in the singles spectra (<2% of the total decay), the cascades through the 2.5 Mev level are believed to be fairly weak if present, considering that the corresponding level in Si^{29} at 2.43 Mev decays directly to the ground state by an appreciable fraction.[7]

The decay scheme obtained is shown in Fig. 6.

ii) *Gamma-ray energies and Q-value*

The gamma-ray energies were precisely

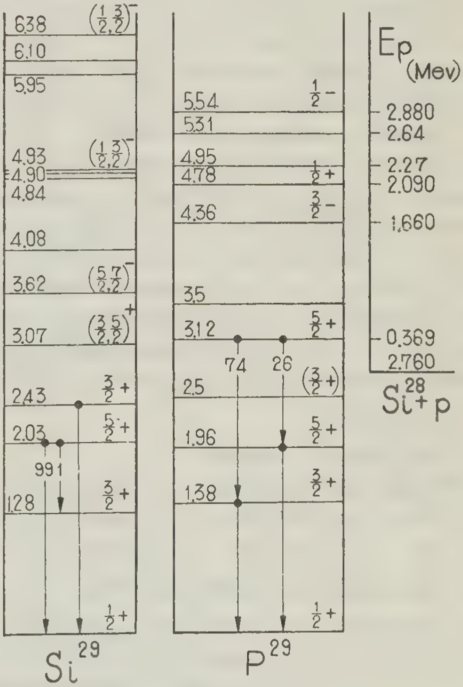

Fig. 6. Level scheme of the mirror pair Si^{29}–P^{29}. The excitation energies of the lower levels in P^{29} were computed from our gamma-ray energies. Higher level energies were calculated from the resonance energies using the measured Q-value of 2.760 Mev. The spin assignements of the lower levels in P^{29} are discussed in the text.

determined using a 10-channel pulse height analyzer. Overall linearity of the measuring system was better than 1% and care was taken to reduce the counting rate so as no shift of the peak to occur. Energy calibration was carried out before and after each run of experiments with the gamma-rays from the following radioisotopes; ThC″ (2.615 Mev), Sb^{124} (2.088, 1.692 Mev), Y^{88} (1.851 Mev), Co^{60} (1.332, 1.172 Mev), Na^{22} (1.277 Mev), Zn^{65} (1.119 Mev). Several measurements were performed at $\theta=0°$ for the 1.96 and 1.16 Mev lines as well as at $\theta=90°$ for the 1.73 and 1.38 Mev lines. The results obtained are cited in Table I. From these gamma-ray energies the excitation energies of the first, second and fourth excited states were determined to be 1.384±0.008, 1.961±0.013 and 3.116±0.012 Mev, respectively. These values are approximately in agreement with the results of the $Si^{28}(d, n)P^{29}$ reaction, yielding levels at 1.30, 1.92 and 2.9 Mev.[8] An alternative order of the cascade gamma-rays would yield levels at 1.16 and 1.73 Mev, which are incompatible with the (d, n) measurements. The Q-value of the $Si^{28}(p, \gamma)P^{29}$ reaction is calculated to be 2.760±0.013 Mev, using the resonance energies of 368.9±0.7 kev, reported by Kuperus, Smulders and Endt.[13]* This Q-value is by about 36 kev larger than the published value, $Q=2.724$ Mev,[15] which was based on the end-point energy measurement of the P^{29} positron decay ($E_{\beta+}(\max)=3.945\pm 0.005$ Mev)[7] and on the Q-value of the $Si^{28}(d, p)Si^{29}$ reaction ($Q=6.246\pm0.010$ Mev).[16] This discrepancy may be due to some instrumental error in the measurement of the positron end-point energy.

iii) *Angular distributions*

The angular distributions of four gamma-ray lines were measured at $\theta=0°$, 15°, 30°, 45°, 60°, 75° and 90° with respect to the proton beam. The earlier experiments were performed at the closer distance of $d=10$ cm between the counter and the target to reduce the natural background counts, but the distance was increased to 15 cm in the later measurements to reduce the attenuation effect of the finite solid angle of the detector on the coefficients of $P_4(\cos\theta)$ term. This was essentially necessary to establish the spin of the 1.96 Mev level. The distance between the counter and the target was held constant within one millimeter at each angular setting. The radiation yield was monitored by an integrated proton current, since the intensity of the contaminant 2.3 Mev gamma-ray varied considerably with time. Several data taken at each angle were checked to be consistent with each other and were decomposed into five component gamma-rays as described in section i). After correcting the absorption in the target and target backing, angular distributions were fitted into the formula $W'(\theta)=1+G_2A_2P_2(\cos\theta)+G_4A_4P_4(\cos\theta)$ by the method of least squares. The attenuation factors due to the finite solid angle of the counter were taken from the curves calculated by Gove and Rutledge.[17] The data obtained at $d=10$ cm and at $d=15$ cm were separately analyzed, and the resultant A_2 and A_4 coefficients are tabulated in Table II, to-

Table II. Angular distribution coefficients and their standard deviations obtained by the least squares fit of the data taken at $d=10$ cm as well as at $d=15$ cm, to an expansion of the form, $W'(\theta)=1+G_2A_2P_2(\cos\theta)+G_4A_4P_4(\cos\theta)$. The adopted values for the attenuation factors G_2 and G_4 are also listed.

E_γ (Mev)	Measurements at $d=10$ cm			
	G_2	A_2	G_4	A_4
1.96	0.839	0.211±0.039	0.536	0.120±0.080
1.73	0.838	−0.809±0.041	0.534	0.026±0.074
1.38	0.837	−0.568±0.017	0.530	−0.017±0.031
1.16	0.836	0.372±0.036	0.527	0.097±0.071

E_γ (Mev)	Measurements at $d=15$ cm			
	G_2	A_2	G_4	A_4
1.96	0.914	0.275±0.027	0.731	0.111±0.039
1.73	0.913	−0.860±0.016	0.730	0.049±0.021
1.38	0.912	−0.557±0.017	0.727	−0.027±0.023
1.16	0.911	0.272±0.041	0.724	−0.015±0.058

---

* *Note added in proof*:—From this Q-value, the mass of P^{29} is calculated to be 28.990980±17 a.m.u., using the mass excess of −13.223±0.009 Mev for Si^{28}. This is in excellent agreement with the recent results of Hinds and Middleton obtained by the magnetic analyses of the $Si^{28}(He^3, d)P^{29}$ reaction products, yielding the mass of P^{29} as 28.990978±16 a.m.u. They also locate the first and second excited states in P^{29} at 1.368±0.010 Mev and 1.960±0.010 Mev, respectively. [S. Hinds and R. Middleton: Proc. Phys. Soc. **75** (1960) 444].

gether with the adopted attenuation factors, G_2 and G_4. The errors quoted in Table II are to be understood as standard errors and are mainly of statistical origin. In Figs. 7 and 10, the angular distributions measured at $d=15$ cm are shown as a function of $\cos^2\theta$, together with the least squares fitted curves.

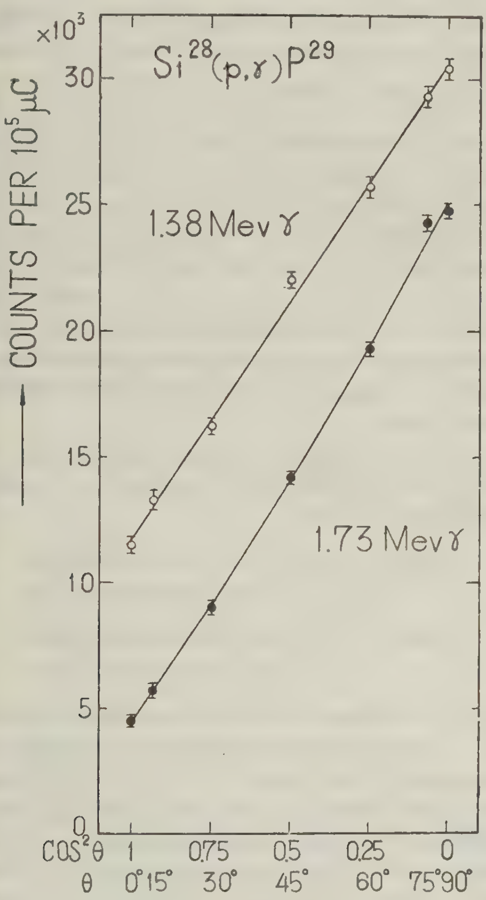

Fig. 7. Angular distributions of the 1.73−1.38 Mev cascade lines measured at $d=15$ cm. The solid lines represent the least squares fitted curves, $A_0(1-0.785\,P_2+0.036\,P_4)$ for the 1.73 Mev line and $A_0(1-0.518P_2)$ for the 1.38 Mev line.

As the angular distributions of the 1.73 Mev–1.38 Mev cascade lines, we have adopted the mean values of the two data, i.e.

$$1.73\text{ Mev}: \quad W(\theta)=1-(0.84_3\pm0.02)P_2(\cos\theta) + (0.04_4\pm0.02)P_4(\cos\theta) \,,$$

$$1.38\text{ Mev}: \quad W(\theta)=1-(0.56_2\pm0.02)P_2(\cos\theta) - (0.02_4\pm0.02)P_4(\cos\theta) \,.$$

From these angular distributions we can deduce spins and parities of the levels concerned. Since the ground state of Si^{28} is $J=0+$, the resonance state formed is expected to be $J_1=1/2+$ for *s*-wave capture, $J_1=1/2-$ or $3/2-$ for *p*-wave capture, and $J_1=3/2+$ or $5/2+$ for *d*-wave capture. Higher wave capture is highly improbable as will be discussed in the next section. Then the resonance state at 3.12 Mev must be either $J_1=3/2\pm$ or $5/2+$, since the obvious anisotropies observed eliminate the case of $J_1=1/2\pm$. On the other hand, the first excited state at 1.38 Mev has been assigned as either $J_2=3/2+$ or $5/2+$ on the basis of the $l_p=2$ stripping pattern from the $Si^{28}(d, n)P^{29}$ reaction. These informations propose four possible cases of $3/2(DQ)3/2$, $3/2(DQ)5/2$, $5/2(DQ)3/2$ and $5/2(DQ)5/2$ as the spin sequence involving the 1.73 Mev transition. Calculated A_2 coefficients for

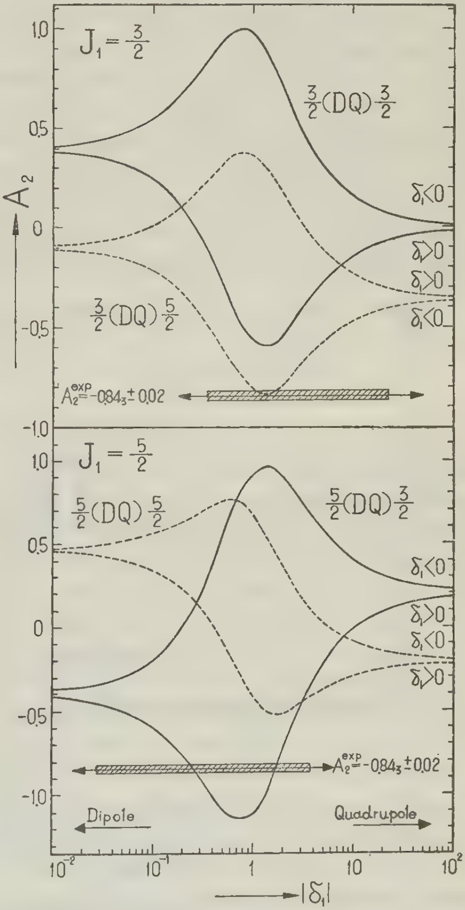

Fig. 8. Theoretical A_2-coefficients, calculated as a function of dipole-quadrupole mixing ratio δ_1, for the first gamma-ray de-exciting a resonance state with spin $J_1=3/2$ (upper figure) or $5/2$ (lower figure) to the state with $J_2=3/2$ (solid curve) or $5/2$ (dotted curve).

these cases are illustrated in Fig. 8, as a function of mixing ratio δ_1. Here Huby phase correction[18] which affects the sign of mixing ratio has been taken into account. As is clearly seen, experimental A_2 coefficient of the 1.73 Mev gamma-ray cannot be fitted with the sequence 3/2(*DQ*)3/2 or 5/2(*DQ*)5/2. A slight possibility exists for the 3/2(*DQ*)5/2 sequence with the mixing ratio $-1.52<\delta_1<-1.02$. In the case of 5/2(*DQ*)3/2, experimental A_2-coefficient can be fitted to the theoretical one with either $\delta_1=0.251\pm0.014$ or $\delta_1=1.69\pm0.05$. These mixing ratios yield the coefficient of $P_4(\cos\theta)$ term as $A_4=0.039\pm 0.004$ or 0.483 ± 0.008 respectively, which, compared with the experimental value of $A_4{}^{\text{exp}}=0.04_4\pm0.02$, eliminates the larger value of δ_1.

In order to distinguish between the two spin sequences 3/2(*DQ*)5/2(*QO*)1/2 and 5/2(*DQ*)·3/2(*DQ*)1/2, which were not uniquely selected by the above considerations, the measured A_2-coefficient of the 1.38 Mev second gamma-ray is also compared with the calculated value in Fig. 9, with the mixing ratio δ_2 as a parameter. Here use was made of the mixing ratio of the first gamma-ray determined above, and the known character of $J=1/2+$ for the ground state of P^{29}. Obviously only in the case of the sequence 5/2(*DQ*)3/2·(*DQ*)1/2 the measured distribution can be fitted to the calculated one with either $\delta_2=-0.167\pm0.021$ or $\delta_2=-1.215\pm0.051$, although unique choice between these two solutions cannot be made from our present informations. Thus the resonance state at 3.12 Mev was found to have $J=5/2+$ due to *d*-wave capture and to decay by a transition of predominatly *M*1 character with (6.3±0.8)% *E*2 admixture to the first excited state at 1.38 Mev, which was together determined to be $J=3/2+$ and to decay to the $J=1/2+$ ground state by a transition involving either (3.0±0.6)% or (146±10)% *E*2 mixture to *M*1 component. Here we have used the angular distribution $W(\theta)=1-(0.570\pm0.015)P_2(\cos\theta)$ for the 1.38 Mev second transition, excluding the $P_4(\cos\theta)$ term on account of the $J=3/2$ nature of the initial level.

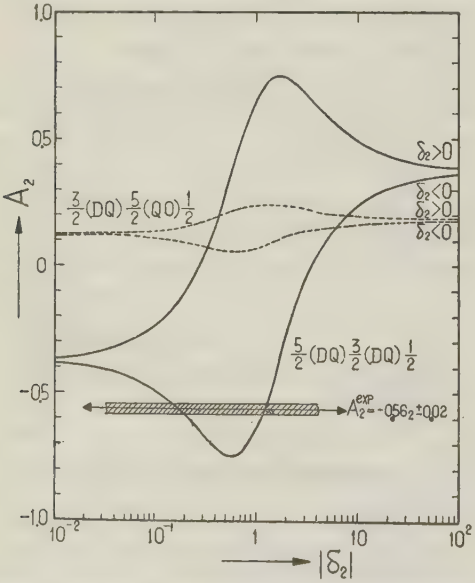

Fig. 9. Theoretical A_2-coefficients, calculated as a function of multiple mixing ratio δ_2, for the second gamma-ray of the spin sequence 5/2(*DQ*)3/2(*DQ*)1/2 (solid curve) or 3/2(*DQ*)·5/2(*QO*)1/2 (dotted curve), involving the cascade from the resonance to the ground state through the first excited state.

Next we consider angular distributions of the 1.16 Mev–1.96 Mev cascade lines which were found to be,

$$1.16\text{ Mev}:\quad W(\theta)=1+(0.31_9\pm0.04)P_2(\cos\theta)+(0.01_9\pm0.05)P_4(\cos\theta)\,,$$

$$1.96\text{ Mev}:\quad W(\theta)=1+(0.26_6\pm0.03)P_2(\cos\theta)+(0.11_2\pm0.04)P_4(\cos\theta)\,,$$

after averaging the two data cited in Table II. The intermediate state at 1.96 Mev is expected to be either $J=3/2+$ or $5/2+$ from the $l_p=2$ pattern in the $\text{Si}^{28}(d,n)\text{P}^{29}$ stripping reaction.[8] Of these two assignments, $J=3/2+$ may at first seem to be preferable since the level decays directly to the ground state. The corresponding level in Si^{29} at 2.03 Mev, however, has been assigned as $J=5/2+$ from the angular distribution measurements of gamma-rays following the inelastic scattering of protons on Si^{29}.[5] Theoretical predictions also support this assignment. On the other hand, our experimental A_2-coefficients indicate that if the $J=5/2+$ assignment is correct, the 1.96 Mev second gamma-ray must be an *E*2-*M*3 mixture, with the mixing ratio $\delta_2=-0.23\pm 0.09$ or -1.58 ± 0.28, although alternative 3/2+ assignment requires only several percents of *E*2 mixture to *M*1 for both the first and second gamma-rays. To clarify these situations definitely, the existence of $P_4(\cos\theta)$ term in the distribution of the 1.96 Mev line was carefully checked with improved geometry. The results showed evidently the existence of $P_4(\cos\theta)$ term, as illustrated in Fig. 10, which eliminates the case of $J=3/2+$ and establishes the $J=5/2+$ assignment for the 1.96 Mev level. Then the 1.16 Mev first transition is calculated to include $\left(1.4_5\,{}^{-0.7}_{+0.9}\right)\%$ $E2$ component to $M1$, while the 1.96 Mev direct ground state transition must involve $\left(5{\cdot}2^{-2.8}_{+5.0}\right)\%$ $M3$ component to $E2$, as noted above. With these assignments, the A_4-coefficients for the 1.16 and 1.96 Mev gamma-rays are calculated to be -0.005 ± 0.003 and 0.144 ± 0.017 respectively, in agreement with the experimental values, $0.01_9\pm0.05$ and 0.11_2 ±0.04.

iv) *Resonance Strength*

From the absolute thick target yield of gamma-radiations, the resonance strength $\omega\gamma=(2J_1+1)\Gamma_p\Gamma_\gamma/(\Gamma_p+\Gamma_\gamma)$ was calculated to be $(4.7_2\pm0.8)\times10^{-3}$ ev, or $\gamma=(0.78_6\pm0.13)\times10^{-3}$ ev, using the calculated efficiencies of NaI crystal and the mean intensities of cascade lines. The proton width Γ_p of this resonance is then 0.79×10^{-3} ev or larger, and the reduced proton width in units of sum rule limit, *i.e.* $\gamma_p^2/(\hbar^2/\mu R^2)$ is calculated to be 2.1×10^{-2} or larger for *d*-wave capture, using a nuclear radius of $1.5A^{1/3}\times10^{-13}$ cm. If we assume *f*-wave capture, the corresponding figure is computed to be 110×10^{-2}, which safely eliminates the assignment of *f*- or higher wave capture to this resonance. The value 2.1×10^{-2} for *d*-wave capture is consistent with the general trend of the dimensionless reduced proton widths in nuclei with $22<A<35$,19) but was found to be by about a factor of ten larger than the value calculated for the 3.07 Mev mirror level in Si^{29}, using the (d,p) stripping reaction cross sections.20)

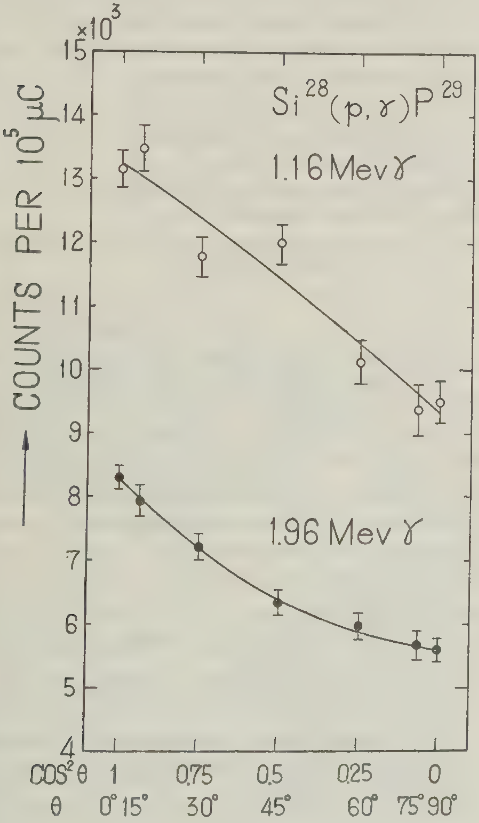

Fig. 10. Angular distributions of the 1.16-1.96 Mev cascade lines measured at $d=15$ cm. The solid lines represent the least squares fitted curves, $A_0(1+0.248P_2-0.011P_4)$ for the 1.16 Mev line and $A_0(1+0.252P_2+0.081P_4)$ for the 1.96 Mev line.

On the other hand, the radiative width of the 3.12 Mev state expressed in units of single particle width is calculated as $|M|^2\geqslant6.2\times10^{-3}$, the lower limit being by a factor of four smaller than the mean value, $|M|^2_{\text{ave.}}\approx25\times10^{-3}$, found for $M1$ transitions in nuclei in the region $22<A<35$. But it is not sure which of Γ_p or Γ_γ limits the resonance strength in the present case.

§ 4. Discussion

The results obtained in the present investigation well establish the mirror properties of the low levels in Si^{29} and P^{29}. $J=3/2+$ assignment to the 1.38 Mev level in P^{29} is in accord with that to the 1.28 Mev level in Si^{29}, which is considered to be mainly of a $d_{3/2}$ single-particle nature. $J=5/2+$ character of the 1.96 Mev level in P^{29} also agrees with that of the 2.03 Mev level in Si^{29}, as discussed already in the previous section, and the strong $E2$ decay of this level to the ground state was observed in both nuclides. The 3.07 Mev level in Si^{29} has been assigned to be either $J=3/2+$ or $5/2+$ from the $l_p=2$ pattern of the $Si^{28}(d,p)Si^{29}$ stripping reaction products, which is consistent with our $J=5/2+$ assignment to the corresponding 3.12 Mev level in P^{29}.

The strong *p*-wave resonances in P^{29} established at $E_p=1.66$ and 2.88 Mev9) ($E_x=4.36$ and 5.54 Mev) seem to have a single-particle nature and to correspond to the 4.93 and 6.38

Mev levels in Si^{29} which have been assigned to be single-particle $p_{3/2}$ and $p_{1/2}$ states. Then, it should be noted that an f-wave resonance, corresponding to the 3.62 Mev level in Si^{29}, which is known to be either $J=5/2-$ or $7/2-$ from the $Si^{28}(d, p)Si^{29}$ reaction and is presumably a single-particle $f_{7/2}$ state, still remains to be found at $E_p=700\sim900$ kev region.[21] The 3.5 Mev level found by the (d, n) measurements might be of this character.

Bromely *et al.* have applied a strong coupling collective model to the description of the low levels of Si^{29}, and assigned 0, 2.43 and 2.03 Mev levels as a $K=1/2$ rotational band based on the 1/2+ ground state ($2s_{1/2}$ Nilsson orbit) and the levels at 1.28 and 3.07 Mev as a $K=3/2$ band based on the 3/2+ 1.28 Mev level ($1d_{3/2}$, $K=3/2$ orbit), assuming a negative spheroidicity with $\delta=-0.15$.[2] Recently Pandya has calculated the energy levels of Si^{29} assuming a weakly coupled system of the collective vibrational motion of the spherical core with the $2s_{1/2}$ and $1d_{3/2}$ single-particle orbitals.[3] Both models predict $J=5/2+$ for the 3.07 Mev level, as was experimentally confirmed for the corresponding 3.12 Mev level of P^{29} in the present investigation. Other spin values found in P^{29} are also consistent with these pictures, and application of the collective description to this mirror pair seems to be appropriate, although detailed structure of the model must further be checked and improved. In particular, it seems still doubtful in the present stage whether the Si^{29} and P^{29} are really deformed or not.

Strong $E2$ enhancement compared to $M1$ observed in the decay of the 1.96 Mev level seems to indicate collective effects, and the weakness of the 3.12 Mev $E2$ direct ground state transition from the resonance state may be due to the different K-values of the states concerned. The relatively strong $M1$ component to $E2$ ($\Gamma_{M1}/\Gamma_{E2}=35.5$ or 0.68) observed in the decay of the 1.38 Mev $d_{3/2}$ level indicates the existence of mixing of s-d orbitals in these levels, as was suggested to explain the magnetic moment of Si^{29} and the ft-value of P^{29} positron decay. The transition rate observed in this experiment would further serve to check the model if explicit numerical calculations are performed.

We would like to thank Prof. K. Kimura and Dr. S. Yasumi for their supports, encouragements and advices throughout the course of this work. We also wish to thank Dr. H. Ikegami of the Institute for Nuclear Study, University of Tokyo, and Dr. M. Kawamura and Dr. A. Aoki of Kyoto Prefectural University for their kind supports. This work was financially aided by the Ministry of Education.

Note added in proof:—We were informed recently that Van Oostrum and Olness *et al.* have also investigated the gamma-rays from the $Si^{28}(p, \gamma)P^{29}$ reaction in some detail. Their results are consistent with those presented here. [K. J. Van Oostrum: Thesis (Delft) (1959) unpublished. J. W. Olness and J. L. Parker: Bull. Amer. Phys. Soc. **5** (1960) 56.]

References

1) E. Feenberg: *Shell Theory of the Nucleus* (Princeton Univ. Press. 1955) Chap. IX.
2) D. A. Bromley, H. E. Gove and A. E. Litherland: Canad. J. Phys. **35** (1957) 1057.
3) S. P. Pandya: Prog. Theor. Phys. **21** (1959) 431.
4) J. R. Holt and T. N. Marsham: Proc. Phys. Soc. London A, **66** (1953) 467.
5) D. A. Bromley, H. E. Gove, E. B. Paul, A. E. Litherland and E. Almqvist: Canad. J. Phys. **35** (1957) 1042.
6) B. B. Kinsey and G. A. Bartholomew: Canad. J. Phys. **31** (1953) 537.
7) H. Roderick, O. Lönsjö and W. E. Meyerhof: Phys. Rev. **97** (1955) 97.
8) J. M. Calvert, A. A. Yaffe and E. E. Maslin: Proc. Phys. Soc. London A, **70** (1957) 78.
9) J. Vorona, J. W. Olness, W. Haeberli and H. W. Lewis: Phys. Rev. **116** (1959) 1563.
10) K. J. Van Oostrum, J. Alster, N. Hazewindus and A. H. Wapstra: Physica **24** (1958) 1051.
11) J. Muto: J. Phys. Soc. Japan **15** (1960) 17.
12) K. Okano: J. Phys. Soc. Japan **15** (1960) 28.
13) J. Kuperus, P. J. M. Smulders and P. M. Endt: Physica **25** (1959) 600.
14) C. Van der Leun and P. M. Endt: Phys. Rev. **110** (1958) 96.
15) P. M. Endt and C. M. Braams: Rev. Mod. Phys. **29** (1957) 683.
16) D. M. Van Patter and W. W. Buechner: Phys. Rev. **87** (1952) 51.
17) H. E. Gove and A. R. Rutledge: Atomic Energy of Canada, Limited, Report CRP-755 (Chalk River 1958).
18) R. Huby: Proc. Phys. Soc. London A, **67** (1954) 1103.
19) C. Van der Leun: Thesis, Utrecht (1958).
20) Y. Fujimoto, K. Kikuchi and S. Yoshida: Prog. Theor. Phys. **11** (1954) 264.
21) H. Ohmura: Genshikaku Kenkyu **4**, No. 1, (1959) 77 (in Japanese).

Journal of the Physical Society of Japan, Vol. 15, No. 9, September, 1960

On the Electronic Component of Extensive Air Showers near the Axis

By Tadashi Kameda, Yoshio Toyoda and Toshio Maeda
Department of Physics, Kobe University, Japan

(Received February 9, 1960)

Using two multiplate cloud chambers and five density detectors consisting of 250 G.M.-counter hodoscopes, characters of the electronic component of extensive air showers were investigated for various distances from the axis in the range $r \leq 10$ m at 2770 m altitude. The size N of the selected showers extended from 1×10^5 to 2×10^6.

The following results were obtained :

(1) The integral size spectrum can be represented by a power law of the form $N^{-\gamma}$, where the value of γ varies from 1.5 to 2.0 as the size increases.

(2) The lateral density distribution of the high-energy electronic component with the energy $E \geqslant 1$ Bev fits well to that of the pure electronic shower with the age parameter $s=1.4$.

(3) The ratio of the density of high-energy electrons and photons to that of all electrons is independent of the atmospheric depth.

(4) The integral energy spectrum can be expressed by the E^{-n} within the energy region 250 Mev $\leqslant E \leqslant 1$ Bev, and the value of n shifts from 0.7 to 1.2 with increasing r.

(5) The lateral distribution of the energy flux carried by the electronic component is expressed by the form $r^{-(1.57\pm0.24)}$.

(6) The showers having steeper lateral distribution of electrons than the average one near the axis contain more high-energy rays.

(7) The averge zenith angle distribution is represented by the form $\cos^{6.7\pm1.4}\theta$, however that of showers containing more high-energy rays by the form $\cos^{10.0\pm2.0}\theta$.

§ 1. Introduction

The experiments on the extensive air showers (EAS) at the mountain altitude have been carried out by many authors from various points of view. Owing to them, we have fairly precise knowledge on the lateral distribution of the electrons and the density distribution of EAS. Moreover, the mean characters of EAS were revealed by these authors for electronic component, penetrating component, and nuclear active component. The studies on the high-energy electrons and photons near the axis of EAS are reported by a few authors[1),2),3)]. However, character of the individual shower from a viewpoint of high-energy electronic component is scarcely studied hitherto.

The comprehensive knowledge on the high-energy electronic component in EAS is of necessity not only to research into the development of the EAS, but also to study the mechanism of the nuclear interaction of ultra high-energy nucleons.

Our experiments were intended to make researches on the high-energy electronic component near the axis in great detail as could be possible, study the character of the individual shower through it, and increase the reference materials on the structure of EAS at the mountain altitude. For this purpose, we especially gave attentions to the followings:

i) The location of shower axis was determined by the method of the maximum electron density, because the determination of axis by the core selector (for example, the type used by Cocconi etc.) was found to be inadequate on account of giving a considerable bias to some EAS.

ii) Two cloud chambers were used to obtain informations as much as possible on the individual shower. Moreover, they were separately located and set up at right angle with each other, giving the accurate zenith angle of EAS.

§ 2. Apparatus

The arrangement of the apparatus is shown in Fig. 1. D_1, D_2, D_3, D_4, and D_5 in the figure are the electron density detectors, each of which contains 20 large counters of 122 cm² sensitive area each, and 30 small counters of 38 cm². The long axes of every counters were directed to south-north direction. All counters are connected to the 250 channel neon-hodoscope separately. The error of the electron density determined by these detectors are within 30% in the range from 50/m² to 600/m², and it increases outside the above range. The density more than 1000/m² is not determined. A and B in the Fig. 1. are the similar rectangular cloud chambers. Each of them has effective area of 0.08 m², and contains 9 lead plates of 1 cm thickness which serve to estimate the energy of electrons and photons. The top of the chamber is made of 2.7 g/cm² thickness of Dulalmin (0.11 r. 1.), and the dead space under the Dulalmin plate is filled up with 2.5 g/cm² thickness of paraffin (0.05 r. 1). Both chambers were placed apart by 3.5 m at their centres, and at right angle each other, as seen in the figure. The cloud chambers and neon-hodoscope are triggered by the master pulses, which are the coincidence pulses of discharges of one or more counters of the specified three large counters in each of the density detectors D_2, D_3, D_4, and D_5, and simultaneous discharge of the specified two large counters in D_1, *i.e.* 6-fold coincidence (Master Pulse I). Most of the measurements were performed by triggering the apparatus by this master pulse, but in some of the measurements, the above mentioned three counters in D_2, D_3, D_4, and D_5 were increased to five, and simultaneously the number of the specified large counters in double coincidence in D_1 was increased to four, (Master Pulse II). The more stringent bias for large density of D_1 is based on the intention that we are concerned in selecting EAS whose axis fall within the square area subtended by D_2, D_3, D_4, and D_5, and in its vicinity. D_1 and both cloud chambers were placed in wooden hut whose roof has 1.5 g/cm² wood and 0.2 g/cm² copper, and D_2, D_3, D_4, and D_5 were placed in wooden boxes which were covered by 0.4 g/cm² wood.

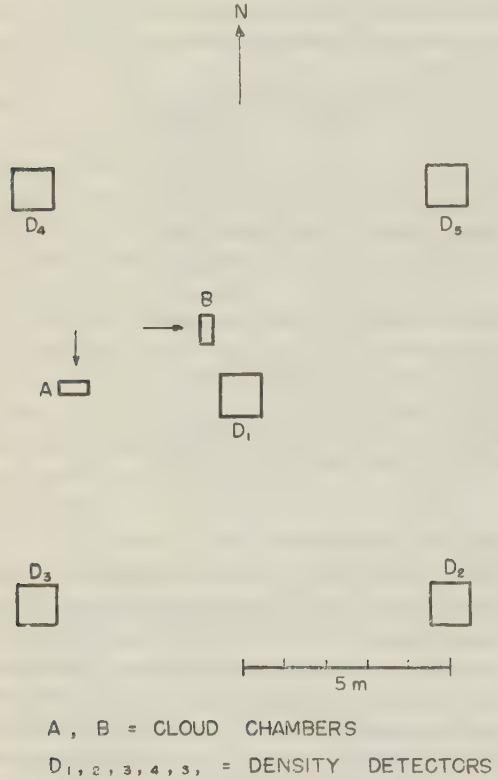

Fig. 1. Arrangement of apparatus.

The experiment was carried out at Mt. Norikura, 2770 m elevation, 741 g/cm² average atmospheric pressure in the measuring period, in 1957.

§ 3. Size Spectrum

The location of the axis and the size of EAS were determined simultaneously by the electron densities at D_1, D_2, D_3, D_4, and D_5*, using the AS computer of the I.N.S. type and assuming the vertical incidence of the electrons**. The following procedures were taken for analysing density data:

i) The densities at every place are tried to fit to the lateral distribution curve of the density, derived from the N-K function[4] of $s=1.25$,[5] taking account of the errors of densities obtained by the density detectors.

ii) If the densities at every place do not fit to the above mentioned curve, the most smoothly fit distribution curve is assumed, and the total number of such EAS is determined by the density at the farthest place, assuming that the density at a great distance should obey the lateral distribution of $s=1.25$.

---

* The number of particles in the top sections of A and B cloud chambers is also referred to the determination of the axis location.

** For the EAS of zenith angle of 45°, the difference of the location of the axis determined by this assumption is 0.8 m in the extreme case, and usually is within 0.5 m.

The error of determination of the location of shower axis is within 1 m in the interior of the square of D_2, D_3, D_4, and D_5, in most of the showers, and outside the area the accuracy decreases gradually in different way, depending on the size of EAS and on the position of axis. The probability of generating the master pulses was calculated numerically for 196 positions (centres of 1 m² area) and for several size, assuming the vertical incidence of EAS and the lateral distribution of $s=1.25$. It is a very tedious work to obtain the accurate triggering probability when the effect of zenith angle distribution of EAS is considered, because the probability depends on the azimuth as much as the zenith angle owing to the parallel arrangement of counters. According to the calculated results on the EAS which is detected by MP (I) and whose axis falls within a square area subtended by D_2, D_3, D_4, and D_5 and at 37° of zenith angle, the triggering probability increases by 6% and 7% for EAS which are incident from east-west direction with $N=5\times10^5$ and 2.5×10^5, respectively, compared with the vertical incident EAS of the same sizes, and decreases by the same amount for EAS from the north-south direction. Taking into account the above mentioned results, and the zenith angle distribution of the form $\cos^7\theta$, our assumption of vertical incidence seems to give a negligible errors in the determination of the triggering probability.

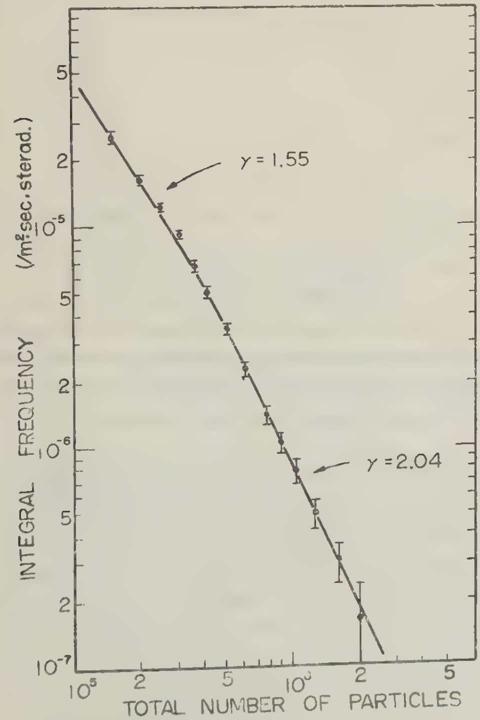

Fig. 2. Integral size spectrum of EAS

The size spectra of EAS were separately obtained in the following four cases; a) EAS detected by MP (I) or MP (II), the axes of which fell inside a 10 m square with D_1 at the centre, and b) EAS detected by the same master pulses in a those in a), the axes of which fell within the area of a 14 m square substracted by a 10 m square, each with D_1 at the centre. As no significant differences are found between them, each results is summarized, and the size spectrum thus obtained is shown in Fig. 2. The ordinate in the figure is the absolute frequencies calculated assuming the zenith angle distribution of $\cos^7\theta$ (§ 5).

Representing the size spectrum by the power law of

$$F(\geqslant N)=a\left(\frac{N}{10^5}\right)^{-\gamma}$$

where N is the total number of the charged particles, a and γ take the following values, respectively,

$$\left.\begin{array}{l}a=4.9\times10^{-5}/\text{m}^2.\ \text{sec. sterad.}\\ \gamma=1.55\pm0.10\end{array}\right\}\ \text{for}\ N\leqslant4\times10^5$$

$$\left.\begin{array}{l}a=8.2\times10^{-5}/\text{m}^2.\ \text{sec. sterad.}\\ \gamma=2.04\pm0.20,\end{array}\right\}\ \text{for}\ N\geqslant4\times10^5$$

where the errors are standard deviations. (Hereafter the errors are shown by standard deviations).

Here it should be noted that the above mentioned size spectrum was obtained assuming that the lateral distribution of all EAS obeyed that of $s=1.25$. In actual the individual shower is divergent in the age, and it is not appropriate to represent the lateral distribution of all showers with an unique one, as seen in the distribution near the axis (§ 4e). However, as it is estimated that the proportion of showers having young age and old one to all showers is about 30%, and the ratio of the showers of young age to those of old age is nearly one, the drastic change may not occur in the size spectrum obtained by us, and so the above mentioned variation of values of γ may occur in actual in the range observed.[2] The similar variation of γ was observed on EAS near the sea level in the same range of size.[6],[7] This fact seems to be connected with the variation of character of nuclear interaction in super high energy region, as pointed out by Russian authors,[8] or with the shortening of the absorption mean free path for nucleons of higher energy.

§ 4. Electronic Component near Shower Axis

Characters of high-energy electronic component were investigated for various distances from the shower axis in the range of $r \leqslant 10$ m. The energy E of electrons and photons was determined from the total number of the track segments of the cascade showers initiated in the lead plates in the cloud chambers. We estimated the shower energy to be 50 Mev per segment for lead plates of 1 cm thickness according to the experimental results of Bender[9] and Hazen[10] and took account of the effective thickness for oblique incidence. This value might be over-estimated if compared with that of Danilova *et. al.*[3] based on the calculation of Ivanenko. We selected the showers whose axes fell within a 12 m square around D_1, in order to keep errors of the distances from the axis to the chambers within about 1 m. The sizes of the selected showers extend from 1 to 15×10^5 and the mean size was $\bar{N} = 4 \times 10^5$.

(a) *Lateral Density Distribution of High-energy Electronic Component*

The lateral density distributions of the high-energy electronic components with $E \geqslant 1$ Bev, $E \geqslant 2$ Bev and $E \geqslant 5$ Bev were investigated by inspecting 1100 photographs of the cloud chambers, making use of the determined sizes and distances from the axis. The high-energy cascade showers originating in the first or the second lead plate were accepted to find the density of high-energy particles. This limitation was taken in order to decrease the chance of confusing the cascade showers from the nucleonic showers originating in the lead plates, and avoid to overestimate the density of high-energy particles in oblique showers. Accordingly, this has such a tendency that the density of high-energy rays is apt to be underestimated in oblique showers, but the effect is small.[1]

To decide the distribution, at first, the data were divided into three groups according to the shower size, $1 \times 10^5 \leqslant N \leqslant 2.7 \times 10^5$ ($\bar{N} = 1.8 \times 10^5$), $2.8 \times 10^5 \leqslant N \leqslant 4.4 \times 10^5$ ($\bar{N} = 3.5 \times 10^5$) and $4.5 \times 10^5 \leqslant N \leqslant 1.5 \times 10^6$ ($\bar{N} = 7.5 \times 10^5$). The distributions of the high-energy electronic component with $E \geqslant 1$ Bev are given in Fig. 3 for each size, where the densities are normalized for EAS with $\bar{N} = 4 \times 10^5$ (those that follow are the same). We did not find for these distributions to have any difference within the limits of experimental errors, and moreover the densities of high-energy rays were approximately in proportion to each size for the same r.

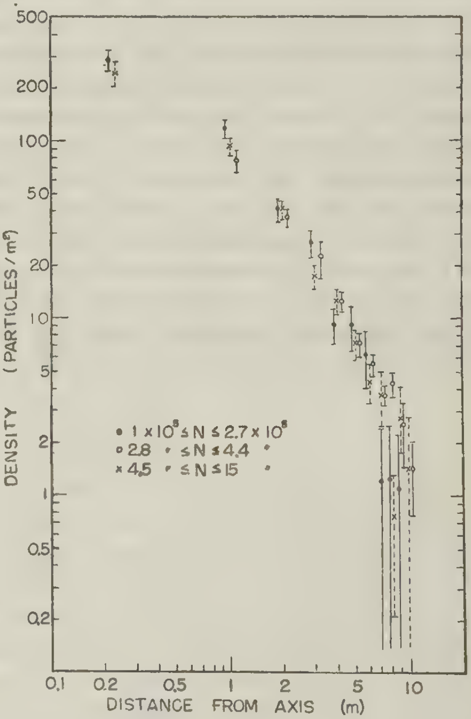

Fig. 3. Lateral density distribution of the electronic-component with the energy $E \geqslant 1$ Bev in EAS for three shower sizes. The density is normalized to showers with $\bar{N} = 4 \times 10^5$.

Accordingly, we treated all showers of different size altogether for the purpose of decreasing the statistical errors. The results obtained are presented in Fig. 4. For comparison of the experimental results with the theoretical distributions of the pure electronic shower, the integral lateral distributions of electrons with the age parameter $s = 1.0$ and $s = 1.4$ for each energy are shown in the figure, They were calculated from the structure function based on Approximation A, assuming that primary energy is infinite in the result of Kamata and Nishimura.[4] In the figure, the experimental distributions are very close to the curves of $s=1.4$ in the range $1\,\mathrm{m} \leqslant r \leqslant 10\,\mathrm{m}$. This means that those of $s=1.4$ are the closest in available ones ($s=0.6$, 1.0, 1.4, and 2.0). The experimental values include, however, both electrons and photons, but theoretical distributions only electrons.

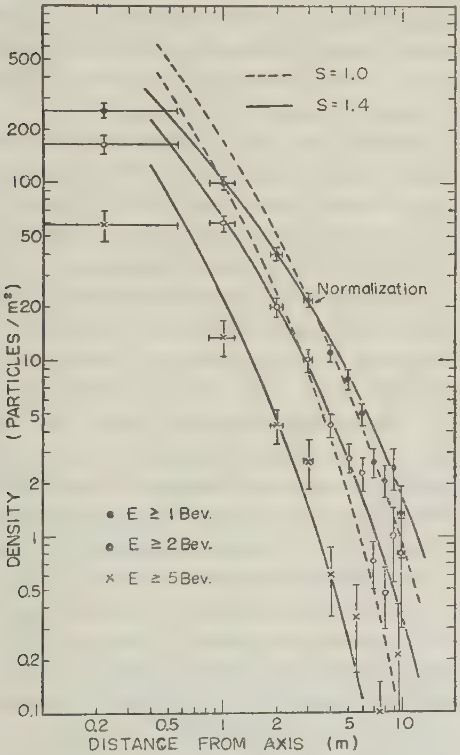

Fig. 4. Lateral density distribution of high-energy electronic-component in EAS with $\bar{N}=4\times10^5$ for three energy region. Theoretical curves are normalized for $E\geqslant1$ Bev at 3 m.

Therefore, if the lateral spread of photons is not very different from that of electrons, this fact shows that the lateral spread of the high-energy electronic component with the energy of $E\geqslant1$ Bev can be explained only by Coulomb scattering in the range $r>1\,\mathrm{m}$ just as that of the low-energy electronic component. Namely, it seems that the main source of the energy supply of EAS is confined in the narrow region $r\leqslant1\,\mathrm{m}$.

(b) *Ratio of the Density of High-energy Electrons and Photons to that of Electrons of all Energies*

These ratios can be calculated by the results of (a) and the assumed lateral density distribution of all electrons, but we tried to get the ratios experimentally using about one-third of the data in (a). In estimating the density of all electrons from the number of electrons in the top section of the chamber, the transition effect in the top wall of the chamber and the roof of the hut must be taken into account. With the aim of doing this the lateral density distribution of electrons in the top section was investigated. The result shows that the distribution is the form $r^{-(1\cdot00\pm0\cdot05)}$ in the range $1\,\mathrm{m}\leqslant r\leqslant10\,\mathrm{m}$ and $r^{-(0\cdot55\pm0\cdot35)}$ in $r\leqslant1\,\mathrm{m}$. The form r^{-1} distribution is close to that of $s=1.25$ in $1\,\mathrm{m}\leqslant r\leqslant10\,\mathrm{m}$. As the energy spectrum does not suffer a radical change in the investigated range of r as shown by (c), the dependence of the transition effect on r in our apparatus does not vary

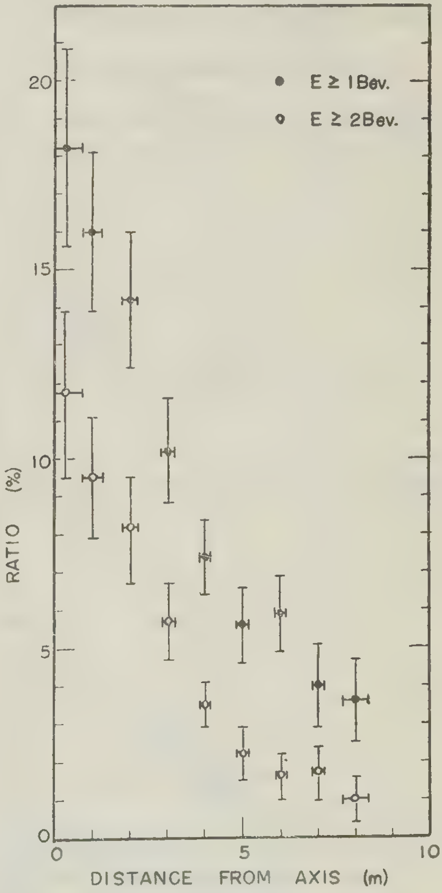

Fig. 5. Ratio of the density of the electronic-component with $E\geqslant1$ Bev and $E\geqslant2$ Bev to that of all electrons versus distance from the axis.

so much. But the absolute values of the density in the top sections is 26% more than that of $s=1.25$ at the distance $r=1$ m and 18% at $r=8$ m. Consequently the number of electrons in the sections was corrected by the above quantities. (These quantities of correction may be possessed of the error of about −10% because the boundaries of the illuminated regions were not necessarily very clear). The ratios found for high-energy rays with $E \geqslant 1$ Bev and $E \geqslant 2$ Bev are given in Fig. 5. These absolute values are higher than that of Danilova *et. al.*[3] because of the difference of the energy estimate.

Further, in an attempt to see the variation of the fraction of the high-energy component, $\Delta(e+\gamma, E \geqslant 1 \text{ Bev})/\Delta(e, E \geqslant 0)$, with the atmospheric depth, we picked up the data which satisfied the following criterion among the preceding data, and investigated the variation with the projected zenith angle: the distance from the shower axis to the chamber is 3 m, 5 m and 7 m or less for showers of the size $1\times10^5 \leqslant N \leqslant 3.4\times10^5$, $3.5\times10^5 \leqslant N \leqslant 6.4\times10^5$ and $6.5\times10^5 \leqslant N \leqslant 1.5\times10^6$ respectively. Only 9% of the data picked up by this criterion was ruled out on account of the indetermination of their projected zenith angles. Therefore, the investigated variation is hardly biased, but the values of the ratio become a little higher because the data ruled out did not contain a high-energy ray (see § 5). The mean space angles corresponding to the respective intervals of the projected angle were calculated using the zenith angle distribution seen in § 5, and those were further reduced to the mean atmospheric depth.

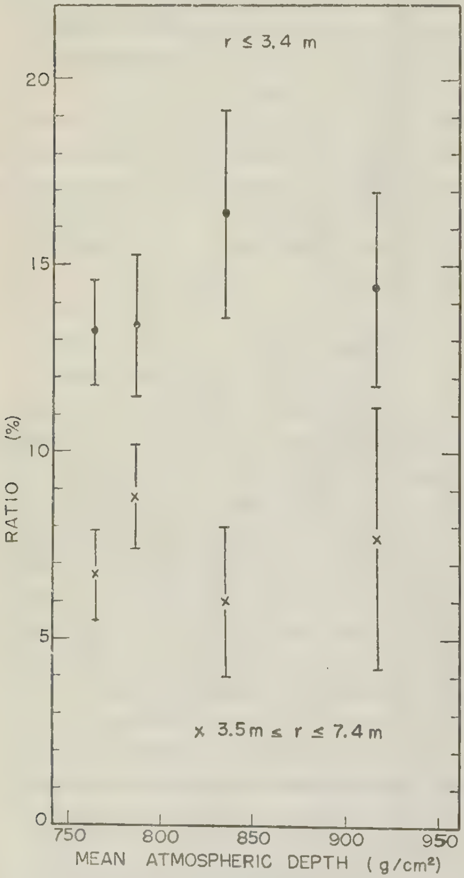

Fig. 6. Variation of $\Delta(E \geqslant 1 \text{ Bev}, e+\gamma)/\Delta(E \geqslant 0, e)$ with mean atmospheric depth.

The results in the range $r \leqslant 3.4$ m and $3.5 \text{ m} \leqslant r \leqslant 7.5$ m are shown in Fig. 6, where the ratios hardly vary with the atmospheric depth. Hereupon, this comparison of the ratio is not done for EAS with the same primary energy, but for EAS with the same size under the different atmospheric depth. However, as stated at the beginning of (a), the density of high-energy rays was in proportion to the size for the same distance from the axis, namely, this ratio is independent on the size within the investigated region. Accordingly, this ratio does not vary with the atmospheric depth for EAS with the same primary energy, too. This result agrees with that of Danilova *et. al.*[3] which was obtained by comparing the measurement at sea level with that at 3860 m.

It seems that this fact shows a state of equilibrium between the electronic component and the high-energy nucleonic component.

(c) *Energy Spectrum*

The integral energy spectra of the electronic component with $E \geqslant 250$ Mev were investigated in the three intervals, $r \leqslant 3.4$ m, $3.5 \text{ m} \leqslant r \leqslant 6.4$ m and $6.5 \text{m} \leqslant r \leqslant 10$m. In this analysis, we adopted only the showers, the project zenith angle of which is less than eight degrees in the vertical plane perpendicular to the front glass of the chamber. This treatment was done to eliminate cascade showers whose particles come out of the illuminated region on the half way in the chamber, and thus to avoid the accuracy of estimated energy of showers to be reduced. As little difference was recognized between those of two groups divided according to the size, we investigated all showers of different size altogether. The results are given in Fig. 7, and in the range $250 \text{ Mev} \leqslant E \leqslant 1$ Bev each spectrum can be represented by a power law of the form E^{-n} and the values of n are given below,

$n=0.75\pm0.08$ for $r\leqslant 3.4$ m
1.03 ± 0.09 for $3.5\text{ m}\leqslant r\leqslant 6.4$ m
1.22 ± 0.13 for $6.5\text{ m}\leqslant r\leqslant 10$ m.

In the energy range $E\geqslant 1$ BeV, the values of n become larger.

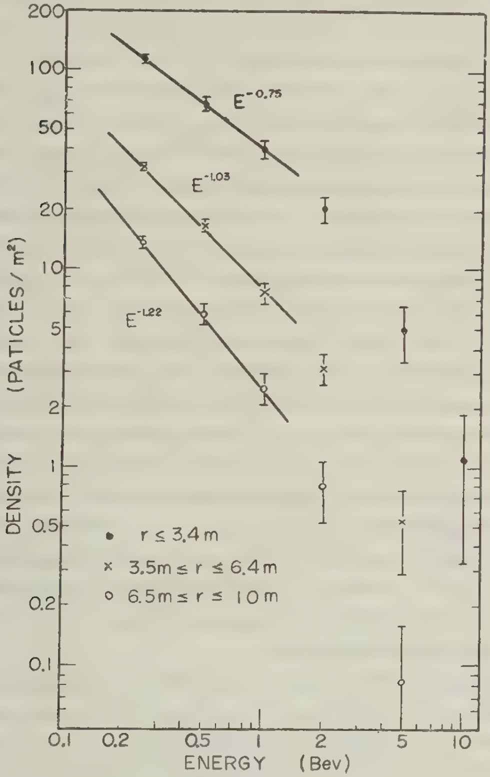

Fig. 7. Integral energy spectrum of electronic-component in EAS with $\bar{N}=4\times10^5$ for three distance intervals.

(d) *Lateral Distribution of the Energy Flux*

Using the results given in (c), it is possible to construct the lateral distribution of the energy flux carried by the electronic component. In doing so, the curves of the energy spectrum were extrapolated to the very high-energy region, and the flux in the low energy region were estimated, using the number of electrons of all energies and the number of photons obtained from the spectrum of Richard and Nordheim.[11] The errors based on these assumptions were estimated in a reasonable way. The result found for the showers with $\bar{N}=4\times10^5$ is shown in Fig. 8. Generally, the form of the distribution for the size N in the

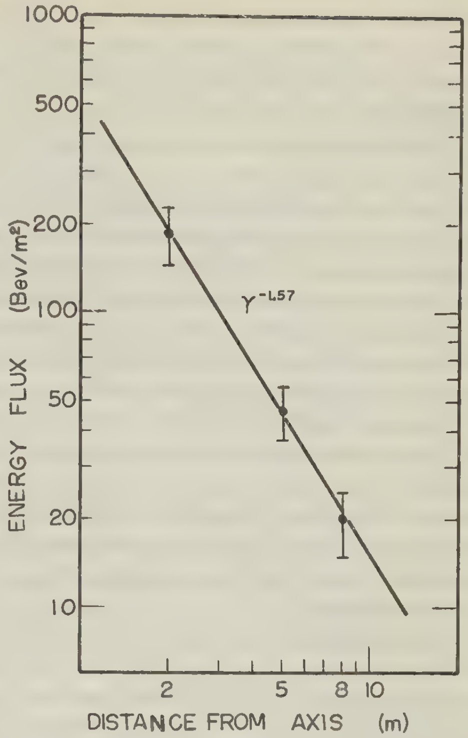

Fig. 8. Lateral distribution of the energy flux of electronic-component in EAS with $\bar{N}=4\times10^5$.

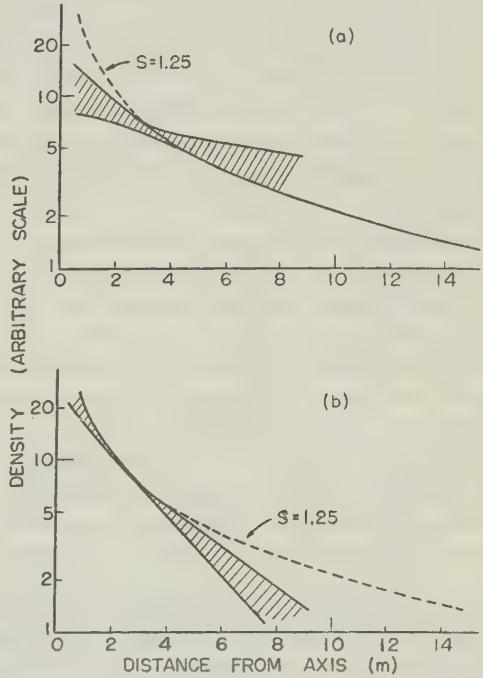

Fig. 9. Lateral distribution of charged particles near the shower axis. Density lies in the hatched region. 9(a) F-distribution; 9(b) S-distribution.

investigated region can be written as follows

$$E_p=(1.38\pm0.48)\cdot N\cdot r^{-(1.57\pm0.24)}\text{Mev}\cdot\text{m}^{-2}.$$

The value of this power index agrees with the result of Danilova *et al.*[3]

(e) *Lateral Density Distribution of All Electrons near the Axis*

In most of the showers, the lateral distribution of charged particles is well fit to the one expected from the N-K function of $s=1.25$. However, there are some showers whose distribution of particles does not fit clearly to the expected one, and their distributions are divided into two groups as follows:

a) The distribution in which the density near the axis (1~3 m from the axis) is remarkably less than the expected one, as shown in Fig. 9(a). This type of distribution is designated as *F*-distribution, and that which is expected from the N-K function of $s=1.25$ as *N*-distribution.

(b) The distribution in which the density at $r>3$ m is less than the expected one, and is well represented by exp $(-\alpha r)$, where $\alpha=0.25\sim0.4$/m, as shown in Fig. 9(b). This type of distribution is named as *S*-distribution.

The proportion of showers with each distribution is studied for EAS whose axis fall within 3 m from the density detectors, and the results obtained are listed in Table I. This proportion is nearly independent on the shower size of less than 8×10^5, and for $N\geqslant8\times10^5$ the fraction of *F*-distribution decrease, and that of *S*-distribution increases gradually, and seems to tend to $S/N\sim1/3$ at $N=2\times10^6$.

Table I.

N	F	S
74±8%	16±3%	10±2%

Table II.

	N	F	S
AcS	65±19%	3±3%	32±12%
NAcs	61±18%	39±14%	0

As mentioned in § 5(a), the lateral distribution of the high-energy electrons and photons ($E\geqslant1$ Bev) does not depend on the shower size, and so the mean number of them in each cloud chamber is known from the position of the axis and the size of showers. We pick up the two kinds of EAS in which the number of high-energy electrons and photons falling on both cloud chambers is thrice as many as the mean number, and less than one third of it. The former may be regarded as the active showers (AcS), and the latter the non-active showers (NAcS). The types of the lateral distribution of these showers are examined, and the results are listed in Table II.

As seen in Table II, the proportion of the showers with *S*-distribution and *F*-distribution is reversed in AcS and NAcS.

From these results, the followings may be concluded qualitatively:

i) Considerable parts of EAS, which contain more high-energy electronic component than the average, reveal *S*-distribution, and this shows that the showers of *S*-distribution are relatively young age. The reverse holds for the showers of *F*-distribution.

ii) The result that for EAS of large size ($N\geqslant8\times10^5$) the showers of *F*-distribution decrease and those of *S*-distribution increase, means that there are few showers of large size which are of old age, and this result seems to give some suggestions on the development of EAS in the air. However, the narrow arrangement of our apparatus used and poor data of the showers of large size obtained, make it dangerous to go deep into more consideration.

iii) In some period of the measurement, we used the core selector similar to the one used by Cocconi *et al*,[12] to trigger the whole apparatus. Almost all of EAS selected by this method are of *N*- and *S*-distribution. This shows the correctness of the above mentioned results, and also implies that the lateral distribution of EAS selected by the core selector has a tendency to reveal that of the showers of young age.

§ 5. Zenith Angle Distribution

The projected zenith angle distribution of EAS was measured, using the two cloud chambers which were set at right angles with each other. Generally, low-energy electrons being scattered to various directions, it is difficult to determine the angle of the showers containing no high-energy cascade shower and having small densities in the chambers. Accordingly, if only the showers whose angles are easily determined were picked up for the analysis, the obtained distribution would have some biases, characters of which are not known well.

At first, we investigated the zenith angle distribution averaged for all showers having various characters. If most of showers whose zenith angles are undecided are showers with specific characters, and their zenith angle distribution is different from the average one, the obtained distribution does not answer the purpose. Therefore, in order to reduce the above mentioned biases as much as possible and to increase the accuracy of the angle, the showers which satisfied together the following two criteria were accepted for analysis:

(i) The distance from the shower axis to the chamber is 3 m, 5 m and 7 m or less for the showers of the size $1\times10^5 \leqslant N \leqslant 3.4\times10^5$, $3.5\times10^5 \leqslant N \leqslant 6.4\times10^5$ and $6.5\times10^5 \leqslant N \leqslant 1.5\times10^6$ respectively. (In these regions, on the average, about one or more rays with $E \geqslant 1$ Bev are expected to fall into the chamber from the result of § 4(a).)

(ii) The picture of the chamber contains either at least one high-energy ray with $E \geqslant 1$ Bev and a few parallel tracks, or five or more parallel tracks, where tracks were regarded to be parallel if their projected angles did not differ by more than 8°.

On the above criteria, the projected zenith angles of EAS were determined mainly by high-energy rays, and for 85% of the showers accepting the criterion (i), their projected zenith angles could be determined. The number of selected data was 393 and the mean size was $\bar{N}=4.5\times10^5$.

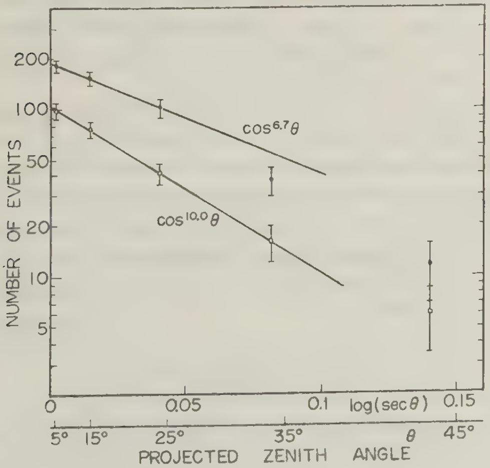

Fig. 10. Projected zenith angle distribution of EAS The upper curve shows distribution averaged for all showers, and the lower curve shows that of young showers.

As every triggering counter was arranged in the north-south direction, inclined showers have the different triggering efficiency according to the azimuth angle. As the result of this effect, the projected zenith angle distribution of A chamber becomes flatter than the space-angle distribution and on the contrary that of B becomes steeper. This tendency was verified experimentally. In order to exclude it, the total data of A and those of B were averaged with equal weight, and moreover the variation of effective area in registering EAS was taken into account.

The result is shown by the upper curve in Fig. 10, and the distribution is of the form of $\cos^{6.7\pm1.4}\theta$ in the range 0–30°. This form should be agreed with that of the space-angle, and accordingly we get the absorption mean free path Λ of the intensity of EAS

$$\Lambda=113\pm22 \text{ g cm}^{-2}.$$

This value is in agreement with the result of Miura *et al.*[13] measured at Mt. Norikura, but they did not measure the size. Moreover, the value agrees with the result of Clark[14] measured for EAS with the primary energy approximately equal to ours at sea level. The absorption m.f.p. of the number of particles λ defined by $\lambda=\gamma\Lambda$ can be determined to be

$$\lambda=203\pm42 \text{ g cm}^{-2}.$$

with $\gamma=1.8\pm0.15$ in § 3.

In addition, we investigated the zenith angle distribution of the EAS in which the number of high-energy electrons and photons with $E \geqslant 1$ Bev falling in the chamber is more than twice as many as the mean number seen from § 4(a). Of course, the above criterion (i) was not imposed on these EAS. The rate of high-energy rays is independent on the zenith angle, as seen from § 4(b). Hence, the data selected in such a manner contain mostly showers with specific character, but their zenith angle distribution is not biased in favor of specific angles. The number of the selected data was 238 and the mean size was $\bar{N}=5\times10^5$. The zenith angle distribution obtained from them is given by the lower curve in Fig. 10, where the distribution well represented by the form $\cos^{10.0\pm2.0}\theta$ in the range 0°–30°. From this, we get the following absorption m.f.p. Λ^* of intensity

$$\Lambda^* = 76 \pm 15 \text{ g cm}^{-2}.$$

This value is pretty smaller than the average m.f.p. Λ.

This result can be interpreted as follows; the majority of the selected showers are young, namely, they develope mainly near the apparatus, and accordingly the obtained value Λ^* seems to show the effective collision m.f.p. of the primary particles of EAS.

§ 6. Conclusion

From the experimental results of EAS measured at 2770 m elevation (741 $\text{g}\cdot\text{cm}^{-2}$ atmospheric pressure), the following conclusions were obtained:

(1) The integral size spectrum can be represented by the following form

$$F(\geqslant N) = 4.9\times10^{-5}(N/10^5)^{-(1.55\pm0.10)}\text{m}^{-2}\cdot\text{sec}^{-1}\cdot\text{sterad}^{-1}.$$

$$\text{for} \quad 1\times10^5 \leqslant N \leqslant 4\times10^5$$

$$F(\geqslant N) = 8.2\times10^{-5}(N/10^5)^{-(2.04\pm0.20)}\text{m}^{-2}\cdot\text{sec}^{-1}\cdot\text{sterad}^{-1}.$$

$$\text{for} \quad 4\times10^5 \leqslant N \leqslant 2\times10^6.$$

(2) The lateral spread of the high-energy electronic component can be explained only by Coulomb scattering in the range $r > 1$ m. Namely, the main source of the energy supply of EAS is confined in the narrow range $r \leqslant 1$ m.

(3) In a greater part of the EAS with the size $1\times10^5 \leqslant N \leqslant 1\times10^6$, the electronic component is in a state of equilibrium with the high-energy nucleonic component in the region of the atmospheric pressure 700∼1000 $\text{g}\cdot\text{cm}^{-2}$.

(4) In the range 1 m $\leqslant r \leqslant$ 10 m, the integral energy spectrum can be represented by the form E^{-n} within the energy region 250 Mev $\leqslant E \leqslant$ 1 Bev, and the value of n shifts from 0.7 to 1.2 as the distance from the axis r increases. In the energy region $E \geqslant 1$ Bev, the value n becomes larger.

(5) The lateral distribution of the energy flux carried by the electronic component can be expressed by the form $r^{-(1.57\pm0.24)}$ in the range $1 \leqslant r \leqslant 10$ m.

(6) The lateral distribution of electrons near the axis is not expressed by an unique distribution. Generally, the showers having steeper distribution seem to contain more high-energy electronic component and to be young in age, and those of flatter distribution have the reverse character. The proportion of the showers with S-distribution increases with increasing size in the range $N \geqslant 8\times10^5$.

(7) The absorption m.f.p. of the intensity of the EAS with the mean size $\bar{N} = 5\times10^5$ is 113 ± 22 $\text{g}\cdot\text{cm}^{-2}$, and the absorption m.f.p. of the number of the particles is 203 ± 42 $\text{g}\cdot\text{cm}^{-2}$. The effective collision m.f.p. of the primary particles is nearly 76 ± 15 $\text{g}\cdot\text{cm}^{-2}$.

We wish to express our gratitude to Prof. O. Minakawa for his valuable discussions and encouragement. We are also grateful to Prof. G. Fujioka and I. Kita for their useful discussions and kind advices and to Mr. K. Watanabe for his cooperation, and to Prof. S. Kikuchi, the director of Mt. Norikura Cosmic Ray Laboratory of Tokyo University, who offered us facilities to achieve the experiment. This study was supported partly by the Scientific Research Expenditure of the Ministry of Education.

References

1) W. E. Hazen, R. W. Williams and C. A. Randal: Phys. Rev. **93** (1954) 578.
2) S. Miyake, K. Hinotani, T. Kaneko and I. Katsumata: J. Phys. Soc. Japan **13** (1958) 782.
3) T. V. Danilova, O. I. Dovzhenko, S. I. Nikolskii and I. V. Rakovolskaia: Sov. Phys. JETP **7** (1958) 374.
4) K. Kamata and J. Nishimura: Progr. Theor. Phys. Suppl. **6** (1958) 93.
5) G. B. Khristiansen Oxford Conf. Ext. Air Shower: A.E.R.E. Publication 1956 London.
6) G. V. Kulikov and G. B. Khristiansen: Sov. Phys. JETP **8** (1959) 441.
7) private communication from I.N.S. Air Shower Group.
8) S. I. Nikolskii, Y. N. Vavilov and V. V. Batov: Dokl. Akad. Nauk SSSR **111** (1956) 71.
9) P. A. Bender: Nouvo Cimento II (1955) 980.
10) W. E. Hazen: Phys. Rev. **99** (1955) 911.
11) J. A. Richard and L. W. Nordheim: Phys. Rev. **74** (1948) 1106.
12) G. Cocconi, V. Cocconi Tongiorgi and K. Greisen: Phys. Rev. **76** (1949) 1020.
13) I. Miura, Matano, Y. Toyoda and T. Murayama: J. Phys. Soc. Japan **10** (1955) 595.
14) G. W. Clark: Phys. Rev. **108** (1957) 450.

JOURNAL OF THE PHYSICAL SOCIETY OF JAPAN, Vol. 15, No. 9, SEPTEMBER, 1960

Lattice Frequency of Ionic Crystals

By S. S. MITRA and S. K. JOSHI

Department of Physics, The University, Allahabad-2, U. P., India

(Received February 17, 1960)

"Using an inverse power type repulsive potential two different expressions for the lattice frequency of ionic crystals are obtained, one in terms of the cohesive energy and the other in terms of the compressibility of the crystal."

In a recent communication1) the authors have derived an expression for the lattice frequency, ν, of ionic crystals in terms of the cohesive energy, E_0, using a simplified Born-Mayer potential of the type

$$u=-\frac{\alpha e^2z^2}{r}+Mbe^{-\sigma(r/r_0)}$$

The relation is

$$\nu=\frac{1}{2\pi}\left(\frac{E_0}{r_0^2NM\mu}\right)^{1/2}\left[\frac{2\sigma(\sigma-2)}{(\sigma-1)}\right]^{1/2}$$

where r_0 is the closest equilibrium distance between two unlike ions, M is coordination number, μ is the reduced mass of the ions, N is Avogadro's number and σ a potential parameter. The lattice frequency calculated from the above relation compares well with the experimental values of $\nu_{\max}$, the infrared eigen frequency as determined by Barnes2) for some of these crystals.

The purpose of the present communication is to derive a similiar expression for the lattice frequency using a repulsive energy of the inverse power type. The following potential energy has been used:

$$u=-\frac{\alpha e^2z^2}{r}+\frac{Mb}{r^n} \tag{1a}$$

symbols having their usual meanings. In the above expression for the potential energy the overlap potentials between other than nearest neighbours, van der Waal interactions and zero point energy have been neglected.

Neglecting anharmonicity, the frequency, ν, is given by

$$\nu=\frac{1}{2\pi}\sqrt{\frac{f}{\mu}}$$

where the force constant, f, is the coefficient of Δr, the change in inter nuclear distance, in the expression for $\frac{du}{d\Delta r}$, and μ the reduced mass.

For a crystal of the NaCl type, equation (1a) may be rewritten in terms of Δr as

$$u=-e^2z^2\left[\frac{1}{r_0-\Delta r}+\frac{1}{r_0+\Delta r}+\frac{4}{(r_0^2+\Delta r^2)^{1/2}}\right]+b\left[\frac{1}{(r_0-\Delta r)^n}+\frac{1}{(r_0+\Delta r)^n}+\frac{4}{(r_0^2+\Delta r^2)^{n/2}}\right] \tag{1b}$$

for convenience $(\Delta r)^2$ has been denoted as Δr^2. Differentiating u with respect to Δr and collecting terms in Δr, one obtains for f

$$f=2n(n-1)br_0^{-(n+2)}$$

In equation (1b) we have confined ourselves only to the six nearest neighbours. The poor convergence of the first sum (coulomb part) demands the consideration of the next nearest and farther neighbours. But because of origin being a centre of symmetry, irrespective of the number of neighbours considered, the first sum will not have any term in Δr. In other words electrostatic interactions between the various ions contribute nothing to f. The highly convergent nature of the second sum (repulsive part) in equation (1b) justifies the consideration of only the nearest neighbours.

The cohesive energy, E_0, is given by

$$E_0=-N(u)_{r_0}=N\left(\frac{\alpha e^2z^2}{r_0}-\frac{Mb}{r_0^n}\right)$$

The constant b is determined from the condition $\left(\frac{du}{dr}\right)_{r_0}=0$ giving

$$b=\frac{\alpha e^2z^2}{Mn}r_0^{n-1}$$

Thus

$$\nu=\frac{1}{2\pi}\sqrt{\frac{2nE_0}{MN\mu r_0^2}} \tag{2}$$

The lattice frequency may also be expressed in terms of compressibility, x. The compressibility is given by

$$\frac{1}{x}=V\frac{d^2U}{dV^2}$$

Table I.

Crystal	n^a	$E_0{}^b$ (K. Col/Mole)	$r_0{}^c$ (10^{-8} cm)	χ^c (10^{-12}/barye)	ν cm^{-1} (Eqn. 2)	ν cm^{-1} (Eqn. 3)	ν cm^{-1} (Exptl.)
LiF	6.0	240.1	2.010	1.17	526	529	307
LiCl	7.0	198.1	2.572	3.41	373	363	
LiBr	7.5	189.3	2.745	4.31	341	303	
LiI	8.5	181.1	3.000	6.01	320	277	
NaF	7.0	213.4	2.310	2.11	326	326	246
NaCl	8.0	182.8	2.814	4.26	182	227	164
NaBr	8.5	173.3	2.981	5.08	191	182	134
NaI	9.5	166.4	3.231	7.07	175	154	117
KF	8.0	189.7	2.665	3.30	257	253	
KCl	9.0	164.4	3.140	5.63	178	175	141
KBr	9.5	156.2	3.293	6.70	143	138	113
KI	10.5	151.5	3.526	8.54	130	118	98
RbF	8.5	181.6	2.815	4.10	177	211	
RbCl	9.5	160.5	3.270	6.65	150	141	118
RbBr	10.0	153.3	3.427	7.94	139	103	88
RbI	11.0	149.0	3.663	9.57	97	87	78
CsF	9.5	173.7	3.004	4.25	208	207	

a See reference 4). b See reference 5). c reference 6).

where V and U are volume and energy per unit cell. In terms of crystal parameters one obtains

$$x=\frac{18r_0{}^4}{\alpha e^2z^2(n-1)}$$

for the NaCl type lattice.

Hence

$$\nu=\frac{1}{2\pi}\sqrt{\frac{36r_0}{xM_\mu}} \qquad (3)$$

which is very similiar to the expression obtained by Huggins[3] using an exponential type repulsive energy.

In Table I, ν calculated from relations (2) and (3) are compared with the experimental values of $\nu_{\max}$ due to Barnes.

The authors wish to thank Prof. K. Banerjee for his interest in the investigation. Thanks are also due to the University Grants Commission, Govt. of India for the award of a senior fellowship to one of them (S.S.M.).

References

1) S. S. Mitra and S. K. Joshi: Physica, **26** (1960) 284.
2) R. B. Barnes: Z. Phys. **75** (1932) 723.
3) M. L. Huggins: J. Chem. Phys. **5** (1937) 143.
4) F. Seitz: The Modern Theory of Solids (McGraw Hill, New York, 1940) 80.
5) C. Kittel: Introduction to Solid State Physics (John Wiley, New York, 1957) 80.
6) M. Born and K. Huang: Dynamical Theory of Crystal Lattices (Clorendon, Oxford, 1954) 26.

JOURNAL OF THE PHYSICAL SOCIETY OF JAPAN, Vol. 15, No. 9, SEPTEMBER, 1960

The Resonance Type Absorption of Very Thin Silver and Gold Films

By Shigeo YAMAGUCHI

Department of Physics, Faculty of Science,
Tokyo Metoropolitan University

(Received April 19, 1960)

The spectral transmission from 200 mμ to 1,200 mμ of silver and gold thin films was measured. It was found that for heated silver films a strong resonance type absorption appeared with the peak at 435 mμ ~ 480 mμ and then the absorption due to electrons in the conduction band disappeared. For heated gold films, the similar results were also obtained but the absorption strength was rather weak and the peak position shifted to 510 mμ ~ 550 mμ.

By taking into account the two dimensional aggregations, some discussions were made from the view point of the collective motion of conduction electrons within small metallic particles of which the film was composed.

§ 1. Introduction

It is known that very thin films have optical properties different from those of the bulk metal. The optical constants as determined in connection with metallic films change remarkably with film thickness. While the refractive index n increases as the thicknes becomes smaller, the extinction coefficient k decreases promptly in many cases, thus the thinner metallic film having the more properties of an insulator. On the other hand, thin films of many metals absorb light selectively, and the absorbing manner varies with thickness. For example, silver films viewed by transmitted light show light yellow at a thickness of about 10Å and deep blue for thickness thicker than some value.

A number of experimental and theoretical works on this subject has already been made.[1] The phenomena are owing to the fact that thin metallic films are not homogeneous slab of the metal, but are composed of small agregates of metallic atoms. Application of Maxwell-Garnett theory in which the film is regarded as a three dimensional suspenoid of spherical metallic particles possessing the same optical constants as those of the bulk metal can explain many experimental features, but seems to be still unsatisfactory from a quantitative point of view.[3)-5)] The theory modified by Schopper[6] in which the film was considered to be a two-dimensional set of rotational ellipsoids having the same optical constants as the bluk metal, and the dipole interaction among ellipsoids was ignored showed the result which agreed with his experiment relating to the evaporated gold film.

In the work to be reported here, the author investigated spectral transmission of thin metallic films, and found a resonance type absorption, which for the thinnest silver films had the maximum at about 435 mμ and completely isolated from the absorption due to the electronic interband transition and also from the absorption due to the electrons in the conduction band. The letter will be refered to the conductive absorption hereafter. The absorption band was though to be the similar kind one to that observed by Hampe[7] in gold film at about 550 mμ. In accordance with Hampe, the author ascribed it to the resonance oscillation of the electron gas in the metallic particles composing the film. Some calculations were made in order to test the propriety of the above explanation and to get some information about the film structure.

§ 2. Experimental

Films were prepared by the deposition of the evaporated metal from a heated molybenum ribbon in an evacuated vessel in which the pressure was maintained below 2×10^{-5} mmHg. Evaporated metals were silver and gold. The substrate was either fused sillica plate or collodion film. During evaporation the substrate was kept at a constant temperature between room temperature and 160°C controlled by an electrical heater behind the substrate. The deposit was laid between the two aquadac coatings on substrate, which were served as the electrodes for the measurement of the electrical conductivity of film. The electrical current across the film with terminal voltage 45V～135V was recorded by an electromagnetic oscillograph through a high gain d.c. amplifier during and after deposition of metal. Samples of various thicknesses were prepared and their spectral transmission was measured in the wavelength region from 200 mμ to 1,200 mμ using a Beckman type spectrophotometer. The transmission was determined in reference to that of a clear substrate. The error of transmission measurement was within about 0.5%. It was found that the anomalous absorption which is to be stated became sharper, if the film was heated for some time after its preparation. This heat treatment for silver was done successively to the deposition in the same evacuated vessel, while for gold films it was done in a separate vacuum oven, as it required a higher temperature, 400～500°C.

The determination of the film thickness is the most important factor to decide the optical properties of film. The author determined three thicknesses in following ways: the first was estimated from the evaporation speed and the evaporation time, the second from the transmission at $\lambda=265$ mμ and the third from the activation analysis.

The speed of evaporation was controlled by the heating current, and was estimated previously for several values of heating current in two ways: one from the weight change of the metal source and the other from the thickness of the formed film determined by means of multiple beam interference. If the deposition was done on substrate at room temperature, and the evaporation occurred into solid angle 2π, the rates of deposition estimated in the above two ways fairly agreed. Hence we obtained a thickness d_w' of each sample from the relation:

$$d_w' = \frac{(\text{deposition weight per unit area per unit time}) \times (\text{deposition time})}{(\text{bulk density of the metal})}$$

assuming that the deposition occurred in constant rate throughout that time. Another thickness, sybolized by d_{265} below, was obtained from the optical transmission at $\lambda=265$ mμ. The reason and procedure will be explained in the next section. In order to check the above thicknesses and to estimate the actual mass thickness correctly, the activation analysis for several samples was made using reactions $\mathrm{Ag}^{109}(\mathrm{n}\gamma)\mathrm{Ag}^{110}$ and $\mathrm{Ag}^{107}(\mathrm{n}\gamma)\cdot\mathrm{Ag}^{108}$ in following procedure*: a sample activated in an atomic reactor for 30 sec. was dissolved into 2 c.c. of 8 Normal $\mathrm{HNO_3}$ and its activity was measured by a γ-ray scintillation counter. For reference the weighed silver and the relatively thick film deposited on substrate at room temperature were used. The results are shown in Table II and Fig. 5.

§ 3. Experimental Results

(A) *Silver on Fused Silica*

An example of a series of spectral transmission for silver films of gradually varying thickness is shown in Fig. 1(a). The figure given to each curve is the sample number. The samples were made with the same condition but different evaporation times, the

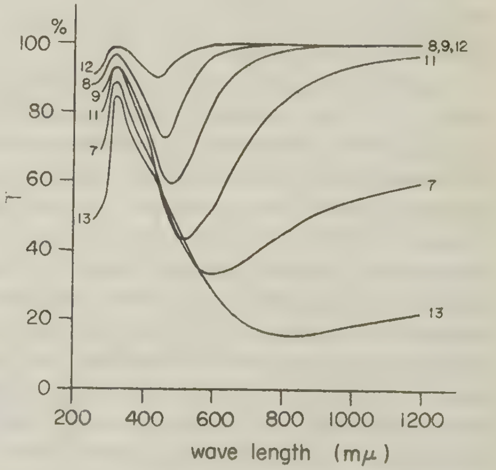

Fig. 1(a) Transmission curves of silver films deposited on fused silica at room temperature with the deposition rate 7Å/sec.

---

* The author thanks Mr. F. Ichikawa, Japan Atomic Energy Research Institute, for his kindness to give many conveniences for this measurement.

latter values being given on the horizontal time axis of Fig. 1(b). Fig. 1(b) shows the electrical conductivity record of a film for which the evaporation was continued longer than usual but under the same evaporation conditions as for the above samples.

The conduction does not occurr for some period after opening the shutter of atomic beam, and when it occurred, increases nearly exponentially. If the shutter was closed in this stage, the conduction begins to decrease at once, and falls to zero as a function of the substance of substrate, its temperature, and the rate of deposition. These behaviours indicated that silver atoms arriving at the surface of substrate moved easily to agglomerate into minute grains, thus remaining non-conductive in the early of evaporation. When the grains grew by continued evaporation, and bridges were formed among them, the current begins to flow. As the agglomeration continues still after the stop of evaporation, the unstable bridges will be broken, and the film becomes again non-conductive.

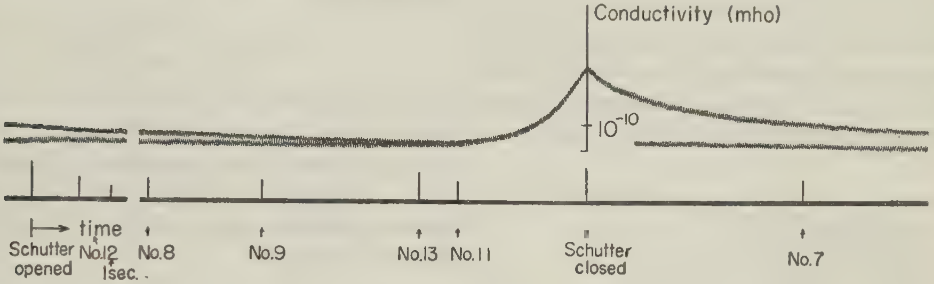

Fig. 1(b) The electrical conductivity record for a silver film formed under the same conditions.

All the samples but No. 7 and No. 13 given in Fig. 1(a) are those for which the evaporations were stopped within the period of non-conductive.

The spectrophotometric curves of thinnest films Nos. 12, 8 show, in addition to the absorption band at ultraviolet end, which is already known to be due to the electronic interband transition, the existence of an absorption band with a peak at 434~450 mμ. We will call provisionally the latter an anomalous absorption band. There does not appear the usual conductive absorption for these films. Such thin films exhibit light yellow when viewed by transmitted light. As thickness is increased, and the anomalous absorption band becomes stronger, its peak is slightly displaced to longer wavelength and begins to broaden on the same side. In this stage, films viewed by transmitted light exhibit ruddy orange. For still thicker films the broadening on the longer wavelength side of anomalous absorption continues, and finally there remains only the transmission gap at 320 mμ. Such films display blue colour in the transmitted light. That the considerable decreasing in transmission due to conductive absorption occurs for the film such as No. 7 for which the electrical conduction has decayed may be understood by considering that for electrical conduction it needs long metal chains eventually joing the electrodes, while for the conductive absorption not so long chains is needed.

For all cases of the various evaporation conditions, the above mentioned results are similar except minute details, but there is no constant relation between each stage and the mass thickness. Generally films formed on substrate at higher temperature have their electrical and optical properties belonging to the second and the third stage for the thicker mass thickness on lower temperature substrate.

It was found that the anomalous absorption band of films of such thickness as No. 9 and 11 or even No. 7 and No. 13 was changed into that corresponding to the thinnest one with respect to the peak position and breadth, and the conductive absorption was disappeared, if the films were heated at a temperature above 100°C for 30 min.~1 h. successively to their formation. Examples of transmission curve of heated films are shown in Fig. 2. The thickness are given here by d_{265}.

The effect on the band-breadth was conspicuous, while the peak position still depended on the thickness as shown in Fig. 3.

The ratio of transmission through the film and substrate, which was measured directly in the present experiment, is to be expressed with the good approximation by[8)]

$$T=\frac{1}{\left[1+\frac{1}{\mathrm{n}_2+1}\frac{2\pi d}{\lambda}(2\mathrm{nk})\right]^2} \tag{1}$$

when $2\pi(\mathrm{n}-i\mathrm{k})d/\lambda \ll 1$. Here the film is considered to be optically homogeneous slab having the optical thickness d and the optical constants n, k. λ is the wavelength of light and n_2 the refractive index of the substrate.

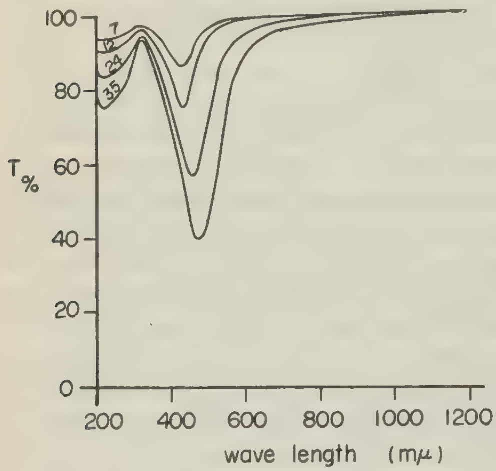

Fig. 2. Transmission curves of heated silver films of fused silica at about 160°C for one hour.

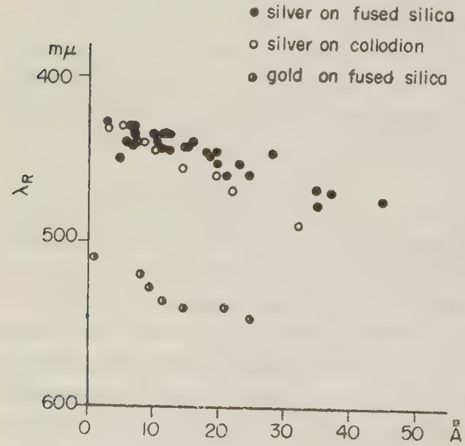

Fig. 3. The peak position of resonance type absorption vs. thickness for heated silver and gold films.

The quantity

$$X=\frac{2}{\mathrm{n}_2+1}\frac{2\pi d}{\lambda}(2\mathrm{nk}) \tag{2}$$

represents the amount of energy dissipated in the film per unit time and per unit area, and was obtained from the experiment for heated films. This quantity in the region of the anomalous absorption band can be expressed very well by the following resonance type formula as a function of the light angular frequency:

$$X=X_{\max}\frac{\gamma_0^2x^2}{(1-x^2)^2+\gamma_0^2x^2} \tag{3}$$

where $X_{\max}$ is the peak value of X, γ_0 is known from the half breadth $\Delta\omega/\omega_R$, and x is ω/ω_R, ω_R being the frequency of peak position. Example of experimental curve and the fitted resonance curve of the formula (3) is shown in Fig. 4.

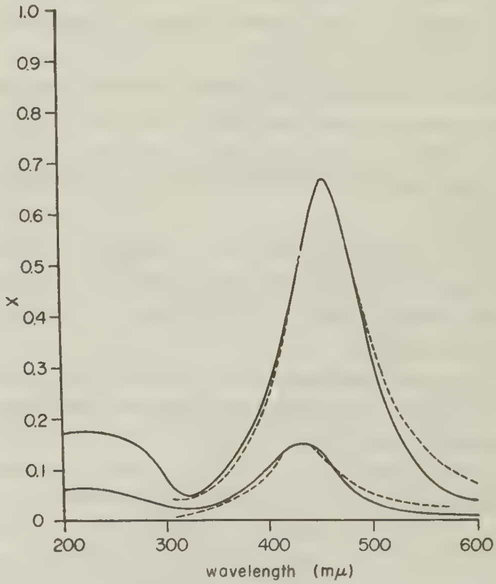

Fig. 4. The anomalous absorption curve of heated silver films and the fitted resonance curve.

In Table I are given the values of d_w', λ_R, $X_{\max}$ and γ_0 obtained for heated films. As is seen in the table, the dependence of $X_{\max}$ on d_w' is very irregular. This is the circumstance that metallic atoms re-evaporate during the heat treatment very irregulary and so the d_w' does not correspond to the actual mass thickness. On the other hand, the $X_{\max}$ of anomalous absorption band is nearly proportional to the X value at $\lambda=265$ mμ. In the films not heated, the X value at 265 mμ is

Table I. Characteristic data of heated thin silver films on fused silica.

Sample No.	d_w'(Å)	d_{265}(Å)	d_A(Å)	λ_R(mμ)	$X_{\max}$	γ_0
25	8.2	3.0	1.4	428	0.065	0.212
23	10.7	4.9	2.25	450	0.080	0.240
24	15.5	6.0	2.9	440	0.135	0.219
36	7.4	6.3	3.0	440	0.110	0.198
32	5.8	6.3	3.0	430	0.122	0.190
18	16.4	6.9	3.25	442	0.115	0.242
1	7.0	7.0	3.5	435	0.100	0.246
7	6~8	7.0	3.5	430	0.150	0.215
35	7.4	7.0	3.5	430	0.137	0.204
30	10.3	7.5	3.9	440	0.187	0.200
28	13.9	9.3	4.8	440	0.215	0.232
31	9.0	10.0	5.2	440	0.213	0.202
33	13.1	10.0	5.2	435	0.222	0.230
14	15.4	10.5	5.6	440	0.275	0.238
15	21.0	11.3	6.3	444	0.295	0.208
27	9.0	11.5	6.5	435	0.240	0.210
20	22.6	12.0	7.0	435	0.250	0.230
9	13.6	12.5	7.5	435	0.305	0.200
13	9.8	12.5	7.5	435	0.225	0.240
21	10.7	14.5	9.8	443	0.375	0.200
22	40.4	15.5	11.0	443	0.430	0.207
26	20.4	16.0	11.5	440	0.380	0.200
12	33.6	18.0	13.8	446	0.485	0.230
29	40.4	18.5	14.4	448	0.525	0.259
5	21.0	19.5	15.5	453	0.525	0.220
11	20.5	19.5	15.5	445	0.525	0.200
34	27.1	21	17.4	460	0.660	0.195
8	30.4	23	19.6	454	0.695	0.208

Table II. Data of the activation analysis.†

Sample No.	d_w'(Å)	d_{625}(Å)	total weight**		activity (min.)*
			W'(gr.)	W_{265}(gr.)	
1	7.4	10.5	3.96×10^{-6}	5.61×10^{-6}	3.6
2	14	11.8	7.35	6.2	3.6
3	16.8	16.5	8.76	8.65	1.65
4	26.6	18.75	15.6	11.1	1.5
5	12.3	8.5	7.45	5.6	3.6
6	32.8	18.75	21.1	12	0.88
7	41	41.6	25.6	25.9	0.47
8***	—	—	11160	—	0.00125

* The reduced time for 10^4 counts at 8 min. after neutron bombarding.

** The total weight of silver estimated from the relation:

$$W=(\text{density of bulk silver})\times(\text{film area})\times(\text{thickness})$$

*** The reference sample of weighed silver.

† The error of activation analysis is said to be about 10%.

almost proportional to d_w' and if we put $2nk = 3.7$ in the formula (2) the thickness d_{265} calculated from the observed X agrees well with d_w'. Moreover the heat treatment has almost no effect on the shape of absorption band in ultraviolet region. Hence also for heated films, we calculated the thickness d_{265} in the same way from their X value at 265 mμ, which seems to correspond to the actual mass thickness and is given in Table I as d_{265}. The dependence $X_{\max}$ of anomalous absorption on d_{265} is shown in Fig. 5. As is seen in Fig. 5, $X_{\max}$ is nearly proportional to d_{265}, but more exactly $(d_{265})^{1.37}$. γ_0 does not change remarkably for all thickness and has the mean value 0.223.

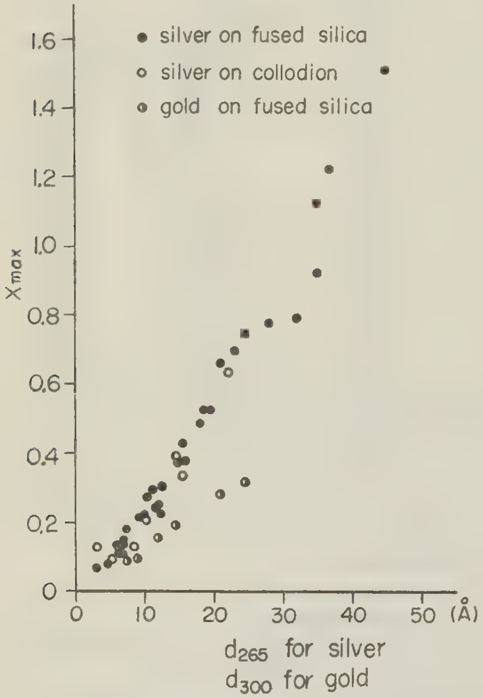

Fig. 5. The dependence of the $X_{\max}$ value of anomalous absorption on thickness for heated silver and gold film.

The results of the activation analysis is shown in Table II. In this case, the activity again correlates more to d_{265} than to d_w'. Thus the thickness d_{265} corresponds better to the actual mass thickness, and the relation between the mass thickness d_A estimated from the activity and d_{265} is shown in Fig. 6. For larger thickness than $d_{265}=40$Å, the thickness d_{265} agree with the thickness d_A but for small thickness than $d_{265}=40$Å, it gives larger than d_A. Using this relation, the linearity in the dependence of $X_{\max}$ on thickness is fairly improved d_A values estimated by using the curve shown in Fig. 6 for each sample are tabulated in Table I.

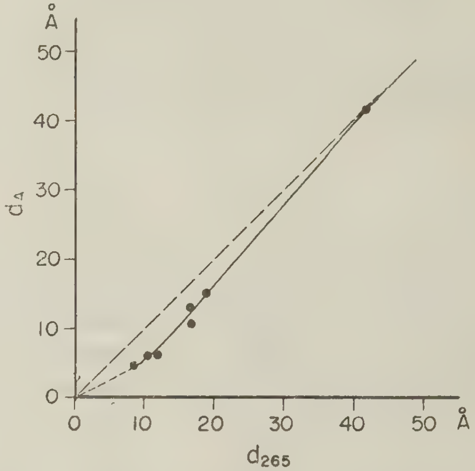

Fig. 6. The relation between thicknesses d_A estimated by activation analysis and d_{265} estimated from transmission at $\lambda = 265$ mμ.

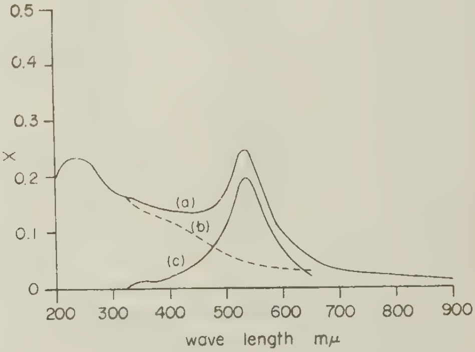

Fig. 7. The absorption curve of a heated gold film on fused silica at about 500°C for one hour.

(B) *Silver on Collodion*

The electrical conductivity records showed that silver atoms on collodion surface moved rather slowly to agglomarate than those on fused silica.

The transmission curve was similar to that for a film on fused silica, but the conductive absorption appeared for thinner film and the anomalous absorption band was displaced more rapidly and its breadth was somewhat larger than those for films on fused silica. The peak position of anomalous absorption band and the $X_{\max}$ value are shown in Fig. 3 and Fig. 5 respectively. The average γ_0

value is 0.25.

(C) *Gold on Fused Silica*

The absorption of a thin evaporated gold film is shown in Fig. 7 by the curve (a). The film was formed on fused silica and heated at about 500°C for 1 h.. The anomalous absorption as in the case of silver is perceived with a peak at about 550 mμ, but it is overlapped now by the tail of the absorption due to the interband transition. The separation of them was made by using the result of Joos and Kropfer[9] relating to the temperature dependence of absorption edge of thick gold film. Assuming that the anomalous absorption falls to zero already at 300 mμ, this portion of the curve (a) is extended to longer wavelengths according to nk curve obtained by Joos and Kropfer. The extended portion is shown in Fig. 7 by the broken curve (b). The anomalous absorption proper (curve (C)) is obtained by subtracting (b) from (a). The curve (C) is well represented by the formula (2) with $\gamma_0=0.17$. The thickness d_{300} was determined from the X values at 300 mμ in similar way as done in silver. The $X_{\max}$ value of anomalous absorption is proportional to d_{300} as shown in Fig. 4.

The electrical conductivity record showed that the agglomeration of gold atoms occurred more slowly and its dependence on temperature is slighter than in the case of silver. In parallel with this, it was more difficult to remove perfectly the conductive absorption and to narrow the anomalous absorption band by heating.

§ 4. Discussion of Results

The shape of absorption curve suggests that the anomalous absorption was induced by the resonance oscillation of the conduction electrons in the metallic particles of the film. The electron within a particle may oscillate collectively, if the dipole approximation can be used, and the oscillation frequency ω satisfies the condition $2\pi/\omega \ll \tau_{\text{coll}}$, where τ_{coll} is the mean collision time of electrons. We assume that the electron gas is bounded around the equilibrium position by a restoring force $-\kappa\xi$, ξ being the displacement of the electron gas as a whole. Let the electron density in a metal be n_0 and the volume of the particle V. The restoring force must be due to the depolarizing force of the particle $L\cdot P/V$, where $p=-Vn_0e\xi$ is the dipole moment resulting from the displacement and L the depolarizing factor. Hence we have

$$\kappa = L V n_0^2 e^2$$

and, dividing this by the total mass Vn_0m

$$\omega_0^2 = L\frac{n_0e^2}{m}\,^{*} \tag{4}$$

as the natural frequency.

To obtain the actual resonance frequency ω_R, we must take into account of the dipole interaction among the particles composing the film. Assuming that N dipoles per unit area lie with average spacing 'a', and their moments are all equal and in the same direction parallel to the plane, the interaction field R is given by (Appendix I)

$$R = 2\pi\frac{N}{a}p\,. \tag{5}$$

The equation of motion of the electron gas in the film is

$$\ddot{p}+\gamma\dot{p}+\omega_0^2 p = \frac{Vn_0e^2}{m}[E_0e^{i\omega t}+R] \tag{6}$$

where $E_0e^{i\omega t}$ is the electric vector of incident light. We obtain the resonance frequency ω_R and the amplitude of oscillation p_0 as follows:

$$\omega_R^2 = \frac{4\pi n_0 e^2}{m}\left(\frac{L}{4\pi}-\frac{d_w}{2a}\right) \tag{7}$$

$$p_0 = \frac{Vn_0e^2}{m}\,\frac{1}{\omega_R^2-\omega^2+i\gamma\omega}E_0 \tag{8}$$

where the notation $d_w=NV$ means the true mass thickness of the film. If we imagine a substance which is formed by piling up such films with interval τ, the optical constants n, k of it are given by

$$(\mathrm{n}-i\mathrm{k})^2 = 1+\frac{d_w}{\tau}\,\frac{4\pi n_0e^2}{m\omega_R^2}\,\frac{\gamma_0 x}{(1-x^2)^2+\gamma_0^2x^2}\,. \tag{9}$$

Considering again the single film, we obtain the quantity as

$$X = \frac{2}{\mathrm{n}_2+1}\,\frac{2\pi d_w}{\lambda}\,\frac{4\pi n_0e^2}{m\omega_R^2\gamma_0}\,\frac{\gamma_0^2 x}{(1-x^2)^2+\gamma_0^2x^2} \tag{10}$$

---

* From Eq. (4), one may see that the conduction electrons, for example, in a spherical metallic particle resonate at the frequency $\omega_R=\omega_p/\sqrt{3}$. It was suggested by Dr. H. Kanazawa, University of Tokyo, that the similar phenomenon could also be expected in the characteristic energy loss of fast electrons due to the electron plasma in such particle. (private communication from Dr. H. Kanazawa.)

where $x=\omega/\omega_R$ and $\gamma_0=\gamma/\omega_R$. Eq. (9) becomes the formula used to represent the experimental result, if we put

$$X_{\max}=\frac{2}{n_2+1}\,\frac{2\pi d_w}{\lambda_R}\,\frac{4\pi n_0 e^2}{m\omega_R{}^2\gamma_0}\,. \qquad (11)$$

Assuming that the conduction electrons are perfectly free, we can calculate the value d_w from experimental values $X_{\max}$, λ_R, and γ_0 for each sample.

The calculated d_w values are 0.6~0.7 times d_A. This result may be reasonable, but, for the more quantitative discussions, the assumptions made in the above consideration are needed to examine.

By Eq. (7) we can determine d_w/a from the experimental value ω_R, if the depolarizing factor L is assumed. We assume that the particles are of the form of flat rotational ellipsoid with the axis of symmetry perpendicular to the film and axial ratio m. $L/4\pi$ as the function of m has the value 1/3 for $m=1$ and decreases with increasing m. For obtained experimental results several models for films structure are possible, that is, the possible range of m value is given by $d_w/2a=L/4\pi-m\omega_R{}^2/4\pi n_0e^2>0$. The interparticle spacing 'a' relaties to the true mass thickness d_w as below:

$$a=\frac{d_w}{2\left(\dfrac{L}{4\pi}-\dfrac{m}{4\pi n_0 e^2}\omega_R{}^2\right)}\,. \qquad (12)$$

For $m=1$, 2, and 3, the above equation gives the value $a\approx 3d_w$, $6d_w$ and ∞, respectively.

As for gold films, the circumstance is more complicated by the superposition of anomalous absorption on interband transition absorption band. This may be counted for one of the reasons for the smaller peak value of anomalous absorption than that of silver film.

The breadth of anomalous absorption band is of the same order as that of Hampe, but there is no appreciable dependence on thickness in contrast with his results. Before one states the damping mechanism, one will have to make clear the origin of the disagreement between experimental results.

Many features of optical anomaly appearing in their metallic films can be qualitatively understood from present view point. For example, the displacement of peak position of anomalous absorption and the wide band breadth are owing to longer joining among particles and the fluctuation of joining order. In order to explain quantatively, the exact knowledge of actual film structure is needed (Appendix II). Since the effect of heating on the film structure is large as seen in silver case, the electronmicroscopic observation does not always give us the information of film structure exactly corresponding to the optical properties.

The author wishes to thank Professor M. Kiuchi for his kind guidance and encouragement throughout the present work.

Appendix I. Calculation of Dipole Interaction Field

Suppose that N dipoles per unit area uniformly distribute on the film plane with spacing 'a', and their moments are equal and parallel. The electrostatic energy between two parallel dipoles of equal moment is given by

$$\frac{p^2}{r^2}(1-3\cos^2\psi) \qquad \text{(AI 1)}$$

where r is the distance between them and ψ is the angle between $\boldsymbol{r}$ and $\boldsymbol{p}$. Total energy is obtained from (AI 1) by summation over all dipoles, i.e.

$$\begin{aligned} I&=\Sigma_i\frac{p^2}{r_i{}^2}(1-3\cos^2\psi_i)\\ &=p^2\int_{a/2}^{\infty}\int_0^{2\pi}\frac{1}{r^2}(1-3\cos^2\psi)Nrdrd\psi \qquad \text{(AI 2)}\end{aligned}$$

where for $r>a/2$, isolated dipoles was replaced by the continuous distribution. The dipole interacting force R can be calculated by following equation:

$$(-Vn_0e)R=-\frac{\partial}{\partial\xi}I(\xi)\,. \qquad \text{(AI 3)}$$

Thus we have

$$R=2\pi\frac{N}{a}p\,. \qquad \text{(AI 4)}$$

Surface density N relates to interparticle spacing 'a' with $N=f\cdot 1/a^2$, where f is the correction factor of the order of unity. Then the field in another form is given by

$$R=f\frac{2\pi}{a^3}p\,. \qquad \text{(AI 5)}$$

It should be noted that in three dimensional case the Lorentz field was $4\pi/3\cdot 1/a^3\cdot p$ and now $2\pi\cdot 1/a^3\cdot p$, which is 3/2 times as much as that in three dimensional case.

Appendix II.

Here we consider the film composed of various type of particle form and size. We classify particles by the depolarizing factor L and volume V. The natural frequency of conduction electrons in the particle having L and V is given by

$$\omega_R^2(L)=L\frac{n_0e^2}{m}. \quad \text{for all } V \qquad (\text{AII } 1)$$

If such particles uniformly distribute on a plane with surface density N_{LV} and the average spacing a_{LV}, the dipole interacting field R is approximately given by

$$R=\Sigma_{LV}e\pi\frac{N_{LV}}{a_{LV}}P_{LV}. \qquad (\text{AII } 2)$$

The equation of motion of the electron gas in such film is

$$\ddot{p}_{LV}+\gamma_{LV}\dot{p}_{LV}+\omega_0^2(L)p_{LV} = \frac{Vn_0e^2}{m}(E_0e^{i\omega t}+R) \qquad (\text{AII } 3)$$

We take the average in following meaning:

$$\Sigma_V\frac{1}{a_{LV}^3}=\frac{1}{a_L^3},\quad \Sigma_V\frac{V}{a_{LV}^3}=\frac{V_V}{a_L^3},$$
$$\Sigma_V\frac{p_{LV}}{a_{LV}^3}=\frac{p_L}{a_{LV}^3} \qquad (\text{AII } 4)$$

and ignore the dependence γ_{LV} on L, and V. Then the equation of motion is reduced to

$$\ddot{p}_L+\gamma\dot{p}_L+\omega_0^2(L)p_L = \frac{V_Ln_0e^2}{m}\left(E_0e^{i\omega t}+\Sigma_{L'}\frac{2\pi}{a_{L'}^3}p_{L'}\right). \qquad (\text{AII } 5)$$

It is difficult to obtain the concrete solution for an actual film, but one may say that the resonance frequency distributes around the mean value so that the wide breadth of anomalous absorption band occurs.

Present view point is equal to that of Maxwell-Garnett theory. For simplicity we consider the optical properties of the three dimensional suspensoid of small spherical particles possessing the optical constants $\mathcal{E}=(\mathrm{n}-i\mathrm{k})^2$. The optical constants of the suspensoid $\mathcal{E}_e=(\mathrm{n}_e-i\mathrm{k}_e)^2$ is given by

$$\frac{\mathcal{E}_e-1}{\mathcal{E}_e+2}=q\frac{\mathcal{E}-1}{\mathcal{E}+2} \qquad (\text{AII } 6)$$

where q is the full factor of suspensoid. If the optical properties of particles is well represented by Drude-Zener formula such as sodium the optical constants $\mathcal{E}=(\mathrm{n}-i\mathrm{k})^2$ is

$$\mathcal{E}=1-\frac{\omega_p^2}{\omega^2-i\gamma\omega} \qquad (\text{AII } 7)$$

where $\omega_p^2=4\pi n_0e^2/m$, and $1/\gamma$ is the mean collision time of conducting electrons in the bulk metal. Substituting Eq. (AII 7) into Eq. (AII 6), we have

$$\mathcal{E}_e=(\mathrm{n}_e-i\mathrm{k}_e)^2=1+\frac{\omega_p^2q}{\frac{1}{3}\omega_p^2(1-q)-\omega^2+i\gamma\omega} \qquad (\text{AII } 8)$$

which is the same formula given by Hampe. Thus all the authors including the present author stand the same physical origin.. Sennett and Scott's criterion of the apperance of a maximum in the absorption vs. thickness is satisfied in the wavelength region in which the conductive absorption lay the main role for the optical properties of metal.

References

1) H. Mayer: Physik der Dünner Schichten *Teil I* (Stuttgart, 1950). O. S. Heavans: Optical Properties of Thin Solid Films (London, 1955).
2) J. C. Maxwell-Garnett: Trans. Roy. Soc. (Lond.) **203A** 385.
3) R. S. Sennett, and G. D. Scott: J. Opt. Soc. Amer. **40** (1950) 203.
4) P. L. Clegg: Proc. Phys. Soc. **65** (1952) 774.
5) J. Krautkrämer: Ann. Physik **32** (1938) 537.
6) H. Schopper: Z. Phys. **130** (1951) 565.
7) W. Hampe: Z. Phys. **152** (1958) 476.
8) H. Wolter: Z. Phys. **105** (1937) 269.
9) G. Joos and A. Kropfer: Z. Phys. **138** (1954) 251.

JOURNAL OF THE PHYSICAL SOCIETY OF JAPAN, Vol. 15, No. 9, SEPTEMBER, 1960

Electrical Properties of Pseudo-binary Systems of Ag_2VI's; $Ag_2Te_xSe_{1-x}$, $Ag_2Te_xS_{1-x}$, and $Ag_2Se_xS_{1-x}$

By Shin-ya MIYATANI

Department of Physics, Faculty of Science, Niigata University

(Received March 2, 1960)

The electrical properties such as the electronic and ionic conductivities, Hall coefficients, etc. of the alloys Ag_2 (Te, Se; Te, S; Se, S) are studied with use of the galvanic cell Ag|AgI|specimen|Pt, the excess Ag content being controlled by sending a current across the cell. The electrical properties of these alloy systems change continuously in the α phase as the mixing ratio x is varied, while they change discontinuously or rapidly at certain x's in the β phase. The experimental results are compared with theory under simplifying assumptions such as the energy-independent relaxation time and the energy-momentum relation given by $\varepsilon=\hbar^2k^2(1-Bk^2)/2m^*$.

§ 1. Introduction

In previous works[1,2] it was shown that the comparatively large mobility of Ag ions in Ag_2VI's, namely Ag_2S, Ag_2Se and Ag_2Te, makes the study of these substances easy. This is due to the fact that the galvanic cell Ag|AgI| specimen|Pt is available and hence the excess Ag amount and free electron density in the specimen can be easily controlled by sending a proper current across the cell, from Ag-saturated state to S, Se, or Te-saturated state, and moreover the e.m.f. of the cell E gives a useful information about the position of the Fermi level in the specimen. This cell is also available in the present systems since Ag ions are as mobile in them as in Ag_2VI's. Hence we can expect that the present alloy systems can be studied with similar easiness by the help of this cell.

Before describing the electrical properties of the alloys, let us review the properties of their components, namely Ag_2Te, Ag_2Se and Ag_2S. Fig. 1 shows the electrical conductivity σ_e vs temperature for these three substances and corresponding E curves. The ionic conductivity σ_i is $1\sim4\ \Omega^{-1}\,\mathrm{cm}^{-1}$ in the α phase and much smaller in the β phase[2]. The transport number σ_i/σ_e is therefore very small (1% or less) except β-Ag_2S. See first the E graphs in Fig. 1. Since the value of E can be varied from zero (Ag-saturated state) to about 0.2 volt (VI-saturated in vacuum), it can be seen from these curves whether a given state is near to Ag- or VI-saturated state. More exactly, E is given by

$$eE=(\zeta_i^0+\zeta_e^0)-(\zeta_i+\zeta_e)\ , \qquad (1)$$

where ζ_i and ζ_e are the chemical potentials of Ag ion and electron in a sample respectively and ζ_i^0 and ζ_e^0 are those in the sample in Ag-saturated state. The α phase of these substances is known as 'average crystal' which possesses many available sites with similar occupation energies for each Ag ion[10].

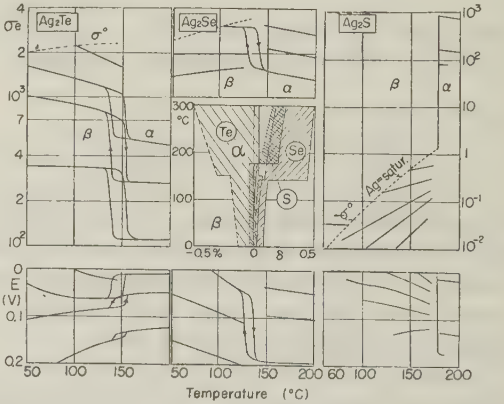

Fig. 1. $\sigma_e(\Omega^{-1}\,\mathrm{cm}^{-1})$ and corresponding E vs temperature for three Ag_2VI's. In the center is shown the permissible range of δ by hatching somewhat schematically.

In such a case, ζ_i is equal to ζ_i^0 and then eE is equal to $\zeta_e^0-\zeta_e$. In other words, E represents the position of the Fermi level relative to that in the Ag-saturated state. The crystal structure of the β phase is different and hence ζ_i will be in general different from ζ_i^0. As mentioned in the previous paper[2], such a composition-dependence of ζ_i seems remarkable in

β-Ag_2Se, negligible in β-Ag_2S and appreciable at lower temperatures in β-Ag_2Te. Thus it may be said that the E curves in Fig. 1 represent the position of the Fermi level relative to the Ag-saturated state except for β-Ag_2Te below 100°C and β-Ag_2Se. Now the figure shows that E changes suddenly at the phase transition. In particular such a change of E is so large for Ag_2S that even Ag-saturated sample is changed to S-supersaturated one at $\beta \rightarrow \alpha$ transition, accompanying precipitation or evaporation of S. In other words there is a remarkable difference of Ag-solubility between α and β phases.

We next consider the electrical conductivity curves in Fig. 1. The σ_e values are comparatively large except β-Ag_2S, while β-Ag_2S shows typical semiconducting behaviors. As for the mobility of conduction electron, see Fig. 4. From Figs. 1 and 4 we see that the change of σ_e at $\beta \rightarrow \alpha$ phase transition has different causes for different Ag_2VI's; for Ag_2Te it is due to the decrease of the electron density caused by the increase of the energy gap, for Ag_2Se it is due to the decrease of the electron mobility, the electron density being conserved, and for Ag_2S it is mainly due to the increase of the electron density caused by the escape of S.

Finally we consider the deviation from the stoichiometric composition. As mentioned above, the Ag content can be varied in a certain range. In other words the deviation lies in a certain permissible range. Hence Ag_2VI should be, exactly speaking, written as $Ag_{2+\delta}VI$ though we have omitted δ so far and shall also omit henceforth because of its smallness. Now at supply or removal of Ag across the cell the excess Ag density D is of course changed by the density of Ag supplied or removed, D being obviously related to δ by $D = N_A \delta d/A$ (N_A=Avogadro's number, d=density, and A=molecular weight). The value of D can be thus determined relatively. The absolute value of D is estimated as follows. The concentration of free electron n_1 obtained from Hall coefficient is changed at supply of Ag nearly by the change of D, for α-Ag_2Se and α-Ag_2S, indicating the simple relation $n_1 = D$. The analysis of experimental data for α-Ag_2Te shows also that the concentration of holes n_2 becomes dominant in this case but the similar simple relation

$$n_1 - n_2 = D \qquad (2)$$

seems valid, the former relation $n_1 = D$ being a special case of $n_1 \gg n_2$. Thus we have the absolute value of D. It may be noted that the validity of such a simple relation means that there is no neutral defect such as Ag ion vacancy with trapped hole.

We can now construct the permissible δ range diagram as shown in the center of Fig. 1. We see from this figure that α-Ag_2Te can contain a large amount of Ag ion vacancies while α-Ag_2Se can contain a large amount of excess Ag ions. Corresponding to these facts, the hole conductivity dominates the electron conductivity at large negative δ for α-Ag_2Te while the former is negligible and the electron gas is highly degenerate for α-Ag_2Se. In contrast, the β-Ag_2S can contain only a very small amount of excess Ag, resulting in its typical semiconducting behavior.

We have so far reviewed the general features of three Ag_2VI's. They are similar to each other in some points, e.g. they have the large ionic conductivity and plasticity in the α phase, which will be due to the similar crystal structure. On the other hand they have of course their characteristic features, and in particular β-Ag_2S is remarkably different from other β phases. When two of Ag_2VI's are mixed, the similar natures will be conserved but the different points will be gradually changed from one to the other as x is varied. In §2 such gradual changes will be surveyed. The more detailed data will be described in §3 and compared with the theory.

§2. General Survey

(a) *Experimental arrangements*

The sample is prepared by melting two of Ag_2VI's of proper proportion in a sealed silica tube. The sample obtained is soft at the α phase and so it is pressed or rolled to a plate of proper thickness at the α phase temperature. Then the specimen is cut from it to proper size. The β phase of S-rich sample (β_S phase mentioned later) is as soft as the α phase and so the S-rich samples can be rolled to thin foil at room temperature. Other β phases are rather brittle.

The volume of a specimen is estimated from its weight under the assumption that the density (A_2Te: 8.5, Ag_2Se: 8.0, Ag_2S: 7.3

g/cm³) is linearly changed with mixing ratio x. The method of measurement is the usual direct current method. To the specimen are attached Pt electrodes, Pt-headed potential probes, Ag|AgI probes, and copper constantan thermocouples on the electrodes (Fig. 10). They are set in a glass tube which is evacuated by a rotary pump. The potential differences between the probes are measured by means of a potentiometer through a rotary switch. When the temperature is lower than the phase transition point of AgI (~140°C), AgI+5%AgCl is more suitable than pure AgI for our purpose.

When a direct current is sent through Pt electrodes, the ionic current flows together with the electronic current. The former decays out soon with the time constant τ_i given by $(L/\pi)^2|d(eD)/dE|\sigma_i^{-1}$, L being the length of the specimen[2)]. The potential drop between two Pt-headed potential probes changes at such a decaying process. This change is obviously of order of σ_i/σ_e and so negligibly small in our cases except β-Ag_2S and its neighboring compositions. On the other hand the potential drop between two AgI|Ag probes appears at the instant of switching-on and off of the current and decays as such a polarization builds up and decays out. The ionic conductivity σ_i can be obtained from the time constant τ_i of this decay. In order to get a proper value of τ_i, the length of specimen should be properly chosen, e.g. 3 cm for α phases and 1~0.3 cm for β phases.

(b) *Examples of σ_e and E vs temperature and α-β transition point*

The space does not permit to describe the σ_e and E curves for many mixing ratios, so that only two examples for each system are shown in Fig. 2, where we write three systems $Ag_2Te_xSe_{1-x}$, $Ag_2Se_xS_{1-x}$ and $Ag_2Te_xS_{1-x}$ as Te-Se, Se-S, and Te-S for simplicity. From such measurements we can construct the phase diagram as shown in Fig. 3, where the curves dividing the phases are double owing to the hysteresis effect, the upper one representing the transition point at increasing temperature and the lower one at decreasing temperature.

Let us now give some explanations about Fig. 2. Comparing it with Fig. 1, we see that (d) and (f) are Ag_2S-like, (a) and (e) are Ag_2Te-like but (b) and (c) are somewhat singular, that is, the phase transition takes place twice. This double transition will be more apparent if one see Fig. 3, which shows that for $x=0.6$~0.7 in Te-Se there appears an intermediate phase between α and β phase and for Se-S the β phase is divided into two different phases. The appearance of the intermediate phase is also justified by the appearance of a step of the ionic conductivity shown by the dotted line in (b). As for the α-β transition temperature, it is not very much lowered for Te-Se and Se-S systems but it is so lowered for Te-S system that the α phase is stable at 20°C for $x=0.2$~0.8.

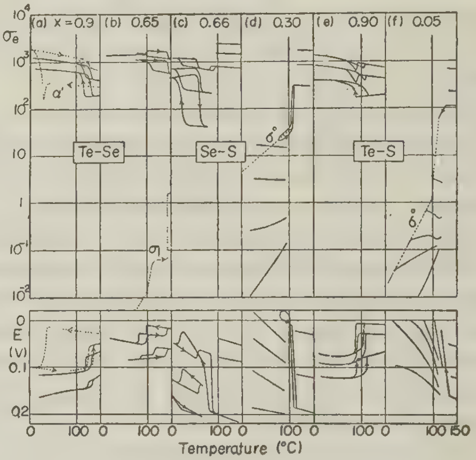

Fig. 2. $\sigma_e(\Omega^{-1}\,\mathrm{cm}^{-1})$ and corresponding E vs temperature for two examples of each system.

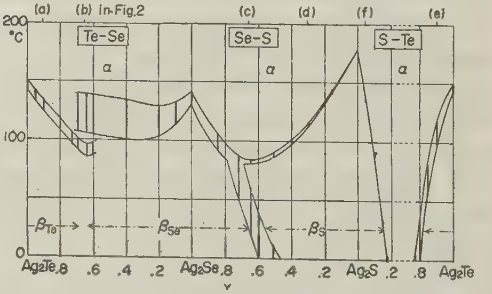

Fig. 3. Phase diagram of three systems. The examples shown in Fig. 2 correspond to the x-values shown on the upper axis.

At measurements of those transition temperatures, some complex situation appears for Te-Se system. That is, for $x=0.9$~0.6 the α-β transition is suppressed when Ag is too much removed at the α phase. As mentioned later, the α phase seems to change to another phase α' if Ag is removed over a certain amount. Once such a change occurs, α' phase does not change to β at the normal $\alpha \rightarrow \beta$ transition temperature. For example, $\alpha' \rightarrow \beta$ change is suppressed down to 40∼30°C for $x=0.9$ as shown by the dotted line in (a). For $x=0.8$ or less, α' is stable even at room temperature. When the temperature is raised up to above 300°C, α' is changed back to the previous α phase. The similar phase change is also observed for Te-S system but the suppression of the transition is not so remarkable as Te-Se system.

(c) *Mobility of conduction electron*

Fig. 4 shows $R\sigma_e$ vs temperature. Actually $R\sigma_e$ depends on eE/kT or δ (Fig. 8 (b)), especially in the case of high degeneracy as Ag_2Se and in the case of high hole density as Ag_2Te.

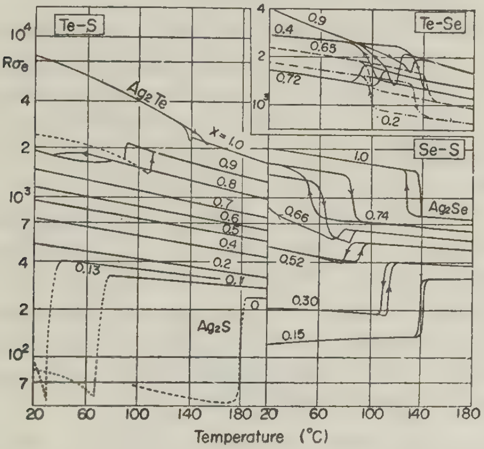

Fig. 4. $R\sigma_e$($cm^2 s^{-1} v^{-1}$) vs temperature for three systems. The $R\sigma_e$ value for $x \leq 0.13$ of Te-S is small and inaccurate and so is shown by the dotted line. For $x=0.9$ of Te-S it is somewhat affected by a heat treatment right below the transition point (quenching of the lattice disturbance at a pre-stage of the transition ?).

The values shown in Fig. 4 are almost their maximum values and may be taken as representing the electron mobilities. In order to see the x-dependence of the mobility thus obtained, Fig. 4 is rewritten to Fig. 5. We see from this figure that there are two types of x-dependence in the β phase; that is, the sensitive one in the Te-side and S-side as expressed by $\exp bx$ and rather insensitive one in the Se-side. Thus the whole β phase is divided into three regions β_{Te}, β_{Se} and β_S, as shown in Fig. 5 and also in Fig. 3. This division is in fact justified by the X ray study mentioned later. In contrast to the β phase, $R\sigma_e$ in the α phase (dotted curve in Fig. 5) is varied rather smoothly with x, suggesting the structure of the α phase is similar to each other in the whole range. In addition, Fig. 5 shows also $E_\alpha - E_\beta$ roughly which is the maximum value of the change of E at the α–β transition and so gives a measure of the difference of the Ag-solubility between two phases.

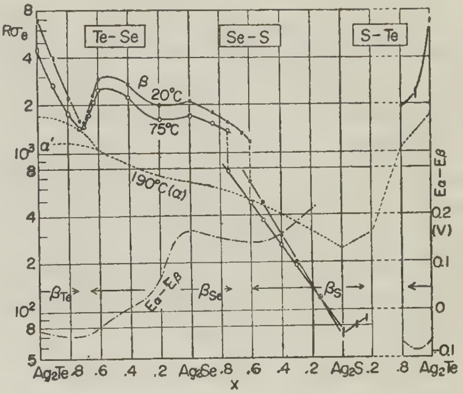

Fig. 5. $R\sigma_e$($cm^2 s^{-1} v^{-1}$) vs x. The change of E at $\alpha \rightarrow \beta$, $E_\alpha - E_\beta$, is also shown roughly in the linear scale on the right-hand ordinate axis.

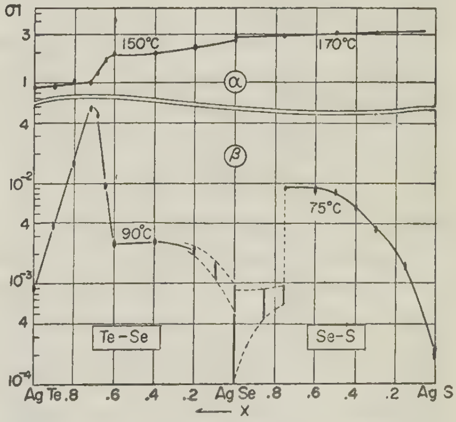

Fig. 6. σ_i($\Omega^{-1} cm^{-1}$) vs x for two systems. The graph is shortened by unit in logarithmic scale between the curves for α and for β.

(d) *Ionic conductivity*

Fig. 6 shows the x-dependence of the ionic conductivity σ_i for two systems where σ_i is estimated by the ionic polarization method mentioned already in (a) of this paragraph. As seen from the figure, σ_i is not only D-independent but also nearly x-independent in the α phase, while it is D-dependent in the

β_{Se} phase as shown by the broken lines and it is D-independent but sensitively x-dependent in the β_{Te} and β_S phases. Thus the ionic conductivity also shows that the β_{Se} phase should be distinguished from the β_{Te} and β_S phases. As for the temperature-dependence, σ_i increases slightly in the α phase but it increases rapidly (The activation energy is of the order of 0.7 ev.) in the β phase with increasing temperature.

(e) *X-ray study at room temperature*

In order to confirm the conclusion that the β phase is divided into three regions, X-ray diffraction profiles are recorded for the plates of the present systems with use of X-ray diffractometer (‘*Geigerflex*’). The result is shown in Fig. 7, twice of Bragg angle being plotted against the mixing ratio. This shows clearly that X-ray profiles are different between three β phases β_{Te}, β_{Se} and β_S, and discontinuous at their borders, justifying the conclusion mentioned above.

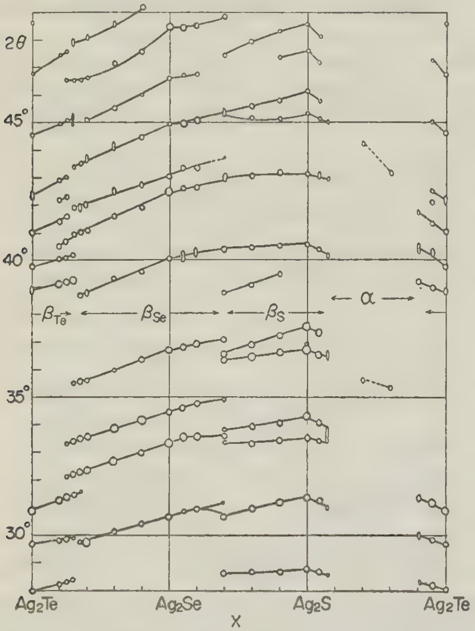

Fig. 7. 2θ (θ: Bragg angle) vs x at room temperature. The intensity of each reflection is roughly shown by the magnitude of each circle. Cu target with Ni filter.

The crystal structures of β-Ag_2VI's are of low symmetry; β-Ag_2S is reported as monoclinic ($a=9.47$Å, $b=6.92$Å, $c=8.28$Å, $\beta=124°$)[8] and β-Ag_2Te is as rhombic (16.27Å, 26.68Å, 7.55Å)[9], while β-Ag_2Se seems unknown (missing in Landolt-Börnstein (1955)). On the other hand, α-Ag_2VI's are reported as cubic[10] and so have a few reflections. In our case the α phase is stable at room temperature for $x=0.2\sim0.8$ in S–Te system, showing only two peaks in the angle range shown in Fig. 7. Further the background is dominant like amorphous substances for the α phase. The analysis of the crystal structures for our systems is thus difficult and will be left to the future. Finally we add a note on α' phase. As mentioned in (b) of this paragraph, α phase is changed to α' in a certain x range of Te–Se system and α' is stable at room temperature. The X-ray profiles of this α' are recorded, showing that they are quite different from the β phase, though not shown in Fig. 7.

§ 3. Electrical Properties as Functions of eE/kT and Discussions

In the preceding paragraph, we surveyed the general features of the present systems. In this paragraph we treat them a little more in detail. As mentioned in Introduction, E represents the relative position of the Fermi level if the chemical potential of Ag ion is D- or E-independent. Then the electrical properties such as σ_e and $R\sigma_e$ (in logarithmic scale) plotted against eE/kT can be directly compared with the corresponding theoretical curves plotted against the reduced Fermi energy. We first consider the α phase and then β phase briefly.

(a) σ_e, $R\sigma_e$ and $d(eD)/dE$ *vs* eE/kT *in the* α *phase*

Fig. 8 shows the plots vs eE/kT; (a) is of σ_e, (b) is of $R\sigma_e$, and (c) is of $d(eD)/dE$ approximated by $\Delta S/\Delta E$, where ΔS is the amount of electricity sent across AgI divided by the volume of the specimen, and ΔE is the change of E at that time. Also, the right-hand half is for Se–S system, and the left-hand half is for Te–Se and Te–S systems. Let us consider first $d(eD)/dE$, since it is not related to the scattering process. If we assume that Eq. (2) $n_1-n_2=D$ is valid and further the energy-momentum relation is of the standard form $\mathcal{E}=\hbar^2k^2/2m_1$, then we have

$$-\frac{d(eD)}{dE}=\frac{e^2}{kT}\frac{2}{\sqrt{\pi}}\left\{N_1\frac{1}{2}F_{-1/2}(\eta_1)+N_2\frac{1}{2}F_{-1/2}(\eta_2)\right\}, \qquad (3)$$

where N_1 stands for $2(2\pi m_1kTh^{-2})^{3/2}$, N_2 for the similar quantity for hole with the effective mass m_2, and $F_r(\eta)$ is the Fermi integral of order r with reduced Fermi energy η, η_2 being related to η_1 and energy gap E_G by $\eta_1+\eta_2=-E_G/kT$. As seen in Fig. 8 (c), the hole contribution given by the second term in Eq. (3) may be negligible for Se–S system in the whole range of x, while it predominates for Te-rich samples of Te–Se and –S systems. We consider therefore first Se–S system where we may assume $n_1=D$ always. Comparing Fig. 8 (c) with theoretical curve log $(F_{-1/2}/2)$ vs η (Fig. 12), e.g. overlapping two graphs (one being written on a semitransparent paper), we find that any adjustment of the origin does not make them coinside with each other. The discrepancy between them becomes larger as Se is richer or degeneracy is higher. It can be, however, removed by giving up the assumption of the standard form of conduction band as follows.

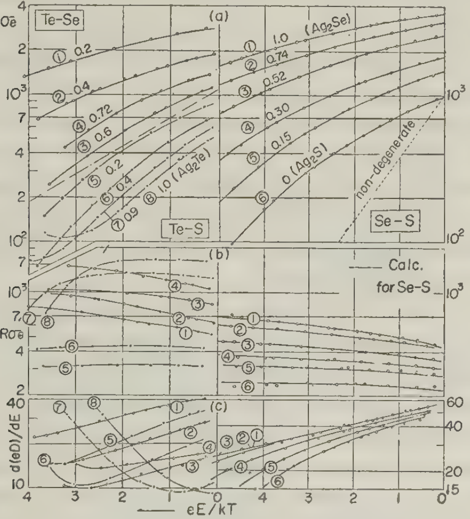

Fig. 8. (a) $\sigma_e(\Omega^{-1}\,\mathrm{cm}^{-1})$, (b) $R\sigma_e(\mathrm{cm}^2\,\mathrm{s}^{-1}\,\mathrm{v}^{-1})$, and (c) $d(eD)/dE(\mathrm{C\,cm}^{-3}\,\mathrm{v}^{-1})$ vs eE/kT in the α phase. The temperature is 170°C for Se–S except 180°C for $x=0$ (Ag_2S), 190°C for Te–Se (No. 1∼4) and 195°C for Te–S (No. 5∼8). The effect of the small temperature difference between them is not so serious as to give a notifiable change to these curves.

Let the energy of electron be given, as usually done6), by

$$\mathcal{E}=\frac{\hbar^2k^2}{2m_1}(1-Bk^2)\,, \qquad (4)$$

or reducing $\mathcal{E}$ and k to non-dimensional,

$$y=\kappa^2\left(1-\frac{a}{2}\kappa^2\right);$$

$$\kappa=\frac{\hbar}{\sqrt{2m_1kT}}|k|\,,\quad a=\frac{4m_1kT}{\hbar^2}B\,, \qquad (5)$$

where y stands for $\mathcal{E}/kT$. Then $F_{-1/2}/2$ in Eq. (3) should be replaced by G_n' defined in Appendix (Fig. 12). We choose the value of a as 0.035 so as to get best fit with experiment, assuming the same value is valid even for small x, for which a-value can not be so definitely chosen as for large x.

We next consider σ_e and $R\sigma_e$ which are related to the scattering process. Here we must assume some energy dependence of the relaxation time τ or mean free path l of free electrons. As discussed by several authors5,7), the energy dependence of τ or l relies on the scattering mechanism; e.g. the accoustical or disorder scattering leads to l=constant, the optical scattering to τ=constant for slow electrons and to $\tau\propto k$ for fast electrons, and the impurity scatterings also to their characteristic energy dependences. Furthermore two or more scatterings are present in general, making the quantitative treatment for this problem very difficult unless we have full understanding to the substance under consideration. Unfortunately, our knowledge about the scattering mechanism for the present systems characterized by the 'average, mixed, and ionic crystal with degenerate electron gas' is as yet so poor that we only choose a simple energy dependence so as to get a good agreement with the experiment as possible. The result of trial shows that the energy-independence of τ can account for the experimental data fairly well, as seen shortly. The more convincing treatment will be left to the time when we have the more detailed knowledge such as the Debye temperature, the most effective mode of lattice vibration, and the effect of average structure and alloying.

Under such a simplification, the theoretical expressions for σ_e and $R\sigma_e$ are given by

$$\sigma_e=e\mu N_1\frac{4}{3\sqrt{\pi}}G_\sigma\,,\quad R\sigma_e=\mu G_{R\sigma}\,, \qquad (6)$$

where G_σ and $G_{R\sigma}$ are as defined in Appendix, and μ stands for $e\tau/m_1$. We can draw, therefore, these theoretical curves (Fig. 12) on the experimental plots so as to get best fit. The curves for Se–S in Fig. 8 are such theoretical one, showing a good agreement with experiment. The result of such a comparison reveals that the values of μ obtained from $R\sigma_e$

are larger by a factor of about 20% than those obtained from σ_e with use of m_1-value determined from $d(eD)/dE$, or obtained from $d\sigma_e/d(eD)$, showing the experimental systematic error of such a extent which may come from the roughness of measuring magnetic field, specimen size, etc.

We consider next the Te–S and Te–Se systems. In these cases it is difficult to determine the reliable a-value for a large range of x, since the hole contribution in Fig. 8 (c) becomes predominant and further the available range of eE/kT is narrowed by the α–α' change. Hence we assume the same a-value 0.035 for every case. We may expect that this value can account for, at least, the Se-side and nearly the S-side of the systems under consideration. At any rate, under this a-value, the experiment plots can be compared with the theoretical curves although not shown in the figure. For Te-rich case, further, the energy gap can be estimated from Fig. 8 (c) if we assume the value of N_2 or m_2.

(b) *x-dependence of the electrical properties*

By the analyses mentioned above we obtain the position of the Fermi level, the effective mass of free electron m_1, and the mobility of electron μ, and further the energy gap for Te-rich case. Fig. 9 shows the result of analyses, where $\zeta_e{}^0$ is the Fermi energy in Ag-saturated state and $\mu m_1/m$ gives the τ-value (sec) by being multiplied by 5.7×10^{-16}. The lower limit of ζ_e is also shown roughly by the chain line. Thus we have the permissible range of ζ_e which corresponds to the permissible range of δ mentioned in Introduction. Seeing the $\zeta_e{}^0$ curve, we notice that it varies smoothly but has two minima near $x=0.6$ in Te-Se and –S systems. The dotted lines representing $\zeta_e{}^0$ of the α' phase continue to the $\zeta_e{}^0$ of the α phase without such minima, suggesting that, if the α and α' are different phases or of different structures, the α is Ag_2Te-like structure while the α' might be Ag_2Se (or Ag_2S)-like one rather than Ag_2Te-like. The figure shows also the positions of the top of the valence band for Te-rich samples, which is estimated, as mentioned in (a), from the hole contribution (non-degenerate) in Fig. 8 (c) under the assumption of $m_2/m=1.6$ (the mean value obtained for Ag_2Te). For comparison, those obtained optically are shown by the circles marked by ' From I. R. ' for Te–S, where they are obtained from the absorption edge at transmission of infrared ray at 20°C[4], 20°C being of course in the α phase range in this case as known from the phase diagram Fig. 3.

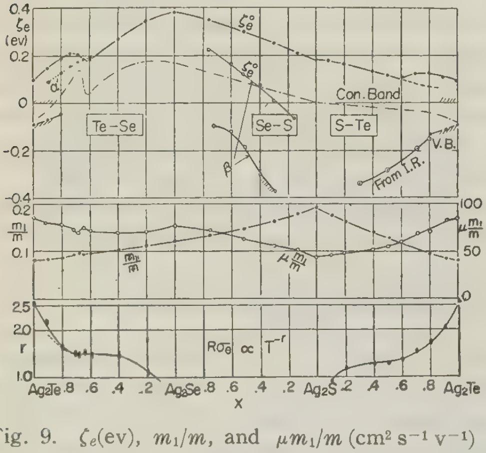

Fig. 9. ζ_e(ev), m_1/m, and $\mu m_1/m$ ($cm^2\,s^{-1}\,v^{-1}$) in the α phase (170∼200°C). The two curves in Se–S marked by β are $\zeta_e{}^0$ and valence band position at 75°C (β_s) refered later. The lowest graph shows the temperature-dependence of $R\sigma_e$ by the r-values for the α phase.

On the other hand, the middle graph of Fig. 9 shows that the electron mobility is minimum in Ag_2S because of the largest effective mass and smallest relaxation time, while it is maximum in Ag_2Te because of the opposite extrema. Further, the lowest graph shows the r-value, where $R\sigma_e$ (electron mobility) is assumed to be proportional to T^{-r} in the α phase below 300°C. The r-value for Te-rich samples is fairly large while it is small for Se–S system and not shown.

(c) *An example of α–α' transition*

In this section we consider the α–α' transition with an example of $Ag_2Te_{0.9}Se_{0.1}$ shown in Fig. 10. It shows $R\sigma_e$, σ_e, $d(eD)/dE$, the reduced thermoelectric power $\theta=e\Theta/k$ and the reduced Nernst coefficient $q=eQ/(kR\sigma_e)$. On the σ_e curve, σ_e decreases e.g. from the point A to B as Ag is removed. If Ag is supplied back without approaching B, the previous A is recovered. If B or its neighboring point is attained, σ_e begins to decrease without further removal of Ag and reaches C after sufficient waiting. Then σ_e changes on the lower curve CD and never returns to upper curve at this temperature. We call this lower state α' in contrast to the upper state α.

The two curves corresponding to α and α'

are connected by the broken lines which show the same composition or D. Comparing two values connected, we notice that the decrease of σ_e is about twice as large as the decrease of $R\sigma_e$ at B–C, that means, the concentration of free electron n_1 becomes about half, while n_1 is almost conserved at A–D as expected from the validity of $n_1=D$. This decrease of n_1 will be due to the increase of the energy gap as far as $n_1-n_2=D$ is assumed. In fact, the σ_e and θ curves in the figure show that the bottom of the conduction band shifts to the right by $1.5\,kT$ on this figure while the $d(eD)/dE$ curves show that the top of the valence band shifts to the left by about $0.7kT$.

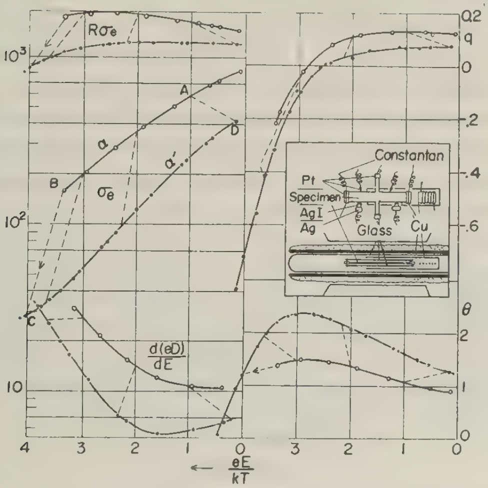

Fig. 10. An example of the $\alpha-\alpha'$ transition. $R\sigma_e$ ($cm^2\,s^{-1}\,v^{-1}$), σ_e($\Omega^{-1}\,cm^{-1}$), $d(eD)/dE$ ($C\,cm^{-3}\,v^{-1}$) in logarithmic scale and q, θ in linear scale are plotted against eE/kT at about 185°C for $Ag_2Te_{0.9}Se_{0.1}$. The schematic diagram to illustrate sample-holding is also shown.

Then the increase of the energy gap will be, summing them, about $2.2kT=\sim 90$ mv. Thus we conclude that the α–α' change is a kind of phase transition accompanying the change of the energy gap. It is also accompanied by the decrease of the electron mobility and of $\zeta_e{}^0$ or Ag-solubility. The experimental plots in Fig. 10 can not, to be regret, be satisfactorily accounted for under the assumptions taken above and so their detailed analysis will be left to the future. We only note here that the q-value and the η-dependence of $R\sigma_e$ in the small η range (0~2, where the hole contribution is negligible) decrease at $\alpha\to\alpha'$, suggesting that this transition is also accompanied by the decrease of a-value or the change of energy-dependence of τ, or both.

(d) *σ_e and $d(eD)/dE$ vs eE/kT for β_S*

As mentioned in Introduction, if the chemical potential of Ag ion ζ_i is composition-dependent, the comparison between theory and experiment as done in the preceding sections becomes impossible unless E is properly corrected. The physical meaning of this correction is in general not clear. In this respect, the β phase is more difficult to study than the α phase. This composition-dependence of ζ_i, however, decreases as the temperature is raised, and becomes negligible at sufficiently high temperatures except the β_{Se} phase, as expected from the composition-independence of σ_i in β_S and β_{Te} in contrast to the composition-dependence of σ_i in β_{Se}, as mentioned in § 2 (d). Then the comparison is possible again. As an example of such a case we shall describe the eE/kT plots for Se–S system in the β_S phase.

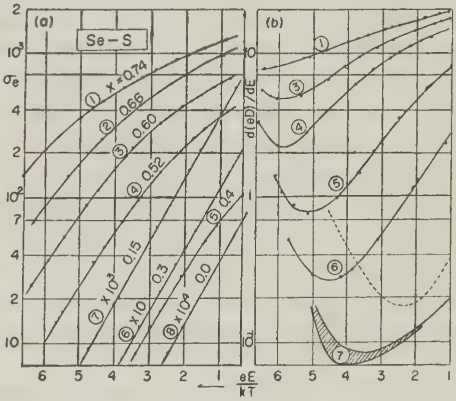

Fig. 11. (a) σ_e($\Omega^{-1}\,cm^{-1}$), (b) $d(eD)/dE$ ($C\,cm^{-3}\,v^{-1}$) vs eE/kT at 75°C for the β_S phase of Se–S. The corresponding plots for β_{Se} are very Ag_2Se-like though not shown.

Fig. 11 shows σ_e and $d(eD)/dE$ at 75°C for this case. The values of $R\sigma_e$ are almost composition- or eE/kT-independent though not shown. These curves show clearly that the non-degenerate feature of S-rich sample changes gradually to the degenerate features as seen in the α phase. In the non-degenerate case, σ_e is of course proportional to $\exp\eta$ and $d(eD)/dE$ is to be given by

$$-\frac{d(eD)}{dE}=\frac{e^2}{kT}(N_1\exp\eta_1+N_2\exp\eta_2)\,, \quad (7)$$

which is illustrated by the dotted line in (b) in the figure, showing the similarity to the experimental curves (No. 5 and 6). When x is as small as 0.15, the gradual change at supply or removal of Ag becomes ramarkable as in Ag_2S, making the value of $d(eD)/dE$ undefinite as shown by hatching (No. 7).

When the degeneracy is not very high, the position of $\eta=0$ can not determined from the curves of σ_e or $d(eD)/dE$. Therefore, it is determined from the θ (reduced thermoelectric power) vs eE/kT plots where the value of a is temporarily assumed as 0.03 which can account for the η-dependence of $d(eD)/dE$ for high degenerate case as $x=0.74$ (No. 1). The ζ_e^0-values thus determined are shown in Fig. 9, repsesenting its considerable lowering in comparison with ζ_e^0 in the α phase. To be regret, the position of $\eta=0$ estimated from θ is somewhat displaced from that obtained by the σ_e-curve in the degenerate case, showing the experimental systematic error or invalidity of our assumptions or both. Overlooking such a discrepancy, the effective mass of electron is estimated as $0.1\sim0.14m$. Next, the energy gaps are roughly estimated from Fig. 11 (b) assuming $m_2=m$, which are also shown in Fig. 9. On the other hand, the energy gap at 20°C is estimated, as the case of α Te–S, from the absorption edge at the infrared transmission in non- or slightly-degenerate samples, as 0.4 ev ($x=0.6$), 0.45 (0.52), 0.56 (0.40), and 0.65 (0.30). They have the same x-dependence with those shown in Fig. 9, although they are considerably larger than those.

Finally, we shall give a short comment about the β_S–β_{Se} transition as seen in Fig. 2 (c). The change of σ_e in this case indicates that the energy gap decreases at $\beta_S\rightarrow\beta_{Se}$. In the case of $x=0.6$, both phases are stable at 20°C; β_S is stable when the temperature is lowered down to 20°C while β_{Se} is stable when it is raised up from below 0°C as known from the phase diagram. Making use of this fact, the infrared transmission at 20°C is compared between two phases for a specimen of $x=0.6$. The result is just as expected; as the cooling time is longer, the transmission decreases remarkably. This decrease is obviously due to the shift of the absorption edge and the increase of the free carrier absorption.

We have so far tried to show how the electrical properties of Ag_2VI's are varied from one to the other by mixing two of them. As mentioned already the assumption of constant τ has no convincing theoretical basis at the present stage. We can only say which energy dependence leads to better agreement with experiment. At such a choice of the energy dependence, the introduction of the a-value makes the definite choice very difficult. For example, the η-dependence of $R\sigma_e$ and the positive q-value observed in α-Ag_2Se can not be accounted for by constant τ but fairly well accounted for by constant l[1)] as far as the a-value is assumed zero. If the assumption of $a=0$ is abandoned, however, the situation becomes quite different, that is, constant τ is better than constant l under proper a-value, as seen already. For Ag_2Te and Ag_2S, the ambiguity in such a choice is more profound, since the a-value can not exactly determined in these cases. Thus we see that we should have more detailed informations for our systems in order to proceed farther.

The author wishes to express his sincere thanks to Mr. Suzuki, Mr. Yokota, and Mr. Haga in our Department of Physics for their kind advices and discussions. The present work was supported by the Scientific Research Fund of the Ministry of Education.

Appendix

Every expression in the reference (3), treating two-band semiconductor under the assumptions of $a=0$ and $l=l_0y^r$ ($y=\mathcal{E}/kT$), keeps its validity for the more general case where $y=y(\kappa^2)$ and $\tau=\tau_0t(y)$, κ being defined in Eq. (5), if

$$\left\{p\left(r-\frac{1}{2}\right)+\frac{3}{2}+n\right\}F_{p\{r-(1/2)\}+(1/2)+n};\quad p=1,2,3\,,\quad n=0,1\,,\tag{8}$$

used there is replaced by its generalized expression given by[5,6,7]

$$K_{pn}=-\int\kappa^{3-p}\left(\frac{t}{2}\frac{dy}{d\kappa}\right)^p y^n\frac{\partial f}{\partial y}dy\,.\tag{9}$$

The μ defined there by $el_0(2m^*kT)^{-1/2}$ is to be taken here as $e\tau_0/m^*$ and α, β, γ, δ, φ and ψ are accordingly generalized as

$$\left.\begin{aligned}\alpha=\frac{K_{20}}{K_{10}}\,,\quad\beta=\frac{K_{11}}{K_{10}}\,,\quad\gamma=\frac{K_{21}}{K_{10}}\,,\\ \delta=\frac{K_{13}}{K_{10}}\,,\quad\varphi=\frac{K_{30}}{K_{10}}\,,\quad\psi=\frac{K_{31}}{K_{10}}\,.\end{aligned}\right\}\tag{10}$$

It is easily seen that the expression (9) is reduced to (8) if $t=y^{r-(1/2)}$, and $y=\kappa^2$. As another special case, if $t=1$ and $y=\kappa^2(1-a\kappa^2/2)$ as Eq. (5), K_{pn} is reduced to L_{pn} expressed as

$$L_{pn}=-\int\left(\frac{1-z}{a}\right)^{3/2}z^p y_n\frac{\partial f}{\partial y}dy;\qquad z=\sqrt{1-2ay}\,. \tag{11}$$

Then we have, for single carrier,

$$-\frac{d(eD)}{dE}=\frac{e^2}{kT}\frac{2}{\sqrt{\pi}}N_1G_n';$$

$$G_n'=\int\left(\frac{1-z}{a}\right)^{1/2}\frac{1}{z}\frac{\partial f}{\partial y}dy\,, \tag{12}$$

$$\sigma_e=\frac{4e\mu N_1}{3\sqrt{\pi}}L_{11}\,,\quad R\sigma_e=\mu\frac{L_{20}}{L_{10}}\,,\quad q=\frac{L_{11}}{L_{10}}-\frac{L_{21}}{L_{20}}\,. \tag{13}$$

Rewritting L_{11} and L_{20}/L_{10} in Eq. (13) as G_σ and $G_{R\sigma}$, we have Eq. (6).

These integrals G_n', G_σ, etc. can be evaluated, the a-value being chosen properly, by expanding the integrands in terms of y and using the numerical table of F_r (r: half integer)[7] for small η-values (<5), while by using the high degeneracy approximation for large η-values (>5)[5]. Fig. 12 shows various theoretical curves thus obtained together with the special cases of (1) $a=0$, τ=constant and (3) $a=0$ and l=constant. Further, it shows two examples of experimental q-value at 170°C, indicating the better applicability of curve (2) or (2′) in comparison to (1) or (3).

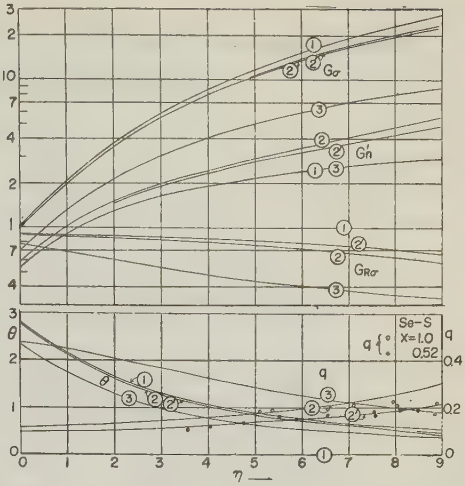

Fig. 12. Theoretical curves; (1) $a=0$, (2) $a=0.035$, (2′) $a=0.03$, where τ is energy-independent, while (3) $a=0$ and the mean free path is energy-independent, or $\tau=\tau_0y^{-1/2}$. The examples of experimental q-value are also shown.

References

1) S. Miyatani: J. Phys. Soc. Japan **10** (1955) 786 (*Ag_2S*); **13** (1958) 317 (*Ag_2Se*); **13** (1958) 341 (*Ag_2Te*).
2) S. Miyatani: J. Phys. Soc. Japan **14** (1959) 996.
3) S. Miyatani and I. Yokota: J. Phys. Soc. Japan **14** (1959) 750.
4) S. Miyatani: J. Phys. Soc. Japan **14** (1959) 1634.
5) A. H. Wilson: *The Theory of Metals* (Cambridge Univ. Press, 1953).
6) R. Barrie: Proc. Phys. Soc. London **B 69** (1956) 553.
7) O. Madelung: *Handbuch der Physik* **20** (1957) 53.
8) L. S. Ramsdell: Amer. Mineral. **28** (1943) 401.
9) J. F. Rowland: Amer. Mineral. **36** (1951) 471.
10) P. Rahlfs: Z. physik. Chem. **B 31** (1935) 157.

JOURNAL OF THE PHYSICAL SOCIETY OF JAPAN, Vol. 15, No. 9, SEPTEMBER, 1960

Temperature Dependence of the Optical Absorption Edge of Tungsten Trioxide Single Crystal

By Tsuruji IWAI

Faculty of Science, Osaka University, Osaka

(Received March 4, 1960)

The optical absorption edge of WO_3 single crystal has been measured with polarized light over the temperature range from −100°C to 900°C. From 0°C to about 700°C, the absorption edge shifts linearly toward red with increasing temperature, the temperature coefficients being -9.0×10^{-4} ev/deg for the case of light polarized in the direction parallel to the a-axis (a-polarized light) and -6.5×10^{-4} ev/deg for the case of light polarized in the direction parallel to the c-axis (c-polarized light), respectively.

In the vicinity of −50°C, an anomalous shift of the absorption edge takes place. This is attributed to the phase transition. In the low temperature phase, the extinction position is different from that in the high temperature phase. In addition, when the temperature is raised through 740°C, a sudden red shift takes place for the case of a-polarized light, the magnitude being about 0.35 ev, while no anomaly occurs for c-polarized light.

§ 1. Introduction

A report has previously been published on the optical absorption edge of WO_3 single crystals[1]. But it is limited to the case in which natural light falls on a platelike crystal having its c-axis perpendicular to the plate (c-crystal). According to the measurements of the optical indices of refraction[2], the optical anisotropy of WO_3 is larger than that of other perovskite-type ferroelectrics. Furthermore, it has been observed that WO_3 shows pleochroism at room temperature[3]. Judging from these facts, it may be desired that the temperature dependence of the optical absorption will be measured by use of the polarized light corresponding to the symmetry of the crystal.

The color of WO_3 crystals becomes deeper when the temperature is raised as seen in many other polar crystals. When the orthorhombic-to-tetragonal transition takes place at 740°C, the color shows an abrupt change from reddish yellow to dark red. According to the visual observation of a b-plane by S. Sawada *et al.*[4], this sudden change occurs only in the case of observations with the light polarized in the direction parallel to the a-axis (a-polarized light).

WO_3 has several transition points at about −50°C, (or −40°C and 17°C)[5], 330°C, 740°C, and 910°C etc. The optical absorption edge has been measured with polarized light over the temperature range covering almost all of these transition points. Above 900°C, however, no measurement has been done because of strong radiation from the background. Furthermore, when WO_3 is kept above 700°C for a long time, its surface becomes pitted and dirty owing to sublimation. Therefore, the measurements at temperatures above 700°C was possible only in the heating procedure.

§ 2. Experimental

The greater part of the WO_3 single crystals prepared with a sublimation method were c-crystals. From among them, several c-crystals about 50 μ thick were chosen and used as specimens. Some b-crystals about 100 μ thick were also obtained by cleaving the larger c-crystals. These samples had not the so-called 90° domains i.e. a-b or a-c domains.

1) b-plane: When a- or c-polarized light was incident perpendicularly upon the b-plane of WO_3, the light transmitted through the crystal was examined with the aid of a small quartz prism spectrograph. A tungsten lamp was used as a continuous light source and polarized light was obtained with Nicols. In Fig. 1, (a) is the continuous spectrum of the light source, while (b)- and (c)-series are the absorption spectra of a thin crystal at room temperature for a- and c-polarized light. Each series shows the dependence of the spectrum on the exposure time. As seen in Fig. 1, if an exposure time is sufficiently long, the end of the continuum at the shorter wavelength side is hardly changed for any longer exposure. At any temperature, the wavelength of the terminal for such a long exposure is adopted as the absorption edge. This value may correspond to that at the steep part of the usual absorption curves. The temperature dependence of the absorption edge was measured over the range from −100°C to 900°C. The result obtained is shown in Fig. 2.

At any temperature, the wave-length of the absorption edge for *a*-polarized light is a little longer than that for *c*-polarized light. However, the absorption edge shifts linearly toward red simlarly in both cases, as the temperature is raised from room temperature to about 700°C, and we can not observe any anomaly associated with the monoclinic-to-orthorhombic transition at 330°C. In this linear region, the temperature coefficients of the shifts are as follows:

-9.0×10^{-4} ev/deg for *a*-polarized light,

and

-6.5×10^{-4} ev/deg for *c*-polarized light.

Around the transition point at −50°C, anomalous shifts are observed for both polarized light cases. In each case, the shift occurs along a different path on heating and cooling. The most remarkable shift takes place at 740°C, the orthorhombic-to-tetragonal transition point. Namely, for *a*-polarized light, the absorption edge suddenly shifts far into the near infrared, the magnitude being about 0.35 ev, while, for *c*-polarized light, such a sudden shift does not take place.

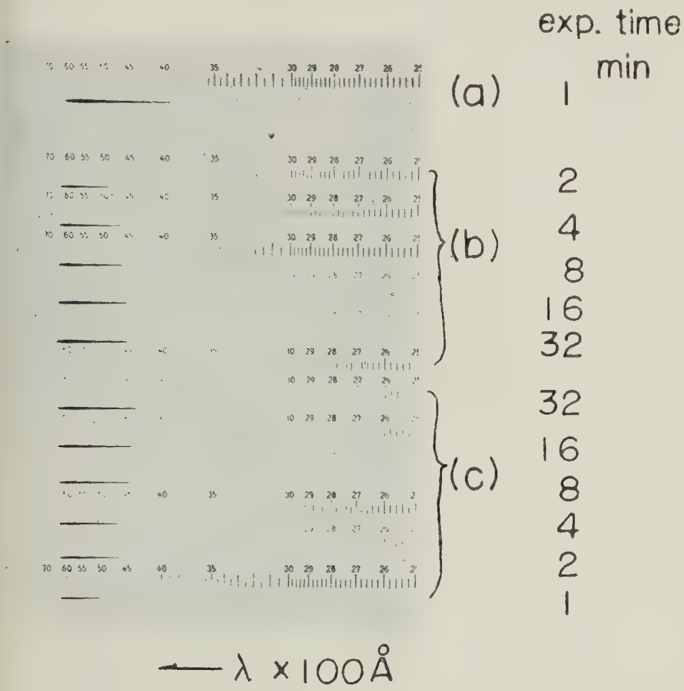

Fig. 1. Optical absorption in *b*-crystal

2) *c-plane*: By use of *a*- and *b*-polarized light, the same experiments as in the case of *b*-plane were carried out. The results are shown in Figs. 3 and 4. Roughly speaking, the temperature dependence of the absorption edge is in agreement with the result for *b*-plane with *a*-polarized light. However, there seems to be some difference between the two cases

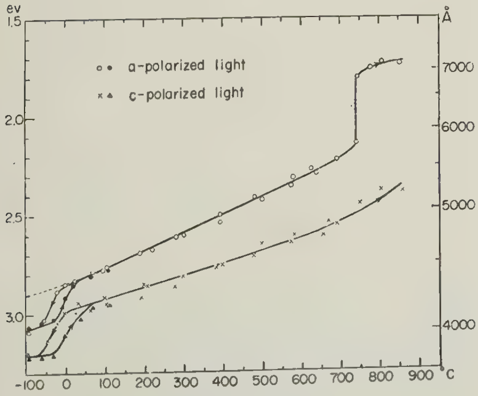

Fig. 2. Optical absorption edge *versus* temperature in *b* plane

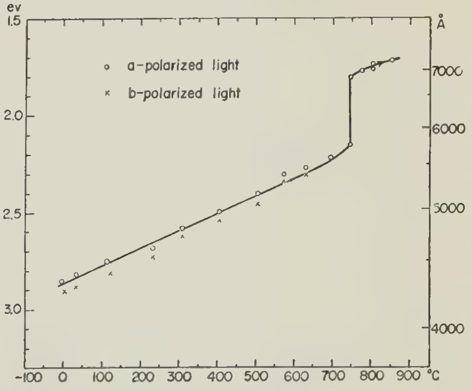

Fig. 3. Optical absorption edge *versus* temperature in *c*-plane

with *a*- and *b*-polarized light. In the temperature range from room temperature to about 700°C, the absorption edge for *a*-polarized light always appears on the longer wave-length side than that for *b*-polarized light, though the difference is small (about 50 Å~100 Å), while they coincide with each other below −50°C as shown in Fig. 4.

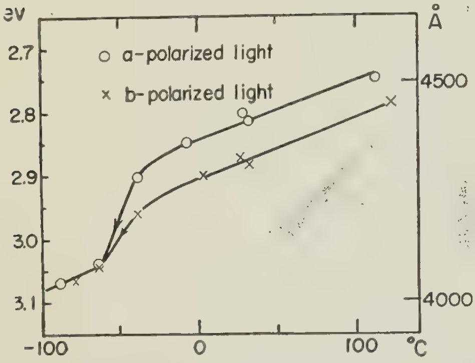

Fig. 4. Optical absorption edge *versus* temperature in *c*-plane

§3. Discussions

1) *From 0°C to 700°C*: In this temperature range, the absorption edge shifts toward longer wave-lengths for any polarized light, as the temperature is elevated. The red shift of the absorption edge has been investigated theoretically[6], and explained by the interactions between the lattice vibrations and the electrons in the crystal. These theories show that the shift is represented qualitatively by

$$E=\alpha-\beta T \quad (T\gg\Theta),$$

where E is the energy of the absorption edge, α and β are the constants characteristic to the crystal, T is the absolute temperature of the crystal, and Θ is the Debye temperature of the crystal. Since the symmetry of WO_3 is not cubic, and several physical constants (*e.g.* Debye temperature etc.) are unknown, the experimental results can not be compared with the theory directly. At any rate, the experimental curve is satisfied with the above expression, qualitatively. The values of α and β estimated in this temperature region are as follows:

$\alpha=3.1_1$ ev, $\beta=9.0\times10^{-4}$ ev/deg,
for *a*-polarized light,

and

$\alpha=3.1_5$ ev, $\beta=6.5\times10^{-4}$ ev/deg,
for *c*-polarized light.

These temperature coefficients are close to the values which have been well known in normal ionic crystals[7] and $BaTiO_3$[8]. Thus, these linear shifts may be due to the interactions between the lattice vibrations and the electrons in the crystals.

2) *Below 0°C*: According to the measurements with $BaTiO_3$ single crystals[8], at the orthorhombic-to-rhombohedral transition point the transparency decreases very much, and the absorption edge shifts suddenly toward red in appearance, because of multidomains in the low temperature phase (rhombohedral phase). When WO_3 is cooled, the multidomain structure as shown in Fig. 5 appears at about −50°C, at the same time as the transition to the low temperature phase happens. Therefore, the anomalous shifts about this transition point might be apparent as in the case of $BaTiO_3$. If so, the shifts should take place toward longer wave-lengths in contradiction to the experimental curves. Therefore the shifts of the absorption edge accompanied with this transition can not be attributed to the multidomain effect. In fact, by the microscopic inspection, the color of WO_3, light green just above this transition point, becomes pale, as soon as the multidomains have appeared.

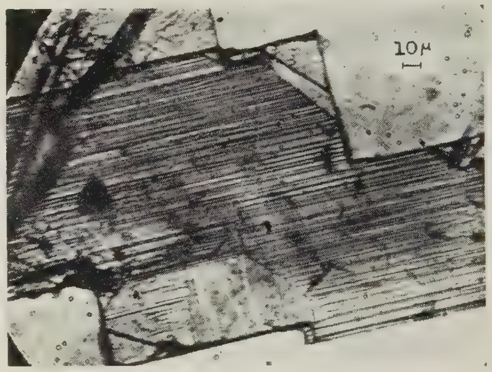

Fig. 5. The domain structure of WO_3 below −50°C

The extinction position of a *c*-plane changes abruptly with this transition. In the low temperature phase it makes an angle of about 45° with the monoclinic *b*-axis, while it is parallel or perpendicular to the *b*-axis in the high temperature phase. Then the direction of a- or b-polarized light is no longer parallel to anyone of the optic elasticity axes in the low temperature phase. This may be the reason why any distinction of the absorption edge between a- and b-polarized light cases is not observed in the low temperature phase as shown in Fig. 4. On the other hand, such an abrupt change in regard to the extinction position of a b-plane does not occur, and the discrepancy of the absorption edge between the a- and c-polarized light cases is also seen in the low temperature phase.

According to T. Muto *et al.*[6], the shift of the absorption edge due to the interactions between the lattice vibrations and the electrons at low temperatures is expressed by

$$E=\alpha'-\beta' \exp(\Theta/T) \quad (T \ll \Theta) .$$

This means simply a deviation from the linear dependence on temperature. The experimental curves, however, are not so simple, but exhibit obviously the temperature hysteresis loops. Thus, it is difficult to believe that the anomalous shift is a deviation from the linear dependence as mentioned above*. Then, it is natural to suppose that the shift should be attributed to the phase transition. Such an anomalous shift related to the phase transition has not yet been observed in the case of $BaTiO_3$.

3) *From 700°C to 900°C*: Accordingly to S. Sawada *et al.*[4], a polydomain structure appears in the tetragonal phase above 740°C, and then vanishes at about 810°C. Therefore, in the range from 740°C to 810°C, the incident ray of light may be refracted or reflected at plenty of domain walls. As a result, there is some possibility that the absorption edge may suddenly shift in appearance at 740°C just as in the case of the low temperature phase of $BaTiO_3$. However, such an apparent absorption should disappears above 810°C. Moreover, any abrupt shift is not observed for c-polarized light. From these facts, the sudden shift observed in the case of a-polarized light can not be considered to be a mere apparent phenomenon.

Then, some other mechanisms should be taken into consideration to explain this anomaly. There are two mechanisms at least that must not be neglected. The first is based on migrations of some oxygen atoms. When WO_3 single crystals are kept in vacuum above 740°C for a long time, they are likely to be reduced and the surfaces assume metallic luster. Magnèli and Hagedüs *et al.*[9] have shown that there are several kinds of reduced forms of tungsten oxides. Judging from this situation, it may be supposed that some oxygen atoms in the interior of WO_3 are apt to move from their normal sites at high temperatures. Therefore, if one assumes that the concentration of oxygen vacancies increases when the phase changes from orthorhombic to tetragonal, the optical absorption due to such a lattice imperfection is expected to be much more intense in the tetragonal phase than in the orthorhombic phase[1]. This optical absorption band might appear on a little longer wavelength side than the intrinsic absorption band edge. Accordingly, the superposition of the intrinsic absorption with the absorption band due to such a lattice imperfection in the tetragonal phase may give rise to the optical anomaly at 740°C. Such being the case, the anisotropic character of the absorption edge, that is, the fact that the sudden shift takes place only for the case of a- or b-polarized light may be attributed to the anisotropic character of a lattice imperfection**.

---

* According to S. Sawada[10] the value of specific heat begins to decrease gradually at about 0°C, when the temperature is lowered. Then assuming $\Theta=300°K$, and using the temperature coefficients of the linear red shift, the calculated curve on the low temperature side is a dotted line in Fig. 2 for the case of a-polarized light.

** If oxygen ions lining up in the direction of the a-, b-, and c-axes are called O_a, O_b, and O_c respectively, as discussed in the previous paper[1], it may be expected that the O_a is especially movable in the tetragonal phase. Then, suppose that any one of O_a-site becomes vacant, and two electrons will be trapped around the vacancy to keep the electrical neutrality. Since two W ions always close to the vacancy, the trapped electrons may roughly be considered to move around the two W ions. Such a model resembles a hydrogenlike molecule. When the electron in such a hydrogenlike molecule makes the optical transition from its ground state to the first excited state, the dominant component of the transition matrix element of the dipole moment will be that along the direction joining the two nuclei. Since this direction coincides with the a-axis in the present case, such optical absorption can be observed for a-polarized light case, but not for c-polarized light in the dipole transition approximation.

The second is based on energy band considerations. The energy band scheme would depend on the nature of the crystalline field and vary with the symmetry of the crystal. Then, the energy band structure of WO_3 can be expected to change with the phase transition. As many authors[11] pointed out in wurtzite structure materials, the optical transition between the valence and conduction bands follows the proper selection rule for the crystal structure, which depends on polarization of the incident light in the anisotropic crystal. In tetragonal $BaTiO_3$, R. C. Casella *et al.*[12] have observed the dichroic effect at the absorption edge, which disappears in the cubic phase. They also treated this phenomenon in terms of band-band transitions. Therefore, energy band considerations would lead one to expect the anisotropy of the optical absorption edge (pleochroism) and also the sudden shift of the absorption edge associated with the phase transition in WO_3 without assuming any lattice defect***. From this point of view, the intrinsic absorption edge itself would be expected to show a shift, owing to the change of the band structure, when the phase changes from orthorhombic to tetragonal.

At the present stage, however, it may be too early to decide which one of the two mechanisms mentioned above is more important, because the low resolving power of the spectrograph used prevented the author from getting information about any detailed structure of the absorption edge.

This work has been carried out under the guidance of Professor T. Horie, to whom the author wishes to express his sincere gratitude. The author wishes to express his sincere thanks to Professor S. Sawada of Tokyo Institute of Technology for valuable suggestion and kind advice. The author also wishes to express his gratitude to Lect. K. Kawabe of Kobe University, Dr. T. Kojima of Osaka City University and Mr. T. Kojima of Kinki University for their valuable discussions and criticisms. He wishes to thank Mr. E. Hirota and Mr. A. Tsubaki for their valuable assistance.

References

1) T. Horie, K. Kawabe and T. Iwai: Ann. Rep Sci. Works, Fac, Sci. Osaka Univ. **4** (1956) 45.
2) S. Sawada and G. C. Danielson: Phys. Rev. **113** (1959) 1008.
3) R. Ueda and T. Ichinokawa: Phys. Rev. **80** (1950) 1106.
4) S. Sawada and G. C. Danielson: Phys. Rev. **113** (1959) 1005.
5) S. Tanisaki: J. Phys. Soc. Japan, **15** (1960) 566.
6) T. Muto and S. Ôyama: Prog. Theor. Phys. **5** (1950) 833.
A. Radkowsky: Phys. Rev. **73** (1948) 749.
H. Y. Fan: Phys. Rev. **82** (1951) 900.
7) H. Fesefeldt: Z. Physik **64** (1930) 627, 741.
8) T. Horie, K. Kawabe and S. Sawada: J. Phys. Soc. Japan **9** (1954) 823.
9) A. Magnèli: Nova Acta Regiae Soc. Sci. Upsaliensis (4) **14** (1950) 20; Acta Cryst. **6** (1953) 495.
A. J. Hagedüs, T. Millner, J. Neugebauer und K. Sasvári: Z. anorg. Chem. **281** (1955) 64.
10) S. Sawada: J. Phys. Soc. Japan **11** (1956) 1237.
11) G. Dresselhaus: Phys. Rev. **105** (1957) 135.
J. L. Birman: Phys. Rev. **114** (1959) 1490.
R. C. Casella: Phys. Rev. **114** (1959) 1514.
12) R. C. Casella and R. P. Keller: Phys. Rev. **116** (1959) 1469.

*** Going along this line, the pleochroism of WO_3 may be attributed to the splitting of the electronic state, of which the energy band is composed, due to the crystalline field. If the wave-lengths of the absorption edge for *a*-, *b*-, and *c*-polarized light are called λ_a, λ_b, and λ_c respectively, from the experimental result it follows:

$\lambda_a-\lambda_b\approx100$ Å (0.05 ev), $\lambda_a-\lambda_c\approx700$ Å (0.3 ev) in the orthorhombic phase, $\lambda_a=\lambda_b$, $\lambda_a-\lambda_c\approx1800$ Å (0.6 ev) in the tetragonal phase. This value is considerably larger than that roughly estimated from the dichroic data in tetragonal $BaTiO_3$[12] (0.02～0.03 ev) in the region where the dichroic peak is located.

JOURNAL OF THE PHYSICAL SOCIETY OF JAPAN, Vol. 15, No. 9, SEPTEMBER, 1960

Association of Vacancies with Calcium Impurities in Potassium Chloride Crystals

By Tosiyuki NINOMIYA

The Institute for Solid State Physics, the University of Tokyo, Tokyo

(Received June 4, 1960)

Measurements are made on the dc conductivity and dielectric loss in quenched KCl crystals doped with small amount of $CaCl_2$. The evidence for formation of higher complexes is obtained from the decay of the conductivity during annealing after quenching. It is also found that there exists a relation between the number of free vacancies, n_v, and that of impurity-vacancy associated pairs, n_p, during the decay at a fixed temperature,

$$n_p = K' n_v^{1.92}.$$

The number of the free vacancies is found to decay exponentially with time. The activation energy for the decay is estimated to be 0.63 ± 0.1 eV.

§1. Introduction

One of the conventional methods of investigation of atomic defects in ionic crystals is to add small amount of divalent impurities to the host crystals[1]. Results obtained are usually analysed on the assumptions that these impurity ions are dissolved substitutionally in the lattice and there exist free vacancies and impurity-vacancy associated pairs in it besides isolated impurity ions. On the other hand, Haven suggested the existence of higher complexes, that is, impurity-vacancy clusters[2]. He measured dielectric loss in NaCl containing $CaCl_2$ at 110°C and estimated the concentration of the free vacancies from the low frequency conductivity and that of the pairs from the height of the loss peak. A sum of these two concentrations was found to be smaller than the concentration of the added impurity. It seems, however, to remain some ambiguity in his analysis, because we have neither reliable knowledge about the mobility of the free vacancies at these low temperatures nor about the dipole moment of the pairs[3].

The purpose of the present paper is to investigate the state of the impurities in KCl and provide a new evidence for formation of the aggregates of calcium impurities in the crystal.

§2. Theory

In ionic crystals the addition of divalent cation impurities leads to the formation of cation vacancies. These vacancies tend to associate with isolated impurity ions owing to the Coulomb interaction between these opposite charges. The degree of association decreases with increasing temperature. Then, in a quenched crystal an excess concentration of free vacancies and isolated impurity ions is retained and they migrate to form impurity-vacancy associated pairs and higher complexes, when the crystal is held at a fixed temperature after quenching.

Under the condition that crystals are quenched from a temperature, in which positive ion vacancies introduced with divalent impurities are predominant, a sum of the number of the free vacancies, $n_v(t)$, and that of the pairs, $n_p(t)$, should remain constant during annealing after quenching unless precipitates or higher complexes are created. Then,

$$n_v(t) + n_p(t) = N. \qquad (1)$$

Eq. (1) gives a straight line as shown in curve *a* of Fig. 1, when plotted in a n_v versus n_p curve.

In the case in which the formation of higher complexes occurs during the annealing process, a sum of the numbers of the vacancies and the pairs decreases with time and a trajectory becomes curvilinear. (Fig. 1 curve *b* or *c*) Curve *c* can be expected if a rate of formation of higher complexes is slower than that of formation of simple associated pairs.

So long as quenching strain has no influence on the mobility of free vacancies, their number is proportional to dc conductivity or ac conductivity at low frequencies. The existence of associated pairs gives rise to dielectric loss in a crystal and its peak height is proportional to their number. Therefore, if observed dc conductivity is plotted against tan δ due to the pairs, a valuable information about the higher complexes or precipitates may be obtained from the shape of the obtained curve.

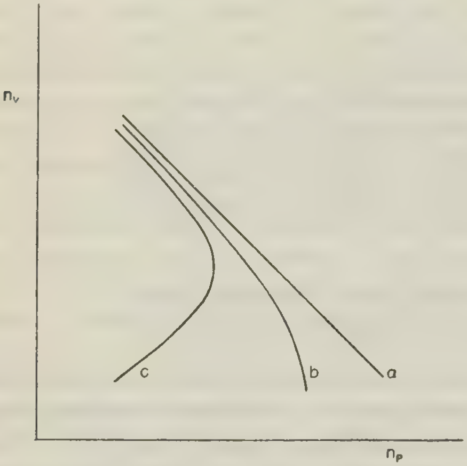

Fig. 1. Trajectory of the numbers of defects after quenching.

§ 3. Experimental Procedure

KCl crystals used as source material were purified beforehand by normal freezing of powder of Wako reagent grade purity. These pure crystals show neither dielectric loss of Debye type due to associated pairs, nor change in their conductivity after quenching.

Specimen crystals were grown from the melt of the above source material, into which $1\times10^{-2}\sim5\times10^{-2}$ mole per cent of $CaCl_2$ had been added, by the normal freezing method using a platinum boat in the atmosphere of purified nitrogen. The end of crystals solidified in a boat was turbid and milky looking, when cooled slowly to room temperature. Only transparent portions were used in the measurements.

The concentration of Ca^{++} impurities was estimated from the dc conductivity at 372°C by making reference to the data given by Kelting and Witt[4] for KCl-$CaCl_2$ system. Those for pure crystals were also estimated to be about 2×10^{-4} mole per cent.

The crystals were cleaved into pieces about $4\times5\times2$ mm for quenching experiments. After heating these crystals at about 530°C, which is still in the impurity range, in a vacuum vessel for several hours, quenching was done by removing the vessel from a furnace and making air flow into it. Most of the quenched crystals were cleaved into three pieces as shown in Fig. 2, and the hatched section was used for measurements in order to avoid an effect of inhomogeneity. Some crystals were measured after all surface layers of about 0.8 mm thickness were removed by cleavage in order to investigate an effect of surface contamination. These gave the same results as those crystals shown in Fig. 2.

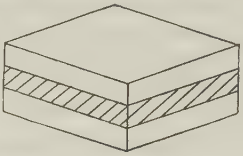

Fig. 2. Cleavage of a quenched crystal. The hatched section was used for measuremets of conductivity.

The ac conductivity was measured with the ac bridge.[5] Measurements of the dc conductivity were made with the $\mu\mu$-A meter which has a time constant of 1 second. Electrodes were applied with silver paints. Colloidal graphite was also used for the measurements of the dc conductivity up to high temperatures.

The decay of the conductivity was measured at various selected temperatures after keeping quenched crystals for about 20 hours

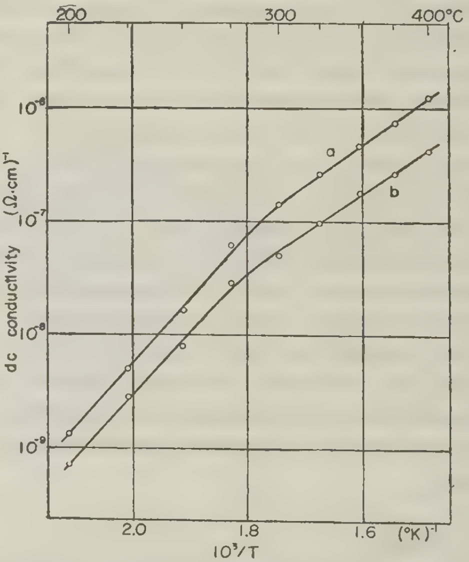

Fig. 3. Dc conductivity of annealed crystals doped with Ca^{++}. Impurity concentration
a: 0.01 mole per cent
b: 0.003 mole per cent

at room temperature. It took 30~60 minutes to raise the temperature of crystals to the selected one from room temperature. Therefore, we could not observe a change which took place during the resting and the temperature increasing.

§ 4. Experimental Results

a) *Dc conductivity of annealed crystals*

The dc conductivity of the doped crystals, which were annealed in the atmosphere of nitrogen at 650°C for 11 hours and cooled to room temperature at a rate of 10 deg/hr, were shown in Fig. 3. The curve for a crystal containing 0.01% Ca^{++} shows a portion of steeper slope below 300°C and, when the measurements were made while the crystal was cooled from 400°C at a more rapid rate than 150°C/hr, an increasing cooling rate results in a larger conductivity in this temperature range.

b) *Dielectric loss in annealed and quenched crystals*

The dielectric loss curve plotted against frequency for annealed crystals shows one peak, which is 1.25 times wider than a simple Debye type loss as shown in Fig. 4. This peak is supposed to be the loss due to impurity-vacancy associated pairs in comparison with the results by Dryden.[6]

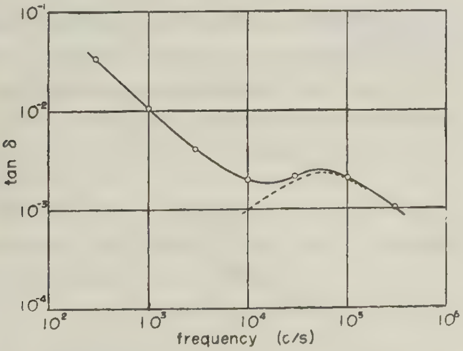

Fig. 4. Dielectric loss in an annealed crystal containing 0.01% Ca^{++} at 143°C.

Dielectric loss in a quenched crystal was also measured. Curve *a* and *b* in Fig. 5 show losses which were measured 10 min. and 5.5 hours after the beginning of decay observation, respectively. Curve *b* is shifted down to make the figure distinctive. The magnitude of the loss peak of curve *b* is smaller than that of curve *a* by 22%. Changes of neither the position nor the shape of the loss peak due to the pairs were observed during annealing at 144°C.

From those results we may conclude that we can follow a change of the number of the pairs during a decay if we measure a magnitude of dielectric loss at a fixed frequency. We chose 100 kc/s as the measuring frequency.

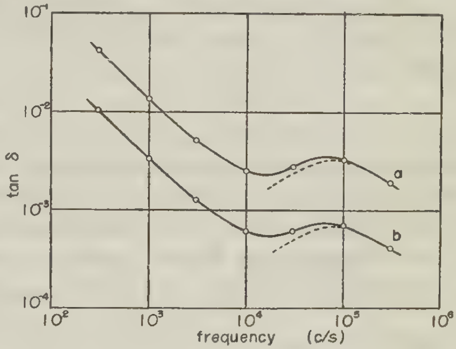

Fig. 5. Dielectric loss in a quanched crystal containing 0.006% Ca^{++} at 144°C. Curve *b* is shifted down to make the figure distinctive. (see text)

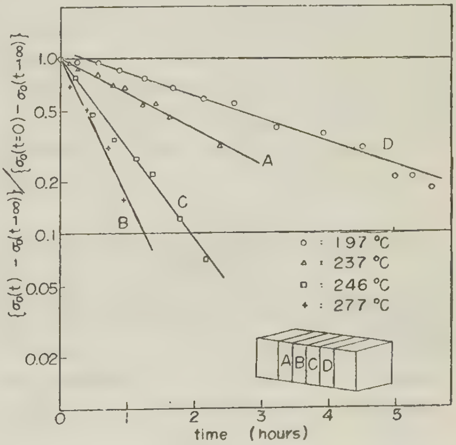

Fig. 6. Decay of dc conductivity after quenching.

c) *Decay of dc conductivity*

The dc conductivity was found to decay exponentially with time. The temperature dependence of the relaxation time for decay was investigated on the four pieces A, B, C and D, which were obtained by cleavage from one quenched crystal containing 0.01% Ca^{++}, as shown in Fig. 6. The origin of time was the time at which the temperature of crystal reaches the selected one. The activation energy for the decay was obtained to be 0.63±0.1 eV. (Fig. 7) Decay could not be observed above 200°C for a crystal containing 0.003% Ca^{++}, but at 144°C the conductivity decayed slightly (a few per cent).

d) *Ac conductivity decay*

Simultaneous measurements were made on dc conductivity, ac conductivity at 300 c/s and dielectric loss at 100 kc/s during annealing at 144°C for a quenched crystal containing 0.01% Ca^{++}. The dc conductivity, σ_0, and the conductivity at 300 c/s, σ_{300}, decayed, keeping a relation

$$\sigma_{300}=K_1\sigma_0 \qquad (2)$$

as shown in Fig. 8. K_1 was about 1.6 and this suggests that the measured value of the dc conductivity was affected by polarization. But, at the same time, this relation shows that the magnitude of the dc conductivity is proportional to the number of the free vacancies in spite of polarization effect.

To the dielectric loss at 100 kc/s both the simple associated pairs and the free vacancies contribute. The magnitude of the contribution from the latter can be estimated from the conductivity at 300 c/s. This was only 3~4% of the total loss. By subtracting this value from the observed loss, the contribution from the former could be obtained. Fig. 9 shows a curve of the logarithum of $\sigma_0(t)$ versus the logarithum of $\tan\delta$ due to the pairs, $\tan\delta_{\rm pair}$. This curve can be fitted by a relation

$$\tan\delta_{\rm pair}=K_2\ \sigma_0^{1.92}. \qquad (3)$$

The nearly same value of K_2 was obtained for crystals containg Ca^{++}, the concentration of which is 0.003% to 0.02%, at the same temperature.

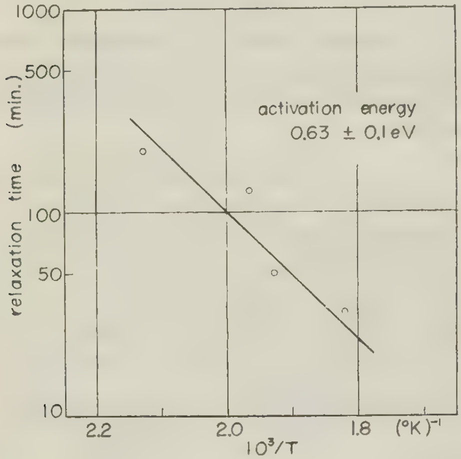

Fig. 7. Relaxation time for decay of dc conductivities.

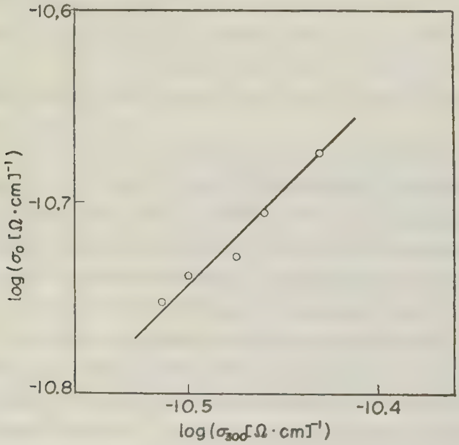

Fig. 8. Relation of dc conductivity and ac conductivity at 300 c/s during decay at 144°C.

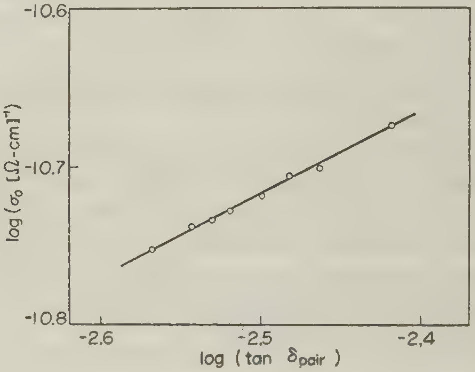

Fig. 9. Trajectry of conductivity during annealing at 144°C.

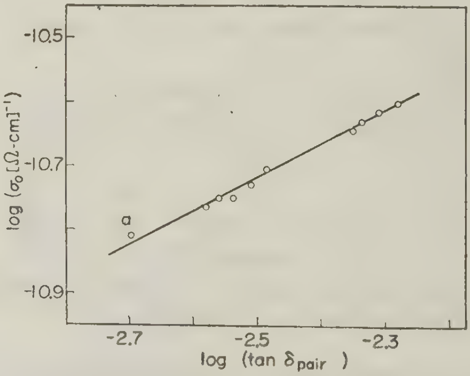

Fig. 10. Trajectory of conductivity during annealing at 144°C.

A quenched crystal containing 0.02% Ca^{++} was cooled slowly to room temperature after the decay of the conductivity was measured at 144°C for several hours, and was again heated to 144°C after keeping at room temperature for 19 hours and the measurement was continued. The result is shown in Fig. 10. The point *a* is that obtained in the measurement after resting at room temperature. The other points are those in first annealing. A straight line could be drawn through all these points and the same relation as the formula (3) was obtained.

For another crystal we made a similar measurement, but by heating the crystal for several hours up to higher temperature by 10 degrees in the course of annealing instead of cooling. The same relation was also available.

§ 5. Discussion

a) *Possible influence of quenching strains on the conductivity*

In ionic crystals the thermal conductivity is very small and thermal stresses cause plastic deformations. If quenching strains had an influence on the jump frequency of the bound vacancy around a Ca^{++} ion, its change would result in a shift of the peak frequency of loss. As shown in Fig. 5, we could not find any change either in the peak frequency or in the shape of the curve of loss due to the simple associated pairs during annealing. This implies that the observed decay of the loss is not affected by quenching strains, but is due to the decrease of the number of the pairs.

As for the free vacancies, we may conclude that quenching stains have little influence on their mobility, when we take into account the fact that measurements of ionic conductivity of pure crystals after quenching by air cooling reveal no change in either the ac or dc values.

Therefore, a relation between the free vacancies, n_v, and of the pairs, n_p, can be deduced from the formala (3),

$$n_p = K'_2 \, n_v^{1.92}. \tag{4}$$

b) *Association of vacancies with the impurity ions*

In quenched crystals, there exists an excess of the free vacancies and the isolated impurity ions. They will attract each other and form simple associated pairs. These pairs also tend to form precipitates or higher complexes.

These reactions can be formulated in terms of the following equations:

Reaction I [free vacancy]+[isolated imprity ion] $\leftrightarrows$ [simple associated pair], (5)

Reaction II $n \times$[simple associated pair] $\rightleftarrows$ [precipitate or higher complex]. (6)

Charged higher complexes may also be formed.

From the experimental results shown in Fig. 9 and 10, following conclusions can be obtained:

1) The deviation of the curve in Fig. 9 from the curve *a* in Fig. 1 is the direct evidence for the formation of higher complexes or precipitates during the annealing.

2) Reaction I can reach an equilibrium in a short time at 144°C, but for the other reaction the time required to reach equilibrium is long. In this situation an expected curve of n_v *vs.* n_p is curve *c* in Fig. 1. We, however, observed only a part of the trajectory because of our experimental condition that it took about one hour to raise the temperature of crystals to the selected one.

From the present experiment, we can not decide which are formed during the annealing, precipitates or higher complexes. But, the formation of higher complexes seems more likely, because the density of KCl crystals containing small amount of $CaCl_2$ changes linearly with the concentrations of the impurity.[7)]

Since the reaction 1 reaches equilibrium in a short time, the following relation may be expected between the concentrations of the defects:

$$K \, n_v \cdot n_i = n_p, \tag{7}$$

where n_i is the number of isolated impurity ions. K is slightly dependent on the concentration of unassociated defects, because there exist long range Coulomb interactions among these defects.

Unless charged complexes are formed,

$$n_v = n_i, \tag{8}$$

and Eq. (7) is reduced to an explicit form as[1),8)]

$$x_p = 12 \, x_v^2 \exp\left[\frac{T_0}{T} - \frac{2(2\pi\sqrt{2})^{1/2} (T_0/T)^{3/2} x_v^{1/2}}{\{1+4(\pi\sqrt{2})^{1/2} (T_0/T)^{1/2} x_v^{1/2}\}} \right], \tag{9}$$

where x_p and x_v are the molar fractions of the pairs and of the vacancies respectively and T_0 is a binding energy of the pairs divided by Boltzmann's constant. In the derivation of this equation, purely Coulombic interactions among the defects are assumed at all separations and only nearest association is considered as pair.

The experimental results in NaCl containing $CdCl_2$ agree well with the prediction of Eq. (9), if we take the binding energy as 0.34 eV.[8] This value is in fairly good agreement with the calculated one by Bassani and Fumi.[9] They obtained the value of the binding energy of 0.32 eV for Ca^{++} in KCl.[9] When a sum of the concentrations of free vacancies and pairs is $1\times10^{-3}\%$, $5\times10^{-3}\%$ and $1\times10^{-2}\%$, $d(\log x_p)/d(\log x_v)$ is estimated to be 1.8, 1.7 and 1.6 respectively from Eq. (9), using the binding energy of 0.32 eV. In these estimations, the long range interactions are somewhat underestimated, because the energy value of 0.32 eV is smaller by a factor of about 2 than that obtained on the assumption of purely Coulombic interactions, and correction of this will further reduce the value of $d(\log x_p)/d(\log x_v)$.

On the other hand, from the experiment of the conductivity decay, we obtained the formula (4), where $d(\log x_p)/d(\log x_v)=1.92$. The disagreement between the experiment and the above estimation suggests that the number of free vacancies may not be equal to that of isolated impurity ions or the distribution of defects may not be homogeneous.

In the former case charged complexes or charged dislocations will be formed. Owing to the lack of information about the concentration of isolated Ca^{++} ions, we can make no further discussion. If similar experiments as above are made for crystals containing manganese impurities, more definite conclusions may be obtained, because we expect to have detailed information about the behaviors of manganese ions from electron spin resonance.

As to the existence of heterogeneity in crystals, we may conclude that quenching strains do not play important role, taking into account that both crystals cleaved as shown in Fig. 2 and those, for which all surface layers were removed, showed the same results.

The author wishes to express his sincere thanks to Professor H. Kanzaki and Professor T. Suzuki for their encouragement and many valuable discussions. He is also much indebted to Mr. K. Kido for his help and to Profesor J. Yamashita for his advice.

Reference

1) For a review, see A. B. Lidiard: *Handbuch der Physik*, **20**, (Springer Verlag, Berlin, 1957)
2) Y. Haven: *Defects in Crystalline Solids* (The Physical Society, London, 1955) 261p.
3) Y. Haven: Philips Tech. Rev. **20**, (1958), 69.
4) H. Kelting and H. Witt: Z. Phys. **126** (1949) 697.
5) S. Takahashi and I. Matsuzaki: Bulletin of the Electrotechnical Laboratory, **19** (1955) 99. in Japanese. This bridge is constructed after Gross and Cole (Rev. Sci. Instr. **20** (1949) 252) with some improvements.
6) J. S. Dryden and R. J. Meakins: Disc. Farad. Soc. **23** (1957) 39.
7) H. Pick and H. Weber: Z. Phys. **128** (1950) 409.
8) A. B. Lidiard: Phys. Rev. **94** (1954) 29.
9) F. Bassani and F. G. Fumi: Nuovo Cimento **11** (1954) 274.

JOURNAL OF THE PHYSICAL SOCIETY OF JAPAN, Vol. 15, No. 9, SEPTEMBER, 1960

Measurement of the Intensity in Electron Diffraction by a CdS Single Crystal

By Satio TAKAGI and Fuminori FUJIMOTO

Institute of Physics, College of General Education,
University of Tokyo, Komaba, Meguro-ku, Tokyo

(Received May 7, 1960)

A method of measuring the intensity of electron in electron diffraction patterns by the electron-bombardment-induced-current (EBIC) in a CdS single crystal is described. The CdS detector is moved in the diffraction camera by a screw which is driven by a synchronous motor. EBIC is measured directly by a automatic recording millivoltmeter. EBIC properties of good crystals selected from those prepared by Frerichs' method are given. It is shown that the intensity can be measured within 2–3% error, if suitable precautions are made. An example of the measurement on TlCl is also given.

§1. Introduction

The photographic method is usually employed for the intensity measurement in electron diffraction. For the purpose of precise measurement, however, this method requires rather elaborate procedures and for all these procedures an accuracy better than a few percent cannot be expected. In X-ray diffraction, the direct method of intensity measurement with a G–M or other counters is widely used with satisfactory results. Lennander[1] has developed the G–M counter method in electron diffraction and succeeded in obtaining on accuracy as high as that in X-ray diffraction. However, the resolving time of the G–M counter is too long for the beam intensity conveniently used in electron diffraction experiment and moreover the detector is not suitable to be put in the ordinary diffraction camera.

One of the authors and his collaborator[2] have pointed out that the electron-bombardment-induced-current (EBIC) in CdS crystal can be utilized for the intensity measurement in electron diffraction, and Simon[3] applied this method to X-ray diffraction. It was pointed out in the electron case, that drawback of this method were relatively long response time (1 min.) of, and the hysteresis effect in EBIC. By proper choise of the CdS crystal, the characteristics of the detector are now greatly improved, the response time and the hysteresis effect being reduced to a negligible extent.

Characteristic of the photoconduction[4] and of EBIC[5] have been studied by many authors. However, the results obtained are not always satisfactory for the present purpose.

Experimental results on the EBIC characteristics of CdS detector for use in electron diffraction are presented in this paper together with an example of the intensity measurement.

§2. Preparation of CdS Detector

The CdS single crystals were prepared by Frerichs' method, no impurity being added purposely. Crystals suitable for the detector of electron beam were selected under the following directions: i) the stick-like crystals 0.5–1.0 mm in diameter and about 3 mm in length, ii) with orange colour, iii) no luminescence with ultra-violet irradiation, iv) with extremely small dark current and v) with relatively large photocurrent induced with daylight.

Indium metal which makes ohmic contact with CdS was evaporated directly onto the crystal surface with a narrow gap at the centre of the crystal. The gap was made by placing a fine wire on the crystal during the evaporation. Deposited indium served as electrodes and the gap as the slit of the detector. Suitable thickness of indium electrode is 1500–3000 A, for 0.03 mm gap. Thicker electrodes made electrical contact with each other and with thinner ones the effective width of the slit became larger than the true width of the gap. This is probably due to the fact that the conductivity of thin electrodes is comparable with the conductivity of CdS crystal induced by electron beam which can penetrate through thin electrode and reach the crystal underneath.

The crystal detector prepared by the above procedures was set between two copper electrodes, making electrical contact with them with conductive paste.

§ 3. Apparatus

The diffraction camera used in this experiment is of a usual type with a focussing coil. CdS detector is placed in front of a box containing the photographic plates and can be driven perpendicular to the incident beam by a screw which is rotated either by hand or by a synchronous motor. The maximum stroke is 9 cm. The driving system of the detector is shown in Fig. 1. D is the detector composed of a insulator base, two copper electrodes and an CdS crystal, P is a metal shield which protect the insulator base from being charged up by electron beam, S is the driving screw, C is the incident beam stop and F is a Faraday cylinder, 6.5 mm in diameter, which is used in obtaining the characteristic curve (i.e. EBIC vs. electron intensity curve) of the crystal.

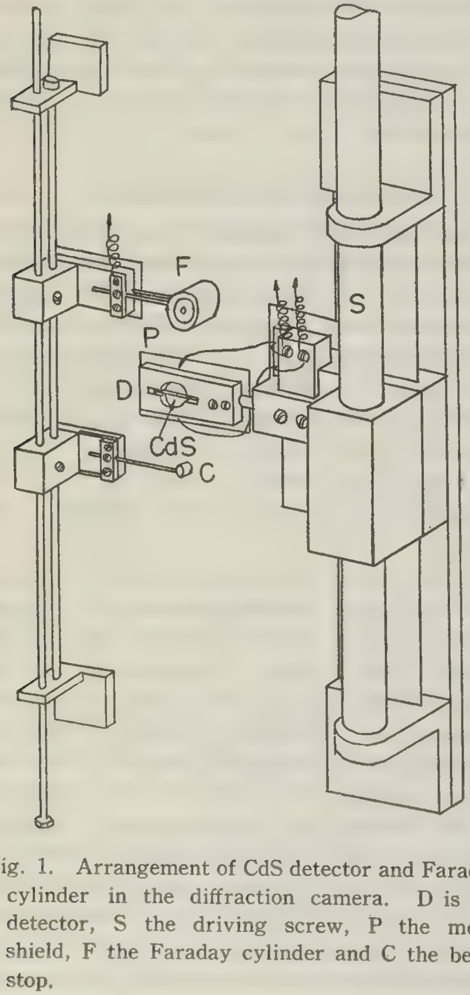

Fig. 1. Arrangement of CdS detector and Faraday cylinder in the diffraction camera. D is the detector, S the driving screw, P the metal shield, F the Faraday cylinder and C the beam stop.

The detector D is connected in series with a battery and an automatic recording millivoltmeter which are placed outside the camera and F with a DC amplifier of maximum sensitivity 10^{-13} A.

Photographic plates can be stored in a box not shown in the figure and the diffraction pattern can be photographed whenever desired.

The primary voltage of the high-tension transformer was kept constant by an automatic stabilizer which was controlled by a variable impedance connected in series with the primary circuit of the transformer. No especials tabilizer of the electron current was used, but following precautions were taken: i) the voltage on the Wehnelt cylinder was applied by self-biasing, ii) tungsten filament with fresh surface was used as the cathode which was heated by a battery, iii) the residual pressure in the diffraction camera was kept as low as

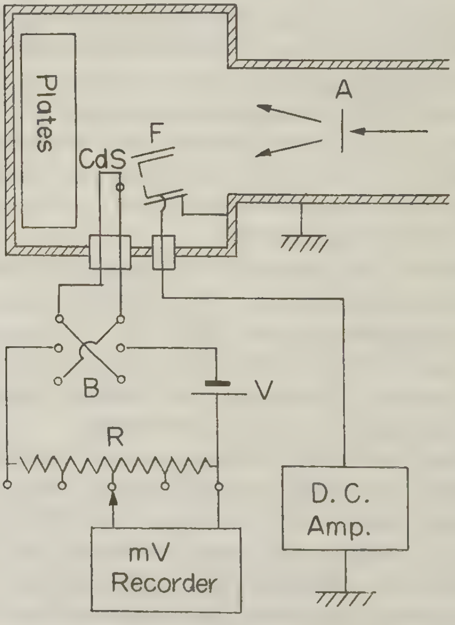

Fig. 2. Schematic diagram showing the arrangement of obtaining the EBIC vs. electron intensity curve.

8×10^{-5} mmHg. Under these conditions the fluctuation in the total electron current was less than 1%.

§ 4. Characteristics of the CdS Detector

i) *EBIC vs. electron intensity curve*

Fig. 2 schematically shows arrangement of obtaining the sensitivity curve and measuring EBIC and the electron current. The scatterer A is a thick film of amorphous substance such as glass, which gives diffraction pattern of almost uniform intensity distribution, the incident spot disappearing in the pattern. The Faraday cylinder is set at high scattering angle where the intensity distribution of electrons over the openning of the cylinder is sufficiently constant, and the CdS crystal is held behind the hole at the bottom of the cylinder. The electron current onto the crystal is calculated from the current onto the Faraday cylinder assuming the proportionality between the beam current and the cross section. The voltage applied to the crystal and the mean electric field in the crystal are given in Table I.

Table I. Properties of CdS detectors.

Dector No.	Slit width mm	Cryst. width mm	Applied voltage Volt (kV/cm)	n*	Gain*
1	0.2	0.70	45 (2.25)	0.82	4.8×10^6
2	0.08	1.00	6 (0.75)	0.90	1.2×10^7
3	0.08	0.69	6 (0.75)	0.97	5.1×10^7
4	0.03	0.68	1.5 (0.50)	0.87	1.3×10^7
5	0.03	0.75	45 (15.0)	0.90 ($>3.1\times10^{-10}$ A/cm²) 0.98 ($<3.1\times10^{-10}$ A/cm²)	2.3×10^7
6	0.03	0.74	1.5 (0.50)	0.82	4.3×10^7
7	0.03	0.53	6 (2.0)	0.96	4.9×10^7
8	0.03	0.67	1.5 (0.50)	0.97	4.3×10^7

* for 41.3 keV electrons.

The results for 41.7 keV electrons are shown in Fig. 3, Fig. 9 (a) and (b). Dark current for each crystal was negligibly small. The relation between EBIC and the electron current is given by the well known formula

$$i\propto I^n\,,$$

where i and I are EBIC and the electron current, respectively. Values of n are given in Table I, which are constant in the whole range of measurement except in the case of Dectector No. 5 for which n is 0.9 for intensities higher than 3.1×10^{-10} A/cm² and 0.98 for lower intensities. The deviation of the individual points from the curve is within 3%, except a few points which show larger deviations. These larger deviations might arise not from the error in the measurement of the intensity of EBIC but from that in the measurement of the electron current. The measurement of the latter is more difficult owing to the stray electrons scattered or se-

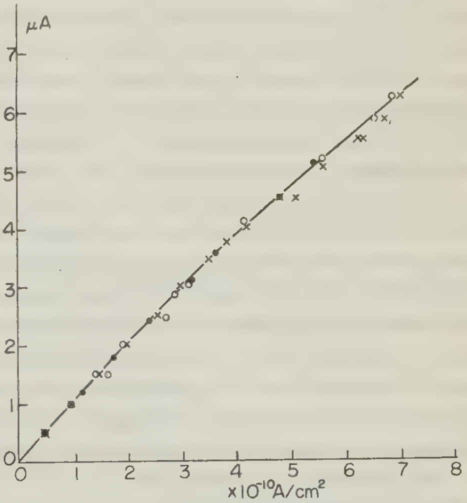

Fig. 3. Characteristic curve for Detector No. 2. The ordinate is EBIC and the abssisa is the electron intensity. Electron energy=41.3 keV.

●: the measurement on the 1st day,

○: the measurement on the 2nd day,

×: the measurement on the 3rd day.

condarily emmitted from the surroundings of the Faraday cylinder.

The characteristic curve did not change for 48 hours so long as the crystal was kept in vacuum. When, however, the crystal was exposed to air, the characteristic curve changed. An example is shown in Fig. 4.

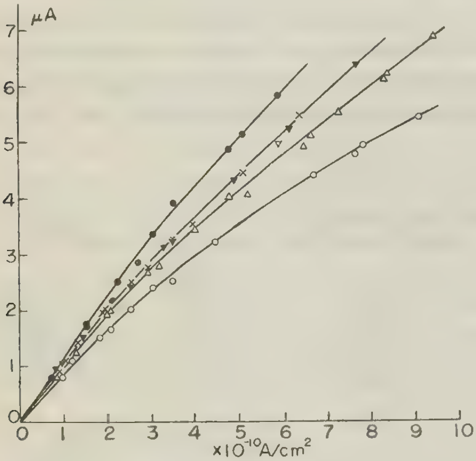

Fig. 4. Change of the characteristic curve upon exposure to air and subsequent evacuation. Electron energy=41.3 keV.

●: before the exposure,
○: 1^h 30′ after the exposure,
△: 3^h 00′ after the exposure,
×: 4^h 30′ after the exposure,
▼: 24^h after the exposure.

Black circles represent results before the exposure to air, and white circles those 1.5 hours after 15 minutes exposure to air and subsequent evacuation, triangles and crosses those of later measurements. The time of measurement after the exposure is given in the legend. It is shown in the figure that after 4.5 hours the curve did not change any more, but it did not coincide with the initial curve, while for Detector No. 8 the characteristic curve coincided with the initial one about 20 minutes after the exposure. After repeated exposure to air, not only the gain but also the value of n changes. So it is necessary to check the characteristic curve for each intensity measurement.

The sensitivity of CdS crystals changed on irradiation with very strong electron beam. The EBIC then gradually increased with constant beam intensity. When the direction of the applied voltage was reversed by B in Fig. 2, the EBIC suddenly decreased and then gradually increased.

The irradiation with such a strong beam must be avoided, hence use was made of beam stop C in Fig. 1. By the irradiation with diffracted electrons used in this experiment none of the crystals showed such decrease of EBIC on reversing of the field, except Detector No. 1 which showed a slight decrease at the beam intensity higher than 5×10^{-10} A/cm².

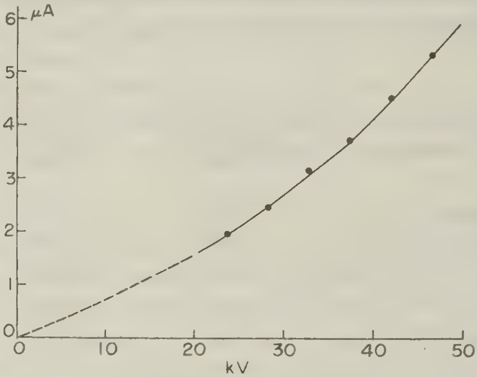

Fig. 5. Change of sensitivity with electron energy for Detector No. 2. Electron intensity=3.5 $\times 10^{-10}$ A/cm².

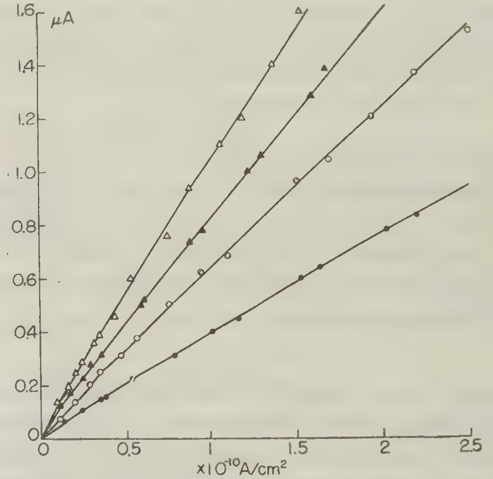

Fig. 6. Characteristic curves for Detector No. 8 with various electron energy. ●: 23.5 keV; ○: 32.4 keV; ▲: 41.3 keV; △: 50.2 keV.

Fig. 5 shows the variation of EBIC with the accelerating voltage at constant electron current for Detector No. 2 and Fig. 6, the characteristic curve of Detector No. 8 for 23.5, 32.4, 41.3 and 50.2 keV electrons. The change of the characteristic curve was reversible with the change of the accelerating voltage.

ii) *Response time*

The speed of response of EBIC is an important factor in the present method. It has been reported[4] that the response of photoconduction consists of two distinct parts: an initial rapid portion and a much slower portion of which response times are several μ sec. and several sec., respectively.

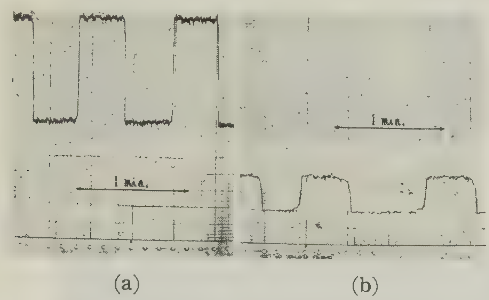

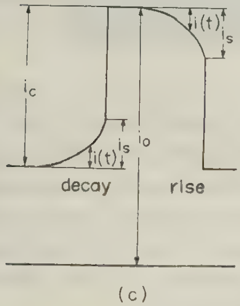

Fig. 7. Response of EBIC on Detector No. 8, (a) for $I_0=1.2\times10^{-10}$A/cm², (b) for $I_0=3.2\times10^{-12}$A/cm², (c) showing the meaning of symboles used in the text.

Fig. 7 shows the results of the experiment on EBIC. The electron intensity was instantaneously reduced to about half of the initial value and then increased to the initial value. (a) and (b) show the results for strong and weak irradiation, respectively. (c) shows schematically two portions of response time and the meaning of symbols used in the text and in Table II where values of response time T in rising case are given. The value of T, which is here refered to as "the response time" is defined as the time required for $i(t)$ to become $i_s/2$ (see Fig. 7(c)). Note that T does not mean the time required for $i(t)$ to become $i_c/2$. The value of T for decaying case is generally a little smaller than that for rising case. In Table III, values of T and i_s/i_0 of Detector No. 8 are shown for various change of the irradiation intensities in the case of medium and weak irradiations. EBIC reaches to the constant value within a few second even with very weak irradiation, and the response time is the shorter, the smaller the variation of irradiation intensity.

Table II. Values relating to the response of detectors in the rise case. $I_c/I_0=1/2$ and electron energy=41.3 keV.

Detector No.	i_s/i_0 (%)	T (sec.)	I_0 (A/cm²)
2	0.5	<0.5	8.6×10^{-10}
	0.5	1	4.4×10^{-10}
	1.5	1	2.1×10^{-10}
	3	1.5	9.3×10^{-11}
3	1	0.5	4.1×10^{-10}
	3	1	7.5×10^{-11}
	5	1.5	3.1×10^{-11}
	9	1.5	1.6×10^{-11}
4	2	1	6.4×10^{-10}
	2	1	3.2×10^{-10}
	5	1.5	1.4×10^{-10}
	8	1.5	2.6×10^{-11}
5	0.5	<0.5	3.8×10^{-9}
	1	0.5	1.2×10^{-9}
	1	1	6.3×10^{-10}
	4	1	2.8×10^{-10}
6	1.5	1	2.0×10^{-9}
	2	1	8.6×10^{-10}
	3	1	2.2×10^{-10}
	4	1.5	1.1×10^{-10}
7	2	1	2.3×10^{-9}
	3	1	1.0×10^{-9}
	4	1.5	3.5×10^{-10}
	7	1.5	1.3×10^{-10}
8	<0.5	<0.5	1.2×10^{-10}
	2	1	5.7×10^{-11}
	3	1	2.4×10^{-11}
	5	1.5	1.1×10^{-11}
	15	1.5	3.2×10^{-12}

The response time was smaller than the response time of the recorder for the intensity variation usually met with in practical diffraction work.

iii) *Other Properties*

a) *Noise of EBIC.* For the detector with slit width larger than 0.08 mm, the noise of EBIC was less than the fluctuation in the incident electron intensity and was negligible. For smaller slit width, e.g. 0.03 mm, the magnitude of noise was often larger than 10% of the EBIC for weak irradiation, and did not decrease with decrease of the electron intensity, though the fluctuation in the

Table III. Values relating to the response corresponding to various changes of electron intensity for Detector No. 8. (electron energy=41.3 keV).

		In the rise case		In the decay case	
I_0 (A/cm^2)	I_e/I_0	i_s/i_0 (%)	T (sec.)	i_s/i_0 (%)	T (sec.)
9.5×10^{-11}	1/4	0.5	0.5	0.5	<0.5
	1/2	1	0.5	1	0.5
	3/4	2	1	1	0.5
	7/8	2.5	1.5	1.5	1
	1	3	1.5	2	1.5
2.5×10^{-11}	1/4	2.5	1	2.5	1
	1/2	3	1	3	1
	3/4	5	2	3	2
	7/8	7	2.5	3.5	2.5
	1	9	2.5	6	2.5

electron intensity became smaller with the decrease of the electron intensity. After prolonged use with large noise, the crystal was often broken down and became conductive.

When there is a large noise, it is better to reduce the applied field and diminish the noise. For this reason the strength of the applied field to the crystal is limited.

b) *The infra-red quenching.* It was reported in the previous note, that the illumination with infra-red light improved the hysteresis effect in the sensitivity curve. This method, however, was not adopted in the present experiment, because (1) the hysteresis effect in the sensitivity curve was not observed so long as the electron intensity was kept less than a reasonable value, (2) the response of EBIC was not improved, (3) the sensitivity decreased and (4) the variation of the EBIC increased probably by the fluctuation in the infra-red intensity.

§ 5. Measurement of Debye Ring for Electron Diffraction

Fig. 8 (a) and (b) show the intensity curves of electron diffraction pattern from a polycrystalline TlCl which was preparated in the camera by vacuum evaporation onto collodion film. CdS Detector No. 8 with slit width 0.03 mm was used. (a) and (b) show the intensity curves for which the divider resistance R shown in Fig. 2 were 1 kΩ and 10 kΩ, respectively. (c) shows the photograph which was taken subsequently. Fig. 9 (a) and (b) show the characteristic curves for Fig. 8 (a) and (b) respectively, by which the absolute values of electron intensity of (a) and (b) can be obtained.

The detector speed was 2 mm/min. and the time required for the measurement was 7 min. This time is determined by the line width (0.08 mm for 110-reflection in this case) and the pen speed of the recorder (2 sec. for full scale). If we measure more broad line or use the high speed recorder, we can shorten the time of measurement.

§ 6. Discussion

The main cause of error in the present method are as follows: (1) slow response of EBIC, (2) the shift of EBIC, (3) the noise and (4) the shift and fluctuation of the intensity of scattered electrons. The former three of these are concerned with the properties of crystals, and can be avoided by proper choise of the crystal and of the intensity of electrons. Detector No. 8, for example, can safely be used with current density from 5×10^{-12} A/cm^2 to more than 2.5×10^{-10} A/cm^2. This range covers the whole range of current densities in usual diffraction pattern. The change of the characteristic curve of the crystal on exposure to air is a troublesome problem, because it necessitates frequent calibration of the characteristic curve. This will be avoided, however, by employing suitable air lock for the replacement of specimens and photographic plates used in ordinary electron microscopes.

(4) arises from the fluctuation of the inci-

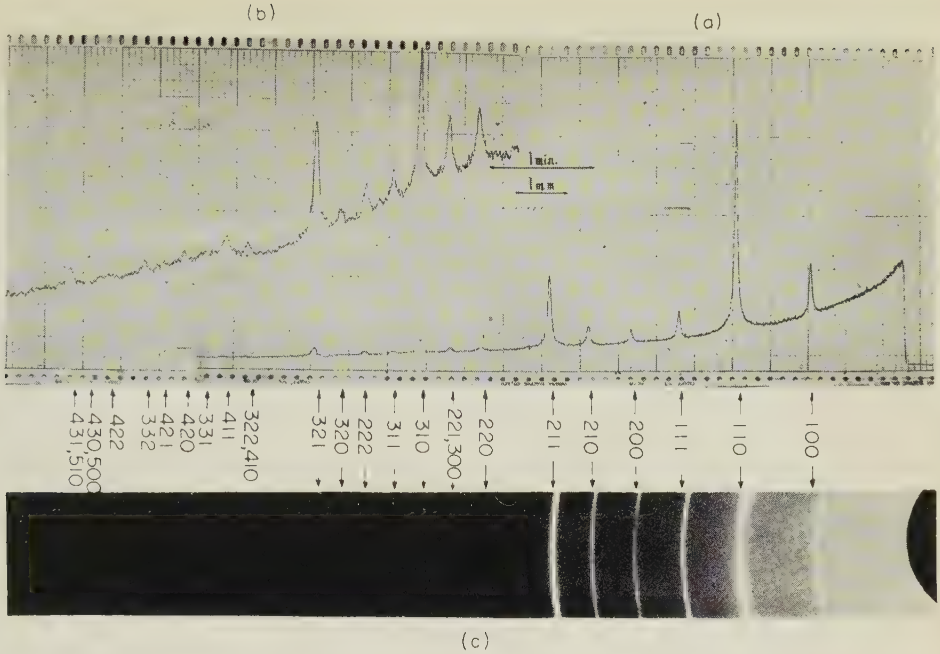

Fig. 8. Example of the measurement on TlCl. The distance in the acctual pattern and the time of measurement are indicated in the figure. Electron energy=41.3 keV.

(a) for R (Fig. 2)=1 kΩ, (b) for R=10 kΩ, (c) the diffraction pattern.

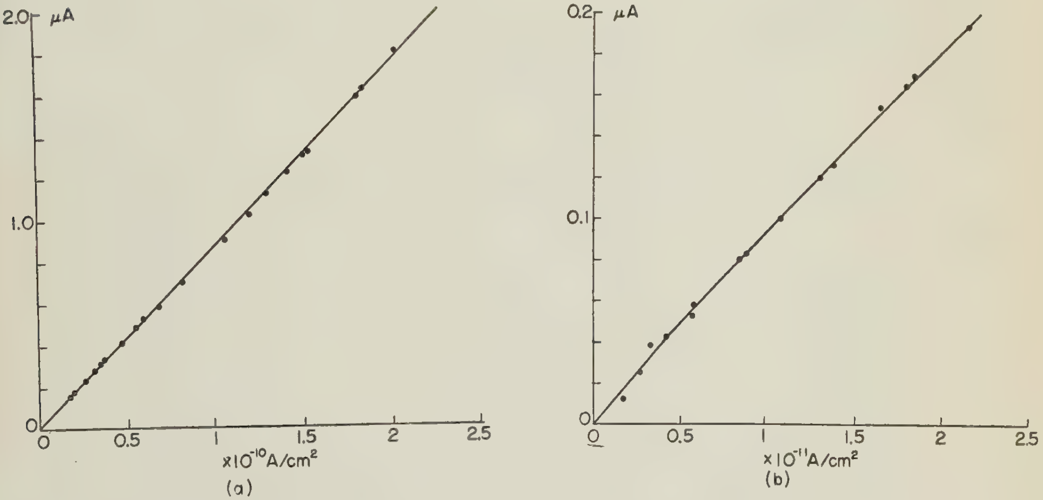

Fig. 9. Characteristic curves of Detector No. 8. (a) and (b) are those corresponding to Fig. 8 (a) and (b), respectively.

dent beam and the change of the specimen on irradiation with electron beams. The fluctuation of the intensity of the total electron current from the cathode to the anode can easily be kept constant within 1%, so long as suitable precautions stated in § 3 are taken into account. The fluctuation in the intensity of actual incident beam, i.e. the beam passed through slits, is somewhat larger and is 2–3% in ordinary conditions. The intensity of the diffracted beam, however, sometimes changed gradually, even if the incident beam intensity was kept constant. This may be due to the change in specimen: e.g. the contamination of the specimen, the vapourization in the case of volatile speci-

mens and the chemical change in the case of chemically unstable substances. To avoid this effect, weak electron beam should be used which, however, is limited by rather slow response of EBIC and relatively large noise for weak electron beams. The present method is not adequate for the diffraction by unstable substances.

In the present study, we do not considered in detail the mechanism of EBIC, but merely quote the data on properly selected crystals and show that these crystals can be used for the present purpose. The study of photoconductivity of CdS and other crystals has made a progress in recent years, and the production of good crystals suitable for the detection of electron beam i.e. crystals with short response time, small noise and with n nearly equal to 1 etc. may be expected.

This work was partly supported by a research grant of the Ministry of Education.

References

1) S. Lennander: Ark. Fys. **8** (1954) 551.
2) S. Takagi and T. Suzuki: Acta Cryst. **8** (1955) 441.
3) H. Simon and M. v. Heimendahl: Ann. Physik **20** (1957) 355.
4) R. H. Bube: Proc. IRE (1955) 1836. A. Rose: Proc. IRE (1955) 1850.
5) H. Kallmann and R. Warminsky: Ann. Physik **6** (1949) 229. H. Benda: Ann. Physik **9** (1951) 419. S. M. Ryvkin, B. M. Konnvalenko and Y. S. Smetanikova: Sh. Techn. Fis. **24** (1954) 961. C. E. Bleil, D. D. Synder and Y. T. Sihvonen: Phys. Rev. **111** (1958) 1522. F. Lappe: Zeit. Physik **154** (1959) 267.

Journal of the Physical Society of Japan, Vol. 15, No. 9, September, 1960

Elektronische Wechselwirkung zwischen Wasserstoff und aufgedampften Nickelfilmen

Von Yoshihiko Mizushima

Electrical Communication Laboratory, Nippon Telegraph and Telephone Public Corporation, Musashino-shi, Tokyo

(Recived December 28, 1959)

Adsorption of hydrogen on nickel film was measured, which was evaporated under an ultra-high vacuum condition. The relation between the adsorption and the change of electrical resistance of the film was closely studied to find apparently complicated results, which were very different from those of the previous reports. The effect of film thickness, measuring temperature and annealing temperature were separately examined. Adsorption kinetics were also regarded. From the experimental facts it was concluded that the adsorbed species were: (1) negatively charged atom, (2) positively charged atom and (3) molecule. The charge is, however, relatively small. An explanation for the resistance change was suggested.

§ 1. Problemstellung

Die Adsorption von Wasserstoff an Übergangsmetallen ist wegen ihrer grundlegenden Bedeutung für die heterogene Katalyse in den letzten Jaharzehnten besonders weitgehend untersucht worden. Seit 20 Jahren gewinnt die Messung an im Hochvakuum aufgedampften Metallschichten[1),2)] wegen der Sauberkeit solcher Filme zunehmend an Interesse.

Das Verhalten der elektrischen Leitfähigkeit von Metallfilmen bei der Adsorption von Fremdmolekeln[3)] wird neuerdings vielfach und mit Erfolg für die Untersuchungen herangezogen. Die von den verschiedenen Autoren erhaltenen Ergebnisse bezüglich des Systems Ni/H_2 sind aber noch nicht in guter Übereinstimmung[3),4),5)], was zur Folge hat, daß der Mechanismus der Adsorption von Wasserstoff an Nickel noch nicht restlos geklärt ist.

Das Ziel der vorliegenden Arbeit ist, das Verhalten der elektrischen Leitfähigkeit von im Ultrahochvakuum[6)] aufgedampften Nickelschichten bei der Adsorption von Wassestoff unter saubersten Bedingungen zu verfolgen und den Einfluß der Meßtemperatur, der Aufdampf- und Temperungsbedingungen zu studieren, um damit Aufschluß über den Adsorptionsmechanismus zu gewinnen. Ein Teil der experimentellen Ergebnisse ist kurz mitgeteilt[7)].

§ 2. Experimentelles

In Abb. 1 ist die Versuchsapparatur dargestellt. Meßzelle Z und Ionisationometer I.M. können mit elektrischem Ofen auf über 400°C, alle anderen Teile, mit Ausnahme des McLeodschen Manometers, mit Hilfe einer Heizbandumwickelung auf 300°C geheizt werden. Das Quecksilber ist vorher mit kleiner Flamme gut entgast worden. Nach einer 20 Stunden dauerunden Ausheizung und Elektronenbombardment der nicht heizbaren Metallteile des Ionisationsmanometers ist ein Endvakuum von 10^{-11} Torr erreichbar. Als Kriterium für die Vakuumdichtigkeit soll die gesamte Apparatur über Nacht Klebvakuum halten, d.h. der Leckwert soll kleiner als 3.10^{-12} l. Torr/Sek. sein.

Der Verschluß S_6 ist mit einem Schliffeinsatz versehen, damit keine Rückdiffusion von Gas, das langsam vom Quecksilber abgegeben wird, in den Meßteil stattfindet. Dadurch kann der Meßteil beliebig lange unter gutem Vakuum gehalten werden. Solange das Ionisationsmanometer läuft, bleibt dieser Teil im Bereich von 10^{-10} Torr. Wenn das Ionisationsmanometer nicht eingeschaltet ist, nimmt der Druck dieses Teils langsam zu (über Nacht 10^{-9} Torr).

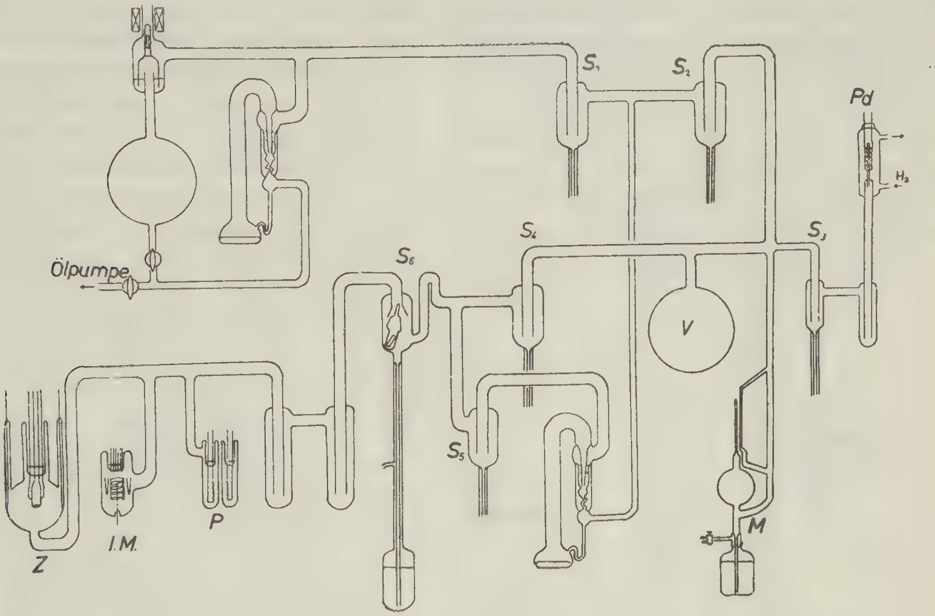

Abb. 1. Versuchsapparatur

Bei der Durchführung der Versuche muß das Vakuum beim Glühen der Nickelwendel gerade vor dem Äufdampften 10^{-10} Torr erreichen. Dann wird die Meßzelle auf 90°K abgekühlt, und der Nickelfilm wird aufgedampft bis zum gewünschten Widerstandswert, normalerweise 100 Ω (Schichtdicke ca. 100 Å), innerhalb 15 Min. Danach wird die Zelle auf Zimmertemperatur erwärmt und weiter im kochenden Wasserbad eine Stunde lang getempert. Nach Sennett u. Scott[8)] und Reynolds u. Stilwell[9)] ist die Kristallstruktur des aufgedampften Films umso kompakter, je größer die Aufdampfgeschwindigkeit ist. Es ist aber in diesem Falle wichtiger, daß die aufgedampfte Oberfläche gasfrei bleibt. Deshalb wird die geringere Wendeltemperatur gewählt, zumal bei Übergangsmetallen die Gefahr einer Koagulation nicht so groß ist.

Bei der Entkühlung der Zelle nach dem Aufdampfen kann man einen kurzzeitigen Druckanstieg beobachten, der bei ungenügender Entgasung der Nickelwendel über 10^{-7} Torr erreichen kann. Wendet man jedoch die Methode mit vier Zuführungsdrähten[5] an, so tritt dieses Druckmaximum nicht mehr auf, soweit die Wendel gut entgast wurde.

Durch die einstündige Temperung bei 373°K erreicht man, daß der Widerstand bei Zimmertemperatur konstant bleibt, daß also kein Ordnungsvorgang mehr festzustellen ist.

Dann wurde die Messung begonnen.

Nach der Messung wird die aufgedampfte Schicht in verdünnter Salpetersäure gelöst und nach einer Methode von Sandell[10] photometrisch bestimmt.

Das in den meisten Fällen zum Versuch benutzte Nickel hat etwa 1.7% Verunreinigungen, wie Co, Al, Si. Um einerseits die Verunreinigung der Schicht möglichst gering zu halten und anderseits did Entgasung möglichst vollkommen durchzuführen, wurde bei Verwendung einer neuen Nickelwendel zunächst ein Film aufgedampft, der nicht zu einer Messung diente. Erst nach Herauslösen dieses ersten Films und Reinigung der Zelle wurde der richtige Versuch mit einem neuen aufgedampften Film begonnen. Der versuch mit spektroskopisch reinem Nickel zeigte, daß die vorliegende Meßergebnisse bei beiden Nickelproben fast dieselben sind, solange die Entgasung sehr vorsichtig durchgeführt wird.

§ 3. Experimentelle Ergebnisse

Soweit nicht besonders erwähnt, sind die Bedingungen der Schichtherstellung: Aufdampfen bei 90°K unter 10^{-10} Torr, Schichtdicke ca. 100 Å und Temperung bei 373°K 1 Stunde lang.

3–1. *Adsorption bei 273°K*

Ein typischer Verlauf des Widerstandes und

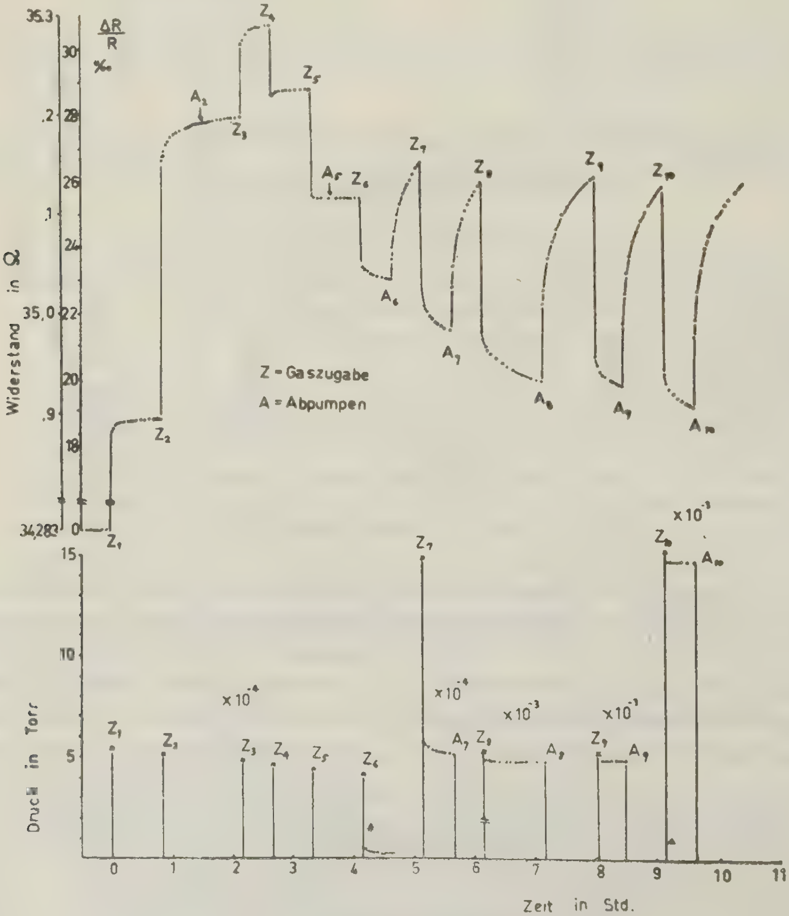

Abb. 2. Adsorption bei 273°K

des Drucks bei 273°K als Funktion der Zeit nach verschiedenen Zugaben von Wasserstoff ist in Abb. 2 dargestellt. Bei der jeweiligen Zugaben Z_1 bis Z_5 ist nach 20 Sek. kein Druck mehr festzustellen. Der Widerstand steigt nach der Gaszugabe zunächst sehr rasch an, dann langsamer. Die geringfügige zeitliche Widerstandszunahme dauert auch dann noch an, wenn der Druck praktisch auf Null abgesunken ist. Das läßt auf irgeneinen Vorgang schließen, der unabhänging ist vom Gasdruck. Nach der Zugabe einer gewissen Wasserstoffmenge erreicht der Widerstand schließlich ein Maximum (Z_3) und nimmt dann bei weiteren Zugaben ab. Die langsame Widerstandszuanhme nach jeder Zugabe bleibt jedoch erhalten. Der Druck fällt immer noch rasch innerhalb einer halben Minute bis auf Null ab. Bei weiteren Gaszugaben wird die langsame Widerstandszunahme schwächer. Schließlich erreicht man einen Punkt, von dem ab nicht mehr die ganze abgegebene Gasmenge adsorbiert wird. Nach diesem Punkt ist das Adsorptionsgleichgewicht so langsam, daß man mit dem Piranimanometer verfolgen kann.

Der Druck- und Widerstandsverlauf ist jetzt mit einem beträchtlichen Zeitbedarf verknüpft. Der Sättigungswert wird innerhalb einiger Stunden nicht erreicht. Während vor diesem Grenzpunkt durch Abpumpen kein Gas desorbiert werden kann und der Widerstand sich folglich beim Abpumpen auch nicht ändert, läßt sich nach dem Grenzpunkt durch Abpumpen innerhalb der Fehlergrenze die gesamte (nach diesem Grenzpunkt) adsorbierte Gasmenge desorbieren, wobei die Widerstandsänderung rückläufig ist. Dieser Grenzpunkt ist also eine wichtige Größe und wird im folgenden als irreversible Grenze bezeichnet. Die Gasmenge, die bis zu dieser Grenze adsorbiert ist und nicht mehr desorbiert werden kann, wird n_{irr} genannt. Die reversibel, unter dem Druck 5.10^{-3} Torr und in 1 Stunde adsorbierte Menge wird n_{rev} genannt. Unter $n_{\max}$ versteht man die Menge, die bis zum Erreichen des Widerstandsmaximum adsorbiert ist. Die entsprechende Widerstandsänderung vom Anfangswert R_0 wird $\Delta R_{\max}$ genannt.

Wird eine genügend große Wasserstoffmenge auf einmal zugegeben, so erreicht die Adsorption innerhalb einer halben Minute die irreversible Grenze, nach der die Adsorption langsam vor sich geht, wie in Abb. 3 dargestellt ist. Der Widerstand erreicht also das Maximum sehr rasch, so daß nur der reversible Teil der Beobachtung zugänglich wird.

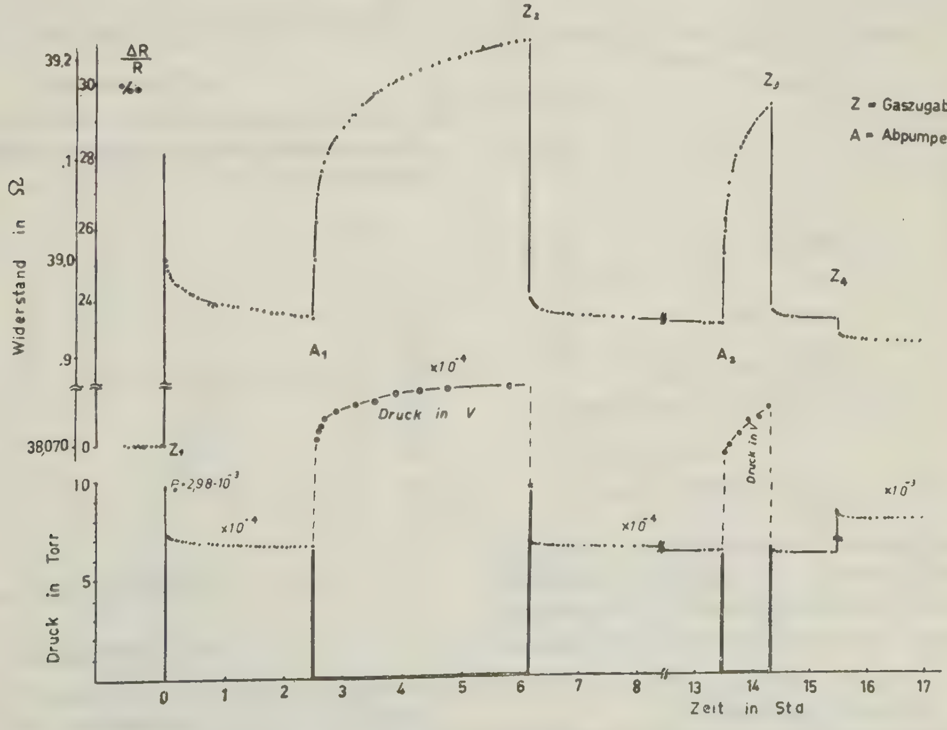

Abb. 3. Adsorption bei 293,5°K

Die Widerstandsänderung ist durchaus proportional der adsorbierten Menge.[7] Diese Tatsache deutet darauf hin, daß der gemessenen Widerstandsänderung und gemessenen Adsorption ein und derselbe Mechanismus zu Grunde liegt.

In Abb. 4 sind die Werte für die Widerstandsänderungen aus Abb. 2 über log $(t+t_0)$ aufgetragen. Alle Kurven, die bei der Desorption erhalten werden, folgen ohne Ausnahme und bis zum Ende der sogenannten Zeldovich-Gleichung[11]

$$n=\frac{1}{\alpha}\,[\log (t+t_0)+\text{const}] \tag{1}$$

oder

$$R=\frac{1}{\alpha}\,[\log (t+t_0)+\text{const}]\,. \tag{2}$$

Die Abb. 5 gibt den Zusammenhang zwischen der relativen Widerstandsänderung $\Delta R/R$ und der adsorbierten Menge pro Makrooberfläche mit den aus Abb. 2 zu entnehmenden Werten.

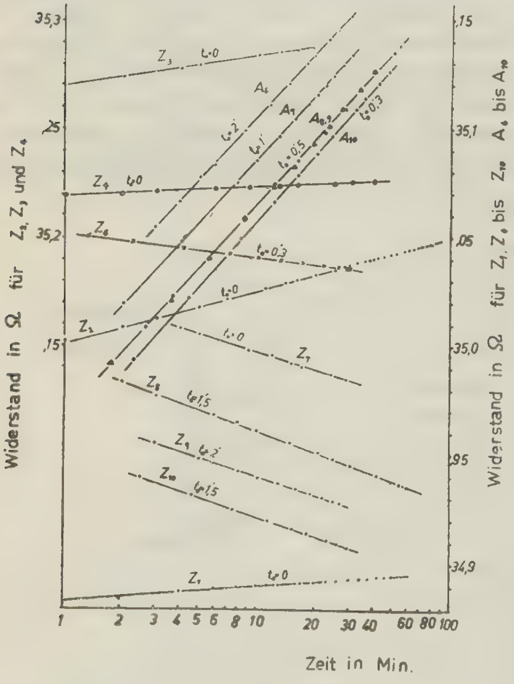

Abb. 4. Kinetik bei 273°K in Abb. 2

Die Meßpunkte entsprechen noch nicht ganz dem Gleichgewicht, da sich der Widerstand noch weiter entsprechend der Zeldovich'schen Gleichung ändert wie aus Abb. 3 zu ersehen ist.

3–2. *Adsorptionsisotherme*[7]

Die isotherme Widerstands- bzw. Druckänderung wurde bei Zimmertemperatur und bei tiefer Temperatur untersucht. Die Absorptionsenthalpie ΔH wird im reversiblen Bereich errechnet und in Abb. 6 als Funktion der Belegung pro Makrooberfläche aufgetragen.

Bei der Temperaturänderung im Isothermenversuch läßt sich die Aktivierungsenergie der Chemisorption bei Zimmertemperatur ermitteln. Die Aktivierungsenergie nimmt mit jeder Zugabe schwach zu. Sie ist im irreversiblen Bereich nicht zu berechnen und beträgt wahrscheinlich Null, da sowohl bei Zimmertemperatur als auch bei tiefer Tem-

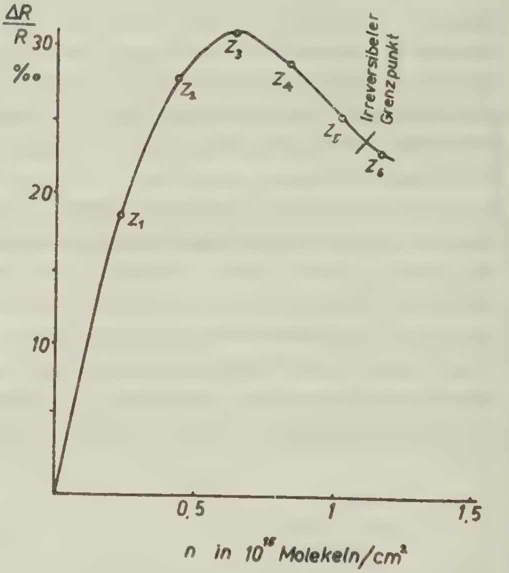

Abb. 5. Widerstandsänderung in Abhängikeit von der adsorbierten Zahl von Wasserstoffmolekeln bei 273°K nach Abb. 2

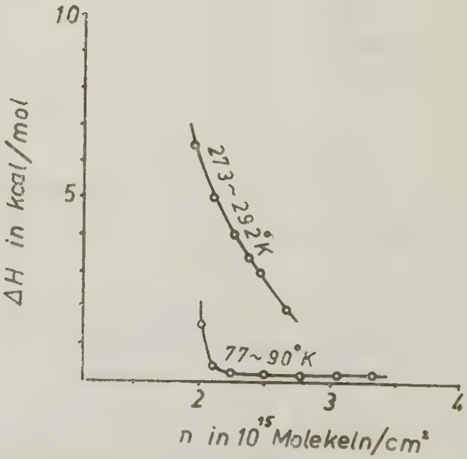

Abb. 6. Die aus Isothermen berechnete Adsorptionswärme ΔH in Abhängigkeit von der Besetzung mit Wasserstoff

peratur die irreversible Adsorption ohne Zeitbedarf vor sich geht.

3–3. *Adsorption bei 90°K*

Der typische Adsorptionsverlauf—durchgeführt genau wie bei 273°K—ist in Abb. 7 dargestellt. Am Anfang finden sehr schnelle Adsorptionen mit irreversibler Widerstandszunahme statt. Bis zum Widerstandsmaximum sind die Verhältnisse sehr ähnlich wie bei 273°K. Der einzige Unterschied besteht darin, daß die ständige langsame Widerstandszunahme, die nach jeder Zugabe unabhängig vom Gasdruck verläuft, bei 90°K nicht der Zeldovich-Gleichung gehorcht, sondern nahezu linear ist. Nach dem Maximum nimmt der Widerstand—auch wie bei 273°K—ab. Bei jeder Zugabe ist ein kleiner Widerstandspeak vorhanden, der jedoch schnell durch eine Widerstandsabhahme überkompensiert wird. Nach einigen weiteren Zugaben nimmt der Widerstand wie vorher zu, doch erfolgt die Abnahme bedeutend langsamer und in so geringem Maße, daß als Endeffekt eine geringe Widerstandszunahme resultiert. Der irreversible Grenzpunkt wird dann (Z_{10}) erreicht und der Druckverlauf ist meßbar.

Bei weiterer Zugabe ändern sich die Verhältnisse wieder. Der Peak bei der Zugabe

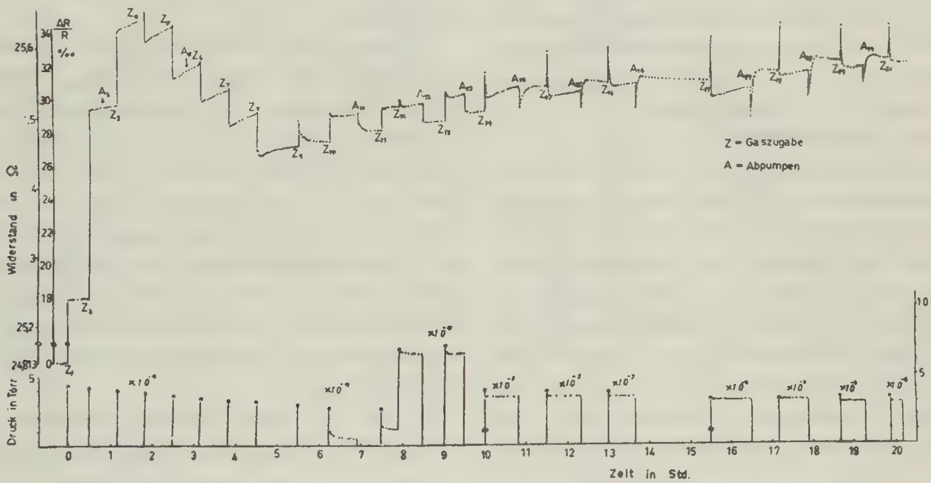

Abb. 7. Adsorption bei 90°K

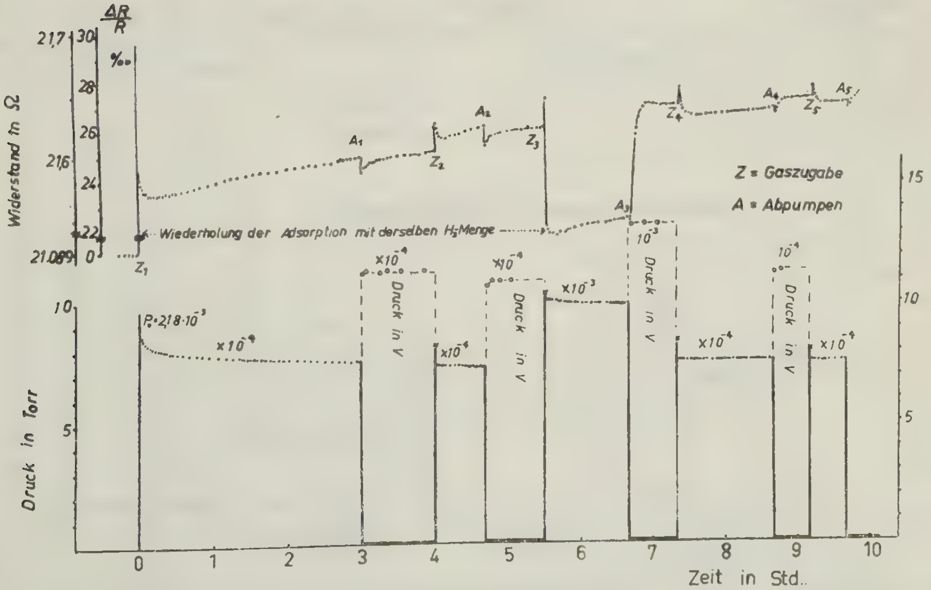

Abb. 8. Durch zwischenzeitliche Druckerhöhung bewirkte Umkehr des Widerstandseffktes bei 90°K

bleibt, doch ist die nachfolgende Widerstandsabnahme so groß, daß sie die Zunahme überwiegt. Beim Abpumpen geht dieser reversible Teil nach Auftreten eines umgekehrten Peaks wieder zurück. Je höher der Zugabedruck wird, desto stärker diese Umkehr der Widerstandsänderung.

Wenn auf einmal eine hinreiched große Gasmenge zugegeben wird, erhält man eine Kurve, wie sie in Abb. 8 und 9 dargestellt ist. Die Adsorption erreicht schon in einer halben Minute über Maximum und Minimum des Widerstandes die irreversible Grenze. Danach findet eine langsame, teilweise reversible Adsorption statt. Beim Abpumpen desorbiert nur wenig. Der Obserflächenprozeß geht immer—auch während des Abpumpens—unabhängig vom Gasdruck weiter, so daß lei der nochmaligen Zugabe der abgepumpten Gasmengen der Druck weiter abnimmt.

Um die Umkehr (Inversion) der Widerstandseffekte eingehender zu prüfen, wurden folgende Versuche unternommen. In Abb. 8 ist der Einfluß des Gasdrucks auf die Inversion gezeigt. Mit kleinem Zugabedruck wurde zunächst die Reversibilität geprüft. Danach wurde ein großer Druck zugegeben (Z_3). Nach dem Abpumpen wurde nochmals wie vorher ein kleiner Druck zugegeben. Es zeigt sich, daß nun die Inversion stattgefunden hat, d.h., daß die Widerstandsabnahme nach dem Peak bei der Zugabe diesen überkompensiert und daß beim Abpumpen die Widerstandszunahme stärker als die Widertsandsabnahme ist.

Bei dem andern Versuch (Abb. 9) wurde zunächst die Reversibilität geprüft. Dann wurde die Zelle auf 273°K erwärmt, ohne daß vorher abgepumpt war. Dabei erfolgte eine merkliche Adsorption wie am Gleichgewichtsdruck und am Widerstand zu erkennen war. Nach Abkühlung auf 90°K wurde wiederum die Reversibilität geprüft. Durch die zwischenzeitliche Temperaturerhöhung ist die Umkehr der Widerstandsänderung eingetreten und macht sich auch bei dem kleinen Druck bemerkbar.

Eine proportionalität zwischen Widerstandsänderung und adsorbierte Menge ist nicht mehr vorhanden. Der Druckverlauf folgt der Zeldovich'schen Gleichung unabhängig vom zwischenzeitlichen Abpumpen wie in Abb. 10 (aus Abb. 8) dargestellt ist. Der Widerstandsverlauf ist dagegen sehr kompliziert. Es gilt die Zeldovich-Gleichung bei der Desorption nicht mehr, da die Desorption nach wenigen Minuten endet. Diese Tatsachen deuten darauf hin, daß mehrere Adsorptionsmechanismen bei 90°K vorliegen.

In Abb. 11 ist die relative Widerstandsänderung aufgetragen als Funktion der Zahl von

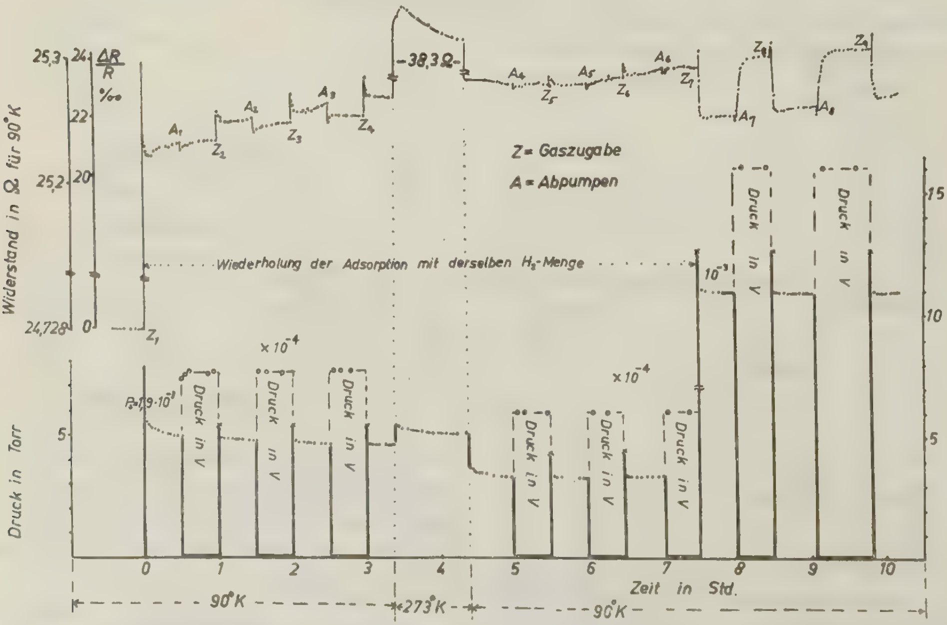

Abb. 9. Durch zwischenzeitliche Temperaturerhöhung bewirkte Umkehr des Widerstandseffektes bei 90°K

bei 90°K adsorbierten Wasserstoffmolekeln unter Zugrundelegung des in Abb. 7 dargestellten Versuchs.

3–4. *Einfluß der Schichtdicke*

Es wurden Schichten mit einer Dicke d von 25 Å bis 500 Å aufgedampft. Die Adsorption wurde jeweils unter gleichen Bedingungen durchgeführt. In Abb. 12 sind die Widerstände der Schichten als Funktion der Schichtdicke bei 273°K und 90°K angegeben. Wie ersichtlich ist, gilt für dickere Schichten ungefähr die Gesetzmäßigkeit

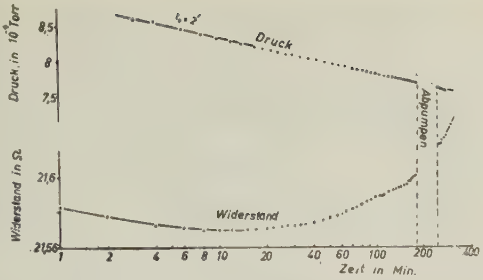

Abb. 10. Beziehung zwischen der zeitlichen Änderung von R und p in Abb. 11 zwischen Z_1 und Z_2

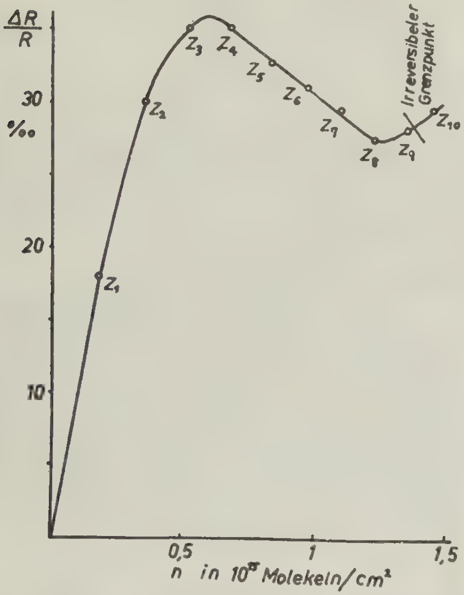

Abb. 11. Widerstandsänderung in Abhängigkeit von der adsorbierten Zahl von Wasserstoffmolekeln bei 90°K nach Abb. 10

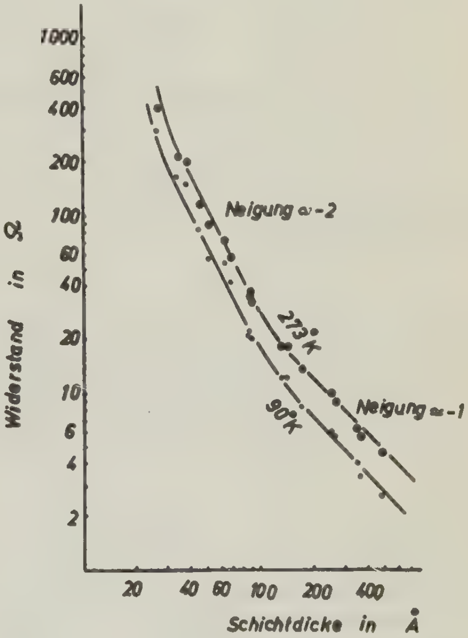

Abb. 12. Widerstand und Schichtdicke unbelegter Ni-Schichten

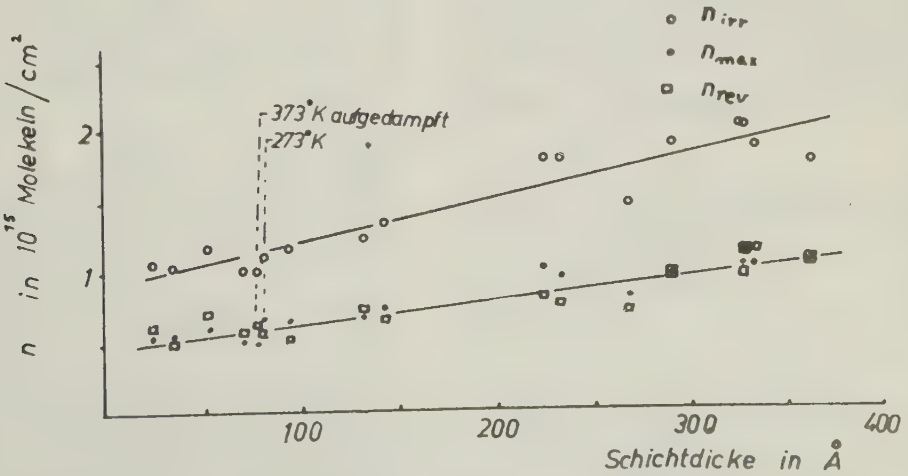

Abb. 13. Adsorbierte Menge H_2 in Abhängigkeit von der Schichtdicke, 273°K

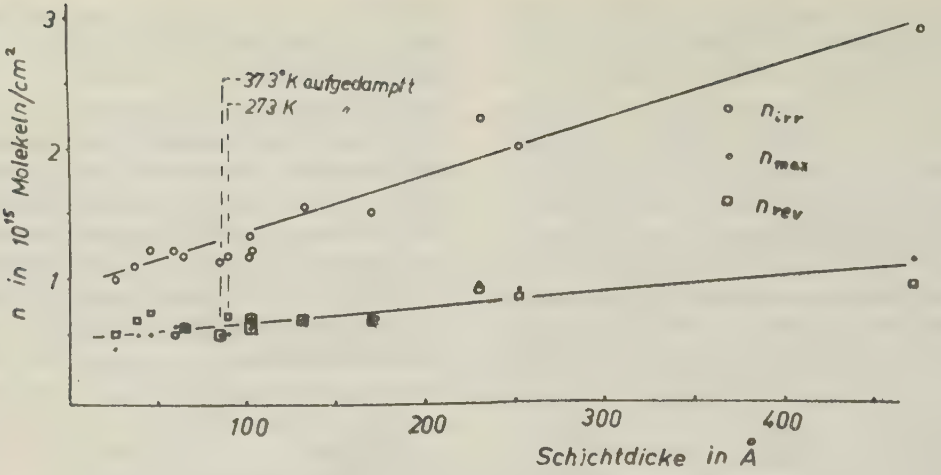

Abb. 14. Adsorbierte Menge H_2 in Abhängket von der Schichtdicke, 90°K

$$1/R = \text{const}\,(d - \text{const}), \tag{3}$$

sowie für dünnere Schicht näherungsweise im gemessenen Bereich

$$1/R = \text{const} \cdot d^2. \tag{4}$$

Exakt liegt hier natürlich keine Linearität zwischen log R und log d vor. Grenzdicke zwischen beider Gleichungen liegt etwa bei 100Å.

Die charakterischtischen Größen n_{max}, n_{irr} und n_{rev} sind für verschiedene Schichtdicken in Abb. 13 und 14 dargestellt. Die Meßwerte ergeben eine Gerade, die nicht durch den Ursprung geht. Diese Tatsache deutet darauf hin, daß die Adsorption an dünne Schicht auf Oberfläche stattfindet. Es gibt nur wenige Mitteilungen[12),13)], die besagen, daß die Gerade nicht durch den Koordinatenanfangspunkt geht. Extrapoliert man die in Abb. 13 und 14 angegebenen Werte nach größeren Schichtdicken hin, so erhält man eine ungefähre Übereinstimmung mit anderen in der Literatur angegebenen Werten[2),14)].

In Abb. 15 ist $\Delta R_{\text{max}}/R$ gegen log d aufgetragen. Die Kurve zerfällt in zwei Teile. Bei dünneren Schichten ist $\Delta R_{\text{max}}/R$ unabhängig von Meß-temperatur und von Schichtdicke, bei dickeren dagegen abhängig von Temperatur und von Schichtdicke.

3–5. *Einfluß der Temperaturbedingung*

Alle Nickelschichten wurden bei 90°K bis 100 Ω aufgedampft und später bei verschiedener Temperatur 1 Stunde lang getempert. In Abb. 16 sind n_{max}, n_{irr}, n_{rev} sowie $\Delta R_{\text{max}}/R$ für die gleiche Schichtdicke (ca. 100 Å) dargestellt. Der Ordnungszustand nimmt mit steigender Tem-

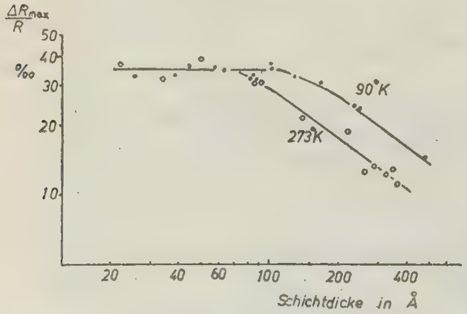

Abb. 15. Maximale Widerstandsänderung als Funktion der Schichtdicke

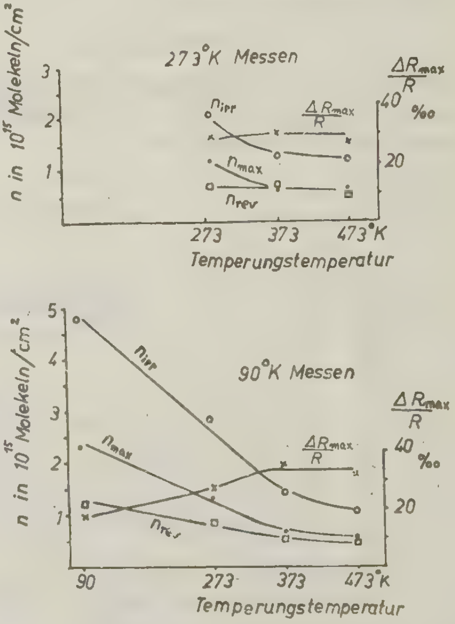

Abb. 16. Einfluß der Temperung auf die adsorbierte Menge H_2 und auf die maximale Widerstandszunahme

erungstemperatur zu und die Oberflächenrauhigkeit nimmt entsprechend ab. Infolgedessen werden die absorbierten Mengen $n_{\max}$, n_{irr}, n_{rev} kleiner, die relative Widerstandsänderung $\Delta R_{\max}/R$ dagegen größer. Aus Abb. 17 ist zu entnehmen, daß die Verhältnisse $n_{\text{rev}}/n_{\text{irr}}$ bzw. $n_{\max}/n_{\text{irr}}$ unabhängig von der Temperungstemperatur sind.

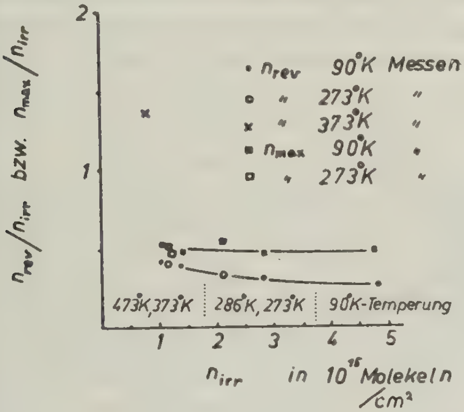

Abb. 17. Einfluß der Temperung auf das Verhältnis $n_{\text{rev}}/n_{\text{irr}}$ bzw. $n_{\max}/n_{\text{irr}}$

Während die Änderung des elektrischen Widerstandes bei allen getemperten Schichten ähnlich verläuft, ist bei ungetemperten Schichten die zweite Widerstandszunahme (molekular) viel größer als bei den getemperten.

Die Temperung bei 473°K ruft keine wesentliche Änderung gegenüber der Temperung bei 373°K hervor.

3–6. *Einfluß der Aufdampftemperatur*

Die Abb. 13 und 14 zeigen, daß beim Aufdampfen bei 273°K oder 373°K die charakteristischen Werte, $n_{\max}$, n_{irr} und n_{rev}, nicht von denen bei normaler Aufdampftemperatur (90°K) verschieden sind. Der Verlauf der Widerstandskurve zeigt auch keine Abweichung vom üblichen Verhalten. Die Adsorption von Wasserstoff ist also unabhängig von der Aufdampftemperatur, jedoch abhängig von der höchsten Temperatur, auf der die Schicht erwärmt wurde, d.h. von der Temperungstemperatur.

3–7. *Einfluß der Sauberkeit der Arbeitsbedingungen*

Versuche, bei denen die Vorentgasung nicht vollkommen durchgeführt war, zeigen; (1) Auch *bei 273°K* ein negativer Widerstandspeak beim Abpumpen auftritt. (2) $\Delta R_{\max}$ erfolgt weniger und von Mal zu Mal verschieden[15] (Durch Vorbelegung ist der Widerstand vor der Messung schon erhöht, wodurch $n_{\max}$ entsprechend weniger wird.). (3) Die langsame, vom Gasdruck unabhängige Widerstandszunahme ist verschwunden. (4) Im irreversiblen Bereich bei tiefer Temperatur zeigt sich keine Inversion, und bei der Gaszugabe nimmt der Widerstand lediglich zu, beim Abpumpen ab.

§ 4. Diskussion

4–1. *Sauberkeit der Schichten*

Nach Becker[16] erhält man zuverlässige Ergebnisse nur, wenn die Partialdrucke von O_2 und H_2O unter 10^{-10} Torr liegen. Das ist wahrscheinlich der Grund dafür, daß die vorhergehenden Arbeiten[3,4,5,15,17,18,19,20] nicht übereinstimmten und widersprechende Ergebnisse zeigten. Oda et al.[21] haben gezeigt, daß der Sauerstoff im Restgas eine wichtige Rolle auf Meßergebnisse spielt. Die beschriebene Resultate sind innerhalb der Meßfehler gut reproduzierbar, welcher Erfolg nur durch die Methode der vier Zuführungsdrähten erreicht wurde, denn das Gas, das während des Aufdampfens herausgetrieben wird, an die neu aufgedampfte Schicht sofort adsorbiert und nicht mehr desorbiert, dessen Effekt durch Ionisationsmanometer auch nicht zu beobachten ist.

4–2. *Diskussion einer Diffusion in das Innere der Schicht*

Beeck[2] hat für aufgedampfte Nickelschichten eine anfängliche sehr rasche Adsorption von Wasserstoff und eine nachfolgende langsame Druckabnahme gefunden. Diese langsame Adsorption ist nach seiner Deutung eine Diffusion in das Kristallgitter. Später haben Porter u. Tompkins[12] am System Fe/H_2 und Gundry u. Tompkins[22] am System Ni/H_2 diese Annahme genau nachgeprüft und geschlossen, daß die langsame Adsorption eine Art von Oberflächenadsorption sei.

Auch in der vorliegenden Arbeit sind diese Verhältnisse mit einer anderen Methode nachgeprüft, Wie aus Abb. 17 hervorgeht will, das Verhältnis $n_{\max}/n_{\text{irr}}$ bzw. $n_{\text{rev}}/n_{\text{irr}}$ bei Messungen unterhalb Zimmertemperatur nicht so stark geändert wie die Mengen $n_{\max}$, n_{irr} und n_{rev} selbst. Ferner zeigen Abb. 13 und 14, daß dieses Verhältnis fast unabhängig von der Schichtdicke und auch von der Meßtemperatur ist. Mit Änderung der Schichtdicke ändert sich die Oberflächenrauhigkeit und dadurch auch das Verhältnis Oberfläche zu Volumen. Übrigens, wenn eine Diffusion in Filminnere stattfindet, so muß sie bei 273°K stärker als bei 90°K sein. Adsorptionsverhalten bei beider Temperatur sind bis zu dem Punkt sehr ähnlich, der etwa $n_{\min}$ bei 90°K entspricht. All diese Tatsachen deuten darauf hin, daß den vorliegenden Versuchen unterhalb Zimmertemperatur und unter 5.10^{-8} Torr keine innere Diffusion stattfindet. Bei 373°K nimmt jedoch das Verhältnis $n_{\text{rev}}/n_{\text{irr}}$ sehr stark zu. Hier liegt wahrscheinlich eine innere Diffusion vor.

4–3. *Adsorptionssisotherme und Rauhigkeitsfaktor*

Die Adsorptionsisothermen im reversiblen Bereich bei Zimmertemperatur ergibt sich gegen $\sqrt{p}$ ein geradeliniger Verlauf.[7] Erfolgt die Langmuir'sche Adsorption mit Dissoziation in zwei verschiedenen Zuständen, so gilt allgemein:

$$n=b_1\sqrt{a_1p}/(1+\sqrt{a_1p})+b_2\sqrt{a_2p}/)(1+\sqrt{a_2p}) \tag{5}$$

Wenn eine der Adsorptionswärmen bzw. eine der Konstanten a sehr groß ist, hat Gl. (5) folgende Näherung für *niedrige* Drucke:

$$n=b_1+b_2\sqrt{a_2p} \tag{6}$$

Diese Gleichung erklärt die Lage wobei die obengenannte Gerade nicht durch den Koordinatenanfangspunkt geht. Der irreversible Anteil b_1 liegt vor, wenn die Adsorptionswärme dieses Anteils so groß ist, daß das Gas nicht mehr desorbiert. In Abb. 18 wird die Langmuir'sche Gerade für reversible Mengen geprüft. Man erhält eine Gerade, aus deren Neigung der Wert b_2 zu errechen ist. Die Summe b_1+b_2 entspricht der Menge der Sättigungsadsorption 3, 7.10^{15} Molekeln/cm². Wenn man annimmt, daß die drei kristallographischen Flächen, (110), (111), (100), für nicht orientierte, dünne Schicht gleichäufig sind, bekommt man einen Oberflächen-ranhig-keitsfaktor von 4.8.

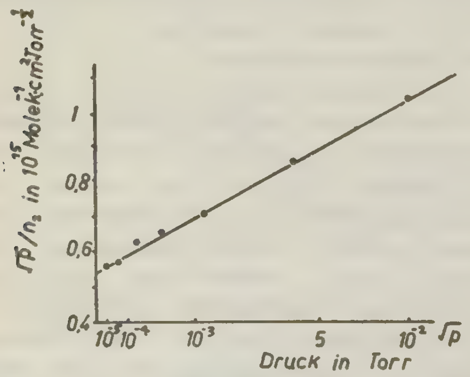

Abb. 18. Langmuir-Gerade bei 273°K nach Abb. 7

Wenn man eine Annahme von Trapnell[23] als Kriterium für $\theta=1$ übernimmt, dann beträgt die adsorbierte Menge bis 2,5 kcal, physikalische Adsorptionswärme, bei Zimmertemperatur nach Abb. 6 $2{,}5.10^{15}$ Molekeln/cm², entsprechend einem Rauhigkeitsfaktor von 3 für die Schichtdicke von ca. 100 Å.

4–4. *Molekulare Adsorption bei tiefer Temperatur*

Die Adsorptionsisotherme bei tiefer Temperatur und die daraus ermittelte Adsorptionsenthalpie (Abb. 6) lassen sich eine Schlußfolgerung herausziehen, daß die molekulare Adsorption bei tiefer Temperatur und im reversiblen Bereich voliegen[7] wobei im Widerstandsverlauf eine zweite Widerstandszunahme vorhanden ist. Somit ist anzunehmen, daß diese zweite Widerstandszunahme von der molekularen Adsorption versursacht wird. Eine Deutung der Ergebnisse geht davon aus, daß die H_2-Molekel im Oberflächenfeld des Metalls als Dipol polarisiert ist, dessen positives Ende nach außen gerichtet ist[24]. Für den Schichtwiderstand wird sich das negative Ende stärker auswirken, da es näher an der Oberfläche sitzt. Damit $\Delta R>0$.

Bei Gaszugabe bei tiefer Temperatur treten viele Peaks auf, besonders im Falle der ungetemperten Schichten. Das hat seinen Grund im folgenden. Bei stärker Besetzung wird die Wahrscheinlichkeit kleiner, daß zwei leere Plätze nebeneinander vorhanden sind, auf denen eine Molekel sofort dissozieren kann. Deshalb muß die Molekel zunächst auf einem leeren Platz molekular adsorbieren ($\Delta R>0$). Später, wenn durch Oberflächendiffusion ein zweiter benachbarter leerer Platz in der günstigen Richtung entsteht, kann die Molekel langsam auch diesen besetzen und dissozieren ($\Delta R<0$). Bei tiefer Temperatur ist die Rotationsschwingung kaum angeregt, und außerdem die Geschwindigkeit der Oberflächendiffusion geringer.

4–5. *Eigenschaften der atomaren Adsorption*

Die Adsorption von Wasserstoff an sauberem Ubergangsmetall ist zuerst von Roberts[25] untersucht worden, der fand, daß der Wasserstoff bei Zimmertemperatur in Atome dissoziert und daß die Adsorptionsgeschwindigkeit sehr groß ist. Später wurde diese Annahme auch an aufgedampften Schichten weiter bestätigt2),16),26). Die anfängliche rasche Adsorption wird als ein Charakteristikum für Sauberkeit betrachtet27),28),29),30).

Bei der Wasserstoffadsorption auf Nickel nimmt die Photoemission ab7),31), und das Oberflächenpotential wird negativ24). Dieser Befund deutet darauf hin, daß der adsorbierte Wasserstoff auf Nickel negativ polarisiert ist. Die größe des Dipolmomentes läßt sich aus verschienenen Meßergebnissen berechnen. Es wurde gefunden4), daß sie viel kleiner ist, als zu erwarten wäre, wenn der Wasserstoff als Ion adsorbiert ist. Die Adsorptionswärme ist trotzdem sehr hoch32) und auch die Widerstandsänderung ist sehr stark. Es wurde eine Theorie33),34) entwickelt, daß der Wasserstoff hauptsächlich kovalent adsorbiert ist. Man kann annehmen, daß sich eine negative Polarisation teilweise überlagert. Nach einer Theorie von Higuchi *et al*35) ist der ionische Anteil etwa 26% zu berechnen.

4–6. *Atomare Adsorption und Widerstandsänderung*

Bei atomarer Adsorption nimmt der Widerstand zunächst stark zu, dann schwächer ab. Für die Deutung dieser Erscheinung sind folgende Ursachen zu diskutieren.

a) Es findet eine Adsorption an aktiven Zentren bzw. an Gitterstörungen statt36). Solche Zentren sind sehr empfindlich gegenüber Sinterung. Die erhaltenen Meßkurven und charakteristischen Größen sind aber sämtlich ähnlich, unabhängig von der Temperung und von der Aufdampftemperatur. Aus dem Grunde ist diese Möglichkeit abzulehnen.

b) Einfluß verschiedener Kristallflächen. Aus demselben Grunde wie bei a) und deshalb, weil die Vehältnisse $n_{\max}/n_{\mathrm{irr}}$ bzw. $n_{\max}/n_{\min}$ unabhängig von der Temperung konstant bleiben, ist nicht anzunehmen, daß die verschiedenen Kristallflächen einen so verschiedenen Einfluß auf die Wasserstoffadsorption an Nickel ausüben, wie das beim Wolfram der Fall ist. Diese Differenz der Austrittsarbeiten kann nur eine untergeordnete Rolle spielen, da die atomare Adsorption hauptsächlich kovalent ist. Wortmann *et al*32) haben bei sehr sauberen Bedingungen mit dem Feldelektronenmikroskop gearbeitet und mitgeteilt, daß die Adsorption von Wasserstoff an Nickel-Einkristallen bei sehr tiefer Temperatur, anders als beim System W/H_2, sehr homogen verläuft, und daß ein Effekt durch die verschiedenen Kristallflächen nicht zu bemerken ist30).

c) Zunächst findet eine Adsorption an der äußeren Oberfläche statt, dann an der inneren, d.h. an der Grenzoberfläche der einzelnen Kristallkörnchen5). Wenn die Widerstandszunahme auf eine Adsorption an der äußeren Oberfläche, und die Abnahme auf eine Adsorption an der inneren zurückzuführen wäre, dann ist es nicht zu verstehen, daß nach dem Maximum der Widerstand bei Gaszugabe sofort abfällt und nachher langsam zunimmt.

d) Temperaturerhöhung infolge Adsorptionswärme15). Die angeführten Versuche zeigen, daß die Zunahme lange Zeit erhalten bleiten, unabhängig davon, ob die Schicht abgekühlt oder nicht. Diese Theorie kann also nicht bestätigt werden.

e) Es gibt zwei Arten der atomaren Adsorption, eine gibt die Widerstandszunahme; die andere die Abnahme. Nur diese Deutung erscheint möglich. In folgenden Paragraphen werden alle experimentellen Ergebnisse mit dieser Annahme gedeutet.

Bis zum Widerstandsmaximum ist der Wasserstoff teilweise negativ aufgeladen, da der Widerstand zunimmt und die Photoemission abnimmt7). Die Elektronen werden aus dem Metall in die Adsorptionsschicht gezogen. Dieser teilweise negativ aufgeladene Zustand sei mit $H^{(-)}$ bezeichnet. Nach dem Wider-

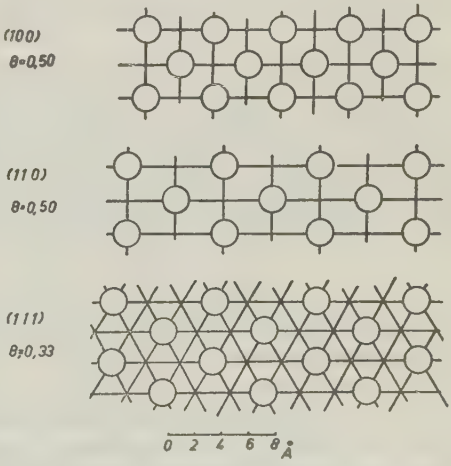

Abb. 19. Atomare Adsorption von $H^{(-)}$ auf den Ni-Kristallflächen (100), (110) und (111)

tandsmaximum soll der Wasserstoff entsprechend mit $H^{(+)}$ bezeichet werden, da der Widerstand abnimmt. In diesem Falle aber ändert sich die Photoemission wenig oder sogar nicht7). Von der Vakuumseite gesehen, wird sich das Oberflächenpotential nicht so stark ändern wie der Widerstand, denn $H^{(+)}$ ist kleiner als $H^{(-)}$ und haftet dichter an der Oberfläche.

Weil der Wasserstoff auf der Oberfläche beweglich ist32), wird sich $H^{(-)}$ am Anfang so gleichmäßig verteilen, daß die Repulsion gegeneinander möglich klein ist. Am Widerstandsmaximum liegt eine Verteilung der $H^{(-)}$ auf den einzelnen Flächen vor wie in Abb. 19 dargestellt ist. Der mittlere θ—Wert beträgt $\theta=0{,}44$, wenn alle 3 Kristallflächen als gleich häufig angenommen werden. Dieser Wert ist ein Sättigungswert und, wie nachher erklärt wird, nicht zu erreichen. Aus dem Grunde ist der beobachtete Wert $\theta(R_{\max})$ kleiner. $n_{\max}$ entspricht einer Oberflächenbelegung von ca. $\theta=0{,}2$, unter der Annahme, daß der Rauhigkeitsfaktor 4 ist.

Nach diesem Maximum folgt stärkere Repulsion zwischen den adsorbierten Atomen. Von diesem Moment an wird die Adsorption für $H^{(+)}$ günstiger, weil einerseits die elektrostatische Energie damit verringert wird und anderseits $H^{(+)}$ kleiner ist. Dann kann es auch im Gegensatz zu $H^{(-)}$ leichter in die feinen Spalten eindringen und dort adsorbieren. Deshalb ist bei Zimmertemperatur weitere Adsorption von $H^{(+)}$ möglich, während bei 90°K beim Überschreiten einer gewissen Belegung molekulare Adsorption stattfindet.

4–7. *Elektronische Begründung der Adsorption*

In Abb. 20 ist das Potentialprofil des System Ni/H_2 dargestellt, dessen Berechnung auf Morse'scher Kurve und auf Literaturenwerte erfolgt. Die Abb. 20 zeigt, daß die Wasserstoffmolekel keine Aktivierungsenergie braucht, um zu dissozieren und zu chemisobieren27).

Dowden37) hat auf Grund theoretischer Überlegungen auf die Möglichkeit hingewiesen, daß zwei Adsorptionstypen für Waserstoff am Nickel vorliegen können. Diese Theorie ist später von Gundry u. Tompkins38) zur Deutung ihrer Ergebnisse aufgegriffen worden. Eine Deutung erfolgt mit kombinierten d-s-p-Orbitals, die andere lediglich mit d-Orbital. Im folgenden wird eine vorläufige Annahme gemacht, daß $H^{(-)}$ der d-s-p-Bindung und $H^{(+)}$ der d-Bindung entspricht. Es ist nicht unbedingt nötig, aber dient zur Veranschaulichung.

In Abb. 21 ist das gesamte Schema der Potentialkurven dargestellt. Es ist zu beachten, daß die Potentialkurven für die d-s-p-Bindung und für die d-Bindung auf der Abszisse getrennt dargestellt sind. Das bedeutet nicht, daß die Bindungsabstände so verschieden sind, sondern nur, daß die d-s-p-Bindung nach der d-Bindung erreicht wird und deshalb von der Gasphase weiter entfernt dargestellt ist. Die zunächst stattfindende einfache d-Bindung kann in die stärkere d-s-p-Bindung übergehen ohne daß ein Platzwechsel erfolgt.

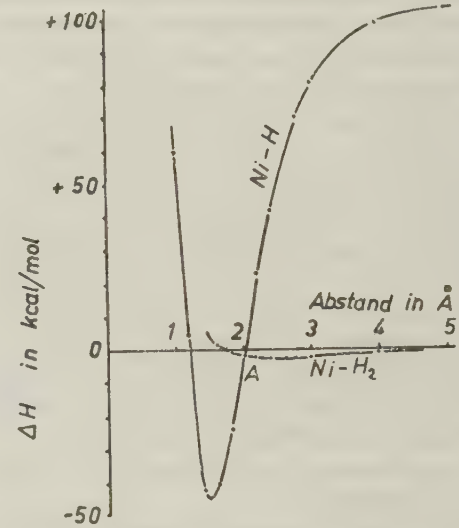

Abb. 20. Potentialprofil des Systems Nickel-Wasserstoff

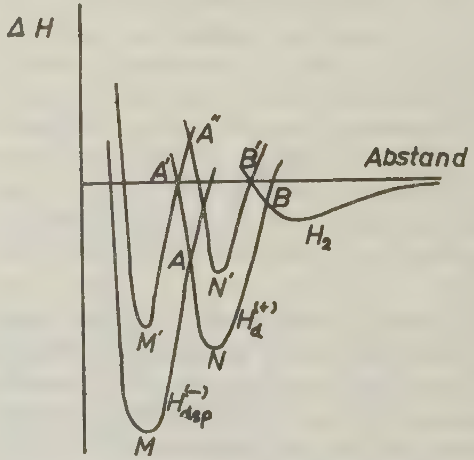

Abb. 21. Potentialprofil nach der Theorie von Dowden

Wenn eine Molekel auf die Schicht trifft, wird sie sofort dissozieren und in die tiefste Mulde M fallen. Dabei ist $\Delta R>0$ und die Adsorptionsenthalpie am größten. Mit der Besetzung wird die d-s-p-Kurve angehoben, bis der Schnittpunkt A die Nulllinie erreicht (A'). Danach adsorbiert Wasserstoff zum größten Teil als $H^{(+)}$ mit d-Bindung aber noch ohne Aktivierungsenergie; denn B liegt unter der Nulllinie. Mit der Besetzung steigt auch diese Kurve an, bis der Schnittpunkt B mit der Kurve für die van der Waal'schen Adsorption (H_2) die Nulllinie erreicht (B'). Danach wird bei 90°K der Wasserstoff nur noch zunächst molekular adsorbiert (H_2). Bei Zimmertemperatur kann wegen der thermischen Energie der Wasserstoff über die Potentialmauer in die d-Bindung gelangen. Der Schnittpunkt zwischen den Potentialkurven für $H^{(-)}$ und $H^{(+)}$ ist nun sehr stark gestiegen (A'') und sehr schwer übersteigbar. Bevor der tiefste Punkt M der d-s-p-Kurve und der tiefste N der d-Kurve die Nullinie nicht erreichen, ist keine wahre Sättigungsadsorption anzunehmen. Diese ist wegen der hohen Potentialmauer sehr schlecht erreichbar.

Die Aktivierungsenergie für die Desorption ist anfänglich sehr hoch und viel größer als für die Adsorption. Desorption findet deshalb noch nicht statt, auch wenn abgepumpt wird. Beim Auftreten der reversiblen Adsorption sind die Rotentialkurven so weit gestiegen, daß die Aktivierungsenergie für die Desorption bedeutend kleiner geworden ist. Bei 90°K ist die thermische Energie aber so klein, daß praktisch nur Molekeln desorbiert werden, während bei Zimmertemperatur immerhin die Atome über den molekularen Zustand langsam desorbieren, wie es aus Abb. 3 und Abb. 9 entnommen kann.

Bei allen Meßkurven ist eine stets zunehmende Tendenz des Widerstandes vorhanden. Solange M niedriger als N und N niedriger als die Nulleinie liegt, wird $H^{(+)}$ aus der d-Binding nicht desorbieren, sondern langsam in die d-s-p-Bindung übergehen. Dieser Übergang ist der langsamen, ständigen Widerstandserhöhung zuzuschreiben, die bei Zimmertemperatur relativ schnell zu einem Abschluß kommt (Abb. 2), während sie bei tiefer Temperatur lange Zeit benötigt.

Die Verhältnisse betreffs der Widerstandsänderung sind bei 90°K recht kompliziert. Bei der Gaszugabe überschreitet der Widerstand einen Peak (H_2), bevor er abnimmt. Bei noch größeren Zugabedrucken tritt die Inversion ein. Diese Inversion wird, wie in Abb. 8 und 9, verstärkt durch großen Druck und durch Temperaturerhöhung. Durch die beiden Effekte geht die Umwandlung $H_2\rightarrow H_d^{(+)}\rightarrow H_{dsp}^{(-)}$ schneller. Wenn die für die d-s-p-Bindung in Frage kommenden Plätze alle besetzt sind, wird die langsame Widerstandszunahme geringer. Die Stellen, die bei niedrigem reversiblem Druck von H_2 besetzt waren, sind jetzt von stärker gebundenen $H_{dsp}^{(-)}$ eingenommen. Nach dieser Druck- bzw. Temperaturerhöhung sind im reversiblen Bereich unter niedrigem Druck nur noch sehr wenig Stellen für stabiles H_2 verfügbar. Bei weiteren Gaszugaben entsteht der instabile Peak, aber es schließt sich der folgende, reversible Vorgang an $H_2\rightleftarrows H_d^{(+)}$. Der Widerstand nimmt bei der Zugabe nach dem Peak ab. Es ist also Inversion eingetreten.

Das Oberflächenpotential im reversiblen Bereich und bei Zimmertemperatur wird bei der Zugabe durch den Übergang $H_d^{(+)}\rightarrow H_{dsp}^{(-)}$ etwas negativer, und damit wird die Photoemission verringert, da der Effekt von $H_{dsp}^{(-)}$ stärker als der von $H_d^{(+)}$ ist. Bei der Zugabe von noch höheren Drucken wird der Adsorptionszustand von $H_{dsp}^{(-)}$ allmählich gesättigt, und nun bleibt der Wasserstoff meistens als $H_d^{(+)}$. Das Oberflächenpotential wird somit etwas positiv, wie auch bei Photoemission7) gefunden worden ist.

4–8. *Reaktionskinetik*

a) Zimmertemperatur

Erst im reversiblen Bereich ist die Geschwindigkeit dn/dt bzw. dR/dt meßbar. In diesem Falle ist, wie Abb. 21 zeigt, die Potentialkurve nach oben zu verschoben. Die Aktivierungsenergie E ist entsprechend höher7), ihre Zunahme ΔE in erster Näherung proportional der adsorbierten Menge. Diese Proportionalität ist theoretisch und experimentell bestätigt worden26),39),40).

$$\Delta E=\mathrm{Const}\cdot n \tag{7}$$

$$dn/dt=\mathrm{Const}\cdot\exp\left(-\frac{E+\mathrm{Const}\cdot n}{kT}\right)=a\cdot e^{-\alpha n} \tag{7'}$$

Daraus folgt durch Integration

$$n=\frac{1}{\alpha}[\ln(t+t_0)-\ln \alpha a] \tag{8}$$

$$t_0=\frac{e^{\alpha n_0}}{\alpha a},\quad n_0=n_{(t=0)},$$

also Zeldovich-Gleichung. In diesem Falle spielt eine Reaktionsordnung eine untergeordnete Rolle. Die Gesetzmäßigkeit gilt sowie bei Widerstandsänderung, da sie proportional der adsorbierten Menge ist, als auch bei der Desorption, da die Aktivierungsenergie für Desorption auch zunimmt.

b) 90°K

b–1) Adsorption als Molekel

Wie an dem Peak im reversiblen Bereich zu erkennen ist, geht die Adsorption als Molekel sehr rasch vor sich. Die molekulare Adsorption geht beim Abpumpen sofort zurück.

b–2) Dissoziation in Atome

Die Molekel kann sich zersetzen und $H^{(+)}$ bilden soweit noch ein benachbarter leerer Platz verfügbar ist. Der zeitliche Verlauf des Peaks bei einer jeden Zugabe ist nicht genau zu verfolgen, da der Vorgang sehr schnell ist. Bei ungetemperter Schicht jedoch ist der Peak größer und der Gang verfolgbar. Nach Eliminierung des Ordnungsvorgangs der Schicht selbst ist die Kurve in Abb. 22 dargestellt.

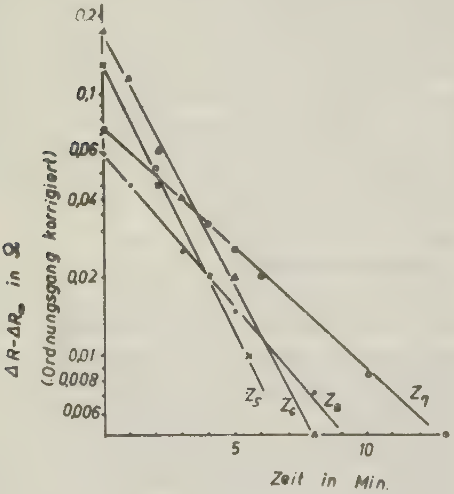

Abb. 22. Zeitlicher Verlauf der Dissoziation bei einer ungetemperten Schicht

Die Reaktion 1. Ordnung ist für die beiden Mechanismen möglich, die in § 4–4 vorgeschlagen waren.

Auch der Peak im zweiten Widerstandszunahmebereich (Z_9 in Abb. 7) kann untersucht werden. Hier ist die atomare d-Bindung bereits stark besetzt, so daß der Schnittpunkt B fast zur Nullline angehoben ist. Die Molekel kann nicht mehr sofort dissozieren und zunächst als polarisierte Molekel adsorbiert. Die für die molekulare Adsorption in Betracht kommenden Stellen sind aber noch nicht ganz besetzt, weshalb die Adsorption immer noch rasch vor sich geht. Die Dissoziation wird in dem Falle bestimmt durch die Geschwindigkeit, mit der der Punkt B überwunden wird. Die Analyse ergibt also eine Zeldovich-Gleichung, die experimentell bestätigt werden kann.

b–3) Stets zunehmende Tendenz des Widerstandes

Wie vorher häufig erwähnt wurde, gibt es bei 90°K eine lineare Widerstandszunahme. Bei tiefer temperatur geht die Überwindung der Potentialmauer zwischen d- und d-s-p-Bindung langsam vor sich. Die Zeldovich-Gleichung wird dann für die Bedingung: kleines T bzw. großes α umgeformt

$$n=\frac{1}{\alpha}\left[\frac{t}{t_0}+\ln t_0-\ln\frac{1}{\alpha a}\right]. \tag{9}$$

Das besagt; die d-Bindung wandelt sich mit der Zeit linear in die d-s-p-Bindung um. Der gesamte Widerstand nimmt linear zu, denn es ist $|\varDelta R_{asp}|>|\varDelta R_d|$. Der lineare Vorgang wird durch eine Druckerhöhung und eine Temperaturerhöhung zur Sättigung beschleunigt (vgl. Abb. 9).

b–4) Schlußfolgerung für 90°K

Die H_{dsp}-Bindung wird am Anfang des Versuchs zuerst besetzt, dann H_d und H_2. In den späteren Versuchsstufen ist wegen der Anhebung der Potentialkurven diese Reihe umgekehrt, nämlich zuerst wird H_2 besetzt, dann H_d und langsam H_{dsp}. Diese Tatsache ist nur durch die Wechselwirkungstheorie mit zwei Bindungstypen zu verstehen.

4–9. *Elektronische Begründung der Widerstandsänderung*

Die folgenden Ausführungen beziehen sich auf die Widerstandsänderung bis zum Erreichen der maximalen Widerstandszunahme. Nach der semi-klassischen Sommerfeld'schen Theorie gilt die Gleichung

$$R=\frac{1}{\sigma}=\frac{\text{Const}}{N.1.d}\,, \tag{10}$$

wobei σ die Leitfähigkeit, N die Zahl der effektiven Leitungselektronen pro cm³, l die mittlere freie Weglänge der Leitungselektronen bedeuten.

Für die Leitfähigkeit σ bei Schichtdicken, die Größer als die freie Weglänge sind, gilt theoretisch folgende Formel[41],

$$\frac{\sigma}{\sigma_\infty}=1-\frac{3}{8}\frac{l}{d}\,, \qquad (11)$$

wobei σ_∞ sich auf unendlich dicke Schichten bezieht. Sie entspricht der empirischen Formel Gl. (3). Nach dieser Gleichung beträgt die freie Weglänge ca. 110 Å (umgerechnet aus Abb. 12), während in der Literatur[42] für massives Nickel 266 Å angegeben ist. Für aufgedampfte, feinkörnige Schichten ist 110 Å plausibel.

Für Widerstandsänderung infolge der Adsorption folgt es aus Gl. (10):

$$-\frac{\Delta R}{R}=\frac{\Delta N}{N}+\frac{\Delta l}{l}+\frac{\Delta d}{d}\,. \qquad (12)$$

Zu erster Näherung wird $-\Delta R/R=\Delta N/N$ angenommen[3]. Die Widerstandsänderung wird in Elektronenzahländerung umgerechnet und in Einheiten pro adsorbiertes Wasserstoffatom in Abb. 23 dargestellt. Dabei wird angenommen, daß ein Nickelatom 0,6 freie Leitungselektronen liefert. (Die unteren Kurven stellen die für $H^{(+)}$ berechnete Werte dar.).

Die Elektronenbeanspruchung ist temperaturabhängig, wie aus Abb. 15 und 23 hervorgeht. Wenn die Widerstandsänderung durch Beanspruchung bzw. Lieferung von Leitungselektronen besteht, ist die Tatsache sehr schwierig zu verstehen; denn die Leitungselektronenzahl ist temperaturunabhängig. Der berechnete Wert von ca. 3 Elektronen pro H-Atom für dicke Schichten ist auch viel zu groß, sowohl bei kovalenter als auch ionischer Bindung.

In Abb. 24 ist der Absolutwert $\Delta R/_{\max}$ gegen

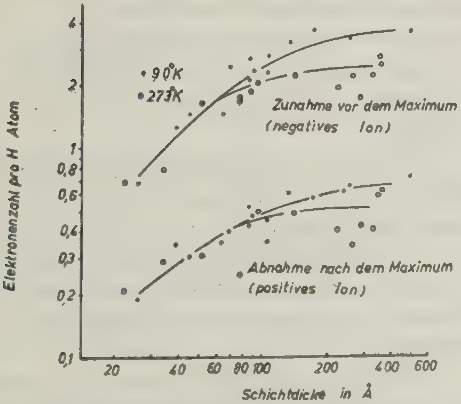

Abb. 23. Elektronenbeanspruchung pro Wasserstoffatom in Abhängikeit von der Schichtdicke

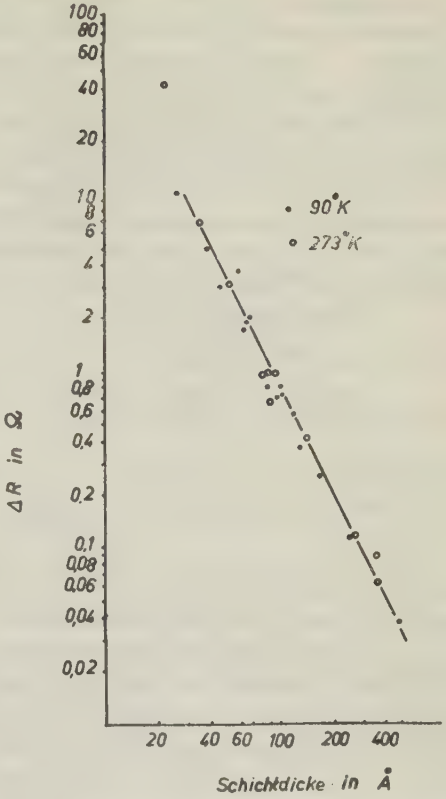

Abb. 24. Maximale absolute Widerstandszunahme bei 90°K und 273°K als Funktion der Schichtdicke

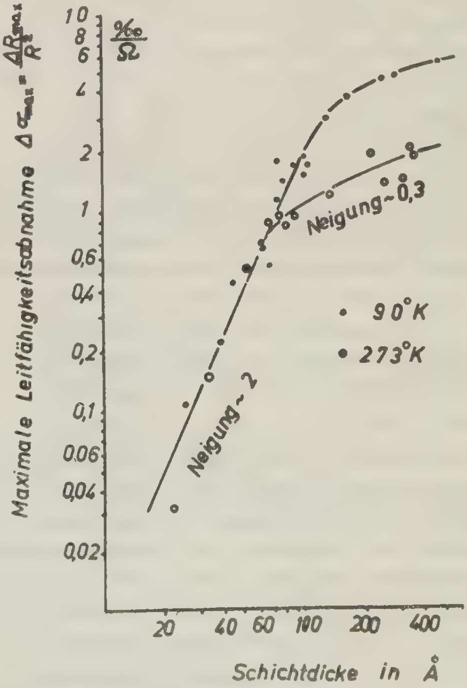

Abb. 25. Maximale Leitfähigkeitsabnahme bei 90°K und 273°K als Funktion der Schichtdicke

d aufgetragen. Der durch Adsorption hervorgerufene Zusatzwiderstand ist temperaturunabhängig. Diese Tatsache deutet genau wie bei der Matthiessen'schen Regel daraufhin, daß die Widerstandsänderung durch eine Behinderung der Leitung verursacht wird und nicht durch die Änderung der Elektronenzahl.

In Abb. 25 ist $\Delta\sigma_{\max}$ gegen d aufgetragen. Nach Abb. 15 kann man näherungsweise folgende Gleichung erhalten

$$1/R=\mathrm{Const}\cdot N.l.d^m \tag{13}$$

wobei $m\geq 1$. Daraus folgt

$$-\frac{\Delta R}{R}=\frac{\Delta N}{N}+\frac{\Delta l}{l}+m\frac{\Delta d}{d} \tag{14}$$

und ferner

$$\Delta\sigma=-\frac{\Delta R}{R^2}=\Delta N.l.d^m+\Delta l.N.d^m+md.N.l.d^{m-1} \tag{15}$$

Aus Abb. 12 erhält man für dickere Schichten einen Wert $m\gtrsim 1$, und für dünnere $m\simeq 2$.

Zur Deutung des Kurvenverlaufs in Abb. 25 für *dickere* Schichten, bei denen $\Delta\sigma$ temperaturabhängig ist und die Neigung etwas größer als 0 ist, kann nur das letzte Glied der rechten Seite in Gl. (15), $\Delta d.N.l.d^{m-1}$, herangezogen werden. Das Auftreten von Δd im letzten Glied könnte in folgender Weise gedeutet werden. Durch die Wechselwirkung werden die s-Elektronen teilweise in die d-Lücken[4)18)] und teilweise für die Aufladung des Wasserstoffs übergehen, um damit eine Bindung aufzuführen, was zur Folge hat, daß die Oberflächennickelschicht freie Elektronen verliert und eine Elektronenmangelschicht sich bildet. Als Endeffekt wird diese unmittelbare Oberflächennähe für die Stromleitung unwirksam. Die effektive Dickenänderung beträgt ca. 4Å, also 1∼2 Nickelatomschichten.

Bei *dünneren* Schichten (<110Å) gilt $m\simeq 2$ und dann kommt als einzige Möglichkeit für eine Deutung des Kurvenverlaufs in Abb. 25 das Glied $\Delta l.N.d^2$, bei dem einerseits die Neigung ca. 2 ist und das anderseits temperaturunabhängig ist. Bei dünneren Schichten spielt die Oberflächenrauhigkeit eine wichtige Rolle. Die Streuung der Leitungsselektronen durch das in Spallen sleckende $H^{(-)}$ wirkt viel stärker aus, als auf einer glatten Schicht. Dabei sollte man den Effekt nicht als gleich mäßige Querschnittänderung betrachten, denn in der Schicht, bei der die Schichtdicke kleiner als die freie Weglänge ist, ändert sich der Widerstand durch die Querschnittänderung nicht.

Der Effekt beruht also auf eine Änderung der freien Weglänge. In Analogie zur Matthiessen'schen Regel bei Legierungen kann die wahre Elektronenbeanspruchung bei einer dünnen Schicht sehr grob abschätzen. Massive Legierung und Oberflächenadsorption sind natürlich nicht dasselbe, doch in dem Punkte ähnlich, daß jede freie Weglänge von der zusätzlichen Streuung beeinflußt wird. Da $n_{\max}$ ca. $1{,}10^{15}$ Atome/cm² beträgt, und da auf ein Ni-Oberflächenatom 1 H-Atom kommt [2),12),22)], werden ebenso viele Nickelatom aufgeladen. Man nimmt also an, daß ebenso viele zusätzlich geladene Gitterbausteine gleichmäßig verteilt sind. Die effektive geänderte Ladungszahl ΔZ ist wie folgt abzuschätzen: Bei Gültigkeit der Gleichung[44)]

$$\Delta R=\mathrm{Const}\ (\Delta Z)^2 n\,, \tag{16}$$

in der n der prozentuale Zusatz an Störatomen ist, beträgt ΔZ für Adsorption ca. 0,3, denn die Widerstandsänderung bei einer Schichtdicke von 50Å beträgt ca. 3%, und ein Zusatz von 1 Atom—% Cu eine Widerstandsänderung ergibt von 15% bei einer Ladungsdifferenz[42)]. Die Aufladung des Wasserstoffs ist somit nicht so stark.

§ 5. Zusammenfassung

1. Sehr saubere Ni-Schichten wurden im Ultrahochvakuum hergestellt. Die Wasserstoffadsorption wurde im Temperaturbereich von 77°K bis 373°K gemessen.

2. Die Adsorption ist im wesentlichen eine Oberflächenerscheinung, wenn die Adsorption unter Zimmertemperatur stattfindet.

3. Der elektrische widerstand wird bei dem Adsorption zunächst vergrößert.

4. Bei tiefer Temperatur gibt es ein Widerstandsmaximum und anschließend ein Minumum, bei Zimmertemperatur nur ein Maximum.

5. Es findet anfänglich eine rasche irreversible Adsorption statt, danach eine langsame reversible Adsorption.

6. Die Adsorption bei Zimmertemperatur ist atomar, die bei tiefer Temperatur ist ein Gemisch von atomarer und molekularer Adsorption.

7. Unter der Annahme, daß bei atomarer Adsorption zwei Bindungstypen möglich sind, lassen sich alle komplizierten Erscheinungen

und die Kinetik erklären.

8. Die Widerstandsänderung wird durch eine Störung des Leitungszustandes im Metall verursacht, d. h. durch eine Änderung des wirksamen Querschnittes oder Streuung der Elektronen.

9. Die Polarisation des adsorbierten Wasserstoffs ist verhältnismäßig gering, obgleich der Effekt auf Elektronenleitung ausgeprägt ist.

Der Deutsche Akademische Austauschdienst und die Deutsche Forschungsgemeinschaft haben die Arbeit durch Stipendien unterschützt. Herrn Prof. Dr. R. Suhrmann möchte ich für die Anregung zu dieser Arbeit, die Bereitstellung der nötigen Mittel und die sorgfältigen Diskussionen meinen herzlichen Dank aussprechen. Herr T. Ichimiya, der ein Stipendium ermöglichte, sei auch bestens gedankt.

Schrifttumsverzeichnis

1) O. Beeck, A. E. Smith u. A. Wheeler; Proc. Roy. Soc. **A117**, (1940) 62.
2) z. B., O. Beeck: Adv. in Catalysis **2** (1950) 151.
3) z. B., R. Suhrman: Adv. in Catalysis **7** (1955) 303. R. Suhrmann, G. Wedler u. D. Schliephake: Phys. Chem. NF **12** (1957) 128.
4) z. B., J. J. Broeder, L. L. van Reijen, W.M.H. Sachtler u. G.C.A. Schuit: Z. Elektrochem. **60** (1956) 838.
5) W.M.H. Sachtler u. G. J. H. Dorgelo: Bull. Soc. Chim. Belg. **67** (1958) 465.
6) D. Alpert: J. Appl. Phys. **24** (1953) 860.
7) R. Suhrmann, Y. Mizushima, A. Hermann u. G. Wedler: Z. Phys. Chem. NF **20** (1959) 332.
8) R. S. Sennett u. G. D. Scott: J.O.S.A. **40** (1950) 203.
9) F. W. Reynolds u. G. R. Stilwell: Phys. Rev. **88** (1952) 418.
10) E. B. Sandell: Colorimetric Determination of Traces of Matals, 2. ed. Interscience Publ. N.Y. (1950)
11) H. A. Taylor u. N. Thon: J.A.C.S. **74** (1952) 4169. P. T. Landsberg: J. Chem. Phys. **23** (1955) 1079.
12) A. S. Porter u. F. C. Tompkins: Proc. Roy. Soc. **A217** (1953) 544.
13) J. Bagg u. F. C. Tompkins: Trans. Faraday Soc. **51** (1955) 1071.
14) z. B., D. F. Klemperer u. F. S. Stone: Proc. Roy. Soc. **A243** (1957) 375.
15) J. H. Singleton: J. Phys. Chem. **60** (1956) 1606.
16) J. A. Becker, Adv. in Catalysis **7** (1955) 135.
17) R. Suhrmann u. K. Schulz: Z. Phys. Chem. NF **1** (1954) 69.
18) E. L. Lee, J. A. Sabatka u. P. W. Selwood: J.A.C.S. **79** (1957) 5391. P. W. Selwood: Adv. in Catalysis **9** (1957) 93.
19) G. Rienäcker u. N. Hansen: Z. Elektrochem. **60** (1956) 887.
20) W. M. H. Sachtler: J. Chem. Phys. **25** (1956) 751.
21) Z. Oda u. H. Arata: J. Phys. Chem. **62** (1958) 1471. T. W. Hickmott u. G. Ehrlich: J. Phys. Chem. Soc. **5** (1958) 47.
22) P. M. Gundry u. F. C. Tompkins: Trans. Faraday Soc. **53** (1957) 218.
23) B. M. W. Trapnell: Proc. Roy. **A206** (1951) 39.
24) J. C. P. Mignolet: Disc. Faraday Soc. **8** (1950) 105. J. C. P. Mignolet: J. Chem. Phys. **23** (1955) 753.
25) J. K. Roberts: Proc. Roy. Soc. **A152** (1953) 445.
26) A. S. Porter u. F. C. Tompkins: Proc. Roy. Soc. **A217** (1953) 529.
27) M. W. Roberts u. Sykes: Trans. Faraday Soc. **54** (1958) 548.
28) J. H. de Boer: Adv. in Catalysis **8** (1956) 17.
29) B. M. W. Trapnell: Chemisorption, Butterworths Sci. Publ. London (1955)
30) T. Kwan: Adv. in Catalysis **6** (1954) 67.
31) R. Suhrmann: Z. Elektrochen. **60** (1956) 804.
32) z. B., R. Wortmann, R. Gomer u. R. Lundy: J. Chem. Phys. **27** (1957) 1099.
33) D. D. Eley: Disc. Faraday Soc. **8** (1950) 34.
34) R. Culver, J. Pritchard u. F. C. Tompkins: Z. Elektorochem. **63** (1959) 741.
35) I. Higuchi, T. Ree u. H. Eyring: J.A.C.S. **79** (1957) 1330.
36) M. McD. Baker, G. I. Jenkins u. E. K. Rideal: Trans. Farady Soc. **51** (1955) 1952.
37) D. A. Dowden: J. Chem. Soc (1950) 242., Chemisorption, Butterworth Sci. Publ. (1957)
38) P. M. Gundry u. F. C. Tompkins: Trans. Faraday Soc. **52** (1956) 1609.
39) S. Glassstone, K. J. Laidler u. H. Eyring: The Theory of Rate Process, McGraw-Hill Co. N.Y. (1941)
40) J.J.F. Scholton u. P. Zwietering: Trans. Faraday Soc. **53** (1957) 1363.
41) H. Mayer: Physik dünner Schichten II, Wissenschaftliche Verlagsgesellschaft Stuttgart (1955)
42) N. F. Mott u. H. Jones: The Theory of the Properties of Metals and Alloys, Oxford atthe Clarendon Press (1936)

JOURNAL OF THE PHYSICAL SOCIETY OF JAPAN, Vol. 15, No. 9, SEPTEMBER, 1960

The Binding Energy of the σ Bond. IV.
Discussion on the Higher Order Terms

By Kiyosi O-OHATA

Physics Department, Tokyo Institute of Technology,
Oh-okayama, Meguro-ku, Tokyo

(Received March 5, 1960)

It has been shown in the previous report that the bond orbital method gives the total energy of the molecule as the expanded power series of the overlap integrals between the bond orbitals. It is here shown that the contribution of the third order terms of these overlap integrals, which are neglected hitherto, to the binding energy of the σ bond is by no means negligible though smaller than that of the second order terms. In the case where the third order terms are taken into account, the validity of the additivity rule of the binding energies of the saturated hydrocarbons is discussed.

§1. Introduction

In the previous report[1] we considered the binding energy of the saturated molecules with only σ bonds, assuming that the total energy of these molecules can be obtained in good approximation if we take into account the terms up to the second order of the overlap integrals between orbitals involved in the different bonds. It is very difficult to discuss generally the contribution of the higher terms than the third order to the binding energy of the σ bond. We here propose a method to discuss this problem with the use of the bond orbital method. In the bond orbital method the ground electronic state of the saturated molecule is expressed by a closed shall like structure, in which individual orbitals are filled with two electrons with the opposite spins. There arises no difference in the expectation value of the total energy whether we use, as bond orbitals, a set of nonorthogonal orbitals or that of the mutually orthogonal bond orbitals constructed by the linear combinations of the former orbitals. We follow the method of orthogonalization due to Landshoff and Loewdin.[2] Then we can easily obtain the expression of the total energy of the molecule which takes into account the higher order terms of the non-orthogononality between the different bonds. We shall particularly discuss the magnitude of the contribution of the third order terms to the binding energy of the saturated molecule.

§2. The Bond Orbitals

We consider a chemical bond A-B, which binds the atoms A and B in the saturated molecule. The bond orbital τ_α, which is in charge of the bond A-B, is given by a linear combination of ϕ_i the atomic valence orbitals of the atom A and ϕ_j that of the atom B, namely,

$$\tau_\alpha=\frac{1}{\sqrt{N_\alpha}}(\lambda\phi_i+\mu\phi_j)\ , \tag{2.1}$$

where $N_\alpha=\lambda^2+\mu^2+2\lambda\mu S_{ij}$, λ and μ are the parameters, and S_{ij} is the overlap integral between the orbitals ϕ_i and ϕ_j. The electronic ground configuration of the molecule is given by

$$\tau_\alpha)^2\tau_\beta)^2\tau_\gamma)^2\cdots\tau_\zeta)^2\ . \tag{2.2}$$

We here exclude the lone-pair and core electrons, but even if we include them to the configuration (2.2), it is still valid that the electronic configuration is given by a closed shell like structure. We shall assume that the bond orbitals are orthogonal to the lone-pair and core orbitals. If it is not the case, we can follow the orthogonalization process to make the valence orbitals to be orthogonal to the core orbitals, as discussed in §2 of I.

We here apply the Loewdin method of orthogonalization to the set of bond orbitals (2.2) to make them mutually orthogonal. According to Loewdin, the relation between the column matrix of the orthogonal bond orbitals (τ^0) and the one of the non-orthogonal bond orbitals (τ) is given by

$$(\tau^0)=(\mathbf{1}+\boldsymbol{T})^{-1/2}(\tau)\ , \tag{2.3}$$

where $\mathbf{1}$ is the unit matrix, $\boldsymbol{T}$ is the matrix constructed from the overlap integrals $T_{\alpha\beta}$

between the bond orbitals τ_α and τ_β, and $T_{\alpha\alpha}$ is assumed to be zero. As the state is given by a closed shell like structure the wave function constructed from the configuration (2.2) is the same as that from the configuration

$$\tau_\alpha{}^o)^2\tau_\beta{}^o)^2\tau_\gamma{}^o)^2\cdots\tau_\zeta{}^o)^2 \tag{2.4}$$

and the electronic energry of the molecule obtained by the former function is the same as that by the latter one.

The detailed form of the orthogonal bond orbital $\tau_\alpha{}^o$ is

$$\begin{aligned}\tau_\alpha{}^o=&\left\{1+\frac{8}{3}\sum_\xi T^2_{\alpha\xi}-\frac{5}{16}\sum_\xi T_{\alpha\xi}\left(\sum_\eta T_{\alpha\eta}T_{\xi\eta}\right)\right\}\tau_\alpha\\&-\sum_\beta\left\{\frac{1}{2}T_{\alpha\beta}-\frac{3}{8}\sum_\xi T_{\alpha\xi}T_{\beta\xi}\right.\\&\left.+\frac{5}{16}\sum_\xi T_{\alpha\xi}\left(\sum_\eta T_{\beta\eta}T_{\xi\eta}\right)\right\}\tau_\beta\,,\end{aligned} \tag{2.5}$$

where we neglect the terms of the higher than the fourth order in the powers of the overlap integrals, the subscripts denote the individual bonds and the summation is taken over all the constituent bonds. The total energy of the molecule is expressed as

$$E=2\sum_\alpha I^o_{\alpha\alpha}+\sum_\alpha\sum_\beta(2C^o_{\alpha\beta}-K^o_{\alpha\beta})+\sum_{(XY)}\frac{Z_XZ_Y}{R_{XY}}\,, \tag{2.6}$$

where

$$I^o_{\alpha\alpha}=(\tau_\alpha{}^o|h|\tau_\alpha{}^o)=\int\tau_\alpha{}^o(1)h(1)\tau_\alpha{}^o(1)dv_1\,,$$

$$\begin{aligned}C^o_{\alpha\beta}&=(\tau_\alpha{}^o\tau_\alpha{}^o;\tau_\beta{}^o\tau_\beta{}^o)\\&=\iint\tau_\alpha{}^o(1)\tau_\beta{}^o(2)\frac{1}{r_{12}}\tau_\alpha{}^o(1)\tau_\beta{}^o(2)dv_1dv_2\,,\end{aligned}$$

and

$$\begin{aligned}K^o_{\alpha\beta}&=(\tau_\alpha{}^o\tau_\beta{}^o;\tau_\beta{}^o\tau_\alpha{}^o)\\&=\iint\tau_\alpha{}^o(1)\tau_\beta{}^o(2)\frac{1}{r_{12}}\tau_\beta{}^o(1)\tau_\alpha{}^o(2)dv_1dv_2\,.\end{aligned}$$

$h(1)$ is a part of the total Hamiltonian which depends on only one electron, and we assumed all the orbitals to be real. The last term in Eq. (2.6) shows the nuclear repulsion. If we substitute the relation (2.5) into Eq. (2.6) and omit the terms higher than fourth order of the overlap integrals, we obtain an approximate formula for the total energy. Based on the order of the overlap integrals we can devide the total energy as follows:

1. The zeroth order terms:

$$\sum_\alpha E_0(\alpha)=\sum_\alpha\left(2I_{\alpha\alpha}+C_{\alpha\alpha}+2\sum_{\beta\neq\alpha}{}'C_{\alpha\beta}\right)+\sum_{(XY)}\frac{Z_XZ_Y}{R_{XY}}\,, \tag{2.7}$$

2. The second order terms:

$$\begin{aligned}\sum_{(\alpha\beta)}E_2(\alpha\beta)=2\sum_{(\alpha\beta)}&\Big[T^2_{\alpha\beta}\Big\{I_{\alpha\alpha}+I_{\beta\beta}+C_{\alpha\alpha}+C_{\beta\beta}+3C_{\alpha\beta}+2\sum_{\xi\neq\alpha,\beta}{}''(C_{\alpha\xi}+C_{\beta\xi})\Big\}\\&-2T_{\alpha\beta}\Big(I_{\alpha\beta}+D_{\alpha,\alpha\beta}+D_{\beta,\alpha\beta}+2\sum_{\xi\neq\alpha,\beta}{}''C_{\xi,\alpha\beta}\Big)-K_{\alpha\beta}\Big]\,,\end{aligned} \tag{2.8}$$

3. The third order terms:

$$\begin{aligned}\sum_{(\alpha\beta\gamma)}E_3(\alpha\beta\gamma)=-4\sum_{(\alpha\beta\gamma)}&\Big[T_{\alpha\beta}T_{\beta\gamma}T_{\gamma\alpha}\Big\{I_{\alpha\alpha}+I_{\beta\beta}+I_{\gamma\gamma}+C_{\alpha\alpha}+C_{\beta\beta}+C_{\gamma\gamma}\\&+3(C_{\alpha\beta}+C_{\beta\gamma}+C_{\gamma\alpha})+2\sum_{\xi\neq\alpha,\beta,\gamma}{}'''(C_{\alpha\xi}+C_{\beta\xi}+C_{\gamma\xi})\Big\}\\&-T_{\beta\gamma}T_{\gamma\alpha}\Big(I_{\alpha\beta}+D_{\alpha,\alpha\beta}+D_{\beta,\alpha\beta}+D_{\gamma,\alpha\beta}+2\sum_{\xi\neq\alpha,\beta,\gamma}{}'''D_{\xi,\alpha\beta}\Big)\\&-T_{\gamma\alpha}T_{\alpha\beta}\Big(I_{\beta\gamma}+D_{\alpha,\beta\gamma}+D_{\beta,\beta\gamma}+D_{\gamma,\beta\gamma}+2\sum_{\xi\neq\alpha,\beta,\gamma}{}'''D_{\xi,\beta\gamma}\Big)\\&-T_{\alpha\beta}T_{\beta\gamma}\Big(I_{\gamma\alpha}+D_{\alpha,\gamma\alpha}+D_{\beta,\gamma\alpha}+D_{\gamma,\gamma\alpha}+2\sum_{\xi\neq\alpha,\beta,\gamma}{}'''D_{\xi,\gamma\alpha}\Big)\\&+T_{\alpha\beta}L_{\gamma,\alpha\beta}+T_{\beta\gamma}L_{\alpha,\beta\gamma}+T_{\gamma\alpha}L_{\beta,\gamma\alpha}\Big]\,.\end{aligned} \tag{2.9}$$

In the above expression, $\sum_\alpha$ in the zeroth order terms, $\sum_{(\alpha\beta)}$ in the second order terms, and $\sum_{(\alpha\beta\gamma)}$ in the third order terms mean the summations over all the constituent bonds, over all the pairs of the bonds, and over all the sets of three bonds, respectively, and

$$I_{\alpha\beta}=(\tau_\alpha|h|\tau_\beta)\ , \qquad C_{\alpha\beta}=(\tau_\alpha\tau_\alpha;\tau_\beta\tau_\beta)\ ,$$
$$K_{\alpha\beta}=(\tau_\alpha\tau_\beta;\tau_\alpha\tau_\beta)\ , \qquad D_{\alpha,\beta\gamma}=(\tau_\alpha\tau_\alpha;\tau_\beta\tau_\gamma)\ ,$$
$$L_{\alpha,\beta\gamma}=(\tau_\alpha\tau_\beta;\tau_\alpha\tau_\gamma)\ .$$

The discussion on the zeroth order and the second order terms in the preceding articles can of course be applied in the present case. In fact, it is easy to show the equivalence between H_0/Δ_0 in I and Eq. (2.7) and that between $H_2/\Delta_0-H_0\Delta_2/\Delta_0^2$ in I and Eq. (2.8).

§ 3. The Contribution of the Third Order Terms

We compute the magnitude of the contribution of the third order terms Eq. (2.9) to the binding energy of the C–C bond in the diamond crystal. In this case, we can put $\lambda=\mu=1$ from the symmetry consideration of the bond. The structure diagram of the diamond crystal is shown schematically in Fig. 1. Eq. (2.9) consists of the summation over the sets of three bonds. We classify the various sets of three bonds in the diamond crystal into the following groups:

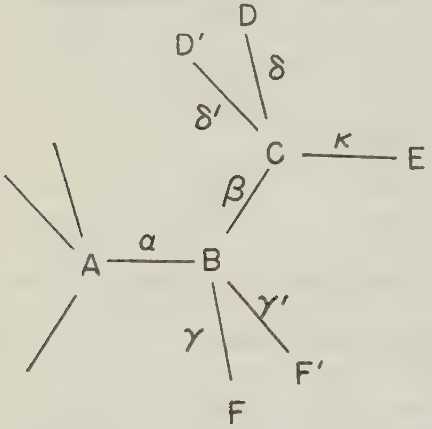

Fig. 1. Schematical Diagram of the Diamond Crystal. Capital letters show the constituent atoms and Greek small letters denote the constituent bonds.

1. (α, β, γ), where α, β and γ are the adjacent bonds with each other.

2. (α, β, δ), where β is adjacent to both of α and δ, but δ is the second nearest neighbouring bond to α and locates at the gauche position for α.

3. (α, β, κ), where α and β, β and κ are the adjacent bonds as in the preceding case, but κ, the second nearest neighbour bond of α, locates at the trans position for α.

4. (α, γ, κ), where α and γ are the adjacent bonds, and κ is the second nearest neighbouring bond for both of α and γ and locates at the trans position for α and at the gauche position for γ.

5. $(\alpha, \gamma, \delta')$, where α and γ are the adjacent bonds, and δ' is the second nearest neighbouring bond for both of α and γ and locates at the gauche position for both of α and γ.

6. (α, δ, η), where α, δ and η are the second nearest neighbouring bonds with each other.

7. Other sets of three bonds.

The sets of three bonds having the same geometrical structure give the same contribution to the binding energy of a bond. The total contribution of the third order terms to the binding energy of a bond is expressed as

$$2E_3(\alpha\beta\gamma)+6E_3(\alpha\beta\delta)+3E_3(\alpha\beta\kappa)$$
$$+12E_3(\alpha\gamma\kappa)+6E_3(\alpha\gamma\delta')+2E_3(\alpha\delta\eta)\ , \qquad (3.1)$$

where we neglect the contribution from the 7th group. In the calculation of each term in Eq. (3.1), the values of the molecular integrals appearing in Eq. (2.9) are readily evaluated, as they are expressed as the linear combinations of the molecular integrals involving the atomic orbitals used already in the previous paper of this series. The values of many center energy integrals are estimated by an approximation like Mulliken's one. In the evaluation of the value of $E_3(\alpha\beta\gamma)$ of the first group, we take into account only the potential of the atoms A, B, C and F in Fig. 1. This corresponds to the assumption that the molecular integrals are approximated by the following formulae:

$$C_{\alpha\xi}\simeq\frac{1}{2}(C_{\alpha x}+C_{\alpha y}),\quad D_{\xi,\alpha\beta}\simeq\frac{1}{2}(D_{x,\alpha\beta}+D_{y,\alpha\beta})\ ,$$

where ξ shows a bond other than α, β, and γ, and $\tau_\xi=(\phi_x+\phi_y)/\sqrt{2(1+S_{xy})}$. This may not introduce any significant error in the calculation of the value of $E_3(\alpha\beta\gamma)$ because of the same reason as we have already given for the approximate validity of Mulliken's approximation. The similar treatments have been applied to compute the values of the other terms in Eq. (3.1), that is, only the effect from the atoms in the set of the three bonds is considered explicitly and other atoms are assumed to be completely shielded by their valence electrons. The result of the computation is given in Table I.

Table I. The Contribution from Each Group (in eV).

$2E_3(\alpha\beta\gamma)$	$6E_3(\alpha\beta\delta)$	$3E_3(\alpha\beta\kappa)$	$12E_3(\alpha\gamma\kappa)$	$6E_3(\alpha\gamma\delta')$	Total
−0.83	−0.59	+0.44	+0.73	−0.42	−0.67

We neglect the contribution from the term $2E_3(\alpha\delta\eta)$ of the sixth group, the magnitude of which is estimated roughly as about 0.1 eV, namely about 1/8 of the first term. As the values of the overlap integrals between the bonds are: $T_{\alpha\beta}\simeq 0.1$, $T_{\alpha\delta}\simeq 0.05$ and $T_{\alpha\kappa}\simeq -0.05$, the order of magnitude of the contribution from each term is found roughly proportional to the product of the corresponding overlap integrals and the total number of the terms belonging to the same group, that is, $2E_3(\alpha\beta\gamma)\simeq 2CT_{\alpha\beta}T_{\beta\gamma}T_{\gamma\alpha}$, where C is a constant. It may, then, be resonable that the contribution from the second to fifth groups almost cancels out each other and the total contribution of the third order terms is roughly equal to the value of the term of the first group, as seen from Table I. The total contribution of the third order terms seems to be by no means negligibly small in the quantitative discussion of the binding energy of the C–C bond in the diamond crystal, but it is smaller than the total contribution of the second order terms, $3E_2(\alpha\beta)+6E_2(\alpha\delta)+3E_2(\alpha\kappa)$, the value of which is about 1.5 eV, though there is an ambiguity in the treatment of the intra-atomic exchange integrals. If we assume that the atomic valence orbital ϕ_i is the eigenfunction of the Hartree-Fock type equation (5.8) of I, we obtain −0.47 eV as the value of $2E_3(\alpha\beta\gamma)$. Furthermore it seems that Mulliken's type approximation used for the calculation of the values of the many center energy integrals is rather crude for the case of the exchange type molecular integrals and gives comparatively small values for these integrals, as seen from the application of this approximation to the two center energy integrals. The last three terms in Eq. (2.9) are almost determined by the three center energy integrals. According to the above consideration it might be possible to obtain a smaller value as the total contribution of the third order terms than that given in Table I. Then it seems that the contribution of the third order terms does not play any essential role in the binding energy of the σ bond. It may also be plausible to assume that the contribution of the fourth order terms is smaller than that of the third order terms and can be neglected.

§ 4. Consideration on the Additivity Rule

In the preceding section we have found that the contribution of the third order terms to the binding energy of the C–C bond is rather small and the fourth order terms may be completely neglected. We shall show that the additivity rule in the binding energies of the saturated hydrocarbons is valid under some assumptions even if the third order terms cannot be neglected. Usually we define the bond energy of a C–H bond as one fourth of the total energy of methane. In terms of Eq. (2.7)–(2.9), it can be expressed as

$$D(CH)=E_0(\alpha)+\frac{3}{2}E_2(\alpha\beta)+E_3(\alpha\beta\gamma)+\frac{1}{4}(E_\sigma^*-E_\sigma)\,, \qquad (4.1)$$

where α, β and γ are the nearest neighbouring C–H bond with each other and $E_\sigma^*-E_\sigma$ is the promotional energy in the free carbon atom. It is not necessary to consider the promotional energy for the hydrogen atoms. If we cannot neglect the second and third order terms in Eq. (4.1), the bond energy of a C–H bond is not determined soley by the quantities of the bond itself but involves the interaction energies between the bonds. The values of the second and third order terms are, however, rather small and approximately determined by the values of the overlap integrals between the bond orbitals. The overlap integral $T_{\alpha\beta}$ has an almost equal value in either case where the nearest neighbouring bonds are C–H or C–C. Then we shall assume that the values of $E_2(\alpha\beta)$ and $E_3(\alpha\beta\gamma)$ in the methane are equal to those of $E_2(\alpha'\beta')$ and $E_3(\alpha'\beta'\gamma')$ in the diamond if $(\alpha\beta)$ and $(\alpha'\beta')$, and $(\alpha\beta\gamma)$ and $(\alpha'\beta'\gamma')$ belong to the same geometrical group, in the sense explained above, respectively. Furthermore, each term in Eq. (4.1) contains the contribution from the potential of the whole molecule, but the potential of the remote atoms is not so important as the C–H bond is expected to be approximately homopolar. If we can ignore in Eq. (4.1) the difference between the corresponding quantities in the second and third order terms of the C–H and C–C bonds, the bond energy of a C–C bond can be calculated using the quantities defined for the ethane as

$$D(CC)=E_0(\beta)+3E_2(\alpha\beta)+6E_2(\alpha\delta)+3E_2(\alpha\kappa)$$
$$+2E_3(\alpha\beta\gamma)+6E_3(\alpha\beta\delta)+3E_3(\alpha\beta\kappa)$$
$$+12E_3(\alpha\gamma\kappa)+6E_3(\alpha\gamma\delta')+\frac{1}{2}(E_C^*-E_C)\,, \tag{4.2}$$

where β denotes the C–C bond and the others represent the C–H bonds. The notation of the bond $\alpha, \beta, \gamma\cdots$ is the same as that explained in the preceding section, and so the geometrical relation among the bonds in the individual terms of Eq. (4.2) can be understood easily. There are two kinds of overlap integrals between the orbitals involved in the second nearest neighbouring bonds. The value of the overlap integral between the orbitals of the bonds locating at the gauche position with each other is almost equal in magnitude to that between the orbitals of the bonds locating at the trans position with each other, but they have the opposite sign, so that the total effect of the second neighbouring bonds to the third order term may be small enough to be neglected. This has been shown for the C–C bond of the diamond crystal in the preceding section. This may be the case even if we take into account the third nearest or more remote neighbouring bonds in the third order terms. Furthermore, the overlap integrals between the orbitals of the third nearest or more remote neighbouring bonds are exceedingly small. Then we may be allowed to neglect their effect. Though each term of Eq. (4.2) involves the potential of the whole molecule, it depends mainly, as discussed in § 3 of II, on the potential of the atoms which are connected by the bond orbitals involved in the term under consideration. The values of the second and third order terms seem to be roughly determined by the product of the overlap integrals considered in the term, for example, we may put approximately $E_3(\alpha\beta\gamma)=CT_{\alpha\beta}T_{\beta\gamma}T_{\gamma\alpha}$, as shown in the preceding section. The value of the overlap integral $T_{\alpha\beta}$ between the bond orbitals τ_α and τ_β is almost equal in any case where the bond orbitals are responsible for the C–H or the C–C bonds. If we assume that the value of each term in Eq. (4.2) is equal to that in the diamond crystal, we can calculate the binding energy of a C–C bond in the diamond from the total binding energies of propane, butane and so on.

Although the above discussion involves a serious assumption, it can be expected that the additivity rule in the binding energies of the saturated hydrocarbons is valid, even if we take the non-orthognality between the bond orbitals into account. Even if we recognize the difference between the C–H and C–C bonds in the second and third order terms, we can show that the additivity rule is asymptotically valid in the long chain molecule of saturated hydrocarbon, if we use the appropriate definitions of the C–H and C–C bond energies which are expressed as

$$\left.\begin{aligned} D(CH)&=D_0(CH)+\frac{1}{2}E_2(\bar{\alpha}\bar{\beta})+2E_2(\bar{\alpha}\beta)+E_3(\bar{\alpha}\bar{\beta}\gamma)\,,\\ D(CC)&=D_0(CC)+2E_2(\bar{\alpha}\beta)+E_2(\alpha\beta)+2E_2(\bar{\alpha}\bar{\delta})+4E_2(\bar{\alpha}\delta)\\ &\quad+2E_2(\bar{\alpha}\bar{\kappa})+E_2(\alpha\kappa)+2E_3(\bar{\alpha}\beta\gamma)+2E_3(\bar{\alpha}\beta\bar{\delta})+4E_3(\bar{\alpha}\beta\delta)+2E_3(\bar{\alpha}\beta\bar{\kappa})\\ &\quad+E_3(\alpha\beta\kappa)+4E_3(\bar{\alpha}\bar{\gamma}\bar{\kappa})+4E_3(\bar{\alpha}\gamma\bar{\kappa})+4E_3(\bar{\alpha}\gamma\kappa)+2\overline{E_3}(\alpha\bar{\gamma}\delta')+4E_3(\bar{\alpha}\gamma\bar{\delta}')\,,\end{aligned}\right\} \tag{4.3}$$

where $D_0(CH)$ and $D_0(CC)$ are the zeroth order bond energies of the C–H and C–C bonds, respectively, the superscript bar means the C–H bond orbitals and the others represent the C–C bond orbitals.

§ 5. Discussion

In this article, we used the bond orbital method to describe the electronic state of the saturated molecule and made the bond orbitals to be orthogonal with each other by Loewdin's method. In this method the operator $(\mathbf{1}+\boldsymbol{T})^{-1/2}$ is defined by a power series of the overlap integrals and the condition for the convergence of the series is

$$|\sum_{\xi}{}' T_{\alpha\xi}|<1\,. \tag{5.1}$$

In our case, as it is found that

$$|\sum_{\xi}{}' T_{\alpha\xi}| \simeq 1\ , \tag{5.2}$$

we cannot expect the rapid convergence of the power series. Schmid[3] also calculated the cohesive energy of the diamond crystal by the use of the orthogonalized atomic orbitals obtained by Loewdin's method, but in this case Loewdins method may be unable to be applied because the condition (5.1) does not hold at all. Under the assumption that the exchange integral $K_{\alpha\beta}$ between the bond orbitals τ_α and τ_β is a quantity of the order of $T^2_{\alpha\beta}$, we rearranged the terms in the expanded series, taking account of the order of magnitude of the overlap integral between the bond orbitals, and obtained the result that the contribution of the third order terms is smaller than that of the second order terms and may not play any essential role in the discussion of the binding energy of the σ bond, though it may be by no means negligible quantitatively. Niira[4] reported that if the total energy of the methane is expanded in the same way as that in this article, the convergence of series is not so simply discussed. However, his calculation showed that the total energy is given in good approximation by the terms up to the second order of the overlap integrals. The same was reported by Lundqvist,[5] who calculated the cohesive energy of LiH by the use of Loewdin's method, though the expanded power series for $(\mathbf{1}+\boldsymbol{T})^{-1/2}$ diverges. We should like to receall here Nukasawa's discussion[6] on the higher order terms, which was already cited in § 6 of I. The fundamental formula in his discussion is written in the previous notation as

$$E_3(\alpha\beta\gamma) = -T_{\alpha\beta}T_{\beta\gamma}T_{\gamma\alpha}\sum_{(\lambda\mu)}\frac{E_2(\lambda\mu)}{T^2_{\lambda\mu}}\ , \tag{5.3}$$

where the summation $\sum\limits_{(\lambda\mu)}$ extends over the pairs of bonds $(\alpha\beta)$, $(\beta\gamma)$ and $(\gamma\alpha)$. He showed that it may be sufficient to consider the terms up to the second order in the calculation of the total energy, if the relations analogous to Eq. (5.3) still hold for the terms higher than the third order and the overlap integrals under consideration are sufficiently small. It is easily shown from Eqs. (2.8) and (2.9) that the condition for the validity of Eq. (5.3) is

$$\begin{aligned} &T_{\alpha\beta}T_{\beta\gamma}T_{\gamma\alpha}(C_{\alpha\beta}+C_{\beta\gamma}+C_{\gamma\alpha})-2(T_{\beta\gamma}T_{\gamma\alpha}D_{\gamma,\alpha\beta}+T_{\gamma\alpha}T_{\alpha\beta}D_{\alpha,\beta\gamma}+T_{\alpha\beta}T_{\beta\gamma}D_{\beta,\gamma\alpha}) \\ &\quad -\left(\frac{T_{\beta\gamma}T_{\gamma\alpha}}{T_{\alpha\beta}}K_{\alpha\beta}+\frac{T_{\gamma\alpha}T_{\alpha\beta}}{T_{\beta\gamma}}K_{\beta\gamma}+\frac{T_{\alpha\beta}T_{\beta\gamma}}{T_{\gamma\alpha}}K_{\gamma\alpha}\right)+2(T_{\alpha\beta}L_{\gamma,\alpha\beta}+T_{\beta\gamma}L_{\alpha,\beta\gamma}+T_{\gamma\alpha}L_{\beta,\gamma\alpha})=0\ , \end{aligned} \tag{5.4}$$

which holds approximately for the actual values of the molecular integrals given in § 3. In our previous calculation of the C–C bond of the diamond crystal it was shown that the effect of the non-orthogonality between the orbitals of the second nearest neighbouring bonds is not significant to the binding energy of the σ bond. Then, the discussion due to Nukasawa is applicable to our system and we may conclude that the approximate value of the binding energy of the σ bond is obtained if we stop at the second order terms with respect to the overlap integrals between the orbitals of the adjacent bonds, in other words, most of the terms higher than the third order is considered to be included effectively in the second order terms by the use of the relations analogous to Eq. (5.3). However, if we consider the approximations assumed in Nukasawa's theory, the error of the value of the binding energy of the σ bond which is calculated in the second order approximation of the overlap integrals between the bond orbitals may be comparable to the contribution of the third order term given in this article.

The author wishes to express his sincere thanks to Professor K. Niira for his incessant encouragement and for his kind reading of the manuscript and to Professor E. Ishiguro for his valuable suggestions. The author is indebted to the Ministry of Education for this research grant.

References

1) K. O-ohata: J. Phys. Soc. Japan, **15** (1960), 1048, 1258, 1449. These papers are refered to as I, II, and III, respectively.
2) P. O. Loewdin: Advance in Phys. **5** No. 17 (1956).
3) L. A. Schmid: Phys. Rev. **92** (1953), 1373.
4) K. Niira: Busseiron Kenkyu, No. **93** (1956), 53. (in Japanese).
5) S. O. Lundqvist: Arkiv Fysik, **8** (1954), 177, **9** (1955), 453, A. Morita: Chemical Physics I, (Kyoritsu-sha, 1958), p. 216. (in Japanese).
6) K. Nukasowa: Busseiron Kenkyu, No. **49** (1952), 41. (in Japanese).

JOURNAL OF THE PHYSICAL SOCIETY OF JAPAN, Vol. 15, No. 9, SEPTEMBER, 1960

The Dipole Moment and End-to-end Length of the Isotactic Vinyl Polymer, II.
A Special Simplified Model and Numerical Calculations

By Tsugio MORI

Ôtsu Senior High School, Ôtsu, Shiga-ken, Japan

(Received March 28, 1960)

In the preceding paper[1], fundamental formulas for $\langle\mu^2\rangle_0$, $\langle R^2\rangle_0$, $\langle\mu^2\rangle$ and $\langle R^2\rangle$ are derived. In the present paper, these formulas are brought into the more convenient forms for numerical calculations, and the square well potential of internal rotation of polymer and a linear function $\varphi'(\varphi)$ are introduced. The results of calculations explain that $\langle\mu^2\rangle/n\mu_0^2$ must be 0.3~1.0 when effective bond length is 5~10 Å. These values agree satisfactory with experimental data.

§ 1. Matrix Elements

Principal results of the preceding paper[1] are collected below:—

$$\frac{\langle\mu^2\rangle_0}{n\mu_0^2}=1+2(0\ 0\ 1)\mathbf{Y}^{\mathrm{T}}\mathbf{X}(\mathbf{1}-\mathbf{X})^{-1}\mathbf{Y}\begin{bmatrix}0\\0\\1\end{bmatrix}, \tag{1}$$

$$\frac{\langle R^2\rangle_0}{Nb_0^2}=(0\ 0\ 1)(\mathbf{1}+\mathbf{Z})(\mathbf{1}-\mathbf{X})^{-1}(\mathbf{1}+\mathbf{Z}')\begin{bmatrix}0\\0\\1\end{bmatrix}, \tag{2}$$

$$\frac{\langle\mu^2\rangle}{n\mu_0^2}=1+\frac{\rho^2-P}{1-P}\left(\frac{\langle\mu^2\rangle_0}{n\mu_0^2}-1\right), \tag{3}$$

$$\frac{\langle R^2\rangle}{Nb_0^2}=\rho^2\frac{\langle R^2\rangle_0}{Nb_0^2} \tag{4}$$

and

$$P=(1+\alpha)\frac{Nb_0^2}{\langle R^2\rangle_0}, \tag{5}$$

where we use the notations

$$\mathbf{X}=\langle\mathbf{D}(\varphi')\mathbf{D}(\varphi)\rangle, \tag{6}$$

$$\mathbf{Y}=\left\langle\mathbf{D}\left(\varphi'-\frac{2\pi}{3}\right)\right\rangle, \tag{7}$$

$$\mathbf{Z}=\langle\mathbf{D}(\varphi)\rangle \tag{8}$$

and

$$\mathbf{Z}'=\langle\mathbf{D}(\varphi')\rangle. \tag{9}$$

Therefore we must calculate the elements of these matrices (6)~(9). The (1, 1)-element of **X** is given by

$$\mathrm{X}_{11}=-\alpha\langle\sin\varphi'\sin\varphi\rangle+\alpha^2\langle\cos\varphi'\cos\varphi\rangle+\beta^2\langle\cos\varphi'\rangle.$$

In order to write such formula simply, we introduce the following abbreviations:—

$$\left.\begin{aligned}\langle\mathrm{s's}\rangle&=\langle\sin\varphi'\sin\varphi\rangle,\\ \langle\mathrm{s'c}\rangle&=\langle\sin\varphi'\cos\varphi\rangle,\\ \langle\mathrm{s'}\rangle&=\langle\sin\varphi'\rangle,\\ \langle\mathrm{c's}\rangle&=\langle\cos\varphi'\sin\varphi\rangle,\\ \langle\mathrm{c'c}\rangle&=\langle\cos\varphi'\cos\varphi\rangle,\\ \langle\mathrm{c'}\rangle&=\langle\cos\varphi'\rangle,\\ \langle\mathrm{s}\rangle&=\langle\sin\varphi\rangle,\\ \text{and}\quad \langle\mathrm{c}\rangle&=\langle\cos\varphi\rangle.\end{aligned}\right\} \tag{10}$$

If we put

$$\mathbf{X}=\begin{bmatrix}\mathrm{X}_{11}&\mathrm{X}_{12}&\mathrm{X}_{13}\\ \mathrm{X}_{21}&\mathrm{X}_{22}&\mathrm{X}_{23}\\ \mathrm{X}_{31}&\mathrm{X}_{32}&\mathrm{X}_{33}\end{bmatrix}, \tag{11}$$

we can write down the following formulas:—

$$\left.\begin{aligned}\mathrm{X}_{11}&=-\alpha\langle\mathrm{s's}\rangle+\alpha^2\langle\mathrm{c'c}\rangle+\beta^2\langle\mathrm{c'}\rangle,\\ \mathrm{X}_{12}&=-\langle\mathrm{s'c}\rangle-\alpha\langle\mathrm{c's}\rangle,\\ \mathrm{X}_{13}&=\beta\{\langle\mathrm{s's}\rangle+\alpha(\langle\mathrm{c'}\rangle-\langle\mathrm{c'c}\rangle)\},\\ \mathrm{X}_{21}&=\alpha\langle\mathrm{c's}\rangle+\alpha^2\langle\mathrm{s'c}\rangle+\beta^2\langle\mathrm{s'}\rangle,\\ \mathrm{X}_{22}&=\langle\mathrm{c'c}\rangle-\alpha\langle\mathrm{s's}\rangle,\\ \mathrm{X}_{23}&=-\beta\{\langle\mathrm{c's}\rangle+\alpha'(\langle\mathrm{s'c}\rangle-\langle\mathrm{s'}\rangle)\},\\ \mathrm{X}_{31}&=\alpha\beta(1-\langle\mathrm{c}\rangle),\\ \mathrm{X}_{32}&=\beta\langle\mathrm{s}\rangle,\\ \mathrm{X}_{33}&=\alpha^2+\beta^2\langle\mathrm{c}\rangle.\end{aligned}\right\} \tag{12}$$

We denote the cofactor matrix of $(\mathbf{1}-\mathbf{X})$ by **A**, namely,

$$(\mathbf{1}-\mathbf{X})^{-1}=\frac{\mathbf{A}}{|\mathbf{1}-\mathbf{X}|}=\frac{1}{|\mathbf{1}-\mathbf{X}|}\begin{bmatrix}\mathrm{A}_{11}&\mathrm{A}_{12}&\mathrm{A}_{13}\\ \mathrm{A}_{21}&\mathrm{A}_{22}&\mathrm{A}_{23}\\ \mathrm{A}_{31}&\mathrm{A}_{32}&\mathrm{A}_{33}\end{bmatrix}, \tag{13}$$

where $|\mathbf{1}-\mathbf{X}|$ is the determinant of $(\mathbf{1}-\mathbf{X})$, and

$$|\mathbf{1}-\mathbf{X}|=\begin{vmatrix}1-X_{11} & -X_{12} & -X_{13}\\ -X_{21} & 1-X_{22} & -X_{23}\\ -X_{31} & -X_{32} & 1-X_{33}\end{vmatrix}. \tag{14}$$

Then the relation

$$\mathbf{X}(\mathbf{1}-\mathbf{X})^{-1}=\frac{\mathbf{A}}{|\mathbf{1}-\mathbf{X}|}-\mathbf{1} \tag{15}$$

is easily verified.

Although the matrix **Y** has nine elements, we need to know only its third column elements, which are denoted by B_1, B_2, B_3 respectively, and abbreviated to the one column matrix **B**, namely,

$$\mathbf{Y}\begin{bmatrix}0\\0\\1\end{bmatrix}=\begin{bmatrix}B_1\\B_2\\B_3\end{bmatrix}=\mathbf{B}\,, \tag{16}$$

where

$$\left.\begin{aligned}&B_1=\beta\left\langle \cos\left(\varphi'-\frac{2\pi}{3}\right)\right\rangle,\\ &B_2=\beta\left\langle \sin\left(\varphi'-\frac{2\pi}{3}\right)\right\rangle,\\ &B_3=\alpha\,.\end{aligned}\right\} \tag{17}$$

We also need the third row elements of $(\mathbf{1}+\mathbf{Z})$, and the third column elements of $(\mathbf{1}+\mathbf{Z}')$. They are given by

$$(0\ 0\ 1)(\mathbf{1}+\mathbf{Z})=(\beta,\ 0,\ 1+\alpha) \tag{18}$$

and

$$(\mathbf{1}+\mathbf{Z}')\begin{bmatrix}0\\0\\1\end{bmatrix}=\begin{bmatrix}\beta\langle c'\rangle\\ \beta\langle s'\rangle\\ 1+\alpha\end{bmatrix}. \tag{19}$$

Substitution of (15) and (16) in Eq. (1) yields

$$\frac{\langle \mu^2\rangle_0}{n\mu_0{}^2}=1+\frac{2\mathbf{B}^{\mathrm{T}}\mathbf{A}\mathbf{B}}{|\mathbf{1}-\mathbf{X}|}-2\mathbf{B}^{\mathrm{T}}\mathbf{B}\,, \tag{20}$$

where

$$\mathbf{B}^{\mathrm{T}}\mathbf{A}\mathbf{B}=B_1{}^2A_{11}+B_2{}^2A_{22}+B_3{}^2A_{33}+B_2B_3(A_{23}+A_{32})+B_3B_1(A_{31}+A_{13})+B_1B_2(A_{12}+A_{21}) \tag{21}$$

and

$$\mathbf{B}^{\mathrm{T}}\mathbf{B}=B_1{}^2+B_2{}^2+B_3{}^2\,. \tag{22}$$

While the substitution of (13), (18) and (19) in Eq. (2) yields

$$\begin{aligned}\frac{\langle R^2\rangle_0}{Nb_0{}^2}=\frac{1}{|\mathbf{1}-\mathbf{X}|}&[\beta\langle c'\rangle\{\beta A_{11}+(1+\alpha)A_{31}\}\\ &+\beta\langle s'\rangle\{\beta A_{12}+(1+\alpha)A_{32}\}+(1+\alpha)\{\beta A_{13}+(1+\alpha)A_{33}\}]\,.\end{aligned} \tag{23}$$

Now, the details of the determinant $|\mathbf{1}-\mathbf{X}|$ and elements of the matrix **A** are needed. They are collected below:—

$$\begin{aligned}|\mathbf{1}-\mathbf{X}|=\beta^2[&(1-\langle c'\rangle)(1-\langle c\rangle)(1-\langle c'c\rangle)+(1-\langle c'\rangle)\langle s\rangle\langle c's\rangle+(1-\langle c\rangle)\langle s'\rangle\langle s'c\rangle-\langle s'\rangle\langle s\rangle\langle s's\rangle\\ &+\alpha\{(1-\langle c'\rangle)(1-\langle c\rangle)\langle s's\rangle+(1-\langle c'\rangle)\langle s\rangle\langle s'c\rangle\\ &\quad+(1-\langle c\rangle)\langle s'\rangle\langle c's\rangle-(1-\langle c'c\rangle)\langle s'\rangle\langle s\rangle\}]\,,\end{aligned} \tag{24}$$

$$\left.\begin{aligned}&A_{11}=\beta^2[(1-\langle c\rangle)(1-\langle c'c\rangle)+\langle s\rangle\langle c's\rangle+\alpha\{(1-\langle c\rangle)\langle s's\rangle+(\langle s'c\rangle-\langle s'\rangle)\langle s\rangle\}]\,,\\ &A_{12}=-\beta^2[(1-\langle c\rangle)\langle s'c\rangle-\langle s\rangle\langle s's\rangle+\alpha\{(1-\langle c\rangle)\langle c's\rangle-(\langle c'\rangle-\langle c'c\rangle)\langle s\rangle\}]\,,\\ &A_{13}=\beta[(1-\langle c'c\rangle)\langle s's\rangle+\langle s'c\rangle\langle c's\rangle\\ &\qquad+\alpha\{(1-\langle c'c\rangle)(\langle c'\rangle-\langle c'c\rangle)+\langle s's\rangle^2+\langle c's\rangle^2+(\langle s'c\rangle-\langle s'\rangle)\langle s'c\rangle\}\\ &\qquad\quad+\alpha^2\{(\langle c'\rangle-\langle c'c\rangle)\langle s's\rangle+(\langle s'c\rangle-\langle s'\rangle)\langle c's\rangle\}]\,,\\ &A_{21}=\beta^2(1-\langle c\rangle)\langle s'\rangle\,,\\ &A_{22}=\beta^2(1-\langle c'\rangle)(1-\langle c\rangle)\,,\\ &A_{23}=-\beta[(1-\langle c'\rangle)\langle c's\rangle-\langle s'\rangle\langle s's\rangle+\alpha\{(1-\langle c'\rangle)\langle s'c\rangle-(1-\langle c'c\rangle)\langle s'\rangle\}]\,,\\ &A_{31}=\beta[\langle s'\rangle\langle s\rangle+\alpha\{(1-\langle c\rangle)(1-\langle c'c\rangle)+\langle s\rangle\langle c's\rangle\}\\ &\qquad\qquad\qquad+\alpha^2\{(1-\langle c\rangle)\langle s's\rangle+(\langle s'c\rangle-\langle s'\rangle)\langle s\rangle\}]\,,\\ &A_{32}=\beta[(1-\langle c'\rangle)\langle s\rangle-\alpha\{(1-\langle c\rangle)\langle s'c\rangle-\langle s\rangle\langle s's\rangle\}\\ &\qquad\qquad\qquad-\alpha^2\{(1-\langle c\rangle)\langle c's\rangle-(\langle c'\rangle-\langle c'c\rangle)\langle s\rangle\}]\,,\end{aligned}\right\} \tag{25}$$

and

$$\left.\begin{aligned}A_{33}=&(1-\langle c'\rangle)(1-\langle c'c\rangle)+\langle s'\rangle\langle s'c\rangle\\&+\alpha\{(2-\langle c'\rangle-\langle c'c\rangle)\langle s's\rangle+(\langle s'c\rangle+\langle s'\rangle)\langle c's\rangle\}\\&+\alpha^2\{(1-\langle c'c\rangle)(\langle c'\rangle-\langle c'c\rangle)+\langle s's\rangle^2+\langle c's\rangle^2+(\langle s'c\rangle-\langle s'\rangle)\langle s'c\rangle\}\\&+\alpha^3\{(\langle c'\rangle-\langle c'c\rangle)\langle s's\rangle+(\langle s'c\rangle-\langle s'\rangle)\langle c's\rangle\}\,.\end{aligned}\right|$$

It is remarked that we can easily verify

$$\beta A_{11}+(1+\alpha)A_{31}=\frac{1+\alpha}{\beta}(\beta^2\langle s'\rangle\langle s\rangle+A_{11})\,,$$

and

$$\beta A_{12}+(1+\alpha)A_{32}=\frac{1+\alpha}{\beta}\{\beta^2(1-\langle c'\rangle)\langle s\rangle+A_{12}\}$$

from (25). Then Eq. (23) becomes

$$\frac{\langle R^2\rangle_0}{Nb_0^2}=\frac{1+\alpha}{|\mathbf{1}-\mathbf{X}|}[\beta^2\langle s'\rangle\langle s\rangle+\langle c'\rangle A_{11}+\langle s'\rangle A_{12}+\beta A_{13}+(1+\alpha)A_{33}]\,. \tag{26}$$

If the rotation of each bond were to be independent of the others, we would replace $\langle s's\rangle$, $\langle s'c\rangle$, $\langle c's\rangle$, $\langle c'c\rangle$ by $\langle s'\rangle\langle s\rangle$, $\langle s'\rangle\langle c\rangle$, $\langle c'\rangle\langle s\rangle$, $\langle c'\rangle\langle c\rangle$ respectively, and would reduce (26) to

$$\frac{\langle R^2\rangle_0}{Nb_0^2}=\frac{(1+\alpha)\{1+2(\langle s'\rangle\langle s\rangle-\langle c'\rangle\langle c\rangle)+(\langle s'\rangle^2+\langle c'\rangle^2)(\langle s\rangle^2+\langle c\rangle^2)\}}{(1-\alpha)\{(1-\langle c'\rangle)(1-\langle c\rangle)-(\langle c'\rangle-\langle c'\rangle^2-\langle s'\rangle^2)(\langle c\rangle-\langle c\rangle^2-\langle s\rangle^2)\}}\,. \tag{27}$$

In this paper, however, we have no regard for the independent bond rotation. Eq. (27) has been derived by Nagai[2].

§2. Potential of Internal Rotation

Since the method of numerical calculations in this paper is quite primitive, it is disirable that assumptions concerning with the internal rotation are as simple as possible. In the preceding paper[1], two notations φ and φ' are introduced in order to represent the rotations of adjoining bonds. In the present paper, we put two assumptions for φ and φ'. First a linear function

$$\varphi'=\lambda\varphi+\frac{2\pi}{3} \tag{28}$$

is assumed, where λ is a constant, and the constant term $2\pi/3$ corresponds to $\varphi'(0)=2\pi/3$, which conforms with the assumption in the preceding paper. On the other hand, a square well potential V defined by

$$\left.\begin{aligned}V&=0\quad(\text{when}\quad 0\leqq|\varphi|\leqq\mathcal{E})\\&=\infty\quad(\text{when}\quad|\varphi|>\mathcal{E})\end{aligned}\right\} \tag{29}$$

is assumed for the internal rotation, where $\mathcal{E}$ is a parameter which varies with some conditions, that is, temperature, interaction between polymer and solvent, etc. The first assumption (28) means an imagination that two kinds of potential widths, $2\mathcal{E}$ and $2|\lambda|\mathcal{E}$, may alternate in the polymer chain, since the asymmetric carbon atoms appear every two bonds in the chain. The second assumption (29) defines the mean of any physical quantity ξ, namely,

$$\langle\xi\rangle=\frac{\int_{-\infty}^{\infty}\xi\exp(-V/kT)d\varphi}{\int_{-\infty}^{\infty}\exp(-V/kT)d\varphi}=\frac{1}{2\mathcal{E}}\int_{-\varepsilon}^{\varepsilon}\xi d\varphi\,. \tag{30}$$

For example, we have

$$\langle s's \rangle = \frac{1}{2\varepsilon}\int_{-\varepsilon}^{\varepsilon} \sin\left(\lambda\varphi + \frac{2\pi}{3}\right) \sin\varphi \, d\varphi \, .$$

Some of such means are collected below:—

$$\left.\begin{aligned}
\langle s's \rangle &= \frac{1}{2}\left\{\frac{\sin(1-\lambda)\varepsilon}{(1-\lambda)\varepsilon} - \frac{\sin(1+\lambda)\varepsilon}{(1+\lambda)\varepsilon}\right\}\cos\frac{2\pi}{3}\,, \\
\langle s'c \rangle &= \frac{1}{2}\left\{\frac{\sin(1-\lambda)\varepsilon}{(1-\lambda)\varepsilon} + \frac{\sin(1+\lambda)\varepsilon}{(1+\lambda)\varepsilon}\right\}\sin\frac{2\pi}{3}\,, \\
\langle s' \rangle &= \frac{\sin\lambda\varepsilon}{\lambda\varepsilon}\sin\frac{2\pi}{3}\,, \\
\langle c's \rangle &= -\frac{1}{2}\left\{\frac{\sin(1-\lambda)\varepsilon}{(1-\lambda)\varepsilon} - \frac{\sin(1+\lambda)\varepsilon}{(1+\lambda)\varepsilon}\right\}\sin\frac{2\pi}{3}\,, \\
\langle c'c \rangle &= \frac{1}{2}\left\{\frac{\sin(1-\lambda)\varepsilon}{(1-\lambda)\varepsilon} + \frac{\sin(1+\lambda)\varepsilon}{(1+\lambda)\varepsilon}\right\}\cos\frac{2\pi}{3}\,, \\
\langle c' \rangle &= \frac{\sin\lambda\varepsilon}{\lambda\varepsilon}\cos\frac{2\pi}{3}\,, \\
\langle s \rangle &= 0\,, \\
\langle c \rangle &= \frac{\sin\varepsilon}{\varepsilon}\,, \\
B_1 &= \beta\frac{\sin\lambda\varepsilon}{\lambda\varepsilon}\,, \\
B_2 &= 0 \\
\text{and}\qquad B_3 &= \alpha\,.
\end{aligned}\right\} \qquad (31)$$

Here we consider three typical cases, namely, $\lambda=0, 1, -1$. If $\lambda=0$, two adjoining bonds compose a rigid segment holding asymmetric carbon atom and dipolar substituent between them, and the rotation is possible only at joints of segments. If $0<\lambda<1$, φ' is an increasing function of φ, but the scale of rotation in a segment is smaller than that of a whole segment. The assumption $0<\lambda<1$ is equivalent to the imagination that a relaxation effect may exist between excitation φ and response φ'. If $\lambda=1$, the scale of rotation in a segment is the same order as that of a whole segment. If $\lambda<0$, φ' is a decreasing function of φ, and it may be shown after numerical calculations that the case $\lambda=-1$ cannot explain the experimental data.

We substitute $\lambda=0, 1, -1$ one after another in (31), and put the notations

$$f_1 = \frac{\sin\varepsilon}{\varepsilon}\,, \quad f_2 = \frac{\sin 2\varepsilon}{2\varepsilon}\,. \qquad (32)$$

The results are collected in Table I.

Table I.

	$\lambda=0$	$\lambda=1$	$\lambda=-1$
$\langle s's \rangle$	0	$-\frac{1}{4}(1-f_2)$	$\frac{1}{4}(1-f_2)$
$\langle s'c \rangle$	$\frac{\sqrt{3}}{2}f_1$	$\frac{\sqrt{3}}{4}(1+f_2)$	$\frac{\sqrt{3}}{4}(1+f_2)$
$\langle s' \rangle$	$\frac{\sqrt{3}}{2}$	$\frac{\sqrt{3}}{2}f_1$	$\frac{\sqrt{3}}{2}f_1$
$\langle c's \rangle$	0	$-\frac{\sqrt{3}}{4}(1-f_2)$	$\frac{\sqrt{3}}{4}(1-f_2)$
$\langle c'c \rangle$	$-\frac{1}{2}f_1$	$-\frac{1}{4}(1+f_2)$	$-\frac{1}{4}(1+f_2)$
$\langle c' \rangle$	$-\frac{1}{2}$	$-\frac{1}{2}f_1$	$-\frac{1}{2}f_1$
$\langle s \rangle$	0	0	0
$\langle c \rangle$	f_1	f_1	f_1
B_1	β	βf_1	βf_1
B_2	0	0	0
B_3	α	α	α

§ 3. Numerical Calculations and Conclusions

The first step of our numerical calculations is to deal with the quantities for the unperturbed configuration, i.e., $\langle\mu^2\rangle_0/n\mu_0^2$ and $\langle R^2\rangle_0/Nb_0^2$. If we substitute the formulas of Table I in (24), (21) and (22) and make use of the values

$$\alpha=\frac{1}{3}\,,\qquad \beta=\frac{\sqrt{8}}{3}\,, \tag{33}$$

then we have the following relations.

$$\left.\begin{aligned}&\lambda=0:\\ &\qquad |\mathbf{1}-\mathbf{X}|=\frac{4}{3}(1-f_1^2)\,,\\ &\qquad \mathbf{B}^{\mathrm{T}}\mathbf{AB}=\frac{1}{3}(3-f_1-f_1^2)\,,\\ &\qquad \mathbf{B}^{\mathrm{T}}\mathbf{B}=1\,.\end{aligned}\right\} \tag{34}$$

$$\left.\begin{aligned}&\lambda=1:\\ &\quad |\mathbf{1}-\mathbf{X}|=\frac{2}{27}(1-f_1)\{9+(1+2f_1)(5+4f_2)\}\,,\\ &\quad \mathbf{B}^{\mathrm{T}}\mathbf{AB}=\frac{1}{972}[81+\{11+16f_1-4(1-f_2)\}(5+4f_2)\\ &\qquad\qquad -32f_1\{(1-f_2)(5+4f_2)-3(1-f_1)(2+f_2)\}\\ &\qquad\qquad +128f_1^2(1-f_1)(7+2f_2)]\,,\\ &\quad \mathbf{B}^{\mathrm{T}}\mathbf{B}=\frac{1}{9}(1+8f_1^2)\,.\end{aligned}\right\} \tag{35}$$

$$\left.\begin{aligned}&\lambda=-1:\\ &\quad |\mathbf{1}-\mathbf{X}|=\frac{2}{27}(1-f_1)\{9+(1+2f_1)(7+2f_2)\}\,,\\ &\quad \mathbf{B}^{\mathrm{T}}\mathbf{AB}=\frac{1}{972}[81+\{11+16f_1+2(1-f_2)\}(7+2f_2)\\ &\qquad\qquad +16f_1\{(1-f_2)(7+2f_2)+3(1-f_1)(5+f_2)\}\\ &\qquad\qquad +128f_1^2(1-f_1)(8+f_2)]\,,\\ &\quad \mathbf{B}^{\mathrm{T}}\mathbf{B}=\frac{1}{9}(1+8f_1^2)\,.\end{aligned}\right\} \tag{36}$$

Then we can calculate the values of $\langle\mu^2\rangle_0/n\mu_0^2$ according to the formula (20) as the function of ε within the interval

$$0\leqq\varepsilon\leqq\pi\,. \tag{37}$$

The results are given in Table II.

On the other hand, we have the following relations by the use of (26) and Table I, and refering (33).

$$\left.\begin{aligned}&\lambda=0:\\ &\qquad \frac{\langle R^2\rangle_0}{Nb_0^2}=\frac{4(1+f_1+f_1^2)}{3(1-f_1^2)}\,.\end{aligned}\right\} \tag{38}$$

$$\left.\begin{aligned}&\lambda=1:\\&\quad\frac{\langle R^2\rangle_0}{Nb_0^2}=\frac{2\{27+(1+4f_1^2+4f_2)(5+4f_2)\}}{3(1-f_1)\{9+(1+2f_1)(5+4f_2)\}}\,.\end{aligned}\right\}\tag{39}$$

$$\left.\begin{aligned}&\lambda=-1:\\&\quad\frac{\langle R^2\rangle_0}{Nb_0^2}=\frac{2\{27+(7+4f_1^2-2f_2)(7+2f_2)\}}{3(1-f_1)\{9+(1+2f_1)(7+2f_2)\}}\,.\end{aligned}\right\}\tag{40}$$

Table II. $\langle\mu^2\rangle_0/n\mu_0^2$.

ε	$\lambda=0$	$\lambda=1$	$\lambda=-1$
0	∞	∞	∞
0.2	37.1	36.5	37.9
0.4	9.31	8.67	10.10
0.6	4.132	3.609	4.955
0.8	2.316	1.953	3.187
1.0	1.484	1.303	2.405
1.2	1.042	1.048	2.005
1.4	0.785	0.968	1.779
1.6	0.628	0.966	1.638
1.8	0.531	0.990	1.538
2.0	0.474	1.017	1.458
2.2	0.444	1.035	1.385
2.4	0.433	1.043	1.314
2.6	0.438	1.041	1.246
2.8	0.454	1.033	1.179
3.0	0.479	1.019	1.117
π	0.500	1.008	1.076

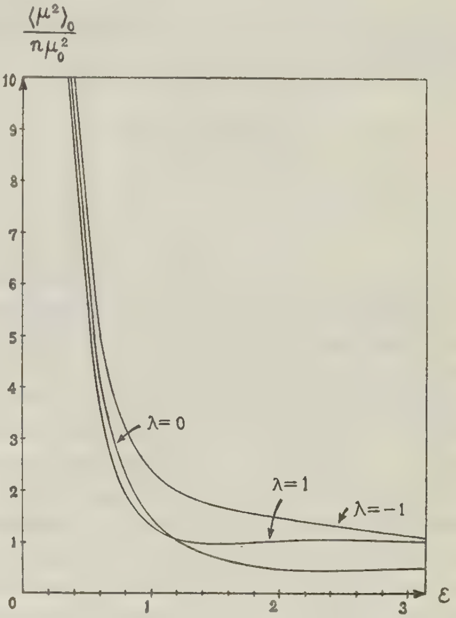

Fig. 1. Plots of $\langle\mu^2\rangle_0/n\mu_0^2$ against ε.

Table III. $\langle R^2\rangle_0/Nb_0^2$.

ε	$\lambda=0$	$\lambda=1$	$\lambda=-1$
0	∞	∞	∞
0.2	297	296	299
0.4	74.5	72.6	76.5
0.6	32.98	31.13	34.94
0.8	18.38	16.67	20.34
1.0	11.65	10.098	13.58
1.2	7.999	6.640	9.906
1.4	5.813	4.663	7.691
1.6	4.407	3.472	6.257
1.8	3.457	2.731	5.281
2.0	2.792	2.254	4.594
2.2	2.316	1.941	4.102
2.4	1.970	1.736	3.747
2.6	1.718	1.608	3.495
2.8	1.534	1.539	3.323
3.0	1.402	1.518	3.213
π	1.333	1.524	3.167

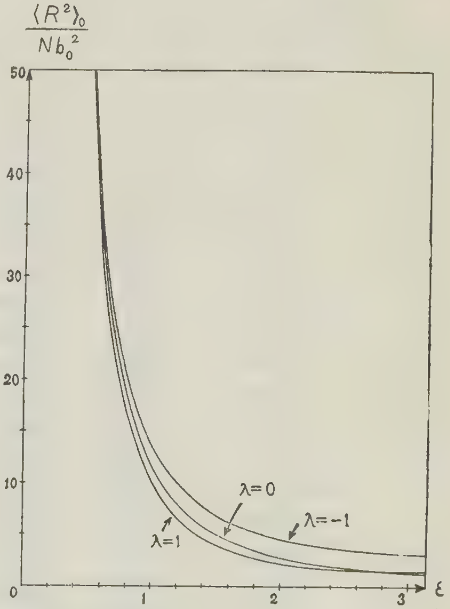

Fig. 2. Plots of $\langle R^2\rangle_0/Nb_0^2$ against ε.

Then we can calculate the values of these quantities within the interval (37), and have Table III.

According to these Tables, $\langle\mu^2\rangle_0/n\mu_0^2$ and $\langle R^2\rangle_0/Nb_0^2$ are plotted against ε in Figs. 1 and 2, respectively.

Here we define the effective bond length b' by

$$b'=(\langle R^2\rangle/N)^{1/2}\,, \tag{41}$$

and that corresponding to the unperturbed configuration b_0' by

$$b_0'=(\langle R^2\rangle_0/N)^{1/2}\,. \tag{42}$$

It is reported experimentally that

$$\langle\mu^2\rangle/n\mu_0^2=0.3\sim0.8 \qquad (43)$$[3),4)]

and

$$b'=5\sim11\,[\text{Å}]\,. \qquad (44)$$[5),6)]

The unperturbed configuration cannot explain these experimental values according to the reason described below. If we put $b_0'=9\,[\text{Å}]$ and $b_0=1.54\,[\text{Å}]$, we have $\langle R^2\rangle_0/Nb_0^2=34$ which corresponds to $\varepsilon\simeq0.6$ in Table III. While, in Table II, the same ε-value corresponds to $\langle\mu^2\rangle_0/n\mu_0^2\simeq4$ which confricts the experimental value (43). This disagreement is common to each case $\lambda=0,\ 1,\ -1$. However, the above disagreement is rather natural in the case in which the parameter ρ concerning with the excluded volume effect is not considered.

Now we take the second step of numerical calculations. The preceding step is equivalent to set the value $\rho=1$, but we consider $\rho>1$ in the present step. Let us put $\rho^2=2$ as a test case and calculate the values of $\langle R^2\rangle/Nb_0^2$ and $\langle\mu^2\rangle/n\mu_0^2$ from (3), (4) and (5). We neglect the insertion of the former values, because they are easily got by doubling each value of Table III. The latter values are shown in Table IV, and plotted against ε in Fig. 3.

Table IV. $\langle\mu^2\rangle/n\mu_0^2$ for $\rho^2=2$.

ε	$\lambda=0$	$\lambda=1$	$\lambda=-1$
0	∞	∞	∞
0.2	73.3	72.1	75.1
0.4	17.8	16.5	19.4
0.6	7.396	6.335	9.067
0.8	3.735	2.989	5.527
1.0	2.031	1.652	3.962
1.2	1.092	1.107	3.166
1.4	0.505	0.924	2.722
1.6	0.094	0.910	2.449
1.8	−0.205	0.971	2.259
2.0	−0.533	1.058	2.102
2.2	−0.867	1.147	1.954
2.4	−1.320	1.228	1.803
2.6	−2.076	1.285	1.643
2.8	−3.724	1.278	1.479
3.0	−10.15	1.177	1.317
π	−∞	1.071	1.208

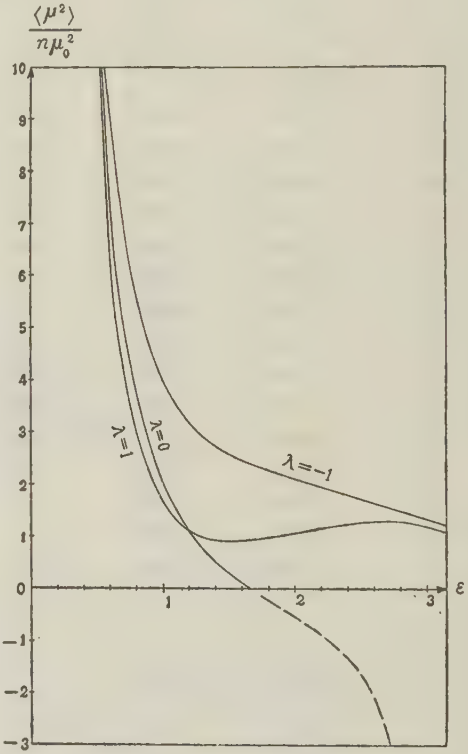

Fig. 3. Plots of $\langle\mu^2\rangle/n\mu_0^2$ against ε for $\rho^2=2$.

From this result, we have two suggestions. In the first place, the internal rotation corresponding to $\lambda=-1$ may be neglected, because $\langle\mu^2\rangle/n\mu_0^2$ is in this case always larger than 1 contrary to the experimental value (43). The second suggestion originates from the fact that $\langle\mu^2\rangle/n\mu_0^2$ in the case $\lambda=0$ is negative within the interval $1.7<\varepsilon<\pi$, and $-\infty$ at $\varepsilon=\pi$. Of course, the negative value of $\langle\mu^2\rangle$ is impossible, then the internal rotation of the rigid segment is limited within the interval $0<\varepsilon<1.7$. In general, it is conceived that the free rotation of the rigid segment may bring a confrict saying that a kind of mean square quantity becomes negative as $\langle\mu^2\rangle$ in this paper.

Table V. Calculated values at $\varepsilon=1.3$ (74°29′)

ρ^2	b'[Å]		$\langle\mu^2\rangle/n\mu_0^2$	
	$\lambda=0$	$\lambda=1$	$\lambda=0$	$\lambda=1$
1	4.01	3.62	0.897	0.993
2	5.67	5.11	0.769	0.984
4	8.02	7.24	0.512	0.966
6	9.83	8.86	0.256	0.948

Therefore we conclude that we should adopt $\lambda\geqq 0$ and $1.2<\mathcal{E}<1.4$ in order to explain the experimental value (43).

We have discussed above the test case of $\rho^2=2$, which brings to us some suggestions. Then we put on the next trial

$$\lambda=0,\ 1;\quad \mathcal{E}=1.3;\quad \rho^2=1,\ 2,\ 4,\ 6$$

and calculate $\langle\mu^2\rangle/n\mu_0^2$ and effective bond length b'. The results are shown in Table V, where $b_0=1.54$ [Å] is used. In this Table, values of the row of $\rho^2=1$ are calculated from Tables II and III by the interporation at $\mathcal{E}=1.3$, and values of other rows are calculated from the row of $\rho^2=1$ and the formulas (4), (5) and (3).

Now, Table V indicates to us that the experimental values (43) and (44) may be simultaneously interpreted by making choice of $\lambda=0\sim1$, $\rho^2=2\sim6$ and $\mathcal{E}\simeq1.3$.

On the other hand, it is also remarked that the $\mathcal{E}$-value 1.3 is nearly the minimum point of $\langle\mu^2\rangle/n\mu_0^2$ in the case of $\lambda\simeq1$.

The author wishes to express his thanks to Mr. K. Shindô of Shiga University for his kind discussions and constant encouragement.

References

1) T. Mori: J. Phys. Soc. Japan **15** (1960) 1482.
2) K. Nagai: J. Chem. Phys. **30** (1959) 660.
3) P. Debye and F. Bueche: J. Chem. Phys. **19** (1951) 589.
4) W. R. Krigbaum and A. Roig: J. Chem. Phys. **31** (1959) 544.
5) B. H. Zimm: J. Chem. Phys. **16** (1948) 1093, 1099.
6) F. W. Peaker: J. Polym. Sci. **22** (1956) 25.

JOURNAL OF THE PHYSICAL SOCIETY OF JAPAN, Vol. 15, No. 9, SEPTEMBER, 1960

The Superexchange Interaction between Cr^{+3} pair in Chromium Bi-nuclear Complex Ions.

By Hanako KOBAYASHI, Taiichiro HASEDA and Eizo KANDA

Research Institute for Iron, Steel and Other Metals,
Tohoku University, Sendai, Japan

and Masayasu MORI

Institute of Polytechnics, Osaka City University, Osaka, Japan

(Received May 6, 1960)

The investigation of the magnetic properties of chromium bi-nuclear complex compounds was made. The results of the magnetic susceptibility measurements were analyzed on the assumption that their magnetic behaviours are determined mainly by the superexchange interaction between two Cr^{+3} ions in the same complex unit. The coefficient of the superexchange interaction J was estimated to be about $-30\,k$ in the cases of $[(NH_3)_5Cr\text{-}OH\text{-}Cr(NH_3)_5]^{+5}$ and $[(NH_3)_5Cr\text{-}OH\text{-}Cr(NH_3)_4OH]^{+4}$ complex ions. In the case of $[(NH_3)_5Cr\text{-}O\text{-}Cr(NH_3)_5]^{+4}$, the susceptibility is very small below room temperature, hence a large absolute value of J is required to account for the experimental result. The susceptibility of $[Cr(NH_3)_5Cl]Cl_2$ which is a usual mononuclear complex salt, was measured for the sake of comparison with the above mentioned bi-nuclear complex salts. The susceptibility obeys in this case the Curie-Weiss law in the range between 2.5°K and room temperature. The Weiss constant Θ is $-0.8°K \pm 0.1°K$ and the Curie constant C is 1.82. The X-ray powder patterns of these complexes were taken and examined in comparison with the magnetic properties.

§1. Introduction

The structures and the magnetic and optical properties of the bi-nuclear complex compounds of chromium were investigated by Wilmarth, Graff and Gustin(1) and by Mori, Ueshiba and Yamatera(2). In these compounds, two chromium ions in a complex unit have the oxygen or hydroxyl bridge between them. The spins of the two Cr^{+3} ions will interact through the brige. This may be regarded as a type of the superexchange interaction. On the other hand, the interaction between the spins of Cr^{+3} ions belonging to the different complex units, will be much weaker than the interaction between those in the same complex unit. Thus, the magnetic properties of these compounds are considered to be predominantly determined by the interaction between a couple of ions through the bridge in each complex unit. The situation resembles in some respects the case of copper acetate(3) which is a sort of bi-nucler complex compound of Cu^{+2} ions. In the latter case the magnetic properties are considered to be determined by the direct mutual interaction of two Cu^{+2} ions in a complex unit. Welo(4) in 1928 and Gijsman, Karantassis and Wucher(5) in 1954 measured the magnetic susceptibilities of some tri-nuclear complex compounds of Cr^{+3} and Fe^{+3}. Kambe(6) estimated the magnitude of the mutual interaction between Cr^{+3} and Fe^{+3} ions by analysing the Welo's results. The Hamiltonian used was, $\mathscr{H}=-2J[(\boldsymbol{S}_1\boldsymbol{S}_2)+(\boldsymbol{S}_2\boldsymbol{S}_3)+\alpha(\boldsymbol{S}_3\boldsymbol{S}_1)]$ in which $\boldsymbol{S}_1$, $\boldsymbol{S}_2$ and $\boldsymbol{S}_3$ were the spins of the three magnetic ions in one complex unit. The values of J consistent with the experimental results were $-14k \langle J \langle -18k$ assuming $\alpha=1$.

Bi-nuclear complex ions of chromium investigated in the present work are as follows:

$$[(NH_3)_5Cr\text{-}OH\text{-}Cr(NH_3)_5]^{+5} \cdots\cdots\cdots (A)$$

$$[(NH_3)_5Cr\text{-}OH\text{-}Cr(NH_3)_4OH]^{+4} \cdots\cdots (B)$$

and $$[(NH_3)_5Cr\text{-}O\text{-}Cr(NH_3)_5]^{+4} \cdots\cdots\cdots (C).$$

The bridges in the complex units are expected to be almost linear in the former two complexes and definitely linear in the last one. The purpose of the present investigation is to obtain information about the superexchange interaction through these bridges.

§2. Experiments

The measurements of the magnetic susceptibility were carried out by the Hartshorn bridge method. The a.c. frequency used was 90 cycles per sec. and the strength of the magnetic field in the measuring coil was 20~100 Oe. The measurements were made in the temperature range down to 1.5°K. As the samples are unstable in light and moisture, special care was taken to avoid them. The measuring apparatus used is capable to detect the susceptibility of a sample of 1 g which has the gram susceptibility of 1×10^{-5} (c.g.s.e.m.u.) in the accuracy of ±1%. However the accuracies on the whole in the present experiments were about ±3% below 20.4°K and about ±10% above 20.4°K.

Samples

$[(NH_3)_5Cr\text{-}OH\text{-}Cr(NH_3)_5]_2Cl_3(ClO_4)_7H_2O$ (Decammine-μ-ol-dichromium (III) chloride perchlorate) (A)

This salt was prepared by precipitation with perchloric acid from aqueous solution of decammine-μ-ol-dichromium (III) chloride which was prepared using Jφrgensen's procedure. The salt precipitates in the form of needle crystal of rose colour. The colour changes into pale purple light and moisture.

$[(NH_3)_5Cr\text{-}OH\text{-}Cr(NH_3)_4OH]Cl_4H_2O$ (Hydroxononammine-μ-ol-dichromium (III) chloride 1-hydrate) (B)

This salt was prepared according to the direction of Jφrgensen for the preparation of erythrochromium (III) chloride. The dark red complex salt thus prepared contained nine moles of ammonia per each pair of two chromium atoms, in accordance with the observation of Wilmarth et al.⁽¹⁾. This salt also turns violet in light and moisture.

$[(NH_3)_5Cr\text{-}O\text{-}Cr(NH_3)_5](ClO_4)_4$ (Decammine-μ-oxo-dichromium (III) perchlorate) (C)

This salt was prepared by the reaction of (A) with ammonia sodium perchlorate solution. The colour of this sample is deep blue, but it becomes blue if it is dried after washing with ether. The colour changes into red purple in light and moisture.

$[Cr(NH_3)_5Cl]Cl_2$ (Chloropentamminechromium (III) chloride)

This salt was prepared by boiling a mixture of hexamminechromium (III) chloride and hydrochloric acid for 30 min.. The crude chloride thus obtained was dissolved in water and recrystallized by adding hydrochloric acide. The bright red chloride was washed with ethanol and dried in air.

Magnetic Susceptibility

Complex compounds A and B. The magnetic susceptibilities of these complex compounds χ_{2M}* are shown in Fig. 1. The values are corrected for small amount of impurity and diamagnetism⁽⁹⁾**. The susceptibilities in the room temperature range obey the Curie-Weiss law with $\Theta\cong-30$°K and the Curie constant C is consistent with the spin value $S=3/2$ of a Cr^{+3} ion. The susceptibilities of these two salts have their maximum values at about 50°K and have very small values at liquid helium temperatures.

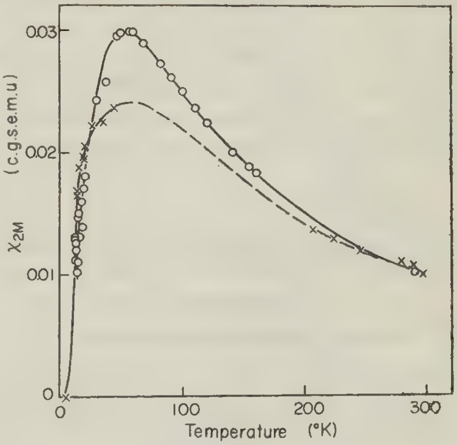

Fig. 1. Magnetic susceptibilities.
O: $\{[(NH_3)_5CrOHCr(NH_3)_5]Cl_{1.5}(ClO_4)_{3.5}\cdot\frac{1}{2}H_2O\}$,
×: $[(NH_3)_5CrOHCr(NH_3)_4OH]Cl_4\cdot H_2O$.

Complex compound C. The magnetic susceptibilities of this salt, χ_{2M} were 0.0010 (±0.0001) (c.g.s.e.m.u.) between 14.5°K and 20.4°K, 0.0010 (±0.0001) (c.g.s.e.m.u.) at 80°K, 0.0010 (±0.0001) (c.g.s.e.m.u.) at 105°K and 0.0020 (±0.0002) (c.g.s.e.m.u.) at 290°K. Any remarkable hump of susceptibility could not be detected between 105°K and 290°K. This complex compound is decomposed above the room temperature by warming up even in the dark place and the decomposed sample shows a normal paramagnetic susceptibility.

---

* The symbol χ_{2M} used here for bi-nuclear complex compounds stands for the value for one mole of complex compound, which contains two gram ions of Cr^{+3}.

** The following values multiplied by -1×10^{-6} were used for the calculstion of the diamagnetic molar susceptibilities. Cl^-:25, ClO_4^-:33, Cr^{+3}:15, H_2O:13, NH_3:1.1, -O-:5, and OH^-, -OH-:9.

$[Cr(NH_3)_5Cl]Cl_2$. The molar magnetic susceptibility of this salt χ_M is shown in Fig. 2 and Table I, in which the diamagnetic correction has not been made. The paramagnetic susceptibility follows the Curie-Weiss law between 2.5°K and room temperature. The values of C and Θ are 1.82 and −0.8°K respectively.

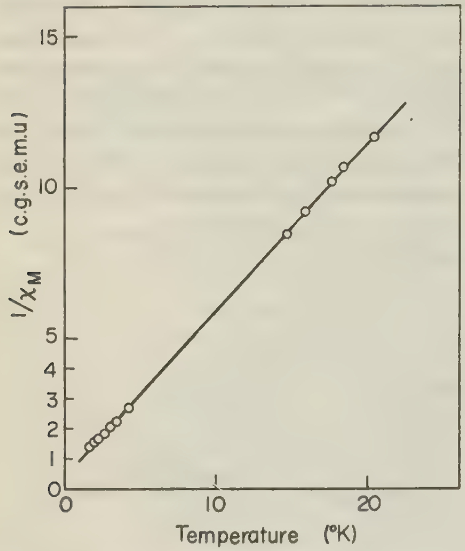

Fig. 2. Molar magnetic susceptibility.
O: $[Cr(NH_3)_5Cl]Cl_2$

Table I. Molar magnetic Susceptibility of $[Cr(NH_3)_5Cl]Cl_2$

T (°K)	χ_M (c.g.s.e.m.u.)
98.3	0.0198
20.4	0.0860
18.4	0.0938
17.6	0.0984
15.9	0.109
14.7	0·118
4.20	0.366
3.41	0.439
2.93	0.484
2.49	0.547
2.16	0.605
1.92	0.641
1.61	0.704
1.52	0.718

§ 3. Discussion.

Complex compounds A and B. Though the single crystals of the two complex compounds have not been obtained, their X-ray patterns of powder samples were taken. They resemble very much each other as are shown later and their magnetic behaviours are also alike as indicated in Fig. 1. The analysis of the data on one of them may be applied to the other. The bond angle of the bridge in these complex compound is not exactly 180°, because there is a H-atom attached to the oxygen of the bridge. In the following, it is assumed that the orbital anguler momentum of each Cr^{+3} ion is quenched and only the spin angular momentum remains free, and so the Cr^{+3} ion is effectively in the $S=3/2$ state. If the electron spins of two Cr^{+3} ions are denoted by S_1 and S_2 and the coefficient of the mutual exchange interaction between S_1 and S_2 by J, the Hamiltonian of this bi-nuclear complex ions under the external magnetic field H will be given as follows.

$$\mathscr{H}=J\cdot \boldsymbol{S}_1\cdot \boldsymbol{S}_2+g\beta \boldsymbol{H}(\boldsymbol{S}_1+\boldsymbol{S}_2)$$

Energy levels are obtained as shown in Fig. 3. Then, the magnetic susceptibility of a complex unit is calculated by means of the partition function obtained from these energy levels, as follows:

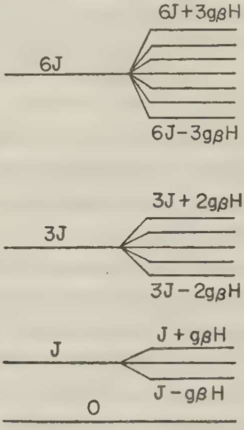

Fig. 3. Energy levels of bi-nuclear complex ion of Cr^{+3}.

$$\chi_{2M}=\frac{Ng^2\beta^2}{kT}\;\frac{2e^{5J/kT}+10e^{3J/kT}+28}{e^{6J/kT}+3e^{5J/kT}+5e^{3J/kT}+7},$$

where β is the Bohr magneton, k Boltzman's constant, T absolute temperature, g spectroscopic splitting factor, (2.00 was adopted.) and N Avogadro's number.

The calculated χ_{2M} are shown in Fig. 4. as function of absolute temperature in which J

is used as a parameter. The best fit was obtained by assuming $J=-28\,k$ in the complex A and $J=-36\,k$ in the complex B. The agreement between the experimental values and the calculated ones is sufficient in the temperature range above 50°K in the former complex compound. The deviation from the calculated values at lower temperatures may be attributed to some slight deformation in crystal structure in the complex. In the latter complex, $|J|$ is somewhat larger than in the former. The detailed structure determination of these complex compounds by X-ray analysis has not been made, as mentioned above, because of the difficulty in getting a perfect single crystal. It is probable, however, from the chemical and optical investigations⁽¹⁾⁽²⁾ that the bridge between two Cr^{+3} ions in these complex units, is

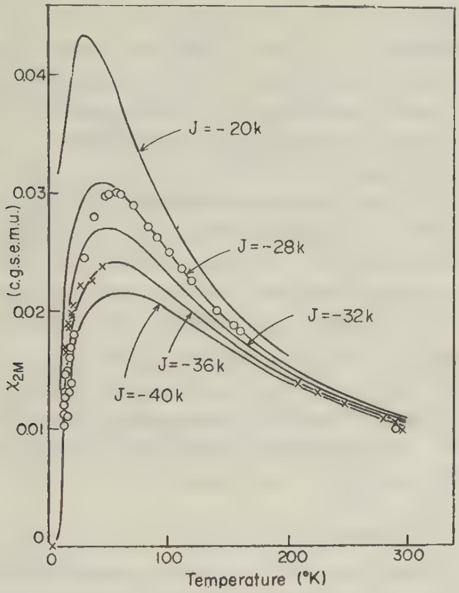

Fig. 4. Magnetic susceptibilities.
O: $\{[(NH_3)_5CrOHCr(NH_3)_5]Cl_{1\cdot5}(ClO_4)_{3\cdot5}\cdot\frac{1}{2}H_2O\}$,
×: $[(NH_3)_5CrOHCr(NH_3)_4OH]Cl_4\cdot H_2O$.

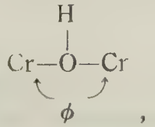

$$\overset{\displaystyle H}{\overset{|}{Cr-O-Cr}}\ ,\quad \phi$$

in which the angle ϕ is almost 180°. The mutual interaction between two Cr^{+3} ions is thought of as the superexchange interaction of the 3d electrons of Cr^{+3} through O^{-2} in -OH- bridge. The superexchange interaction of Cr^{+3} $(3d^3)$ through 180° bridge is thought to be antiferromagnetic ($J<0$) in nature⁽¹⁰⁾. The obtained value of J ($-28\,k\sim-36\,k$) may be compared with J in the bulk crystals such as Cr_2O_3. The value of about $-30\,k$ is not unreasonable considering the number of the nearest neighbours and the Weiss constant ($\Theta=500$°K) in Cr_2O_3⁽¹¹⁾. Recently, some attempts have been made to decide the value of J by the paramagnetic resonance method in highly diluted crystals such as Mn^{+2} in MgO (1:100)⁽¹²⁾ or Cr^{+3} in ruby (1:100)⁽¹³⁾ In the Mn–O–Mn case, $J=28k\pm4\,k$ was found out and in the case of Cr^{+3} pair in ruby, the estimated value of J was about $-359\,k$. The present value of $J=-30\,k$ for Cr^{+3} pair is considerably different from the above value though the bridge between Cr^{+3} pair is not -O- (as in the ruby case) but -OH- in the present case.

Complex compound C. The salt C was expected to show the most typical superexchange interaction in the case of 180° bridge. The observed susceptibility of a complex unit is about 0.001 (c.g.s.e.m.u.) in the wide temperature range. It has a little temperature dependence increasing with increasing temperature, but it could not definitely be determined whether there is any hump of susceptibility between 80°K and 300°K or not according to our apparatus. In the case of complex A, the model of two localized spins of $S=3/2$ interacting with each other via the -OH- bridge was taken. If the same model is assumed in this case, it is required that the coefficient of the exchange interaction J is negative and its absolute value should be larger than $200\,k$ to account for the experimental results. This absolute value of J is extremely large, in contrast to the values of J which was found in the range between $28\,k$ and $36\,k$ by Kambe⁽⁶⁾ and others⁽⁷⁾ and in almost the same range in the case of complexes A and B in our experiments.

The compound $K_4Ru_2Cl_{10}O\cdot H_2O$ which has a complex anion $[Cl_5Ru\text{-}O\text{-}RuCl_5]^{-4}$ shows diamagnetic susceptibility at room temperature. Dunitz and Orgel⁽¹⁴⁾ explained this diamagnetisum by applying the molecular orbital theory. Structure of the complex C is thought similar to this anion and the application of the molecular orbital theory may also be not unreasonable in this case. But, the straight-forward application of the molecular orbital theory analogous to the treatment by Dunitz and Orgel gives rise to the paramagnetic state of S=1 which comes from the two unpaired electrons remaining in the doubly degenerated non-bonding orbital. And this is not consistent with our experimental result if any mechanism which brings the two spins into an interaction is not considered.

$[Cr(NH_3)_5Cl]^{+2}$. As is expected, this complex ion is found to be a normal paramagnetics and the susceptibility follows the Curie-Weiss law. The obtained Curie constant C=1.82 is in reasonable agreement with Cr^{+3} ($3d^3$), S=3/2. The Weiss constant $\Theta=-0.8°K$ is somewhat larger than is usually expected. The crystal structure of this salt has not been determined, but it is sure that each Cr^{+3} ion is surrounded octahedrally by five NH_3's and one Cl^- ion. If the passages or paths of the superexchange interaction are considered to lie between Cr^{+3} ions, they will be such as follows:

$$Cr^{+3}\text{-}NH_3\text{—}Cl^-\text{-}Cr^{+3} \qquad \text{(I)}$$

$$Cr^{+3}\text{-}NH_3\text{—}NH_3\text{-}Cr^{+3} \qquad \text{(II)}$$

$$Cr^{+3}\text{-}NH_3\text{—}Cl^-\text{—}NH_3\text{-}Cr^{+3} \qquad \text{(III)}$$

$$Cr^{+3}\text{-}NH_3\text{—}Cl^-\text{—}Cr^{+3} \qquad \text{(IV)}$$

etc..
One of the present authors (T.H.) has pointed out the importance of hydrogen bond in the superexchange interaction, discussing the antiferromagnetic nature in $CoCl_2\cdot 6H_2O$⁽¹⁵⁾. Although the conclusion has not definitly been obtained in the $[Cr(NH_3)_5Cl]Cl_2$ case, it is noteworthy to refer that the large Weiss constant Θ may have some connection with the possible existence of hydrogen bond such as N-H—Cl on the path I or III etc.,.

X-ray powder patterns.

The X-ray powder patterns of the bi-nuclear complex salts investigated were obtained by Norelco camera. They are shown in Fig. 5. The results obtained are very well consistent with the data by Wilmarth, Graff and Gustin⁽¹⁾. As is apparent from Fig. 5, the complexes A and B resemble each other, but are quite different from the complex C. These facts are consistent with the magnetic behaviours mentioned above.

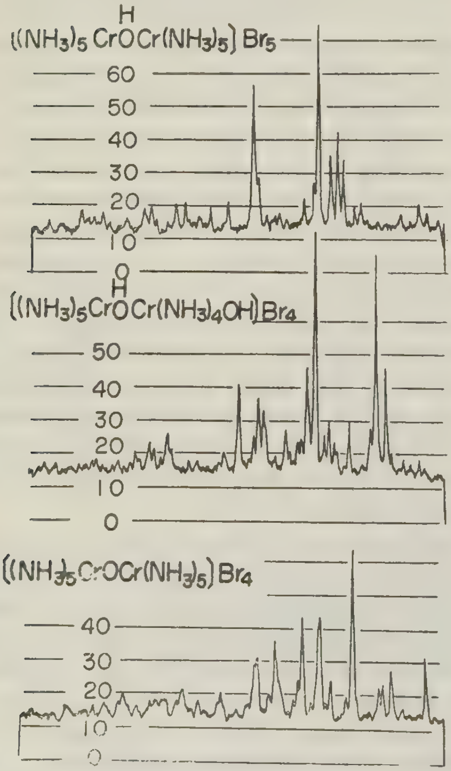

Fig. 5. X-ray powder patterns.

§ 4. Summary.

It was intended to obtain experimentally the magnitude and the sense of the superexchange interaction of Cr^{+3} pair through the investigation on the bi-nuclear complex compounds of chromium. Because, the magnetic properties of the bi-nuclear complex are thought to be determined for the most part by the superexchange interaction between the pair of the two magnetic ions through an intervening diamagnetic oxygen ion. The coefficient of the superexchange interaction in the pair of Cr^{+3} ions coupled by the almost linear $\overset{\mathrm{H}}{\overset{|}{-\mathrm{O}-}}$ bridge was found out in the range of $-28k\sim-36k$. In the case of -O- bridge, the extremely large absolute value of J, which amounted to $200k\sim400k$, was required to explain the experimental results, if the same model is used as in the case of the $\overset{\mathrm{H}}{\overset{|}{-\mathrm{O}-}}$ bridge.

The susceptibility of $[Cr(NH_3)_5Cl]Cl_2$ which is a usual mono-nuclear complex, obeys the Curie-Weiss law from 2.5°K to room temperature. The Weiss constant Θ obtained is $-0.8°K$. A comparatively large value such as this may be understood in connection with the possibility of existance of hydrogen bond on the interaction paths which are considered between two Cr^{+3} ions.

We are now intending to investigate the other bi-nuclear complex compounds of Cr^{+3} in which the bond angle of the bridge is almost 90°. From the preliminally experiments, rather small $|J|$ value is expected in such salts.

The authors wish to express their sincere thanks to Dr. H. Yamatera in St. Pauls Univ. Tokyo, for his valuable discussion especially on the chemical properties of the salts investigated. Their thanks are also due to Messers. I. Tsubokawa and T. Watanabe for the measurements of the susceptibility at higher temperatures.

References

1) W. K. Wilmarth, H. Graff and S. T. Gustin: J. Amer. Chem. Soc. **78** (1956) 2683
2) M. Mori, S. Ueshiba and H. Yamatera: Bull. Chem. Soc. Japan. **32** (1959) 88
3) B. Bleaney, and K. D. Bowers: Proc. Roy. Soc. **A 214** (1952) 451
4) L. A. Welo: Phil. Mag. 7th ser. **6** (1928) 481
5) J. Wucher and H. M. Gijsman: Physica **20** (1954) 361, H. M. Gijsman: T. Karantassis and J. Wucher: ibid. **20** (1954) 367
6) K. Kambe: J. Phys. Soc. Japan **5** (1950) 48
7) A. Abragam, J. Horowitz. and J. Yvon: J. Phys. radium **13** (1952) 489
8) S. M. Jørgensen: J. prakt. Chem. (2) **25** (1882) 321
9) A. V. Jagannadham: Proc. Rajasthan Acad. Sci. **1** (1950) 6; C. A. **45** (1951) 9948
10) J. Kanamori: J. Phys. Chem. Solids **10** (1959) 87
11) G. Foex and M. Graff: Compt. rend. **209** (1939) 160
12) B. A. Coles, J. W. Orton and J. Owen: Phys. Rev. Letters **4** (1960) 116
13) L. Rimai, H. Statz, M. J. Weber, G. A. de Mars and G. F. Koster: Phys. Rev. Letters **4** (1960) 125
14) J. D. Dunitz and L. F. Orgel: J. Chem. Soc. **111** (1953) 2594
15) T. Haseda; J. Phys. Soc. Japan **15** (1960) 483

JOURNAL OF THE PHYSICAL SOCIETY OF JAPAN Vol. 15, No. 9, SEPTEMBER, 1960

A Study of Sorbed Water on Cellulose by Pulsed NMR Technique

By Masahumi SASAKI,* Takao KAWAI**, Akira HIRAI*,
Tsuneo HASHI* and Akira ODAJIMA***.

* *Department of Physics, Faculty of Science, Kyoto University.*
** *Yoshida College, Kyoto University.*
*** *Research Institute of Applied Electricity, Hokkaido University.*

(Received May 6, 1960)

The state of sorbed water on cellulose has been studied by pulsed NMR technique. From the experimental results of spin-lattice relaxation time (T_1) and spin-spin relaxation time (T_2), observed as a spin echo decay time, following conclusions have been derived. (1) Two phases of the sorbed water are classified; the localized and the mobile. (2) The correlation time (τ_N) derived from T_1 using BPP theory, is consistent with that (τ_D) derived from dielectric measurements. (3) T_1 is by one or two order longer than T_2 in contradiction to BPP theory for extremely narrowing case. As an explanation for this fact, we propose that, when we consider about T_2, the effects of magnetic nuclei contained in the absorbent must be taken into account, though no theory is given. (4) The average life-time of water molecule sorbed on cellulose in the localized state is estimated to be several hundredths of a second and to decrease with temperature.

§ 1. Introduction

The spin-lattice relaxation time (T_1) and the spin-spin relaxation time (T_2) are very useful quantities for studying the state of sorbed water, as well as the dielectric relaxation time and other thermodynamical quantities.

One of the authors (A.O.) has measured the line-width of proton of water molecule sorbed on cellulose by using a high resolution NMR spectrometer[1] and compared the apparent correlation time (τ_N) derived from his data by BPP theory[2] with that (τ_D) from dielectric measurements[3,4,5]. The result is that τ_N is by about one order longer than τ_D.

If both τ_N and τ_D are the correlation times of rotational Brownian motion of water molecule in the sorbed state, they should be connected by the relation $\tau_N=\frac{1}{3}\tau_D$. So our initial purpose of this study is to clarify whether τ_N is consistent with τ_D or not, by means of T_1 measurement. As a result, we have found that τ_N derived from T_1 is consistent with τ_D from dielectric data.

Furthermore, it was found that there coexist two T_1's, but not two T_2's. It is very interesting that Zimmerman *et al.*[6,7,8] have found a similar result for T_1 and T_2 of sorbed water on silica gel by using the pulsed NMR technique. In their case, two T_2's coexisted, but two T_1's only in a limited range of water content. In a recent journal, we noticed that Winkler[9] studied sorbed water on allumina by using the pulsed NMR technique, observing the same kind of phenomena as Zimmerman's and ours.

The experimental data obtained and their interpretations and discussions will be given in detail below.

§ 2. Experimental Results

We have measured T_1 of proton of sorbed water on cellulose as a function of water content (x) and of temperature (T), by using 90°–90° pulse method[10] at 25 Mc/sec. The water content is defined as the ratio of weight of the sorbed water to the weight of the cellulose. The samples used were of the water contents of 12.5%, 16.5%, 20.3%, 36%, 44%, 55%, and 148%. The apparatus used has been described in detail elsewhere[11].

One example of our measurements is shown in Fig 1, where the difference between the nuclear signal just after the first pulse (y_1) and that after the second (y_2) is shown as a function of the pulse interval (τ) in a semi-logarithmic scale. In many cases, the curve of ln (y_1-y_2) *versus* τ is a straight line, whose slope gives T_1. But in our case, y_1-y_2 is given by the following expression:

$$y_1-y_2=y_{11}\exp\left(-\frac{\tau}{T_{11}}\right)+y_{12}\exp\left(-\frac{\tau}{T_{12}}\right).$$

From this figure, we can obtain three quantities: T_{11}, T_{12} and $y_{11}/(y_{11}+y_{12})$.

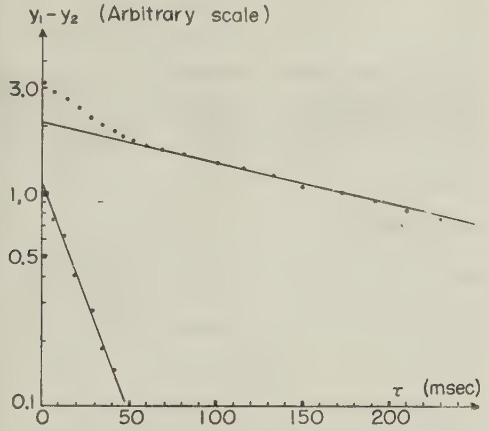

Fig. 1. Semi-logarithmic plots of the differences between the nuclear signal amplitude after the first pulse (y_1) and that after the second (y_2) *versus* the pulse interval (τ). Experimental plots are represented as

$$y_1-y_2=y_{11}\exp\left(-\frac{\tau}{T_{11}}\right)+y_{12}\exp.\left(-\frac{\tau}{T_{12}}\right),$$

giving three quantities; $T_{11}=20$ msec, $T_{12}=165$ msec, and $y_{11}/(y_{11}+y_{12})=0.35$.

Sample: Proton of sorbed water molecule on cellulose.

Water content (Weight of sorbed water/Weight of cellulose): 16.5%.

Temperature: 13°C.

Then the question arises whether these two T_1's are entirely due to the sorbed water, since cellulose molecule $(C_6H_{10}O_5)_n$ also contains protons. In order to check this point, we have measured the signal amplitude just after the first pulse, $(y_1=y_{11}+y_{12})$ as a function of the water content. The data obtained are shown in Fig. 2. The experimental points are on a straight line, which passes through the origin. If some protons in the cellulose contribute to nuclear signals, this straight line would displace to intersect the ordinate axis, and, if some protons in the sorbed water do not contribute to nuclear signals, this straight line would displace to intersect the abscissa axis. From this fact, we can conclude that the nuclear signal is wholly due to the sorbed water, and that all protons in the sorbed water contribute to the nuclear signal. That the protons in the cellulose do not contribute to the nuclear signal is consistent with the circumstances that our apparatus cannot detect the signal produced by protons in a rigid state, as alreary stressed in our previous article concerning the apparatus[11] and protons in the cellulose are considered to be in a rigid state. The half line-width of proton in the cellulose was measured by Varian spectrometer and found to be broader than 10 gauss.

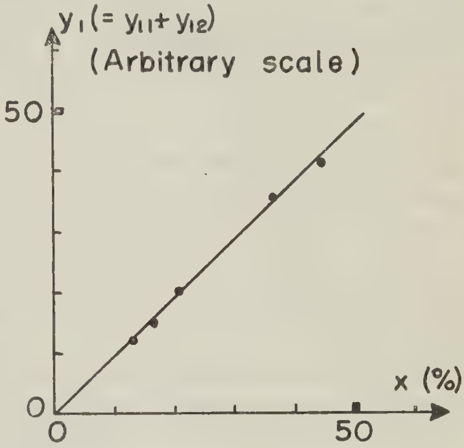

Fig. 2. Water content dependence of y_1 $(=y_{11}+y_{12})$ at room temperature, showing that three quantities (T_{11}, T_{12}, and $y_{11}/(y_{11}+y_{12})$) are all concerned with sorbed water. (See § 2).

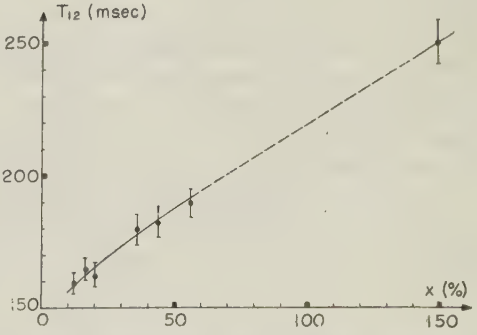

Fig. 3 (a). Water content dependence of T_{12} (longer T_1) at room temperature.

The values of T_{11}, T_{12} and $y_{11}/(y_{11}+y_{12})$ as functions of water content (x) and of temperature (T) are shown in Figs. 3~6. Rough measurements of spin echo decay time (T_2) have also been made only at room temperature as a function of water content, and shown in

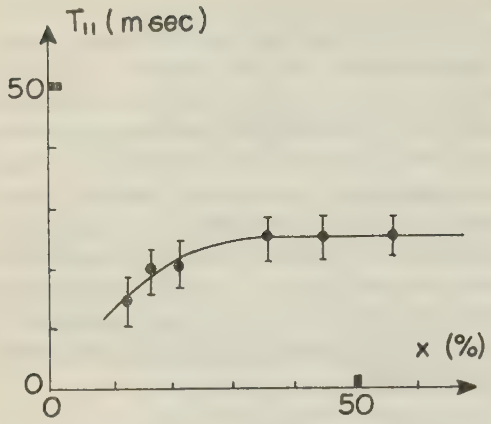

Fig. 3 (b). Water content dependence of T_{11} (shorter T_1) at room temperature.

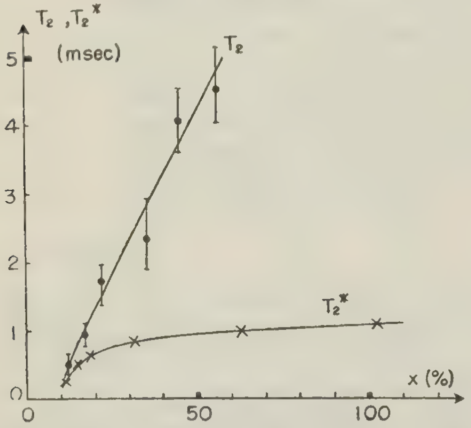

Fig. 3 (c). Water content dependence of T_2 (spin echo decay time) and $T_2{}^*=(\pi\Delta H_{1/2})^{-1}$ at room temperature. $\Delta H_{1/2}$ (half line-width) is obtained from the steady state measurement (reference 1).

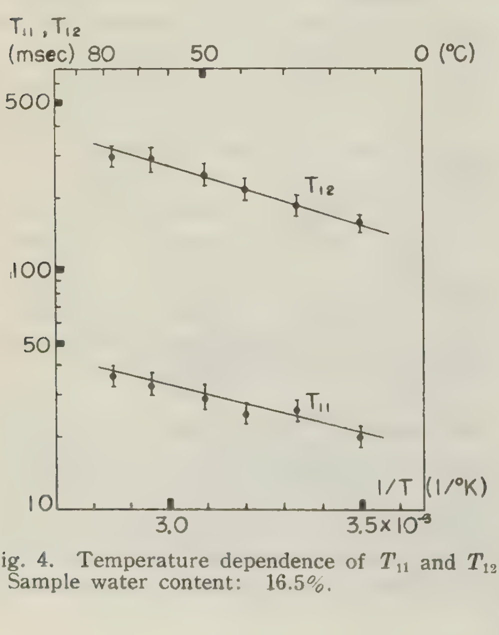

Fig. 4. Temperature dependence of T_{11} and T_{12}. Sample water content: 16.5%.

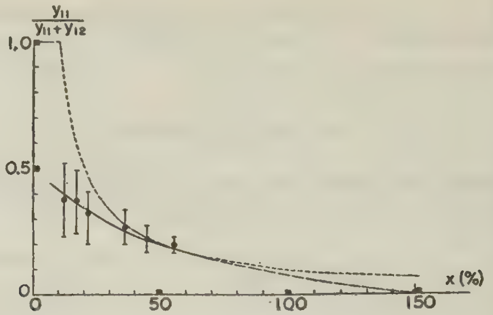

Fig. 5. Water content dependence of $y_{11}/(y_{11}+y_{12})$ at room temperature. Dotted curve is obtained from the simplified model of sorption (cf. § 3 (d).)

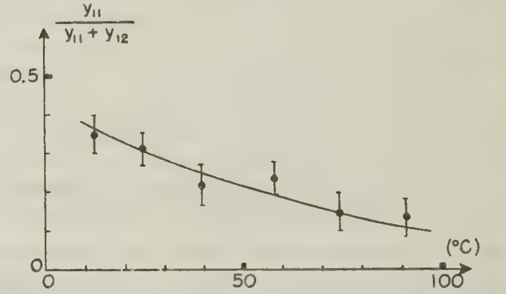

Fig. 6. Temperature dependence of $y_{11}/(y_{11}+y_{12})$. Sample water content: 16.5%.

Fig. 3 (c). In Fig. 3 (c), $T_2{}^*=(\pi\Delta \mathrm{H}_{1/2})^{-1}$ obtained from line-width measurement[1] is also shown for reference. Using these data, we shall discuss the sorbed state of water molecule in the next section.

§ 3. Discussions

a) Coexistence of two T_1's

As already mentioned, we have obtained two T_1's of proton of sorbed water on cellulose. From this fact, we can conclude that there are two different phases of the sorbed water. This is consistent with Zimmerman's data[6,7,8], Winkler's data[9], and dielectric data[12,13]. Now we propose that the shorter T_1 (T_{11}) is due to protons of the localized water, perhaps hydrogen-bonding with OH groups of cellulose, and the longer T_1 (T_{12}) to protons of the mobile water, not directly adhering to cellulose, but perhaps hydrogen-bonding with other water molecules.

The nuclear magnetic resonance of multiphase system has been studied by many workers[7,8,14,15]. Among them, Zimmerman-Brittin's analysis[7] based on the stochastic theory, seems to be very suitable for the analysis of our data. Now, we analyse our data by their theory.

At this point, there is something to note, from the experimental point of view, about the possibility of the observation of two or more T_1's, which is particularly interesting in high polymer NMR researches[16]. We draw the curves, as in Fig. 1,

$$y_1-y_2=Ae^{-a\tau}+Be^{-b\tau},$$

for various values of a, b and $A/(A+B)$ ($A+B$ being normalized to unity). Then we find that the condition that two T_1's can be measured separately is that $b/a>5$ or $b/a<1/5$, and $10>\frac{B}{A}>\frac{1}{10}$. These conditions are rather strict limitations. We have measured, indeed, T_1's of various high polymers, but we could not have so far measured two T_1's separately.

b) Values of T_{11} and T_{12}.

T_{11} is of the order of 20 msec and T_{12} of the order of 200 msec. Both increase slightly when the water content is increased (Fig. 3 (a), (b)). For simplicity, we assume that the exchange rate between the localized state and the mobile state is so low that the average life-time of a water molecule in the localized state (τ_{ex}) is very much longer compared with T_1. In this case, T_{11} gives the exact spin-lattice relaxation time for protons of the localized water and T_{12} that for protons of the mobile water.

As far as T_1 is concerned, we take the simplest model that the energy of spin system relaxes to the rotational Brownian motion of water molecules by the magnetic dipole-dipole interaction. Then, following BPP theory[2] revised by Kubo and Tomita[17], T_1 is given by

$$\frac{1}{T_1}=\frac{3}{10}\gamma^4h^2b^{-6}\left(\frac{\tau_N}{1+\omega^2\tau_N^2}+\frac{4\tau_N}{1+4\omega^2\tau_N^2}\right),$$

where b is the inter-proton distance in a water molecule, which is taken to be 1.5 A, and ω, is 2π times the resonance frequency, 25 Mc/sec in our case. Now, from the data of temperature dependence of both T_{11} and T_{12} (Fig. 4), it is obvious that we are dealing with extremely narrowing case in BPP theory, where $\omega\tau_N\ll1$. Then we can derive the correlation times τ_{N1} and τ_{N2} to be of the order of 10^{-10} sec and 10^{-11} sec corresponding to T_{11} and T_{12} respectively. Based on our model already mentioned, τ_N and τ_D should be connected by the following relation:

$$\tau_N=\frac{1}{3}\tau_D=\frac{4\pi\eta a^3}{3kT},$$

where η is the viscosity coefficient, and a the radius of water molecule. Our value of τ_{N2} of the mobile water is favorably compared with τ_D derived from dielectric measurements[3,4,5], which is of the order of 10^{-10} sec.

If the exchange between two states cannot be neglected, which would be the actual situation (see § 3 (d)), the apparent values of T_1's are shorter than the actual T_1's[7,8]. This effect is serious at high temperature. Even if we take this effect into account, it is obvious that we are dealing with the extremely narrowing case, and the orders of magnitude of τ_N's would not be altered.

We have assumed that the relaxation mechanisms for both of water molecules, the localized and the mobile, are the same, and have attributed the difference between T_{11} and T_{12} to the difference between their τ_N's. But, in the actual situation, the relaxation mechanisms for both may be different. For instance, the relaxation mechanisms for the localized water may be via non-spherical Brownian motion such as considered by one of the authors (A.O.)[18], or via paramagnetic impurities contained in cellulose. These points are not clear at the present stage of our investigation.

Finally, our data must be compared with T_1's of protons of sorbed water on silica gel obtained by Zimmerman and Lasater[8]. Their values of T_1 corresponding to our data are of the order of 20 msec, only single T_1 existing except for 10.6, 12.6, and 13.6% samples. The reason for the difference between their data and ours is not clear, and perhaps the difference of the adsorbent is its origin, and it is a further task to clarify this difference.

c) Values of T_2

Since our apparatus is not suitable for accurate measurement of T_2, we made only rough measurements of T_2, where we could not separate two T_2's so far. We think it is a great task left for us to solve the question whether we can separate two T_2's in our sample. We are now proceeding to modify our apparatus to measure the spin echo decay time accurately.

T_2 varies from 0.5 msec to 4.5 msec, with the water content increasing (Fig. 3 (c)) and T_2 is by about one order of magnitude shorter than T_{11}. In general, if the mechanisms for T_1 and T_2 are of the same origin, BPP theory gives the relation $T_1=T_2$ in the extremely narrowing case with which we are dealing. Now we explain this disagreement by considering that the main mechanisms responsible for T_1 and T_2 are different. For T_1 we have considered that the main mechanism is due to the rotational Brownian motion of water molecule. For T_2 we propose that the protons contained in the cellulose, which themselves are not detected in the signal, make some local field at the positions of sorbed water molecules, varying from position to position, and shorten T_2. The formulation of the spin echo decay time in this situation is another task left for us and we shall discuss this point after we shall have completed the accurate measurement of T_2.

d) Values of $y_{11}/(y_{11}+y_{12})$

First we consider the dependence of $y_{11}/(y_{11}+y_{12})$ on water content. $y_{11}/(y_{11}+y_{12})$ decreases with the water content. Eor 148% sample at room temperature, we could not separate two T_1's i.e. $y_{11}/(y_{11}+y_{12})\simeq 0$ (Fig. 5).

The quantity $y_{11}/(y_{11}+y_{12})$ represents the ratio of the number of water molecules in the localized state to the total number of water molecules, if the exchange between the localized and the mobile states is neglected.

Then we consider a simplified model of sorption, such that, with the water content increasing, water molecules make hydrogen bonds with OH groups of cellulose until there are no OH groups left for hydrogen bonding, and only after that the mobile water appears. The degree of crystallinity of our cellulose sample is about 70% and the OH groups inside the crystalline part do not take part in the sorption. According to this model, a simpe calculation shows that the dependence of $y_{11}/(y_{11}+y_{12})$ on water concent is represented by the dotted curve in Fig. 5. In the general tendency, this dotted curve is like the experimental curve. In order to make more precise comparison, however, the following facts must be taken into account. First, when the water content is increasing, the mobile water would appear before the monolayer is fully completed. Second, there may be some swelling effects. Finally, the exchange between the localized and the mobile states cannot be neglected, and then $y_{11}/(y_{11}+y_{12})$ is smaller than the actual population ratio[7,8].

Next, we consider the temperature dependence of the value of $y_{11}/(y_{11}+y_{12})$, which decreases with the temperature increasing (Fig. 6). We explain this phenomenon in the following way. The average life-time of a water molecule in the localized state (τ_{ex}) would not be so much longer than T_{11} and it would vary with the temperature as τ_{exo} exp $\Delta H/RT$, where ΔH is the activation energy for the hydrogen bond between water molecule and OH group of cellulose. When the temperature is increased, the actual relaxation time T_{11} increases and τ_{ex} decreases, and gradually T_{11} becomes comparable with τ_{ex}. So, $y_{11}/(y_{11}+y_{12})$ decreases with the temperature. Of course, the above explanation is one of the possible explanations for the data of Fig. 6. Following the above explanation, we estimate τ_{ex} to be of the order of several tens of msec at room temperature. Since we can separately measure T_{11}'s of the order of 20 msec, the average life-time in the localized state of the sorbed water on cellulose is not shorter than 20 msec at room temperature. On the other hand, for the sorbed water on silica gel, Zimmerman *et al.* obtained the value of 3 msec for the average life-time in the localized state, which is again by one order of magnitude shorter than ours. This difference is also a task for further investigation, as the difference in the values of T_1.

§ 4. Conclusions

We have measured the spin-lattice relaxation time of proton of sorbed water on cellulose. There are two different phases of water molecule. the localized and the mobile. The data of T_1 was analysed by BPP theory. The correlation time derived from T_1 is consistent with the value from dielectric measurements. The value of T_2 is by about one or two order of magnitude shorter than T_1, contradicting with the theoretical prediction $T_1=T_2$ for extremely narrowing case, we are dealing with. We have qualitatively explained this discrepancy by considering the effects of protons contained in cellulose. But a more quantitative treatment, that is, the theory of T_2 of the heterogeneous system, which is constituted by two sets of spins in different environments, one being in the fluctuating lattice (protons of sorbed water) and the other in the rigid lattice (protons in cellulose), must be developed. The average life-time in the localized state of sorbed water molecule on cellulose would be of the order of several tens of msec.

By this study, many points left for questions in the previous study by one of the authors (A.O.) have become clear. Further points left for us are to measure accurately the spin echo decay time, to develop the theory of the T_2 of the heterogeneous system, and to clarify the difference between the sorption mechanisms on cellulose and on silica gel.

The authors would like to express their sincere thanks to Professor I. Takahashi for his continual interest and discussions. It is also our pleasure to acknowledge the assistance of Mr. S. Inoue of Hokkaido University.

References

1) A. Odajima: J. Phys. Soc. Japan **14** (1959) 308.
2) N. Bloembergen, E. M. Purcell and R. V. Pound: Phys. Rev. **73** (1948) 679.
3) M. Takeda: Bull. Chem. Soc. Japan **24** (1951) 169.
4) R. Seidman and S. G. Mason: Canad. J. Chem. **32** (1954) 744.
5) S. Ono, T. Kuge and N. Koizumi: Bull. Chem. Soc. Japan **31** (1958) 34 and 40.
6) J. R. Zimmerman, B. G. Holms, and J. A. Lasater: J. Phys. Chem. **60** (1956) 1157.
7) J. R. Zimmerman and W. E. Brittin: J. Phys. Chem. **61** (1957) 1328.
8) J. R. Zimmerman and J. A. Lasater: J. Phys. Chem. **62** (1958) 1157.
9) H. Winkler: Archives des Sciences, **12** (1959) 161.
10) E. L. Hahn: Phys. Rev. **80** (1950) 580.
11) T. Hashi, A. Hirai, M. Sasaki, and T. Kawai: Memoirs of the College of Science, University of Kyoto, Series A **29** (1959) 205.
12) J. J. Windle and T. M. Shaw: J. Chem. Phys. **22** (1954) 1752.
13) J. J. Windle and T. M. Shaw: J. Chem. Phys. **25** (1956) 435.
14) A. Miyake: J. Chem. Phys. **27** (1957) 1425.
15) S. Broersma: J. Chem. Phys. **24** (1956) 153 and 639.
16) G. W. Wilson and G. E. Pake: J. Chem. Phys. **27** (1957) 115.
17) R. Kubo and K. Tomita: J. Phys. Soc. Japan **9** (1954) 888.
18) A. Odajima: J. Phys. Soc. Japan **14** (1959) 777.

JOURNAL OF THE PHYSICAL SOCIETY OF JAPAN, Vol. 15, No. 9, SEPTEMBER, 1960

Study of Aqueous Solution of Strong Electrolyte—Reexamination of Molecular Refraction*

By Takeshi SATOH and Koreaki HAYASHI

Department of Physics, Defense Academy, Obaradai, Yokosuka, Japan

(Received, May 11, 1960)

Molecular refraction of 1–1 electrolyte aqueous solution was reexamined in the light of a proposed model. So-called Lorentz-Lorenz function was plotted against molar fraction of electrolyte. Linear relationships and critical phenomenon dividing the whole range into two were found. By applying our theory we obtain total number of hydration, $n_I^{(+)}+n_I^{(-)}+n_{II}^{(+)}+n_{II}^{(-)}$, where the hydration numbers around each cation and anion are defined as $n_I^{(+)}$, $n_I^{(-)}$ referred to the primary region and $n_{II}^{(+)}$, $n_{II}^{(-)}$ referred to the secondary region respectively. We could also estimate the polarizability α_* of water molecule which are considered as 'solvent in concentrated range' and subjected to the sufficient effect of polarization from surrounding ions.

§1. Introduction

Recently one of the authors (T.S.) has offered a model (1) of aqueous solution of strong electrolyte, which is to be applied throughout the whole range of concentration. In short the kernel of our model consists in two points: one is an extension of definition of so-called hydration layer and the other is perception that there exists critical range of concentration and consequently we can divide the whole into two, distinctly different ranges from structural viewpoint. Then we use primary hydration numbers $n_I^{(+)}$, $n_I^{(-)}$ and secondary hydration numbers $n_{II}^{(+)}$, $n_{II}^{(-)}$. The superscript (+) or (−) refers that a layer concerned is one located arond a cation or an anion respectively.

Now we are going to reexamine molecular refraction from an above-mentioned standpoint. Of course this problem had been studied three decades ago and a trial, theoretical explanation has been given by Böttcher(2). As well-known, 'law of additivity of molecular refraction' is valid in multi-component systems. The application of this law is unexpectedly capable in wider field. Let the molecular refraction of a solution considered be denoted by R, that of each component by R_i and molar fraction of each component by f_i, the law is formulated in the equation,

$$R=\sum_i R_i f_i. \tag{1}$$

On the other hand molecular refraction R is defined as $(\mu/\rho)\,(n^2-1)/(n^2+2)$, where the notations are used as following:

n = refractive index of solution,

ρ = density of solution,

μ = average molecular weight of solution,

$= \sum_i \mu_i f_i$.

In this paper we restrict our consideration in two-component systems. Then it is easily seen that if we plot so-called Lorentz-Lorenz function $\rho^{-1}(n^2-1)/(n^2+2)$ against molar fraction of solute f, we will obtain such a curve as shown in Fig. 1. Fig. 1. shows an example of water-methylalcohol solution at 22°C, where

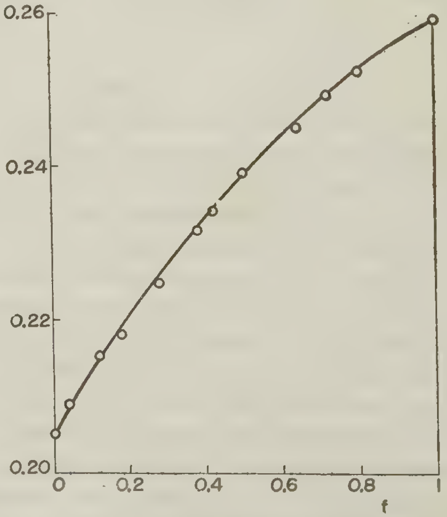

Fig. 1. Methylalcohol (22°C)

---

* Read at the annual meeting of the Physical Society of Japan held at University of Tokyo on April 6, 1960.

methylalcohol is taken as solute.

§ 2. Experimental Data

Let us back and consider our systems. Since dissociation can be assumed perfect because of 1–1 electrolytes, it turns out that variable f representing molar fraction of cation and anion simultaneously is the same to that of electrolyte solute. And then f is limited to the order of only several percent. Consequently we notice that Lorentz-Lorenz function is expected to be approximately linear to f.

In the literatures we find available data for analysis which were done by Fayans' collaborators, H. Kohner(3), W. Geffcken(4), and P. Hölemann and H. Kohner(5). The Plots of $\rho^{-1}(n^2-1)/(n^2+2)$ versus f are shown in Fig. 2 to Fig. 6. In these figures we find distinctive features that relation can be approximately indicated by two straight lines having different slopes. But we must recognize that there is only small number of points, particularly in dilute range. For this reason we tried reobservations for supplemental data by preparing more detailed points of concentration.

Here we describe the outline of the experimental. Sodium chloride, sodium bromide, potassium chloride, potassium bromide and potassium iodide have been studied as electrolyte solutes. All samples were special-class

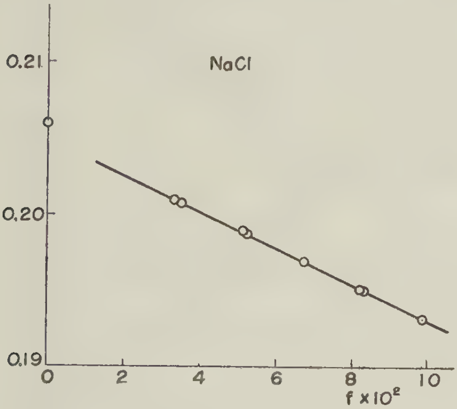

Fig. 2. Sodium chrolide (25°C)

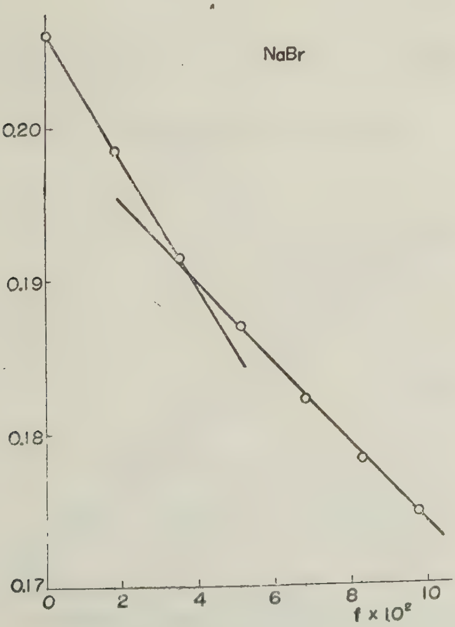

Fig. 3. Sodium bromide (27°C)

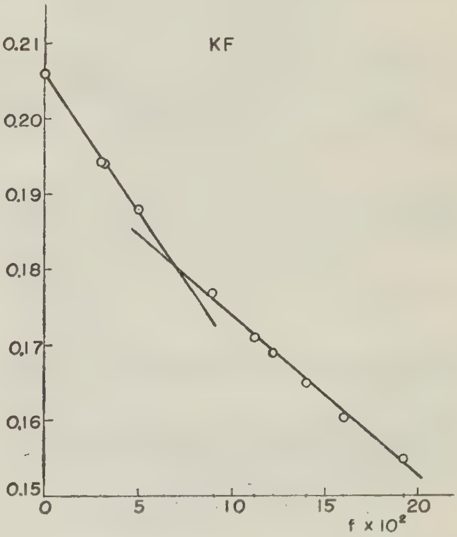

Fig. 4 Potassium fluoride (25°C)

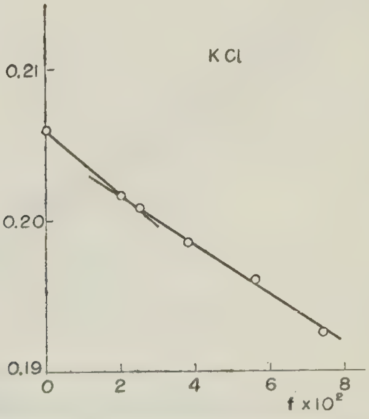

Fig. 5. Potassium chrolide (55°C)

commercial products, which were dried in a thermostat for several hours before making solutions. Refractive indices of solutions have been measured by Abbe refractometer using light source of a sodium discharge tube.

Temperature of specimen was kept constant by passing water through jacket from water works. Error of refractive index was limited within ±2 at the fourth decimal, while that of temperature of specimen cell ± (0.1 or 0.2)°C. The density of solution has beed measured by a picnometer. The results are shown in Fig. 7 to Fig. 11. From these figures we can probably draw our conclusion upon experimental facts.

§ 3. Theoretical Interpretation

We take cation, anion and water as the

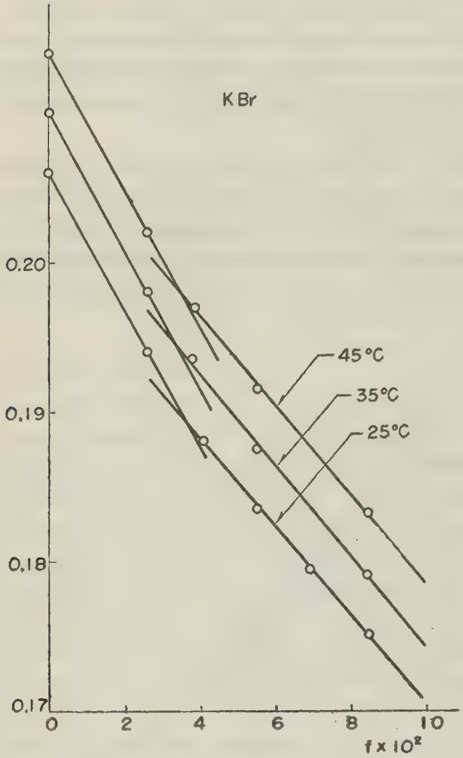

[Measuring points corresponding to 35° and 45°C are plotted in a way of translation by constant.]

Fig. 6. Potassium bromide (25 C)

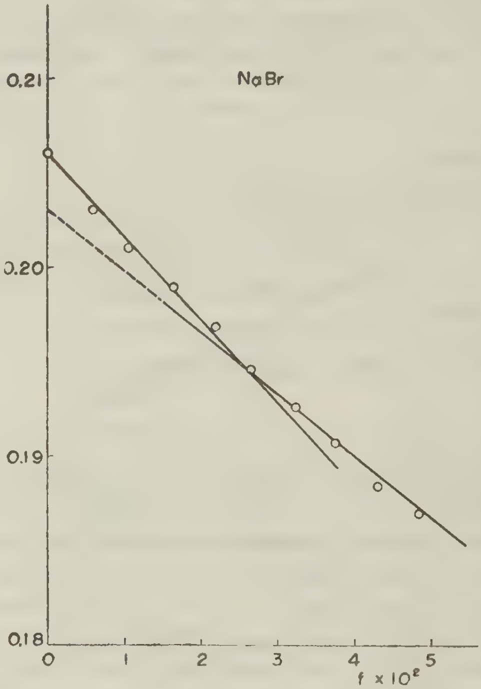

Fig. 8. Sodium bromide (20°C)

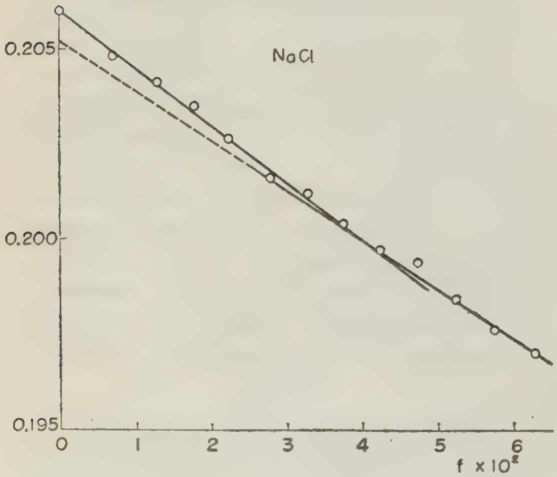

Fig. 7. Sodium chrolide (19°C)

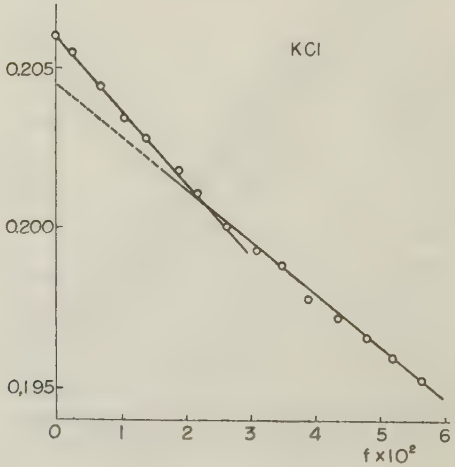

Fig. 9. Potassium chrolide (19°C)

components. However, from above situation based upon our model simple treatment of water might not be permitted. That is, we should consider molecular refraction of water molecular which corresponds to different state; $R_{\mathrm{I}}^{(+)}$, $R_{\mathrm{I}}^{(-)}$ referred to waters in primary hydration region, $R_{\mathrm{II}}^{(+)}$, $R_{\mathrm{II}}^{(-)}$ referred to those in secondary hydration region and R_0 referred to the normal, free water molecules. R_+ and R_- denote those of cation and anion.

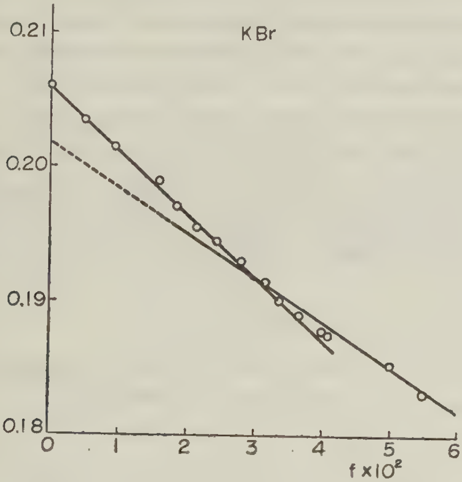

Fig. 10. Potassium bromide (19°C)

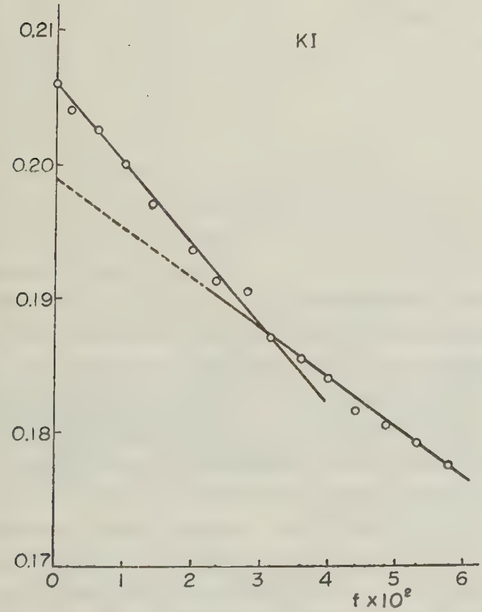

Fig. 11. Potassium iodide (19°C)

(i) *dilute range*

Since molar fraction of the cation and the anion is f, that of water is $1\text{-}2f$. Molar fractions of different types of water are, therefore, given in the following from.

types of water molecule	molar fraction
primary layer of cation	$n_{\mathrm{I}}^{(+)}f$
primary layer of anion	$n_{\mathrm{I}}^{(-)}f$
secondary layer of cation	$n_{\mathrm{II}}^{(+)}f$
secondary layer of anion	$n_{\mathrm{II}}^{(-)}f$
normal	$1-(n_{\mathrm{I}}^{(+)}+n_{\mathrm{I}}^{(-)}+n_{\mathrm{II}}^{(+)}+n_{\mathrm{II}}^{(-)}+2)f$

Consequently, $\sum\limits_j R_j f_j$ can be written:

$$\begin{aligned}\sum R_j f_j &= (R_+ + R_-)f \\ &+ (R_{\mathrm{I}}^{(+)} n_{\mathrm{I}}^{(+)} + R_{\mathrm{I}}^{(-)} n_{\mathrm{I}}^{(-)} \\ &+ R_{\mathrm{II}}^{(+)} n_{\mathrm{II}}^{(+)} + R_{\mathrm{II}}^{(-)} n_{\mathrm{II}}^{(-)})f + R_0\{1-(n_{\mathrm{I}}^{(+)} \\ &+ n_{\mathrm{I}}^{(-)} + n_{\mathrm{II}}^{(+)} + n_{\mathrm{II}}^{(-)} + 2)f\} \\ &= R_0(1+Af),\end{aligned} \tag{2}$$

where coefficient A is written by an equation,

$$\begin{aligned}A = \{&(R_+ + R_-) + (R_{\mathrm{I}}^{(+)} n_{\mathrm{I}}^{(+)} + R_{\mathrm{I}}^{(-)} n_{\mathrm{I}}^{(-)} \\ &+ R_{\mathrm{II}}^{(+)} n_{\mathrm{II}}^{(+)} + R_{\mathrm{II}}^{(-)} n_{\mathrm{II}}^{(-)}) - R_0(n_{\mathrm{I}}^{(+)} \\ &+ n_{\mathrm{I}}^{(-)} + n_{\mathrm{II}}^{(+)} + n_{\mathrm{II}}^{(-)} + 2)\}/R_0.\end{aligned} \tag{3}$$

While $\bar{\mu}(=\sum\limits_j \mu_j f_j)$ is $\mu_0(1+Bf)$, where μ_0 is denoted as molecular weight of water and coefficient $(\mu_+ + \mu_- - 2\mu_0)/\mu_0$ is abbreviated by B.

Of course $\mu_+ + \mu_-$ equals to molecular weight of solute. Hence Lorentz-Lorenz equation can be written in the following from:

$$\begin{aligned}\rho^{-1}(n^2-2)/(n^2+2) &= (R_0/\mu_0)(1+Af)(1+Bf)^{-1} \\ &\approx (R_0/\mu_0)\{1-(B-A)f\}.\end{aligned} \tag{4}$$

Here we neglect higher order terms more than square of f. Eq. (4) shows that $\rho^{-1}(n^2-1)/(n^2+2)$ is approximately linear to f and so our theoretical derivation agrees satisfactorily with experimental result.

(ii) *concentrated range*

When concentration reaches to a critical point, almost no free water molecule exists in solution. We must, therefore, consider different members of component, namely water molecules can be now classified into three. Hence molar fractions of these three types of water are given in the same manner.

types of water molecule	molar fraction
primary layer of cation	$n_{\mathrm{I}}^{(+)}f$
primary layer of anion	$n_{\mathrm{I}}^{(-)}f$
over-all secondary layer	$1-(n_{\mathrm{I}}^{(+)}+n_{\mathrm{I}}^{(-)}+2)f$

If R corresponding to secondary-region water molecule is designated as R_*, $\sum\limits_j R_j f_j$ can be written:

$$\sum R_j f_j = (R_+ + R_-)f + (R_{\mathrm{I}}^{(+)} n_{\mathrm{I}}^{(+)} + R_{\mathrm{I}}^{(-)} n_{\mathrm{I}}^{(-)})f + R_*\{1-(n_{\mathrm{I}}^{(+)} + n_{\mathrm{I}}^{(-)} + 2)f\} = R_*(1+A_*f), \tag{5}$$

where coefficient A_* is written as follows:

$$A_*=\{(R_+ + R_-)+(R_{\mathrm{I}}^{(+)}n_{\mathrm{I}}^{(+)}+R_{\mathrm{I}}^{(-)}n_{\mathrm{I}}^{(-)} - R_*(n_{\mathrm{I}}^{(+)}+n_{\mathrm{I}}^{(-)}+2)\}/R_*. \tag{6}$$

Hence,

$$\rho^{-1}(n^2+1)/(n^2+2)=(R_*/\mu_0)(1+A_*f)(1+Bf)^{-1}\approx(R_*/\mu_0)\{1-(B-A_*)f\}, \tag{7}$$

where higher order terms more than square of f are neglected as in Eq. (4). Eq. (7) is also seen to be able to explain experimental fact. By using available graphs we are now going to determine hydration number. In Eq. (4) and Eq. (7) we can obtain absolute value of gradient, say g and g_*, and constant factor term, R_0/μ_0 and R_*/μ_0 (consequently R_0 and R_*) respectively. Hence we have,

$$(R_0/\mu_0)(B-A)=g \tag{8}$$

and

$$(R_*/\mu_0)(B-A_*)=g_*. \tag{9}$$

Substituting Eq. (3) and Eq. (6) into these equations,

$$(R_+ + R_-)+(R_{\mathrm{I}}^{(+)}n_{\mathrm{I}}^{(+)}+R_{\mathrm{I}}^{(-)}u_{\mathrm{I}}^{(-)}+R_{\mathrm{II}}^{(+)}n_{\mathrm{II}}^{(+)}+R_{\mathrm{II}}^{(-)}n_{\mathrm{II}}^{(-)})-R_0(n_{\mathrm{I}}^{(+)}+n_{\mathrm{I}}^{(-)}+n_{\mathrm{II}}^{(+)}+n_{\mathrm{II}}^{(-)}+2)=B-g(\mu_0/R_0), \tag{10}$$

$$(R_+ + R_-)+(R_{\mathrm{I}}^{(+)}n_{\mathrm{I}}^{(+)}+R_{\mathrm{I}}^{(-)}n_{\mathrm{I}}^{(-)})-R_*(n_{\mathrm{I}}^{(+)}+n_{\mathrm{I}}^{(-)}+2)=B-g_*(\mu_0/R_*). \tag{11}$$

When Eq. (10) is subtracted from Eq. (11), the following equation is obtained,

$$(R_0-R_*)(n_{\mathrm{I}}^{(+)}+n_{\mathrm{I}}^{(-)}+n_{\mathrm{II}}^{(+)}+n_{\mathrm{II}}^{(-)}+2)=\mu_0\{(g/R_0)-(g_*/R_*)\}.$$

The over-all hydration number is, therefore, determined by:

$$n_{\mathrm{I}}^{(+)}+n_{\mathrm{I}}^{(-)}+n_{\mathrm{II}}^{(+)}+n_{\mathrm{II}}^{(-)}=\{\mu_0/(R_0-R_*)\}\times\{(g/R_0)-(g_*/R_*)\}-2. \tag{12}$$

Values of $n_{\mathrm{I}}^{(+)}+n_{\mathrm{I}}^{(-)}+n_{\mathrm{II}}^{(+)}+n_{\mathrm{II}}^{(-)}$ for several 1-1 electrolyte species calculated from Eq. (12) are tabulated in Tab. 1.

Table 1. Values of α_*, $n_{\mathrm{I}}^{(+)}+n_{\mathrm{I}}^{(-)}+n_{\mathrm{II}}^{(+)}+n_{\mathrm{II}}^{(-)}$ and $C_{\mathrm{crit.}}$

	B	temp. (°C)	g	g_*	R_* (cm³/mol.)	α_*(A³)	$n_{\mathrm{I}}^{(+)}+n_{\mathrm{I}}^{(-)}+n_{\mathrm{II}}^{(+)}+n_{\mathrm{II}}^{(-)}$	$C_{\mathrm{crit.}}$ (mol./lit.)	Reference
NaCl	1.25	25	0.15	0.12	3.69	1.46	20	2.1	(5)
		19	0.15	0.13	3.69	1.46	15		
NaBr	3.72	27	0.41	0.26	3.60	1.43	19	2.7	(3)
		20	0.44	0.32	3.67	1.45	32		
KF	1.23	25	0.36	0.22	3.53	1.40	29		(4)
KCl	2.14	25	0.21	0.16	3.69	1.46	35	1.4	(4)
		19	0.23	0.16	3.68	1.46	39		
KBr	4.61	25	0.47	0.30	3.60	1.43	23	1.7	(4)
		19	0.48	0.34	3.63	1.43	27		
KI	7.22	19	0.61	0.38	3.58	1.42	24	1.6	

§ 4. Discussion

Böttcher has thought that the experimental fact that apparent dependency of molecular refraction of component upon the concentration is caused by a limited validity of the Lorentz-Lorenz formula and all the deviations can be explained by his corrected Lorentz-Lorenz formula⁽²⁾. While our treatment is based upon the assumption that the additivity law of molecular refraction holds widely. We consider that the knick phenomena are to be attributed rather to structural change in the solution. Then, if we adopt a conventional relationship that polarizability α of a particle is proportional to molecular refraction R, we obtain the values of α_* corresponding to R_*, which are listed in Tab. 1. Clearly α_* is smaller than α_0, although the difference is not so remarkable. (The value of polarizability α_0 at 25°C is 1.470 A^3, which should be distinguished from Böttcher's value 1.303 A^3 because of different definition.) This is easily understandable since in the region in which α_* is defined water molecule undergoes sufficiently the polarization effect from ion. Moreover, it seems interesting and meaningful that α_* has a general tendency of decrease against the increasing of ionic radius.

We can quote glass as an appropriate example in concentrated range. Although glass is super-cooled liquid, it is just like our systems in extremely concentrated ionic solution. A similar treatment to this paper are found to be applied successfully in the structural study of glass(6).

The neglect of higher order terms more than f^2 in Eq. (4) and Eq. (7), particularly in the latter, must be examined in such a case as KBr or KI, which has large value of B. Because, in these samples f^2-term may become to be somewhat comparable to f^1-term around larger value of concentration near saturation. But we cannot detect these trend in our experimental ranges as seen in Fig. 10 and Fig. 11. Bjerrum has pointed out that we must consider an influence of ion association, which may occur mainly in high concentrations. Since ion association increases proportional to the square of concentration, its contribution to Eq. (7) is of the order of f^3. We might, therefore, neglect this effect.

Table 2. Estimation of secondary hydration number $n_{II}^{(+)}+n_{II}^{(-)}$

	$n_I^{(+)}+n_I^{(-)}$	$n_{II}^{(+)}+n_{II}^{(-)}$
NaCl	6	28
NaBr	6	26
KCl	5	34
KBr	5	22
KI	5	19

It should be remembered that the value of $n_I^{(+)}+n_I^{(-)}+n_{II}^{(+)}+n_{II}^{(-)}$ calculated by Eq. (12) might not be regarded to be very accurate, because that values of g and g_* obtained graphically can only be determined fairly rough. After allowing this circumstance, we try to estimate total number of secondary hydration. If we use total number of primary hydration that has been simply called hydration number, we can obtain total number of secondary hydration to each electrolyte. Mean values of $n_I^{(+)}+n_I^{(-)}$(7) used for estimation and those of $n_{II}^{(+)}+n_{II}^{(-)}$ determined thus are listed in Tab. 2. Hydration number is supposed almost independent on temperature. This is verified by a fact that all the slopes of straight lines corresponding to various temperatures are determined nearly the same whithin experimental error as seen in Fig. 6.

The values of critical concentration $C_{crit.}$ may be compared with ones determined with other hydration-dependent quantities. At present we have only few examples available for this comparison. Here we will refer a result of viscosity. With NaCl we can find good agreement between present work and recent report by Suryanarayana and Venkatesan(8).

The authors takes this opportunity to thank Prof. J. Itoh for his suggestion concerning the subject of hydration. Special thanks are due to Dr. I. Oshida and Prof. K. Ishiguro for their deep interests and invaluable discussions. Finally, we would like to thank Mrs. M. Hakuya for her assistance of measurement and calculation during this work.

References

(1) T. Satoh, J. Phys. Soc. Japan, **15**, 1134 (1960).
(2) C. J. F. Böttcher, Rec. trav. chim., **65**, 39, 19 (1946)
C. J. F. Böttcher, "Theory of Electric Polarization" Chap. VIII, p. 273, Elsevier Publ. Co., Amsterdam (1952)
(3) H. Kohner, Z. physik. Chem., B **1**, 427 (1928)
(4) W. Geffcken, Z. physik. Chem., B **5**, 81 (1929)
(5) P. Hölemann and H. Kohner, Z. physik. Chem., B **13**, 338 (1931)
(6) e.g. J. E. Stanworth, "Physical Properties of Glass", Chap. 2, p. 56, Oxford (1950)
(7) e.g. J. O'M. Bockris, "Modern Aspects of Electrochemistry" Chap. 2, p. 62, Butterworths Scie. Publ. (1954)
(8) C. V. Suryanarayana and V. K. Venkatesan, Trans. Faraday Soc., **54**, 1709 (1958)

JOURNAL OF THE PHYSICAL SOCIETY OF JAPAN, Vol. 15, No. 9, SEPTEMBER, 1960

On the Magnetic Properties of a $CrBr_3$ Single Crystal

By Ichiro TSUBOKAWA

The Research Institute for Iron, Steel and Other Metals,
Tohoku University, Sendai, Japan.

(Received May , 1960)

Magnetic properties of single crystals of $CrBr_3$ have been measured with a magnetic balance and also with a torque magnetometer. The ferromagnetic Curie point has been found to be 37°K from the temperature dependences of magnetization and of torque. Based on the data of the magnetic susceptibility above the Curie point, the paramagnetic Curie point θ_p, Curie constant C_M and the effective Bohr magneton number have been determined to be 47°K, 1.84 and 3.85 μ_B respectively. From the saturation magnetization at 4 2°K, the moment of chromium ion is estimated to be 3 μ_B, coinciding with the spin moment obtained from the susceptibility measurement above the Curie temperature. Direction of easy magnetization lies along the c-axis of the hexagonal lattice, and the second order and the fourth order anisotropy constants are estimated to be $K_1=-5.08\times10^5$ and $K_2=0.65\times10^5$ erg/cc respectively. In the present results, there is found a small deviation in the torque curves from simple sinusoidal form, $L=K \sin 2\theta$, which is discussed on the basis of the higher order term of magnetic anisotropy in the high field strength range and also of the domain-theoretical consideration in the low field strength range.

§ 1. Introduction

Several anhydrous di- or trihalides of the elements of the iron group shown an interesting magnetic property which is known to be metamagnetism. For these compounds, the paramagnetic Curie temperatures θ_p have a positive sign, and in the temperature range below these points the magnetic susceptibilities depend on the magnetic field strength. In spite of $\theta_p > 0$, it was discovered by neutron diffraction experiments that the magnetic spin ordering in the crystal lattice of these compounds is antiferromagnetic. On the other hand, the chromium trihalides, $CrCl_3$⁽¹⁾ and $CrBr_3$⁽²⁾⁽³⁾, are considered to have different magnetic properties in comparision with those mentioned above, but any detailed study was not yet undertaken. On this point of view, the magnetic properties of a single crystal of $CrBr_3$ were investigated by the present author.

§ 2. Experimental Results

A single crystal of $CrBr_3$ was prepared by heating the powdered chromium (99.3%) in the vapour of bromine (99.9%) up to about 750°C. A schematic diagram of the apparatus for growing $CrBr_3$ crystals is shown in Fig. 1. The crystals were grown up to about $4\times7\times7$ mm³ in dimension and were cooled in the furnace F_1. The $CrBr_3$ crystals appeared in the form of hexagonal plates with a cleavage plane of (0001), dark green in color.

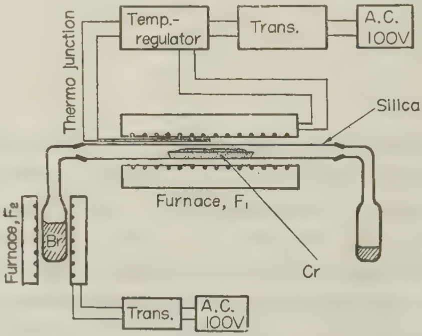

Fig. 1 A schematic diagram of the apparatus for growing the $CrBr_3$ crystals: Powdered chromium was placed in furnace F_1 and heated to 750°C. Bromine vapor was prepared by heating bromine in a glass container to 50°C by furnace F_2.

Chemical analysis showed that the $CrBr_3$ crystals thus obtained contained only trivalent chromium ions. It was also confirmed by a Debye-Scherrer X-ray pattern that the crystal was hexagonal in structure with the lattice constants $a=3.66$ Å and $c=18.30$ Å, which agreed closely with the results of the previous work(4).

Temperature dependence of specific magnetization σ and of susceptibility χ above the Curie point were also measured and the results are shown in Figs. 2 and 3. The ferromagnetic Curie temperature was estimated to be about 37°K by plotting the σ^2–T curve. In Fig. 3, the inverse susceptibility is also plotted against the temperature, which shows that the paramagnetic susceptibility above the Curie temperature obeys the epuation

$$\chi=\frac{0.0063}{T-47},$$

whence the paramagnetic Curie point was determined to be $\theta_p=47$°K and the Curie constant, C_M, and the effective Bohr magneton number, p_{eff}, are 1.84 and 3.84 μ_B respectively.

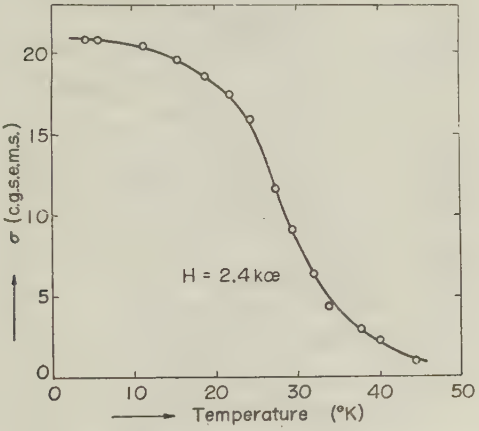

Fig. 2. Temperature dependence of magnetization.

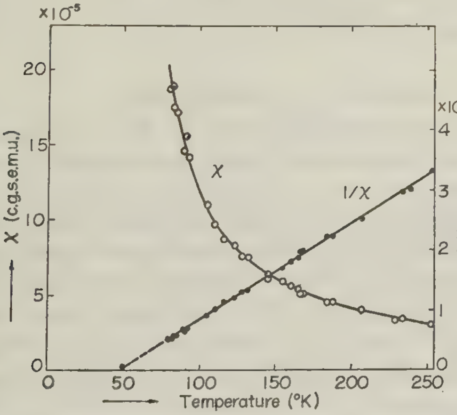

Fig. 3. Temperature dependence of the susceptibility above the Curie point. (Inverse susceptibility is also plotted).

Torque measurement was performed by means of a torque magnetometer. A single crystal specimen used in the present experiment was spherical in shape, 2 mm in diameter. Some typical torque curves at 4.2°K in the a–c placn are shown in Fig. 4. The stable position for the specimen could not be found when the magnetic field was oriented near a-direction of the crystal. When the applied field was 2.4 koe, the torque maximum appeared at $\theta=48°$, θ representing the poler angle of the field direction from c-axis, but it displaced towards the a-axis with increasing field strength. The deflection θ reached its maximum value 62° at about 7 koe and then decreased with the further increase of magnetic field strength. The maximum

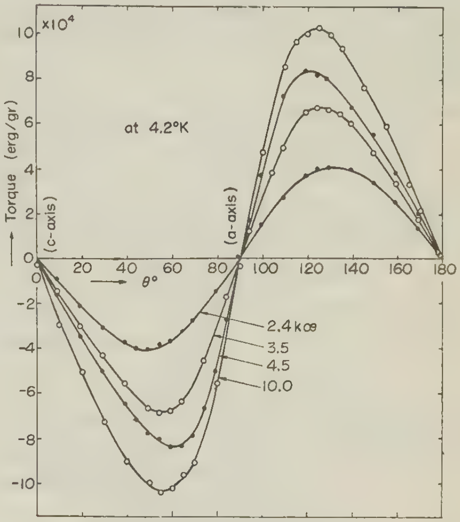

Fig. 4. Torque curves at 4.2°K.

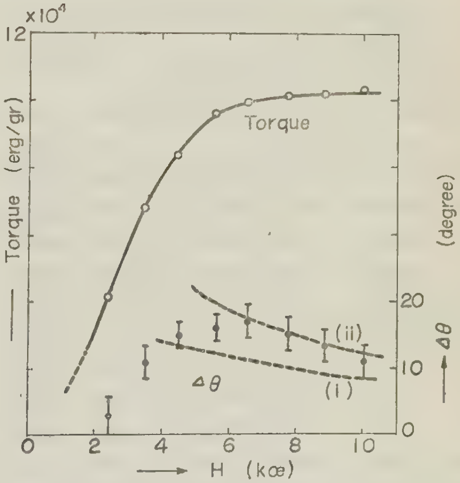

Fig. 5. Field dependences of the value of the torque maximum and of $\Delta\theta$.

torques and deviations $\Delta\theta$ of the torque maximum position from 45° for each curve are plotted against the applied field strength in Fig. 5. A temperature dependence of the value of the torque maximum measured in the field strength of 10 koe is shown in Fig. 6. Further torque measurements were performed above the Curie temperature, and $(\chi_c-\chi_a)$ calculated by using the value of torque is shown in Table 1.

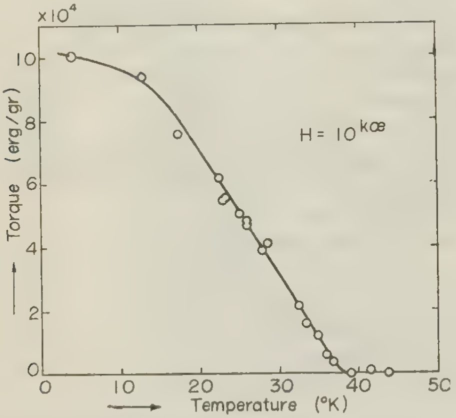

Fig. 6. Temperature dependence of torque.

Table I. The values of $\chi_c-\chi_a$.

Temp.	$\chi_c-\chi_a$	Temp.	$\chi_c-\chi_a$	Temp.	$\chi_c-\chi_a$
43.0°K	116×10^{-6}	64.3°K	4.6×10^{-6}	101°K	0.80×10^{-6}
43.5	106	66.0	3.7	106	0.75
43.8	96	70.0	2.5	109	0.71
43.9	84	73.0	2.1	124	0.57
44.0	67	74.7	1.85	141	0.45
45.0	52	76.3	1.68	154	0.38
45.5	47	77.5	1.59	159	0.37
50.0	26	78.0	1.36	166	0.35
51.2	20	80.0	1.31	178	0.32
53.2	17.0	81.0	1.25	190	0.30
54.0	14.6	86.0	1.14	203	0.27
56.5	11.9	91.0	1.00	223	0.26
56.7	11.6	94.0	0.91	239	0.24
58.0	10.6	97.0	0.86	269	0.23
60.5	8.3	99.0	0.84	293	0.21

The magnetization curves at 4.2°K for the direction of c–axis and that perpendicular to it were taken by means of a magnetic balance, and the results are shown in Fig. 7. As it shows, c–axis is the direction of easy magnetization and the technical saturation is reached by the field strength of 4 koe. The saturation value at 4.2°K is estimated to be 58 gauss/gr, which corresponds to 270 gauss/cc. The dotted curve in Fig. 7 shows the average value of magnetizations for the directions of easy and difficult magnetization, which agrees very well with that of the powder specimen reported by Hansen(3).

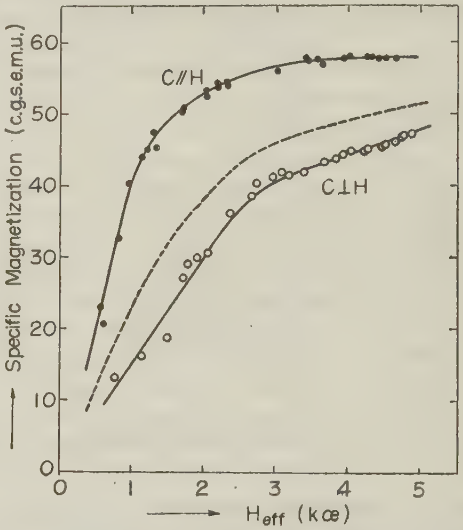

Fig. 7. Magnetization curves parallel to a–axis and c–axis.

§ 3. Discussions of the Results

A lot of hexagonal halides of the elements of the iron group show metamagnetic properties, whereas, the present compound is considered to be ferromagnetic since this compound does not show any antiferromagnetic behaviors for low magnetic field strength. Also the Curie-Weiss law holds above the critical point and the paramagnetic Curie temperature is higher than the ferromagnetic Curie point.

From the results of the magnetization curves of single crystals and of the torque measurement, it is concluded that the direction of easy magnetization lies along c–axis of the crystal. The saturation moment in c–direction at 4.2°K would be supposed to be about 3 μ_B from the results obtained. On the other hand, from the susceptibility measurement above the Curie temperature, we determined that the spin quantum number is 3/2. These values agree well with the spin magnetic moment of Cr^{3+} ion.

Paths of superexchange interaction in the present compound may be classified into those in the c-plane as well as along the c-direction. The crystal structure of $CrBr_3$ is shown in Fig. 8, and the path of the interaction in the c-plane is A—O—B which passes through one intermediate anion, while the other along the c-direction is C—O′—O″—D which passes through two intermediate anions. All other kinds of paths are considered to have a negligible contribution to the net interaction since overlapping of the charge clouds of ions in these paths is not expectable to be large from the view point of the ionic radii of Cr^{3+} and Br^-. The angle of A—O—B linkage is calculated to be about 89°. Kanamori(5) suggested that if the cations are Cr^{3+} and the angle of the linkage, 90°, the sign of superexchange interaction is ferromagnetic. Hence, the interaction along the c-directions is considered to be also ferromagnetic.

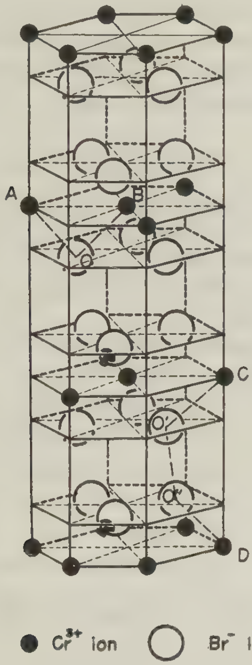

Fig. 8. Crystal sturcture of $CrBr_3$.

Next the behavior of the torque curve is discussed. In the strong field range, the maximum of the torque curve shown in Fig. 4 reaches a saturation value; Based on the uniaxial anisotropy energy,

$$U=K\cos^2\theta,$$

(K represents the anisotropy constant) and from the saturation value of torque maximum, K is estimated to be -4.8×10^5 erg/cc. In this case the dependence of the position of torque maximum, $\theta_m=\pi/4+\varDelta$, on the magnetic field strength is given by

$$\sin(2\varDelta)=\left[\sqrt{1+32\,(K/HI_s)^2}-1\right]\Big/(8K/HI_s)$$

neglecting the higher order terms in K/HI_s[*], where H is the magnetic field strength and I_s, the value of the saturation magnetization. Putting the obtained values of K and I_s mentioned above into the equation, the value of $\varDelta$ is obtained as shown by the dotted curve (i) in Fig. 5. As it shows, discrepancy of the order of a few degrees exists between theoretical and experimental results. Such a difference may be due to the higher order term of the anisotropy energy. Introducing a higher order term of the anisotropy energy

$$U=K_1\cos^2\theta+K_2\cos^4\theta,$$

the saturation value of maximum torque is expressed by

$$L_{max}=-(K_1+K_2),$$

at sufficiently strong field strengths. On the other hand, the position θ_m of maximum torque is given by

$$\theta_m=\pi/4+\varDelta+\varDelta',$$

$$\varDelta=K_2/(K_1+K_2),$$

$$\varDelta'=\frac{(A\cos 2\varDelta-4B\sin 4\varDelta)(A\cos 2\varDelta-\mathrm{B}\sin 4\varDelta)}{A\cos 2\varDelta-}$$

$$\frac{-(A\sin 2\varDelta+2B\cos 4\varDelta)^2}{4B\sin 4\varDelta}\cdot\frac{1}{HI_s}$$

with $A=-(K_1+K_2)$ and $B=-\frac{K_2}{2}$. The fittest curve (ii) shown in Fig. 5 has been obtained by choosing the values

$$K_1=-5.08\times10^5 \text{ and } K_2=0.65\times10^5 \text{ erg/cc.}$$

On the other hand, as the field strength decreases, the torque curve takes again a sinusoidal form as expressed by

$$L=A\sin 2\theta,$$

where A is a canstant. Such a fact is qualitatively explained by the fact that the magnetic moment of the specimen I lies along easy direction of magnetization by the application of very weak fields and is also proportional to the effective field strength in the direction: The magnetization in c-direction is expressed to be

$$I(H)\backsim H\cos\theta.$$

---

[*] The value of K/HI_s takes a value 0.18 at $H=10$ koe.

The torque value is expressed by

$$L = IH \sin\theta .$$

Eliminating I, from the above equations the following expression for L is obtained

$$L \backsim H^2 \sin 2\theta .$$

Hence in this case the torque curve approaches to a sinudoidal form, as is observed by the field strength of 2.4 koe.

The anisotropy constant is also calculable from the area between the magnetization curves along the direction of easy and difficult magnetization. Extrapolating the magnetization curves of the a-direction, we can evaluate the anisotropy constant to be about -5×10^5 erg/cc which agrees closely with the value K_1 estimated from the torque curve.

The anisotropy constant calculated basing on the dipole-dipole interaction is 3.66×10^5 erg/cc, which has the opposite sign as compared with the experimental value. Such discrepancy will be solved by considering the interaction energy between the spin and the orbital moment of chromium ion under the influence of bromine ions, especially that of the polarized bromine ions in the crystal lattice of this compound. A detailed calculation by Dr. Yamada of this Institute is now in progress.

Acknowledgements

The author wishes to express his cordial thanks to Professors T. Hirone and H. Watanabe for their encouragement and useful discussions. Also he wishes to express his hearty thanks to Drs. S. Maeda and N. Tsuya for their valuable discussions.

References

1) W. J. de Haas, B. H. Schultz and J. Koolhaas: Physica, **7** (1940) 57, H. J. Woltjer: Leiden Comm. (1925) 173 b.
2) W. N. Hansen and M. Griffel: J. Chem. Phys. **30** (1959) 913.
3) W. N. Hansen: J. Appl. Phys. **30** (1959) 304 S.
4) Wyckoff: *Crystal Structures.*
5) J. Kanamori: J. Phys. Chem. Solid **10** (1959) 87.
6) M. Yamada: *Private Communication.*

JOURNAL OF THE PHYSICAL SOCIETY OF JAPAN, Vol. 15, No. 9, SEPTEMBER, 1960

The Three-Level Gas Maser as a Microwave Spectrometer

By Tatsuo YAJIMA and Koichi SHIMODA

Department of Physics, Faculty of Science,
University of Tokyo, Tokyo

(Received June 4, 1960)

A method of microwave spectroscopy using three-level maser action is described, and some preliminary experiment on HDCO is given. A b-type transition, $3_{03}\leftarrow2_{12}$, which is connected with a a-type transition $2_{11}\leftarrow2_{12}$, has been definitely assigned by the observation of three-level maser action. Moreover, the weak transition, $3_{03}\leftarrow2_{12}$, was observed with very good signal to noise ratio by using the strong transition, $2_{11}\leftarrow2_{12}$, as a detecting transition. Theories of the three-level maser action in gases are also compared with experiment and shown to be in good agreement. Further applications of the three-level gas maser as a spectrometer as well as an amplifier are discussed.

§ 1. Introduction

The principle of the three-level maser was first proposed for a gas system by Bassov and Prokhorov in 1955¹⁾. The successful operation of the three-level maser was performed using paramagnetic crystals²⁾ at liquid helium temperature following the proposal by Bloembergen³⁾. One of the authors employed a three-level gas maser as a spectrometer to observe a direct l-type doubling transition of OCS at 12.78 Mc[4].

The three-level gas maser amplifier has the following advantages over the solid state maser. The gas maser is operated at room temperature or at dry-ice temperature rather than at liquid helium temperature. The maser material of gas may be filled in a sealed-off waveguide cell, without using a vacuum pump or a liquid nitrogen trap as in beam-type masers. The band-width of a gas maser is variable in a wide range from some ten kilocycles to more than 10 Mc simply by changing the pressure of the working gas, although larger pumping power is required as the band-width increases. Another feature of the gas maser is its feasibility for shorter waves than conventional microwaves, while the paramagnetic solid state maser will find it difficult to apply to higher frequencies, (say above 100 Gc). Because the traveling wave type gas maser employs a simple waveguide structure, it is more favorable for millimeter waves than the solid state traveling wave maser which employs an intricated structure. The noise temperature of the gas maser should generally be larger than that of the solid state maser but considerably lower than the room temperature, even though the temperature of the gas is high.

On the other hand, operation of the three-level maser as an amplifier or an oscillator becomes difficult at lower frequencies, because the absorption coefficient of spectral lines decreases in proportion to the square of the transition frequency. At higher frequencies, however, sufficient pumping power is not easily available. Therefore, the three-level gas maser has not yet been tested as an amplifier at the present stage.

However, besides the use as an amplifier or an oscillator, the three-level gas maser has some spectroscopic applications as mentioned before. As a microwave spectrometer, it has following advantages. First, the three-level gas maser can be used in obtaining concrete assignment of transitions in a complicated microwave spectrum. Secondly, a weak transition can be detected with much improved sensitivity by using the three-level maser action, if another strong transition which involves one common energy level with the former one is used as a detecting transition.

This paper describes a microwave double resonance experiment on HDCO molecule to demonstrate the behavior described above, including a study on the three-level maser action itself inherent in the gas system.

§ 2. Sensitivity of the Three-level Microwave Spectrometer

Suppose that a molecule has three energy levels as shown in Fig. 1. Two transitions, (1↔3) and (2↔3), are allowed and their frequencies are written as ν_p and ν_s, respectively. The three-level maser action may be considered as the change in intensity of one transition (2↔3) due to a relatively strong radiation corresponding to the other transition (1↔3). The transitions (1↔3) and (2↔3) are called the pumping transition and the signal transition respectively.

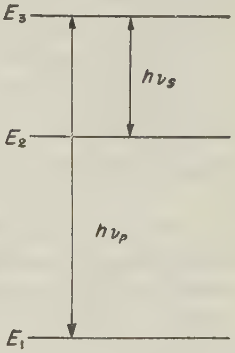

Fig. 1. A three-level system.

A semi-classical explanation of the three-level maser action based on a change in population difference alone is well known. The relaxation times between various levels may be asumed to be equal in a gaseous state, and $h\nu_p$, $h\nu_s \ll kT$ where T is the temperature of the gas. Then, the relative change of absorption coefficient at the center of the transition (2↔3) due to the pumping radiation of frequency ν_p can be derived from Eq. (6) in reference (5). The absorption coefficient α_s* of the transition (2↔3) under pumping radiation is expressed in the form

$$\frac{\alpha_s}{\alpha_{s0}}=\frac{1+2w(2-r)}{1+4w} \tag{1}$$

$$r=\nu_p/\nu_s$$

$$w=\frac{2\pi|\mu_p|^2P_0}{3v_gh^2(\Delta\nu)^2S}$$

---

* For the net induced emission of power, α_s is negative.

where α_{s0} is the absorption coefficient without pumping, w the usual saturation parameter for the plane polarized wave, P_0 the pumping power, μ_p the dipole matrix element for the transition $(1\leftrightarrow 3)$, $\Delta\nu$ the half half-width of the line, v_g the group velocity of the pumping radiation in the waveguide, and S the cross-sectional area of the waveguide.

The semi-classical theory gives a good approximation for most solid state masers, unless pumping power is not very large, because $T_1 \gg T_2$ holds usually, where T_1 and T_2 are the longitudinal and transverse relaxation times respectively. However, in the case of a gas system where the relaxation occurs through molecular collisions $(T_1 \approx T_2)$, the semi-classical treatment may not be correct. The quantum mechanical treatment of the three-level maser has already been given by A. Javan[5] and A. M. Clogston[6]. The ratio of the gas absorption coefficient with and without pumping can also be derived from Eq. (21) in reference (5).

$$\frac{\alpha_s}{\alpha_{s0}}=\frac{1+w(4-3r)}{(1+4w)\,(1+w)} \tag{2}$$

Eqs. (1) and (2) will be compared with experimental results in the next section. Notice that in some cases Eq. (1) gives larger values than Eq. (2), and vice versa in other cases.

Now, let us consider the sensitivity of a three-level gas maser for spectroscopic purposes. When $\nu_p \gg \nu_s$, saturation between states 1 and 3 by a strong radiation results in an enormous increase in the population difference between states 2 and 3, and hence the absolute value of absorption coefficient at the signal frequency increases in a large amount. A semi-classical treatment of the sensitivity of this type of three-level spectrometer and an experimental study on OCS has already been reported[4]. A quantum-mechanical evaluation for the case when $\nu_p=24{,}355.50$ Mc and $\nu_s=12.78$ Mc, at the pumping power level of $w=\frac{1}{2}$* gives

$$|\alpha_s|/\alpha_{s0}=630$$

An increase of sensitivity by such a large factor enables one to observe low frequency transition of the molecule.

Next, let us consider a case when both ν_p and ν_s are in the microwave frequency range. Then the ratio ν_p/ν_s is not very large so that the method described above is not effective. For example, taking values of $\nu_p/\nu_s=10$ and $w=\frac{1}{2}$, we have only

$$|\alpha_s|/\alpha_{s0}=2.7$$

However, there is another method of using the three-level maser as a sensitive spectrometer. Consider a case when the transition probability between states 1 and 3 is much smaller than that between states 2 and 3. Accordingly the absorption coefficient of the gas in its thermal equilibrium at the frequency ν_p is much smaller than that at the signal frequency ν_s. A change in absorption coefficient of the strong transition $(2\leftrightarrow 3)$ caused by the weak pumping transition $(1\leftrightarrow 3)$ may be observed in order to detect the weak transition $(1\leftrightarrow 3)$. The increase of sensitivity which is obtained by this method is calculated as follows.

The change in absorption coefficient, $|\Delta\alpha_s| = |\alpha_s-\alpha_{s0}|$, is assumed to be observed by a usual waveguide-type spectrometer. The signal to noise ratio of a spectral line with the absorption coefficient α is proportional to $\alpha\sqrt{P}$, were P is the microwave power. The signal to noise ratio increases with the input power P, but the saturation effect and the increase of detector noise put a limit for input power. Then the maximum available signal to noise ratio of the line turns out to be proportional to approximately $\alpha^{1\cdot 0\sim 0\cdot 5}$.

Therefore, a direct observation of the transition $(1\leftrightarrow 3)$ may be assumed to exhibit the signal to noise ratio proportional to the absorption coefficient in thermal equilibrium, α_{p0}, while the change of absorption at the frequency ν_s can be observed with the signal to noise ratio proportional to $|\Delta\alpha_s|$, if the sensitivity of the spectrometer is the same at the frequencies ν_p and ν_s. For the case of interest when $\alpha_{p0} \ll \alpha_{s0}$, the increase of the signal to noise ratio is quite large since $|\Delta\alpha_s|/\alpha_{p0} \gg 1$, so long as the sufficient power at the frequency ν_p is used. A measure of the increase of sensitivity is obtained from Eq. (2) as

$$\frac{|\Delta\alpha_s|}{\alpha_{p0}}=\frac{w(3r+1+4w)}{(1+4w)(1+w)}\,\frac{\alpha_{s0}}{\alpha_{p0}} \tag{3}$$

---

* This corresponds to $|y|^2\tau^2=\frac{1}{2}$ in ref. (5), and is an approximate condition for maximum power of net induced emission, when $\nu_p \gg \nu_s$

For example, when $w=\frac{1}{2}$, one obtains

$$\frac{|\Delta\alpha_s|}{\alpha_{p0}}=\frac{1+r}{3}\frac{\alpha_{s0}}{\alpha_{p0}}\gg 1$$

Because the microwave spectrometer is generally more sensitive at lower frequencies, the actual increase of sensitivity will be somewhat larger than the value given by Eq. (3).

It seems worth noticing that the sensitive detection of weak lines by such a method can also be applied for a case when $\nu_p < \nu_s$ or $r < 1$. Now the lower frequency transition is detected by the change in absorption of the higher frequency transition. It is quite obvious that the method described above is not restricted for the level system with $E_3 > E_2 > E_1$, but can be applied generally for any three-level systems if one weak transition is connected to another strong transition through a common level. Three-level systems, where the levels are $E_2 > E_3 > E_1$, $E_1 > E_2 > E_3$ and in other cases, are essentially the same as that described above.

The three-level maser detector for ultra-microwaves proposed by one of the authors[7] is also closely related to the present case. However, the three-level maser spectrometer of this type differs from the three-level maser detector, since the former is intended to detect weak absorption using a large power at the frequency ν_p, while the latter is to detect a small power using the strong absorption at the pumping frequency.

§ 3. Experimental Results on HDCO

A number of three-level systems can be found in the energy levels of molecules. A three-level gas maser of formaldehyde-d_1, HDCO, was experimentally investigated for spectroscopic purposes. The microwave spectrum of HDCO has been studied in our laboratory[8),9)] and a fairly complete report by T. Oka will be published in near future. Since the molecular axis of HDCO differs from the inertia axis by some angle, the component of electric dipole moment along the b-axis enables one to observe b-type transition which are absent in H_2CO and D_2CO. In order to use the b-type transition for the study of molecular structure a search for a b-type transition, $3_{03} \leftarrow 2_{12}$, was carried out, but resulted in a doubtful assignment because the molecular constants determined from a-type transitions were not accurate enough to discriminate spectral lines of other rotational states or those due to impurities. This R^b-type transition, $3_{03} \leftarrow 2_{12}$, constitute a three-level system with a strong Q^a-type transition, $2_{11} \leftarrow 2_{12}$, as shown in Fig. 3. Therefore a definitive assigning of the R^b-type transition was intended by the effect of its pumping action on the Q^a-type transition, $2_{11} \leftarrow 2_{12}$. Another purpose of the experiment on this level system was to investigate the sensitivity consideration of the three-level spectrometer as described in § 2. There is a large difference of absorption coefficient between two allowed transitions, since the component of dipole moment on the b-axis is much smaller than that on the a-axis. Namely, by using the strong transition, $2_{11} \leftarrow 2_{12}$, as a detecting transition, the weak transition, $3_{03} \leftarrow 2_{12}$, was expected to be observed with better signal to noise ratio.

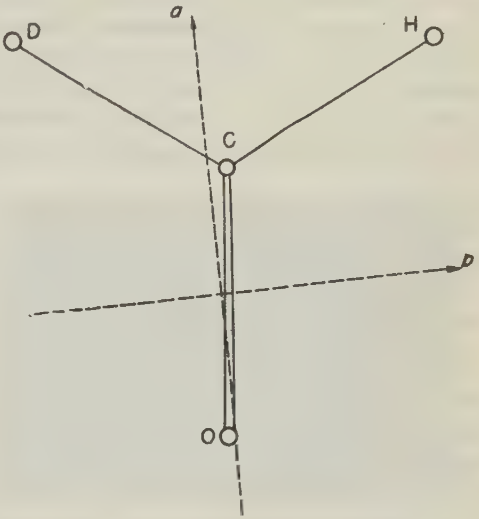

Fig. 2. Molecular structure of HDCO. a and b represent the principal axes of inertia.

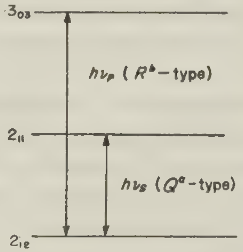

Fig. 3. A three-level energy diagram of HDCO

The frequencies, the components of electric dipole moment, the squares of the dipole matrix elements, and the calculated absorption coefficients in thermal equilibrium at room temperature of the two transitions, $3_{03}\leftarrow 2_{12}$ and $2_{11}\leftarrow 2_{12}$, are listed in Table I.

Table I. A set of three-level transitions in HDCO

	pumping	signal
transition	$3_{03}\leftarrow 2_{12}$	$2_{11}\leftarrow 2_{12}$
frequency (Mc)	34916.4	16038.06
component of the dipole moment (Debye)	$\mu_b=0.21$	$\mu_a=2.30$
square of the dipole matrix element (Debye²)	0.0095	0.88
absorption coefficient* (cm⁻¹)	1.9×10^{-6}	3.7×10^{-5}

* calculated under the assumptions of $\Delta\nu=10$ Mc/mmHg and 100% purity.

From the values in Table I the expected increase of sensitivity, $|\Delta\alpha_s|/\alpha_{p0}$, in observing the transition, $3_{03}\leftarrow 2_{12}$, was calculated as a function of P_0 and $\Delta\nu$ as shown in Fig. 4. It may be seen from the figure that one can easily obtain a large increase of sensitivity by the use of the pumping power of the order of several ten milliwatts which is easily attainable by a commercially available klystron.

Fig. 5 shows a block diagram of the experimental setup of a three-level spectrometer. The absorption cell is made of a K-band waveguide of 1 meter length, with the cross section of 10.7 mm×4.3 mm I.D., in which the usual Stark electrode is inserted. In order to increase the pumping effect, it is preferable to use the waveguide of smaller cross-sectional area, as long as the signal frequency is above the cut-off frequency of the waveguide.

Gaseous sample was obtained by heating powdered paraformaldehyde-d_1 of about 90% purity. The gas pressure must be low to reduce the line-width so as to increase the pumping effect. But the line-width is limited by the broadening due to the wall collision

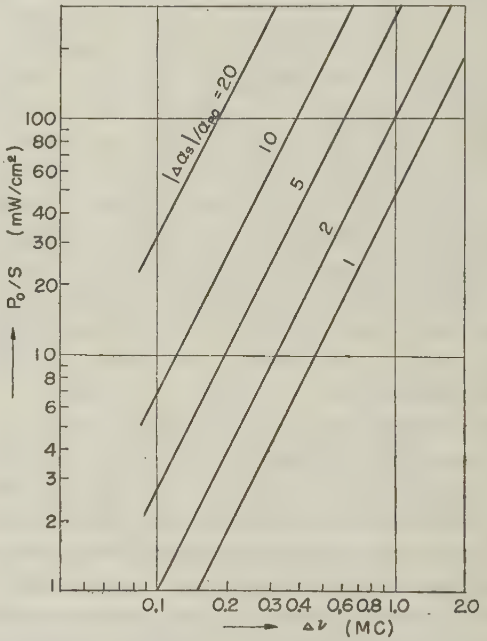

Fig. 4. Calculated increase of sensitivity, $|\Delta\alpha_s|/\alpha_{p0}$, as a function of line-width, $\Delta\nu$, and pumping power, P_0/S, in observing the transition $3_{03}\leftarrow 2_{12}$ of HDCO by the three-level maser technique.

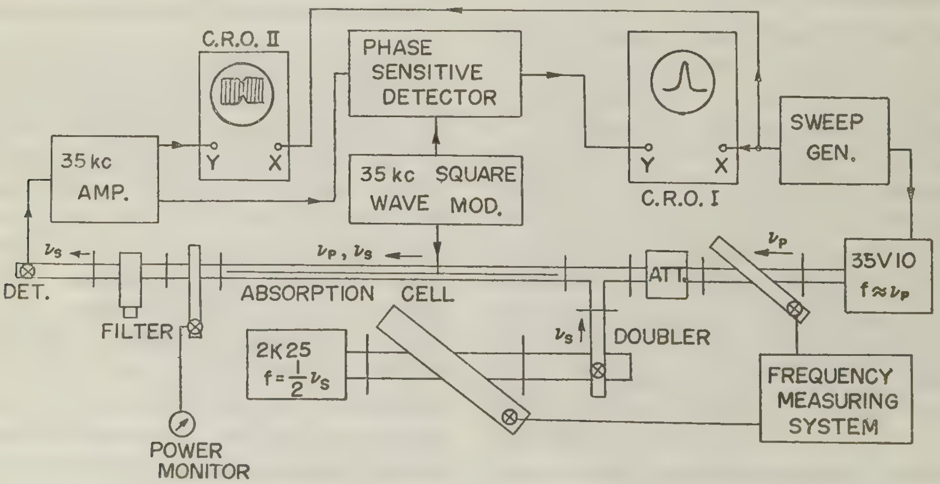

Fig. 5. Block diagram of the three-level microwave spectrometer.

and the Doppler effect which are calculated as 19 kc for the cell used and 39 kc for the frequency, 35 Gc, respectively.

The signal power was supplied by a crystal doubler driven by a 2K25 klystron, and the strong pumping power was delivered by a 35V10 milimeter-wave klystron. In order to prevent the pumping power from entering the detector, a filter made of a rectangular cavity with $Q \approx 800$ is placed between the cell and the detector. The pumping power is monitored by a crystal detector in an auxiliary waveguide.

The three-level maser action can be observed by two methods. For one case, the signal frequency is fixed and the pumping frequency is swept; and for the other case, the signal frequency is swept. For the spectroscopic purpose to detect the pumping transition, the former method is appropriate. The experimental study was carried out in this case. A square-wave Stark modulation at a frequency of 35 kc was employed to observe the change of absorption at the signal frequency due to pumping. The signal frequency was fixed at the center of the line, ν_s, by monitoring a maximum amplitude of the 35 kc amplifier output on the screen of C.R.O.–II. An automatic frequency control of the signal frequency might be desirable, but it was not necessary for a short time observation.

Now, the three-level maser action was observed, when the pumping frequency was swept in a certain range including the correct frequency of the transition, $3_{03} \leftarrow 2_{12}$. This was explicitly displayed on the screen of C.R.O.–II as shown in Fig. 6, where the horizontal axis represents the change of pumping frequency. The dip in the figure which indicates the decrease of absorption coefficient at the center of the signal transition, $2_{11} \leftarrow 2_{12}$, occurs at the expected frequency of 34916.4 Mc. Thus the *b*-type transition, $3_{03} \leftarrow 2_{12}$, has been definitely assigned. The dip increased, of course, with decreasing linewidth and with increasing pumping power. About 80% decrease of the absorption coefficient could be obserbed with the pumping power of 60 milliwatts. With more power, one might observe the induced emission.

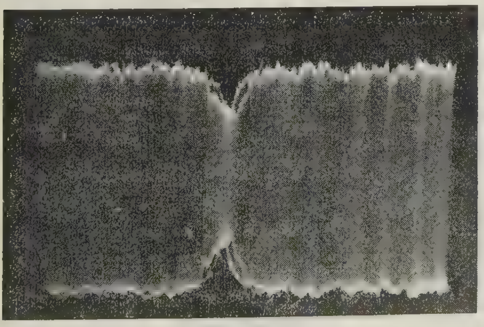

Fig. 6. Three-level maser action in HDCO displayed on an oscilloscope screen. The ordinate shows absorption intensity at the center of the transtion $2_{11} \leftarrow 2_{12}$, and the abscissa represents the change of pumping frequency including the transition frequency of $3_{03} \leftarrow 2_{12}$.

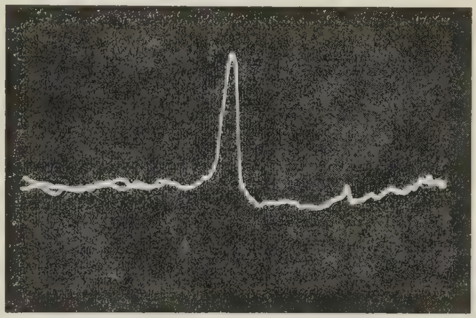

Fig. 7. Spectral line of the pumping transition, $3_{03} \leftarrow 2_{12}$, of HDCO detected by the change of the signal transition, $2_{11} \leftarrow 2_{12}$.

After a phase sensitive detector with a low pass filter, a spectral line was obtained with a very good signal to noise ratio on the screen of C.R.O.–I as shown in Fig. 7. This is the pumping transition, $3_{03} \leftarrow 2_{12}$, detected by the absorption change of the signal transition, $2_{11} \leftarrow 2_{12}$. The signal to noise ratio of the $3_{03} \leftarrow 2_{12}$ line obtained by this method was found to be better by about 10 times than that observed directly in the same absorption cell with a conventional method. This is considered as a verification of the sensitivity of the three-level spectrometer.

The three-level maser action was also observed by the other method with the fixed pumping frequency and the swept signal frequency. However, the stable measurement was difficult because of the frequency instability of the klystron at the pumping frequency.

Now, the theoretical formulae (1) and (2) can be compared with experimental results by plotting α_s/α_{s0} versus P_0 or $\Delta\nu$. The experimental values α_s/α_{s0} can be obtained immediately from Fig. 6, and shown in Fig. 8. The line-width, $\Delta\nu$, was varied by changing the gas pressure and the pumping power, P_0, was constant to nearly 60 milliwatts. Theoretical curves were calculated for the power and $v_g = 0.84\,c$. The agreement between the quantum mechanical theory and the experiment seems to be good within the experimental accuracy. It is noted that the curve of the semi-classical theory deviates considerably from the observed values.

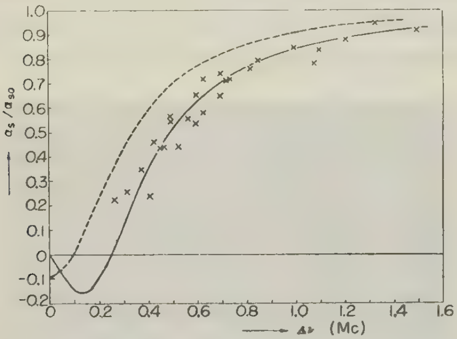

Fig. 8. Relative change of absorption coefficient at the center of transition $2_{11} \leftarrow {}_{12}$ by the pumping of transition $3_{03} \leftarrow 2_{12}$ in HDCO.

× observed point for $P_0 = 60$ mW
- - - - theoretical curve of Eq. (1) (semi-classical)
—— theoretical curve of Eq. (2) (quantum-mechanical)

§ 4. Concluding Remarks

The application of three-level maser technique to microwave spectroscopy was discussed and a successful experiment on HDCO molecule was described. There are many three-level systems of molecules for which the present technique can be applied, because for spectroscopic purposes the method is not restricted to the level scheme of Fig. 1 as mentioned before. For the cases of more complicated spectra where the hyperfine structure and the effect of internal motions are present, or the isotopically substituted molecules and some unknown impurities are present among the molecules under study, the method described here may also be applied effectively in identifying some paticular lines.

To use the three-level system of gas as an amplifier, the required conditions are, of course, much more severe. A K-type doubling transition of an asymmetric top molecule may be used at the signal and a transition of $\Delta J = \pm 1$ as pumping for that purpose. Several examples which are estimated to exhibit a relatively intense induced emission power with the pumping frequency of below 100 Gc are listed in Table II.

Further investigation on the quantum mechanical behavior of the three-level maser needs stronger pumping. Experimental studies on three-level systems of other molecules are in progress.

Table II. Three-level systems in which appreciable net induced emission is expected.

	(1)	(2)	(3)	(4)	(5)
molecule	HDS	HDO	HDCO	HDCO	HDCO
pumping	$2_{2,0} \leftarrow 3_{0,3}$	$4_{3,1} \leftarrow 5_{2,4}$	$3_{0,3} \leftarrow 2_{1,2}$	$7_{1,6} \leftarrow 6_{2,5}$	$12_{2,10} \leftarrow 11_{3,9}$
signal	$2_{2,0} \rightarrow 2_{2,1}$	$4_{3,1} \rightarrow 4_{3,2}$	$2_{1,1} \rightarrow 2_{1,2}$	$6_{2,4} \rightarrow 6_{2,5}$	$11_{3,8} \rightarrow 11_{3,9}$
ν_p* (Mc)	28.8×10^3	62.4×10^3	34916.4	25.6×10^3	27.1×10^3
ν_S (Mc)	11283.83	5702.78	16038.06	8922.6	5702.6
$-\alpha_{s,\max.}$ (mW/cm^2)	4.6×10^{-6}	1.4×10^{-5}	6.0×10^{-6}	4.5×10^{-6}	3.5×10^{-6}
$P_{0,\mathrm{opt.}}$ (mW/cm^2)	980	4.6	87	140	120

* The values of ν_p have not been measured excepting the case of (3).

$-\alpha_{s,\max}$ is the maximum intensity of net induced emission expressed as negative absorption coefficient at room temperature; and $P_{O,\mathrm{opt}}$ is the optimum pumping power of the plane wave per unit area giving maximum net induced emission when the line-width $\Delta\nu$ is 100 kc.

The authors are indebted to Mr. T. Oka for his helpful discussions and informations on the microwave spectrum of HDCO.

References

1) N. G. Bassov and A. M. Prokhorov: J. Exp. Theor. Phys. USSR **28** (1955) 249
2) See, for example, a review, J. Weber: Rev. Mod. Phys. **31** (1959) 681
3) N. Bloembergen: Phys. Rev. **104** (1956) 324

4) K. Shimoda: J. Phys. Soc. Japan **14** (1959) 954
5) A. Javan: Phys. Rev. **107** (1957) 1579
6) A. M. Clogston: J. Phys. Chem. Solids **4** (1958) 271
7) K. Shimoda: J. Phys. Soc. Japan **14** (1959) 966
8) H. Hirakawa, T. Oka and K. Shimoda: J. Phys. Soc. Japan **11** (1956) 1207
9) K. Kondo, H. Hirakawa, A. Miyahara, T. Oka and K. Shimoda: J. Phys. Soc. Japan **15** (1960) 303

JOURNAL OF THE PHYSICAL SOCIETY OF JAPAN, Vol. 15, No. 9, SEPTEMBER 1960

Monte Carlo Calculations of Motion of Electrons in Helium

By Tomizo ITOH and Toshimitsu MUSHA
Electrical Communication Laboratory, Musashino-shi, Tokyo

Monte Carlo calculations are performed with an electronic computor to investigate the behavior of electrons in helium gas in a uniform electric field. The ionization and excitation coefficients and the drift velocities of electrons in helium for $E/p_0=40$, 80 and 160 v/cm/mmHg are obtained. The velocity distributions of electrons are also calculated.

§ 1. Introduction

For an investigation of an electrical discharge in a gas, it is important to know the behavior of electrons in an electric field. The fundamental quantities such as ionization and excitation coefficients and the velocity distribution of electrons were calculated approximately by other workers only when an electric field is uniform and/or weak[1)2)3)]. The present work is performed in the hope to offer a new method of calculation applicable to the case of strong and/or non-uniform electric fields which often appear in actual discharges in gases.

The essential feature of the gas discharge phenomena consists in the motion of charged particles and the mutual interaction among the particles, i.e., electrons, ions, and neutral molecules. When the charged-particle density is very low compared with that of the gas molecules, only two-body collisions between an electron and a neutral molecule become important. In such a case, if we take one electron in the gas and trace its orbit with an electronic computing machine considering the influence of an electric field and electron-molecule collisions, information on the fundamental quantities of the discharges may be obtained.

In this paper a Monte Carlo method is presented for calculating the motion of electrons in a static uniform electric field; and its application to helium is described.

§ 2. Method of the Calculation

In a uniform electric field E an electron moves on a parabolic orbit until it collides with a gas molecule. The kinetic energy which the electron gains in the electric field is lost in collisions. In the case of large E/p_0 (p_0 is the gas pressure at 0°C), the rate of energy lost in elastic collisions is negligible compared with that in inelastic ones[4)]. We assume, therefore, that in an elastic collision an electron is scattered by a gas molecule with its kinetic energy unchanged. On the other hand, when it excites or ionizes a gas molecule in a collision it loses a certain amount of energy corresponding to the excitation or the ionization potential of the gas molecule respectively, changing its direction of motion. In the latter case another electron is deprived of the gas molecule and a part of the energy of the primary electron is shared with the secondary one. After the ionizing collision either of two electrons may be trace thereafter. Consequently we select one arbitrarily here.

As to the angle of scattering, it is assumed to distribute isotropically in any kind of collision. This assumption has to be introduced from the memory capacity of our computing machine.

2.1 *Decision of the Collision Occurrence*

In a Monte Carlo calculation dealing with a problem of neutron passage in a medium, a free path length of a neutron is determined by a simple exponential law with a random number since the particle does not change its kinetic energy in the flight. Regarding an electron accelerated in an electric field, however, another method must be employed to decide a collision occurrence because the collision cross section of a gas molecule for an electron varies with the electron energy. The method adopted here is as follows:

The probability P that an electron collides with gas molecule in the small distance dx along its path is expressed as

$$P=dx/\lambda, \tag{1}$$

where λ is the mean free path of the electron dependent on the electron energy. Suppose that the orbit of an electron in an electric field is divided into small sections, then the probability that the electron collides with gas molecules in each section can be calculated from λ. On the contrary when the probability has been given previously the length of each section l is computed from Eq. (1) provided $p \ll 1$. The smaller l is, the longer the calculation time becomes while we have better approximation. Hence we give the probability 0.1 to each section so that $l=0.1\lambda$ in approximation. The mean free path λ of an electron in helium at 0°C and 1 mmHg is calculated for any electron energy from the formula which is a good approximation to the observed values[5]. In every section, whether the electron collides or not is decided by a pseudo-random number q provided by a subroutine (taking the middle part of the square of the preceding random number) stored in our computing machine. Since q takes a value between 0 and 1 arbitrarily the probability that q falls on the interval from 0 to 0.1 is equal to the collision probability of the electron in each section. Consequently when q falls between 0 and 0.1 the electron is judged to collide with a gas molecule in the section. If a collision does not occur after such a decision, the length of the next section is calculated, and a decision of collision occurrence will be given again. The procedure described above is repeated unitil a collision occurs.

2.2 *Calculation of Particle Parameters*

The coordinate axis z being set antiparallel to the electric field, the state of the motion of an electron is specified by its speed V, the direction cosine $\cos\theta$, where θ is the angle made by the line of flight with the z axis, and the time t. If an electron is in a state (V, $\cos\theta$, z, t) it will take, after a flight along the orbit by a length l, a new state (V', $\cos\theta'$, $z+\Delta z$, $t+\Delta t$). These parameters are connected by the following relations:

$$V'\sin\theta'=V\sin\theta \tag{2}$$

$$mV'\cos\theta'=mV\cos\theta+eE\Delta t \tag{3}$$

$$\frac{1}{2}mV'^2=\frac{1}{2}mV^2+eE\Delta z \tag{4}$$

where m and $-e$ are the mass and the electric charge of the electron, respectively; Δz is the projection of l on the z axis. The exact expression of Δz as a function of l is complicated containing terms of a logarithm and square roots. The calculation of such terms with the computing machine requires relatively long time and, moreover, Δz must be calculated in each small section, so that it is suitable to be expressed approximately as (see Fig. 1)

$$\Delta z=l\cos\theta. \tag{5}$$

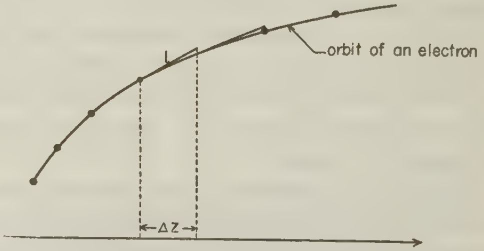

Fig. 1. Illustration of the tangential approximation. The length l of the electron flight is measured on a tangent at each dividing point of the orbit of an electron.

2.3 *Decision of the Kind of Collisions*

Whenever a collision occurs the kind of collision has to be decided. In the present work for helium the electron-atom collisions are classified in four kinds, i.e., that of electric, ionizing, exciting to the metastable state 2^3S_1, and exciting to the other levels. The three kinds of inelastic-collision probabilities P per 1 cm of the electron flight are calculated for

Table I. Values of the constants in eq. (5) for three kinds of inelastic collisions.

Kind of collisions	A (ev^2)	B (eV·cm)$^{-1}$	C (cm^{-1})	ε_0 (ev)
Excit. to the 2^3S_1 level	2.50×10^{-1}	1.09×10^{-1}	3.11×10^{-2}	19.8
Excit. to the other levels	1.85×10^{3}	6.88×10^{1}	0	19.0
Ionization	4.90×10^{3}	1.72×10^{2}	0	24.46

any electron energy ε according to the formulas which approximate the experimental results[6] up to the electron energy of 100 eV. These formulas are expressed in the form

$$P=\frac{B(\varepsilon-\varepsilon_0)}{A+(\varepsilon-\varepsilon_0)^2}+C \tag{6}$$

where A, B, C and ε_0 are constants dependent on the kind of collision. Table I lists these constants for helium. In Fig. 2 the experimental data and the values calculated from Eq. (6) for the ionizing collision are shown.

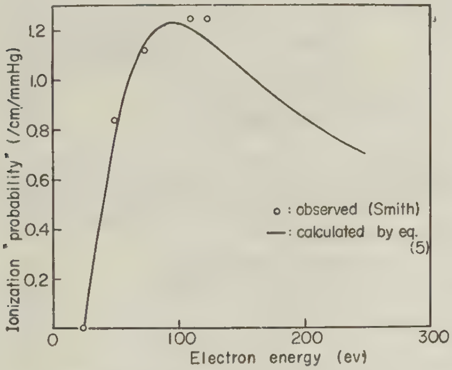

Fig. 2. Ionization "probability" of electrons in helium.

Table II. Excited levels of the helium atom with relatively large excitation cross sections.

State	Excitation energy (ev)
2^1S_0	20.6
2^3P_1	20.9
2^1P_1	21.2
3^1P_1	23.1
Average	21.45

The values of energy loss of an electron in an exciting collision in helium are 19.8 ev to the metastable 2^3S_1 level and 21.4 ev to the other excitation levels; the latter is the average value over four levels which have relatively large cross sections (Table II). In an ionizing collision the energy loss is not definite since a part of the energy of the primary electron is shared with the secondary one. The energy distribution of electrons produced in ionizing collisions of 100 ev incident electrons with helium were measured by Goodrich[7] (Fig. 3). Such a distribution is assumed to hold in the other incident electron energy. Immediately after an ionizing collision the energy of an electron is determined by a random number submitting to such a distribution.

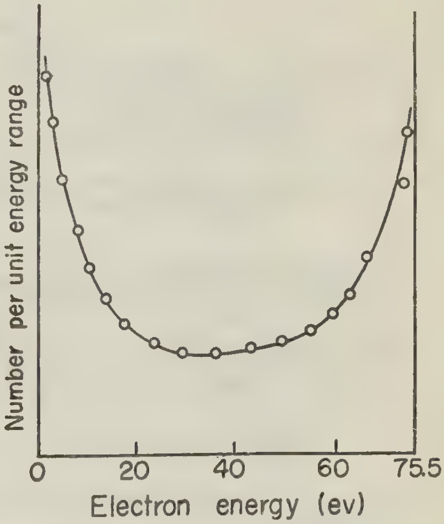

Fig. 3. Energy distribution of electrons produced in ionizing collisions of 100 volt electrons with helium as observed by Goodrich.

As previously stated when a random number q takes any value between 0 and 0.1 we consider that an electron collides with a gas molecule. If the electron energy is less than the lowest excitation energy (19.8 ev of the 2^3S_1 level) it must be an elastic collision. When the electron has enough energy to excite this level the excitation-collision probability P_{met} to this level in this small section l is calculated from Eq. (6) and compared with q. In case $q\leq P_{\text{met}}$ occurs an excitation to this level.

When $q>P_{\rm met}$ the excitation-collision probability $P_{\rm exc}$ to the other levels is to be calculated provided that the electron energy is more than 21.45 ev, and this kind of excitation is considered to occur for $q \leq P_{\rm net}+P_{\rm exc}$. Contrarily when the electron energy is less than 21.45 ev it must be an elastic collision. The similar process for ionization collision is repeated $q>P_{\rm met}+P_{\rm exc}$. If we have $q>P_{\rm met}+P_{\rm exc}+P_{\rm ion}$, where $P_{\rm ion}$ is the probability of ionizing collision in the section, this means an elastic collision (see Fig. 4).

Thus decided the kind of collision, the speed V'' and the direction cosine $\cos\theta''$ after the collision are computed from the angle of scattering and the loss of the electron energy. The scattering angle (and also the electron energy in case of an ionizing collision) is determined using another random number.

2.4 *Velocity Distribution of Electrons*

As mentioned above, the motion of an electron is traced throughout the calculations. This electron can be taken arbitrarily among the ensemble of electrons under the same physical conditions. The values of the velocity of one electron are sampled in every constant time interval τ in the process of calculation. As the whole system may be considered in stationary state, this sequence of samples would be taken as an ensemble and, the ergodicity of the random process in the system being assumed, this new ensemble is statistically equivalent to the original one. Based on such considerations the velocity distributions of electrons are obtained. Fig. 4 shows the flow chart of the calculations.

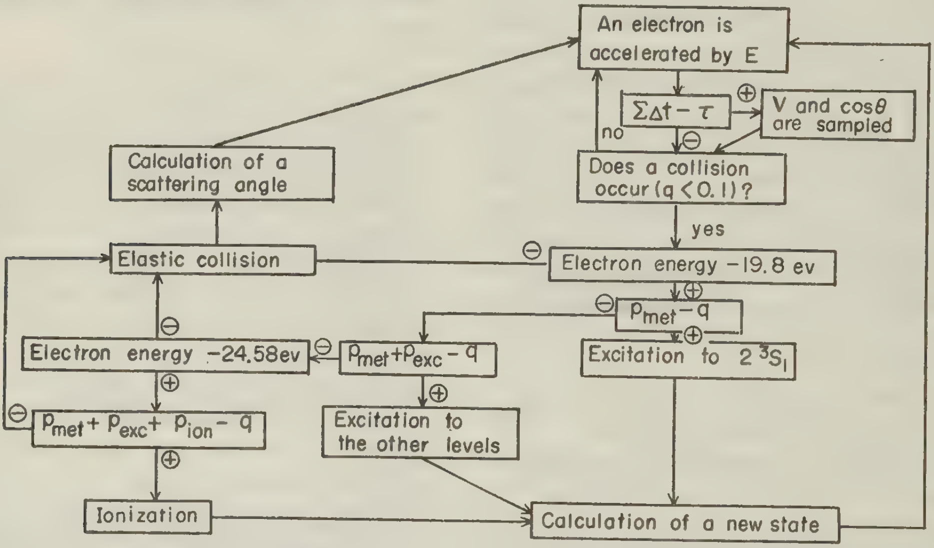

Fig. 4. Flow chart of the Monte Carlo calculation of the motion of an electron in an electric field.

§ 3. Results

As the calculation proceeds, the following data are punched out as the outputs of the computing machine.

(a) V and $\cos\theta$ sampled in the constant time interval τ.

(b) z and t at which an inelastic collision occurs with suitable marks to distinguish the kind of them.

Appropriate statistical treatments of data (a) yield the velocity distributions of electrons. The drift velocities, and the ionization and the excitation coefficients of electrons are derived from the data (b) in the following manner.

The plots of z versus t are on a nearly straight line whose slope z/t gives the drift velocity of an electron. The ionization coefficient α is defined as

$$\alpha = \lim_{z\to\infty} N_i(z)/z \tag{7}$$

where $N_i(z)$ is the number of ionization collisions that occur during the electron flight from $z=0$ to $z=z$. Calculated values of $N_i(z)/z$ versus z in the case of $E/p_0=80$ v/cm/mmHg are shown in Fig. 5. As seen in this figure values of $N_i(z)/z$ scatter widely for small z's, tending to converge to a certain value as z increases. In the present work we take as α a value of $N_i(z)/z$ at the largest z, whose deviation from the limiting value would be within few percents. The excitation coefficients are treated in the same way.

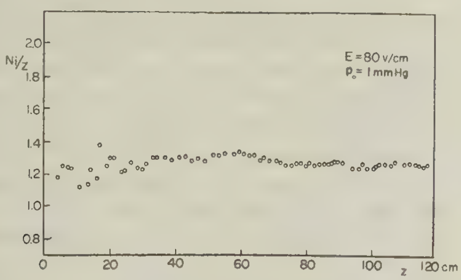

Fig. 5. The number of ionizations per *cm* averaged over the distance z of the electron drift.

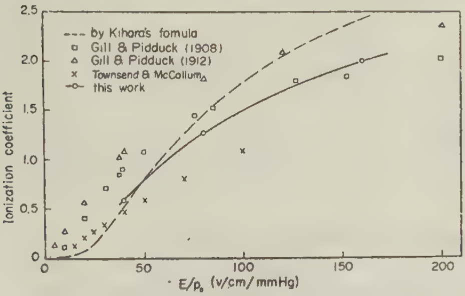

Fig. 6. Ionization coefficients of electrons in helium *vs*. E/p_0 with the observed and calculated values by other workers.

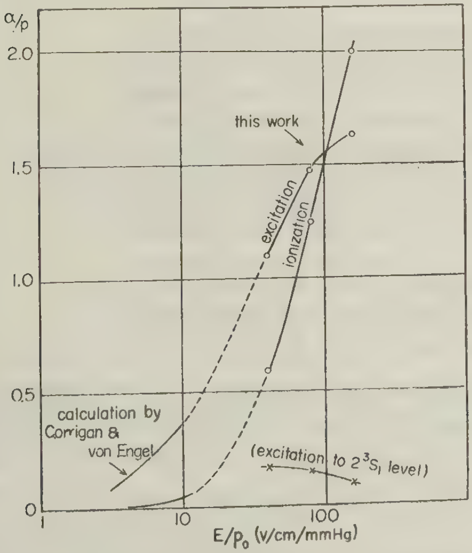

Fig. 7. Coefficients of ionization and excitation. The excitation coefficient to the 2^3S_1 metastable level is plotted separately, and the results calculated by Corrigan & von Engel for 10 of E/p_0 are also plotted which are connected with the results of this work by broken lines.

The ratios of α to the gas pressure p_0 are plotted against E/p_0 in Fig. 6. In this figure the experimental values by other workers[8] and calculated values from Kihara's[3] formula (9.5) are shown. In Fig 7 the coefficients of ionization and excitation to the metastable level 2^3S_1 and to the other levels are shown.

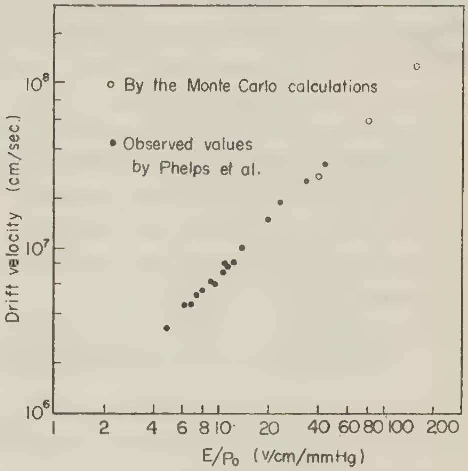

Fig. 8. Drift velocity of electrons in helium.

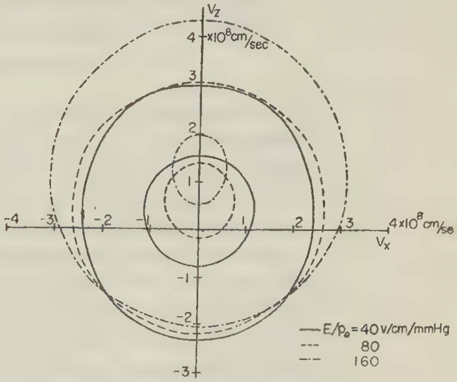

Fig. 9. Velocity distributions of electrons in helium. The inner contour denotes the density three times as much as that of the outer one.

For comparison the calculated values by Corrigan and von Engel[2] in the low E/p_0 region making use of the energy distributions of electrons calculated theoretically by Smit[9] are also illustrated in this figure. The excitation coefficient of helium in high E/p_0 has not yet been calculated or measured by other workers. The drift velocity of an electron in helium is plotted in Fig. 8 against E/p_0 together with the observed values by Phelps et al[10]. The drift velocity increases nearly proportionally to E/p_0. Fig. 9 is the velocity distributians of electrons each of which is compiled from about 15000 data.

We are deeply indebted to Dr. K. Takatsu for his kind advices and encouragements throughout this investigation. We also wish to thank Dr. Z. Kiyasu and Dr. T. Shindo for many fruitful discussions and suggestions, and to members of the electronic computor group in our laboratory for their technical assistances.

References

1) I Abdelnabi and H. S. W. Massey: Proc. Phys. Soc. **A, 66** (1953) 288.
2) S. J. B. Corrigan and A. von Engel: Proc. Phys. Soc. **72** (1958) 786
3) T. Kihara: Rev. Mod. Phys. **24** (1952) 45.
4) M. J. Druyvesteyn and F. M. Penning: Rev. Mod. Phys. **12** (1940) 87.
5) C. E. Normand: Phys. Rev. **35** (1930) 1217.
6) P. T. Smith: Phys. Rev. **36** (1930) 1297. H. Maier-Leibnitz: Z. Phys. **95** (1935) 489. Hdb. d. Phys. **36** (1956) 360. G. J. Schulz and R. E. Fox. Phys. Rev. **106** (1957) 1179.
7) M. Goodrich: Phys. Rev. **52** (1937) 259.
8) E. W. B. Gill. and F. B. Pidduck: Phil. Mag. **16** (1908) 280. ibid. **23** (1912) 837. J. S. Townsend and S. P. McCallum: Phil Mag **17** (1934) 678.
9) J. A. Smit: Physica **3** (1936) 543.
10) A V. Phelps, J. L. Pack and L. S. Frost: Phys. Rev. **117** (1960) 470.

JOURNAL OF THE PHYSICAL SOCIETY OF JAPAN, Vol. 15, No. 9, SEPTEMBER, 1960

Ion Optics in Long, Multistage Accelerator Tubes

By Masateru SONODA, Akira KATASE, Masao SEKI and Yoshihisa WAKUTA

Department of Nuclear Engineering, Faculty of Engineering,
Kyushu University, Fukuoka

(Received May 23, 1960)

The recurrence formulae for the cardinal elements of a multistage accelerator tube are derived. The calculated results for an equidiameter cylinder lens obtained by the consecutive applications of the formulae are not so different from those obtained by assuming a uniform acceleration and still show the appreciable deviations from the experimental data. The errors would, therefore, become large, unless the experimental values are used for the cardinal elements of an individual accelerating lens on which the calculation for multistage accelerator tube is based. As an example, the cardinal elements for a 12-stage accelerator tube is shown The comparison with those obtained by the assumption of a uniform acceleration shows that the latter results are not satisfactorily accurate for such a multistage accelerator.

§ 1. Introduction

The rectilinear multistage accelerator made up of many cylindrical accelerating electrodes has been used frequently because of its simplicity of mechanical construction. The ion optics for this case has, however, been investigated, by assuming that the electric field in the accelerator is uniform,[1)2)] or by the consecutive multiplications of lens matrices.[3)] In the former method, the results deviate considerably from practice, if the appreciable lengths of field free spaces exist between the accelerating gaps, whereas the latter method is much cumbrous. To solve these difficulties, we have found the recurrence formulae for the cardinal elements of the accelerating system and have succeeded in obtaining the ion optical characteristics accurately and comparatively simply.

§ 2. Method of Calculation

It is assumed that the electric potential distribution in the accelerating system can be represented schematically as shown in Fig. 1. The potential in this case is taken relative to zero potential at zero ion kinetic energy (negative for positive ions).

We denote here as follows (see Fig. 2).

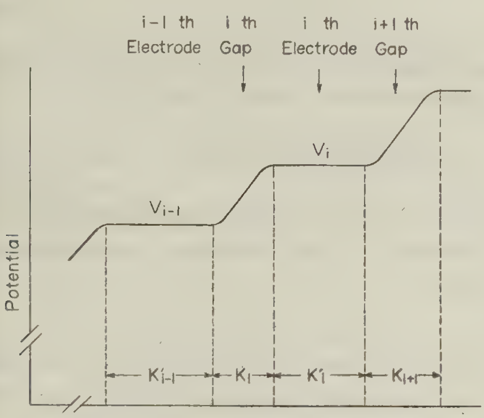

Fig. 1. Potential distribution in an accelerating system.

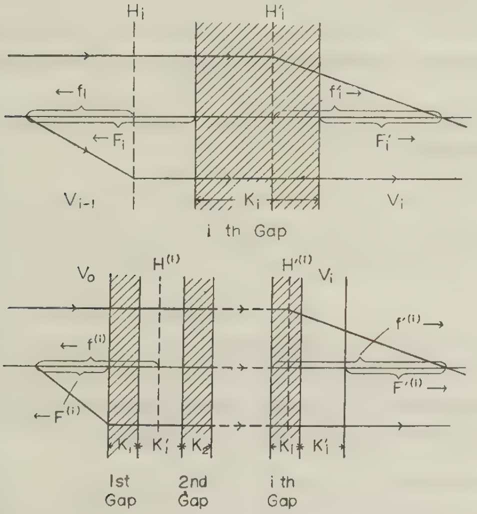

Fig. 2. Cardinal elements. H and H' are the principal plane in the source space side and image space side respectively. The shaded portions show the space where an electric field is applied.

K_i: the length of the i-th space where an electric field is applied,

K'_i: the length of the field free space between the i-th and $(i+1)$-th gaps,

V_i: the potential of the i-th electrode,

$N_i = V_i/V_{i-1}$: the ratio of potential of the i-th and $(i-1)$-th electrodes,

F_i, F'_i: the distance of the focal point of the i-th gap lens from the i-th gap field boundary in the source space side and image space side respectively,

f_i, f'_i: the focal length of the i-th gap lens in the source space side and image space side respectively,

$F^{(i)}$, $F'^{(i)}$: the distance of the focal point of the system composed of the first i gap lenses and i field free spaces, from the lens boundary in the source space side and image space side respectively,

$f^{(i)}$, $f'^{(i)}$: the focal length of the system composed of the first i gap lenses and i field free spaces, in the source space side and image space side respectively,

$\boldsymbol{A}_i$: the lens matrix of the system composed of the i-th gap and the i-th field free space,

$\boldsymbol{A}^{(i)}$: the lens matrix of the system composed of the first i gap lenses and i field free spaces,

D_i: the determinant of $\boldsymbol{A}_i$,

and

$D^{(i)}$: the determinant of $\boldsymbol{A}^{(i)}$.

(a) *Recurrence formulae for $f^{(i)}$ and $f'^{(i)}$*

According to U. Timm,[3] the lens matrix of the i-th gap is

$$\begin{bmatrix} \dfrac{F'_i}{f'_i} & \dfrac{f_i f'_i - F_i F'_i}{f'_i} \\ -\dfrac{1}{f'_i} & \dfrac{F_i}{f'_i} \end{bmatrix},$$

where

$$\left.\begin{aligned} \frac{F'_i}{K_i} &= -\frac{4}{3}\,\frac{N_i(N_i^{1/2}-3)}{(N_i-1)(N_i^{1/2}-1)}, \\ \frac{F_i}{K_i} &= \frac{4}{3}\,\frac{3\,N_i^{1/2}-1}{(N_i-1)(N_i^{1/2}-1)}, \\ \frac{f'_i}{K_i} &= \frac{8}{3}\,\frac{N_i}{(N_i-1)(N_i^{1/2}-1)}, \\ \frac{f_i}{K_i} &= \frac{8}{3}\,\frac{N_i^{1/2}}{(N_i-1)(N_i^{1/2}-1)}. \end{aligned}\right\} \qquad (1)$$

in the case of a uniform field.

Whereas, the matrix for the field free space is

$$\begin{bmatrix} 1 & K'_i \\ 0 & 1 \end{bmatrix}.$$

Hence, the matrix $\boldsymbol{A}_i$ becomes

$$A_i=\begin{bmatrix}1 & K'_i\\ 0 & 1\end{bmatrix}\times\begin{bmatrix}\frac{F'_i}{f'_i} & \frac{f_if'_i-F_iF'_i}{f'_i}\\ -\frac{1}{f'_i} & \frac{F_i}{f'_i}\end{bmatrix}$$

$$=\begin{bmatrix}\frac{F'_i-K'_i}{f'_i} & \frac{f_if'_i-F_iF'_i+K'_iF_i}{f'_i}\\ -\frac{1}{f'_i} & \frac{F_i}{f'_i}\end{bmatrix}. \qquad (2)$$

And the determinant of lens matrix is

$$D_i=|A_i|=f_i/f'_i\ . \qquad (3)$$

Furthermore,

$$A^{(i)}=A_i\cdot A_{i-1}\cdot\cdots\cdots A_1\ . \qquad (4)$$

Then, $D^{(i)}$ is given as

$$D^{(i)}=f^{(i)}/f'^{(i)}=D_i\cdot D_{i-1}\cdot\cdots\cdots D_1$$

$$=\frac{f_i\cdot f_{i-1}\cdots\cdots f_1}{f'_i\cdot f'_{i-1}\cdots\cdots f'_1}\ . \qquad (5)$$

Next, we consider $f^{(i)}$ and $f'^{(i)}$. From Eq. (4),

$$A^{(i)}=\begin{bmatrix}a_{11}^{(i)} & a_{12}^{(i)}\\ a_{21}^{(i)} & a_{22}^{(i)}\end{bmatrix}=A_i\cdot A^{(i-1)}$$

$$=\begin{bmatrix}\frac{F'_i-K'_i}{f'_i} & \frac{f_if'_i-F_iF'_i+K'_iF_i}{f'_i}\\ -\frac{1}{f'_i} & \frac{F_i}{f'_i}\end{bmatrix}$$

$$\times\begin{bmatrix}a_{11}^{(i-1)} & a_{12}^{(i-1)}\\ a_{21}^{(i-1)} & a_{22}^{(i-1)}\end{bmatrix}, \qquad (6)$$

and

$$a_{11}^{(i)}=F'^{(i)}/f'^{(i)}\ , \qquad (7)$$

$$a_{21}^{(i)}=-1/f'^{(i)}\ , \qquad (8)$$

$$a_{22}^{(i)}=F^{(i)}/f'^{(i)}\ . \qquad (9)$$

Therefore,

$$a_{11}^{(i)}=\frac{F'_i-K'_i}{f'_i}a_{11}^{(i-1)}$$

$$+\frac{f_if'_i-F_iF'_i+K'_iF_i}{f'_i}a_{21}^{(i-1)}\ , \qquad (10)$$

$$a_{21}^{(i)}=-\frac{1}{f'_i}a_{11}^{(i-1)}+\frac{F_i}{f'_i}a_{21}^{(i-1)}\ . \qquad (11)$$

Substituting $a_{11}^{(i-1)}$ of Eq. (11) into Eq. (10), we obtain

$$a_{11}^{(i)}=-(F'_i-K'_i)a_{21}^{(i)}+f_ia_{21}^{(i-1)}. \qquad (12)$$

Replacing i by $i-1$,

$$a_{11}^{(i-1)}=-(F'_{i-1}-K'_{i-1})a_{21}^{(i-1)}+f_{i-1}a_{21}^{(i-2)}. \qquad (13)$$

Eliminating $a_{11}^{(i-1)}$ from Eqs. (11) and (13), we get

$$a_{21}^{(i)}=\frac{\Delta_{i-1}}{f'_i}a_{21}^{(i-1)}-\frac{f_{i-1}}{f'_i}a_{21}^{(i-2)}\ , \qquad (14)$$

where $\Delta_{i-1}=F'_{i-1}+F_i-K'_{i-1}\ .$ (15)

By Eq. (9), Eq. (14) becomes

$$\frac{f'_i}{f'^{(i)}}=\frac{\Delta_{i-1}}{f'^{(i-1)}}-\frac{f_{i-1}}{f'^{(i-2)}}\ . \qquad (16)$$

This is the recurrence formula for $f'^{(i)}$.

Expressing $f'^{(i)}$ by $f^{(i)}$ by Eq. (5), we obtain as the recurrence formula for $f^{(i)}$:

$$\frac{f_i}{f^{(i)}}=\frac{\Delta_{i-1}}{f^{(i-1)}}-\frac{f'_{i-1}}{f^{(i-2)}}\ . \qquad (17)$$

(b) *Recurrence formula for $F^{(i)}$ and $F'^{(i)}$*

By Eqs. (7) and (8), Eqs. (11) and (12) become

$$\frac{f'^{(i)}}{f'^{(i-1)}}=\frac{f'_i}{F'^{(i-1)}+F_i}\ ,$$

$$F'^{(i)}=F'_i-K'_i-f_i\frac{f'^{(i)}}{f'^{(i-1)}}\ .$$

Substituting the former equation into the latter one, we obtain the recurrence formula for $F'^{(i)}$:

$$F'^{(i)}=F'_i-K'_i-\frac{f_if'_i}{F'^{(i-1)}+F_i}\ . \qquad (18)$$

The above equation can also be written as follows:

$$F'^{(i)}=F'_i-K'_i-\frac{f_if'_i}{\Delta_{i-1}+F'^{(i-1)}-(F'_{i-1}-K'_{i-1})}$$

$$=F'_i-K'_i$$

$$-\frac{f_if'_i}{\Delta_{i-1}-\frac{f_{i-1}f'_{i-1}}{\Delta_{i-2}+F'^{(i-2)}-(F'_{i-2}-K'_{i\ 2})}}\ .$$

Therefore, $F'^{(i)}$ can be expressed finally as the following continued fraction:

$$F'^{(i)}=F'_i-K'_i-\frac{f_if'_i}{\Delta_{i-1}}\,\underset{-}{}\,\frac{f_{i-1}f'_{i-1}}{\Delta_{i-2}}\,\underset{-}{}$$

$$\cdots\cdots\underset{-}{}\,\frac{f_3f'_3}{\Delta_2}\,\underset{-}{}\,\frac{f_2f'_2}{\Delta_1}\ . \qquad (19)$$

Next, we consider $F^{(i)}$. From Eq. (6), the following equations are obtained:

$$a_{12}^{(i)}=\frac{F_i'-K_i'}{f_i'}a_{12}^{(i-1)}$$

$$+\frac{f_if_i'-F_iF_i'+K_i'F_i}{f_i'}a_{22}^{(i-1)}\ , \qquad (20)$$

$$a_{22}^{(i)}=-\frac{1}{f_i'}a_{12}^{(i-1)}+\frac{F_i}{f_i'}a_{22}^{(i-1)}\ . \qquad (21)$$

Replacing i by $i-1$ in Eq. (20) and substituting into Eq. (21), we obtain

$$a_{22}^{(i)}=\frac{1}{f_i'}\Big[F_i\,a_{22}^{(i-1)}-f_{i-1}\,a_{22}^{(i-2)}$$
$$-(F'_{i-1}-K'_{i-1})\Big(\frac{a_{12}^{(i-2)}}{f'_{i-1}}-\frac{F_{i-1}}{f'_{i-1}}a_{22}^{(i-2)}\Big)\Big]$$
$$=\frac{1}{f_i'}\Big[\Delta_{i-1}\,a_{22}^{(i-1)}-f_{i-1}\,a_{22}^{(i-2)}\Big]. \qquad (22)$$

By Eq. (9), this equation becomes

$$\frac{F^{(i)}}{f'^{(i)}}=\frac{1}{f_i'}\Big[\Delta_{i-1}\frac{F^{(i-1)}}{f'^{(i-1)}}-f_{i-1}\frac{F^{(i-2)}}{f'^{(i-2)}}\Big]. \qquad (23)$$

This is the recurrence formula for $F^{(i)}/f'^{(i)}$. As $f'^{(i)}$ can be obtained by the consecutive applications of Eq. (16), $F^{(i)}$ can easily be calculated from Eq. (23).

Furthermore, we put

$$\left.\begin{aligned}p^{(i)}&=f'_i f'_{i-1}\cdots f_1'\,a_{22}^{(i)}\,,\\ q^{(i)}&=f'_i f'_{i-1}\cdots f_1'\,a_{21}^{(i)}\,.\end{aligned}\right\} \qquad (24)$$

Substituting these equations into Eqs. (14) and (22), and cancelling denominators, we obtain

$$\left.\begin{aligned}p^{(i)}&=\Delta_{i-1}\,p^{(i-1)}-f'_{i-1}f_{i-1}\,p^{(i-2)}\,,\\ q^{(i)}&=\Delta_{i-1}\,q^{(i-1)}-f'_{i-1}f_{i-1}\,q^{(i-2)}\,.\end{aligned}\right\} \qquad (25)$$

By the theorem about the continued fraction, the above equations mean that $F^{(i)}$ can be expressed as the following continued fraction:

$$F^{(i)}=\frac{p^{(i)}}{q^{(i)}}=F_1-\frac{f_1f_1'}{\Delta_1}\;-\;\frac{f_2f_2'}{\Delta_2}\;-\;\cdots\;-\;\frac{f_{i-1}f'_{i-1}}{\Delta_{i-1}}\,. \qquad (26)$$

Eqs. (19) and (26) may be used to obtain directly the values of $F'^{(i)}$ and $F^{(i)}$.

(c) *Newton's formula*

If the number of accelerating stages is n, the relation between the source and image is given by the following Newton's formula:

$$(S-F^{(n)})\;(I-F'^{(n)})=f^{(n)}f'^{(n)} \qquad (27)$$

where S and I are the distance of source and image from the lens boundary respectively.

The magnification can be expressed as

$$M=-(I-F'^{(n)})/f'^{(n)}. \qquad (28)$$

It is necessary to make the value of M as small as possible, if a well-defined small spot of accelerated beam is required on a target.

§ 3. Applications

In order to calculate the ion optical characteristics of a multistage accelerator tube, the cardinal elements of individual accelerating lens must be known. However, there are very few experimental data except those by K. Spangenberg and L. M. Field[4], in which the cardinal elements of equidiameter cylinder lens are given against the voltage ratio N for several values of the gap spacing. These results show the considerable deviations especially for the cases of smaller voltage ratio and larger gap spacing from those calculated by the assumption that the electric field is uniform and protrudes by half the cylinder diameter into both electrodes. Therefore, we try to improve the approximation by the consecutive applications of our recurrence formulae obtained above.

At first, we assume that the potential distribution along the axis of the lens composed of two coaxial equidiameter cylinders is given by[5)]

$$V(z)=\frac{V_1+V_2}{2}+\frac{V_2-V_1}{2.6304\,S/R}\log\frac{1.3152\,(z+S/2)/R}{1.3152\,(z-S/2)/R}\,, \qquad (29)$$

where R is the cylinder diameter, S is the gap spacing between the two cylinders and the coordinate z is taken along the axis from the center of gap. The whole range of z is

Table I. The cardinal elements of the lens composed of two coaxial equidiameter cylinders for the case of $S=2R$.

Cardinal elements	N	Calculated by the recurrence formulae.	Calculated by the assumption of a single uniform field.	Experimental values.[4)]
f/R	4	7.3	7.1	13.6
	6	3.6	3.6	5.8
	8	2.6	2.4	3.0
	10	2.1	1.7	2.2
f'/R	4	14.5	14.2	25.0
	6	8.9	8.8	13.4
	8	7.3	6.7	8.9
	10	6.5	5.5	6.8
F/R	4	8.0	8.9	14.4*
	6	3.1	4.7	5.7*
	8	1.9	3.1	2.6*
	10	1.2	2.3	1.5*
F'/R	4	7.7	7.1	18.0*
	6	3.6	2.4	8.2*
	8	0.68	0.57	4.0*
	10	−0.84	−0.44	2.1*

* These are derived from the original values, assuming that the field boundaries are at the distance of $2R$ from the center of gap.

divided into a large number of small intervals, in which the field is taken to be uniform and the potential distribution given by Eq. (29) is replaced by a sequence of such uniform fields. The cardinal elements of each interval are calculated by Eq. (1). Then, the cardinal elements for the whole lens can be obtained by the consecutive applications of Eqs. (16), (17), (18) and (23), taking $K'=0$. The calculated results do not show any appreciable improvement as shown in Table I, in which the comparison for the case of $S=2R$ is given as an example. The situation can not be improved, even if the higher order terms[6] are taken into account. The reasons can not yet be well explained. The errors would, therefore, become large in calculating the cardinal elements of a multistage accelerator, unless the experimental values are used for each accelerating lens.

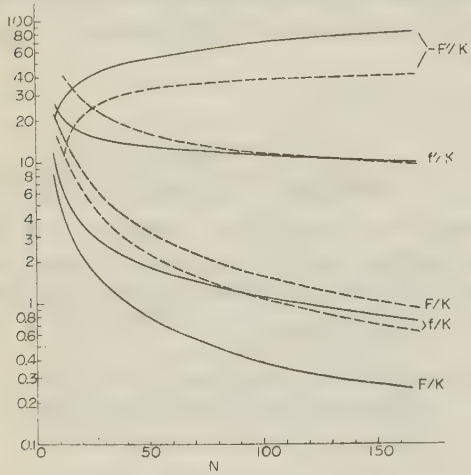

Fig. 3. Cardinal elements for our accelerator plotted against the ratio N of the energy of accelerated ions to that of incident ions. The accelerator consists of 12 coaxial equidiameter cylinders of 13.5 cm in length and 3 cm in inner diameter. The gap spacings are 2.5 cm. The case for a uniform acceleration is shown by the broken curves for the sake of comparison.

An example of the cardinal elements of a multistage accelerator tube is shown in Fig. 3, in which the calculated results for our 12-stage Cockcroft accelerator are given. As the applied accelerating voltage is assumed to be divided equally on each gap, the cardinal elements depend only on the ratio N of the energy of accelerated ions to that of incident ions. The broken curves in the figure represent the case in which a single uniform electric field is assumed in the accelerating system. Appreciable deviations are seen in f/K and f'/K for $N<50$, and in F/K and F'/K for the whole range of N. It is, therefore, clear that the calculation by the assumption of a uniform acceleration can not give satisfactorily accurate results in the case of such a multistage accelerator tube.

References

1) M. M. Elkind: Rev. Sci. Instr. **24** (1953) 129.
2) W. Dähnick *et al*: Z. Naturforsch. **10a** (1955) 603.
3) U. Timm: Z. Naturforsch. **10a** (1955) 593.
4) F. E. Terman: *Radio Engineer's Handbook* (McGraw-Hill Book Co., Inc., New York, 1943) 322.
5) S. Bertram: Proc. Inst. Radio Eng. **28** (1940) 418.
6) E. Bruche and O. Scherzer: *Geometrische Elektronenoptik* (Springer-Verlag, Berlin, 1934).

JOURNAL OF THE PHYSICAL SOCIETY OF JAPAN, Vol. 15, No. 9, SEPTEMBER, 1960

Transport Coefficients of Plasmas in a Magnetic Field

By Shobu KANEKO

Department of Physics, Faculty of Science,
University of Tokyo

(Received June 4, 1960)

The electric and the thermal conductivities, and the coefficient of the thermal diffusion of plasmas in a magnetic field are calculated under the assumption that the mass ratio m_2/m_1 is considerably smaller than unity, where m_1 and m_2 are masses of an ion and an electron, respectively. Thereby the terms of the order $(m_2/m_1)^{\frac{1}{2}}$ are retained considering the application to the deuterium plasma, but the higher order terms than those are neglected. For various strengths of the magnetic field, these coefficients are evaluated by the Chapman-Enskog method up to the 6th approximation, and the convergence of this method is examined. The probable error of our approximation varies from 0.1% to 10% with the strength of the magnetic field.

§ 1. Introduction

The investigation of the transport coefficients of plasmas is an important problem of the plasma physics. To calculate these coefficients we need, in general, the velocity distribution function which satisfies the Boltzmann equation. The electrical and thermal conductivites of plasmas have been calculated by many authors, i.e. Landshoff[1], Spitzer and Härm[2], and Schirmer and Friedrich[3] when there is no magnetic field. In the presence of a magnetic field, the calculations of these coefficients have been made by Cowling[4], Landshoff[5], Fradkin[6], Braginskii[7], Marshall[8], and Kihara, Midzuno, and Kaneko[9].

Using the Chapman-Enskog method[10] we calculate in this article these transport coefficients for various strengths of the magnetic field up to the 6th approximation, and examine the convergence of this method. In the absence of the magnetic field the calculation was also made by Landshoff[1] up to the 5th approximation under the same purpose.

The following assumptions have been made in carrying through the calculations.

(i) The plasma is composed of one type of ions as species *1* and electrons as species *2*. The particle mass, charge and number density of the ion will be denoted by m_1, $e_1=Ze$, and n_1 respectively and those of the electron by m_2, $e_2=-e$, and n_2.

(ii) The plasma is charge neutral as a whole, i.e. $Zn_1=n_2$.

(iii) Since the mass ratio, $m_2/m_1=M_2$, is considerably smaller than unity, we neglect the terms of the order M_2 or higher, but retain the terms of the order $M_2^{1/2}$ considering the practical application to the deuterium plasma.

(iv) The plasma is so hot that the Coulomb logarithm, $\ln\left(\frac{kTl_D}{e_1e_2}\right)$, is much larger than unity, where l_D is the Debye characteristic length and T the temperature of the plasma.

(v) The electric field $\boldsymbol{E}$, and the magnetic flux $\boldsymbol{B}$ are uniform in space. Both the field $\boldsymbol{E}$ and the temperature gradient $-\operatorname{grad} T$ are perpendicular to $\boldsymbol{B}$. By this assumption it is sufficient to consider only the transport coefficients across the magnetic field. The transport coefficients along the magnetic field are the same as in the absence of the magnetic field.

§ 2. Method of Calculation

Since the Chapman-Enskog method used in this paper has been explained in detail by many authors[10], only a short account will be given in this and the next section.

For the treatment of conduction phenomena it is sufficient to look for the stationary velocity distribution function. The velocity distribution function f_i for particles of species i, interacting with particles of species j is determined by the Boltzmann equation[10]

$$\boldsymbol{c}_i\frac{\partial f_i}{\partial \boldsymbol{r}}+\frac{e_i}{m_i}\left(\boldsymbol{E}+\frac{1}{c}\boldsymbol{c}_i\times\boldsymbol{B}\right)\cdot\frac{\partial f_i}{\partial \boldsymbol{c}_i}$$
$$=\sum_{j=1}^{2}\iiint d\boldsymbol{c}_j g_{ij} b\,db\,d\varepsilon\left[\,f_i(\boldsymbol{c}_i')f_j(\boldsymbol{c}_j')-f_i(\boldsymbol{c}_i)f_j(\boldsymbol{c}_j)\,\right], \tag{1}$$

where $\boldsymbol{c}_i$ and $\boldsymbol{c}_i'$ are the velocities of a particle of species i before and after the collision, $g_{ij}=|\boldsymbol{c}_i-\boldsymbol{c}_j|$ is the relative speed between particles i and j; b is the impact parameter, ε the azimuthal angle of the orbit of relative motion, and c the velocity of light.

Supposing that the electric field $\boldsymbol{E}$ and the temperature gradient $-\text{grad}\ T$ are small, the distribution functions f_i are expanded as

$$f_i=f_i^{(0)}[1+\varphi_i]\,, \tag{2}$$

where $f_i^{(0)}$ and φ_i are respectively the distribution functions in the equilibrium state and their distortion. The distribution functions $f_i^{(0)}$ are determined by

$$\begin{aligned}&\frac{e_i}{m_i c}\boldsymbol{c}_i\times\boldsymbol{B}\cdot\frac{\partial f_i^{(0)}}{\partial \boldsymbol{c}_i}\\&\quad=\sum_{j=1}^{2}\iiint d\boldsymbol{c}_j g_{ij} b\,db\,d\varepsilon\Big[f_i^{(0)}(\boldsymbol{c}_i')f_j^{(0)}(\boldsymbol{c}_j')-f_i^{(0)}(\boldsymbol{c}_i)f_j^{(0)}(\boldsymbol{c}_j)\Big]\,,\end{aligned} \tag{3}$$

and solutions of these equations are the well-known Maxwell distributions;

$$f_i^{(0)}=n_i\left(\frac{m_i}{2\pi kT}\right)^{3/2}\exp\left(-\frac{m_i c_i^2}{2kT}\right), \tag{4}$$

where k is the Boltzmann constant.

The distortions φ_i of the distribution functions which are of the order $\boldsymbol{E}$ and $-\text{grad}\ T$, are given as the solutions of following equations;

$$\begin{aligned}&-f_i^{(0)}\left(\frac{5}{2}-w_i^2\right)(\boldsymbol{c}_i\cdot\text{grad}\ln T)-f_i^{(0)}\frac{e_i}{kT}(\boldsymbol{c}_i\cdot\boldsymbol{E})=-f_i^{(0)}\frac{e_i}{m_i c}\boldsymbol{c}_i\times\boldsymbol{B}\cdot\frac{\partial\varphi_i}{\partial\boldsymbol{c}_i}\\&\quad+\sum_{j=1}^{2}\iiint d\boldsymbol{c}_j g_{ij} b\,db\,d\varepsilon\, f_i^{(0)}f_j^{(0)}\Big[\varphi_i(\boldsymbol{c}_i')+\varphi_j(\boldsymbol{c}_j')-\varphi_i(\boldsymbol{c}_i)-\varphi_j(\boldsymbol{c}_j)\Big]\,,\end{aligned} \tag{5}$$

where $\boldsymbol{w}_i$ are the non-dimensional velocities $\sqrt{\dfrac{m_i}{2kT}}\,\boldsymbol{c}_i$.

Because the left hand sides of the equations (5) have linear dependence on $\boldsymbol{E}$ and $-\text{grad}\ T$, the solutions φ_i may be written as

$$\varphi_i=-\boldsymbol{D}_i\cdot\boldsymbol{E}-\boldsymbol{A}_i\cdot\text{grad}\ln T\,, \tag{6}$$

where the quantities $\boldsymbol{D}_i$ and $\boldsymbol{A}_i$ are vectors which involve only the vectors $\boldsymbol{c}_i$ and $\boldsymbol{B}$ and scalars. Since $\boldsymbol{B}$ is a pseudo-vector, the independent true vectors which we need under the assumption (v) are $\boldsymbol{w}_i$ and $\boldsymbol{w}_i\times\boldsymbol{b}$ ($\boldsymbol{b}=\boldsymbol{B}/B$). Then the vectors $\boldsymbol{D}_i$ and $\boldsymbol{A}_i$ can be written as

$$\begin{aligned}\boldsymbol{A}_i&=A_i^{\mathrm{I}}\boldsymbol{w}_i+A_i^{\mathrm{II}}\boldsymbol{w}_i\times\boldsymbol{b}\,,\\\boldsymbol{D}_i&=D_i^{\mathrm{I}}\boldsymbol{w}_i+D_i^{\mathrm{II}}\boldsymbol{w}_i\times\boldsymbol{b}\,,\end{aligned} \tag{7}$$

where the coefficients A_i^{I}, etc. are scalar functions of w_i^2, B^2, and $(\boldsymbol{w}_i\cdot\boldsymbol{B})^2$.

Substituting the equations (6) and (7) into the equations (5), we obtain the equations for D and A as

$$\begin{aligned}&-f_i^{(0)}\frac{e_i}{kT}\boldsymbol{c}_i=i\omega_i D_i f_i^{(0)}\boldsymbol{w}_i\\&\quad-\sum_{j=1}^{2}\iiint d\boldsymbol{c}_j g_{ij} b\,db\,d\varepsilon\, f_i^{(0)}f_j^{(0)}\Big[(D_i\boldsymbol{w}_i)'+(D_j\boldsymbol{w}_j)'-(D_i\boldsymbol{w}_i)-(D_j\boldsymbol{w}_j)\Big]\,,\end{aligned} \tag{8}$$

$$\begin{aligned}&-f_i^{(0)}\left(\frac{5}{2}-w_i^2\right)\boldsymbol{c}_i=i\omega_i A_i f_i^{(0)}\boldsymbol{w}_i\\&\quad-\sum_{j=1}^{2}\iiint d\boldsymbol{c}_j g_{ij} b\,db\,d\varepsilon\, f_i^{(0)}f_j^{(0)}\Big[(A_i\boldsymbol{w}_i)'+(A_j\boldsymbol{w}_j)'-(A_i\boldsymbol{w}_i)-(A_j\boldsymbol{w}_j)\Big]\,,\end{aligned} \tag{9}$$

where we have used the complex notations, i.e.

$$D_i = D_i^{\mathrm{I}} + iD_i^{\mathrm{II}} \,,$$
$$A_i = A_i^{\mathrm{I}} + iA_i^{\mathrm{II}} \,, \tag{10}$$

and $\omega_i = e_iB/m_ic$ is the Larmer frequency of the species i.

First of all, we can derive a following relation between A and D from the equations (8) and (9)

$$\sum_i \frac{e_i}{kT}\int d\boldsymbol{c}_i(\boldsymbol{c}_i\cdot\boldsymbol{w}_i)\, f_i^{(0)} A_i = \sum_i \int d\boldsymbol{c}_i\left(\frac{5}{2} - w_i^2\right)(\boldsymbol{c}_i\cdot\boldsymbol{w}_i) f_i^{(0)} D_i . \tag{11}$$

Besides the equations (8) and (9), D_i and A_i, must satisfy a subsidiary condition that the plasma as a whole is at rest:

$$\sum_i m_i \int d\boldsymbol{c}_i\, f_i \boldsymbol{c}_i = 0 \,. \tag{12}$$

By substitution of the equations (2), (4), (6), and (7), this condition becomes

$$\sum_i n_i\sqrt{m_i}\int d\boldsymbol{w}_i e^{-w_i^2} w_i^2 D_i = 0 \,, \tag{12'}$$
$$\sum_i n_i\sqrt{m_i}\int d\boldsymbol{w}_i e^{-w_i^2} w_i^2 A_i = 0 \,.$$

For convenience in later work, we introduce a system of orthogonal functions;

$$S_1^{(0)} \equiv -\frac{n_2\sqrt{m_2}}{n_1\sqrt{m_1}} S^{(0)}{}_{3/2}(w_1^2) \,, \qquad S_2^{(0)} \equiv S^{(0)}{}_{3/2}(w_2^2) \,,$$

and for values of r greater than zero,

$$S_1^{(r)} \equiv S_{3/2}{}^{(r)}(w_1^2) \,, \qquad S_2^{(r)} \equiv 0 \,,$$
$$S_1^{(-r)} \equiv 0 \,, \qquad S_2^{(-r)} \equiv S^{(r)}{}_{3/2}(w_2^2) \,, \tag{13}$$

where $S_{3/2}{}^{(r)}(x)$ are Sonie's polynomials of the order ³⁄₂ whose orthogonal relation is

$$\int_0^\infty e^{-x} S_m{}^{(p)}(x) S_m{}^{(q)}(x) x^m dx = 0 \qquad \text{for } p \neq q \tag{14}$$
$$= \frac{1}{p!}\Gamma(m+p+1) \qquad \text{for } p = q \,.$$

By use of this system of orthogonal functions we expand D_i and A_i as

$$D_i = \sum_{m=-\infty}^{\infty} d^{(m)} S_i^{(m)} \,, \tag{15}$$
$$A_i = \sum_{m=-\infty}^{\infty} a^{(m)} S_i^{(m)} \,,$$

where

$$d^{(m)} = d^{\mathrm{I}(m)} + id^{\mathrm{II}(m)} \,, \tag{16}$$
$$a^{(m)} = a^{\mathrm{I}(m)} + ia^{\mathrm{II}(m)} \,.$$

The equality of the coefficients of $S_1^{(0)}$ and $S_2^{(0)}$ follows from the conditions (12′), which D and A must satisfy; it can easily be verified by substituting (15) and (16) into the equations (12′). The equations which determine the coefficients $d^{(m)}$ and $a^{(m)}$ are obtained from the equations (8) and (9) by substituting the equations (15) and operating $\sum_i \int d\boldsymbol{c}_i\boldsymbol{w}_i S_i^{(r)}$. The results are

$$\frac{3}{2}\frac{n_2 e}{kT}\left(\frac{2kT}{m_2}\right)^{1/2}\delta_{r,o}=\sum_{-\infty}^{\infty}\left[h^{(m)}\delta_{r,m}+\{\boldsymbol{w}S^{(r)},\boldsymbol{w}S^{(m)}\}\right]d^{(m)}\,,$$

$$\frac{15}{4}\left[n_1\left(\frac{2kT}{m_1}\right)^{1/2}\delta_{r,1}+n_2\left(\frac{2kT}{m_2}\right)^{1/2}\delta_{r,-1}\right] \tag{17}$$

$$=\sum_{-\infty}^{\infty}\left[h^{(m)}\delta_{r,m}+\{\boldsymbol{w}S^{(r)},\boldsymbol{w}S^{(m)}\}\right]a^{(m)}\,,$$

where

$$h^{(r)}=\begin{cases} i\dfrac{2n_1\omega_1}{\sqrt{\pi}}\dfrac{\Gamma(r+\frac{5}{2})}{r!} & \text{for } r>0 \\ i\dfrac{2n_2\omega_2}{\sqrt{\pi}}\dfrac{\Gamma(|r|+\frac{5}{2})}{|r|!} & \text{for } r\leqq 0\,, \end{cases} \tag{18}$$

and

$$\{F,G\}=-\sum_{ij}\iiiint d\boldsymbol{c}_i d\boldsymbol{c}_j g_{ij} b\,db\,d\varepsilon\, f_i^{(0)}(c_i)\,f_j^{(0)}(c_j)F_i(\boldsymbol{c}_i)\cdot$$

$$\left[G_i(\boldsymbol{c}'_i)+G_j(\boldsymbol{c}'_j)-G_i(\boldsymbol{c}_i)-G_j(\boldsymbol{c}_j)\right]$$

$$=n_1^2[F,G]_1+n_2^2[F,G]_2+n_1n_2[F_1+F_2,\,G_1+G_2]_{12}\,, \tag{19}$$

$$[F,G]_i=-\frac{1}{n_i^2}\iiiint d\boldsymbol{c}_i d\bar{\boldsymbol{c}}_i g_{ii} b\,db\,d\varepsilon\, f_i^{(0)}(c_i)\,f_i^{(0)}(\bar{c}_i)F_i(\boldsymbol{c}_i)\,.$$

$$[G_i(\boldsymbol{c}_i')+G_i(\boldsymbol{c}_i')-G_i(\boldsymbol{c}_i)-G_i(\bar{\boldsymbol{c}}_i)]\,,$$

$$[F_1+F_2,\,G_1+G_2]_{12}$$

$$=-\frac{1}{n_1n_2}\iiiint d\boldsymbol{c}_1 d\boldsymbol{c}_2 g_{21} b\,db\,d\varepsilon\, f_1^{(0)}(c_1)\,f_2^{(0)}(c_2)\,[F_1(\boldsymbol{c}_1)+F_2(\boldsymbol{c}_2)]\,.$$

$$[G_1(\boldsymbol{c}_1')+G_2(\boldsymbol{c}_2')-G_1(\boldsymbol{c}_1)-G_2(\boldsymbol{c}_2)]\,,$$

$$\delta_{m,n}=\begin{cases}1 & \text{for } m=n \\ 0 & \text{for } m\neq n\,.\end{cases}$$

These equations (17) are infinite simultaneous linear equations, and can be solved approximately by taking r and m within some finite value.

§ 3. Transport Coefficients

Among the electric current $\boldsymbol{j}$, the reduced heat flow $\boldsymbol{q}$ due to conduction, the electric field $\boldsymbol{E}$, and the temperature gradient $-\text{grad}\ln T$ there exist the well-known linear relations[9]:

$$\boldsymbol{q}=-T\lambda\,\text{grad}\ln T+\alpha\boldsymbol{j}$$

$$\boldsymbol{E}=\ \alpha\,\text{grad}\ln T+\sigma^{-1}\boldsymbol{j}\,. \tag{20}$$

Here λ and σ are respectively the thermal and electric conductivities and α is the coefficient which represents the interference between the thermal and electric phenomena. These transport coefficients in a magnetic field are represented by tensors of the type,[9]

$$\lambda=\begin{pmatrix}\lambda^{\mathrm{I}} & -\lambda^{\mathrm{II}} \\ \lambda^{\mathrm{II}} & \lambda^{\mathrm{I}}\end{pmatrix}. \tag{21}$$

for example.

By definition, the electric current is written as

$$\begin{aligned} \boldsymbol{j} &\equiv \sum_i n_i e_i \overline{\boldsymbol{c}_i} = \sum_i e_i \int d\boldsymbol{c}_i f_i^{(0)} \varphi_i \boldsymbol{c}_i \\ &= -\frac{n_2 e_2}{2} \left(\frac{2kT}{m_2}\right)^{1/2} \left[d^{\mathrm{I}(0)} \boldsymbol{E} + d^{\mathrm{II}(0)} (\boldsymbol{b} \times \boldsymbol{E}) \right] \\ &\quad -\frac{n_2 e_2}{2} \left(\frac{2kT}{m_2}\right)^{1/2} \left[a^{\mathrm{I}(0)} \operatorname{grad} \ln T + a^{\mathrm{II}(0)} (\boldsymbol{b} \times \operatorname{grad} \ln T) \right], \end{aligned} \tag{22}$$

where we have used equations (6), (7), (15), and (16). Hence the electric conductivity σ and the coefficient of the thermal diffusion φ are expressed as follows

$$\sigma \equiv \sigma^{\mathrm{I}} + i \sigma^{\mathrm{II}} = -\frac{n_2 e_2}{2} \left(\frac{2kT}{m_2}\right)^{1/2} d^{(0)}, \tag{23}$$

$$\varphi \equiv \varphi^{\mathrm{I}} + i \varphi^{\mathrm{II}} = -\frac{n_2 e_2}{2T} \left(\frac{2kT}{m_2}\right)^{1/2} a^{(0)}, \tag{24}$$

where the assumption (iii) has been used.

In the same way the heat flow $\boldsymbol{q}^*$ can be calculated as

$$\begin{aligned} \boldsymbol{q}^* &\equiv \sum_i n_i \frac{1}{2} \overline{m_i c_i^2 \boldsymbol{c}_i} = \sum_i \frac{1}{2} m_i \int d\boldsymbol{c}_i c_i^2 \boldsymbol{c}_i f_i^{(0)} \varphi_i \\ &= \frac{n_2 e_2}{2} \left(\frac{2kT}{m_2}\right)^{1/2} \left[a^{\mathrm{I}(0)} \boldsymbol{E} + a^{\mathrm{II}(0)} (\boldsymbol{b} \times \boldsymbol{E}) \right] + \frac{5}{2} \frac{kT}{e_2} \boldsymbol{j} \\ &\quad + \frac{5}{4} n_1 kT \left(\frac{2kT}{m_1}\right)^{1/2} \left[a^{\mathrm{I}(1)} \operatorname{grad} \ln T + a^{\mathrm{II}(1)} (\boldsymbol{b} \times \operatorname{grad} \ln T) \right] \\ &\quad + \frac{5}{4} n_2 kT \left(\frac{2kT}{m_2}\right)^{1/2} \left[a^{\mathrm{I}(-1)} \operatorname{grad} \ln T + a^{\mathrm{II}(-1)} (\boldsymbol{b} \times \operatorname{grad} \ln T) \right]. \end{aligned}$$

In this calculation we have used the relation (11) and the assumption (iii). Hence the reduced heat flow $\boldsymbol{q} = \boldsymbol{q}^* - \frac{5}{2} \frac{kT}{e_2} \boldsymbol{j}$ may be written

$$\boldsymbol{q} = -T [\varphi^{\mathrm{I}} \boldsymbol{E} + \varphi^{\mathrm{II}} (\boldsymbol{b} \times \boldsymbol{E})] - T \lambda^{\mathrm{I}} \operatorname{grad} \ln T - T \lambda^{\mathrm{II}} (\boldsymbol{b} \times \operatorname{grad} \ln T),$$

where

$$\lambda \equiv \lambda^{\mathrm{I}} + i \lambda^{\mathrm{II}} = -\frac{5}{4} n_2 k \left(\frac{2kT}{m_2}\right)^{1/2} \left[a^{(-1)} + \frac{n_1}{n_2} \left(\frac{m_2}{m_1}\right)^{1/2} a^{(1)} \right]. \tag{25}$$

From these results we can see that only the coefficients $d^{(0)}$, $a^{(0)}$, $a^{(-1)}$ and $a^{(1)}$ are needed to calculate the transport coefficients and are determined by the equations (17). These equations can be simplified by use of the assumption (iii).

First of all we consider the collision integrals $\{wS^{(r)}, wS^{(m)}\}$. By use of the definitions (19) these collision integrals become

$$\{wS^{(r)}, wS^{(m)}\} = \begin{cases} n_1^2 [w_1 S_1^{(r)}, w_1 S_1^{(m)}]_1 + n_1 n_2 [w_1 S_1^{(r)}, w_1 S_1^{(m)} + w_2 S_2^{(m)}]_{12} & \text{for } r > 0 \\ n_1 n_2 \Big[-\frac{n_2 \sqrt{m_2}}{n_1 \sqrt{m_1}} \big\{ [w_1, w_1 S_1^{(m)}]_{12} + [w_1, w_2 S_2^{(m)}]_{12} \big\} & \\ \quad + [w_2, w_2 S_2^{(m)}]_{12} + [w_2, w_1 S_1^{(m)}]_{12} \Big] & \text{for } r = 0 \\ n_2^2 [w_2 S_2^{(r)}, w_2 S_2^{(m)}]_2 + n_1 n_2 [w_2 S_2^{(r)}, w_1 S_1^{(m)} + w_2 S_2^{(m)}]_{12} & \text{for } r < 0, \end{cases} \tag{26}$$

where we have used the conservation of the momentum:

$$[w_i, w_i S^{(m)}_{\frac{3}{2}} (w_i^2)]_i = 0 .$$

Various collision integrals which appeared in the above equation (26) are calculated in Appendix: the results are

$$
\begin{aligned}
&[w_1 S_{3/2}^{(r)}, w_1 S_{3/2}^{(m)}]_1 = M_2^{1/2}[w_2 S_{3/2}^{(r)}, w_2 S_{3/2}^{(m)}]_2 \ , \\
&[w_1 S_{3/2}^{(r)}, w_1 S_{3/2}^{(m)}]_{12} = O(M_2) \qquad , \\
&[w_1 S_{3/2}^{(r)}, w_2 S_{3/2}^{(m)}]_{12} = O(M_2^{r+1/2})
\end{aligned}
\tag{27}
$$

Using this mass ratio dependence in the equations (26) and (17), we get the equations for $d^{(0)}$, $a^{(0)}$, $a^{(-1)}$, and $a^{(1)}$ as follows

$$\frac{3}{2}\frac{n_2 e}{kT}\left(\frac{2kT}{m_2}\right)^{1/2}\delta_{r,o} = \sum_{m=-\infty}^{0}\{h^{(m)}\delta_{r,m} + n_2^2[w_2 S_2^{(r)}, w_2 S_2^{(m)}]_2 + n_1 n_2[w_2 S_2^{(r)}, w_2 S_2^{(m)}]_{12}\}\, d^{(m)} \qquad (r \leq 0)\ , \tag{28}$$

$$-\frac{15}{4} n_2\left(\frac{2kT}{m_2}\right)^{1/2}\delta_{r,-1} = \sum_{m=-\infty}^{0}\{h^{(m)}\delta_{r,m} + n_2^2[w_2 S_2^{(r)}, w_2 S_2^{(m)}]_2 + n_1 n_2[w_2 S_2^{(r)}, w_2 S_2^{(m)}]_{12}\} a^{(m)} \qquad (r \leq 0)\ , \tag{29}$$

$$-\frac{15}{4}\left(\frac{2kT}{m_2}\right)^{1/2}\delta_{r,1} = n_1 \sum_{m=1}^{\infty}[w_2 S_2^{(r)}, w_2 S_2^{(m)}]_2\, a^{(m)} \qquad (r \geq 1)\ . \tag{30}$$

In the equations (30) the influence of the magnetic field to the motion of ions is neglected. Because, as can be easily seen from the equations (18) and (27), it is higher order, at least, by $M_2^{1/2}$ compared with that of the ion-ion collisions and the contribution of the $a^{(1)}$ itself to the thermal conductivity λ is of the order $M_2^{1/2}$. The equations (28) and (29) were used by Landshoff[5] to calculate the transport coefficients.

For convenience we introduce the notations $e^{(m)}$ and $b^{(m)}$ by relations

$$
\begin{aligned}
d^{(m)} &= \frac{e}{kT}\left(\frac{2kT}{m_2}\right)^{1/2}\tau e^{(m)} \ , \\
a^{(m)} &= -\frac{5}{2}\left(\frac{2kT}{m_2}\right)^{1/2}\tau b^{(m)} \ ,
\end{aligned}
$$

where τ is the mean collision time for electrons and is defined by

$$\frac{1}{\tau} \equiv \frac{2}{3} n_1 [w_2, w_2]_{12} = \frac{16}{3} n_1 \left(\frac{2\pi kT}{m_2}\right)^{1/2}\left(\frac{Ze^2}{2kT}\right)^2 \ln\frac{kT\, l_D}{Ze^2}\ . \tag{31}$$

By use of these new notations transport coefficients are expressed by

$$\sigma = \frac{n^2 e^2}{m_2}\tau e^{(0)} \qquad , \tag{32}$$

$$\varphi = -\frac{5k}{2}\frac{n_2 e}{m_2}\tau b^{(0)} \qquad , \tag{33}$$

$$\lambda = \frac{25}{4}\frac{n_2 k^2 T}{m_2}\tau\left[b^{(-1)} + \frac{n_1}{n_2}\left(\frac{m_2}{m_1}\right)^{1/2} b^{(1)}\right] \qquad , \tag{34}$$

and $e^{(0)}$, $b^{(0)}$, $b^{(-1)}$ ane $b^{(1)}$ are determined by

$$\sum_{-\infty}^{0} E_{rm} e^{(m)} = \delta_{r,o} \qquad (r \leq 0) \qquad , \tag{35}$$

$$\sum_{-\infty}^{0} E_{rm} b^{(m)} = \delta_{r,-1} \qquad (r \leq 0) \qquad , \tag{36}$$

$$\sum_{1}^{\infty} F_{rm} b^{(m)} = \delta_{r,1} \qquad (r \geq 1) \qquad , \tag{37}$$

where

$$E_{rm}=\frac{4}{3}\,i\,\frac{\omega_2\tau}{\sqrt{\pi}}\,\frac{\Gamma\left(|r|+\frac{3}{2}\right)}{|r|!}\,\delta_{r,m}+\frac{n_2[w_2S_2^{(r)},\,w_2S_2^{(m)}]_2+n_1[w_2S_2^{(r)},\,w_2S_2^{(m)}]_{12}}{n_1[w_2,\,w_2]_{12}}, \tag{38}$$

$$F_{rm}=\frac{[w_2S^{(r)}{}_{3/2},\,w_2S^{(m)}{}_{3/2}]_2}{[w_2,\,w_2]_{12}}$$

The transport coefficient α, which is defined by the equation (20), is related to σ and φ by

$$\alpha=-T\sigma^{-1}\varphi \tag{39}$$

or

$$\alpha^{\mathrm{I}}=-T\frac{\varphi^{\mathrm{I}}\sigma^{\mathrm{I}}+\varphi^{\mathrm{II}}\sigma^{\mathrm{II}}}{(\sigma^{\mathrm{I}})^2+(\sigma^{\mathrm{II}})^2}=\frac{5}{2}\frac{kT}{e}c^{\mathrm{I}(0)},$$

$$\alpha^{\mathrm{II}}=-T\frac{\varphi^{\mathrm{II}}\sigma^{\mathrm{I}}-\varphi^{\mathrm{I}}\sigma^{\mathrm{II}}}{(\sigma^{\mathrm{I}})^2+(\sigma^{\mathrm{II}})^2}=\frac{5}{2}\frac{kT}{e}c^{\mathrm{II}(0)},$$

where

$$c^{\mathrm{I}(0)}=\frac{b^{\mathrm{I}(0)}e^{\mathrm{I}(0)}+b^{\mathrm{II}(0)}e^{\mathrm{II}(0)}}{\{e^{\mathrm{I}(0)}\}^2+\{e^{\mathrm{II}(0)}\}^2}, \tag{40}$$

$$c^{\mathrm{II}(0)}=\frac{b^{\mathrm{II}(0)}e^{\mathrm{I}(0)}-b^{\mathrm{I}(0)}e^{\mathrm{II}(0)}}{\{e^{\mathrm{I}(0)}\}^2+\{e^{\mathrm{II}(0)}\}^2}.$$

Table I. Computed values of $e^{\mathrm{I}(0)}$ and $e^{\mathrm{II}(0)}$ for the electric conductivity in a plasma with $Z=1$.

$e^{\mathrm{I}(0)}$

$\omega_2\tau$ \ M	2	3	4	5	6	∞ *)
0	1.93198	1.94986	1.96357	1.96930	1.97111	1.975
0.2	1.55365	1.58748	1.59352	1.59811	1.60005	
0.5	0.79979	0.86014	0.86632	0.86747	0.86834	
1.0	0.34111	0.36036	0.37058	0.37264	0.37307	
2.0	0.13795	0.12456	0.12628	0.12841	0.12932	
4.0	0.04981	0.04272	0.03995	0.03945	0.03968	
6.0	0.02482	0.02224	0.02047	0.01964	0.01941	

$e^{\mathrm{II}(0)}$

$\omega_2\tau$ \ M	2	3	4	5	6
0	0.00000	0.00000	0.00000	0.00000	0.00000
0.2	−0.74588	−0.72881	−0.73320	−0.73623	−0.73667
0.5	−0.90260	−0.91865	−0.91814	−0.91982	−0.92102
1.0	−0.65513	−0.70249	−0.70660	−0.70692	−0.70723
2.0	−0.39856	−0.41910	−0.42778	−0.43003	−0.43038
4.0	−0.22808	−0.22865	−0.23128	−0.23315	−0.23407
6.0	−0.15908	−0.15807	−0.15844	−0.15916	−0.15976

*) Value calculated by Spitzer and Härm, see reference 2).

§ 4. Results

Following to Chapman and Enskog we cut off the matrices E_{rm} and F_{rm} beyond $|r|$, $|m|=M$ to solve the equations (35), (36), and (37) and examine the convergence of this method by taking $M=2, 3, 4, 5$, and 6. The simultaneous linear equations so obtained are solved by the Parametron Computor PC-1 at the University of Tokyo.

Considering the application to the deuterium or tritium plasma which plays an important role in the thermonuclear fusion devices, we

Table II. Computed values of $b_{\mathrm{I}}^{(0)}$ and $b_{\mathrm{II}}^{(0)}$ for the coefficient of thermal diffusion in a plasma with $Z=1$.

$b_{\mathrm{I}}^{(0)}$

$\omega_2\tau$ \ M	2	3	4	5	6	∞ *)
0	−0.62132	−0.55455	−0.56073	−0.55873	−0.55773	−0.5555
0.2	−0.46855	−0.37820	−0.37466	−0.37482	−0.37386	
0.5	−0.16740	−0.09710	−0.08844	−0.08739	−0.08733	
1.0	+0.00251	+0.00806	+0.02125	+0.02370	+0.02406	
2.0	0.04329	0.02399	0.02595	0.02871	0.02976	
4.0	0.02524	0.01704	0.01407	0.01371	0.01408	
6.0	0.01380	0.01091	0.00901	0.00820	0.00802	

$b_{\mathrm{II}}^{(0)}$

$\omega_2\tau$ \ M	2	3	4	5	6
0	0.00000	0.00000	0.00000	0.00000	0.00000
0.2	0.29010	0.28334	0.29050	0.29005	0.28955
0.5	0.33514	0.27137	0.27684	0.27798	0.27770
1.0	0.20934	0.14535	0.14126	0.14237	0.14260
2.0	0.08177	0.06046	0.05083	0.04885	0.04884
4.0	0.01924	0.01926	0.01642	0.01444	0.01354
6.0	0.00677	0.00809	0.00769	0.00690	0.00628

*) Value calculated by Spitzer and Härm, see reference 2).

Table III. Computed values of $b_{\mathrm{I}}^{(-1)}$, $b_{\mathrm{II}}^{(-1)}$ and $b_{\mathrm{I}}^{(1)}$ for the thermal conductivity in a plasma with $Z=1$.

$b_{\mathrm{I}}^{(-1)}$

$\omega_2\tau$ \ M	2	3	4	5	6	∞ *)
0	0.41421	0.66358	0.66636	0.66706	0.66761	0.6679
0.2	0.35105	0.52777	0.51959	0.51955	0.51998	
0.5	0.22331	0.27375	0.28228	0.28126	0.28125	
1.0	0.13789	0.12084	0.13774	0.13961	0.13954	
2.0	0.08016	0.05364	0.05610	0.05950	0.06055	
4.0	0.03449	0.02506	0.02188	0.02168	0.02218	
6.0	0.01789	0.01466	0.01263	0.01184	0.01172	

$b_{\mathrm{II}}^{(-1)}$

$\omega_2\tau$ \ M	2	3	4	5	6
0	0.00000	0.00000	0.00000	0.00000	0.00000
0.2	−0.13093	−0.25620	−0.25376	−0.25375	−0.25415
0.5	−0.16763	−0.30277	−0.28812	−0.28754	−0.28759
1.0	−0.14123	−0.22012	−0.22387	−0.22095	−0.22061
2.0	−0.11223	−0.13329	−0.14398	−0.14554	−0.14516
4.0	−0.08013	−0.07934	−0.08240	−0.08449	−0.08533
6.0	−0.05972	−0.05803	−0.05846	−0.05931	−0.05995

$b_{\mathrm{I}}^{(1)}$

$\omega_2\tau$ \ M	2	3	4	5	6
0	0.70711	0.88388	0.89379	0.89382	0.89385

*) Value calculated by Spitzer and Härm, see reference 2).

have made calculations for the plasma with $Z=1$. The collision integrals which we need are calculated in Appendix. Computed values of $e^{(0)}$, $b^{(0)}$, $b^{(-1)}$ and $b^{(1)}$ for various strengths of the magnetic field are shown in Tables I through III. In the absence of the magnetic field Spitzer and Härm's values[2], which are obtained by solving the Fokker-Planck's equation, are also presented in these tables.

From these tables we see that, for all transport coefficients in a magnetic field of any strength, the values in the 6th approximation have accuracy of three decimal places. Especially our values of the 6th approximation coincide perfectly well with values of Spitzer and Härm.

The similar calculations with ours were also made by Landshoff for cases: (i) the 3rd approximation in the presence of the magnetic field[5], (ii) up to the 5th approximation in the absence of the magnetic field.[1]

For convenience of the practical uses, the $e^{(0)}$, $c^{(0)}$, and $b^{(-1)}$ in the 6th approximation have been computed in detail and presented in Table IV. The $b^{(1)}$ in this approximation has been already shown in Table III. For the deuterium plasma, for example, the $M_2^{1/2}$ is 0.0165 so the correction term $M_2^{1/2}b^{\mathrm{I}(1)}$ for λ^{I} is necessary to get values which are accurate to three places of decimals.

In conclusion the author wishes to express his sincere thanks to Prof. T. Kihara for his continual guidance and his kindness in reading the original manuscript. Thanks are also due to Mr. Y. Ishibashi for the permission to use his program for solving the simultaneous linear equations. The present work has been supported by the Asahi Fellowship for Nuclear Fusion Research.

Table IV. Computed values of $e^{\mathrm{I}(0)}$, $e^{\mathrm{II}(0)}$, $c^{\mathrm{I}(0)}$, $c^{\mathrm{II}(0)}$, $b^{\mathrm{I}(-1)}$, and $b^{\mathrm{II}(-1)}$ in the 6th approximation as function of $\omega_2\tau$.

$\omega_2\tau$	$e^{\mathrm{I}(0)}$	$e^{\mathrm{II}(0)}$	$c^{\mathrm{I}(0)}$	$c^{\mathrm{II}(0)}$	$b^{\mathrm{I}(-1)}$	$b^{\mathrm{II}(-1)}$
0	1.97111	0.00000	−0.28295	0.00000	0.66761	0.00000
0.05	1.94167	−0.22950	−0.28132	0.01735	0.65500	−0.08449
0.1	1.85948	−0.43693	−0.27672	0.03364	0.62070	−0.15819
0.15	1.73976	−0.60762	−0.26986	0.04813	0.57290	−0.21496
0.2	1.60005	−0.73667	−0.26153	0.06055	0.51998	−0.25415
0.3	1.31451	−0.88418	−0.24297	0.07954	0.42004	−0.29136
0.4	1.06615	−0.92981	−0.22434	0.09215	0.34058	−0.29635
0.5	0.86834	−0.92102	−0.20695	0.10030	0.28125	−0.28759
0.6	0.71512	−0.88684	−0.19123	0.10535	0.23705	−0.27406
0.7	0.59667	−0.84261	−0.17718	0.10827	0.20347	−0.25954
0.8	0.50433	−0.79589	−0.16469	0.10971	0.17734	−0.24553
0.9	0.43142	−0.75025	−0.15359	0.11012	0.15650	−0.23251
1.0	0.37307	−0.70723	−0.14370	0.10982	0.13954	−0.22061
1.5	0.20456	−0.53897	−0.10751	0.10337	0.08726	−0.17516
2.0	0.12932	−0.43038	−0.08503	0.09470	0.06055	−0.14515
2.5	0.08930	−0.35676	−0.07004	0.08646	0.04464	−0.12381
3.0	0.06546	−0.30405	−0.05963	0.07928	0.03431	−0.10778
3.5	0.05012	−0.26462	−0.05205	0.07316	0.02723	−0.09530
4.0	0.03968	−0.23407	−0.04632	0.06801	0.02218	−0.08533
4.5	0.03225	−0.20976	−0.04189	0.06370	0.01846	−0.07720
5.0	0.02678	−0.18997	−0.03828	0.06004	0.01564	−0.07046
5.5	0.02263	−0.17357	−0.03527	0.05691	0.01345	−0.06478
6.0	0.01941	−0.15976	−0.03273	0.05418	0.01172	−0.05995

Appendix

A part of the collision integrals which we need are treated by many authors[3][10], especially for the case of the Coulomb interaction, by Landshoff[5].

For convenience we introduce the velocities of the center of masses $\boldsymbol{G}$ and of the relative motion $\boldsymbol{g}_{21}$, instead of the velocities of two particles $\boldsymbol{c}_1$ and $\boldsymbol{c}_2$, i.e.

$$\boldsymbol{c}_1=\boldsymbol{G}-M_2\boldsymbol{g}_{21}\ , \qquad \boldsymbol{c}_2=\boldsymbol{G}+M_1\boldsymbol{g}_{21}\ , \tag{A·1}$$

or in a non-dimensional form

$$\begin{aligned} \boldsymbol{w}_1&=M_1{}^{1/2}\boldsymbol{X}-M_2{}^{1/2}\boldsymbol{g}\ , \\ \boldsymbol{w}_2&=M_2{}^{1/2}\boldsymbol{X}+M_1{}^{1/2}\boldsymbol{g}\ , \end{aligned} \tag{A·2}$$

where

$$M_1=\frac{m_1}{m_1+m_2}\ ; \qquad M_2=\frac{m_2}{m_1+m_2}\ ,$$

$$\boldsymbol{X}=\sqrt{\frac{m_1+m_2}{2kT}}\boldsymbol{G}\ , \quad \boldsymbol{g}=\sqrt{\frac{m_1m_2}{2(m_1+m_2)kT}}\boldsymbol{g}_{21}\ .$$

The Jacobian of this transformation is given by

$$\frac{\partial(\boldsymbol{X},\boldsymbol{g})}{\partial(\boldsymbol{c}_1,\boldsymbol{c}_2)}=\frac{(m_1m_2)^{3/2}}{(2kT)^3}\ . \tag{A·3}$$

The collision integral $[\boldsymbol{w}_1S_{3/2}{}^{(p)}(w_1{}^2),\ \boldsymbol{w}_2S_{3/2}{}^{(q)}(w_2{}^2)]_{12}$ is, by definition, equal to

$$\frac{1}{n_1n_2}\iiiint d\boldsymbol{c}_1d\boldsymbol{c}_2g_{21}bdbd\varepsilon\ f_1{}^{(0)}f_2{}^{(0)}\{\boldsymbol{w}_1S_{3/2}{}^{(p)}(w_1{}^2)-\boldsymbol{w}_1{}'S_{3/2}{}^{(p)}(w_1{}'^2)\}\cdot\boldsymbol{w}_2S_{3/2}{}^{(q)}(w_2{}^2).$$

Using the generating function of the Sonie polynomials

$$(1-s)^{-5/2}e^{-xs/1-s}=\sum s^pS_{3/2}{}^{(p)}(x)\ ,$$

we obtain the collision integral $[\boldsymbol{w}_1S_{3/2}{}^{(p)}(w_1{}^2),\ \boldsymbol{w}_2S_{3/2}{}^{(q)}(w_2{}^2)]_{12}$ as the coefficient of s^pt^q in the expansion of

$$(1-s)^{-5/2}(1-t)^{-5/2}\ \pi^{-3}\iiint\{H_{12}(0)-H_{12}(\chi)\}g_{21}\ bdbd\varepsilon\ d\boldsymbol{g} \tag{A·4}$$

in powers of s and t. Here $H_{12}(\chi)$ is defined by

$$H_{12}(\chi)=\int(\boldsymbol{w}_1{}'\cdot\boldsymbol{w}_2)\exp-(X^2+g^2+Sw_1{}'^2+Tw_2{}^2)d\boldsymbol{X}$$

where

$$S=\frac{s}{1-s}\ , \qquad T=\frac{t}{1-t}\ ,$$

and χ is the diffraction angle for the orbit of relative motion, i.e. $\boldsymbol{g}\cdot\boldsymbol{g}=g^2\cos\chi$.

The integral $H_{12}(\chi)$ becomes after straight forward calculations

$$\begin{aligned} &\pi^{-3/2}(1-s)^{-5/2}(1-t)^{-5/2}(M_1M_2)^{-1/2}H_{12}(\chi) \\ &\qquad=\exp(-j_{12}g^2)(1-M_2s-M_1t)^{-5/2}\{\frac{3}{2}+(1-j_{12}-\cos\chi)g^2\}\ , \end{aligned} \tag{A·5}$$

where $\qquad j_{12}=\{1-2M_1M_2st\,(1-\cos\chi)\}/(1-M_2s-M_1t)\ .$

Now we expand $\{H_{12}(0)-H_{12}(\chi)\}$ in terms of $(1-\cos\chi)$ and need only the linear term, because the Rutherford scattering cross section is proportional to $(1-\cos\chi)^{-2}$, so the contributions of large angle scattering are negligible. Then we get

$$\pi^{-3/2}(1-s)^{-5/2}(1-t)^{-5/2}(M_1M_2)^{-1/2}\{H_{12}(0)-H_{12}(\chi)\}=-(1-M_2s-M_1t)^{-5/2}\exp\left(-\frac{g^2}{1-M_2s-M_1t}\right)$$

$$\times g^2(1-\cos\chi)\left[1+\frac{5M_1M_2}{1-M_2s-M_1t}st-\frac{2M_1M_2st}{(1-M_2s-M_1t)^2}g^2\right].$$

Substituting this equation into the equation (A·4) we finally obtain

$$\sum_p\sum_q s^pt^q[w_1S_{3/2}{}^{(p)}(w_1{}^2),\, w_2S_{3/2}{}^{(q)}(w_2{}^2)]_{12}$$
$$=-8(M_1M_2)^{1/2}\left(\frac{2\pi kT}{m_{12}}\right)^{1/2}\left(\frac{Ze^2}{2kT}\right)^2\ln\left(\frac{kTl_D}{Ze^2}\right)$$
$$\times\frac{1}{(1-M_2s-M_1t)^{3/2}}\left[1+\frac{3M_1M_2st}{1-M_2s-M_1t}\right], \tag{A·6}$$

where m_{12} is the reduced mass.

We note here that M_1 and M_2 appear only in the combination M_1t, M_2s, so the collision integral $[w_1S_{3/2}{}^{(p)},\, w_2S_{3/2}{}^{(q)}]_{12}$ has $M_1{}^{q+1/2}\,M_2{}^{p+1/2}$ as a factor.

By similar method the collision integral $[w_1S_{3/2}{}^{(p)}(w_1{}^2),\, w_1S_{3/2}{}^{(q)}(w_1{}^2)]_{12}$ can be calculated and we write here only the results:

$$\sum_p\sum_q s^pt^q[w_1S_{3/2}{}^{(p)}(w_1{}^2),\, w_1S_{3/2}{}^{(q)}(w_1{}^2)]_{12}=$$
$$8M_2\left(\frac{2\pi kT}{m_{12}}\right)^{1/2}\left(\frac{Ze^2}{2kT}\right)^2\ln\left(\frac{kTl_D}{Ze^2}\right)$$
$$\times\frac{a^{-3/2}}{1-st}\left[1+\frac{5M_1{}^2}{a}st+\frac{2M_1M_2}{a}\frac{st(1-s)(1-t)}{1-st}\right], \tag{A·7}$$

where $a=1-M_2(s+t)+(M_2-M_1)st$.

From this we obtain

$$\sum_p\sum_q s^pt^q[w_1S_{3/2}{}^{(p)}(w_1{}^2),\, w_1S_{3/2}{}^{(q)}(w_1{}^2)]_{12}$$
$$=8M_2\left(\frac{2\pi kT}{m_2}\right)^{1/2}\left(\frac{Ze^2}{2kT}\right)^2\ln\left(\frac{kTl_D}{Ze^2}\right)\frac{1}{(1-st)^{5/2}}\left[1+\frac{5st}{1-st}\right]+O(M_2{}^2), \tag{A·8}$$

$$\sum_p\sum_q s^pt^q[w_2S_{3/2}{}^{(p)}(w_2{}^2),\, w_2S^{5/2(q)}(w_2{}^2)]_{12}$$
$$=8\left(\frac{2\pi kT}{m_2}\right)^{1/2}\left(\frac{Ze^2}{2kT}\right)^2\ln\left(\frac{kTl_D}{Ze^2}\right)\frac{1}{(1-s)^{3/2}(1-t)^{3/2}(1-st)}+O(M_2) \tag{A·9}$$

It is clear from the definition, the collision integrals $\sum\limits_p\sum\limits_q s^pt^q[w_2S_{3/2}{}^{(p)},\, w_2S_{3/2}{}^{(q)}]_2$ can be obtained from

$$\sum_p\sum_q s^pt^q\{w_2S_{3/2}{}^{(p)}(w_2{}^2),\, w_1S_{3/2}{}^{(q)}(w_1{}^2)]_{12}$$
$$+[w_2S_{3/2}{}^{(p)}(w_2{}^2),\, w_2S_{3/2}{}^{(q)}(w_2{}^2)]_{12}\}$$

by taking $M_1=M_2=\frac{1}{2}$, $m_{12}=\frac{m_2}{2}$, and $Z=1$.

Hence we get

$$\sum_p\sum_q s^pt^q[w_2S_{3/2}{}^{(p)}(w_2{}^2),\, w_2S_{3/2}{}^{(q)}(w_2{}^2)]_2=8\sqrt{2}\left(\frac{2\pi kT}{m_2}\right)^{1/2}\left(\frac{e^2}{2kT}\right)^2\ln\left(\frac{kTl_D}{e^2}\right)$$
$$\times\frac{st}{[1-\frac{1}{2}(s+t)]^{5/2}(1-st)^2}\left[1-\frac{1}{2}(s+t)-\frac{1}{8}st+\frac{1}{4}st(s+t)-\frac{3}{8}(st)^2\right]. \tag{A·10}$$

From the mass dependence of this equation we can deduce the relation

$$[w_1S_{3/2}{}^{(p)}(w_1{}^2),\, w_1S_{3/2}{}^{(q)}(w_1{}^2)]_1=M_2{}^{1/2}[w_2S_{3/2}{}^{(p)}(w_2{}^2),\, w_2S_{3/2}{}^{(q)}(w_2{}^2)]_2 . \tag{A·11}$$

The equations (A·9) and (A·10) are also obtained by Landshoff.[5]

References

1) R. Landshoff: Phys. Rev. **82** (1951) 442.
2) L. Spitzer, Jr. and R. Härm: Phys. Rev. **89** (1953) 977.
3) H. Schirmer and J. Friedrich: Z. Phys. **151** (1958) 174; **153** (1959) 563.
4) T. G. Cowling: Proc. Roy. Soc. (London) **A183** (1945) 453.
5) R. Landshoff: Phys. Rev. **76** (1949) 904.
6) E. S. Fradkin: J. Exp. Theor. Phys. (U.S.S.R.) **32** (1957) 1176.
7) S. I. Braginskii: J. Exp. Theor. Phys. (U.S.S.R.) **33** (1957) 459.
8) W. Marshall: A.E.R.E. T/R 2419.
9) T. Kihara, Y. Midzuno, and S. Kaneko: J. Phys. Soc. Japan **15** (1960) 1101.
10) See, for example, S. Chapman and T. G. Cowling: The Mathematical Theory of Non-Uniform Gases (Cambridge University Press, London, 1953).

Errata

Study on Some Tl Base Alloys, with Reference to their Electronic Structure

By Ryōji SUGANUMA

J. Phys. Soc. Japan **15** (1960) 1395

Page	Column	Line		Shoubd be rerd
1396	right	8	**Pase Diagrams**	**Phase Diagrams**
1404	Fig. 8		Lattic constant	Lattice Constant
1405	right	2 from the bottom	Billouin	Brillouin
1406	left	1	considerably	considerable
1407	Fig. 12, caption		per lattice at site	per lattice site

Short Notes

This section is intended to secure prompt publication of important discoveries in physics. The reports should not exceed 800 words in length. A figure of size 7 cm × 7 cm will be counted as 150 words.

J. PHYS. SOC. JAPAN **15** (1960) 1697

Effect of Heat-Treatment upon Sintered Cadmium Sulphide Photoconductive Films

by Saburo KITAMURA

Central Research Laboratories, Matsushita Electric Industrial Co., Osaka

(Received June 23, 1960)

When the sintered CdS:Cl:Cu photoconductive films[1,2] prepared by the flux method using $CdCl_2$ as flux material were heated in vacuum or in inert gas, the relation between dark current and temperature became irreversible, the activation energy decreased, and the trap concentration increased, and it was found that there appeared a peak at room temperature in thermally stimulated current curve.

The sintered CdS:Cl:Cu photoconductive films were obtained by sintering on a base plate of fused quartz of 20 × 20 mm size. The material of electrodes was gold evaporated on the surface of fused quartz before sintering CdS layers. The distance between two electrodes was 0.5 mm and the length of electrodes was 20 mm. With evaporated gold electrodes, the contact between electrodes and CdS was nonohmic below 0.1 volt while ohmic above 0.1 volt. When the sintered films were heated at a rate of 1°C/min and the dark current was measured by applying a D. C. voltage of 100 volts, the relation between dark current and temperature was reversible below 90°C, but it became irreversible above 90°C.

The relations between conductivity and $1/T$(°K) of both untreated films and films treated at 160°C in vacuum are shown in Fig. 1. It is seen that by heat-treatment in vacuum, the activation energy of sintered films decreases to a value of one twentieth of the initial one. The results of the measurements on thermally stimulated current are plotted in Fig. 2. Sintered films cooled at liquid air temperature were irradiated by a light from an incandescent lamp and a D. C. voltage of 30 volts was applied in darkness, and then they were heated at a rate of about 1°C per second. The variation of current in heating process was recorded by an X–Y recorder. The trap concentration of sintered film heat-treated in vacuum is about twenty times that of the initial value, and there is a peak at about room temperature in thermally stimulated current curve of the sintered film heat-treated in vacuum.

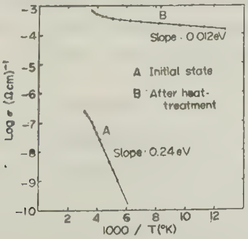

Fig. 1. Conductivity *versus* $1/T$(°K).

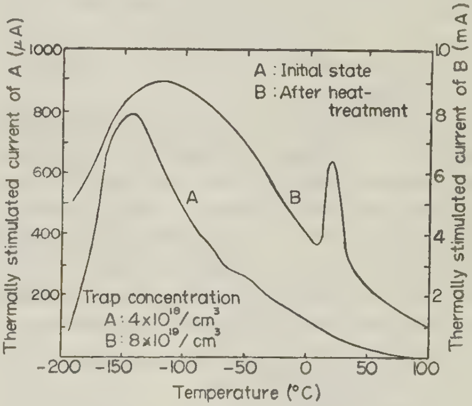

Fig. 2. Temperature dependence of thermally stimulated current; 30 volts D. C. was applied, heating rate about 1°C/sec.

Muscheid[3] and Woods[4] reported that CdS single crystal heated at 200∼300°C in vacuum had high conductivity due to sulphur vacancies. In sintered films these phenomena were found to appear above 90°C. By measuring the thermally stimulated current it is proved that the sintered films have large trap concentrations, but it is still unknown whether the peak at room temperature in thermally stimulated current curve of sintered films heated in vacuum is produced by sulphur vacancies or by other defects. Experiments are now carried on in order to investigate the peak at room temperature.

The author wishes to thank Professor K. Tanaka, Kyoto University, for his advice.

References

1) S. Kitamura: Conference, Soc. Appl. Phys, Japan, March (1960).
2) C. P. Hadley and E. Fischer: RCA Rev. **20** (1959) 635.
3) W. Muscheid: Ann. d. Phys. **13** (1959) 322.
4) J. Woods: J. Electron. Control **3** (1957) 225.

J. PHYS. SOC. JAPAN **15** (1959) 1698

Ferroelectricity in The Potassium Ferrocyanide Group Ferroelectrics Substituted by Deuterium for Hydrogen

By Shigeru WAKU, Kunio MASUNO and Toshisuke TANAKA

Electrical Communication Laboratory, Nippon Telegraph and Telephone Public Corporation, Tokyo

(Received July 13, 1960)

In the previous papers,[1)2)] we reported the ferroelectric behavior in potassium ferrocyanide, $K_4Fe(CN)_6 \cdot 3H_2O$, and its isomorphous substances, $K_4Ru(CN)_6 \cdot 3H_2O$ and $K_4Os(CN)_6 \cdot 3H_2O$ and $K_4Mn(CN)_6 \cdot 3H_2O$. We attempted to substitute the water of crystallization of these cyano complexes by deuterium oxide.

After the dehydration of powdered samples of these cyano complexes by heating for 6 hours at 110°C, mother solutions were prepared by dissolving these dehydrated powders in heavy water containing 99.9% D_2O. Single crystals were grown by slow cooling of these mother solutions. In the case of $K_4Mn(CN)_6 \cdot 3D_2O$, as it was very unstable, we could not obtain deuterated compounds.

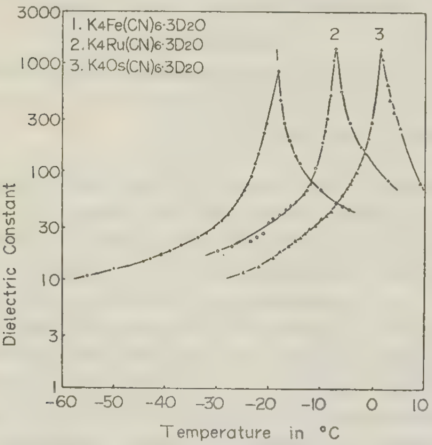

Fig. 1. Dielectric constant along [10$\bar{1}$] direction of deuterated potassium ferrocyanide group ferroelectrics.

Ferroelectric behavior of these deuterated cyano complexes were not significantly different from those of the normal cyano complexes except a little shifting of the Curie point toward the higher temperature side. Fig. 1 shows the temperature dependence of the small signal dielectric constant of these cyano complexes in [10$\bar{1}$] direction. Only one peak coresponding to the Curie point is shown in each curve. In [101] and [010] directions, no more than very weak anomaly is etected. Ferroelectric hysteresis loop appears only in [10$\bar{1}$] direction. Fig. 2 shows the temperature dependence of the spontaneous polarization P_s and coercive field E_c of these deuterated cyano complexes. The spontaneous polarization of the deuterated cyano complexes are somewhat larger than that of the normal cyano complexes. Table 1 shows the transition temperature of the normal and deuterated cyano complexes. Temperature sifting of the transition point by deuterium substitution is the smallest among the ready examined ferroelectrics.

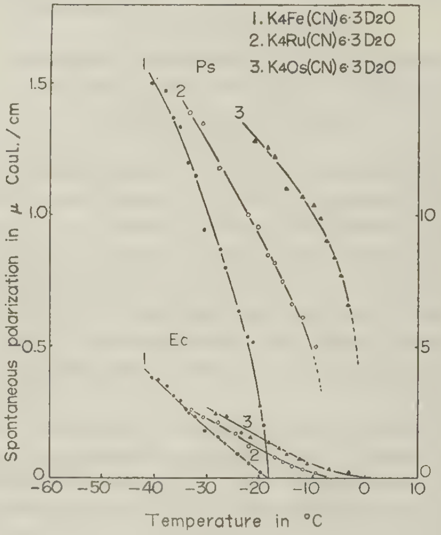

Fig. 2. Spontaneous polarization and coercive field along [10$\bar{1}$] direction of deuterated potassium ferrocyanide group ferroelectrics.

Table 1. The transition temperature of the normal and deuterated potassium ferrocyanide group ferroelectrics.

$K_4Fe(CN)_6 \cdot 3H_2O$	−24.5°C	$K_4Ru(CN)_6 \cdot 3H_2O$	−14.5°C
$K_4Fe(CN)_6 \cdot 3D_2O$	−18.0°C	$K_4Ru(CN)_6 \cdot 3D_2O$	− 7.3°C
$K_4Os(CN)_6 \cdot 3H_2O$	− 2.4°C	$K_4Mn(CN)_6 \cdot 3H_2O$	−40 °C
$K_4Os(CN)_6 \cdot 3D_2O$	1.8°C		

Authors are very grateful to Dr. H. Hirabayashi for his helpful discussions.

References

1) S. Waku, H. Hirabayashi, H. Toyoda, H. Iwasaki and R. Kiriyama: J. Phys Soc. Japan. **14** (1959) 973.
2) S. Waku, K. Masuno, T. Tanaka and H. Iwasaki: J. Phys. Soc. Japan. **15** (1960).

J. PHYS. SOC. JAPAN **15** (1960) 1699

Impurity Shift of Pure Quadrupole Resonance Frequency

By Yoshiro IMAEDA

Faculty of Engineering, Tokushima University, Tokushima

(Received July 6, 1960)

It is well known that the line width of pure quadrupole resonances increases and its intensity decreases with the increase of impurity content in samples[1], but the frequency shift caused by the impurities has not been noticed except for a few cases[2,3] with exceptionally large shifts.

A careful measurement, however, revealed that an observable amount of the impurity shift exists in almost all cases. It is the purpose of this note to present the examples of these impurity shifts for bromates and chlorates.

In the present experiment, stable and sensitive regenerative spectrometers[4,5] operated at a low rf level are found to be essential in order to get faithful absorption curves without any dielectric heating of the samples which, if appreciable in magnitude, might result in a "temperature shift". And the temperature of the samples (0°C in the present experiment) ought to be kept constant with an accuracy of a few thousandths of a degree in every run in order to keep the temperature shift of the resonance frequency below the amount of the impurity shift.

Some of the experimental results are tabulated in Table I. The sign of the impurity shift is either positive or negative with respect to the frequency of pure specimen depending upon the kinds of the impurities. The general tendency is such that the larger size impurities than the original ions, when some of the latter ones are replaced by the former ones, decrease the frequency (−shift), and the smaller size impurities increase the frequency (+shift). The lines are always Gaussian, and no asymmetry in the line shape is observed for all specimens.

The dominant cause of the present impurity shift is believed to be due to a successive distortion of electronic wave functions about the impurities. And the change in the amplitude of the lattice vibrations due to impurities[3] would not be responsible for the present impurity shift, because the temperature dependence of the impurity shift for bromates is not noticed[6].

The details of the discussions as well as the experimental procedure will be published in the comming issue of the Journ. Sci. Hiroshima Univ. Ser. A.

It is a pleasure of the author to express his indebtedness to Professor H. Tazaki of Hiroshima University for the stimulating interest he has taken in the progress of this work and to Professor T. Kushida of the same University for the suggestion of the present investigation and his helpful advice and discussions and also to Professor Y. Kôi of Tokushima University for his valuable comments.

Table I. Impurity shift of P.Q.R. frequency. The observed shift in the resonance frequency caused by impurities in the lattice is shown in the fourth column, where a +sign and a −sign correspond to the increase and the decrease in the center frequency respectively. And the first column designates the host material whose halogen nuclei are observed.

Host material	Impurity	Impurity content (mol%)	Frequency shift (cps)	Halfwidth (cps)
$KClO_3$	$NaClO_3$	0.9±0.1	+1100±200	2280±200
$KClO_3$	KNO_3	0.44±0.03	+135±45	1600±150
$KClO_3$	$KBrO_3$	0.39±0.03	−250±20	1880±100
$KClO_3$	$AgClO_3$	0.97±0.05	+630±30	1450±100
$KClO_3$	$LiClO_3$		0±50	1100±100
$KClO_3$	$Ba(ClO_3)_2$	0.13±0.03	0±40	1350±100
$KClO_3$	$Ni(ClO_3)_2$	0.16±0.03	0±30	1100±100
$NaClO_3$	$KClO_3$	7.2 ±0.1	−760±30	1800±100
$NaClO_3$	$NaNO_3$	2.23±0.03	+90±30	1650±100
$NaClO_3$	$NaBrO_3$	0.48±0.03	−1015±70	2100±100
$NaClO_3$	$AgClO_3$	1.3 ±0.15	−1320±40	2100±100
$KBrO_3$	$NaBrO_3$		0±500	10,000±500
$KBrO_3$	$KClO_3$		+3000±300	9,700±500
$NaBrO_3$	$KBrO_3$		−2700±300	13,000±500
$NaBrO_3$	$NaClO_3$		+3300±150	8,300±500
$NaBrO_3$	$NaIO_3$		−2000±200	7,000±500
$NaBrO_3$	$LiBrO_3$		0±200	8,000±500

References

1) For example, J. Duchesne and A Monfils: Compt. rend. **238** (1954) 1801.
2) C. Dean: J. Chem. Phys. **23** (1955) 1734.
3) B. Dreyfus: Ann. physique **3** (1958) 683.
4) G. Watkins: thesis, Harvard University, 1952 (unpublished).
5) G. B. Benedek and T. Kushida: Phys. Rev. **118** (1960) 46.
6) K. Saiki: private communication.

J. Phys. Soc. Japan **15** (1960) 1700

Measurement of Temperature Dependence of T_1 of Proton in Some High Polymers by Pulsed NMR Technique

By Takao Kawai,* Masahumi Sasaki,**
Akira Hirai,** Tsuneo Hashi,**
and Akira Odajima***

**Yoshida College, Kyoto University*
***Department of Physics, Faculty of Science, Kyoto University*
****Research Institute of Applied Electricity, Hokkaido University*

(Received June 10, 1960)

In order to add to the information about the internal motion in high polymer, we have measured the spin-lattice relaxation time (T_1) of proton in some high polymers, in the temperature region from 20°C to 300°C, by 90°-90° pulse method at 25 Mc/sec. The description of the apparatus was already given.[1] The samples were poly-vinyle acetate (PVAc), poly-methyl acrylate (PMA), poly-methyl methacrylate (PMMA), etc. The error in the measurement was about ±10%.

The results obtained are shown in Fig. 1. For PVAc and PMA, the curves of log T_1 *versus* $1/T$ are simply V-shaped, and the dominant mechanism which determines T_1 is considered to the segmental motion. For PMMA, the curve is not V-shaped but has a tendency to have another minimum at lower temperature.

The correlation time of the internal motion in high polymer is distributed over a wide range, as well-known from the dielectric and mechanical relaxation experiments. Since simple analytic formulas relating T_1 with distributed correlation time are not available at present, we have tentatively used BPP theory for analysis, namely.

$$\frac{1}{T_1}=\frac{3}{10}\frac{\gamma^4\hbar^2}{b^6}\left\{\frac{\tau_c}{1+\omega^2\tau_c^2}+\frac{4\tau_c}{1+4\omega^2\tau_c^2}\right\},$$

$$\tau_c=\tau_0\exp\left(\frac{\Delta E}{RT}\right)$$

The results thus obtained are shown by the dashed curves in Fig. 1.

For further study, it is desirable to measure T_1 at lower temperature and at various resonance frequencies, and the spin-echo decay time. We are now proceeding along this line.

The authors express their sincere thanks to Prof. I. Takahashi for his continual interest and discussions. Their thanks are also due to the members of our laboratory for their assistances.

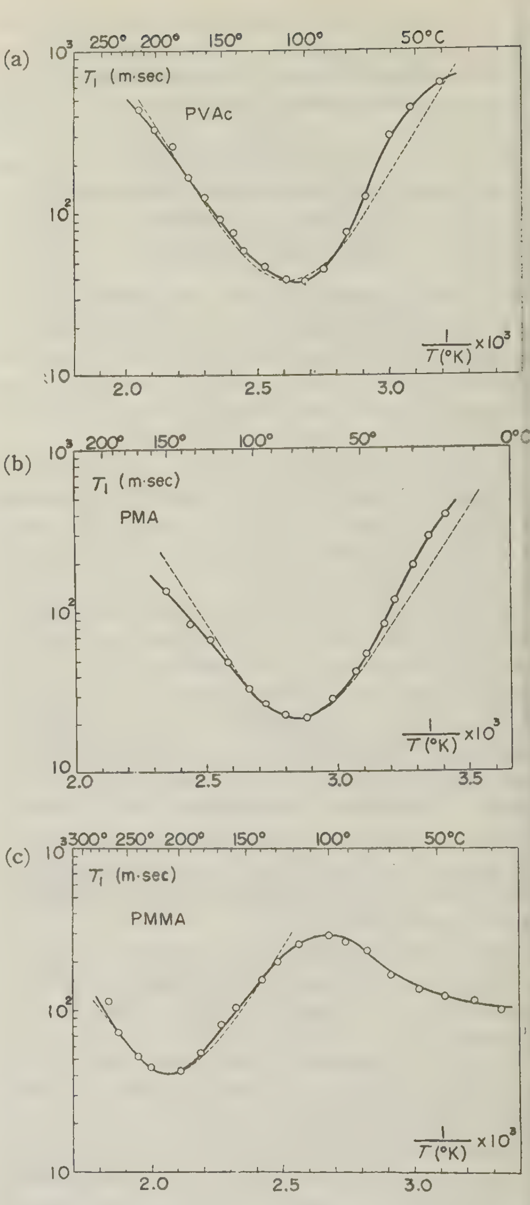

Fig. 1. Temperature dependence of T_1 of proton in some polymers. Solid curve represents the experimental results. Dashed curve represents the temperature dependence obtained by BPP theory, using following parameters.

(a) Sample; PVAc,
b=1.9Å, $\tau_0=6\times10^{-16}$ sec, ΔE=12 Kcal/mole.
(b) Sample; PMA,
b=1.8Å, $\tau_0=2\times10^{-16}$ sec, ΔE=11 Kcal/mole.
(c) Sample; PMMA,
b=1.9Å, $\tau_0=2\times10^{-14}$ sec, ΔE=12 Kcal/mole.

References

1) T. Hashi, A. Hirai, M. Sasaki and T. Kawai: Memoirs of the College of Science, University of Kyoto, Series A **29** (1959) 205.

J. Phys. Soc. Japan **15** (1960) 1701

On the Mechanism of the Electrical Conduction in CdSe

By Hirosi Tubota, Hiromichi Suzuki
and Kazuyoshi Hirakawa

General Education Department, Kyushu University, Fukuoka

(Received June 28, 1960)

In order to study the mechanism of the electrical conduction in CdSe, the following experiments were performed. On the surface of single crystals of n-type CdSe obtained by slow cooling from the melt of stoichiometric composition, various elements of Group I, II, III, IV and VI were evaporated, and the crystals were heat-treated at various temperatures for various durations so that the elements diffused into the bulk material. These treatments were performed in vapor of the corresponding elements. The changes of resistivities of the treated specimens are shown in following figures.

Fig. 1 shows the behaviors of room-temperature resistivities of the specimens as functions of the duration of heat treatment at 350°C.

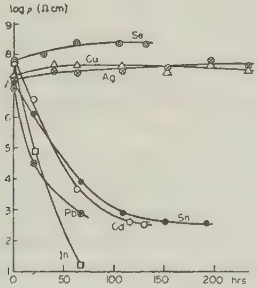

Fig. 1. Electrical resistivity against the duration of heat treatment for specimens treated at 350°C.

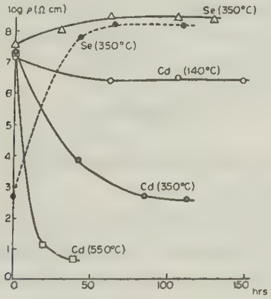

Fig. 2. Electrical resistivity of samples doped with Cd and Se.

Fig. 2 shows the effects of doping with Se and also with Cd at different temperatures. The result shown by the dashed curve in the figure was obtained for the specimen doped with Se after doping with Cd at 350°C.

It was found that resistivities of the heat-treated specimens changed toward the value of those of CdSe as grown when specimens were kept in air at room temperature.

Considering these results, we can conclude that the impurity centers contributing to the electrical conduction in CdSe may presumably be Se vacancies. Hence, if a specimen was treated with Se, its resistivity may increase because of the decrease of Se vacancies, whereas if treated with Cd the reverse is the case. As the doped atoms of Group III and IV may locate in the interstitial sites, resistivities decrease. In the case of Group I, resistivities increase slightly, This may be because these elements may substitute Cd atoms, but their diffusion constants are small. In the cases of foreign elements, it may be determined by consideration of atomic radii that whether they substitute the lattice atoms or locate in the interstitial sites. The atomic radii of the elements are given in Table I after Wyckoff. Since the atomic radii of Cu and Ag are smaller than that of Cd, they substitute Cd atoms. On the other hand, since the radii of In and Pb are larger than those of Cd and Se, they locate in the interstitial sites. As the diffusion through the interstitial sites are easier, it can be understood that in the cases of In and Pb the changes of resistivity are large. In the case of Sn, however, the result is difficult to understand from this consideration.

As seen above, the electrical conduction in CdSe might be due to the presence of Se vacancies. This implies that the CdSe crystals obtained from the melt of stoichiometric composition are excess in Cd. This is in agreement with the suggestion¹⁾ that in chalcogenides the compound contains the excess of the element with higher boiling point.

The authers wish to express their sincere thanks to Prof. T. Okada for his kind advice.

Table I. Atomic radii after Wyckoff (in Å)

I	II	III	IV	VI
Cu				Se
1.27				1.16
Ag	Cd	In	Sn	
1.44	1.48	1.62	1.40	
			Pb	
			1.74	

Reference

1) Taromír Horák, Mojmír Machovec and František Kosak: C. A. Vol. 52, (1957), 16043C.

J. Phys. Soc. Japan **15** (1960) 1702

Characteristics of Krypton Counters

By Tatsusaburo Suzuki & Jiro Yuhara
Research & Development Institute, Japan
Tecchu Majima
Defence Agency, Tokyo
Japan Radio Company, Tokyo

(Received July 15, 1960)

In 1956 W. Parrish and T. R. Kohler⁽¹⁾ reported that they used a krypton counter (total pressure 500 mmHg) having 10% ethylene added to analyze the soft X-rays. But they did not describe the characteristics of the counter in detail. The authors experimented with the characteristics of krypton counter, since it seemed advantageous to use a krypton counter in order to analyze the soft X-rays because of high gas absorption obtained in the short length. The glass wall counters having gold sputtered cathodes and 0.05 mm.φ center wires were filled with 99.9% krypton gas made by Linde, and pure ethylene added as quenching gas. The partial pressures of krypton and ethylene were 150–500 mmHg and 2.5–52 mmHg, respectively. The counter out-puts were connected to the cathode-follower pre-amplifier plus Tracerlab pulse amplifier and counted by a Tracerlab super-scaler. The γ-ray 100 μc source of Cs^{137} was placed at the positions 10 cm, 20 cm, or 1 m distant from the counters.

The obtained discharging characteristics vs the partial pressures are shown in Fig. 1. It is evident from Fig. 1 that the characteristics of the counters depend mainly upon the partial pressures of ethylene, but not upon that of krypton. Because the counters having equal partial pressures of ethylene give similar plateau curves in spite of the differences of that of krypton, it seems possible to conclude that the characteristics of the counters are dependent upon only partial pressures, and not on the percentage of ethylene. At the partial pressures of ethylene which are lower than 8.5 mmHg the counters usually discharge continuously or semi-continuously at the voltages slightly higher than the starting voltages. At the partial pressure of ethylene higher than 45 mmHg they give only poor plateau curves. But at the partial pressures 17.5–35 mmHg of ethylene they give appreciable good plateau curves. The counting-rate of the counters giving good plateau curves was measured at the different sensitivities of the Tracerlab pulse amplifier from 1 mV to 100 mV. The counters out-puts were connected to the Tracerlab GM counter pre-amplifier and were counted. In this case the counts obtained agreed very well with the counts in the cases of pulse amplifier sensitivities 2–50 mV. Therefore it is evident that the counters experimented have Geiger-Müller counters properties. The counters containing mixtures of krypton and methane were also experimented. The partial pressures of methane were 10, 20, 30, 40, and 50 mmHg. They give poor plateau curves or discharge continuously. The counters containing mixtures of krypton and ethylene have good self-quenching properties. On the other hand the counters containing mixtures of krypton and methane have poor self-quenching properties. This fact can be accounted for by the fact that the ionization potential of the krypton is larger than that of the ethylene and less than that of the methane, and therefore the secondary emissions at the cathodes can be quenched in the krypton counter containing the ethylene and not in that containing the methane⁽²⁾. At the ethylene partial pressures which are less than 8.5 mmHg the counters discharge continuously, because the appreciable number of krypton ions can reach the cathodes after many collisions.

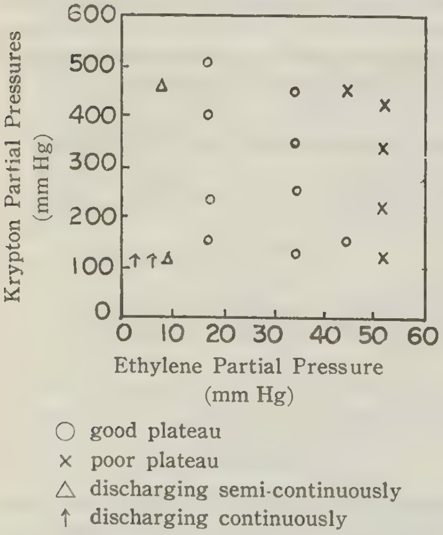

Fig. 1. Plotts of the krypton and ethylene partial pressures.

References:

1) W. Parrish & T. R. Kohler; Rev. Sci. Instr. **27** (1956) 795
2) S. A. Korff; Electron ane Nuclear Counters (2nd ed.) Chapt. 4

J. PHYS. SOC. JAPAN **15** (1960) 1703

Magnetoresistance Effect in the Magnetization Reversal of Permalloy Films

By Eiji TATSUMOTO, Kaizo KUWAHARA and Mitita GOTO

Department of Physics, Faculty of Science, Hiroshima University, Hiroshima

(Received June 23, 1960)

In Permalloy films, it has been accepted that the magnetization reversal takes place by domain wall motion and rotation in low frequency fields parallel and perpendicular to the easy direction, respectively[1)2)]. In the present work, this was confirmed by measuring the magnetoresistance effect which is expressed as

$$\Delta R/R = A \sin^2\theta \qquad (1)$$

where A is a constant and θ is the angle between the magnetization vector and primary current[3)].

The specimens used were two kinds of rectangular films of 80 Ni Permalloy (10 mm × 20 mm) which will be denoted by (//) and (⊥) depending on whether the lengthwise direction is parallel or perpendicular to the easy direction, respectively. They were made on glass substrates heated at 200°C by depositing in the presence of fields in vacuum and their thickness is about 2×10^3 A.

While the anisotropy field H_k has usually been determined by measuring the linear relation between B and H in low driving fields perpendicular to the easy direction[1)], it can also be determined by measuring the relation of $\Delta R/R$ and H in that case, because Eq. (1) can be rewritten as $\Delta R/R = A(1-H^2/H^2_k)$, since $\cos\theta = H/H_k$. Both linear relations, B–H and $\Delta R/R$–H^2, were found to be equally applicable, and the H_k obtained is 4.0 oe in the (//) specimen and 4.5 oe. in the (⊥) specimen.

Figs. 1 and 2 show B–H, dB/dt–H and $\Delta R/R$–H curves from the top to the bottom which were measured on the (//) and (⊥) specimens in a 60 cps field of 10 oe. peak. The observed B, dB/dt and $\Delta R/R$ and H are all parallel to the long side direction of the specimens.

In the (//) specimen, according to the B–H and dB/dt–H curves in Fig. 1, the magnetization reversal is interpreted as due to nucleation of reverse domains and their growth, as is commonly accepted. This interpretation is confirmed by the $\Delta R/R$–H curve in Fig. 1 (c), because it indicates the fact that very little rotation occurs. In detail, however, a small variation in $\Delta R/R$ is observed near the coercive force H_c as seen faintly in the figure. We suspect that it may be attributed not to a small coherent rotation but to local rotation on account of the fluctuation of H_k in direction and magnitude. The local rotation would presumably be responsible for nucleation of the reverse domains.

In the (⊥) specimen, it has been assumed that the B–H and dB/dt–H curves in Fig. 2 are due to coherent rotation. This is also confirmed by the $\Delta R/R$–H curve in Fig. 2 (c) which illustrates that there occurs almost coherent and continuous rotation with the variation of fields. In detail, however, the rotation does not seem to be perfectly coherent, because the maximum variation of $\Delta R/R$ is slightly smaller than A which is the maximum in the coherent rotation corresponding to the value at 90° in Eq. (1). We also suspect that, as in case of the (//) specimen, it may be attributed to the local fluctuation of H_k. In this magnetization process, the clockwise and anti-clockwise rotations must start simultaneously in different regions so that the boundaries would be fuzzy in the initial process but probably be converted abruptly to the distinct ordinary walls. Then, we suspect that the Barkhausen discontinuities observed near H_c in Fig. 2 (b) would be due to the abrupt conversion.

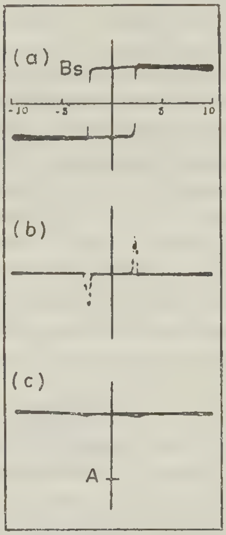

Fig. 1. The (//) specimen: (a) is B–H curve, (b) dB/dt–H curve and (c) $\Delta R/R$–H curve.

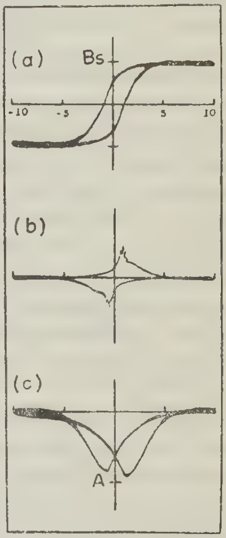

Fig. 2. The (⊥) specimen: (a) is B–H curve, (b) dB/dt–H curve and (c) $\Delta R/R$–H curve.

References

1) D. O. Smith: J. Appl. Phys. **29** (1958) 264.
2) C. D. Olson and A. V. Pohm: J. Appl. Phys. **29** (1958) 274.
3) R. M. Bozorth: *Ferromagnetism* (D. Van Nostrand Company, 1951) 752.

J. PHYS. SOC. JAPAN **15** (1960) 1704

Magnetostriction of Yttrium Iron Garnet

By Akira NAKAMURA and Yoshikazu SUGIURA
Electrotechnical Laboratory, Nagatacho,
Tokyo, Japan

(Received July 25, 1960)

The magnetostriction of polycrystalline Y.I.G. was measured by the method using the adhesive strain gauge. In order to measure the rather small change in length, the output signal of the strain gauge bridge was amplified by the chopper amplifier. The over-all sensitivity of the relative change in length reached nearly 2×10^{-8}. Somewhat modified method using coaxial cavity[1] was also used for checking the sign of the magnetostriction. Although the sensitivity is in the vicinity of 1×10^{-7}, the same sign for pure nickel metal was observed.

The sample was prepared from 99.9% Y_2O_3 and 99.99% Fe_2O_3 by sintering in air at 1350°C. The X-ray diffraction patterns showed no extra lines. The sample was placed in a Dewar vessel to avoid temperature fluctuation. The saturation magnetostriction of polycrystalline material is expressed as

$$\frac{\delta l}{l}=\frac{3}{2}\lambda_s(\cos^2\theta-1/3)$$

where θ is the angle between the magnetic field and the measured direction of length.

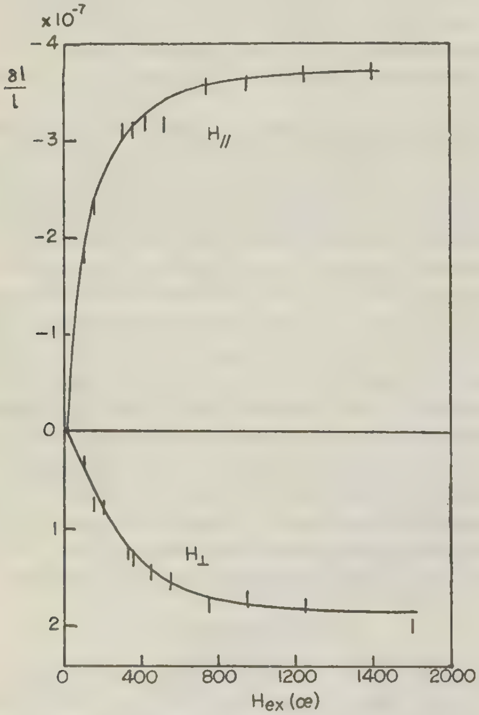

Fig. 1. The fractional change in length of polycrystalline Y.I.G. vs external magnetic field at room temperature.
The dimension of the sample: $6.9\times2.4\times0.9$ (mm).

The relative change in length is plotted against the applied magnetic field in Fig. 1. From this curve we obtain the saturation magnetostriction constant $\lambda_s=-(3.7\pm0.5)\times10^{-7}$. This rather small value seems to be explained by the dipolar interaction.[2] Since Tsuya[3] has explained the magnetostriction of Mn-ferrite by the dipolar interaction.

In the case of the dipolar interaction the magnetostriction constants for Y.I.G. is expressed as follows,

$$\lambda_{100}=2U/(C_{11}-C_{12}),\quad \lambda_{111}=-2U/3c_{44}$$
$$U=(2S_{AA}+3S_{BB}-4S_{AB})\cdot32M^2$$

where c_{ij} is the elastic constants and M is the saturation magnetization per cc. The values of S_{lk} are calculated by the lattice sum method as follows;

$$S_{AA}=0.046,\quad S_{BB}=0.094,\quad S_{AB}=-0.099.$$

As the elastic constants for Y.I.G. has not been obtained, we substitute the values for Ni-ferrite.[4] Taking $M=138$ gauss and

$$c_{11}=21.99\times10^{11},\quad c_{12}=10.94\times10^{11},\quad c_{44}=8.12\times10^{11}$$

(dyne cm^{-2}), the calculated value are

$$\lambda_{100}=8.4\times10^{-7},\quad \lambda_{111}=-3.8\times10^{-7}$$
$$\lambda_s=1/5(2\lambda_{100}+3\lambda_{111})=1.1\times10^{-7}$$

If we take as c_{ij} the value of magnetite or Co-Zn ferrite[5] λ_s becomes 0.2×10^{-7} or 0.8×10^{-7}.

The order of magnitude of the calculated value for λ_s is not so far apart from the experimental value, but its sign is different from the measured one. The shape effect[6] and the magneto-caloric effect may be smaller than 0.2×10^{-7}. Thus we may probably have to consider some other effect originating from the higher order perturbation relating to the L-S coupling, in order to explain the measured negative λ_s.

The authors express their sincere thanks to Drs. M. Tachiki, E. Sawaguchi, and N. Sakamoto K. Matsuura for their kind discussions.

References

1) K. Matsuura: Bull. E.T.L. **19** (1955) 24 (in Japanese).
2) R. Becker: ZS. f. Physik **62** (1930) 253.
3) N. Tsuya: Sci. Research Inst. Tohoku Univ. **B8** (1957) 161.
4) D. F. Gibbons: J. Appl. Phys. **28** (1957) 810.
5) R. F. S. Hearmon: Advance in Physics **5** (1956) 323.
6) R. Becker: ZS. f. Physik **87** (1933–1934) 547.

J. Phys. Soc. Japan **15** (1960) 1705

The Influence of Aging Treatment on the Temperature Dependence of the Electric Resistance in Alnico 5 Magnet

By Tatsuo Fujiwara and Tetsuo Kato
Daido Steel Co., Research Lab. Nagoya

(Received July 22, 1960)

In Alnico 5 Magnet, it has been believed that its magnetic anisotropy and high coercivity are principally founded on the shape anisotropy of elongated fine precipitates oriented to the direction of magnetic field which is applied during heat-treatment. However, the reversibility discovered recently in its magnetic properties during aging process has brought out a certain presumption that some other mechanisms except the precipitation may affect them, too.1)2) It was pointed out by Clegg and co-workers3) that the perfect separation of phases would not take place in the structure of Alnico 5 magnet which gives best magnetic properties. Its best magnetic properties brought out by aging treatment at about 600°C may also depend upon another mechanism, except the growth of precipitates. In order to interpret its phenomenon, the present authors investigated first the influence of aging treatment on the temperature dependence of the electric resistance associated with its magnetic properties. The heating-rate in measurement is about 4.5°C/min. In Fig. 1, the curvatures as indicated by AB, BC, and CD can be noticed on the curves of the specimens aged at and under 600°C, and in aging at 625°C the curvature as indicated by AB vanishes. This phenomenon suggests that there is a transformation which starts at about 300°C and finishes at about 600°C.

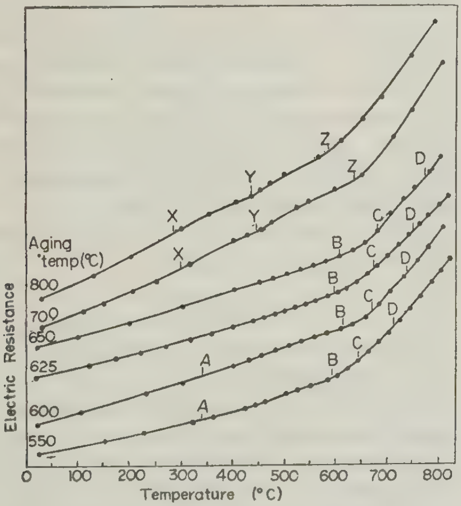

Fig. 1. Electric resistance-temperature curves in Alnico 5 aged 4 hrs. at each temperature from 550 to 800°C after solution heating and subsequent cooling at about 1.5°C/sec.

Moreover points C and curvatures CD on the curves correspond to the decreases of reversibility of its magnetic properties originated from aging treatment at about 650°C.4) This fact suggests the perfect separation to two phases to be commenced from this temperature. At the specimens aged at above 700°C, each curve shows a kink point at 450°C as indicated by Y. This change corresponds to the change at the temperature dependence of the saturated induction.3)

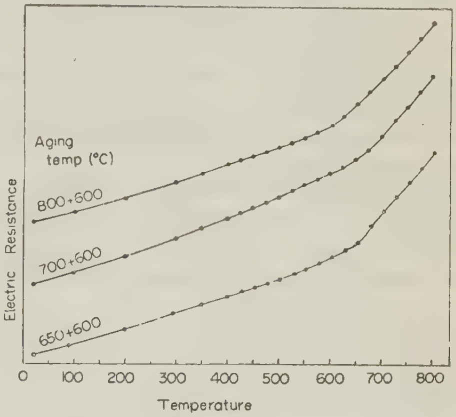

Fig. 2. Electric resistance-temperature curves in Alnico 5 aged 4 hrs. at each temperature from 650 to 800°C after solution heating and subsequent cooling at about 1.5°C/sec, and re-aged 4 hrs. at 600°C.

Fig. 2. shows the curves for the case reaged for 4 hours at 600°C. These curves do not show the curvature and the kink point like AB and Y indicated in Fig. 1, respectively. From this fact, it is suggested that the nature of the transformation caused by aging treatment at 600°C differs from one caused by aging treatment above 650°C.

From these experimental results, it is concluded that there are two different mechanisms during aging process of Alnico 5 magnet. One will occur during aging process at about 600°C that gives the best magnetic properties, and may be something like order-disorder transformation. And the other will be lapped over the former mechanism during aging process above 650°C, which is precipitation.

References

1) M. G. von der Steeg and K. J. de Vos: J. Appl. Phys. **27** (1956) 1250.
2) J. R. Hansen, Conference on Mag. and Mag. Mat.: (1955) 198.
3) A. G. Clegg and M. McCaig, Proc. Phys. Soc.: **B70** (1957) 817.
4) T. Fujiwara and T. Kato: to be published.

J. PHYS. SOC. JAPAN **15** (1960) 1706

Preparation of Ferromagnetic Chromium Dioxide

By Buichi KUBOTA

Technical Research Department, Wireless Division,
Matsushita Electric Industrial Co., Ltd.
Kadoma, Osaka, Japan

(Received June 14, 1960)

Since it has been reported[1][2][3][4] that ferromagnetic chromium dioxide, CrO_2, was formed by the thermal decomposition of chromium trioxide CrO_3, an increasing interest is being shown in the magnetic properties of chromium dioxide.[5] The present paper describes a new preparation method based on the thermal decomposition of CrO_3 under a high oxygen pressure resulting from the oxygen liberated from CrO_3 itself.

Chemically pure CrO_3 containing 0.059% of sulfate ion and 0.2% of absorbed water was used as a starting material. Various amounts of dry CrO_3 were charged in the high pressure bomb which was made of stainless steel and whose inner volume was about 36 cm³ (30 mmϕ, 50 mm height), and then heated at a constant rate of 10°C per hour in an electric furnace. The temperature was measured at the top and bottom of the bomb, and the temperature difference between them was controlled within 1°C. The high oxygen pressure in the bomb was caused by the oxygen liberated from CrO_3 itself and increased with the temperature. The pressure was measured with a Bourdon gauge set in the bomb. The relations between the temperature and oxygen pressure are shown in Fig. 1. by solid lines. The lines show that the pressure increases by step with the temperature. It will be concluded that the decomposition promotes remarkably in the temperature regions of the vertical parts of these curves and does not occur in those of the horizontal parts.

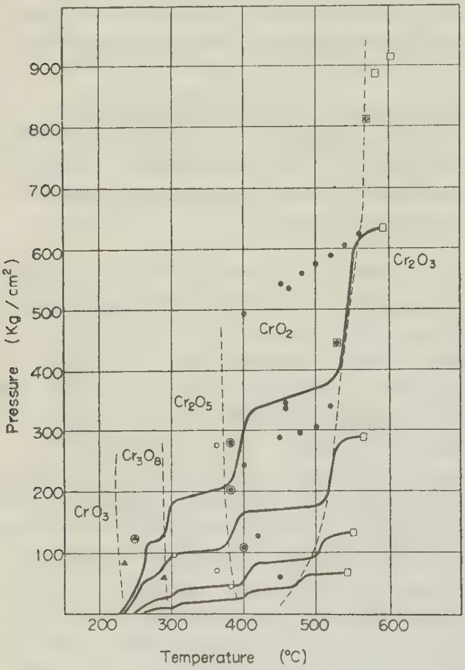

Fig. 1. The relation between the heating temperature and oxygen pressure in the thermal decomposition of chromium anhydride, CrO_3. ▲, ○, ● and □ show the results of isothermal heat treatments, indicating that the crystal structure are Cr_3O_8, Cr_2O_5, CrO_2 and Cr_2O_3, respectively.

Dotted lines show roughly the boundaries among the various oxides.

In order to confirm this conclusion, isothermal heat treatments were also carried out. As above mentioned, dry CrO_3 in the bomb was heated up to the various temperatures and kept for several hours at each temperature and quenched in air. The X-ray powder patterns of the products were observed. The results are shown in Fig. 1, indicating that their crystal structures were either one or two of Cr_3O_8, Cr_2O_5, CrO_2 and Cr_2O_3. From decomposition losses of the samples heated at 1000°C for 2 hours, the ratios of the oxygen to chromium ion were determined. From the available data, it was found that their chemical formula were $CrO_{2.6\sim2.7}$, $CrO_{2.4\sim2.5}$, $CrO_{1.9\sim2.1}$ and $CrO_{1.5}$, respectively.

The magnetic properties of the chromium dioxide prepared by heating CrO_3 at 480°C for 4 hours under the oxygen pressure of about 560 kg/cm², were measured with a magnetic balance in the temperature range from 77°K to 500°K. The ratio of the oxygen to chromium ion was 1.997, as a result of the thermogravimetric analysis. The Curie temperature was 117°C and the saturation magnetization at O°K was 133.7±2 gausses/gram, from which the Bohr magneton number of a Cr^{4+} ion was calculated to be 2.01±0.03.

The author wishes to thank Mr. F. Kanamaru and Mr. H. Chiba for their help.

References

1) A. Michel and J. Bénard: Bull. Soc. Chim. France, **10** (1943) 315.
2) C. Guillaud, A. Michel, J. Bénard and M. Fallot: Compt. rend. **219** (1944) 58.
3) R. S. Schwartz, I. Fankuchen and R. Ward: J. A. Chem. Soc. **74** (1952) 1676.
4) S. M. Ariya et al.: Zhur. Obshchei Khim. **23** (1953) 1241.
5) K. Siratori and S. Iida: J. Phys. Soc. Japan **15** (1960) 210.

J. PHYS. SOC. JAPAN **15** (1960) 1707

A New Method to Determine Hydration Energy of Ion

By Yoshio ISHIDA

Department of Physics, Faculty of Education Shimane Univerity, Matsue

(Received June 10, 1960)

The method reported here is based upon the double-shell model for hydration of ion and the idea was got from the following experimental facts. The molal volume of the hydration sphere can be obtained by measurement of either of the compressibility and the dielectric constant versus the concentration of the aqueous solution of metallic salt. The molal volume Φ_β which can be obtained from the compressibility measurement, is represented by

$$\Phi_\beta=-\frac{1000A}{\beta_1}-\frac{1000B}{\beta_1}C^{1/2} \tag{1}$$

assuming that the sphere is imcompressible. A and B are the constants in the relation $\beta=\beta_1+Ac+Bc^{3/2}$, where β and β_1 are the compressibilities of the solution and the pure water respectively, and C the molal concentration. The molal volume $\Phi_{\varepsilon 0}$ which can be obtained from the dielectric measurement, is given by

$$\varepsilon=\varepsilon_1-\frac{C}{1000}\Phi_{\varepsilon 0}(\mathcal{E}_1-\mu^2)\frac{1+2\varepsilon_1}{\mu^2+2\varepsilon_1}, \tag{2}$$

assuming that the dielectric constant of the sphere reduces to its optical value. In the expression, ε and ε_1 are the dielectric constants and μ the refractive index of pure water. The values of $\Phi_{\beta 0}$ (Φ_β at infinite dilution C→O) of several salts were calculated from the data of Bachem,[1] Yasunaga[2] and the present author, and those of $\Phi_{\varepsilon 0}$ from the data of Hasted, Ritson and Collie.[3] We find that $\Phi_{\beta 0}$ is nearly equal to $\Phi_{\beta 0}$ for NaCl and KCl, but greater than $\Phi_{\beta 0}$ for $MgCl_2$ and $BaCl_2$. Therefore, it is reasonable to assume the double-shell structure for hydration sphere. The first shell which is conceived referring to $\Phi_{\beta 0}$ responds to neither the change of the mechanical pressure nor of the electric field. The second shell which is referring to $\Phi_{\varepsilon 0}-\Phi_{\beta 0}$, however, does respond to the change of the mechanical pressure but not of the electric field. In order to discuss matters about separate ion, we divided $\Phi_{\beta 0}$ and $\Phi_{\varepsilon 0}$ into the values of respective ions according to ionic mobilities and then obtained the coordination numbers n_1 and n_2 constituting the first and the second shell. The effective radius R_{eff} of the shell was also obtained. Referring to Bernal-Fowler's study,[4] we have attained the formula to calculate the hydration energy U_h as follows:

$$U_h=\frac{\varepsilon_1-1}{2\varepsilon_1}\frac{Z^2e^2}{R_{eff}}+n_1P_1+n_2P_2-(n_1+n_2)u_w, \tag{3}$$

where the first term gives the change of the free energy outside the shell, P_1 is a mutual potential energy between a water molecule in the first shell and the ion, P_2 that between a water molecule in the second shell and the ion, and u_w energy which a water molecule in the shell had in pure water. From Fig. 1, we can get

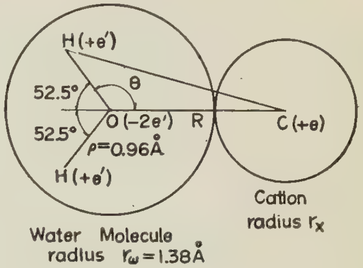

Fig. 1. A water molecule attaching to a univalent cation.

$$P_1=\frac{2e'e}{R}-\frac{2e'e}{\sqrt{R^2+\rho^2+2R\rho\cos\theta}}-\frac{b}{R^9}, \tag{4}$$

where e', effective charge of H, is approximately equal to $e/2$. The last term gives the quantum mechanical repulsive potential, in which b can be obtained by $\partial P_1/\partial R=0$. As to P_2 we can calculate it, assuming that the radius of ion becomes r_x+2r_w. We can evaluate u_w as 8.3 [kcal/mol] from the definition. Thus, we calculated the values of U_h of several ions, which are tabulated in Table I with other related values. They coincide roughly with the values given by different researchers and in different ways.

Table I. Hydration energy U_h calculated and other related values

Ion	n_1	n_2	R_{eff} [Å]	U_h[kcal/g.ion]
Na^+	4	0	3.38	121
K^+	3	0	2.92	81.1
Mg^{2+}	8	8	4.99	455
Ba^{2+}	10	4	4.82	429
Cl^-	2	0	2.51	67.4

The author wishes to thank Professor I. Takahashi of Kyoto University for his continual encouragement and valuable discussion.

References

1) Ch. Bachem: ZS. f. Phys. **101** (1936) 541.
2) T. Yasunaga: J. Chem. Soc. Japan **72** (1951) 87.
3) J. B. Hasted, D. M. Ritson, and C H. Collie: J. Chem. Phys. **16** (1948) 1.
4) J. D. Bernal and R. H. Fowler: J. Chem. Phys. **1** (1933) 515.

J. Phys. Soc. Japan **15** (1960) 1708

On the Stripe Pattern during Rolling of Viscous Materials

Toshimaro Sone, Masayoshi Fukushima
Research Laboratory, Snow Brand Milk Products Co. Ltd. Higashi-Sinagawa Tokyo
Eiichi Fukada
Kobayashi Institute of Physical Research Kokubunji, Tokyo

(Received July 11, 1960)

A regular pattern of stripe has been observed in a number of viscous materials during rolling on the roll mill. The photograph shows the stripe pattern that appeared in the butter during rolling. The roll mill employed is the ordinary type of two duplicate cylinders which is originally designed for the calendering of synthetic resins at high temperature. The length and diameter of roll are 17.5 cm and 7.6 cm respectively and the speed of rotation can be varied from 18 to 45 r.p.m.

As is seen in the photograph, the pattern appears on both surfaces of rolls, parallel to the direction of rotation and with the same distances between successive peaks. The distance between peaks in the stripe is closely associated with the viscosity of the material on roll. Fig. 1. depicts the relation between the distance between peaks D and the viscosity η of the butter during rolling. a is the clearance between two rollers. The experimental formula derived for the relation is $\eta=\eta_0 \exp C/(D_0-D)$, where C and D_0 are constants which are determined by experiments. The viscosity η has been measured at 600 c/s by an oscillation-plate viscometer. Some results for the condensed milk is also plotted in the same curve.

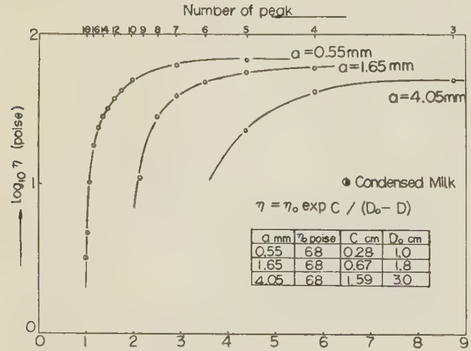

Fig. 1.

When the butter is subjected to working by the roll mill, the viscosity of butter decreases gradually with the rolling time. The number of peaks in stripe increases, in another words, the distance between peaks decreases with the decrease of viscosity. When the effective length of roller is varied by moving the two spacers located in both ends of roll, the distance between peaks is never changed, although the number of peak is inevitably altered.

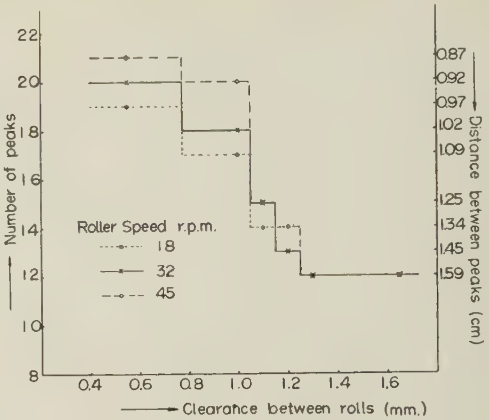

Fig. 2.

The generation of the stripe pattern is quite stable. Even if the pattern is broken by stirring the butter mechanically, it reappears again directly after passing of material through the clearance of rolls. The stripe with a certain number of peaks is stable for a certain range of viscosity. If the viscosity decreases further, the alignment of peaks becomes unstable and fluctuating, then a new peak adds the stripe and makes the pattern stable again. Therefore, the correlation curve between the viscosity and the distance between peaks is not continuous but discontinuous one with the zig-zag breaks.

The similar behaviour during rolling has been observed in many materials other than butter, for example, honey, syrup, grease, silicone oil etc. Fig. 2. illustrates the relation between the clearance of rolls and the distance between peaks in the stripe observed in a printing ink on the roll mill. The apparent viscosity of printing ink decreases with the increase of shear rate of flow, which is determined by the roller speed and the clearance between rolls. Fig. 2. reflects, therefore, the close correlation between the distance between peaks and the apparent viscosity of printing ink.

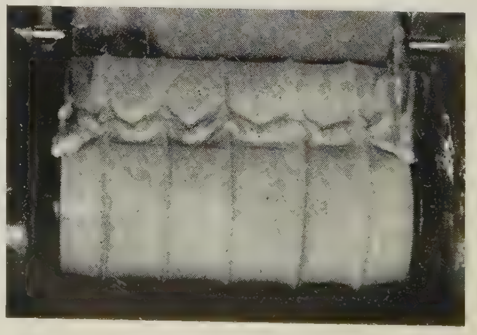

J. Phys. Soc. Japan **15** (1960) 1709

α-Trapping Centers in n-Type Silicon

By Jun'ichi OKADA and Tetsuro SUZUKI
Matsuda Research Laboratory
Tokyo Shibaura Electric Co., Ltd.,
Kawasaki Japan

(Received July 26, 1960)

It has been known that there are several kinds of trapping centers1),2) in a silicon crystal which is pulled from a melt in a fused silica crucible. Kaiser, Frisch and Reiss3) have suggested that these trapping centers would correspond to the electrically active complexes containing two or three oxygen atoms. They have also shown that the complexes containing four oxygen atoms are ascribed to the thermal donors formed during heat treatment at 450°C, and have postulated that these electrically active complexes are generated by the successive reactions from atomically dispersed oxygen atoms. And the density of these dispersed oxygen atoms can be assumed to remain nearly constant3),4) in the initial stage of the annealing process. According to this assumption, it can be shown that the increase of these electrically active complexes is monotonous against the annealing time. In order to see whether this expected behavior of the complexes is in accordance with that of the density of α-trapping centers or not, we have investigated the rate of formation of α-trapping centers and thermal donors in n-type silicon crystals grown from quartz crucible due to annealing at 450°C.

Our experimental procedure and results are as follows. In the first step, the etched specimen was heated on a molybdenum boat in a purified hydrogen atomosphere for 30 minutes at 1350°C. Then, it was quenched by sliding the molybdenum boat to room temperature part of the furnace. In the succeeding steps, the specimen was heated in the same furnace for definite time intervals at 450°C, repeatedly. After each step of the heat treatments, the densities of added electrons and α-trapping centers were measured. The former was estimated from the resistivity, and the latter was estimated from the time dependence of the photoconductivity. An example of our experimental results is shown in Fig. 1. The increase of electron densities is monotonous in the initial stage of annealing. However the density of α-trapping centers is zero after quenching from 1350°C and shows maximum for annealing time of about 30 minutes at 450°C. Thus, this result indicates that α-trpping centers in n-type silicon cannot be described as the complexes containing two or three oxygen atoms. On the other hand, it has been confirmed that an oxygen-free silicon crystal which is grown by floating-zone technique contains no trapping center. This fact indicates that a trapping center has something to do with the presence of oxygen atoms dispersed in a silicon crystal. Accordingly, it may be predicted that α-trapping centers would correspond to the complexes which contain not only oxygen atoms but also other impurity atoms or crystal defects, i.e. vacancies, interstitials or dislocations.

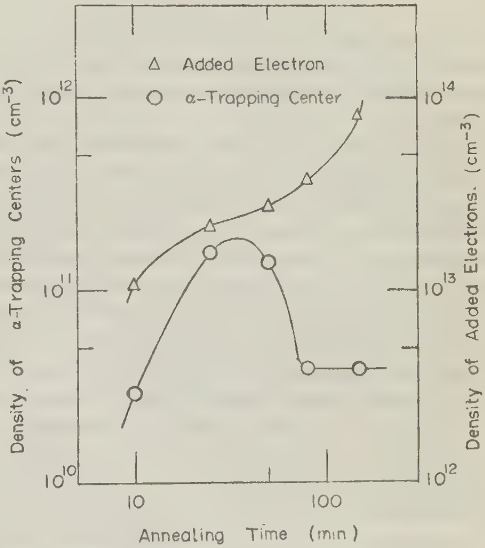

Fig. 1. Densities of α-trapping centers and added electrons *versus* annealing time at 450°C.

The behavior of trapping center is now being investigated against the following conditions: (1) speed of quenching from 1350°C (2) dislocation density (3) concentration of dissolved oxygen atoms.

We are indebted to Mr. Toshio Abe and Mr. Teruo Kobayashi for their kind advices and discussions.

References

1) J. A. Hornbeck and J. R. Haynes: Phys. Rev. **97** (1955) 311.
2) J. R. Haynes and J. A. Hornbeck: Phys. Rev. **100** (1955) 609.
3) W. Kaiser, H. L. Frisch and H. Reiss: Phys. Rev. **112** (1958) 1546.
4) W. Kaiser: Phys. Rev. **105** (1957) 1751.

J. PHYS. SOC. JAPAN **15** (1960) 1710~1711

Die Schwankung der Zündstelle eines brennbaren Gemisches bei der Selbst-Zündung in Stosswellen

von Kunio TERAO

Institut für physikalische Chemie der Universität Göttingen

(Received July 9, 1960)

Die Induktionszeit der Selbstzündung eines brennbaren Gemisches hat allgemein eine Schwankung(1), die aus physikalischen Gründen unvermeidlich ist.

Um diese Schwankung der Zündstelle zu messen, wurde ein Stoßrohr von 4 m Länge und 3 cm × 3 cm Querschnitt benutzt, und der Versuch wurde genau so wie bei der Messung(1) der Induktionszeit der Selbstzündung durchgeführt, nämlich das Rohr wurde mit einer Membrane aus Aluminiumfolien in zwei Teile getrennt. In den ersten Teil wurde Hochdrucktreibluft eingeführt und in den andern wurde das Gemisch eingeführt. Wenn die Versuchsbedingungen erfüllt waren, wurde die Membrane mit einer Stechnadel zerbrochen, so daß die Stoßwelle in das Gemisch läuft. Die Entzündung entsteht in der reflektierenden Stoßwelle an der Endwand.

Als Endwand wurde eine Plexiglasplatte eingesetzt, so daß man von draußen mit einem Photomultiplier die Entzündung im ganzen Stoßrohr messen kann. An einer Seite des Endteils des Stoßrohrs wurde ein Fenster aus Plexiglas angebracht, so daß man von dieser Seite mit einem andern Photomultiplier die Entzündung im Raum des Stoßrohrs hinter dem Fenster messen kann.

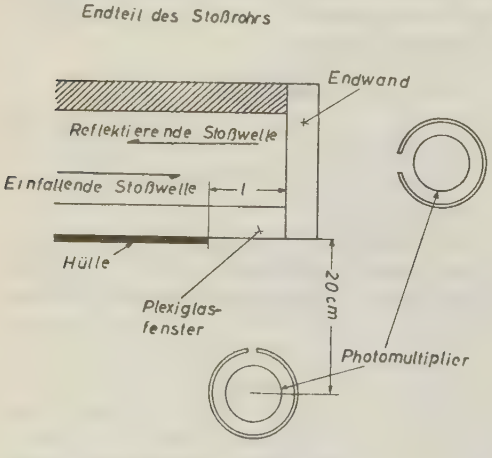

Die beiden Photomultiplier* wurden an einen Zweistrahloszillographen angeschlossen, so daß sie gleichzeitig gemessen werden konnten. Wenn die Entzündung im Raum direkt hinter dem Fenster losgeht, muß die Induktionszeit, die mit dem Photomultiplier von der Seite gemessen wird, gleich der Induktionszeit sein, die mit dem andern Photomultiplier vor der Endwand gemessen wird. Wenn die Entzündung im andern Raum losgeht, muß die Induktionszeit, die mit dem Photomultiplier von der Seite gemessen wird, länger sein, als die mit dem andern Photomultiplier gemessene.

Wenn man die Breite des Fenster ändert und mehrere Male denselben Versuch macht, bekommt man eine Verteilungskurve der Zündstelle. Bei diesem Experiment wurde der Versuch bei Verschiedenen Fensterbreirte ausgeführt. Die Breite des Fensters betrug: 20,0 mm, 22,5 mm, 25,0 mm, 27,5 mm und 30,0 mm von der Endwand. Bei jeder Breite des Fensters wurde 20 Mal unter derselben Bedingungen gemessen.

Von dieser Verteilungskurve der Zündstelle kann man die Wahrscheinlichkeit der Entzündung in einer Volumeneinheit bekommen, aber dabei muß die Zeitänderung berücksichtigt werden, genau so wie bei der Messung der Wahrscheinlichkeit der Entzündung in einer Zeiteinheit die Volumänderung berücksichtigt wurde. Wenn man Folgende darstellt:

$P(l)$: die Wahrscheinlichkeit dafür, daß im Abstand l von der Endwand des Stoßrohrs keine Entzündung und in größeren Abstand Entzündung auftritt; $\mu(l)$: die Wahrscheinlichkeit der Entzündung in einem Mol und in einer Millisekunde an einer Stelle l; t:Zeit nach der Reflektion der Stoßwelle an der Endwand; l: Abstand von der Endwand; D_2: Geschwindigkeit der reflektierenden Stoßwelle; A: Querschnittsfläche des Stoßrohrs dann(1)(2) folgt

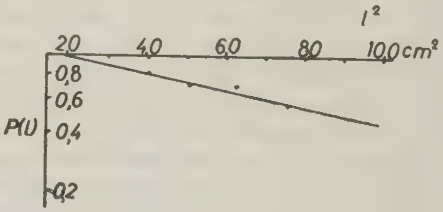

$$\mu(l) = -\frac{\{2 \cdot D_2 \ln P(l) - \ln P(l_2)\}}{A \cdot (l_1^2 - l_2^2)},$$

Bild 2 zeigt das Versuchsergebnis eines Methan-Luftgemisches (Konzentration 5,5%) und die Kurve ist wirklich eine Gerade. Daraus erhält man

$\mu(l) = 140 \times 10^2/\text{Mol}\cdot\text{msec.}$, $\mu(l)$ wirklich von l unabhängig.

Dabei konnte man nur das Druckverhältnis Treibdruck zu Unterdruck messen.

$$\frac{P_T}{P_0} = \frac{21{,}0at}{0{,}15at} = 140$$

Von der Schwankung der Induktionszeit wurde die Wahrscheinlichkeit der Entzündung in einer Millisekunde und in einem Mol unter ähnlichen

Bedingungen ($\frac{P_T}{P_0}=152$, die Temperatur der Rückwelle 773°K) berechnet. Sie ergibt sich $\mu(t)=50\times10^2$/Mol·msec. Eigentlich ist $\mu(t)$ nicht anders als $\mu(l)$, und sie müssen miteinander übereinstimmen, wenn die Bedingungen gleich sind. Das Resultat des Experiments zeigt, daß sie miteinander ziemlich gut übereinstimmen, wenn man Versuchsfehler berücksichtigt.

Damit wurde bewiesen, daß die Zündstelle der Selbstzündung eines brennbaren Gemisches eine Schwankung hat, und daß auch die Menge des Gemisches auf die Entzündung großen Einfluß hat.

Schrifttum

1) K. Terao: J. phys. Soc. Japan Vol. 15, 6, (1960)
2) M. Hirata: Bull. Math. Stat. **3** (1947) 57
Kikai no Kenkyu, **1** (1949) 182, 231
Ooyotokeigaku (Angewandte Statistik) 1949, 11, 01.

J. PHYS. SOC. JAPAN **15** (1960) 1711

Electron Spin Resonance of Manganese in Ammonium Chloride

By Hidetaro ABE and Hiroko SHIRAI
The Institute for Solid State Physics, University of Tokyo

(Received July 11, 1960)

Recently, divalent manganese ion incorporated into cubic crystals of monovalent alkali halides has been extensively investigated with the electron spin resonance techniques[1)2)] which give us detailed informations about the electronic structure of the ion and its environments.

The crystal structure of alkali halides belongs to the NaCl type, one of the simplest lattices. In the present report, ammonium chloride, NH_4Cl, is used as the host crystal which belongs to the CsCl type, another of the simplest crystal lattices. It is known that ammonium chloride has three crystal modifications. The β modification is stable at a temperature range from 184.3°C to −30.5°C (the λ temperature) and has the crystal structure of CsCl type, if an ammonium group, NH_4^+, is treated as a monovalent positive ion.[3)4)]

The sample crystals were grown from the mixed aqueous solution of ammonium chloride and manganese chloride, $MnCl_2\cdot4H_2O$, with a weight ratio about 100: 1. The ESR spectra were observed at room temperature (about 20°C) with the static magnetic field rotated within the (001) and the (110) plane. The spectrometer works at about 23,110 Mc which was used to study the copper butylate monohydrate.[5)]

In our preveous study[6)] with 9000 Mc spectrometer, the observed spectra could not been analyzed because the influence of crystalline field was much larger than the Zeeman energy. With our 24,000 Mc spectrometer, the Zeeman energy just exceeds the former. The ESR spectrum consists of many lines which spread over a wide range of magnetic field, e.g. at the [100] direction they appear from 1,705 oer, to 14,940 oer. The results are fairly well expressed with a spin-Hamiltonian:

$$\mathscr{H}=g\beta\vec{H}\vec{S}+DS_z^2+A\vec{I}\vec{S} \qquad (1)$$

with parameters of $g=1.984$ (isotropic), $D=1600\pm25$ oer., and $A=93\pm4$ oer. The crystalline field seems to have no rhombic part ($E\approx0$). There are three equivalent choices in direction of z-axis which are three cubic axes of the crystal: [100], [010], and [001] axes. This suggests the manganese ion substitutes an ammonium group (NH_4^+) and one of the six nearest neighbour ammonium ions becomes vacant to secure the requirement of charge neutrality. This model satisfies the axially symmetric field by a consideration on atomic arrangements.

The crystalline field parameter, D, in the present case is anomalously large compared with the case of manganese ion in some hydrated crystals[7)] (100∼200 oer.) or in NaCl[1)] (130 oer.).

Results at reduced temperatures, in bromide crystals, and further discussions will be published in a forthcoming paper.

References

1) G. D. Watkins: Phys. Rev. **113** (1959) 79.
2) K. Morigaki, M. Fujimoto and J. Itoh: J. Phys. Soc. Japan **13** (1958) 1174.
3) E. L. Wagner and D. F. Hornig: J. Chem. Phys. **18** (1950) 296.
4) G. E. Bacon: Neutron Diffraction. (Oxford 1955) P. 173.
5) H. Shirai and H. Abe: to be published.
6) H. Abe: J. Phys. Soc. Japan **12** (1957) 435.
7) K. D. Bowers and J. Owen: Rept. Prog. Phys. **18** (1955) 304.

J. PHYS. SOC. JAPAN **15** (1960) 1712~1713

A Note on the Magnetic Resonance in Metals

By Ko SUGIHARA
Technical Research Department, Wireless Division,
Matsushita Electric Industrial Co.,
Kadoma, Osaka

(Received June 13, 1960)

The effect of the normal skin effect on the line shape of the magnetic resonance of the localized spins was studied by Bloembergen[1]. For a pure metal at liquid helium temperatures, the free path of the conduction electrons is large compared to the skin depth in the radio-frequency range, actually typical values of the free path are $l \gtrsim 10^{-3}$ cm and the penetration depth δ for angular frequency $\omega \sim 10^8$ sec^{-1} is 10^{-4} cm. In this note we shall derive the absorption curve in N M R in the anomalous skin effect region.[*]

The theories of the anomalous skin effect in the presence of a static magnetic field have been given by Heine,[4] Azbel'-Kaner[5] and Mattis-Dresselhaus[6] in connection with the cyclotron resonance in metals.

A semi-infinite sample is considered with its boundary in the $z=0$ plane and positive z direction is towards the interrior of the metal. The oscillating field $H_1 \exp(i\omega t)$ and the static field are parallel to the y-axis and to the z-axis respectivelly. The absorption rate is given by

$$P=(c/4\pi)^2 H_1^2 (R_e Z) \qquad (1)$$

where Z represents the surface impedance. Taking into the consideration of the permeability μ, Z is written in the form

$$Z=-4\pi i\omega\mu c^{-2}\, E_x(0)/E'_x(0), \qquad (2)$$

where $E_x(0)$ stands for the x-component of the electric field and $E'_x(0)$ its derivative at $z=0$. Neglecting the displacement current, $E_x(0)/E'_x(0)$ can be written as

$$\frac{E_x(0)}{E'_x(0)}=-\frac{2}{3}\left(1-\frac{i}{\sqrt{3}}\right)\left(\frac{c^2 l}{3\pi^2\sigma\mu\omega}\right)^{1/3} \times \tanh^{1/3}\left[\frac{\pi}{\omega_c\tau}(1+i\omega\tau)\right], \qquad (3)^{\dagger)}$$

where σ is the D. C. conductivity, ω_c the cyclotron frequency and τ is the time of relaxation of the conduction electrons. As $\omega\tau$, ω/ω_0 and $|\chi|$ are very small, the real peal part of Z becomes

$$R_e Z=R_0\left\{1+\frac{8\pi}{3}\left(\frac{\chi'}{\sqrt{3}}+\chi''\right)\right\}, \qquad (4)$$

$$R_0=\frac{8}{9}\left(\frac{\sqrt{3}\,\pi\omega^2 l}{c^4\sigma}\right)^{1/3}\left[\frac{\sinh(\pi/\omega_c\tau)}{\cosh(\pi/\omega_c\tau)}\right]^{1/3}. \qquad (4)'$$

If the electron's orbit are not quantized, (4)′ reduces to the result given by Reuter-Sondheimer.[7] From Eq. (4) it is concluded that the absorption rate by the spin system is proportional to $(\chi'/\sqrt{3}+\chi'')$ in the anomalous region, on the other hand to $(\chi'+\chi'')$ in the normal region. For simplicity, we assume that the line shape is given by the Bloch-type and far from saturation, then the ratios of the absorption maximum and minimum and their positions are easily obtained and they are summarized in the following table.

	position of max	position of min.	ratio of absorption max. and min.
Normal	$\Delta\omega T_2=\sqrt{2}-1$	$\Delta\omega T_2=-(1+\sqrt{2})$	14: -1
Anomalous	$\Delta\omega T_2=2-\sqrt{3}$	$\Delta\omega T_2=-(2+\sqrt{3})$	5.8: -1

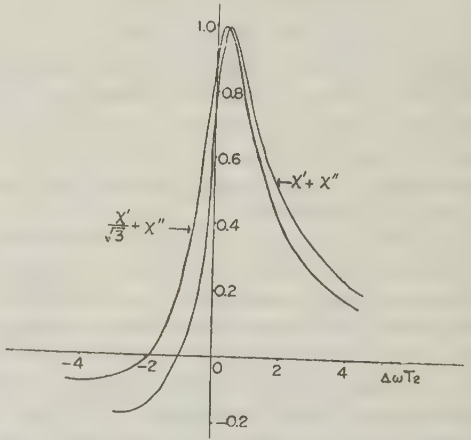

Fig. 1. Absorption curves in the normal and the anomalous region.

Absorption curve in which the maximum values are normalized to 1 are shown in Fig. 1. Unitil now, we limit our discussion to the semiinfinite sample but it is desirable to analize the relation between the dimension of the sample and the absorption curve. Particularly, it seems to be interesting to us to investigate the problem in the region $l>d>\delta$, where d is the thickness of the sample.

---

[*] The extension of the Dyson's theory[2] of paramagnetic resonance by the conduction electrons in the normal region was carried out by Kittel[3], but his theory can not be applicable to the problem of the localized spin system.

†) Putting $\mu=1$, we obtain the Eq. (27) given by Mattis-Dresselhaus.

References

N. Bloembergen: J. App. Phys. **23** (1952) 1383.
F. Dyson: Phys. Rev. **98** (1955) 349.
G. Feher and A. F. Kip: Phys. Rev. **98** (1955) 3´7.
V. Heine: Phys. Rev. **107** (1957) 431.
M. Ya Azbel and E. A. Kaner: J. Phys. Chem. Solid. **6** (1958) 113.
D. C. Mattis and G. Dresselhaus: Phys. Rev. **111** (1958) 403.
G. E. Reuter and E. H. Sondheimer: Proc. Roy. Soc **A195** (1948) 336.

J. Phys. Soc. Japan **15** (1960) 1713~1714

$1/f$ Noise and Channel in Ge PN Junction

By Kiichi Komatsubara*, Yoshio Inuishi, Hiroshi Edagawa* and Tsutomu Shibaike

College of Engineering, Osaka Uuiversity.
**Kobe Kogyo Co..*

(Received June 25, 1960)

We have been studying the mechanism of $1/f$ noise in semiconductor pn junctions,⁽¹⁾⁽²⁾ and suggested that the channel is a predominant source of the $1/f$ noise in reversely biased pn junctions. Now some direct evidence of this suggestion have been found in our measurement of "field effect" on excess noise. Ge grown pn junctions were placed like Fig. 1, where surface field electrode of conducting glass were attached to the cleaned junction surface through a thin mica separator. The glass tubes containing the specimen were evacuated at 10^{-6} mm Hg for several hours and sealed. Ge pn junction thus prepared were reversely biased at the voltage V_c and various surface fields were applied on the junction by the voltage V_F on the field electrode as shown in Fig. 1. The mean reverse current I through the junction and the mean square short-circuit noise current $\langle \Delta i^2\rangle$ at 1 kc were measured at various values of V_F and V_c.

As an example, Fig. 2 shows the noise $\langle \Delta i^2\rangle$ and current I in n^+p junctions as function of surface field voltage V_F. For $V_F>0$, inversion layer or channel grows in the high resistivity (p) side and for $V_F<0$ accumulation layer grows in the high resistivity side as will be mentioned later. Now we can see in Fig. 2 that the channel produces the remarkable increase both in excess current and in excess noise. Judging from the frequency spectrum of the noise as shown in Fig. 3, the channel noise is mainly $1/f$ type. Similar data for p^+n junction are shown in Fig. 4, which also show that the channel formation in high resistivity n side at $V_F<0$ produces large $1/f$ noise accompanied by the increase in excess current.

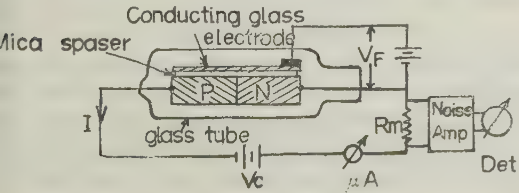

Fig. 1.

This channel formation was confirmed by illuminating the reversely biased junction surface by fine beam of chopped light through conducting glass electrode at various voltage V_F and examin-

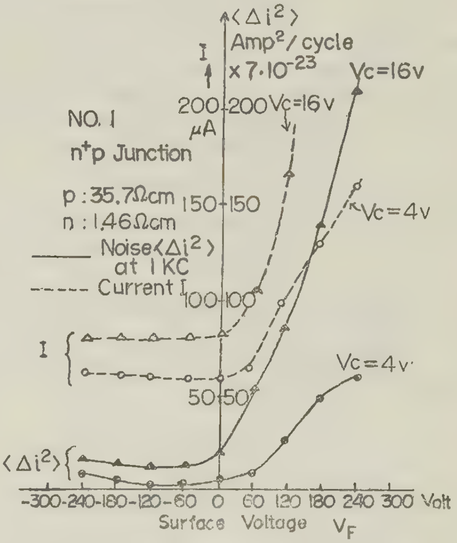

Fig. 2.

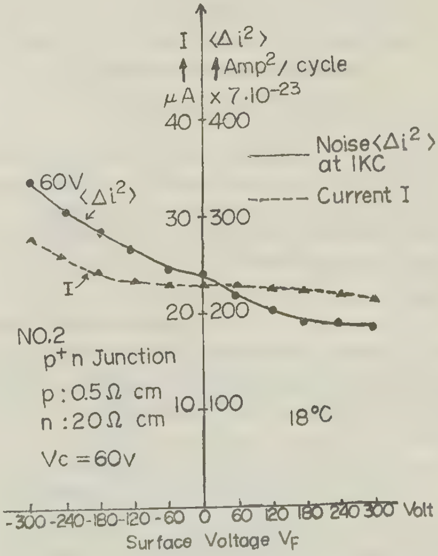

Fig. 3.

ing the photo-current as the function of beam position. The details of these experiment will be published in a full paper soon.

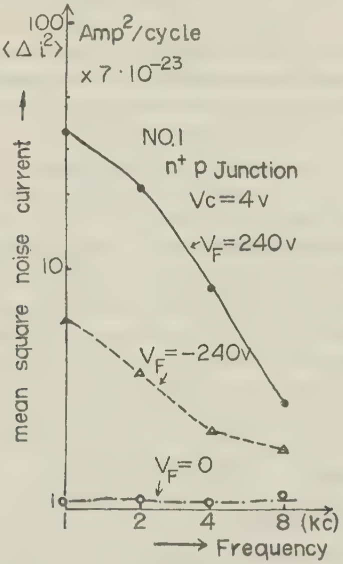

Fig. 4.

References

1) Y. INUISHI; Tech. Rep. osaka University **7**, 11 (1957)
2) Y. INUISHI; J. Phys. Soc. of Japan **12**, 439 (1957)

J. PHYS. SOC. JAPAN **15** (1960) 1714~1715

Spin Wave Resonance in Ni Films

By Hiroshi NOSÉ

Department of Physics, Faculty of Science,
Tokyo Metropolitan University

(Received June 14, 1960)

The "*Spin Wave Resonance*" (*S.W.R.*) proposed by Kittel[1] was confirmed from the observation in 80 Ni-Fe film by Seavey and Tannenwald.[2] The present report shows that it was confirmed also in Ni film provided that a certain condition was satisfied.

In the thin film, it was suggested by Macdonald[3] that the usual expressions of ferromagnetic resonance condition had to be modified. When an external magnetic field $H_{\parallel}$ is applied parallel to the film plane,

$$\left(\frac{\omega}{\gamma}\right)^2=\left(H_{\parallel}+4\pi M+\frac{3\lambda\sigma}{M}+\frac{3\lambda\sigma_u}{M}\cos^2\theta\right)\times\left(H_{\parallel}+\frac{3\lambda\sigma_u}{M}\cos 2\theta\right),$$

where M and λ are the saturation magnetizatio and magnetostriction constant of the bulk, respec tively; σ is a planer stress isotropic in the fil plane; σ_u is a uniaxial stress lying in the film plan at an angle θ out of the direction of M. Th stresses are positive for tension, and negative fo compression as usual. The uniaxial stress ha been introduced in place of the uniaxial anisotropy though the latter is commonly used.

Similarly in the case of the magnetic field H perpendicular to the film plane,

$$\left(\frac{\omega}{\gamma}\right)^2=\left(H_{\perp}-4\pi M-\frac{3\lambda\sigma}{M}-\frac{3\lambda\sigma_u}{M}+\frac{2A}{M}k^2\right)\times\left(H_{\perp}-4\pi M-\frac{3\lambda\sigma}{M}+\frac{2A}{M}k^2\right),$$

where the term $2Ak^2/M$ expresses the *S.W.R.*; th exchange coupling constant $A=4JS^2/a$ (a: th lattice constant for f.c.c., J: the exchange energy S: the spin angular momentum); the magnitude o the wave number $k=p\pi/L$ (p: an odd integer, L the film thickness).

Ni films in the present work were prepared b evaporating on the mica- and glass-substrates heate at 15~320°C in vacuum (4×10^{-5} mmHg). The film thicknesses measured by the multiple beam inter ferometer were 1000~3000Å. The presence of magnetic field about 50 Oe in the course of th evaporation or annealing affected hardly the *S.W.R* in these films.

Some of the results obtained by the ferro magnetic resonance at 9,300 Mc/s, and the crystal line structures examined by the electron diffractio are briefly reported.

i) The films evaporated on the mica heated a 320°C had $\sigma=5.3\times10^9$ and $\sigma_u=-1.9\times10^8$ dyne/cm in agreement with the observation by Macdonal carried out only in the case of the parallel field a 23,000 Mc/s. These values did not remarkably depend on the substrate temperature. This is pre sumably due to the fact that the cleavage surface of mica is fairly clean and smooth. The *S.W.R* in these films was not clearly observed.

ii) In the films evaporated on the glass main tained at room temperature, magnitudes of stresses considerably fluctuated: that is $\sigma=(6\sim12)\times10^9$ and $\sigma_u=-(1\sim5)\times10^8$ dyne/cm². This fluctuation as well as these magnitudes, however, decreased with the rising substrate temperature, for example at 320°C $\sigma=(4.0\sim4.5)\times10^9$ and $\sigma_u=-(0.2\sim0.5)\times10^8$ dyne/cm². These results are quite different from the films on the mica and somewhat attributable to inhomogenities on the surface structure of glass substrate. The *S.W.R.* in these films could be definitely observed provided that the films prepared at room temperature had not only larger stresses but also sharper absorption line. They had $L=$ 2000~2500Å, $p=4\sim7$, and $A=(0.47\sim0.59)\times10^{-6}$

erg/cm. Even if they were annealed at 100～300°C for one hour in vacuum immediately following the evaporation, the definite *S.W.R.* disappeared.

iii) While the half-widths (ΔH between maximum slopes) were about $\Delta H_{\parallel}=300\sim600$ and $\Delta H_{\perp}=250$ Oe in the films prepared on the mica at any substrate temperature they were $\Delta H_{\parallel}=200\sim600$ and $\Delta H_{\perp}=180\sim300$ Oe, and $\Delta H_{\parallel}=250\sim350$ and $\Delta H_{\perp}=180\sim280$ Oe in the films prepared on the glass at room temperature and at 320°C, respectively. They also depend on the condition of substrate surface as described above. Though its fine structure of absorption line could not be made clear, the *S.W.R.* seems to exist also in parallel field taking account of the skewed absorption line and $\Delta H_{\parallel}\geqq\Delta H_{\perp}$.

iv) By investigations with the electron diffraction, it was found that the preparation of the single crystal films on the mica by socalled *Epitaxy* failed at any substrate temperature. On the other hand, the films prepared on the glass maintained at lower temperatures had the fibre textures whose axes were [110] and/or [111] normal to the films, but the ones prepared at the temperature higher than 200°C had no fibre texture and the sharper diffraction lines. According to the results obtained, these fibre textures are presumed to have no relation with the excitation of the *S.W.R.* and the magnitude of stresses.

The author wishes to express his thanks to Prof. R. Kimura for his continued encouragement and to Dr. M. Kuriyama for his cooperation.

References

1) C. Kittel: Phys. Rev. **110** (1958) 1295.
2) M. H. Seavey and P. E. Tannenwald: Phys. Rev. Letters **1** (1958) 168; J. Appl. Phys. **30** (1959) 227S.
3) J. R. Macdonald: Proc. Phys. Soc. London **A64** (1951) 968; Phys. Rev. **106** (1957) 890.

J. PHYS. SOC. JAPAN **15** (1960) 1715

Magnetic Property of Cr_2O_5

By Eiichi HIROTA and Buichi KUBOTA

Research Division, Wireless Department,
Matsushita Electric Industrial Co., Ltd.
Osaka, Japan

(Received July 4, 1960)

Various intermediate chromium oxides between CrO and Cr_2O_3 are obtained by heating CrO_3 under high oxygenic pressure. These oxides are Cr_3O_8, Gr_2O_5 and CrO_2. Of these oxides, chromium dioxide, CrO_2, is ferromagnetic. A number of investigations on this dioxide have been reported, but there are few reports of the other oxides. In the present note the result of magnetic measurements on Cr_2O_5 is reported.

The specimen was prepared by heating CrO_3 up to 305°C under an oxygenic pressure of 95 Kg/cm² for 12 hours. The X-ray powder pattern of the specimen showed only the Cr_2O_5 phase, but the background was remarkable. The oxygen content of the specimen was determined from the ignition loss at 1,000°C for 1 hour, and the result showed that the specimen was $CrO_{2.41}$. From thermogravimetric and differential thermal analysis, it was found that the oxide was stable up to about 380°C in air. The density was about 3.24. Impurities of the specimen were also examined by spectroscopic analysis and traces of Ca, Cu, Fe, Mg, Na, Pb and Si were detected.

Magnetic measurements were carried out with the use of an automatic recording magnetic balance in the temperature range between 77°K and 500 K. The paramagnetic susceptibility of Cr_2O_5 at room temperature was obtained as

$$\chi=(19.4\pm0.5)\times10^{-6}\ \text{e.m.u./g},$$

where an aqueous solution of Ni Cl_2 was used as the standardizing solution.

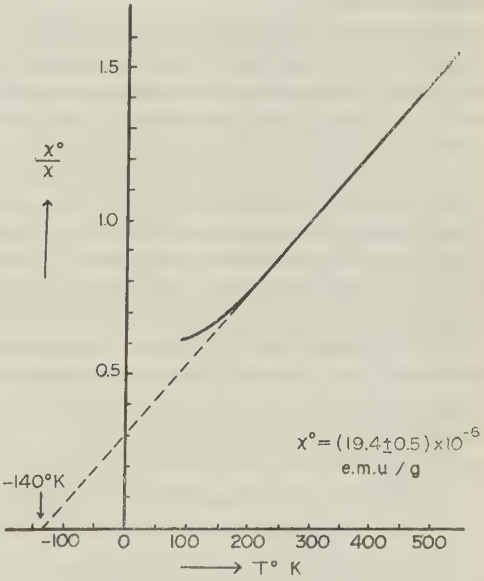

Fig. 1. Inverse susceptibility versus temperature curve for Cr_2O_5.

From thermomagnetic measurements the $1/\chi$–T curve was obtained. The result is shown in Fig. 1. In the high temperature range the $1/\chi$–T curve is well described by the Curie-Weiss law, $\chi=C/(T+\theta$, where $C=8.44\times10^{-3}$ e.m.u./g-deg, $\theta=140$°K. It seems resonable to conclude that Cr_2O is antiferromagnetic. To make this conclusion more definite, measurements below 77°K are desirable.

J. PHYS, SOC. JARAN **15** (1960) 1716~1717

Thermal Bleaching of F-Centers of Gamma-Irradiated KCl at Low Temperatures

By Noriaki ITOH, and Tokuo SUITA

Department of Nuclear Engineering, College of Engineering, Osaka University.

(Received July 29, 1960)

In order to investigate the nature of color centers in KCl formed by gamma-irradiation at low temperatures and the mechanism of their formation, the thermal bleaching curve of F-centers was measured.

The specimens which were obtained from the ingot purchased from Harshaw Chemical Co. were kept in the cryostat with quartz window set in the Co^{60} 10,000 Curie cave in Japan Atomic Energy Research Institute (JAERI). After irradiation the change in the optical absorption was measured by the Cary spectrophotometer. The coloration of the quartz window is small as compared with that of KCl crystals in the interesting wave length range and can be subtracted without causing substantial error.

The irradiated specimens were warmed at a rate of about 1°C/min and during that the absorption coefficient of the specimen was measured intermittently by sweeping the spectrometer at the speed of 5 mμ/sec. The temperature dependence of the band width of the F-band was obtained by measuring the temperature dependence of the peak value of the F-band of gamma-irradiated KCl at room temperature, in which case, the change of the absorption coefficient with temperature was reversible showing that the absorption intencity is constant. The dependence of the band width on the temperature thus obtained is nearly the same as that obtained by Russel and Klick[1], and used to calculate the concentration of F-centers from the peak value of the F-band at various temperatures during warming up.

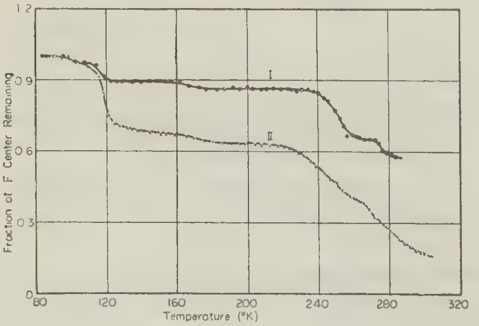

Fig. 1. Annealing curve of F-centers of KCl gamma-irradiated at liquid nitrogen temperature. I; 9.4×10^4 r, n_0 (initial F center concentration) $= 3.8 \times 10^{15}$/cc, II; 1.7×10^6 r, $n_0 = 4.6 \times 10^{16}$/cc.

Fig. 1 shows the bleaching curue of F centers of KCl irradiated at liquid nitrogen temperature by various gamma dose. It is clear that the sharp decrease of F centers occur at the temperatures of 98°K, 116°K, 172°K, 250°K and 278°K. It should also be noted that the gradual decrease of the concentration of F centers can be observed besides the sharp decreases especially when the crystal was heavily colored. This is more clearly seen in the bleaching curve of KCl irradiated at dry ice temperatures.

As F centers are stable thermally in these temperature range[2], the decrease shown in Fig. 1 seems to be due to the thermal decomposition of V centers. Measurements were also done on the change of V bands during warming up. In the temperature range in which the first decrease of F centers occur, most of V_1 centers disappeared, showing that this decrease is due to the decomposition of V_1 centers. From the results of Delbecq et al[3], the second stage seems to be related to the V_K centers. The forth and fifth stage were observed to correspond to the V_2 band and the band having the peak near 270 mμ, respectively.

The decrease of the concentration of F centers in each stage seems to be a measure of the concentration of each V centers formed by gamma-irradiation. It is interesting to know that the concentration of V_1 centers is nearly proportional to the initial concentrations of F centers, whereas the concentration of V_K centers increased superlinearly with increasing gamma ray dose. Corresponding to the superlinear incaease of V_K centers, the concentration of F centers which remain stable after warming up to room temperature saturates in the case when irradiated at liquid nitrogen temperature.

The gradual decrease of the F center concentration during warming up may occur if some clustering of V type centers lowers their activation energy for thermal decomposition. In this connection it is interesting to note that Markham et al have shown[4] that the distribution of F centers are not so uniform in KBr irradiated at room temperature, from their bleaching experiments at liquid helium temperature. In order to clear these points and effects of impurity on the annealing curve more experiments are now in progress.

Most parts of this work was done while Nuclear Engineering one of the authors (N. I.) was in the course of School of JAERI. The authors would like to express our gratitude to Prof. Y. Takagi, Dr. K. Kubo and other staffs of the Solid State Physics Division of JAERI and

also to the members of solid state group of Suita's Laboratory.

References

1) G. A. Russel and C. C. Klick: Phys. Rev. **101** (1956) 1473.
2) N. F. Mott and R. W. Gurney: *Electronic Processes in Ionic Crystals* (Oxford, 1948).
3) C. J. Delbecq, B. Smaller and P. H. Yuster: Phys, Rev. **111** (1958) 1235.
4) J. J. Markham, R. T. Platt, and I. L. Mador: Phys. Rev. **92** (1953) 597.

J. PHYS. SOC. JAPAN **15** (1960) 1717

Oscillatory Magnetoresistance in N-Type PbTe

By Yasuo KANAI, Riro NII and Naozo WATANABE

Electrical Communication Laboratory, Musashinoshi, Tokyo

(Received July 5, 1960)

As is well known[1)], the mobilities of electrons and holes in PbS, PbSe and PbTe become very large at liquid helium temperature. This fact suggests us that the oscillatory galvanomagnetic effects could be observed in these semiconductors at very low temperatures.

Hall effect and megnetoresistance of n-type PbTe were measured at 4.2°K in a pulsive strong (over 100 KG) magnetic field. The transverse magnetoresistance *versus* magnetic field strength curve of one of our samples is shown in Fig. 1. This sample had the following character at 4.2°K; electrical resistivity $\rho_0=2.15\times10^{-5}$ ohm-cm, Hall coefficient $R_H=-35.6$ cm^3/Coul., hence Hall mobility $\mu_H\equiv|R_H|/\rho_0=1.65\times10^6$ cm^2/V. sec. As we can see in Fig. 1, it is quite clear that there are some oscillatory parts in the magnetoresistance effect in n-type PbTe. But we could not find any anomaly in the Hall effect of the same sample.

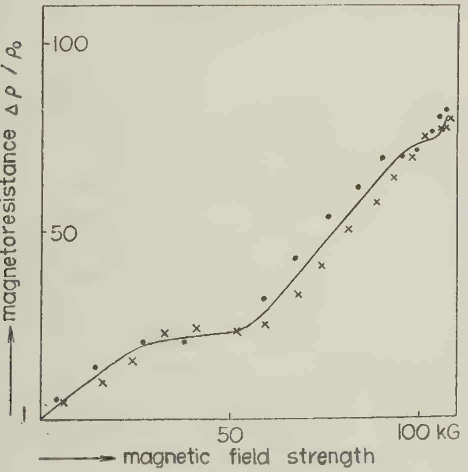

Fig. 1. The transverse magnetoresistance *versus* magnetic field strength curve of an n-type PbTe crystal at 4.2°K. The symbols · and × show the values obtained when the magnetic field increased and decreased respectively.

Further systematic investigations on the oscillatory galvanomagnetic effects in PbTe are now in progress and the results will be reported in this Journal.

References

1) For instance, W. W. Scanlon: Solid State Physics Vol. 9 (Academic Press Inc., New York, 1959) 83.

J. PHYS. SOC. JAPAN **15** (1960) 1717~1718

Sign Reversal of Hall Coefficients at Low Temperatures in Heavily Compensated *p*-type Germanium

Hiroo YONEMITSU, Hajime MAEDA, and Hisao MIYAZAWA

Matsuda Research Laboratory, Toshiba Electric Co., Kawasaki

(Received July 8, 1960)

Impurity center conduction in germanium has been well examined by Fritzsche et al[1] and other authors[2]. However, no one has successfully observed sign reversal of Hall coefficients even in deliberately compensated specimens. According to the two carrier model[1] of free holes and acceptor electrons, there might be the sign reversal provided the mobility and the concentration of free holes are very small while those of acceptor electrons are quite large. These conditions will be realized if the crystal is quite heavily compensated, as illustrated in Fig. 1.

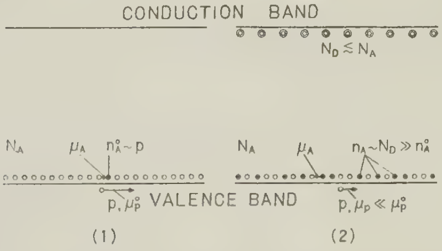

Fig. 1. Comparison between (1) uncompensated and (2) heavily compensated p-type Ge. Note that $n_A \gg n^0_A$ and $\mu_p \ll \mu_p^0$ because of added donors.

The present authors, therefore, prepared such a crystal in which the ingot initially containing $\sim 2\times 10^{16}$ Ga cm^{-3} and having resistivity of 0.2 ohm·cm was heavily compensated with Sb. The resultant specimens cut from this crystal indicate resistivity of ~0.32 ohm-cm and p-type Hall coefficient of ~740 cm^3 coul^{-1}. at room temperature, suggesting ~40% compensation. When the measurements were carried out at low temperatures, The Hall coefficients at 5,000 gauss, as plotted in Fig. 2, indicated a maximum at 10°K, then decreased as usual with decreasing temperature, and eventually the sign reversal occurred nearly at 5°K. Thereafter the Hall coefficients flattened off, showing temperature insensitive behaviors. Meanwhile, the resistivity showed typical characteristics of impurity conduction below 10°K. Similar results have been obtained on several specimens.

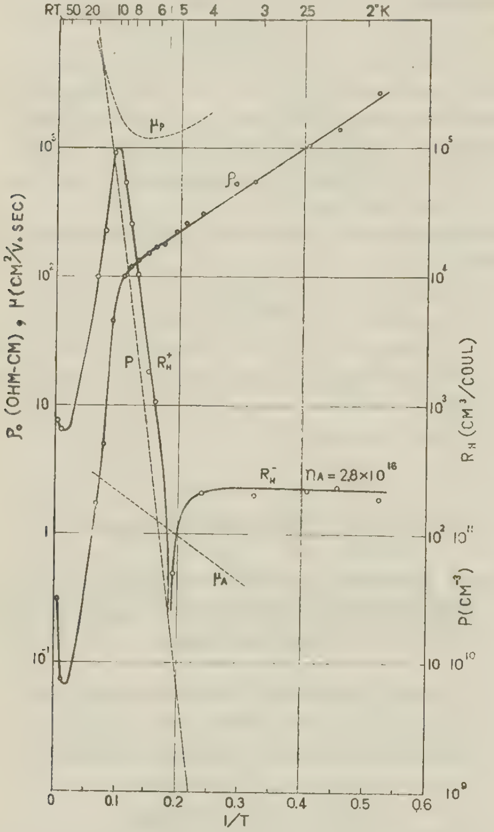

Fig. 2. An example of behaviors of Hall coefficient and resistivity for a heavily compensated p-type Ge.

The data were analysed by the two carrier model, which is expressed by

$$R_H = \frac{1}{e}\frac{r_p p \mu_p{}^2 - r_A \mu n_A{}^2{}_A}{(p\mu_p + n\mu_A)^2}, \quad \rho_0 - e^{-1}(p\mu_p + n_A\mu_A)^{-}$$

where r_p and r_A are assumed to be unity in the present case. Some quantities thus determined are presented in Fig. 2. The values of μ_p and μ_A seem reasonable[3,4] except n_A slightly exceeds N_A.

References

1) H. Fritzsche and K. Lark-Horovitz: Physica **20** (1954) 834
H. Fritzsche: Phys. Rev. **99** (1955) 406

2) C. S. Hung and J. R. Gliessman: Phys. Rev. **96** (1954) 1226
W. C. Dunlap, Jr.; Phys. Rev. **94** (1954) 1419

3) E. Conwell and V. F. Weisskopf: Phys. Rev. **77** (1950) 388

4) J. S. Blakemore: Phil. Mag. **4** (1959) 560

JOURNAL OF THE PHYSICAL SOCIETY OF JAPAN, Vol. 15, No. 10, OCTOBER, 1960

Energy Dependence of Angular Distributions of the Reaction $Al^{27}(p, \alpha)Mg^{24}$ in the Energy Region between 10.5 and 14.5 Mev*

By Hiroshi OGATA, Hidehiko ITOH,
Department of Nuclear Science, Faculty of Science, Kyoto University
Yoshiko MASUDA, Kunio TAKAMATSU, Maumi KAWASHIMA,
Akira MASAIKE and Isao KUMABE
Department of Physics, Faculty of Science, Kyoto University

(Received June 13, 1960)

The angular distributions of the reactions $Al^{27}(p, \alpha)Mg^{24}$ resulting in the ground and first excited states of Mg^{24} were measured at 37 energies between 10.5 and 14.5 Mev, making use of proportional counters.

Similar behaviour was obtained for both reactions. The variation of the shape of the angular distributions with the bombarding energy is rather smooth in the higher energy region, but becomes rapid with decreasing the bombarding energy. There appear some resonance-like peaks and valleys in the excitation curves at laboratory angles of 50°, 90° and 130° but their positions are not coincident with one another and in the higher energy region these peaks disappear in the excitation curves for the total cross sections.

The variations of the excitation curves for the total cross sections and of the shape of the angular distributions with energy in the lower energy region may be due to the fluctuations in the number or properties of the compound nucleus levels and to the interference between the compound nucleus and direct interaction processes. The smoothing-outs of the excitation curves for the total cross sections and of the variation of the shape of the angular distributions in the higher energy region seem to be due to the effects of decreasing level spacing in the compound nucleus and of increasing contribution from the direct interaction process. However, in the entire energy region, the interference between the compound nucleus and direct interaction processes and some contribution from the heavy particle stripping process cannot be neglected.

§1. Introduction

The sharp energy dependence of the differential cross sections for the (p, α) and (p, p') reactions in the medium weight nuclei was reported by several authors. Fischer *et al.*[1] have measured the angular distributions of the reactions $Al^{27}(p, \alpha_0)Mg^{24}$ and $Al^{27}(p, \alpha_1)Mg^{24*}$ resulting in the ground and first excited states of Mg^{24}, respectively, at 10.87 and 10.97 Mev, as well as the excitation curves for these reactions in the energy region between 9.6 and 11 Mev. It has been found that these excitation curves show a sharp energy dependence which is not expected from the view-point of direct interaction theories.

In a previous paper,[2] we have reported the excitation curves at a laboratory angle of 50° with respect to the bombarding beam, from 12.7 to 14.1 Mev and the angular distributions at 14.1, 13.0 and 12.8 Mev for the reactions $Al^{27}(p, \alpha_0)Mg^{24}$ and $Al^{27}(p, \alpha_1)Mg^{24*}$. It has been found that the excitation curves show a sharp energy dependence, and some angular distributions show strong backward peaking, although the $Al^{27}(p, \alpha_0)Mg^{24}$ data can be partially fitted by $[j_2(Qr_0)]^2$ of Butler's theory.[3]

For Ni and Si^{28} targets, the dependence of the yield of the inelastic scattering resulting in the first excited state on the bombarding energy has been measured in detail by Hu *et al.*[4] by changing the incident proton energy finely at intervals of about 50 kev. They have recognized that there were resonance-like behaviours with spacing of about several hundred kev. In order to interpret such sharp energy dependence, Igarasi *et al.*[5] have proposed a nuclear model based on some kind of partial heating of the nucleus.

---

* This experiment was performed using a 160 cm variable energy cyclotron at the Institute for Nuclear Study, University of Tokyo.

Numerical data obtained in this experiment will be published in Memoirs of the College of Science, University of Kyoto.

In this situation the accumulation of more detailed experimental data is desirable for further development. In this paper the results of measurements on the angular distributions of the reactions $Al^{27}(p, \alpha_0)Mg^{24}$ and $Al^{27}(p, \alpha_1)Mg^{24*}$ at 37 energies between 10.5 and 14.5 Mev are reported as a part of our extensive investigations on the (p, α) reaction.

§ 2. Experimental Procedure

Proton beam was obtained from a 160 cm variable energy cyclotron[6] at the Institute for Nuclear Study, University of Tokyo. The detector[7] is a proportional counter, as shown in Fig. 1, filled with argon and 5% CO_2 at such pressures that the fast alpha particles from the individual (p, α) reaction lose their energies completely inside the sensitive volume of the counter. In this way alpha particle groups were easily separated from proton and deuteron groups. Two proportional counters making an angle of 40° to each other were placed on the turn table in the scattering chamber to save the time of the observation. In order to stop completely the alpha particles resulting in the ground state of Mg^{24}, the counters were filled with $A\text{-}CO_2$ at pressures of 75.0, 64.4, 60.1, 51.0 and 45.3 cmHg for 14.55∼14.28, 14.16∼13.31, 13.16∼12.25, 12.17∼11.70 and 11.53∼10.65 Mev respectively. The counter pressures could be easily varied from the outside of the scattering chamber.

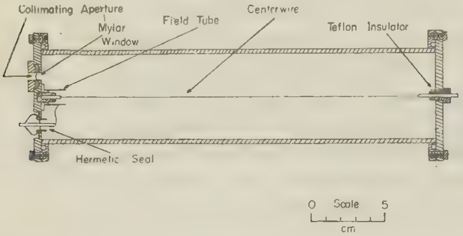

Fig. 1. Proportional counter used for the detection of the alpha particles.

As a target a foil of aluminium of 0.668 mg/cm² in thickness was used which was placed at 45° with respect to the bombarding beam, and corresponds to the energy loss of about 30 kev at 14 Mev proton energy. The beam current was measured by a Faraday cup and a beam current integrator, and furthermore monitored by a CsI(Tl) scintillation counter located at one of the side windows of the scattering chamber making an angle of 75° with the beam direction. The detector bias was chosen to count only the pulses due to the protons scattered elastically by aluminium.

The beam energy was varied at intervals of about 100 kev by varying the magnetic field and the frequency of the cyclotron. The energy of protons was measured carefully at the beginning and the end of each measurement of the angular distributions by the combination of aluminium absorbers and a shallow ionization chamber. Using the range energy relation obtained by Bichsel *et al.*,[8] the absolute value of beam energy was determined within the experimental error of 100 kev, and the relative value is considered to be much more accurate. The energy spread of the incident beam was not determined precisely but it seems to be less than 50 kev.

A typical pulse height distribution of the alpha particles from the reaction $Al^{27}(p,\alpha)\cdot Mg^{24}$ is shown in Fig. 2. Two peaks in Fig. 2 correspond to the reaction $Al^{27}(p, \alpha_0)\cdot Mg^{24}$ ($Q=+1.595$ Mev[9]) resulting in the ground state and the reaction $Al^{27}(p, \alpha_1)Mg^{24*}$

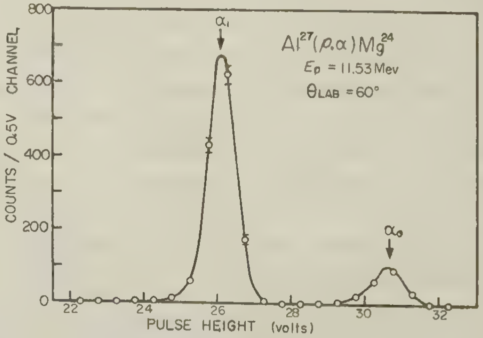

Fig. 2. Typical pulse height distribution of the alpha particles from the reactions $Al^{27}(p, \alpha)Mg^{24}$ resulting in the ground and first excited states of Mg^{24} at a laboratory angle of 60° for 11.53 Mev protons.

($Q=+0.227$ Mev[9]) in the first excited state of Mg^{24}. The energy resolution (full width at half maximum) was about 2.8% and the complete separation of the two peaks was obtained. Background due to oxygen and carbon contamination and reactions other than (p, α) reactions, for instance (p, p') reaction, is expected to have no influence upon the spectra, considering the Q values ($Q=-5.208$ Mev[10]) for $O^{16}(p, \alpha)N^{13}$ and $Q=-7.563$ Mev[10]) for $C^{12}(p, \alpha)B^{9}$) and the energy losses in the counter volume.

§ 3. Results and Discussion

Examples of the angular distributions are shown in Fig. 3. Error bars represent the uncertainties due to counting statistics. All the angular distributions measured here are collected and the three-dimensional views of them as a function of the incident proton energy and the C.M. angle are shown in Figs. 4 and 5. The curves in these figures were drawn smoothly among experimental points as those in Fig. 3. Measured angle and magnitude of experimental errors are similar to those in Fig. 3. As can be seen from Fig. 4 and 5, for both reactions the variation of the shape of the angular distributions with the bombarding energy is rather smooth in the higher energy region, but becomes rapid gradually with decreasing energy.

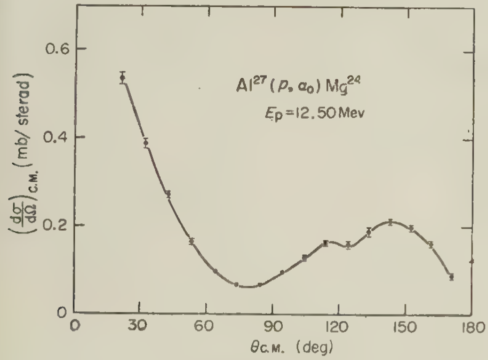

Fig. 3a.

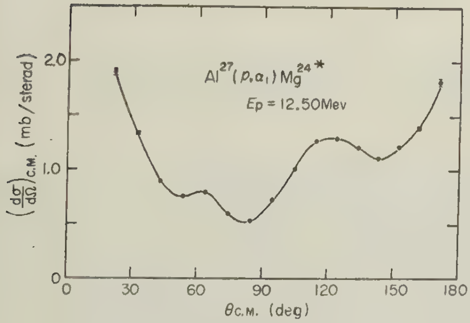

Fig. 3b.

Fig. 3. Angular distributions of the alpha particles from the reactions $Al^{27}(p, \alpha_0)Mg^{24}$ and $Al^{27}(p, \alpha_1)Mg^{24*}$ at 12.5 Mev incident proton energy. The solid curves were drawn smoothly among experimental points. The errors are smaller than the points, unless shown otherwise.

Fig. 6 shows the excitation curves at laboratory angles of 50°, 90° and 130° for the reactions $Al^{27}(p, \alpha_0)Mg^{24}$ and $Al^{27}(p, \alpha_1)\cdot Mg^{24*}$ as well as those for the total cross sections integrated from the angular distributions. For both reactions there appear some resonance-like peaks and valleys in the excitation curves at laboratory angles of 50°, 90° and 130°, but their positions are not coincident with one another and in the higher energy region these peaks disappear in the excitation curves for the total cross sections. Therefore these facts are considered to come from the variation of the shape of the angular distributions with the bombarding energy and not from the presence of the intermediate resonance levels proposed by Igarasi *et al.*[5]) Thus it should be noted that without the measurement of the total cross sections it is dangerous to ascribe the resonance-like peaks in the excitation curves for the differential cross sections to the presence of the intermediate resonance levels.

It is interesting to compare these results with the triton pickup or exchange theories. According to the simple theories of these surface direct interactions,[3]) the angular distribution for the reaction $Al^{27}(p, \alpha)Mg^{24}$ is found to be essentially expressed as follows:

$$\frac{d\sigma}{d\Omega} \propto [j_l(Qr_0)]^2 ,$$

where j_l is the spherical Bessel function of order l, and Q is the momentum transfer as obtained by following equation:

$$Q=\left| \boldsymbol{k}_p - \frac{M_i}{M_f} \boldsymbol{k}_\alpha \right| ,$$

where $\boldsymbol{k}_p$ and $\boldsymbol{k}_\alpha$ are the center of mass momenta in units of $\hbar$ of the incident protons and emergent alpha particles, respectively, and M_i and M_f are the masses of Al^{27} and Mg^{24}, respectively, and r_0 is the interaction radius. No angular distributions in the pre-

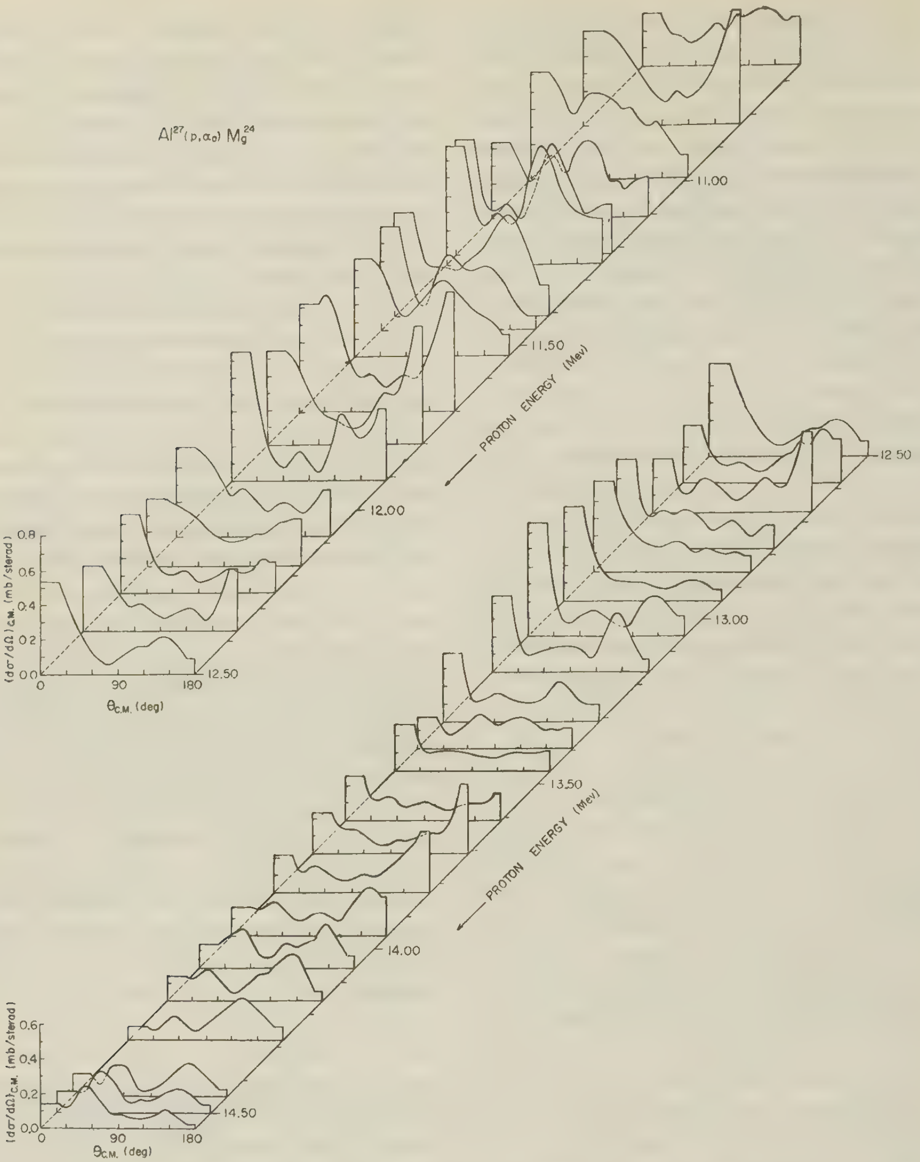

Fig. 4. Three dimensional view of the angular distributions for the reaction $\mathrm{Al^{27}}(p, \alpha_0)\mathrm{Mg^{24}}$ as a function of the incident proton energy and the C.M. angle.

sent experiment are expected to be well fitted by the direct interaction theories but partial fitting may be expected at least in the higher energy region.

To interpret the present data, the peak positions in the angular distributions were plotted in Fig. 7 as a function of the incident proton energy and the C.M. angle. It can be seen that there are several mountain ranges, that is, groups of the peak positions in this figure. The presence of these mountain ranges suggests that the direct interaction process plays an important role in these reactions. The movement of the peak positions to the forward angle with increasing energy agrees in general with the prediction of the direct interaction theories. The triangles in Fig. 7 indicate the peak positions calculated from the direct interaction theory with radii of the denoted values in this figure and with the values of $l=2$ and $l=0$ for the reactions $\mathrm{Al^{27}}(p, \alpha_0)\mathrm{Mg^{24}}$ and $\mathrm{Al^{27}}(p, \alpha_1)\mathrm{Mg^{24*}}$, respectively, at 11, 12, 13 and 14 Mev. These values of the radius were chosen to give the best fit to the mountain ranges. It can be seen that the general behaviours of the

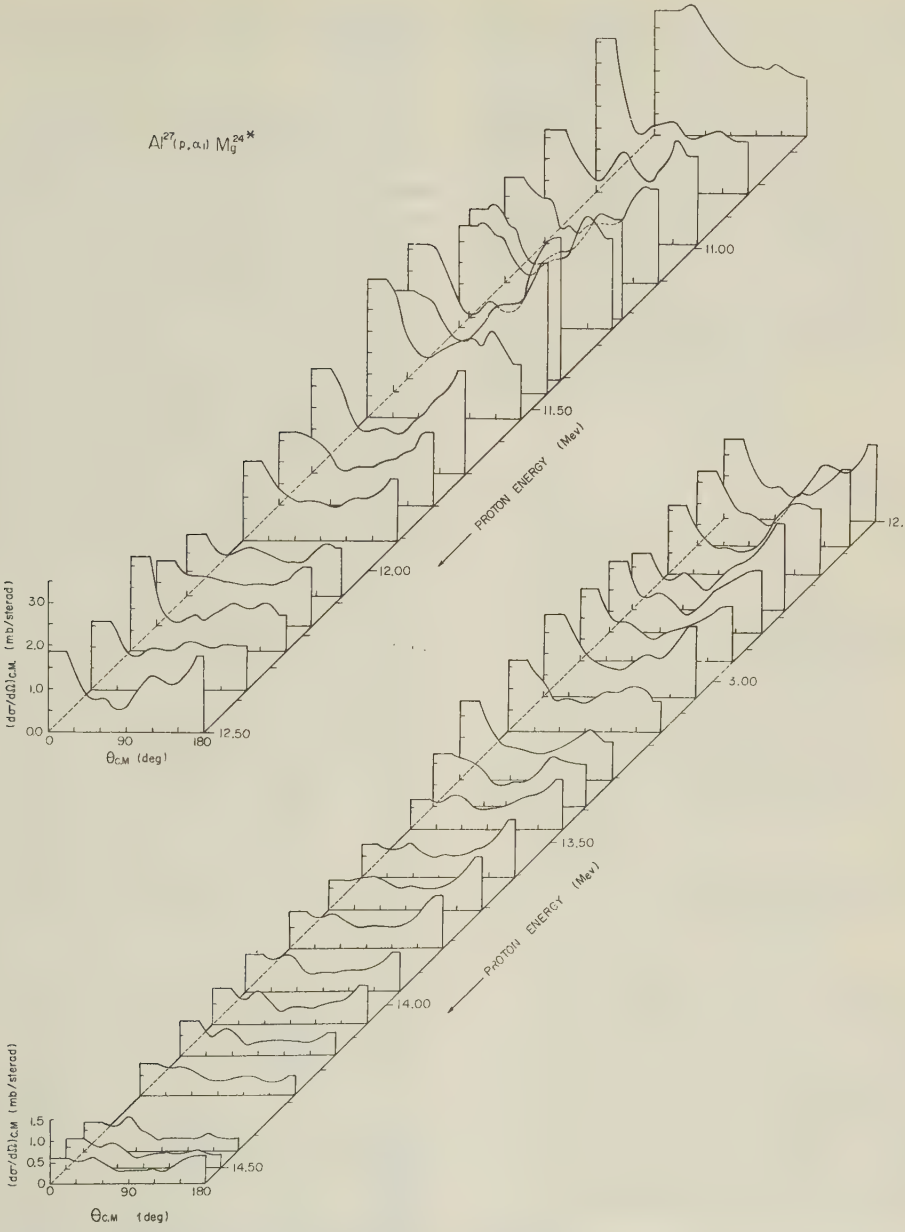

Fig. 5. Three dimensional view of the angular distributions for the reaction $Al^{27}(p, \alpha_1)Mg^{24*}$ as a function of the incident proton energy and the C.M. angle.

mountain ranges are reproduced by the triton pickup theory, although these values of the radius are considerably larger as compared with those used commonly and vary with the incident proton energy. Therefore the direct interaction process seems to play an important role in these reactions in the entire energy region observed here.

The observed sharp energy dependence cannot be explained by the simple theories of direct interaction which predict very slowly changing differential cross sections. Modification of the direct interaction theories,[11] including the distorted wave treatments, would probably also not produce such a sharp energy dependence. Owen and Madansky[12] have obtained good qualitative agreement with the angular distributions for the reactions $B^{11}(d, n)C^{12}$ and $C^{13}(He^3, \alpha)C^{12}$ which show large energy dependence, extending the ordinary deuteron stripping theory to include the effect of heavy particle stripping. This heavy particle stripping process gives the angular distribution having backward peaks for emitted alpha particles. The backward peakings which appear in the angular distributions at several incident energies in the present results show possibly the evidence of considerable contribution of the heavy particle stripping process.

On the other hand, assuming that the reaction $Al^{27}(p, \alpha)Mg^{24}$ occurs through the compound nucleus formation, the sharp energy dependence cannot be expected from the statistical theory,[13] which is based on the assumptions that there are many levels of all types at the excitation energy of the compound nucleus (continuum assumption), and the corresponding wave functions have a random phase so that when phase averages are performed all interference terms will vanish (statistical assumption). In this case, therefore, the continuum or statistical assumption cannot be satisfied. The compound nucleus, Si^{28}, would have up to 22.2 and 25.6 Mev of excitation at 11.0 and 14.5 Mev of bombarding energy respectively. Since there are 29 levels[14] in Si^{28} between 13.75 and 14.69 Mev, assuming the level density $\omega(E) \propto \exp(E^{1/2})$,[15] $\omega(22.2)$ and $\omega(25.6)$ are calculated to be about 80 and 115 levels/Mev respectively, although there is some uncertainty connected with the

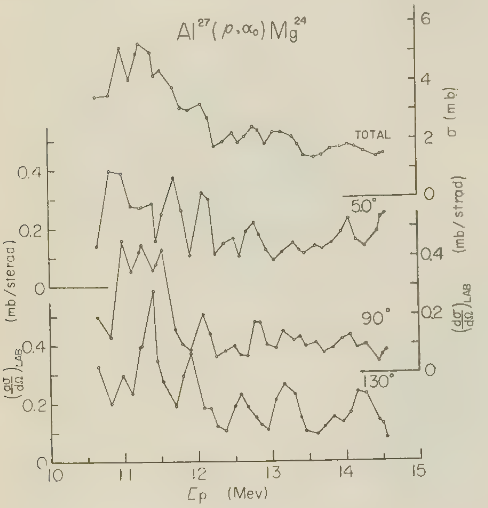

Fig. 6a.

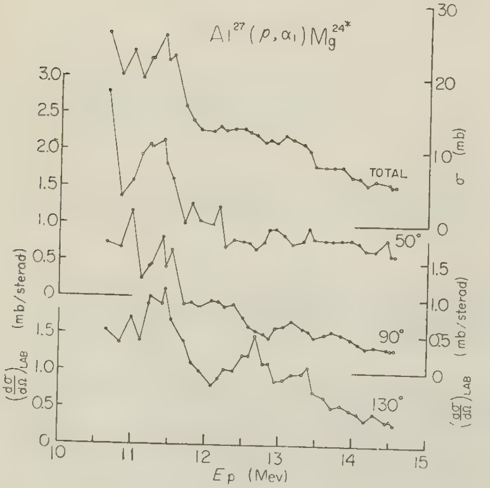

Fig. 6b.

Fig. 6. Differential cross sections at laboratory angles of 50°, 90° and 130° and the total cross sections for the reactions $Al^{27}(p, \alpha_0)Mg^{24}$ and $Al^{27}(p, \alpha_1)Mg^{24*}$ as a function of the incident proton energy.

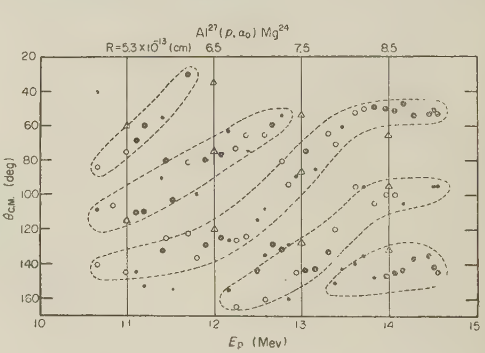

Fig. 7a.

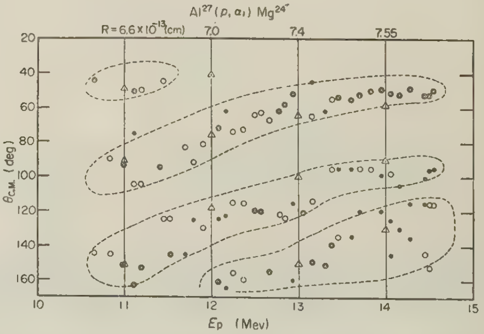

Fig. 7b.

Fig. 7. Peak positions in the angular distributions as a function of the incident proton energy and the C.M. angle. Double open circles, open circles and filled circles indicate the positions of large, medium and small peaks in the angular distributions respectively. Triangles indicate the peak positions calculated from the direct interaction theory for radii of the denoted values in the figure at 11, 12, 13 and 14 Mev.

calculation oft he level density by this equation.

In the lower energy region, since level spacing in the compound nucleus is such that several levels should be excited at each energy, the variations of the excitation curves for the total cross sections and of the shape of the angular distributions with energy may be due to the fluctuations in the number or properties of the compound nucleus levels and to the interference between the compound nucleus and direct interaction processes. The smoothing-outs of the excitation curves for the total cross sections and of the variation of the shape of the angular distributions with increasing energy could be the effects of decreasing level spacing in the compound nucleus and of increasing contribution from the direct interaction process which is seen from the shape of the angular distributions.

Recently we have studied the angular distributions for the reactions $Co^{59}(p, \alpha)Fe^{56}$ and $Mn^{55}(p, \alpha)Cr^{52}$ [16] resulting in the ground and first excited states at 7.7∼14.1 and 7.6∼12.9 Mev respectively. It has been found that the direct interaction processes are predominant at the proton energies above about 11 Mev. This behaviour seems to be similar to that of the present result.

Since misdetermination of the solid angle in the previous work was found, absolute values of the cross sections in the previous (p, α) experiments on Al, Cr[2] and F[7] should be multiplied by a factor of 1.39. Corrected values of the cross sections for the previous $Al(p, \alpha)$ data[2] are in agreement with the present values.

In conclusion, the variations of the excitation curves for the total cross sections and of the shape of the angular distributions with energy in the lower energy region may be due to the fluctuations in the number or properties of the compound nucleus levels and to the interference between the compound nucleus and direct interaction processes. The smoothing-outs of the excitation curves for the total cross sections and of the variation of the shape of the angular distributions in the higher energy region seem to be due to the effects of decreasing level spacing in the compound nucleus and of increasing contribution from the direct interference between the interaction process. However, in the entire energy region, the compound nucleus and direct interaction processes, and some contribution from the heavy particle stripping process cannot be neglected.

The authors wish to thank Professor K. Kimura and Professor T. Sidei for their interests and encouragements throughout this work. Their thanks are also due to the cyclotron crew of the Institue for Nuclear Study, University of Tokyo, for their kind hospitality and patient cooperation.

References

1) G. E. Fischer, V. K. Fischer, E. A. Remler and M. D. Tatcher: Phys. Rev. **110** (1958) 286 (L).
2) I. Kumabe, C. L. Wang, M. Kawashima, M. Yada and H. Ogata: J. Phys. Soc. Japan **14** (1959) 713.
3) S. T. Butler: Phys. Rev. **106** (1957) 272.
4) C. Hu, K. Kikuchi, S. Kobayashi, K. Matsuda, Y. Nagahara, Y. Oda, N. Takano, M. Takeda and T. Yamazaki: J. Phys. Soc. Japan **14** (1959) 861; **15** (1960) 760.
5) S. Igarasi, K. Izumo and T. Udagawa: Progr. Theor. Phys. **21** (1959) 468.
6) S. Kikuchi *et al.*: J. Phys. Soc. Japan **15** (1960) 41.
7) H. Ogata: J. Phys. Soc. Japan **14** (1959) 707.
8) H. Bichsel, R. F. Mozley and W. A. Aron: Phys. Rev. **105** (1957) 1788.
9) P. M. Endt and C. M. Braams: Rev. Mod. Phys. **29** (1957) 683.
10) F. Ajzenberg-Selove and T. Lauritsen: Nuclear Phys. **11** (1959) 1.
11) W. Tobocman and M. H. Kalos: Phys. Rev. **97** (1955) 132. S. Hayakawa and S. Yoshida: Progr. Theor. Phys. **14** (1955) 1.
12) G. E. Owen and L. Madansky: Phys. Rev. **105** (1957) 1766. G. E. Owen, L. Madansky and S. Edwards, Jr.: Phys. Rev. **113** (1959) 1575.
13) W. Hauser and H. Feshbach: Phys. Rev. **87** (1952) 366.
14) D. E. Alburger and E. M. Hafner: Rev. Mod. Phys. **22** (1950) 373.
15) J. M. Blatt and V. F. Weisskopf: *Theoretical Nuclear Physics* (John Wiley and Sons, Inc., New York 1952), p. 371.
16) H. Ogata, H. Itoh, Y. Masuda, K. Takamatsu, M. Kawashima, A. Masaike and I. Kumabe: subsequent paper.

JOURNAL OF THE PHYSICAL SOCIETY OF JAPAN, Vol. 15, No. 10, OCTOBER, 1960

Angular Distributions of the Reactions $Co^{59}(p, \alpha)Fe^{56}$ at 7.7~14.1 Mev and $Mn^{55}(p, \alpha)Cr^{52}$ at 7.6~12.9 Mev*

By Hiroshi OGATA and Hidehiko ITOH
Department of Nuclear Science, Faculty of Science, Kyoto University
Yoshiko MASUDA, Kunio TAKAMATSU, MAUMI KAWASHIMA, Akira MASAIKE and Isao KUMABE
Department of Physics, Faculty of Science, Kyoto University

(Received June 13, 1960)

The angular distributions of the reactions $Co^{59}(p, \alpha)Fe^{56}$ and $Mn^{55}(p, \alpha)Cr^{52}$ resulting in the ground and first excited states of the residual nuclei have been measured at 7.7, 8.7, 9.8, 10.85, 11.9, 13.1 and 14.1 Mev and at 7.65, 8.85, 9.65, 10.7, 11.8 and 12.9 Mev of the incident proton energy, respectively, making use of proportional counters.

Similar behaviour was obtained for these four reactions. For the reaction $Co^{59}(p, \alpha)Fe^{56}$ the forward peak in the angular distribution is prominent at 14.1 and 13.1 Mev and disappears gradually with decreasing proton energy, and the angular distribution is approximately 90° symmetrical below about 11 Mev. For the reaction $Mn^{55}(p, \alpha)Cr^{52}$ the angular distribution is considerably forward peaked at 12.9 and 11.8 Mev and it approximately 90° symmetrical below about 10 Mev. It was found that the total cross section integrated from the angular distributions for both reactions decrease smoothly with increasing proton energy.

It is considered that the reactions $Co^{59}(p, \alpha)Fe^{56}$ and $Mn^{55}(p, \alpha)Cr^{52}$ resulting in the ground and first excited states of the residual nuclei occur through the similar reaction process, that is, in the lower energy region the compound nucleus process plays a predominant role, although some contribution from the direct interaction process cannot be neglected, and the contribution from the direct interaction process becomes gradually significant with increasing proton energy and is predominant above about 11 Mev.

§ 1. Introduction

The studies of the (p, α) reactions for various elements play an important role in the investigation of the nuclear reaction mechanism. A number of studies of the (p, α) reactions have been reported, but most of them have been carried out for light elements. For light elements, such as C^{12} 1) or F^{19},2),3) the reactions resulting in lower states of the residual nuclei appear to favour description by the simple direct interaction theories. Recently we have studied the angular distributions for the reactions $Al^{27}(p, \alpha)Mg^{24}$ 4) resulting in the ground and first excited states of Mg^{24} at 37 energies between 10.5 and 14.5 Mev. The sharp energy dependence of the angular distributions shows that these reactions occur through the complicated processes.

For medium and heavy elements, Brady5) has measured the angular distribution for the reaction $Rh^{103}(p, \alpha)Ru^{100}$ resulting in the ground state. The strong forward peaking of the angular distribution suggests that the alpha particles are produced by direct interactions. Investigations of the (p, α) reactions in targets of wide range of atomic number have been performed by Fulmer and Cohen6) at 23 Mev and by Fulmer and Goodman7) at the proton energies between 9.5 and 23 Mev. It has been reported that the alpha particles from the heaviest elements and the high energy parts of the spectra from lighter targets are strongly forward peaked and are produced by direct interactions, and an alpha particle model may be important for the nuclei for which the compound nuclei are integral number of alpha particles.

---

* This experiment was performed using a 160 cm variable energy cyclotron at the Institute for Nuclear Study, University of Tokyo.

Numerical data obtained in this experiment will be published in Memoirs of the College of Science, University of Kyoto.

In a previous paper,[8] we have reported the angular distributions of two alpha particle groups from the reaction $Cr^{52}(p, \alpha)V^{49}$, one of which corresponds to the alpha particles resulting in the first three levels and the other corresponds to the levels up to about 1 Mev excitation except the first three levels. It has been found that the reactions $Cr^{52}(p, \alpha)V^{49}$ occur mostly through the compound nucleus formation at lower incident energies below 11 Mev and then the contribution from the direct interactions becomes significant gradually with increasing energy.

For medium weight nuclei studies of the (p, α) reactions to a single level of the residual nucleus have not been reported, but they give probably more reliable information concerning the reaction mechanism. Therefore the present work was undertaken to investigate the angular distributions of the reactions $Co^{59}(p, \alpha)Fe^{56}$ resulting in the ground and first excited states of Fe^{56} at 7.7~14.1 Mev and of the reactions $Mn^{55}(p, \alpha)Cr^{52}$ resulting in the ground and first excited states of Cr^{52} at 7.6~12.9 Mev, as a part of our extensive investigations on the (p, α) reaction.

§2. Experimental Procedure

The experiment was performed with the proton beam from a 160 cm variable energy cyclotron at the Institute for Nuclear Study, University of Tokyo. The general experimental method has been described in the preceding paper.[4]

For the reaction $Co^{59}(p, \alpha)Fe^{56}$, the target was a self-supporting cobalt foil of 0.62 mg/cm² in thickness which was obtained by an electroplating method. For the reaction $Mn^{55}(p, \alpha)Cr^{52}$, manganese metal evaporated onto a mylar film (0.8 mg/cm² thick) was used and the thickness of the manganese target was 0.55 mg/cm².

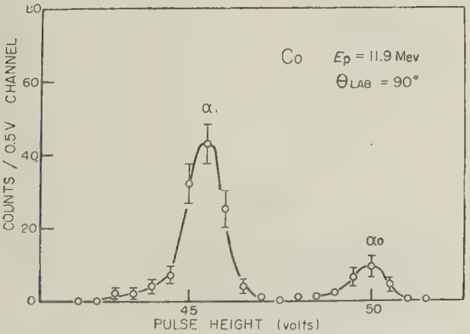

Fig. 1. Typical pulse height distribution of the alpha particles from the reactions $Co^{59}(p, \alpha)Fe^{56}$ resulting in the ground and first excited states of Fe^{56} at a laboratory angle of 90° for 11.9 Mev protons.

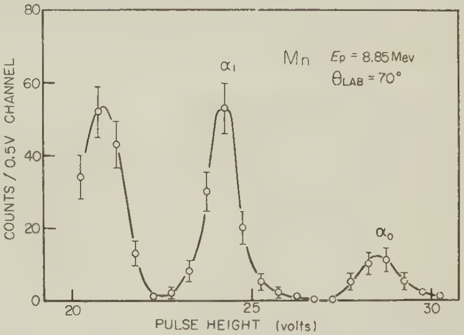

Fig. 2. Typical pulse height distribution of the alpha particles from the reactions $Mn^{55}(p, \alpha)Cr^{52}$ resulting in the ground and first excited states of Cr^{52} at a laboratory angle of 70° for 8.85 Mev protons.

Figs. 1 and 2 show typical pulse height distributions of the alpha particles from the reaction $Co^{59}(p, \alpha)Fe^{56}$ at a laboratory angle of 90° for 11.9 Mev protons and from the reaction $Mn^{55}(p, \alpha)Cr^{52}$ at a laboratory angle of 70° for 8.85 Mev protons, respectively. Two peaks in Fig. 1 correspond to the reactions $Co^{59}(p, \alpha_0)Fe^{56}$ resulting in the ground state of Fe^{56} ($Q_0 = +3.23$ Mev[9]) and the reaction $Co^{59}(p, \alpha_1)Fe^{56*}$ resulting in the first excited state of Fe^{56} ($Q_1 = +2.39$ Mev[9],[10]). The energy resolution (full width at half maximum) was about 2.5% and complete separation of these two peaks was obtained. While, in Fig. 2, there appear three peaks of which first two correspond to the reactions $Mn^{55}(p, \alpha_0)Cr^{52}$ resulting in the ground state of Cr^{52} ($Q_0 = +2.58$ Mev[9]) and the reaction $Mn^{55}(p, \alpha_1)Cr^{52*}$ resulting in the first excited state of Cr^{52} ($Q_1 = +1.13$ Mev[9],[10]). The energy resolution was about 3.5% and complete separation of these two peaks was obtained. In both reactions $Co^{59}(p, \alpha)Fe^{56}$ and $Mn^{55}(p, \alpha)Cr^{52}$ for larger angles and at higher proton energies, the separation was slightly worse and the spectrum analysis was necessary. However, the ambiguity accompanied by this analysis was rather small.

Since the results of spectroscopic analysis for Co and Mn metals used as targets scarcely showed the existence of impurities, for both reactions the background due to impurities is expected to have no influence upon the experimental results. Furthermore, for the reaction $Mn^{55}(p, \alpha)Cr^{52}$ the background due to carbon and oxygen contained in the mylar film does not affect the experimental results owing to the large negative Q-values of the reactions $C^{12}(p, \alpha)B^{9}$ and $O^{16}(p, \alpha)N^{13}$.

§ 3. Results and Discussion

Figs. 3 and 4 show the angular distributions for the reactions $Co^{59}(p, \alpha_0)Fe^{56}$ and $Co^{59}(p, \alpha_1)Fe^{56*}$, respectively, at 7.7, 8.7, 9.8, 10.85, 11.9, 13.1 and 14.1 Mev of the incident proton energy. It can be seen from Fig. 3 that the forward peak in the angular distribution for the reaction $Co^{59}(p, \alpha_0)Fe^{56}$ is prominent at 14.1 and 13.1 Mev and disappears gradually with decreasing proton energy, and the angular distribution is approximately 90° symmetrical below about 11 Mev. For the reaction $Co^{59}(p, \alpha_1)Fe^{56*}$ quite similar behaviour can be seen from Fig. 4.

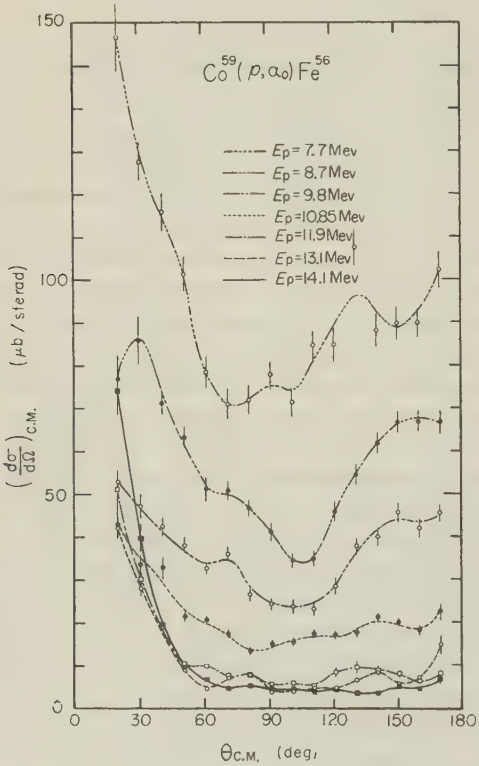

Fig. 3. Angular distributions of the alpha particles from the reaction $Co^{59}(p, \alpha_0)Fe^{56}$ at 7.7, 8.7, 9.8, 10.85, 11.9, 13.1 and 14.1 Mev. The error bars represent the uncertainties due to counting statistics.

The reactions $Co^{59}(p, \alpha_0)Fe^{56}$ and $Co^{59}(p, \alpha_1)Fe^{56*}$ at 14.1 and 13.1 Mev seem to occur predominantly through the direct interaction processes. It is interesting to compare these angular distributions with the simple theory of the surface direct interaction by triton pickup or knockon process. According to this theory,[11] the angular distribution for the (p, α) reaction is expressed as follows:

$$\frac{d\sigma}{d\Omega} \propto [j_l(Qr_0)]^2 , \qquad (1)$$

where j_l is the spherical Bessel function of order l and Q is the momentum transfer as obtained by following equation;

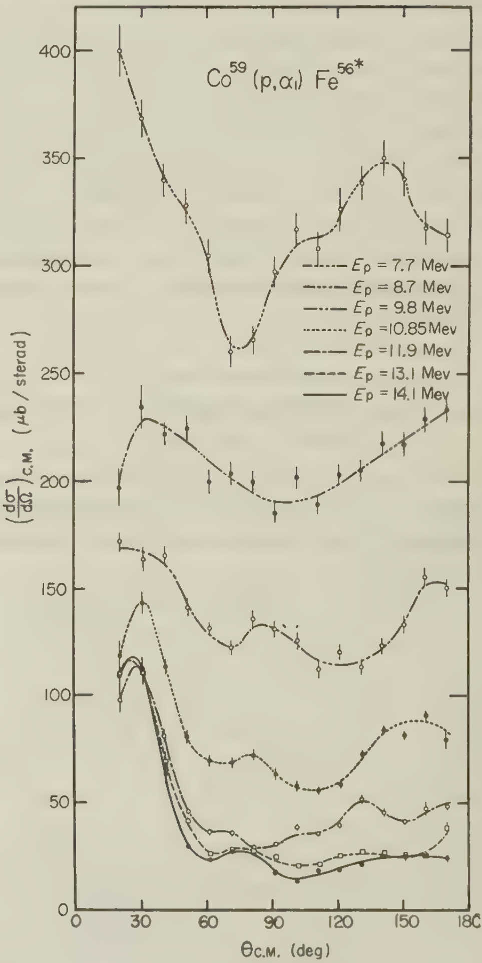

Fig. 4. Angular distributions of the alpha particles from the reaction $Co^{59}(p, \alpha_1)Fe^{56*}$ at 7.7, 8.7, 9.8, 10.85, 11.9, 13.1 and 14.1 Mev. The error bars represent the uncertainties due to counting statistics.

$$Q=\left| k_p - \frac{M_i}{M_f} k_\alpha \right| ,$$

where k_p and k_α are the center of mass momenta in units of $\hbar$ of the incident protons and the emergent alpha particles, respectively, M_i and M_f are the masses of the target and the residual nuclei, respectively, and r_0 is the interaction radius. The dashed curves in Figs. 5 and 6 have been calculated from Eq. (1) with the values of $l=3$ and $r_0=4.8\times10^{-13}$ cm for the reaction $Co^{59}(p, \alpha_0)Fe^{56}$ and with $l=1$ and $r_0=5.4\times10^{-13}$ cm for the reaction $Co^{59}(p, \alpha_1)Fe^{56*}$, respectively, at 14.1 Mev. These theoretical curves are considered to fit qualitatively the experimental data, although the magnitudes of interaction radii differ slightly from one another, and seem to be rather smaller as compared with those used commonly. The approximately 90° symmetrical angular distributions at 9.8, 8.7 and 7.7 Mev are consistent with the prediction of the statistical theory of the compound nucleus. The total cross sections integrated from the angular distributions, for the reactions $Co^{59}(p, \alpha_0)Fe^{56}$ and $Co^{59}(p, \alpha_1)Fe^{56*}$ are shown in Fig. 9, and it can be seen that they decrease monotonously with increasing proton energy.

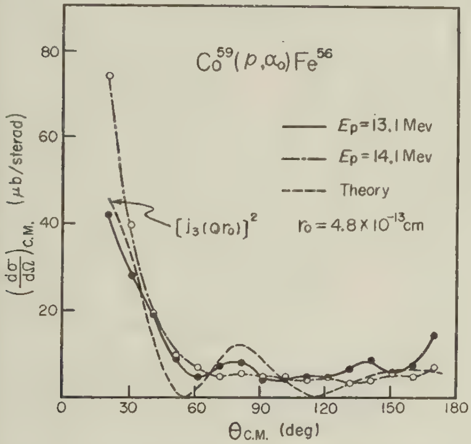

Fig. 5. Angular distributions of the alpha particles from the reaction $Co^{59}(p, \alpha_0)Fe^{56}$ at 13.1 and 14.1 Mev. The dashed curve shows the theoretical angular distribution at 14.1 Mev.

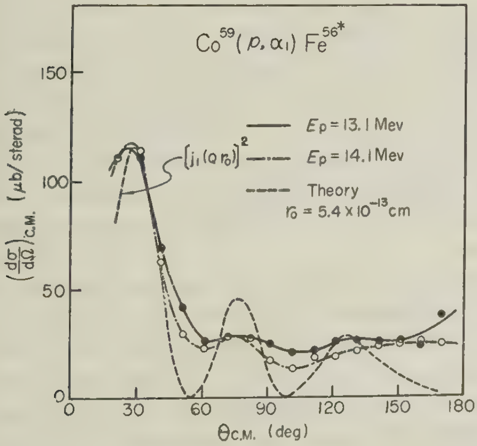

Fig. 6. Angular distributions of the alpha particles from the reaction $Co^{59}(p, \alpha_1)Fe^{56*}$ at 13.1 and 14.1 Mev. The dashed curve shows the theoretical angular distribution at 14.1 Mev.

Figs. 7 and 8 show the angular distributions of the alpha particles from the reactions $Mn^{55}(p, \alpha_0)Cr^{52}$ and $Mn^{55}(p, \alpha_1)Cr^{52*}$, respectively, at 7.65, 8.85, 9.65, 10.7, 11.8 and

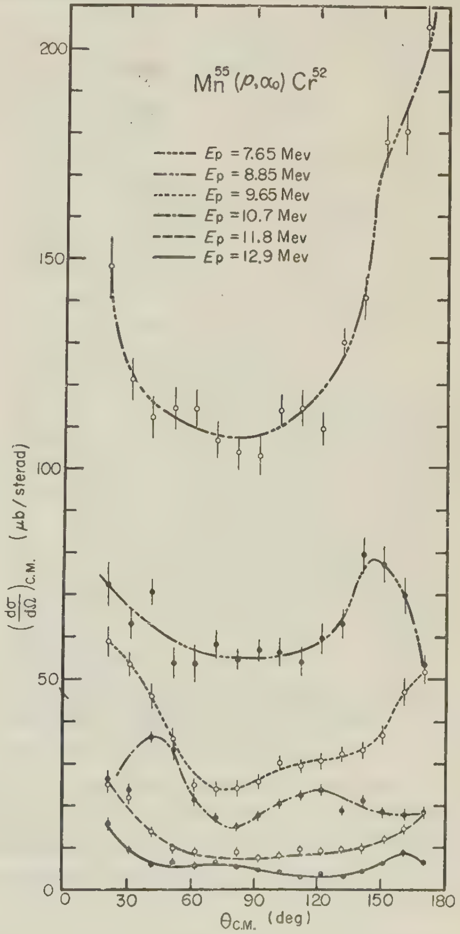

Fig. 7. Angular distributions of the alpha particles from the reaction $Mn^{55}(p, \alpha_0)Cr^{52}$ at 7.65, 8.85, 9.65, 10.7, 11.8 and 12.9 Mev. The error bars represent the uncertainties due to counting statistics.

12.9 Mev. It can be seen from Figs. 7 and 8 that the angular distributions for both reactions are considerably forward peaked at 12.9 and 11.8 Mev, and are approximately 90° symmetrical below about 10 Mev. These behaviours are very similar to those in the case of Co^{59}, although the forward peakings in the higher energy region are not so conspicuous and in general the angular distributions are more smooth. It can also be said that the direct interaction processes play a main role in these reactions above about 11 Mev and the compound nucleus process becomes predominant with decreasing proton energy. The total cross sections for the reactions $Mn^{55}(p, \alpha_0)Cr^{52}$ and $Mn^{55}(p, \alpha_1)Cr^{52*}$ are shown in Fig. 9 with those for the reaction $Co^{59}(p, \alpha)Fe^{56}$. They also decrease monotonously with increasing proton energy.

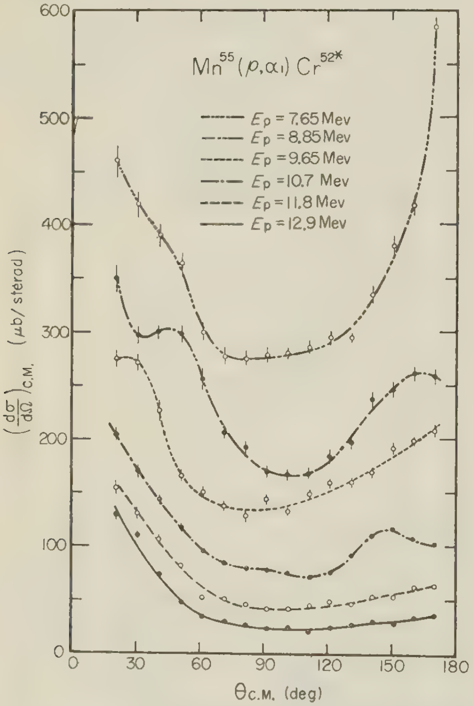

Fig. 8. Angular distributions of the alpha particles from the reaction $Mn^{55}(p, \alpha_1)Cr^{52*}$ at 7.65, 8.85, 9.65, 10.7, 11.8 and 12.9 Mev. The error bars represent the uncertainties due to counting statistics.

For the reaction $Mn^{55}(p, \alpha)Cr^{52}$, the behaviours of the angular distributions, the absolute values of the total cross sections and the energy dependence of the total cross sections are quite similar to those for the reaction $Co^{59}(p, \alpha)Fe^{56}$. In both reactions the mass numbers of the target elements and the reaction Q values are similar to each other, and the targets are the odd-even nuclei. Therefore, it can be expected that the reactions $Co^{59}(p, \alpha)Fe^{56}$ and $Mn^{55}(p, \alpha)Cr^{52}$ occur through the similar reaction process.

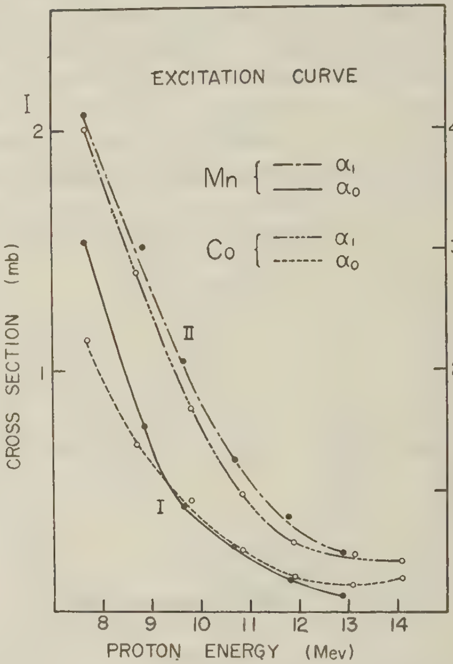

Fig. 9. Total cross sections integrated from the angular distributions for the reactions $Co^{59}(p, \alpha_0)Fe^{56}$, $Co^{59}(p, \alpha_1)Fe^{56*}$, $Mn^{55}(p, \alpha_0)Cr^{52}$ and $Mn^{55}(p, \alpha_1)Cr^{52*}$ as a function of the proton energy.

The difference between the cross sections for the reaction $Cr^{52}(p, \alpha)V^{49}$ [8] and the reactions $Co^{59}(p, \alpha)Fe^{56}$ and $Mn^{55}(p, \alpha)Cr^{52}$ may be due to following facts for the reaction $Cr^{52}(p, \alpha)V^{49}$ that Cr^{52} is an even-even nucleus, the reaction Q value is -2.59 Mev[10] and some levels of the residual nucleus are concerned.

Recently experimental investigations of the (p, p') reactions for medium weight nuclei at 8~14 Mev have been carried out by Kikuchi *et al.*[12] and Hu *et al.*[13] It has been found that the angular distributions of inelastically scattered protons are prominently forward peaked, and these (p, p') reactions occur mostly through the direct interaction processes down to 8 Mev. The difference between the angular distributions for the (p, α) and (p, p')

reactions is considered to be due to larger contributions from the direct interaction processes relative to the compound nucleus process in the (p, p') reactions than in the (p, α) reactions. It must also be noted that the absolute cross sections for the (p, p') reactions are by two orders of magnitude larger than those for the (p, α) reactions. These facts may suggest that the reduced widths for the (p, α) reactions are quite smaller as compared with those for the (p, p') reactions.

It is expected that the monotonic decrease of the total cross sections with increasing energy up to about 11 Mev could be explained with the statistical theory of the compound nucleus, but the slower decrease or flattening in the higher energy region could not. Since it was shown from the angular distributions that the reaction $Co^{59}(p, \alpha)Fe^{56}$ proceeds predominantly through the compound nucleus process at 8 Mev, a rough calculation of the total cross sections from the evaporation theory[14] was performed and the result was normalized to the experimental one at 8 Mev. The calculated cross sections are nearly in agreement with experimental ones up to about 11 Mev, but become smaller in the higher energy region and are about one fifth at 14 Mev. This fact also means that the direct process is predominant in the higher energy region. This fact is consistent with that obtained from the angular distribution.

In conclusion, it is considered that the reactions $Co^{59}(p, \alpha)Fe^{56}$ and $Mn^{55}(p, \alpha)Cr^{52}$ resulting in the ground and first excited states of the residual nuclei occur through the similar reaction process, that is, in the lower energy region the compound nucleus process plays a predominant role, although some contribution from the direct interaction process cannot be neglected, and the contribution from the direct interaction process becomes gradually significant with increasing proton energy and is predominant above about 11 Mev.

The authors wish to express their thanks to Professor K. Kimura and Professor T. Sidei for their interests and encouragements throughout this work. They are also indebted to the cyclotron crew of the Institute for Nuclear Study, University of Tokyo, for their kind hospitality and patient cooperation.

References

1) D. R. Maxson and J. H. Terrell: Bull. Amer. Phys. Soc. Ser. II, **3** (1958) 381.
2) J. G. Likely and F. P. Brady: Phys. Rev. **104** (1956) 118.
3) H. Ogata: J. Phys. Soc. Japan **14** (1959) 707.
4) H. Ogata, H. Itoh, Y. Masuda, K. Takamatsu, M. Kawashima, A. Masaike and I. Kumabe: preceding paper.
5) These data were introduced by P. C. Gugelot in Physica **22** (1956) 1019.
6) C. B. Fulmer and B. L. Cohen: Phys. Rev. **112** (1958) 1672.
7) C. B. Fulmer and C. D. Goodman: Phys. Rev. **117** (1960) 1339.
8) I. Kumabe, C. L. Wang, M. Kawashima, M. Yada and H. Ogata: J. Phys. Soc. Japan **14** (1959) 713.
9) V. J. Ashby and H. C. Catron: University of California Radiation Laboratory Report UCRL-5419, 1959 (unpublished).
10) K. Way, R. W. King, C. L. McGinnis and R. van Lieshout: Nuclear Schemes $A=40-A=92$ TID-5300, (United States Atomic Energy Commission 1955), p. 40 and p. 54.
11) S. T. Butler: Phys. Rev. **106** (1957) 272.
12) K. Kikuchi, S. Kobayashi and K. Matsuda: J. Phys. Soc. Japan **14** (1959) 121.
13) C. Hu, K. Kikuchi, S. Kobayashi, K. Matsuda, Y. Nagahara, Y. Oda, N. Takano, M. Takeda and T. Yamazaki: J. Phys. Soc. Japan **14** (1959) 861.
14) J. M. Blatt and V. F. Weisskopf: *Theoretical Nuclear Physics* (John Wiley and Sons, Inc., New York 1952), p. 371.

JOURNAL OF THE PHYSICAL SOCIETY OF JAPAN, Vol. 15, No. 10, OCTOBER, 1960

A Study of Pulse Height Distribution of Boron—Trifluoride Proportional Counters

By Mikiya YAMANE

Hitachi Central Research Laboratory, Kokubunji-machi, Tokyo

(Received May 28, 1960)

The pulse height distribution of boron trifluoride counter under overall irradiation by slow neutron has been treated allowing for the wall effect of the counter. Energy spectra, $R(\varepsilon')$, is given under assumption of a Gaussian resolution function by,

$$R(\varepsilon')\approx\frac{s}{2RE_0}\int_0^{E_0}\frac{1}{\sqrt{2\pi}\sigma}\exp\left\{-\frac{(\varepsilon'-\varepsilon)^2}{2\alpha^2}\right\}d\varepsilon+\left(1-\frac{S}{2R}\right)\frac{1}{\sqrt{2\pi}\sigma}\exp\left\{-\frac{(\varepsilon'-E_0)^2}{2\sigma^2}\right\},$$

where s and E_0 are the whole range and initial energy of alpha-particle respectively, and R is the radius of the counter. Agreement between theoretical and experimental distribution has been discussed for appropriate filling pressures.

§ 1. Introduction

Neutron counters filled with boron trifluoride gas have been used extensively and studied by many investigators since the first experiment of Korff and Danforth[1]. The principle of the operation of the counter is based on the reactions

$$B^{10}+n\rightarrow Li^7+\alpha+2.78\ \mathrm{MeV}$$

or

$$B^{10}+n\rightarrow Li^{*7}+\alpha+2.3\ \mathrm{MeV}$$

and thus it is expected that the shape of pulse height distribution for an ideal counter should show two sharp peaks. However several experiments revealed the appreciable broadening of the peaks because of (a) fluctuation of the number of initial ion pairs and (b) fluctuation of the gas multiplication. The fluctuation of the number of initial ion pairs is primarily due to the counter wall effect which produces a long tail on the low energy side of the peak[2]. The fluctuation of the gas multiplication is mainly due to electron capture which is ascribed to unsatisfactory purification of the filling gas[3].

The purpose of this paper is to investigate the wall effect and to afford a quantitative basis to the spectral properties of the counter.

§ 2. Calculation

While the full energy of the slow neutron-induced disintegration, when spent in the counter gas, gives rise to a full energy pulse, the case in which the disintegration fragments suffer the wall effect gives lower energy pulses depending on path length of the particles through the counter gas. We shall first consider the distribution of the path length of the particles for a counter, of which the end effect is much smaller than the wall effect.

Assumptions employed for calculation are as follows:

(1) The slow neutron-induced disintegration takes place uniformly throughout the counter. This assumption will be justified for counters of reasonable dimension and of reasonable filling pressure, since the mean free path of neutron is much longer than the diameter of the counter.

(2) The track of the disintegration fragments occurs in random direction. This is most probable for fully thermalized neutrons.

(3) The Li^7 fragment has a much smaller range than alpha particle. Thus the wall effect will be mainly due to alpha particles.

A fraction of alpha-particles whose track intercepts the counter wall be expressed by,

$$n_1=\int_0^s f(l)dl\ , \qquad (1)$$

where $f(l)$ is the distribution function of the path length of alpha-particles and s is the whole range of alpha-particle in the gas. The length of the path of alpha-particle originating at a distance r from the axis, moving in direction θ, ϕ and hitting the wall is given by, (Fig. 1)

$$l^2\sin^2\phi\cos^2\theta+2rl\cos\theta+r^2+l^2\cos^2\phi-R^2=0\ , \qquad (2)$$

where θ is an angle between OX and the rack.

ϕ is an angle between OY and the projection of the track on the plane YOZ.

R is the radius of the counter.

Now, from the assumptions (1) and (2), n_1 is also expressed by the following equation:

$$n_1=\frac{1}{\pi R^2}\int_{R-s}^{R} 2\pi r dr\cdot\frac{4}{4\pi}\int_0^{\pi/2} d\phi\int_0^{\theta_0}\sin\theta d\theta\ , \tag{3}$$

vhere

$$\theta_0=\cos^{-1}\frac{-r+\sqrt{r^2\cos^2\phi+R^2\sin^2\phi-s^2\sin^2\phi\cos^2\phi}}{s\sin^2\phi}\ , \tag{4}$$

Using eq. (2) and transforming the variable from θ to l, eq. (3) becomes then

$$\begin{aligned} n_1&=\frac{2}{\pi R^2}\int_{R-s}^{R} rdr\int_0^{\pi/2} d\phi\int_{R-r}^{s}\frac{1}{l^2\sin^2\phi}\left\{\frac{r^2\cos^2\phi+R^2\sin^2\phi}{\sqrt{r^2\cos^2\phi+R^2\sin^2\phi-l^2\sin^2\phi\cos^2\phi}}-r\right\}dl \\ &=\frac{2}{\pi R^2}\int_0^{s}\frac{dl}{l^2}\int_0^{\pi/2}\frac{d\phi}{\sin^2\phi}\int_{R-l}^{R}\left\{\frac{r^2\cos^2\phi+R^2\sin^2\phi}{\sqrt{r^2\cos^2\phi+R^2\sin^2\phi-l^2\sin^2\phi\cos^2\phi}}-r\right\}dr \\ &=\frac{2}{\pi R^2}\int_0^{s}\frac{dl}{l^2}\int_0^{\pi/2}\left\{\frac{4R^2}{3\sin^2 2\phi}\left(\sqrt{R^2-\frac{l^2}{4}\sin^2 2\phi}-R\right)\right. \\ &\qquad\left.+\frac{3}{2}l^2\sqrt{R^2-\frac{l^2}{4}\sin^2 2\phi}-\frac{l^2}{3}+\frac{2}{3}l^2\cos^2\phi\right\}d\phi\ . \end{aligned} \tag{5}$$

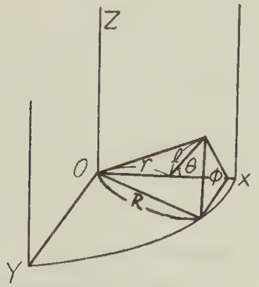

Fig. 1. Path length of alpha-particle in the counter.

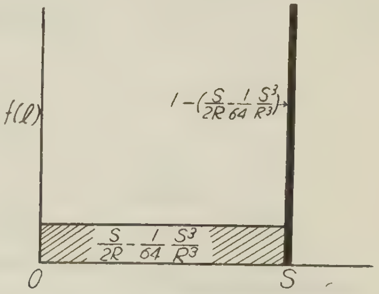

Fig. 2. Distribution of path length of alpha-particles in the counter.

When the range of alpha-particle is smaller than the diameter of the counter, this integral is evaluated by expanding into power series and integrating each term:

$$n_1=\int_0^{s}\left(\frac{1}{2R}-\frac{3}{64}\frac{l^2}{R^3}-\frac{15}{6144}\frac{l^4}{R^5}\cdots\right)dl\ . \tag{6}$$

By equating the integrands of eqs. (1) and (6) we obtain the distribution of the path length through the counter:

$$f(l)=\frac{1}{2R}-\frac{3}{64}\frac{l^2}{R^3}-\frac{15}{6144}\frac{l^4}{R^5}\cdots\ . \tag{7}$$

Since the first term is large compared with other terms, this distribution is nearly constant from 0 to s. Now, a fraction of alpha-particles which strike the wall of the counter is given by,

$$n_1=\frac{s}{2R}-\frac{1}{64}\frac{s^3}{R^3}-\frac{3}{6144}\frac{s^5}{R^5}\cdots\ . \tag{8}$$

This expression indicates that the degree of the wall effect is approximately the ratio of the range of alpha-particles to the diameter of the counter, the result of which is consistent with our anticipation. Thus the remainder, $n_2=1-\left(\frac{s}{2R}-\frac{1}{64}\frac{s^3}{R^3}\cdots\right)$, will be accounted for the line spectrum of the slow neutron-induced reaction. Calculated distribution of the path length is shown in Fig. 2.

In the calculation of energy spectra, an account must be taken of the total ionization along the track of alpha-particles. Assuming that the total ionization is proportional to the path length of alpha-particles in the gas, energy loss spectrum will be obtained from eq. (8),

$$I(\mathcal{E})=\frac{s}{2R}\frac{1}{E_0}-k(\mathcal{E})\,, \tag{9}$$

where E_0 is the initial energy of alpha-particle and $k(\mathcal{E})$ corresponds to all terms except the first in eq. (7), and is much small compared with $s/2R\cdot 1/E_0$.

Finally we return to resolution effect accompanying the multiplication process of the counter. By analogy with the resolution function of the photomultiplier system proposed in the paper by Miller and Snow[4], we assume a Gaussion resolution for the counter:

$$\frac{1}{\sqrt{2\pi}\sigma}\exp\left\{-\frac{(\mathcal{E}'-\mathcal{E})^2}{2\sigma^2}\right\},$$

where σ is empirically determined from the width of the peak. Thus the expression for the energy spectra of α-particles is

$$\begin{aligned}R(\mathcal{E}')&=\int_0^{E_0}\frac{1}{\sqrt{2\pi}\sigma}\exp\left\{-\frac{(\mathcal{E}'-\mathcal{E})^2}{2\sigma^2}\right\}I(\mathcal{E})d\mathcal{E}+n_2\frac{1}{\sqrt{2\pi}\sigma}\exp\left\{-\frac{(\mathcal{E}'-E_0)^2}{2\sigma^2}\right\}\\&\approx\frac{s}{2RE_0}\int_0^{E_0}\frac{1}{\sqrt{2\pi}\sigma}\exp\left\{-\frac{(\mathcal{E}'-\mathcal{E})^2}{2\sigma^2}\right\}d\mathcal{E}+\left(1-\frac{s}{2R}\right)\frac{1}{\sqrt{2\pi}\sigma}\exp\left\{-\frac{(\mathcal{E}'-E_0)^2}{2\sigma^2}\right\}.\end{aligned} \tag{10}$$

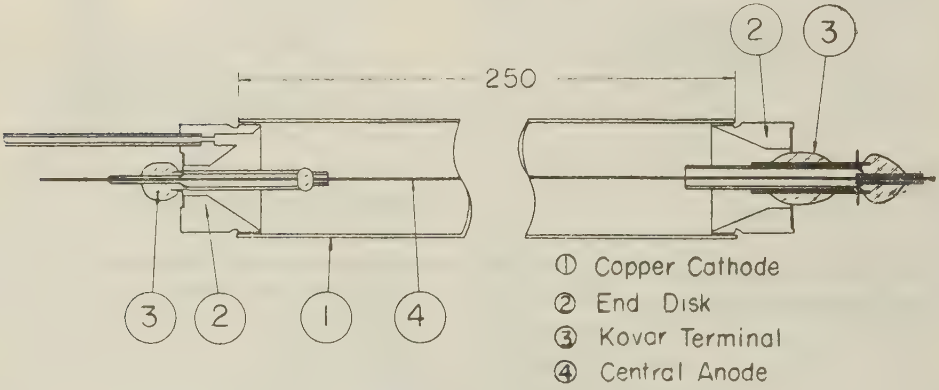

Fig. 3. Construction of the counter.

The first term is an error integral and readily evaluated, for instance, from the table of Jahnke and Emde.

§ 3. Experimental

Fig. 3 shows the construction of our experimental counter. Counter cathode ① is copper cylinder 12.5 mm in radius and 250 mm in length, which at both ends is soldered with copper end discs ② together with open skirt Kovar glass terminals ③. The radius of tungsten central wire ④ is 0.05 mm and the active length is 205 mm.

The counter was evacuated using a mercury diffusion pump and outgassing is performed at 300°C, and then filled with boron trifluoride gas.

Boron trifluoride gas for counter filling was generated by thermal decomposition of enriched boron trifluoride-calcium fluoride complex. The subsequent purification of the gas was performed in similar way as described by F. Hudswell et al.[5] The purity of the gas was examined by mass spectrometer and traces of impurities (mainly BFOH) was detected.

Measurement was made under overall irradiation by slow neutron using a 20 mc Ra–Be source and paraffin moderator. Pulses obtained were fed via a cable of about 1 meter (≈70 pF) to A–1 type amplifier having rise and fall time constants of 0.3 μ sec and 3 μ sec respectively. They were then fed to Baird Atonic type one channel pulse height analyzer.

§ 4. Results and discussion

Pulse height distributions for a counter containing 50 cm Hg BF_3 are shown in dashed lines in Figs. 4–6. Operating voltages are 1900 V, 2400 V and 3100 V, and the gas multiplication at those voltages are 9, 70 and 1000 respectively. It is seen that at lower operating voltage the two peaks arising from transitions to excited state and ground state of Li^7 are completely resolved as shown in Fig. 4, whereas at higher operating voltage 2.8 MeV peak is masked by 2.3 MeV peak.

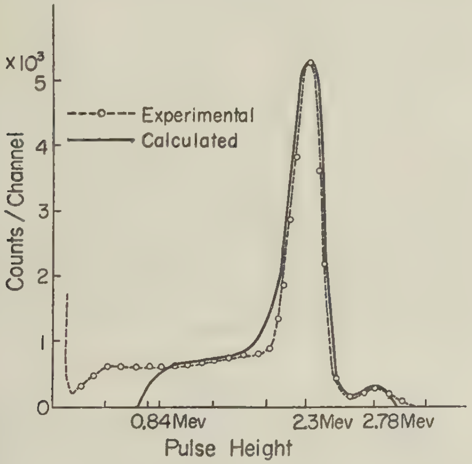

Fig. 4. Pulse height distribution of the counter. H.T=1900 V. Gas multiplication=9. Pressure =50 cmHg of BF_3.

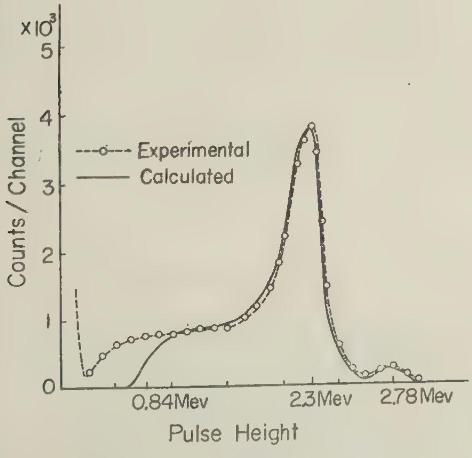

Fig. 5. Pulse height distribution of the counter. H.T=2400 V. Gas multiplication=70. Pressure =50 cmHg of BF_3.

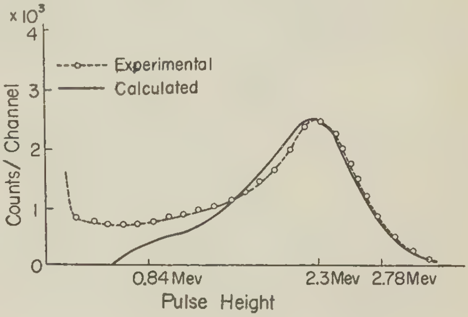

Fig. 6. Pulse height distribution of the counter. H.T=3100 V. Gas multiplication=1000. Pressure=50 cmHg of BF_3.

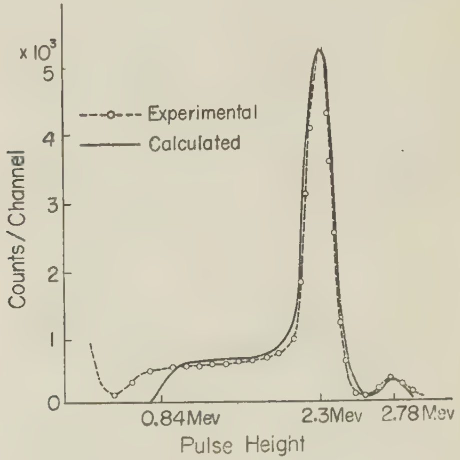

Fig. 7. Pulse height distribution of the counter. H.T=2200 V. Gas multiplication=9. Pressure =60 cmHg of BF_3.

The widths of 2.3 MeV peak at $1/e$ maximum are 0.34 MeV, 0.49 MeV and 0.92 MeV and thus the values constant σ of Gaussian resolution function are 0.12 MeV, 0.174 MeV and 0.326 MeV respectively.

The increase in width of the peak with operating voltage will be due to the fluctuation of gas multiplication.

The marked tail on the low energy side of the peak is apparently due to the wall effect of the counter. Since the whole range of alpha-particle with energy 2.3 MeV×7/11, in 50 cm Hg BF_3 is about 12 mm, calculated wall effect ($s/2R$) in our 25 mm diameter counter is about 48%. Substituting the values of σ and $s/2R$ in eq. (10), the energy spectra of alpha-particles are readily obtained. With addition of energy of Li^7 fragments, 2.3 MeV× 4/11, the general shapes of the calculated spectra are shown in full lines in Figs. 4–6.

The slight discrepancy between the theoretical and experimental curves, in which the tail of the experimental curves extends much further to low energy region, will be attributed to the wall effect of Li^7 fragments of which no account is taken in theoretical treatment because of much shorter length of the track.

Measurements for counters of different filling pressure was also made in order to make clear the effect of the range of the particles. The results are shown in Figs. 7 and 8 for counters containing 60 cm Hg and 70 cm Hg BF_3. The gas multiplication is about 9 and operating voltages are 2200 V and 2500 V respectively. It is seen that the wall effect of of Li^7 fragments observed at the lower end of the distribution, and of alpha-particles measured as intensity at the tail of the distribution reduces with increased filling pressure. The ratio of the area of low energy tail to total area of the spectra and the values of theoretically calculated wall effect are summarized in Table I.

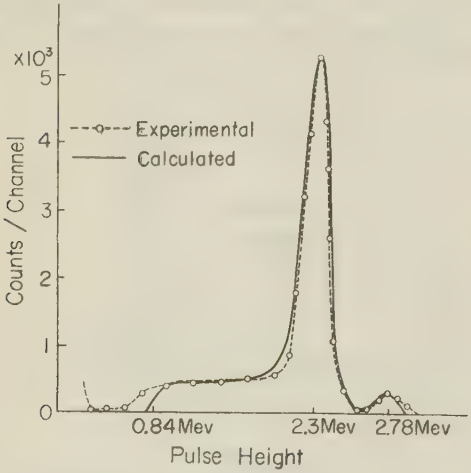

Fig. 8. Pulse height distribution of the counter. H.T=2500 V. Gas multiplication=9. Pressure =70 cmHg of BF_3.

Table I. Wall effect of the counters.

Filling pressure	H.T.	Calculated ($s/2R$)	Experimental
50 cm Hg	1900 V	48%	57%
60 cm Hg	2200 V	40%	45%
70 cm Hg	2500 V	34%	40%

Acknowledgements

The writer wishes to express his cordial thanks to Dr. J. Nakamura and Dr. M. Sugawara for their encouraging guidance throughout this work. His thanks are also due to Mr. N. Mitsuhashi for his untiring assistance throughout the experiment.

References

1) S. A. Korff and W. E. Danforth: Phys. Rev. **55** (1939) 980.
2) I. L. Fowler and P. R. Tunnicliffe: Rev. Sci. Instr. **21** (1950) 734.
3) J. A. Bistline: Rev. Sci. Instr. **19** (1948) 842.
4) W. F. Miller and W. J. Snow: Rev. Sci. Instr. **31** (1960) 39.
5) F. Hudswell et el: A. E. R. E. C/R 651 (1951).

JOURNAL OF THE PHYSICAL SOCIETY OF JAPAN, Vol. 15, No. 10, OCTOBER, 1960

Mixing Ratio of the 440-keV Gamma Radiation in ^{23}Na

By Akira MIZOBUCHI, Toshio KATOH and Jian-zhi RUAN

Department of Physics, Faculty of Science, Osaka University, Osaka

(Received May 30, 1960)

The angular distribution and the direction-polarization of the 440-keV gamma rays in ^{23}Na$(p, p'\gamma)^{23}$Na reaction have been measured at the 1.29-MeV resonance. For these measurements the following results were observed; for the angular distribution, $W(\theta)=1-(0.091\pm0.004)P_2$ $(\cos\theta)$ and for the polarization parameter, $p=+0.69\pm0.02$. From the observed results, the mixing ratio of the 440-keV gamma radiation was obtained as $(\mathrm{E2/M1})^{1/2}=+0.045\pm0.015$. This value agrees with the prediction from the collective model.

§ 1. Introduction

The properties of low lying states of the nuclide ^{23}Na have been investigated by many workers$^{1-5)}$. The ground and the first excited states are known to have spins 3/2 and 5/2, respectively, and both even parities. In addition, the spins and the excitation energies for low lying states agree with the predictions from the collective model$^{3)}$. It is of interest, therefore, to investigate the pattern of the gamma radiation from the excited state. The angular distribution and the direction-polarization correlation of the 440-keV gamma radiation from the first excited state in ^{23}Na$(p, p'\gamma)^{23}$Na reaction were measured at the 1.29-MeV resonance. The angular distribution of the 440-keV gamma radiation was fitted to the form $W(\theta)=1+A_2P_2(\cos\theta)$. Moreover the direction-polarization correlation was mesured by a polarimeter using the Compton effect, and this kind of the measurement was pointed out by Metzger and Deutch$^{6)}$, and Fagg and Hanna$^{7)}$. The polarization was measured for the gamma rays emitted to the direction $\theta=90°$. The mixing ratio, $\delta=(\mathrm{E2/M1})^{1/2}$, of the 440-keV gamma radiation has been obtained from the coefficient of the angular distribution, A_2, and the polarization parameter, p.

§ 2. Experimental procedure

The Osaka University static generator provided protons for this experiment. The energy of the protons was analyzed by a magnet controlled by the proton resonance. A sodium target was prepared by evaporation of NaCl on a 0.1 mm copper backing. Its thickness was estimated at a few keV at the 1.29-MeV from the excitation function. A resonance in the ^{23}Na$(p, p'\gamma)^{23}$Na reaction is found at $E_p=$ 1.29-MeV and this resonance state have spin 1 and odd parity$^{4)}$. The bombarding energy of protons was set at this resonance peak.

The gamma ray detector used was a 1.5″$\phi\times$1.5″ NaI(Tl) scintillation spectrometer. For the observation of the angular distribution of the 440-keV gamma rays, a single channel pulse height analyzer was employed, which was set to count the full-peak portion of the 440-keV gamma rays in the pulse height spectrum shown in Fig. 1.

In the case of the measurement of angular distribution, the gamma detector having a slit of 25 mmϕ was mounted at 25 cm from the target, and on a angle-changer centered on the target.

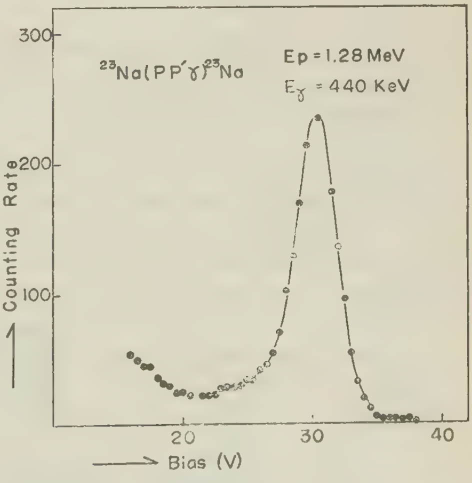

Fig. 1. Pulse height spectrum of gamma rays in ^{23}Na$(p, p'\gamma)^{23}$Na reaction at the 1.29-MeV resonance. These data were obtained using 2.5″$\phi\times$2.5″ NaI(Tl) scintillation spectrometer.

The experimental geometry for the direction-polapization measurement is shown in Fig. 2 The polarimeter using the Compton effect was a $2''\phi\times2''$ plastic scintillator. The gamma rays scattered by the polarimeter had been detected by a NaI(Tl) scintillation spectrometer, and the coincidence spectrum of the gamma rays which coincided with the Compton recoil electron in the polarimeter were determined. The typical coincidence spectrum is shown in Fig. 3. A schematic diagram of the electronics is shown in Fig. 4. The fast coincidence circuit[8] had the resolving time, $2\tau=30\times10^{-9}$ sec.

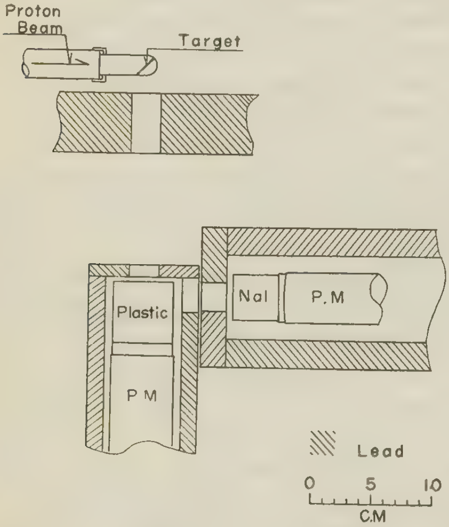

Fig. 2. Plan view of the geometrical arrangement in direction-polarization measurement. The plastic scintillator was used as a polarimeter and the gamma rays scattered by the polarimeter were detected by NaI scintillation spectrometer, which was set at the positions parallel to and vertical to the plane of the paper, by means of rotation of the detector.

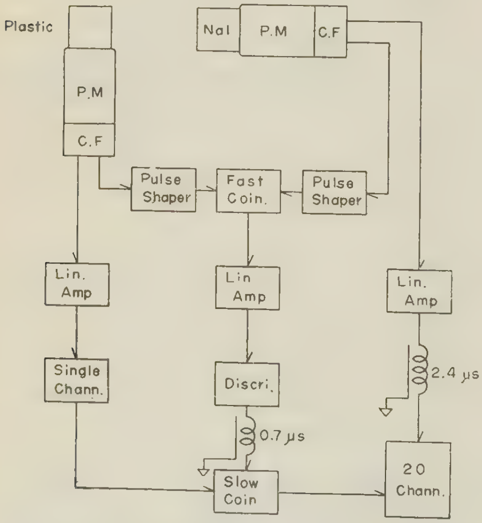

Fig. 3. Schematic diagram of the circuits used in this experiment.

The polarimeter is arranged so that $\theta=90°$, where θ is the angle between the direction of the incident beam and the emitted gamma rays. $N_{//}/N_{\perp}$ is defined as the ratio of the coincidence rate for the position when the detector of the Compton scattered photons is in the plane defined by the incident proton beam and the emitted gamma rays to the coincidence rate for the perpendicular position.

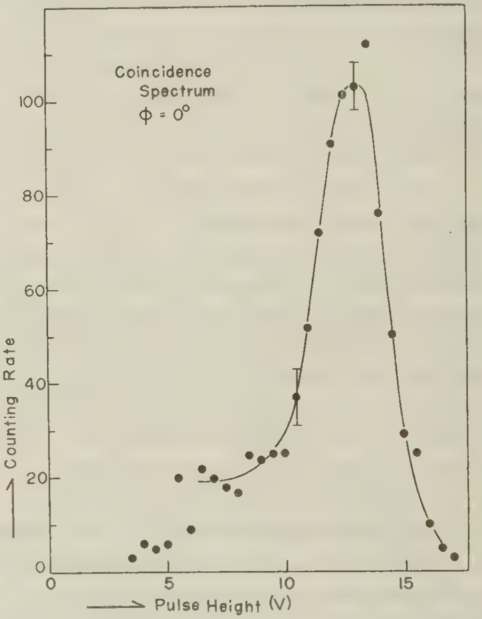

Fig. 4. Pulse height spectrum of the scattered gamma rays in coincidence with Compton recoil electron in the polarimeter.

The ratio $N_{//}/N_{\perp}$ and polarization parameter p are related through the following expression:

$$N_{//}/N_{\perp}=(p+R)/(1+pR),$$

where R is the sensitivity of the polarimeter. For the case of the ideal geometry, R is simply the ratio of two differential cross sections for Compton scattering, $d\sigma_{\phi=90}/d\sigma_{\phi=0}$, where ϕ is the angle between the direction of polarization of gamma rays and the plane defined by the incident and scattered gamma rays. The polarimeter used in this experiment had a value $R\risingdotseq5.9\pm1.0$, which was calculated by the Klein-Nishina formula considering the effect of the solid angle.

§ 3. Results and Discussion

The angular distribution of the 440-keV gamma rays in the $^{23}\mathrm{Na}(p, p'\gamma)^{23}\mathrm{Na}$ reaction was measured at the 1.29-MeV resonance. It is shown in Fig. 5. The experimental data were fitted to the form $W(\theta)=1+B_2\cos^2\theta$ using the method of least-squares. In Fig. 5 the solid line indicates the least-square fit. The result obtained exhibits $B_2=-0.142\pm0.005$. And this value were rewritten by the coefficient, A_2, of the distribution in the Legendre polynominal, *i.e.* $W(\theta)=1+A_2P_2(\cos\theta)$. Then, $A_2=-0.091\pm0.004$ was obtained.

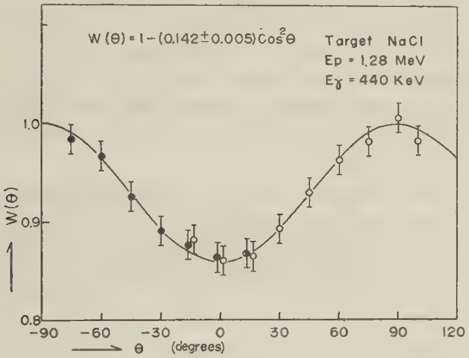

Fig. 5. The angular distribution of the 440-keV radiation. The solid curve is least-square fit of the distribution to the form $W(\theta)=1+B_2\cos^2\theta$.

Next, at the same resonance $N_{//}/N_{\perp}=1.30\pm0.04$ was determined for the polarization measurement. The polarization parameter, p, was obtained as $p=0.69\pm0.02$ from the above result.

The coefficient of the distribution and the polarization parameter of the gamma radiation for $^{23}\mathrm{Na}(p, p'\gamma)^{23}\mathrm{Na}$ reaction depend on the mixing ratio of the multipole order for gamma rays, and on the angular momentum and the channel spin for incident protons. These values, A_2 and p, have been expressed in a convenient form by Biedenharn and Rose[9] and Sharp *et al*[10].

The assignments of the ground and the first excited states of ^{23}Na and the resonance state of $^{23}\mathrm{Na}(p, p'\gamma)^{23}\mathrm{Na}$ reaction at the 1.29-MeV are known to have $3/2^+$, $5/2^+$ and 1^-, respectively[1-5]. Using these spin assignments, δ and t which agree with the experimental values A_2 and p were obtained as shown in Fig. 6, where δ and t are $(E2/M1)^{1/2}$ and the ratio of the intensities of incident protons entered a resonance state with $l=3$ to with $l=1$, respectively. By way of the experimental results, the mixing ratio of the 440-keV gamma radiation was obtained as $\delta=+0.045\pm0.015$.

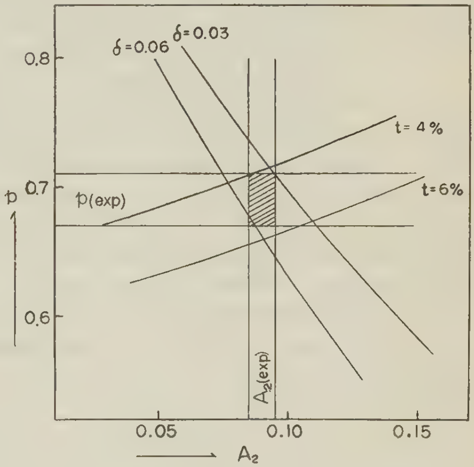

Fig. 6. The values of A_2 and p calculated as function of δ and t. The parameters δ and t are $(E2/M1)^{1/2}$ for the 440-keV gamma rays and (intensity of f-wave) (intensity of p-wave), for incident protons respectively.

It is assumed that the angular momentum of inelastically scattered protons has $l=1$, and the channel spin of incident protons has $S=2$. This assumption is reasonable from following consideration: (1) Since the inelastically scattered protons have low energy, the angular momentum $l=3$ would be excluded. (2) If the channel spin of incident protons mixed $S=1$ with $S=2$, t would be more large without changes of δ.

According to the independent particle model,

Table I. The values of $(E2/M1)^{1/2}$.

Paul and Montague[13]	0.02	Theoretical value
Rasmussen et al.[15]	+0.057	Experiment of mean life for resonance scattering
Present experiment	+0.045±0.015	

the ground and the first excited states of ^{23}Na are states of abnormal coupling of three like particles$^{11)}$, such as $(d_{5/2})^3\,3/2$ and $(d_{5/2})^3\,5/2$, respectively. The selection rule given by Moszkowski$^{12)}$ forbids M1 transition between these states. Paul and Montague$^{13)}$ studied the low lying states of ^{23}Na for rotation particle coupling$^{14)}$. The level energy and the spins agreed with the experimental data were obtained. Their calculated value of the mixing ratio of the 440-keV gamma radiation is given as $\delta=0.02$. As shown in Table I, this value agrees with the present result and the experimental result of Rasmussen, Metzger and Swann$^{15)}$. It is, therefore, supported that the nuclide ^{23}Na has the collective charactor.

Acknowledgements

It is a great pleasure to acknowledge the continued interest and encouragement by Professor T. Wakatsuki and Dr. S. Yamabe in this work. The authors would like to thank Mr. H. Iwata for his technical assistance.

References

1) A. P. French and J. O. Newton: Phys. Rev. **85** (1952) 1041.
2) W. G. Read and R. W. Krone: Phys. Rev. **104** (1956) 1018.
3) G. M. Temmer and N. P. Heydenburg: Phys. Rev. **104** (1956) 986. E. B. Paul and J. H. Montague: Nuclear Physics **8** (1958) 61.
4) P. H. Stelson: Phys. Rev. **96** (1954) 1584.
5) R. Berenbaum, J. H. Towle and H. Matthews: Proc. Phys. Soc. **69A** (1956) 858.
6) F. Metzger and M. Deutsch: Phys. Rev. **78** (1950) 551.
7) L. W. Fagg and S. S. Hanna: Rev. Mod. Phys. **31** (1959) 711.
8) Z. Bay: Nucleonics, **14** (1956) 56.
9) L. C. Biedenharn and M. E. Rose: Rev. Mod. Phys. **25** (1953) 729.
10) Sharp, Kennedy, Sears and Hoyle: *Chalk River Laboratory Report* CRT-556 (unpublished).
11) M. G. Mayer and J. H. D. Jensen: *Elementary Theory of Nuclear Shell Structures*, John Wiley and Sons, New York, 1955.
12) S. A. Moszkowski: Phys. Rev. **89** (1953) 474.
13) E. B. Paul and J. H. Montague: Nuclear Physics **8** (1958) 61.
14) A. K. Kerman: Mat. Fys. Modd. Dan. Vid. Selsk. **30** No. 15 (1956).
15) V. K. Rasmussen, F. R. Metzger and C. P. Swan: Nuclear Physics **13** (1959) 95.

JOURNAL OF THE PHYSICAL SOCIETY OF JAPAN, Vol. 15, No.10 OCTOBER, 1960

(d, α) Reactions on Some Light Nuclei

By Chuin HU

Faculty of Science, Osaka University

(Received May 30, 1960)

Angular distributions of the emergent alpha particles from the reactions $O^{16}(d, \alpha_0)N^{14}$(g'nd.), $N^{14}(d, \alpha_0)C^{12}$(g'nd.), $N^{14}(d, \alpha_1)C^{12*}$(4.44 Mev state), $F^{19}(d, \alpha_0)O^{17}$(g'nd.), $F^{19}(d, \alpha_1)O^{17*}$(0.872 Mev state) and $P^{31}(d, \alpha_0)Si^{29}$(g'nd) were investigated at several bombarding energies in the region from 10.3 Mev to 11.4 Mev. The distributions which cover the angular range between approximately 25° and 160° in the center-of-mass system, exhibit generally oscillatory and forward peaking behavior.

The intensity of the transition to the 2.31 Mev ($T=1$) state of N^{14} was measured in the range from 10.5 to 11.4 Mev in the step of 100 keV interval by aluminum absorber. The alpha particles from the targets were detected by a thin CsI(Tl) crystal scintillation spectrometer.

The experimental results were compared with the theoretical curves calculated by simplified direct-interaction model of Butler and the model which includes heavy particle stripping process. The attempts to fit some data were also made by using an approximate expression derived by Newns for double stripping process.

§1. Introduction

A number of investigators pointed out that a large majority of particle-nuclear reactions at bombarding energies from 10 to 50 MeV, which leave the final nucleus at low-lying excited levels, are induced by the direct-interaction process, and that the observed angular distributions show generally stripping-like patterns.

By the development of the theory of deuteron stripping by Butler[1] and others[2], the analysis of the angular distributions in these reactions, which leave the residual nucleus in some definite quantum state, have provided many useful informations on the properties of these states in nuclei. The (d, p) or (d, n) reaction receives a predominant contribution from a direct interaction. There are, however, few reasons why only this particular type of reactions should show clearly a direct interaction feature compared to other reactions. According to Butler[3], when the direct process plays a remarkable role, the predicted shapes of the angular distributions of (d, p), (p, α), (p, p'), (α, α'), etc. have no sharp distinction to each other and are expected to have a similar form. The theoretical differential cross sections for the direct process exhibit generally oscillatory behavior with a rapid decrease in intensity at angles larger than that of the primary peak.

On the other hand, many other theoretical treatments were given by several authors[4] assuming individual character involved in each special reaction on the standpoint of direct interaction.

In contrast with the reactions of (d, p), (p, p'), etc., little effort was done in the experimental studies for the angular distribution of (d, α) reaction, and also little is yet known about the possible reaction mechanism for this reaction on light nuclei with the medium bombarding energy. Therefore, in addition to the investigations which had been reported previously[6),7),12),13)], the present data on the angular distribution of (d, α) reaction on light nuclei with about 11 MeV incident energy, may be expected to have the possibility to give useful informations concerning the reaction mechanism, and will offer some facts to check the validity of the theory which has been derived by Newns[5] in a similar way as deuteron stripping reaction.

Another important process of nuclear reaction which competes with the direct process stated above is the compound nuclear process, by which many nuclear reactions at low bombarding energies are explained reasonably. Of course, it is expected that the contributions from the compound nucleus formation can not be neglected for our case. The energy dependence would be observed in the shape of angular distribution, if both the continuum and statistical assumption about compound nucleus are violated in the compound nucleus process. The angular distribution would be symmetric about 90° in two limiting cases in which the reaction proceeds through single compound nucleus level or through a large numbers of the compound nucleus levels involved in the energy width of incident beam[14]. In order to observe the contribution of the compound process, this work was investigated at several bombarding deuteron energies in the region from 10.3 to 11.4 MeV.

In the $O^{16}(d, \alpha_1)N^{14*}$ (2.31 MeV state) reaction, minor breakdown of the isotopic spin selection rule governing transition to the first excited state of the N^{14} nucleus had been observed by Dalton, Hinds and Parry[6] at the bombarding energies of 6.8, 7.1, 7.2 and 8.7 MeV, and by Browne[7] from 5 MeV up to 7.5 MeV. The failure of the selection rule in this reaction was explained by Browne[7] on the basis of Coulomb force admixing the isotopic spin impurities into the intermediate state configurations. Therefore, the appearance of the forbidden group suggests the existence of $T=1$ level in the compound nucleus F^{18}, and the compound process plays considerable roles in the nuclear reactions. Isotopic spin conservation fails at low bombarding energies, but such breakdown cannot be expected at the bombarding energies where the reaction proceed through direct interaction[24]. It is, therefore, interesting to extend the range of bombarding energy in order to determine whether the forbidden group appears or not.

§ 2. Experimental procedures

The experiments were performed with 11.4 MeV deuterons from the Osaka University 44-inch cyclotron. The layout of the cyclotron and associated equipments had been shown elsewhere[8]. The beam was collected in a Faraday cup which was always held at ground potential, and was measured by a vibrating reed electrometer. The measurements of the angular distribution were made at angles ranging from 20° to 130° or 160° in the laboratory system with steps of 10° interval. The counter angle could be set to ±0.1° by means of a varnier scale and the angular resolution was ±1.0°.

The emergent alpha particles were detected by a thin uniform CsI(Tl) crystal on a R. C. A. 6342 photomultiplier. To resolve the product alpha particles from the longer ranged charged particles, such as protons and deuterons, which

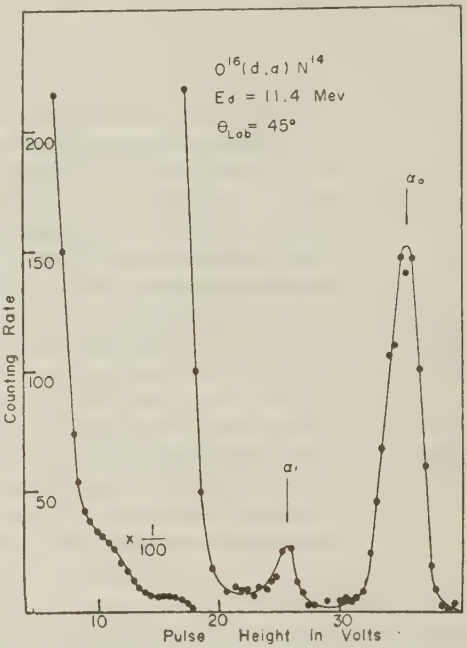

Fig. 1. Pulse-height spectrum of alpha-particles emitted at $\theta_{lab.}=45°$ from a mylar target bombarded with 11.4 MeV deuterons. An aluminum absorber (3 mg/cm²) was inserted in front of a counter.

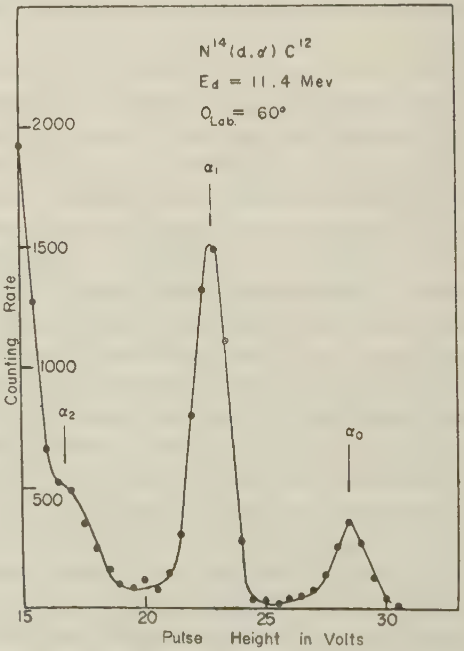

Fig. 2. Pulse-height spectrum of alpha-particles emitted at $\theta_{lab.}=60°$ from a melamin target bombarded with 11.4 MeV deuterons.

were produced by the reactions (*d*, *p*), (*d*, *d*) and (*d*, *d′*), the thickness of the CsI(Tl) crystal was chosen so thin as to be nearly equal to the range of the highest energy alpha-particle group from (*d*, *α*) reaction with 11.4 MeV incident energy at 90° in the laboratory system. At the forward angles smaller than 90°, aluminum absorbers were inserted in front of the scintillator until the pulse height of the highest energy alpha-particle group reached a maximum at each angular position. Actually CsI(Tl) crystals of 50 or 40 mg/cm² and 17 mm ×20 mm were used in the O^{16} experiments, but these were replaced by the crystals of 80 or 90 mg/cm² in other runs. The output pulses were amplified, shaped, and then analysed by a multichannel pulse height analyser. In the case of earlier measurements for $O^{16}(d, \alpha_0)N^{14}$(g'nd.) and $O^{16}(d, \alpha_1)N^{14*}$ (2.31 MeV state), a commercial 20-channel pulse height analyser was used, and in another experiments this was replaced by a 30-channel pulse height analyser, which had been constructed in our laboratory.

In order to identify the levels in the (*d*, *α*) reaction, the author used the range-energy relation for protons in aluminum[9] and the fact that the CsI(Tl) crystal responds linearly to the *α* particle energy loss in crystal[10]. Using alpha particles from the reaction $O^{16}(d, \alpha_0)N^{14}$ and $O^{16}(d, \alpha_2)N^{14*}$(2nd.), a measure-

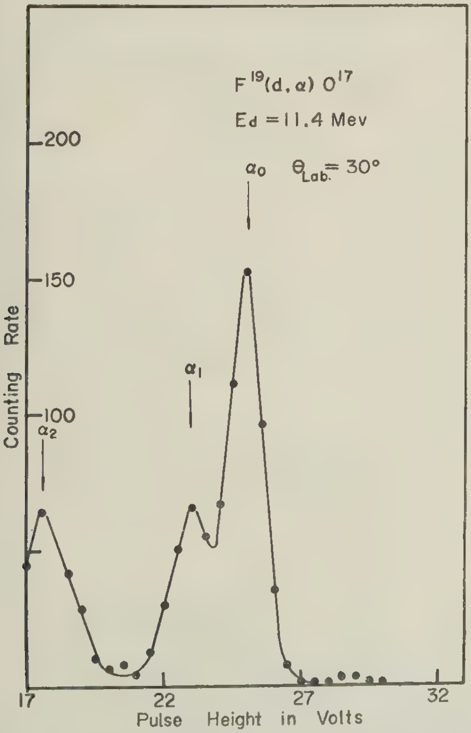

Fig. 3. Pulse-height distribution of alpha-particles at $\theta_{lab.}=30°$ from a teflon target bombarded with 11.4 MeV deuterons.

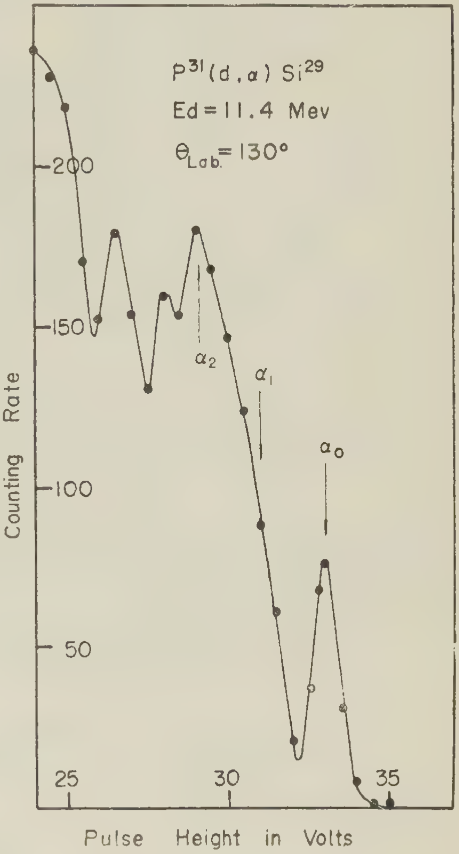

Fig. 4. Pulse-height distribution of alpha-particles at $\theta_{lab.}=130°$ from a phosphor target bombarded with 11.5 MeV deuterons.

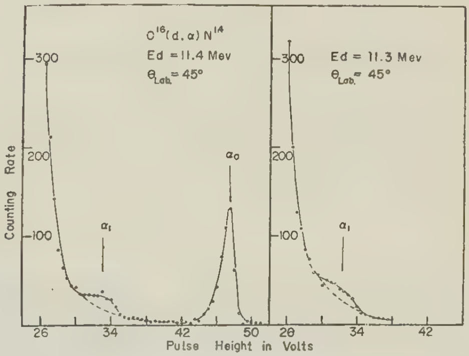

Fig. 5. Pulse-height spectrum of alpha-particles from a mylar target with 11.4 MeV and 11.3 MeV deuterons. An aluminum absorber (5 mg/cm²) was inserted in front of a counter.

ment was carried out on the CsI(Tl) crystal, which were used in this work, to obtain the pulse height ratio as a function of the energy of the emergent alpha particles. Then the comparison was performed between the output voltage from a linear amplifier and the results calculated kinematically.

A mylar film (0.8 mg/cm^2), was used in the measurements of $O^{16}(d, \alpha)N^{14}$ reaction, and a teflon film (0.9 mg/cm^2) was used in the $F^{19}(d, \alpha)O^{17}$ reaction. These targets are essentially $C_5H_4O_2$ and CF_2 respectively. The alpha-particle group under investigation was not contaminated with alpha particles of the same energy from reactions on other constituents. These substances were not so strong under deuteron bombardment that the calibrations were employed frequently for each run. The targets for the $N^{14}(d, \alpha)C^{12}$ and $P^{31}(d, \alpha)Si^{29}$ reactions, were prepared as follows; A melamin film ($C_3H_6N_6$, 2.2 mg/cm^2) was painted uniformly on the myler film (0.8 mg/cm^2), and commercial red phosphor powder (0.3 mg/cm^2) was molded uniformly in a thin polystylene film (1.0 mg/cm^2). These targets were supported by a 3 cm×3 cm frame, and were placed in the center of a cylindrical scattering chamber at 45° to the incident beam.

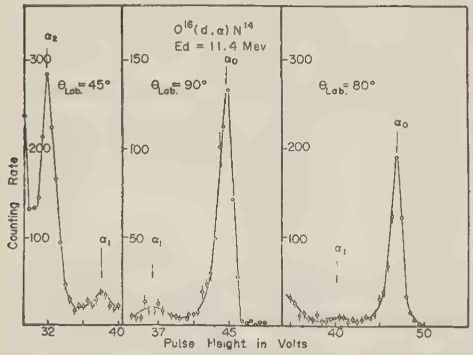

Fig. 6. Pulse-height spectrum of alpha-particles resulting from the bombardment of a mylar target at several angles without an aluminum absorber at 11.4 MeV deuterons.

§ 3. Result

In Figs. 1 to 6 are shown the typical CsI(Tl) scintillation counter spectra obtained by the targets mentioned above, and the expected positions of peaks corresponding to the discrete states in the residual nuclei.

The alpha-particle group from $F^{19}(d, \alpha_0)O^{17}$ (g'nd.) and that from $F^{19}(d, \alpha_1)O^{17*}$(1st.) were not well resolved. In the results of $P^{31}(d, \alpha)Si^{29}$ experiments, the groups leading to the excited states could not be resloved adequately, except

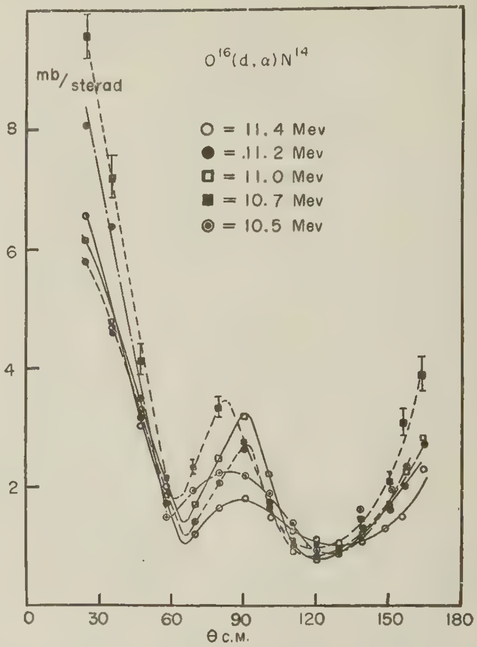

Fig. 7. Differential cross sections for the $O^{16}(d, \alpha_0)N^{14}$ (g'nd. state) reaction with several bombarding energies.

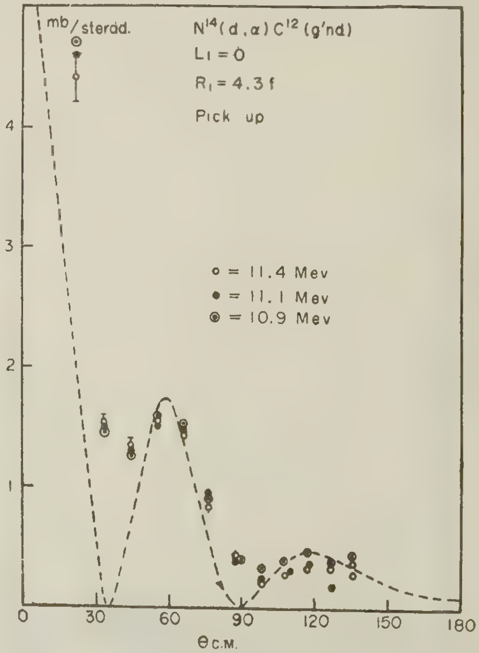

Fig. 8. Differential cross sections for the $N^{14}(d, \alpha_0)C^{12}$ (ground state) reaction. The dotted curve was calculated for pick up process with $r_1=4.3$ *f*., and $l_1=0$.

the group corresponding to the transition the ground state of Si^{29}.

The observed angular distributions for (d, α) nsitions induced by the deuterons of about MeV, which correspond to the ground and first excited states of the residual nuclei shown in Figs. 7 to 12.

The indicated relative errors of differential ss sections were due to the counting sta- tics, uncertainty in separation of alpha- rticle groups, and the background substrac- n, and the overall errors did not exceed 10%. The estimated errors in the absolute fferential cross sections are as follows: oxy- n target ±70%, nitrogen target ±80%, orin target ±50% and phosphor target 70%.

To assert the existence of the yield leading the first excited state ($T=1$) in N^{14}, almi- um absorbers (3 mg/cm^2 and 5 mg/cm^2) were serted respectively in front of the CsI(Tl) ystal, and the measured spectra are shown Figs. 1 and 5. The spectra without almi- um absorber are shown in Fig. 6. In all ses, the forbidden group appeared, and the eld for this state was much less than the

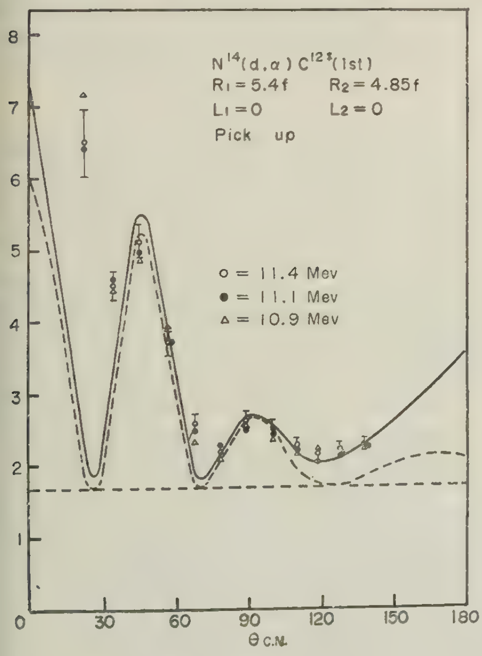

Fig. 9. Differential cross sections for the $N^{14}(d, \alpha_1)C^{12}$ (4.44 MeV state) reaction. The dotted curve was calculated for pick up process with $r_1=5.4f.$, $l_1=0$ while the solid curves included heavy particle stripping process with $r_1=4.85f.$, $l_1=0$, $r_2=4.85f.$, and $l_2=0$.

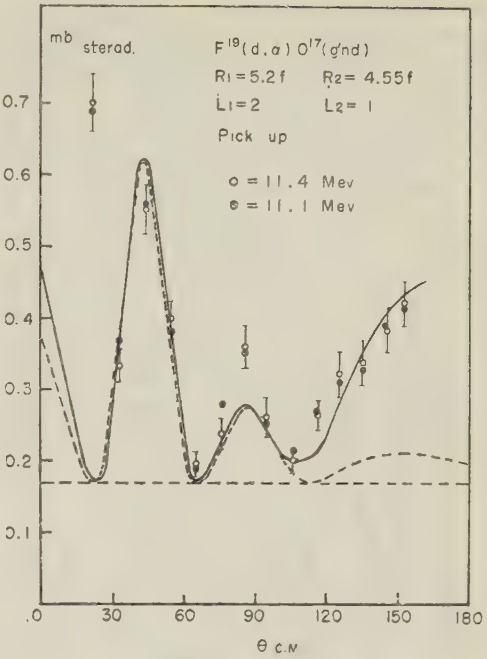

Fig. 10. Differential cross sections for the $F^{19}(d, \alpha_0)O^{17}$ (ground state) reaction. The dotted curve was calculated for pick up process with $r_1=5.2$ $f.$, $l_1=2$, which the solid curve included heavy particle stripping process with $r_1=5.2f.$, $l_1=2$, $r_2=4.55f.$, and $l_2=1$.

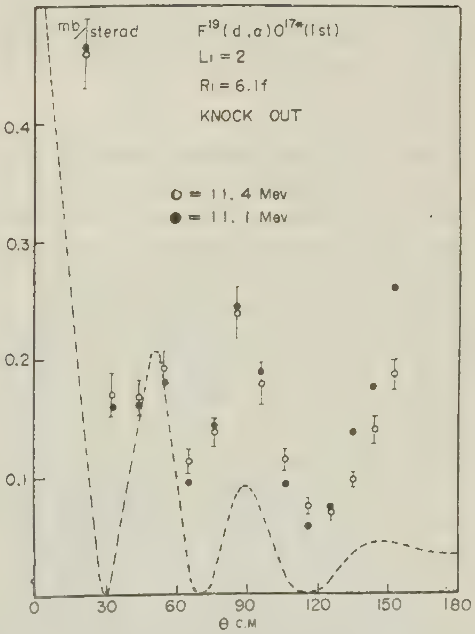

Fig. 11. Differential cross sections for the $F^{19}(d, \alpha_1)O^{17}$ (0.872 MeV state). The dotted curve was calculated for knock out process with $r_1=6.1f.$, and $l_1=2$.

yield for the ground state. The ratio of intensity of transition to 2.31 MeV to ground state is 10±5% at 45° in the laboratory system at 11.4 MeV bombarding energy.

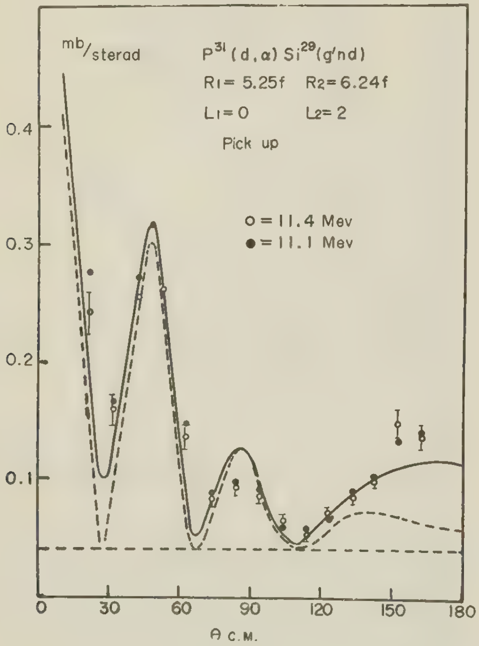

Fig. 12. Differential cross sections for the $P^{31}(d, \alpha_0)Si^{29}$ (ground state). The dotted curve was calculated for pick up process with $r_1=5.25f.$, $l_1=0$, while the solid curve included heavy-particle stripping process with $r_1=5.25f.$, $l_1=0$, $r_2=6.24f.$, and $l_2=2$.

§ 4. Discussion

The angular distributions investigated in this work show strong forward peaking and oscillatory behavior. Some of them have another peak in the backward direction. In addition to these facts, the large energy dependency of the angular distribution was not observed except for the $O^{16}(d, \alpha)N^{14}$ reaction. Accordingly, it is reasonable to assume that the direct interaction process is playing an important role.

The fits to these angular distributions were made with the theoretical differential cross sections derived by Butler[3] for direct interaction, in the same way as, for example, a (d, p) reaction. The theoretical curves calculated with the formula derived by Butler, in which the alpha-particle was treated as a single particle, showed good agreement with experimental results. The effect of internal structure of alpha-particle was not considered in the calculation. In our treatment, the deuteron and alpha-particle were also considered as single particles even around the nucleus. The used expression for the theoretical differentia cross section was,

$$\frac{d\sigma}{d\Omega}\propto|F_1(K_1)\,W\{j_{l1}(Q_1r),\,h_{l1}(i\kappa_1r)\}_{r=r_1}|^2 \qquad (1$$

where $F_1(K_1)$ is a form factor. Q_1 and κ_1 are related to the appropriate momentum transfer vector defined below and binding energy. r_1 is the interaction radius, and l_1 is the change of angular momentum. The allowed l_1-values are found by the selection rule.

$$I_f=I_i+l_1+S \qquad (2$$

Here I_i is the spin of the target nucleus, I_f is the spin of the final state and S is the resultant spin of the incident and emerging particles. l_1 must be odd as the parity is changed.

For a given (d, α) reaction, the both processes of "Knock out" and "Pick up" were considered, and these processes are characterized respectively as follow; "Knock out"

$$\left.\begin{aligned} Q_1&=\frac{M_f}{M_i}\left[K_\alpha-\frac{M_i}{M_f}K_d\right]\\ \kappa_1&=\frac{1}{\hbar}(2M_\alpha\mathcal{E}_{\alpha i})^{1/2}+(2M_d\mathcal{E}_{df})^{1/2}\} \end{aligned}\right\} \qquad (3)$$

"Pick up"

$$\left.\begin{aligned} Q_1&=K_\alpha-\frac{M_f}{M_i}K_d\\ \kappa_1&=\frac{1}{\hbar}(2M_d\mathcal{E}_{di})^{1/2} \end{aligned}\right\} \qquad (4)$$

where M_i, M_f, M_d and M_α are the masses of the initial nucleus, final nucleus, deuteron and alpha-particle. $\mathcal{E}_{\alpha i}$, $\mathcal{E}_{di}$ and $\mathcal{E}_{df}$ are the binding energies, respectively, of alpha-particle in the initial nucleus, a deuteron in the initial nucleus, and a deuteron in final nucleus corresponding to the ground or the first excited state.

To get better agreement with the large cross sections at backward angles in the experimental results, the interaction which have been neglected in the theory mentioned above, must be considered. Therefore, the heavy particle stripping interaction[11] was added to the so-called ordinary direct interaction process. These two processes are coherent to each other, so that interference occurs between them. The differential cross section including heavy particle stripping is

$$\frac{d\sigma}{d\Omega}\propto|F_1(K_1)\,W\{j_{l1}(Q_1r),\,h_{l1}(i\kappa_1r)\}_{r=r_1}$$
$$+A\cdot F_2(K_2)j_{l2}(Q_2r_2)|^2 \tag{5}$$

ere A is an adjustable constant and the subcript 1 and 2 refer to knock out (or pick up) nd heavy particle stripping respectively. Vhen these are evaluated, the theoretical ifferential cross section becomes,

$$\frac{d\sigma}{d\Omega}\propto|F_1(K_1)\,W\{j_{l1}(Qr),\,h_{l1}(i\kappa_1r)\}_{r=r_1}|^2$$
$$+a\cdot F_1(K_1)F_2(K_2)\,W\{j_{l1}(Q_1r),\,h_{l1}(i\kappa_1r)\}$$
$$\times j_{l2}(Q_2r_2)\cos\beta$$
$$+b\cdot|F_2(K_2)j_{l2}(Q_2r_2)|^2 \tag{6}$$

vhere $\cos\beta$ arises from the transformation rom the heavy particle stripping axis of uantization K_2 to the knock out (or pick up) xis K_1, and β is the angle between K_1 and K_2, and " *a* " and " *b* " are adjustable constants.

The parameters used in the differential ross section for heavy particle stripping are

$$\left.\begin{aligned} Q_2&=K_d+\frac{M_d}{M_f}K_\alpha \\ K_2&=K_\alpha+\frac{M_\alpha}{M_i}K_d \end{aligned}\right\} \tag{7}$$

nd the form factor is calculated by the folowing equation.

$$F_2(K_2)=\int_0^\infty \psi_l(r)j_2(K_2r)r^2dr\,. \tag{8}$$

Iere $\psi_l(r)$ is the internal wave function of he alpha-particle in the initial nucleus, and is the orbital angular momentum of alphaarticle in the initial nucleus relative to the ore. In this case alpha-particle was treated s single particle. In almost all cases, the implified $\psi_l(r)$ was used in the calculation or convenience, so that $F_2(K_2)$ varies so slowly ver the angles that it has little effect on he final results.

The dotted curves calculated by Eq. (1) for ll reactions studied in this work with " Knock ut " or " Pick up " for all allowed angular nomentum transfers and for several values f the interaction radii are shown in Figs. 8 o 13. Some of them were lifted by adding n isotropic contribution to the theoretical ross section. A chief fraction of this additional ross section probably is due to the compound uclear process and the rest may be caused by he interference between various direct interctions or between direct interaction and comound nuclear process.

On the whole, a good agreement was obtained between theoretical curves and the experimental results for positions of maxima and minima, except for their height, and the marked disagreement between them appeared in the shapes over the backward angles.

Table I. Comparison of the positions of maxima and minima of experimental differential cross sections from (*d*, *α*) reactions with the predictions of Eq. (1)

The final state	Maximum or Minimum	Alpha-particle angle in the center of mass system	
		Experiment	Theory
C^{12}(g'nd.)	Min.	~ 40°	37°
	Max.	~ 60°	60°
	Min.	~100°	90°
C^{12}(1st.)	Min.	35°	28°
	Max.	45°	45°
	Min.	75°	70°
N^{14}(g'nd.)	Max.	65°	65°
	Min.	90°	90°
	Max.	~120°	120°
O^{17}(g'nd.)	Min.	~ 32°	24°
	Max.	43°	44°
	Min.	65°	65°
	Max.	90°	88°
	Min.	102°	105°
O^{17}(1st.)	Min.	~ 67°	70°
	Max.	87°	90°
	Min.	~120°	120°
Si^{29}(g'nd.)	Min.	30°	30°
	Max.	50°	50°
	Min.	74°	75°
	Max.	84°	95°

In Table I are summarized the locations of maxima and minima of the experimental results and the predictions of a simplified calculation based on the Eq. (1). The solid curves in Figs. 8 to 13 were calculated by Eq. (6). It is recognized that these curves are in better agreement with the data over the entire range of angles studied with reasonable radii and l-values than those predicted by Eq. (1). However, the theoretical curves for heavy particle stripping can be reproduced with slight variation in the interaction radius for the other values of the change in angular momentum. This is caused by the fact that the minimum value of Q_2 is relatively large. Accordingly, it is impossible to distinguish between various

l_2-values for heavy particle stripping, though, the use of this interaction improves the fit to the data.

In addition to these attempts, we tried to make fit the data to the formula derived by Newns[5] for double stripping (or double pick up) process. An approximate expression derived on this assumption is.

$$\frac{d\sigma}{d\Omega}\propto \exp\left(\frac{K^2}{8\gamma^2}\right)\cdot|A(L)j_L(\kappa r_0)|^2 \tag{9}$$

where the exponential term depends upon the internal motion of incident particle and corresponds to the form factor introduced in deuteron stripping. $A(L)$ is a constant and can be determined by fitting the theoretical curve to the experimental results, and r_0 is interaction radius. L is the total orbital angular momentum transfer in final nucleus by nucleons and is defined as follow.

$$\boldsymbol{L}=\boldsymbol{l}_p+\boldsymbol{l}_n \tag{10}$$

Here l_p and l_n are orbital angular momenta of proton and neutron which are captured by target nucleus. Between the spin of initial state I_i and that of final state I_f, the selection rule is required

$$|I_f-I_i|-1\leqq l_p+l_n\leqq I_i+I_f+\frac{1}{2}+\frac{1}{2} \tag{11}$$

and there is a parity change only when L is odd. The momentum transfer vectors K and k are,

$$\left.\begin{aligned}\boldsymbol{K}&=\frac{1}{2}\boldsymbol{K}_\alpha-\boldsymbol{K}_d\\ \boldsymbol{k}&=\boldsymbol{K}_\alpha-\left(\frac{M_f}{M_i}\right)\boldsymbol{K}_d\end{aligned}\right\} \tag{12}$$

The results obtained by Eq. (9) are shown in Figs. 14 and 15. Though more detailed discussion is given in latter section, it may be noted that the curves calculated by Eq. (9) illustrate better agreement than that obtained by Eq. (1) for this reaction. In the following we shall make further detailed discussions on individual targets.

4.1 $O^{16}(d, \alpha)N^{14}$(g'nd.)

The result of angular distribution for the transition to the ground state N^{14} was given by Freemantle[12] et al., at deuteron bombarding energy of 19 MeV, which was nearly symmetric about 90°. Fischer and Fischer[13] showed that the angular distribution observed by Freemantle could be fitted with a curve derived from Eq. (1) with $r_1=4.2f.$ and $l_1=0$. Recently, Browne[7] measured the angular distribution and excitation function of the alpha particle group leading to the ground state of N^{14} with bombarding energy up to 7.5 MeV. The observed angular distribution at 7.03 MeV was not symmetric about 90°, and the excitation function for the group leading to ground state varied rapidly with bombarding energy.

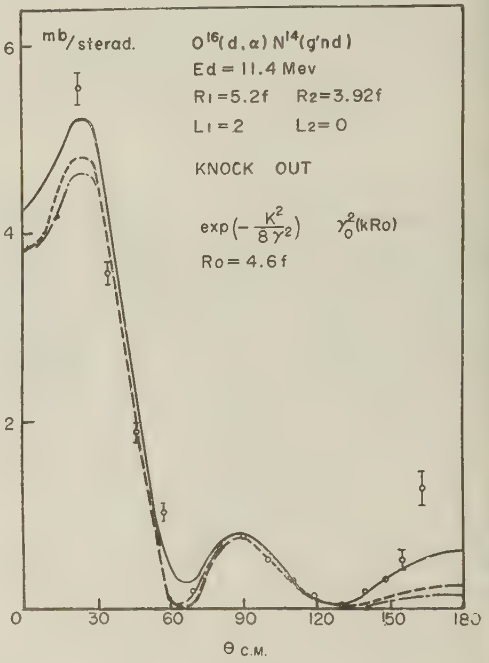

Fig. 13. Differential cross section substracted the isotropic part from the observed data of the $O^{16}(d, \alpha_0)N^{14}$ (g'nd.) reaction. The dotted curve was calculated for knock out process with $r_1=5.2f.$, and $l_1=2$. The solid curve included heavy particle stripping process with $r_1=5.2f.$, $l_1=2$, $r_2=3.92f.$, and $l_2=0$. The dashed curve was calculated for double stripping process with $r_0=4.6f.$ and $L=2$.

More recently Dalton et al.[15] investigated this reaction at 6.8, 7.1, 7.2 and 8.9 MeV, and the observed angular distributions at 6.8 and 8.9 MeV showed a forward peak. Especially the result at 8.9 MeV was essentially similar to the distributions obtained in the present work. Therefore the reaction mechanism governing this transition is explained more easily on the base of direct-interaction process than that of compound nucleus formation. The distributions investigated at various bombarding energies between 10.5 and 11.4 MeV are illustrated in Fig. 7. As shown in Fig. 13 fairly good agreements were obtained between distribution curve obtained at 11.4 MeV and the theoretical curves derived from Eq. (1) with $l_1=2$, $r_1=5.2f.$, and from Eq. (6) with $l_1=2$, $r_1=5.2f.$, $l_2=0$, $r_2=3.92f.$, if the isotropic part is subtracted from the experimental curve. It is recognized that relatively large cross sections in back ward angles suggest the existence of heavy particle stripping process. The yields, however, change too rapidly with bombarding energies to be accounted for by the heavy particle stripping alone. If one ignores the variation of interaction radius deduced from the data and Eq. (6), the main feature of these distributions can be represented theoretically. Moreover, the curve calculated from Eq. (9) with $L=2$, $r_0=4.6f.$, was nearly the same in shape with the curve obtained by Eq. (1), and the contribution from anther L-value, namely, $L=0$, was negligible in the angular distribution at 11.4 MeV.

On the other hand, it is remarkable that the total cross section shown in Fig. 14 obtained by integrating the angular distribution curves shows gradual change with bombarding energy and reaches a maximum at 10.7 MeV, and the shape of the angular distribution at 10.7 MeV is slightly different from others.

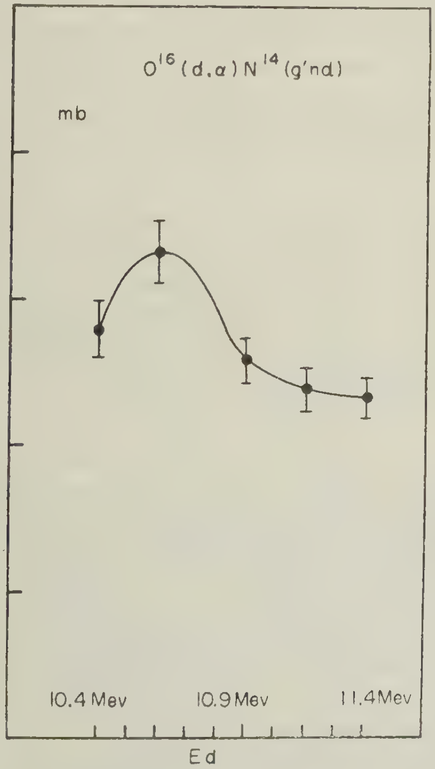

Fig. 14. Energy dependence of the total cross sections for the $O^{16}(d, \alpha_0)N^{14}$ (ground state) reaction.

Accordingly, it is expected that a direct process does play a leading role, and the process of compound nucleus formation undertakes a subsidiary role.

4.2 $O^{16}(d, \alpha_1)N^{14*}$ ($T=1$, 1st.)

The investigations relating to the 2.31 MeV level of N^{14} by (d, α) reaction was reported in detail in references 6 and 7. On the small appearance of these forbidden group, the detailed explanation was given by Browne[7] and by Lane and Thomas[15]. The violation of the isotopic spin selection rule was not observed clearly at 8.9 MeV deuteron bombarding energy, though the yield curve of the 2.31 MeV level indicated the excistence of this forbidden group up to 7.5 MeV bombarding energies. The excitations of compound nucleus with the deuteron bombarding energies of 8.9 MeV and 7.5 MeV are about 15 MeV and 14 MeV. In the latter case, the situation of compound nucleus are expected to exist in the region which is intermediate of those satisfying criteria (5.2) and (5.3) in the paper of Lane and Thomas[15]. The yield of the forbidden group shows resonance-like anomalies at 6.2, 6.7 and 7.2 MeV[7),8]. It is possible to assume that disappearance of this forbidden group at 8.9 MeV is due to the isolated resonances, so that the situation of the states excited with the deuteron bombarding energy of 11 MeV is expected to be similar to the situation excited with 7.5 MeV deuteron. Certainly a minor break-down in the isotopic spin selection rule was observed at 11.4 and 11.3 MeV as illustrated in Figs. 1, 5 and 6. Moreover, the yield of this forbidden group could be observed at 45° in the laboratory system at 11.2, 11.1, 10.7 and 10.6 MeV bombarding energies, with the comparable order to the intensity at 11.3 MeV.

4.3 $N^{14}(d, \alpha_0)C^{12}$(g'nd.) and $N^{14}(d, \alpha_1)C^{12*}$(1st.)

Previous study on the $N^{14}(d, \alpha)C^{12}$ reaction was made by Gibson and Thomas[16] at 8 MeV. Fischer and Fischer[13] measured the angular distributions for this reaction at 21 MeV. These results show the forward peaking and oscillatory behavior. As illustrated in Figs. 8 and 9, the angular distributions investigated at 11.4, 11.1 and 10.9 MeV also show direct interaction feature distinctly.

When one attempts to compare these data

with the theoretical curve calculated by Eq. (1), it is expected qualitatively that the pick-up process would be more probable than knock out process for the $N^{14}(d, \alpha)C^{12}$ reaction in contrast to the $O^{16}(d, \alpha)N^{14}$ reaction. Then the fits to the angular distribution are shown in Figs. 8 and 9, with reasonable interaction radii.

In the case of transition to ground state, considerable energy dependency of the angular distribution in the region greater than 90° may be due to the similar reason as discussed in previous section.

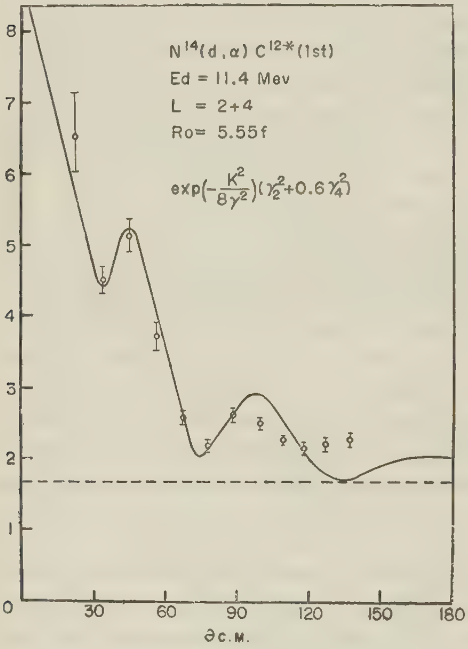

Fig. 15. Theoretical fit to the differential cross section of $N^{14}(d, \alpha_1)C^{12}$ (4.44 MeV state) using Eq. (9) with $L=2+4$ and $r_0=5.5f.$.

The distribution corresponding to the first excited stated deviates considerably in the forward angles from the theoretical ones which are obtained from Eqs. (1) and (6) by using one allowed l_1-value. This marked discrepancy may be reduced by summing up for all allowed l_1-values in Eq. (1). In fact, as illustrated in Fig. 15, the curve calculated by Eq. (8) with $r_0=5.55f.$, $L=2$ and 4, and $[A(4)/A(2)]^2=0.6$, shows a better agreement with the datum at forward angles than the curve derived from Eq. (1) with $r_1=5.4f.$, $l_1=0$, for pick up process.

4.4 $F^{19}(d, \alpha_0)O^{17}$(g'nd.) and $F^{19}(d, \alpha_1)O^{17*}$(1st.)

Measurements of the angular distributions of the alpha-particle group leading to the ground and low-lying state in O^{17} were not reported before this study. However, remarkable theoretical studies were made by several authors[17),18),19)] on the character of the ground and low-lying states. According to their interpretation, these states are described successfully on the bases of the shell[17),18)] and collective models[19)], and F^{19} is treated as a nucleus which has three particles outside the O^{16} core closed shells. Therefore, pick up process is more preferable than knock out process for the $F^{19}(d, \alpha)O^{17}$ reaction.

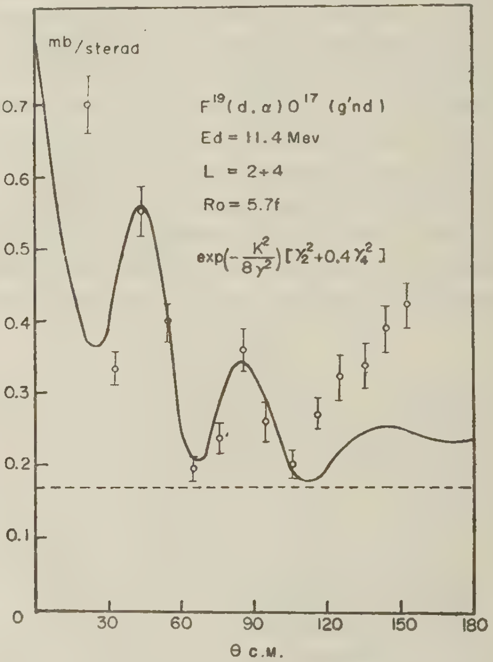

Fig. 16. Theoretical fit to the differential cross section of $F^{19}(d, \alpha_0)O^{17}$ (ground state) using Eq. (9) with $L=2+4$ and $r_0=5.7f.$.

Among the angular distributions of alpha-particle groups leading to the ground and first excited states, our data corresponding to the transition to ground state in O^{17} exhibit good agreement with the curve calculated from Eq. (6) with $r_1=5.2f.$, $l_1=2$, $r_2=4.55f.$, $l_2=1$ in pick up case. A better agreement could be obtained with the curve calculated by Eq. (9) with $r_0=5.5f.$, $L=2$ and 4, and $[A(4)/A(2)]^2=0.33$ as shown in Fig. 16.

Since the observed angular distribution of the $F^{19}(d, \alpha_1)O^{17*}$(1st.) reaction shows that the first maximum is smaller than that of the second maximum, the curves given by Eqs. (6) and

(9) did not show any agreement with the shape of the theoretical curve for any reasonable choice of parameter. The marked disagreement in the neighborhood of the secondary maximum may be caused by either the interference between the direct and compound nuclear process or by the fact that the used differential cross sections rest on gross simplification, so that, the disagreement between datum and curve may not be said to be real one.

4.5 $P^{31}(d, \alpha_0)Si^{29}$(g'nd.) and $P^{31}(d, \alpha_1)Si^{29*}$(1st.)

The ground and low-lying state of P^{31} and Si^{29} had been adequately characterized on the asumption of a strong-coupling collective model by Broude, Green and Willmott[21] and by Bromley[20] et al.. The ground state of P^{31} was interpreted as a base of $K=1/2$ (Nilsson orbit 9)[22] rotational band with negative (oblate) deformation parameter $\delta=-0.15\sim-0.3$. Here K, the quantum number introduced by Bohr and Mottelson[23], is the angular momentum along the nuclear symmetry axis. On the other hand, in the case of Si^{29}, the sequence of states corresponding to the ground, 2.03 and 2.43 MeV levels were explained as a rotational band for $K=1/2$ (Nilsson orbit 9). The state at 1.28 MeV was assigned as a $K=3/2$ (Nilsson orbit 8) rotational spectrum. Moreover, it was demonstrated that Si^{29} has also an oblate shape with negative deformation parameter $\delta=-0.15$.

From these facts, the probability leading to the 1.28 MeV state by the (d, α) reaction is expected to be smaller than the probability corresponding to the transition to the $K=1/2$ rotational states in Si^{29}. In order to excite the 1.28 MeV state via direct-interaction process, the reconstruction must be required not only in core but also for the structure of extra-particles.

Adequate separation in the pulse height spectrum for the alpha-particle group leading to 1.28 MeV state in Si^{29} could not be obtained as illustrated in Fig. 4, but the group corresponding to 2.03 MeV state appeared at all observation angles with intensity comparable to the ground state yield.

In Fig. 12 is shown one of the fits of data for the $P^{31}(d, \alpha_0)Si^{29}$(g'nd.) reaction. The theoretical curve given in the figure for pick up process corresponds to $r_1=5.25f.$, $l_1=0$, $r_2=6.24f.$ and $l_2=2$. The curve for the knock out process with $r_1=5.6f.$, $l_1=0$, $r_2=6.24$ and $l_2=2$ was practically identical with the above one.

Before the discussion is concluded, the author wishes to emphasize that the preceding discussions on the angular distributions are only qualitative, so that further works both experimental and theoretical, are required in order to derive quantitative results. The angular distribution for the (d, α) reaction on light nuclei with intermediate bombarding energy, may, however, be explained qualitatively on the assumption of double pick up process, such as the theory derived by Newns. Such theory will become one of the powerful tools in nuclear spectroscopy in the further investigation for (d, α) reaction.

I would like to express my thanks to Professor T. Wakatsuki and Assistant professor S. Yamabe for their continued encouragement and helpful suggestions, and to Professor Y. Oda for his advice during the early part of this experiment. For useful discussions and cooperations I am indebted much to M. Takeda, S. Kato and the member of the cyclotron group. The valuable discussions on the theory with Dr. M. Sano and T. Kammuri were indispensable. My thanks are also due to Dr. H. C. Newns for communicating the results of his work on the double stripping process.

References

1) S. T. Butler: Proe. Roy., Soc. (London) A, **208** (1951) 559.
2) A. B. Bhatia, K. Huang, R. Huby and H. C. Newns: Phil. Mag. **43** (1952) 485. P. B. Datch and J. B. French: Phys. Rev. **87** (1952) 980. W. Tobocman and M. H. Kalos: Phys. Rev. **97** (1955) 132. J. Sawicki: Nuc. Phys. **6** (1958) 575. G. R. Satchler: Ann. Phys. **3** (1958) 275.
3) S. T. Butler: Phys. Rev. **106** (1957) 272.
4) Austern, Butler and McManus: Phys. Rev. **92** (1953) 350. Hayakawa, Kawai and Kikuchi: Progr. Theoret. Phys. Japan **13** (1955) 415, **14** (1955) 1. S. Yoshida: Proc. Phys. Soc. (London) A, **69** (1956) 668. J. R. Lamarsh and H. Feshbach: Phys. Rev. **104** (1956) 1633. C. A. Levinson and K. K. Banerjee: Ann. Phys. N. Y. **2** (1957) 471. J. Sawicki: Nuc. Phys. **6** (1958) 613. N. Austern and S. T. Butler: Phys. Rev. **109** (1958) 109. G. F. Pieser and N. P. Heydenburg: Phys. Rev. **111** (1958) 264. K. Glendenning: Phys. Rev. **114** (1959) 1297. E. M. Henley: Nuc. Phys. **13** (1959) 317.

5) H. C. Newns: (to be published)

6) A. W. Dalton, S. Hinds and G. Parry: Proc. Phy. Soc. **71** (1958) 253.

7) C. P. Browne: Phys. Rev. **104** (1956) 1598.

8) Y. Oda, M. Takeda, C. Hu and S. Kato: Phys. Soc. Japan **14** (1959) 396.

9) Bidhel, Mozeley and Aron: Phys. Rev. **105** (1957) 1788. H. Bichel: Phys. Rev. **112** (1958) 1089. R. M. Sternheimer: Phys. Rev. **115** (1959) 137.

10) C. B. Fulmer and B. L. Cohen: Phys. Rev. **112** (1958) 1672. C. B. Fulmer: Phys. Rev. **108** (1957) 1113.

11) L. Madansky and G. E. Owen: Phys. Rev. **99** (1955) 1608. G. E. Owen and L. Madansky: Phys. Rev. **105** (1957) 1766.

12) Freemantle, Gibson, Prowse and Rotblat: Phys. Rev. **92** (1953) 1268.

13) G. E. Fischer and V. K. Fischer: Phys. Rev. **114** (1959) 533.

14) W. Hauser and H. Feshbach: Phys. Rev. **87** (1952) 366.

15) A. M. Lane and R. G. Thomas: Revs. Moder Phys. **30** (1958) 257.

16) W. M. Gibson and E. E. Thomas: Proc. Roy. Soc. (London) **A**, **210** (1952) 543.

17) Elliot. J. P. and B. H. Flowers: Proc. Roy Soc. (London) **A**, **229** (1955) 536.

18) M. G. Redlich: Phys. Rev. **98** (1955) 199.

19) E. B. Paul: Phil. Mag. **2** (1957) 311.

20) D. A. Bromley, H. E. Gove and Litherland: Canad. J. Phys. **35** (1957) 1057. D. A. Bromley, H. E. Gove, E. B. Paul, A. E. Litherland and E. Almquist: Canada. J. Phys. **35** (1957) 1047.

21) C. Broude, L. L. Green and J. C. Willmot: Proc. Phys. Soc. **71** (1958) 1097, **71** (1958) 1115, **71** (1958) 1122.

22) S. G. Nilsson: Kgl. Danske, Videnskab, Mutt., Phys. Modd. (1955) No. 16. R. Mottelson and S. G. Nilson: Matt. Phys. Modd. Dan. Vid. Selsk. **1** (1959) No. 8.

23) A. Bohr and Mottelson: Kgl. Danske, Videnskab., Matt. Phys. Modd. **27** (1953) No. 16.

24) H. Morinaga: Phys. Rev. **97** (1954) 444.

JOURNAL OF THE PHYSICAL SOCIETY OF JAPAN, Vol. 15, No. ,10 OCTOBER, 1960

Emission of ^{8}Li, ^{9}Li and ^{8}B Fragments from Stars Produced by 4.3 Gev π^--Mesons in Nuclear Emulsion

By Kuni IMAEDA*, Mitsuko KAZUNO* and Nobuo ITO**

Department of Physics, Yamanashi University, Kofu, Japan

(Received May 11, 1960)

9.300 stars with more than 5 black prongs were examined to study ^{8}Li, ^{9}Li and ^{8}B fragments emitted from these stars. Thus, we found 90 examples of hammer tracks produced by ^{8}Li or ^{8}B fragments, 11 examples of tracks produced by $^9\mathrm{Li}\rightarrow{}^9\mathrm{Be}+e^-\rightarrow{}^4\mathrm{He}+{}^4\mathrm{He}+n+e^-$ and the one by $^9\mathrm{Li}\rightarrow{}^9\mathrm{Be}+e^-\rightarrow{}^5\mathrm{He}+{}^4\mathrm{He}+e^-$.

The experimental result of angular distribution, energy distribution, and frequency of emission of these fragments are given. Comparison is made between the experimental result and the prediction of evaporation theory on the frequency of emission of these fragments. The effect of the ^{8}B fragments on the estimation of the Coulomb barrier of the residual nucleus for ^{8}Li fragment is discussed.

§1. Introduction

Hammer track was first reported by Occhialini and Powell[1)] and was established to be due to a ^{8}Li fragment coming out of a nuclear disintegration and decaying at rest into two alpha-particles and an electron by Franzinetti and Payne[2)] and other. A similar event which is due to a ^{9}Li fragment decaying at rest into two alpha-particles, a neutron and an electron was reported by Fry[3)] and several authors[4)]. Similar event should also be due to a ^{8}B fragment, and this was first pointed out by Alvarez[5)] and has shown by Gilbert[6)].

Many investigations were performed on the emission of ^{8}Li fragments and its mechanism of emission. But relatively few experiments have described at the same time the distinction between ^{8}B fragment and ^{8}Li fragment[7)].

The aim of this paper is to investigate the relative freqnencies and characteristics of these ^{8}Li, ^{9}Li and ^{8}B fragments emitted from stars produced by 4.3 GeV π^--mesons.

Investigated decays are:

(1) $^8\mathrm{Li}\rightarrow{}^8\mathrm{Be}^*+e^-\rightarrow{}^4\mathrm{He}+{}^4\mathrm{He}+e^-$,

(2) $^8\mathrm{B}\rightarrow{}^8\mathrm{Be}^*+e^+\rightarrow{}^4\mathrm{He}+{}^4\mathrm{He}+e^-$,

(3) $^9\mathrm{Li}\rightarrow{}^9\mathrm{Be}^*+e^-\rightarrow{}^4\mathrm{He}+{}^4\mathrm{He}+n+e^-$,

and

(4) $^9\mathrm{Li}\rightarrow{}^9\mathrm{Be}^*+e^-\rightarrow{}^5\mathrm{He}+{}^4\mathrm{He}+e^-$.

§2. Experimental Procedure and Results

A stack of Ilford G5 emulsion pellicles of 3″×4″, 600 μm thickness 36 sheets have exposed to the 4.3 GeV π^--meson beams from Bevatron at Berkeley. After the exposure, the emulsions were processed by amidolbisulphite temperature development method. Area scanning was made under 150 magnification of microscope to pick up double stars, hyperfragments, hammer tracks and ^{9}Li hammer tracks. The events were tentatively classified by visual criteria, into hammer tracks, ^{9}Li hammer tracks, hyperfragments and others. Hammer track includes those produced by ^{8}B fragment.

The definition of the hammer tracks and ^{9}Li hammer tracks are as follows. Two tracks by helium nuclei (^{4}He or ^{5}He) and a track by an electron or a positron associate with the common centre where ^{8}Li or ^{8}B or ^{9}Li fragments stopped. The experimental determination that an apparent hammer track or an apparent ^{9}Li hammer track are those produced by ^{8}Li or ^{8}B fragments or ^{9}Li fragments, respectively, was made by the following criteria.

(A) The criteria for the ^{8}Li and ^{8}B hammer tracks

(a) Two alpha-particles should be emitted in opposit direction and their ranges in emulsion should be equal.

(b) The experimental Q-value of the decay obtained from the sum of the energy of the two alpha-particles should agree with the Q-

---

* Now at Dublin Institute for Advanced Studies, Dublin, Ireland.

** Now at Institute of Polytechnics, Osaka City University, Osaka, Japan.

vaule of the decay of an excited ^{8}Be nucleus into two alpha-particles.

(c) An electron track for ^{8}Li or a position track for ^{8}B shuld be associated at the point of decay of the fragment.

All the hammer tracks analysed in this paper satisfy the criteria (a) and (b). And out of 90 hammer tracks 8 events are missing the electron track, and these may be due to the crowded prongs of the parent star or short available path length for electron track in the same emulsion. The distribution of the Q-values of 8 events are in good agreement with those which have an electron track. There remains, however, some possibilities that the tracks are due to hyperfragments, but such a possibility can be neglected, because probability that hyperfragments satisfy the creteria (a) and (b) are extremely small.

In the course of analysis, we found out two examples which satisfy the criteria (a) and (c) but not (b). Their Q-values, assuming the decay (1) are 1.75 MeV and 1.5 MeV, respectively. But there are no levels of the excited ^{8}Be nucleus corresponding to the values. There was doubt about these hammer tracks, because the two tracks are too short to determine exactly that the tracks satisfy the criteria (a) or not.

After the examination, we concluded that the events are due to ^{9}Li fragments. The experimental Q-values are well fit to the decay of excited ^{9}Be nuclei and included in ^{9}Li hammer tracks.

(B) Criteria for ^{9}Li hammer tracks.

(d) An electron track should be associated with the decay for all ^{9}Li hammer tracks. In the case of the decay (3): $^9\text{Li}\rightarrow{}^4\text{He}+{}^4\text{He}+n+e^-$.

(e) Two alpha-particles are in general neither collinear nor equal range.

(f) By assuming that the event is due to the decay scheme (3) and the magnitude of the momentum of the neutron is equal to the sum of that of the two alpha-particles, the experimental Q-value obtained should agree with the Q-value calculated of the decay of an excited ^{9}Be*: $^9\text{Be}^*\rightarrow{}^4\text{He}+{}^4\text{He}+n$.

In the case of the decay (4): $^9\text{Li}\rightarrow{}^5\text{He}+{}^4\text{He}+e^-$.

(g) As expected from the decay of excited ^{9}Be* nucleus into ^{4}He and ^{5}He nuclei, two tracks of the alpha-particles should be collinear and their ranges are such that the momenta of the ^{4}He and ^{5}He particles should be equal in magnitude and opposite in direction.

(h) The experimental Q-value of the decay of an excited ^{9}Be nucleus into a ^{4}He nucleus and a ^{5}He nucleus should agree with the Q-value calculated from the decay scheme (4).

Table I.

Parent Star					Hammer track				^{9}Li Hammer track	
					No. of ^{8}Li Fragment			No. of ^{8}B Fragment	No. of ^{9}Li Fragment	
									Decay	
No. of black prongs	Mean Prong No.			No. of Stars	Observed	Corrected,	Frequency	Observed	Type (1)	Type (2)
	Total	Black	Grey						Observed	Observed
5- 8	9.8	6.3	2.0	4483	16	17.3	0.39±0.09	0	1	0
9–11	14.4	10.0	2.9	2248	23	24.9	1.11±0.22	0	3	1
12–14	17.8	12.9	3.6	1411	20	21.6	1.53±0.33	0	2	0
15–20	22.2	16.5	3.6	1099	27	29.2	2.66±0.47	0	2	0
21	29.6	21.8	6.2	63	2	2.2	3.49±2.53	2	3	0
Mean	13.7	9.5	2.7		88	95.2	1.02±0.15	2	11	1
Total				9304						
Total No. of Hammer					97.4				14.5	

All the ^{9}Li hammer tracks used are accompanied by an electron track and could be definitely distinguished from hyperfragments.

The number of the ^{8}Li, ^{8}B and ^{9}Li hammer tracks are shown in Table I.

There may be, however, some ^{9}Li hammer tracks whose electron tracks could not be observed and in this case it was excluded from ^{9}Li fragment. Thus, the corrections were made by assuming the same missing probability of the electron track as in the case of ^{8}Li hammer tracks. Also the correction were made in Table I for the hammer tracks whose prongs do not end in the same emulsion sheet and cannot be picked up as hammer tracks.

In order to distinguish between ^{8}Li and ^{8}B hammer tracks, attempt was made to distinguish ^{8}B hammer tracks from ^{8}Li hammer tracks.

The δ-ray measurement were performed on all the hammer tracks longer than 200 μm and the dip angle of less than 56° in unprocessed emulsion. The experimental number of δ-rays of more than two grains, and of more than three grains are shown in Table II and III.* The number of δ-rays attached to track No. 10 is distinctly different from the others.

The total number N_δ of δ-rays attached to a track of the range R of a particle of the charge Z and the mass M is expressed as follows:

$$N_\delta = M \cdot G(RZ^2/M) \qquad \text{(A)}$$

where $G(\quad)$ is a function which depends only on (RZ^2/M).

The range R_{Li} and R_{B} of the tracks of ^{8}Li and ^{8}B fragments, are such that the tracks contain the same number of δ-rays, then the expression (A) shows that, as the mass is the same, the range is inversely proportional to the square of charge: $R_{\text{Li}}/R_{\text{B}} = (Z_{\text{B}}/Z_{\text{Li}})^2 = (5/3)^2$.

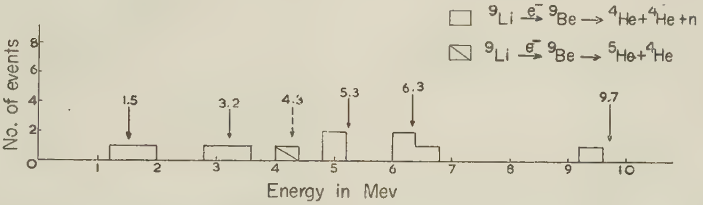

Fig. 1. Q-value obtained of the decay of ^{9}Be (produced by β- decay of ^{9}Li) into ^{4}He+^{4}He+n+Q and ^{4}He+^{5}He+Q.

Assuming that the track No. 10 is due to a ^{8}B fragment, the expected curve for δ-rays obtained of ^{8}Li from those of track No. 10 is shown in Fig. 2.

That the width for ^{8}B fragment is larger than that for ^{8}Li fragment results in under estimate of the number of δ-rays of more than two grains in the track of ^{8}B fragment. Taking into account of the fact, the result agrees with that the track No. 10 is due to a ^{8}B fragment.

For shorter tracks, the profile measurement were made on all the hammer tracks whose dip angles are less than 35° and the length exceeds 60 μm. The tracks were divided into 5 micron cells and for each segment of the track, the mean width was measured under the microscopic magnification 1.500 and summed up those values for each track.

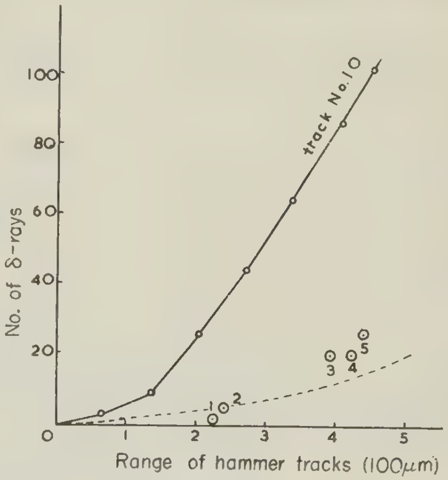

Fig. 2. The number of δ-rays in the tracks of hammer. ---- indicates the number of δ-rays for Li fragments expected from Z^2 law and assuming the track No. 10 is due to a ^{8}B fragment.

---

* (Note by the Editor) These tables are missing here owing to an accident; they will be printed in the Errata reaction of the forthcoming issue.

Thus, we get a measure of area on each track. The values obtained are plotted in Fig. 3. The area is not depend on the dip angle of track of the dip angle less than 35°[9]. The distribution shows that track No. 15 is distinctly different from the other group. The mean values of the group is 0.95±0.08 μm^2. The value for the track No. 15 is 1.246 μm^2 and the value is deviated more than twice the standard deviation.

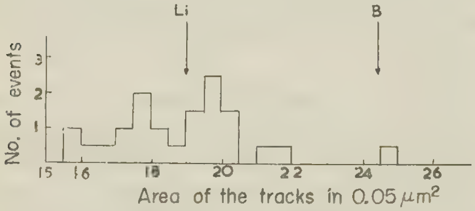

Fig. 3. Profile measurement (area of the tracks of 60 μm track length).

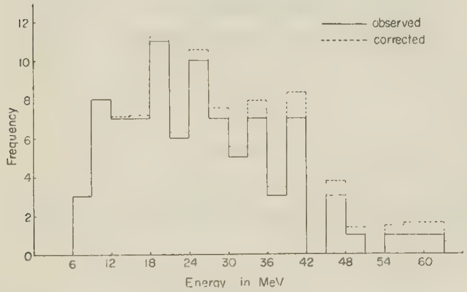

Fig. 4, Energy distribution of ^{8}Li fragments emitted from stars produced by 4.3 GeV π^--mesons in emulsion.

From the mean value of the group of 0.948 μm^2 for ^{8}Li fragment, and applying $z^{1/2}$ law of the track width, we obtain the track width for ^{8}B fragment, 1.22 μm^2 which is in good agreement with the observed value of 1.25 μm^2. Thus, the track No. 15 is concluded to be due to a ^{8}B fragment. Our result also agrees with 1.27 for the ratio of the area of 100 μm tracks of ^{8}B and ^{8}Li fragments which was obtained by O. Skjeggested et al.[7].

The frequency of emission of ^{8}Li, ^{8}B and ^{9}Li fragments in stars of different number of black prongs are given in Table I. The corrections for the hammer tracks which are escaped from emulsion before decaying at rest are made in Appendix (I) and included in Table I.

The energy distribution of 88 ^{8}Li fragments assuming that all the hammer tracks are produced by ^{8}Li fragments and that of 12 ^{9}Li fragments are shown in Fig. 5 and in Fig. 6, respectively. The angular distribution of ^{8}Li fragments and ^{9}Li fragments to the incident π^--meson beam are shown in Fig. 7. The energy distribution of ^{8}Li and ^{9}Li fragments in the backward direction as well as the forward direction with regard to the direction of the incident π^--meson are shown in Fig. 8. The ratio of the number of ^{8}Li fragments emitted in the forward to backward obtained is 1.29±0.26 for all fragments and 2.4±0.9

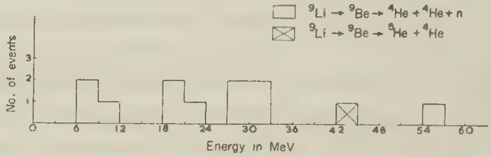

Fig. 5. Energy distribution of ^{9}Li fragments.

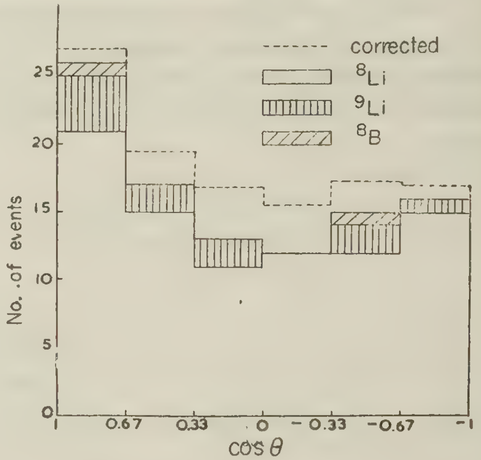

Fig. 6. Angular distribution of hammer tracks to the incident π-meson beam.

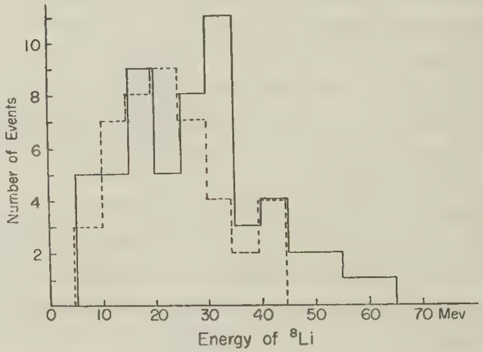

Fig. 7. Energy distribution of hammer tracks emitted in forward and backward direction. —— forward, - - - - Backward.

for energy greater than 30 MeV.

§ 3. Discussion

Frequency of emission of ^{8}B fragment

Based on the observed ^{8}B fragment, an estimate of the total number of ^{8}B fragments is made. The number of fragment A of the energy between E and $E+dE$ emitted from nucleus of the temperature T at rest is given as follows:

$$\text{(I)}\quad dN_{\rm A}=N_{\rm A}\frac{E_{\rm A}-V_{\rm A}}{T^2}\exp\left(-\frac{E_{\rm A}-V_{\rm A}}{T}\right)dE_{\rm A},$$

where $N_{\rm A}$, $V_{\rm A}$ are the total number, the height of Coulomb potential for fragment A.

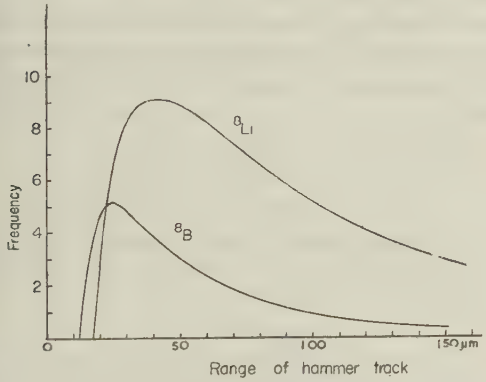

Fig. 8. Range distribution of hammer tracks of the mixture of ^{8}Li fragments and ^{8}B fragments with the ratio of 10:3.

According to (I), when $E_{\rm B}-V_{\rm B}=E_{\rm Li}-V_{\rm Li}$ holds, the ratio of the number of ^{8}B and ^{8}Li fragments of the energy greater than $E_{\rm B}$ and $E_{\rm Li}$, respectively, is equal to the ratio of the total number of ^{8}B and ^{8}Li fragments i.e. $N_{\rm B}/N_{\rm Li}$. Putting for $V_{\rm Li}=7$ MeV and 8 MeV and $E_{\rm B}=40$ MeV (which is the energy of ^{8}B fragment distinguishable from ^{8}Li fragment) and taking into account of the experimental restriction for the identification of ^{8}B fragments, we get $N_{\rm B}/N_{\rm Li}=0.1\sim0.3$. The result is in conformity with that obtained by Skjeggested *et al.* and also the prediction from the evaporation theory which gives the ratio $N_{\rm B}/N_{\rm Li}=1/3.2$ for $T=10.3$ MeV. (Appendix II)

In order to know the contribution of ^{8}B fragment, the range distribution of hammer tracks when the ratio $N_{\rm B}/N_{\rm Li}$ is equal to 0.3, is given in Fig. 9. The best fit curve to the experimental distribution is given by $T=10.3$ MeV and $V_{\rm Li}=8.0$ MeV.

As can be seen from Fig. 8, the low energy cut in the range distribution is determined by that of ^{8}B fragment. The height of Coulomb potential thus obtained from the low energy end of the distribution correspond to that of ^{8}B and not to that of ^{8}Li fragments as ordinarily assumed.

This conclusion is scarcely affected by the motion of the emitting nuclei and the tunnel effect of the evaporating fragments through barrier.

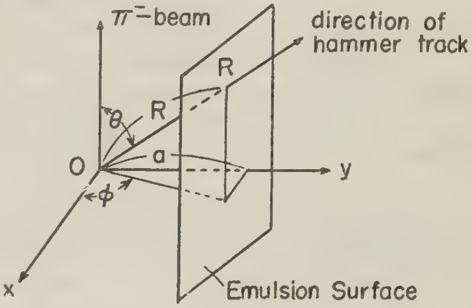

Fig. 9.

The above conclusion, however, depends on the ratio $N_{\rm B}/N_{\rm Li}$ and the number of hammer tracks observed in the experiment. In the case where $N_{\rm B}/N_{\rm Li}=0.1$, and the number of hammer tracks observed is less than 100, which is not incompatible with the present experimental results, the possibility of observation of ^{8}B fragments which range is less than that of the shortest ^{8}Li fragments will be small as the observed number of hammer tracks decrease and the value of the potential thus obtained become more likely to be that of ^{8}Li fragment rather than that of ^{8}B fragment.

The ratio $N_{\rm B}/N_{\rm Li}=0.1\sim0.3$ is also in agreement with that of Skjeggested *et al.* But the experimental result obtained so far is not sufficient to draw any difinite conclusion on the potential barrier, and the further experiment is desirable.

Frequency of emission of ^{9}Li fragment

The frequency r_2 of emission of ^{9}Li fragment relative to that of ^{8}Li fragment is 0.15 ±0.05. The value is much higher than that expected from the one by 950 MeV proton by Munir *et al.* in which a ^{9}Li fragment in 50 ^{8}Li fragments.

One of the reason for this is due to the dependence of the frequency on the temperature of emitting nuclei. But the temperature is not sufficient for the explanation of the difference between the two experiments. But the evaporation theory gives the ratio $N(^9\mathrm{Li})/N(^8\mathrm{Li})=1/17.8$ or $1/10.7$ for the spin of ^{9}Li is 1 or 2, respectively. (Appendix II) The value is in conformity with our experimental value of 0.15.

§ 4. Conclusion

1. 90 examples of hammer tracks observed in which two ^{8}B fragments are identified.

2. 12 examples of ^{9}Li fragment decays are observed. 11 examples of which are the decay of $^9\mathrm{Li}\rightarrow{}^9\mathrm{Be}+e^-\rightarrow{}^4\mathrm{He}+{}^4\mathrm{He}+n+e^-$, and an example is the decay of $^9\mathrm{Li}\rightarrow{}^9\mathrm{Be}+e^-\rightarrow{}^5\mathrm{He}+{}^4\mathrm{He}+e^-$.

3. Frequency of emission of ^{8}Li fragment is estimated to be $(0.94\pm0.11)\times10^{-2}$ and that of ^{9}Li fragment is $(0.15\pm0.05)\times10^{-2}$ per star, respectively.

4. Frequency of emission of ^{8}B fragment is estimated to be $(0.1\sim0.3)\times10^{-2}$ per star of heavy nuclei.

5. Frequency of emission of ^{9}Li fragment is in conformity with that of evaporation theory.

6. The height of Coulomb potential determined from the shortest range cut off of the range distribution of hammer track is more likely to be that of V_{B} and not V_{Li}. The value obtained is $V_{\mathrm{Li}}=(3/5)V_{\mathrm{B}}=8$ MeV.

7. $N(\text{forward})/N(\text{backward})=1.30\pm0.26$ for all ^{8}Li fragments, and 2.4 ± 0.9 for ^{8}Li of the energy greater than 30 MeV.

As ^{8}B and ^{9}Li nuclei are isobar and isotope of ^{8}Li nucleus, the study of ^{8}B and ^{9}Li fragments emitted from stars will give another light to the mechanism of emission of those fragments from nuclear disintegration. Care should be paid for the distinction between these hammer tracks, hyperfragments and strange particle when the energy of primary goes up and is sufficient for the production of these particles.

We are very grateful to Professor E. J. Lofgren who arranged the exposure of the stack and to Dr. W. W. Chupp and Dr. T. Kotani who exposed the stack in perfect conditions.

Appendix I. Correction factors for the hammer tracks escaped from emulsion

The coordinate is taken as in Fig. 9.

Then, the fraction of hammer tracks whose residual range is $R\,\mu$m and emitted from stars at a depth of a in a direction of θ to the incident π^--meson, escape from the surface of the emulsion is $(2/\pi)\cos^{-1}(a/R\sin\theta)$.

The fraction of the escaping hammer tracks of the residual range of $R\,\mu$m and emitted in the direction θ from the stars which are uniformly distributed from the depth 0 to $D\,\mu$m is

$$2R\sin\theta/(\pi D)$$

where we have assumed that D is larger than R and no hammer tracks which range exceeds $D\,\mu$m. The energy distribution of the fragments is given by the evaporation theory:

$$dN=\frac{E-V}{T}\exp\left(\frac{E-V}{T}\right)d\left(\frac{E}{T}\right).$$

Then, the fraction of the hammer tracks of all the energy but emitted in a specified angle θ is

$$\text{(II)}\qquad I=\int_{E=V}^{\infty}\left(\frac{2R}{\pi D}\sin\theta\right)dN\Big/\int_{E=V}^{\infty}dN$$

where R and E are given by the range-energy relation:

$$R=kE^{l}\,,\qquad l\simeq3/2\,,$$

where k is a constant.

Integrating (II), we obtain

$$I=\frac{2}{\pi}\left(\frac{R_v}{D}\right)\left(1+\frac{l(l+1)}{(V/T)}+\varepsilon\right)\sin\theta\,,$$

where

$$\varepsilon=\frac{(l+1-(V/T))l(l-1)}{(V/T)^{l}}e^{V/T}\int_{\sqrt{V/T}}^{\infty}x^{l-2}e^{-x}dx\,,$$

and R_v is the range of hammer tracks of the energy corresponds to V of the Coulomb barrier height, ε is small compared with 1.

Summing up for all directions, we get, assuming the isotropic distribution of emission of the fragments from stars,

$$C=\frac{R_v}{2D}\left(1+\frac{l(l+1)}{(V/T)}+\varepsilon\right).$$

Now, putting for $l=3/2$, $V=9.7$ MeV, and $T=10.3$ MeV, we obtain for $C=0.075$ for ^{8}Li and 0.025 for ^{8}B fragment.

The correction for the number of the fragments is given by

$$N_{\mathrm{corr.}}=N_{\mathrm{observed}}/(1-C)\ .$$

Appendix II

According to evaporation theory, the probability N_A per unit time for the emission of a particle A with kinetic energy $E \geqq V_A$ is[7]

$$N_A=kT^2\exp\{(-V_A+b_A+DF)/T\}\ ,$$

where $k=\sigma_0 gm/\pi^2\hbar^3$, σ_0=geometrical cross-section of the residual nucleus, m=mass of the emitted particle, b_A=binding energy of the emitted particle, V_A=height of the Coulomb potential barrier, T=nuclear temperature of the residual nucleus, F=Helmholtz free energy of the residual nucleus of $A(N, Z)$, ΔF the difference between F of the nucleus before and after the emission of that of the nucleus.

F of a heavy nucleus $A(N, Z)$, is given by, based on Fermi-gas model of nucleus,

$$F=A[-\alpha+\beta(\Theta-\Theta_0)^2-0.07(1+1.2\Theta^2)T^2]$$

where $\Theta=(N-Z)/A$ and Θ_0 is the value of Θ for the most stable nucleus of mass A, α =8.5 MeV, β=22.3 MeV, and is well represented by the semi-empirical formula:

$$\Theta_0=\frac{A^{2/3}}{A^{2/3}+132}\ .$$

Taking Br^{80}_{35} as a mean nucleus of the characteristics of the evaporating heavy nucleus in emulsion, we find for V_{Li}=8 MeV,

$$r_1=\frac{N(^8\mathrm{B})}{N(^8\mathrm{Li})}=\exp\left[\frac{1}{T}(-12.8+0.011T^2)\right],$$

$$r_2=\frac{N(^9\mathrm{Li})}{N(^8\mathrm{Li})}=\frac{g_{^9\mathrm{Li}}}{5}\exp\left[\frac{1}{T}(-15.2-0.09T^2)\right],$$

where $g_{^9\mathrm{L}}=3$ or 5, according to the spin of ^{9}Li equal to 1 or 2.

For T=8, 9, 10.3 MeV, we obtain $r_1=1/4.8$, 1/3.9 and 1/3.2 and $r_2=g_{^9\mathrm{Li}}/13.0$, $g_{^9\mathrm{Li}}/11.7$ and $g_{^9\mathrm{Li}}/10.7$, respectively.

References

1) G. P. S. Occhialini and C. F. Powell: Nature, London **159** (1947) 93.
2) C. Franzinetti and R. M. Payne: Nature, London **161** (1948) 735.
3) W. F. Fry: Phys. Rev. **89** (1953) 325.
4) K. Imaeda and M. Kazuno: Memo. Faculty Liberal Art and Education, Yamanashi Univ. **4** (1953) 275.
5) L. W. Alvarez: Phys. Rev. **93** (1950) 518.
6) F. C. Gilbert: Phys. Rev. **93** (1954) 499.
7) O. Skjeggestad and S. O. Sörensen: Phys. Rev. **113** (1959) 1115. O. Skjeggestad, An Investigation of Heavy Fragments Dmitted From Stars In Nuclear Emulsions. Archiv For Mathematik og Naturcidenskab. B. LIV Nr. 7.
8) B. A. Munir: Phil. Mag. **1** (1956) 355.
9) S. Nakagawa, E. Tamai, H. Fuzita and K. Okudaira: Journ. Phys. Soc. of Japan, **11** (1956) 191; **12** (1957) 747.

JOURNAL OF THE PHYSICAL SOCIETY OF JAPAN, Vol. 15, No. 10, OCTOBER, 1960

X-ray observations on Cleavage Faces of LiF Single Crystals

By Mitsuru YOSHIMATSU
Rigaku Denki Co Ltd., Haijima, Akijima City, Tokyo
and Kazutake KOHRA
Institute of Physics, College of General Education, University of Tokyo, Komaba, Meguro, Tokyo

(Received January 9, 1960)

Cleavage faces of LiF single crystals were studied by the Berg-Barrett method of X-rays. (i) Boundary lines of subgrains with small tilt angle show the intensity enhancement. The intensity enhancement is also seen for boundaries lying closely to the surface. (ii) As to deformations produced by cleaving, more informations such as slip directions are obtained than in etce-pit photographs. (iii) Furthermore, outcrops of individual dislocations arrayed in a boundary line or scattered in the interior of a grain are resolved. Dislocation half-loops lying closely to the surface in a slip line are also observed. In each type of the defects above mentioned the direction of Burgers vector is determined.

§ 1. Introduction

X-ray diffraction microscopy which presents us topographical information about lattice defects in a crystal has been recently developed to such an extent that individual dislocations have been able to be detected[1]. In comparison with light and electron microscopy, X-ray diffraction microscopy has several advantages: specimens do not suffer from any change of state with such a treatment as etching or decoration; they need not be so thin as in electon microscopy; and furthermore the direction of the dislocation Burgers vector can be determined. In X-ray microscopy, three different natures of diffraction are utilized to discriminated distorted region from the perfect one, or to obtain the image contrast; that is, (i) enhancement of integrated intensity or reduction of primary extinction; (ii) displacement of diffraction angle (in order of second) and (iii) decrease or disappearance of anomalous transmission. With the use of (i), Lang[2] established a fine technique to observe clearly dislocation lines in the interior of crystals. With the refined Berg-Barrett mehtod[3] where the nature of (i) is also used, Newkirk[4] observed outcrops of individual dislocations at the surface of Fe-Si single crystal, and furthermore fine structures of plastic deformations and dislocation outcrops at the cleavage face of a slightly compressed LiF single crystal. Bonse and Kappler[5] studied outcrops of dislocations at the surface of a Ge single crystal wifh the double crystal spectrometer using (ii), where the fine structure of the image was compared with the theory. With the use of (iii) Borrmann et al[6] observed dislocation lines in the interior of Si single crystal with a point source of X-rays, while Bardt and Hosemann[7] and Gerold and Meyer[8] observed dislocation lines with a parallel beam arrangement, the latter having also obtained the stereographic pattern. By the same technique one of the author and his coworkers showed that the anomalous transmission phenomenon was useful to detect lattice defects or strain field caused by other sources than the dislocation, that is, the strain field produced by external force in a Ge single crystal[9] and the layer structure probably due to oxygen in a Si single crystal[10], the latter of which had been observed by Dash with the decoration technique and infra-red microscopy[11].

We have observed cleavage faces of LiF single crystals by the refined Berg-Barrett method as Newkirk*. This method needs neither any special micro-focus X-ray tube as the one of Lang, nor any complicated instruments as the one of Bonse or Lang.

The surface of LiF single crystal has been intensively studied especially using the chemical etching technique[13]. As mentioned above, a general study of LiF single crystals by X-ray microscopy has been reported by Newkirk. While Newkirk studied mainly plastic deformations procuced by a slight compression, we studied more details of lattice defects on surfaces as cleaved, such as grain boundaries, plastic deformations produced by cleaving, individual dislocation outcrops found at the subgrain boundary or within the subgrain and dislocation half-loops lying near the surface.

---

* The preliminary report has been given[12].

§ 2. Experiments

a. *Apparatus*

The experimental arangement is shown in Fig. 1. The distance between the specimen and the photographic plate was made as small as possible to obtain the high resolution from the reason described in § 2c. The LiF single crystals were purchased from the Harshaw Chemical Company. The usual sealed-off X-ray tube of Cr target with the focal size 1×10 mm was used and operated at 40 KVP and 10 mA. For the case of high magnification (about 100 times), high resolution spectrographic plates 649-0 of Kodak were used, where the exposure time was several hours.

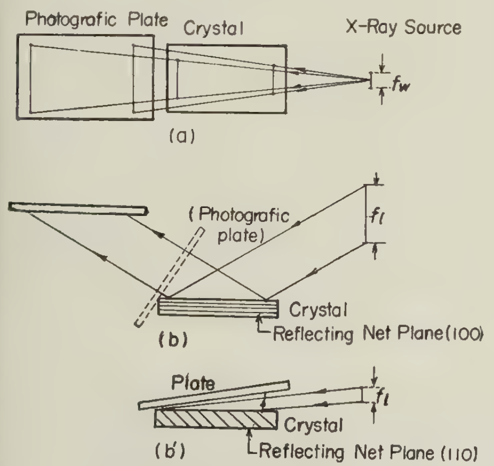

Fig. 1. Experimental arrangement.
(a) Projection on the plane perpendicular to the incident plane.
(b) Projection on the plane parallel to the incident plane. For the (200) reflections, the photographic plate is put at the position indicated with the dotted line.
(b′) Projection is the same as in (b), but for the case of {220} reflections.

In the present experiment, the apparent focal size is $f_w=1$ mm and $fl=1$ mm, the true focal size being 1×10 mm².

In order to obtain the good image contrast, a foil of Be 0.2 mm thick was used instead of black paper for shielding the photographic plate from the light and cleavage surfaces as flat as possible were used.

b. *Direction of Burgers vector and reflecting plane*

For the LiF crystals, the slip planes are {110} and the slip directions or the direction of the Burgers vector are ⟨110⟩ as shown in Fig. 2. It is usually known that the reduction of extinction is the strongest, when the reflecting plane is normal to the direction in which the lattice distortion is the strongest. Accordingly it is expected that the image contrast is the largest when the Burgers vector directs normal to the reflecting plane. For this reason the {220} reflections were mainly utilized as in case of Newkirk. The (200)

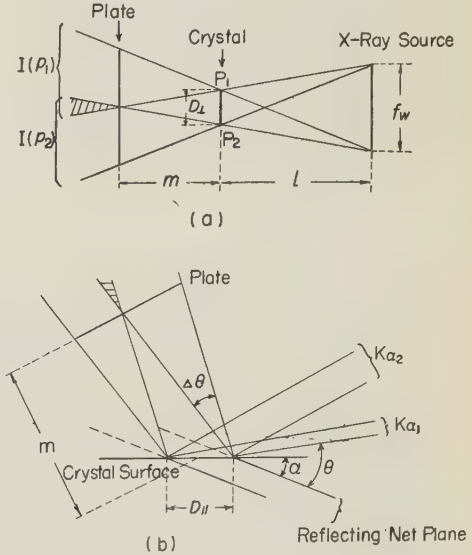

Fig. 3. Schematic diagram showing resolution of the image.
(a) Projection on the plane perpendicular to thd incident plane. In the hatched region, the two images $I(p_1)$ and $I(p_2)$ can not be separated.
(b) Projection on the plane parallel to the incident plane. The difference in the direction of K_{α_1} and K_{α_2} is exaggerated.

$\boldsymbol{D}_\perp$ and $\boldsymbol{D}_{//}$ are the component of the shortest separable distances in the direction perpendicular and parallel to the incident plane respectively.

l and m are the distances from the crystal to X-ray source and to the photographic plate respectively. θ is the Bragg angle, α, the angle between the reflecting plane and the crystal surface, $\Delta\theta$, the angle of dispersion K_{α_1} and K_{α_2}, f_w, the apparent X-ray focal width.

reflection was also sometimes used for comparison. In Table I the angles between the reflecting planes used and various slip directions are given. In the present experiment the {220} reflections have also the advantage that the image is hardly distorted: the magnification in the direction parallel to the incident plane is usually only several per cent larger than in the direction perpendicular to the incident plane.

In the experiment four planes of {220}, that is, $(2\bar{2}0)$, (220), (202) and $(20\bar{2})$, can be practically used as the reflecting plane. The direction (not sign) of the Burgers vector will be determined by knowing the reflection plane giving the strongest contrast. This is, how-

Table. I. Angles between the reflecting planes used and the slip directions. (in degree)

Reflecting planes \ Slip directions	[101]	$[10\bar{1}]$	[110]	$[1\bar{1}0]$	$[0\bar{1}1]$	[011]
(202)	90	0	30	30	30	30
$(20\bar{2})$	0	90	30	30	30	30
(220)	30	30	90	0	30	30
$(2\bar{2}0)$	30	30	0	90	30	30
(200)	45	45	45	45	0	0
	(screw)				edge	

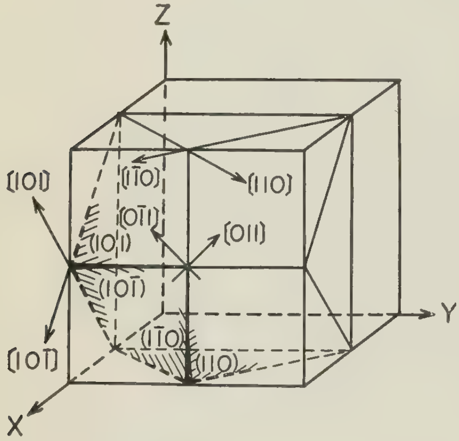

Fig. 2. Slip planes and slip directions. In the figure only the planes and directions which can be used for X-ray observation are shown. The cleavage face is (100).

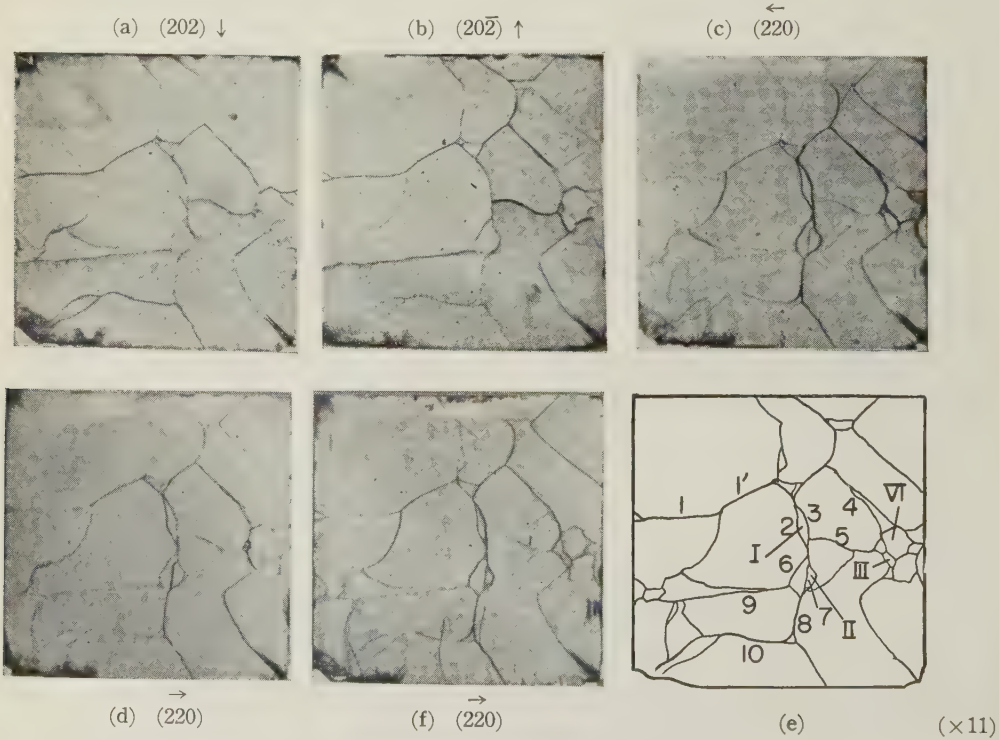

(a) (202) ↓ (b) $(20\bar{2})$ ↑ (c) $\overleftarrow{(220)}$

(d) $\overrightarrow{(220)}$ (f) $\overrightarrow{(220)}$ (e) (×11)

Fig. 4. X-ray photographs of snbgrain boundaries for different reflections.
(a), (b), (c) and (d) were taken from the same surface of a crystal, and (f) was taken from the matched surface of the pair produced by cleaving. For comparison the mirror image is shown in (f). The arrow indicates the direction of the incident beam.

ever, possible only if the Burgers vector direction is [110], $[1\bar{1}0]$, [101] or $[10\bar{1}]$, but not if the direction is [011] or $[01\bar{1}]$. In the latter case, the image contrast is expected to be the same for above four reflections, and it cannot be determined to which direction the Burgers vector is parallel.

c. *Instrumental resolving power*

One of the factors limiting the resolution of the image is the grain size of the photographic plate. We can practically use the special plate, for example, Kodak 649-0, the grain size of which is smaller than 1μ, at the cost of a long exposure.

Another factor determining the resolution is the diffuseness of the image of an isolated defect such as a dislocation outcrop or a dislocation line. This factor is further classified into the one due to the state of defects, and the one due to the experimental arrangement.

The fomer is dependent of the aggregating state of dislocations, the relative direction of the Burgers vector to the reflecting plane and others. The latter is here called the instrumental resolving power, and involves the factors such as the property of the incident beam source, and the relative position of the source, specimen and the photographic plate. The former is an important but complicated problem, and will be mentioned a little in § 5a and § 6, but should be studied in detail in the

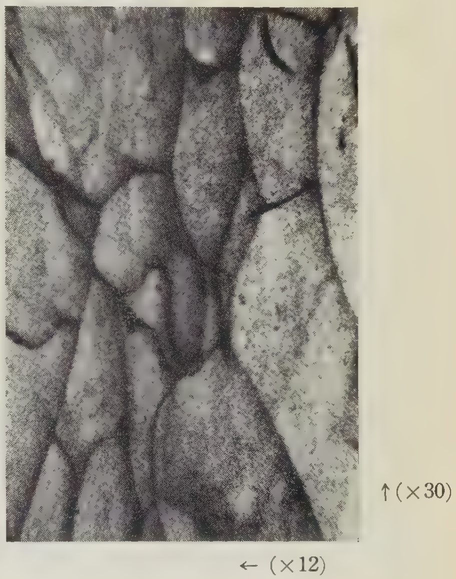

Fig. 5. Subgrain boundaries showing the asymmetric intensity distribution. (200) reflection.

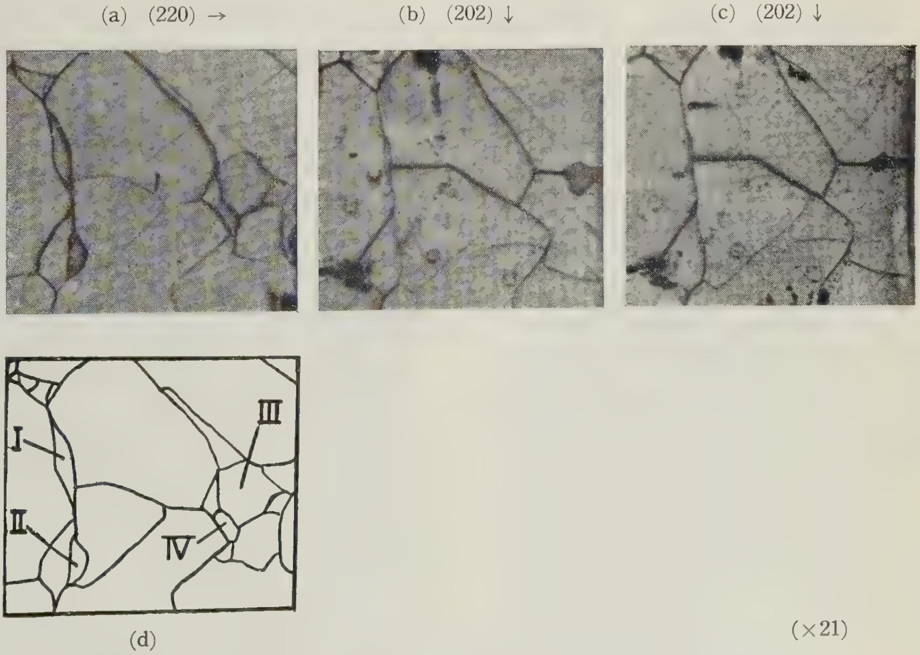

Fig. 6. The change in appearance of subgrain boundaries with chemical polishing.
(a) as-cleaved, (b), chemically polished for 15 min. ($\sim 12\mu$), (c), furthermore chemically polished for 6 min. ($\sim 5\mu$). (d), the schematic diagram of (a).

(geometrical divergence, spectral distribution of the wave length), dimension of the X-ray future. Here we consider only the latter.

The instrumental resolving power can be roughly estimated by the following consideration for two components parallel and perpendicular to the indident plane. The schematic diagramm is given in Fig. 3. Here the case that the diffracted rays lie in the incident plane is considered for simplicity. This condition is realized in our experiment. The shortest separable distances of two points lying on the crystal surface are given for two components respectively as follows:

$$D_{//}=\frac{m\Delta\vartheta}{\sin(\vartheta+\alpha)}, \qquad (1)$$

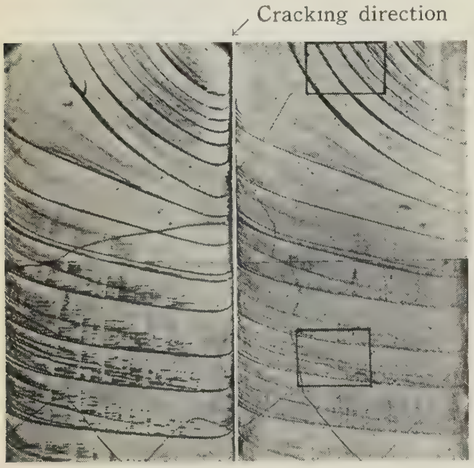

(a) (202) ↓ (b) (220) ← (×8)

Fig. 7. X-ray photographs from a cleavage face for different reflections when the cracking speed is pretty slow. The similar pattern to (a) was obtained with $(20\bar{2})$ reflection, and also the similar one to (b) was obtained with $(2\bar{2}0)$.

(a) (220) ← (b) (220) ←

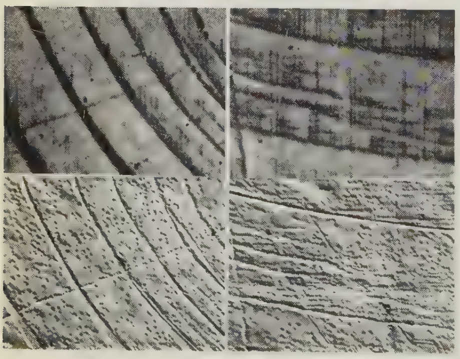

(a′) (b′) (×23)

Fig. 8. Correspondence of diffraction and etch-pit photographs of lattice defects produced by cleaving.
The photographs were taken from the regions marked in Fig. 7(b). The etch-pit photographs were taken after the deep etching of the cleaved surface (about 3 min.) in order to separate well individual pits.

(a) $(20\bar{2})$ ↑ (b) $(2\bar{2}0)$ →

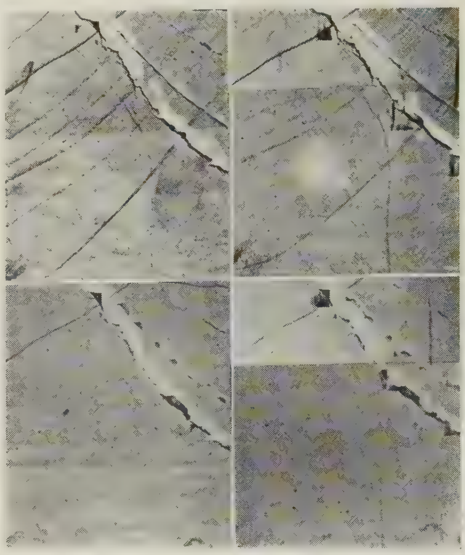

(c) $(20\bar{2})$ ↑ (d) $(2\bar{2}0)$ → (×11)

Fig. 9. The change of the pattern with heat-treatment.
(a) and (b), as cleaved. (c) and (d), heat-treated at 400°C for 20 min.. No more change was observed with heat-treatment for 30 hours at this temperature.

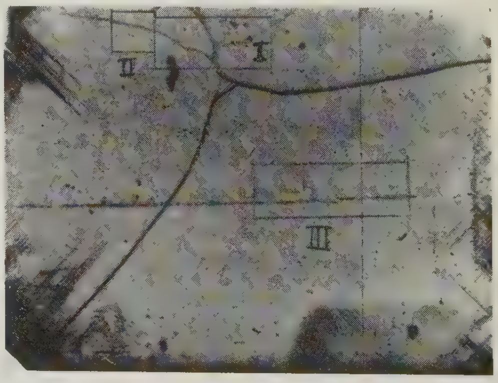

$(20\bar{2})$ ↑ (×17)

Fig. 10. Original X-ray photograph from which three regions were enlarged to observe individual dislocations as shown in Figs. 11, 13 and 14. This photograph was taken at the final stage after the surface layer about 28μ thick had been removed with chemical polishing, corresponding to the stage c of Fig. 11 or 14.

and

$$D_\perp = \frac{m}{l+m} \doteqdot \frac{m}{l} f_w . \qquad (2)$$

As seen from (1), $D_{//}$ may be considered to be mainly determined by the divergence of $K\alpha_1$ and $K\alpha_2$, when m is given. It is practically meaningless that $D_\perp$ is far smaller than $D_{//}$. Therefore f_w needs not be very small, and

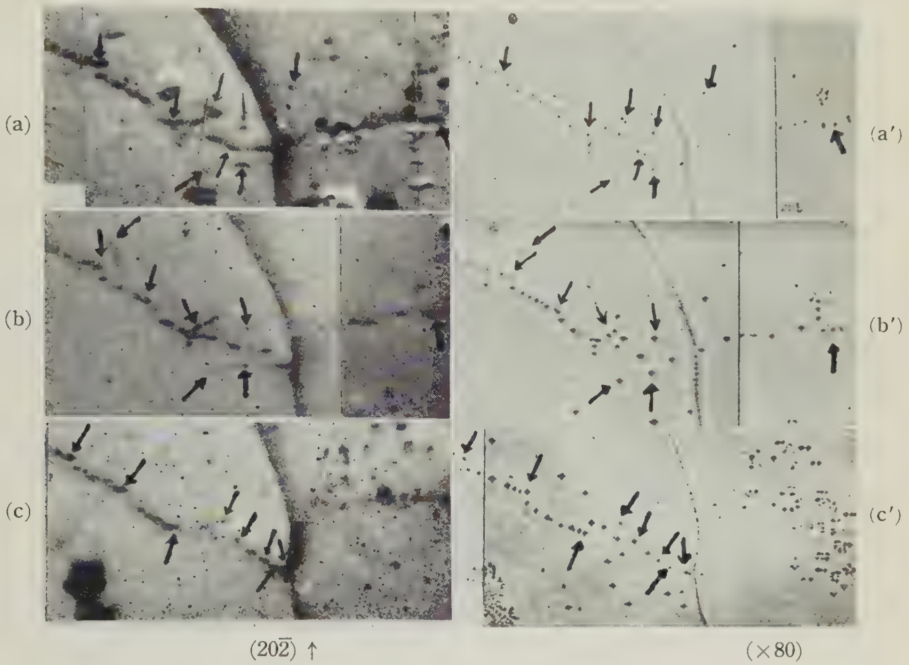

Fig. 11. Charge of X-ray and etch-pit photographs with chemical polishing.
(a) The cleaved face was chemically polished for 10 min., (b), chemically polished further for 5 min. after having been etched to obtain the etch-pit pattern, (c), furthermore chemically polished for 15 min. after (b).
For comparison some outcrops of dislocations are indicated by arrows.

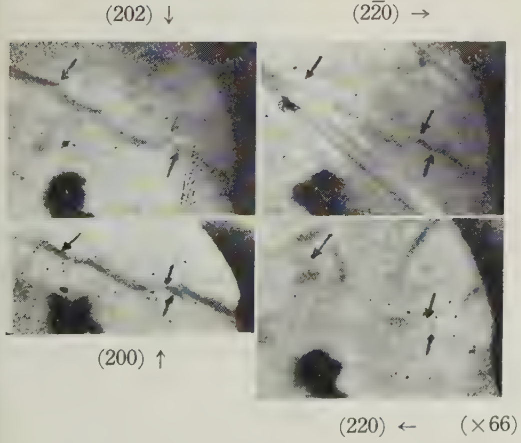

Fig. 12. X-ray photographs of dislocations in the sub-grain boundary with different reflections. The photograph for (2$\bar{2}$0) reflection is given in the Fig. 12 (c).

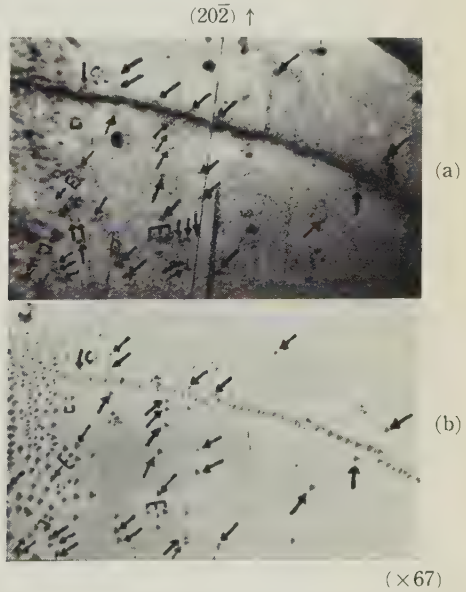

Fig. 13. X-ray and etch-pit photographs showing scattered dislocations in the interior of sub-grains.

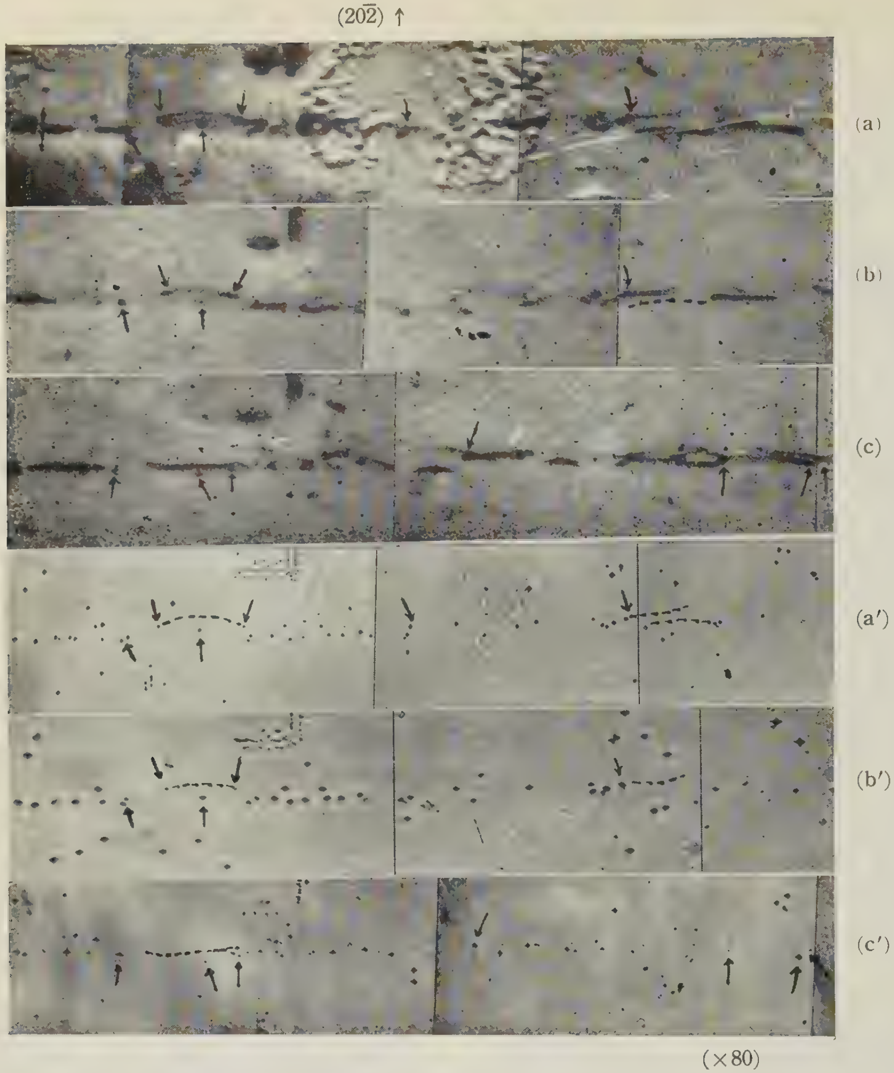

Fig. 14. Change of X-ray and etch-pit photographs of the dislocations on a slip line with chemical polishing. Polishing treatment is the same as in Fig. 12.

we can use the usual X-ray tube of the focal size 1×10 mm. In the present experiment, the following dimensions were used: $m=0.2\sim1.0$ mm, $l=150$ mm and $f_w=1$ mm. For the {220} reflections we have $\vartheta=53.5°$ and $\alpha=45°$, and for the (200) reflection $\vartheta=34.7°$ and $\alpha=0°$. With $\Delta\vartheta(\mathrm{K}\alpha_1, \mathrm{K}\alpha_2)=2\times10^{-3}$ radians, and $m=0.5$ mm, we have from (1) and (2) $D_{//}=1.0\mu$ and $D_{\perp}=3.3\mu$ for {220}, and $D_{//}=1.8\mu$ and $D_{\perp}=3.3\mu$ for (200). The order of resolutions may be said to be several microns.

§ 3. Subgrain Boundaries

a. *Intensity enhancement at the subgrain boundaries.*

When the crystal is of high quality, the network pattern with the enhanced intensity is observed on the diffraction photograph

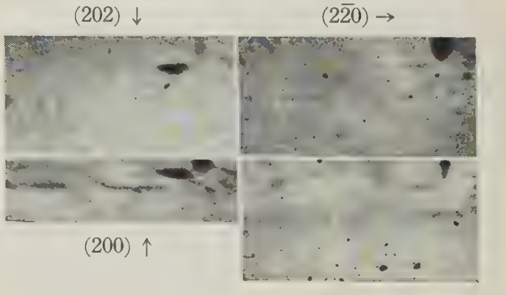

Fig. 15. X-ray photographs of a part (left) of Fig. 14 with different reflections. The chemical stage is the same to the one of Fig. 14 (c).

from the cleavage face. A series of photographs for various net planes from a face are shown in Fig. 4. From the etch-pit photograph the network was confirmed to correspond to the subgrain boundary on which etch pits were arryed, as seen in Fig. 11. As will be mentioned in § 5a, the boundary line could be also resolved in individual dislocations even in the diffraction photograph, if the dislocation density is sufficiently low. The intensity enhancement at the boundary is attributed to the reduction of the extinction effect due to the strain field around the dislocation array.

It is known[14] that if the dislocation density at the boundary is sufficiently high and accordingly the tilt angle is sufficiently large, the intensity enhancement as mentioned above is not seen at the boundary, but the intensity anomaly of another type appears. The images of grains shift against each other, being separated from or overlapped each other according to the sense of the tilt agnle. In the former case the region of zero intensity appears, while in the latter case the intensity enhancement is seen as the result of overlapping, but the enhancement is not so remarkable and the region is usually not so narrow as in case of the small tilt-angle boundary. As the case of the large tilt-angle boundary has been studied by many investigators, it will not be considered in the present paper.

b. *Change in the intensity contrast with the reflecting planes.*

As seen in Fig. 4, the intensity contrast of the boundary is remarkably changed with the different reflecting planes.

Most boundaries have the strongest intensity for one reflecting plane, for example, the lines 1 and 10 for the (202) reflection, 5 and 9 for $(20\bar{2})$, 3, 6 and 8 for (220) and 7 for $(2\bar{2}0)$. From the reason mentioned in § 2b. it can be concluded that the Burgers vectors of dislocations for these lines are normal to the reflecting planes giving the strongest contrast, respectively. On the other hand, some boundaries, for example, 1′ and 4, do not show any remarkable intensity change with different planes. In this case the Burgers vector of dislocation is considered to be normal to eithe (011) or $(01\bar{1})$ plane, neither of which can be used as the reflecting plane in the experiment.

Some lines have almost equal intensity for two reflections, for example, the line 2 for the (220) and $(2\bar{2}0)$ reflections. This facts cannot be explained by the consideration in § 2b. Some other factors, such as the coexistence of dislocations with different Burgers vector directions, the difference of the strain field between an isolated dislocation and a dislocation assembly or a boundary wall, seem to be considered. Some considerations in relation to these problem will be given in § 5 and § 6.

c. *Intensity enhancement in the whole region of subgrain and asymmetric intensity distribution of the boundary line*

It is to be noted that some small subgrains show the intensity enhancement in the whole region: for example, grains indicated with I, II, III and IV in Fig. 4(e) show the intensity enhancment in Fig. 4(f), which was taken from the matched face of the piece making the pair with the one of Fig. 4(a)∼(d).

It is also noticed that some boundary lines show the asymmetric intensity distribution in the direction normal to the line, being diffuse at one side, while sharp at another side. This tendency is more clearly seen in another photograph, Fig. 5.

To explain these phenomena the following experiment was carried out. After the cleavage face, from which Fig. 4f was taken, was chemically polished with the NH_4OH (2% in volume) solution following Gilman[15], the X-ray photograph was taken again. This procedure was twice repeated. The thicknesses of layers removed at both polishings are estimated to be about 12 and 5μ respectively. Corresponding patterns are given in Fig. 6. The change of the pattern is especially remarkable for the small grains having the intensity enhancement as above mentioned: Grains II and IV have disappeared already with one time polishing, and grains I and III become smaller. From this fact it can be concluded that the boundary walls of these subgrains found themselves so closely to the surface (at the deepness of ten μ in order) that X-rays reflected at the boundary walls are less absorbed in the path, resulting in the intensity enhancment for the whole subgrain.

The asymmetric intensity distribution of the boundary line is also explained in the similar way: the boundary wall lies much inclined to the surface, and accordingly lies very closely to the surface.

§ 4. Plastic Deformations produced by Cleaving

Besides the network pattern of subgrain bondary, another type of patterns as shown in Fig. 7 was sometimes observed, which seems, at first sight, to be consisted of parallel streaks (horizontal and vertical) and curved lines. As a general tendency the pattern of this kind appeared more clearly when the cracking speed was lower. Similar patterns were taken and studied by Gilman[15] with the etch-pit technique, and the X-ray diffraction photograph of the pattern was also taken by Newkirk.[15]* We examined the pattern of the X-ray photograph in more detail and especially tried to obtain some complementary informations to those from the etch-pit photograph.

The appearance of the streak pattern is changed noticeably with different reflecting planes, that is, only horizontal parallel streaks are seen for (202) or $(20\bar{2})$ reflection, while only vertical ones for (220) or $(2\bar{2}0)$. It can be concluded that the plastic deformations produced by cleaving are consisted of four kinds of slip: the [101] direction in the $(10\bar{1})$ plane and $[\bar{1}01]$ in (101) for the horizontal streaks, and [110] in $(1\bar{1}0)$ and $[1\bar{1}0]$ in (110) for the vertical streaks.

As another feature, a group of curved lines like the wave front is observed. Both kinds of horizontal and vertical streaks above mentioned are broken at the curved line. According to Gilman, when the propagation speed of cracking is slowed down or stopped, many dislocations are generated. The curved lines correspond to the crack fronts at various instants. For comparison, the enlarged photographs of two regions in Fig. 7(b) and the corresponding etch-pit photographs are given in Fig. 8.

The etch pit photographs was taken after the cleaved surface was etched, in order to obtain the clear pattern of etch pits. Therefore the exact comparison can not be made, but some essential differences of both patterns are clearly seen. Needless to say, at first, the information as to the Burgers vector direction is obtained only from the diffraction photograph. Secondly, in the diffraction photograph the spotty images of the dislocation outcrops can be hardly observed, but the streaks are only observed. These facts suggest that a streak corresponds to one or a few dislocation lines, which lie very closely to the surface. A similar case will be mentioned in § 5(c). The concept that the defects responsible for the streaks are very shallow is also supported by the experimental fact that the streaks disappears with a slight chemical etching or with the heat-treatment such as at 400°C for 20 min., as seen in Fig. 9.

§ 5. Dislocation Outcrops and Dislocation Half-Loops

In the diffraction photograph from the LiF single crystal, outcrops of individual dislocations are usually difficult to be observed, because the dislocation density is generally not so low as in case of Ge and Si. In the present experiment, however, individual dislocation outcrops, arrayed in the subgrain boundary or scattered in the interior of the subgrain, could be resolved. Furthermore, the image of dislocation half-loops was also confirmed.

In Fig. 10 a general view of the diffraction photograph of a specimen is given, three regions of which were enlarged to study various types of dislocations.

a. *Dislocations in the subgrain boundary*

In Fig. 11 the diffraction as well as etch-pit photographs of the region I of Fig. 10 are given, where the change of the pattern with successive chemical polishing is also shown. The chemical polishing was carried out as follows. At first the cleaved face was chemically polished in the same way as in § 3c to obtain the photographs of good contrast by removing the distorted layer produced on cleaving. Then the X-ray photograph (Fig. 11(a)) was taken. Next, the surface was slightly etched by Gilman's method, to obtain the etch-pit photograph (Fig. 11(a′)). Repeating this procedure, a series of photographs were obtained. The times of chemical polishing were 10, 5 and 15 minutes, respectively, which means that the layers about 8, 4 and 12μ respectively were removed at each polishing. The thickness of the layer taken away with the etching before obtaining the etch-pit photograph is considered to be negligible, because the time of etching was a few minutes.

---

* Furthermore it is seen in Fig. 7(a) that horizontal streaks are broken at some white lines running about vertically. The latter lines are likely to be the cleavage step.

As seen in the diffraction photographs, Fig. 11 (a), (b) and (c), the boundary running nearly horizontally is consisted of the array of points. One point corresponds sometimes to one etch pit and sometimes to an assembly of a few etch pits. The dimension of one point image, several microns, seems to limit the resolution. It is a little larger than the instrumental resolving power discussed in § 2c. This is probably because the resolution of the image becomes poorer by the effect of lattice distortion as mentioned in § 2c.

The distribution of dislocations near the cross-point of the boundaries is changed remarkably with etching in both diffraction and etch-pit photographs. The horizontal boundary line which is seen as one line in Fig. 11a, is divided into two boundaries in Fig. 11(c)*.

The image contrast of the dislocation outcrops in the diffraction photographs is varied sensitively with the reflecting plane, as shown in Fig. 12. These photographs were taken at the same stage of chemical polishing to the one of Fig. 11(c′). Among the series of the {220} reflection photographs, Fig. 11(c) and Fig. 12, the intensity contrast of the point image is the strongest for the $(20\bar{2})$ reflection**. From the consideration in § 2b, it can be said that the Burgers vector direction of the dislocation is $[10\bar{1}]$.

b. *Scattered dislocations in the interior of subgrains*

Outcrops of dislocations scattered in the interior of subgrains are usually difficult to be observed in the diffraction photograph. But with a careful treatment, they could be also observed as shown in Fig. 13, where the etch-pit photograph is also given for comparison. In both photographs, which were taken from the region II of Fig. 10, one-to-one correspondence could be established for many points.

The intensity contrast of these scattered isolated dislocations is generally far weaker than one of the dislocations arrayed in the subgrain boundary. This fact might be probably attributed to the following circumstances. According to the dislocation theory, the strain field around a single dislocation decreases more gradually than the one around the dislocation row or the boundary wall, and accordingly the strain gradient in the former is smaller than in the latter. On the other hand, it is usually known that the extinction effect is weaker or the intensity contrast is stronger when the strain gradient is larger.

c. *Dislocation array and half-loops*

In Fig. 14 the diffraction photographs from the region III of Fig. 10, are given together with the etce-pit photographs. The series of photographs were taken at the same stages of chemical polishing to these of Fig. 11.

The difference in appearance between the diffraction and etch-pit photographs is remarkable. while etch pits are observed to be arrayed nearly on a line in the etch-pit photograph, many streaks and a few points are observed in the diffraction photograph. The both ends of the streak were proved in most cases to correspond to etch pits.

It may be concluded that the streaks in the diffraction photograph is the image of the half-loop of the dislocation: the half-loop lies so closely to the surface that not only the dislocation outcrops but also dislocation loops themselves are observed. The appearance of the pattern in the diffraction as well as etch-pit photograph is changed remarkably with a slight etching of the order of ten microns.

For the left region of Fig. 14 the diffraction photographs were taken with (200) and various reflections {220} other than $(20\bar{2})$, as shown in Fig. 15, where the stage of chemical polishing corresponds to the one of Fig. 14(c). The intensity contrast is very weak for all reflections {220} in Fig. 15. Therefore it can be concluded that the Burgers vector direction of the dislocation loop is $[10\bar{1}]$. The slip plane is also considered to be parallel to (101). It is to be noted that the streaks or the etch pits are not arrayed exactly on a straight line, suggesting that the slip does not occur exactly in one plane.

§ 6. Conclusions and Discussions

The Berg-Barrett method of X-ray diffraction microscopy proved useful to study the defects on the surface or lying closely under the surface of single crystals. In favourable cases, individual dislocations could be resolved (§ 5).

---

* In Fig. 11(c′) it seems that other imperfections appear and mask the boundary.

** It is to be noted that the intensity contrast is not completely zero for other reflection than $(20\bar{2})$, being pretty strong for (202) and weak but still obserbable for $(2\bar{2}0)$ and (220).

As an advantage common to the X-ray diffraction microscopy, the specimen can be observed without disturbing the state of the specimen, being different from light microscopic observation by the use of etching or decoration. Accordingly the Berg-Barrett method is useful to study the surface phenomena, which might disappear by a slight etching or the heat-treatment necessary for decoration. Furthermore the X-ray diffraction microscopy is generally suitable for the study of structural changes of lattice defects. As an example, the polygonization process of bent crystals of LiF is being studied by us and will be reported in the near future.

Another advantage common to the X-ray diffraction microscopy, that the intensity contrast of the image is dependent of the relative direction of the strain gradient to the reflecting plane, was utilized to the fullness in the present study. In many cases, the Burgers vector direction of dislocation could be determined (§ 3b, § 4, § 5a and b).

For some cases (§ 3b), however, the change in intensity contrast of the boundaries could not be explained by the simple consideration mentioned in § 2. The dimension of the image is also a problem to be studied in the future, in relation to the resolution of the image (§ 2c). Theoretical considerations are necessary, taking account of factors such as the modified strain field arround the dislocation array, not a single dislocation, and the relative directions of the Burgers vector as well as the dislocation line to the reflecting plane.

The authors should like to express their sincere thankfulness to Profs. E. Fukushima, A. Ookawa and M. Sakamoto for their helpful discussions, and to Mr. Y. Shimura, president of Rigaku Denki Co. Ltd., for his interests and encouragements, and also to Mr. Y. Sugiyama for his technical assistance.

References

1) For example, as a general survey, K. Kohra: Kinzoku Butsuri (Metal Physics, in Japanese) **5** (1959) 91.
2) A. R. Lang: J. Appl. Phys. **29** (1958) 597; Acta Cryst. **12** (1959) 249; J. Appl. Phys. **30** (1959) 1748. A. R. Lang and G. Meyrick: P1il. Mag. **4** (1959) 878.
3) W. Berg: Naturwiss. **19** (1931) 391. C. S. Barrett: AIME Trans. **161** (1945) 15. Also refer to J. B. Newkirk: AIME Trans. **215** (1959) 483.
4) J. B. Newkirk: J. Appl. Phys. **29** (1958) 995; Phys. Rev. **110** (1958) 1465; AIME Trans. **215** (1959) 483.
5) U. Bonse und E. Kappler: Zs. f. Naturforsch. **13a** (1958) 348; U. Bonse: Zs. f. Phys. **153** (1958) 278.
6) G. Borrmann, W. Hartwig und H. Irmler: Zs. f. Naturforsch. **13a** (1958) 423.
7) H. Bardt und W. Hosemann: Zs. f. Naturforsch. **13a** (1958) 680.
8) V. Gerold und F. Meier: Zs. f. Phys. **155** (1959) 387.
9) Z. Ishii and K. Kohra: J. Phys. Soc. Japan **14** (1959) 1250.
10) Z. Ishii, T. Furuoya, Y. Sasaki and K. Kohra: J. Phys. Soc. Japan **15** (1960) 206.
11) W. C. Dash: J. Appl. Phys. **30** (1959) 459.
12) M. Yoshimatsu and K. Kohra: J. Phys. Soc. Japan **14** (1959) 1249.
13) For example, J. J. Gilman and W. G. Johnston: Dislocations and Mechanical Properties of Crystals (John Wiley, New York, 1957) 116.
14) For example, L. C. Schulz: AIME Trans. **200** (1954) 1082. J. B. Newkirk: J. Appl. Phys. **29** (1958) 995.
15) refer to 13).
16) J. J. Gilman: AIME Trans. **209** (1957) 449.

JOURNAL OF THE PHYSICAL SOCIETY OF JAPAN, Vol. 15, No. 10, OCTOBER, 1960

Study on the Ordered Phases with Long Period in the Gold-Zinc Alloy System

I. Survey of Crystal Structures and Calorimetric Measurement

By Hiroshi IWASAKI, Makoto HIRABAYASHI, Kunio FUJIWARA[†]
Denjiro WATANABE and Shiro OGAWA

The Research Institute for Iron, Steel and Other Metals,
Tohoku University, Sendai

(Received June 2 1960)

The crystal structures of the ordered phases in the Au-Zn alloy system have been studied in detail by means of X-ray and electron diffraction on single crystal samples, and the order-disorder and other kinds of phase transitions involved in the present system have also been studied by the measurement of specific heat.

The previously proposed structures of $Au_{3+}Zn$, Au_3Zn[H], Au_3Zn[R] have substantially been confirmed and that of Au_5Zn_3 only partly. Moreover, the details in these structures have been revealed: in $Au_{3+}Zn$ some type of the strong lattice modulation is present, and in Au_3Zn[R] the two types of structure, $Au_3Zn[R_1]$ and $Au_3Zn[R_2]$, certainly exist. The transition behavior of the alloys with changing temperature has been investigated on samples of various compositions and the thermodynamic data obtained are presented. The phase diagram of the Au-rich side of the present system is reasonably corrected by the present experiment. The orientation distribution of the ordered crystals formed in the originally disordered crystal and the nature of the transition, $Au_3Zn[H] \rightarrow Au_3Zn[R]$, are briefly discussed.

§ 1. Introduction

The formation of the ordered phases with long period in the gold-rich solid solution of the gold-zinc alloy system was first reported by Schubert and his collaborators in 1954[1]. The structures of these ordered phases are characterized by the presence of "anti-phase domains" with definite size, *i.e.* the long range order in the usual sense extends not over the whole crystal volume but only over small domains, and these domains are regularly arranged with a definite phase-shift relation to one another. Examples are found in CuAu II, Cu_3Pd, Ag_3Mg, Au_3Mn etc. Extensive studies by Schubert *et al.* on the gold-zinc alloy system[2),3),4)] by the X-ray powder method made clear the following facts: There are three kinds of the ordered phases with long period, a) $Au_{3+}Zn$*($=Au_4Zn$), b) Au_3Zn[H] and its room temperature modification Au_3Zn[R] and c) Au_5Zn_3. Frequency of the occurrence of anti-phase shift (or out-of-step) in terms of a fundamental face-centered cell**, *i.e.* "*Verwerfungsdichte*", shows a simple dependence on the valence electron concentration of alloys, the dependence being regarded as the characteristic nature of the ordered phases with long period. Recently, one of the present authors (H.I.) proposed[5)] that the phase Au_3Zn[R] is divided furthermore into two types of structure $Au_3Zn[R_1]$ and $Au_3Zn[R_2]$.

Some physical properties, such as electrical resistivity[6),7)], elastic moduli[7)] and thermal dilatation[8)], were measured by several workers on the gold-zinc alloys with various compositions in a wide temperature range, and, in particular, a detailed study using several experimental techniques was performed on Au_3Zn[9)]. These experiments contributed much to our understanding of the nature of the ordered phases and the phase transitions of them.

[†] Now at the Institute for Soild State Physics, Tokyo University, Tokyo.

* The convenient notation $Au_{3+}Zn$ was used by Wilkens and Schubert[3)], because this ordered phase stably exists in the composition range deviating appreciably from the ideal composition Au_3Zn towards Au-rich side, but the fundamental atomic arrangement of this phase is still based on A_3B-type ordered structure. The present authors followed their notation.

** For the meaning of this term, refer to our previously published papers, for example, (12).

However, in view of the complicated character of these ordered phases, a more detailed study on the crystal structures of them with single crystals, on their stable region in the phase diagram and, especially, on their thermodynamic properties seemed to be desirable. We therefore studied the crystal structures by electron diffraction on evaporated single-crystal-like films, and by X-ray diffraction on bulk single crystals. The order-disorder and other kinds of phase transitions involved in the present system were also studied by the measurement of specific heat, from which the changes in configurational energy and entropy were deduced and, at the same time, the type of the transitions could be concluded. In the present paper, the experimental results on the specimens with the composition range from about 15 to 45% Zn* are reported. The details of structure analysis on the ordered phases will be reported in the subsequent paper.

§ 2. Proposed Models for the Structures of the Ordered Phases

From the analysis of powder diffraction patterns of the alloys, Schubert *et al.* proposed the structure models for the three ordered phases in the gold-zinc alloy system, as are shown in the following figures. First, in Fig. 1 the structure of $Au_{3+}Zn$ is shown, which is a two-dimensional anti-phase domain structure ($L1_2VwVw^{\alpha}$) of the Cu_3Pd_{1+} type with an orthorhombic fundamental cell. There occur the anti-phase shifts (or, out-of-steps) simultaneously along two directions in the same region. Au_3Zn[H] is a simple, one-dimensional anti-phase domain structure ($L1_2Vw$) of the Ag_3Mg type with a tetragonal fundamental cell, as is shown in Fig. 2. In this structure, the shift occurs only along one direction. The structure of Au_3Zn[R] is somewhat complicated. The dimensions of its large orthorhombic unit cell are: a and $b \sim \sqrt{2}a_f$ and $c=4c_f$, where a_f and c_f are the axes of the fundamental cell. The atomic arrangement of Au_3Zn[R] is obtained from that of Au_3Zn[H] by shifting many of atoms at the face-centered positions in the latter structure. However, as mentioned before, according to one of the present authors (H.I.)[5] Au_3Zn[R] is divided into the two types of structure, $Au_3Zn[R_1]$ and $Au_3Zn[R_2]$. The latter corresponds to the structure proposed by Schubert *et al.*, while the former has an tetragonal symmetry with the a-axis nearly equal to the a-axis of, and with the c-axis twice the c-axis of the latter. Furthermore, $Au_3Zn[R_1]$ was shown to be an anti-phase structure of $Au_3Zn[R_2]$ with the period of out-of-step, measured in atomic distance, M, being unity. Both the structures are shown in Fig. 3. Au_5Zn_3 has a more complicated structure. According to Schubert *et al.*, the dimensions

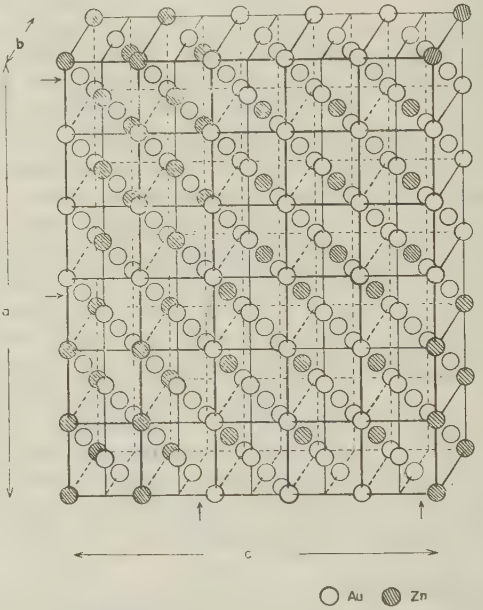

Fig. 1. Model of the two-dimensional anti-phase domain structure, $Au_{3+}Zn$, with $M_1=3$ and $M_3=2.5$. The three axes of the fundamental cell, a_f, b_f and c_f coincide in direction with those of the large unit cell, a, b and c, respectively. Out-of-steps occur at places indicated by arrows.

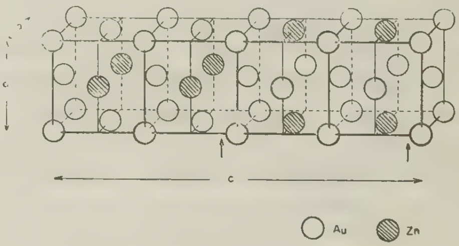

Fig. 2. Model of the one-dimensional anti-phase domain structure, Au_3Zn[H], with $M_3=2$. Out-of-steps occur at places indicated by arrows.

---

* In the present paper, all percentages refer to atomic per cent.

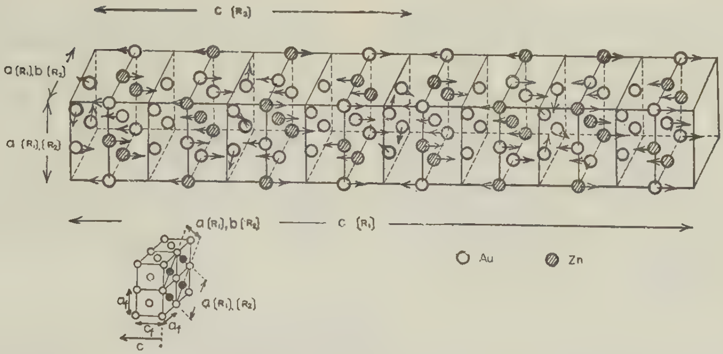

Fig. 3. Model of the ordered structures, Au_3Zn [R_1] and Au_3Zn[R_2]. The two *a*-axes of [R_1] coincide nearly with the *a*- and *b*-axes of [R_2], and the *c*-axis of [R_1] is twice that of [R_2]. Arrows show the directions of atom shift. Geometric relation between the axes of the large unit cell and of the fundamental cell is shown.

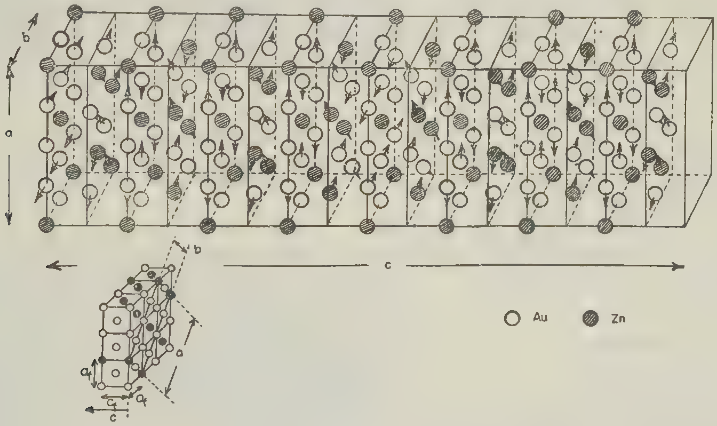

Fig. 4. Model of the ordered structure, Au_5Zn_3. Arrows show the directions of atom shift. Geometric relation between the axes of the large unit cell and of the fundamental cell is shown.

of the large orthorhombic unit cell are: $a=2\sqrt{2}a_f$, $b=\sqrt{2}a_f$ and $c=8c_f$, and, again, atoms in this structure are located at the slightly shifted positions from the face-centered positions, as indicated by arrows in Fig. 4.

§ 3. Experimental Procedures

Alloys were prepared from pure gold (99.99%) and electrolytic zinc (99.95%). In order to avoid oxidation and evaporation loss of zinc, melting and heat treatment of the alloys were always carried out in argon gas atmosphere.

a. Electron diffraction study

Single-crystal-like films for electron diffraction were prepared in the following way: First, well orientated thin gold films were obtained by evaporating gold on cleavage faces of rocksalt kept at high temperatures. Next, different amounts of zinc were evaporated on the gold films at room-temperature, and finally, they were annealed to allow alloy formation. The ordering treatments of the films were carried out at 120°C for a long time. The determination of the composition of films by the measurement of the lattice constant in the region of the *α*-solid solution (disordered state) was not carried out, because the heating of these films up to the disordered state might lead to evaporation loss of zinc.

b. Specific heat and X-ray diffraction study

Gold and zinc were melted together in carbon crucibles and rapidly poured into iron moulds. Each specimen was subjected to preliminary homogenization at temperatures immediately below the solidus for several hours. The composition was determined by chemical analysis.

Specific heat was measured by an adiabatic calorimeter of Nagasaki-Takagi type[10], changing temperature at the rate of about 2 degrees per minute. Specimens employed were cylinders of about 10 mm in diameter and 15 mm in length. To avoid a disturbance due to the heat of oxidation and evaporation of zinc, the vessel of the calorimeter was filled with argon. Before each measurement, the specimen was subjected to an ordering treatment for three or four weeks.

Single crystals were small rod of about 0.2 mm in diameter and 10 mm in length, grown in a thin ceramic tube by the Tammann-Bridgman method. Their composition was examined, when the quenching was effective, by measuring the lattice constant in the disordered state, and utilizing the known relation between the alloy composition and the lattice constant given by Owen and O'Donnell Roberts[11]. Oscillation photographs were taken with cylindrical cameras of 8 cm and 7 cm in diameter by rotating the samples around either a ⟨100⟩ or a ⟨110⟩ direction of the originally disordered cubic cell. Throughout the present work only filtered Cu radiation (wave length=1.5374 kx) was used.

§ 4. Experimental Results

a. Electron Diffraction Study

Seven single-crystal-like films with different compositions were employed, all of which had previously been subjected to the ordering treatment. In Photos. 1, 2, and 3 are reproduced a series of diffraction patterns taken from these films. Zinc composition gradually increases from Photos. 1 to 3. One can recognize gradual changes of the patterns in a rather complicated way. It should be noted that each pattern represents the intensity distribution on a {100} plane section of the reciprocal lattice of the originally disordered cubic cell, though there takes place a slight distortion, and also that the crystallographic axes of the fundamental cell of the ordered phase, which are no longer equivalent to each other on account of the lowered symmetry on ordering, are distributed along the three axes of the original cubic cell. In interpreting the patterns caution was furthermore taken on the possibility that the intensity distribution not lying on the {100} plane of the reciprocal lattice might appear in the pattern owing to bending or twisting of the films.

Adopting the proposed structures shown in § 2, it is able to calculate the intensity distribution in the reciprocal lattice for the ordered phases. In Figs. 5, 6 and 7 are shown the intensity distributions on a {100} plane section calculated by assuming three or sixfold superpositions of possible orientations of the ordered crystal. All the indices are asigned in terms of the original cubic cell.

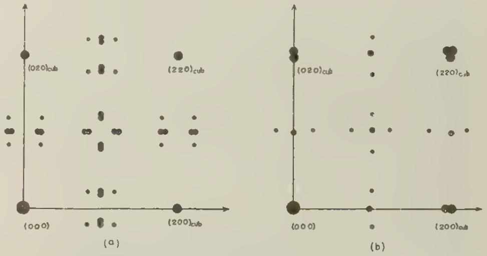

Fig. 5 (a) and (b). Six- and threefold superpositions of the intensity distribution on a {100} plane section of the reciprocal lattice of $Au_{3+}Zn$, (a), and Au_3Zn[H], (b), respectively.

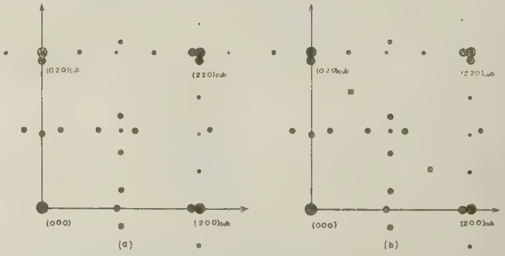

Fig. 6 (a) and (b). Three- and sixfold superpositions of the intensity distribution on a {100} plane section of the reciprocal lattice of Au_3Zn [R_1], (a), and Au_3Zn[R_2], (b), respectively.

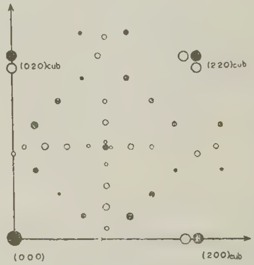

Fig. 7. Sixfold superposition of the intensity distribution on a {100} plane section of the reciprocal lattice of Au_5Zn_3.

The characteristic splitting of the superlattice spots in Photo. 1 (a) can be accounted for by the intensity distribution of $Au_{3+}Zn$ shown in Fig. 5 (a). In Photo. 1 (b), the pattern of $Au_{3+}Zn$ is more clearly observed, though in the same photograph the faint pattern of $Au_3Zn[H]$ is superposed. Photo. 2 (a) shows a diffraction pattern very similar to that of the one-dimensional anti-phase domain structure of Ag_3Mg[12], indicating the fact that only the phase $Au_3Zn[H]$ (Fig. 5 (b)) is present. Photo. 2 (b) can be interpreted as a mixed diffraction pattern of the two phases, namely, $Au_3Zn[H]$ in larger and $Au_3Zn[R_1]$ in less amount. It is noticed in Photos. 3 (a) and (b) that the distribution of the *c*-axis of the ordered phase Au_5Zn_3 is unequal along the three directions, showing the preferential orientation of the *c*-axis in the direction of the film normal. This fact is in contrast to the case of the other ordered phases of the present system. The intensity distribution from an Au_5Zn_3 crystal with such a preferential orientation is shown by solid circles in Fig. 7, and diffraction spots due to the crystals with their *c*-axis lying in the film surface are shown by open circles. Taking the above fact into account, the diffraction patterns in Photos. 3 (a) and (b) are explained as the mixing of $Au_3Zn[R_2]$ and Au_5Zn_3.

Similarly as in other ordered alloys with long period, such as CuAu II[13], Cu_3Pd[14], Au_3 Mn[15] etc., satellites flanking the direct spot can be observed in all the present diffraction patterns, though weak in their intensity. In the X-ray diffraction pattern, however, the satellite spots could hardly be detected around the direct spot.

The structure data obtained by electron diffraction are summarized in Table I.

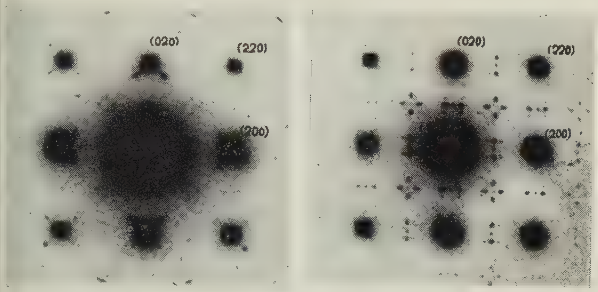

(a)　(b)

Photo. 1. Electron diffraction patterns of (a) $Au_{3+}Zn$ and (b) $Au_{3+}Zn+Au_3Zn[H]$. In (b), the former excels the latter in amount.

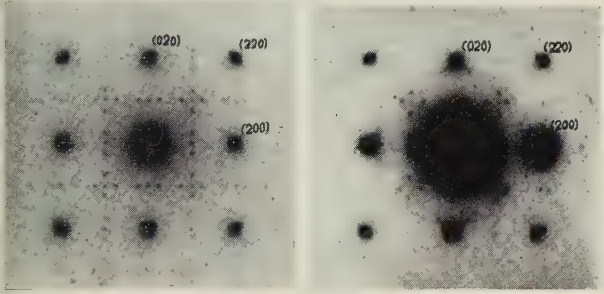

(a)　(b)

Photo. 2. Electron diffraction patterns of (a) $Au_3Zn[H]$ and (b) $Au_3Zn[H]+Au_3Zn[R_1]$. In (b), the former excels the latter in amount.

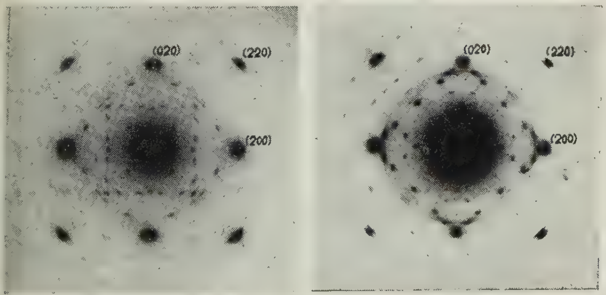

(a)　(b)

Photo. 3. Electron diffraction patterns of (a) $Au_3Zn[R_2]+Au_5Zn_3$ and (b) $Au_3Zn[R_2]+Au_5Zn_3$. In (a), the former and in (b), the latter excel the others in amount.

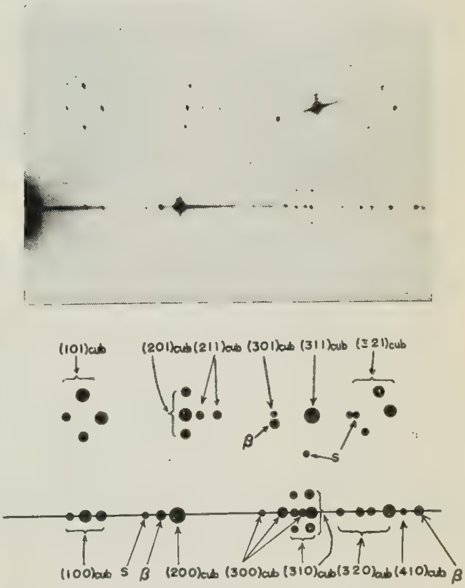

Photo. 4. X-ray oscillation pattern of $Au_{3+}Zn$ from the 19% Zn single crystal and its schematic diagram. $[001]_{cub}$. is vertical and oscillation angle is 30°. *s* and *β* represent satellite and *Kβ* spots, respectively.

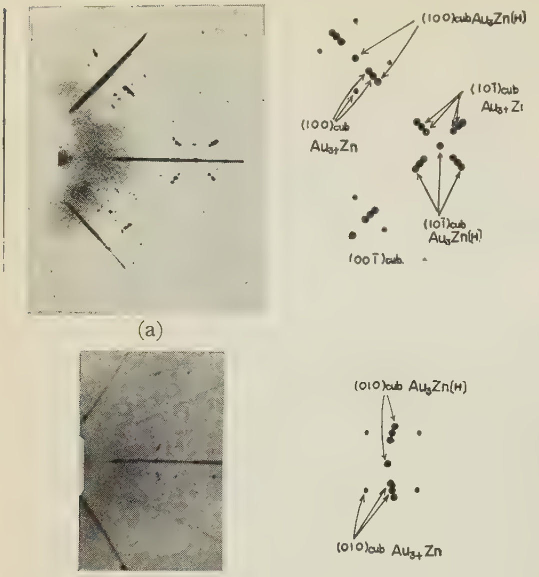

Photo. 5. X-ray oscillation patterns of $Au_{3+}Zn$+Au_3Zn[H] from the 20% Zn single crystal and their schematic diagrams. $[101]_{cub}$. is vertical and oscillation angles are 11° in (a) and 30° in (b). (a) $(100)_{cub}$. and $(10\bar{1})_{cub}$. superlattice spots. (b) $(010)_{cub}$. superlattice spots.

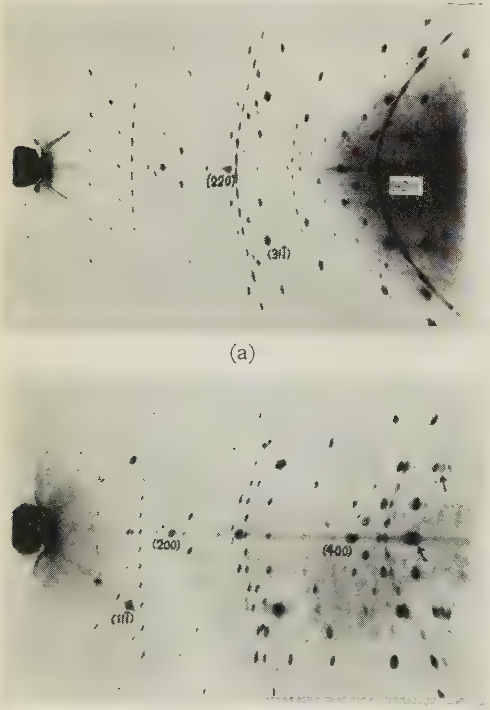

Photo. 6. X-ray oscillation patterns of (a) Au_3Zn [R_1] (23.5% Zn crystal) and (b) Au_3Zn[R_2] (26% Zn crystal). In both, the *c*-axis of the ordered crystal is vertical and oscillation angle is 80°. In (b), spots from a slight amount of Au_5Zn_3 are also observed. (indicated by arrows.)

b. X-ray Diffraction Study

X-ray diffraction study was carried out on single crystal samples. Since, unfortunately, single crystal with the composition range 30 to 40% Zn could by no means be prepared, the ordered phase Au_5Zn_3 was not studied by X-rays.

Photo. 4 shows the oscillation pattern of the crystal of 19% Zn, with the schematic diagram. Each superlattice reflexion splits in a characteristic group of spots, though some of groups

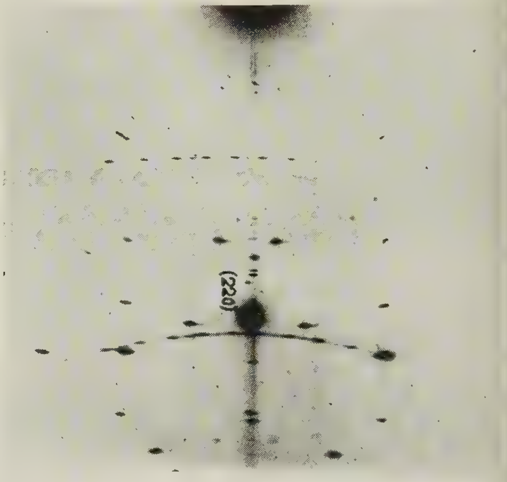

Photo. 7. X-ray oscillation pattern of Au_3Zn[R_1]+Au_3Zn[R_2] from the 24% Zn single crystal. In this crystal, the *c*-axis of the ordered crystal is distributed not only in vertical but also in horizontal orientation. Oscillation angle is 30°.

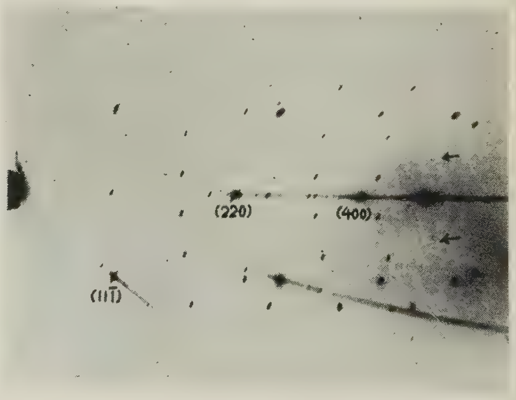

Photo. 8. X-ray oscillation pattern of Au_3Zn[H] from the quenched 26% Zn single crystal. The *c*-axis of the ordered crystal is vertical and oscillation angle is 60°. On account of incomplete quenching, transition into Au_3Zn[R] has slightly taken place. (Very weak spots indicated by arrows.)

Table I. Structure data obtained by electron diffraction.

Specimen No.	Phases	a_f* (kx)	c_f* (kx)	c_f/a_f	$\sqrt[3]{a_f{}^2c_f}$ (kx)	M_1**	M_3**
1	$Au_{3+}Zn$	4.05***	4.05	1.00	4.05	2.9	2.6
2	$Au_{3+}Zn$	4.04***	4.06	1.00_5	4.05	3.0	2.6
	Au_3Zn[H]	4.02	4.08	1.01_5	4.04		2.0
3	$Au_{3+}Zn$	4.02***	4.04	1.00_5	4.03	2.9	2.5
	Au_3Zn[H]	4.02	4.08	1.01_5	4.04		2.0
4	Au_3Zn[H]	4.01	4.12	1.02_7	4.05		2.0
5	Au_3Zn[H]	****	****	1.02_2			2.0
	$Au_3Zn[R_1]$	****	****	1.04_2			
6	$Au_3Zn[R_2]$	3.96	4.18	1.05_6	4.03		
	Au_5Zn_3	3.90	4.21	1.08	4.00		
7	$Au_3Zn[R_2]$	3.95	4.20	$1{\cdot}06_3$	4.03		
	Au_5Zn_3	3.89	4.23	1.08_7	4.00		

* Lattice constants of the fundamental face-centered cell.

** Period of out-of-step or half the reciprocal of "*Verwerfungsdichte*", measured in atomic distance. M_1 and M_3 correspond to the a_f and c_f directions, respectively.

*** It was not able to detect the fine structure of the diffraction spots due to an orthorhombic symmetry of $Au_{3+}Zn$.

**** Lattice constants could not be determined because of lack of the standard pattern.

ook incomplete. Here it must be noted that he present diffraction pattern can be accounted or by the only twofold superposition of the ingle crystal of $Au_{3+}Zn$ unlike the electron liffraction pattern. In Fig. 8 is shown the corresponding intensity distribution of $Au_{3+}Zn$. Examination of the diffraction pattern revealed he following fact: In Photo. 4, for example, he superlattice spots $(321)_{cub.}$ consist of four spots split crosswise, the vertical pair of spots being indexed as $(1+1/2M_1, 3, 2)$ and $(1-1/2M_1, 3, 2)$ and the horizontal pair as $(3+1/2M_1, -1, 2)$ and $(3-1/2M_1, -1, 2)$. In each of the pairs the asymmetry in intensity is recognized. Generally speaking, a spot at the higher diffraction angle side, $(h+1/2M_1, k, l)$ is always stronger than that at the lower angle side, $(h-1/2M_1, k, l)$ and this asymmetry becomes more conspicuous with increasing h. A similar

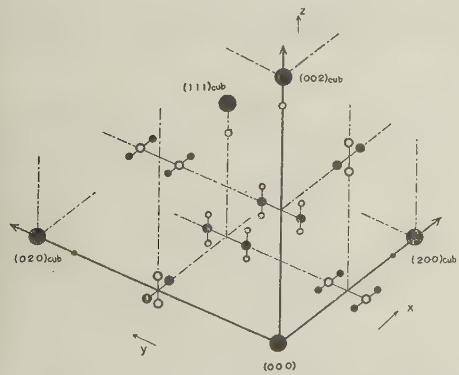

Fig. 8. Twofold superposition of the intensity distribution in the reciprocal lattice of $Au_{3+}Zn$. Solid and open circles represent the diffraction spots from the crystals with the following two orientations: in one, c-axis in y, a-axis in x direction, and in the other, c-axis in y, a-axis in z direction, respectively.

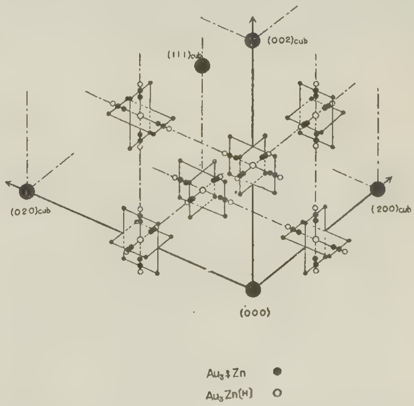

Fig. 9. Intensity distribution in the reciprocal lattice of the crystal, in which $Au_{3+}Zn$ and Au_3Zn[H] coexist. Solid and open circles represent the superlattice spots from $Au_{3+}Zn$ and Au_3Zn[H], respectively. The former corresponds to the sixfold, and the latter to the threefold superpositions.

asymmetry is also recognized in another set of split superlattice spots, (horizontal paris in $(310)_{cub}$. spots), which are generally indexed as $(h, k, l+1/2M_3)$ and $(h, k, l-1/2M_3)$. These two kinds of asymmetry were previously noticed by Wilkens and Schubert[3] in their powder diffraction pattern. In addition to the asymmetry in intensity, another fact was found in our diffraction pattern, that is, the appearance of the very weak satellite spots flanking the fundamental spots. The satellite spots are indicated as "s" in Photo. 4. They can be indexed as, for example, $(h+1/M_1, k, l)$ and $(h-1/M_1, k, l)$. Both the facts suggest a complicated atomic arrangemet in the structure of $Au_{3+}Zn$.

Coexistence of the two ordered phases $Au_{3+}Zn$ and Au_3Zn[H] is recognized in the diffraction patterns of the single crystal of 20% Zn shown in Photo. 5 (a) and (b). All spots may be classified into two groups as shown in Fig. 9, each group corresponding to the intensity distribution of the constituent ordered phase. In this case, the orientation of the ordered phase is equally probable in the directions of the three axes of the original cubic cell.

Photos. 6 (a) and (b) show the oscillation patterns of the single crystals of 23.5 and 26% Zn, respectively, and in both crystals the c-axis of the ordered crystal lies in the direction of the rotation axis, altough weak spots can be observed which are reflected from the crystals with the c-axis in the direction approximately perpendicular to the rotation axis. From Photo. 6 (a) the three-dimensional intensity distribution was directly obtained as shown in Fig. 10, and this corresponds to that of the tetragonal phase $Au_3Zn[R_1]$ with single orientation. Although the diffraction pattern in Photo. 6 (b) show apparently a fourfold symmetry about the c-axis, it seems to be reasonable to assume an orthorhombic symmetry for the structure, because spots at the higher diffraction angle, not seen in this pattern, show diffuse broadening which may be expected as a result of formation of an orthorhombic ordered crystal. Taking this fact into account, the intensity distribution is deduced from Photo. 6 (b) and is shown in Fig. 11, which accords with that calculated from the structure of Au_3Zn[R] of Wilkens and Schubert[4]. This structure was specified as $Au_3Zn[R_2]$. In spite of the resemblance between

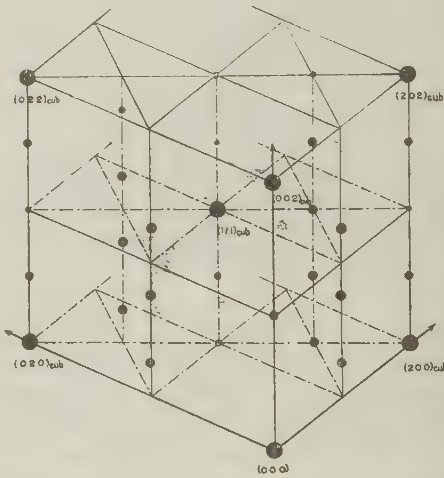

Fig. 11. Intensity distribution in the reciprocal lattice of $Au_3Zn[R_2]$ with single orientation.

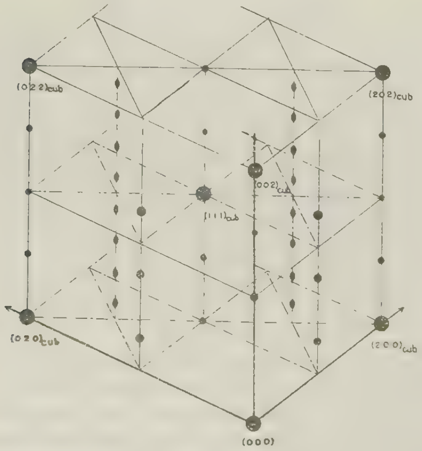

Fig. 10. Intensity distribution in the reciprocal lattice of $Au_3Zn[R_1]$ with single orientation.

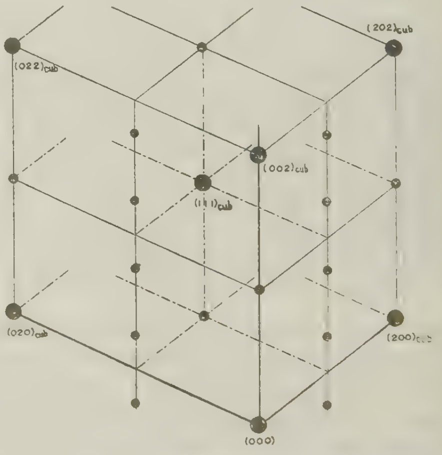

Fig. 12. Intensity distribution in the reciprocal lattice of the "true" single crystal of Au_3Zn[H].

Table II. Structure data obtained by X-ray diffraction.

omposition Zn %	Heat treatment	Phases	a_f (b_f) (KX)	c_f (KX)	$\sqrt[3]{a_f^2 c_f}$ (KX)	c_f/a_f (a_f/b_f)	M_1	M_3
19	330° C-100° C 25 days	$Au_{3+}Zn$	4.028 (4.017)	4.053	4.033	1.009* (1.003)	2.9	2.4
20	350° C- 80° C 62 days	$Au_{3+}Zn$ Au_3Zn[H]	4.025** 3.992	4.049 4.080	4.033 4.022	1.006 1.022	2.9	2.4 2.0
21	330° C- 80° C 62 days	$Au_{3+}Zn$ Au_3Zn[H]	***	***	***	1.01 1.02	2.9	2.4 2.0
23.5	330° C-100° C 41 days	$Au_3Zn[R_1]$	3.942	4.167	4.016	1.057		
24	350° C- 80° C 62 days	$Au_3Zn[R_1]$ $Au_3Zn[R_2]$	3.942	4.151	4.010	1.053		
26	330° C-100° C 38 days	$Au_3Zn[R_2]$ Au_5Zn_3	3.938 3.88	4.143 4.15	4.005 3.97	1.052 1.07		
26	290° C 6 hrs. quenched	Au_3Zn[H]						2.0
28	330° C-100° C 38 days	$Au_3Zn[R_2]$ Au_5Zn_3	3.938 3.89	4.147 4.15	4.007 3.97	1.053 1.07		
30	330° C-100° C 38 days	$Au_3Zn[R_2]$ Au_5Zn_3	***	***	***			
45	330° C-100° C 25 days	AuZn	3.142		3.142	1.000		

* In this case, the value of c_f/b_f is cited instead of that of c_f/a_f.

** It was not able to detect the fine structure of the diffraction spots due to an orthorhombic symmetry of $Au_{3+}Zn$.

*** Lattice constants could not be determined on account of imperfection of the crystal.

two structures, there is an evidence that ey coexist with a thermodynamic stability the intermediate composition, as is indicated Photo. 7. Spots on chains lining up vertically long alternately to either structure. In oto. 6 (b), faint spots belonging neither to $Au_3Zn[R_1]$ nor to $[R_2]$ are also observed. These spots can be accounted for by the model for Au_5Zn_3 proposed by Schubert *et al.*

Finally, Photo. 8 shows the oscillation pattern of the high temperature phase Au_3Zn[H], the specimen being quenched after annealing at 290°C for 6 hours. The pattern almost

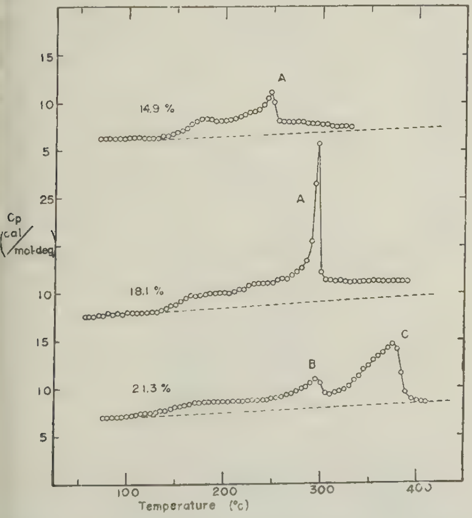

ig. 13. Specific heat versus temperature curves of 14.9, 18.1 and 21.3% Zn alloys.

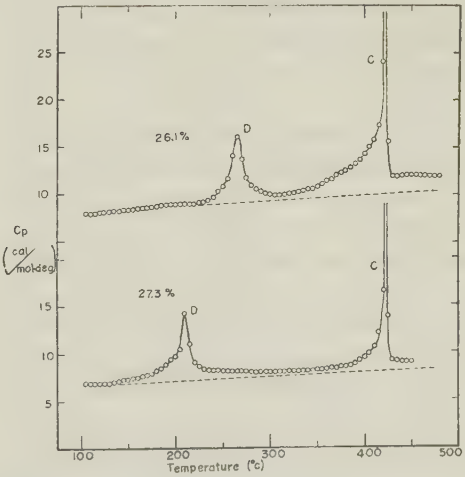

Fig. 14. Specific heat versus temperature curves of 26.1 and 27.3% Zn Alloys.

corresponds to a "true" single crystal of the ordered phase without superposition of orientations. The dimension of this crystal is estimated to be about 0.5 mm. The intensity distribution shown in Fig. 12 corresponds to a typical one-dimensional anti-phase domain structure.

In Table II are summarized the structure data from X-ray diffraction.

c. *Specific heat measurement*

Twelve samples were employed to the specific heat measurement, their composition ranging from 14.9 to 38.4% Zn. Some of the measured Cp-T curves are shown in Figs. 13, 14 and 15. It is possible to interpret these curves by taking account of the results of the diffraction study.

Disordering of the phase $Au_{3+}Zn$ is seen as an anomalous peak *A* in both 14.9 and 18.1% samples. The transition energy is rather small and a fair amount of heat absorption remains even after the transition temperature has been passed, indicating the persistence of short range order. A peak *B* in 21.3% (also in 19.6%), which appears at the same temperature, 300°C, for both samples, may be considered as due to the reaction, $Au_{3+}Zn + Au_3Zn[H] \rightarrow \alpha$(disordered solid solution)$+ Au_3Zn[H]$, *i.e.* the peritectoid reaction[*]. In 26.1 and 27.3%, a very sharp peak *C* can be seen with the latent heat, indicating that the order-disorder transition in Au_3Zn is of the first order. In 21.3%, peak *C* due to the same transition is recognized, though less marked. Persistence of the short range order is again recognized in this transition, and the tendency is the more prominent, the nearer the ideal composition Au_3Zn is approached. Existence of the two phase region, the ordered and disordered phases, could not clearly be detected in the measurements. There appears another smaller peak *D* in 26.1 and 27.3%, which is an evidence of the transition between $Au_3Zn[H]$ and $Au_3Zn[R]$. That a small energy (about 210 cal./mol. at 27.3%) is associated in this case is consistent with the result of the diffraction study that no marked atomic diffusion but only slight shift of atoms is accompanied with the present transition. In the Cp-T curves of 29.9, 35.3 and 38.4%, a common peak *E* at about 300°C is interpreted as due to the decomposition of Au_5Zn_3 into $Au_3Zn[H] + AuZn$ (CsCl-type ordered phase), which is another peritectoid reaction. The latent heat of the order of about 90−30 cal./mol. was observed at 410°C in 29.9 and 35.3% as a sharp peak *F*, which corresponds to the eutectoid reaction, $Au_3Zn[H] + AuZn \rightarrow \alpha + Au_3Zn$. A small kink *G* in 38.4% may be due to crossing over the solubility limit of AuZn.

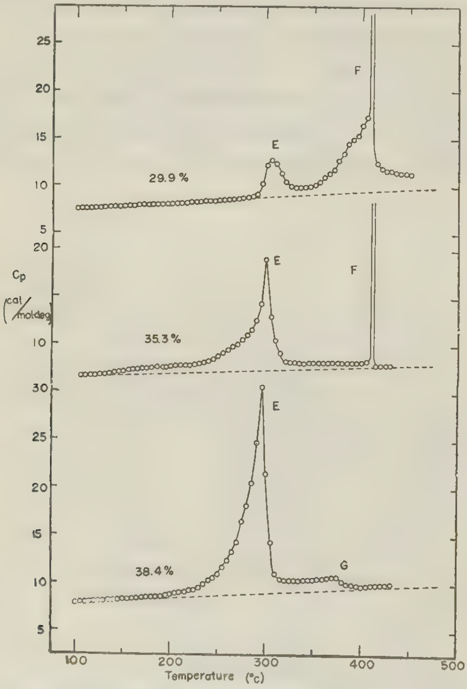

Fig. 15. Specific heat versus temperature curves of 29.9, 35.3 and 38.4% Zn alloys.

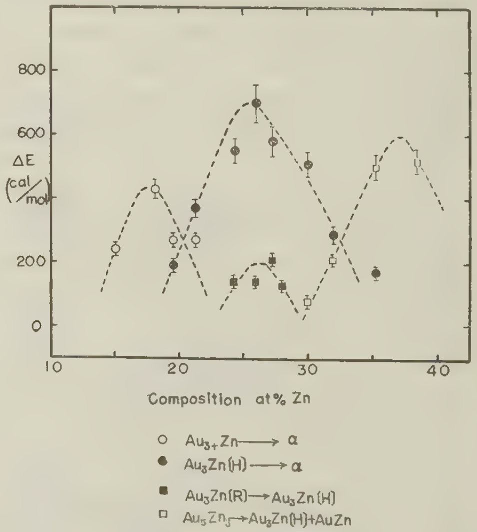

Fig. 16. Changes in configurational energy associated with various types of the transitions, plotted against the alloy composition.

[*] Latent heat was not observed, presumably because the reaction was too slow to be observed.

Energy changes associated with each type of the transitions are plotted against the alloy composition in Fig. 16.

§ 5. Interpretation and Discussion of the Experimental Results

On the basis of the information obtained from the diffraction study as well as from the calorimetric measurement, it is possible to construct the phase diagram of the gold-rich side of the gold-zinc alloy system, as is shown in Fig. 17, in which open circles represent the transition temperatures obtained from the present measurements, though these temperatures were obtained from the heating experiments only. It should be noted that the transition at about 140°C, which was observed by Soldau[6] in his resistometric measurement on samples with composition range 31 to 35% Zn, could not be detected in the present measurements. It seems, however, to be reasonable to assume the existence of the phase boundary at about 140°C shown by the dotted horizontal line in Fig. 17 in order to account consistently for the results of the diffraction study. The phase diagram thus constructed is roughly similar to that proposed by Wilkens and Schubert[4], but a phase boundary between $Au_3Zn[R_1]$ and $Au_3Zn[R_2]$ is added, and the phase relation at about 20% Zn and at 300°C is changed from the eutectoid to the peritectoid in the present diagram.

By the present diffraction study on single crystals, the proposed structures of the ordered phases in the gold-zinc system were substantially confirmed, though the phase Au_5Zn_3 was not fully investigated, because bulk single crystals of this phase were not available.

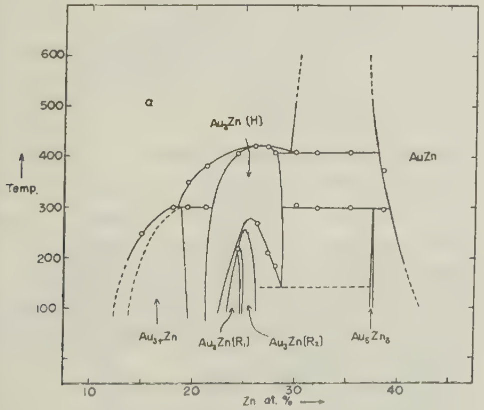

Fig. 17. The phase diagram of the Au-rich side of the Au-Zn alloy system concluded from the present work.

The asymmetry in intensity of the split superlattice spots and the appearance of satellite spots around the fundamental spots in the diffraction pattern of $Au_{3+}Zn$ cannot be derived from the simple model of the structure shown in Fig. 1. Presumably, the phenomena would be accounted for by assuming the presence of deviation in atomic arrangement from the simple model. Wilkens and Schubert[3] tried to explain the asymmetry of the spots by assuming the presence of the displacements of atoms at the anti-phase boundary. Another model is possible according to one of the present authors (H.I.), in which the non-stoichiometry in the alloy composition of $Au_{3+}Zn$ and the variation of lattice spacing with maximum spacing at the boundary are taken into account: in other words, the modulations of both the scattering factor and the lattice spacing in the structure are considered. By this model, it is possible to account for to some extent the intensity asymmetry of the split spots and the observed intensities of the satellite spots. The detailed discussion on this subject will be presented in the subsequent paper.

When the crystal is cooled down from the disordered state across the transition temperature of the order-disorder, one of the three axes of the disordered cubic cell may become the *c*-axis of the ordered cell, and this axis in the ordered state is generally expected to distribute equally along the directions of the three axes of the disordered cell. However, in some cases, as was shown in § **4**, the unequal orientation distribution of the ordered crystals can be observed. Examination of many of the diffraction patterns from the ordered phases in the present and other alloy systems revealed the following tendencies. In thin films, the manifoldly superposed diffraction patterns of single crystals of the ordered phase are very often observed, indicating that each single-crystalline region extends only over small volume. On the other hand, in bulk crystals, regions with single orientation of the ordered phase are so large that, in the case of $Au_3Zn[H]$, the diffraction pattern from the "true" single crystal can sometimes be obtained, as is shown in Photo. 8. In the nucleation of ordered phases such as Au_5Zn_3

Table III. Comparison between the theories and the data of calorimetry in various. ordered alloys of the A_3B type.

	Experiments					Theories		
	Au_3Zn	Au_3Cd	Ag_3Mg	Cu_3Pd	Cu_3Au	Bragg-Williams	Peierls	Cowley
at. % B atom	26.1	24.4	25.4	24.9	24.9			
T_c (°K)	696	685	666	738	664			
ΔE (cal./mol.)	700	680	560	510	530			
Q (cal./mol.)	145	110	150	—	122			
$RT_c/\Delta E$	1.98	2.00	2.37	2.87	2.49	2.19	2.38	2.68
$\Delta\Phi/R$	0.51	0.52	0.47	—	0.40	0.562	0.46	
RT_c/Q	9.6	12.3	9.1	—	10.8	10.07	3.69	6.39
Reference		(16)	(12)	(17)	(18)			
Valence electron concentration	1.25	1.25	1.25	0.75	1.00			
Period of out-of-step	2.0	2.0	1.8	4.4				

and CuAu II, in which the c/a ratio of the fundamental cell deviates appreciably from unity, the preferential distribution of the c-axis is observed even in the case of thin films.

One of the peculiar phenomena in the ordered phase with long period in the present system is the occurrence of the phase transition between Au_3Zn[H] and Au_3Zn[R]. Au_3Zn[H] is thermally stable only in a definite temperature range and transforms by cooling into the room temperature modification Au_3Zn[R]. Though a few experimental facts have been reported on the stability of the phase Au_3Zn[H] by previous workers[8),2)], they could not elucidate thoroughly the nature of the transition. Since, as was shown in § **4**, there occurs only slight shift of atoms in the transition $Au_3Zn[H] \rightleftarrows [R]$, *i.e.*, the transition is martensitic, it is conceived that any rapid cooling cannot quench the high temperature phase Au_3Zn[H] into room temperature. In the present experiment, however, the quenching was not always impossible. A specimen, which was annealed for a short time at the temperature range of [H], *e.g.* for 6 hrs. at 290°C, was incomplete in atomic ordering, but yet enough to give fairly intense superlattice spots. If this specimen was rapidly cooled by water, it was possible to suppress practically the atomic movement on passing the transition point of $[H] \rightleftarrows [R]$. The transition $A_3uZn[H] \rightarrow [R]$ may thus be dependent on the degree of order, and this supposition seems to be consistent with the empirical fact that if the composition of the alloy deviates from the ideal value (3:1), or the third element is added to Au_3Zn, *i.e.*, if the development of the perfect order is disturbed by changing the alloy composition, the temperature range of the stable existence of Au_3Zn[H] becomes lower.

In Table III are compared the data of calorimetry obtained from the present alloy and other ordered alloys of the A_3B type with the theoretical predictions, where ΔE, $\Delta\Phi$ and Q represent the configurational energy, entropy just above the transition temperature and the latent heat, respectively. All of the ordered alloys cited in the Table, except Cu_3Au, have the ordered structure with long period.

References

1) K. Schubert, B. Kiefer and M. Wilkens: Z. Naturforschg. **9a** (1954) 987.

2) K. Schubert, B. Kiefer, M. Wilkens and R. Haufler: Z. Metallkde. **46** (1955) 692.

3) M. Wilkens and K. Schubert: Z. Metallkde. **48** (1957) 550.

4) M. Wilkens and K. Schubert: Z. Metallkde. **49** (1958) 633.

5) H. Iwasaki: J. Phys. Soc. Japan **14** (1959) 1456.

6) P. Soldau: J. Inst. Metals **30** (1923) 351.

7) W. Köster: Z. Metallkde. **32** (1940) 151.

8) E. Raub, P. Walter and A. Engel: Z. Metallkde. **40** (1949) 401.

9) E. Feingold: Dissertation of the Temple University, 1959.

10) S. Nagasaki and Y. Takagi: J. Appl. Phys. Japan **17** (1948) 104.

11) E. A. Owen and E. A. O'Donnell Roberts: J.

Inst. Metals **71** (1945) 213.
12) K. Fujiwara, M. Hirabayashi, D. Watanabe and S. Ogawa: J. Phys. Soc. Japan **13** (1958) 167.
13) S. Ogawa and D. Watanabe: J. Phys. Soc. Japan **9** (1954) 475.
14) D. Watanabe and S. Ogawa: J. Phys. Soc. Japan **11** (1956) 226.
15) D. Watanabe: J. Phys. Soc. Japan **13** (1958) 535, **15** (1960) 1030.
16) M. Hirabayashi and S. Ogawa: To be published in Acta Meta.
17) F. W. Jones and C. Sykes: J. Inst. Metals **65** (1939) 419.
18) C. Sykes and F. W. Jones: Proc. Roy. Soc. A **157** (1936) 213.

JOURNAL OF THE PHYSICAL SOCIETY OF JAPAN, Vol. 15, No. 10, OCTOBER, 1960

On the Superconducting Ground State

By Ziro MIKURA
Research Institute for Iron, Steel and Other Metals,
Tohoku University, Sendai

(Received May 7, 1960)

The energy difference ΔE between the superconducting and normal states is recalculated as a function of half an energy gap μ_0, manipulating the unrenormalized Hamiltonian of Fröhlich by the method of Bogoliubov. The result is in disagreement with experiment, in contrast to Bogoliubov's one. Extension to higher orders of perturbation calculation does not remove the discrepancy. It is then shown that the agreement with experiment is recovered if the theory is reformulated on the principle of minimum energy in place of the principle of compensation of dangerous diagrams. The screened Coulomb repulsions between electrons do not change the qualitative aspect of the result. No detailed discussion is offered on the electromagnetic properties, but it is suggested that a successful theory in predicting a correct ΔE-μ_0 relation would not necessarily lead to a full understanding of them.

§ 1. Introduction

Recently, Bardeen, Cooper and Schrieffer[1] developed a new theory of superconductivity and successfully explained many of the properties of superconductors. They started from the renormalized Hamiltonian of Fröhlich[2]. It is not evident, however, that this simplified Hamiltonian reflects all the essential features of the original, unrenormalized Hamiltonian. Bogoliubov[3], on the other hand, advanced another, ingenious method of attacking the same problem, and stated that he could arrive at the same result as Bardeen et al. His method can be applied to the unrenormalized Hamiltonian, and this is a great advantage over the BCS method. It is to be noted, however, that Bogoliubov based his theory, without giving legitimate justification, on an unfamiliar principle of compensation of dangerous diagrams. He chose a canonical transformation on this principle, merely for the reason that the subsequent mathematical treatments could be made easiest thereby. However, it should be noted that in the problem of superconductivity physically different solutions are expected for different canonical transformations adopted, and that, in consequence, mathematical convenience cannot be a guiding principle to find the best transformation from the physical point of view.

The object of the present work is to show:

(1) The principle of compensation leads to a relation in disagreement with experiment between an energy gap $2\mu_0$ and the difference in energy, ΔE, between the superconducting and normal states.

(ii) If the principle of minimum energy is adopted instead of the principle of compensation, then a satisfactory agreement is obtained between theory and experiment as regards the above-mentioned relation.

(iii) The screened Coulomb repulsion does not affect these results.

No attempt is made to account for the electromagnetic properties, but it is suggested that a successful theory in predicting an energy gap $2\mu_0$ and its relation to the energy difference ΔE would not necessarily lead to a full understanding of them.

§ 2. Second-Order Perturbation Calculation of the Energy on the Principle of Compensation

According to Fröhlich[2] the Hamiltonian of a system of electrons interacting with phonon fields, with the Coulomb interactions omitted, is written as

$$H=\sum_{k,\sigma}(\varepsilon_k-\lambda)a_{k\sigma}^+a_{k\sigma}+\sum_{w}\omega(w)\left(b_w^+b_w+\frac{1}{2}\right)+H_{\text{int}}\ , \tag{2.1}$$

$$H_{\text{int}}=(ig/\sqrt{2V})\sum_{\left(\substack{k,k',\sigma\\ k'-k=w}\right)}\sqrt{\omega(w)}\,a_{k\sigma}^+a_{k'\sigma}b_w^+ +\text{c.c.}\ , \tag{2.2}$$

where we employ a nomenclature of common use. The electron-phonon coupling constant g is assumed to be small in the sense that

$$g^2N(0)<1\ , \tag{2.3}$$

where $N(0)$ is the number of Bloch states of one spin per unit energy per unit volume a the Fermi surface. The parameter λ should be determined by requiring the expectatio value of $\sum_{k\sigma}a_{k\sigma}^+a_{k\sigma}$ for the state under examination to be equal to N, number of electron in the system.

Following Bogoliubov we introduce a set of new Fermion operators defined by a canonica transformation

$$a_{k\uparrow}=u_k\alpha_{k0}+v_k\alpha_{-k1}^+\ ,\qquad a_{k\downarrow}=u_k\alpha_{k1}-v_k\alpha_{-k0}^+\ , \tag{2.5}$$

$$u_k^2+v_k^2=1;\qquad u_k=u_{-k}\ ,\qquad v_k=v_{-k}\ . \tag{2.6}$$

In terms of these variables the Hamiltonian is expressed in the form

$$H=U+H_0+H'\ ,\qquad H'=H_1+H_2+H_3\ , \tag{2.7}$$

$$U=\sum_k 2(\varepsilon_k-\lambda)v_k^2\ , \tag{2.8}$$

$$H_0=\sum_k(\varepsilon_k-\lambda)(u_k^2-v_k^2)(\alpha_{k0}^+\alpha_{k0}+\alpha_{k1}^+\alpha_{k1})+\sum_w\omega(w)\left(b_w^+b_w+\frac{1}{2}\right)\ , \tag{2.9}$$

$$H_1=\sum_k(\varepsilon_k-\lambda)u_kv_k(\alpha_{k0}^+\alpha_{-k1}^+ +\alpha_{-k1}\alpha_{k0})\ , \tag{2.10}$$

$$\begin{aligned}H_2=(ig/2V)\sum_{\left(\substack{k,k'\\ k'-\ \ =w}\right)}\sqrt{\omega(w)}\{&u_kv_{k'}(\alpha_{k0}^+\alpha_{-k'1}^+ +\alpha_{-k'0}^+\alpha_{k1}^+)\\ &+u_{k'}v_k(\alpha_{-k1}\alpha_{k'0}+\alpha_{k'1}\alpha_{-k0})\}b_w^+ +\text{c.c.}\ ,\end{aligned} \tag{2.11}$$

$$\begin{aligned}H_3=(ig/2V)\sum_{\left(\substack{k,k'\\ k'-k=w}\right)}\sqrt{\omega(w)}\{&u_ku_{k'}(\alpha_{k0}^+\alpha_{k'0}+\alpha_{k1}^+\alpha_{k'1})\\ &-v_kv_{k'}(\alpha_{-k'1}^+\alpha_{-k1}+\alpha_{-k'0}^+\alpha_{-k0})\}b_w^+ +\text{c.c.}\ .\end{aligned} \tag{2.12}$$

When the energy of the lowest eigenstate of this Hamiltonian is formally calculated according to the Goldstone-Hugenholtz perturbation theory[4],[5] taking H' as a perturbation, the result is expected to depend on the choice of the transformation. The specific choice

$$\left.\begin{aligned}&u_k=0\ ,\qquad v_k=1\ ,\qquad &\varepsilon_k<\zeta\ ,\\ &u_k=1\ ,\qquad v_k=0\ ,\qquad &\varepsilon_k>\zeta\ ,\end{aligned}\right\} \tag{2.13}$$

(ζ: energy of an electron on the Fermi surface) is assumed to correspond to the normal state. Following Bogoliubov, perturbation calculation of the energy is carried out in the present section to terms in second order in g. No dangerous energy denominators arise in the perturbation expansion of the normal state energy. For an arbitrary choice of u_k, v_k [satisfying the condition (2.6)], however, there are in general some diagrams that give rise to dangerous denominators. The principle of compensation of dangerous diagrams states that the superconducting ground state corresponds to the special choice of u_k, v_k for which the contributions from such dangerous diagrams disappear by mutual compensation. In order to secure this compensation, it is necessary and sufficient to guarantee the mutual compensation of those processes in which a pair of quasi-particles with equal and opposite momenta is created from the vacuum without phonon creation. A diagram corresponding to such a process will be called a pair-creating diagram. Actually, it suffices, to second order in g, that the H_1-process illustrated in Fig. 1 is compensated by the sum of the H_2H_3-processes in Fig. 2. In these and all other figures, solid lines directed to the left or to the right represent respectively $\boldsymbol{k}0$ or $\boldsymbol{k}1$ particles and broken lines are phonons. There are many other diagrams which are of second order in g and lead to the same process, as some typical examples are illustrated in Fig. 3. However, they are found to have little effect on the determination of u_k, v_k provided that the condition (2.3) is satisfied. This may be realized if one examines the contribution of these diagrams to the compensation equation by making use of the approximate solution for u_k, v_k to be obtained on requiring the mutual compensation of diagrams in Figs. 1 and 2. The compensation of those processes illustrated in Figs. 1 and 2 requires

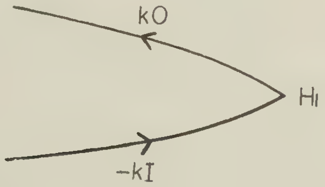

Fig. 1. Pair-creating diagram effected by H_1.

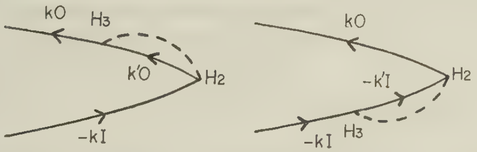

Fig. 2. Important pair-creating diagrams in second order in g.

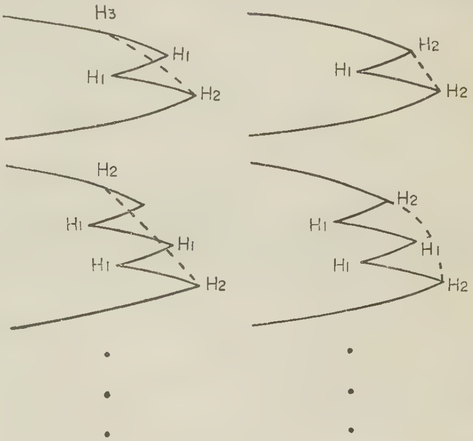

Fig. 3. Examples of unimportant pair-creating diagrams in second order in g. Particle lines may be directed either clockwise or counter-clockwise.

$$\alpha_{-k1}\alpha_{k0}H_1|0\rangle-\alpha_{-k1}\alpha_{k0}H_3H_0^{-1}H_2|0\rangle=0\ , \tag{2.14}$$

where $|0\rangle$ is the quasi-particle vacuum state. Making use of the explicit expressions (2.9)-(2.12) gives

$$\begin{aligned}2(\varepsilon_k-\lambda)u_kv_k-(u_k^2-v_k^2)\sum_{k'}\frac{g^2}{V}\frac{\omega_{kk'}u_{k'}v_{k'}}{\omega_{kk'}+E_k+E_{k'}}\\-u_kv_k\sum_{k'}\frac{g^2}{V}\frac{\omega_{kk'}(u_{k'}^2-v_{k'}^2)}{\omega_{kk'}+E_k+E_{k'}}=0\ ,\end{aligned} \tag{2.15}$$

where

$$E_k\equiv(\varepsilon_k-\lambda)(u_k^2-v_k^2);\qquad \omega_{kk'}\equiv\omega(\boldsymbol{k}-\boldsymbol{k}')\ . \tag{2.16}$$

E_k may be interpreted as the energy of a free quasi-particle. Setting

$$\overline{\varepsilon}_k=\varepsilon_k-\frac{1}{2}\sum_{k}\frac{g^2}{V}\frac{\omega_{\boldsymbol{kk}'}(u_{k'}^2-v_{k'}^2)}{\omega_{\boldsymbol{kk}'}+E_k+E_{k'}}\,, \tag{2.17}$$

$$\xi_k=\overline{\varepsilon}_k-\lambda\,, \tag{2.18}$$

$$c(k)=\sum_{k'}\frac{g^2}{V}\frac{\omega_{\boldsymbol{kk}'}u_{k'}v_{k'}}{\omega_{\boldsymbol{kk}'}+E_k+E_{k'}}\,, \tag{2.19}$$

we can transform (2.15) into the form

$$2\xi_k u_k v_k=(u_k^2-v_k^2)c(k)\ . \tag{2.20}$$

Besides the trivial solution (2.13), this has another solution:

$$u_k=\left[\frac{1}{2}\left(1+\frac{\xi_k}{\sqrt{c^2(k)+\xi_k^2}}\right)\right]^{1/2},\quad v_k=\left[\frac{1}{2}\left(1-\frac{\xi_k}{\sqrt{c^2(k)+\xi_k^2}}\right)\right]^{1/2}. \tag{2.21}$$

It follows easily that

$$u_k v_k=c(k)/2\sqrt{c^2(k)+\xi_k^2}\ ;\quad u_k^2-v_k^2=\xi_k/\sqrt{c^2(k)+\xi_k^2}\,. \tag{2.22}$$

Introducing (2.21) into (2.19) and solving the resulting equation

$$c(k)=\frac{1}{2}\sum_{k'}\frac{g^2}{V}\frac{\omega_{\boldsymbol{kk}'}}{\omega_{\boldsymbol{kk}'}+E_k+E_{k'}}\frac{c(k')}{\sqrt{c^2(k')+\xi_{k'}}}\,, \tag{2.23}$$

we can determine $c(k)$. Going over from summation to integration we have an integral equation for $c(k)$

$$c(k)=\frac{1}{2(2\pi)^3}\int g^2\frac{\omega_{\boldsymbol{kk}'}}{\omega_{\boldsymbol{kk}'}+E_k+E_{k'}}\frac{c(k')}{\sqrt{c^2(k')+\xi_{k'}^2}}d\boldsymbol{k}'\ . \tag{2.24}$$

We shall now attempt to solve this equation approximately. The following facts are taken into consideration: (i) $c(k)$ need not be exactly determined for large $|\xi_k|$ because the contribution of dangerous diagrams to the energy from this region is negligible, and (ii) the main contribution to the integral arises from the region $|\boldsymbol{k}'|\simeq k_0$ (k_0: wave number corresponding to $\xi_k=0$). It is to be noted that we may put, in a good approximation, for $g^2N(0)<1$

$$\lambda=\zeta;\quad k_0=k_F\ (k_F\text{: wave number corresponding to }\zeta)\ . \tag{2.25}$$

We shall first carry out the integration with respect to angle variables. We take approximately $|\boldsymbol{k}|$, $|\boldsymbol{k}'|\simeq k_0$, and, in consequence, assume

$$\omega_{\boldsymbol{kk}'}=\begin{cases}\hbar s_0 k_0\sqrt{2(1-t)}\,, & -t_0<t<1\,,\\ 0\,, & -1<t<-t_0\,,\end{cases} \tag{2.26}$$

s_0 being the velocity of sound and t the cosine of the angle between $\boldsymbol{k}$ and $\boldsymbol{k}'$. For $t=-t_0$ we have the maximum value of $\omega_{\boldsymbol{kk}'}$, which may be put equal to the phonon quantum at the Debye frequency, giving

$$\hbar s_0 k_0\sqrt{2(1+t_0)}=\omega_D=k\Theta_D\ . \tag{2.27}$$

Using (2.26) we can easily carry out the integrations with respect to angle variables in (2.24). The result is found to be represented by

$$c(k)=\frac{1}{(2\pi)^2}\int g^2\frac{\omega}{\omega+E_k+E_{k'}}\frac{c(k')}{\sqrt{c^2(k')+\xi_{k'}^2}}k'^2dk' \tag{2.28}$$

in a sufficient approximation, employing an average phonon energy

$$\omega=(3/5)k\Theta_D\ . \tag{2.29}$$

The maximum error arising from this averaging procedure is about one percent in the important region $E_k+E_{k'}<2\omega$. The procedure is equivalent to replacing, from the outset, $\omega_{kk'}$ by ω in (2.23). To solve the integral equation (2.28) one further approximation is made that E_k' in the denominator is replaced by $\bar{E}_{k'}$ defined by

$$\bar{E}_{k'}=(\bar{\varepsilon}_{k'}-\lambda)(u_{k'}^2-v_{k'}^2)=\xi_{k'}^2/\sqrt{c^2(k')+\xi_{k'}^2}\ . \tag{2.30}$$

Besides a normal state solution $c(k)=0$, we find a nontrivial solution expressed in the following approximate form*

$$c(k)=c_0/(1+E_k/\omega)\ , \tag{2.31}$$

where c_0 is the value of $c(k)$ at $E_k=0$ and can be found by solving

$$1=\frac{1}{2}\int g^2\frac{\omega}{\omega+\xi_{k'}^2/\sqrt{c^2(k')+\xi_{k'}^2}}\,\frac{N(\xi_{k'})}{\sqrt{c^2(k')+\xi_{k'}^2}}d\xi_{k'}\ , \tag{2.32}$$

$N(\xi_{k'})$ being a kind of density of states defined by $N(\xi_{k'})=k'^2(2\pi^2d\bar{\varepsilon}_{k'}/dk')^{-1}$. Since the important contribution to the above integral arises only from a region $|\xi_{k'}|\ll\lambda$, it is permissible to replace $N(\xi_{k'})$ by the value at $\xi_{k'}=0$, which may be approximately identified with the free electron value $N(0)$. Assuming that $c_0\ll\omega$, one is able to carry out the integration in (2.32) to get

$$1=Ax-A \tag{2.33}$$

with the abbreviations $A\equiv g^2N(0)$; $x\equiv\ln(2\omega/c_0)$. From (2.33)

$$c_0=2\omega\exp[-A^{-1}-1]\ . \tag{2.34}$$

The relation (2.33) is the same one as that obtained by Bardeen et al.[1] and Bogoliubov[2] except for a correction term of order A. The importance of the exact derivation to this order becomes apparent in § 5. Combination of (2.21), (2.31) and (2.34) fully determines the transformation fulfilling the principle of compensation to second order in g.

We are now able to proceed to the calculation of the energy of the "superconducting ground state", in Bogoliubov's sense, relative to the normal state energy. In second order perturbation theory it reads

$$\Delta E_c^{(2)}=D(U-\langle 0|H_2H_0^{-1}H_2|0\rangle)\ , \tag{2.35}$$

where D means the subtraction of the normal state value corresponding to (2.13). We have omitted not only the contributions from the dangerous ground state diagrams related to the pair-creating ones in Figs. 1 and 2, but also the contributions from those related to the diagrams in Fig. 3 and like ones, in the same spirit as stated before in discussing the compensation condition. As has been shown by Bogoliubov, Eq. (2.35) gives

$$\Delta E_c^{(2)}=D\sum_k 2\xi_k v_k^2-\sum_{k,k'}\frac{g^2}{V}\frac{\omega_{kk'}u_kv_ku_{k'}v_{k'}}{\omega_{kk'}+E_k+E_k'}-D\sum_{k,k'}\frac{g^2}{V}\frac{\omega_{kk'}u_k^2v_{k'}^2}{\omega_{kk'}+E_k+E_{k'}}\ ,$$

where $\varepsilon_k-\lambda$ has been replaced by ξ_k $(\equiv\bar{\varepsilon}_k-\lambda)$ in the first term without loss of accuracy. With (2.19) this yields

$$\Delta E_c^{(2)}=D\sum_k 2\xi_k v_k^2-\sum_k c(k)u_kv_k-D\sum_{k,k'}\frac{g^2}{V}\frac{\omega_{kk'}u_k^2v_{k'}^2}{\omega_{kk'}+E_k+E_{k'}}\ . \tag{2.36}$$

With (2.21) the first two members on the right side gives

---

* In all applications of this equations E_k may be replaced by $\bar{E}_k$ defined by a similar equation as (2.30). Moreover, c_0 may be used in place of $c(k)$ in the expression of $\bar{E}_k$.

$$-(D\sum_{k}\xi_k^2/\sqrt{c^2(k)+\xi_k^2}+(1/2)\sum_{k}c^2(k)/\sqrt{c^2(k)+\xi_k^2})\,. \tag{2.37}$$

In going over to this we have neglected $D\sum_k(1/2)\xi_k$ which is clearly very small. To evaluate (2.37), we divide the k-space into two parts, the inner and outer regions of a spherical shell $|\xi_k|<P$ with P appropriately chosen so as to satisfy the condition $c_0 \ll P \ll \omega$. (Note that we are assuming that $c_0 \ll \omega$.) Putting $c(k)=c_0$ without loss of accuracy for $|\xi_k|<P$, we have

$$\begin{aligned}
&-(D\sum_{\substack{k\\(|\xi_k|<P)}}\xi_k^2/\sqrt{c^2(k)+\xi_k^2}+(1/2)\sum_{\substack{k\\(|\xi_k|<P)}}c^2(k)/\sqrt{c^2(k)+\xi_k^2})\\
&\quad=-N(0)V\{P\sqrt{c_0^2+P^2}-c_0^2\ln(2P/c_0)-P^2+c_0^2\ln(2P/c_0)\}\\
&\quad=-(1/2)N(0)c_0^2\,.
\end{aligned}\tag{2.38}$$

For the outer region we have

$$\begin{aligned}
&\lim_{\Lambda\to\infty}|D\sum_{\substack{k\\(P<|\xi_k|<\Lambda)}}\xi_k^2/\sqrt{c^2(k)+\xi_k^2}+(1/2)\sum_{\substack{k\\(P<|\xi_k|<\Lambda)}}c^2(k)/\sqrt{c^2(k)+\xi_k^2}|\\
&\quad<\lim_{\Lambda\to\infty}|\sum\xi_k^2/\sqrt{c_0^2+\xi_k^2}+(1/2)\sum c_0^2/\sqrt{c_0^2+\xi_k^2}-\sum|\xi_k||\\
&\quad=(1/8)N(0)c_0^4/P^2\,,
\end{aligned}\tag{2.39}$$

which is neglected compared with the contribution from the first region.

We shall next evaluate the last term in (2.36). Replacing E_k, $E_{k'}$ by $\bar{E}_k$, $\bar{E}_{k'}$ without loss of accuracy and making use of the same procedure of angle integrations used for (2.24), we have

$$-D\sum_{k,k'}\frac{g^2}{V}\frac{\omega_{kk'}u_k^2v_{k'}^2}{\omega_{kk'}+E_k+E_{k'}}=-\lim_{\Lambda\to\infty}AN(0)VD\int_{-\lambda}^{\Lambda}\int_{-\lambda}^{\Lambda}\frac{(\omega/4)d\xi_{k'}d\xi_k}{\omega+\xi_k^2/\sqrt{c^2(k)+\xi_k^2}+\xi_{k'}^2/\sqrt{c^2(k')+\xi_{k'}^2}}\,.$$

Setting $\eta=\xi_k/c_0$, $\eta'=\xi_{k'}/c_0$, $\delta=\omega/c_0$, $L=\Lambda/c_0$, $K=\eta^2/\delta\sqrt{1+\eta^2}$ and $\delta_K=(1+K)\delta$ and extending the integration to $-\infty$, we get

$$-\lim_{L\to\infty}AN(0)VD\int_0^L\int_0^L\frac{c_0^2d\eta'd\eta}{1+\eta^2/\delta\sqrt{(1+K)^{-2}+\eta^2}+\eta'^2/\delta\sqrt{(1+K')^{-2}+\eta'^2}}\,. \tag{2.40}$$

Integrating first with respect to η' with due regard to the inequality $1\ll\delta\ll L$, we obtain from (2.40)*

$$-\lim_{L\to\infty}AN(0)VD\int_0^L c_0^2\left\{\delta\ln(L/\delta)+\frac{\ln(2\delta)}{2\delta(1+K)^2}-\delta\ln(1+K)+\delta\ln\left(1+\frac{\delta_K}{L}\right)\right\}d\eta\,. \tag{2.41}$$

No contribution arises from the first term in the brackets, because the quantity after the symbol D becomes independent of c_0 for this term. To evaluate the remaining terms use is made of

$$\int_0^L\frac{d\eta}{(1+K)^2}=\delta+\delta^{-1}\ln(2\delta)\,,$$

$$\int_0^L\ln(1+K)d\eta=(L+\delta)\ln(L/\delta)-L+\delta-(2\delta)^{-1}\ln(2\delta)\,,$$

$$\int_0^L\ln(1+\delta_k/L)d\eta=L\ln(1+\delta/L)+L\times[\text{func. of } L/(L+\delta)]-(L+\delta)^{-1}\ln(2L)\,,$$

which are valid for δ, $L\gg1$. The final result is then

---

* The η'-integration is carried out by dividing it into three parts, $(0,\delta)$, (δ,δ_k) and (δ_k, L) and expanding the integrand in powers of η'/δ and η'/δ_k in the first region, in powers of δ/η' and η'/δ_k and in powers of δ/η' and δ_k/η', respectively, in the second and third regions.

$$-\boldsymbol{D}\sum_{k,k'}\frac{g^2}{V}\frac{\omega_{kk'}u_k^2v_{k'}^2}{\omega_{kk'}+E_k+E_{k'}}=-AN(0)Vc_0x\,. \tag{2.42}$$

This is exact in the approximation ignoring terms of relative order x^{-1}.

Combining (2.38) and (2.42) gives

$$\Delta E_c^{(2)}/V=-(1/2)N(0)c_0^2-AxN(0)c_0^2\,. \tag{2.43}$$

The right-hand side with the second term omitted is just that was found by Bogoliubov. It is felt that he thought the last term of (2.36) to be negligibly small. We find the contrary; if the relation (2.33) is substituted into (2.43), it becomes

$$\Delta E_c^{(2)}=-(3/2)N(0)c_0^2\,. \tag{2.44}$$

This is three times as large as the value obtained by Bogoliubov.

We shall next investigate the energy $\mu(\boldsymbol{k})$ for an elementary excitation of momentum $\boldsymbol{k}$. In second-order perturbation calculation

$$\mu(\boldsymbol{k})=E_k-\langle \boldsymbol{k}s|H'(H_0-E_k)^{-1}H'|\boldsymbol{k}s\rangle\,, \tag{2.45}$$

where $|\boldsymbol{k}s\rangle=\alpha_{ks}^+|0\rangle$, $s=0,\ 1$. Following Bogoliubov it is easily shown that the minimum excitation energy μ_0 occurs at $E_k=0$ and is given by

$$\mu_0=2u_kv_k\sum_{k'}\frac{g^2}{V}\frac{\omega_{kk'}u_{k'}v_{k'}}{\omega_{kk'}+E_{k'}}=c_0\,. \tag{2.46}$$

Since a pair of quasi-particles should be excited in real excitation phenomena, μ_0 is to be compared with half an observed energy gap.

Summarizing this section, we can say that, if one calculates the difference in energy between the superconducting and normal states in second-order perturbation theory based on the principle of compensation, the result is expressed, in terms of half an energy gap μ_0, by

$$\Delta E_c^{(2)}=-(3/2)N(0)\mu_0^2\,. \tag{2.47}$$

The earlier result due to Bogoliubov

$$\Delta E_c^{(2)}=-(1/2)N(0)\mu_0^2 \tag{2.48}$$

seems to have been derived by incorrectly disregarding the contribution of the last term in (2.36).

§3. Comparison with Experimental Data

It is interesting to see what relation exists between the energy gap and the difference in energy between the superconducting and normal states for real superconductors. We know a relation $\Delta E/V=-H_0^2/8\pi$ (H_0: critical field at absolute zero) thermodynamically, and an expression $\gamma_n=(2/3)\pi^2k^2N(0)$ for the normal specific heat constant (per unit volume) of electrons in a metal according to the Sommerfeld theory. It is then easy to derive the following formula

$$\Delta E/V=-\kappa N(0)\mu_0^2 \tag{3.1}$$

with a dimensionaless quantity

$$\kappa=(\pi/3)(H_0^3/n^2\gamma_nT_c^2)\,, \tag{3·2}$$

where n is the energy gap measured in the unit of kT_c.

The theory in the preceding section predicts that the value of κ calculated from experimental data on H_0, T_c, γ_n and n should be the same constant for all superconductors and be equal to 3/2. In Table I the calculated values of κ are listed for some superconductors together with the observed data employed to derive them. Note that the semi-empirical value of κ is nearly equal to 1/2 for all these cases. This fact suggests that the relation (3.1) holds for all superconductors with $\kappa=1/2$, and that there must be something wrong in the theoretical treatments of the preceding section where κ is found to be 3/2. Despite the agreement with experiment, Bogoliubov's derivation of (2.48) cannot be acceptable for the very reason that it was only possible by missing an important contri-

Table I. Semi-empirical values of κ, ratio between $-\Delta E/V$ and $N(0)\mu_0^2$, together with various experimental data used to derive them.

Metal	H_0 gauss	T_c °K	γ_n (erg/cm^3 deg^2)$\times 10^{-3}$	$n \equiv 2\mu_0/\kappa T_c$	κ
Al	106	1.171	1.35a)	3.25d)	0.60
Sn	305	3.72	1.03b)	3.4d)	0.59
Pb	805	7.22	1.72c)	4.1e)	0.45

a) Phillips[6], b) Corak and Satterwaite[7], c) Horowitz et al.[8], d) Biondi and Garfunkel[9] e) Richards and Tinkham[10].

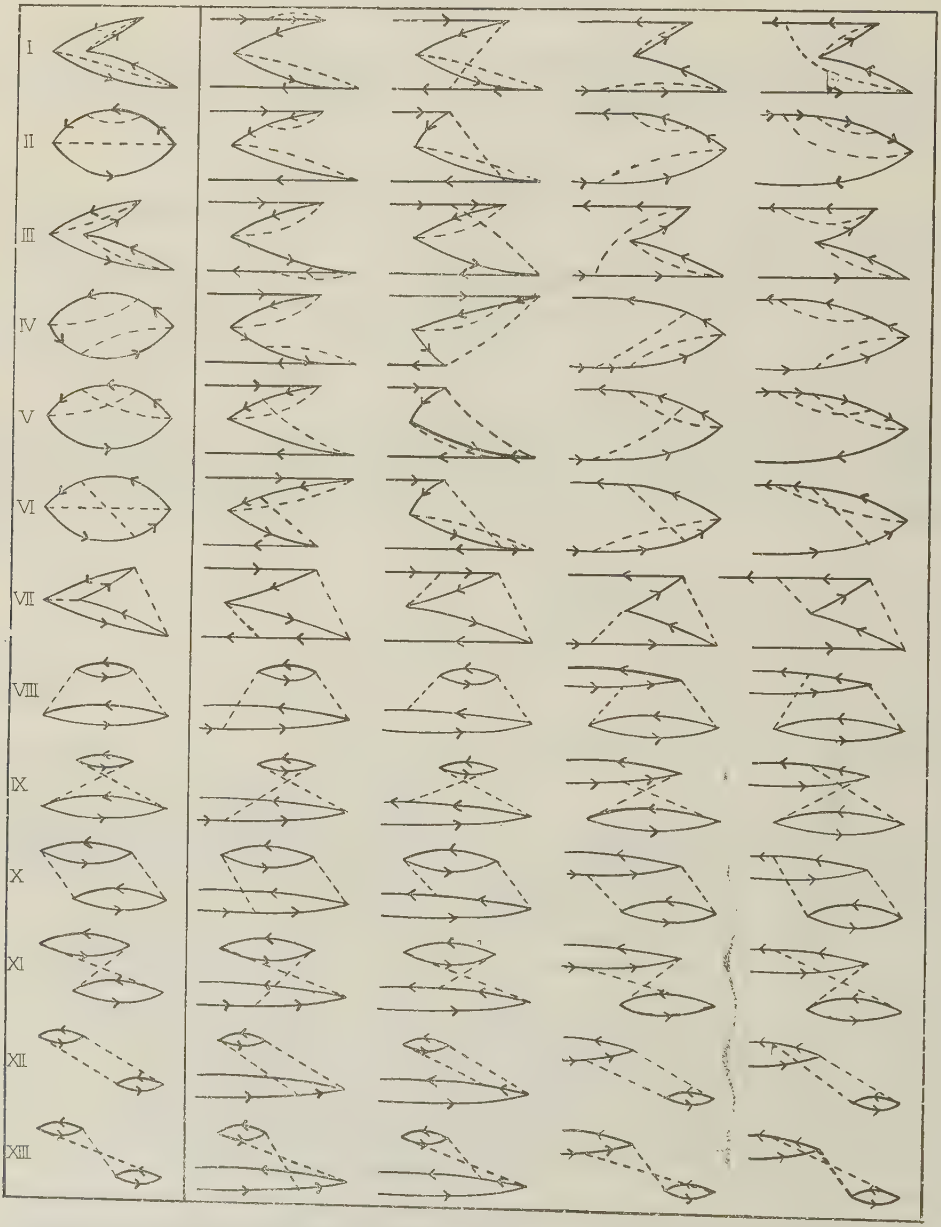

Fig. 4. Important ground state diagrams in fourth order in g (at the left end) and important pair-creating diagrams in the same order constructed therefrom. To each diagram in groups I-VII there is a conjugate diagram not shown in the figure.

bution to the energy.

§ 4. Fourth-Order Perturbation Calculation Based on the Principle of Compensation

First of all, we note that the principal contribution of the second order term in the perturbation expansion of ΔE in § 2 was exactly cancelled by the principal contribution of the zeroth order term. This is easily seen if one evaluates separately the two terms in the parentheses of (2.37) substituting (2.31) for $c(k)$. As a result of this cancellation the main part of ΔE consists of the next order contributions of the zeroth and second order terms in the perturbation expansion*. In view of these situations we are led to study the contribution to ΔE from the diagrams of fourth order in g, which may possibly be of the same order of magnitude as the next lowest order contribution from the second order diagrams. In this section we shall see that this really happens. The fact invalidates in principle the calculation of ΔE in second-order perturbation theory, but it will also be shown that the consideration of fourth order diagrams does not change the final relation between the difference in energy, ΔE, and half an energy gap μ_0 and, in consequence, cannot answer the purpose to avoid the discrepancy between theory and experiment discussed in the preceding section.

We have stated that the fourth order term in the perturbation expansion for ΔE is an order of magnitude smaller than the second order term, and, as expected, we find a similar situation for any two successive order terms except for the zeroth and second order terms. We are thus justified to restrict ourselves to the calculation of ΔE to fourth order in g.

Before proceeding to the calculation of the energy, it is necessary to extend the principle of compensation so as to eliminate the dangerous diagrams to fourth order in g. We need first of all to construct all important pair-creating diagrams of fourth order in g contributing to the compensation equation. They are conveniently constructed from the important, connected ground state diagrams of fourth order shown at the left end of Fig. 4. Note that there is a conjugate diagram with all arrows reversed to each of the ground state diagrams labelled as I–VII. To every ground state diagram belong four pair-creating diagrams, which are shown in the same figure and whose construction from the original ground state diagram will be explained immediately. Note that every ground state diagram has two or three points where particles are annihilated. If we modify a ground state diagram at one of these points in such a manner as illustrated in Fig. 5, then we have one pair-creating diagram for each case**. As easily observed, all important pair-creating diagrams of fourth order in g can be constructed in this way from the ground state diagrams in Fig. 4 without duplication. We disregard the unimportant pair-creating diagrams in fourth order in g which involve H_1-processes. This conforms to the earlier neglect of the second order diagrams such as shown in Fig. 3.

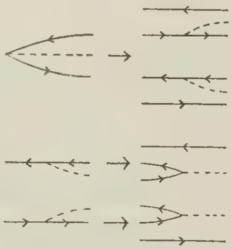

Fig. 5. Procedures in constructing pair-creating diagrams from a ground state diagram.

We have now to investigate the contribution of the pair-creating diagrams in Fig. 4 to the last term in the compensation equation

$$\alpha_{-k1}\alpha_{-k0}H_1|0\rangle-\alpha_{-k1}\alpha_{k0}H_3H_0^{-1}H_2|0\rangle-\alpha_{-k1}\alpha_{k0}H'H_0^{-1}H'H_0^{-1}H'H_0^{-1}H'|0\rangle_{\text{connected}}=0\,, \qquad (4.1)$$

which is the extension of (2.14). Making use of the explicit expressions for H_2 and H_3, we find that the contributions of all the diagrams belonging to one and the same group are always possible to be summed up into the form

$$-(u_k^2-v_k^2)\Phi_i(k)-u_kv_k\Psi_i(k)\,, \qquad i=\text{I}, \cdots, \text{XIII}, \quad (4.2)$$

---

* Note that we are assuming an inequality $c_0 \ll \omega \ll \lambda$.

** In Fig. 5 we illustrate only the cases where a phonon is annihilated, in order to save space.

where $\Phi_i(k)$ and $\Psi_i(k)$ are approximately constant for $E_k<\omega$ and approach zero with E_k increasing beyond ω. Since the expressions both for $\Phi_i(k)$ and $\Psi_i(k)$ are complicated and their evaluation is tedious, we omit details of them and give only a brief account of the evaluation of $\Phi_i(k)$ in the Appendix. An important remark should be made that all $\Phi_i(k)$'s vanish for the normal state solution (2.13). This is evident at first sight for the diagrams labelled as I-IV and VIII–XIII, and can be seen after some reduction for those labelled as V–VII. The compensation condition to fourth order in g reads now

$$2(\varepsilon_k-\lambda)u_kv_k-(u_k^2-v_k^2)\left\{\sum_{k'}\frac{g^2}{V}\frac{\omega_{kk'}u_{k'}v_{k'}}{\omega_{kk'}+E_k+E_{k'}}+\sum_i\Phi_i(k)\right\}$$
$$-u_kv_k\left\{\sum_{k'}\frac{g^2}{V}\frac{\omega_{kk'}(u_{k'}^2-v_{k'}^2)}{\omega_{kk'}+E_k+E_{k'}}+\sum_i\Psi_i(k)\right\}=0\,. \qquad (4.3)$$

If we put

$$\overline{\varepsilon_k}=\varepsilon_k-\sum_{k'}\frac{g^2}{V}\frac{\omega_{kk'}(u_{k'}^2-v_{k'}^2)}{\omega_{kk'}+E_k+E_{k'}}-\sum_i\Psi_i(k);\qquad \xi_k=\overline{\varepsilon}_k-\lambda\,,$$
$$c(k)=\sum_{k'}\frac{g^2}{V}\frac{\omega_{kk'}u_{k'}v_{k'}}{\omega_{kk'}+E_k+E_{k'}}+\sum_i\Phi_i(k)\,, \qquad (4.4)$$

then we have from (4.3)

$$2\xi_ku_kv_k=(u_k^2-u_k^2)c(k)\,, \qquad (4.5)$$

which is formally identical with (2.20). The nontrival solution is again

$$u_k=\left[\frac{1}{2}\left(1+\frac{\xi_k}{\sqrt{c^2(k)+\xi_k^2}}\right)\right]^{1/2},\qquad v_k=\left[\frac{1}{2}\left(1-\frac{\xi_k}{\sqrt{c^2(k)+\xi_k^2}}\right)\right]^{1/2}, \qquad (4.6)$$

which keeps both relations in (2.22). From the inspection of the expressions for $\Phi_i(k)$, we see that every $\Phi_i(k)$ can be assumed in the form $c_i/(1+E_k/\omega)$, c_i=const., taking account of the fact that the exact E_k-dependence is not essential for $E_k/\omega\lesssim 1$. (See the Appendix.) We can then solve Eq. (4.4) approximately by assuming $c(k)$ in the same form as in § 2, namely,

$$c(k)=c_0/(1+E_k/\omega)\,. \qquad (4.7)$$

Before proceeding to the determination of c_0, we shall study the energy of the "superconducting ground state" measured relative to that of the normal state, and the energy gap, both as a function of c_0. The former is given by

$$\varDelta E_c^{(4)}=\boldsymbol{D}(U-\langle 0|H_2H_0^{-1}H_2|0\rangle-\langle 0|H'H_0^{-1}H'H_0^{-1}H'H_0^{-1}H'|0\rangle_{\text{connected}})\,. \qquad (4.8)$$

The ground state diagrams of importance contributing to the last term in the parentheses are just those shown at the left end of Fig. 4. Careful examination of the contribution from each diagram reveals that it is expressed, to a reasonable approximation, in the form $-\sum_k u_kv_k\Phi_i(k)$, using the same $\Phi_i(k)$ as in (4.3) and (4.4). Application of (4.4) to the following expanded form of (4.8)

$$\varDelta E_c^{(4)}=\boldsymbol{D}\sum_k 2\xi_kv_k^2-\sum_{k,k}\frac{g^2}{V}\frac{\omega_{kk'}u_kv_ku_{k'}v_{k'}}{\omega_{kk'}+E_k+E_{k'}}$$
$$-\boldsymbol{D}\sum_{k,k'}\frac{g^2}{V}\frac{\omega_{kk'}u_k^2v_{k'}^2}{\omega_{kk'}+E_k+E_{k'}}-\sum_k u_kv_k\sum_i\Phi_i(k) \qquad (4.9)$$

gives

$$\varDelta E_c^{(4)}=\boldsymbol{D}\sum_k 2\xi_kv_k^2-\sum_k c(k)u_kv_k-\boldsymbol{D}\sum_{k,k'}\frac{g^2}{V}\frac{\omega_{kk'}u_k^2v_{k'}^2}{\omega_{kk'}+E_k+E_{k'}}\,. \qquad (4.10)$$

This is the same equation as that obtained earlier in the second order calculation [Eq. (2.36)].

If one replaces again the density of states $N(\xi_{k'})$ at $\xi_{k'}=0$ by the free electron value $N(0)$ and assumes $c(k)\ll\omega$, then the right-hand side of (4.10) can be manipulated in the same way as before with the result

$$\Delta E_0^{(4)}=-(1/2)N(0)c_0^2-AxN(0)c_0^2\,,\qquad [x\equiv\ln(2\omega/c_0)],\quad(4.11)$$

which is, of course, identical to (2.43) though a different value ought to be substituted for c_0. As described in the Appendix, the last term in (4.4) arising from the fourth order diagrams is of order $c(k)A^2x$ and, in consequence, is smaller than the second order contribution by factor A. This means that Eq. (4.4) must lead to the same relation (2.33), which was derived from (2.19), except for the correction term of order A. We have then $Ax=1+O(A)$. With this Eq. (4.11) gives

$$\Delta E_0^{(4)}=-(3/2)N(0)c_0^2\,,\qquad(4.12)$$

which is identical with the result of second order calculation, (2.44).

We shall now calculate half an energy gap μ_0. As before it is identified with the minimum energy required to excite a single quasi-particle from the vacuum. Considering, for example, an excitation of a $\boldsymbol{k}0$ particle, we have

$$\mu_0=\langle \boldsymbol{k}0|H'H_0^{-1}H'|\boldsymbol{k}0\rangle+\langle \boldsymbol{k}0|H'H_0^{-1}H'H_0^{-1}H'H_0^{-1}H'|'\boldsymbol{k}0\rangle_{\text{connected}}\,,\qquad(4.13)$$

where $|\quad|'$ means that no intermediate state should be taken equal to $|\boldsymbol{k}0\rangle$. The second order contribution has already been studied and found to equal c_0. To deal with the second term, we need to construct all the important diagrams contributing to it. It is easily seen that they have one-to-one correspondence to the pair-creating diagrams in Fig. 4 and are derived from the latter by merely exchanging the external $-\boldsymbol{k}1$-line for a new, external $\boldsymbol{k}0$-line running from the right and ending at the same point. Careful study of the contribution from each group of such diagrams reveals that it is given by $\Phi_i(k_0)$. As is shown in the Appendix, $\Phi_i(k_0)\sim c_0A$. Thus, we can neglect the fourth order contribution to the excitation energy and get $\mu_0=c_0$ as in second order calculation. Thus, from (4.12) we obtain

$$\Delta E_0^{(4)}=-(3/2)N(0)\mu_0^2\,.\qquad(4.14)$$

This means that the consideration of fourth order diagrams does not change the relation between the energy difference $\Delta E/V$ and half an energy gap μ_0 while it may possibly change both quantities. We are led then to conclude that the discrepancy between theory and experiment discussed in § 3 should be attributed not to lack of accuracy in mathematical manipulations but to some conceptional origin.

Both for the sake of completeness and later requirements we shall now express the constant c_0 in terms of the interaction parameter A. For this purpose it suffices to evaluate only the main part of $\Phi_i(k)$, linear in c_0, to the lowest order in A (assuming $x\sim A^{-1}$). A brief account of this evaluation is found in the Appendix. The result is

$$\sum_i\Phi_i(k)=-\gamma c_0A^2x/(1+E_k/\omega);\qquad\gamma\fallingdotseq0.1\,.\qquad(4.15)$$

On account of the difficulty in evaluating some of $\Phi_i(k)$'s accurately, we have confidence only in the order of magnitude of the above value for γ. However, we shall require no exact knowledge of γ to advance further arguments in subsequent sections.

Substituting (4.15) into (4.4) and solving it for c_0 give

$$1=Ax-(1+\gamma)A\quad\text{or}\quad c_0=\mu_0=2\omega\exp[-A^{-1}-(1+\gamma)]\,.\qquad(4.16$$

This means that the energy gap $2\mu_0$ is modified by a factor $\exp[-\gamma]$ and the difference in energy, $\Delta E/V$, by a factor $\exp[-2\gamma]$ if one takes into account the contribution of fourth order diagrams.

§ 5. Reformulation on the Basis of the Principle of Minimum Energy

In view of the results obtained in the preceding section as well as the considerations in Introduction, we are led to doubt the validity of the principle of compensation of dangerous diagrams due to Bogoliubov. Consequently, we attempt in this section to reformulate the theory on the basis of another, more legitimate principle, namely, the principle of minimum energy.

We shall start from the transformed Hamiltonian (2.7)-(2.12). Put

$$\xi_k=\varepsilon_k-\lambda\ , \qquad E_k=(\varepsilon_k-\lambda)(u_k^2-v_k^2) \tag{5.1}$$

and assume u_k and v_k in the form

$$u_k=\left[\frac{1}{2}\left(1+\frac{\xi_k}{\sqrt{c^2(k)+\xi_k^2}}\right)\right]^{1/2}, \qquad v_k=\left[\frac{1}{2}\left(1-\frac{\xi_k}{\sqrt{c^2(k)+\xi_k^2}}\right)\right]^{1/2}, \tag{5.2}$$

where $c(k)$ is a function to be determined on a variational principle. The results obtained in preceding sections suggest that the electron-phonon interaction affects less effectively those electronic states which are at distances more than ω apart from the Fermi surface, and also that one may assume Eq. (4.7) for $c(k)$ in (5.2). Thus, we put

$$c(k)=c_0/(1+E_k/\omega) \tag{5.3}$$

with c_0 now considered as a variational parameter.

The parameter c_0 will now be determined by minimizing the energy of the lowest state calculated on perturbation theory taking H' as a perturbation. It is assumed that

$$c_0 \ll \omega\ , \tag{5.4}$$

$$g^2N(0)\ln(2\omega/c_0)\equiv Ax=1+O(A)\ . \tag{5.5}$$

We shall see later that both conditions are really fulfilled by c_0 in the vicinity of its best choice. A mathematical difficulty arises, of course, in connection with the dangerous diagrams, which are generally not compensated in the present treatment. We believe on physical grounds that the dangerous diagrams would provide us with a finite result if their contributions could be collected in an appropriate way. We expect further that the solution u_k, v_k satisfying the principle of minimum energy is not largely distinct from that satisfying the principle of compensation so that the contribution of dangerous diagrams is small enough to be dropped from the energy to be minimized. We assume it for a while, but some discussion on this point will be presented in the next section.

The energy of the lowest state corresponding to any set of u_k, v_k which is defined by (5.2) and (5.3) with c_0 satisfying (5.4) and (5.5), can be expressed in the same form as that obtained in the preceding section, namely, by Eq. (4.9), provided all dangerous diagrams are disregarded as assumed above. In applying this equation to the present case, however, ξ_k and E_k are, of course, differently defined, namely, by (5.1). Suggested by the inspection of this expression, we can reach the following general aspect of perturbation expansion of $\Delta E/V$. It is naturally a power series of A beginning with a constant term. The coefficient of any order term can be expressed by a double series expanded in powers of $(c_0/\omega)^2$ and x $[\equiv\ln(2\omega/c_0)]$. If one is interested only in terms linear in c_0^2, assuming $c_0\ll\omega$, then he does not meet with any higher powers of x than the second because x is always accompanied by factor c_0. This enables us to disregard diagrams contributing to the energy in sixth or higher order in g on assuming $Ax\sim1$. We have thus

$$\Delta E/V=N(0)c_0^2\{x-Ax^2+\alpha+\beta Ax+\gamma A^2x^2+O(A)\}\ , \tag{5.6}$$

where α, β and γ are numerical coefficients of order 1. The numerical coefficients in the first and second terms, 1 and -1 respectively, are easily found by evaluating the first two terms of (4.9) in a crude way. The values to be assigned to α, β and γ may be obtained by manipulating the right-hand side of the same equation accurately. We shall leave for a moment these three coefficients undetermined for a reason which becomes apparent later.

On minimizing $\varDelta E/V$ with respect to c_0 we find

$$Ax=1+(\alpha+\beta+\gamma+1/2)A\ , \tag{5.7}$$

which is reliable to the term of order A. It is easy to see that the value of c_0 corresponding to (5.7) really affords the minimum (not the maximum) energy. If it is denoted by $\bar{c}_0$, Eq. (5.7) gives

$$\bar{c}_0=2\omega\ln[-A^{-1}-(\alpha+\beta+\gamma+1/2)]\ . \tag{5.8}$$

It is to be noted that the final results, (5.7) and (5.8), are fully consistent with the initially made assumptions, (5.4) and (5.5), provided that A is fairly smaller than 1 and $\alpha+\beta+\gamma+1/2$ is not a large negative number. Actual evaluation of α, β and γ will show that the latter condition is really satisfied, as we see later.

Introduction of (5.7) in (5.6) gives the energy of the superconducting ground state measured relative to that of the normal state:

$$\begin{aligned}\varDelta E_m/V=N(0)\bar{c}_0^2\{&A^{-1}+(\alpha+\beta+\gamma+1/2)+\alpha-A^{-1}[1+(\alpha+\beta+\gamma+1/2)A]^2\\&+\beta[1+(\alpha+\beta+\gamma+1/2)A]+\gamma[1+(\alpha+\beta+\gamma+1/2)A]^2\}\\=-(1/2)&N(0)\bar{c}_0^2\ .\end{aligned} \tag{5.9}$$

Terms of relative order A should not be retained in the final result because it would be unreliable unless terms of order $N(0)c_0^2A$ were included in the initial equation (5.6). It is rather surprising that the final result does not explicitly depend on α, β and γ.

We shall next investigate half an energy gap μ_0. It is calculated in quite a similar way as in the theory based on the principle of compensation as long as all dangerous diagrams are disregarded, giving*

$$\bar{\mu}_0=2u_kv_k\sum_{k'}(g^2/V)u_{k'}v_{k'}/(1+E_{k'}/\omega)\ . \tag{5.10}$$

With (5.1), (5.2), (5.3) and (5.5) this yields $\bar{\mu}_0=\bar{c}_0A\bar{x}=\bar{c}_0$. Combining this with (5.9) we have

$$\varDelta E_m/V=-(1/2)N(0)\bar{\mu}_0^2\ , \tag{5.11}$$

which is a result in satisfactory agreement with experiment (c.f. § 3). We have thus confirmed that the discrepancy between theory and experiment, which was found in the theory based on the principle of compensation, can completely be removed by reformulating theory on the principle of minimum energy. Furthermore, it should be emphasized that the final result (5.11) can be obtained with any arbitrary values assigned to α, β and γ as long as an inequality $\alpha+\beta+\gamma+1/2>-1$ is fulfilled. We have left so far the above three numerical factors undetermined to find this situation most easily.

We shall now show that the superconducting ground state arrived at in the present section has really a lower energy than the " ground state " obtained earlier on the principle of compensation. To do so, we need the actual values for α, β and γ. They are obtained by evaluating the right-hand side of (4.9) employing (5.1), (5.2) and (5.3). Actual calculations are as follows.

$$\begin{aligned}\boldsymbol{D}\sum_k 2\xi_kv_k^2&=-N(0)V\lim_{\Lambda\to\infty}\left\{\int_{-\lambda}^{\Lambda}\xi_k^2/\sqrt{c^2(k)+\xi_k^2}\,d\xi_k-\int_{-\lambda}^{\Lambda}|\xi_k|d\xi_k\right\}\\&=2N(0)V\lim_{\Lambda\to\infty}\int_0^{\Lambda}\xi_k(1-\xi_k/\sqrt{c^2(k)+\xi_k^2})d\xi_k\end{aligned}$$

---

* Quantities fixed on the principle of minimum energy will be denoted by barred letters.

$$=N(0)V\lim_{\Lambda\to\infty}\left\{\Lambda^2-2\int_0^{\omega}\xi_k^2/\sqrt{c_0^2(1+\xi_k^2/\omega\sqrt{c_0^2+\xi_k^2})^{-2}+\xi_k^2}\,d\xi_k\right.$$
$$\left.-2\int_{\omega}^{\Lambda}\xi_k^2/\sqrt{c_0^2(1+\xi_k^2/\omega\sqrt{c_0^2+\xi_k^2})^{-2}+\xi_k^2}\,d\xi_k\right\}$$
$$=N(0)V\lim_{\Lambda\to\infty}\left\{\Lambda^2-\omega\sqrt{c_0^2+\omega^2}+c_0^2\ln(2\omega/c_0)-\left(\frac{1}{2}+\ln 2\right)c_0^2-\Lambda^2+\omega^2\right.$$
$$\left.+\left(\ln 2-\frac{1}{2}\right)c_0^2\right\}$$
$$=N(0)Vc_0^2(x-3/2)\,, \tag{5.12}$$

$$-\sum_{k,k'}\frac{g^2}{V}\frac{\omega_{kk'}u_kv_ku_{k'}v_{k'}}{\omega_{kk'}+E_k+E_{k'}}$$
$$=-g^2N(0)Vc_0^2\lim_{\Lambda\to\infty}\lim_{\Lambda'\to\infty}\int_0^{\Lambda}\int_0^{\Lambda'}\left(1\Big/\left(1+\frac{\xi_k^2}{\omega\sqrt{c^2(k)+\xi_k^2}}+\frac{\xi_{k'}^2}{\omega\sqrt{c^2(k')+\xi_{k'}^2}}\right)\right)$$
$$\times\left(1+\frac{\xi_k^2}{\omega\sqrt{c^2(k)+\xi_k^2}}\right)^{-1}\left(1+\frac{\xi_{k'}^2}{\omega\sqrt{c^2(k')+\xi_{k'}^2}}\right)^{-1}$$
$$\times\frac{d\xi_{k'}d\xi_k}{\sqrt{c^2(k)+\xi_k^2}\sqrt{c^2(k')+\xi_{k'}^2}}$$
$$=-g^2N(0)Vc_0^2\lim_{\Lambda\to\infty}\int_0^{\Lambda}\frac{1}{\left(1+\dfrac{\xi_k^2}{\omega\sqrt{c_0^2+\xi_k^2}}\right)^2\sqrt{c_0^2+\xi_k^2}}$$
$$\times\left\{\ln(2\omega/c_0)-\frac{\omega\sqrt{c_0^2+\xi_k^2}}{\xi_k^2}\ln\left(1+\frac{\xi_k^2}{\sqrt{c_0^2+\xi_k^2}}\right)\right\}d\xi_k$$
$$=-g^2N(0)Vc_0^2\{\ln(2\omega/c_0)[\ln(2\omega/c_0)-1]-\ln(2\omega/c_0)\}$$
$$=-N(0)Vc_0^2(Ax^2-2Ax)\,. \tag{5.13}$$

Reduction of the last two terms in (4.9) is carried out in exactly the same way as described before (in § 2 and in the Appendix), giving

$$-D\sum_{k,k'}\frac{g^2}{V}\frac{\omega_{kk'}u_k^2v_{k'}^2}{\omega_{kk'}+E_k+E_{k'}}=-N(0)Vc_0^2Ax\,, \tag{5.14}$$

$$-\sum_k u_kv_k\sum_i \Phi_i(k)=\gamma N(0)Vc_0^2A^2x^2\,. \tag{5.15}$$

Substitution of the above results in (4.9) yields

$$\Delta E/V=N(0)c_0^2(x-3/2-Ax^2+Ax+\gamma A^2x^2)\,,$$

showing that the three numerical coefficients in (5.6) are as follows:

$$\alpha=-3/2\,,\qquad \beta=1\,, \tag{5.16}$$

and γ is identical with γ used in § 4 to express $\sum_i \Phi_i(k)$. Note that

$$\alpha+\beta+\gamma+1/2=\gamma;\qquad |\gamma|\ll 1 \text{ (c.f. Appendix)}, \tag{5.17}$$

which satisfies the earlier requirements that $\alpha+\beta+\gamma+1/2$ should not be a large negative number.

By use of these values Eqs. (5.7) and (5.8) are found to become

$$A\bar{x}=1+\gamma A\,, \tag{5.18}$$

$$\bar{c}_0=\bar{\mu}_0=2\omega\exp[-A^{-1}-\gamma]\,. \tag{5.19}$$

Comparing (5.19) with (4.16) we see that the energy gap derived here on the principle of minimum energy is e times larger than that obtained in the theory based on the principle of compensation. Comparison of the energy difference reads $\Delta E_m/\Delta E_c=e^2/3$. This means that the energy of the superconducting ground state defined here, measured relative to that of the normal state, is about 2.5 times lower than that of the earlier "superconducting ground state" defined on the principle of compensation.

§ 6. Discussion of the Contribution of Dangerous Diagrams

In the preceding section a very reasonable result has been obtained by reformulating the theory on the principle of minimum energy. However, the arguments advanced there can be justified only when the contributions from the dangerous diagrams can be collected by an appropriate mathematical device to give a finite and sufficiently small amount. Although we have not yet found any device to collect these contributions, some discussion will be given to suggest that they are really of little importance, at least, in the present procedure assuming $c(k)$ in the form (5.3).

In the first place it will be shown that we can find a state which lies very close to the "ground state" reached in the preceding section and whose energy can be calculated without suffering from the difficulty due to vanishing denominators to give the same energy and energy gap as those given by (5.11) and (5.19).

Consider a state which corresponds to assuming $c(k)$ slightly different from (5.3), namely, in the form

$$c(k)=\begin{cases}\bar{c}_0(1-A)/(1+E_k/\omega)\ , & |\xi_k|<\bar{c}_0\ ,\\ \bar{c}_0/(1+E_k/\omega)\ , & |\xi_k|>\bar{c}_0\ .\end{cases} \tag{6.1}$$

It is then easy to show that the principle of compensation of dangerous diagrams is fulfilled in the region $|\xi_k|<\bar{c}_0$. In fact, the right-hand side of the compensation equation (4.4) can be reduced, within the approximations keeping terms to relative order A, to the form

$$\frac{\bar{c}_0}{1+\xi_k^2/\omega\sqrt{c^2(k)+\xi_k^2}}(A\bar{x}-A-\gamma A^2\bar{x})=\frac{\bar{c}_0}{1+\xi_k^2/\omega\sqrt{c^2(k)+\xi_k^2}}(A\bar{x}-A-\gamma A) \tag{6.2}$$

in the present choice of $c(k)$. Applying Eq. (5.18) which holds as well with $c(k)$ given by (6.1), we have from (6.2)

$$\bar{c}_0(1-A)/(1+\xi_k^2/\omega\sqrt{c^2(k)+\xi_k^2})\ ,$$

which is just equal to the left-hand side of (4.3) when $|\xi_k|<\bar{c}_0$. Then, the so-called dangerous diagrams are no longer dangerous; they are compensated in the region $|\xi_k|<\bar{c}_0$ and do not bring forth difficulties in the region $|\xi_k|>\bar{c}_0$. Their contribution to the energy, ΔE, is finite and can be estimated to be negligible in the following way.

In Fig. 6 some lower order dangerous diagrams contributing to the energy are shown. The vertex represents either H_1 or the combined action H_2H_3 illustrated in Fig. 2 (or the reverse). The contribution from these diagrams may be expressed in the form

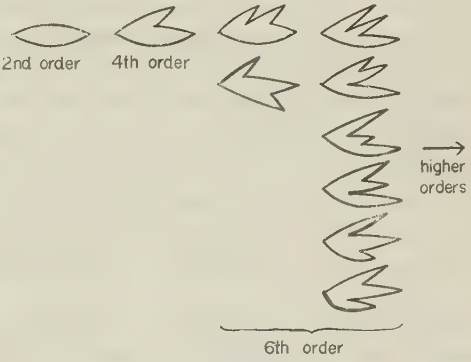

Fig. 6. Typical dangerous diagrams. Every vertex may represent either H_1 or the combined action of H_2 and H_3. Two alternative labellings are allowed for each diagram (except for the first one).

$$-\frac{1}{2}\sum_k{}'\frac{[c(k)-b_1(k)]^2}{\sqrt{\bar{c}_0^2+\xi_k^2}}+\frac{1}{2}\sum_k{}'\frac{[c(k)-b_1(k)]^2}{\sqrt{\bar{c}_0^2+\xi_k^2}}\frac{[c(k)-b_2(k)]^2}{4\xi_k^2}$$
$$-\frac{1}{2}\sum_k{}'\frac{[c(k)-b_1(k)]^2}{\sqrt{\bar{c}_0^2+\xi_k^2}}\frac{[c(k)-b_2(k)]^2}{4\xi_k^2}\left\{\frac{[c(k)-b_2(k)]^2}{4\xi_k^2}+\frac{[c(k)-b_3(k)]^2}{4\xi_k^2}\right\}+\cdots\ , \tag{6.3}$$

where the summation is limited to the region $|\xi_k|>\bar{c}_0$ and the successive terms correspond to the successive groups of diagrams in Fig. 6. The quantity denoted by $b_n(k)$ is introduced by the H_2H_3-process (or the reverse) and expressed in the form

$$b_n(k)=\sum_{k'}\frac{g^2}{V}\frac{\omega_{kk'}u_{k'}v_{k'}}{\omega_{kk'}+(2n-1)E_k+E_{k'}}+\sum_i \Phi_{in}(k)\ , \tag{6.4}$$

where $\Phi_{in}(k)$ is of the same form as $\Phi_i(k)$ introduced in §4 except that all energy denominators are increased by the same amount $2(n-1)E_k$. Note that

$$b_1(k)=\bar{c}_0(1-A)/(1+E_k/\omega)=c(k)(1-A)\ , \qquad |\xi_k|>\bar{c}_0\ . \tag{6.5}$$

Considering that the summation is carried out only in the region $|\xi_k|>\bar{c}_0$, we can expect the major contribution in (6.3) to arise from the first term. By use of (6.5) this is easily evaluated to give

$$-A^2N(0)\bar{c}_0{}^2\bar{x}\simeq -AN(0)\bar{c}_0{}^2\ . \tag{6.6}$$

There are many other complicated types of dangerous diagrams (which are of course not dangerous now) contributing to the energy, but it is possible to show that the sum of their contributions is small compared to that arising from the above-mentioned simplest diagrams.

The change in the originally non-dangerous part of energy, brought about by the modification of u_k, v_k under consideration, arises mainly from the first two terms on the right hand side of (4.9). In the approximations keeping only terms to relative order A, these terms give rise respectively to a change

$$-AN(0)\bar{c}_0{}^2\{2\ln(\sqrt{2}+1)-\sqrt{2}\} \qquad \text{and} \qquad -AN(0)\bar{c}_0{}^2\{-2\ln(\sqrt{2}+1)+\sqrt{2}\}\ ,$$

resulting in a vanishing sum. Thus, we have found that the non-dangerous part of energy of the new state introduced by the modification (6.1) differs from the value obtained for the original state in the preceding section [(5.9) with (5.19)] at most in terms of relative order A^2. In comparison with this part, the contribution of dangerous diagrams in (6.6) can be neglected. Since it is quite evident that half an energy gap μ_0 is again equal to $\bar{c}_0$ given in (5.19), we have reached all the final results in the preceding section without suffering from dangerous diagrams in the present case.

From these considerations it can be seen that the procedure advanced in the preceding section is practically equivalent to the following one. Let us asseme $c(k)$ in the form

$$c(k)=c_0(k)/(1+E_k/\omega)\ ,$$

$$c_0(k)=\begin{cases} c_0(1-pA)\ , & |\xi_k|<c_0\ , \\ c_0\ , & |\xi_k|>c_0\ , \end{cases} \tag{6.7}$$

instead of (5.3). Then, for any choice of c_0 ($\ll\omega$), the contribution to the energy from dangerous diagrams vanishes by mutual compensation for $\boldsymbol{k}$ such that $|\xi_k|<c_0$ and becomes negligibly small for $\boldsymbol{k}$ such that $|\xi_k|>c_0$ if p is chosen so as to satisfy

$$Ax=1+(1+\gamma-p)A\ ; \qquad x\equiv\ln(2\omega/c_0)\ . \tag{6.8}$$

This is easily verified in quite the same way as in the earlier case dealing with (6.1). To determine the best value of c_0, the variational procedure can be carried through in the same way as in the preceding section, neglecting dangerous diagrams with full justification in the present case as explained above. If we note that the perturbation series for the energy is the same as before in the approximation neglecting terms of order $AN(0)c_0{}^2$, it is easy to get the earlier result (5.18) and (5.19) [$c_0=\bar{c}_0$; $Ax=1+\gamma A$], and, hence, $p=1$ from (6.8) in agreement with (6.1). It may be said that we have chosen the best transformation among those which do not give rise to vanishing denominators in perturbation series.

In spite of the success of the present procedure in predicting the correct $\Delta E-\mu_0$ relation, it seems necessary to make the following remark: It is open to question that the transformation to give the true ground state needs to meet the above requirements of mathematical convenience.

§ 7. Effect of the Screened Coulomb Repulsion

So far, we have ignored entirely the effect of the Coulomb repulsion between electrons. A rigorous treatment of this repulsion is a difficult problem, and so we investigate here the effect of a model repulsion in the form such as considered by Abrikosov et al.[11]

A repulsive interaction may generally be written in the form

$$(2V)^{-1}\sum_{\left(\substack{\boldsymbol{k},\boldsymbol{l},\boldsymbol{k}',\boldsymbol{l}',\sigma,\rho\\ \boldsymbol{k}'-\boldsymbol{k}=\boldsymbol{l}-\boldsymbol{l}'}\right)} h(\boldsymbol{k},\,\boldsymbol{l},\,\boldsymbol{l}',\,\boldsymbol{k}')a_{\boldsymbol{k}\sigma}{}^+a_{\boldsymbol{l}\rho}{}^+a_{\boldsymbol{l}'\rho}a_{\boldsymbol{k}'\sigma}\,;\qquad h(\boldsymbol{k},\,\boldsymbol{l},\,\boldsymbol{l}',\,\boldsymbol{k})\geqq 0\,. \tag{7.1}$$

Adding this term to the earlier Hamiltonian (2.1) and applying the Bogoliubov transformation, we have*

$$H=U+H_0+H'\,,\qquad H'=H_1+H_2+H_3+H_4\,, \tag{7.2}$$

where

$$U=\sum_{\boldsymbol{k}}(2\xi_k v_k{}^2-V^{-1}v_k{}^2\sum_{\boldsymbol{k}'}\bar{h}_{\boldsymbol{k}\boldsymbol{k}'}v_{k'}{}^2+V^{-1}u_kv_k\sum_{\boldsymbol{k}'}h_{\boldsymbol{k}\boldsymbol{k}'}u_{k'}v_{k'})\,, \tag{7.3}$$

$$\begin{aligned}H_0=\sum_{\boldsymbol{k}}\{\xi_k(u_k{}^2-v_k{}^2)-V^{-1}u_kv_k\sum_{\boldsymbol{k}'}2h_{\boldsymbol{k}\boldsymbol{k}'}u_{k'}v_{k'}\}(\alpha_{\boldsymbol{k}0}{}^+\alpha_{\boldsymbol{k}0}+\alpha_{-\boldsymbol{k}1}{}^+\alpha_{-\boldsymbol{k}1})&\\ +\sum_{\boldsymbol{w}}\omega(\boldsymbol{w})\left(b_w{}^+b_w+\frac{1}{2}\right),&\end{aligned} \tag{7.4}$$

$$H_1=\sum_{\boldsymbol{k}}\{2\xi_ku_kv_k+V^{-1}(u_k{}^2-v_k{}^2)\sum_{\boldsymbol{k}'}h_{\boldsymbol{k}\boldsymbol{k}'}u_{k'}v_{k'}\}(\alpha_{\boldsymbol{k}0}{}^+\alpha_{-\boldsymbol{k}1}{}^++\alpha_{-\boldsymbol{k}1}\alpha_{\boldsymbol{k}0}) \tag{7.5}$$

with the abbreviations

$$\left.\begin{aligned}&\xi_k\equiv\varepsilon_k-\lambda+V^{-1}\sum_{\boldsymbol{k}'}\bar{h}_{\boldsymbol{k}\boldsymbol{k}'}v_{k'}{}^2\,,\\ &\bar{h}_{\boldsymbol{k}\boldsymbol{k}'}\equiv h(\boldsymbol{k},\,-\boldsymbol{k}',\,-\boldsymbol{k}',\,\boldsymbol{k})+h(\boldsymbol{k},\,\boldsymbol{k}',\,\boldsymbol{k}',\,\boldsymbol{k})-h(\boldsymbol{k},\,\boldsymbol{k}',\,\boldsymbol{k},\,\boldsymbol{k}')\,,\\ &h_{\boldsymbol{k}\boldsymbol{k}'}\equiv h(\boldsymbol{k},\,-\boldsymbol{k},\,-\boldsymbol{k}',\,\boldsymbol{k}')\,.\end{aligned}\right\} \tag{7.6}$$

H_2 and H_3 stand for the same expressions as given in (2.11) and (2.12), and H_4 is a sum of terms expressed in products of four creation and destruction operators, arising from the repulsive interaction term. It is to be noted that H_4 is non-diagonal and can be disregarded in the calculation of the ground state and singly excited state energies to the present approximation. As a model of the screened Coulomb repulsion, Abrikosov et al. considered the following case

$$\bar{h}_{\boldsymbol{k}\boldsymbol{k}'}=h_{\ \ \boldsymbol{k}'}=\begin{cases}h\ \text{(a positive constant)}, & |\xi_k|,\ |\xi_{k'}|<\omega_c,\\ 0\,, & \text{otherwise},\end{cases} \tag{7.7}$$

where ω_c is assumed to be much larger than ω (average phonon energy) taking account of the fact that the Coulomb repulsion in metals is screened at very short distances comparable to the lattice spacing. Furthermore, we assume a weak repulsion, that is,

$$hN(0)\equiv B<1\,. \tag{7.8}$$

Taking account of the difference in force range of the two kinds of interactions, we put

$$u_k=\left[\frac{1}{2}\left(1+\frac{\xi_k}{\sqrt{c^2(k)+\xi_k{}^2}}\right)\right]^{1/2},\quad v_k=\left[\frac{1}{2}\left(1-\frac{\xi_k}{\sqrt{c^2(k)+\xi_k{}^2}}\right)\right]^{1/2}, \tag{7.9}$$

---

* See Beliaev's article in reference[12].

assuming

$$c(k)=\begin{cases} c_0/(1+\xi_k^2/\omega\sqrt{c_0^2+\xi_k^2})+c_1\ , & |\xi_k|<\omega_c\ , \\ c_0/(1+\xi_k^2/\omega\sqrt{c_0^2+\xi_k^2})\ , & |\xi_k|>\omega_c\ , \end{cases} \tag{7.10}$$

where c_0 and c_1 are independent parameters which are to be determined variationally on the principle of minimum energy.

Proceeding in exactly the same way as in § 4, we have the energy difference in the following form

$$\begin{aligned} \Delta E=D\Big\{&\sum_k 2\xi_k v_k^2-V^{-1}\sum_{k,k'} h v_k^2 v_{k'}^2+V^{-1}\sum_{k,k'} h u_k v_k u_{k'} v_{k'} \\ &-\sum_{k,k'}\frac{g^2}{V}\frac{\omega_{kk'} u_k v_k u_{k'} v_{k'}}{\omega_{kk'}+E_k+E_{k'}}-\sum_{k,k'}\frac{g^2}{V}\frac{\omega_{kk'} u_k^2 v_{k'}^2}{\omega_{kk'}+E_k+E_{k'}}-\sum_k u_k v_k\sum_i \Phi_i(k)\Big\}\ , \end{aligned} \tag{7.11}$$

where $E_k=\xi_k(u_k^2-v_k^2)-2V^{-1}u_k v_k \sum_{k'} h u_{k'} v_{k'}$. The last term in the brackets which arises from the diagrams in fourth order in g has the same expression as the corresponding one in (4.9). Substitution of (7.9) with (7.10) for u_k and v_k shows that the second term in the brackets has a negligible contribution and the other contributions are as follows:

$$D\sum_k 2\xi_k v_k^2=N(0)V\Big\{(c_0+c_1)^2x+c_1^2D-(c_0+c_1)^2\Big[\frac{1}{2}+\frac{c_0^2}{(c_0+c_1)^2}\Big]\Big\}\ , \tag{7.12}$$

$$V^{-1}\sum_{k,k'} h u_k v_k u_{k'} v_{k'}=N(0)VB(c_0x+c_1y)^2\ , \tag{7.13}$$

$$\sum_{k,k'}\frac{g^2}{V}\frac{\omega_{kk'} u_k v_k u_{k'} v_{k'}}{\omega_{kk'}+E_k+E_{k'}}=N(0)VA\{(c_0+c_1)^2x^2-2c_0(c_0+c_1)x\}\ , \tag{7.14}$$

$$D\sum_{k,k'}\frac{g^2}{V}\frac{\omega_{kk'} u_k^2 v_{k'}^2}{\omega_{kk'}+E_k+E_{k'}}=N(0)VA(c_0+c_1)^2x\ , \tag{7.15}$$

$$\sum_k u_k v_k\sum_i \Phi_i(k)=-N(0)V\gamma A^2(c_0+c_1)^2x^2\ , \tag{7.16}$$

where

$$x\equiv\ln[2\omega/(c_0+c_1)],\quad y\equiv\ln[2\omega_c/(c_0+c_1)],\quad D\equiv y-x=\ln(\omega_c/\omega)$$

and γ in (7.16) is the same numerical factor as in (4.15). By use of these results we have from (7.11)

$$\begin{aligned} \Delta E/V=N(0)(c_0+c_1)^2\Big\{x+\alpha\Big(\frac{c_0}{c_0+c_1}\Big)-Ax^2+\beta\Big(\frac{c_0}{c_0+c_1}\Big)Ax+\gamma A^2x^2\Big\}& \\ +N(0)c_1^2D+N(0)B(c_0x+c_0y)^2\ ,& \end{aligned} \tag{7.17}$$

where

$$\alpha(r)=-(1/2+r^2);\qquad \beta(r)=2r-1\ . \tag{7.18}$$

Comparison of this equation with the earlier one (5.6) shows that we have two additional terms other than all corresponding to those in the latter equation.

We shall now minimize $\Delta E/V$ by taking independent variations with respect to c_0 and c_1. From $\delta\Delta E/\delta c_0=\delta\Delta E/\delta c_1=0$ it follows, neglecting small quantities,

$$\begin{aligned} &(c_0+c_1)x-(1/2)(c_0+c_1)+(c_0+c_1)\alpha+(1/2)c_1\alpha'-(c_0+c_1)Ax^2+(c_0+c_1)Ax \\ &\qquad+(c_0+c_1)\beta Ax+(1/2)\beta' c_1 Ax+\gamma(c_0+c_1)A^2x^2+B(x-1)(c_0x+c_1y)=0\ , \end{aligned} \tag{7.19}$$

$$\begin{aligned} &(c_0+c_1)x-(1/2)(c_0+c_1)+(c_0+c_1)\alpha-(1/2)c_0\alpha'-(c_0+c_1)Ax^2+(c_0+c_1)Ax \\ &\qquad+(c_0+c_1)\beta Ax-(1/2)\beta' c_0 Ax+\gamma(c_0+c_1)A^2x^2+B(y-1)(c_0x+c_1y)=0\ , \end{aligned} \tag{7.20}$$

The difference gives

$$c_1+B(c_0x+c_1y)=(c_0+c_1)S/D\,, \tag{7.21}$$

where

$$S=(1/2)(\alpha'+Ax\beta') \tag{7.22}$$

which is a quantity of order 1. Introducing (7.21) into (7.19) gives

$$Ax=1-c_1/(c_0+c_1)+S/D\,, \tag{7.23}$$

where we have neglected terms of order A. The energy difference corresponding to the minimum condition, $\varDelta E_m/V$, can be obtained, by combining (7.16) and (7.19), in the form

$$\begin{aligned}\varDelta E_m/V=N(0)(c_0+c_1)^2\Big\{\frac{1}{2}-Ax-\frac{1}{2}\,\frac{c_1}{c_0+c_1}(\alpha'+\beta' Ax)+\frac{c_1{}^2}{(c_0+c_1)^2}D\\ -B(x-1)\frac{c_0x+c_1y}{c_0+c_1}+Bx\frac{(c_0x+c_1y)^2}{(c_0+c_1)^2}\Big\}\,.\end{aligned} \tag{7.24}$$

By use of (7.21), (7.22) and (7.23) this equation can be reduced to

$$\varDelta E_m/V=-(1/2)N(0)(\bar{c}_0+\bar{c}_1)^2\,, \tag{7.25}$$

where the letters $\bar{c}_0$ and $\bar{c}_1$ are used to show that they are now fixed values corresponding to the minimum energy.

The excitation energy for a particle $\boldsymbol{k}s$ is given (neglecting higher order effects) by

$$\mu(\boldsymbol{k})=E_k-2u_kv_k\sum hu_{k'}v_{k'}-\langle \boldsymbol{k}s|H'(H_0-E_k)^{-1}H'|\boldsymbol{k}s\rangle\,.$$

Putting $E_k=0$ gives half an energy gap

$$\begin{aligned}\bar{\mu}_0&=-B(\bar{c}_0\bar{x}+\bar{c}_1\bar{y})+A(\bar{c}_0+\bar{c}_1)\bar{x}\\ &=(\bar{c}_0+\bar{c}_1)\{\bar{c}_1/(\bar{c}_0+\bar{c}_1)-\bar{S}/D+A\bar{x}\}=\bar{c}_0+\bar{c}_1\end{aligned} \tag{7.26}$$

Combining this result with (7.25) yields

$$\varDelta E_m/V=-(1/2)N(0)\bar{\mu}_0{}^2\,, \tag{7.27}$$

which is exactly the same equation that has been obtained earlier and found to agree with experiment.

In order to study the effect of the repulsion on the energy gap, we need to find the actual value of $\bar{c}_0+\bar{c}_1$ as a function of interaction parameters A and B. For this purpose, we first transform Eq. (7.19), using (7.22), into the following form

$$A\bar{x}=1+B\frac{\bar{c}_0\bar{x}+\bar{c}_1\bar{y}}{\bar{c}_0+\bar{c}_1}-\frac{1}{\bar{x}}\Big(\frac{1}{2}-A\bar{x}-\bar{\alpha}-\bar{\beta}A\bar{x}-\frac{\bar{c}_1}{\bar{c}_0+\bar{c}_1}\bar{S}-\gamma A^2\bar{x}+B\frac{\bar{c}_0\bar{x}+\bar{c}_1\bar{y}}{\bar{c}_0+\bar{c}_1}\Big)\,. \tag{7.28}$$

Making use of (7.21) and the following relation to be derived therefrom

$$\bar{c}_1/(\bar{c}_0+\bar{c}_1)=-B\bar{x}/(1+BD)+\bar{S}/D(1+BD)\,,$$

we can reduce Eq. (7.28) further to the form

$$A\bar{x}=1+\frac{B\bar{x}}{1+BD}-\frac{1}{\bar{x}}\Big\{\frac{1}{2}-A\bar{x}-\bar{\alpha}-\bar{\beta}A\bar{x}-\frac{\bar{S}^2}{D(1+BD)}-\gamma A^2\bar{x}^2+\frac{B\bar{x}}{1+BD}\Big\}\,. \tag{7.29}$$

In the first approximation, we have $A\bar{x}=1+B\bar{x}/(1+BD)$, which, introducing an effective interaction parameter

$$A'\equiv A-B/(1+BD)\,, \tag{7.30}$$

can be written as

$$A'\bar{x}=1\,. \tag{7.31}$$

Employing the approximate relation (7.31) to estimate the last term and assuming that $D\equiv\ln(\omega_c/\omega)\gg 1$, we have finally from (7.29)

$$A'\bar{x}=1+\left\{\alpha\left(\frac{A}{A'}\right)+\beta\left(\frac{A}{A'}\right)\frac{A}{A'}+\gamma\frac{A^2}{A'^2}+\frac{1}{2}\right\}A'\,, \tag{7.32}$$

where an approximate relation $\bar{c}_0/(\bar{c}_0+\bar{c}_1)=1+B\bar{x}/(1+BD)=A\bar{x}=A/A'$ has been used to transform the last term. From (7.32) we get

$$\begin{aligned}\bar{c}_0+\bar{c}_1=\bar{\mu}_0&=2\omega\exp\left[-\frac{1}{A'}-\left\{\alpha\left(\frac{A}{A'}\right)+\beta\left(\frac{A}{A'}\right)\frac{A}{A'}+\gamma\frac{A^2}{A'^2}+\frac{1}{2}\right]\right.\\&=2\omega\exp\left[-\frac{1}{A'}+\frac{A}{A'}-(1+\gamma)\frac{A^2}{A'^2}\right],\end{aligned} \tag{7.33}$$

where the last equality is effected by the definition (7.18). The last expression in (7.33) coincides with the right-hand side of the earlier equation (5.19) when $A'=A$, and in general cases such that $A'<A<1$ the former is always smaller, indicating that the repulsive interaction diminishes the energy gap. Comparison of the above result with (5.19) shows further that the major effect of the repulsive interaction on the energy gap and the energy difference between the superconducting and normal states can be taken into account by changing the interaction parameter in the old equation into A' given by (7.30). This was the conclusion reached by Abrikosov et al. dealing with the renormalized Fröhlich Hamiltonian in a rough way by Bogoliubov's method. As was pointed out by these authors and can be seen from (7.30), the repulsive interaction is less effective on account of a large difference in force ranges $[D\gg 1]$.

Finally, we shall give, for comparison, some results to be obtained when the same problem is treated on the principle of compensation. We need again to introduce two constants, c_0 and c_1, to express $\Delta E/V$ and μ_0. They are found to be given by

$$\Delta E_c/V=-(1/2+A/A')N(0)(c_0+c_1)^2; \qquad \mu_0=c_0+c_1\,, \tag{7.34}$$

thus yielding

$$\Delta E_c/V=-(1/2+A/A')N(0)\mu_0^2\,, \tag{7.35}$$

where A' is the same quantity as that used in the preceding case and defined by (7.30). We can find for the minimum excitation energy

$$\mu_0=c_0+c_1=2\omega\exp\left[-\frac{1}{A'}-(1+\gamma)\frac{A^2}{A'^2}\right]. \tag{7.36}$$

Note that the ratio of $\Delta E_c/V$ to $N(0)\mu_0^2$ is no longer independent of the interaction parameters. The fact that $1/2+A/A'>3/2$ indicates that the deviation from the semi-empirical law is even larger in the presence of a repulsive interaction.

To compare the energy difference between the superconducting and normal states calculated on different principles, we consider the ratio $\Delta E_m/\Delta E_c=\exp[2(A/A')]/[1+2(A/A')]$, which is always larger than $e^2/3$ when $A/A'>1$, indicating that the ground state reached on the principle of minimum energy has really a much lower energy than the one presumed on the principle of compensation.

§ 8. Concluding Remarks

We have been suspiscious of Bogoliubov's idea that the perturbation treatment based on the principle of compensation of dangerous diagrams provides the superconducting ground state of the electron-phonon system. Recalculation of the ground state energy, $\Delta E/V$, and the energy gap, $2\mu_0$, shows indeed the invalidity of this principle in predicting a well-established semi-empirical relation. A satisfactory agreement between theory and experiment is obtained if the theory is reformulated on the principle of minimum energy.

It is found that the difference in energy between the superconducting and normal states is always given correctly as a function of an energy gap if we have lowest order terms of the form $N(0)c_0{}^2x$ and $-N(0)c_0{}^2Ax^2$ in the energy expansion such as (5.6) and if the parameter c_0 is determined on the principle of minimum energy. Note that the next order terms of order $N(0)c_0{}^2$ have no importance to the derivation of the final result [Eq. (5.9)], in spite of the fact that $\varDelta E_m/V$ is just of this order of magnitude. We believe that this is the reason for the success of the BCS theory in which both the model and the mathematical treatment were much simplified but nevertheless both quoted terms were found in the expression of the energy.

In connection to this fact, an important remark should be made. First of all note that the lowest order terms just mentioned are quite insensitive to change in the form of $c(k)$ within a very narrow region for $\boldsymbol{k}$ surrounding the Fermi surface (e.g., in $|\xi_k|<c_0$). Note further that in the present theory we have assumed $c(k)$ to be nearly constant for $\boldsymbol{k}$ such that $|\xi_k|<c_0$ in order to circumvent the mathematical difficulty due to vanishing denominators. From these facts, we see that, although we have reached a correct relation between $\varDelta E$ and μ_0, this does not necessarily mean the validity of the obtained distribution function u_k, v_k in the immediate vicinity of the Fermi surface. On the other hand, it is evident that some of the electromagnetic properties (e.g., a non-vanishing Knight shift or low frequency Fourier components of current) may be closely connected to the behaviour of quasi-particles in this narrow region*. Thus, it may be concluded that a successful theory in predicting a correct $\varDelta E-\mu_0$ relation would not necessarily lead to a full understanding of the electromagnetic properties of superconductors.

Appendix

The contributions to the equation of compensation (4.1) from the pair-creating diagrams in fourth order in g (shown in Fig. 4) are found to be collected for each group into the form

$$-(u_k{}^2-v_k{}^2)\varPhi_i(k)-u_kv_k\varPsi_i(k)\ , \tag{A.1}$$

where the index i discriminates the group (i=I–XIII) and both $\varPhi_i(k)$ and $\varPsi_i(k)$ are functions of k^2 expressed in a complicated form. Careful examination of the expressions for $\varPhi_i(k)$'s shows that all $\varPhi_i(k)$'s vanish for the normal state solution, resulting in the vanishing total expression (A.1). Since we have no space to write down all the explicit expressions for $\varPhi_i(k)$'s and $\varPsi_i(k)$'s and to describe the procedures of their evaluation, we shall only present approximate expressions and evaluations of $\varPhi_i(k)$ in some typical cases.

First of all we have approximately**

$$\varPhi_{\mathrm{I}}(k)=-\left(\frac{g^2}{2V}\right)^2\sum_{k',k''}\left\{\omega_{kk'}u'v'\left[\frac{\omega_{kk''}}{(D_{kk''}+2E)(D_{kk'}+D_{kk''})D_{kk''}}+\frac{\omega_{k'k''}}{(D_{k'k''}+2E)(D_{kk'}+D_{k'k''})D_{k'k''}}\right]\right.$$
$$\left.+\frac{\omega_{kk''}u''v''}{D_{kk''}{}^2}\left[\frac{\omega_{kk'}}{D_{kk'}+D_{kk''}}+\frac{\omega_{k'k''}}{D_{kk'}+D_{k'k''}}\right]\right\}, \tag{A.2}$$

---

* Note that if one modifies the distribution function in this region in such a way that it tends to the normal one ($u_kv_k=0$) when the Fermi surface is approached, then the excitation energy vanishes for a quasi-particle on the Fermi surface although the value of $\sum_{k'}(g^2/V)u_{k'}v_{k'}/(1+E_{k'}/\omega)$ remains almost unchanged. [c.f. (5.10).]

** Eqs. (A.2) and (A.3), and (A.7) below are obtained from the exact expressions after some reduction taking the best advantage of the fact that $c(k)\ll\omega\ll\lambda$. We need only to retain the main part of the term linear in c_0. We can further omit all terms linear in $u_{k'}{}^2-v_{k'}{}^2$ provided that they have either a product $u_{k'}v_{k'}$ as a factor or a denominator involving $E_{k'}$, because in this case the important region for the summation over $\boldsymbol{k}'$ is limited to $\boldsymbol{k}'$ in a close vicinity of the Fermi surface, where the density of states $k'^2/(2\pi^2d\xi_{k'}/dk')$ is approximately constant (according to the condition c_0, $\omega\ll\lambda$), and the quantity $u_{k'}{}^2-v_{k'}{}^2$ is an odd function of $\xi_{k'}$.

$$\Phi_{\rm II}(k)=-\left(\frac{g^2}{2V}\right)^2\sum_{k',k''}\left\{\omega\ u'v'\left[\frac{\omega_{kk''}}{(D_{kk''}+2E)(D_{kk'}+D_{kk''})D_{kk''}}\right.\right.$$

$$\left.+\frac{\omega_{k'k''}}{D_{k'k''}+2E)(D_{kk'}+D_{k'k''}-2E')D_{k'k''}}\right]$$

$$\left.-\frac{\omega_{kk''}u''v''}{D_{kk''}{}^2}\left[\frac{\omega_{kk'}}{D_{kk'}+D_{kk''}-2E}+\frac{\omega_{k'k''}}{D_{kk''}+D_{k'k''}-2E''}\right]\right\}, \qquad \text{(A.3)}$$

where the suffix k, k', $\cdots$ are suppressed for clarity (except for $\omega_{kk'}$, $D_{kk'}$, $\cdots$) and $D_{kk'}\equiv\omega_{kk'}+E_k+E_{k'}$, etc. It is convenient to evaluate $\Phi_{\rm I}(k)+\Phi_{\rm II}(k)$ instead of evaluating $\Phi_{\rm I}(k)$ and $\Phi_{\rm II}(k$ separately. The evaluation is rather straightforward if one goes over from summation to integration and replaces all phonon energies by the average value ω $[=(3/5)k\Theta_D]$ introduced in § 2, giving

$$\Phi_{\rm I}(k)+\Phi_{\rm II}(k)=-2(1-\ln 2)c_0A^2x/(1+E/\omega)\ . \qquad \text{(A.4)}$$

Evaluation of $\Phi_{\rm III}(k)$ and $\Phi_{\rm IV}(k)$ can be carried out similarly with the result

$$\Phi_{\rm III}(k)=-(2\ln 2)c_0A^2x/(1+E/\omega)\ , \qquad \text{(A.5)}$$

$$\Phi_{\rm IV}(k)=(1/2)c_0A^2x/(1+E/\omega)\ . \qquad \text{(A.6)}$$

These results are not very accurate for $E>\omega$, but this fact does not affect any final result obtained in the text.

Straightfoward evaluation of $\Phi_{\rm V}(k)-\Phi_{\rm XIII}(k)$ is a difficult problem, since in these cases we encounter summations over three momenta which are not independent but are connected by the momentum conservation law. We devise a shortcut means of evaluating them at the sacrifice of accuracy. The actual procedure will be described taking $\Phi_{\rm VIII}(k)$ as a typical example. We have to evaluate

$$\Phi_{\rm VIII}(k)=\left(\frac{g^2}{2V}\right)^2\sum_{k',k'',k'''}{}'\frac{\omega_{kk'}{}^2u'v'}{E+E'+E''+E'''}\left\{\frac{1}{(D_{kk'}+2E)D_{kk'}}+\frac{1}{(D_{k''k'''}+2E)D_{k''k'''}}\right\}, \qquad \text{(A.7)}$$

where the prime over the summation symbol indicates that the momentum conservation $\boldsymbol{k}'-\boldsymbol{k}=\boldsymbol{k}'''-\boldsymbol{k}''$ should be satisfied. Since we need not an accurate result for $E>\omega$, we can drop $2E$ from the second denominators. We can also omit E' from the first denominator because we have a factor $u'v'$ in the numerator. Furthermore, E', E'' and E''' can be replaced by $|\xi'|$, $|\xi''|$ and $|\xi'''|$, respectively, in all denominators without loss of accuracy. We introduce polar coordinates k', θ', φ' and k'', θ'', φ'', taking the z-axis coinciding with the vector $\boldsymbol{k}$. We have then

$$k'''^2=k_0{}^2\{2+(k''/k_0)^2-2\cos\theta'-2(k''/k_0)\cos\theta''$$
$$+2(k''/k_0)[\cos\theta'\cos\theta''+\sin\theta'\sin\theta''\cos(\varphi'+\varphi'')]\}\ , \qquad \text{(A.8)}$$

where both $|\boldsymbol{k}|$ and $|\boldsymbol{k}'|$ are replaced approximately by the momentum such that $\lambda=\hbar^2k_0{}^2/2m$. If we introduce new variables such as $\eta'=\xi'/c_0$, $\eta''=\xi''/c_0$, $\eta'''=\xi'''/c_0$, $t'=\cos\theta'$, $t''=\cos\theta''$, $\varphi=\varphi'+\varphi''$ together with the dimensionless quantities $L=\lambda/c_0$, $\delta=\omega/c_0$, then we have, after integrating with respect to ϕ',

$$\Phi_{\rm VIII}(k)=\frac{A^2c_0\delta}{32\pi^2}\int_{-L}^{\infty}d\eta'\int_{-L}^{\infty}d\eta''\int_{-t_0}^{1}dt'\int_{-1}^{1}dt''\int_{0}^{2\pi}d\varphi$$

$$\times\frac{1}{(E/c_0+|\eta''|+|\eta'''|)\sqrt{1+\eta'^2}}\left\{\frac{1}{(\delta+E/c_0+|\eta'|)^2}+\frac{1}{(\delta+|\eta''|+|\eta'''|)^2}\right\}, \qquad \text{(A.9)}$$

where

$$\eta'''=2L+\eta''-2Lt'-2L\sqrt{L(L+\eta'')}\,t''$$
$$+2\sqrt{L(L+\eta'')}(t't''+\sqrt{1-t'^2}\sqrt{1-t''^2}\cos\varphi)\ . \qquad \text{(A.10)}$$

The last relation has been derived from (A.8) by putting approximately $k''^2=k_0^2+2mc_0\eta''/\hbar^2$ and $k'''^2=k_0^2+2mc_0\eta'''/\hbar^2$. The lower limit of the t'-integration is chosen as $-t_0$, which was introduced in (2.26) and related to the maximum phonon energy by Eq. (2.27). The approximations made so far have little effect on the accuracy of the final result as long as we are interested in the main term of $\Phi_{\text{VIII}}(k)$.

To proceed further, we put, first of all, $-t_0=-1$. We believe that this approximation does not bring forth any large error, because the largest possible value of θ' is not largely apart from π and, moreover, $dt'/d\theta'$ is very small for θ' close to π.

Before taking a next step, we shall attempt to find a conventional method of evaluating the following integral

$$I(\eta'')=(8\pi)^{-1}\int_{-1}^{1}dt'\int_{-1}^{1}dt''\int_{0}^{2\pi}d\varphi f(\eta'''), \tag{A.11}$$

where $f(\eta''')$ may be any arbitrary function of η''' and is assumed to be expressed as a function of t', t'' and φ according to (A.10). We try to replace this triple integral approximately by a single integral

$$I'(\eta'')=\int_{-L}^{\infty}P(\eta'',\eta''')f(\eta''')d\eta''', \tag{A.12}$$

introducting an appropriately chosen probability density $P(\eta'',\eta''')$. Graphical consideration suggests that one may put, with a fairly good approximation,

$$P(\eta'',\eta''')=\begin{cases} P(\eta''), & -L<\eta'''<Y(\eta''), \\ 0, & \text{otherwise.}\end{cases}$$

In the actual procedure we determine $P(\eta'')$ and $Y(\eta'')$ so that we get an exact result for a simple case, $f(\eta''')\equiv\eta'''$. It follows then

$$P(\eta'')=(6L+2\eta'')^{-1}, \qquad Y(\eta'')=5L+2\eta'', \tag{A.13}$$

as easily verified by directly integrating both integrals and comparing the results. To check up to what extent this procedure is useful, we apply it to the evaluation of some directly integrable functions and compare the result, $I'(\eta'')$, with that of direct integration, $I(\eta'')$, in the following table.

	η''	$f(\eta''')\equiv\eta'''$	η'''^2	η'''^4	η'''^6	$[(5L-2\eta'')^2-\eta'''^2]^3$
$\left(\frac{I'-I}{I}\right)\times 100$ (errors in %)	$-L$	0	0	0	0	0
	0	0	+14	+84	+227	+6
	L	0	+9	+62	+86	+5

Note that the method is fairly reliable when aplied to the function $[(5L-2\eta'')^2-\eta'''^2]^3$, to which the actual integrand in (A.7) bears the best resemblance. Both functions have a maximum at $\eta'''=0$ and descreasing on both sides. We may thus expect errors of the same order of magnitude as those listed in the last columm when the present method is applied to the evaluation of $\Phi_{\text{VIII}}(k)$. Applying (A.12) with (A.13), we can transform (A.9) into the form

$$\Phi_{\text{VIII}}(k)=\frac{A^2c_0\delta}{4}\int_{-L}^{L}\frac{d\eta'}{\sqrt{1+\eta'^2}}\int_{-L}^{L}\frac{d\eta''}{6L-2\eta''}\int_{-L}^{5L-2\eta''}\left\{\frac{1}{(\delta+E/c_0+|\eta'|)^2}+\frac{1}{(\delta+|\eta''|+|\eta'''|)^2}\right\} \times\frac{d\eta'''}{E/c_0+|\eta''|+|\eta'''|}. \tag{A.14}$$

The approximate evaluation of the right-hand side is now possible. The first term in the brackets gives

$$-(1.38/4)c_0A^2x/(1+E/\omega)^2 \tag{A.15}$$

and the second term is found to be

$$-c_0 A^2 x(\omega/\lambda) \ln(\lambda/\omega) \tag{A.16}$$

except for numerical factor of order 1. Assuming $\omega/\lambda \ll 1$ we neglect (A.16) and get

$$\Phi_{\mathrm{VIII}}(k) = -(1.38/4) c_0 A^2 x/(1+E/\omega)^2 \,. \tag{A.17}$$

Evaluating all remaining $\Phi_i(k)$'s in similar ways, we find that $\Phi_{\mathrm{IX}}(k)$, $\Phi_{\mathrm{XII}}(k)$ and $\Phi_{\mathrm{XIII}}(k$ have the same contribution as $\Phi_{\mathrm{VIII}}(k)$ except for unimportant difference in E-dependent factor and all other $\Phi_i(k)$'s can be neglected. Thus, we have

$$\Phi_{\mathrm{IX}}(k) = \Phi_{\mathrm{XII}}(k) = \Phi_{\mathrm{XIII}}(k) = -(1.38/4) c_0 A^2 x/(1+E/\omega)^2 \,, \tag{A.18}$$

where we have assumed the same E-dependence as in $\Phi_{\mathrm{VIII}}(k)$.

By use of (A.4), (A.5), (A.6), (A.17) and (A.18), we get finally

$$\sum_i \Phi_i(k) = -\gamma c_0 A^2 x/(1+E/\omega) \tag{A.19}$$

with

$$\gamma = 2(1-\ln 2) + 2\ln 2 - 1/2 - 4(1.38/4) \doteqdot 0.1 \,, \tag{A.20}$$

where a common factor $(1+E/\omega)^{-1}$ is applied to all $\Phi_i(k)$'s. Since the positive and negative contributions to γ nearly cancels each other, there might be a large error in the value of γ arising from the rough estimate (A.17) and (A.18). We believe, however, that this does not exceed two hundred percents.

References

1) J. Bardeen, N. L. Cooper and J. R. Schrieffer: Phys. Rev. **106** (1957) 1175.
2) H. Fröhlich: Proc. Roy. Soc. **A215** (1952) 291.
3) N. N. Bogoliubov: Zh. eks. teor. Fiz. **34** (1958) 58 (Soviet Phys. JETP **7**, 41).
4) J. Goldstone: Proc. Roy. Soc. **A239** (1957) 267.
5) N. M. Hugenholtz: Physica **23** (1957) 481.
6) N. E. Phillips: Phys. Rev. **114** (1959) 676.
7) W. S. Corak and C. B. Satterwaite: Phys. Rev. **102** (1956) 662.
8) H. Horowitz: A. A. Silvidi, S. F. Malaker and J. G. Daunt: Phys. Rev. **88** (1952) 1182.
9) M. A. Biondi and M. P. Garfunkel: Phys. Rev. Letters **2** (1959) 143.
10) R. L. Richards and M. Tinkham: Phys. Rev. Letters **1** (1958) 318.
11) A. A. Abrikosov, L. P. Gor'kov and I. M. Khalantnikov: Zh. eks. teor. Fiz. cited in I. M. Khalatnikov and A. A. Abrikosov: Advances in Phys. **8** (1959) 45.
12) C. Dewitt (ed.): *The Many Body Problems* (Wiley, 1959) 343p.

JOURNAL OF THE PHYSICAL SOCIETY OF JAPAN, Vol. 15, No. 10, OCTOBER, 1960

Impurity Trapped Interstitials and the Low Temperature Annealing Stages of Irradiated Copper

By Ryukiti R. HASIGUTI

Department of Metallurgy, University of Tokyo

(Received May 7, 1960)

A semi-empirical method was developed to evaluate interaction energies of close impurity-atom-interstitial pairs. It was found that an undersize impurity atom provides with a deep trap for an interstitial, while an oversize impurity atom furnishes to an interstitial several shallow traps with different interaction energies. These results were applied to the annealing temperature problem of irradiated copper. Stage II was interpreted as due to the liberations and annihilations of several kinds of shallow trapped interstitials, and stage III was explained as due to the liberations and annihilations of deep trapped interstitials.

1. Introduction

The behaviors of lattice defects introduced into noble metals such as copper, gold and silver by electron, deuteron or neutron irradiations have been extensively investigated by many workers1). Copper is especially well investigated among these metals from both experimental and theoretical standpoints1). Nevertheless several most important problems are not yet solved. One of these important unsolved problems is the low temperature annealing stage problem of irradiated copper.

Annealing of lattice defects in copper takes place in five successive temperature stages1),2),3). The stage I ranges from about 14°K to about 65°K. The stage II has so wide a range that it is often called a garbage annealing stage. It extends from the end of stage I to the advent of stage III. The stage III has a fairly sharp range, which extends from about 240°K to about 300°K. The temperature range of stage IV is considerably different according to different authors, but it extends usually from about 100°C to about 200°C. The stage V is usually found in the range from about 300°C to about 400°C.

As far as the stage V is concerned, the interpretations by different authors agree with each other. We shall omit, therefore, to consider the stage V. The interpretations of lower four stages are quite confusing today, as will be shown in the next section.

The present author will propose in this paper a new interpretation which explains the lower four stages consistently. Interstitial atoms trapped by impurity atoms will play important roles in the interpretation of stages II and III. We shall investigate the behaviors of these impurity trapped interstitials from various points of view.

§ 2. Previous Interpretations of Annealing Stages

Earlier interpretations appeared in literatures up to 1955 were reviewed and tabulated by Glen4). Interpretations appeared since 1956 will be summerized in Table I. The last row shows the interpretation proposed by the present author in this paper.

Now we shall consider the five views shown in Table I. Earlier views up to 1955 will be

Table I. Interpretations of annealing temperature stages by different authors.

Annealing stages	I	II	III	IV
Seeger2) (1958)	c.p. m.r.	c.p. (V_2)	I	V
Van Bueren3) (1957)	c.p, m.r.	I	V_2	V
A.I. group5) (1956)	c.p.	c.p. (V_m)	I	V, I_m I^*, V^*
G.E. group6),7),8) (1959)	c.p. I	I^* (V_2)	V(?)	(?)
Illinois group9),10) (1956) (1958)	c.p. I	V_m	V	—
Present author	c.p. I	I^* (V_2, I_m)	I^{**}	V

c.p.: close-pair, m.r.: micro-recrystallization, I: interstitial, V: vacancy, V_2: divacancy, V_m: multivacancy, I_m: multi-interstitial, V^*: trapped vacancy, I^*: trapped interstitial, I^* in the lowest row: shallow trapped interstitial, I^{**}: deep trapped interstitial.

considered, when it will be necessary to do so. The ways of allocations of various lattice defects to four annealing stages in Table I are roughly divided into two categories. The views expressed by the first three groups of investigators belong to the first category, and those shown by the second two research groups make the second category.

The chracteristics of the first category are in that stage IV is considered to be due to the migration of free vacancies and that the stage III is considered to be due to the migration of free interstitials except the case of van Bueren[3]. In the second category, it is considered that the free interstitials migrate in the stage I and the free vacancies migrate in the stage III. All the research groups agree with each other in two points; i.e. in the first place close vacancy-interstitial (V–I) pairs annihilate at least partly in stage I, and in the second place free interstitials migrate always at lower temperatures than free vacancies.

It must be emphasized here that G. E. group[6),7),8] and Illinois group[10] have performed most beautiful experimental works concerning the stage I. More detailed works have never been done concerning the other stages. The results published by these two groups will be shown in Table II.

Table II. Interpretations of annealing sub-stages.

Sub-stages	I_A	I_B	I_C	I_D	I_E
Corbett et al.	c.p. (1)	c.p. (2)	c.p. (3)	I (corr.)	I (uncorr.)
Ill, group	c.p.	c.p.	c.p.	I	

c.p. (1), etc.: first closest pair, etc., (corr.): correlated recombination, (uncorr.): uncorrelated recombination.

G. E. group found five sub-stages in the stage I. After careful analyses of their results, they conclude that the first three substages are due to recombinations of close V–I pairs with different interaction energies, and that the last two sub-stages are due to migrations of free interstitials to recombine with correlated vacancies (sub-stage I_D) or with uncorrelated vacancies (sub-stage I_E). Illinois group also found a fine structure of the stage I.

It may be considered that the mechanisms of annealing in stage I were clarified as the results of investigations of G. E. group and Illinois group to such an extent as we can believe that free migrating interstitials, besides close V–I pairs, do contribute to the annealing processes in stage I. This means that the interpretations which include the allocations of free interstitials to stage II or III must be revised. On the other hand, it is highly probable from the experimental results on cold-worked copper[11] and quenched copper[12] that the stage IV is due to the migration of free vacancies. It seems that the confusion of interpretations by various schools comes mainly from the unclearness of stages II and III. It is the main objective of this paper to make these two stages clear.

§ 3. Evidences for trapping of Interstitials by Impurity Atoms

Impurity trapping of interstitials is by no means a new concept. It was first discussed by Lomer and Cottrell[13] in 1955. It was not, however, on the firm foundation of knowledges that they considered the impurity trapping of interstitialcies*, because important informations concerning the behaviors of interstitials in stage I annealing processes were lacking at that time. Many authors, who treated the annealing stage problems since 1956, rather disregarded the important roles of impurity trapped interstitials, although they considered, so to say, the auxiliary functions of these trapped interstitials, as some examples are seen in Table I.

There are many experimental evidences for impurity trapping of interstitials. We shall show here an evidence which is important from the point of view of the present paper.

According to Blewitt and others[14], the stage I annealing process is partially or completely suppressed in properly impurity doped copper as shown in Fig. 1. In this figure the lower curve shows the isochronal annealing behavior of 99.999+% copper neutron-irradiated at 14.5°K. The stage I is suppressed about 60% in 0.1% Be-doped specimen as shown by the middle curve. The complete suppression is seen in the upper curve, where the specimen is doped with 1% Be. The suppression of stage I annealing process can be understood, if it is considered that the defects, which migrate in the stage I, are trapped by beryllium atoms. If the migrating defects are interstitials, it is natural that they are trapped by undersize impurity atoms like beryllium. It is also possible for an oversize impurity atom to trap an interstitial by Eshelby's elastic interaction[15)]. This point will be discussed in detail later.

---

* As far as the static nature is concerned, an interstitialcy is considered to be the same as an interstitial.

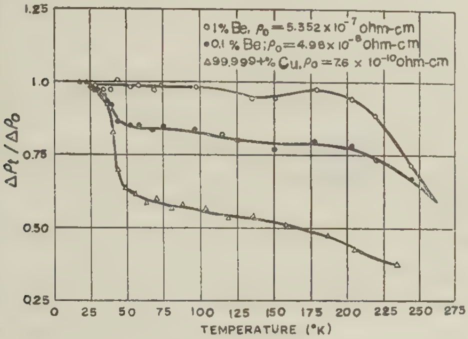

Fig. 1. The isochronal annealing curve of beryllium-doped copper following a reactor irradiation at 14.5°K. $\Delta\rho_t/\Delta\rho_0$ is the fraction of the radiation-induced resistivity remaining after each annealing pulse. (After Blewitt et al.[14)])

§ 4. Elastic Interaction between an Interstitial Atom and an Impurity Atom

Now we shall consider the interactions between an interstitial atom and an impurity atom. First of all let us consider the interaction calculated by the elasticity theory. According to Eshelby[15)], the interaction energy E_{int} between two defects with dilatations Δv_1 and Δv_2 is expressed by

$$E_{\text{int}}=-\frac{15d}{8\pi\gamma^2}\Delta v_1\Delta v_2\frac{\Gamma}{r^3}\,, \tag{1}$$

$$\gamma=3(1-\sigma)/(1+\sigma)\,, \tag{2}$$

$$\Gamma=\frac{2}{5}-2(l^2m^2+m^2n^2+n^2l^2)\,, \tag{3}$$

where d is a constant with negative value in the case of metals which is derived from elastic constants, σ is Poisson's ratio, r is the distance between two point defects, and l, m and n are direction cosines. The dilation Δv should be taken here as that in a body with a free surface. If $\Delta v_1\Delta v_2$ is negative and Γ is positive, the interaction will be attractive, because d is always negative in the case of metals.

The interaction can, however, be either attractive or repulsive for a given pair of defects, if the configuration of two defects changes, because the value of Γ can either be positive or negative according to the values of direction cosines. In other words an attractive interaction is expected from both negative and positive values of $\Delta v_1\Delta v_2$, which means that an interstitial is trapped by an oversize impurity atom as well as by an undersize impurity atom. This was pointed out in section 3.

An interstitial atom in a face-centered cubic lattice can take various forms in the crystal lattice, i.e. (1) an ordinary interstitial form, in which the interstitial atom occupies the the body center of cubic unit cell, (2) Huntington's C configuration[16)], and (3) a crowdion form. An atom in the ordinary interstitial form will be called simply an interstitial atom or an interstitial in this paper.

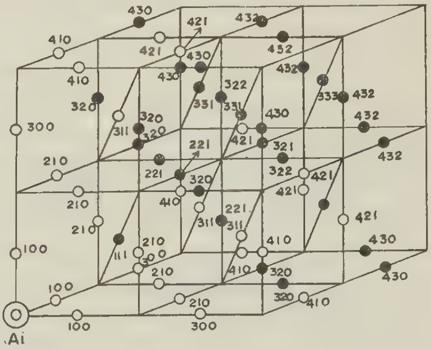

Fig. 2. Various configurations of impurity-atom-interstitial pairs in face-centered cubic lattice. ◎: substitutional impurity atom, ○: interstitial for $\Gamma>0$, ●: interstitial for $\Gamma<0$. No distinction is made between (100), (010), (001), etc. The unit of the coordinates is $a/2$.

Various possible configurations of impurity-atom-interstitial (A_i–I) complexes or associations are shown in Fig. 2. A double circle at the left *h* and lower corner shows a substitutional impurity atom (A_i) and open and solid circles indicate the possible positions of interstitial atoms. The figures at these circles show the coordinates of interstitials, of which the unit is in $a/2$, where a is the lattice constant. No distinction is made between (100), (010), (001), etc. in the figure. Open circles show the interstitial positions for $\Gamma>0$, and solid ones show those for $\Gamma<0$. The values of Γ for various configurations are given in

Table III. The distance r is expressed in unit of $a/2$ in the table.

The dilatations of interstitial (I), vacancy (V) and various impurity atoms are shown in Table IV. Impurity atoms in the middle columns of the table are those used in the experiments by Blewitt et al.[14], as some of them are shown in Figs. 1, 5 and 6. The right hand columns of the table contain impurity atoms usually found in high purity copper. They are shown in the order of decreasing amount in copper except phosphorus. Phosphorus is found in considerable amount in copper in some cases, and is not found at all in other cases.

Table III. r and Γ in the equation (1).

r^2		Γ	r^2		Γ
1	(100)	+0.400	19	(331)	−0.148
3	(111)	−0.267	21	(421)	+0.018
5	(210)	+0.080	25	(500)	+0.400
9	(300)	+0.400	25	(430)	−0.060
9	(221)	−0.192	27	(511)	+0.260
11	(311)	+0.086	27	(333)	−0.267
13	(320)	−0.026	29	(520)	+0.162
17	(410)	+0.290	29	(432)	−0.180
17	(322)	−0.210			

Table IV. Dilatations Δv of interstitial, vacancy and impurity atoms in copper.

Point defect	Δv in Ω	Impurity atom	Δv in Ω	Impurity atom	Δv in Ω
I	+2.8*	Be	−0.40	S	−0.57
I	+2.01**	Au	+0.42	Fe	−0.04
V	−0.6*	Zn	+0.26	As	−0.07
V	−0.45**	Ni	−0.07	Te	+0.47
		Si	−0.28	Se	−0.31
				Sb	+0.89
				Sn	+0.80
				P	−0.49

Ω: atomic volume of copper.
* From Tucker and Sampson (Acta Met. **2** (1954) 433).
** From Tewordt (Phys. Rev. **109** (1958) 61).

Fig. 3 shows interaction energy vs. A_i–I distance curves calculated from the equation (1) with $\Delta v_1 \Delta v_2 = 0.9\Omega^2$, where Ω is the atomic volume of copper. Energies are expressed in their absolute values. Curves 1 and 2 are for $\Gamma = +0.400$ and $\Gamma = -0.267$, respectively. Interaction energies of various A_i–I configurations with these two values of Γ are shown as open circles on the curves, and those with other values of Γ than these two are shown as triangles without accompanying curves.

As the Eshelby's equation is based on the elasticity theory, it cannot be applied to very close A_i–I pairs. Corbett et al.[6] hesitatingly use the elasticity equation to calculate the interaction energy of vacancy-interstitial pair as close as (300) configuration. Magnuson et al.[10] apply the same equation to estimate the interaction energy of interstitial pair in (222) configuration, although they point out that a careful atomic calculation should be made to obtain more reliable value. It seems after

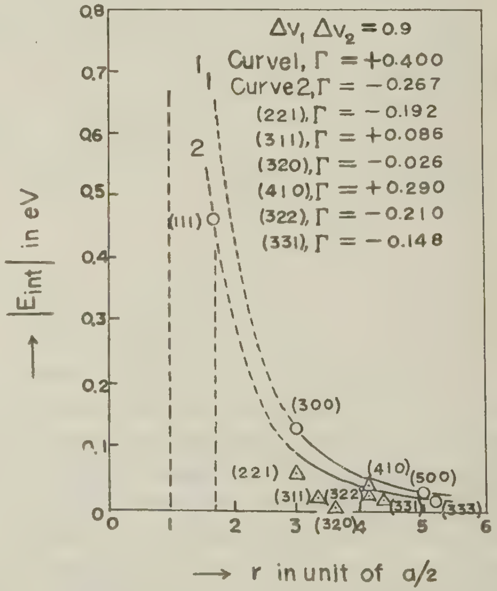

Fig. 3. Interaction energies calculated by elasticity theory. Dotted portions of the curves are rather meaningless, because elasticity theory fails there. Interaction energies are expressed in their absolute values.

all that the elasticity equation is not applicable inside $r=3\sim4$. The dotted portions of the curves in Fig. 3 are rather meaningless, because they are in the region where the equation (1) fails.

However, the interaction energies of close A_i–I pairs, where the elasticity theory fails, are what we want to know the most to elucidate the trapping behaviors of interstitials by impurity atoms. We shall consider this problem from a different point of view in the next section.

§ 5. Interaction Energies of Close Impurity-Atom-Interstitial Pairs

As mentioned above, the interaction energies of close A_i–I pairs with separations less than $r=3\sim4$ cannot be calculated by the elasticity equation. We shall use some experimental data to estimate the interaction energies at moment to avoid rather complicated straightforward atomic calculations.

In section 3, we referred to the experiments by Blewitt et al.[14] on the suppression of stage I annealing processes by impurity doping. Fig. 1 shows of examples of beryllium doped copper. These results can be interpreted as follows. In 1% beryllium doped copper (the upper curve in Fig. 1) all the interstitials produced by neutron irradiation are trapped by beryllium atoms, resulting in a disappearance of annealing stage I. These trapped interstitials are released from impurity atoms above about 200°K as is seen from the upper curve in Fig. 1. If the annealing kinetics for the temperature range above 200°K, which is evidently the annealing stage III, are known, we can calculate the activation energy, E, of this annealing process. If this annealing process is considered to be due to the release of impurity trapped interstitials, and if E is known, we are able to obtain the interaction energy from the equation

$$E=E_{\text{int}}+E_{\text{mig}}\ , \tag{4}$$

where E_{mig} is the migration energy of an interstitial. As the released interstitials will migrate very quickly to appropriate sinks and will disappear there, the dissociation of A_i–I pairs will form the rate determining process. Hence the above equation (4) is justified.

It would be possible to assume appropriate kinetics for the annealing process to obtain the activation energy, E, from the data of Blewitt et al., if necessary. However, the accurate estimation of activation energy from insufficient data is not necessarily important for the objective of this paper. We shall choose, therefore, the simplest possible way to estimate the activation energy.

It is recognized that the average absolute temperature, T_a, at which the annealing process is observed in usual measurements, is proportional to the activation energy, when the annealing processes in question are similar in nature to each other. This may be expressed as

$$T_a=cE\ , \tag{5}$$

where c is a proportionality constant. This equation is easily derived from the rate equations of annealing processes, if the same entropy of activation is assumed for different annealing processes. And this relation can be well checked experimentally, if well-defined suitable experimental data are chosen.

Now it may be assumed that the constants c's obtained from different experiments give the same values, if the annealing temperature stages concerned are the same with each other, because it is considered that the annealing modes are the same in the same annealing temperature stages. This assumption may be especially well applied in the case of such a well-defined stage as the stage III, with which we are concerned now. We shall use, therefore, the data of T_a and E of annealing stage III by several workers including those of deuteron irradiated copper by Overhauser[17] to obtain the value of c. Then c is calculated as

$$c=380°\text{K/eV}\ . \tag{6}$$

Taking the average annealing temperature as 230°K in the case of beryllium doped copper (Fig. 1), we obtain 0.49 eV for $A_{i(\text{Be})}$–I interaction energy from the equations (4) and (5) and the value (6). E_{mig} was put as 0.12 eV according to Corbett et al.[6] Now we shall put as

$$E_{\text{int(Be)}}=0.5\text{ eV}\ , \tag{7}$$

instead of 0.49 eV, considering the low accuracy of the method to obtained the interaction energy.

This energy, $E_{\text{int(Be)}}$, is considered to be for the closest $A_{i(\text{Be})}$–I pair with (100) configuration, because beryllium is an undersize atom. This point will be discussed later in detail.

The next problem is to combine the above obtained E_{int} with elasticity curve (Fig. 3). This was done in Fig. 4. An open circle at the left end of curve (2) indicates the $E_{\mathrm{int(Be)}}$ value for (100) configuration. The curve (1), which is the same as the curve (1) in Fig. 3, represents the elasticity equation (1).

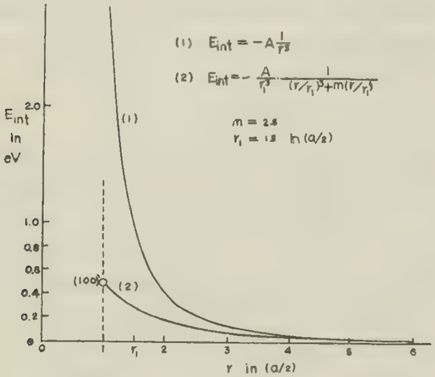

Fig. 4. Interaction energies between a beryllium atom and an interstitial in copper. Curve (2) is calculated from the equation (8). Curve (1) is calculated from the elasticity equation for comparison.

Now we assume a relation between E_{int} and r as

$$E_{\mathrm{int}}=-\frac{A}{r_1^3}\cdot\frac{1}{(r/r_1)^3+m(r/r_1)}\,, \qquad (8)$$

to obtain the values of interaction energy at various separations. The equation (8) is just a conventional expression which reduces to the elasticity equation at large separations as is seen from the curve (2) in Fig. 4. The curve (2) is obtained, putting $m=2.5$ and $r_1=1.5$ (in $a/2$).

Now the interaction energies of various A_i–I configurations are calculated by means of the equation (8). The results are shown in Tables V and VI. These values are only to obtain a knowledge of the order of magnitudes.

§ 6. Stable and Unstable Configurations

Various A_i–I configurations were shown in Fig. 1 in section 3. We have to distinguish, however, between stable and unstable configurations as follows. Let us first examine an undersize impurity atom, which attracts an interstitial, if Γ is positive. (100) configuration is of course stable, because it is the closest pair with attractive force.

Table V. Various configuration of impurity-atom-interstitial pairs in the case of undersize beryllium atoms in copper crystal. The (300) configuration and others are unstable and will change to the (100) configuration as indicated by the arrow.

$\Gamma>0$, undersize atom (attraction)			
(100)	stable	$E_{\mathrm{int}}\approx0.5$,	$E\approx0.62$
(300)	⟶ (100)		
(210)	⟶ (100)		
(311)	stable	$E_{\mathrm{int}}\approx0.01$,	$E\approx0.13$
(410)	⟶ (210)	⟶ (100)	
(421)	⟶ (410)	⟶ (210)	⟶ (100)

Table VI. Various configurations of impurity-atom-interstitial pairs in the case of oversize gold atoms in copper crystal. The arrows indicate the change to the stable configuration.

$\Gamma<0$, oversize atom (attraction)			
(111)	stable	$E_{\mathrm{int}}\approx0.17$,	$E\approx0.29$
(221)	stable	$E_{\mathrm{int}}\approx0.03$,	$E\approx0.15$
(320)	stable	$E_{\mathrm{int}}\approx0.003$,	$E\approx0.12$
(322)	⟶ (221)		
(331)	stable	$E_{\mathrm{int}}\approx0.01$,	$E\approx0.13$
(430)	⟶ (320)		
(333)	⟶ (331)		
(432)	⟶ (322)	⟶ (221)	

It is usually considered that an interstitial moves always in ⟨100⟩ direction[10]. This means that an interstitial makes interstitialcy movements, when it migrates through the crystal lattice. In other words it has the "C configuration" of Huntington[16] as the saddle point, when it makes migration through the lattice. This restriction of the migrating direction is a condition for considering stable configurations.

Now the (300) configuration will be considered. An interstitial at (300) position will move towards the impurity atom by the attractive force, resulting in an (100) configuration. Thus the (300) is an unstable configuration. The results of this kind of considerations are shown in Table 5 for an undersize impurity atom with $\Gamma>0$. It is seen that (300), (210), (410), (421), etc. are all unstable, all reducing to (100) configuration. The only one stable position other than (100) is (311), which has $E_{\text{int}} \approx 0.01$ eV. (311) is stable, because (111) is a repulsive position.

It should be emphasized here, however, that the occurence of (311) is rather seldom, because it cannot be reached from any other position in the eight unit cells in Fig. 2, while all the open circled positions other than (311) reduce to (100) positions as shown in Table V. (311) cannot be reached from (331), because (331) is a repulsive position. It is possible of course to reach (311) from (511), but (511) configuration has an almost negligible interaction. It may be concluded after all that (100) is almost the unique stable configuration for an undersize impurity atom, although it may be an over-simplification to neglect completely the (311) positions.

The activation energy of annealing process due to the dissociation of $A_{i(\text{Be})}$–I pairs is 0.62 eV as shown in Table V. This is for the stage III annealing process. Dissociated interstitials disappear very quickly recombining with vacancies, resulting in second order kinetics.

§ 7. Oversize Impurity Atoms

The situation for an oversize impurity atom is quite different. The results of considerations along the same line as before are given in Table 6 for an impurity gold atom, which is an oversize atom. An oversize atom attracts an interstitial, when Γ is negative. As are shown in the table, there are four stable configurations in the eight unit cells of Fig. 1. The occurrences of these configurations are comparatively evenly distributed. The values of activation energies range from 0.12 eV to 0.29 eV as shown in Table VI. The interaction energies for $A_{i(\text{Au})}$–I pairs were calculated using the equation (8) with constants obtained through $A_{i(\text{Be})}$–I interaction.

The results in Table VI should be compared with Fig. 5, which is a reproduction of the experimental results on gold-doped copper by Blewitt et al.[14] As are expected from the results in Table VI, the annealing stages of irradiated gold-doped copper should extend rather continuously from the end of stage I to some higher temperatures as a result of overlapping of several annealing processes with different activation energies. This type of annealing is found in Fig. 5. In other words Blewitt's results on gold-doped copper are explained at least qualitatively by our model. Incidentally Blewitt et al. explain their results in a different way[14].

Blewitt et al. performed further experiments on nickel-, silicon-, and zinc-doped copper. These results are all explained at least qualitatively by our model.

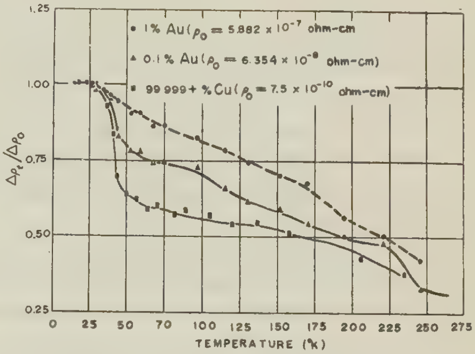

Fig. 5. The isochronal annealing curve of gold-doped copper following a reactor irradiation at 14.5°K. $\Delta\rho_t/\Delta\rho_0$ is the fraction of the radiation induced resistivity remaining after each annealing pulse. (After Blewitt et al.[14])

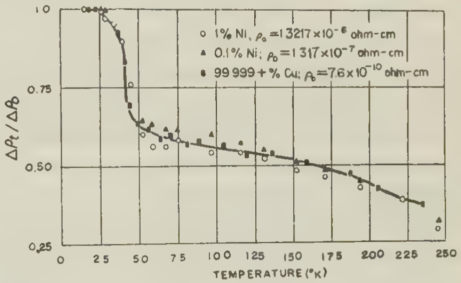

Fig. 6. The isochronal annealing curve of nickel-doped copper following a reactor irradiation at 14.5°K. $\Delta\rho_t/\Delta\rho_0$ is the fraction of the radiation-induced resistivity remaining after each annealing pulse. (After Blewitt et al.[14])

The addition of 1% nickel shows almost no influence on the annealing behaviors of copper, as is seen from Fig. 6. This is understandable from the small dilatation of nickel (see Table IV). But if the interaction energy of $A_{i(\text{Ni})}$–I is calculated from the equation (8) with constants obtained through beryllium-atom-interstitial interaction, there should be a small interaction, which is not found in Fig. 6. This discrepancy may be due to some effects other than atomic radius effect.

Although the behaviors of silicon (undersize) and zinc (oversize) are understood qualitatively on the basis of atomic radius concept, it seems there are some additional effects again in these cases. These effects may presumably be valence effects. To inquire further, however, into this problem is not the aim of this paper.

§ 8. Conclusions

(1) Both undersize impurity atoms and oversize impurity atoms trap interstitials.

(2) Various configurations of impurity-atom-interstitial pairs were considered.

(3) An undersize impurity atom provides with a deep trap, if the dilatation is large. An undersize atom with a small dilatation gives rise of course to a shallow trap.

(4) An oversize impurity atom furnishes several shallow traps with different interaction energies.

(5) Annealing temperature stages of irradiated copper are interpreted as follows.

(5a) Stage I is considered after G. E. group and Illinois group to be due to the annihilations of close V–I pairs and free migrating interstitials.

(5b) Stage II is interpreted as due to the liberations and annihilations of several kinds of shallow trapped interstitials (I*) with different interaction energies. The annihilations of divacancies and the dissociations and annihilations of multi-interstitials will take place in this stage, if they exist.

(5c) Stages III is considered to be due to the liberations and annihilations of deep trapped interstitials (I**) with almost unique interaction energy. The annihilation of liberated interstitials is achieved by the recombination with vacancies, which results in second order kinetics.

(5d) Stages IV is considered to be due to the annihilation of vacancies.

(5e) These interpretations are summarized in the last row of Table I.

Note added in proof. We have recently received a preprint of an article entitled "Thermally Activated Point Defect Migration in Copper" by C. J. Meechan, A. Sosin and J. A. Brinkman, in which A. I. group have modified their annealing model from the one presented in the present paper as the A. I. model.

References

1) See the following review articles. G. H. Kinchin and R. S. Pease: Rep. Progr. Phys. **18** (1955) 1.
J. W. Glen: Adv. Phys. **4** (1955) 381.
K. Lintner and E. Schmid: Ergebn. exakt. Naturw. **28** (1955) 302.
F. Seitz and J. S. Koehler: Solid State Phys **2** (1956) 305. See also ref. (2).
2) A. K. Seeger: Second U. N. Int. Conf. Peacef Uses Atomic Energy, P/998 (1958).
3) H. G. van Bueren: Philips Res. Rep. **12** (1957) 1; **12** (1957) 190.
4) J. W. Glen: Adv. Phys. **4** (1955) 381.
5) C. J. Meechan and J. A. Brinkman: Phys. Rev. **108** (1956) 1193.
6) J. W. Corbett, R. B. Smith and R. M. Walker: Phys. Rev. **114** (1959) 1452.
7) J. W. Corbett, R. B. Smith and R. M. Walker: Phys Rev. **114** (1959) 1460.
8) J. W. Corbett and R. M. Walker: Phys. Rev. **115** (1959) 67.
9) F. Seitz and J. S. Koehler: Solid State Phys. **2** (1956) 305.
10) G. D. Magnuson, W. Palmer and J. S. Koehler: Phys. Rev. **109** (1958) 1990.
11) D. Bowen, R. R. Eggleston and R. H. Kropschot: J. Appl. Phys. **23** (1952) 630. See also ref. (3).
12) G. Airoldi, G. L. Bacchella and E. Germagnoli: Phys. Rev. Letters, **2** (1959) No. 4, p. 145.
13) W. M. Lomer and A. H. Cottrell: Phil. Mag. **46** (1955) 711.
14) T. H. Blewitt, R. R. Coltman, C. E. Klabunde and T. S. Noggle: J. Appl. Phys. **28** (1957) 639.
15) J. D. Eshelby: Acta Met. **3** (1955) 487.
16) H. B. Huntington: Phys. Rev. **91** (1953) 1092.
17) A. W. Overhauser: Phys. Rev. **94** (1954) 1551.

JOURNAL OF THE PHYSICAL SOCIETY OF JAPAN, Vol. 15, No. 10, OCTOBER, 1960

The Structure Analysis of $AuCu_3$ by Means of a Fourier Transformation of X-ray Diffuse Scatterings

By Kenji DOI

Japan Atomic Energy Research Institute, Tokai-mura, Naka-gun, Ibaraki-ken, Japan

(Received December 10, 1959)

The method of analysing the two-dimensional disordered structure using the function;

$$\varphi_H(x_1, x_2)=\iint A(s_1,s_2)\frac{\sin \pi a_1(s_1-s_1{}^H)}{\pi(s_1-s_1{}^H)}\cdot\frac{\sin \pi a_2(s_2-s_2{}^H)}{\pi(s_2-s_2{}^H)}\exp 2\pi i\{(s_1-s_1{}^H\cdot x_1)+s_2-s_2{}^H\cdot x_2)\}ds_1ds_2$$

is described, where $s_1{}^H$ and $s_2{}^H$ mean the coordinates of a relpoint $H(=hk0)$, and $A(s_1, s_2)$ the *amplitude* of the diffuse scattering at the point (s_1, s_2) in reciprocal space.

The method is applied to the disordered structure of Cu_3Au projected upon (001), giving the statistical parameters describing the atomic composition of each atomic site. The unit cell compositions, which are readily derived from the atomic site compositions, are found appreciably deviated from those corresponding to the bulk composition of Cu_3Au, the Au-rich cell being surrounded by the Cu-rich ones. This suggests that the ordering of this alloy progresses rather by the inter- changes of neighbouring atoms than by the growth of domains in which Au atoms are supposed not to come in contact with each other.

In Appendices remarks are given in relation to the short-range order parameters, and the significances of phase assignments for diffuse scatterings are discussed.

§ 1. Introduction

The diffuse scatterings produced by the disordered alloy crystals have been usually interpreted in terms of the short-range order parameters which specify the statistical characters of atom *pairs* of given separation and orientation. For instance Cowley[1] has developed a method of deriving the short-range order parameters from the diffuse scattering of X-rays by the Fourier transformation of *intensity* distribution in reciprocal space. It is noted, however, that the short-range order parameters alone cannot be considered as a full description of the disordered structure, in the sence that in usual structure analyses Patterson maps cannot be regarded as to give full informations on crystal structures.

Just as in the case of the usual perfect crystal analysis, it was shown[2] that certain plausible assumptions as to the structure examined made it possible to assign phase angles to the diffuse scatterings, and thus to derive more direct informations on the statistical structure of the disordered crystal, than those derived from intensity distribution. In other words, the statistical parameters describing the disordered structure can be deduced not only for the atom *pairs* but also for the configurations of atoms present in the structure examined. An application was given for the structure analysis of Guinier-Preston zone[3] which gives rise to diffuse scatterings in the neighbourhoods of the relpoints of matrix crystal.

In this paper the method is applied to the diffuse scatterings distributed in the neighbourhoods of the superlattice points of the $AuCu_3$ crystal above the critical point; giving as results the statistical parameters specifying more directly the disordered state of alloy structure than the usual short-rang order parameters.

§ 2. The principle of analysis

Let us consider a crystal in which the electron density distribution is represented by a function $\rho(\boldsymbol{x})$ which is not necessarily periodic with respect to the coordinate $\boldsymbol{x}$. The intensity of X-rays diffracted by this is given by

$$I(\boldsymbol{s})=|A(\boldsymbol{s})|^2 \qquad (1)$$

with

$$A(\boldsymbol{s})=\int \rho(\boldsymbol{x}) \exp -2\pi i \boldsymbol{s}\cdot \boldsymbol{x} dv_x \, . \qquad (2)$$

With inversion of (2), we have

$$\rho(\boldsymbol{x})=\int A(\boldsymbol{s}) \exp 2\pi i \boldsymbol{s}\cdot \boldsymbol{x} dv_s \, . \qquad (3)$$

It is noted here that the Fourier reciprocity (2) and (3) need not be restricted to the cases where $\rho(x)$ is strictly periodic, that is to say, structure analyses using the Fourier relations (2), (3) are feasible for disordered structures as well as for the perfectly ordered structures, *provided that the phase angles can be defined without ambiguity and that they can be assigned correctly in reciprocal space*[2),3)].

The principle of analysis here developed consists of taking into account of the intensity distributions only in the limited region of reciprocal space, which permits us to assign phase angles of scattered X-rays with less arbitrary and more plausible assumptions as will be seen at the end of this section.

For example, let us take a two-dimensional structure $\rho(x_1, x_2)$ and consider a function related to it:

$$\varphi_H(x_1, x_2)=\iint A(s_1, s_2) K_{a_1}(s_1-s_1^H) \cdot K_{a_2}(s_2-s_2^H) \exp 2\pi i\{(s_1-s_1^H\cdot x_1)+(s_2-s_2^H\cdot x_2)\} ds_1 ds_2 \qquad (4)$$

with

$$K_{a_1}(s_1)=\frac{\sin \pi a_1 s_1}{\pi s_1} \quad \text{and} \quad K_{a_2}(s_2)=\frac{\sin \pi a_2 s_2}{\pi s_2} \, , \qquad (5)$$

where a_1 and a_2 represent the unit translations in the directions of two crystallographic axes, and s_1^H and s_2^H mean the coordinates of a relpoint $H(=hk0)$. The kernel $K_{a_1}(s_1-s_1^H)\cdot K_{a_2}(s_2-s_2^H)$ permits us to calculate the right-hand side of (4) only with the knowledge of $A(s_1, s_2)$ in the neighbourhood of H, as the kernel decreases with the deviation of (s_1, s_2) from H, and in particular, it vanishes at all the relpoints other than H, where $s_1=s_1^H$ and $s_2=s_2^H$. After rearrangements using the convolution theorem[2),4)], the right-hand side of (4) is written;

$$\varphi_H(x_1, x_2)=\iint \rho(x_1', x_2') \Delta(x_1-x_1', x_2-x_2') \exp -2\pi i(s_1^H x_1'+s_2^H x_2') dx_1' dx_2' \, , \qquad (6)$$

where

$$\Delta(x_1, x_2)=\iint \frac{\sin \pi a_1 s_1}{\pi s_1} \cdot \frac{\sin \pi a_2 s_2}{\pi s_2} \exp 2\pi i(s_1 x_1+s_2 x_2) ds_1 ds_2 \, . \qquad (7)$$

As it is seen that

$$\Delta(x_1, x_2)=\begin{cases} 1 & \text{for} \quad |x_1|<a_1/2 \quad \text{and} \quad |x_2|<a_2/2 \, , \\ 0 & \text{otherwise} \end{cases} \qquad (8)$$

the right-hand side of (6) is interpreted as *the structure factor of index* (H) *for the electrons contained in the rectangular region which is defined by*

$$|x_1-x_1'|<a_1/2 \quad \text{and} \quad |x_2-x_2'|<a_2/2 \qquad (9)$$

Practically, the integration of (4) is replaced by a discrete summation to give the function $\Phi_H(x_1, x_2)$ defined as

$$\Phi_H(x_1, x_2)=\sum_{(n)}\sum A(s_1^n, s_2^n) K_{a_1}(s_1^n-s_1^H) K_{a_2}(s_2^n-s_2^H) \cdot \exp 2\pi i\{(s_1^n-s_1^H\cdot x_1)+(s_2^n-s_2^H\cdot x_2)\} \, , \qquad (10)$$

in place of the function $\varphi_H(x_1, x_2)$ of (4), s_1^n and s_2^n being the coordinates of the discrete points in reciprocal space. When we sample the points *regularly* in reciprocal space, i. e.

$$\left.\begin{aligned} s_1{}^n - s_1{}^H &= \frac{n_1}{a_1 L_1} \qquad (n_1=0,\ \pm 1,\ \pm 2,\ \cdots,\ \pm M_1) \\ s_1{}^n - s_2{}^H &= \frac{n_1}{a_2 L_2} \qquad (n_2=0,\ \pm 1,\ \pm 2,\ \cdots,\ \pm M_2) \end{aligned}\right\} \tag{11}$$

L_1 and L_2 being integers greater than 1, then it is proved that[2)]

$$\Phi_H(x_1, x_2) \propto \overline{\varphi_H(\overline{x_1, x_2})}^{L_1 L_2} \tag{12}$$

provided that M_1 and M_2 in (11) are both sufficiently large, where $\varphi_H(x_1, \overline{x_2})^{L_1 L_2}$ means the values of $\varphi_H(x_1, x_2)$ averaged over the points $(x_1 \pm m_1 a_1 L, x_2 \pm m_2 a_2 L_2)$ with $m_1, m_2 = 0, 1, 2, 3, \cdots$, etc. When we write the values of $\rho(x_1, x_2)$ averaged over the points $(x_1 \pm m_1 a_1 L_1, x_2 \pm m_2 a_2 L_2)$ as $\overline{\rho(x_1, x_2)}^{L_1 L_2}$, we have

$$\overline{\varphi_H(x_1, x_2)}^{L_1 L_2} = \iint \overline{\rho(x_1', x_2')}^{L_1 L_2} \Delta(x_1 - x_1', x_2 - x_2') \exp -2\pi i(x_1' s_1{}^H + x_2' s_2{}^H) dx_1' dx_2' \ . \tag{13}$$

Now we come to the point where the problem of phase assignment for $A(s_1, s_2)$ may be answered correctly, when phase angle can be *defined* at the point (s_1, s_2). In Appendix II we shall consider the case where the phase angles are not to be defined and therefore the substantial phase assignment seems impossible.

Since $A(s_1{}^n, s_2{}^n)$'s for regularly sampled $(s_1{}^n, s_2{}^n)$'s (see Eq. (8)), are the Fourier transforms of $\overline{\rho(x_1, x_2)}^{L_1 L_2}$, they are real if

$$\overline{\rho(x_1, x_2)}^{L_1 L_2} = \overline{\rho(-x_1, -x_2)}^{L_1 L_2} \ . \tag{14}$$

The structure satisfying the condition (14) shall be called *statistically centrosymmetric*. As $A(s_1, s_2)$ is a continuous function of s_1 and s_2, the real function $A(s_1{}^n, s_2{}^n)$ should pass a nodal line $|A(s_1, s_2)| = 0$, when $A(s_1, s_2)$ canges its sign[5)]. Under the statistical centrosymmetry (14) we can thus assign the same sign to all points in a limited region of reciprocal space surrounded by a nodal line.

§ 3. The structure of AuCu₃ above the critical temperature

The intensity distribution of diffuse scatterings of AuCu₃ annealed at 405°C were measured by Cowley[1)]. The observed intensity $I_{\mathrm{dif}}(s_1, s_2, 0)$ in the plane passing through the origin and perpendicular to [001] was sampled according to (11) with $L_1 = L_2 = 15$*. The observed values were normalized to the electronic unit using the following relation[1),6)]

$$\underset{\binom{\text{reciprocal}}{\text{unit cell}}}{\iint} \frac{I_{\mathrm{dif}}(s_1, s_2, 0)}{C_{\mathrm{Au}} C_{\mathrm{Cu}} (f_{\mathrm{Au}} - f_{\mathrm{Cu}})^2} ds_1 ds_2 = \sum_n \alpha(00n) \tag{15}$$

where f_{Au} and f_{Cu} mean the atomic form factors of Au and Cu at the point $(s_1, s_2, 0)$ of the reciprocal space, C_{Au} and C_{Cu}, the atomic composition of Au and Cu, viz. $C_{\mathrm{Au}} = 1/4$ and $C_{\mathrm{Cu}} = 3/4$ for this case. $\alpha(lmn)$'s in the right-hand side are the short-range order parameters which were determined by Cowley by means of the Fourier transformation of intensity distribution.

The phase angles of the structure amplitudes at relpoints (100), (010) and (110) were assumed to be zero**, implying that the origin of direct space was set at an atomic site where Au atoms are of the highest concentration. One can then assign the same phases to all the points sampled after (11), assuming the statistical centrosymmetry (14) for $L_1 = L_2 = 15$. With the normalized values of $I_{\mathrm{dif}}(s_1, s_2, 0)$ (Eq. (15)) and the phase assignment described above, the function

---

* The detailed discussion on the point-samplings in reciprocal space, which is related to the resolving power of intensity observation, is found in the previous paper of the author[2)].

** One may adopt an alternative assumption that they have the values π. It was found, however, that the assumption led to the negative values of $c(ij)$, which are contradictory to the definition of this quantity (see Eq. (20)).

$$A(s_1, s_2, 0)=+\left\{\frac{I_{\mathrm{dif}}(s_1, s_2, 0)}{(f_{\mathrm{Au}}-f_{\mathrm{Cu}})^2}\right\}^{1/2}(Z_{\mathrm{Au}}-Z_{\mathrm{Cu}}) \tag{16}$$

was calculated, where Z_{Au} and Z_{Cu} mean the number of electrons contained in Au and Cu atoms respectively. By the substitution of (16) into (10) the Fourier transforms of amplitude distribution were made, the relpoint H in (10) was set at three superlattice points (100), (010) and (110), so that equation (10) may give us three φ-functions, viz. $\overline{\varphi_{(100)}(x_1, x_2)}^{L_1L_2}$, $\overline{\varphi_{(010)}(x_1, x_2)}^{L_1L_2}$ and $\overline{\varphi_{(110)}(x_1, x_2)}^{L_1L_2}$ as shown in Figs. 1 (a) and (b). The φ-function for (100) was derived from the one for (010) by permuting the axes a_1 and a_2 because of the tetragonal symmetry of $A(s_1, s_2)$. All the φ-functions are found real, the summand of (10) being centro-symmetrical.

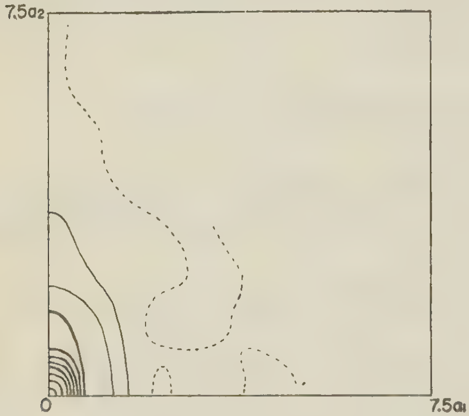

Fig. 1 (a). The function $\overline{\varphi_{(010)}(x_1, x_2)}^{L_1L_2}$. Thick contours represent the levels of 24, 21, 18, 15, 12, 9, 6 and 3 electron units, and thin ones the levels of 1.5 and 0.75 electron units respectively. Zero levels are broken.

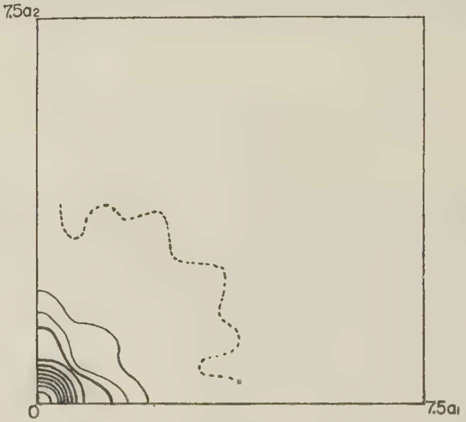

Fig. 1 (b). The function $\overline{\varphi_{(110)}(x_1, x_2)}^{L_1L_2}$. The contours represent the same levels as in (a).

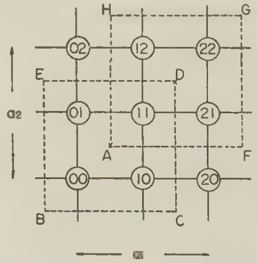

Fig. 2. The structure of Cu$_3$Au projected upon (001). Small circles represent the atomic sites which constitute the projection of face-centred cubic lattice. Points A and D are two sampling points of φ-functions.

The structure of AuCu$_3$ projected upon (001), which is denoted by $\overline{\rho(x_1, x_2)}^{L_1L_2}$ is represented in Fig. 2, where the atomic site at the position $(ia/2, ja/2)$ is denoted by (ij). Now let us consider the φ-functions at point $A(a/4, a/4)$, for which the dotted rectangle $BCDE$ gives the region defined by equation (9). As the Δ-function has a constant value of 1 inside the rectangle, we have, when we assume each atomic site occupied by a point-like atom of electronic content $r(ij)$,

$$\left.\begin{aligned}
\overline{\varphi_{(100)}\left(\frac{a}{4}, \frac{a}{4}\right)}^{L_1L_2} &= r(00)+r(01)-r(10)-r(11)\\
\overline{\varphi_{(010)}\left(\frac{a}{4}, \frac{a}{4}\right)}^{L_1L_2} &= r(00)-r(01)+r(10)-r(11)\\
\overline{\varphi_{(110)}\left(\frac{a}{4}, \frac{a}{4}\right)}^{L_1L_2} &= r(00)-r(01)-r(10)+r(11)
\end{aligned}\right\} \tag{17}$$

As these are three independent linear equations for 4 unknowns, we can solve them for $r(00)$

$-r(10)$, $r(00)-r(01)$ and $r(00)-r(11)$. Next, let us sample the values of φ-functions at point $D(3a/4, 3a/4)$, the region characterized by the non-zero constant value of Δ-function is now given by the rectangle *AFGH*, which holds one atomic site (11) in common with the rectangle *BCDE*. We have three linear equations analogous to (17) for the atomic sites contained in the rectangle *AFGH*, which, combined with (17), permit us to calculate the values of $r(00)-r(12)$, $r(00)-r(21)$ and $r(00)-r(22)$. By sampling the φ-function in such a way that two rectangles defined by (9) for every adjacent sampling points may possess always one atomic site in common, we can derive the values of $r(00)-r(ij)$'s for all (ij)'s.

As a matter of fact, it was found that, for the sites (IJ)'s such that

$$I^2+J^2>X^2\sim 60 \tag{18}$$

the values of $r(00)-r(IJ)$'s were almost constant. We can then assume that

$$c(IJ)\sim C_{\mathrm{Au}}=\frac{1}{4}\,, \tag{19}$$

where $c(ij)$ means the atomic compositon of Au at the site (ij), because we can write $r(ij)$ as

$$r(ij)=Z_{\mathrm{Au}}c(ij)+Z_{\mathrm{Cu}}[1-c(ij)]\ . \tag{20}$$

The we have for the site (IJ)'s

$$r(00)-r(IJ)=r(00)-\frac{1}{4}Z_{\mathrm{Au}}-\frac{3}{4}Z_{\mathrm{Cu}}\ . \tag{21}$$

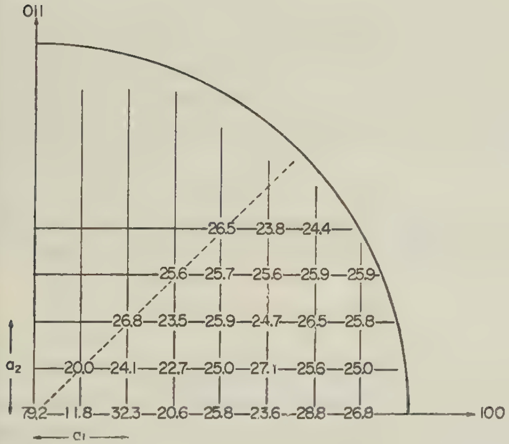

Fig. 3. The percent values of $c(ij)$'s, the Au-concentration at the site (ij)'s. The values for the upper half of the figure are derived from those for the lower half by the reflection with respect to the dotted line. The great circle represents the region outside of which the values of $c(ij)$'s are approximately constant (Eq. (16)).

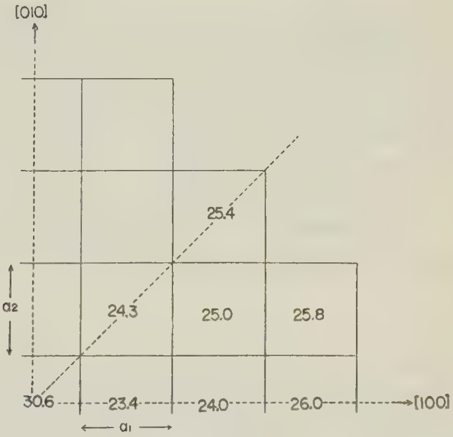

Fig. 4. The percent values of $\kappa(ij)$'s, the Au-concentration of unit cell centred at the site (ij). The values for the upper half of the figure are derived from those for the lower half by the reflaction with respect to the dotted line.

As the left-hand side of (21) is obtained in the electronic scale (Eq. (15)), it is possible to determine the value of $r(00)$ and hence all the values of $r(ij)$'s. The values of $c(ij)$'s are then calculated using Eq. (20) giving the results as shown in Fig. 3. In this figure a large circle represents the region outside of which the condition (19) is approximately satisfied. At the neighbourhood of the origin the Au-rich and Cu-rich sites are arranged almost alternatively.

Whereas the short-range order parameter $\alpha(lmn)$ concerns only to the statistics of atom pairs, the values of $c(ij)$'s here obtained give the information on the statistics of the *squares constituted from* 15×15 *atomic sites* in terms of which the averaged structure $\rho(x_1, x_2)^{L_1L_2}$ ($L_1=L_2=15$) is described.

It is interesting to calculate *the atomic composition of the unit cell centred at the site* (ij), as defined

$$\kappa(ij)=\frac{1}{4}\Big[c(ij)+\frac{1}{2}\{i+1, j)+c(i-1, j)+c(i, j+1)+c(i, j-1)\}$$
$$+\frac{1}{4}\{c(i+1, j+1)+c(i+1, j-1)+c(i-1, j+1)+c(i-1, j-1)\}\Big]. \tag{22}$$

The values of $\kappa(ij)$'s are shown in Fig. 4, where one can see clearly the deviations from $C_{\mathrm{Au}}=25\%$, which may possibly be attributed to the termination errors in the summation of (10). It must be noted, however, that the values in question are those averaged over 9 adjacent sites forming a unit cell, and if we make estimations for those effects[7] it is found that the period of diffraction ripples due to the termination is of the order of $a_1/2$, i. e. the distance between twe adjacent sites. Therefore it is concluded that the finite termination in (10) can be regarded as almost ineffective as far as the values of $\kappa(ij)$'s are concerned. Then it is seen that the unit cell centred at the origin shows the substantial excess in Au-concentration, while in the region surrounding the origin cell there found the unit cells which are in defects of the Au-concentration. The avaraged value of $\kappa(ij)$'s within the circle of Fig. 3 is found to be 25.0%, that is, the value of C_{Au}.

These deviations in the unit cell atomic compositions from those of perfectly ordered structure mean that the diffuse scattering may not be explained by the models as adopted by Wilson[8], where Au atoms are supposed not to come in contact leaving the unit cell compositions unchanged. It is therefore concluded that the ordering of this alloy progresses rather by the interchanges of the neighbouring atoms, than by the growth of the domains in which the perfect order is maintained by keeping all the Au atoms from being in contact with each other. The conclusion is in agreement with that of Edmunds and Hinde[9] arrived at from quite a different point of view. On the other hand Steeple and Edmunds[10] have given a similar result for the ordering of $\mathrm{CdMg_3}$.

Appendix I. The Relation of $c(ij)$ to the Short-range Order Parameters

When we write the short-range order parameter $\alpha(lmn)$ as

$$\alpha(lmn)=1-\frac{1}{C_{\mathrm{Au}}}n_{\mathrm{CuAu}}(lmn) \tag{A. 1}$$

where $n_{\mathrm{CuAu}}(lmn)$ means the proportion of the pairs Cu–Au whose separation and orientation are specified by the triplet of integers (lmn), our result as represented in Fig. 3 should be related to the values of of $\alpha(lmn)$'s projected upon l–m plane, say,

$$\alpha(lm)\equiv\sum_n \alpha(lmn)=1-\frac{1}{C_{\mathrm{Au}}}\sum_n n_{\mathrm{CuAu}}(lmn)\,, \tag{A. 2}$$

because the proportion of pairs $n_{\mathrm{CuAu}}(lmn)$ can be expressed as

$$\sum_{ijk}[1-c(ijk)]c(i+l, j+m, k+n)\,,$$

and

$$n_{\mathrm{CuAn}}(lm)\equiv\sum_n n_{\mathrm{CuAu}}(lmn)=\sum_{ij}[1-c(ij)]c(i+l, j+m)\,. \tag{A. 3}$$

Then (A. 2) runs;

$$\alpha(lm)=1-\frac{1}{C_{\mathrm{Au}}}\sum_{ij}[1-c(ij)]c(i+l, j+m)\,. \tag{A. 4}$$

It is to be noted, however, that the values of $c(ij)$'s in Fig. 3 are the averaged ones in the sence that they are related to the averaged structure $\overline{\rho(x_1, x_2)}^{L_1L_2}$ and not to $\rho(x_1, x_2)$, so that they should be rather denoted by $\overline{c(ij)}^{L_1L_2}$ in order to make clear the differences from the quantities appearing in (A. 4). That is, what we obtain as short-range order parameters using the values given in Fig. 3 is not $\alpha(lm)$ as defined by (A. 2) but $\overline{\alpha(lm)}^{L_1L_2}$ as defined:

$$\overline{\alpha(lm)}^{L_1L_2}=1-\frac{1}{C_{\text{Au}}}\sum_{ij}[1-\overline{c(ij)}^{L_1L_2}]\overline{c(i+l, j+m)}^{L_1L_2} . \tag{A. 5}$$

On the other hand, the short range order parameters obtained by means of the Fourier transformation of intensity distribution, too, cannot be identical as those defined by (A. 1) or (A. 4), because an averaging is inevitably introduced through the replacement of integration by discrete summation which is necessitated by the finite resolving power of intensity observation[2]. In this case the parameter $\alpha(lmn)$ is not related to $P(x_1, x_2)$ but to $\overline{P(x_1, x_2)}^{L_1'L_2'}$, where $P(x_1, x_2)$ is the self-convolution of $\rho(x_1, x_2)$ and L_1', L_2' are the integers greater than 1 which are in general different from L_1 and L_2.

Thus what we obtain is $\overline{\overline{\alpha(lm)}}^{L_1'L_2'}$ defined as

$$\overline{\overline{\alpha(lm)}}^{L_1'L_2'}=1-\frac{1}{C_{\text{Au}}}\overline{\sum_{ij}[1-c(ij)]c(i+l, j+m)}^{L_1'L_2'} . \tag{A. 6}$$

It is seen that the values of $\overline{\alpha(lm)}^{L_1L_2}$ and $\overline{\overline{\alpha(lm)}}^{L_1'L_2'}$ may be different, and in general the one is not derivable from the other unless L_1, L_2, L_1' and L_2' are so large that a_1L_1, a_2L_2, a_1L_1' and a_2L_2' become comparable to the size of the crystal under examination and the values of $\overline{c(ij)}^{L_1L_2}$'s become identical with those of $c(ij)$'s.

Appendix II. A Remark on the Phase Assignment of Diffuse Scattering

In the preceding sections it was supposed implicitely that the disordered structure in question could be represented uniquely by a continuous function $\rho(\boldsymbol{x})$, thus the phase angles could be *defined* without any ambiguity at every point in reciprocal space. In general it cannot be the case because it is known that single crystals are composed of coherent domains (mosaics) which diffract X-rays independently with each other. Let the electron distribution of each coherent domain be represented by $\rho_n(\boldsymbol{x})$ and its Fourier transform by $A_n(\boldsymbol{s})$ $(n=1, 2, 3, \cdots, N)$, the observed diffraction pattern is then expressed as;

$$I(\boldsymbol{s})=\sum_{n=1}^{N}|A_n(\boldsymbol{s})|^2\equiv N|A_0(\boldsymbol{s})|^2 . \tag{A. 7}$$

In this case the phase assignment to the square root of $I(\boldsymbol{s})$ seems quite impossible and even deprived of any substantial significance. The Fourier transformation of *amplitude* distribution, which is nevertheless feasible at least in quite a formal way, leads to the structure $\rho_0(\boldsymbol{x})$ defined as;

$$\rho_0(\boldsymbol{x})\bigstar\rho_0(\boldsymbol{x})=\frac{1}{N}\sum_{n=1}^{N}\{\rho_n(\boldsymbol{x})\bigstar\rho_n(\boldsymbol{x})\} , \tag{A. 8}$$

$\rho_0(\boldsymbol{x})$ being the Fourier transform of $A_0(\boldsymbol{s})$ which is proportional to the square root of $I(\boldsymbol{s})$.

As we have seen in § 2, what we obtain practically is not $\rho_0(\boldsymbol{x})$ itself but the averaged one $\overline{\rho_0(\boldsymbol{x})}^{\boldsymbol{L}}$ defined as;

$$\overline{\rho_0(\boldsymbol{x})}^{\boldsymbol{L}}\bigstar\overline{\rho_0(\boldsymbol{x})}^{\boldsymbol{L}}=\frac{1}{N}\sum_{n=1}^{N}\{\overline{\rho_n(\boldsymbol{x})}^{\boldsymbol{L}}\bigstar\overline{\rho_n(\boldsymbol{x})}^{\boldsymbol{L}}\} , \tag{A. 9}$$

where $\boldsymbol{L}$ stands for the triplet of integers (L_1, L_2, L_3). Although $\rho_n(\boldsymbol{x})$'s at the right-hand side of (A. 8) may vary from domain to domain, and $\rho_0(\boldsymbol{x})$ cannot represent any real structure present in the crystal under examination, one may expect that the averaged structures $\overline{\rho_n(\boldsymbol{x})}^{\boldsymbol{L}}$'s are at little variance among themselves, unless (L_1, L_2, L_3) is so large that L_1a_1, L_2a_2 and L_3a_3 become comparable to the sizes of coherent domains, and therefore that

$$\overline{\rho_0(x)}^L \sim \overline{\rho(x)}^L \,. \qquad \text{(A. 10)}$$

Here $\overline{\rho(x)}^L$ means as a representative structure of the assembly of coherent domains from which the crystal examined is constituted.

The condition (A. 10) may hold for the case of Cu_3Au treated in § 3, and the conclusion of that section need not suffer from possible lack of reality due to the phase assignment given by (16).

References

1) J. M. Cowley: J. Appl. Phys. **21** (1950) 24.
2) K. Doi: Bull. Soc. franç. Minér. Crist. *LXXX* (1957) 325.
3) K. Doi: Acta Cryst. **13** (1960) 45.
4) R. W. James: The Optical Principles of Diffraction of X-rays, Bell and Sons (1954) p. 623.
5) Y. Y. Li and R. Smoluchowski: Phys. Rev. **94** (1954) 866.
6) A. Guinier: Théorie et Technique de la Radiocristallographie, Dunod (1956) p. 574f.
7) K. Doi: Proc. Japan Acad. **30** (1954) 180.
8) A. J. C. Wilson: X-ray Optics., Methuen (1949) p. 81.
9) I. G. Edmunds and R. M. Hinde: Proc. Phys. Soc. **B**, **65** (1952) 716.
10) H. Steeple and I. G. Edmunds; Acta Cryst. **9** (1956) 934.

JOURNAL OF THE PHYSICAL SOCIETY OF JAPAN, Vol. 15, No. 10, OCTOBER. 1960

Visible Light Emission and Microplasma Phenomena in Silicon p-n Junction

II. Classification of weak spots in diffused p-n junctions

By Makoto KIKUCHI

Electrotechnical Laboratory, Tokyo, Japan

(Received June 6, 1960)

In the course of study on the visible light emission and microplasma phenomena in diffused silicon p-n junctions, it has been discovered that there exist several types of weak spots in the junction. They can be roughly classified into two groups, one of them includes tiny weak spots which reveal microplasma current pulses at certain characteristic bias voltages, and the other includes tiny spots which contribute "soft" component to the reverse current without being accompanied with microplasma pulses. The latter type of spots could be produced by scratching the surface of the junction with a tungsten needle, whereas the former could not be produced by the same operation.

In real diffused junctions there are distributed above mentioned types of point defects. Typical experimental results are given, and the correlation between those weak spots and the current-voltage characteristics is discussed.

§ 1. Introduction

Strictly speaking, no definite model is established for the explanation of the microplasma pulses and the visible light emission. The possibility of the visible light emission by the thermal vibration of lattice has already been ruled out because of unbelievable high temperature gradient in the crystal. From the experimental results on the spectral distribution of the emitted light, intra-band transition of energetic carriers has been postulated[1].

However, the switching action of the microplasma spot and the correlation between the light emission and the current pulses are now still in question. Therefore, in the course of investigation on the occurrence of microplasma pulses in reverse-biased diffused silicon p-n junctions, it has been intended to check the carrier multiplication at the microplasma spot. The experimental result was negative, that is, no multiplication could be found in the voltage range where microplasma current pulses were clearly observed on a synchroscope. High value of "apparent" carrier multiplication has already been discussed in the previous paper[2].

During the measurement of multiplication, it has been found out that there exists light emitting spot in the junction which reveals no microplasma pulses at all. Some of them show high value of multiplication but some of them do not. The color of the emitted light from this type of spots is much more brilliant and whitish than that from microplasma spots. In the previous paper[3], only the appearance of the bright spots is mentioned, but it has been found that this kind of spots contribute considerable amount of leakage current component to the reverse characteristic of the junction.

The purpose of this paper is to present the experimental results on the above mentioned weak spots in the junction, as well as to give additional results on the microplasma spots. In the last section, brief discussion and speculation are given.

§ 2. Experimental Procedures

2.1 *Specimens*

The specimens used in this experiment are summarized in Table I with the condition of boron diffusion for making p-n junction on the surface. As shown in the table, resistivity of the samples ranges from 0.1 to 6 ohm-cm. After making a p-type layer on the surface, small area of 1–3 mm in diameter is protected and the remainder of the surface p-type layer is etched off. Four specimens are fixed on a copper plate with silver paste. The copper plate is mounted on a large metal block of the micromanipulator which serves as a heat sink.

2.2 *Experimental apparata and procedures*

Most of the experimental apparata are the same as that described in the previous paper[2].

Table I.

No. of speci-men	resistivity (chm-cm)	diffusion temperature (°C)	diffusion time (min)
B 25	2—6	1050	30
B 26	2—6	1050	40
B 27	2—6	1050	50
B 28	0.02	1050	40
B 29	0.1	1050	40
B 30	1.6	1050	40
B 32	0.15	1050	40
B 33	1.7	1050	40

Essentially, the apparatus for measuring multiplication and for locating weak spots in the junction consists of a chopped light source and micromanipulator with a high sensitivity synchroscope. Micromanipulator is so operated that the maximum performance of certain characteristic can be observed on the synchroscope to find the position of the spot in the junction. Usign an X-Y recorder simultaneously, appearance and disappearance of microplasma pulses can be marked on the reverse current-voltage characteristic of the junction.

§ 3. Experimental Results

3.1 *Microplasma pulses and the current-voltage characteristic*

As has already been described in the previous paper, microplasma pulses appear as reverse bias is increased up to certain voltage. As the voltage is further increased, pluse length and pulse rate is increased and finally the pulses completely disappear. Observing microplasma pulses on a synchroscope, their appearance and disappearance can be indicated on the reverse current-voltage characteristic as shown in Fig. 1. As is shown in the figure, about ten microplasma spots reveal their existence successively as the total current is increased up to 1 mA. The trace of the characteristic as shown in Fig. 1 is quite reproducible.

Fig. 2 shows a part of the characteristic near the appearance of the first microplasma spot. As is shown, the characteristic is rather complex microscopically, i.e., the second derivative is oscillatory. However, the segments (1A), (2B), and (3C) of the curve are meaningless in a sense, since the values of junction current in these regions is only a time average of pulsing current weighted by measuring circuit conditions. It must be noted here that the parts (A2), (B3)··· are quite linear, which has been confirmed on most of the specimens. The above mentioned results, i.e., (1A), (2B), ··· are only the curves of weighted average of "probability", and (A2), (B3)··· are the segments of straight line, must be carefully taken into account for theoretical interpretation of the reverse characteristic of those diffused p-n junctions.

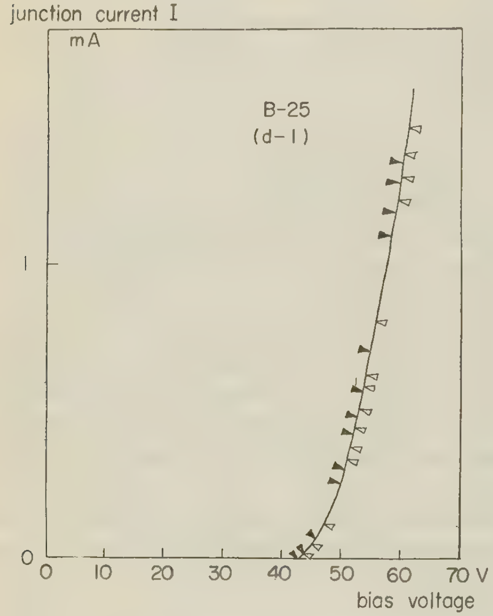

Fig. 1. Typical reverse characteristic of a diffused p-n junction on which appearance and disappearance of microplasma pulses are marked. ▶ and ▷ shows the appearance and disappearance, respectively.

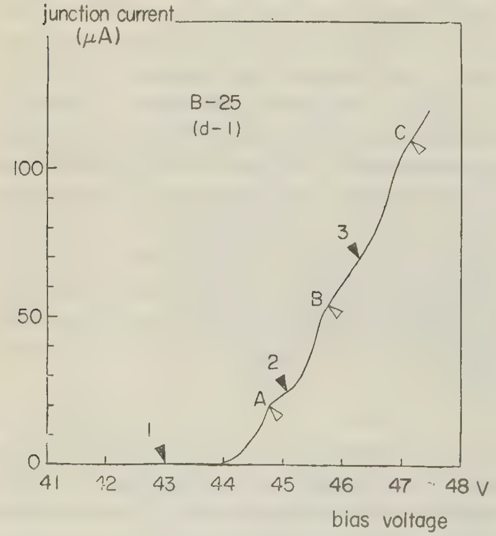

Fig. 2. Part of the current-voltage characteristic curve with the marks of appearance and disappearance of microplasma pulses.

As previously reported, we have succeeded in locating the positions of individual microplasma spots using small chopped light spot. By this technique, it is observed on a synchroscope that the microplasma pulses are most strongly modulated at the chopping frequency when the chopped light just coincides with a microplasma spot. Fig. 3. shows the change in characteristic curve when one of the microplasma spot is illuminated.

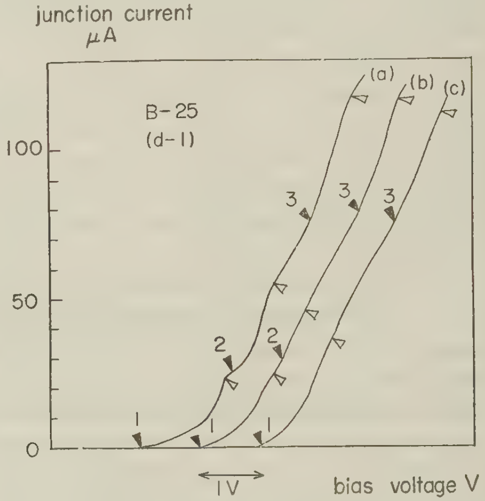

Fig. 3. Change of characteristic curve when certain microplasma spot is selectively illuminated. (The voltage axis is shifted 1 volt for each svccessive measurement) (a) dark, (b) (c) stronger illumination on the spot No. 2.

The voltage axis in the figure is shifted 1 volt for each measurement. As the illumination on the spot No. 2 is made stronger, the variation in the second derivative of the curve is reduced, and finally, appearance of the microplasma pulses from spot No. 2 is shifted to lower voltage. Therefore, it becomes that pulses from spot No. 1 and spot No. 2 can no longer be separated, as shown in the curve (c).

3.2 *Characteristics of microplasma pulses*

In Fig. 4, the grow-up of microplasma pulses is shown. This semi-schematic figure shows the increase of pulse height with increasing bias voltage. The dot circle indicates the time average of the pulsing current.

As is seen in the figure, the pulse height is very small and gradually increases after its appearance, but it is reduced abruptly to zero upon its disappearance. This lack of symmetry must be noted.

The other important feature of the microplasma phenomena is the lack of carrier multiplication, which has already been reported in the previous paper. In our present work, this has been confirmed again. With careless measuring conditions, the apparent multiplication will be confused with the true carrier multiplication but these must be distinguished.

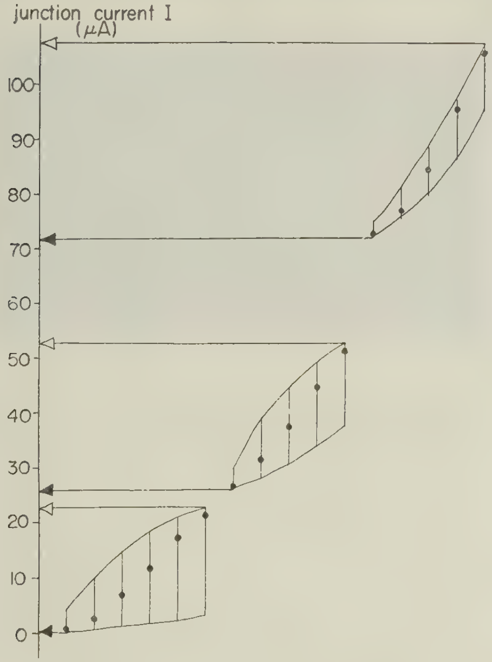

Fig. 4. Grow-up microplasma pulses with increasing bias voltage. The abscissa is reverse bias voltage, but quantitatively meaningless.

Fig. 5 shows the appearance of microplasma pulses with chopped light illumination. The bias voltage is increased from (a) to (d), successively. As is shown, pulse rate of the microplasma current pulses is modulated by the illumination, but the multiplication cannot be found in the case of (d), i.e., the spot is mostly in " ON " state both in the dark and illuminated condition.

3.3 *Weak point in the junction without microplasma pulses*

In the course of study on the above mentioned phenomena, it has been found that there exists light emitting spot in the junction which is not accompanied with the occurrence of microplasma current pulses.

At first, a bright spot was found in the junction through microscope, where the chop-

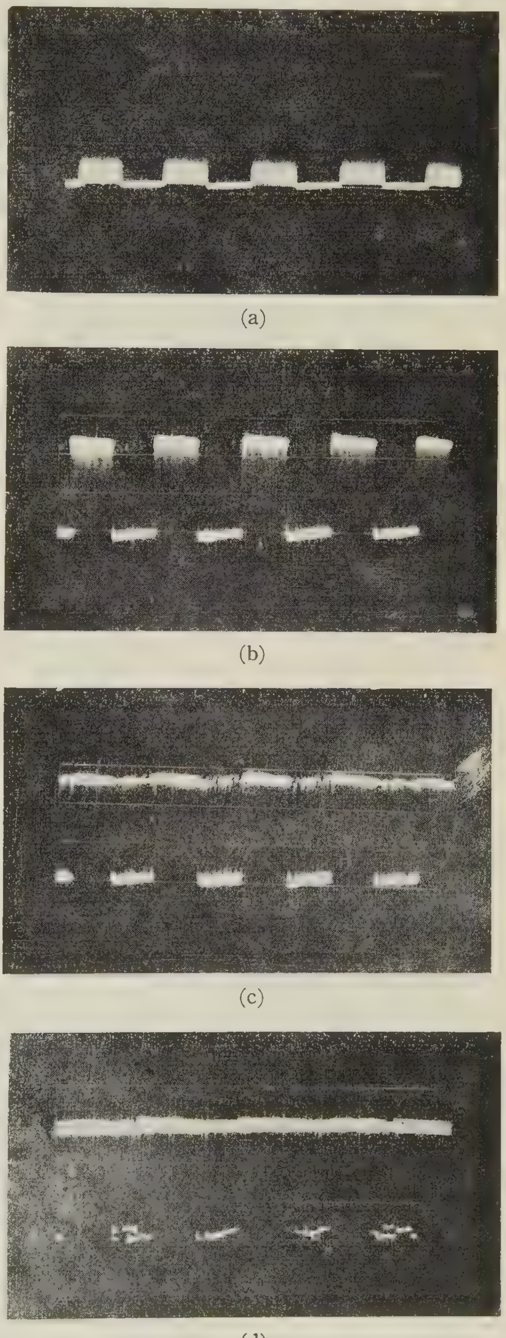

(a)

(b)

(c)

(d)

Fig. 5. Patterns of the microplasma pulses when the junction is illuminated by chopped light. The light is focused on the microplasma spot and the bias voltage is increased from (a) to (d).

ped light was carefully focused. Bias voltage was slowly decreased watching the pattern on the synchroscope. In the case of microplasma spot, the clear pattern like that shown in Fig. 5 should be observed. However, no pattern could be seen even the voltage was decreased as low as 10 volts. It was astonishing that the light emission could be still observed from the spot at this bias. This type of weak spot was found out in this way.

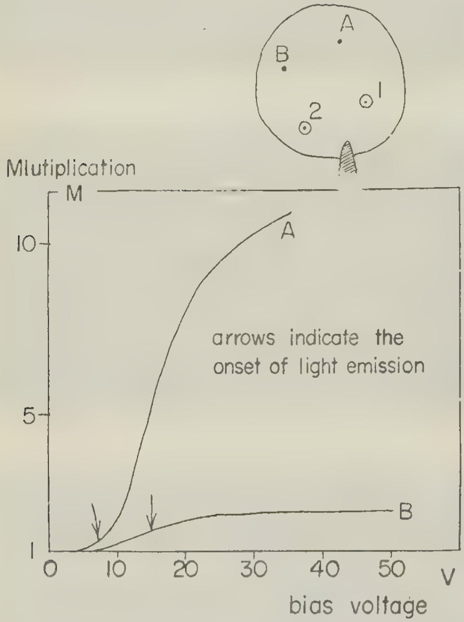

Fig. 6. Examples of weak spots in the junction with multiplication and without microplasma pulses.

By careful observation on many specimens, it has been found that some of those spots reveal high multiplication. In Fig. 6 typical examples are given. In this diffused junction, four weak spots are revealed when the bias voltage is increased up to 65 volts. Two of them are the previously mentioned microplasma spots (1 and 2 in the figure), and the other two are the spots without microplasma pulses which are accompanied with carrier multiplication (A and B). As is shown, multiplication occurs in these spots from the bias valtages as low as 5 and 7 volts, respectively. Moreover, it must be noticed that light emission occurs also at low voltages. In Fig. 7, an example of photoresponse of these kind of spots is shown. It is clearly seen that the nature is essentially different from microplasma spot as shown in Fig. 5.

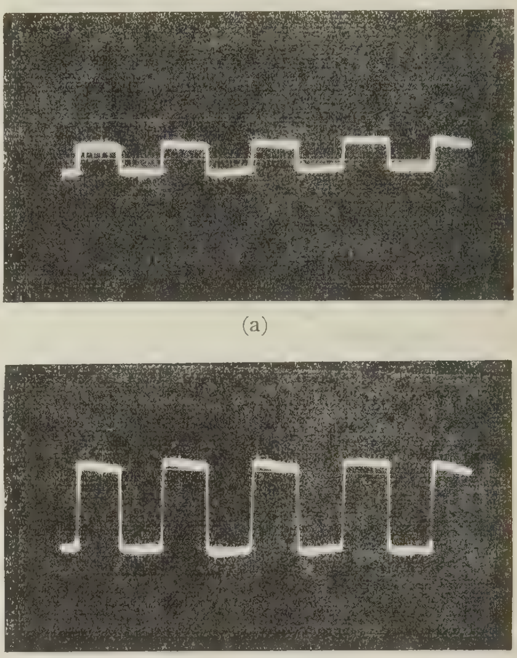

(a)

(b)

Fig. 7. Pattern of photoresponse of the weak spot which reveals no microplasma pulses. Multiplication is clearly observed.

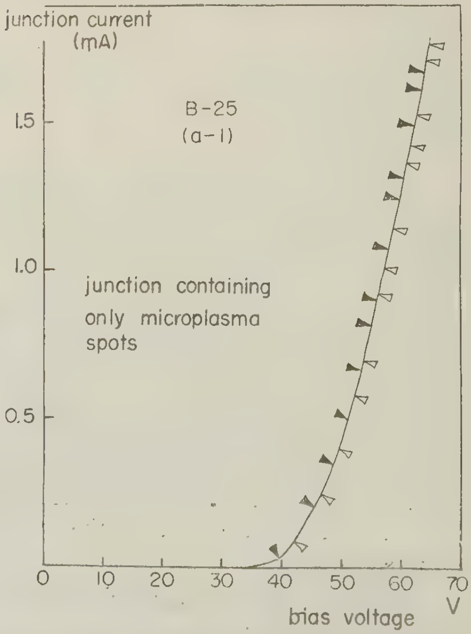

Fig. 8. Current-voltage characteristic of a junction which contains microplasma spots only. (#B-25(a-1)). ▶ and ▷ indicates the appearance and disappearance of microplasma pulses.

It has been found that the existence of this new kind of spot has remarkable influence on the current-voltage characteristic of the junction. Fig. 8 shows the characteristic of the diffused junction which contains only microplasma spots. Although relatively large number of microplasma spots can be found in this junction, the characteristic is pretty hard, i.e., it has sharp breakdown at the voltage where the first microplasma pulses appear.

If the junction contains at least one weak spot without microplasma pulses, however, the characteristic becomes remarkably soft, as shown in Fig. 9. This softness results from the existence of this kind of spots either with or without multiplication. From these experimental results it may well be concluded that the so-called leakage current in the backward characteristic is caused by those kind of weak spots in the junction.

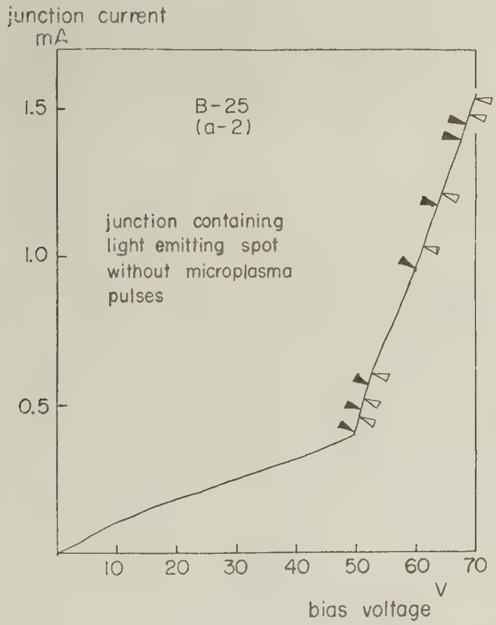

Fig. 9. Current-voltage characteristic of a junction which contains at least one weak spot without microplasma pulses.

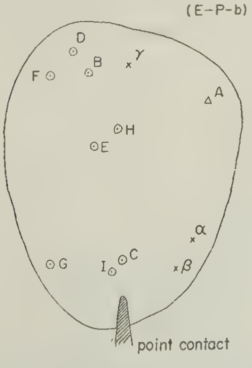

Fig. 10. Map of the light emiting spots in the diffused junction. (#-E-P-b)

In Fig. 10, a result of mapping light emitting weak spots in a diffused junction is given. The sign ⊙ indicates the microplasma spot, △ and × indicates the spot without microplasma pulses, with and without multiplication, respectively. The detailed description of these weak spots are summarized in Table II.

Table II. Detailed description of the weak spots mapped in Fig. 10.

	bias voltage where micro pulses appear (volt)	bias voltage where lighht emission occurs (volt)	micro-plasma pulses	multi-plication
A	7.0	7.0	no	yes
B	71.0		yes	no
C	72.0		yes	no
D	72.5		yes	no
E	79.0		yes	no
F	78.5		yes	no
G	81.2		yes	no
H	85.2		yes	no
I	86.5		yes	no
α		8.5	no	yes
β		9.0	no	yes
γ		9.5	no	yes

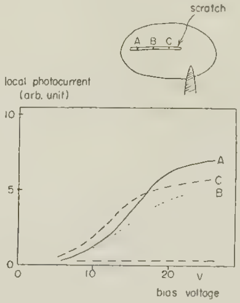

Fig. 11. Multiplication characteristic of the light emitting spots produced by scratching.

3.4 *Effect of scratch on the surface of diffused junction*

On the course of experiment it was sometimes observed that the current-voltage characteristic changed permanently. Recently, it has been found that this change in characteristic can be attributed to the scratch on the surface of the junction made by drawing the metal point electrode by micromanipulator.

It may be very interesting to note that light emitting spot can be produced by the scratch intentionally. The light emitting spots produced by the scratching reveal multiplication as shown in Fig. 11. As is shown, the light emitting spots appear along on the scratch line and the multiplication appears in these spots from the bias voltage as low as 6–10 volts.

It must be noted that none of the spots produced in this way revealed microplasma pulses.

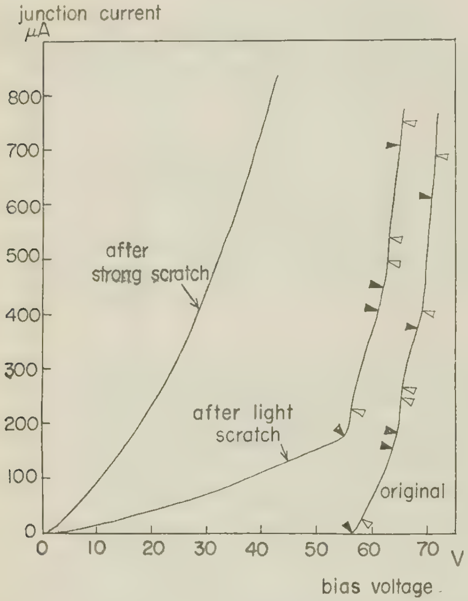

Fig. 12. Effect of scratching on the current-voltage characteristic of a junction.

Fig. 12 shows the effect of scratching on the current-voltage characteristic. From the experimental results mentioned in the previous section, it may be quite natural to expect that the scratching results in the increase of leakage current. It is noted that during the scratching treatment, the ocurrence of microplasma pulses is not influenced.

It must be noticed here that relatively slow response to chopped light has often been observed in the spots produced by scratching. The slow effect appears also in the current, i.e., the increased leakage current by scratching reveals considerable drift (or creep).

3.5 *Summary of the experimental results*

The observed weak spots in the diffused junction can be classified by their characteristics as shown in Table III. Type I is the usual microplasma spot, which is characterized by the occurrence of microplasma pulses and also by the lack of multiplication. Type II is also the microplasma spots, but this seems to be lacking of light emission. In some specimens, no light emitting spots could be observed through microscope after ten or more microplasma breakdown had been observed on the synchroscope. Strictly speaking, however, the existence of type II spot may be still in question.

Table III. Classification of weak spots in the junction.

Type	Microplasma pulses	Light emission	multiplication
I	yes	yes	no
II	yes	no	no
III	no	yes	yes
IV	no	yes	no

Type III and IV are the spots without microplasma pulses. In general, the emitted light from III and IV spots is much brighter than that from I and II spots. The colour is more reddy for I and II, while it is whitish for III and IV. The existence of multiplication is the main feature to distinguish III from IV.

Type III can be produced by scratching on the surface of the junction. III and IV contribute considerable amount of leakage current to the backward characteristic. Therefore, the current-voltage characteristic of the junction containing only I or II spots is hard, while the junction containing at least one of III or IV spots reveals soft characteristic.

It is also noted that visible light emission from III or IV occurs at very low voltages as low as 5–15 volts.

§ 4. Discussions

4.1 *Microplasma spots and current-voltage characteristics*

As has been already mentioned in connection with the experimental result shown in Fig. 2, current-voltage characteristic of a junction containing microplasma spots does not obey the existing simple theories. One of the important features of the characteristic is its linearity between the disappearance and appearance of microplasma as schematically shown in Fig. 13. As is shown in the figure, the parts (BC) and (DE) are linear. As previously noticed, the current is the sum of continuous current and pulses in the regions of (AB) and (CD).

From the above mentioned features of the characteristic curve, it seems natural to have the physical picture as follows. There exist considerable number of weak spots in the junction, and they reveal breakdown successively as the bias voltage is increased. When the bias voltage passes through the breakdown voltage of certain spot, that spot contributes local current which is limited by spreading resistance only. This picture can be represented by the equivalent circuit as shown in Fig. 14. Relay switches are in parallel and each switch has its resistance in series.

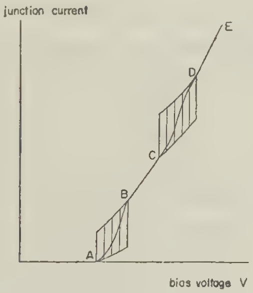

Fig. 13. Schematic representation of the current-voltage relation of a junction containing microplasma spots.

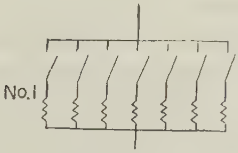

Fig. 14. Equivalent circuit of the junction containing microplasma spots.

When the bias voltage is increased up to the breakdown voltage of the spot No. 1, the relay No. 1 begins to oscillate. The probability of the relay to be in "ON" state is increased as the bias is further increased, and finally the relay is completely switched on.

There are, however, some doubts in the validity of this equivalent circuit. From the experimental results it has been found that the microplasma pulse height grows up at most to 150μA. On the other hand, the resistance of the individual spot (resistance in series to the relay in Fig. 14) has been determined from the derivative of the linear part of the characteristic to be of the order of 20–50 kΩ. From the value of 50 kΩ and equivalent circuit in Fig. 14, the height of the microplasma pulses should be 1 mA, since the first pulses appear nearly 50 volts. Moreover, it should be expected from the equivalent circuit that the extrapolation of the linear part of the characteristic will intersect the origin as shown in Fig. 15 (a). It is observed, however, that the characteristic of real junction is schematically shown as Fig. 15 (b).

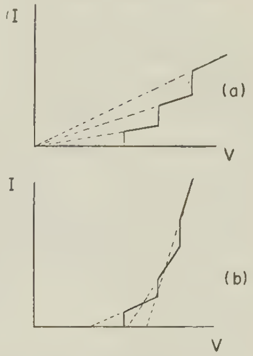

Fig. 15. Schematic representation of the characteristic of (a) equivalent circuit, (b) real junction.

From the resistance determined above and the usual relation

$$R=\frac{\rho}{2d} \qquad (1)$$

for the spreading resistance, where ρ is the bulk resistivity, the diameter d of the spot can be given to be about 0.5 micron. This value is at least one order of magnitude larger than usually believed for the microplasma spot.

Although the detailed mechanism underlying microplasma phenomena is still in question, above mentioned discrepancies seem to show that we must take into account the modulation of spreading resistance in the analysis.

4.2 *Soft characteristic*

It can be concluded that the existence of type III or IV spot give rise to soft reverse characteristic. This may be seen in Table IV where some of the experimental results are summarized.

Characteristic features of type III and IV

Table IV. Summary of the experimental results on the correlation between softness of the current-voltage characteristic and the existence of type III or IV spots.

No. of specimen	Type I or II	Type III or IV	Characteristic
(B-26)			
a-1	yes	no	hard
a-2	yes	yes	soft
a-3	yes	no	hard
a-4	yes	yes	soft
b-1	yes	no	hard

spots are visible light emission and lack of microplasma pulses. Moreover, light emission begins from bias voltages as low as 5 volts. From the results mentioned in 3.4, local damage or highly dislocated region is imagined as the origin of these types of spots. For instance, high density of energy states in the band gap will be responsible for high rate of generation and also for high rate of recombination. On the other hand, high density of energy states will help the Zener mechanism.

At any rate, there must exist high energy carriers since the light emission occurs. However, we are puzzled from the fact that there is clear differecce between type III and IV spots in carrier multiplication characteristic. One possible way to solve this question is to consider the threshold energy $E_s=2.3\,\text{eV}$ for pair creation. Visible light emission may be observed without multiplication if the carriers have energy sufficiently high but less than 2.3 eV. However, this model seems to be too much sophisticated.

4.3 *Microplasma spots*

The most difficult question on the mechanism of microplasma phenomena may be the lack of multiplication after the breakdown where visible light emission can be observed. Light emission occurs after the current pulses appear. Following considerations lead us to believe that the microplasma phenomena is only partly related with avalanche breakdown.

(a) Individual current pulse is not the avalanche induced by a chance carrier, since the pulse width ($10^{-6}-10^{-5}$ sec) it too long compared with the transit time of electrons in the barrier, i.e., 10^{-8} sec..

(b) Above model is not valid also because no carrier multiplication is found after the breakdown.

(c) If it is assumed that the long pulse width is maintained by high density of chance carriers to cause avalanche multiplication, it becomes then difficult to explain long intervals between the pulses.

We have proposed a model taking analogy with the p-n-p-m switch in the previous paper. We have really succeeded to observe similar current pulses in the vicinity of the " turn-on " point of a p-n-p-n four layer diode. However, in the case of this simulation, it is very difficult to keep the " randomness " of the current pulses. The current pulses are apt to fall into relaxation oscillation, and the condition to keep randomness is quite critical.

Therefore, it may be concluded that the first rise of a microplasma pulse is induced by a high energy chance carrier, while its fall is governed by some internal feedback mechanism, which is still in question at present.

The effect of oxygen impurity on the visible light emission has been reported in the previous paper[4]. Recently, it has been found that very few light emiting spots can be observed in the junction formed on a crystal grown by floating-zone method, while the light spots are increased by heating these specimens in oxygen or oxygen-rich atmosphere. Since, however, our equipments to perform heat-treatment are not perfectly free from other chemical impurities, it may not be concluded that only the oxygen impurity is responsible for above mentioned change.

4.4 *Other remarks*

Magnetic field of 6000 Gauss has been applied either in parallel or perpendicular to the surface of the junction, but no effect could be detected on the microplasma pulses.

When the junction is put into vacuum of 10^{-4} mm Hg, leakage current is considerably changed but no change can be detected on the appearance of the microplasma pulses. This result shows that the microplasma spot is rather isolated from the surface condition.

§ 5. **Conclusions**

It has been found that there are four types of weak spots in diffused silicon junctions. They can be classified on light emission, multiplication and microplasma current pulses.

In real junction, these spots are distributed mixed and randomly in the junction, and the current-voltage characteristic is closely correlated with the existence of the spots.

Type III spots have been found to be produced by scratching on the surface by sharp needle.

Experiments are still now being undertaken to clarify the mechanisms underlying microplasma pulses.

The author wishes to express his appreciation to Mr. K. Tachikawa for preparing silicon diffused junctions.

References

1) A. G. Chynoweth, et al: Phys. Rev. **102** (1956) 369.
2) M. Kikuchi and K. Tachikawa: Journ. Phys. Soc. Jap. **15** (1960) 835.
3) Section (3.1) at page 839 of reference (2).
5) M. Kikuchi and K. Tachikawa: Journ. Phys. Soc. Jap. **14** (1959) 1830.

JOURNAL OF THE PHYSICAL SOCIETY OF JAPAN, Vol. 15, No. 10, OCTOBER, 1960

Optical and Structural Anomalies in Potassium Ferrocyanide Trihydrate Crystals

Hiroo TOYODA, Nobukazu NIIZEKI and Shigeru WAKU

Electrical Communication Laboratory, Nippon Telegraph and Telephone Public Corporation

(Received April 16, 1960)

Potassium ferrocyanide trihydrate crystals grown from aqueous solution have been studied with polarizing microscope, X-ray diffraction methods, etching technique, and dielectric measurements at temperature region between 20° and −140°C. Various types of optical anomalies were observed, and the crystals were classified into five types by optical and X-ray investigations. Crystallographic data of monoclinic and tetragonal single crystals were measured. The various optic anomalies were clarified by twinning and parallel growth characteristic to the layer structure of the two modifications. Dislocation pits were observed by etching with a mixture of water and alcohol. Ferroelectric monoclinic phase, and the behaviors of tetragonal phase at low temperatures were studied by low temperature polarizing microscope, dielectric measurements and low temperature precession X-ray photographs. Teteragonal phase was shown to undergo a monotropic phase transition at about −55°C, and transform into a twinned monoclinic phase.

§ 1. Introduction

The authors reported previously the ferroelectricity of potassium ferrocyanide trihydrate ($K_4Fe(CN)_6 \cdot 3H_2O$, hereafter abbreviated as KFCT crystals[1], and pointed out that there appear several peaks in the dielectric constant vs temperature curve, and that the crystal exhibits some peculiar optical behaviors. In a resent study of Waku *et al*[2], it has been revealed for a monoclinic single crystal that the dielectric constant vs temperature curve shows only a single peak, and the polarization axis is along the [10$\bar{1}$] direction.

The authors have found several type of KFCT crystals grown from the aqueous solution with behaviors significantly different from monoclinic single crystals in optical, dielectric, and other properties. The authors have investigated these crystals with X-ray diffraction method, polarizing microscope, dielectric measurement, and etching technique.

1. *Optical classification and X-ray study of crystals*

KFCT is known to crystallize in two types of modifications, one monoclinic and the other tetragonal. Hawever, because of the pseudo-tetragonality of the former structure and also of the layer structure of both of them, samples of single crystals grown from solution show complicated varieties due to twinning and oriented overgrowth. By optical observation and X-ray analysis, the samples can be classified into several types as follows.

I. Monoclinic single crystal: Monoclinic crystal of KFCT is discriminated by its large optic axial angle, $2V=78°10'(-)$, X: ∠[10$\bar{1}$]$=31°50'$, as well as by Laue symmetry 2 (Fig. 1 (a)). By the use of rotation, Weisenberg, and precession methods, the unit cell dimensions were determined as $a=9.380$ A, $b=16.84$ A, $c=9.397$ A and $\beta=90°\pm3'$, where the b axis of the crystal is taken normal to its cleavage face. The space group was assigned to be C2/c. These results are in agreement with those of Posperov and Zdanov[3].

II. Tetragonal single crystal: Tetragonal crystal of KFCT is identified by its uniaxial positive interference figure, and by Laue pattern showing the Laue symmetry 4 (Fig. 1 (b)). The unit cell dimensions were determined as $a=9.410$ A, $c=33.67$ A, where the c axis is chosen normal to the cleavage face. A space group I $4_1/a$ was assigned.

III. Crystal without extinction: In the observation under an orthoscope, the rotation of this type of crystals around the normal to the cleavage face brings out merely a slight change in interference color, and no extinction

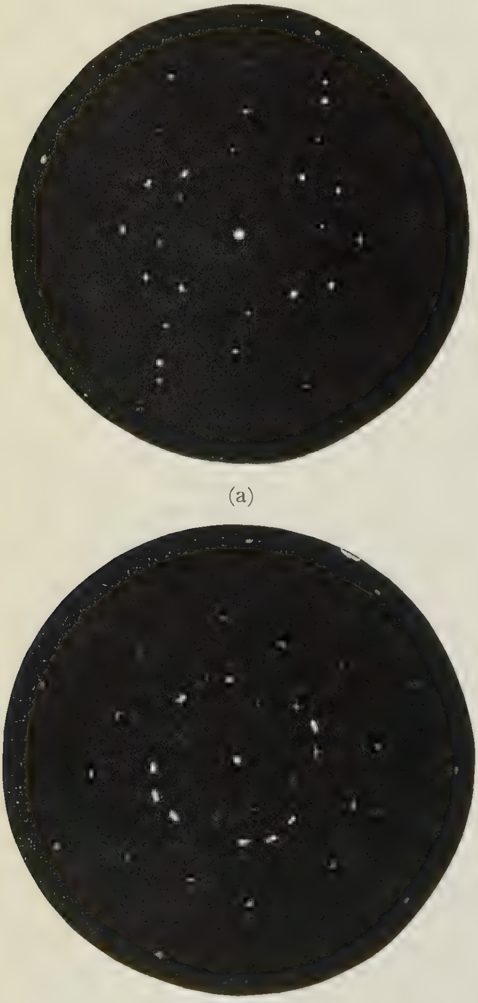

(a)

(b)

Fig. 1. Unfiltered MoK radiation, with crystal to film distance 40 mm. Incident X-ray beam normal to the cleavage faces of crystals.

(a) Laue pattern of monoclinic single crystal.

(b) Laue pattern of tetragonal single crystal.

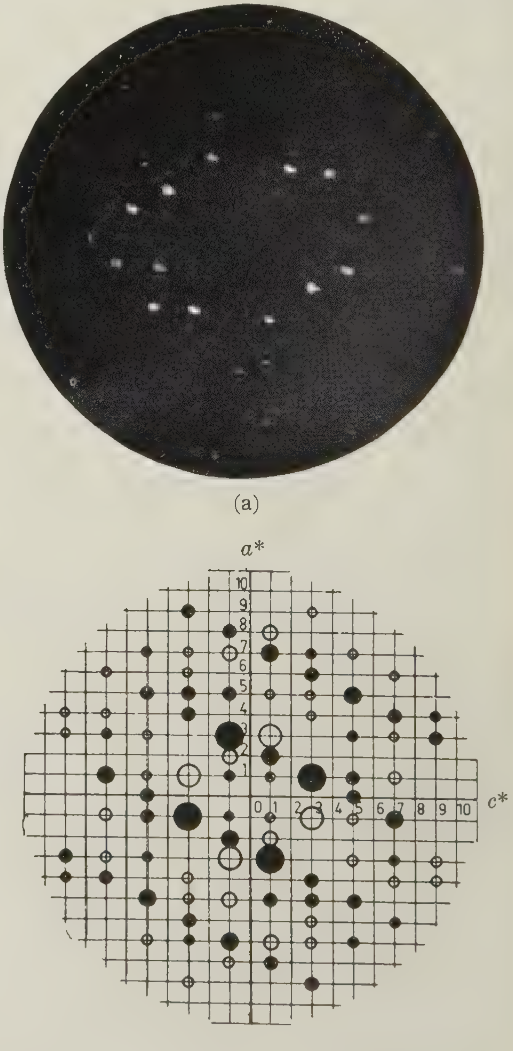

(a)

(b)

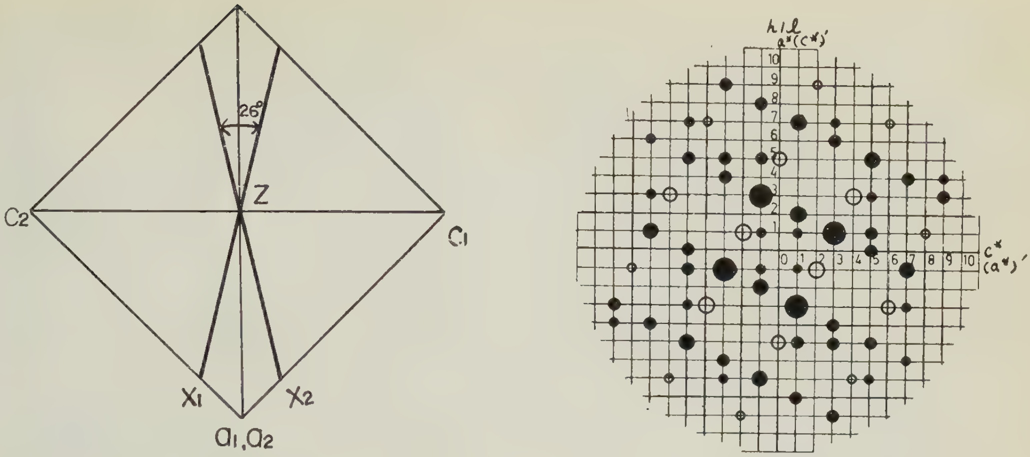

(c) (b)

Fig. 2. Filled-in circles represent one individual of the twinning, and open circles represent the other.
(a) Laue pattern of type III crystal.
(b) Reciprocal lattice level hll of the above crystal.
(c) Schematic representation of the relation between optic planes of two individuals.

positions. The Laue pattern and a schematic representation of the reciprocal lattice level hll are shown in Fig. 2 (a) and 2 (b) respectively. From the analysis, the crystal is interpreted as a macroscopic twin of monoclinic individuals with the twinning axis along [100]. In this type of twinning, the optic axial planes of two individuals make an angle of 26° so that any extinction position cannot exist (Fig. 2 (c)).

IV. Optically biaxial crystal without isogyers: Though the extinction positions exist through an orthoscope for this type of crystals, main isogyers do not appear through a conoscope and two dark points correponding to the apparent optic axes are observed (this unusual feature is explained in Appendix). The Laue pattern and the reciprocal lattice level hll are illustrated in Fig. 3 (a) and 3 (b) respectively. The analysis showed that the crystal is composed of two monoclinic individuals, whose orientations are mutally rotated around their common b axis so that two optic axial plane should be perpendicular to each other, in accordance with the observed optic

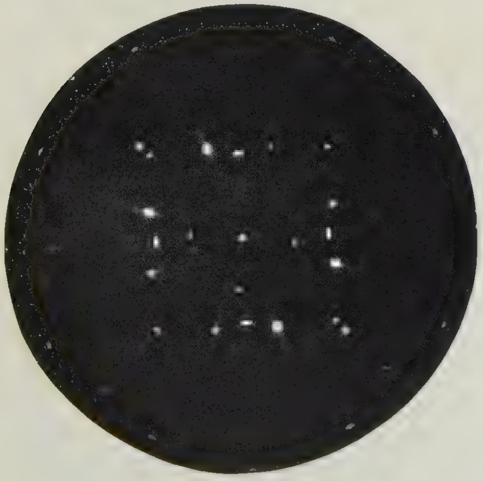

(a)

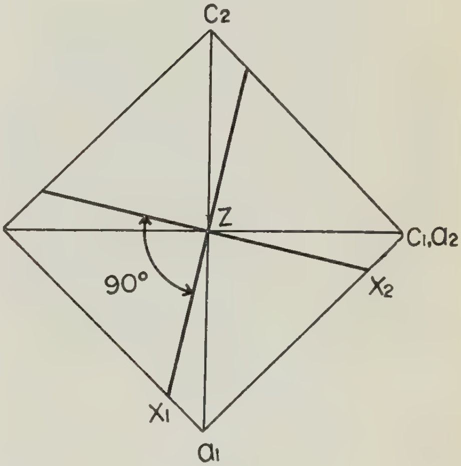

(c)

Fig. 3. Open circles represent the reciprocal lattice points unique to one individual. Those which $h=l=$odd are common to both individuals.
(a) Laue pattern of type IV crystal.
(b) Reciprocal lattice level hll of the above crystal.
(c) Relations between two optic planes.

anomalies (Fig. 3(c)).

V. Optically biaxial crystals with small optic angle: Though main isogyers are observed through a conoscope for this type of crystals, the optic axila angle 2V is not only smaller than that of monoclinic single crystal but indefinite. These crystals do not show any evidence of macroscopic twinning in their Laue pattern. They are either tetragonal pattern containing some diffuse spots and streaks when 2V angle is much smaller or monoclinic pattern with some diffuse spots and streaks when 2V angle is relatively larger. This type of crystals is supposed to be composed of monoclinic and tetragonal crystals which are stacked together with their cleavage planes parallel to each other in a microscopic scale, since, if this is the case, the crystal may be observed as optically homogeneous unit and its 2V angle may decrease according to the proportion of each modification.

Some of the crystal samples actually obtained are found to be composed of combinations of the above five types. It takes place frequently the case in which an individual crystal in the macroscpoic twins or parallel growth is not always a true monoclinic crystal but is a crystal classified under Type V for which 2V angle is smaller than 78°. The crystals divided into biaxial quadrants by a crossed uniaxial band, such as shown in Fig. 5, are also frequently found. It is usual that the neighboring quadrants across an uniaxial part have optic axial planes perpendicular to each other. The angle 2V decreases continuously near the uniaxial band.

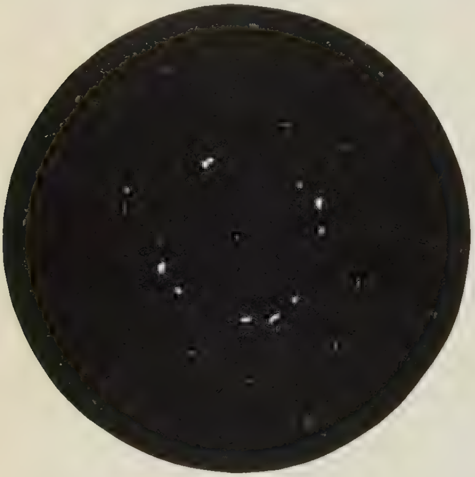

(a)

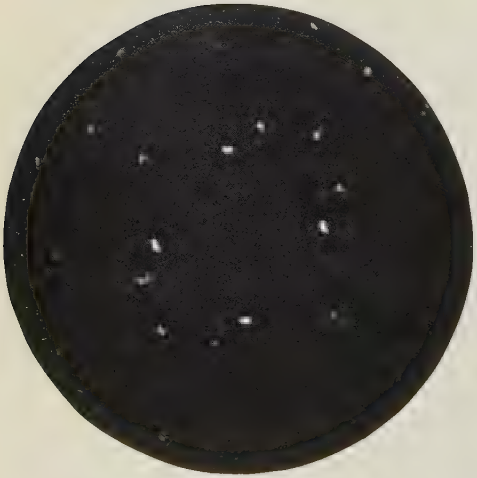

(b)

Fig. 4. Reciprocal lattice analysis of *hll* precession photographs is the same to the one shown in Fig. 3(b).
(a) Laue pattern of tetragonal crystal at −35°C.
(b) Laue pattern of tetragonal crystal at −65°C.

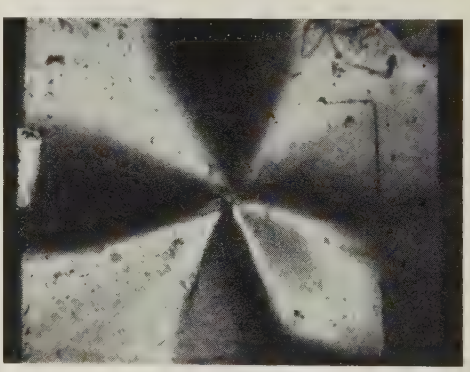

Fig. 5. Photographic picture of an abnormal crystal obtained through a polarized microscope. Dark areas are tetragonal and bright areas are monoclinic twinned crystal.

§2. X-ray Study at Low Temperatures

Low temperature precession photographs of KFCT crystal were taken with the cooling equipment described elsewhere[4]. It has been established that the monoclinic phase (Type I) transforms to ferroelectric phase at −24°C. The unit cell dimensions −90°C were determined as $a=9.332$ A, $b=16.6$ A and $\beta=90°3' \pm 3'$. The space group was assigned as Cc from the observed systematic absences of spectra and the observation that the polarization axis lies in (010) plane.

With the tetragonal crystal, Laue patterns were taken at various temperatures, and it

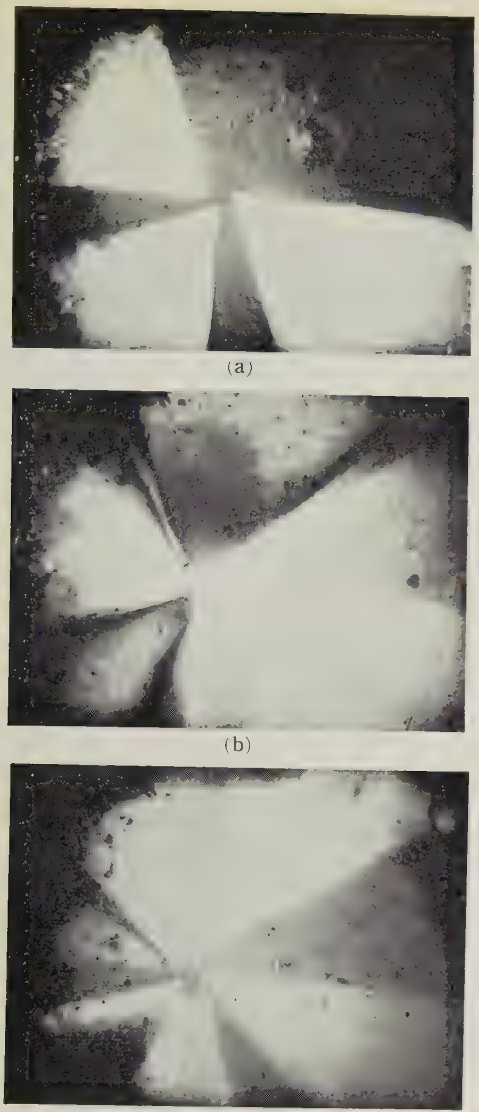
(a)

(b)

(c)

Fig. 6. Change of interference color pattern at low temperatures. (×40)
(a) −38°C. (b) −60°C. (c) −96°C.
The patterns except (a) are all colored and the light and shade do not represent the biaxiality.

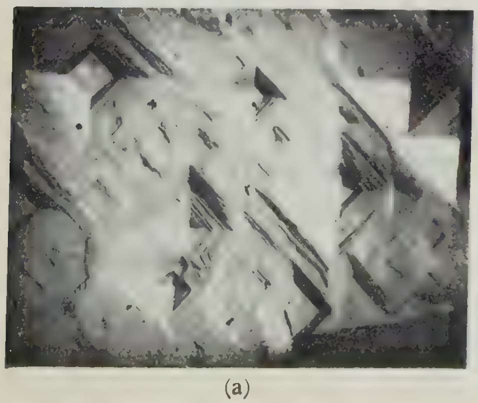
(a)

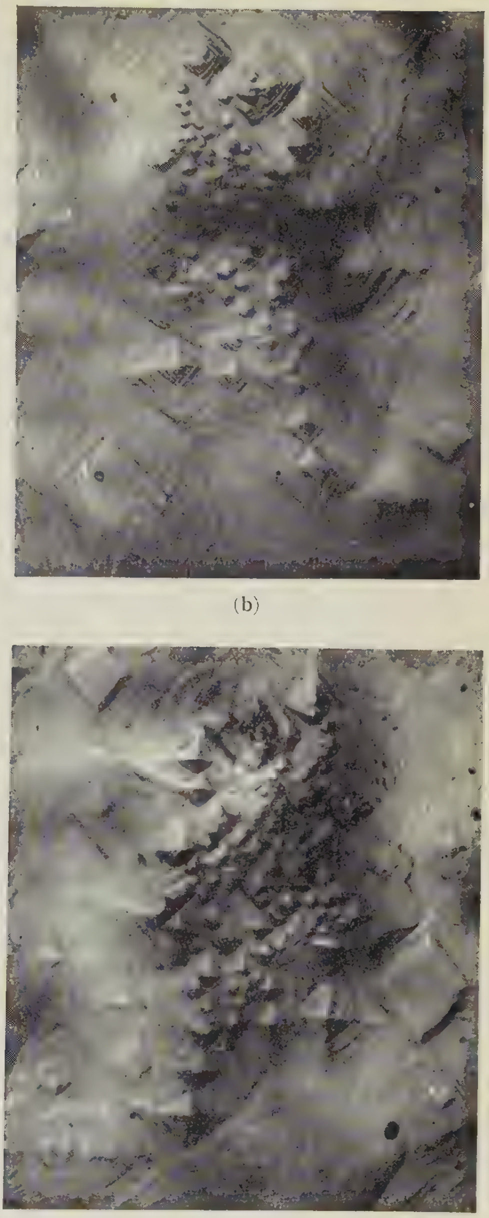
(b)

(c)

Fig. 7. Etch pits on cleavage face.
(a) ×150. (b) and (c) correspond the matching faces. ×75.
The edges of the basal rectangles are parallel to [100] and [001].

was revealed the fact that an irreversible transition to monoclinic phase occurs between −35°C and −60°C (Figs. 4 (a) and 4 (b)). The study by precession method revealved that thus produced monoclinic phase gives the similar pattern as that of Type IV, indicating that the crystal contains two groups of monoclinic components which are related to each other by 90 degrees rotation around the common *b* axis.

§ 3. Optical Observations at Low Temperatures

By the use of an optical stage specifically designed for microscopic observations at low temperature, the observation down to −140°C could be carried out without disturbances due to icings. Dielectric measurement was also carried out in parallel. Conoscopic observation, however, was not successful at low temperatures and was performed only at room temperature.

When a tetragonal crystal (Type II) is cooled down, the interference color does not show any appreciable change down to about −55°C, where a fairly rapid change occurs with the increase of retardation. The color change starts from localized nuclei and spreads over the whole area. The temperature at which the change begins depends more or less on specimen and cooling rate, and it ranges from −55°C to −60°C. The intereference color does not show any rapid change neither by further cooling down to −140°C nor by heating up to room temperature, except a minute change just above −24°C, namely the ferroelectric transition point.

The crystal sample whose optic character is illustrated in Fig. 5 exhibits an interesting change. A typical case is shown in Fig. 6, in which the dark areas are uniaxial and the bright areas contain some biaxial components. As shown by Fig. 6 (b), the boundary movement occurs around a fixed position and the patterns always remain radial. By the conoscopic observation, it is revealed that the apparent optic axial angle has increased over the whole area after the cooling cycle.

§ 4. Etch Figures

When crystals of KFCT are etched in the mixture of water and alcohol, pyramidal etch pits appear on the clevage surface. The pits have some characteristic features such as follows.

(a) Side faces of pyramids are composed of small steps.

(b) The pits appear at definite positions for each sample. When a crystal is cleaved away into two parts and then etched, the pits of two matching faces perfectly fit to each other, as shown in Fig. 7.

(c) The number of etch pits is scanty (a few per millimeter square) for slowly grown crystals, while this number is great many for rapidly grown ones.

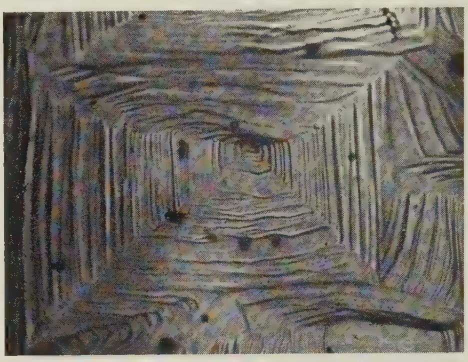

Fig. 8. Inclined etch pits. (×300)

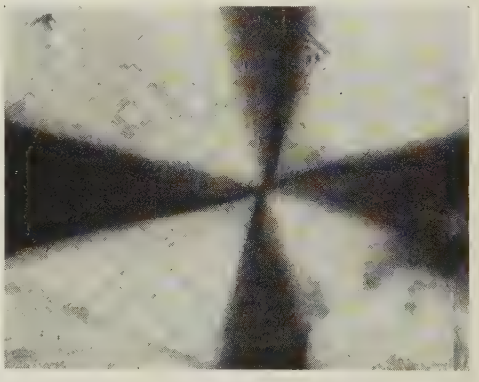

Fig. 9. Etch pit observed through a polarized microscope. ×75

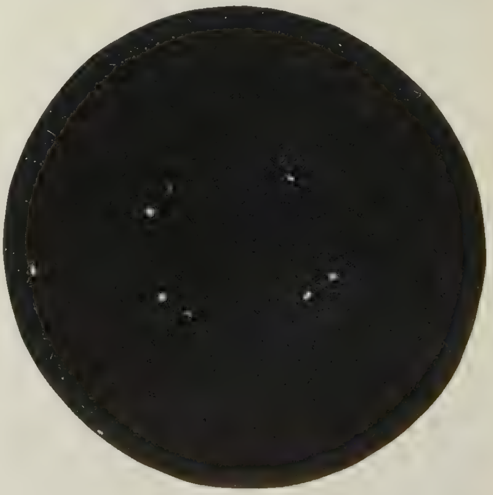

Fig. 15. Laue pattern of type IV crystal taken with monochromatic radiation (Mo Kα, 45 kv 20 ma, 1 hr).

(d) The pyramids are not always perpendicular to the cleavage face as shown in Fig. 8. When etching proceeds, the tip goes ahead along the inclined lines.

(e) Etch pits have a close relation to the optical anomaly. In a crystal with a crossed uniaxial area, the pit density increases near this area and a markedly sharp pit appears at the intersection of the cross (Fig. 9). In the crystals of Type IV, a wedge shaped area distinguishable by difference in birefringence is often observed. In such cases the pit has an octagonal base as schematically shown in Fig. 10.

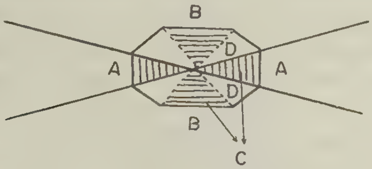

Fig. 10. Etch pit with octagonal base.
Birefringence of area A is smaller than that of B. Side face C of pyramid is composed of steps, while on the face D steps are not so marked.

The observed results are similar to those found in GASH crystals by Nakamura[5], and suggest that the pits are closely related to dislocations in the crystal, and that the various optical anomalies may be caused at least partly by dislocations.

§ 5. Dielectric Measurement

By a dielectric measurement, it has been shown for the Type I crystal that the polarization axis lies in the direction [10$\bar{1}$] which makes an angle of 32° with optic plane, while for an optically abnormal crystal, ferroelectric hysteresis loops are observed in two directions perpendicular to each other. Dielectric measurements so far reported[1),2)] were performed only for heating processes up to room temperature. The results obtained in cooling and heating runs together with optical observation are described below.

When an teragonal crystal (Type II) is cooled down, the dielectric constant shows no appreciable change down to -55°C, where a small peak appears, and the dielectric hysteresis loop appears suddenly, though unsaturated because of a high coercive field. At this temperature the structural transition to the twinned monoclinic phase takes place as mentioned before. In the heating process, the anomaly at about -55°C disappears and the dielectric property shows the features characteristic to Currie point Tc=24°C, where the dielectric constant marks a sharp peak and, at the same time, the dielectric hysteresis loop disappears.

A second cooling cycle differs considerably from the first one, but only slightly from the heating cycle. The Curie point is slightly lower than that for heating. The dielectric peak and the saturated polarization compared at the same (Tc-T) value are also smaller than those in the heating (Fig. 11). Though the temperature where the dielectric anomalies take place changes to some degrees from crystal to crystal, the general trend is common to all.

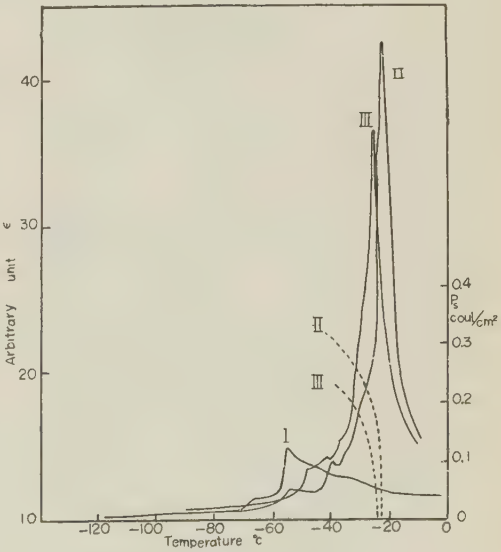

Fig. 11. Dielectric measurement at low temperature.
Full lines represent dielectric constant in arbitrary scale and dotted lines represent saturated polarization.
I. First cooling. II. Heating. III. Second cooling.

The properties as shown in Fig. 11 are obtained with an electric field along the direction inclined by 58° from the apparent optic plane, namely, the direction which is perpendicular to the polarization axis for the monoclinic single crystal. Measurements were repeated on the same crystal but with the filed perpendicular to the previous one. The results are shown in Fig. 12. Since the crystal has been once subjected to the cooling cycle, the ferroelectric transition at −24°C appears even in a first cooling run. The anomaly in dielectric constant is more considerable and the spontaneous polarization is larger than in Fig. 11. Differences of dielectric peaks and spontaneous polarization between the cooling and heating processes are noted again. It is worth mentioning that the summation of spontaneous polarizotion along the two directions in the heating process is nearly equal to that of the monoclinic single crystal.

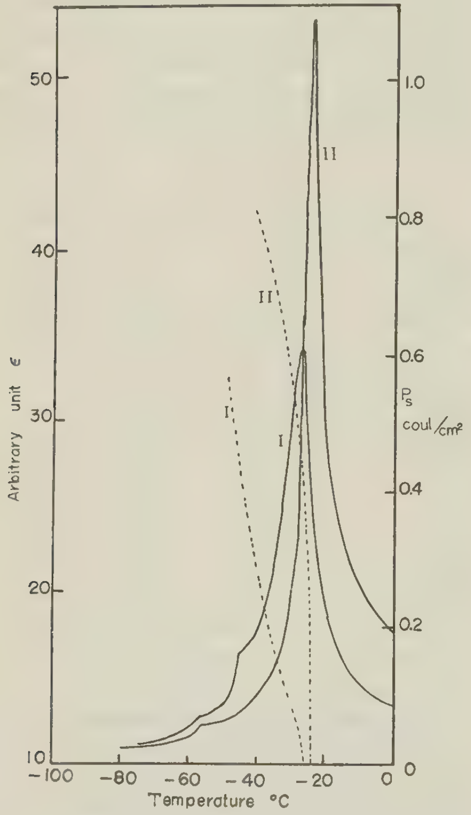

Fig. 12. Dielectric measurement along the direction perpendicular to that in Fig. 18.
Full lines represent dielectric constant in arbitrary scale and dotted lines represent saturated polarization.
I. Cooling. II. Heating.

It is interesting to note that the field cooling has no direct effect on the orientation of the monoclinic components. If the crystal examined was perfectly tetrogonal and if the transition occured homogeneously throughout the crystal, the electric field applied across the transition point would bring out a monoclinic single crystal where $[10\bar{1}]$ axis is parallel to the field direction. The observed fact suggests, therefore, that the original crystal is of the Type V with vanishing 2V angle. The composition of the crystal after the transition seems to be determined by a minute unbalance between the two biaxial components in the original state, and the effect of local crystalline field seems to be larger than that of electric field.

As described in Section 3, a minute change of interference color pattern occurs just above the ferroelectric transition point for a Type II crystal which has been subjected to a cooling process. The color change corresponds to the decrease of retardation due to the partial reappearance of the uniaxial component. The revived tetragonal part can not any ferroelectric contribution down to −55°C and therefore, the ferroelectric behavior in heating run is more conspicuous than that in the second cooling run.

§ 6. Discussion

To understand the optical and dielectric anomalis of KFCT crystals from the structural view point, it is worthy mentioning briefly the present knowledge on the crystal structure of the crystal. The structure determination of monoclidic KFCT (Type I) was performed by Posperov and Zdanov, except for the coordinates of some H_2O molecules. This structure can be considered as a double layer structure, the layer-staking unit of which is illustrated in Figs. 13 (a) and 13 (b). The structure projected on (010) is also shown in Fig. 13 (c).

The monoclinic unit cell is built up with successive double layers stacked with the shift by the amount $\vec{a}/2+\vec{b}/2$, namely by the C-centering vector of space group C2/c. The schematic diagram of this type of stacking is shown in Fig. 14 (a). In terms of the stacking vector, $\vec{C}$, the structure can be expressed by the symbols such as, $\vec{C}\,\vec{C}\,\vec{C}\ldots\vec{C}\,\vec{C}$. In view of pseudo-tetragonality of double layers comprising $Fe(CN)_6$ and K atoms, which can be clearly seen in Fig. 13 (c), we can conceive that the successive stacking operations $\vec{A}\,\vec{A}\,\vec{A}\ldots\vec{A}\,\vec{A}$, where $\vec{A}$ represents a vector $\vec{c}/2+\vec{b}/2$, would also result in a monoclinic structure which is rotated 90° from the former structure around the b axis. The H_2O molecules exist in layers between the double layers of heavier atoms. Among the twelve H_2O molecules in the unit cell, eight molecules are placed on equipoint 8 (f) of C2/c, and specifically at the midpoint of the centers of symmetry 4 (c) and 4 (d), according Posperov *et al.* Although the coordinates of other four molecules were not determined by them, consideration of the space group equipoints and possible interatomic distances should place them at equipoint 4 (e), namely on the two-fold axes, and approximately at the same level as the other eight molecules. Since the arrangement of H_2O molecules in layer has only two-fold symmetry, and not pseudo four-fold symmetry, the orientation of the H_2O layer with respect to double layers in the second type of stacking should be rotated 90° around the *b* axis from that in the first type.

The structure of tetragonal KFCT (Type II) has a very close relations to that of monoclinic one. These relations can be stated as follows: (1) *c* axis of tetragonal crystal is twice as large as the *b* axis of monoclinc one, while the unit cell dimensions of both crystals are otherwise almost identical: (2) The tetragonal reciprocal lattice level *hk*0 is identical to that of monoclinic *hll* except the weak intensities for h=odd, l=even. These facts indicate that the tetragonal structure may pictured as the stacking of double layers such that the unit cell dimension normal to

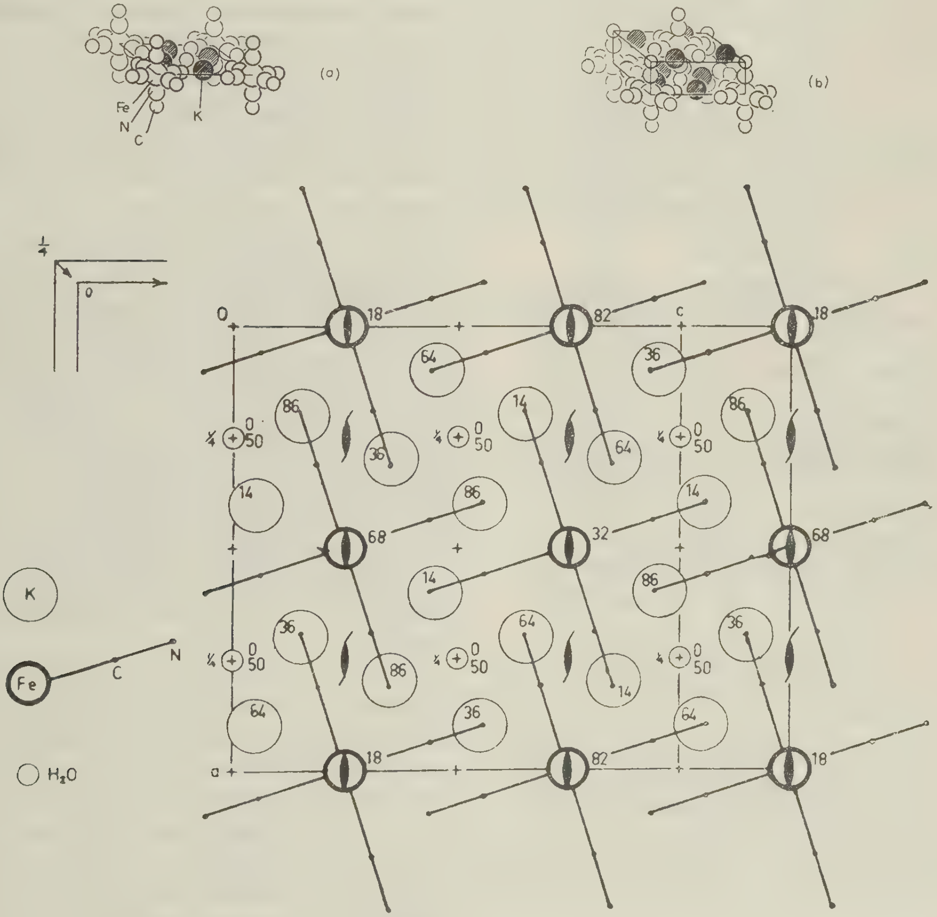

(c)

Fig. 13. Figures indicate the height above the plane in hundredth. (a) and (b) are reproduced from Structure Report XI, pp. 423.

(a) Single layer unit of KFCT crystal.

(b) Double layer unit of KFCT crystal.

(c) Projection of KFCT crystal structure on (010).

the layer is twice as large as that for the monoclinic one. Furthemore, the tetragonal structure shows non-space group extinctions for $l=4\,\mathrm{n}$, h and k=even, and for $=4\,\mathrm{n}\pm2$, h and k=odd. (Space group requires the extiction only for l=even, $h+k$=even). The possible stacking satisfying these observed extra extinction rules is illustrated in Fig. 14(c), referring to the monoclinic unit cell. In this model, the successive double layers are related to each other by four-fold screw axis of $\mathrm{I}\,4_1/a$. Because of the tetragonal symmetry of layers themselves, the relations can be again described by the shifts between layers, and the structure can be expressed by symbols such as, $\vec{A}\,\vec{C}\,\vec{A}\,\vec{C}\ldots\vec{A}\,\vec{C}\,\vec{A}\,\vec{C}$.

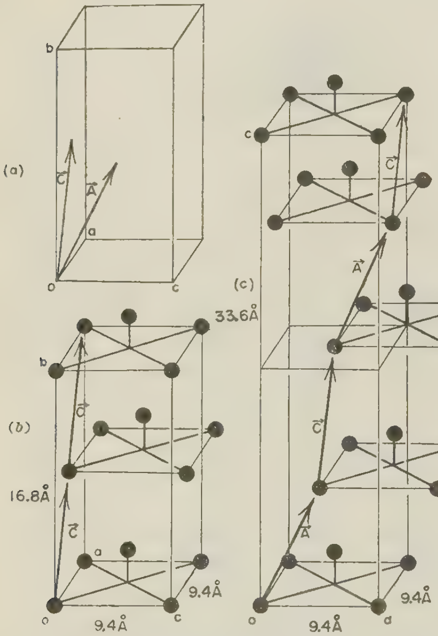

Fig. 14. Double layers are shown only with respect to Fe atoms, and the origin is arbitrarily taken at Fe atom.

(a) Vectors $\vec{A}$ and $\vec{C}$ of monoclinic lattice.

(b) Stacking scheme of double layers in monoclinic unit cell of KFCT crystal structure.

(c) Stacking scheme of double layers in tetragonal unit cell of KFCT structure with monoclinic notations.

In view of the layer structures of two modifications of KFCT, it is most probable that the oriented overgrowth between the two types of structures may take place readily, and that mistakes in stacking may occur frequently. Also the overgrowth between the two types of monoclinic stackings may be conceived to take place readily. If the type of stacking is consistent over some macroscopic dimensions, the resulting crystals may be crystallographically single crystals of Type I and II, or the macroscopic twin or oriented overgrowth described as Type III or IV. Type IV crystals can be then expresssed as; $\vec{A}\,\vec{A}\,\vec{A}\,\vec{A}\ldots\vec{C}\,\vec{C}\,\vec{C}\,\vec{C}$. If the stacking fault takes place in microscopic scale, the resulting crystal can considered as a mixture of tetragonal and monoclinic components. These crystal belong to Type V.

The mistakes in stacking take place if the adjacent layers are related by, say, the shift vector $\vec{A}$ when the normal sequence of layers should be related by vectors $\vec{C}$. Mistakes in a monoclinic structure can be represented as, $\vec{C}\,\vec{C}\,\vec{C}\ldots\vec{C}\,\vec{A}\,\vec{A}\,\vec{C}\,\vec{A}\,\vec{C}\ldots\vec{C}\,\vec{C}$.

These mistakes will give rise to the apperance of diffuse spots in X-ray diffraction photographs, especially around the reciprocal lattice points with indices $h+l$=odd. Qualitatively speaking, these diffuse spots are considered as elongated parallel to b axis of monoclinic crystal, or to c axis of tetragonal crystal. Such diffuse rows are commonly observed in rotation photographs around such axes of Type V crystals. They also appear as diffuse spots in Laue photographs of Type IV crystals, as shown in Fig. 3 (a). The Laue pattern of the same crystal with monochromatized X-ray is illustrated in Fig. 15 to show clearly the arrangement of diffuse spots. Detailed study of diffuse spots as well as the refinement of the crystal structure are in progress.

The optical, X-ray, and dielectric studies of unidirectional transition of the tetragonal phase at about −55°C result in a consistent conclusion that, after the transition of this phase into the monoclinic phase, the crystal becomes composed of oriented parallel growth of individuals with two kinds of orientation. Unidirectional transition, which is well known as monotropy in structural chemistry, may be explained by the free energy-temperature diagrams, and it is usual that the monotropic change takes place in a heating process, However, this is not the case with KFCT crystal.

The authors have recently found some evidences for an irrevercible transition from monoclinic structure to the Type V structures. When a monoclinic crystal is compressed along [101] or [10$\bar{1}$], the retardation observed along [010] decreases and remains unaltered after the removal of the external stress. The retardation increases, however, between −45° and −55°C and does not show any rapid change thereafter in the heating up to room temperature. The dielectric measument was performed also on the pressed crystal powder, and showed that the anomalies at −38°, −45° and 55°C appear both in cooling and heating processes. These facts suggest that the stability of each phase and the peculiar transitions in KFCT crystals may be affected by mechanical stresses. Further theoretical and experimental studies are in progress to understand the processes of transitions.

The authors wish to express their sincere thanks to Dr. H. Hirabayashi for his helpful discussions and to H. Iwasaki, K. Masuno and K. Nagata for their cooperations.

Appendix

Interference of light through a stacking of two thin crystals are considered. The normal to the stacking layer is chosen so as to coincide with the optic axis for uniaxial crystals, or with the X or Z axis for biaxial crystals. We consider the following two cases: A, stacking of an uniaxial and a biaxial crystals; B, two biaxial crystals of the same kind so stacked that the optic planes are perpendicular to each other with common X or Z axis.

When light passing through the stacked crystals breaks up into four linearly polarized lights, the retardations between them are given by

$$\frac{2\pi}{\lambda}d_1(n_1'-n_1''),\ \frac{2\pi}{\lambda}d_2(n_2'-n_2'')\ \text{and}$$
$$\frac{2\pi}{\lambda}\{d_1(n_1'-n_1'')\pm d_2(n_2'-n_2'')\}.$$

Suffix and prime correspond to the stacking individuals and the propagating velocities, respectively. As readily seen from the crystal optical construction, the main isogyer becomes a cross at extinction position and otherwise it suffices to consider two polarized lights with the retardation $\frac{2\pi}{\lambda}\{d_1(n_1'-n_1'')-d_2(n_2'-n_2'')\}$. The directions satisfying the condition $d_1(n_1'-n_1'')=d_2(n_2'-n_2'')$ appear as two dark points in a conoscopic pattern and are observed as the apparent optic axes. The apparent optic plane and optic angle depend on thickness ratio of component crystals.

Actual observations on the isochromats and their changes due to the reduction of thickness revealed that the Type IV crystal of KFCT contains both cases of A and B.

References

1) S. Waku, H. Hirabayashi, H. Toyoda, H. Iwasaki and R. Kiriyama: J. Phys. Soc. Japan **14** (1959) 973.
2) S. Waku, K. Masuno and T. Tanaka: To be published.
3) V. A. Posperov and G. S. Zdanov: Z. fiz. Khim. SSSR, **21** (1947) 405, 521, 879; Structure Report XI 421, 424.
4) N. Niizeki, K. Nagata and S. Waku: Phys. Soc. Japan, Ann. Meeting, April, 1960.
5) T. Nakamura: J. Phys. Soc. Japan **14** (1959) 1022.

JOURNAL OF THE PHYSICAL SOCIETY OF JAPAN, Vol. 15, No. 10, OCTOBER, 1960

Thomas-Fermi-Dirac Model of Compressed Ions

By Shigehiro KOBAYASHI

Department of Physics, Kagawa University, Takamatsu

(Received April 27, 1960)

The Thomas-Fermi-Dirac (TFD) method is extended anew to ions in the compressed state and the series expansion coefficients of its TFD function near the boundary are given.

§ 1. TFD Model of Compressed Ions

In a previous paper[1] we have shown that the simple Thomas-Fermi (TF) model, which has been applied to the treatment for the compressed state of atoms as well as for the free state of atoms and ions[2], can be extended to the compressed state of ions. In this paper, we wish to formulate the TFD model of compressed positive ions in the similar way.

We shall treat a compressed ion with atomic number Z and electron number N.

The requirement that the total energy E of the TFD model of the ion shall be minimum with respect to variation of the electron density ρ, the total number of electrons being kept costant, leads to

$$\frac{5}{3}\kappa_k\rho^{2/3}-\frac{4}{3}\kappa_a\rho^{1/3}-(V-V_0)e=0 \qquad (1)$$

or

$$\rho(r)=\frac{8\pi}{3h^3}(2me)^{3/2}[\{V(r)-V_0+\tau^2\}^{1/2}+\tau]^3, \qquad (2)$$

where V_0 is the Lagrange multiplier expressing the maximum potential for the electron in the ion and

$$\kappa_k=\frac{3}{10}(3\pi^2)^{2/3}e^2a_0, \quad \kappa_a=\frac{3}{4}\left(\frac{3}{\pi}\right)^{1/3}e^2,$$

$$\tau=\left(\frac{4\kappa_a^2}{15\kappa_k e}\right)^{1/2}=\frac{(2me^3)^{1/2}}{h}.$$

Another requirement of self-consistency that the electrostatic potential V shall be created by the electronic cloud of density ρ and the nucleus of the ion is simply expressed in Poisson's equation

$$\Delta V=4\pi\rho e\,. \qquad (3)$$

Combining (2) with (3) and using the ordinary notations

$$r=\mu x, \quad \mu=\frac{1}{4}\left(\frac{9\pi^2}{2Z}\right)^{1/3}a_0\,, \qquad (4)$$

$$V-V_0+\tau^2=\frac{Ze}{r}\psi \qquad (5)$$

and

$$\beta=\tau(\mu/Ze)^{1/2}=6^{1/3}/4(\pi Z)^{2/3} \qquad (6)$$

under the assumption of the spherical symmetry, we can obtain the so-called TFD equation

$$\psi''=x[(\psi/x)^{1/2}+\beta]^3 \qquad (7)$$

and the electron density represented in terms of ψ

$$\rho(x)=\frac{Z}{4\pi\mu^3}\frac{\psi''}{x}=\frac{Z}{4\pi\mu^3}[(\psi/x)^{1/2}+\beta]^3. \qquad (8)$$

By the use of the thermodynamic relation, we can compute the pressure

$$p=-\frac{dE}{dv}=\frac{1}{3}\rho(R)^{4/3}\{2\kappa_k\rho(R)^{1/3}-\kappa_a\} \qquad (9)$$

dependent on the boundary density $\rho(R)$, where v is the volume of the ion.

The solution of (7), namely the TFD function $\psi_{Z,q,X}$ for the state of ionization degree $q=(Z-N)/Z$ and of boundary radius $R=\mu X$

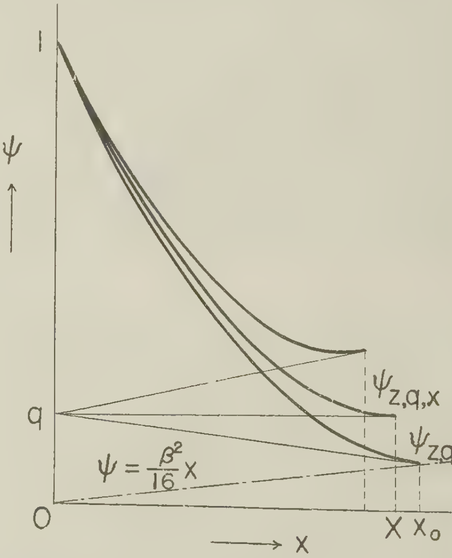

Fig. 1. The TFD function $\psi(x)$ for compressed ions. From Fig. 1 it can be seen that the particular values of Z, q and X determine uniquely a ψ-curve in the assembly of the ψ-curves starting from $\psi(0)=1$ for the particular value of Z.

must satisfy at the nucleus ($x=0$) the condition

$$\psi_{Z,q,X}(0)=1: \text{ nucleus predominates} \tag{10}$$

and at the boundary ($x=X$) the conditions

$$\psi_{Z,q,X}(X)>\frac{\beta^2}{16}X: \text{ finite pressure} \tag{11}$$

and

$$\psi_{Z,q,X}(X)-X\psi'_{Z,q,X}(X)=q: \quad \text{net charge}=(Z-N)e. \tag{12}$$

As is well known, for the free state of the ion with the boundary radius $r_0=\mu x_0(>R)$, which corresponds to the zero pressure, (9) gives the boundary density

$$\rho(r_0)=\left(\frac{\kappa_a}{2\kappa_k}\right)^3=0.002127\ a_0^{-3} \tag{13}$$

independent of Z and N. Accordingly, with $V(r_0)=(Z-N)e/r_0$ we obtain from (1)

$$V_0=\frac{Ze}{r_0}q+\frac{15}{16}\tau^2 \tag{14}$$

and from (5)

$$\psi_{Z,q,x_0}(x_0)=\frac{\beta^2}{16}x_0\,. \tag{15}$$

For the compressed state, V_0 should be chosen, following Slater and Krutter[3], in such a way that the potential V in the immediate neighborhood of the nucleus has a value independent of the boundary radius, that is

$$V=V_0-\tau^2+\frac{Ze}{\mu}\left[\frac{1}{x}+\psi'_{Z,q,X}(0)+\frac{4}{3}x^{1/2}+\dots\right] \quad : \text{ for the compressed state}$$

and

$$V=\frac{(Z-N)e}{\mu x_0}-\frac{1}{16}\tau^2+\frac{Ze}{\mu}\left[\frac{1}{x}+\psi'_{Z,q,x_0}(0)+\frac{4}{3}x^{1/2}+\dots\right] \quad : \text{ for the free state}$$

ought to agree with each other up to the constant terms as well as to those in $1/x$. Thus, V_0 takes the value

$$V_0=\left[\frac{q}{x_0}+\psi'_{Z,q,x_0}(0)-\psi'_{Z,q,X}(0)\right]\frac{Ze}{\mu}+\frac{15}{16}\tau^2 \tag{16}$$

dependent on q and X.

This expression of V_0 for our general case is naturally reduced to (14) for the free state and to the expression (7) in the previous paper[1] for the compressed TF model in which the exchange effect is neglected ($\kappa_a=0$, $\tau=0$).

The expressions (5), (8) and (16) enable us to calculate various physical quantities for ions in the compressed state.

§ 2. Series Expansion Around the Boundary

The TFD function $\psi_{Z,q,X}(x)$ for the compressed ion can be expanded around the boundary point X in a Taylor series such as

$$\psi_{Z,q,X}(x)\equiv a^2X+t_1(X-x)+t_2(X-x)^2+t_3(X-x)^3+\dots, \tag{17}$$

where $a^2\equiv\psi_{Z,q,X}(X)/X$, particularly in the free state $a=\beta/4$ due to (15).

The expansion coefficients up to and including t_7 are given in terms of $\beta(Z)$, q, $a(X)$ and X as follows;

$$t_1=-a^2+\left\{\frac{1}{X}q\right\}$$

$$t_2=\frac{X}{2}(a+\beta)^3$$

$$t_3=-\frac{1}{6}(a+\beta)^3+\left\{\frac{1}{4aX}(a+\beta)^3q\right\}$$

$$t_4=\frac{X}{16a}(a+\beta)^5+\left\{\frac{1}{32a^3X^3}(a^2-\beta^2)q^2\right\}$$

$$t_5=-\frac{1}{80a}(a+\beta)^5+\left\{\frac{3}{160a^3X}(2a-\beta)(a+\beta)^4q\right.$$

$$\left.+\frac{3}{160a^3X^4}(a^2-\beta^2)q^2-\frac{1}{320a^5X^5}(a^2-3\beta^2)q^3\right\}$$

$$t_6=\frac{X}{320a^3}(2a-\beta)(a+\beta)^7+\left\{\frac{1}{120a^3X^2}(a-\beta)(a+\beta)^4q\right.$$

$$+\frac{1}{80a^3X^5}\left[(a^2-\beta^2)+\frac{X^2}{8a^2}(3a^2-5a\beta+6\beta^2)(a+\beta)^3\right]q^2$$

$$\left.-\frac{1}{240a^5X^6}(a^2-3\beta^2)q^3+\frac{1}{1280a^7X^7}(a^2-5\beta^2)q^4\right\}$$

$$t_7=\frac{1}{6720a^3}(2a-5\beta)(a+\beta)^7$$

$$+\left\{\frac{1}{168}\frac{(a+\beta)^4}{a^4X^5}\left[(a-\beta)+\frac{3X^2}{80a^2}(16a^2-18a\beta+15\beta^2)(a+\beta)^2\right]q\right.$$

$$+\frac{1}{112}\frac{a+\beta}{a^3X^6}\left[(u-\beta)+\frac{X^3}{120a^2}(19a^2-69a\beta+150\beta^2)(a+\beta)^2\right]q^2$$

$$+\frac{1}{224}\frac{1}{a^5X^7}\left[(-a^2+3\beta^2)-\frac{X^2}{20a^4}(2a^5+4a^4\beta-4a^3\beta^2-37a^2\beta^3-56a\beta^4-25\beta^5)\right]q^3$$

$$\left.+\frac{3}{1792}\frac{1}{a^7X^8}(a^2-5\beta^2)q^4-\frac{1}{3584}\frac{1}{a^9X^9}(a^2-7\beta^2)q^5\right\}.$$

The bracketted parts depending on q in these expressions are proper to the ion, and the rest parts coincide with the coefficients for compressed neutral atoms given by March[4].

The author would like to express his sincere thanks to Professor K. Umeda of Okayama University for reading the manuscript and giving many advices. This work was supported by the Scientific Research Fund of the Ministry of Education.

References

1) S. Kobayashi: J. Phys. Soc. Japan **14** (1959) 1121; Mem. Fac. Liberal Arts & Educ., Kagawa Univ., II No. 82 (1959).

2) P. Gombás: *Die statistische Theorie des Atoms und ihre Anwendungen* (Springer, Wien, 1949); *Statistische Behandlung des Atoms* (H. B. der Physik Band 36, Springer, Berlin, 1956).

3) J. C. Slater and H. M. Krutter: Phys. Rev. **47** (1935) 559.

4) N. H. March: Proc. Phys. Soc. A **68** (1955) 726, in particular Table 3.

JOURNAL OF THE PHYSICAL SOCIETY OF JAPAN, Vol. 15, No. 10, OCTOBER, 1960

On the Magnetic Properties of the Compound Mn_2As

By Motoyoshi YUZURI and Motohiko YAMADA

The Research Institute for Iron, Steel and Other Metals,
Tohoku University, Sendai

(Received May 6, 1960)

The thermomagnetic properties of a compound Mn_2As were investigated together with the phase diagram of Mn–As system. From the results of measurements of the temperature dependence of magnetic susceptibility and specific heat of the compound Mn_2As, it was found that this alloy is antiferromagnetic with the Néel point at 573°K. The reciprocal of its susceptibility obeys the Curie-Weiss law in the high temperature range, but a considerable deviation therefrom can be seen just above the Néel point as in the case of ferrimagnetism. Based on the Curie constant obtained by the present experiment, the effective magneton number was calculated to be 5.2 per manganese ion. The total heat absorption due to the vanishing of antiferromagnetic order of spins in the present alloy was estimated to be 230 Cal/mol. A discussion based on the molecular field theory is given on the nature of the above-mentioned magnetic properties.

§ 1. Introduction

In the crystal lattice of Cu_2Sb type compounds the cation sites are thought to form a deformed face-centered lattice, which is divisible into two sorts of non-equivalent sublattices. If such cations have magnetic moments, the formation of new types of spin ordering is to be expected because of the presence of such a peculiar type of magnetic lattice structure. But very few magnetic measurements for this type of compounds have hitherto been done, except those for Mn_2Sb.[1) 2) 3)] The present authors undertook a study of the magnetic properties of a compound Mn_2As, whose crystal structure was reported by Nowotny and Halla[4)] as belonging to the above-mentioned type. The phase diagram of manganese-arsenic system was once studied by Guillaud[1)] and Sweeny and Scott.[5)] The results obtained by these authors, however, were not sufficient for the preparation of our specimens. Here, the results of X-ray, thermal and magnetic analyses are also presented which have been carried out in order to study the phase diagram of the present system.

§ 2. Preparation of the Specimen

The specimens used were prepared by the ceramic method. Manganese (99.9%) and arsenic (99.9%) powders were mixed in the desired ratios in the composition range from MnAs to $Mn_{2.3}As$, sealed into evacuated quartz tubes and heated in an electric furnace. To avoid explosion of the tubes during heating, the mixtures were heated up slowly in 72 hours from room temperature up to 900°C at which they were kept for 48 hours. After the reaction was completed, the specimens were cooled slowly down to room temperature in 72 hours. Since the compound Mn_3As_2, which was supposed to be formed by a peritectoid reaction between the compounds MnAs and Mn_2As, had a transition point between 750°C and 775°C, the reaction products whose composition was nearly Mn_3As_2 were annealed more at about 700°C for 72 hours. In order to obtain homogeneous specimens, all the reaction products were crushed, well mixed, again heated to 770°C, kept for 48 hours, and then cooled to room temperature in 72 hours. Such prepared specimens, however, did not show any difference from the original ones in their magnetic properties. Every portion of the specimen thus obtained showed a similar thermo-magnetic behavior.

§ 3. Phase-diagramatic Study of Mn-As System

First, the thermal analysis was made in the composition range from x=1.0 to 2.0, x being the Mn content in the formula Mn_xAs*. The results are shown in Fig. 1. A peak of latent heat type in specific heat vs. temperature was observed invariably at 750°C, for the specimens with compositions $0<x\leq 1.6$; the peak temperature shifts to 775°C for the specimens with $1.7\leq x<2$. The amounts of such endothermic energy are plotted against Mn content in Fig. 2. As shown in the figure, the amount of heat absorption increases almost linearly with Mn atomic percent from the composition of MnAs to Mn_3As_2, reaching a value 260 Cal/mol at ca the latter. It decreases again linearly from $Mn_{1.7}As$ to Mn_2-As starting from a different value of 400 Cal/mol. Besides, the value of specific heat was not influenced by the lowering of the heating rate of the specimen down to one-third of that in the former case. Moreover the transition temperature and the amount of heat absorbed were not influenced by the annealing of the same specimen at 700°C for 24 hours. These facts can be explained by assuming the presence of a narrow single phase field near the composition Mn_3As_2, which involve a phase transition from γ to γ'. The transition point will be 750°C on the As-rich side and 775°C on the Mn-rich side. In the As-rich region, this phase coexists with the compound MnAs, and in the Mn-rich region, with the compound Mn_2As. (Fig. 3)

---

* The compositions of the specimens indicated here are the charged contents.

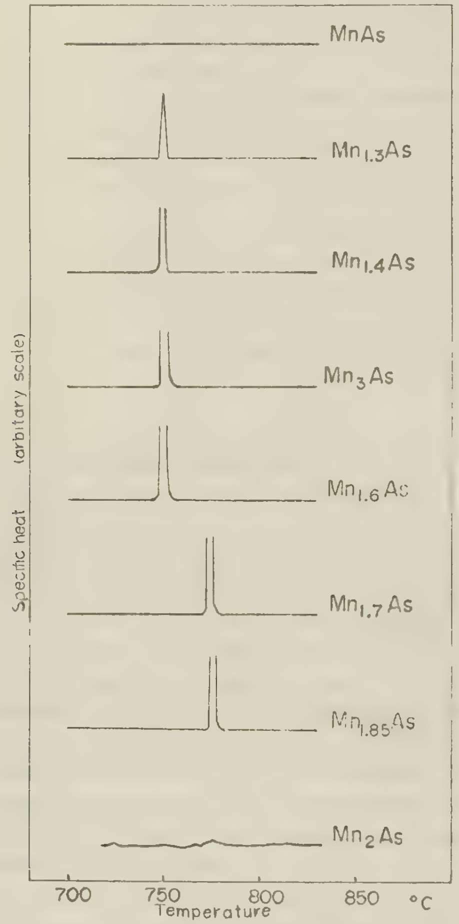

Fig. 1. Thermal analysis curves of Mn_xAs.

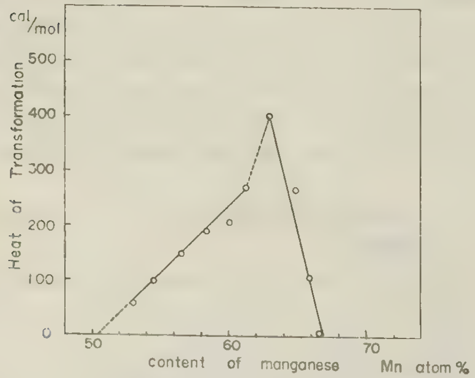

Fig. 2. Transition energy vs. composition in the system *Mn–As*.

Next, the crystal structure was investigated by means of the X-ray powder method. The diffraction lines from the specimen of the composition MnAs could be indexed as those from the NiAs structure with parameters $a=3.72$ Å and $c=5.70$ Å ($c/a=1.53$), which coincided with the result by Oftedals6), and their relative intensities also coincided with the result by calculation. On the other hand, the diffraction lines at the composition $Mn_{2.3}$-As were indexed as those from the crystal structure of Cu_2Sb type with parameters $a=3.78$ Å and $c=6.25$ Å ($c/a=1.65$) in accordance with the result due to Halla and Nowotny4). At intermediate compositions between MnAs and $Mn_{2.3}As$, the diffraction lines from the NiAs structure or that from the Cu_2Sb structure became weak with the increase of x from $x=1$ or with the decrease of x from $x=2$. At the same time, new diffraction lines which could be attributable neither to the NiAs nor to the Cu_2Sb structure became strong correspondingly. In the region between $x=1.5$ and 1.6 only these diffraction lines were seen. Combined with the result of specific heat measurements they are to be attributable to γ'-phase. (Table 1.) The intensity of these lines becomes maximum near $x=1.5$. Diffraction lines from the Cu_2Sb

Table I. The result of X-ray analysis of Mn_3As_2 at room temperature.

Target: Cu

Intensity	Scattering angle	$\sin^2 \theta$
	θ	Observation
VS	20° 45′	0.1253
S	22° 15′	0.1433
S	24° 30′	0.1710
S	26° 36′	0.2005
VS	29° 18′	0.2410
W	31° 48′	0.2780

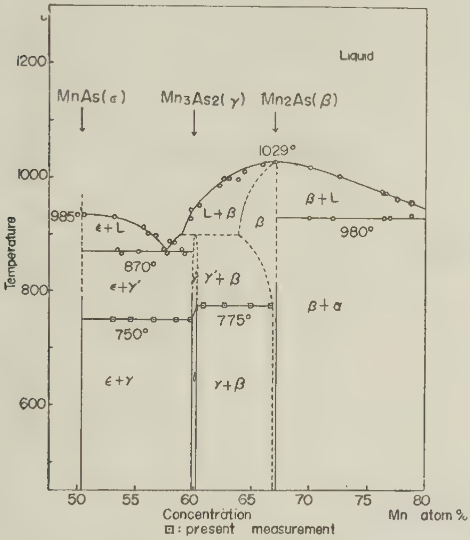

Fig. 3. Phase diagram of *Mn–As* system.

structure begin to appear near $x=1.6$ and only these lines are seen at the region of x greater than 2.0. The lattice parameters corresponding to Mn_2As and γ–phase (the diffraction angles of the lines) remain unchanged for all specimens measured. On the basis of these crystallographic and thermal studies, MnAs, Mn_2As, or γ -phase is stable in a range of composition including $x=1.0$, 2.0 or 1.5 respectively. It is also established that a two-phase field is existing between MnAs and Mn_3As_2 or between Mn_3As_2 and Mn_2As.

In order to investigate the nature of $\gamma \rightleftarrows \gamma'$ transformation mentioned above, powder photographs were taken of the specimen with $x=1.5$ quenched from temperatures above the transition point, however, no change in the diffraction pattern was found. It was also confirmed by means of a high temperature camera that no change in the patterns occurred above this transition point. On the other hand, both diffraction lines from the Cu_2Sb structure and from manganese were observed near $x=2.5$, showing that this composition is inside of the two-phase region with the Cu_2Sb structure and α—Mn.

Based on the results of X-ray and thermal analyses, the phase diagram of Mn–As system was constructed, as shown in Fig. 3.

§ 4. Thermomagnetic Measurements

The magnetic properties of the specimens were measured by means of an automatically recording magnetic balance.[7] The magnetization curves of the compound Mn_3As_2 at liquid air temperature was measured up to the strength of magnetic field of 10,000 Oe, (The technical saturation was reached at 8000 Oe). As shown in Fig. 4, it is also seen the magnetization at high field changes linearly with the inverse square of magnetic field. By extrapolating the value of magnetization to infinitely strong field, the saturation magnetization is obtained to be 17 gauss/gr.

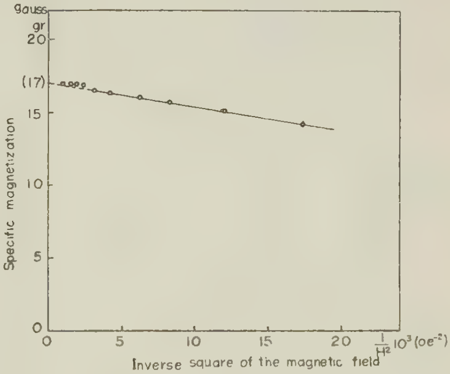

Fig. 4. Specific magnetization of Mn_3As_2 vs. inverse square of the magnetic field.

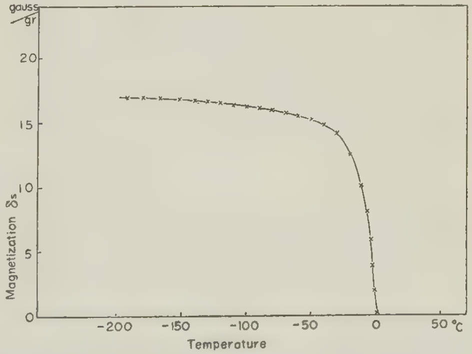

Fig. 5 (A). Thermomagnetic curve below the Curie temperature of Mn_3As_2.

The saturation magnetization varies linearly with $T^{3/2}$ below 150°K. The saturation value at absolute zero of temperature, obtained by extrapolating the linear part of the $\sigma_s - T^{3/2}$ curve, is 17.2 gauss/gr or 0.31 μ_B per Mn atom. The thermomagnetic curve of this compound under the magnetizing field of 8000 Oe is shown in Fig. 5 (A) and Fig. 5 (B), which shows the Curie point lies at 0°C. From the Curie constant, 2.1, obtained from the slope of the $1/\chi - T$ curve, the effective number of magneton per Mn ion was calculated to be 4.1.

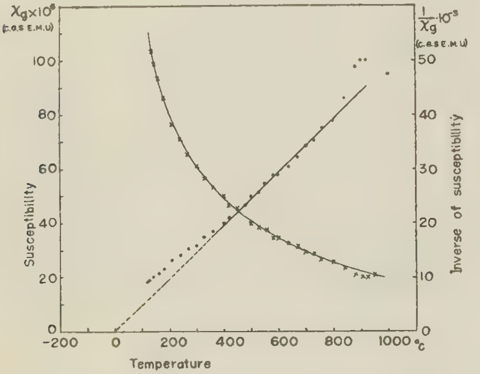

Fig. 5 (B). Thermomagnetic curve above the Curie temperature of Mn_3As_2.

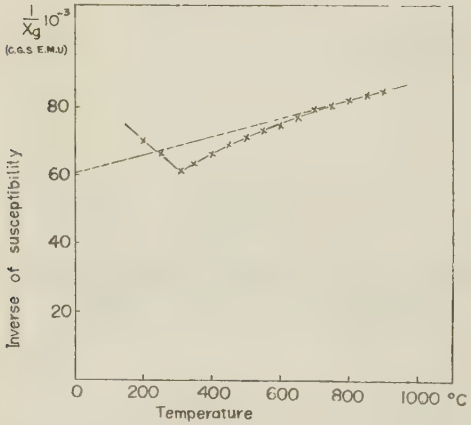

Fig. 6. Reciprocal of susceptibility vs. temperature of $Mn_{2.3}As$.

From the results of thermomagnetic measurement the compound $Mn_{2.3}As$ behaves like an antiferromagnetic substance with the Néel point at 300°C. As shown in Fig. 6, the reciprocal of susceptibility follows the Curie-Weiss law at high temperatures, but decreases rapidly just above the Néel point as is in the case of ferrimagnetism. The specimens with lower Mn concentration show a weak ferromagnetism with Curie point at 0°C as well as an antiferromagnetism with maximum susceptibility at 300°C. The molar magnetization obtained by extrapolating to 0°K at the magnetic field of 8000 Oe decreases linearly, as shown in Fig. 7, with increase of Mn concentration and vanishes at 67%, which again confirms the specimens in the region $1.6 \leq x \leq 2.0$ are the mixtures of Mn_3As_2 and Mn_2As. Actually, however, the specimens with the value of x slightly greater than 2 (e.g. $Mn_{2.1}As$) shows a negligibly weak ferromagnetism with a Curie point at 0°C. It was difficult to avoid a trace of contamination of Mn_3As_2 in this composition range.

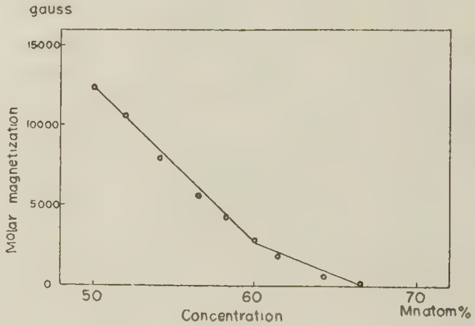

Fig. 7. Saturation magnetization vs Mn concentration.

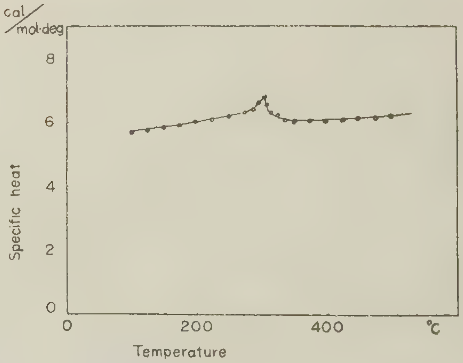

Fig. 8. Specific heat of $Mn_{2.3}As$ vs. temperature.

The measurement of specific heat near the temperature at which the susceptibility of $Mn_{2.3}As$ attained maximum was carried out by means of an adiabatic calorimeter[8]. The result of measurement is shown in Fig. 8. An anomalous peak of specific heat was observed at about 300°C corresponding to the susceptibility maximum of this compound, and the excess heat absorption is estimated to be 230 Cal per mole of mangenese.

§ 5. Discussion of the Result

Now the magnetic properties of the compound Mn_2As will be discussed. In the crystal lattice of Mn_2As there are two sorts of cation sites A and B, as shown in Fig. 9, which are surrounded by arsenic ions tetrahedrally and octahedrally respectively. If we restrict ourselves to a case in which both cation layers, A_1 and B_1, in the present crystal lattice have net spin moment, as is confirmed in the case of Mn_2Sb,[3] it is sufficient to take into account the four molecular field coefficients: (1) inter-layer molecular coefficient n between $B_1(B_4)$, and $B_2(B_3)$, (2) inter-layer molecular coefficient $n\beta_1$ between A_1 and B_1 (B_4), (3) inter-layer molecular coefficient $n\beta_2$ between A_1 and $B_2(B_3)$ and (4) intra-layer molecular coefficient $n\gamma$ in the planes A_1 as well as A_2. The molecular field H_{A1}, H_{B1}, etc. acting on an ion at a lattice point of A_1, B_1 etc. are expressible as

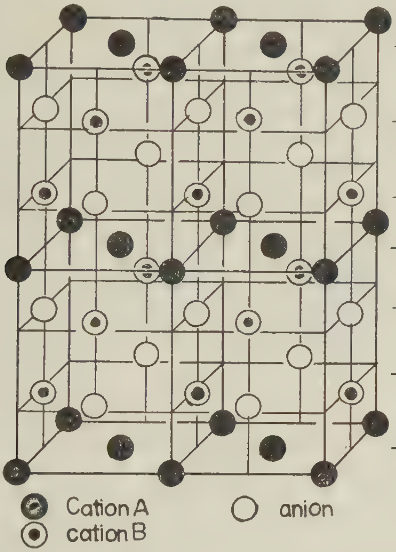

Fig. 9. Mn_2As structure and its sublattices.

$$H_{A1}=n(\beta_1 M_{B1}+\beta_1 M_{B4}+\beta_2 M_{B2}+\beta_2 M_{B3}) \\ +n\gamma M_{A1},$$

$$H_{B1}=n(\beta_1 M_{A1}+\beta_2 M_{A2})+nM_{B1}, \text{ etc.}$$

Here M_{A1} ect, represent the magnetization vectors of sublattice A_1 etc. for one mole of material respectively. In this case four types of spin ordering illustrated in Fig. 10 are expected to occur; one ferromagnetic, one ferrimagnetic and the other two antiferromagnetic (I, II).* The corresponding Néel temperature for the antiferromagnetic cases is given as follows:

$$T_N=\frac{1}{16}[n(2C_A\gamma-C_B)+|n|\{(C_B+2C_A\gamma)^2 \\ +16C_AC_B(\beta_1-\beta_2)^2\}^{1/2}].$$

In each case the paramagnetic susceptibility χ above the Néel temperature is given by following equation:

$$\frac{1}{\chi}=\frac{T-T_a}{1/2\cdot(C_A+C_B)}-\frac{\tau}{T-\theta} \tag{1}$$

Where

$$T_a=-\frac{n}{8(C_A+C_B)}(4C_AC_B\beta+C_B^2+2C_A^2\gamma),$$

$$\theta=\frac{nC_AC_B}{8(C_A+C_B)}(1+2\gamma-4\beta), \quad \beta=\beta_1+\beta_2,$$

$$\tau=\frac{n^2C_AC_B}{32(C_A+C_B)^3}\{C_B(1-2\beta)+C_A(2\beta-2\gamma)\}^2,$$

and C_A and C_B are the molar Curie constants of A and B ions respectively. The second term in the right-hand side of Eq. (1) causes an appreciable deviation from the Curie-Weiss law in the temperature range just above the Néel point.

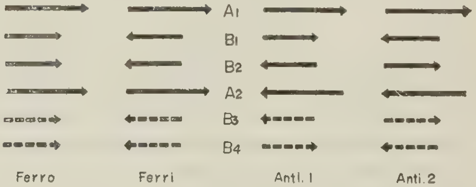

Fig. 10. Four possible types of spin ordering to structure.

If the peak in the susceptibility vs. temperature relation for the compound Mn_2As mentioned above can be attributable to an antiferro-paramagnetic transition as discussed here, the predicted deviation from the Curie-Weiss law can be seen in the magnetic susceptibility of the paramagnetic region of the compound Mn_2As: The full line of the susceptibility curve shown in Fig. 6, is given by putting $T_a=1947$°K, $(C_A+C_B)/2=3.34$, $\tau=10000$°K and $\theta=490$°K (and $T_N=570$°K) in Eq. (1). Using these values, possible values of the molecular field coefficients are calculable. If we assume sextet and quartet states for the manganese ion of A and B sites (the values 4.38 and 2.30 are adopted for C_A and C_B respectively), the molecular field coefficients can be determined as shown in table II. a., and the results for the case in which quintet states are assumed for both ions, are listed in Table II.b. In both cases the calculated Néel temperature based on these coefficents is higher than the calculated ferrimagnetic Curie temperature corresponding to the same values of coefficients, showing that the antiferromagnetic ordering is stable in general, but the calculated internal energy of ferrimagnetic structure at 0°K based on those molecular field constants is lower than that of antiferromagnetic structure, predicting an antiferro-ferrimagnetic transition may occur at low temperature. This prediction is, however, not yet confirmed. The theoretical estimation of the anomalous heat absorption in this antiferro-para transition based on the molecular field treatment is 1150 Cal/mol. Although experimental value of 230 Cal/mol is far smaller than the value, a part of the discrepancy may be attributed to a too crude estimation of the lattice heat which must be subtracted from the above value.

---

* The lattice points in the layer A_i, are also divisible into two sublayers $A_{i'}$ and $A_{i''}$. In such cases some other types of antiferromagnetic ordering are possible such as $M_{Ai'}=-M_{Ai''}$ and $\sum M_{Bi}=0$, and A ions and B ions form respectively antiferromagnetic spin ordering with different Néel temperatures.

Table II* Coefficients of molecular fields.

$(a)^*$		(b)
$C_A=4.38$	$C_B=2.30$	$C_A=C_B=3.34$
$S_A=\frac{5}{2}$	$g_A=2$	$S_A=S_B=\frac{4}{2}$
$S_B=\frac{3.4}{2}$	$g_B=2$	$g_A=g_B=2.12$
or		or
$\Big(S_B=\frac{3}{2}$	$g_B=2.22\Big)$	$\Big(S_A=S_B=\frac{4.3}{2}$
		$g_A=g_B=2\Big)$
$n=-0.61\times10^3$	$n=-1.82\times10^3$	$n=-1.31\times10^3$
$\gamma=1.91$	$\gamma=0.47$	$\gamma=0.84$
$\beta_1+\beta_2=2.3$	$\beta_1+\beta_2=0.84$	$\beta_1+{}_2\beta=1.12$
$\lvert\beta_1+\beta_2\rvert=1.7$	$\lvert\beta_1+\beta_2\rvert=0.18$	$\lvert\beta_1+\beta_2\rvert=0.18$

The authors wish to express their cordial thanks to Professor T. Hirone for his kind guidance throughout the present investigation. Their thanks are also due to Drs. H. Watanabe, S. Maeda and K. Adachi, staff of the Research Institute for Iron, Steel and Other Metals of Tohoku University, and to Dr. S. Nagasaki of Rigaku Denki K. K., who gave their eager and kind discussion.

References

1) G. Guillaud: Thesis, Strasbourg (1943).
2) A. Serres: J. de Phys. (8) **8** (1947) 146.
3) M. K. Wilkinson, N. S. Ginglich and C. G. Shull: J. Phys. Chem. Solids **2** (1957) 289.
4) H. Nowotny and F. Halla: Z. Phys. Chem. (B) **36** (1937) 322.
5) K. H. Sweeny and A. B. Scott: H. Chem. Phys. **22** (1954) 917.
6) I. Oftedals: Z. Phys. Chem. (A) **132** (1927) 208.
7) T. Hirone, S. Maeda and N. Tsuya: Rev. Sci. Instr. **25** (1954) 516.
8) S. Nagasaki and Y. Takagi: Oyobutsuri **17** (1948) 104 (in Japanese).

---

* Note that the free ion states assumed in (a) are different from those found by the neutron diffraction data in Mn_2Sb[3], which give a result with sextet state for B and quartet state for A.

JOURNAL OF THE PHYSICAL SOCIETY OF JAPAN, Vol. 15, No. 10, OCTOBER, 1960

Plasma Oscillations in a Magnetic Field

By Ikuo KAJI
The Research Institute of Applied Electricity, Hokkaido University
Masafumi KITO
The Electrotechnical Laboratory, Tokyo

(Received May 7, 1960)

In the presence of a uniform external magnetic field, the initial value problem for a longitudinal electron oscillation in a fully ionized plasma is treated in the range of the linear theory under the assumption that collisions are negligible and that the angle θ between wave vector and magnetic field is not equal to $\pi/2$, and $\mathrm{Re}(s)\neq 0$ on the complex s-plane. It is shown that, if we determine the indicial condition that the solution of initial value problem varies as $\exp(i\boldsymbol{k}\cdot\boldsymbol{r}+\alpha t)$, where α is a complex valued frequency, then for $\mathrm{Re}(\alpha)<0$ (damped wave) there appears an indeterminancy in the dispersion equation of the potential, and for $\mathrm{Re}(\alpha)>0$ (amplified wave) each dispersion equation of the proper plasma oscillations, the perturbed velocity distribution function, and the potential are coincident. As a typical example, the case in which the equilibrium distribution is Maxwellian is discussed.

Introduction

In the presence of a uniform external magnetic field, a longitudinal small amplitude oscillation of electrons in a fully ionized plasma has been treated by I. B. Bernstein[1] and E. P. Gross[2] when collisions are negligible. The former assumed that the initial perturbed distribution function is an entire function, so that the problem was only restricted to the proper plasma oscillation. The latter discussed only the stationary solution of electron oscillations propagating perpendicular to the magnetic field. However, they did not take into account of the effect of initial perturbed distribution function.

Therefore, we solved the initial value problem for the perturbed distribution function, and determined the indicial condition that the solution of the problem varies as $\exp(i\boldsymbol{k}\cdot\boldsymbol{r}+\alpha t)$ where α is a complex valued frequency, on the condition that the angle θ between the wave vector and the magnetic field is not equal to $\pi/2$, and $\mathrm{Re}(s)\neq 0$ on the complex s-plane. This indicial condition becomes a dispersion equation of a complex valued frequency.

The dispersion equations for the proper plasma oscillation, the perturbed distribution function, and the electrostatic potential are obtained. For amplified wave, we find that these equations are the same, and furthermore these are determined uniquely. However, although for damped wave the dispersion equations of the proper plasma oscillation and the perturbed distribution function are determined uniquely, there exists an indeterminancy in the dispersion equation of the potential, because the equation involves an arbitrary constant. When the constant is zero, the equations for the distribution function and the potential are coincident. Because of the arbitrary constant, there appears the Doppler shift which is determined by $\omega=ku\cos\theta+n\Omega$ in the distribution function providing that an initial distribution function gives a solution of the potential which varies $\exp(i\boldsymbol{k}\cdot\boldsymbol{r}+\alpha t)$.

In §1, basic equations of the plasma oscillation are derived from the linearized Boltzmann equation and Poisson equation by use of the Laplace transform method. Initial value problem is treated in §2 and a dispersion equation for proper plasma oscillation is obtained. An indicial condition that the distribution function and the potential become a solution of the form $\exp(i\boldsymbol{k}\cdot\boldsymbol{r}+\alpha t)$, is determined in §3. As a typical example, the case in which the equilibrium distribution is Maxwellian is discussed in §4.

§1. Basic Equations

Let $f(\boldsymbol{r},\boldsymbol{v},t)$ be the distribution function for electrons, which satisfies the Boltzmann equation

$$\frac{\partial f}{\partial t}+\boldsymbol{v}\cdot\frac{\partial f}{\partial \boldsymbol{r}}-\frac{e}{m}\left\{-\nabla\varphi+\frac{1}{c}\boldsymbol{v}\times\boldsymbol{B}(\boldsymbol{r},t)\right\}\cdot\frac{\partial f}{\partial \boldsymbol{v}}=\left(\frac{\partial f}{\partial t}\right)_{\text{coll}} ,$$

where φ represents the electrostatic potential and $-e$ is the electronic charge. The problem is restricted to merely longitudinal electron oscillation, so that, instead of the full set of Maxwell equations, the Poisson equation is employed. Considering a system which departs only slightly from thermal equilibrium in an external magnetic field, we linearize the Boltzmann equation, neglecting the collision term into

$$\frac{\partial f_1}{\partial t}+\boldsymbol{v}\cdot\frac{\partial f_1}{\partial \boldsymbol{r}}+\frac{e}{m}\nabla\varphi\cdot\frac{\partial f_0}{\partial \boldsymbol{v}}+\frac{e}{mc}\boldsymbol{B}_0\cdot\boldsymbol{v}\times\frac{\partial f_1}{\partial \boldsymbol{v}}=0 , \tag{1.1}$$

and the Poisson equation into

$$\Delta\varphi=4\pi e\int f_1(\boldsymbol{r},\boldsymbol{v},t)\,d^3\boldsymbol{v} , \tag{1.2}$$

where the subscript 0 refers to the steady state, and 1 to a small perturbation. Since (1.1) and (1.2) are linear, it is sufficient to consider a solution of the form $f_{1\boldsymbol{k}}(\boldsymbol{v},t)\,e^{i\boldsymbol{k}\cdot\boldsymbol{r}}$ and $\varphi_{\boldsymbol{k}}(t)\,e^{i\boldsymbol{k}\cdot\boldsymbol{r}}$. In terms of the Fourier component and the Laplace transform, (1.1) and (1.2) become

$$(s+i\boldsymbol{k}\cdot\boldsymbol{v})F(\boldsymbol{v},s)+\frac{e}{mc}\boldsymbol{B}_0\cdot\boldsymbol{v}\times\frac{\partial F(\boldsymbol{v},s)}{\partial \boldsymbol{v}}=-i\frac{e}{m}\psi(s)\boldsymbol{k}\cdot\frac{\partial f_0}{\partial \boldsymbol{v}}-F^*(\boldsymbol{v}) , \tag{1.3}$$

$$-\boldsymbol{k}\cdot\boldsymbol{k}\psi(s)=4\pi e\int F(\boldsymbol{v},s)\,d^3\boldsymbol{v} , \tag{1.4}$$

where

$$F(\boldsymbol{v},s)=\int_0^\infty f_{1\boldsymbol{k}}(\boldsymbol{v},t)\,e^{-st}\,dt , \qquad \psi(s)=\int_0^\infty \varphi_{\boldsymbol{k}}(t)\,e^{-st}\,dt , \tag{1.5}$$

and we use $f_{1\boldsymbol{k}}(\boldsymbol{v},0)=F^*(\boldsymbol{v})$. Introducing the cylindrical co-ordinates in the velocity space

$$\boldsymbol{v}=\boldsymbol{e}_1 w\cos\phi+\boldsymbol{e}_2 w\sin\phi+\boldsymbol{e}_3 u , \tag{1.6}$$

and putting

$$\boldsymbol{k}=\boldsymbol{e}_1 k\sin\theta+\boldsymbol{e}_3 k\cos\theta , \qquad \boldsymbol{B}_0=\boldsymbol{e}_3 B_0 , \tag{1.7}$$

we have from (1.3)

$$\frac{\partial F}{\partial\phi}+\frac{1}{\Omega}(s+i\boldsymbol{k}\cdot\boldsymbol{v})F=\frac{1}{\Omega}\left(F^*-i\frac{e}{m}\psi\boldsymbol{k}\cdot\frac{\partial f_0}{\partial \boldsymbol{v}}\right) , \tag{1.8}$$

where $\Omega=eB_0/mc$ is the gyration frequency. The deduction of (1.8) is essentially the same as in Bernstein's procedure.

Substituting (1.4) into (1.8) we have the equation for $F(\boldsymbol{v},s)$

$$\frac{\partial F}{\partial\phi}+\frac{1}{\Omega}\{s+ik(w\sin\theta\cos\phi+u\cos\theta)\}F=\frac{1}{\Omega}\left\{F^*+i\frac{4\pi e^2}{mk^2}\boldsymbol{k}\cdot\frac{\partial f_0}{\partial \boldsymbol{v}}\int F\,d^3\boldsymbol{v}\right\} . \tag{1.9}$$

From Appendix A, the periodic solution of (1.8) is given by

$$F(\boldsymbol{v},s)=\frac{1}{\Omega}\int_{-\infty}^{\phi}G(s,\phi,\phi')F^*(\boldsymbol{v}')\,d\phi'-\frac{ie}{\Omega m}\psi\int_{-\infty}^{\phi}G(s,\phi,\phi')\boldsymbol{k}\cdot\frac{\partial f_0}{\partial \boldsymbol{v}'}\,d\phi' ; \quad \mathrm{Re}\,(s)>0 , \tag{1.10}$$

where

$$G(s,\phi,\phi')=\exp\left\{-\frac{(s+iku\cos\theta)}{\Omega}(\phi-\phi')-\frac{ikw\sin\theta}{\Omega}(\sin\phi-\sin\phi')\right\}. \tag{1.11}$$

Combining (1.4) and (1.10), we obtain for $\mathrm{Re}(s)>0$

$$\phi(s)=\frac{-\dfrac{4\pi e}{\Omega}\displaystyle\int d^3\boldsymbol{v}\int_{-\infty}^{\phi}G(s,\phi,\phi')F^*(\boldsymbol{v}')\,d\phi'}{k^2-\dfrac{i}{\Omega}\dfrac{4\pi e^2}{m}\displaystyle\int d^3\boldsymbol{v}\int_{-\infty}^{\phi}G(s,\phi,\phi')\boldsymbol{k}\cdot\frac{\partial f_0}{\partial \boldsymbol{v}'}d\phi'}. \tag{1.12}$$

(1.9) and (1.12) are our basic equations.

§ 2. Initial Value Problem

For any given initial distribution function $F^*(\boldsymbol{v})$, we can express the potential, given by (1.12), as a function of the variable t by means of the inversion integral. This integral can be evaluated by using the residues of the poles which arise from the analytic continuation of (1.12) assuming that there does not exist any complication such as a branch point. Then $\varphi_k(t)$ is expressed by the modes corresponding to the poles. After a sufficiently long time, there will remain only a mode having the smallest damping factor, so that we obtain the dispersion equation from this single mode. In (1.12), the poles consist of poles of the numerator which depend on the initial distribution function, and zeros of the denominator which depend on the proper characteristics of the plasma. If $F^*(\boldsymbol{v}')$ in (1.12) is an entire function of u, the numerator is also an entire function providing $\theta\neq(\pi/2)$, as we see in Appendix C. Therefore, the singularities of (1.12) consist only of zeros of the denominator, and these correspond to the proper plasma oscillations. Thus we have, for $\mathrm{Re}(s)>0$, the dispersion equation

$$k^2-\frac{i}{\Omega}\frac{4\pi e^2}{m}\int d^3\boldsymbol{v}\int_{-\infty}^{\phi}G(s,\phi,\phi')\boldsymbol{k}\cdot\frac{\partial f_0}{\partial\boldsymbol{v}'}d\phi'=0\,;\qquad \mathrm{Re}(s)>0\,. \tag{2.1}$$

For $\mathrm{Re}(s)<0$, putting $P\equiv\boldsymbol{k}\cdot\partial f_0/\partial\boldsymbol{v}'$ in (B.3) of Appendix B, we have

$$k^2-\frac{i}{\Omega}\frac{4\pi e^2}{m}\left[\int d^3\boldsymbol{v}\int_{+\infty}^{\phi}G(s,\phi,\phi')\boldsymbol{k}\cdot\frac{\partial f_0}{\partial\boldsymbol{v}'}d\phi'\right.$$
$$\left.+\frac{4\pi^2\Omega}{k\cos\theta}\sum_n\sum_m\exp\left(-i\frac{n\pi}{2}\right)H_{nm}\left(\frac{is+\frac{1}{2}(n-m)\Omega}{k\cos\theta}\right)\right]=0\,;\qquad\mathrm{Re}(s)<0 \tag{2.2}$$

by using (C.4).

§ 3. Dispersion Equations of a Complex Valued Frequency

In this section, let us decide an indicial condition that each solution of the basic equations (1.9) and (1.12) becomes a solution of the form $e^{\alpha t}$ where α is a complex valued frequency, by choosing an initial distribution function $F^*(\boldsymbol{v})$ properly. These conditions are dispersion equations of a complex valued frequency. In what follows, the dispersion equations of the perturbed velocity distribution function and the electrostatic potential will be discussed.

3.1 *Dispersion equation of distribution function*

Consider the indicial condition that $f_{1\boldsymbol{k}}(\boldsymbol{v},t)\,e^{i\boldsymbol{k}\cdot\boldsymbol{r}}$ becomes a solution of the form $\exp(i\boldsymbol{k}\cdot\boldsymbol{r}+\alpha t)$, where α is a complex valued frequency and $\mathrm{Re}(\alpha)\neq0$. Putting

$$f_{1\boldsymbol{k}}(\boldsymbol{v},t)\,e^{i\boldsymbol{k}\cdot\boldsymbol{r}}=F^*(\boldsymbol{v})\,e^{i\boldsymbol{k}\cdot\boldsymbol{r}+\alpha t}\,, \tag{3.1}$$

we have

$$f_{1\boldsymbol{k}}(\boldsymbol{v},t)=F^*(\boldsymbol{v})\,e^{\alpha t}\,. \tag{3.2}$$

Therefore, the Laplace transform of (3.2) gives

$$F(\boldsymbol{v}, s)=\frac{F^*(\boldsymbol{v})}{s-\alpha} . \tag{3.3}$$

Substituting (3.3) into (1.9), and multiplying both sides of (1.9) by $(s-\alpha)$, we have

$$\frac{\partial F^*}{\partial\phi}+\frac{1}{\Omega}\{\alpha+ik(w\sin\theta\cos\phi+u\cos\theta)\}F^*=\frac{i}{\Omega}\frac{4\pi e^2}{mk^2}\boldsymbol{k}\cdot\frac{\partial f_0}{\partial\boldsymbol{v}}\int F^*\,d^3\boldsymbol{v} . \tag{3.4}$$

Normalizing as

$$\int F^*(\boldsymbol{v})\,d^3\boldsymbol{v}=1 , \tag{3.5}$$

we obtain

$$\frac{\partial F^*}{\partial\phi}+\frac{1}{\Omega}\{\alpha+ik(w\sin\theta\cos\phi+u\cos\theta)\}F^*=\frac{1}{\Omega}\frac{4\pi e^2}{mk^2}\boldsymbol{k}\cdot\frac{\partial f_0}{\partial\boldsymbol{v}} . \tag{3.6}$$

This can be solved by using Appendix A; therefore, we have for $\mathrm{Re}(\alpha)>0$ (amplified wave)

$$F^*(\boldsymbol{v})=\frac{i}{\Omega}\frac{4\pi e^2}{mk^2}\int_{-\infty}^{\phi}G(\alpha,\phi,\phi')\boldsymbol{k}\cdot\frac{\partial f_0}{\partial\boldsymbol{v}'}\,d\phi' , \tag{3.7}$$

and for $\mathrm{Re}(\alpha)<0$ (damped wave)

$$F^*(\boldsymbol{v})=\frac{i}{\Omega}\frac{4\pi e^2}{mk^2}\int_{+\infty}^{\phi}G(\alpha,\phi,\phi')\boldsymbol{k}\cdot\frac{\partial f_0}{\partial\boldsymbol{v}'}\,d\phi' . \tag{3.8}$$

If we substitute (3.7) and (3.8) into the indicial condition (3.5) we obtain the dispersion equations;

$$k^2-\frac{i}{\Omega}\frac{4\pi e^2}{mk^2}\int d^3\boldsymbol{v}\int_{-\infty}^{\phi}G(\alpha,\phi,\phi')\boldsymbol{k}\cdot\frac{\partial f_0}{\partial\boldsymbol{v}'}\,d\phi'=0 ; \qquad \mathrm{Re}(\alpha)>0 , \tag{3.9}$$

$$k^2-\frac{i}{\Omega}\frac{4\pi e^2}{mk^2}\int d^3\boldsymbol{v}\int_{+\infty}^{\phi}G(\alpha,\phi,\phi')\boldsymbol{k}\cdot\frac{\partial f_0}{\partial\boldsymbol{v}'}\,d\phi'=0 ; \qquad \mathrm{Re}(\alpha)<0 . \tag{3.10}$$

Inversely, if we take (3.7) and (3.8) as $F^*(\boldsymbol{v})$, on the condition that (3.9) and (3.10) hold, then we obtain a solution $f_1(\boldsymbol{r},\boldsymbol{v},t)$ of the form $\exp(i\boldsymbol{k}\cdot\boldsymbol{r}+\alpha t)$, therefore, we can prove that the solution is uniquely determined by the indicial condition (3.5). Furthermore, under the above indicial condition, we can obtain a solution of the potential $\varphi_k(t)$ which varies as $e^{\alpha t}$, but we find that the solution of the potential satisfies a more general condition than (3.5). These affairs will be seen in the next section.

3.2 *Dispersion equation of electrostatic potential*

In the proceeding section, we have obtained a dispersion equation for the distribution function. But what we observe in the laboratory is a fluctuation of the electrostatic potential. In this section, therefore, we consider a solution of the potential which varies as $\exp(i\boldsymbol{k}\cdot\boldsymbol{r}+\alpha t)$. In what follows, it will be shown that for damped wave an indeterminancy appears in the dispersion relation.

Generalizing (3.6), we consider the equation, provided that $\theta\neq(\pi/2)$,

$$\frac{\partial F^*}{\partial\phi}+\frac{1}{\Omega}\{\alpha+ik(w\sin\theta\cos\phi+u\cos\theta)\}F^*=\frac{i}{\Omega}\frac{4\pi e^2}{mk^2}\left\{\boldsymbol{k}\cdot\frac{\partial f_0}{\partial\boldsymbol{v}}+C\,h(w)\right\} , \tag{3.11}$$

where C is an arbitrary constant, and $h(w)$ is a function of w. From Appendix A, the solution of (3.11) for F^* is given by

$$F^*=\frac{i}{\Omega}\frac{4\pi e^2}{mk^2}\int_{-\infty}^{\phi}G(\alpha,\phi,\phi')\left\{\boldsymbol{k}\cdot\frac{\partial f_0}{\partial\boldsymbol{v}'}+C\,h(w)\right\}d\phi' ; \qquad \mathrm{Re}(\alpha)>0 , \tag{3.12}$$

$$F^*=\frac{i}{\Omega}\frac{4\pi e^2}{mk^2}\int_{+\infty}^{\phi} G(\alpha,\phi,\phi')\left\{\boldsymbol{k}\cdot\frac{\partial f_0}{\partial \boldsymbol{v}'}+C\,h(w)\right\}d\phi' ;\qquad \mathrm{Re}\,(\alpha)<0. \tag{3.13}$$

Ve multiply the derivative of $G(s,\phi,\phi')$ in (1.11),

$$\frac{\partial G(s,\phi,\phi')}{\partial\phi'}=\frac{1}{\Omega}\{s+ik(w\sin\theta\cos\phi'+u\cos\theta)\}G(s,\phi,\phi')\ ,$$

y $F^*(\boldsymbol{v}')$ and multiply (3.11) by $G(s,\phi,\phi')$. We integrate over ϕ' the difference of both quations thus obtained, then we have for $\mathrm{Re}\,(s)>0$

$$\int_{-\infty}^{\phi} G(s,\phi,\phi')F^*d\phi'=\frac{\Omega}{s-\alpha}\left[F^*-\frac{i}{\Omega}\frac{4\pi e^2}{mk^2}\int_{-\infty}^{\phi} G(s,\phi,\phi')\left\{\boldsymbol{k}\cdot\frac{\partial f_0}{\partial \boldsymbol{v}'}+C\,h(w)\right\}d\phi'\right]. \tag{3.14}$$

3y use of this equation, the numerator, I_N, of the basic equation (1.12) is given by

$$I_N=-\frac{4\pi e}{s-\alpha}\left[\int F^*d^3\boldsymbol{v}-\frac{i}{\Omega}\frac{4\pi e^2}{mk^2}\int d^3\boldsymbol{v}\int_{-\infty}^{\phi} G(s,\phi,\phi')\left\{\boldsymbol{k}\cdot\frac{\partial f_0}{\partial \boldsymbol{v}'}+C\,h(w)\right\}d\phi'\right]. \tag{3.15}$$

f we take in (3.15)

$$\int F^*d^3\boldsymbol{v}-\frac{i}{\Omega}\frac{4\pi e^2}{mk^2}\int d^3\boldsymbol{v}\int_{-\infty}^{\phi} G(s,\phi,\phi')C\,h(w)\,d\phi'=1 \tag{3.16}$$

ıs an indicial condition, then for the potential ϕ in (1.12), we have

$$\phi(s)=-\frac{4\pi e}{k^2}\cdot\frac{1}{s-\alpha}\ . \tag{3.17}$$

This shows that for any value of α satisfying (3.16) the potential $\varphi(\boldsymbol{r},t)$ varies as $\exp(i\boldsymbol{k}\cdot\boldsymbol{r}+\alpha t)$. From the substitution of (3.12) and (3.13) into the indicial condition (3.16), we find implicitly the following dispersion equation:

for $\mathrm{Re}\,(\alpha)>0$ (amplified wave)

$$\begin{aligned}\frac{i}{\Omega}\frac{4\pi e^2}{mk^2}\Big[\int d^3\boldsymbol{v}\int_{-\infty}^{\phi} G(\alpha,\phi,\phi')\boldsymbol{k}\cdot\frac{\partial f_0}{\partial \boldsymbol{v}'}\,d\phi'\\ +\int d^3\boldsymbol{v}\int_{-\infty}^{\phi} G(\alpha,\phi,\phi')C\,h(w)\,d\phi'-\int d^3\boldsymbol{v}\int_{-\infty}^{\phi} G(s,\phi,\phi')C\,h(w)\,d\phi'\Big]=1\ ,\end{aligned} \tag{3.18}$$

for $\mathrm{Re}\,(\alpha)<0$ (damped wave)

$$\begin{aligned}\frac{i}{\Omega}\frac{4\pi e^2}{mk^2}\Big[\int d^3\boldsymbol{v}\int_{+\infty}^{\phi} G(\alpha,\phi,\phi')\boldsymbol{k}\cdot\frac{\partial f_0}{\partial \boldsymbol{v}'}\,d\phi'\\ +\int d^3\boldsymbol{v}\int_{+\infty}^{\phi} G(\alpha,\phi,\phi')C\,h(w)\,d\phi'-\int d^3\boldsymbol{v}\int_{-\infty}^{\phi} G(s,\phi,\phi')C\,h(w)\,d\phi'\Big]=1\ .\end{aligned} \tag{3.19}$$

In order to express (3.18) and (3.19) in the form of explicit formulas, let us examine the integral concerning $h(w)$ with the aid of Appendix B. Putting $P\equiv h(w)$ in (B.3), we have

$$\begin{aligned}I^{\pm}(s)&=\int d^3\boldsymbol{v}\int_{\mp\infty}^{\phi} G(s,\phi,\phi')\,h(w)\,d\phi'=2\pi\Omega\sum_m H_m\int_{-\infty}^{\infty}\frac{du}{(s-im\Omega/2)+iku\cos\theta}\\ &=\pm\frac{2\pi^2\Omega}{k\cos\theta}\sum H_m=\pm\frac{2\pi^2\Omega H(0)}{k\cos\theta}\ ;\qquad \mathrm{Re}\,(s)\gtrless 0\ ,\\ &=I^{\pm}(\alpha)\ ;\qquad \mathrm{Re}\,(\alpha)\gtrless 0\ ,\end{aligned}$$

where $H(0)=\int_0^{\infty} w\,h(w)\,dw\neq 0$. These are independent of both s and α. Therefore, (3.18) and (3.19) are reduced respectively to

$$k^2-\frac{i}{\Omega}\frac{4\pi e^2}{m}\int d^3\boldsymbol{v}\int_{-\infty}^{\phi} G(\alpha,\phi,\phi')\boldsymbol{k}\cdot\frac{\partial f_0}{\partial \boldsymbol{v}'}\,d\phi'=0\,;\qquad \mathrm{Re}\,(\alpha)>0\,, \qquad \text{(3.20}$$

$$k^2-\frac{i}{\Omega}\frac{4\pi e^2}{m}\left[\int d^3\boldsymbol{v}\int_{+\infty}^{\phi} G(\alpha,\phi,\phi')\boldsymbol{k}\cdot\frac{\partial f_0}{\partial \boldsymbol{v}'}\,d\phi'-\frac{4\pi^2 C\Omega}{k\cos\theta}H(0)\right]=0\,;\qquad \mathrm{Re}\,(\alpha)<0\,. \qquad \text{(3.21}$$

It is very interesting to note, for a damped wave, as we have seen in (3.21), that ther appears an indeterminancy in the dispersion relation, because (3.21) involves an arbitra constant C. When θ is equal to zero, (3.20) and (3.21) become Berz's result[5], namely, (3.20 and (3.21) correspond to her Eqs. (12) and (10) respectively;

$$\left(\frac{k}{\omega_0}\right)^2=\int_{-\infty}^{\infty}\frac{f_0'(u)}{u-\omega/k}\,du\,,$$

$$\left(\frac{k}{\omega_0}\right)^2=\int_{-\infty}^{\infty}\frac{f_0'(u)}{u-\omega/k}\,du+2\pi ikC_0\,.$$

Next, let us investigate the behaviour of the distribution function $F(\boldsymbol{v},s)$ in (1.10) unde the above indicial condition (3.16). Substituting (3.14) and (3.17) into (1.10), we have

$$F(\boldsymbol{v},s)=\frac{F^*}{s-\alpha}-\frac{i}{\Omega}\frac{4\pi e^2}{mk^2}\cdot\frac{1}{s-\alpha}\int_{-\infty}^{\infty}G(s,\phi,\phi')C\,h(w)\,d\phi'\,. \qquad \text{(3.22}$$

In (3.22), if we take $C=0$, it gives a sufficient condition which the distribution functio varies as $e^{\alpha t}$. Let $C\neq 0$. The relation

$$\exp\{iz\sin\phi\}=\sum_n J_n(z)\,e^{in\phi}$$

leads to

$$\int_{-\infty}^{\phi}G(s,\phi,\phi')\,h(w)\,d\phi'=\sum_n\frac{h(w)J_n(kw\sin\theta/\Omega)}{s+i(ku\cos\theta+\Omega)}\exp\left\{-\frac{ikw}{\Omega}\sin\theta\sin\phi+in\phi\right\}.$$

Substituting this integral into (3.22), we have

$$F(\boldsymbol{v},s)=\frac{1}{s-\alpha}\left\{F^*-\frac{i}{\Omega}\frac{4\pi e^2C}{mk^2}\sum_n\Gamma_n\right\}+\frac{i}{\Omega}\frac{4\pi e^2C}{mk^2}\sum_n\frac{\Gamma_n}{s+i(ku\cos\theta+n\Omega)}\,, \qquad \text{(3.23}$$

where

$$\Gamma_n=\frac{\Omega\,h(w)\,J_n(kw\sin\theta/\Omega)\exp\{-(ikw/\Omega)\sin\theta\sin\phi+in\phi\}}{\alpha+i(ku\cos\theta+n\Omega)}\,.$$

Since $\mathrm{Re}\,(\alpha)\neq 0$, Γ_n is not infinite. From the inverse Laplace transform, we have

$$f_{1\boldsymbol{k}}(\boldsymbol{v},t)=\left\{F^*-\frac{i}{\Omega}\frac{4\pi e^2C}{mk^2}\sum_n\Gamma_n\right\}e^{\alpha t}+\frac{i}{\Omega}\frac{4\pi e^2C}{mk^2}\sum_n\Gamma_n\exp\{-i(ku\cos\theta+n\Omega)t\}\,. \qquad \text{(3.24}$$

Therefore, there appears an angular frequency $\omega=ku\cos\theta+n\Omega$, which is determined by the Doppler shift.

§ 4. The Case of Maxwellian Distribution

As a typical example for each dispersion equation obtained in § 2 and § 3, let us take the case of Maxwellian distribution

$$f_0(v)=N\left(\frac{m}{2\pi\kappa T}\right)^{3/2}\exp\left(-\frac{mv^2}{2\kappa T}\right).$$

Putting $P(u,w,\phi')\equiv\boldsymbol{k}\cdot(\partial f_0/\partial\boldsymbol{v}')$ in (B.3) of Appendix B, we have

$$P(u, w, \phi')=h_{-1}(u, w)\, e^{-i\phi'}+h_0(u, w)+h_1(u, w)\, e^{i\phi'}$$

vhere

$$h_1(u, w)=h_{-1}(u, w)=A_0 w \exp\left\{-\frac{m}{2\kappa T}(u^2+w^2)\right\},$$

$$h_0(u, w)=A_1 u \exp\left\{-\frac{m}{2\kappa T}(u^2+w^2)\right\},$$

$$A_0=-N\frac{m}{2\kappa T}\left(\frac{m}{2\pi\kappa T}\right)^{3/2} k\sin\theta\,,$$

$$A_1=-N\frac{m}{\kappa T}\left(\frac{m}{2\pi\kappa T}\right)^{3/2} k\cos\theta\,.$$

Hence from (B.4), we have

$$H_0(u, \beta)=A_1 u\left(\frac{\kappa T}{m}\right)\exp\left\{-\frac{mu^2}{2\kappa T}-2\lambda\sin^2\beta\right\},$$

$$H_1(u, \beta)=A_0\left(\frac{\kappa T}{m}\right)^2\frac{2k\beta\sin\theta}{\Omega}\exp\left\{-\frac{mu^2}{\kappa T}-2\lambda\sin^2\beta\right\},$$

and

$$H_{-1}=-H_1\,,$$

where

$$\lambda=k^2\frac{\kappa T}{m\Omega^2}\sin^2\theta\,,\qquad \mu=k^2\frac{\kappa T}{m\Omega^2}\cos^2\theta\,.$$

Therefore (B.7) is reduced to

$$I^+(s)=2\pi\int_{-\infty}^{+\infty}du\int_0^{\infty}d(2\beta)\Big[H_0(u, \beta)-i(e^{i\beta}+e^{-i\beta})H_1(u, \beta)\Big]\exp\left\{-(s+iku\cos\theta)\frac{2\beta}{\Omega}\right\}. \tag{4.1}$$

Integrating over u and replacing $2\beta=y$, we have

$$I^+(s)=i\Omega N\left(\frac{m}{\kappa T}\right)\int_0^{\infty}dy(\lambda\sin y+\mu y)\exp\left\{-\frac{sy}{\Omega}-\frac{1}{2}\mu y^2-\lambda(1-\cos y)\right\}. \tag{4.2}$$

Using

$$\frac{d}{dy}\left[\exp\left\{-\frac{1}{2}\mu y^2-\lambda(1-\cos y)\right\}\right]=-(\lambda\sin y+\mu y)\exp\left\{-\frac{1}{2}\mu y^2-(1-\cos y)\right\},$$

we obtain for $\lambda\geqslant 0$, and $\mu>0$, i.e., $\theta\neq(\pi/2)$

$$I^+(s)=i\Omega N\left(\frac{m}{\kappa T}\right)\left\{1-\frac{s}{\Omega}\int_0^{\infty}A(s, y)\,dy\right\};\qquad \mathrm{Re}\,(s)>0 \tag{4.3}$$

where

$$A(s, y)=\exp\left\{-\frac{sy}{\Omega}-\frac{1}{2}\mu y^2-\lambda(1-\cos y)\right\}.$$

For $I^-(s)$, we can apply the same procedure, so that we have

$$I^-(s)=i\Omega N\left(\frac{m}{\kappa T}\right)\left\{1+\frac{s}{\Omega}\int_{-\infty}^{0}A(s, y)\,dy\right\};\qquad \mathrm{Re}\,(s)<0\,. \tag{4.4}$$

On account of the condition $0\neq(\pi/2)$, both $I^+(s)$ and $I^-(s)$ converge for any value of s and define the analytic functions on the s-plane throughout. Moreover, the difference of $I^+(s)$ and $I^-(s)$ gives rise to

$$I^{+}(s)-I^{-}(s)=-iNs\left(\frac{m}{\kappa T}\right)\int_{-\infty}^{\infty}A(s,y)\,dy\,. \qquad (4.5$$

From the above evaluation, each dispersion equation is given as follows.

1) *Amplified waves*; Re $(s)>0$

In this case the dispersion equations for the proper plasma oscillation, the distributio function and the potential are coincident and are given by

$$1+k^2a^2=\frac{s}{\Omega}\int_{0}^{\infty}A(s,y)\,dy\,, \qquad (4.6$$

where a is the Debye length. It is interesting to note that there exists no indeterminan in (4.6). Bernstein showed that there exists no root in this equation.

2) *Damped waves*; Re $(s)<0$

a) The proper plasma oscillation

The dispersion equation is obtained by analytic continuation of (1.12), but since $I^{+}(s)$ is a analytic function throughout the s-plane, the equation is (4.6). Using (4.5) we find that

$$1+k^2a^2=-\frac{s}{\Omega}\int_{-\infty}^{0}A(s,y)+\frac{s}{\Omega}\int_{-\infty}^{+\infty}A(s,y)\,dy=\frac{s}{\Omega}\int_{0}^{\infty}A(s,y)\,dy\,. \qquad (4.7$$

b) The perturbed distribution function

From (3.10) we have

$$1+k^2a^2=-\frac{s}{\Omega}\int_{-\infty}^{0}A(s,y)\,dy\,. \qquad (4.8$$

c) The potential

From (3.21) we have

$$1+k^2a^2=-\frac{s}{\Omega}\int_{-\infty}^{0}A(s,y)\,dy-\frac{4\pi^2 iC}{k\cos\theta}\,\frac{\omega_p{}^2a^2}{N}\,H(0)\,, \qquad (4.9$$

where $\omega_p{}^2$ is defined by $\omega_p{}^2=(4\pi e^2N)/m$.

The writers wish to express their sincere thanks to Professor Y. Ozawa of University o Hokkaido for his continual guidance and encouragement.

Appendix A

Let $H(\phi)$ be a bounded periodic function of the period 2π in ϕ, then the periodic solutio of the period 2π for the equation

$$\frac{dF}{d\phi}+\frac{1}{\Omega}\{s+ik(w\sin\theta\cos\phi+u\cos\theta)\}F=H(\phi) \qquad (A.1$$

is given by

$$F(\phi)=\int_{-\infty}^{\phi}G(s,\phi,\phi')H(\phi')\,d\phi'\;; \qquad \mathrm{Re}\,(s)>0\,, \qquad (A.2$$

$$F(\phi)=\int_{+\infty}^{\phi}G(s,\phi,\phi')H(\phi')\,d\phi'\;; \qquad \mathrm{Re}\,(s)<0\,, \qquad (A.3$$

where

$$G(s,\phi,\phi')=\exp\left\{-\frac{s+iku\cos\theta}{\Omega}(\phi-\phi')-\frac{ikw\sin\theta}{\Omega}(\sin\phi-\sin\phi')\right\}. \qquad (A.4$$

A proof is as follows. For the general solution of (A.1), we have

$$F(\phi)=AG(s,\phi,0)+\int_0^{\phi} G(s,\phi,\phi')H(\phi')\,d\phi' \tag{A.5}$$

where A is an arbitrary constant. Since $F(\phi)=F(\phi+2n\pi)$; $n=\pm1,\pm2,\cdots$, we have

$$AG(s,\phi,0)=\frac{\int_{-2n\pi}^{0} G(s,\phi,\phi')H(\phi')\,d\phi'}{1-\exp(-2n\pi\delta)} \tag{A.6}$$

where

$$\delta=(s+iku\cos\theta)/\Omega\ .$$

To obtain A, which is independent of n, let n be a positive integer and $l=0,1,\cdots,n-1$. Furthermore, if we put $\phi'+2(n-l-1)=\phi''$, and consider the l subdivision of interval $[0,-2n]$, then we have

$$\begin{aligned}&\int_{-2n\pi}^{0} G(s,\phi,\phi')H(\phi')\,d\phi'\\&=[\exp\{-2(n-1)\pi\delta\}+\exp\{-2(n-2)\pi\delta\}+\cdots+1]\int_{-2\pi}^{0} G(s,\phi,\phi')\,H(\phi')\,d\phi'\\&=\frac{1-\exp(-2n\pi\delta)}{1-\exp(-2\pi\delta)}\int_{-2\pi}^{0} G(s,\phi,\phi')\,H(\phi')\,d\phi'\ .\end{aligned}$$

Therefore, (A.6) becomes

$$AG(s,\phi,0)=\frac{\int_{-2\pi}^{0} G(s,\phi,\phi')\,H(\phi')\,d\phi'}{1-\exp(-2\pi\delta)}\ . \tag{A.7}$$

For a negative integer n, it is easily shown that

$$AG(s,\phi,0)=\frac{\int_{2n\pi}^{0} G(s,\phi,\phi')\,H(\phi')\,d\phi'}{1-\exp(2n\pi\delta)} \tag{A.8}$$

and, by the same way, becomes again (A.7). Since (A.6) and (A.8) converge to

$$\int_{-\infty}^{0} GH\,d\phi'\ ; \qquad \text{for}\quad \mathrm{Re}(\delta)>0\ ,$$

and

$$\int_{+\infty}^{0} GH\,d\phi'\ ; \qquad \text{for}\quad \mathrm{Re}(\delta)<0$$

respectively as $n\to\infty$, we obtain (A.2) and (A.3).

Appendix B

We consider the typical integral

$$I^{+}(s)=\int d^3v\int_{-\infty}^{\phi} G(s,\phi,\phi')P(v')\,d\phi'\ ; \qquad \text{for}\quad \mathrm{Re}(s)>0\ , \tag{B.1}$$

$$I^{-}(s)=\int d^3v\int_{+\infty}^{\phi} G(s,\phi,\phi')P(v')\,d\phi'\ ; \qquad \text{for}\quad \mathrm{Re}(s)<0\ , \tag{B.2}$$

where $G(s,\phi,\phi')$ is given by (A.4). If we introduce the cylindrical co-ordinates

$$\boldsymbol{v}'=\boldsymbol{e}_1 w\cos\phi'+\boldsymbol{e}_2 w\sin\phi'+\boldsymbol{e}_3 u$$

in the velocity space, and if we assume that $P(v')$ can be expressed such that

$$P(v')=P(w\cos\phi', w\sin\phi', u)=\sum_{n=-\infty}^{+\infty} h_n(u,w)\,e^{in\phi'} \tag{B.3}$$

$$H_n(u,z)=\int_0^\infty wJ_n(zw)h_n(u,w)\,dw \tag{B.4}$$

$$H_n\left(u, \frac{2k\sin\theta\sin\beta}{\Omega}\right)=\sum_{m=-\infty}^{\infty} H_{nm}(u)\,e^{im\beta}\,, \tag{B.5}$$

if we assume furthermore, that each right hand side of the above relations converges uniformly, then (B.1) and (B.2) are reduced to

$$I^{\pm}(s)=\sum_m\sum_n 2\pi\Omega\exp\left(\frac{-in\pi}{2}\right)\int_{-\infty}^{+\infty}\frac{H_{nm}(u)}{s+i(n-m)\Omega/2+iku\cos\theta}\,du\,; \quad \text{for} \quad \mathrm{Re}\,(s)\gtrless 0\,. \tag{B.6}$$

For $I^+(s)$ a proof is given in the following. (B.3) is obvious since $P(v')$ is a function of the period 2π with respect ϕ'. Substituting $G(s,\phi,\phi')$ given by (A.4) into (B.1) and setting $\phi-\phi'=2\beta$, we have

$$I^+(s)=\sum_{n=-\infty}^{+\infty}\int_{-\infty}^{+\infty}du\int_0^\infty d(2\beta)\exp\left\{-\frac{(s+iku\cos\theta)}{\Omega}2\beta\right\}$$
$$\times\int_0^\infty w\,dw\,h_n(u,w)\int_0^{2\pi}\exp\left\{-\frac{i\beta}{\Omega}2\cos(\phi-\beta)\sin\beta-in(\phi-2\beta)\right\}d\phi\,.$$

Considering the transform $\phi-\beta=\gamma$ of the variables, and the periodicity of the integrand concerning the integral over ϕ, we have

$$I^+(s)=\sum_{n=-\infty}^{+\infty}\int_{-\infty}^{\infty}du\int_0^\infty d(2\beta)\exp\left\{-\frac{(s+iku\cos\theta)}{\Omega}2\beta-in\left(\beta+\frac{\pi}{2}\right)\right\}$$
$$\times 2\pi\int_0^\infty w\,J_n\left(\frac{2k\sin\theta\sin\beta}{\Omega}w\right)h_n(u,w)\,dw\,. \tag{B.7}$$

Let H_n be the Fourier-Bessel transform of h_n, then putting $z=(2k\sin\theta\sin\beta)/\Omega$ we have (B.4). Moreover, noting that H_n is a function of the period 2π for β, we have the Fourier expansion (B.5). Substituting (B.5) into (B.7), after the transform $y=2\beta$, we have

$$I^+(s)=\sum_m\sum_n 2\pi\exp\left(\frac{-in\pi}{2}\right)\int_{-\infty}^{+\infty}du H_{nm}(u)$$
$$\times\int_0^\infty dy\exp\left[-\frac{1}{\Omega}\left\{s+iku\cos\theta+i\frac{\Omega}{2}(n-m)\right\}y\right]. \tag{B.8}$$

For $I^-(s)$, we make the same reduction, and the result is given by

$$I^-(s)=\sum_m\sum_n 2\pi\exp\left(\frac{-in\pi}{2}\right)\int_{-\infty}^{+\infty}du\,H_{nm}(u)$$
$$\times\int_0^{-\infty} dy\exp\left[-\frac{1}{\Omega}\left\{s+iku\cos\theta+i\frac{\Omega}{2}(n-m)\right\}y\right]. \tag{B.9}$$

Integrating (B.8) and (B.9) with respect to y, we have (B.6).

Appendix C

In this appendix, a function is the analytic continuation of $I^+(s)$ given by (B.8), is obtained and compared with $I^-(s)$.

Consider the analytic continuation of the typical integral of $I^+(s)$;

$$Y_{nm}(s)=\int_{-\infty}^{+\infty}\frac{H_{nm}(u)}{u-i\dfrac{s+i(n-m)\Omega/2}{k\cos\theta}}\,du \tag{C.1}$$

to the left half of the s-plane. If all $H_{nm}(u)$ are an entire function of u, $Y_{nm}(s)$ for $\mathrm{Re}(s)>0$ can be continued by Landau's method[3]. Hence, let us displace the path of integration in the complex u-plane in such a way that the point $u=i\{s+i(n-m)\Omega/2\}/k\cos\theta$ always lies above the path of integration, then

$$\tilde{Y}_{nm}(s)=\int_{C}\frac{H_{nm}(u)}{u-i\dfrac{s+i(n-m)\Omega/2}{k\cos\theta}}du$$

is also an entire function. Therefore, we have

$$\tilde{Y}_{nm}(s)=Y_{nm}(s)\ ; \qquad \text{for} \quad \mathrm{Re}(s)>0 \tag{C.2}$$

and

$$\tilde{Y}_{nm}(s)=Y_{nm}(s)+2\pi i H_{nm}\left(i\frac{s+i(n-m)\Omega/2}{k\cos\theta}\right); \qquad \text{for} \quad \mathrm{Re}(s)<0\ . \tag{C.3}$$

Using (C.2) and (C.3) we obtain the analytic continuation of $I^{+}(s)$ to the left half s-plane

$$I^{+}(s)=I^{-}(s)+\frac{4\pi^{2}\Omega}{k\cos\theta}\sum_{m}\sum_{n}\exp\left(-\frac{in\pi}{2}\right)H_{nm}\left(i\frac{s+i(n-m)\Omega/2}{k\cos\theta}\right). \tag{C.4}$$

It should be noted that the condition $\theta\neq(\pi/2)$ is necessary for this continuation.

References

1) I. B. Bernstein: Phys. Rev. **109** (1958) 10.
2) E. P. Gross: Phys. Rev. **82** (1951) 232.
3) L. Landau: J. of Phys. USSR **25** (1946).
4) G. N. Watson: *Theory of Bessel Fnnctions* (1922).
5) F. Berz: Proc. Phys. Soc. **B, 69** (1956) 939.
6) N. G. Van Kampen: Physica **21** (1955) 949.

Journal of the Physical Society of Japan, Vol. 15, No. 10, October, 1960

Pulse Photoconductivity of Additively Colored KBr

By Masami Onuki and Hiroshi Ohkura

Department of Applied Physics, Osaka City University, Osaka

(Received May 18, 1960)

The space charge effect in the measurement of a photocurrent of additively colored KBr was investigated by using the repeated pulsive illumination and applying the d.c. and a.c. electric fields. The space charge polarization may arise from the accumulation of the electrons trapped in the surface states, the depth of which is about 0.3 ev. The condition for the absence of space charge was ascertained to be realized by adopting the a.c. field and the pulsive illumination synchronized with plus and minus peaks of the a.c. field. The temperature-dependence of pulse photocurrent was measured by varying the duration of the pulsive illumination. The time constants of current-decay after switching-off of illumination were also observed. Three kinds of electron-traps were found, the one corresponding to *F* center and the other two to the unknown centers. The activation energies for releasing the electrons trapped in these centers were estimated to be 0.44, 0.35 and 0.43 ev respectively. The growth and bleaching of optical absorption bands were investigated in relation to the above electron-traps. A detailed analysis for the trapping kinetics was made to apply to additively colored KBr crystals.

§1. Introduction

In the measurement of photocurrent in colored alkali halides crystals, the d.c. method has been adopted for its simplicity, in which the d.c. field and the light pulse of comparatively long duration were used in almost all cases.(1)(2)(3) In this method the space charge field should be built up in a specimen. One must decrease light intensity or change the polarity of the applied field alternatively for each measurement, to avoid the undesired effect. Further, in the d.c. method, the time constant of decay of the photocurrent after the switch-off of illumination conld not be measured accurately, because of the non-uniform field in a specimen and the inherent long time constant of a d.c. electrometer.

The photoconductivity due to the F-band light in additively colored alkali halide crystals shows abrupt increases at two different temperature ranges, The first relates to the steep variation of the quantum efficiency of an electron from F center to the conduction band and the second to the thermal release of an electron trapped in F′ center. Von Gerick investigated these problems by means of the pulse photoconductivity measurements in KCl. He used light pulses of 10^{-4} sec and 1.5×10^{-6} sec and applied the d.c. field. He observed that the thermal release of the electron of F′ center occurs at +20°C and +100°C for the above pulse durations respectively.(4) The releasing temperature of F′ electron was known to be −100°C for the light pulse of the order of 1 sec. From these data Seitz estimated the binding evergy ϵ and the time factor τ_0 of F′ electron to be 0.42 ev and 10^{-11} sec, respectively.(5) It is desirable to get ϵ and τ_0 from the direct observation of the decay time of photoconductivity in each temperature.

In the present work we used additively colored KBr crystals purified by the recrystalization technique and adopted both the a.c. field and the light pulse to avoid the space charge effect. The condition for the absence of space charge was ascertained and the temperature-dependence of pulse photoconductivity under the condition was investigated, varying the duration of light pulse. A decay time of conductivity after turn-off of illumination was measured between −170°C and room temperature. From the above two experiments ϵ and τ_0 of some trapping centers which are effective at these temperatures were estimated. The characters of traps were discussed, taking into account the information from the thermal bleaching and recovery of the optical absorption bands.

§ 2. Experimentals and Results

The KBr crystals employed in this investigation were purified by repeating the Kyropoulos method and colored additively. The concentrations of F center were $1\times10^{16}/\text{cm}^3$, $2\times10^{16}/\text{cm}^3$ and $9.7\times10^{16}/\text{cm}^3$, and the dimenssions of specimens were about $1\times2\times3\,\text{mm}^3$. The distance between electrodes was about 1 mm. A specimen was attached to electrodes directly by silver paint, or thin mica sheets were inserted between a specimen and electrodes. The property of photoconductivity was not different so much in the above two cases under the condition free from space charge described latter. For this reason almost all the specimens used in this work were attached to electrodes directly by silver paint unless otherwise stated.

The skelton diagram of measuring apparatus is shown in Fig. 1. The pulsive illumination was synchronized to the commercial power supply of 60 cps. There peated light pulses of the duration ranging from 90μ sec to 800μ sec were made by using a rotating mirror and the light pulses of 30 μ sec by the instant discharge of a Xenon lamp. The light was filtered by an interference filter the transmission peak of which lies in F band of KBr and the pass band of which is about 40 mμ, and was soft-forcused so as to illuminate a surface of a specimen uniformly. The electric field applied to a specimen was supplied from the commercial power line, the peak voltage being synchronized to each light pulse by shifting the phase.

The current pulses caused by pulsive illumination were amplified by the A–1 wide band amplifier improved so as to have a better low frequency characteristics,⁽⁶⁾ and the rejection device for 60 cps was put between the preamplifier and the main one to avoid picking up the 60 cps voltage through a capacity of a specimen. The total gain of the amplifier is 1.4×10^5 in maximum and its band width of amplification ranges from 200 cps to about 10^6 cps. A decay-time shorter than 20 μsec could not be detected practically because of the comparatively dull shape of the illumination pulse.

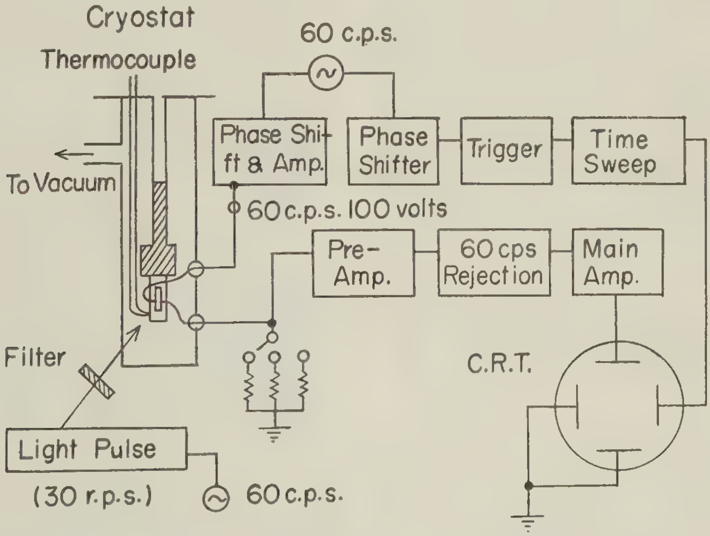

Fig. 1. The measuring device of pulse photocurrent.

A decay-time constant longer than 1.5 msec could not be measured by the above device for the low frequency character of the amplifier used, so the device for measuring the photoconducting Hall effect used by one of us was applied for observing a long decay-time.⁽⁷⁾ This device is applicable for measuring the a c. photoconductivity and consists of a 330 cps oscillator, a tuned amplifier and a differential one, and a cathode-ray oscilloscope. In our experiment a sodium glow lamp was used for a light source because of its rapid quenching illumination. After the stationary alternative photocurrent was built up in the specimen by applying the a.c. 330 cps field and irradiating with the steady F–band light, the illumination was suddenly switched off. Then the horizontal time sweep of the oscilloscope was started to observe the decay-time of the alternative photocurrent in the vertical axis of the oscilloscope. The dacay time was obtained from the envelope curve of the 330 cps photocurrent-decay on the oscilloscope. The band pass amplifier used for this method had a broad band width to avoid the inherent decay effect of the amplifier due to its Q–value. The input impedance was less than 2 MΩ. Using this device, a time constant of current-decay longer than 2×10^{-2} sec was measurable.

(1) *Space Charge Effect*

In the measurement of photocurrent in insulators such as alkali halides and silver halides, it has been well known that the photocurrent decays gradually as time passes on account of the space charge polarization due to accumulation of carriers.(8)(9)(10) To investigate this effect in detail, the variation of photocurrent with time due to the repeating pulsive illumination was measured by applying the a.c. and d.c. fields. The applied electric field was 1×10^3 volts/cm in both cases, and in the case of the a.c. field the pulsive illumination was synchronized to the peak value of the a c. field. Fig. 2 shows the experimental results. In the figure the zero point of the abscissa corresponds to the time when the initial light pulse irradiates the specimen, while the electric field is being applied.

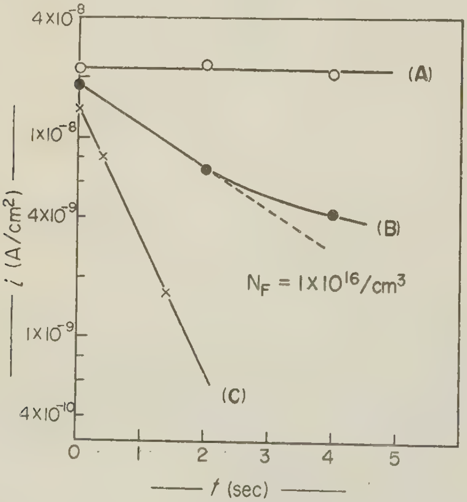

Fig. 2 The variation of pulse photocurrent with time.

(**A**) a.c. field of 60 cps, light pulse of 120 μ sec and 30 rps.

(**B**) d.c. field, light pulse of 120 μ sec and 30 rps.

(**C**) d.c. field, light pulse of 560 μ sec and 30 rps. The field strength is 10^3 volts/cm in all cases.

At room temperature the a.c. field led to the constant value of pulse photocurrent and the values at every time were nearly equal to the initial value of the pulse photocurrent of the d.c. field. Curve **A** in the figure corresponds to i (pulse photocurrent) vs t (time) curve under the condition that the pulse duration was 120 μ sec and the repetition of the pulse was 30 rps and the applied peak field was 10^3 volts/cm. From Curve **A** the condition for the absence of space charge seems to be realized in the a.c. field at least at room temperature. On the contrary, if the applied field was d.c., the pulse photocurrent due to the repeated photopulse decreased as time passed. The larger was the duration of the photopulse and the stronger was the intensity of it, the smaller the decay time of phococurrent resulted. Curve **B** and **C** in the figure show the decays of the repeating pulse photocurrent corresponding to the cases that the durations of the light pulse were 120 μ sec 560 μ sec respectively and the d.c. fields of 10^3 volts/cm were applied. In both cases the intensity of illumination and the repetition of the light pulse were the same. The total charges which flowed before the currents decreased to $1/e$ of their initial value are equal for the above two cases. From the fact, the space charge field due to the charge of about 1.5×10^{-10} coulomb/cm² flowing in one direction decreases the pulse photocurrent, when the d.c. field of 10^3 volts/cm is applied.

We measured the initial photocurrents both under the condition that the pulsive illumination was set on when the d.c. electric field was being applied, and under the condition that the d.c. field was applied suddenly under illumination of the repeating light pulses. In both cases initial currents were equal, so the ionic space charge is negligible in the period of measuring time even at room temperature.

Further, we measured the temperature-dependence of pulse photocurrent under the following condition, (1) the light pulses of

30 rps were synchronized to both the plus and minus peaks of the applied a.c. field (Case **I**), (2) the light pulses of 30 rps were synchronized to only either of plus or minus peaks of the applied a.c. field (Case **II**). The cycles of the applied voltages and the intensities and durations of illumination were the same in both cases. In Fig. 3, Curve **I** corresponds to Case **I** and Curve **II** to Case **II**. In the temperature region above about −80°C. the absolute values of pulse photocurrents in both cases were nearly equal, but in the region below −80°C the photocurrent in Case **II** was smaller than the one in Case **1**. Strictly speaking, in the latter region of temperature the pulse photocurrent in Case **II** was equal to one in Case **1** at the initial time when illumination was turned on, but decayed slowly to the value on Curve **II** after 10∼30 sec. This result indicates that at low temperatures the free charges swept to one direction were immobile and accumulated near the one of the electrodes, neither being drawn backward nor spread uniformly over the specimen by the a.c. field. In conclusion the condition for the absence of space charge in all temperature region of this work can be realized by using the light pulses synchronized to both plus and minus peaks of the applied a.c. field.

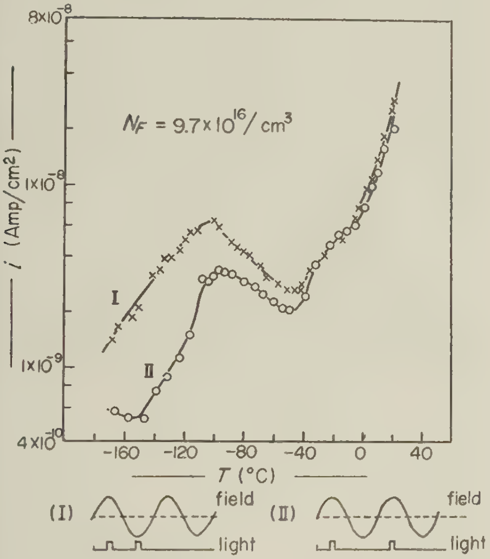

Fig. 3. The temperature-dependence of pulse photocurrent. In the figure the conditions of synchronization between the periods of illuminations and fields are different in the two curves. The periodic relation of the light pulses to the a.c. fields are shown in each case, too.

The field-dependence of the pulse photocurrent under the condition for the absence of space charge was examined at room temperature. Thin mica films were inserted to prevent the field emission effect due to the high electric field used in this experiment. As shown in Fig. 4 the pulse photocurrent is linear to the applied field up to 9×10^3 volts/cm, and then the saturation effect appeared gradually at higher fields. These results show that the condition for the absence of space charge was realized. The effect of inserting mica sheets (about 10^{-3} cm thick) between a specimen and electrodes to the pulse photocurrent was as follows. If the a.c. field synchronized to the pulsive illumination in the peaks was applied and the condition for the space charge free state is satisfied, the insertion of the mica sheets is hardly effective to the pulse photocurrent. But when the d.c. field was applied, a tenth of the initial pulse photocurrent was lasting to flow even after very long time, if mica sheets were not inserted. While the pulse photocurrent disappeared at last completely, if mica sheets were inserted. This effect may be attributed to the fact that the space charge polarization should be weakened by the field emission from the electrode, if the mica sheets were not inserted.

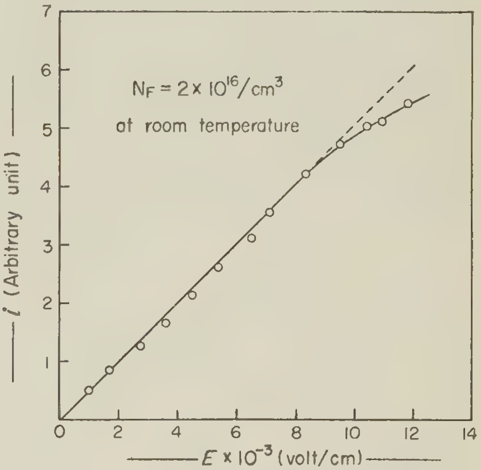

N_F

Fig. 4. The field-dependence of pulse photocurrent. The thickness of the specimen is 4×10^{-1} cm, and the concentration of F center is $2\times10^{16}/\text{cm}^3$.

(2) *The Effect of Light Pulse Duration on the Temperature-Dependence of Photocurrent*

The maximum values of pulse photocurrents for the light pulse durations of 30 μ sec, 90 μ sec and 800 μ sec respectively were measured under the condition free from space charge as mentioned in Subsection (1) of this section, by varying the temperature from −170°C to room temperature. Fig. 5 shows the results of the measurement. The scale of the ordinates in the figure is arbitrary, and we shall discuss only the inclinations of these curves in this figure. Curve **I**, **II** and **III** are the photocurrent vs temperature curves for 30 μ sec, 90 μ sec and 800 μ sec light durations respectively. In the figure the cusps at −32°C and +2°C in Curve **I** correspond to −50°C and −8°C in Curve **II** and to −74°C and −30°C in Curve **III**, respectively. It is observed that the cusp points shift towards lower temperatures, as the pulse duration is increased. However, it is noticable that the cusps at −105°C in all curves do not shift. We shall call these cusps $\mathbf{O}_1$, $\mathbf{O}_2$ and $\mathbf{O}_3$ from low to high temperature. On the other hand, the a.c. photocurrent induced by steady illumination and 330 cps a.c. field was measured. In this case the stationary state was attained in several sec. The temperature-variation of the photocurrent was shown in Curve **IV** of Fig. 5. The definite cusps can hardly be seen in this case. This result is nearly the same as Glaser's one for the d.c. field case.(1)

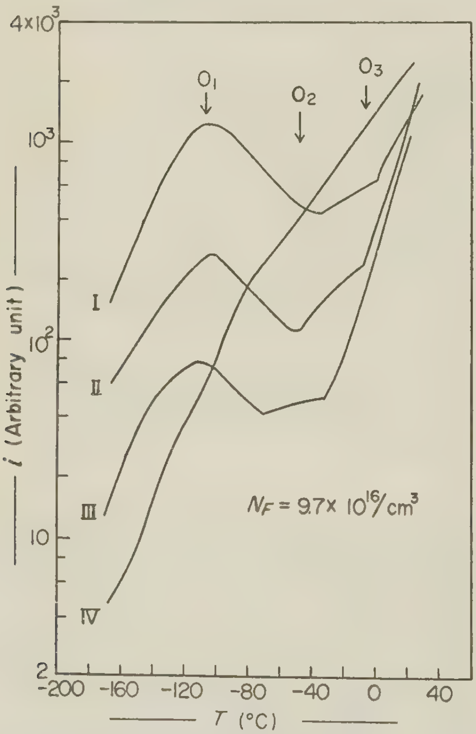

Fig. 5. The temperature-dependence of pulse photocurrent in various pulse durations.

The current-decay were observed at $\mathbf{O}_2$, $\mathbf{O}_3$ and about −100°C. The facts that the pulse photocurrent increases abruptly at the temperatures of $\mathbf{O}_2$ and $\mathbf{O}_3$ and the inclination of the photocurrent-temperature curve under steady illumination differs very much from these of other curves under pulsive illuminations at the higher temperatures above −100°C, are closely related with the temperatures of the current-decay.

(3) *The Current-Decay after Turn-off of Light Pulse*

In this measurement the pulsive illumination synchronized to the plus and minus peaks of the applied a.c. field was used. In Fig. 6 the time constant τ_f for the decay-current after turn-off of pulsive illumination is plotted in each temperature. The extremely small values of τ_f ($\simeq$20 μ sec) at the low temperatures are insignificant. They are only the indication of the upper limits of τ_f. The fast current decay was observed in the vicinities of $\mathbf{O}_2$ and $\mathbf{O}_3$ point, as seen in the figure. Both the maximum value of τ_f and the temperatures for the maximum were almost independent of F-concentration of specimens.

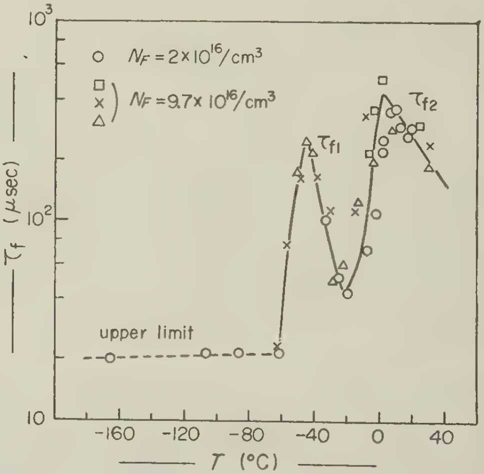

Fig. 6. The temperature-dependence of the fast current-decay.

The maximum values of τ_f decreased to about a quarter of the original values by deforming the specimens by 10%.

(4) *Slow Decay after Steady Illumination*

The apparent difference between the features of pulse and steady photocurrent was seen at the higher temperature than −100°C as seen in Fig. 5. This fact suggested that a slow decay of a comparatively long time constant ($>10^{-2}$ sec) should be concealed in the measurement of pulse photocurrent.

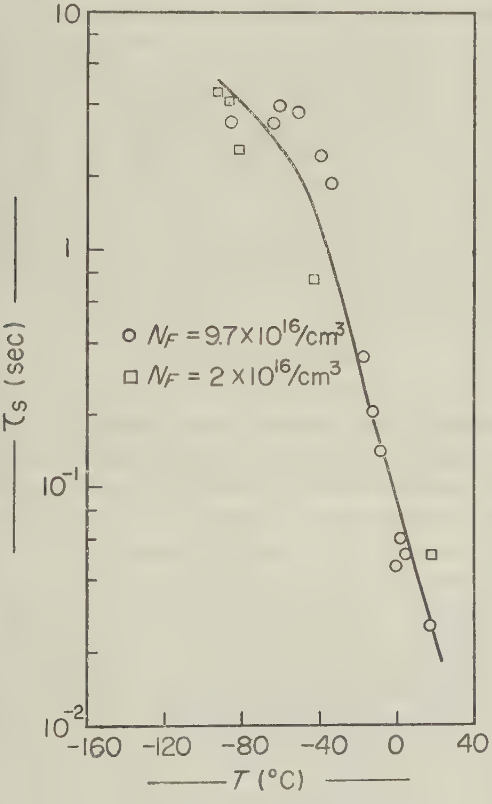

Fig. 7. The temperature-dependence of slow current-decay.

The time constant τ_s of the slow decay was determined by measuring the photocurrent under 330 cps alternative field after switching-off the steady illumination. The results were shown in Fig. 7. The decay of the a.c. photocurrent could not be observed below −100°C. This may be due to the fact that at lower temperatures the number of the electrons trapped in the center is small because of the small yield for photoexcitation of F-electrons to the condition band during illumination and the long time is necessary to release the electrons from the center.

From the results described in this and the last subsection, the slow current-decay of τ_s should be followed by the fast decay of τ_f immediately after the illumination had been switched off in the complete absence of space charge.

(5) *The Field-Dependence of Pulse Photocurrent*

One of us estimated μ_a (apparent mobility of electron)$\times\tau_a$ (apparent lifetime) to be $1\sim3\times10^{-6}$ sec in uncolored KBr crystals, from the observation of the dependence of the internal secondary electron current caused by pulsive electron bombardment with its duration of 10 μ sec on the a.c. field strength applied to the crystal.(11) In the present work the dependence of pulse photocurrent on the applied field was investigated for additively colored crystals. The duration of light pulse was 90 μ sec and F-concentration of the specimen was $9.7\times10^{16}/cm.^3$ Fig. 8 shows the results, where the thickness of the specimen was 5×10^{-2}cm. The saturation effect of the current was not so clearly observed, because the light was irradiated on the whole surface of the specimen. Using the Hecht formula for the points deviated from the straight line by more than 10%, $\mu\tau_a$ was estimated roughly as shown in Fig. 9. In the figure, the values of $\mu\tau_a$ for the specimens of 2×10^{16}/cm F-concentration and for uncolored ones at room temperature are plotted for comparison.

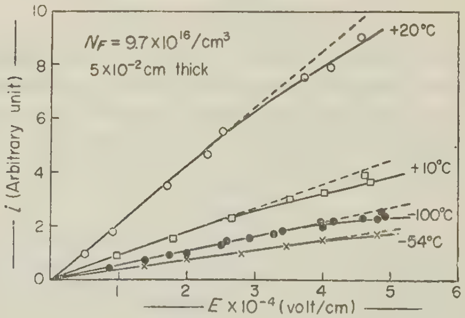

Fig. 8. The field-dependence of pulse photocurrent in each temperature.

§ 2. Discussion

(1) *Space Change Effect*

Space change formation occurs whenever

charge carriers cannot pass freely across the junction between the specimen and one or both of its electrodes. Von Hippel and others performed nearly the same experiment as the present work and proposed that the space charge should be formed near the cathode of a specimen.(8)

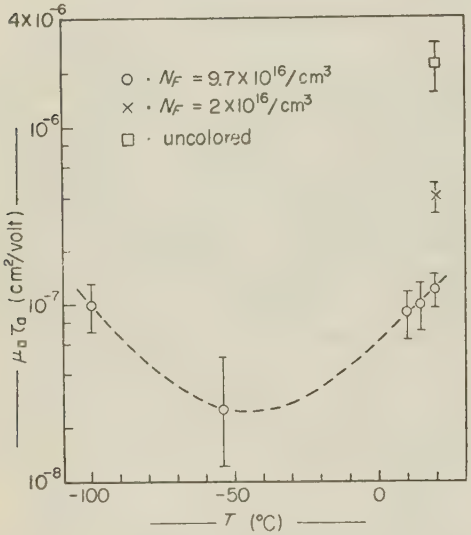

Fig. 9. The temperature and F–concentration dependence of $\mu_a\tau_a$. The circular correspond to $9.7\times10^{16}/cm^3$ of F–concentration, the cross to $2\times10^{19}/cm^3$ of F–concentration and the square to uncolored.

According to the present results, however, an amount of total charge which flowed in the d.c. field untill the space charge field was formed was so small as 1.5×10^{-10} coulomb/cm², which was about several hundredths of the value estimated by von Hippel under the condition for no field-emission.

In our experimental condition electrons may be accumulated near the anode and vacant F centers or negative ion vacancies near the cathode, because both electrodes seem to have the blocking properties. So, it seems to be unsuitable to adopt the von Hippel theory for the present results. Suppose that the electrons are accumulated near the anode and the vacant F centers whose amount is far smaller than the concentration of F center contained are formed near the cathode. The current ceases to flow when the reverse electric field produced by the electrons drawn to the anode becomes sufficient to cancel the applied field. The number of electrons on the surface will be estimated by the following formula,(10)

$$E=4\pi ne/\kappa, \qquad \text{(in e.s.u.)} \qquad (1)$$

where E is the applied field, n the number of electrons on the surface per cm², e the electronic charge and κ the dielectric constant. n is estimated to be 3×10^9 electrons/cm² using (1), for $E=10^3$ volts/cm. This value is nearly equal to the experimental value which was about 1×10^9 electrons/cm².

If the electrons of the space charge were spread uniformly over some region near the anode instead of being concentrated on a plane, the internal electric field should be large enough to flow more current. So, the space charge polarization may arise from the electrons accumulated on a plane near the anode. From the results shown in Fig. 3, it may be reasonable to assume the surface state which can trap electrons. In the current glow curve, the trap-depth will be computed from an approximate equation according to Grossweiner:(12)

$$E\simeq1.51kT_cT'/(T_c-T'), \qquad (2)$$

where T_c is the temperature at the maximum value of the current glow curve, T' the temperature at the half maximum at the low temperature side. Applying this analysis to the differenciation curve $d[(i_I-i_{II})/i_I]/dT$ vs T obtained from Fig. 3, where T is a temperature, and using that $T_c=-90°C$ and $T'=-106°C$, we obtained 0.3 ev as the trap depth of the surface state.

In the case of steady illumination and the a.c. field, the electrons going to the anode surface at a half cycle of the a.c. field may fill the ionized F center formed near the surface at the previous half cycle. For this reason both electrodes should become neutral. The condition for the absence of space charge is supposed to be realized in this case, too.(13) The effect of the capacities of the blocking junctions between a specimen and the electrodes was negligible in the case of the pulsive and steady illumination of the present experiment, because of the applied a.c. field. The investigation for this effect will be published in near future.

(2) *Traps in Colored KBr Crystals*

At least the three kinds of traps should exist in colored KBr, if one considers the characteristics of the temperature-dependence curves of the pulse photocurrent in Fig. 5 and the current-decay effects in Fig. 6 and 7.

At present we shall discuss the time constant of current-decay in term of the trapping kinetics. Supposing that N traps of the one kind normally unfilled exist in the crystal per unit volume, the excess density n of electrons in the conduction band and the excess density n_1 of electrons in traps will vary with time after the turn-off of illumination according to the following formulas,(14)

$$dn/dt = -rn + gn_1 - (N-n_1)nSv, \tag{3}$$

$$dn_1/dt = -gn_1 + (N-n_1)nSv, \tag{4}$$

where $r \equiv 1/\tau_r$ is the rate of recombination of excess electrons in the conduction band (or the rate of trapping by very deep traps), $g \equiv 1/\tau_g$ the rate of generation of electrons from traps, S its cross section for capture of electrons in traps, v the arithmetic mean thermal velocity, and $NSv = 1/\tau_t$ the rate of trapping of electrons when all traps are empty. In the present cases, $N \gg n_1$, because of a small amount of trapped electrons due to small excitation for the case of pulsive light and a large value of N (the number of F center as shown latter) for the case of steady illumination. Using the condition $N \gg n_1$, (3) and (4) lead to the following relation,

$$n \propto \exp(-t/\tau_\infty), \tag{5}$$

where $$\tau_\infty = \tau_r + \tau_g + (\tau_r \tau_g)/\tau_t. \tag{6}$$

The decay current should be proportional to the density n of excess electrons in the conduction band. From the current-decay curve just after the turn-off of illumination, τ_r and τ_t was estimated to be smaller than 20 μ sec at least and negligible in the measurement of a decay time. The time constants observed in this work should be τ_∞ which is simply expressed as follows,

$$\tau_\infty \simeq \tau_g(1 + \tau_r/\tau_t). \tag{7}$$

(τ_r/τ_t) seems to be almost constant over the present temperature region and may be of the order of $1 \sim 10^2$ for the various traps. In conclusion the temperature-dependence of decay times observed in this experiment should be due to τ_g contained in τ_∞.

Fig. 10 shows the time constants τ_{f1} and τ_{f2} of the fast decay as the function of $1/T$. In the figure the points with soild dot of circle and square are obtained from the direct observation of the current-decay and the points with circle and square are obtained from the pulse durations and the shifting temperatures of the cusps in Fig. 5. From Fig. 10, the activation energies $E_{f1} = 0.35$ ev and $E_{f2} = 0.43$ ev are obtained, assuming $\tau_{01} = \tau_{02} = 10^{-11}$ sec in the following formulas,

$$\tau_{f1} = \tau_{01} \exp(E_{f1}/kT), \tag{8}$$

$$\tau_{f2} = \tau_{02} \exp(E_{f2}/kT). \tag{9}$$

None of these traps can be regarded as F center from the following reasons. As shown in Fig. 5, the photocurrent of the steady illumination (Curve **IV**) is about ten times as the pulse photocurrent (Curve **I**~**III**) above −80°C, the above values being adjusted to be equal at **O**$_1$ temperature in the figure. The most effective traps should be F centers. So, it may be reasonable to regard the traps of the slow decay time τ_s to be F centers. In

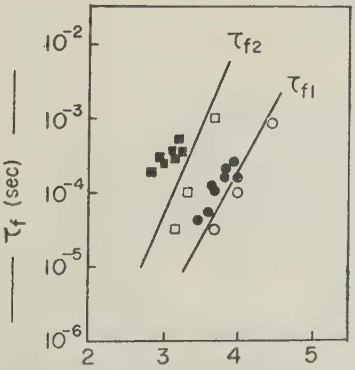

Fig. 10. The time constants τ_{f1} and τ_{f2} of the fast decay as the function of $1/T$.

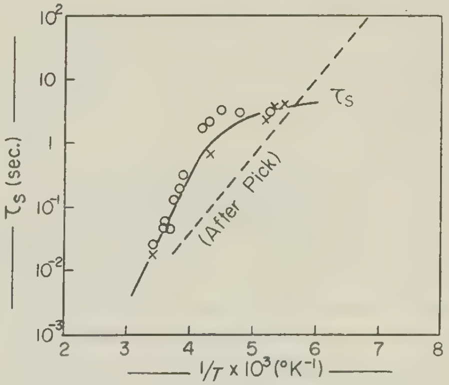

Fig. 11. The time constant τ_s of slow decay as the function of $1/T$. The soild line shows the time constant of slow current-decay, and the dashed line the thermal life of F′ center after Pick.

Fig. 11 the time constant τ_s of the slow decay is plotted against $1/T$. The thermally releasing time of F′ electrons from the optical measurement is plotted against temperature according to Pick for comparison.(15) The optical values for high temperatures are extrapolated from the values measured at low temperatures. From the similarity of the two curves, the trap corresponding to the slow decay may be concluded to be F center. From Fig. 11,

$$\tau_{0s}=1\times10^{-9}\ \text{sec},$$
$$E_s=0.44\ \text{ev},$$

are estimated for this trap. This time factor is inaccurate due to the large value of τ_r/τ_t ($\simeq$100) contained in (7).

Now we shall try to discuss the $\mu_a\tau_a$ in Fig. 8 and 9. μ_a and τ_a are the effective values appeared in the experiment. They are correlated with the microscopic μ and τ through the following relations,

$$\mu_a\simeq(\mu\tau_t)/(\tau_g+\tau_t), \tag{10}$$
$$\tau_a\simeq\tau_g+\tau_t, \tag{11}$$

where $\tau_t\rangle\rangle\tau_r$ is assumed. This assumption is reasonable, because τ_t which is due to F center may be much smaller than τ_r which may due to the unknown imperfections. From (10) and (11), the following formula results,

$$\mu_a\tau_a\simeq\mu\tau_t \tag{12}.$$

In Fig. 9, τ_a can be considered to be equal to τ_t, if we put μ_a equal to μ. Using the law of the temperature-variation of polaron mobility in KBr, μ can be obtained for each temperature. On the other hand, τ_t is written as $1/N_FS_Fv$, where $N_F=$ concentration of F center and $S_F=$ the effective cross section of F center for electron capture. Then S_F is estimated to be $1\sim3\times10^{-16}\text{cm}^2$ and does not vary so much with temperature.

In the uncolored specimen there are about $4\times10^{15}/\text{cm}^3$ traps, if we use the results shown in Fig. 9, the cross section of the unknown traps being taken to be equal to that of F center. The density of the unknown trap in the uncolored specimen in the present case ($<4\times10^{15}/\text{cm}^3$) is nearly equal to the value obtained from the saturation effect of Hall mobility in KCl below 25°K measured by Brown.(16)

For the pulse photocurrent the traps of the fast decay may be as effective as F center. Although these traps seem to be due to thermal treatments or impurities, there is no clear information about their natures. Our optical measurement concerning to these traps shows the following results. (1): The four definite bands lying in the lower energy side of F center are produced by the irradiation of F-light for a long time at −150°C, and the slight bleaching of F-band occurs. These centers vanish thermally at about −50°C completely with the recovery of F-band. (2): By the long time irradiation of F-light at −180°C, F-band bleaches by up to 15% and F′-band is observed. The F′-band changes to F-band thermally by heating the specimen to −150°C in dark. According to our results, the thermal life of F′ center is several hundredths as short as Pick's value in the temperature region below −130°C. F′ center recovered to F center by the irradiation of 2000 mμ light at −180°C.

From the above optical results, it seems that the traps of the fast decay correspond to the centers described in (1) and that of slow decay to F′ center. The short life time of F′ center obtained by our optical measurement almost coincides with τ_s in the measurement of photocurrent decay.

§ 3. Conclusion

In the measurement of photocurrent in colored alkali halide such as KBr, it is better to adopt the a.c. field and pulsive illumination synchronized to plus and minus peaks of the a.c. field, to avoid the space charge polarization effect. The space charge effect may arise from electrons trapped in the surface states whose depth is about 0.3 eV.

The three kinds of traps were found in additively colored KBr purified by the recrystalization technique. One of them is the F center and the other two are the unknown centers probable due to thermal treatments or impurities. The thermal activation energies of the electrons from these traps to the conduction band are 0.44, 0.35 and 0.43 ev respectively.

The mean range of electrons obtained was found to be much larger than the ones obtained by Pohl and Inchauspe.(17)(12) This may be due to the a.c. method adopted and the purer crystal used in this work.

By the measurement of pulse photocurrent under the condition for the absence of space charge, the typical curve of the temperature-dependence of photocurrent in alkali halides such as KCl and NaCl was obtained in KBr. The pulse photocurrent was proportional to μ_H measured by one of us in the temperature region from −100°C to −50°C.(7)

It is expected that the degree of purification of crystal could be determined by the measurement of the mean range of electrons and the time constants of current-decay under the condition free from space charge described in this paper.

We wish to express deep thanks to Prof. Kawamura and Mr. Tomura for their useful discussions and continual encouragements, and to Mr. Kozaki and Mr. Awane for their laborious assistances.

This work was supported by the Scientific Research Fund granted by the Ministry of Education.

References

1) G. Glaser and W. Lehfeldt: Nachr. Akad. Wiss. Göttingen 1936, 91
2) N. Inchauspé: Phys. Rev. **106** (1957) 898
3) G. Kuwabara et al.: J. Phys. Soc. Japan **14** (1959) 1921
4) V. O. von Gericke: Nachr. Akad. Wiss. Göttingen 1950, 1
5) F. Seitz: Rev. Mod. Phys. **26** (1954) 7
6) W. H. Jordan and P. R. Bell: R. S. I. **18** (1947) 10
7) M. Onuki and H. Kawamura: J. Phys. Soc. Japan **14** (1959) 967
8) A. von Hippel et al.: Phys. Rev. **91** (1953) 568
9) F. C. Brown: J. Phys. Chem. Solids **4** (1957) 206
10) C. Kittel: Solid State Physics (second edition) p. 521
11) M. Onuki: Reported in the annual meeting of Physical Society of Japan (1957)
12) L. I. Grossweiner: J. Appli. Phys. **24** (1953) 1306
13) J. R. Macdonald: J. Chem. Phys. **23** (1955) 275
14) J. A. Hornbeck. and J. R. Hayes: Phys. Rev. **97** (1955) 311
15) H. Pick: Ann. d. Physik **31** (1938) 365
16) private communication from F. C. Brown
17) R. W. Pohl: Proc. Phys. Soc. **49** (1937) 16

JOURNAL OF THE PHYSICAL SOCIETY OF JAPAN, Vol. 15, No. 10, OCTOBER, 1960

Dichroism of Z_4 and F Bands

By Masakazu ISHIGURO and Nozomu TAKEUCHI

Institute of Scientific and Industrial Research, Osaka University
Kitahanada, Sakai, Osaka, Japan

(Received June 16, 1960)

To investigate the dichroic property of the Z_4 band, the experiment on the anisotropic bleaching was made. It was found that the symmetry axis of Z_4 center is parallel to <110> direction and the Cole and Friauf's A model is in conformity with this symmetry. It was also found that there exists the same correlation in dichroism between F and Z_4 band as that between F and M band.

§1. Introduction

It is widely known that additively colored KCl crystals doped with strontium show an interesting series of the optical absorption bands called Z_1, Z_2 and Z_3. Pick[1] and Seitz[2] have proposed different models of the centers responsible to these bands.

More recently, Cole and Friauf[3] found a new absorption band of this series at about 860 mμ. It was named Z_4 band and two probable models for the Z_4 center named A and B were proposed by them. (See Fig. 1)

The Z_4 band in KCl:Sr has been found, (1) to be formed by F–irradiation of an additively colored and subsequently quenched crystal, (2) to be thermally bleached at about 110°C accompanying the disappearence of Z_1 band, (3) to give emission at $1.68\,\mu$ with excitation in the F, Z_1, Z_2 or R band whose wavelength is shorter than the Z_4 band, or the Z_4 band itself.3)4).

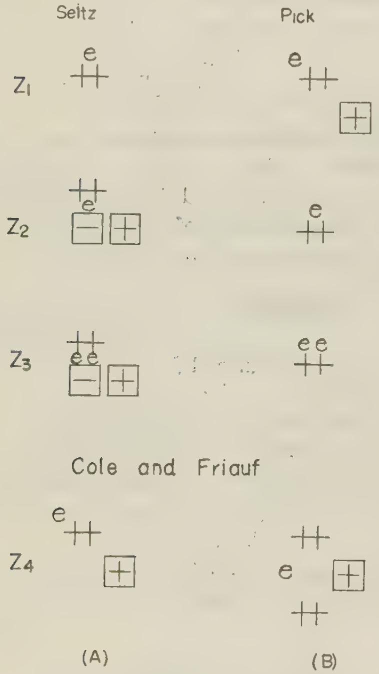

Fig. 1 Models of Z centers.

The present study on the dichroic properties of the Z_4 band of KCl:Sr crystal was undertaken for the following reasons: (1) The two models of Z_4 center above mentioned have different symmetries and the study on the polarization of emission of this center induced with polarized exciting light of 860 mμ reported by West and Compton4) could not decide the orientation of the optical dipole clearly; the degrees of polarization observed were $P(011)=0.39$ and $P(010)=0.34$. If we assume model A or model B for the Z_4 center, the former namely that the optical dipole is solely along the axis of ⟨110⟩, we would predict that $P(010)=0.66$ and $P(010)=0.33$, the later namely that the optical dipole is solely along the axis of ⟨100⟩, we would predict that $P(010)=1.00$ and $P(011)=0.00$. (2) The dichroic F band accompanying the dichroic M band which has been reported by van Doorn and Haven5) in a pure crystal is now one of the intersting problems in this fields. They have suggested that the M center posseses a second and small absorption band hidden under the F band, in addition to the M band. But it leaves a question in the coincidence of the assumed hidden band with the F band for many different kinds of alkali halides. On the other hand, Lambe and Compton6) have suggested another hypothesis dipole-dipole energy transfer between F and M centers. In this case, however, there exist a strong implication that the centers are not situated randomly, but are concentrated mainly in a relatively small volume of the crystal. Besides, it is difficult to interpret the details of the dichroic spectrum by this hypothesis.

In addition to this famous example of F–M dichroism, we have lately reported F–Z_2 dichroism7) which is somewhat more complicated than the former. So it is very attractive to ascertain whether F–Z_4 dichroism also exists or not.

§2. Experimental Procedure

The KCl:Sr crystal was grown in our laboratory by the standard Kyropoulos method and estimated to contain about 10^{-4} mole fraction of strotium—the impurity doping was done in the molton state. The additive coloration of the crystals was made as follows: The block crystals were heated in potassium vapour at about 600°C for 3 hours and then cooled slowly to room temperature. Next, the blocks were cleaved into thin plates between 0.6 and 0.3 mm in thickness and quenched in the dark after heated again at about 600°C for a few minutes. The samples thus prepared show the dominent F

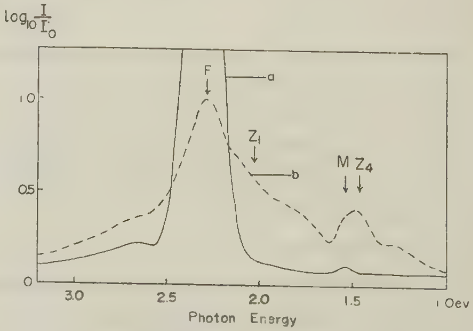

Fig. 2. Absorption spectra
Absorption, (a) before F–light irradiation, (b) after F–light irradiation.

band as in the case of the pure KCl crystal.

Upon irradiating this sample at room temperature with a 500 W tungsten lamp through Matsuda VB3 glass filter for one hour, Z_1, Z_4, M, N and other bands are formed at the expense of the F band. The relative height of the Z_4 band to the F band clearly depends upon the F–irradiation time and quenching rate—the quenching is done quicker, the ratio of Z_4 to F is larger. These situations are shown in Fig. 2, and the characteristic curve of the Matsuda glass filters are shown in Fig. 3.

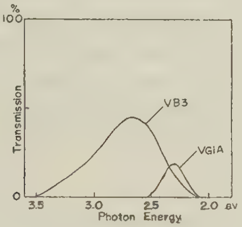

Fig. 3. Gharacteristics of VB3 and VG1A filters.

Throughout this experimental study, we used the samples thus prepared as the virgin crystal. All irradiations were done at room temperature, and all measurements were made at −150°C unless otherwise stated.

In anisotrpic bleaching experiments, the absorption spectra of the crystals were measured with the polarized lights whose electric vectors were perpendicular and parallel to [011] or [010] directions before and after irradiation with [011] or [010] polarized light which were incident on the (100) surface. The dichroic spectra were taken to be the difference between the absorptions as measured with [011] and [0$\bar{1}$1], or with [010] and [001] polarized light.

§ 3. Experimental Results

The absorption curve shown in Fig. 2b was obtained after one hour F–irradiation upon newly quenched crystal at room temperature. Though the F, Z_1 and Z_4 bands are the most prominent, other small absorption bands appear among them. The ratios of Z_1 to Z_4 obtained in various samples were found in largely different values, indicating that Z_1 and Z_4 bands are due to distinct centers—Cole and Friauf[3)] have had the question that both bands might be due to the same center.

The results on the anisotropic bleaching of the Z_4 band where a monochromator or a 100 W tungsten lamp through a set of two filters VV1A and VR1D were used as the light source in the bleaching are shown in Figs. 4A and 4B.

In Fig. 4A, curves b_1 and c_1 show the absorption spectra measured with the light polarized along [011] and [0$\bar{1}$1] respectively after a brief bleaching with the light polarized along [011] direction, and curve a shows

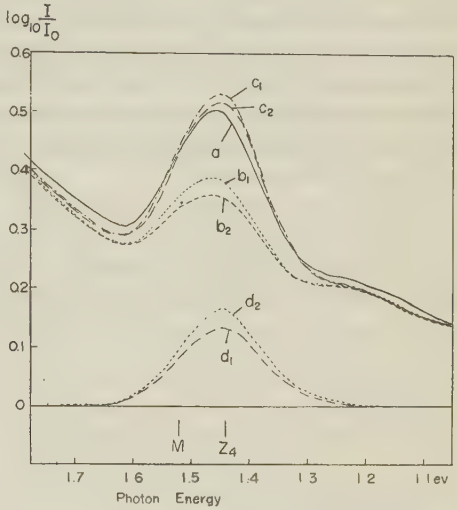

Fig. 4A. Dichroism induced after partial bleaching with [011] polarized light in the Z_4 band. (a) Absorption before bleaching as measured with either [011] or [0$\bar{1}$1] polarized light. Absorption after bleaching, (b) measured with [011] polarized light, (c) measured with [0$\bar{1}$1] polarized light. (d) Dichroic spectra.

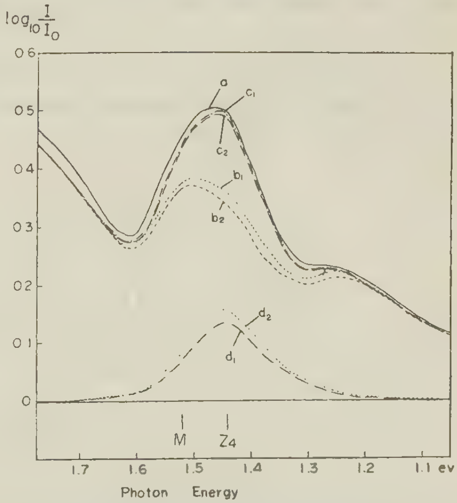

Fig. 4B. The same as Fig. 4A except that [010] and [001] polarized light was used.

the one measured before the bleaching. The absorption measured with the light polarized parallel to the bleaching light decreases markedly, while the one measured with the light polarized perpendicular to the bleaching light increases, indicating that more centers which could absorb $[0\bar{1}1]$ light exist after the bleaching than before. Curves b_2 and c_2 show the succesive bleaching and curves d_1 and d_2 show the dichroic spectra. The above results indicate that not only preferential bleaching of this ceter, but also some reorientation should occur during the polarized light exposure. In Fig. 4B, the similar saturation is observed on the opticalanisotropy induced by the bleaching with the light polarized along [010] direction.

Since both the irradiations with [011] and [010] polarized light induce the dichroism and the peaks of these dichroic spectra precisely coincide with that of the normal Z_4 absorption band, it may be considered that the optical transition corresponding to the Z_4 band is due to an optical dipole oriented parallel to ⟨110⟩ direction. When the anisotropic bleaching is prolonged, the M band also begins to show dichroism considerably.

Then it is striking that during the exposure of the polarized light in Z_4 band there appears another dichroism in the F band region with opposite sign to that in the Z_4 band.

This appearence of the reverse dichroism in the F band region is quite akin to the well-known case of M–F dichroism, but its shape is somewhat different in details. When a crystal is irradiated by the polarized F band light, the dichroism whose sign is opposite to that of the case of the irradiation with Z_4 light appears in both the Z_4 and F band regions. (See Figs. 6A and 6B.)

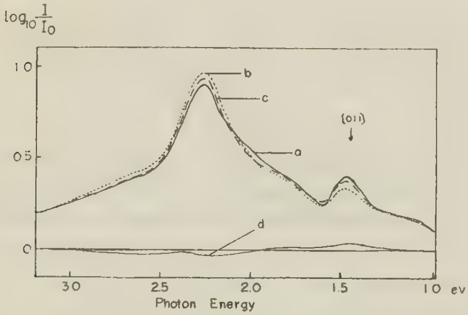

Fig. 5A. Dichroism induced by partial bleaching with [011] polarized light in the Z_4 band. (a) Absorption before bleaching as measured with either [011] or $[0\bar{1}1]$ polarized light.

Absorption after bleaching, (b) measured with [011] polarized light, (c) measured with $[0\bar{1}1]$ polarized light. (d) Dichroic spectra.

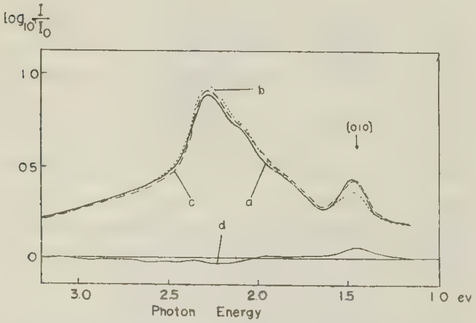

Fig. 5B. The same as Fig. 5A except that [010] and [001] polarized light were used.

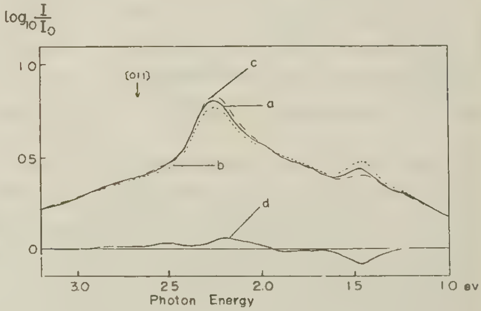

Fig. 6A The same as Fig. 5A except that polarized light in the F band was used as the bleaching light.

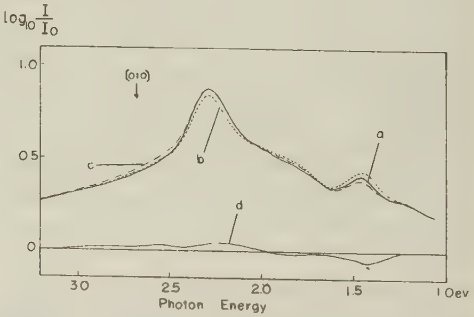

Fig. 6B. The same as Fig. 5B except that polarized light in the F band was used as the bleaching light.

When a virgin crystal is irradiated through VG1A filter, keeping other conditions to be quite the same as in the case of the VB3 filter mentioned above, the strong F–M dichroism appears overlapping with the F–Z_4 dichroism, suggesting that the F–Z_4 dichroism is distinct from the F–M dichroism. (See Fig. 7)

§ 4. Discussion

The results of anisotropic bleaching of the Z_4 band suggest that the center responsible for this band has an axis of symmetry along ⟨110⟩ direction. The A model of this center proposed by Cole and Friauf[3] which is an electron trapped at a divalent ion with a positive ion vacancy bound in the nearest cation site is the one that satisfies the above situation. Thus, Pick's model for Z_1[1] which is quite the same as Cole and Friauf's A model corresponds rather to Z_4.

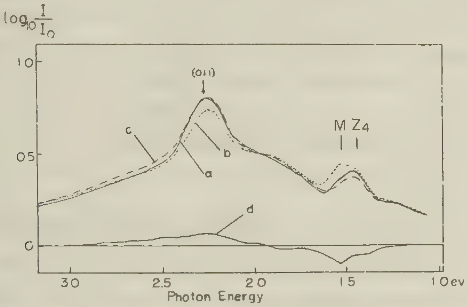

Fig. 7. Dichroism induced by partial bleaching with [011] polarized light through VG1A filter.

Considering the crystalline field of the environment, the symmetry of this center is C_{2V} which is the same as that of the Seitz's model for the M center.

It is interesting that there is the same correlation in dichroism between F and Z_4 bands as that between F and M bands, in addition to that between F and Z_2 bands which has recently been reported by the present authors[7]. Besides, the dichroic spectrum in the F and region is very like that in the case of F–M dichroism.

If the van Doorn hypothesis is taken into account of the correlation in dichroism also in this case, from the C_{2V} symmetry above, the three types of the optical dipoles corresponding to the transitions, A_1–A_1, A_1–B_1 and A_1–B_2 should be taken into consideration for the bands hidden under the F band region. The fact that the F band has a correlation in dichroism also to Z_2 and Z_4 band besides to M band will further add a question to the above hypothesis. Nevertheless, some studies along the van Doorn hypothesis will be reported by the present authors in the near future.

References

1) H. Pick: Ann. Physik **35**, 73 (1939); Z. Physik 114 (1939) 127
2) F. Seitz: Phys. Rev. **83**, 134 (1951)
3) G. R. Cole and H. J. Friauf: Phys. Rev. **107**, (1957) 387
4) E. J. West and W. D. Compton: Phys. Rev. **108**, (1957) 576
5) Th. P. J. Botden, C. Z. van Doorn and Y. Haven: Philips Res. Rep. **9** (1954) 469.
C. Z. van Doorn and Y. Haven: ibid **11** (1956) 479.
C. Z. van Doorn: ibid **12** (1957) 309.
6) J. Lambe and W. D. Comton: Phys. Rev. **106** (1957) 684.
7) M. Ishiguro, E. Sugioka and N. Takeuchi: J. Phys. Soc. Japan **15** (1960) 1302

JOURNAL OF THE PHYSICAL SOCIETY OF JAPAN, Vol. 15, No. 10, OCTOBER, 1960

Wall-effect upon Two-dimensional Stokes Flow of an Electrically Conducting Liquid in a Uniform Magnetic Field

By Yorisaburo TAKAISI

Department of Physics, Faculty of Education,
Ehime University, Matsuyama

(Received June 10, 1960)

This paper deals with the steady slow motion of a circular cylinder in a semi-infinite viscous and electrically conducting liquid parallel to its bounding plane wall in the presence of a uniform magnetic field, using Stokes approximation. Detailed calculation is carried out for the flow produced by the cylinder in two cases: one in a parallel magnetic field and the other in a transverse magnetic field. The expansion formulae for the drag per unit span of the cylinder are obtained in terms of the Hartmann number in each case.

§1. Introduction

In a quite recent paper[1], applying Chester's idea[2] to the two-dimensional Stokes flow, Yosinobu and Kakutani have investigated the effect of magnetic field upon the flow of a viscous and electrically conducting liquid past a circular cylinder in two cases: one in a uniform magnetic field parallel to the main stream and the other in a transverse uniform magnetic field.

In this paper, using Faxén's image method[3], we study the steady slow motion of a circular cylinder in a semi-infinite viscous and electrically conducting liquid parallel to its bounding plane wall on the basis of Stokes approximation in two cases: the first case, where the uniform magnetic field is parallel to the bounding plane wall and the second case, where the uniform magnetic field is perpendicular to the bounding plane wall. The bounding plane wall is assumed to be non-magnetic and non-conducting.

Thus, the expansion formulae for the drag per unit span of the cylinder are obtained in power series of the Hartmann number. Numerical results show that the drag coefficients in both cases are almost independent of the Hartmann number, for its small values, and consequently they are equal to each other and are also equal to that obtained by the classical Stokes approximation.

To this order of approximation, no lift appears in both cases.

§2. Fundamental Equations and Solutions

The fundamental equations for a two-dimensional steady flow of an unbounded, viscous and electrically conducting liquid past a cylindrical body in the presence of a uniform magnetic field have been obtained by Yosinobu and Kakutani to the order of Stokes approximation. Since the equations constitute the starting point of the present study, we shall first recapitulate briefly their analysis for the sake of reference, making modifications so as to be applicable to the motion of the liquid produced by the cylinder moving in the liquid otherwise at rest.

The fundamental equations of magnetohydrodynamics are:

(1) Maxwell's equations:

$$\mathrm{curl}\,\boldsymbol{H}=\boldsymbol{J}\,, \tag{2.1}$$

$$\mathrm{div}\,\boldsymbol{H}=0\,, \tag{2.2}$$

$$\mathrm{curl}\,\boldsymbol{E}=0\,, \tag{2.3}$$

$$\varepsilon\,\mathrm{div}\,\boldsymbol{E}=q\,; \tag{2.4}$$

(2) Ohm's law:

$$\boldsymbol{J}=\sigma(\boldsymbol{E}+\mu\boldsymbol{V}\times\boldsymbol{H})+q\boldsymbol{V}\,; \tag{2.5}$$

(3) The equation of continuity:

$$\mathrm{div}\,\boldsymbol{V}=0\,; \tag{2.6}$$

(4) The modified Navier-Stokes equation:

$$\rho(\boldsymbol{V}\cdot\mathrm{grad})\boldsymbol{V}=-\mathrm{grad}\,P+\rho\nu\nabla^2\boldsymbol{V}+q\boldsymbol{E}+\mu\boldsymbol{J}\times\boldsymbol{H}\,; \tag{2.7}$$

where $\boldsymbol{E}$ is the electric field, $\boldsymbol{H}$ the magnetic field, $\boldsymbol{J}$ the current density, q the excess charge density, ε the dielectric constant, μ

e magnetic permeability, σ the electrical nductivity of the liquid, $\boldsymbol{V}$ the liquid velo-ty, P the pressure, and ρ and ν are respec-vely the density and the kinematic viscosity the liquid. In the above seven equations, e have adopted the rationalized M.K.S. stem. We have also assumed the liquid to homogeneous and isotropic.

We choose the origin of coordinates at the ntre of a cross section of the cylinder and e take the x_1-axis parallel to the direction the undisturbed magnetic field, the x_3-axis ong the axis of the cylinder and the x_2-axis rpendicular to both the x_1- and x_3-axes. The locity of the cylinder is supposed to be rallel to the x_1-axis in the first case and to e x_2-axis in the second case.

First, we neglect the terms involving excess arge q in (2.5) and (2.7) as in usual mag-etohydrodynamic problems. We then assume wo-dimensionality of the problem: namely (1) the quantities in (2.1)~(2.7) are independ-nt of x_3, so that all the derivatives in x_3 sappear in the above equations, and (2) the quid velocity $\boldsymbol{V}$ and the magnetic field $\boldsymbol{H}$ e in the x_1x_2-plane. In consequence of these ssumptions, we have, in both cases,

$$\boldsymbol{J}=\mu\sigma(\boldsymbol{V}\times\boldsymbol{H}) . \qquad (2.8)$$

ubstituting (2.8) into (2.1) and (2.7), and troducing non-dimensional variables $\boldsymbol{v}=\boldsymbol{V}/V_1$, $=\boldsymbol{H}/H_1$, $p=[a/(\rho\nu V_1)]P$ and $(x, y, z)=(x_1/a$, $/a, x_3/a)$, we have, in both cases,

$$R_m(\boldsymbol{v}\times\boldsymbol{h})=\nabla\times\boldsymbol{h} , \qquad (2.9)$$

$$R(\boldsymbol{v}\cdot\nabla)\boldsymbol{v}=-\nabla p+\nabla^2\boldsymbol{v}+M^2(\nabla\times\boldsymbol{h})\times\boldsymbol{h} \qquad (2.10)$$

here a is, for instance, the representative ength of the cylinder, $R_m=\mu\sigma aV_1$ the mag-etic Reynolds number, $R=aV_1/\nu$ the Reynolds umber, $M=(\sigma/\rho\nu)^{1/2}a\mu H_1$ the Hartmann num-er, and ∇ stands for $\boldsymbol{i}(\partial/\partial x)+\boldsymbol{j}(\partial/\partial y)$, here $\boldsymbol{i}, \boldsymbol{j}, \boldsymbol{k})$ are the fundamental unit vectors.

We assume R_m to be small and apply the tokes approximation to Eq. (2.9). Then we ave

$$\nabla\times\boldsymbol{h}=0 . \qquad (2.11)$$

ssuming that the permeabilities of the liquid nd the cylinder are effectively equal, we btain, from (2.2) and (2.11),

$$\boldsymbol{h}=\boldsymbol{i} , \qquad (2.12)$$

so that to the present approximation the magnetic field is everywhere uniform and parallel to the x_1-axis. Inserting (2.12) into (2.10), and assuming R to be small, we have, to the Stokes approximation,

$$-\nabla p+\nabla^2\boldsymbol{v}+M^2(\boldsymbol{v}\times\boldsymbol{i})\times\boldsymbol{i}=0 \qquad (2.13)$$

We now introduce the non-dimensional perturbed velocities $\boldsymbol{v}'=\boldsymbol{v}-\boldsymbol{i}$ in the first case, and $\boldsymbol{v}'=\boldsymbol{v}-\boldsymbol{j}$ in the second case in (2.13). Thus, we have finally the following equation, in both cases:

$$-\nabla p+\nabla^2\boldsymbol{v}'-M^2v\boldsymbol{j}=0 , \qquad (2.14)$$

which should be solved in combination with the equation of continuity for $\boldsymbol{v}'$:

$$\nabla\cdot\boldsymbol{v}'=0 , \qquad (2.15)$$

where (u, v) are the x- and y-components of $\boldsymbol{v}'$, respectively.

Eliminating p from (2.14), we have

$$\nabla^2\omega-M^2\frac{\partial v}{\partial x}=0 , \qquad (2.16)$$

where $\omega=\partial v/\partial x-\partial u/\partial y$ is the vorticity. Eq. (2.15) shows that the perturbed velocity field has a stream function ψ such that

$$u=\frac{\partial\psi}{\partial y} , \qquad v=-\frac{\partial\psi}{\partial x} , \qquad (2.17)$$

and

$$\omega=-\nabla^2\psi . \qquad (2.18)$$

Substituting (2.17) and (2.18) into (2.16) we obtain the equation for ψ as:

$$\left(\nabla^4-M^2\frac{\partial^2}{\partial x^2}\right)\psi=0 . \qquad (2.19)$$

The solution of this equation can be expressed in the form:

$$\psi=\psi_1+\psi_2 , \qquad (2.20)$$

where ψ_1 and ψ_2 are solutions of equations

$$\left(\nabla^2-M\frac{\partial}{\partial x}\right)\psi_1=0 , \qquad (2.21)$$

and

$$\left(\nabla^2+M\frac{\partial}{\partial x}\right)\psi_2=0 , \qquad (2.22)$$

respectively. The appropriate solutions of (2.21) and (2.22) which satisfy the boundary conditions at infinity are given respectively by

$$\psi_1=A_0e^{kx}K_0(kr)+B_1\int_0^{\theta}kr[K_1(kr)+K_0(kr)\cos\theta]e^{kr\cos\theta}d\theta$$
$$+e^{kx}\sum_{n=1}^{\infty}K_n(kr)(A_n\cos n\theta+B_n\sin n\theta) , \qquad (2.23)$$

and

$$\psi_2=C_0e^{-kx}K_0(kr)+D_0\int_0^\theta kr[K_1(kr)-K_0(kr)\cos\theta]e^{-kr\cos\theta}d\theta$$
$$+e^{-kx}\sum_{n=1}^{\infty}K_n(kr)(C_n\cos n\theta+D_n\sin n\theta)\ , \tag{2.24}$$

where $k=\frac{1}{2}M,\qquad x=r\cos\theta,\qquad y=r\sin\theta$ and

$$B_0+D_0=0\ . \tag{2.25}$$

$K_n(x)$ is the modified Bessel function of the second kind. The condition (2.25) ensures that the stream function ψ is one-valued and continuous throughout the whole field of flow.

We introduce conjugate complex velocities w_n's defined as:

$$w_n=u_n-iv_n\qquad(n=1,\ 2)\ . \tag{2.26}$$

Inserting (2.23) and (2.24) into (2.26), and expanding the functions with respect to $e^{i\theta}$, then we have the Fourier series for w_n's as:

$$\begin{aligned}\left.\begin{matrix}w_1\\w_2\end{matrix}\right\}=ik\begin{Bmatrix}A_0\\C_0\end{Bmatrix}&[\pm(K_0I_0-K_1I_1)+e^{-i\theta}(K_0I_1-K_1I_0)+e^{i\theta}(K_0I_1-K_1I_2)\\&\pm e^{-2i\theta}(K_0I_2-K_1I_1)\pm e^{2i\theta}(K_0I_2-K_1I_3)+e^{-3i\theta}(K_0I_3-K_1I_2)]\\+k\begin{Bmatrix}B_0\\D_0\end{Bmatrix}&[\pm(K_0I_0+K_1I_1)+e^{-i\theta}(K_0I_1+K_1I_0)+e^{i\theta}(K_0I_1+K_1I_2)\\&\pm e^{-2i\theta}(K_0I_2+K_1I_1)\pm e^{2i\theta}(K_0I_2+K_1I_3)+e^{-3i\theta}(K_0I_3+K_1I_2)]\\+\frac{1}{2}ik\begin{Bmatrix}A_1\\C_1\end{Bmatrix}&[-K_0I_0+2K_1I_1-K_2I_2\mp e^{-i\theta}(K_0I_1-K_1I_0-K_1I_2+K_2I_1)\\&\mp e^{i\theta}(K_0I_1-K_1I_0-K_1I_2+K_2I_3)-e^{-2i\theta}(K_0I_2-K_1I_1-K_1I_3+K_2I_0)\\&-e^{2i\theta}(K_0I_2-K_1I_1-K_1I_3+K_2I_4)\mp e^{-3i\theta}(K_0I_3-K_1I_2-K_1I_4+K_2I_1)]\\+\frac{1}{2}k\begin{Bmatrix}B_1\\D_1\end{Bmatrix}&[-K_0I_0+K_2I_2\mp e^{-i\theta}(K_0I_1+K_1I_0-K_1I_2-K_2I_1)\\&\mp e^{i\theta}(K_0I_1-K_1I_0+K_1I_2-K_2I_3)-e^{-2i\theta}(K_0I_2+K_1I_1-K_1I_3-K_2I_0)\\&-e^{2i\theta}(K_0I_2-K_1I_1+K_1I_3-K_2I_4)\mp e^{-3i\theta}(K_0I_3+K_1I_2-K_1I_4-K_2I_1)]\\+\cdots\ ,&\end{aligned} \tag{2.27}$$

where the argument kr of the functions K_n and I_n has been omitted for brevity.

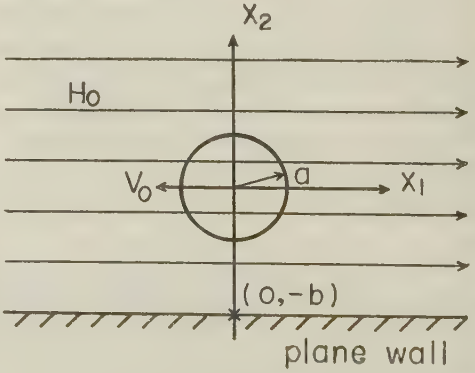

Fig. 1.

§ 3. First Case

Suppose that a circular cylinder of radius a is moving, with constant slow velocity $-V_0$ along the x_1-axis, in the presence of a uniform magnetic field parallel to the x_1-axis, in a semi-infinite viscous and electrically conducting liquid otherwise at rest parallel to its bounding plane wall (Fig. 1). The wall is assumed to be non-magnetic and non-conducting.

3.1. *Method of solution*

If we confine ourselves to the calculation of the forces experienced by the cylinder correct to the order of M^2, the lowest terms being $O(1)$, it suffices to take the first four terms in (2.23) and (2.24) respectively. Then, as shown in our previous paper[4)], we obtain integral expressions for ψ_1 and ψ_2 as:

$$\psi_1=\frac{1}{2}\int_{-\infty}^{\infty}\left\{\frac{1}{\lambda_1}\left(A_0-\frac{i\alpha-k}{k}A_1\right)+\frac{|y|}{y}\left(\frac{i\alpha-2k}{\lambda^2{}_1}B_0+\frac{1}{k}B_1\right)\right\}e^{i\alpha x-\lambda_1|y|}d\alpha\ , \tag{3.1}$$

$$\psi_2=\frac{1}{2}\int_{-\infty}^{\infty}\left\{\frac{1}{\lambda_2}\left(C_0-\frac{i\alpha+k}{k}C_1\right)+\frac{|y|}{y}\left(\frac{i\alpha+2k}{\lambda_2{}^2}D_0+\frac{1}{k}D_1\right)\right\}e^{i\alpha x-\lambda_2|y|}d\alpha\ , \tag{3.2}$$

where $\lambda_1=\sqrt{\alpha^2+2ik\alpha}$ and $\lambda_2=\sqrt{\alpha^2-2ik\alpha}$.

In order to satisfy the boundary conditions on the bounding plane wall, we now superpose, as done by Faxén, a flow due to images, which is derived from a stream function ψ^* defined as:

$$\psi^*=\psi_1{}^*+\psi_2{}^*\ , \tag{3.3}$$

where

$$\psi_1{}^*=\frac{1}{2}\int_{-\infty}^{\infty}f_1(\alpha)e^{i\alpha x-\lambda_1(y+2\delta)}d\alpha\ , \tag{3.4}$$

and

$$\psi_2{}^*=\frac{1}{2}\int_{-\infty}^{\infty}f_2(\alpha)e^{i\alpha x-\lambda_2(y+2\delta)}d\alpha\ , \tag{3.5}$$

where $\delta=b/a$ and $f_n(\alpha)$'s are unknown functions to be determined by the under-mentioned boundary conditions.

The boundary conditions at infinity are satisfied automatically by w_n's and $w_n{}^*$'s. Then, we have only to consider the boundary conditions on the bounding plane wall $y=-\delta$ as well as at the surface of the cylinder. They are

$$(w_1+w_2+w_1{}^*+w_2{}^*)_{y=-\delta}=0\ , \tag{3.6}$$

and

$$(w_1+w_2+w_1{}^*+w_2{}^*)_{r=1}=-1\ . \tag{3.7}$$

3.2. *Determination of the functions $f_n(\alpha)$'s*

Inserting (3.1), (3.2) and (3.4), (3.5) into (3.6), the functions $f_n(\alpha)$'s so far undetermined can be expressed in terms of the unknown constants A_0, B_0, $\cdots$ and D_1 as:

$$\begin{aligned}f_1(\alpha)=&\frac{\lambda_1+\lambda_2}{\lambda_1(\lambda_1-\lambda_2)}\left(A_0-\frac{i\alpha-2k}{\lambda_1}B_0-\frac{i\alpha-k}{k}A_1-\frac{\lambda_1}{k}B_1\right)\\&+\frac{2}{\lambda_1-\lambda_2}\left(C_0-\frac{i\alpha+2k}{\lambda_2}D_0-\frac{i\alpha+k}{k}C_1-\frac{\lambda_2}{k}D_1\right)e^{(\lambda_1-\lambda_2)\delta}\ ,\end{aligned} \tag{3.8}$$

and

$$\begin{aligned}f_2(\alpha)=&-\frac{2}{\lambda_1-\lambda_2}\left(A_0-\frac{i\alpha-2k}{\lambda_1}B_0-\frac{i\alpha-k}{k}A_1-\frac{\lambda_1}{k}B_1\right)e^{-(\lambda_1-\lambda_2)\delta}\\&-\frac{\lambda_1+\lambda_2}{\lambda_2(\lambda_1-\lambda_2)}\left(C_0-\frac{i\alpha+2k}{\lambda_2}D_0-\frac{i\alpha+k}{k}C_1-\frac{\lambda_2}{k}D_1\right)\ .\end{aligned} \tag{3.9}$$

3.3. *Determination of the constants A_0, B_0, $\cdots$ and D_1*

If we insert (3.8) and (3.9) into (3.4) and (3.5) respectively and expand the integrands with respect to $e^{i\theta}$, we obtain, after some lengthy calculations, the Fourier series for w^* as:

$$\begin{aligned}w^*=w_1{}^*+w_2{}^*=&k\{(F_1+iF_2)+k^2r^2(F_5+iF_6)\}A_0+k\{(F_3+iF_4)+k^2r^2(F_7+iF_8)\}B_0\\&+k\{(F_1-iF_2)+k^2r^2(F_5-iF_6)\}C_0+k\{-(F_3-iF_4)-k^2r^2(F_7-iF_8)\}D_0\\&+k(F_9+iF_{10})A_1+k(F_{11}+iF_{12})B_1-k(F_9-iF_{10})C_1+k(F_{11}-iF_{12})D_1\\&+ik^2re^{-i\theta}(F_{13}A_0+F_{14}B_0+F_{13}C_0-F_{14}D_0)\\&+k^2re^{i\theta}\{(F_{15}+iF_{16})A_0+(F_{17}+iF_{18})B_0-(F_{15}-iF_{16})C_0+(F_{17}-iF_{18})D_0\}\\&+\cdot\cdot\cdot\ ,\end{aligned} \tag{3.10}$$

where F_n's are functions of $l=2k\delta$.

We may expand the constants in powers of k as:

$$\left.\begin{aligned}(A_0, B_0, C_0, D_0)&=k^{-1}(A_{00}, B_{00}, C_{00}, D_{00})+k(A_{01}, B_{01}, C_{01}, D_{01})+\cdots ,\\ (A_1, B_1, C_1, D_1)&=k(A_{10}, B_{10}, C_{10}, D_{10})+\cdots .\end{aligned}\right\} \tag{3.11}$$

We insert (2.27) and (3.10) together with (3.11) into (3.7), and we neglect all terms higher than k^3. Then, on equating to zero the terms of the same powers of k in the coefficients of $e^{ni\theta}$ and separating the real and imaginary parts, we obtain linear algebraic equations for the constants A_{00}, A_{01}, $\cdots$ and D_{10}. Solving these equations successively, we obtain

$$\left.\begin{aligned}A_{00}&=C_{00}=0 ,\\ B_{00}&=-D_{00}=-\frac{1}{2\Omega+1+2F_3} ,\\ A_{01}&=C_{01}=-\frac{F_{14}}{2\Omega+1+2F_3} ,\\ B_{01}&=-D_{01}=\frac{4\Omega+1+8F_7-4F_{11}+8F_1F_{14}-16F_9F_{18}}{4(2\Omega+1+2F_3)^2} ,\\ A_{10}&=-C_{10}=\frac{2F_{18}}{2\Omega+1+2F_3} ,\\ B_{10}&=D_{10}=\frac{1}{2(2\Omega+1+2F_3)} ,\end{aligned}\right\} \tag{3.12}$$

where $\Omega=-\gamma-\ln(M/4)$, $\gamma=0.57721\cdots$being Euler's constant.

Making use of the relations $F_{11}=-2F_7$, $F_{14}=-F_1$ and $F_{18}=F_9$, we obtain from (3.11) and (3.12)

$$A_0=C_0=-\frac{2F_{14}}{2\Omega+1+2F_3}\left(\frac{M}{4}\right), \tag{3.13}$$

$$B_0=-D_0=-\frac{2}{M(2\Omega+1+2F_3)}\left\{1-\frac{4\Omega+1-8F_1{}^2+16F_7-16F_9{}^2}{2\Omega+1+2F_3}\left(\frac{M}{4}\right)^2\right\}, \tag{3.14}$$

$$A_1=-C_1=\frac{4F_9}{2\Omega+1+2F_3}\left(\frac{M}{4}\right), \tag{3.15}$$

$$B_1=D_1=\frac{1}{2\Omega+1+2F_3}\left(\frac{M}{4}\right). \tag{3.16}$$

The functions F_n's necessary for the calculation of (3.13)~(3.16) are given by

$$F_1=S_{2,0}(l)+S_{2,1}(l)+\tfrac{1}{2}l\Lambda_0(l)-\tfrac{1}{2}\Lambda_1(l) , \tag{3.17}$$

$$F_3=S_{1,0}(l)+S_{1,1}(l)+C_{1,-1}(l)+C_{1,1}(l)-\Lambda_0(l)-(\tfrac{1}{2}l^{-1}+\tfrac{1}{2}l)\Lambda_1(l)+l , \tag{3.18}$$

$$F_7=\tfrac{1}{2}\{S_{1,-1}(l)-S_{1,1}(l)-C_{1,-1}(l)+C_{1,3}(l)\} , \tag{3.19}$$

$$F_9=S_{2,0}(l)+S_{2,1}(l)+C_{2,-1}(l)-C_{2,3}(l)+\tfrac{1}{2}l^{-1}\Lambda_0(l)-(l^{-2}+\tfrac{1}{2})\Lambda_1(l)+1 , \tag{3.20}$$

where

$$\left.\begin{aligned}S_{1,n}(l)&=\int_0^\infty\frac{1}{(1+\xi^2)^n}e^{-l\xi}\sin\frac{l\xi}{(1+\xi^2)^{1/2}}d\xi ,\\ S_{2,n}(l)&=\int_0^\infty\frac{\xi}{(1+\xi^2)^n}e^{-l\xi}\sin\frac{l\xi}{(1+\xi^2)^{1/2}}d\xi ,\\ C_{1,n}(l)&=\int_0^\infty\frac{1}{(1+\xi^2)^{n/2}}e^{-l\xi}\cos\frac{l\xi}{(1+\xi^2)^{1/2}}d\xi ,\\ C_{2,n}(l)&=\int_0^\infty\frac{\xi}{(1+\xi^2)^{n/2}}e^{-l\xi}\cos\frac{l\xi}{(1+\xi^2)^{1/2}}d\xi ;\end{aligned}\right\} \tag{3.21}$$

and

$$A_n(l)=\pi\{\mathbf{H}_n(l)-Y_n(l)\}\ , \tag{3.22}$$

where $Y_n(x)$ is Neumann's Bessel function of the second kind and $\mathbf{H}_n(x)$ is Struve's function[5] defined as:

$$\mathbf{H}_n(x)=\sum_{m=0}^{\infty}\frac{(-)^m(\frac{1}{2}x)^{n+2m+1}}{\Gamma(m+\frac{3}{2})\Gamma(n+m+\frac{3}{2})}\ . \tag{3.23}$$

3.4. *Forces on the cylinder*

The forces experienced by the cylinder can be calculated by integrating the viscous and Maxwell's stresses on the surface of the cylinder, as done by Yosinobu and Kakutani in the case of no wall. Thus, the lift L^{I} and the drag D^{I} experienced by the cylinder under discussion per unit span can be expressed as:

$$L^{\mathrm{I}}=0\ , \tag{3.24}$$

$$D^{\mathrm{I}}=-4\pi\rho\nu MV_0B_0\ . \tag{3.25}$$

To the present approximation, the Maxwell's stress makes no contributions to the lift and drag. Hence, if use is made of (3.14), we have for the drag coefficient $C_D{}^{\mathrm{I}}$

$$C_D{}^{\mathrm{I}}=\frac{D^{\mathrm{I}}}{\rho\nu V_0}=\frac{8\pi}{2\Omega+1+2F_3}\left\{1-\frac{4\Omega+1-8F_1{}^2+16F_7-16F_9{}^2}{2\Omega+1+2F_3}\left(\frac{M}{4}\right)^2\right\}\ . \tag{3.26}$$

If we expand the functions $\sin\{l\xi/(1+\xi^2)^{1/2}\}$ and $\cos\{l\xi/(1+\xi^2)^{1/2}\}$ in (3.21) into Taylor's series with respect to l, and if use is made of the formula[6]

$$\int_0^\infty(1+\xi^2)^{n-1/2}e^{-l\xi}d\xi=2^{n-1}\pi^{-1/2}\Gamma(n+\tfrac{1}{2})l^{-n}A_n(l)\ , \tag{3.27}$$

together with its derivatives with respect to l, we obtain a series expression with respect to l for the drag coefficient $C_D{}^{\mathrm{I}}$, which is valid for $l\leqq 1$. Thus, an approximate expansion formula correct to $O(l^2)$, for instance, is expressed as:

$$C_D{}^{\mathrm{I}}=\frac{4\pi}{\ln 2\delta-(T-\frac{1}{2})l^2}\left[1+\frac{4l^{-2}-2\Omega-14T+\frac{43}{6}-\frac{64}{3}l+12\left(T^2-\frac{17}{16}T+\frac{10093}{8640}\right)l^2}{\ln 2\delta-(T-\frac{1}{2})l^2}\left(\frac{M}{4}\right)^2\right]\ , \tag{3.28}$$

where $T=-\gamma-\ln(M\delta/2)$.

In the case of no magnetic field so that $M=0$ and $l=0$, (3.28) reduces simply to

$$C_{D0}=\lim_{\substack{M\to 0\\ l\to 0}}C_D{}^{\mathrm{I}}=\frac{4\pi}{\ln 2\delta-\frac{1}{4}\delta^{-2}}\ , \tag{3.29}$$

which is in perfect agreement with the result obtained previously by the present writer for the classical Stokes approximation[7].

On the other hand, for $l>1$, the integrals represented by (3.21) can be evaluated numerically by making use of Simpson's rule. The values of $A_n(l)$ ($n=0$, 1) up to $l=16$ can be found in tables of Bessel functions*. For larger values of l, we make use of the asymptotic expansion[5], which is expressed as:

$$A_n(x)=\sum_{m=0}^{p-1}\frac{\Gamma(m+\frac{1}{2})}{\Gamma(n+\frac{1}{2}-m)(\frac{1}{2}x)^{2m-n+1}}+O(x^{n-2p-1})\ . \tag{3.30}$$

Thus, the drag coefficient $C_D{}^{\mathrm{I}}$ can be evaluated numerically for any value of l.

When the bounding plane wall recedes far away to infinity from the centre of the cylinder, the value of l tends to infinity and our case is reduced to the case of a circular cylinder in an unbounded viscous and electrically conducting liquid in the presence of a parallel magnetic field. The value of M, however, should be kept to be small. Making use of (3.21) and (3.30), we easily find that

---

* See, for example, G. N. Watson: *A Treatise on the Theory of Bessel Functions* (Cambridge, 1922) 666.

$$\lim_{l\to\infty} F_n(l)\to 0 \ .$$

Thus, we have ultimately, from (3.26),

$$C_{D\infty}^{\mathrm{I}}=\lim_{l\to\infty} C_D{}^{\mathrm{I}}=\frac{8\pi}{2\Omega+1}\left\{1-\frac{4\Omega+1}{2\Omega+1}\left(\frac{M}{4}\right)^2\right\} . \tag{3.31}$$

As should be expected, (3.31) is in perfect agreement with the result obtained by Yosinobu and Kakutani for the case of no wall.

§ 4. Second Case

In the case of a transverse magnetic field, the axes of coordinates and the bounding plane wall may be taken as shown in Fig. 2. In this case also the fundamental equations (2.21), (2.22) and their solutions (2.23), (2.24) respectively, and consequently the expressions for the conjugate complex velocities represented by (2.27), hold good. However, as for the integral expressions for ψ_n's and ψ^*'s we have to take

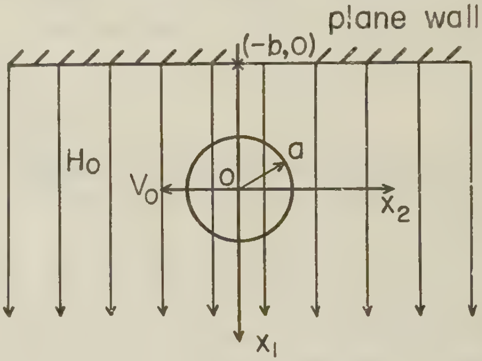

Fig. 2.

$$\psi_1=\frac{1}{2}\int_{-\infty}^{\infty}\left[\frac{1}{\lambda}A_0+\frac{1}{k}\frac{|x|}{x}A_1-i\left\{\frac{1}{\beta}\left(\frac{|x|}{x}+\frac{k}{\lambda}\right)B_0+\frac{\beta}{k\lambda}B_1\right\}\right]e^{i\beta y+kx-\lambda|x|}d\beta\ , \tag{4.1}$$

$$\psi_2=\frac{1}{2}\int_{-\infty}^{\infty}\left[\frac{1}{\lambda}C_0+\frac{1}{k}\frac{|x|}{x}C_1-i\left\{\frac{1}{\beta}\left(\frac{|x|}{x}-\frac{k}{\lambda}\right)D_0+\frac{\beta}{k\lambda}D_1\right\}\right]e^{i\beta y-kx-\lambda|x|}d\beta\ , \tag{4.2}$$

$$\psi_1{}^*=\frac{1}{2}\int_{-\infty}^{\infty}g_1(\beta)e^{i\beta y+(k-\lambda)(x+2\delta)}d\beta\ , \tag{4.3}$$

and

$$\psi_2{}^*=\frac{1}{2}\int_{-\infty}^{\infty}g_2(\beta)e^{i\beta y-(k+\lambda)(x+2\delta)}d\beta\ , \tag{4.4}$$

where $\lambda=\sqrt{\beta^2+k^2}$.

The boundary conditions to be satisfied on the bounding plane wall as well as at the surface of the cylinder are

$$(w_1+w_2+w_1{}^*+w_2{}^*)_{x=-\delta}=0\ , \tag{4.5}$$

and

$$(w_1+w_2+w_1{}^*+w_2{}^*)_{r=1}=i\ . \tag{4.6}$$

By carrying out calculations similar to those in case 1, we have

$$\left.\begin{aligned}
g_1(\beta)=&\left\{-\frac{k+\lambda}{k\lambda}A_0-i\frac{\beta}{k\lambda}B_0+\frac{k+\lambda}{k^2}A_1+i\frac{\beta(k+\lambda)}{k^2\lambda}B_1\right\}e^{-2k\delta}\\
&+\left(-\frac{1}{k}C_0-i\frac{k+\lambda}{k\beta}D_0+\frac{\lambda}{k^2}C_1+i\frac{\beta}{k^2}D_1\right),\\
g_2(\beta)=&\left(\frac{1}{k}A_0-i\frac{k-\lambda}{k\beta}B_0-\frac{\lambda}{k^2}A_1-i\frac{\beta}{k^2}B_1\right)\\
&+\left\{-\frac{k-\lambda}{k\lambda}C_0+i\frac{\beta}{k\lambda}D_0+\frac{k-\lambda}{k^2}C_1+i\frac{\beta(k-\lambda)}{k^2\lambda}D_1\right\}e^{2k\delta}\ ,
\end{aligned}\right\} \tag{4.7}$$

$$\begin{aligned} w^* = w_1^* + w_2^* = {} & ik(G_1 + k^2r^2G_2)A_0 + k(G_3 + k^2r^2G_4)B_0 + ik(G_5 + k^2r^2G_6)C_0 \\ & + k(G_7 + k^2r^2G_8)D_0 + ikG_9A_1 + kG_{10}B_1 + ikG_{11}C_1 + kG_{12}D_1 \\ & + k^2re^{-i\theta}(iG_{13}A_0 + G_{14}B_0 + iG_{15}C_0 + G_{16}D_0) \\ & + k^2re^{i\theta}(iG_{17}A_0 + G_{18}B_0 + iG_{19}C_0 + G_{20}D_0) \\ & + \cdots , \end{aligned} \tag{4.8}$$

where G_n's are functions of $l = 2k\delta$, and

$$\left.\begin{aligned} A_0 = {} & \frac{2}{M(2\Omega - 1 + G_1 - G_5)} \\ & \times \left\{1 - \frac{8\Omega + 1 + 4(G_2 - G_6) - 2(G_9 + G_{11}) - 4(G_9 - G_{11})(G_{17} - G_{19}) - 2(2\Omega - 1 - 2G_5)(G_{13} - G_{15})}{2\Omega - 1 + G_1 - G_5}\left(\frac{M}{4}\right)^2\right\} , \\ C_0 = {} & -\frac{2}{M(2\Omega - 1 + G_1 - G_5)} \\ & \times \left\{1 - \frac{8\Omega + 1 + 4(G_2 - G_6) - 2(G_9 + G_{11}) - 4(G_9 - G_{11})(G_{17} - G_{19}) + 2(2\Omega - 1 + 2G_1)(G_{13} - G_{15})}{2\Omega - 1 + G_1 - G_5}\left(\frac{M}{4}\right)^2\right\} , \\ A_1 = {} & -\frac{2(G_{17} - G_{19}) + 1}{2\Omega - 1 + G_1 - G_5}\left(\frac{M}{4}\right) , \\ C_1 = {} & \frac{2(G_{17} - G_{19}) - 1}{2\Omega - 1 + G_1 - G_5}\left(\frac{M}{4}\right) , \end{aligned}\right\} \tag{4.9}$$

$$B_0 = D_0 = 0 , \qquad B_1 = D_1 = 0 . \tag{4.10}$$

Finally, we have for the drag coefficient C_D^{II}

$$\begin{aligned} C_D^{\mathrm{II}} = \frac{D^{\mathrm{II}}}{\rho\nu V_0} = {} & \frac{8\pi}{2\Omega - 1 + G_1 - G_5} \\ & \times \left\{1 - \frac{8\Omega^2 + 4\Omega + 1 + 4\Omega(G_1 - G_5) + 4(G_2 - G_6) - 2(G_9 + G_{11}) - 2(G_1 + G_5)^2 - 4(G_9 - G_{11})^2}{2\Omega - 1 + G_1 - G_5}\left(\frac{M}{4}\right)^2\right\} \\ & + \pi(\sigma^*/\sigma)M^2 , \end{aligned} \tag{4.11}$$

where σ^* is the electric conductivity of the cylinder, and

$$\left.\begin{aligned} G_1 &= -\tfrac{1}{2}(K_0 - K_2) - \tfrac{1}{2}e^{-l}(K_0 + 2K_1 + K_2) , \\ G_2 &= -\tfrac{1}{8}(2K_0 - K_1 - 2K_2 + K_3) - \tfrac{1}{8}e^{-l}(4K_0 + 7K_1 + 4K_2 + K_3) , \\ G_5 &= \tfrac{1}{2}(K_0 - K_2) + \tfrac{1}{2}e^{l}(K_0 - 2K_1 + K_2) , \\ G_6 &= \tfrac{1}{8}(2K_0 + K_1 - 2K_2 - K_3) + \tfrac{1}{8}e^{l}(4K_0 - 7K_1 + 4K_2 - K_3) , \\ G_9 &= \tfrac{1}{4}(K_1 - K_3) + \tfrac{1}{4}e^{-l}(2K_0 + 3K_1 + 2K_2 + K_3) , \\ G_{11} &= -\tfrac{1}{4}(K_1 - K_3) + \tfrac{1}{4}e^{l}(2K_0 - 3K_1 + 2K_2 - K_3) . \end{aligned}\right\} \tag{4.12}$$

The argument l of the functions K_n's has been omitted for brevity, and the relations $G_{17} = G_9$, $G_{19} = G_{11}$ and $G_{13} - G_{15} = -(G_1 + G_5)$ have been used.

The term $\pi(\sigma^*/\sigma)$ in (4.11) arises from the Maxwell's stress, and the other terms are the contributions from the viscous stress.

In this case also no lift appears.

In the case of no magnetic field, the formula (4.11) reduces also to (3.29), the result for the classical Stokes approximation.

On the other hand, when $\delta \to \infty$ and consequently $l \to \infty$, keeping the value M small, we have

$$\lim_{l\to\infty} G_n\to 0\ ,$$

and consequently

$$C^{\mathrm{II}}_{D\infty}=\lim_{\delta\to\infty} C_D{}^{\mathrm{II}}=\frac{8\pi}{2\Omega-1}\left\{1-\frac{8\Omega^2+4\Omega+1}{2\Omega-1}\left(\frac{M}{4}\right)^2\right\}+\pi\left(\frac{\sigma^*}{\sigma}\right)M^2\ , \tag{4.13}$$

which is in perfect agreement with the result obtained by Yosinobu and Kakutani for the corresponding case.

Table I. Values of $C_D{}^{\mathrm{I}}$.

	By (3.29)	By (3.26)						
δ \ M	0	0.001	0.005	0.01	0.05	0.1	0.5	1
5	5.48	5.48	5.49	5.50	5.67	5.97	8.62	11.31
10	4.20	4.20	4.21	4.23	4.49	4.88	7.39	9.94
50	2.73	2.73	2.78	2.85	3.40	3.86	6.35	8.87
100	2.37	2.38	2.46	2.58	3.18	3.67	6.23	8.75
By (3.30)		1.53	1.90	2.12	2.92	3.48	6.10	8.63

Table II. Values of $C_D{}^{\mathrm{II}}$.

	By (3.29)	By (4.11)					
δ \ M	0	0.001	0.005	0.01	0.05	0.1	0.5
5	5.48	5.48	5.49	5.50	5.74	6.19	10.84
10	4.20	4.20	4.21	4.24	4.64	5.30	10.37
50	2.73	2.73	2.80	2.91	3.89	4.82	10.11
100	2.37	2.38	2.51	2.70	3.83	4.78	10.10
By (4.13)		1.74	2.24	2.56	3.79	4.76	10.09

§ 5. Numerical Discussions

The values of the drag coefficient $C_D{}^{\mathrm{I}}$ have been calculated numerically by using (3.26), as was mentioned in § 3, for various values of the Hartmann number M up to unity as well as for various values ranging from 5 to 100 of the ratio $\delta=b/a$. They are given in Table I and are also plotted in Fig. 3 against M.

The values of $C_D{}^{\mathrm{II}}$ have been calculated by using (4.11) for various values of M up to 0.5 as well as for various values ranging from 5 to 100 of the ratio δ, where we have put $\sigma^*=0$ for simplicity. They are tabulated in Table II and are shown graphically in Fig. 3.

For the sake of reference, the values of $C^{\mathrm{I}}_{D\infty}$ and $C^{\mathrm{II}}_{D\infty}$ have been computed by (3.31) and (4.13) respectively. The results are also given in the corresponding tables, and are shown in Fig. 3.

It is worth noticing that, as can be seen from Tables I, II and Fig. 3, the drag co-

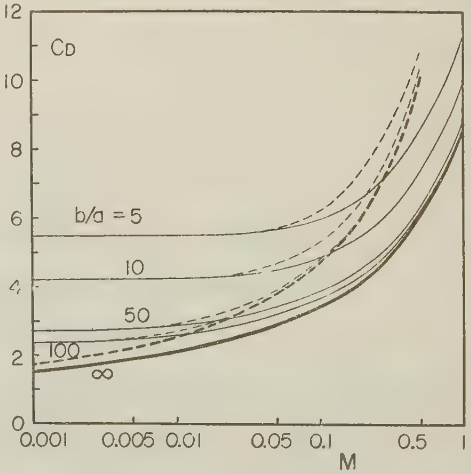

Fig. 3. Drag coefficients *versus* Hartmann number.

—— $C_D{}^{\mathrm{I}}$ calculated by (3.26)

━━ $C^{\mathrm{I}}_{D\infty}$ calculated by (3.31)

- - - - - $C_D{}^{\mathrm{II}}$ calculated by (4.11)

- - - - - $C^{\mathrm{II}}_{D\infty}$ calculated by (4.13) efficients $C_D{}^{\mathrm{I}}$ and $C_D{}^{\mathrm{II}}$ are, for small values of the Hartmann number M, almost independent of M, and consequently they are equal to each other and are also equal to that obtained by the classical Stokes approximation.

Acknowledgement

The writer wishes to express his cordial thanks to Professor S. Tomotika for his continual guidance and also for his kind inspection of the manuscript. The writer's thanks are also due to the Ministry of Education for a grant-in-aid for fundamental scientific researches.

References

1) H. Yosinobu and T. Kakutani: J. Phys. Soc. Japan **14** (1959) 1433.
2) W. Chester: J. Fluid Mech. **3** (1957) 304.
3) H. Faxén: Diss. Uppsala (1921).
4) Y. Takaisi: J. Phys. Soc. Japan **10** (1955) 407.
5) G. N. Watson: *A Treatise on the Theory of Bessel Functions* (Cambridge, 1922).
6) A. Erdélyi: *Tables of Integral Transforms, Vol. I* (McGraw-Hill Book Co., Inc., 1954) 138.
7) Y. Takaisi: J. Phys. Soc. Japan **11** (1956) 1004.

JOURNAL OF THE PHYSICAL SOCIETY OF JAPAN, Vol. 15, No. 10, OCTOBER, 1960

Glass Transition Phenomena and Rheological Properties of Petroleum Asphalt

By Yasaku WADA and Hidenori HIROSE

Department of Applied Physics, Faculty of Engineering, University of Tokyo, Bunkyo-ku, Tokyo, Japan

(Received May 23, 1960)

Volume dilatometry was made for nine kinds of asphalt in a wide range of asphaltene content X. The glass transition temperature T_g becomes higher with increase of X. The discontinuity in thermal expansion coefficient at T_g decreases with X and T_g can no more be observed for $X>70\%$.

The complex shear modulus and shear creep compliance of five samples of asphalt were measured. Above T_g, asphalt is viscoelastic. The temperature-time reducibility applies very well to asphalt. The temperature dependence of retardation times as well as steady flow viscosity obeys to Williams-Landel-Ferry's equation, the standard temperature involved in this equation being 56° higher than T_g for all the samples. The distribution function of retardation times is approximately of a wedge shape when plotted in logarithmic scales, the slope being 0.5 or less according to X. The steady flow viscosity and the maximum retardation time reduced to 20°C markedly increase with X.

These facts allow us some predictions about molecular behaviors in asphalt.

§ 1. Introduction

Asphalts are the highly viscous residue of petroleum obtained by removing most of its volatile components. The elimination of volatile components is often combined with chemical treatment, chiefly oxidation. This treatment is carried out by blowing air through a distilation residue. In this case the products are distinguished by the name "blown asphalt", whereas those prepared by distilation only are called "straight asphalt".

Asphalts are mainly used in protective coatings and as binding materials especially in road constructions. Their suitability for these uses accordingly is largely dependent on their rheological properties. Besides, asphalts are widely used as a material of a polishing disk in glass polishing practice. In this application the rheological properties of asphalts play a particularly important role and for a correct judgement of their suitability, therefore, a thorough knowledge of these properties is indispensable. In fact, the present research has started from this standpoint.

Not a few investigations on the rheological properties of asphalts have so far been carried out by many authors and have been summarized in some reviews.[1-2] In this paper, a more systematic study of rheological properties as well as glass transition phenomena of several kinds of asphalt will be presented. The scheme of the present approach is based on the method which has been developed by Tobolsky, Ferry and many others and found to be very effective in studying the linear viscoelasticity of amorphous polymers.

§ 2. Samples

Asphalt is a mixture of hydrocarbons and compounds of a predominantly hydrocarbon character. Most asphalts contain high-molecular components ("asphaltenes"), which may be precipitated as a solid by diluting the asphalt with low-boiling saturated hydrocarbons. The remaining part is a highly viscous oil of low-molecular weight ("maltenes"). Blown asphalts are richer in asphaltene content than straight asphalts. The elementary analysis reveals[3] that asphaltenes have high carbon/hydrogen ratio, so are rich in cyclic hydrocarbons. On the other hand, maltenes have low carbon/hydrogen ratio and accordingly are rich in linear hydrocarbons.

Nine kinds of samples are used in this investigation (see Table 1). Five samples, C through G, are blown asphalts manufactured for the use of lens polishing. The sample H is a straight asphalt. The content of asphaltenes in these samples was determined by the following procedures: One gram of a sample is completely dissolved in 10 cc of benzene, the solution is added by 50 cc of acetone and leaved at 25°C for one day, then the precipitate is filtered through a filter paper and weighed. The samples A and I are pure asphaltenes and maltenes respectively, being separated from the sample E by the above procedures. The sample B is a mixture of A and I in a weight ratio of 3:1.

In the experiments described in later sections, samples are moulded in suitable forms. In the process of moulding, care must be taken not to overheat the sample in order to prevent it from thermal decomposition. The moulded specimens are leaved in warm water so as to become free from any residual stress.

§ 3. Volume dilatometry

In Table I is given the density of the samples at 20°C measured by the Archimedes method. The density increases with asphaltene content.

Table I.

Sample	Asphaltene (wt. %)	Density (20°C) (g/cc)	Glass transition temp. (°C)	Thermal expansion coeff. (10^{-4}/deg) above T_g	below T_g	difference
A	100	1.079	none			
B	75	1.053	none			
C	61.9	1.039	2	5.8	3.7	2.1
D	58.6	1.034	0	6.0	3.8	2.2
E	57.1	1.030	− 2	6.3	4.0	2.3
F	52.5	1.027	− 6.5	6.6	3.9	2.7
G	50.8	1.026	− 7.5	6.8	3.9	2.9
H	28.6	1.014	−22.5	6.9	3.7	3.2
I	0	1.004	−37.5	7.6	3.4	4.2

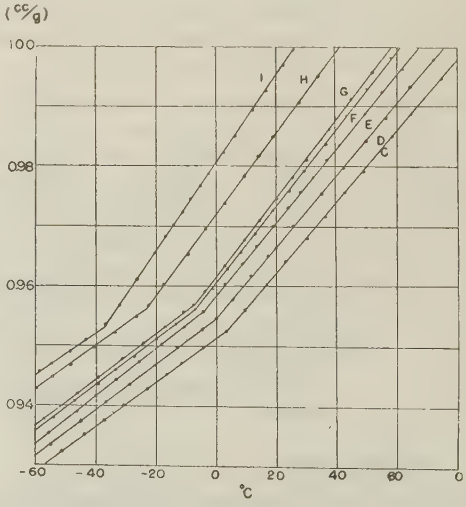

Fig. 1. Cubical thermal expansion of seven kinds of asphalt.

The volume dilatometry was carried out for all the samples. Cubical thermal expansion was determined by placing a specimen in the bulb of a Pyrex-glass dilatometer, surounding it with silicone oil and reading the evel of the oil in the capillary of the dilatoneter as the temperature was lowered. The volume of the dilatomerter bulb was 7.04 cc and the radius of the capillary was 0.633 mm. The temperature range of observation was from 110 down to −60°C and the cooling rate was about 20°C/hour.

The volume-temperature relation of all the samples except A and B shows distinctly a break at a specified temperature, that is, the specific volume continuously varies with temperature, but its slope (thermal expansion coefficient) suddenly decreases below this temperature (Fig. 1). This type of behavior is very widely observed at the glass transition temperature of amorphous polymers and other glass-forming substances. In the case of asphalt also, therefore, the break probably corresponds to the glass transition temperature. In this connection a more positive and convincing discussion will later be given from rheological study.

Anyway, it is clear that the glass transition temperature, so we call here hypothetically, becomes higher with increase of asphaltene content, as is plotted in Fig. 2. Furthermore, one sees that the difference of thermal coefficients above and below the transition temperature, which primarily reflects the "strength" of the transition, decreases with increase of asphaltenes (see Fig. 2) and for the samples A and B, the transition can no more be observed.

The above-mentioned facts suggest some pictures about the glass transition of asphalts. In the transition, linear hydrocarbons, the major component of maltenes, may play a principal role, whereas cyclic hydrocarbons in asphaltenes may have rather a negative influence upon the transition. These considerations will further be discussed and confirmed in the later sections from rheological behaviors above the transition temperature.

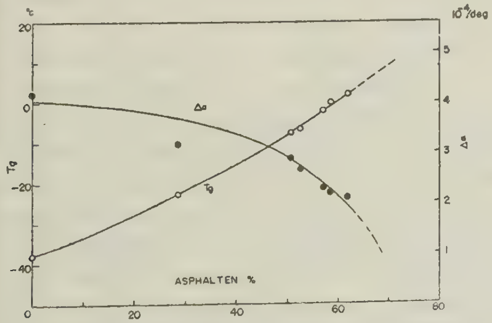

Fig. 2. Glass transition temperature T_g (circle) and difference of thermal expansion coefficient above and below T_g (dot) plotted against asphaltene content.

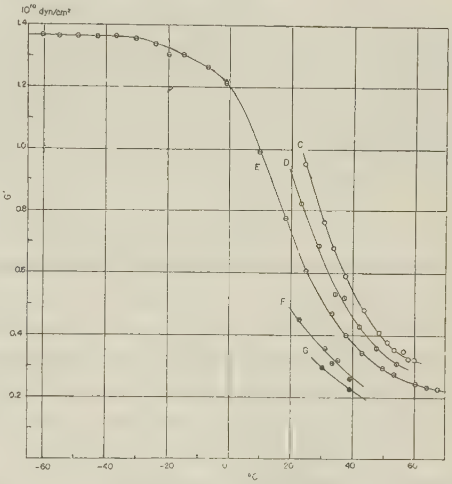

Fig. 3. Real part of complex shear modulus at 33 kc/s *versus* temperature.

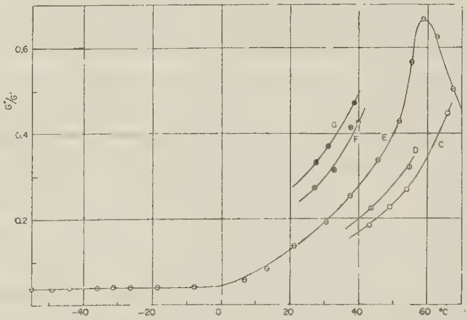

Fig. 4. Loss factor at 33 kc/s *versus* temperature.

§ 4. Complex rigidity of asphalts

The real and imaginary part of complex rigidity were measured at 33 kc/s for samples C through G by means of the composite oscillator method. The details of experimental procedures have been described in a previous paper.[4]

The data are plotted in Figs. 3 & 4, giving typical temperature dispersion curves above the glass transition temperature. One sees in the case of sample E that the storage modulus G′ begins to descend at the transition temperature (−2°C) and, on the other hand, the loss factor G″/G′ begins to rise at this temperature, reaching a maximum at 58°C. The temperature of maximum loss seems to become higher for samples of higher asphaltene content.

No values, according to the authors, have yet been published on the dynamic mechanical properties of asphalt at high frequencies before this work. Dielectric dispersion at frequencies from 50 up to 2×10^6 c/s observed by Saal[5] can only be compared with our data. The temperature region of dispersion observed in both the works very well agrees with each other, when compared at the same frequency.

§ 5. Shear creep compliance measurements

The dynamic test described in the previous section has shown that asphalt is a socalled viscoelastic body. In order to see the overall features of viscoelasticity, it is indispensable to investigate the mechanical properties in as wide a range of times as possible. For this purpose the torsional creep experiment of a specimen in shape of a circular rod was carried out in the present study.

The test specimen was 2.0 cm in length and 0.57 cm in diameter. One end of the specimen was clamped by a fixed chuck, the other end was attached to a rotative chuck which was supported by a ball-bearing. A circular disk of 5.8 cm diameter was fixed to the rotating axis and the torque was applied to the specimen by suspending a weight at the lower end of the thread which was wound around the disk. A small mirror was attached to the disk and the angle of torsion of the specimen after loading was read by a scale and telescope. The whole equipment was set in an air thermostat, whose temperature was regulated within one tenth degree during one run of experiment.

A preliminary test was first made for experimental verification of the proportionality between stress and strain. The curves in Fig. 5 show the plot of torsional deformation for different loads at each time after loading. From the curves we see that, in the measured range of strain at least, the linear relationship between stress and strain holds very well for asphalt. All the experiments in the following, therefore, were made at a constant torque, using a weight of 20 g.

Besides, Fig. 5 gives us another important knowledge. All the straight lines in the figure fall on one point on the abscissa, corresponding to the load of 2.3 g. This value means the frictional force of the bearing, thus the net weight imposed on the specimen was 17.7 g throughout the following study.

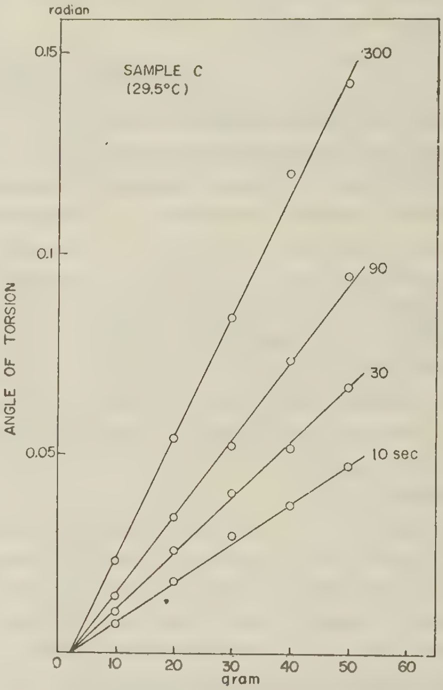

Fig. 5. Torsional creep deformation of sample C for different loads at 29.5°C.

Assuming the linear relationship between stress and strain, the shear creep compliance as a function of time was calculated by

$$J(t)=\frac{\pi r^4}{2l}\cdot\frac{\theta(t)}{N}, \qquad (1)$$

where r and l are the radius and length of the specimen respectively, N the torque, θ the angle of torsion.

Following the above-mentioned procedures, the creep compliance of five samples, C through G, was measured at several temperatures from just above the transition temperature up to about 40°C. The angle of torsion was read from 5 sec to 10 min after loading at appropriate intervals. Fig. 6 illustrates an example of the data over the logarithmic time scale.

In many of the previous investigations on the viscoelasticity of amorphous substances the principle of time-temperature reducibility,[6] developed by Tobolsky, Ferry etc., has been very successfully employed. This principle is founded on the basis that all the retardation times as well as the steady flow viscosity have the same temperature dependence. In the present case also, the creep curves at different temperatures obey very well to this principle. Namely, one can superimpose these curves by a horizontal shift, thus providing a single master curve reduced to an arbitrary reference temperature.

Fig. 7 is the master curve for the sample E reduced to 18°C, the reduced time scale extending from 10^{-3} to 10^{6} sec. In carrying out this reduction, the vertical shift of $J(t)$ was neglected in our case, because, since the temperature range of the data is rather narrow, the vertical shift $T\rho/T_0\rho_0$ would modify only slightly the result and, moreover, the physical meaning of the vertical shift is not *a priori* endent for the asphalt, whose molecular structure is not well understood.

§ 6. Temperature dependence function and activation energy

In the process of determining the master creep curve, the shift factor a_T was evaluated from the amount by which the creep curve at a temperature T was horizontally shifted so as to fit the curve at a reference temperature T_0. Fig. 8 shows the relation between log a_T and temperature for the five samples, T_0 being taken as 20°C.

Since a_T is the factor by which all the re-

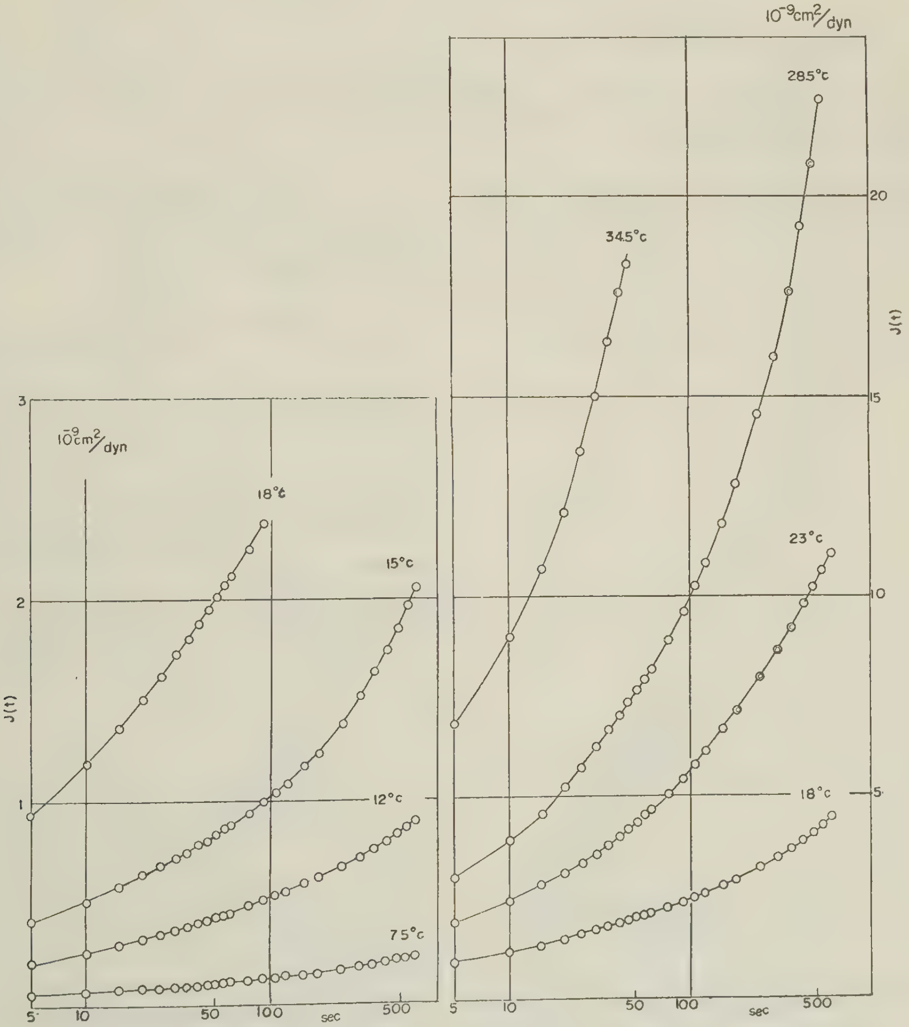

Fig. 6. Creep compliance curves for sample E. Curves below and above 18°C are separately illustrated.

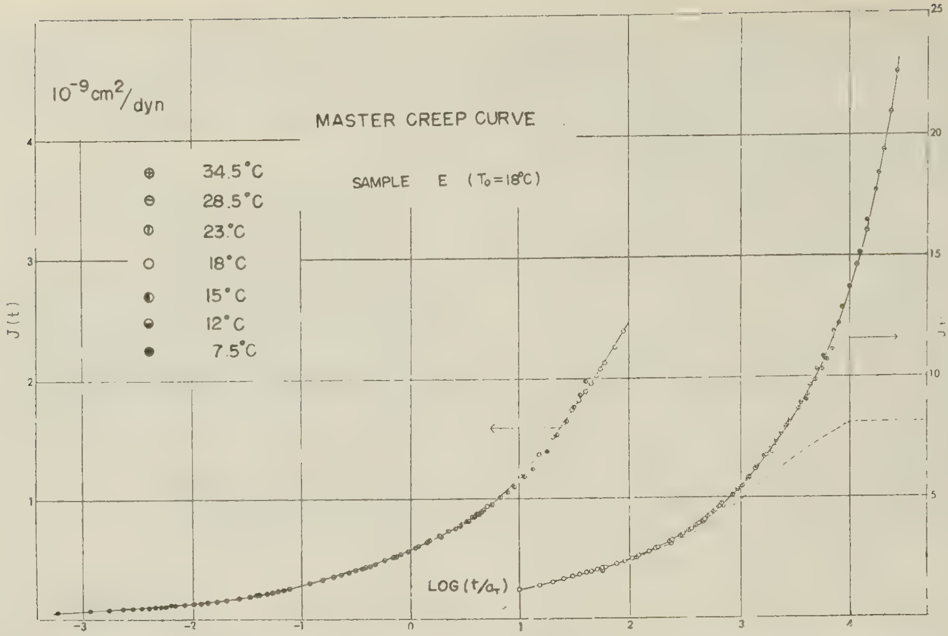

Fig. 7. Master creep compliance for sample E reduced to 18°C, plotted against reduced time (sec). Curve is divided into two portions, each illustrated in different scales. Broken line represents elastic compliance.

tardation times as well as viscosity change when the temperature is changed from T_0 to T, the apparent activation energy H can be expressed by $a_T \infty \exp(H/RT)$, so is calculated by the equation:

$$H = 2.30\,R\,\frac{d(\log a_T)}{d\left(\frac{1}{T}\right)}, \qquad (2)$$

where R is the gas constant and T is absolute temperature. This quantity is plotted in Fig. 9.

Williams, Landel and Ferry have found[7)] that, when the shift factor is reduced to the standard temperature T_s which must be suitably chosen for each substance, the following equation holds to all glass-forming subs-

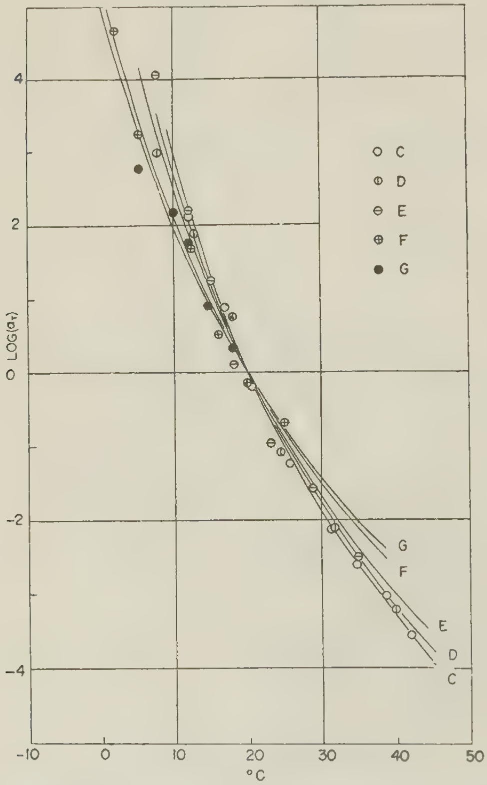

Fig. 8. Shift factor a_T reduced to 20°C for five samples.

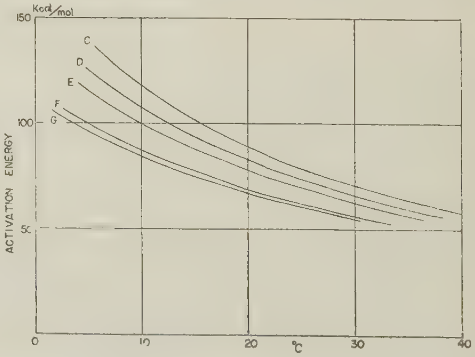

Fig. 9. Apparent activation energy plotted against temperature.

tances ever studied:

$$\log a_T = \frac{-8.86(T-T_s)}{101.6+(T-T_s)} . \qquad (3)$$

Moreover, according to them, T_s is always about 50° higher than the glass transition temperature.

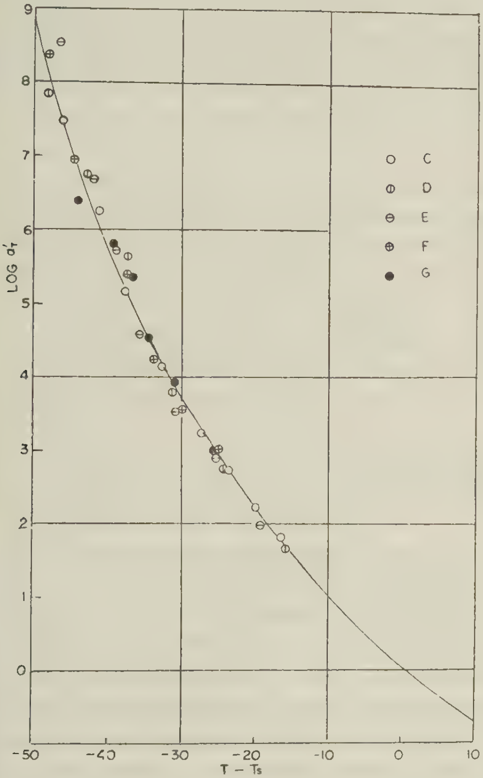

Fig. 10. Temperature dependence of shift factor reduced to standard temperature T_s, which is 56° higher than T_g. Solid line represents Williams-Landel-Ferry's equation.

Fig. 10 shows that Eq. (3) applies very well to asphalt also. T_s was determined by the following procedures: An experimental plot of log a_T (for arbitrary reference temperature) against T is matched to the plot of Eq. (3) with horizontal and vertical translations, using transparent paper, for the best coincidence in shape. T_s can be determined in this manner within ±1°C. The values of T_s thus obtained are listed in Table II. It must be realized that T_s is 56° higher than T_g in Table I for all the samples. This fact offers a clear evidence to the prediction referred in § 3 that the break found in volume-temperature curves should correspond to the glass transition temperature.

§ 7. Steady flow viscosity

The master creep curve, an example of which is shown in Fig. 7, has a linear portion for large values of time when plotted over not logarithmic, but linear time scale (see Fig. 11). Since in this time interval the increase of deformation is only ascribed to viscous flow, the slope of this linear portion is equal to the reciprocal of viscosity. In Table III the viscosity at 20°C is evaluated from the master curves. Viscosities at other temperatures can be obtained from $\eta(T)=\eta(20°\text{C})\,a_T$, using a_T given in Fig. 8. As far as Eq. (3) can be applied, $\eta(T)$ can also be expressed by

Table II.

Sample	T_s(°C)	T_s-T_g
C	58.5	56.5
D	56	56
E	54	56
F	50	56.5
G	49	56.5

Table III. Steady flow viscosity (poise).

Sample	log η(20°C)	Observed viscosity at elevated temperature log η(°C)	Calculated viscosity from Eq. (4) log η(°C)
C	13.15	4.88 (114)	4.64 (114)
D	12.70	4.44 (117)	4.53 (117)
E	12.10	4.02 (110)	4.48 (110)
F	10.45	3.75 (104)	3.65 (104)
G	9.69	3.60 (97)	3.31 (97)

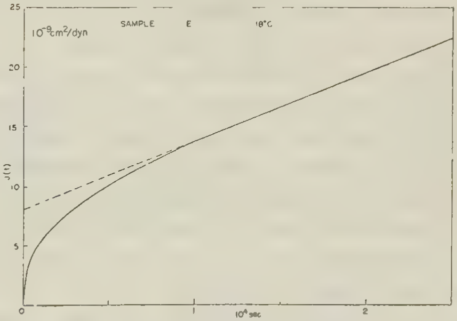

Fig. 11. Master creep compliance for sample E reduced to 18°C plotted in linear time scale.

$$\log \eta(T)=\log \eta(T_s)-\frac{8.86(T-T_s)}{101.6+(T-T_s)}$$
$$=\log \eta(20^\circ\mathrm{C})+\frac{8.86(20-T_s)}{101.6+(20-T_s)}$$
$$-\frac{8.86(T-T_s)}{101.6+(T-T_s)}. \qquad (4)$$

For many glass-forming substances, Eq. (3) has been found approximately valid up to 100 degrees above T_g.[7] This is also the case with asphalt. In Table III the viscosity at elevated temperature, observed by a capillary viscometer, is listed. In this experiment the rate of shear was so small that non-newtonian behaviors were not observed. This values are in fairly good agreement with the calculated ones (see the fourth column in Table 3) from $\eta(20^\circ\mathrm{C})$ using Eq. (4). The agreement is rather surprising, considering that the calculated viscosity is extrapolated from that at 20°C which is higher than the former by the factor of $10^6 \sim 10^9$.

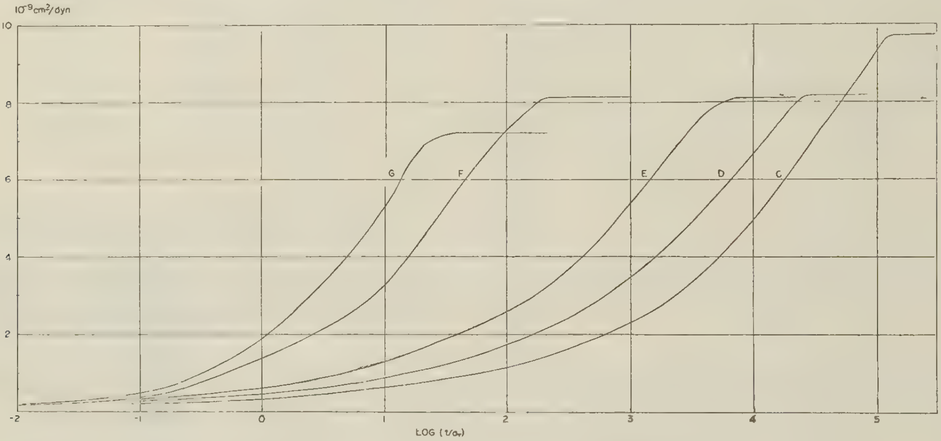

Fig. 12. Elastic compliance reduced to 20°C plotted against reduced time (sec).

§ 8. Retarded elasticity and distribution of retardation times

By substracting viscous flow (t/η) from creep compliance, elastic deformation can be separated out. Since instantaneous elastic compliance is estimated to be less than 10^{-10} cm²/dyn from the rigidity below T_g (see Fig. 3) and gives only a negligible contribution to the total compliance, the elastic part is nearly wholly ascribed to retarded elasticity. This was also experimentally verified by recovery test after creep.

The elastic compliance $J_e(t)$ reduced to 20°C is shown in Fig. 12 for the five samples. Equilibrium elastic compliance $J_e(\infty)$ is about 8×10^{-9} cm²/dyn. From the shape of the curves one sees that they can be expressed by not a single, but multiple retardation times. The distribution function of retardation times can be calculated in a first approximation by the following formula:[8]

$$L(\log \lambda)=0.434\left[\frac{d\,J_e(t)}{d\log t}\right]_{t=\lambda}. \qquad (5)$$

The function $L(\log \lambda)$ reduced to 20°C is illustrated in Fig. 13 in logarithmic scales.

As is readily seen, the function for all the samples is of a wedge shape, that is, log L linearly increases with log λ up to the maximum retardation time and suddenly falls off. The slope of wedge is 0.5 for F and G, and less for C, D and E. It must be noticed here that the distribution function of a wedge

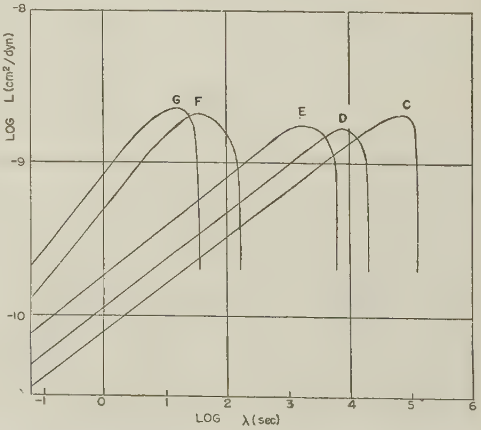

Fig. 13. Distribution function of retardation times reduced to 20°C.

shape is widely observed for linear amorphous polymers above glass transition temperature.[9]

§ 9. Discussions

Summarizing the results, it follows:

(1) Asphalt exhibits glass transition temperature T_g. T_g becomes higher with increase of asphaltene content X. The intensity of transition decreases with increase of X and the transition disappears for X more than 70%.

(2) Above T_g asphalt is viscoelastic. Dynamic loss peak is observed in this region. The temperature of maximum loss becomes higher with increase of X.

(3) The temperature dependence of steady flow viscosity as well as retardation times obeys Williams-Landel-Ferry's equation, when the standard temperature is taken 56° higher than T_g.

(4) The viscosity and maximum retardation time at a given temperature, say at 20°C, markedly increase with X.

(5) The equilibrium elastic compliance and peak intensity of distribution function of retardation times are rather insensitive to X, being about 8×10^{-9} cm²/dyn and 2×10^{-9} cm²/dyn respectively.

(6) The distribution function of retardation times are, when plotted in logarithmic scales, of a wedge shape, the slope being 0.5 for the samples of low X, but less for high X.

From all of these experimental facts, we may deduce some conclusions about the molecular structures of asphalt. From the above facts we can safely conclude that linear hydrocarbons, the major component of maltenes, play the chief role in the glass transition and the mechanical dispersion phenomena accompanied with it, whereas cyclic molecules in asphaltenes perhaps may have rather hindering effect on the brownian motion of linear molecules.

A recent theory of Rouse[10] for the viscoelastic properties of isolated chain molecules predicts that the distribution function of retardation times should be of a wedge shape with the slope of 0.5. The same slope is predicted for a network chain structure from the extension of this theory.[11] In fact, all the amorphous linear polymers have the distribution function of this type above T_g. Since the same behavior is observed in the present case, it may be reasonably said that linear molecules in asphalt form a network structure and the retarded elasticity may be ascribed to microbrownian motions of chain segments between temporary crosslinking points.

A remark, however, must be here noted. Strictly speaking, since the average molecular weight of asphalt is several hundreds[3], molecules in asphalt can only approximately form such a network assumed in the Rouse theory, in which a chain is considered to consist of many submolecules, portions of polymer chain long enough for the separation of their ends to approximate a Gaussian probability distribution. But it may not be unreasonable, as a first step of approach, to assume a network structure in asphalt.

Cyclic molecules may get in the space among the network and disturb its thermal motion. It is not impossible to assume, according to many colloid-chemical studies of asphalt,[3] that cyclic molecules may be in an associated state. Of course, some of the cyclic molecules may form the network together with linear molecules and increase the stiffness of chain.

According to the statistical theory[12] of a network structure, equilibrium elastic compliance $J_e(\infty)$ is written as

$$J_e(\infty)=\frac{M}{\rho RT}\,, \tag{6}$$

where M is the molecular weight of a chain segment between two crosslinks, ρ the density of segment, R the gas constant, T the absolute temperature. Using the observed value of $J_e(\infty)=8\times10^{-9}$ cm²/dyn and assuming $\rho=0.5$ g/cc (ρ is not the density of asphalt as a whole, but of network-forming components only), we get $M=100$. This value is very reasonable compared with the average molecular weight of asphalt.

In conclusion, it is to be hoped that a knowledge of not only viscoelastic properties, but also dielectric dispersion, nuclear magnetic resonance etc. might allow a more precise picture of molecular behaviors in asphalt.

§ 10. Acknowledgements

This work is part of a program of research on the lens polishing supported by the Japan Camera Research Association. The authors are grateful to the members of the Research Group of Lens Polishing in this association for their valuable discussions. The authors also wish to express their gratitude to Mr. S. Sakanoue at the Public Works Research Institute and Dr. S. Iwayanagi and other members at the Polymer Physics Laboratory in the Institute of Physical and Chemical Research for their helpful suggestions.

References

1) J. Ph. Pfeiffer, editor: The Properties of Asphaltic Bitumen (Elsevier Publishing Co. 1950) pp. 49–76.
2) F. R. Eirich, editor: Rheology vol. 2 (Academic Press Inc. 1958) pp. 363–400.
3) J. Ph. Pfeiffer: loc. cit. pp. 13–48.
4) Y. Wada, H. Hirose, T. Asano & S. Fukutomi: J. Phys. Soc. Japan **14** (1959) 1064–1072.
5) J. Ph. Pfeiffer: loc. cit. p. 103.
6) see, for example, F. R. Eirich: loc. cit. pp. 63–70.
7) M. L. Williams, R. F. Landel & J. D. Ferry: J. Am. Chem. Soc. **77** (1955) 3701–3707.
8) see, for example, F. R. Eirich: loc. cit. pp. 467–470.
9) R. S. Marvin: Proc. 2nd Intern. Congr. Rheol. (1954) 156–163.
10) P. E. Rouse, Jr.: J. Chem. Phys. **21** (1953) 1272–1280.
11) J. D. Ferry, R. F. Landel & M. L. Williams: J. Appl. Phys. **26** (1955) 359–362.
12) see, for example, H. Mark & A. V. Tobolsky: Physical Chemistry of High Polymeric Systems (1950) pp. 324–331.

JOURNAL OF THE PHYSICAL SOCIETY OF JAPAN, Vol. 15, No. 10, OCTOBER, 1960

On the Flow of An Electrically Conducting Fluid Near An Accelerated Plate in the Presence of a Magnetic Field

By A. S. GUPTA

Department of Applied Mathematics, Indian Institute of Technology, Kharagpur, India.

(Received May 17, 1960)

The flow of an electrically conducting viscous incompressible fluid due to uniformly accelerated motion of an infinite flat plate is discussed. A uniform magnetic field fixed relative to the fluid is supposed to be present. It is found that when the induced field is negligible compared to the imposed field, velocity at any point and at any instant decreases with the increase in the magnetic field strength. It is further shown that the increase in magnetic field results in an increase in the drag suffered by the plate.

§ 1. Introduction

The magnetohydrodynamics of the flow of a viscous, incompressible and electrically conducting fluid in the presence of an external magnetic field due to the impulsive motion of an infinite flat plate has been discussed by Rossow[1)]. Recently Ong and Nicholls[2)] have extended the problem to cover the case of the flow near an infinite wall which executes simple harmonic motion parallel to itself. In both the problems, however, the induced magnetic field produced by the current has been neglected. Kakutani[3)] has included this induced field while considering the flow of a hydromagnetic fluid in the presence of an oscillating flat plate.

In this paper the flow of an electrically conducting viscous incompressible fluid due to the accelerated motion of an infinite flat plate in the presence of a uniform magnetic field is discussed. The induced magnetic field is neglected as in the case of previous workers. The velocity profile is found in the case when the magnetic lines of force are fixed relative to the fluid and finally the skin friction is calculated.

§ 2. Basic Equations and their Solutions.

Let x denote the coordinate parallel to the direction of motion of the plate and y the coordinate perpendicular to it. At time $t<0$, the fluid and the plate are assumed to be at rest. The plate starts moving at $t=0$. A uniform magnetic field B_0 fixed relative to the fluid is acting along y-axis. The equations of hydromagnetics are:

a) Maxwell's equations (neglecting displacement current)

$$\text{Curl}\,\vec{H}=4\pi\vec{j} \qquad (1)$$

$$\text{Curl}\,\vec{E}=-\frac{\partial\vec{B}}{\partial t} \qquad (2)$$

$$\text{div}\,\vec{B}=0 \qquad (3)$$

$$\vec{B}=\mu_e\vec{H} \qquad (4)$$

b) Ohm's law:

$$\vec{B}=\mu_e\vec{H} \qquad (5)$$

c) The equation of continuity for the fluid:

$$\text{div}\,\vec{q}=0 \qquad (6)$$

d) The modified Navier-Stokes equation:

$$\frac{\partial\vec{q}}{\partial t}+(\vec{q}\cdot\text{grad})\vec{q}=-\frac{1}{\rho}\,\text{grad}\,\rho+\nu\nabla^2\vec{q}+\frac{1}{\rho}\,\vec{j}\times\vec{B} \qquad (7)$$

Where $\vec{E}$ is the electric field, $\vec{B}$ the electromagnetic induction, $\vec{H}$ the magnetic field, μ_e the magnetic permeability, σ the electrical conductivity, $\vec{q}$ the velocity of the fluid. All electromagnetic quantities are measured in electromagnetic units.

In the present problem it is assumed following Meyer[4)] that no applied or polarization voltages exist. i.e., $\vec{E}=0$. This then corresponds to the case where no energy is being added or extracted from the fluid by the electrical means. The magnetic effects are confined to retarding the flow and dissipating energy of motion into heat. Since the plate is infinite, the physical variables will depend on y (the distance from the plate) and t only. Hence if $\vec{q}\equiv(u, v)$ eqn. (6) gives $\partial v/\partial y=0$. This by virtue of the fact that $v=0$ at the plate, gives

$$v=0 \qquad (8)$$

everywhere.

In general, the electrical current flowing in the fluid gives rise to an induced magnetic field which distorts the applied magnetic field, which would exist if the fluid were an electrical insulator. However, since the viscous boundary layer is thin and thermally ionized air is at best a poor electrical conductor it is permissible to neglect the induced field compared to the applied field acting along y-axis. This permits the following simplification for $\vec{B}\equiv(B_x, B_y)$:

$$B_x=0;\quad B_y=\text{Constant}=B_0 \qquad (9)$$

These clearly satisfy eqn. (3). Using eqn. (5) (with $\vec{E}=0$), (8) and (9), the ponderomotive force $\vec{F}=\vec{j}\times\vec{B}/\rho$ in (7) will have the following components

$$F_x=\frac{-\sigma B_0{}^2u}{\rho};\quad F_y=0 \qquad (10)$$

Eqn. (7) now gives with $\vec{q}=(u(y,t), 0)$,

$$\frac{\partial u}{\partial t}=\nu\frac{\partial^2u}{\partial y^2}-\frac{\sigma B_0{}^2u}{\rho} \qquad (11)$$

$$0=-\frac{1}{\rho}\frac{\partial p}{\partial y} \qquad (12)$$

Eqn. (12) gives

$$p=\text{constant} \qquad (13)$$

Eqn. (11) is to be solved subject to the following conditions:

$$u=0 \text{ everywhere for } t<0 \qquad (14)$$

$$\left.\begin{array}{l} u=At^n \text{ at } y=0,\quad t>0 \\ u=0 \text{ or finite at } y=\infty,\quad t>0 \end{array}\right\} \qquad (15)$$

The Laplace transform of (11) with respect to t together with eqn. (14), gives

$$\nu\frac{d^2\bar{u}}{dy^2}-(p+m)\bar{u}=0 \qquad (16)$$

where

$$\bar{u}=\int_0^\infty u(y_1t)e^{-pt}dt,\quad (p>0);\quad m=\frac{\sigma B_0{}^2}{\rho}. \qquad (17)$$

The solution of (16) is

$$\bar{u}=C_1\exp\left[-y\{(p+m)/\nu\}^{1/2}\right]+C_2\exp\left[y\{(p+m)/\nu\}^{1/2}\right] \qquad (18)$$

Eqn. (15) gives

$$\bar{u}=\frac{A\Gamma(n+1)}{p^{n+1}} \text{ at } y=0$$

and $u=0$ or finite at $y=\infty$

Using these conditions, eqn. (18) gives

$$\bar{u}=\frac{A\Gamma(n+1)}{p^{n+1}}\exp\left[-y\{(p+m)/\nu\}^{1/2}\right] \tag{19}$$

Hence

$$u(y,t)=\frac{1}{2\pi i}\int_{c-i\infty}^{c+i\infty}e^{pt}\,\bar{u}(y,p)dp$$

$$=\frac{A\Gamma(n+1)}{2\pi i}\int_{c-i\infty}^{c+i\infty}\frac{e^{pt}}{p^{n+1}}\cdot\exp\left[-y\{(p+m)/\nu\}^{1/2}\right]dp \tag{20}$$

For a uniformly accelerated plate $n=1$, so that eqn. (20) gives

$$u(y,t)=\frac{A}{2\pi i}\int_{c-i\infty}^{c+i\infty}\frac{e^{pt-b\sqrt{p+a^2}}}{p^2}dp \tag{21}$$

where

$$b=\frac{y}{\sqrt{\nu}};\quad a^2=m \tag{22}$$

Putting $p+a^2=v^2$, eqn. (21) gives

$$u(y,t)=\frac{Ae^{-a^2t}}{\pi i}\int_{Br_3}\frac{e^{v^2t-bv}}{(v^2-a^2)^2}v\,dv$$

$$=\frac{Ae^{-a^2t}}{\pi i}\,\frac{1}{4a}\int_{Br_3}e^{v^2t-bv}\left[\frac{1}{(v-a)^2}-\frac{1}{(v+a)^2}\right]dv, \tag{23}$$

where Br_3 is the Bromwich path defined in McLachlahn[5].

Integrating along Br_3, we have

$$\frac{1}{\pi i}\int_{Br_3}\frac{e^{v^2t-bv}}{v-a}dv=e^{a^2t-ab}\,.\ \operatorname{erfc}\frac{b-2at}{2\sqrt{t}} \tag{24}$$

and

$$\frac{1}{\pi i}\int_{Br_3}\frac{e^{v^2t-bv}}{v+a}dv=e^{a^2t+ab}\,.\ \operatorname{erfc}\frac{b+2at}{2\sqrt{t}}. \tag{25}$$

Differentiating equns. (24) and (25) with respect to a under integral sign and substituting in (23), we get

$$u(y,t)=\frac{A}{4a}\Bigg[e^{-ab}\left\{(2at-b)\operatorname{erfc}\frac{b-2at}{2\sqrt{t}}+2\sqrt{\frac{t}{\pi}}\,.\ e^{-\frac{(b-2at)^2}{4t}}\right\}$$
$$+e^{ab}\left\{(2at+b)\operatorname{erfc}\frac{b+2at}{2\sqrt{t}}-2\sqrt{\frac{t}{\pi}}.\ e^{-\frac{(b+2at)^2}{4t}}\right\}\Bigg] \tag{26}$$

which gives the velocity distribution.

For $n=2$,

$$u(y,t)=\frac{A}{2\pi i}\int_{C-i\infty}^{C+i\infty}\frac{e^{pt-b\sqrt{p+a^2}}}{p^3}dp$$

This gives on putting $p+a^2=v^2$ as before,

$$u(y,t)=\frac{Ae^{-a^2t}}{\pi i}\int_{Br_3}\frac{e^{(v^2t-bv)}v}{(v^2-a^2)^2}dv$$

$$=\frac{Ae^{-a^2t}}{8a^2\cdot\pi i}\int\!\!\int_{Br_3}\left[\frac{1}{(v-a)^3}+\frac{1}{(v+a)^3}+\frac{1}{2a}\cdot\frac{1}{(v+a)^2}-\frac{1}{2a}\cdot\frac{1}{(v-a)^2}\right]dv \tag{27}$$

Differentiating eqn. (24) and (25) twice with respect to a under integral sign and substituting in eqn. (27), we get after a lengthy calculation,

$$u(y,t)=\frac{A}{16a^3}\Bigg[e^{-ab}\Big\{(3a^3t^2-4a^2bt+ab^2+b)\operatorname{erfc}\frac{b-2at}{2\sqrt{t}}+\sqrt{\frac{t}{\pi}}\cdot(4a^2t-2ab-2)$$
$$e^{-\frac{(b-2at)^2}{4t}}+e^{ab}\Big\{(4a^3t^2+4a^2bt+ab^2-b)$$
$$\operatorname{erfc}\frac{b+2at}{2\sqrt{t}}-\sqrt{\frac{t}{\pi}}(4a^2t+2ab-2).\ e^{-\frac{(b+2at)^2}{4t}}\Big\}\Bigg] \tag{28}$$

This method can be generalised to calculate $u(y,t)$ from (20) for any positive integral value of n.

Substituting the values of b and a from eqn. (22) in eqn. (26), we get

$$u(y,t)=\frac{A}{4a}\Bigg[e^{-y\sqrt{\frac{m}{\nu}}}\left\{\left(2\sqrt{m}t-\frac{y}{\sqrt{\nu}}\right)\operatorname{erfc}\frac{\frac{y}{\sqrt{\nu}}-2\sqrt{m}t}{2\sqrt{t}}+2\sqrt{\frac{t}{\pi}}e^{-\left(\frac{y}{\sqrt{\nu}}-2\sqrt{m}t\right)^2\Big/4t}\right\}$$
$$+e^{y\sqrt{\frac{m}{\nu}}}\left\{\left((2\sqrt{m}t+\frac{y}{\sqrt{\nu}}\right)\operatorname{erfc}\frac{\frac{y}{\sqrt{\nu}}+2\sqrt{m}t}{2\sqrt{t}}-2\sqrt{\frac{t}{\pi}}e^{-\frac{\left(\frac{y}{\sqrt{\nu}}+2\sqrt{m}t\right)^2}{4t}}\right\}\Bigg] \tag{29}$$

Introducing the non-dimensional variables

$$\Phi(\eta,a_0)=\frac{4u(y,t)}{At};\quad \eta=\frac{y}{\sqrt{\nu t}};\quad a_0=\sqrt{m}t \tag{30}$$

eqn. (29) can be written as

$$\Phi(\eta,a_0)=\frac{1}{a_0}\Bigg[e^{-a_0\eta}\left\{(2a_0-\eta)\operatorname{erfc}\frac{\eta-2a_0}{2}+\frac{2}{\sqrt{\pi}}e^{\frac{-(\eta-2\alpha_0)^2}{4}}\right\}$$
$$+e^{a_0\eta}\left\{(2a_0+\eta)\operatorname{erfc}\frac{\eta+2a_0}{2}-\frac{2}{\sqrt{\pi}}e^{\frac{-(\eta+2\alpha_0)^2}{4}}\right\}\Bigg] \tag{31}$$

It may be noted that $a_0=\sqrt{t\sigma B_0^2/\rho}$ may be looked upon as the non-dimensional Hartman's number in the unsteady motion. A graph is drawn showing the variation of $\Phi(\eta, a_0)$ with η for different values of a_0. It follows from the graph that for a fixed t, velocity at any point in the fluid decreases with increase in a_0 i.e. the magnetic field strength. This is to be expected physically for the effect of magnetic field is to bring about a certain amount of "stiffness" in the fluid resulting in a consequent decrease in the velocity of the fluid.

§ 3. Determination of the skin Friction.

Skin-friction is given by

$$\tau_\omega=-\mu\left(\frac{\partial u}{\partial y}\right)_{y=0}$$

$$=\mu\cdot\frac{At}{4a_0}\cdot\frac{d}{d\eta}\left[e^{-a_0\eta}\cdot\left\{(2a_0-\eta)\,erfc\,\frac{\eta-2a_0}{2}+\frac{2}{\sqrt{\pi}}e^{\frac{-(\eta-2\alpha_0)^2}{4}}\right\}+e^{a_0\eta}\left\{(2a_0+\eta)\,erfc\,\frac{\eta+2a_0}{2}-\frac{2}{\sqrt{\pi}}a_0e^{-a_0^2}\right]$$

This gives after using $\eta=y/\sqrt{\nu t}$

$$\tau_\omega=\frac{\mu A\sqrt{t}}{2a_0}\cdot\left[(2a_0^2+1)erfc\;a_0+\frac{2}{\sqrt{\pi}}a_0e^{-a_0^2}\right] \tag{32}$$

Introducing the drag-coefficient τ_ω^* defined by

$$\tau_\omega^*=\frac{2\tau_\omega}{\mu A}\sqrt{\frac{\nu}{t}}\,, \tag{33}$$

$$\tau_\omega^*=\left(2a_0+\frac{1}{a_0}\right)erfc\;a_0+\frac{2}{\sqrt{\pi}}e^{-a_0^2} \tag{34}$$

The following table shows the variation of τ_ω^* for different values of a_0.

a_0	τ_ω^*	a_0	τ_ω^*
.1	2.259	.7	2.606
.2	2.288	.8	2.710
.3	2.325	.9	2.821
.4	2.374	1.0	2.944
.5	2.438	1.5	3 661
.6	2.519	2.0	4.499

§ 4. Discussion.

The fact that the drag increases with the increase in the magnetic field is due to the following physical considerations.

Because of the motion of the fluid in the magnetic field, an associated electrical field is produced, which according to Ohm's law, sets up electrical currents in the fluid if the latter be a conductor. The interaction of these currents with the magnetic field then produces a body force which must be included in the Navier-Stokes equations for the motion of the fluid. The effect of this body force is to inhibit the motion of the fluid across the lines of force. The natural tendency of the fluid to move along the plate is opposed resulting in an increase in drag.

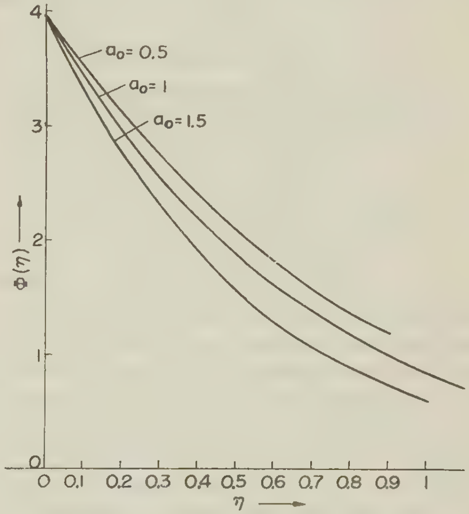

I thank Dr. G. Bandyopadhyay for some helpful suggestions in the preparation of this paper.

References

1) V. J. Rossow: NACA TN-3971 (1957).
2) R. S. Ong and J. A. Nicholls: J. Aero/Space Sciences. **26** (1959) 313.
3) T. Kakutani: J. Phys. Soc. Jap. **13** (1958) 1504.
4) R. C. Meyer: J. Aero/Space Sciences. **25** (1958) 661.
5) N. W. McLachlan: Complex Variable and Operational Calculus with Technical Applications (Cambridge University Press) (1947) 313.

Short Notes

This section is intended to secure prompt publication of important discoveries in physics. The reports should not exceed 800 words in length. A figure of size 7 cm×7 cm will be counted as 150 words.

J. PHYS. SOC. JAPAN **15** (1960) 1898

Time Decrease of Permeability of Substitutional Ferromagnetic Alloys

By Chinji KURODA

Electrical Communication Laboratory
Nippon Telegraph and Telephone Public Corporation
1551, Kichijoji, Musashino-shi, Tokyo, Japan

(Received July 8, 1960)

Decrease of permeability with time after the demagnetization by alternating current is known under the name of disaccommodation (D.A.). It has been proved that D.A. of α-iron is caused by the diffusion of C or N atoms in the interstitial sites. On the other hand, when the substitutional ferromagnetic alloys, which are constituted of Fe, Co, Ni and others, are heat-treated in magnetic field, their magnetic properties are changed more or less. This is well explained by the formation of directional order which can be realized by the diffusion of the elements[1]. Then we can expect that these substitutional alloys also exhibit a magnetic aftereffect at elevated temperatures.[2] Conversely, we can investigate the kinetics of directional ordering by means of the measurements on magnetic aftereffects of permeability.

From this point of view, D.A. of Ni-Co alloys was observed. The specimens whose dimension is 0.2 m/m×7 m/m×300 m/m were obtained by melting the electrolytic Ni and Co in vacuum and cold-rolling. D.A. was measured with a sinusoidal magnetic field of 160 c/s whose amplitude was 0.039 œ. The induced voltages in the secondary coil, after amplified and rectified, were recorded as the permeability. Prior to the measurement of D.A., the specimen was heated to 900°C and maintained for one hour at that temperature, then cooled in magnetic fields of 30 œ to the temperature, at which we could make the measurement, and again maintained for about one hour. The heat-treatments and measurements were done all in dry hydrogen atmospheres. Because of the cooling in a magnetic field, the change of directional order after demagnetization may be supposed to occur almost in 180°-walls.

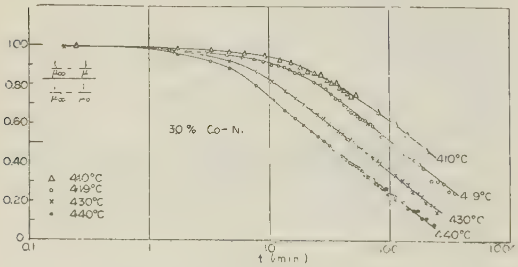

Fig. 1. D.A. of 30% Co-Ni alloy after cooling to the measuring temperature in 30 œrsteds. Ordinate represents $(1/\mu_\infty - 1/\mu)/(1/\mu_\infty - 1/\mu_0)$.

Fig. 1, where ordinate corresponds to $(-1/\mu)$, shows the D.A. at various temperatures. These curves cannot be explained in terms of single relaxation time but present the distinct linear part with $\log t$. According to the representation due to Néel's calculation[3], in which the logarithmic distribution of the relaxation time, τ, was assumed, the ratio of $\tau_{\max}$ to $\tau_{\min}$ could be obtained as about 135 from the linear part for all temperatures of the measurements. Also, activation energy, ca. 2.5 e.v., was obtained from the dependency on temperature of relaxation times. This value agrees with the activation energy obtained by Yamamoto et al.[4] in the case of induced anisotropy energy measured at room temperature after cooling in magnetic field for the alloy of same composition.

From these experimental results, we find out that also for the substitutional alloys in which the number of diffusable atoms is great, the magnetic aftereffect may be described on the assumption of logarithmic distribution of relaxation time. However, the width of distribution in these cases is much broader than in the case of α-iron, in which the ratio is ca. 30[5], although the magnetic structures are simpler due to the cooling in a field. In order to explain this width, it may be necessary to take in the interactions of atoms that migrate under various situations.

We also investigated this alloy with the Co contents from 40% to 70%. Detailed results will be reported later.

References

1) S. Taniguchi and M. Yamamoto: Sci. Rep. Tohoku Univ. **A, 6** (1954) 330. L. Néel: J. phys. radium **15** (1954) 225.
2) S. Taniguchi: Sci. Rep. Tohoku Univ. **A, 7** (1955) 269.
3) L. Néel: J. phys. radium **13** (1952) 249.
4) M. Yamamoto, S. Taniguchi and K. Aoyagi: to be published.
5) P. Brissonneu: J. Phys. Chem. Solids **7** (1958) 22.

J. PHYS. SOC. JAPAN **15** (1960) 1899~1900

The Effect of Cation Vacancies on the Magnetic Annealing of $Co_xFe_{3-x}O_4$

By Tohru INOUE, Hiroshi MIZUTA* and Shūichi IIDA

Department of Physics, Faculty of Science, University of Tokyo

(Received June 3, 1960)

It has been shown experimentally by Iida et al[1] that, in iron cobalt ferrites, the magnitudes of the unixial anisotropy induced by the cooling in a magnetic field depend essentially on the degree of oxidation of the specimens. A postulate has also been presented by them that directional configuration among Co^{++}, Fe^{++}, Fe^{+++} and cation vacancies might play an essential rôle in this phenomenon. On the other hand, Bickford et al[2] have obtained a series of remarkable results for the cobalt poor specimens in highly oxidized states, which can be explained by assuming that the induced anisotropy in these specimens comes from the preferential occupation of Co^{++} ions among four different sites of 16*d* lattice points. Based upon this result they have suggested that, the role of cation vacancies might be only to make the movement of cations easy at high temperatures. In contrast with this suggestion, however, the further experiment made by them[3] for reduced specimens rather shows that the magnitude depends upon the vacancy concentration. Therefore it has become uncertain whether the amount of cation vacancies influences the final equilibrium magnitude of the uniaxial anisotropy or not.

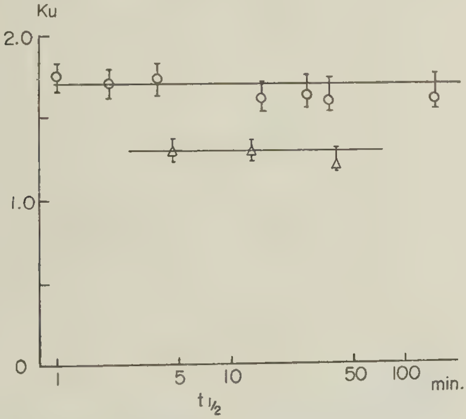

Fig. 1. Relation between final magnitude of anneal induced anisotropy Ku and relaxation time $t_{1/2}$. It should be noticed that the range of permissible errors is not equal for plus and minus side. This is due to the experimental condition of each measurement.
○: $Ku\times10^{-4}$ erg/gr $x=0.063$ $T=100°C$
△: $Ku\times10^{-5}$ erg/gr $x=0.5$ $T=143°C$

Polycrystalline $Co_xFe_{3-x}O_4$ specimens containing cation vacancies in various concentrations were made and the final magnitude of the anneal-induced anisotropy Ku and the relaxation time $t_{1/2}$ (the time at which Ku becomes one half of the initial value) were measured at high temperatures by a torque meter[1]. Special care was taken in order to control and homogenize the concentration of cation vacancies. Adequate reduction of the specimen was made by heat treating each specimen sealed in a small quartz container with a little amount of metallic iron as a reducer. Magnetic measurements were also made with the specimen in the sealed state. It should be emphasized that before measurements each specimen was always annealed at 600~800°C for about two days.

The results for two typical compositions are shown in Fig. 1. As is shown clearly, the final magnitudes of the unixial anisotropy do not depend on the change of the relaxation time of the specimens. Although analysis of the cation vacancy content of each specimen has not yet been performed, the relaxation time observed is considered to be inversely proportional to the density of vacancies in a certain range of the density (this is inferred from a recent stochastic and the statistical thermodynamical analysis)[4],[5]. Therefore, it can be concluded that although the amount of cation vacancies present influences the rate of cation migration very much, it does not affect the final magnitudes of the induced anisotropy, in accordance with the suggestion made by Bickford et al. We believe that this conclusion is hold for the entire range of $Co_xFe_{3-x}O_4$.

From this result it is presumed that, in the case of Bickford et al, the homogeneity of specimens has not been enough. It should be remarked that in our case of $x=0.063$, the homogeneity of the specimens is guaranteed further by the single relaxation time character of all relaxation curves observed.

Observations were also made with specimens which had been reduced severely. The relaxation time increases very much and the measurements could only be made at high temperatures (400~550°C). Moreover, the activation energies calculated are quite different from that of oxidized specimens. It is suggested that the cation migration in this case is taking place by a different diffusion mechanism (interstitialcy diffusion).

References

1) S. Iida, H. Aiyama and H. Sekizawa: J. Phys. Soc. Japan **13** (1958) 58.

---

* Now at Nippon Atomic Industry Group Co. Ltd., Tokyo.

2) R. F. Penoyer and L. R. Bickford, Jr.: Phys. Rev. **108** (1957) 271.
3) L. R. Bickford, Jr., J. M. Brownlow and R. F. Penoyer: J. Appl. Phys. **29** (1958) 441.
4) S. Iida: J. Appl. Phys. **31** (1960) Supplement.
5) S. Iida: to be published.

J. Phys. Soc. Japan **15** (1960) 1900

Colour Center and Gaseous Ions Produced in High Frequency Spark between the Electrodes of Semi-metals, Metal Elements, and Ionic-crystals

By Toshiyoshi Yuasa

Department of Chemistry, School of General Studies, Kyoto University, Kyoto

(Received May 17, 1960)

A double focusing Mattauch-type mass spectrometer with a high-frequency spark ion source was used here. Hintenberger[1], by using the same kinds of apparatus as the author's, has already found the lines of C molecule ions from C_2^+ to C_{28}^+ in the spark between graphite electrodes. However, the mechanism of production of molecular ions is not clear yet. To find out what kinds of electrode elements are capable of producing such molecular ions, experiments were performed by the author in the following way. The material to be examined was prepared in the form of rods. Two such rods were required for each sample and were mounted in the spark ionization source with their tips apart and directly. The source was evacuated and, when the pressure has fallen to about 2×10^{-6} mmHg, a spark voltage was applied to the sample rods. The mass spectrum was recorded on a Ilford Q-II photographic plate.

The experimental results obtained were as shown in Table I. Table I shows that their singly-charged poly-atomic molecular ions are produced for only the semi-metallic samples. When the samples of alkali-halide single crystal were taken out from spark source after examination, it was observed that the crystals were held in their shape and moreover colour centers were formed finely; yellow for NaCl, yellowish brown for LiF, and cobalt blue for KBr. More detailed studies will be reported later.

Table I.

Sample	Ions found										
C		C_5^+,	C_4^+,	C_3^+,	C_2^+,	C^+,	C^{2+},				
Si	Si_6^+,	Si_5^+,	Si_4^+,	Si_3^+,	Si_2^+,	Si^+,	Si^{2+},				
Ge			Ge_4^+,	Ge_3^+,	Ge_2^+,	Ge^+,	Ge^{2+},	Ge^{3+},	Ge^{4+}		
Se				Se_3^+,	Se_2^+,	Se^+,	Se^{2+},				
Te					Te_2^+,	Te^+,	Te^{2+},				
Sb					Sb_2^+,	Sb^+,	Sb^{2+},	Sb^{3+},	Sb^{4+}		
Bi						Bi^+,	Bi^{2+},	Bi^{3+},	Bi^{4+},	Bi^{5+},	Bi^{6+}
Al						Al^+,	Al^{2+},				
Ti						Ti^+,	Ti^{2+},				
Fe						Fe^+,	Fe^{2+},	Fe^{3+}			
Ni						Ni^+,	Ni^{2+},	Ni^{3+}			
Cu						Cu^+,	Cu^{2+},				
Zn						Zn^+,	Zn^{2+},	Zn^{3+}			
Zr						Zr^+,	Zr^{2+},	Zr^{3+}			
In						In^+,	In^{2+},	In^{3+}			
Sn						Sn^+,	Sn^{2+},	Sn^{3+}			
Pt						Pt^+,	Pt^{2+},	Pt^{3+},	Pt^{4+}		
Au						Au^+,	Au^{2+},	Au^{3+}			
NaCl						Na^+,	Na^{2+},	Cl^+			
LiF						Li^+,	Li^{2+},	Li^{3+},	Li^{4+},	F^+	
KBr						K^+,	K^{2+},	K^{3+},	Br^-		

The author wishes to express his thanks to Mr. S. Nasu for his cooperation in the experiments.

Reference

1) E. Dörnenburg and H. Hintenberger: Z. Naturforsch. **14** (1959) 765.

J. Phys. Soc. Japan **15** (1960) 1901

Magnetic Transition in $TiCl_3$

By Shinji Ogawa

Research Institute of Applied Electricity,
Hokkaido University, Sapporo

(Received July 8, 1960)

The nature of the magnetic transition in oxides of titanium and vanadium has been recently discussed by Carr and Foner[1], and Goodenough[2] has pointed out an importance of a direct cation-cation interaction in the ionic crystals which contain the transition metal ions having less-than-half d electrons.

A magnetic transition of similar nature has been observed in $TiCl_3$. Two different results of the magnetic susceptibility of polycrystalline $TiCl_3$ have been reported by Starr, Bitter and Kaufmann[3] and by Klemm and Krose[4]. Our measurement shown in Fig. 1 is in good agreement with the latter's.

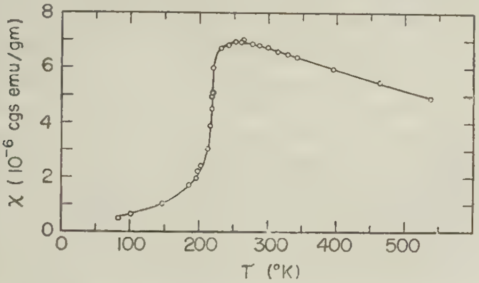

Fig. 1. The magnetic susceptibility of polycrystalline $TiCl_3$.

It was tried to measure the magnetic torque of a small single crystal of hexagonal plate-like shape which had grown up in preparing $TiCl_3$ by the method of reducing $TiCl_4$ with H_2 gas[4], but the amplitude of torque was so small that it could not be measured with the torque magnetometer used. However, the difference between $\chi_{\parallel}$ and $\chi_{\perp}$, the magnetic susceptibilities parallel and perpendicular to the c-axis*, has been estimated to be less than 3×10^{-7} cgs emu/gm in the range of temperature from 77° to 370°K. Combining both results, it is concluded that both $\chi_{\parallel}$ and $\chi_{\perp}$ decreases abruptly at the transition temperature, $T_t=217°\pm2°K$, in contrast to normal antiferromagnetic substances. This anomalous transition suggests a possibility of a lattice distortion at T_t[5]. An X-ray measurement was therefore made. Powder patterns were recorded on a Norelco diffractometer using a copper radiation. The room temperature pattern is in good agreement with that in literature[6], except a slight difference in lattice constants. At T_t, a change in lattice symmetry was not found, although its possibility was not denied because of the broadening of diffraction lines below T_t. However, the lattice spacings changed rather abruptly at T_t. The lattice constants a and c determined from the (30.0) and (00.12) lines respectively are plotted against temperature in Fig. 2. At T_t, the lattice contraction in the plane perpendicular to the c-axis is so large that the expansion in the c-direction cannot prevent a volume contraction.

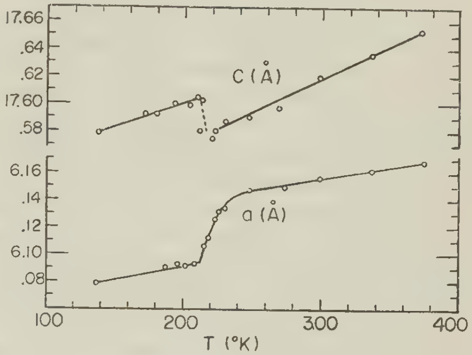

Fig. 2. The temperature dependence of lattice constants a and c.

Ti^{3+} ions in $TiCl_3$ crystal form a honeycomb lattice in the plane perpendicular to the c-axis and each lattice plane is separated from the next plane with intervening two hexagonal lattice planes of Cl^- ions. The observed lattice distortion suggests a formation of the bonding among Ti^{3+} ions in the plane perpendicular to the c-axis below T_t, favoring the model proposed by Goodenough[2]. A long-range antiferromagnetic ordering below T_t is doubtful. An examination by means of neutron diffraction is desired.

The author would like to thank Professor Y. Yokozawa for his continuous interest.

References

1) P. H. Carr and S. Foner: J. Appl. Phys. **31** (1960) 344S.
2) J. B. Goodenough: J. Appl. Phys. **31** (1960) 359S.
3) C. Starr, F. Bitter and A. R. Kaufmann: Phys. Rev. **58** (1940) 977.
4) W. Klemm and E. Krose: Z. anorg. Chem. **253** (1947) 209.
5) E. P. Warekois: J. Appl. Phys. **31** (1960) 346S.
6) W. Klemm and E. Krose: Z. anorg. Chem. **253** (1947) 218.

---

* The crystal structure of $TiCl_3$ is rhombohedral, $C_{3i}^{2}-R\bar{3}$, but a hexagonal representation is used in this note.

J. PHYS. SOC. JAPAN **15** (1960) 1902

On "Screened Impurity Potentials in Metals"

by Ralph J. HARRISON and Arthur PASKIN

Materials Research Laboratory, Ordnance Materials Research Office, Watertown, Massachusetts, U.S.A.

(Received July 6, 1960)

Takimoto[1] has recently derived an expression for the Fourier transform of the screened impurity potential in a cloud of conduction electrons. This expression agrees with that obtained by Silverman and Weiss[2], Langer and Vosko[3] and Izuyama[4]. McIrvine[5] has made an examination of the spatial form of the screened potential obtained by integration of Takimoto's expression for the Fourier transform. McIrvine showed that for one limiting range of values of the screening parameter the integrand has poles on the imaginary axis which contribute an exponentially screened term of the customary Thomas-Fermi (T-F) form. For another range of values of the screening parameter there are complex poles which give rise to an exponentially damped oscillatory term. McIrvine did not consider, however, the contribution to the integral arising from the logarithmic singularity of the integrand in the region $\kappa=2k_0$, where κ is the magnitude of the wave vector in transform space and k_0 is the absolute value of the Fermi wave vector. The importance of this region was pointed out by Langer and Vosko[3]. The second derivative of the integrand has a real pole here which gives rise to an undamped oscillatory term which would becme dominant at large distances for all values of the screening parameter. Langer and Vosko have derived an experession for the change density asymptotically valid at large distances and has also presented results of numerical integration vaild to small distances.

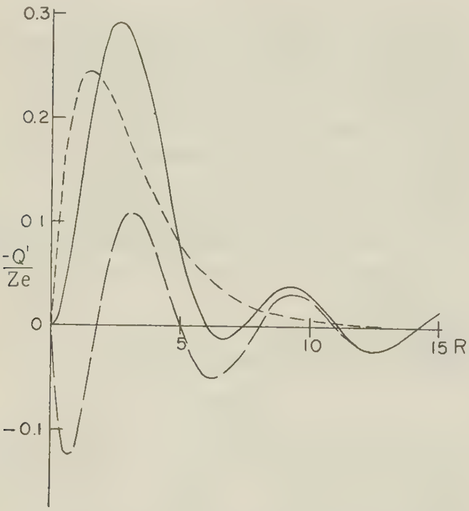

Fig. 1. Radial charge density about an impurity in Cu as function of distance from impurity. $Q'=dQ/dR$.

—— From numerical integration of Takimoto potential.

...... From customary T-F expression.

— — — Difference

In Fig. 1 we present results* obtained from a similar numerical integration of Takimoto's expression using the value of the screening parameter for copper, assuming the free electron value of Fermi energy. For convenience, the quantity plotted as the solid curve is radial charge density, dQ/dR, where dQ is the charge contained in the spherical shell defined by spheres of radius $R+dR$, and where $R\equiv 2k_0r$, with r the distance in real space. For comparison, the customary T-F radial charge density is also plotted in Fig. 1, as well as the difference between it and the Takimoto radial charge density. It is noteworthy that the difference curve is quite close to the values given by the asymptotic expression from large values of R down to about half the nearest neighbor distance, i.e. between $R=3.5$ and ∞, dQ/dR is quite closely given by

$$dQ/dR=(-Ze)\,[\alpha^2R\exp(-\alpha R)-\alpha^2(1+\tfrac{1}{2}\alpha^2)^{-2}R^{-1}\cos R],$$

where Ze=assumed charge on impurity, q=T-F screening parameter, $\alpha=q/2k_0$ and $\alpha R=qr$. In the example illustrated, $\alpha\sim 2/3$. It is possible that for much smaller values of α, a representation as the sum of a damped oscillatory term of the type suggested by McIrvine and the Langer-Vosko asymptotic form would prove useful.

References

1) N. Takimoto: J. Phys. Soc. Japan **14** (1959) 1142.
2) B. D. Silverman and P. R. Weiss: Phys. Rev. **114** (1959) 989.
3) J. S. Langer and S. H. Vosko: J. Phys. Chem. Solids **12** (1959) 196.
4) T. I. Izuyama: Dissertation (See reference 1.)
5) E. C. McIrvine: J. Phys. Soc. Japan **15** (1960) 928.

---

* These result were obtained in connection with a calculation of the nuclear quadrupole interaction in alloys discussed in part in a post-deadline paper presented by Dr. Paul L. Sagalyn and the present authors at the March 1960 (Detroit) Meeting of the American Physical Society.

J. PHYS. SOC. JAPAN **15** (1960) 1903~1304

Electrical Properties of Heavily Doped N-type Germanium

By Yoshitaka FURUKAWA

The Electrical Communication Laboratory, Musashinoshi, Tokyo

(Received August 4, 1960)

It has been reported that[1] for the same electron density, mobility in Sb-doped germanium is higher than that in As-doped germanium, and that[2] phonon assisted tunneling is observed in Sb-doped junctions of germanium but not in P- and As-doped junctions. Therefore, the effect of simultaneous doping of these impurities on the electrical properties of germanium may be an interesting problem.

For this purpose, four crystals containing both As and Sb have been prepared. Rough estimation for As concentration at the top (seed side) of the crystals and at the portion where single crystal breaks is given in Table I.

Table I.

Crystal	As (cm^{-3}) top	n (cm^{-3}) top	As (cm^{-3}) tail	n (cm^{-3}) tail
No. 1	$\sim 2\times 10^{18}$	4.8×10^{18}	$\sim 10^{19}$	1.6×10^{19}
No. 2	$\sim 5\times 10^{17}$	3.0×10^{18}	$\sim 3\times 10^{18}$	8.7×10^{18}
No. 3	$\sim 10^{17}$	1.7×10^{18}	$\sim 10^{18}$	5.2×10^{18}
No. 4	$\sim 2\times 10^{17}$	2.3×10^{18}	$\sim 6\times 10^{17}$	4.7×10^{18}

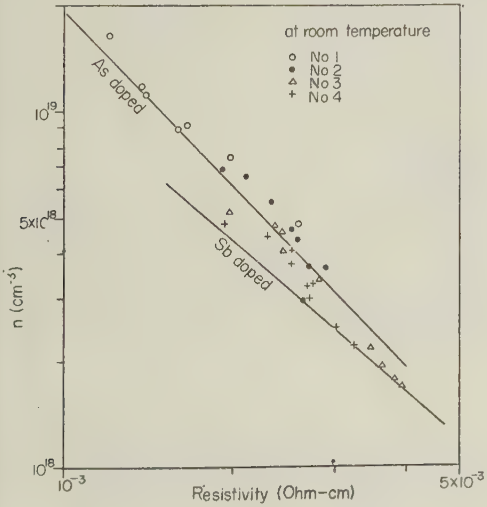

Fig. 1. *n versus* ρ relation.

Fig. 1 shows electron concentration (n) *versus* resistivity (ρ) relation. Solid lines[1] in this figure correspond to As- and Sb-doped germanium. As will be seen from this figure, measured points for samples with small r (r=As concentration/total donor concentration) lie on Sb-doped line, while measured points for samples with large r lie on As-doped line. It has been estimated that the transition of measured points from Sb-doped line to As-doped one occurs at $r \approx 0.2$.

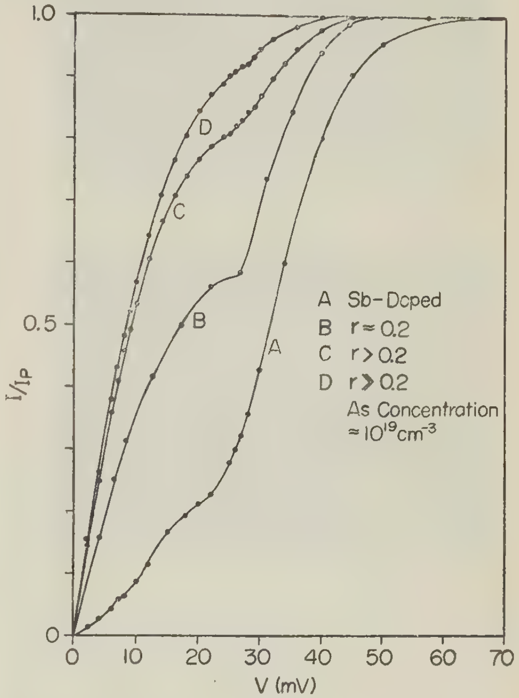

Fig. 2. V-1 characteristic of Sb- and (As+Sb)-Doped Junctions at 4.2°K.

At first, it was expected that indirect tunneling would not be observed in diodes made of (As+Sb)-doped germanium in which $r>0.2$ and n lies on As-doped line shown in Fig. 1. However, the experimental results did not agree with this expectation. Fig. 2 shows a typical example of current-voltage characteristics of Esaki-diodes made of Sb- and (As+Sb)-doped germanium at 4.2°K. Indirect tunneling[2] associated with longitudinal acoustic phonon has been observed even for the samples in which $r \gg 0.2$ and As concentration is about 10^{19} cm^{-3}. However, tunneling associated with transverse acoustic phonon is quite ambiguous for all samples measured in present experiment (except Sb-doped diodes).

Two different interpretations have been given for the difference of tunneling processes (direct and indirect) in As- and Sb-doped junctions. One[2] is based on modification of conduction band edge form, and another[3] is based on the difference of impurity scattering. To explain the present experimental results, the latter interpretation seems to be preferable.

Details will be reported in the near future.

The author thanks Mr. Z. Kiyasu, Associate

Director, and Dr. T. Niimi heartily for the guidance in this work.

References

1) Y. Furukawa: Phys. Soc. Japan **15** (1960) 730.
2) N. Holonyak et al: Phys. Rev. Letter **3** (1959) 167.
3) J. V. Morgan and E. O. Kane: Phys. Rev. Letter **3** (1959) 466.

J. PHYS. SOC. JAPAN **15** (1960) 1304

Radiation of Plasma Oscillation

Shoji KOJIMA and Shigeo HAGIWARA
Tokyo University of Education,
Otsuka, Tokyo

(Received August 1, 1960)

In a previous paper we reported that a radiation having the frequency of the electron plasma oscillation was found with a Yagi antenna in a frequency region of about 700 Mc[1]. Further studies on this radiation have been carried out in microwave region. The discharge tube used was a mercury filled hot cathode tube having a pair of probes and two grids which were first introduced by Takayama to eliminate low frequency oscillations of the discharge[2]. The geometry of the tube is shown in Fig. 1. The radiation was detected with a electromagnetic horn and a superheterodyne receiver whose intermediate frequency was 70 Mc with a band width of 2 Mc.

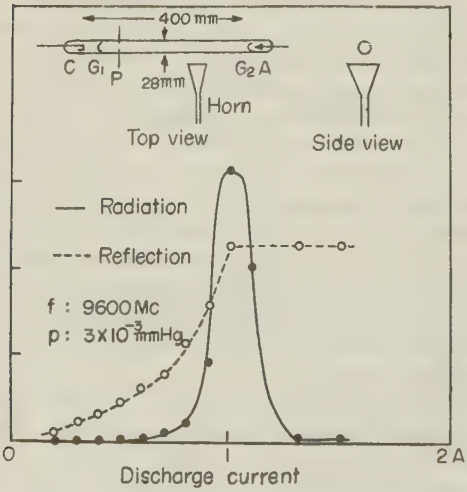

Fig. 1. Resonance curve of radiation.
Full line shows power of radiation in arbitrary scale.
Dotted line shows reflection ratio.

In order to determine the electron concentration of plasma, an experiment on microwave reflection was also carried out by using a klystron signal source. Reflection ratios were measured with a standing wave ratio meter.

Since the electron concentration varies as the discharge current was changed, the power of radiation was measured as a function of discharge current at a fixed frequency of the receiver. A result at a frequency of 9600 Mc is reproduced in Fig. 1 with a full curve. The reflection ratios which were measured at nearly same condition are also shown in the figure with a dotted curve. The radiation shows a predominant resonance at the current where the reflection reaches a saturation. Since at this current the frequency of plasma oscillation becomes 9600 Mc, the radiation seems to originate from the plasma oscillation.

The power of radiation at the resonance peak was roughly estimated to be a order of 10 $\mu\mu$w. The thermal noise of plasma in the above case was very small. The apparent half width of the resonance curve corresponds to about 200 Mc in frequency scale. The true width, however, may be smaller than 60 Mc, because the superheterodyne apparatus receives a image frequency besides the desired frequency. The hight of the resonance was almost constant for the whole region of positive column. In the vicinity of the cathode, the first grid or the probe, however, the radiation was very strong. This fact seems to agree with the previous conclusions that the plasma oscillation is strongly excited in front of the cathode and that the transformation of plasma oscillation into radiation takes place markedly at inhomogenious plasma.

When the pressure of tube increased, the height of resonance decreased and at about 10^{-2} mmHg the resonance sank below the noise level of the apparatus.

Such resonance was not observed in usual fluorescent lamp of 10 watts. However, long tubes of 20 watts or more showed a broad hump at the current which gives rise to the plasma oscillation having the frequency equal to that of the receiver. Above this current the well known noise radiation was observed.

References

1) S. Kojima, K. Kato, S. Hagiwara and R. Matsuzaki: J. Phys. Soc. Japan **14** (1959) 821.
2) K. Takayama: to be published.

---

* Simultaneous measurement on the radiation and reflection will be tried in near future.

J. PHYS. SOC. JAPAN **15** (1960) 1905~1906

The Effect of θ' Phase on the Plastic Deformation of an Age-Hardenable Al-Cu 4% Alloy

By Keisuke MATSUURA and Shigeyasu KODA
The Research Institute for Iron,
Steel and Other Metals,
Tohoku University, Sendai

(Received August 4, 1960)

In the previous short note[1], the effect of G-P aggregates on the plastic deformation was discussed. In the present study, to consider the effect of θ' phase on the plastic deformation, polycrystalline specimens (their grain size was 1/10~1/20 mm, but sometimes a few c.m.) were aged for various times at 240°C after air-cooling from 530°C. The air-cooled state is a supersaturated one with solute atoms, and the heat treatment mentioned above harden the specimens with θ' phase. Wires of 1 mm diameter for tensile testing, and strips of 1 mm thickness for the observation of slip patterns were extended at room temperature and -196°C. Some of the results are shown in Fig. 1 and Photo. 1. The following characteristics were observed.

(1) The initial rate of strain-hardening of aged specimens up to a stress δ_c increases appreciably compared with that of an air-cooled one. The curves are nearly linear, and the slope is $d\delta/d\varepsilon = 5.1\times10^2$ kg/mm^2. Moreover it is insensible to the grain size and the deformation temperature. However, δ_c becomes smaller as the deformation temperature becomes higher. When the applied stress increases over δ_c, the rate of strain-hardening begins to decrease and eventually becomes smaller than that of an air-cooled one.

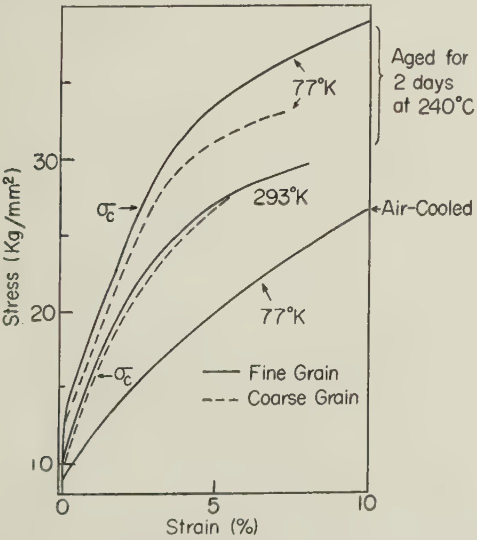

Fig. 1. Stress-strain curves of specimens aged for 2 days at 240°C and the air-cooled one at room temperature and -196°C.

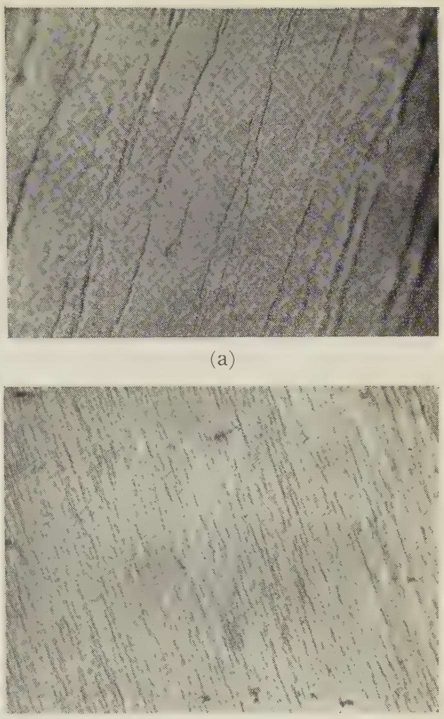
(a)

(b)

Photo. 1. Slip lines of specimens aged for 2 days at 240°C. (a) At the vicinity of fracture by extension at room temperature. (b) After 4.5 % extension at -196°C.

(2) The slip lines are not observed up to a plastic strain ε_c. It may be due to the fact that the slip lines are too fine and wavy to be observed as lines by means of an optical microscope. When the ageing proceeds from 2 hr. to 2 days, the value of ε_c at room temperature deformation varies from 2 % to the fracture strain and the slip lines observed above ε_c become from fine to coarse.

For the room temperature deformation of one aged for 2 days, sharp and coarse slip lines which are frequently connected with cross slip are observed only at the fractured grain, but at -196°C deformation faint and short slip lines connected with cross slip are observed at $\varepsilon_c \sim 5$ %. These facts may be explained as follows. In the specimens, for example the ones aged for 2 days, which θ' phase develops sufficiently, most of dislocations in motion pile up against the precipitates or pass through between them leaving loops around them. Such a process may cause to operate multiple slip as shown by disappearance of slip lines. The increase of strain-hardening is expected because of the interaction of dislocations by the piling up on the precipitates[2] and the operation of multiple slip[3].

Also it is expected that the strain hardening is insensible of the crystal orientation. The same rate of strain-hardening in the fine- and coarse-grained crystals suggests that it is not sensible of the crystal orientation. When the applied stress reaches to δ_c, the piled-up dislocations slip away by cross slip[4] or slip through the precipitates due to the stress concentration in front of the piled up dislocations. If the appearance of slip lines is associated with the slip of precipitates, it follows that, if the deformation temperature is high enough or the precipitates develop sufficiently the cross slip is dominent factor of the decrease in the rate of strain-hardening and if not so the slip of the precipitates is the factor.

References

1) K. Matsuura, S. Izumi and S. Koda: J. Phys. Soc. Japan **13** (1958) 318.
2) J. C. Fisher, E. W. Hart and R. H. Pry: Acta Met. **1** (1953) 336. S. Koda and Y. Hamaguchi: Bulletin, Fac. Eng. Hokkaido Univ. (1954) No. 11, 157.
3) A. H. Cottrell: *Dislocations and Plastic Flow in Crystals* (Oxford, 1953) 168p.
4) A. Seeger: Report of the Lake Placid Conference on *Dislocations and Mechanical Properties of Crystals* (John Wiley Sons, 1957) 241p.

J. PHYS. SOC. JAPAN **15** (1960) 1906

Magnetic Properties of $MgMn_2O_4$

By Kiyoshi MURAMORI and Syohei MIYAHARA

Department of Physics, Faculty of Science, Hokkaido University, Sapporo, Japan

(Received July 1, 1960)

Crystallographical properties of $MgMn_2O_4$ have been studied by Sinha et al.[1] and it has been found that they exhibit an approximate normal spinel structure with a tetragonal deformation at room temperature and most manganese ions are located on octahedral sites. Therefore it is likely that $MgMn_2O_4$ has the same antiferromagnetic properties as the zinc ferrite. However, Jacobs[2] has shown recently that $MgMn_2O_4$ has a spontaneous magnetization of about $0.2\mu\beta$ at 4.2°K which increases linearly with magnetic field at high intensities. In order to clarify the magnetic properties of $MgMn_2O_4$, the crystallographical properties were studied in detail by X-ray diffraction experiments and the susceptibilities of a powdered specimen were measured.

The specimen was prepared from powders of MgO and Mn_2O_3 which were made by calcining the salts. The mixtures were fired for a few hours in air at 1200°C, annealed for a day in air at 900°C in order to complete the conversion of divalent manganese ions to trivalent ones, and cooled slowly to room temperature at the rate of 0.5°C/min. X-ray diffraction patterns of the specimen show a tetragonal spinel-like structure with $c/a=1.15$, which is in agreement with the value determined by Sinha et al.. The cation distribution of the specimen that was determined by the X-ray diffraction intensity ratios of (202)/(004) and (422)/(004) differ about 15% from that of the completely normal spinel structure and is independent of thermal treatments of the specimen within the experimental errors.

Table I. u, x, T_a and C_{mol} mean oxygen positional parameter, fraction of Mg ions located on A-sites, asymptotic Curie temperature and Curie constant.

u	x	T_a	C_{mol}
0.385	0.85	500°K	5.75

Magnetic susceptibility was measured by a Sucksmith's ring balance. From the liquid nitrogen temperature, where the specimen shows no intrinsic magnetic moment, to 550°C, the inverse of the magnetic susceptibility changes linearly with temperature, showing the asymptotic Curie temperature to be −500°K. According to Lotgering[3] the asymptotic Curie temperature of a magnetic spinel is represented by

$$T_a=-(C_A n\alpha/6+C_B n\beta+4nC_AC_B/3)/C_{at}\,, \qquad (1)$$

where C_A and C_B are the Curie constants per mole of tetrahedral (A) and octahedral (B) sites ions respectively, $C_{at}=(C_A+2C_B)/3$; and n, $n\alpha$ and $n\beta$ are the molecular field constants between A-B, A-A and B-B site-ions respectively. It is evident that the first term of the formula (1) has little contribution to T_a. On the other hand, assuming the triangular arrangement of the magnetic moments of cations at B-sites as proposed by Yafet and Kittel[4], the resultant magnetic moment M_0 is expressed

$$M_0=\pm M_A(1-1/\beta)\,, \qquad (2)$$

where + or − sigh is taken for $M_B>M_A$ or $M_A>M_B$ respectively.

Using the relations (1) and (2) and the observed value of T_a (=500°K) and estimated value of M_0 ($=0.2\mu\beta$) by Jacobs, the values of n and $n\beta$ are obtained. For the case $M_B>M_A$ or $M_A>M_B$, $n\beta$ is 100 or 114 respectively. The above values of $n\beta$ are approximately in agreement with that of $n\beta=82\pm12$ obtained from linear increase of magnetic moment by Jacobs[2]. Therefore the magnetic properties of $MgMn_2O_4$ are thought to be consistent with the triangular ferrimagnetic model.

References

1) A. P. B. Shinha, N. R. Sanjana and A. B. Biswas: Acta Crst. **10** (1957) 439.
2) I. S. Jacobs: J. Phys. Chem. Solids **11** (1959) 1.
3) F. K. Lotgering: Philips Res. Rep. **11** (1956) 190.
4) Y. Yafet and C. Kittel: Phys. Rev. **87** (1952) 290.

Errata

Sign Reversal of Hall Coefficients at Low Temperatures in Heavily Compensated *p*-type Germanium

By Hiroo YONEMITSU, Hajime MAEDA and Hisao MIYAZAWA

J. Phys. Soc. Japan **15** (1960) 1718

Right column, the equation "$R_H=\frac{1}{e}\frac{\cdots-r_A\mu n_A{}^2{}_A}{(\cdots+n\mu_A)^2}$, $\rho_0=\cdots$" should be read "$R_H=\frac{1}{e}\frac{\cdots-r_A n_A\mu_A{}^2}{(\cdots+n_A\mu_A)^2}$, $\rho_0=\cdots$".

PROGRESS OF THEORETICAL PHYSICS

CONTENTS

Progress of Theoretical Physics Vol. 23, No. 6, June 1960

Collective Excitations of Electrons in Degenerate Bands. I.—*Spin Waves in Stoner's Model of Ferromagnetism*— .... Takeo IZUYAMA .. 969
Polarization of the Recoil Nucleon from the Photoproduction of Pion .... Masaaki KAWAGUCHI .. 984
On the Representation of the Canonical Commutation Relation of Bose Fields .... Hideo FUKUTOME .. 989
A New Approach to the Theory of Classical Fluids. I .... T. MORITA and K. HIROIKE .. 1003
Ambiguity of $\partial D_c(x)/\partial x^2$ and Causality .... Ichiro FUKADA .. 1028
Pion-Nucleon Interaction, Anomalous Magnetic Moment of Nucleon and Composite Model for Pion .... Chiaki IHARA .. 1035
Origin of the Magnetic Anisotropy Energy of Cobalt Ferrite .. Masashi TACHIKI .. 1055
A Possible Symmetry in Sakata's Model for Bosons-Baryons System. II .... M. IKEDA, S. OGAWA and Y. OHNUKI .. 1073
Bound States in Four-Nucleon Coupling .... Hiroshi YAMAMOTO .. 1100
Interactions Induced by High Energy Neutrinos .... Yoshio YAMAGUCHI .. 1117
Solar Modulation of Primary Cosmic Rays .... Yoshinosuke TERASHIMA .. 1138
Integral Representations of Bethe-Salpeter Amplitudes .... Masakuni IDA .. 1151
Effect of Lattice-Electron Interaction on the Landau Diamagnetism .... Shô-ichiro TANI .. 1157
S-Wave K Meson-Nucleon Interaction .... Shigeo MINAMI .. 1163
A Unified Model for Elementary Particles .... Z. MAKI, M. NAKAGAWA, Y. OHNUKI and S. SAKATA .. 1174
On the Structure of the Elementary Particles .... K. MATUMOTO and M. NAKAGAWA .. 1181
Electromagnetic Structure of the Nucleon. IV.—*Charge Distribution of the Proton*— .... K. HIIDA, N. NAKANISHI and T. SHIOZAKI .. 1189

Letters to the Editor:

Form Factor and Structure of Particles .... K. YAMAMOTO .. 1204
On the Inelastically Scattered Proton at High Energy .... Y. SAKAMOTO .. 1205
Anomalous Creation of μ-Mesons Originating in Weak Interactions .... H. NAGAI and D. ITÔ .. 1207
Phenomenological Model of Elementary Particle Interactions .... D. ITÔ, K. IWATA, S. FURUI, K. FUJII and T. SAKUMA .. 1210
Virial Expansion Formulae for the Microfield and Micropotential Distribution Functions and Their Application to a High Temperature Plasma .... T. MORITA .. 1211
Polarization in Heavy Particle Stripping .... M. A. NAGARAJAN .. 1214
The Effect of π^2 Term in the S-Wave π-N Scattering .... I. UMEMURA .. 1216
Contents and Author Index to Vol. 23 .... i–xii

Price $ 1.25 per copy
$ 15.00 per year (postage inclusive)
Annual dues for foreign members (individual subscribers)
$ 12.00 (postage inclusive)
〃 for foreign members of the Physical Society of Japan
$ 10.00 (postage inclusive)

Application for membership, subscriptions and orders for back numbers should be sent, directly or through book-dealers, to

The Publication Office
in
Yukawa Hall, Kyoto University, Kyoto, Japan

. . . .

JOURNAL OF THE PHYSICAL SOCIETY OF JAPAN, Vol. 15, No. 11, NOVEMBER, 1960

Decay of Potassium 44

By Kazusuke SUGIYAMA, Tsutomu TŌHEI, Masumi SUGAWARA
Department of Physics, Faculty of Science, Tohoku University, Sendai
Tsunekichi DAZAI and Yukinori KANDA
Tokyo Institute of Technology, Tokyo

(Received June 6, 1960)

An investigation of the decay scheme of K^{44} has been made with anthracene- and 5″×5″ NaI(Tl)-scintillation counters, and coincidence techniques. In addition to the 4.91-, 3.55- and 2.63-MeV beta rays, the following gamma rays has been assigned to Ca^{44}: 0.48-, 0.63-, 0.74-, 0.90-, 1.06-, 1.16-, 1.5-, 1.74-, 2.08-, 2.17-, 3.4-, 4.4-, 4.6- and 5.0-MeV. A decay scheme is proposed.

§1. Introduction

It is interesting to get an information about the level structure of Ca^{44} which situates between double magic nuclei Ca^{40} and Ca^{48}. Hitherto this has been investigated by the negatron decay of K^{44} and the positron decay of Sc^{44}. B. L. Cohen[1] has reported the 1.13-, 2.07- and 2.48-MeV gamma rays in his study of K^{44} and suggested that there was 1.5-MeV beta ray to higher level, though no comment on the level structure was offered. J. W. Blue and E. Bleuler[2] have reported the presence of 1.16- and 2.54-MeV gamma rays in their study on the Sc^{44} decay.

According to the beta ray energy systematics[3], the K^{44}–Ca^{44} energy difference is about 6.1-MeV and is higher than the Sc^{44}–Ca^{44} energy difference of 3.6-MeV, then one may have more information in the higher levels of Ca^{44} from the study of K^{44}.

§2. Experimental Procedure and Results

a) *Source sample*

Natural Calcium ($CaCO_3$) was irradiated with 18-MeV deuteron-carbon neutrons by the 160-cm cyclotron of the Institute of Nuclear Study, University of Tokyo. Irradiated samples were dissolved in a solution of HCl, and chemically separated by means of a method using tetraphenyl-boron-soda. Gamma ray spectra were measured at each stage of chemical process to confirm that Calcium (Ca–49) and Argon (A–41) were removed.

Decay life of the chemically separated sample was measured by a G–M counter and an anthracene scintillation counter which was used for the beta ray spectrum in the high energy portion. The decay curve measured by a G–M counter is shown in Fig. 1. Half life of K^{44} then assigned as 22.3-min., though it had measured 18-min.[4], 20-min.[5] and 22-min.[1] so far.

b) *Beta rays*

Beta ray spectra were obtained using a 1-in. dia. 1-in. long anthracene crystal with a multichannel pulse height analyser. The anthracene scintillation counter was calibrated with the Cs^{137} conversion line, Zn^{65}, Na^{22}, Na^{24}, Co^{60} gamma ray Compton edges and the Sr^{90} beta ray spectrum. The Fermi-Kurie plot is shown in Fig. 2. The maximum energies of beta rays were obtained as the 4.91-, 3.55- and 2.63-MeV from the Fermi-Kurie plot. Lower energy beta rays were covered by gamma ray background. Though the 3.55-MeV beta ray has been found in the decay of K^{42}, it may exist in the decay of K^{44} also.

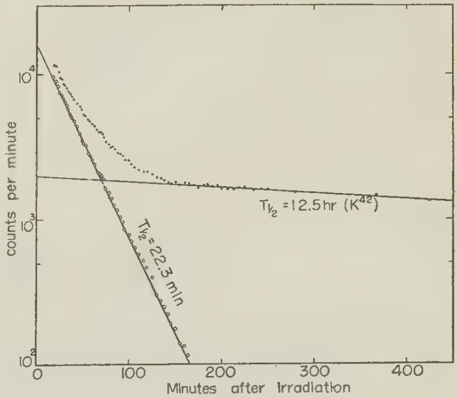

Fig. 1. Decay of K^{44}. ● shows the experimental count, and ○ shows the value that subtracted the K-42 (12.5-hr) from the experimental count.

c) *Gamma rays*

Gamma ray spectrum study was made using 5-in. dia. 5-in. long NaI(Tl) crystal. A lead collimating slit (see Fig. 3) was used for the sum peak measurement. Extreme cases of the measurement are shown in Fig. 3.

Though B. L. Cohen has suggested that the 3.6-MeV peak is the sum peak, it was confirmed as a single peak in our spectrum. Furthermore higher energy gamma rays could be observed, as the large 5-in. dia. 5-in. long NaI(Tl) crystal was used. The gamma ray spectrum was measured at 14-min., 34-min. and 56-min. after irradiation, and each peaks showed 22-min. decay life except the 1.5-MeV peak. The 1.5-MeV peak was found to be mixed gamma rays of Ca^{44} and Ca^{42}, since this peak had two decay components of 22-min. and a longer one in the decay life measurement. The gamma ray spectrum in lower energy portion is shown in Fig. 4.

d)· *Gamma-gamma coincidence measurements*

Gamma-gamma coincidences were studied with 5-in. dia. 5-in. long and 3-in. dia. 3-in.

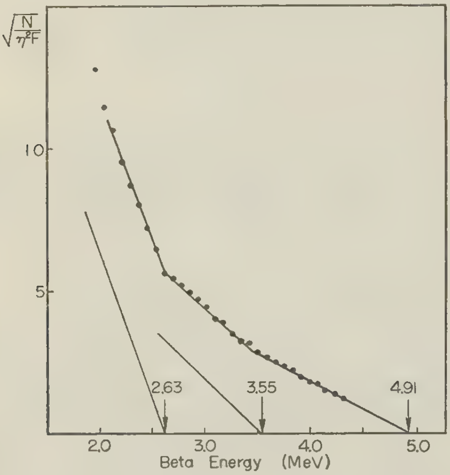

Fig. 2. Fermi-Kurie plot of the beta spectrum of K^{44}.

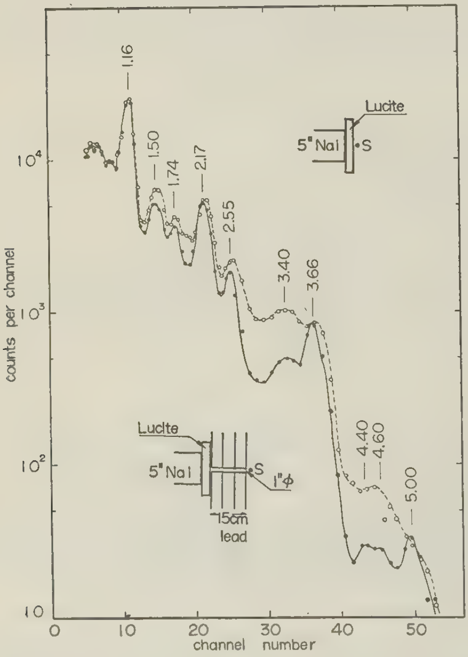

Fig. 3. Gamma ray spectra in K^{44}. Arrangements for sum peak measurements are also shown in this figure.

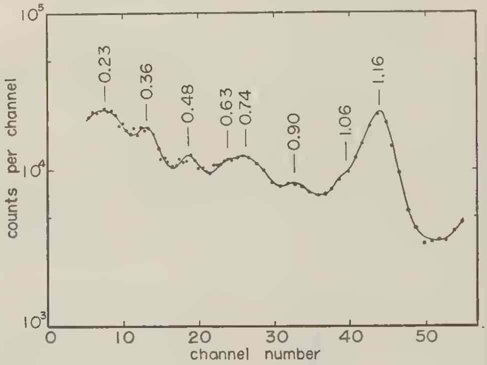

Fig. 4. The gamma ray spectrum in lower energy portion of K^{44}.

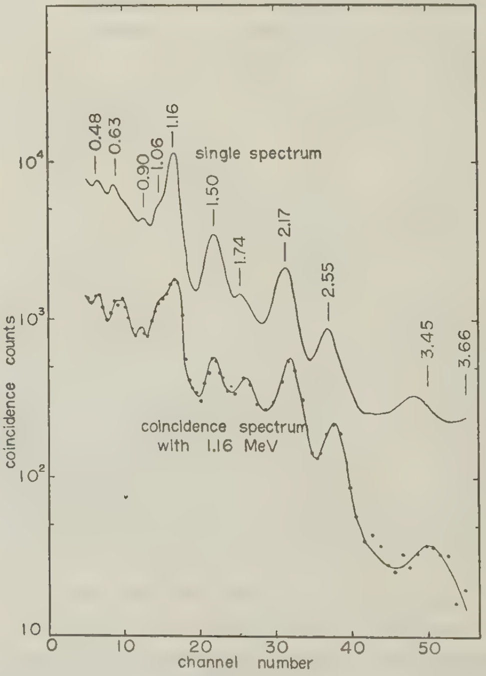

Fig. 5. Coincidence spectrum with the 1.16-MeV Gamma ray peak.

long NaI(Tl) crystals. The 1.16-, 1.5-, 2.1- and 2.5-MeV peaks were employed as gates. In each coincidence experiment the chance coincidence spectrum was subtracted from the observed coincidence spectrum using the gate counts as the source intensity normalization. The net coincidence spectra are shown in Fig. 5 and Fig. 6. It was found that the 2.1-MeV peak was a superposition of the 2.08- and 2.17-MeV and the 2.55-MeV line was also a doublet. These results are tabulated in Table I.

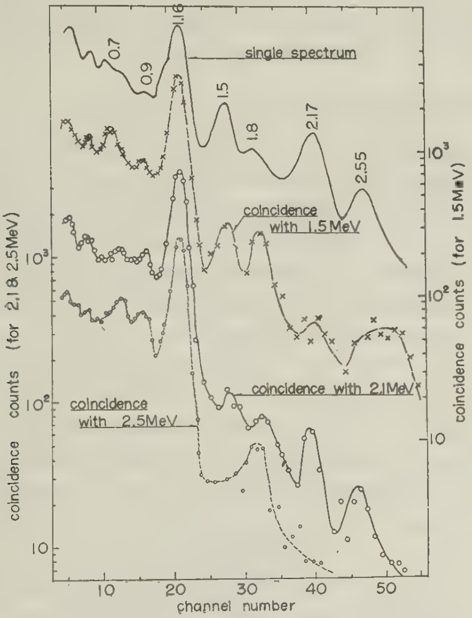

Fig. 6. Coincidence spectra with the 1.5-MeV Gamma ray peak (---×---), the 2.1-MeV Gamma ray peak (——○——) and the 2.5-MeV Gamma ray peak (----●----).

Table I. Summary of gamma-gamma coincidence measurements.

gate	1.16	1.5	2.1	2.5
coincident gamma rays	0.48	0.48	0.48	0.48
	0.63	0.63	?	0.63
	0.74	—	0.74	0.74
	0.90	0.90	0.90	0.90
	1.06	—	—	—
	?	1.16	1.16	1.16
	1.53	1.5	—	?
	1.74	1.74	—	1.74
	2.17	?	2.08	—
	2.55	?	2.55	—
	3.45	—	—	—

§ 3. Conclusion and Discussion

a) *Results*

At the result of above measurements, gamma rays belonging to Ca^{44} were assigned, and they are tabulated in Table II with their relative intensities. The relative intensities of lower energy gamma rays could not be determined since they suffered from disturbances due to higher energy gamma-rays. For the determination of the relative intensity, the efficiency of 5-in. dia. 5-in. long NaI(Tl) crystal with the lead slit was determined experimentally using several gamma rays of Cs^{137}, Na^{22}, Na^{24}, and Co^{60}, the efficiency in our source position (see Fig. 2) being found to be lower than the calculation[6] for parallel beam.

Table II. Energy and relative intensity of gamma radiations in K^{44}.

γ-ray energy	relative intensity
0.48-MeV	—
0.63	—
0.74	—
0.90	1
1.06	1
1.16	100
1.5	—
1.74	13
2.08 2.17	60
2.55	12
3.4	—
3.66	6.2
4.4	—
4.6	—
5.0	0.6

b) *Decay scheme*

There are reaction data on the levels of Ca^{44}, $K^{41}(d, p)Ca^{44}$ by J. P. Schiffer[7] and $Ca^{44}(p, p')Ca^{44}$ by C. M. Braams[8]. These data were referred to our proposed level scheme shown in Fig. 7.

No measurement have been reported to far on the spin and parity assignment of the K^{44} ground state. Since this configuration is p: $(d\ 3/2)^3$ and n: $(f\ 7/2)^5$, according to Nordheim rule it might be 2^-. Although K^{40} and K^{42} have the same configuration with K^{44}, however, there are measurements[3] in which K^{40} has 4^- and K^{42} has 2^- and K^{40} is an exception of the Nordheim's rule. According to the beta energy systematics, the K^{44}–Ca^{44} transition energy is expected to be about 6.1-MeV. Since our measurement has shown that the highest energy of the beta ray is 4.91-MeV and it is known that the first excited state of Ca^{44} is at 1.16-MeV the 4.91-MeV beta ray therefore may correspond the transition to the 1.16-MeV 2^+ state. The branching ratio of this transition is about ten percent and so $\log ft=8.0$ which is rather lower than the value for the first unique forbidden transition.

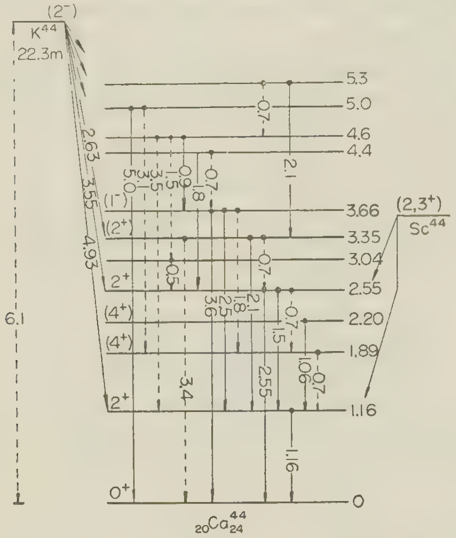

Fig. 7. Proposed decay scheme of K^{44}. The decay scheme of Sc^{44} proposed by J. W. Blue and E. Bleuler is also shown in this figure.

So, it may be expected that the spin and the parity of the ground state of K^{44} is 2^-. We could not find the 6.1-MeV beta ray within the intensity limit of one percent. This transition would be the first unique forbidden because $\log f_0t=7.4$ and $\log ft>9.5$. It is therefore reasonable that K^{44} ground state is 2^-. The 1.89-MeV second excited state and the 2.2-MeV third excited state may be 0^+ or 4^+, since we could find neither the cross over gamma rays to the ground state nor beta rays to these states. However, it would be 0^+ if the ground state of K^{44} is 4^-. As to this problem, it is interesting that the second excited state of Ca^{42} is recently measured as 0^{+} [9),10)].

The 2.55-MeV state is expected to be 2^+ because of the presence of the 2.55-MeV gamma ray to the ground state, the 3.55-MeV beta transition ($\log f_0t=6.1$) and the K-Capture transition from the Sc^{44} ground state (2^+ or 3^+)[2)].

The 2.63-MeV beta transition ($\log f_0t=5.7$) was assigned as the transition to the 3.35-MeV state which was assigned as 2^+.

Although we could not assign the spins of the higher energy levels from our data, the 3.66-MeV state may be the lowest odd spin state and probably 1^- according to the odd spin state systematics, found by H. Morinaga.

§ 4. Acknowledgement

The authors would like to thank Dr. H. Morinaga who suggested the present work and showed his unpublished data studied at Purdue University. They are also indebted to Professor M. Kimura for his continual encouragements throughout this work. It is a pleasure to acknowledge their indebtedness to Dr. S. Iwata who suggested the method of the chemical treatment. Further, they are greatly indebted to the beta group, the chemist group and the cyclotron crew in the Institute of Nuclear Study, Tokyo University.

References

1) B. L. Cohen: Phys. Rev. **94** (1954) 117.
2) J. W. Blue and E. Bleuler: Phys. Rev. **100** (1955) 1324.
3) K. Way, R. W. King, C. L. McGinnis and R. van Lieshout: Nuclear Level Schemes (TID-5300).
4) H. Walke: Phys. Rev. **52** (1937) 663.
5) W. W. Buechner: quoted by K. Way et al. ref. 3.
6) W. F. Miller, J. Reynolds and W. J. Snow: Rev. Sci. Instr. **28** (1957) 717.
7) J. P. Schiffer: Phys. Rev. **97** (1955) 428.
8) C. M. Braams: quoted by P. M. Endt and C. M. Braams: Rev. Mod. Phys. **29** (1957) 683.
9) H. Morinaga, N. Mutsuro, M. Sugawara: Phys. Rev. **114** (1959) 1146.
10) I. Asplund and T. Wiedling: Arkiv f. Fysik **15** (1959) 303.
11) H. Morinaga: Phys. Rev. **103** (1956) 503.

JOURNAL OF THE PHYSICAL SOCIETY OF JAPAN, Vol. 15, No. 11, NOVEMBER, 1960

Absolute Cross Section of the Reaction $Cu^{63}(\gamma, n)Cu^{62}$ for Lithium Gamma Rays

By Shinjiro YASUMI, Minoru YATA*, Kunio TAKAMATSU,
Akira MASAIKE and Yoshiko MASUDA**

Department of Physics, Faculty of Science, Kyoto University, Kyoto

(Received July 13, 1960)

The cross section of the reaction $Cu^{63}(\gamma, n)Cu^{62}$ for Li gamma rays was measured in order to discover some causes of the existing discrepancy between values measured by bremsstrahlungs and by nuclear gamma rays. Experimental procedures used in this experiment were much improved as compared with those used in previous measurements performed in our laboratory for the same purpose.

The present results were as follows:

$$\sigma_{\mathrm{Li}-\gamma}=62\pm4 \text{ mb for Li gamma rays,}$$

and

$$\sigma_{17.6}=76\pm5 \text{ mb for 17.6 Mev } \gamma\text{-rays.}$$

This value is about 30 per cent lower than the average cross section value determined by the photon difference method in several bremsstrahlungs' experiments. Therefore, we suggest that the modified spectrum method proposed by Penfold and Leiss might eliminate not only the above-mentioned discrepancy but also the discrepancy between theoretical and experimental values in the form $\sigma_{-2}\equiv\int\sigma E^{-2}dE$, as pointed out by Levinger.

§1. Introduction

It is a very interesting problem to study the interactions between electromagnetic waves and various nuclei by comparing experimental values with theoretical predictions on total photoreaction cross sections. Usually, for this purpose, experimental cross sections determined by using electron bremsstrahlungs are compared with the various sum rules in such forms as $\int\sigma dE$, $\int\frac{\sigma}{E}dE$, $\int\frac{\sigma}{E^2}dE$, etc.

In a previous paper¹⁾, using lithium gamma rays, we determined a value for the cross section of $Cu^{63}(\gamma, n)Cu^{62}$ reaction, which has been frequently used as the standard for photoreaction cross sections; and we compared this value with other experimental values hitherto published by several authors at $E_\gamma=17.6$ Mev. Then we found that the values measured by various investigators did not agree with one another, and they can be roughly divided into two groups, one of which averages about 100 mb and the other about 50 mb. Moreover, it appears generally that the former group contains mainly bremsstrahlungs' data and the latter mainly Li gamma rays' ones.

These facts seem to be very important for the above-mentioned problem, and further we found that our previous experiment¹⁾ included the following defects: (1) There are comparatively large statistical errors in the absolute measurement of the γ-flux; (2) We had used the values determined by another experiment as the correction factors for the absolute β counting, instead of determining these factors directly, and the geometries of the two β countings were found to be not identical with each other. Therefore, the correction factors used in the previous work seem to be inappropriate. (3) When we converted the cross section for cross section for Li gamma rays into the one for 17.6 Mev gamma rays, the most suitable values were not necessarily used. In order to discover the causes for such discrepancies among the measured values, we tried to improve the experimental procedures to obtain a more accurate value on the $Cu^{63}(\gamma, n)Cu^{62}$ cross section. Refinements performed in this study are as follows: (1)

---

* Present address: Sumitomo Electric Industries Co. Ltd.

** Radiation Center of Osaka Prefecture.

Hough's method[2),3)] in the absolute determination of the γ-ray flux was improved by using a transparent 4π Geiger counter specially designed at our laboratory; (2) As another calibration of the γ-ray intensity, a large NaI ($5''\phi \times 4''$) scintillation counter was used, whose detection efficiency for gamma rays was calculated by Wolicki *et al.*;[4)] (3) The absolute β counting method by which we obtained a true specific activity from counting rates measured for samples with finite thickness, was also improved not only by using 4π β counter whose construction was designed to be almost the same as that of the transparent 4π Geiger counter, but also by using very intense Cu^{62} thin samples activated by T-d 14 Mev neutrons at the same irradiation geometry as γ-rays' one; (4) The γ-ray source was more sharply defined than in the previous experiment.

§ 2. Experimental Procedures and Results

The γ-rays were produced by the $Li^7(p, \gamma)Be^8$ reaction: Li metal of about 0.5 mm in thickness, attached firmly* on molybdenum plates sufficiently cooled with water from behind, was bombarded with magnetically analysed protons ($\sim$50 μA) which were accelerated to about 450 kev by a Cockcroft generator. Sample discs made of natural copper, which were 20 mm in diameter and 0.9 mm in thickness, were irradiated by these γ-rays, and (γ, n) cross sections were determined by the activation method.

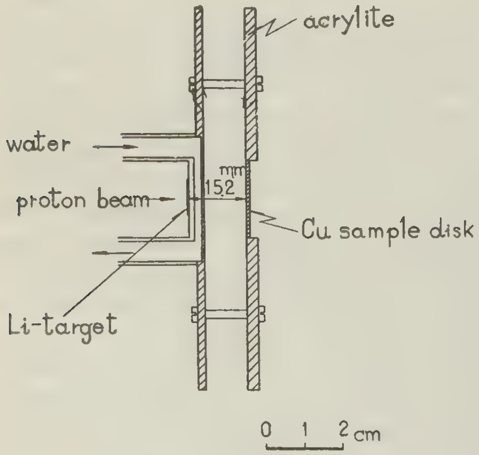

Fig. 1. Schematic drawing of the γ-ray irradiation geometry.

The size of the proton beam spot was well-defined to about 5 mm×4 mm by a slit of 4 mmϕ and the γ-irradiation geometry used in this work was the same as for the previous experiment[1)], as shown in Fig. 1.

Measurement of γ-quanta

The γ-ray intensities were measured by using an end-window Geiger counter enclosed with thick lead walls, as indicated in Fig. 2, which we shall call the "γ-monitor" hereafter; and its detection efficiency for Li-p γ-ray was calibrated by the improved Hough's method of which we will give an account subsequently.

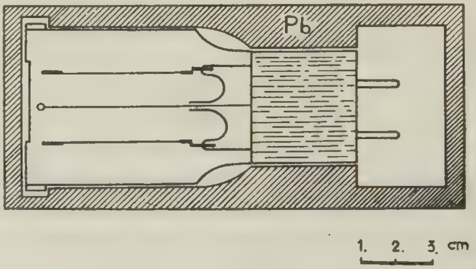

Fig. 2. An end-window Geiger counter enclosed with thick lead walls, which we call the "γ-monitor" in this paper.

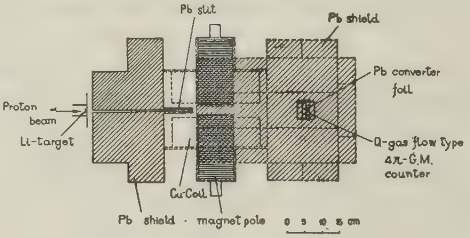

Fig. 3. Hough's arrangement for determining the γ-ray flux used in this experiment. A detailed construction of the Q-gas flow type 4π-Geiger counter represented in this figure is shown in Fig. 4.

Hough's arrangement for determining the γ-ray flux used in this experiment is schematically represented in Fig. 3. The counter which we used to count secondary electrons emitted from a converter foil by γ-rays has the construction as shown in Fig. 4. This is a 4π Geiger counter of Q-gas** flow type and is made transparent along the γ-rays' passage by the use of two windows consisting of mylar and wire gauze. A converter attached to a converter holder by "cello-tape" can be put in the centre of this counter.

---

* Lithium metal was melted on a molybdenum plate in a vacuum chamber.

** Q-gas consists of helium (99%) and isobutane (1%), and it was purchased from Takachiho Shoji Co. Ltd.

As converters, lead foil discs 8 mm in diameter were used, their dimension being carefully determined, taking account of the dimensions of the Pb-slits and the windows of the counter.

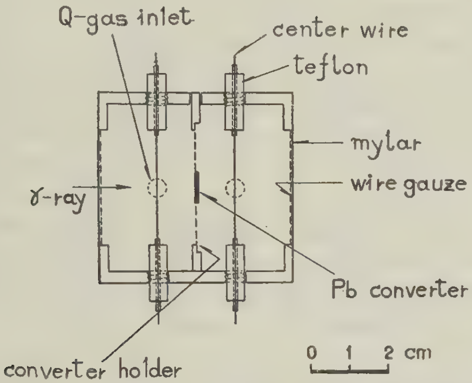

Fig. 4. Construction of the Q-gas flow type 4π-Geiger counter used in Hough's arrangement.

We can expect from the arrangement shown in Fig. 3 that the counter will be able to count all secondary electrons produced from a Pb converter disc if the latter is sufficiently thin.

In this case, the count of the converter counter is given by

$$N_c(w)=N_{c0}+n_\gamma\frac{N_0}{M}w\bar{\sigma}_e\ , \qquad (1)$$

where

$N_c(w)$: counts of the counter with a Pb converter of w weight,
N_{c0}: counts of the counter without a Pb converter,
n_γ: number of γ-quanta per cm² at the position of a Pb converter,
$\bar{\sigma}_e$: electronic absorption cross section of lead for Li-p γ-rays (averaged over 17.6 Mev and 14.8 Mev γ-rays),
w: weight of lead converter discs,
N_0: Avogadro's number,
M: Molecular weight of lead.

The γ-monitor (Fig. 2) to be calibrated was in operation together with the 4π counter, and we measured the ratio of $N_c(w)$ to the count of the γ-monitor N_M for various weights of converters. Then, Eq. (1) becomes,

$$\frac{N_c(w)}{N_M}=\frac{N_{c0}}{N_M}+\frac{n_\gamma N_0}{M\cdot N_M}\cdot w\bar{\sigma}_e\ . \qquad (2)$$

The ratio N_{c0}/N_M should be as small as possible to ensure the accuracy of measurements. For this purpose, special care was taken with the arrangements in Fig. 3: (1) The dimensions of the Pb-slit were so chosen that the γ-ray flux through it sufficiently covered the converter disc (8 mmϕ) and never collided with the thick walls of the 4π counter; (2) No lead shields were placed behind the counter; (3) The magnetic field of an electromagnet was used to remove secondary electrons from the forward direction.

In this experiment, it is obvious that the correct alignment of the γ-source—slit—counter—converter foil-system is very essential, and the transparency of the converter counter was found to be very helpful in aligning it exactly and easily.

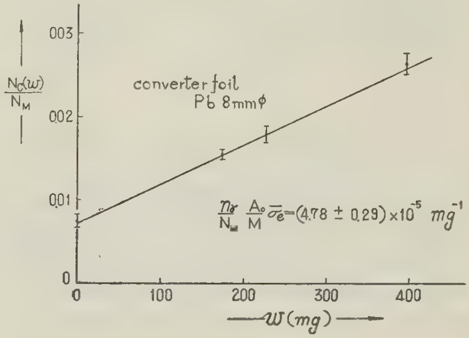

Fig. 5. Plot of $N_c(w)/N_M$ *versus* w, the thickness of converter foils. The solid straight line is the best fit by least square calculation. From the slope of this straight line, we obtain, $(n_\gamma/N_M)(N_0/M)=(4.78\pm0.29)\times10^{-5}\ \text{mg}^{-1}$.

The ratio $N_c(w)/N_M$[*] is plotted against various thicknesses ($w=0$, 172.0 mg, 225.3 mg, 397.3 mg) of the foil converter discs in Fig. 5, in which the solid straight line is the best fit by least square calculation. From the slope of this straight line, we obtain

$$\frac{n_\gamma N_0\bar{\sigma}_e}{N_M M}=(4.78\pm0.29)\times10^{-5}\ \text{mg}^{-1}\ . \qquad (3)$$

Then, if we use $\bar{\sigma}_e=(19.6\pm0.12)$ barns as the electronic absorption cross section of lead for

---

[*] For Li-p γ-rays, as naturally expected, the counting rates of the forward-half counter was almost constant for changing thickness of foils. Therefore we adopted the counts by the backward-half counter only as $N_c(w)$.

Li-p γ-rays, averaged over 17.6 Mev and 14.8 Mev γ-rays, we get

$$\frac{n_\gamma}{N_M}=0.8331\,\mathrm{cm}^{-2}\,.$$

Consequently, if we assume that γ-rays are emitted isotropically[5], the total number of γ-quanta, N_γ, emitted from a target is given as follows for one count of the γ-monitor placed at a distance of 50.05 cm from the γ-source:

$$\frac{N_\gamma}{N_M}=\frac{n_\gamma}{N_M}4\pi R^2=(4.09\pm0.25)\times10^4\,. \qquad (4)_1$$

This value agrees very well with the previous measurement[3] performed by us, which however has less accuracy than the present work.

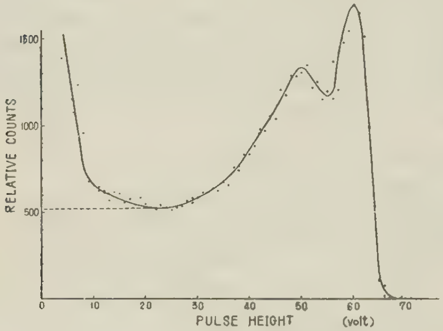

Fig. 6. Pulse-height distribution from an NaI crystal ($5''\phi\times4''$) irradiated by Li-p gamma rays. The shape of pulse-height distribution at low energy range is assumed to be represented by a dotted straight line parallel to the abscissa.

Another calibration of the γ-monitor was performed using an NaI (Tl) crystal ($5''\phi\times4''$) scintillation counter, which was operated together with the γ-monitor during the irradiations of γ-rays. Pulse-height distributions from the NaI counter were obtained with a 10 channel pulse-height analyser, and these are shown in Fig. 6. If the shape of pulse-height distribution at lower energy ranges is assumed to be represented by a dotted straight line parallel to the abscissa as shown in Fig. 6, the following value is obtained from the detection efficiencies of the NaI (Tl) scintillator for γ-rays calculated by Wolicki *et al.*[4], and from the geometries of arrangements:

$$\frac{N_\gamma}{N_M}=(4.41\pm0.44)\times10^4\,. \qquad (4)_2$$

This value agrees fairly well with the value $(4)_1$ obtained by Hough's method, taking into account the absorption by target materials.

Thus, we adopted the value determined by Hough's method as the detection efficiency of the γ-monitor, namely: For the case where the γ-monitor is placed at a distance of 50.05 cm from the γ-source,

$$\frac{N_\gamma}{N_M}=\frac{4\pi}{\omega\cdot\mathcal{E}}=(4.095\pm0.25)\times10^4\,, \qquad (5)$$

where ω is the solid angle which the γ-monitor subtends at the γ-ray source and $\mathcal{E}$ is the detection efficiency of the γ-monitor.

Determination of the Cross Section

The cross section of $\mathrm{Cu}^{63}(\gamma, n)\mathrm{Cu}^{62}$ reaction was determined by the activation method.

γ-ray intensities were measured by the γ-monitor for every one minute interval throughout irradiations, and we can regard γ-ray intensities as almost constant in each interval. After irradiations, produced activities on sample discs of 20 mm in diameter and 0.9 mm in thickness were measured by an end-window Geiger counter for about ten minutes.

Then, the cross section σ was determined by the following equation:

$$\sigma=\frac{M\left[N\Big/\sum_{i=1}^{T}N_{Mi}\exp\{-(T-i+t_0)\lambda\}\right]\cdot S'\cdot C_k}{N_0\eta\Omega A[(1-e^{-\lambda})(1-e^{-t'\lambda})/\lambda)]\cdot(4\pi/\omega\cdot\mathcal{E})}\,, \qquad (6)$$

where

N_0: Avogadro's number
M: molecular weight of the sample
η: isotopic abundance
S': $=S\cdot C_G=\lim\limits_{w\to0}\dfrac{N_s}{N\cdot w}$ where S is a correction factor related to the self-absorption and the self-scattering of the sample; C_G is a geometrical correction factor for the β-counting concerning the solid angle, the absorption by air and a mica window of an end-window Geiger counter, and the back scattering; N_s is the β count on thin samples, and N is the β count for the same time interval on samples of 0.9 mm in thickness, after neutron irradiations.
Ω: solid angle of the sample under irradiation; it is equal to $(1/4)\log\{(R^2+a^2)/a^2\}$, where R is the radius of the sample and a is the distance between the γ-source and the front surface of the sample disc.
A: correction factor concerning the finite

dimension of the γ-source.

N_{Mi}: γ-counts by the γ-monitor for one minute of the i-th interval

T: time of irradiation

t_0: time elapsed from the end of irradiation to the beginning of the β counting

i: number of the order of each time interval during irradiation (integer)

t': time interval of β-counting on the sample after irradiation

N: β-counts per t' minute on the sample of 0.9 mm in thickness

C_k: correction factor concerning the branching ratio between the positron emission and the orbital electron capture

ω: solid angle which the γ-monitor subtends at the γ-ray source

$\mathcal{E}$: detection efficiency of the γ-monitor, where $4\pi/\omega\mathcal{E}=4.095\times10^4$ by Eq. (5)

λ: decay constant of the isotope Cu^{62}

S' can be defined to be the product of S factor by C_G-factor, the former being the correction factor related to the self-absorption and self-scattering of the the sample, and the latter being the geometrical correction factor concerning the solid angle, the absorption by air and mica window of an end-window Geiger counter, and the back scattering of the sample and the other materials.

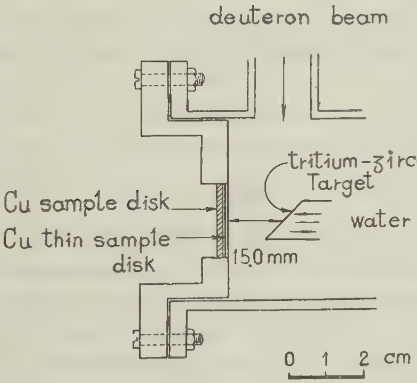

Fig. 7. Schematic drawing of the neutron irradiation geometory.

In order to obtain the S'-value, thin copper discs of various thickness with the same diameter as the sample disc were irradiated with T-d neutrons in juxtaposition with it, as indicated in Fig. 7. After irradiations, produced activities on the former (thin sample) were counted by a 4π-Geiger counter of Q-gas flow type whose construction is shown in Fig. 8 and on the latter (so-called sample disc) by an end-window Geiger counter for the same time interval.

When the ratio $N_s/(N\cdot w)$ is plotted against w, we obtain a curve as shown in Fig. 9. If this curve is extrapolated to zero thickness, then the limiting value $\lim_{w\to0}\{N_s/(N\cdot w)\}\equiv S'$ can be obtained, which may be taken as the value proportional to the product of the "true" specific activity by the geometrical correction factor.

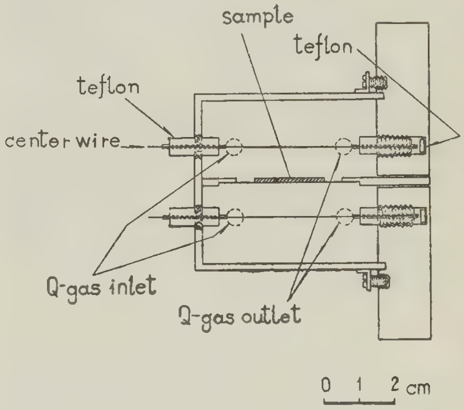

Fig. 8. Construction of a 4π-Geiger counter of Q-gas flow type used in the activation measurement.

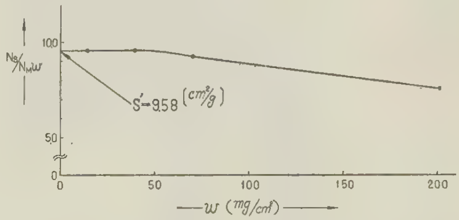

Fig. 9. Plot of $\{N_s(w)\}/(N\cdot w)$ *versus* the thickness of thin samples. Extrapolating this curve to zero thickness, the limiting value $\lim_{w\to0}(N_s)/(N\cdot w)=S'=9.58\ \mathrm{cm^2/g}$ can be obtained.

The result is as follows:

$$S'=9.58\ (\mathrm{cm^2/g})\ . \qquad (7)$$

We measured the decay curve at each run in the above-mentioned measurement, and it was verified that the same residual activity on samples irradiated by T-d neutrons was measured as in the case of Li-gamma rays.

The half-life of Cu^{62} was determined as 9.79 ± 0.13 min. in our previous work[1] and then the decay constant λ becomes:

$$\lambda=0.0708\,\mathrm{min}^{-1}\,. \tag{8}$$

Thus, substituting (5), (7), (8) into Eq. (6), the cross section of $Cu^{63}(\gamma, n)Cu^{62}$ for lithium gamma rays was obtained as follows:

$$\sigma_{\mathrm{Li}\text{-}\gamma}=62\pm4\ \mathrm{mb}\,. \tag{9}$$

The uncertainty indicated above is the overall error which results from the measurements for the following values, namely: S', $\omega\mathcal{E}$, N, λ, and N_{Mi}.

§ 3. Conclusions and Discussions

Lithium gamma rays, as is well known, consist of 17.6 Mev lines with a half-width of 12 kev and 14.8 Mev lines with a half-width of about 1.9 Mev[6]. When we want to convert the cross section value for Li gamma rays to that for 17.6 Mev gamma rays, it is necessary for us to know the intensity ratio between the above two γ-rays and the ratio of (γ, n) cross sections of Cu^{63} for these two γ-rays.

By simple calculations, the relation between $\sigma_{17.6}$ and $\sigma_{\mathrm{Li}\text{-}\gamma}$ is given by

$$\frac{\sigma_{17.6}}{\sigma_{\mathrm{Li}\text{-}\gamma}}=\frac{1+R}{(1/r)+R}\,, \tag{10}$$

where $I_{17.6}/I_{14.8}=R$ (intensity ratio) and $\sigma_{17.6}/\sigma_{14.8}=r$ (cross section ratio). For the intensity ratio R, the value determined by Stearns and McDaniel[7] is widely used, and we also adopted this value, namely $R=1.7\pm0.2$.

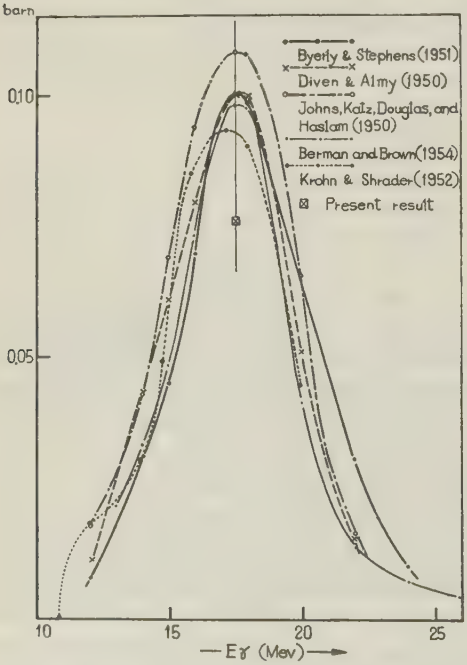

Fig. 10[8]. Excitation curves of the reaction $Cu^{63}(\gamma, n)Cu^{62}$ obtained by various authors. A point represents the value for 17.6 Mev γ-ray determined in the present experiment.

For the cross section ratio r, excitation curves determined by many authors give somewhat different values as indicated in Fig. 10. If we adopt the average value of these measurements for r, namely $r=2.0$, the cross section for 17.6 Mev γ-ray can be obtained by (10):

$$\sigma_{17.6}=76\pm5\ \mathrm{mb}\,.$$

This value is about 30 per cent lower than the average value of cross section values determined with bremsstrahlungs as is shown in Fig. 10.

Recently, Penfold and Leiss[9] proposed the "modified spectrum method" instead of the "photon difference method" originated by Katz and Cameron[10]. In the reaction $Ni^{58}(\gamma, n)Ni^{57}$, Roalsvig *et al.*[11] found that the absolute value of $\sigma_{\max}$ obtained by using the modified spectrum method was about 40 per cent lower than the value obtained by the photon difference method. If we assume a similar situation in the case of $Cu^{63}(\gamma, n)Cu^{62}$ as in the case of nickel, it seems very probable that $\sigma_{17.6}$ obtained by the present experiment will agree nicely with bremsstrahlung's data obtained by the modified spectrum method, since all bremsstrahlungs' data reproduced in Fig. 10 were obtained by the photon difference method.

Moreover, it was pointed out by Levinger[12] that the sum rule calculation in the form of $\sigma_{-2}\equiv\int\sigma E^{-2}dE$ by Migdal[13] gave $2.25\,A^{5/3}$ μb/Mev, while the experimental data for seven nuclei from Al to U agree with the equation of the same form but with a larger coefficient, namely, $\sigma_{-2}=3.5\,A^{5/3}$ μb/Mev. Considering* the fact that the above experimental data were all based on the $Cu^{63}(\gamma, n)Cu^{62}$ reaction cross section obtained from bremsstrahlungs' data by the photon difference method, it seems likely to us that the modified spectrum method for measurements with bremsstrahlungs might eliminate the above discrepancy between the theoretical and the experimental equations about σ_{-2}, as well as the discrepancy between the cross section value obtained by bremsstrahlungs and that obtained by lithium gamma rays.

---

* For these discussions we are greatly indebted to Dr. K. Okamoto.

Acknowledgements

The authors wish to express their sincere gratitude to Prof. K. Kimura for his encouragement throughout this experiment.

They are deeply indebted to Drs. K. Okamoto, T. Nakamura, I. Kumabe, and Prof. M. Kimura of Tohoku University for their valuable discussions. They wish also to express their sincere thanks to Mr. K. Okano for his kind help in γ-ray flux measurement by a scintillation counter. The authors' thanks are also due to Professor S. Tomotika and Mr. H. Hackett jr. for their kind inspection of the manuscript. The work was partly supported by a grant-in-aid for scientific research from the Ministry of Education.

References

1) T. Nakamura, K. Takamatsu, K. Fukunaga, M. Yata and S. Yasumi: J. Phys. Soc. Japan **14** (1959) 693.
2) P. V. C. Hough: Phys. Rev. **80** (1950) 1069.
3) T. Nakamura, K. Fukunaga, K. Takamatsu and S. Yasumi: Mem. Coll. Sci. Kyoto Univ. **A29** (1959) 141.
4) E. A. Wolicki, R. Jastrow and F. Brooks: Naval Research Laboratory Report, **NRL-4833**, Washington, D. C. 1956.
5) Devons and Lindsey: Proc. Phys. Soc. (London) **63A** (1950) 1202.
M. B. Stearns and B. D. McDaniel: Phys. Rev. **82** (1951) 450.
Nabholz, Stoll, and Wäffler: Helv. Phys. Acta **25** (1952) 153.
6) F. Ajzenberg-Selove and T. Lauritsen: Nucl. Phys. **11** (1959) 49.
7) M. B. Stearns and B. D. McDaniel: Phys. Rev. **82** (1951) 450.
8) P. R. Byerly and W. E. Stephens: Phys. Rev. **83** (1951) 54.
B. C. Diven and G. M. Almy: Phys. Rev. **80** (1950) 407.
H. E. Johns, L. Katz, R. A. Douglas and R. N. H. Haslam: Phys. Rev. **80** (1950) 1062.
A. I. Berman and K. L. Brown: Phys. Rev. **96** (1954) 83.
V. F. Krohn and E. F. Shrader: Phys. Rev. **87** (1952) 685.
9) Penfold and Leiss: *Analysis of Photo Cross Section* (Physics Research Laboratory, University of Illinois, 1958).
10) Katz and Cameron: Can. J. Phys. **29** (1951) 518.
11) J. P. Roalsvig, R. N. H. Haslam, and D. J. McKenzie: Can. J. Phys. **37** (1959) 607.
12) J. S. Levinger: Phys. Rev. **107** (1957) 554.
13) A. Migdal: J. Exptl. Theoret. Phys. U.S.S.R. **15** (1945) 81.

JOURNAL OF THE PHYSICAL SOCIETY OF JAPAN, Vol. 15, No. 11, NOVEMBER, 1960

Multipole Interaction Stabilizing Cubic Molecular Crystals

By Taro KIHARA

Department of Physics, Faculty of Science, University of Tokyo

(Received July 1, 1960)

The stability of several cubic molecular crystals is investigated on the basis of multipole interaction between the molecules. The stability of the cubic close-packed structure of heavy rare-gas crystals is due to the repulsion between electrical octapoles induced in atoms in the hexagonal close-packed structure. The face-centered cubic structures of carbon dioxide and cyclohexane-hexahalides and the body-centered cubic structures of silicon-tetrafluoride and hexamethylene-tetramine are configurations with the maximum electrostatic attraction between permanent charge distributions in the molecules. Pingpong balls containing two or four pieces of magnet represent these molecules with permanent multipoles; and it is demonstrated that a proper "crystal" of such balls (suspended in water) is stable.

§1. Introduction

Spherically symmetric molecules crystallize into a close-packed structure. Thus neon, argon, krypton, xenon, and also methane CH_4 and adamantan (sym-tricyclodecane) $(CH_2)_6(CH)_4$ crystallize into the face-centered cubic lattice. There have been several attempts to explain the stability of the cubic close packing for rare-gas atoms over the hexagonal close packing (except helium for which quantum effect is predominant), but the problem has not been settled. A purpose of the present paper is to answer from a very simple and presumably correct point of view.

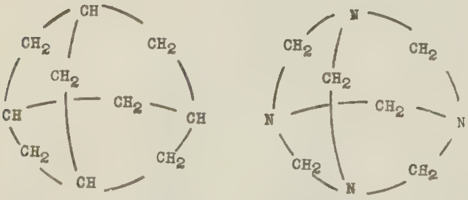

Fig. 1. Two nearly spherical molecules, adamantan and hexamethylene-tetramine, for which crystal structures are different.

Silicon-tetrafluoride SiF_4 and hexamethylene-tetramine $(CH_2)_6N_4$ are both nearly spherical like methane and adamantan (Fig. 1). They crystallize, however, not into a close-packed structure, but into the body-centered cubic lattice keeping the molecular orientations parallel (Fig. 2). On the other hand crystals of carbon-dioxide CO_2, cyclohexane-hexachloride $C_6H_6Cl_6$ and cyclohexane-hexabromide $C_6H_6Br_6$ have face-centered cubic structures. The molecular axes are then distributed equally in four orientations $(1,1,1)$, $(1,1,-1)$, $(1,-1,1)$, and $(-1,1,1)$; and the structures are not close packing for these prolate and oblate molecules (Fig. 3). All these molecules have strong electric multipoles; and another purpose of the present paper is to explain, by use of artificial molecules, the stability of these structures from the multipole interaction between molecules.

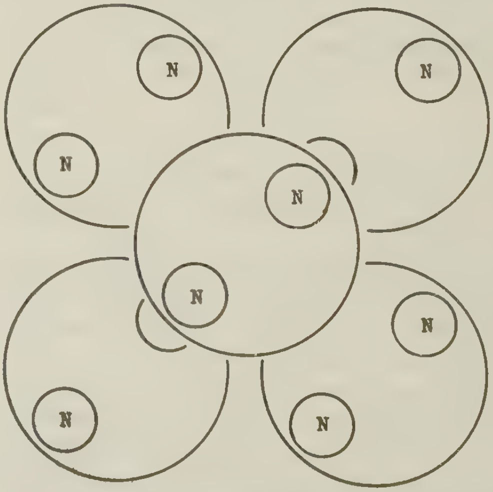

Fig. 2. Molecular orientation in the body-centered cubic crystal of hexamethylene-tetramine.

§2. Crystals of Heavy Rare-Gas Atoms

Much of the empirical research in molecular physics has been based on a two-body potential function such as

$$U(r)=\frac{U_0}{s-6}\left[6\left(\frac{r_0}{r}\right)^s-s\left(\frac{r_0}{r}\right)^6\right] \qquad (1)$$

or

$$U(r)=\frac{U_0}{\sigma-6}\left[6\exp\frac{\sigma(r_0-r)}{r}-\sigma\left(\frac{r_0}{r}\right)^6\right], \qquad (2)$$

where r is the intermolecular distance, and U_0 and r_0 are potential parameters. If the potential is assumed to be additive and if only the first-neighbor interaction in a crystal is considered, then the cubic and hexagonal close-packed structures have equal cohesive energies, because in both cases an atom has equal number (twelve) of first neighbors.

Interactions between second and farther neighbors were calculated in detail by Kihara and Koba[1]. It was shown, however, that the stability of the cubic close-packed lattice does not follow from the additive potential (1) for any value of s greater than 6 nor from the potential (2) for $\sigma > 8.675$. For these potentials the hexagonal close-packed lattice is more stable, although it is favored over the cubic by only 0.01 percent of the cohesive energy. The cubic close-packed lattice becomes more stable than the hexagonal for σ less than 8.675. But the potential (2) with $\sigma < 8.765$ has too wide a bowl to be accepted as a very accurate two-body intermolecular potential. This work was supplemented and confirmed by Jansen and Dawson[2], who took account of the zero-point energy.

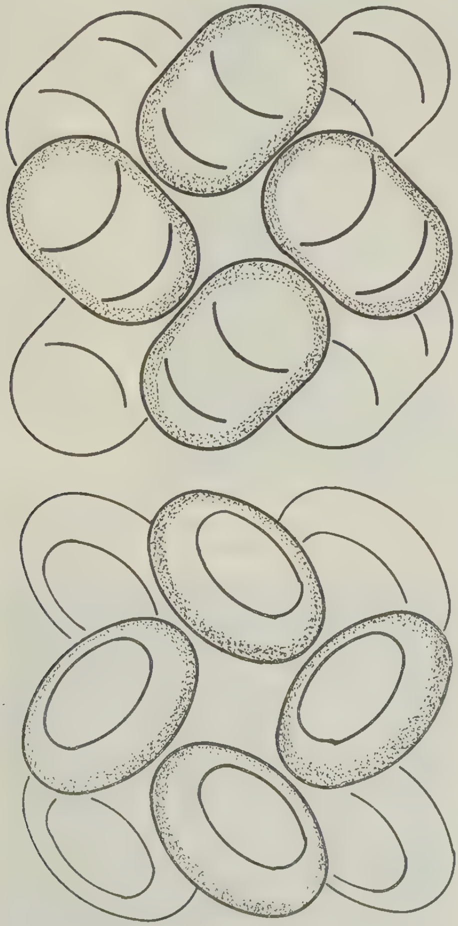

Fig. 3. Molecular orientations in the face-centered cubic crystals of carbon-dioxide (top) and cyclohexane-hexahalides.

Explanation of the stability of the cubic crystals on the basis of a two-body potential function was thus unsuccessful. As a next step three-body interactions were considered by several authors. Axilrod[3] summed the triple-dipole interaction, a nonadditive part of the van der Waals attraction, in both the cubic and hexagonal close packings. He concluded: " The difference in the triple-dipole interaction for the cubic and hexagonal close-packed lattice, although favoring the former structure, is less than 0.01 percent of the cohesive energy and hence cannot account for the structure of these rare-gas solids ".

The second and third virial coefficients in the equation of state of rare gases calculated by use of the potential (1) with $s=12$ agree with observed values when the nonadditivity of the intermolecular potential is taken into account[4]. If we assume the potential additivity, on the other hand, then we must use an effective intermolecular potential with a wider bowl in order to explain the temperature dependence of the third virial coefficient[5]. In other words, the influence of nonadditivity of the intermolecular potential can, to some extent, be eliminated by using an effective (additive) intermolecular potential with a wider bowl. An appropriate choice may be not far from the potential (2) with $\sigma=8.675$, for which two structures of close packing have exactly equal cohesive energies.

Thus we have seen that no essential difference exists between cubic and hexagonal cohesive energies so far as a central force is assumed between molecules. An alternative approach is therefore needed; non-central forces must be considered, as it was pointed out by Prins et al.[6] and Barron and Domb[7].

A rare-gas atom is spherically symmetric in free space, but not in a crystal because of the compression by surrounding atoms. An atom in a close-packed lattice has twelve nearest neighbors and has six "windows" facing the second neighbors (Fig. 4). At these windows the electron density should be different from other parts, and hence the atom has an electrical multipole. It is easily seen that, in a hexagonal close-packed lattice, this multipole is an octapole and the octapole interaction between first neighbors is repulsive.

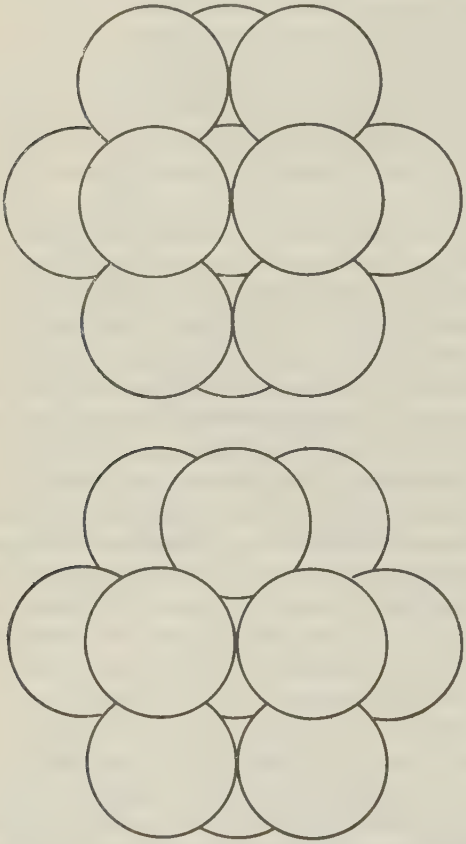

Fig. 4. First neighbor configurations for hexagonal (top) and cubic close packings.

In a cubic close-packed lattice, on the other hand, an atom has a higher symmetry, the lowest-order non-vanishing multipole being hexadecapole. Although this hexadecapole interaction is also repulsive, the effect is definitely smaller than the octapole repulsion in the hexagonal case.

Thus we reach the following conclusion: *The stability of the cubic close-packed structure of heavy rare-gas crystals is due to the repulsion between electrical octapoles induced in atoms in the hexagonal case.*

§ 3. Cubic Crystals of Molecules with Permanent Multipoles

In a previous paper Kihara and Koba[8] discussed the cohesive energy of the face-centered cubic crystal of carbon-dioxide, and showed that 20 percent of the cohesive energy is the quadrupolar attraction between the molecules. If the carbon-dioxide crystallized into a close-packed lattice, keeping the molecular axes parallel, then the quadrupolar interaction, which is repulsive in this case, would reduce its total cohesive energy.

The crystal structures of cyclohexane-hexahalides can be understood in a similar way. It should be noted, however, that quadrupoles of these molecules are not point quadrupoles but the molecules have their nonvanishing sizes of charge distribution.

The electric charge distribution in a carbon-dioxide or cyclohexane-hexahalide molecule can be represented by a "magnetic charge distribution" in a convex body, a sphere, say. A system of these models of molecules will then crystallize into the corresponding cubic lattice, if the stability of the real crystal is due to this orientation-sensitive interaction.

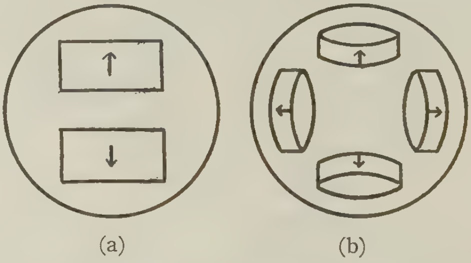

(a) (b)

Fig. 5. Pingpong balls containing pieces of magnetized barium-ferrite, which are our molecular models for carbon-dioxide and for hexamethylene-tetramine.

In order to make this type of artificial molecule, place appropriately two pieces of magnet inside a pingpong ball (Fig. 5a); let the ball have unit density and be suspended in water. A "crystal" of such balls in the configuration of carbon-dioxide or cyclohexane-hexahalide (Fig. 6) is in fact satisfactorily stable against disturbances.

A system of pingpong balls, each containing four smaller pieces of magnet in configuration of a tetrahedral symmetry (Fig. 5b), can "crystallize" in a body-centered cubic lattice which is characteristic of silicon-tetrafluoride

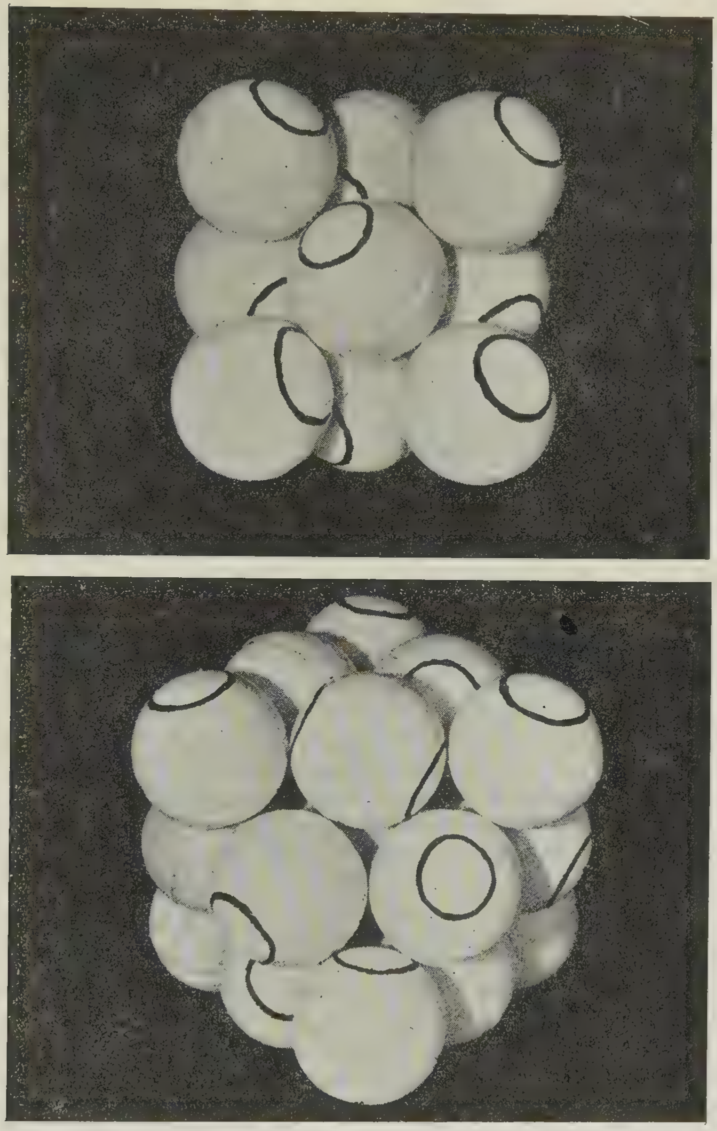

Fig. 6. Face-centered cubic crystals of the magnetized balls for carbon-dioxide or cyclohexane-hexahalide. Circles on the spherical surface indicate the positions of the magnets.

or hexamethylene-tetramine, the position of a piece of magnet corresponding to the position of a fluorine or nitrogen atom. (Fig. 7).

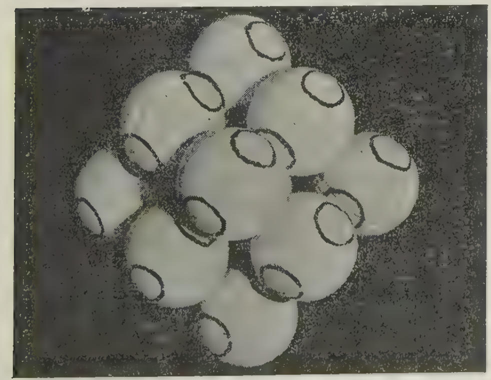

Fig. 7. Body-centered cubic crystal of the magnetized balls for silicon-tetrafluoride or hexamethylene-tetramine.

Thus we reach the following conclusion: *The face-centered cubic structures of carbon dioxide and cyclohexane-hexahalides and the body-centered cubic structures of silicon-tetrafluoride and hexamethylene-tetramine are configurations with the maximum electrostatic attraction between permanent charge distributions in the molecules.*

This work was partly done at the University of Wisconsin, Theoretical Chemistry Laboratory, in February and March, 1960.

References

1) T. Kihara and S. Koba: J. Phys. Soc. Japan **7** (1952) 348.
2) L. Jansen and J. M. Dawson: J. Chem. Phys. **22** (1954) 1619, **23** (1955) 482.
3) B. M. Axilrod: J. Chem. Phys. **19** (1951) 724.
4) S. Koba, S. Kaneko, and T. Kihara: J. Phys. Soc. Japan **11** (1956) 1050.
5) T. Kihara: Rev. Mod. Phys. **25** (1953) 831, **27** (1955) 412, Sec. 18.
6) J. A. Prins, J. M. Dumoré, and Lie Tiam Tjoan: Physica **18** (1952) 307.
7) T. H. K. Barron and C. Domb: Proc. Roy. Soc. A **227** (1955) 447.
8) T. Kihara and S. Koba: J. Phys Soc. Japan **14** (1959) 247.

JOURNAL OF THE PHYSICAL SOCIETY OF JAPAN, Vol. 15, No. 11, NOVEMBER, 1960

Anisotropic Hall Coefficients in n-Type Germanium

Hisao MIYAZAWA and Hajime MAEDA

Matsuda Research Laboratory, Tokyo-Shibaura Electric Co.,
Komukai-Toshiba-cho, Kawasaki

(Received July 13, 1960)

Precise measurements of Hall effect have been made at 77°K, 90°K, 195°K, and 298°K up to 11,000 gauss on oriented single crystals of n-type germanium containing 5×10^{14} antimony per cm^3 as donor centers. The results should principally indicate the variations of μ_H/μ with the magnetic field and with the temperature, since the carrier concentration may be practically constant under the present conditions.

Absolute values of μ_H/μ have been deduced from R_∞ and R_0. R_∞ for which μ_H/μ always equals unity is fortunately obtained by extraporating $R_H^{\langle001\rangle}$(77°K) vs $1/H^2$ data. Then $R_H^{\langle001\rangle}/R_\infty$ will straightway give $\mu_H/\mu \cdot \langle001\rangle_H$. On the other hand, μ_H/μ for other orientations may be indirectly estimated from their extraporated R_0 for which μ_H/μ is independent of the orientation and should be equal to $R_0^{\langle001\rangle}/R_\infty$ at respective temperatures, neglecting the effect due to slightly different impurity concentration between specimens.

Values of μ_H/μ thus determined are always smaller than unity, while those of $\langle001\rangle_H$ approach to unity most rapidly with increasing field and those of $\langle110\rangle_H$ most slowly. They are of course temperature dependent and the zero magnetic field values are equal to 0.83 at 77°K, 0.84 at 90°K, 0.90 at 195°K and 0.92 at 298°K respectively.

Numerical evaluation of the Boltzmann's equation taking account of ellipsoid model and mixed scatterings can give the observed values fairly well. It appears, however, preferable to introduce some correction term, e.g., reasonable amount of optical phonon scattering for the best agreement.

§1. Introduction

Hall measurements are the most popular and fundamental techniques to obtain many information about electronic properties in semiconductor physics. In most cases thus far, however, little attention has been paid to μ_H/μ appearing in the Hall coefficient, sometimes assuming it equals unity while sometimes equating it to $3\pi/8$ without considering scattering mechanisms in detail.

According to theoretical calculations, on the other hand, it is generally predicted that μ_H/μ is more or less dependent on the applied magnetic field and not a unique constant unless free carriers are perfectly degenerated. Usually, the behavior is rather complicated even if the semiconductor material is isotropic. For instance, Johnson and Whitesell[1] have indicated interesting results in which magnetic field dependence of μ_H/μ is considerably influenced by mixing a small amount of ionized impurity scattering into the acoustic phonon scattering in the case of isotropic semiconductor, although no experimental verifications have been given because of the lack of proper isotropic materials. Theoretical analysis of anisotropic Hall coefficients in n-type germanium has been briefly dealt with by Abeles and Meiboom[2] and also by Shibuya[3] who have aimed to explain anisotropic magnetoresistance data[4] by assuming ellipsoid band model and isotropic thermal scattering. Putting the effective mass ratio at 20, they obtained 0.93 for the values of μ_H/μ at zero magnetic field. As compared with the calculations by Johnson et al, the only regreatful point in their analysis is the neglection of slight impurity scattering in the real crystals, which may considerably affect the field dependence of Hall coefficient.

As for the experimental examinations of μ_H/μ, there have been little works chiefly because of the requirements for accurate instrumentations detecting rather small effects. It is noteworthy that anisotropic variations of relative μ_H/μ values with magnetic field strengths were first observed in n-type germanium at room temperatures by Mason, Hewitt and Wick[5] and ingeniously analysed on the phenomenolygical basis of cubic symmetry only. Though their beautiful results can elucidate the relation between crystal direction and Hall coefficient, absolute values of μ_H/μ and its temperature effect have not been given and remained obscure. A drastic determination of μ_H/μ in germanium was reported by Morin[6] who compared the conductivity mobility, which was calibrated by the drift mobility of minority carriers injected in p- or n-type specimens at 300°K, with the Hall mobility of respective type. He has quoted an experimental value of 1.05 for n-type independent of temperature between 25 and 300°K. In his case, however, despite of epoch-making method, observed data were too dispresed to discuss the agreement with theory and moreover no anisotropic characteristics were considered. His brilliant success was a disclosure of extraordinary behavior of μ_H/μ in *p*-type germanium which will not be referred here.

Since the ellipsoid model for n-type germanium has been well established by cyclotron resonance experiments[7], theoretical investigations of transport phenomena thereafter have been pointed to the anisotropy in the relaxation time. General aspect on such a basis has been discussed by Herring and Vogt[8]. Under these circumstances, reexamination of the Hall effect as well as other transport phenomena taking account of crystal orientation and scattering anisotropy was a desirable subject for many valley semiconductors. Bullis and Krag[9] have reported a timely work on n-type germanium specimens of highly symmetric orientations, in which they have shown that observed data for μ_H/μ at 77°K agree reasonably well with calculations using ellipsoid model and constant mean free time hypothesis, especially the agreement is good when the magnetic field is in $\langle 001\rangle$ direction and exceeds several kilo-gauss. In the second paper[10], Bullis has extended his measurements including other galvanomagnetic effects to another temperature of 300°K in addition to 77°K in order to evaluate the anisotropy factor principally due to the relaxation, where he has quoted the behaviors of Hall coefficients could not be quantitatively explained. Though these investigations have almost clarified qualitative features of μ_H/μ, there is some further information yet to be desired for better understandings.

The authors have carried out similar measurements on specimens of several selected crystal orientations at four different temperatures in the exhaustion region, and obtained the explicit variations of anisotropic μ_H/μ with temperatures and magnetic field strengths making an attempt at the highest accuracy. The present paper will describe those experimental results and the theoretical calculations aiming more quantitative approach without neglecting anisotropic factors both in effective mass and in mixed scatterings.

§2. Experimental Procedures

The techniques used here are almost similar to those by Bullis and Krag[9] and will be described briefly. Highly uniform and stable magnetic field up to 11,000 gauss was produced by an electromagnet for high resolution nuclear magnetic resonance of which pole face diameter was 30 cm and gap was 4.5 cm. The field strengths were determined within

0.01% errors by measuring proton resonance frequencies with a heterodyne frequency meter. The measurements of Hall voltage and sample current were carried out by a YEW Type P–7 potentiometer, where the observed values were reproducible at most within ±0.1%. Therefore, the whole accuracy was limited only by potential measurements.

Four measuring temperatures chosen here were 77°, 90°, 195°, and 298°K which were respectively provided by liquid nitrogen, liquid oxygen, mixture of dry ice and ethyl ether, and air-conditioned room temperature. In all cases the sample mounted on a holder was directly immersed in a Dewar vessel containing each refrigerant or no refrigerant.

The specimens were zone-leveled n-type germanium single crystals of about 3 ohm-cm containing nearly 5×10^{14} antimony per unit volume. Since these crystals are so well controlled that the concentrations of uncontrolled centers less than 10^{13} may be easily realizable, one may suppose an essential condition for the present purpose that the carrier concentrations are practically constant irrespective of temperatures even in the worst case. After the crystals were oriented by X-ray analysis, the specimens were cut out of the crystals in the shape as shown in Fig. 1 by a supersonic dice. The selected orientations are also indicated in Fig. 1. Angle θ varying from 0° to 90° was chosen as a parameter. In the following, a notation $R_H^{\langle\theta\rangle}(T°\mathrm{K})$ will represent the Hall coefficient at magnetic field strength of H gauss and at temperature of T°K in a specimen for which magnetic field is applied in the direction of angle θ. In place of θ, Miller indices will be used in the case of high symmetry orientations, for example, $\langle 0° \rangle$ will be represented bv $\langle 001 \rangle$ and so on. As either sample current or Hall voltage is in $\langle 1\bar{1}0 \rangle$ direction in the present case and both are permutable each other[4], indication of the direction is omitted in the notation. Although no cross magneto-resistance effect[4] appears in these orientations, Hall coefficient is determined according to the usual way by reversing the magnetic field and the sample current and averaging the observed Hall voltages. It was found in our case that the reversal of current had no important effect upon the results. First of all, the vital point for precise experiments was to

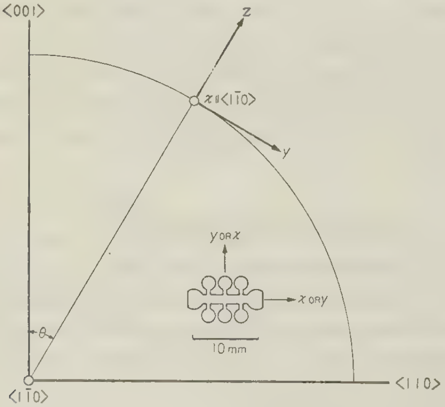

Fig. 1. Geometry of specimen and direction of magnetic field $\boldsymbol{H}$, sample current $\boldsymbol{I}$ and Hall voltage $\boldsymbol{V_H}$. θ is chosen as a parameter.

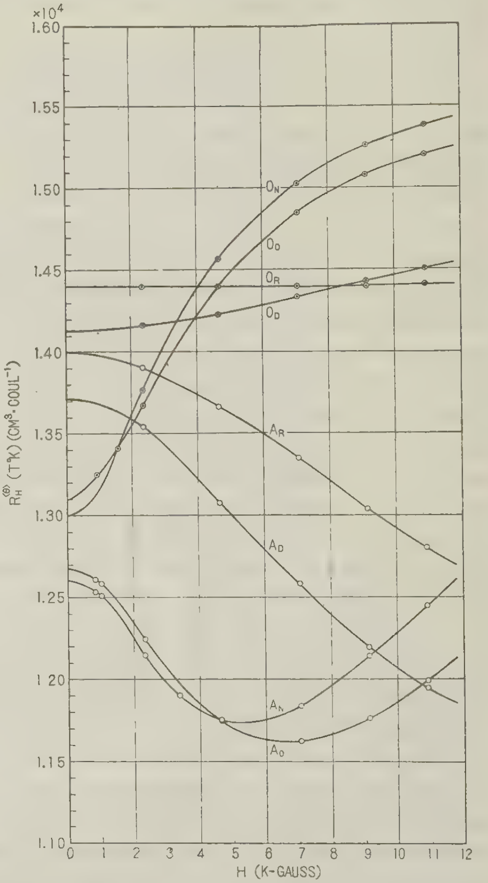

Fig. 2. $R_H^{\langle001\rangle}(T°\mathrm{K})$ and $R_H^{\langle110\rangle}(T°\mathrm{K})$ plotted against H. ⟨001⟩ sample is designated as " O ", and ⟨110⟩ as " A ". Subscripts R, D, etc. represent specified temperatures: i.e., R≡room temperature (298°K), D≡dry ice (195°K), O≡liquid oxygen (90°K), and N≡liquid nitrogen (77°K).

obtain low-resistance contacts for the specimens. In order to realize good ohmic contacts, electrode- and probe-arms were electroplated with rhodium or alloyed with tin-antimony alloy so as to be more n-type before soldering. There was no difference at room temperature between both treatments, where the contacts were always satisfactory, while at low temperatures the latter showed better results in contrast with facts that the former sometimes cracked or frequently made potentiometer balance insensible with slight contact resistance. Hence the alloying contacts were used in most specimens, though they required somewhat elaborate processes.

§ 3. Experimental Results

A. $R_H^{\langle\theta\rangle}$ vs H at several specified temperatures

Several curves of Hall coefficients for two typical high symmetry orientations are shown in Fig. 2. The following facts are notable here;

(1) that both $R_0^{\langle 001\rangle}(T°\mathrm{K})$ and $R_0^{\langle 110\rangle}(T°\mathrm{K})$ increase with increasing temperatures in the same proportion, and

(2) that $R_H^{\langle 001\rangle}(298°\mathrm{K})$ is strikingly field insensitive while other R_H's in both orientations vary in quite different manners.

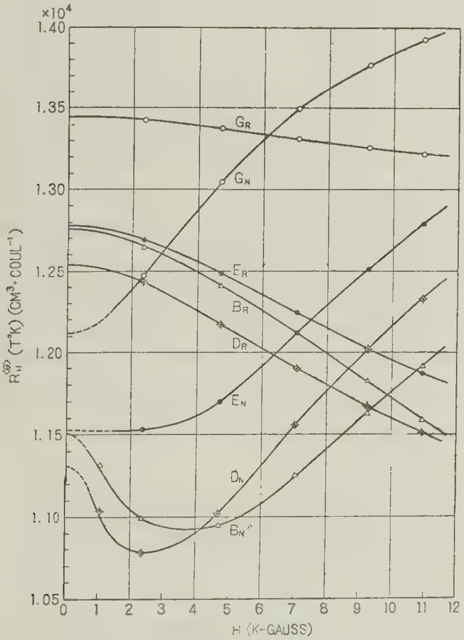

Fig. 3. $R_H^{\langle\theta\rangle}(T°\mathrm{K})$ vs H for several orientations. $\langle\theta\rangle=\langle 75°\rangle$ for sample B, $\langle 111\rangle$ for D, $\langle 112\rangle$ for E, and $\langle 15°\rangle$ for G. Subscripts are the same to Fig. 2.

Since carrier concentrations never decrease with increasing temperatures or hardly depend upon magnetic field strengths and directions, it is evident that behaviors of these curves should be ascribed to relative changes in μ_H/μ.

Fig. 3 shows several sets of Hall coefficients for specimens of other orientations.

B. Determination of $R_\infty^{\langle 001\rangle}(77°\mathrm{K})$ and $\mu_H/\mu\cdot\langle 001\rangle_H$

At high magnetic field and low temperatures a constant mean free time approximation for $R_H^{\langle 001\rangle}$ is very good as demonstrated by Bullis et al[9], and the Hall coefficient for an inifinite magnetic field, $R_\infty^{\langle 001\rangle}(77°\mathrm{K})$, is determined by plotting $R_H^{\langle 001\rangle}(77°\mathrm{K})$ as a function of $1/H^2$ and extraporating linearly to the value of $H=\infty$ as shown in Fig. 4. Since μ_H/μ at infinite magnetic field always equals unity irrespective of the crystal orientations, the mass ratio and the scattering mechanism as discussed in the theory. $R_H^{\langle 001\rangle}(T°\mathrm{K})/R_\infty^{\langle 001\rangle}\cdot(77°\mathrm{K})$ in the specimen should straightway give the absolute values of $\mu_H/\mu\langle 001\rangle_H$ provided the carrier concentration is constant. The constancy of the carrier will be discussed in the later section.

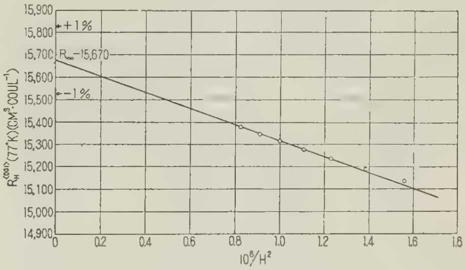

Fig. 4. $R_H^{\langle 001\rangle}(77°\mathrm{K})$ vs $1/H^2$. Determination of R_∞.

C. Evaluation of $\mu_H/\mu\langle\theta\rangle_H$

Since $R_\infty^{\langle\theta\rangle}(77°\mathrm{K})$ cannot be determined by simple extraporation method, $\mu_H/\mu\langle\theta\rangle_H$ must be indirectly evaluated in some other way. This is possible by noting a fact that the Hall coefficient for zero field is also independent of the crystal orientations, that is to say, $R_0^{\langle\theta\rangle}(T°\mathrm{K})ne$ should be equal to $R_0^{\langle 001\rangle}(T°\mathrm{K})n'e$ where n and n' are carrier concentrations of respective specimens and e is electronic charge. In the ideal case n and n' should be equal, but actually slight difference is inevitable because of the fluctuation in impurity concentration, even if the specimens are cut from the same ingot. Fortunately, $\mu_H/\mu(T°\mathrm{K})$ is a rather slowly varying function of the impurity concentration. Therefore, the effect of the difference in n on μ_H/μ will be neglected here, regarding it as insignificant. Fig. 5 shows the values of $\mu_H/\mu\langle\theta\rangle_H$ determined in these manners.

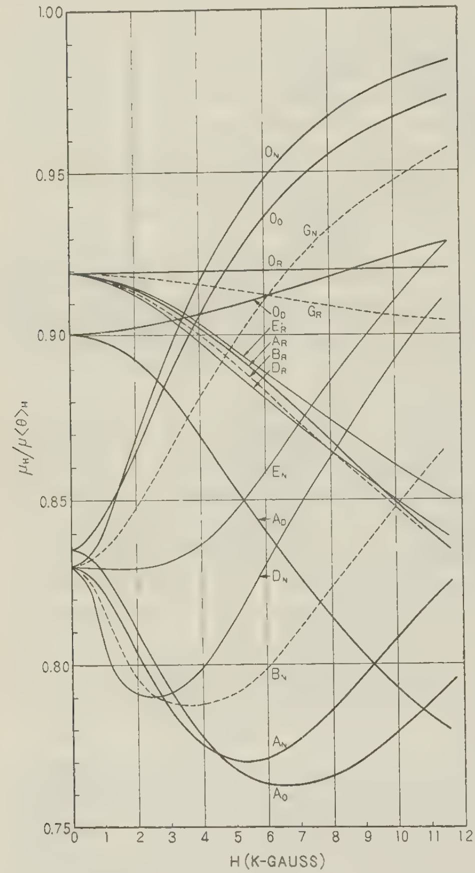

Fig. 5. Variations of $\mu_H/\mu\langle\theta\rangle_H$ at four temperatures with H.

In addition to the fact that considerably anisotropic features observed by Mason et al[5] and also by Bullis[9],[10] were reproduced here, it was explicitly examined for the first time that the values of μ_H/μ at usual magnetic field strengths and at usual exhaustion temperatures pass through a region fairly lower than unity in contrast with Morin's data[6].

As for the room temperature data, low field expansion formula,

$$R_H^{\langle\theta\rangle}=R_0(1+\xi^{\langle\theta\rangle}H^2+\eta^{\langle\theta\rangle}H^4+\zeta^{\langle\theta\rangle}H^6) \quad (3.1)$$

is valid in the whole range of measured magnetic field, and empirical values of coefficients, $\xi^{\langle\theta\rangle}$, $\eta^{\langle\theta\rangle}$ and $\zeta^{\langle\theta\rangle}$, are summarized in Table I, which also gives R_0, ρ_0 and μ_H. Theoretically calculated $\xi_c^{\langle\theta\rangle}$'s are also listed in Table I, where agreement between $\xi^{\langle\theta\rangle}$ and $\xi_c^{\langle\theta\rangle}$ seems to be satisfactory.

D. Reproductibility of $\mu_H/\mu(T°\mathrm{K})$

It will be desirable to check whether the assumption of constant carrier concentration irrespective of temperature is allowable or not. Though any orthodox examination is not available since variations of carrier concentration and μ_H/μ with temperatures is inseparable in the experiments, it may be worth-while to examine the reproducibility of μ_H/μ on specimens cut from different ingots which may contain different concentrations of uncotrolled centers. These uncontrolled centers which capture electrons at low temperatures may be ionized in some degree at room temperature, resulting in the increase in conduction electrons which, in turn, may cause the decrease in Hall coefficients. If observed values of $R_H^{\langle\theta\rangle}(T°\mathrm{K})/R_\infty(77°\mathrm{K})$ in each specimen were too much random, reliable determination of $\mu_H/\mu(T°\mathrm{K})$ may be hopeless,

Table I. Weak field expansion data at room temperature for 3 or 4 ohm-cm n-type Ge.

sample $\langle\theta\rangle_H$	A <110>	B <75°>	D <111>	E <112>	G <15°>	O <001>
R_0 (cm³/coul)	13,998	12,743	12,532	12,767	13,439	14,400
ρ_0 (ohm-cm)	4.1	3.5	3.3	3.9	4.15	3.84
μ_H (cm²/v·sec)	3,414	3,641	3,798	3,274	3,238	3,750
$\xi^{\langle\theta\rangle}$ (gauss^{-2})×10⁹	−1.245	−1.298	−1.582	−1.144	−0.278	0
$\eta^{\langle\theta\rangle}$ (gauss^{-4})×10¹⁸	7.112	7.952	14.00	7.676	1.762	
$\zeta^{\langle\theta\rangle}$ (gauss^{-6})×10²⁶	−2.211	−2.811	−5.366	−2.495	−0.503	
$\xi_c^{\langle\theta\rangle}$ (gauss^{-2})×10⁹	−1.135	−1.275	−1.517	−1.135	−0.289	0

Table II. Reproducibility of $R_0^{<001>}(298°\text{K})/R_\infty^{<001>}(77°\text{K})$ for specimens cut from different ingots.

sample	$R_0(298°\text{K})$* (cm³/coul)	$R_\infty(77°\text{K})$ (cm³/coul)	$R_0(298°\text{K})/R_\infty$
5-04-D	17,124	18,400	0.930
5-04-B	13,312	14,525	0.917
2-03-A	10,811	11,780	0.918
2-18-01	10,689	11,595	0.922
3-22-03	9,806	10,740	0.913
2-13-02	7,567	8,330	0.909

* $R_H^{<001>}(298°\text{K})$ is field independent, and the value at 2355 gauss is taken as $R_0(298°\text{K})$.

though larger values are favorable.

The check was carried out on several ⟨001⟩ specimens, of which results always showing fairly good reproducibility are given in Table II. From these results it may be concluded (1) that the carrier contribution from the uncontrolled centers is fortunately insignificant, or otherwise, (2) that the contribution, if any, is very similar for all ingots. If the latter were the case, the present deduction for $\mu_H/\mu(T°\text{K})$ will be confused, and further discussion will be done in the later section.

§ 4. Theoretical Analysis

A. Model for scattering mechanism

An empirical fact of strikingly field independent R_H (298°K) cannot be explained by Abeles-Meiboom's theory[2] and will suggest that slight impurity scattering is important[1] even at room temperature. In the present case, therefore, mixed scattering will be taken into account, where the relaxation time will be treated not as a power function of electron energy but as a combination of lattice and impurity scatterings. Following Herring-Vogt[8], consider an ellipsoid model for relaxation time similar to effective mass, and denote the principal value along longitudinal axis ⟨111⟩ of an energy ellipsoid as τ_l and that along transverse axis as τ_t. Then,

$$\begin{aligned} 1/\tau_t &= \sqrt{kT}/l\ (x^{1/2}+\delta^2 x^{-3/2}) \\ 1/\tau_l &= \sqrt{kT}/l(x^{1/2}+r\delta^2 x^{-3/2}) \qquad (4.1) \\ x &\equiv \mathcal{E}/kT \end{aligned}$$

where $\mathcal{E}$ is energy of electron, k Boltzmann's constant, l mean free path associated with acoustic phonon scattering, δ^2 a parameter indicating mixing rate of impurity scattering in the direction of transverse axis and r is an anisotropy parameter for pure ionized impurity scattering. It has been cleverly determined by Laff and Fan's magnetoresistance experiment[11] that r equals 1/12, while acoustic phonon scattering is isotropic. These results will be utilized here, too. According to deformation potential theory[12] and Conwell-Weisskopf's theory[13], temperature dependence of δ^2 will be approximately given by

$$\delta^2 \infty (kT)^{-3}\ . \qquad (4.2)$$

If the anisotropy of impurity scattering is neglected, δ^2 corresponds to β or $6\mu_L/\mu_I$ given by Johnson-Whitesell[1]. That is to say,

$$\delta^2 \simeq 6\mu_L/\mu_I\ . \qquad (4.2a)$$

B. Conductivity tensor and expression of Hall Coefficient

Now let us consider non-degenerate case and Boltzmann satistics will be assumed. From Boltzmann's equation, the conductivity tensor associated with principal axes of an ellipsoid will be given in the following form, when magnetic field $\boldsymbol{H}(H_1, H_2, H_3)$ is applied,

$$\begin{aligned} \sigma_{11} &= uK\alpha + uv^2K^2\gamma H_1^2 \\ \sigma_{22} &= uK\alpha + uv^2K^2\gamma H_2^2 \\ \sigma_{33} &= u\alpha^* + uv^2K^2\gamma H_3^2 \\ \sigma_{12} &= -uvK^2\beta H_3 + uv^2K^2\gamma H_1H_2 = \sigma_{21}(-\boldsymbol{H}) \\ \sigma_{23} &= -uvK\beta^* H_1 + uv^2K^2\gamma H_2H_3 = \sigma_{32}(-\boldsymbol{H}) \qquad (4.3) \\ \sigma_{31} &= -uvK\beta^* H_2 + uv^2K^2\gamma H_3H_1 = \sigma_{13}(-\boldsymbol{H}) \\ K &\equiv m_3/m_1 = m_3/m_2 \\ u &\equiv Ne^2(l/m_3)(kT)^{-1/2}4/3\sqrt{\pi} \\ v &\equiv (e/c)(l/m_3)(kT)^{-1/2} \end{aligned}$$

where suffix 3 corresponds to longitudinal one and 1, 2 transverse, m_1, m_2 and m_3 are principal values for respective axis of effective mass tensor, K anisotropy parameter for effective mass, N carrier concentration per valley, $-e$ electronic charge. $K=20$ will be used[7] in the present analysis.

α, β etc. are integrals as shown in the following:

$$\begin{aligned}
\alpha(\delta^2,\ p;\ s) &\equiv \int_0^\infty F^{-1}(x^2+\delta^2)(x^2+r\delta^2)x^3 e^{-x} dx \\
\alpha^*(\delta^2,\ p;\ s) &\equiv \int_0^\infty F^{-1}(x^2+\delta^2)^2 x^3 e^{-x} dx \\
\beta(\delta^2,\ p;\ s) &\equiv \int_0^\infty F^{-1}(x^2+r\delta^2)x^{9/2} e^{-x} dx \\
\beta^*(\delta^2,\ p;\ s) &\equiv \int_0^\infty F^{-1}(x^2+\delta^2)x^{9/2} e^{-x} dx \\
\gamma(\delta^2,\ p;\ s) &\equiv \int_0^\infty F^{-1} x^6 e^{-x} dx
\end{aligned} \tag{4.4}$$

where

$$\begin{aligned}
&F(x,\ \delta^2,\ p;\ s) \equiv (x^2+\delta^2)^2(x^2+r\delta^2)+p(x^5+s\delta^2x^3) \\
&p \equiv v^2(KH_1^2+KH_2^2+K^2H_3^2) \\
&s \equiv (KH_1^2+KH_2^2+rK^2H_3^2)/(KH_1^2+KH_2^2+K^2H_3^2).
\end{aligned}$$

Let $\{\Sigma\}$ be conductivity tensor viewed from the observing coordinate system as chosen in Fig. 1, where magnetic field $\boldsymbol{H}$ is in z direction, current $\boldsymbol{J}$ in x and Hall voltage V_H in y direction. Then, the Hall coefficient is given by

$$R_H^{\langle\theta\rangle} = \frac{1}{H} \frac{-\Sigma_{yx}}{\Sigma_{xx}\Sigma_{yy}-\Sigma_{yx}\Sigma_{xy}} . \tag{4.5}$$

Assuming four ellipsoid model possessing [111] longitudinal axes, transformation of $\{\sigma\}$ to the observing coordinate system can be performed in two steps just like Abeles-Meiboom's fashion[2]. (See Appendix.)

Several expressions interested in the present experiment will be given in the following.

(1) Isotropic quantities

Zero field Hall coefficient is independent of orientations and expressed by

$$R_0 = -\left(\frac{3\pi}{8}\right)\frac{1}{nec}\left\{\frac{2}{\sqrt{\pi}}\frac{3K(K\beta_0+2\beta_0^*)}{(2K\alpha_0+\alpha_0^*)^2}\right\} \tag{4.6}$$

where n is total carrier concentration and equal to $4N$. As for conductivity and Hall mobility,

$$\sigma_0 = (4/3)u(2K\alpha_0+\alpha_0^*) \tag{4.7}$$

$$\mu_H = |R_0\sigma_0| = |v| \frac{K(K\beta_0+2\beta_0^*)}{2K\alpha_0+\alpha_0^*} . \tag{4.8}$$

Here α_0, β_0, etc. are the values for $H=0$ or $p=0$, i.e.[14],

$$\begin{aligned}
\alpha_0 &= \int_0^\infty \frac{x^3 e^{-x} dx}{x^2+\delta^2} \equiv 3!\,\mathfrak{L}_3(\delta) \\
\alpha_0^* &= 3!\,\mathfrak{L}_3(\delta\sqrt{r}) \\
\beta_0 &= \int_0^\infty \frac{x^{9/2} e^{-x}\, dx}{(x^2+\delta^2)^2} \equiv (9/2)!\,\vartheta_{9/2}(\delta) \\
\beta_0^* &= \frac{1}{1-r}(9/2)!\,\frac{1}{\delta^2}\{\mathfrak{L}_{9/2}(\delta\sqrt{r})-\mathfrak{L}_{9/2}(\delta)\} .
\end{aligned} \tag{4.9}$$

Meanwhile, infinite field Hall coefficient is also isotropic and simply given by

$$R_\infty = -\frac{1}{nec}\ . \tag{4.10}$$

(2) Anisotropic quantities

$$\frac{R_H^{\langle 001\rangle}}{R_0} = \frac{\dfrac{K\beta+2\beta^*}{K\beta_0+2\beta_0^*}}{\left(\dfrac{2K\alpha+\alpha^*}{2K\alpha_0+\alpha_0^*}\right)^2 + \left(\dfrac{K\beta+2\beta^*}{K\beta_0+2\beta_0^*}\right)^2(\mu_H H)^2} \tag{4.11}$$

where

$$r=1/12\ ,$$
$$s=(rK+2)/(K+2)=1/6$$
$$p=(1/3)\frac{(K+2)}{K}\left(\frac{2K\alpha_0+\alpha_0^*}{K\beta_0+2\beta_0^*}\right)^2(\mu_H H)^2\ .$$

$$\frac{R_H^{\langle 111\rangle}}{R_0} = \frac{\dfrac{K(3\beta^{(1)}+\beta^{(2)})+8\beta^{*(2)}}{4(K\beta_0+2\beta_0^*)}}{\left\{\dfrac{3K\alpha^{(1)}+5K\alpha^{(2)}+4\alpha^{*(2)}}{4(2K\alpha_0+\alpha_0^*)}\right\}^2 + \left\{\dfrac{K(3\beta^{(1)}+\beta^{(2)})+8\beta^{*(2)}}{4(K\beta_0+2\beta_0^*)}\right\}^2(\mu_H H)^2} \tag{4.12}$$

where superscripts (1) or (2) indicate that the following p and s should be substituted into α or β.

$$p=\left(\frac{2K\alpha_0+\alpha_0^*}{K\beta_0+2\beta_0^*}\right)^2(\mu_H H)^2\ , \qquad s=r=1/12$$

for superscript (1), and

$$p=\left(\frac{K+8}{9K}\right)\left(\frac{2K\alpha_0+\alpha_0^*}{K\beta_0+2\beta_0^*}\right)^2(\mu_H H)^2\ , \qquad s=\frac{rK+8}{K+8}=29/84$$

for superscript (2).

C. Numerical values and comparison with experiments

(1) Weak field behavior of R_H

Low field Hall coefficients may be expanded in a series with even powers of $\mu_H H$, of which form is expected from Eqs. (4.4) and (4.8) to be

$$R_H^{\langle\theta\rangle} = R_0\{1+a^{\langle\theta\rangle}(\mu_H H)^2 + b^{\langle\theta\rangle}(\mu_H H)^4 - \cdots\}\ . \tag{4.13}$$

In order to determine the coefficients $a^{\langle\theta\rangle}$ and $b^{\langle\theta\rangle}$ for specific orientations, integrals in (4.11) and (4.12) should be expanded in power series of p.

$$\begin{aligned}
\alpha &= \sum_{n=0}^{\infty}(-1)^n\alpha_n p^n, & \alpha_n &= \int_0^\infty \frac{(x^5+s\delta^2x^3)^n x^3 e^{-x}}{(x^2+\delta^2)^{2n+1}(x^2+r\delta^2)^n}dx \\
\alpha^* &= \sum_{n=0}^{\infty}(-1)^n\alpha_n^* p^n, & \alpha_n^* &= \int_0^\infty \frac{(x^5+s\delta^2x^3)^n x^3 e^{-x}}{(x^2+\delta^2)^{2n}(x^2+r\delta^2)^{n+1}}dx \\
\beta &= \sum_{n=0}^{\infty}(-1)^n\beta_n p^n, & \beta_n &= \int_0^\infty \frac{(x^5+s\delta^2x^3)^n x^{9/2} e^{-x}}{(x^2+\delta^2)^{2n+2}(x^2+r\delta^2)^n}dx \\
\beta^* &= \sum_{n=0}^{\infty}(-1)^n\beta_n p^n, & \beta^*_n &= \int_0^\infty \frac{(x^5+s\delta^2x^3)^n x^{9/2} e^{-x}}{(x^2+\delta^2)^{2n+1}(x^2+r\delta^2)^{n+1}}dx\ .
\end{aligned} \tag{4.14}$$

Numerical values of several α_n's and β_n's are summarized in Table III. Substituting (4.14) in (4.11) and (4.12), $a^{\langle\theta\rangle}$ and $b^{\langle\theta\rangle}$ in (4.13) will be given by

Table III.

δ	α_0	α_0^*	$(4/3\sqrt{\pi})\beta_0$	$(4/3\sqrt{\pi})\beta_0^*$	α_1 $(s=1/6)$	α_1^* $(s=1/6)$
0	1	1	0.66667	0.66667	1	1
0.1	0.98134	0.99789	0.61617	0.63293	0.78028	0.81155
0.2	0.94825	0.99256	0.55660	0.59083	0.63141	0.68095
0.3	0.91035	0.98520	0.50127	0.54986	0.52184	0.58245
0.4	0.8712	0.97663	0.45163	0.51147	0.43545	0.50449
0.5	0.83183	0.96734	0.40760	0.47611	0.36785	0.44039
0.6	0.7938	0.95760	0.36859	0.44347	0.31310	0.38552
0.8	0.7218	0.93705	0.30338	0.38620	0.23151	0.29982
1.0	0.6564	0.91488	0.25184	0.33834	0.17435	0.23849
1.2	0.59832	0.89146	0.21074	0.29830		
1.4	0.54630	0.86982	0.17758	0.26357		
1.6	0.49998	0.84684	0.15069	0.23431		

δ	$(4/3\sqrt{\pi})\beta_1$ $(s=1/6)$	$(4/3\sqrt{\pi})\beta_1^*$ $(s=1/6)$	α_1 $(s=1/12)$	α_1^* $(s=1/12)$	$(4/3\sqrt{\pi})\beta_1$ $(s=1/12)$	$(4/3\sqrt{\pi})\beta_1^*$ $(s=1/12)$
0	1.33333	1.33333	1	1	1.33333	1.33333
0.1	0.63309	0.67312	0.77717	0.80752	0.62957	0.66842
0.2	0.43574	0.48094	0.62675	0.67464	0.43189	0.47581
0.3	0.32123	0.36383	0.51634	0.57475	0.31750	0.35858
0.4	0.24580	0.28564	0.42952	0.49594	0.24232	0.28061
0.5	0.19278	0.22943	0.36175	0.43137	0.18959	0.22471
0.6	0.15399	0.18740	0.30698	0.37626	0.15109	0.18302
0.8	0.102215	0.12968	0.22561	0.29064	0.099881	0.12595
1.0	0.069914	0.093062	0.16883	0.22963	0.067987	0.089913

δ	α_1 $(s=29/84)$	α_1^* $(s=29/84)$	$(4/3\sqrt{\pi})\beta_1$ $(s=29/84)$	$(4/3\sqrt{\pi})\beta_1^*$ $(s=29/84)$
0	1	1	1.33333	1.33333
0.1	0.78695	0.82018	0.64065	0.68318
0.2	0.64141	0.69447	0.44399	0.49191
0.3	0.53363	0.59894	0.32923	0.37507
0.4	0.44816	0.52282	0.25327	0.29640
0.5	0.38093	0.45971	0.19963	0.23953
0.6	0.32622	0.40534	0.16021	0.19679
0.8	0.24415	0.31950	0.10733	0.13766
1.0	0.18618	0.25746	0.074044	0.099811

$$a^{\langle\theta\rangle}(\delta)=2A_1/S-B_1/S-1\ ,$$
$$b^{\langle\theta\rangle}(\delta)=1-4A_1/S+3B_1/S-2A_2/S^2+B_2/S^2+3(A_1/S)^2-2A_1B_1/S^2 \tag{4.15}$$

where in the case of $\langle 001\rangle_H$,

$$S\equiv\frac{2K}{K+2}\left(\frac{K\beta_0+2\beta_0^*}{2K\alpha_0+\alpha_0^*}\right)^2$$
$$A_n\equiv\frac{2K\alpha_n+\alpha_n^*}{2K\alpha_0+\alpha_0^*}$$
$$B_n\equiv\frac{K\beta_n+2\beta_n^*}{K\beta_0+2\beta_0^*} \tag{4.16}$$
$$s\equiv\frac{rK+2}{K+2}=\frac{1}{6}$$

and in the case of $\langle 111\rangle_H$,

$$\begin{aligned}
S &\equiv \left(\frac{K\beta_0+2\beta_0{}^*}{2K\alpha_0+\alpha_0{}^*}\right)^2 \\
A_n &\equiv \frac{1}{4(2K\alpha_0+\alpha_0{}^*)}\{3K\alpha_n{}^{(1)}+5K\alpha_n{}^{(2)}t^n+4\alpha_n{}^{*(2)}t^n\} \\
B_n &\equiv \frac{1}{4(K\beta_0+2\beta_0{}^*)}\{3K\beta_n{}^{(1)}+K\beta_n{}^{(2)}t^n+8\beta_n{}^{*(2)}t^n\} \\
t &\equiv \frac{K+8}{9K}=\frac{7}{45} \\
s &\equiv r=1/12 \qquad \text{for superscript (1)} \\
s &\equiv \frac{rK+8}{K+8}=\frac{29}{84} \qquad \text{for superscript (2)}
\end{aligned} \tag{4.17}$$

Fig. 6 indicates $a^{\langle\theta\rangle}(\delta)$ thus calculated.

It is a remarkable result that sign reversal of $a^{\langle 001\rangle}$ takes place at $\delta\sim0.1$. In view of the fact that $R_H^{\langle 001\rangle}$(298°K) is independent of field strength at weak field, it is believed that δ must be nearly 0.1 at room temperature in the present crystals. Another information about δ can be obtained from (4.2a) using Conwell's μ_I for $N_I=5\times10^{14}$ and μ_L at room temperature[13], resulting in $\delta\sim0.14$, which agrees fairly well with the value above mentioned.

In order to compare (4.13) with (3.1), $\xi_c^{\langle\theta\rangle}\equiv a^{\langle\theta\rangle}\mu_H{}^2$'s were calculated by assuming δ 0.1 at 298°K and by using $\mu_H\sim3{,}800$ together with the theoretical curves for $a^{\langle\theta\rangle}$ shown in Fig. 6. Cubic symmetry relations[5] were used to calculate $\xi_c^{\langle\theta\rangle}$ except $\xi_c^{\langle 001\rangle}$ and $\xi_c^{\langle 111\rangle}$. As indicated in Table I, satisfactory agreement between $\xi^{\langle\theta\rangle}$ and $\xi_c^{\langle\theta\rangle}$ was obtained. These features will predict weak field behaviors of Hall coefficients for crystals of any resistivity or at any temperature not actually measured, by sliding δ with the relations of (4.2) and (4,2a).

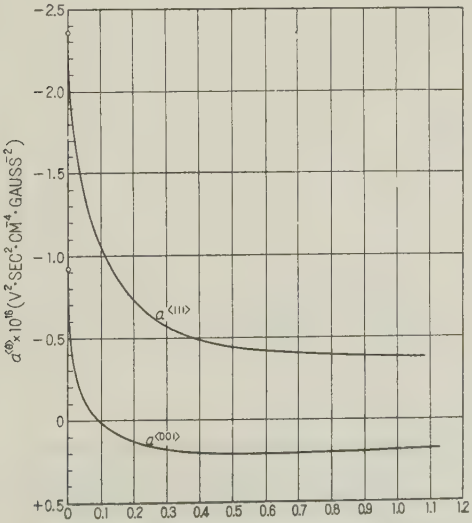

Fig. 6. Weak field expansion coefficient $a^{\langle\theta\rangle}(\delta)$.

(2) Temperature dependence of R_0/R_∞

From (4.6) and (4.10) R_0/R_∞ or μ_H/μ at zero field is easily obtained.

$$\begin{aligned}
\frac{R_0}{R_\infty} &= \frac{3\pi}{8}\frac{3K(K+2)}{(2K+1)^2}I(\delta) \\
I(\delta) &= \frac{2}{\sqrt{\pi}}\frac{(2K+1)^2}{K+2}\frac{(K\beta_0+2\beta_0{}^*)}{(2K\alpha_0+\alpha_0{}^*)^2}
\end{aligned} \tag{4.18}$$

Fig. 7 shows the behavior of $I(\delta)$, where solid curve is calculated with $K=20$ and $r=1/12$, while two broken curves correspond (1) to the one in which $K=15$ and $r=1/12$ are assumed, and (2) to the one in which $K=20$ and $r=1$, respectively. It is found that

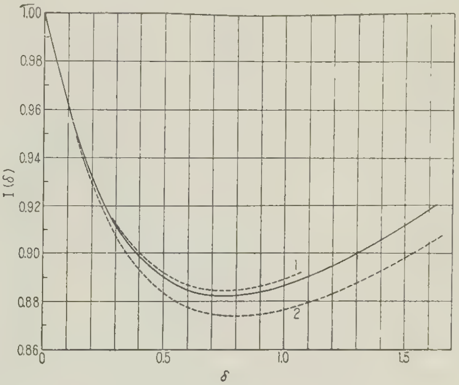

Fig. 7. $I(\delta)$ vs δ. Solid curve; $K=20$, $r=1/12$.
Broken curve 1; $K=15$, $r=1/12$.
Broken curve 2; $K=20$, $r=1$.

isotropic impurity scattering depresses the minimum of $I(\delta)$ to some extent, while mass ratio does not too much affect $I(\delta)$. When $\delta=0$, (4.18) coincides with Abeles-Meiboom or Shibuya's formula[2),3)].

For the purpose of comparison with experimental data, it will be convenient to draw the R_0/R_∞ curve not against δ but against temperature. From (4.2) and previous inference on δ, let us now assume

$$\delta(T)=0.1(300/T)^{3/2}\,. \tag{4.19}$$

Substituting (4.19) in (4.18), R_0/R_∞ will become a function of temperature. The resultant R_0/R_∞ vs T curve is illustrated in Fig. 8. It is seen that R_0/R_∞ has a minimum of 0.82 near liquid nitrogen temperature in the present case. Meanwhile, under constant mean free time assumption investigated by Bullis and Krag[9)] the minimum of R_0/R_∞ was 0.79. Of course, better agreement with experiments can be obtained in the present case, though exact experimental determination of R_0's is somewhat difficult at 77°K and 90°K. The discrepancy at zero field may be a fault of the constant mean free time approximation.

In Fig. 8 two other R_0/R_∞ vs T curves, in which (1) δ is chosen by Conwell-Weisskopf's formula or (2) isotropic impurity scattering is assumed, are also presented. It seems theoretical R_0/R_∞'s have qualitatively explained the behavior of experimental data. However, a tendency cannot be overlooked that the observed values deviate upwards from the theoretical curves, especially at higher temperatures, where no possibility depressing the observed points is expected. As will be discussed in the later section, this might suggest that some correction such as optical phonon scattering is necessary. Remarks on the curve 3 in Fig. 8 will be given in the next section.

§ 5. Discussions

A. Constancy of carriers

Applying Fermi satistics to a semiconductor containing 5×10^{14} donors, N_d, per cm^3 of which energy level, E_d, lies at 0.01 eV below the conduction band edge, the rate of exhaustion can be easily determined at any temperature. This is the ideal case in the pre-

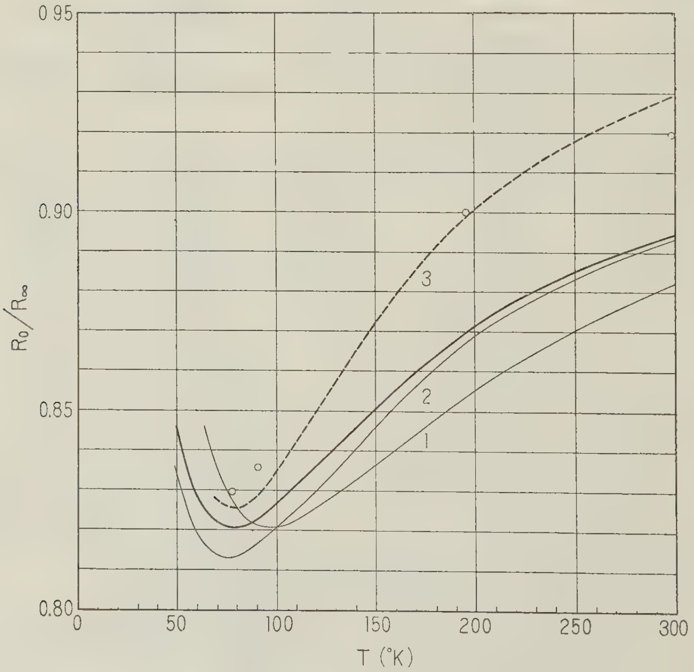

Fig. 8. R_0/R_∞ vs T. Open circles are experimental. Solid curve; calculated with $\delta=0.1\cdot(300/T)^{3/2}$, $K=20$, $r=1/12$. Thin curve 1; $\delta=0.14(300/T)^{3/2}$, derived from Conwell's μ_I is used instead of above δ. Thin curve 2; $r=1$ or isotropic impurity scattering is assumed, leaving δ and K unchanged. Broken curve 3; modified by optical phonon scattering.

Table IV. Rate of exhaustion and corresponding Fermi energy in a semiconductor, in which $N_d=5\times10^{14}$ cm^{-3}, $E_d=0.01$ eV and $(m^*/m)^{3/2}=0.4$.

	77°K	90°K	195°K	298°K
$N_d/n(T\,°\mathrm{K})$	1.0017	1.0011	1.0002	1.00006
$n(T\,°\mathrm{K})/n(77\,°\mathrm{K})$	1.0000	1.0006	1.0015	1.0016
$\zeta(T\,°\mathrm{K})$ eV	−0.052	−0.063	−0.156	−0.254

sent specimens. Table IV shows the ratio $N_d/n(T\,°\mathrm{K})$, $n(T\,°\mathrm{K})/n(77\,°\mathrm{K})$ and Fermi energy $\zeta(T\,°\mathrm{K})$. It is seen that the assumption of constant carriers is well assured in the ideal case.

However, actual specimens may naturally contain some uncontrolled imperfections, from which ionization is possible at higher temperatures. Then, let us consider the maximum concentration of these uncontrolled centers. One clue will be to measure the mean lifetime of injected minority carriers. In most crystals used here the lifetime by means of photoconductivity decay method was about 200 μsec at room temperature. According to Burton et al[15] the value of 200 μsec is their highest limit for 3 ohm-cm n-type germanium, where the concentration of the unknown recombination centers, N_x, may be estimated to be less than 1×10^{13} per cm^3. Though it is not clear what the sources of N_x are, probably they consist of crystal imperfections such as dislocations or vacancies and chemical impurities. As a matter of fact main centers concerned with the carrier contribution are those having energy levels near or between Fermi levels at liquid nitrogen and room temperatures. Therefore, dislocations, which have been proved to have an acceptor level about 0.2 eV below the conduction band[16], must be considered in the first place, since they are substantially empty at room temperature but can occupy electrons at low temperatures. According to the reciprocal law between lifetime and dislocation density[17], the lifetime of nearly 500 μsec, which is two or three times was large as the observed one, will be expected at room temperature using measured dislocation density of about 5×10^3 per cm^2 or less in our crystals. Thus it would appear that dislocations are an important factor among N_x concerned with the carrier contribution, even if Read's theory has concluded[18] that only relatively few of dislocation sites will be filled at low temperatures because of space charge effect. The remaining fraction of N_x might be due to chemical impurities, copper for example, and frozen-in vacancies, though their solubility[19] is rather small. These centers possess their energy levels near or below the middle of the gap[20] and do not much affect the number of carriers.

In consequence, the temperature effect of uncontrolled centers on number of carriers would be fortunately insignificant, and the resultant undesirable shift of $R_H(T\,°\mathrm{K})$ due to carrier change should be at most within 2 percent even in the worst case.

B. Thermomagnetic effect

Since the Ettinghausen effect cannot be excluded in the experiment, it will be necessary to confirm negligible contribution of the effect to Hall voltage. Ettinghausen effect, entirely the same with Hall effect, can be written in the form

$$\Delta T=PIH/d \tag{5.1}$$

where ΔT, P, I, and d are temperature difference across the specimen, Ettinghausen coefficient, total current and thickness of the specimen respectively. As for P, Mette et al[21] have obtained the value of nearly 10^{-6} deg. cm. amp.$^{-1}$ gauss^{-1} for 3 ohm-cm n-type germanium at 300°K. Using this result with the present experimental conditions of $I\sim0.5$ mA and $d\sim1$ mm, (5.1) gives $\Delta T\sim5\times10^{-5}$ deg. at $H=10^4$ gauss. Considering the Seebeck effect of which order is 1 mV per deg. carried out by Geballe and Hull,[22] the resultant electromotive force should be approximately equal to 0.05 μV. Consequently, this is quite negligible as compared with Hall voltage of about 10 mV at 10^4 gauss, and it may be concluded that even phonon-drag effect at low temperatures is out of the question.

C. Optical phenon scattering

Plotting the observed values of R_0/R_∞ against temperature, it seems that they are somewhat lager than the theoretical ones as already shown in Fig. 8. Furthermore, there may be a possibility that $R_0/R_\infty(298°\text{K})$ shifts within 2 per-cent toward higher value, in view of the doubt in carrier constancy. Though the discrepancy is not so definite that the theoretical analysis may be radically modified, it is yet suggested that some correction is desirable.

One resonable approach will be to consider the effect of optical phonon scattering, which has bee used to explain a fact that the temperature dependence of conduction electron mobility does not obey the exact $-3/2$ power law but rather follows -1.66 power law[6] in very pure crystals. In order to understand this behavior, Herring[23] has proposed to take account of intervalley scattering, while Weinreich et al[24] have insisted that the effect should be ascribed not to intervalley scattering but to optical phonon scattering with their experiments on acousto-electric effect.

Then, a trial calculation was carried out by adding a term $1/\tau_0$ due to optical phonon to Eq. (4.1). Here, $1/\tau_0$ is given by

$$1/\tau_0=\frac{\sqrt{kT}}{l}\begin{cases} C\dfrac{\gamma}{e^\gamma-1}\sqrt{x+\gamma}+C\dfrac{\gamma}{1-e^{-\gamma}}\sqrt{x-\gamma} & x>\gamma \\ C\dfrac{\gamma}{e^\gamma-1}\sqrt{x+\gamma} & x<\gamma. \end{cases} \tag{5.2}$$

where $\gamma\equiv\theta_0/T$. Using $\theta_0\sim432°\text{K}$ obtained by Brockhouse et al[25] by means of neutron diffraction, and by assuming $C=0.125$ which seems to be acceptable, broken curve 3 shown in Fig. 8 has been calculated, resulting in better agreement with the observed values.

§ 6. Conclusions and Acknowledgments

Anisotropic values of μ_H/μ appearing in Hall coefficients in n-type germanium have been precisely observed at four specifield temperatures and theoretically discussed under ellipsoid model and mixed scattering. Experimental results have elucidated the importance of slight impurity scattering. It has been also clarified that μ_H/μ's at usual magnetic field strengths are considerably anisotropic and almost always smaller than unity. These features are well explained by the theoretical analysis.

In case μ_H/μ is assumed to be $3\pi/8$ in ordinary Hall measurements, it is rather recommended that a value of 0.9, in place of $3\pi/8$, is used in non-degenerate n-type germanium. For further arguments, the following facts should be remembered even if number of carriers remains unchanged:

(1) R_0 decreases at first with decreasing temperature, reaches a minimum, and then begins to rise again.

(2) Unless θ is very small, $R_H^{\langle\theta\rangle}$ generally decreases at first with increasing field, reaches a minimum, and then increases toward its infinite field value.

(3) $R_H^{\langle 001\rangle}$ approaches its infinite field value in most straightforward way without initial decreasing.

Careful experiments of this kind may be utilized to detect the small mixing rate of ionized impurity scattering into lattice scattering or may be helpful to determine the symmetry property of energy band structure in a semiconductor. These knowledges will be also useful to apply the Hall effect to some devices.

Finally, the authors wish to acknowledg the support of Dr. H. Muraoka and Mr. T. Abe of Toshiba Transistor Plant who prepared and oriented the crystal. They are also greateful to Dr. M. Shibuya of the Electrotechnical Laboratory for many helpful suggestions and discussions. Mr. T. Kikuchi and Miss E. Komiyama assisted with many of the numerical calculations and the experimental measurements.

Appendix I. Transformation of $\{\sigma\}$ into $\{\Sigma\}$

(1) {S}, Conductivity tensor in respect to crystal axis system

The transformation must be performed in two steps. First, the components of $\{\sigma\}^{(i)}$, the conductivity tensor viewed from the i-th valley system (i), are transformed into the crystal axis system (c), while $\boldsymbol{H}^{(i)}$ in $\{\sigma\}^{(i)}$ are fixed as parameters. Here $\boldsymbol{H}^{(i)}$ is the set of the components of magnetic field $\boldsymbol{H}$ viewed from the i-th valley system. Let the transformation tensor be $\{\mathrm{A}\}^{(i)}$, defined for a vector $\boldsymbol{v}$ as

$$\boldsymbol{v}^{(i)}=\{\mathrm{A}\}^{(i)}\cdot\boldsymbol{v}^{(c)}\ . \tag{A.1}$$

Then we obtain

$$\{\mathrm{S}'\}=\sum_{i}\{\mathrm{A}\}^{(i)-1}\cdot\{\sigma(\boldsymbol{H}^{(i)})\}^{(i)}\cdot\{\mathrm{A}\}^{(i)}\ . \tag{A.2}$$

Secondly, $\boldsymbol{H}^{(i)}$'s in $\{\mathrm{S}'\}$ are replaced by the original magnetic field referred to the new system. This can be performed by substituting

$$\boldsymbol{H}^{(i)}=\{\mathrm{A}\}^{(i)}\cdot\boldsymbol{H}^{(c)} \tag{A.3}$$

in (A.2).

Table A—I.

$\{\mathrm{A}\}^{(1)}$ $\langle 111\rangle,\ \langle\bar{1}\bar{1}\bar{1}\rangle$	$\{\mathrm{A}\}^{(2)}$ $\langle 1\bar{1}1\rangle,\ \langle\bar{1}1\bar{1}\rangle$	$\{\mathrm{A}\}^{(3)}$ $\langle\bar{1}\bar{1}1\rangle,\ \langle 11\bar{1}\rangle$	$\{\mathrm{A}\}^{(4)}$ $\langle\bar{1}11\rangle,\ \langle 1\bar{1}\bar{1}\rangle$
$\begin{bmatrix}\frac{-1}{\sqrt{2}} & \frac{1}{\sqrt{2}} & 0\\ \frac{-1}{\sqrt{6}} & \frac{-1}{\sqrt{6}} & \frac{2}{\sqrt{6}}\\ \frac{1}{\sqrt{3}} & \frac{1}{\sqrt{3}} & \frac{1}{\sqrt{3}}\end{bmatrix}$	$\begin{bmatrix}\frac{1}{\sqrt{2}} & \frac{1}{\sqrt{2}} & 0\\ \frac{-1}{\sqrt{6}} & \frac{1}{\sqrt{6}} & \frac{2}{\sqrt{6}}\\ \frac{1}{\sqrt{3}} & \frac{-1}{\sqrt{3}} & \frac{1}{\sqrt{3}}\end{bmatrix}$	$\begin{bmatrix}\frac{1}{\sqrt{2}} & \frac{-1}{\sqrt{2}} & 0\\ \frac{1}{\sqrt{6}} & \frac{1}{\sqrt{6}} & \frac{2}{\sqrt{6}}\\ \frac{-1}{\sqrt{3}} & \frac{-1}{\sqrt{3}} & \frac{1}{\sqrt{3}}\end{bmatrix}$	$\begin{bmatrix}\frac{-1}{\sqrt{2}} & \frac{-1}{\sqrt{2}} & 0\\ \frac{1}{\sqrt{6}} & \frac{-1}{\sqrt{6}} & \frac{2}{\sqrt{6}}\\ \frac{-1}{\sqrt{3}} & \frac{1}{\sqrt{3}} & \frac{1}{\sqrt{3}}\end{bmatrix}$

In n-type germanium, $\{\mathrm{A}\}^{(i)}$'s are given in Table A.I. Thus we obtain, denoting the field components referred to the crystal axis system as H_1, H_2, H_3,

$$\begin{aligned}
S_{11}&=u\sum_{i=1}^{4}[(1/3)\{2K\alpha(p^{(i)},\ s^{(i)})+\alpha^*(p^{(i)},\ s^{(i)})\}+v^2K^2H_1^2\gamma(p^{(i)},\ s^{(i)})\\
S_{12}&=u\sum_{i=1}^{4}[(-1)^i(1/3)\{K\alpha(p^{(i)},\ s^{(i)})-\alpha^*(p^{(i)},\ s^{(i)})\\
&\quad-(1/3)(vK\{Kq^{(i)}\beta(p^{(i)},\ s^{(i)})+q^{*(i)}\beta^*(p^{(i)},\ s^{(i)})+v^2K^2H_1H_2\gamma(p^{(i)},\ s^{(i)})\\
S_{12}(\boldsymbol{H})&=S_{21}(-\boldsymbol{H})\ .
\end{aligned} \tag{A.4}$$

Here we must substitute the following relations into $p^{(i)}$'s, $s^{(i)}$'s, $q^{(i)}$'s and $q^{*(i)}$'s according to Eq. (A.3).

$$\begin{aligned}
p_1&=(1/3)v^2K\{(K+2)(H_1^2+H_2^2+H_3^2)+2(K-1)(H_1H_2+H_2H_3+H_3H_1)\}\\
p_2&=(1/3)v^2K\{(K+2)(H_1^2+H_2^2+H_3^2)+2(K-1)(-H_1H_2-H_2H_3+H_3H_1)\}\\
p_3&=(1/3)v^2K\{(K+2)(H_1^2+H_2^2+H_3^2)+2(K-1)(H_1H_2-H_2H_3-H_3H_1)\}\\
p_4&=(1/3)v^2K\{(K+2)(H_1^2+H_2^2+H_3^2)+2(K-1)(-H_1H_2+H_2H_3-H_3H_1)\}\\
s_1p_1&=(1/3)v^2K\{(rK+2)(H_1^2+H_2^2+H_3^2)+2(rK-1)(H_1H_2+H_2H_3+H_3H_1)\}\\
s_2p_2&=(1/3)v^2K\{(rK+2)(H_1^2+H_2^2+H_3^2)+2(rK-1)(-H_1H_2-H_2H_3+H_3H_1)\}\\
s_3p_3&=(1/3)v^2K\{(rK+2)(H_1^2+H_2^2+H_3^2)+2(rK-1)(H_1H_2-H_2H_3-H_3H_1)\}\\
s_4P_4&=(1/3)v^2K\{(rK+2)(H_1^2+H_2^2+H_3^2)+2(rK-1)(-H_1H_2+H_2H_3-H_3H_1)\}
\end{aligned} \tag{A.5}$$

$$\begin{aligned}
q_1&=H_1+H_2+H_3 & q_1^*&=-H_1-H_2+2H_3\\
q_2&=H_1-H_2+H_3 & q_2^*&=-H_1+H_2+2H_3\\
q_3&=-H_1-H_2+H_3 & q_3^*&=H_1+H_2+2H_3\\
q_4&=-H_1+H_2+H_3 & q_4^*&=H_1-H_2+2H_3\ .
\end{aligned} \tag{A.6}$$

The other components of S_{jk} are obtained by cyclic permutation of indices of H_l in Eqs. (A.4), (A.5) and (A.6).

(2) $\{\Sigma\}$, Conductivity tensor in respect to observing system

The transformation can be performed in the same way as in (1). Now let us define the tensor {G} as follows

$$\boldsymbol{v}^{(o)}=\{\mathrm{G}\}\cdot\boldsymbol{v}^{(c)}\,, \tag{A.7}$$

or

$$\begin{aligned} &\boldsymbol{J}/\!/\langle G_{11},\ G_{12},\ G_{13}\rangle \\ &\boldsymbol{V_H}/\!/\langle G_{21},\ G_{22},\ G_{23}\rangle \\ &\boldsymbol{H}/\!/\langle G_{31},\ G_{32},\ G_{33}\rangle\,. \end{aligned} \tag{A.8}$$

Then we obtain

$$\{\Sigma'\}=\{\mathrm{G}\}\cdot\{\mathrm{S}\}\cdot\{\mathrm{G}\}^{-1}\,. \tag{A.9}$$

Subsequently, $\boldsymbol{H}$ in (A.9) must be replaced as

$$H_1=G_{31}H,\ H_2=G_{32}H,\ H_3=G_{33}H\,. \tag{A.10}$$

In the present experimental situation,

$$\{\mathrm{G}\}=\begin{bmatrix} -1/\sqrt{2} & 1/\sqrt{2} & 0 \\ -(1/\sqrt{2})\cos\theta & -(1/\sqrt{2})\cos\theta & \sin\theta \\ (1/\sqrt{2})\sin\theta & (1/\sqrt{2})\sin\theta & \cos\theta \end{bmatrix} \tag{A.11}$$

in accordance with Fig. 1.

For $\langle 001\rangle_H$ case, for instance, we obtain from (A.9), (A.10) and (A.11),

$$\begin{aligned} \Sigma_{11}&=(1/2)(S_{11}+S_{22}-S_{12}-S_{21}) \\ \Sigma_{22}&=(1/2)(S_{11}+S_{22}+S_{12}+S_{21}) \\ \Sigma_{12}&=(1/2)(S_{11}-S_{22}+S_{12}-S_{21}) \\ \Sigma_{21}&=(1/2)(S_{11}-S_{22}-S_{12}+S_{21})\,, \end{aligned} \tag{A.12}$$

where

$$\begin{aligned} S_{11}&=S_{22}=(4/3)u\{2K\alpha(p,\ s)+\alpha^*(p,\ s)\} \\ S_{12}&=-S_{21}=-(4/3)uvK\{K\beta(p,\ s)+2\beta^*(p,\ s)\}H\,. \end{aligned} \tag{A.13}$$

In this case, following parameters have been used which are derived from (A.5) and (A.6) together with (A.10) and (A.11).

$$\begin{aligned} p&\equiv p_1=\cdots=p_4=(1/3)v^2K(K+2)H^2 \\ s&\equiv s_1=\cdots=s_4=(rK+2)/(K+2) \\ q_1&=\cdots=q_4=H \\ q_1^*&=\cdots=q_4^*=2H\,. \end{aligned} \tag{A.14}$$

We obtain $R_H^{\langle 001\rangle}$ by substituting (A.12) and (A.13) into (4.5), and then R_0 by taking $p=0$, from which (4.11) can be derived. (4.12) is also obtained in the similar way.

Appendix II. Condition for weak field expansion

Expansion of α etc. in respect to p is performed by rewriting the denominator of integrand in the following form,

$$\frac{1}{(x^2+\delta^2)^2(x^2+r\delta^2)+px^3(x^2+s\delta^2)}=\frac{1}{(x^2+\delta^2)^2(x^2+r\delta^2)}\left[1-\sum_{n=1}^{\infty}\left\{\frac{x^3(x^2+s\delta^2)}{(x^2+\delta^2)^2(x^2+r\delta^2)}\right\}^n p^n\right]. \tag{A.15}$$

In the integration of every term the expansion is meaningless unless

$$\alpha_n p^n > \alpha_{n+1} p^{n+1}\ , \quad \text{etc.} \tag{A.16}$$

Therefore the condition will be sought here. Since $s<1$, the sufficient condition will be given by

$$\frac{px^3(x^2+s\delta^2)}{(x^2+\delta^2)^2(x^2+r\delta^2)} < \frac{px^3}{(x^2+\delta^2)(x^2+r\delta^2)} < 1 \qquad \text{for } 0 \leq x < \infty\ , \tag{A.17}$$

or

$$(x^2+\delta^2)(x^2+r\delta^2) - px^3 = \delta^4\{(\xi^2+1)(\xi^2+r) - \varphi\xi^3\} \equiv \delta^4 f(\xi) > 0\ , \tag{A.18}$$

where

$$\xi \equiv x/\delta\ , \qquad \varphi \equiv p/\delta\ .$$

From

$$f'(\xi) = \xi\{4\xi^2 - 3\varphi\xi + 2(1+r)\} = 0\ , \quad \text{and} \quad r = 1/12$$

the minimum value of $f(\xi)$ is given at

$$\xi_0 = (3\varphi + \sqrt{9\varphi^2 - (104/3)})/8\ . \tag{A.19}$$

Numerical evaluation of $f_{\min} > 0$ must result in the condition

$$\varphi \equiv p/\delta < 0.2\ . \tag{A.20}$$

References

1) V. A. Johnson and W. J. Whitesell: Phys. Rev., **89** (1953) 941. See also A. Beer, J. A. Armstrong, and I. N. Greenberg: Phys. Rev., **107** (1957) 1506 for further extension.
2) B. Abeles and S. Meiboom: Phys. Rev., **95** (1954) 31.
3) M. Shibuya: Phys. Rev., **95** (1954) 1385.
4) G. L. Pearson and H. Suhl: Phys. Rev., **83** (1951) 768.
5) W. P. Mason, W. H. Hewitt, and R. F. Wick: J. Appl. Phys., **24** (1953) 166.
6) F. J. Morin: Phys. Rev., **93** (1954) 62.
7) B. Lax, H. J. Zeiger, and R. N. Dexter: Physica **20** (1954) 818. G. Dresselhaus, A. F. Kip, and C. Kittel: Phys. Rev., **98** (1955) 368.
8) C. Herring and E. Vogt: Phys. Rev., **101** (1956) 944.
9) W. M. Bullis and W. E. Krag: Phys. Rev., **101** (1956) 580.
10) W. M. Bullis: Phys. Rev., **109** (1958) 292.
11) R. A. Laff and H. Y. Fan: Phys. Rev., **112** (1958) 317.
12) J. Bardeen and W. Shockleye: Phys. Rev., **80** (1950) 72.
13) E. Conwell and V. F. Weisskopf: Phys. Rev., **77** (1950) 388. E. Conwell: Proc. Inst. Radio Engrs., **40** (1952) 1327.
14) R. B. Dingle, D. Arndt, and S. K. Roy: Appl. Sci. Res., **B6** (1957) 155.
15) J. A. Burton, G. W. Hull, F. J. Morin, and J. C. Severiens: J. Phys. Chem., **57** (1953) 853.
16) G. L. Pearson, W. T. Read, and F. J. Morin: Phys. Rev., **93** (1954) 666.
17) G. K. Wertheim and G. L. Pearson: Phys. Rev., **107** (1957) 694.
18) W. T. Read, Jr.: Phil. Mag., **45** (1954) 775 1119.
19) R. Newman and W. W. Tyler: "Solid State Physics", F. Seitz and D. Turnbull, Eds., Vol. 8 (Acad. Press Inc., New York) p. 75 S. Mayburg: Phys. Rev., **95** (1954) 38.
20) R. Newman and W. W. Tyler: loc. cit., p. 71.
21) H. Mette, W. W. Gärtner, and C. Loscoe: Phys. Rev., **115** (1959) 537.
22) T. H. Geballe and G. W. Hull: Phys. Rev., **94** (1954) 1134.
23) C. Herring: B. S. T. J., **34** (1955) 237.
24) G. Weinreich, T. M. Sanders, Jr., and H. G. White: Phys. Rev., **114** (1959) 33.
25) B. N. Brockhouse and P. K. Iyengar: Phys. Rev., **111** (1958) 747.

JOURNAL OF THE PHYSICAL SOCIETY OF JAPAN, Vol. 15, No. 11, NOVEMBER, 1960

On the Electrical and Optical Properties of p-type Cadmium Telluride Crystals

By Shôji YAMADA

Institute of Electronics, Fuculty of Engineering, Shizuoka University, Hamamatsu, Japan

(Received March 23, 1960)

The electrical and optical properties were measured with p-type synthetic CdTe single crystals. The Hell coefficients of the crystals increased by the heat treatment or the growth in the cadmium vapor. From the present measurements it will be shown that the intrinsic energy gap is about 1.43 e.v., the ionization energy of acceptors is about 0.20 e.v. and the Hall mobility of holes is about 80 cm^2/volt-sec. at room temperature. It seems that the data of Hall mobilities are in agreement with the theory of intercation with the optical mode of lattice vibrations.

§1. Introduction

CdTe is one of the II-VI compound semiconductors whose photoconductive, photovoltaic and luminescent properties have been investigated by many authors. CdTe surpasses any other II-VI compound in obtaining relatively large crystals from the melt and in preparing both n- and *p*-type crystals[1)2)3)].

Concerning CdTe crystals, relatively few papers have been published[4)5)] and only few properties have been clarified.

In this paper the method of the preparation of the single crystals and the treatment of them in Cd vapor will be reported. The measurements of optical absorption, reflection and refractive index, dielectric constant, photoconducting properties and Hall effects will also be described.

§2. Preparation of Samples

The crystals used in this experiment were synthetic single ones. For the purification the cadmium and tellurium were distilled in vacuum. The resulting materials were mixed in the proportion of atomic equivalents, and they were put into a fused silica tube crucible which had a capillary bottom in order to grow only one seed. Then the crucible was evacuated and sealed off. For the growth of the single crystal the double furnace of Stockbarger-type was used (Fig. 1). The crucible was heated at about 1150°C for 3 hours in the furnace, and it was gradually lowered down to the lower temperature region in the furnace. The speed of lowering was about 2 cm/hr. Thus the crystal was grown from the bottom of the crucible.

The crystals obtained were of cylindrical form of about 10 mm in diameter and 50 mm in length. The X-ray examination indicates that all these crystals had the lattice structure of zinc blende type, and that all the cleaved surfaces were (110) planes.

One of the crystals was first heated at the temperature of about 950°C, and then immediately immersed in water so as to be cooled down rapidly. This crystal also revealed an X-ray pattern of the cublic structure. The above result means that the transformation from cubic to hexagonal structure which was suggested by Miyasawa and Sugaike[4)6)7)] could not be observed at the temperature used.

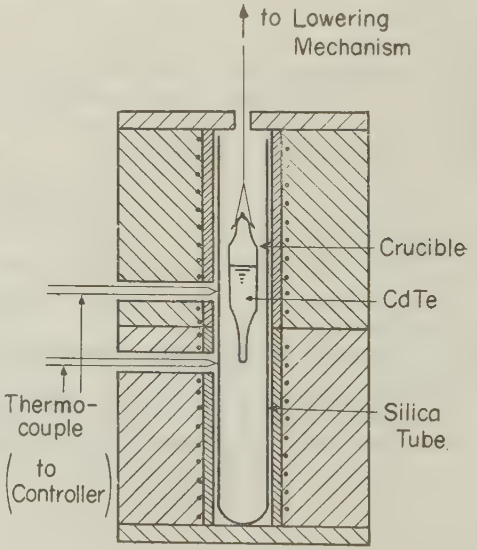

Fig. 1. Shematic diagram of the Stockbarger-type furnace.

All the crystals as grown showed *p*-type electrical conductivity, and the resistivies were of the order of $10^2 \sim 10^3\ \Omega$-cm. These crystals will be designated as *A*-type in this paper. The *p*-type crystals of high resistivity ($10^6 \sim 10^8\ \Omega$-cm) were obtained, however, by the crystal growth in the saturated vapor pressure of cadmium. These high resistivities were not altered both by the zone refining the elements and by the recrystallization of CdTe. These crystals will be called H-type. More doping of excess Cd could not change the crystals into *n*-tpye ones but made them porous.

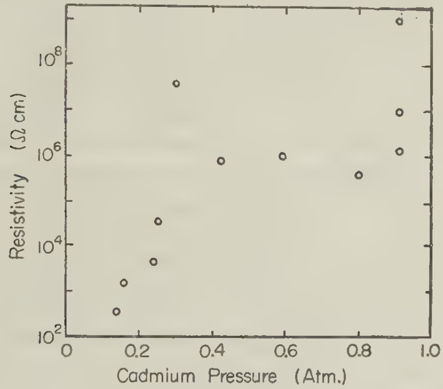

Fig. 2. The resistivity of samples as a function of Cd vapor pressure under the heat treatment. All the samples used were cut from the same A-type crystal and treated at 900°C for 5 hours.

Similar result were obtained under the heat treatment of samples in various cadmium vapor pressures. After the treatment the surfaces of about 0.1 mm in thickness of the samples (the dimension was about $9 \times 3 \times 2\ \mathrm{mm}^3$) were turned into *n*-type, but the bulk remained in *p*-type. This result was observed within the temperature range of 800∼950°C throughout the period of 3∼10 hours during which the treatment was conducted. Furthermore, it could not be altered when the rapid cooling was applied to the samples by means of immersion in water after the treatment. With the treated samples, the resistivity of the bulk was shown in Fig. 2. As the pressure increased, the resistivity of sample became higher, but under the pressure of more than 0.27 atmosphere the change of the resistivity with pressure was hardly observable. These samples will be designated as *C*-type.

By the addition of Ga into the melt, crystals obtained showed *n*-type condnction, but, so long as the amount of Ga was very small, the crystals remained *p*-type. These crystals will be called *G*-type.

§3. Experimental Results

1) *Optical Properties.* All the optical properties were measured at room temperature. Fig. 3 is the transmission data on the single crystals. It will be seen from the figure that there is the absorption edge at about 1.43 e.v. of the incident photon energy.

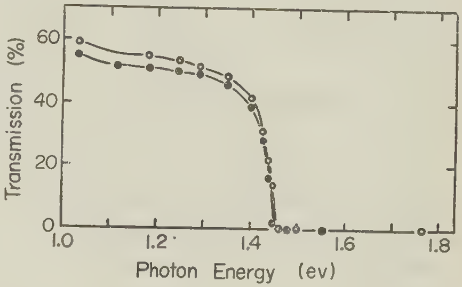

Fig. 3. Transmission measurements of CdTe single crystals.

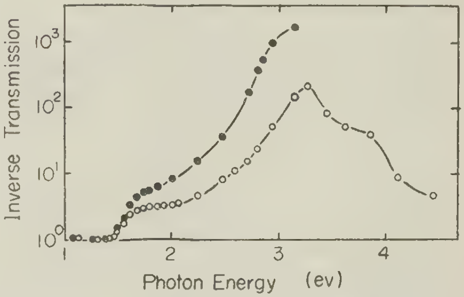

Fig. 4. Absorption spectra of thin films.

The absorption spectra of the evaporated thin films are shown in Fig. 4. There is also the absorption edge at about 1.43 e.v. Unless the correction is made relative to the reflection loss, the absorption coefficient is about $7 \times 10^4\ \mathrm{cm}^{-1}$ at 2 e.v. of the incident photon energy. From the fact the absorption edge is considered to be attributed to the fundamental absorption.

Fig. 5 shows the reflectivity of light on the cleaved surface of a single crystal, and the reflectivity spectrum seems to correspond well with the absorption ones.

The photoconducting phenomena could be observed on the crystals of high resistivity. The photoconducting spectra are shown in Fig. 6. With the *H*-type samples main peak is situated at about 1.42 e.v. According to the Hall measurements these crystals showed *p*-type conduction under illumination as well as in the dark. *G*-type crystals of *p*-type in the dark became *n*-type under illumination of light. There are three peaks of sensitivity at about 1.0, 1.37 and 1.43 e.v.

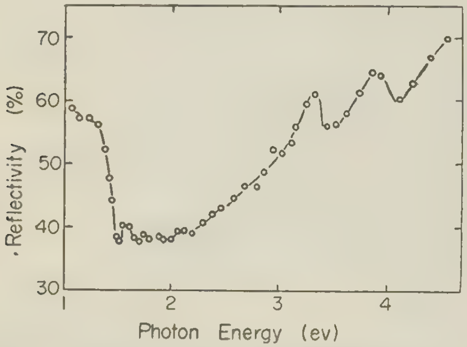

Fig. 5. Reflection on a cleaved surface of a crystal.

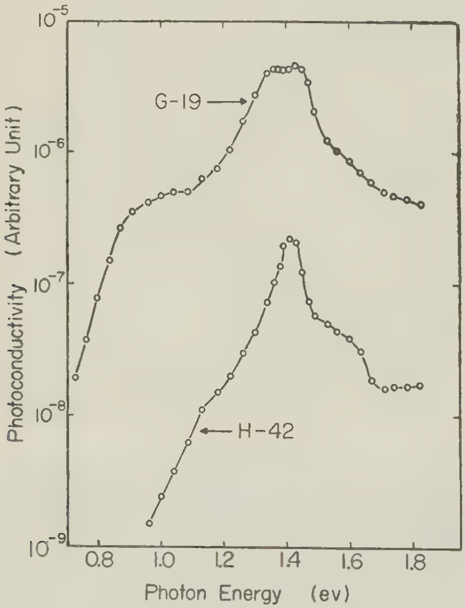

Fig. 6. Typical photoconducting spectra.

The refractive index *n* of the crystal was determined by the means of measurements of minimum deviation angle of light through the crystal cut into the prism. When the light of about 1 μ in wavelength was used, the value of *n* obtained was 2.83±0.03.

2) *Electrical Properties*. The Hall effects of the samples were measured with the ordinary d.c. method. The Hall coefficients of eight representative samples are shown in

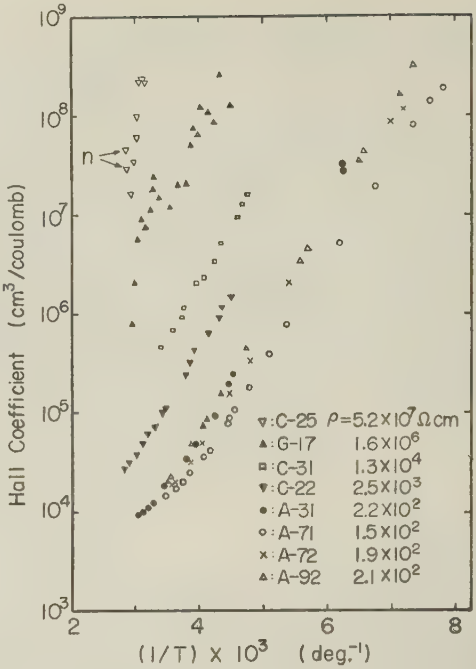

Fig. 7. Hall coefficients of eight samples as a function of inverse temperature. Hall coefficients observed in n-type are noted as n, and ρ is the resistivity of samples at room temperature.

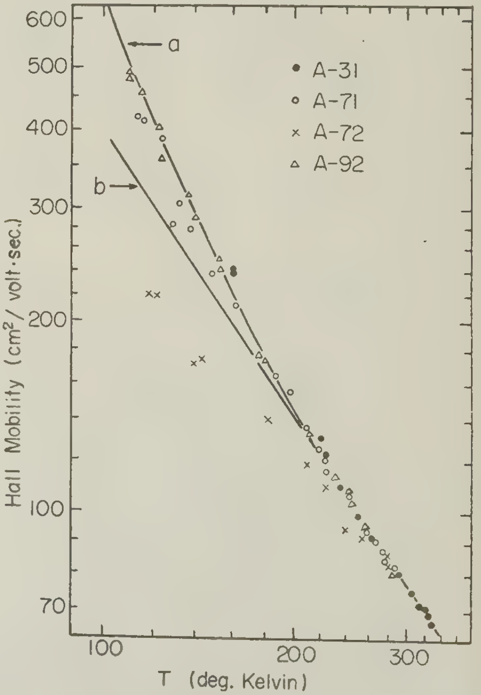

Fig. 8. Temperature dependence of the Hall mobilities with several A-type samples. Curve ***a*** and ***b*** are calculated from

$\mu_H=57\{\exp(252/T)-1\}$ and

$\mu_H=4\times10^5\,T^{-3/2}$ respectively.

Fig. 7. Except for the data on the samples of very high resistivity at high temperature range, all the coefficients obtained were of p-type, and the slopes of the curves are about the same. At temperatures higher than room one Hall coefficients of the samples of comparatively low resistivity have an inclination of saturation.

The Hall mobility of holes was determined from the data. The temperature dependence of Hall mobility μ_H for several A-type samples is shown in Fig. 8. The Hall mobility was about 80 cm²/volt-sec. at room temperature. With C-type samples the values were observed somewhat smaller than the above.

The dielectric constant $\mathcal{E}$ of the CdTe crystals was determined through the measurement of the capacities of condensers in which the CdTe plates were inserted as the dielectric media. When an osillator of 1 MC frequency was used, it was found that $\mathcal{E}$ is 10.3 ± 0.2 at room temperature.

§4. Discussions

It is known from the absorption and reflection data that the fundamental absorption edge is situated at about 1.43 e.v. This value coincides well with the main peak of photoconductivity. On the other hand, in the absorption and reflection spectra, some structures were also observed. Through the results may be interpreted with various possibilities, it is probable that the energy gap is about 1.43 e.v. unless the further informations are obtained.

Excess Te or Cd vacancies seem to be one of the most predominant impurity centers contained in the present crystals, since some amount of Cd is vaporized at the melting point of CdTe, and the resultant crystals grown from the mixture of atomic equivalent proportion may contain some excess Tellurium. In fact relatively low resistivities of p-type were observed in such crystals, and insulating crystals were grown in the saturated Cd vapor pressure. Simillarly, by the heat treatment in Cd vapor p-type samples of high resistivity could be obtained.

On the other hand, CdTe could hardly contain more than definite quantity of Cd excess impurity, becuse Cd added could not change carrier sign into n-type.

All the curves that represent the relation between the Hall coefficient and temperature data formed approximately the same slope in the case of p-type samples. Let $p=(3\pi/8)(1/Re)$ be the hole concentration, then we can obtain the concentration from the Hall coefficient R. In this case the hole concentration will be expressed as follows:

$$\frac{p(p+N_D)}{(N_A-N_D-p)N_V}=\left(\frac{m_d}{m_e}\right)^{3/2} D^{-1} \exp(-E_A/kT) \tag{1}$$

where N_A and N_D are the concentration of acceptors and donors included in the samples, and E_A and D the ionization energy and degeneracy of acceptor, respectively. Quantity m_d is the density-of-state mass of holes in the valence band, m_e is the free electron mass, and N_V is the density of state in the valence band with $m_d=m_e$.

If the logarithm of the left-hand side of Eq. (1) is plotted against the reciprocal of the absolute temperature, one should obtain a straight line whose slope gives E_A and whose intercept is $(m_d/m_e)^{3/2} D^{-1}$. In making such a plot the values of the parameters, N_A and N_D, must be chosen. Such plots of A-type samples were shown in Fig. 9. If we chose the other values of (N_A-N_D) or too small vales of N_D, the plots could not fit in with a straight line as shown in the figure. The intercept gives the value of $(m_d/m_e)^{3/2} D^{-1}$ as a reasonable value of about 0.5. If the value of N_D is too large, $(m_d/m_e)^{3/2} D^{-1}$ has an unreasonably large value. The slope of the line corresponds with $E_A=0.20$ e.v. Then it seems that in the A-type samples there are both acceptors and donors of $10^{15}\sim10^{16}$/cc and the ionization energy of acceptors will be about 0.20 e.v.

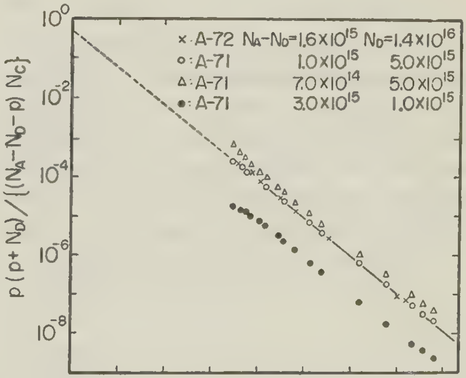

Fig. 9. Carrier concentration analysis of A-type samples.

In Fig. 8 curve ***b*** is drawn in accordance with the following equation:

$$\mu_H=4\times10^5\ T^{-3/2}\ \text{(practical unit)},$$

which is expected from the scattering by the acoustical mode of lattice vibrations. Our data show the larger values than the curve at low temperature and those data agree with neither the acoustical nor the impurity scattersng formulas.

Fröhlich and Mott[8] have studied the optical mode scattering in the weak coupling approximation, and Low and Pines[9] have developed the problem in the intermediated coupling range.

According to them the optical mode could be approximated with a single frequency ω. Then the following expression is given for the mobility μ below the Debye temperature $\Theta=\hbar\omega/k$:

$$\mu=\frac{1}{2\alpha\omega}\frac{e}{m}\left(\frac{m^*}{m}\right)^3 f(\alpha)\{\exp(\Theta/T)-1\}$$

$$\text{(electro-magnetic unit)}, \qquad (2)$$

where m and m^* are the effective mass of the electron and polaron respectively, α the strength of the interaction of the electron with the lattice, and $f(\alpha)$ a slowly varying function of α which is a little larger than unity at the low values of α. The quantities m and m^* are related as follows:

$$m^*=m(1+\alpha/6), \qquad (3)$$

and ω could be calculated from the *Reststrahl* wavelength λ_t as follows:

$$\omega=(\varepsilon/n^2)^{1/2}\ 2\pi c/\lambda_t \qquad (4)$$

and also α is given by

$$\alpha=\frac{e^2}{\hbar}\left(\frac{m}{2\hbar\omega}\right)^{1/2}\left(\frac{1}{n^2}-\frac{1}{\varepsilon}\right). \qquad (5)$$

Mitsuishi, Yoshinaga and Fujita[10] have observed the *Reststrahlen* of CdTe and found the wevelength to be about 66.7 μ. Using the values of dielectric constant and refractive index obtained, we cauld calculate the Debye temperature as 252°K.

In Fig. 8 curve ***a*** represents

$$\mu_H=57\{\exp(252/T)-1\}\ \text{(practical unit)}.$$

This expression seems to be better fitted to the experimental data and it may be considered that the deviation of the data from the curve ***a*** would be explained by the experimental errors and some contributions from the impurity and/or acoustical scattering.

If the Hall mobility μ_H meassured could be supposed to be the good approximation of true mobility μ, effective mass m, polaron effective mass m^* and coupling constant α could be calculated from the data. The values obtained for CdTe are as follows:

$$m=(0.63\pm0.06)m_e, \quad m^*=(0.69\pm0.07)m_e,$$

$$\alpha=0.57\pm0.08.$$

Assuming that $\mu_H=(3\pi/8)\,\mu$ we must enlarge the above values in about 9%.

§5. Acknowledgement

In conclusion, the author wishes to express his sincere thanks to Drs. K. Mizushima, O. Mikami and Y. Kamiya of Electrical Communication Laboratory for the instructions during the course of this work. The author is also indebted to Drs. T. Horii and S. Narita for their invaluable guidance and encouragements and to Messrs. A. Nakata and A. Takahashi for their laborious assistance.

References

1) D. A. Jenny and R. H. Bube: Phys. Rev. **96** (1954) 1190.
2) F. A. Kröger and D. de Nobel: J. Electronics **1** (1955) 190.
3) D. de Nobel: Phylips Res. Rep. **14** (1959) 361.
4) H. Miyasawa and S. Sugaike: J. Phys. Soc. Japan **9** (1954) 648.
5) S. U. Svenchnikov and V. T. Aleksandrov: Soviet Physics Technical Physics **2** (1957) 842.
6) R. Frerichs: Phys. Rev. **72** (1947) 594.
7) J. Appel and G. Lauts: Physica **XX** (1954) 1110.
8) H. Fröhlich and N. F. Mott: Proc. Phys. Soc. (London) **A171** (1939) 4694, **A62** (1949) 446.
9) F. Low and D. Pines: Phys. Rev. **98** (1955) 414.
10) A. Mitsuishi, H. Yoshinaga and S. Fujita: J. Phys. Soc. Japen **13** (1958) 1235.

JOURNAL OF THE PHYSICAL SOCIETY OF JAPAN, Vol. 15, NOVEMBER, 1960

Concentration Dependence of the Hall Coefficient in the Magnesium-Cadmium Alloys

By Seiichiro NOGUCHI and Takao SATO

Department of Physics, Faculty of Science, Tokyo Metropolitan University, Tokyo

(Received May 7, 1960)

The Hall coefficients of magnesium-cadmium alloys have been measured as a function of composition at both room temperature and 300°C with the magnetic field up to 6.5 KG. For all the compositions, the Hall coefficients are independent of magnetic field. An electronic structure of this system has been discussed with results of the lattice-spacing relations obtained by Hume-Rothery and Raynor. A relation between energy gap and concentration is discussed by comparing their results with the Hall coefficients measured by us. The present experimental results indicate that the energy gaps show a tendency to increase with the addition of cadmium to magnesium.

§1. Introduction

The Hall coefficients of magnesium and cadmium are negative and positive respectively. Both are divalent metals with the close-packed hexagonal structure. In pure magnesium or cadmium the number of overlapped electrons is equal to the number of holes in the first Brillouin zone. Thus a positive Hall coefficient means predominating hole mobility, while, if it is negative, an electron conduction must be more important.

Magnesium and cadmium make a continuous solid solution at higher temperatures, while at lower temperatures the existence of three ordered phases Mg_3Cd, MgCd and $MgCd_3$ has been confirmed by several investigators[1]. In the continuous solid solution region the axial ratio of the close-packed hexagonal lattice varies monotonically with concentration[2]. The electronic structure of the alloys should undergo a change with the variation of the axial ratio.

The purpose of the present paper is to obtain an information about the electronic structure of this system by means of the Hall effect measurements. The temperature at which a part of our measurements was performed is high enough for the existence of the continuous series of solid solutions. As it has been noted above, three ordered phases appear at room temperature, and correspond to three extreme values of the Hall coefficient.

§2. Experimental Procedure

Specimen preparation

The cadmium and magnesium used in this investigation have the purity of 99.9%. A series of 13 alloys is prepared to cover the whole concentration range. These alloys are melted under no flux, and cast into iron molds, so as to give plates 3 cm in length, 1 cm in width, and 0.2 cm in thickness, which are at once sealed in evacuated glass tubes, and annealed for 5 weeks at 300∼310°C. The tubes are then cooled in a blast of air, since quenching in water are responsible for the development of cracks as Hume-Rothery and Rayner had noted. After this treatment these alloys are polished to be 0.2∼0.3 mm in thickness as rapid as possible in order to prevent oxidization. They are sealed again in evacuated glass tubes, annealed for several days at 300°C, and then rapidly cooled to room temperature.

Measurement

All samples are approximately $25\times8\times0.3$ mm. The samples are joined by spot welding to annealed copper wires. A primary sample current of about 2A is supplied by batteries, and measured with a mirror-backed ammeter. The Hall voltage is measured with a DC amplifier[3] using a galvanometer which has a high sensitivity of about 7×10^{-9} V/div. and the technique has been developed in our laboratory. As mentioned by Hume-Rothery and Raynor, in quenched alloys the superlattice transformations took place on keeping the alloys at room temperatures, therefore, we measure the Hall coefficients at 300°C in an atmosphere of argon using an electric furnace which are put into the pole-pieces of electromagnet. The relatively shorter period fluctuations of the temperature of the specimen cause a variation of thermoelectric force at the probe-junctions, and therefore they disturb the measurement of Hall effect. The current of the furnace is supplied by a current stabilizer in order to eliminate fluctuations of a line voltage, because the Hall voltage to be measured in our work is less than 10^{-6} Volt and even a slight fluctuatians of the temperature difference between the probe-junctions can screen the Hall voltage.

§ 3. Results

The Hall coefficients of the magnesium-cadmium alloys at both room temperature and 300°C are given in Table I and Fig. 1.

Table I.

Composition (at. % Mg)	Hall Coefficient (m^3/A sec)	
	room temp.	300°C
0	6.0×10^{-11}	3.4×10^{-11}
10	10.0	3.3
20	16.9	3.3
25	17.8	3.3
30	17.0	3.2
40	11.9	0.3
50	6.0	0.0
60	10.4	− 0.4
70	15.9	− 0.5
75	14.0	− 0.7
80	7.7	− 1.6
90	5.8	− 4.7
100	−10.6	−10.6

(a) *The continuous solid solution*

The data at 300°C show that the Hall coefficients vary monotonically from a positive value for cadmium to a negative value for magnesium. The addition of cadmium to magnesium causes a rapid increase of the Hall coefficient, while the addition of magnesium to cadmium causes no changes. There is an abrupt change in the concentration-Hall coefficient diagram in the range of 60–70 at. % Cd.

(b) *The ordered phases*

The data at room temperature are given for the alloys which are annealed long enough to form ordered peases. In Fig. 1 the dependence of Hall coefficient on concentration has a minimum at 50 at. % and two maxima at 25 at. % and 75 at. % Cd correspoding to ordered alloys MgCd, Mg_3Cd and $MgCd_3$ respectively. Also included are the data of Salkovitz et al.[4] for magnesium-rich magnesium-cadmium alloys, and their results are in good agreement with our observations over the corresponding concentrations.

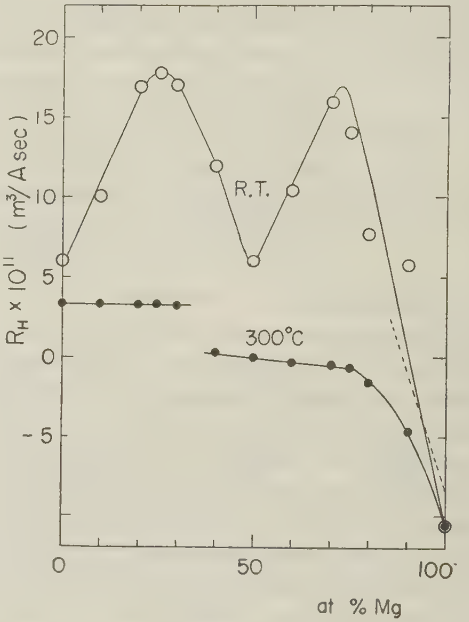

Fig. 1. The Hall coefficient at room temperature and 300°C as a function of concentration of cadmium. The dotted line shows the data of Salkovitz et al..

§ 4. Discussions

Many investigators have explained the peculiar variation of the lattice parameters of the metals with the close-packed hexagonal structure[5]. In 1940 Hume-Rothery and Raynor investigated the lattice parameters of magnesium-cadmium alloys at 310°C and made a discussion about onsets of electron overlaps across the faces of the Brillouin zone. They concluded that the observation was well interpreted with the Brillouin zone theory developed by Jones. A direct consequence of this theory is that a significant effect should be found on the Hall coefficient, when overlap occurs. Further, even if no new overlap occurs, the variation of concentration of the alloys should cause a distortion of Brillouin zone, i.e. a distortion of crystal structure on account of an interaction of Brillouin zone boundaries with Fermi surface[6].

The information of such a change of Fermi surface has come from X-ray data, but a more direct approach can be achieved by examining the concentration dependence of the Hall coefficient. The present measurements have shown that the Hall coefficients of the solid solutions of this system vary smoothly with composition except in the range of 60–70 at. % Cd.

Magnesium and cadmium have the same valency, i.e., divalent and almost the same volume, but have different axial ratios of their close-packed hexagonal structures. There is, however, much difference between the Hall coefficients of them, that is to say, the Hall coefficient of magnesium is -10.6×10^{-11}, and that of cadmium is 6.0×10^{-11} m^3/A sec. The Hall coefficient of magnesium does not vary with temperature, while that of cadmium shows a considerable decrease with the increase of the temperature in this temperature range. The Hall coefficient of cadmium is still positive, on the contrary, magnesium has a negative value in the temperature range of this measurements.

Since magnesium and cadmium are conductors of electricity, there must be an overlap into a second zone, the two band model might be adopted, and one can write

$$R_H=-\frac{1}{|e|}\left\{\frac{n_1\mu_1{}^2-n_2\mu_2{}^2}{(n_1\mu_1+n_2\mu_2)^2}\right\}\,, \qquad (1)$$

were R_H is the Hall coefficient, μ is the mobility, and n is the number of charge carriers per unit volume, and subscripts 1 and 2 refer to electrons and holes. Since both metals are divalent, each atom contributes two electrons in all the concentrations of these alloys. As the first Brillouin zone of close-packed hexagonal structure can contain two electrons per atom, the number of electrons which are effective as carriers is equal to the number of holes. Therefore, Eq. (1) can be written as follows,

$$R_H=-\frac{1}{n|e|}\left(\frac{\mu_1-\mu_2}{\mu_1+\mu_2}\right)\,, \qquad (2)$$

$$R_H\sigma=-(\mu_1-\mu_2)\,, \qquad (3)$$

were σ is the total conductivity. The values of $(\mu_1-\mu_2)$ for both the continuous solid solution and the ordered phases are calculated by using both the Hall coefficient obtained in our present work and the conductivity measured by Grube and Schiedt. The values for the ordered phases may be meaningless because the electron number n_1 may differ from the hole number n_2 due to the splitting of the Brillouin zone by a formation of new periodicity and a distortion of the structures. The variations of these $(\mu_1-\mu_2)$ with compositions are presented in Fig. 2. Also included are the data of Salkovitz et al. for the magnesium-rich region in magnesium-cadmium system. Their results are in good agreement with the present results in the corresponding compositions.

The first Brillouin zone of the close-packed hexagonal structure is shown in Fig. 3, and the energy of an electron varies continuously within this zone which is surrounded every-

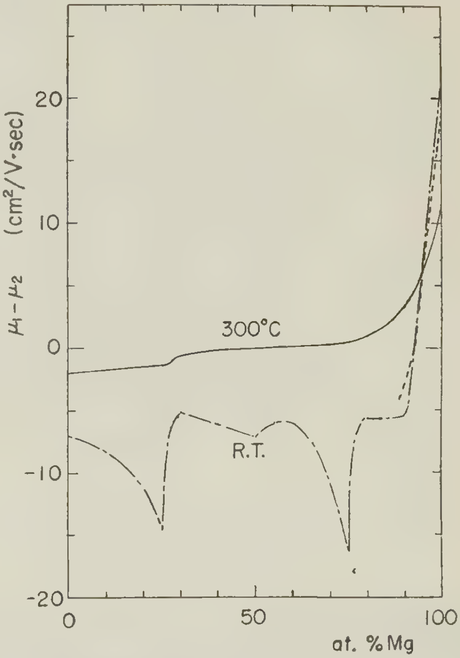

Fig. 2. The difference between electron and hole mobilities versus composition curves at room temperature and 300°C. The dotted line is the results obtained by Salkovitz et al..

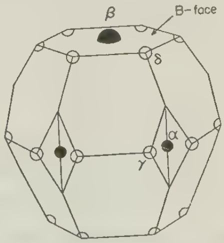

Fig. 3. The first Brillouin zone of the close-packed hexagonal structure.

where by an energy discontinuity, and contains exactly two electrons per atom. As mentioned above, magnesium and cadmium are conductors of electricity, then there must be an overlap into a second zone. In order to explain the present results, two types of electron overlaps and holes are employed. Mott and Jones have shown that the overlaps may occur either at β or at the re-entrant corners, point α, in Fig. 3. As it has been noted above, in magnesium-cadmium alloys at higher temperatures, there must be the same number of holes as that of electrons. From the shape of the Brillouin zone it will be plausible to consider that the holes may exist at both γ and δ. The most important factors affecting these electron overlaps and holes are the magnitude of the energy gaps at the corresponding faces of the Brillouin zone and the axial ratio, c/a, of the structure. If the energy gaps are not changed by a variation of the axial ratio, the electron overlap α and hole δ decrease and the β and the γ increase with the increase of axial ratio. On the contrary, when we take an effect of only the energy gaps on the overlaps and holes in consideration, increasing energy gaps decrease the corresponding electron overlaps and holes, i.e., if the energy gap associated with the B face of the Brillouin zone increases, the overlap β and the hole δ decrease.

Such a model may be adopted, and R_H is given by

$$R_H=-\frac{1}{|e|}\left\{\frac{n_\alpha\mu_\alpha{}^2+n_\beta\mu_\beta{}^2-n_\gamma\mu_\gamma{}^2-n_\delta\mu_\delta{}^2}{(n_\alpha\mu_\alpha+n_\beta\mu_\beta+n_\delta\mu_\delta+n_\delta\mu_\delta)^2}\right\}, \tag{4}$$

where the subscripts α, β, γ and δ refer to the α and β overlaps, and the γ and δ holes, respectively. By assuming that the relative variation of mobilities of the electrons and holes with respect to composition is not very large, a large concentration dependence of the Hall coefficient in magnesium-cadmium alloys will be explained by the change of magnitude of the electrons and holes with composition. According to the calculation of Mott and Jones there is no α overlap for cadmium with axial ratio 1.885 but no β overlap for magnesium with axial ratio 1.6237. And hence the results of our present experiment indicate that the following relation holds among the mobilities of overlaps and holes: $\mu_\delta>\mu_\alpha>\mu_\beta\sim\mu_\gamma$. By neglecting the effect of energy gap, a relation between the axial ratio and the concentration should indicate that the Hall coefficient makes a large change in the region of 60–100 at. % Cd, while in the region of pure magnesium to 60 at. % Cd the change is very small. Contrary to the expectation, little change was found in the region of 60–100 at. % Cd, and a rapid variation of the Hall coefficient in the region of 0–40 at. % Cd. In order to explain such a dependence of the Hall coefficient on the composition, it is sufficient that the energy gaps for the α and β overlaps increase with the increase of the contents of cadmium. Namely, the rapid decrease of the axial ratio with increasing magnesium contents in cadmium-rich regions will tend to decrease the β overlap but the decreasing energy gaps will counterwork. Then the observed Hall coefficients keep almost a constant value. In contrast with this, the axial ratio shows only a very slight increase with the addition of cadmium to pure magnesium, so that the Hall coefficient should be scarcely affected by taking into account of the effect of only the axial ratio on the overlaps and holes. When the effect of the increasing energy gap is taken into account, it may be expected that a considerable increase of the Hall coefficient is shown with the increase of cadmium contents.

The results at room temperature demonstrate the larger positive values of the Hall coefficient of Mg_3Cd and $MgCd_3$, than that of MgCd. The Brillouin zones of both types which are formed by an additional periodicity of super-lattice appreciably differ from each other[7]. It is reasonable to consider that such a difference will cause a different interaction of the Brillouin zone boundaries with the Fermi surface. A considerable distinction of the Hall coefficients may be due to the difference of the interaction.

The writers wish to thank Mr. K. Yonemitsu for the discussions and his helpful assistance with their experiments.

References

1) G. Grube and E. Schiedt: Z. anorg. Chem. **194** (1930) 190. M. Hirabayashi: J. Japan Inst. Met. **16** (1952) 295. M. Hirabayashi, S. Nagasaki, H. Maniwa and H. Nagasu: J. Japan Inst. Met. **B 13** (1946) 6. A. Moore and G. V. Raynor: Acta Met. **5** (1957) 601.
2) W. Hume-Rothery and G. V. Raynor: Proc.

Roy. Soc. **A 174** (1940) 471.
3) K. Yonemitsu and T. Sato: J. Appl. Phys. Japan **26** (1957) 153.
4) E. I. Salkovitz, A. I. Schindler and E. W. Kammer: Phys. Rev. **105** (1957) 887.
5) G. V. Raynor: Proc. Roy. Soc. **A 174** (1940) 457. T. B. Massalski: Acta Met. **5** (1957) 541. T. B. Massalski and B. Cockayne: Acta Met. **7** (1959) 762. C. B. Walker and M. Marezio: Acta Met. **7** (1959) 769.
6) J. B. Goodenough: Phys. Rev. **89** (1953) 282. J. W. McClure: Phys. Rev. **98** (1955) 449.
7) K. Yonemitsu and T. Sato: J. Phys. Soc. Japan **13** (1958) 15.

JOURNAL OF THE PHYSICAL SOCIETY OF JAPAN, Vol. 15, No. 11, NOVEMBER, 1960

Theory of Thermoelectric Power of Ionic Crystals, IV.

By Eijiro HAGA

Department of Physics, Faculty of Science, Niigata University

(Received May 10, 1960)

The thermoelectric power Q associated with the movement of silver ions in Ag_2X (X=S, Se, Te) is discussed, where Q is obtainable by measuring the potential difference between silver electrodes in an arrangement as $Ag(T_1)|AgI(T_1)|Ag_2X|AgI(T_2)|Ag(T_2)$. When a temperature gradient is applied, Q, in general, changes with time because of the thermal diffusion of both electrons and silver ions, and then reaches its steady value. An information on the heat of transport of a silver ion is obtained from the comparison between theory and experiment.

An explanation on the heat of transport in ionic crystals is given taking into account the variation of vibration frequency of lattice due to the presence of defects. The theory is compared with the experimental data on silver halides and Ag_2X available at present.

§1. Introduction

In §2 we shall discuss the thermoelectric power of Ag_2X (X=S, Se, Te). The thermoelectric power associated with silver ions in these substances has been measured by Reinhold under the arrangement: $Ag(T_1)|Ag_2X|Ag(T_2)$, where T_1 and T_2 are temperatures in the respective places[1]. In this arrangement, silver atoms in Ag(T_1 or T_2) enter into Ag_2X until the equilibrium is attained, when $T_1=T_2$. When a temperature gradient is applied between the two silver electrodes, it is not sure that the thermal equilibrium for silver ions holds at junctions, since it may happen that silver atoms enter into Ag_2X from $Ag(T_2(>T_1))$ and deposit at $Ag(T_1)$, resulting in the net current of silver atom through Ag_2X. The measurements of Reinhold hence will not give the ionic thermoelectric power. This ambiguity on the thermal equilibrium can be removed by inserting a purely ionic conductor such as AgI between Ag and Ag_2X, as

$$Ag(T_1)|AgI(T_1)|Ag_2X|AgI(T_2)|Ag(T_2)\,. \quad (1)$$

In this arrangement, the electrochemical potential of a silver ion, ζ_{Ag^+}, is continuous everywhere and so the difference of the Fermi levels between the two electrodes is related to $d\zeta_{Ag^+}/dx$, which can be obtained by the similar procedure to that in ***III***[2] reported already. When a temperature gradient is applied to the specimen, $d\zeta_{Ag^+}/dx$ changes with time because of the appearance of the current of silver atoms and then reaches the steady value. It will be obvious that, in the steady state, the presence of electrons in the specimen has no effect on the thermoelectric power in the arrangement (1).

Next, in §3, we shall give a theoretical consideration on the heat of transport in ionic crystals. Concerning the heat of transport, the values of $h_F + Q_i^* + Q_v^*$ and $-Q_v^*/T + \partial\mu_v^0/\partial T$ have been obtained from the comparison of the theory of thermoelectric power with experiments in AgCl[3] and AgBr[4], where Q_i^* and Q_v^* and the heat of transport of an interstitial Ag^+ and an Ag^+ vacancy, respectively, h_F is the enthalpy of forming a pair of Frenkel defects and μ_v^0 is the Gibbs free energy of taking out a silver ion from a lattice site in a perfect crystal to the vacuum. The theory of Wirtz[5] on the mechanism of thermal diffusion can not explain these values and hence we shall make a theoretical consideration on the heat of transport, showing a fairly good agreement with experimental values.

§ 2. Ionic Thermoelectric Powers of Ag_2S, Ag_2Se and Ag_2Te

The thermoelectric power Q in the arrangement (1) is related to Q_{Ag^+}, with the same procedure as that in ***I***[6], by

$$eQ = eQ_{Ag^+} + s_{Ag}^{Ag}\,, \tag{2}$$

where eQ_{Ag^+} is the value value obtained by subtracting ζ_{Ag^+} in Ag_2X at a certain point from that at an other point at higher temperature by 1°C, and s_{Ag}^{Ag} is the entropy of a silver atom in a silver atom in a silver metal. Hence we have merely to calculate $d\zeta_{Ag^+}/dx$ as follows.

The electrical current densities of silver ions and electrons, j_i and j_e, are given, respectively, by

$$\left.\begin{aligned} j_i &= \frac{\sigma_i}{e}\left(eE - \left(\frac{\partial\mu_i}{\partial n_i}\right)_T \frac{\partial n_i}{\partial x} - \frac{Q_i^*}{T}\frac{\partial T}{\partial x}\right), \\ j_e &= \frac{\sigma_e}{e}\left(eE + \left(\frac{\partial\mu_e}{\partial n_e}\right)_T \frac{\partial n_e}{\partial x} + \frac{Q_e^*}{T}\frac{\partial T}{\partial x}\right), \end{aligned}\right\} \tag{3}$$

where σ_i, n_i and μ_i are the partial conductivity, the concentration and the chemical potential per ion, of silver ions, respectively, and σ_e, n_e and μ_e are similar quantities on electrons. With use of the condition that the total current does not exist; $j_i + j_e = 0$ and the charge neutrality condition; $\partial n_i/\partial x = \partial n_e/\partial x$, we obtain

$$\begin{aligned} \frac{d\zeta_{Ag^+}}{dx} &= -eE + \frac{d\mu_i}{dx} \\ &= \left[t_e\left(\frac{\partial\mu_{Ag}}{\partial n_{Ag}}\right)_T \frac{(n_i)_{x=L} - (n_i)_{x=0}}{\Delta T}\right. \\ &\quad \left. + \left(\frac{\partial\mu_i}{\partial T}\right)_{n_i} - \frac{t_i Q_i^* - t_e Q_e^*}{T}\right]\frac{\partial T}{\partial x}\,, \end{aligned} \tag{4}$$

where μ_{Ag} and n_{Ag} are the chemical potential per atom and the concentration of silver atom in Ag_2X, t_i and t_e are the transport numbers of silver ions and electrons, respectively, and ΔT is the temperature difference between the ends of the specimen of length L. The difference of n_i between the ends of the specimen, $(n_i)_{x=L} - (n_i)_{x=0}$, changes with time t, after ΔT is applied at $t=0$, since n_i or n_e depends on time because of the thermal diffusion of both electrons and ions. Therefore it is seen from Eqs. (2) and (4) that the thermoelectric power depends on time. This time dependence can be found with use of the similar procedure to that in ***III***[2] as follows. Here, let us consider only the case that L is so long that the time constant τ is much longer than the time required to set up ΔT in the specimen.

The continuity equation for ions

$$\frac{\partial n_i}{\partial t} = -\frac{\partial j_i/e}{\partial x} \tag{5}$$

is reduced with use of Eq. (3) differentiated with respect to x, higher order term than that of $\partial T/\partial x$ being neglected, to

$$\frac{\partial n_i}{\partial t} = \frac{\sigma t_e t_i}{e^2}\left(\frac{\partial\mu_{Ag}}{\partial n_{Ag}}\right)_T \frac{\partial^2 n_i}{\partial x^2}\,, \tag{6}$$

where σ is the total conductivity, $\sigma_i + \sigma_e$. The boundary condition to Eq. (6) is given by

$$(j_i)_{x=0} = (j_i)_{x=L} = 0\,, \tag{7}$$

which is rewritten as

$$\left(\frac{\partial n_i}{\partial x}\right)_{x=0} = \left(\frac{\partial n_i}{\partial x}\right)_{x=L} = -\frac{Q_e^* + Q_i^*}{T(\partial\mu_{Ag}/\partial n_{Ag})_T}\frac{\partial T}{\partial x}\,. \tag{8}$$

On the other hand, the initial condition is $n_i = n_i^0$, n_i^0 being a constant independent of x. Then, solving Eq. (6), we obtain

$$\begin{aligned} &\frac{(n_i)_{x=L} - (n_i)_{x=0}}{\Delta T} \\ &\quad = -\frac{Q_e^* + Q_i^*}{T(\partial\mu_{Ag}/\partial n_{Ag})_T}\left[1 - F\left(\frac{t}{\tau}\right)\right], \end{aligned} \tag{9}$$

where $F(t/\tau)$ is given by Eq. (21) in ***III***[2], and

$$\tau = \frac{e^2L^2}{\pi^2\sigma t_i t_e(\partial\mu_{Ag}/\partial n_{Ag})_T}\,. \tag{10}$$

From Eqs. (2), (4) and (9), we obtain the expression for the thermoelectric power:

$$\begin{aligned} eQ = &-\frac{Q_i^*}{T} + \left(\frac{\partial\mu_i}{\partial T}\right)_{n_i} \\ &+ \frac{t_e}{T}(Q_e^* + Q_i^*)F\left(\frac{t}{\tau}\right) + s_{Ag}^{Ag}\,. \end{aligned} \tag{11}$$

The electrical conduction in Ag_2X has been studied by Miyatani[7], according to whom the concentration of silver atoms can be freely varied within a certain range, and μ_i is independent of n_i in α-phase, while it depends on n_i in β-phase in fairly complicated way. In α-phase, the time constant τ is so short that the usual measurement of the thermoelectric power gives the steady value and so the third term in Eq. (11) is neglected. The value of $Q_i^*/T-\partial\mu_i/\partial T$ is therefore found from the experimental value of Q with use of the value of $s_{\mathrm{Ag}}^{\mathrm{Ag}}$ estimated from the specific heat of Ag. On the other hand, in the β-phase, the thermoelectric power is expected to change with time, since τ is not so small. Accordingly the value of $Q_e^*+Q_i^*$ will be obtained if the time dependence of Q is measured, besides the value of $Q_i^*/T-\partial\mu_i/\partial T$ obtained in the steady state.

In addition, the change of Q, after ΔT is removed at $t=0$ in the steady state, is calculated as follows, where τ is assumed to be much longer than the time required to remove ΔT. The potential difference between the ends of the specimen, ΔV, is given in such a case by

$$e\Delta V=\int_0^L\left(-eE+\left(\frac{\partial\mu_i}{\partial n_i}\right)_T\frac{\partial n_i}{\partial x}\right)dx$$

$$=t_e\left(\frac{\partial\mu_{\mathrm{Ag}}}{\partial n_{\mathrm{Ag}}}\right)_T[(n_i)_{x=L}-(n_i)_{x=0}]\,. \qquad (12)$$

The diffusion equation (6) and the boundary condition (8), $\partial T/\partial x$ being zero, are valid at the present case, while the initial condition is given by

$$n_i=n_i^0-\left(\frac{x}{L}-\frac{1}{2}\right)\frac{Q_e^*+Q_i^*}{T(\partial\mu_{\mathrm{Ag}}/\partial n_{\mathrm{Ag}})_T}\Delta T\,, \qquad (13)$$

which is the solution at $t=\infty$ of Eq. (6). From Eqs. (12) and (13), we obtain

$$e\frac{\Delta V}{\Delta T}=-\frac{t_e}{T}(Q_e^*+Q_i^*)F\left(\frac{t}{\tau}\right), \qquad (14)$$

which is equal to the third term of Eq. (11) depending on time. Such a situation is similar to the case treated in ***III***[2]. The transport number of electrons t_e in Eqs. (11) and (14) can be taken as unity except β-Ag_2S, for any electron density according to the measurement of Miyatani (t_i is of the order of 1% except β-Ag_2S).

The measurement of the thermoelectric power of the α-Ag_2X in the arrangement (1) has been made by Endo for the various concentration of silver ions[8]. Theory predicts that the ionic thermoelectric power is independent of the concentration of silver atoms, since the α-Ag_2X is of an average structure and all silver ions contribute to the ionic conduction. This Ag-concentration-independence of Q has been experimentally confirmed by Endo[8]. The experimental values under the arrangement (1) is remarkably different from those by Reinhold[1] as seen in Table I. The measurement of Reinhold seems to give roughly the electronic thermoelectric power of Ag-saturated specimen, which is obtainable with electrodes like *Pt*. From the experimental values of Endo[8], we obtain the values of $Q_i^*/T-\partial\mu_i/\partial T$ with use of Eq. (11), its third term being neglected, as shown in Table I.

Table I. The experimental values of ionic thermoelectric power of α-Ag_2X and the values of $Q_i^*/T-\partial\mu_i/\partial T$ obtained from Q-values by Endo.

Ag_2S

°C	$-Q(\mu v/°C)$		$\frac{1}{e}\left(\frac{Q_i^*}{T}-\frac{\partial\mu_i}{\partial T}\right)(\mu v/°C)$
	Reinhold	Endo	
200	−70	230	780
250	−70	230	810
300	−70	230	840

Ag_2Se

°C	$-Q(\mu v/°C)$		$\frac{1}{e}\left(\frac{Q_i^*}{T}-\frac{\partial\mu_i}{\partial T}\right)(\mu v/°C)$
	Reinhold	Endo	
200	−40	250	800
250	−40	250	830
300	−40	250	860

Ag_2Te

°C	$-Q(\mu v/°C)$		$\frac{1}{e}\left(\frac{Q_i^*}{T}-\frac{\partial\mu_i}{\partial T}\right)(\mu v/°C)$
	Reinhold	Endo	
200	−120	440	990
250	−120	420	1000
300	−120	415	1020

§ 3. Heat of Transport

We first consider a homogeneous substance like AgCl possessing mobile particles under a constant temperature and pressure. Let us imagine that it is divided into two parts **A** and **B** by an imaginary plane and N particles move from **A** to **B**. If such a movement occurs under a constant temperature and pressure, the heat of NQ^* must be, in general, supplied from the environment into **A** and the same amount of heat must be taken away from **B** to the environment. The heat Q^* is called the heat of transport of the particle transported, in the present paper.

We now consider the heat of transport, Q_i^*, of an interstitial ion which is doing thermal vibration around its equilibrium position in **A**. To calculate Q_i^*, let us trace the movement of an interstitial ion which first wanders within **A** and at last enter into **B**. In order for the ion to move from one interstitial site to the next one, it must climb the potential barrier, and, at this time, a certain amount of heat, $\varDelta H$, must be supplied from the environment to **A**. The magnitude of $\varDelta H$, can be obtained as follows. Let x' be the x-coodinate of a (100) plane in **A**, x_1 and x_2 be the x-coordinates of interstitial positions nearest to the (100) plane, x' lying in the middle of x_1 and x_2, and n be an average number of interstitial ions at x_1 or x_2. When an interstitial ion moves from x_1 to x_2, the energy is transported by the amount U_i^*, which can be obtained according to Wert who has computed the transition probability per unit time, w_i, for an ion to move from x_1 to x_2 by means of the statistical mechanics[9]. Let (x, y, z), (p_x, p_y, p_z) and m be the space-coordinate, the conjugate momentum and the mass of an interstitial ion, Q, P and $K(P)$ be the collective coordinate, the conjugate momentum and the total kinetic energy of the lattice ions vibrating at normal sites in **A**, and $\varphi(x, y, z; Q; v)$ be the total potential energy of the system consisting of lattice ions and an interstitial ion in **A** of volume v. Then, the mean energy transported across the plane $x=x'$ in time interval δt is given by

$$nw_iU_i^*\delta t=\frac{\int N_0\frac{p_x}{m}\delta t\,dp_x\int\exp\left[-\frac{T(x',y,z;Q;v)}{kT}\right]S(x',y,z;Q;v)\,dp_y\,dp_z\,dy\,dz\,dP\,dQ\,dv}{\int\exp\left[-\frac{T(x,y,z;Q;v)}{kT}\right]dp_x\,dp_y\,dp_z\,dx\,dy\,dz\,dP\,dQ\,dv}, \tag{15}$$

where

$$\left.\begin{aligned}T(x',y,z;Q;v)&=K(P)+\varphi(x',y,z;Q;v)+\frac{1}{2m}(p_x^2+p_y^2+p_z^2)+p_0v\,,\\ S(x',y,z;Q;v)&=\varphi(x',y,z;Q;v)+\frac{1}{2m}(p_x^2+p_y^2+p_z^2)\,,\end{aligned}\right\} \tag{16}$$

N_0 and p_0 are the total number of interstitial ions in **A** and the pressure, respectively, and the integration with respect to (x, y, z) is taken over the volume in **A**. From Eq. (15), with use of

$$w_i=\nu_i\exp(-\varDelta g_i/kT)\,, \tag{17}$$

where ν_i and $\varDelta g_i$ are the vibration frequency, and the Gibbs free energy of activation, of an interstitial ion, respectively, we easily obtain

$$U_i^*=V(x')+2kT\,, \tag{18}$$

where

$$V(x')=\frac{\int\exp-\frac{1}{kT}[\varphi(x',y,z;Q;v)+p_0v]\varphi(x',y,z;Q;v)\,dy\,dz\,dQ\,dv}{\int\exp-\frac{1}{kT}[\varphi(x',y,z;Q;v)+p_0v]\,dy\,dz\,dQ\,dv} \tag{19}$$

is the mean potential energy of the system which consists of lattice ions in **A** and an interstitial ion at x'. Since $\varDelta H$ is equal to the difference of the enthalpy of the system between when the interstitial ion is at x' and when it is at x_1, we obtain

$$\varDelta H=(V(x')+2kT)-(V(x_1)+K_i)+p_0\varDelta v\,, \tag{20}$$

where K_i is the sum of the kinetic energy of the interstitial ion due to the vibration in (yz) plane and the total energy due to the vibration in x direction, and Δv is the volume increase of **A** when an interstitial ion is activated from x_1 to x'.

Next, when an interstitial ion moves away from the position x' in **A** to **B**, the entropy of lattice ions in **A** varies because of the variation of vibration frequency of lattice ions around x'. Since the movement of an interstitial ion from **A** to **B** takes place reversibly, the contribution of the entropy variation to the heat of transport is $-T\Delta s(x')$, where $\Delta s(x')$ is the increase of the entropy of lattice ions due to the presence of an ion at x'. Hence, we have

$$Q_i^* = \Delta H - T\Delta s(x') \ . \tag{21}$$

From Eqs. (20) and (21), we obtain

$$Q_i^* = -(K_i - Ts_i^{osc}) + T\frac{\partial \mu_i^0}{\partial T} + 2kT + \Delta u_i \ , \tag{22}$$

where

$$\Delta u_i = (V(x') - V(x_1)) - T(\Delta s(x') - \Delta s(x_1)) + p_0\Delta v \ , \tag{23}$$

μ_i^0 is the Gibbs free energy of bringing an ion from the vacuum to the state of thermal vibration at an interstitial position in a perfect crystal, and s_i^{osc} is the vibration entropy of an interstitial ion.

The movement of an Ag^+ vacancy from **A** to **B** is equivalent to that of an lattice ion from **B** to **A**. Hence we have, corresponding to Eq. (22),

$$Q_v^* = K_L - Ts_L^{osc} + T\frac{\partial \mu_v^0}{\partial T} - 2kT - \Delta u_v \ , \tag{24}$$

where K_L, s_L^{osc}, and Δu_v are defined for an lattice ion in a similar way to those for interstitial ion. Summing up Eqs. (22) and (24), we have

$$Q_i^* + Q_v^* = \Delta u_i - \Delta u_v - Ts_F + 3kT \ln \nu_0/\nu_i \ , \tag{25}$$

where ν_0 is the mean vibration frequency of lattice ions, K_L and K_i are both taken as $2kT$, and the entropy of forming a pair of Frenkel defects, s_F, may be written as

$$s_F = -\frac{\partial(\mu_i^0 + \mu_v^0)}{\partial T} = k\sum \ln\frac{\nu}{\nu'} + k\sum \ln\frac{\nu}{\nu_i'} + 3k\ln\frac{\nu_0}{\nu_i} \ , \tag{26}$$

ν, ν', and ν_i' being the frequency of a normal mode of vibration of lattice ions in the perfect crystal, that in the presence of a vacancy, and that in the presence of an interstitial ion, respectively. In Eq. (26), it is expected that the first term is positive and the other terms are negative. The values of s_F found from the conductivity data on AgCl and AgBr by Teltow[10] lead to an extraordinarily large difference between ν and ν'.[10] Hence, we shall assume $\nu_0 \sim \nu_i$ and neglect the last term in Eq. (25). We shall further assume that s_L^{osc} may be approximately taken as a half of the vibration entropy of a pair of positive and negative ions at normal sites, and $\Delta u_{i,v}$ may as the activation energy of the mobility $u_{i,v}$:

$$u_{i,v} = \frac{u_{i,v}^0}{T}\exp\left(-\frac{\Delta u_{i,v}}{kT}\right) , \tag{27}$$

where $u_{i,v}^0$ is a parameter independent of temperature.

Now we can compare the theoretical values obtained from Eqs. (24) and (25) with the experimental values as shown in Table II, where we use the values obtained from the data of Teltow[10] as follows; $h_F=1.69$(AgCl) and 1.27 ev(AgBr), $s_F=1270$ and 1020×10^{-6} ev/°C, $\Delta u_i=0.19$ and $0.19\,ev$, and $\Delta u_v=0.39$ and $0.40\,ev$, two values being of AgCl and AgBr, respectively.

Let us next consider the case of α-Ag_2X. The activation energy of the mobility, Δu, is obtained from the conductivity data of Endo[8] with use of

$$\sigma = \frac{\sigma^0}{T}\exp\left(-\frac{\Delta u}{kT}\right) , \tag{28}$$

where σ is the conductivity and σ^0 is a parameter independent of temperature. From this equation, the values of Δu in Ag_2S, Ag_2Se and Ag_2Te are obtained as 0.093, 0.099 and 0.137 *ev*, respectively. Assuming $s^{0sc}=\frac{1}{3}s^{0sc}_{Ag_2X}$, the value obtained from Eq. (22) can be compared with the values obtained in § 2, as shown in Table III.

Further, the thermoelectric power of α-AgI has been measured as 560 $\mu v/°C$ at 200∼300°C by Reinhold under an arrangement: $Ag(T_1)|AgI|Ag(T_2)$. The activation energy Δu is obtained as 0.101 *ev* from the data of Tubandt, et al.[11] with use of Eq. (28). Assuming $s^{0sc}=\frac{1}{2}s^{0sc}_{AgI}$, the comparison between theory and experiment is also possible as shown in Table III.

Table II. The comparison between theory and experiment for the heat of transport in AgCl and AgBr.

AgCl

°C	$h_F+Q_i^*+Q_v^*(ev)$		$\frac{1}{e}\left(-\frac{Q_v^*}{T}+\frac{\partial\mu_v^0}{\partial T}\right)(\mu v/°C)$	
	Exp.	Theory	Exp.	Theory
250	0.78	0.83	1360	1420
300	0.63	0.76	1480	1380
350	0.52	0.70	1500	1360

AgBr

°C	$h_F+Q_i^*+Q_v^*(ev)$		$\frac{1}{e}\left(-\frac{Q_v^*}{T}+\frac{\partial\mu_v^0}{\partial T}\right)(\mu v/°C)$	
	Exp.	Theory	Exp.	Theory
175	0.70	0.60	1380	1560
250	0.58	0.53	1370	1480

Table III. The comparison between theory and experiment for $(Q_i^*/T-\partial\mu_i/\partial T)/e$ (in $\mu v/°C$) in Ag_2S, Ag_2Se, Ag_2Te and AgI.

°C	Ag_2S		Ag_2Se		Ag_2Te		AgI	
	Exp.	Theory	Exp.	Theory	Exp.	Theory	Exp.	Theory
200	780	860	800	920	990	1170	1110	960
250	810	870	830	930	1000	1170	1140	970
300	840	880	860	940	1020	1180	1170	990

From Tables II and III, it is seen that the theory developed in the present section fits fairly well with experiments though we made several rough assumptions under a simple model. The present theory will be also available to the case of $NaCl+CdCl_2$ and will be compared with experiment if Q is measured with *e.g.* chlorine gas electrodes, though such a measurement seems not to be carried out as yet.

The writer wishes to express his cordial thanks to Mr. S. Endo who kindly carried out the measurements on α-Ag_2X, available to the comparison with theory. The writer is also very much indebted to Drs. S. Miyatani, I. Yokota, T. Kurozawa and Profs. Y. Suzuki, R. Kubo for their useful discussions. The present work was supported by the Scientific Research Fund of the Ministry of Education.

References

1) H. Reinhold: Z. Anorg. Allg. Chem. **171** (1928) 181. H. Reinhold and A. Blachny: Z. Elektrochem. **39** (1933) 290.
2) E. Haga: J. Phys. Soc. Japan **14** (1959) 1176.
3) Y. Suzuki, S. Endo, and E. Haga: J. Phys. Soc. Japan **14** (1959) 729.
4) R. W. Christy, E. Fukushima and H. T. Li: J. Chem. Phys. **30** (1959) 136.
5) K. Wirtz: Z. Phys. **44** (1943) 221.
6) E. Haga: J. Phys. Soc. Japan **13** (1958) 1090.
7) S. Miyatani: J. Phys. Soc. Japan **10** (1955) 786; **13** (1958) 317; **13** (1958) 341; **14** (1959) 996.
8) S. Endo: Unpublished.
9) C. A. Wert: Phys. Rev. **79** (1950) 601.
10) J. Teltow: Ann. Physik **15** (1955) 268; **5** (1949) 63, 71.
11) C. Tubandt and E. Lorenz: physik. Chem. **87** (1914) 513.

JOURNAL OF THE PHYSICAL SOCIETY OF JAPAN, Vol. 15, No. 11, NOVEMBER, 1960

Measurement of Microwave Dielectric Constants of Ferroelectrics

Part I. Dielectric Constants of $BaTiO_3$ Single Crystal at 3.3 KMc/s.

By Eiji NAKAMURA and Jiro FURUICHI

Department of Physics, Faculty of Science,
Hokkaido University, Sapporo, Japan

(Received May 12, 1960)

Horner et al's method of dielectric measurement at microwave region has been extended so that it can be applied for cylindrical specimens of arbitrary cross-sections with relatively high loss tangent and high permittivity. Small amount of Specimen is good enough for our method. As the first application of our method, dielectric constants of $BaTiO_3$ single crystal have been measured from room temperature to 170°C at a frequency of 3.3KMc/s. Above the Curie point, dielectric constants measured at 3.3KMc/s agree well with those measured at 24KMc/s by Benedict and Durand, while the loss tangents slightly above the Curie point are 0.01 ± 0.007 in our case compared to 0.1 in the case of Benedict and Durand.

§1. Introduction

Investigations of dielectric properties of ferroelectrics at microwave region provide an information on the mechanism of ferroelectric phase transition, as well as on their usefulness in microwave circuits. That is, if a dielectric dispersion is observed in a single crystal at microwave region, it can be considered as a strong evidence that the transition is order-disorder type. Several workers measured microwave dielectric constants of ferroelectrics. Yager[1] had found dielectric dispersion of Rochelle salt in microwave region about ten years ago, and Akao et al[2] did very detailed investigation of this dispersion. Very recently Nishioka and Takeuchi[3] have observed dielectric behaviour of $(glycine)_3 H_2SO_4$, at about 10 KMc/s, and found that dielectric anomaly at the Curie point still occurs in this region though the dielectric constant at room temperature is smaller than that of low frequency value. Several workers measured dielectric constants of ceramic $BaTiO_3$, and found dispersions at microwave frequencies. But since phase transition in $BaTiO_3$ cannot be considered as order-disorder type[4] it was doubted whether single crystal exhibited the same dispersion in microwave region. Because of the difficulties in growing big single crystals and in measuring microwave dielectric constants of small specimens, this question had not been answered until the paper of Benedict and Durand.[5] They have shown that the dielectric constants at 24 KMc/s are not so small compared to low frequency values as in ceramics though loss tangents are not very small. The present authors planned measurements of microwave dielectric constants of $BaTiO_3$ single crystal before the paper of Benedict and Durand appeared, and developed a method of measuring dielectric constants of small specimens. Although our results are almost the same as those of Benedict and Durand's, it was thought worthwhile to publish our results by the following reasons: (1) Our method is different from theirs, and it seems worthwhile to introduce our method and to compare our results to those of Benedict and Durand's especially since we are intending to apply our method to other ferroelectrics. (2) Our frequency (3.3 KMc/s) is different from theirs (24 KMc/s) and our values of loss tangents were quite different from those reported by them.

This paper is the first part of our reports on microwave measurements of ferroelectrics. In part II measurements on other ferroelectrics will be reported.

§2. Principle of Measurement

Horner et al[6] studied the field of TM_{010} mode in a cylindrical cavity which has a cylindrical dielectric specimen placed coaxially in it. They assumed that the specimen has a small radius, low dielectric constant and negligible loss, and obtained the following expressions for the dielectric constant $\mathcal{E}'$ and the loss factor tan δ;

$$\mathcal{E}'=0.539\frac{a^2}{b^2}\frac{\Delta f}{f}+1\ ,$$

and

$$\tan\delta=\frac{0.269}{\mathcal{E}'}\frac{a^2}{b^2}\left(\frac{1}{Q_2}-\frac{1}{Q_1}\right)\ , \tag{1}$$

where a and b are radii of the cavity and the sample respectively, f is a resonant frequency of the cavity and Δf is the difference between a resonant frequency of the empty cavity and that of the cavity containing the specimen, respectively.

The main purpose of this section is to prove that practically the same equation as Eq. (1) can be derived with less restrictions on shapes and properties of the dielectric specimen than those put by Horner et al, and show that the resonant cavity method is applicable also for ferroelectrics. Below, discussions will be made under the following assumption: the dielectric specimen is cylindrical, and placed parallel to the axis of the circularly cylindrical cavity, both ends of the cylindrical specimen being in contact with the cavity wall; cross-section of the specimen has a very small area, but may have any shape; real and imaginary parts of the dielectric constants of the specimen may be reasonably high as far as they are finite; the specimen may be dielectrically anisotropic, but one of the principal axes of dielectric tensor is parallel to the axis of the cavity. In the present section, discussions will be limited to TM_{010} mode. Of course, similar discussions can be applied to other modes, and we can also treat other shapes of specimens if we consider depolarization effects. However, these will lead us too far afield in this section.

According to Bethe and Schwinger[7], deviation of the cavity resonant frequency due to existence of an isotropic dielectric specimen is given by

$$\frac{\Delta f}{f_2}=\frac{\int_{v_s}(\mathcal{E}_2-1)\boldsymbol{E}_1\cdot\boldsymbol{E}_2dv+\int_{v_s}(\mu_2-1)\boldsymbol{H}_1\cdot\boldsymbol{H}_2\,dv}{\int_{v_s}(\boldsymbol{E}_1\cdot\boldsymbol{E}_2+\boldsymbol{H}_1\cdot\boldsymbol{H}_2)dv}\ , \tag{2}$$

where $f=f'+if''$ is the complex resonant frequency, and $\Delta f\equiv f_1-f_2$. Here and throughout the paper, subscripts 1 and 2 mean that the quantities are those of the empty cavity and those of the cavity containing a specimen, respectively. $\mathcal{E}$ and μ are complex dielectric constant and complex magnetic permeability, respectively. $\int_{v_s}dv$ and $\int_{v_s}dv$ mean that the integrations should be carried out within the specimen and within the cavity respectively. Eq. (2) can be applied to any dielectric specimen of any shape, and, as proved in Appendix, it holds also for anisotropic dielectrics if we use a tensor dielectric constant.

Due to our assumptions, the dielectric specimen has its side surface and its principal axis of dielectric tensor parallel to $\boldsymbol{E}_1$ in case of TM_{010} mode, therefore, no electric charge seems to be induced on its side surface. Since $\boldsymbol{E}_2$ is parallel to $\boldsymbol{E}_1$ for such a case, and $\mu_2=1$, Eq. (2) can be rewritten as

$$\frac{\Delta f}{f_2}=\frac{(\mathcal{E}_{20}-1)\int_{v_s}\boldsymbol{E}_1\cdot\boldsymbol{E}_2\,dv}{\int_{v_c}(\boldsymbol{E}_1\cdot\boldsymbol{E}_2+\boldsymbol{H}_1\cdot\boldsymbol{H}_2)dv}\ , \tag{3}$$

where is $\mathcal{E}_{20}$ is the principal dielectric constant along the cavity axis.

If field distortion due to insertion of the specimen is negligible, $\boldsymbol{E}_2$ may be approximated by

$$\boldsymbol{E}_2=A\boldsymbol{E}_1\ , \tag{4}$$

where A is a scalar constant. In the present case Eq. (2) may hold approximately even inside the specimen owing to the boundary conditions for $\boldsymbol{E}$. This approximation may hold if $|\Delta f/f_2|$ is very small, as shown by Spencer et al[8]. On this assumption Eq. (3) can be rewritten as

$$\frac{\Delta f}{f_2}=\frac{(\mathcal{E}_{20}-1)\int_{v_s}E_1{}^2dv}{2\int_{v_c}E_1{}^2dv}\ . \tag{5}$$

Here use was made of the relation, $\int_{v_c}E_1{}^2dv=\int_{v_c}H_1{}^2\,dv$. Using the cylindrical coordinates (r, θ, z), the components of E_1 for the TM_{010} mode are given by

$$\left.\begin{array}{l}E_r=E_\theta=0\ ,\\ E_z=J_0(kr)\ ,\end{array}\right\} \tag{6}$$

where $J_0(kr)$ is the zeroth order Bessel function, and k is the wave number constant. Using Eq. (6) and assuming that the specimen is placed near the center axis of the cavity, Eq. (5) becomes

$$\varepsilon_{20}=0.539\frac{v_c}{v_s}\frac{\Delta f}{f_2}+1 \qquad (7)$$

where v_c and v_s stand for volumes of the cavity and of the specimen, respectively. It should be mentioned here that there is no restrictions on the magnitude of dielectric constant and loss factor insofar as $|\Delta f/f_2|$ remains very small. According to Eq. (7), one can make $|\Delta f/f_2|$ small by making v_s small. The dielectric constant ε_{20} and resonance frequencies f_1 and f_2 are complex quantities by their definitions, and therefore, one can calculate the real dielectric constant ε'_{20} and loss factor $\tan\delta$ using Eq. (7). The results obtained are

$$\left.\begin{aligned}&\varepsilon'_{20}=0.539\frac{v_c}{v_s}\frac{\Delta f}{f_2}+1\,,\\ &\text{and}\\ &\tan\delta=\frac{0.269}{\varepsilon'_{20}}\frac{v_c}{v_s}\left(\frac{1}{Q_2}-\frac{1}{Q_1}\right).\end{aligned}\right\} \qquad (8)$$

These equations are identical with Eq. (1) if the specimen has a circular cross-section.

§ 3. Experimental Set-up and Specimens

The block diagram of the microwave circuit is shown in Fig. 1. A klystron of 726A type was used as the oscillator. Sawtooth voltage was supplied to its reflector electrode for frequency modulation. The out put signals from the test cavity and the cavity wavemeter were fed to an oscilloscope. f and the Q-factor of the test cavity were determined from patterns on the oscilloscope screen.

The test cavity is 67.7 mm in diameter and 5.3 mm in height. Frequency deviation associated with temperature change was −0.068 Mc/deg. The Q–factor of the empty cavity was about 500 and practically independent of temperature.

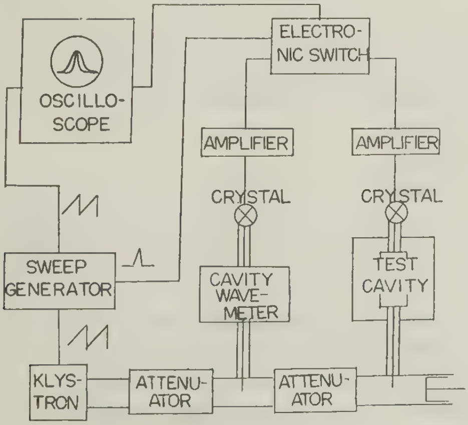

Fig. 1. Block diagram of the experimental set-up.

Table I.

Sample	Cross-section (cm²)	$\lvert\Delta f/f_2\rvert_{max}$
1 (single crystal)	1.70×10^{-4}	0.043
2 (single crystal)	1.50×10^{-4}	0.053
3 (ceramics)	0.96×10^{-4}	0.011

Table I gives cross-sections and maximum frequency deviations for the samples used in our measurement. All the samples are cylindrical-shapes with square cross-sections. The single crystals were supplied by Bell Telephone Laboratory.* Ceramic samples which were used as a check of the method were supplied by Kobayashi Institute of Physical Research.**

The crystals were cut by ultrasonic cutter* and then finished up by polishing with fine SiC powder. We tried to make the specimen a single domain crystal of which the long axis is parallel to the c-axis. However, small domains of which the c-axis are perpendicular to the long axis were observed at room temperature.

In the case of high permittivity specimen, even a small gap is a source of large error. To avoid this error, we painted conductive plastics between the ends of the specimen and the cavity wall.

§ 4. Experimental Results

Measured dielectric constants are shown as a function of temperature in Fig. 2 in comparison with Benedict and Durand's results[5]. These values are calculated by Eq. (8). The data of the samples 1 and 2 agreed well with those of Benedict and Durand's data above the Curie temperature. For ceramic sample (sample 3), the data are consistent with those of Powles and Jackson's[9].

---

*, ** The authors are indebted to Dr. J. W. Nielsen and Mr. J. P. Remeika of Bell Telephone Laboratory, Dr. T. Mitsui of Laboratory for Insulation Research of Massachusetts Institute of Technology and Dr. M. Marutake and Dr. Y. Tokita of Kobayashi Institute of Physical Research for supplying samples.

*** The authors wish to thank Dr. N. Sakamoto of Electrotechnical Laboratory and Dr. S. Kawaji of Gakushuin University for their kindness for cutting crystals by ultrasonic cutter.

Below the Curie temperature our results are quite different from those of Benedict and Durand's. This seems to come from differences in domain structure as will be discussed in the next section.

Dielectric loss could be measured with reliable accuracy only above the Curie point. The results are shown in Fig. 3.

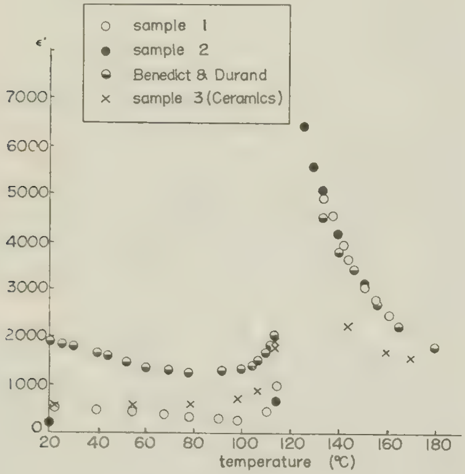

Fig. 2. ε' vs temperature.

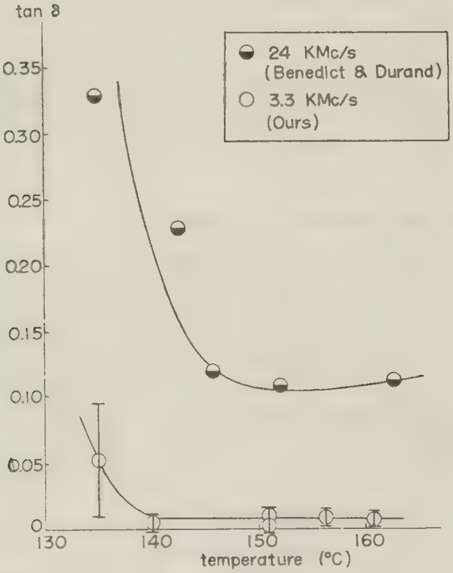

Fig. 3. tan δ vs temperature.

The difference between our results and those of Benedict and Durand is more than experimental error, ±0.007. As Table 1 shows the sample 3 (ceramics) is smaller than samples 1 and 2 in cross-section, but tan δ of the ceramics was too high to be measured even for this small specimen.

§ 5. Discussion

1) *Above the Curie temperature.*

Figs. 2 and 3, show that the $BaTiO_3$ single crystal does not exhibit dielectric dispersion up to 3 KMc/s region above the Curie temperature. Using ceramic samples, Powles and Jackson and others[8] observed decrease of ε' and increase of $\tan\delta$ with increasing frequency even above the Curie point, though that dispersion was smaller above the Curie point than below the Curie point. According to their results, $\tan\delta$ at 10 KMc/s and at 1.5 Mc/s are about 10^{-1} and 10^{-2}, respectively. The former value agrees with those which have been obtained by Benedict and Durand at 24 KMc/s for single crystals. Of course, the value of $\tan\delta=0.1$ at microwave region is too large to be attributed to conductivity. Then, it can be considered that dielectric dispersion occur near 24 KMc/s in the single crystal. And discrepancy of $\tan\delta$ between our result and Benedict and Durand's suggests that ionic resonance absorption frequency which appears in infrared region in ordinary ionic crystals is shifted to millimeter wave region in $BaTiO_3$, at temperature slightly above the Curie point, as Landauer[10] showed theoretically.

2) *Below the Curie temperature.*

Since our samples are multi-domain crystals our results may differ from the results on the single domain crystals below the Curie temperature. On the single domain crystals, as Benedict and Durand have shown, $\tan\delta$ is approximately the same above and below the Curie point except for temperatures close to the Curie point where $\tan\delta$ is large. Large dielectric loss observed below the Curie point in our measurement, though it could not be measured quantitatively, suggests the existence of some mechanism of dielectric dispersion due to multi-domain structure, which could also be the origin of the dispersion in ceramics.

As shown in Fig. 2, the sample 1 has a region where $\partial\varepsilon'/\partial T$ is negative. No definite interpretation is given for this fact, but one possible explanation seems to be that a tension, which was originated from the difference of expansion coefficients between cavity material and $BaTiO_3$, forced the c-axis of small domains to reorientate parallel to the field direction.

Appendix

We will show here that Eq. (2) is applicable for a specimen having anisotropic dielectric constant, by using Slater's normal mode method[11].

From the Maxwell's equations

$$\operatorname{curl} \boldsymbol{E}_1 = -i\omega_1 \boldsymbol{H}_1 \qquad \text{(A 1)}$$

and

$$\operatorname{curl} \boldsymbol{H}_1 = i\omega_1 \boldsymbol{E}_1 \qquad \text{(A 2)}$$

following wave equations hold in the cavity 1,

$$\left.\begin{aligned} &\nabla^2 \boldsymbol{E}_1 + \boldsymbol{k}_1 \boldsymbol{E}_1 = 0\,, \\ \text{and}\quad &\nabla^2 \boldsymbol{H}_1 + \boldsymbol{k}_1 \boldsymbol{H}_1 = 0\,. \end{aligned}\right\} \qquad \text{(A 3)}$$

To each eigen value $\boldsymbol{k}_i$ corresponds solutions of $\boldsymbol{E}_{1i}$ and $\boldsymbol{H}_{1i}$. It is easy to show that sets of solutions $(\boldsymbol{E}_{11},\cdots, \boldsymbol{E}_{1i},\cdots)$ and $(\boldsymbol{H}_{11},\cdots \boldsymbol{H}_{1i}\cdots)$ form complete systems of orthogonal functions. The fields $\boldsymbol{E}_{1i}$ and $\boldsymbol{H}_{1i}$ are the field of ith mode.

In cavity 2, the Maxwell's equations become as

$$\operatorname{curl} \boldsymbol{H}_2 = i\omega_2 \mathcal{E}_2 \boldsymbol{E}_2 \qquad \text{(A 4)}$$

and

$$\operatorname{curl} \boldsymbol{E}_2 = -i\omega_2 \mu_2 \boldsymbol{H}_2 \qquad \text{(A 5)}$$

where $\mathcal{E}_2$ is a tensor, in general, and expressed by a matrix $(\mathcal{E}_{jk})$ $(j, k=1,2,3)$. Expanding the left hand side of (A 4) with $\boldsymbol{E}_{1i}$,

$$\operatorname{curl} \boldsymbol{H}_2 = \sum_i \boldsymbol{E}_{1i} \int_{v_c} \operatorname{curl} \boldsymbol{H}_2 \cdot \boldsymbol{E}_{1i}{}^* dv = \sum_i \boldsymbol{E}_{1i} \left[\int_{v_c} i\omega_1 \boldsymbol{H}_2 \cdot \boldsymbol{H}_{1i}{}^* dv + \int_{v_c} \operatorname{div}(\boldsymbol{H}_2 \times \boldsymbol{E}_{1i}{}^*) dv \right],$$

where $\boldsymbol{E}_{1i}{}^*$ is the complex conjugate of $\boldsymbol{E}_{1i}$, and so on. From the boundary conditions,

$$\int_{v_c} \operatorname{div}(\boldsymbol{H}_2 \times \boldsymbol{E}_{1i}{}^*) dv = \int_s \boldsymbol{n} \cdot (\boldsymbol{H}_2 \times \boldsymbol{E}_{1i}{}^*) ds = \int_s (\boldsymbol{E}_{1i}{}^* \times \boldsymbol{n}) ds \simeq 0$$

where S is surface of the cavity and $\boldsymbol{n}$ is a normal unit vector. Expanding the right hand side of (A 4) with $\boldsymbol{E}_{1i}$ and comparing coefficients of $\boldsymbol{E}_{1i}$, following relation can be derived

$$\omega_1 \int_{v_c} \boldsymbol{H}_2 \cdot \boldsymbol{H}_{1i}{}^* dv = \omega_1 \int_{v_c} (\mathcal{E}_2 \boldsymbol{E}_2) \cdot \boldsymbol{E}_{1i}{}^* dv = \omega_2 \int_{v_c} \sum_j \sum_k \mathcal{E}_{jk} E_{2,j} \cdot E_{1i,k}{}^* dv\,, \qquad \text{(A 6)}$$

where $E_{2,j}$ is a component of the vector $\boldsymbol{E}_2$, and so on. Similary, development of (A 5) with $\boldsymbol{H}_{1i}$ gives

$$\omega_1 \int_{v_c} \boldsymbol{E}_2 \cdot \boldsymbol{E}_{1i}{}^* dv = \omega_2 \int_{v_c} \mu_2 \boldsymbol{H}_2 \cdot \boldsymbol{H}_{1i}{}^* dv\,, \qquad \text{(A 7)}$$

where $\int_s \boldsymbol{E}_{1i}{}^* \cdot (\boldsymbol{n} \times \boldsymbol{E}_2) ds \simeq 0$ is used. Then, from (A 6) and (A 7)

$$\frac{\omega_1}{\omega_2} = \frac{\displaystyle\int_{v_c} \sum_j \sum_k \mathcal{E}_{jk} E_{2,j} \cdot E_{1i,k}\, dv + \int_{v_c} \mu_2 \boldsymbol{H}_2 \cdot \boldsymbol{H}_{1i}{}^* dv}{\displaystyle\int_{v_c} \boldsymbol{E}_{1i}{}^* \cdot \boldsymbol{E}_2\, dv + \int_{v_c} \boldsymbol{H}_{1i}{}^* \cdot \boldsymbol{H}_2\, dv}\,,$$

therefore

$$\frac{\omega_1 - \omega_2}{\omega_2} = \frac{\displaystyle\int_{v_s} \left[\sum_j \sum_k \mathcal{E}_{jk} E_{2,j} E_{1i,k}{}^* - \boldsymbol{E}_2 \cdot \boldsymbol{E}_{1i}{}^* \right] dv + \int_{v_s} (\mu_2 - 1) \boldsymbol{H}_2 \cdot \boldsymbol{H}_{1i}{}^* dv}{\displaystyle\int_{v_c} (\boldsymbol{E}_{1i}{}^* \cdot \boldsymbol{E}_2 + \boldsymbol{H}_{1i}{}^* \cdot \boldsymbol{H}_2)\, dv} \qquad \text{(A 8)}$$

because $\mathcal{E}_2 = \mu_2 = 1$ in the cavity 2 except in v_s. If we introduce the unit matrix $\mathbf{1} = \begin{pmatrix} 100 \\ 010 \\ 001 \end{pmatrix}$, (A 8) can be written as

$$\frac{\omega_1 - \omega_2}{\omega_2} = \frac{\displaystyle\int_{v_s} \{(\mathcal{E}_2 - \mathbf{1}) \boldsymbol{E}_2\} \cdot \boldsymbol{E}_{1i}{}^*\, dv + \int_{v_s} (\mu_2 - 1) \boldsymbol{H}_2 \cdot \boldsymbol{H}_{1i}{}^*\, dv}{\displaystyle\int_{v_c} (\boldsymbol{E}_{1i}{}^* \cdot \boldsymbol{E}_2 + \boldsymbol{H}_{1i}{}^* \cdot \boldsymbol{H}_2)\, dv}\,.$$

Acknowledgements

The authors wish to express their thanks to Dr. T. Mitsui for his illuminating discussions throughout this work. They also wish to express their thanks to Dr. J. W. Nielsen and Mr. J. P. Remeika for their kindness of supplying the single crystals, and Mr. Y. Tsuji for his help of the measurements. The authors thanks are also due to the members of Furuichi laboratory for their kind discussions.

References

1) W. P. Mason: Piezoelectric Crystals and their Applications to Ultrasonics. Van Nostrand, (1950) 251.
2) H. Akao and T. Sasaki: J. Chem. Phys. **23** (1955) 2210. H. Akao, T. Takakura and T. Sasaki: J. Phys. Soc. Japan **7** (1952) 361.
3) A. Nishioka and M. Takeuchi: J. Phys. Soc. Japan **14** (1959) 971.
4) P. W. Anderson: Ceramic Age, Newark, N. J., April (1951).
5) T. S. Benedict and J. L. Durand: Phys. Rev. **109** (1958) 191.
6) F. Horner, T. A. Tailor, R. Dunsmuir, J. Lamb and W. Jackson: J. Inst. Elec. Eng. (London) **93**, Part III, (1946) 53.
7) H. A. Bethe and J. Schwinger: N.D.R.C. Rpt. **D1**-117, Cornell University (March 1943)
8) E. G. Spencer, R. C. Le Craw and L. A. Ault: J. Appl. Phys. **28** (1957) 130.
9) J. G. Powles and W. Jackson: Proc. I. R. E. **96** (1949) 971. von H. J. Schmitt: Z. Angew. Phys. **9**(1957) 107.
10) R. Landauer: unpublished.
11) J. Slater: Rev. Mod. Phys. **18** (1946) 467.

JOURNAL OF THE PHYSICAL SOCIETY OF JAPAN, Vol. 15, No. 11, NOVEMBER, 1960

Theory of Resistance Minimum in Dilute Paramagnetic Alloys

By Kensuke TANI*

Department of Physics, Faculty of Science, Osaka University, Osaka

(Received May 18, 1960)

We have calculated the electrical resistance of dilute paramagnetic alloys from the standpoint of seeing if the resistance minimum could arise from the short range order of the spins of the solute atoms.

In order that the resistivity minimum appears it is found that (i) the magnetic ion pairs which make the dominant contribution must be those ferromagnetically coupled and the scattering due to them must be dominantly elastic, and (ii) the functional form of the exchange integral $J(r)$ must be similar to that of the radial distribution of the 3d electrons.

A difficulty in the present interpretation is that the temperature at which the resistance minimum occurs is about ten times higher than that of experiments.

In the October 1 issue of the Physical Reivew Letters, Brailsford and Overhauser[1] published a paper with the same title as above. The present author has independently performed** a similar calculation from the same standpoint in order to see if the resistance minimum could arise from the short range order of the spins of the solute paramagnetic atoms.

The paramagnetic atoms are here assumed to have spins of magnitude of 1/2, and the neighbouring atoms are assumed to couple each other either ferromagnetically or antiferromagnetically. (Brailsford and Overhauser assumed spins of arbitrary magnitude, but considered only the case of ferromagnetic coupling). We take a pair of paramagnetic atoms at positions $\boldsymbol{R}_1$ and $\boldsymbol{R}_2$ $(\boldsymbol{R}_2-\boldsymbol{R}_1=\boldsymbol{R})$

---

* Now at the Research Institute for Fundamental Physics, Kyoto University, Kyoto.

** Read before the 14th Annual Meeting of the Physical Society of Japan held at Hiroshima, October 8-12, 1959.

which interact with the Hamiltonian:

$$H_0=-2\mathfrak{J}(\boldsymbol{R})\boldsymbol{S}_1\cdot\boldsymbol{S}_2 \qquad (S_1=S_2={}^1/_2). \tag{1}$$

The scattering potential for a conduction electron due to this pair may be written as[2]:

$$H^1=-N^{-1}\sum_{n\boldsymbol{kk}'\uparrow\downarrow}\{V(\boldsymbol{kk}')\pm S_n^z J(\boldsymbol{kk}')\}e^{i(\boldsymbol{k}-\boldsymbol{k}')\boldsymbol{R}_n}a^*_{\boldsymbol{k}'\uparrow\downarrow}\,a_{\boldsymbol{k}\uparrow\downarrow}$$
$$-N^{-1}\sum_{n\boldsymbol{kk}'}J(\boldsymbol{kk}')e^{i(\boldsymbol{k}-\boldsymbol{k}')\boldsymbol{R}_n}(a^*_{\boldsymbol{k}'\downarrow}\,a_{\boldsymbol{k}\uparrow}\,S_n{}^+ + a^*_{\boldsymbol{k}'\uparrow}\,a_{\boldsymbol{k}\downarrow}\,S_n{}^-) \tag{2}$$

Making use of these two assumptions (1) and (2), the temperature-dependent part of the resistivity was calculated, obtaining

$$R=\frac{3\pi^2}{e^2}\frac{m}{E_f}\left(\frac{\hbar}{2m}\right)^{3/2}B\,,^{(*)} \tag{3}$$

$$B\equiv\int\frac{V}{8\pi^3}\frac{1}{2}\left(\frac{2m}{\hbar^2}\right)^{3/2}\frac{2\pi}{\hbar}N^{-2}\left|J(2k_F\sin\theta/2)\right|^2(1$$
$$-\cos\theta)\sin\theta\times\left\{3A^{-1}e^{J\beta/2}\left[1+\frac{\sin(2k_FR\sin\theta/2)}{2k_FR\sin\theta/2}\right]\right.$$
$$\left.+\frac{5}{2}A^{-1}\frac{2e^{J\beta/2}}{e^{2J\beta}+1}\left[1-\frac{\sin(2k_FR\sin\theta/2)}{2k_FR\sin\theta/2}\right]\right\}d\theta\,,$$

with $A=3e^{J\beta/2}+e^{-3J\beta/2}$ and $\beta=1/kT$, V being the volume of the sample and θ the scattering angle.

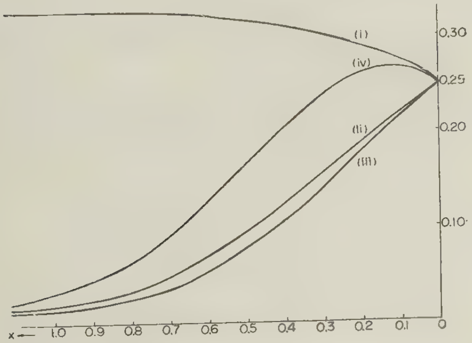

Fig. 1. Temperature dependences of elastic factor $A^{-1}e^{J\beta/2}$ are given by curve (i) for $J>0$ and curve (ii) for $J>0$. Curve (iii) and (iv) draw the temperature dependence of inelastic factor $A^{-1}\,2e^{J\beta/2}/(c^{2J\beta}+1)$ for $J>0$ and $J>0$, respectively.

The first term in the curly brackets in B comes from the elastic scattering by the triplet state, while the second term corresponds to inelastic scattering associated with the transition between the triplet and singlet states. The temperature dependence of the elastic term is given through the factor $A^{-1}\exp(J\beta/2)$, and its explicit form is shown in Fig. 1 by the increasing difficulty for them to lose their curve (i) for the case of ferromagnetic coupling ($J>0$) and by curve (ii) for the case of antiferromagnetic coupling ($J>0$), the abscissa being $x=J\beta/2$. On the other hand, the temperature dependence of the inelastic term is due to the factor $A^{-1}\exp(J\beta/2)/[\exp(2J\beta)+1]$, and it is shown by curve (iii) for $J>0$ and by curve (iv) for $J<0$. The physical interpretation of these behaviours is as follows.

Curve (i): the population of the triplet state increases monotonously with lowering temperature, thus $1/4\rightarrow1/3$ as $\beta=0\rightarrow\infty$.

Curve (ii): the population of the triplet state decreases monotonously as the temperature is lowered, thus $1/4\rightarrow0$ as $\beta=0\rightarrow\infty$.

In curves (iii) and (iv), the decrease of the resistivity at low temperatures comes from the fact that the population of the upper level decreases and therefore the inelastic scattering occurs mainly by exciting the pair, the conduction electron giving its energy. However, this is difficult because of the increasing degeneracy of the conduction electrons and thus energy. The second in each of the solid brackets in B represents the interference effect between the scattering by one of the paired paramagnetic atoms and that by the other. Contributions to the resistivity of these interference terms depend sensitively on the functional of $J(2k_F\sin\theta/2)$.

The integrals

Table I. Values of the integrals (4) divided by $J_0{}^2$. a and b are chosen to be $(0.093\text{Å})^{-1}$ and $(0.51\text{Å})^{-1}$, respectively, which have been determined to represent approximately the radial distribution function of the 3d electron cloud of Mn^{++}.

	$J(r)=J_0\delta(r)$		$J_0r\exp(-ar)$		$J_0\exp(-b^2r^2)$	
	elastic	inelastic	elastic	inelastic	elastic	inelastic
$R_{\text{n.n.}}$	6.42	5.35	12.69	1.18	3.10	3.17
$R_{\text{2.n.}}$	6.26	4.79	nearly the same as above		3.44	2.64

(*) In this calculation we neglect $\mathfrak{J}$ compared with E_F,

$$\int \left|J(2k_F \sin\theta/2)\right|^2 (1-\cos\theta)\sin\theta \times\left[1\pm\frac{\sin(2k_F R\sin\theta/2)}{2k_F R\sin\theta/2}\right]d\theta \qquad (4)$$

have been calculated for $J(r)$ of the three types as shown in Table I, where are shown their numerical values for the nearest neighbour distance $R=R_{\text{n.n.}}$ and the second neighbour distance $R=R_{\text{2.n.}}$ for the f.c.c. lattice.

If we know, for instance, the concentration of the Mn atoms in Cu, we can calculate the concentration of the pairs of nearest neighbours, that the pairs of second neighbours, and so on. The resistivity of the Cu-Mn dilute alloy is then calculated as the sum of the contributions from these pairs.

In order that the resistivity minimum appears, curve (i) in Fig. 1 must make the dominant contribution to the resistivity, since the resistivity due to lattice vibrations, which has to be added, increases rapidly with increasing temperature. In other words, the pairs which make the dominant contribution must be those ferromagnetically coupled and the scattering due to them must be dominantly elastic. These conditions are satisfied if the n.n. pairs and 2.n. pairs are the main contributors and they are ferromagnetically coupled, and also the functional form of $J(r)$ is similar to that of the radial distribution of the 3d electrons (the second column in Table I).

A difficulty in the present interpretation of the resistivity minimum is that it should occur at a high temperature of the order of J/k, while the observed temperature is only several times higher than the temperature of the resistivity maximum which corresponds to the Néel temperature of the interactining Mn atoms, the latter being expected to be at czJ/k (c=concentration, $z=12$) which is $\sim 10^{-2}$ J/k for $c=10^{-3}$. However, in the lack of detailed theoretical knowledge of the Néel temperature of the dilute alloys at the present moment, this difficulty cannot be taken too seriously.

Acknowledgements

I would like to to express my sincere thanks to Professor T. Nagamiya for suggesting the present problem and kind discussions. My thanks are also due to the Yukawa Foundation of Osaka University for their grant of a Research Fellowship.

References

1) A. D. Brailsford and A. W. Overhauser: Phys. Rev. Letters **3** (1959) 331.
2) T. Kasuya: Prog. Theor. Phys. **16** (1956) 45.
K. Yosida: Phys. Rev. **107** (1957) 396.

JOURNAL OF THH PHYSICAL SOCIETY OF JAPAN, Vol. 15, No. 11, NOVEMBER, 1960

Direct Observation of Lattice Defects in Cold-worked High Manganese Steels by Means of Electron Microscopy*

By Zenji NISHIYAMA and Ken-ichi SIMIZU

Institute of Scientific and Industrial Research, Osaka University, Sakai, Osaka-fu, Japan

(Received June 20, 1960)

Thin foils have been made by electrolytic polishing from bulk specimens of cold-worked high manganese steel. They have been observed by electron microscopy with the object of studying lattice defects formed by cold-working. From the micrographs and the selected area electron diffraction patterns obtained it is concluded that on {111} planes of the austenite matrix very thin (<100Å) plates of a hexagonal close-packed phase (ε) are formed, which correspond to the origins of strain markings formerly found on the etched surface by using the replica, and that ordinary stacking faults as found in 18–8 stainless steels are also present.

§ 1. Introduction

It is expected from the dislocation theory that in the face-centred cubic (FCC) metals stacking faults are easily formed in {111} planes by cold-working if the energy of the faults is small. Actually Hirsch et al.[1] observed the interference fringes due to the stacking faults in cold-worked 18–8 stainless steels by means of transmission electron microscopy.

If the stacking fault is induced, every two-layers of (111) planes in the FCC phase a hexagonal close-packed (HCP) phase is formed. Such a phenomenon will easily occur for the alloy having an equilibrium diagram in which there is a HCP phase region close to the FCC phase region. High manganese (Had-field) steel as well as Cu–Si alloy will belong to such a category.

As is well known, the high manganese steel is so much hardened by cold-working that it is very difficult to explain the reason only in terms of the ordinary work hardening. To clarify this fact a number of works[2] have been made, but the reason remains in question. In the preceding paper[3], it was tried to solve this problem by investigating the nature of strain markings seen on the etched surface of the cold-worked specimen. The observation was made by electron microscopy using the replicas of the surface. From the results it was suggested that there would be a very thin plate of HCP (ε) phase passing through every strain marking.

Thereafter the present writers succeeded in making thin foils of the steel for transmission electron microscopy, and so could test the former presumption, the result of which will be described in this paper dealing with the lattice defect produced by cold-working.

§ 2. Experimental method

For specimens a steel plate containing 0.97% C and 9.75% Mn was hot-forged to 1 mm thick, and the surface layers on both sides were ground off to a thickness of 0.5 mm. To austenitize the steel, it was solution-treated by heating for four hours at 1000°C in vacuum, followed by quenching into water. After it was electrolytically polished down to 0.3 mm thick for removing the surface layers, it was beaten with a hammer to cold-work. Lastly the plate was again electrolytically polished down to a thin foil by Bollmann's[4] method using electrolyte

Phosphoric acid	200 c.c.
Chromic acid	100 gr.

with the current of 1.5 Amp, 20 Volt at 70°C for the plate having an area of 2 cm in diameter.

It was subjected to direct observation by an electron microscope (JEM-5G) with 100 kV for Figs. 1, 2 (a), 6, 7, 8 and with 80 kV for Figs. 4, 5 (a).

§ 3. Experimental results

Fig. 1 is a transmission electron micrograph of an area in the specimen cold-worked. In

---

* This paper was read before the 9th Annual Meeting of the Physical Society of Japan held at Hiroshima University, in October, 1959.

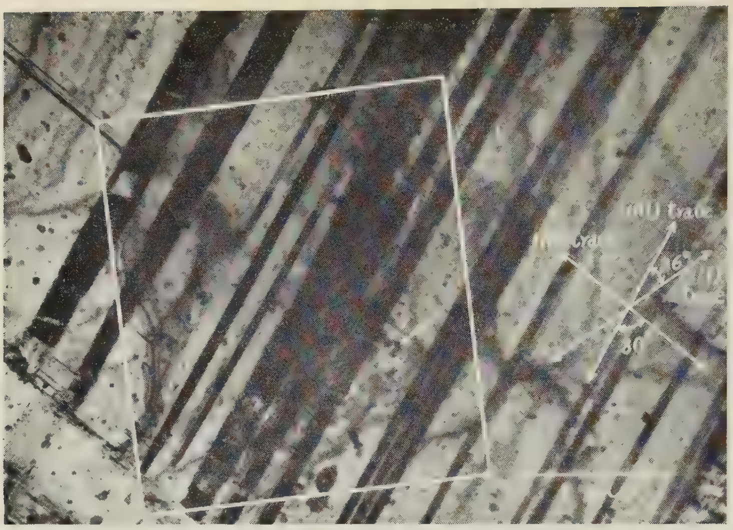

Fig. 1. Transmission elecron micrograph of a thin foil made by electrolytic polishing from a beaten sheet of high manganese steel, showing parallel bands of ε-phase.

this photograph a number of dark parallel bands are seen, which appear to have been formed in {111} planes of the FCC matrix (white ground) by cold-working. To study the crystal structure of these bands, the selected area electron diffraction pattern was taken of the white-framed region. Fig. 2 (a) is the pattern taken, which is considered to consist mainly of reflections from the parallel bands, because the darkness of the bands in Fig. 1 indicates that they have made stronger Bragg reflections than from the matrix. The main spots appeared in this diffraction pattern constitute a distribution of hexagonal array somewhat deformed. The distances between these spots are as shown in Fig. 3: A=8.28 mm, B=8.31 mm, C=7.25 mm (equivalent camera length=430 mm).

Let us first assume that the bands seen in Fig. 1 are due to parallel plates of ε-phase occurred parallel to its basal plane (0001). When the plates are very thin, their reciprocal lattice points will elongate in the direction of c-axis. If so, their diffraction pattern will appear as the section of the reciprocal lattice (elongated in the c direction) by a plane parallel to the foil. On this assumption and considering that AB direction (Fig. 3) was nearly parallel* to the bands in Fig. 1, we can calculate the orientation of the foil with respect to the crystallographic axes of the ε-phase plate using the distances between spots, Fig. 3. The result of the calculations** is

		H	K	I	L
	(i)	0.201	0.193	−0.404	1
or	(ii)	−0.201	−0.193	0.404	1

Assuming the orientation relationships between HCP plate and FCC matrix to be Shoji-Nishiyama's[5], we have the orientation*** of the foil referred to the FCC matrix axes to be

		h	k	l
	(i)	0.492	0.864	0.105
or	(ii)	0.482	0.110	0.869

From these orientations, we expect the traces of $(\bar{1}11)$, $(1\bar{1}1)$, $(11\bar{1})$ to be at (i) 78.7°, 29.1°, 180°-41.8° or (ii) 79.8°, 180°-43.6°, 27.9° from (111) trace. Actually, of these traces, $(\bar{1}11)$

---

* The rotation of the pattern due to the change of current through the intermediate lens was taken into account.

** $K=\pm(a/c)L$

$$\times\sqrt{3\{1-(A/B)^2\}/\{(2\rho+1)^2(A/B)^2-(\rho+2)^2\}}$$

$H=\rho K$, $L=1$

where

$$\rho=\sigma-1\pm\sqrt{1-\sigma+\sigma^2}\ ,$$

$$\sigma=\{(B/C)^2-1\}/\{(A/C)^2-1\}$$

In the calculations, the following values were used: a=3.574Å for the matrix and a=2.522Å, c=4.066Å, c/a=1.612 for ε-phase. These are estimated from the data given in the papers of reference (6) and (7).

*** $h=(1/4)\sqrt{3/2}(a/c)L+(2/3)(H-K)$,

$k=h+2K$, $l=h-2H$,

the hexagonal axes $(HK\cdot L)$ being taken parallel to $[10\bar{1}]$, $[\bar{1}10]$, $[111]$ of the cubic axes, respectively.

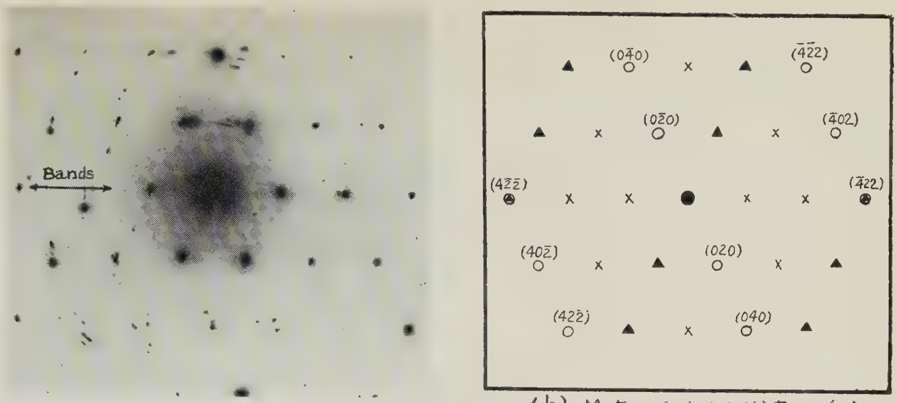

(a)

(b) Matrix(o) + (111) twin (▲)
Electron beam ∥ $[\bar{1}0\bar{2}]$

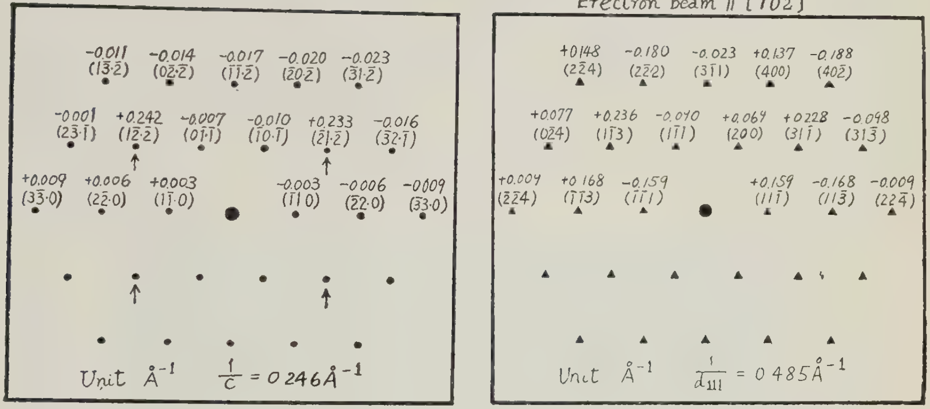

(c) Thin ε (HCP)
Electron beam ⊥ (−0.201, −0.193, •, 1)

(d) Thin (111) twin
Electron beam ∥ [021]

Fig. 2 (a). Selected area electron diffraction pattern of the white-framed portion in Fig. 1.
(b). Predicted pattern of FCC matrix and its twin produced in $(111)_{FCC}$, the orientation of the specimen being assumed to be $(102)_{FCC}$.
(c). Predicted pattern of thin HCP produced in $(111)_{FCC}$, the figures noted above the indeces indicating the distances of the non-elongated reciprocal lattice points from Ewald sphere in the direction of *c*-axis.
(d). Predicted pattern of thin FCC twins produced in $(111)_{FCC}$, the figures indicating the distances of the non-elongated reciprocal lattice points from Ewald sphere in the [111] direction.

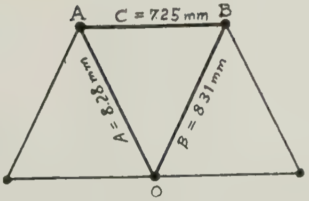

Fig. 3. Diagrammatical illustration of the spot distances in Fig. 2 (a) (equivalent camera length 430 mm).

Table I.

	Angle between (111) trace and other traces		Inclination of plates, calc.		Width of unit band (smallest), obs.
	Calc.	Obs.	Angle	Cosine	
(111) trace			32.4°	0.844	360Å
($\bar{1}$11) trace	79.8°	80°	73.3°	0.287	120Å
(11$\bar{1}$) trace	27.9°	26°	80.8°	0.160	<100Å

trace is realized at the left upper corner of Fig. 1, and (11$\bar{1}$) trace is seen very weakly at the middle region shown by an arrow. Their observed trace angles 80°, 26° are fairly coincident with the calculated ones of orientation (ii) (Table I). Moreover the observed widths of these traces are approximately proportional to the calculated cosine of the inclination of the plates of orientation (ii). These facts justify the orientation (ii).

Since this orientation is near $(102)_{\rm FCC}$ deviating only by 6.8°, spots due to the matrix will be also predicted to appear near the reciprocal lattice points on a plane parallel to (102) if the Bragg conditions are satisfied. These predicted positions, however, are only part of the observed spots as shown in Fig. 2 (b), mark ○. While, ε-phase of orientation (ii) can interprete almost all the observed regular spots as the small elongation ($0.02\,\text{Å}^{-1}$ at most) of the reciprocal lattice points on $(\bar{1},\bar{1}\cdot 1)$ plane, except four spots marked by arrows, as shown in Fig. 2 (c). The latter four, however, can be interpreted as the large elongation of the reciprocal lattice points $\{11\cdot 2\}$ which is about $0.24\,\text{Å}^{-1}$ apart from Ewald sphere in the c direction. Such a large amount of elongation may be allowable owing to very thin plates.

An alternative interpretation of the dark bands in Fig. 1 is that they are merely twins produced at {111} planes of the matrix. If so and if the orientation of the matrix is near (102), we predict the spots as shown by mark ▲ in Fig. 2 (b), besides the spots of the matrix marked by ○. In this way some of the observed spots can be interpreted, but there still remain some spots (×) unexplained*. But if we consider that the reciprocal lattice points of the thin twin plates are elongated in the direction perpendicular to the twin plane, all the observed spots can be interpreted, as shown in Fig, 2 (d), provided that the amount of the elongation reaches $0.24\,\text{Å}^{-1}$. Thus the bands seen in Fig. 1 can be attributed to the thin plates of twins as well as of ε-phase, so far as Figs. 1 and 2 (a) are concerned.

Fig. 4 is a photograph of another region in the foil. Of the white-framed portion in this photograph a selected area electron diffraction pattern was taken, which is shown in Fig. 5 (a). For analysis of this pattern, we assume the orientation of the matrix such that the foil plane is parallel to $(0\bar{1}1)$, since two sets of bands seen in Fig. 5 are both narrow and intersect with an angle of 71° which is almost equal to the angle (70°32′) between two of {111} planes. Then we expect the diffraction spots of the matrix at position, as shown by mark (o) in Fig. 5 (b), (c) and (d), if they appear. Spots are found at those positions in the actual photograph (a). The other spots,

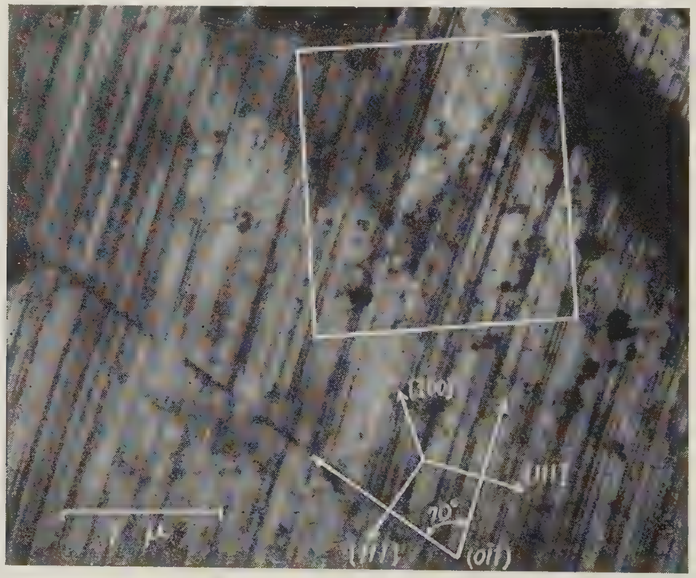

Fig. 4. Transmission electron micrograph of a thin foil of beaten high manganese steel, showing a parallel-line structure of ε-phase.

---

* If there exists the periodic error due to the coherency between the matrix and the twins, the junction spots may appear at positions unexplained. But such a possibility is very little, because the bands in question are formed running through the region near the selected area for electron diffraction.

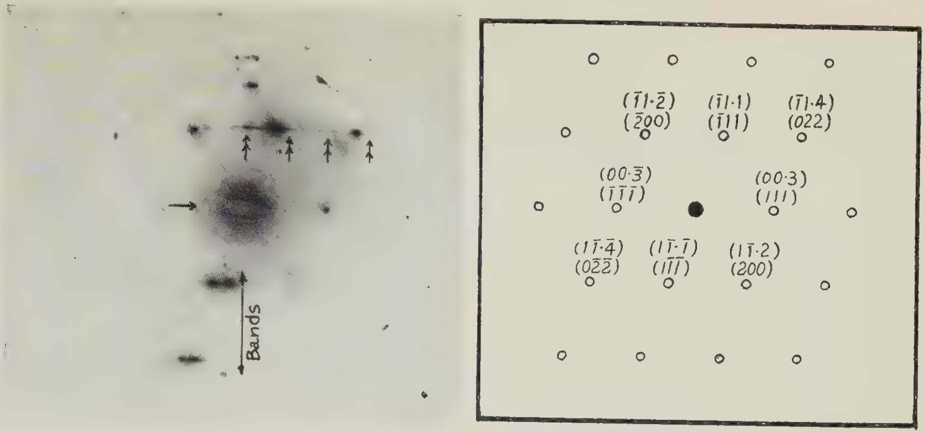

(a)

(b) Matrix Upper figure : hexagonal index
Lower figure : cubic index
Electron beam // $[01\bar{1}]$

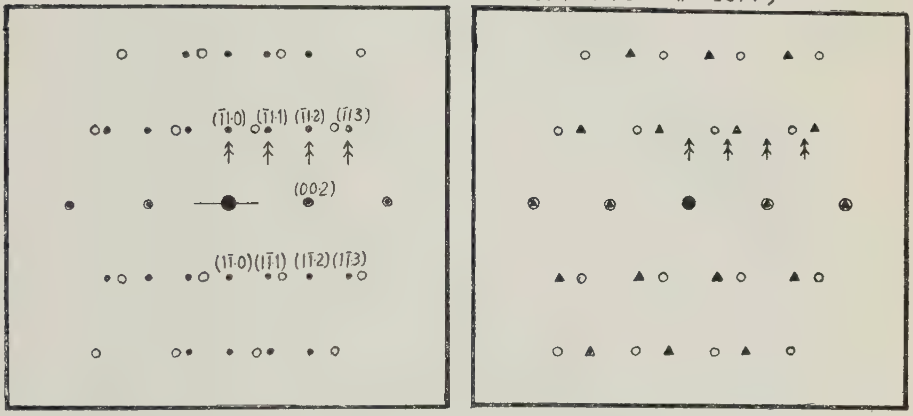

(c) Matrix (○) + HCP (●)
Electron beam // $[01\bar{1}]$ // $[11\cdot0]$

(d) Matrix (○) + Twin (▲)

Fig. 5 (a). Selected area diffraction pattern of the white-framed portion in Fig. 5.
(b), (c), (d) Predicted patterns, the orientation of the specimen being as-sumed to be $(0\bar{1}1)_{\mathrm{FCC}}$.

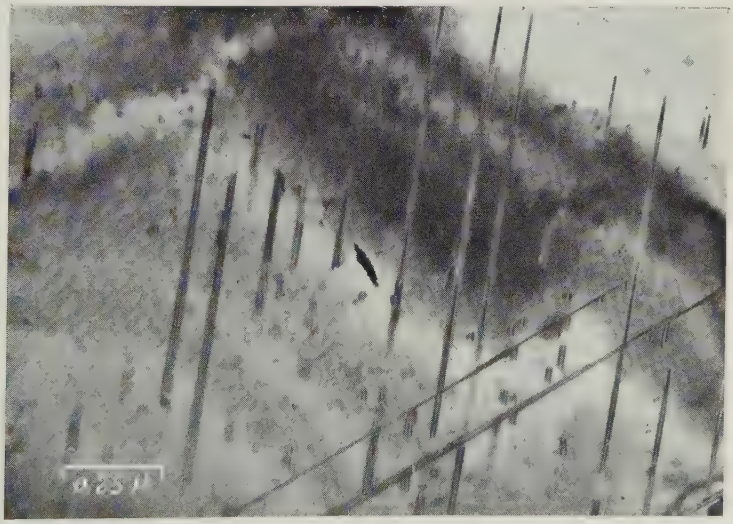

Fig. 6. Transmission electron micrograph of a thin foil of beaten high manganese steel, showing parallel fringes due to the stacking fault.

especially marked by ↑, can be interpreted as due to HCP (ε) phase in the bands but not due to twins.

If the above interpretation is correct, the plates of ε phase must be almost perpendicular to the foil, and the thickness of each plate can be directly estimated from the photograph. The estimated value is less than 100 Å. From these thin plates it is expected that the HCP spots and the central spot are accompanied by streaks in the direction perpendicular to the bands, as actually observed in the horizontal direction. It is moreover noted that the spots $H-K\neq 3n$ (in hexagonal index) of the matrix are not accompanied by such streaks. This indicates that there are no stacking faults in the matrix of this region, although we cannot say so for the interior of the ε-plate.

Fig. 6 is a micrograph of another region in the specimen, where the degree of cold-working may be different from those in Figs. 1 and 4. In Fig. 6, many bands are also seen, each band consisting of a few lines of fringes which exhibit the reversal in intensity in the region where extinction contours (broad dark

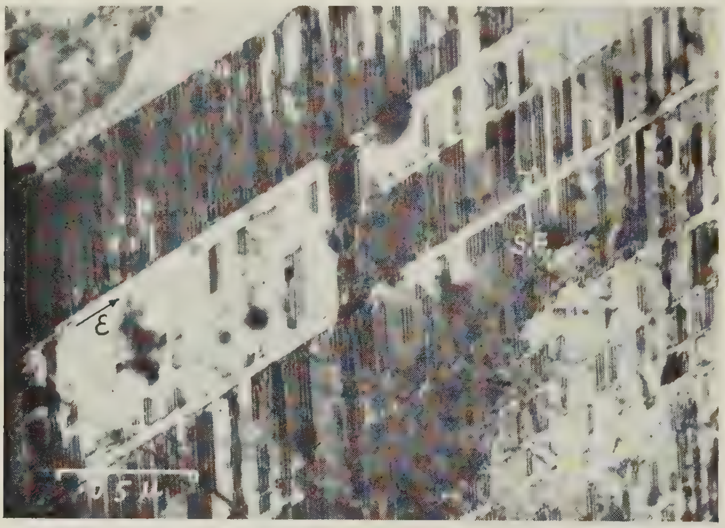

Fig. 7. Transmission electron micrograph of a thin foil of beaten high manganese steel, showing parallel fringes due to the stacking fault (S.F.) and no-reflecting bands of ε-phase.

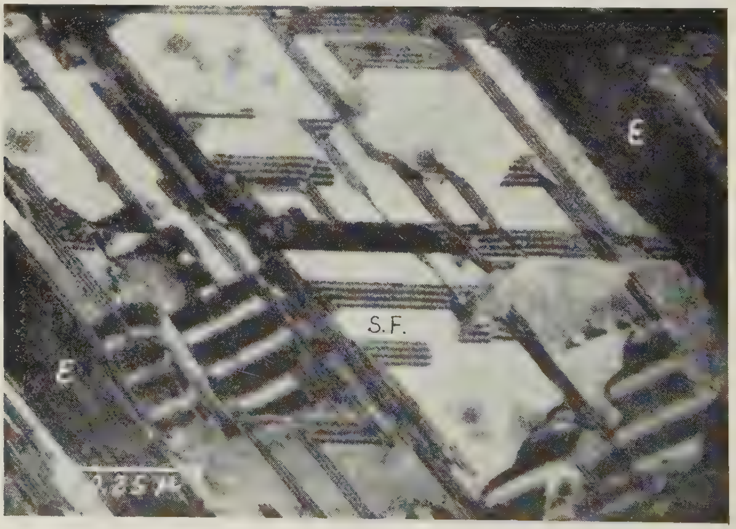

Fig. 8. Transmission electron micrograph of a thin foil of beaten high manganese steel, showing parallel fringes due to the stacking fault (S.F.) and reflecting bands of ε-phase.

region running from right-bottom to left-top) are appeared. As in the case of the photograph given by Hirsch et al.[1] in 18–8 stainless steel, the behaviors of these fringes indicate that each band is due to a stacking fault plane inclined to the foil. The short fringe seen here and there are due to dislocations which are just to begin to extend. In this figure there are also seen three bands intersecting with the stacking fault fringes. From their behaviors it seems that they are rather due to HCP (ε) plates as mentioned before.

Fig. 7 is a photograph of another region, in which two kinds of bands are also seen: Fringes marked by S. F. are due to a stacking fault and white (no-reflecting) bands marked by ε are due to ε plates.

Fig. 8 is another enlarged micrograph, in which various kinds of bent stacking faults having a stair-rod dislocation are clearly seen, and ε phase regions which are reflecting look to consist of many thin plates.

§ 4. Discussion

As shown in the micrographs described above, there are present stacking faults in some regions but ε plates in other regions. This inhomogenuity is caused by non-uniformity of the degree or rate of cold-working due to hand-hammering. Any way, from the experimental facts we recognize the formation of ε plates as well as stacking faults in {111} planes of FCC matrix.

The ε plate seems to be less than 100 Å in thickness and of less amount than the matrix. The reason why the diffracton pattern of such plates of less amount was seen is on the condition that the matrix did Bragg reflection less in intensity than ε plates. And it is highly probable that this ε plate corresponds to the origin of the strain markings revealed on the etched surface. By this means, it may be said that the present experiment confirmed the former presumption that the origin of the strain marking is the thin ε plate but not the cluster of stacking faults as assumed in the case of Cu–Si alloy by C. S. Barrett[8].

From these facts it may be concluded that the enormous work-hardening of the high manganese steel is because of the formation of stacking faults and thin plates of ε-phase.

The authors wish to express their gratitute to Mr. A. Tanaka, the Faculty of Medicine, Osaka University, for his help to take electron micrographs.

References

1) M. J. Whelan, P. B. Hirsch, R. W. Horne and W. Bollmann: Proc. Roy. Soc., **A**, **240** (1957) 524.
2) H. M. Otte: Acta Met., **5** (1957) 614.
3) Z. Nishiyama, K. Shimizu, M. Oka and T. Hiromoto: Mem. Inst. Sci. and Ind. Res., Osaka Univ., **16** (1959) 73.
4) W. Bollmann: Phys. Rev., **103** (1956) 1588.
5) H. Shoji: Zeits. f. Krist., **77** (1931) 381; Z. Nishiyama: Sci. Rep. Tohoku Univ., **25** (1936). 79.
6) A. R. Troiano and F. T. McGuire: Trans. ASM, **31** (1943) 340.
7) J. G. Parr: J. Iron and Steel Inst., **171** (1952) 137.
8) C. S. Barrett: Trans. AIME, **188** (1950) 123.

JOURNAL OF THE PHYSICAL SOCIETY OF JAPAN, Vol. 15, No. 11, NOVEMBER, 1960

Antiferromagnetic Resonance in NiO in Far-infrared Region

By Hisamoto KONDOH

Department of Physics
University of Osaka Prefecture

(Received June 23, 1960)

Using the far-infrared spectrometer constructed recently in Osaka University, measurements of the optical absorption were made on the single crystal of NiO (Néel temperature=523°K) in the wave-length range of 210 to 385 microns and at temperatures 90° to 470°K. No magnetic field was applied. An absorption peak was clearly observed whose wave-length varied with temperature. With increasing temperature it shifted toward the longer wave-length side and at the same time the peak height diminished. At room temperature (291°K) the peak was at 293±5 microns ($34.1\pm0.6\,\mathrm{cm}^{-1}$) and the wave-length value extrapolated to absolute zero was 274 microns ($36.5\,\mathrm{cm}^{-1}$). This absorption peak is attributed to the antiferromagnetic resonance of the mode in which the antiparallel sublattice magnetizations oscillate perpendicularly to the easy plane of magnetization, (111). The constant, K, of the anisotropy energy which constrains the sublattice magnetizations in the easy plane is calculated to be 4.96×10^6 erg/cc at 0°K from the theoretical formula $\omega=(ge/2mc)(2K/\chi_\perp)^{1/2}$, assuming $g=2.23$. This can be compared with theoretical value, 7.01×10^6 erg/cc, based on the magnetic dipolar interaction between Ni^{++} ions, but the experimental value is smaller.

§ 1. Introduction

Since Nagamiya[1] and Kittel[2] initiated the theory of the antiferromagnetic resonance (AFMR), the microwave resonance experiments in centimeter and millimeter regions have been made on a number of antiferromagnetic materials, and it was found that the expermental results were essentially in good agreement with the theory. The microwave resonance experiments with moderate fields on $\mathrm{CuCl_2\cdot2H_2O}$ ($T_N=4.3$°K) by Leiden Group[3] and on $\mathrm{CuCl_2\cdot2H_2O}$ ($T_N=4.7$°K) and $\mathrm{CuBr_2\cdot2H_2O}$ ($T_N=5°\sim6.5$°K) by Date[4] could be interpreted by the theory of Yosida[5] and Nagamiya[6] for orthorhombic crystal. For antiferromagnetics having higher Néel temperature and hence larger exchange field, a very high frequency or a very high magnetic field is necessary to observe the AFMR. Johnson and Nethercot[7] measured the AFMR in $\mathrm{MnF_2}$ ($T_N=68$°K) with short millimeter waves and Foner[8] used high pulse magnetic field to observe AFMR in $\mathrm{MnF_2}$ and $\mathrm{Cr_2O_3}$ ($T_N=308$°K). An earlier experiment on $\mathrm{Cr_2O_3}$ by Dayhoff[9] using lower fields could not reveal the whole behavior of the resonance phenomenon. These experiments could be well interpreted by the theory of Nagamiya[1] and Keffer and Kittel[10] for uniaxial crystal and gave valuable informations about the temperature-dependent anisotropy energy constant of these crystals.

The technique of far-infrared spectroscopy should also be valuable for this study. In Berkeley, Tinkham[11] has succeeded to measure with a far-infrared spectrometer the AFMR in $\mathrm{FeF_2}$ ($T_N=79$°K) which has a high crystalline field anisotropy energy. A far-infrared spectrometer[12] was constructed a few years ago in Osaka University by Prof. Yoshinaga, and by his courtesy the present author was able to study the AFMR in NiO ($T_N=523$°K). The range of wave-length studied was 210 to 385 microns, since the theoretical estimate of the resonance wavelength, based on the dipolar anisotropy energy constant, was 231 microns ($43.3\,\mathrm{cm}^{-1}$) at 0°K. The resonance was detected, and the present paper will give the detailed account of our experimental procedure and theoretical interpretation of the results.

§ 2. Theoretical Estimate of the Antiferromagnetic Resonance Frequency

The crystal structure of NiO is of the NaCl type with a slight rhombohedral deformation below the Néel temperature. Neutron diffraction experiments[13),22),23)] showed that the spin arrangement is of the Néel type, i.e., there are alternating (111) sheets of plus spins and minus spins, and that the spin axis is confined in the (111) plane. Since the Ni^{++} ions in the cubic crystalline field of NiO should possess an isotropic g-value, no crystalline field anisotropy energy can be expected, and the anisotropy energy in NiO should arise for the most part from the magnetic dipolar interaction among the Ni^{++} ions. This anisotropy energy can be expressed in the form

$$U=(2/3)K(\alpha\beta+\beta\gamma+\gamma\alpha)\,, \qquad (1)$$

where α, β, and γ are the direction cosines of the spin axis relative to the cubic principal axes. The constant K has been calculated by Kaplan[14)] and it is positive, so that the spin axis is to be confined in the (111) plane. For absolute zero, K is expressed in the form

$$K=(3/2)(57.41)(gS\mu_B)^2a^{-6}\,, \qquad (2)$$

(a is the lattice constant and $S=1$ for Ni^{++}) and it is calculated to be

$$K=7.01\times10^6\ \mathrm{erg/cc} \qquad \text{for NiO}\,, \qquad (3)$$

assuming $g=2.23$ and using $a=4.17\times10^{-8}$ cm. This g-value was taken from Low's[15)] paramagnetic resonance measurement of the g-value of Ni^{++} in MgO.

There are two modes of eigen-oscillation of the sublattice magnetizations. One is such that the antiparallel sublattice magnetizations oscillate with a large amplitude in the (111) plane and the net magnetization oscillates with a phase difference of $\pi/2$ in the direction perpendicular to the plane. The frequency of this oscillation in the absence of any external field is proportional to the square root of the product between the molecular field constant, A, which is the reciprocal perpendicular susceptibility, and the small (if any) anisotropy energy constant within the easy plane. The other mode is such that the large motion takes place perpendicularly to the easy plane and the small bending oscillation within the easy plane. This mode has a frequency

$$\omega=(ge/2mc)(2AK)^{1/2}=(ge/2mc)(2K/\chi_\perp)^{1/2}\,, \qquad (4)$$

where K is the anisotropy energy constant for the out-of-plane motion.

With the use of the observed perpendicular susceptibility $\chi_\perp=80.5\times10^{-6}$ emu/cc[16)]* and the value of K given by (3), we can estimate the frequency of the second mode at absolute zero to be $\nu_0(\text{theor.})=\omega/2\pi=43.3\ \mathrm{cm}^{-1}$, the corresponding wave-length being 231 microns.

Since K arises from the dipolar interaction, it should vary with temperature proportionally to the square of the magnitude of the sublattice magnetizations if the temperature is sufficiently high. With the Brillouin function formula, the K value at room temperature is estimated to be by 21 percents less than that at absolute zero, and correspondingly the resonance wave-length at room temperature comes out at 259 microns (38.6 cm^{-1}).**

With these expectations, the author has carried out an absorption experiment on NiO crystal in the wave-length range of 210 to 385 microns, varying the temperature from 90° to 470°K.***

§ 3. Experimental

NiO samples used in the present experiment were slabs cut from single crystals grown by the flame fusion method by Dr. Nakazumi[20)]. Results given in Figs. 1–3 were obtained with slabs whose basal surfaces were parallel to (111). These samples were obtained by cutting and polishing the mother crystals into plates 1 to 2 mm thick.**** This procedure was followed, since at first a measurement with a sample cleaved along a (100) plane gave only a faint absorption peak. Later we found that crystals cleaved along (100) gave as good results as crystals polished along (111); when both kinds of samples were annealed well at 1600°~1670°C in argon atomosphere, as Roth and Slack[22] did, the crystals became much more perfect, but the position and shape of the absorption peak measured at room temperature remained the same.

---

* This value of $\chi_\perp$ was taken from Singer's measurements on stress-annealed single crystal. It is the value at 523°K where there is the maximum of the specific heat and where the present author has found[17)] the torque in magnetic field to vanish, i.e., the parallel and perpendicular susceptibilities to coincide with each other. The susceptibility has a maximum at 630°K and the maximum value is 88.7 emu/cc.

** The spin wave treatment shows that[18)] at low temperatures K is proportional to the cube of the magnetization, and the resonance frequency[19)] is then not given by $\sqrt{2AK(T)}$ but it is given by $\sqrt{2AK(T)}\cdot(M(O)/M(T))^{1/2}$, therefore the frequency is proportional to $M(T)$. We assume here the classical molecular field picture.

*** It was not possible to detect the peak beyond 430°K due to decreasing incident beam intensities for longer wave-lengths than 385 microns and diminishing peak height.

**** This thickness was chosen as being smaller than the skin depth, which could be estimated from the conductivity measurements by Yamaka[21)] to be of the order of 30 cm at room temperature and 0.2 cm at 440°K for wave-lengths of 300 microns. (The values of the resistivity are 5×10^7 ohm-cm at 300°K and 2×10^3 ohm-cm at 440°K),

At room temperature, a single slab with an area of about 1.5 cm^2 could be used, which was put close to the Golay detector[12]. For measurements at higher and lower temperatures, the sample had to be put at the entrance slit (maximum area$=50\times20$ mm^2) which is far away from the detector, and therefore a large area was required for the sample to obtain a sufficient beam intensity at the detector. For this purpose, a plate of aluminium with a dozen holes was prepared and NiO slabs, all with (111) surfaces and with thickness of 1.5 ~1.7 mm, were fitted in them. Furthermore, to make a good thermal contact, two other plates of aluminium having smaller holes were pressed on it from the both sides. The total effective area of the crystals was then 9.3 cm^2. The beam was made to focus at the slit with an aperture of 6°. At room temperature, both samples gave the same main absorption peak, although some differences were found in the side peaks which appeared in some of the curves as seen in Figs. 1 and 2. Temperature measurements of the sample were made with a copper-constantan thermocouple whose one end was made to contact with a crystal which was mounted near the center of the aluminium plate. The temperature difference between the crystals and the thermo-bath was estimated to be within 5° in thermally stationary state.

The sample, the thermo-bath, and the optical system were all set in a vacuum tank and they were remote-controlled. Thermal radiation from the bath could be eliminated with the use of the technique of chopping the beam and detecting the corresponding alternating intensity[12]. The resolution of the spectrum was about 10 microns in the neighborhood of 300 microns. As the beam intensity fell rapidly above 375 microns, it was not possible to extend our measurements beyond 385 microns (26.0 cm^{-1}).

Observations were made of the intensity, I', in the presence of the sample and the intensity, I, in the absence of the crystal. The ratio I'/I gives the transmission rate. The plots of this ratio for different thickness of the sample and different temperature are given in Figs. 1 and 2.

§ 4. Results

Optical absorptions were all measured in the absence of external field. Measurements at room temperature (291°K) were made with single slabs of thickness 1.0 mm, 1.3 mm, and 2.0 mm. The corresponding values of the transmission rate, I'/I, are shown in Fig. 1.

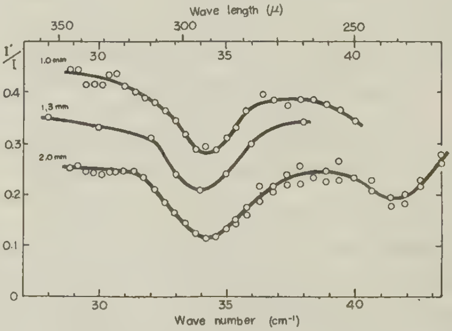

Fig. 1. Transmission rate, I'/I, through single slabs of thickness 1.0 mm, 1.3 mm, and 2.0 mm at room temperature. Incident beam is perpendicular to the (111) surface of the crystal.

These curves indicate clearly an absorption peak at 293±5 microns (34.1±0.6 cm^{-1}) and show further that the absorption rate increases with increasing thickness. In order to check that this absorption peak is characteristic of NiO, a sample of CoO was examined in the neighborhood of this wave-length. No absorption anomaly was found, however.

Variation with temperature of the absorption curve was studied with another kind of sample (having a dozen crystals) mentioned in the preceding section. The results are shown in Fig. 2. The frequency of the absorption maximum shifts to smaller values with increasing temperature, and these values are plotted in Fig. 3. As the incident beam intensity decreased with decreasing frequency and the transmission rate decreased with increasing temperature, no absorption peak was detectable beyond 430°K (the Néel tempera-

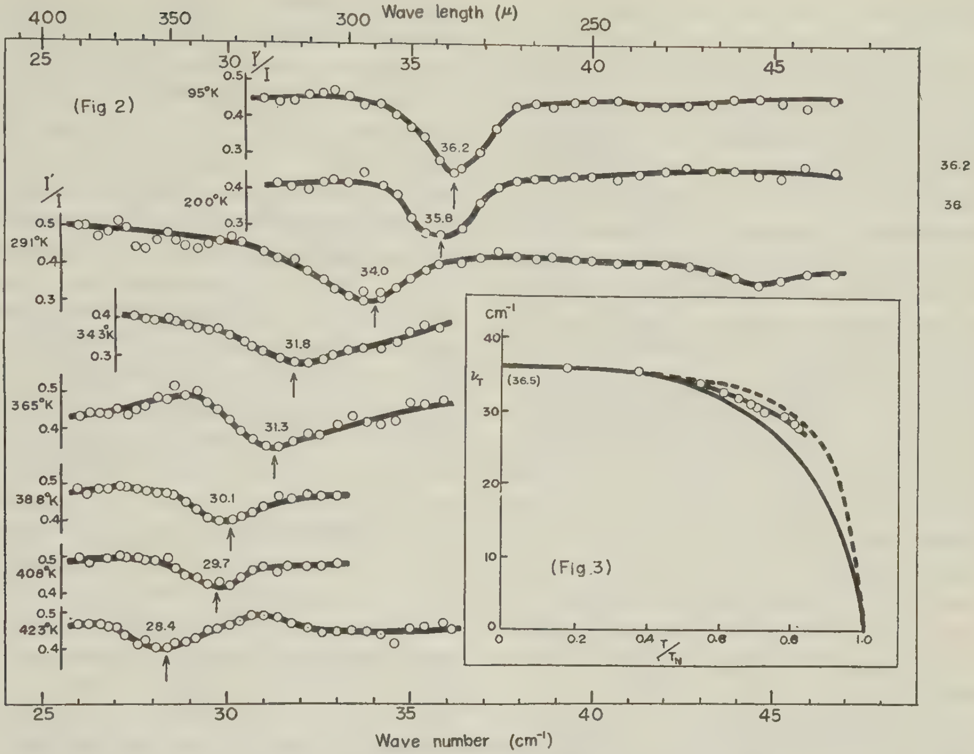

Fig. 2. Transmission rate, I'/I, through a sample having a dozen crystals, at various temperature. Incident beam is perpendicular to the (111) surfaces of the crystals.

Fig. 3. Temperature dependence of the frequency of the absorption maximum. Experimental points are plotted from the data of Fig. 2. A thin curve is the Brillouin curve with $S=1$ and a dotted curve the variation of sublattice magnetizations with temperature obtained from the neutron diffraction experiment by Roth. These two curves are so normalized as to coincide with our experimental value of wave number at 0°K and at room temperature, respectively.

ture is at 523°K). The wave number extrapolated in Fig. 3 to absolute zero is found to be 36.5 cm^{-1} (274 microns).

From the formula (4), and with this absorption frequency value at 0°K and the perpendicular susceptibility $\chi_{\perp}=80.5\times10^{-6}$ emu/cc, the value of the magnetic anisotropy constant, $K(exp.)$, is calculated to be 4.96×10^6 erg/cc at 0°K. On the other hand, the value of the corresponding anisotropy energy due to the magnetic dipolar interaction between Ni^{++} ions, $K(theor.)$, is given by (3), i.e., 7.01×10^6 erg/cc. This theoretical value of the anisotropy constant corresponds to an absorption frequency of $\nu_0(theor.)=43.3$ cm^{-1}. (If the g-value were taken to be 2.00, one would have obtained $K(exp.)=6.16\times10^6$ erg/cc and $K(theor.)=5.64\times10^6$ erg/cc).

Since $K(theor.)$ should be proportional to the square of the magnitude of the sublattice magnetizations, if only dipolar anisotropy energy is taken into account, the temperature dependence of the resonance wave-number snould be theoretically given by the Brillouin curve with $S=1$. In Fig. 3 this theoretical curve is shown together with the experimental one.

§ 5. Discussion

We see from Fig. 3 that at absolute zero $\nu_0(exp.)=36.5$ cm^{-1} is smaller than $\nu_0(theor.)=43.3$ cm^{-1} and that the measured resonance wave number decreases with temperature more steeply near the Néel temperature than that predicted by the theory. The temperature dependence of the sublattice magnetzaitions has been measured by the neutron diffraction experiment by Roth[13] and it is also shown in Fig. 3 by a dotted curve, which was so normalized that it coincides with our resonance wave number curve at 291°K. It is seen that the behavior of this curve is more similar to that of our resonance wave number curve.

In the estimate of ν_0(*theor.*), ambiguities are introduced by the use of the value of $\chi_\perp$ and the isotropic g-value. Roth and Slack[22] have recently prepared a very good single crystal of NiO which contained untwinned domain to 98.7 percents, and they measured the magnetic anisotropy by the torque method. Combining their data with Singer's measurements of the single crystal susceptibility, they estimated the value of $\chi_\perp$ to be 71.5×10^{-6} emu/cc. This value is smaller by about 10 percents than that used in the present paper which was based on Singer's measurements alone. If this smaller value of $\chi_\perp$ is assumed, the discrepancy between ν_0(*theor.*) and ν_0(*exp.*) becomes even greater. As for the g-value, we have used that of Ni^{++} in MgO, since the g-value of Ni^{++} in NiO is not known. The g-value comes into the frequency formula by a factor g^2, so that a small change in g can influence ν_0(*theor.*) rather drastically.

The difference between ν_0(*theor.*) and ν_0(*exp.*), as well as the difference in the temperature dependence of the resonance wave number, could partly be due to the contribution of the crystalline field anisotropy energy. However, the value of the latter expected from rhombohedral deformation of the order of 0.1 percents should be very small.

Interaction between different antiferromagnetic domains may also give rise to a shift in the resonance frequency. However, we have observed in specimens annealed at 1670° C in argon atomosphere the same wave number for the absorption peak at room temperature. The origin of the discrepancy is therefore not clear at the present moment.

It was found that the temperature dependence of the line width of the absorption peak differs from that of the AFMR in other antiferromagnetic materials hitherto investigated: (1) the line width is much broader than that of MnF_2 or $CuCl_2\cdot2H_2O$ at the same reduced temperature T/T_N, and (2) the line width changes little with temperature and only the height of the absorption peak decreases with increasing temperature. In vergin NiO crystals prepared by the flame fusion method, we observed a number of small twin domains of a dimension of ~10 microns, but in crystals annealed at 1670°C in argon atmosphere and then cooled slowly to room temperature, we may have large domains. For both these samples we observed the same line width and the same position of the absorption peak. Therefore the twin domains may be little responsible for the line width. Roth and Slack[22] observed that the line intensities of the neutron diffraction pattern for a twinless NiO crystal changed with the intensity of the external field, and from this result, together with his result of the torque measurements, they concluded that in low fields NiO may consist of small antiferromagnetic domains with random distribution of the axis of magnetization. These antiferromagnetic domains may give rise to a fluctuation of the molecular field for individual spins and may broaden and shift the absorption peak. The anisotropy field will also fluctuate and produce a similar effect. Furthermore, motion of the domain walls and demagnetizing field from free poles produced at the walls due to different precessions in different domains may also have some effect. If these were the origin of the line width (and a possible line shift), we could expect that the absorption line becomes sharper by application of a high field. However, we have done no such experiment.

§ 5. Acknowledgements

The author would like to express his great appreciation to Professor T. Nagamiya for suggesting this problem and for his continual guidance during the course of this research. The author would like also to express his sincere thanks to Professor H. Yoshinaga for allowing the author to use his spectrometer and giving him instructions concerning the measurements. Furthermore, he is indebted to Dr. A. Mitsuishi for kind assistance and discussion as regards instrumental problems, Dr. A. Tachiki for stimulating discussion, Dr. Y. Nakazumi for providing him with crystals, Mr. N. Fukuoka for helpful assistance, and finally to Professor E. Uchida for warm encouragement throughout this work.

References

1) T. Nagamiya: Prog. Theor. Phys. **6** (1951) 342, 350.
2) C. Kittel: Phys. Rev. **82** (1951) 565.
3) J. Ubbink, J. A. Poulis, J. H. Gerritsen and L. J. Gorter: Physica **18** (1952) 361; **19** (1953) 928. J. H. Gerritsen: Thesis (Leiden, 1955).

4) M. Date: Phys. Rev. **104** (1956) 623.
5) K. Yosida: Prog. Theor. Phys. **6** (1951) 691; **7** (1952) 25, 425.
6) T. Nagamiya: Prog. Theor. Phys. **11** (1954) 309.
7) F. M. Johnson and A. H. Nethercot: Phys. Rev. **114** (1959) 705.
8) S. Foner: Phys. Rev. **107** (1957) 683.
9) E. S. Dayhoff: Phys. Rev. **107** (1957) 84.
10) F. Keffer and C. Kittel: Phys. Rev. **85** (1952) 329.
11) Private communication.
12) H. Yoshinaga, S. Fujita, S. Minami, A. Mitsuishi, R. A. Oetjen and Y. Yamada: J. Opt. Soc. America **48** (1958) 315.
13) W. L. Roth: Phys. Rev. **110** (1958) 1333; **111** (1958) 772.
14) J. I. Kaplan: J. Chem. Phys. **22** (1954) 1709.
15) W. Low: Phys. Rev. **109** (1958) 247.
16) J. R. Singer: Phys. Rev. **104** (1956) 929.
17) H. Kondoh, E. Uchida, Y. Nakazumi and T. Nagamiya: J. Phys. Soc. Japan **13** (1958) 579.
18) T. Oguchi: Phys. Rev. **111** (1958) 1063.
19) T. Oguchi: to be published. (Private communication.)
20) Y. Nakazumi: J. Chem. Soc. Japan Ind. Chem. Soc. **59** (1956) 1304.
21) E. Yamaka and K. Sawamoto: Phys. Rev. **112** (1958) 1861.
22) W. L. Roth and G. A. Slack: Memo. Rep. G. E. Research Lab., No. MD-**42**, P-212 (1959). W. L. Roth and G. A. Slack: J. App. Phys. **31** (1960) 352.
23) H. A. Alperin: J. App. Phys. **31** (1960) 354.

JOURNAL OF THE PHYSICAL SOCIETY OF JAPAN, Vol. 15, No. 11, NOVEMBER, 1960

Magnetostriction and Crystal Anisotropy of Nickel-Chromium and Nickel-Vanadium Alloys

By Tokuo WAKIYAMA

Kobayashi Institute of Physical Research, Tokyo

and Sōshin CHIKAZUMI

Institute for Solid State Physics, University of Tokyo, Tokyo

(Received June 27, 1960)

Magnetostriction constants, λ_{100} and λ_{111}, of nickel-chromium and nickel-vanadium alloys were measured at room and liquid nitrogen temperatures by a strain gauge method. Both constants were negative and their magnitudes decreased monotonically with increasing the composition of adding elements. Magnetocrystalline anisotropy constants were also measured at the same temperatures. The concentration dependence of the anisotropy constants was more drastic than that of the magnetostriction constants.

The present data and other available data of nickel binary alloys were analysed on the basis of Néel's theory and the coefficients of dipole-dipole and quadrupole-quadrupole interactions of atom pairs in nickel alloys were estimated. The dipole-dipole interactions of Ni-M (where M=V, Cr, Mn, Fe, Co, Ni and Cu) atom pairs were fairly well explained under the assumption of the spin-orbit interaction.

§1. Introduction

It is well known that the magnetostriction constants are closely related with the dipole-dipole interaction between magnetic atoms and its dependence on the lattice spacing. L. Néel[1] showed this relation in a phenomenological way in connection with the theory of magnetic annealing. The purpose of the present investigation is to determine the coefficient of dipole-dipole interaction between various sorts of magnetic atoms by using the magnetostriction constants measured by various investigators[2)-4)]. Unfortunately we could not find out the experimental data on Ni–Cr and Ni–V alloys, so we measured these constants at room and liquid nitrogen temperatures. Crystal anisotropy constants were also measured at the same temperatures and a phenomenological quadrupole-quadrupole interaction coefficient was determined for various atom paris[5)-8)].

§2. Specimens and Experimental Procedure

Specimens used in this experiment were prepared by melting electrolytic nickel and chromium, and high-purity vanadium in a high vacuum induction furnace. Large crystals were obtained by solidifying the alloy slowly in a crucible. These crystals were cut into disk plates parallel to (110). The size of the specimen was 8∼15 mm in diameter and 0.3∼1 mm in thickness. The compositions of Ni–Cr crystals are 0, 1.47, 2.52 and 4.08 at.% chromium and those of Ni–V crystals are 1.28 2.95 and 3.93 at.% vanadium. In advance to the measurement, all specimens were annealed for 2 hours at 1300°C and quenched from 700°C to secure the disorder state.

Measurement of the magnetostriction constants was carried out by means of strain gauge technique, using the apparatus as shown in Fig. 1. Strain gauges were placed on the crystals in both [001] and $[\bar{1}11]$ crystallographic directions. The change in the electric resistace of the strain gauge was measured by an ordinary Wheatstone bridge. An unbalanced current was measured by a galvanometer directly. The strain sensitivity was the order of 0.65×10^{-6} per 1 mm deflection of the scale. Magnetostricton was plotted against the direction of the field at every 5° from 0 to 180°. The angle θ is always measured from [001] direction.

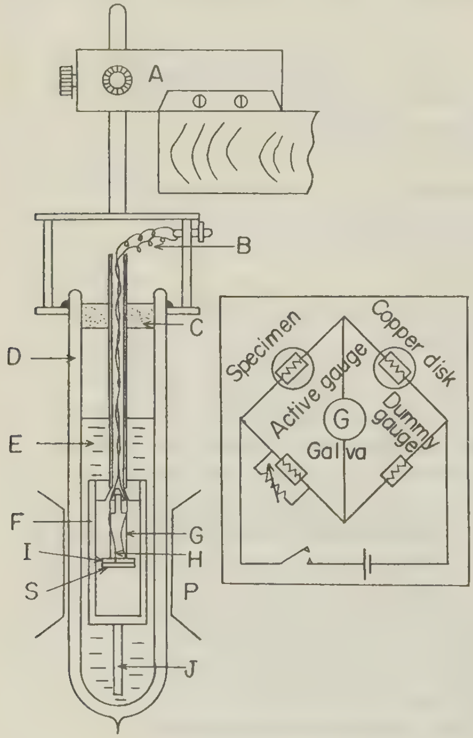

Fig. 1. Measuring apparatus of magnetostriction. A: leveling device, B: leads of strain gause and thermocouple, C: cork, D: dewar vessel, E: liquid nitrogen, F: hollow copper case, G: specimen holder, H: thermocouple, I: copper disk with dummy gauge, S: specimen with active gauge, J: copper thermoresistance, P: pole piece.

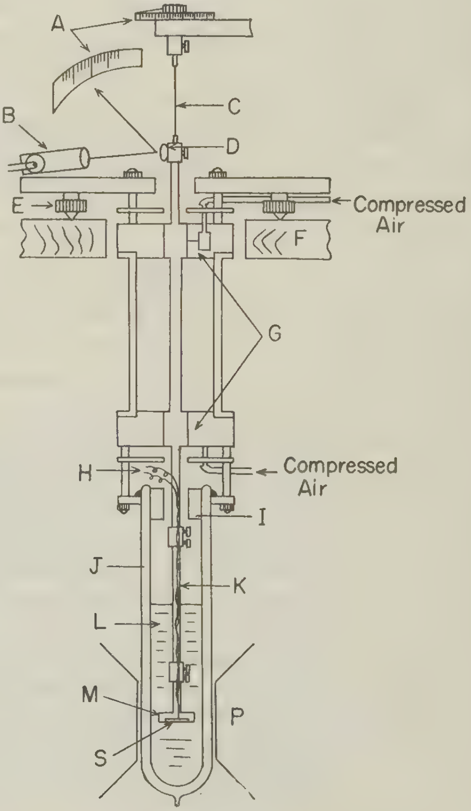

Fig. 2. Torque magnetometer. A: scale, B: light source, C: elastic string, D: mirror, E: leveling device, F: wooden table, G: two combined air-flow bearings, H: leads of thermocouple, I: cork, J: dewar vessel, K: porcelain tube, L: liquid nitrogen, M: specimen holder, S: specimen, P: pole piece.

Measurement of the anisotropy constant was carried out by means of the torque magnetometer as shown in Fig. 2. This apparatus is characterized by a pair of two air-flow bearings, almost the same as used by R. F. Penoyer[9], which enable the frictionless rotation of specimen holder about the vertical axis.

The intensity of the magnetic field is about 8000 œ, which is strong enough to saturate the specimen, at room and liquid nitrogen temperatures.

§3. Experimental Results

One of the results of magnetostriction measurement in the [001] and [$\bar{1}$11] direction in (110) plane is shown in Fig. 3 as a function of θ. These curves were analyzed by assuming the two-constants expression

$$\lambda=\frac{3}{2}\lambda_{100}\left(\alpha_1{}^2\beta_1{}^2+\alpha_2{}^2\beta_2{}^2+\alpha_3{}^2\beta_3{}^2-\frac{1}{3}\right)$$
$$+3\lambda_{111}(\alpha_1\alpha_2\beta_1\beta_2+\alpha_2\alpha_3\beta_2\beta_3+\alpha_3\alpha_1\beta_3\beta_1),\qquad (1)$$

where λ is the spontaneous saturation magnetostriction, α_1, α_2 and α_3 are the direction cosines of the spontaneous magnetization β_1, β_2 and β_3 are those of the direction of measurement with respect to the crystal axes. This formula well expresses the experiment as shown by the solid curves in Fig. 3. The values of the magnetostriction constants thus obtained are tabulated in Table I, and are also plotted as a function of the alloy composition in Figs. 4 and 5 for Ni-Cr and Ni-V alloys respectively. In both cases the obtained curves are similar in shape and λ_{100} and λ_{111} are negative values for any chromium or vanadium content and their absolute values

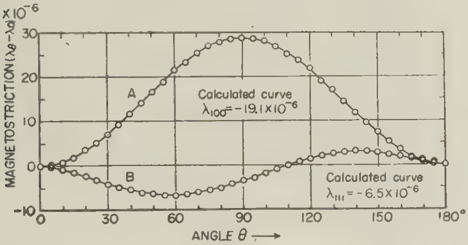

Fig. 3. Magnetostriction measured in the [001] and [$\bar{1}$11] directions as a function of angle θ in (110) plane of 3.93 atomic-percent V-Ni crystal. A: strain gauge parallel to [001], B: strain gauge parallel to [$\bar{1}$11].

Table I. The experimental values of λ_{100} and λ_{111}.

Specimen (at. %)	300° K		77° K	
	$\lambda_{100}\times10^6$	$\lambda_{111}\times10^6$	$\lambda_{100}\times10^6$	$\lambda_{111}\times10^6$
Ni	−55.8	−29.5	−58	−37
1.47% Cr-Ni	−44.6	−19.6	−46	−26
2.52% Cr-Ni	−34.8	−14.2	−43	−21
4.08% Cr-Ni	−20.6	− 7.9	−35	−17
1.28% V-Ni	−43.0	−21.0	−51	−29
2.95% V-Ni	−29.6	−13.4	−39	−22
3.93% V-Ni	−19.1	− 6.5	−34	−15

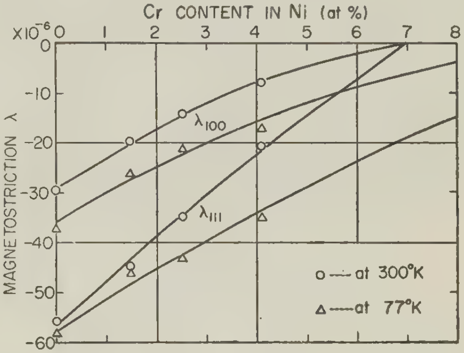

Fig. 4. Concentration dependence of the magnetostriction constants of Ni-Cr alloys. Solid curves are the quadratic functions of atomic concentration of Cr.

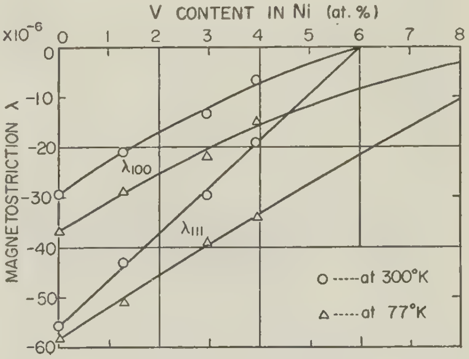

Fig. 5. Concentration dependence of the magnetostriction constants of Ni-V alloys. Solid curves are the quadratic functions of atomic concentration of V.

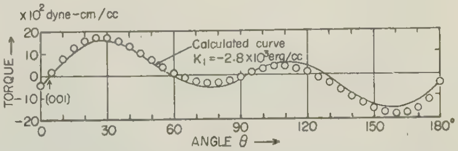

Fig. 6. Torque curve for (110) plane of 3.93 atomic-percent V-Ni crystal measured at 300°K.

decrease monotonically with increasing concentration. At liquid nitrogen temperature, both constants were increased in their absolute values, though the general feature of the curves was not changed.

One of the torque curves is shown in Fig. 6. The values of the anisotropy constant K_1 were calculated by the Fourier analysis. The values of K_1 thus obtained are tabulated in Table. II, and are also graphically shown in Figs. 7 and 8 as a function of the alloy composition. The anisotropy constant K_1 of Ni–Cr or Ni–V alloys remains negative for any chromium or vanadium content, and fades out much more rapidly with increasing chromium or vanadium content than the intensity of magnetization does. It is interesting to note that the concentration dependence of K_1 of Ni–Cr alloys is more drastic than that of Ni–V alloys, whereas its saturation magnetization decreased more slowly with concentration than that of Ni–V alloys[10].

Table II. The experimental values of crystal anisotropy constants.

Specimen (at. %)	K_1 ($\times 10^4$ erg/cc)	
	300° K	77° K
Ni	−4.9	−73
1.47% Cr–Ni	−1.1	−27
2.52% Cr–Ni	−0.38	−17
4.08% Cr–Ni	0	− 6.5
1.28% V–Ni	−2.4	−36
2.95% V–Ni	−0.73	−18
3.93% V–Ni	−0.28	−13

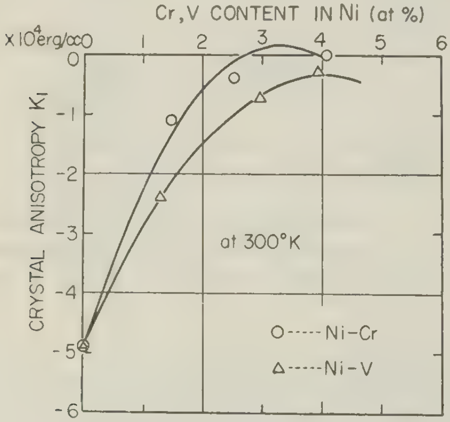

Fig. 7. Concentration dependence of the crystal anisotropy constants of Ni-Cr and Ni-V alloys measured at 300°K. Solid curves are the quadratic functions of atomic concentration of Cr and V, respectively.

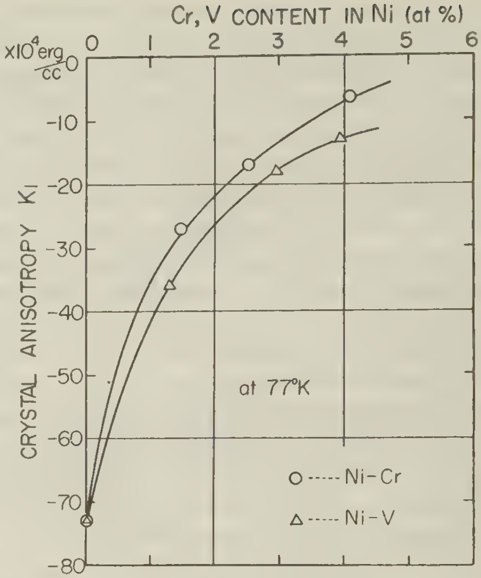

Fig. 8. Concentration dependence of the crystal anisotropy constants of Ni-Cr and Ni-V alloys measured at 77°K.

§4. Analysis of the Experimental Results

Magnetostriction is the phenomenon that the crystal lattice is deformed by the interaction of atomic magnetic moments. According to L. Néel[1], the energy due to interaction between neighboring atoms should be a function of the distance between the two atoms and also of the angle φ between magnetization and pair direction, so that it can be expressed by the Legendre polynomials.

$$w=g+\left(l+m\delta r\right)\left(\cos^2\varphi-\frac{1}{3}\right)+\left(q+s\delta r\right)\left(\cos^4\varphi-\frac{6}{7}\cos^2\varphi+\frac{3}{35}\right)+\cdots, \quad (2)$$

where g is the isotropic interaction such as exchange interaction, l and q are the coefficient of dipole-dipole and quadrupole-quadrupole interaction respectively, m and s are the differential coefficients of l and q with respect to r and δr is the variation of the distance r. Starting from the formula (2), Néel calculated the magnetostriction constants and obtained for face-centered cubic crystal

$$\left.\begin{aligned}\lambda_{100}&=-\frac{nN}{72VC_2}(6l+mr_0),\\ \lambda_{111}&=-\frac{nN}{36VC_3}(2l+mr_0),\end{aligned}\right\} \quad (3)$$

where n is the number of the nearest neighbors, N the Avogadro number, V the atomic volume, C_2 and C_3 the elastic constants, and r_0 the distance between the nearest neighbors for undeformed lattice. From these relations, we can solve l and m, thus

$$\left.\begin{aligned}\frac{nNl}{2V}&=\frac{9}{2}(C_3\lambda_{111}-2C_2\lambda_{100})\,,\\ \frac{nNmr_0}{2V}&=9(2C_2\lambda_{100}-3C_3\lambda_{111})\,.\end{aligned}\right\}\tag{4}$$

Now in the case of the alloy, interaction between the atoms should be different for different pair of atoms, so that l and m for AA, BB and AB pairs should be denoted by l_{AA}, m_{AA}, l_{BB}, m_{BB} and l_{AB}, m_{AB} respectively. In the case of disordered state, the number of each kind of pairs is proportional to $C_A{}^2$, $C_B{}^2$ $2C_AC_B$, where C_A and C_B are the concentration of A and B atoms, so the average value of l and m should be given by

$$l=l_{AA}C_A{}^2+2l_{AB}C_AC_B+l_{BB}C_B{}^2\,,\tag{5}$$

$$m=m_{AA}C_A{}^2+2m_{AB}C_AC_B+m_{BB}C_B{}^2\,.\tag{6}$$

Since λ_{100} and λ_{111} are expressed as a linear function of l and m as shown in (3), they should also depend upon the atomic concentration in the same way as (5) or (6). In other words, λ versus C_B curves are expected to be parabolic. This is actually the case for most of ferromagnetic alloys.

Figs. 4 and 5 show the concentration dependence of magnetostriction constants measured for Ni–Cr and Ni–V alloys, just fitted by quadratic functions by adjusting the parameters. Using the values of the parameters and $V=6.55$ cc, $C_2=0.45\times10^{12}$ dyne/cm^2 and $C_3=1.185\times10^{12}$ dyne/cm^2, which are observed for nickel, we can calculate the values of l and m for Ni–Ni, Ni–V and V–V pairs. The values are tabulated in Table III together with the values for other nickel alloys.

Table III. Coefficient of the dipole-dipole interaction and its differential coefficient with respect to r of each atom pair in various face-centered cubic nickel alloys.

A–B	Nl_{AA}	Nl_{AB}	Nl_{BB}	$Nm_{AA}r_0$	$Nm_{AB}r_0$	$Nm_{BB}r_0$
Ni–V	0.73×10^8 erg/mol 0.42*	0.54×10^8 erg/mol 4.5*	-193×10^8 erg/mol −116*	5.4×10^8 erg/mol 7.7*	-73×10^8 erg/mol −75*	965×10^8 erg/mol 720*
Ni–Cr	0.79 0.47*	0.90 3.3*	−167 − 74*	5.2 7.3*	−76 −68*	110×10 611*
Ni–Mn	1.0	−3.7	13	4.3	−14	43
Ni–Fe	0.8**	−3.8**	12**	4.6**	−7.3**	− 28**
Ni–Co	1.0	−6.9	− 11	3.1	28	17
Ni–Cu	1.1	0.23	−4.5	3.0	−5.5	9.9

(*: at 77°K, **: after L. Néel[1)])

The crystalline anisotropy constant K_1 can be related to the third term of (2), as shown by Néel, thus

$$K_1=\frac{N}{V}q\,.\tag{7}$$

Since there is a possibility that dipole-dipole interaction can gives rise to the cubic anistropy[11)], the value of q thus obtained from K_1 should involve both of the dipole and quadrupole interaction terms.

Fig. 6 shows the torque curve measured for (110) plane of 3.93 at.% V–Ni at 300°K. The concentration depence of K_1 is also fitted by quadratic function of atomic concentration as shown in Fig. 7. The values of q thus determined for various atom pairs are tabulated in Table IV.

Table IV. Coefficient of quadrupole-quadrupole interaction of each atom pair in various face centered cubic nickel alloys.

A–B	Nq_{AA}	Nq_{AB}	Nq_{BB}
Ni–V	-0.32×10^6 erg/mol	7.4×10^6 erg/mol	-183×10^6 erg/mol
Ni–Cr	−0.31	9.6	−280
Ni–Mn	−0.28	2.9	− 26
Ni–Fe	−0.33	0.58	−0.49
Ni–Co	−0.20	1.0	−5.0
Ni–Cu	−0.37	0.84	−2.0

At 77° K, $Nq_{NiNi}=-4.8\times10^6$ erg/mol

§5. Discussion

Since we determined the values of l and m by using nickel-rich alloys, the values for B–B pair are not reliable. The values of l_{NiNi} and m_{NiNi} are almost the same for all alloys. This is simply because the parabolic curves drawn to fit the experimental points pass the vicinity of nickel point in every cases. The most significant values obtained from magnetostriction constants are those of l and m for Ni–B pairs. In Fig. 9 we plotted the l_{NiB} as a function of electron concentration of B atom, where we can see a fairly regular dependence of l value upon the number of $3d$ electrons.

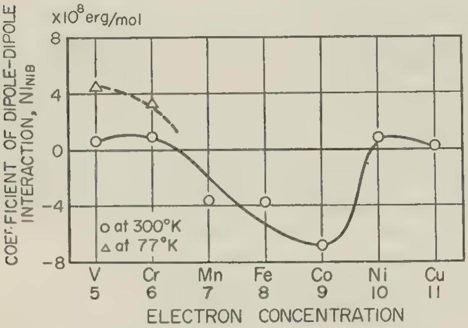

Fig. 9. Dependence of the coefficient of dipole-dipole interaction for Ni–B pairs on the electron concentration of B atom.

The features of this curve are summarized as follows:

i) Negative part of the curve starts from $n=6.5\sim7.0$, where n is the number of electrons outside the argon shell of the B atom, and takes the muximum at about $n=9$.

ii) l_{NiB} takes the positive value in the regions $n<6.5\sim7.0$ and $n>9.8$.

iii) The order of magnitude of l_{NiB} is $10^8\sim10^9$ erg/mol.

The origin of dipole-dipole interaction in ferromagnetic crystals was first discussed by N.S. Akulov[12)] and by R. Becker[13)], who showed that the purely magnetic dipole-dipole interaction is too small to account for the actual magnitude of uniaxial crystal anisotropy and that of magnetostriction. As pointed by Van Vleck[11)], the actual origin is belived to be a combined effect of spin-orbit interaction and overlapping wave functions between the neighboring atoms. The presence of some orbital angular mometum and overlapping of the neighboring $3d$ orbits are, therefore, prerequisite for the pseudo-dipole interaction. From this point of view, we can interprete several features of the experimental curve.

Since the number of $4s$ conduction electrons is believed to be about one at Cr or Mn[14)], the remaining $3d$ electrons should take $3d^5$ state (S state) at about $n=6$, where the atom should have no orbital angular momentum, so that we cannot expect any pseudo-dipole interaction at this point. As the number of electrons increases from this point, the orbital angular momentum should be increased, provided the atom stays in a free state. Actually, however, the atom is under the action of the strong crystalline field. In the case of the face-centered cubic metals, each atom is surrounded by 12 cations, each of which is found in ⟨110⟩ direction from the center atom. In such a case, d-orbits should split into $d\varepsilon$ and $d\gamma$ orbits, where $d\varepsilon$ orbits extend towards ⟨110⟩ directions, while $d\gamma$ oribits extend along the coordinate axes. Since each atom shoud find neighboring cations in ⟨110⟩ directions, $d\varepsilon$ orbits might be more stable than $d\gamma$ orbits, as is the case for octahedral sites of ferrite. In this case, $3d^6$ and $3d^7$ should have triply degenerate ground state, where the orbital angular momentum is remained unchanged. This is not exactly the case for actual metal, where the large part of the orbital angular momentum is quenched as being expected from the g-value. The tendency of leaving some orbital angular momentum at about $n=7\sim8$, however, is found for the actual metals, because the observed value of g-factor, which is nearly equal to 2 at $n=7$, begin to deviate from 2 with an increase of n, and its deviation takes the maximum at about $n=9$.[15)] This behavior of the orbital angular momentum seems to explain the experimental fact i) fairly well.

When $n<6$ and $n>9$, the last electron should occupy $d\gamma$ orbits. These regions are corresponding to those indicated in ii). It is, however, not clear whether or not the positive value of l_{NiB} can be related to the $d\gamma$ orbit.

As pointed out by C. Kittel[16),17)], the order of magnitude of pseudo-dipole interaction can be given by

$$|l| \approx J(g-2)^2, \qquad (8)$$

where J is the exchange integral. Since $J\approx10^{10}\sim10^{11}$ erg/mol and $g-2\approx0.05\sim0.08$, (8) gives the value of l of the order of magnitude $10^7\sim10^9$ erg/mol, which is in good agreement with the experimental value stated in iii).

It should be noted here that the value of

m_{NiB} depends upon the electron concentration n of the B atom almost in the same way as that of l_{NiB}. This fact may be explained by assuming that the dependence of l_{NiB} upon the lattice constant is mainly caused by a change in the overlapping of $3d$ shells between Ni and B atoms.

Acknowledgements

The authors express their hearty thanks to Dr. J. C. Slonczewski of IBM Research Laboratory, Dr. T. Moriya of Bell Telephone Laboratories and Dr. M. Tachiki of the Osaka University for their valuable advices about theoretical argument of this paper and also to Dr. T. Nakamichi of the Research Institute for Iron, Steel and Other Metals, who informed his data of Ni-Mn alloys.

References

1) L. Néel: J. Phys. et Rad. **15** (1954) 225.
2) F. Lichtenberger: Ann. Phys. **10** (1932) 45.
3) R. M. Bozorth: Rev. Mod. Phys. **25** (1953) 42.
4) M. Yamamoto and T. Nakamichi: Sci. Rep. RITU **11** (1959) 168.
5) R. M. Bozorth and J. G. Walker: Phys. Rev. **89** (1953) 624.
6) H. J. Williams and R. M. Bozorth: Phys. Rev. **55** (1939) 673.
7) J. W. Shih: Phys. Rev. **50** (1936) 376.
8) L. W. Mckeehan: Phys. Rev. **51** (1937) 136.
9) R. F. Penoyer: Boston Conf. (1956) 365.
10) C. Sadron: Ann. Phys. **10** (1932) 26.
11) J. H. Van Vleck: Phys. Rev. **52** (1937) 1178.
12) N. S. Akulov: Z. f. Phys. **52** (1928) 389.
13) R. Becker: Z. f. Phys. **62** (1930) 253.
14) W. J. Carr, Jr.: Phys. Rev. **85** (1952) 590.
15) R. M. Bozorth: Ferromagnetism (D. Van Nostrand Co., Inc., N. Y., 1951) 453.
16) J. H. Van Vleck: J. de Phys. et Rad. **12** (1951) 262.
17) C. Kittel: Nuov. Cim. **6** Ser. X (1957) 895.

JOURNAL OF THE PHYSICAL SOCIETY OF JAPAN, Vol. 15, No. 11, NOVEMBER, 1960

Studies on the Preparation of Pure Alkali Chlorides*

By Koichi KOBAYASHI and Tetsuhiko TOMIKI

Department of Physics, Tohoku University, Sendai

(Received June 27, 1960)

Systematic studies were made on the preparation of pure KCl and NaCl crystals. Effects of the starting material on the purity of crystal were studied with KCl and NaCl powders of reagent grade of several different brands and with those prepared from bicarbonate and hydrochloric acid. Methods by distillation and crystallization in vacuum and by Kyropoulos technique in air were used for the crystallization procedures to study on each of their advantages. To estimate the concentration of impurities in crystals, the measurement of ionic conductivity was made for multivalent metallic ions, optical absorption for hydroxyl ions, and chemical analysis for bromine ions. The purest crystal in respect of these impurities was found to be the one grown from its powder prepared from bicarbonate and hydrochloric acid by the method of distillation and crystallization in vacuum. After the studies on the edge of the fundamental absorption in connection with the concentration of bromine, an absorption band due to the presence of bromine was found in KCl of which maximum is at 7.12 ev at room temperature.

§ 1. Introduction

In the past three decades, considerable efforts have been devoted to study on alkali chloride crystals by a number of workers to investigate their intrinsic natures as a typical example of an ionic crystal. It is well known, however, that some of their properties are found to be different from crystal to crystal and the experimental results are influenced strongly by chemical impurities and physical imperfections in the crystal. One example is a growth rate of color centers at room temperature. This is known to be so sensitive to the density of impurities and of dislocations that one has to be careful in measuring the true magnitude of the energy of formation of a color center by an ionizing radiation from its growth curve. One does not know also whether the very poor photoelectric response of alkali chloride during an irradiation in the fundamental optical absorption region is characteristic of its perfect crystal, since the Schubweg of electrons might be shortened considerably by the presence of imperfections. Even on a color center itself, it is not so certain whether the experimental results are completely free from any effects due to imperfections, since the color center concentration with which investigations have been carried is of the same order as or less than the concentration of impurities in most cases. Therefore, it may be important to study with a very perfect crystal to reduce any influences due to the presence of imperfections for investigating the intrinsic nature of alkali chloride. This is the reason for the present studies on the preparation on pure crystals.

In the present work, we have studied on KCl and NaCl as typical examples of alkali chlorides. At the first step of our systematic studies on the preparation of perfect crystals, our interests have been concentrated on their chemical impurities. We have investigated on multivalent metallic ions, hydroxyl ions, and halogen ions of other kinds present in KCl and NaCl as impurities, and have developed a method of preparation of pure crystal in respect of these impurities. After examinations of the edge of the fundamental absorption in both crystals, it has been found that its position is related primarily to the concentration of impurity bromine, which has been found to be one of the most abundant impurities in the crystals. Furthermore, a new absorption band due to the presence of bromine has been found in KCl just at the edge of its fundamental absorption band.

---

* A part of the present work has been carried out during our temporary stay in Prof. Kanzaki's laboratory of the Institute for Solid State Physics, University of Tokyo.

§ 2 Experimental

1) *Preparation of Crystals*

Crystals were grown from their powders of defferent kinds by different methods of crystallization to investigate their effects on the purity of the crystals.

a. Starting materials

Alkali chloride powders of two different kinds were used as a starting material. One was the powder made from alkali bicarbonate and hydrochloric acid through a chemical reaction. The other was powders obtained from different companies as reagent grade chemicals. The former was prepared for trying to make a starting material as pure as possible by a conventional chemical technique before the crystallization. The following are the reasons of using bicarbonate and hydrochloric acid: Firstly, it is possible to purify alkali and chloride ions separately by chemical means. The second is that the chemical purification of bicarbonate and hydrochloric acid is much easier than that of alkali chloride. Thirdly, the purity of alkali bicarbonate and hydrochloric acid available commercially is believed to be better than that of commercial alkali chlorides.

Synthetic KCl powders were made from $KHCO_3$ and HCl in their aquous solution. HCl was purified through two times ether extractions followed by a careful distillation. The aquous solution of $KHCO_3$, which was prepared from this salt of reagent grade without further chemical purification, was then mixed with this HCl. The resultants were KCl, H_2O, and CO_2, the last of which was able to be eliminated easily just by heating. KCl powder was obtained after cooling its saturated solution and was dried in vacuum.

Synthetic NaCl powders were made from $NaHCO_3$ and HCl. $NaHCO_3$ was purified by a chloroform solution of dithizone and 8-hydroxyquinoline. NaCl powder was prepared with HCl purified by ether extraction through the same procedure as for KCl, except the precipitation of this salt by an addition of alcohol to its saturated solution. No trace of metal impurity was found in this NaCl by a spectroscopic analysis except potassium.

Commercial KCl and NaCl powders were of G.R. grade made by the Kanto Chemical Company, the Wako Pure Chemical Industries, and the Merck Company in Germany.

b. Crystal growing

Two methods were used for growing single crystals in this study. One was the usual Kyropoulos technique and crystals were pulled up in air from their melts in a platinum crucible. The other was the method through distillation and crystallization in vacuum inside a quartz tube which was developed by Kanzaki and Kido[1].

Crystals prepared by the above methods are listed in Tables I and II. In the column of starting material, powder made from alkali bicarbonate and hydrochloric acid is denoted as *a*, while powders obtained from Kanto, Wako, and Merck are indicated as *b*, *c*, and *d*, respectively. In the column of crystal growing, *K* and *V* represent the method of Kyropoulos and of distillation and crystallization in vacuum, respectively.

It should be noted that the crystals grown by the method of distillation and crystallization in vacuum did not show good planes after cleavage and may contain dislocations in much higher concentration than Kyropoulos crystals. Particularly, NaCl crystals grown in this way were found to be deformed severely. NaCl–aV–2 listed in Table II is the worst crystal in this respect, of which cleavage planes are curved.

2) *Ionic Conductivity*

As a mearsure of an amount of multivalent metallic ion impurities, an ionic conductivity was measured on each of crystals with d.c. technique.

Fig. 1 indicates the results of the ionic conductivity of KCl prepared in this study. The conductivity of Harshaw crystal is also shown in this figure for the purpose of comparison. It was found usually that the conductivity in its structure sensitive region varies within a factor of two between crystals prepared from commercial powders in different bottles obtained from the same company.

The concentrations of electric carriers in KCl were estimated from the present conductivity data in the structure sensitive region and the vacancy mobility measured by Kelting and Witt[2]. They are listed in Table I as *n*/cc.

Among Kyropoulos KCl crystals in Table I, KCl–aK–1, the crystal which was grown from

Table I. KCl crystals.

Crystal	Starting material	Crystal growing	*n*/cc	OH/cc	ev at $k=10$ cm^{-1}	Bromine concentration
KCl-aK-1	*a*	*K*	1×10^{15}	2×10^{15}	7.027	$9\ \times10^{-6}$
KCl-HA-1	Harshaw		9×10^{15}	8×10^{15}	6.985	7.1×10^{-5}
KCl-bc2K-1	*b*+*c*	*K*	8×10^{15}	2×10^{15}	6.919	1.1×10^{-4}
KCl-bK-1	*b*	*K*	4×10^{15}	2×10^{15}	6.904	1.3×10^{-4}
KCl-dK-1	*d*	*K*	7×10^{15}	2×10^{15}	6.847	3.6×10^{-4}
KCl-bc2K-2	*b*+*c*	*K*	1×10^{16}	2×10^{15}	6.822	8.1×10^{-4}
KCl-B-II-3*	*b*	*V*	1×10^{15}	$<3\times10^{14}$	6.828	—

* Kindly supplied by Prof. H. Kanzaki of the Institute for Solide State Physics, University of Tokyo.

KCl powder prepared from $KHCO_3$ and HCl, has the lowest *n* of which magnitude is as small as 1×10^{15} per cc. One may note that this amount is smaller than that of Harshaw KCl by a factor of nine and is comparable to that of KCl–B–II–3 which was purified through careful distillation and crystallization in vacuum. If one assumes that the concentration of electric carriers is related directly to that of multivalent metallic ion impurities, one can say that the concentration of multivalent metallic ions in KCl–aK–1 is considerably lower than that of crystals grown directly from commercial KCl powders.

To estimate an amount of reduction of multivalent metallic ions in KCl by the Kyropoulos procedure, crystallization from the melt was repeated carefully four times in air and the ionic conductivity was measured with the crystal after each step. The starting meterial was the commercial KCl powder of G.R. grade. The concentration of electric carriers was found to be decreased in the manner, 1.1×10^{16}, 8.2×10^{15}, 3.6×10^{15}, and 2.3×10^{15} per cc according to the successive crystallization from the melts. This would indicate that the concentration of multivalent metallic ion impurities can be reduced to one fifth of its original amount by applications of Kyropoulos technique in three times. The concentration of multivalent metallic ions in the final crystal is about twice that of KCl–aK–1 in magnitude.

Electric conductivities were measured also on NaCl crystals prepared by different procedures. The results are shown in Fig. 2. Concentrations of electric carriers, *n*, were estimated with the vacancy mobility given by Etzel and Maurer[3)] and are tabulated in Table

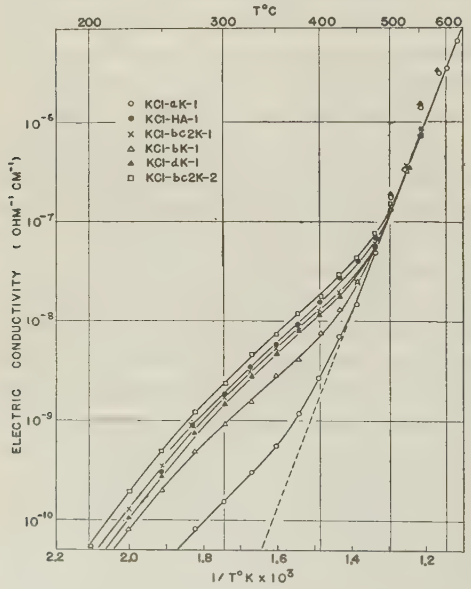

Fig. 1. Ionic conductivities of KCl crystals.

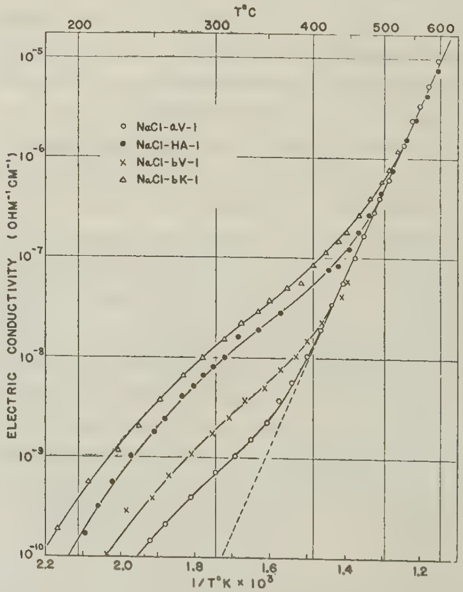

Fig. 2. Ionic conductivities of NaCl crystals,

II. One may notice that n for NaCl–bV–1 is smaller by six times than that for NaCl–bK–1. The former was grown from the commercial KCl powder by the method of distillation and crystallization in vacuum, while the latter was grown from the same material but by the Kyropoulos method.

Both NaCl–aV–1 and NaCl–bV–1 are grown by the method of distillation and crystallization in vacuum. However, the former was started with NaCl prepared from bicarbonate and hydrochloric acid and the latter was with the commercial one. The magnitude of n for NaCl–aV–1 was found to be smaller by three times than that for NaCl–bV–1. One may note also that this magnitude is smaller by a factor of more than ten than that for Harshaw NaCl.

It may be interesting to note that the concentrations of electric carriers at the both ends of the boule of NaCl–aV–1 were found to be different only by a factor of 1.1, while those of the boule of NaCl–bV–1 by a factor of 2.2. Therefore, it would be very probable that the NaCl powder which was prepared from bicarbonate and hydrochloric acid already contain little multivalent metallic ions which can be removed effectively by the crystallization from the melts.

NaCl–aV–2 in Table II is the crystal prepared from the same starting material and by the same growing procedure as NaCl–aV–1. However, the large deformation of the former has been found to be introduced during the course of crystallization in vacuum.

Table II. NaCl crystals.

Crystal	Starting material	Crystal growing	n/cc	OH/cc	ev at $k=10$ cm^{-1}	Bromine concentration
NaCl–aV–1	*a*	V*	2.5×10^{15}	$<6\times10^{14}$	7.222	1.1×10^{-5}
NaCl–HA–1	Harshaw		3×10^{16}	3×10^{16}	7.213	1.4×10^{-5}
NaCl–bV–1	*b*	V*	8×10^{15}	$<6\times10^{14}$	7.174	—
NaCl–bK–1	*b*	K	5×10^{16}	2×10^{16}	7.158	4.0×10^{-5}
NaCl–aV–2	*a*	V*	5×10^{15}	$<6\times10^{14}$	7.190	—

* Distillation and crystallization in vacuum was performed kindly by Mr. K. Kido at the Institute for Solid State Physics, University of Tokyo.

3) *Optical absorption*

Optical absorptions were measured on KCl and NaCl crystals at room temperature to find any absorptions due to the presence of impurities. In the infrared region, a Perkin-Elmer Model 21 infrared spectrophotometer was used to cover from 2.5 to 15μ. No absorption band was found in KCl and NaCl listed in Tables I and II in this spectral range. In the region from visible up to 2.5 μ, a Hitachi recording spectrophotometer was used and again no absorption band was detected in these crystals.

Optical absorption measurements in the range from 240 mμ down to the fundamental absorption edge, however, indicate significant differences between crystals. They were measured at 12°C with a vacuum ultraviolet spectrophotometer which was constructed by Ueta and his collaborators. The results are shown in Fig. 3 for KCl and in Fig. 4 for NaCl. The thickness of the crystal used in this measurement was ranging from 0.6 mm to 1.0 mm. The absorption coefficient was determined by taking into account of the reflection loss. The reflectivity used in this calculation was estimated from the index of refraction for both KCl and NaCl given by Gyulai[4] in the range from 240 to 185 mμ. In the wave length region shorter than 185 mμ, the reflectivity measured by Hartman et al[5] was used after having been normalized to the one calculated from the index of refraction at 185 mμ. One may notice in both figures the presence of so called OH-band and the large difference in the position of the fundamental absorption edge between crystals.

a. OH band

The results in Fig. 3 indicate the presence of absorption band at 204 mμ in all KCl crystals except KCl–B–II–3. This is known to be the absorption due to OH ion present as an impurity in KCl[6]. The absorption coefficient of KCl–B–II–3 which was prepared by distillation and crystallization in vacuum was almost zero in the range from 190 to 240 mμ and therefore no OH absorption was observed within our experimental error. The intensity of this absorption band was found to be the highest in KCl–HA–1, the Harshaw KCl, among the KCl crystals studied. All other crystals which were grown from different KCl powders by the same procedure, that is the Kyropoulos method in air, show the presence of OH band with small but almost the same intensity. The concentration of OH ion in KCl was estimated under the assumption that its oscillator strength is 1.9[6]. The results are listed in Table I.

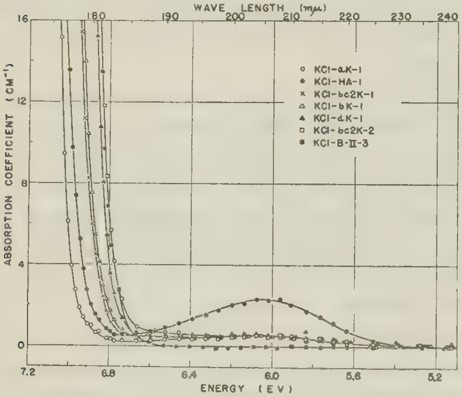

Fig. 3. Absorption spectra of KCl crystals in the ultraviolet region.

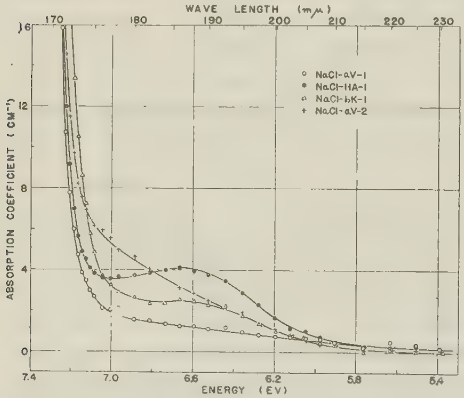

Fig. 4. Absorption spectra of NaCl crystals in the ultraviolet region.

In Fig. 4, one may find that the absorption band at 185 mμ due to OH ion in NaCl[6] is present apparently in NaCl–HA–1, the Harshaw crystal, and in NaCl–bK–1 which was grown in air by the Kyropoulos method. Its intensity is much higher in the former crystal than in the latter. Crystals NaCl–aV–1 and NaCl–aV–2 have a pronounced tail extending from the edge of the fundamental absorption to the region of OH band but there is no sign of a hump in their absorption curves in the region of OH band. Both crystals have been grown from the same starting material and by the same vacuum distillation and crystallization method. However, NaCl–aV–2 has been deformed much more severely than NaCl–aV–1, so that the only significant difference between them may be of their concentration of dislocations. Since the tail is much larger in the former crystal than in the latter, the tails of both crystals are possibly due to the dislocations but not to the chemical impurities. Therefore, it may be said that no hydroxyl ions detectable by optical means are present in NaCl crystals prepared by the distillation and crystallization in vacuum. In Table II, the concentrations of hydroxyl ion in NaCl are listed which were estimated under the assumption that the oscillator strength is unity.

b. Edge of the fundamental absorption

In Fig 3, considerable difference is observed in the position of the edge of the fundamental absorption between KCl crystals. The photon energies where the absorption coefficient, k, is 10 cm^{-1} are listed in ev in Table I for the indication of the position of the edge of each crystals. The difference of the position of this kind was found also in NaCl crystals as shown in Fig. 4. The photon energies at $k=10$ cm^{-1} for NaCl are list in Table II. It is clear from these tables and figures that the absorption edge positioned at the shortest wave length was of KCl–aK–1 among KCls and of NaCl–aV–1 among NaCls, both of which were grown from their powders prepared from bicarbonate and hydrochloric acid.

From the data in Tables I and II, one may find that there is no definite relation between the position of the fundamental edge and the concentration of electric carriers or of hydroxyl ions. Therefore, the shift of the position of the edge may not be due to the presence of multivalent metallic ions or hydroxyl ions in KCl and NaCl. It may be possible to imagine that the difference of the edge position might be explained by the different concentrations of dislocations in the crystals. However, the positions of the edge of NaCl–HA–1 and NaCl–bK–1 are in the longer wave length side than that of NaCl–aV–1 while the dislocation densities of the former two are believed to be much lower than that of the latter. Also, in Fig. 3, all of the KCl crystals do not show any tail with appreciable intensity in spite of their different position of the fundamental absorption edge. Therefore, one may conclude that the difference in the position of the edge is not caused by the difference in the dislocation density in crystals.

Other impurity possibly present in alkali chlorides is halogen of other kinds, particularly bromine. Therefore the colorimetric chemical analysis of bromine[7] was made on each crystal of KCl and NaCl. The amount of bromine was determined by measuring the intensity of the optical absorption at 580 mμ due to bromophenol blue resulting from the addition of sodium hypochlorite and phenol red to the aqueous solution of the sample. The minimum amount of bromine in a crystal which was able to be determined by this method was about 3×10^{-6} in mole fraction. The results are listed in Tables I and II in the unit of mole fraction of the bromine ions to the total halogen ions. The concentrations of bromine thus found are of surprisingly large, so that the bromine may be one of the major impurities in alkali chlorides. The crystal which contains the least bromine among KCls was KCl–aK–1 and among NaCls was NaCl–aV–1, both of which were grown from their powders prepared from bicarbonate and hydrochloric acid.

It may be clear in Tables I and II that the position of the fundamental absorption edge of both KCl and NaCl is related directly to the concentration of bromine in the crystal in such a way that the former is shifted to the longer wave length side with the increase of the latter. Therefore, one may conclude that the position of the edge of the fundamental absorption in both KCl and NaCl commonly used depends primarily upon the amount of impurity bromine in the crystal.

To investigate further details of the absorption edge in KCl, absorption measurements were made in higher absorption coefficient region with thin crystals of about 0.15 mm in their thickness. Absorption coefficients thus measured on the thin crystals were found to be in good agreement with those obtained on the thick crystals in Fig. 3, in the range between $k=10\ \mathrm{cm}^{-1}$ and $40\ \mathrm{cm}^{-1}$. In Fig.5, the absorption coefficient at the edge of KCl crystals is plotted in a logarithmic scale as a function of the photon energy in much wider range than in Fig. 3. These data are taken from absorption coefficients of the thin crystals in the range of $k>20\ \mathrm{cm}^{-1}$ and from those of the thick crystals below it. Below $k=40\mathrm{cm}^{-1}$, it is found that there is a linear relation between log k and the photon energy for all crystals, and their slopes are almost the same between each other except that of KCl–aK–1 which is the purest in respect of the impurity bromine. Above $40\ \mathrm{cm}^{-1}$ in k, however, absorption curves bend over and appear to approach asymptotically at high k value to the absorption curve of KCl–aK–1 which is linear in log k versus energy relation in the entire range of the measurement.

The absorption curve of KCl–aK–1 was extrapolated linearly in this semilogarithmic scale to $k=10^6\ \mathrm{cm}^{-1}$ which is assumed as the maximum absorption coefficient of the first exciton absorption in KCl. Then the photon energy at this point was given as 7.59 ev. This value is very close to 7.56 ev which is estimated from the absorption curve given by Hartman et al[5] as the photon energy at the maximum of the long wave length side absorption band of the first exciton doublet in KCl at 300° K. Extrapolations of absorptions curves for other crystals led to the

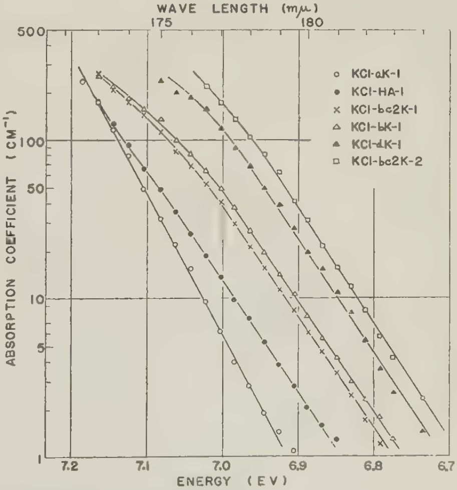

Fig. 5. Fundamental absorption edges of KCl crystals.

photon energies at $k=10^6\ cm^{-1}$ which are completely different from 7.56 ev.

To investigate the efficiency of the method of crystallization from the melt on the elimination of the impurity bromine from alkali halides, the chemical analysis for bromine was made also on the starting materials for the crystals KCl-bK-1, KCl-dK-1, and NaCl-bK-1. It was found that only 10% of bromine in KCl and 20% of bromine in NaCl was able to be removed during a single process of crystallization though the Kyropoulos technique. This may indicate that the method of crystallization from the melt, such as Kyropoulos or zone melting technique, seems not to be so efficient on the purification of alkali chlorides in respect of the impurity bromine.

§ 3. Discussion

1) *Preparation of pure alkali chloride crystals*

In Table I, we have seen that the concentration of the electric carriers or of the multivalent metallic ions in KCl-aK-1, which was grown from the powder prepared from $KHCO_3$ and HCl, is considerably smaller than those in other Kyropoulos KCl crystals. Therefore, it would be clear that it is of advantage to the preparation of pure crystal by the Kyropoulos method to use this KCl powder as the starting material. In the case of NaCl, it has been shown that the magnitude of n for NaCl-bV-1 is much smaller than that for NaCl-bK-1. This would indicate that the method of distillation and crystallization in vacuum is more effective than the Kyropoulos method on the elimination of multivalent metallic ions from NaCl. This result is similar to the one found by Kanzaki and Kido in KCl[1]. However, we have also found that n for NaCl-aV-1 is smaller by a factor of three than that for NaCl-bV-1. Then it may be said that the method started with bicabonate and hydrochloric acid is better than that started directly with commercial NaCl powder even in the case of the application of vacuum distillation and crystallization technique.

The presence of hydroxyl ions has not been detected optically in all KCl and NaCl crystals as far as they are prepared through distillation and crystallization in vacuum, while all other Kyropoulos crystals show the presence of hydroxyl ions. Therefore, the method of distillation and crystallization in vacuum may be an excellent one for the preparation of alkali chlorides free from hydroxyl ions.

It has been indicated that little bromine can be removed from alkali chloride during the process of the crystallization from the melt. Therefore, to prepare a pure crystal of KCl and of NaCl in respect of bromine, it must be necessary to start with their powders of which bromine concentrations are as small as possible. Commercial KCl and NaCl have been found to contain a large amount of bromine of an order of 10^{-4} in mole fraction which is difficult to be removed from alkali chloride by a usual chemical technique. However, if one looks at the procedure of the preparation of alkali chloride powder from bicarbonate and hydrochloric acid, one may find that the only possible source of bromine in alkali chloride is hydrochloric acid. Hydrochloric acid is believed to contain less bromine than alkali chloride and can be purified easily by fractional distillations. Crystals KCl-aK-1 and NaCl-aV-1 show certainly the presence of bromine in smaller concentrations than other crystals grown directly from their commercial powders.

The efficiency of the elimination of bromine from alkali chlorides by the method of distillation and crystallization in vacuum has not been studied. However, the bromine concentration of KCl-B-II-3, which is grown directly from the commercial KCl by the above method, is estimated as high as 7×10^{-4} from the position of its fundamental edge by the interpolation of the relation between the edge position and the bromine concentration. Therefore, the vacuum distillation of alkali chlorides seems not to be so effective on the elimination of the bromine.

At the present stage of this study, it is concluded that the following way would be recommeded for the preparation of pure KCl and NaCl crystals in respect of multivalent metallic ions, hydroxyl ions, and bromine ions: Alkali chloride powders are prepared from bicarbonate and hydrochloric acid both of which are purified chemically. Then they are crystallized by the method of distillation and crystallization in vacuum. It should be noted that, although the crystal thus prepared is quite pure in chemical impurity, its density of dislocations is always higher than that of the Kyropoulos crystal. This is the serious problem of this method, and the preparation of crystal free from dislocations has been left to future studies.

2) *Absorption band due to the presence of bromine in KCl**

We have shown that the edge of the fundamental absorption in KCl is shifted to the longer wave length side with an increase of the concentration of bromine. At the fundamental absorption edge, the absorption curves of the crystals with bromine in appreciable amount have been found to deviate from the linear relation and bend over as have been shown in Fig. 5. Since the concentration of bromine in KCl–aK–1 is far lower than those of other KCls and so the position of its fundamental edge is at the shortest wave length, it may be reasonable to assume that the absorption edge of KCl–aK–1 is almost of pure KCl. This assumption may also be supported by the previously mentioned fact that only the position of the fundamental edge of KCl–aK–1 at $k=10^6$ cm^{-1}, which is estimated by the extrapolation, is close to that of the first excition peak of KCl. Therefore, the difference between the absorption coefficients of KCl–aK–1 and those of other KCl crystals would be an excess absorption due to the presence of bromine. In Fig. 6, these differences are plotted in a logarithmic scale as a function of photon energy. The curves thus obtained are the bands which shapes are similar to one another, although their shape at the short wave length side of the band is not so clear because of the error in measurements at high absorption coefficient. Moreover, the positions of the maximum of the bands for KCl–HA–1, KCl–bc2K–1, and KCl–bK–1 are all at 7.12 ev, so that they are the bands of one kind with different intensities.

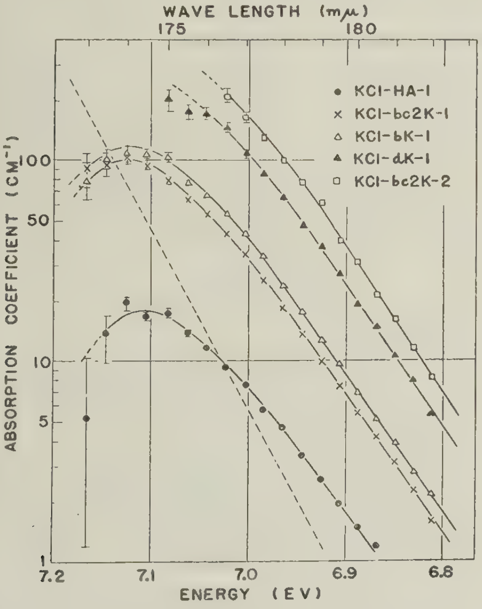

Fig. 6. Absorption band due to the presence of bromine in KCl. Edge of the fundamental absorption band of pure KCl is shown as a straight broken line.

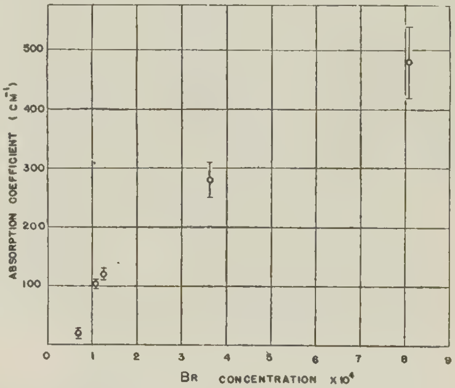

Fig. 7. Plots of the maximum absorption coefficient of the band at 7.12 ev as a function of bromine concentration in KCl.

In Fig. 7, the maximum heights of these absorption bands are plotted as a function of their bromine concentration. It is seen in this figure that the band grows certainly with the increase of the bromine concentration. Therefore, one may conclude that the absorption band at 7.12 ev is due to the presence of bromine in KCl.

It may be noted that the absorption curve at the long wave length side of this band is represented by a straight line below one third of its maximum in the plot of log k versus photon energy. This is exactly the same relation as has been found in the fundamental absorption edge of silver halides[8] and other alkali halides[9]. Therefore, it can be said that the Urbach rule where the temparature is constant holds nicely even in the case of the absorption due to the small amount bromine in KCl lattice.

The half width of this band is found to be

---

* A preliminary account of the work in this section was published as a *short note* in J. Phys. Soc. Japan **15** (1960) 1350.

0.18 ev if the band shape is symmetric. This value is very close to 0.20 ev, the half width of the first exciton absorption band in KBr at room temperature which is estimated roughly from the absorption curve given by Eby et al.[10] However, the position of the maximum of this band is at 7.12 ev which is far from 6.61 ev[10], the position of the maximum of the first excition band in KBr. From these facts, one may say that the nature of the absorption band due to the presence of small amount bromine in KCl is not so different from that of the exciton band due to the excitation of bromine in KBr, except the difference in the position of their absorption maxima, which is probably due to the difference of the lattice distance around the bromine.

One may estimate the oscillator strength of this absorption from the data in Fig. 7 assuming that the absorption is due to the bromine itself. However, the relation between the maximum height and the bromine concentration is not so perfectly linear, so that only a rough estimation was made. The oscillator strength was estimated as 0.07 ± 0.02 by the aid of the Smakula's formula in the first approximation.

We have assumed so far that the edge of the fundamental absorption of KCl–aK–1 is of pure KCl, and all of the estimations in this section has been based upon this assumption. However, this crystal actually contains bromine of 9×10^{-6} in mole fraction, so that its absorption edge is not of pure KCl. If we use 0.07 as the oscillator strength of the absorption due to bromine, then this excess absorption in KCl–aK–1 can be calculated as $8\,\mathrm{cm}^{-1}$ at 7.12 ev, the position of the maximum of this absorption. The absorption coefficient of KCl–aK–1 measured at this photon energy is $67\,\mathrm{cm}^{-1}$. Then, about 12% of the measured absorption of KCl–aK–1 at 7.12 ev may come from the absorption due to bromine. However, since the difference in absorption coefficient between KCl–aK–1 and other KCls at the edge is much larger than $8\,\mathrm{cm}^{-1}$, the estimations of the absorption due to bromine with the assumption that the absorption edge of KCl–aK–1 is of pure KCl may not be incorrect. We have seen in Fig. 6 that the slope of the absorption band due to bromine is smaller than that of the absorption edge of pure KCl. Then, the contribution of the bromine absorption to the measured absorption at the edge of KCl should become larger at the longer wave length. Therefore, the true absorption edge of the pure KCl may be a little steeper than that of KCl–aK–1. This may be one of the reasons for that 7.59 ev, the assumed value of the photon energy of KCl–aK–1 at $k=10^6\,\mathrm{cm}^{-1}$ by the linear extrapolation, is larger than 7.56 ev, the position of the maximum of the exciton band of KCl.

In Fig. 6, the edge of the fundamental absorption of KCl–aK–1, which is almost of pure KCl, is indicated as a straight broken line. One may notice in this figure that the absorption due to bromine in KCl commonly used is much stronger than the fundamental absorption of pure KCl at the absorption tail. Therefore, cares must be taken on the optical excitation at the edge to study the true nature of the exciton absorption in KCl crystal.

Acknowledgement

We wish to thank Professor M. Ueta for his giving us an opportunity to use his vacuum ultraviolet spectrophotometer, and Professor H. Kanzaki for his stimulating discussions and letting us use some of his instruments. Thanks are also due to Mr. S. Tamura for his many valuable suggestions on chemistry and to Mr. K. Kido for his growing some crystals by the method of distillation and crystallization in vacuum. A part of this work was supported by the Research Grant from the Ministry of Education.

References

1) H. Kanzaki and K. Kido: J. Phys. Soc. Japan **15** (1960) 529.
2) H. Kelting and H. Witt: Z. Phys. **126** (1949) 697.
3) H. W. Etzel and R.J. Maurer: J. Chem. Phys. **18** (1950) 1003.
4) Z. Gyulai: Z. Phys. **46** (1927) 80.
5) P. L. Hartman, J. R. Nelson and J. G. Siegfried: Phys. Rev. **105** (1957) 123.
6) H. W. Etzel and D. A. Patterson: Phys. Rev. **112** (1958) 1112.
7) D. F. Boltz: *Colorimetric Determination of Nonmetals* (Interscience Publishers, New York, 1958) 193p.
8) F. Urbach: Phys. Rev. **92** (1953) 1324. F. Moser and F. Urbach: Phys. Rev. **105** (1957) 406.
9) W. Martienssen: J. Phys. Chem. Solids **2** (1957) 257. U. Haupt: Z. Phys. **157** (1959) 232.
10) J. E. Eby, K. J. Teegarden and D. B. Dutton: Phys. Rev. **116** (1959) 1099.

JOURNAL OF THE PHYSICAL SOCIETY OF JAPAN, Vol. 15, No. 11, NOVEMBER, 1960

On the Magnetic Anisotropy of Single Crystal of Chromium Telluride

By Tokutaro HIRONE and Shôko CHIBA

The Research Institute for Iron, Steel and Other Metals, Tohoku University, Sendai

(Recieved June 27, 1960)

The anisotropy of a ferromagnetic single crystal of CrTe with NiAs structure was investigated by magnetic torque measurements. From the experiment it was seen that the axis of easy magnetization is [001] and it does not change from room temperature to liq. He temperature. At 0°K the uniaxial anisotropy constant will be about 5×10^6 erg per cm^3. As for the origin of anisotropy, the dipole-dipole energy can account for only about 20 percent of the observed value.

§ 1. Introduction

Recently the magnetic anisotropy of single crystals of ferro- or ferrimagnetic compounds with nickel arsenide structure was investigated by several authors. In the case of MnBi[1] the axis of easy magnetization was found to be [001] near room temperature and change to [100] at 85°K, being associated with a gradual change of the magnetic anisotropy constant with temperature. It has also been shown that in the case of MnSb[1] the axis of easy magnetization is invariantly [001] and moreover the magnetic anisotropy constant remains unchanged with the decrease of temperature down to 20°K. In the case of ferrimagnetic compound Fe_7Se_8[2] the axis of easy magnetization lies in the c-plane at room temperature and it approaches to the c-axis with lowering temperature. In this paper the authors report the variation of the magnetic anisotropy of the ferromagnetic chromium telluride with the same crystal structure.

§ 2. Specimen and Experimental Procedure

For the pupose of the preparation of single crystals of the compound CrTe, powder of chromium (96% purity) and crushed grains of tellurium (99.99%) were mixed in proper raito. The mixture was sealed in an evacuated silica tube, heated in an electric furnace to 1100°C for 24 hours, and cooled slowly. The reaction product was crushed again and mixed well in a mortar. From this reaction product a single crystal was prepared by the Bridgann method. As shown in Fig. 1, the reaction product was put into a fused silica tube (10 mm in diameter), one end of which was joined to a balloon filled with argon gas. The sample in the silica tube was set so as to put the meniscus of the molten specimen in the hottest part of the furnace, as shown in Fig. 1. After keeping several hours at high temperature it was cooled at a rate of 50° per hour. When the temperature of the specimen reached 1050°C on the cooling the specimen was quenched into water.

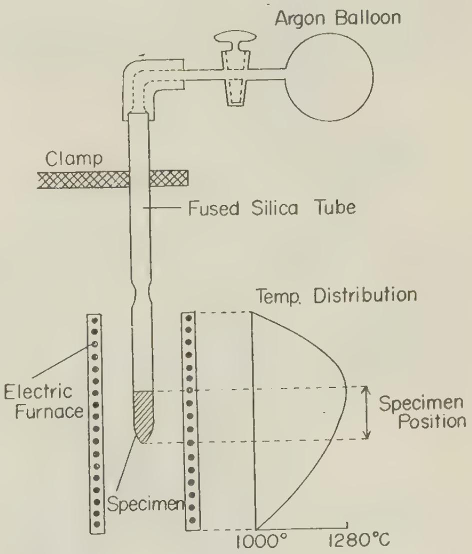

Fig. 1. The apparatus to prepare a single crystal.

A part of the single crystal thus obtained was crushed and a Debye-Scherrer photograph was taken, which showed that the structure was of NiAs type with $a=3.93$Å, $c=6.15$Å and $c/a=1.56$. These results coincide with the results previously reported by Oftedal[3]. Circular disks with the disk plane (100) as well as (001) were prepared with the aid of the Laue photograph. The size of the disks was 4.5 mm in diameter and 1 mm in thickness. The composition of the specimen was confirmed by chemical analysis to be 53 at % Te.

§ 3. Experimental Results

Magnetic torque curves were measured for the disk with (100) plane at room temperature, −77°, −183° and −268°C. The maximum field used in the measurements was 22,000 oe above −183° and was 17,000 oe at liquid He temperature. The curves obtained are shown in Figs. 2, 3, 4 and 5. As seen from these figures the curves obtained show two-fold symmetry. The orientation of easy magnetization lies along the *c*-axis. The value of the torque in the direction of difficult magnetization was not easily determined. The axis of easy magnetization does not show any change with a drop in temperature down to the helium point. Let the polar angle of the

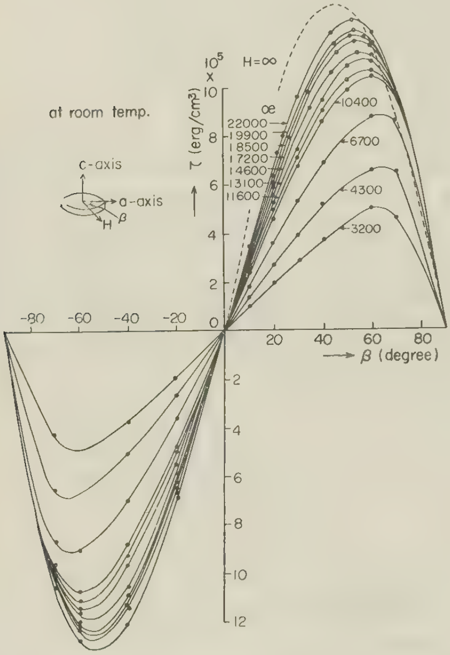

Fig. 2. The magnetic torque curves at room temperature.

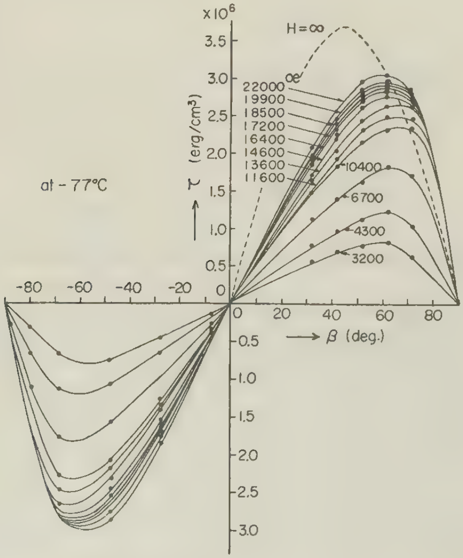

Fig. 3. The magnetic torque curves at −77°C.

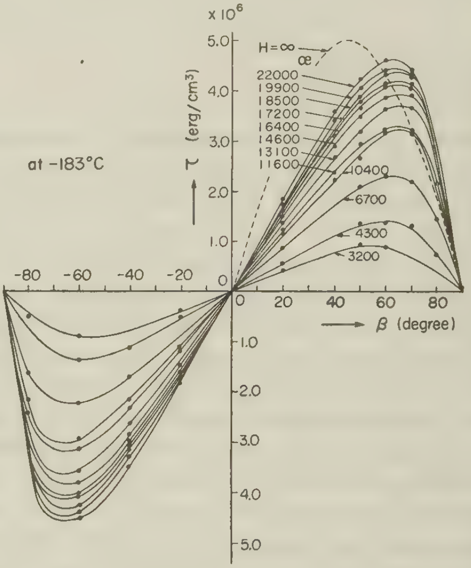

Fig. 4. The magnetic torque curves at −183°C.

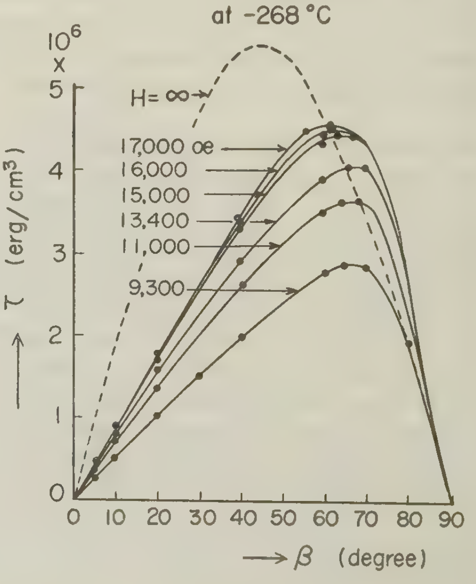

Fig. 5. The magnetic torque curves at −268°C.

field direction from the c-axis be β. At low field strength the maximum of the torque was found to lie a little near $\beta=90°$, and with the increase of the field it approachs $\beta=45°$, with the increase in amplitude of the torque curve.

Next, the magnetizing curve in the direction of easy magnetization was taken by means of an induction type magnetometer due to Chiba's design[4], the results at room temperature being shown in Fig. 6. It was seen from this curve that the saturation magnetisation is already attained at about H=2,000 oe. The magnetization vs. temperature curve at 8,000 oe was taken in the region above the liquid nitrogen temperature. The curve obtained is shown in Fig. 7. As seen in the figure, the temperature dependence of the saturation magnetization is given by the Weiss curve with the spin quantum number $S \geq 2$. The value shown by the symbol ■ at T=0°K is the presumed value at 0°K for the present composition calculated from the data of $\sigma_0=74.57$ which is obtained for stoichiometric chromium-telluride by Guillaud[5]. This is consistent with the present data. The value of saturation moment per Cr atom at 0°K is 2.39μ_b. The extrapolation of σ^2-T curve gives that the Curie point of this specimen is 61°C. It should be mentioned here that Tsubokawa[6] has measured the change of susceptibility with temperature above the Curie point with the specimens from the same source as that of the present study. According to his results the Curie-Weiss law holds in the paramagnetic region with the paramagnetic Curie point, θ_p of 57°C, the Curie constant, C_m of 2.08, the effective magneton, number, μ_{eff} of 4.08, and S of 1.6 if g-value is assumed to be two. Therefore, the S value obtained from the magnetization at low temperatures does not coincide with that obtained from the Curie constant in the high temperature region.

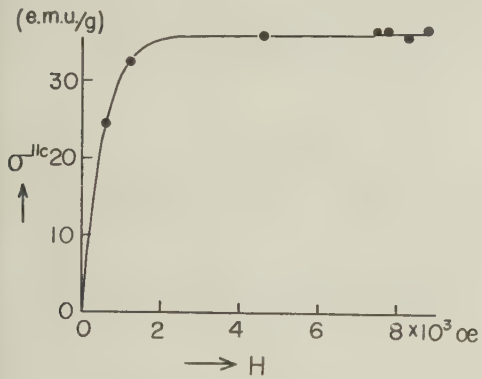

Fig. 6. Magnetization vs. magnetic field curve for a single crystal.

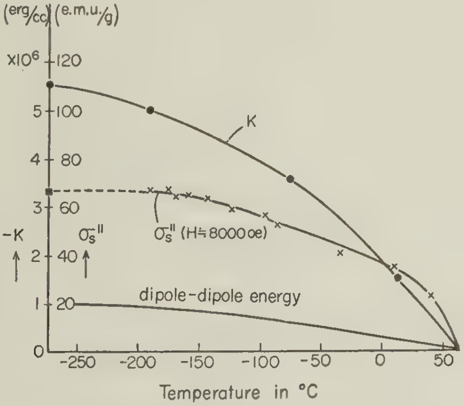

Fig. 7. Anisotropy K vs. temperature curve. Magnetization σ_s vs. temperature curve. Dipole-dipole interaction energy vs. temperature curve.

§ 4. The Value of Anisotropy Constant K

Based on the torque curves shown in the foregoing section the anisotropy constant K was calculated by using the following relation.

$$\frac{1}{2K}=\frac{1}{HJ_s}-\left(\frac{d\beta}{d\tau}\right)_0 , \tag{1}$$

τ; torque per unit volume, cm³ .

$\left(\frac{d\beta}{d\tau}\right)_0$; derivative of τ near $\beta=0$.

The value $(d\beta/d\tau)_0$ was obtained from the torque curves of each field and the experimental value of saturation magnetization per unit volume was used as J_s. The K value is

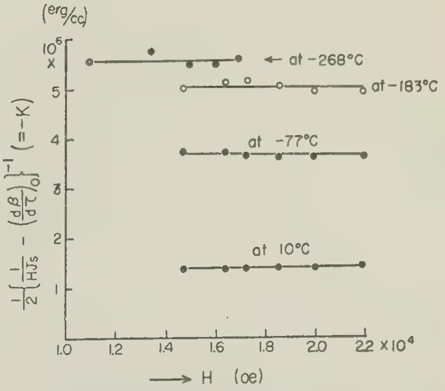

Fig. 8. The value of K as derived from equation (1) vs. magnetic field curvcs.

calculated from equation (1). In Fig. 8, calculated K values were plotted against the field strengths used for the measurement of torque curves. As seen from this figure, K shows a constant value irrespective of the field strength at each temperature, which shows that the equation (1) is reasonably hold in this case. The anisotropy constant K vs. temperature curve is shown in Fig. 7, which shows that the anisotropy of this compound decreases gradually with the increase of temperature. The saturation torque curves calculated from the obtained anisotropy constant are shown by dotted curves in Figs. 2, 3, 4 and 5.

Some considerations will be given to the origin of the anisotropy energy mentioned above. The dipole-dipole interaction was calculated for this compound, the result of which is shown in Fig. 6. As seen in Fig. 6. this term is consistent in sign with the experimental result but the value reaches only about 20 percent of the result of observation. The gap between theory and experiment will be filled by the calculation of the anisotropy due to the spin-orbit interaction of Cr ions influenced by the crystalline field. But in this case a simple ionic model is not sufficient to start the calculation of the anisotropy since the ionic moment in the low temperature region was found to be far less than that in the high temperature region. So that, in the interpretation of this experimental result a detailed discussion on the electronic structure of this compound will be required.

Finally the authors wish to express their hearty thanks to Dr. Maeda and Dr. Watanabe for their useful discussions, and to Mr. Adachi for valuable suggesions.

References

1) C. Guillaud: C. Thesis. Strasburg, 1-127.
2) K. Hirakawa: J. Phys. Soc., Japan, **12** (1957) 929.
3) I. Oftedal: Z. Physik. Chem., **128** (1927) 135.
4) S. Chiba: J. Phys. Soc., Japan, **15** (1960) 581.
5) C. Guillaid and S. Barbezat: Compt. Rend., **222** (1946) 386.
6) I. Tsubokawa: J. Phys. Soc., Japan, **11** (1956) 662.

JOURNAL OF THE PHYSICAL SOCIETY OF JAPAN, Vol. 15, No. 11, NOVEMBER, 1960

Total Cross Sections of Carbon, Oxygen, Fluorine and Thorium for Fast Neutrons

By Kineo TSUKADA and Takayoshi FUSE*

Japan Atomic Energy Research Institute Tokai-mura, Ibaraki-ken

(Received July 25, 1960)

The neutron total cross sections of carbon, oxygen, fluorine and thorium have been measured in the energy range of 3.3 to 5.0 MeV. Measurements were made with a good-geometry arrangement and an energy resolution of about 20 keV, using a neutron detector which had a high efficiency and a good characteristic for gamma-ray discrimination. For carbon, oxygen and fluorine, several resonances in the cross sections were analyzed to give spin assignments. For thorium, a giant resonance was observed at 4.2±0.2 MeV.

§1. Introduction

The neutron total cross sections are of great interest in nuclear physics aside from their importance in practical problems. The resonances appearing in the total cross sections are associated with quasi-stationary energy states of the compound system of the target nucleus plus a neutron. The knowledge about

---

* On leave of absence from Transportation Technical Research Institute, Mitaka, Tokyo.

the characteristics of levels or the statistics of their distribution can be obtained from the measurement of the height or the number of the resonance peaks. Sharp resonances disappear with the increase of neutron energy, because of the overlapping of levels and the spread of neutron energy. This phenomenon occurs at low energy region for heavy nuclei (e.g. at 1 keV for thorium as compared with 10 MeV for oxygen)1). But the resonance of another type, that is, the giant resonance, is seen in this continuum region. This is due to the size effect of nuclei, which is explained by the optical model2).

It is not so easy to measure the neutron total cross sections with high accuracy and resolution because of the large spread of the incident neutron energy, the high background of neutrons and gamma rays, the low efficiency of neutron detectors and the difficulty involved in determining neutron energies. The measurement of this sort is so tedious and time-consuming that the experiment with complicated arrangements are troublesome. Recently, a simple scintillation detector3) which has a good characteristic for the discrimination of gamma rays against neutrons has been developed. In an organic phosphor the decay time of the fluorescence4) excited by neutrons is different from that by gamma rays, and one can make use of this difference for the purpose of discrimination of gamma rays with only a minor change in the conventional photomultiplier circuit. This detector has an efficiency higher than that of the Hornyack button, because of its large sensitive for neutron counting. A detector of high efficiency is especially indispensable in the high resolution work with a good geometry, because neutron flux available is in general very low.

In the present work an attempt was made to measure the neutron total cross sections of carbon, oxygen, fluorine and thorium in an energy range of 3.3 to 5.0 MeV using the detector mentioned above. The assignment of the spin and parity was tried for several resolved resonances. For thorium, a giant resonance was observed as expected by the systematics5).

§ 2. Experimental

The measurements were made at the JAERI 2-MV Van de Graaff accelerator. Neutrons, energy of which was 3.3 to 5 MeV, were produced by using the $D(d,n)He^3$ reaction. The experimental area was 3.6 meters above the ground and had little amount of neutron scattering material nearby in order to minimize the background. By a couple of electrostatic quadrupole lenses, deuterium beam was focused on a target, which was located 8 meters away from a 90-degree beam analyzing magnet. This decreased the machine background remarkably. The experimental arrangement was designed for a good-geometry transmission measurement, as shown in Fig. 1.

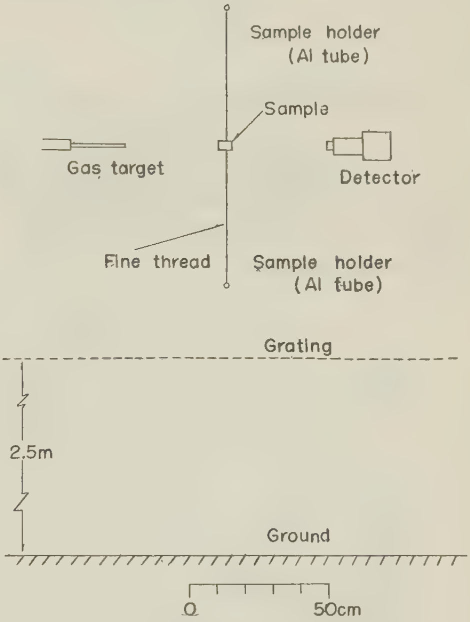

Fig. 1. Experimental Arrangement.

Thorium dioxide (ThO_2, purity 99.9%), Teflon (C_nF_{2n+2}, commercial product), and graphite (C, reactor grade) were used as samples. The thorium oxide sample was of powder form and filled in a lucite cylinder, whose inner diameter and length were 3.7 and 9.0 cm, respectively. The Teflon and graphite samples were 3.0 cm in diameter, and 5.0 and 4.5 cm in length, respectively. The neutron transmission was about 50% in each case. The samples were placed at the middle of the neutron source and the detector, and alined with a transit. The distance from the source to the detector was 75 cm in almost all cases*.

---

* This distance was 50 cm for dots " · " in Fig. 3, in the energy range of 3.3 to 4.4 MeV.

The neutron source was composed of a gas chamber, whose length and inside diameter were 3 cm and 1 cm, respectively. Its entrance window was nickel foil of 0.00005″ thickness. The pressure of deuterium was 5.0 cm Hg* in almost all cases. The neutron energy and its spread were estimated by calculating the loss and straggling of the deuteron energy in the nickel window and the gas. The energy value obtained by the calculation was lower by 20 keV than that obtained by the comparison of the resonance energies of oxygen with those in the results of Becker et al.[6] and Walton et al.[7] In Fig. 3, the corrected value is shown. The neutron detector consisted of a 1″×1″ϕ anthracene crystal and a Du Mont 6467 photomultiplier. In order to discriminate gamma rays against neutrons by the method stated in § 1, the voltage difference between the last dynode and the anode was decreased to 18 volts.** This introduced a serious space charge limitation and magnified the difference between the decay of the fluorecence by the neutrons and that by the gamma rays. The output signal was delivered from the last dynode. Fig. 2 shows the energy dependence of the maximum pulse height of the output signal for the neutrons

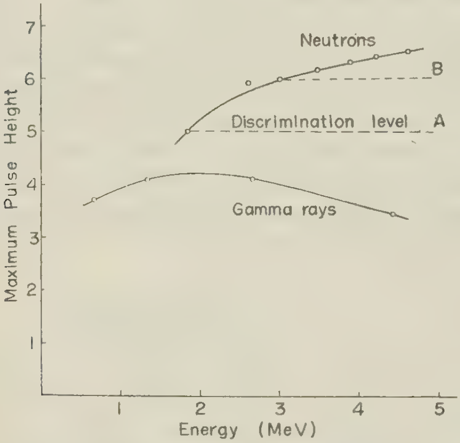

Fig. 2. Energy dependence of the maximum pulse height of the output signal from the anthracene scintillation counter with the space-charge-limited photomultiplier.

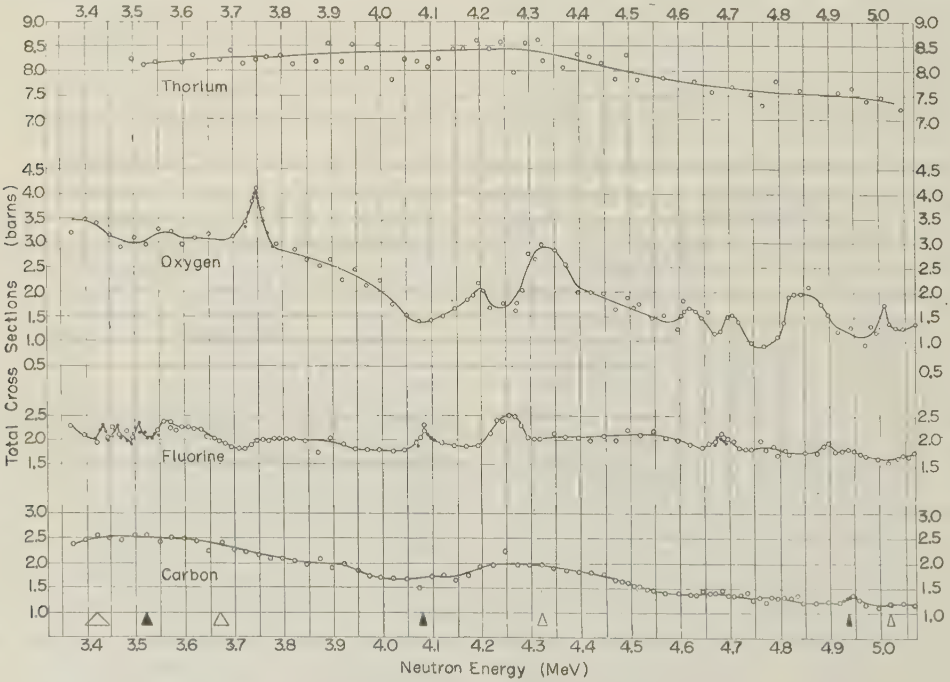

Fig. 3. Neutron total cross sections of carbon, oxygen, fluorine and thorium. The energy resolution is shown as equivalent triangles at several energies. The open and solid triangles correspond to the open and solid circles respectively.

---

* This pressure was 2.5 cm Hg for dots "·" in Fig. 3.

** The voltage differences of the other parts were kept at a normal rate and the total voltage difference between the photo-cathode and the anode was 1,400 volts.

and gamma rays. In this detector system, precaution had to be paid for overloading because of its rather long pulse processing time.

Evaluation of the background counts was done by using a copper bar, whose length and diameter were 50 cm and 3 cm, respectively. The background was less than 0.7%. Existence of energy-degraded neutrons due to the deuterium adsorbed in the window and the wall of the target chamber was checked by counting the neutrons with the chamber evacuated, which yielded less than 1% of the normal output. Neutrons were monitored with a current integrater and two long counters.

§ 3. Results and Discussions

Counts obtained were processed by the following formula to give the total cross section σ.

$$\exp(-N\sigma)=\frac{C_{\text{sample in}}-C_{\text{copper bar}}}{C_{\text{sample out}}-C_{\text{copper bar}}}, \qquad (1)$$

$C_{\text{sample in}}$: counts per charge Q of the incident deuterons when the sample was placed,

$C_{\text{sample out}}$: counts per charge Q when the sample was taken out or the empty can was placed instead of the thorium sample,

$C_{\text{copper bar}}$: counts per charge Q when the copper bar (§ 2) was placed,

N: number of nuclei per unit area in the sample.

An in-scattering correction to be applied to the results obtained through the procedure written above were calculated by Eq. (2)[8] and found to be less than 2%.

$$\frac{\Delta\sigma}{\sigma}=\frac{1}{2}[D/L)(kr+1)]^2\,, \qquad (2)$$

L: distance between the neutron source and the detector,

D: diameter of the sample,

k: neutron wave number,

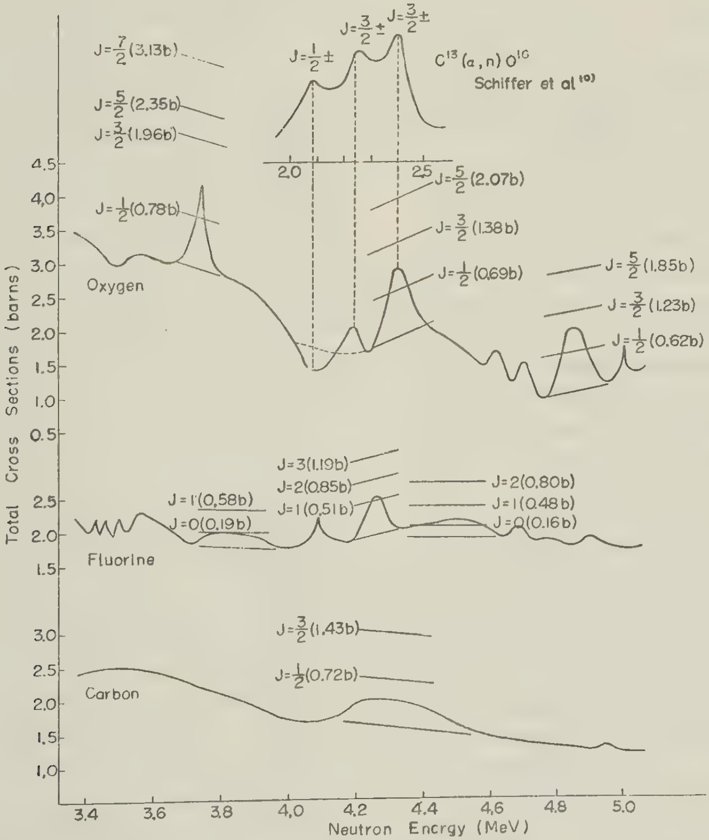

Fig. 4. Spin assignments for several resonaces in the neutron total cross sections of carbon, oxygen and fluorine. The figures in the brackets show the calculated values of $4\pi\lambda\!\!\!^{-2}g_J$.

r: nuclear radius given by $1.4A^{1/3}\times10^{-13}$ cm.

The total cross section of fluorine was obtained from the transmission data of Teflon by subtracting the contribution of carbon. In order to obtain the cross sections of oxygen and thorium, following procedure was adopted. At first, the cross section of thorium was assumed to have gradual change and no sharp resonances and the cross section of oxygen which had been published by Becker et al.[6] and Walton et al.[7] was subtracted from the transmission data of thorium oxide and then the curve of the remainder was smoothed out to give the cross section curve for thorium. The necessity for this procedure was due to the fact that data of different origin had different energy resolution. Next, the cross section of thorium was subtracted from the transmission data of thorium oxide and the

Table I. Levels of the compound nuclei C^{13}, O^{17} and F^{20}. J shows the spin and parity, and $\Gamma_{\mathrm{c.m.}}$ the observed width at half maximum of the resonances in the center-of-mass system.

	Present Results				Other Nuclear Data			
Element	Neutron Energy (MeV) at Resonance	Level (MeV)	J^π	$\Gamma_{\mathrm{c.m.}}$ (keV)	Level (MeV)	J^π	Nuclear Reaction	References
C^{13}*	3.520±0.050	8.193		large	8.33	3/2+	(n, n)	P.R. 109,891
	4.320±0.050	8.931	1/2+	~300	9.0		(n, n)	P.R. 78,508
	4.940±0.010	9.503		~20	9.51		(n, n)	P.R. 102,1384
O^{17}+					7.373	5/2	(α, n)	P.R. 107,1065
					7.560	≥7/2	(α, n)	P.P.S. A69,830
	3.745±0.010	7.669	3/2, 5/2	~20	7.676	≥5/2	(α, n)	P.R. 102,1384
					7.94	1/2±	(α, n)	P.R. 105,1811
	4.200±0.010	8.102			8.07	3/2±	(α, n)	P.R. 102,1348
	4.330±0.010	8.225	3/2	~90	8.20	3/2±	(α, n)	
	4.470(group)	8.351			8.34	1/2	(α, n)	
					8.39	5/2	(α, n)	
	4.625±0.010	8.491			8.46	7/2±	(α, n)	
	4.705±0.010	8.572						
	4.845±0.010	8.704	3/2	~90	8.70	(3/2∓)	(α, n)	
	5.010±0.010	8.859		<20				
					8.89	3/2∓	(α, n)	
F^{20}#	3.433±0.010	9.866			9.8		(n, α)	P.R. 100,69
	3.460±0.010	9.892						
	3.505±0.010	9.934						
	3.560±0.010	9.987						
	3.605±0.010	10.029			10.04		(n, α)	P.R. 100,69
					10.11		(n, α)	〃
	3.820±0.020	10.233	0−, 1	~200	10.19		(n, α)	〃
	4.085±0.010	10.485		~10	10.53		(n, α)	〃
	4.255±0.010	10.652	1, 2	~60				
	4.430±0.050	10.813	0−, 1	~330	10.81		(n, α)	〃
	4.680±0.010	11.050		~30	11.07		(n, α)	P.R. 99,643A
	4.770±0.010	11.136		<25				
	4.890±0.010	11.250		<25	11.22		(n, α)	P.R. 100,69
	(4.935	11.307)						
					11.39		(n, α)	〃

* Binding energy of a neutron was taken as 4.946 MeV.[11]
Binding energy of a neutron was taken as 4.146 MeV.[11]
Binding energy of a neutron was taken as 6.606 MeV.[11]

cross section of oxygen measured with the energy resolution of the present work was thus obtained. The resolution was about two times better than that in the Walton's measurement, and nearly equal to that in the Becker's. These results are shown in Fig. 3.

The statistical error was about 1% in the whole range. The neutron energy spread calculated from each energy is shown in Fig. 3. These values, however, may be increased a little, because of the local variation in the thickness of the nickel foil (may be less than a few keV).

The comparison of the present data with the others[1] shows that, for carbon, there are some apparent systematic disagreements* amounting to more than 10%. But these disagreements can be eliminated by taking account of the difference in the spread of neutron energies. For fluorine, the published data[1] has an energy resolution too poor to be compared with the present result. For oxygen, present data agree with those of Becker et al.[6] and Walton et al.[7] fairly well. For thorium, there has been no published data in the energy region of the present work.

Some informations about the energy levels of the compound nuclei, C^{13}, O^{17} and F^{20}** have been obtained from the position and the peak height of the resonances. The height of a resonance peak is given by $4\pi\lambda\!\!\!^{-2} g_{Jl}$***, which is a function of the spin J of the compound nucleus and the neutron anguler momentum l, as far as the elastic scattering is predominant over other reactions and, moreover, the resonance is isolated and well-resolved. In Fig. 4, the calculated values of $4\pi\lambda\!\!\!^{-2} g_J$ are inserted. The dip of the oxygen cross section at 4.06 MeV may correspond to a s resonance ($l=0$), as seen by the comparison with that of the (α, n) reaction[10] inserted in the same figure. Estimation of the J value was tried for each resolved resonance and the results are shown in Table I with those obtained from other sources[11]. The resonances listed in Table I do not cover all of the resonances in this energy region, even for carbon.

For thorium, a giant resonance was observed at 4.2±0.2 MeV. The peak cross section was 8.5 barns****. Fig. 5 shows not only the present data for thorium but also the results in the lower energy region[1] and at 14 MeV[1].

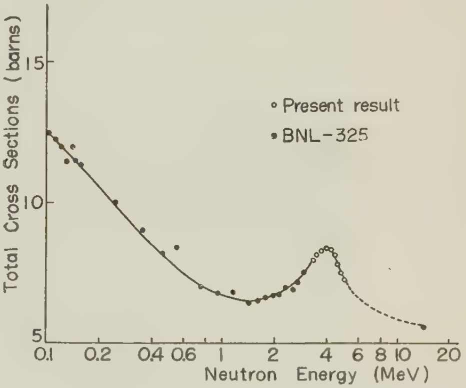

Fig. 5. Neutron total cross section of thorium.

The authors would like to express their appreciation to Dr. T. Momota for his invaluable help and advice. The authors are greatly indebted to Mr. C. Kobayashi, Mr. Y. Sato and members of the fast neutron group for operation and maintenance of the Van de Graaff accelerator, and to Mr. R. Ito for his assistance in the measurements.

References

1) D. J. Hughes and R. B. Schwartz: BNL 325.
2) H. Feshbach, C. E. Porter and V. F. Weisskopf: Phys. Rev. 96 (1954) 448.
3) R. B. Owen: AERE EL/R 2712.
4) G. T. Wright: Proc. Phys. Soc. (London) 69B (1956) 358.
5) R. J. Howerton: UCRL-5226.
6) R. L. Becker and H. H. Barschall: Phys. Rev. 102 (1956) 1384.
7) R. B. Walton, J. D. Clement and F. Borell:

---

* In the energy range of 3.4 to 4.2 MeV, there is a rather large difference between the present data and those of Freier et al.[1]. The spread of the neutron energies in Freier's experiment is ±200 keV, about ten times as large as ours. By taking the average of points in a range of 400 keV, our curve will be shifted towards Freier's.

** Isotopic abundance

$$\begin{cases} \text{carbon: } C^{12}\ (98.90\%),\ C^{13}\ (1.10\%) \\ \text{oxygen: } O^{16}\ (99.7\%),\ O^{17}\ (0.04\%),\ O^{18}\ (0.20\%) \\ \text{fluorine: } F^{19}\ (100\%) \end{cases}$$

*** For a single isolated level[9],

$$\begin{cases} \sigma_{\max}=4\pi\lambda\!\!\!^{-2}[gl_{Jl}\cos^2\delta_l+\sum\limits_l(2l+1)\sin^2\delta_l] \\ \sigma_{\min}=4\pi\lambda\!\!\!^{-2}[-g_{Jl}\sin^2\delta_l+\sum\limits_l(2l+1)\sin^2\delta_l] \\ \text{and } \sigma_{\max}-\sigma_{\min}=4\pi\lambda\!\!\!^{-2}g_{Jl},\ \text{if } \Gamma_n\sim\Gamma_{\text{total}}. \end{cases}$$

**** Howerton[5] estimated the position and the peak cross section of this resonance to be 3.5 MeV and 8.1 barns respectively, from the systematics of the total cross section data.

Bull. Am. Phys. Soc. Ser. II, 1 (1956) 326.
8) R. B. Day and R. L. Henkel: Phys. Rev. 92 (1953) 358.
9) C. T. Hibdon: Phys. Rev. 114 (1959) 179.
10) J. P. Schiffer, A. A. Kraub and J. R. Risser: Phys. Rev. 105 (1957) 1811.
11) F. Ajemberg-Selove and T. Lauritsen: Nuc. Phys. 11 (1959) 1.

JOURNAL OF THE PHYSICAL SOCIETY OF JAPAN, Vol. 15, No. 11, NOVEMBER, 1960

Temperature Dependence of Surface Potential in Silver Chloride Single Crystals

By Hisawo WAKABAYASI

Faculty of Engineering, Chuo University, Tokyo

(Received July 27, 1960)

The temperature dependence of the surface potential of silver chloride single crystals is similar to that of silver bromide single crystals. The knee point moves to the higher temperature as the content of cadmium in the specimen is increased. The formation energy of Frenkel defect and other quantities are obtained. Comparing with the results of ionic conductivity measurements, the intrinsic and the structure-sensitive regions of silver chloride single crystal determined by surface potential were found to correspond to those determined by ionic conductivity, respectively. From the difference between the reciprocals of the knee point temperatures determined by the two methods, the ratio of the mobility of an interstitial silver ion to a silver vacancy may be obtained.

§ 1. Introduction

In the previous paper[1)], we have shown the following things. The surface potential versus temperature curve for a silver bromide single crystal is composed of two straight lines, one of which corresponds to the structure-sensitive region of the crystal and the other to its intrinsic region. They, when extended, intersect each other at a knee point, the temperature of which is determined by the amount of doped divalent cations which are supposed to dissolve into the crystal lattice. Of course, the curve deviates from the straight lines near the knee point. The knee point moves to higher temperature with increasing amount of divalent cations doped into the crystal. We also proposed the interpretation for these facts. The variation of the surface potential with temperature is due to the change in the space charge potential on the side of the silver-coated surface of a silver halide crystal. Near and on its free surface, silver ions and electrons move under the condition that their change cancels the variation of potential due to the space charge on this side.

To verify whether the surface potential in a single crystal of silver chloride varies similarly with temperature as in a silver bromide, the surface potential measurements were carried out the same as before. We also measured the ionic conductivity and each region determined by surface potential measurements was concluded to correspond to that determined by the ionic conductivity measurements, respectively.

§ 2. Apparatus

The apparatus is that used for measurements of surface potential in silver bromide single crystals. The specimens were cut by Ti-saw from silver chloride single crystals which were made from the melt in air by Kyropoulos method. They were lapped and etched in series by sodium thiosulfate, ammonium hydroxide and hydrochloric acid. After etching, they were rinsed in flowing water for about twenty minutes and at last washed by distilled water. They were nearly

1 mm thick. All measurements were carried out after keeping the specimens at measuring temperature for about twenty minutes in the case of surface potential measurements.

To measure the temperature of the surface of specimens, a thermocouple was attached to their surfaces. It indicated too low temperature degrees, which might be attributed to the low thermal conductivity of the specimens and the thermal loss through the thermocouple wires. When the thermocouple was welded on a silver metal block placed on the platinum plate electrode, on which a specimen was placed for measurements, a curve was obtained from which the concentration of Frenkel defect was calculated to be too large, and the results were contradictory to ionic conductivity measurements. According to our interpretation, the surface potential variation with temperature is attributed to the change of potential due to the ionic space charge layer on the side of the silver-coated surface, so that the temperature of this side must been measured. The thermal loss of radiation from the surface of a specimen is hindered by the vibrating reed of the electrometer over it and specimens are thin, so that the temperature of their surfaces may be assumed to be equal to that of their silver-coated surfaces. We might identify the temperature of a specimen with that of the surface of the plate electrode to which a specimen is in contact. It was at last decided to measure the temperature by the thermocouple pressed against the plate electrode.

The concentration of doped impurity—cadmium ions in our case—was chemically analysed. Cadmium in silver chloride was extracted by the method of Church. The amount of cadmium was quantitatively analysed by the colorimetrical method, using Hitachi photoelectric spectrometer. Standard samples were made by solving cadmium acetate into water, and they contained 5γ, 10γ, 30γ, 50γ of cadmium, respectively. The chemical analysis was carried out in Japan Analytical Chemistry Research Institute.

§ 3. Experimental Results

(1) *Surface potential variation with temperature*

The peculiar variation of surface potential in the first run which appeared in the case of silver bromide single crystals, was not observed in silver chloride single crystals[1].

Experimental results are plotted in Fig. 1. It is easily seen that the temperature dependence of surface potential in a silver chloride single crystal is also represented by two straight lines and the knee point temperature moves to higher temperature as more divalent cations are doped into the crystal. It is higher in silver chloride than in silver bromide when doped with the same amount of divalent cations. The values for various other quantities were obtained by the same way as in silver bromide crystals. They are shown in Table I. The symbols are the same as in the previous paper[1].

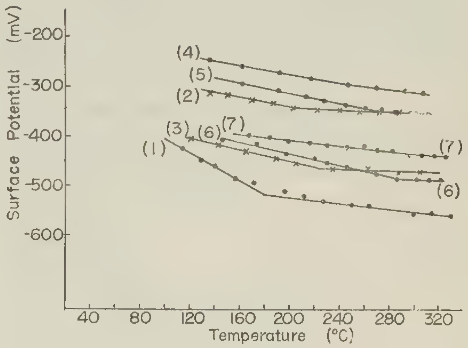

Fig. 1. The variation of the surface potential of silver chloride crystals with temperature. The associated numbers which ascend from 1 to 7 indicate the specimens which are doped with 0, 0.125, 0.25, 0.5, 1.0, 2.5, and 5.0 Mol.-% of cadmium ions, respectively. The knee point moves to higher temperature as more amount of cadmium is doped into crystal.

The values of N_1B_1/N_2B_2 which contains only the internal factors are seen to be in agreement with each other, but the values of A_1A_2/B_2 differ from specimen to specimen and this must be attributed to the different values of A_2. The N_1B_1/N_2B_2 versus α and the A_1A_2/B_2 versus α curves are shown in Fig. 2. N_1B_1/N_2B_2 seems to be independent of α which is due to the surface condition. There is a tendency that A_1A_2/B_2 decreases as α increases. A_1A_2/B_2 is large for specimens in which the straight line in the intrinsic region has a steep slope. α seems to become smaller as the slope of the straight line in the structure-sensitive region increases.

The knee point temperature —T_S— is de-

Table I.

Specimen	Concentration of cadmium ions	$2e\cdot(V_{1S}-V_{2S})$	α	$\frac{N_1B_1}{N_2B_2}$	$\frac{A_1A_2}{B_2}$	T_S
OCIP-3	0.51×10^{-3} Mol.-%	0.90 eV	0.44	1.7×10^7	4820	453°K
OCII′Cd 0.125-1	1.66	0.45	0.72	2.0	25	478
OCI Cd 0.25-1	2.8	0.44	0.73	2.6	61	488
OCI Cd 0.5-2	5.6	0.18	0.89	2.3	54	507
OCI′Cd 1-1	1.66×10^{-2}	0.40	0.75	1.5	26	548
OCI Cd 2.5-2	2.8	0.51	0.68	2.7	57	556
OCII Cd 5-1	6.0	0.21	0.87	3.2	13	578

termined by the following equation.

$$c^2=N_1B_1/N_2B_2 \exp-(E_{F0}/kT_S) \qquad (1)$$

where no factors appear which are related to the surface condition. The logarithm of the concentration of dissolved divalent cations versus the reciprocal of the knee point temperature (in the absolute unit) curve is shown in Fig. 3. From the slope of the line, the formation energy at 0°K of Frenkel defect in a silver chloride single crystal was found to be 1.6 eV, which is nearly equal to 1.69 eV[2]. N_1B_1/N_2B_2 is equal to 2.1×10^7. The temperature dependence of the formation energy of Frenkel defect in silver chloride is given by

$$E_F=1.6-1.4\times10^{-3}T\,.$$

From the experimental curves, the value of $N_1B_1/N_2B_2c^2$ is obtained but the values of N_1B_1/N_2B_2 and c are not determined separately. The amount of cadmium ions which replace silver ions at normal lattice sites would not be equal to the chemically analyzed amount, but we have no knowledge about the difference between two quantities. The above obtained values in Table I are calculated under the assumption that c is either equal to or

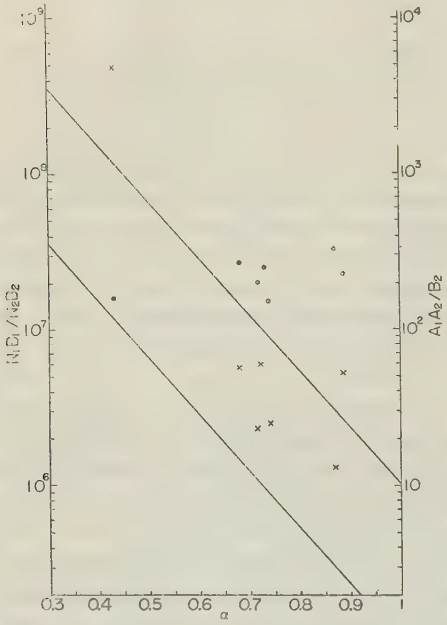

Fig. 2. N_1B_1/N_2B_2 and A_1A_2/B_2 plotted against α, being denoted by solid circles and crosses, respectively. N_1B_1/N_2B_2 is independent of α, but A_1A_2/B_2 decreases with α. The lower and upper straight lines are

$$\log A_1A_2/B_2=(1-\alpha)/2\cdot\log 2\times10^7\,,$$

and

$$\log A_1A_2/B_2=(1-\alpha)/2\cdot\log 2\times10^7+\log 10\,,$$

respectively.

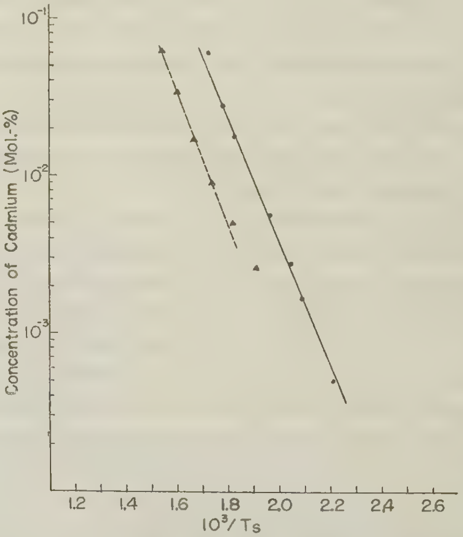

Fig. 3. The logarithm of the concentration of the dissolved cadmium ions plotted against $1/T_S$, where T_S is the knee point temperature for the specimens doped with the above-mentioned amount of cadmium ions. From the slope of the line we have E_{F0}=1.6 ev, and $N_1B_1/N_2B_2=2.1\times10^7$. The broken curve is one obtained by Ebert and Teltow[2].

not far different from the value determined by chemical analysis. The weighed amount of doped cadmium before melting and the chemically analyzed amount in the samples are tabulated in Table II.

It is seen from Table II that the ratio B/A lies between 1 and 1.3, except for the specimen denoted by OCI′Cd 1, and cadmium impurities are more soluble in the crystal than in the melt. It is contrary to the results in the case of potassium chloride. It seems probable that the amount of impurities would increase by recrystalization because the sample denoted by OCII′Cd 1 (R) was recrystalized from the sample denoted by OCII′Cd 1.

Table II.

Specimens	Doped amount of Cd —A—	Chemically analyzed amount of Cd —B—	B/A
	Mol.-%	Mol.-%	
OCIP	0.	$5. \times 10^{-4}$	
OCII′Cd 0.125	1.25×10^{-3}	$1.6_6 \times 10^{-3}$	1.3
OCI Cd 0.25	2.5×10^{-3}	2.8×10^{-3}	1.1
OCI Cd 0.5	5.0×10^{-3}	5.6×10^{-3}	1.1
OCII′Cd 0.5	5.0×10^{-3}	6.5×10^{-3}	1.3
OCI′Cd 1	1.0×10^{-2}	$1.6_6 \times 10^{-2}$	1.7
OCI′Cd 2.5	2.5×10^{-2}	2.8×10^{-2}	1.1
OCII Cd 5	5.0×10^{-2}	6.0×10^{-2}	1.2
OCI′Cd 1 S 1	1.0×10^{-2}	$1.2_7 \times 10^{-2}$	1.3
OCI′Cd 1 S 5	1.0×10^{-2}	$1.2_4 \times 10^{-2}$	1.2_4
OCII′Cd 1	1.0×10^{-2}	1.3×10^{-2}	1.3
OCII′Cd 1 (R)		$1.7_8 \times 10^{-2}$	1.8

(2) *Results of ionic conductivity measurements*

To ascertain whether the intrinsic region can be identified to that determined from the ionic conductivity measurements, the variation of ionic conductivity of each specimen with temperature was measured.

Silver was developed on the two faces to be electrodes of a specimen, which together with silver blocks on its silver-developed faces, was pushed between nickel electrodes fixed in a crucible. The temperature was measured by a copper-constantan thermocouple welded on the nickel electrode. The crucible was set into an electric furnace. The direct current conductivity was measured by a galvanometer in series with the specimen. Their reproducibility was good. The logarithm of specific conductivity is plotted against the reciprocal of absolute temperature of a specimen in Fig. 4.

The curve for each specimen consists of two parts, one of which is steeper than the other, and the steep parts for various specimens overlap each other in higher temperature range. The specific conductivity in the gentle range seems to be nearly proportional to the concentration of the cadmium content, but it is not strictly established. The steep part for undoped specimens lies in the right side of those doped with Cd, and it does not overlap them. Nevertheless, the activation energies of both groups were nearly equal and about 1 eV. The specimens doped with sulpher ions showed the similar behaviour as undoped specimens. The activation energies in each region of the curve are about 1 eV and about 0.4 eV, respectively. It is apparent

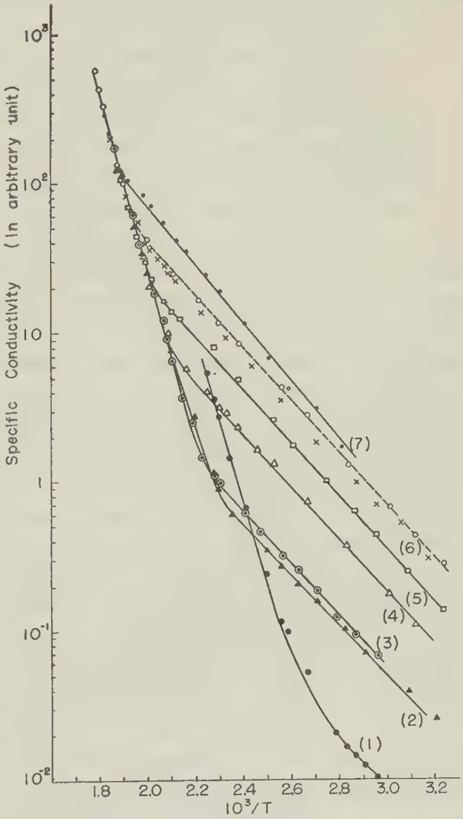

Fig. 4. The specific conductivity of silver chloride crystals doped with cadmium chloride as a function of $10^3/T$. The numbers on the curves refer to 1) the specific conductivity of "pure" AgCl, 2) 0.00125 Mol.-% of $CdCl_2$, 3) 0.0025 Mol.-%, 4) 0.005 Mol.-%, 5) 0.01 Mol.-%, 6) 0.025 Mol.-%, and 7) 0.05 Mol.-%.

that the steep range of the curve corresponds to the intrinsic region and the gentle to the structure-sensitive region. The intrinsic region of specimens seems to begin at a little lower temperature than in the surface potential measurements. The mobility of an interstitial silver ion is larger than a silver vacancy, so that the results are reasonable. The relation between two kinds of knee point temperatures will be discussed later.

§ 4. Discussion

1.6 eV was obtained for the value of the formation energy at 0°K of Frenkel defect in a silver chloride crystals. Considering the errors in the concentration of effective cadmium doped into the crystal and temperature, it may be regarded as agreeing with 1.69 eV obtained by Ebert and Teltow[2]. Taking account of the fluctuation of obtained data from a straight line when $\ln c$ is plotted against $10^3/T$, the value of the formation energy may not be larger than 1.7 eV, and not smaller that 1.5 eV. When the temperature of specimens was elevated above about 330°C, surface potential showed irregular behaviour which was different from specimen to specimen. So, it was difficult to determine accurately the knee point temperature for specimens doped with high concentration of cadmium ions. Below about 140°C, the curves of surface potential plotted against temperature followed various paths, some of which were bent upwards. In such a range of temperature, the association of silver vacancies and cadmium ions may have a role to play and the curve would bend downwards and its slope would become gentler, which is contrary to the present results. It was confirmed that surface potential is higher in lower range of vacuum than in higher range of vacuum, so that gases absorbed on and near the free surface may be contributing to these phenomena, for which we have not a definite interpretation. The logarithm of the concentration of Frenkel defect in silver chloride plotted against $10^3/T$ which was obtained by Ebert and Teltow[2] seems to consist of two lines and the slope of the line below 280°C decreases corresponding to the value of the formation energy, 1.27 eV. According to the present results, the curve seems to retain the same slope down to 170°C.

From the Eq. (1), it is apparent that the concentration of Frenkel defect at knee point temperature is equal to the concentration of impurity cations which replace silver ions at lattice sites. The concentration of Frenkel defect so obtained is several times higher than that obtained by ionic conductivity measurements[2], as was the case in silver bromide crystals. A part of the discrepancy might have been caused by errors in the temperature measurement on the surface of the crystal in our case.

A_1A_2/B_2 may be equal to the square root of $(N_1B_1/N_2B_2)^{1-\alpha}$ under the assumption that the surface potential in the intrinsic region is independent of temperature. In reality, it decreases linearly with temperature, and from Fig. 2, the experimental values of A_1A_2/B_2 fall within the strip bounded by the two curves, $A_1A_2/B_2=(N_1B_1/N_2B_2)^{(1-\alpha)/2}$ and $A_1B_1/B_2=10\times(N_1B_1/N_2B_2)^{(1-\alpha)/2}$. In this temperature range, A_1 and B_2 may be independent of α, and A_1 is nearly equal to unity. We may assume that as temperature is elevated, the work required for taking away an electron on the surface to infinity will decrease and A_2 must be smaller than unity and A_2 is dependent on α. From Fig. 2, the maximum variation might be larger than 10^3 to 1. It follows that B_2 is smaller than unity and B_2

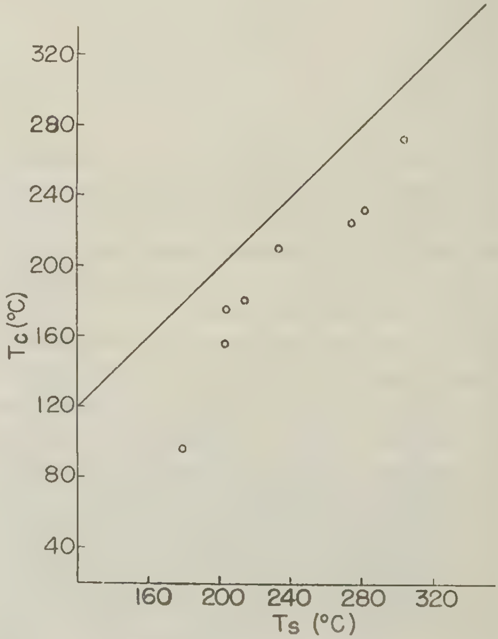

Fig. 5. T_C plotted against T_S. All points lie below the solid line $T_C=T_S$.

is not smaller than 10^{-5} because A_1 may be nearly equal to unity and B_2 may be between $(2\times10^7)^{-1/2}$ and $(2\times10^9)^{-1/2}$ when α is 0. Then B_1 must be larger than one. The energy level for an interstitial silver ion would drop and that for a silver ion at a lattice site would elevate as temperature rises.

By the variation of the ionic conductivity with temperature the intrinsic and the structure-sensitive regions of silver halide crystals can be determined as well as by the variation of surface potential with temperature. The knee point temperature of the surface potential curve will be higher than that of the logarithmic curve of ionic conductivity versus the reciprocal temperature (absolute unit), since an interstitial silver ion has larger mobility than a silver vacancy and the mobility plays the important role only in the latter curve. This point will be ascertained by Fig. 5, in which T_C is plotted against T_S. T_S is always higher than T_C. Suffixes C and S denote measurements of conductivity and surface potential, respectively.

It is apparent under a qualitative view that the intrinsic region determined by surface potential corresponds to that determined by ionic conductivity and the same for the structure-sensitive region.

We will now examine whether this can be established quantitatively. From the Eq. (1), we have:

$$(E_{F0}/k)\times x_S=\ln N_1B_1/N_2B_2-\ln c^2$$

where x_S stands for the reciprocal of T_S, which is the knee point temperature determined from the surface potential measurement. The specific conductivity for silver chloride —σ— is determined by the following equation[3]:

$$\sigma=\sigma_0\left\{\sqrt{\left(\frac{c}{2y_0}\right)^2+1}-\frac{c}{2y_0}\frac{\varphi-1}{\varphi+1}\right\}$$

where σ_0 stands for the intrinsic conductivity which would be displayed by an ideally pure crystal, and we denote the concentration of Frenkel defect in such a crystal by y_0 and the ratio of the mobility of an interstitial silver ion μ_1 to that of a silver vacancy μ_2 by φ.

In the intrinsic region, where $y_0\gg c$

$$\sigma=\sigma_0=Ney_0(\varphi+1)\mu_2$$

where N is the number of silver ion lattice sites per unit volume and $-e$ is electronic charge.

In the structure-sensitive region, where $c\gg y_0$

$$\sigma=\sigma_0\cdot\frac{c}{y_0(\varphi+1)}=cNe\mu_2$$

μ_1, μ_2, and y_0 contain reciprocal temperature only in the exponential function. Then, σ versus $1/T$ curve will be a straight line in each region. The knee point will be determined by extended lines, where extrapolated values of conductivity are equal, and we have

$$N_1B_1/N_2B_2\exp-(E_{F0}/kT_C)\times(\varphi+1)^2=c^2\,. \quad (2)$$

Then, we get

$$x_C=x_S+3.99\times10^{-4}/E_{F0}\log(\varphi+1)$$

where E_{F0} is the formation energy at 0°K in electron volt unit. From this relation we can obtain the mobility ratio φ, which is plotted against $10^3/T$ in Fig. 6.

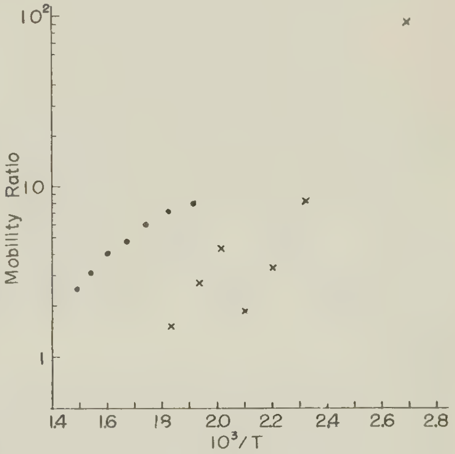

Fig. 6. The logarithm of the ratio of the mobility of an interstitial silver ion to that of a silver vacancy as a function of $10^3/T$. Ebert and Teltow's values[2] are denoted by solid circles and our results are denoted by crosses. Except for "pure" samples, the values of φ are in a resonable range with fluctuation and show a tendency to increase with decreasing temperature.

The values of φ have a tendency that they seem to increase as temperature decreases. The calculated values are subject to great error since they are determined as a small difference between the reciprocal temperatures of two knee points, both of which are determined with some uncertainty on the experimental curves.

With such uncertainty in mind, values of φ may be in a resonable range.

These results showed merely qualitative correctness of our interpretation about surface potential variation with temperature. However, a remarkable difference does appear between φ's for samples doped with a little amount of cadmium ions and undoped samples. The knee point of "pure" samples is at about 180°C in the case of surface potential but is below 100°C in the case of ionic conductivity. The knee point in ionic conductivity of a specimen doped with 1.25 Mol.-% of cadmium is at about 150°C and the value of φ for it is a resonable one. The knee point of an undoped specimen is at about 80°C and φ seems to be large though we have no accurate knowledge of φ at such a low temperature. This difference seems to be attributed to the facts that in higher temperature range the curves for "pure" specimens do not overlap those for doped ones. If the former is displaced to overlap the latter, φ would be reduced from 90 to 20.

In the case of AgBr, the same results were obtained, that is, the knee point temperature obtained from surface potential is higher than that from ionic conductivity, and the ratio of mobilities is smaller than that by Teltow. Also the discontinuity of the knee point temperature between "pure" and a little-doped samples appeared in ionic conductivity measurements.

With increaseing amount of cadmium doped into the crystal, the ionic conductivity decreases and attains to the minimum, and then increases[2]. So, doped cadmium ions make the logarithmic curve of the ionic conductivity versus the reciprocal temperature complex near the knee point. Our experimental temperature range might be in such a peculiar range, and if the range is extended to higher temperature, the discrepancy would disappear and all curves would overlap one another. In suce temperature range, the polarization makes measurement difficult and measurements in such a range did not been carried out.

The size of specimens are about 3×2×2 (mm), and undesirable stress field may remain to change μ_1 and μ_2. It is desirable to use large and well-annealed samples. Stress field may have contributions to both measurements which are not controlled, and make φ fluctuate. The dislocations in a specimen doped with Cd may trap interstitial silver ions and make the conductivity decrease.

The surface potential measurements were carried out in vacuum, and the ionic conductivity measurements in air. To compare the former's knee point temperature with that of the latter, it is necessary to carry out both measurements in the same atmosphere. The specimens for surface potential were thinner than 1 mm, and the electrodes could not been attached to them. We used different specimens for both measurements which were neighbouring parts of the sample.

The above-mentioned three ways involve contradictory characters, but through these ways, more accurate values of φ may be obtained.

Acknowledgements

The author acknowledges with pleasure his debt to Dr. S. Sonoike for his guidance. The author is also grateful to Prof. Dr. H. Takahasi (the University of Tokyo) for helpful suggestions and criticium to manuscript. He wishes to acknowledge the courtesy of Dr. T. Asari and Mr. Y. Watanabe in Japan Analytical Chemistry Research Institute for quantitative analysis of a little amount of cadmium in the crystals. Thanks are extended to the assistance of Mr. H. Motoi throughout the course of this work. The present investigation has been partly supported by this special Research Grant from Chuo University.

References

1) S. Sonoike and H. Wakabayasi: J. Phys. Soc. Japan **14** (1959) 1664.
2) I. Ebert and J. Teltow: Ann. Phys. **15** (1955) 268.
3) A. B. Lidiard: Handbuch der Physik **20** (Springer, 1957) 286.

JOURNAL OF THE PHYSICAL SOCIETY OF JAPAN, Vol. 15, No. 11, NOVEMBER, 1960

On the Magnetic Properties of Cr_2As and Cu_2Sb

By Motoyoshi YUZURI*

The Research Institute for Iron, Steel and Other Matals,
Tohoku University, Sendai, Japan

(Received August 1, 1960)

The thermomagnetic properties of the compound Cr_2As and Cu_2Sb were investigated together with the phase diagram of Cr–As system. From the results of thermal and thermomagnetic measurements for Cr_2As and Cu_2Sb it was found that they show antiferromagnetic behavior with the Néel point at 393°K and at 373°K respectively. Their reciprocal susceptibilities obey the Curie-Weiss law in high temperature range, but a considerable deviation therefrom is seen just above the Néel point. From the Curie constant obtained by the present experiment, the effective magneton number μ_{eff} of the magetic carrier was calculated to be 3.6 and 2.6 for these compounds, Cr_2As and Cu_2Sb, respectively. The total heat absorptions due to the vanishing of antiferromagnetic order in spin arrangement were 50 Cal/mol and 20 Cal/mol. A discussion is given on the origin of the above-mentioned magnetic properties.

§1. Introduction

Various types of spin ordering are expected to be formed[1] for the magnetic compounds with the crystal structure of Cu_2Sb type. Previously the present author reported[1] the antiferromagnetic behavior of the compound Mn_2As with this structure. Now he undertook to study the magnetism of the compounds Cr_2As and Cu_2Sb with the same crystal structure. Since the range of existence of the compound Cr_2As in the phase diagram of Cr–As binary system was not yet clear, X-ray, thermal and magnetic analyses were treid in the composition range near Cr_2As, and, based on the results obtained, the phase diagram near this stoichiometric composition was also established. In the following are given the results of the measurement and the discussion on the spin ordering in Cr_2As and Cu_2Sb.

§2. Preparation of the Specimen

The specimens used were prepared by the usual ceramic method. Chromium (99.3%) and arsenic (99.9%) powder or copper (99.9%) and antimony (99.9%) powder were mixed in the desired ratio, respectively, sealed in evacuated silica tubes and then heated in an electric furnace. To avoid explosion of the tubes during heating, the mixtures were heated up slowly, in 72 hours from room temperature to 900°C in the case of arsenide, and in 96 hours from room temperature to 500°C in the case of antimonide, and they were kept at the terminal temperatures for 48 hours. After the reaction was completed they were cooled down slowly to room temperature. In order to obtain homogeneous specimens, all the reaction products were crushed, mixed well, again heated, to 900°C in the case of Cr_2As and to 500°C in the case of Cu_2Sb, kept at these temperatures for 48 hours and cooled down to room temperature in 72 hours. Such prepared specimens, however, did not show any difference from the original ones in their magnetic properties. Every portion of the specimen thus obtained showed the same thermomagnetic behavior.

§3. Phase-diagramatic Study of Cr–As system

First, the change in crystal structure due to the composition of chromium in Cr–As binary system was investigated by means of X-ray powder method. The diffraction lines in the specimens with the composition CrAs were found to be indexed as those due to the orthorhombic structure with parameters $a=3.48$Å, $b=6.21$Å, $c=5.73$Å; this result almost coincides with that by Nowotny and Arstad[2]. The diffraction lines due to the orthorhombic structure became weak and new lines began appear with an increase of Cr content from $X=1$ in the formula Cr_XAs. The diffraction angles* in the case of $X=1.5$ are shown in Table I. The intensity of the lines became maximum near $X=1.5$ and they disappeared near $X=1.9$. They are indexed as those due to the tetragonal system, in which $a=7.05$Å, $c=9.05$Å, $c/a=1.18$.

---

* Now at the Faculty of Science, Kyoto University.

Table I. X-ray analysis of Cr_3As_2.

Target: Cu

Intensity	Scattering angle	Index	$\sin^2\theta$	
I	θ	$h\ k\ l$	Observation	Calculation
w	14°45′	0 0 3	0.0648	0.0651
w	15°15′	2 0 2	0.0692	0.0689
vw	16°00′	1 0 3	0.0760	0.0751
vs	16°28′	2 2 0	0.0804	0.0800
vs	16°54′	1 1 3	0.0845	0.0851
w	18°12′	3 0 1	0.0975	0.0972
vw	19°57′	0 0 4	0.1164	0.1157
s	20°30′	1 0 4	0.1227	0.1257
s	21°38′	1 1 4	0.1359	0.1357
s	21°48′	2 3 1	0.1379	0.1372
m	22°38′	2 2 3	0.1479	0.1451
w	23°15′	2 0 4	0.1558	0.1557
vs	24°21′	1 4 0	0.1700	0.1698
m	25°56′	1 0 5	0.1912	0.1908
m	28°17′	2 0 5	0.2245	0.2208
vw	35°39′	2 2 6	0.3397	0.3403
w	44°06′	1 1 8	0.4828	0.4827

On the other hand, the diffraction lines of the compound with the composition Cr_2As could be indexed as those of the crystal structure of Cu_2Sb type and its parameters a and c were 3.58Å and 6.25Å respectively (axial ratio $c/a=1.76$); the results coincide again with those by Nowotny and Arstad. The diffraction lines of Cu_2Sb structure were found for specimens in which $X=1.6$. In intermediate compositions between Cr_2As and Cr, the intensity of diffraction lines due to Cu_2Sb structure became weak with an increase of X beyond $X=2.0$ and new diffraction lines appeared, which could be indexed as those of a tetragonal structure with $a=2.90$Å and $c=6.25$Å. These lines became strong at about $X=5$, but the precise value of X for the compound with this structure was not determined in the present study. In Table II is given the result of analysis of this structure. All the lattice parameters or diffraction angles mentioned above remain unchanged with the change in composition.

Table II. Result of X-ray analysis of a compound appearing near $X=5$ at room temperature.

Target: Cu

Intensity	Scattering angle	Index	$\sin^2\theta$	
I	θ	$h\ k\ l$	Observation	Calculation
m	19°29′	1 0 1	0.1115	0.1124
s	22°00′	1 1 0	0.1405	0.1412
s	24°12′	0 0 2	0.1680	0.1680
s	25°27′	1 1 1	0.1846	0.1828
s	34°19′	2 0 1	0.3180	0.3236
m	38°45′	1 2 1	0.3940	0.3940
w	40°57′	1 0 3	0.4460	0.4484
w	41°57′	2 0 2	0.4499	0.4496

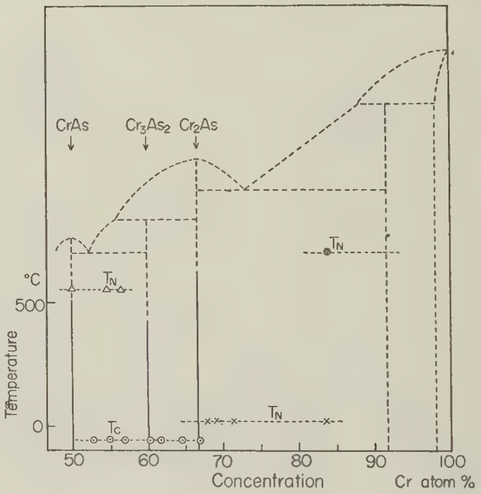

Fig. 1. Phase diagram of Cr–As system.

On the basis of these crystallographic studies, several phases are considered to be existing, that is, orthorhombic phase in a narrow range of composition including $X=1.0$, a phase with Cu_2Sb structure near $X=2.0$, a compound with tetragonal structure near $X=1.5$ and another compound with tetragonal struuture near $X=5.0$. It is conceivable that two phase regions exist between CrAs and Cr_3As_2, Cr_3As_2 and Cr_2As, Cr_2As and Cr_5As, and Cr_5As and Cr. Based on the results of X-ray analysis and the magnetic analysis which will be given in the next section, a tentative phase-diagram of Cr–As system was constructed, as shown in Fig. 1.

---

* Cr-As system was once investigated by Nowotny and Arstad, but they could not ascertain the presence of Cr_3As_2 phase by X-ray analysis, so that their results do not agree with the present ones in Cr_3As_2 phase.

The diffraction lines of the compound Cu_2Sb could be indexed as those of the crystal structure of Cu_2Sb type, its parameters a and c being 3.99Å and 6.07Å respectively (axial ratio $c/a=1.54$). These results coincide also with those by Elander, Hagg and Westgren[3].

§ 4. Thermomagnetic Measurement

The measurement of the magnetic susceptibility was made by means of an automatically recording magnetic balance[4]. First the thermomagnetic curve for CrAs was taken at a field strength of 3500 Oe in the temperature range from the boiling point of liquid nitrogen to 1000°C. The result is shown by a curve in Fig. 2. A peak of susceptibility was observed at 550°C. A similar peak was also observed in $Cr_{1.3}As$.

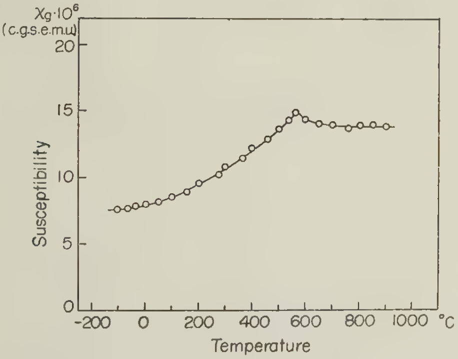

Fig. 2. Thermomagnetic curve of CrAs.

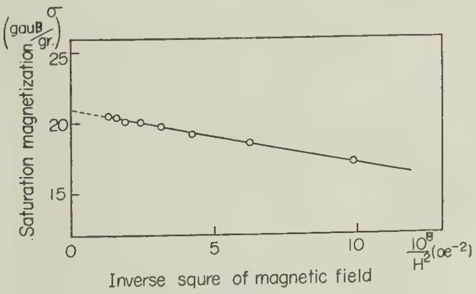

Fig. 3. Specific magnetization of Cr_3As_2 versus inverse square of the magnetic field.

It was also found that the compound Cr_3As_2 shows ferromagnetism. The magnetization curve of the compound Cr_3As_2 was measured to a field strength of 10000 Oe, as shown in Fig. 3. The magnetization varies linearly with inverse of the magnetic field. And the saturation magnetization σ_s was obtained by by extraporation. Now the $\sigma_s - T^{3/2}$ curve (Fig. 4(A)) indicates that the saturation magnetization varies linearly with T below 150°K. The saturation value at absolute zero of temperature obtained by extrapolating the linear part of the $\sigma_s - T^{3/2}$ curve reaches 21.0 gauss/gr, or 0.38 μ_B per Cr atom. Moreover, the molar magnetization obtained by extrapolating to 0°K at a magnetic field of 8000 Oe changes with Cr concentration, as given in Fig. 5, showing that the magnetization increases linearly from the composition of 50% Cr, reaches its maximum at Cr_3As_2, and then decreases again linearly until it vanishes at 67.8% Cr (near Cr_2As). Such an aspect confirm the existance of two phase regions between CrAs and Cr_3As_2 and

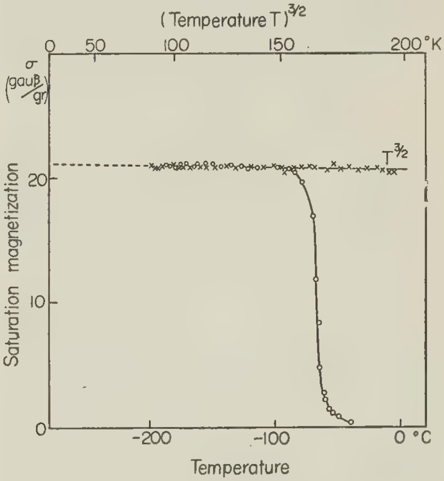

Fig. 4. (A) Thermomagnetic curve (ferromagnetic range) of Cr_3As_2. Where the scale of vertical axis is common for two curves.

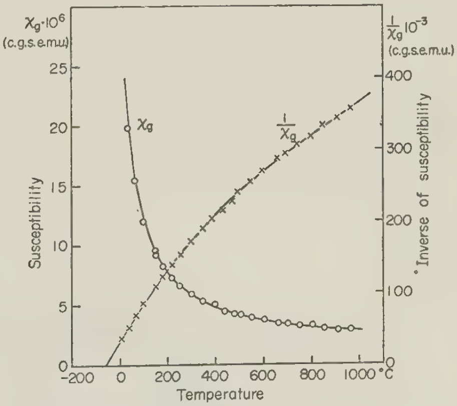

Fig. 4. (B) Thermomagnetic curve (paramagnetic range) of Cr_3As_2.

between Cr_3As_2 and Cr_2As, as shown in Fig. 1.

On the other hand, the thermomagnetic curve of this compound under a magnetizing field of 8000 Oe is shown by the curve in Fig. 4(A), showing that the Curie point lines at −60°C. The susceptibility of the compound above the Curie point was found to change like as a ferrimagnetic compound (Fig. 4(B)). From the Curie constant obtained from the slope of the $1/\chi_g - T$ curve at high temperature, the effective magneton number per Cr ion was calculated to be 2.0. If the Landé factor is assumed to be 2, the mean spin quantum number S will be 1.2/2. According to Haraldsen[5], the saturation value and effective magneton number of Cr_3As_2 were 0.68 μ_B and 2.3 per Cr atom, which are somewht different from the present result.

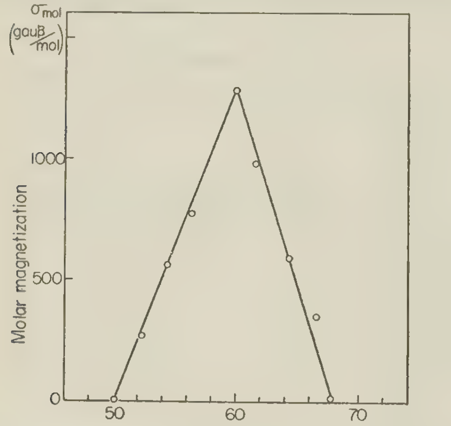

Fig. 5. Saturation magnetization versus Cr concentration.

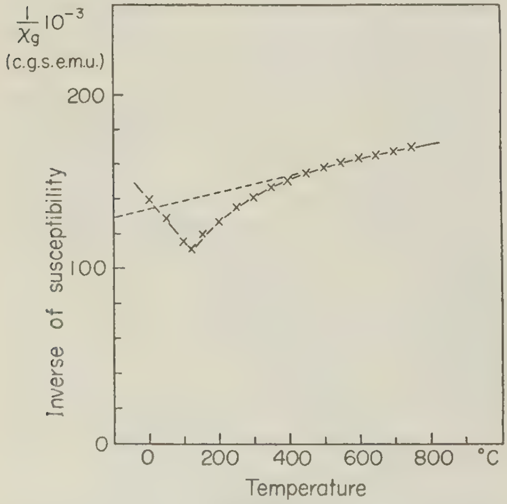

Fig. 6. Reciprocal susceptibility versus temperature of $Cr_{2.1}As$.

The result of thermomagnetic measurement for $Cr_{2.1}As$* at a magnetic field of about 3500 Oe in the temperature range from the boiling point of liquid nitrogen to 1000°C is given in Fig. 6. The peak of susceptibility at 120°C seen from the same figure is attributable to the compound with Cu_2Sb structure (compound Cr_2As). As shown in Fig. 6, the reciprocal susceptibility of $Cr_{2.1}As$ decreases linearly with the lowering of temperature in the high temperature range, but it falls more rapidly just above the point of susceptibility maximum, as in the case of Mn_2As.

The thermomagnetic curve for Cr_5As in the magnetic field of about 3500 Oe in the temperature range from the boiling point of liquid nitrogen to 1000°C is shown in Fig. 7. The magnetic anomaly at 120°C is due to the contamination of the compound Cr_2As, and the magnetic anomaly at 700°C is attributable

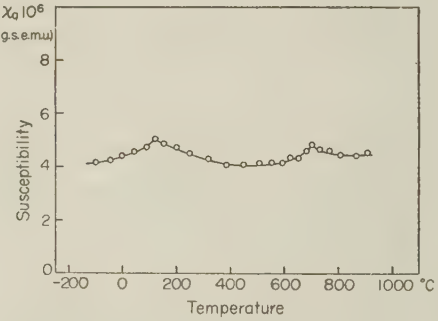

Fig. 7. Thermomagnetic curve of Cr_5As.

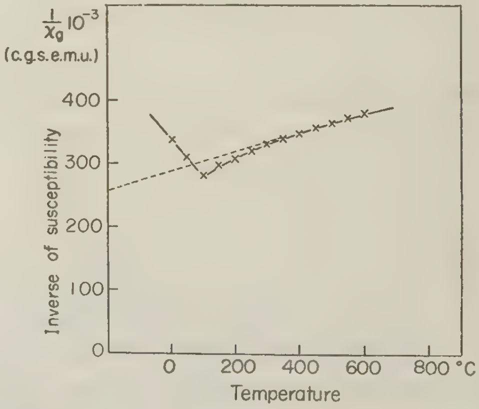

Fig. 8. Reciprocal susceptibility versus temperature of Cu_2Sb.

---

* The composition given here is based not on the chemical analysis but on the charged content, so that we can not attach too much significance to non-stoichiometry of the composition.

to the phase richer in chromium. All these results are considered to confirm the phase diagram mentioned in the previous section.

Next, the thermomagnetic curve for Cu_2Sb under the magnetic field of about 3500 Oe in the temperature range from the boiling point of liquid nitrogen to 1000°C is Fig. 8. It shows a peak of susceptibility at 100°C. Just above the temperature of maximum suceptibility the inverse susceptibility falls rapidly with the lowering of the temperature just as in the case of Cr_2As and Mn_2As.

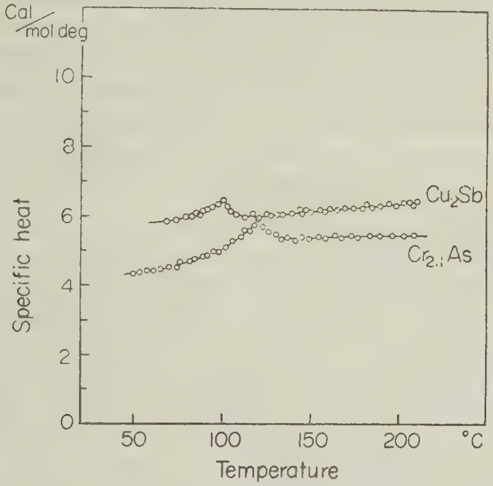

Fig. 9. Specific heats of $Cr_{2.1}As$ and Cu_2Sb versus temperature.

The measurement of the specific heat near the maximum point of susceptibility of the compound $Cr_{2.1}As$ and Cu_2Sb was made by means of an adiabatic caloriemeter, the detailed discription of which is given elsewhere[6]. The results of measurement are shown in Fig. 9. The anomalous peak of the specific heat at about 120°C for $Cr_{2.1}As$ and at about 100°C for Cu_2Sb are considered to correspond to the susceptibility maximum of these compounds respectively, and total heat absorptions at these points are estimated to be 50 and 20 Cal/mol of Cr and Cu, respectively.

§ 5. Discussion on the Antiferromagnetic Behavior of Compounds Cr_2As and Cu_2Sb

Now a suggestion is made here that the peak in susceptibility at 120°C in the case of $Cr_{2.1}As$ and at 100°C in the case of Cu_2Sb can reasonably be attributed to the antiferro-paramagnetic transition in the spin ordering in this type of crystal lattice. The temperature dependence of susceptibility above the maximum point in these substances shown in Fig. 6 and 8 may be expressed as follows:

$$\frac{1}{\chi_M}=\frac{T+2067}{1.61}-\frac{13.6\times10^3}{T-360} \quad \text{for the case of } Cr_2As \qquad (1)$$

and

$$\frac{1}{\chi_M}=\frac{T+1694}{0.85}-\frac{14.5\times10^3}{T-290} \quad \text{for the case of } Cu_2Sb \qquad (2)$$

Now the lattice for cations in Cu_2Sb type crystal is divisible into two sublattices, and if different kinds of cations (s.g. Mn^0 and Mn^{3+} occupy both of these sublattices, respectively, then antiferromagnetic or ferrimagnetic ordering can be expected to occur due to the proper exchange interaction between the ions. In such a case the suceptibility above the Néel or the Curie point is shown[1] to be given by

$$\frac{1}{\chi}=\frac{T+T_a}{\frac{1}{2}(C_A+C_A)}-\frac{\tau}{T-\theta} \qquad (3)$$

where

$$T_a=-\frac{n}{8(C_A+C_B)}(C_B+2C_A+4C_AC_B)$$

$$\theta=\frac{n}{8(C_A+C_B)}(1+2\gamma-4\beta), \quad \beta=\beta_1+\beta_2$$

$$\tau=\frac{n^2\,C_AC_B}{32(C_A+C_B)}\{C_B(1-2\beta)+2C_A(\beta-\gamma)\},$$

and

$$T_A=\frac{1}{16}[n(2C_A-C_B)+|n|\{(C_B+2C_A)^2+16C_AC_B(\beta_1-\beta_2)\}^{\frac{1}{2}}].$$

In these expression T_a is the asymptotic Curie point, C_A and C_B the molar Curie constants of both kinds of cations, respectively, and $n\gamma$, $n\beta_1$, $n\beta_2$ and n represent the intra- as well as inter-layer molecular field coefficients as is defined elsewhere[1]. By comparing expression (3) with the empirical expression (1) and (2), possible values of the molecular field coefficients were determined. If quintet and triplet states for both kinds of Cr ions (2.42 and 0.8 for C_A and C_B) and triplent and doublet states for Cu (1.24 and 0.46 for C_A and C_B) are assumed, then the molecular field coefficient can be determined as shown in Table III.

For the sake of comparison the ferrimagnetic Curie temperature corresponding to the same

Table III. Coefficients of molecular field.

Cr_2As		Cu_2Sb	
$C_A=2.42,\quad C_B=0.80$		$C_A=1.24,\quad C_B=0.46$	
$S_A=4/2,\ g_A=1.80$ (or $S_A=3.5/2,\ g_A=2$)		$S_A=2/2,\ g_A=2.22$ (or $S_A=2.3/2,\ g_A=2$)	
$S_B=2/2,\ g_B=1.79$ (or $S_B=1.7/2,\ g_B=2$)		$S_B=1/2,\ g_B=2.21$ (or $S_B=1.2/2,\ g_B=2$)	
$n=-1.15\times10^3$	$n=-3.71\times10^3$	$n=-2.61\times10^3$	$n=-6.05\times10^3$
$\gamma=2.29$	$\gamma=0.600$	$\gamma=1.56$	$\gamma=0.57$
$\beta_1+\beta_2=2.43$	$\beta_1+\beta_2=0.87$	$\beta_1+\beta_2=1.69$	$\beta_1+\beta_2=0.82$
$\|\beta_1-\beta_2\|=1.86$	$\|\beta_1-\beta_2\|=0.24$	$\|\beta_1-\beta_2\|=1.23$	$\|\beta_1-\beta_2\|=0.17$

values of coefficients was calculated in both cases and it can be shown that the Néel temperature corresponding to these values of coefficients is higher than the ferrimagnetic Curie point, and the antiferromagnetic ordering is, in general, stable, as compared with the case of ferrimagnetic ordering. But the result of calculation for the corresponding internal energy of ferrimagnetic structure, based on the molecular field constants shown above, is lower than that of antiferromagnetic ordering, which predicts a transition from antiferro- to ferrimagnetic state at low temperatures. In the present experiment such a transition was not found in either compound at least above the liquid nitrogen temperature, so that it may be interesting to extend the measuremet to lower temperature. It may be noted, however, that a slight change of molecular field coefficient for the case $C_A>C_B$ in the above Table can make the free energy of the antiferromagnetic state lower than that of the ferrimagnetic state in the whole temperature range, eliminating the possibility of the transition suggested above.

Based on the present theory, the anomalous heat absorption of Cr_2As and Cu_2Sb due to antiferro-para transition is calculated to be 670 and 530 Cal/mol, respectively. The experimental values seem to be smaller than those due to the order-disorder change of spin arrangement. Although, since the estimation of the specific heat due to the thermal vibration of atoms is not rigorous, it might be possible that the exact value of the amount of heat absorption at the Néel point lies far beyond the present value, this is a theoretical problem to be studied in future.

Acknowledgement

The author wishes to express his cordial thanks to Professor T. Hirone for his kind guidance throughout the present work. His thanks are also due to Drs. H. Watanabe, S. Maeda, K. Adachi and M. Yamada, staff members at the Research Institute for Iron, Steel and Other Metals of Tohoku University and Dr S. Nagasaki at Rigaku Denki K. K., who gave eager discussions in the course of the present investigation.

References

1) To be published shortly in this journal.
2) H. Nowotny and O. Arstad: Z. Phys. Chem. **38** (1939) 461.
3) M. Elunder, G. Hagg and A. Westgren: Arkiv Kem. Mineral. Geolg. (B) **12** (1935) No. 1.
4) T. Hirone, S. Maeda and N. Tsuya: Rev. Sci. Instr. **25** (1954) 516.
5) H. Haraldsen and E. N. Blindesen: Z. Elektrochem. **45** (1939) 686.
6) S. Nagasaki and T. Tokagi: J. Appl. Pnys. Japan (in Japanese) **17** (1948) 104.

JOURNAL OF THE PHYSICAL SOCIETY OF JAPAN, Vol. 15, No. 11, NOVEMBER, 1960

X-ray Studies on the Ferrite-Haematite Solid Solutions

By Chisato OKAZAKI

Research Department, Wireless Division, Matsushita Elect.
Ind. Co. Ltd., Kadoma, Osaka

(Received April 27, 1960)

The variation of the lattice dimension of the solid solution system, $NiFe_2O_4$-Fe_2O_3, and the precipitation process of α-Fe_2O_3 therefrom were investigated by X-ray analysis. These quenched solid solutions possess unstable inhomogeneities originating in the localized oxidization. When annealed at certain temperatures, the solid solution tends to become stabilized by the precipitation of α-Fe_2O_3. The activation energy for the precipitation was found to be ca 1.03 ev.

The solubility of Fe_2O_3 in $NiFe_2O_4$ was determined at various temperatures, and the heat of dissolution was found to be 1.3 ev.

§1. Introduction

It is well known that ferrites can dissolve a considerable amount of ferric oxide at high temperatures.[1), 2)] After a rapid cooling, these soild solutions appear to be homogeneous even at room temperature. However, their electrical conductivity[3)], magnetic field annealing effect[4)] and disaccomodation phenomenon[5)], etc., are dependent not only upon their compositions but also upon the process of preceding heat treatment. These properties should be interpreted in terms of the dissolved ferric oxide in these solid solutions.

Among numerous ferrites, nickel ferrite is known to be the most stable with respect to its atomic arrangement and the valency state, therefore it is a suitable material for the study of examining the behavior of the dissolved ferric oxide. In this paper, a study on the stability of the nickel ferrite-ferric oxide system against the precipitation of ferric oxide will be given.

Some qualitative reports concerning such a precipitation have been published by other investigators[6), 7)], but, no quantitative consideration has been reported.

§2. Preparation of the nickel ferrite-ferric oxide solid solutions

Different proportions of nickel oxide and ferric oxide, both of the c.p. grade were mixed in a steel ball mill. These mixtures were fired at 1300°C in air or in an oxygen atmosphere for four hours, and cooled rapidly (about 100°C/min.) to room temperature.

The products fired in air and quenched were found to be a solid solution having the spinel-type structure if the mole ratio Fe_2O_3/NiO, which we shall designate by x hereafter, was below 2.2. On the other hand, the products fired in an oxygen atmosphere and the quenched are solid soultions if x is below 1.8. Both of these two kinds of preparations contain large amounts of ferrous iron Fe^{2+}. The amounts of Fe^{2+} in these solid solutions were determined by the chemical analysis proposed by Gorter and others[8)], and are shown in Table I.

Table I. Contents of Fe^{2+} ions in $NiFe_2O_4$-Fe_2O_3 solid solutions

Original mole ratios of Fe_2O_3 to NiO x	Atomic ratios of Fe^{2+} to the total Fe ions %		Atomic ratios of Fe^{2+} to the total excess Fe ions %	
	fired in air, quenched	fired in oxygen, quenched	fired in air, quenched	fired in oxygen, quenched
1.5	5.0	4.8	15.8	14.4
1.75	6.5	6.5	15.2	15.2
2.00	7.6	7.4	15.2	14.8

§3 The lattice constants of the solid solutions, $NiFe_2O_4$-Fe_2O_3, and the role of excess iron ions

In order to find in what manner the excess amounts of ferric oxide are dissolved in the ferrite, the variation of lattice constant with the excess amount of ferric oxide was measured.

Using an automatic recording X-ray diffractometer, X-ray powder patterns of these solid solutions were taken with filtered Co-Kα radiation. Lattice constants were obtained by the extrapolation method against $1/2\,(\cos^2\theta/\sin\theta+\cos^2\theta/\theta)$ using a number of diffraction peaks at high angles, which were calibrated with pure Si (99.99%).

The results are shown in Fig. 1, where the unit cell dimension a_0 is plotted as a function of the excess amount of ferric oxide; curve (1) is for the specimens fired and quenched in the oxygen atmosphere, and curve (2) is for the ones in the air.

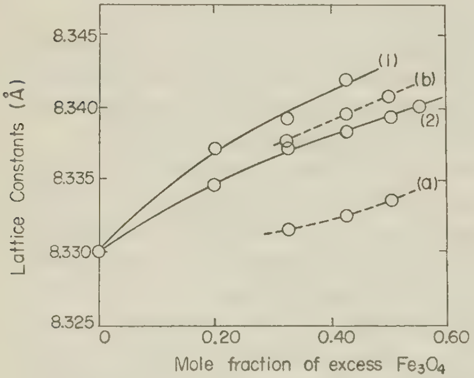

Fig. 1. Lattice constants of quenched $NiFe_2O_4$-Fe_2O_3 soild solutions.
(1) Specimens fired at 1300° C in the oxygen atmosphere
(2) Specimens fired at 1300° C in air
(a) Calculated values using "Vegard's law" -assumtion (a)-
(b) Calculated values using "Vegard's law" -assumption (b)-

In order to accomodate the excess amount of Fe^{3+}, the following there processes may take place:

(1) Soild solution of magnetite phase (reduction of Fe^{3+} to Fe^{2+})

(2) Soild solution of γ-haematite phase

(3) Precipitation of α-Fe_2O_3.

Since the ionic radius of Fe^{2+} ion is larger than those of Ni^{2+} and Fe^{3+} ions, the solid solution of magnetite phase will be followed by an expansion of the lattice ($a_{\text{magnetite}}-a_{\text{nickel-ferrite}}=0.06$Å).[9] The solid solution of γ-haematite phase may lead to a contraction of the lattice ($a_{\text{nickel-ferrite}}-a_{\gamma\text{-haematite}}=0.03$Å)[10]. Using "Vegard's law", and assuming the concentrations of Fe^{2+} ions determined by the chemical analysis, the lattice constants of the air-fired specimens having different x-values were calculated in two ways, based on the following two assumptions (a) and (b). Namely, the lattice dimensions change in proportion to the molar fraction of

(a) both the magnetite and γ-haematite phases,

or

(b) the magnetite phases alone.

Results are shown in Fig. 1, by the curves (a) and (b). Observed values agree fairly well with the calculated values for (b). This suggests that the contraction effect due to the presence of γ-haematite phase is not large in these solid solutions.

On the other hand, the lattice constant of the specimens fired in the oxygen atmosphere is always larger than that of the air-fired specimens with equal amounts of excess ferric oxide. This fact can not be explained by the assumption given above.

Ferric oxide tends to be more reduced at higher temperatures. It is expected that, during the process of rapid cooling, the oxidization of the solid solution localizes on the surface of each individual grain. But, when the localized ferric oxide does not crystallize sufficiently or when its amount is less than 2∼3% of the spinel matrix, it is impossible to detect the precipitate positively by the X-ray analysis. In this case, the observed value of the lattice constant of solid solution may be larger than that calculated by assuming a homogeneous ferrite-magnetite-haematite solid solution, with equal amounts of both the Fe^{2+} ions and the excess ferric oxide. It is expected that, in the oxygen atmosphere, such a formation of localized precipitation on the surface of grain is larger than that in the air. Because of this effect, the lattice constants of the oxygen-fired specimens may tend to be larger than those of the air-fired specimens. Even in the air-fired specimens, their lattice constants may be larger to some extent than the calculated values by this effect.

§ 4 Precipitation of α-ferric oxide from the solid solutions

As stated in the preceding chapter, the quenched solid solution possesses a somewhat unstable inhomogeneity. In order to consider the stability of these solid solutions, precipitation processes of α-ferric oxide therefrom were investigated in various annealing conditions.

4–1 *Temperature dependence*

The solid solutions obtained by quenching were heated in air at temperatures between room temperature and 1300°C, followed by a slow cooling. The rate of heating and cooling were about 1°C/min.[11] in these cases. The amounts of crystalline phases in these powders at different temperatures were measured continually using a high temperature X-ray diffraction camera with Co–Kα ray.

Within a certain definite temperature region, each specimen was found to contain α-ferric oxide, precipitated from the solid solutions. The amount of precipitated ferric oxide was determined from measurements of the intensity ratio of (111) of α-Fe_2O_3 to (220) of the spinel matrix. A calibration curve prepared from the measurements of unheated mixtures of α-ferric oxide and nickel ferrite in various mole ratio was used.

Results obtained can be summarized as follows (see Fig. 2):

(1) It was found that the precipitation of α-ferric oxide first occurs at about 550°C.

(2) Between 800°C and 900°C, the amount of precipitation reaches a maximum value, which is nearly equal to the amount of the excess portion of ferric oxide contained in each solid solution, $NiFe_2O_4$–Fe_2O_3.

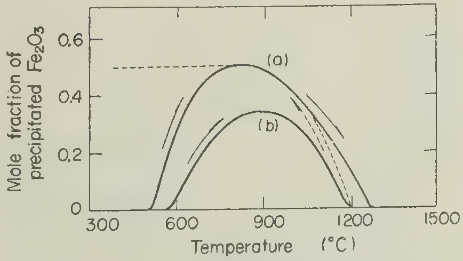

Fig. 2. The temperature dependence of the precipitation of α-Fe_2O_3 from $NiFe_2O_4$–Fe_2O_3 solid solution.
(a) $NiFe_2O_4\cdot Fe_2O_3$
(b) $NiFe_2O_4\cdot(0.5)Fe_2O_3$

(3) As temperature becomes higher than 900°C, the amount of precipitated α-ferric oxide decreases. This means that the α-ferric oxide becomes again soluble in the nickel ferrite at high temperatures. The precipitation disappears completely at about 1250°C.

(4) When a specimen is slowly cooled from higher temperatures, the precipitation of α-ferric oxide begins to occur at about 1200°C. At about 800°C, the precipitation appears to be complete. Below 800°C, the amounts of the precipitates remain constant down to room temperature.

4–2 *Time dependence*

The precipitation of α-ferric oxide from the quenched solid solution depends not only upon the annealing temperature but also upon

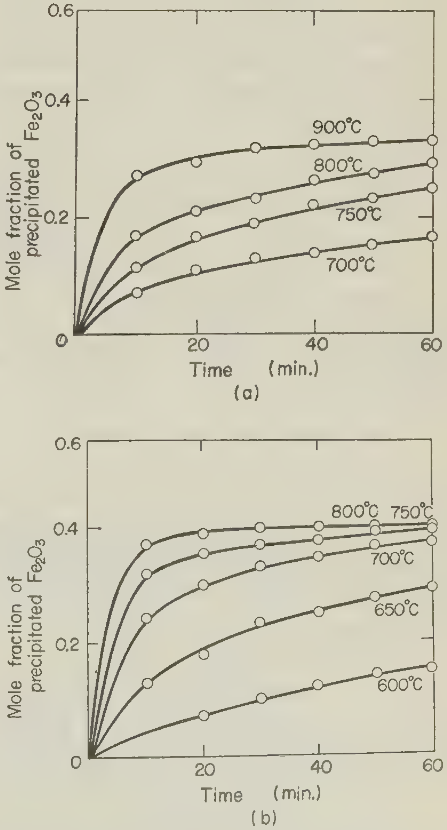

Fig. 3. The time dependence of the precipitation of α-Fe_2O_3 from $NiFe_2O_4$–Fe_2O_3 solid solution.
(a) $NiFe_2O_4\cdot(0.5)Fe_2O_3$
(b) $NiFe_2O_4\cdot(0.75)Fe_2O_3$

the time during which the specimen is annealed.

After various annealing times at certain definite temperatures, the specimens were quenched in air to room temperature in order to stop the precipitation. The rates of precipitation were determined by the same method that was used in the study of the temperature dependence. Results are shown in Fig. 3 (a) and 3 (b). In Fig. 3, the amount of the precipitated α-ferric oxide, expressed in mole fraction in the solid solution, is plotted as a function of reaction time for different annealing temperatures. With a specimen annealed at about 900°C, the precipitation completes after about one hour.

In these cases, end values are always nearly equal to the excess amount of ferric oxide contained in the initial solid solution. But, when the annealing temperature is higher than 1000°C, the amount of precipitate reaches very rapidly a certain saturation value, which is smaller than the amount of excess ferric oxide contained in the initial solid solution. It is likely that the equilibrium take place between the solid solution and the precipitate at these temperatures.

4-3 *Analysis of the experimental results*

The kinetics of the growth of precipitates will be discussed briefly. If each individual grain of the specimen possesses an equal probability for the precipitation and the rate of precipitation is simply proportional to the concentration of dissolved ferric oxide in the solid solution, then we have,

$$\frac{dn}{dt}=K_1(1-n)\,, \qquad (1)$$

where n is the fraction of the precipitated α-ferric oxide to the initial amount of ferric oxide dissolved in the ferrite, and K_1 is the rate constant of precipitation. If K_1 is independent of n, then

$$\ln\frac{1}{1-n}=K_1 t\,. \qquad (2)$$

Regarding K_1 as a constant of reaction for the precipitation, it may be expressed

$$K_1=K_0\,exp(-E_A/kT)\,. \qquad (3)$$

Using these equations, $\log\{1/(1-n\}$ vs. t and $\log K_1$ vs. $1/T$ curves are calculated from the experimental results. They are shown in Figs. 4 and 5, suggesting that equations (2) and

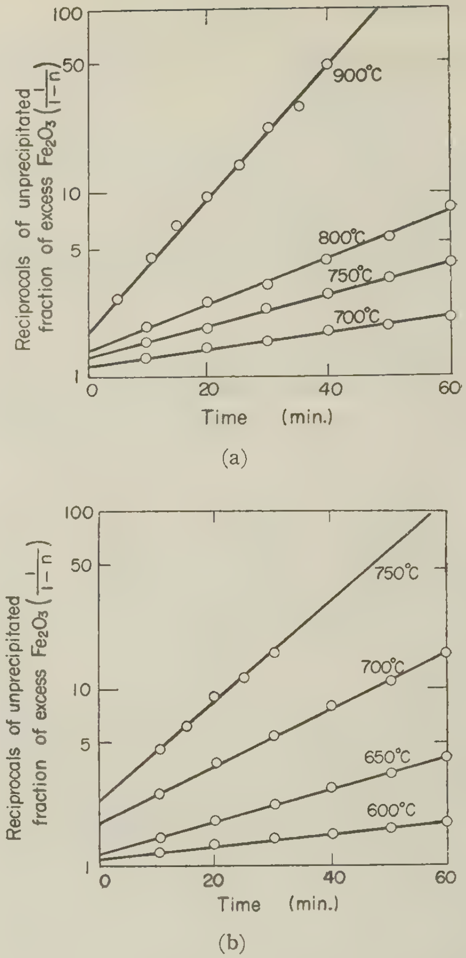

Fig. 4. Ratio of the total amounts to the unprecipitated amounts, of the excessively dissolved Fe_2O_3, versus the time of annealing.
(a) $NiFe_2O_4\cdot(0.5)Fe_2O_3$
(b) $NiFe_2O_4\cdot(0.75)Fe_2O_3$

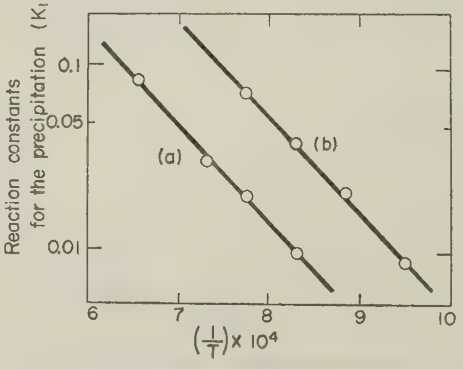

Fig. 5. Reaction rate constants versus the reciprocals of the absolute temperatures.
(a) $NiFe_2O_4\cdot(0.5)Fe_2O_3$
(b) $NiFe_2O_4\cdot(0.75)Fe_2O_3$

(3) are approximately valid for our present experiments. The activation energy, E_A, is found to be about 1.03 ev.

§ 5 Solubility of the *α*-ferric oxide in the nickel ferrite

Let us assume that the solubility of *α*-ferric oxide in a nickel ferrite can be expressed by the same way as that of a solid in a liquid phase. Then, the equilibrium solubility of *α*-ferric oxide in a nickel ferrite as well as its temperature dependency may be expressed by the following equation,

$$(C_{sat})=A\cdot exp\{-(\Delta H_{sat})/RT\}, \qquad (4)$$

where (C_{sat}) is the mole fraction of ferric oxide in a saturated solid solution, and (ΔH_{sat}) is the heat of dissolution of *α*-ferric oxide in the saturated solution of nickel ferrite-haematite.

Using this equation, $\log(C_{sat})$ vs. $1/T$ curve is calculated from the experimental results obtained for a solid solution having the mole ratio 1:1 (i.e., $x=2$), and is shown in Fig. 6. From these results, the heat of dissolution is estimated to be approximately 1.3 ev.

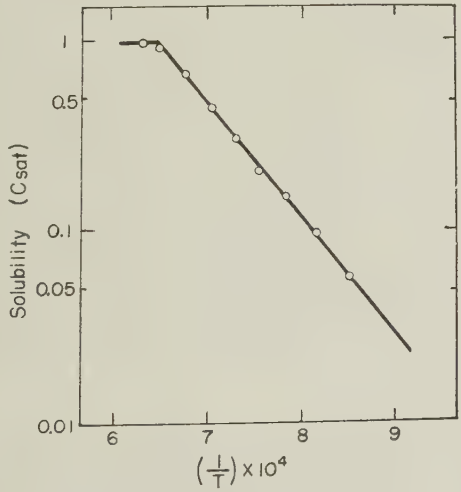

Fig. 6. Solubilities of α-Fe_2O_3 to $NiFe_2O_4$ versus the reciprocals of the absolute temperatures.

§ 6 Conclusion

For the nickel ferrite-haematite solid solution system, the variation of the lattice dimention, the precipitation and redissolution of *α*-ferric oxide were investigated by X-ray analysis. Conclusions drawn from these investigations are as follows:

(1) These solid solution systems, which are obtained by quenching, possess somewhat unstable inhomogeneities originating in the localized oxidixation on the surface of grain.

(2) Above ca. 600°C, these solid solutions tend to become stabilized by the precipitation of *α*-ferric oxide.

(3) At relatively low temperatures, the reaction rate for the precipitation depends upon the amount of the dissolved ferric oxide in the solid solution. The activation energy for the precipitation is about 1.03 ev.

(4) At high temperatures, a definite amount of *α*-ferric oxide is soluble in the ferrite in a state of thermal equilibrium. The heat of dissolution in this process is found to be 1.3 ev.

Acknowledgement

The author wishes to express his sincere thanks to Prof. T. Nagamiya and Prof. T. Watanabe, of Osaka University, for criticizing this manuscript. Thanks are also due to Mr. S. Kisaka, Manager of our department, for his support and to Mr. S. Mori and Mr. F. Kanamaru for their helps throughout the course of this work.

References

1) A. E. Van Arkel, E. J. W. Verwey and M. G. Van Bruggen: Rec. Trav. Chim. Pays-bas, **55** (1936) 331
2) E. J. W. Verwey, A. E. Van Arkel and M. G. Van Bruggen: Ibid., **55** (1936) 340
3) L. G. Van Unitert: J. Chem. Phys., **23** (1955) 1883
4) S. Iida, H. Sekizawa and Y. Aiyama: J. Phys. Soc. Japan, **13** (1958) 58
5) K. Ohta: Kobayashi-Riken Hokoku: **8** (1958) 17 (in Japanese)
6) I. Kushime and T. Amanuma: Mem. Fac. Eng. Kyoto University, **19** (1957) 191
7) I. Kushima and T. Amanuma: Metal Physics, **2** (1956) 103 (in Japanese)
8) E. W. Gorter: Philips Res. Rep., **9** (1954) 341
9) C. F. Jefferson and E. F. Westrum, Jr: J. Phys. Chem., **61** (1957) 1430
10) P.B. Braun, Nature **170** (1952) 1123
11) S. Mori and C. Okazaki: National Tech. Rep., **5** (1959) 158 (in Japanese)

JOURNAL OF THE PHYSICAL SOCIETY OF JAPAN, Vol. 15, No. 11, NOVEMBER, 1960

X-Ray Study on the Binding Properties of Cu_2O and Ag_2O Crystals

By Tadasu SUZUKI

Institue of Physics, College of General Education, University of Tokyo, Meguro-ku, Komaba, Tokyo

(Received May 5, 1960)

Crystallographical properties of the chemically prepared powder samples of Ag_2O and Cu_2O were investigated by an X-ray diffractometer, in relation to their bonding characters. The lattice constant is 4.720±0.004A for Ag_2O and 4.268±0.001A for Cu_2O. The thermal expansion coefficient of the lattice is 1.9×10^{-6} for Cu_2O. The root-mean-square amplitude of the thermal lattice vibration is determined as 0.26A for Cu_2O and 0.40A for Ag_2O at room temperature. The mean lattice strain is 1.4% for Ag_2O and 0.15% for Cu_2O, respectively. The thermal decomposition of Ag_2O was also observed. The obtained results suggest that the binding force between metallic and oxygen atoms is much weaker in Ag_2O than in Cu_2O, which can not be expected from the purely ionic model for the present crystals.

§ 1. Introduction

The crystal structure of cuprous oxide (Cu_2O), which is known as of the cuprite type[1], has a cubic symmetry with copper and oxygen atoms in the unit cell at the positions as follows:

oxygen: (1/4, 1/4, 1/4) (3/4, 3/4, 3/4)
copper: (0, 0, 0) (0, 1/2, 1/2) (1/2, 0, 1/2) (1/2, 1/2, 0)

Each oxygen atom is surrounded tetrahedrally by four copper neighbours, while each copper atom has two oxygen neighbours at equal distance.

The nature of the bonding in this crystal structure has been discussed sometimes by ionic model and sometimes by co-valent model. Pauling proposed that the co-valent bonding is more important in the Cu_2O-type structure[2]. In fact, if oxygen atom is a doubly charged *positive* ion, the *sp* bonds in four directions may form the tetrahedral frame-work of the crystal.

On the other hand, there are some experimental facts favouring the ionic model. For instance, spectroscopic analysis[3], quadrupole resonance study[4] and measurement of dielectric dispersion[5] are explained fairly well by the ionic model.

Silver oxide (Ag_2O) is the only substance possessing the cuprite type structure besides cuprous oxide.[*],[**] Like Cu_2O, Ag_2O is known to be semiconductive and show a photoconductivity. However, Ag_2O and Cu_2O are quite different in stability. The melting point of the latter is as high as 1236°C[8], while the former begins to decompose at about 200°C. Such a large difference in stability suggests that the binding energy of the Ag_2O lattice is too smaller than that of the Cu_2O lattice to be explained by assuming the ionic models for both structures.

In the present work, the properties of Ag_2O and Cu_2O were investigated by the X-ray diffraction method in order to clarify their bonding character. In this paper, a study dealing with thermal lattice vibration, thermal expansion, lattice strain of both specimens and thermal decomposition of Ag_2O is reported. The study of the electron distribution in the structure by an accurate intensity measurement will be reported in a subsequent paper.

§ 2. Samples

The red fine powder samples of Cu_2O, supplied from the Furukawa Mining Company, were prepared by dehydration and desiccation of the copper hydrate deposits which were obtained in the course of electrolysis of copper in NaCl solution.

---

[*] It is reported that lead mono-oxide (Pb_2O) also belongs to the cuprite type structure. However, there seems to be some ambiguity about its structure.[6]

[**] Since gold oxide (Au_2O) may exist,[7] an attempt to prepare the mono-oxide of gold by applying some intense oxidizing agents was tried in relation with the present work, but the X-ray diffraction examination showed only a diffuse halo pattern with its first intensity maximum at the scattering angle of 33° and the second small maximum at 60°.

The black powder samples of Ag_2O, supplied from the Tokuriki Noble Metal Company, were prepared by the neutralization of $AgNO_3$ with NaOH. The oxidation of Ag is difficult[9] and the above method is the only known procedure for preparing an appreciable quantity of the sample. In this procedure, too less NaOH produces a mixture of Ag_2O and Ag_2CO_3, while too much NaOH results in the reduction of $AgNO_3$ to Ag. The adequate quantity of NaOH against $AgNO_3$ was controlled by X-ray examination of the prepared specimens.

The diffraction patterns and the X-ray fluorescent analysis of the present samples showed no trace of impurity. The particle size of the samples observed by a microscope is about one micron for Cu_2O and about two microns for Ag_2O. Such a particle size is small enough for a flat specimen of the diffractometer.

§ 3. Instrumentals

For convenience of surveying many samples, the Norelco X-ray diffractometer was used with its rate-meter and scaler. The measurements were performed mainly with the Cu $K\alpha$ radiation filtered by a nickel foil of 0.013 mm thick, although Mo, Fe, Co and Cr $K\alpha$ radiations were also used when necessary. A proportional counter was employed as radiation detector. The study of the thermal expansion and of the lattice vibration were performed with low- and high-temperature attachments. The cooling was achieved by the gas flow generated from liquid nitrogen, by controlling the evaporation rate of nitrogen with an electronic heater immersed in a Dewer flask[10]. For heating, an electronic furnace was set up behind the sample holder. By these attachments the temperature of the samples could be changed from −150°C to 200°C.

§ 4. Lattice Constant and Thermal Expansion

For the determination of the lattice constants, the higher angle reflections (400), (331), (420), (422) and (511)+(333) of Cu_2O and (400), (331) and (420) of Ag_2O were used. The observed value of the lattice constant 4.720±0.004A for Ag_2O and 4.268±0.001A for Cu_2O coincides within the experimental error with the reported values by previous workers, 4.720A for Ag_2O[1] and 4.269A for Cu_2O[11].

The variation of the lattice constant was measured in the temperature range between −150°C and 200°C. The thermal lattice expansion coefficient of Cu_2O estimated by the (511)+(333) reflection is 1.9×10^{-6}.[*] The value for the bulk crystal of Cu_2O was reported as $2.8\sim1.8\times10^{-6}$.[12]

For Ag_2O, the expansion coefficient could not be determined precisely due to the broadening of lines, and was estimated as the same order with that of Cu_2O.

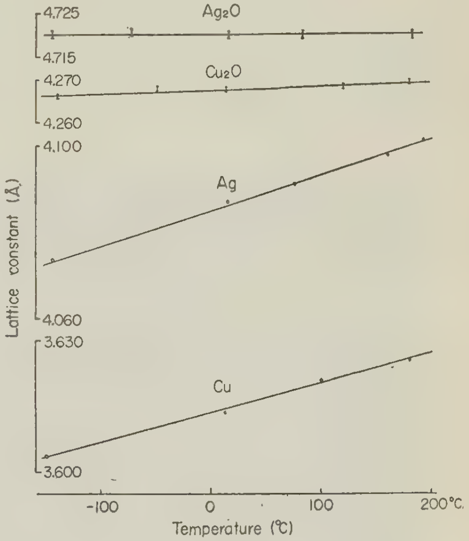

Fig. 1. Thermal expansion of lattice.

The powder samples of Ag and Cu were also measured for instrumental calibration under the same condition. The observed expansion coefficient is 1.0×10^{-5} for Ag and 1.7×10^{-5} for Cu, respectively, and agrees well with the reported values of 0.96×10^{-5} for Ag and 1.71×10^{-5} for Cu[13]. The variation of the lattice constant of the specimens against the covered temperature range is shown in Fig. 1.

§ 5. Thermal Decomposition of Ag_2O

A continuous observation of the thermal decomposition of sputtered Ag_2O by means of the electron diffraction method has been formerly reported[14]. In the present experiment, the decomposition process of Ag_2O was followed quantitatively by X-ray diagram. The powder samples of Ag_2O were packed into a specimen holder and kept at temperatures, say 100°C, 150°C and 200°C, for about 20 hours in an electrical furnace and then the samples were examined by the X-ray diffractometer at room temperature. As shown in Fig. 2(b), the lines of Ag appeared and, at the same time, the intensity of Ag_2O-lines at low angles diminished gradually by the heat treatment. After the heat treatment above 220°C, the pattern showed only the lines of Ag.

---

[*] This value coincides approximately with the unpublished value 2.3×10^{-6}, obtained by T. Takenaka in Prof. S. Miyake's laboratory with the use of the X-ray photographic method.

As is well known, Cu_2O does not decompose but is liable to oxidize by heat treatment.

The observed intensity-decrease of the Ag_2O-lines at low angles can be explained by assuming that the decomposition proceeds from the surface to the interior of the sample. Let x denote the ratio of the Ag_2O quantity in a small volume dV at the depth y from the surface of the samples to its initial quantity. x is considered to be a decreasing function of y, and we assume, for simplicity, the following exponential form,

$$x=1-(1-a)\,e^{-by}\,,$$

where a and b are appropriate constants. Then, the diffracted intensity dI' from Ag_2O in that part is

$$dI'=\{1-(1-a)\,e^{-by}\}e^{-\mu s}\,dV\,,$$

where s denotes the optical path length in the sample and μ the linear absorption coefficient of the sample. The absorption coefficient of the mixture of Ag_2O and Ag is assumed to be equal to that of Ag_2O. Then the integrated intensity I' from a heat-treated sample is given

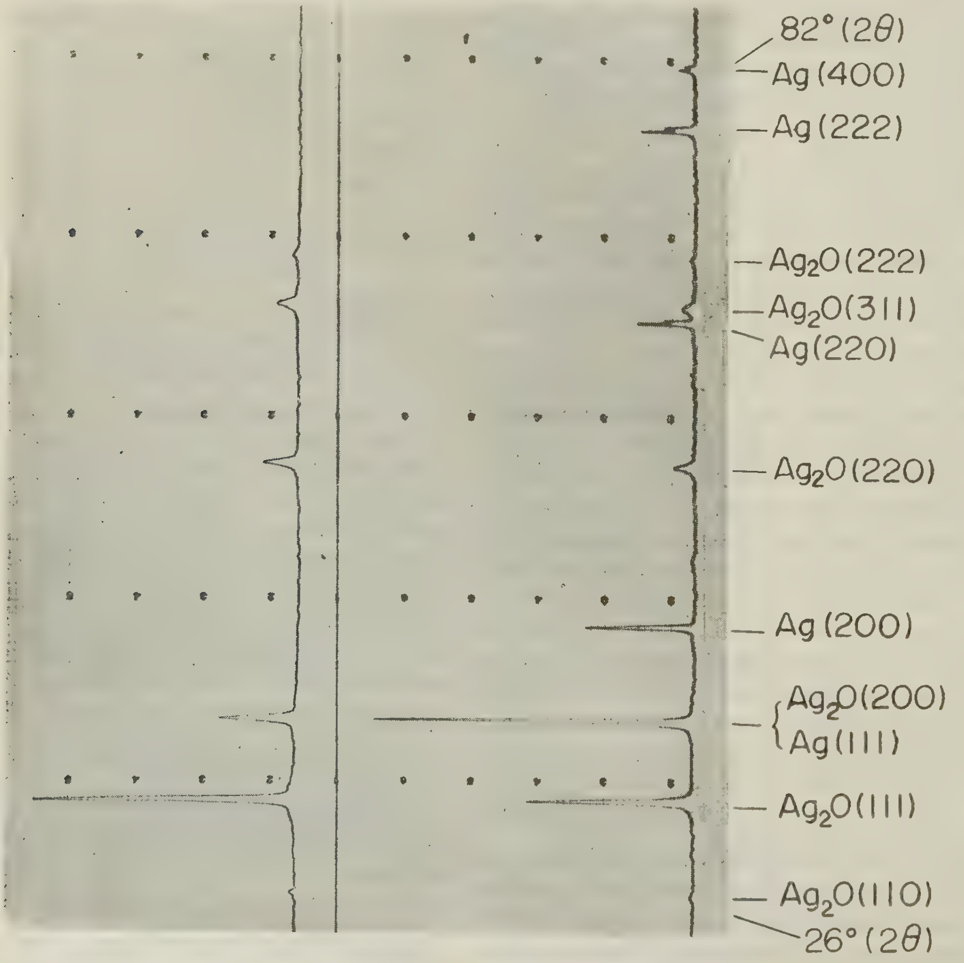

Fig. 2. Debye-Scherrer diagram of Ag_2O: (a) before the heat treatment and (b) after heated at 150°C for 20 hours.

by

$$I'=I\{1+(a-1)\}\frac{2\mu}{b\sin\theta+2\mu},$$

where θ is the Bragg angle and I signifies the integrated intensity for the flat powder sample[15] before the heat treatment. From the above equation we have

$$\frac{I}{I-I'}=\frac{b\sin\theta+2\mu}{2\mu(1-a)},$$

which shows a linear relation of $I/I-I'$ to $\sin\theta$. This relation is confirmed to be the case by Fig. 3. In short, the intensity-diminution of the Ag_2O-lines at low angles is due to the thinness of the decomposed layer of Ag_2O at the surface of the specimen.

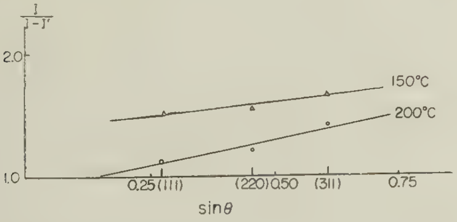

Fig. 3. I/I−I′ against sin θ, I and I′ being the integrated intensity before and after the heat treatment.

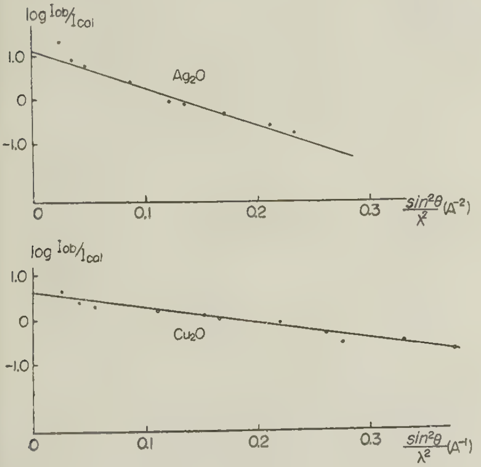

Fig. 4. The logarithmic ratio of the observed intensity to the calculated one plotted against $\sin^2\theta/\lambda^2$.

§ 6. Thermal Lattice Vibration

The root-mean-square amplitude $\sqrt{\bar{u}^2}$ of the thermal lattice vibration was determined by plotting the logarithmic ratio of the observed intensity to the calculated one against $\sin^2\theta/\lambda^2$, as shown in Fig. 4. From the well-known relation

$$I_{ob}/I_{cal}=\text{const}\cdot\exp\left(-2B\frac{\sin^2\theta}{\lambda^2}\right)$$

B can be obtained by the slope of the plot. For cubic crystals B is related to $\bar{u}^2$ as follows:

$$B=\frac{8\pi^2}{3}\bar{u}^2=8\pi\,\bar{u}_s^2\ ,$$

where $\bar{u}_s^2$ signifies the mean square-amplitude of vibration in a particular direction. The theoretical value of the intensity was calculated by the relation

$$I_{c.l}=C\frac{1+\cos^2 2\theta}{\cos\theta\sin^2\theta}\,j\,F^2\ ,$$

where F is the structure factor, j is the multiplicity of the diffraction, θ is the Bragg angle and C is the constant depending on the intensity of the incident X-ray beam. The structure factor F was calculated using the atomic scattering factors of copper and oxygen computed by Berghuis *et al*[16], and that of silver computed by Thomas and Umeda[17]. The dispersion effect of Ag and Cu atoms for

Table I. The calculated and observed values of the integrated intensities and the rms amplitude of the thermal vibration $\sqrt{\bar{u}^2}$ at room temperature. The theoretical values, taking no account of temperature effect, were computed by the relation in § 7. The constant C is put 400 only for the convenience of the calculation. The observed value of (222) is normalized to the theoretical value.

hkl	Cu_2O		Ag_2O	
	I_{cal}	I_{ob}	I_{cal}	I_{ob}
110	154	291	164	720
111	3145	4783	10244	17260
200	1230	1653	4336	10400
220	1123	1367	3892	5960
311	1019	1089	4016	4050
222	244	244	1028	1028
400	165	147	628	498
331	483	350	1824	947
420	405	241	1556	704
422	585	343		
511 333	869	396		
$B=\frac{8\pi^2}{3}\bar{u}^2$	1.75 A²		4.25 A²	
$\sqrt{\bar{u}^2}$	0.26 A		0.40 A	

the Cu Kα radiation was corrected by the tabulation given by Dauben and Templeton[18]. The values of I_{cal}, I_{ob}, B and $\sqrt{\bar{u}^2}$ for room temperature are tabulated in Table I.

The influence of the extinction effect on the observed intensities was studied by using the Kα radiations of Mo, Cu, Fe, Co and Cr. For Cu_2O, the ratio of the F-values of (111) reflection to that of (222) was plotted against the various wave lengths. For Ag_2O, the ratio of (111) to (311) was examined, since its (222) reflection for Cr Kα was too weak. The above ratios were nearly constant within the standard deviation of about 6%, and no dependence on the wave length could not be recognized. It is thus assumed that the effect of primary extinction is not appreciable in the present samples. Secondary extinction was assumed to be negligible for these fine powder samples.

The thermal lattice vibration was observed in the temperature range between −150°C and 200°C. Since, as was described in the previous section, Ag_2O begins to decompose above about 100°C, the surface of the flat specimens was covered with a thin Myler foil of 0.01 mm thick in order to prevent the thermal decomposition. The Myler foil was also used for the measurements on Cu_2O and Cu in order to prevent the oxidation. The absorbing effect of the foil was corrected at low diffraction angles. The rms amplitudes for the various temperatures are shown in Fig. 5, together with those for Ag and Cu obtained by the same procedure. The values of $\sqrt{\bar{u}^2}$, 0.14A for Cu and 0.16A for Ag agree well with the reported values of 0.145A and 0.16A for Cu and Ag, respectively[19]. The observed values of the rms amplitude of Ag_2O is remarkably large, as can be expected from the diffracted pattern shown in Fig. 2(a), in which the intensities at higher angles are strongly reduced.

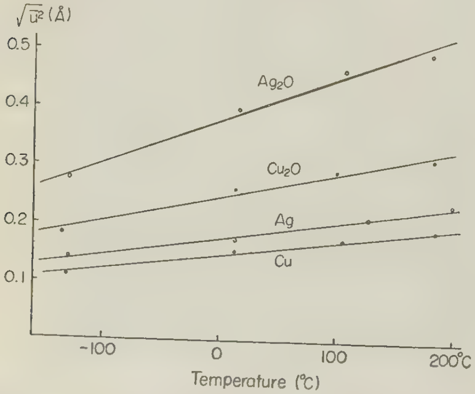

Fig. 5. The change of the rms amplitudes with temperature.

For a crystal containg two kinds of atoms, as is the present case, the mean amplitudes of vibration are to be determined separately to each atom. The above obtained value of $\sqrt{\bar{u}^2}$ should be regarded as an empirical quantity representing an average for metallic and oxygen atoms in the crystals. In a similar sence, the Debye characteristic temperature Θ of an empirical meaning can be determined from the mean-square ampliture $\bar{u}^2$, using the relation

$$\bar{u}^2=\frac{9h^2\,T}{4\pi^2k\,m\Theta^2}\left\{\phi(x)+\frac{x}{4}\right\}^{20)},$$

where $x=T/\Theta$, $\phi(x)$ is a function relating to the frequency distribution of lattice vibration evaluated by Debye, k the Boltzman constant and m the mean atomic weight. The obtained value of Θ are tabulated in Table II. The temperature dependence of $\bar{u}^2$ can be approximately put $\bar{u}^2=aT$, as is known from the above relation. The constant a is related to the elastic constant[21], and determined to be 1.3×10^{-20} for Cu_2O and 6.0×10^{-20} for Ag_2O. The value of a for NaCl is reported to be 5.7×10^{-21} [22].

Table II. The Debye characteristic temperature of Ag_2O and Cu_2O.

	Cu_2O	Ag_2O
T (°C)	Θ (°K)	Θ (°K)
−130	176	85
17	180	90
190	190	95

§ 7. Lattice Strains

Diffraction lines from Ag_2O were very broad, as an example is shown in Fig. 6. It was, therefore, expected that the chemically prepared samples might contain lattice strain. The strain distribution in the present samples was measured by the line broadening analysis. To obtain the integral breadth, the broadening due to the Kα doublet was corrected by the method of Jones[23]. The instrumental broadening was calibrated by the standard strain-free specimens of silicon.

If both the particle size and the strain effect are present, the line breadth β is in most cases expressed by the following linear equation[24)]

$$\beta\cos\theta=\lambda/\varepsilon+2\eta\sin\theta,$$

where ε, λ, η and θ are the particle size, the X-ray wave length, the effective strain and the Bragg angle, respectively. The line breadth of the present samples, determined by the above procedures, satisfies this relation as shown in Fig. 7. The magnitude of strain may be obtained from slopes of straight lines.

Recently Kuriyama showed[25)] that, if the lattice strain distribution is of a Cauchy type and that of the particle size is of an exponential form, the above relation is strictly correct.

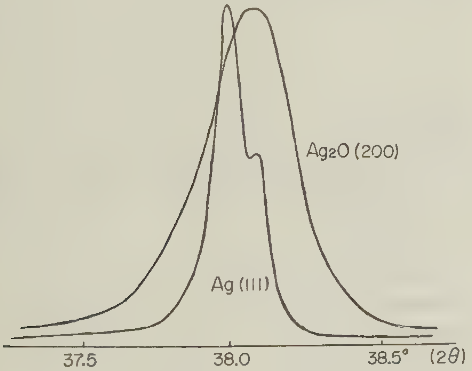

Fig. 6. Line breadth of Ag_2O in comparison with Ag. The maximum values are adjusted to the same level.

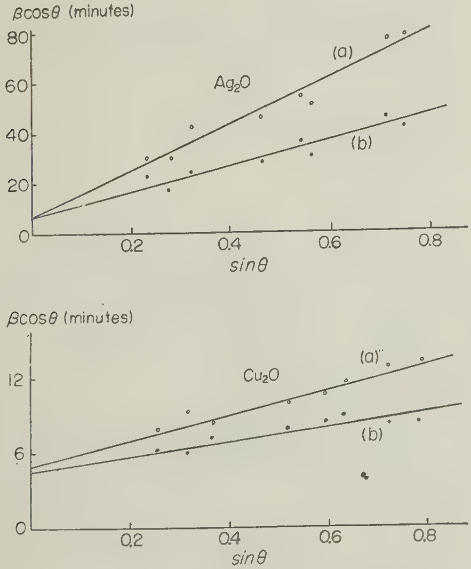

Fig. 7. Angular dependence of the integral line breadth.

The mean strain found in this way was 1.4% for Ag_2O and 0.15% for Cu_2O. By annealing the samples, these strain decreased to about one half of the initial values, but did not disappear. The electrolytically prepared powder samples of Ag and Cu are also measured and both samples showed no lattice strain.

§ 8. Conclusion and Discussion

The experimental results can be summarized as follows. The thermal lattice expansion coefficient of Cu_2O is 1.9×10^{-6} and the same order is estimated for Ag_2O. The rms amplitude of the thermal lattice vibration $\sqrt{\bar{u}^2}$ is 0.40A for Ag_2O and 0.25A for Cu_2O at room temperature. The lattice vibration of Ag_2O is comparatively large even at room temperature and becomes as large as 0.5A at about 200°C, as is shown in Fig. 6. The mean value of lattice strain, so far as the examined samples are concerned, is 1.4% for Ag_2O and 0.15% for Cu_2O, respectively. The former substance decomposes at above 100°C. The decomposition begins from the surface of the specimen and at about 200°C Ag_2O decomposes nearly completely.

The large lattice strain observed in Ag_2O seems to be ascribed to lattice deffects, for instance such as those caused by isolated silver which is formed in the lattice as a result of the instability of the structure. The above results on thermal decomposition, thermal lattice vibration and the lattice strain all suggest that the binding force between the metallic atom and the oxygen atom is much weaker in Ag_2O than in Cu_2O.

As was mentioned in § 1, Cu_2O has been considered in many cases to be ionic from the experimental facts. Taking the purely ionic model for both crystals, the lattice energy can be estimated from the Born theory by the use of Madelung constant for the cuprite type structure. The values are shown in Table III from the tabulation of Seitz[26)]. Calculated values of the lattice energy of some typical ionic oxides are also tabulated for comparison. The Table shows that the difference of the lattice energy between Cu_2O and Ag_2O calculated by the ionic model is not especially large in spite of the marked difference in observed properties of the both substances.

In this connection, it is interesting that the thermal lattice expansion of Ag_2O and Cu_2O

Table III. Crystal structure, lattice constant, melting point and the lattice energy calculated by ionic model of Cu_2O and Ag_2O, and of di-valent oxides.

	Crystal structure	Lattice constant	Melting point	Theoretical lattice energy
MgO	NaCl type	4.20 A	2800°C	940 Kcal/mol
CaO	〃	4.80	2572	842
SrO	〃	5.14	2430	790
BaO	〃	5.52	1923	747
Cu_2O	cuprite type	4.27	1236	682
Ag_2O	〃	4.72	decomposes above 100°C	585

is comparatively small, in spite of the large lattice vibration in them. As the result, the thermal lattice expansion coefficient deviates from Megaw's rule[27] between thermal expansion coefficient and ionicity. Megaw's rule states the following empirical relation. Let q denote the "electronic share", namely the charge number of a ion divided by the number of its nearest neighbour atoms, and α signify the thermal expansion coefficient, then the relation $\alpha q^2 \times 10^6 \doteqdot 1$ holds in typical ionic crystals. For example, the values of $\alpha q^2 \times 10^6$ for NaCl, CsCl and CaF_2 are 1.1, 0.8 and 1.2, respectively. This value for Cu_2O, being 0.48, deviates considerably from unity.

These circumstances seem to suggest that the *purely* ionic model is not adequate for the present crystals. It is probable that the cohesive energy of the cuprite type crystal is partly contributed by an overlap of electron distribution or by atomic polarization[28].

In conclusion the author wishes to express his thanks to Prof. S. Miyake for his kind permission to perform a part of this work in his laboratory in the Institute for Solid State Physics of the University of Tokyo. Thanks are also due to Profs. S. Miyake and S. Takagi and S. Hosoya and to Dr. M. Kuriyama for his kind discussions. This work was partly supported by the Scientific Research Grant of the Ministry of Education.

References

1) P. Niggli: Z. Krist. **57** (1922) 253.
2) L. Pauling: *The Nature of the Chemical Bond* (Cornel Univ. Press, New York, 1949) 196 p.
3) M. Hayashi: J. Phys. Soc. Japan **14** (1959) 681.
4) T. P. Das and E. L. Hahn: *Solid State Physics*, Suppl. 1. ed. by F. Seitz and D. Turnbull (Akademic Press, New York, 1958) 180 p.
5) T. D. Schultz: Technical Rep. No. 9. Solid State and Molecular Theory Broup MIT.
6) R. W. G. Wyckoff: *The structure of Crystals* 2nd ed. (Chemical Catalogue, New York, 1931) 238 p.
7) J. W. Mellor: *A Comprehensive Treaties on Inorganic and Theoretical chemistry* Vol. **3**. (1922) 578 p.
8) *International Critical Table*: **7** (1921) 265.
9) E. Menzel and C. Menzel-Kopf: Z. Naturforsch. **13** (1958) 985.
10) T. Sakurai and T. Suzuki: Norelco Reporter **6** (1959) 122.
11) Swanson and Fuyat: NBS Circular **539**, II (1953) 23.
12) R. Uno and T. Okada: J. Phys. Soc. Japan **1** (1950) 23.
13) C. J. S. Smithells: *Metals Reference Book* (Butterworths Scientific Pub. London, 1955) Vol. **2**. 637 p.
14) T. Suzuki: Z. Naturforsch. **12** (1957) 497.
15) H. P. Klug and L. E. Alexander: *X-Ray Diff. Procedures*, (John Willy, New York, 1958) 377 p.
16) J. Berghuis *et al*: Acta Cryst. **8** (1955) 478.
17) L. H. Thomas and K. Umeda: J. Chem. Phys. **26** (1957) 293.
18) C. H. Dauben and D. H. Templeton: Acta Cryst. **8** (1948) 841.
19) K. Lonsdale: Acta Cryst. **1** (1948) 142.
20) R. W. James: *Optical Principles of the Diffraction of X-Rays* (Bell, London, 1954) 237 p.
21) I. Waller: Dissertation, Upsala (1925).
22) I. Waller and R. W. James: Proc. Roy. Soc. **A117** (1927) 214.
23) F. W. Jones: Pro. Roy. Soc. **A166** (1938) 16.
24) W. H. Hall: Pro. Phys. Soc. **A62** (1919) 741.
25) M. Kuriyama: J. Phys. Soc. Japan **15** (1960) 1429.
26) F. Seitz: *Modern Theory of Solid* (McGraw-Hill, New York, 1940) 83 p.
27) H. D. Megaw: Z. Krist. **100** (1938) 58.
28) F. W. DeWette: Physica **25** (1959) 1225.

JOURNAL OF THE PHYSICAL SOCIETY OF JAPAN, Vol. 15, No. 11, NOVEMBER, 1960

Dislocation Networks and Moiré Patterns of Molybdenite

By Yoshihiro KAMIYA, Keiichi ANDO, Minoru NONOYAMA
and Ryozi UYEDA

Physical Institute, Nagoya University, Nagoya, Japan

(Received August 2, 1960)

In electron micrographs of molybdenite films, various network-patterns were observed. They are interpreted as images of dislocation networks. Several electron micrographs are reproduced and remarkable features observed in them are explained in terms of dislocations. One of the remarkable observations is that each line of a network sometimes becomes broader and the network changes into a moiré pattern. The gradual change from a sharp image of dislocation to a broad moiré fringe can be explained by a simple consideration. The former implies that the strain accompanying the dislocation is concentrated and the latter, that the strain is spread.

§ 1. Introduction

In the course of an experiment on epitaxy[1], various network-patterns were observed in electron micrographs from molybdenite films evaporated with silver. Similar patterns were also observed for bare molybdenite films and it has become clear that the patterns represent dislocation networks in molybdenite.

In the present paper several of the electron micrographs are reproduced and remarkable features of the patterns are interpreted in terms of dislocations. One of the remarkable observations is that each line of a network sometimes becomes broader and the network changes into a moiré pattern. The gradual change from a sharp image of dislocation to a broad moiré fringe can be explained by a simple consideration. The former implies that the strain accompanying the dislocation is concentrated and the latter, that the strain is spread.

§ 2. Experimental

Thin films of molybdenite were made by pealing good molybdenite of Korean origin. Near peripheries of pealed samples, small transparent areas were usually found which were adequate for observation by electron microscopy. The thickness was not uniform and it could not be measured. In the following sections, thin, medium, and thick may correspond to a few hundred Ångströms, several hundred Ångströms and more than several hundred to a few thousand Ångströms, respectively. These are rough estimates from diffraction patterns. Thin films produce net-patterns while thick films produce mainly Kikuchi-patterns. Electron micrographs were taken at accelerating voltages 75 or 100 kv. Direct magnification was about ×5,000. Exposure time was a few seconds for thin films while for thick films a few ten seconds.

§ 3. Results

Photos. 1–4* were obtained in the course of an experiment on epitaxy[1]. The specimen was a molybdenite film evaporared with silver. Various patterns were obtained from different parts of the specimen. The silver deposit does not form a uniform film and is clearly observed in Photo. 2 as the fine irregular pattern in each cell of the network. In the present paper the silver deposit is not important.

Photos. 5–14 were obtained from bare molybdenite films. Most of molybdenite films produced some network-patterns which were usually irregular and unconspicuous. Sometimes, however, various remarkable patterns were observed. The pictures reproduced in the present paper are some examples from an immense variety.

Photos. 5–8 were obtained from thin films. In these pictures, extinction contours show high contrast. Extinction contours and network-lines usually move when specimens are first irradiated by the electron beam. After several minutes they become gradually stationary. Photos. 9 and 10 were from films of medium thickness, and Photo. 11 from thick

---

* Taken in Hitachi Central Laboratory in July, 1957.

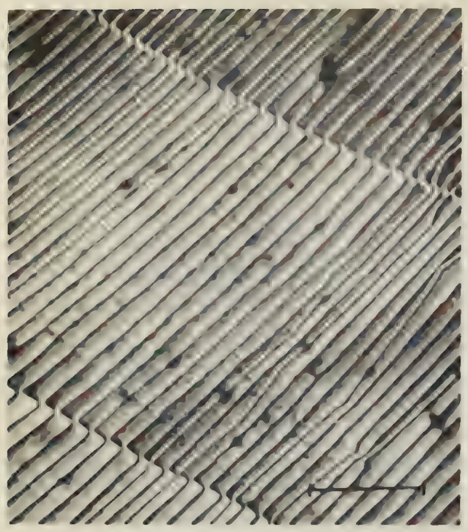

Photo. 1. 1μ

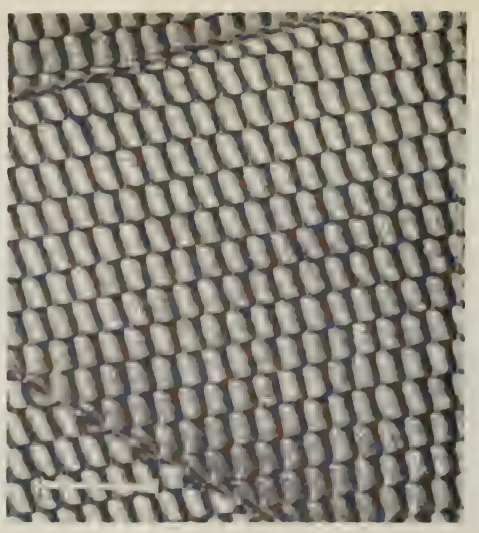

1μ Photo. 2.

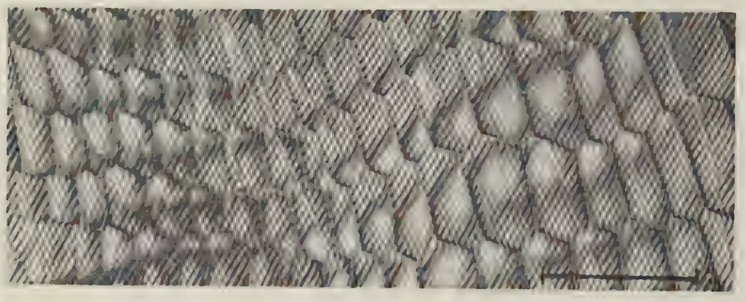

Photo. 3. 1μ

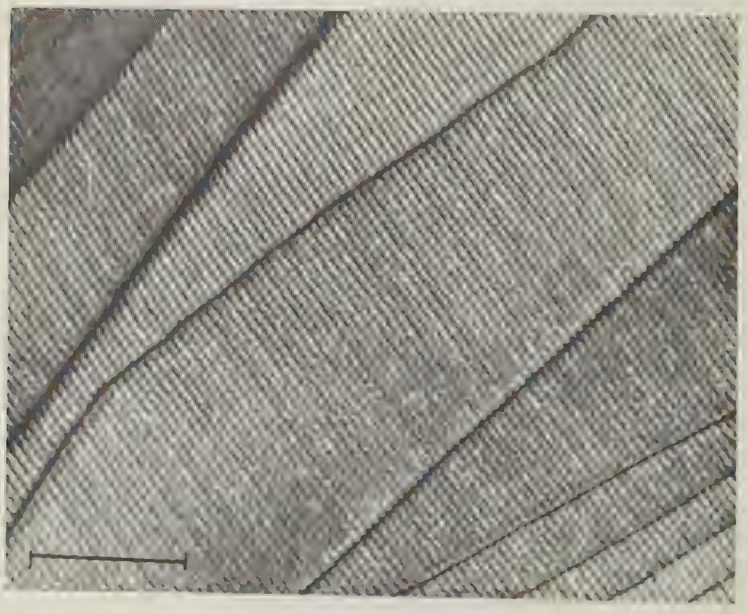

1μ Photo. 4.

Photos. 1-4. Network patterns from molybdenite-silver.
Magnification: 15,000 for Photos. 1 and 2,
20,000 for Photos. 3 and 4.

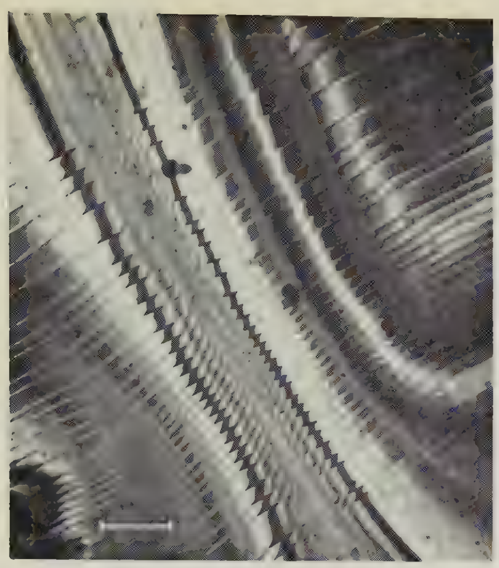

1μ Photo. 5.

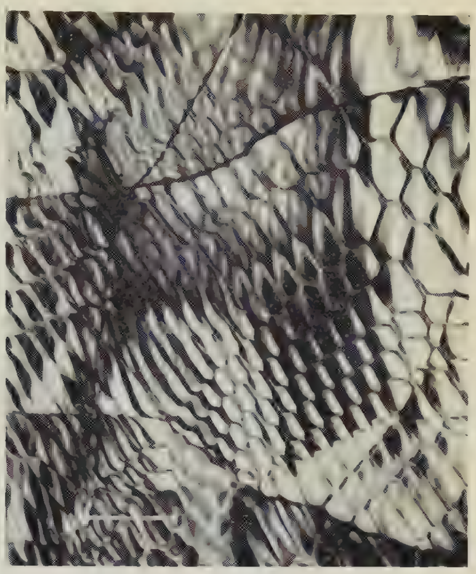

1μ Photo. 6.

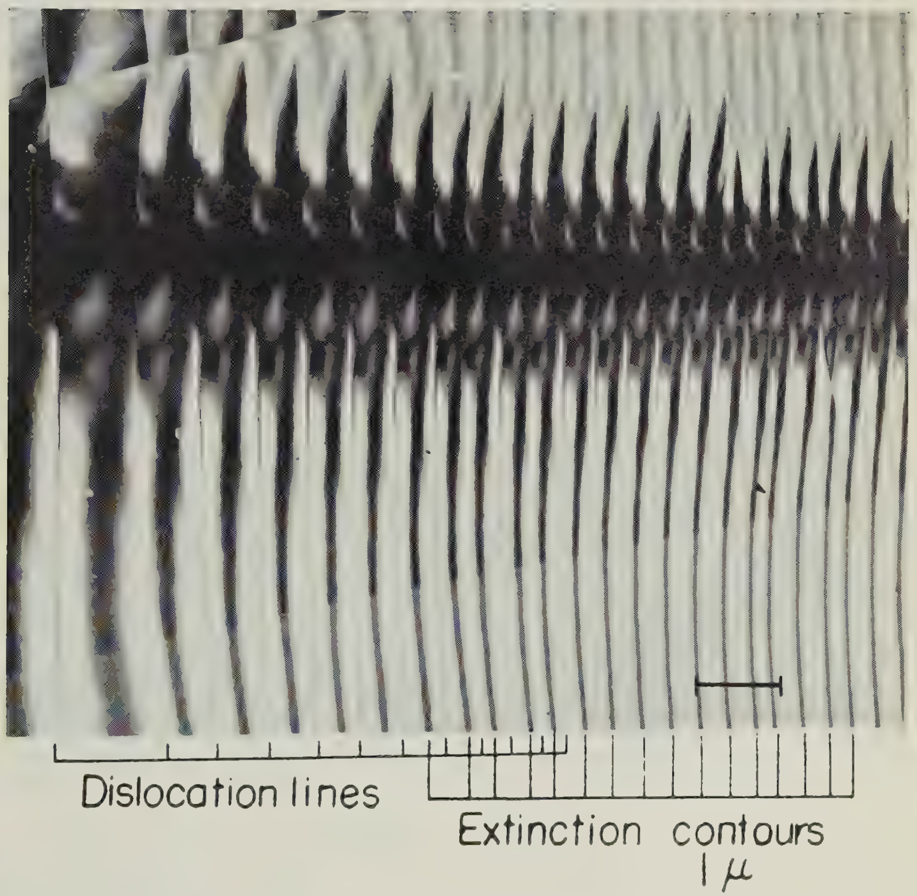

Photo. 7.

Photos. 5–7. Thin films of molybdenite.
Magnification: 9,000 for Photo. 5,
12,000 for Photos. 6 and 7.

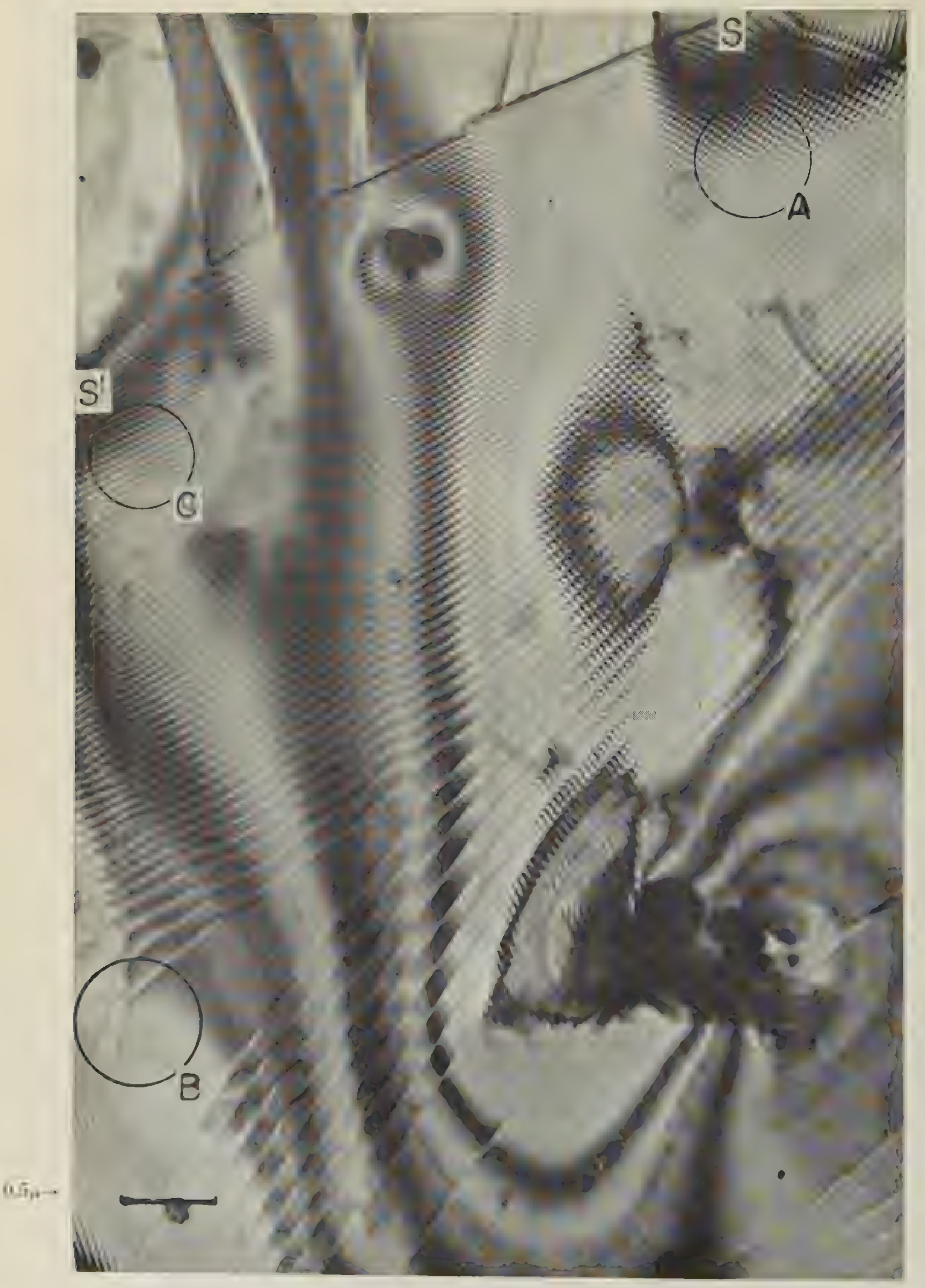

Photo. 8. Thin film of molybdenite.
Magnification: 30,000.

films. Extinction contours are less conspicuous for thicker films. The specimen of Photo. 11 was so thick that it produced only Kikuchi bands and the incident spot was observed only when the anomalous transmission took place[2]. Photos. 12 and 13 were taken at high temperature of about 600°C. So far, only a few pictures were taken at high temperatures and it is not yet clear whether or not this type of patterns is specific

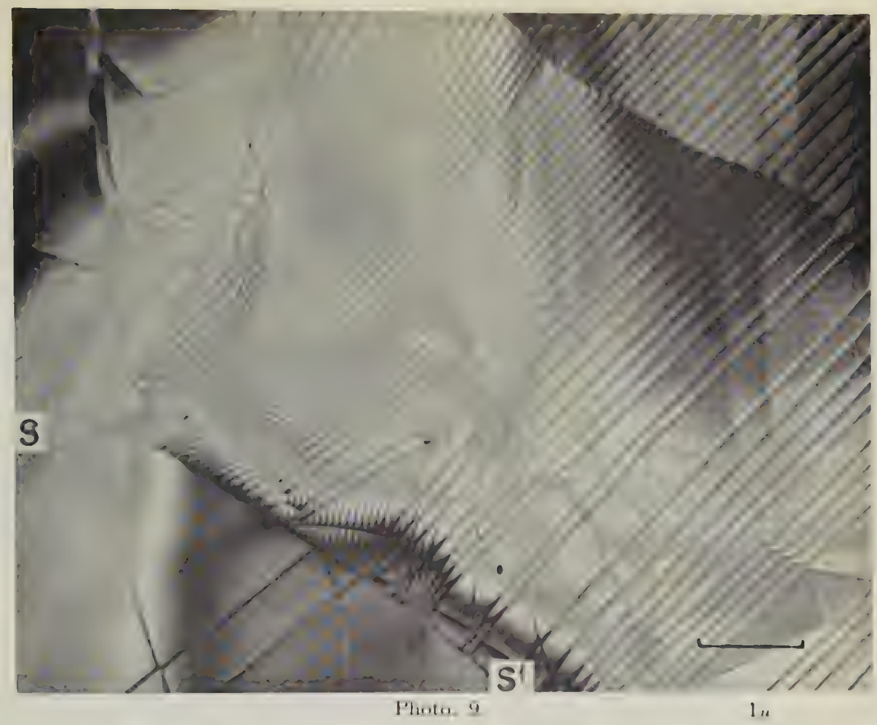

Photo. 9

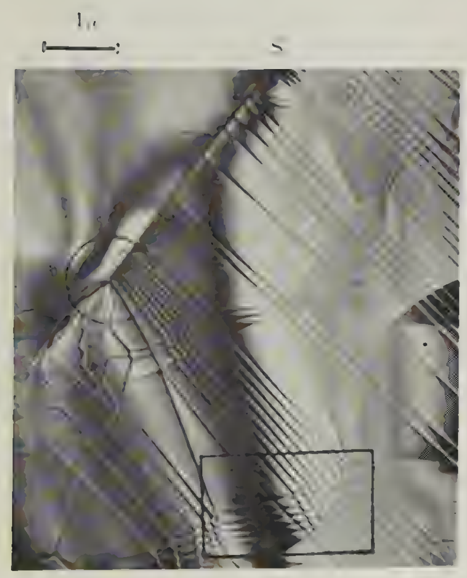

Photo. 10a.

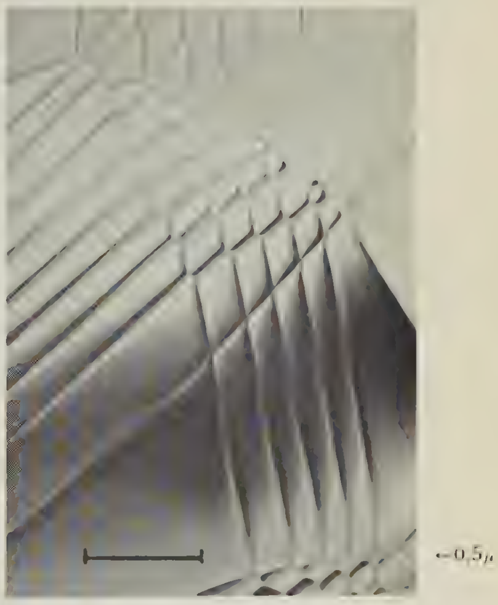

Photo. 10b.

Photos. 9 and 10. Molybdenite films of medium thickness.
Magnification: 15,000 for Photo. 9,
9,000 and 35,000 respectively for Photos. 10a and 10b.

to high temperatures.

§ 4. Interpretations and Discussions

Photo. 1 is very similar to one of the images of dislocations obtained by Hirsch et al[3]. Photos. 9–11 look similar to network-patterns of bismuth tellulide obtained by Geach and Phillips[4]. They have concluded that the patterns are images of dislocations because the majority of the patterns may be interpreted

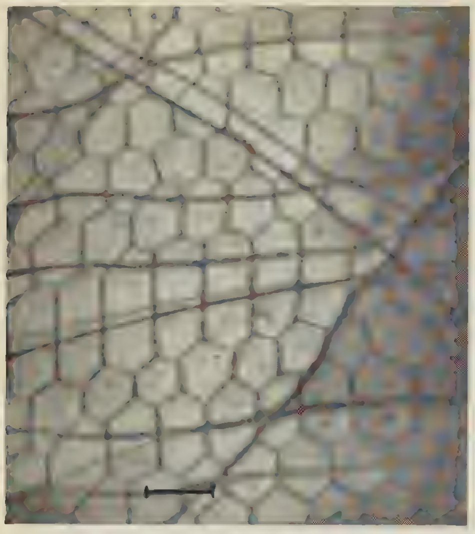

Photo. 11.

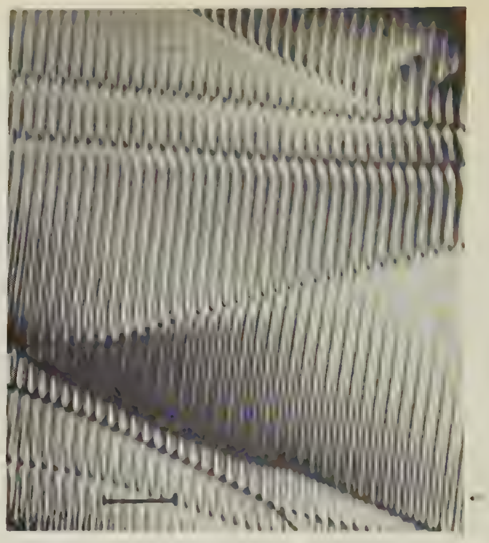

Photo. 12.

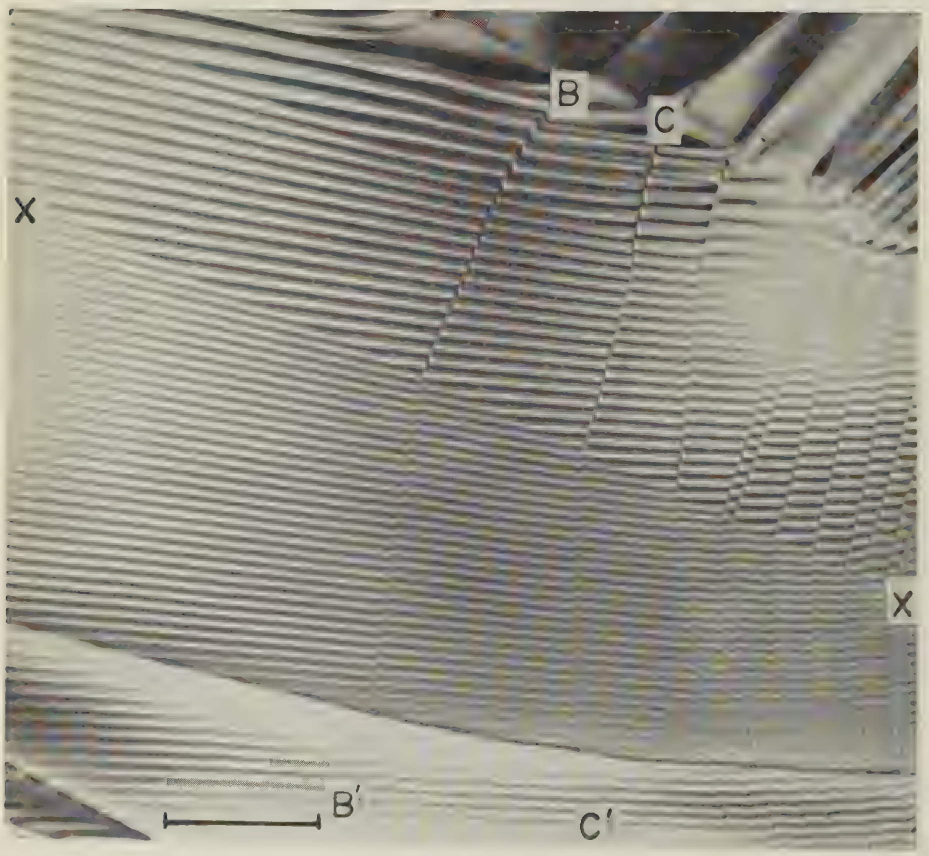

Photo 13.

Photo. 11. Thick film of molybdenite. Magnification: 9,000.
Photo. 12. Taken at 600°C. Magnification: 13,000.
Photo. 13. Taken at 600°C. Magnification: 21,000.

by dislocation theory. For the same reason, we also conclude that most of the patterns represent dislocations. A few exceptions are surface steps as explained in subsection (f) (SS' in Photos. 8 and 9).

(a) *Distortion of extinction contours*

Pictures similar to Photo. 5 were previously obtained by Hibi[5] in the case of mica. Uyeda[6] reproduced one of them and stated that the line patterns are " without a doubt due to imperfections ". It has now become clear that the line patterns represent dislocations.

Extinction contours are remarkably distorted across each dislocation lines when the films are thin (Photos. 5–8). The same phenomenon was observed by Hashimoto[7] for MoO_3 films. He concluded that the distortion is due to bending of the films. We attribute the cause of the bending to the stress around dislocations. Fig. 1 illustrates a rubber model of a film with two edge dislocations. Regular parts of the model is made merely by pasting two rubber sheets on which parallel lines have been drawn. To make a dislocated part, the lower sheet is stretched normal to the parallel lines so that one edge dislocation is produced between the stretched (lower) and the unstretched (upper) sheets. Keeping the lower sheet stretched, the two sheets are pasted together. When the tension stretching the lower sheet is released, the pasted part buckles as observed in Fig. 1.

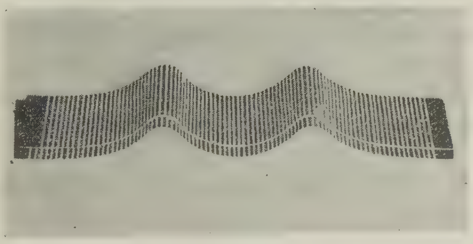

Fig. 1. Rubber model of a thin film with two edge dislocations.

(b) *Moiré fringes and images of dislocations*

It may be worth-while to make clear the relation between moiré fringes and images of dislocations before going into detailed interpretations of reproduced pictures. For the sake of simplicity, the explanation is given by the use of a simple two-dimensional model.

Let us consider two sheets of net as shown in Fig. 2a. Draw an arbitrary curve on one of them and shift the part rightside the curve by a Burgers vector b, resulting in a strain along the curve (Fig. 2b). Then superpose Fig. 2a over Fig. 2b so that the lattices coincide perfectly over the unstrained part (Fig. 2c). A band is observed along the curve, corresponding to an image of dislocation. If the strain is limited in a narrow region along the curve, the band is narrow corresponding to a sharp image of dislocation. If, however, the strain is spread over a broader region, the band becomes broader. The broadened band may adequately be called moiré fringe, because many of moiré fringes observed in

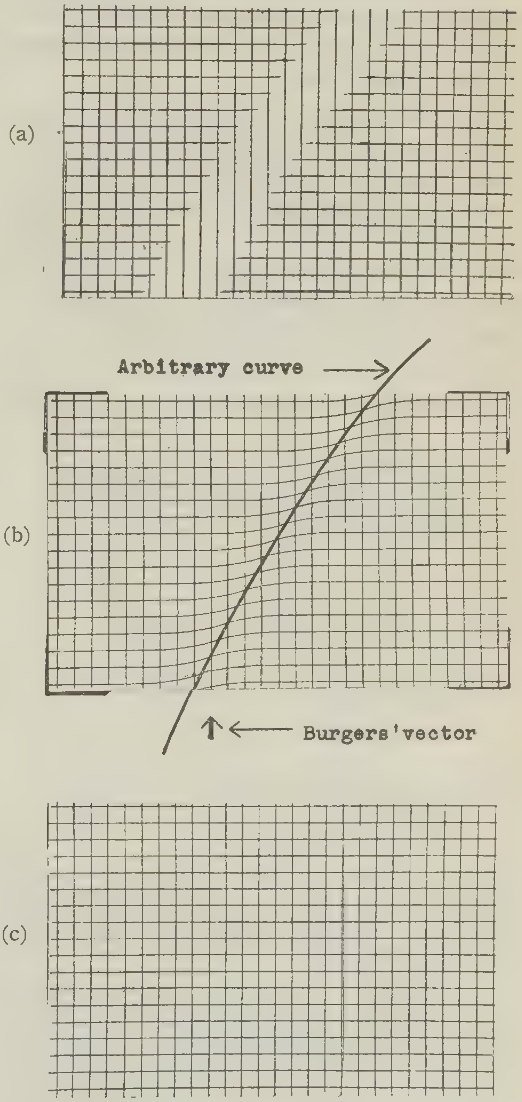

Fig. 2. Illustrating an image of dislocation superposition of (a) over (b) results in (c).

everyday life, *e.g.*, moiré patterns on window curtains, are produced by some kind of strain. Thus it has become clear that there is no discrete difference between a sharp image of dislocation and a broad moiré fringe. It may be said that a sharp image of dislocation is an extreme case of moiré fringes. In the following discussions, however, the term, moiré fringe, is used only for relatively broad bands.

In Photo. 9, the network consists of sharp images of dislocations in most part. Near the curve SS' however, the network looks like moiré pattern. This is understood according to the above discussion. It is often observed that fine networks change to moiré patterns. This change may be caused by the interaction between dislocations.

(c) *Moiré patterns and grid of dislocations*

It is known in dislocation theory that a regular grid of screw dislocations causes a rotation[8]. When, however, the strain accompanying the dislocation is concentrated, the rotation is stepwise (Fig. 3). The steps become gradual as the strain is spread and finally a uniform rotation is obtained*.

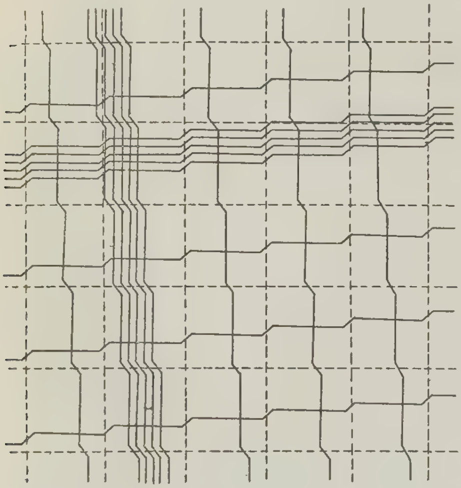

Fig. 3. Stepwise rotation caused by dislocation grid**. Lines indicate the net planes just above the dislocation grid and broken lines indicate screw dislocations.

In part A of Photo. 8 a two-dimensional moiré pattern is observed. It may be a rotation moiré and thus each fringe in part A may correspond to a screw dislocation. The fringes in part A are not perfectly periodic, and the grid is somewhat distorted. The distortion is more remarkable in other parts of Photo. 8. In part B, one set of parallel fringes in part A changes to irregular curves while the other set remains as parallel lines. The structure similar to part B is found also in Photos. 4 and 9. Parallel lines and irregular curves look very different. However, it is sure that both of them represent dislocations with Burgers vectors parallel to the cleavage plane, because in Photo. 8 both of them are extensions of screw dislocations in part A.

Photos. 12 and 13 have also the structure of parallel lines and irregular curves. In Photo. 13 parallel lines are so broad that they may better be called moiré fringes and the irregular curves indicated by BB' etc. are relatively sharp. The broad fringes and sharp curves look so different that they seem to represent different things. However, we conclude that both of them represent dislocations because the structure of parallel lines and irregular curves is similar to that in part B of Photo. 8. This conclusion is supported in the next subsection.

It is supposed that most of the observed dislocations have Burgers vectors parallel to the cleavage plane. Dislocations with Burgers vectors normal to the cleavage plane are also probable. However, they have not yet been identified. Although the mechanism of the formation of dislocations is not clear, it is highly probable that a set of dislocations such as parallel lines is produced from a source by the severe stress applied when the specimen is pealed.

(d) *Parallel lines*

According to dislocation theory, a set of parallel screw dislocations causes a shear[8]. We first considered that parallel lines observed in Photos. 4, 8, 9, and 13 are screw dislocations. Similar to the case of rotation, the shear is stepwise when parallel lines are sharp (Photo. 9) and is uniform* when they are broad (Photo. 13). In part B of Photo. 8, the spacing of parallel lines is only 200Å. This indicates a very strong shear stress. The irregular curves which intersects the parallel lines may cancel the stress more or less. It is often observed that two sets of parallel lines make a grid when the spacings become small. By the formation of a grid, the stress may be released, resulting in a rotation.

---

* It should be noted that the grid of screw dislocations corresponding to a uniform rotation is not unique. For this reason, the dislocation interpretation of rotation moiré includes some ambiguity.

** A better illustration is available in: W. T. Read: *Dislocations is Crystals* (McGraw-Hill, 1953), p. 179.

* Similar to the case of uniform rotation [footnote to subsection (c)], the set of dislocations corresponding to a uniform shear is not unique.

The spacing of the broad fringes in Photo. 13 is as large as 1,000Å. For such a large spacing no spreading of strain has been observed in pictures taken at room temperatures. Thus it is likely that the spreading is an effect of the high temperature (Sec. 3). The fringes refract on boundary XX' and the phase of fringes shifts across the irregular curves BB', CC' etc. (Photo. 13). A tentative interpretation of the refraction and the phase shift is illustrated in Fig. 4. The refraction may imply a discontinuous change of shear on the boundary. If the parallel fringes were rotation moiré, the so-called moiré dislocations[9] should have been observed instead of the refraction. The phase shift implies that the dislocation lines corresponding to the irregular curves have an edge component as predicted by Hashimoto[10]. Similar phenomenon was also observed by Izui[11] for graphite.

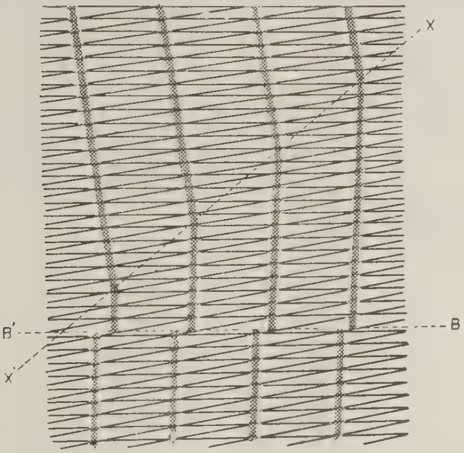

Fig. 4. Illustrating the refraction and phase shift of moiré fringes in Photo. 13.

The above discussions are based upon the assumption that the parallel lines are screw dislocations. On the other hand, Geach and Phillips[4] believed that the parallel lines observed by them are edge dislocations. The parallel fringes observed by us may also be interpreted as edge dislocations. At the present stage, it is not yet decided whether parallel lines are screw or edge. Probably, they are sometimes screw, sometimes edge and sometimes have both components.

(e) *Contrast of dislocations*

Hirsch et al.[3] developed the theory of diffraction contrast which explains images of dislocations. According to them, a Bragg reflection which is weakly excited in the surrounding of a dislocation is enhanced by the strain accompanying the dislocation. The enhancement causes the contrast in the image of dislocation. If two Bragg reflections are simultaneously excited, the image is doubled. Hirsch et al.[3] have proved that the image of a dislocation vanishes under the condition

$$(b \cdot h) = 0 , \qquad (1)$$

where b is the Burgers vector of the dislocation and h is the reciprocal lattice vector corresponding to the Bragg reflection which is weakly excited in the surrounding of the dislocation.

In part C of Photo. 8 only one set of parallel fringes is remarkable and the other set is almost invisible. Since it is certain that there is a grid of dislocations in part C, the vanishing of one set must be due to relation (1).

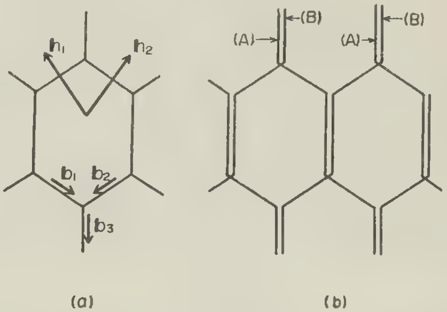

Fig. 5. Explanation of hexagonal network in Photo. 11.

The structure of the hexagonal network in Photo. 11 can also be explained by relation (1). We assume that the network is composed of screw dislocations and that two Bragg reflections h_1 and h_2 are simultaneously excited (Fig. 5a). Since neither $(h_1 \cdot b_3)$ nor $(h_2 \cdot b_3)$ vanishes, the parts of the network with Burgers vector b_3 appear as double lines. On the other hand, since $(h_1 \cdot b_2)$ vanishes but $(h_2 \cdot b_2)$ does not, the parts with Burgers vector b_2 appears as single lines. Similarly, the parts with b_1 are also single. The zigzag lines indicated by (A) are produced by reflection h_1 and those (B) by h_2 (Fig. 5b). The pattern illustrated in Fig. 5b agrees with Photo. 11. It should be noted that the specimen of Photo. 11 is so thick that the incident spot does not appear in the diffraction pattern (Sec. 3). Therefore the simple theory of diffraction contrast must be modified to explain the detail of contrast observed in Photo. 11.

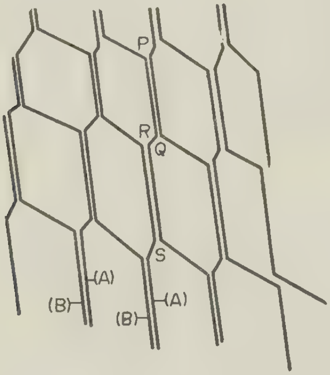

Fig. 6. Network in Photo. 10b.

In Photo. 10b a pattern as illustrated in Fig. 6 is observed. If we assume that the two sets of zigzag lines (A) and (B) in the figure are produced by reflections h_1 and h_2, respectively, we see that (A) is on the left and (B) is on the right along the segment RS, while the relation is reversed along the segment PQ. This cannot be understood if both segments have the same Burgers vector. An alternative interpretation is based upon a conjecture that a single Bragg reflection produces n-ple images according to n given by

$$(h\,b)=n\,. \tag{2}$$

Relation (1) is a special case of this relation. If we assume that the network in the figure is composed of screw dislocations and h is parallel to the segment RS, it is possible that $n=2$ for the segment parallel to RS and $n=1$ for the other segments. Anyway, no conclusion has yet been obtained.

In Photo. 6, hexagonal networks as illustrated in Fig. 7a are observed which are essentially the same as that in Fig. 6. In this case, however, the film is thin and distortion of extinction contours is remarkable. Thus it is probable that a part of the hexagonal network is caused by extinction contours as illustrated in Fig. 7b. A similar tendency is also observed in Photo. 3.

Photo. 12, which was taken at a high temperture, shows lines which are doubled in some parts. This may be interpreted similar to Photo. 7. In Photo. 7, however, images of dislocations are sharply distinguished from extinction contours, while in Photo. 12 they cannot be distinguished. This complicacy may be caused not only by the deformation of the film but also by the spreading of strains accompanying dislocations. In general, images of dislocations, moiré fringes and extinction contours are not sharply distinguished from each other.

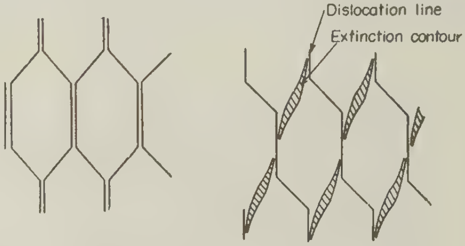

Fig. 7. Schematic illustration of hexagonal network in Photo. 6.

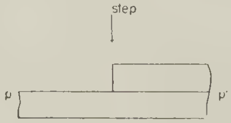

Fig. 8. Surface step.

(f) *Surface steps*

Curves indicated by SS' in Photos. 8 and 9 may be surface steps or grain boundaries. Taking into acccount that molybdenite has a layer structure, surface steps are more probable. In Photo. 8, for example, the upper part is assumed to be thinner than the lower part. Many dislocations in the thicker part stop at the step. This is understood by assuming that the dislocations lie on the plane PP' in Fig. 8. It is also observed in Photos. 8 and 9 that a few dislocations in the thinner part also stop at the steps. This is not yet interpreted.

In Photo. 10a we see a boundary line indicated by S at the top. The line resembles surface step SS' in Photo. 9. However, at the center of the circle (Photo. 10a), the feature of the line changes suddenly and near the left side of the picture the continuation of the line looks like a usual dislocation line rather than a step. It may be possible to interpret that the step running from S terminates at the center of the circle, indicating that there is a bundle of screw dislocations normal to the film at the center. Similar situation is often observed in other pictures and sometimes it is most difficult to distinguish surface steps from usual dislocations.

§ 5. Acknowledgement

We wish to express our sincere thanks to Dr. B. Tadano and the electron microscope group of the Hitachi Central Laboratory for taking many electron micrographs in the preliminary experiment. We also wish to thank to Dr. P. B. Hirsch, Dr. J. W. Menter and their co-workers for showing us many of their unpublished pictures and for valuable comments.

The present work was supported by the Scientific Research Grant of the Japanese Ministry of Education in 1958.

References

1) Y. Kamiya and R. Uyeda: Acta Cryst: to be published.
2) G. Borrmann: Phys. Z. **42** (1940) 157.
K. Kohra and H. Watanabe: J. Phys. Soc. Japan **14** (1950) 1119.
3) P. B. Hirsch, A. Howie and M. J. Whelan: Vierter Internationaler Kongress für Elektronenmikroskope p 527 (1958).
P. B. Hirsch, A. Howie and M. J. Whelan: Phil. Trans. Roy. Soc. **A 252** (1960) 499.
4) G. A. Geach and R. Phillips: Vierter Internationaler Kongress für Elektronenmikroskope p 571 (1958).
5) T. Hibi and S. Takahashi: Sci. Rep. RITU. **11** (1955) 490.
6) R. Uyeda: J. Phys. Soc. Japan **10** (1955) 256.
7) H. Hashimoto: J. Phys. Soc. Japan **9** (1954) 150.
8) A. H. Cottrell: *Dislocation and Plastic Flow in Crystals* (Oxford, 1953) Chap. III.
W. T. Read: *Dislocation in Crystals* (McGraw-Hill, 1953) Chap. XII.
9) H. Hashimoto and R. Uyeda: Acta Crysi. **10** (1957) 143.
10) K. Izui: J. Phys Soc. Japan **14** (1969) 1829.

JOURNAL OF THE PHYSICAL SOCIETY OF JAPAN, Vol. 15, No. 11, NOVEMBER, 1960

Beam-Type Masers for Radiofrequency Spectroscopy

By Koichi SHIMODA, Hiroshi TAKUMA,* and Tadao SHIMIZU

Department of Physics, Faculty of Science,
University of Tokyo, Tokyo

(Received June 28, 1960)

Beam-type masers for radiofrequency spectroscopy of molecules are considered. The theoretical estimate of sensitivity is discussed and a table of minimum detectable beam intensity and estimate of available beam intensity for some of the low frequency transitions is given. A K-type doubling transition, $4_{31}\rightarrow 4_{32}$, of formaldehyde was observed as an emission line at 4.5769 ± 0.0023 Mc, and compared with theories. The observed saturation in focusing is probably due to the non-adiabatic change of rotational states in the focuser. The saturation broadening of the line with increasing rf field shows agreement with theory.

§ 1. Introduction

The radiofrequency molecular spectroscopy using three-level maser action was previously developed by one of the authors.[1] Although it was proved to be useful in detecting low frequency transitions of molecules, the properly spaced third level was necessary in order to perform an effective pumping.

On the other hand, the beam maser can be operated on two levels, between which the transition is allowed, if molecules in either of the two levels are selected by an appropriate method. It is well known that the beam maser spectroscopy has been developed in the microwave frequency range. Although the application of the technique to still higher or much lower frequencies seems promising, very little experimental work has been explored in these ranges.

The energy of a single photon is very small at low frequencies, but the noise figure of an amplifier is much smaller than that for microwaves. Therefore, it is probable that not a few transitions of molecules are detectable by a beam maser even in the megacycle range.

Theoretical considerations on the sensitivity and behavior of the beam-type rf maser are given in this paper. An experimental work on a K-type doubling transition of formaldehyde molecule, $4_{31}\rightarrow 4_{32}$, and the result are also described.

§ 2. Theoretical Considerations

A simplified diagram of the beam-type maser for radiofrequencies is shown in Fig. 1. The beam source and the focuser are essentially the same as those used for microwave masers. Molecules in the beam make transitions inside a parallel-plate condenser, instead of a cavity resonator in a microwave maser. A resonant circuit tuned to the transition frequency is formed with the capacitance of the parallel-plate condenser, C_x, and an external inductance, L. The resonant circuit is excited by a signal generator and the rf voltage across the electrodes is amplified, rectified and displayed on a cathode ray oscilloscope and a recorder. Low frequency Stark modulation and a narrow-band lock-in detector can be used to attain a good sensitivity.

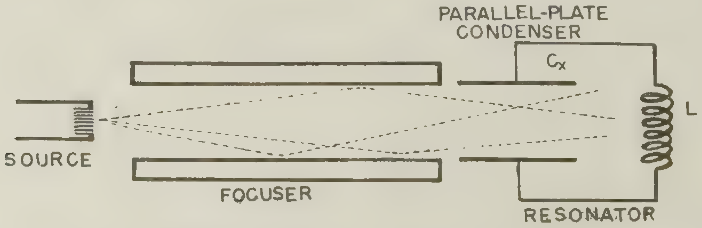

Fig. 1. Simplified diagram of the beam-type rf maser.

---

* Present address: Department of Applied Physics, Faculty of Engineering, University of Tokyo, Tokyo.

(i) Focusing

The Stark energy of a slightly asymmetric rotor can be expressed by

$$W_E=\pm\left[\sqrt{\left(\frac{h\nu_0}{2}\right)^2+\left\{\frac{\mu KME}{J(J+1)}\right\}^2}-\frac{h\nu_0}{2}\right] \quad (1)$$

where E is the intensity of electro-static field, ν_0 the frequency corresponding to the transition between k-type doublets. Because $\frac{\mu KME}{J(J+1)}\gg h\nu_0$ in the focusing field of an rf maser, electro-static focusing seems to be generally more effective compared to the focusing of molecules in doublet levels corresponding to microwave frequencies.

However, the behavior of the rotational state in a focusing field may not be assumed to be adiabatic, when the Stark energy is much larger than the rf photon energy $h\nu_0$ and when the time of flight of the molecules in the focuser, Δt, is not very large compared with $1/\nu_0$. Besides, a rapid change of electric field which the molecules see between the focuser and the parallel-plate condenser must stimulate transitions from focused to unfocused state.

Therefore, the focusing efficiency in the rf maser should show stronger saturation effect with increasing focuser voltage than in a microwave maser. Any further consideration of the theory of saturation character of the focuser is not given in this paper, but an experimental result will be described in the next section.

(ii) Sensitivity

Emission (or absorption) of rf power by the molecules between the parallel electrodes is detected by the increase (or decrease) of rf voltage across the electrodes. It may be expressed by the increase (or decrease) of the quality factor Q of the resonant circuit. The rf electric field between the electrodes of separation d,

$$E(\nu,t)=E\cos 2\pi\nu t=\frac{V}{d}\cos 2\pi\nu t\,,$$

is given by a loosely coupled signal generator. The power emitted form the molecules is written in the form[2)]

$$\Delta P=nh\nu_0\frac{x^2}{(\omega-\omega_0)^2+x^2}\sin^2\{(\omega-\omega_0)^2+x^2\}^{\frac{1}{2}}\frac{t}{2}\,, \quad (2)$$

where n is the number of excited molecules entering the parallel-plate condenser in a unit time, $x=E\bar{\mu}/\hbar$, $\omega_0/2\pi$ the frequency of transition, and L the lengh of the electrodes. Here $\bar{\mu}$ is the average for the component of the molecular dipole matrix element along the direction of rf field in the parallel-plate condenser.

At the center frequency of the line, $\omega=\omega_0$, the emitted power is

$$\Delta P=nh\nu_0\sin^2\frac{xL}{2v}\,, \quad (3)$$

where $v=\frac{2}{\sqrt{\pi}}\alpha=\frac{2}{\sqrt{\pi}}\sqrt{\frac{2kT}{M}}$ is the average velocity of molecules.

The change of the quality factor becomes

$$\Delta\left(\frac{1}{Q}\right)=-\frac{2\Delta P}{\omega_0 CV^2}\,,$$

where $C=C_x+C_s$, C_s being the stray capacitance.

Since the resonant circuit can be assumed to be driven by a constant current generator, the increase of rf voltage is given by

$$\Delta V=-VQ\,\Delta\left(\frac{1}{Q}\right)=\frac{2n\bar{\mu}Q}{Cd}\,\frac{\sin^2\left(\frac{xL}{2v}\right)}{x}\,. \quad (4)$$

The optimum value of rf voltage for maximum ΔV is calculated by differenciating Eq. (4).

$$x_{\rm opt}=2.33\frac{v}{L}\,, \quad (5)$$

$$V_{\rm opt}=2.33\frac{\hbar}{\bar{\mu}}\,\frac{vd}{L}\,. \quad (6)$$

The resonator noise voltage v_n is calculated from

$$\frac{v_n{}^2}{2Z}=FkT\Delta f\,, \quad (7)$$

where F is the over-all noise figure and Δf the bandwidth of the spectrometer, and $Z=\frac{Q}{C\omega}$ the impedance of the resonant circuit.

Then the emission (or absorption) of rf power is detectable, when $\Delta V>v_n$. From Eqs. (4), (5) and (7) the minimum detectable intensity of the beam flux is

$$n_{\rm min}\approx\frac{2vd}{\bar{\mu}L}\sqrt{\frac{C}{\omega_0 Q}FkT\Delta f} \quad (8)$$

in a unit time. Values of $n_{\rm min}$ for rf transitions of some molecules are calculated and shown in Table I, from the assumed values of $F=2$, $C=20$ pF, $T=300$°K, $\Delta f=1$ cps, $Q=100$, $d=0.5$ cm, and $L=10$ cm.

Now the flux of state-selected molecules from the focuser can be evaluated according to the theory by one of the authors.[3] From equation (3.9) in reference (3), the flux of focused molecules is given by

$$n \approx n_0 f \frac{4A}{\pi^2 A_0}\left(\frac{l}{R}\right)^2 \left(\frac{\bar{\mu}E}{kT}\right)^2 , \qquad (9)$$

since

$$\frac{v_0^2}{\alpha^2} \approx \frac{\bar{\mu}E}{kT} , \quad \text{and} \quad N = \frac{\sqrt{\pi}\, n_0 f}{A_0 \alpha} ,$$

where n_0 is the total flux of molecules flowing out from the source of area A_0, f the fraction of molecules in a particular rotational state, l the length of the focuser, R the radius, and E the maximum intensity of electric field in the focuser. The average of dipole matrix element of molecules entering the focuser, $\bar{\mu}$, is given by

$$\bar{\mu}^2 = \mu^2 \frac{K^2 \langle M^2 \rangle_{av}}{J^2(J+1)^2} = \frac{\mu^2 K^2}{3J(J+1)} , \qquad (10)$$

Then for a slightly asymmetric rotor, when $\bar{\mu}E \gg h\nu_0$, the flux of focused molecules can be written by

$$n \approx n_0 f \frac{4A}{3\pi^2 A_0}\left(\frac{l}{R}\right)^2 \frac{\mu^2 K^2 E^2}{J(J+1)k^2 T^2} . \qquad (11)$$

Numerical examples for some molecules are calculated and compared with $n_{\min}$ in Table I. These values have been calculated from Eqs. (8) and (11) with the following values, $n_0 = 10^{17}$ molcules/sec and, $A/A_0 = 1$, $l = 40$cm, $R = 0.5$cm, and the eight-pole focuser voltage of 10 kV corresponding to $E = 40$ kV/cm. The ratio of n to $n_{\min}$ may be considered as a theoretical estimate of signal-to-noise ratio of the line. Table I shows that many of the low frequency

Table I. Rf transistions of some slightly asymmetric molecules for beam-type masers. Transition frequencies, ν_0, are calculated by a rigid rotor approximation. Values of $n_{\min}$ and n are calculated from Eqs. (8) and (11).

Molecule	Transition	f	ν_0	$n_{\min}$	n	$n/n_{\min}$
H_2CO	$3_{30} \to 3_{31}$	0.48%	0.65Mc	2.4×10^{11}	176×10^{11}	75
	$4_{31} \to 4_{32}$	0.59	4.58	1.1	139	121
	$5_{32} \to 5_{33}$	0.68	18.3	0.48	100	206
	$6_{33} \to 6_{34}$	0.75	54.8	0.33	80	234
	$6_{42} \to 6_{43}$	0.19	0.23	3.8	36	10
	$7_{43} \to 7_{44}$	0.20	0.85	2.3	28	12
HDCO	$3_{30} \to 3_{31}$	0.27	1.96	1.4	96	70
	$4_{31} \to 4_{32}$	0.33	13.8	0.67	69	104
	$5_{32} \to 5_{33}$	0.38	54.7	0.41	54	130
	$5_{41} \to 5_{42}$	0.32	0.22	4.8	81	17
	$6_{42} \to 6_{43}$	0.35	1.10	2.9	63	22
D_2CO	$3_{30} \to 3_{31}$	0.15	2.68	1.1	54	49
	$4_{31} \to 4_{32}$	0.19	18.7	0.55	42	77
	$5_{32} \to 5_{33}$	0.21	75.0	0.34	32	95
	$5_{41} \to 5_{42}$	0.37	0.38	3.6	96	27
	$6_{42} \to 6_{43}$	0.43	1.8	1.9	80	41
	$7_{43} \to 7_{44}$	0.45	6.96	1.1	64	57
H_2CCO	$2_{20} \to 2_{21}$	0.04	0.40	4.4	5	1.2
	$3_{21} \to 3_{22}$	0.06	1.98	2.7	4	1.3
	$4_{22} \to 4_{23}$	0.07	5.94	2.1	3	1.3
	$5_{23} \to 5_{24}$	0.09	13.9	1.7	2	1.3
HCOOH	$2_{20} \to 2_{21}$	0.05	30.4	0.41	9	22.0
	$3_{30} \to 3_{31}$	0.07	0.35	3.6	14	3.9
	$4_{31} \to 4_{32}$	0.09	2.46	1.8	11	6.2
	$5_{32} \to 5_{33}$	0.11	9.89	1.1	9	8.2
	$7_{43} \to 7_{44}$	0.13	0.56	4.6	10	2.2
	$8_{44} \to 8_{45}$	0.14	1.68	3.0	8	2.8
	$9_{45} \to 9_{46}$	0.15	4.35	2.1	7	3.5

rotational transitions of molecules are detectable.

(iii) Line-width

The line-width of the spectrum is determined by the time of flight of the molecules in the parallel-plate condenser. The half-width is[2),4)]

$$2\Delta\nu_0=0.9\,\frac{v}{L}\,,$$

when the amplitude of rf field is sufficiently small.

The saturation broadening of the line can be calculated by taking average of Eq. (2) multiplied by a weight factor, $\bar{e}^{t/\tau}$. The saturation broadened line-width is

$$2\Delta\nu_{\text{sat}}=2\sqrt{(\Delta\nu_0)^2+\left(\frac{x}{2\pi}\right)^2}\,. \qquad (12)$$

For a given rotational transition, there are $2J+1$ different components corresponding to different values of M. The component with larger value of M shows stronger saturation than the component with smaller value of M. It should be noted that the space quantization in the rf field is independent of the space quantization in the focusing field, although the same notation M is used in either field.

§ 3. Experimental Results

A radiofrequency spectral line of formaldehyde, corresponding to the transition between K-type doublets, $4_{31}\rightarrow4_{32}$, was investigated by a beam-type maser. A block diagram of the spectrometer is shown in Fig. 2. The rf electrodes of three parallel plates are 12 cm long with the spacings of 0.4 cm. They are held in a shield box by two sheets of polystyrene at their edges. The state-selected molecular beam enters the rf field through a hole in one side of the shield box.

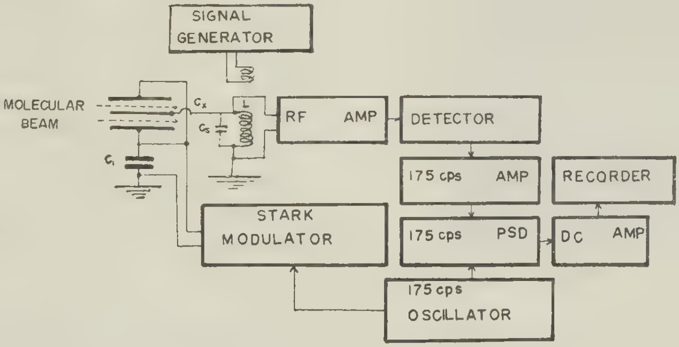

Fig. 2. Block diagram of the maser spectrometer.

A square wave modulation voltage is applied to the outer two electrodes with variable dc bias. The rf by-pass capacitor C_1 is 0.1 μF, C_x=8pF, $C=C_x+C_s=25$ pF. The Q value of the LC resonator is about 70. A signal generator which feeds the rf signal is swept by a small synchronous motor.

The noise figure of the spectrometer was measured to be 3, including the noise of the rf signal generator and of the 175 cps oscillator. The time constant of the dc amplifier used in the following work was $\tau=2.5$ seconds, so that the effective bandwidth Δf is

$$\Delta f=2\times\frac{1}{4\tau}=0.2\,\text{cps}\,,$$

including the 175 cps image noise.

The molecules of formaldehyde were produced by heating powdered paraformaldehyde. A dry ice trap was used in order to remove impurities and polymers of H_2CO. The beam source and the eight-pole focuser are the same ones as used for microwave works.[5)6)] The intensity of the beam flux was estimated to be $10^{17}\sim10^{18}$ molecules per second.

A typical trace of record of the observed spectrum with a focuser voltage of 15 kV and an rf voltage of 3 mV peak is shown in Fig. 3 The observed center frequency is

$$\nu_0=4.5769\pm0.0023\ \text{Mc}\,,$$

where the error is 3 times the standard deviation.

The observed signal-to-noise ratio of the line in Fig. 3 is nearly 40, while the theoretical estimate from Eqs. (8) and (11) gives a value of 1200 for a total beam flux $n_0=5\times10^{17}$ molecules/sec, $V=10$ kV, $v=4.6\times10^4$ cm/sec, $\bar{\mu}=$

0.907 D, ($\mu=2.34$ D), and $L=12$ cm. The difference may be due to the divergence of the beam within the parallel-plate condenser, and to the non-adiabatic behavior of molecules in the focuser region as described before.

The intensity of the emission line was observed as a function of focuser voltage, and the result is plotted in Fig. 4. According to the theoretical estimate given by Eq. (9), the number of focused molecules is proportional to the square of focuser voltage. But Fig. 4 shows strong saturation and confirms violation of adiabatic assumption in the focusing field, as described in § 2 (i). At a focuser voltage of 1 kV for example, the observed signal-to-noise ratio is about 4, while the calculated value of $n/n_{\min}$ is 12, and the discrepancy is smaller.

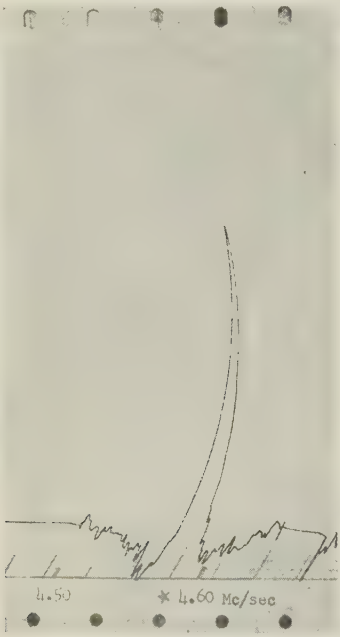

Fig. 3. Typical trace of the $4_{31}\rightarrow 4_{32}$ transition of H_2CO.

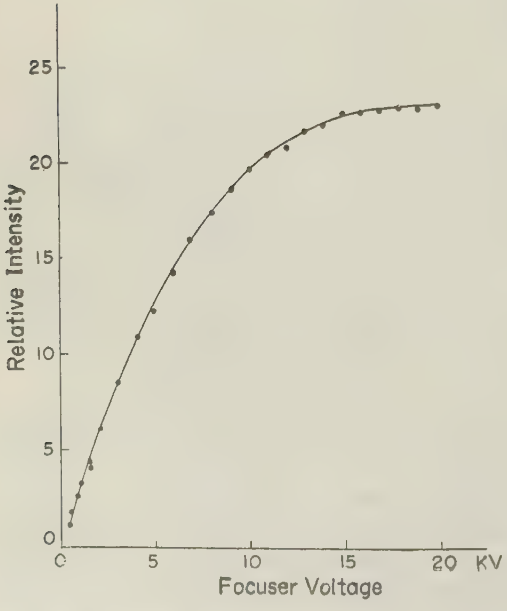

Fig. 4. Observed saturation in focusing.

The half-width of the line was measured as a function of rf valtage on the parallel plate condenser as shown in Fig. 5. A theoretical curve of Eq. (12) for the average value of dipole moment $\bar{\mu}$ is also shown. Agreement between theory and experiment seems good.

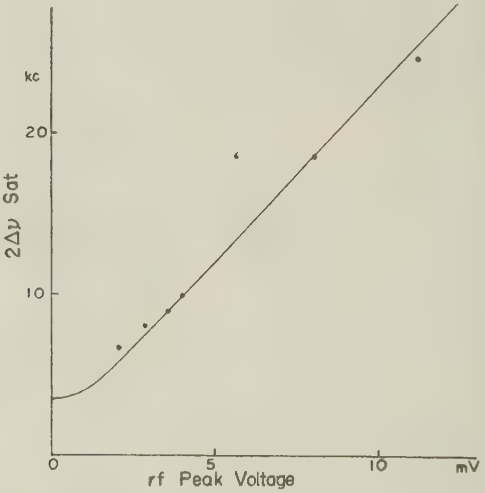

Fig. 5. Half-width of the line as a function of rf voltage.

It may be noted that the Stark shift of an rf transition in a dc field is larger than the shift of a microwave transition in general. Thus the broadening by inhomogeneous dc field becomes large in the rf maser. Even a surface potential difference of the electrodes of the order of some ten millivolts is large enough to somewhat broaden the line. For example, a dc field of 100 mV/cm produces a Stark shift of 2.1 kc for the $M=4$ component in the $4_{31}\rightarrow 4_{32}$ transition of H_2CO.

§ 4. Discussions

The centrifugal distortion of formaldehyde molecule was discussed by Lawrance and Strandberg,[7] and recently by Oka.[8] The calcuated frequencies of the $4_{31}\rightarrow 4_{32}$ transition by these two methods are 4.572 Mc and 4.575 Mc, respectively. They differ from each other, and the value from Oka's theory agrees well with our experimental result. Oka has solved the secular equation based on the Hamiltonian by Kivelson and Wilson.[9] Thus it seems natural that his theory gives more correct value than the semi-empirical calculation according to Lawrance and Strandberg.

According to the theory of the magnetic hyperfine structure of formaldehyde,[6] the $4_{31} \to 4_{32}$ line consists of three strong $\Delta F=0$ transitions and four weak $\Delta F=\pm 1$ transitions. Because the splitting between $\Delta F=0$ components are calculated to be several cycles per second, it is reasonable that the line is observed as a singlet. The $\Delta F=\pm 1$ components are very weak and could not be observed in the present experiment. However, by improving the sensitivity the $\Delta F=\pm 1$ transitions would be observed since the separation is expected to be of the order of 10 kc.

The Stark and Zeeman effects of the rf transition can also be studied by the high resolution beam maser spectrometer. The Stark voltage can be applied to the parallel-plate condenser. The measurement of the Stark pattern of the $4_{31} \to 4_{32}$ line of H_2CO is now in progress.

References

1) K. Shimoda: J. Phys. Soc. Japan **14** (1959) 954.
2) K. Shimoda, T. C. Wang, and C. H. Townes: Phys. Rev. **102** (1956) 1308.
3) K. Shimoda: J. Phys. Soc. Japan **12** (1957) 1006.
4) J. P. Gordon, H. J. Zeiger, and C. H. Townes: Phys. Rev. **99** (1955) 1264.
5) K. Shimoda: J. Phys. Soc. Japan **13** (1958) 939.
6) H. Takuma, T. Shimizu, and K. Shimoda: J. Phys. Soc. Japan **14** (1959) 1595.
7) R. B. Lawrance and M.W.P. Strandberg: Phys. Rev. **83** (1951) 363.
8) T. Oka: Thesis submitted to the Department of Chemistry, University of Tokyo; to be publised.
9) D. Kivelson, and E.B. Wilson: J. Chem. Phys. **20** (1952) 1575.

JOURNAL OF THE PHYSICAL SOCIETY OF JAPAN, Vol. 15, No. 11, NOVEMBER, 1960

On the Paramagnetic Susceptibility of Sm^{3+} ion

By Norikiyo URYU
Department of Physics, Faculty of Science, Kyusyu University, Fukuoka, Japan

(Received July 25, 1960)

Synopsis:

The paramagnetic susceptibility of Sm^{3+} ion measured by Borovik-Romanov and Kreines are explained on the basis of crystalline field theory. Postulatiug an appropriate cubic or trigonal potential for two modifications of Sm_2O_3, the magnetic behaviours are well explained with the best choice of the coefficients of each potential. Total separations of the ground manifold $216k$ and $432k$ are obtained for the two cases and are compared with the above author's rough estimations 52 cm^{-1} and 150 cm^{-1}. Further, their erroneous assignment for the lowest state is pointed out.

§1. Introduction

The paramagnetism of the rare earth salts has been investigated in detail both theoretically and experimentally. The $4f$ electrons which contribute to the magnetism are sufficiently screened by outer electrons and the magnetic behaviours, for instance, the effective Bohr magneton number, are well explained as that of free ion. In Sm^{3+} or Eu^{3+}, the excited energy levels which are split by L–S coupling are near the ground level, and the contribution of the high frequency part pointed out by Van Vleck[1] is large. Taking this into account, the paramagnetic susceptibilities of rare earth ion can be explained satisfactorily.

For the ions in crystals, the effects of the crystalline field are not so large and the intra-ionic L–S coupling is the predominant perturbation for the free ion. Accordingly, as the stationary state, we have the Russel-Saunders coupling in which $2S+1$ or $2L+1$ energy levels of different J values are split by above perturbation. The crystalline field affects the energy states of each J values and removes the $2J+1$ degeneracy partially or wholly except for the Kramers doublets. The studies of the rare earth salts which take into account the effect of the crystalline field are that of Pr^{3+} and Nd^{3+} by Penney and Schlapp[2], and that of $Sm_2(SO_4)_3 7H_2O$ crystal by Miss Frank[3]. Her study ranged over the temperature 70°K∼300°K, and she concluded unimportance of the crystalline field for the susceptibility.

Recently, Borovik-Romanov and Kreines[4] investigated the paramagnetic susceptibilities of Eu^{3+} and Sm^{3+} ions over the temperature range of 12°K∼300°K and found that the magnetic properties of Sm^{3+} depend on its crystal structure. The samples investigated are the microcrystalline powder of Sm_2O_3 (Sample I of purity lower than 99.0% and Sample II of purity 99.99%) and $Sm_2(C_2O_4)_3$ $10H_2O$. Ordinary Sm_2O_3 has cubic structure (b. c. c.) and Sample II does not change its crystal structure by heating, whereas Sample I takes an essentially different structure of pseudotrigonal by heating over 720°C. Consequently, as to Sample I, the susceptibility curves for heated and unheated one separate into two, whereas that for Sample II agrees with either one of Sample I in both cases. The results of $Sm_2(C_2O_4)_3$ $10H_2O$ agrees well with Van Vleck's theoretical curve.

In order to explain these result, Borovik-Romanov and Kreines have made a simple estimation of the energy states of the ion in a crystalline field. They take the expression of the susceptibility as follows:

$$\chi=\frac{Ng^2\mu_B{}^2}{kT}\,\frac{M^2{}_{1eff}+M^2{}_{2eff}\exp\{-\varDelta W_1/kT\}+M^2{}_{3eff}\exp\{-\varDelta W_2/kT\}}{1+\exp\{-\varDelta W_1/kT\}+\exp\{-\varDelta W_2/kT\}}+N\alpha,$$

where $\varDelta W_1$, $\varDelta W_2$ are the energy differences between two upper levels and the lowest level which are split from the ground state of six-fold degeneracy, and are of $J_z=\pm 1/2$, $\pm 3/2$, $\pm 5/2$ respectively. They assume that these three doublet states are eigenstates in the presence of crystalline field and take $M_1=\pm 1/2$, $M_2=\pm 3/2$ and $M_3=\pm 5/2$. $N\alpha$ is the high frequency part. Treating $\varDelta W_1$ and $\varDelta W_2$ as the parameter, they determined their values of the best fit for the susceptibility curves, and the values thus determined are $\varDelta W_1=0$, $\varDelta W_2=52\,\mathrm{cm}^{-1}$ (73°K) in the case of cubic modification and $\varDelta W_1=20\,\mathrm{cm}^{-1}$ (29°K), $\varDelta W_2=150\,\mathrm{cm}^{-1}$ (218°K) in the case of pseudotrigonal modification. In fact, they have shown the curves of good agreement with experiments by using these values. However, the eigenstates of ${}^6H_{5/2}$ in cubic or trigonal field are not of $J_z=\pm 1/2$, $\pm 3/2$, $\pm 5/2$ but are their linear combinations, because non-diagonal matrix elements are present. Accordingly, the ground of their arguments to deduce the values of $\varDelta W_1$, $\varDelta W_2$ is meaningless.

Our present purpose is to investigate the energy level splittings by using an appropriate cubic or trigonal potential, and estimate the values of its coefficient in order to explain their experimental results. In this case, the contribution from the excited states can be considered only as the constant susceptibility and may be neglected for the temperature dependent part. Thus we shall consider the effect of crystalline field only in the manifold of $J=5/2$, or of $J=7/2$ if necessary.

§2. Crystalline Potential

We can expand the potential in spherical harmonics by assuming that it satisfies Laplace's equation, thus

$$V=\sum_{n,\,m}A_n{}^m r^n Y_n{}^m(\theta,\,\varphi). \tag{2.1}$$

For our present purpose, the number of terms in (2.1) can be considerably reduced as follows. In evaluating an integral such as $\int\chi^* V\psi d\tau$ where χ and ψ denote f-electron wave function, all terms for which $n>6$ will have zero matrix elements by the orthogonality relations for spherical harmonics and can be omitted. Similarly all terms for which n is odd have zero element because the product

$\chi^*\psi$ is unchanged by the substitution $x, y, z \rightarrow -x, -y, -z$ whereas V reverses its sign. Accordingly, as fas as we consider the f-electron, V takes the form

$$V = \sum_{m=-2}^{2} A_2^m r^2 Y_2^m(\theta, \varphi) + \sum_{m=-4}^{4} A_4^m r^4 Y_4^m(\theta, \varphi)$$
$$+ \sum_{m=-6}^{6} A_6^m r^6 Y_6^m(\theta, \varphi)\ , \tag{2.2}$$

and, being real, $A_2^m = A_2^{-m}$, $A_4^m = A_4^{-m}$ and $A_6^m = A_6^{-m}$.

Now, if we consider the case of cubic potential, the form which V takes is one for a regular octahedron of the six nearest neighbours and we have

$$V_c = A_4^0 r^4 \Big[Y_4^0(\theta, \varphi) + \sqrt{\frac{5}{14}}$$
$$\Big\{ Y_4^4\ \theta, \varphi) + Y_4^{-4}(\theta, \varphi) \Big\} \Big], \tag{2.3}$$

or by changing to Cartesian coordinates

$$V_c = D\left(x^4 + y^4 + z^4 - \frac{3}{5} r^4 \right), \tag{2.3a}$$

where $D = 15\ A_4^0/4\sqrt{\pi}$.

As for the trigonal potential, its three-fold symmetry axis can be considered as (1 1 1) direction of the regular octahedron, and we suppose that the dominant part of the trigonal potential is given as

$$V' = Fr^4 \Big[Y_4^0(\theta, \varphi) - \sqrt{\frac{10}{7}}$$
$$\Big\{ Y_4^3(\theta, \varphi) + Y_4^{-3}(\theta, \varphi) \Big\} \Big], \tag{2.4}$$

which is obtained by the coordinate transformation of (2.3). The general form of V, showing a distortion along (1 1 1) direction is, thus,

$$V_t = A_2^0 r^2 Y_2^0(\theta, \varphi) + A_4^0 r^4 Y_4^0(\theta, \varphi) + V'$$
$$+ \sum_{m=-6}^{6} A_6^m r^6 Y_6^m(\theta, \varphi). \tag{2.5}$$

Now, in the calculation of the matrix elements of these crystalline potentials it is convenient to use the method of operator equivalence by Stevens[5)], according to which we have the following relations

$$\sum A_2^0 r^2 Y_2^0(\theta, \varphi) = \sum B_2^0 (3z^2 - r^2) \equiv B_2^0 \overline{r^2} \alpha \{3J_z^2 - J(J+1)\}$$

$$\sum A_4^0 r^4 Y_4^0(\theta, \varphi) = \sum B_4^0 (35z^4 - 30r^2z^2 + 3r^4)$$
$$\equiv B_4^0 \overline{r^4} \beta \{35J_z^4 - 30J(J+1)J_z^2 + 25J_z^2 - 6J(J+1) + 3J^2(J+1)^2\},$$

$$\sum r^4 \equiv \beta \overline{r^4} \left\{ \{J^2(J+1)^2 - \frac{1}{3} J(J+1) \right\},$$

$$\sum \left(x^4 + y^4 + z^4 - \frac{3}{5} r^4 \right) \equiv \frac{\beta}{20} \overline{r^4} \{35J_z^4 - 30J(J+1)J_z^2 + 25J_z^2 - 6J(J+1)$$
$$+ 3J^2(J+1)^2\} + \frac{\beta}{8} r^4 (J_+^4 + J_-^4),$$

$$\sum A_6^0 r_6 Y_6^0(\theta, \varphi) = \sum B_6^0 (231z^6 - 315r^2z^4 + 105r^4z^2 - 5r^6)$$
$$\equiv B_6^0 \gamma \overline{r^6} [231J_z^6 - 315J(J+1)J_z^4 + 735J_z^4 + 105J^2(J+1)^2J_z^2$$
$$- 525J(J+1)J_z^2 + 294J_z^2 - 5J^3(J+1)^3 + 40J^2(J+1)^2 - 60J(J+1)], \tag{2.6}$$

where the constants α, β and γ are given with regard to the ground manifold ($4f^5\ {}^6H_{5/2}$) by

$$\alpha = \frac{13}{7.45}\ , \qquad \beta = \frac{26}{33.7.\ 45}\ , \quad \gamma = 0. \tag{2.7}$$

For the first excited state ($J = 7/2$),

$$\beta' = -\frac{26}{45.33.\ 7} \frac{8}{99} \tag{2.8}$$

is to be used instead of β. From the relation of (2.7), the last term of (2.5), i. e., the term for $n = 6$ can be neglected as far as the ground state is concerned. The expression of V' in terms of Cartesian coordinates is

$$V'=\frac{3}{16\sqrt{\pi}}F\{35z^4-30r^2z^2+3r^4+60\sqrt{2}\,xz(r^2-z^2)-80\sqrt{2}\,x^3z\}, \tag{2.9}$$

and its equivalent operator is given by

$$\begin{aligned}F'\beta\overline{r^4}[35J_z^4-30J(J+1)J_z^2+25J_z^2-6J(J+1)\\ +3J^2(J+1)^2-5\sqrt{2}\{J_z(J_+^3+J_-^3)+(J_+^3+J_-^3)J_z\}],\end{aligned} \tag{2.10}$$

where the relation $D=-30F'$ holds.

Below, we shall calculate the susceptibility treating the coefficients $D\overline{r^4}$, $B_2^0r^2$, $B_4^0r^4$ and $F'r^4$ as parameters and estimate the values of the best fit with experimental results. The cubic modification causes no trouble, as in this case only one parameter is involved. However, the case of trigonal modification has three unknown parameters and the problem becomes complicated. Now, in view of the susceptibility curves of Sample I and II, the magnitudes of the crystalline potential in each cubic structure can be inferred to be nearly the same. But, as to the change of the crystalline field when Sample I transforms into trigonal phase, nothing is revealed. As stated before, the dominant part of trigonal potential is V' which is obtained by transforming (2.3a) into the direction of (1 1 1), together with the additional field of axial symmetry due to distortion along this direction. But for the essential change, we could expect the relation $D=-30F'$ between the coefficients of crystalline field in the two phases, and it might be possible to diminish the number of parameters in this way. However, there is no definite reason for doing this. We shall take into account only the term of the second degree as the part of axial symmetry and neglect the term of the fourth degree for the time being, and estimate the coefficients of crystalline potential assuming $F\gg B_2^0$.

§ 3. The Energy Eigenvalues and the Susceptibility

The normal state of Sm^{3+} is $^6H_{5/2}$, and from the recent spectroscopic estimation we have the separation 1100 cm^{-1} (1540k) between the states of $J=5/2$ and $J=7/2$ which is caused by the L-S coupling. This almost agrees with the theoretical estimation 1070 cm^{-1} by Van Vleck with the use of shielding constant σ of 33. For our present purpose to calculate the susceptibility below 100°K, the excited states contribute only as the so-called high frequency part. Thus, for the time being, we have only to consider the crystalline field splitting in the manifold of $J=5/2$.

If we take as the perturbation the cubic potential (2.3a) or pseudotrigonal potential (2.5), the secular determinant of sixth degree for the ground state decomposes into three secular determinants of second degree. The necessary matrix elements are given as follows:

$$\begin{aligned}&<J, M|J_+^4+J_-^4|J, M-4>=<J, M-4|J_+^4+J_-^4|J, M>\\ &\quad=\{(J+M)!(J-M+4)!/(J+M-4)!(J-M)!\}^{1/2},\\ &<J, M|J_zJ_+^3|J, M-3>=\frac{M}{M-3}<J, M|J_+^3J_z|J, M-3>\\ &\quad=[(J-M+3)!(J+M)!/(J-M)!(J+M-3)!]^{1/2}M,\\ &<J, M|J_zJ_-^3|J, M+3>=\frac{M}{M+3}<J, M|J_-^3J_z|J, M+3>\\ &\quad=[(J-M)!(J+M+3)!/(J-M-3)!(J+M)!]^{1/2}M.\end{aligned} \tag{3.1}$$

Below, for convenience' sake, we shall consider the cubic or trigonal case separately.

I) The case of cubic modification.

The secular equation in this case can be decomposed into two as follows:

$$\begin{array}{l|cc|l} <\mp\frac{5}{2}| & 3a-W & 3\sqrt{5}\,a & =0 \\ <\pm\frac{3}{2}| & 3\sqrt{5}\,a & -9a-W & , \\ \end{array} \tag{3.2}$$

$$\begin{array}{l|cc|l} <-\frac{1}{2}| & 6a-W & 0 & =0 \\ <+\frac{1}{2}| & 0 & 6a-W & , \\ \end{array}$$

where $a=\beta D\overline{r^4}$. The energy eigenvalues are $W=6a$, $-12a$ and the eigenfunctions corresponding to them are given respectively as

$$\left.\begin{aligned} \psi &=\sqrt{\frac{5}{6}}\left|-\frac{5}{2}\right>+\frac{1}{\sqrt{6}}\left|\frac{3}{2}\right>, \\ \varphi &=\sqrt{\frac{5}{6}}\left|\frac{5}{2}\right>+\frac{1}{\sqrt{6}}\left|-\frac{3}{2}\right>, \\ \phi &=\left|\frac{1}{2}\right>, \qquad \phi'=\left|-\frac{1}{2}\right>, \end{aligned}\right\}\ (W=6a)$$

$$\left.\begin{aligned} \psi' &=\frac{1}{\sqrt{6}}\left|-\frac{5}{2}\right>-\sqrt{\frac{5}{6}}\left|\frac{3}{2}\right> \\ \varphi' &=\frac{1}{\sqrt{6}}\left|\frac{5}{2}\right>-\sqrt{\frac{5}{6}}\left|-\frac{3}{2}\right> \end{aligned}\right\}\ (W=-12a) \tag{3.3}$$

Now, the susceptibility can be calculated by the use of well known formula

$$\begin{aligned} \chi &=\frac{B}{kT}\sum_{jmj'm'}|\mu_B(jm;\,j'm')|^2\,e^{-W^0{}_{nj}/kT} \\ &\quad+2B\sum_{jmn'j'm'(n\neq n)}\frac{|p_B{}^0(njm;\,n'j'm'|^2}{h\nu(n';\,n)}\,e^{-W^0{}_{nj}/kT}, \\ B&=N\sum_{jm}e^{-W^0{}_{njm}/kT} \end{aligned} \tag{3.4}$$

In the present case, we have $\mu_B=g\mu_B J_z$ and $g=2/7$. The second term contains the temperature-independent part which comes from the lowest manifold and the excited state of $J=7/2$. $p^0{}_B$ equals μ_B as regards the lowest manifold. If we abbreviate the part of the second term which comes from the excited state as $N\alpha_J$, we have

$$\begin{aligned} \alpha_J&=\frac{\mu_B{}^2}{6(2J+1)}\left[\frac{F(J+1)}{h\nu(J+1;\,J)}-\frac{F(J)}{h\nu(J\colon J-1)}\right], \\ F(J)&=\frac{1}{J}\,[(S+L+1)^2-J^2]\,[J^2-(S-L)^2]. \end{aligned} \tag{3.5}$$

Thus the result is given as follows:

$$\begin{aligned} \chi_0=\frac{Ng^2\mu_B{}^2}{a}&\left[\frac{40}{81}-\frac{40}{81e}{}^{-18a/kT}+\frac{2a}{kT}\left\{\left(\frac{5}{6}\right)^2+\left(\left(\frac{1}{2}\right)^2+\left(\frac{11}{6}\right)^2\right)e^{-18a/kT}\right\}\right] \\ &+2\{1+2\,e^{-18a/kT}\}+N\alpha_J. \end{aligned} \tag{3.6}$$

$N\alpha_J$ may be replaced by (3.22). See below.

II) The case of trigonal modification.

As stated at the end of the previous section, we shall take the crystalline potential as

$$\begin{aligned} V_t=B_2{}^0\overline{r^2}\alpha\{3J_z{}^2-J(J+1)\}+F'\beta\overline{r^4}[35J_z{}^4-30J(J+1)J_z{}^2 \\ +25J_z{}^2-6J(J+1)+3J^2(J+1)^2-5\sqrt{2}\{J_z(J_+{}^3+J_-{}^3)+(J_+{}^3+J_-{}^3)J_z\}]. \end{aligned} \tag{3.7}$$

If we neglect the term of B_2^0, we have the splitting into two energy levels of four-fold and two fold degeneracy as in the case of cubic potential. However, the secular determinant inclusive of the term B_2^0 is decomposed as

$$\begin{array}{l} \langle -\frac{5}{2}| \\ \langle +\frac{1}{2}| \end{array} \begin{vmatrix} b+5c-W & \sqrt{20}\,b \\ \sqrt{20}\,b & 2b-4c-W \end{vmatrix} =0$$

$$\begin{array}{l} \langle +\frac{5}{2}| \\ \langle -\frac{1}{2}| \end{array} \begin{vmatrix} b+5c-W & -\sqrt{20}\,b \\ -\sqrt{20}\,b & 2b-4c-W \end{vmatrix} =0 \tag{3.8}$$

$$\begin{array}{l} \langle +\frac{3}{2}| \\ \langle -\frac{3}{2}| \end{array} \begin{vmatrix} -3b-c-W & 0 \\ 0 & -3b-c-W \end{vmatrix} =0$$

where $60F'\beta\overline{r^4}=b$, $2B_2^0\alpha\overline{r^2}=c$.

In the approximation of $b \gg c$, we obtain the energy eigenvalues $W_1=b(6+20/9\,\varepsilon^2)$, $W_2=-b(3-\varepsilon+20/9\,\varepsilon^2)$, $W_3=-b(3+\varepsilon)$ by neglecting the higher term than ε^3, and the eigenfunction belonging to them are given by

$$\left.\begin{aligned} \psi_1 &=\alpha_1\left|-\frac{5}{2}\right> +\beta_1\left|\frac{1}{2}\right> \\ \varphi_1 &=\gamma_1\left|\frac{5}{2}\right> +\delta_1\left|-\frac{1}{2}\right> \end{aligned}\right\} \quad (W=W_1)$$

$$\left.\begin{aligned} \psi_1' &=\alpha_2\left|-\frac{5}{2}\right> +\beta_2\left|\frac{1}{2}\right> \\ \varphi_1' &=\gamma_2\left|\frac{5}{2}\right> +\delta_2\left|-\frac{1}{2}\right> \end{aligned}\right\} \quad (W=W_2)$$

$$\phi_1=\left|\frac{3}{2}\right>, \quad \phi_1'=\left|-\frac{3}{2}\right>, \qquad (W=W_3) \tag{3.9}$$

where $\varepsilon=c/b \ll 1$, and each coefficients of (3.9) are obtained as

$$\begin{aligned} \alpha_1 &=\gamma_1=\frac{2}{3}\left(1+\frac{5}{9}\varepsilon-\frac{5}{81}\varepsilon^2\right), \\ \beta_1 &=-\delta_1=\frac{\sqrt{5}}{3}\left(1-\frac{4}{9}\varepsilon-\frac{14}{81}\varepsilon^2\right), \\ \alpha_2 &=\gamma_2=\frac{\sqrt{5}}{3}\left(1-\frac{4}{9}\varepsilon-\frac{14}{81}\varepsilon^2\right), \\ \beta_2 &=-\delta_2=-\frac{2}{3}\left(1+\frac{5}{9}\varepsilon-\frac{5}{81}\varepsilon^2\right). \end{aligned} \tag{3.10}$$

Following (3.4), we consider the contribution from the lowest manifold. As the measurements are made on the microcrystalline powder, it is necessary to compare the experimental result with the mean value of the susceptibilities along x, y, z directions unlike the cubic case. Let us first calculate the low frequency part of the parallel and the perpendicular susceptibilities.

a) Parallel susceptibility

Taking up to ε^2, the necessary matrix elements in (3.4) are given by

$$
\begin{aligned}
|(\psi_1|J_z|\psi_1)|^2 = |(\varphi_1|J_z|\varphi_1)|^2 &= \frac{25}{36}+\frac{200}{81}\varepsilon+\frac{1900}{27^2}\varepsilon^2,\\
|(\psi_1'|J_z|\psi_1')|^2 &= \frac{49}{36}-\frac{280}{81}\varepsilon+\frac{1180}{27^2}\varepsilon^2,\\
|(\varphi_1|J_z|\varphi_1')|^2 = (\psi_1|J_z|\psi_1')|^2 &= \frac{20}{9}+\frac{40}{81}\varepsilon-\frac{1540}{27^2}\varepsilon^2.
\end{aligned}
\tag{3.11}
$$

Then denoting as $W_2-W_1=\Delta E$, $W_3-W_1=\Delta E'$, we have

$$
\begin{aligned}
\chi_{t//} = \frac{2Bg^2\mu_B^2}{kT}&\left\{\left(\frac{25}{36}+\frac{200}{81}\varepsilon+\frac{1900}{27^2}\varepsilon^2\right)+\frac{9}{4}e^{-\Delta E'/kT}\right.\\
&\left.+\left(\frac{49}{36}-\frac{280}{81}\varepsilon+\frac{1180}{27^2}\varepsilon^2\right)e^{-\Delta E/kT}\right\}\\
&+4Bg^2\mu_B^2\,\frac{\dfrac{20}{9}+\dfrac{40}{81}\varepsilon-\dfrac{1540}{27^2}\varepsilon^2}{\Delta E}\{1-e^{-\Delta E/kT}\}.
\end{aligned}
\tag{3.12}
$$

b) Perpendicular susceptibility

Putting $\mu_x=g\mu_BJ_x$ and $J_x=(J_++J_-)/2$ in this case, we can obtain the non vanishing matrix elements which appear in (3.4). Then in the following formula

$$
\begin{aligned}
\chi_{t\perp} = {}&\frac{2Bg^2\mu_B^2}{kT}\{|(\psi_1|J_x|\varphi_1)|^2+|(\psi_1'|J_x|\varphi_1')|^2\,e^{-\Delta E/kT}\}\\
&+2Bg^2\mu_B^2\Big[\{|(\psi_1|J_x|\phi_1)|^2+|(\psi_1|J_x|\phi_1')|^2+|(\varphi_1|J_x|\phi_1)|^2\\
&+|(\varphi_1|J_x|\phi_1')|^2\}/\Delta E'+\{|(\psi_1|J_x|\varphi_1')|^2+|(\varphi_1|J_x|\psi_1')|^2\}/\Delta E\\
&+\left\{\frac{|(\psi_1|J_x|\phi_1)|^2+|(\psi_1|J_x|\phi_1')|^2+|(\varphi_1|J_x|\phi_1)|^2+|(\varphi_1|J_x|\phi_1')|^2}{-\Delta E'}\right.\\
&\left.+\frac{|(\phi_1|J_x|\varphi_1')|^2+|(\phi_1|J_x|\psi_1')|^2+|(\phi_1'|J_x|\varphi_1')|^2+|(\phi_1'|J_x|\psi_1')|^2}{\Delta E-\Delta E'}\right\}\\
&\times e^{-\Delta E/kT}-\left\{\frac{|(\psi_1|J_x|\varphi_1')|^2+|(\varphi_1|J_x|\psi_1')|^2}{\Delta E}\right.\\
&\left.+\frac{(\phi_1|J_x|\varphi_1')|^2+|(\phi_1|J_x|\psi_1')|^2+|(\phi_1'|J_x|\varphi_1')|^2+|(\phi_1'|J_x|\psi_1')|^2}{\Delta E-\Delta E'}\right\}e^{-\Delta E/kT}\Big],
\end{aligned}
\tag{3.13}
$$

each matrix element are obtained up to the term of ε^2 and after tedious calculation, we finally have

$$
\begin{aligned}
\chi_{t\perp} = {}&\frac{g^2\mu_B^2}{kT}B\left\{\frac{25}{18}\left(1-\frac{16}{9}\varepsilon+\frac{40}{81}\varepsilon^2\right)+\frac{8}{9}\left(1+\frac{20}{9}\varepsilon+\frac{130}{81}\varepsilon^2\right)e^{-\Delta E/kT}\right\}\\
&+2g^2\mu_B^2B\Big[-\frac{10}{27}\frac{1}{b}\left(1-\frac{1}{3}\varepsilon-\frac{20}{81}\varepsilon^2\right)-\frac{10}{81}\cdot\frac{1}{b}\left(1+\frac{1}{3}\varepsilon-\frac{114}{81}\varepsilon^2\right)\\
&+\left\{\frac{10}{27}\frac{1}{b}\left(1-\frac{1}{3}\varepsilon-\frac{20}{81}\varepsilon^2\right)+\frac{19}{12}\frac{1}{b\varepsilon}\left(1+\frac{230}{171}\varepsilon+\frac{2480}{19.9^2}\varepsilon^2\right)\right\}e^{-\Delta E/kT}\\
&+\left\{\frac{10}{81}\frac{1}{b}\left(1+\frac{1}{3}\varepsilon-\frac{114}{81}\varepsilon^2\right)-\frac{19}{12}\frac{1}{b\varepsilon}\left(1+\frac{230}{171}\varepsilon+\frac{2480}{19.9^2}\varepsilon^2\right)\right\}e^{-\Delta E/kT}\Big].
\end{aligned}
\tag{3.14}
$$

c) High frequency part.

As in the temperature-dependent part, the temperature-independent part may have different contributions to parallel and perpendicular susceptibilities, and this must be taken into account in the averaging process. However, the anisotropy of this constant susceptibility may be neglected as shown in the following.

Let us consider only the state of $J=7/2$ as the excited one. If the splittings of this level due to crystalline field are neglected, $\chi_{\parallel}$ is given by $N\alpha_J$ of (3.5) and $\chi_{\perp}$ coincides with $\chi_{\parallel}$. In order to show it, we notice that the matrix elements

$$\begin{aligned}
&<\frac{5}{2},\ \pm\frac{1}{2}\Big|L_x+2S_x\Big|\frac{7}{2},\ \pm\frac{3}{2}>=\pm\sqrt{5}\,f\left(\frac{7}{2}\right),\\
&<\frac{5}{2},\ \mp\frac{1}{2}\Big|L_x+2S_x\Big|\frac{7}{2},\ \pm\frac{1}{2}>=\pm\sqrt{3}\,f\left(\frac{7}{2}\right),\\
&<\frac{5}{2},\ \pm\frac{3}{2}\Big|L_x+2S_x\Big|\frac{7}{2},\ \pm\frac{5}{2}>=\pm\frac{\sqrt{30}}{2}f\left(\frac{7}{2}\right),\\
&<\frac{5}{2},\ \mp\frac{3}{2}\Big|L_x+2S_x\Big|\frac{7}{2},\ \mp\frac{1}{2}>=\pm\frac{\sqrt{6}}{2}f\left(\frac{7}{2}\right),\\
&<\frac{5}{2},\ \pm\frac{5}{2}\Big|L_x+2S_x\Big|\frac{7}{2},\ \pm\frac{7}{2}>=\pm\frac{\sqrt{42}}{2}f\left(\frac{7}{2}\right),\\
&<\frac{5}{2},\ \pm\frac{5}{2}\Big|L_x+2S_x\Big|\frac{7}{2},\ \pm\frac{3}{2}>=\mp\frac{1}{\sqrt{2}}f\left(\frac{7}{2}\right).
\end{aligned}\tag{3.15}$$

are used for $\chi_{\perp}$, where $f(J)=\sqrt{\frac{\{J^2-(L-S)^2\}\{(L+S+1)^2-J^2\}}{4J^2(2J-1)(2J+1)}}$ and $f\left(\frac{7}{2}\right)=\sqrt{\frac{15}{98}}$.

From (3.5) we have,

$$N\alpha_{5/2}=\frac{20N\mu_B^2}{7h\nu}\tag{3.16}$$

On the other hand, the corresponding perpendicular component

$$\chi_{c\perp}=\frac{2N\mu_B^2}{6}\sum\frac{|(L_x+2S_x)(njm;\,n'j'm')|^2}{h\nu(n':n)},\tag{3.17}$$

turns out to be equal to

$$\frac{2N\mu_B^2}{h\nu}\times 56\times\frac{15}{98}=N\alpha_{5/2},\tag{3.18}$$

if we use (3.15). This result can be seen from another point of view (see, for instance, reference 1). This will provide some suggestion for the consideration of anisotropy.

By taking only (2.10), the secular determinant in the manifold of $J=7/2$ are given by

$$\begin{array}{l}
\begin{array}{l} <\frac{7}{2},\ \pm\frac{7}{2}| \\ <\frac{7}{2},\ \pm\frac{1}{2}| \\ <\frac{7}{2},\ \mp\frac{5}{2}| \end{array}
\begin{vmatrix} 7b'-W & \mp2\sqrt{70}\,b' & 0 \\ \mp2\sqrt{70}\,b' & 9b'-W & \pm4\sqrt{10}\,b' \\ 0 & \pm4\sqrt{10}\,b' & -13b'-W \end{vmatrix}=0\ ,\\[2ex]
\begin{array}{l} <\frac{7}{2},\ \frac{3}{2}| \\ <\frac{7}{2},\ -\frac{3}{2}| \end{array}
\begin{vmatrix} -3b'-W & 0 \\ 0 & -3b'-W \end{vmatrix}=0\ ,
\end{array}\tag{3.19}$$

and the eigenvalues $W_1=-21b'$, $W_2=-3b'$ and $W_3=27b'$ are obtained. Their eigenfunctions are written as

$$\Phi_i=\alpha_i'\Big|-\frac{7}{2}>+\beta_i\Big|-\frac{1}{2}>+\gamma_i\Big|\frac{5}{2}>,$$

$$\begin{aligned}&\Phi_i'=\alpha_i'\left|+\frac{7}{2}\right>+\beta_i'\left|+\frac{1}{2}\right>+\gamma_i'\left|-\frac{5}{2}\right>,\\ &\left|\pm\frac{3}{2}\right> \qquad (W=W_2)\\ &(i=1,\ 2,\ 3)\end{aligned} \tag{3.20}$$

where $b'=60F'\beta'\overline{r^4}$, and the coefficients are determined by the relations

$$\alpha_i^2+\beta_i^2+\gamma_i^2=1,$$

and

$$\frac{\alpha_1}{2\sqrt{70}}=\frac{\beta_1}{30}=-\frac{\gamma_1}{4\sqrt{10}} \qquad \text{etc.}$$

These values α_i, β_i and γ_i are not so different from each other, and the original $|J, M>$ states make roughly equal contribution to the eigenstates except for $|7/2, \pm3/2>$. Moreover, as b' amounts to about one tenth of b, the matrix elements which connect with the lowest state have similar effects as in (3.5) and (3.18) (if we denote the splitting from the unperturbed level by ΔW, the order of error is less than $(\Delta W/h\nu)^2$). This is the reason for neglecting the anisotropy of constant part.

Thus, considering only the splitting of the lowest state, we can take safely the high frequency part as follows:

$$\chi_{tc}=B\mu_B^2\left\{\frac{1}{h\nu-6b}\,\frac{20}{7}+\frac{1}{h\nu+3b}\,\frac{40}{7}\,e^{9b/kT}\right\}, \tag{3.21}$$

and also we calculate $N\alpha_J$ of (3.6) with replacing by

$$\chi_{cc}=\frac{N\mu_B^2}{1+2e^{-18a/kT}}\left\{\frac{1}{h\nu+12a}\,\frac{20}{7}+\frac{1}{h\nu-6a}\,\frac{40}{7}\,e^{-18a/kT}\right\} \tag{3.22}$$

by the same reason.

From (3.21) and (3.14), the final expression of the susceptibility for the powder sample becomes

$$\begin{aligned}\chi_t&=(\chi_{t\parallel}+2\chi_{t\perp})/3\\ &=\frac{0.06125}{\mu T}\Bigg[-\frac{40}{9}+\left(\frac{19}{18}\cdot\frac{1}{\mathcal{E}'}+15+\frac{1180}{9}\mathcal{E}'\right)e^{\mu(1+\mathcal{E}')}\\ &\quad+\left(-\frac{19}{18}\,\frac{1}{\mathcal{E}'}-\frac{95}{9}-\frac{1180}{9}\mathcal{E}'\right)e^{\mu(1-\mathcal{E}')}\\ &\quad+\mu\left\{\frac{25}{36}+\frac{3}{4}e^{\mu(1+\mathcal{E}')}+\left(\frac{3}{4}-\frac{40}{9}\mathcal{E}'\right)e^{\mu(1-\mathcal{E}')}\right\}\Bigg]\\ &\quad\div 2\{1+e^{\mu(1+\mathcal{E}')}+e^{\mu(1-\mathcal{E}')}\}+\chi_{tc},\end{aligned} \tag{3.23}$$

where $9b/kT=\mu$, $\mathcal{E}=9\mathcal{E}'$ and $2Ng^2\mu_B^2/k=0.06125$.

§ 4. Results and Discussion

The experimental values of $1/\chi$ by Borovik-Romanov and Kreines are shown in Fig. 1 and Fig. 2. The experimental points in Fig. 1 are the one for cubic modification of Sm_2O_3 and ○ denotes for Sample I and ● for Sample II. Fig. 2 shows the results for pseudotrigonal modification where ○ denote for Sample I and ● are the results of Leiden group,

In Fig. 1, the theoretical curve 1 is plotted by Eq. (3.6) using the value $a=12\,k$ so as to get the best fit at high temperatures, and for comparison curve 2 is plotted using the value $a=15\,k$. Taking $a<0$, the fitting seems to be impossible in view of the slope of tangential line for $1/\chi$ curve at 0°K; In the limit $T\rightarrow 0$, (3.6) are written asymptotically as

$$a>0\ \ldots.\ 1/\chi\sim 47.05\ T,$$
$$a<0\ \ldots.\ 1/\chi\sim 18.08\ T$$

and we can only give reasonable results when $a>0$.

In Fig. 2, the theoretical curve (a) is plotted by using the values $b=-48k$ and $\mathcal{E}'=-0.1$. In this case, the sign of b is not definite from the comparison of the experiment with asymptotic form of $1/\chi$ in the limit $T\to 0$, ($1/\chi\sim 47.02T$ for negative b and $1/\chi\sim 43.53T$ for positive b), though the fitting at high temperature region can be achieved by taking $b<0$ in agreement with the sign of cubic case. We obtained above value from the intersection of the curves for b and $\mathcal{E}'$ of the best fit at temperatures of 100°K and 60°K respectively. As b depends slightly on $\mathcal{E}'$, the value of $\mathcal{E}'$ has some arbitrariness, but on the value of b we can have fair reliance. For comparison, the curves for $b=-60k$ and $b=-90k$ in the case of $\mathcal{E}'=-0.1$ are shown. In Fig. 3, the anisotropy of the susceptibility for the pseudotrigonal case are also shown.

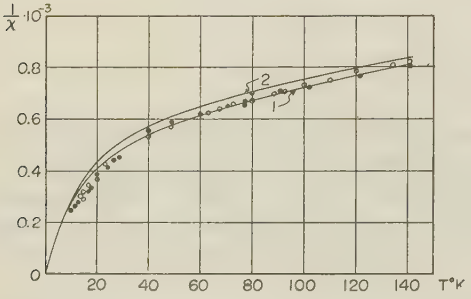

Fig. 1. Experimental points and theoretical curves of $1/\chi$ for cubic modification.

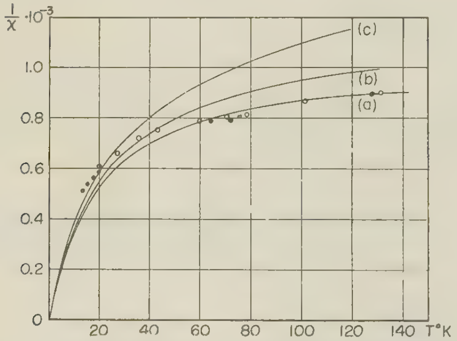

Fig. 2. Experimental points and theoretical curves of $1/\chi$ for pseudotrigonal modification.
(a): curve for $b=-48\,k$ $(\varepsilon'=-0.1)$
(b): curve for $b=-60\,k$ 〃
(c): curve for $b=-90\,k$ 〃

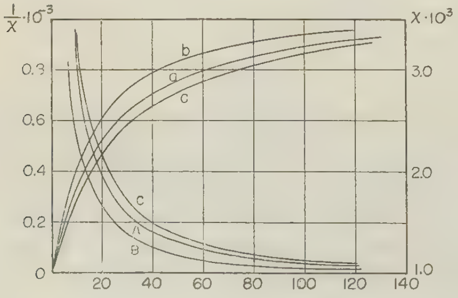

Fig. 3. Anisotropy of susceptibility in the case of pseudotrigonal modification ($b=-48\,k$, $\varepsilon'=-0.1$)
(a): $1/\chi=3/(\chi_{\parallel}+2\chi_{\perp})$ (A): $\chi=(\chi_{\parallel}+2\chi_{\perp})/3$
(b): $1/\chi_{\parallel}$ (B): $\chi_{\parallel}$
(c): $1/\chi_{\perp}$ (C): $\chi_{\perp}$

One of the conclusions of the simple consideration by Borovik-Romanov and Kreines is that if six states of $J_z=\pm 1/2,\ \pm 3/2,\ \pm 5/2$ in the manifold of $J=5/2$ are the eigenstates, the state of small J_z lies as lower one. This means the opposite sign of the coefficient of cubic potential to what is obtained by us, and in the case of trigonal potential the lowest state contains $\pm 5/2$, $\pm 1/2$ states nearly equally. Thus we cannot assent to their conclusion. Rather, our results agrees with the results of Giesekus[6] who estimated the crystalline potential of $Sm(BrO_3)_3 9H_2O$.

The total separation $52\,cm^{-1}$ which they obtained in cubic case may be compared with our $18a=216k$. As for the trigonal case, our result $9b=432k$ is more than twice of their estimation $150\,cm^{-1}$. With respect to these overall splittings in two modifications, their estimations and also our results are not necessary equal. The essential change in the crystalline structure due to thermal treatment of the sample may be a cause of this, but further discussion is not possible at the present stage.

In conclusion, the author wishes to express his cordial thanks to Professor T. Nakamura of Ôsaka University for his valuable discussions and also to members of laboratory for their discussions.

References

1. J. H. Van Vleck: The Theory of Electric and Magnetic Susceptibilities, Oxford, (1932).
2. W. G. Penney and R. Schlapp: Phys. Rev. **41** (1932) 194.
3. A. Frank: Phys. Rev. **48** (1935) 765.
4. A. S. Borovik-Romanov and N. M. Kreines: Soviet Physics, J.E.T.P. USSR **2** (1956) 657.
5. K. W. H. Stevens: Proc. Phys. Soc. **A65** (1952) 209.
6. H. Giesekus: Ann. der Physik **8** (1951) 350.

Journal of the Physical Society of Japan, Vol. 15, No. 11, November, 1960

Electroluminescence of Insulated Particles, II

By Keiji Maeda

Matsuda Research Laboratory, Tokyo Shibaura Electric Co., Kawasaki

(Received July 1, 1960)

Lehmann's experimental results on the emission intensity of a single electroluminescent phosphor particle embedded in an insulating dielectric as a function of the applied voltage are analysed on the model proposed in the Part I of this report. In this model the local field enhancement is attributed to the disturbance of the applied field due to the conducting phase of the phosphor particle. The results are reasonable and the validity of the model is confirmed.

§ 1. Introduction

For the origin of the local field enhancement, which is a fundamental problem in the theory of electroluminescence, many workers have adopted the barrier model. However, we have proved in the Part I of this paper[1] (hereafter refered as Part I) that the barrier model is not reasonable for the electroluminescence of phosphor particles dispersed in an insulating dielectric. We have also shown several reasons why the model proposed by Zalm is not suitable for the actual situations[2]. As an alternative mechanism, we have proposed a model that the local field enhancement takes place around the edge of highly conducting phase which is deposited on or segregated within the poorly conducting ZnS phosphor particle. It has been shown that the various experimental facts can be explained consistently by this model.

In Part I it has deen predicted that the voltage dependence of the electroluminescence intensity of an emitting spot is represented by

$$B_s=\alpha_s \exp(-\beta_s/V) \qquad (1)$$

where α_s and β_s are constants depending on the shape and size of the conducting phase which produces the local field enhancement for this emitting spot. Since the values of α_s and β_s differ from spot to spot, the experimental relationship between the applied voltage and the brightness of an electroluminescent cell

$$B_c=\alpha_c \exp(-\beta_c/\sqrt{V}) \qquad (2)$$

should be obtained by summing Eq. (1) over the emitting spots within the cell. However, when Part I was published there were no definite experimental results in support of our model.

§ 2. Analysis of Lehmann's Experiments

Recently Lehmann[3] has measured the voltage dependence of emission intensity of a single phosphor particle on six particles. He has found that the intensity is represented by Eq. (1) for one particle and by the sum of two or more of Eq. (1) for other five particles respectively. The former one particle has a single emitting spot and the latter particles have two or more emitting spots in each of them. Further he has demonstrated that Eq. (2) can be obtained from Eq. (1) by numerical calculations. His experimental results are in complete agreement with our prediction but his numerical calculations have been made on the particle size distribution of the phosphor as he assumed the barrier model.

We shall consider the absolute value of β_s. From Lehmann's measurements which are

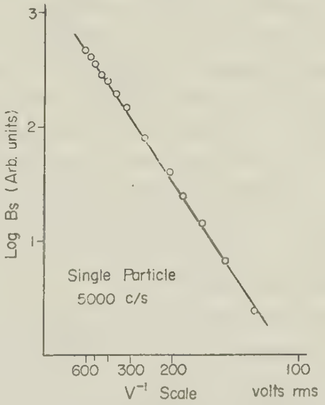

Fig. 1. Voltage dependence of electroluminescence intensity of a single phosphor particle measured by Lehmann.

shown in Fig. 1, we obtain the value of β_s to be 770 V rms and the thickness of the cell is considered to be about 100 μ. On the other hand, we have assumed in Part I that the conductive phase is spheroid in shape as a simple model. The field strength is calculated around the edge of the spheroid when it is placed parallel to the applied field with its major axis. From the probability of carrier multiplication in this local field, the above Eq. (1) is obtained. Using Eqs. (2), (3), (10), (14) and (16) of Part I, we have

$$\beta_s = \frac{\pi C d}{4\sqrt{2}\, r_0 K} \tag{3a}$$

for the oblate spheroid and

$$\beta_s = \frac{C d}{\sqrt{2}\, r_p^2 K} \tag{3b}$$

for the prolate spheroid when V in Eq. (1) is expresed by rms value for a sinusoidal applied voltage. Here, C is the constant in the exponential term of the probability of secondary electron production, d is the thickness of the cell, K is the factor of the field strength in ZnS due to the difference in the dielectric constant between the embedding dielectric and ZnS, and r_0 and r_p are the ratio of the major axis to the minor axis of the oblate and the prolate spheroid respectively. We obtain the values of r_0 or r_p when it is assumed that the field enhancement for the spot is due to either an oblate or a prolate spheroidal conducting phase by inserting the following values in Eqs. (3a) or (3b); $C=8\times 10^5$ V/cm as stated in Part I, $\beta_s=770$ V/cm, $d=100\,\mu$ and $K=2$. Then we have $r_0=2.9$ or $r_p=1.9$. Exactly speaking, Eqs. (3a) and (3b) are derived on the assumption of large axial ratio. But we have made use of them for the sake of simplicity and semi-quantitative nature of our discussion as stated in the next section. When we make exact but complicated calculation, we have $r_0=1.9$ and $r_p=2.0$. It becomes clear that the value of β_s obtained by Lehmann can be explained by our model assuming the plausible shape of the conductive spheroid.

It seems reasonable from Fig. 1 to assume that the minimum applied voltage necessary for the appreciable photon emission in this spot is 100 V rms. Then the average field strength in the cell E_{th} at the peak of this ac voltage cycle is $\sqrt{2}\times 10^4$ V/cm. We have derived the equations for this field strength on the assumption of large axial ratio, i.e. Eqs. (6) and (7) of Part I. However, it becomes clear from Eqs. (4)* and (5) of Part I that these equations are poor approximation for the above values of r_0 and r_p. The exact equations are too complicated to be treated here for our semi-quantitative calculation. Therefore, we shall adopt a simple method. The potential drop in the average field over the distance of the major axis a of the spheroid is concentrated, superposing on the average field, around the edge of the sheroid over the distance of the minor axis. This potential drop should be at least equal to the energy of the forbidden gap of ZnS I_G for the occurrence of appreciable electroluminescence, i.e.

$$I_G = E_{th} K a. \tag{4}$$

Inserting $I_G=3.7$ eV and other values stated above into Eq. (4), we obtain $a=1.3\,\mu$. The obtained value is small compared with the dimension of the phosphor particle, i.e. from 10 to 20 μ in diameter. The presence of the conducting phase of this order of magnitude indimension is reasonable from the various characteristics of the phosphor particle.

§ 3. Discussion

Although we do not know the actual shape of the conducting phase, the assumption of the spheroidal shape may be considered too simple. However, in the first approximation, emphasis should be placed on the shape of the edge in question relative to the whole dimension of the conducting phase. Of course, some actual edges would be more or less sharp than the above spheroidal approximation. Since our discussion is semi-quantitative first approximation in order to demonstrate the consistency of the various quantities, the above approximation is considered to be satisfactory. For instance, even if the dimension of the conducting phase should be multiplied by two in order to avoid the uncertainty of the approximations involved, Lehmann's experiments can be explained reasonably by our model.

As stated before, the derivation of the

---

* Eq. (4) of Part I should be read $\delta=(ac^2/2)^{\frac{1}{3}}$ instead $\delta=(ac^2/2)^{\frac{1}{2}}$.

emission intensity of a cell Eq. (2) from the emission intensity of a spot involves summation of Eq. (1) over the emitting spots. We cannot show the derivation explicitly, since we do not know the distribution of the size and shape of the conducting phase. However, since the number of spots having small values of β_s, i.e. large axial ratio, would be small in a similar way as that of particles having large diameter in the particle size distribution treated by Lehmann, it is expected that the summation of Eq. (1) over emitting spots leads to Eq. (2).

Although the structure of the electroluminescent particle is very complicated and only a little is known on the conducting phase, it is concluded from the above analysis that the validity of our model is further confirmed.

A short explanation will be added for the estimation of efficiency of electroluminescent cell described in Part I in order to avoid misunderstanding. It has been reported to show that the low efficiency of electroluminescent cell can be explained by reasonable estimation on the various processes. It is based on the data by the Philips group and different values would be obtained by analysing other data. Exactly speaking, we should compare the estimated value with the efficiency measured by the Philips group on the same cell, i.e. about 7 lm/W from the efficiency curve shown in Fig. 2 of Part I. Therefore, it does not represent the maximum obtainable efficiency in future.

Note added in proof — Very recently Lehmann has made microscopic observations on ihe electroluminescent phosphor particles (J. Electrochem. Soc. **107** (1960) 657). Within the particles he observed dark segregations, which are frequently thin and elongated, almost needle-like. The emission spots are visibly located directly at the ends of the segregations. Therefore, it seems that our simple assumptions on the shape of the conductive phase are justified. Further, according to his observation the segregations are larger, on the average, in larger particles and vice versa. From this result we can explain the relations between the voltage dependence of emission intensity of a cell, i.e. α_c and β_c, and the particle size distribution (for example, Lehmann: J. Electrochem. Soc. **105** (1958) 585) on our model.

References

1) K. Maeda: J. Phys. Soc. Japan **13** (1958) 1351
2) K. Maeda: Physica **25** (1959) 721
3) W. Lehmann: J. Electrochem. Soc. **107** (1960) 20

JOURNAL OF THE PHYSICAL SOCIETY OF JAPAN, Vol. 15, No. 11, NOVEMBER, 1960

Pseudokinematical Approximation in Electron Diffraction by Crystal

By Mitsuhiko HAYASHI*

Physical Institute, Nagoya University, Nagoya, Japan

(Received August 1, 1960)

The pseudokinematical theory of electron diffraction is considered to be a good approximation for gas molecules. When, the theory is applied to crystals, however, there is an ambiguity concerning the nature of the approximation. In the present paper, the ambiguity is removed by comparing the result of the theory with the exact solution. The higher order Born approximation applied to the entire crystal is used as the exact solution. It is concluded that the pseudokinematical approximation is better than that of the usual kinematical theory and coincides almost with the exact solution under the condition that the crystal is very thin and there is no overlap of atoms when the crystal is seen from the direction of the incident beam.

§1. Introduction

Glauber & Schomaker[1)] pointed out that the kinematical theory of diffraction (KT) is not adequate for the electron diffraction by gas molecules containing heavy atoms. They attributed the cause of this fact to the multiple scatterings of electrons in the heavy atoms. They modified the kinematical theory by substituting the rigorous atomic scattering amplitudes for the usual ones, and succeeded in explaining the electron diffraction patterns from such molecules. The modified theory was called by Hoerni[2)] the pseudokinematical theory (PKT). KT is equivalent to Born approximation in which the multiple scatterings of electrons are entirely neglected. In PKT, the multiple scatterings in individual atoms are taken into account, while those on different atoms are neglected. PKT has been proved to be satisfactory for the electron diffraction by gas molecules.

Hoerni[2)] studied the applicability of PKT to crystals. He compared the result of PKT with that of the dynamical theory (DT) in the case of thin crystals. Based upon numerical calculations, he concluded that the agreement was good for the reflections of low indices, but in general there was no agreement for higher indices. In his calculations of DT, only the systematic interactions* are taken into account. This is not adequate because in the case of thin crystals the accidental interactions** should also be taken into account (Appendix IV).

Recently, Miyake[3)] studied the change of the intensity from DT value to KT value and inferred that PKT would be misleading when applied to crystals. Fujimoto[4)] succeeded in formulating the dynamical theory taking into account many reflected waves. He made numerical calculations[5)] of a number of examples using his formula. According to the result, the exact value does not coincide with PKT value, but it does with KT value when the crystal is thin ($\lesssim$15A). In his calculations, however, only the systematic interactions were taken into account as in Hoerni's[2)].

The purpose of the present paper is to make clear the applicability of PKT to crystals. By comparing the result of PKT with the exact solution, it is concluded that the approximation of PKT is better than that of KT and is very near the exact value in the case of very thin crystals.

---

* Now at Department of Applied Physics, Nagoya University, Nogoya, Japan.

** When the intensity of a given reflection ***h*** is calculated by DT, it is necessary to take into account the coupling of ***h***-reflection with all the other reflections. The reflection ***h*** remains in the Bragg position when the crystal is rotated around the vector ***h***. As the crystal is rotated the amplitudes of other reflections change, except those corresponding to the reciprocal lattice points lying on the rotation axis. Thus some of the dynamical interactions depend on the azimuthal orientation, whereas the others do not. Hoerni[2)] called the latter the systematic interactions and the former the accidental interactions.

§ 2. The pseudokinematical theory and the exact solution of diffraction

(A) *Pseudokinematical theory* (PKT)

When incident wave $\Psi^{(0)}(\mathbf{r})$ with wave vector $\mathbf{K}_0$ falls upon a free atom, a scattered wave $\phi^S(\mathbf{r})$ is produced. $\phi^S(\mathbf{r})$ can be expressed as a series of successive approximations;

$$\phi^S(\mathbf{r})=\phi^{(1)}(\mathbf{r})+\phi^{(2)}(\mathbf{r})+\cdots. \tag{1}$$

If the atom is assumed to have a potential $V_a(\mathbf{r})$, the first approximation $\phi^{(1)}(\mathbf{r})$ is given by[8]

$$\phi^{(1)}(\mathbf{r})=\frac{1}{4\pi}\int\frac{\exp[2\pi iK_0|\mathbf{r}-\mathbf{r}'|]}{|\mathbf{r}-\mathbf{r}'|}\times U_a(\mathbf{r}')\exp[2\pi i\mathbf{K}_0\cdot\mathbf{r}']\,d\mathbf{r}', \tag{2}$$

where

$$U_a(\mathbf{r})=\frac{2me}{\hbar^2}V_a(\mathbf{r}). \tag{3}$$

Using the relations

$$U_a(\mathbf{r})=4\pi\int_\infty f(\mathbf{b})\exp[2\pi i\mathbf{b}\cdot\mathbf{r}]\,d\mathbf{b}, \tag{4}$$

$$\frac{1}{4\pi}\frac{\exp[2\pi iK_0|\mathbf{r}-\mathbf{r}'|]}{|\mathbf{r}-\mathbf{r}'|}=\frac{1}{(2\pi)^2}\times\int\frac{\exp[2\pi i\mathbf{k}\cdot(\mathbf{r}-\mathbf{r}')]}{\mathbf{k}^2-\mathbf{K}_0^2}\,d\mathbf{k}\,{}^{9)} \tag{5}$$

and

$$\int_\infty\exp[2\pi i(\mathbf{K}_0+\mathbf{b}-\mathbf{k})\cdot\mathbf{r}']\,d\mathbf{r}'=\delta(\mathbf{K}_0+\mathbf{b}-\mathbf{k}),{}^{10)} \tag{6}$$

where $f(\mathbf{b})$ is the usual atomic scattering amplitude for electrons, eq. (2) is rewritten as

$$\phi^{(1)}(\mathbf{r})=\frac{1}{\pi}\int\frac{\exp[2\pi i\mathbf{K}\cdot\mathbf{r}]}{\mathbf{K}^2-\mathbf{K}_0^2}f(\mathbf{K}-\mathbf{K}_0)\,d\mathbf{K}. \tag{7}$$

Similarly, the second approximation is given by

$$\phi^{(2)}(\mathbf{r})=\frac{1}{\pi^2}\int d\mathbf{K}\frac{\exp[2\pi i\mathbf{K}\cdot\mathbf{r}]}{\mathbf{K}^2-\mathbf{K}_0^2}\times\int\frac{f(\mathbf{K}-\mathbf{k})f(\mathbf{k}-\mathbf{K}_0)}{\mathbf{k}^2-\mathbf{K}_0^2}\,d\mathbf{k}. \tag{8}$$

PKT wave function $\Psi^P(\mathbf{r})$ for a crystal is given by

$$\Psi^P(\mathbf{r})=\Psi^{(0)}(\mathbf{r})+\sum_n\sum_i\phi^S{}_{n,i}(\mathbf{r}). \tag{9}$$

Here, $\phi^S{}_{n,i}(\mathbf{r})$ is the wave scattered from the i-th atom in the n-th unit cell. $\sum\limits_n$ and $\sum\limits_i$ represent the summations over all lattice points in the crystal and over all atoms in the unit cell, respectively. If the first approximations $\phi^{(1)}{}_{n,i}(\mathbf{r})$ given by (7) are substituted for $\phi^S{}_{n,i}(\mathbf{r})$ in eq. (9), KT wave function is obtained. From eqs. (1), (7), (8) and (9) we have

$$\Psi^P(\mathbf{r})=\Psi^{(0)}(\mathbf{r})+\Psi^{P(1)}(\mathbf{r})+\Psi^{P(2)}(\mathbf{r})+\cdots, \tag{10}$$

where

$$\Psi^{P(1)}(\mathbf{r})=\frac{1}{\pi}\int\frac{\exp[2\pi i\mathbf{K}\cdot\mathbf{r}]}{\mathbf{K}^2-\mathbf{K}_0^2}\times F(\mathbf{K}-\mathbf{K}_0)L(\mathbf{K}-\mathbf{K}_0)\,d\mathbf{K}, \tag{11}$$

$$\Psi^{P(2)}(\mathbf{r})=\frac{1}{\pi^2}\sum_i\int d\mathbf{K}\frac{\exp[2\pi i\mathbf{K}\cdot\mathbf{r}]}{\mathbf{K}^2-\mathbf{K}_0^2}\times\exp[-2\pi i(\mathbf{K}-\mathbf{K}_0)\cdot\mathbf{r}_i]\times L(\mathbf{K}-\mathbf{K}_0)\int\frac{f_i(\mathbf{K}-\mathbf{k})f_2(\mathbf{k}-\mathbf{K}_0)}{\mathbf{k}^2-\mathbf{K}_0^2}\,d\mathbf{k}, \tag{12}$$

....

Here $F(\mathbf{b})$ is the usual structure factor for electrons and $L(\mathbf{b})$ the diffraction function of the crystal. They are given by

$$F(\mathbf{b})=\sum_i f_i(\mathbf{b})\exp[-2\pi i\mathbf{b}\cdot\mathbf{r}_i], \tag{13}$$

$$L(\mathbf{b})=\sum_n\exp[-2\pi i\mathbf{b}\cdot\mathbf{R}_n], \tag{14}$$

where $\mathbf{R}_n$ and $\mathbf{r}_i$ represent the position of the n-th lattice point and the i-th atom in the unit cell, respectively.

(B) *Exact solution* (SBAC)

Applying the successive Born approximation to the entire crystal[6] (SBAC), we have for the exact wave function

$$\Psi(\mathbf{r})=\Psi^{(0)}(\mathbf{r})+\Psi^{(1)}(\mathbf{r})+\Psi^{(2)}(\mathbf{r})+\cdots, \tag{15}$$

where

$$\Psi^{(1)}(\mathbf{r})=\frac{1}{\pi}\int\frac{\exp[2\pi i\cdot\mathbf{K}\cdot\mathbf{r}]}{\mathbf{K}^2-\mathbf{K}_0^2}\times F(\mathbf{K}-\mathbf{K}_0)L(\mathbf{K}-\mathbf{K}_0)\,d\mathbf{K}, \tag{16}$$

$$\Psi^{(2)}(\mathbf{r})=\frac{1}{\pi^2}\int d\mathbf{K}\frac{\exp[2\pi i\cdot\mathbf{K}\cdot\mathbf{r}]}{\mathbf{K}^2-\mathbf{K}_0^2}\times\int\frac{F(\mathbf{K}-\mathbf{k})F(\mathbf{k}-\mathbf{K}_0)}{\mathbf{k}^2-\mathbf{K}_0^2}\times L(\mathbf{K}-\mathbf{k})L(\mathbf{k}-\mathbf{K}_0)\,d\mathbf{k}, \tag{17}$$

....

(C) *Derivation of Fraunhofer formula*

The formulae (10) and (15) are Fresnel formulae. It is desirable to obtain Fraunhofer formulae which correspond to the usual experimental condition of electron diffraction. This is carried out by the following mathematical procedure.

Eqs. (11), (12), (16) and (17) are all of the form

$$\Psi(\boldsymbol{r})=C\int_{\infty}\frac{\exp[2\pi i\boldsymbol{K}\cdot\boldsymbol{r}]}{K^2-K_0{}^2}P(\boldsymbol{K})d\boldsymbol{K}. \tag{18}$$

For eq. (17), for instance, $P(\boldsymbol{K})$ represents

$$P(\boldsymbol{K})=\int\frac{F(\boldsymbol{K}-\boldsymbol{k})F(\boldsymbol{k}-\boldsymbol{K}_0)}{k^2-K_0{}^2}\times L(\boldsymbol{K}-\boldsymbol{k})L(\boldsymbol{k}-\boldsymbol{K}_0)d\boldsymbol{k}.$$

Since for large $|\boldsymbol{r}|$ the function $P(\boldsymbol{K})$ varies slowly compared to $\exp[2\pi i\boldsymbol{K}\cdot\boldsymbol{r}]/(K^2-K_0{}^2)$, eq. (18) is reduced to a surface integral on Ewald sphere.

$$\Psi(\boldsymbol{r})=C\frac{i\pi}{k_0}\int_{\substack{\text{Ewald}\\ \text{sphere}}}\exp[2\pi i\boldsymbol{K}\cdot\boldsymbol{k}]P(\boldsymbol{K})\,d\sigma, \tag{19}$$

where $d\sigma$ is the surface element on Ewald sphere. Taking the direction of $\boldsymbol{r}$ as the polar axis, we can express $P(\boldsymbol{K})$ on Ewald sphere as $P(\theta,\varphi)$, where θ and φ are the polar and the azimuthal angle, respectively. Then, eq.(19) can be rewritten as

$$\Psi(\boldsymbol{r})=Ci\pi K_0\int_0^{2\pi}d\varphi\int_0^{\pi}P(\theta,\varphi)\times\exp[2\pi iK_0r\cos\theta]\sin\theta d\theta. \tag{20}$$

Integrating the inner integral by parts, and taking into account the facts that $P(\pi,\varphi)$ is vanishingly small and that $\partial P/\partial\theta$ changes with θ much more slowly than $\exp[2\pi iK_0r\cos\theta]$, we have finally[11]

$$\Psi(\boldsymbol{r})=C\pi\frac{\exp[2\pi iK_0r]}{r}P(\boldsymbol{K}_r), \tag{21}$$

where $\boldsymbol{K}_r$ is the wave vector in the direction of $\boldsymbol{r}$.

By applying the relation (21) to eqs. (11), (12), (16) and (17), we obtain Fraunhofer formulae.

$$\Psi^P(\boldsymbol{r})=\Psi^{(0)}(\boldsymbol{r})+\frac{\exp[2\pi iK_0r]}{r}\times[\varPhi^{P(1)}(\boldsymbol{K}_r,\boldsymbol{K}_0)+\varPhi^{P(2)}(\boldsymbol{K}_r,\boldsymbol{K}_0)+\cdots], \tag{22}$$

$$\Psi(\boldsymbol{r})=\Psi^{(0)}(\boldsymbol{r})+\frac{\exp[2\pi iK_0r]}{r}\times[\varPhi^{(1)}(\boldsymbol{K}_r,\boldsymbol{K}_0)+\varPhi^{(2)}(\boldsymbol{K}_r,\boldsymbol{K}_0)+\cdots\cdot], \tag{23}$$

where

$$\varPhi^{P(1)}(\boldsymbol{K}_r,\boldsymbol{K}_0)=F(\boldsymbol{K}_r-\boldsymbol{K}_0)L(\boldsymbol{K}_r-\boldsymbol{K}_0), \tag{24}$$

$$\varPhi^{P(2)}(\boldsymbol{K}_r,\boldsymbol{K}_0)=\frac{1}{\pi}\sum_i\exp[-2\pi i(\boldsymbol{K}_r-\boldsymbol{K}_0)\cdot\boldsymbol{r}_i]L(\boldsymbol{K}_r-\boldsymbol{K}_0)\int\frac{f_i(\boldsymbol{K}_r-\boldsymbol{k})f_i(\boldsymbol{k}-\boldsymbol{K}_0)}{k^2-K_0{}^2}d\boldsymbol{k}, \tag{25}$$

.... ,

$$\varPhi^{P(n)}(\boldsymbol{K}_r,\boldsymbol{K}_0)=\frac{1}{\pi^{n-1}}\sum_i\exp[-2\pi i(\boldsymbol{K}_r-\boldsymbol{K}_0)\cdot\boldsymbol{r}_i]L(\boldsymbol{K}_r-\boldsymbol{K}_0)\times\int\cdots\int\frac{f_i(\boldsymbol{K}_r-\boldsymbol{k}_1)f_i(\boldsymbol{k}_1-\boldsymbol{k}_2)\cdots f_i(\boldsymbol{k}_{n-1}-\boldsymbol{K}_0)}{(k_1{}^2-K_0{}^2)(k_2{}^2-K_0)\cdots(k^2{}_{n-1}-K_0{}^2)}d\boldsymbol{k}_1d\boldsymbol{k}_2\cdots d\boldsymbol{k}_{n-1}, \tag{26}$$

.... ;

$$\varPhi^{(1)}(\boldsymbol{K}_r,\boldsymbol{K}_0)=F(\boldsymbol{K}_r-\boldsymbol{K}_0)L(\boldsymbol{K}_r-\boldsymbol{K}_0), \tag{27}$$

$$\varPhi^{(2)}(\boldsymbol{K}_r,\boldsymbol{K}_0)=\frac{1}{\pi}\int\frac{F(\boldsymbol{K}_r-\boldsymbol{k})F(\boldsymbol{k}-\boldsymbol{K}_0)}{k^2-K_0{}^2}L(\boldsymbol{K}_r-\boldsymbol{k})L(\boldsymbol{k}-\boldsymbol{K}_0)d\boldsymbol{k}, \tag{28}$$

.... ,

$$\varPhi^{(n)}(\boldsymbol{K}_r,\boldsymbol{K}_0)=\frac{1}{\pi^{n-1}}\int\cdots\int\frac{F(\boldsymbol{K}_r-\boldsymbol{k}_1)F(\boldsymbol{k}_1-\boldsymbol{k}_2)\cdots F(\boldsymbol{k}_{n-1}-\boldsymbol{K}_0)}{(k_1{}^2-K_0{}^2)(k_2{}^2-K_0{}^2)\cdots(k_{n-1}-K_0{}^2)}\times L(\boldsymbol{K}_r-\boldsymbol{k}_1)L(\boldsymbol{k}_1-\boldsymbol{k}_2)\cdots L(\boldsymbol{k}_{n-1}-\boldsymbol{K}_0)d\boldsymbol{k}_1d\boldsymbol{k}_2\cdots d\boldsymbol{k}_{n-1}, \tag{29}$$

....

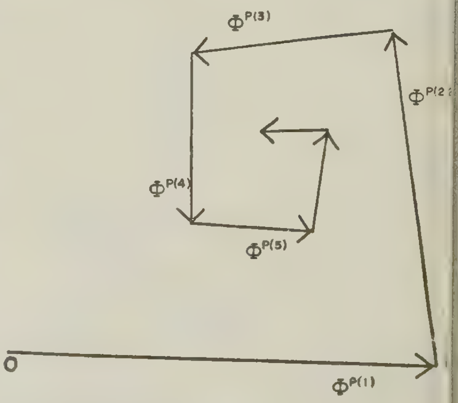

Fig. 1. Illustration of $\varPhi^{P(1)}+\varPhi^{P(2)}+\cdots$ on the complex plane.

Scattering amplitude $\varPhi^{P(1)}+\varPhi^{P(2)}+\cdots$is diagramatically illustrated in Fig. 1. If the crystal is centrosymmetric and the Bragg condition is satisfied, $\varPhi^{P(1)}$ is in the positive direction of the real axis, $\varPhi^{P(2)}$ nearly in the positive direction of the imaginary axis, $\varPhi^{P(3)}$ nearly in the negative direction of the real axis, etc. The same holds also for $\varPhi^{(1)}+\varPhi^{(2)}+\cdots\cdots$.

§ 3. Comparison of PKT with SBAC

In the first approximation, PKT and SBAC coincide with each other [eqs.(24) and (27)], and they coincide also with KT.

The second approximation of PKT (25) can be rewritten for a plane parallel crystal as (Appendix I)

$$\Phi^{P(2)}(\boldsymbol{K},\boldsymbol{K}_0)\approx\frac{1}{\pi S_0}L(\boldsymbol{b})\sum_G\frac{1}{2K_{gz}}\sum_i\exp\left[-2\pi i\boldsymbol{b}\cdot\boldsymbol{r}_i\right]$$
$$\times\left[i\pi f_i(\boldsymbol{b}-\boldsymbol{g})f_i(\boldsymbol{g})+\mathrm{P}\int_{-\infty}^{\infty}\frac{f_i(\boldsymbol{b}-\boldsymbol{g}-\rho\boldsymbol{\nu}+\boldsymbol{g})f_i(\rho\boldsymbol{\nu}+\boldsymbol{g})}{\rho}d\rho\right]. \tag{30}$$

Here $\boldsymbol{K}_r$ in eq.(25) is simply denoted by $\boldsymbol{K}$ and P represents the principal value. Unit cell vectors $\boldsymbol{a}_1$ and $\boldsymbol{a}_2$ lie in the plane of crystal surface and

$$\left.\begin{aligned}&\boldsymbol{b}=\boldsymbol{K}-\boldsymbol{K}_0,\\&\boldsymbol{G}=G_1\boldsymbol{a}_1{}^*+G_2\boldsymbol{a}_2,\\&\boldsymbol{g}=\boldsymbol{G}+\rho_g\boldsymbol{\nu},\\&\boldsymbol{K}_g=\boldsymbol{K}_0+\boldsymbol{g},\\&S_0=|\boldsymbol{a}_1\times\boldsymbol{a}_2|,\end{aligned}\right\} \tag{31}$$

where G_1 and G_2 are integers and ρ_g is the excitation error for $\boldsymbol{G}$ (Fig. 2). The z- axis is taken normal to the crystal surface and $\boldsymbol{\nu}$ is the unit vector in z-direction. In the derivation of (30), the integral over Ewald sphere is replaced by the summation over reciprocal lattice points. This is a good approximation as explained in Appendix I.

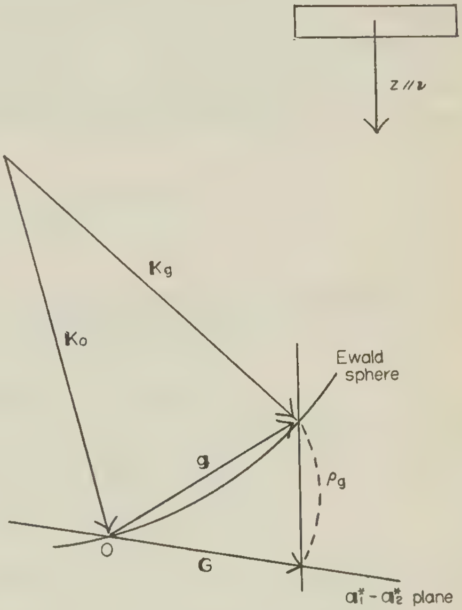

Fig. 2.

For simplicity, we assume a crystal of one unit cell thickness with an area $|M_1\boldsymbol{a}_1\times M_2\boldsymbol{a}_2|$, where M_1 and M_2 are integers. Under this assumption, the second approximation of SBAC (28) becomes (Appendix II)

$$\Phi^{(2)}(\boldsymbol{K},\boldsymbol{K}_0)=\frac{1}{\pi S_0}L(\boldsymbol{b})\sum_G\frac{1}{2K_{gz}}\sum_i\sum_j\exp\left[-2\pi i(\boldsymbol{b}-\boldsymbol{g})\cdot\boldsymbol{k}_i\right]\exp\left[-2\pi i\boldsymbol{g}\cdot\boldsymbol{r}_j\right]$$
$$\times\left[i\pi f_i(\boldsymbol{b}-\boldsymbol{g})f_j(\boldsymbol{g})+\mathrm{P}\int_{-\infty}^{\infty}\frac{f_i(\boldsymbol{b}-\boldsymbol{g}-\rho\boldsymbol{\nu})f_j(\rho\boldsymbol{\nu}+\boldsymbol{g})}{\rho}\cos 2\pi(z_i-z_j)\,\rho d\rho\right.$$
$$\left.+i\int_{-\infty}^{\infty}\frac{f_i(\boldsymbol{b}-\boldsymbol{g}-\rho\boldsymbol{\nu})f_j(\rho\boldsymbol{\nu}+\boldsymbol{g})}{\rho}\sin 2\pi(z_i-z_j)\,\rho d\rho\right], \tag{32}$$

where z_i is the z-component of $\boldsymbol{r}_i$.

Eqs.(30) and (32) can be written as

$$\left.\begin{aligned}&\Phi^{P(2)}(\boldsymbol{K},\boldsymbol{K}_0)=A+B,\\&\Phi^{(2)}(\boldsymbol{K},\boldsymbol{K}_0)=A+A'+B+B'+B''.\end{aligned}\right\} \tag{33}$$

The expressions of A, B, A' etc. are given in Appendix III. Terms A and B come from double scatterings within the same atom, whereas terms A', B' and B'' come from double scatterings on different atoms. In reciprocal space, a double scattering is a successive transition of state from $\boldsymbol{K}_0$ to $\boldsymbol{k}$ and then to $\boldsymbol{K}$. $\Phi^{P(2)}(\boldsymbol{K}, \boldsymbol{K}_0)$ and $\Phi^{(2)}(\boldsymbol{K}, \boldsymbol{K}_0)$ are made up of such transitions with all possible intermediate states $\boldsymbol{k}$'s. Thus every point in the reciprocal space contributes to $\Phi^{P(2)}$ and $\Phi^{(2)}$ as an intermediate state. Terms A and A' are the contribution from the points on Ewald sphere, while terms B, B' and B'' from all the points of the reciprocal space except those on Ewald sphere.

It is easily seen that terms B' and B'' are quite negligible in comparison to B for the usual wave length of electrons (10 KV~500 KV). Terms A' is negligible in comparison to A, provided that the central parts of atoms where the atmic potential has considerable value do not overlap when the crystal is seen from the direction of $\boldsymbol{K}_0$ (Appendix IV). Thus it is concluded that PKT is a better approximation than KT, and particularly when the condition of non-overlap is satisfied, PKT is almost equal to the exact solution i.e. $|\Phi^{P(2)}-\Phi^{(2)}|\ll|\Phi^{(2)}|$.

Under the condition of non-overlap, it is also found that $|\Phi^{P(3)}-\Phi^{(3)}|\ll|\Phi^{(3)}|$, $|\Phi^{P(4)}-\Phi^{(4)}|\ll|\Phi^{(4)}|$ etc.

The conclusion reached above applies to crystals of any size and also to amorphous substances as shown in the following. If we assume an amorphous scatterer, we obtain from eqs.(25) and (28) for the second approximations of PKT and SBAC

$$\Phi^{P(2)}(\boldsymbol{K},\boldsymbol{K}_0)=\frac{1}{\pi}\frac{1}{2K_0}\sum_i \exp\left[-2\pi i(\boldsymbol{K}-\boldsymbol{K}_0)\cdot\boldsymbol{r}_i\right]\int_{\substack{\text{Ewald}\\\text{sphere}}}\left[i\pi f_i(\boldsymbol{K}-\boldsymbol{k})f_i(\boldsymbol{k}-\boldsymbol{K}_0)\right.$$
$$\left.+\mathrm{P}\int_{-\infty}^{\infty}\frac{f_i(\boldsymbol{K}-\boldsymbol{k}-\rho\boldsymbol{\nu})f_i(\rho\boldsymbol{\nu}+\boldsymbol{k}-\boldsymbol{K}_0)}{\rho}d\rho\right]d\sigma, \tag{34}$$

$$\Phi^{(2)}(\boldsymbol{K},\boldsymbol{K}_0)=\frac{1}{\pi}\frac{1}{2K_0}\sum_i\sum_j\int_{\substack{\text{Ewald}\\\text{sphere}}}\exp\left[-2\pi i(\boldsymbol{K}-\boldsymbol{k})\cdot\boldsymbol{r}_i\right]\exp\left[-2\pi i(\boldsymbol{k}-\boldsymbol{K}_0)\cdot\boldsymbol{r}_j\right]$$
$$\times\left[i\pi f_i(\boldsymbol{K}-\boldsymbol{k})f_j(\boldsymbol{k}-\boldsymbol{K}_0)+\mathrm{P}\int_{-\infty}^{\infty}\frac{f_i(\boldsymbol{K}-\boldsymbol{k}-\rho\boldsymbol{\nu})f_j(\rho\boldsymbol{\nu}+\boldsymbol{k}-\boldsymbol{K}_0)}{\rho}\cos 2\pi(z_i-z_j)\rho d\rho\right.$$
$$\left.+i\int_{-\infty}^{\infty}\frac{f_i(\boldsymbol{K}-\boldsymbol{k}-\rho\boldsymbol{\nu})f_j(\rho\boldsymbol{\nu}+\boldsymbol{k}-\boldsymbol{K}_0)}{\rho}\sin 2\pi(z_i-z_j)\rho d\rho\right]d\sigma, \tag{35}$$

Here $L(\boldsymbol{b})$ is taken as unity, and $\sum_i$ and $\sum_j$ are extended over all atoms in the scatterer. The derivation of (34) from (25) is exact and any approximation as used in that of (30) from (25) is not necessary. Eqs. (34) and (35) are compared in the same way as in the case of eqs.(30) and (32). Then it is found that PKT approximation almost coincides with the exact solution provided that the number of atoms which overlap one another when the scatter is seen from the directon of $\boldsymbol{K}_0$ is negligibly small compared to the number of atoms which do not overlap any other (Appendix V).

In Appendixes (IV) and (V), the atomic numbers of the atoms in the crystal are assumed to be nearly the same. If the crystal cotains heavy and light atoms, the overlap of two heavy atoms are important and that of a heavy atom and a light atom or of two light atoms can be neglected. This is verified because S_{ij} given by (A8) and (A12) predominates only when both the i-th and the j-th atom are heavy.

§ 4. Discussions

It is concluded in the previous section that the result of PKT coincides with that of the exact theory under the condition that there is no overlap of atoms when the crystal is seem from the direction of the incident beam. This conclusion may be physically interpreted as follows. The scattering of electrons by an atom is considerable only for small scattering angles for the usual accelerating voltages (≳10 KV). Therefore, when the condition of non-overlap is satisfied, the multipe scatterings on different atoms are negligible compared to those in individual atoms. The reason that PKT is satisfactory for gas molecules may be understood as follows. Since gas molecules take random orientations, the probability that two atoms in a molecule arrange themselves along the direction of the incident beam is very small. Thus the condition of non-overlap is satisfied for most molecules.

Our result that PKT gives more exact value than KT for very thin crystals does not contradict the conclusion by Miyake,[3] Fujimoto[4] and Fujiwara[6] that the exact value approaches KT value in the limit $\lambda D \to 0$, where λ is the wave length of electrons and D the crystal thickness.

First, we consider the variation of I_h with D fixing λ to a definite value, where I_h is the intensity* of a given reflection $\boldsymbol{h}$. It is well known[2] that, according to KT and PKT, the curve $\sqrt{I_h}$ vs. D is a straight line if Bragg condition is exactly satisfied. This can be seen also from eqs. (22), (24), (25) etc. The curve for the exact value is tangent to the straight line for KT at the origin (Miyake, Fujimoto and Fujiwara) and it may cross the straight line for PKT at $D=D_0$ (Present theory), where D_0 is the one unit cell thickness. Thus the curves $\sqrt{I_h}$ vs. D for a definite value of λ may be as illustrated in Fig. 3.

Next, we consider the variation of $\sqrt{I_h}$ with λ for a fixed value of D. KT intensity is independent of λ. From eqs. (22) to (29) it is found that PKT intensity and the exact intensity approaches KT value in the limit $\lambda \to 0$. Thus the intensity may change with λ for a fixed D as illustrated in Fig. 4.

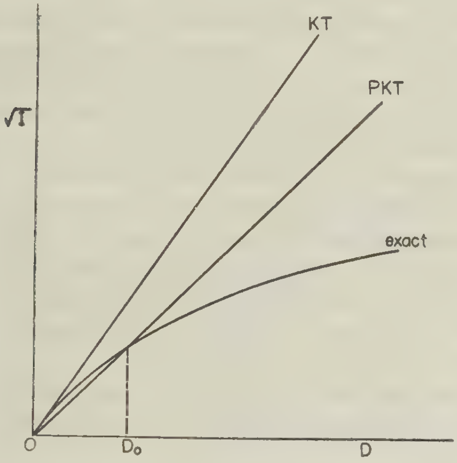

Fig. 3. Dependence of $\sqrt{I}$ on D for fixed λ.

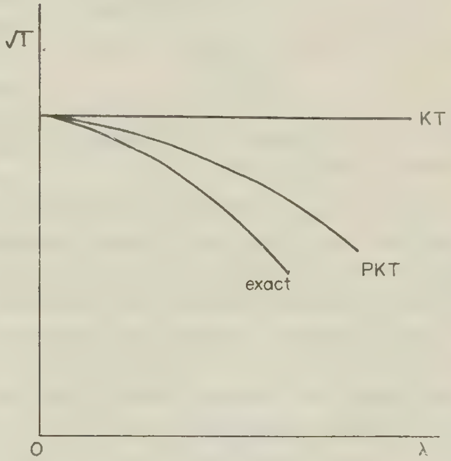

Fig. 4. Dependence of $\sqrt{I}$ on λ for fixed D.

From Fig. 3 and Fig. 4, it is clear that the three intensities all coincide with each other in the limit $\lambda D \to 0$. It is noted that the structure factor of PKT $F^P(\boldsymbol{K}, \boldsymbol{K}_o)=\sum_i f^P{}_i(\boldsymbol{K}, \boldsymbol{K}_o) \times \exp[-2\pi i(\boldsymbol{K}-\boldsymbol{K}_o)\cdot \boldsymbol{r}_i]$ depends upon λ and approaches the structure factor of KT $F(\boldsymbol{K}-\boldsymbol{K}_o)$ in the limit $\lambda \to 0$. Here f^P is the rigorous atomic scattering amplitude in which the multiple scatterings within the atom are taken into account.

Ibers & Hoerni[13] calculated f^P for 40 KV by the method of partial waves for selected atoms of the atomic numbers ranging from 1 to 98 using the Thomas-Fermi potential in the approximate from the Rozental.[14] According to the result, the value of $|f^P|$ differs for heavy atoms considerably from the Born approximation value f calculated for the same potential (Fig. 5). Thus, at the usual voltages the discrepancy between the exact and KT value may be considerable for thicknesses around D_0 when heavy atoms are contained. This is supported by the fact[1] that the electron diffraction by gas molecules can be explained by PKT but it can not by KT at the voltages 10 -80 KV. Thus, when we say that the exact value approaches KT value in the limit $\lambda D \to 0$, it implies that D must be reduced to a value smaller than the atomic diameter if the voltage is fixed to say 80 KV, or that the voltage must be increased much higher than 80 KV if D is fixed to a physically possible value.

According to the numerical calculation by Fujimoto,[5] the exact intensity coincides with

---

* Peak intensity. The conclusion of this section holds also for the integrated intensity.

KT value within the error of 3% for 111-reflection from Au of the thicknesses smaller than 15 A at $2\pi/\lambda=100$ A^{-1} (37 KV). On the other hand, from the value of $|f^{P}{}_{An}|$ calculated by Ibers & Hoerni, it is found that $I^{P}{}_{111}/I^{K}{}_{111}=0.784$ for 40 KV for the same crystal, where $I^{P}{}_{111}$ and $I^{K}{}_{111}$ are the intensity of 111-reflection given by PKT and by KT, respectively. Thus the exact intensity must differ from that of KT by about 20% for $D\approx D_0=4.07$ A. The conflicting result of the two calculations may be caused by the neglecting of the accidental interactions in Fujimoto's calculation.

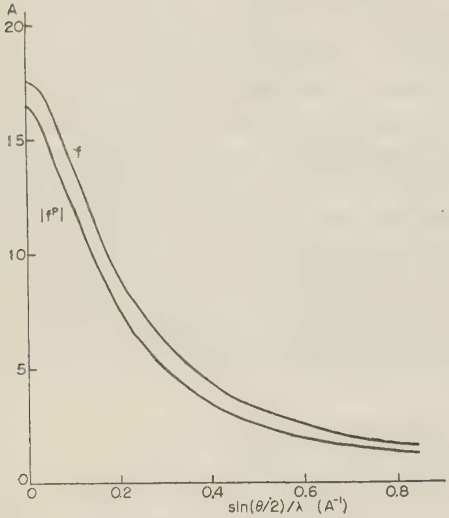

Fig. 5. Comparison of $|f^P|$ for 40KV and f for Tl. Thomas-Fermi potential (Rozental form) is used.

For usually available values of λ and D, the exact intensity can neither be approximated by KT value nor by PKT value. Therefore, the method of extrapolation is needed in order to obtain the intensity of KT or PKT. If we extrapolate the observed (exact) intensity to $\lambda=0$ at a fixed value of D, KT intensity will be obtained, In the method proposed by Honjo & Kitamura[7] the diffraction patterns are taken for various λ and the intensity in the limit $\lambda\to 0$ is obtained. It is also possible in principle to extrapolate the intensity to $D=D_0$ at a fixed value of λ and obtain PKT intensity. But the reflections for which the procedure is valid are limited on account of the condition of non-overlap. Moreover the procedure is experimentally impossible even for the reflections for which the condition of non-overlap is satisfied. Thus, PKT is not applicable to the structure analysis of crystals, while KT is convenient for the purpose. Theories by Miyake,[3] Fujimoto[4] and Fujiwara[6] provide the theoretical basis for the method by Honjo & Kitamura.

The present problem was suggested to the author by Prof. Ryozi Uyeda.

In conclusion, the author wishes to express his sincere thanks to Prof. Ryozi Uyeda for his kind guidance throughout this work. The author's thanks are also due to Dr. Y. Kainuma for his valuable suggestions and discussions.

Appendix

(I) Derivation of (30)

The integral in eq. (25) is calculated as follows.[12]

$$\int\frac{f_i(\boldsymbol{K}-\boldsymbol{k})f_i(\boldsymbol{k}-\boldsymbol{K}_0)}{\boldsymbol{k}^2-\boldsymbol{K}_0{}^2}\,d\boldsymbol{k}=\mathrm{P}\int d\boldsymbol{k}+\int\limits_{\text{singular}}d\boldsymbol{k}\qquad.$$

Taking the polar and the azimuthal angle θ,φ and writing $f_i(\boldsymbol{K}-\boldsymbol{k})\,f_i(\boldsymbol{k}-\boldsymbol{K}_0)\equiv g(k,\,\theta,\,\varphi)$,

$$\int\limits_{\text{singular}}d\boldsymbol{k}=\iiint\limits_{\text{singular}}\frac{g(k,\theta,\varphi)}{k^2-K_0{}^2}k^2\sin\theta dkd\theta d\varphi=\iint\sin\theta d\theta d\varphi\int\limits_{\text{singular}}\frac{g(k,\theta,\varphi)}{(k-K_0)(k+K_0)}k^2dk$$

$$=\iint\sin\theta d\theta d\varphi\pi i\frac{g(K_0,\theta,\varphi)}{2K_0}K_0{}^2=\frac{i\pi}{2K_0}\int\limits_{\substack{\text{Ewald}\\\text{sphere}}}f_i(\boldsymbol{K}-\boldsymbol{k})f_i(\boldsymbol{k}-\boldsymbol{K}_0)d\sigma.$$

Thus eq.(25) can be written as

$$\Phi^{P(2)}(\boldsymbol{K},\boldsymbol{K}_0)=\frac{1}{\pi}L(\boldsymbol{b})\sum_i\exp\left[-2\pi i\boldsymbol{b}\cdot\boldsymbol{r}_i\right]\left[\frac{i\pi}{2K_0}\int\limits_{\substack{\text{Ewald}\\\text{sphere}}}f_i(\boldsymbol{K}-\boldsymbol{k})f_i(\boldsymbol{k}-\boldsymbol{K}_0)d\sigma\right.$$

$$\left.+\mathrm{P}\int\frac{f_i(\boldsymbol{K}-\boldsymbol{k})f_i(\boldsymbol{k}-\boldsymbol{K}_0)}{\boldsymbol{k}^2-\boldsymbol{K}_0{}^2}d\boldsymbol{k}\right].\qquad\text{(A1)}$$

Taking into account that $f(\boldsymbol{b})$ changes only a little when $\boldsymbol{b}$ changes by an amount of the order of a^*, we have

$$\left.\begin{aligned}&\int\limits_{\substack{\text{Ewald}\\\text{sphese}}} f_i(\boldsymbol{K}-\boldsymbol{k})f_i(\boldsymbol{k}-\boldsymbol{K}_0)d\sigma \approx \frac{1}{S_0}\sum_G \frac{K_0}{K_{gz}} f_i(\boldsymbol{K}-\boldsymbol{K}_g)f_i(\boldsymbol{K}_g-\boldsymbol{K}_0),\\ &\mathrm{P}\int \frac{f_i(\boldsymbol{K}-\boldsymbol{k})f_i(\boldsymbol{k}-\boldsymbol{K}_0)}{\boldsymbol{k}^2-\boldsymbol{K}_0^2}d\boldsymbol{k} \approx \frac{1}{S_0}\sum_G \frac{1}{2K_{gz}}\,\mathrm{P}\int_{-\infty}^{\infty}\frac{f_i(\boldsymbol{K}-\boldsymbol{K}_g-\rho\boldsymbol{\nu})f_i(\rho\boldsymbol{\nu}+\boldsymbol{K}_g-\boldsymbol{K}_0)}{\rho}d\rho.\end{aligned}\right\} \tag{A2}$$

Substituting (A2) into (A1), we obtain eq. (30)

(II) Derivation of (32)

For a crystal plate of one unit cell thickness with an area $|M_1\boldsymbol{a}_1\times M_2\boldsymbol{a}_2|$, we have from (14), for large M_1 and M_2,

$$L(\boldsymbol{b})\approx\sum_{G1}\sum_{G2}\delta(\xi-G_1)\,\delta(\eta-G_2), \tag{A3}$$

where G_1 and G_2 are integers and $\boldsymbol{b}=\xi\boldsymbol{a}_1^*+\eta\boldsymbol{a}_2^*+\zeta\boldsymbol{a}_3^*$. Eq. (32) is obtained from eq. (28) by the help of eqs. (13) and (A3).

(III) Expressions of A, B, A', B' and B''

$$A=\frac{i}{S_0}L(\boldsymbol{b})\sum_G\frac{1}{2K_{gz}}\sum_i\exp[-2\pi i\boldsymbol{b}\cdot\boldsymbol{r}_i]f_i(\boldsymbol{b}-\boldsymbol{g})f_i(\boldsymbol{g}), \tag{A4}$$

$$B=\frac{1}{\pi S_0}L(\boldsymbol{b})\sum_G\frac{1}{2K_{gz}}\sum_i\exp[-2\pi i\boldsymbol{b}\cdot\boldsymbol{r}_i]\mathrm{P}\int_{-\infty}^{\infty}\frac{f_i(\boldsymbol{b}-\boldsymbol{g}-\rho\boldsymbol{\nu})f_i(\rho\boldsymbol{\nu}+\boldsymbol{g})}{\rho}d\rho,$$

$$A'=\frac{i}{S_0}L(\boldsymbol{b})\sum_G\frac{1}{2K_{gz}}\sum_{i\neq j}\sum\exp[-2\pi i(\boldsymbol{b}-\boldsymbol{g})\cdot\boldsymbol{r}_i]\exp[-2\pi i\boldsymbol{g}\cdot\boldsymbol{r}_j]f_i(\boldsymbol{b}-\boldsymbol{g})f_j(\boldsymbol{g}), \tag{A5}$$

$$\begin{aligned}B'=\frac{1}{\pi S_0}L(\boldsymbol{b})\sum_G\frac{1}{2K_{gz}}\sum_{i\neq j}\sum\exp[-2\pi i(\boldsymbol{b}-\boldsymbol{g})\cdot\boldsymbol{r}_i]\exp[-2\pi i\boldsymbol{g}\cdot\boldsymbol{r}_j]\\ \times\mathrm{P}\int_{-\infty}^{\infty}\frac{f_i(\boldsymbol{b}-\boldsymbol{g}-\rho\boldsymbol{\nu})f_j(\rho\boldsymbol{\nu}+\boldsymbol{g})}{\rho}\cos 2\pi(z_i-z_j)\,\rho d\rho,\end{aligned}$$

$$\begin{aligned}B''=\frac{i}{\pi S_0}L(\boldsymbol{b})\sum_G\frac{1}{2K_{gz}}\sum\sum_j\exp[-2\pi i(\boldsymbol{b}-\boldsymbol{g})\cdot\boldsymbol{r}_i]\exp[-2\pi i\boldsymbol{g}\cdot\boldsymbol{r}_j]\\ \times\int_{-\infty}^{\infty}\frac{f_i(\boldsymbol{b}-\boldsymbol{g}-\rho\boldsymbol{\nu})f_j(\rho\boldsymbol{\nu}+\boldsymbol{g})}{\rho}\sin 2\pi(z_i-z_j)\rho d\rho\ .\end{aligned}$$

(IV) Comparison of A' with A

Eqs. (A4) and (A5) can be approximately written as

$$A\approx\frac{i}{S_o}L(\boldsymbol{b})\ \frac{1}{2K_{oz}}\sum_i\exp[-2\pi i\boldsymbol{b}\cdot\boldsymbol{r}_i]\ S_{ii}(\boldsymbol{b}), \tag{A6}$$

$$A'\approx\frac{i}{S_o}L(\boldsymbol{b})\ \frac{1}{2K_{oz}}\sum_i\exp[-2\pi i\boldsymbol{b}\cdot\boldsymbol{r}_i]\sum_j{}'\ S_{ij}(\boldsymbol{b}), \tag{A7}$$

where $\sum_j{}'$ represents the summation over j excluding $j=i$. $S_{ij}(\boldsymbol{b})$ is given by

$$S_{ij}(\boldsymbol{b})=\sum_G f_i(\boldsymbol{b}-\boldsymbol{g})f_j(\boldsymbol{g})\exp[-2\pi i\boldsymbol{g}\cdot(\boldsymbol{r}_j-\boldsymbol{r}_i)]. \tag{A8}$$

In the case where the number of atoms in the unit cell is small and their atomic numbers are nearly equal,

$$\frac{A'}{A}\sim\frac{\sum_j{}'\ S_{ij}(\boldsymbol{b})}{S_{ii}(\boldsymbol{b})}\equiv\sum_j{}'\ Q_{ij}\ . \tag{A9}$$

For the reflections of low indices, $|Q_{ij}|$ is determined almost solely by s_{ij}, where s_{ij} is the smallest distance between i-atom and j-atom projected on the plane perpendicular to $\boldsymbol{K}_o$ (Fig. 6.). $|Q_{ij}|$ decreases monotonously from unity to zero when s_{ij} increases from zero to infinity. $|Q_{ij}|$ is negligibly small in comparison to unity when s_{ij} is larger than the sum of the screening distances (a_i+a_j) of the atomic potentials of i-atom and j-atom. Here the screening distance a_i is such a distance that $\phi_i(r)\ll 1$ for $r>a_i$, where $\phi_i(r)$ is the screening function of the atomic potential of i-atom. An example of curve $Q_{ij}(s_{ij})$ is given in Fig. 7.

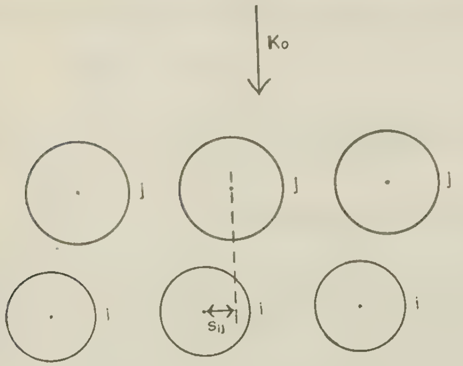

Fig. 6. Illustration of overlap of atom.

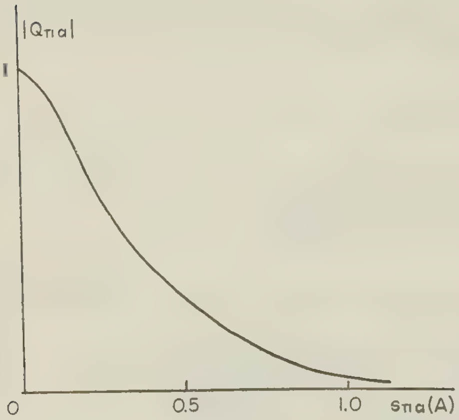

Fig. 7.

Thus we see that A' is small in comparison to A when s_{ij} is larger than (a_i+a_j) for every pair of atoms i, j. This is the condition of non-overlap mentioned in § 3.

The rapid decrease of $|Q_{ij}(s_{ij})|$ with increasing s_{ij} is due to the summation over all $\boldsymbol{G}$'s in (A8). The summation means that the accidental interactions as well as the systematic interactions are taken into account. If the summation is made only over the systematic interactions, $|Q_{ij}(s_{ij})|$ does not decrease so rapidly.

(V) Comparison between (34) and (35)

Eqs. (34) and (35) are written in the form of (33). The expressions of A, B, A' etc. in this case are easily found by comparing (34) and (35) with (30) and (32). An order estimation of these quantities shows that also in this case B' and B'' are negligible compared to B. A, A', S_{ij} and Q_{ij} are given by

$$A=\frac{i}{2K_o}\sum_i \exp\left[2\pi i(\boldsymbol{K}-\boldsymbol{K}_o)\cdot\boldsymbol{r}_i\right] S_{ii}(\boldsymbol{K}-\boldsymbol{K}_o), \tag{A10}$$

$$A'=\frac{i}{2K_o}\sum_i \exp\left[2\pi i(\boldsymbol{K}-\boldsymbol{K}_o)\cdot\boldsymbol{r}_i\right]\sum_j{}' S_{ij}(\boldsymbol{K}-\boldsymbol{K}_o), \tag{A11}$$

$$S_{ij}(\boldsymbol{K}-\boldsymbol{K}_o)=\int_{\substack{\text{Ewald}\\ \text{sphere}}}\exp\left[-2\pi i(\boldsymbol{k}-\boldsymbol{K}_o)\cdot(\boldsymbol{r}_j-\boldsymbol{r}_i)\right] \times f_i(\boldsymbol{K}-\boldsymbol{k})f_j(\boldsymbol{k}-\boldsymbol{K}_o)d\sigma, \tag{A12}$$

$$Q_{ij}=S_{ij}/S_{ii}$$

Q_{ij} is found to decrease rapidly with increasing s_{ij} as in the case of Appendix (IV). In the summation over j in $\sum_j{}' S_{ij}(\boldsymbol{K}-\boldsymbol{K}_o)$ of (A11), only the atoms in the neighbourhood of the i-th atom must be taken into account. If non of those atoms overlap the i-th atom, then $\sum_j{}' S_{ij}\ll S_{ii}$. When the condition $\sum_j{}' S_{ij}\ll S_{ii}$ holds for most of the i-th atom, we have $A'\ll A$ from (A10) and (A11) assuming the randomness of the phases $\exp\left[2\pi i(\boldsymbol{K}-\boldsymbol{K}_o)\cdot\boldsymbol{r}_i\right]$.

References

1) R. Glauber & V. Schomaker: Phys. Rev. **89** (1953) 667.
2) J. A. Hoerni: Phys. Rev. **102** (1956) 1534.
3) S. Miyake: J. Phys. Soc. Japan **14** (1959) 1347,
4) F. Fujimoto: J. Phys. Soc. Japan **14** (1959) 1558.
5) F. Fujimoto: J. Phys. Soc. Japan **15** (1960) 859.
6) K. Fujiwara: J. Phys. Soc. Japan **14** (1959) 1513.
7) G. Honjo & N. Kitamura: Acta Cryst. **10** 533.
8) N. F. Mott & H. S. W. Massey: *The Theory of Atomic Collisions* (Clarendon Press, Oxford, 1949) Chap. VII, Sec. 1.

9) L. I. Schiff: *Quantum Mechanics* (McGraw-Hill Book Co. Inc., New York, 1948) p. 161.
10) I. N. Sheddon: *Fourier Transforms* (McGraw-Hill Book Co. Inc., New York, 1951) p. 3[illegible].
11) N. Kato: J. Phys. Soc. Japan **7** (1952) 408.
12) H. Yoshioka: J. Phys. Soc. Japan **12** (1957) 618.
13) J. A. Ibers & J. A. Hoerni: Acta Cryst. **7** (1954) 405.
14) S. Rozental: Z. Phys. **98** (1936) 742.

Journal of the Physical Society of Japan, Vol. 15, No. 11, November, 1960

Magnetic Properties of Potassium Iron Group Fluorides KMF_3

By Kinshiro HIRAKAWA*, Kazuyoshi HIRAKAWA** and
Takasu HASHIMOTO*

**Department of Physics, **General Education Department, Kyusyu University, Fukuoka*

(Received August 5, 1960)

Evidence of antiferromagnetism in perovskite-type potassium iron group fluoride KMF_3 was found through the susceptibility measurements made between 80°K and 700°K. The obtained results are as follows:

Compounds	T_N(°K)	θ(°K)	C_M	p
$KMnF_3$	88	158	4.73_5	6.15
$KFeF_3$	113	—	—	—
$KCoF_3$	114	125	3.07_5	4.95
$KNiF_3$	275	843	2.41_5	4.39
$KCuF_3$	243	355	0.58_7	2.16

T_N: Néel point, θ: paramagnetic Curie temperature,
C_M: Curie constant, p: effective Bohr-magneton number.

Additional thermal analysis was also made in order to confirm the Néel points. The magnetic properties of these compounds are reviewed and brief discussions of our results are given.

§ 1. Introduction

Recently, the magnetic properties of compounds with relatively simple structures, for example, MO, MF_2, MF_3, $LaMO_3$, etc.,[1] have been investigated experimentally and theoretically in detail. We have been interested in the magnetic properties of the series of KMF_3, which has the perovskite structure. Although $LaMO_3$[2] and MF_3[3] are similar to KMF_3 as regards crystal structure, the M ions in the former two series are trivalent and it is not always easy to obtain the compounds with ideal composition or to prepare the specimens in the form of single crystals. On the other hand, the M ions in the latter are divalent and cover all of the more-than-half transition metal ions ranging from Mn^{2+} to Cu^{2+}, and it is possible to obtain their single crystals. In these materials, we may expect to obtain plenty of information about the superexchange and anisotropy mechanisms, since the M ions are arranged on the simple cubic lattice with a F^- ion in the center of each two adjacent M^{2+} ions. A detailed X-ray investigation on the crystals prepared by us have been performed by Okazaki et al.,[4] whose results are shown in Table I.

Table I. Lattice parameters of KMF_3

Compounds	values at 298°K (Å)
$KMnF_3$	a; 4.191 ± 0.001
$KFeF_3$	a; 4.122 ± 0.001
$KCoF_3$	a; 4.069 ± 0.001
$KNiF_3$	a; 4.015 ± 0.001
$KCuF_3$	$A(=\sqrt{2}a)$; 5.855 ± 0.002 $C(=2c)$; 7.852 ± 0.004 (Tetragonal)

On the course of our studies, we came to know the results of investigation made by Martin et al.[5] They have found the Néel points of this series to be $KMnF_3$(incomplete), $KFeF_3$(115°K), $KCoF_3$(135.3°K), $KNiF_3$(275°K), $KCuF_3$(<100°K) respectively. Recently, Shulman et al observed the N.M.R. shift of F^{19} and Co^{59}, F^{19} in $KMnF_3$[6] and $KCoF_3$[7] respectively. Ogawa[8] measured the susceptibility of $KMnF_3$. Their results are not always in agreement with our results. In this paper, our measurements of the powder susceptibility will be described and the magnetic properties of this series will be reviewed.

§2. Preparation of the Specimens

All specimens were prepared from the reagent grade of chemicals. The employed methods of preparation will be described for each compound.

$KMnF_3$:

We obtained $KMnF_3$ in the precipitated form from the aqueous solutions of the weighted 3KF and $MnCl_2 \cdot 4H_2O$. The precipitates packed in the carbon crucible were dried in vacuum and melt in the argon atmosphere to crystallize. Another method is to melt the precipitates in the nitrogen atmosphere with KCl or KI as a flux. Thus we obtained white transparent (with a dash of pink) crystals. The specimens obtained by these two methods showed completely the same magnetic properties.

$KFeF_3$:

The preparation of $KFeF_3$ is the most difficult. The precipitates obtained from $FeCl_2$ and KF reaction have a pseudo-perovskite structure and are ferrimagnetic below ~110°K. This ferrimagnetism may perhaps arise from the Fe^{3+} contamination in the starting material $FeCl_2$. By melting there precipitates in the argon atmosphere, we could obtain rectangular brown crystals of $KFeF_3$, which were proved to be cubic by X-ray analysis. As these crystals are mixed with a little amount of magnetite, we could not obtain a quantitative results; they are however not ferrimagnetic but antiferromagnetic below 113°K.

$KCoF_3$ and $KNiF_3$:

The concentrated aqueous solutions of $CoCl_2$ and $KF \cdot HF$ were mixed and the water was evapolated at 90°C. When a proper amount of $KCoF_3$ precipitated, the remained KCl and HF were fully washed out by boiled water. The powder was then dried in vacuum at about 200°C. $KNiF_3$ was also prepared by the same method.

$KCuF_3$:

At first, $CuCO_3$ was dissolved into an excess equeous solution of HF, then an adequate composition of KF was added. This dilute solution was kept in the temperature controlled (90°C) drying furnace, then excess water and HF were evaporated. By using this method we could obtain crystals of $KCuF_3$ slightly with coloured violet and about 2×2×1 m/m in size.

Because of the difficulty of the chemical analysis of F^-, we could not know the precise composition of these compounds. Only comparison between the diffracted intensity and density gave information or regards the composition.

§3. Susceptibility measurements

Susceptibility was measured in the nitrogen atmosphere by the use of the automatic recording magnetic balance of Hirone type.[9] For the determination of the absolute value, Gouy's method was employed. Temperatures were measured by a fine copper-constantan thermocouple (~0.1 mmϕ). The correction for the exerted force due to the constantan wire becomes considerably significant at temperatures below ~150°K, especially in the measurements of the low susceptibility compounds such as $KNiF_3$ and $KCuF_3$. The errors of the susceptibility measurements are estimated to be less than one percent.

§4. Results and discussions

$KMnF_3$*: Fig. 1 shows the measured, gram susceptibility χ in the case of heating run. The Néel point is estimated to be 88°K, below which the susceptibility strongly depends upon the field strength, suggesting that the crystal has a weak ferromagnetic component. Under field strengths higher than 5,000 gauss the susceptibility in the antiferromagnetic region does not depend on temperature showing that the spin moment is flopped into a plane perpendicular to the field direction. Such an easy flopping is convincing if we consider that Mn^{2+} is in ^{6}S state and is on the simple cubic lattice points for which there should be no dipole-dipole interaction. At a temperature a little above the Néel point the susceptibility curve shows a kink. The origin of the occurrence of this kink is not understood at present, but the observed curve for KMnF$_3$ is very similar to that for MnCO$_3$.[12] The susceptibility follows the Curie-Weiss law above about 200°K but not below it. X-ray determination of our sample shows that, below about 200°K, the crystal becomes tetragonally deformed. The observed paramagnetic Curie temperature θ is 158° and the effective Bohr-magneton number p is 6.15, which is somewhat larger than the free spin value 5.92 for Mn^{2+}.

---

* Dr. Portis et al have made torque[10], X-ray[11] and microwave[10] measurements on $KMnF_3$. Their results are consistent to our results. We would like to express our thanks to Dr. Portis for kindly supplying their preprints.

KFeF$_3$: As the preparation of this specimen is difficult, the measured susceptibility will be reported very briefly. Fig. 2 shows the measured results. This specimen contains evidently a trace of magnetite, but it may be pointed out that below 113°K KFeF$_3$ becomes antiferromagnetic.

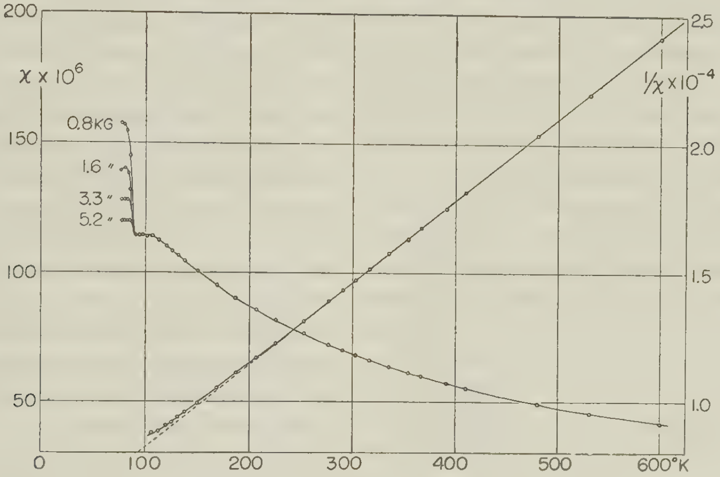

Fig. 1. Gram susceptibility (inverse susceptibility) versus temperature curve for KM$_n$F$_3$.

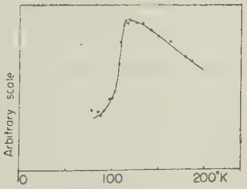

Fig. 2. The susceptibility-temperature curve for KF$_e$F$_3$, which contains a trace of magnetite.

KCoF$_3$: Fig. 3 shows the measured susceptibility of KCoF$_3$. Below 114°K χ decreases monotonically with falling temperature, thus 114°K is thought to be the Néel point. In some specimens the $\chi_{\max}$ point was about 20 degrees higher than 114°K. But the results

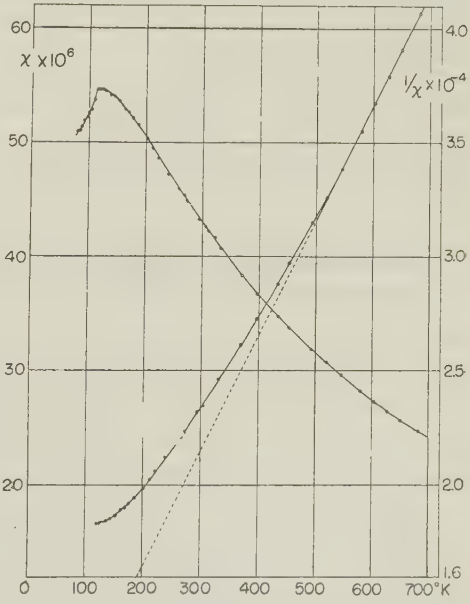

Fig. 3. Gram susceptibility (inverse susceptibility) versus temperature curve for KC$_0$E$_3$.

of X-ray and calorimetric measurements suggest that 114°K is more preferrable*. The paramagnetic susceptibility follows the Curie-Weiss law above~500°K, but deviates below it. The values of θ, C_M and p obtained in the region between~500°K and 700°K are 125°, 3.07 and 4.95, respectively.

θ/T_N is 1.09 which is the smallest in this series. As the θ/T_N value of $KMnF_3$ is 1.80, the lower θ/T_N value in $KCoF_3$ may be, as pointed out by Kanamori[13] for CoO, the effect of the residual orbital moment of Co^{2+} in the cubic field. The temperature dependence of χ, the value of C_M and p are very similar to those of CoO measured by La' Blanchetais[14]. As is well known, the lowest orbital triplet of Co^{2+} in the cubic field is split into three levels with $j=1/2$, $3/2$ and $5/2$ by the L-S coupling. As these level separations are of the order of kT which corresponds to the temperatures of measurements, one may be able to expect a considerable deviation of χ from the Curie-Weiss law. An analysis of such a case has been made with success by Kanamori[13] for CoO.

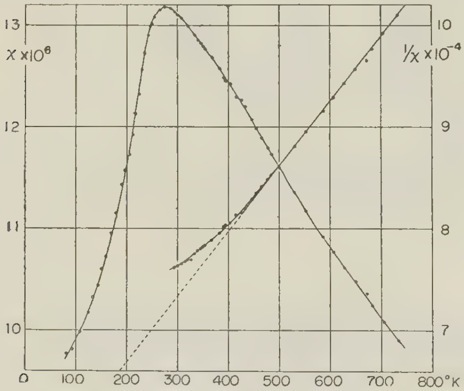

Fig. 4. Gram susceptibility (inverse susceptibility) versus temperature curve for KN_iF_3.

$KNiF_3$: The measured susceptibilities of $KNiF_3$ are shown in Fig. 4. A fairly broad maximum was found at 275°K, below which χ decreases in the usual manner and the ratio $\chi_{T=0}/\chi_{max}$ is 9.0/13.2=0.68 which is very nearly 2/3. We examined further the field dependence of susceptibility below the Néel point, but no change was detected at all. Thus we suggest that the spin moment of Ni^{2+} in $KNiF_3$ is fixed to the crystal axis. In the paramagnetic region χ obeys the Curie-Weiss law with $\theta=840°$ and $p=4.39_4$, but again deviates from it below~400°K. This deviation may be the effect of short range order still remaining above the Néel point. It is noted, however, that the observed θ and p are unusually large compared with $T_N=275°K$ and $p=2\sqrt{S(S+1)}=2.82$ for the free spin value of Ni^{2+}. Such a high p has also been observed in NiO (p=4.6) by Singer.[15]

In order to interpret this, we subtract tentatively a temperature independent susceptibility $\chi_c=3.5\times10^{-6}$ (or $\chi_{mol\ c}=5.6=10^{-4}$) from the observed paramagnetic susceptibilities and get the corrected value of θ and p as 300° and 2.80, respectively, both of which are reasonable value. In the cubic field the orbital levels of Ni^{2+} consist of higher two triplets and the lowest singlet and the separations are usually fairly large compared with kT. Thus the temperature independent term χ_c may be the Van Vleck paramagnetism plus a small part of diamagnetism due to the constituent nonmagnetic ion cores.

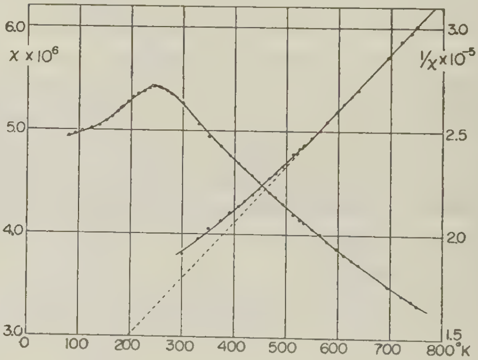

Fig. 5. Gram susceptibility (inverse susceptibility) versus temperature curve for $KCuF_3$.

$KCuF_3$: Fig. 5 shows the susceptibility of $KCuF_3$. A broad maximum in $\chi-T$ curve was observed at 243°K, below which χ decreases slowly with falling temperature. The Curie-Weiss law is applicable at temperatures higher than 500°K. Because of the small susceptibility, the magnetic properties of $KCuF_3$ are very sensitive to diamagnetic corrections or contamination of other paramagnetic salts. From the observed data, without any diamagnetic corrections for K^+ and F^-, we obtained $\theta=355°$ and p=2.16. As the lowest orbital state for Cu^{2+} in the cubic field is $d\gamma$, p should be very nearly 1.73, which is the free spin value of Cu^{2+}. The experimentally obtained p=2.16 is considerably higher than 1.73, and if suitable diamagnetic corrections are made p will become still larger. As in the case of $KNiF_3$, we may be able to consider the Van Vleck paramagnetism due to the upper $d\varepsilon$ orbits, but no reasonable explanation for θ and p has been found at present. It may possible that $KCuF_3$ has an A-type[16] antiferromagnetic spin structure as in $LaMnO_3$ and MnF_3 because the Cu^{2+} has, like Mn^{3+}, an unpaired electron in $d\gamma$ orbits and by X-ray studies[17] it has been confirmed that the crystal has a large Jahn-Teller distortion very similar to that in $LaMO_3$ or MF_3. Thus, $KCuF_3$ would might have an A-type structure, and one might expect a small or rather negative θ/T_N, because in the A-type structure there exists ferromagnetic nearest neighbour coupling within the {001} planes. This is the case for MnF_3 studied by Bozorth and Nielson[18]. In our case, however, θ/T_N is positive and not so small compared to unity. Thus at present we are not certain whether or not $KCuF_3$ has an A-type structure.

---

* T_N for $KCoF_3$ has been reported to be 135.3°K after Martin et al[5] and 137°K in the paper of Schulman.[7]

§ 5. Thermal analysis

In order to ascertain in another way the antiferromagnetic transition of the substances thermal analysis was made by a simple method (a type of conduction calorimeter). Measurements were made on $KCoF_3$, $KNiF_3$ and $KCuF_3$. A typical sharp anomalous hump in specific heat curve was observed at 109°K for $KCoF_3$, 253°K for $KNiF_3$ and 220°K for $KCuF_3$. These temperatures are all somewhat lower than the corresponding temperatures T_N, found by susceptibility measurements. Although any marked changes of the crystal symmetry of $KNiF_3$ and $KCuF_3$ have not been observed by X-ray, we believe that the antiferromagnetic transition was comfirmed. The fact that T_N determined from susceptibility measurements are higher than those from thermal analysis is a common fact, and it has been explained by Nakamura[19] as due to statistical effects.

§ 6. Conclusion

The details of the present experiment and discussions of the results were already des-

Table II

Compounds	Mol. Wt.	T_N°K			C_M	p	θ/T_N
		Mag.	Sp.h.	X-ray*			
$KMnF_3$	151.04	88			4.73_5	6.15_3	1.80
$KFeF_3$	151.95	113		102			
$KCoF_3$	155.04	114	109	112	3.07_5	4.95_8	1.09
$KNiF_3$	154.81	275	253	—	2.41_5	4.39_4	3.07
$KCuF_3$	159.64	243	220	—	0.58_7	2.16	1.48

* After Okazaki[17]

Table III. Comparison of Neel temperatures of various cubic compounds in °K.

	d^4	d^5	d^6	d^7	d^8	d^9
$LaMO_3$	$LaMnO_3$ 100	$LaFeO_3$ 750	$LaCoO_3$ —			
MF_3	MnF_3 43	FeF_3 394	CoF_3 460			
MO		MnO 118	FeO 189	CoO 290	NiO 520	CuO* 230
KMF_3		$KMnF_3$ 88	$KFeF_3$ 113	$KCoF_3$ 114	$KNiF_3$ 275	$KCuF_3$** 243

* Monoclinic complicated structure.

** Tetragonally deformed perovskite structure.

cribed for each compound KMF_3. In Table II the characteristic magnetic properties of this series are summarized.

It is interesting to compare the T_N of the KMF_3 series to those of other cubic compounds such as MF_3, $LaMO_3$ and MO, because in the crystal of perovskite structure T_N may be a direct measure of the superexchange among the M ions. This is shown in Table III. Unfortunately, full comparison with other perovskite type compounds can not be made. But it may be pointed out that in the MO series T_N becomes successively higher toward high d electron compounds, while in the KMF_3 series it may be classified into high T_N group of more than $d\varepsilon^6 d\gamma^2$($KNiF_3$ and $KCuF_3$) and low T_N group of less than $d\varepsilon^6 d\gamma^2$ ($KMnF_3$, $KFeF_3$, and $KCoF_3$).

Lastly it is pointed out that the susceptibilities of this series show not necessarily a sharp maximum at their Néel point and the Curie-Weiss law is applicable only at higher temperatures than twice as large as their Néel temperatures. As a matter of fact, we observed in some of the crystallized specimen of KMF_3, a temperature independent susceptibility in a wide range immediately above the Néel temperature, like in the case of $ZnFe_2O_4$.[20] It is not certain at present whether this result is due to the effect of some special properties of short range order in such a type of crystal or to a certain incompleteness of their crystals.

We wish to express our hearty thanks to Prof. Nagamiya and Dr. Nakamura of Osaka University for their kind interests and encouragements, to Mr. Okazaki for showing us his unpublished X-ray data and to Osaka Oxygen Company for kindly supplying us liquid nitrogen. A part of this research was supported by the scientific expenditure of Ministry of Education.

References

1) T. Nagamiya, K. Yoshida and R. Kubo: Adv. in Phys. **4** (1955) 1.
E. O. Wollan, H. R. Child, W. C. Koehler and M. K. Wilkinson: Phys. Rev. **112** (1958) 1132.
W. C. Koehler and E. O. Wollan: J. Phys. Chem. Solids. **2** (1957) 100.
2) H. L. Yakel, Jr: Acta Cryst. **8** (1955) 394.
3) M. A. Hepworth, K. H. Jack, R. D. Peacock and G. J. Westland: Acta Cryst. **10** (1957) 63.
4) A. Okazaki, Y. Suemune and T. Fuchikami: J. Phys. Soc. Japan **14** (1959) 1823.
5) R. L. Martin, R. S. Nyholm and N. C. Stephenson: Chemistry and Industry (1956) 83.
6) R. G. Shulman, K. Knox and B. J. Wyluda: Bull. Amer. Phys. Soc. S. II **4** (1959) 166.
7) R. G. Shulman: Phys. Rev. Let. **2** (1959) 459.
8) S. Ogawa: J. Phys. Soc. Japan **14** (1959) 1115.
9) T. Hirone, S. Maeda and N. Tsuya: Sci. Rep. R.I.T.U. **A6** (1954) 67.
10) O. Beckman, A. J. Heeger, A. M. Portis and D. T. Teaney: Detroit Meeting of the Amer. Phys. Soc. (1960).
11) O. Beckman, I. Olovsson and K. Knox: to be published in Acta. Cryst..
12) A. S. Borovik-Romanov: Sov. Phys. JETP **9** (1959) 539.
13) J. Kanamori: Prog. Theor. Phys. **17** (1956) 177.
14) C. H. La' Blanchetais: Jour. de Phys. et le Rad. **12** (1951) 765.
15) J. R. Singer: Phys. Rev. **104** (1956) 929.
16) E. O. Wollan and W. C. Koehler: Phys. Rev. **100** (1955) 88.
17) A. Okazaki: private communication.
18) R. M. Bozorth and J. W. Nielson: Phys. Rev. **110** (1958) 879.
19) T. Nakamura: Reported at the research meeting held at Yukawa Hall (1956).
20) A. Arrott and J. E. Goldman: Phys. Rev. **98** (1955) 1201.

JOURNAL OF THE PHYSICAL SOCIETY OF JAPAN Vol. 15, No. 11, NOVEMBER, 1960

The Perturbation Method due to the Small Change in the Shape of the Boundary*

By Tomoyuki SAITO*

*Tokyo University of Agriculture and Technology***
Koganei, Tokyo

(Received April 25, 1960)

A general method is presented for estimating the effect caused by a small change in the boundary shape (or the hypersurface shape in the many-dimensional space, the time-coordinate being included) upon the solutions or eigenvalues of linear partial differential equations (elliptic, parabolic or hyperbolic). When the given boundary is slightly deformed from a shape favorable for obtaining the solutions, this method gives the approximate solutions or eigenvalues based upon the exact or unperturbed ones for the case of the favorable shape, where many solutions can be obtained easier. The following illustrative examples are given, showing the validity of the method presented: (1) The eigenfrequencies of the lateral vibration of a uniform membrane fixed at its boundary close to a circle in shape, e.g. elliptic, oval, cinquefoil-shaped, etc. (2) The eigenvalue problem concerning the heat conduction of a "corned-beef-can"-shaped uniform matter, close to a rectangular parallelepiped in shape and with its temperature being kept constant on the boundary surface. (3) Three boundary-value problems representing the parabolic, hyperbolic and elliptic cases, respectively.

§ 1. Introduction

Generally speaking, the partial differential equations in physics are laid to be solved, not alone, but always together with boundary-conditions. For boundaries of favorable shapes (or "favorable boundaries" for short), such as circle, sphere, rectangular parallelepiped, etc., many have been solved analytically. For boundaries of rather irregular or unfavorable shapes (or "unfavorable boundaries"), however, it is generally difficult to solve the equations analytically, except in some special cases. But, when the deviation of the given boundary from a favorable one is small, the very situation makes a method for approximate solutions possible.

Two ways of approach have been presented; the one commenced by Brillouin(1) consists in expanding the perturbed solution by the eigenfunctions of the unperturbed, exactly solvable problem. It needs to solve a secular equation of infinite order, the solution obtained diverges in most cases, and so only a few problems have been solved by this method.

The other method, introduced by Oshida et al.,(2) seems more promising, for it surmounts the difficulty by the use of an appropriate transformation of the variables, changing the shape of the boundary to a favorable one. In general, this transformation makes the original equation more complicated, but, if the transformation is small, the transformed equation can be treated by a method similar to the one familiar in the ordinary theory of perturbation.

The latter method is not generally known, nor to be said well-established, in spite of its applicability to the wide field of mathematical physics. In this paper, the present author generalizes the method extensively, giving the formulae in a form immediately applicable to the vast field of mathematical physics. These formulae are sufficiently compact and are as easily handled as those in the ordinary perturbation method.

Concerning the extension of the method, a new technique is presented in boundary-value problems (in the broader sense, including so-called initial-value problems), which makes the problems with time-dependent boundary-conditions solvable, by admitting the time-coordinate into the method.

Although the practical terminology, "unfavorable" and "favorable", is used from the point of view of contributing to the intimate connection between the theory and its practical application, the discussion concerns only the two categories of boundaries, "given or deformed" and "undeformed", and so it is not necessary that the former should be always "unfavorable" and the latter "favorable", since the present paper aims originally at the effect which a slight deformation of the boundary has upon the solutions or eigenvalues.

---

* Read at the 15th Annual Meeting of the Physical Society of Japan, on April 5, 1960.

** Tokyo Noko Daigaku

§2. General Principles

1. *The introduction of the one-to-one mapping between the two boundaries, given and favorable.*

A linear partial differential equation (or simply "equation" for short, when there is no fear of confusion)

$$L\Psi(x) = -h(x) \tag{1}$$

is given with some specified boundary-condition on its specified boundary

$$C: \quad S(x)=0 \quad \text{or} \quad x=X(\lambda) \tag{2}$$

in the N-dimensional space (including the time-axis, as the case may be). **L** is a linear partial differential operator, $\Psi(x)$ the solution to be sought for, $h(x)$, $S(x)$ and $X(\lambda)$ the given functions of x and λ, respectively, continuously differentiable with respect to their arguments up to the requested order, x and λ representing symbolically the independent variables x^α and the independent parameters λ^i, with the indices α and i obeying the following rule:

Any index is assumed (unless any special mention is made) to vary from 1 to N, or from 1 to N–1, according as it is Greek or Latin, respectively. Also, any index appearing twice in one term should be regarded as a "summation-index", as is familiar in tensor calculus.

If the given boundary C is slightly deviated from the favorable one

$$C: \quad S^{(0)}(x)=0 \quad \text{or} \quad x=X^{(0)}(\lambda) \tag{3}$$

the functions S and X in Eq. (2) will be expanded in power series of a small quantity ϵ ($|\epsilon| \ll 1$), respectively, as follows:

$$S(x)=S^{(0)}(x)+\epsilon S^{(1)}(x)+\epsilon^2 S^{(2)}(x)+\dots$$
$$X(\lambda)=X^{(0)}(\lambda)+\epsilon X^{(1)}(\lambda)+\epsilon^2 X^{(2)}(\lambda)+\dots \tag{4}$$

where $S^{(n)}(x)$ and $X^{(n)}(\lambda)$, $n=0, 1, 2, \dots$, are the known functions of x and λ, respectively, sufficiently qualified concerning their differentiability with respect to their arguments, etc.

Now, suppose that the following transformations (5) and (6) are one-to-one mappings, of the given domain D (together with the surrounding boundary C) onto the favorable domain D_0 (together with the surrounding boundary C_0), and merely of the given boundary C onto the favorable one C_0, respectively:

$$x^\alpha=\bar{x}^\alpha+\epsilon\varphi^{(1)\alpha}(\bar{x})+\epsilon^2\varphi^{(2)\alpha}(\bar{x})+\dots$$

or, symbolically,

$$x=\bar{x}+\epsilon\varphi^{(1)}(\bar{x})+\epsilon^2\varphi^{(2)}(\bar{x})+\dots \tag{5}$$

and

$$\lambda^i=\bar{\lambda}^i+\epsilon\Lambda^{(1)i}(\bar{\lambda})+\epsilon^2\Lambda^{(2)i}(\bar{\lambda})+\dots$$

or, symbolically,

$$\lambda=\bar{\lambda}+\epsilon\Lambda^{(1)}(\bar{\lambda})+\epsilon^2\Lambda^{(2)}(\bar{\lambda})+\dots \tag{6}$$

where $\varphi^{(1)\alpha}(x)$, $\varphi^{(2)\alpha}(x)$, ... and $\Lambda^{(1)i}(\lambda)$, $\Lambda^{(2)i}(\lambda)$, ... are the functions of x and λ, respectively, the former ("domain-to-domain deviation functions", so to speak) being defined in and in the neighborhood of D_0, and the latter ("boundary-to-boundary deviation functions", so to speak) being defined on C_0, both qualifying the geometrical deviation of the given boundary from the favorable one. not independent of each other as a matter of course, as is shown in Eq. (13), and being, of course, assumed to be continuously differentiable with respect to their arguments up to the requested order.

Here, ϵ is assumed to be sufficiently small to make the Jacobian to be positive, therefore permitting the following "inverse" transformations (writing symbolically):

$$\bar{x}=x-\epsilon\varphi^{(1)}(x)-\epsilon^2\{\varphi^{(2)}(x)-\boldsymbol{D}^{(1)}\varphi^{(1)}(x)\}-\cdots \tag{7}$$

and

$$\bar{\lambda}=\lambda-\epsilon\Lambda^{(1)}(\lambda)-\epsilon^2\{\Lambda^{(2)}(\lambda)-\boldsymbol{D}^{(1)}{}_{(\lambda)}\Lambda^{(1)}(\lambda)\}-\cdots \tag{8}$$

respectively, with $\boldsymbol{D}^{(1)}$ and $\boldsymbol{D}^{(1)}{}_{(\lambda)}$ being defined in Eq. (11).

Eqs. (4) are rewritten in terms of $\bar{x}$ and $\bar{\lambda}$, respectively, by means of Eqs. (5) and (6), as follows:

$$\begin{aligned}S(x)=S^{(0)}(\bar{x})&+\epsilon\{S^{(1)}(\bar{x})+\boldsymbol{D}^{(1)}S^{(0)}(\bar{x})\}\\&+\epsilon^2\{S^{(2)}(\bar{x})+\boldsymbol{D}^{(1)}S^{(1)}(\bar{x})+\boldsymbol{D}^{(2)}S^{(0)}(\bar{x})\}+\cdots\end{aligned} \tag{9}$$

and

$$X(\lambda)=X^{(0)}(\bar{\lambda})+\in\{X^{(1)}(\bar{\lambda})+\boldsymbol{D}^{(1)}{}_{(\lambda)}X^{(0)}(\bar{\lambda})\}$$
$$+\in^2\{X^{(2)}(\bar{\lambda})+\boldsymbol{D}^{(1)}{}_{(\lambda)}X^{(1)}(\bar{\lambda})+\boldsymbol{D}^{(2)}{}_{(\lambda)}X^{(0)}(\bar{\lambda})\}+\cdots \tag{10}$$

where

$$\boldsymbol{D}^{(1)}\equiv\varphi^{(1)\alpha}\frac{\partial}{\partial x^{\alpha}},$$
$$\boldsymbol{D}^{(2)}\equiv\frac{1}{2}\varphi^{(1)\alpha}\varphi^{(1)\beta}\frac{\partial^2}{\partial x^{\alpha}\partial x^{\beta}}+\varphi^{(2)\alpha}\frac{\partial}{\partial x^{\alpha}}$$
$$\boldsymbol{D}^{(1)}{}_{(\lambda)}\equiv\Lambda^{(1)i}\frac{\partial}{\partial\lambda^{i}},$$
$$\boldsymbol{D}^{(2)}{}_{(\lambda)}\equiv\frac{1}{2}\Lambda^{(1)i}\Lambda^{(1)k}\frac{\partial^2}{\partial\lambda^{i}\partial\lambda^{k}}+\Lambda^{(2)i}\frac{\partial}{\partial\lambda^{i}}. \tag{11}$$

Therefore, the above-adopted mappings or transformations (5) and (6) should be such ones as transform the equation of the given boundary (2) to the following series of equations, respectively:

$$S^{(0)}=0,\ (S^{(1)}+\boldsymbol{D}^{(1)}S^{(0)})_{S^{(0)}=0}=0,$$
$$(S^{(2)}+\boldsymbol{D}^{(1)}S^{(1)}+\boldsymbol{D}^{(2)}S^{(0)})_{S^{(0)}=0}=0,\cdots \tag{12}$$

and

$$x=X^{(0)}(\lambda),\ (\varphi^{(1)})_{x=X^{(0)}}=X^{(1)}+\boldsymbol{D}_{(\lambda)}{}^{(1)}X^{(0)},$$
$$(\varphi^{(2)})_{x=X^{(0)}}=X^{(2)}+\boldsymbol{D}^{(1)}{}_{(\lambda)}X^{(1)}+\boldsymbol{D}^{(2)}{}_{(\lambda)}X^{(0)},\cdots \tag{13}$$

as are easily verified.

2. *Introduction of "virtual" scalar functions.*

Corresponding to an arbitrary scalar function $u(x)$, a new or "virtual" function $\bar{u}(x)$ is defined by the following relation:

$$\bar{u}(\bar{x})=u(x) \tag{14}$$

where $\bar{x}$ and x are related to each other through Eq. (5), and, just because of Eq. (5) being one-to-one mapping, $\bar{u}$ and u are defined by each other in such a way as $\bar{u}$ is defined in D_0 by means of u defined in D, and vice versa.

By making use of Eq. (5), the relation between $\bar{u}$ and u is obtained as follows:

$$\bar{u}(x)=\bar{u}(\bar{x}+\in\varphi^{(1)}(\bar{x})+\in^2\varphi^{(2)}(\bar{x})+\ \ldots)$$
$$=\bar{u}(\bar{x})+\in\boldsymbol{D}^{(1)}\bar{u}(\bar{x})+\in^2\boldsymbol{D}^{(2)}\bar{u}(\bar{x})+\ \ldots$$
$$=u(x)+\in\boldsymbol{D}^{(1)}u(x)+\in^2\boldsymbol{D}^{(2)}u(x)+\ \ldots$$

i.e.

$$\bar{u}=(1+\in\boldsymbol{D}^{(1)}+\in^2\boldsymbol{D}^{(2)}+\ \ldots)\,u \tag{15}$$

or, inversely,

$$u=[1-\in\boldsymbol{D}^{(1)}-\in^2(\boldsymbol{D}^{(2)}-\boldsymbol{D}^{(1)}\boldsymbol{D}^{(1)})-\ldots]\bar{u} \tag{16}$$

as is easily verified.

For instance, by making use of Eqs. (12),

$$\bar{S}=S^{(0)}$$

which shows that the virtual expression of the given boundary C is the favorable boundary C_0.

3. *Introduction of "virtual" tensor functions.*

Corresponding to an arbitrary covariant or contravariant tensor function, $u_{\alpha_1\alpha_2\cdots\alpha_n}(x)$ or $u^{\alpha_1\alpha_2\cdots\alpha_n}(x)$, a new or "virtual" covariant or contravariant tensor function, $\bar{u}_{\alpha_1\alpha_2\cdots\alpha_n}(x)$ or $\bar{u}^{\alpha_1\alpha_2\cdots\alpha_n}(x)$, is defined by the following relations, respectively:

$$\bar{u}_{\alpha_1\alpha_2\cdots\alpha_n}(\bar{x})=\frac{\partial x^{\beta_1}}{\partial\bar{x}^{\alpha_1}}\cdot\frac{\partial x^{\beta_2}}{\partial\bar{x}^{\alpha_2}}\cdots\frac{\partial x^{\beta_n}}{\partial\bar{x}^{\alpha_n}}u_{\beta_1\beta_2\cdots\beta_n}(x)$$

and

$$\bar{u}^{\alpha_1\alpha_2\cdots\alpha_n}(\bar{x})=\frac{\partial\bar{x}^{\alpha_1}}{\partial x^{\beta_1}}\cdot\frac{\partial\bar{x}^{\alpha_2}}{\partial x^{\beta_2}}\cdot\cdot\frac{\partial\bar{x}^{\alpha_n}}{\partial x^{\beta_n}}u^{\beta_1\beta_2\cdots\beta_n}(x) \tag{17}$$

where $\bar{x}$ and x are related to each other through Eq. (5) and the correspondence between the tensors, given and virtual, is also one-to-one.

By making use of Eqs. (5), (7), (15) and (16), the relations between the original and the virtual tensors are obtained as follows:

$$\bar{u}_{\alpha_1\cdot\cdot\alpha_n}=u_{\alpha_1\cdot\cdot\alpha_n}+\in[\sum_{s=1}^{n}\varphi^{(1)\beta_s}{}_{,\alpha_s}u_{\alpha_1\cdot\cdot\alpha_{s-1}\beta_s\alpha_{s+1}\cdot\cdot\alpha_n}$$
$$+\boldsymbol{D}^{(1)}u_{\alpha_1\cdot\cdot\alpha_n}]+\ldots$$

and

$$\bar{u}^{\alpha_1\cdot\cdot\alpha_n}=u^{\alpha_1\cdot\cdot\alpha_n}-\in[\sum_{s=1}^{n}\varphi^{(1)\alpha_s}{}_{,\beta_s}u^{\alpha_1\cdot\cdot\alpha_{s-1}.\beta_s\cdot\alpha_{s+1}\cdot\cdot\alpha_n}$$
$$-\boldsymbol{D}^{(1)}u^{\alpha_1\cdot\cdot\alpha_n}]-\ldots \tag{18}$$

or, inversely,

$$u_{\alpha_1\cdot\cdot\alpha_n}=\bar{u}_{\alpha_1\cdot\cdot\alpha_n}-\in[\sum_{s=1}^{n}\varphi^{(1)\beta_s}{}_{,\alpha_s}\bar{u}_{\alpha_1\cdot\cdot\alpha_{s-1}\beta_s\alpha_{s+1}\cdot\cdot\alpha_n}$$
$$+\boldsymbol{D}^{(1)}\bar{u}_{\alpha_1\cdot\cdot\alpha_n}]-\ \ldots$$

and

$$u^{\alpha_1\cdot\cdot\alpha_n}=\bar{u}^{\alpha_1\cdot\cdot\alpha_n}+\in[\sum_{s=1}^{n}\varphi^{(1)\alpha_s}{}_{,\beta_s}\bar{u}^{\alpha_1\cdot\cdot\alpha_{s-1}\cdot\beta_s.\alpha_{s+1}\cdot\cdot\alpha_n}$$
$$-\boldsymbol{D}^{(1)}\bar{u}^{\alpha_1\cdot\cdot\alpha_n}]+\ldots \tag{19}$$

where the indices attached to the right-hand foot of any function, with a comma ahead of them, mean its differentiation with respect to the coordinates or arguments denoted by them as follows:

$$f_{,\alpha}\equiv\frac{\partial f}{\partial x^{\alpha}},\ f_{,\alpha_1\alpha_2\cdot\cdot\alpha_n}\equiv\frac{\partial^n f}{\partial x^{\alpha_1}\partial x^{\alpha_2}\cdot\cdot\partial x^{\alpha_n}}\ \text{etc.},$$

as is usual in differential geometry.

Especially, as regards the fundamental metrical tensors, covariant and contravariant,

$$\bar{g}_{\alpha\beta}=g_{\alpha\beta}+\in g^{(1)}{}_{\alpha\beta}+\ \ldots$$

and

$$\bar{g}^{\alpha\beta}=g^{\alpha\beta}-\in g^{(1)\alpha\beta}-\ \dots \qquad (20)$$

where

$$g^{(1)}{}_{\alpha\beta}\equiv\varphi^{(1)\gamma}{}_{,\alpha}g_{\gamma\beta}+\varphi^{(1)\gamma}{}_{,\beta}g_{\alpha\gamma}+\boldsymbol{D}^{(1)}g_{\alpha\beta}$$
$$=g_{\alpha\rho}g_{\beta\sigma}g^{(1)\rho\sigma}$$
$$g^{(1)\alpha\beta}\equiv\varphi^{(1)\alpha}{}_{,\gamma}g^{\gamma\beta}+\varphi^{(1)\beta}{}_{,\gamma}g^{\alpha\gamma}-\boldsymbol{D}^{(1)}g^{\alpha\beta}$$
$$=g^{\alpha\rho}g^{\beta\sigma}g^{(1)}{}_{\rho\sigma}$$

which will be used later in the transformation of boundary-conditions, etc.

4. *Introduction of "virtual" functions corresponding to the functions defined on the given boundary C.*

Corresponding to an arbitrary scalar function $F(\lambda)$ defined on the boundary C, a virtual function $\bar{F}(\lambda)$ is defined by the following relation:

$$\bar{F}(\bar{\lambda})=F(\lambda) \qquad (21)$$

where $\bar{\lambda}$ and λ are related to each other through Eq. (6) and, just because of Eq. (6) being one-to-one mapping, the correspondence between $\bar{F}$ and F is one-to-one.

The relation between $\bar{F}$ and F is obtained as follows:

$$\bar{F}(\lambda)=\bar{F}(\bar{\lambda}+\in \Lambda^{(1)}(\bar{\lambda})+\in^2\Lambda^{(2)}(\bar{\lambda})+\dots)$$
$$=\bar{F}(\bar{\lambda})+\in \boldsymbol{D}^{(1)}{}_{(\lambda)}\bar{F}(\bar{\lambda})+\in^2\boldsymbol{D}^{(2)}{}_{(\lambda)}\bar{F}(\bar{\lambda})+\ \dots$$
$$=F(\lambda)+\in \boldsymbol{D}^{(1)}{}_{(\lambda)}F(\lambda)+\in^2\boldsymbol{D}^{(2)}{}_{(\lambda)}F(\lambda)+\ \dots$$

i.e.

$$\bar{F}=(1+\in \boldsymbol{D}^{(1)}{}_{(\lambda)}+\in^2\boldsymbol{D}^{(2)}{}_{(\lambda)}+\ \dots)F \qquad (22)$$

or, inversely,

$$F=[1-\in \boldsymbol{D}^{(1)}{}_{(\lambda)}$$
$$-\in^2(\boldsymbol{D}^{(2)}{}_{(\lambda)}-\boldsymbol{D}^{(1)}{}_{(\lambda)}\boldsymbol{D}^{(1)}{}_{(\lambda)})-\dots]\,\bar{F} \qquad (23)$$

as is easily verified.

It is easily shown by making use of Eqs. (4), (13), (15) and (22), that, corresponding to the equation of the given boundary C: $x=X(\lambda)$, its virtual expression is $x=X^{(0)}(\lambda)$, the equation of the favorable boundary C_0 (which might be, therefore, referred to as the "virtual" boundary).

5. *Introduction of "virtual" linear partial differential operators.*

Corresponding to an arbitrary linear partial differential operator L (or merely "operator" for short, when there is no fear of confusion), a new or "virtual" operator $\bar{L}$ is defined as follows:

$$\bar{L}\bar{u}=\overline{Lu} \qquad (24)$$

where the correspondence between $\bar{L}$ and L is also one-to-one.

By making use of Eqs. (15) and (16), the relation between the operators, given and virtual, is obtained as follows:

$$\bar{L}\bar{u}=\overline{Lu}=(1+\in \boldsymbol{D}^{(1)}+\in^2\boldsymbol{D}^{(2)}+\ \dots)Lu$$
$$=(1+\in \boldsymbol{D}^{(1)}+\in^2\boldsymbol{D}^{(2)}+\dots)L$$
$$[1-\in \boldsymbol{D}^{(1)}-\in^2(\boldsymbol{D}^{(2)}-\boldsymbol{D}^{(1)}\boldsymbol{D}^{(1)})-\ \dots]\bar{u}$$

therefore

$$\bar{L}=L+\in L^{(1)}+\in L^{(2)}+\ \dots \qquad (25)$$

where

$$L^{(1)}\equiv \boldsymbol{D}^{(1)}L-L\boldsymbol{D}^{(1)}$$
$$L^{(2)}\equiv \boldsymbol{D}^{(2)}L-L\boldsymbol{D}^{(2)}-L^{(1)}\boldsymbol{D}^{(1)}$$

or, inversely,

$$L=\bar{L}-\in \bar{L}^{(1)}-\in^2\bar{L}^{(2)}-\ \dots \qquad (26)$$

where

$$\bar{L}^{(1)}\equiv \boldsymbol{D}^{(1)}\bar{L}-\bar{L}\boldsymbol{D}^{(1)}$$
$$\bar{L}^{(2)}\equiv \boldsymbol{D}^{(2)}\bar{L}-\bar{L}\boldsymbol{D}^{(2)}-\boldsymbol{D}^{(1)}\bar{L}^{(1)} \quad .$$

The virtual expressions or "transformations" of several important operators are given in explicit forms, convenient to use, to the first order of approximation here, where the chief aim is to have the extensive scope of the subject rather than the elevation of the order of approximation, as follows:

[1] Laplacian operator

$$\bar{\Delta}=\Delta+\in L^{(1)}{}_{\triangle}+\ \dots \qquad (27)$$

where

$$\Delta\equiv\frac{1}{\sqrt{g}}\frac{\partial}{\partial x^\alpha}\sqrt{g}\,g^{\alpha\beta}\frac{\partial}{\partial x^\beta}$$
$$L^{(1)}{}_{\triangle}\equiv-\left[\frac{1}{\sqrt{g}}\frac{\partial(\sqrt{g}\,\varphi^{(1)\gamma})}{\partial x^\gamma}\Delta\right.$$
$$\left.+\frac{1}{\sqrt{g}}\frac{\partial}{\partial x^\alpha}\sqrt{g}\,\Phi^{\alpha\beta}\frac{\partial}{\partial x^\beta}\right]$$
$$\Phi^{\alpha\beta}\equiv g^{(1)\alpha\beta}-\frac{g^{\alpha\beta}}{\sqrt{g}}\frac{\partial(\sqrt{g}\,\varphi^{(1)\gamma})}{\partial x^\gamma}=\Phi^{\beta\alpha}$$
$$g\equiv|g_{\alpha\beta}|$$

the time-coordinate being here assumed to be not included among x or to be a mere parameter at most, if it appears.

[2] The "heat-conduction" operator

$$\bar{L}_{h.c.}=L_{h.c.}+\in L^{(1)}{}_{h.c.}+\ \dots \tag{28}$$

where

$$L_{h.c.}\equiv\kappa^2\Delta-\frac{\partial}{\partial t}$$

$$L^{(1)}{}_{h.c.}\equiv\kappa^2(L^{(1)}{}_{\triangle}+L^{(1)}{}_{t\triangle})+L^{(1)}{}_{\partial/\partial t}$$

$$L^{(1)}{}_{\triangle}\equiv[L^{(1)}{}_{\triangle}\text{ of Eq.(27)}]_{\alpha=i,\beta=k,\gamma=l}$$

$$L^{(1)}{}_{t\triangle}\equiv-\Big[2g^{kl}\varphi^{(1)N}{}_{,k}\frac{\partial^2}{\partial x^l\partial x^N}$$

$$+\frac{1}{\sqrt{g}}\frac{\partial(\sqrt{g}g^{kl}\varphi^{(1)N}{}_{,k})}{\partial x^l}\frac{\partial}{\partial x^N}\Big]$$

$$L^{(1)}{}_{\partial/\partial t}\equiv\varphi^{(1)N}{}_{,N}\frac{\partial}{\partial x^N}+\varphi^{(1)l}{}_{,N}\frac{\partial}{\partial x^l}$$

$$g\equiv|g_{ik}|,\quad x^N\equiv t.$$

[3] D'Alembertian operator

$$\bar{\Box}=\Box+\in L^{(1)}{}_{\Box}+\ \dots \tag{29}$$

where

$$\Box\equiv\frac{1}{\sqrt{g}}\frac{\partial}{\partial x^\alpha}\sqrt{g}g^{\alpha\beta}\frac{\partial}{\partial x^\beta}$$

$$L^{(1)}{}_{\Box}\equiv-\Big[\frac{1}{\sqrt{g}}\frac{\partial(\sqrt{g}\varphi^{(1)\gamma})}{\partial x^\gamma}\Box$$

$$+\frac{1}{\sqrt{g}}\frac{\partial}{\partial x^\alpha}\sqrt{g}\Phi^{\alpha\beta}\frac{\partial}{\partial x^\beta}\Big]$$

$$g\equiv|g_{\alpha\beta}|,\quad x^N\equiv ct\text{ or }t.$$

Especially, when $x^N=ct$, $g_{NN}=g^{NN}=-1$ and $g_{Nk}=g^{Nk}=0$, the above expression is reduced to the following:

$$\overline{\left(\Delta-\frac{1}{c^2}\frac{\partial^2}{\partial t^2}\right)}=\left(\Delta-\frac{1}{c^2}\frac{\partial^2}{\partial t^2}\right)$$

$$+\in L^{(1)}{}_{\Box}+\dots \tag{30}$$

where

$$L^{(1)}{}_{\Box}\equiv L^{(1)}{}_{\triangle}+L^{(1)}{}_{(\Box-\triangle)}$$

$$L^{(1)}{}_{\triangle}\equiv[L^{(1)}{}_{\triangle}\text{ of Eq.(27)}]_{\alpha=i,\beta=k,\gamma=l}$$

$$L^{(1)}{}_{\Box-\triangle}\equiv2\varphi^{(1)N}{}_{,N}\frac{\partial^2}{\partial(x^N)^2}$$

$$+2(\varphi^{(1)l}{}_{,N}-g^{kl}\varphi^{(1)N}{}_{,k})\frac{\partial^2}{\partial x^l\partial x^N}+\varphi^{(1)l}{}_{,NN}\frac{\partial}{\partial x^l}$$

$$+\left\{\varphi^{(1)N}{}_{,NN}-\frac{1}{\sqrt{g}}\frac{\partial(\sqrt{g}g^{kl}\varphi^{(1)N}{}_{,k})}{\partial x^l}\right\}\frac{\partial}{\partial x^N}$$

$g\equiv|g_{ik}|.$

[4] The operator $\partial/\partial x^\alpha$

$$\overline{\frac{\partial}{\partial x^\alpha}}=\frac{\partial}{\partial x^\alpha}-\in D^{(1)}{}_\alpha-\in^2D^{(2)}{}_\alpha-\ \dots \tag{31}$$

where

$$D^{(1)}{}_\alpha\equiv\frac{\partial}{\partial x^\alpha}D^{(1)}-D^{(1)}\frac{\partial}{\partial x^\alpha}=\varphi^{(1)\gamma}{}_{,\alpha}\frac{\partial}{\partial x^\gamma}$$

$$D^{(2)}{}_\alpha\equiv\frac{\partial}{\partial x^\alpha}D^{(2)}-D^{(2)}\frac{\partial}{\partial x^\alpha}-D^{(1)}{}_\alpha D^{(1)}$$

$$=\varphi^{(2)\gamma}{}_{,\alpha}\frac{\partial}{\partial x^\gamma}-(D^{(1)}{}_\alpha\varphi^{(1)\gamma})\cdot\frac{\partial}{\partial x^\gamma}\ .$$

[5] The operator $L_n\equiv\partial/\partial n$, differentiating to a direction normal to the given boundary C

$$\bar{L}_n=L_n-\in L^{(1)}{}_n-\in^2L^{(2)}{}_n-\ \dots \tag{32}$$

where

$$L_n\equiv\frac{g^{\alpha\beta}S_{,\alpha}}{\sqrt{g^{\rho\sigma}S_{,\rho}S_{,\sigma}}}\frac{\partial}{\partial x^\beta}\text{ or }\frac{g^{\alpha\beta}\Delta_\alpha}{\sqrt{g^{\rho\sigma}\Delta_\rho\Delta_\sigma}}\frac{\partial}{\partial x^\beta}$$

$$L^{(1)}{}_n\equiv L_nD^{(1)}-D^{(1)}L_n$$

$$L^{(2)}{}_n\equiv L_nD^{(2)}-D^{(2)}L_n-L^{(1)}{}_nD^{(1)}$$

Δ_α being the cofactor of c^α in the following determinant of the order N, consisting of the derivatives $X^\alpha{}_{,i}(\equiv\partial X^\alpha/\partial\lambda^i)$ and of the mere letters c^α introduced only to specify their own cofactors, respectively:

$$\begin{array}{ccccccc}
c^1 & c^2 & \cdots\cdots & c^\alpha & \cdots\cdots & c^N \\
X^1{}_{,1} & X^2{}_{,1} & \cdots\cdots & X^\alpha{}_{,1} & \cdots\cdots & X^N{}_{,1} \\
\vdots & \vdots & & \vdots & & \vdots \\
X^1{}_{,i} & X^2{}_{,i} & \cdots\cdots & X^\alpha{}_{,i} & \cdots\cdots & X^N{}_{,i} \\
\vdots & \vdots & & \vdots & & \vdots \\
X^1{}_{,N-1} & X^2{}_{,N-1} & \cdots\cdots & X^\alpha{}_{,N-1} & \cdots\cdots & X^N{}_{,N-1}
\end{array}$$

or

$$\Delta_\alpha=(-1)^{\alpha-1}\varepsilon^{i_1\cdots i_{\alpha-1}i_{\alpha+1}\cdots i_N}$$

$$X^1{}_{,i_1}X^2{}_{,i_2}\cdots X^{\alpha-1}{}_{,i_{\alpha-1}}X^{\alpha+1}{}_{,i_{\alpha+1}}\cdots X^N{}_{,i_N}$$

with $\varepsilon^{i_1\cdots i_{\alpha-1},i_{\alpha+1}\cdots i_N}$ being $+1$ or -1 according as the permutation

$$\begin{pmatrix}1,\cdots,\alpha-1,\alpha,\cdots,N-1\\ i_1,\cdots,i_{\alpha-1},i_{\alpha+1},\cdots\cdots,i_N\end{pmatrix}$$

is even or odd and being zero otherwise.

Eq.(32) is rewritten by means of Eqs.(4) and (12) as follows:

$$\bar{L}_n=L^{(0)}{}_n-\in N^{(1)}-\ \dots \tag{33}$$

where

$$L^{(0)}{}_n\equiv\frac{g^{\alpha\beta}S^{(0)}{}_{,\alpha}}{\sqrt{g^{\rho\sigma}S^{(0)}{}_{,\rho}S^{(0)}{}_{,\sigma}}}\frac{\partial}{\partial x^\beta}$$

$$\text{or }\frac{g^{\alpha\beta}\Delta^{(0)}{}_\alpha}{\sqrt{g^{\rho\sigma}\Delta^{(0)}{}_\rho\Delta^{(0)}{}_\sigma}}\frac{\partial}{\partial x^\beta}$$

$$N^{(1)}\equiv\frac{g^{(1)\alpha\beta}S^{(0)}{}_{,\alpha}}{\sqrt{g^{\rho\sigma}S^{(0)}{}_{,\rho}S^{(0)}{}_{,\sigma}}}\frac{\partial}{\partial x^\beta}$$

$$-\frac{1}{2}\frac{(g^{(1)\alpha\beta}S^{(0)}{}_{,\alpha}S^{(0)}{}_{,\beta})}{(g^{\rho\sigma}S^{(0)}{}_{,\rho}S^{(0)}{}_{,\sigma})}L^{(0)}{}_n$$

or $$\frac{g^{(1)\alpha\beta}\Delta^{(0)}{}_\alpha}{\sqrt{g^{\rho\sigma}\Delta^{(0)}{}_\rho\Delta^{(0)}{}_\sigma}}\frac{\partial}{\partial x^\beta}$$

$$-\frac{1}{2}\frac{(g^{(1)\alpha\beta}\Delta^{(0)}{}_\alpha\Delta^{(0)}{}_\beta)}{(g^{\rho\sigma}\Delta^{(0)}{}_\rho\Delta^{(0)}{}_\sigma)}L^{(0)}{}_n$$

$$\Delta^{(0)}\equiv(\Delta)_{X=X^{(0)}}$$

6. *The Dirichlet condition (or the question, what value the virtual function $\bar{\Psi}$ should take on the boundary C_0 of the domain D_0, when a scalar function $\Psi(x)$ takes the given value $f(x)$ or $F(\lambda)$ on the boundary C of the domain D).*

If the given function $f(x)$ is assumed to be defined in some neighborhood of C_0, the answer is obtained by making use of Eqs.(14) and (15), as follows:

$$\bar{\Psi}(\bar{x})=\Psi(x)=f(x)=\bar{f}(x)$$
$$=(1+\in D^{(1)}+\in^2 D^{(2)}+\ .\ .\ .)f(\bar{x}) \text{ on } C_0$$

i.e.

$$(\bar{\Psi})_{C_0}=[(1+\in D^{(1)}+\in^2 D^{(2)}+\ .\ .\ .)f\,]_{C_0} \quad (34)$$

Or, if the boundaries, C and C_0, are represented in terms of their respective parameters (related to each other through Eq.(6)), like Eqs.(2) and (3), what value should the virtual function $\bar{\Psi}$ take on C_0, when the boundary-value of the scalar function Ψ on C is $F(\lambda)$?

Making use of Eqs.(14), (21) and (22), the answer is obtained as follows:

$$\bar{\Psi}(X^{(0)}(\bar{\lambda}))=\bar{\Psi}(\bar{x})=\Psi(x)=\Psi(X(\lambda))=F(\lambda)=\bar{F}(\bar{\lambda})$$
$$=(1+\in D^{(1)}{}_{(\lambda)}+\in D^{(2)}{}_{(\lambda)}+\cdots)F(\bar{\lambda})$$

i.e.

$$(\bar{\Psi})_{C_0}=(1+\in D^{(1)}{}_{(\lambda)}+\in^2 D^{(2)}{}_{(\lambda)}+\cdots)F \quad (35)$$

Eqs.(34) and (35) are the virtual expressions, respectively, of the inhomogeneous Dirichlet condition

$$(\Psi)_C=(f(x))_C \text{ or } (\Psi)_C=F(\lambda)$$

given on the boundary C. Also, by combining the above results, Eqs. (34) and (35), when the following identity holds on the boundary C:

$$(f(x))_C=F(\lambda) \quad ,$$

then

$$[(1+\in D^{(1)}+\in^2 D^{(2)}+\ .\ .\ .\ )f]_{C_0}$$
$$=(1+\in D^{(1)}{}_{(\lambda)}+\in^2 D^{(2)}{}_{(\lambda)}+\ .\ .\ .\ )F$$

where the function $f(x)$ is required only to be equal to $F(\lambda)$ on the boundary C, and free elsewhere, as far as it is continuated "smoothly" from the value on the boundary.

Eq.(35) tells that, when F is a constant, the virtual function $\bar{\Psi}$ should take the same constant value on the boundary C_0, too.

7. *The Neumann condition.*

The given function $f(x)$ is assumed to be defined smoothly in the neighborhood of C_0 (therefore, also of C).

For the Neumann condition

$$L_n\Psi=f(x) \quad \text{on } C,$$

making use of Eqs.(24) and (33),

$$(L^{(0)}{}_n-\in N^{(1)}-\ .\ .\ .\ )\bar{\Psi}=\bar{L}_n\bar{\Psi}=\overline{L_n\Psi}$$
$$=(1+\in D^{(1)}+\ .\ .\ .\ )L_n\Psi=(1+\in D^{(1)}+\ .\ .\ .\ )f$$

or, carrying the perturbed part on the first side to the last side and assuming the expression

$$\bar{\Psi}\equiv\bar{\Psi}^{(0)}+\in\bar{\Psi}^{(1)}+\in^2\bar{\Psi}^{(2)}+\ .\ .\ . \quad (36)$$

the "virtual" Neumann condition is

$$(L^{(0)}{}_n\bar{\Psi})_{C_0}=[\,f+\in(N^{(1)}\bar{\Psi}^{(0)}+D^{(1)}f)+\ .\ .\ .\ ]_{C_0} \quad (37)$$

Or, when the boundaries, C and C_0, are represented in terms of the parameters, like Eqs.(2) and (3), and the Neumann condition is given as follows:

$$(L_n\Psi)_C=F(\lambda) \quad ,$$

then, by making use of Eqs.(14), (22), (24) and (33),

$$[L^{(0)}{}_n-\in N^{(1)}-\ .\ .\ .\ )\bar{\Psi}(\bar{x})]_{\bar{x}=X^{(0)}(\bar{\lambda})}$$
$$=[\bar{L}_n\bar{\Psi}(\bar{x})]_{\bar{x}=X^{(0)}(\bar{\lambda})}=[\overline{L_n\Psi}(\bar{x})]_{\bar{x}=X^{(0)}(\bar{\lambda})}$$
$$=[L_n\Psi(x)]_{x=X(\lambda)}=F(\lambda)=\bar{F}(\bar{\lambda})$$
$$=(1+\in D^{(1)}{}_{(\lambda)}+\ .\ .\ .)F(\bar{\lambda})$$

therefore, from the first and the last sides, and also assuming the expression (36), the corresponding virtual Neumann condition is obtained as follows:

$$(L^{(0)}{}_n\bar{\Psi})_{C_0}=F+\in\{(N^{(1)}\bar{\Psi}^{(0)})_{C_0}+D^{(1)}{}_{(\lambda)}F\}+\ .\ .\ . \quad (38)$$

8. *The mixed boundary-condition.*

The corresponding virtual expression is derived by combining the results already obtained. In the following, the given functions $p(x)$, $q(x)$ and $f(x)$ are assumed to be defined smoothly in the neighborhood of the boundary C therefore of C_0, and their values on the boundary C are assumed to be expressed in terms of the parameters as follows:

$$[p(x)]_{x=X(\lambda)}\equiv P(\lambda),\quad [q(x)]_{x=X(\lambda)}\equiv Q(\lambda),$$
$$[f(x)]_{x=X(\lambda)}\equiv F(\lambda).$$

Now, a mixed bondary-condition

$$[p(x)\boldsymbol{L}_n\Psi+q(x)\Psi]_C=[f(x)]_C$$

or

$$P(\lambda)(\boldsymbol{L}_n\Psi)_C+Q(\lambda)(\Psi)_C=F(\lambda)$$

is expressed "virtually" as follows:

$$[p\boldsymbol{L}^{(0)}{}_n\bar{\Psi}+q\bar{\Psi}]_{C_0}=[f+\in f^{(1)}+\ .\ .\ .]_{C_0}$$

or

$$P(\boldsymbol{L}^{(0)}{}_n\bar{\Psi})_{C_0}+Q(\bar{\Psi})_{C_0}=F+\in F^{(1)}+\ .\ .\ . \tag{39}$$

where

$$(f^{(1)})_{C_0}\equiv[\boldsymbol{D}^{(1)}f$$
$$+\{p\boldsymbol{N}^{(1)}-(\boldsymbol{D}^{(1)}p)\cdot\boldsymbol{L}^{(0)}{}_n-(\boldsymbol{D}^{(1)}q\}\bar{\Psi}^{(0)}]_{C_0}$$

or

$$=[p\{\boldsymbol{N}^{(1)}\bar{\Psi}^{(0)}+\boldsymbol{D}^{(1)}\boldsymbol{L}^{(0)}{}_n\bar{\Psi}^{(0)}\}+q\boldsymbol{D}^{(1)}\bar{\Psi}^{(0)}]_{C_0}$$

with $\boldsymbol{L}^{(0)}{}_n\bar{\Psi}^{(0)}$ in the last side being, of course, considered to be given in the neighborhood of the bondary C_0 before being acted on by the operator $\boldsymbol{D}^{(1)}$, and

$$F^{(1)}\equiv\boldsymbol{D}^{(1)}{}_{(\lambda)}F$$
$$+[\{P\boldsymbol{N}^{(1)}-(\boldsymbol{D}^{(1)}{}_{(\lambda)}P)\boldsymbol{L}^{(0)}{}_n-(\boldsymbol{D}^{(1)}{}_{(\lambda)}Q)\}\bar{\Psi}^{(0)}]_{C_0}$$

or

$$=P[(\boldsymbol{N}^{(1)}\bar{\Psi}^{(0)})_{C_0}+\boldsymbol{D}^{(1)}{}_{(\lambda)}(\boldsymbol{L}^{(0)}{}_n\bar{\Psi}^{(0)})_{C_0}]$$
$$+Q\boldsymbol{D}^{(1)}{}_{(\lambda)}(\bar{\Psi}^{(0)})_{C_0}$$

[Example] *The virtual expression of a mixed boundary-condition* $p_0\dfrac{\partial\Psi}{\partial n}+q_0\Psi=F(\theta,\varphi)$, *with* p_0 *and* q_0 *being constants, on the boundary* $r=a(1+\in\phi)$, *with* ϕ *being a function of* θ *and* φ, *which is close to the spherical surface* $r=a$ *in shape.*

The equations of the two boundaries are rewritten as follows:

$$S\equiv r-a-\in a\phi=0$$
$$S^{(0)}\equiv r-a=0$$

and the following transformation is adopted as an appropriate one:

$$r=\bar{r}[1+\in\varphi(\bar{\theta},\bar{\varphi})],\ \theta=\bar{\theta},\ \varphi=\bar{\varphi}.$$

Then, according to Eq. (39), the mixed boundary-condition

$$\left(p_0\frac{\partial\Psi}{\partial n}+q_0\Psi\right)_{r=a(1+\epsilon\phi)}=F(\theta,\varphi)$$

is transformed to the following virtual one:

$$\left(p_0\frac{\partial\bar{\Psi}}{\partial r}+q_0\bar{\Psi}\right)_{r=a}=F+\in p_0(\boldsymbol{N}^{(1)}\bar{\Psi}^{(0)})_{r=a}+\ .\ .\ .$$

where

$$\boldsymbol{N}^{(1)}\equiv\left(\phi\ \frac{\partial}{\partial r}+\frac{\phi_{,\theta}}{r}\frac{\partial}{\partial\theta}+\frac{\phi_{,\varphi}}{r\sin^2\theta}\frac{\partial}{\partial\varphi}\right)$$

9. *The procedure for solving the problem.*

The given problem i.e. Eq.(1) with some boundary-condition on the given boundary C is transformed to the corresponding "virtual" problem i.e. the "virtual" equation

$$\bar{\boldsymbol{L}}\bar{\Psi}=-\bar{h} \tag{40}$$

or, assuming the expression (36),

$$\boldsymbol{L}\bar{\Psi}=-h-\in(\boldsymbol{L}^{(1)}\bar{\Psi}^{(0)}+\boldsymbol{D}^{(1)}h)$$
$$-\in^2(\boldsymbol{L}^{(2)}\bar{\Psi}^{(0)}+\boldsymbol{L}^{(1)}\bar{\Psi}^{(1)}+\boldsymbol{D}^{(2)}h)-\ .\ .\ . \tag{41}$$

with the "virtual" boundary-condition to be obtained according to Eqs. (34), (35), (37), (38) or (39) on the boundary C_0.

This virtual problem is solved, by subjecting Eq.(40) to the ordinary perturbation method, as is shown in the next section, or by treating Eq.(41) by means of Green's formula or otherwise, respectively, according as it is an eigenvalue problem or a boundary-value one (elliptic, parabolic or hyperbolic). The solution thus obtained, being "virtual", must be transformed to the corresponding "real" solution, so to speak, by means of Eq. (7), which is the solution sought for of the given problem. For the virtual solution of the form (36), the corresponding "real" solution Ψ is written, according to Eq. (16), as follows:

$$\Psi=\bar{\Psi}^{(0)}+\in(\bar{\Psi}^{(1)}-\boldsymbol{D}^{(1)}\bar{\Psi}^{(0)})$$
$$+\in^2[\bar{\Psi}^{(2)}-\boldsymbol{D}^{(1)}\bar{\Psi}-(\boldsymbol{D}^{(2)}-\boldsymbol{D}^{(1)}\boldsymbol{D}^{(1)})\bar{\Psi}^{(0)}]+\ .\ .\ . \tag{42}$$

Unlike the functions, the eigenvalues are not varied by the last transformation (7).

§ 3. Eigenvalue problems

The equation

$$\boldsymbol{L}\Psi=-\kappa\Psi \tag{43}$$

which is obtained from Eq.(1) by replacing $h(x)$ by $\kappa\Psi$, and coupled with an appopriately specified boundary-condition on the given boundary C, presents an eigenvalue problem.

Since the main object here is to show the procedure to meet such a case, the problem is assumed to be of a non-degenerate type.

By means of Eq.(5), the given equation (43) with its boundary C is transformed to the corresponding virtual euqation

$$\bar{\boldsymbol{L}}\bar{\Psi}=(\boldsymbol{L}+\in \boldsymbol{L}^{(1)}+\in^2\boldsymbol{L}^{(2)}+\ldots)\bar{\Psi}=-\kappa\bar{\Psi} \quad (44)$$

with the boundary C_0, to which the well-developed ordinary perturbation method[3] is applied, yielding the following eigen-functions $\bar{\Psi}_n$ and eigenvalues κ_n, n denoting the order:

$$\begin{aligned}\bar{\Psi}_n&=\bar{\Psi}^{(0)}{}_n+\in\bar{\Psi}^{(1)}{}_n+\in^2\bar{\Psi}^{(2)}{}_n+\ldots\\ \kappa_n&=\kappa^{(0)}{}_n+\in\kappa^{(1)}{}_n+\in^2\kappa^{(2)}{}_n+\ldots\end{aligned} \qquad (45)$$

where

$$\boldsymbol{L}\bar{\Psi}^{(0)}{}_n=-\kappa^{(0)}{}_n\bar{\Psi}^{(0)}{}_n\,, \quad (\bar{\Psi}^{(0)}{}_n,\bar{\Psi}^{(0)}{}_n)=1$$

$$\bar{\Psi}^{(1)}{}_n=\sum_{m(\neq n)}\frac{L^{(1)}{}_{mn}}{\kappa^{(0)}{}_m-\kappa^{(0)}{}_n}\bar{\Psi}^{(0)}{}_m \quad \text{etc.}$$

$$\kappa^{(1)}{}_n=-L^{(1)}{}_{nn}\,,$$

$$\kappa^{(2)}{}_n=-\left(L^{(2)}{}_{nn}+\sum_{m(\neq n)}\frac{L^{(1)}{}_{nm}L^{(1)}{}_{mn}}{\kappa_m{}^{(0)}-\kappa_n{}^{(0)}}\right), \quad \text{etc.}$$

$$L^{(i)}{}_{mn}\equiv(\bar{\Psi}^{(0)}{}_m\boldsymbol{L}^{(i)}\bar{\Psi}^{(0)}{}_n)\,, \quad i=1,2,\ldots$$

The "virtual" eigenfunctions (45) must be transformed, according to Eq.(42), to the "real" ones

$$\Psi_n=\bar{\Psi}^{(0)}{}_n+\in(\bar{\Psi}^{(1)}{}_n-\boldsymbol{D}^{(1)}\bar{\Psi}^{(0)}{}_n)+\in^2[\bar{\Psi}^{(2)}{}_n-\boldsymbol{D}^{(1)}\bar{\Psi}^{(1)}{}_n-(\boldsymbol{D}^{(2)}-\boldsymbol{D}^{(1)}\boldsymbol{D}^{(1)})\bar{\Psi}^{(0)}{}_n]+\ldots$$

while the "virtual" eigenvalues (45) are the "real" ones, as they are, since they are not varied by the last transformation.

[Example 1] *The eigenfrequencies ω_{ns} of the lateral vibration of a uniform membrane, under a constant tension T and fixed at its boundary $r=a$ $[1+\in\phi(\theta)]$, close to a circle $r=a$ in shape.*

As is easily seen by comparing the equations of the boundaries, given and favorable, an appropriate mapping or transformation is

$$r=\bar{r}[1+\in\phi(\bar{\theta})] \text{ and } \theta=\bar{\theta}$$

($t=\bar{t}$ having no connection here).

The differential equation governing the lateral displacement $\Psi(r,\theta)$ is

$$(\Delta+k^2)\Psi=0$$

where $k\equiv\omega/c$, $c\equiv\sqrt{T/\sigma}$, with ω and σ being the angular frequency and the surface density, respectively.

The above equation, together with its boundary-condition $\Psi=0$ at $r=a(1+\in\phi)$, is transformed to the following:

$$(\Delta+k^2+\in\boldsymbol{L}^{(1)}{}_\triangle+\ldots)\bar{\Psi}=0, \quad \bar{\Psi}=0 \text{ at } r=a,$$

where

$$\boldsymbol{L}^{(1)}{}_\triangle=-\left[2\phi\Delta+\left(2\phi_{,\theta}\frac{\partial}{\partial\theta}+\phi_{,\theta\theta}\right)\frac{1}{r}\frac{\partial}{\partial r}\right]$$

The unperturbed eigenfunctions $\bar{\Psi}^{(0)}{}_{ns}$, such as

$$(\Delta+k^{(0)2}{}_{ns})\bar{\Psi}^{(0)}{}_{ns}=0, \quad \bar{\Psi}^{(0)}{}_{ns}=0 \text{ at } r=a,$$

are written as follows:

$$\bar{\Psi}^{(0)}{}_{ns}=A_{ns}\cos(n\theta-\alpha_{ns})\cdot J_n(k^{(0)}{}_{ns}r), \quad n\geqq0, \ s\geqq1,$$

where A_{ns} and α_{ns} are constants concerning normalization and phase, respectively, and $k^{(0)}{}_{ns}$ are such as $J_n(k^{(0)}{}_{ns}a)=0$.

The boundary-deviation $\phi(\theta)$ is assumed to be expanded in a Fourier series as follows:

$$\phi(\theta)=\sum_{m=0}^{\infty}B_m\cos(m\theta-\beta_m)$$

where B_m and β_m are appropriate amplitude- and phase-constants, respectively.

Then, according to Eq. (45), the eigenfrequencies ω_{ns}, perturbed by the boundary-deviation $\phi(\theta)$, are obtained, to the first order of approximation, as follows:

$$\omega_{ns}=\omega^{(0)}{}_{ns}\left[1-\frac{\epsilon}{2}\sum_{m=0}^{\infty}B_m\frac{2\delta_{m,0}\cos\beta_m+\delta_{m,2n}\cos(2\alpha_{ns}-\beta_m)+\delta_{m+2n,0}\cos(2\alpha_{ns}+\beta_m)}{1+\delta_{n,0}\cos(2\alpha_{ns})}\right]$$

where δ's are usual Kronecker's deltae, therefore e.g. $\delta_{m+2n,0}$ being equal to 1 only when $m+2n=0$ or $m=n=0$ now, and zero otherwise.

This result coincides with Rayleigh's one(4), where his δr is the equivalent of $\epsilon a\phi$ in the present paper.

A glance at the above result obtained for the general from of $\phi(\theta)$ gives immediately the following information about the contributions from the individual terms $B_m\cos(m\theta-\beta_m)$:
(a) The term with $m=0$ expresses the uniform enlargement (or reduction) of a circular membrane with the tension being kept constant. $B_0\cos\beta_0$, being a constant, can be put 1, without losing the generality. Then, the term means that the eigenfrequencies $\omega^{(0)}{}_{ns}$ are decreased (or increased) to $\omega^{(0)}{}_{ns}(1-\epsilon)$, as the radius a is increased (or decreased) to $a(1+\epsilon)$.
(b) For $m\geqq1$, only the terms with $m=$even can perturb only the eigenfrequencies ω_{ns} with $n=m/2$, whereas the terms with $m=$odd not any one, to the first order of approximation.

To the former, an elliptic boundary ($m=2$), etc. belong, whereas an oval boundary ($m=1$), a cinquefoil-shaped (or "umebachi-gata" in Japanese) boundary ($m=5$), etc. belong to the latter.

[Example 2] *The eigenvalue problem concerning the heat conduction of a "corned-beef-can"-shaped uniform matter, close to a rectangular parallelepiped in shape and with its temperature being kept constant or zero on the boundary surface.*

The equation $(\Delta+\kappa)\Psi=0$, which is derived from the original equation of heat conduction $(k^2\Delta-\partial/\partial t)T=0$ (k^2: thermal diffusibility) by putting the temperature $T=\Psi(xyz)\exp(-k^2\kappa t)$, together with the boundary-condition $\Psi=$const. $=0$ on the given boundary surface, presents an eigenvalue problem.

The corned-beef-can-shaped domain and its surrounding boundary $OADBCFHE$, with the corner O at the origin of the orthogonal Cartesian coordinate-system, with the edges OA and OB on the x- and the y-axes, respectively, with a pair of faces $OBEC$ and $ADHF$ making a small inclination ϵ_1 $(0<\epsilon_1\ll1)$ against the yz-plane, and with another pair of faces $OAFC$ and $BDHE$ making a small inclination ϵ_2 $(0<\epsilon_2\ll1)$ against the xz-plane, are mapped or transformed to the rectangular-parallelepiped-shaped domain and the surrounding boundary $OADBC_0F_0H_0E_0$ respectively, by the following transformation:

$$x=\bar{x}+\epsilon_1\bar{z}\left(1-\frac{2\bar{x}}{a}\right)$$

$$y=\bar{y}+\epsilon_2\bar{z}\left(1-\frac{2\bar{y}}{b}\right)$$

$$z=\bar{z}+\epsilon_3\bar{z}\,,\qquad \epsilon_1\sim\epsilon_2\sim\epsilon_3\,,$$

where

$$a\equiv OA=BD=\overline{C_0F_0}=\overline{E_0H_0}$$

$$b\equiv\overline{OB}=\overline{AD}=\overline{C_0E_0}=\overline{F_0H_0}\,.$$

The last equation shows that the height c of the corned-beef-can-shaped matter is related to the height c_0 of the rectangular parallelepiped in the way $c=c_0(1+\epsilon_3)$, and so the former's volume $V\equiv abc[1-\epsilon_1(c/a)-\epsilon_2(c/b)]$ is equal to the latter's volume $V_0\equiv abc_0$, when $\epsilon_3=\epsilon_1(c/a)+\epsilon_2(c/b)$.

The virtual equation with its own boundary-condition is

$$(\Delta+\kappa+\epsilon L^{(1)}{}_{\triangle}+\ldots)\bar{\Psi}=0\,,\quad \bar{\Psi}=0 \text{ on } OADBC_0F_0H_0E_0$$

where

$$\in L^{(1)}{}_{\triangle}=2\left[\in_1\frac{2z}{a}\frac{\partial^2}{\partial x^2}+\in_2\frac{2z}{b}\frac{\partial^2}{\partial y^2}-\in_3\frac{\partial^2}{\partial z^2}-\in_1\left(1-\frac{2x}{a}\right)\frac{\partial^2}{\partial x\partial z}-\in_2\left(1-\frac{2y}{b}\right)\frac{\partial^2}{\partial y\partial z}\right]$$

The unperturbed eigenvalues $\kappa^{(0)}{}_{lmn}$ and the normalized eigenfunctions $\overline{\Psi}^{(0)}{}_{lmn}$ such as $(\Delta+\kappa^{(0)}{}_{lmn})\overline{\Psi}^{(0)}{}_{lmn}=0$ and $\overline{\Psi}^{(0)}{}_{lmn}=0$ on $OADBC_0F_0H_0E_0$, are given as follows:

$$\kappa^{(0)}{}_{lmn}=\left(\frac{l\pi}{a}\right)^2+\left(\frac{m\pi}{b}\right)^2+\left(\frac{n\pi}{c_0}\right)^2,\quad 1\leqq l,m,n$$

$$\overline{\Psi}^{(0)}{}_{lmn}=\sqrt{\frac{8}{abc_0}}\sin\left(\frac{l\pi x}{a}\right)\cdot\sin\left(\frac{m\pi y}{b}\right)\cdot\sin\left(\frac{n\pi z}{c_0}\right)$$

Then, according to Eq.(45), the eigenvalues κ_{lmn} are obtained to the first order of approximation as follows:

$$\kappa_{lmn}=\kappa^{(0)}{}_{lmn}+2\pi^2\left[\in_1\frac{c_0}{a}\left(\frac{l}{a}\right)^2+\in_2\frac{c_0}{b}\left(\frac{m}{b}\right)^2-\in_3\left(\frac{n}{c_0}\right)^2\right]$$

or, in terms of c instead of c_0,

$$\kappa_{lmn}=\pi^2\left[\left(\frac{l}{a}\right)^2+\left(\frac{m}{b}\right)^2+\left(\frac{n}{c}\right)^2+2\left\{\in_1\frac{c}{a}\left(\frac{l}{a}\right)^2+\in_2\frac{c}{b}\left(\frac{m}{b}\right)^2\right\}\right]$$

When $\in_3=\in_1(c/a)+\in_2(c/b)$, κ_{lmn} and $\kappa^{(0)}{}_{lmn}$ are interpreted to concern the corned-beef-can shape and the rectangular parallelepiped shape, respectively, of the same matter of the equal volume. For an arbitrary order lmn of the eigenvalues,

$$(\kappa_{lmn}-\kappa^{(0)}{}_{lmn})_{\text{equal volume}}=2\pi^2\left[\in_1\frac{c}{a}\left\{\left(\frac{l}{a}\right)^2-\left(\frac{n}{c}\right)^2\right\}+\in_2\frac{c}{b}\left\{\left(\frac{m}{b}\right)^2-\left(\frac{n}{c}\right)^2\right\}\right]$$

whose sign varies according to the values of l,m and n.

However, it is determined by the respective smallest eigenvalues κ_{111} and $\kappa^{(0)}{}_{111}$, which shape is more efficient for the matter cooling off, the corned-beef-can shape or the rectangular parallelepiped shape, under the condition of the equal volume and of the same quality. As regards ordinary corned-beef cans,

$$a<c \quad\text{and}\quad b<c, \quad\text{therefore}\quad (\kappa_{111}-\kappa^{(0)}{}_{111})_{\text{equal volume}}>0$$

which means that they cool off more rapidly than when they take the shape of a rectangular parallelepiped of the equal volume.

§ 4. Boundary-Value Problems

The fundamental line along which a given boundary-valve problem should be solved is already given in the last subsection of § 2, and so the detailed explanation is omitted here. Instead, some examples are given to illustrate the present method.

[**Example 1.**] (Parabolic Case) *The heat conduction in an "infinitely large" flat-plate-shaped uniform matter, with its temperature $\Psi(x, t)$ being initially equal to the specified value $f(x)$ as a function of x within it and being kept always at a constant value θ_0 on its two flat surfaces $x=0$ and $x=a(1+\in\phi)$, of which the latter is assumed to move slightly to the direction normal to the surface itself, such as $\phi=\phi(t)$, with $\phi(0)=0$, without breaking the constancy of the thermal diffusibility κ^2 and without introducing any appearance or disappearance of heat except through the conduction.*

By making use of the transformation $x=\bar{x}\{1+\in\phi(\bar{t})\}$ and $t=\bar{t}$, the solution $\Psi(x, t)$ which satisfies the equation $(\kappa^2\partial^2/\partial x^2-\partial/\partial t)\Psi=0$ as well as the boundary-condition

$$(\Psi)_{t=0}=f(x)\ \text{for}\ 0<x<a\ \text{and}\ (\Psi)_{x=0}=(\Psi)_{x=a(1+\epsilon\phi)}=\theta_0\ \text{for}\ t\geqq 0,$$

to the first order of approximation, is obtained as follows:

$$\Psi=\theta_0+\sum_{l=1}^{\infty} A_l \sin(\alpha_l x)\left[1+2\epsilon\kappa^2\alpha_l^2\int_0^t \phi(\tau)d\tau\right]\exp(-\kappa^2\alpha_l^2 t)-\epsilon\sum_{l=1}^{\infty} A_l\alpha_l x\cos(\alpha_l x)\cdot\phi(t)\exp(-\kappa^2\alpha_l^2 t)$$
$$-2\epsilon\sum_{l=1}^{\infty}\sum_{n=1}^{\infty} A_n\frac{ln(-1)^{l+n}}{(l^2-n^2)+4l^2\delta_{l,n}}\sin(\alpha_l x)\int_0^t\frac{d\phi(\tau)}{d\tau}\exp\{\kappa^2(\alpha_l^2-\alpha_n^2)\tau\}d\tau\cdot\exp(-\kappa^2\alpha_l^2 t)$$

where

$$A_l\equiv\frac{2}{a}\int_0^a\{f(\xi)-\theta_0\}\sin(\alpha_l\xi)d\xi\ ,\quad \alpha_l\equiv\frac{l\pi}{a}\ .$$

[Example 2] (Hyperbolic Case) *The lateral vibration of a uniform string, strained between the two ends at* $x=0$ *and at* $x=a\{1+\epsilon\phi(t)\}$, *with* $\phi(0)=0$, *respectively, with the tension being kept constant, as is realized by the use of a smooth pulley, which is made to move longitudinally according to* $x=a(1+\epsilon\phi)$, *also playing the role of a fixed end for the lateral vibration, and through which the string is extended to be attached with a constant load.*

By making use of the transformation $x=\bar{x}\{1+\epsilon\phi(\bar{t})\}$ and $t=\bar{t}$, the lateral displacement $\Psi(x.\ t)$ which satisfies the equation $(\partial^2/\partial x^2-\partial^2/\partial t^2)\Psi=0$ (putting the velocity $c=1$ for the sake of simplicity) as well as the boundary-condition

$$(\Psi)_{t=0}=f(x),\qquad (\partial\Psi/\partial t)_{t=0}=v(x)\qquad \text{for}\quad 0<x<a,$$
$$(\Psi)_{x=0}=(\Psi)_{x=a(1+\epsilon\phi)}=0\qquad\qquad \text{for}\quad t\geqq 0\ ,$$

to the first order of approximation, is obtained as follows:

$$\Psi=\sum_{l=1}^{\infty}\{\sin(\alpha_l x)-\epsilon\phi(t)\alpha_l x\cos(\alpha_l x)\}\{A_l\cos(\alpha_l t)+\frac{B_l}{\alpha_l}\sin(\alpha_l t)\}$$
$$+2\epsilon\sum_{l=1}^{\infty}\sin(\alpha_l x)\int_0^t\sin\{\alpha_l(t-\tau)\}\{\alpha_l A_l\cos(\alpha_l\tau)+B_l\sin(\alpha_l\tau)\}\phi(\tau)d\tau$$
$$-2\epsilon\sum_{l=1}^{\infty}\sum_{n=1}^{\infty}\frac{(-1)^{l+n}\alpha_n}{(\alpha_l^2-\alpha_n^2)+4\alpha_l^2\delta_{l,n}}\sin(\alpha_l x)\left[A_n\sin(\alpha_l t)\cdot\left(\frac{d\phi}{dt}\right)_{t=0}+\int_0^t\sin\{\alpha_l(t-\tau)\}\chi_n(\tau)d\tau\right]$$

where

$$\chi_n(t)\equiv\{A_n\cos(\alpha_n t)+\frac{B_n}{\alpha_n}\sin(\alpha_n t)\}\frac{d^2\phi}{dt^2}-2\{\alpha_n A_n\sin(\alpha_n t)-B_n\cos(\alpha_n t)\}\frac{d\phi}{dt}$$

$$A_n\equiv\frac{2}{a}\int_0^a f(\xi)\sin(\alpha_n\xi)d\xi\ ,\qquad B_n\equiv\frac{2}{a}\int_0^a v(\xi)\sin(\alpha_n\xi)d\xi$$

$$\alpha_n\equiv\frac{n\pi}{a}\ .$$

[Example 3] (Elliptic Case) *The electrostatic potential* $\Psi(r,\theta,\varphi)$ *around a conductor at rest, whose shape* $r=a\{1+\epsilon\phi(\theta,\varphi)\}$ *is close to a sphere* $r=a$ *and whose own potential is held at a constant value* V_0.

By making use of the transformation $r=\bar{r}\{1+\epsilon\phi(\bar{\theta},\bar{\varphi})$, $\theta=\bar{\theta}$, $\varphi=\bar{\varphi}$, and by assuming the expression of ϕ in terms of the spherical harmonics

$$\phi(\theta,\varphi)=\sum_{l=0}^{\infty}\sum_{m=0}^{l}B_{lm}P_l^m(\cos\theta)\cdot\cos(m\varphi-\beta_m)$$

the solution $\Psi(r,\theta,\varphi)$ which satisfies the equation $\Delta\Psi=0$ as well as the boundary-condition $(\Psi)_{r=a(1+\epsilon\phi)}=V_0$ to the first order of approximation, is obtained as follows:

$$\Psi=V_0\frac{a}{r}\left[1+\epsilon\sum_{l=0}^{\infty}\sum_{m=0}^{l}B_{lm}\left(\frac{a}{r}\right)^l P_l^m(\cos\theta)\cos(m\varphi-\beta_m)\right]$$

Especially, when the conductor takes the shape of an ellipsoid (close to a sphere), it is easily verified that the above result coincides with what is derived from the well-known formula

$$\Psi(\mu)=\frac{Q}{2}\int_{\mu}^{\infty}\frac{d\nu}{\sqrt{(a^2+\nu)(b^2+\nu)(c^2+\nu)}}$$

with Q being the electric charge on the ellipsoid-shaped conductor and with the lower limit of integration μ depending upon the observer's point (x,y,z) through the equation

$$\frac{x^2}{a^2+\mu}+\frac{y^2}{b^2+\mu}+\frac{z^2}{c^2+\mu}=1\ ,$$

as is expected.

Acknowledgement

The author wishes to express his sincere thanks to Prof. Isao Oshida for his kind guidance and encouragements throughout this work.

References

1) P. M. Morse and H. Feshbach: *Methods of Theoretical Physics* (McGraw-Hill Co., New York, Toronto and London, 1953) 1052.
2) I. Oshida et al.: Research Journal of the Faculty of Technology, Nagoya University, Vol. **3**, No. 1 (1950) 13 (in Japanese).
3) R. Courant and D. Hilbert: *Methoden der Mathematischen Physik* I (Springer, Berlin, 1931, 2nd ed.) 296.
T. Kato et al.: *Methods of Solving Differential Equations Approximately* (Iwanami Press, Tokyo, 1958) 164 (in Japanese).
4) J. W. S. Rayleigh: *Theory of Sound*, Vol. **1** (1877) 336.

JOURNAL OF THE PHYSICAL SOCIETY OF JAPAN, Vol. 15, No. 11, NOVEMBER, 1960

Transonic Flow past a Wavy Wall

By Iwao HOSOKAWA

National Aeronautical Laboratory of Japan, Shinkawa, Mitaka, Tokyo

(Received July 28, 1960)

Transonic flow past an infinitely long sinusoidal wall has not hitherto been thoroughly investigated, although some studies of the high subsonic flow near the critical have been made by Kaplan and others by use of the thin-wing-expansion method and the transonic approximation method. In this paper the author studied transonic flows past a sinusoidal wall including shock waves by use of his new method, and could find the velocity and pressure distributions on the wall with success. The result gives a reasonable model for understanding the transition of the flow pattern from subsonic to supersonic.

§ 1. Introduction

In order to investigate the problem of the existence or non-existence of continuous mixed flows, it seems to be very convenient to study the transonic flow past a wavy wall. In 1940, Görtler[1] found a continuous solution of a high subsonic flow with local supersonic regions past a kind of wavy wall which is correct up to the third approximation and he conjectured it to be convergent. For the case of an exactly sinusoidal wall, the solution of Imai and Oyama[2] by the thin-wing-expansion method seems to be divergent above the critical Mach number. On the other hand, Kaplan[3] showed on the basis of the transonic approximation that a continuous, symmetrical wave solution would diverge above the critical Mach number. According to him, the critical value of the transonic similarity parameter defined after von Kármán is ξ_{crit}, $\kappa=-(0.83244/\pi)^{-2/3}$. Thus the solution of the supercritical flow may be asymmetric and would cease to be continuous.

The present work is concerned with this problem. The author makes use of his new method[4], which will be summarized in the next section. This method can give the reasonable features: shock waves appear whenever mixed flows occur, and the solution tends to the same form as that given by the usual linear theory in the sub- and supersonic extremities. The solution, however, has a weak point in the present problem : shock waves in the real flow are always accompanied by entropy increase, which would destroy periodicity of the flow, while the present hypothetical flow is assumed to be isentropic and periodic. But the present investigation seems to be still significant, because the increase of entropy is comparatively small and the periodicity remains locally.

§ 2. Summary of the Method

The basic equation of the two-dimensional transonic flow can be written as:[4]

$$(1-M_\infty^2)\Phi_{xx}+\Phi_{yy}=(\gamma+1)M_\infty^2\Phi_x\Phi_{xx} \qquad (2.1)$$

where $U_\infty\Phi$ is the perturbation velocity potential, U_∞ and M_∞ are the free stream velocity and Mach number respectively, γ is the ratio of specific heats, and the x-axis is taken in the direction of the free stream.

According to Oswatitsch and Maeder, the approximate potential φ satisfies the linearized equation :

$$(1-M_\infty^2)\varphi_{xx}+\varphi_{yy}=K\varphi_x \qquad (2.2)$$

where K is an appropriately chosen constant. The solution of (2.2) can be found in a simple way with the given boundary conditions, apart from the selection of the value of K.

Here we put

$$\Phi=\varphi+g \qquad (2.3)$$

and establish the equation governing the nonlinear correction term g. Then, with the aid of the order estimation of the equation, g_x can be calculated approximately in the neighbourhood of the boundary and it can be found that g_x and φ_x are of the same order of magnitude. (From this point of view, the linearized theory due to Maeder cannot be of the first order approximation in itself, because of the tacit assumption, $\varphi\gg g$.)

Finally g_x can be integrated as follows:

$$g_x=-\varphi_x+(1-M_\infty^2)/\{(\gamma+1)M_\infty^2\} \pm\sqrt{Y(x)} \qquad (2.4)$$

where

$$Y(x)=\left\{\varphi_x-\frac{1-M_\infty^2}{(\gamma+1)M_\infty^2}\right\}^2 -2\int_{c^*}^{x}\left\{\varphi_{cx}-\frac{K}{(\gamma+1)M_\infty^2}\right\}\varphi_x\,dx \qquad (2.5)$$

and the double sign corresponds to

$$\varphi_x\gtrless(1-M_\infty^2)/\{(\gamma+1)M_\infty^2\} \qquad (2.6)$$

On the proper physical and mathematical grounds, c^* and K are uniquely determined in the following manner :

$$\varphi_x(x=c^*,\ y=0;\ K) =(1-M_\infty^2)/\{\gamma+1)M_\infty^2 \qquad (2.7)$$

$$\varphi_{xx}(x=c^*,\ y=0;\ K) =K/\{(\gamma+1)M_\infty^2\} \qquad (2.8)$$

The former is the condition that $x=c^*$ is the sonic point on the boundary, and the latter means that K should be taken as the value of the acceleration at the sonic point. In treating usual transonic flows, (2.7) and (2.8) constitute the simultaneous equations for finding c^* and K. Next, for purely subsonic or supersonic flows, the value of c^* should be kept fixed at its lower or upper critical value just when the sonic point disappears out of the flow, on account of the continuous transition of the flow field with changing Mach number. And then K should be determined by (2.8) alone.

§ 3. Linearized Transonic Flow Potential

At first we require the solution of (2.2) subject to the boundary conditions:

i) $\varphi_y=f'(x)=i\omega f_0\,e^{i\omega x}$, for $y=0$ (3.1)

ii) grad $\varphi\to0$, for $y\to\infty$ (3.2)

where the wavy boundary is expressed as

$$f(x)=f_0\,e^{i\omega x}\quad (f_0,\ \omega:\ \text{real constants}) \qquad (3.3)$$

Here and hereafter we shall consider only the real parts of the complex expressions.

Now this solution is

$$\varphi=-(i\omega f_0/\mu)\exp\left(-\mu y+i\omega x\right) \qquad (3.4)$$

where

$$\mu=(\beta^4\omega^4+K^2\omega^2)^{1/4}\exp\left(\frac{i}{2}\tan^{-1}\frac{K}{\beta^2\omega}\right) \tag{3.5}$$

$$\beta^2=1-M_\infty^2 \tag{3.6}$$

so that

$$\varphi=-(\omega f_o/|\mu|)\exp[-\mathrm{Re}(\mu)y+i\{\omega x-\mathrm{Im}(\mu)y-\arg(\mu)+\pi/2\}] \tag{3.7}$$

By differentiation we have

$$\varphi_x=(\omega^2 f_o/|\mu|)\exp[-\mathrm{Re}(\mu)y+i\{\omega x-\mathrm{Im}(\mu)y-\arg(\mu)\}] \tag{3.8}$$

$$\varphi_{xx}=(i\omega^3 f_o/|\mu|)\exp[-\mathrm{Re}(\mu)y+i\{\omega x-\mathrm{Im}(\mu)y-\arg(\mu)\}] \tag{3.9}$$

In (3.8), we can see a rough feature of the transonic flow. First, in a supercritical flow in which $K\doteqdot 0$, the perturbed velocity and so the pressure have a phase lag, arg (μ), relative to the wall, which approaches $\pi/2$ as $\beta^2\to-\infty$ so that the solution would agree with that given by the supersonic linear theory. It is interesting to note that arg (μ) becomes $\pi/4$ when $M_\infty^2\to1\pm0$. Secondly, as is seen from (3.7)-(3.9), the perturbed wave is propagated along the straight line:

$$y=\{\omega/\mathrm{Im}(\mu)\}x+\text{const.} \tag{3.10}$$

which tends to the Mach line as $\beta^2\to-\infty$, as should be expected.

§4. Procedure of Refinement

1) *Constants c^* and K*

In the present case, (2.7) and (2.8) become

$$(1-M_\infty^2)/\{(\gamma+1)M^2_\infty\}=\omega^2 f_o/|\mu|\exp[i\{\omega c^*-\arg(\mu)\}] \tag{4.1}$$

$$K/\{(\gamma+1)M^2_\infty\}=i\omega^3 f_o/|\mu|\exp[i\{\omega c^*-\arg(\mu)\}] \tag{4.2}$$

with the aid of (3.8) and (3.9). If we introduce the transonic similarity parameter after Spreiter, $\xi_\infty=(M_\infty^2-1)/[(\gamma+1)M_\infty^2(2f_o)]^{2/3}$, where the wave length is assumed as unity, and another parameter after Maeder, $\alpha=K/2\beta^2$, the equation can be simplified as

$$\pm|\xi_\infty|^{3/2}=\frac{\pi}{(1+\alpha^2/\pi^2)^{1/4}}\times\exp\left[i\left(2\pi c^*-\frac{1}{2}\tan^{-1}\frac{\alpha}{\pi}\right)\right] \tag{4.3}$$

$$\pm2\alpha|\xi_\infty|^{3/2}\ i\,\frac{2\pi^2}{(1+\alpha^2/\pi^2)^{1/4}}\times\exp\left[i\left(2\pi c^*-\frac{1}{2}\tan^{-1}\frac{\alpha}{\pi}\right)\right] \tag{4.4}$$

where the double sign corresponds to $M_\infty\lesseqgtr1$.

Taking the real parts of the above equations, and eliminating $|\xi_\infty|$, we can obtain

$$2\pi c^*=-(1/2)\tan^{-1}(\alpha/\pi) \tag{4.5}$$

and hence the solutions for c^* and α:

$$\cos4\pi c^*=-\xi_\infty/\pi^{2/3} \tag{4.6}$$

$$\alpha=\pm\pi\sqrt{(\pi^{4/3}/\xi_\infty^2)-1} \tag{4.7}$$

where $|\xi_\infty|\leqq\pi^{2/3}$ is assumed.

Next we know from (4.6) that $\mp\pi^{2/3}$ should be the lower and upper critical values of ξ_∞, respectively and then c^*'s are N and $(-1/4)+N$ where N is an integer. Thus in order to know α in the case of $|\xi_\infty|\geqq\pi^{2/3}$, we have only to fix c^* at these values and solve for α by (4.4) in accordance with the prescription given in §2. As a result, it is assured that $\alpha=0$ holds irrespective of the values of ξ_∞ when $|\xi_\infty|\geqq\pi^{2/3}$.

Consequently we obtain the following explicit expressions of the linearized flow velocity.

$$\varphi_x=(\pi^{2/3}/|\beta|)2f_o|\xi_\infty|^{1/2}\exp[i\{2\pi x-(1/2)\tan^{-1}(\pm\sqrt{(\pi^{4/3}/\xi_\infty^2)-1})\}] \tag{4.8}$$

$$=\frac{\pi^{2/3}(2f_o)^{2/3}}{(\gamma+1)^{1/3}M_\infty^{2/3}}\exp\left[i\left\{2\pi x-\frac{1}{2}\tan^{-1}\left(\pm\sqrt{\frac{\pi^{4/3}}{\xi_\infty^2}-1}\right)\right\}\right] \tag{4.9}$$

$$\text{for}\quad|\xi_\infty|\leqq\pi^{2/3}$$

$$=\{\pi(2f_o)/\beta\}\,e^{i(2\pi x)}\qquad\text{for}\quad\xi_\infty\leqq-\pi^{2/3} \tag{4.10}$$

$$=\{\pi(2f_o)/|\beta|\}\,e^{i(2\pi x-\pi/2)}\qquad\text{for}\quad\xi_\infty\geqq\pi^{2/3} \tag{4.11}$$

2) *Sonic Point and Shock Wave Position*

When $|\xi_\infty|\leqq\pi^{2/3}$, we can find another root c^{**} in place of c^* from (4.3) and (4.7) as follows:

$$-\xi_\infty=\pi^{2/3}\cos\{2\pi c^{**}-(1/2)\tan^{-1}(\pm\sqrt{(\pi^{4/3}/\xi_\infty^2)-1})\} \tag{4.12}$$

$x=c^{**}$ is a point located in the decelerated flow region and it is known from (2.4)-(2.6) that there appears some velocity discontinuity at c^{**}. As was known from the previous paper[4),

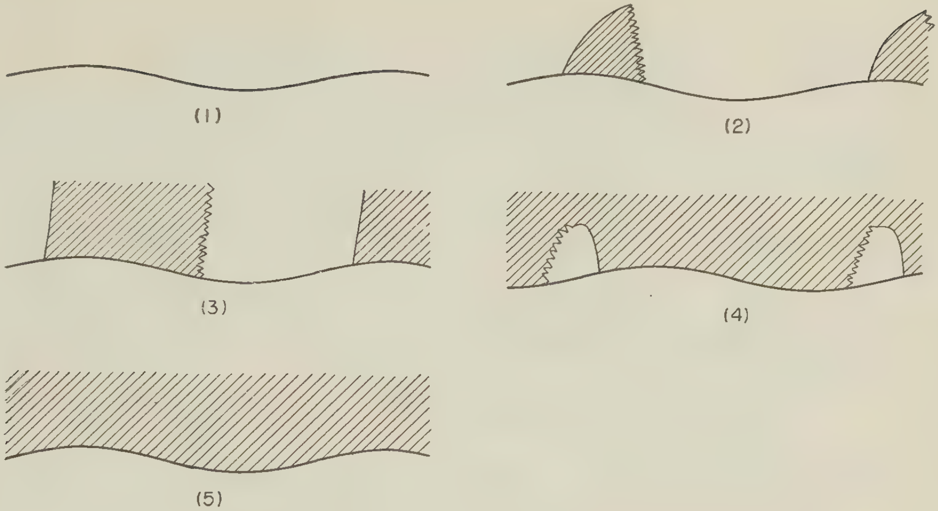

Fig. 1. Pictures of various transonic flows.
(a) subsonic flow.
(b) subsonic supercritical flow.
(c) sonic flow.
(d) supersonic but below upper critical flow.
(e) supersonic flow.
Shaded portions indicate supersonic regions, which are enclosed by sonic lines and shock lines drawn with solid and saw-toothed lines respectively.

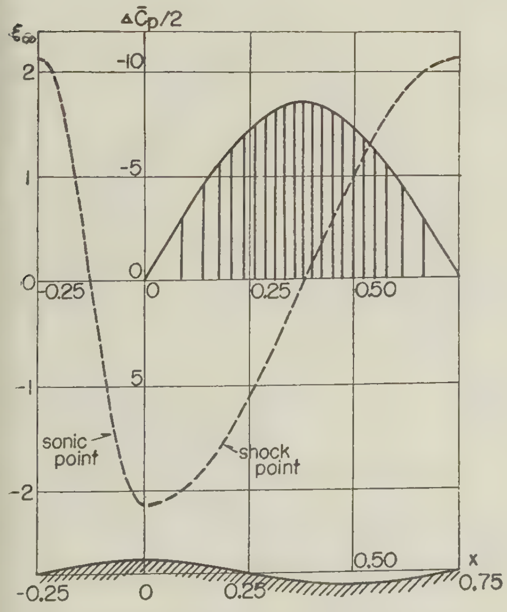

Fig. 2. Movement of sonic point and shock wave position on the wall with varying ξ_∞ and pressure jump at the shock.

it is considered as the position of the shock wave on the wall.

The manners in which the sonic point and the shock point on the wall change with ξ_∞ are shown in Fig. 2. Both of them first appear at the summits of the wavy wall at the instant when M_∞ reaches the lower critical value; then the sonic points move upstream and the shock points downstream with increasing Mach number, until each sonic point joins, at the upper critical Mach number, the receding shock point which has originated at the preceding summit of the wavy wall: thus all the sonic points coincide with the shock points and hence the subsonic regions disappear. This result may be interpreted as shown roughly in Fig. 1.

3) *Results of the Procedure of Refinement*

If we write

$$\varphi_x=(2f_o)/|\beta|\cdot F(x;\ \xi_\infty) \tag{4.13}$$

the following expressions for Φ_x are obtained with the aid of (2.4) and (2.5);

$$\Phi_x=\frac{1-M_\infty{}^2}{(\gamma+1)M_\infty{}^2}\pm\sqrt{2}\sqrt{\frac{(1-M_\infty{}^2)^2}{(\gamma+1)^2M_\infty{}^4}-\frac{(1-M_\infty{}^2)(2f_o)}{(\gamma+1)M_\infty{}^2|\beta|}F(x)+\frac{K(2f_o)}{(\gamma+1)M_\infty{}^2|\beta|}\int_{c^*}^{x}F(x)dx} \tag{4.14}$$

$$=\frac{2f_o}{|\beta|}\left\{(\pm)_1|\xi_\infty|^{3/2}\pm\sqrt{2}\sqrt{|\xi_\infty|^3(\mp)_1|\xi_\infty|^{3/2}F(x)+2|\alpha||\xi_\infty|^{3/2}\int_{c^*}^{x}F(x)dx}\right\} \tag{4.15}$$

for $|\xi_\infty|\leqq\pi^{2/3}$

and

$$\Phi_x=\frac{1-M_\infty^2}{(\gamma+1)M_\infty^2}\pm\sqrt{\frac{(1-M_\infty^2)^2}{(\gamma+1)^2M_\infty^4}+\frac{(2f_o)^2}{|\beta|^2}F(c^*)^2-2\frac{(1-M_\infty^2)}{(\gamma+1)M_\infty^2}\left(\frac{2f_o}{|\beta|}\right)F(x)} \tag{4.16}$$

$$=\frac{2f_o}{|\beta|}\{(\pm)_1|\xi_\infty|^{3/2}\pm\sqrt{|\xi_\infty|^3+F(c^*)^2\,(\mp)_1\,2|\xi_\infty|^{3/2}\,F(x)} \tag{4.17}$$

$$\text{for}\quad |\xi_\infty|\geqq\pi^{2/3}$$

where the double signs with and without the parenthesis $(\ \ )_1$ correspond respectively to $M_\infty\lessgtr 1$ and

$$F(x)\,(\mp)_1|\xi_\infty|^{3/2}\gtrless 0 \tag{4.18}$$

Here if the reduced pressure coefficient,

$$\bar{C}_p=\frac{\{(\gamma+1)M_\infty^2\}^{1/3}}{(2f_o)^{2/3}}C_p=\frac{|\beta|}{(2f_o)|\xi_\infty|^{1/2}}C_p \tag{4.19}$$

is introduced, we can obtain, using the approximate relation $C_p=-2\Phi_x$,

$$\bar{C}_p=-2\left\{(\pm)_1|\xi_\infty|\pm\sqrt{2}\sqrt{|\xi_\infty|^2(\mp)_1|\xi_\infty|^{1/2}F(x)+2|\alpha||\xi_\infty|^{1/2}\int_{c^*}^{x}F(x)\alpha x}\right\} \tag{4.20}$$

$$\text{for}\quad |\xi_\infty|\leqq\pi^{2/3}$$

and

$$C_p=-2\{(\pm)_1|\xi_\infty|\pm\sqrt{|\xi_\infty|^2+F(c^*)^2|\xi_\infty|^{-1}(\mp)_1\,2|\xi_\infty|^{1/2}\,F(x)}\} \tag{4.21}$$

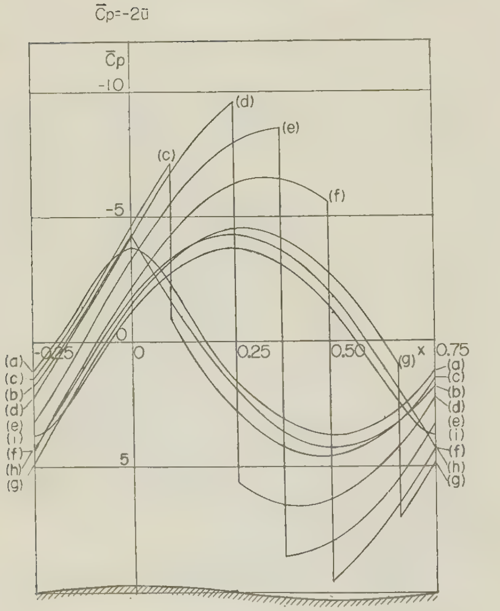

Fig. 3. Pressure distributions on the wall in terms of $\bar{C}_p$.

(a) $\xi_\infty=-2.8$
(b) $=-\pi^{2/3}$
(c) $=-2.0$
(d) $=-1.0$
(e) $=\ 0$
(f) $=\ 1.0$
(g) $=\ 2.0$
(h) $=\ \pi^{2/3}$
(i) $=\ 2.8$

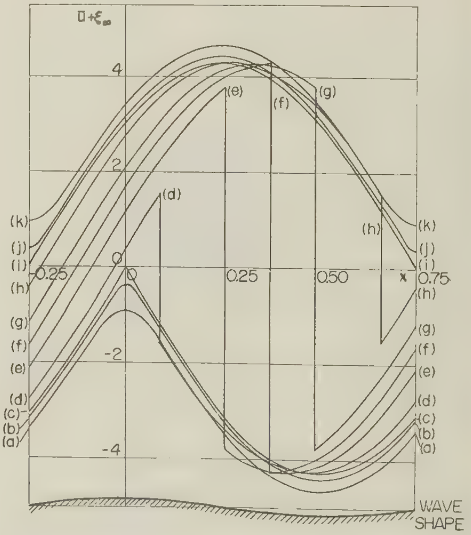

Fig. 4. Velocity distributions on the wall in terms of $\bar{u}+\xi_\infty$.

(a) $\xi_\infty=-2.8$
(b) $=-2.4$
(c) $=-\pi^{2/3}$
(d) $=-2.0$
(e) $=-1.0$
(f) $=\ 0$
(g) $=\ 1.0$
(h) $=\ 2.0$
(i) $=\ \pi^{2/3}$
(j) $=\ 2.4$
(k) $=\ 2.8$

$$=-2|\xi_\infty|^{1/2}\begin{Bmatrix} e^{i(2\pi x)} & (\xi_\infty<o) \\ e^{i(2\pi x-\pi/2)} & (\xi_\infty>o) \end{Bmatrix}+O(|\xi_\infty|^{-2}) \tag{4.22}$$

$$\text{for} \quad |\xi_\infty|\geqq\pi^{2/3}$$

All these results are consistent with the transonic similarity law.

(4.22) may be rewritten in the usual form of the pressure coefficient as follows:

$$C_p=-2\frac{(2f_o)}{|\beta|}\pi\begin{Bmatrix} e^{i(2\pi x)} & (\xi_\infty<o) \\ e^{i(2\pi x-\pi/2)} & (\xi_\infty>o) \end{Bmatrix}+O[(2f_o)^2] \tag{4.23}$$

This agrees with the result given by the usual linear theory.

Next, in order to see directly the velocity distribution in a reduced form that is invariant under the transonic similarity transformation, we introduce the following quantity:

$$\bar{u}+\xi_\infty\equiv\frac{\{(\gamma+1)M_\infty{}^2\}^{1/3}}{(2f_o)^{2/3}}\left\{\Phi_x+\frac{M_\infty{}^2-1}{(\gamma+1)M_\infty{}^2}\right\}=\frac{M^2-1}{\{(\gamma+1)(2f_o)M^2{}_\infty\}^{2/3}} \tag{4.24}$$

Then it indicates the local Mach number distribution in such a manner that

$$\bar{u}+\xi_\infty \gtreqless 0 \qquad \text{when} \qquad M \gtreqless 1 \tag{4.25}$$

Thus we can see our results for the pressure and local Mach number distributions in terms of the respective reduced quantities in Figs. 3 and 4. Now, the half of the pressure jump at the shock is found from (4.20), that is,

$$\Delta\bar{C}_p/2=2\sqrt{2}\sqrt{|\xi_\infty|^2(\mp)_1|\xi_\infty|^{1/2}F(c^{**})+2|\alpha||\xi_\infty|^{1/2}\int_{c^*}^{c^{**}}F(x)dx} \tag{4.26}$$

which is shown in Fig. 2, for a given shock wave position c^{**}.

§ 5. Discussion and Conclusion

A comparison with Kaplan's result for the lower critical flow is shown in Fig. 5. For the wall of the waviness ratio $2f_o=0.01$, the critical Mach number is about 0.91 in his case, according to Shapiro's sample calculation[5], while it is 0.917 in our case. With respect to the peak negative pressure there is no great difference. Thus, our approximation method is more satisfactory in comparison with Kaplan's one which requires more lengthy calculation, in order to inquire into the general feature of transonic flows.

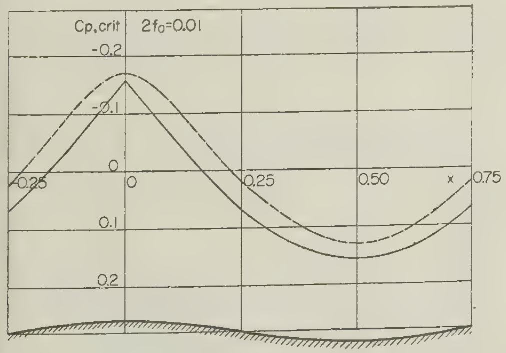

Fig. 5. Comparison of pressure distributions on the wall in the lower critical flow, predicted by Kaplan and by the present method. (The former is based on the figure given in Ref. 5.)
- - - - - - Kaplan, $M_{\infty,\,\mathrm{crit}}=0.91$
———— Present, $M_{\infty,\,\mathrm{crit}}=0.917$

Further, we can find a close analogy between the flows through a one-dimensional Laval nozzle and past a sinusoidal wall. Namely, the flow patterns shown in Figs. 3 and 4 are quite similar to those of the former if the sonic point of the latter is considered as corresponding to the throat, although in our case the sonic point moves upstream along the wall with increasing Mach number. Therefore it is not strange that the curves of $\bar{C}_p(x)$ and $\bar{u}(x)+\xi_\infty$ have sharp angles at the sonic points when the flow is critical (lower or upper). It will be interesting to compare this fact with Wood and Clarke's recent work[6] on the transonic flow in cascades, in which they evaluated, with success, the effect of the nonlinear term of the fundamental

equation (2–1) by replacing the term by the corresponding quantity of the one-dimensional flow.

Thus, it is found that our new approximation method can be applied successfully to the transonic flow past a sinusoidal wall and hence it may be expected that our method would be useful for the consideration of the general feature of the transonic flows.

In conclusion, the author wishes to express his sincere gratitude to Professor R. Kawamura and Mr T. Shigemi for their kind advice and valuable discussions.

References

1) H. Görtler: Z. a. M. M. **20** (1940) 254.
2) I. Imai and S. Oyama: Rep. Inst. Sci. Tech., Univ. Tokyo **2** (1948) 39.
3) C. Kaplan: NACA Tech. Note 2748 (1952).
4) I. Hosokawa: J. Phys. Soc. Japan **15** (1960) 149.
5) A. H. Shapiro: *The Dynamics and Thermodynamics of Compressible Fluid Flow* II (Ronald Press, New York, 1954) 841 p.
6) A. D. Wood and J. H. Clarke: J. Aero. Sci. **26** (1959) 318.

JOURNAL OF THE PHYSICAL SOCIETY OF JAPAN, Vol. 15, No. 11, NOVEMBER 1960

Selbstzündung von Kohlenwasserstoff-Luftgemischen in Stosswellen

von Kunio TERAO
Institut für physikalische Chemie der Universität Göttingen

(Received July 4, 1960)

The ignition mechanism of hydrocarbon-air mixtures is discussed. Thus, the ignition probabilities of various hydrocarbon-air mixtures were computed from the fluctuations of their ignition lags in shock waves. From these ignition probabilities, the activation energies of the primary and secondary reactions were calculated.

Next, the activation energies for the C–H and C–C bonds in the reaction with oxygen are estimated, as well as the amount of heat liberated for secondary reactions.

The mean ignition lags of other n-paraffin-air mixtures were, in accord with the experimental conditions, estimated from the above determined values.

Einleitung

Wie in der letzten Arbeit(1) über die Selbstzündung des n–Hexan-Luft-Gemisches in Stoßwellen berichtet wurde, hat die Induktionszeit der Entzündung eines brennbaren Gemisches immer eine Schwankung, von der man aber die Wahrscheinlichkeit der Entzündung des Gemisches in einer Zeiteinheit ausrechnen kann, damit man den Zündmechanismus genauer betrachten kann.

Um den Zündmechanismus der verschiedenen Brennstoffe zu vergleichen, werden in dieser Arbeit Methan–, Äthan–, Äthylen-Luft-Gemische und Äthan-Sauerstoff-Gemisch genau so wie beim n–Hexan-Luft-Gemisch untersucht.

Versuchsergebnisse

Das Experiment wurde genau so wie beim n–Hexan - Luftgemisch durchgeführt, d. h. unter derselben Bedingung wurden zahlreiche Versuche gemacht, so daß man die Schwankung der Induktionszeit der Entzündung messen kann. Von der Schwankung der Entzündungsinduktionszeit wurde die Wahrscheinlichkeit der Entzündung in einer Millisekunde

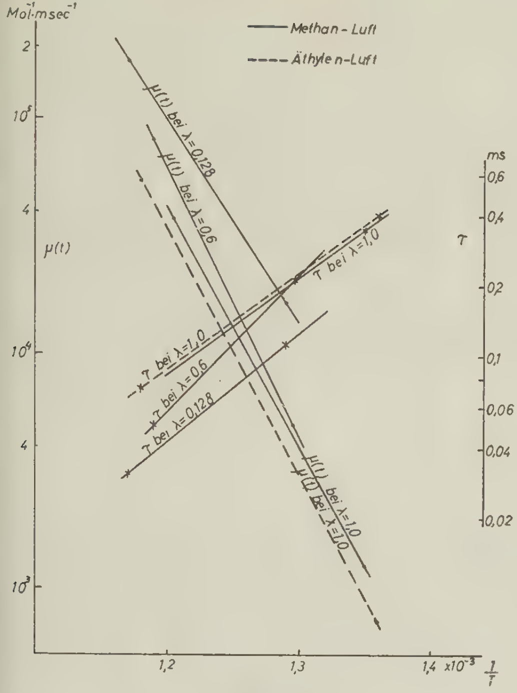

Bild 1.

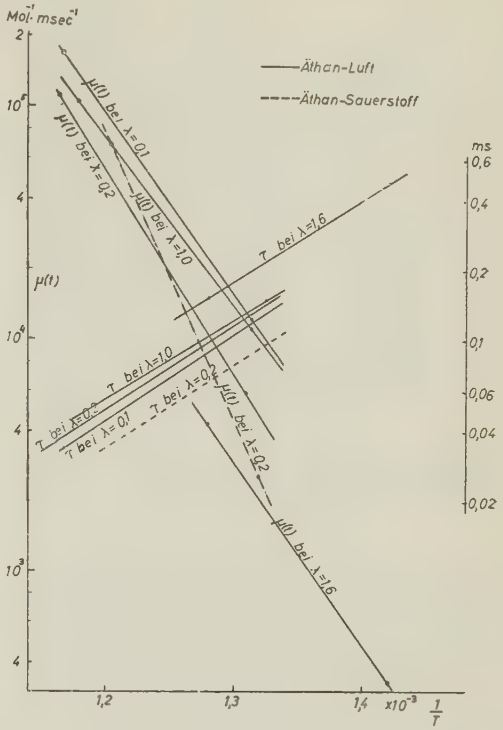

Bild 2.

Tabelle I.

Brennstoff	λ	M_1	T °K	P at	$\mu(t)$ $Mol^{-1} \cdot msec^{-1}$	τ msec	t_i msec
Äthan-Luft	1,6	2,11	705	3,00	$32{,}3 \times 10$	0,47	0,70
		2,27	780	2,92	$44{,}0 \times 10^2$	0,15	0,20
	1,0	2,14	755	3,20	$91{,}2 \times 10^2$	0,148	0,19
		2,32	850	3,26	$106{,}0 \times 10^3$	0,047	0,06
	0,2	2,12	765	3,00	$59{,}5 \times 10^2$	0,126	0,19
		2,3	860	3,00	$112{,}0 \times 10^3$	0,037	0,05
	0,1	2,11	762	2,95	$122{,}0 \times 10^2$	0,12	0,16
		2,28	857	2,90	$170{,}0 \times 10^3$	0,034	0,045
Methan-Luft	1,0	2,08	740	2,85	$10{,}3 \times 10^2$	0,345	0,56
		2,25	830	2,84	$38{,}2 \times 10^4$	0,086	0,11
	0,6	2,09	773	3,00	$50{,}0 \times 10^2$	0,2100	0,265
		2,27	840	2,88	$82{,}0 \times 10^3$	0,050	0,064
	0,13	2,097	777	2,90	$14{,}7 \times 10^3$	0,11	0,148
		2,25	855	2,94	$18{,}1 \times 10^4$	0,030	0,041
Äthylen-Luft	1,0	2,10	735	2,93	$7{,}2 \times 10^4$	0,40	0,55
		2,33	850	2,98	$55{,}0 \times 10^3$	0,071	0,09
Äthan-Sauerstoff	0,2	2,19	756	3,28	$25{,}7 \times 10^2$	0,09	0,199
		2,34	830	3,05	$69{,}0 \times 10^3$	0,035	0,055

λ: Mischungsverhältnis
M: Mach-Zahl der einfallenden Stoßwelle
T: Temperatur der reflektierenden Stoßwelle
P: Druck der reflektierenden Stoßwelle
$\mu(t)$: Wahrscheinlichkeit der Entzündung in einer Millisekunde in einem Mol.
τ: Zeitlänge, in der keine Entzündung entsteht
t_i: Mittelwert der Induktionszeit der Entzündung

Tabelle II.

Brennstoff	Konzentration % Vol.	E_1+E_2-W kcal/Mol	E_1 kcal/Mol	E_2-W kcal/Mol	A	B
n-Hexan-Luft	2,21(λ=1.0)	24,0	17,0	7,0	$67{,}5\times10^{8}$	$3{,}5\times10^{-3}$
	1,33(λ=0.6)	24,6	15,7	8,9	$22{,}3\times10^{9}$	$8{,}5\times10^{-4}$
	0,67(λ=0.3)	32,7	16,3	16,4	$60{,}6\times10^{11}$	$8{,}0\times10^{-6}$
	0,33(λ=0.15)	35,3	16,3	19,0	$50{,}7\times10^{12}$	$9{,}0\times10^{-7}$
Äthan-Luft	9,0 (λ=1.6)	35,6	19,4	16,2	$32{,}7\times10^{12}$	$47{,}0\times10^{-7}$
	5,7 (λ=1.0)	33,6	17,9	15,7	$48{,}8\times10^{12}$	$45{,}0\times10^{-7}$
	1,13(λ=0.2)	40,0	23,2	16,8	$59{,}0\times10^{13}$	$27{,}0\times10^{-7}$
	0,6 (λ=0.1)	35.8	19,1	16,8	$24{,}0\times10^{13}$	$27{,}0\times10^{-7}$
Methan-Luft	9,1 (λ=1.0)	49,5	30,6	18,9	$38{,}0\times10^{16}$	$13{,}0\times10^{-7}$
	5,5 (λ=0.6)	53,0	26,0	27,0	$50{,}0\times10^{17}$	47.5×10^{-10}
	1,27(λ=0.13)	46,9	25,3	21,6	$23{,}0\times10^{16}$	$7{,}0\times10^{-8}$
Äthylen-Luft	6,5 (λ=1.0)	48,0	28,8	19,2	$16{,}1\times10^{16}$	$7{,}5\times10^{-7}$
Äthan-Sauerstoff	5,7 (λ=0.2)	56,5	40,3	16.2		

und in einem Mol Gemisch ausgerechnet. Davon wurden weiter die Aktivierungsenergien der Start- und Sekundärreaktion, Konstante A und B in den Gleichungen 5 und 6 in der letzten Arbeit usw. für Methan-, Äthan-, Äthylen-Luft-Gemische und Äthan-Sauerstoff in verschiedener Temperatur mit verschiedener Konzentration berechnet.

Bild 1, 2, Tabelle I und II zeigen die Ergebnisse. In der Tabelle sind die Verschsergebnisse des n-Hexan-Luftgemisches auch ersichtlich.

1) *Aktivierungsenergie der Startreaktion E_1:*

Nach diesen Ergebnissen kann man erst die Aktivierungsenergie der Startreaktion der Methan-, Äthan-, und n-Hexan-Luftgemische vergleichen. Wie Bild 3 zeigt, ist die Aktivierungsenergie des Methan-Luftgemisches durchschnittlich 27,3 kcal/Mol und viel größer als die der andern, aber der Unterschied der Aktivierungsenergie des Äthan Luftgemisches (19.9 kcal/Mol) und des n-Hexan-Luftgemisches (16.4 kcal/Mol) ist nicht so groß. Es ergibt sich wahrscheinlich aus dem Unterschied der Molekülstruktur. Nämlich Methan hat nur 4 C–H Bindungen. Dagegen hat Äthan 1 C–C und 6 C–H Bindungen und n-Hexan 5 C–C und 14 C–H Bindungen.

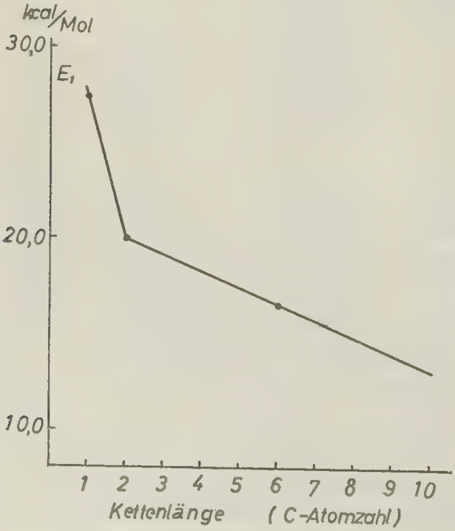

Bild 3.

Bei der Entzündung des Äthan-Luftgemisches soll erst die C–C Bindung auseinandergehen und mit Sauerstoff eine chemische Reaktion machen, weil ihre Bindungskraft kleiner ist als die der C–H Bindung⁽²⁾ und sie sogar den größten Kraftmoment hat. Mit dem n-Hexan-Luftgemisch soll es auch genau so gehen, nämlich die C–C Bindung in der Mitte der C–C Kette muß erst auseinandergehen und mit O_2 eine Reaktion machen. Deshalb muß die Aktivierungsenergie der Startreaktion in den beiden Fällen die Energie sein, mit der eine C–C Bindung auseinandergeht und mit Sauerstoff eine chemische Reaktion macht. Daß die Aktivierungsenergie des Äthan-Luftgemisches etwas größer ist als die des n-Hexan-Luftgemisches, ist deswegen, weil die Kette des n-Hexan viel länger ist und sein Kraftmoment größer sein muß als Äthan.

Beim Methan-Luftgemisch muß erst irgendeine C–H Bindung auseinandergehen, aber die

Bindungskraft der C–H Bindung ist viel größer als die der C–C Bindung. Deshalb ist die Aktivierungsenergie der Startreaktion des Methan-Luftgemisches viel größer als die des Äthan– und *n*–Hexan-Luftgemisches.

Hieraus und aus den Versuchsergebnissen könnte man schließen, daß die Aktivierungsenergie der C–H Bindung für die Reaktion mit O_2 etwa 27,0 kcal/Mol und die der C–C für die Reaktion mit O_2 etwa 20 bis 15 kcal/Mol, aber immer verschieden je nach der Kettenlänge ist, d.h. je länger die Kette ist, um so geringer ist die Aktivierungsenergie der C–C Bindung für die Reaktion mit O_2, wie Bild 3 zeigt.

2) *Reaktionsstufenzahl*:

Wie in der letzten Arbeit beim *n*–Hexan-Luftgemisch erklärt wurde, kann man von dem Zusammenhang zwischen der Konzentration des Brennstoffes und Konstanten A oder B die Reaktionsstufenzahl n_1 und n_2 ausrechnen. Beim Äthan– und Methan-Luftgemisch ist es nicht so deutlich und man kann daraus die Reaktionsstufenzahl nicht gut schätzen, vielleicht deswegen, weil die Reaktionsstufenzahl dabei nicht so groß ist und die Änderung des A oder B mit der Konzentration ziemlich klein ist. Da man aber schon beim *n*–Hexan-Luftgemisch n_1 und n_2 ungefähr schätzen konnte, kann man davon weiter n_1 und n_2 bei andern Brennstoffen schätzen. Da nämlich A proportional $\left(\frac{1}{\lambda}\right)^{n_1+n_2}$ ist, kann man die Reaktionsstufenzahl des verschiedenen Brennstoffes mit derselben Konzentration vergleichen, weil der Unterschied der Molekülsgröße hier fast keine Rolle spielt, und sie damit erhalten. Daraus kann man schließen, daß die Reaktionsstufenzahl des Äthan-Luftgemisches 4 und die des Methan Luftgemisches 3 ist, wenn n_1+n_2 beim *n*–Hexan-Luftgemisch 5 ist, wie schon in der letzten Arbeit geschätzt wurde. Von B kann man n_2 bestimmen. Beim *n*–Hexan-Luftgemisch ist es 4. Daraus wurde n_2 beim Äthan-Luftgemisch 3 und beim Methan-Luftgemisch 2 geschätzt.

3) *Reaktionsvorgänge*:

Da die Aktivierungsenergie der Startreaktion und die Reaktionsstufenzahl schon bekannt sind, könnte man damit die Reaktionsvorgänge einigermaße vermuten.

Beim Methan-Luftgemisch sollte erst eine C–H Bindung mit Stoß eines Sauerstoffmoleküls auseinander gehen und mit O_2 eine Reaktion machen, und dann anschließend andere 2 C–H Bindungen genau so wie die erste aber mit der Wärme von jeder vorgehenden Reaktion nacheinander auseinandergehen und in die Reaktion mit O_2 kommen. Beim Äthan-Luftgemisch kommt erst die C–C Bindung in die Reaktion und anschließend kommen 3 C–H Bindungen nacheinander in die Reaktion mit der Wärme von jeder vorgehenden Reaktion.

Beim *n*–Hexan-Luftgemisch geht vielleicht, wie schon gesagt, erst die C–C Bindung in der Kettenmitte auseinander und das Molekül wird in zwei getrennt.

$$-C-C-C-C-C-C \rightarrow -C-C-C-O \quad -O-C-C-C-$$

Dann wirkt jeder Teil schon wie ein Molekül, d.h. sie haben miteinander keinen besondern Zusammenhang mehr. Eins davon trennt sich weiter und vielleicht geht nochmals eine C–C Bindung auseinander, weil die Bindungskraft der C–C kleiner ist als die der C–H Bindung. Anschließend gehen noch 2 C–H Bindundgen auseinander und kommen in die Reaktion mit O_2. Nämlich an der Primärreaktion nimmt eine C–C Bindung teil und an der Sekundärreaktion nehmen 2 C–C und 2 C–H Bindungen teil. Inzwischen können natürlich mehrere komplizierte Kettenreaktion von sich gehen, aber solange man von solcher konkreten Reaktion absieht und nur die Reaktion mit Sauerstoffmolekülen betrachtet, könnte es mit größer Möglichkeit so wie oben erklärt gehen.

Um diese Sache nochmals klar zu machen, wurde noch ein Experiment mit Äthylen-Luftgemisch gemacht. Wie es in Bild 1 oder Tabelle II gezeigt ist, sind sowohl die Aktivierungsenergien der Primär- und Sekundärreaktion wie A und B fast gleich denen von Methan-Luftgemischen. Das bedeutet nämlich, daß die Entzündungsreaktion des Äthylen-Luftgemisches genau so vor sich geht wie die des Methan-Luftgemisches. Da die C=C Bindung, die Äthylen hat, viel größere Bindungskraft hat als C–H Bindung, geht erst eine C–H Bindung auseinander und dann schließen 2 C–H Bindungen an, genau so wie beim Methan-Luftgemisch.

4) *Die Aktivierungsenergie der Sekundärreaktion E_2 und die zur Sekundärreaktion zugeführte Wärme W:*

Da die Aktivierungsenergien der C–C und C–H Bindung für die Reaktion mit O_2 klar geworden sind und die Reaktionsvorgänge vermutet werden können, kann man daraus die Aktivierungsenergie der Sekundärreaktion ausschätzen.

Beim Methan-Luftgemisch kommt erst 1 C–H Bindung in die Reaktion, die zur Startreaktion gehört, und dann schließen 2 C–H Bindungen in der Sekundärreaktion an. Die Aktivierungsenergie einer C–H Bindung für die Reaktion mit O_2 ist nach dem Experimentsresultat 27,0 kcal/Mol. Deshalb soll die Aktivierungsenergie der Sekundärreaktion $E_2=2\times 27{,}0=54{,}0$ kcal/Mol. Beim Äthan-Luftgemisch kommen 3 C–H Bindungen in die Sekundärreaktion. $E_2=3\times 27{,}0=81{,}0$ kcal/Mol.

Beim *n*-Hexan-Luftgemisch kommen 2 C–C und 2 C–H Bindungen in die Sekundärreaktion. Aber dabei soll die Aktivierungsenergie der C–C Bindung zwischen denen der C–C Bindung in der Mitte der *n*-Hexankette und der Methankette, d.h. 16,4 und 19,9 kcal/Mol, weil die Kettenlänge zur Sekundärreaktion länger ist als Äthan, aber kürzer als *n*-Hexan. Je weiter die Sekundärreaktion vor sich geht, um so kürzer wird die Kettenlänge und um so weniger wird das Kraftmoment, d.h. um so mehr braucht man die Aktivierungsenergie. Hier wurde der Mittelwert 18,0 kcal/Mol genommen.

$$E_2=2\times 18{,}0+2\times 27{,}0=90 \text{ kcal/Mol.}$$

Da E_2-W schon vom Experiment bekannt ist, kann man leicht die zur Sekundärreaktion zugeführte Wärme W ausrechnen. Beim *n*-Hexan-Luftgemisch ist W von 71.0 bis 83,0 kcal/Mol, beim Äthan-Luftgemisch 64,2 bis 65,3 kcal/Mol und beim Methan-Luftgemisch 27,0 bis 35,1 kcal/Mol. Je magerer das Gemisch ist, desto geringer ist die Wärme.

5) *Die ausgeführte Totalwärme bei der Reaktion W_T:*

Die Wärme W, die zur Sekundärreaktion zugeführt wird, ist nur ein Teil der gesammten Wärme W_T, die bei der ganzen Reaktion entsteht. Jetzt denken wir nur an eine C–C bzw. C–H Bindung. Nehmen wir ε als die Aktivierungsenergie für die Reaktion, w_t als die Totalwärme, die gleich der Aktivierungsenergie für die Reversreaktion ist, und Δh als die Reaktionswärme, die man nach der Reaktion merkt und gleich $w_t-\varepsilon$ ist. Für die nachfolgende Reaktion wirkt nicht die Reaktionswärme Δh, sondern die Totalwärme der vorgehenden Reaktion w_t, die der Unterschied zwischen dem angeregten Zustand und dem nach der Reaktion ist. Dabei kann jede nachfolgende Reaktion nicht die ganze Wärme bekommen, sondern einen Teil davon, weil sich die Wärme durch die Stöße mit nichtaktivierten Molekülen vermindern muß.

Die Reaktionswärme Δh kann man nach der Bindungsenergie(2) ausrechnen, wenn man die Reaktionsvorgänge kennt.

Δh bei der Reaktion einer C–H Bindung mit O_2 33,8 kcal/Mol und Δh bei der Reaktion einer C–C Bindung 22,3 kcal/Mol

Die Summe der Aktivierungsenergie und der Reaktionswärme soll die ausgeführte Totalwärme sein.

w_t einer–C–H Bindung bei der Reaktion mit O_2
$=33{,}8+27{,}0\approx 61{,}0$ kcal/Mol

w_t einer C–C Bindung bei der Reaktion mit O_2
$=22{,}3+18{,}0\approx 40$ kcal/Mol

Daraus kann man die ausgeführte Totalwärme von jedem Gemisch errechnen.

Beim Methan-Luftgemisch ist W_T $3\times 61=183$ kcal/Mol, weil dabei 3 C–H Bindungen in Frage kommen. Beim Äthan-Luftgemisch ist es $1\times 40+3\times 61=223$ kcal/Mol und beim *n*-Hexan-Luftgemisch $3\times 40+2\times 61=242$ kcal/Mol.

Die Differenz zwischen der Totalwärme W_T und der zur Sekundärreaktion zugeführten Wärme W ist die Wärme, die in die Umgebung des betreffenden Moleküls übergeht, oder im Molekül bleibt, um es zu wärmen.

Bei der Entzündung muß die Wärme von der Entzündungsreaktion oder der sogenannten Vorreaktion zur Umgebung des betreffenden Moleküls ausgeführt werden, so daß die Reaktion sich zur Verbrennung erweitern kann. Wie bis dahin erklärt wurde, braucht man bis zur Entzündung nicht die vollkommenen Reaktion des Brennstoffsmoleküls, sondern einige Stufen, z.B. bei Methan 3, bei Äthan 4 und bei *n*-Hexan 5. Denn die Wärme von der unvollkommenen Reaktion genügt schon, um einen Teil der Umgebung des Brennstoffsmoleküls zu erwärmen, so daß die Reaktion sich erweitern kann. Diese Wärme soll die Wärme sein, die die Differenz von der Wärme W_T und W ist. Merkwürdig ist es, daß die von der Entzündgsreaktion in die Umgebung ausgeführte Wärme bei jedem Gemisch fast immer gleich etwa 150 kcal/Mol ist. Das bedeutet nämlich, daß man für die Entzündung immer so viel Wärmeausfuhr braucht.

Beim Äthan-Sauerstoffgemisch ist die Aktivierungsenergie der Startreaktion 40 kcal/Mol (Bild 1 und Tabelle II) und die der Sekundärreaktion fast gleich der beim Äthan-Luftgemisch. Vielleicht kommen in die Startreaktion eine C–C und eine C–H Bindung gleichzeitig, weil die Aktivierungsenergie ungefähr gleich der Summe der von C–C und C–H Bindung ist. Deshalb muß die Reaktion der Entzündung der Äthan-Sauerstoffgemisches gesamt 5 Reaktionsstufen haben, nämlich 1 C–C und 4 C–H Bindung kommen in die Reaktion. Das kommt vielleicht daher, daß es so viel Wärme ausführen muß, um die Umgebung zu erwärmen, daß die Reaktion weiter in der Umgebung vor sich gehen kann, weil die spezifische Wärme etwas mehr ist als die der Luft und zwar auch daher, daß es sich mit Sauerstoff leicht Reaktion machen kann, weil es in der Umgebung des Brennstoffsmoleküls viel Sauerstoff gibt.

6) *Wärmeerhaltungskoeffizient*:

Wieviel Prozent von der Totalwärme zur Sekundärreaktion effektiv wirkt, wird von dem Verhältnis der zur sekundären Reaktion zugeführten Wärme W und gegen die Summe der Totalwärme jeder Reaktionsstufe außer der letzten gezeigt. Die Wärme, die in der letzten Reaktionsstufe entsteht, spielt keine Rolle zur Sekundärreaktion. Dieser Wärmeerhaltungskoeffizient ist verschieden je nach der Konzentration, besonders je nach dem Brennstoff. Beim n-Hexan-Luftgemisch ist es 40 bis 46%, beim Äthan-Luftgemisch etwa 40% und beim Methan-Luftgemisch 23 bis 30%. Das ist vielleicht deswegen, weil die Reaktionsvorgänge verschieden sind, nämlich verschiedene chemische Bindungen in die Reaktion kommen. Daraus wurde jeder Wärmeerhaltungskoeffizient für C–C und C–H Bindung bei der Reaction mit O_2 geschätzt. Für C–C Bindung ist es etwa 57% und für C–H 27%, bei der Konzentration etwa 1,3%.

Verallgemeinerung

In der vorigen Arbeit[1] über Selbstzündung des n-Hexan-Luftgemisches wurde erklärt, daß man je nach dem Zustand die Induktionszeit der Entzündung theoretisch ausrechnen kann, wenn die Wahrscheinlichkeit der Entzündung in einer Zeiteinheit und die Zeitlänge, in der keine Entzündung entsteht, bekannt sind. Dazu braucht man aber die Aktivierungsenergien der Start- und Sekundärreaktion E_1 und E_2, die zur Sekundärreaktion zugeführte Wärme W, Konstante A und B. Wenn man die Reaktionsvorgänge der Entzündung kennt, d.h. welche chemische Bindung sich wie oft an der Reaktion beteiligt, kann man schon diese Werte schätzen.

Die Reaktionsvorgänge der n-Paraffine, die man von ihrem Molekülstruktur und von ihrer in die Umgebung des betreffenden Moleküles ausgeführten Wärme schätzen kann, sind Folgende:

Brennstoff	Startreaktion	Sekundärreaktion
CH_4	C–H	2 C–H
C_2H_6	C–C	3 C–H
C_3H_8 und C_4H_{10}	C–C	2 C–C, 2 C–H
C_5H_{12}, C_6H_{14}, C^7H_{16}, C_8A_{18} und $C_{10}H_{22}$	C–C	2 C–C, 2 C–H

Damit kann man jede Reaktionsstufenzahl der Start- und Sekundärreaktion n_1 und n_2

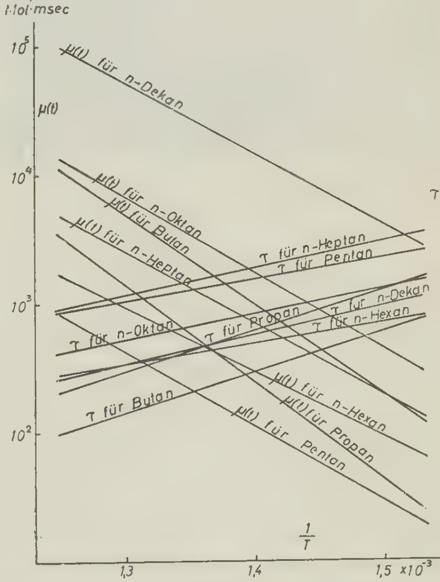

Bild 4.

erhalten, und gleich weiter A und B halbempirisch von den Resultaten des oben berichteten Experiments, E_1 und E_2 kann man auch genau so bekommen. Mit diesen Werten kann man schon die Wahrscheinlichkeiten der Entzündung in einer Millisekunde in einem Mol Gemisch und τ ausrechnen, mit denen man weiter alle Entzündungsinduktionszeiten beliebter n-Paraffin-Luftgemische je nach dem Zustand theoretisch errechnen kann. Bild 4 zeigt die theoretisch berechneten τ und Wahrscheinlichkeiten der Entzündung in einer Millisekunde in einem Mol Gemisch von Propan-, Butan-, Pentan-, n-Heptan, n-Oktan und n-Decan-Luft Im Bild 5 werden die durchschnittlichen Induktionszeiten, die nach dieser Theorie ausgerechnet werden, und die empirisch gemessenen von der Arbeit(3) von A. Martinengo verglichen, in der das Gemisch in einem Stahlzylinder mit einem Kolben schnell adiabatisch gedruckt und gezündet wurde. Die Temperatur verschiebt sich allgemeine nach unten, aber solcher Fehler kommt oft vor, wenn Experiments- und Meßmethode anders ist. Aber sonst stimmen beide Werte ziemlich gut überein, besonders die anschaulichen Aktivierungsenergien E, die von den Neigungen der Kurve $ln\ \tau_i$ in Bezug auf $1/T$ nach Gleichung $\tau_i = \text{Konst.} \times e^{\frac{E}{RT}}$ errechnet werden sollen, stimmen sehr gut überein.

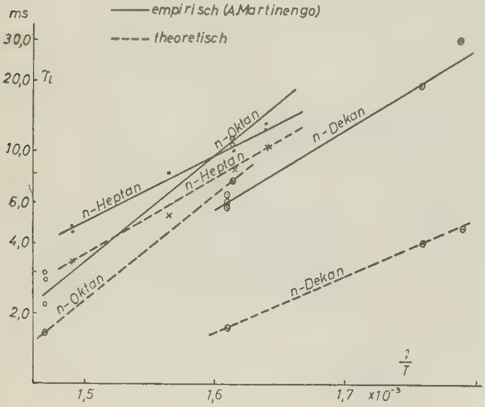

Bild 5.

Zusammenfassung

Mit der letzten und dieser Arbeit ist klar geworden, daß man von der Wahrscheinlichkeit der Entzündung in einer Zeiteinheit, die man aus der Schwankung der Induktionszeit der Entzündung errechnen kann, viel neues wissen und vermuten kann, z.B. welche chemische Bindung an welcher Reaktion teilnimmt, wie groß jede Aktivierungsenergie, die Totalwärme, die Sekundärreaktion zugeführte Wärme, Konstante A und B usw. Nach diesen empirischen und theoretischen Ergebnissen kann man auch die durchschnittlichen Induktionszeiten der Entzündung beliebiger n-Paraffin-Luftgemische schätzen.

Zum Schluß danke ich Herrn Prof. W. Jost und Herrn Dr. Wagner, die mir die Chance gegeben haben, diese Arbeit zu tun, und für die freundliche Leitung.

Schrifttum

1) K. Terao: J. Phys. Soc. Japan Vol. 15, 6 (1960).
2) J. C. Jungers: Cinétique Chimique Applique (1958) 7.
3) A. Martinengo: Doktorarbeit (1958) Universität Göttingen, Z. f. phys. Chemie Neue Folge 20, 3/4, 1959, 22, 3/4, 1959.

JOURNAL OF THE PHYSICAL SOCIETY OF JAPAN, Vol. 15, No. 11, NOVEMBER, 1960

Glass Cracking Caused by Underwater Spark

By Shin-ichi HYODO
Department of Applied Physics, University of Tokyo, Tokyo
Fumiko OKUDA
Department of Physics, University of Tokyo, Tokyo

(Received July 5, 1960)

Using a Beckman & Whitley high-speed framing camera, the velocity of glass fracture caused by an underwater disruptive electric spark was measured. The observed maximum velocity was about 2.4 km/sec, 60% higher than the usually accepted normal limiting value. A gradual decrease of fracture velocity was also observed. From these observations it has been deduced that the maxium fracture velocity is, contrary to the hitherto assumed theory, dependent on the increasing rate of applied stress.

§ 1. Introduction

Since in 1937 Schardin and Struth[1,2] studied the spread of impact fractures in glass by the use of their multiple-spark camera, not a few investigations have been carried out for the determination of glass-fracture velocity.[3,4,5,6,7,8] They unanimously indicated that for any kind of glass there existed a certain constant maximum velocity corresponding to its chemical composition (about 1500 m/sec for normal glass), which was not affected either by the over-all stress at the moment of fracture or by the temperature of glass specimen. According to Dimmick[5], the effect of the latter on a soda-lime glass can be expressed as the temperature coefficient on the order of -0.15 m/sec/°K. This maximum velocity is approximately equal to one half of the velocity of transverse waves and to one third of that of longitudinal waves in the material studied. Theoretical considerations supporting this limiting value from the standpoint of its correlations with elastic waves were also developed by Poncelet[9], Yoffe[10], Mott[11], and Robert and Wells[12].

In some of his earlier works, however, Hirata[13] presented a photograph like the one in Fig. 1, which shows the initial state of glass fracture produced by underwater spark discharge. It should be noticed that this shadowgraph of growing cracks was taken in the light emitted from the underwater spark itself with some suitable arrangement of a reflecting spherical mirror placed under the glass plate. Therefore, even if the light duration of the spark be 1 μsec (this is rather an over-estimation for ordinary spark shadowgraphs), the velocity of glass fracture in this case would surpass the above-mentioned limiting value.

The main purpose of our work was to check this point by means of successive high-speed photography.

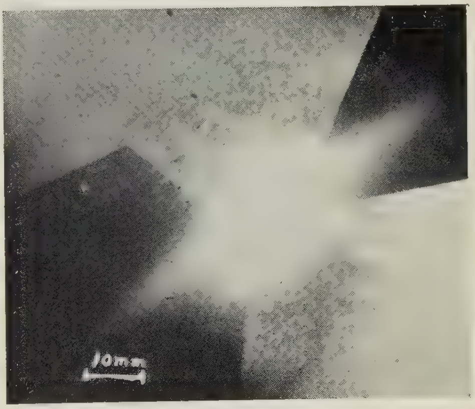

Fig. 1. A silhouette photograph of growing glass cracks initiated by an underwater electric spark.

§ 2. Experimental Procedure

The specimen was prepared by cutting an ordinary sheet glass. Between this specimen having a square form of about 7×7 cm^2 and 1.4 mm thickness and the glass plate having the same form but a larger thickness were sandwiched two pieces of aluminium foil cut in a spear-like shape as a couple of electrodes as shown in Fig. 2. The tips of the foils were placed facing each other with a gap of about 1 mm between them. After such procedure was carried out wholly in the water with special care to extrude any trace of air bubbles, the specimen assembly was left in a water tank equipped with a glass window in its bottom.

The schematic diagram of the whole experimental arrangement is shown in Fig. 3. In order to catch the sequence of the events, a high-speed framing camera (Beckmen & Whitley Model 189) was used. As this instrument is not equipped with any adequate shutter, a Xenon flash lamp of sufficiently short duration was adopted as the illumination source so as to prevent the film from double exposure. When the rotating mirror in the camera attained a definite speed, a sharp pulse was brought out from the camera by manual switching just before the mirror came to the position of the first frame. This pulse served both for firing the flash lamp immediately and for triggering the main underwater spark after the delay of 2 μsec or so.

When the third electrode of the three-point gap was triggered, a high voltage of 50 KV, at which the Leyden jar had been kept, was

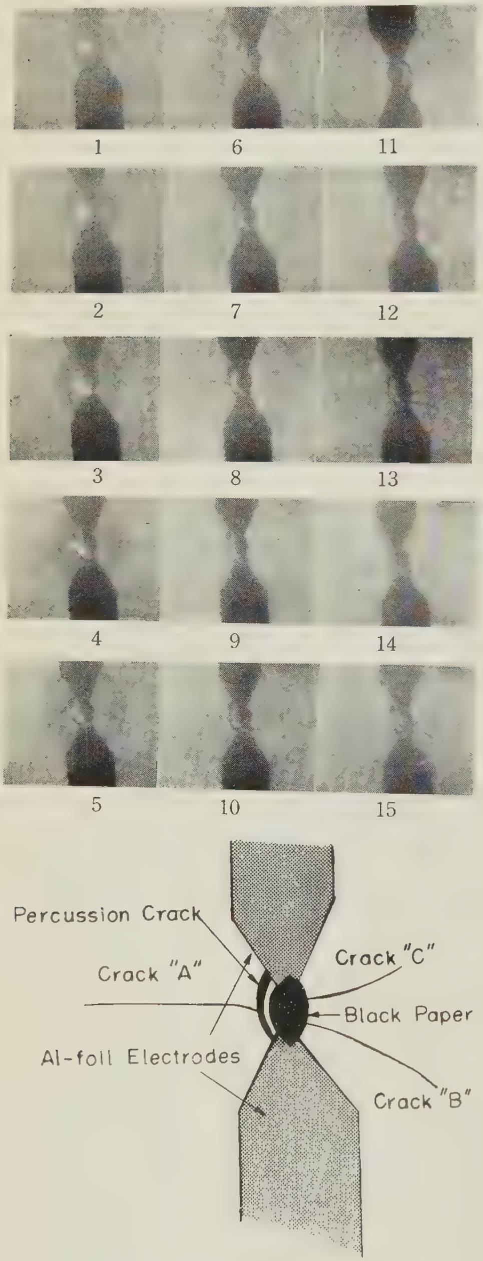

Fig. 4. A sequence of 15 pictures taken at a rate of 1.8×10^6/sec, using the Beckman & Whitley high-speed framing camera. The sequence shows the initial stage of glass fracture produced by underwater spark discharge.

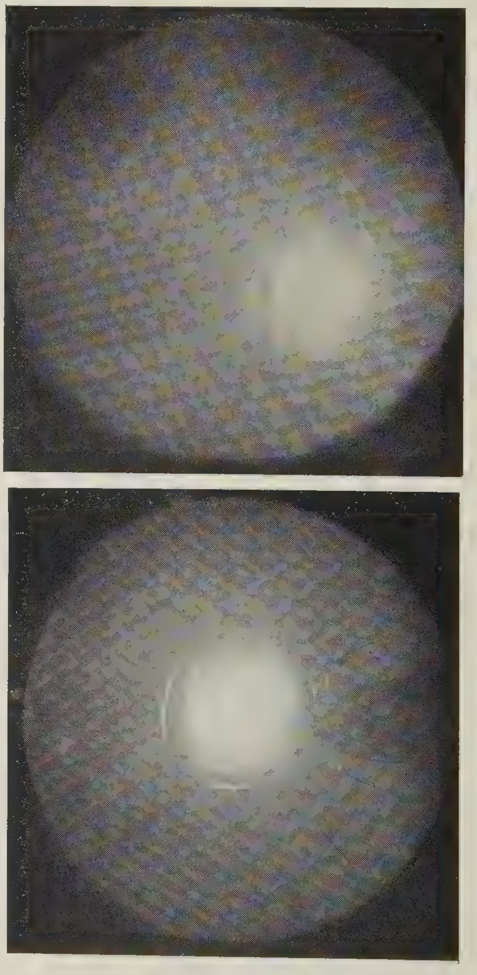

Fig 8. Two successive views, taken with a high-speed cine-micrograph, of a fast-cracking of a thin glass sheet. Exposure time for each was 6×10^{-7} sec; interval between frames was 2.4×10^{-6} sec.

suddenly applied to the underwater electrodes. Then a gaseous conduction channel formed across the gap. The rate of current rise was so great that the growth of the gaseous conduction channel was strictly restrained by the inertia of the water, and this resulted in high pressure upon the gas of the channel and cosequently also upon the water around. It was the pressure wave thus generated in the water that caused the glass specimen to fracture. It may be said that the loading time in this method is extremely short as compared with other mechanical impacts.

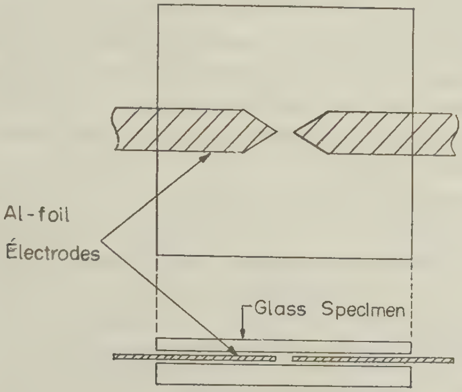

Fig. 2. Arrangement of Al-foil electrodes sandwiched between glass plates.

After illuminating the phenomenon in silhouette, light from the source was deflected to the horizontal direction by the plane mirror placed above the water tank and finally fell into the objective lens of the high-speed camera through a large condenser lens. As the pictures were liable to be spoiled by the light directly coming from the luminous underwater spark, a tiny piece of black paper was placed over the position of the electrode gap.

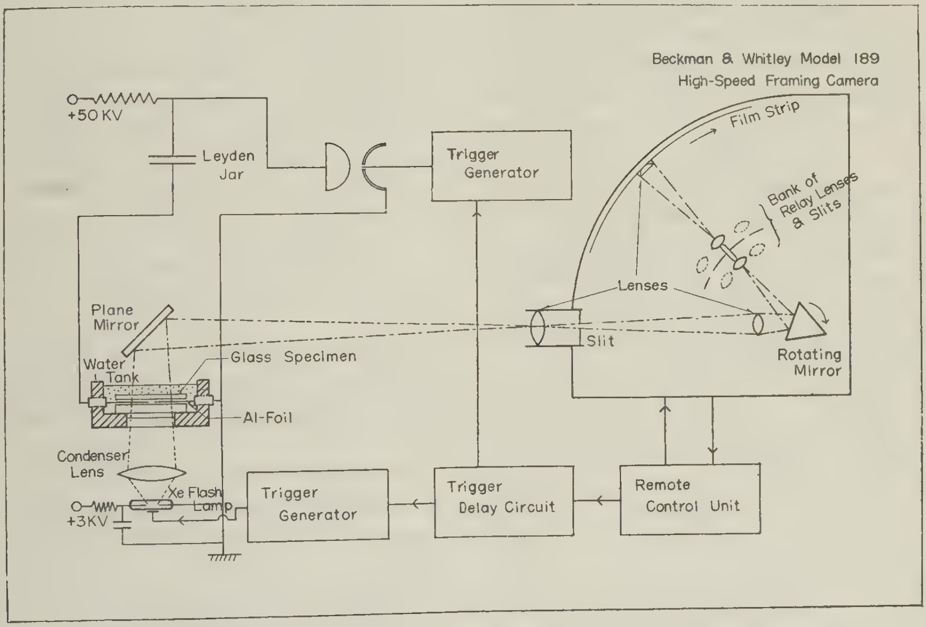

Fig. 3. A schematic diagram of the whole experimental arrangement.

§ 3. Results and Discussions

In Fig. 4 is illustrated a typical sequence of pictures of glass fracture produced by underwater spark. They were taken at a rate of 1.8×10^6 frames per sec. It can be seen that at first a percussion crack of ellipitic form appears and then from its margin a few cracks commence to grow in the directions radially outward from the center of percussion. In addition, the pressure wave in the water is also clearly photographed propagating in a circular form ahead of the cracks. The propagation-time curves of these cracks and a pressure wave are indicated in Fig. 5.

Partly because of the scattering of light at a number of glass-water boundaries through which the illuminating light from the Xenon lamp passes and partly because of slight defects in the condenser lens which is located not so far out of the focus of the objective lens, the resolution of fine details in the shadowgraphs cannot be very satisfactory. For the determination of the propagation distance, therefore, measurement was repeated seven to ten times for each shot on the enlarged positive photographs either by direct scaling or by a travelling microscope. The mean square root deviations of such observed values are 0.40 mm, and are indicated by the bars annexed to each of the points in Fig. 5. It may be natural to assume here that the very early stage of the appearance of a crack is not detectable in these photographs if the length of the crack does not exceed the order of 0.4 mm. A smoothed out curve is drawn covering the system of plotted points in Fig. 5, and at the successive points along this curve the respective gradients to the curve are obtained graphically. The relation between the crack velocity thus obtained and the time elapsed after the beginning of the fracture is shown in Fig. 6, while Fig. 7 shows the velocity versus the extending length of the crack.

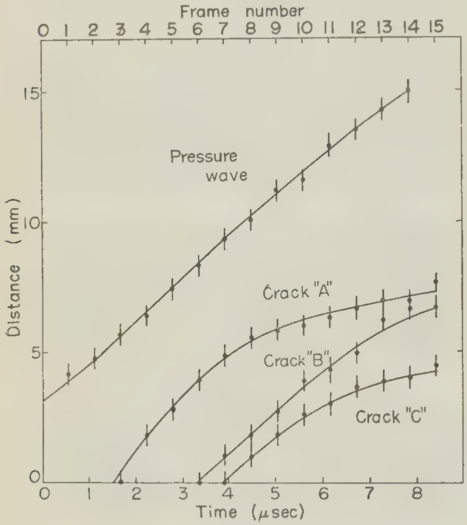

Fig. 5. Measurement of three cracks and a pressure wave shown in Fig. 4.

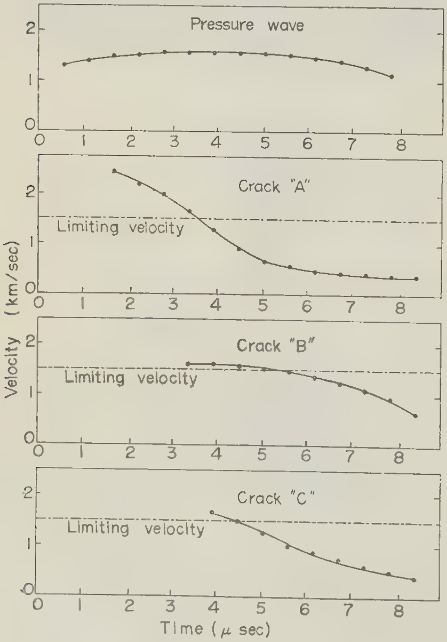

Fig. 6. Velocity versus time.

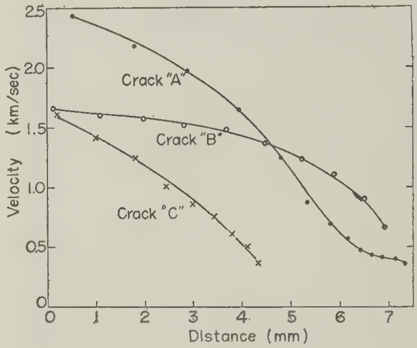

Fig. 7. Velocity versus length of cracks.

According to Figs. 6 and 7, the fracture velocity of the crack "A" at its initial stage attains a value as large as 2.4 km/sec, which is about 60% larger than the generally accepted maximum velocity. Although the precision of velocity determination by means of differentiation of the length-time curve is not sufficiently high, yet it is unbelievable that the maximum velocity in this case is higher not than the normal limit, even if a conceivable range of errors is taken into account.

As is already known, there are some cracks running apparently faster than the limiting velocity. For example, if a fine scratched line exists in the internal part, or on the surface, of a glass plate and the direction of maximum loading tension coincides approximately with this line, a crack with secondary fractures will follow this line with enormous velocity. Secondary fractures can also be initiated sucessively at numerous points with some distances apart in front of the normal cracks, as is reported by Pugh *et al.*[14)15)] when violent shock waves much faster than the fracture velocity are applied. This view, however, does not apply to the present case, for although the cracks we observed are those that have developed secondarily from the margin of the ellipitic percussion crack, the velocity we measured is that of the extension of those secondary cracks themselves, not the superposed one.

It might be supposed that the observed supervelocity is due to an extraordinarily large impact energy. But this cannot be the case, because the impact energy is by no means conspicuous; this would have been less than 10^8 erg, even if the whole energy reserved in the Leyden jar had been dissipated for producing fractures, whereas, in the experiment of Schardin and Struth who shot rifle bullets against glass targets, the consumed energy should have been greater than that in our experiment in the order of magnitude. Thus we are lead to the idea that the normal maximum fracture velocity can be surpassed if the loading rate of an impact attains some extremely high value. In other words, we are suggesting that the most important factor that influences the maximum fracture velocity may be $\dot{S}$ or $\ddot{S}$, where S denotes the overall stress at the moment of fracture and the dot means the time derivative.

Recently Schardin[16)] stated that the fracture velocity V_f should be determined by an equation of the following form:

$$V_f = F(T, \rho, E, \mu, X)$$

where T indicates the surface energy in the material, ρ the density, E Young's modulus, μ Poisson's ratio, X the residual plastic energy. His equation will hold, so long as $\dot{S}$ or $\ddot{S}$ is not so large.

Further he gave interesting remarks as follows. "It is an astonishing fact that during the twenty years that high-speed photography has been used to study fracture phenomena no continuous velocity decrease of a crack once running at maximum speed could be observed. Very often a crack stops rapidly, and no transition phase can be detected within the space and time resolution of the applied equipment (order of magnitude; 1 mm and 1 μsec, respectively). This is true for high-speed as well as for low-speed loading."

As a fundamental reason for the non-existence of a gradual decrease of fracture velocity, he presumed that a certain value of exterior stress is indispensable for the proceeding of a fracture and it stops abruptly when the exterior stress comes below this value owing to the consumption of kinetic energy through the fracture. His presumption, however, seems to be somewhat hasty when viewed in the light of the results of our study.

The only condition under which a velocity decrease is observed by high-speed photography is when hackle marks appear, he states[17)]. In our case no hackle marks could be observed so far as the resolution by the unaided eye is concerned.

In the crack "B" of Fig. 5 the marked points are seen much scattered around the mean smoothed curve. This is due to the fact that we drew the curve so that its time derivative might be a monotonically decreasing function. However, it may be more natural to consider that the variation of the fracture velocity is not always monotonic on the way of crack propagation, for Schardin already found evidences of cracks stopping and starting again.

In Fig. 8 two photographs are given which were taken with a high-speed cine-micrograph[18)19)]. They also show the fracture of a thin plate (0.25 mm in thickness) of the microscope cover glass caused by the underwater spark. While in the first frame no radial cracks can be found, several cracks have developed in the second frame. As the framing rate in this case was 4.2×10^5 per sec and the magnification was $4.2\times$, the estimated velocity of the longest crack is higher than 2.2 km/sec, which agrees well with the value in Fig. 6.

In conclusion of these discussions, we should like to comment upon Hirata's remarks on the single-exposure photograph such as in Fig. 1. Though the duration of light output from the spark was much longer than his estimation probably because of the vaporization of the foil electrodes, it took time of the same order before radial cracks started from the margin of initially formed percussion cracks, so the two effects compensated each other and his estimation of fracture velocity did not differ so widely from the results of our investigations.

§ 4. Conclusion

While there has been a generally accepted view that the maximum fracture velocity of glass is quite independent of the method of application of impact, we have found, by measurement, a higher fracture velocity when the fracture was initiated by the underwater electric spark. Such supervelocity could be observed only transiently and was confined to the initial region around the origin of the cracks. The fracture velocity went down soon to the normal value, and after that gradually decreased. This phenomenon was found for the cracks which began to appear at a comparatively early stage of fracture. For the cracks developing later no such remarkable supervelocity was observed, though the gradual decrease of fracture velocity could be traced, contrary to the usual assumption made according to the results hitherto obtained from the usual high-speed photography.

We wish to express our best thanks to Prof. Moriso Hirata for his stimulating guidance and suggestions. Cordial thanks are also due to Mr. Taijirō Uchida of Nihon University who operated the Beckman & Whitley high-speed framing camera.

References

1) H. Schardin and W. Struth: Z. tech. Phys. **11** (1937) 474
2) ,, ,, : Glastech. Ber. **16** (1938) 219
3) F. E. Barstow and H. E. Edgerton: J. Amer. ceram. Soc. **22** (1939) 302
4) A. Smekal: Glastech, Ber. **23** (1950) 186
5) H. M. Dimmick and J. M. McCormick: J. Amer. ceram. Soc. **34** (1951) 240
6) N. Lundborg and C. H. Jahansson: Arkiv. Fysik **4** (1952) 555
7) D. G. Christie and H. Kolsky: J. Soc. Class. Tech. **36** (1952) 65
8) F. Kerkhof: Naturwiss. **40** (1953) 478
9) E. F. Ponce'et: *Fracturing of Metals*, Amer. Soc. for Metals (1948) 201
10) E. H. Yoffe: Phil. Mag. **42** (1951) 739
11) N. F. Mott: Engineering **165** (1948) 16
12) D. K. Roberts and A. A. Wells: Engineering **178** (1954) 820
13) M. Hirata: Oyo-butsuri (or J. Appl. Phys. Japan) **5** (1936) 482
14) M. E. Pugh *et al*: J. Appl. Phys. **23** (1952) 48
15) K. M. Baird: Nature **160** (1947) 24
16) H. Schardin: *Fracture*, Technol. Press of M. I. T. (1959) 297
17) ,, : Proc. Intern. Comm. Glass **1** (1954) 81
18) J. S. Courtney-Pratt and D. P. Thackeray: J. Photogr. Sci. **5** (1957) 32
19) S. Hyodo: Oyo-butsuri **29** (1960) 544

Short Notes

This section is intended to secure prompt publication of important discoveries in physics. The reports should not exceed 800 words in length. A figure of size 7 cm×7 cm will be counted as 150 words.

J. Phys. Soc. Japan **15** (1960) 2099

Fatigue Properties of Zinc Single Crystals and Polycrystals

Mikio Yamamoto and Jirô Watanabé

The Research Institute for Iron Steel and Other Metals, Tôhoku University
Sendai

(Received September 9, 1960)

Zinc single crystals with the [0001], $[10\bar{1}0]$, and $[11\bar{2}0]$ orientations and zinc polycrystals having the grain size of 130∼400 grains/cm², have been subjected to the cantilever rotating fatigue tests at room temperature. 99.99% pure zinc was used for the preparation of the specimens; single crystals were made by the Bridgman method, and polycrystals were produced by sucking up the melt into galss tubes, in argon atmosphere or vacuum. The specimens were polished carefully with emery papers 0∼0.5, then polished chemically with ethyl alcohol plus nitric acid plus hydroperoxide (1:1:1), and finally annealed at 350°C for 2 hours in the state sealed in a vacuum.

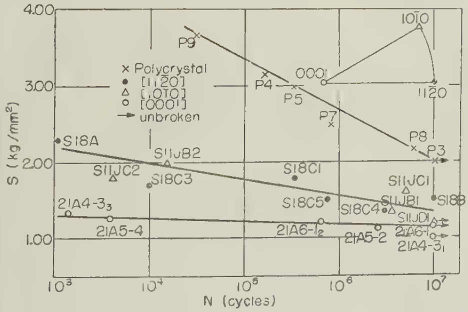

Fig. 1. Fatigue properties of zinc single crystals and polycrystals.

The maximum alternating bending strees, S, *versus* the logarithm of the number of cycles to fractur, N, curves are shown in Fig. 1, which indicates that the curves are linear and that both the slope of the curve and the fatigue strength are the greatest for polycrystals and become less in the order of $[11\bar{2}0]\cong[10\bar{1}0]$ and [0001] single crystals. The S–N curve for [0001] crystals lies nearly parallel to the abscissa, showing that the fatigue failure occurs in a very narrow stress range above which the crystals cleavage-fracture along the (0001) plane immediately after the load was applied. Similar S–N curves were observed in the low temperature fatigue tests on zinc and iron polycrystals which showed brittle fracture.[1] These facts may indicate that brittle or less plastic crystals show no or less fatigue. The S–N curves are nearly the same for $[11\bar{2}0]$ and $[10\bar{1}0]$ crystals, in which the plastic deformation proceeds by multiple slips of $\{11\bar{2}2\}[\bar{1}\bar{1}23]$ system as well as by twinning of the $\{10\bar{1}2\}[10\bar{1}\bar{1}]$ system and finally the failure occurs by stepped-like cleavage along the $\{10\bar{1}0\}$ planes of the matrix and along the {0001} planes of the twin.

The endurance limit, defined conviniently as the fracture stress at 10^7 cycles, is 2.0 kg/mm² for polycrystals, 1.30 kg/mm² for $[11\bar{2}0]$ and $[10\bar{1}0]$ crystals, and 1.10 kg/mm² for [0001] crystals. The comparison of these data with those of the statical strength, determined from tests made on single crystals of the same orientations as the fatigued ones, indicates that, in [0001] crystals, the normal stress operating on the (0001) cleavage plane at the endurance limit is about a half of the normal fracture stress observed in the statical test, but the resolved shear stress operating along the (0001) $[11\bar{2}0]$ direction at the endurance limit coincides very well with the critical resolved shear stress of the $(0001)[11\bar{2}0]$ slip in the static deformation. The latter relation also holds for the $\{11\bar{2}2\}[\bar{1}\bar{1}23]$ slip system and for the $\{10\bar{1}2\}[10\bar{1}\bar{1}]$ twinning in $[11\bar{2}0]$ and $[10\bar{1}0]$ crystals. These findings mean that the fatigue stress below which the specimen crystal never break equals to the minimum stress at which slip or twinning starts, in consistent with the observation by Hempel et al.[2] that the endurance limit of iron single crystals coincides with their yield strength.

It is to be added that the fatigue properties of polycrystals are independent on the grain size in accordance with the observation by Fegredo and Greenough.[3]

References

1) R. D. McCammon and H. M. Rosenberg: Proc. Roy. Soc., **A242** (1957) 203.
2) M. Hempel, A. Kochendörfer, and E. Hillnhagen: Arch. Eisenhütt., **28** (1957), 417.
3) D. M. Fegredo and G. B. Greenough: J. Inst. Metals, **87** (1958–59), 1.

J. PHYS. SOC. JAPAN **15** (1960) 2100

NMR of Co^{59} in Ferromagnetic Hexagonal Cobalt Metal

By Yoshitaka KÔI and Akira TSUJIMURA
Faculty of Engineering, Tokushima University, Tokushima, Japan
and Toshimoto KUSHIDA
Department of Physics, Faculty of Science, Hiroshima University, Hiroshima, Japan

(Received July 13, 1960)

The NMR in ferromagnet was first observed in *cubic* cobalt metal by Gossard and Portis[1]. The resonance frequency of Co^{59} is 213 Mc/sec at room temperature, and the frequency extrapolated to 0°K is 217.2 Mc/sec,[2,3] implying an effective field of 217.5×10^3 oersteds at the site of the nucleus. The field arises from the hyperfine interaction between the nucleus and both the core and the conduction electrons, as has been discussed by Marshall[4]. Therefore, the resonance frequency gives useful information about the electronic configuration. From this point of view, the resonance in *hexagonal* cobalt is very interesting. Portis and Gossard[3] searched for the resonance, but did not succeed probably because of the insufficient sensitivity of their spectrometer. The present authors have succeeded in observing the resonance, and it is the purpose of this note to report the results of the experiment.

The sample was about 0.5 gm. of finely divided and well annealed Co metal. A superregenerative spectrometer was used for detecting the resonance. It was frequency-modulated, and the resonance signal was displayed on an oscilloscope. As is well known, superregenerative scheme is adapted for detecting weak resonaeces because of its high sensitivity, but its serious disadvantage is that the apparent shape of the resonance signal varies appreciably with the condition of the quenching. Therefore, accurate determinations of the line width, the intensity, and the frequency were impossible.

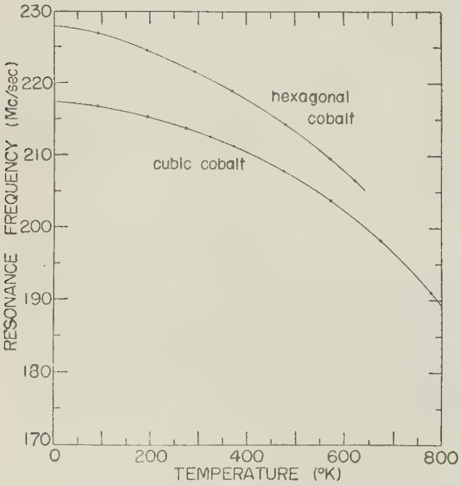

Fig. 1. The resonance frequency of Co^{59} as a function of temperature. The error in the determination of the frequency is ±0.5 Mc/sec for hexagonal cobalt.

The line width is estimated to be about 0.4 Mc/sec by comparing the signal with that in cubic cobalt[3]. The intensity is much weaker than that in cubic phase. It is obvious that a large anisotropy energy in hexagonal cobalt is responsible for this reduction in intensity. In fact, the intensity increases with increasing temperature and reaches the maximum at about 230°C where the anisotropy constant K_{u1} changes its sign[5]. The maximum intensity is about ten times as strong as that at room temperature.

The frequency-*versus*-temperature curve is shown in Fig. 1 together with the curve for cubic cobalt.[2,3,6] It is seen that the frequency decreases with increasing temperature more rapidly in hexagonal cobalt than in cubic one. The frequency extrapolated to 0°K is 228.0±0.5 Mc/sec, which corresponds to an effective field of $(228.4\pm0.5)\times10^3$ oersteds. This value is slightly larger than that determined by the specific-heat measurement at low temperature[7,8] and also than the value in cubic cobalt. The difference of about 11×10^3 oersteds between the values in hexagonal and cubic cobalt would be due to the contribution from the dipolar field of 3d electrons, though it is only one seventh of Marshall's estimation.

Co^{59} resonances in Co alloys are now being investigated.

References

1) A. C. Gossard and A. M. Portis: Phys. Rev. Letters **3** (1959) 164.
2) V. Jaccarino: Bull. Am. Phys. Soc. Ser. **II, 4** (1959) 461.
3) A. M. Portis and A. C. Gossard: J. Appl. Phys. **31** (1960) 205 S.
4) W. Marshall: Phys. Rev. **110** (1957) 1280.
5) W. Sucksmith and J. E. Thompson: Proc. Roy. Soc. **A, 225** (1954) 326.
6) Y. Kôi, A. Tsujimura and Y. Yukimoto: J. Phys. Soc. Japan **15** (1960) 1342.
7) V. Arp, D. Edmonds and R. Petersen: Phys. Rev. Letters **3** (1959) 212.
8) C. V. Herr and R. A. Erickson: Phys. Rev. **108** (1957) 896.

J. PHYS. SOC. JAPAN **15** (1960) 2101

Dielectric Constants and Loss Tangents of $(\text{Glycine})_3\text{H}_2\text{SO}_4$(TGS) at 3.3 KMc/s

By Eiji NAKAMURA and Jiro FURUICHI
Department of Physics, Faculty of Science, Hokkaido University, Sapporo Japan

(Received August 11, 1960)

Dielectric constants, ε', and loss tangents, $\tan\delta$, of TGS were measured at the 3.3 KMc/s from room temperature to about 80°C. The experimental method was almost the same as that of previous one[1]. But instead of the cylindrical cavity in the previous paper, a rectangular parallelepiped cavity resonating in TE_{105} mode was used. The electric field of this mode was given by

$$\left.\begin{aligned} &\boldsymbol{E}_x=\boldsymbol{E}_z=0\,, \\ &\boldsymbol{E}_y=a\sin\frac{\pi}{A}x\sin\frac{5\pi}{C}z \qquad (a\text{: constant})\,, \end{aligned}\right\} \quad (1)$$

where A and C are dimensions of the cavity along the x and z directions. If a cylindrincal dielectric specimen is placed at one of the positions at which the electric field is maximum, and if its sides are parallel to the electric field and both ends are in perfect contact with the cavity wall, the dielectric constant and the loss tangent of the specimen can be obtained by following expressions;

$$\left.\begin{aligned} &\varepsilon'=\frac{v_c}{2v_s}\cdot\frac{f_1-f_2}{f_2}+1\,, \\ &\tan\delta=\frac{1}{4\varepsilon'}\frac{v_c}{v_s}\left(\frac{1}{Q_2}-\frac{1}{Q_1}\right), \end{aligned}\right\} \quad (2)$$

as far as f_1-f_2 is small, where v_c, v_s, f and Q stand for the volume of the cavity, the volume of the specimen, resonant frequency and Q value of resonance, respectively, and also suffix 1 and 2 mean the empty cavity and cavity containing the specimen, respectively. Since the specimen is cylindrical, v_c/v_s equals the ratio of cross-sectional area of the cavity and the specimen perpendicular to the y direction. A resonant cavity of $7\times0.4\times30\,\text{cm}^3$ was used in our measurements. Loaded Q value of the empty cavity was about 1,400. The measured values of ε' and $\tan\delta$ did not depend on the specimen volumes.

Table I.

Specimen	Cross-sectional Area (cm²)
1*	0.86×10^{-4}
2	$4.8\ \times10^{-3}$
3	$7.8\ \times10^{-3}$
4	1.11×10^{-2}
5	2.30×10^{-2}

* Cross-sectional area of the specimen 1 is estimated from f_1-f_2.

Table I gives the dimensions of the used TGS specimens. All the specimens have square cross-sections, and monoclinic b-axis is orientated to the field direction. In Fig. 1 the temperature variations of both the dielectric constant and loss tangent along the b-axis are shown. The data at 1 Mc/s were obtained by using an inductive-ratio-arm bridge. The relaxation frequency of TGS at the Curie point has been reported to be 500 Mc/s[2]. However, the dielectric constants at 3.3 KMc/s were found not to be appreciably smaller in the measured temperature region except near the Curie temperature compared with the values at lower frequencies, and also the observed loss tangents were not very large in these regions. Hence, we may say that the dielectric dispersion is not effective even at 3.3 KMc/s in these temperature regions. We may expect, therefore, that relaxation frequency has a minimum at the Curie point, as was shown in Rochelle salt[3]. In order to verify this expectation, it would be necessary to extend the measurement to higher frequencies.

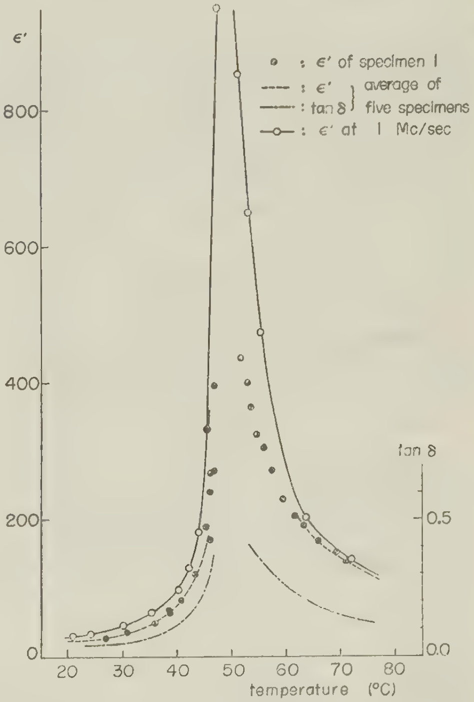

Fig. 1. ε' and $\tan\delta$ of TGS along the b-axis.

References

1) E. Nakamura and J. Furuichi: J. Phys. Soc. Japan **15** (1960) .
2) A. Lurio and E. Stern: J. Appl. Phys. **31** (1960) 1125.
3) H. Akao and T. Sasaki: J. Chem. Phys. **23** (1955) 2210.

J. PHYS. SOC. JAPAN **15** (1960) 2102

Some Properties of Titanium Sesquioxides Containing Vanadium Ions

By Tatsuyuki KAWAKUBO, Taketoshi YANAGI
and Shoichiro NOMURA

Physics Department, Tokyo Institute of Technology O-okayama, Meguro-ku, Tokyo

(Received August 22, 1960)

Experimental data have been presented that show marked changes in the electrical[1], magnetic[2] and thermal[3] properties of Ti_2O_3 in the temperature range of 160°~200°C. It has also been examined by X-ray diffraction studies[2] that the lattice parameters of Ti_2O_3, which has the corundum type structure with the trigonal symmetry, change abruptly in the same temperature region. The sudden change in magnetic susceptibility has suggested that an antiferromagnetic ordering would be present below the transition temperature, but any positive evidence for antiferromagnetism has not been obtained by a recent neutron diffraction study[4]. The present report is concerned with studies on Ti_2O_3-V_2O_3 solid solutions containing up to ten molar percents of V_2O_3.

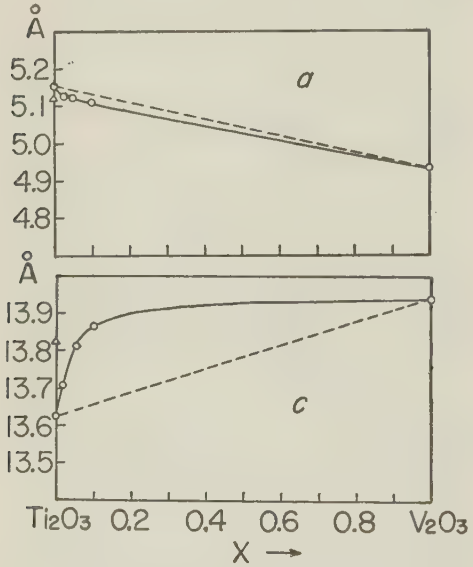

Fig. 1. Lattice parameters a and c of $(Ti_{1-x}V_x)_2O_3$ at room temperature. The values for Ti_2O_3 at 280°C[2] are given by the marks Δ and the values for V_2O_3 are due to ASTM Card.

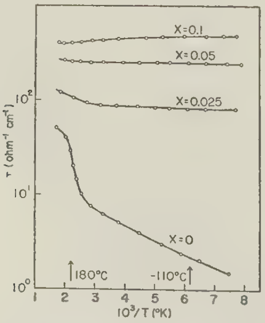

Fig. 2. Electrical conductivity of $(Ti_{1-x}V_x)_2O_3$ as a function of reciprocal temperature.

The specimens used were prepared by sintering the mixture of Ti, TiO_2 and V_2O_5 powders of desired ratio in a carbon resister vacuum furnace under the pressure of 10^{-4} mmHg, at 1450°C, for about 5 hours. The hexagonal lattice parameters a and c for $(Ti_{1-x}V_x)_2O_3$ at room temperature are shown in Fig. 1. An outstanding fact found in our work is that the lattice parameters observed in the solid solution series show a great deviation from that of Vegard's law and their values lie nearly to those of pure Ti_2O_3 obtained above the transition temperature. A marked difference was also observed between the electrical conductivities of pure Ti_2O_3 and its solid solutions. The result is shown in Fig. 2. The electrical conductivity of pure Ti_2O_3 shows a characteristics of semiconductor and has a stepwise increase near 180°C. This anomalous feature, when some amount of Ti^{3+} ions in Ti_2O_3 are replaced by V^{3+} ions, becomes extremely indistinct and the semiconducting character of the electrical conduction changes to the metallic one. For $Ti_{1.8}V_{0.2}O_3$, the electrical conductivity apparently decreases with increasing temperature.

It may be said from these expeaimental facts that the transition observed in pure Ti_2O_3 is sensitively affected by the existence of a small content of V^{3+} ions. Assuming one electron per cation to be available in stoichiometric Ti_2O_3, we may say that a small deviation of the number of electrons in cation from one causes a large effect on the properties of Ti_2O_3. Further, the facts observed in our study seem to favor a model proposed by Goodenough[5], which gives an idea of the electron pair bond formation between cations in Ti_2O_3 at low temperatures.

The authers wish to express their sincere thanks to Professor Shozo Sawada for his helpful discussions and continual encouragement.

References

1) F. J. Morin: Phys. Rev. Letters **3** (1959) 34.
2) A. D. Pearson: J. Phys. Chem. Solids **5** (1957) 316.
3) B. F. Naylor: J. Amer. Chem. Soc. **68** (1948) 1077.
4) G. Shirane, S. J. Pickart and R. Newnham: J. Phys. Chem. Solids **13** (1960) 167.
5) J. B. Goodenough: Phys. Rev. **117** (1960) 1442.

J. PHYS. SOC. JAPAN **15** (1960) 2103

Photoconductivity of Cu-activated Cadmium Sulphide-Selenide

By Sumitada ASANO

Department of Physics, Faculty of Science, Okayama University

(Received September 24, 1960)

Spectral response of photoconductivity of CdS has been extensively investigated. On the other hand, we know that the emission band and absorption edge of ZnS phosphor shift towards longer wave-lengths by adding increasing quantity of CdS, ZnSe or CdSe1). In this paper we report the spectral response of photoconductivity of Cu-activated Cd(S:Se) at room temperature. The starting materials, pure CdS and CdSe powder, were prepared by careful procedures mentioned in the previous paper2). The mixture of CdS and CdSe powder was dried at 110°C after adding 5×10^{-2} mole % of $CuCl_2$ as activator and 2 mole % of KCl as co-activator. Then it was put on a silica boat and fired in a silica tube for 15 minutes at 1000°C in nitrogen atomosphere.

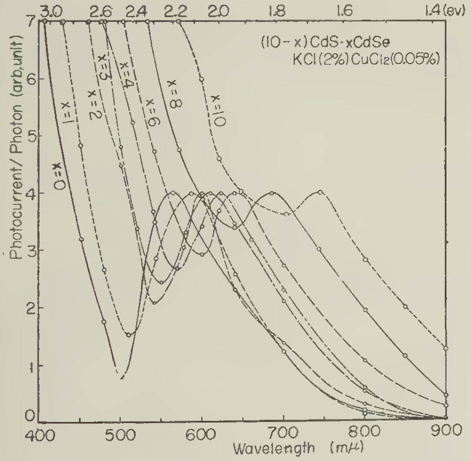

Fig. 1. Spectral response of photoconductivity. The peak of each sample is arranged to have the same height.

The sample was ground and settled on a conducting glass plate by sedimentation in ethyl-alcohol without any binder, and pressed to a flat metal sheet mounted in an evacuated glass vessel so that the sample was sandwitched between the conducting glass plate and the metal sheet. The sample then became a uniform layer about 0.3 mm in thickness. A uniform light beam from a tungsten lamp was led onto the conducting glass plate through a glass monochromator. The spectral energy distribution of the beam incident on the sample through the conducting glass had been measured previously by a vacuum thermocouple. A DC voltage of several volts was applied across the sample from a battery source. The results are shown in Fig. 1.

As is shown in the figure, the peak due to copper shifts regularly towards longer wave-lengths, as in the case of the emission band in Cu-activated Zn(S:Se) phosphors. The trough observed between the fundamental and copper absorption bands becomes shallower with increasing proportion of CdSe. Besides, the spectral reflectance of each sample was measured in comparison with standard MgO powder by using the same apparatus as in the reference cited3). Then the value of forbidden gap of each sample was determined from the position of absorption edge in the reflectance spectra. The average rate of reduction in the forbidden gap is about 0.69×10^{-2} eV/mole % of CdSe, whereas that in the energy gap for copper absorption obtained from Fig. 1 is about 0.52×10^{-2} eV/mole % of CdSe. These facts show that the forbidden gap is decreased more rapidly than the energy gap for copper absorption and that the ground state of copper, in the samples containing large proportion of CdSe, tends to be immerged in the valence band4).

The response time in the decay of photocurrent after sufficient irradiation at the wave-length of copper peak was measured for various irradiances using an electromagnetic oscillograph. The response time t_0 of the sample approximately obeys the relation

$$t_0=kL^{-n}\,,$$

where L is the photon density incident upon the sample, k the constant characteristic to the sample and $n\simeq0.5$. k decreases rapidly with increasing proportion of CdSe. This will be attributed mainly5) to the fact that the thermal depth of shallow traps concerned in current decay decreases and trapped electrons may be easily released into the conduction band with increasing proportion of CdSe. This fact is observed also in thermoluminescence experiments on (Zn:Cd)S and Zn(S:Se) phosphors6).

Details will be published later.

References

1) H. W. Leverents: *Introduction to Luminescence of Solids* (John Wiley and Sons, Inc., N.Y. 1950) pp. 196–205.
2) S. Asano: Science of Light **4** (1955) 32, 48.
3) Jh. P. J. Botden and F. A. Kroeger: Physica **15** (1949) 747.
4) M. Avinor and G. Meijer: J. Chem. Phys. **32** (1960) 1456.
5) C. Kittel: *Introduction to Solid State Physics* (John Wiley and Sons, Inc., N.Y. 1956) p. 518.
6) W. Hoogenstraaten: Philips Res. Rept. **13** (1958) pp. 75–77.

J. Phys. Soc. Japan **15** (1960) 2104

On the Ferrimagnetic Resonance of Europium Iron Garnet

By W. P. Wolf
Clarendon Laboratory, Oxford, England

(Received June 22, 1960)

Recent microwave experiments on polycrystalline europium iron garnet (EuIG) have shown⁽¹⁾ that this substance has a rather low *g*-value, (1.34 at 300°K), which varies with temperature. The purpose of this note is to account semi-quantitatively for the observed magnitude of *g* and its temperature variation.

In any strongly coupled ferrimagnetic system the effective *g*-value which determines the resonance condition, is given by⁽²⁾

$$g_{eff}=\frac{2mc}{e}\frac{\boldsymbol{M}}{\boldsymbol{A}}\quad,$$

where $\boldsymbol{M}$ is the total magnetic moment, in units of Bohr magnetons per molecule, and $\boldsymbol{A}$ is the total angular momentum, in units of $h/2\pi$ per molecule. The magnitude of $\boldsymbol{M}$ in EuIG and its variation with temperature has been measured by Pauthenet⁽³⁾, and it has recently been explained theoretically.⁽⁴⁾ The theory showed that $\boldsymbol{M}$ can be accounted for in terms of the algebraic sum of the magnetic moment of the Fe^{3+} sublattices behaving very much as in yttrium iron garnet (YIG), and an antiparallel magnetic moment due to the Eu^{3+} ions. The latter arises from an exchange interaction with the Fe^{3+} ions as in other substances, but with the difference that it is almost entirely of an *induced* nature, due to off diagonal matrix elements from the spectroscopic ground state $J=0$ to the first excited state $J=1$. This mechanism gives rise to an induced magnetic moment because $\boldsymbol{L}+2\boldsymbol{S}$ is not a constant of the motion, but it does not produce any angular moment, which is proportional to $\boldsymbol{L}+\boldsymbol{S}$. Therefore we would expect $\boldsymbol{A}$ in EuIG to be very similar to its magnitude in YIG, in which it has value

$$A_{\mathrm{YIG}}=\frac{2mc}{e}\cdot\frac{M_{\mathrm{YIG}}}{g_{\mathrm{YIG}}}\quad,$$

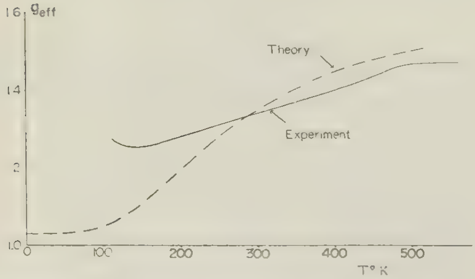

Variation of the resonance *g*-value with temperature. Solid line, experimental results⁽¹⁾; broken line, theoretical results calculated from $2M_{\mathrm{EuIG}}/M_{\mathrm{YIG}}$, taken from curves 1 and 2 of reference (4).

where g_{YIG} is very close to 2.⁽⁵⁾ Thus the *g*-value in EuIG should be close to $2M_{\mathrm{EuIG}}/M_{\mathrm{YIG}}$.⁽⁶⁾ Using curves 1 and 2 in Figure 1 of reference 4, this gives the broken line shown in the Figure. The agreement with the experimental results is quite reasonable, in view of the simplifying assumptions, and the fact that the theory contains no adjustable constants other than the coefficient a which normalizes curve 2 at $T=0°K$.

At the lowest temperatures there is a systematic divergence which is not explained. It may be connected with the observed broadening and doubling of the lines, which were ascribed to anisotropy effects in the polycrystalline material.⁽¹⁾ If this is so the theory should apply better to single crystal data.⁽⁷⁾ Another possible explanation for the discrepancy might be the effect of rare earth or other impurities, either in the resonance samples or in Pauthenet's magnetic moment samples.

The present theory is very crude. Improvements could be made a) by allowing for the small amount of angular momentum due to the $J=1$ state in Eu^{3+}; b) the change in the Fe^{3+} sublattice magnetization, and hence $\boldsymbol{A}$, due to the back-action of the Eu^{3+} ions on the Fe^{3+} sublattices; c) inadebuacies of the molecular field theory, especially at the highest and lowest temperatures. All these effects are potentially quite important (~10%), but the considerable complications do not seem worthwhile at present in view of the reasonable agreement of the simple theory.

The author would like to thank Professor J. H. Van Vleck for stimulating discussions.

References

1) Y. Shichijo, T. Miyadai and H. Takata: J. Phys. Soc. Japan **15** (1960) 530.
2) N. Tsuya: Progr. Theor. Phys. **7** (1952) 263. R. K. Wangsness: Phys. Rev. **91** (1953) 1085.
3) R. Pauthenet: Ann. de Chim. et de Phys. **3** (1958) 424.
4) W. P. Wolf and J. H. Van Vleck: Phys. Rev. **118** (1960) 1492.
5) J. F. Dillon Jr: Phys. Rev. **105** (1957) 759.
6) This form is superficially similar to the recent explanation of *g*-values in other rare earth garnets (C. Kittel, Phys. Rev. **115** (1959), 2587, but its origin is quite different. In other rare earths the angular momentum is quenched by rapid relaxation, while in Eu^{3+} it is suppressed by the spin-orbit coupling.

J. PHYS. SOC. JAPAN **15** (1960) 2105∼2106

Reflection and Absorption Spectra of LiF in the Extreme Ultraviolet Region

By Riso KATO, Kaizo NAKAMURA,
Atsuo MATSUI and Yoichi UCHIDA

Depertment of Physics, Faculty of Science,
Kyoto University.

(Received September 10, 1960)

Fundamental optical absorptions of alkali halides in the extreme ultraviolet region have been investigated by several authors$^{1)-3)}$. The absorption spectra were measured on evaporated thin films because of their large absorption coefficients in the region. For LiF, however, the absorption method cannot be used to investigate the fundamental optical absorption for the lack of appropriate substrates, and the reflection method is expected to be the most useful for this purpose.

Thus, in the present experiment the reflection spectrum of LiF was measured. A single crystal of LiF had been kindly offered by Prof. Pringsheim, and its newly cleaved surface was used. The cryostat for reflection measurements is shown schematically in Fig. 1. It is a modified one of Walker's type$^{4)}$. The vacuum monochromator$^{5)}$ used was the Seya-Namioka type. Since it has no window in the optical path, measurements could be carried out down to 800 Å with the band width of about 2 Å.

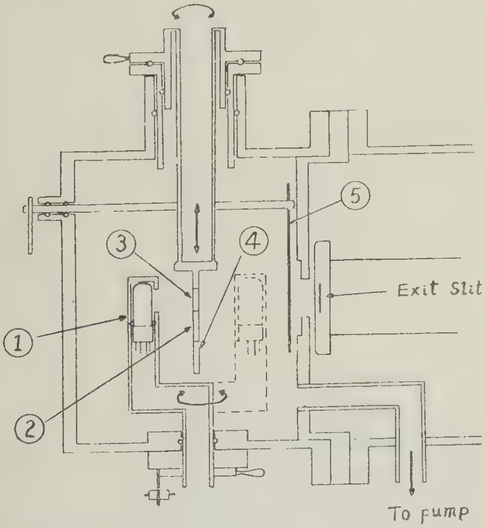

Fig. 1. Shematic diagram of the cryostat for reflection measurements.
(1): photomultiplier rotatable around the sample holder.
(2): sample holder movable along the vertical axis.
(3): window for sample.
(4): window for reference.
(5): turret with several filters.

The obtained reflection spectrum is shown by curve (1) in Fig. 2. Curve (2) shows the absorption spectrum of the same crystal with the correction of reflection effect. The reflection measurements were carried out with the incident angle of 15° at room temperature. The values of reflectivity may contain the experimental errors of about 10% which might arise from mechanical operation of the cryostat and from incompleteness in the correction of stray light. But the tendency of the curve is not affected by the errors, because the reflection measurements were made by recording each about 100 Å segment of the spectrum.

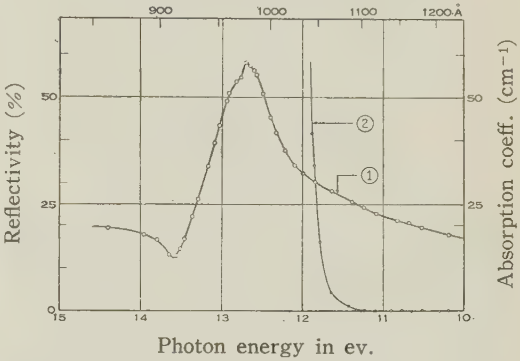

Fig. 2. Reflection and absorption spectra of LiF single crystal measured at room temperature.
Curve (1): reflection spectrum.
Curve (2): absorption spectrum.

As seen in curve (1), a peak was found at 12.7 ev and a "shoulder" was observed at about 13.8 ev. In accordance with the fact$^{2)}$ and the theoretical consideration that reflection peaks nearly coincide with absorption peaks, the newly found 12.7 ev peak and 13.8 ev "shoulder" in the reflection spectrum of LiF at room temperature are assigned to the exciton peak and the onset of the band-to-band transition respectively. Furthermore, as seen in curve (1), the shape of the reflection spectrum near the peak suggests that the exciton band in LiF has a mutiplet structure which will be confirmed with success in measurements at low temperatures.

References

1) R. Hilsch and R.W. Pohl: Z. Physik **59** (1930) 812, E. G. Schneider and H.M. O'Bryan: Phys. Rev. **51** (1937) 293, W. Martienssen: J. Phys. Chem. Solids **2** (1957) 257, J. E. Eby, K. J. Teegarden and E. B. Dutton: Phys. Rev. **116** (1959) 1009.
2) P. L. Hartman, J. R. Nelson and J. G. Siegfried: Phys. Rev. **105** (1957) 123, E. A. Taft

and H. R. Phillip: J. Phys. Chem. Solids **3** (1957) 1.
3) J. N. Ferguson, Jr: Phys. Rev. **66** (1944) 220. J. W. Taylor and P. L. Hartman: Phys. Rev. **113** (1959) 1421.
4) W. C. Walker, O. P. Rustgi and G. L. Weissler: J.O.S.A. **49** (1959) 471.
5) Y. Uchida *et al.*: J. Appl. Phys. Japan **29** (1960) 492.

J. PHYS. SOC. JAPAN **15** (1960) 2106~2107

The Effect of Plastic Deformation on the Cluster Formation in an Al-Cu 4% Alloy

By Keisuke MATSUURA and Shigeyasu KODA

The Sesearch Institute for Iron,
Steel and Other Metals,
Tohoku University, Sendai

(Received September 22, 1960)

According to recent investigations1),2) the high rate of cluster formation in Al-Cu alloys quenched from a temperature of a uniform solid solution range is ascribed to the quenched-in vacancies. In the present work, the effect of plastic deformation on such a clustering of solute atoms is examined with a 4% Cu alloy by measuring the electric resistivity, and the roles of dislocations and vacancies in the clustering process are also discussed. The polycrystalline specimens, 0.7 mm in diameter, were water-quenched or air-cooled after being solution-treated between 520 and 530°C, and were dipped without delay in liquid nitrogen. After being streched to various extents (0~17.8%) in liquid nitrogen, they were transferred to a bath of constant temperature to make ageing. The determination of the electric resistance at any stage of ageing process was carried out in a liquid nitrogen bath in order to suppress any further progress of ageing during resistance measurement. Some of the results are shown in Fig. 1, where ΔR is the increase of resistivity during ageing and R_0 the initial resistivity just after water-quenching or air-cooling. The following tendencies are recognized.

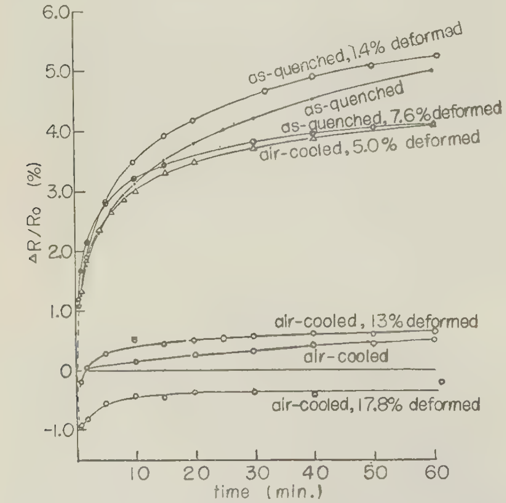

Fig. 1. Change of electric resistivity on ageing at 0°C.

(1) Both for water-quenched and air-cooled specimens, resistivity increases during ageing process after plastic deformation if the latter is small as in the case of several percent or less elongation. Such an increase is ascribed to cluster formation. However, in air-cooled specimens a decrease of resistivity is observed at the beginning of ageing after large deformation such as elongation exceeding about 13%. This decrease may be due to the annihilation of defects produced by plastic deformation.

(2) Except such an initial decrease of resistivity the plastic deformation after water-quenching or air-cooling increases the increasing rate of resistivity in the early stages of ageing. In air-cooled specimens the effect is more evident.

(3) On the other hand, the rate of increase in resistivity of deformed specimens decreases with ageing time more rapidly than that of the undeformed water-quenched one. This rapid decrease becomes more pronounced with increasing amount of elongation.

(4) The initial rate of resistivity increase in an air-cooled, 4-5% elongated specimen is about the same as that of a water-quenched. The results obtained for both specimens in the range of ageing temperature between 18 and −30°C were compared. From a curve of $\{d(\Delta R)/R_0 dt\}_{t=0}$ plotted against $1/T$ the activation energy of about the same value 0.47~0.52 eV was obtained for both cases. These results suggest that the initial rate of cluster formation is enhanced by the excess vacancies produced by plastic deformation. On the other hand, the fact that the rate decreases rapidly with ageing time for deformed specimens may be explained by the fact that dislocations are the effective sinks of excess vacancies3): that is, the increase in dislocation density leads to the rapid annihilation of excess vacancies and, therefore, to the rapid decrease of the rate of clustering. However, there may be another possibility that the clusters formed at distorted regions are stable and their development is hindered, as pointed out by Graf and Guinier4). It has been reported that the cluster formation is hindered by prestrain after quenching5),6). On the other hand, it is known that small clusters form immediately after or during plastic deformation at

room temperatures[7),8)]. All these facts which seem inconsistent at first sight fully confirm to the results obtained in the present investigation.

References

1) W. Desorbo, H. N. Treaftis and D. Turnbull: Acta Met. **6** (1958) 401.
2) T. Federighi: Acta Met. **6** (1958) 379.
3) M. Winterberger: Acta Met. **7** (1959) 549.
4) R. Graf and A. Guinier: Compt. Rend. **238** (1954) 2175.
5) J. M. Silcock: Phil. Mag. **4** (1959) 1187.
6) Y. Murakami and O. Kawano: Japan Inst. light Metals **10** (1960) No. 2, 11.
7) K. Matsuura, Y. Hamaguchi and S. Koda: J. Phys. Soc. Japan **12** (1957) 1424.
8) K. M. Carlsen and R. W. K. Koneycombe: J. Inst. Metals **83** (1954–55) 449.

J. PHYS. SOC. JAPAN **15** (1960) 2107

Distribution Coefficient of Zinc in Gallium Arsenide

By Akikazu SHIBATA

Sony Coporation, Shinagawa, Tokyo

(Received August 24, 1960)

The distribution coefficients of many substances in Ge and Si are reported though, not so many are reported in compound semiconductors. During the course of study of intermetallic semiconductor compounds in our laboratory, the distribution coefficient of Zn in GaAs was obtained through the impurity distribution study in GaAs ingots. The well-known formula giving the impurity distribution of a solidified ingot in the case of normal freezing was the basis of the determination of the distribution coefficient in this work; that is[1)],

$$C^S(g)=KC_0^L(1-g)^{K-1}\ ,$$

therefore,

$$\log C^S(g)=(K-1)\log+\log KC_0^L\ ,$$

where g, the fraction of the melt which has been solidified; C^S, the impurity concentration of the solid as a function of the fraction; C_0^L, the original impurity concentration involved in the melt; and K, the distribution coefficient. Thus, by plotting $\log C^S(g)$ vs $\log(1-g)$, a straight line can be obtained, and the tangent of the line, δ, gives the distribution coefficient as $K=(1+\delta)$.

Among the possible dopants in Group III–V intermetallic compounds, Zn and Cd are the most favorable dopants for p-type materials and Se and Te for n-type. In this work, the distribution coefficient of Zn in GaAs, which has not yet been reported so far as the author awares, was determined.

A vacuum sealed quartz tube, $ID=16$ mm, containing about 15 g of Zn doped GaAs was held in a horizontal furnace and kept at about 1280°C for several hours. The uniform distribution of the impurity concentration in the melt was not examined, however, the uniformity was assumed. The melt was then pulled out from the furnace to be solidified with a speed of 25 mm/hr. The obtained ingot was a large grain polycrystal and had a length of about 65 mm. The direction of the crystal growth was not examined.

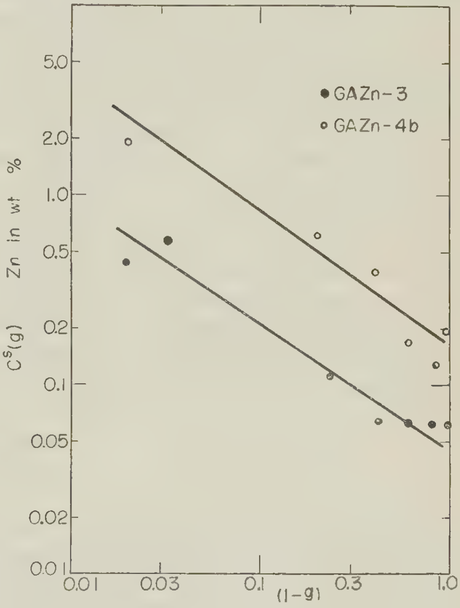

Fig. 1. Zn distribution as a function of position.

The initial concentrations of Zn in the two samples used, GAZn-3 and GAZn-4b, were 0.45 and 0.9 wt% respectively. Six to seven specimens were cut from each ingot and the Zn concentration was determined chemically using Polarography Method.

From the results, $\log C^S(g)$ vs $\log(1-g)$ were plotted which are shown in the Fig. 1. Two best fit straight lines were drawn and the tangents of the lines were determined graphically. The resultant tangents were -0.68 and -0.70 for GAZn-3 and GAZn-4b respectively. The distribution coefficients were then determined as 0.32 and 0.30 respectively. Consequently, the distribution coefficient of Zn in GaAs was concluded as 0.31.

Reference

1) A. Hayes, and J. Chipman, J. Trans. AIME, **135** (1939) 85.

J. PHYS. SOC. JAPAN **15** (1960) 2108~2109

Interaction Types and Selection Rules in Baryon Processes

By Seitaro NAKAMURA

Department of Physics, Faculty of Science, University of Tokyo, Tokyo, Japan

(Received September 13, 1960)

In the previous letter[1)], we have introduced an interaction Hamiltonian of the strong interaction for baryons by assuming new symmetry—"κ-charge independence"—which is an extension of the idea of symmetrical meson theory. κ-charge of baryons is defined from the 2×2 Pauli matrices: $Q_\kappa=(1+\kappa_3)/2$, just as electric charge of nucleons is defined from the ordinary τ matrices, $Q_e=(1+\tau_3)/2$. We assign $\kappa_3=1/2$ for the Ξ-particles and nucleons, $\kappa_3=-1/2$ for the Σ and Λ-particles, just as we assign $\tau_3=1/2$ for proton and $\tau_3=-1/2$ for neutron. Instead of using the ordinary isospin space, we adopt a three dimensional charge space, called N-space, where electric charge is defined by the relationship $Q_e=N_3$. This is not identical with the M-space representation proposed by d'Espagnat, Prentki and Salam[2)], and by Takeda[3)], because strangeness is not used in our representation. In order to give a Hamiltonian symmetric in κ-space and also in N-space, (both of which are three dimensional and orthogonal to each other,) we assume the existence of sixteen kinds of mesons which mediate the strong interactions among baryons. They are in the states with $Q_\kappa=\kappa_3=1, 0, -1$ ($|\kappa|=1$) and $Q_\kappa=\kappa_3=0$ ($|\kappa|=0$), to each of which there correspond four values $Q_e=N_3=1, 0, -1$ (triplet) and 0 (singlet). It is shown that kaons correspond to mesons with $Q_\kappa=\pm1$, strangeness-two mesons to those with $Q_\kappa=0$ ($|\kappa|=1$) and pions to those with $Q_\kappa=0$ ($|\kappa|=0$). We assume the existence of two kinds of kaons, the one coupling the Ξ-particle with the Σ and Λ-particles and which we denote L-kaons, and the other coupling nucleons with the Σ and Λ-particles and which we denote K-kaons.

Now we shall determine the interaction types by introducing two assumptions which follow: i) Parity is conserved in the strong interactions. ii) Invariance under time-reversal of the Wigner type is required. As a result, the interaction Hamiltonian for $H_{\Sigma\Sigma\pi}$ (given in (14) in the previous letter[1)]) will be cancelled out by adding the hermitian conjugate part.

$$H_{\Sigma\Sigma\pi}=0\,,\qquad H_{\Sigma\Lambda\pi}=0\,,\qquad g'\text{: pure imag.}\qquad \Omega_{\Sigma\Sigma\pi}=\gamma_5, \gamma_5\gamma_\mu\,;\qquad \Omega_{\Sigma\Lambda\pi}=\gamma_5, \gamma_\mu, \gamma_5\gamma_\mu\,.$$

$$H_{\Sigma\Sigma\pi}\equiv g'\overline{\boldsymbol{\Sigma}}\times\Omega_{\Sigma\Sigma\pi}\boldsymbol{\Sigma}\cdot\pi+\text{h.c.}\,;\qquad H_{\Sigma\Lambda\Pi}\equiv g'(\overline{\boldsymbol{\Sigma}}\Omega_{\Sigma\Lambda\Pi}\Lambda\cdot\pi+\overline{\Lambda}\Omega_{\Sigma\Lambda\Pi}\boldsymbol{\Sigma}\cdot\pi)+\text{h.c.}\,.$$

Thus we have not global symmetry[4)] in the pion-baryon interaction. Analyses[5)-6)] on the branching ratios for the inelastic scattering of K^--meson by proton seem to support the present result.

With regard to the other interactions, we are open to many possibilities, depending on the relative parities of baryons and the intrinsic parities of mesons. For instance, we may consider the following two possibilities for the strong interaction between Σ and Λ through D-mesons.

A) $H_{\Sigma\Sigma D}=0\,,\qquad H_{\Sigma\Lambda D}\neq0\,,\qquad g\text{: pure imag.}\qquad \Omega_{\Sigma\Sigma D}=\gamma_5, \gamma_5\gamma_\mu\,;\qquad \Omega_{\Sigma\Lambda D}=\gamma_5, \gamma_\mu, \gamma_5\gamma_\mu\,.$

B) $H_{\Sigma\Sigma D}=0\,,\qquad H_{\Sigma\Lambda D}=0\,,\qquad g\text{: pure imag.}\qquad \Omega_{\Sigma\Sigma D}=\gamma_5, \gamma_5\gamma_\mu\,;\qquad \Omega_{\Sigma\Lambda D}=1\,.$

$$H_{\Sigma\Sigma D}\equiv g\overline{\boldsymbol{\Sigma}}\times\Omega_{\Sigma\Sigma D}\boldsymbol{\Sigma}\cdot\boldsymbol{D}+\text{h.c.}\,;\qquad H_{\Sigma\Lambda D}\equiv g(\overline{\boldsymbol{\Sigma}}\Omega_{\Sigma\Lambda D}\Lambda\cdot\boldsymbol{D}+\overline{\Lambda}\Omega_{\Sigma\Lambda D}\boldsymbol{\Sigma}\cdot\boldsymbol{D})+\text{h.c.}\,.$$

For the case A), we must find the selection rule to prove the metastability of $D^\pm$-meson, lest the Ξ-particle should be unstable against the decay process $\Xi\rightarrow\pi+N$. For the case B), we have no trouble about the metastability of $D^\pm$-mesons as the strangeness-two mesons recently reported.

From the final expressions for the interaction Hamiltonians (9)-(12) in the previous letter[1)], with the present assumptions i), ii) and B), we can infer the selection rules to determine the baryon-processes.

For the strong interactions:

(I) $\Delta n_1=0\,,$ (II) $\Delta n_2=0\,,$ (III) $\Delta n_3=0\,,$

where

$$n_1=n_N+n_\Sigma+n_\Lambda+n_\Xi\,,$$

$$n_2=n_N+n_K+n_\Xi+n_L\,,$$

$$n_3=n_N+n_K+2n_D-n_\Xi-n_L\,.$$

Here n_N, n_Σ, n_Λ and n_Ξ are the particle numbers for the respective particles; for mesons we assign:

$n_K=+1\quad(K_+{}^+, K_+{}^0)\,,\qquad n_L=+1\quad(L_+{}^-, L_+{}^0)\,,$

$=-1\quad(K_-{}^-, K_-{}^0)\,,\qquad =-1\quad(L_-{}^+, L_-{}^0)\,,$

$n_D=+1\quad(D^+)\,,\qquad n_D=0\quad(D^0)\,,\qquad n_D=-1\quad(D^-)\,.$

The selection rule (I) implies conservation of the baryon number. The selection rule (II) denotes conservation of κ-charge. The selection rule (III) corresponds to conservation of strangeness strictly when we are not involved with strangeness-two particles. It is remarkable, however, to have reached the law of strangeness in this case, because we did not start by assuming strangeness as a quantum number of particles. On the other hand, the present theory introduces a new selection rule of conservation of κ-charge in (II). For instance, the process $\Xi^- + P \to \Lambda + \Lambda$ is forbidden by (II), but it is allowed by the strangeness rule alone. As a result, we are led to assume the necessary existence of Ξ-hyperfragments, which from the strangeness rule alone should decay instantaneously.

References

1) S. Nakamura: J. Phys. Soc. Japan **15** (1960) 2122.
2) B. D'Espagnat, J. Prentki and A. Salam: Nuclear Phys. **5** (1958) 447.
3) G. Takeda: Prog. Theor. Phys. **19** (1958) 631.
4) M. Gell-Man: Phys. Rev. **106** (1957) 1296.
5) K. Kawarabayashi: Prog. Theor. Phys. **20** (1958) 117. K. Kawarabayashi and T. Sawada: ibid. **23** (1959) 451.
6) A. Salam and P. T. Mathews: Kiev Conference on High Energy Physics, 1959.
7)

J. PHYS. SOC. JAPAN **15** (1960) 2109

The Magnetic Properties of NiBr$_2$

By Ichiro TSUBOKAWA

The Research Institute for Iron, Steel and Other Metals, Tohohu University, Sendai, Japan

(Received September 8, 1960)

It has been shown by several authors[1),2)] that the hexagonal di-chloride of iron, cobalt and nickel show interesting magnetic properties, meta-magnetism. Also the antiferromagnetic spin ordering of these compounds was ascertained by means of neutron diffraction experiments[3)]. During the course of the investigation of bromides of the iron group elements, the present author will report the magnetic properties of NiBr$_2$.

A specimen of NiBr$_2$ was prepared by the same method described in the previous paper[4)]; powder nickel (99.9%) was heated to about 720°C in bromine vapor (99.9%). The compound thus obtained had an appearence of a thin hexagonal-like plate and tinged red color. It was confirmed by Debye-Scherrer X-ray photographs that the crystal structure of the compound was the CdCl$_2$ type.

The magnetic susceptibility of the compound obtained was measured at intervals from the liquid helium point to room temperature by using a magnetic balance. The result is shown in Fig. 1. The temperature variation of the susceptibility shows antiferromagnetic behavior having a maximum susceptibility at a temperature close to 60°K. This temperature is considered to be the antiferromagnetic Néel point. The inverse susceptibility above the Néel point is also plotted in Fig. 1. An asymptotic Curie temperature θ_p was estimated as -20°K from $1/\chi - T$ relation. Now, Kanamori[5)] suggested that the superexchange interaction in the c-plane of the hexagonal structure containing Ni^{2+} ions is ferromagnetic. Hence the superexchange interaction along the c-axis is antiferromagnetic, and is weak compared to the former, because the metal ions are separated by two layers of anions. On the other hand, for NiCl$_2$, $T_N = 52$°K $\theta_p = 68.2$°K$>$0°K. Consequently, the antiferromagnetic exchange interaction along the c-axis of NiBr$_2$ is stronger than that of NiCl$_2$.

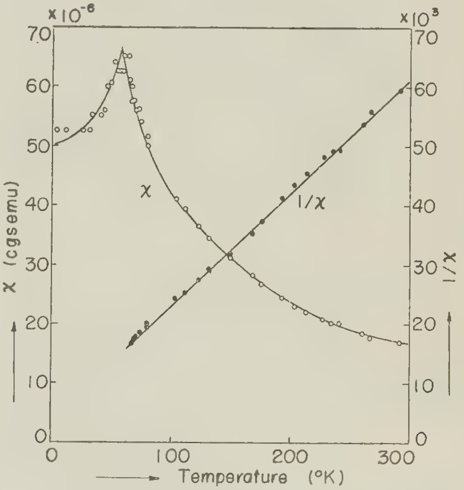

Fig. 1. Susceptibility and inverse susceptibility vs. temperature curves.

From the relation $1/\chi - T$, we estimated the Curie constant C_M and the effective Bohr magneton number p_{eff} as 1.12 and $3.0\mu_B$ respectively. The spin quantum number S is also obtained as 2.1/2 assuming that the Landé factor is two. This value corresponds to S of the Ni^{2+} ion.

References

1) W. J. de Haas and B. N. Schultz: Physica **6** (1939) 481.
2) Starr, Bitter and Kaufman: Phys. Rev. **58** (1940) 977.
3) M. K. Wilkinson, J. W. Cable, E. O. Wollan and W. C. Koehler: Phys. Rev. **113** (1959) 497.
4) I. Tsubokawa: J. Phys. Soc. Japan **15** (1960) 1664.
5) J. Kanamori: J. Phys. Chem. Solid **10** (1959) 87.

J. PHYS. SOC. JAPAN **15** (1960) 2110~2111

Infrared Absorption of Electrons Through Piezoelectric Scattering

By Toshio TANAKA
Department of Applied Physics,
Faculty of Engineering,
Tokyo University, Tokyo

(Received September 1, 1960)

The absorption of a photon by free carriers cannot occur unless the free carriers gain the momentum by collisions with some lattice imperfection. The infrared absorption due to the interactions of electrons with lattice vibtrations of acoustic mode was treated first by Fan, Spizer and Collins[1] basing on the deformation potential model and thereafter has been analyzed in more detail by many authors[2],[3], indicating that the absorption coefficient varies with the photon frequency as

$$\alpha\propto\omega^{-n}\,,$$

where

$$n=3/2 \text{ for } \hbar\omega\gg kT\,,\qquad n=2 \text{ for } \hbar\omega\ll kT\,.$$

Recently the results measured by Thomas[4] in ZnO crystals represent that the absorption coefficient shows a stronger frequency dependence.

Here, we shall consider the absorption of an infrared photon by conduction electron in crystals with wurtzite structure through piezoelectric scattering.

In ionic crystals with wurtzite structure, which show piezoelectric effects, the acoustic lattice vibrations can produce an electric polarization which scatters electrons. The polorization is

$$\boldsymbol{P}=\boldsymbol{P}_{\text{piezo}}+\alpha\boldsymbol{E}=\boldsymbol{P}_{\text{piezo}}-4\pi\alpha\frac{(\boldsymbol{P}\cdot\boldsymbol{q})}{q^2}\boldsymbol{q}\,, \tag{1}$$

where $\boldsymbol{q}$ is the wave vector, the first and second terms represent respectively the piezoelectric polarization and the polarization induced by the macroscopic electric field, which is obtained from Maxwell equation or microscopic consideration of the lattice. Accordingly, Eq. (1) becomes

$$\boldsymbol{P}\cdot\boldsymbol{q}=(\boldsymbol{P}_{\text{piezo}}\cdot\boldsymbol{q})/1+4\pi\alpha=(1/\varepsilon_s)(\boldsymbol{P}_{\text{piezo}}\cdot\boldsymbol{q})\,.$$

Here $\boldsymbol{P}_{\text{piezo}}$ can be expressed as follows;

$$\boldsymbol{P}_{\text{piezo}}=(P_1,\ P_2,\ P_3)\,,$$

$$P_1=-i\sum_{q,\alpha}\left(\frac{\hbar}{2\rho\omega(\boldsymbol{q},\ \alpha)\Omega}\right)^{1/2}e_{15}(\varepsilon_1q_3+\varepsilon_3q_1)(be^{i\boldsymbol{qr}}-b^*e^{-i\boldsymbol{qr}})\,,$$

$$P_2=-i\sum_{q,\alpha}\left(\frac{\hbar}{2\rho\omega(\boldsymbol{q},\ \alpha)\Omega}\right)^{1/2}e_{15}(\varepsilon_2q_3+\varepsilon_3q_2)(be^{i\boldsymbol{qr}}-b^*e^{-i\boldsymbol{qr}})\,,$$

$$P_3=-i\sum_{q,\alpha}\left(\frac{\hbar}{2\rho\omega(\boldsymbol{q},\ \alpha)\Omega}\right)^{1/2}\{e_{31}(\varepsilon_1q_1+\varepsilon_2)+e_{33}\varepsilon_3q_3\}(be^{i\boldsymbol{qr}}-b^*e^{-i\boldsymbol{qr}})\,,$$

where ρ the density, Ω the volume of the crystal, e_{15}, e_{31}, e_{33} the piezoelectric constants, $\omega(\boldsymbol{q},\alpha)$ and $\boldsymbol{\varepsilon}(\boldsymbol{q},\alpha)$ are the frequency and the unit polarization vector belonging to mode $(\boldsymbol{q},\alpha)$ of acoustic lattice vibrations, and b and b^* denote the annihilation and production operators of a phonon, respectively.

The interaction energy between an electron and the lattice vibrations

$$\mathscr{H}(\boldsymbol{r}_{el})=-\frac{4\pi}{\varepsilon_s}e\sum_{q,\alpha}\left(\frac{\hbar}{2\rho\omega(\boldsymbol{q},\ \alpha)\Omega}\right)^{1/2}a(\boldsymbol{q},\ \alpha)\{b\exp(i\boldsymbol{qr}_{el})+b^*\exp(-i\boldsymbol{qr}_{el})\}\,,$$

where

$$a(\boldsymbol{q},\ \alpha)=\frac{1}{q^2}\{e_{15}(\varepsilon_1q_1q_3+\varepsilon_2q_2q_3+\varepsilon_3q_1{}^2+\varepsilon_3q_2{}^2)+e_{31}(\varepsilon_1q_1q_3+\varepsilon_2q_2q_3)+e_{33}\varepsilon_3q_3{}^2\}\,,$$

from which the first- order phonon scattering matrix elements $(\overset{a}{V_s{}^e})$ are derived;

$$(\overset{a}{V_s{}^e})=\frac{8\pi^2e^2\hbar}{\varepsilon_s{}^2\Omega\rho}\cdot\frac{\{a(\boldsymbol{q},\ \alpha)\}^2}{\omega(q,\ \alpha)}\begin{cases} n(\boldsymbol{q},\ \alpha) & \text{for phonon absorption}\\ n(\boldsymbol{q},\ \alpha)+1 & \text{for phonon emission}\,.\end{cases}$$

Using these scattering matrix elements, we can calculate easily the absorption cross section in second-order Born approximation

$$\sigma(\omega)=\frac{2\pi}{\hbar}\left[\frac{2\pi e^2\hbar^4}{3\sqrt{\varepsilon_0}\,cm^{*1/2}}\cdot\frac{1}{(kT)(\hbar\omega)^3}\right]\sum_{x}Av_0\sum_{f}|(V_s)|^2q^2\sum_{p=0}^{1}(-)^P\delta\Big\{(E(\boldsymbol{k}_f)-E(\boldsymbol{k}_0))/kT$$
$$\mp\frac{\hbar\omega(q,\ \alpha)}{kT}-(-)^P\frac{\hbar\omega}{kT}\Big\}\,,$$

where Av_0 means the thermal average on initial states $\boldsymbol{k}_0$ of electrons, $\sum_f$ means the sum on final states $\boldsymbol{k}_f$, and the summation on α indicates that the longitudinal and transverse lattice vibrations should be taken into account. The term of $P=1$ in the last summation has been introduced by taking account of stimulated emission. Here, for simplicity, we have considered that the conduction band is spherical. Inserting Eq. (4) into Eq. (5),

$$\sigma(\omega)=\frac{2\sqrt{2}\,\pi^{3/2}}{3\varepsilon_s{}^2\sqrt{\varepsilon_0}\,\rho}\cdot\frac{e^4e_{15}{}^2}{c\cdot m^{*1/2}}(kT)^{-3/2}z^{-2}e^z K_1(z)(1-e^{-2z})\left\{\frac{4}{105}\,\frac{1}{u_l{}^2}\left(32+32\frac{e_{31}}{e_{15}}+24\frac{e_{33}}{e_{15}}+12\frac{e_{31}e_{33}}{e_{15}{}^2}+8\frac{e_{31}{}^2}{e_{15}{}^2}+15\frac{e_{33}{}^2}{e_{15}{}^2}\right)\right.$$
$$\left.+\frac{8}{105}\,\frac{1}{u_t{}^2}\left(19-2\frac{e_{31}}{e_{15}}+2\frac{e_{33}}{e_{15}}-6\frac{e_{31}e_{33}}{e_{15}{}^2}+3\frac{e_{31}{}^2}{e_{15}{}^2}+3\frac{e_{33}{}^2}{e_{15}{}^2}\right)\right\},$$

where $z=\frac{\hbar\omega}{2kT}$, u_l and u_t are the sound velocities belonging to each mode and $K_1(z)$ is the modified Bessel function of order 1, which, has the following asymptotic forms

$$K_1(z)\sim\left(\frac{\pi}{2z}\right)^{1/2}e^{-z}\left(1+\frac{3}{8z}-\frac{15}{128z^2}+\cdots\right)\quad\text{for}\quad z\gg1\,,$$
$$\sim\frac{1}{z}\qquad\text{for}\quad z\ll1\,.$$

Therefore,

$$\sigma(\omega)\propto T\cdot\omega^{-5/2}\quad\text{for}\quad z\gg1\,,$$
$$\propto T^{1/2}\omega^{-2}\quad\text{for}\quad z\ll1\,,$$

For CdS crystals, $\sigma=1.4\times10^{-17}\,\text{cm}^2$ at $T=300°\text{K}$ and $\lambda=10\mu$. This manitude is comparable with one derived by the deformation-potential model. Unfortunately, we have no knowledge about physical constants for other crystals with wurtzite structure. Although we expect that the effect is more dominant in ZnO crystal the effects of electron scattering due to the optical-lattice vibrations may predominate[5] there. The author would express his sincere thanks to Prof. Y. Suge for his encouragement.

J. Phys. Soc. Japan **15** (1960) 2111～2112

Optical Properties of Irradiated LiF Crystals in the Extreme Ultraviolet Region

By Riso Kato, Shin-ichi Nakashima*,
Kaizo Nakamura and Yoichi Uchida

Department of Physics, Faculty of Science, Kyoto University

(Received June 16, 1960)

Optical absorptions of LiF single crystals irradiated with β- or γ-rays were measured in the extreme ultraviolet and some relations to the results[1] hitherto obtained were found.

A vacuum spectrophotometer of Seya-Namioka type with a concave grating of 1 m radius and 1200 line/mm constructed in our laboratory[2] were used. The light source was a cold cathode hydrogen discharge tube operated on D.C. 1 ampere at about 1 mm Hg. With these apparatus the useful spectral range reached down to about 900 Å and measurements could be carried out within the band width of about 2 Å. Present studies were done on LiF crystals obtained from Prof. Pringsheim and from the Harshaw Chem. Co. They were found the purest among those available.

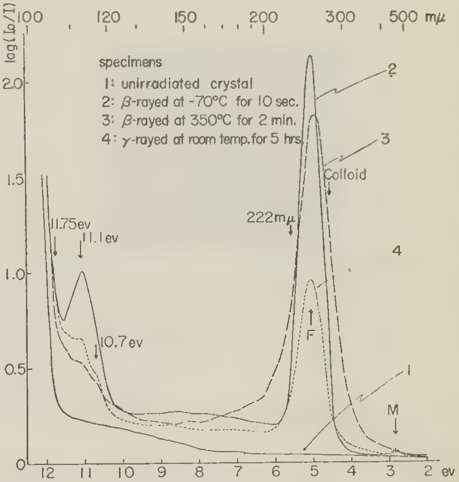

Fig. 1. Absorption spectra of LiF crystals irradiated with 0.9 MeV β-rays from a Van de Graaff machine or with γ-rays from Co^{60} (measured at room temperature).

As seen in Fig. 1, specimen 2 was found to have an absorption band at 11.1 eV well separated from the fundamental band. The band seems to be proportional in height to F band. In specimens 3 and 4, however, a composite shoulder was observed and seems to consist of at least two bands at 11.75 and 11.1 eV. The much longer wavelength components were seen faintly at about 10.7 and 9.5 eV. They became also appreciable in specimen 2 when it was irradiated with F light. Their intensities depend sensitively on histories of sample treatment and differ from crystal to crystal (Fig. 2). The width of each band at 5 eV in Fig. 1 suggests that specimens 3 and 4 contain 222 mμ and collid bands[1] overlapping on F bands. It was found that when specimen 2 was bleached with F light the band at 11.1 eV decreased and the absorption at 11.75 eV increased as 222 mμ band appeared (Fig. 2 (a)). Thus the existence of 222 mμ band is closely related to 11.75 eV band. The behavior of 11.1 eV band reminds us of β band[3], but its separation from the 1st exciton band exceeds 1 eV and the appearance of 11.75 eV and 222 mμ bands accompanying the irradiation with F light made the analysis difficult. Further experiments are required to confirm the nature of 11.1 eV band. With the assumption that the concen-

---

* Now at Matsushita Electronics Co.

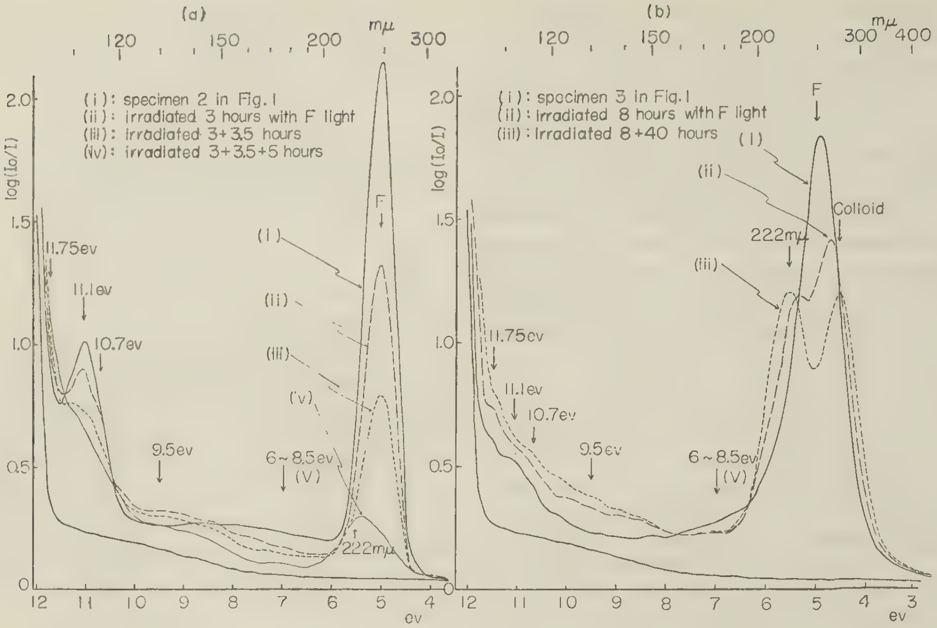

Fig. 2. Absorption spectra of irradiated LiF after bleaching with F light (measured at room temperature).

tration of 11.1 eV center is equal to F center, the oscillator strength of the band is estimated to be about 0.25.

As seen in Fig. 2(a), a broad absorption from 6 to 8.5 eV (curve (i)) disappeared with F light irradiation and is considered tentatively as a V band. As for the nature of 222 mμ band, our knowledge has been meager. Now in this experiment it appeared strongly in specimen 3 (Fig. 2(b)). Having been quenched to room temperature immediately after β-ray irradiation at 350°C, specimen 3 is likely to contain many defects. Then it is reasonable to consider that electrons released from F centers by the F light irradiation are trapped in some kind of the defects to form 222 mμ centers. In fact, in specimen 2 irradiated with β-rays at −70°C, the rate of change from F to 222 mμ band is much smaller than in specimen 3 as seen in Fig. 2. Finer experiments and quantitative discussions will be reported in the near future.

References

1) P. Pringsheim and P. Yuster: Phys. Rev. **78** (1950) 293. C. J. Delbecq and P. Pringsheim: J. Chem. Phys. **21** (1953) 794. P. Pringsheim: Z. Physik **136** (1954) 573. C. J. Delbecq, P. Pringsheim and P. Yuster: Z. Physik **138** (1954) 226.
2) Y. Uchida, et al: J. Appl. Phys. Japan **29** (1960) 492.
3) J. C. Delbecq, P. Pringsheim and P. Yuster: J. Chem. Phys. **19** (1951) 574. F. Bassani and N. Inchauspé: Phys. Rev. **105** (1957) 819. D. L. Dexter: Phys. Rev. **83** (1951) 1044.

J. Phys. Soc. Japan **15** (1960) 2112~2113

Study of Solid-Solution Single Crystals Containing BaTiO$_3$

By Tunetaro Sakudo
Electrotechnical Laboratory, Nagatacho, Tokyo

(Received September 3, 1960)

Recently many investigations have been made about the single crystals of solid-solutions of the perovskite-type ferroelectrics. The present note reports several results obtained in the cases of $BaTiO_3$-$SrTiO_3$ and $BaTiO_3$-$PbTiO_3$ solid-solution single crystals.

Crystals have been grown by modified Remeika's method using KF as flux. Solid-solution ceramics of the pertinent composition were chosen as solute materials. Maximum soaking temperatures were varied according to the compositions of solute. The soaking temperature was raised in the case of (Ba-Sr) TiO_3 and was lowered in (Ba-Pb) TiO_3, than in the case of $BaTiO_3$.

In the course of growing crystals it was observed that the butterfly-wing habit of pure $BaTiO_3$ disappeared gradually and the crystal size became smaller with increasing mole-ratio of Sr and Pb to Ba, as reported earlier by Kisaka et al.[1] Rather large square-plate crystals with {100} faces, as shown in

Fig. 1, were used in dielectric measurements. This crystal habit was denoted by DeVries[2] as untwinned [110] dendrite in the case of $BaTiO_3$.

Fig. 2 shows the plot of dielectric constant as function of temperature for (Ba-Pb) TiO_3 crystals. It is noticed from the figure that compositions of the grown crystals differ from those of the starting materials, as the Curie points of the crystals are different from those of the ceramics of the pertinent compositions.[3] Such phenomena were observed also in the case of (Ba-Sr) TiO_3. Compositions of the crystals were ascertained by the fluorescent X-ray analysis and the lattice-constant measurement. The relations between the compositions of solutes and grown crystals are shown in Fig. 3. These results are in disagreement with those of Kisaka et al. in (Ba-Sr) TiO_3.[1]

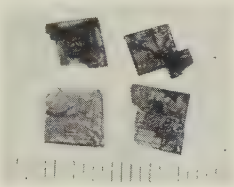

Fig. 1. Crystals grown from $(Ba_{0.9}Pb_{0.1})TiO_3$.

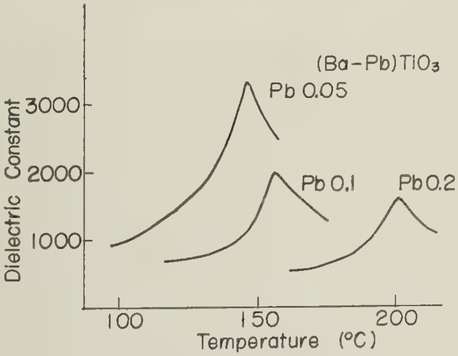

Fig. 2. Dielectric constant *vs* temperature for $(Ba\text{-}Pb)TiO_3$.

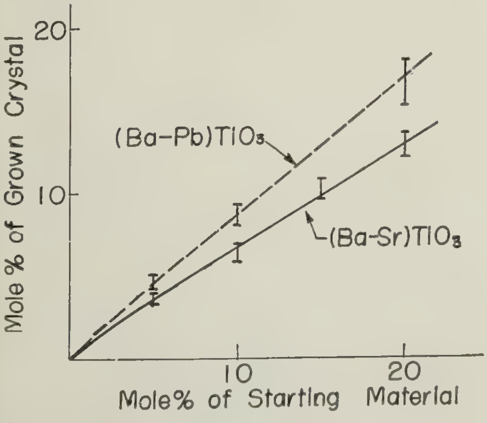

Fig. 3. Relation between the compositions of solutes and grown crystals.

In the series of (Ba-Pb) TiO_3, the spontaneous polarization and the coercive field were measured by observing the dielectric hysteresis loop. The birefringence was obtained by measuring the separation of birefringence bands in Na monochromatic light. The results are listed in Table I. In the measured region, the spontaneous polarization and the coercive field are seen to increase almost linearly with Pb content.

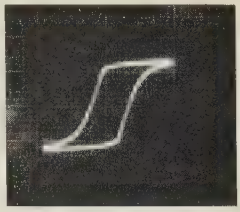

Fig. 4. Hysteresis loop of the crystal grown from $(Ba_{0.8}Pb_{0.2})TiO_3$.

Table I. Characteristics of (Ba-Pb) TiO_3 crystals.

Mole % of $PbTiO_3$ in Solute	0	0.05	0.1	0.2
Mole % of $PbTiO_3$ in Crystal	0	0.04	0.078	0.18
Curie temperature (°C)	125	144	165	202
Spontaneous polarization $\left(\frac{\mu\,\text{coul}}{\text{cm}^2}\right)$	23	27	28.5	36
Coercive field $\left(\frac{\text{kV}}{\text{cm}}\right)$	0.9	1.7	4.8	11
Birefringence $\frac{\Delta n}{n}$	0.053	/	0.050	0.048

Khodakof et al.[4] have reported that the thermal treatment remarkably changed the dielectric properties of the crystals of (Ba-Sr) TiO_3, but such phenomena were not observed in our experiment.

This work was supported by the Scientific Research Expenditure of the Ministry of Education.

References

1) Kisaka, Ikegami and Sasaki: J. Phys. Soc. Japan **14** (1959) 1680.
2) R. C. DeVries: J. Amer. Cer. Soc. **42** (1959) 547.
3) Shirane et al.: J. Phys. Soc. Japan **6** (1951) 256.
4) Khodakof et al.: Dokl. Akad. Nauk USSR **108** (1956) 825.

J. Phys. Soc. Japan **15** (1960) 2114～2115

On the Reversible Optical Conversion Between A- and B-centers in Colored KCl Crystals

By Hiroshi Ohkura and Takeshi Uchida

Department of Applied Physics, Osaka City University, Osaka, Japan

(Received September 3, 1960)

We have observed a new reversible process in the optical conversion between A-and B-centers. Optical absorption measurements were carried out at about −180°C. KCl crystals made by repetitions of Kyropoulos' method were colored additively in the atmosphere of a previously distilled sodium metal vapor.

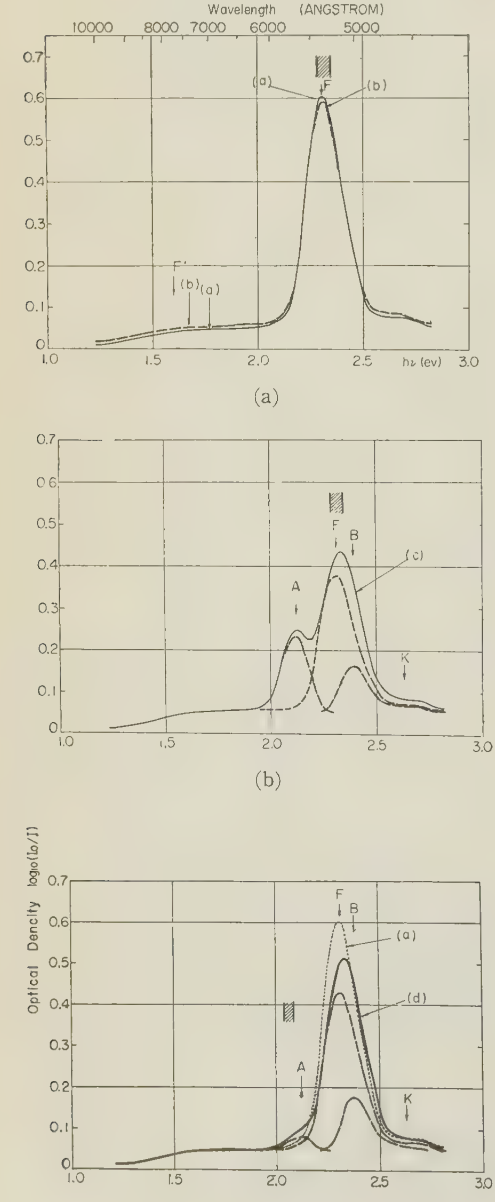

(a)

(b)

(c)

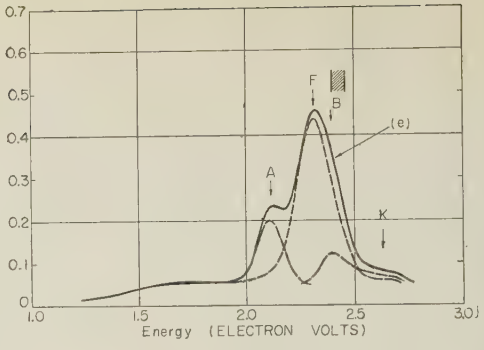

(d)

Fig. 1. A sequence of absorption measurements on additively colored KCl of 1.80 mm thickness subject to subsequent irradiation with F–, A–, and B-light. The absorption measurements were made at about −180°C. Curve (a), unbleached; Curve (b), after ten minutes F-light bleaching at −180°C; Curve (c), after ten minutes F-light bleaching at −20°C; Curve (d), after forty minutes A-light bleaching at −180°C; Curve (e), after one hour B-light bleaching at −180°C. The shaded area represents the wavelength region covered by the irradiating light during bleaching.

The results will be discussed (subsequently) with the reference to a typical example for a specimen of 1.80 mm in thickness shown in Fig. 1. Curve (a), Fig. 1, shows the optical absorption spectrum of the additively colored crystal of KCl exhibiting only F-centers. Curve (b), shown as the dashed curve, is the saturated absorption curve after ten minutes F-light (5300 A) bleaching at −180°C. Before carrying out next procedures, the F' band in curve (b) was reverted to the F band by warming the crystal to room temperature. Curve (c), obtained after ten minutes F-light bleaching at −20°C, shows the F band bleach together with the simultaneous increase of the A and B bands. These bands are illustrated as the dashed curves on the same graph, which are obtained by substracting appropriately the F band absorption (the dashed curve) from the curve (c). In addition to these bands, there is a slight increase of absorption at the high frequency side of the B band, a part of which is overlapped on it.

The crystal is now subjected to A-light (6000 A) bleaching at −180°C. Curve (d), obtained after forty minutes A-light bleaching, is compared with the curve (a), shown as the dotted curve on the same graph. It shows the bleaching of A-centers together with the simultaneous increase of B-centers, without the appreciable change of both

F- and F'- bands. These bands are illustrated by the dashed curves on the same graph. The crystal is then subjected to B-light (5100 A) bleaching at −180°C, the result is shown in curve (e), in which each band is illustrated by the dashed curve. We now find that the A band recovers at the expense of the B band during B-light irradiation.

The occurrence of this conversion between A and B band depends on the temperature. For instance, no change was observed when above mentioned optical excitations were carried out at −200°C.

We wish to thank Professor H. Kawamura and Mr. M. Tomura for their advice and encouragement in the course of this work.

This work was supported by the Scientific Research Found of the Ministry of Education.

J. PHYS. SOC. JAPAN **15** (1960) 2115

Anomalous Paramagnetic Resonance in $Ni(NH_3)_6Cl_2$

By Muneyuki DATE

Department of Physics, Faculty of Science,
Osaka University, Osaka

(Received August 6, 1960)

An anomalous paramagnetic resonance was observed in the single crystal of $Ni(NH_3)_6Cl_2$ below the liquid nitrogen temperature. This ammine complex of nickel has a cubic crystalline structure in which each nickel ion is surrounded by six NH_3 groups forming a regular octahedron$^{1)}$. Isotropic paramagnetic resonance absorption was observed above the liquid nitrogen temperature with $g=2.16$. The observed line width was 150 oersted, which is independent of the orientation of the crystal within experimental errors. Accordingly, it may be concluded that the crystalline electric field acting on each nickel ion is perfectly cubic and that therefore there is no splitting in the lowest spin triplet.

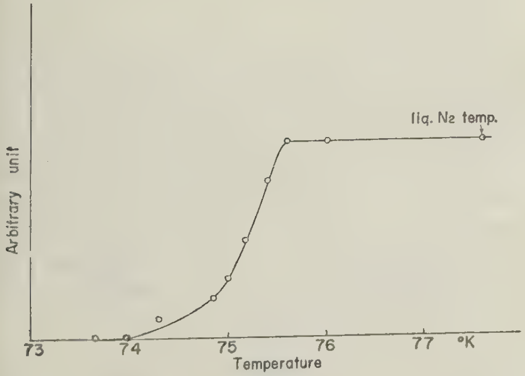

Fig. 1. Temperature dependence of absorption intensities at 36.17 kMc/sec. magnetic field is along the {100} direction.

Below 76°K, however, the resonance line vanishes suddenly, the variation of the relative intensity being shown in Fig. 1. This vanishing is independent of the orientation of the crystal and no line broadening of the paramagnetic resonance, which is usually observed above the antiferromagnetic transition temperature, is observed near the transition temperature in the present case.

The observed transition may be due to the quenching of the free rotations of the NH_3 groups below 76°K. Hindered rotation of ammonia or ammonium radicals in solid is frequently observed in various compounds. In our case, the quenching of the rotational motion of the NH_3 groups will produce a crystalline electric field of a lower symmetry acting upon each nickel ion and this field will induce an initial splitting of the ground state spin triplet. Then the resonance point will shift largely from that which corresponds to $g=2.16$, and thus one will observe the vanishing of the normal resonance below the transition point. Although there is a possibility of observing the spin resonance of the distorted crystal below the transition temperature if the distortion of the unit octahedron were regular in space, and the magnitude of distortion were not extremely large, there was no resonance absorption below 74°K at 36 kMc/sec up to 10 kilo oersted.

The vanishing of the paramagnetic resonance does not seem to occur from magnetic origin. By susceptibility measurements Kido and Watanabe$^{2)}$ have shown that there is no remarkable change near the liquid nitrogen temperature. Recently, however, Watanabe$^{3)}$ observed the temperature dependence of the g-value by careful susceptibility measurements and showed that $g=2.18\pm0.03$ at room temperature and $g=2.21\pm0.03$ near the liquid hydrogen temperature. These data are consistent with ours, so far as we assume the variation of the g-value to be due to a slight deformation of the unit octahedron below 76°K. Proton resonance experiment performed by Kim and Sugawara$^{4)}$ showed that the line disappeared below 1.6°K, which may be due to the antiferromagnetic transition and may have no relation to our observation.

References

1) R. W. G. Wyckoff: Crystal Structures, vol. **2**, Interscience Pub., New York (1951) 34.
2) K. Kido and T. Watanabe: J. Phys. Soc. Japan **14** (1959) 1217.
3) T. Watanabe: private communication.
4) P. H. Kim and T. Sugawara: J. Phys. Soc. Japan **13** (1958) 968.

J. PHYS. SOC. JAPAN **15** (1960) 2116~2117

Absorption Spectra of Potassium Bromide-Thallium Phosphors

By Tokumichi TAMAI

Research Laboratory, Matsushita Electronics Corporation, Takatsuki, Osaka

(Received September 10, 1960)

The absorption spectra of potassium bromide-thallium phosphors have been studied at both liquid nitrogen and room temperatures. Single crystals were prepared by dissolving a small quantity of thallous bromide in a melt of potassium bromide and growing up by the well-known Kyropoulos method in this laboratory. Concentrations of thallous ions are 0.001, 0.01, and 0.1 mol% in the melt. An automatic recording spectrophotometer was used to measure the absorption spectra of these crystals. Although a considerable amount of information can be found in the literatures concerning the properties of the potassium bromide-thallium phosphors,[1-7] yet absorption band in the region of 210 mμ have not been clearly resolved. Muuss[7] has reported the bands at 4.76, 5.57, 5.81, and 6.12 eV at room temperature, and the last three bands have been only partly resolved. In the present experiment three bands at 4.79, 5.60, and 5.92 eV have been clearly resolved at liquid nitrogen temperature, but the band at 6.12 eV was not observed at both liquid nitrogen and room temperatures. Fig. 1 shows typical absorption curves.

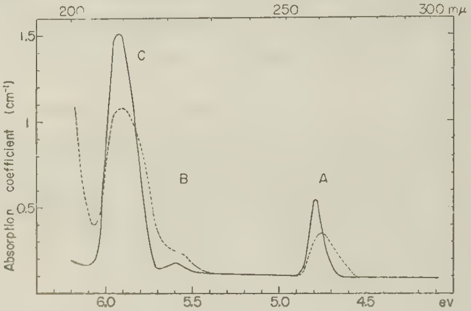

Fig. 1. Typical absorption spectra of the potassium bromide-thallium phosphor, solid line was taken at liquid nitrogen temperature and dotted line taken at room temperature.

Table I. The absorption peaks and the half-widths of various bands at both liquid nitrogen and room temperatures, and the values of the oscillator strengths of A, B and C bands, taking the value of the oscillator strength of C band as unity.

		A	B	C
Absorption peaks	Room Temperature	4.76 (eV)	5.56 (eV)	5.90 (eV)
	Liquid Nitrogen Temperature	4.79 (eV)	5.60 (eV)	5.92 (eV)
Half-width	Room Temperature	0.17 (eV)	not clear	0.265 (eV)
	Liquid Nitrogen Temperature	0.096 (eV)	0.088 (eV)	0.19 (eV)
Oscillator strength of the absorption transitions at liquid nitrogen temperature, taking that of C band as unity		0.155	~0.014	1

The absorption bands at 4.79 and 5.92 eV correspond to A and C bands as denoted by Seitz[8] respectively. The band at 5.60 eV should be assiged to B band because height of the absorption band varies linearly with the concentration of thallous ion and the ratio of the oscillator strength of this B band to that of A or C band is nearly equal to the corresponding ratio in the case of the bands in potassium iodide-thallium phospors.[9,10] The absorption peaks and the half widths are summarized in Table I.

The half-widths of A and C bands are narrower than the values reported by Lorentz,[2] and that of A is equal to Muuss' value.[7] As seen in Fig. 1, the half-width of C band is wider than those of A and B bands, and the shape of C band is clearly asymmetric. Thus it is likely to consisted of at least two bands, and it will be suggested that $^1P_1$ level is probably perturbed by the crystalline field which is not a cubic symmetry, and separated by three levels.[10] Further discussion with detailed measurements will be reported later on.

The author would like to express his gratitude to Prof. Y. Uchida for his guidance and discussions on the work.

References

1) R.Hilsch: Z. Phys. **44** (1956) 860.
2) H. Lorenz: Z. Phys. **46** (1927) 558.
3) R. Hilsch and R. W. Pohl: Z. Phys. **48** (1928)

384.
4) M. Forro: Z. Phys. **56** (1929) 534; **58** (1930) 613.
5) W. v. Meyeren: Z. Phys. **61** (1930) 321.
6) P. Pringsheim: Rev. Mod. Phys. **14** (1942) 132.
7) H. Leuts and H. Muuss: Z. Phys. **155** (1959) 531.
8) F. Seitz: J. Chem. Phys. **6** (1938) 163.
9) A. Smakula: Z. Phys. **59** (1930) 603.
10) P. H. Yuster and C. J. Delbecq: J. Chem. Phys. **21** (1953) 892.

J. PHYS. SOC. JAPAN **15** (1960) 2117~2118

N Bands in Alkali Halide Crystals

By Sadao HATTORI

Department of Natural Science, Nagoya Branch,
Aichi Gakugei University, Nagoya

(Received September 10, 1960)

The N bands of some alkali halide crystals were investigated. The samples, cleaved out of the single crystals grown from the melts of KCl, NaCl, KBr, KI and LiF were colored at room temperature with the irradiation of X rays from a tungsten target through a beryllium window, operated at about 50 kv and 15 ma. The colored samples were bleached with their respective F light at room temperature to develop the N_1 and N_2 bands, except for LiF for which the whole light from a low pressure Hg lamp was used and furthermore at about 100° to 150°C to develop the N bands in reasonable times.

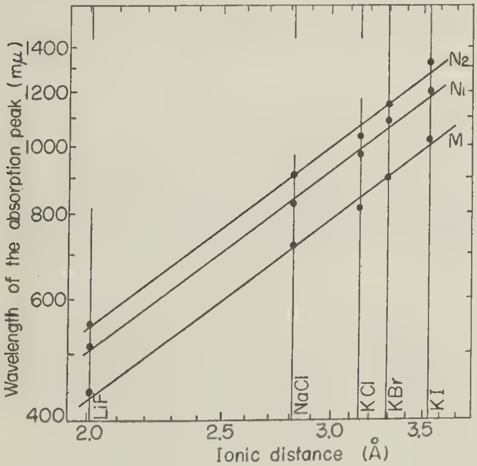

Fig. 1. The relation between the wavelengths of absorption peaks of N_1, N_2 and M bands and the ionic distances of various salts, measured at −170°C.

The N_1 and N_2 bands thus obtained, as well as the M bands of these salts were shown in Fig. 1 satisfying well Ivey's relation.[1] The N bands, except for the N_2 bands of KBr and KI, were obtained earlier[2] and the results obtained here were in good agreement with them. The N_2 bands of KBr and KI were so slight that it was uncertain that they were in fact the N_2 bands, but these bands, as shown in the figure satisfied comparatively well Ivey's relation together with the N_2 bands of the other salts investigated here.

The N_1 and N_2 bands were investigated in more details with NaCl, for which the two bands were well separated even at room temperature, with the following results:

1) The N_2 band was destroyed while the N_1 band was enhanced with the irradiation of the M band light at room temperature. This is shown in Fig. 2. (Similar results were also obtained with KCl.) However, the rate of the destruction of the former band was much larger than that of the enhancement of the latter band.

2) When the crystal was irradiated with the M band light after the X ray coloring, only the N_1

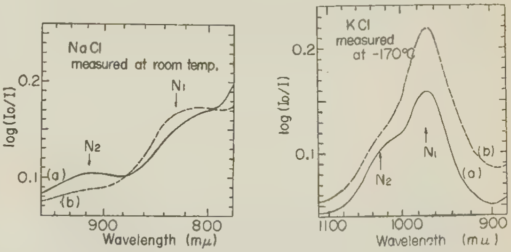

Fig. 2. The N_1 and N_2 bands of the X ray colored NaCl and KCl crystals irradiated, (a) with the F band light and (b) with the M band light at room temperature, after the irradiation with the F band light.

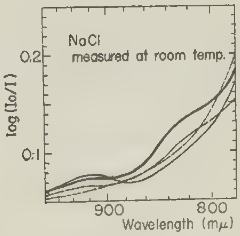

····· X rayed 41 KV. 12 ma. 15 hours (0.47)*
—— 10 min. at 98°C (0.42)*
━━ 100 min. at 98°C (0.39)*
— — — 15 hours at 98°C (0.25)*

* The number means the optical density of the M-band for each curve.

Fig. 3. The thermal behaviors of the N_1 and N_2 bands of the X ray colored NaCl crystals, when the crystal was kept at 98°C in the dark.

band was enhanced.

3) Only the N_2 band was enhanced appreciably in the X ray colored crystal which was kept at about 30°C during 20 hours in the dark. At higher temperatures, e.g. at 98°C, both bands were enhanced but the rate of growth in this thermochemical reaction was much larger for the N_2 band than for the N_1 band. After reaching their maxima, they decayed gradually (Fig. 3).

These results seem to indicate that the N_1 and N_2 bands are rather due to different centers. Further details of the nature of these two bands are now under investigation.

The author wishes to express his thanks to Professor Y. Uchida of Kyoto University for his kind interests and encouragement.

References

1) H. F. Ivey: Phys. Rev. **72** (1947) 341, 873.
2) For example, KCl—R. Herman, M. C. Wallis and R. F. Wallis: Phys. Rev. **103** (1956) 87. NaCl:—W. D. Compton and C. C. Klick: Phys. Rev. **112** (1958) 1620. KBr and KI:—D. H. Goode and P. A. Schroeder: Phys. Rev. **115** (1959) 1426. LiF:—N. Itoh, K. Kubo and T. Suita: Presented at the annual meeting of the Physical Society of Japan, Oct. 1959.

J. PHYS. SOC. JAPAN **15** (1960) 2118

A Correction to my Paper "The Dipole Moment and End-to-end Length of the Isotactic Vinyl Polymer, I."

By Tsugio MORI
Ôtsu Senior High School, Ôtsu,
Shiga-ken, Japan

(Received September 13, 1960)

In the two papers published under the title "The Dipole Moment and End-to-end Length of the Isotactic Vinyl Polymer, I[1] and II[2]", the author maintained that we should replace the expression

$$\frac{1}{n}\sum_{i<j}^{n}\sum \mathbf{X}^{j-i-1} \qquad \mathrm{I(20)}$$

by

$$\{1+g(n)\}(\mathbf{1}-\mathbf{X})^{-1}\,. \qquad \mathrm{I(23)}$$

This replacement was needed in order to compare the calculated values of $\langle\mu^2\rangle$ and $\langle R^2\rangle$ with their experimental values, although we did not know whether $\lim(\mathbf{X}^n/n)$ was $\mathbf{0}$ or infinity. But, after the publication of the texts I and II, the author found a way of the verification of the formula

$$\lim_{n\to\infty}\frac{1}{n}\mathbf{X}^n=\mathbf{0}\,. \qquad \mathrm{I(22)}$$

Therefore, the statements in p.1485 of this volume, running from Eq. (22) to Eq. (24), must be corrected as the following.

" However, the verification of the formula

$$\lim_{n\to\infty}\frac{1}{n}\mathbf{X}^n=\mathbf{0} \qquad (22)$$

is not simple, for $\mathbf{X}$ is not orthogonal. Some authors have neglected the verification of (22), and put (22) as the assumption. On the other hand, there was another group of authors who have stated that they were interested only in the case of (22). The difference between their standpoints was small, and many authors have reduced (20) to

$$\frac{1}{n}\sum_{i<j}^{n}\sum \mathbf{X}^{j-i-1} \longrightarrow (\mathbf{1}-\mathbf{X})^{-1}\,.$$

However, it is remarked that the above reduction brings $\lim(\sum\sum \mathbf{X}^{j-i-1}/n)$ into a quantity which is independent of n. In other words, the formula (19) reduces into

$$\langle\mu^2\rangle=(\mathrm{const.})\, n\mu_0^2\,,$$

which corresponds to the random coil, or the unperturbed (Gaussian) coil in general. If we wish to treat an interrupted configuration which is neither the Gaussian coil nor the crystalline configuration, a jump of thought is needed. In this paper, we use the replacement

$$\frac{1}{n}\sum_{i<j}^{n}\sum \mathbf{X}^{j-i-1} \longrightarrow \{1+g(n)\}(\mathbf{1}-\mathbf{X})^{-1}\,, \qquad (23)$$

where $g(n)$ is a function of n. The replacement (23) may be unaccountable so far as we stick to (22). However, it must be rather significant that we can make a progress from the Gaussian coil by the use of (23). If $\lim g(n)$ is a constant which is independent of n, we have the Gaussian coil. In this way, we can write

$$\lim_{n\to\infty} g(n)\begin{cases} =\infty \text{ (for most chain configurations)} \\ = \text{a const. (for the Gaussian coil)} \end{cases}\text{''}. \qquad (24)$$

The verification of

$$\lim_{n\to\infty}\frac{1}{n}\mathbf{X}^n=\mathbf{0} \qquad \mathrm{I(22)}$$

may be treated in the next paper under the title "The Dipole Moment and End-to-end Length of the Isotactic Vinyl Polymer, III."

References

1) T. Mori: J. Phys. Soc. Japan **15** (1960) 1482.
2) T. Mori: J. Phys. Soc. Japan **15** (1960) 1638.

J. PHYS. SOC. JAPAN **15** (1960) 2119

Analysis of the NMR Spectra of Acrylic Acid and Ethyl Acrylate

By Yoji ARATA,
University of Electro-Communications, Chofu, Tokyo
Hiroshi SHIMIZU,
Faculty of Pharmaceutical Sciences, The University of Tokyo, Tokyo
and Shizuo FUJIWARA
Department of Chemistry, Faculty of Science, The University of Tokyo, Tokyo

(Received September 28, 1960)

The NMR spectra of acrylic acid and ethyl acrylate were measured at 56.4 Mc and analyzed by the method proposed by McConnell, McLean and Reilly[1] with the aid of parametron digital computer PC-1 at the University of Tokyo. The spectrum of acrylic acid is very complicated as shown in Fig. 1. The values of chemical shifts and spin-spin coupling constants are shown in Table I as well as those for ethylenic protons obtained in the literature[2]. The values in Table I were obtained by means of the least squares method, which made the analysis of the spectrum very easy; the details of the analysis will be published elsewhere[3]. As we examine the results of Table I, we notice that the spin-spin coupling constant between gem protons of acrylic acid is considerably larger than those of ester and of normal ethylene groups. This may be interpreted in terms of decreasing HCH angle[4] of this acid.

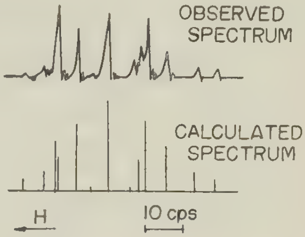

Fig. 1. The observed and calculated spectra of acrylic acid.

Table I. Values of chemical shifts and spin-spin coupling constants of acrylic acid and ethyl acrylate.

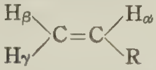	Chemical shifts (cps)	Spin-spin coupling constants (cps)		
		J_{trans}	J_{cis}	J_{gem}
Acrylic acid (R: COOH)	$\nu_\gamma-\nu_\beta=30.8$ $\nu_\alpha-\nu_\beta=12.5$	13.4	8.3	5.7
Ethyl acrylate (R: $COOC_2H_5$)	$\nu_\beta-\nu_\alpha=43.7$ $\nu_\gamma-\nu_\alpha=36.3$	16.4	7.8	−0.2
Normal ethylenic group[2]		17∼18	8∼11	1∼2

It is pleasure for us to thank Mr. Ichiro Yamaguchi and Mr. Naohiro Hayakawa of the Japan Atomic Energy Research Institute who gave us the opportunity to make measurements by the NMR spectrometer, Varian V-4300C, in their laboratory.

References

1) H. M. McConnell, A. D. McLean and C. A. Reilly: J. Chem. Phys. **23** (1955) 1152.
2) J. A. Pople, W. G. Schneider and H. J. Bernstein: *High-Resolution Nuclear Magnetic Resonance*, (McGraw-Hill, 1959) p. 193.
3) to be submitted for publication in J. Chem. Phys.
4) H. S. Gutowsky, M. Karplus and D. M. Grant: J. Chem. Phys. **31** (1959) 1278.

J. PHYS. SOC. JAPAN **15** (1960) 2119∼2120

On the Resistance Anomaly of Dilute Zinc Alloys at Low Temperatures

By Yoshio MUTO
The Research Institute for Iron, Steel and Other Metals, Tohoku University, Sendai

(Received September 20, 1960)

In the previous note[1], we reported that the dilute alloys of zinc with manganese show a minimum in the electrical resistance-temperature curves and the decrease of the electrical resistance in the magnetic field. It was planned to obtain further information by extending the study on the electrical properties of the dilute alloys. As zinc used previously was not good in purity, high purity zinc (99.999%) was adopted as the solvent metal and melted with small amounts of manganese, chromium and tin, respectively. The method of preparation of the specimens was the same as described in the previous note. Then the specimens were placed in a furnace heated at 350°C and rapidly quenched into water. Judging from the equilibrium diagrams, all specimens are considered to be within the solubility range. In these specimens, no important impurity could be detected.

Fig. 1 shows that the electrical resistance of Zn–Mn alloys increases with decreasing temperature. We believe that Zn–Mn alloys show a resistance minimum above 4.2°K. It is also noted that for the case of the most concentrated Zn–Mn (0.12 at. %) alloy prepared the rate of increase of the electrical resistance decreases with decreasing temperature. Thus, it may be expected that a resistance maximum will appear at an extremely low temperature. In Fig. 2, it is seen that the electrical resistance of dilute Zn–Cr alloys also increases with decreasing temperature. Zn–Cr alloys have also a resistance minimum above 4.2°K. Fig. 3 shows the electrical resistance of a Zn–Sn alloy revealing no anomalous behaviour. The absolute value of electrical resistance of this specimen is much smaller than that of Zn–Mn and Zn–Cr alloys.

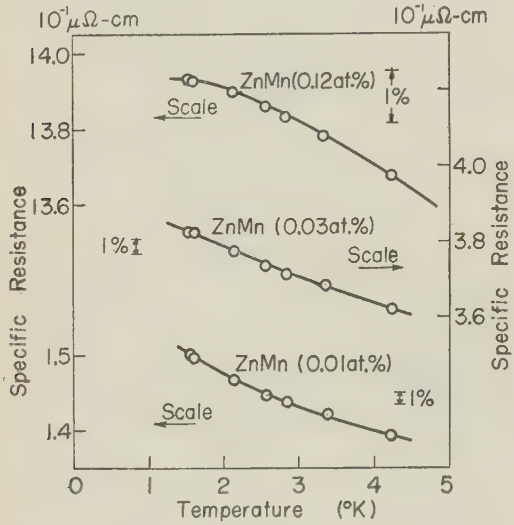

Fig. 1. Specific resistance versus temperature of zinc alloyed with manganese.

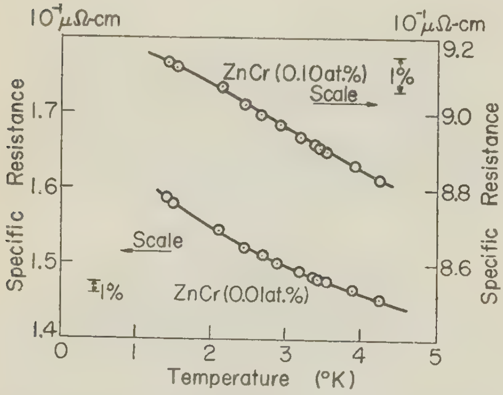

Fig. 2. Specific resistance versus temperature of zinc alloyed with chromium.

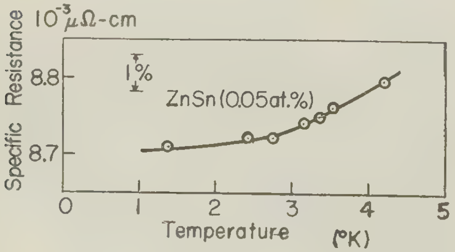

Fig. 3. Specific resistance versus temperature of zinc alloyed with tin.

Judging from the above experimental results, the electrical resistance of zinc alloy containing a non-transition metal shows no anomaly, while the zinc alloys containing transition metals have a resistance minimum. Recently, Hedgcock, Muir and Wallingford[2] obtained the similar results on magnesium alloys. On the other hand, Pearson, Rimek and Templeton[3),4] observed that the electrical resistances of both poly- and single crystal of Cu–Fe alloy show a minimum, and the electrical resistance of polycrystalline Cu–Sn alloy shows a minimum while that of single crystal shows no anomalous behaviour. In view of these results, it seems that the electronic properties of the dilute alloys containing transition metals show the anomalous behaviour probably due to the exchange interaction between the conduction electrons and the magnetic ions, while the electronic properties of the dilute alloys containing non-transition metals are to be explained by spin-independent scattering mechanisms.

The author wishes to express his sincere thanks to Prof. T. Fukuroi, Assist. Prof. Y. Shibuya and Assist. Prof. S. Tanuma for their kindness and stimulating discussions concerning the present work.

References

1) Y. Muto, Y. Tawara, Y. Shibuya and T. Fukuroi: J. Phys. Soc. **14** (1959) 380.
2) F. T. Hedgcock, W. B. Muir and E. Wallingford: Can. J. Phys. **38** (1960) 376.
3) W. B. Pearson, D. M. Rimek and I. M. Templeton: Phil. Mag. **41** (1959) 612.
4) W. B. Pearson: Phil. Mag. 41 (1959) 622.

J. PHYS. SOC. JAPAN **15** (1960) 2121

Infrared Absorption of Free Carriers in Ionic Crystals

By Toshio TANAKA

Department of Applied Physics, University of Tokyo, Tokyo, Japan

(Received Sep. 6, 1960)

In the previous short note[1)] we estimated the infrared photon absorption cross section through piezoelectric scattering of free carriers, whereby we pointed out that the appreciable effect on the infrared absorption of the interactions between electrons and the lattice vibrations of the longitudinal optical mode in crystals such as ZnO, CdS etc. might be expected. Here we shall estimate the magnitude and the photon frequency dependence of the infrared absorption of free carriers in ionic crystals.

The electronic polarization produced by the optical lattice vibrations has a strong interaction with electrons. The interaction Hamiltonian[2)] is

$$H_{\mathrm{int}}=\sum_q\{V_q b_q e^{iq\mathrm{II}}+V_q{}^* b_q{}^* e^{-iq\mathrm{II}}\}$$

where

$$V_q=4\pi i\sqrt{e^2\hbar/2\gamma\omega_l V}\cdot 1/q,\quad \gamma\equiv\omega_l{}^2/4\pi(1/\varepsilon_\infty-1/\varepsilon_s)\,.$$

Here ω_l is the frequency of the longitudinal optical mode of the lattice vibration, ε_∞ and ε_s are the high-frequency-and the static-dielectric constants respectively, and b_q and $b_q{}^*$ are phonon destruction and creation operators. Due to the interactions electrons can gain the momentum from the phonons and, therefore, can absorb photons. The absorption cross section is calculated in Born approximation[3)];

$$\sigma(\omega)=\frac{2\pi}{\hbar}\left[\frac{4\pi^2}{3}\cdot\frac{e^4\hbar^5\omega_l}{\sqrt{\varepsilon_\infty}\cdot C\cdot V\cdot m^{*2}}\left(\frac{1}{\varepsilon_\infty}-\frac{1}{\varepsilon_s}\right)(\hbar\omega)^{-3}\right]Av_0\sum_f\left(n_q\sum_{p=0}^{1}(-1)^p\delta(E(\boldsymbol{k}_f)-E(\boldsymbol{k}_0)-\hbar\omega_l-(-1)^p\hbar\omega\right)$$

$$+(n_q+1)\sum_{p=0}^{1}(-1)^p\delta(E(\boldsymbol{k}_f)-E(\boldsymbol{k}_0)+\hbar\omega_l-(-1)^p\hbar\omega))$$

$$=\frac{8\sqrt{2}\sqrt{\pi}}{3}\cdot\frac{e^4\hbar\omega_l(kT)^{1/2}}{\sqrt{\varepsilon_\infty}\cdot C\cdot m^{*1/2}}\left(\frac{1}{\varepsilon_\infty}-\frac{1}{\varepsilon_s}\right)(\hbar\omega)^{-3}$$

$$\times\left\{\begin{array}{ll}\left[nz_1e^{z_1}K_1(z_1)+(n+1)z_2e^{z_2}K_1(z_2)-(n+1)\dfrac{e^{-2z_1}}{2}(1+z_1+z_1e^{z_1}K_1(z_1))-nz_2e^{-z_2}K_1(z_2)\right] & \text{for } \omega\geq\omega_l\\ \left[nz_1e^{z_1}K_1(z_1)+\dfrac{(n+1)}{2}(1+z_3+z_3e^{z_3}K_1(z_3))-nz_3e^{z_3}K_1(z_3)-\dfrac{e^{-2z_1}}{2}(n+1)(1+z_1+z_1e^{z_1}K_1(z_1))\right] & \text{for } \omega\leq\omega_l\end{array}\right\}$$

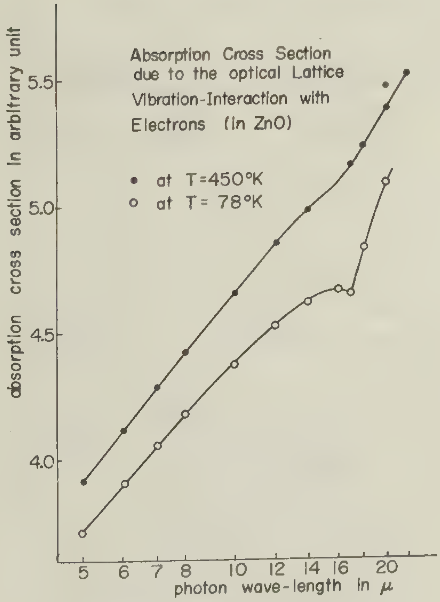

Fig. 1.

In the above equation the terms of $p=1$ have been introduced by taking account of the stimulated emission of photon. $K_1(z)$ is the modified Bessel function of order 1; and $z_1\equiv\hbar(\omega+\omega_l)/2kT$, $z_2\equiv\hbar(\omega-\omega_l)/2kT$ and $z_3\equiv\hbar(\omega_l-\omega)/2kT$; and n is the mean phonon number.

Let us attempt to apply the equation to the case of ZnO crystal. Using the following values, $m^*=0.06\,\mathrm{m}$, $\varepsilon_\infty=4$, $\varepsilon_s=8.15$ and $\hbar\omega_l=0.0733\,\mathrm{ev}$, we find that $\sigma\doteqdot1.7\times10^{-15}\,\mathrm{cm}^2$ at $\lambda=10\,\mu$ and $T=300$°K. This magnitude is comparable with the experimental value $\sigma=1.2\times10^{-15}\,\mathrm{cm}^2$[4)]. The dependence of the absorption cross section on the photon wavelength is shown in Fig. 1 for $\tau\omega>1$.

The λ^3-dependence in short wavelength region measured[4)] in ZnO crystals seems not to be explained.

The author wishes to express his sincere thanks to Prof. Y. Suge for his encouragement.

References

1) T. Tanaka: J. Phys. Soc. Japan in press.
2) Fröhlich: Advances in Phys. **3** (1954) 325.
3) R. Rosenberg and M. Lax: Phys. Rev. **112** (1958) 843.
4) D. G. Thomas: Phys. Chem. Solids **10** (1959) 47.

J. PHYS. SOC. JAPAN **15** (1960) 2122~2123

Strong Interaction of Baryons

Hy Seitaro NAKAMURA
Department of Physics, University of Tokyo,
Tokyo, Japan

(Received September, 8, 1960)

On the three dimensional charge space, we can write a Hamiltonian of the weak interaction as an invariant[1)–3)], while the formulation on the usual isospin space enforces us to give a spinor Hamiltonian for that. For the strong interaction, however, the three dimensional representation leads us to violation of strangeness. As a trial case, let us forget strangeness[4)–5)] and find a new quantum number which takes place of strangeness.

We shall introduce a two component spinor Ψ_μ, and define 2×2 matrices, κ_L, in this κ space.

$$\left.\begin{aligned}\Psi_\mu=\begin{pmatrix} p_\mu \\ q_\mu \end{pmatrix},\quad & p_1=(\Xi^-+p)/\sqrt{2}\,, && p_2=(\Xi^--p)/\sqrt{2}\,i, \\ & p_3=(\Xi^0-n)/\sqrt{2}\,, && p_0=(\Xi^0+n)/\sqrt{2} \\ & q_1=(\Sigma^-+\Sigma^+)/\sqrt{2}\,, && q_2=(\Sigma^--\Sigma^+)/\sqrt{2}\,i, \\ & q_3=\Sigma^0, && q_0=\Lambda \end{aligned}\right\} \tag{1}$$

$$\kappa_1=\begin{pmatrix} 0 & 1 \\ 1 & 0 \end{pmatrix},\ \kappa_2=\begin{pmatrix} 0 & -i \\ i & 0 \end{pmatrix},\ \kappa_3=\begin{pmatrix} 1 & 0 \\ 0 & -1 \end{pmatrix},\ \kappa_0=\begin{pmatrix} 1 & 0 \\ 0 & 1 \end{pmatrix}. \tag{2}$$

We consider a new charge $Q_\kappa=(1+\kappa_3)/2$, which is 1 for p and 0 for q. According to the principle[6)] of interchange-ability of particles which is an extension of symmetric meson theory, we assume a strong interaction between p and q through four groups of mesons, $\mathfrak{K}_+$, $\mathfrak{K}_0$, $\mathfrak{K}_-$ and $\mathfrak{K}_0'$.

$$p_+\to q_0+\mathfrak{K}_+\ , \qquad q_0\to p_++\mathfrak{K}_-\ , \tag{3}$$

$$p_+\to p_++\mathfrak{K}_0(\mathfrak{K}_0')\ , \qquad q_0\to q_0+\mathfrak{K}_0(\mathfrak{K}_0')\ . \tag{4}$$

Each group is assumed to be composed of four members in the states of $Q_e=N_3=1,\ 0,\ -1$ (triplet) and 0 (singlet) in the three dimensional charge space, which we shall call N-space.

$$\left.\begin{aligned}\mathfrak{K}_+ &=\left(K^+,\ \frac{L_+{}^0-K_+{}^0}{\sqrt{2}},\ L^-,\ \frac{L_+{}^0+K_+{}^0}{\sqrt{2}}\right) \\ \mathfrak{K}_- &=\left(L^+,\ \frac{L_{-0}-K_-{}^0}{\sqrt{2}},\ K^-,\ \frac{K_-{}^0+L_-{}^0}{\sqrt{2}}\right)\end{aligned}\right\} \tag{5}$$

$$\left.\begin{aligned}\mathfrak{K}_0 &=(D^+,\ D^0,\ D^-,\ D^{0\prime}) \\ \mathfrak{K}_0' &=(\pi^+,\ \pi^0,\ \pi^-,\ \pi^{0\prime})\end{aligned}\right\} \tag{6}$$

Here the upper suffices are electric charge, and the lower suffices κ-charge. Thus we can write down an interaction Hamiltonian of the strong interaction among baryons through mesons, $\mathfrak{K}_+$, $\mathfrak{K}_-$, (κ-charge exchange terms) and $\mathfrak{K}_0$, $\mathfrak{K}_0'$ (κ-charge neutral terms). We assume that H is of κ-charge independence which follows;

$$\begin{aligned}H=\ & a\overline{\Psi}_{[i}\kappa_L\Phi_{Lj}\psi_{k]}+b\overline{\Psi}_0\kappa_L\Phi_{Lj}\Psi_j+c\overline{\Psi}_j\kappa_L\Phi_{L0}\Psi_j \\ & +d\overline{\Psi}_j\kappa_L\Phi_{Lj}\Psi_0+e\overline{\Psi}_0\kappa_L\Phi_{L0}\Psi_0+a'\overline{\Psi}_{[i}\kappa_0\Phi_{0j}'\Psi_{k]} \\ & +b'\overline{\Psi}_0\kappa_0\Phi_{0j}'\Psi_j+c'\overline{\Psi}_j\kappa_0\Phi_{00}\Psi_j+d'\overline{\Psi}_j\kappa_0\Phi_{0j}\Psi_0 \\ & +e'\overline{\Psi}_0\kappa_0\Phi_{00}\Psi_0+\text{h.c.} \\ & \qquad i,\ j,\ k=1,\ 2,\ 3, \qquad L=1,\ 2,\ 3.\end{aligned} \tag{7}$$

$$\begin{aligned}\Phi_{+,\mu} &=\left(\frac{L^-+K^+}{\sqrt{2}},\ \frac{L^--K^+}{\sqrt{2}\,i},\ \frac{L_+{}^0-K_+{}^0}{\sqrt{2}},\ \frac{L_+{}^0+K_+{}^0}{\sqrt{2}}\right), \\ \Phi_{0,\mu} &=\left(\frac{D^-+D^+}{\sqrt{2}},\ \frac{D^--D^+}{\sqrt{2}},\ D^0,\ D^{0\prime}\right), \\ \Phi_{-,\mu} &=\left(\frac{K^-+L^+}{\sqrt{2}},\ \frac{K^--L^+}{\sqrt{2}\,i},\ \frac{L_-{}^0-K_-{}^0}{\sqrt{2}},\ \frac{L_-{}^0+K_-{}^0}{\sqrt{2}}\right), \\ \Phi_{0,\mu}' &=\left(\frac{\pi^-+\pi^+}{\sqrt{2}},\ \frac{\pi^--\pi^+}{\sqrt{2}\,i},\ \pi^0,\ \pi^{0\prime}\right). \\ & \qquad \mu=1,\ 2,\ 3,\ 0.\end{aligned}$$

Here a, b, c, d, e and a', b', c', d', e' are coupling constants. If we assume further

$$ai=b=c=d=e\equiv g\ , \quad -a'i=b'=c'=d'=e'\equiv g'\ , \tag{8}$$

we get using the matrix representation[7)]

$$\begin{aligned}H_{\mathfrak{K}_+}=g\Big[& (\overline{p}\,\overline{n})\begin{pmatrix} \Sigma^0 & \sqrt{2}\,\Sigma^+ \\ \sqrt{2}\,\Sigma^- & -\Sigma^0 \end{pmatrix}\begin{pmatrix} K^+ \\ K^0 \end{pmatrix} \\ & +(\overline{\Xi}{}^0\overline{\Xi}{}^-)\begin{pmatrix} \Sigma^0 & \sqrt{2}\,\Sigma^+ \\ \sqrt{2}\,\Sigma^- & -\Sigma^0 \end{pmatrix}\begin{pmatrix} L^0 \\ L^- \end{pmatrix} \\ & +(\overline{p}\,\overline{n})\begin{pmatrix} \Lambda & 0 \\ 0 & \Lambda \end{pmatrix}\begin{pmatrix} K^+ \\ K^0 \end{pmatrix} \\ & +(\overline{\Xi}{}^0\overline{\Xi}{}^-)\begin{pmatrix} \Lambda & 0 \\ 0 & \Lambda \end{pmatrix}\begin{pmatrix} L^0 \\ L^- \end{pmatrix}\Big]+\text{h.c.}\ ,\end{aligned} \tag{9}$$

$$\begin{aligned}H_{\mathfrak{K}_-}=g\Big[& (\overline{K}{}^+\overline{K}{}^0)\begin{pmatrix} \Sigma_0 & \sqrt{2}\,\Sigma^+ \\ \sqrt{2}\,\Sigma^- & -\Sigma^0 \end{pmatrix}\begin{pmatrix} p \\ n \end{pmatrix} \\ & +(\overline{L}{}^0\overline{L}{}^-)\begin{pmatrix} \Sigma^0 & \sqrt{2}\,\Sigma^+ \\ \sqrt{2}\,\Sigma^- & -\Sigma^0 \end{pmatrix}\begin{pmatrix} \Xi^0 \\ \Xi^- \end{pmatrix} \\ & +(\overline{K}{}^+\overline{K}{}^0)\begin{pmatrix} \Lambda & 0 \\ 0 & \Lambda \end{pmatrix}\begin{pmatrix} p \\ n \end{pmatrix} \\ & +(\overline{L}{}^0\overline{L}{}^-)\begin{pmatrix} \Lambda & 0 \\ 0 & \Lambda \end{pmatrix}\begin{pmatrix} \Xi^0 \\ \Xi^- \end{pmatrix}\Big]+\text{h.c.}\ ,\end{aligned} \tag{10}$$

$$\begin{aligned}H_{\mathfrak{K}_0}=g/\sqrt{2}\Big[& (\overline{p}\,\overline{n})\begin{pmatrix} \sqrt{2}\,D^+ & 0 \\ 0 & \sqrt{2}\,D^+ \end{pmatrix}\begin{pmatrix} \Xi^0 \\ \Xi^- \end{pmatrix} \\ & +(\overline{\Xi}{}^0\overline{\Xi}{}^-)\begin{pmatrix} \sqrt{2}\,D^- & 0 \\ 0 & \sqrt{2}\,D^- \end{pmatrix}\begin{pmatrix} p \\ n \end{pmatrix} \\ & +(\overline{p}\,\overline{n})\begin{pmatrix} D^0 & 0 \\ 0 & -D^0 \end{pmatrix}\begin{pmatrix} p \\ n \end{pmatrix} \\ & +(\overline{\Xi}{}^0\overline{\Xi}{}^-)\begin{pmatrix} D^0 & 0 \\ 0 & -D^0 \end{pmatrix}\begin{pmatrix} \Xi^0 \\ \Xi^- \end{pmatrix} \\ & -\left(\overline{\boldsymbol{\Sigma}}\times\boldsymbol{\Sigma}\cdot\boldsymbol{D}+\overline{\boldsymbol{\Sigma}}\cdot\boldsymbol{D}\Lambda+\overline{\Lambda}\boldsymbol{D}\cdot\boldsymbol{\Sigma}\right)\Big] \\ & +g/\sqrt{2}\,[(P\overline{P}+\overline{\Xi}{}^-\Xi^-+\overline{n}n+\overline{\Xi}{}^0\Xi^0) \\ & -(\overline{\Sigma}{}^+\Sigma^++\overline{\Sigma}{}^-\Sigma^-+\overline{\Sigma}{}^0\Sigma+\overline{\Lambda}\Lambda)]D^{0\prime}+\text{h.c.}\ ,\end{aligned} \tag{11}$$

$$
\begin{aligned}
H_{\mathfrak{K}_0}{}' = g'/\sqrt{2}\Big[(\bar{p}\bar{n})&\begin{pmatrix} \pi^0 & \sqrt{2}\pi^+ \\ \sqrt{2}\pi^- & -\pi^0 \end{pmatrix}\begin{pmatrix} p \\ n \end{pmatrix} \\
&+(\bar{\Xi}^0\bar{\Xi}^-)\begin{pmatrix} \pi^0 & \sqrt{2}\pi^+ \\ \sqrt{2}\pi^- & -\pi^0 \end{pmatrix}\begin{pmatrix} \Xi^0 \\ \Xi^- \end{pmatrix} \\
&+(\bar{\boldsymbol{\Sigma}}\times\boldsymbol{\Sigma}\cdot\boldsymbol{\pi}+\bar{\boldsymbol{\Sigma}}\cdot\boldsymbol{\pi}\cdot\Lambda+\bar{\Lambda}\cdot\boldsymbol{\pi}\boldsymbol{\Sigma})\Big] \\
&+g'/\sqrt{2}\,[(\bar{P}P+\bar{\Xi}^-\Xi^-+\bar{n}n+\bar{\Xi}^0\Xi^0) \\
&+(\bar{\Sigma}^+\Sigma^++\bar{\Sigma}^-\Sigma^-+\bar{\Sigma}^0\Sigma^0+\bar{\Lambda}\Lambda)]\pi^{0\prime}+\text{h.c.}\,.
\end{aligned}
\tag{12}
$$

It is seen in (9)-(12) that charge independence[7] in the ordinary isospin representation is valid in the strong interactions (3)-(4), except in the processes involving D^0-mesons. From (9)-(10) we see that the K-kaons couple only nucleons with the Σ and Λ-particles, while the L-kaons couple only the Ξ-particles with the Σ and Λ-particles. In (11) $D^{\pm}$-mesons are of strangeness-two mesons for the nucleon-Ξ coupling, but are of strangeness-zero mesons for the $\Xi-\Lambda(\Sigma)$ coupling. In (12), the pion-baryon interactions are given just as we expect.

References

1) S. Nakamura: J. Phys. Soc. Japan **15** (1960) 1543.
2) B. d'Espagnat, J. Prentki, A. Salam: Nuclear Physics **4** (1958).
3) G. Takeda: Prog. Theor. Phys. **19** (1958) 631.
4) T. Nakano and K. Nishijima: Prog. Theor. Phys. **10** (1953) 581. T. Nishijima, ibid, **13** (1955) 285.
5) M. Gell-Mann: Phys. Rev. **92** (1953) 833.
6) S. Nakamura: Nuclear Physics **14** (1959) 155.
7) O. Klein: Arkiv for Fysik, 16 nur 17 (1959) 91.

Errata

(Note by the Editor) The following tables should be inserted into the paper

Emission of ^{8}Li, ^{9}Li and ^{8}B Fragments from Stars Produced by 4.3 GeV π^--Mesons in Nuclear Emulsion

By Kuni IMAEDA, Mitsuko KAZUNO and Nobuo ITO

J. Phys. Soc. Japan **15** (1960) 1753

Table II. Number of δ-rays in the track of No. 10.

Range (μm)	No. of δ-rays		Total number of δ-rays ≧2 grains
	≧3 grains	≧2 grains	
0- 67	0	3	3
67-135	1	6	9
135-202	1	17	26
202-270	8	18	44
270-337	8	20	64
337-404	19	22	86
404-451	29	16	102

Table III. Number of δ-rays (≧2 grains) in hammer tracks of the range exceeds 200 μm.

Track number	Range (μm)	tan (dip angle)	No. of δ-rays (≧2 grains)
3	227	0.17	1
124	239	0.28	5
19	359	0.82	1
112	390	0.84	20
57	420	0.01	20
27	438	0.85	26
10	451	1.10	102

PROGRESS OF THEORETICAL PHYSICS

CONTENTS

Progress of Theoretical Physics Vol. 24, No. 3, September 1960

On the Quantization of Physical Space-Time Operators ....Ichie WATANABE..465
Scattering of Electrons by the Thermal Motion of Impurity Ions ....Shigeharu KOSHINO..484
Collective Correlation between Vacuum Nucleons and the S-Wave Pion-Nucleon Scattering ....Osamu HARA..495
Field Theoretical Interpretation of "*B-Matter*". I ....Hiroshi YAMAMOTO..512
The Electric Polarizability of the Neutron ....T. UEDA and M. SAWAMURA..519
The Theory of the Nucleon Level Structure in Terms of the Pion-Pion Resonance. I........K. ITABASHI, M. KATO, K. NAKAGAWA and G. TAKADA..529
Mathematical Foundation of the Quantum Theory of Free Fields .... Hitoshi WAKITA..555
Symmetry in Sakata's Model and Weak Interactions .... M. IKEDA, Y. MIYACHI and S. OGAWA..569
Theory of Classical Fluids and the Convolution Approximation (*Note on Papers by Tohru Morita*) ....Emmanuel MEERON..588
On the Concept of Regraduation in General Relativity..H. NARIAI and Y. UENO..593
Non-Locality in the Second Order Potential ....Robert L. CAROVILLANO..614
The Hyperon and Nucleon Interactions. I—*Potentials*— ......Masayuki UEHARA..629
Vibrational Thermodynamic Properties of Lattices with Defects. II—*Two- and Three-Dimensional Simple Cubic Lattices*— ....J. MAHANTY, A. A. MARADUDIN and G. H. WEISS..648
On a Unified Description of Elementary Particles........................... ....M. TAKETANI and Y. KATAYAMA..661

Letters to the Editor:

A New Approach to the Theory of Classical Fluids. IIIa............ ....T. MORITA and K. HIROIKE..679
Charge Distribution in Be^9 ....Y. R. WAGHMARE..681
Causality and Local Commutativity ....K. YAMAMOTO..684
Synthesis of Iron Group Elements by the Rapid Nuclear Process ....M. NISHIDA, H. TSUDA and H. TSUJI..685

Errata:

Electromagnetic Structure of the Nucleon. V—*Numerical Results of Three-Pion-State Contributions*—(Vol. 24, p. 414)............... ....K. HIIDA and N. NAKANISHI..688

Price $ 1.25 per copy
$ 15.00 per year (postage inclusive)
Annual dues for foreign members (individual subscribers)
$ 12.00 (postage inclusive)
" for foreign members of the Physical Society of Japan
$ 10.00 (postage inclusive)

Application for membership, subscriptions and orders for back numbers should be sent, directly or through book-dealers, to

The Publication Office
in
Yukawa Hall, Kyoto University, Kyoto, Japan

. . . .

JOURNAL OF THE PHYSICAL SOCIETY OF JAPAN, Vol. 15, No. 12, DECEMBER, 1960

Excitation Functions for Alpha-particle Reactions on Fe^{56} and Fe^{57}

By Shigeo TANAKA, Michiaki FURUKAWA, Shiro IWATA*, Masuo, YAGI**
Hiroshi AMANO*** and Takashi MIKUMO
Institute for Nuclear Study, University of Tokyo
Tanashi-Machi, Tokyo

(Received July 1, 1960)

Excitation functions for the (α, pn), $(\alpha, p2n)$, $(\alpha, 3n)$ and $(\alpha, \alpha pn)$ reactions on Fe^{56} and the $(\alpha, \alpha p)$ reaction on Fe^{57} were measured by the activation method using a stacked-foil technique, the alpha-particle energies ranging from 17 to 40 MeV. The measured excitation functions for the alpha-particle reactions on Fe^{56} (present work) were compared with those for the proton reactions on Co^{59} (Sharp et al.); the compound nucleus Ni^{60} being the same for two cases. The comparison gives a test of the validity of compound nucleus theory. The ratios of corresponding cross sections seem to agree well with the theory (except in the case of resulting Co^{57}). However, it may be seen that the two curves corresponding to the same residual nucleus in each case do not entirly coincide in energy.

§1. Introduction

Ghoshal tested the applicability of Bohr's[1] compound nucleus hypothesis of nuclear reaction to the medium-energy region[2]. According to Bohr's hypothesis, we may write $\sigma(a,b)/\sigma(a,b')=\sigma(a',b)/\sigma(a',b')$ provided that the excitation energy of the compound nucleus is the same. In Ghoshal's experiment, the compound nucleus, Zn^{64}, was formed both by proton bombardment of Cu^{63} and by alpha-particle bombardment of Ni^{60}. The relation

$$\sigma(p,\ n):\sigma(p,\ 2n):\sigma(p,\ pn)$$
$$=\sigma(\alpha,\ n):\sigma(\alpha,\ 2n):\sigma(\alpha,\ pn)$$

was observed to hold when 7 MeV was added to the proton energy to match the excitation energy of the compound nucleus. The validity of Bohr's hypothesis was also confirmed to the reactions in heavy elements by John.[3] He compared the excitation functions for $Pb^{206}(\alpha, xn)$ with those for $Bi^{209}(p, xn)$, where $x=2$, 3 or 4. The cross sections of the alpha-particle and proton reactions were in good agreement with each other provided that the proton energy was shifted by adding 11.9 MeV.

It has been pointed out, however, by Eastman, Isenor, Bainbridge and Duckworth[4] and also by John[3] that the energy shift required to fit the experiment to the compound nucleus theory is not exactly equal to the value derived from mass measurement. This discrepancy might throw some doubt on the validity of the compound nucleus theory.

The present experiment has been undertaken in order to give a further test of the above considerations. The excitation functions measured here for the (α, pn), $(\alpha, p2n)$, $(\alpha, 3n)$ and $(\alpha, \alpha pn)$ reactions on Fe^{56} are compared with those for the corresponding proton reactions on Co^{59} measured by Sharp, Diamond and Wilkinson.[5]

This experiment is also a part of the present authors' systematic study in which the cross sections of the alpha-particle reactions on medium-weight nuclei at intermediate energies are investigated. The $(\alpha, \alpha p)$ reaction on Fe^{57} is also reported here.

§2. Experimental

The bombardments were performed with the external alpha-particle beam from the 160 cm INSJ variable energy cyclotron by means of a "stacked-foil" technique. The beam was collected in a Faraday cup and the total charge of the beam was measured by a current integrator. A more detailed description of the bombarding system is given in the previous reports.[6-7] In different experiments, the initial alpha-particle energies were 40.2, 32.1 and 32.0 MeV, and certain energy region was overlapped in different runs. The energy dependence of cross sections was measured by using the stacked-foil technique in which target foils were interspaced with aluminum absorbers. The value of the energy loss of alpha-particles in aluminum absorber was taken from the works of Bichsel, Mosley and Aron,[8] Burkig and MacKenzie,[9] and Sternheimer,[10] whereas that in iron target was calculated from the stopping power formula of Bethe et al. using the estimated mean excitation potential ($I=13\ Z$ and $Z=26$).

---

* Engineering Research Institute, Kyoto University, Kyoto.

** Department of Chemistry, Faculty of Science, Tohoku University, Sendai.

*** Japan Atomic Energy Research Institute, Tokai-Mura, Ibaragi.

The targets consisted of natural-iron foils (7.7±0.1 mg/cm^2) whose purity was approximately 99.8%.

After the bombardment, the target foil was dissolved in acid and nickel, manganese, cobalt and iron were chemically separated by means of an anion exchange resin.

The disintegration rates of the samples were determined with a calibrated GM counter, a $4\pi\beta$-counter and an (1−3/4 in. dia.×2 in. high, 1−1/2 in. dia.×1 in. high and well type) NaI scintillation counter. The counting procedure is given in detail in the Appendix.

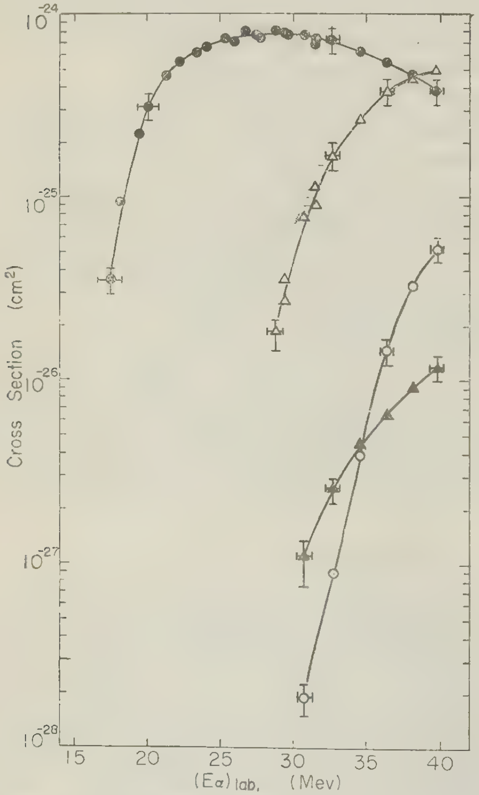

Fig. 1. Excitation functions for the aplha-particle reactions on Fe^{56}.

● Fe$^{56}(\alpha, pn)$Co^{58} △ Fe$^{56}(\alpha, p2n)$Co^{57}
▲ Fe$^{56}(\alpha, 3n)$Ni^{57} ○ Fe$^{56}(\alpha, \alpha pn)$Mn^{54}

§ 3. Results and Discussion

The absolute cross sections are plotted as a function of alpha-particle energy in Fig. 1, which also includes the energy spread in target foil and the estimated error of the magnitude of cross section for some experimental points. The Fe$^{56}(\alpha, p2n)$Co^{57} and the Fe$^{56}(\alpha, 3n)$Ni^{57} cross section were not calculated below 29 MeV because of the interference of the Fe$^{54}(\alpha, p)$Co^{57} and the Fe$^{54}(\alpha, n)$Ni^{57} reaction, respectively.

The interference above 29 MeV is estimated from the data of Fe^{54} [11] and included as a source of error in the vertical line in Fig. 1.

The comparison between the alpha-particle

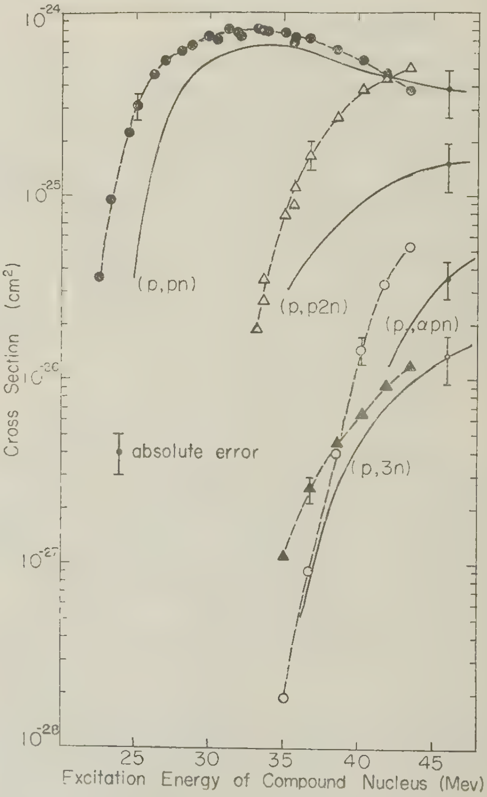

Fig. 2. Comparison between the alpha-particle reactions on Fe^{56} and the proton reactions on Co^{59}.

● Fe$^{56}(\alpha, pn)$Co^{58} △ Fe$^{56}(\alpha, p2n)$Co^{57}
▲ Fe$^{56}(\alpha, 3n)$Ni^{57} ○ Fe$^{56}(\alpha, \alpha pn)$Mn^{54}

Solid line represents the excitation function for each corresponding proton reaction on Co^{59} (Sharp et al.)

reactions on Fe^{56} and the proton reactions on Co^{59} is illustrated in Fig. 2. The compound nucleus produced in both cases is Ni^{60}. According to the compound nucleus theory, the relative yields of these reactions should be the same regardless of target provided that the excitation energy of the compound nucleus is the same. The excitation energy of the compound nucleus is $B_\alpha + 56/60\,E_\alpha$ for the alpha-particle reactions; or, $B_p + 59/60\,E_p$ for the proton reactions. Where B_α and B_p represent the binding energies of an alpha-particle to Ni^{60} and of a proton to Ni^{60}, respectively; E_α and E_p are the kinetic energies of an alpha-particle and of a proton in the laboratory system. The quantities B_α and B_p are deduced from the mass values which have recently been measured with high precision by Quisenberry, Scolman and Nier[12]; $B_\alpha = 6.31$ MeV and $B_p = 9.54$ MeV.

It will be seen in Fig. 2 that the two curves corresponding to the same residual nucleus in each case do not entirely coincide in energy. The difference is about 2 MeV and is in the opposite direction to what appears in both Ghoshal's and John's experiments. The uncertainty in energy may come from the uncertainties in the bombarding energies. The alpha-particle energy is estimated to be accurate to ± 0.5 MeV at 20 MeV; taking into account the uncertainties of incident energy, target thickness and estimated value of energy loss. The present authors have experienced good agreement in series of bombardments. The precision of the alpha-particle energy at 20 MeV is estimated to be ± 0.3 MeV. The proton bombardment was performed by Sharp, Diamond and Wilkinson[5] with the internal scattered beam of the Harvard University 95 in. synchrocyclotron. The available initial proton energies were 73.5 and 100.3 MeV, and it was estimated that the energy at the front of the target stack was accurate to ± 0.6 MeV. The bombardments were also made by them with the 32 MeV proton linac at Berkeley to get good resolution in the low-energy portions of Ni^{57} and Co^{58} excitation functions, and the energy of the incident protons was known to ± 0.2MeV. Hence the uncertainty in energy may amount 1 MeV at $E_{\mathrm{exc}} = 25$ MeV in their experiment and ours. On the other hand, it might be thought that the errors in absolute cross sections also reduce the discrepancy in energy. These two uncertainties are not altogether impossible to eliminate the discrepancy in energy at all. However, it is more likely to see that there is a discrepancy in energy in this comparison. More accurate experiments are required to see exactly whether the discrepancy is significant.

When the proton curve in Fig. 2 is made to shift by subtracting about 2 MeV, the two curves corresponding to the same residual nucleus in each case seem to match quite well (except in the case of producing Co^{57}) both in the shape of excitation function and in the magnitude of cross section. The difference between the value of the cross section for the Fe^{56} $(\alpha, p2n)Co^{57}$ reaction and that for the $Co^{59}(p, p2n)Co^{57}$ reaction should be again checked experimentally.

The excitation function for the $Fe^{57}(\alpha, \alpha p)Mn^{56}$ reaction is shown in Fig. 3.

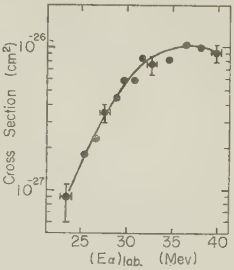

Fig. 3. Excitation function for the reaction $Fe^{57}(\alpha, \alpha p)Mn^{56}$.

Acknowledgements

Authors' thanks are due to Prof. I. Nonaka and the other members of staff of Low Energy Division in this Institute for their constant interest and encouragement. The help of Messrs. T. Karasawa, A. Suzuki, H. Ogawa, H. Adachi, Y. Miyazawa, and T. Yamada in operating the cyclotron is gratefully acknowledged. The continued assistance of Mr. T. Ando throughout the work is also acknowledged.

Appendix

Counting procedures

Ni^{57}—After Ni^{57} was allowed to decay to Co^{57}, *Ni^{57}* was measured as Co^{57}.

Co^{58}—The 810 KeV γ-ray photopeak was measured with an 1–3/4 in. dia. ×2 in high NaI scintillation counter. The contribution

of Co^{56} was subtracted by comparing the sample with a Co^{56} standard source. The disintegration rate of Co^{58} was obtained by applying the photopeak efficiency to the counting rate. The photopeak efficiency in the present equipment was obtained by calibrating with the various standard sources of known disintegration rates. The disintegration rate was also checked by a $4\pi\beta$-counting assuming the positron emission probability of 15% per total disintegration. Both values agreed each other within 10%.

Co^{57}—The 122 and 137 KeV γ-ray photopeaks were measured in an 1—3/4 in. dia. ×2 in. high well-type NaI scitillation counter. The photopeak efficiency was estimated as 0.85.

Mn^{56}—The disintegration rate was obtained by counting the β-rays with a calibrated GM counter.

Mn^{54}—The 845 KeV γ-ray photopeak was measured with an 1—3/4 in. dia. ×2 in. high NaI scintillation counter. The disintegration rate was obtained by applying photopeak efficiency to the counting rate as in the case of Co^{58}.

"Note added in proof"

After this work, one of the present authors* has studied the alpha-particle reactions on Ni^{60}. He has compared, after Ghoshal's work, the alpha-particle reactions on Ni^{60} with the proton reactions on Cu^{63}. In the comparison all the cross sections on both reactions which have been measured up to date by many authors are included. He has obtained the conclusion that the energy values in the experiments compared might not be so accurate that it seems inadequate to discuss strictly whether the discrepancy in energy is significant.

References

1) N. Bohr: Nature **137** (1936) 344.
2) S. N. Ghoshal: Phys. Rev. **80** (1950) 939.
3) W. John: Phys. Rev. **103** (1956) 704.
4) Eastman, Isenor, Bainbridge and Duckworth: Phys. Rev. **103** (1956) 145.
5) Sharp, Diamond and Wilkinson: Phys. Rev. **101** (1956) 1493.
6) S. Kikuchi et al.: J. Phys. Soc. Japan **15** (1960) 41.
7) Tanaka, Furukawa, Mikumo, Iwata, Yagi and Amano: J. Phys. Soc. Japan **15** (1960) 545.
8) Bichsel, Mosley and Aron: Phys. Rev. **105** (1957) 1788.
9) V. C. Burkig and K. R. MacKenzie: Phys. Rev. **106** (1957) 848.
10) R. M. Sternheimer: Phys. Rev. **115** (1959) 137.
11) Tanaka, Furukawa, Iwata, Yagi, Amano and Mikumo: J. Phys. Soc. Japan **15** (1956) 1547.
12) Quisenberry, Scolman and Nier: Phys. Rev. **104** (1956) 461.

---

* S. Tanaka: to be published in J. Phys. Soc. Japan.

JOURNAL OF THE PHYSICAL SOCIETY OF JAPAN, Vol. 15, No. 12, DECEMBER, 1960

Multipolarity of γ-ray Absorption in $U^{238}(\gamma, f)$ Reaction produced by $F(p, \alpha\gamma)$ γ rays

By Eiko TAKEKOSHI

Japan Atomic Energy Research Institute Tokai Laboratory

(Received July 4, 1960)

Multipolarity of γ-ray absorption in $U^{238}(\gamma, f)$ reaction, produced by monochromatic γ rays from $F(p, \alpha\gamma)$ reactions, has been investigated by the analysis of the angular distribution of 1018 tracks of fission fragments in uranium-impregnated nuclear emulsions. It can be explained by mixing two sorts of interaction; *electric dipole* ($E1$) and *electric quadrupole* ($E2$). The ratio of $E2$ to $E1$ absorption cross section, denoted by σ_{fq}/σ_{fd}, has been found to be 0.13 ± 0.05. This value is compared with other results with bremsstrahlung. The angular distribution is consistent with those of Baz *et al.*, however, the analysis and interpretation of the results are different from those of Baz *et al.*.

§ 1. Introduction

As mentioned by A. Bohr[1], the nucleus, which is passing over the saddle point and whose excitation energy is not too far above the fission threshold, is "*cold*", since major part of its energy content is bound in potential energy of deformation. The quantum states available to the nucleus at the saddle point of the "*fission channels*" are then widely separated and represent relatively simple types of motion of the nucleus. These channels are expected to form a similar spectrum to that of observed low-energy excitations of the ground state of the nucleus.

This character of the motion of the nucleus at the saddle point gives rise to a number of regularities in the fission phenomena. Thus, fission process passing through a single channel may exhibit a marked anisotropy in the angular distribution of the fragments, depending on the angular momentum quantum numbers of the channel. Moreover, the wide spacing of the channels implies that the fission threshold may depend significantly on the spin-parities of the compound nucleus. Experimental data on these aspects of the fission phenomenon may thus provide valuable information on the structure of fissioning nuclei at a crucial state of the process.

The case of photofission of even-even nuclei presents some extremely simple features, since in this case the compound nucleus is always produced in a (1–) state, when *electric dipole* absorption is assumed. The lowest (1–) fission channel at the saddle point corresponds to a $K=0$ configuration, with the nuclear angular momentum taken up by rotational motion. For photon energies near the fission threshold, the majority of the fissioning nuclei are therefore expected to pass through this particular channel. In this case the angular distribution of the emitted fragments is expected to be mainly of the type expressed by the following form

$$I(\theta)=b\cdot\sin^2\theta\ , \tag{1}$$

where θ is an angle of nuclear symmetry axis from the photon direction and b is a constant.

As the photon energy increases, other channels of (1–) type representing intrinsic nuclear excitations become available. Those channels having $K=1$ give an anisotropy of opposite character to that of the form (1) and in consideration of the two characters a nearly isotropic distribution is expected for the nuclei passing through the saddle point in a state of intrinsic excitation. Thus, the total angular distribution becomes

$$I(\theta)=a+b\cdot\sin^2\theta\ . \tag{2}$$

According to L. Katz *et al.*[2], the ratio b/a was given by the empirical relation $b/a=x/(E_\gamma-z)^y$, where x, y and z were empirically determined constants equal to 40, 2.6 and 4 respectively for U^{238} nucleus. Therefore, the ratio b/a decreases as photon energy increases.

This circumstance provides an explanation of the observed angular anisotropy of the fission fragments. The experimental studies by E. J. Winhold *et al.*[3] and L. Katz *et al.*, with the bremsstrahlung of maximum energies between 6.0 MeV and 20 MeV produced by a linear accelerator and by a betatron, have shown that the angular distribution is expressed by the form (2) and that γ-ray absorption process can be assumed to be $E1$ absorption only. Winhold *et al.* measured intensities of fission fragments which were emitted at 90° and parallel to incident photons, using a scattering chamber in which fission products were caught on aluminium foils, and thus measuring β activities. Katz *et al.* tried to measure ratios of intensities at various angles to that at incident direction, using a fission chamber in which fission pulses from a uranium target were amplified by linear amplifiers and were introduced to a coincidence circuit gated by expander pulses from betatron.

The situation obtained by V. P. Bannik *et al.*[4] and Baz *et al.*[5] with bremsstrahlung of maximum energies, between 6.5 MeV and 26.5 MeV produced by a synchrotron, has been expressed by a different form from the form (2). The angular distribution is then expressed by the following form

$$I(\theta)=a+b\cdot\sin^2\theta+c\cdot\sin^2\theta\cdot\cos^2\theta\ , \qquad (3)$$

and the γ-ray absorption process can be regarded as the mixture of $E1$ and $E2$ characters. Thus, a detailed angular distribution was shown, in which intensities of fission fragments of various angles to that at incident photon direction were measured by means of uranium-impregnated nuclear emulsion; and the ratio of absorption cross section of $E2$ to $E1$ was discussed.

These experiments were carried out with bremsstrahlung. When this bremsstrahlung is in use, these x-rays have a continuous spectrum extending from zero to the maximum energy of electrons which strike a target. The x-ray spectrum, however, may have various forms, even if these maximum energies have the same value. Thus, the experimental results using bremsstrahlung do not seem to contribute to the explanation of the structure of uranium-238 nuclei. The study obtained by using monochromatic γ rays is rather preferable for this study to bremsstrahlung, because the compound nucleus excited by monochromatic γ rays splits into fission fragments while it passes through a few fission channels; and the analysis of the angular distribution is believed to give a clear information on the structure of the deformed nucleus. The angular distribution of the fission fragments in $U^{238}(\gamma, f)$ reaction, produced by $F(p, \alpha\gamma)$ γ rays, $E_\gamma=6.13$ MeV, is very characteristic for an aspect of the γ-ray absorption process near the threshold in $U^{238}(\gamma, f)$ and $U^{238}(\gamma, n)$ U^{237} reaction.

In the present experiment the angular distribution of the fission fragments for $U^{238}(\gamma, n)$ reaction was measured by using uranium-impregnated nuclear emulsions irradiated by $F(p, \alpha\gamma)$ γ rays under a good geometrical condition. This results shows that the γ-ray absorption process is the mixture of $E1$ and $E2$, and the ratio of $E2$ to $E1$, denoted by σ_{fq}/σ_{fd}, is 0.13 ± 0.05. This result is compared with other results with bremsstrahlung and is discussed.

§ 2. Procedure

Natural uranium-impregnated nuclear emulsions were irradiated for about 10 hours under γ rays produced by proton bombardment of a CaF thick target. The proton beam was accelerated up to 2 MeV by Van de Graaff of the J.A.E.R.I., and the intensity of the magnetically analysed beam was 25 μA. Diameters of the CaF thick target and the proton-beam spot was 8 mm and 3 mm respectively. Sakura NR–M1 uranium-impregnated nuclear plates (1.5″×1″, 200 μ thickness) were used. Each plate was arranged in the manner that the 1″ edges was 12 cm apart from the target and the 1.5″ edges parallel to the γ rays, giving glancing incidence.

The uranium-impregnated nuclear plates were made by immersing the Sakura NR–MI nucler plates (Ilford C2 class) into 25 percent uranyl acetate solution in which the ratio of admixture of glycerine is 3 percent. Immersing of the plates was continued to reach saturation. The immersing time was 3 hours at 25°C. When the plates were immersed into the uranyl acetate solution concentrated over 25 percent, the action of development and fixing of the plates was disturbed by crystallization of the uranyl acetate in the nuclear plates.

The developing procedure of the two bath method[6] was chosen as the most suitable method. For the best condition of the second stage in this procedure of the two bath method, it was found that the developing time is 25 minutes at 17°C. At this condition, very sharp tracks of fission fragments and faint tracks of spontaneous α particles from uranium were obtained, which made the scanning of the plates considerably easier. The microphotographs of the representative type of these very sharp tracks and the faint tracks are shown in Fig. 1.

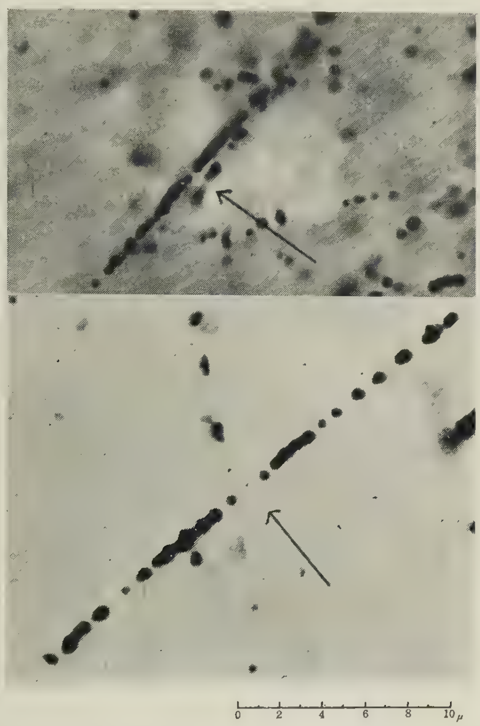

Fig. 1. Microphotographs of typical fission tracks. The arrows show the fission point of U^{238} nucleus.

The very sharp tracks of the fission fragments are dense at the middle and faint at both ends; that is why they are called "*taper track*". The faint tracks of spontaneous α particles from uranium are dotted with black grains in tatters.

The shrinkage factor was obtained by measuring the horizontal and vertical components of the lengths[11] of spontaneous α tracks from uranium in uranium-impregnated nuclear emulsion un-exposed to γ rays. The shrinkage factor was 1.9.

The processed emulsions were scanned using "Tiyoda" and "Nippon Kogaku" microscopes at a magnification of ×1350 and ×1500 respectively. Each depth measurement (mean of three readings) was subject to about $\pm 0.3\,\mu$ standard deviation. Errors in the horizontal projections were $\pm 0.5\,\mu$.

The quantity of the uranium in uranium-impregnated nuclear emulsion was about 0.03 g/cm^3[8].

The total florine γ-ray doses in position of emulsions were about 10^8 quanta/cm^2[9].

Since discrimination between α tracks and fission tracks has ambiguity due to non-uniformity of emulsion sensitivity, it is considered that 1708 fission tracks contain the impurity of spontaneous α tracks from uranium. This impurity was eliminated by using the following method; the uranium-impregnated nuclear plates, un-irradiated by γ rays, were developed intensely in the grade of sharp tracks for α particles. The range distribution of these α tracks and that of fission tracks in these plates are shown in Figs. 2 and 3 respectively.

In the Fig. 2 the peaks at $16\,\mu$ and $19\,\mu$ represent the length of range of α particles from uranium-I and uranium-II+Ac-uranium respectively. From the Figs. 2 and 3, it was pointed out that the fission tracks shorter

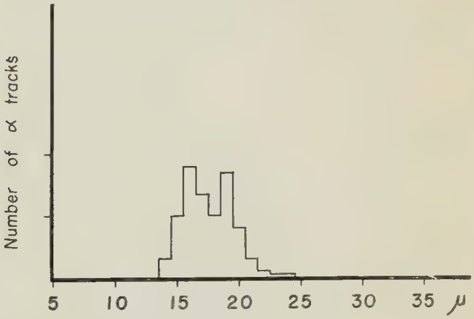

Fig. 2. Range distribution of spontaneous α tracks in uranium-impregnated nuclear plates, un-exposed to γ rays.

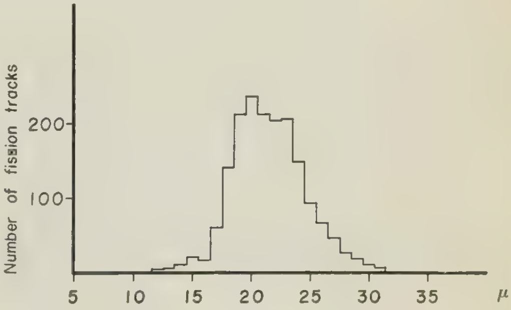

Fig. 3. Range distribution of fission tracks in uranium-impregnated nuclear plates, exposed to γ rays.

than 20 μ may involve the impurity of the spontaneous α tracks. It was very difficult to estimate the fraction of the impurity to fission tracks. However, the difference was not found between the angular distributions for the fission tracks longer than 21 μ and 22 μ.

Thus, by using the angular distribution for the fission tracks longer than 21 μ, the process of $U^{238}(\gamma, f)$ reaction was analyzed. The number of these tracks was 1018.

§ 3. Results and Discussions

The angular distribution for the fission tracks longer than 21 μ is shown in Fig. 4 and that longer than 22 μ is shown in Fig. 5.

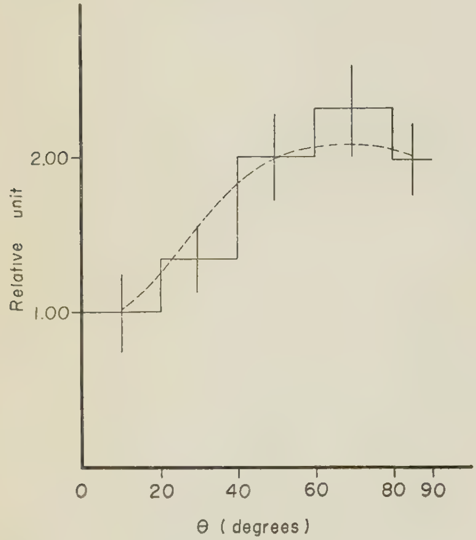

Fig. 4. Angular distribution for the fission tracks longer than 21 μ. Dotted line curve was calculated by least square fitting; this is expressed by

$$I(\theta)=1+(1.02\pm0.49)\sin^2\theta +(1.63\pm0.52)\sin^2\theta\cdot\cos^2\theta\,.$$

The experimental data of the angular distribution were taken at 20° interval. The value at θ° is expressed by a relative number of tracks between θ°−10° and θ°+10° to that between 0° and 20°. Correction for the escape of tracks from the emulsion surface was done. In Figs. 4 and 5 the vertical lines indicate only the statistical standard deviations.

For the purpose of observation of the systematic error in angular distribution measurement, the angular distribution of the tracks from spontaneous α decay of uranium was measured by using uranium-impregnated nuclear emulsions (not exposed to γ rays). This is shown in Fig. 6.

Since this proved to be flat with respect to the angle, as was expected, it was understood that there was no systematic error in the present angular distribution measurement of fission tracks. After the examination of control plates placed outside the γ rays, the

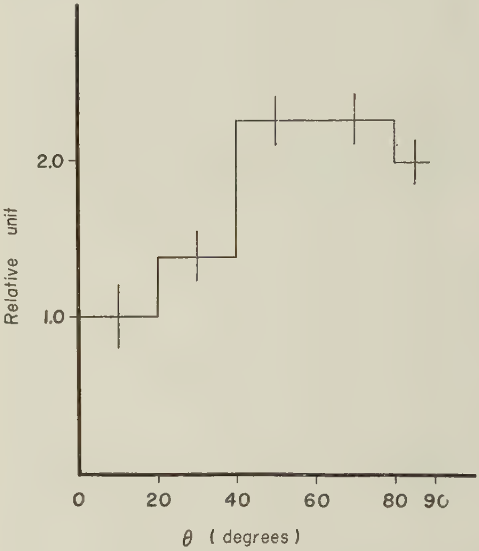

Fig. 5. Angular distribution for the fission tracks longer than 22 μ

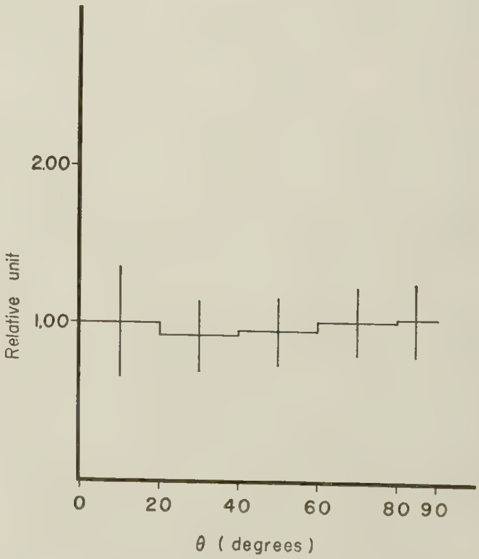

Fig. 6. Angular distribution of spontaneous α tracks in uranium-impregnated nuclear plates (not exposed to γ rays).

fission tracks due to the background neutrons were confirmed to be negligible.

As mentioned in § **1**. there were two experimental results for photon absorption resulting in nuclear fission. In the first, as done by Winhold *et al.* and Katz *et al.*, the photon absorption was assumed to be *electric dipole* character ($E1$). In the second, as done by Bannik *et al.* and Baz *et al.*, the *electric quadrupole* absorption was added to $E1$.

Winhold and Halpern measured only the anisotropy of the angular distribution. They measured only at two angle points, so their results were interpreted by $E1$ absorption alone.

Katz *et al.* measured detailed angular distribution and found that in all cases the data were represented by the form (2). Their results show that the photon absorption is due to $E1$ only and $E2$ process is negligibly small.

Baz *et al.* studied detailed angular distributions by using uranium-impregnated nuclear emulsions, and the change of the angular distribution with energy $E_{\gamma\,\mathrm{max}}$ was studied. In their experimental results, it was pointed out that $E1$ should be mixed with $E2$ and that the ratio $E2$ to $E1$ depend on the energy $E_{\gamma\,\mathrm{max}}$.

In the present experiment the detailed angular distribution was studied by using uranium-impregnated nuclear emulsions irradiated by monochromatic γ ray from $F(p, \alpha\gamma)$ reaction. As shown in Figs. 4 and 5, it was considered that $E2$ must be added to $E1$, since the angular distribution curve at the neighborhood of 90° descend lower than the value given by $I(\theta)=a+b\cdot\sin^2\theta$. Thus, these angular distribution must be described by

$$I(\theta)+I(\pi-\theta)=a+b\sin^2\theta+c\sin^2\theta\cdot\cos^2\theta\,, \tag{4}$$

where the summation $I(\theta)+I(\pi-\theta)$ is done, since it is impossible to distinguish either one of the fissions tracks from the other.

From the present experimental data, the coefficients " a ", " b " and " c " in the form (4) were calculated by using the least mean square fitting. It was given by the following expression;

$$I(\theta)=1+(1.01\pm0.49)\sin^2\theta+(1.63\pm0.52)\sin^2\theta\cdot\cos^2\theta\,.$$

The present results were compared with those of Baz *et al.* and others[2),3)] for (**i**) the graph of angular distribution, (**ii**) the ratios of b/a, c/a and c/b and (**iii**) the b/a ratio calculated in the assumption of the angular dependence to be of the form $I(\theta)=a+b\cdot\sin^2\theta$.

(**i**) The comparison of the angular distributions produced by $F(p, \alpha\gamma)$ γ rays and the bremsstrahlung is shown in Fig. 7. (***a***), (***b***) and (***d***) show the angular distributions produced by bremsstrahlung at $E_{\gamma\,\mathrm{max}}=9.4$ MeV, 8 MeV and 6.5 MeV, respectively, obtained by

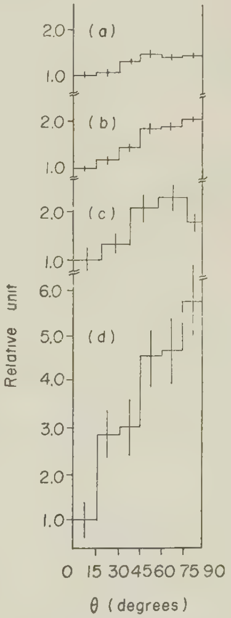

Fig. 7. Comparison of the angular distributions. (***a***), (***b***) and (***d***) show the results obtained by Baz *et al.*, and (***c***) shows the results obtained in the present experiment.

Table I. Comparison with the ratios b/a, c/a and c/b produced by $F(p, \alpha\gamma)$ γ rays and bremsstrahlung.

$E\gamma$	b/a	c/a	c/b	Reference
$E_{\gamma\,\mathrm{Max}}$ $=6.5$ MeV	4.2 ±1.8	3.1 ±3.2	0.75 ±0.71	A. I. Baz *et al.*
$E_{\gamma\,\mathrm{Max}}$ $=8.0$ MeV	1.12 ±0.12	0.60 ±0.38	0.54 ±0.34	〃
$E_{\gamma\,\mathrm{Max}}$ $=9.4$ MeV	0.54 ±0.08	1.34 ±0.34	2.46 ±0.68	〃
$F(p\,\alpha\gamma)$ γ rays				
$E\gamma$ $=6.13$ MeV	1.02 ±0.49	1.63 ±0.52	1.59 ±0.49	Present Experiment

Baz *et* al., and (*c*) shows the angular distribution produced by F(p, $\alpha\gamma$) γ rays, $E_\gamma=6.13$ MeV, obtained from the present experiment.

(**ii**) The comparison of the ratios of b/a, c/a and c/b produced by F(p, $\alpha\gamma$) γ rays and the bremsstrahlung are expressed in Table I.

(**iii**) The graph comparing the ratios b/a, obtained by Winhold *et al.*, Katz et al. and Baz *et al.* with the present results, is shown by Fig. 8.

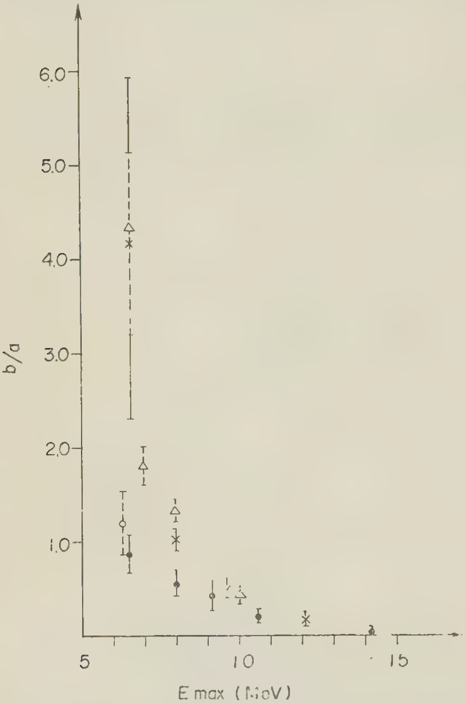

Fig. 8. Graph comparing the ratios b/a.

● results obtained by Winhold *et al.*

△ results obtained by Katz *et al.*

× results obtained by Baz *et al.*

○ results obtained in the present experiment.

These b/a ratios were calculated in the assumption of the angular dependence to be of the form $I(\theta)=a+b\cdot\sin^2\theta$. The discrepancy at each value of the same photon maximum energy may, possibly, be due to difference in the spectrum form of bremsstrahlung and monochromatic γ rays.

§4. Interpretation and Conclusions

Baz *et al.* derived, from the angular distribution of the form (4), the ratio of the $E2$ absorption process to the $E1$ absorption process in the following way. The coefficients "a", "b" and "c" were considered to express isotropic part of angular distribution and the anisotropic parts related to the $E1$ and $E2$ absorption cross section, respectively. Then expressing $E1$ and $E2$ photon absorption cross section in nuclear fission by σ_{fa} and σ_{fq}, respectively, the value of σ_{fq}/σ_{fa} was given by

$$\sigma_{fq}/\sigma_{fa}=c/5b\ . \qquad (5)$$

The values of σ_{fq}/σ_{fa} for each $E_{\gamma\max}$ are also given in Table II, where it is seen that the values increase with increase of E_γ.

Table II. Comparison with the values σ_{fq}/σ_{fa} obtained from the form (5) for data by Baz *et al.* and in the present experiment.

$E\gamma$	σ_{fq}/σ_{fa}	Reference
$E\gamma_{\mathrm{Max}}=6.5$ MeV	0.15 ± 0.14	A. I. Baz *et al.*
$E\gamma_{\mathrm{Max}}=8.0$ MeV	0.11 ± 0.07	〃
$E\gamma_{\mathrm{Max}}=9.4$ MeV	0.49 ± 0.14	〃
F(p, $\alpha\gamma$) γ rays $E\gamma=6.13$ MeV	0.32 ± 0.05	Present Experiment

However, different possibilities are suggested by A. Sugie[10]. According to him, the isotropic part "a" must also be due to either $E1$ or $E2$ or both. The existence of the isotropic part means that the states with K-value one are involved in addition to those with $K=0$. If $K=1$ states are mixed to $K=0$ states in both $E1$ and $E2$ process, we cannot determine the ratios uniquely from the experimentally obtained ratios b/a and c/a. However, we can calculate the ratio σ_{fq}/σ_{fa} by putting several plausible assumptions about the ratio of the processes with different K-values. Then we find that the energy dependence of the ratio σ_{fq}/σ_{fa} changes as follows.

(**i**) As the simplest case; assuming only $K=0$ and $K=1$ contribute to $E1$ and only $K=0$ to $E2$, the value of σ_{fq}/σ_{fa} is given by

$$\sigma_{fq}/\sigma_{fa}=2/15\cdot c/a/(1+2/3\cdot b/a)\ . \qquad (6)$$

The values, calculated from the ratios of "*c*/*a*" and "*b*/*a*" in Table I by using form (6), are represented in Table III; where the values of σ_{fq}/σ_{fa} is nearly constant, when the maximum energies of bremsstrahlung increase.

Table III. Comparison with the values σ_{fq}/σ_{fa} obtained from the form (6) for data by Baz *et al.* and in the present experiment.

E_γ	σ_{fq}/σ_{fa}	Reference
$E_{\gamma\,\mathrm{Max}}=6.5$ MeV	0.11 ± 0.26	A. I. Baz *et al.*
$E_{\gamma\,\mathrm{Max}}=8.0$ MeV	0.05 ± 0.03	〃
$E_{\gamma\,\mathrm{Max}}=9.4$ MeV	0.13 ± 0.03	〃
$F(p, \alpha\gamma)$ γ rays		
$E_\gamma=6.13$ MeV	0.13 ± 0.05	Present Experiment

(**ii**) However, if it is assumed that both $K=0$ and $K=1$ contribute to both $E1$ and $E2$ and that the mixing ratio of $K=1$ to $K=0$ be the same for both $E1$ and $E2$, the ratios of $E2$ to $E1$ increase with increase of photon energy.

(**iii**) Moreover, when an assumption of $K=2$ for $E2$ is added with the same ratio as that of $K=1$ to $K=0$, the similar trend to the above case exist.

(**iv**) However, in case that both $K=0$ and $K=1$ contribute to $E1$ and $K=0$ and $K=2$ to $E2$ and the both mixing ratios are the same, the values σ_{fq}/σ_{fa} are shown to be constant in the region.

Thus, it is found that any unique answer is not drawn as the above discussion, since the values of σ_{fq}/σ_{fa} depend on K-value combination.

As the case stands, however, the author considered that the suggestion given by A. Sugie is reasonable. Therefore, the form (6) is taken for the calculation of the value σ_{fq}/σ_{fa}. As shown in Table III, it is 0.13 ± 0.05. This value, being able to be considered to correspond to that for bremsstrahlung of maximum energy between 8.0 and 9.4 MeV, is consistent with that of Baz *et al.*, after re-calculation by form (6).

The above mentioned consideration must be examined from another point of view, since any unique answer is not drawn from the angular distribution analysis. In other words the competition between $U^{238}(\gamma, f)$ and $U^{238}(\gamma, n)U^{237}$ reaction must be considered, because the energy is somewhat above the threshold of $U^{238}(\gamma, n)U^{237}$ reaction. The relative probability of $U^{238}(\gamma, f)$ and $U^{238}(\gamma, n)$ reaction was studied by Duffield and Huizenga[11] and Gindler *et al.*[12], using radiochemical techniques. They found that the photofission branching ratio, which may be regarded as roughly constant in the region of $E_{\gamma\,\max}=8$ to 11 MeV, was 0.2 for U^{238}. Also Lazareva *et al.*[13] used neutron and fission-counting techniques in order to obtain fission branching ratio. They obtained a value of 0.24 for U^{238}, roughly constant in the region from $E_{\gamma\,\max}=6.5$ MeV to 11 MeV. Thus, it is necessary to consider the photon absorption leading to $U^{238}(\gamma, n)$ reaction near the threshold ($E_\gamma=5.97$ MeV).

The following situation was presented by Baz and Smorodinsky[14]. The $E1$ absorption process leads to $U^{238}(\gamma, n)$ as well as $U^{238}(\gamma, f)$, but the $E2$ absorption process leads only to $U^{238}(\gamma, f)$, not to (γ, n). Then, as the energy becomes higher than the (γ, n) threshold, (γ, f) reaction through the $E1$ process will decrease due to the competition with the (γ, n) reaction, but the (γ, f) reaction through the $E2$ process will not. Thus the ratio σ_{fq}/σ_{fa} increases with increase of photon energy.

However, a different possibility is pointed out by A. Sugie. The photon absorption leading to the $U^{238}(\gamma, n)$ reaction near the threshold is determined mainly by spin-parties of lowlying levels, in U^{237} nucleus disintegrated from $U^{238}(\gamma, n)U^{237}$, since the ground state of U^{238} is 0^+ and neutrons from the $U^{238}(\gamma, n)$ reaction near the threshold may be S-wave. If the ground state of U^{237} is $1/2-$, as suggested by J. O. Rasmussen *et al.*[15] presence of a competing (γ, n) reaction in $E1$ should bring increase of the value of σ_{fq}/σ_{fa} with increase of photon energy. However, if the ground state of U^{237} is $1/2+$, as represented by B. N. Mottelson and S. G. Nilsson[16], the S-wave neutrons of $U^{238}(\gamma, n)$ reaction near the threshold, in case of $E1$ in $U^{238}(\gamma, n)$ reaction, should decay to the levels of excited states of U^{237}. If, in the excited states of U^{237}, the positive parity levels lie close to negative parity levels, the photon absorption of $U^{238}(\gamma, n)$ might be, possibly, given by both $E1$ and $E2$. Thus, without the knowledge of the spin-parities of the levels of U^{237}, both conclusions, σ_{fq}/σ_{fd} is constans or increases with energy, are permissible.

In conclusion, it is not firmly determined whether the ratio of σ_{fq}/σ_{fd} derived from the analysis of angular distribution is constant or increases with increase of photon energy and whether proper value of mixing ratio of $E2$ to $E1$ is found or not, even if the competition between $U^{238}(\gamma, n)$ and $U^{238}(\gamma, f)$ reaction is considered. The author can draw no definite conclusion, since the spin-parities of ground state and excited states of U^{237} are not unambiguously assigned. However, when the spin-parities of levels for U^{237} nucleus is assigned, the aspect of the ratio σ_{fq}/σ_{fd} in $U^{238}(\gamma, f)$ may be proposed from the competition between $U^{238}(\gamma, f)$ and $U^{238}(\gamma, n)$ reactions. Then, an important clue may be given for the levels at the saddle point of the fission, especially for the levels having $K=1$ and positive parity, through the angular distribution analysis.

Acknowledgements

The author wishes to thank Mr. T. Momota and the member of the laboratory for helpful advices. Her thanks are also expressed to Mr. A. Sugie and Mr. K. Moriguchi for valuable theoretical discussion, to Mr. T. Nakajima for chemical analysis and to Miss H. Ishiwa and Miss H. Sasaki for scanning many plates and for numerical calculations.

References

1) A. Bohr: Geneva Conf. **Vol. II.** (1959) 151.
2) L. Katz, A. P. Baerg and F. Brown: Geneva Conf. A/Conf. 15/P/205 U.S.A. (1958)
3) E. J. Winhold and I. Halpern: Phys. Rev. **103** (1956) 990.
4) V. P. Bannik, N. M. Klikova, L. E. Lazareva and W. Yakovlet: J.E.T.P. **33**, **1** (1957) 53.
5) A. I. Baz, N. M. Klikova, L. E. Lazareva, N. V. Nikitina and V. A. Semenov: Geneva Conf. A/Conf. 15/P/2037 USSR. (1958).
6) Arthur Beiser: Rev. Mod. Phys. **24** (1952) 273.
7) J. Rotblat and C. T. Tai: Fundamental Mechanism of Photographic Sensitivity (1951) 331.
8) The chemical analysis was performed by T. Nakajima (the research member of Japan Atomic Energy Research Institute).
9) Eiko. Takekoshi: Genshikaku.Kenkyu **3** (1958) **45** (in Japanese).
10) A. Sugie: Private communication.
11) R. B. Duffield and J. R. Huizenga: Phys. Rev. **89** (1953) 1042.
12) J. E. Gindler, J. R. Huizenga and R. A. Schmitt: Phys. Rev. **104** (1956) 425.
13) L. E. Lazareva, B. I. Gavrilov, B. N. Valnev, G. N. Zatsepina and V. S. Stavinsky: Conference of the Academy of Sciences on the Peaceful Uses of Atomic Energy (1955).
14) A. I. Baz. and Smorodinsky: Geneva Conf. (1958).
15) J. O. Rasmussen, F. L. Canavan and J. M. Hollander: Phys. Rev. **107** (1957) 141.
16) B. N. Mottelson and S. G. Nilsson: K. Danske Vidensk. Selsk. Mat. Fys. Medd. **1**, 8 (1959).

JOURNAL OF THE PHYSICAL SOCIETY OF JAPAN, Vol. 15, No. 12, DECEMBER, 1960

Search for Weak Gamma-Rays in the Positron Decay of Mn^{51}

Masao NOZAWA*, Hisashi YAMAMOTO and Yasukazu YOSHIZAWA
Department of Physics, Faculty of Science, Osaka University, Osaka
and Yujiro KOH
Department of Physics, Faculty of Science, Osaka City University, Osaka

(Received July 20, 1960)

Weak gamma-rays following the decay of Mn^{51} were investigated by a NaI(T1) scintillation spectrometer. To eliminate the effect of the strong annihilation gamma-ray, a new method was used. Gamma-rays of 0.74 and 1.17 MeV were found and these intensities were 0.4 ± 0.2 and 0.2 ± 0.1 percent of the positrons, respectively. The half-life of Mn^{51} was determined as 44 ± 1 min.

§ 1. Introduction

Mn^{51} having half-life of 44 min decays to Cr^{51} by the emission of 2.16 MeV positrons[1]. No gamma-ray has been found in this decay[2][3]. On the other hand, the investigations of the reaction V^{51} (p, n) Cr^{51} indicated the excited states of Cr^{51} to be 0.74, 1.42 and 1.53 MeV, but the spins and parities of these levels have not been known. The spin and parity of the ground state of Cr^{51} are 7/2−, *i.e.* $(f_{7/2})^{-1}$ in the shell model and those of Mn^{51} are estimated to be 5/2− or 7/2−, *i.e.* $(f_{7/2})^{-3}{}_{J=5/2 \text{ or } 7/2}$. Therefore, if the spins and parities of the excited states of Cr^{51} are 3/2, 5/2, 7/2, or 9/2−, the beta transition from Mn^{51} to those levels may be allowed. Then weak gamma-rays from such a excited state can be found, when log $ft=5\sim7$.

In the case of the investigation of Mn^{52m} (21 min)[4] the weak gamma-ray of about 0.74 MeV with a long half-life was found in the scintillation spectra, and it is estimated to belong to the decay of Mn^{51}. The strong gamma-ray and the annihilation radiation of Mn^{52m} disturbed to detect weak gamma-rays of Mn^{51}. Hence we bombarded the chromium target by low energy deuterons of about 6 MeV which do not produce Mn^{52m} by the $(d, 2n)$ reaction[4]. As the strong annihilation gamma-ray of Mn^{51} and its high energy tail due to the annihilation in flight and the bremsstrahlung of the positrons disturbed the measurement of weak gamma-rays, we devised a new method which decreases above mentioned effect of the annihilation gamma-ray.

In § 2 this method will be introduced. The application of this method to Mn^{51} and the result will be discussed in § 3.

§ 2. A Method for Elimination of the Annihilation Gamma-Ray.

The annihilation radiation often disturbs the NaI scintillation spectrometer measurement for weak gamma-rays, especially, near and lower than 0.5 MeV gamma-rays. If the effect of this radiation is removed, weak gamma-rays, can be easily measured. For this purpose coincidence methods are commonly used. But they are not practical for very weak

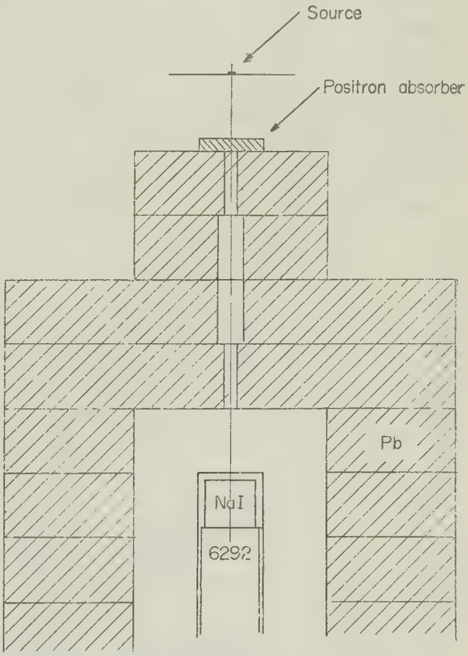

Fig. 1. Schematic diagram of the experimental arrangement for elimination of the annihilation gamma-ray.

---

* Now at Japan Atomic Energy Research Institute, Tokai, Ibaraki, Japan.

gamma-rays.

In our experiment a new method was adopted. Such thin material as the beta-ray source of no self-absorption must be used for gamma-ray source, in order to decrease the annihilation of positrons near the source. A $1\frac{1}{2}'' \times 1\frac{1}{2}''$ NaI scintillation probe was shielded by the lead which has a collimation system as shown in Fig. 1. A plastic plate used as the absorber for positrons was put between the lead collimater and the source. The solid angle for the gamma-ray is denoted by ω_γ, that of the effective area of the plastic plate by ω_+ and that for the annihilation radiation converted in the plastic plate by ω_a. Counting rates for the gamma-ray and the annihilation radiation are $N\delta_\gamma\omega_\gamma\epsilon_\gamma$ and $N\delta_+\omega_+\omega_a\epsilon_a$, respectively, where N is the disintegration rate and δ_γ, δ_+, ϵ_γ, and ϵ_a are the branching ratios and the efficiencies of the scintillation counter. In the present experiment ω_γ, ω_a and $\omega_+ < 10^{-2}$. Then the counting rate for the annihilation radiation can be remarkably decreased.

For preliminary experiments Na^{22} deposited on thin mylar film was used. Fig. 2 shows the pulse height spectra for different conditions. The effect of this method can be seen by the comparison with 1.28 MeV gamma-ray. The annihilation gamma-ray was decreased to 10~30 percent. In order to take away the annihilation in air, the source was placed in vacuum chamber, but its effect was not so large.

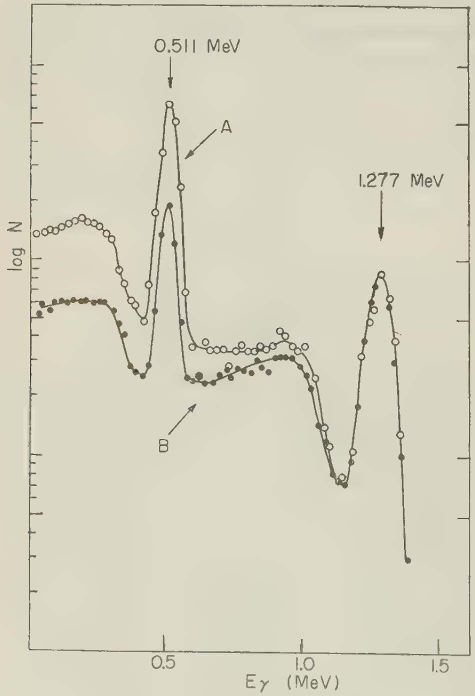

Fig. 2. Scintillation spectra of Na^{22}. Curve A shows spectrum using a gamma-ray source in a thick plastic vessel, and Curve B collimated spectrum with a plastic positron absorber using the thin source (the condition shown in Fig. 1).

The annihilation in the neighbourhood of the source is so small for high energy positrons that this method is more effective than low energy positions. The strong source more than 0.1 mc is necessary, because the small solid angle must be used. A typical case is shown in the investigation of Mn^{52m}4).

§ 3. Experimental Procedure and Result

Chromium foils of about 10 mg/cm^2 thick were bombarded by 6 MeV deuterons of Osaka University cyclotron degraded by aluminum absorber. Target foils were used without

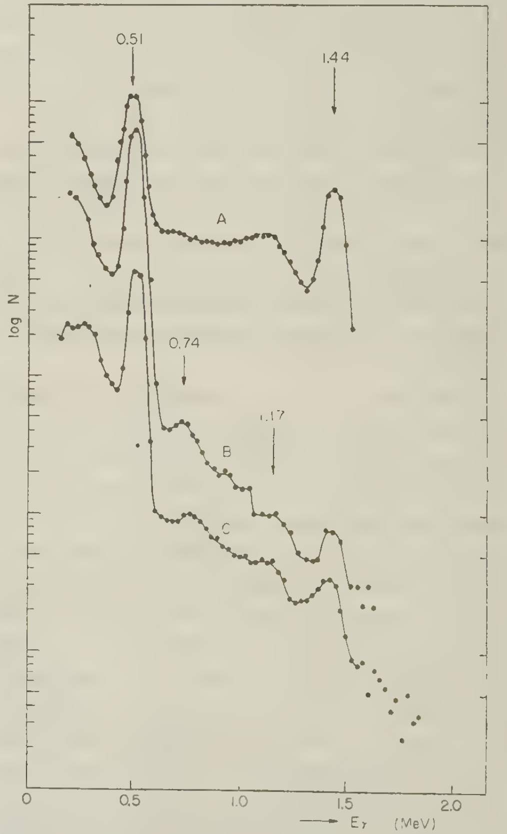

Fig. 3. Scintillation spectra of Mn^{51}. Curve A is the usual gamma-ray spectrum of the source bombarded by 11.4 MeV deuterons, Curve B that by 6 MeV deuterons, and Curve C the spectrum by the new method of the source by 6 MeV deuterons.

chemical process for the gamma-ray sources. The gamma-ray was measured in the worse condition than that as shown in Fig. 1, because the strong enough source could not get. Curve *A* in Fig. 3 shows an usual gamma-ray spectrum from the foil bombarded by 11.4 MeV deuterons. There were the strong 1.435 MeV and the annihilation gamma-rays of Mn^{52m}. Curve *B* is also the usual spectrum from the foil bombarded by 6 MeV deuterons. The spectrum using the new method is shown by Curve *C*. To determine the intensity of positrons, during the measurement of the decay of the spectrum, the source foil was placed between plastic plates. In this arrangement most of positrons are expected to annihilate at the plastic plates.

New gamma-rays of 0.74 and 1.17 MeV were found. A gamma-ray of about 1.4 MeV was estimated to be that of Mn^{52m}, though it is curious that Mn^{52m} was produced at lower energy than (*d*, 2*n*) threshould as Kafaras, *et al.*[5] pointed out. To confirm whether these gamma-rays belong to Mn^{51}, the decay curves are plotted as indicated in Fig. 4. The half-life of Mn^{51} was determined as 44±1 min from these curves. The relative intensities of weak gamma-rays were determined by comparison with the annihilation radiation. Estimated intensities are 0.4±0.2 and 0.2±0.1 percent of the positrons for 0.74 and 1.17 MeV gamma-rays, respectively.

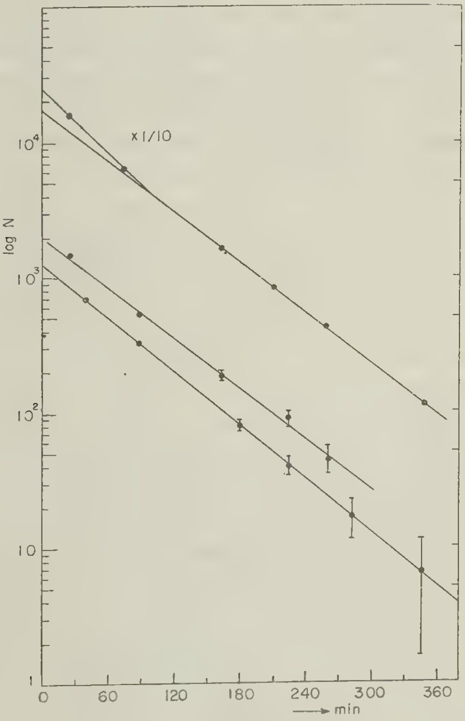

Fig. 4. Decay curves of gamma-ray peak. *A*, *B* and *C* shows annihilation, 0.74 and 1.17 MeV gamma-rays, respectively.

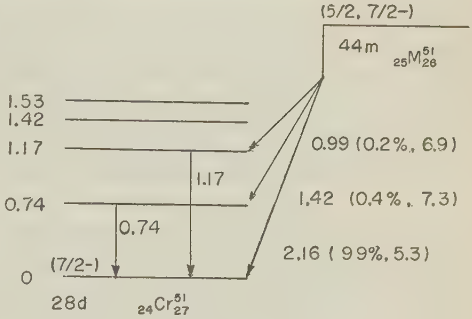

Fig. 5. Decay scheme of Mn^{51}.

The decay scheme is shown in Fig. 5. *EC*/β^+ and log *ft* for the ground state transition are 0.03 and 5.2 from Zweifel[6], Brysk and Rose[7] and Feenberg and Trigg[8]. From these intensities log *ft* are 7.3 and 6.9 for beta-decays to 0.74 MeV and 1.17 MeV levels. These values are large compared with 5.2 for the ground state transition. There is no such a a large log *ft* value except Ca^{47} in the $f_{7/2}$ shell region. The spin and parity of Mn^{51} are 5/2− or 7/2−, *i.e.*, $(f_{7/2})^{-3}{}_{J=5/2 \text{ or } 7/2}$. Then 0.75 and 1.17 MeV levels of Cr^{51} is not expected to have a single particle excited state such as $f_{5/2}$, but to have to more complex configuration. Because there is no even parity configuration and beta transition to these levels cannot be first forbidden.

References

1) K. Way, R. W. King, C. L. McGinnis, R. van Lieshout: Nuclear Level Schemes, Nuclear Data Project, Washington D. C. 1955.
2) A. H. W. Aten, Jr., J. Kooi, B. de Vries and A. L. Veenendeal: Physica **19** (1953) 1051.
3) L. Koester: Z. Naturf. **9a** (1954) 104.
4) T. Katoh, M. Nozawa, Y. Yoshizawa and Y. Koh: J. Phys. Soc. Japan, **15** (1960) 2140.
5) P. Kafaras and J. W. Irvine, Jr.: Phys. Rev. **104** (1956) 703.
6) P. F. Zweifel: Phys. Rev. **96** (1954) 1572; **107** (1957) 329.
7) H. Brysk and M. E. Rose: Rev. Mod. Phys. **30** (1958) 1169.
8) E. Feenberg and G. Trigg: Rev. Mod. Phys. **22** (1950) 399.

JOURNAL OF THE PHYSICAL SOCIETY OF JAPAN, Vol. 15, No. 12, DECEMBER, 1960

Beta- and Gamma-Ray Spectroscopy of Mn^{52} and Mn^{52m}

Toshio KATOH, Masao NOZAWA* and Yasukazu YOSHIZAWA
Department of Physics, Faculty of Science, Osaka University, Osaka
and Yujiro KOH
Department of Physics, Faculty of Science, Osaka City University, Osaka

(Received July 20, 1960)

Excited levels of Cr^{52} were studied by investigating the decays of Mn^{52}(5.7 days) and Mn^{52m}(21 min), produced by $Cr^{52}(d, 2n)Mn^{52,52m}$. By means of a two-directional focusing beta-ray spectrometer, NaI(TI) scintillation spectrometers and a 20-channel pulse height analyzer, following results were obtained: (1) Energies of the main three gamma-rays from Mn^{52} are 746.8±0.2, 938.1±0.4 and 1434.7±0.8 keV. (2) The maximum energies of the positrons from Mn^{52} and Mn^{52m} are 0.572±0.006 and 2.61±0.03 MeV, respectively. (3) The spins and parities of the levels of 3120, 2373 and 1435 keV were determined to be 6+, 4+ and 2+, from measurements of conversion electrons and angular correlations. (4) Several weak gamma-rays were found, which could be inferred to belong to these decays. (5) The half-life of Mn^{52m} is 21±1 min. Its branching ratio $IT/(\beta^+ + EC)$ was determined as 2±1 percent. (6) The energy of isomeric transition is 0.383±0.003 MeV, which was decided as $E4$ from $K/L+M$ and the transition probability.

§1. Introduction

From many investigations[1),2)] it has been well established that Mn^{52} decays with the half-life of 5.7 days through the emission of the positron of 0.58 MeV to a excited level of Cr^{52}, which emits gamma-rays of 0.73, 0.94 and 1.45 MeV in turn. Besides, a isomeric state Mn^{52m} with the half-life of 21 min has been found which decays by the emission of the 2.6 MeV positron to the 1.45 MeV level of Cr^{52}, and in small fraction through the isomeric transition of the 0.39 MeV gamma-ray to Mn^{52}. The values of log *ft* for the positron emission from Mn^{52} and that from Mn^{52m} are 5.3 and 5.6, respectively, and both can be regarded as the allowed transitions. V^{52}(3.8 min) also decays to the 1.45 MeV level of Cr^{52} through the negatron emission. This decay has, however, not yet been reported in detail.

Mazari, Buechner and Sperduto[3)] measured exactly the energy spectra in the reactions $Cr^{52}(p, p')Cr^{52*}$ and $Mn^{55}(p, \alpha)Cr^{52*}$, and found many levels which had not yet been seen in the decays from Mn^{52} and Mn^{52m}. New levels of 2.648, 2.767, 2.965 and 3.161 MeV are shown in Fig. 1.

By Seaborg, *et al.*[2)], the 3.161 MeV level was assigned to be identical as the 3.13 MeV level[3)] in the decay of Mn^{52}. The small difference of energy between them cannot, however, be negligible. According to the K. Way, *et al.*[1)], it is concluded that the three main gamma de-excitation of Cr^{52} are quadrupole transitions and the spins of the concerned levels are 6, 4, 2 and 0. Then the spin of Mn^{52m}, which decays to the 1.45 MeV level, will be 2 or 3. If the 1.45 MeV level is assumed to have the

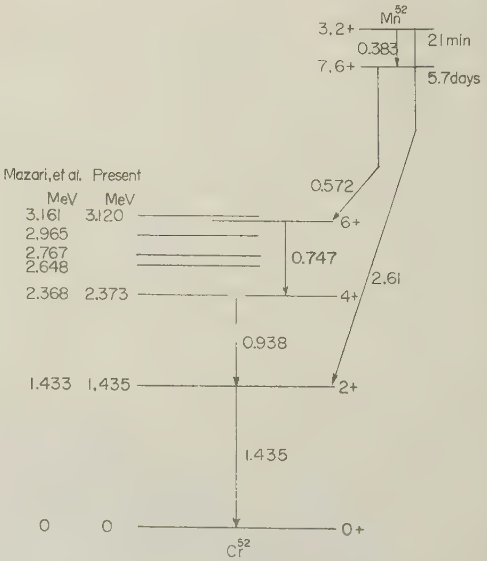

Fig. 1. The decay scheme of Mn^{52} and Mn^{52m}.

---

* Now at Japan Atomic Energy Research Institute, Tokai, Ibaraki, Japan.

even parity according to the systematics of even-even nuclei, Mn^{52m} will have the same parity. Similarly, the spin and parity of Mn^{52} is either 6+ or 7+ from the selection rule of beta-decay. This spin has been also measured by the paramagnetic resonance method[4]. These results are also supported from the conclusion of Huiskamp[5], that the spins and parities of the above-mentioned levels are 6+, 4+, 2+ and 0+, derived from the measurement of gamma-ray directional and polarization angular distributions at low temperature. We have no information concerning spins of new levels found by Mazari, *et al.*, but can infer that they have low spins as they are levels resulting from excitation by the low energy protons. Therefore, a detection of unknown weak gamma-rays between these levels may be possible in the decay of Mn^{52m} rather than Mn^{52}. And it is questionable to consider that the 3.161 MeV level found by Mazari, *et al.* and the 3.13 MeV level in the decay of Mn^{52} are the identical, as they suggested[3].

In this paper, the following results are reported: (1) The energies of three main gamma-rays from Mn^{52} were precisely measured by means of the magnetic beta-ray spectrometer. It was tried to clarify the above mentioned problem from these gamma-ray energies. (2) By measuring the relative total conversion ratios of the three main gamma-rays and those angular correlations, the spins and parities of the concerned levels were re-examined. (3) Unknown weak gamma-rays from Mn^{52} and higher spin levels were looked for. (4) The energy of main gamma-ray from Mn^{52m} was measured, and it was ascertained that it comes from the first excited level of Cr^{52} and is coincident with the annihilation gamma-ray. (5) New weak gamma-rays from Mn^{52m}, especially, the expected from the results of Mazari, *et al.*, were searched. Several weak gamma-rays were found. (6) Beta-ray spectra of Mn^{52} and Mn^{52m} were measured by the beta-ray spectrometer and analyzed. (7) For the isomeric transition of Mn^{52m}, $K/L+M$ and the half-life were measured by the beta-ray spectrometer, and the energy and the intensity of the gamma-ray by the scintillation spectrometer.

Bombarding the natural chromium by 11.4 MeV deuterons of a cyclotron in Osaka University, Mn^{52} and Mn^{52m} were obtained. The cross section of this reaction was reported by Irvin, *et al.*[6].

§ 2. Source Preparation

For the production of Mn^{52} and Mn^{52m} natural metalic chromium was bombarded by the 11.4 MeV deuteron beam of the cyclotron in Osaka University[7], of which the maximum values of beam currents were about 100μA for the internal target and about 50μA for the external. However, the current was limited to 30～50μA and 15～25μA, respectively.

2.1 Mn^{52}

The internal target was mainly used. Target material was natural chromium metal of 100～300 micron thickness electroplated on a copper plate of 1 mm thickness, which was set with ordinary solder to a water-cooled copper pipe of 25 mm diameter.

Impurities in chromium were lower than the spectroscopical limit, except a trace of iron. Considerable products with half-life longer than 5 days are due to $Cr^{50}(d, p)Cr^{51}$ and $Cr^{50}(d, \alpha)V^{48}$ other than $Cr^{52}(d, 2n)Mn^{52}$. The most serious problem in the chemical separation was the removal of V^{48} (16 days). The energies of gamma-rays from V^{48} are 0.99, 1.04 and 1.33 MeV, thus V^{48} and Mn^{52} can be hardly separated by the scintillation spectrometer. Really, the admixture of V^{48} in Mn^{52} brought the ambiguity for weak gamma-rays, angular correlation measurements, etc. The following radiocolloid method was finally adopted by Otozai, *et al.*[8]. The separated sample was tested by observing the positron spectra of V^{48} and Mn^{52} of which the maximum energies are 693 and 572 keV, respectively, and by measuring the half-life difference in the scintillation spectra: (1) The target is treated with 6 N nitric acid to remove base metal from the electroplated chromium, and the resulted chromium foil is then dissolved in 1 ml of concentrated hydrochloric acid. (2) The solution is diluted to about 10 ml with distilled water and added dropwise to the bromine-saturated 2.5 N caustic soda solution (200 ml reagent solution per 100 mg chromium). (3) To this solution, about 5 mg of ammonium vanadate solution containing 20 mg of vanadate is added. (4) The excess bromine is distilled off completely. (5) The solution is filtered with a 3G5 sintered-glass filter to catch manganese activities as radiocolloid. (6) The colloid caught on the filter is washed five times with 2 ml aliquots of water, and successively eluted five times with 2 ml aliquots of concentrated hydrochrolic acid. (7) The eluted solutions are dried up, and carrier-free manganese activities are finally obtained.

The source for the beta-ray spectrometer was carrier free $MnCl_2$ which was deposited on 0.8 mg/cm^2 myler film with insulin solution. Myler film was coated before hand with thin aluminium. Sources for the scintillation spectrometer were also deposited on myler film and padked in Acrylite vessels of about 1 mm wall thickness. Especially the source for the angular correlation was aqueous solution of $MnCl_2$, sealed in an Acrylite pipe of inner diameter 1 mm and wall thickness 1 mm.

2.2 Mn^{52m}

As its half-life is short, the chemical separation was hardly possible and it was practical that chromium foils were bombarded and used without further treatment. Chromium foils were produced by the method of Irvin, *et al.*[5]. Chromium was electroplated on thin copper plates from aqueous solution of chromic acid. Then plates were annealed in vacuum at aboot 200°C within about 5~8 hours, and copper plates were taken away by HNO_3. In the case of sources of the beta-ray spectrometer, chromium foils of 5~10 mg/cm^2 thickness and 5×30 mm^2 dimension were bombarded by external deuteron beam of ~20 μA for 20~30 min. Sources for the scintillation spectrometer were prepared with smaller current and shorter time. As the foils are thin, the ratio of the (d, n) and (d, p) reaction yields to the $(d, 2n)$ yield is relatively small. Because of short bombardments, long life activities of Mn^{52}, V^{48} and Cr^{51} do not cause trouble. Mn^{51}(44 min) was not also an obstacle to observation as shown in § 4.

§ 3. Instruments

The two-directional focusing beta-ray spectrometer was used for observation of beta-spectra and internal conversion electrons. For observations of the gamma-ray single and coincidence spectra and the γ-γ angular correlation, $1\frac{1}{2}'' \times 1\frac{1}{2}''$ and $3' \times 3'$ NaI(Tl) scintillators mounted on 5819 and 6364 photomultipliers were used.

3.1 *Beta-ray spectrometer*

The spectrometer shown in Fig. 2 is of the mushroom type as reported by Hedgran, Siegbahn and Svartholm[9]. The mean radius of electron path is 40 cm, the weight of the magnet 2.2 ton, the diameter 124 cm and the gap at the mean radius 22 cm.

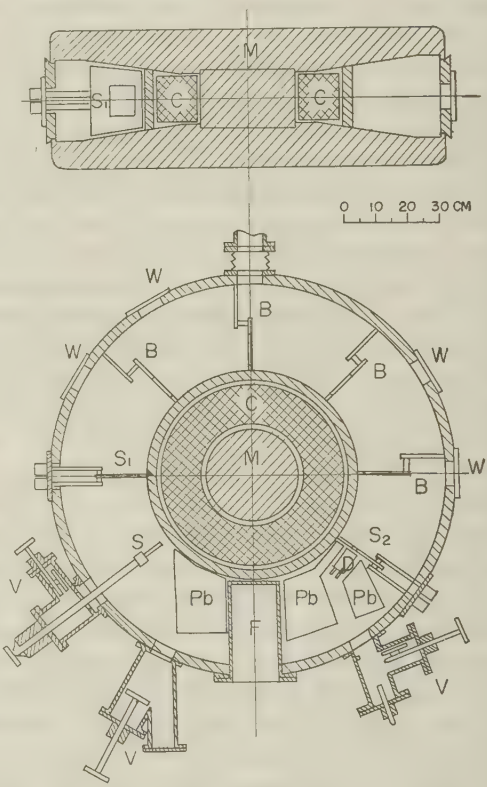

Fig. 2. Two-directional focusing beta-ray spectrometer. M indicates the magnet iron; C, the magnet coil; S, the source; S_1 and S_2, the defining and the exit slits; B, the baffles; D, the detector; V, the valve for the vacuum seals; W, the glass windows; Pb, the lead shield; and F, the chamber for the magnetic field measurement apparatus.

The power source of the magnet is storage batterys of 100 volts and controled by slide resistances. Error due to the hysterisis of the I-B curve can be restricted to less than 0.1 percent, by demagnetization and measurement starting from zero current.

The slit system is made up of two slits and four baffles, as shown in Fig. 2. The defining slit is placed at angular distance 36° from the source, and the exit slit just in front of the GM counter. The slits are adjustable in the directions both radial and vertical. The position of the source is also adjustable in the radial direction. Electrons scattered from inner walls of vacuum chamber are removed by the four aluminium baffles. Upper limit of scattered electrons was about one thousandth. This limit was estimated from counting rates in the energy regions lower than the cut-off energy of the counter window and higher than the maximum energy of various beta sources, e.g. that of Y^{90}.

The GM counter is of the end window type with 3 mg/cm^2 mica. It was seen by measuring the spectrum of Y^{90} that the absorption of the window begins at about 300 keV and its cut-off energy is about 50 keV.

3.2 *Scintillation spectrometer*

Scintillators were the $1\frac{1}{2}'' \times 1\frac{1}{2}''$ NaI(Tl) covered with lead and graded shields, and their resolutions were 11 percent for 662 keV gamma-ray of Cs^{137}. A $3'' \times 3''$ ascintillator was also used for high energy gamma-rays. Linear amplifiers were of the Higinbotham tybe. Single channel pulse height analyzers of the sweep type and a 20-channel pulse height analyzer were used. Fig. 3 shows the block diagram which was used in the coincidence measurement.

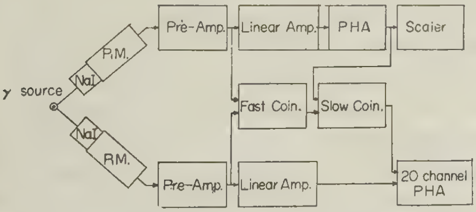

Fig. 3. Blook diagram of the coincidence spectrometer.

For the measurement of the angular correlation were used two single channel P.H.A. and a goniometer made of alminium. The solid angle correction factors for the angular correlation coefficients A_2 and A_4 were 1.07 and 1.25, respectively. The energy dependence of these factor were less than 0.2 percent in the range 0.7∼1.5 MeV.

§ 4. Spectra of Beta-Rays and Internal Conversion Electrons

4.1 Mn^{52}

The source was prepared by the method stated in § 2. The removal of V^{48} was satisfactory. The admixture of Mn^{54} did not cause trouble, because it decays through a electron capture and a 838 keV gamma transition[10].

(1) Beta-ray spectrum. In Fig. 4 is shown the momentum spectrum obtained by our beta-ray spectrometeter. Assuming the $B\rho$ vs. current curve for positrons was the same for negatrons, the energy was calibrated by using the K conversion lines of the 1173 keV gamma-ray of Co_{60} and the 662 keV gamma-ray of Cs^{137}.

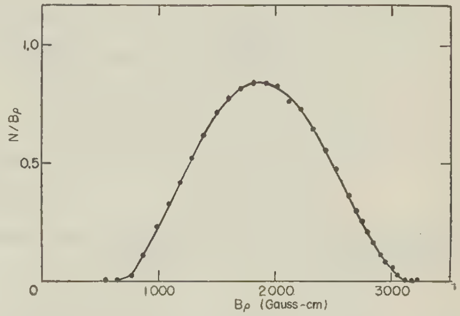

Fig. 4. Momentum spectrum of the positrons emitted in the decay of Mn^{52}.

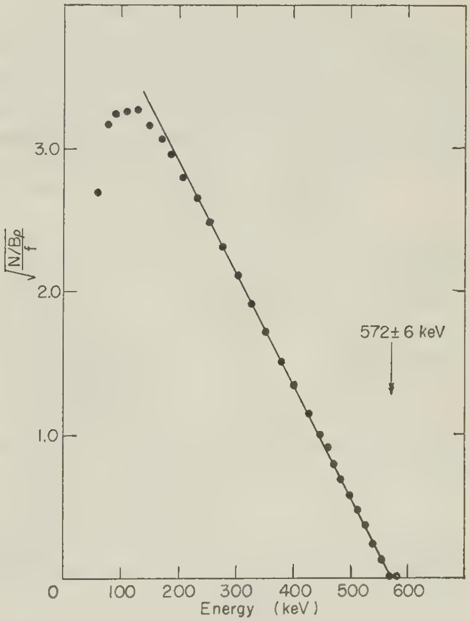

Fig. 5. Kurie plot of the positrons emitted in the decay of Mn^{52}.

Fig. 5 shows the Kurie plot, from which the maximum energy 572±6 keV is determined. As shown in the Figure the Kurie plot is straight from the maximum energy down to about 200 keV, where the absorption

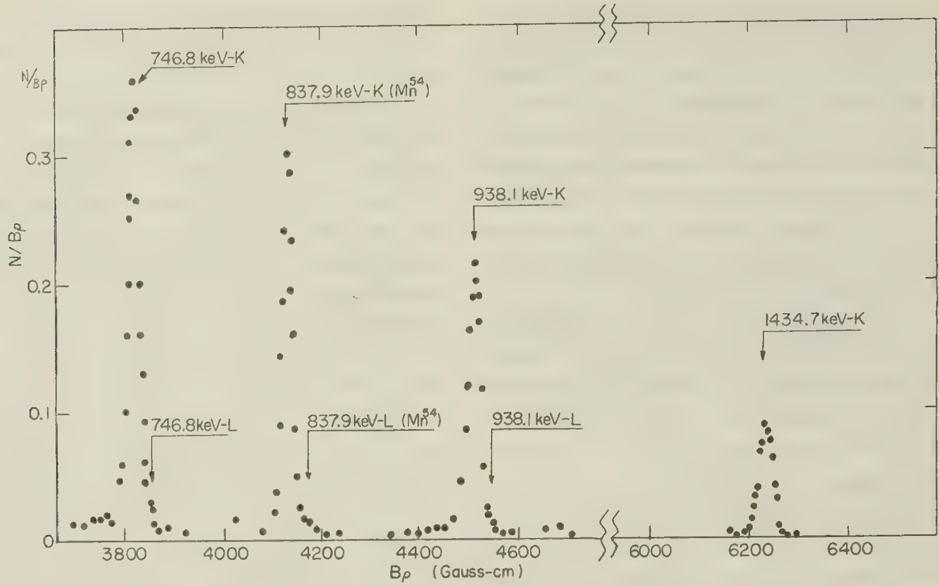

Fig. 6. Spectrum of the Conversion electrons in the 600~1000 keV region and the 1400~1500 KeV region emitted in the decay of Mn^{52}.

by the counter window can be thought to begin. Then if the value of half-life 5.72 days[11] is adopted, the value of log *ft* is 5.4.

(2) Internal conversion electrons Fig. 6 shows the spectrum of the internal conversion lines using the same source as that of beta-ray spectrum. The relative half maximum width of each line is 0.6 percent. The values of energies of each gamma-rays are tabulated in Table I, where energy standards were the *K*-conversion lines of Cs^{137} and Co^{60}.

Table I. Gamma-ray energies in the decay of Mn^{52} (MeV).

Peacock and Dutsch [a]	Keister [b]	Present
0.734±0.015	0.74	0.7468±0.0002
0.94±0.02	0.93	0.9381±0.0004
1.46±0.03	1.46	1.4347±0.0008

a) W. C. Peacock and M. Deutsch, Phys. Rev. **69** (1946) 306.
b) G. L. Keister, Phys. Rev. **96** (1954) 855A.

Table II. $K/L+M$ ratios of the gamma-rays in the decay of Mn^{52}.

$E\gamma$(keV)		746.8	938.1
Exp.		8.5±0.6	8.9±0.9
Theor.	E1	8.3	8.6
	E2	7.8	7.8
	M1	8.0	8.0
	M2	7.8	7.8

The *K*-lines and the $L+M$ lines can be barely separated for 747 and 938 keV gamma-yays. In Table II values of the observed $K/L+M$ ratios are compared with those calculated from the tables of Rose[12]. Here the calculated ratios are taken into consideration only for cases of E1, E2, M1 and M2, because the gamma-rays are restricted to be quadrupole from the results of angular correlation as shown in §6, and ratios other than these four are far from the observed values. The Rose's values for *M*-shell which do not contain the correction for the screening effect should be multiplied by factor about 0.6[13]. The calculated values in Table II were thus obtained and agree well with the observed within experimental error

Instead of measuring the conversion coefficents, the relative intensity ratios of the total conversion electrons of the three gamma-rays were measured. As intensities of weak gamma-rays other than the main three were estimated less than 5 percent (§5), the main three can be said to have equal intensities within the same error. Therefore the ratios of the total conversion electrons are regarded as the ratios of the total conversion coefficients. These ratios compared with calculated

Table III. Relative total conversion ratios of the three main gamma-rays in the decay of Mn^{52}.

E_γ(keV)		746.8	938.1	1434.7
Exp.		5.3±0.5	2.7±0.3	1.0
Theor.	I	1.95(E1)	1.20(E1)	1(M1)
	II	5.26(E2)	2.85(E2)	1(M1)
	III	8.87(M2)	4.94(M2)	1(M1)
	IV	4.82(E2)	2.62(E2)	1(E2)
	V	4.91(M2)	2.73(M2)	1(M2)
	VI	8.13(M2)	2.62(E2)	1(E2)
	VII	3.20(M1)	2.62(E2)	1(E2)

values for all combinations of E1, E2, M1 and M2 transitions. Table III shows the observed values and some of the calculated ones, normalized for the 1435 keV gamma-ray. It can be concluded that combinations except E2–E2–E2, M2–M2–M2 and E2–E2–M1 are rejected.

4.2 Mn^{52m}

The relatively short half-life of Mn^{52m} necessitated several devices for source preparation of beta-ray spectrometer as stated in § 2.

(1) Beta-ray spectrum Runs of measurements for twenty momentum values were repeated several times until the source decayed out. Decay curves obtained for three momentum values are illustrated in Fig. 7. All decay curves showed the half-life of 21 min. A momentum spectrum derived from these decay curves is shown in Fig. 8. Fig. 9 is its Kurie plot. It shows the maximum energy 2.61±0.03 MeV and the allowed shape down to 0.2 MeV from the maximum energy. Decay curves of the low energy part in Fig. 7 deviate from the straight line with the passage of time. This seems to be the admixture of Mn^{51}(44 min). This effect is, however, negligible as seen from the decay curves.

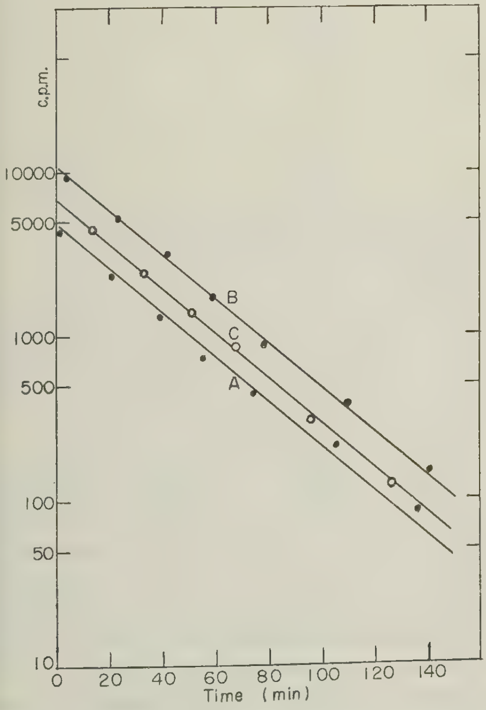

Fig. 7. Decay of the positron spectrum of Mn^{52m}. *A*, *B* and *C* are the decay curves of the points indicated by the same letters in Fig. 8.

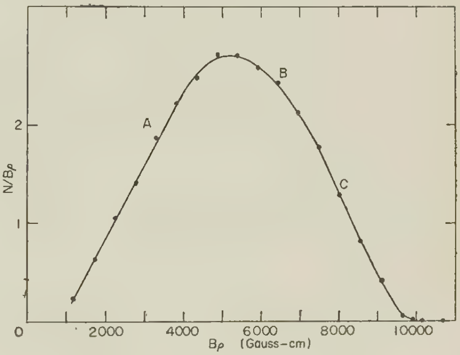

Fig. 8. Momentum spectrum of the positrons emitted in the decay of Mn^{52m}. The intensities of the measured points were normalized at the same time.

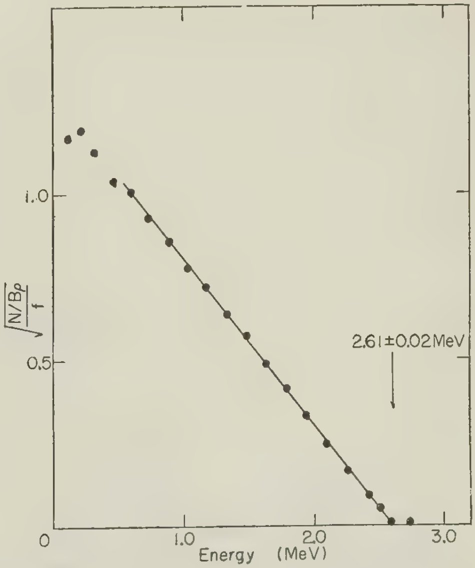

Fig. 9. Kurie plot of the positrons emitted in the decay of Mn^{52m}.

(2) Internal conversion A spectrum of con-

version electrons containing two strong lines was obtained as shown in Fig. 10. Energies of these gamma-rays are tabulated in Table IV. Fig. 11 is the decay plots of the conversion line of 383 keV gamma-ray, which shows the half-life is 24±5 min.

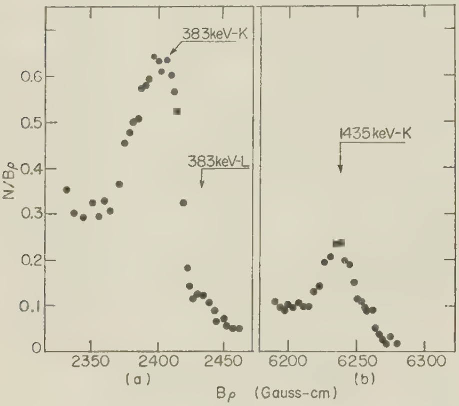

Fig. 10. Spectrum of the conversion electrons emitted in the decay of Mn^{52m}. (a) Region between 350 and 390 keV. (b) Region between 1400 and 1450 keV.

Table IV. Gamma-ray energies in the decay of Mn^{52m}(MeV).

Osborne and Deutsch[a)]	Present
0.39	0.383±0.003
1.46±0.04	1.435±0.003

a) R. K. Osborne and M. Deutsche, Phys. Rev. **71** (1947) 467A.

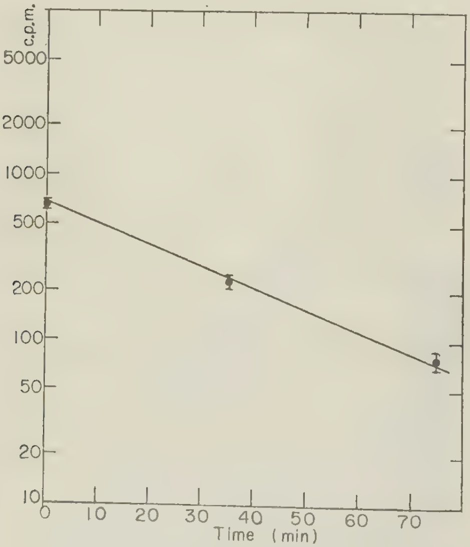

Fig. 11. Decay of the conversion electrons of the 383 keV transition emitted in the decay of Mn^{52m}.

The 1435 keV gamma-ray can be said to be emitted from the first excited state of Cr^{52} as in the case of Mn^{52}. The 383 keV gamma transition can be thought to be isomeric. The observed and the calculated *K*/*L* ratios tabulated in Table V show that it is a *E*4 transition. Besides the above two strong gamma-rays we searched for whether conversion electrons of weak gamma-ray exist between 0.5 and 1.5 MeV, but found nothing. It will be concluded that there is no conversion electron of intensity more than 20 percent of 1435 keV conversion electrons.

Table V. *K*/*L*+*M* ratio of the 383 keV gamma-ray in the decay of Mn^{52m}.

		K/*L*+*M*
Exp.		7.2±0.4
Theor.	E1	8.6
	E2	8.4
	E3	8.1
	E4	7.5
	E5	6.9
	M1	8.6
	M2	8.3
	M3	8.0
	M4	7.7
	M5	7.2

§ 5. Scintillation Gamma Spectra

5.1 Mn^{52}

(1) Single spectra Fig. 12 shows the scintillation spectrum of the well-known three gamma-rays of Mn^{52} measured by using the 1½″×1½″ NaI(Tl) scintillator and the single channel pulse height analyzer.

The energies of these three gamma-rays have been reported by Peacock and Deutsch and others. Table I contains some of these values. The preceding values for 938 keV gamma-ray agree well with the present values but values for other two gamma-rays do not well. Here, we reexamined the energies of these two gamma-rays by means of the scintillation spectrometer calibrated with the annihilation and 938 keV gamma-rays, and obtained the values of 0.746 and 1.433 MeV. The fact that present results from two dif ferent methods are not contradictory means hat there is no such a gamma-ray in the eighbourhood of these gamma-rays as to ause a deviation of a peak in the scintillation spectrum. It can be concluded that the 3.161 MeV level found by Mazari, *et al.* differs from the 3.121 MeV level in the decay of Mn^{52} over the experimental errror as shown in Fig. 1. Therefore, the positron decay to the 3.161 MeV level from Mn^{52} is estimated to be forbidden.

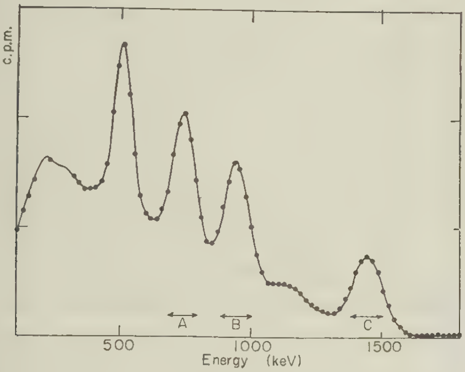

Fig. 12. Gamma spectrum of Mn^{52}. A, B and C indicate the gate-windows for the angular correlation.

The intensities of the three gamma-rays were estimated to be nearly equal, using the energy-efficiency curve of the scintillation counter. Besides, the levels of 2.648, 2.767, 2.965 and 3.161 MeV found by Mazari, *et al.* and shown in Fig. 1 may cause weak gamma-rays other than the main three, if they have appropriate spins and parities. We attempted the search of weak gamma-rays between 0.94~1.43 MeV, comparing the shape of the 1.435 MeV gamma-ray spectrum with that of the 1.12 MeV gamma-ray of Zn^{65} and estimated their intensities less than 10 percent at most.

The energy range higher than 1.435 MeV was swept carefully, using the $1\frac{1}{2}'' \times 1\frac{1}{2}''$ NaI(Tl) scintillator and 20-channel P.H.A. A weak 1.73 MeV gamma-ray was found in this way. Fig. 13 is the result of the more detailed measurement of this gamma-ray by use of the $3'' \times 3''$ scintillator and the single channel P.H.A. The intensity is estimated as about 0.5 percent of the main gamma-rays from Fig. 13.

(2) Coincidence spectra Coincidence spectra were observed using 20-channel P.H.A. Opening a gate window at the full width of the 1.435 MeV photo-peak, the coincidence spectrum of the annihilation, 0.747 and 0.938 MeV gamma-rays were observed in the range lower

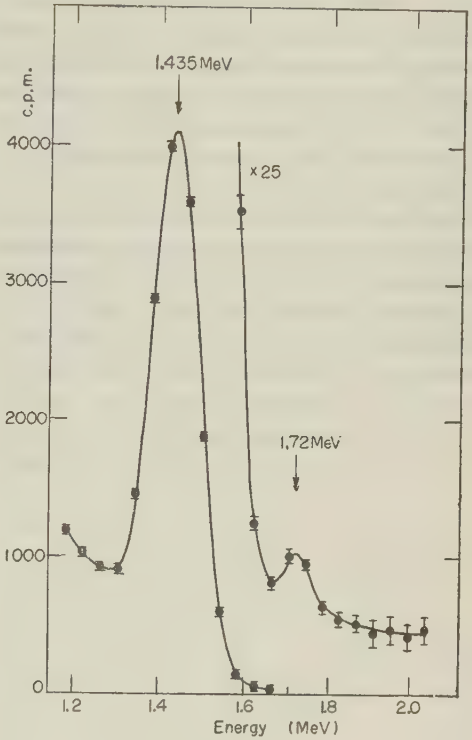

Fig. 13. Weak high energy gamma-ray of Mn^{52}.

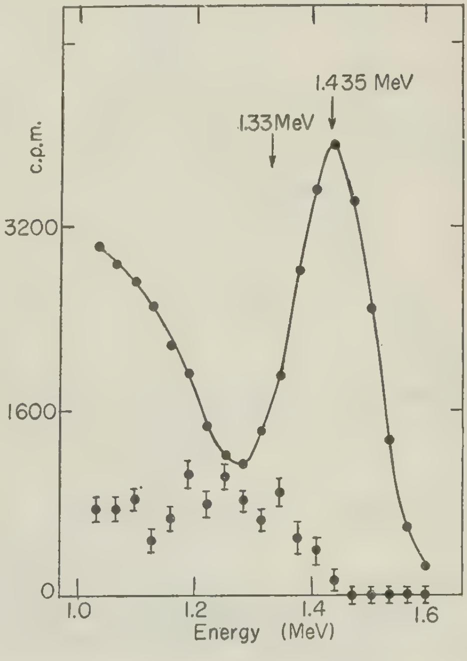

Fig. 14. Gamma-ray spectrum coincident with the 1.435 MeV gamma-ray of Mn^{52}.

than 1 MeV. The coincidence of the 0.747 MeV gamma-ray with 0.938 MeV was also confirmed. These facts show the main three gamma-rays are successive. Fig. 14 is a coincidence spectrum with a gate window opened at the higher side of the photo-peak of 1.435 MeV gamma-ray. This shows weak 1.33 and 1.2 MeV gamma-rays about 5 and 3 percent of the main three, respectively.

5.2 Mn^{52m}

(1) Single spectra Fig. 15 shows single and summing spectra of chromium foils bombarded by deuterons as stated in § 2. The NaI(Tl) scintillators were of 1½″×1½″ and 3″×3″. The latter was placed at 30 cm as well as 0.5 cm in front of the sources for the purpose to identify summing peaks.

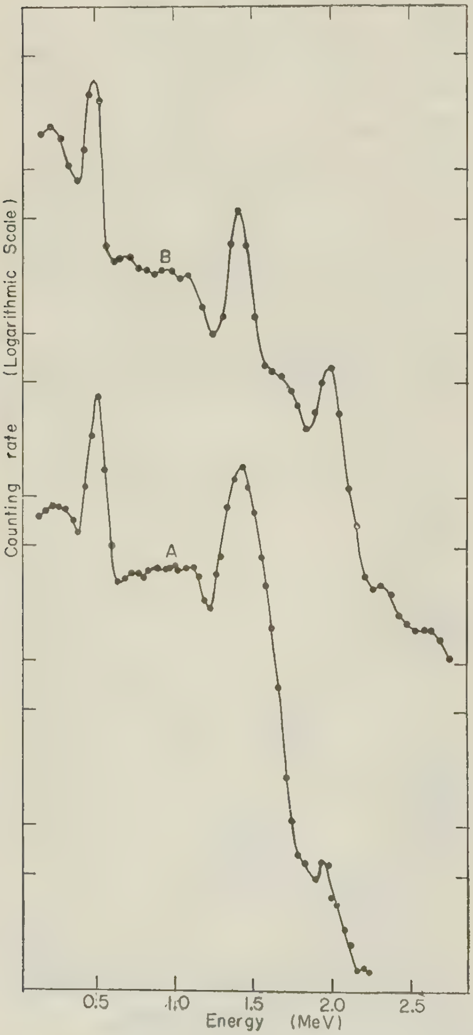

Fig. 15. Gamma-ray spectra of Mn^{52m}. A indicates single spectrum, and B summing spectrum.

Both the 1.435 MeV and the annihilation gamma-rays decayed with the half-life of Mn^{52m} at the start, and with the half-life of Mn^{52} after a few hour. The decay curves of these two gamma-rays are shown in Fig. 16, from which the half-life of Mn^{53m} 21±1 min is obtained.

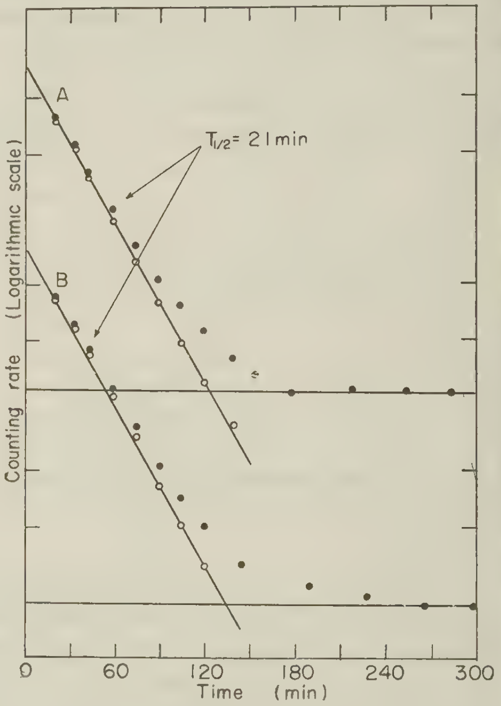

Fig. 16. Decay curves of the 1.435 MeV and the annihilation gamma-rays of Mn^{52m}. A indicates the decay curve of the 1.435 MeV gamma-ray, and B the decay curve of the summing peak of the two gamma-rays.

The search of weak gamma-rays was tried with the two methods corresponding to the energy regions lower and higher than the energy of the annihilation gamma-ray. For the higher region shapes of spectra were compared with those of known single gamma-rays, and several weak gamma-rays were found between 0.511 and 1.435 MeV, but they could not be said to be conclusive. For the lower region, on the other hand, the method of such simple comparison as the above-mentioned is practically impossible, because the region is covered by the strong Compton peak of the annihilation gamma-ray. We eliminated the effect of the annihilation gamma-ray with the same method as used for the detection of weak gamma-rays from the positron emitter Mn^{51} [14].

The annihilation of positrons was avoided in the vicinity of the source foil as carefully as possible. The $1\frac{1}{2}'' \times 1\frac{1}{2}''$ NaI (Tl) scintillator was covered by the lead shield of 20 cm thickness with a collimating hole of 1 cm diameter. The sourse was placed at 30 cm in front of the scintillator and the positrons were stopped just before the hole by the plastic plate of 1 cm thickness. Fig. 17 is the obtained result, which shows distinctly the 0.383 MeV gamma-ray, in comparison with the spectrum of the source in a glass vessel without the lead shield which is shown in Fig. 15. The half-life 23±4 min of this gamma-ray was also checked. From the relative intensity to the 1.435 MeV gamma-ray, the branching ratio of the 0.383 MeV gamma-ray to the positron decay plus the electron capture could be estimated as 2±1 percent considering the efficency of the detector, and the partial half-life of gamma transition not containing conversion electrons as 18 hours.

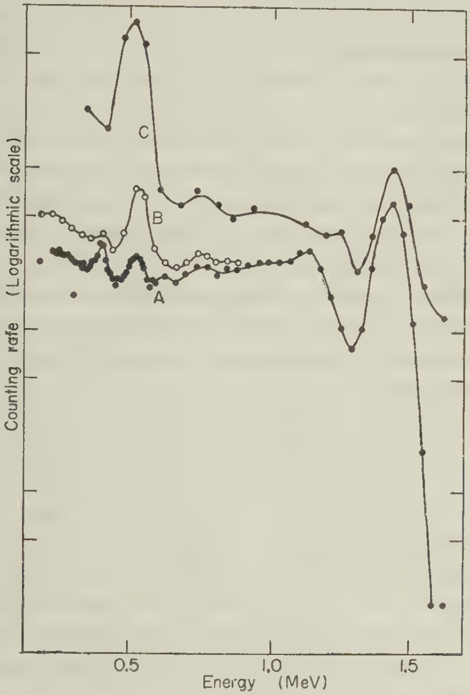

Fig. 17. Gamma-ray spectrum of Mn^{52m}. Curve A shows the spectrum measured with the plastic plate, Curve B the spectrum without the plate, and Curve C the ordinary spectrum of the source in a glass vessel without the lead shield.

(2) Coincidence spectra Coincidence spectra were observed using the $1\frac{1}{2}'' \times 1\frac{1}{2}''$ scintillators. The gate-windows were opened at the full width of the photo-peaks of 1.435 and 0.511 MeV as well as the high energy and the low energy sides of the photo-peak of 1.435 MeV and near 1.2 MeV. Fig. 18 is the result of the former case, shows the some of these coincidence spectra compared with the single.

From those experiments, the coincidences of the positrons with the 1.435 MeV gamma-ray were confirmed and several weak gamma-rays were found as follows: 0.70(3%), 0.94(4%), 1.02(3%), 1.15(2%), 1.37(%) and 1.52 MeV(2%). The percentages in parentheses are ratios of those intensities to the intensity of the 1.435 MeV gamma-ray. However, statistial errors were large, the decisive conclusions were difficult.

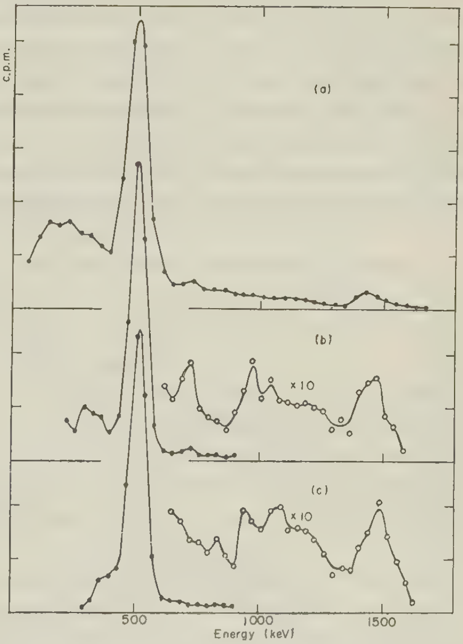

Fig. 18. Single and coincidence gamma spectra of Mn^{52m}. (a) Single spectrum. (b) Coincidence spectrum with the 1.435 MeV photo-peak. (c) Coincidence spectrum with the 1.2 MeV region.

§ 6. Directional Angular Correlation

6.1 *Experimental results*

The directional angular correlation among the three gamma-rays were observed. As mentioned in § 2, the admixture of V^{48} is a serious obstacle, especially for the observation of the angular correlations. The source of present measurement was prepared carefully in this point.

The gate-windows were set at the full width of the respective photo-peaks indicated by arrows *A*, *B* and *C* in Fig. 12. Combinations of the gate-windows are denoted by *B-C*, *A-C* and *A-B*. Of the three combinations, *B-C* of the two higher energy gamma-rays are not questionable in the following means. But the combinations *A-C* and *A-B* are not simple. Some parts of the Compton-peaks of the higher energy gamma-rays always pile up on the photo-peaks of the lower energy gamma-rays. Therefore, the counting rates of *A-C* and *A-B* are complex ones which are dependent upon the Compton as well as the photoelectric cross sections of the three gamma-rays. Though the correction in this point is difficult, it can be said that, in a special case where the observed three angular correlations are equal to each other, the correlation functions of three gamma-rays themselves are common and this correction becomes unnecessary. The results in Fig. 19 and Table 6 show that the observed correlations differ only slightly with each other and are relatively close to the theoretical for the spin-multipole sequence $J+2(2)J(2)J-2$. However it will be noticeable that the combination *B-C*, which is expected to be not disturbed by other gamma-rays, deviates from the other two observed and the theoretical correlations beyond the experimental error.

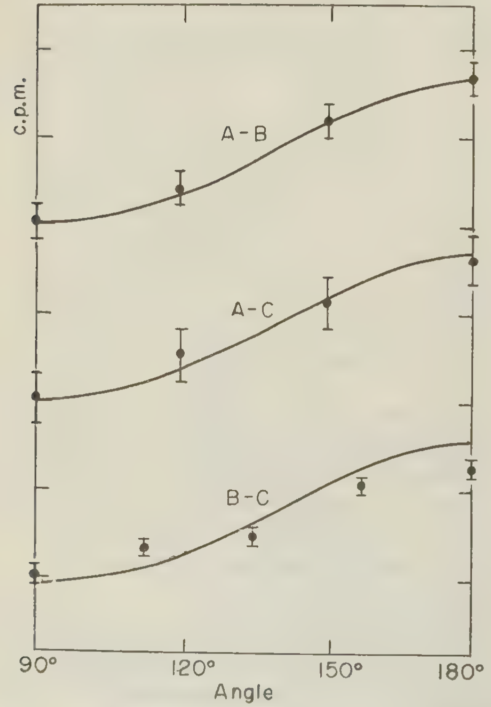

Fig. 19. Angular correlations of the three gamma-rays of Mn^{52}.

6.2 *Analysis*

Generally, for three quadrupole gamma-rays γ_1, γ_2 and γ_3 emitted succesively with dipole mixing it can be said as follows. Measurements of the three combinations of them γ_1-γ_2, γ_1-γ_3 and γ_2-γ_3 are possible. Assume each of three has a correlation function close to the theoretical one for $J+2(2)J(2)J-2$, as the present case of Mn^{52}. It is noticed that two sequences $J\pm1(1+2)J(2)J-2$ and $J(1+2)J(2)J-2$ give same correlation functions as that of $J+2(2)J(2)J-2$ within the usual experimental error, if the mixing ratios are appropriate. However, in the case of the triple cascade with the same correlation functions the possibilities of the mixed transitions can be excluded, except for the case where the only first gamma-ray is mixed, similarly the only third is so.

Table VI. Angular correlation coefficients of Mn^{52}.

		A_2	A_4
Teor.	$J+2(2)J(2)J-2$	0.1020	0.0091
Exp.	0.938−1.435	0.079±0.013	0.003±0.018
	0.747−1.435	0.102±0.019	−0.003±0.036
	0.747−0.938	0.114±0.018	0.005±0.034

In the case of Mn^{52}, the spin and parity of the ground state of Cr^{52} is 0+, and then γ_3 must be a pure multipole. Hence γ_2 and γ_3 are pure quadrupole transition from Table IV, but γ_1 is a pure or mixed quadrupole transition and the spin of the third excited level is not determined uniquely. As a consequence it can be concluded that following four sequences are left as possible, 6(2)4(2)2(2)0, 5(2+1)4(2)2(2)0, 4(2+1)4(2)2(2)0 and 3(2+1)4(2)2(2)0. In § 7 we shall compare these results with the values of the internal conversion coefficients and determine the third level spin.

Far the fact that the coefficients A_2 and A_4 of the combination γ_2-γ_3 are slightly smaller than those of the other combinations and the calculated, several reasons can be considered as follows: (1) The half-life of the 1.435 MeV level may be relatively long. (2) The atomic excited or ionized state after the decay may have a sufficiently long life and an intense field of the extranuclear effect. This effect is often remarkable for the electron capture. (3) Some weak gamma-rays other than the main three cause A_2 and A_4 to attenuate. The first and the second reasons are unnatural. Because, estimated half-lives of excited levels of about 1 MeV in nuclei near Mn^{52} are so short that they can not cause small A_2 and A_4 unless perturbing field is extremely intense. It is confirmed by the observed half-life of order 10^{-13} sec by the method of the resonance fluorescence[15]. It is also difficult to consider that the extranuclear field due to atomic excited levels perturbes the first excited level only and does not the second and the third levels. The third reason seems to be relatively natural. As stated in § 5, we found weak gamma-rays of 1.33 and 1.2 MeV which were coincident with the 1.435 MeV gamma-ray. If an appropriate decay scheme was assumed, the explanation of this attenuation was possible.

§ 7. Discussions

According to the *j-j* coupling shell model, ${}_{24}Cr^{52}_{28}$ is the nucleus, of which neutrons fill the $f_{7/2}$ orbit and protons leave four holes in the same orbit. Therefore, low lying excited states of this nucleus seem to be attributable to the proton excitation. Levels of the neutron excitations will come higher than a few MeV. The application of the shell model is considerably successful in the region near Cr^{52}. From the viewpoint of the collective model Cr^{52} is a neutron magic number nucleus for which vibration of spherical core may be considered to be pertinent. This model, however, has not yet succeeded in the Cr^{52} region. The nuclear structure of this region is not discussed here in detail, but will be an interesting problem in future.

${}_{25}Mn^{52}_{27}$ is the odd-odd nucleus, of which neutrons and protons have one and three holes in the $f_{7/2}$ shell respectively. Thus the ground state spin of Mn^{52} must be larger than zero, obeying the Nordheim's weak rule.

7.1 *Beta-decay*

Using our values of maximum energies of positron spectra, the log *ft* values of Mn^{52} and Mn^{52m} were determined as 5.4 and 5.3 respectively. For the half-lives, 5.72 days reported by Backofen and Herber[11] for Mn^{52} and 21 min of the present measurement for Mn^{52m} were adopted. From the values of log *ft* and the shapes of the spectra shown in Figs. 5 and 9, both transitions are allowed, i.e., $\Delta J=0$, ± 1 and no parity change.

In addition, we can estimate that low energy components of the beta-rays are less than 10 percent from the shapes of both spectra.

7.2 *Isomeric transition*

The energy and intensity of the gamma-ray of the isomeric transition were measured. The transition is $E4$, $E5$ or $M5$ from $K/L+M$, as shown in Table V. The partial half-life of the gamma-transition were estimated as 6×10^4 sec. Compared with the single particle estimate the transition is $E4$ or $M4$. As mentioned in § 4.1 the three combinations of multipolarities are possible for the three gammma-rays. For any one of these combinations the 1435 keV and 3120 keV levels have same parities. Thus the parities of Mn^{52} and Mn^{52m}, which decay to the levels of same parities through the allowed transitions, should be the same. Therefore, the isomeric transition is concluded to be $E4$.

If the first excited state of Cr^{52} has even parity, it can be decided the parities of Mn^{52} and Mn^{52m} are even.

7.3 *Excited states of* Cr^{52}

The energies of the gamma-rays from Mn^{52} were precisely measured. The obtained levels except the 3120 keV level agree well with those of Mazari, *et al.* The 3120 keV level differs from 3160 keV level of Mazari, *et al.* beyond the experimental error.

We conclude that there are close lying two levels. The 3120 keV level was not excited in the experiment of Mazari, *et al.* It is interesting that protons of a few MeV do not excite such a high spin level, as infered from the multipolarities of the triple cascade gamma-rays.

The spins and parities of the levels 1435, 2373 and 3120 keV were decided as follows. The relative ratio of the internal conversion coefficients and $K/L+M$ of the three gamma-rays led to the conclusion that their multipolarities are restricted to the three combinations: $E2$–$E2$–$E2$, $M2$–$M2$–$M2$ and $E2$–$E2$–$M1$(§ 4.1). By the experiment of the angular correlation, the gamma-ray from the first excited level was decided to be quadrupole, using the ground state spin of zero[16]. The three gamma-rays was restricted to either $E2$–$E2$–$E2$ or $M2$–$M2$–$M2$. This was consistent with the result of the angular correlations (§ 6.2). The correlation experiment can decide uniquely the spin values of the excited levels except that of the 3120 keV level. Besides, from the well-established systematics that both the first excited and ground levels of even-even nuclei have even parities, the combination $M2$–$M2$–$M2$ is excluded and the spins and parities become (3, 4, 5 or 6)+, 4+, 2+ and 0+.

As the positrons from Mn^{52m} decay to the first excited level but do not to the ground level, the spin and parity of Mn^{52m} will be 2 or 3+. As the transition from Mn^{52m} to Mn^{52} is $E4$ (§ 7.2), the spin and parity of Mn^{52} is 6 or 7+. On the other hand the 0.94 MeV gamma-ray of about 4 percent which is presumably emitted from the second excited level was present in the coincidence spectra (§ 5.2). This gamma-ray can be considered to follow the beta transition to the second excited level, of which the weak positron spectrum was not observed because of its low intensity. If it is so, long ft for the beta transition to the second excited level is 5.8, and the spins and parities of Mn^{52m} and Mn^{52} are reasonably assigned to be 3+ and 7+ rather than 2+ and 6+. 2+ and 6+ cannot, however, be excluded from the discussion in § 7.4. In addition, Jeffries, *et al.*[4] obtained the spin 6 for Mn^{52} from the paramagnetic resonance measurement. Then, the spin and parity of 3120 keV level of Cr^{52} is restricted to 5, 6, 7 or 8+ by the above-mentioned spin and parity of Mn^{52} and the selection rule of beta-decay. Combining above two discussions, the spins and parities of the levels of Cr^{52} are concluded to be (5 or 6)+, 4+, 2+ and 0+. 5+ of the 3120 keV level is excluded from a following reason. If 5+ is assumed the mixing ratio $E2/M1 \approx 0.08$ of the 747 keV gamma-ray is necessary in order to explain the angular correlation experiment. Such a dominance of $M1$ is inconsistent with the result of the relative internal conversion ratio.

It should be emphasized that the above arguments are based upon our observed results using only two assumptions, the even parities of the first excited and ground states of the even-even nuclei. Our final results agree well with the experiment of Huiskamp, *et al.*[5] for the distribution of the gamma-ray from polarized nuclei.

7.4 *Week gamma-rays*

As stated in § 5, many weak gamma-rays other than the main three were found. As preliminary interpretations, it is tried to connect these gamma-rays with levels found by Mazari, *et al.*

The 1.73 MeV gamma-ray from Mn^{52} can be regarded as the transition between the 3161 and 1435 keV levels. Considering the 1435 keV level of 2+ and the selection rule of beta-decay, the spin of the 3161 keV level is presumably 3 or 4.

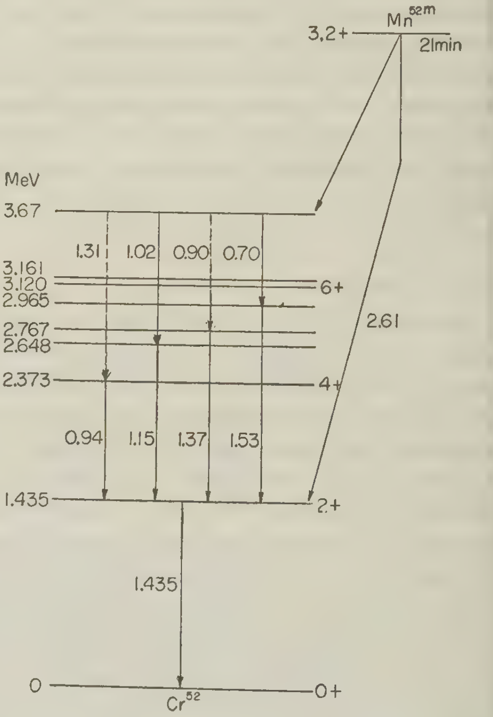

Fig. 20. Tentative decay scheme for the weak gamma-rays of Mn^{52m}.

The 1.2 and 1.33 MeV gamma-ray of Mn^{52} which are coincident with the 1.435 MeV gamma-ray can be interpreted to be the transitions trom the 2648 and 2767 keV level to the 1435 keV level. Assuming that the transitions from the 3120 keV level to both levels are $E2$, the observed branching ratios of the two weak gamma-rays to the 0.747 MeV gamma-ray from the 3120 keV level are agree with the single particle estimate. Then the assignment of 4+ to the both levels found by Mazari, *et al.* seems to be reasonable.

For Mn^{52m} the transitions of the 1.52, 1.37, 1.15 and 0.94 MeV gamma-rays, which are coincident with the 1.435 MeV gamma-ray, can be interpreted as those from the 2965, 2767, 2648 and 2373 keV levels to the 1435 keV level. The left weak 0.70 and 1.02 MeV gamma-rays cannot be explained by use of the known levels. Assuming a new level of 3.67 MeV, it is considered that these gamma-rays are due to transitions to 2965 and 2647 keV levels, as shown in Fig. 20. The intensities of the gamma-rays are consistent within experimental error. The beta transition to the 3.67 MeV level gives rather small log *ft* value 4.

One the other hand the low energy gamma-rays from Mazari's level to the 2767 and 2373 keV levels were observed within the upper limit of 1 percent. The gamma-rays from the 3.67 MeV level to the 2767 keV and 2373 keV levels could not be distinguished from the 1.37 and 0.94 MeV gamma-rays which were assumed to be emitted in the transition from these two levels to the 1435 keV level. Thus the decisive conclusion could not be obtained for the beta transition to the 2373 keV level as mentioned in § 7.3.

Acknowledgement

The authors would like to thank Prof. S. Kikuchi, Prof. T. Wakatsuki, Prof. J. Itoh and the members of the cyclotron group in Osaka University for their helps and interests. They are also indebted to Dr. J. Sanada for his contribution to the construction of the spectrometer and to Prof. K. Otozai, Mr. S. Kume, Mr. S. Iwata, Mr. Y. Yamamoto and Mr. I. Fujisawa for the chemical separation.

References

1) K. Way, R. W. King, C. L. McGinnis and R. van Lieshout: Nuclear Level Scheme, $A=20-A=92$ (United States Atomic Energy Commission, June 1955).
2) D. Strominger, J. M. Hollander and G. T. Seaborg: Rev. Mod. Phys. **30** (1958) 585.
3) M. Mazari, W. W. Buechner and A. Sperduto: Phys. Rev. **107** (1957) 1383.
4) M. Abraham, C. D. Jeffries, R. W. Kedzie and O. S. Leifson: Bull. Am. Phys. Soc. Ser. II, **2** (1957) 382. C. D. Jeffries: Phys. Rev. **117** (1960) 1056. R. W. Kedzie and C. D. Jeffries: private communication.
5) W. J. Huiskamp, A. N. Diddens, J. C. Severiens, A. R. Miedema and M. J. Steenland: Physica **23** (1957) 605.
6) P. Kafaras and J. W. Irvine, Jr.: Phys. Rev. **104** (1956) 703.
7) S. Kikuchi, T. Wakatsuki, S. Yamaguchi, Y. Oda, J. Sanada, S. Yamabe, Y. Yoshizawa, M. Takeda, M. Nozawa, E. Okada, Y. Hirao, S. Kobayashi, M. Kondo, S. Ozaki, T. Katoh, K. Okano, S. Kato, C. Hu and Y. Koh: Ann. Rep. Scient. Works Fac. Sci. Osaka Univ. **3** (1955) 1.
8) K. Otozai, S. Kume, S. Iwata, Y. Yamamoto and I. Fujisawa: Isotopes and Radiation (Tokyo) **1** (1958) 39.
9) A. Hedgran, K. Siegbahn and N. Svartholm: Proc. Phys Soc. **A63** (1950) 960. A. Hedgran: Ark. f. Fysik **5** (1952) 1.
10) T. Katoh, M. Nozawa, Y. Yoshizawa and Y. Koh: J. Phys. Soc. Japan **13** (1958) 1410.
11) E. W. Backofen and R. H. Herber: Phys. Rev. **97** (1955) 743.
12) M. E. Rose: Internal Conversion Coefficients (North-Holland Publishing Co., Amsterdam, 1958).
13) M. E. Rose: private communication.
14) M. Nozawa, H. Yamamoto, Y. Yoshizawa and Y. Koh: J. Phys. Soc. Japan **15** (1960) 2137.
15) S. Ofer and A. Schwarzschild: Phys. Rev. Letters **3** (1959) 384.
16) P. Brix, J. T. Eisinger, H. Lew and G. Wessel: Phys. Rev. **92** (1953) 647.

JOURNAL OF THE PHYSICAL SOCIETY OF JAPAN, Vol. 15, No. 12, DECEMBER 1960

Polarization of Protons Scattered from Complex Nuclei

By Shotaro YAMABE, Michiya KONDO, Shohei KATO,
Takashi YAMAZAKI, and Jian-zhi RUAN

Department of Physics, Osaka University, Osaka, Japan

(Received August 4, 1960)

The experimental results for the angular dependence of polarization of elastically scattered protons from carbon at 14 and 16 MeV, and the polarization at 45° laboratory angle in the elastic scattering by 12 target nuclei at the energy of 12~17 MeV are described. Qualitative agreement with the calculation in terms of optical potential with spin-orbit interaction is obtained for elastic scattering of protons by carbon.

§ 1. Introduction

In recent years the measurements[1)–9)] of the polarization of nucleons scattered from nuclei have been performed at low energy region. From these experiments large amounts of polarization have been observed which are unexpected from the extrapolation of some high energy experiments[10)]. This indicates that the spin-orbit interaction plays an important role in nucleon scattering phenomena as in bound nuclei, and some analyses[11),12)] in terms of optical potential with spin-orbit component have been performed.

The experimental results for the angular dependence of polarization of elastically scattered protons from carbon at 14 and 16 MeV, and the polarizations at 45° laboratory angle in the elastic scattering by 12 target nuclei at the energy of 12~17 MeV are described in this paper.

§ 2. Experimental Procedure

This experiment was performed using the INS 160 cm variable energy cyclotron of University

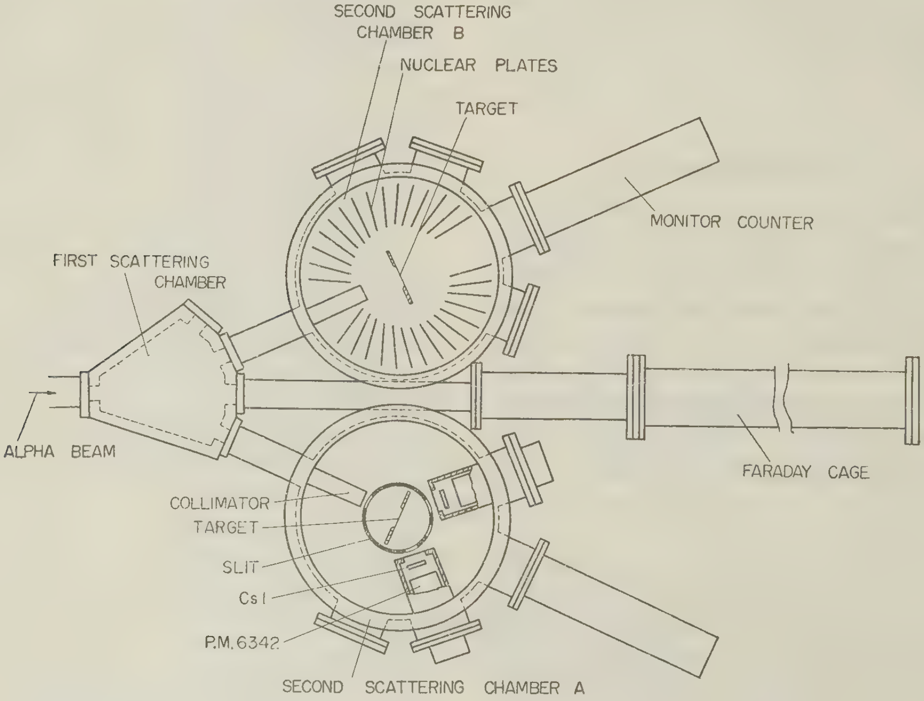

Fig 1. The second scattering chamber A is for the measurements of the left-right asymmetries by cesium-iodide scintillation counters. The chamber B shows a part of the arrangement used for the measurements of the angular dependences of the left-right asymmetries by nuclear emulsion. The details such as the shield and the pumping system are not shown in this figure.

of Tokyo. The experimental arrangement is shown in Fig. 1. 30~40 MeV α particles were extracted from cyclotron, focused by a pair of quadrupole magnets and a sector magnet, and led through the vacuum pipe to the first scattering chamber in the next room. The entrance window of the first scattering chamber was stainless steel foil of 30 mg/cm^2 and its diameter was 2.0 cm. The beam spread in the scattering volume of the first scattering chamber was adjusted to 8 mm width and 10 mm height by a pair of slits in front of the chamber. The beam, passed through the first scattering chamber and exit window of a stainless steel foil, entered into a system of Faraday cage. The beam current, about 0.3 μA, was integrated by a conventional integrator circuit, and a small fraction of this beam was led through a aluminum foil to outside of the vacuum system and its energy was determined by measuring the range in aluminum.

The first scattering chamber was filled with tank hydrogen gas 5 to 10 atmospheric pressures. Protons recoiled to ±25° with respect to the direction of the incident α particles, passed through the stainless steel foil (30 mg/cm^2) and collimator system, were led to the evacuated second scattering chamber. The energy of these recoil protons was varied from 12 MeV to 17 MeV by changing the primary energy of α particles and the pressure of hydrogen gas of the first scattering chamber. These protons are expected to be nearly completely polarized from the phase-shift analysis of the p-He scattering experiments(7),(13).

At the center of the second scattering chambers the foil targets (Be, C etc.) were placed. The recoiled beams were collimated to 10 mm × 20 mm at the target position. These second scattering chambers and collimator systems were carefully aligned within ±0.5°.

Changing the energy of the recoiled protons, excitation functions of the left-right asymmetries of the second scattering were measured by cesium-iodide scintillation counters combined with 6342 photomultiplier tubes which were set at ±45° to the direction of the recoiled proton in the second scattering chamber. The scintillation counters could be exchanged to each other, and no systematic error could be found in this system. The target and the slit system were set in ditches which were concentrically machined in the bottom of the chamber. This slit system was a cylinder of 11 cm dia. which had four windows in the middle of its height, entrance and exit holes and two circular slits of 1.5 cm dia. Geometrical asymmetries were check-

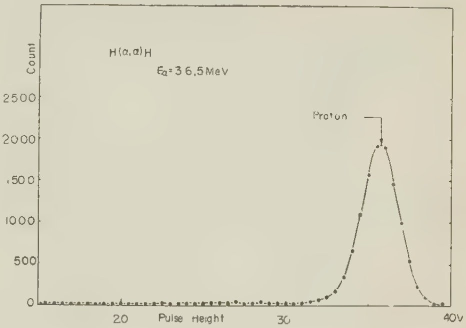

Fig. 2. The energy spectrum of the recoil protons.

Table I. Polarization (%) of protons elastically scattered from nuclei at 45° in the laboratory system.

Ep (MeV)	11.7	14.3	14.8	15.9	16.9
Be	−31.0±1.5	−30.4±1.8	−32.7±1.4	−31.2±2.1	−24.6±1.9
C	−16.0±1.3	−51.4±1.9	−55.4±1.0	−54.6±1.6	−47.1±1.6
Mg			−16.7±3.8		−9.3±4.1
Al			−8.0±4.3		
Ti			−6.3±2.9		+9.5±3.9
Ni	−9.3±1.5		−5.3±2.2		
Cu			−11.3±1.6		−13.2±2.1
Ag			−9.4±1.9		−18.5±2.3
Cd			−11.6±2.1		
Sn			−15.0±2.1		
Au		−1.5±1.4	−6.4±1.6	−6.3±1.8	−4.4±2.2
Pb			−0.8±1.1		−0.9±2.1

ed by inversing this cylinder, and satisfactory results were obtained. Pulses from the counters were amplified and analyzed by 20 channel pulse height analyzers.

A small fraction of the recoiled proton beam, which entered into the second scattering chamber, was led through a aluminum foil at the end of this chamber to outside of the vacuum system, and the energy spectrum of the recoil protons was measured by a scintillation counter and is shown in Fig. 2.

The angular dependences of the left-right asymmetries of the second scattering were measured by nuclear emulsion, in this case plate holders were placed in the second scattering chambers. We used two plate holders the one is for both forward and backward angle, the other is for around ±90°. The angular range covered was ±30° to ±160° by an interval of 10° in the laboratory system. The glancing angle of the plates was 10° and overall angular resolution was ±3°. We used Ilford C-2 200 μ plates of 1″×3″.

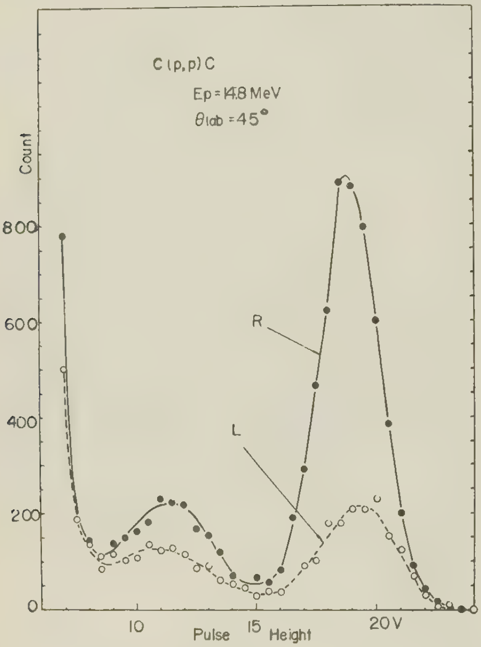

Fig. 3. Pulse height spectra of the polarized protons scattered by C.

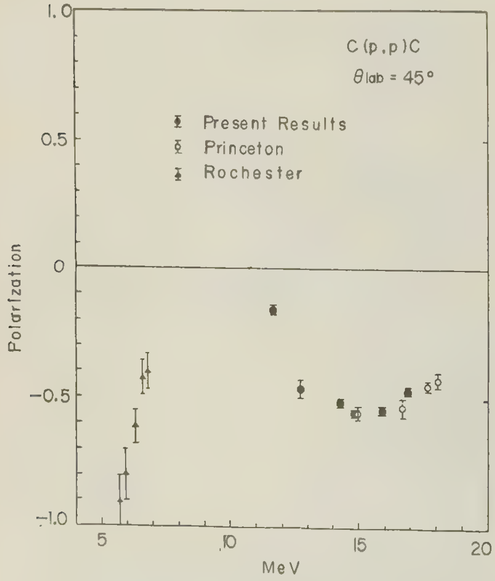

Fig. 4. Excitation function of the polarization of the elastically scattered protons from C.

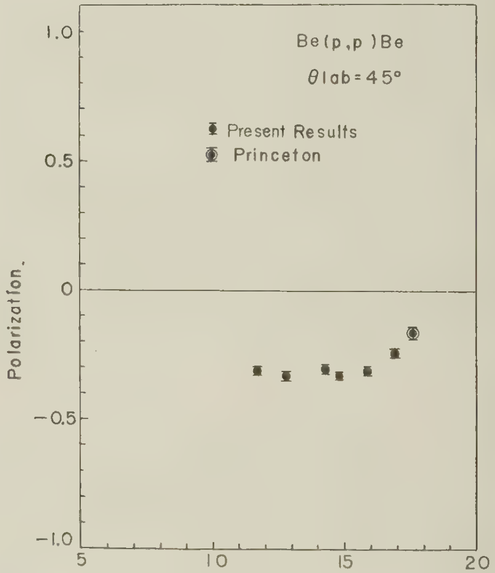

Fig. 5. Excitation function of the polarization of the elastically scattered protons from Be.

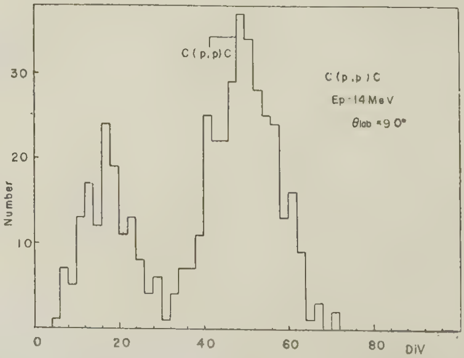

Fig. 6. A typical histogram of the protons scattered by C.

3. Results and Discussion

The measured left-right ratio R of the scat-ered intensities in the second scattering is xpressed by the product of the polarization f the first and the second scattering as the ollowing relation

$$\frac{R-1}{R+1}=P_1\cdot P_2\ ,$$

vhere P_1 and P_2 are the polarization of the irst and the second scattering, respectively. The sign convention for the polarization is hat the positive direction is that of $k_{\rm inc}\times k_{\rm sc}$, where $k_{\rm inc}$ and $k_{\rm sc}$ are the incident and scattered wave vectors, respectively. We assumed that P_1 was equal to $+100\%$ which was not contradictory to both a direct measurement[14] and a calculation from the value of the scattering phase-shift, then P_2 could be obtained.

The results obtained for elastically scattered protons using scintillation counters are listed in Table I and typical pulse height spectra are shown in Fig. 3. Errors indicated are only statistical ones throughout this article. The scattering angle was 45° in the laboratory system and the values of the proton energy were expressed approximately at the center of the target. It is noticeable that all the values except the one for Ti at 16.9 MeV have negative sign. In Figs. 4 and 5 excitation functions for C and Be are shown with other results in this energy region.

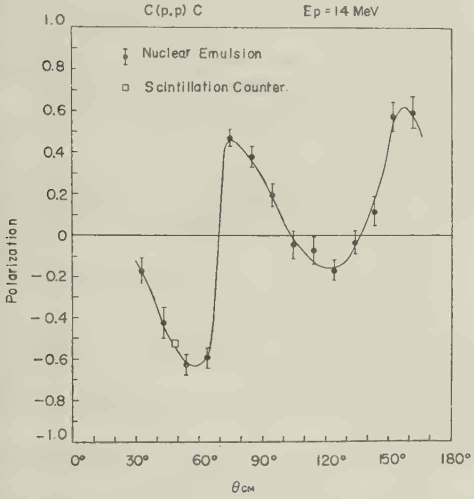

Fig. 7. The angular dependence of the polarization for C at 14 MeV.

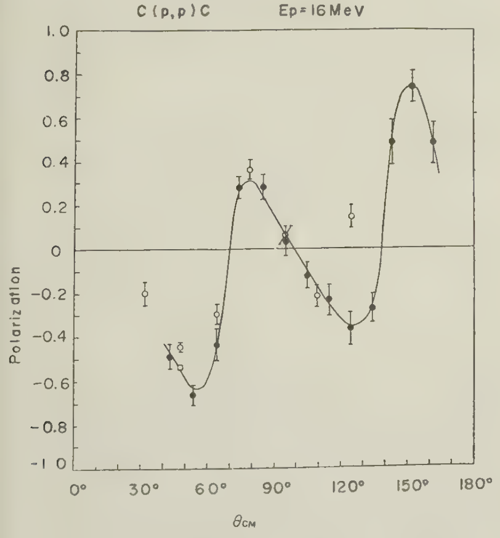

Fig. 8. The angular dependence of the polarization for C at 16 MeV. The open circles represent the result obtained by Brockman at 17.7 MeV.

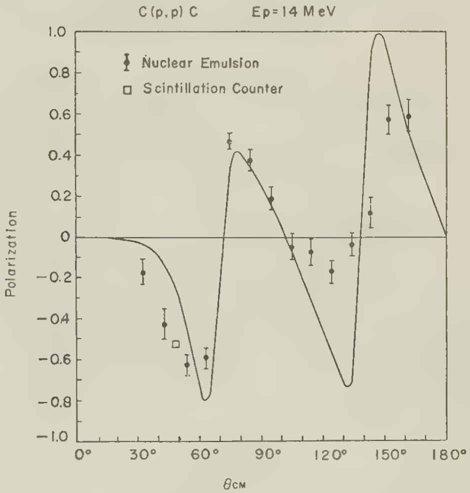

Fig. 9. Comparison with optical model calculation. Theoretical prediction given by Erickson and Cheston is indicated.

The angular dependence of the polarization for elastically scattered proton from C at 14 and 16 MeV was measured by nuclear emulsion. A typical histogram is shown in Fig. 6.

The results of the angular dependence of the polarization are shown in Figs. 7 and 8. These angular dependences were very similar in shape to each other. The result obtained by Brockman[7] at 17.7 MeV was also very similar to our present results, and these circumstances are shown in Fig. 8. From these facts we may conclude that the energy dependence of the polarization of protons elastically scattered from C is not so remarkable in this energy region.

Theoretical calculation using the optical model with spin-orbit potential for 14 MeV proton on C was given by G. W. Erickson and W. B. Cheston[12)], and our result at 14 MeV can be fitted qualitatively with this calculation, as shown in Fig. 9. In this figure, theoretical prediction by Erickson and Cheston is shown by solid curve. The optical potential adopted in the calculation is

$$V(\vec{r},\vec{\sigma}) = V_c(r)+[(V+iW)+(v+iw)\vec{\sigma}\vec{L}]\frac{1}{1+e^{(r-R)/a}},$$

where $V_c(r)$ is the Coulomb potential. The values of the parameters are as follows, $R=2.845\times10^{-13}$ cm, $a=0.5\times10^{-13}$ cm, $V=-50$ MeV, $W=-8.5$ MeV, $v=-2$ MeV and $w=0$.

Table II. The left-right asymmetries (%) for inelastically scattered protons from $C^{12}(Q=-4.43$ MeV).

Ep (MeV)	14.8	15.9	16.9
asymmetry	-32.4 ± 2.6	-32.6 ± 3.3	-41.3 ± 2.5

The left-right asymmetries at 45° laboratory angle for inelastically scattered protons from C^{12} ($Q=-4.43$ MeV) are listed in Table II. As to the angular dependence we could not obtained reliable data because of the large background of neutron and γ-radiation.

Acknowledgments

We are indebted to the INS cyclotron group of University of Tokyo for the very reliable operation of the machine. We also wish to express our gratitudes to Professor T. Wakatsuki for his guidance and to Dr. J. Sanada for his helpful discussions throughout this work.

References

1) M. Heusinkveld and G. Freier: Phys. Rev. **85** (1952) 80.
2) P. Huber and E. Baumgartner: Helv. Phys. Acta. **26** (1953) 423.
3) Adair, Darden and Fields: Phys. Rev. **96** (1954) 503.
4) A. Remund: Helv. Phys. Acta **29** (1956) 545.
5) M. Scott: Phys. Rev. **110** (1958) 1398.
6) L. Rosen and J. Brolley: Phys. Rev. **107** (1957) 1454.
7) K. W. Brockman: Phys. Rev. **110** (1958) 163.
8) W. A. Blanpied: Phys. Rev. **113** (1959) 1099.
9) R. E. Warner and W. P. Alford: Phys. Rev. **114** (1959) 1338.
10) Dickson, Rose and Salter: Proc. Phys. Soc. (London) **A68** (1955) 361.
11) Culler, Fernbach and Sperman: Phys. Rev. **101** (1956) 1047.
12) G. Erickson and W. Cheston: Phys. Rev. **111** (1958) 891.
13) K. W. Brockman: Phys. Rev. **102** (1956) 391, Phys. Rev. **108** (1957) 1000.
14) J. Sanada, K. Nishimura, S. Suwa, I. Hayashi, K. Fukunaga, N. Ryu and M. Seki: Jour. Phys. Soc. Japan **15** (1960) 754.

JOURNAL OF THE PHYSICAL SOCIETY OF JAPAN, Vol. 15, No. 12, DECEMBER, 1960

Reactions of Nickel with Alpha-Particles

By Shigeo TANAKA

Institute for Nuclear Study, University of Tokyo,
Tanashi-Machi, Tokyo

(Received August 5, 1960)

Excitation functions for the alpha-particle induced reactions on Ni^{58}, Ni^{60}, Ni^{61}, Ni^{62} and Ni^{64} have been measured at incident energies up to 40 Mev. The sum of the measured cross sections for Ni^{58} appears to agree with the total reaction cross section calculated from the continuum theory for $r_0=1.7\times10^{-13}$ cm. The sum almost agrees with the optical-model analysis of reaction cross section for alpha-particles by Igo, but his prediction seems to give a little higher value. In the excitation function for the $(\alpha, \alpha n)$ reaction on Ni^{58}, there is a small "knee" immediately after the effective threshold (around 23 Mev). The alpha-particle reactions on Ni^{60} have been compared with the proton reactions on Cu^{63}, the compound nucleus Zn^{64} being the same for two cases. The prediction from the compound nucleus theory seems to hold roughly, and it seems inadequate to discuss strictly whether the discrepancy in energy is significant. The same is observed in the comparison between the alpha-particle reactions on Ni^{62} and the proton reactions on Cu^{65}.

§1. Introduction

Present author and his colaborators[1-4] are studying systematically the cross sections of alpha-particle reactions on medium-weight nuclei at intermediate energies. As a part of their systematic study, the excitation functions for the reactions listed in Table I have been measured in this study for alpha-particle energies up to 40 Mev.

Table I. List of the reactions studied.

Target Nuclide	Type of Reaction
Ni^{58}	$(\alpha,\ p+\alpha,\ n)$, $(\alpha,\ pn+\alpha,\ 2n)$, $(\alpha,\ \alpha p)$, $(\alpha,\ \alpha n)$, $(\alpha,\ \alpha pn)$, $(\alpha,\ \alpha 2n)$
Ni^{60}	$(\alpha,\ n)$, $(\alpha,\ pn)$, $(\alpha,\ 2n)$, $(\alpha,\ \alpha pn)$, $(\alpha,\ p2n+\alpha,\ 3n)$
Ni^{61}	$(\alpha,\ p)$
Ni^{62}	$(\alpha,\ n)$, $(\alpha,\ pn)$, $(\alpha,\ \alpha p)$
Ni^{64}	$(\alpha,\ p)$, $(\alpha,\ 3n)$

Recently, Houck and Miller[5] measured the excitation functions for the $(\alpha, \alpha p)$, $(\alpha, \alpha n)$, $(\alpha, \alpha pn)$ and $(\alpha, \alpha 2n)$ reactions on Ni^{58} for alpha-particle energies up to 40 Mev. They compared the ratios of $\sigma(\alpha, \alpha p)/\sigma(\alpha, \alpha n)$ and $\sigma(\alpha, \alpha pn)/\sigma(\alpha, \alpha 2n)$ for Ni^{58} with those of $\sigma(\alpha, p)/\sigma(\alpha, n)$ and $\sigma(\alpha, pn)/\sigma(\alpha, 2n)$ for Fe^{54}, respectively. They themselves and also Dostrovsky, Fraenkel and Friedlander[6] discussed their results in terms of the evaporation theory of compound nucleus. The $(\alpha, p+\alpha, n)$ and $(\alpha, pn+\alpha, 2n)$ reactions on Ni^{58} have been also measured in this study. The sum of the measured cross sections has been compared with the total reaction cross section predicted by the continuum theory and by the optical model analysis.

The alpha-particle reactions on Ni^{60} and the proton reactions on Cu^{63} were previously measured by Ghoshal[7]. They gave the experimental evidence for the Bohr's compound nucleus hypothesis to the medium energy region. It has been pointed out, however, by Eastman, Isenor, Bainbridge and Duckworth[8] and also by John[9] that the energy shift required to fit Ghoshal's experiment to the compound nucleus theory is not exactly equal to the value derived from mass measurement The measurement of the alpha-particle reactions on Ni^{60}, after Ghoshal's work, would be of use to examine this discrepancy. The similar discrepancy was shown, very recently, by the present author and his colaborators[4] for the comparison between the alpha-particle reactions on Fe^{56} and the proton reactions on Co^{59}. Further, the comparison between the alpha-particle reactions on Ni^{62} in this study and the corresponding proton reactions on Cu^{65} would be of use for the test of this discrepancy.

Very recently, McGowan, Stelson and

Smith[10] measured the cross sections for the reactions $Ni^{58}(\alpha, n)Zn^{61}$, $Ni^{58}(\alpha, p+\alpha, n+\alpha, \gamma)$, $Ni^{60}(\alpha, n)Zn^{63}$ and $Ni^{62}(\alpha, n)Zn^{65}$ up to $E_\alpha=11.0$ Mev. And present results are compared with theirs.

§ 2. Experimental

The bombardments were performed with the external alpha-particle beam from the 160 cm INSJ variable energy cyclotron by means of a stacked-foil technique. The stack of the target foils was placed at the bottom of the long cylindrical cup which was served also as a Faraday cup. The beam was measured by a 100% feed-back type current integrator. Each stack generally consisted of 10 to 12 target foils which were interspaced with aluminum absorbers. The value of the energy loss of alpha-particles in aluminum absorber was taken from the works of Bichsel, Mozley and Aron[11], Burkig and MacKenzie[12] and of Sternheimer[13], whereas that in nickel target was calculated from the stopping power formula of Bethe et al. using the estimated mean excitation potential; $I=13Z$ (ev) and $Z=28$. In different experiments, the initial alpha-particle energies were 40.0, 38.5, 32.0 and 31.3 Mev, and energy region was overlapped in different runs by a few Mev. After the bombardment, the target foil was dissolved in acid and nickel, cobalt, copper and zinc were chemically separated by means of an anion exchange resin. Each fraction was then submitted to counting. For the shorter-lived nuclides (mainly for Cu^{60}, Cu^{62} and Zn^{63}) short time irradiation (from 30 seconds to a few minutes) was performed several times with 5 to 6 target foils in the stack. The shorter-lived activities were counted, with and without a chemical separation. Copper and zinc were separated from nickel and other constituents by means of an organic co-precipitation method.[14,15] The chemical process completed within 25 minutes. A more detailed description of the bombarding system is given in the previous reports[1,16], and that of the chemical procedure in the Appendix.

The targets consisted of natural-nickel foils (8.7±0.2 mg/cm²) whose impurities were chemically analyzed.

Table II. Impurities of natural-nickel target.

Impurity	C	Si	Mn	Co	Fe	Mg
Content (%)	0.02	0.03	0.05	0.05	0.01	0.11

The disintegration rates of the residual nuclides were determined with a calibrated GM counter, a $4\pi\beta$-counter and an (1−3/4 in. dia. ×2 in. high, 1−1/2 in. dia. ×1 in. high and well-type) NaI scintillation counter. The counting technique and the calibration method are presented in detail in the Appendix.

§ 3. Results and Discussion

Reactions of Ni^{58}

The excitation functions for the alpha-particle reactions on Ni^{58} are shown Fig. 1 and Fig. 2, which also include the estimated error of the magnitude of cross section and the energy spread in target foil for some experimental points. The cross sections measured by McGowan, Stelson and Smith[10] for the low-energy part of the $(\alpha, p+\alpha, n+\alpha, \gamma)$ reaction agree well with the present results. (See: Fig. 1) Natural-nickel was used as target material; hence the $(\alpha, p+\alpha, n)$ cross section for Ni^{58} and the $(\alpha, p2n+\alpha, 3n)$ cross section for Ni^{60} could not be obtained separately, above the threshold for the latter reaction.

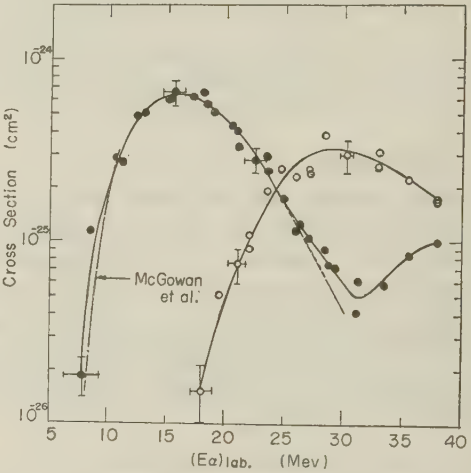

Fig. 1. Excitation functions for the alpha-particle reactions on Ni^{58}. (Part 1)

● $Ni^{58}(\alpha, p)Cu^{61}+Ni^{58}(\alpha, n)Zn^{61}$.

○ $Ni^{58}(\alpha, pn)Cu^{60}+Ni^{58}(\alpha, 2n)Zn^{60}$.

–·– $\sigma(\alpha, p+\alpha, n+\alpha, \gamma)$ measured by McGowan et al.[10]

- - - - Estimated curve of $\sigma(\alpha, p+\alpha, n)$ after subtraction of the contribution from the reactions $Ni^{60}(\alpha, p2n)Cu^{61}$ and $Ni^{60}(\alpha, 3n)Zn^{61}$.

The excitation functions for the reactions (α, αp), (α, αn) and (α, αpn) obtained by Houck and Miller[5)] and by the present author agree completely with each other. (See: Fig. 2)

The sum of the measured cross sections is compared with the total reaction cross section calculated from the continuum theory (according to Shapiro's calculation[17)]) and from the optical model analysis (according to Igo's calculation[18)]). A shallow minimum around 22 Mev in the sum of the measured cross sections may reflect a substantial contribution of the unmeasured cross sections. The most probable reactions which are missed in this experiment may be the (α, $\alpha\gamma$) reaction and particularly the (α, $2p$) reaction. The threshold for the (α, $2p$) reaction is lower than that for the (α, pn) reaction by about 8.1 Mev (Quisenberry et al.[19)]), thus the (α, $2p$) reaction may be quite important in spite of the Coulomb barrier of the proton emission. According to Shapiro's calculation, a value of $r_0=1.7\times10^{-13}$ cm appears to give a reliable fit to the sum of the measured cross sections. Igo's prediction almost agrees with the present experiment, but seems to give a little higher value.

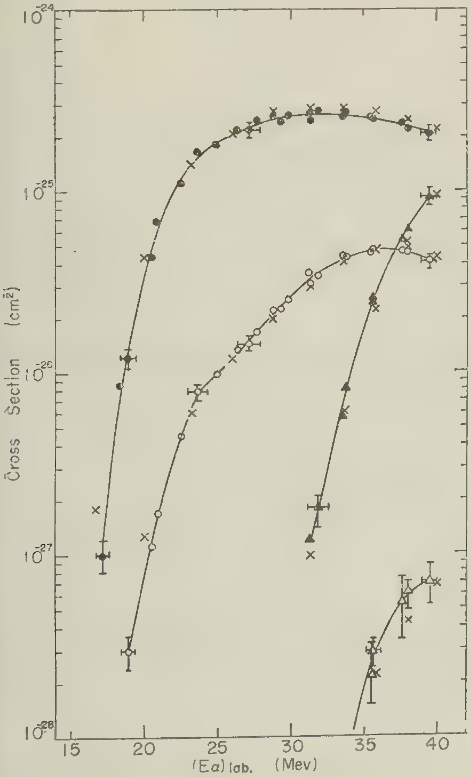

Fig. 2. Excitation functions for the alpha-particle reactions on Ni^{58}. (Part 2)

- ● $Ni^{58}(\alpha, \alpha p)Co^{57}$ ▲ $Ni^{58}(\alpha, \alpha pn)Co^{56}$
- ○ $Ni^{58}(\alpha, \alpha n)Ni^{57}$ △ $Ni^{58}(\alpha, \alpha 2n)Ni^{56}$
- × The cross sections measured by Houck and Miller[5)] for each corresponding reaction.

The next value is not shown in the Figure.
$\sigma(\alpha, \alpha n)$ at 33.5 Mev = 6×10^{-29} cm².

It can be seen that there is a small "knee" immediately above the effective threshold (around 23 Mev) in the excitation function for the (α, αn) reaction. (See: Fig. 2) The "knee" was carefully determined by two different runs. The contamination of cobalt into nickel fraction was reduced below $\sim1\times10^{-5}$ by careful procedures. It is thought that this "knee" is beyond experimental errors. This anomaly was also observed in the excitation function for the (α, 2n) reaction on Fe^{54} by the present author and his colaborators[3)] and also by Houck and Miller[5)], the reason remains uncertain.

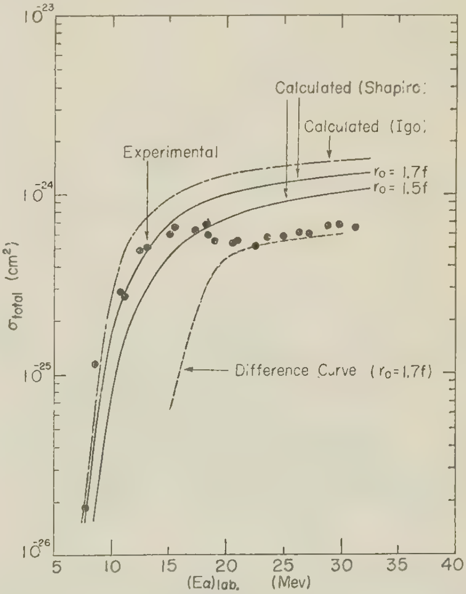

Fig. 3. The total reaction cross section for the alpha-particle reactions on Ni^{58}.

- ● Sum of the measured cross sections.
- —— Total reaction cross section calculated from the continuum theory of $r_0=1.7\times10^{-13}$ cm and of $r_0=1.5\times10^{-13}$ cm. (According to Shapiro's calculation[17)])
- —·— Total reaction cross section predicted from Igo's optical model analysis.[18)]
- ---- Difference curve between continuum theory of $r_0=1.7\times10^{-13}$ cm and sum of the measured cross sections.

The energy dependences of the ratios of $\sigma(\alpha, \alpha p)/\sigma(\alpha, \alpha n)$ and $\sigma(\alpha, \alpha pn)/\sigma(\alpha, \alpha 2n)$ for Ni^{58} are shown in Fig. 4. The predominance of proton emission over neutron emission has been reported for the cross section ratios of various reactions resulting the isobaric pairs of Co^{57}–Ni^{57} and Co^{56}–Ni^{56}.[3,5,20–24] The shallow concave which can be seen around 23 Mev in the ratio curve of $\sigma(\alpha, \alpha p)/\sigma(\alpha, \alpha n)$ is a consequence of the "knee" observed in the $(\alpha, \alpha n)$ excitation function.

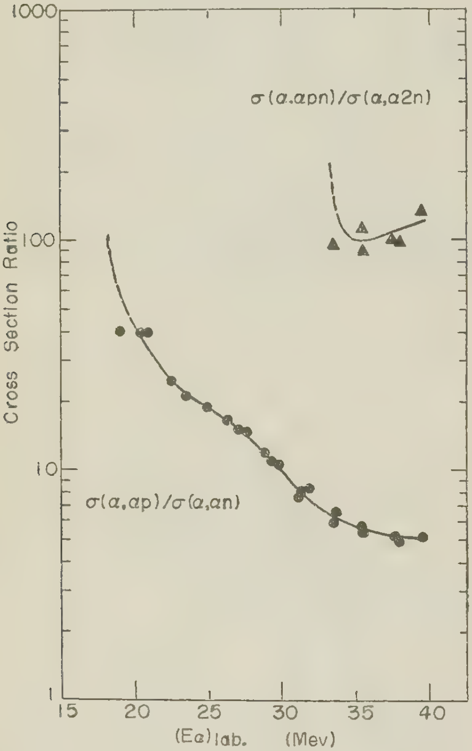

Fig. 4. The energy dependences of the cross section ratios of $\sigma(\alpha, \alpha p)/\sigma(\alpha, \alpha n)$ and $\sigma(\alpha, \alpha pn)/\sigma(\alpha, \alpha 2n)$ for Ni^{58}.

Reactions of Ni^{60}

The excitation functions for the (α, n), (α, pn) and $(\alpha, 2n)$ reactions on Ni^{60} are shown in Fig. 5 together with the data of Ghoshal.[7] The present results do not entirely agree with Ghoshal's, especially for the energy dependences of the (α, n) and the (α, pn) reaction. The low-energy part of the (α, n) excitation function measured by McGowan et al. agrees rather with the present experiment than with Ghoshal's. The experiment of McGowan et al. is considered to be most accurate among the three for the energy values at the low-energy part. The disagreement in energy between Ghoshal's and the present experiment may have an influence on the discussion made by Eastman et al.[8] and John.[9] They have pointed out that the energy shift to fit Ghoshal's experiment to the compound nucleus theory is not exactly equal to the value derived from mass measurement.

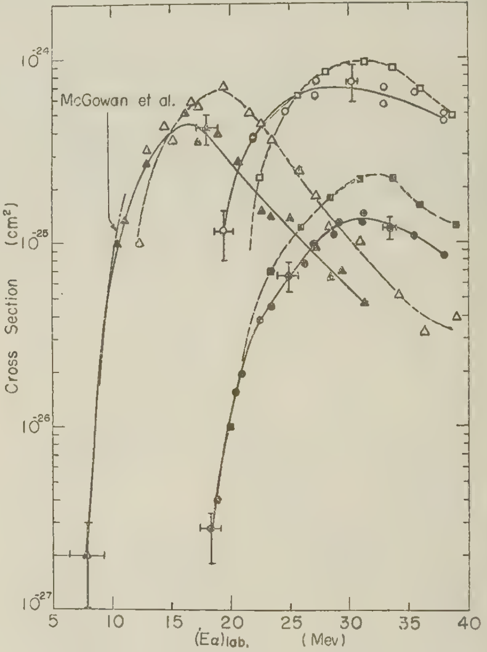

Fig. 5. Excitation functions for the alpha-particle reactions on Ni^{60}. (Part 1)

▲	$Ni^{60}(\alpha, n)Zn^{63}$	Present data*
○	$Ni^{60}(\alpha, pn)Cu^{62}$	
●	$Ni^{60}(\alpha, 2n)Zn^{62}$	
△	$Ni^{60}(\alpha, n)Zn^{63}$	Ghoshal's data
□	$Ni^{60}(\alpha, pn)Cu^{62}$	
▨	$Ni^{60}(\alpha, 2n)Zn^{62}$	
---	$\sigma(\alpha, n)$ measured by McGowan et al.[10]	

* With regard to the interfering reactions of Ni^{61}, no corrections is applied to the present results.

The comparison between the alpha-particle reactions on Ni^{60} and the proton reactions on Cu^{63} is illustrated in Fig. 6. All the available cross sections of both reactions are compared schematically with the excitation energy of the compound nucleus, Zn^{64}. The binding energies of an alpha-particle to Zn^{64} and of a proton to Zn^{64} are deduced from the mass values which have recently been measured with high precision by Quisenberry, Scolman and Nier[19];

B_α=3.93 Mev and B_p=7.71 Mev. The magnitude of cross section obtained by Ghoshal is somewhat larger than that obtained by other authors in every case. And the energy values in the experiments of both Ghoshal and Meadows might not be so accurate that it seems inadequate to discuss strictly whether the discrepancy in energy is significant. However, it seems certain that the (α, n) and the (p, n) excitation function disagree in energy with each other by about 1 Mev. Further accurate experiment is desirable to see whether the discrepancy is significant. On the whole, this comparison is not necessarily in disagreement with the prediction from the compound nucleus theory; i.e. the relation $\sigma(\alpha, n):\sigma(\alpha, pn):\sigma(\alpha, 2n)=\sigma(p, n):\sigma(p, pn):\sigma(p, 2n)$ is roughly satisfied provided that the excitation energy of compound nucleus is the same.

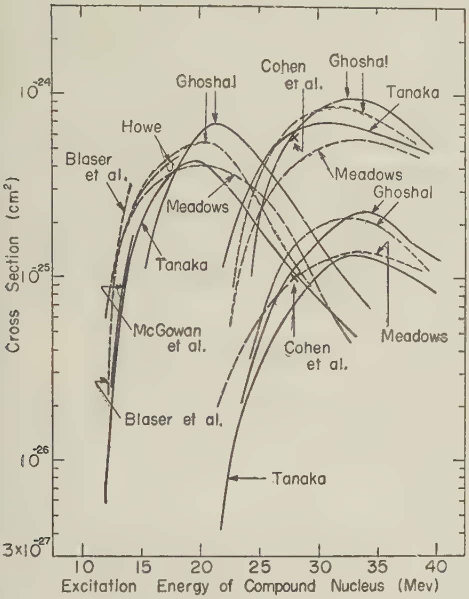

Fig. 6. The comparison between the alpha-particle reactions on Ni^{60} (solid curves) and the proton reactions on Cu^{63} (dashed curves), the compound nucleus Zn^{64} being the same for two cases.

Reaction	Bombarding Energy	Author	Reference
$Ni^{60}+\alpha$	40 and 32Mev	Tanaka	This work
$Ni^{60}+\alpha$	40	Ghoshal	7
$Ni^{60}+\alpha$	11.0	McGowan et al.	10
$Cu^{63}+p$	32	Ghoshal	7
$Cu^{63}+p$	100 and 75	Meadows	25
$Cu^{63}+p$	12	Howe	26
$Cu^{63}+p$	6.7	Blaser et al.	27
$Cu^{63}+p$	21.5	Cohen et al.	28

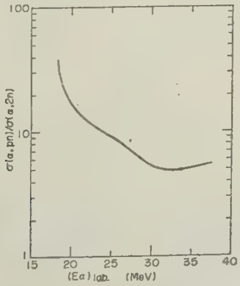

Fig. 7. The energy dependence of the cross section ratio of $\sigma(\alpha, pn)/\sigma(\alpha, 2n)$ for Ni^{60}.

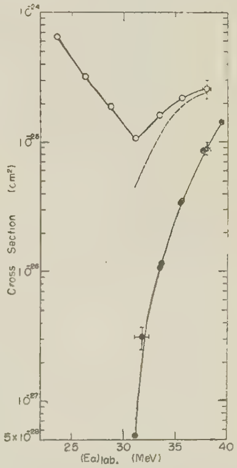

Fig. 8. Excitation functions for the alpha-particle reactions on Ni^{60}. (Part 2)

- ● $Ni^{60}(\alpha, \alpha pn)Co^{58}$
- ○ $Ni^{60}(\alpha, p2n)Cu^{61}+Ni^{60}(\alpha, 3n)Zn^{61}$
- ---- Estimated curve of $\sigma(\alpha, p2n+\alpha, 3n)$ after subtraction of interfering reaction. (See: text)

The energy dependence of the ratio of $\sigma(\alpha, pn)/\sigma(\alpha, 2n)$ for Ni^{60} is shown in Fig. 7.

The excitation functions for the $(\alpha, \alpha pn)$ and $(\alpha, p2n+\alpha, 3n)$ reactions on Ni^{60} are also shown in Fig. 8. The $(\alpha, p2n+\alpha, 3n)$ cross section was estimated by subtracting the contribution of the $(\alpha, p+\alpha, n)$ cross section for Ni^{58}. (Dashed curve in Fig. 8)

Reactions of Ni^{62}

The excitation functions for the (α, n), (α, pn) and $(\alpha, \alpha p)$ reactions on Ni^{62} are shown in Fig. 9. The use of natural-nickel as target material made it impossible to distinguish between the $Ni^{62}(\alpha, n)Zn^{65}$ and the $Ni^{64}(\alpha, 3n)Zn^{65}$ cross section above the threshold for the latter reaction. And, what is worse, the $Ni^{62}(\alpha, pn)Cu^{64}$ and the $Ni^{61}(\alpha, p)Cu^{64}$ cross section could not be distinguished exactly. The yield of producing Cu^{64} was classified into two reactions assuming a smooth curve of each excitation function. The estimated excitation functions are indicated by the dashed curves in Fig. 9 and Fig. 11. The rough estimation may not cause much ambiguities.

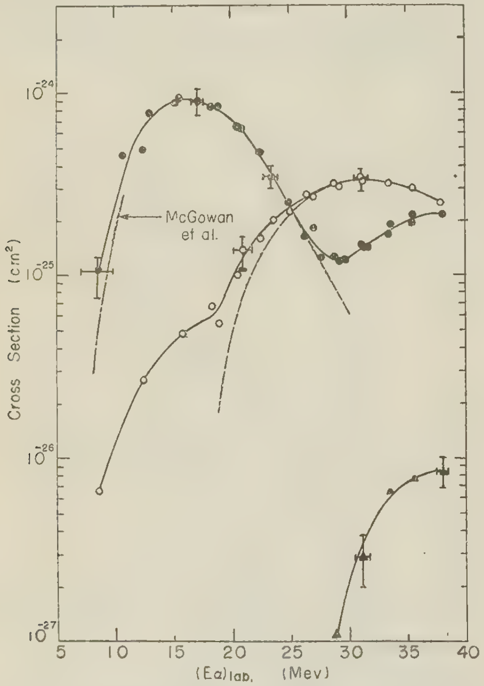

Fig. 9. Excitation functions for the alpha-particle reactions on Ni^{62}.

● $Ni^{62}(\alpha, n)Zn^{65}$ ○ $Ni^{62}(\alpha, pn)Cu^{64}$
▲ $Ni^{62}(\alpha, \alpha p)Co^{61}$
---- Estimated curve after subtraction of interfering reaction. (See: text)

The present results for the alpha-particle reactions on Ni^{62} are compared in Fig. 10 with the corresponding proton reactions on Cu^{65}, with the excitation energy of the compound nucleus, Zn^{66}. The binding energies of an alpha-particle to Zn^{66} and of a proton to a Zn^{66} are assumed 4.56 Mev and 8.90 Mev, respectively. These values are deduced from the mass values measured by Quisenberry et al.[19] The prediction from the compound nucleus theory seems to hold roughly and the discrepancy in energy between the experiment and the theory can not be observed. However, the difference between the value of cross section for the $Ni^{62}(\alpha, pn)Cu^{64}$ reaction and that for the $Cu^{65}(p, pn)Cu^{64}$ reaction

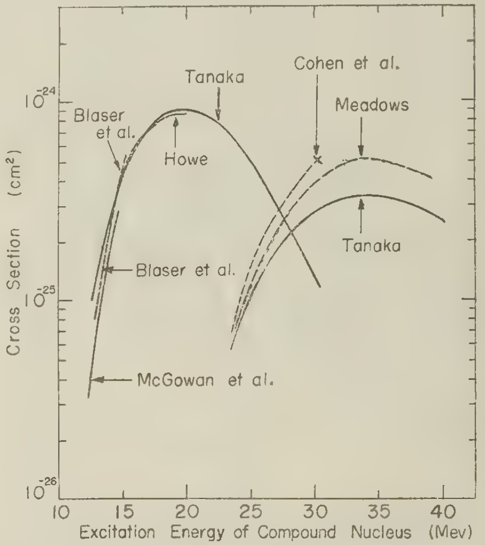

Fig. 10. The comparison between the alpha-particle reactions on Ni^{62} (solid curves) and the proton reactions on Cu^{65} (dashed curves), the compound nucleus Zn^{66} being the same for two cases.

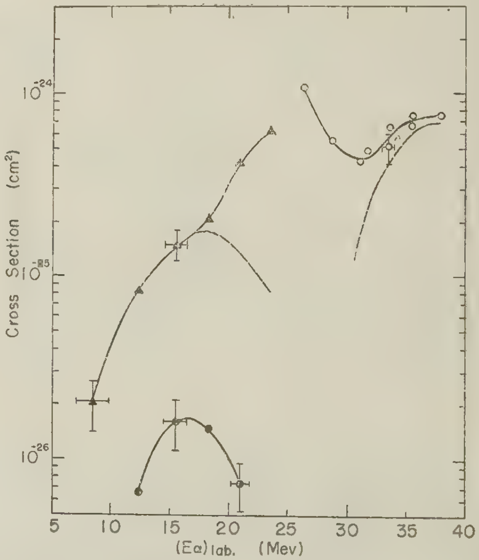

Fig. 11. Excitation functions for the alpha-particle reactions on Ni^{61} and Ni^{64}.

▲ $Ni^{61}(\alpha, p)Cu^{64}$ ○ $Ni^{64}(\alpha, 3n)Zn^{65}$
● $Ni^{64}(\alpha, p)Cu^{67}$
---- Estimated curve after subtraction of interfering reaction. (See: text)

should be again checked experimentally.*

Reactions of Ni^{61} and Ni^{64}

The results of the reactions on Ni^{61} and Ni^{64} are shown in Fig. 11. The excitation functions for the $Ni^{61}(\alpha, p)Cu^{64}$ and the $Ni^{64}(\alpha, 3n)Zn^{65}$ reaction were estimated by subtracting the contribution of the $Ni^{62}(\alpha, pn)Cu^{64}$ and the $Ni^{62}(\alpha, n)Zn^{65}$ reaction, respectively.

All the excitation functions measured in this study may be useful in the comparison with the evaporation calculation based on the statistical theory of nuclear reaction. However, such a discussion is not made in this paper.

Acknowledgements

The close association with Messrs. M. Furukawa, S. Iwata, M. Yagi and Dr. H. Amano has contributed immeasurablly to this work, and their continued colaboration and helpful advice are gratefully acknowleded. Thanks are also due to Prof. I. Nonaka and the other members of staff of Low Energy Division in this Institute for their constant interest and encouragement. The cyclotron bombardments could not have been done without the co-operation and help of Messrs. T. Karasawa, A. Suzuki, H. Ogawa and the other Cyclotron Crew of this Institute. The continued assistance of Messrs. T. Ando, A. Iguchi and M. Chiba throughout this work are also acknowledged.

Appendix

A. Chemical Procedures

For shorter-lived nuclides

The target foil was dissolved in 2 ml of conc. HCl with the aid of 10 drops of 30% H_2O_2. The excess of H_2O_2 was decomposed by adding 25% $NaHSO_3$. After the addition of zinc carrier (200 γ of Zn), 6N–NH_4OH was added to the solution until the blue color of Ni-ammin complex appeared. The solution was neutralized to methyl orange with 1N–HCl. 5 ml of 5% NH_4I and 3 ml of 3% methyl violet were added. The Cu-precipitate was separated by centrifuge and washed with 10 ml of 0.5% NH_4I. The precipitate was dissolved in ethyl alcohol and submitted to counting. The united solution of supernatent and washing was adjusted to pH 10～12 by adding 6N–NH_4OH drop by drop, and then 5 ml of 5% NH_4SCN and 3 ml of 3% methyl violet were added. The zinc precipitate was separated by centrifuge, and dissolved in alcohol.

For longer-lived nuclides

The target foil was dissolved in aqua regia.

Table III. Nuclear data necessary for the calculation.

Nucleide	Half-life	Radiation and Energy (Mev)	Emission Probability of β- and γ-ray (%)
Co^{56}	77 d	β^+ 1.50	18
		β^+ 1.00	
		β^+ 0.44	
		γ 0.845	100
Co^{57}	270 d	γ 0.122	100
		γ 0.137	
Co^{58}	71 d	β^+ 0.485	15
		γ 0.810	100
Co^{61}	1.65 h	β^- 1.22	100
Ni^{56}	6.0 d	——	—
Ni^{57}	37 h	β^+ 0.85	47
		β^+ 0.72	
		β^+ 0.35	
Cu^{60}	24 m	β^+ 2.00	93
		β^+ 3.00	
		β^+ 3.92	
Cu^{61}	3.3 h	β^+ 1.21	66
		β^+ 0.94	
		β^+ 0.56	
Cu^{62}	10.0 m	β^+ 2.91	98
Cu^{64}	12.8 h	β^+ 0.656	19
		β^- 0.571	39
Cu^{67}	59 h	β^- 0.577	100
		β^- 0.484	
		β^- 0.395	
Zn^{60}	2.1 m	——	—
Zn^{61}	1.5 m	——	—
Zn^{62}	9.3 h	β^+ 0.66	12
Zn^{63}	38.3 m	β^+ 2.4	93
		β^+ 1.4	
Zn^{65}	245 d	γ 1.114	45

---

* *Note added in proof*—H. P. Yule and A. Turkevich [Phys. Rev. **118** (1960) 1591] measured the $Cu^{65}(p, pn)Cu^{64}$ cross section in the energy range 82–426 Mev. Their result is lower than Meadows's by a factor of about 0.6. The value of Yule and Turkevich reduces the discrepancy in the magnitude of cross section between the proton and the alpha-particle reaction.

the solution was evaporated nearly to dryness and the residue was dissolved in 1 ml of 8N–HCl. The solution was then passed through a column (13 mm dia. × 150 mm high) of anion exchange resin Dowex-1X 8 (200～400 mesh) followed by washing with about 25 ml of 8N–HCl. Nickel was eluted with 8N–HCl, cobalt with 4N–HCl, copper with 2.5N–HCl and zinc with 2N–HNO_3.

B. Counting and Calibration Procedures

The nuclear data shown in Table III were used for the calculation of disintegration rates. These data were obtained mainly from the compilation of Strominger et al.[29]

Co^{56} The γ-rays above 1.6 Mev were measured in a well-type NaI scintillation counter to discriminate against other activities. The disintegration rate was obtained by comparing the sample with a calibrated Co^{56} standard source. (See: reference 3 for the detailed calibration procedures)

Co^{57} The 122 and 137 kev γ-ray photopeaks were counted in an 1−3/4 in. dia. × 2 in. high well-type NaI scintillation counter. The counting efficiency was assumed as 0.85. (See: reference 1)

Co^{58} The 810 kev γ-ray photopeak was counted in a well-type NaI scintillation counter. The contribution of Co^{56} was subtracted by comparing the sample with a Co^{56} standard source. (See: reference 1 for the detailed subtraction procedure). The disintegration rate was obtained by applying the intrinsic photopeak efficiency to the counting rate. (See: reference 4)

Co^{61} The decay of cobalt fraction was followed with the GM counter whose efficiency had been calibrated with various β^--emitters of known disintegration rates.

Ni^{56} After Ni^{56} was allowed to decay to Co^{56}, the disintegration rate of Ni^{56} was measured as Co^{56}.

Ni^{57} After Ni^{57} was allowed to decay to Co^{57}, it was counted as Co^{57}.

Cu^{60} Immediately after the bombardment, the target foil was sandwiched by two brass plates of sufficient thickness to stop the positrons, and the two 0.51 γ-rays were detected in coincidence with two 1−1/2 in. dia. × 1 in. high NaI scintillation counters positioned 180° from each other with respect to the source. The decay was followed for about 10 hours to distinguish Cu^{60} from Cu^{61}, Cu^{62} and Zn^{63}. The counting efficiency of the instrument was calibrated by the Na^{22} standard source, the absolute activity of which had been determined by both the γ-γ coincidence and the $4\pi\beta$-counting method. In the experiment with chemical separation, copper fraction counted similarly. The counting with a calibrated GM counter was also performed.

Cu^{61} After chemical separation, the positrons were counted with a calibrated GM counter. The decay was also followed with a $4\pi\beta$-counter to determine the disintegration rate. In the experiment with short time irradiation, the decay was followed by measuring the coincident annihilation radiation. (See: Cu^{60}) The disintegration rates from the different experiments agreed with each other within 10%.

Cu^{62} Without chemical separation, the coincident annihilation radiation was measured. (See: Cu^{60})

Cu^{64} and *Cu^{67}* The disintegration rates were obtained by following the decay of copper fraction with a calibrated GM counter.

Zn^{62} The decay of zinc fraction was followed with a calibrated GM counter. A $4\pi\beta$-counting was also performed.

Zn^{63} After chemical separation, an aliquot of zinc fraction was counted with a calibrated GM counter and another aliquot was submitted to counting the coincident annihilation radiation. (See: Cu^{60})

Zn^{65} The 1.11 Mev γ-ray photopeak was counted in a well-type NaI scintillation counter. The photopeak efficiency was obtained by comparing the sample with a Zn^{65} standard source.

References

1) Tanaka, Furukawa, Mikumo, Iwata, Yagi and Amano: J. Phys. Soc. Japan **15** (1960) 545; Errata: ibid. **15** (1960) 1357.
2) Tanaka, Furukawa, Mikumo, Iwata, Yagi and Amano: J. Phys. Soc. Japan **15** (1960) 952.
3) Tanaka, Furukawa, Iwata, Yagi, Amano and Mikumo: J. Phys. Soc. Japan **15** (1960) 1547.
4) Tanaka, Furukawa, Iwata, Yagi, Amano and Mikumo: to be published in J. Phys. Soc. Japan.
5) F. S. Houck: *Atomic Energy Commission Report* NYO-7332, June, 1959 (unpublished); F. S. Houck and J. M. Miller: (private communication).
6) Dostrovsky, Fraenkel and Friedlander: Phys. Rev. **116** (1959) 683.

7) S. N. Ghoshal: Phys. Rev. **80** (1950) 939.
8) Eastman, Isenor, Bainbridge and Duckworth: Phys. Rev. **103** (1956) 145.
9) W. John: Phys. Rev. **103** (1956) 704.
10) F. K. McGowan: (private communication); McGowan, Stelson and Smith: Bull. Am. Phys. Soc. II **5** (1960) 266. P. H. Stelson and F. K. McGowan: Bull. Am. Phys. Soc. II **5** (1960) 266.
11) Bichsel, Mozley and Aron: Phys. Rev. **105** (1957) 1788.
12) V. C. Burkig and K. R. MacKenzie: Phys. Rev. **106** (1957) 848.
13) R. M. Sternheimer: Phys. Rev. **115** (1959) 137.
14) I. M. Korenman: Usp. khim. (USSR) **23** (1954) 89.
15) H. Goto, S. Ikeda and H. Amano: (to be published).
16) S. Kikuchi et al.: J. Phys. Soc. Japan **15** (1960) 41.
17) M. M. Shapiro: Phys. Rev. **90** (1953) 171.
18) G. Igo: Phys. Rev. **115** (1959) 1665.
19) Quisenberry, Scolman and Nier: Phys. Rev. **104** (1956) 461.
20) S. Kaufman: Phys. Rev. **117** (1960) 1532.
21) J. J. Pinajian (private communication); Pinajian, Need and Webb: Bull. Am. Phys. Soc. II **5** (1960) 267.
22) J. H. Carver and W. Turchinetz: Proc. Phys. Soc. (London) **73** (1959) 585.
23) K. H. Purser and E. W. Titterton: Australian J. Phys. **12** (1959) 103.
24) Cohen, Newman and Handley: Phys. Rev. **99** (1955) 723.
25) J. W. Meadows: Rev. **91** (1953) 885.
26) H. A. Howe: Phys. Rev. **109** (1958) 2083.
27) Blaser, Boehm, Marmier and Peaslee: Helv. Phys. Acta **24** (1951) 3.
28) B. L. Cohen and E. Newman: Phys. Rev. **99** (1955) 718; Cohen, Newman, and Handley: Phys. Rev. **94** (1954) 620.
29) Strominger, Hollander and Seaborg: Rev. Modern Phys. **30** (1958) 585.

JOURNAL OF THE PHYSICAL SOCIETY OF JAPAN, Vol. 15, No. 12, DECEMBER, 1960

Excitation Function for the Reaction $B^{11}(p, n)C^{11}$ up to E_p=15 MeV and Energy Levels of C^{12}

By Michiaki FURUKAWA, Yoshihide ISHIZAKI, Yoshihiro NAKANO*,
Tadashi NOZAKI**, Yoshio SAJI and Shigeo TANAKA
Institute for Nuclear Study, Universty of Tokyo, Tanashi-machi, Tokyo

(Received August 5, 1960)

Excitation function for the $B^{11}(p, n)C^{11}$ reaction was measured by the activation method with improved energy resolution for the proton energies ranging from 4.7 to 15.0 MeV. The excitation function exhibited rather clear peaks at proton energies of 8.5, 9.9, 10.9, 11.5 and 13.6 MeV in the laboratory system and a broad peak at the energy region between 13.8 MeV and 14.5 MeV. A considerable number of uncertain peaks were also observed. The excitation function for the $O^{16}(p, \alpha)N^{13}$ reaction was also obtained above E_p=9.7 MeV.

§1. Introduction

The excitation function for the $B^{11}(p, n)C^{11}$ reaction was measured using a stacked-foil method by Blaser *et al.*[1] for the proton energies up to 6.7 MeV; by Kalinin, Ogloblin and Petrov[2] up to 12.2 MeV; and by Hintz and Ramsey[3] up to 100 MeV. The excitation function below 5.5 MeV was also confirmed by Gibbons and Macklin[4] from the measurement of total neutron yield. The energy levels of C^{12} were compiled by Ajzenberg-Selove and Lauritsen[5].

---

* Hokkaido Gakugei University, Sapporo, Hokkaido.

** The Electrical Communication Laboratory, Musashino, Tokyo.

Some of the present authors[6] are under study about the angular distributions of neutrons from the $B^{11}(p, n)C^{11}$ reaction at various incident proton energies from 8 to 15 MeV. For this work, it is desirable to obtain more precise information on the energy dependence of the cross sections over the region $E_p=8\sim15$ MeV.

In the experiment reported here, the excitation function for the (p, n) reaction on B^{11} was measured by the activation method for the proton energies ranging from 4.7 MeV to 15.0 MeV. Borax was used as a target material, so that the excitation function for the $O^{16}(p, \alpha)N^{13}$ reaction above $E_p=9.7$ MeV was simultaneously obtained.

§ 2. Experimental

The external beam from the 160 cm INSJ variable energy cyclotron was used to irradiate the targets. The deflected beam was focused by a pair of quadrupole magnets and a sector-type focusing magnet, and was collimated successively by narrow graphite slits. The energy dependence of the cross sections for the reaction $B^{11}(p, n)C^{11}$ was measured by a stacked-foil technique in which every ten target foils were stacked. In different seven bombardments, the initial energies were 15.0, 14.0, 13.0, 11.5, 10.0, 8.5 and 7.5 MeV which were calculated from the cyclotron frequencies. Each stack covered a range of from 1.5 to 2.8 MeV and this range overlapped that of adjacent stacks by about 0.5 MeV. The bombardments were generally performed with the protons of 75 μC for 3.5 minutes. The energy uncertainty of the incident beam was estimated to be less than ±1%. The beam was monitored by a Faraday cup and the total charge of the beam was measured by a 100% feed-back type current integrator.

The targets were of sodium borate bihydrate ($Na_2B_4O_7 \cdot 2H_2O$) prepared as follows. The powdered pure borax ($Na_2B_4O_7 \cdot 10H_2O$) was suspended in acetone with polyvinyl acetate as a binding material, and deposited onto a thin aluminum backing fail after evaporation of acetone. Then, it was heated in an oven at about 80°C in order to convert $Na_2B_4O_7 \cdot 10H_2O$ into $Na_2B_4O_7 \cdot 2H_2O$. The boron contents in some targets were chemically analyzed

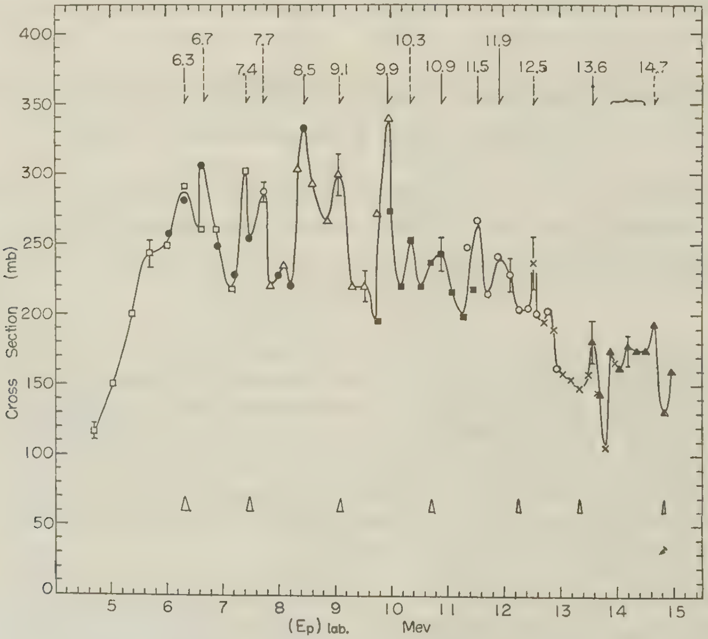

Fig. 1. Excitation function for the reaction $B^{11}(p, n)C^{11}$. The different marks of points represent the results from the separate bombardments, while the solid line is the composite curve for the excitation function. The peaks are pointed out by the arrows with the energies in the laboratory system. (The arrows with dashed lines indicate the peaks less certain than those indicated by solid lines.) The vertical bars at some experimental points indicate the estimated errors of relative cross sections. The wedges show the energy resolution in the targets.

after bombardments and they were consistent with the form of $Na_2B_4O_7 \cdot 2H_2O$. The thicknesses of targets were almost about 2 mg/cm^2 and the inhomogeneity in thickness was estimated to be less than 10%. The energy loss in 1 mg/cm^2 of $Na_2B_4O_7 \cdot 2H_2O$ was 30 keV for the 15.0 MeV protons and 62 keV for the 6.0 MeV protons.

After the bombardment, the target was sandwiched by brass plates of appropriate thickness, and the two 0.51 MeV γ-rays from positron annihilation were detected in coincidence by two 1-1/2 in. dia. ×1 in. high NaI scintillation counters positioned 180° from one another with respect to the source. The decay was followed for about 2 hours in order to distinguish between the activity of C^{11} from the $B^{11}(p, n)C^{11}$ reaction and that of N^{13} from the $O^{16}(p, n)N^{13}$ reaction. The disintegration rate was obtained by applying the counting efficiency calibrated with a Na^{22} standard source, the absolute activity of which had been determined by both the γ-γ coincidence and the 4π β-counting method.

§ 3. Results

The excitation function for the $B^{11}(p, n)C^{11}$ reaction is shown in Fig. 1.

The prominent peaks occur at energies of 8.5 MeV and 9.9 MeV in the laboratory system. These two peaks appeared already in the previous work of Kalinin *et al.*[2] and were confirmed in this experiment with improved energy resolution. There is also evidence that fairly clear peaks might be present at 6.3, 6.7, 7.4, 7.7, 9.1, 10.3, 10.9, 11.5, 11.9, 12.5, 13.6 and 14.7 MeV, among which the four peaks at 10.9, 11.5, 11.9 and 13.6 MeV might be most reliable. It is not certain whether there are separate peaks at 6.3 and 6.7 MeV or whether there might be one resonance instead of two. And it is similarly situated for the peaks at 7.4 and 7.7 MeV. An improved resolution was not attained for the low-energy portion of the excitation function. It can be seen that a broad peak appears at the energy region between 13.8 MeV and 14.5 MeV. In this broad peak a few overlapping resonances must be involved. Further experiment is desirable for the confirmation of a number of uncertain peaks in this experiment.

The absolute cross section obtained here agrees well with that reported by Kalinin *et al.*[2], but differs rather greatly from those of Blaser *et al.*[1] and of Hintz and Ramsey[3].

The enegy levels of C^{12} derived from this experiment are shown in Fig. 2, together with the references of Blaser *et al.*[1] and Kalinin *et al.*[2]

The exciation function for the reaction O^{16}

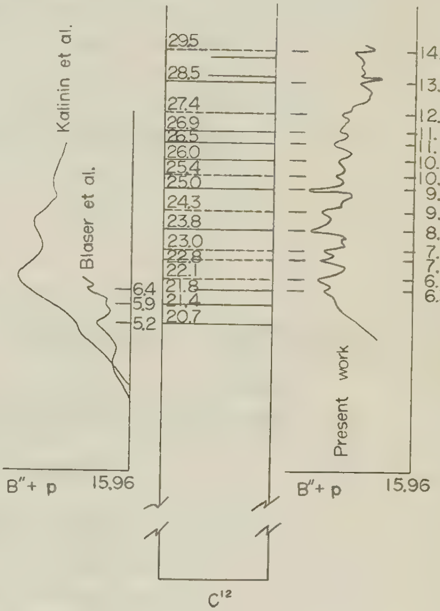

Fig. 2. Energy levels of C^{12} derived from this experiment. Energy values are plotted vertically in MeV. Uncertain levels are indicated by dashed lines; broad levels are cross-hatched. Excitation functions for the $B^{11}(p, n)C^{11}$ reactions are shown schematically, with the yield plotted horizontally and the bombarding energy vertically. Bombarding energies are indicated in laboratory coordinates and plotted to scale in centre-of-mass coordinates.

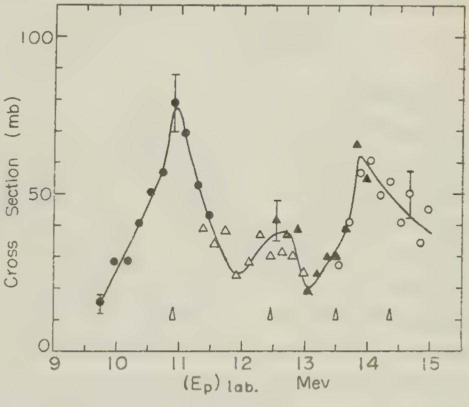

Fig. 3. Excitation function for the reaction $O^{16}(p, \alpha)N^{13}$.

$(p, \alpha)N^{13}$ is also shown in Fig. 3. This agrees well with the previous work of Whitehead and Foster[7].

Acknowledgements

Authors are indebted to Mr. A. Iguchi for his help in preparing the targets. They are also grateful to Dr. K. Saito for his help in chemical analysis and to Mr. A. Suzuki for his assistance in cyclotron operation.

References

1) Blaser, Boehm, Marmier and Scherrer: Helv. Phys. Acta **24** (1951) 465.
2) Kalinin, Ogloblin and Petrov: Atomnaya Energya **2** (1957) 193.
3) H. N. Hintz and N. F. Ramsey: Phys. Rev. **88** (1952) 19.
4) J. H. Gibbons and R. L. Macklin: Phys. Rev. **114** (1959) 571.
5) F. Ajzenberg-Selove and T. Lauritsen: Nucl. Phys. **11** (1959) 117.
6) Hisatake, Ishizaki, Isoya, Nakamura, Nakano, Saheki, Saji and Yuasa: J. Phys. Soc. Japan **15** (1960) 741.
7) A. B. Whitehead and J. S. Foster: Can. J. Phys. **36** (1958) 1276.

JOURNAL OF THE PHYSICAL SOCIETY OF JAPAN, Vol. 15, No. 12, DECEMBER, 1960

The $N^{14}(d, n)O^{15}$ Reaction in the Energy Range from 1.5- to 2.9-MeV

By Susumu MORITA, Nawoyuki KAWAI, Yorio GOTÔ,
Takashi MAKI, and Masahiro MUKAE.

Department of Physics, Faculty of Science,
Kyushu University, Fukuoka.

(Received August 8, 1960)

The angular distributions of neutrons emitted from the $N^{14}(d, n)O^{15}$ reation were investigated by means of the neutron detector made of a thin plastic scintillator to eliminate the gamma ray background, at the deuteron energies of 1.53-, 1.72-, 1.96-, 2.24-, 2.54-, 2.65_5-, and 2.90-MeV.

The results were compared with the stripping theory including the heavy particle stripping, and qualitative agreements were obtained. The excitation curve of this reaction was also estimated and compared with those of the $N^{14}(d, p)N^{15}$ and $N^{14}(d, \alpha)C^{12}$ reactions. The excitation curves of the $N^{14}(d, n)$ and $N^{14}(d, p)$ reactions show similar resonance-like structures, while that of the $N^{14}(d, \alpha)$ reaction shows somewhat different behavior.

§ 1. Introduction

In our previous experiment[1], the angular distribution of the $N^{14}(d, n)O^{15}$ reaction at the deuteron energy of 1.96 MeV was measured and a sharp increase in the backward directions, besides the forward peak was found. And also, one of the authors[2] observed the excitation curves of this reaction at the directions of 0°, 90°, and 165° to the deuteron beam in the energy range of deuteron from 1.0- to 2.2-MeV. These results suggested that the angular distributions change remarkably with deuteron energy. J. L. Weil and K. J. Jones[3] observed the excitation curve at the direction of 0° at deuteron energies 1.0- to 5.5-MeV.

The aim of this experiment is to observe in detail the angular distributions in the energy range of deuterons from 1.5- to 2.9-MeV with small intervals of deuteron energy and to obtain informations concerning the reaction mechanism, by comparing the angular distributions and excitation curve with theory, Retz-Schmidt and Weil[4] have made the same measurements in the energy range of deuteron from 0.91- to 5.27-MeV with larger energy intervals than in this work.

§ 2. Experimental Procedure

The magnetically analyzed deutron beam from the Van de Graaff accelerator of Kyushu University passed through a window of 0.00005- or 0.0001-in. thick nickel foil, and entered into the target chamber filled with nitrogen gas. Fig. 1 shows a sectional view of the target chamber and beam duct. The amount of materials constructing the beam duct and the target chamber was minimized to reduce the scattering and absorption of neutrons in these materials, and the inner surface of the wall exposed to the deuteron beam was covered with silver plates to avoid neutron production. The target chamber, 2.0 cm in depth, was filled with commercial nitrogen gas to the pressure of 20.0 cm Hg and the energy loss of deuteron of 2 MeV in the nickel foil was estimated to be 120- and 320-KeV for the two foils respectively, and the energy loss in the nitrogen gas was estimated to be 140 KeV.

A disk of thin plastic scintillator of 1 mm in thickness and 10 mm in diameter was used for neutron detection at bombarding deuteron energies below 2.24 MeV and that of 1.5 mm in thickness and of the same diameter was used at deuteron energies above 2.54 MeV.

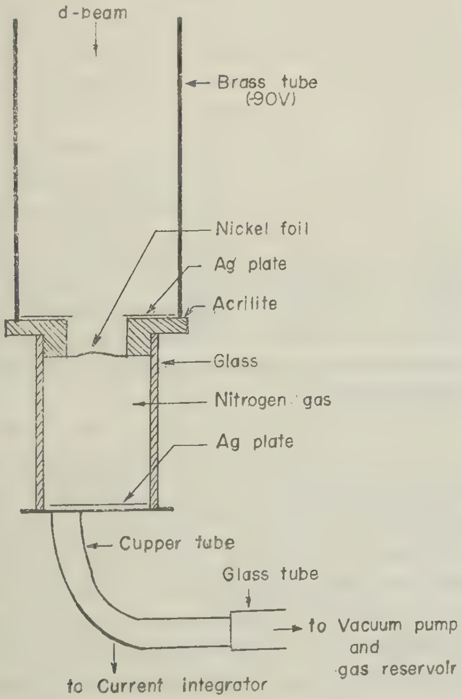

Fig. 1. Sectional view of the target chamber and the beam duct.

The plastic scintillator was mounted on a EMI 6097 photomultiplier tube, and output pulses from this tube were linearly amplified and fed to a 20-channel pulse-height analyzer. The pulse-height spectra obtained by this manner are similar to those shown in the previous paper[2]. The principle of discrimination of the associated gamma rays by means of a neutron detector of this type, has been described previously.

The background due to scattered neutrons was measured by inserting an iron absorber between the target chamber and the detector, and that due to *d-d* neutrons produced in deuterium contaminants on the inner surface of the chamber wall was measured by deuteron bombardment of the empty chamber, and they were found to be negligible.

The pulse-height spectra obtained by the 20-channel pulse-height analyzer, were corrected for escapes of recoil protons from the scintillator, add then transformed to the energy spectra using the pulse-heigot vs. proton-energy relation for the plastic scintillator. Then, the energy spectra were integrated from the energies of 85% of maximum energies to the maximum energies, to give the measures of neutron intensities, since this portion of the spectrum represents the energy distribution of recoil protons in the plastic scintillator and include no γ-ray background.

Either of the two plastic scintillators of 0.1 cm and 0.15 cm in thickness, having same diameters of 1.0 cm, mounted on a DuMont 6291 photomultiplier tube was used as a monitor counter according as energies of neutrons to be counted. The monitor counter was placed at the direction of 90° and at a distance of 14.0 cm from the center of the target.

In order to obtain the angular distribution, the above mentioned integrals of energy spectra of recoil protons obtained at different detector angles and at a certain deuteron energy, were corrected for the variation of the *n-p* scattering cross section with neutron energy and normalized to a definite number of monitor counts.

§ 3. Results and Discussion

Fig. 2 shows the seven angular distributions obtained at the deuteron energies of 1.53-, 1.72-, 1.96-, 2.24-, 2.54-, 2.68-, and 2.90-MeV. The angular resolutions ranged from ±4° at the detector angle of 0°, to ±6° at 90°. The errors shown in the figure are statistical ones, which range from 5% to 2%. Besides the statistical uncertainties, uncertainties in the evaluation of neutron intensities from the pulse-height spectra of recoil protons in the plastic scintillator, and those in the estimation of neutron scatterings in materials present between the target and detector, and so on, were considered and the over-all relative uncertainties of every experimental points in angular distribution were estimated to be less

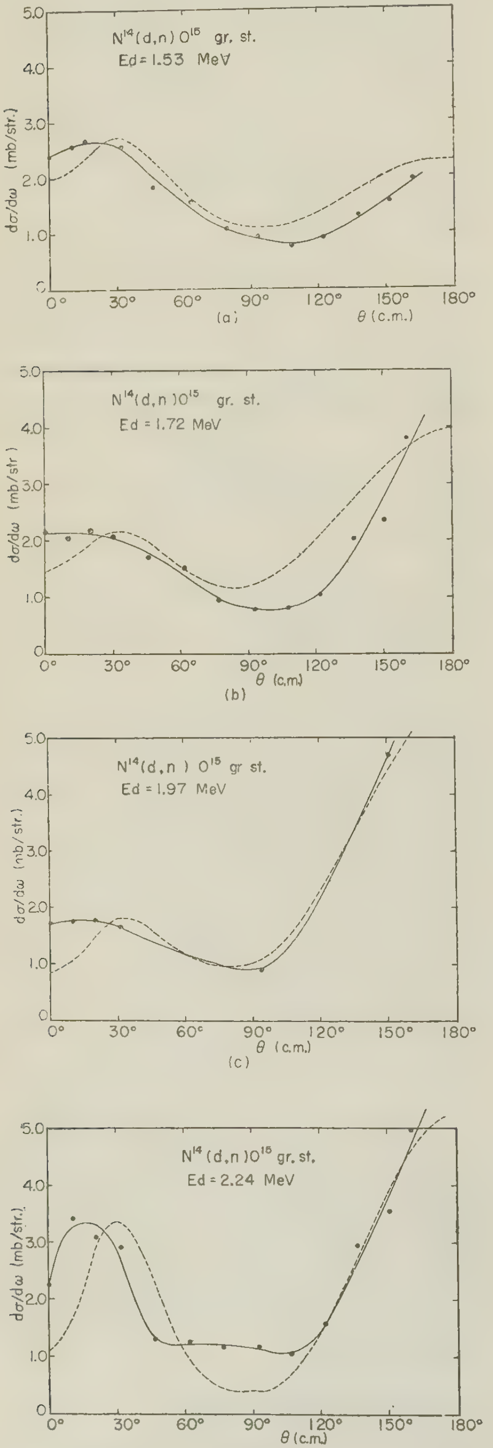

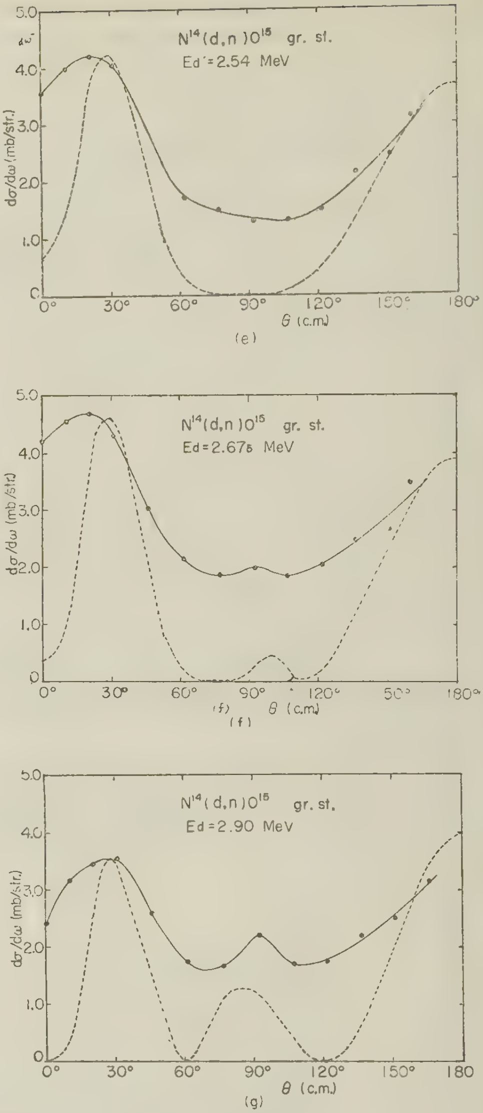

Fig. 2. The angular distributions of the neutrons from the N^{14}(d, n)O^{15} reaction. The energy of deuteron is shown for each distributions. Solid curves are experimentals, and dotted curves are the theoreticals, calculated by the heavy particle stripping process.

than 10%. The relative uncertainties of the total cross sections derived from the angular distributions were thought to be about to be about 15%.

These angular distributions are consistent with those obtained by Retz-Schmidt and Weil[4] at the deuteron energies of 1.50_7-, 1.88_1-, and 3.13_1-MeV, although some discrepancies are found between the angular distribution obtained by us at $E_d=2.54$ MeV and that obtained by Retz-Schmidt and Weil at $E_d=2.58$ MeV. At this deuteron energy, their result shows smaller rise in the backward directions than ours. As was expected from the previous work[2], the shape of the angular distribution at the backward directions varies remarkably with the deuteron energy, but the forward peak does not. Moreover, it must be noted that this behavior of angular distribution of neutrons from the $N^{14}(d, n)O^{15}$ ground state reaction shows a strong resemblance to that of protons from the $N^{14}(d, p)N^{15}$ ground state reaction in the same range of deuteron energy, obtained in our laboratory[5]. We attempted to analyze these angular distributions of the $N^{14}(d, n)O^{15}$ ground-state reaction with the heavy particle stripping theory of Owen and Madansky[6]. Although this theory includes some inconsistency, as was pointed out by Hasegawa and Ichikawa[7], we used the formula of Owen and Madansky because of its simplicity. Their formula would be sufficient for qualitative discussions.

The heavy particle stripping means the stripping of neutron from the target N^{14} nucleus and the capture of N^{13} by the deuteron. The orbital angular momentum of captured N^{13} are limited by the conservation of angular mementum and parity. The ground state of O^{15} has been known to have spin of 1/2 and odd parity, the deuteron has spin of one and even parity, and the N^{13} core has odd parity. So that the orbital angular momentum l_c of the captured N^{13} must be limited to 0 or 2. Since the d-wave penetrability is much less than that for s-wave, we can neglect the $l_c=2$ terms.

According to Owen and Madansky,

$$\frac{d\sigma}{d\omega}\propto\left|G_D(K_1)j_1(k_1R_1)+\frac{\lambda_2}{\lambda_1}G_H(K_2)j_0(k_2R_2)\right|^2 ,$$

where,

$$G_D(K_1)=\frac{1}{K_1^2+0.0529\times10^{26}} ,$$

$$G_H(K_2)=\left[\frac{1}{1.423\times10^{26}-K_2^2}+\frac{1}{0.5098\times10^{26}+K_2^2}\right]\times[0.1423\sin(K_2r_N)+j_1(K_2r_N)] ,$$

λ_2/λ_1 is the ratio of the amplitude for the heavy particle stripping to that of the ordinary deuteron stripping. Other symbols have usual meanings as quoted in reference[6]. This ratio is assumed to be a function of deuteron energy and was adjusted to get the fit with experimental results. The radius and depth of the potential well used to determine the neutron wave function for the calculation of $G_H(K_2)$, were 3.37×10^{-13} cm and 40 MeV, respectively, and to assume these values means

$$\alpha_N r_N=\left[\frac{2M}{\hbar^2}|E-V|\right]^{1/2}r_N=4.03 ,$$

$$\beta_N r_N=\left[\frac{2M}{\hbar^2}|E|\right]^{1/2}r_N=2.41 .$$

The value of 7.0×10^{-13} cm was chosen for both interaction radii, R_1 and R_2.

Although these interaction radii, as well as the ratio of amplitudes λ_2/λ_1, can be taken as adjustable parameters depending on the deuteron energy, we could obtained, as can be seen in Fig. 3, qualitative agreements with the experimental angular distributions with this constant value of interaction radii.

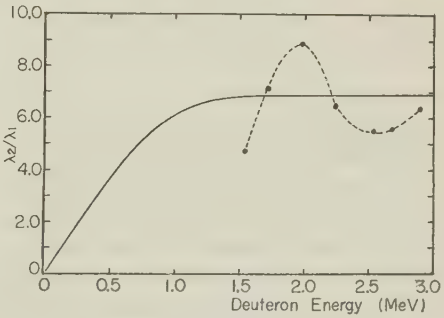

Fig. 3. The ratio of amplitude λ_2/λ_1 of the heavy particle stripping to that of the ordinary stripping.

In the analysis of the reaction $B^{11}(d, n)C^{12}$ [6], these interaction radii were assumed to be constant independent of deuteron energy but Weil and Jones[3], and Hasegawa and Ichikawa[7] used energy dependent interaction radii. In the formula of Ichikawa and Hasegawa, one more adjustable parameter was introduced in the interference term of the both stripping processes. Accordingly, much better fit to the experimental distributions would be obtained by using Ichikawa's formula. The values of λ_2/λ_1, which were adopted in the calculation of the curves in Fig. 2, were plotted against the deuteron energy and are shown in Fig. 3 connected with a broken line. As was pointed out by Retz-Schmidt and Weil, λ_1/λ_1 does not show monotone increase with deuteron energy, in contract to the cases of reactions $B^{11}(d, n)$ and $N^{15}(d, n)$, where the ratio increases gradually up to the deuteron energy corresponding to the height of Coulomb barrier, which is 2.2 MeV and then becomes nearly flat, as is shown by the full curve in this figure. Anomalously large value of λ_2/λ_1 was found at the deuteron energy of 2 MeV, where the excitation curve shows a small peak and the angular distribution has a remarkable rise in the backward direction.

In order to obtain some information on the reaction mechanism, the excitation curve of this reaction is shown in Fig. 4, together with the data obtained by Retz-Schmidt and Weil and also with the excitation curves of the $N^{14}(d, p)N^{15}$ and $N^{14}(d, \alpha)C^{12}$ ground-state reactions, which were obtained in our laboratory[5].

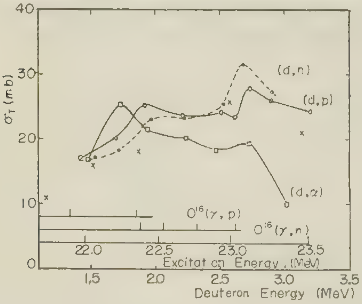

Fig. 4. Excitation curves of the reactions $N^{14}(d, n)$, $N^{14}(d, p)$[8], and $N^{14}(d, \alpha)$[8] reactions. Retz-Schmidt and Weil's results on the $N^{14}(d, n)$ reaction are also shown with crosses.

The absolute valve of cross section of the $N^{14}(d, n)$ reaction in the present experiment, was determined by normalizing the angular distribution to the absolute cross section obtained at the direction of 30° by Retz-Schmidt and Weil.

As the reactions $N^{14}(d, n)O^{15}$ and $N^{14}(d, p)N^{15}$ are considered to be mirror reactions, it may be natural that the angular distributions of these reactions behave quite similarly, whether the reactions proceed through the compound nucleus formation or the striping process. Moreover, it must be noted that the excitation curve of the $N^{14}(d, n)$ reaction shows similar behavior to that of the $N^{14}(d, p)N^{15}$ reaction and some resonance-like structures were found in these excitation functions. We can not decide whether these structures are due to the compound nucleus formation or the distortion effects of the wave function in the stripping reaction. As for the (d, α) reaction, such a surface direct interaction has been considered as double pick-up process. However, it will be reasonable to consider that in the lower energy range of deuteron the compound nucleus formation is more predominant than in the (d, n) and (d, p) reactions, and in fact, the angular distributions of α-particles from the $N^{14}(d, \alpha)C^{12}$ ground-state reaction have quite different behavior, showing rapid change with deuteron energy[8]. Nevertheless, in the excitation curve of the $N^{14}(d, \alpha)$ reaction, the resonances are less predominant than in the other two curves, and the dip in this curve, observed at deuteron energy of 2.7 MeV, corresponds to the peaks in the excitation curves of (d, p) and (d, n) reactions. This fact will suggest that the resonance-like structures found in the excitation of (d, p) and (d, n) reactions are to be interpreted by the distortion effect of wave function in the stripping reaction. But, the effects of compound nucleus formation on the (d, p) and (d, n) reactions can not be entirely excluded.

The level structure of the compound nucleus O^{16} obtained from other reactions[9] are shown in the lower insert of Fig. 4. Most of these were observed in the breaks of the yield curves of induced activity. However, the levels, observed in the photo-reactions, are not necessarily found in the present excitation curves because of the isotopic spin selection rule. As the isotopic spins of N^{14} and deuteron are equal to zero ($T=0$), the levels of compound nucleus O^{16}, excited by the deuteron bombardment of N^{14}, must have the isotopic spin of zero. On the other hand, the levels of O^{16}, excited by photon, are expected to have the isotopic spin of unity.

The authors express their cordial thanks to Prof. I. Nonaka for his discussions and all the other members of the nuclear laboratory of Kyushu University for their cooperation throughout this work.

References

1) I. Nonaka, S. Morita, N. Kawai, T. Ishimatsu, K. Takeshita, Y. Nakajima, and N. Takano: J. Phys. Soc. Japan **12** (1957) 841.
2) S. Morita: J. Phys. Soc. Japan **12** (1958) 126.
3) J. L. Weil and K. W. Jones: Phys. Rev. **112** (1958) 1975.
4) J. Retz-Schmidt and J. L. Weil: Private communication.
5) N. Kawai: To published in J. Phys. Soc. Japan.
6) G. E. Owen and L. Madansky: Phys. Rev. **105** (1957) 1766.
7) K. Hasegawa and H. Ichikawa: Prog. Theor. Phys. **21** (1959) 569.
8) To be published in J. Phys. Soc. Japan.
9) B. M. Penfold and A. S. Spicer: Phys. Rev. **100** (1955) 1377.
L. Cohen, A. K. Mann, B. J. Patton, K. Reibel, W. E. Stephens, and E. J. Winhold: Phys. Rev. **104** (1956) 108.
C. Milone, S. Milone-Tamburino, R. Rinzivillo, A. Rubbino and C. Tribuno: Nuovo Cimento. **7** (1958) 729.

JOURNAL OF THE PHYSICAL SOCIETY OF JAPAN, Vol. 15, No. 12, DECEMBER, 1960

Gamma Radiation Following the Decay of Dy^{165}

By Akira HASHIZUME, Tan TAKAHASHI, Yoshihiko TENDO
and Yohko ENOMOTO

The Institute of Physical and Chemical Research, Bunkyo, Tokyo

(Received June 16, 1960)

The transition of gamma-rays in Ho^{165} emitted in the decay of Dy^{165} (140 min) has been studied with γ-γ coincidence and sum coincidence techniques. In addition to previously reported gamma-rays, (178), ~483, and ~515 keV gamma-rays are found in coincidence experiment. About 1 MeV gamma-rays is resolved into 998 and 1055 keV gamma-rays. A proposed decay scheme is presented. The measured half-life of Dy^{165} is 142.4 ± 0.5 min.

§ 1. Introduction

The strong radioactivity of dysprosium induced by slow neutrons was first observed by Marsh and Sugden[1] and independently by Hevesy and Levi[2]; its half-life was reported to be 2.5 hours. Later, this activity was assigned to mass 165 by Inghram *et al.*[3], and the most accurately measured half-life was 139.19 ± 0.14 min.[4] The activity with a half-life of 1.25 min. was first reported by Flammersfeld[5] and was assigned to a metastable state of Dy^{165} by Inghram[6]. Since then, the decay of Dy^{165} has been investigated by a number of authors[7]–[12], yet its decay scheme cannot be regarded as thoroughly investigated.

The beta-ray energies measured by Slätis[8] with a magnetic spectrometer were reported to have the values 0.24, 0.42 and 0.88 MeV, while, according to Bonhoeffer *et al*[12], they are 0.305, 1.00, 1.22 and 1.3 MeV which were found by the use of the beta- and gamma-ray coincidence technique with scintillation counters. In addition to the several gamma-ray previously reported[11], Bonhoeffer found 555 keV gamma-rays. The largest energy value of the gamma-rays reported is nearly 1 MeV, and the authors have resolved this into two gamma-rays, 998 and 1055 keV in the investigation of gamma-ray transitions with a sum coincidence technique, and the decay scheme of Dy^{165} is considered.

§ 2. Experimental Procedure

The gamma-ray sources of dysprosium were produced in the research reactor JRR-1* by neutron irradiation of dysprosium oxide** of the spectrographic purity of 99.9%. After one or two hour irradiation the samples were left to decay for few hours to allow the short lived activities to die away.

---

* Japan Atomic Energy Research Institute at Tokai.

** Obtained from Société des Terres Rares, Paris.

The gamma-rays were investigated with a NaI(Tl) crystal of 1″ diameter and 1″ height, optically coupled to a 6292 DuMont photomultiplier, together with a sum conincidence[14] and a coincidence scintillation spectrometers. A schematic diagram of the sum coincidence spectrometer is shown in Fig. 1. The output pulses from White cathod-followers (CF-1, CF-2) are clipped by 1 m of RG/65-U cable and make to either into a linear adding network. The linear adding network and the adjustment of the height of the pulses from two counters with potentiometers are nearly the same as described by Hoogenboom[13]. The accidental coincidence is examined by a delay line either connected to the adding network or inserted between the output of a single channel pulse height analyzer and the gate input of a multichannel analyzer. Pulse heights are analyzed with a 256 channel pulse height analyzer which is gated with 2 μsec pulses of the output of a single channel pulse height analyzer. The energy resolution of the sum coincidence spectrometer examined with Co^{60} was 5.6% at 1.33 MeV. The gamma-sources used to calibrate the energy scale of the spectrometer over the range from 75 to 2500 deV were Co^{60}, Se^{75}, Cs^{137} and Hg^{203}.

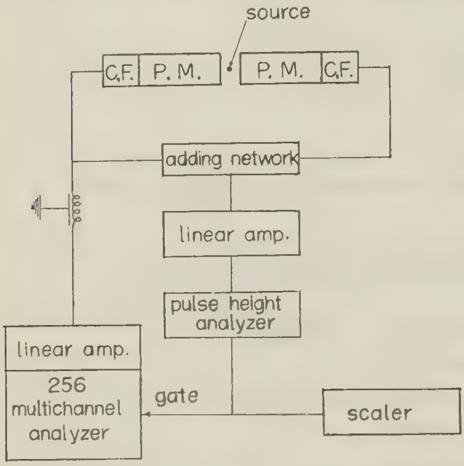

Fig. 1. Block diagram of the sum coincidence spectrometer.

§ 3. Experimental Results and Conclusions

Fig. 2 shows the gamma-ray spectra of dysprosium obtained with a single crystal scintillation spectrometer. The curve 1 shows the spectrum obtained with the distance of 20 cm between the source and the surface of the crystal and the curve 2 that with the distance of 3 mm to indicate the summing effect. Previously reported 1 MeV gamma-ray was resolved into two photopeaks of 998±5 and 1055±5 keV gamma-rays. It is evident from the curve 1 and 2 that the 998 keV gamma-ray reveals the summing effect. This indicates that the gamma-rays emitted from the level of this energy decay partly in cascade to the ground state. The decay of these two peaks were followed for 16 hours, the half-life of which was found to be 144 min proving that the peaks are caused by the gamma-rays from decaying Dy^{165}. The other gamma-ray energies were 95±2, 277±5, 364±6, 577±6, 627±4, 714±4 keV. The gamma-ray spectrum was also examined by using a large NaI(Tl) crystal (4″φ×1″1/2), and it is concluded that the 557 keV peak is neither Compton peak nor a scattering peak but a photopeak. The 1 MeV gamma-ray did not resolve into two peaks when the large crystal was used.

A least-square analysis of the decay curve obtained with the total counts of a scintillation counter yielded for Dy^{165} the half-life of 142.4±

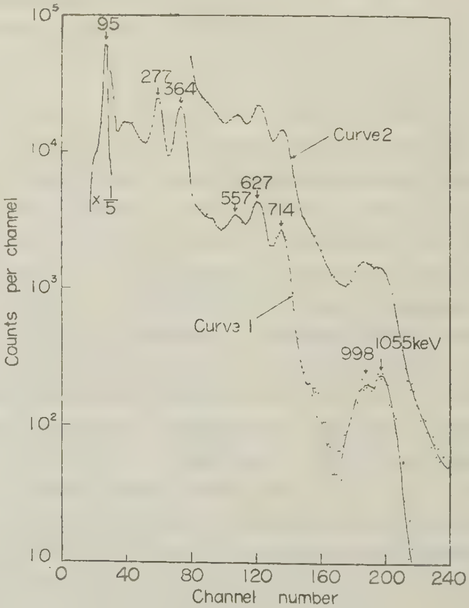

Fig. 2. The scintillation spectra was measured with 1″φ×1″ NaI (Tl) crystal. The curve 1 shows the spectrum with the distance of 20 cm between the source and the crystal, and the curve 2 that with the distance of 3 mm.

).5 min. The contribution of long lived activities due to impurities was found to be egligible. The half-life reported by Slätis is 145±3 min[8] and by Sher 139.17±0.14 min[4] nd recently by Mayquez 143.0±2.6 min[15].

As the spectra of single scintillation counter uggest the presence of the aforementioned oublet near 1 MeV, a careful search was ade in the 1 MeV region with the technique of the sum coincidedce. The gate of the sum coincidence was set from 990 to 1150 keV at intervals of every 3 keV. The typical sum coincidence spectra of gamma-rays obtained with the channel settings of the differential discriminator at 1055 and 998 keV are shown in Figs. 3 and 4. With the gate set at 998 keV (Fig. 4), the previously reported[11] 714–277, 627–364 keV cascade gamma-rays are clearly shown. Furthermore there occurs a broad peak at 500 keV, which suggests the presence of another cascade gamma-rays. The small rises of about 200 and 800 keV are due to Compton scattering. With the gate set at 1060 keV, there appeared no significant peaks (Fig. 3), that is there is no cascade gamma-rays.

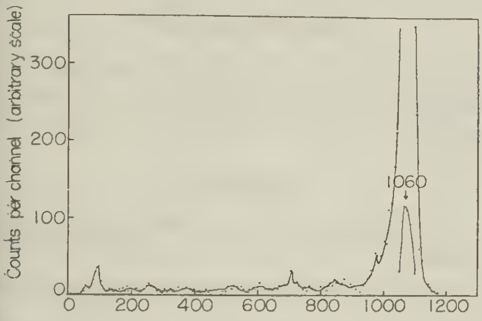

Fig. 3.

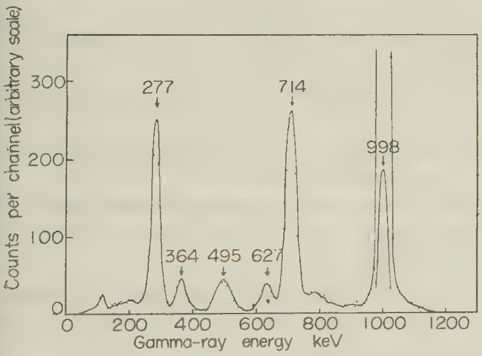

Fig. 4.

Fig. 3 and 4. The sum coincidence spectra of dysprosium. The sum-channel settings are at 1060 and 998 keV.

The coincidence spectra gated with 714, 627 and 557 keV photopeaks are shown in Figs. 5, 6 and 7 by dashed lines. For comparison a spectrum of single crystal scintillation counter normalized at 277 keV is shown in Figs. 5 and 6 and at 178 keV in Fig. 7. The width of coincidence gate is shown on the direct gamma-ray spectrum by arrows with oblique lines. With the coincidence gate opened at 714 keV, a strong peak at 277 keV is seen (Fig. 5) and when opened at 627 keV, the 364 keV peak rises (Fig. 6) and another peak of 277 keV observed is thought to be coincident with Compton scattered 714 keV gamma-rays. When opened at 557 keV, there appeared 178 keV peak (Fig. 7). Other peaks observed at 277 and 364 keV may also due to the Compton scattered 627 and 714 keV gamma-rays. From these considerations the coincidences of 277–714, 364–627 and (178–557) keV are concluded. The

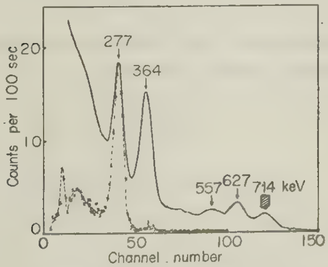

Fig. 5. Coincidence spectrum with 714 keV photopeak.

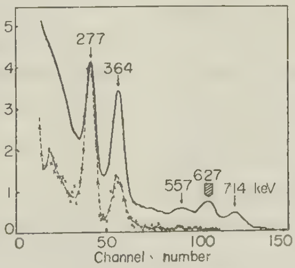

Fig. 6. Coincidence spectrum with 627 keV photopeak.

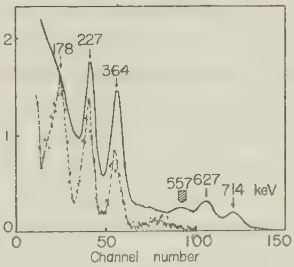

Fig. 7. Coincidence spectrum with 557 keV photopeak.

The dashed lines represent coincidence spectra which are normalized at the 227 keV photopeak of single crystal gamma-ray spectrum in Fig. 5 and Fig. 6. In Fig. 7 the coincidence spectrum is normaliged at 178 keV. The width of each coincidence gate is shown on the single crystal gamma-ray spectrum by arrows with obligue lines.

coincidences of 277–714 and364–627 keV gamma-rays correspond with sum coincidence results of Fig. 4.

From the results of single crystal gamma-ray spectra and of the sum coincidence experiment, about 1 MeV level is composed of two levels is composed of two levels of 998 and 1055 keV. Cork[11)] reported the existence of 515 keV level from the decay of Dy^{165m}, and the 495 keV peak in Fig. 4 is presumed to be the unresolved peak composed of two peaks of 483 and 515 keV by assuming that the 988 keV level decays in two-step cascade, first to 515 keV level second to the the ground level. For an interpretation of the coincidence between 178–555 keV gamma-rays, 733 keV level may be suggested.

From the Nilsson model, the estimated values of the spins and parities of the ground states of Dy^{165} and Ho^{165} and are 7/2+ and 7/2−. The gamma-ray transition from the first excited level to the ground state is M1 M1+E2[7),10)], that is, $\Delta l=1$ with no parity change. From the Coulomb excitation experiment[14)] this level is known as rotational level hence the spin and parity of the first excited state are 9/2−. The proposed nuclear energy level scheme is shown in Fig. 8. The energy and intensity of beta-rays for this scheme were taken from the results of Bonboeffer *et al.*[12)]

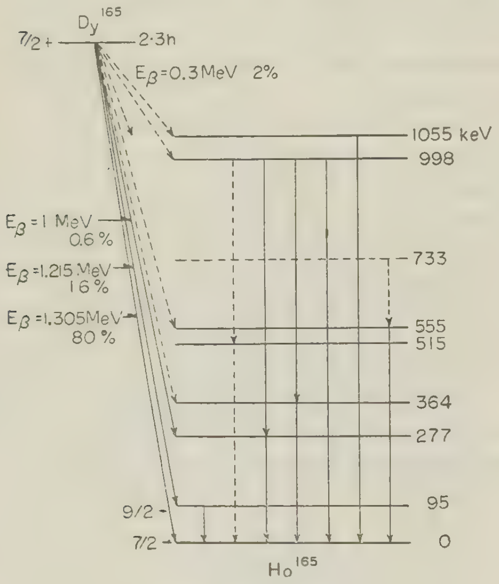

Fig. 8. Proposed decay scheme of D_y^{165}.

Acknowledgement

The authors are greatly indebted to Dr. F Yamasaki for his valuable advice in this experiment.

References

1) J. K. Marsh and S. Sugden: Nature **136** (1935) 102.
2) G. Hevesy and H. Levi: Nature **136** (1935) 103.
3) M. G. Inghram, R. J. Hayden and D. Hess: Phys. Rev. **71** (1947) 270.
4) R. Sher, H. J. Kouts and K. W. Downes: Phys. Rev. **87** (1952) 523.
5) A. Flammersfeld: Z. Naturforsch. **1** (1946) 190.
6) M. G. Inghram, A. E. Shaw and D. Hess: Phys. Rev. **72** (1947) 515.
7) O. Weber: Z. Naturforsch. **94A** (1954) 115.
8) H. Slätis: Arkiv. Math. Astron. Fysik **33A** (1949) No. 17.
9) R. L. Caldwell: Phys. Rev. **78** (1950) 408.
10) J. W. Mihelich and E. L. Church: Phys. Rev. **85** (1952) 690.
11) W. C. Jordan, J. M. Cork and S. B. Burson: Phys. Rev. **92** (1953) 1218.
12) F. Bonhoeffer, H. H. Hennies and A. Flammersfeld: Z. Phys. **155** (1959) 488.
13) A. M. Hoogenboom: Nucl. Instr. **3** (1958) 57
14) G. M. Temmer and N. P. Heydenburg: Phys. Rev. **94** (1954) 1399.
15) E. R. Mayquez: An. Real Soc. Españ. Fís. Quím. **50(A)** (1954) 95.

JOURNAL OF THE PHYSICAL SOCIETY OF JAPAN, Vol. 15, No. 12, DECEMBER, 1960

Decays of Photoreaction Products of Selenium

By Tokihiro KUROYANAGI*

Department of Physics, Tohoku University, Sendai

(Received June 21, 1960)

The decay properties of Se^{73m}, Se^{81} and As^{79} have been studied by scintillation methods. Gamma-ray spectra showed lines of energy 170, 275, 335, 410, 480, 550, 650 and 840 KeV belonging to the decay of Se^{81}. The decay scheme of Se^{81} was proposed with the aid of single and coincidence measurements of radiations. The mass difference between the ground states of Se^{81} and Br^{81} is represented by the 1.56-MeV beta ray. In As^{79}, new gamma rays of 360, 440, 725 and 890 KeV were found. Beta-gamma and gamma-gamma coincidence measurements confirmed that a 44-min activity in selenium is attributed to Se^{73m}. It is found that the beta-decay energy is 1.86-MeV and that there is no appreciable gamma ray.

§ 1. Introduction

Natural selenium consists of the stable isotopes of mass number 74, 76, 77, 78, 80 and 82. When a selenium sample is irradiated by 25-MeV bremsstrahlung, many radioactive isotopes of selenium and arsenic are produced by (γ, n) and (γ, p) reactions. If the time of irradiation is comparatively short (several tens minutes), the radiations from Se^{73}, Se^{73m}, Se^{77m}, Se^{79m}, Se^{81}, Se^{81m}, As^{79} and As^{81} are expected to be observed. Since the activities of Se^{77m}, Se^{79m} and As^{81} have short halflives of 17.5 sec, 3.9 min and 32 sec, respectively, the dominant radiations at about ten minutes after the termination of the bombardment may be caused by Se^{73}, Se^{73m}, Se^{81}, Se^{81m} and As^{79}. The decay characteristics of these isotopes have been known in some extent but not with good accuracy, although the isotopes of Se and As region with long half-lives are very well studied. It, therefore, seemed to be worth while studying the decays of Se^{73m}, Se^{81} and As^{79}.

Using an internal bombarding technique[1] recently developed in our laboratory and scintillation spectrometers, such unknown radiations were investigated.

§ 2. Experimental Arrangement

The gamma-ray spectrometer consisted of a $1\frac{1}{2}$-inch in height and $1\frac{1}{2}$-inch in diameter NaI(T1) crystal attached to the end of a DuMont type 6292 photomultiplier tube. In order to eliminate the beta background, it was necessary to place a 2 g/cm² polystyrene absorber between the sample and the crystal. Pulses from the photomultiplier tube were fed through a cathode follower and linear amplifier to a 100-channel pulse-height analyzer.

Because of the complexity of gamma-ray spectra to be analyzed with the scintillation spectrometer, a careful analysis of resolution and respone function was necessary. The energy calibrations were done using all or some of the following gamma-ray sources: In^{114}, Hg^{203}, Au^{198}, Cs^{137}, Zn^{65} and Na^{22}. The errors in energy measurements of gamma rays were within ±5 KeV.

The energy resolution as a function of energy E was determined from the full width ΔE at the half maximum of the various monoenergetic photopeaks of Hg^{203}, Cs^{137}, Zn^{65} and Na^{22} corresponded fairly well to the formula:

$$\frac{(\Delta E)^2}{E} = AE + B$$

with $A = -0.011$, $B = 15$ KeV. Measured pulse-height spectra were resolved with the aid of the reference spectra obtained using standard sources of Hg^{203}, Au^{198}, Cs^{137} and Zn^{65} under conditions similar to this experiment. A contribution due to bremsstrahlung of beta rays was subtracted from the pulse-height spectra using the spectra of bremsstrahlung of beta-ray sources of P^{32} and Sr^{90} which have no gamma ray. A calibration of the photopeak efficiency vs energy was obtained by the coincidence method using sources of Se^{75}, Na^{22} and In^{114} (Fig. 1). In order to determine the intensities of the gamma rays $I(\gamma)$, use is made of the following eqation:

---

* Now at Japan Atomic Energy Reserch Institute, Tokai-Mura, Ibaraki-ken, Japan.

$$I(\gamma)=\epsilon_p(\gamma)\Omega(\gamma)A(\gamma)\exp(-\mu d),$$

where $\epsilon_p(\gamma)$ and $\Omega(\gamma)$ are the photopeak efficiency and the solid angle for the detection of γ, $\exp(-\mu d)$ is the fraction of transmitted through the beta absorber. $A(\gamma)$ is the photopeak area which was calculated by assuming a Gaussian shape as photopeak shape, and by using the energy resolution of the crystal and the observed maximum height of the peak. The errors of the obtained intensities were few tens percents.

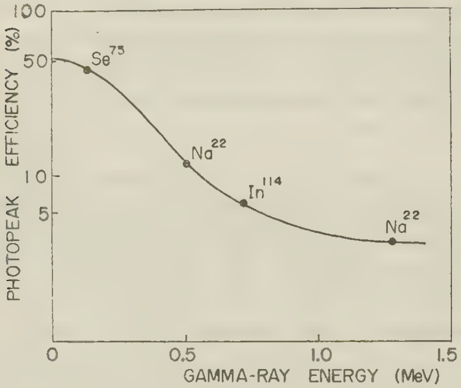

Fig. 1. Photopeak efficiency *vs* energy.

The beta-ray counter consisted of an anthracene scintillator 0.6-cm thick and 2-cm in diameter, attached to a DuMont 6292 photomultiplier tube and protected from light by a 2 mg/cm² aluminum foil. The electronic system was identical with that of the gamma-ray spectrometer. In order to obtain the energy calibration curve of the spectrometer, the end points of well known sources, In^{114}, P^{32} and Au^{198}, were determined using the Kurie plots without correction of the resolution of the phosphor. It has been proved that such a calibration without correction of the resolution is quite enough for our purpose. The errors in measured end-point energies were within ±50 KeV. The irradiated samples were melted and spread on an aluminum foil 2 mg/cm² thick to make thin beta-ray sources. The average thickness of the sources was about 50 mg/cm².

In order to determine which of the observed gamma rays is in coincidence with beta rays, beta-gamma coincidence measurements were made using a conventional "fost-slow" coincidence circuit whose resolving time $2\tau=80$ mμ sec in the energy range between 0.07 and 1.3 MeV. The radiations were viewed by a 1½-inch×1½-inch NaI(T1) crystal and a 0.6-cm×2-cm anthracene crystal which were mounted on DuMont 6291 photomultiplier tubes. To determine the coincidence ralationship of the gamma-rays, the beta-ray counter was replaced with a second gamma-ray spectrometer. In the gamma-gamma coincidence experiments, the same "fast-slow" coincidence circuit mentioned previously was employed. In all the coincidence measurements, a correction for the accidental coincidence counts was neglible because of the fast resolving time of the coincidence circuit.

§ 3. Results and Discussion

A sample of natural selenium metal of 300 mg was exposed to the 25-MeV betatron bremsstrahlung for twenty minutes and displaced in front of the gamma-ray spectrometer the spectrometer was turned on for an appropriate time interval and the measurement was continued successibly for seven hours after the irradiation. Fig. 2 shows the spectra counted at 4, 36 and 513 min after the termination of the bombardment. In this spectrum, there are seven outstanding peaks at 100, 275, 345, 410 485, 725 and 875 KeV. Following the decays of these peaks, it was found that the gamma rays displayed on the spectrum contained

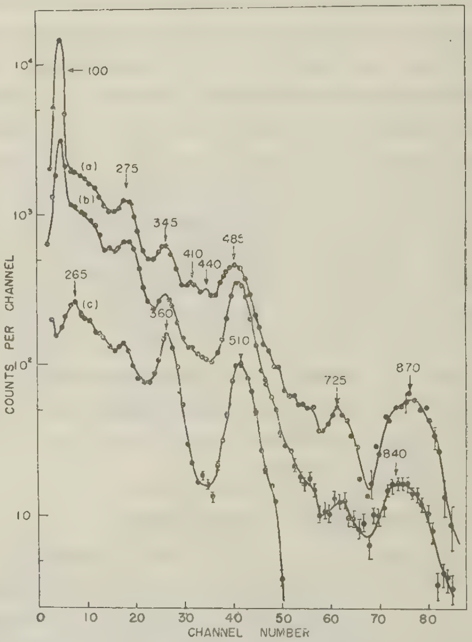

Fig. 2. Gamma-ray spectra of irradiated selenium sample with 25-MeV bremsstrahlung. (a), (b) and (c) show the spectra at 4, 36 and 513 min after the termination of bombardment.

radiations of the isotopes, Se^{73}, As^{79} and Se^{81}, and the isomers, Se^{73m} and Se^{81m}. The spectra were not disturbed by the (γ, p) product (As^{81}) of Se^{82}, since the activity has a short half-life of 32 sec[2]. In order to assign the decay properties of Se^{73m}, As^{79}, Se^{81} and Se^{81m}, radiations of the activities were studied separately.

3.1 Se^{73m}

The radioactive decay of Se^{73} has been investigated by F. Scott[3] and R. W. Hayward and D. D. Hoppes[4]. In selenium, the 44-min radioactivity[5] having the beta-decay energy of 1.7±0.2 MeV has been proposed to Se^{73m}.

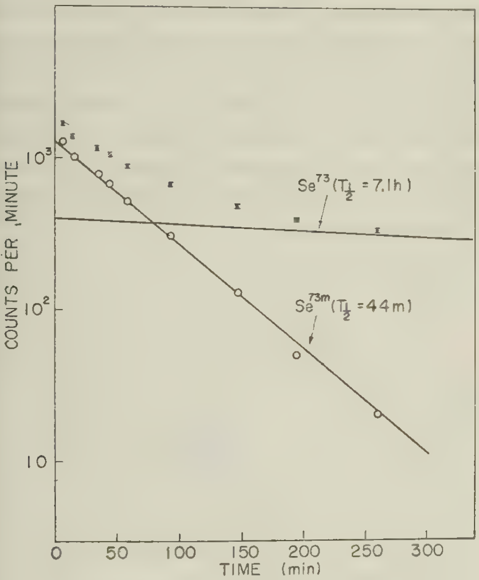

Fig. 3. Decay curve of gamma rays in coincidence with 510-KeV annihilation radiations.

In order to verify the existence of the 44-min isomer without disturbance of other background radiations, the gamma rays in coincidence with the 510-KeV annihilation quanta were measured. A natural selenium metal was irradiated with 25-MeV bremsstrahlung for twenty minutes, and the decay of the coincidence gamma ray was followed for about six hours. The decay curve consisted of two components of 44-min and 7.1-hour half-lives as shown in Fig. 3. The gamma-gamma coincidence spectrum between 10 min and 80 min after a 20 min bombardment was compared with the coincidence spectrum of Na^{22} taken under conditions similar to this experiment, which is shown in Fig. 4. Moreover, no intensive gamma rays were found when the coincidence spectrum was observed with two spectrometers at 90° each other. These results show that an upper limit of the gamma-ray intensity ratio for annihilation quanta does not exceed 1%. It is supported from these evidences that the radiation with the 44-min half-life belongs to the positron decay of Se^{73m}.

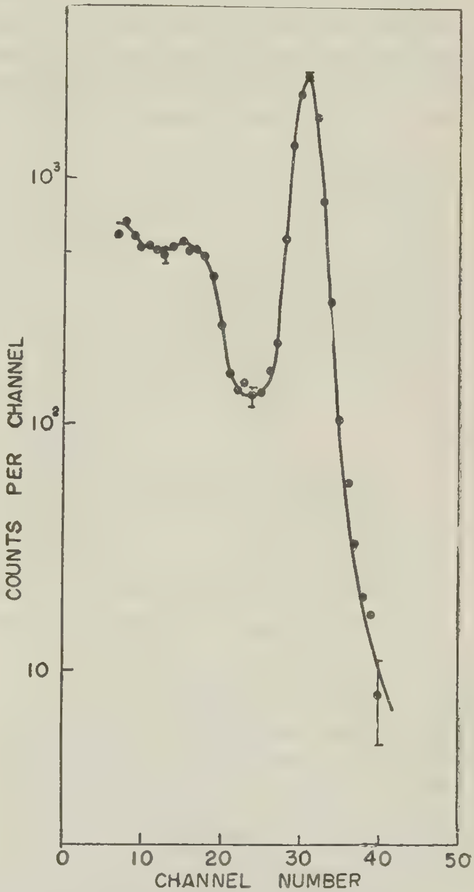

Fig. 4. Gamma-rey spectrum in coincidence with annihilation quanta. The solid line shows coincidence spectrum of Na^{22} taken under similar conditions.

Using the beta-gamma coincidence method, the positron decay energy of the isomer was measured. In this measurement coincidence gates were opened with the pulses corresponded to the photopeak of the 275-KeV gamma ray for an investigation of Se^{81} decay characteristic. However, the beta rays emitted from Se^{73m} could be mearured for the existence of Compton pulses of the annihilation quanta in this gate. The Kurie plot of the obtained beta-ray spectrum is shown in Fig. 5. In this Kurie plot three beta-ray groups having the end point energies of 1.01, 1.32 and 1.86 MeV were found. Following the decays of each beta-ray group, the 1.86-MeV beta group was identified as positrons of Se^{73m} with the half-life of 44 min, and the beta rays of the 1.32-MeV end point was found to belong to the wellknown 7.1-hour decay of Se^{73}. (The 1.01-MeV beta group will be disscused in the later section of Se^{81}). The energy of this isomeric level was determined to be 130±50 KeV from the beta-ray end-point energy of 1.86 MeV and the decay scheme of Se^{73}.

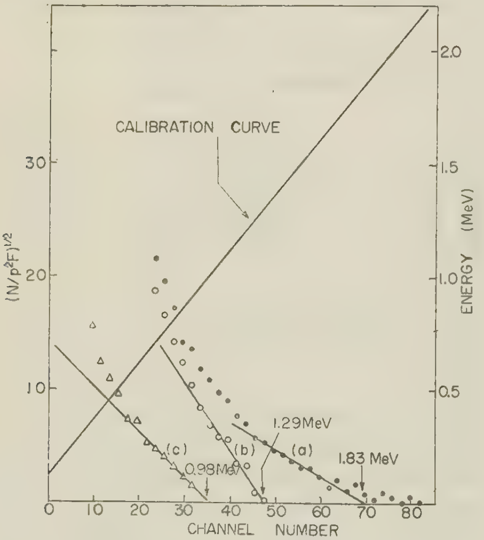

Fig. 5 (a). Fermi analysis of the beta-ray spectrum in coincidence with Compton pulses of annihilation quanta. (b). Fermi analysis of the positron group of Se^{73}. (c). Fermi analysis of the beta group in coincidence with the 275 KeV gammr-ray. The second and third groups obtained by the subtraction method. The self-absorption corrections are not yet applied.

The nuclear shell model predicts that for nuclei with 39 neutrons the two lowest lying states will be $p\,1/2$ or $g\,9/2$ levels with nearly the same energy. From the knowledge that Zn^{69} and Ge^{71} with 39 neutrons have an isomer of $M\,4$ type, and that the ground state spin of Se^{73} is $g\,9/2$, the isomeric state of Se^{73} should be expected to be $p\,1/2$. The isomeric transition of $M\,4$ type in Se^{73} will be expected. However, according to Weisskopf's single particle estimate with correction for the internal conversion process a partial half-life of such an $M\,4$ transition must have an order of 10^8 hours, which makes the branching of such a transition negligible. Since the isomer has no gamma ray, the log ft value is determined to be 4.9, which suggest an allowed transition. Therefore, it is concluded that the positron group leads to the ground state of As^{73} which has a $p\,3/2$ single particle state, and that the isomeric level is a $p\,1/2$ state. A $p\,3/2$ state cannot be expected, since its isomeric transition must be E 3 type and then the partial halflife must have an order of second. A systematic change of the energy splitting between $p\,1/2$ and $g\,9/2$ states in each of three isomers of Zn^{65}, Ge^{71} and Se^{73} is shown in Fig. 6.

Using the decay curve of the annihilation quanta, the yield ratio of the ground and isomeric states of Se^{73} by the photo-neutron emission was calculated to be 1:0.3 with the correction of the K electron capture decay which was done using the table of Wapstra Nijgh and van Lieshout[6]. Again, the value is one of the supports of the assignment of this activity to Se^{73m}.

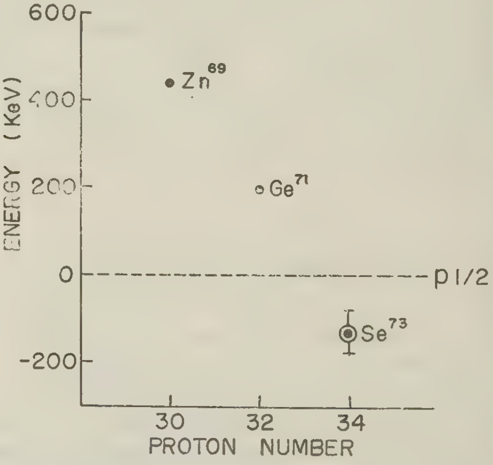

Fig. 6. Change of the energy splitting between $p1/2$ and $g9/2$ states in $n=39$ isomers.

3.2 As^{79}

Butement, Cuningham and Ythier[7] pointed out in their studies that As^{79} decayed to the 96-KeV isomeric level of Se^{79} with the half-life of nine minutes without any appreciable gamma ray.

In the present investigation, chemical separations were performed in order to see the gamma-ray associated with As^{79} without confusing radiations. Selenium dioxide powder was irradiated for ten minutes and then dissolved into hot 10N HCl with arsenic carrier and the arsenic was extracted by CCl_4.

Fig. 7 shows the gamma-ray spectrum which was taken from 4 min to 24 min after the termination of the bombardment. As shown in Fig. 7, there are four outstanding peak at 95, 360, 440 and 510 KeV. Following the decays of these peaks, the former three lines were found to be the radiations associated with As^{79}. The 510-KeV gamma ray was assigned to O^{15} activity from the decay period. Moreover, it was found that weak gamma rays of energies of 725 and 890 KeV belong to As^{79}. These results were consistent with the spectrum (Fig. 2) obtained from the photoactivated selenium sample which was not treated chemically.

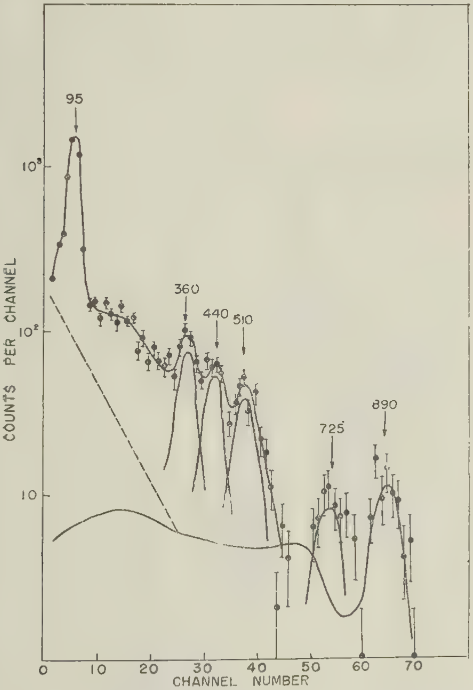

Fig. 7. Gamma-ray spectrum of As^{79}. The dashed line shows the contribution by bremsstrahlung of the beta rays.

Since the ground state of As^{79} is expected to be 3/2− and the ground and isomeric states of Se^{79} have been identified to be 7/2+ and 1/2−, respectively, it is considered that the observed gamma rays are the cascade transition with the 96-KeV isomeric transition. Consequently, the total disintegration of As^{79} should be obtained from the number of the 96-KeV transition correcting for the 3.9-min half-life of Se^{79m}. From these spectra, the intensity ratios per total decay were calculated, which is shown in Table I.

Table I. Relative intensities of the gamma radiations of As^{79}

Energy (KeV)	Percent of total decay
360	2.5
440	2.5
725	1.0
890	1.5

3.3 Se^{81}

The radioactive decay of Se^{81} has been investigated by several experimenters7), and a 57-min isomeric level7) has been found. The beta ray spectrum of Se^{81} has been studied with a 180° type spetrometer by Bergström and Thulin8), Rutledge, Cork and Burson9), who reported the the beta-ray endpoint energies of 1.38 and 1.5 MeV, Respectively. However the respective gamma rays have not been reported previously.

Heydenburg and Temmer10), Wolicki, Fagg and Geer11) reported the 275-KeV level of Br^{81} by means of Coulomb excitation. In 1958 and 1959, Duffield and Vegor12), Goodman and Schardt13) found the 550-KeV level with 37 μ sec half-life of Br^{81} by the reactions (γ, γ') and (p, γ).

In order to determine the beta decay energy and gamma rays of Se^{81}, a natural selenium sample was irradiated by 12-MeV bremsstrahlung for twenty minutes. Only the Se^{81} activity was produced by bremsstrahlung of this energy, since the threshould energies in the (γ, p) reactions are above 12 MeV, and Se^{74} and Se^{82} have the neutron binding energies of 12.1 and 9.4 MeV, respectively.

The Kurie plot (Fig. 8) of the beta-ray spectrum yielded a value of 1.56±0.05 MeV as the beta-decay energy. This agrees with the results by Rutledge etal within the experimental error. In this Kurie plot the energy parts higher than 0.5 MeV were linear, and the summing of Compton electrons from gamma rays causes considerable distortion in the lower energy parts. The gamma rays of the sample were measured by a single crystal scintillation spectrometer. The peaks were found at 103, 170, 275, 410, 480, 550, 640 and 840 KeV, and these gamma rays except the 103-KeV gamma ray of Se^{81m} were assigned to Se^{81} by following the decay periods.

In order to determine the decay from the isomeric level of Se^{81} (57 min), the gamma ray spectrum of an irradiated sample by 25-MeV bremsstrahlung for sixty minutes was measured. No drastic change was seen. Beta-gamma coincidence spectrometry was also very helpful in determining the position of gamma rays in a decay scheme. Fig. 5 shows the Kurie plot of the beta-ray spectrum in coincidence with the gamma ray of 275 KeV which is one of the most strong gamma rays. A beta-ray group of 1.01 MeV was found besides 1.3- and 1.8-MeV beta groups belonging to Se^{73} and Se^{73m}, which were mentioned previously. A beta-ray group in the energy region lower than 500 KeV may be questionable, since backscattering from the source and counts of electrons probably introduced a considerable Compton distortion of the low energy beta-ray spectrum.

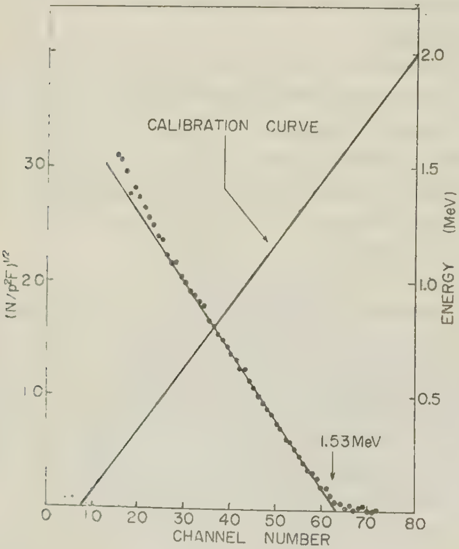

Fig. 8. Kurie plot of the beta spectrum of Se^{81}. Self-absorption correction is not yet applied.

To determine the decay scheme, gamma-gamma coincidence measurements were made. The gamma rays of 105 and 275 KeV were found in coincidence with 170-KeV gamma ray. The 105- and 275-KeV gamma rays were in coincidence with the 275-KeV gamma ray. Besides these gamma rays, weak coincidence gamma rays of 170, 205 and 410 KeV were seen by a careful analysis of the spectrum. The 170- and 275-KeV gamma ray was in coincidence with the 410-KeV gamma ray. Fig. 9 shows one of examples of the coincidence gamma-ray spectra. In this figure the peak at 510 KeV is due to the annihilation radiation of Se^{73} in coincidence with its Compton pulses, which was verified by following the decay. When the coincidence gates were opened by the pulses from the gamma rays of 550, 650 and 840 KeV, no intensive photopeaks were observed. In the case of the 550-KeV gate, the radiations were viewed with two spectrometers at 90° each other in order to avoid the suprious coincidence by the annihilation quanta in the Se^{73} decay and the Se^{73m}. In this coincidence spectrum, a weak gamma ray of 290 KeV was observed. In all measurements, no gamma ray which is in coincidence with the 335-KeV gamma ray was observed.

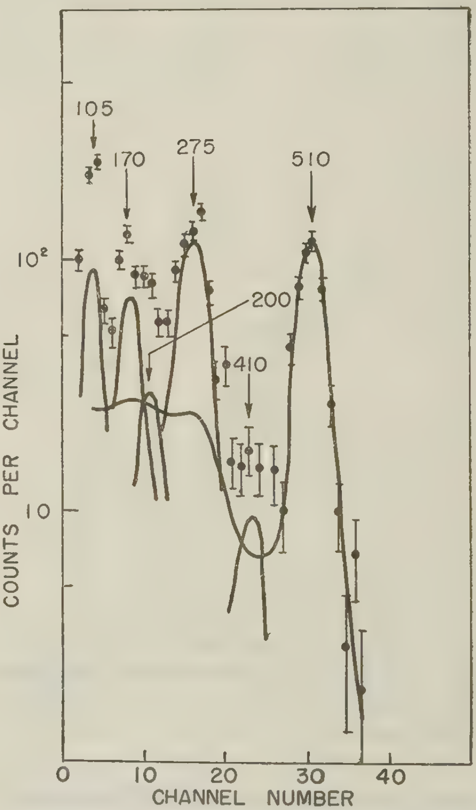

Fig. 9. Se^{81} gamma-ray spectrum in coincidence with the 275 KeV gamma rays.

From the gamma-gamma coincidence measurements and the single crystal spectrometer result which is analyzed to each gamma ray (Fig. 2), the intensity ratios of the gamma rays were calculated. The spectrum of Fig. 10 was obtained from Fig. 2(a), from which

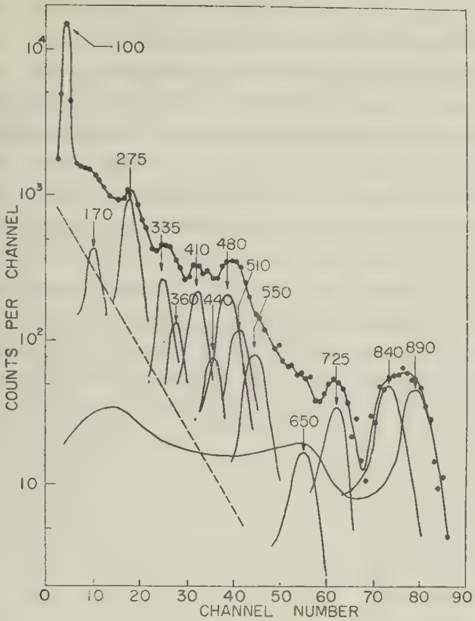

Fig. 10. Analyzed gamma-ray spectrum of irradiated selenium sample with 25-MeV bremsstrahlung. The dashed line shows the contribution by bremsstrahlung of the beta ray.

Table II. Relative intensities of the gamma ray of Se^{81}

Energy (KeV)	Percent of total decay
105	0.1
170	1.4
205	0.5
275	1.8
275	1.2
335	0.9
280	?
290	0.1
410	1.0
415	0.2
480	1.8
550	0.9
650	0.3
840	0.9

the contribution of the gamma radiations belonging to Se^{73} has been subtracted. The results are summarized in Table II.

3.4 Decay Scheme of Se^{81}

The above results indicate that the radioactive decay of Se^{81} is accompanied by the gamma rays of energies of 105, 170, 275, 410, 480, 550, 650 and 840 KeV. The measurements of the half-lives in all experiments and the measurements of the radiation of the source irradiated by 12-MeV bremsstrahlung also indicated that these gamma rays must be attributed to Se^{81}. The Kurie plot of beta-ray spectrum measured by the single crystal beta-ray spectrometer shows that the beta-decay energy of Se^{81} is 1.56 MeV. and that there is no intensive branching since the Kurie plot is quite linear over the region from the end-point energy to about 0.5 MeV.

The beta-gamma coincidence measurement indicates that the gamma ray of 275 KeV is fed by the beta ray of 1.01 MeV. A difference between this energy and the 1.56 MeV beta-decay energy propose that there is a level at 550 KeV in Br^{81}. On the other hand, the 275-KeV level in Br^{81} has been known as a 5/2− state from the Coulomb excitation, (p, γ) and (γ, γ') reaction experiments, and the ground state of Se^{81} has been assigned to be a 1/2− state. Since a beta decay between the 1/2− state and the 5/2− comes to be a second forbidden transition, a beta ray populating the 275-KeV level of Br^{81} will not compete with other transitions. The information from the gamma-gamma coincidence spectrum gated by the photopeak pulses of 275-KeV gamma ray strongly suggests that there is a level at 550 KeV which feeds two equal energy gamma rays of 275 KeV. It is supported by the fact that there is the gamma ray of energy of 550 KeV in the spectrum measured by the single crystal spectrometer. The gamma-gamma coincidence spectra in coincidence with 275- and 170-KeV gamma rays suggest the energies of four levels at 170, 275, 550 and 690 KeV in Br^{81}. It is consistent with the gamma-gamma coincidence result gated by the 410-KeV gamma ray, and the intensity relations are consistent with the fact that the 275-KeV level is not populated by a beta ray as found in the beta-gamma coincidence experiment. Since the coincidence counts with the 410-KeV gamma ray are very small, it is considered that there is a level at 410-KeV. An absence of strong gamma rays in coincidence with 550, 650, and 840 KeV shows the levels at 550, 650 and 840 KeV. The weak gamma ray of 290 KeV in coincidence with the 550-KeV gamma ray may be a transition between levels at 840 and 550 KeV.

The relative intensity ratios of the beta rays were calculated to see if the intensity ratios of the gamma rays might be interpreted to be consistent with each other. Then the intensities of each beta ray per total disintegration of Se^{81} were determined from the comparison between the intensities of the 103–KeV gamma ray (isomeric transition of Se^{81m} with the 57–min half-life) and the 57–min component of each gamma ray. In this determination, the intensity of the 103–KeV transition was corrected by the internal conversion coefficient of the value of $\alpha=11$, and the number of disintegration of the Se^{81} ground state made from the Se^{81m} isomeric transition was calculated. The branching of the beta group having the 1.01–MeV end-point energy and populating the 550–KeV level of Br^{81} was obtained to be 2% for the total disintegration of Se^{81}. According to verification of the branching ratio, the gamma-ray spectrum and the beta-ray counts of a source were simultaneously measured by a NaI(T1) spectrometer and a Geiger Muller counter. The source was irradiated by 12–MeV bremsstrahlung for 20 minutes. The branching ratio of the beta ray feeding the 550–KeV level of Br^{81} was obtained to be 2%, which was in good agreement with the previous result. The obtained intensities of various beta groups are listed in Table III together with their associated log *ft* valus which are computed from Moszkowski's nomographs. The relative intensities of gamma radiations were normalized to total decay due to the similar way. A tentative decay scheme which is consistent with the observations is shown in Fig. 11. The 335–KeV gamma ray cannot be illustrated on the decay scheme, since any gamma ray has not been observed in coincidence with the 335–KeV gamma ray.

Table III. Relative intensities and log *ft* values of the various beta-ray transitions in the decay of Se^{81}

Energy (MeV)	Percent of total decay	log *ft*
1.56	92	5.2
1.39	1.3	6.6
1.15	1.0	6.2
1.08	1.8	5.9
1.01	2.0	5.7
0.88	0.5	6.1
0.72	1.0	5.6

In the experiment of (p, γ) and (γ, γ') reactions, a level at 550 KeV has been assigned to be a 9/2+ state which is an isometric state with the half-life of 37 μsec. However, the 550–KeV level in this experiment must not be the 9/2+ state, since the log *ft* value of the 1.01–MeV beta ray is 5.7 which suggests that the 1.01–MeV beta decay is either allowed or first forbidden transition. Therefore, it is concluded that the 550–KeV level in the present investigation is a new level near the 9/2+ state, and has a low spin value and an odd parity.

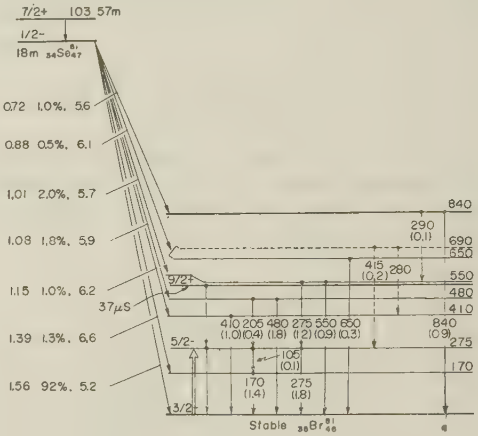

Fig. 11. Tentative decay scheme of Se^{81}.

The 550–KeV level of the 9/2+ state may be populated directly from Se^{81m} having the spin and the parity of 7/2+, since the beta transition is expected to be an allowed type. Therefore, the decay of the 275–KeV photopeak must contain a component with the half-life of 57 min. However, the experimental results shows an absence of this component. An upper limit of the beta branching was determined to be about 0.005% for the 103–KeV isomeric transition, and the associated log *ft* value was computed to be 8.9. Such large values of log *ft* in allowed transitions between the high spin states have often appeared in this mass range. For example, in the case of transition from the 7/2+ to the 9/2+ state in $Ge^{77} \rightarrow As^{77}$, the log *ft* value has been known to be 8.0[14].

Since the other beta rays have comparatively low values of log *ft* and the Se^{81} ground state has been known as a 1/2− state, the various leves of Br^{81} appearing in the decay of Se^{81} are expected to be low spin and odd parity states; 1/2−, 3/2−. In this mass range it is characteristic that many levels are seen having low spins and odd parities.

The author is deeply indebted to Prof. H. Morigana for interesting discussions in this study.

References

1) H. Morinaga and T. Kuroyanagi: Nuclear Instruments and Methods **6** (1960) 66.
2) H. Morinaga, T. Kuroyanagi, H. Mitsui and K. Shoda: J. Phys. Soc. Japan **15** (1960) 213.
3) F. Scott: Phys. Rev. **84** (1951) 659.
4) R. W. Hayward and D. D. Hoppes: Phys. Rev. **101** (1956) 93.
5) F. N. Hooge and A.H.W. Aten junior: Physica **19** (1953) 1074.
6) A. H. Wapstra, G. J. Nijgh, R. van Lieshout: Nuclear Spectroscopy Table (1959) p. 65.
7) See K. Way, R. W. King, C. L. McGinnis and R. van Lieshout: Nuclear Level Scheme, U. S.A.E.C. TID-5300 (1955), and B. S. Dzelepow and L. K. Peker: Decay Schemes of Radioactive Nuclei, Moskow, Lenningrad (1958).
8) I. Bergström and S. Thulin: Phys. Rev. **76** (1949) 1718.
9) W. C. Rutledge, J. M. Cork and S. B. Berson: Phys. Rev. **86** (1952) 775.
10) N. P. Heydenberg and G. M. Temmer: Phys. Rev. **93** (1954) 906.
11) E. A. Wolicki, L. W. Fagg and E. H. Geer: Phys. Rev. **105** (1957) 238.
12) R. B. Duffield and S. H. Vergors: Phys. Rev. **112** (1958) 1958.
13) A. Goodman and A. W. Schardt: Bull. Am. Phys. Soc. **4** (1959) No. 1, 56 VA2.
14) See, for example, A. W. Schardt: Phys. Rev. **108** (1957) 398.

JOURNAL OF THE PHYSICAL SOCIETY OF JAPAN, Vol. 15, No. 12, DECEMBER, 1960

^{8}Li Emission from Nuclear Disintegrations Produced by 4.3 GeV Negative π-Mesons

By Masaomi (Takahata) OHTA
Department of Physics, Osaka City University

(Received July 14, 1960)

Fifty-five ^{8}Li fragments from heavy element disintegrations produced by 4.3 GeV negative π-mesons were found. The frequency, the energy and angular distributions of these ^{8}Li fragments were compared with those of the fragments produced by 5.7 GeV proton beam reported by Goldsack et al. No appreciable difference has been found between the two cases. Of light element disintegrations, the frequency of ^{8}Li fragments was found to be about 0.006.

§1. Introduction

In 1957, Goldsack et al.[1] studied ^{8}Li emission from heavy element disintegrations produced by 5.7 GeV protons and reported energy and angular distributions and frequency of those fragments. The present work involves an investigation of ^{8}Li fragments from nuclear disintegrations produced by 4.3 GeV negative π-mesons.

It has been found in this laboratory that both the mean number of black prongs in the stars ($N_h \geqq 7$) produced by 6.2 GeV proton beam and that produced by 4.3 GeV negative pion beam are nearly equal to 10. Thus, it may be plausible to assume that the average excitation energies of both stars are nearly equal (~380 MeV), and, in consequence, the frequencies of emission of ^{8}Li fragments may also be equal. A similar consideration may be allowed in the case for 4.3 GeV pion and 5.7 GeV proton. On the other hand, since there is a certain difference between the two incident energies, if the frequency of emission of heavier particles is assumed to depend on the incident energy, the frequency in the present case may be expected to decrease with decreasing energy. Hence, an attempt has been made to compare the frequency, the energy and angular distribution of the two cases.

^{8}Li fragments from light element disintegrations are also studied.

§ 2. Experimental Procedure and Results

A stack of Ilford G5 emulsions 600 μ thick and of size 3″×4″, exposed to 4.3 GeV negative pion beam from the Berkeley Bevatron was used.

Each star with a minimum track in the direction of negative π-mesons was examined under a ×60 oil objective, and all black prongs were followed up either to their ends in the emulsion or to the points at which they left the plates. All the "hammer tracks" found were assumed to be due to ^{8}Li nuclei, it has been known that a small proportion of the hammer tracks may be due to ^{8}B or ^{9}Li nuclei[2].

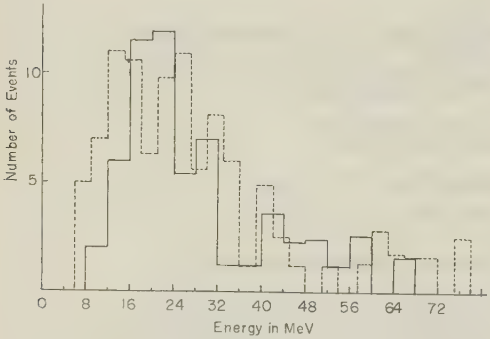

Fig. 1. Energy distribution of the ^{8}Li fragments. The solid histogram represents that of 4.3 GeV negative π-mesons. The dotted histogram represents that of 5.7 GeV protons obtained by Goldsack et al.

In total 6700 stars examined, 65 examples of ^{8}Li emission were observed. One star with two hammer tracks was also found. Of the parent stars, 54 had 7 or more heavily ionizing prongs, and hence correspond to heavy element disintegrations; of the remainder only 6 which had no short recoils were considered to be due to light element disintegrations.

Using the range-energy relation, the energy of each fragment was estimated. The energy distribution of ^{8}Li fragment from the heavy element disintegrations is shown in Fig. 1. The distribution has been corrected for the loss of fragments leaving the emulsion before coming to rest.

The angular distribution of the fragments is plotted with an interval of equal solid angle with respect to the direction of incident beam in Fig. 2, in which the forward to backward ratio was found to be nearly unity.

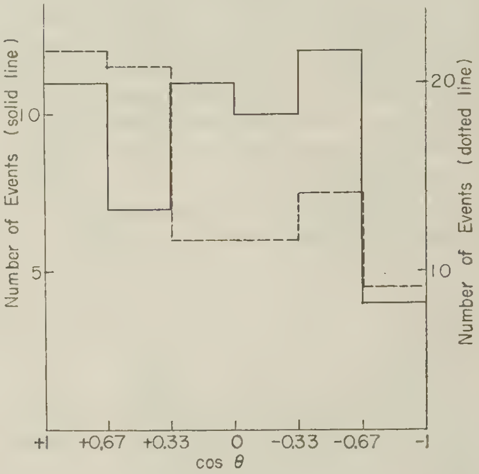

Fig. 2. Angular distribution of the ^{8}Li fragments, plotted in equal intervals of solid angles, and measured with respect to the direction of the incident negative π-mesons or protons. The solid histogram represents that of 4.3 GeV negative π-mesons. The dotted histogram represents that of 5.7 GeV protons obtained by Goldsack et al.

The stars having ^{8}Li fragments have been divided into some groups with respect to their different number of heavy prongs, as shown in Table I, in the same manner as had been done in the case of 5.7 GeV proton reported by Goldsack et al. The frequency of emission of ^{8}Li fragments for each group was estimated and is listed in Table I together with the data of 5.7 GeV proton. The mean value of the frequency was found to be 0.014 ±0.001.

The stars ($N_h \geqq 3$) with less than five black prongs were tentatively classified as light element disintegrations, if they had no short recoil. Although some uncertainty is inevitably included in this classification, the frequency of the ^{8}Li emission has been evaluated to be about 0.006.

Table I.

No. of Black Prongs	No. of Stars	No. of Fragments		Frequency (4.3 GeV π^-) Present author	Frequency (5.7 GeV proton) Goldsack et al.
		Observed	Corrected		
5- 8	2134	11	12.2	0.0057±0.0018	0.0059±0.0012
9–11	1072	6	6.8	0.0064±0.0026	0.0186±0.004
12–14	672	18	20.2	0.030 ±0.007	0.0186±0.004
15–20	378	19	20.8	0.055 ±0.013	0.0275±0.007
≧21	45	1	1.1	0.03	0.05
Mean value	4301	55	61.1	0.014 ±0.001	0.013 ±0.001

§ 3. Discussion

The energy distribution in Fig. 1 shows that most of the fragments have energies between 8 and 40 MeV but that there is a considerable high energy tail. It is readily seen that this distribution is similar to the case of 5.7 GeV proton obtained by Goldsack et al. which is indicated by dotted line in the same Figure. However, the nearly isotropic angular distribution in Fig. 2 indicates that most of the fragments may be emitted as part of the evaporation process. This seems to differ from the results of 5.7 GeV proton.

In order to interpret the above fact, it may be of use to follow energy and angular distributions more in detail. Hence, the data are divided into two groups depending on the number of black prongs in the parent stars. The fragments from stars with less than 12 black prongs (' small ' stars) and those with 12 or more black prongs (' large ' stars) were compared with corresponding data of proton, respectively. There are 17 observed events in the first group and 38 in the second.

The energy and angular distributions of the fragments from small stars and large stars except the angular distribution of small stars are all similar to those of 5.7 GeV proton. According to Goldsack et al.[1] the fragments from the large stars are ejected as the part of evaporation process, since their angular distribution was essentially isotropic, as it should be for an evaporation process. This does not differ from the present case. On he contrary, the angular distribution of the small stars obtained by them was markedly anisotropic, which differs from the present distribution as shown in Fig. 3.

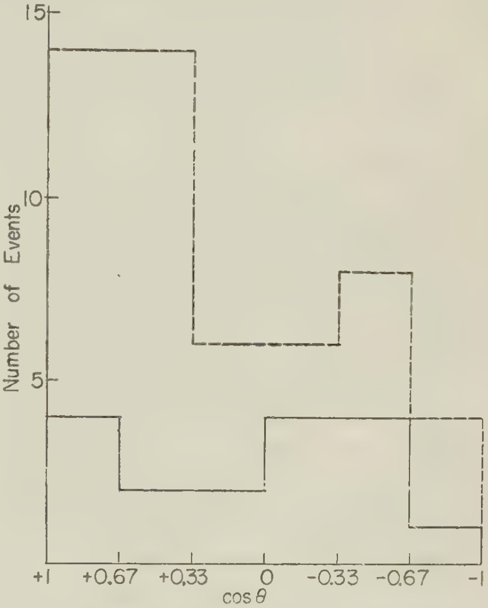

Fig. 3. Angular distribution of the ^{8}Li fragments ejected from stars with less than 12 black prongs. The solid histogram represents that of 4.3 GeV negative π-mesons. The dotted histogram represents that of 5.7 GeV protons obtained by Goldsack et al.

In the present experiment, the ratio of the fragments from the small stars to that from the large one is about one half, while in the case studied by Goldsack et al. the ratio is about 4/3. Further, as seen in Table I the frequency of such small stars is smaller than that of the large stars. Hence, it may be said that the present result is not essentially inconsistent with that obtained by Goldsack et al. as most of the fragments are due to the evaporation process. Namely, the proportion of the fragments which have relatively high energies and may be ejected in the forward direction seen in the case of the small stars is small in the present case, and consequently the contribution of these fragments to the total angular distribution may be inappreciable. However, the isotropic distribution in Fig. 3 may be partly considered to be due to its poor statistics. Since Imaeda et al.[2] have studied the angular distribution of the fragments under the same beam exposure as in the present investigation, the data may be more reliable in statistics if the present result is combined with theirs. The combined result is shown in Fig. 4, in which the difference from the case of proton is hardly recognized.

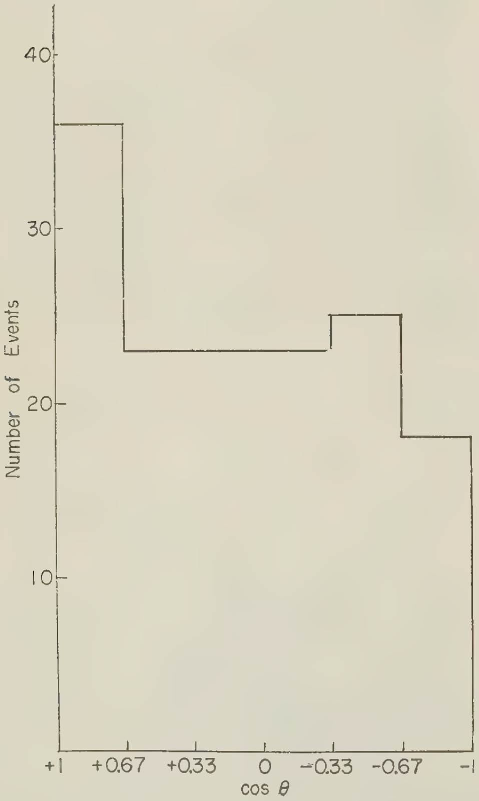

Fig. 4. Angular distribution of the ^{8}Li fragments, the data of Imaeda et al. were combined with ours.

The mean value of the frequency agrees quite well with that of 5.7 GeV proton, though a certain difference is seen for each group. This indicates that, on the average, the frequency of emission of ^{8}Li fragments rather depends on the excitation energy of stars than on the incident energy.

For the ^{8}Li fragments from light element distributions, only a paper by Munir has been reported[3]. He studied the frequency of the fragments from nuclear disintegrations induced by 950 MeV protons. From 3400 light element disintegrations with four or more prongs he obtained the number of ^{8}Li nuclei to be 22.5 from which the frequency can be obtained to be about 0.007 which is very close to the present result of 0.006. The coincidence of the frequencies of the above two cases, in spite of the difference in their energies, may be interpreted, if it is assumed that ^{8}Li fragments are due to nuclei after a light element breakup.

Acknowledgements

The author wishes to express his sincere thanks to Prof. Y. Watase and Dr. S. Kaneko for their encouragement throughout this work. The author is also indebted to Mr. O. Kusumoto and Mr. S. Matsumoto for their helpful advices and discussions. Thanks are also due to Prof. E. J. Lofgren, Dr. W. W. Chupp and Dr. T. Kotani who made the present work possible by exposing the emulsion stack in the negative π-meson beam of Bevatron Berkeley.

References

1) S. T. Goldsack, W. D. Lock and B. A. Munir: Phil. Mag. **2** (1957) 149.
2) K. Imaeda, K. Kazuno and N. Ito: Univ. of Yamanashi, Faculty of Education and Liberal Arts, **No. 9** (1958) 148 (in Japanese). W. F. Fry: Phys. Rev. **89** (1953) 325. L. W. Alvarez: Phys. Rev. **80** (1950) 518. F. C. Gilbert: Phys. Rev. **93** (1954) 499.
3) B. A. Munir: Phil. Mag. **1** (1956) 355.

JOURNAL OF THE PHYSICAL SOCIETY OF JAPAN, Vol. 15, No. 12, DECEMBER, 1960

A Model Theory of Liquid

By Akiya OOKAWA

Department of Physics and Chemistry, Gakushuin University,
Mejiro, Tokyo

(Received March 1, 1960)

As a structural model of liquid, a crystal threaded by fine network of dislocations is proposed. The main prepositions characterizing the model system are the elastic distortion of the mesh material in bulk rather than the local distortion at the core of the constituent dislocations, the frequency modulation for the transversal shear waves due to the anharmonicity of the potential, and the introduction of degenerated non-harmonic shearing translations. With the prepositions, the model system is shown to display a kind of first order phase transition between an imperfect crystal as representative for the liquid phase and a perfect crystal as representative for the solid phase. The order of magnitude of the frequency modulating coefficient, the only adjustable parameter, is estimated under comparison with the experimental data of noble metals.

§1. Introduction

Any model theory of liquid, regarding the liquid state near the melting point as a kind of imperfect crystal, makes use of lattice imperfections known in the field of crystalline solid, such as the vacant site[1], the dislocation[2], and the grain boundary[3]. In these theories, as to the excess entropy stabilizing the liquid phase compared to the solid phase, the interest is rather directed to the configurational entropy such as those due to the randomness in distributing the said imperfections.

The concentration of lattice imperfections representing the liquid state, however, is expected very large and the interactions between the constituent imperfections is expected accordingly very strong to the order unusually experienced in the field of crystalline solid. Under the circumstances, the individuality of the constituent lattice imperfections could not necessarily be preserved, in the sense that the distortion of the lattice might not be restricted locally near the core of each imperfections.

In the field of the theory of liquid, the importance of the modulation of lattice vibrations due to the anharmonicity of potential is well recognized. Mott[4] has succeeded in early days in relating the change at melting of electric resistivity to the modulation of eigen frequency, although the theory did not stand on any structural background. In the field of crystalline solid, the modulation of lattice vibrational spectrum due to anharmonic potential is discussed by several authors[5],[6],[7],[8], for cases of point lattice defects such as the vacant site and the interstitial atom.

Under the circumstances, in the representative model of liqid crowded with lattice imperfections, the elastic distortion of the lattice in bulk is expected large enough to contribute much to the entropy gain of the system due to anharmonic modulation of eigen frequency[9]. Here we present, standing on these characteristics, a model theory of liquid constituted of aggregate of crystallities in state of self-strain stabilized thermodynamically.

§2. Model Proposed

We consider a crystalline solid threaded by fine network of dislocations. When the dislocation segments are far apart from each other as it is usually in the field of crystal plasticity, the lattice distortion is localized near the core of dislocations. But, as the dislocation segments constituting the present model of liquid are expected neighbouring at a distance of the order of several atom spacings, we assume, instead of the localized distortion at the core of dislocations, rather the distortion in bulk of each lattice material at the mesh of the dislocation network. For a given density of lattice imperfections, the excess energy as well as the excess entropy of the system over those of the perfect crystal are functions of the degree of *diffuseness* of the said imperfections. We ought in general to evaluate the degree of diffuseness by variation principle to minimize the free energy. For system of scarce density of lattice imperfections at low temperature, as it is usually in the solid state, the excess energy favours the lattice distortion well localized at the core of imperfections. For system of large density of imperfections at high temperature, however, the predominance of the excess entropy is expected to favour the lattice distortion rather diffused out in bulk material[9]. The present model assumes the extreme case of the latter as to the diffuseness of lattice distortion in liquid state.

The model is shown schematically in Fig. 1 for the case of two-dimensional simple cubic lattice, where the lattice points at the mesh are disposed in state of self-strain in bulk so as to relax the local strain at the core of dislocations. It can be seen that almost all the material is under shearing strain to the order of $a/\alpha a$, where a is the atom spacing and $2\alpha a$ is the average spacing between the like dislocations. The excess energy of the model system in three dimension over that of a perfect crystal without dislocations can be approximated by

$$U_0=\frac{3}{2}N\mu(a/\alpha a)^2 v_0 \,, \tag{1}$$

where N, μ and v_0 are the number of atoms, the rigidity, and the atomic volume, respectively, The factor 3 is due to the three independent components of shear strain.

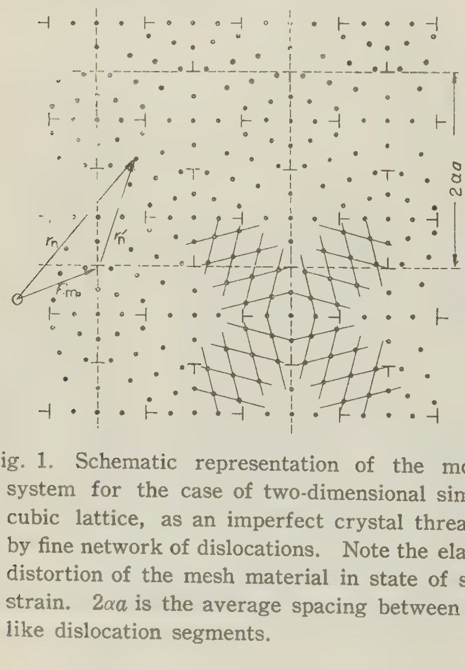

Fig. 1. Schematic representation of the model system for the case of two-dimensional simple cubic lattice, as an imperfect crystal threaded by fine network of dislocations. Note the elastic distortion of the mesh material in state of self-strain. $2\alpha a$ is the average spacing between the like dislocation segments.

The dislocation is the lattice imperfection originally introduced in the field of crystal plasticity. Its prominent feature discriminating it from other lattice imperfections is that the elastic shearing strain energy can be dissipated by the movement of dislocations introduced[10]. Now, in the present model of liquid threaded by dislocation network, the constituent dislocation segments are forced, under the influence of the thermal shear waves, to move in such a manner as to result a kind of plastic flow of the material to annihilate the elastic shear strain energy associated with the thermal shear waves. Taking account of such a dynamical character of the constituent dislocations of the present model, the transversal shear waves with the wave length longer than the average spacing $2\alpha a$ of the constituent dislocation segments are expected to be attenuated by the appropriate movement of the dislocation segments. For sake of simple treatment, we assume, defining a critical wave length $\lambda^*=2\alpha a$ or a corresponding critical wave number

$$k^*=2\pi/\lambda^*=\pi/\alpha a \,, \tag{2}$$

that in the model lattice the thermal shear waves with wave number $k>k^*(\lambda<\lambda^*)$ shall survive as vibrational modes but that the thermal shear waves with wave number $k<k^*$ $(\lambda>\lambda^*)$ shall degenerate into translational modes. This means that we expand the solenoidal displacement $\boldsymbol{u}(\boldsymbol{r}_n, t)$ of atom at coordinate $\boldsymbol{r}_n$ in the form

$$\boldsymbol{u}(\boldsymbol{r}_n,t)=\frac{1}{\sqrt{N}}\sum_{(k>k^*)}\sum_i \boldsymbol{B}_{ki}\exp(i\boldsymbol{k}\boldsymbol{r}_n) +\frac{1}{\sqrt{M}}\sum_{(k<k^*)}\sum_i \boldsymbol{B}'_{ki}\exp(i\boldsymbol{k}\boldsymbol{R}_m) \tag{3}$$

with $\boldsymbol{B}_{ki}\perp\boldsymbol{r}_n$ and $\boldsymbol{B}'_{ki}\perp\boldsymbol{R}_m$, $i=1$, 2 specifying the polarization. The coordinate $\boldsymbol{R}_m$ is defined as such a representative coordinate for each mesh material that the same $\boldsymbol{R}_m$ stands for every $\boldsymbol{r}_n$ belonging to all lattice points of the m-th crystallite (see Fig. 1). $M=N/\alpha^3$ is the total number of the crystallites. These translational thermal modes correspond to the relative shearing translation between the mesh material, each material or the crystallite behaving as a kinetic unit, so to speak. It is to be noted, however, that the translational freedom is introduced as to the solenoidal displacement but not as to the irrotational displacement, and so the total number of degenerated translational modes is equal to twice the number of crystallites.

Thus the Hamiltonian of the model system, of atomic mass m, is assumed in the form

$$\mathscr{H}=U_0+\sum_k \frac{1}{2m}(C_k^2+m^2\omega_{1k}^2 A_k^2)$$
$$+\sum_{(k>k^*)}\sum_i \frac{1}{2m}(D_{ki}^2+m^2\omega_{2ki}'^2 B_{ki}^2)$$
$$+\sum_{(k<k^*)}\sum_i \frac{1}{2m\alpha^3} D_{ki}'^2 \,. \tag{4}$$

The first term U_0 in the right hand side is the configurational excess energy given by Eq. (1), the second term represents the longitudinal vibrational modes each of eigen frequency ω_{1k}, the third term represents the surviving transversal vibrational modes, each of modified eigen frequency ω_{2ki}', and the fourth term represents the transversal translational modes. A_k and B_{ki} are the normal coordinates, and C_k, D_{ki} and D_{ki}' are the momenta, respectively.

As to the modulation of eigen frequency for the transversal shear waves, the main cause of modulation is the shear strain of the material in state of self-strain, $x=a/\alpha a$. To evaluate this anharmonic modulation of the eigen frequency $\omega_{2ki}'(x)$ for strained material, we tentatively assume, by symmetry consideration, a functional relation

$$\omega_{2ki}'(x)/\omega_{2ki}=\exp\left(-\tfrac{1}{2}\gamma x^2\right) \tag{5}$$

with constant coefficient γ, where ω_{2ki} is the natural eigen frequency for unstrained crystal. It can not be denied that, as it is with the Grüneisen's constant in the classical treatment of lattice expansion, this assumption is open to much debate, such as the different modulation for waves of different wave vector, the dependence of the coefficient on the strain, and also the *a posteriori* variation of the constant with temperature. Eq. (5) is assumed for the present provisionally to develope the treatment of the model.

§ 3. Partition Function

As the classical liquid is under consideration in the present treatment, the partition function of the system is gived by

$$Z=h^{-3N}\int\cdots\int \exp\left(-\mathscr{H}/kT\right)d\tau \,,$$

where the integration extends over all the configurations available for N atoms. In the present crystallite model theory, all the configurations of the system can be grouped into subgroups, the members of each subgroup representing the configurations with a specified average mesh size αa. So we may wright in the form

$$Z=\sum_\alpha Z_\alpha \,. \tag{6}$$

The specific partition function for each subgroup is

$$Z_\alpha=h^{-3N}\int\cdots\int^{1} \exp\left(-\mathscr{H}/kT\right)d\tau \,,$$

where the integration extends over configurations available for each specified average mesh size αa. With the Hamiltonian (4), the specific partition function is calculated through

$$Z_\alpha=h^{-3N}\,e^{-U_0/kT}\prod_k\iint \exp\left\{-\frac{1}{2mkT}C_k^2-\frac{m\omega_{1k}^2}{2kT}A_k^2\right\}dA_k dC_k$$
$$\times\prod_{(k>k^*)}\prod_i\iint \exp\left\{-\frac{1}{2mkT}D_{ki}^2-\frac{m\omega_{2ki}'^2}{2kT}B_{ki}^2\right\}dB_{ki}dD_{ki}$$
$$\times\prod_{(k<k^*)}\prod_i\iint \exp\left\{-\frac{1}{2m\alpha^3 kT}D_{ki}'\right\}dB_{ki}'dD_{ki}' \,. \tag{7}$$

The integration range for the harmonic coordinates, A_k and B_{ki}, can be extended from $-\infty$ to $+\infty$, due to neglegible contribution from the extreme configurations. The integration range $\Delta B_{ki}'$ for the translational coordinates, B_{ki}', is estimated to of the order of

$$\Delta B_{ki}'=\frac{k^*}{k}\Delta B_{k^*i}'=\frac{k^*}{k}a \qquad (k<k^*) \tag{8}$$

as follows. As to the critical mode characterized by the wave vector k^*, the transversal translational motion between two neighbouring layers of crystallites, the one in positive and the other in negative direction, is realized by means of one intervening layer of constituent dislocations (see Fig. 1). Because of the quasi-periodic distribution of the constituent dislocation segments, the identical arrangement of dislocations is resumed each after one layer of dislocations moves by the period $2\alpha a$, accompanying relative displacement between two halves of the crystal seperated by the dislocation layer amounting to the lattice constant a. Thus we expect an integration range of amount a for the critical mode. As to the other modes with smaller wave number ($k<k^*$), we have $\lambda/\lambda^*(=k^*/k)$ times as many intervening layers of dislocations, each contributing by the amount a to the relative displacement between two layers of crystallite at maximum displacement. With the integration ranges thus specified, we obtain

$$\ln Z_\alpha=-\frac{U_0}{kT}+\sum_k \ln\left(\frac{kT}{\hbar\omega_{1k}}\right)+2\sum_{(k>k^*)}\ln\left(\frac{kT}{\hbar\omega'_{2k}}\right)+2\sum_{(k<k^*)}\ln\left\{\frac{\sqrt{2\pi m\alpha^3 kT}}{h}\frac{k^*}{k}a\right\}. \tag{9}$$

By use of the spectra, g_l and g_t, each for the longitudinal and for the transversal modes, we have, refering Eq. (1),

$$\begin{aligned}\ln Z_\alpha=&-\frac{3N\mu v_0}{2kT}\alpha^{-2}+\int_0^{k_c}\ln\left(\frac{kT}{\hbar\omega_{1k}}\right)g_l dk+2\int_{k^*}^{k_c}\ln\left(\frac{kT}{\hbar\omega'_{2k}}\right)g_t dk\\&+2\int_0^{k^*}\ln\left\{\frac{\sqrt{2\pi mkT}a}{h}\alpha^{3/2}\frac{k^*}{k}\right\}g_t dk\,.\end{aligned} \tag{10}$$

Now we want to introduce the Debye approximation for the spectra

$$g_l=g_t=3Nk^2/k_c^3\,, \tag{11}$$

normalized to $\int_0^{k_c} g dk=N$, independently of the introduction of network of dislocations. This approximation is not inconsistent with the introduction of the translational shearing modes by Eq. (3), as the total number of these degenerated translational modes

$$2\int_0^{k^*} g_t dk=2N\left(\frac{k^*}{k_c}\right)^3=2N\left(\frac{\pi/\alpha a}{\pi/a}\right)^3=2N/\alpha^3 \tag{12}$$

is equal to twice the number of crystallites.

The partition function Z_0 for an ideally perfect crystal is obtained as the limiting case of infinite mesh size, $\alpha\to\infty$ and $k^*\to 0$;

$$\ln Z_0=\int_0^{k_c}\ln\left(\frac{kT}{\hbar\omega_{1k}}\right)g_l dk+2\int_0^{k_c}\ln\left(\frac{kT}{\hbar\omega_{2k}}\right)g_t dk\,. \tag{13}$$

From Eqs. (10) and (13), it follows

$$\ln\left(\frac{Z_\alpha}{Z_0}\right)=-\frac{3N\mu v_0}{2kT}\alpha^{-2}+2\int_{k^*}^{k_c}\ln\left(\frac{\omega_{2k}}{\omega'_{2k}}\right)g_t dk+2\int_0^{k^*}\ln\left\{\frac{\sqrt{2\pi mkT}a}{h}\frac{k^*}{k}\alpha^{3/2}\Big/\frac{kT}{\hbar\omega_{2k}}\right\}g_t dk\,,$$

which can be transcribed, with the natural frequency $\omega_{2k}=\sqrt{\mu v_0/m}\,k$ and refering Eqs. (5) and (11), to

$$\begin{aligned}\ln\left(\frac{Z_\alpha}{Z_0}\right)&=-\frac{3N\mu v_0}{2kT}\alpha^{-2}+2\ln\left(\frac{\omega_{2k}}{\omega'_{2k}}\right)\int_{k^*}^{k_c}g_t dk+2\ln\left\{\sqrt{\frac{\mu v_0}{2\pi kT}}ak^*\alpha^{3/2}\right\}\int_0^{k^*}g_t dk\\&=-\frac{3N\mu v_0}{2kT}\alpha^{-2}+\gamma\alpha^{-2}\cdot N(1-\alpha^{-3})+2\ln\left\{\sqrt{\frac{\mu v_0}{2kT}}\alpha^{1/2}\right\}\cdot N\alpha^{-3}\,.\end{aligned} \tag{14}$$

Defining the atomic quantities z_α and z_0 by $Z_\alpha=z_\alpha^N$ and $Z_0=z_0^N$, we have

$$\ln\left(\frac{z_\alpha}{z_0}\right)=\left(\gamma-\frac{\Theta}{T}\right)\alpha^{-2}+\ln\left(\frac{\pi}{3}\frac{\Theta}{T}\alpha\right)\alpha^{-3}-\gamma\alpha^{-5}\,, \tag{15}$$

where the reference temperature Θ is defined by

$$k\Theta=\frac{3}{2}\mu v_0\,. \tag{16}$$

§ 4. Thermodynamical Characters

The specific partition sunction $Z_\alpha=z_\alpha{}^N$ represents the relative thermodynamical probability of each subgroup specified by the average mesh size αa. As the relevent number of atoms N is sufficiently large, the total partition function Z is substantially approximated by the specific one Z_{α^*} for most probable subgroup. The mesh size $\alpha^*(T)$ for such a stable configuration is determined, by maximizing expression (15) as function of α for each temperature, by

$$\ln\frac{\pi}{3}-\frac{1}{3}+\ln\alpha^*-\frac{5}{3}\gamma\alpha^{*-2}$$
$$=-\ln\frac{\Theta}{T}+\frac{2}{3}\left(\frac{\Theta}{T}-\gamma\right)\alpha^*\,. \tag{17}$$

In the followings, the stable size α^* will be abbreviated merely by α.

As to the thermodynamical stability of the present system relative to the solid, we may presume that the solid can be represented by the limiting case of infinite mesh size, that is the ideal crystal without any imperfections. It might be argued that the real solid is not perfect but contains many lattice imperfections, which give rise to the well-known structure sensitive properties of the solid. In respect to the thermodynamical quantities, however, we may assume these quantities characteristic to the solid rather insensitive to existing lattice imperfections. Under the circumstances, the melting temperature T_m can be determined by the equilibrium condition between the two phases, $z_\alpha=z_0$. So we have, from Eq. (15) with the stable mesh size α^* of Eq. (17), at the melting point

$$\left(\gamma-\frac{\Theta}{T_m}\right)\alpha_m+\ln\left(\frac{\pi}{3}\,\frac{\Theta}{T_m}\,\alpha_m\right)=\gamma\alpha_m^{-2}\,. \tag{18}$$

For each specified value of the frequency modulating coefficient γ, Eqs. (18) and (17) determine the ratio Θ/T_m between the melting temperature T_m and the reference temperature Θ as well as the stable mesh size α_m at the melting point.

The excess free energy Δf per atom in liquid state over that in the solid state is given by

$$\Delta f=-kT\ln(z_\alpha/z_0)$$

with the stable α^* given by Eq. (17). The excess energy $\Delta e=\partial(\Delta f/T)/\partial(1/T)$ is calculated, noting that $\partial z_\alpha/\partial\alpha=0$ for α^*, to be

$$\Delta e=kT\left(\frac{\Theta}{T}\alpha^{-2}-\alpha^{-3}\right)=\frac{3\mu v_0}{2}\alpha^{-2}-kT\alpha^{-3}\,, \tag{19}$$

the first term in the right hand side being the configurational excess energy and the second term being the energy deficit due to degeneration of $2M(=2N/\alpha^3)$ degrees of freedom from vibrational to translational. The melting entropy $\Delta s(T_m)=\Delta e(T_m)/T_m$ is, accordingly, given by

$$\Delta s(T_m)=k\left(\frac{\Theta}{T_m}\alpha_m^{-2}-\alpha_m^{-3}\right), \tag{20}$$

where α_m is the stable mesh size at the melting point satisfying simultaneously Eqs. (17) and (18).

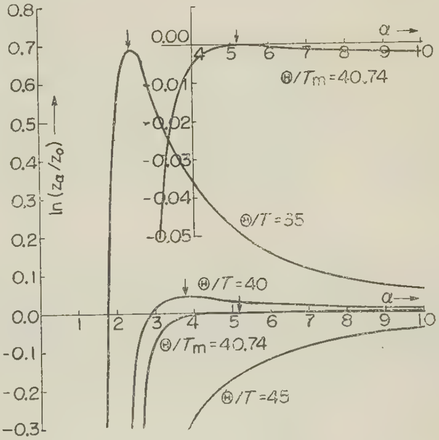

Fig. 2. Relative thermodynamical probability of subgroup at each constant temperature, for a specified value of $\gamma=40$. In the inset, the ordinate is magnified ten times.

§ 5. Discussions

The general trend of the relative thermodynamical probability z_α/z_0 is plotted, according to Eq. (15), in Fig. 2 as function of the mesh size α at each constant temperature, assuming a tentative value $\gamma=40$ for the frequency modulating coefficient. It can be seen that at low enough temperature, $\Theta/T=45$, z_α increases with increasing α monotonously to z_0, thus stabilizing the perfect crystal as representative for the solid phase, while at a high enough temperature, $\Theta/T=35$, z_α takes, at the stable mesh size α^* satisfying Eq. (17), a maximum value exceeding z_0, thus stabilizing the imperfect crystal as representative for the liquid phase. At an intermediate temperature T_m satisfying Eq. (18) as well as Eq. (17) for each specified γ, $\Theta/T_m=40.74$ for $\gamma=40$, the most probable imperfect crystal represented by the average mesh size α_m that maximizes z_α is in equilibrium with the perfect crystal of infinite mesh size, being seperated from each other by an intervening minimum of z_α, which is shown in the inset of Fig. 2. We have accordingly at the temperature T_m a kind of first order transition. The numerical value $\Theta/T_m=40.74$ is estimated graphically from ln $(z_\alpha{}^*/z_0)$ *versus* Θ/T plot for the case $\gamma=40$. The melting entropy $\varDelta s(T_m)$ for the transition is estimated by Eq. (20) to $1.51k$ in this case. Similar results obtained for each specified value of γ are summarized in Table I.

Table I. Predicted values at the melting point.

γ	30	40	50
α_m	4.71	5.18	5.30
Θ/T_m	30.78	40.74	50.67
$\varDelta s(T_m)/k$	1.37	1.51	1.79

The present model theory has, as can be seen in the above procedure, just one adjustable parameter, the frequency modulating coefficient γ. The reference temperature Θ, defined by Eq. (16), is determined by the rigidity μ and the atomic volume v_0 or by the atomic mass m and the propagation velocity v_t of the transversal wave through

$$k\Theta=\frac{3}{2}\mu v_0=\frac{3}{2}\rho v_t{}^2\cdot v_0=\frac{3}{2}mv_t{}^2\ . \tag{21}$$

As the coefficient γ is introduced in the present treatment rather tentatively, we want to estimate the probable value of this coefficient *a posteriori* in comparison with the experimental data. It seems legitimate to choose metals as the material for comparison, because the dislocation characterizing the present model is the lattice imperfection well established in the field of crystal plasticity of metals among others. The experimental data for noble metals is shown in Table II.

As to the ratio Θ/T_m, the experimental value for these metals is very close to 40, which suggests, refering Table I, a value nearly equal to 40 for the frequency modulating coefficient γ. For other face-centred cubic metals, the experimental value of the ratio ranges between 30 and 50. For body-centred cubic metals, iron and tungsten, the ratio is of order of 60. In the poor state of the present theory inherent from many approximations, we are reluctant from discussing specifically solely on the coefficient γ, but it seems that the order of magnitude of the coefficient can be evaluated empirically on these lines.

Table II.

Metal	T_m (°K)	Q_m (kcal/mol)	$\varDelta s/k$	v_t (m/sec)	atomic weight	Θ (°K)	Θ/T_m
copper	1,356	3.1	1.15	2,260	63.54	59,000	43.5
silver	1,233	2.69	1.10	1,590	107.88	49,200	39.9
gold	1,336	3.05	1.15	1,200	197.0	51,100	38.3

As to the melting entropy $\varDelta s(T_m)$, the estimated value exceeds the experimental one, and the discrepancy does not seem remediable by mere adjustment of value for γ. Now, in reviewing the prepositions introduced in § 2, the expression (1) for the configurational excess energy of the model system seems to be criticized. We see in Table I that the stable mesh size α^*a for the model system is less than several atom spacings. The average shear strain, $a/\alpha a$, is accordingly larger than 1/10 and so, because of the anharmonic nature of the strain energy, the expression (1) is expected to overestimate the configurational excess energy. This overestimation in the configurational energy may be the cause resulting in the said discrepancy of the melting entropy.

The author wishes to express his cordial thanks to Prof. M. Kotani and Prof. T. Muto for criticizing discussions throughout.

References

1) J. E. Lennard-Jones and A. F. Devonshire: Proc. Roy. Soc. **A165** (1938) 1; **169** (1938) 317; **170** (1939) 464.

2) S. Mizushima: J. Phys. Soc. Japan **15** (1960) 70.
3) A. Ookawa: J. Phys. Soc. Japan **2** (1947) 108; **3** (1948) 295; **6** (1952) 543.
4) N. F. Mott: Proc. Roy. Soc. **A 146** (1934) 465.
5) K. F. Stripp and J. G. Kirkwood: J. Chem. Phys. **22** (1954) 1579.
6) H. B. Huntington, G. A. Shirn and E. S. Wajda: Phys. Rev. **99** (1955) 1085.
7) K. Yamahuzi and T. Tanaka: Prog. Theor. Phys. **20** (1958) 327.
8) K. Fischer: Z. Phys. **155** (1959) 59.
9) E. Fukushima and A. Ookawa: J. Phys. Soc. Japan **10** (1955) 970.
10) A. H. Cottrell: Dislocations and Plastic Flow in Crystals (Oxford, 1953).

JOURNAL OF THE PHYSICAL SOCIETY OF JAPAN, Vol. 15, No. 12, DECEMBER, 1960

Surface Free Energy of a Dilute Gas

By Takuji TSUZUKI

Yokohama Municipal University Kanazawa-ku, Yokohama

(Received August 6, 1960)

The effect of boundary wall on a dilute gas of hard spheres is discussed. The free energy of the system is given as a function, not only of the volume, but also of the surface area of the container. The formula for the excess free energy due to the surface (surface tension) is given both for classical as well as for quantum mechanics. The quantum correction substitutes the effective diameter σ_{eff} for the classical diameter σ of a molecule.

§1. Introduction

In the current theories of statistical mechanics, systems are usually treated in the limit of infinite volume keeping the density constant. The physical quantities thus evaluated are therefore independent of the shape and the size of the vessel containing the system. These treatments are however inconvenient when the size of the system is small, or when the thickness of container becomes very small. For example, the spin wave theory for thin ferromagnetic materials has been developed by M. J. Klein and R. S. Smith[1]. They have shown theoretically that the spontaneous magnetization decreases with decreasing thickness. Their results are qualitatively in good agreement with experimental data of E. C. Crittendon and R. W. Hoffman[2]. Besides magnetic properties, we may cite many anomalous properties of thin substances, e. g., lowering of melting point[3], increasing of electric resistance[4], and decreasing of specific heat[5].

Another typical example of a small system is an atomic nucleus. Even for the heaviest atom, the number of nucleons at the surface of a nucleus is by no means negligible compared with the total number of nucleons. The surface tension and the surface energy play undoubtedly very important roles in determining the properties of nuclei. However statistical mechanics of nuclei, taking the effect of nuclear surface into account, is not yet fully developed.

In these problems we are more or less concerned with the surface free energy, that is, the surface tension. This is defined as the excess free energy per unit surface area. In general the structure near the surface of any system is obviously different from that in bulk. Particularly, the surface tension of liquid has been investigated by many authors[6] from the theoretical view-point. In the quantum treatment, A. Harasima et al.[7] has introduced the zero-point energy into the evaluation of surface energy, and M. Toda[8] has derived the general expression of surface tension in terms of density matrix.

Since, in general, the quantum treatment of the surface effect on a system of many particles with mutual interaction is of great difficulty, only the case of a dilute gas is investigated in this paper. Section 2, is devoted to classical dilute gas composed of hard spheres. Molecules interacting with square well potential is also treated in Appendix III. In Section 3, it is shown that by the quantum correction, the effective diameter of a particle must be larger than the diameter of a classical molecule.

§ 2. Classial Gas

We shall begin with the case of a gas of very low density. The constituent molecules are assumed to be hard spheres of diameter σ. If we increase area of the surface by the amount A, the volume which is accessible to the molecules diminishes by the amount $A\sigma/2$, since any molecule can not come closer to the surface than its radius $\sigma/2$. For a very dilute gas the part of the free energy which depend on the volume V is given by $-NkT\log V$, where N is the number of gas molecules. Therefore the increment of the free energy due to the new surface is given, for unit area, by

$$\gamma=-\frac{1}{A}NkT\log\{(V-A\sigma/2)/V\}\cong\frac{N}{V}kT\frac{\sigma}{2}\,. \tag{2.1}$$

This is the first approximation for the excess free energy γ per unit area of the surface. We may also apply Eq. (2.1) to the change in surface tension of liquid caused by solute molecules (Appendix I).

When the density of the gas is higher, collision between molecules is to be taken into consideration. For the equation of state this corresponds to the calculation of the second virial coefficient. If, in general, the interaction energy between molecules is given in the form

$$U=\sum_{i>j=1}^{N}u(i,j)\,,$$

the configurational partition function is given by the integral of

$$e^{-\beta U}=1+\sum_{i>j=1}^{N}(e^{-\beta u(i,j)}-1)+\cdots\,. \tag{2.2}$$

The first term on the right-hand side of Eq. (2.2) gives Eq. (2.1) for the surface free energy. For hard sphere molecules under consideration, each of the second term is -1 when $r_{ij}<\sigma$ and vanishes when $r_{ij}>\sigma$.

When we integrate Eq. (2.2), especially each of the second term, with respect to a molecule, we are to subtract that part of the volume which is not accessible to that molecule. If the area of the vessel is A and if any molecule can not come closer to the wall than the distance a, the region with volume Aa near the surface and the interaction sphere with volume $4\pi\sigma^3/3$ around any other molecule are not accessible. The region common to these is not to be counted twice. For a molecule which is at x from the wall, this part of the interaction sphere is

$$v(x)=\int_{x-a}^{\sigma}d\xi\,\pi(\sigma^2-\xi^2)=\frac{\pi}{3}(x-\sigma-a)^2(x+2\sigma-a)\,. \tag{2.3}$$

We find thus the free energy F expressed by the formula

$$\begin{aligned}\lambda^{3N}N!\exp(-\beta F)&=\int\cdots\int dx_1\cdots dx_N e^{-\beta U}\\&=(V-Aa)^N+N(N-1)/2\cdot(V-Aa)^{N-2}\\&\quad\times\left\{\left(-\frac{4}{3}\pi\sigma^3-Aa\right)(V-Aa)+A\int_a^{a+\sigma}v(x)dx\right\}+\cdots\\&=(V-Aa)^N\left\{1-\frac{N(N-1)}{2(V-Aa)}\left(\frac{4}{3}\pi\sigma^3-\frac{\pi}{4}\sigma^4\frac{A}{V-Aa}\right)\right\}+\cdots\,.\end{aligned} \tag{2.4}$$

Or, expanding the logarithm, we obtain the result configurational part of the free energy F_0

$$F_c=-NkT\left(\log V-\frac{2\pi}{3}\sigma^3\frac{N}{V}\right)+\gamma A\,, \tag{2.5}$$

where

$$\gamma=\frac{NkT}{V}\left\{a+\frac{\pi}{24}(16a-3\sigma)\sigma^3\frac{N}{V}\right\}\,. \tag{2.6}$$

If we define the effective volume $V_{\rm eff}$ as follows

$$\lambda^{3N} N! \exp(-\beta F) = V_{\rm eff}^{N}\,, \tag{2.7}$$

then it becomes from Eq. (2.4)

$$V_{\rm eff} = V - Aa - N\left(\frac{2}{3}\pi\sigma^3 - \frac{\pi}{8}\sigma^4\frac{A}{V}\right). \tag{2.8}$$

W. A. Steele and G. D. Halsey, Jr.[9] have calculated the effective volume assuming the attractive force of Lennard-Jones type, and obtained

$$V_{\rm eff} = V - Aa + Aa\sum_{\tau=1}^{\infty}\{1/\tau!(3\tau-1)\}(\mathcal{E}/kT)^{\tau}\,. \tag{2.9}$$

The third term in the right-hand side of Eq. (2.9) is derived from the attractive forces between the gas molecules and the wall. In the present paper, however, the effect of the attractive force caused by the square-well potential will be expanded in Appendix III.

Putting $a=\sigma/2$, we get the second approximation for the surface free energy:

$$\gamma = \frac{NkT\sigma}{2V}\left(1+\frac{5\pi}{12}\sigma^3\frac{N}{V}\right). \tag{2.10}$$

The equation of state is, from Eq. (2.5),

$$p = \frac{NkT}{V}\left(1+\frac{2\pi}{3}\sigma^3\frac{N}{V}\right). \tag{2.11}$$

We may interprete Eq. (2.1) the other way: the most convenient way of estimating surface effect is to introduce a very thin wall at the middle of the system and thus divide it into two parts keeping the total volume unaltered. As is shown in Fig. 1, if we want to introduce a wall amidst the vessel, we have to push aside those molecules which lies on that plane. To do this we first introduce two hypothetical membranes side by side. These membranes are such that through which the center of any molecule can not pass. Introduction of these membranes does not affect the free energy of the total system. Then we push one of the membrane to the right and the other to the left by the same amount $\sigma/2$ (see Fig. 1). At this stage we can introduce, without any work, a wall of infinitesimal thickness amidst the membranes to divide the system into two parts. Increase in the free energy is equal to the work done by moving the membranes. Since the gaseous pressure exerting on each membrane is, in the first approximation, equal to the pressure p of the gas, the work per unit area of each membrane is $p\sigma/2$ which is the excess free energy given by Eq. (2.1) because $p=NkT/V$ is satisfied in this approximation.

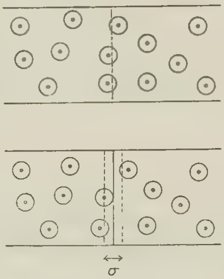

Fig. 1.

A similar interpretation for Eq. (2.10) is not difficult. After some calculations given in Appendix II, we see that the pressure on the membranes when separated mutually by the distance s is

$$p(s) = \frac{NkT}{V}\left\{1+\frac{\pi}{3}(3\sigma^2 s - s^3)\frac{N}{V}\right\}.$$

Therefore the work done by unit surface of the membranes is

$$\frac{1}{2}\int_0^{\sigma} p(s)ds = \frac{NkT\sigma}{2V}\left(1+\frac{5\pi}{12}\sigma^3\frac{N}{V}\right),$$

which is identical to the surface free energy given by Eq. (2.10).

It is straight-forward to extend the calculation to more general case in which attractive force is present (Appendix III).

§ 3. Quantum Corrections

When the gas is very dilute we can treat the molecules as free particles. Then we have exact density matrix

$$\rho^{(1)}(\boldsymbol{x}, \boldsymbol{x}')=\sum_{k=1}^{\infty} \varphi_k{}^*(\boldsymbol{x}') \exp(-h^2k^2/8\pi^2mkT)\varphi_k(\boldsymbol{x}) , \tag{3.1}$$

where

$$\varphi(\boldsymbol{x})= \prod_{x,y,z}\sqrt{\frac{2}{L_x}} \sin\frac{\pi n_x}{L_x}x , \qquad n_x=1, 2, \cdots \tag{3.2}$$

and L_x etc. mean the widths of the container.

From Eq. (3.1) we get the well-known expression for the density $\rho(x)$ at distance $x(\ll L_x)$ from the surface wall. When $\rho(x)$ is normalized so that $\rho\rightarrow 1$ as x becomes large, we have

$$\rho(x)=1-\exp(-4\pi x^2/\lambda^2) , \tag{3.3}$$

with

$$\lambda^2=h^2/2\pi mkT , \tag{3.4}$$

where h stands for the Planck's constant, k the Boltzmann constant and T the temperature.

The surface free energy in this case has been given by Toda[8]. The result is

$$\gamma=\frac{N}{V}\frac{\lambda}{4}kT . \tag{3.5}$$

This formula affords following interpretation. If there is no wall $\rho(x)$ stays 1 up to $x=0$. Introduction of the wall at $x=0$ causes a decrease in the density. The amount of this decrease can be expressed by the length δ:

$$\delta=\int_0^\infty \exp(-4\pi x^2/\lambda^2)dx=\lambda/4 . \tag{3.6}$$

In other words, the volume accessible to a molecule is diminished by $A\delta$, where A denoted the area of the surface as before. The surface free energy is therefore obtained by substituting δ for $\sigma/2$ in Eq. (2.1). This gives immediately Eq. (3.5).

When the diameter of molecules is finite and is σ, we have to substitute $\sigma/2+\delta$ for $\sigma/2$ in Eq. (2.1). We obtain thus the first approximation for a very dilute gas at low temperatures:

$$\gamma=\frac{N}{V}kT\left(\frac{\sigma}{2}+\frac{\lambda}{4}\right) . \tag{3.7}$$

We see that $\gamma/\gamma_{\text{class}}$ increases with decreasing temperature.

The second approximation, which takes molecular collision into account, can be obtained if the counter-part of Eq. (2.2) in quantum mechanics is evaluated. This is given as[10]

$$\begin{aligned}\exp(-\beta H^{(N)})&=\exp(-\beta H_0{}^{(N)})\\ &\quad+\sum_{i>j} \exp(-\beta H_0{}^{(N-2)}(\{i, j\})[\exp(-\beta H^{(2)}(i, j)-\exp(-\beta H^{(2)}(i, j))]+\cdots ,\end{aligned} \tag{3.8}$$

where $H^{(N)}$ denotes the hamiltonian of N particles and $H_0{}^{(N)}$ that without interaction. The bracket $\{i, j\}$ means that the i-th and the j-th molecules are excluded.

The first term on the right-hand side of Eq. (3.8) gives Eq. (3.7). Up to the second term we have

$$e^{-\beta F}=\frac{\lambda^{-3N}}{N!}\left\{V-A\left(\frac{\sigma}{2}+\frac{\lambda}{4}\right)\right\}^{N}$$
$$\times\left\{1+\frac{N(N-1)}{2}\left[V-A\left(\frac{\sigma}{2}+\frac{\lambda}{4}\right)\right]^{-2}\iint d\boldsymbol{x}_1 d\boldsymbol{x}_1(S-1)+\cdots\right\}, \tag{3.9}$$

where S is defined by

$$\langle \boldsymbol{x}_1, \boldsymbol{x}_2| \exp[-\beta H^{(2)}(1,2)]|\boldsymbol{x}_1, \boldsymbol{x}_2\rangle=\lambda^{-6}S(\boldsymbol{x}_1, \boldsymbol{x}_2) . \tag{3.10}$$

The integral appearing in Eq. (3.9) is difficult to evaluate.

If we neglect the effect of the boundary, however, S is obtained and gives the second virial coefficient, which is given by

$$B(T)=2\pi N\int_0^\infty r^2 dr(1-S(r)) , \tag{3.11}$$

where

$$S(r)=S(|\boldsymbol{x}_1-\boldsymbol{x}_2|) . \tag{3.12}$$

Noting that $\rho^{(2)}=\exp(-\beta H^{(2)})$ satisfies the Bloch equation we can calculate its diagonal element. The result is (cf. reference 11)

$$S(r)=\frac{\sqrt{2}\,\lambda^3}{\pi^2 r^2}\sum_l (2l+1)\int_0^\infty dk \exp(-\lambda^2k^2/2\pi)v_l^2(k, r) , \tag{3.13}$$

where

$$v_l(k, r)=\sqrt{\frac{\pi kr}{2}}\,\frac{J_{-l-(1/2)}(k\sigma)J_{l+(1/2)}(kr)-J_{l+(1/2)}(k\sigma)J_{-l-(1/2)}(kr)}{\{J^2_{l+(1/2)}(k\sigma)+J^2_{-l-(1/2)}(k\sigma)\}^{1/2}} , \tag{3.14}$$

in which σ means the diameter of a molecule.

Making use of the definition of Bessel functions we can show, for large value of kr, that

$$v_l^2(kr)\sim\begin{cases}\dfrac{1}{\sqrt{1-(l/kr)^2}}\sin^2\{k(r-\sigma)\sqrt{1-(l/kr)^2}\} , & (l<kr)\\ 0 , \quad (l>kr) . & \end{cases} \tag{3.15}$$

For high temperatures we get finally

$$\begin{aligned}S(r)&=\frac{\sqrt{2}\,\lambda^3}{\pi^2 r^2}\int_0^\infty dk\int_0^{kr}\frac{2l dl}{\sqrt{1-(l/kr)^2}}\sin^2\{k(r-\sigma)\sqrt{1-(l/kr)^2}\}\exp(-\lambda^2k^2/2\pi)\\&=\frac{\sqrt{2}\,\lambda^3}{\pi^2 r^2}\int_0^\infty dk(kr)^2\left\{1-\frac{\sin 2k(r-\sigma)}{2k(r-\sigma)}\right\}\exp(-\lambda^2k^2/2\pi)\\&=1-\exp\{-2\pi(r-\sigma)^2/\lambda^2\} .\end{aligned} \tag{3.16}$$

The second virial coefficient can be calculated easily with the use of (3.16), namely

$$B(T)=\frac{2}{3}\pi N\sigma^3+\frac{\pi}{\sqrt{2}}N\sigma^2\lambda+N\sigma\lambda^2+\frac{1}{4\sqrt{2}}N\lambda^3 , \tag{3.17}$$

which agrees with calculation by other authors except for the last term. Quantum effect appears in our theory, in the deviation of $S(r)$ from unity in the range $\sigma\leq r$. The same argument used in deriving Eq. (3.6) applies to Eq. (3.16). Thus the effective diameter σ_{eff} defined by

$$\sigma_{\text{eff}}=\sigma+\frac{\lambda}{2\sqrt{2}} \tag{3.18}$$

must be substituted for the classical diameter σ. The meaning of the density matrix in quantum theory is illustrated in Appendix IV.

A temporal second appoximation for the surface free energy is given, in quantum mechanics, by replacing σ by σ_{eff} and a by $\sigma/2+\lambda/4$ in Eq. (2.6). That is

$$\gamma=\frac{NkT}{V}\left[\left(\frac{\sigma}{2}+\frac{\lambda}{4}\right)+\left\{\frac{2}{3}\pi\left(\frac{\sigma}{2}+\frac{\lambda}{4}\right)-\frac{\pi}{8}\left(\sigma+\frac{\lambda}{2\sqrt{2}}\right)\right\}\left(\sigma+\frac{\lambda}{2\sqrt{2}}\right)^3\frac{N}{V}\right]. \tag{3.19}$$

§ 4. Concluding Remarks

When statistical effect is introduced, we have to consider exchange of particles. Exchanging $\boldsymbol{x}_1$ and $\boldsymbol{x}_2$ in Eq. (3.13), the same formula is given for even l, and sign changes for odd l. namely

$$S(r)=1-\exp\{-2\pi(r-\sigma)^2/\lambda^2\}\pm\frac{\sqrt{2}\,\lambda^3}{\pi^2 r^2}\sum_l(-)^l\int_0^\infty dk\exp(-\lambda^2k^2/2\pi)v_l^2(kr)\,, \tag{3.20}$$

in which the upper sign corresponds to Bose-Einstein statistics and the lower to Fermi-Dirac statistics. However in the approximation for high temperature, the third term in the right hand side of Eq. (3.20) nearly vanishes. The Slater sum of pair particles is scarcely influenced by the statistical effect in high temperature region.

The evaluation of the surface tension of a dilute gas has a certain relation to the calculation of the third virial coefficient in the sense that the wall can be introduced by making the diameter of the third molecule infinite. Recently A. Pais and G. E. Uhlenbeck[12] have investigated the third virial coefficient in quantum treatment. However, application of this theory to the problem of the surface tension does not seem to be possible.

Acknowledgement

In conclusion the author wishes to express his hearty thanks to Professor M. Toda of Tokyo University of Education for his helpful discussions and encouragement.

Appendix I.

There is intimate similarity between the behaviors of a dilute gas and of a dilute solution. The pressure p of a gas corresponds to the osmotic pressure π of a solution, and the surface tension γ of a gas corresponds to the increase in the surface tension of the solution $\Delta\gamma=\gamma-\gamma_0$, in which γ is the surface tension of the solutions and γ_0 is that of pure solvent.

If we assume that the solute molecules are hard spheres which do not make their appearance the free surface of the solution we can apply the above results to this case and obtain

$$\Delta\gamma=\frac{1}{2}\pi\sigma\,. \tag{A.1}$$

For example, for aqueous solution of saccharose with one molal concentration, $\Delta\gamma=1.2$ dyne/cm and $\pi=27$ atm., thus we obtain from Eq. (A.1) $\sigma\approx9$ Å. This value seems reasonable qualitatively, though the molecule ($C_{12}H_{22}O_{11}$) is not a hard sphere.

Appendix II.

The membranes considered in § 2 are separated by the distance s in Fig. 2. At any instant, there are molecules whose interaction spheres cut the membranes. A and B in Fig. 2 are those areas of one of the membranes cut by the molecules in the right and in the left halves of the vessel respectively. Let S_A and S_B be the total area of these per unit area of the membrane. Then we have

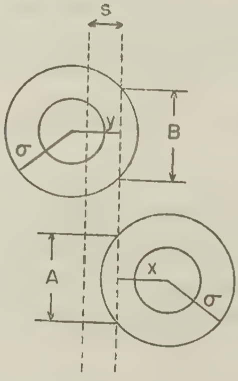

Fig. 2.

$$S_A=\frac{N}{V}\int_0^{\sigma}\pi(\sigma^2-x^2)\,dx=\frac{2\pi}{3}\sigma^3N/V$$

$$S_B=\begin{cases}\dfrac{N}{V}\displaystyle\int_s^{\sigma}\pi(\sigma^2-y^2)\,dy=\left(\dfrac{2\pi}{3}\sigma^3+\dfrac{\pi s^3}{3}-\pi\sigma^2 s\right)\dfrac{N}{V}\,, & (s<\sigma)\\ 0\,, \quad (s>\sigma)\,. \end{cases} \tag{A.2}$$

In the calculation of the impact on the membrane due to a molecule the areas S_A and S_B covered by other molecules are to be excluded. Since the probability density for a molecule is $1/(V-4\pi N\sigma^3/3)$, the pressure on the membrane is

$$p(s)=\frac{NkT}{V-4\pi N\sigma^3/3}(1-S_A-S_B)\cong\frac{NkT}{V}\left\{1+\frac{\pi}{3}(3\sigma^2 s-s^3)\frac{N}{V}\right\}\,,\qquad (s<\sigma) \tag{A.3}$$

$p(s)$ increases with increasing s, and reaches at $s=\sigma$ the actual pressure of the gas given by Eq. (2.11).

Appendix III.

M. P. Freeman and G. D. Halsey, Jr.[13] have investigated the adsorption phenomena of gases to solids. They assumed the hard sphere repulsion and the cube law attraction between each molecule and the surface, and only the hard sphere repulsion between the gas molecules. We shall here treat the gas molecules with attraction. Besides the interaction between molucules $u(r)$, we shall introduce the potential energy between a molecule and the boundary wall $u_w(x)$, which is a function of the shortest distance x from the center of a molecule to the surface of the wall. Both $u(r)$ and $u_w(x)$ may be very large where r and x become smaller compared with molecular dimension, and may have negative values at appropriate values of r and x, and vanish in the limit $r\to\infty$ and $x\to\infty$. Tendency of cohesion and adhesion can be expected from the negative values of $u(r)$ and $u_w(x)$ respectively. It may be allowed to approximate the function $u(r)$ by a square-well potential of the form

$$u(r)=\begin{cases}\infty & \text{for} \quad 0\leq r\leq\sigma\\ -\varepsilon & \text{for} \quad \sigma<r\leq g\sigma\\ 0 & \text{for} \quad g\sigma<r\,,\end{cases} \tag{A.4}$$

where σ denotes the diameter of a molecule, g is a dimensionless constant. It has been shown by T. Kihara[14] that Eq. (A.4), with $g=2$, gives the second virial coefficient in good agreements with experimental results for rare gases.

For $u_w(x)$ we assume the analogous form

$$u_w(x)=\begin{cases}\infty & \text{for} \quad 0\leq x\leq a\\ -\Delta & \text{for} \quad a<x\leq b\\ 0 & \text{for} \quad b<x\end{cases} \tag{A.5}$$

where a means the collision radius between a molecule and the wall and is nearly equal to or slightly larger than the molecular radius $\sigma/2$. $c\equiv b-a$ means the width of the well. For brevity's sake, we introduce dimensionless quantities

$$F\equiv e^{\beta\varepsilon}-1\,,\qquad G\equiv e^{\beta\Delta}-1\,. \tag{A.6}$$

The total potential energy U is written

$$U(\boldsymbol{x}_1,\boldsymbol{x}_2,\cdots,\boldsymbol{x}_N)=\sum_{i>j}^{N}u(|\boldsymbol{x}_i-\boldsymbol{x}_j|)+\sum_{i=1}^{N}u_w(\boldsymbol{x}_i) \tag{A.7}$$

and the formula $\exp(-\beta U)$ can be expanded when the density of the gas is dilute. After some calculations, the free energy F is given by

$$\lambda^{3N}N!\exp(-\beta F)=(V-aA+cGA)^N + \frac{N(N-1)}{2}(V-aA+cGA)^{N-2}\left\{(V-aA)\frac{4}{3}\pi\sigma^3[-1+(g^3-1)F]+IA\right\}, \quad \text{(A.8)}$$

in which

$$I=FG^2\pi\left(g^2\sigma^2c^2-\frac{4}{3}\sigma^3c+\frac{1}{2}\sigma^4-\frac{1}{6}c^4\right)+G^2\pi\left(\frac{1}{2}\sigma^4-\frac{4}{3}\sigma^3c\right) +FG\pi\left(\frac{4}{3}g^3\sigma^3c+g^2\sigma^2c^2-\frac{8}{3}\sigma^3c+\frac{1}{2}\sigma^4-\frac{1}{6}c^4\right) +G\pi\left(\frac{1}{2}\sigma^4-\frac{8}{3}\sigma^3c\right)+F\pi\left(-\frac{1}{4}g^4\sigma^4+\frac{1}{4}\sigma^4\right)+\pi\frac{1}{4}\sigma^4. \quad \text{(A.9)}$$

The pressure p becomes

$$\frac{p}{kT}=-\frac{1}{kT}\left(\frac{\partial F}{\partial V}\right)_T=\frac{N}{V}-\frac{N^2}{V^2}\frac{2}{3}\pi\sigma^3[-1+(g^3-1)F]. \quad \text{(A.10)}$$

The second term in the right-hand side of Eq. (A. 10) is identical with the second virial coefficient in the limit of infinite volume.

The surface tension γ is derived as follows

$$\frac{\gamma}{kT}=\frac{N}{V}(a-cG)-\frac{N^2}{V^2}\left\{\frac{2}{3}\pi\sigma^3[-1+(g^3-1)F](a-2cG)+\frac{1}{2}I\right\}, \quad \text{(A.11)}$$

where I was defined in Eq. (A.9). When the hard sphere model is adopted, Eq. (A.11) reduces to Eq. (2.6).

The surface energy U_A, which is defined as the derivative of the energy with respect of the surface area, becomes

$$U_A=-\frac{N}{V}cG'-\frac{N^2}{V^2}\left\{\frac{2}{3}\pi\sigma^3[-a(g^3-1)F'-2(-1+(g^3-1)F)cG']+\frac{1}{2}I'\right\}, \quad \text{(A.12)}$$

where prime denotes the derivative with respect to β, namely

$$I'=\frac{\partial}{\partial\beta}I, \qquad F'=\frac{\partial F}{\partial\beta}=\mathcal{E}e^{\beta\varepsilon} \qquad \text{and} \qquad G'=\frac{\partial G}{\partial\beta}=\varDelta e^{\beta\Delta}.$$

Appendix IV.

The diagonal element of the density matrix can be written, in terms of the path-integral, as

$$\rho^{(N)}(\boldsymbol{x}_1,\cdots,\boldsymbol{x}_N;\ \boldsymbol{x}_1,\cdots\boldsymbol{x}_N) =\int\exp\left[-\int_0^\beta\left\{\frac{2\pi^2m}{h^2}\left|\frac{d\boldsymbol{x}(u)}{du}\right|^2+U[\boldsymbol{x}(u)]\right\}du\right]\mathscr{D}\boldsymbol{x}(u), \quad \text{(A.13)}$$

where the paths are such that

$$\boldsymbol{x}_1(0)=\boldsymbol{x}_1(\beta)=\boldsymbol{x}_1,\ \boldsymbol{x}_2(0)=\boldsymbol{x}_2(\beta)=\boldsymbol{x}_2,\cdots,\ \boldsymbol{x}_N(0)=\boldsymbol{x}_N(\beta)=\boldsymbol{x}_N.$$

For small β (high temperatures) the paths which contribute to the integral are nearly straight. In this case, we get the classical expression. For large β (low temperatures) the paths may wiggle and the molecules may collide even if they are separated in the initial or final state. This is the quantum effect that the effective diameter of molecules increases with decreas ing temperature.

References

1) M. J. Klein and R. S. Smith: Phys. Rev. **81** (1951) 378.
2) E. C. Crittendon and R. W. Hoffman: Rev.

Mod. Phys. **25** (1953) 310; Phys. Rad. **17** (1956) 270.
3) Y. Sayama: Proc. Phys.-Math. Soc. Japan **23** (1941) 869. Y. Fujiki and R. Suganuma: J. Phys. Soc. Japan **8** (1953) 427. M. Takagi: J. Phys. Soc. Japan **9** (1954) 359.
4) R. Nossek: Z. Physik **142** (1955) 321.
5) H. P. R. Frederikse: Physica **15** (1948) 860.
6) R. H. Fowler: Proc. Roy. Soc. **A, 159** (1937) 229. J. G. Kirkwood and F. P. Buff: J. Chem. Phys. **17** (1949) 338.
7) A. Harasima and Y. Simura: J. Phys. Soc. Japan **11** (1956) 14.
8) M. Toda: J. Phys. Soc. Japan **10** (1955) 512.
9) W. A. Steele and G. D. Halsey, Jr.: J. Chem. Phys. **22** (1954) 979; J. Phys. Chem. **59** (1955) 57.
10) T. Yokota: J. Phys. Soc. Japan **15** (1960) 779.
11) G. E. Uhlenbeck and E. Bethe: Physica **III** (1936) 729; ibid. **IV** (1937) 915. R. Abe: Progr. Theor. Phys. **19** (1958) 699.
12) A. Pais and G. E. Uhlenbeck: Phys. Rev. **116** (1959) 250.
13) M. P. Freeman and G. D. Halsey, Jr.: J. Phys. Chem. **59** (1955) 181.
14) T. Kihara: Rev. Mod. Phys. **25** (1953) 831.

JOURNAL OF THE PHYSICAL SOCIETY OF JAPAN, Vol. 15, No. 12, DECEMBER, 1960

Ferrimagnetic Reasonance in Europium-Iron Garnet

Tomonao MIYADAI

Electrical Communication Laboratory Nippon Telegraph and Telephone Public Corporation Tokyo Japan

(Received June 13, 1960)

Ferrimagnetic reasonance experiment in a single crystal and polycrystalline samples has been carried out by a usual microwave technique. It has been found, for the single crystal, that the temperature variations of the g-factor and the line width are similar to those of erbium-iron garnet (ErIG) except for the existence of a broad maximum in line width at about 200°K. These behaviors agree well with Kittel's theory proposed recently. At room temperature, $g_{\rm eff}=1.32$, $\Delta H=600$ œ (anisotropy in line width having been hardly observed) and $K_1/M_s=-400$ œ (which is an order of magnitude larger than that of YIG). For polycrystalline samples, $g_{\rm eff}$ is essentially the same as for the single crystal sample. In the absorption curve, a secondary peak appears, below 200°K, in the lower magnetic field side of the main absorption peak. Electronic state of Eu^{3+} in the garnet crystal is briefly discussed.

§1. Introduction

Yttrium-iron garnet (YIG)[1),2)] and lutethium-iron garnet (LuIG)[3)] show a very narrow ferrimagnetic resonance line width, while all the other garnets reported so far[4)] show very broad one. Furthermore, both line widths and g-factors differ considerably among them. It is, therefore, obvious that rare earth ions in the garnet considerably affect the behavior of ferrimagnetic resonance. This is contrasted to the role of rare earth ions in optical properties[5)] to which they make little contribution. Now we are interested in the role of rare earth ions in ferrimagnetic resonance in rare earth-iron garnets.

Recently, Kittel et al.[6),7)] proposed a theory of ferrimagnetic resonance in rare earth-iron garnets. The temperature dependences of line widths and g-factors for erbium-iron garnet (ErIG) and holumium-iron garnet (HoIG)[4)] are explained very well by the theory. For samarium-iron garnet (SmIG) and ytterbium-iron garnet (YbIG), however, it appears that the theory should be modified to some extent.[4)] For gadolinium-iron garnet (GdIG)[4)], Tsuya-Wangsness' model[8),9)] is found to hold.[4),10)] For the other grants, there are little data.

We have, here, chosen europium-iron garnet (EuIG), Eu$_3$Fe$_5$O$_{12}$. One of the reasons for the choice is that no data have been reported so far and another reason is as follows: the multiplet terms of Eu^{3+} in free ion state are so closely located near the lowest state (the ground state has $J=0$, $^7F_0$) that magnetic properties of Eu^{3+} in crystals cannot be explained without taking into account the mixing of excited states having $J\neq 0$.[11] For example, Eu^{3+} in garnet crystal (EuIG) has a magnetic moment of about 0.8 μ_B per ion,[12] even at 4.2°K. Accordingly it may be expected that these special situations for Eu^{3+} affect the character of ferrimagnetic resonance in EuIG. In this paper, it is shown that the behavior of ferrimagnetic resonance in EuIG can be explained very well by kittel's theory and that the ground state for Eu^{3+} in EuIG may be mixed with higher states having $J\neq 0$ in some way.

§ 2. Samples and Experimental Procedures

The single crystal sample was prepared by flux method.[13] The starting proportion of the oxides, Eu_2O_3 (99.9%)*), Fe_2O_3 and PbO was somewhat different from that**) proposed by Nielsen[13]; a little less in contents of Eu_2O_3 and PbO than that of Nielsen. It was found that our proportion was preferable in order to get large single crystals under the conditions used here. Our treatment was as follows: the mixed powder was maintained to melt for 5 hours and then cooled very slowly down to about 900°C at various rates of 1 to 5°C/hr according to temperature ranges and finally drawn out of the furnance into air. The temperature control system[14] used in the heat treatments had a detecting unit which was operated by magnetic modulation system and could detect the difference between the temperature inside the furnance and a reference one given by a precision potentiometer. The polycrystalline sample was prepared by coprecipitation method[15]; the mixed powder obtained was prefired at 1000°C for about 2 hours and then sintered at 1330°C for 5.3 hours, both in air. The apparent density of the sample was equal to 5.36, corresponding to relative density of 90%, and the Curie temperature measured by a magnetic balance[16] was equal to 292°C, which agreed with the value obtained by Pauthenet.[12] The shape of the single crystal- and polycrystalline samples used for resonance absorption measurement were sphers of 0.59 mm and 0.54 mm in diameters, respectively. For polycrystalline samples, several spheres with different diameters were also measured at room temperature. Since no difference between them was observed for g-factor and line width within the experimental errors, a sphere of 0.54 mm in diameter alone was used for measurement at various temperatures.

The resonance absorption measurement were made in the temperature range between liquid nitrogen and Curie point at 18320 Mc/sec, the power of which was obtained by frequency doubling of microwave power of 9160 Mc/sec from a 2K25 klystron. The experimental procedures were a usual microwave technique. A frequency-modulation method was used***) (its modulation amplitude being so as to cover the Q-curve for the cavity), and the static magnetic field was slowly sweeped manually through the resonance field and the absorption curve was recorded automatically on an X-Y recorder.

§ 3. Experimental Results

Single crystal sample At room temperature, the measurement was made by rotating the sample around a ⟨110⟩ direction at every 10 degrees. At other temperatures, it was made for three principal axes; with magnetic fields parallel to ⟨100⟩, ⟨110⟩ and ⟨111⟩ directions. At low temperatures, no absorption could be observed for ⟨100⟩ direction, because the resonant field required at those temperatures is beyond the available field (~16000 œ). The g-factor and the first order cubic anisotropy field K_1/M_s at room temperature was obtained from the relation[18] for a (110) plane in which the saturation magnetization M_s lies;

$$\left.\begin{aligned}\omega^2=\gamma^2&\left\{H_0+(2-\sin^2\theta-3\sin^2 2\theta)\frac{K_1}{M_s}\right\}\\&\times\left\{H_0+2\left(1-2\sin^2\theta-\frac{3}{8}\sin^2 2\theta\right)\frac{K_1}{M_s}\right\}\\\gamma&=g_{\mathrm{eff}}\frac{e}{2mc}\end{aligned}\right\} \qquad (1)$$

---

*) Product of Davison Chem. Co., USA. It contains $Sm_2O_3+Gd_2O_3$ of 0.1% as impurities according to chemical analysis by the company.

**) $Y_2O_3:Fe_2O_3:PbO=3.5:44:52.5$ (mol %).

***) The details of the equipment are described elsewhere[17].

where H_0 stands for the resonant field, θ for the angle between M_s (or H_0) and a ⟨100⟩ direction which lies in the (110) plane. The observed resonant fields are plotted as a function of θ in Fig. 1 in which is also shown the curve calculated from Eq. (1) with $g=1.32$ and $K_1/M_s=-410$ œ.

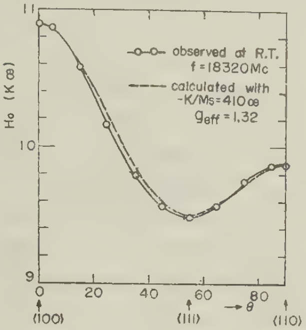

Fig. 1. Reasonant fields *vs* θ in a (110) plane at room temperature. θ is the angle between M_s and <100>.
Dashed curve represents the calculated one by Eq. (1).

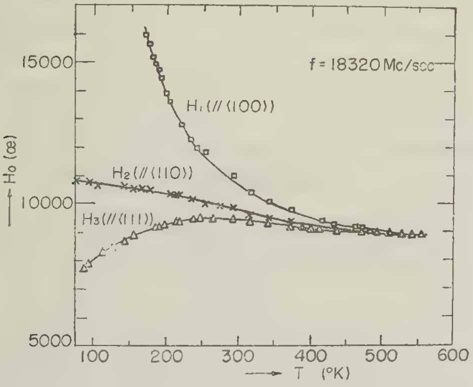

Fig. 2. Temperature variations of resonant fields for three principal axes.

The resonant fields for three principle axes ⟨100⟩, ⟨110⟩ and ⟨111⟩ are plotted as a function of temperature in Fig. 2. The g-faotcr and cubic anisotropy fields K_1/N_s and K_2/M_s are calculated from the relations[19]:

$$\left.\begin{aligned}&\omega^2=\gamma^2(H_1+2K_1/M_s)^2\ ,\\&\omega^2=\gamma^2(H_2-2K_1/M_s)(H_2+K_1/M_s+K_2/2M_s)\ ,\\&\omega^2=\gamma^2(H_3-4K_1/3M_s-4K_2/9M_s)^2\ ,\end{aligned}\right\}\tag{2}$$

where H_1, H_2 and H_3 refer to resonant fields parallel to ⟨100⟩, ⟨110⟩ and ⟨111⟩, respectively. In the calculation, the values for H_1, H_2 and H_3 were read on the smoothed out curves in Fig. 2. The errors of K_1/M_s and K_2/M_s were 100 and several hundreds, oersteds, respectively.

K_2/M_s vanishes at room temperature, but it becomes comparable with K_1/M_s at about 200°K, although it involves rather large uncertainty, namely the observed value is comparable with that of experimental error. Values of K_2/M_s at low temperatures are tabulated in Table I.

Table I.

T (K°)	K_1/M_s (œ)	K_2/M_s (œ)	g_{eff}
230	− 870	0	1.24
210	−1180	+ 300	1.22
190	−1670	+ 500	1.20
170	−2170	+1000	1.15

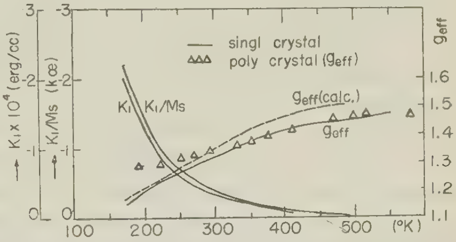

Fig. 3. K_1/M_s, K_1 and g_{eff} for single crystal sample are shown as functions of temperature. Dashed curve represents the calculated one by Eq. (3). g_{eff} for polycrystalline sample is also plotted.

There are temperature dependences of g-factor as well as K_1/M_s. They are shown in Fig. 3. Similar temperature dependences of g-factor were also found in other garnets.[4]

$-K_1/M_s$ seems to increase rapidly with decreasing temperature in the temperature range where K_2/M_s is also appreciable. K_1/M_s is equal to about −400 œ at room temperature. Such a value is an order of magnitude larger than that of YIG. K_1/M_s reaches about −2000 œ at 180°K. In Fig. 3 is also shown the anisotropy constant K_1 calculated by using Pauthenet's data[12] for saturation magnetization. The full line width varies with temperature as shown in Fig. 4.

Anisotropy in line width was hardly detected within the experimental errors (~10%), although the line width for ⟨100⟩ $(H_{\langle 100\rangle})$ seemed to be the narrowest. A broad maximum occurs near 200°K; such a peak has not been observed so far in other garnets except for YIG containing terbium (Tb) as an impurity.[20] Such a behavior that the line width decreases with increasing temperature and increases rapidly just below Curie temperature, is common to other garnets.[21]

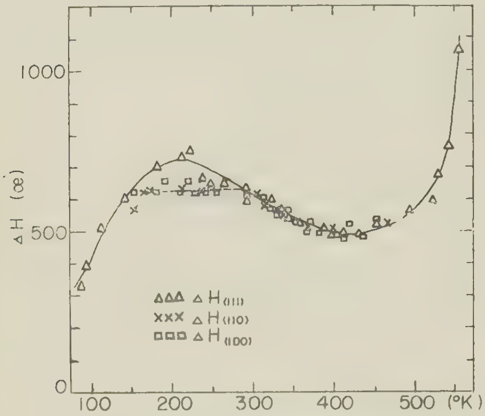

Fig. 4. Line width for single crystal *vs* temperature. There is little anisotropy in line width except near 200°K.

Polycrystalline sample The *g*-factor and line width were measured under the same conditions as above. The *g*-factor of polycrystalline sample has almost the same values as that of single crystal above room temperature, whereas below room temperature the former has values slightly larger than the latter and are less temperature-dependent (Fig. 3). The line width at room temperature is about 1200 œ, which is about two times larger than that for single crystal. Below about 200°K, a secondary peak appears on the lower magnetic field side of the main peak, and it becomes more intense and shifts further away from the main peak as the temperature decreases.[22] It is interesting that the temperature at which the secondary peak appears, coincides with that at which the maximum in line width for single crystal occurs. The line width involving the secondary peak increases rapidly at low temperature and reaches 5000 œ at 80°K.

§ 4. Discussion

g-factor Recently Kittel et al[6),7)] proposed a theory of ferromagnetic resonance in rare earth garnets. The theory assumes that a) rare earth garnet can be treated as a ferrimagnetics with two sublattices (one consisting of Fe^{3+} on 16–a sites and Fe^{3+} on 24–d sites, the other consisting of M^{3+} on 24–c sites); b) rare earth ions (except for ions having $L=0$ or $J=0$) are highly damped, while ferric ions are not damped except through ferric-rare earth exchange coupling. On these assumptions, the theory predicts that the effective *g*-factor g_{eff} of the granet is given by

$$g_{\text{eff}}=g(Y)\frac{M_s(M)}{M_s(Y)} \qquad (3)$$

where M_s denotes saturation magnetization, M refers to MIG and Y to YIG. Eq. (3) holds in the intermediate temperature region i.e. below Curie point down to such a temperature that relaxation frequency τ^{-1} of rare earth ions becomes comparable to ferric-rare earth exchange frequency ω_{AB}. At lower temperatures, where $\tau^{-1}<\omega_{AB}$,

$$g_{\text{eff}}=M_s(\mathrm{M})/\{M_s(\mathrm{Y})/g(\mathrm{Y})+M_s(\mathrm{M}^{3+})/g(\mathrm{M}^{3+})\} \qquad (4)$$

in which M^{3+} refers to rare earth sublattice. Eq. (4) is identical with Tsuya-Wangsness formula[8),9)] for a two-sublattice ferrimagnet.

The calculated curve by Eq. (3) is shown in Fig. 3. In the calculation, *g*(Y) was assumed to be equal to 2.0 independent of temperature. For M_s(Eu) and M_s(Y), the data of Pauthenet[12)] were adopted. If Eu^{3+} is in a state having $J=0$, as Kittel noted, it could not work on the movement of Fe^{3+} as a damper since it does not interact with lattice. In such a case, the Kittel's theory will not apply. The calculated g_{eff} of EuIG is actually in good agreement with the observed one. This is an indication that Eu^{3+} does interact with lattice, in other words, that it is in a state of which J does not completely vanish.

The *g*-factor for the polycrystal is, below room temperature, slightly larger and less temperature dependent than that for the single crystal. This can be explained according to Schlömann[23)] who calculated ferromagnetic resonance condition in polycrystalline ferrites. He showed that there exists in a polycrystalline sample having cubic anisotropy, an additive internal field H_i, which is given by

$$H_i=\frac{|K_1|}{M_s}+1.5(4\pi M_s)\frac{\Delta v}{V} \qquad (5)$$

where $\Delta v/V$ is the ratio of the total pore-volume to the sample volume. As the reults, $g_{\rm eff}$ for polycrystal can show an apparent temperature dependence and have a larger value than true $g_{\rm eff}$. Since both $|K_1|/M_s$ and M_s are decreasing functions of temperature $g_{\rm eff}$ for polycrystalline sample would decrease with increasing temperature or would suppress tendency of increase. For example, at about 200°K, $H_i \approx 1000$ œ. This is about 10% of the resonant field (~ 10000 œ) and a reasonable value in order to explain the g-value for polycrystal which is about 10% larger than for single crystal.

Line width The theory of Kittel et al[7)] predicts that the line width varies schematically with temperature as shown in Fig. 5.

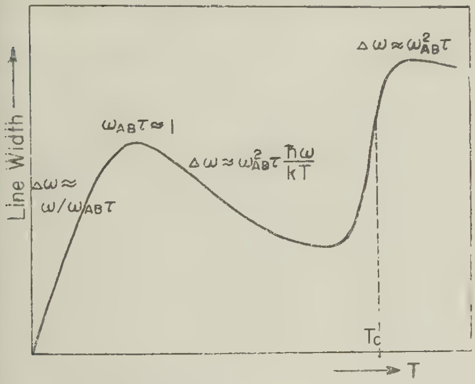

Fig. 5. Schematic temperature dependence of line width by Kittel's theory.

For the sincle crystal, the temperature dependence of line width has just the same form as Fig. 5. A secondary peak, which appears in the polycrystalline sample at low temperatures, may be explained by Schlöman's mechanism.[24)] According to it, in polycrystalline samples having cubic anisotropy and $M_s \ll H_a$ ($H_a = 2|K_1|/M_s$), a secondary peak appears in the lower magnetic field side of the main resonance peak when k ($\equiv H_a/\omega$)>0.5 is satisfied. In our case in which the condition $M_s \ll H_a$ is well satisfied below room temperature,[12)] since a secondary peak appears at about 200°K, k is thought to have reached about 0.5 at the temperature. In other words $|K_1|/M_s$ is to be equal to ≈ 2500 œ at 200°K. But the measured value is only 1500 œ. It is possible that this discrepancy is due to the fact that K_2/M_s becomes significant there.

Anisotropy The first order cubic anisotropy constant K_1 or anisotropy field K_1/M_s for EuIG is about an order of magnitude larger than that for YIG.[1)] If Eu^{3+} were in a state with $J=0$ in the garnet crystal, the anisotropy for EuIG would be comparable with that for YIG.

Electronic state for Eu^{3+} in the garnet crystal As described in preceding paragraphs, we are led to conclude that Eu^{3+} in EuIG is in a state mixed with higher states having $J \neq 0$ in some way, say, with the aid of crystal fields and polarization effect pointed out by van Vleck and Frank,[25)] because of the following reasons; a) g-factor for Eu^{3+} does not contribute to the effective g-factor for EuIG as the result of having been damped out of rare earth spins; b) above 200°K, line width decreases montonically with increasing temperature up to below Curie point (this may be interpreted as motional narrowing by high relaxation frequency τ^{-1} of rare earth spins); c) Eu^{3+} makes a large contribution to anisotropy for EuIG; d) Eu^{3+} has a magnetic moment of 0.8 μ_B per ion in EuIG.[12)]

Above conclusion and our experimental results are somewhat contradictory with the experiment of Dillon et al[20)] in which there has not been observed, below room temperature, any maximum in line width for YIG single crystal containing Eu-impurity of 1%. According to our results and Kittel's theory which predicts linear dependence of line width upon impurity concentration, the sample of Dillon et al would have a maximum in line width of about 7 œ near 200°K since the temperature, at which a maximum occurs, does not depend on resonance frequency.

§ 5. Conclusion

The temperature dependence of $g_{\rm eff}$ for EuIG is in good quantitative agreement with the prediction of Kittel's theory[6),7)] and the temperature dependence of line width shows a qualitative agreement with it. From this fact and others, it is concluded that the state for Eu^{3+} in the garnet crystal is considered to be mixed with higher states having $J \neq 0$. The difference between the g-factor of single- and polycrystals, and also the occurance of a secondary peak in the polycrystal can be explained by Schlömann's mechanism.[23),24)]

Acknowledgement

The author wishes to express his sincere appreciation to Dr. N. Tsuya of Tohoku

University and Mr. Y. Shichijo, Chief of the magnetic materials research section of our laboratory for their general guidance and continued encouragement. He is much indebted to Mr. H. Takata of our laboratory for his very able assistance. It is also a pleasure to acknowledge the assistance of Mr. T. Ito in measurements.

Note added in proof:

As for the electronic state of Eu^{3+}, there exists a possibility that local uniaxial crystalline fields at each 24–C site cause level mixing of $J=0$ state (ground state for free Eu^{3+}) and $J\neq0$ states.

References

1) J. F. Dillon, Jr.: Phys. Rev. **105** (1957) 759.
2) E. G. Spencer, R. C. LeCraw and A. M. Clogston: Phys. Rev. Letters **3** (1959) 32.
3) J. I. Masters and R. W. Roberts, Jr.: J. Appl. Phys. **30** Suppl. (1959) 179S.
4) G. P. Rodrigue, H. Meyer and R. V. Jones: to be published in J. Appl. Phys.
5) A. M. Clogston: J. phys. radium **20** (1959) 151.
6) C. Kittel: Phys. Rev. **115** (1959) 1587.
7) P. G. de Gennes, C. Kittel and A. M. Portis: Phys. Rev. **116** (1959) 323.
8) N. Tsuya: Progr. Theor. Phys. **7** (1952) 263.
9) R. K. Wangsness: Phys. Rev. **91** (1953) 1085.
10) B. A. Calhoun, W. V. Smith and J. Overmeyer: J. Appl. Phys. **29** (1958) 427.
11) J. H. Van Vleck: *The Theory of Electric and Magnetic Susceptibilities* (Clarendon Press, Oxford, 1932)
12) R. Pauthenet: Ann. physique **3** (1958) 424.
13) J. W. Nielsen and E. F. Dearborn: J. Phys. Chem. Solids **5** (1958) 202.
14) A. Terajima: to be published in Sci. Rep. Tohoku Univ.
15) W. P. Wolf and G. P. Rodrigue: J. Appl. Phys. **29** (1958) 105.
16) T. Hirone, S. Maeda and N. Tsuya: Rev. Sci. Instr. **25** (1954) 344.
17) Y. Shichijo and T. Miyadai: Rev. Electr. Comm. Labor. **8** (1960) 12.
18) L. R. Bickford, Jr.: Phys. Rev. **78** (195 449.
19) J. F. Dillon, Jr., S. Geschwind and V. Jaccarino: Phys. Rev. **100** (1955) 750.
20) J. F. Dillon, Jr. and J. W. Nielsen: Phys. Rev. Letters **3** (1959) 30.
21) G. P. Rodrigue, J. E. Pippen, W. P. Wolf and C. L. Hogan: IRE Trans. MTT **6** (1958) 83.
22) Y. Shichijo, T. Miyadai and H. Takata: J. Phys. Soc. Japan **15** (1960) 530.
23) E. Schlömann: *Conference on Magnetism and Magnetic Materials,* AIEE, 600 Oct. 1956, Boston.
24) E. Schlömann: J. phys. radium **20** (1959) 327.
25) J. H. Van Vleck and A. Frank: Phys. Rev. **34** (1929) 1494, 1625.

Journal of the Physical Society of Japan, Vol. 15, No. 12, December, 1960

Thermal Conduction in Ferroelectric Ceramics

By Ikushi Yoshida

The Institute for Solid State Physics, University of Tokyo,
and Tokyo Institute of Technology, Tokyo

(Received June 28, 1960)

Apparatuses were constructed and measurements were made on the thermal conductivity of insulating crystals over the temperature ranges from −200°C to 600°C. For the lower temperature range, the absolute measurement was used, while for the higher one, the comparative method was adopted. The thermal conductivities of ferroelectric $PbTiO_3$ and anti-ferroelectric $PbZrO_3$ showed a rather large step-wise increase, in contrast to the case of $BaTiO_3$, as they passed into the paraelectric state. Discussions are given of the relation between the magnitude of thermal conductivity and the crystal structure. It is pointed out that the anharmonic potential for the smaller ions should be responsible for the scattering of phonons in these substances.

1. Introduction

Phase transitions of crystals are in general accompanied by anomalies in many physical properties. In dielectric substances, anomalies are often found in the specific heat, the coefficient of thermal expansion (change of volume), the dielectric constant and other quantities, and they supply us with a useful clue to discovering and confirming a new transition, and in further investigations of it. On the other hand, the main carriers of heat are thought to be the lattice waves in dielectric substances, and so it is expected that the thermal conductivity of them would show some peculiar features when phase changes take place.

Eucken and Schöder found no appreciable change of thermal conductivity of solid hydrogen bromide on passing through the two transitions at 117°K and 113°K, but found a steep increase with decreasing temperature for the transition at 89°K.[1] This increase began somewhat above 89°K and continued down to 78°K. They attributed the heat conduction to the waves of the torsional motion of individual HBr molecules and explained the sudden decrease of thermal conductivity as due to the onset of random molecular orientation. Gerritsen and van der Star found a peak of thermal conductivity of solid methane around the phase transition at 20°K[2] and explained it by a simple formula based on a consideration of rotations of CH_4 groups. According to them, CH_4 molecules are rotating above the transition and their rotational kinetic energy is propagated by resonance, resulting in a peak of thermal conductivity which corresponds to that of specific heat and is proportional to the latter. According to v. Simson, the thermal conductivity of ammonium chloride shows a steep increase with decreasing temperature around the transition at −30°C[3], but no positive explanation is given.

Crystallographically, ferroelectrics belong to the crystal classes having pyroelectricity but are characterized by the fact that their polar structures are caused by a slight distorsion of nonpolar ones. It is well expected that such a distorsion of ion arrangement would affect the behaviour of the vibration of ions, and hence the mutual couplings of phonons. The phase change from polar to non-polar states, or *vice versa*, may, therefore, cause some anomaly in the thermal conductivity.

It was reported that the thermal conductivity of barium titanate ceramic actually shows a small anomaly around the transition at 120°C[4], where the phase change from the ferroelectric to paraelectric state takes place. The anomaly is, however, fairly small and it was difficult to make a sufficient discussion.

We have now measured the thermal conductivity of lead titanate ceramic with a hope that its large tetragonality ratio c/a compared with of barium titanate might result in a larger anomaly in the thermal conductivity, supplying us with a clearer knowledge on a relation between phase transition and thermal conductivity.

A mersurment has also been made on the antiferroelectric lead zirconate for the purpose of comparing the effect of antiferroelectric lattice deformation on the thermal conductivity with that of ferroelectric one. Temperature ranges of the measurement have been extended to lower side for both barium titanate and strontium titanate ceramics.

§ 2. Apparatus and Measurement

Absolute measurement was used for the measurement of thermal conductivity at temperatures lower than room temperature. However, heat leak due to radiation, which is almost inevitable in calorimetric measurements, rapidly increases with temperature, so that we were obliged to give up the plan of measuring the thermal conductivity of a substance from liquid nitrogen temperature up to about 600°C using the same apparatus. At temperatures higher than room temperature, we therefore decided to resort to the comparative method. Details of apparatuses for these two methods will be described in the following.

2. 1. *Low-Temperature Apparatus*

In Fig. 1 is shown the main part of the apparatus. A heater H_1 attached to one end of the specimen S with a cross-sectional area A supplies heat of constant rate Q. It consists of a zigzag strip of silver metal formed on the basal face of the ceramic specimens by air-drying silver paste and has a resistance of several ohms. This structure was adopted in order to reduce the heat leak from the surface and to eliminate excess heat capacity which would lower the accuracy of measurement. T_1 and T_2 are Cu-constantan thermocouples with 0.1 mm diameter, and were used to measure the temperature difference ΔT between the two points separated l longitudinally in the specimen. T_3 was used to measure the temperature difference between the specimen and the radiation shield which was necessary to evaluate the side-wise heat leak.

C is a radiation shield of stainless steel and is provided with a copper basal cap D and a heater H_2. E serves as a sink of the heat flow through the specimen and has a heater H_3. Using H_2 and H_3, it is in principle possible to make measurements at temperatures higher than the coolant, but difficulty arises in maintaining the whole of the inner part of the apparatus at a temperature higher than the outer vessel for a long time without any appreciable fluctuation, and necessarily lowers the accuracy of measurement, so that our measurements were restricted to discrete temperatures determined by the temperature of the coolant, with the exceptions of a few cases.

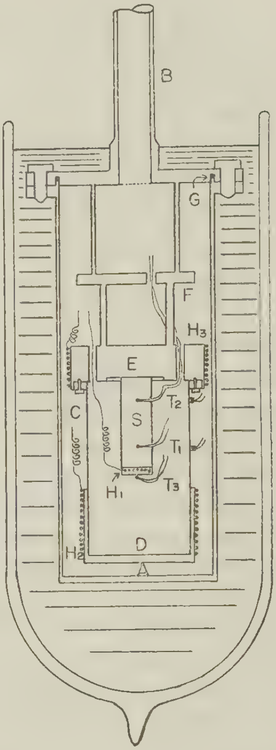

Fig. 1. Main part of the low-temperature apparatus.

The heat sink is connected to the thermal damper F and the latter to the outer vessel A. G is a lead gasket. All leads of heaters and thermocouples go through the stainless steel pipe B, which is long enough to decrease the consumption of the coolant due to heat conduction, and come out of the vessel through vacuum seals. The degree of vacuum was better than 10^{-4} mm Hg. Under the vacuum of this degree the heat leak due to convection was practically negligible, but when the vacuum was only of the order of $1\sim0.1$ mm Hg. at room temperature the leak was from a few to ten percent of Q.

Liquid nitrogen, dry ice with alcohol or ice flakes with or without salt was used as coolant.

Thermal conductivity of the specimen κ is obtained by the formula

$$\kappa = Q \frac{l}{A \cdot \Delta T}. \qquad (1)$$

The validity of this formula rests on the assumption that there is no heat leak from the surface of the heater by radiation or any other mechanism. If this heat leak is Q_{loss}, (1) must be modified to

$$\kappa = (Q - Q_{loss}) \frac{l}{A \cdot \Delta T}, \qquad (2)$$

Q_{loss} due to convection or conduction through heater leads and thermocouples was found to be negligible compared to Q, but that due to radiation, which strongly depends on the temperature and increases as the cube of absolute temperature, becomes appreciable at higher temperatures. At room temperature Q_{loss} due to radiation was about 20% of Q or so, and we adopted the corrected formula (2) for the determination of κ. The following two reasons seem to secure the plausibility of the correction;

(i) κ's obtained by correcting for Q_{rad}'s for different Q's are in good accordance.

(ii) κ's so corrected agree with those obtained by the comparative method.

2. 2. *High-Temperature Apparatus*

At high temperatures the radiation loss becomes exceedingly large, and so the comparative method had to be adopted. In Fig. 2, A and B are two rods with known thermal conductivities and S is a disc specimen. In the stationary state, the following equation holds provided that there is no side-wise heat leak:

$$\kappa_A \left(\frac{dT}{dx}\right)_A = \kappa_S \left(\frac{dT}{dx}\right)_S = \kappa_B \left(\frac{dT}{dx}\right)_B. \qquad (3)$$

By measuring the temperature gradients in A, S and B one can obtain the thermal conductivity of the specimen κ_S.

Difficulty in boring holes into the specimen to insert thermocouples made us adopt a method in which the temperature gradient in the specimen was not directly measured, but calculated from the difference between the temperatures at both sides of the specimen obtained by extrapolation. Temperature drops at the surfaces of specimen in contact with the reference substances were eliminated by pasting the surfaces of contact with air-drying silver paste and by giving a large mechanical pressure.

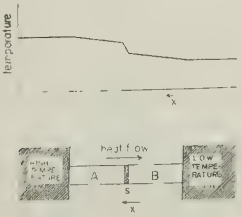

Fig. 2. Principle of the comparative method.

The main part of the apparatus is shown in Fig. 3. The specimen S is placed between two rods A and B, both of which are made of pure iron. Two pairs of reference rods were prepared, the diameters of which were 2 cm (rod 1) and 3 cm (rod 2), respectively. Thermal conductivity for these reference substances were taken from the "*American Institute of Physics Hand-book, 2nd ed.* (1957)".

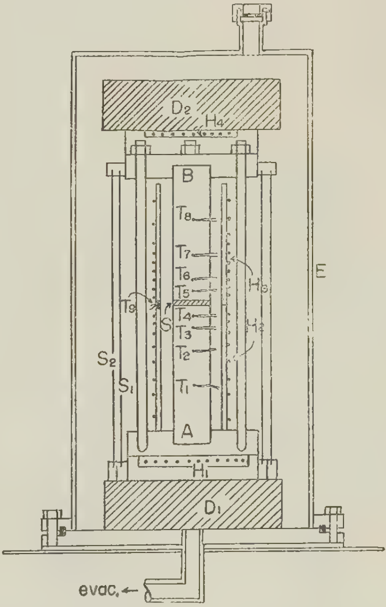

Fig. 3. Main part of the high-temperature apparatus.

The temperature gradients established in the rods A and B, generated by two main heaters H_1 and H_4, were measured by eight alumel-chromel thermocouples $T_1 \sim T_8$ with 0.3 mm diameter. T_9 is a subsidiary thermocouple to measure the temperature of side heaters which also serve as thermal shields. Two subsidiary heaters H_2 and H_3 serve to give a suitable temperature distribution to the thermal shields lest the side-wise heat leak from the rods and specimen should cause a non-linear temperature distribution. S_1 and S_2 are copper radiation shields, and D_1 and D_2

are insulating bricks. E is a vacuum vessel which was evacuated by a rotary pump.

An example of the temperature distribution along the rods and the specimen is shown in Fig. 4. The thermal conductivity of rutile was measured as a calibration of the apparatus, and the result is shown in Fig. 5 along with that due to Kingery et al[5]., the correction for the porosity being made for both of them. Agreement is quite satisfactory.

§ 3. Preparation of Specimens.

For the preparation of lead titanate ceramic, powdered raw materials of PbO and TiO_2 were mixed together with water, pressed into a disc and fired in a Siliconit furnace. The product was crashed, well pulverized and meshed, then pressed into the desired form and sintered. Other specimens were prepared by a similar procedure. Sizes and conditions of fabrication are listed in Table I.

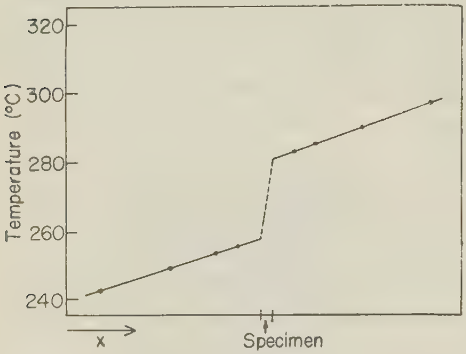

Fig. 4. An example of the temperature distribution along the rods and the specimen ($PbTiO_3$ ceramic).

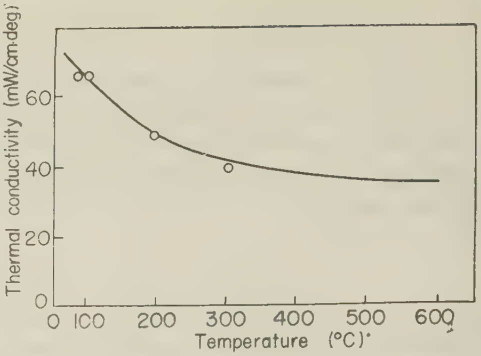

Fig. 5. Thermal conductivity of rutile.
circles: our measurement.
real line: Kingery et al.[5]

§ 4. Results of Measurements

4. 1. *Lead Titanate*

Main efforts were concentrated on the investigation of the behaviour of thermal con-

Table I. Sizes and characteristics of specimens.

	$PbTiO_3$	$PbZrO_3$	$BaTiO_3$		$SrTiO_3$	
			No. 1	No. 2	No. 1	No. 2
2r (cm)	2.235	2.12	3.195	2.06	2.80	2.18
d (cm)	0.395	0.3274	0.837		0.678	
l (cm)				1.45		2.47
ρ (g/cm^3)	6.86	6.05	5.35	5.03	4.35	4.01
P (%)	14.6	25.5	10.6	16.0	12.8	19.5
grade	C S	S C	S S	S C	S S	S S
pressure (tons/cm^2)	0.53	0.53	2.2	1.3	2.2	0.53
time (hr)	2	2	4	6.5	4	8
temp. (°C)	1250	1200	1370	1300	1370	1400

2r : diameter
d : thickness
ρ : density
grade : of raw materials; S for "special" and C for "chemical pure" grade. The left symbol refers to "A" element (Pb, Ba or Sr) and the right symbol refers to "B" element (Ti or Zr).
pressure : of second forming
time : of second sintering
temperature : of second sintering.

ductivity about the phase transition at 490°C, where the ferroelectricity disappears. In Fig. 6 is shown the temperature dependence of the thermal conductivity of lead titanate. The thermal conductivity decreases with increasing temperature up to about 350°C, then begins to increase until a maximum is reached at about 500°C, and then decreases again.

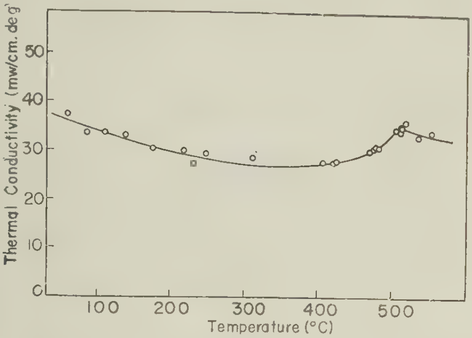

Fig. 6. Thermal conductivity of $PbTiO_3$.

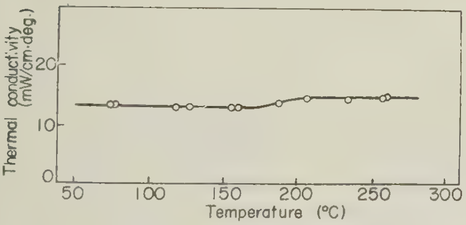

Fig. 7. Thermal conductivity of $PbZrO_3$.

4. 2. *Lead Zirconate*

In Fig. 7 is shown the temperature dependence of the thermal conductivity of lead zirconate ceramic. The phase transition is known to occur at about 230°C, and above this temperature the antiferroelectricity disappears. The change of thermal conductivity observed somewhat below this temperature may correspond to the transition.

Reproducibility of measurement was good below the transition temperature, but at higher temperatures the thermal conductivity was somewhat increased with the repetition of measurements. It seems possible that some changes in the state of aggregation of grains took place by repeated heating and cooling under a large mechanical pressure.

4. 3. *Barium Titanate*

Temperature dependence of thermal conductivity of barium titanate ceramic above room temperature (specimen No. 1) has already been published,[4] and that below room temperature (specimen No. 2) is shown in Fig. 8. The temperature coefficient is slightly positive, and the magnitude of thermal conductivity at room temperature is compatible with that given in the previous paper which was measured by a different method.

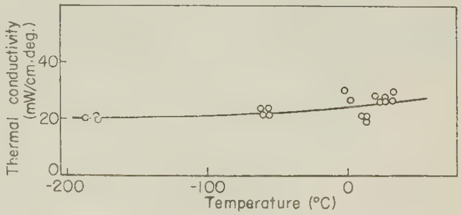

Fig. 8. Thermal conductivity of $BaTiO_3$

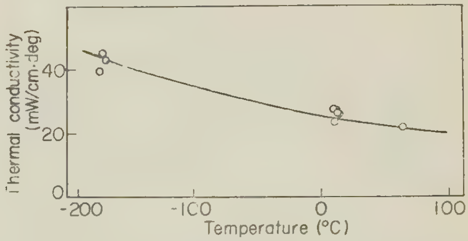

Fig. 9. Thermal conductivity of $SrTiO_3$.

4. 4. *Strontium Titanate*

Fig. 9 shows the temperature dependence of thermal conductivity at low temperatures (specimen No. 2), and that at higher temperatures (specimen No. 1) will be found in the previous paper.[4] Thermal conductivity of strontium titanate increases fairly steeply with decreasing temperature.

§ 5. Discussions

5. 1. *Magnitude of Thermal Conductivity*

In discussing the absolute value of the thermal conductivity of ceramic substances, appropriate considerations must be taken of the porosity effect. Through pores embedded in a continuum heat may be transmitted by convection and radiation, when a temperature gradient is set up in the medium. An apparent thermal conductivity of a pore κ_P may be defined so that the pore can be replaced by a medium with thermal conductivity equal to κ_P .

Several theoretical formula have been proposed to express the dependence of the thermal conductivity of a porous substance κ upon its porosity P[6][7], using thermal conductivities of the dense material κ_0 and of the pore κ_P. When pores are sufficiently small and the temperature is not so extremely high, κ_P/κ_0 becomes negligibly small and all formulae approximately reduce to

$$\kappa=(1-P)\kappa_0 . \tag{4}$$

Table II gives some typical values for the perovskite type substances with correction for the porosity by using the formula (4). The result on rutile is also given for comparison. Corrected values of specimens with different porosities agree well with each other for barium titanate and lead titanate, and as has already been stated, our corrected value of rutile agrees well with that obtained by Kingery et al. The specimen of strontium titanate used for low temperature measurement had a crack perpendicular to the length, which might have increased its thermal resistance.

Table II. Corrected values of thermal conductivities of some ceramics.

Substance	Thermal conductivity (mW/cm.deg.)	Temperature (°C)	Porosity (%)	Corrected for porosity (mW/cm.deg.)	Apparatus
$BaTiO_3$	30.2	55	10.6	33.4	High
	27.0	27	16.0	32.2	Low
$SrTiO_3$	59.0	60	12.8	67.8	High
	43.0	64	19.5	53.5	Low
$PbTiO_3$	33.6	110	14.6	39.4	High
	31.6	64	15.7	37.6	High
$PbZrO_3$	13.3	75	25.5	17.9	High
TiO_2	57.2	100	13.4	66.0	High

Although purely theoretical evaluation of the thermal conductivity of insulators seems rather difficult and no satisfactory theory has yet been proposed, the formula by Dugdale and MacDonald[8] giving the mean free path l of phonons

$$l=A_0/3\beta\gamma T \tag{5}$$

seems to give a tolerable accordance with experiments for alkali halide crystals, where A_0, β and γ mean the nearest neighbour distance, linear coefficient of thermal expansion and Grüneisen constant. γ is expressed as

$$\gamma=3\beta/\chi c , \tag{6}$$

where χ is the compressibility and c the specific heat per unit volume.

We shall now apply (5) to the case of barium titanate as an example. Using $\beta=0.9\times10^{-5}$ deg.$^{-1}$, $A_0=2\times10^{-8}$ cm, $\chi=0.617\times10^{-12}$ cm^2/dyn., and $c=0.78$ cal/deg. cm^3, we have $\gamma=1.34$ and $l=180$ Å (at 300°K). On the other hand, the experimental value of l is defined by

$$\kappa=\frac{1}{3}cvl , \tag{7}$$

where v is the mean group velocity of phonons. Using $\kappa=32.2$ mW/cm. deg. (at 300°K) and $v=3.73\times10^5$ cm/sec, we have $l=7.95$ Å. This is much shorter than the calculated value.

Some ambiguity is always involved in the interpretation of experimental data on the specific heat of crystal with a complex lattice, when a comparison is to be made with theories which are usually based on a simple lattice.

A unit cell of barium titanate contains one molecule, or five ions with fifteen degrees of freedom, which can be classified into three degrees of freedom associated with lattice translations, three associated with torsional motions of the unit cell, and nine associated with vibrational motions of a TiO_6 octahedron. Each of these vibrational modes will be approximated by an Einstein model, and the characteristic temperatures of them were determined by Last[9], from the infrared absorption, as 720°K for three modes and 490°K for other six modes respectively. These modes are considered to contribute scarecely to the thermal conduction because of their low group velocities. If these modes of vibrations were omitted in the discussions of thermal conduction, barium titanate crystal can be regarded as a diatomic lattice having the CsCl structure and may be compared with alkali halides, many of which, however, have the NaCl structure. The specific heat of barium titanate to be inserted into (6) and (7) is thus estimated as

0.3 cal/deg. cm^3, which changes γ and the theoretical and the experimental l's as follows;

$\gamma=3.50$

$l=71.0$ Å, theoretical

$l=20.7$ Å experimental.

A large discrepancy between theoretical and experimental value is still seen, and it would be far more serious at lower temperatures for (5) predicts that the theoretical mean free path length increases with decreasing temperature while the experiment does not show any such tendency. Similar discrepancy between the theoretical mean free path and that calculated from the thermal conductivity is also found in other crystals measured in our experiment. A tentative explanation of this contradiction, though qualitative, is as following.

Taking an ionic model of barium titanate we may regard its lattice to be composed of larger ions Ba^{--} (r=1.43 Å) and O^{--} (r=1.32 Å), together forming a face-centered, approximately cubic lattice, and of smaller ions Ti^{4+} (r=0.64 Å) occupying one kind of interstitial positions — the body center, but not the edge centers. This interstitial position assigned to Ti^{4+} is spacious enough for the ion to move about*, and it can really be shifted to a position near one of six neighbouring O^{--}, thus causing the ferroelectricity. Ti^{4+} ion is therefore considered to be bound with a highly anharmonic restoring force, and according to Devonshire[11] and to Slater[12] this anharmonicity is the origin of a linear increase of polarizability with decreasing tempearture, which causes the $4\pi/3$ catastrophe in barium titanate. This anharmonicity associated with the relative displacement of Ti ions against O ions is now not directly connected to the thermal expantion of the whole crystal, for the latter is mainly determined by anharmonicities in potentials between larger ions constituting the framework of the crystal. It seems probable that the translational waves propagating heat may be coupled with the motion of Ti ion, and the anharmonic potential energy of the latter comes into the Hamiltonian describing the system of phonons as a perturbation, resulting in an increase of collision probability of phonons and therefore of thermal resistivity. A similar argument will be made also for other crystals.

It is noteworthy and moreover suggestive that the thermal conductivities of barium titanate, lead titanate and strontium titanate increase in this order, while the infrared absorption frequencies change also in the same order[9], (545 cm^{-1}, 590 cm^{-1} and 610 cm^{-1}), which are thought to show the character of the potentials for the Ti ion in these substances.

5. 2. *Temperature Dependence of Thermal Conductivity*

According to Peierls[13] the thermal conductivities of simple crystals decrease nearly proportionally to 1/T with increasing temperature at higher temperatures ($T \gtrsim \theta_D$), and this temperature dependence was experimentally confirmed[14]. The thermal conductivity of glassy substance, on the other hand, generally increases with increasing temperature and is said to be proportional to the specific heat[14]. There are many substances of which the thermal conductivity has the temperature dependence between 1/T and that of specific heat. In this connection the ratio of the thermal conductivity at 83°K to that at 273°K, obtained by Eucken and Kuhn for many substances[15], is interesting. A few of the values of this ratio are cited in Table III, together with those of barium titanate and strontium titanate ceramics.

An examination of the Table III shows a general tendency that the complexity of structure lowers the ratio and the aggregation of crystallites still more. Though the scantiness of measurements does not permit us to say much about the temperature dependence of thermal conductivity of strontium titanate, the fact that there exists no phase transition would secure a discussion of general tendency. The ratio 1.80 is considerably smaller than 3.29, the inverse ratio of 83°K, to 273°K, and this would suggest that a considerable portion of thermal resistance has come from other sources than the U-process of three phonons, i. e., couplings of translational waves with vibrations of Ti ions or many other modes of vibrations, grain boundary scattering of phonons, etc.

---

* In this estimation Goldschmidt's ionic radii were used. Kittel insists[10] that the Ti-O contact determines, using Zachariazen's ionic radii, the lattice constant as 4.12 Å, which is larger than the actual value 4.004 Å, suggesting a mixture of covalency into the bonding.

Some complication may be involved in the case of barium titanate because of the existence of three phase transitions at 120°C, 5°C and −90°C, respectively, but the deviation from 1/T law has probably, or even more certainly, the same reason as in strontium titanate.

The thermal resistivity of lead titanate ceramic versus temperature is shown in Fig. 10, and the following empirical formula was found to hold in a rather wide temperature range.

$$1/\kappa = 14.0 + 0.042\ T\ \text{(cm.deg./W)}, \tag{8}$$

or

$$\kappa = 23.9/(T+334)\ \text{(W/cm.deg.)}. \tag{9}$$

Table III. Ratios of low- to high-temperature thermal conductivity

Substance	K_{83}/K_{273}
marble	1.21
calcite (crystal, ⊥)	4.09
sylvine	2.09
KCl (crystal)	4.27
NaCl (crystal)	3.78
KNO_3 (crystal aggregation)	0.89
$K_2Cr_2O_7$ (crystal, ⊥)	0.851
$K_2Cr_2O_7$ (crystal, //)	0.922
$BaTiO_3$ (ceramic)	0.80
$SrTiO_3$ (ceramic)	1.80

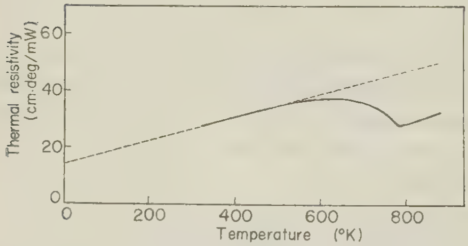

Fig. 10. Thermal resistivity of $PbTiO_3$.

5. 3. *Thermal Conductivity Anomalies*

The anomaly of thermal conductivity observed in barium titanate at about 120°C is small and it seems difficult to decide whether this anomaly is truly of the peak type, as was found in solid methane by Gerritsen and van der Star, or of the step type, as in lead titanate and lead zirconate.

Anyhow, the simple explanation that the anomaly in the thermal conductivity would be merely a direct reflection of that in the specific heat, supposing that v and l in the expression (7) do not appreciably change with temperature, seems incorrect, for the anomalous specific heat does not come from the vibrational energy of propagating waves but from the potential energy of Ti ions, which, in the first approximation, are considered to be oscillating independently. There seem to be two competing factors; the increase of symmetry which would operate to increase the thermal conductivity, and the augmentation in amplitude of Ti ions, detected by Känzig[16], in going into the paraelectric state which may operate to lower the thermal conductivity.

The increase of thermal conductivity is far more clearly manifested in lead titanate and lead zirconate. The additional part of the thermal conductivity of lead titanate, obtained by subtracting the " normal " part of thermal conductivity (experimental formula (9)) from the observed one, is shown in Fig. 11. It is reasonable to attribute the increase of thermal conductivity to the increase of symmetry, due to the restoring back of Pb and Ti ions to their positions of symmetry from the much shifted positions in the ferroelectric state. It is interesting to compare the behaviours of ion-shifting in barium titanate and lead titanate in this connection. In the former, Ti ion is responsible for the main part of the crystal deformation and the relative shift of Ba ion against O ion is considered small, while in lead titanate, the shift of Pb ion is larger than that of Ti ion and so the face-centered cubic lattice composed of Pb and O is much deformed. This latter affair seems to explain why the thermal conductivity of the cubic structure is much larger than that of the tetragonal structure in lead titanate.

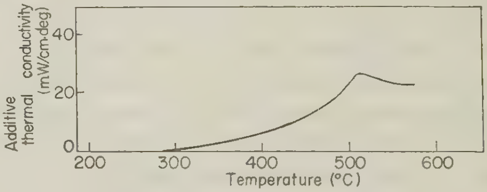

Fig. 11. Additional thermal conductivity of $PbTiO_3$.

The situation would be nearly the same for lead zirconate, and no essential difference between the ferroelectric and antiferroelectric substances was observed in this point.

§ 6. Summary

Two apparatuses for the measurement of thermal conductivity were described.

The thermal conductivities of barium titanate, strontium titanate, lead titanate and lead zirconate were measured on ceramic specimens, and suitably corrected for the porosity. The low value of thermal conductivity of barium titanate cannot be explained by the application of the formula due to Dugdale and MacDonald, and similar discrepancies between the experiment and the theory were observed for the other substances. A possibility was pointed out that Ti ions loosely bound in the O octahedron scatter the phonon waves and lower the thermal conductivity.

The temperature dependences of thermal conductivities of them were far from the 1/T law, and the grain boundary resistance and couplings of translational waves with vibrations of Ti ions were proposed as possible causes of the discrepancy. The thermal resistance of the well sintered lead titanate specimen was analyzed as the sum of the two components, one being proportional to the absolute temperature and the other one constant.

Little was discussed on the small anomaly of thermal conductivity of barium titanate, but the large step-wise increase of thermal conductivity of lead titanate was considered to have originated from the increase of symmetry, i. e., from the restoring-back of the shifted ions Ti and Pb to the positions of symmetry. The general affair was considered not much different in anti-ferroelectric lead zirconate.

§ 7. Acknowledgement

The author should like to express his sincere thanks to Prof. S. Sawada for his kind guidance, whose incessant advices and criticisms were indispensable for the accomplishment of the work. Hearty thanks are also due to Prof Y. Kakiuchi for showing interest and for many valuable suggestions, who was very generous in affording every facilities for the investigation. The author wishes to thank Prof. S. Nomura for many useful discussions.

References

1) A. Eucken and E. Schröder: Ann. Physik **36** (1939) 609.
2) A. N. Gerritsen and P. van der Star: Physica **9** (1942) 503.
3) Cl. v. Simson: Naturwiss. **38** (1951) 559.
4) I. Yoshida, S. Nomura and S. Sawada: J. Phys. Soc. Japan **13** (1958) 1550.
5) W. D. Kingery, J. Francl, R. L. Coble and T. Vasilos: J. Am. Ceram. Soc. **37** (1954) 107.
6) H. W. Russel: J. Am. Ceram. Soc. **18** (1035) 1.
7) A. L. Loeb: J. Am. Ceram. Soc. **37** (1954) 96.
8) J. S. Dugdale and D. K. C. MacDonald: Phys. Rev. **98** (1955) 1751.
9) J. T. Last: Phys. Rev. **105** (1957) 1740.
10) C. Kittel: *Introduction to Solid State Physics, 2nd ed.* (1956).
11) A. F. Devonshire: Phil. Mag. **40** (1949) 1040; **42** (1951) 1065.
12) J. C. Slater: Phys. Rev. **78** (1950) 748.
13) R. Peierls: Ann. Physik. **3** (1929) 1055.
14) R. Berman: Adv. Phys. **2** (1953) 103.
15) A. Eucken and G. Kuhn: Z. phys. Chem. **134** (1928) 193.
16) W. Känzig: Helv. Phys. Acta **24** (1951) 175.

Journal of the Physical Society of Japan, Vol. 15, No. 12, December, 1960

Paramagnetic Susceptibility of an Electron Gas in Alkali Metals

By Masao Shimizu

Department of Physics, Tokyo Metropolitan University

(Received July 4, 1960)

The paramagnetic susceptibilily of an electron gas is calculated by making use of the Bohm-Pines description of electron interactions. The contribution from the long-range correlation to the susceptibility calculated by Pines is modified by using the larger cutoff wave vector of plasma oscillations and including the new contribution from the zero-point energy of plasma oscillations. The contribution from the second-order perturbation-theoretic calculation of the screened Coulomb interactions is obtained by a proper approximation. The contribution from the third-order perturbation-theoretic calculation of the interactions is obtained by a rather crude approximation. The comparisons of paramagnetic susceptibility with experimental values for alkali metals are made and the agreements for Li and Na are satisfactory. The volume dependences of paramagnetic susceptibility for alkali metals are examined by comparing the experimental results on the pressure dependence of the Knight shift with the Brooks calculations of the Fermi interaction.

§ 1. Introduction

The paramagnetic susceptibility of conduction electrons was first calculated by Pauli[1]. Sampson and Seitz[2] took into account the effect of the exchange interaction between electrons and the correlation in the calculation of paramagnetic susceptibility of conduction electrons. Pines[3,4] calculated the paramagnetic susceptibility of conduction electrons using the Bohm-Pines collective description of electron interactions[5], and obtained satisfactory agreements with the experimental values for alkali metals. In this paper, however, we shall extend Pines' calculation by making use of the better approximation.

In the first place, as seen from the calculation of susceptibility for an electron gas at high density by Brueckner and Sawada[6], the contribution from the short-range correlation to the susceptibility obtained by Pines[5] is smaller than the value at high density limit and must be corrected.

In the second place, we must use a larger maximum wave vector k_c of plasma oscillations than that used by Pines. Ferrell[7] and Sawada et al.[8] obtained the relation,

$$\beta=k_c/k_0=0.47r_s^{1/2}\ , \tag{1.1}$$

in the case of the non-magnetic state, where k_0 is the wave vector at the Fermi surface and r_s is the radius, measured in atomic units, of a sphere having the same volume with the volume per electron. We use this relation in determining the screening of the Coulomb interaction.

In the paramagnetic state of an electron gas, β would be dependent on its magnetization. Since, however, the total energy of an electron gas in the non-magnetic state should be independent of β, we may also use in the paramagnetic state the constant β given by (1.1) as long as the magnetization is very small.

In the third place, the dispersion relation of plasma oscillations depends on the distribution of electrons, that is, their magnetization. Then we must take into account the change of the zero-point energy of plasma oscillations due to the magnetization and the contribution to paramagnetic susceptibility.

In the fourth place, as seen from the Pines calculation[3),4)] the effect of the short-range correlation energy, that is, the second-order perturbation energy of the screened Coulomb interaction, on the susceptibility is considerable in comparison with the effect of the exchange interaction. Accordingly it will be expected that the contribution from the third-order perturbation calculation of the screened Coulomb interaction may also be considerable.

The energy of the first-order perturbation calculation of the screened Coulomb interaction, that is, the exchange energy, decreases if the number of parallel spins of electrons increases. On the contrary the energy of the second-order perturbation calculation increases as a correction to the first-order energy if the number of parallel spins increases. Then the energy of the third-order perturbation calculation is expected to behave like the energy of the first-order perturbation calculation.

Taking into consideration the four points mentioned above, we shall calculate the paramagnetic susceptibility of an electron gas by means of the B–P collective description of interaction. The results on the first and third points have been already reported[9].

At 0°K we consider an aggregate of N electrons embedded in a background of a uniform positive charge, whose density is equal to that of the electrons. We assume that the spin directions of N_+ electrons are left-hand (positive) and that of N_- electrons are right-hand (negative). The state of electrons is specified by wave vectors. The maximum wave vector occupied by electrons of positive and negative spin directions are k_+ and k_- respectively. Then we have

$$(V/6\pi^2)k_+{}^3=N_+\ ,\quad (V/6\pi^2)k_-{}^3=N_-\ . \tag{1.2}$$

Let the difference between N_+ and N_- be n, and we define ξ as follows:

$$n/N=\xi\ ,\quad N_+-N_-=n\ ,\quad N_++N_-=N\ . \tag{1.3}$$

When $\xi \ll 1$, the total kinetic energy of an electron gas and its total exchange energy of the ordinary long-range Coulomb interactions are expanded by ξ, a well-known fact, as follows:

$$E_F=E_F^0+\gamma_F\xi^2\ ,\quad E_{\text{ex.}}=E_{\text{ex.}}^0+\gamma_{\text{ex.}}\xi^2\ . \tag{1.4}$$

respectively, where

$$\gamma_F=1.228r_s^{-2}(m/m^*)\ , \tag{1.5}$$

$$\gamma_{\text{ex.}}=-0.2036/r_s\ . \tag{1.6}$$

m^* is an effective mass of electrons and we assume that the effective mass reduces only the thermal kinetic energy as Pines pointed out[4]. Energies are measured by Rydberg unit per electron.

In §2, the contribution of the long-range cerrelation is calculated. The second-order perturbation calculation of the screened Coulomb interaction is worked out in §3. In §4 the third-order perturbation calculation is worked out.

In §5 we obtain the values of paramagnetic susceptibility for alkali metals and compare them with the experimental results.

In §6 the volume dependences of susceptibility are compared with the experimental results of the pressure dependence of the Knight shifts by making use of the Brooks calculation on the effective masses and the hyperfine interactions for alkali metals.

§2. Contribution from the Long-Range Correlation

When $n\neq 0$, the following four terms of the long-range correlation energies which depend on n are considered.

The first term is the zero-point energy of plasma oscillations, and has been given in (I) as follows:

$$\varDelta E_P=\gamma_P\xi^2\ ,\quad \gamma_P=0.008981\ . \tag{2.1}$$

The second term is the correction of (1.6) when the Coulomb interaction is screened by plasma oscillations and has been calculated by Pines[4]. This is (see (3.16) in (I))

$$E'_{\text{ex.}}=\gamma'_{\text{ex.}}\xi^2\ ,\quad \gamma'_{\text{ex.}}=0.01125\ . \tag{2.2}$$

The third term is the exchange energy of the weak velocity dependent interactions which are deduced from the second-order perturbation calculation of the electron-plasma interaction. The exchange integral of this interaction between electrons with wave vectors $\boldsymbol{k}$ and $\boldsymbol{k}'$ is approximately given by

$$\left.\begin{aligned} J^{r.p.}_{\boldsymbol{kk}'} &= -\frac{\pi e^2\hbar^2}{Vm^2}\,\frac{(k^2-k'^2)}{\{\omega^2-\hbar^2(k^2-k'^2)^2/4m^2\}(\boldsymbol{k}-\boldsymbol{k}')^2}\ , && \text{if}\quad |\boldsymbol{k}-\boldsymbol{k}'|<k_c;\\ &=0\ , && \text{if}\quad |\boldsymbol{k}-\boldsymbol{k}'|>k_c\ . \end{aligned}\right\} \tag{2.3}$$

where ω is the plasma angular frequency.

When $n\neq 0$, the total exchange energy of $J^{r.p.}_{\boldsymbol{kk}'}$ in (2.3) is

$$E^{r.p.}(n)=-\frac{1}{2}\sum_{k<k_+,}\ \sum_{k'<k_+} J^{r.p.}_{\boldsymbol{kk}'}-\frac{1}{2}\sum_{k<k_-,}\ \sum_{k'<k_-} J^{r.p.}_{\boldsymbol{kk}'}\ . \tag{2.4}$$

This is approximately calculated as follows:

$$E^{r.p.}(n)=\frac{e^2\hbar^2 V}{4\pi^3 m^2\omega_p^2}\left\{\frac{2}{45}(k_+{}^5+k_-{}^5)k_c{}^3-\frac{1}{16}\frac{0.98}{0.517}(k_+{}^4+k_-{}^4)k_c{}^4\right.$$
$$\left.+\frac{1}{30}(k_+{}^3+k_-{}^3)k_c{}^5-\frac{1}{144}(k_+{}^2+k_-{}^2)k_c{}^6\right\}, \qquad (2.5)^*$$

by taking into account the results when $n=0$, that is,

$$E^{r.p.}=-\sum_{k<k_0,\, k'<k_0}\sum J^{r.p.}_{kk'}=\frac{e^2\hbar^2 V k_0{}^8}{2\pi^3 m^2\omega_p{}^2}\left(\frac{2\beta^3}{45}-\frac{0.98}{0.517}\frac{\beta^4}{16}+\frac{\beta^5}{30}-\frac{\beta^6}{144}\right), \qquad (2.6)^*$$

where $\omega_p{}^2=(4\pi e^2N/mV)$. The terms proportional to $k_c{}^4$ or β^4 in (2.5) and (2.6) are correctec by the factor (0.98/0.517) which is expected from the higher-order perturbation calculation[10]

If $\xi\ll 1$, (2.5) is expanded from (1.1), (1.2) and (1.3) as follows**:

$$\left.\begin{aligned}&E^{r.p.}(n)/N=E^{r.p.}/N+\gamma_{r.p.}\xi^2\,,\\&\gamma_{r.p.}=-0.01065+0.02124r_s{}^{-1/2}+0.00006893r_s\,.\end{aligned}\right\} \qquad (2.7$$

The fourth term is the energy of the reaction to the self-energy of electrons coming from the interaction between electrons and plasma oscillations. This is given by the following expression.

$$\left.\begin{aligned}&E'_F(n)=-\frac{\beta^3}{6N}\frac{\hbar^2}{2m}\left(\sum_{k<k_+}k^2+\sum_{k<k_-}k^2\right)=E'_F+\gamma'_F\xi^2\,,\\&\gamma'_F=-0.02124r_s{}^{-1/2}\,,\end{aligned}\right\} \qquad (2.8$$

where E'_F is the energy of the reaction when $n=0$.

The part of the long-range correlation energy which depends on n is given, from (2.1), (2.2), (2.7) and (2.8), by

$$\left.\begin{aligned}&\Delta E_{l.r.}=\gamma_{l.r.}\xi^2\,,\\&\gamma_{l.r.}=\gamma_P+\gamma'_{\mathrm{ex.}}+\gamma_{r.p.}+\gamma'_F=0.009580+0.00006893r_s\,.\end{aligned}\right\} \qquad (2.9)$$

$4\gamma_{l.r.}$ corresponds to $\alpha_{l.r.}$ given by Pines[4)], but there is a considerable difference between them. The difference may be attributable to the different approximations which are made use of in the calculation of energy of the electron gas as an expansion of r_s.

§ 3. Effect of the Short-Range Correlation

The short-range correlation energy is obtained from the second-order perturbation calculation of the screened Coulomb interaction. This energy when $n\neq 0$ is given by[4)]

$$\left.\begin{aligned}&E^{s.r.}_{\mathrm{corr.}}(n)=E^{s.r.}_{+-}+\tfrac{1}{2}(E^{s.r.}_{++}+E^{s.r.}_{\mathrm{ex.}++})+\tfrac{1}{2}(E^{s.r.}_{--}+E^{s.r.}_{\mathrm{ex.}--})\,,\\&E^{s.r.}_{xy}=-\frac{m}{\hbar^2}\left(\frac{4\pi e^2}{V}\right)^2\sum_{\boldsymbol{k}_1}\sum_{\boldsymbol{k}_2}\sum_{\boldsymbol{p}}\frac{1}{p^4\boldsymbol{p}\cdot(\boldsymbol{p}+\boldsymbol{k}_1+\boldsymbol{k}_2)}\,,\\&E^{s.r.}_{\mathrm{ex.}xy}=\frac{m}{\hbar^2}\left(\frac{4\pi e^2}{V}\right)^2\sum_{\boldsymbol{k}_1}\sum_{2}\sum\frac{1}{p^2(\boldsymbol{p}+\boldsymbol{k}_1+\boldsymbol{k}_2)^2\boldsymbol{p}\cdot(\boldsymbol{p}+\boldsymbol{k}_1+\boldsymbol{k}_2)}\,,\end{aligned}\right\} \qquad (3.1)$$

where the regions of the sums are given by $k_1<k_x$, $|\boldsymbol{k}_1+\boldsymbol{p}|>k_x$, $k_2<k_y$, $|\boldsymbol{k}_2+\boldsymbol{p}|>k_y$, $p>k_c$, and $E^{s.r.}_{\mathrm{ex.}xy}$ is subject to an additional restriction, $|\boldsymbol{p}+\boldsymbol{k}_1+\boldsymbol{k}_2|>k_c$. $E^{s.r.}_{+-}$ is the correlation energy between electrons with antiparallel spins. $\frac{1}{2}(E^{s.r.}_{\pm\pm}+E^{s.r.}_{\mathrm{ex.}\pm\pm})$ are the correlation energies between electrons with parallel spins.

---

* In (2.5) and (2.6) the ordinary unit of energy is used.

** In the previous paper, (I), the formula for $\gamma_{r.p.}$, (4.20), was misprinted. $\gamma_{r.p.}$ in (2.7) is the correct result. Moreover, the coefficient of r_s in (5.7) of (I), 0.2272, should be replaced by 0.2744.

For the calculation of $E^{s.r.}_{\pm\pm}$ we make use of the results calculated by Pines[4] and Fletcher and Larson[11] when $n=0$. For the calculation of $E^{s.r.}_{\mathrm{ex.}\pm\pm}$ we make use of the results obtained by Gell-Mann and Brueckner[12] and Nozières and Pines[10].

When $n=0$ and $\beta<2$[4,11],

$$E^{s.r.}_{+-}(0)=E^{s.r.}_{\pm\pm}(0)\equiv E^{s.r.}(0)=-\frac{m}{\hbar^2}\left(\frac{4\pi e^2}{V}\right)^2\sum_{\substack{k_1<k_0,\\|\boldsymbol{k}_1+\boldsymbol{P}|>k_0,}}\sum_{\substack{k_2<k_0,\\|\boldsymbol{k}_2+\boldsymbol{P}|>k_0,}}\sum_{p>k_c}\frac{1}{p^4\boldsymbol{p}\cdot(\boldsymbol{p}+\boldsymbol{k}_1+\boldsymbol{k}_2)}$$

$$=\frac{e^2}{2a_0}\frac{Vk_0{}^3}{3\pi^4}\left\{-\frac{11}{6}+\frac{\pi^2}{4}-\frac{8}{3}\ln 2+2(\ln 2)^2+2(1-\ln 2)\ln\beta-\frac{\beta^2}{16}+\frac{\beta^4}{960}\right\}. \tag{3.2}$$

If $n=0$, $E^{s.r.}_{\mathrm{ex.}++}+E^{s.r.}_{\mathrm{ex.}--}$ becomes[12,10]

$$\tfrac{1}{2}E^{s.r.}_{\mathrm{ex.}++}(0)+\tfrac{1}{2}E^{s.r.}_{\mathrm{ex.}--}(0)\equiv E^{s.r.}_{\mathrm{ex.}}(0)$$

$$=\frac{m}{\hbar^2}\left(\frac{4\pi e^2}{V}\right)^2\sum_{\substack{k_3<k_0,\\|\boldsymbol{k}_1+\boldsymbol{P}|>k_0,}}\sum_{\substack{k_2<k_0,\\|\boldsymbol{k}_2+\boldsymbol{P}|>k_0,}}\sum_{\substack{p>k_c\\|\boldsymbol{P}+\boldsymbol{k}_1+\boldsymbol{k}_2|>k_c}}\frac{1}{p^2(\boldsymbol{p}+\boldsymbol{k}_1+\boldsymbol{k}_2)^2\boldsymbol{p}\cdot(\boldsymbol{p}+\boldsymbol{k}_1+\boldsymbol{k}_2)}$$

$$=\frac{e^2}{2a_0}\frac{Vk_0{}^3}{3\pi^2}(0.046-0.015\beta^2\pm0.002). \tag{3.3}$$

In $n\neq0$, $E^{s.r.}_{++}$ and $E^{s.r.}_{--}$ are written from (3.2) as

$$E^{s.r.}_{\pm\pm}=\frac{e^2}{2a_0}\frac{Vk_\pm{}^3}{3\pi^4}\left\{-\frac{11}{6}+\frac{\pi^2}{4}-\frac{8}{3}\ln 2+2(\ln 2)^2+2(1-\ln 2)\beta_\pm-\frac{\beta_\pm{}^2}{16}+\frac{\beta_\pm{}^4}{960}\right\}, \tag{3.4}$$

where $\beta_\pm=k_c/k_\pm$. Similarly $E^{s.r.}_{\mathrm{ex.}++}+E^{s.r.}_{\mathrm{ex.}--}$, when $n\neq0$, is written from (3.3) as

$$\tfrac{1}{2}E^{s.r.}_{\mathrm{ex.}++}+\tfrac{1}{2}E^{s.r.}_{\mathrm{ex.}--}=\frac{e^2}{2a_0}\frac{V}{6\pi^2}\{k_+{}^3(0.046-0.015\beta_+{}^2)+k_-{}^3(0.046-0.015\beta_-{}^2)\}. \tag{3.5}$$

$E^{s.r.}_{+-}$, when $n\neq0$, is analytically calculated by replacing the sums in (2.1) by integrations, and is written as a function of k_+, k_- and k_c in the case of $k_+>k_-$ and $2k_->k_c$ as follows:

$$\begin{aligned}E^{s.r.}_{+-}=&-(e^2/2a_0)(V/3\pi^4)\Big[\{13/40-(\ln 2)^2+(\ln 2)(\ln k_c)\}(k_+{}^3+k_-{}^3)\\&+(4/15+\ln 2-\ln k_c)k_+k_-(k_++k_-)+k_c{}^2(k_++k_-)/120-(k_-{}^3\ln 2+k_+{}^3/3-k_+{}^2k_-)\ln k_+\\&-(k_+{}^3\ln 2+k_-{}^3/3-k_-{}^2k_+)\ln k_-+(1/24)(-7k_+{}^3+15k_+{}^2k_-+15k_+k_-{}^2-7k_-{}^3)\ln(k_++k_-)\\&+(5/8)(k_+{}^3-k_+{}^2k_--k_+k_-{}^2+k_-{}^3)\ln(k_+-k_-)+\{k_c{}^3/120-k_c(k_+{}^2+k_-{}^2)/4\\&+3(k_+{}^2-k_-{}^2)^2/8k_c+(k_+{}^5-5k_+{}^3k_-{}^2-5k_+{}^2k_-{}^3+k_-{}^5)/20k_c{}^2\}\ln\{(k_++k_--k_c)/(k_++k_-+k_c)\}\\&-(1/12)(k_+{}^3-6k_+{}^2k_--6k_+k_-{}^2+k_-{}^3)\ln\{1-k_c{}^2(k_++k_-)^{-2}\}+\{(k_c{}^3/384)-(3k_+{}^2k_c/16)\\&+(3k_+{}^4/8k_c)\}\ln\{(2k_-+k_c)/(2k_--k_c)\}-(k_-{}^3/6)\ln\{1-(k_c{}^2/4k_-{}^2)\}\\&-\frac{1}{2}(k_+{}^3+k_-{}^3)\int_{2k_+}^{\infty}\frac{dp}{p}\ln\frac{p+k_++k_-}{p-(k_++k_-)}+\frac{1}{2}(k_+{}^3-k_-{}^3)\int_{2k_+}^{\infty}\frac{dp}{p}\ln\frac{p+k_+-k_-}{p-k_++k_-}\\&-\frac{1}{2}(k_+{}^3+k_-{}^3)\int_{2k_-}^{2k_+}\frac{dp}{p}\ln(p+k_++k_-)+\frac{1}{2}(k_+{}^3-k_-{}^3)\int_{2k_-}^{2k_+}\frac{dp}{p}\ln(p+k_+-k_-)\\&+\frac{1}{2}k_-{}^3\int_{2k_-}^{2k_+}\frac{dp}{p}\ln(p^2+4k_-{}^2)+\frac{1}{2}k_-{}^3\int_{k_c}^{2k_-}\frac{dp}{p}\ln(4k_-{}^2-p^2)\\&-\frac{1}{2}(k_+{}^3+k_-{}^3)\int_{k_c}^{2k_-}\frac{dp}{p}\{(k_++k_-)^2-p^2\}+\frac{1}{2}k_+{}^3\int_{k_c}^{2k_-}\frac{dp}{p}\ln(4k_+{}^2-p^2)\Big].\end{aligned} \tag{3.6}$$

If $n=0$, that is, $k_+=k_-=k_0$, this formula completely coincides with the formula for $E^{s.r.}(0)$ obtained by Fletcher and Larson[11].

In the case where $\xi=n/N\ll1$, using (1.2) and (1.3) we obtain from (3.2) and (3.6)

$$\left.\begin{aligned} E^{s.r.}_{+-} &= E^{s.r.}(0)+\frac{e^2N}{2a_0}\gamma^{+-}_{s.r.}\xi^2\,, \\ \gamma^{+-}_{s.r.} &= \frac{1}{\pi^2}\left(\frac{1}{2}-\frac{1}{9}\ln 2-\frac{1}{3}\ln\beta-\frac{\beta^2}{720}-\frac{\beta^4}{8640}\right). \end{aligned}\right\} \tag{3.7}$$

and from (3.2), (3.3), (3.4) and (3.5) we obtain

$$\left.\begin{aligned} \frac{1}{2}(E^{s.r.}_{++}+E^{s.r.}_{\text{ex.}\,++})+\frac{1}{2}(E^{s.r.}_{--}+E^{s.r.}_{\text{ex.}\,--}) &= E^{s.r.}(0)+E^{s.r.}_{\text{ex.}}(0)+\frac{e^2N}{2a_0}(\gamma^{++}_{s.r.}+\gamma^{--}_{s.r.})\xi^2\,, \\ (\gamma^{++}_{s.r.}+\gamma^{--}_{s.r.}) &= \frac{1}{\pi^2}\left\{-\frac{1}{3}(1-\ln 2)+\frac{\beta^2}{144}+\frac{\beta^4}{4320}\right\}+\frac{0.015\beta^2}{9}\,. \end{aligned}\right\} \tag{3.8}$$

Then, the total short-range correlation energy, $E^{s.r.}_{\text{corr.}}(n)$ in (3.1), is expanded in powers of ξ as follows:

$$\left.\begin{aligned} E^{s.r.}_{\text{corr.}}(n) &= 2E^{s.r.}(0)+E^{s.r.}_{\text{ex.}}(0)+\frac{e^2N}{2a_0}\gamma_{s.r.}\xi^2\,, \\ \gamma_{s.r.} &= \gamma^{+-}_{s.r.}+\gamma^{++}_{s.r.}+\gamma^{--}_{s.r.}=\frac{1}{\pi^2}\left(\frac{1}{6}+\frac{2}{9}\ln 2-\frac{1}{3}\ln\beta+\frac{\beta^2}{180}+\frac{\beta^4}{8640}\right)+\frac{0.015\beta^2}{9}\,. \end{aligned}\right\} \tag{3.9}$$

From (1.1), $\gamma_{s.r.}$ is rewritten as

$$\gamma_{s.r.}=0.05799-0.01689\ln r_s+0.0004925r_s+0.0000005722r_s{}^2\,. \tag{3.10}$$

The coefficient of $\ln r_s$ in $\gamma_{s.r.}$ is $-(1/6\pi^2)$ and coincides with the result for the electron gas at high density obtained by Brueckner and Sawada, and the constant term in $\gamma_{s.r.}$ is nearly equal to their result[6].

§4. Third-Order Perturbation Calculation of the Screened Coulomb Interaction

In an unperturbed ground state, electrons are assumed to compactly occupy up to the levels with k_+ and k_- for positive and negative spins respectively. We consider only the excited states in which two electrons are excited over the Fermi surface by the screened Coulomb interaction. Using the vector model we calculate the third-order perturbation energy of the screened Coulomb interaction. The details of the calculation are given in Appendix I. The results are as follows:

$$E^{(3)}=E_1{}^{(3)}+E_2{}^{(3)}+E_3{}^{(3)}\,, \tag{4.1}$$

$$\begin{aligned} E_1{}^{(3)} &= \frac{1}{2}\left(\frac{4\pi e^2}{V}\right)^3\frac{m^2}{\hbar^4}\sum_{\mathbf{k}_i,}\sum_{\mathbf{k}_j,}\sum_{\mathbf{p},}\sum_{\mathbf{p}'}\Bigg[\frac{1}{p^2p'^2\mathbf{p}\cdot(\mathbf{p}+\mathbf{k}_i+\mathbf{k}_j)\mathbf{p}'\cdot(\mathbf{p}'+\mathbf{k}_i+\mathbf{k}_j)} \\ &\quad\times\{(\mathbf{p}-\mathbf{p}')^{-2}-(\mathbf{p}+\mathbf{p}'+\mathbf{k}_i+\mathbf{k}_j)^{-2}P_{ij}{}^{\sigma}\}\Bigg]\,, \end{aligned} \tag{4.2}$$

$$\begin{aligned} E_2{}^{3)} &= \frac{1}{2}\left(\frac{4\pi e^2}{V}\right)^3\frac{m^2}{\hbar^4}\sum_{\mathbf{k}_i,}\sum_{\mathbf{k}_j,}\sum_{\substack{\mathbf{k}_l\neq\mathbf{k}_i,\\ \neq\mathbf{k}_j,}}\sum_{\mathbf{p}}\Bigg[\Bigg[\frac{1}{\mathbf{p}\cdot(\mathbf{p}+\mathbf{k}_i+\mathbf{k}_j)\mathbf{p}\cdot(\mathbf{p}+\mathbf{k}_l+\mathbf{k}_j)} \\ &\quad\times\Bigg\{\frac{1}{p^6}-\frac{P_{ij}{}^{\sigma}}{p^4(\mathbf{p}+\mathbf{k}_i+\mathbf{k}_j)^2}-\frac{P_{jl}{}^{\sigma}}{p^4(\mathbf{p}+\mathbf{k}_j+\mathbf{k}_l)^2}-\frac{P_{il}{}^{\sigma}}{p^4(\mathbf{k}_i-\mathbf{k}_l)^2}+\frac{P_{ij}{}^{\sigma}P_{il}{}^{\sigma}}{p^2(\mathbf{k}_i-\mathbf{k}_l)^2(\mathbf{p}+\mathbf{k}_i+\mathbf{k}_j)^2} \\ &\quad+\frac{P_{ij}{}^{\sigma}P_{il}{}^{\sigma}}{p^2(\mathbf{k}_i-\mathbf{k}_l)^2(\mathbf{p}+\mathbf{k}_j+\mathbf{k}_l)^2}+\frac{P_{ij}{}^{\sigma}P_{jl}{}^{\sigma}}{p^2(\mathbf{p}+\mathbf{k}_i+\mathbf{k}_j)^2(\mathbf{p}+\mathbf{k}_j+\mathbf{k}_l)^2} \\ &\quad-\frac{P_{il}{}^{\sigma}}{(\mathbf{k}_i-\mathbf{k}_l)^2(\mathbf{p}+\mathbf{k}_i+\mathbf{k}_j)^2(\mathbf{p}+\mathbf{k}_j+\mathbf{k}_l)^2}\Bigg\}\Bigg] \\ &\quad+\text{[Here insert the above term with } i \text{ and } j \text{ interchange]}\Bigg]\,, \end{aligned} \tag{4.3}$$

$$E_3{}^{(3)}=\frac{1}{2}\left(\frac{4\pi e^2}{V}\right)^3\frac{m^2}{\hbar^4}\sum_{\boldsymbol{k}_i,}\sum_{\boldsymbol{k}_j,}\sum_{\substack{\boldsymbol{k}_l\neq\boldsymbol{k}_i,\\ \neq\boldsymbol{k}_j,}}\sum_{\boldsymbol{p}}\left[\frac{1}{\underline{p}^2\{\boldsymbol{p}\cdot(\boldsymbol{p}+\boldsymbol{k}_i+\boldsymbol{k}_j)\}^2}\left\{-\frac{P_{il}{}^\sigma}{\underline{p}^2}\left(\frac{1}{(\underline{\boldsymbol{p}+\boldsymbol{k}_i+\boldsymbol{k}_l})^2}-\frac{1}{(\underline{\boldsymbol{k}_i-\boldsymbol{k}_l})^2}\right)\right.\right.$$

$$-\frac{P_{jl}{}^\sigma}{p^2}\left(\frac{1}{(\underline{\boldsymbol{p}+\boldsymbol{k}_j+\boldsymbol{k}_l})^2}-\frac{1}{(\underline{\boldsymbol{k}_j-\boldsymbol{k}_l})^2}\right)+\frac{P_{ij}{}^\sigma P_{il}{}^\sigma}{(\boldsymbol{p}+\underline{\boldsymbol{k}_i+\boldsymbol{k}_j})^2}\left(\frac{1}{(\underline{\boldsymbol{p}+\boldsymbol{k}_j+\boldsymbol{k}_l})^2}-\frac{1}{(\underline{\boldsymbol{k}_j-\boldsymbol{k}_l})^2}\right)$$

$$\left.\left.+\frac{P_{ij}{}^\sigma P_{jl}{}^\sigma}{(\underline{\boldsymbol{p}+\boldsymbol{k}_i+\boldsymbol{k}_j})^2}\left(\frac{1}{(\underline{\boldsymbol{p}+\boldsymbol{k}_i+\boldsymbol{k}_l})^2}-\frac{1}{(\underline{\boldsymbol{k}_j-\boldsymbol{k}_l})^2}\right)\right\}\right]. \tag{4.4}$$

$P_{ij}{}^\sigma$ is an operator which exchanges the spin coordinates of i and j electrons and so on. We have $P_{ij}{}^\sigma=\frac{1}{2}(1+4\boldsymbol{S}_i\cdot\boldsymbol{S}_j)$, where $\boldsymbol{S}_i$ and $\boldsymbol{S}_j$ are spin operators of i and j electrons respectively. If i and j spins are parallel $P_{ij}{}^\sigma=1$, and if they are antiparallel $P_{ij}{}^\sigma=0$. In (4.2), (4.3) and (4.4) the summations over $\boldsymbol{k}_i$, $\boldsymbol{k}_j$, $\boldsymbol{k}_l$, $\boldsymbol{p}$ and $\boldsymbol{p}'$ are taken such that the absolute values of the vectors underlined are larger than k_c, $|\boldsymbol{k}|<k_+$ and $|\boldsymbol{k}+\boldsymbol{p}|>k_+$ or $|\boldsymbol{k}+\boldsymbol{p}'|>k_+$ when the state with the wave vector $\boldsymbol{k}$ is a positive spin state, and $|\boldsymbol{k}|<k_-$ and $|\boldsymbol{k}+\boldsymbol{p}|>k_-$ or $|\boldsymbol{k}+\boldsymbol{p}'|>k_-$ when the state with the wave vector $\boldsymbol{k}$ is a negative spin state.

As shown in (A15) of Appendix I, each term in $E_1{}^{(3)}$, (4.2), is derived from the processes in which two electrons jump out of the Fermi surface because of the screened Coulomb interaction between them and again jump into other states and finally they go back to the original states. Each term in $E_2{}^{(3)}$, (4.3), as shown in (A16) of Appendix I, is derived from the processes, in which two electrons jump out of the Fermi surface, and then, one of these electrons goes back to one of the original states occupied by them before and another new electron jump out of the Fermi surface simultaneously, and finally two electrons above the Fermi surface go back under the Fermi surface. As shown in (A17) of Appendix I, each term in $E_3{}^{(3)}$, (4.4), corresponds to the processes, in which two electrons jump out of the Fermi surface, and then, one of these electrons and another electron are exchanged because of the exchange interaction between them and finally two electrons go back as before.

In the case of the high-density limit of the electron gas, only the term being proportional to p^{-6} in (4.3) is taken into account.

We can write $E_1{}^{(3)}$, $E_2{}^{(3)}$, $E_3{}^{(3)}$ for the electron configuration, in which electrons with positive and negative spins occupy compactly up to the states with the wave vectors k_+ and k_- respectively, in the following way. Hereafter we replace the sums by integrations and wave vectors are measured in units of k_0. We use $\alpha=(4/9\pi)^{1/3}$ and the Rydberg units per electron as the unit of energy.

When the spins of electrons with $\boldsymbol{k}_i$ and $\boldsymbol{k}_j$ are positive and negative respectively, $E_1{}^{3)}$, (4.2), becomes

$$E_1{}^{(3)}(+-)=\frac{3\alpha r_s}{32\pi^7}\int d^3\boldsymbol{k}_1\int d^3\boldsymbol{k}_2\int d^3\boldsymbol{p}\int d^3\boldsymbol{p}'\frac{1}{\underline{p}^2\underline{p}'^2(\boldsymbol{p}-\boldsymbol{p}')^2\boldsymbol{p}\cdot(\boldsymbol{p}+\boldsymbol{k}_1+\boldsymbol{k}_2)\boldsymbol{p}'\cdot(\boldsymbol{p}'+\boldsymbol{k}_1+\boldsymbol{k}_2)}, \tag{4.5}$$

where the regions of integrations are given by $p>\beta$, $p'>\beta$, $|\boldsymbol{p}-\boldsymbol{p}'|>\beta$, $0<k_1<n_+$, $|\boldsymbol{k}_1+\boldsymbol{p}|>n_+$, $|\boldsymbol{k}_1+\boldsymbol{p}'|>n_+$, $0<k_2<n_-$, $|\boldsymbol{k}_2+\boldsymbol{p}|>n_-$ and $|\boldsymbol{k}_2+\boldsymbol{p}'|>n_-$. n_+ and n_- are k_+/k_0 and k_-/k_0 respectively.

When both spins of electrons with $\boldsymbol{k}_i$ and $\boldsymbol{k}_j$ are positive or negative, we have from (4.2)

$$E_1{}^{(3)}(\pm\pm)=\frac{3\alpha r_s}{64\pi^7}\int d^3\boldsymbol{k}_1\int d^3\boldsymbol{k}_2\int d^3\boldsymbol{p}\int d^3\boldsymbol{p}'\frac{1}{\underline{\boldsymbol{p}}^2\underline{\boldsymbol{p}}'^2\boldsymbol{p}\cdot(\boldsymbol{p}+\boldsymbol{k}_1+\boldsymbol{k}_2)\boldsymbol{p}'\cdot(\boldsymbol{p}'+\boldsymbol{k}_1+\boldsymbol{k}_2)}$$

$$\times\{(\underline{\boldsymbol{p}-\boldsymbol{p}'})^{-2}-(\underline{\boldsymbol{p}+\boldsymbol{p}'+\boldsymbol{k}_1+\boldsymbol{k}_2})^{-2}\}. \tag{4.6}$$

The regions of these integrations are given by the ones in which $n_\mp$ is replaced by $n_\pm$ in the regions for $E_1{}^{(3)}(+-)$, (4.5).

Similarly, $E_2{}^{(3)}$, (4.3), and $E_3{}^{(3)}$, (4.4), when the spins of electrons with $\boldsymbol{k}_i$, $\boldsymbol{k}_j$ and $\boldsymbol{k}_l$ are determined as positive or negative, are given as follows:

$$E_2^{(3)}(\pm\pm\mp)=\frac{3\alpha r_s}{32\pi^7}\int d^3\boldsymbol{k}_1\int d^3\boldsymbol{k}_2\int d^3\boldsymbol{k}_3\int d^3\boldsymbol{p}\,\frac{1}{\boldsymbol{p}\cdot(\boldsymbol{p}+\boldsymbol{k}_1+\boldsymbol{k}_2)\boldsymbol{p}\cdot(\boldsymbol{p}+\boldsymbol{k}_2+\boldsymbol{k}_3)}$$
$$\times\{\underline{p}^{-6}-\underline{p}^{-4}(\underline{\boldsymbol{p}+\boldsymbol{k}_1+\boldsymbol{k}_2})^{-2}\}\ , \tag{4.7}$$

where the regions of integrations are $p>\beta$, $0<k_1<n_\pm$, $|\boldsymbol{k}_1+\boldsymbol{p}|>n_\pm$, $0<k_2<n_\pm$, $|\boldsymbol{k}_2+\boldsymbol{p}|>n_\pm$, $0<k_3<n_\mp$, and $|\boldsymbol{k}_3+\boldsymbol{p}|>n_\mp$;

$$E_2^{(3)}(\pm\mp\mp)=\frac{3\alpha r_s}{64\pi^7}\int d^3\boldsymbol{k}_1\int d^3\boldsymbol{k}_2\int d^3\boldsymbol{k}_3\int d^3\boldsymbol{p}\,\frac{1}{\boldsymbol{p}\cdot(\boldsymbol{p}+\boldsymbol{k}_1+\boldsymbol{k}_2)\boldsymbol{p}\cdot(\boldsymbol{p}+\boldsymbol{k}_2+\boldsymbol{k}_3)}$$
$$\times\{2\underline{p}^{-6}-\underline{p}^{-4}(\underline{\boldsymbol{p}+\boldsymbol{k}_2+\boldsymbol{k}_3})^{-2}-\underline{p}^{-4}(\underline{\boldsymbol{k}_2-\boldsymbol{k}_3})^{-2}-(\underline{\boldsymbol{k}_2-\boldsymbol{k}_3})^{-2}(\underline{\boldsymbol{p}+\boldsymbol{k}_1+\boldsymbol{k}_2})^{-2}(\underline{\boldsymbol{p}+\boldsymbol{k}_1+\boldsymbol{k}_3})^{-2}\}\ , \tag{4.8}$$

where the regions of integrations are $p>\beta$, $0<k_1<n_\pm$, $|\boldsymbol{k}_1+\boldsymbol{p}|>n_\pm$, $0<k_2<n_\mp$; $|\boldsymbol{k}_2+\boldsymbol{p}|>n_\mp$ $0<k_3<n_\mp$, and $|\boldsymbol{k}_3+\boldsymbol{p}|>n_\mp$;

$$E_2^{(3)}(\pm\mp\pm)=\frac{3\alpha r_s}{64\pi^7}\int d^3\boldsymbol{k}_1\int d^3\boldsymbol{k}_1\int d^3\boldsymbol{k}_3\int d^3\boldsymbol{p}\,\frac{1}{\boldsymbol{p}\cdot(\boldsymbol{p}+\boldsymbol{k}_1+\boldsymbol{k}_2)\boldsymbol{p}\cdot(\boldsymbol{p}+\boldsymbol{k}_2+\boldsymbol{k}_3)}$$
$$\times\{2\underline{p}^{-6}-\underline{p}^{-4}(\underline{\boldsymbol{k}_1}-\underline{\boldsymbol{k}_3})^{-2}-\underline{p}^{-4}(\underline{\boldsymbol{p}+\boldsymbol{k}_1+\boldsymbol{k}_3})^{-2}-(\underline{\boldsymbol{k}_1-\boldsymbol{k}_2})^{-2}(\underline{\boldsymbol{p}+\boldsymbol{k}_1+\boldsymbol{k}_2})^{-2}(\underline{\boldsymbol{p}+\boldsymbol{k}_2+\boldsymbol{k}_3})^{-2}\}\ , \tag{4.9}$$

where the regions of integrations are $p>\beta$, $0<k_1<n_\pm$, $|\boldsymbol{k}_1+\boldsymbol{p}|>n_\pm$, $0<k_2<n_\mp$, $|\boldsymbol{k}_2+\boldsymbol{p}|>n_\mp$ $0<k_3<n_\pm$, and $|\boldsymbol{k}_3+\boldsymbol{p}|>n_\pm$;

$$E_2^{(3)}(\pm\pm\pm)=\frac{3\alpha r_s}{32\pi^7}\int d^3\boldsymbol{k}_1\int d^3\boldsymbol{k}_2\int d^3\boldsymbol{k}_3\int d^3\boldsymbol{p}\,\frac{1}{\boldsymbol{p}\cdot(\boldsymbol{p}+\boldsymbol{k}_1+\boldsymbol{k}_2)\boldsymbol{p}\cdot(\boldsymbol{p}+\boldsymbol{k}_2+\boldsymbol{k}_3)}$$
$$\times\{\underline{p}^{-6}-\underline{p}^{-4}(\underline{\boldsymbol{p}+\boldsymbol{k}_1+\boldsymbol{k}_2})^{-2}-\underline{p}^{-4}(\underline{\boldsymbol{p}+\boldsymbol{k}_2+\boldsymbol{k}_3})^{-3}-\underline{p}^{-4}(\underline{\boldsymbol{k}_1-\boldsymbol{k}_3})^{-2}$$
$$+\underline{p}^{-2}(\underline{\boldsymbol{k}_1-\boldsymbol{k}_3})^{-2}(\underline{\boldsymbol{p}+\boldsymbol{k}_1+\boldsymbol{k}_2})^{-2}+\underline{p}^{-2}(\underline{\boldsymbol{k}_1-\boldsymbol{k}_3})^{-2}(\underline{\boldsymbol{p}+\boldsymbol{k}_2+\boldsymbol{k}_3})^{-2}$$
$$+\underline{p}^{-2}(\underline{\boldsymbol{p}+\boldsymbol{k}_1+\boldsymbol{k}_2})^{-2}(\underline{\boldsymbol{p}+\boldsymbol{k}_2+\boldsymbol{k}_3})^{-2}-(\underline{\boldsymbol{k}_1-\boldsymbol{k}_3})^{-2}(\underline{\boldsymbol{p}+\boldsymbol{k}_1+\boldsymbol{k}_2})^{-2}(\underline{\boldsymbol{p}+\boldsymbol{k}_2+\boldsymbol{k}_3})^{-2}\}\ , \tag{4.10}$$

where the regions of integrations are $p>\beta$, $0<k_1<n_\pm$, $|\boldsymbol{k}_1+\boldsymbol{p}|>n_\pm$, $0<k_2<n_\pm$, $|\boldsymbol{k}_2+\boldsymbol{p}|>n_\pm$, $0<k_3<n_\pm$, and $|\boldsymbol{k}_3+\boldsymbol{p}|>n_\pm$; and

$$E_3^{(3)}(\pm\pm\pm)=\frac{3\alpha r_s}{64\pi^7}\int d^3\boldsymbol{k}_1\int d^3\boldsymbol{k}_2\int d^3\boldsymbol{k}_3\int d^3\boldsymbol{p}\,\frac{1}{\underline{p}^2\{\boldsymbol{p}\cdot(\boldsymbol{p}+\boldsymbol{k}_1+\boldsymbol{k}_2)\}^2}$$
$$\times[-\underline{p}^{-2}\{(\underline{\boldsymbol{p}+\boldsymbol{k}_1+\boldsymbol{k}_3})^{-2}-(\underline{\boldsymbol{k}_1-\boldsymbol{k}_3})^{-2}\}-\underline{p}^{-2}\{(\underline{\boldsymbol{p}+\boldsymbol{k}_2+\boldsymbol{k}_3})^{-2}-(\underline{\boldsymbol{k}_2-\boldsymbol{k}_3})^{-2}\}$$
$$+(\underline{\boldsymbol{p}+\boldsymbol{k}_1+\boldsymbol{k}_2})^{-2}\{(\underline{\boldsymbol{p}+\boldsymbol{k}_1+\boldsymbol{k}_3})^{-2}+(\underline{\boldsymbol{p}+\boldsymbol{k}_2+\boldsymbol{k}_3})^{-2}-(\underline{\boldsymbol{k}_1-\boldsymbol{k}_3})^{-2}-(\underline{\boldsymbol{k}_2-\boldsymbol{k}_3})^{-2}\}]\ , \tag{4.11}$$

$$E_3^{(3)}(\pm\pm\mp)=0\ , \tag{4.12}$$

$$E_3^{(3)}(\pm\mp\mp)=\frac{3\alpha r_s}{64\pi^7}\int d^3\boldsymbol{k}_1\int d^3\boldsymbol{k}_2\int d^3\boldsymbol{k}_3\int d^3\boldsymbol{p}\,\frac{1}{\underline{p}^4\{\boldsymbol{p}\cdot(\boldsymbol{p}+\boldsymbol{k}_1+\boldsymbol{k}_2)\}^2}$$
$$\times\{(\underline{\boldsymbol{k}_2-\boldsymbol{k}_3})^{-2}-(\underline{\boldsymbol{p}+\boldsymbol{k}_2+\boldsymbol{k}_3})^{-2}\}\ , \tag{4.13}$$

$$E_3^{(3)}(\mp\pm\mp)=\frac{3\alpha r_s}{64\pi^7}\int d^3\boldsymbol{k}_1\int d^3\boldsymbol{k}_2\int d^3\boldsymbol{k}_3\int d^3\boldsymbol{p}\,\frac{1}{\underline{p}^4\{\boldsymbol{p}\cdot(\boldsymbol{p}+\boldsymbol{k}_1+\boldsymbol{k}_2)\}^2}$$
$$\times\{(\underline{\boldsymbol{k}_1-\boldsymbol{k}_3})^{-2}-(\underline{\boldsymbol{p}+\boldsymbol{k}_1+\boldsymbol{k}_3})^{-2}\}\ , \tag{4.14}$$

where the regions of integrations are the same with the ones in the respective cases of the spin configurations for $E_2^{(3)}$ given above.

As the necessary integrations in (4.5)–(4.14) have not been carried out analytically, we obtain the coefficients of ξ^2 approximately in the form of the expansions of the order of ξ using four approximations which are expected to hold when β is nearly equal to 1 or $r_s\sim4.5$, as shown in Appendix II. The result is given by (A34) and shown in Fig. 1 by a dotted line.

As shown in Appendix III, from the calculation of $E^{(3)}$ in the case of the high-density imit of the electron gas, we obtain (A39). Then, from the above two calculations we determine $E^{(3)}$ approximately as follows (see Appendix III):

$$E^{(3)}=E_0{}^{(3)}+\gamma^{(3)}_{\text{corr.}}\xi^2\ ,$$

$$\gamma^{(3)}_{\text{corr.}}=-0.0658\exp(-0.278r_s)\ , \qquad (4.15)$$

and this is shown in Fig. 1.

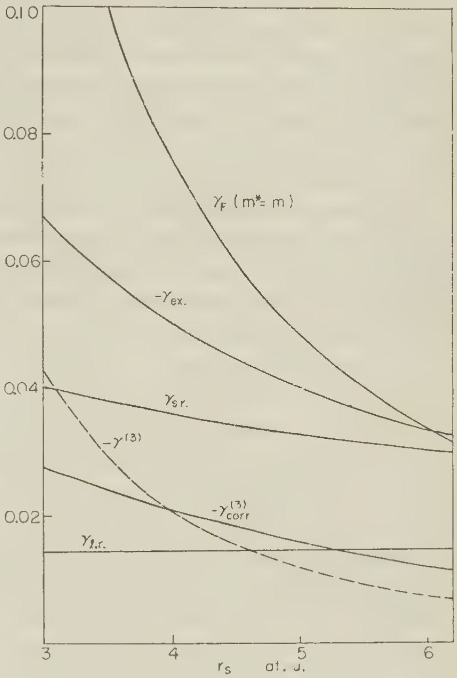

Fig. 1. Various contributions to γ, e.g. γ_F (1.5), $\gamma_{\text{ex.}}$ (1.6), $\gamma_{l.r.}$ (2.9), $\gamma_{s.r.}$ (3.10), $\gamma^{(3)}$ (A34), $\gamma^{(3)}_{\text{corr.}}$ (4.15) are shown as functions of r_s.

§ 5. Comparisons with Paramagnetic Susceptibilities of Alkali Metals

The total energy of the completely degenerate electron gas in the external magnetic field is given by the sum of the Fermi energy, exchange energy, long-range correlation energy, short-range correlation energy, third-order perturbation-theoretic energy of the screened Coulomb interaction and the Zeeman energy as follows:

$$E_{\text{total}}=E_0+\xi^2\gamma-\mu_B(n/N)H/(e^2/2a_0)\ , \qquad (5.1)$$

where E_0 is the total energy of the electron gas when $\xi=0$ and $H=0$, and from (1.5), (1.6), (2.9), (3.10) and (4.15) γ becomes

$$\gamma=\gamma_F+\gamma_{\text{ex.}}+\gamma_{l.r.}+\gamma_{s.r.}+\gamma^{(3)}_{\text{corr.}}\ . \qquad (5.2)$$

By looking for n so as to minimize the total energy (E_{total}), we can obtain the paramagnetic susceptibility in c.g.s. unit as follows:

Table I. Paramagnetic susceptibilities of alkali metals.

Metal	Li	Na	K	Rb	Cs
r_s at. u.	3.24	3.99	4.90	5.31	5.79
m^*/m	1.39	0.984	0.93	0.939	0.807
γ_F	0.0842	0.0784	0.0550	0.0464	0.0454
$\gamma_{\text{ex.}}$	−0.0629	−0.0510	−0.0416	−0.0384	−0.0352
$\gamma_{l.r.}$	0.0098	0.0099	0.0099	0.00995	0.0100
$\gamma_{s.r.}$	0.0397	0.0366	0.0335	0.0324	0.0312
$\gamma^{(3)}_{\text{corr.}}$	−0.0268	−0.0217	−0.0170	−0.0149	−0.0131
γ	0.0441	0.0521	0.0399	0.0354	0.0383
$\chi_{\text{cal.}}\cdot10^6$ c.g.s.	2.12	0.967	0.677	0.0599	0.428
$\chi_{\text{exp.}}\cdot10^6$ c.g.s.	1.90a 2.08±0.1c 1.96±0.1d	0.764a 0.95±0.1c 0.89±0.04e	0.793b	0.706a	0.887a

a Calculated from the measurements of the Knight shift by G. B. Benedek and T. Kushida: J. Phys. Chem. Solids **5** (1958) 241 and the calculations of the hyperfine interaction by H. Brooks (quoted by G. B. Benedek and T. Kushida).

b Calculated from the measurement of the Knight shift by W. B. Gager and F. J. Milford: Bull. Am. Phys. Soc. **5** (1960) 176 and the calculation of the hyperfine interaction by J. Callaway: *Solid State Physics* vol. 7 (Academic Press Inc., New York, 1958) 144.

c Obtained from the paramagnetic resonance experiments at 77°K by R. T. Schumacher and C. P. Slichter: Phys. Rev. **101** (1956) 58.

d Obtained in the same way as c by R. Hecht and A. G. Redfield: Bull. Am. Phys. Soc. **4** (1959) 240.

e Obtained like c at 4°K by R. T. Schumacher and W. E. Vehse: Bull. Am. Phys. Soc. **5** (1960) 296.

$$\chi=(n\mu_B/HV)=(N\mu_B^2/2\gamma V)=3.18\times10^{-6}r_s^{-3}\gamma^{-1}\ . \tag{5.3}$$

From (5.3) the paramagnetic susceptibilities for alkali metals are calculated and are shown in Table I. In this table, the values of r_s are the values at room temperature (300°K)[13] and we use the values of the effective mass calculated by Brooks[14].

The paramagnetic susceptibilities calculated for alkali metals are compared with the observed values, obtained from the intensity-measurement of the paramagnetic resonance of conduction electrons, for Li[15),16)] and Na[15),17)].

Table II. Volume dependence of $\chi\Omega$.

Metal	Li	Na	Rb	Cs
q	$\simeq -0.03$	$+0.635$	$+0.516$	$+0.601$

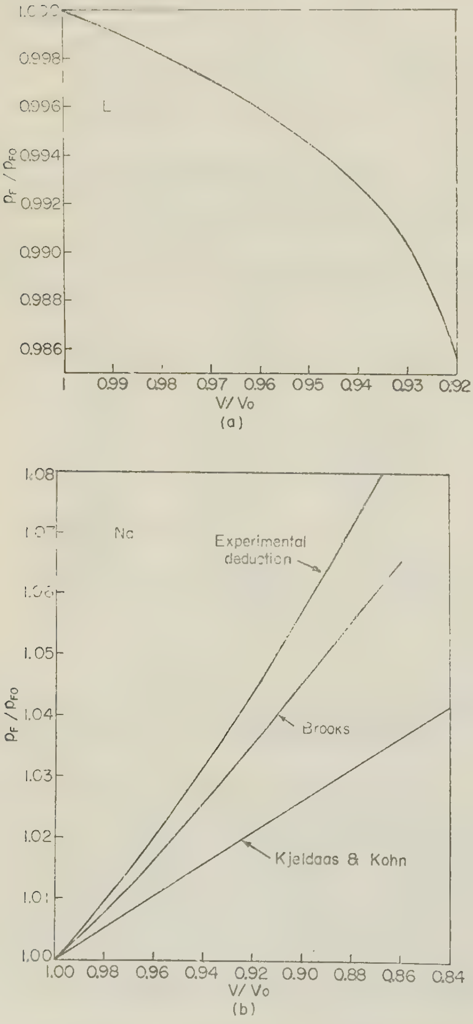

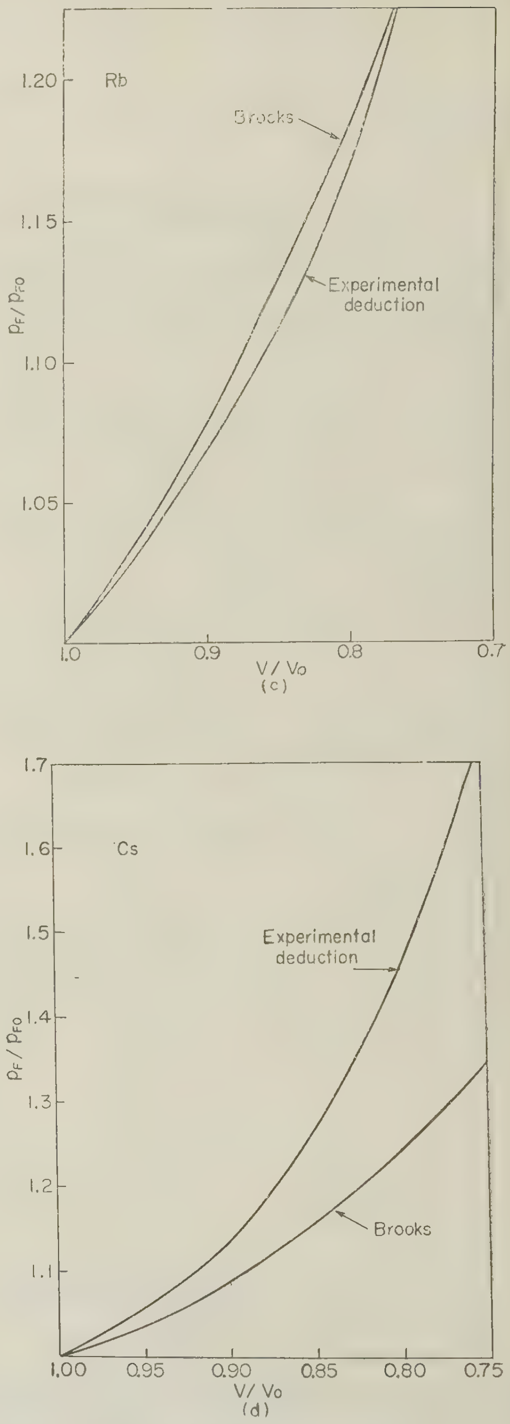

Fig. 2. Volume dependences of P_F for Li, Na, Rb and Cs derived from (5.3) and (5.4) using the Benedek and Kushida data[13)], together with the theoretical results obtained by Kjeldaas and Kohn[24)] for Na and those obtained by Brooks[25)] for Na, Rb and Cs.

On the other hand, the Knight shift K is given by[18)]

$$K=(8\pi/3)\chi\Omega P_F\ , \tag{5.4}$$

where Ω is atomic volume, $P_F=\langle|\Psi_F(0)|^2\rangle$ is the probability density of an electron, whose energy is equal to the Fermi energy, at the nucleus. From the measurements of the Knight shifts for Li, Na, Rb, Cs[13)] and K[19)] and the calculations of P_F for Li, Na, Rb, Cs by Brooks[20)] and for K by Callaway[21)], we can obtain χ using (5.4) and show the results in the eleventh row of Table I.

The agreements between the theoretical values and the experimental values of paramagnetic susceptibility for Li and Na are satisfactory. Generally it will be expected that the theoretical value obtained here is greater than the experimental one because we take into account up to the third-order perturbation calculation which contributes to γ as negative. However, for K, Rb, Cs the latter is greater than the former. This disagreement will be due to the fact that the higher-order terms of r_s in γ which are neglected in our calculation become important for K, Rb, Cs.

§ 6. Comparison with Pressure-Effect of the Knight Shift for Alkali Metals

Benedek and Kushida measured the pressure dependence of the Knight shift for Li, Na, Rb and Cs[13)], and determined the volume dependence of the Knight shift using Bridgman's data[22)] on the $P-V$ isotherms for the alkali metals. Following their analysis we shall discuss the volume dependence (or r_s dependence) of the paramagnetic susceptibility calculated in § 5.

In order to find the volume dependence of χ, (5.3), for alkali metals, we use the values of effective mass and its volume dependence* which were calculated by Brooks[14)] and Brooks and Ham[23)]. Expressing the volume dependence of $\chi\Omega$ as $\chi\Omega/(\chi\Omega)_0=(V/V_0)^q$, where V_0 is the volume at room temperature (300°K), from (5.3) we obtain the values of q as shown in Table II.

From the volume dependence of the Knight shift determined by Benedek and Kushida and that of the $\chi\Omega$ determined above, the volume dependences of P_F for Li, Na, Rb and Cs are obtained by (5.4) and are shown in Fig. 2. In Fig. 2b the comparisons with the calculated values by Kjeldass and Kohn[24)] and Brooks[25)] for Na are made. In Fig. 2c and 2d the comparisons with the calculated values of P_F by Brooks[25)] for Rb and Cs are made respectively. Although we could not make any comparison with the calculated values of P_F for Li, it is interesting to note that the volume dependence of P_F for this metal is very small.

Appendix I

Using the vector model of electron spins we calculate the third-order perturbation-theoretic energy of the screened Coulomb interaction. We consider N electrons in the volume V. The energy of the perturbation is as follows:

$$H'=\sum_{i>j} H_{ij}'\ , \tag{A1}$$

$$H_{ij}'=(4\pi e^2/V)\sum_{|\boldsymbol{p}|>k_c} p^{-2}\exp(i\boldsymbol{p}\cdot(\boldsymbol{r}_i-\boldsymbol{r}_j))\ . \tag{A2}$$

Let the unperturbed states be the states of the completely free electrons. In the ground state we assume that N electrons occupy the states with the wave vectors $\boldsymbol{k}_1, \boldsymbol{k}_2, \cdots, \boldsymbol{k}_N$

---

* For the r_s dependence of effective mass m^* of Cs we use the following data calculated by Brooks (private communication):

r_s	4.2	4.6	5.0	5.4	5.8	6.2
m/m^*	1.7297	1.4858	1.3068	1.2862	1.2370	1.2004

We should like to express our sincere thanks to Professor H. Brooks and Dr. T. Kushida for informing us of these results.

respectively and the spin function is expressed by Θ_0. Then, the total wave function $\Psi_0(\boldsymbol{k}_1, \boldsymbol{k}_2, \cdots, \boldsymbol{k}_N)$ is

$$\Psi_0(\boldsymbol{k}_1, \boldsymbol{k}_2, \cdots, \boldsymbol{k}_N)=(N!)^{-1/2}\sum_P \varepsilon_P P\varphi_{\boldsymbol{k}_1}(1)\varphi_{\boldsymbol{k}_2}(2)\cdots\varphi_{\boldsymbol{k}_N}(N)P^\sigma\Theta_0 \,, \tag{A3}$$

where

$$\varphi_{\boldsymbol{k}_j}(i)=V^{-1/2}\exp(i\boldsymbol{k}_j\cdot\boldsymbol{r}_i) \,. \tag{A4}$$

P and P^σ are permutation operators on electron coordinates and spin coordinates respectively and $\varepsilon_P=+1$ or -1 if P is an even or an odd permutation.

In the state in which i and j electrons jump to other orbits with the wave vectors $\boldsymbol{k}_i'$ and $\boldsymbol{k}_j'$ and the total spin states is described by $\Theta_{m'}$, the total unperturbed wave function is as follows:

$$\begin{aligned}\Psi_{m'}(\boldsymbol{k}_i', \boldsymbol{k}_j')=(N!)^{-1/2}\sum_P \varepsilon_P P\varphi_{\boldsymbol{k}_1}(1)\cdots\varphi_{\boldsymbol{k}_{i-1}}(i-1)\varphi_{\boldsymbol{k}_i'}(i)\varphi_{\boldsymbol{k}_{i+1}}(i+1)\cdots\\ \times\varphi_{\boldsymbol{k}_{j-1}}(j-1)\varphi_{\boldsymbol{k}_j'}(j)\varphi_{\boldsymbol{k}_{j+1}}(j+1)\cdots\varphi_{\boldsymbol{k}_N}(N)P^\sigma\Theta_{m'} \,.\end{aligned} \tag{A5}$$

Using the formula of the third-order perturbation-calculation,

$$E_\lambda{}^{(3)}=\sum_\mu{}'\sum_\gamma{}'\frac{H_{\lambda\mu}'H_{\mu\gamma}'H_{\gamma\lambda}'}{(E_\lambda-E_\mu)(E_\lambda-E_\gamma)}-\sum_\mu{}'\frac{H_{\lambda\mu}'H_{\mu\lambda}'H_{\lambda\lambda}'}{(E_\lambda-E_\mu)^2} \,, \tag{A6}$$

we can obtain the third-order perturbation-theoretic energy of the screened Coulomb interactions as follows:

$$E^{(3)}=E_1{}^{(3)}+E_2{}^{(3)}+E_3{}^{(3)} \,, \tag{A7}$$

$$\begin{aligned}E_1{}^{(3)}=\frac{1}{8}\sum_{\boldsymbol{k}_i,\boldsymbol{k}_j,}\sum_{\boldsymbol{k}_i',\boldsymbol{k}_j',}\sum_{\boldsymbol{k}_i'',\boldsymbol{k}_j'',}\sum_{m',m''}\frac{(0;\,\boldsymbol{k}_i\boldsymbol{k}_j|H_{ij}'|m';\,\boldsymbol{k}_i'\boldsymbol{k}_j')(m';\,\boldsymbol{k}_i'\boldsymbol{k}_j'|H_{ij}'|m'';\,\boldsymbol{k}_i''\boldsymbol{k}_j'')}{\{\varepsilon(\boldsymbol{k}_i', \boldsymbol{k}_j')-\varepsilon(\boldsymbol{k}_i, \boldsymbol{k}_j)\}\{\varepsilon(\boldsymbol{k}_i'', \boldsymbol{k}_j'')-\varepsilon(\boldsymbol{k}_i, \boldsymbol{k}_j)\}}\\ \times(m'';\,\boldsymbol{k}_i''\boldsymbol{k}_j''|H_{ij}'|0;\,\boldsymbol{k}_i\boldsymbol{k}_j) \,,\end{aligned} \tag{A8}$$

$$\begin{aligned}E_2{}^{(3)}=\frac{1}{8}\sum_{\boldsymbol{k}_i,\boldsymbol{k}_j,}\sum_{\substack{\boldsymbol{k}_l\neq\boldsymbol{k}_i,\\ \neq\boldsymbol{k}_j,}}\sum_{\boldsymbol{k}_i',\boldsymbol{k}_j',}\sum_{m',m''}\\ \times\Bigg[\sum_{\boldsymbol{k}_i'',\boldsymbol{k}_l'}\frac{(0;\,\boldsymbol{k}_i\boldsymbol{k}_j|H_{ij}'|m';\,\boldsymbol{k}_i'\boldsymbol{k}_j')(m';\,\boldsymbol{k}_i\boldsymbol{k}_l|H_{il}'|m'';\,\boldsymbol{k}_i''\boldsymbol{k}_l')(m'';\,\boldsymbol{k}_i''\boldsymbol{k}_j'\boldsymbol{k}_l'|H_{jl}'|0;\,\boldsymbol{k}_i\boldsymbol{k}_j\boldsymbol{k}_l)}{\{\varepsilon(\boldsymbol{k}_i', \boldsymbol{k}_j')-\varepsilon(\boldsymbol{k}_i, \boldsymbol{k}_j)\}\{\varepsilon(\boldsymbol{k}_i'', \boldsymbol{k}_j', \boldsymbol{k}_l')-\varepsilon|\boldsymbol{k}_i, \boldsymbol{k}_j, \boldsymbol{k}_l)\}}\\ +\sum_{\boldsymbol{k}_j'',\boldsymbol{k}_l'}\frac{(0;\,\boldsymbol{k}_i\boldsymbol{k}_j|H_{ij}'|m';\,\boldsymbol{k}_i'\boldsymbol{k}_j')(m';\,\boldsymbol{k}_j'\boldsymbol{k}_l|H_{jl}'|m'';\,\boldsymbol{k}_j''\boldsymbol{k}_l')(m'';\,\boldsymbol{k}_i'\boldsymbol{k}_j''\boldsymbol{k}_l'|H_{il}'|0;\,\boldsymbol{k}_i\boldsymbol{k}_j\boldsymbol{k}_l)}{\{\varepsilon(\boldsymbol{k}_i', \boldsymbol{k}_j')-\varepsilon(\boldsymbol{k}_i, \boldsymbol{k}_j)\}\{\varepsilon(\boldsymbol{k}_i', \boldsymbol{k}_j'', \boldsymbol{k}_l')-\varepsilon(\boldsymbol{k}_i, \boldsymbol{k}_j, \boldsymbol{k}_l)\}}\Bigg] \,,\end{aligned} \tag{A9}$$

$$\begin{aligned}E_3{}^{(3)}=\frac{1}{4}\sum_{\boldsymbol{k}_i,\boldsymbol{k}_j,}\sum_{\boldsymbol{k}_i',\boldsymbol{k}_j',}\sum_{m',m''}\\ \times\Bigg[\frac{(0;\,\boldsymbol{k}_i\boldsymbol{k}_j|H_{ij}'|m';\,\boldsymbol{k}_i'\boldsymbol{k}_j')(m';\,\boldsymbol{k}_i'\boldsymbol{k}_j'|H'|m'';\,\boldsymbol{k}_i'\boldsymbol{k}_j')(m'';\,\boldsymbol{k}_i'\boldsymbol{k}_j'|H_{ij}'|0;\,\boldsymbol{k}_i\boldsymbol{k}_j)}{\{\varepsilon(\boldsymbol{k}_i', \boldsymbol{k}_j')-\varepsilon(\boldsymbol{k}_i, \boldsymbol{k}_j)\}^2}\\ -\frac{(0;\,\boldsymbol{k}_i\boldsymbol{k}_j|H_{ij}'|m';\,\boldsymbol{k}_i'\boldsymbol{k}_j')(m';\,\boldsymbol{k}_i'\boldsymbol{k}_j'|H_{ij}'|m'';\,\boldsymbol{k}_i\boldsymbol{k}_j)(m'';\,\boldsymbol{k}_i\boldsymbol{k}_j|H'|0;\,\boldsymbol{k}_i\boldsymbol{k}_j)}{\{\varepsilon(\boldsymbol{k}_i', \boldsymbol{k}_j')-\varepsilon(\boldsymbol{k}_i, \boldsymbol{k}_j)\}^2}\Bigg] \,,\end{aligned} \tag{A10}$$

where

$$\varepsilon(\boldsymbol{k}_i, \boldsymbol{k}_j)=\frac{\hbar^2}{2m}(k_i{}^2+k_j{}^2) \,, \tag{A11}$$

$$\varepsilon(\boldsymbol{k}_i, \boldsymbol{k}_j, \boldsymbol{k}_l)=\frac{\hbar^2}{2m}(k_i{}^2+k_j{}^2+k_l{}^2) \,, \tag{A12}$$

$$(m';\, \boldsymbol{k}_i'\boldsymbol{k}_j'|H_{ij}'|m'';\, \boldsymbol{k}_i''\boldsymbol{k}_j'')=\int \Psi^*_{m'}(\boldsymbol{k}_1\cdots\boldsymbol{k}_i'\cdots\boldsymbol{k}_j'\cdots\boldsymbol{k}_N)H_{ij}'$$
$$\times\Psi_{m''}(\boldsymbol{k}_1\cdots\boldsymbol{k}_i''\cdots\boldsymbol{k}_j''\cdots\boldsymbol{k}_N)d\tau_1\cdots d\tau_N=\frac{4\pi e^2}{V}\sum_{|\boldsymbol{P}|>k} p^{-2}$$
$$\times\{\delta(-\boldsymbol{k}_i'+\boldsymbol{p}+\boldsymbol{k}_i'')\delta(-\boldsymbol{k}_j'-\boldsymbol{p}+\boldsymbol{k}_j'')-\delta(-\boldsymbol{k}_i'+\boldsymbol{p}+\boldsymbol{k}_j'')\delta(-\boldsymbol{k}_j'-\boldsymbol{p}+\boldsymbol{k}_i'')P^{(ij)}_{m'm''}\}\,, \tag{A13}$$

and $P^{(ij)}_{mm'}=\int\Theta^*_m P^{(ij)}\Theta_{m'}d\xi_1\cdots d\xi_N$, where $P^{(ij)}$ is an exchange operator between i and j spin coordinates, and

$$(m;\, \boldsymbol{k}_i\boldsymbol{k}_j\boldsymbol{k}_l|H_{jl}'|m';\, \boldsymbol{k}_i'\boldsymbol{k}_j'\boldsymbol{k}_l')=\int\Psi^*_m(\boldsymbol{k}_1\cdots\boldsymbol{k}_i\cdots\boldsymbol{k}_j\cdots\boldsymbol{k}_l\cdots\boldsymbol{k}_N)H_{jl}'$$
$$\times\Psi_{m'}(\boldsymbol{k}_1\cdots\boldsymbol{k}_i'\cdots\boldsymbol{k}_j'\cdots\boldsymbol{k}_l'\cdots\boldsymbol{k}_N)d\tau_1\cdots d\tau_N$$
$$=\frac{4\pi e^2}{V}\sum_{|\boldsymbol{P}|>k_c} p^{-2}[\delta(\boldsymbol{k}_i-\boldsymbol{k}_i')\{\delta(-\boldsymbol{k}_j+\boldsymbol{p}+\boldsymbol{k}_j')\delta(-\boldsymbol{k}_l-\boldsymbol{p}+\boldsymbol{k}_l')\delta_{mm'}$$
$$-\delta(-\boldsymbol{k}_j+\boldsymbol{p}+\boldsymbol{k}_l')\delta(-\boldsymbol{k}_l-\boldsymbol{p}+\boldsymbol{k}_j')P^{(jl)}_{mm'}\}-\delta(\boldsymbol{k}_i-\boldsymbol{k}_j')\{\delta(-\boldsymbol{k}_j+\boldsymbol{p}+\boldsymbol{k}_i')\delta(-\boldsymbol{k}_l-\boldsymbol{p}+\boldsymbol{k}_l')P^{(ij)}_{mm'}$$
$$-\delta(-\boldsymbol{k}_j+\boldsymbol{p}+\boldsymbol{k}_l')\delta(-\boldsymbol{k}_l-\boldsymbol{p}+\boldsymbol{k}_i')(P^{(ij)}P^{(il)})_{mm'}\}]\,. \tag{A14}$$

(4.2) is obtained from (A8), (A11) and (A13) if we leave the spin permutation operators in the vector model without integrations. The processes of the perturbation in this case are shown as follows:

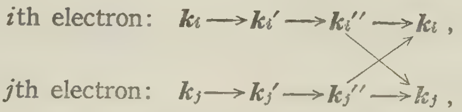

*i*th electron: $\boldsymbol{k}_i \longrightarrow \boldsymbol{k}_i' \longrightarrow \boldsymbol{k}_i'' \longrightarrow \boldsymbol{k}_i$,
*j*th electron: $\boldsymbol{k}_j \longrightarrow \boldsymbol{k}_j' \longrightarrow \boldsymbol{k}_j'' \longrightarrow \boldsymbol{k}_j$,

(A15)

where the crossing of the two arrows means the exchange of the two electrons.

(4.3) is obtained from (A9), (A11), (A12), (A13), and (A14) as before. In this case there are the following 16 processes:

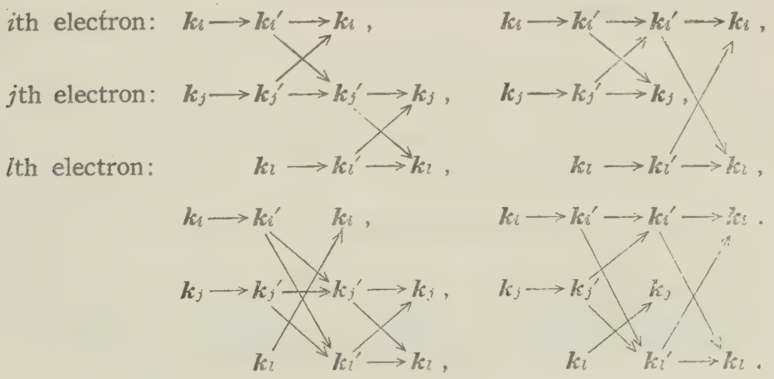

*i*th electron: $\boldsymbol{k}_i \longrightarrow \boldsymbol{k}_i' \longrightarrow \boldsymbol{k}_i$,
*j*th electron: $\boldsymbol{k}_j \longrightarrow \boldsymbol{k}_j' \longrightarrow \boldsymbol{k}_j' \longrightarrow \boldsymbol{k}_j$,
*l*th electron: $\boldsymbol{k}_l \longrightarrow \boldsymbol{k}_l' \longrightarrow \boldsymbol{k}_l$,
$\boldsymbol{k}_i \longrightarrow \boldsymbol{k}_i' \longrightarrow \boldsymbol{k}_i' \longrightarrow \boldsymbol{k}_i$,
$\boldsymbol{k}_j \longrightarrow \boldsymbol{k}_j' \longrightarrow \boldsymbol{k}_j$,
$\boldsymbol{k}_l \longrightarrow \boldsymbol{k}_l' \longrightarrow \boldsymbol{k}_l$,
$\boldsymbol{k}_i \longrightarrow \boldsymbol{k}_i'$ $\boldsymbol{k}_i$,
$\boldsymbol{k}_j \longrightarrow \boldsymbol{k}_j' \longrightarrow \boldsymbol{k}_j' \longrightarrow \boldsymbol{k}_j$,
$\boldsymbol{k}_l$ $\boldsymbol{k}_l' \longrightarrow \boldsymbol{k}_l$,
$\boldsymbol{k}_i \longrightarrow \boldsymbol{k}_i' \longrightarrow \boldsymbol{k}_i' \longrightarrow \boldsymbol{k}_i$.
$\boldsymbol{k}_j \longrightarrow \boldsymbol{k}_j'$ $\boldsymbol{k}_j$
$\boldsymbol{k}_l$ $\boldsymbol{k}_l' \longrightarrow \boldsymbol{k}_l$.

(A16)

(4.4) is obtained from (A1), (A10), (A11), and (A13) and there are 8 processes in this case, that is,

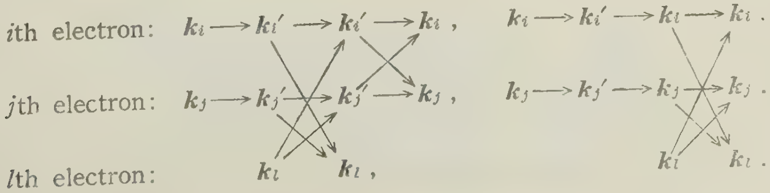

*i*th electron: $\boldsymbol{k}_i \longrightarrow \boldsymbol{k}_i' \longrightarrow \boldsymbol{k}_i' \longrightarrow \boldsymbol{k}_i$,
*j*th electron: $\boldsymbol{k}_j \longrightarrow \boldsymbol{k}_j' \longrightarrow \boldsymbol{k}_j' \longrightarrow \boldsymbol{k}_j$,
*l*th electron: $\boldsymbol{k}_l$ $\boldsymbol{k}_l$,
$\boldsymbol{k}_i \longrightarrow \boldsymbol{k}_i' \longrightarrow \boldsymbol{k}_i \longrightarrow \boldsymbol{k}_i$.
$\boldsymbol{k}_j \longrightarrow \boldsymbol{k}_j' \longrightarrow \boldsymbol{k}_j \longrightarrow \boldsymbol{k}_j$.
$\boldsymbol{k}_l$ $\boldsymbol{k}_l$.

(A17)

Appendix II

As we have not succeeded in carrying out the necessary integrations in (4.5)–(4.14) analytically, we calculate the integrations using the following four approximations:

(1) The scalar products of two independent vectors are neglected, e.g. $\boldsymbol{p}\cdot(\boldsymbol{p}+\boldsymbol{k}_1+\boldsymbol{k}_2)\to p^2$, $(\boldsymbol{p}-\boldsymbol{p}')^2\to p^2+p'^2$.

(2) k_1^2, k_2^2 and k_3^2 in the integrands are replaced by the mean values in the Fermi sphere, that is, 3/5.

(3) Taking into account the fact that $p>\beta$, $\beta\sim1$ in alkali metals, and the contribution from the lower value of p is considered to be predominant in the integrations of p, we use the following approximation $(p^2+k_1^2+k_2^2)^{-1}\to p^{-2}-(k_1^2+k_2^2)/(2p^4)$ when $p^2\sim k_1^2+k_2^2$.

(4) By making use of the above three approximations, $\boldsymbol{k}_1$, $\boldsymbol{k}_2$, and $\boldsymbol{k}_3$ in all the integrands disappear. Then, for the integrations over $\boldsymbol{k}_1$, $\boldsymbol{k}_2$, and $\boldsymbol{k}_3$, we use the following approximation. In the equations which define the regions of integrations for $\boldsymbol{k}_1$ in (4.5) and (4.6), $|\boldsymbol{k}_1+\boldsymbol{p}|>n_+$ and $|\boldsymbol{k}_1+\boldsymbol{p}'|>n_+$ are assumed to be independent of each other because $|\boldsymbol{p}-\boldsymbol{p}'|>\beta$. The region of integration for $\boldsymbol{k}_1$ is shown in Fig. 3 as the shaded area, but we neglect the portion where the three spheres O, P, and Q overlap trebly.

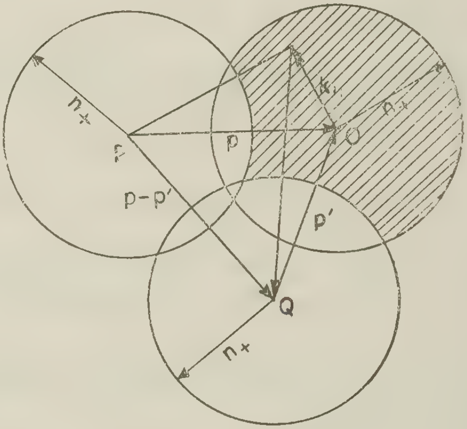

Fig. 3. Allowed regions of integrations for $\boldsymbol{k}_1$, $\boldsymbol{k}_2$ and $\boldsymbol{k}_3$ in (4.5) and (4.6).

Then, when $p<2n_+$, $p'<2n_+$, the integration of $\boldsymbol{k}_1$ over the region $0<k_1<n_+$, $|\boldsymbol{k}_1+\boldsymbol{p}|>n_+$, $|\boldsymbol{k}_1+\boldsymbol{p}'|>n_+$, becomes $\int d^3\boldsymbol{k}_1=\pi\{4n_+^3/3-(4n_+^3/3-n_+^2p+p^3/12)-(4n_+^3/3-n_+^2p'+p'^3/12)\}$, where $\pi((4/3)n_+^3-n_+^2p+(p^3/12))$ is the volume that the spheres O and P in Fig. 3 overlap each other. Similarly the integrations for $\boldsymbol{k}_2$ and the integrations when n_+ is replaced by n_- are carried out.

Furthermore we use the expansions:

$$n_\pm=k_\pm/k_0=1\pm\frac{1}{3}\xi-\frac{1}{9}\xi^2\,, \tag{A18}$$

in the integrations and we calculate the coefficients of ξ^2 only.

Therefore, when $p<2$ and $p'<2$ we have

$$\left.\begin{aligned}K_{+-}&=\int\limits_{\substack{k_1<n_+,\\ |\boldsymbol{k}_1+\boldsymbol{P}|>n_+,\\ |\boldsymbol{k}_1+\boldsymbol{P}'|>n_+.}} d^3\boldsymbol{k}_1\int\limits_{\substack{k_2<n_-,\\ |\boldsymbol{k}_2+\boldsymbol{P}|>n_-,\\ |\boldsymbol{k}_2+\boldsymbol{P}'|>n_-.}} d^3\boldsymbol{k}_2=C_{+-}+\xi^2I_{+-}\,,\\ I_{+-}&=(\pi^2/54)\{-96+112(p+p')-36(p+p')^2+(p+p')(p^3+p'^3)\}\,;\end{aligned}\right\} \tag{A19}$$

when $p<2$ and $p'>2$,

$$K_{+-}=C'_{+-}+\xi^2I'_{+-}\,,\qquad I'_{+-}=-(2\pi^2/3)p^2+(\pi^2/54)p^4\,; \tag{A20}$$

when $p>2$ and $p'<2$,

$$K_{+-}=C''_{+-}+\xi^2I''_{+-}\,,\qquad I''_{+-}=-(2\pi^2/3)p'^2+(\pi^2/54)p'^4\,; \tag{A21}$$

when $p>2$ and $p'>2$,

$$K_{+-}=(16\pi^2/9)(1-\xi^2)\,. \tag{A22}$$

After all, the part of $E_1^{(3)}(+-)$, (4.5), which is proportional to ξ^2 is as follows:

$$E_1^{(3)}(+-)=\frac{3\alpha r_s}{2\pi^5}\xi^2\left[\left\{\int_\beta^2 dp\int_\beta^2 dp' I_{+-}+\int_\beta^2 dp\int_2^\infty dp' I'_{+-}\right.\right.$$
$$\left.\left.+\int_2^\infty dp\int_\beta^2 dp' I''_{+-}-\frac{16\pi^2}{9}\int_2^\infty dp\int_2^\infty dp'\right\}\frac{1}{p^2p'^2(p^2+p'^2)}\right]. \tag{A23}$$

By carrying out the integrations for p and p' and from (1.1), we have

$$E_1^{(3)}(+-)/\xi^2=\gamma_1^{(3)}(+-)=-0.1071r_s^{-1}+0.2042r_s^{-1/2}-0.1331$$
$$+0.01986r_s^{1/2}+0.005284r_s+0.0001167r_s(\ln r_s)^2-0.002108r_s\ln r_s$$
$$-0.0001426r_s^{3/2}+0.00003265r_s^2+1.346\times10^{-6}r_s^{5/2}-1.338\times10^{-8}r_s^{7/2}\,. \tag{A24}$$

The integrations for $\boldsymbol{k}_1$ and $\boldsymbol{k}_2$ in (4.6) are worked out as before, and when $p<2$ and $p'<2$ we have

$$\left.\begin{aligned}
K_{\pm\pm}&=\int\limits_{\substack{k_1<n_\pm,\\ |\boldsymbol{k}_1+\boldsymbol{P}|>n_\pm,\\ |\boldsymbol{k}_1+\boldsymbol{P}'|>n_\pm,}} d^3\boldsymbol{k}_1\int\limits_{\substack{k_2<n_\pm,\\ |\boldsymbol{k}_2+\boldsymbol{P}|>n_\pm,\\ |\boldsymbol{k}_2+\boldsymbol{P}'|>n_\pm,}} d^3\boldsymbol{k}_2=C\pm D\xi+\xi^2 I\,,\\
I&=\pi^2\left\{\frac{16}{9}-\frac{40}{27}p+\frac{2}{9}p^2+\frac{p^4}{54}+\left(-\frac{40}{27}+\frac{4}{9}p+\frac{p^3}{54}\right)p'+\frac{2}{9}p'^2+\frac{pp'^3}{54}+\frac{p'^4}{54}\right\};
\end{aligned}\right\} \tag{A25}$$

when $p<2$ and $p'>2$ we have

$$K_{\pm\pm}=C'\pm D'\xi+\xi^2 I'\,,\qquad I'=(\pi^2/54)p^2(12+p^2)\,; \tag{A26}$$

when $p>2$ and $p'<2$ we have

$$K_{\pm\pm}=C''\pm D''\xi+\xi^2 I''\,,\qquad I''=(\pi^2/54)p'^2(12+p'^2)\,; \tag{A27}$$

and when $p>2$ and $p'>2$ we have

$$K_{\pm\pm}=(16\pi^2/9)(1\pm2\xi+\xi^2)\,. \tag{A28}$$

From (A25)-(A28), (4.6) becomes

$$E_1^{(3)}(++)+E_1^{(3)}(--)=\frac{3\alpha r_s}{2\pi^5}\,\frac{6}{5}\xi^2\left[\left\{\int_\beta^2 dp\int_\beta^2 dp' I+\int_\beta^2 dp\int_2^\infty dp' I'\right.\right.$$
$$\left.\left.+\int_2^\infty dp\int_\beta^2 dp' I''+\frac{16\pi^2}{9}\int_2^\infty dp\int_2^\infty dp'\right\}\frac{1}{p^2p'^2(p^2+p'^2)^2}\right]. \tag{A29}$$

By carrying out the integrations for p and p' and from (1.1), we have

$$\{E_1^{(3)}(++)+E_1^{(3)}(--)\}/\xi^2=\gamma_1^{(3)}(++)+\gamma_1^{(3)}(--)$$
$$=0.07060r_s^{-2}-0.07796r_s^{-3/2}+0.01664r_s^{-1}+0.001354-4.171\times10^{-4}r_s^{1/2}$$
$$+2.198\times10^{-5}r_s-4.075\times10^{-6}r_s^{3/2}+1.657\times10^{-6}r_s^2+6.851\times10^{-9}r_s^{5/2}\,. \tag{A30}$$

Then from (A24) and (A30) $E_1^{(3)}$, (4.2), becomes

$$E_1^{(3)}=E_1^{(3)}(+-)+E_1^{(3)}(++)+E_1^{(3)}(--)=\text{const.}+\xi^2\gamma_1^{(3)}\,,$$
$$\gamma_1^{(3)}=\gamma_1^{(3)}(+-)+\gamma_1^{(3)}(++)+\gamma_1^{(3)}(--)$$
$$=0.07060r_s^{-2}-0.07796r_s^{-3/2}-0.09050r_s^{-1}+0.2042r_s^{-1/2}$$
$$-0.1318+0.01945r_s^{1/2}+0.005306r_s-1.467\times10^{-4}r_s^{3/2}$$
$$+3.431\times10^{-5}r_s^2+1.353\times10^{-6}r_s^{5/2}-1.338\times10^{-8}r_s^{7/2}$$
$$+1.167\times10^{-4}r_s(\ln r_s)^2-2.108\times10^{-3}r_s\ln r_s\,. \tag{A31}$$

For the calculations of $E_2^{(3)}$ and $E_3^{(3)}$ the same approximations with the ones used for the calculation of $E_1^{(3)}$ are made use of and the results are as follows:

$$\left.\begin{aligned}E_2^{(3)}=&E_2^{(3)}(+++)+E_2^{(3)}(++-)+E_2^{(3)}(+-+)+E_2^{(3)}(-++)\\&+E_2^{(3)}(---)+E_2^{(3)}(--+)+E_2^{(3)}(-+-)+E_2^{(3)}(+--)=\text{const.}+\xi^2\gamma_2^{(3)}\ ,\\ \gamma_2^{(3)}=&-0.1819r_s^{-2}-0.09327r_s^{-1}+0.04218-0.004582r_s-5.371\times10^{-6}r_s^2+0.001002r_s\ln r_s\ ,\end{aligned}\right\}\tag{A32}$$

and

$$\left.\begin{aligned}E_3^{(3)}=&E_3^{(3)}(+++)+E_3^{(3)}(++-)+E_3^{(3)}(+-+)+E_3^{(3)}(-++)\\&+E_3^{(3)}(---)+E_3^{(3)}(--+)+E_3^{(3)}(-+-)+E_3^{(3)}(+--)=\text{const.}+\xi^2\gamma_3^{(3)}\ ,\\ \gamma_3^{(3)}=&-0.6318r_s^{-5/2}+0.2214r_s^{-3/2}-0.003347r_s^{-1/2}+5.518\times10^{-4}r_s^{1/2}+8.321\times10^{-5}r_s\ .\end{aligned}\right\}\tag{A33}$$

Then, from (A31), (A32) and (A33) $E^{(3)}$, (4.1), becomes

$$\left.\begin{aligned}E^{(3)}=&E_0^{(3)}+\gamma^{(3)}\xi^2\ ,\\ \gamma^{(3)}=&\gamma_1^{(3)}+\gamma_2^{(3)}+\gamma_3^{(3)}=-0.6318r_s^{-5/2}-0.1113r_s^{-2}+0.1435r_s^{-3/2}-0.1838r_s^{-1}\\&+0.1708r_s^{-1/2}-0.08959+0.02000r_s^{1/2}+8.073\times10^{-4}r_s\\&-1.467\times10^{-4}r_s^{3/2}+2.894\times10^{-5}r_s^2+1.353\times10^{-6}r_s^{5/2}\\&-1.338\times10^{-8}r_s^{7/2}-0.001106r_s\ln r_s+1.167\times10^{-4}r_s(\ln r_s)^2\ .\end{aligned}\right\}\tag{A34}$$

In (A34) there are several terms which diverge if r_s tends to zero. This comes from the fact that we use the approximations, in obtaining (A34), which are reasonable at actual metallic densities ($r_s\sim4$) and undoubtedly will be wrong approximations at $r_s=0$, as seen from the dotted curve in Fig. 1.

Appendix III

At the high-density limit of the electron gas, the most important term in the third-order perturbation-calculation energies of the screened Coulomb interactions is the term which is independent on the spin orientations in $E_2^{(3)}$, (4.3). This is given by

$$\begin{aligned}E_h^{(3)}(\xi)=&f(n_+,n_+,n_+)+f(n_+,n_+,n_-)+f(n_+,n_-,n_-)+f(n_+,n_-,n_+)\\&+f(n_-,n_-,n_-)+f(n_-,n_-,n_+)+f(n_-,n_+,n_+)+f(n_-,n_+,n_-)\ ,\end{aligned}\tag{A35}$$

where $f(x_1, x_2, x_3)$ is defined as follows:

$$f(x_1,x_2,x_3)=\frac{3\alpha r_s}{32\pi^7}\int_{\substack{k_1<x_1,\\|\boldsymbol{k}_1+\boldsymbol{P}|>x_1,}}d^3\boldsymbol{k}_1\int_{\substack{k_2<x_2,\\|\boldsymbol{k}_2+\boldsymbol{P}|>x_2,}}d^3\boldsymbol{k}_2\int_{\substack{k_3<x_3,\\|\boldsymbol{k}_3+\boldsymbol{p}|>x_3.}}d^3\boldsymbol{k}_3\int_{p>\beta,}d^3\boldsymbol{p}\,\frac{1}{p^6\boldsymbol{p}\cdot(\boldsymbol{p}+\boldsymbol{k}_1+\boldsymbol{k}_2)\boldsymbol{p}\cdot(\boldsymbol{p}+\boldsymbol{k}_2+\boldsymbol{k}_3)}\ .\tag{A36}$$

From $n_\pm=1\pm(1/3)\xi-(1/9)\xi^2$, $E_h^{(3)}(\xi)$ is expanded in powers of ξ^2 as follows:

$$E_h^{(3)}(\xi)-E_h^{(3)}(0)=\frac{4}{3}\xi^2\left\{-2\frac{\partial f(x,1,1)}{\partial x}+\frac{\partial^2 f(x,1,1)}{\partial x^2}\right\}_{x=1}.\tag{A37}$$

We calculate $f(x_1, x_2, x_3)$ at the limit $\beta\to0$ in the following way. Let the direction cosines between $\boldsymbol{p}$ and $\boldsymbol{k}_1$, $\boldsymbol{k}_2$, $\boldsymbol{k}_3$, be λ_1, λ_2, λ_3 respectively. When $p\to0$, the regions of the integrations for $\boldsymbol{k}_i$ become $0\leq\lambda_i\leq1$, $k_i>x_i>k_i-p\lambda_i$ ($i=1, 2, 3$). Then we have

$$f(x_1,x_2,x_3)=\frac{3\alpha r_s}{\pi^3}\int_\beta^\infty\frac{dp}{p^3}\int_0^1d\lambda_1\int_0^1d\lambda_2\int_0^1d\lambda_3\,\frac{\lambda_1\lambda_2\lambda_3x_1^2x_2^2x_3^2}{(x_1\lambda_1+x_2\lambda_2)(x_2\lambda_2+x_3\lambda_3)}\ .\tag{A38}$$

From (A38) and $\beta=0.47r_s^{1/2}$, (A37) becomes

$$E_h^{(3)}(\xi)-E_h^{(3)}(0)=\xi^2\gamma_h^{(3)}\ ,\qquad\gamma_h^{(3)}=-0.0658\ ,\tag{A39}$$

When $r_s \rightarrow 0$, $\gamma^{(3)}$, given by (A34), of course does not coincide with $\gamma_h{}^{(3)}$, then we correct $\gamma^{(3)}$ as follows: assuming that at $r_s=0$ $\gamma^{(3)}$ becomes $\gamma_h{}^{(3)}$ and at $r_s=4$ $\gamma^{(3)}$ takes the value given by (A34) and taking account of the fact that $\gamma^{(3)}$ must become zero at $r_s \rightarrow \infty$, we approximate $\gamma^{(3)}$ by the formula

$$\gamma^{(3)}_{\text{corr.}} = \gamma_h{}^{(3)} \exp(-0.278 r_s) \,. \tag{A40}$$

This $\gamma^{(3)}_{\text{corr.}}$ is shown in Fig. 1.

References

1) W. Pauli: Zeits f. Phys. **41** (1927) 81.
2) J. B. Sampson and F. Seitz: Phys. Rev. **58** (1940) 633.
3) D. Pines: Phys. Rev. **95** (1954) 1090.
4) D. Pines: *Solid State Physics* vol. 1 (Academic Press Inc., New York, 1955) 367.
5) see reference 4.
6) K. A. Brueckner and K. Sawada: Phys. Rev. **112** (1958) 328.
7) R. A. Ferrell: Phys. Rev. **107** (1957) 450.
8) K. Sawada, K. A. Brueckner, N. Fukuda and R. Brout: Phys. Rev. **108** (1957) 507.
9) M. Shimizu: J. Phys. Soc. Japan **15** (1960) 376, hereafter referred to as (I).
10) P. Nozières and D. Pines: Phys. Rev. **111** (1958) 442.
11) J. G. Fletcher and D. C. Larson: Phys. Rev. **111** (1958) 455.
12) M. Gell-Mann and K. A. Brueckner: Phys. Rev. **106** (1957) 364.
13) G. B. Benedek and T. Kushida: J. Phys. Chem. Solids **5** (1958) 241.
14) see reference 13 and H. Brooks: Phys. Rev. **91** (1953) 1027.
15) R. T. Schumacher and C. P. Slichter: Phys. Rev. **101** (1956) 58.
16) R. Hecht and A. G. Redfield: Bull. Am. Phys. Soc. **4** (1959) 240.
17) R. T. Schumacher and W. E. Vehse: Bull. Am. Phys. Soc. **5** (1960) 296.
18) W. D. Knight: *Solid State Physics* vol. 2 (Academic Press. Inc., New York, 1956) 128.
19) W. B. Gager and F. J. Milford: Bull. Am. Phys. Soc. **5** (1960) 176.
20) see reference 13.
21) J. Callaway: *Solid State Physics* vol. 7 (Academic Press, Inc., New York, 1958) 144.
22) P. W. Bridgman: Proc. Amer. Acad. Arts Sci., **58** (1923) 166; **60** (1925) 385.
23) F. Ham: *Solid State Physics* vol. 1 (Academic Press. Inc., New York, 1955) 127.
24) T. Kjeldaas and W. Kohn: Phys. Rev. **101** (1955) 66.
25) see reference 13.

JOURNAL OF THE PHYSICAL SOCIETY OF JAPAN, Vol. 15, No. 12, DECEMBER, 1960

Magnetic Susceptibilities of Non-Ferromagnetic Transition Metals

By Masao SHIMIZU

Department of Physics, Faculty of Science, Tokyo Metropolitan University, Tokyo

and Takeshi TAKAHASHI

Faculty of Liberal Arts, Meijo University, Nagoya

(Received August 1, 1960)

The increases of the magnetic susceptibilities with temperature for non-ferromagnetic transition metals are investigated by making use of the band picture. If the Fermi surface at the absolute zero of temperature is in the neighbourhood of a minimum of the electron state density, the susceptibility increases with temperature at lower temperatures. Instead of the band with a minimum of the electron state density we use the band where two standard bands are superposed. The spin paramagnetic susceptibilities of this band are calculated numerically at arbitrary temperatures in the several cases of the position of the Fermi surface and the shape of the band, and it is shown that the susceptibilities increase with temperature at higher temperatures. By comparing our theoretical results with the experimental results for the susceptibilities of pure chromium and dilute alloys of iron in chromium at higher temperatures, the position and the shape of the Fermi surface in the neighbourhood of the minimum of the state density for chromium are discussed.

§ 1. Introduction

Among non-ferromagnetic transition metals there are many metals whose paramagnetic susceptibilities increase with temperature. We show in Table I their susceptibilities and the temperature dependences at room temperature [1),2),3),4)], where the signs of plus and minus represent the increase and the decrease with temperature respectively.

It will be difficult to understand this phenomenon by the Heitler-London model. Of course, it may be possible to consider that these transition metals are antiferromagnetic and their Néel temperatures are rather high. However, for some metals their susceptibilities increase even at about 2000°K. If these metals were antiferromagnetic, their Néel temperatures should be higher than 2000°K. Such an interpretation is improbable.

Making use of the band theory, Stoner[5)] has shown that if there is a minimum in the state density of the band and if the Fermi energy at 0°K is at the minimum, the magnetic susceptibility increases with temperature. This fact will be explained simply in the following way. The number of electrons and the total magnetic moment of electrons are given respectively by

$$\left.\begin{aligned} N&=\int_0^\infty \frac{\nu(\mathcal{E})d\mathcal{E}}{\exp[(\mathcal{E}-\mathcal{E}_F-\mu_B H)/kT]+1}+\int_0^\infty \frac{\nu(\mathcal{E})d\mathcal{E}}{\exp[(\mathcal{E}-\mathcal{E}_F+\mu_B H)/kT]+1}\,, \\ \frac{M}{\mu_B}&=\int_0^\infty \frac{\nu(\mathcal{E})d\mathcal{E}}{\exp[(\mathcal{E}-\mathcal{E}_F-\mu_B H)/kT]+1}-\int_0^\infty \frac{\nu(\mathcal{E})d\mathcal{E}}{\exp[(\mathcal{E}-\mathcal{E}_F+\mu_B H)/kT]+1}\,, \end{aligned}\right\} \tag{1}$$

where $\mathcal{E}$ is the energy of an electron, $\mathcal{E}_F$ the Fermi energy and $\nu(\mathcal{E})$ the density of states. From the first equation $\mathcal{E}_F$ is determined as a function of temperature, then from the second the susceptibility is obtained.

At low temperature integrals in (1) are expanded by series, and the paramagnetic susceptibility is given by

$$\chi=\frac{M}{H}=2\mu_B^2\nu(\mathcal{E}_0)\left\{1+\frac{\pi^2}{6}\left[\frac{\nu''(\mathcal{E}_0)}{\nu(\mathcal{E}_0)}-\left(\frac{\nu'(\mathcal{E}_0)}{\nu(\mathcal{E}_0)}\right)^2\right](kT)^2\right\}, \tag{2}$$

where $\mathcal{E}_0$ is the Fermi energy at 0°K, $\nu'(\mathcal{E})=d\nu(\mathcal{E})/d\mathcal{E}$ and $\nu''(\mathcal{E})=d^2\nu(\mathcal{E})/d\mathcal{E}^2$. If we assume for $\nu(\mathcal{E})$ the usual form $\mathcal{E}^{1/2}$ or $\mathcal{E}^n$, the sign of the temperature coefficient of the susceptibility is negative. Elcock *et al.*[6] calculated susceptibilities numerically from (1), and found that for these cases the temperature coefficients are negative at all temperatures.

On the other hand, if $\mathcal{E}_0$ is at a minimum of the state density the temperature coefficient becomes positive, because $\nu'(\mathcal{E}_0)$ is zero and $\nu''(\mathcal{E}_0)$ is positive. The transition metals, whose susceptibilities increase with temperature, have the lower values of susceptibilities and specific heats at low temperature (both are proportional to $\nu(\mathcal{E}_0)$) than those of two neighbouring elements in Table I. This fact is consistent with the above discussion. But (2) is valid for $T \ll \mathcal{E}_0/k$, and at arbitrary temperature where this condition is not necessarily satisfied we must work out numerical calculations with (1).

The purpose of this paper is to investigate the temperature dependence of the magnetic susceptibility at arbitrary temperature in the case where the Fermi energy at 0°K is in the neighbourhood of a minimum of the state density and to discuss the band shape in the neighbourhood of the minimum by comparing our results with the experimental results.

On the other hand it is supposed that the thermal expansion of these metals may affect their susceptibilities. But a simple calculation by the Stoner theory shows that this effect is considerably small (Appendix).

Table I. The magnetic susceptibilities, $\chi_{\mathrm{mole}} \times 10^6$, and their temperature dependences, $d\chi_{\mathrm{mole}}/dT \times 10^8$, at room temperature of non-ferromagnetic transition metals are shown. $d\chi_{\mathrm{nole}}/dT \times 10^8$ are shown in parentheses. The values are adopted from references 1, 2, 3 and 4. The susceptibility of W is nearly independent of temperature at room temperature, but at high temperature it increases with temperature ($d\chi_{\mathrm{mole}} dT \times 10^8 = 0.5$ at 1500°K).

Sc 315 (−24)	Ti 153 (+4)	V 230 (−1)	Cr 188 (+1)	Mn 533 (−14)	Fe —	Co —	Ni —
Y 191 (− 7)	Zr 120 (+2.5)	Nb 212 (−2)	Mo 89 (+0.2)	Tc —	Ru (44) (0)	Rh 102 (+3)	Pd 558 (−140)
La 122 (− 3)	Hf 81 (+1)	Ta 154 (−1)	W 58 (+0)	Re 69 (0)	Os 10 (+1)	Ir 26 (+2)	Pt 190 (− 12)

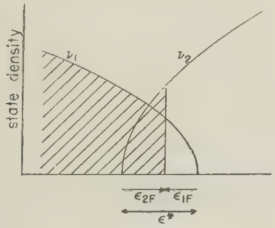

Fig. 1. Superposition of two "standard" bands. ε^* is the overlapping of bands, ε_{1F} and ε_{2F} are the Fermi energies.

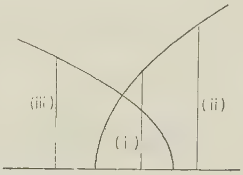

Fig. 2. Three cases in Eq. (6).

§ 2. Calculation of Paramagnetic Susceptibilities for Two Standard Bands Superposed

By superposition of two "standard" bands we approximate a band which has a minimum in the state density (Fig. 1); the state density is given by

$$\nu(\mathcal{E}) = \nu_1(\mathcal{E}) + \nu_2(\mathcal{E}), \quad \nu_1(\mathcal{E}) = a_1 \mathcal{E}^{1/2}, \quad \nu_2(\mathcal{E}) = a_2 \mathcal{E}^{1/2}. \tag{3}$$

For the left band in Fig. 1 $\mathcal{E}$ is measured from the top to the left, while for the right band $\mathcal{E}$ is measured from the bottom to the right. We represent the overlapping of bands by $\mathcal{E}^*$, the Fermi energies by $\mathcal{E}_{1F}$ and $\mathcal{E}_{2F}$ ($\mathcal{E}^* = \mathcal{E}_{1F} + \mathcal{E}_{2F}$), and their values at 0°K by $\mathcal{E}_{10}$ and $\mathcal{E}_{20}$ respectively.

For this band (1) becomes as follows:

$$\left.\begin{aligned}(N_1-N)/(kT)^{3/2}&=a_1[F_{1/2}(\eta_1+\beta')+F_{1/2}(\eta_1-\beta')]-a_2[F_{1/2}(\eta_2+\beta')+F_{1/2}(\eta_2-\beta')]\,,\\ M/\mu_B(kT)^{3/2}&=a_1[F_{1/2}(\eta_1+\beta')-F_{1/2}(\eta_1-\beta')]+a_2[F_{1/2}(\eta_2+\beta')-F_{1/2}(\eta_2-\beta')]\,,\end{aligned}\right\} \tag{4}$$

where

$$F_{1/2}(\eta)=\int_0^\infty\frac{x^{1/2}dx}{e^{x-\eta}+1}\,,\quad x=\mathcal{E}/kT,\quad \eta_1=\mathcal{E}_{1F}/kT,\quad \eta_2=\mathcal{E}_{2F}/kT,\quad \beta'=\mu_BH/kT\,,$$

and N_1 is the total number of states in the left band. Putting $\mathcal{E}^*=kT^*$, we have

$$\eta_1+\eta_2=T^*/T. \tag{5}$$

The first equation of (4) becomes

$$F_{1/2}(\eta_1)-pF_{1/2}(\eta_2)=\left\{\begin{array}{ll}\dfrac{2}{3}\dfrac{1-pr^{3/2}}{(1+r)^{3/2}}\left(\dfrac{T^*}{T}\right)^{3/2}, & \text{for } \mathcal{E}_{10}>0,\ \ \mathcal{E}_{20}>0 \text{ (Fig. 2 (i))};\\ -\dfrac{2}{3}p\left(\dfrac{r}{1+r}\right)^{3/2}\left(\dfrac{T^*}{T}\right)^{3/2}, & \text{for } \mathcal{E}_{10}<0,\ \ \mathcal{E}_{20}>0 \text{ (Fig. 2 (ii))};\\ \dfrac{2}{3}\dfrac{1}{(1+r)^{3/2}}\left(\dfrac{T^*}{T}\right)^{3/2}, & \text{for } \mathcal{E}_{10}>0,\ \ \mathcal{E}_{20}<0 \text{ (Fig. 2 (iii))},\end{array}\right\} \tag{6}$$

where $p=a_2/a_1$ and $r=\mathcal{E}_{20}/\mathcal{E}_{10}$.

From the second equation of (4)

$$\chi/(2\,\mu_B{}^2a_1\mathcal{E}^{*1/2})=[F'_{1/2}(\eta_1)+pF'_{1/2}(\eta_2)](T/T^*)^{1/2}\,, \tag{7}$$

where $F'_{1/2}(\eta)=dF_{1/2}(\eta)/d\eta$. The first term in the right-hand side of (7) is the contribution from the holes of the left band and the second is that from the electrons of the right band. η_1 and η_2 are determined as functions of temperature from (5) and (6), and then χ is given as a function of temperature by (7).

If $T\to0$,

$$\frac{\chi}{2\mu_B{}^2a_1\mathcal{E}^{*1/2}}\to\left\{\begin{array}{ll}\dfrac{1+pr^{1/2}}{(1+r)^{1/2}}\,, & \text{for } 0<r;\\ \dfrac{1}{(1+r)^{1/2}}\,, & \text{for } -1<r<0;\\ p\left(\dfrac{r}{1+r}\right)^{1/2}, & \text{for } r<-1\,.\end{array}\right\} \tag{8}$$

If $T\to\infty$, η_1 and η_2 approach their limiting values $\eta_1{}^\infty$ and $\eta_2{}^\infty$ given by

$$F_{1/2}(\eta_1{}^\infty)=pF_{1/2}(\eta_2{}^\infty)\,, \tag{9}$$

then

$$\chi/(2\mu_B{}^2a_1\mathcal{E}^{*1/2})\to[F'_{1/2}(\eta_1{}^\infty)+pF'_{1/2}(\eta_2{}^\infty)](T/T^*)^{1/2}\,. \tag{10}$$

At intermediate temperatures we calculate susceptibility numerically from (5), (6) and (7) We make use of the numerical values of $F_{1/2}(\eta)$ which have been given by McDougall an Stoner[7]. The results of our calculations for the temperature variations of the susceptibilit at several values of r when $p=1$ and 10 are shown in Fig. 3.

At higher temperatures susceptibilities increase infinitely with temperature. This behavio is due to the fact that we use the "open" band shown in Fig. 1, because in this case th number of the electrons which contribute to the susceptibility increases infinitely with increasin temperature. According to Elcock[8] a "closed" band composed of the superposition of tw standard bands (Fig. 4) gives a temperature decrease of susceptibility at higher temperature Of course, since the real band is closed, our calculation is not appropriate at higher tempera tures. However, because the usual temperature region will be rather "low" compared with the total width of a band, it is enough to use an open band.

On the other hand, at low temperature susceptibility is determined by $\nu(\mathcal{E}_0)$. There are two dips in the band given by (3). The shape of the band given by (3) will be rather different from that of the real band in the neighbourhood of the "minimum", then the calculated susceptibilities at low temperature will be unreliable.

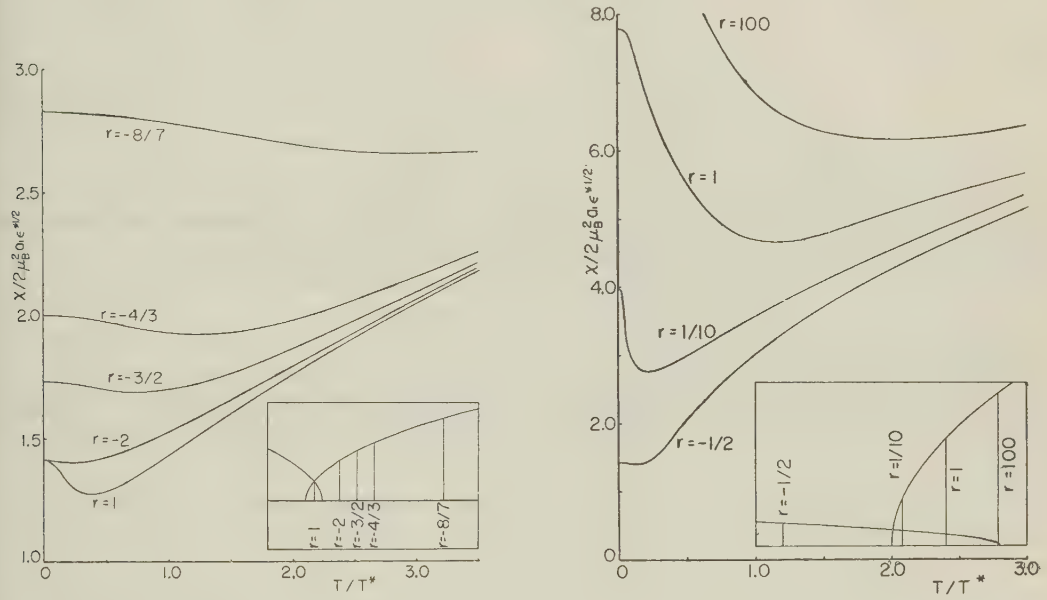

Fig. 3 (a). Fig. 3 (b).

Fig. 3. The calculated temperature-variations of the susceptibilities. (a) $p=1$, and (b) $p=10$.

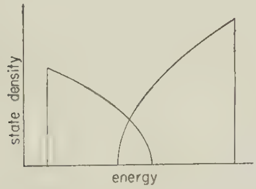

Fig. 4. "Closed" band composed by the superposition of two standard bands.

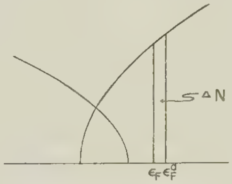

Fig. 5. Variation of the Fermi energy due to alloying. ε_F and $\varepsilon_F{}^a$ represent the Fermi energies of a pure metal and a dilute alloy respectively.

§ 3. Paramagnetic Susceptibilities of Dilute Alloys of Transition Metals

Now we consider dilute alloys in which a small amount of another metal is alloyed in the transition metals discussed above. Let the susceptibility of a transition metal be χ and that of its dilute alloy with another metal be $\chi+\Delta\chi$ and we obtain

$$\frac{\mathcal{E}^*}{\mu_B{}^2}\frac{\Delta\chi}{\Delta N}=\frac{pF''_{1/2}(\eta_2)-F''_{1/2}(\eta_1)}{pF'_{1/2}(\eta_2)+F'_{1/2}(\eta_1)}\frac{T^*}{T}, \tag{11}$$

where $F''_{1/2}(\eta)=d^2F_{1/2}(\eta)/d\eta^2$ and ΔN is the increase of the number of electrons (Fig. 5). Here we have assumed that the band shape is not affected by alloying and the additional electrons are distributed in the same band.

With these assumptions and assuming a proper band we can easily explain the increase of the specific heat, which is proportional to T at low temperature, when another metal is alloyed.

For $T\to 0$,

$$\frac{\varepsilon^*}{\mu_B^2}\frac{\Delta\chi}{\Delta N}\to\left\{\begin{array}{ll}\frac{1}{2}\frac{(1+r)(p-r^{1/2})}{pr+r^{1/2}}, & \text{for } 0<r;\\ \frac{1}{2}(r+1), & \text{for } -1<r<0;\\ \frac{1}{2}\frac{r+1}{r}, & \text{for } r<-1,\end{array}\right\} \tag{12}$$

and for $T\to\infty$,

$$\frac{\varepsilon^*}{\mu_B^2}\frac{\Delta\chi}{\Delta N}\to\frac{pF''_{1/2}(\eta_2^\infty)-F''_{1/2}(\eta_1^\infty)}{pF'_{1/2}(\eta_2^\infty)+F'_{1/2}(\eta_1^\infty)}\frac{T^*}{T}\propto T^{-1}. \tag{13}$$

As shown in the following section, this result agrees qualitatively with the experimental results obtained by Newmann and Stevens[9], *i.e.* in dilute alloys of iron in chromium $\Delta\chi$ follows the Curie law at higher temperatures (they explain this result with the Mott-Stevens model, namely they attribute $\Delta\chi$ to the effect of the two localized electrons of an iron atom).

§ 4. Comparison with Experimental Results

The results obtained above contain many parameters which cannot be determined definitely. So we ought to be satisfied with rather rough estimations in the following way. Now, we rewrite (11) and (13), and compare with the experimental results obtained by Newmann and Stevens[9].

If we neglect the difference between densities of pure chromium and dilute alloys of iron in chromium, and that between the atomic weights of chromium and iron,

$$\Delta N=1.16\times 10^{22}\,qx \quad \text{per gram,} \tag{14}$$

where x is the fraction of Fe atoms and q the increase of electrons per iron atom. Then (11) and (13) become

$$\Delta\chi=0.00721\,qx\frac{pF''_{1/2}(\eta_2)-F''_{1/2}(\eta_1)}{pF'_{1/2}(\eta_2)+F'_{1/2}(\eta_1)}\frac{1}{T}, \tag{11'}$$

and for $T\to\infty$

$$\Delta\chi\to 0.00721\,qx\frac{pF''_{1/2}(\eta_2^\infty)-F''_{1/2}(\eta_1^\infty)}{pF'_{1/2}(\eta_2^\infty)+F'_{1/2}(\eta_1^\infty)}\frac{1}{T}. \tag{13'}$$

η_1^∞ and η_1^∞ are determined by the value of p (see (9)), and then the slope of $1/\Delta\chi$ vs. T is determined by p, also.

Although it seems to be reasonable to take 2 for the value of q, we will regard q as a parameter for the time being. It is possible to obtain an agreement between our theoretical calculations and the experimental observations of susceptibilities if q is larger than 2 and p is larger than 10. We will use $p=10$ in the following consideration.

In Fig. 6 the measured values of susceptibilities for chromium are compared with the theoretical values of susceptibilities for $p=10$, $r=-2$, $T_{20}(=\mathcal{E}_{20}/k)=350°\text{K}$ and $p=10$, $r=1/10$, $T_{20}=250°\text{K}$. In Fig. 7 the measured $\Delta\chi$ of Cr-Fe alloy (1.05% Fe) is compared with the theoretical $\Delta\chi$ for the same parameters with those mentioned above. The values of a_1 in Fig. 6 and of q in Fig. 7 are determined to get an agreement between the theoretical values and the experimental values for susceptibilities at high temperature. It is difficult to determine the value of r precisely, because the curves are not so different for both cases where $r=-2$ and 1/10.

If the Fermi energy is nearer to the "minimum" (r is smaller) than these cases, it seems to be impossible to fit the calculated curves with the experimental results for both χ and $\Delta\chi$ by using the same values of parameters.

And if the Fermi energy is in the left-hand of the "minimum" ((iii) in Fig. 2), it is quite mpossible to get a satisfactory agreement between our calculations and experimental results or both χ and $\Delta\chi$. Anyhow it can be said that the order of magnitude of T_{20} for Cr is iven by the value obtained above($\sim$300°K).

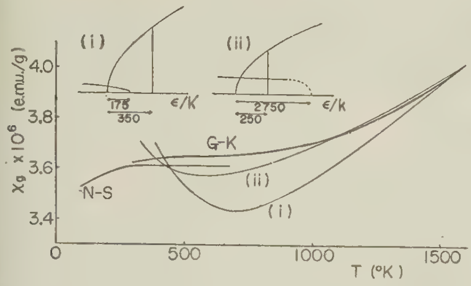

Fig. 6. Comparison between the theoretical susceptibilities and the experimental ones for chromium.

(i) Calculated for $p=10$, $r=-2$, $T_{20}=350$°K and $\mu_B{}^2k^{1/2}a_1=1.56\times10^{-8}$, e.m.u. g^{-1} deg$^{-1/2}$,

(ii) Calculated for $p=10$, $r=1/10$, $T_{20}=250$°K and $\mu_B{}^2k^{1/2}a_1=1.23\times10^{-8}$ e.m.u. g^{-1} deg$^{-1/2}$,

G-K: Experimental result by McGuire and Kriessman[1],

N-S: Experimental result by Newmann and Stevens[9].

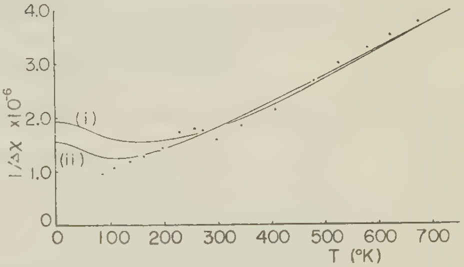

Fig. 7. Comparison between the theoretical susceptibilities and the experimental ones for 1.05% Fe in Cr.

(i) Calculated for $p=10$, $r=-2$, $T_{20}=350$°K, $q=4.8$,

(ii) Calculated for $p=10$, $r=1/10$, $T_{20}=250$°K, $q=5.8$,

Dots are experimental results by Newmann and Stevens[9].

The above-mentioned analysis is consistent with the experimental results on the low-emperature specific heat of Cr-Fe alloy obtained by Wei *et al.*[11] According to their neasurements, when the fraction of Fe atom, x, is small, γ increases rapidly with x, where T is the low-temperature specific heat. Because γ is proportional to $\nu(\mathcal{E}_0)$, if we assume that he band shape is not different from that of pure chromium when a small amount of iron toms is alloyed, we can expect that the slope of the state density vs. energy at $\mathcal{E}_0$ is steeper. To obtain a rough estimation we neglect the left half of the band shown in Fig. 1, *i.e.* $(\mathcal{E})=a\mathcal{E}^{1/2}$ and $a=(3/4)N\mathcal{E}_0{}^{-3/2}$, and we have $C/Nk=(\pi^2/2)(kT/\mathcal{E}_0)$, where C is the electronic pecific heat per mole. Then $\Delta\gamma/\Delta N=\pi^2k^2/(6\,\mathcal{E}_0)=\pi^2k/(6\,T_0)$. As $\Delta N=Lq\,x$, $\Delta\gamma=3.2\,qx/T_0$ cal. nole^{-1} deg^{-2}, where L is Avogadoro's number. Comparing this with the observed value, $\gamma/x=0.041$ cal. mole^{-1} deg^{-2}, we get

$$T_0=80\,q\,.$$

his is consistent with the result obtained above from the analysis of the magnetic suscepti-ility.

5. Conclusion

From the theoretical point of view we see that if the Fermi energy is at the minimum of he state density the magnetic susceptibility increases not only at low temperature but also t any temperature. Especially, from the comparison between the theoretical result and the xperimental one for chromium we can conclude as follows; (1) there is a minimum in the tate density of the band of chromium and the slope of the state density vs. energy above he minimum is considerably steeper than that below the minimum (*i.e.* $p\gg1$), (2) the Fermi nergy of chromium at 0°K is a little higher than the minimum, and (3) the magnetic sus-eptibility of Cr-Fe alloy can also be interpreted qualitatively by the band model.

This work was completed while one of the authors (T. T.) held a grant from Foundation or In-service Trainining and Welfare of the Private School Personnel.

Appendix

According to (2) in the text the magnetic susceptibility at low temperature is

$$\chi=2\,\mu_B^2\nu(\mathcal{E}_0)\,. \qquad \text{(A-1}$$

In order to estimate the effect of the thermal expansion on the susceptibility, we put

$$\nu(\mathcal{E})=4N\mathcal{E}^{1/2}/(3\,\mathcal{E}_0^{3/2}),\quad \mathcal{E}_0=(\hbar^2/2\,m^*)(3\pi^2N/V)^{2/3}\,,$$

where m^* is an effective mass of the electrons. Then

$$\chi=3^{1/3}\pi^{-4/3}N^{1/3}\mu_B^2\hbar^{-2}m^*V^{2/3}\,. \qquad \text{(A-}$$

The temperature variation of χ is

$$\begin{aligned}\left(\frac{\partial\ln\chi}{\partial T}\right)_P&=\left(\frac{\partial\ln\chi}{\partial\ln V}\right)_T\left(\frac{\partial\ln V}{\partial T}\right)_P+\left(\frac{\partial\ln\chi}{\partial T}\right)_V\\&=\left(\frac{2}{3}+\frac{\partial\ln m^*}{\partial\ln V}\right)_T\left(\frac{\partial\ln V}{\partial T}\right)_P+\left(\frac{\partial\ln m^*}{\partial T}\right)_V\,.\end{aligned}$$

As $(\partial\ln V/\partial T)_P=3\alpha$ and $(\partial\ln m^*/\partial\ln V)_T=\frac{1}{3}[\partial\ln(m^*/m)/\partial\ln r_s]_T$, we obtain

$$\left(\frac{\partial\ln\chi}{\partial T}\right)_P=\left\{2+\left(\frac{\partial\ln(m^*/m)}{\partial\ln r_s}\right)_T\right\}\alpha\,, \qquad \text{(A-}$$

Table II. The temperature increases of the magnetic susceptibilities and the thermal expansion coefficients of Cr, Mo and Ti.

		Cr	Mo	Ti
$\left(\frac{\partial\ln\chi}{\partial T}\right)_P\times10^4$	room temp.	+0.5	+0	+3.5
	1500°K	+2	+1	—
$\alpha\times10^4$	room temp.	0.08	0.05	0.09
	1500°K	0.14		—

where α is the thermal expansion coefficient and r_s the mean distance between electrons. Here we neglect the explicit temperature dependence of the effective mass.

According to the results obtained by Brooks *et al.* the values of $[\partial\ln(m^*/m)/\partial\ln r_s]_T$ for Li, Na, and Rb are -0.01, $+0.07$ and $+0.12$ ($\ll 2$) respectively[12]. Assuming that the second term of the right-hand side of (A-3) can also be neglected for transition metals we obtain

$$(\partial\ln\chi/\partial T)_P=2\alpha\,. \qquad \text{(A-4)}$$

For example the temperature increases of the magnetic susceptibilities and the thermal expansion coefficients of Cr, Mo and Ti are shown in Table II. It is seen that the effect of the thermal expansion is considerably small to explain the temperature increases of the magnetic susceptibilities for these metals.

References

1) T. R. McGuire and C. J. Kriessman: Phys. Rev. **85** (1952) 452.
2) C. F. Squire and A. R. Kaufmann: J. Chem Phys. **9** (1941) 637.
3) C. J. Kriessman: Rev. Mod. Phys. **25** (195 122.
4) E. C. Stoner: Acta Met. **21** (1954) 259.
5) E. C. Stoner: Proc. Roy. Soc. **A, 154** (193 656.
6) E. W. Elcock, P. Rhodes and A. Teviotdal Proc. Roy. Soc. **A, 221** (1954) 53.
7) J. McDougall and E. C. Stoner: Phil. Tran Roy. Soc. **237** (1938) 67.
8) E. W. Elcock: Proc. Roy. Soc. **A, 222** (195 239.
9) M. M. Newmann and K. W. H. Stevens: Pro Phys. Soc. London **74** (1959) 290.
10) N. F. Mott and K. W. H. Stevens: Phil. Ma **2** (1957) 1364.
11) C. T. Wei, C. H. Chang and P. A. Beck: Phy Rev. Letters **2** (1959) 95.
12) Quoted by G. B. Benedek and T. Kushida: Phys. Chem. Solid **5** (1958) 241.

JOURNAL OF THE PHYSICAL SOCIETY OF JAPAN, Vol. 15, No. 12, DECEMBER, 1960

The Magnetic Properties of Single Crystals of Chromium Selenide

By Ichiro TSUBOKAWA

The Research Institute for Iron, Steel and Other Metals, Tohoku University, Sendai, Japan.

(Received August 4, 1960)

The magnetic susceptibilities of the single crystals as well as powder specimen of chromium selenides with the composition, $CrSe_{1.00}$, $CrSe_{1.04}$ and $CrSe_{1.07}$ were measured from the boiling point of liquid helium up to 900°K. The susceptibility vs. temperature curves showed a break at 279°K, 271°K and 232°K for $CrSe_{1.00}$, $CrSe_{1.04}$ and $CrSe_{1.07}$ respectively. The anisotropy of the susceptibility increases rapidly from these breaking points to lower temperatures. There exists also a peak of the specific heat just above the room temperature which, however, lies a little higher than the breaking point mentioned above. This peak temperature of specific heat is considered to be the antiferromagnetic Néel point. Asymptotic Curie temperature, θ_p, Curie constant C_M and spin quantum number S were determined from the susceptibility data in the paramagnetic region.

1. Introduction

The magnetic susceptibility of chromium selenide, CrSe, was once measured by Haraldsen and Kowalski[1] in the temperature range from the boiling point of liquid air to 630°K and by the author[2] from the helium temperature to 400°K. From these results, it was seen that the susceptibility of the powdered specimen of this compound increases steadily with decreasing temperature. Since the asymptotic Curie temperature, θ_p, obtained from the measurements mentioned above takes a value -200°K, an antiferromagnetic ordering of spins will be expected in the crystal lattice of this compound at low temperatures. Recently Corliss and Hastings[3] observed by means of neutron diffractometer an antiferromagnetic spin ordering below room temperature. However, no peak of susceptibility corresponding to the antiferromagnetic Néel point was found by the above authors. It was also shown theoretically that a relation $T_N \geq |\theta_p|/5$[4] holds for the antiferromagnetic substances with NiAs structure. Hence, the Néel temperature is expected to be sufficiently higher than 4.2°K. From these points of view, magnetic and thermal properties of a single crystal of this compound were investigated.

§2. Specimens and Experimental Results

Three powder specimens of chromium selenides with the compositions $CrSe_{1.00}$, $CrSe_{1.04}$ and $CrSe_{1.07}$, were prepared by the solid reaction method. Powdered chromium (99.3%) and selenium (99.99%) were sealed in evacuated silica tubes in the desired ratios and heated in an electrical furnace. The highest temperatere reached 1100°C. All the specimens were confirmed to be of the NiAs structure by means of the Debye–Scherrer technique. In order to prepare single crystals of these compounds, the powdered specimens obtained above were put again into evacuated silica tubes, 15 mm in diameter, as shown in Fig. 1. This silica tube was connected to a balloon of soft rubber, half filled with argon gas, so as to keep normal pressure in the silica tube. Since the melting point of the compound lies just above 1500°C, the specimen was heated in a siliconit furnace up to about 1600°C and cooled slowly at the rate of 1.5°C per minute. A single crystal obtained by this method, 15 mm in diameter and about 20 mm in length, had a cleavage plane $(10\bar{1}0)$. No appreciable deviation in the composition of the crystal from that of the original powder specimen was detected by chemical analysis.

The temperature depencence of the susceptibility of the compound in powdered form was taken from the helium temperature up to 900°K with a magnetic balance[5], the result being shown in Fig. 2. As it shows, the susceptibility decreases at first rapidly and then slowly and after showing a breaking point at

279°K, it decreases again rapidly with a further rise of temperature. With the increase of selenium content, the breaking point falls down slightly, although the general aspect of the curve remains unchanged. As seen from the inverse susceptibility curves plotted in Fig. 2, the Curie-Weiss law holds for the susceptibilities of these compounds above th breaking point. The asymptotic Curie point θ_p and the Curie constant C_M obtained ar tabulated in Table I, together with the averag spin quantum number, S for chromium ion which is calculated from C_M with assumin that the Landé factor is equal to two,

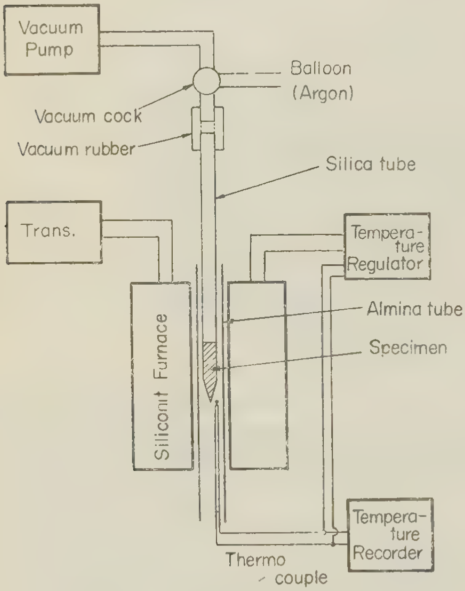

Fig. 1. Schematic diagram of the apparatus to make a single crystal.

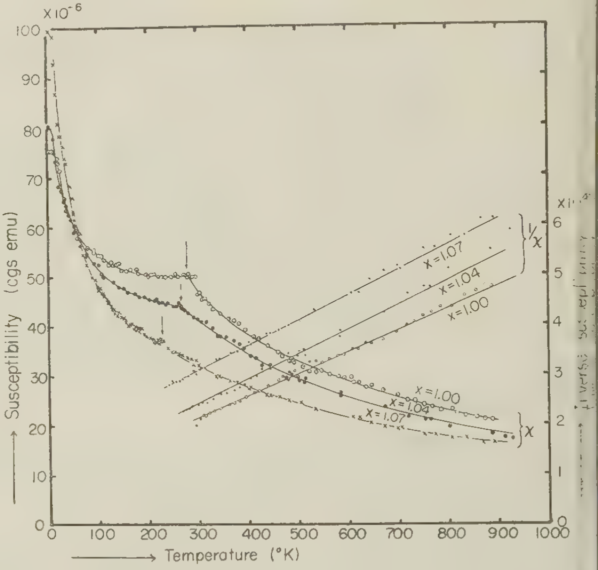

Fig. 2. Susceptibility vs. temperature curves for polycrystalline $CrSe_{1.00}$, $CrSe_{1.04}$ and $CrSe_{1.07}$. Inverse susceptibilities are also ploted.

Teble I. Paramagnetic Curie point θ_p, Curie constant C_M, spin quantum number S and the temperature of breaking point on χ–T curve, of $(\chi_c-\chi_a)=0$ and of C_p maximum.

Compounds	θ_p	C_M	S	Temperature		
				of breaking point on χ–T curve	of $(\chi_c-\chi_a)=0$	of C_p max.
$CrSe_{1.00}$	−200° K	∼ 3.0	4/2	279° K	278° K	320° K
$CrSe_{1.04}$	−190° K	∼ 2.7	3.8/2	271°	271°	—
$CrSe_{1.07}$	−320° K	∼ 2.7	3.8/2	232°	256°	—

Next, the susceptibilities, χ_c, along c-axis and χ_a, along a-axis, were measured with a magnetic balance. These results are shown in Fig. 3 (a), (b) and (c) for each specimen. As is shown, a remarkable anisotropy in the susceptibility is present below the temperature of the breaking point. χ_a decreases slightly with the rise of temperature from helium point, then reaches a constant value at about 60°K, while χ_c decreases continuously with rising temperature.

The torque curves in the a-c plane of th crystal mentioned above were taken with magnetic torsion balance, a few of the result being shown in Fig. 4 (a) and (b). The curve in the figures were taken for a specimen wit the composition $CrSe_{1.00}$ at the temperature of 4.2°K and 86°K respectively. The angula dependence of torque value in the a-c plan is expressed simply by sin 2θ. Also the H plot of the measured torque value is show in Fig. 5. As seen from it the torque valu changes linearly with the square of the field strength. Hence, the torque value will be expressed by the expression

$$L=\frac{1}{2}m(\chi_c-\chi_a)H^2\sin 2\theta\ .$$

$(\chi_c-\chi_a)$ is obtained from the torque values at $\theta=45°$, as a function of temperature, the result being shown in Fig. 6. It was confirmed that the result obtained agrees with that from the direct measurement of susceptibility of the single crystal. The difference takes a positive value at low temperatures, decreases in value with rising temperature and shows a negative value just below room temperature. With the increase of the selenium content the difference of the susceptibility changes its sign at lower temperatures.

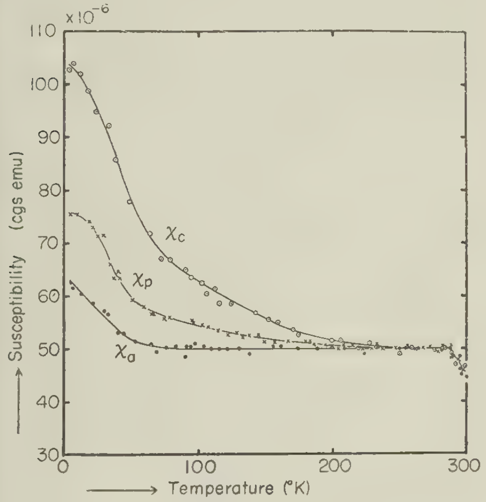

(a)

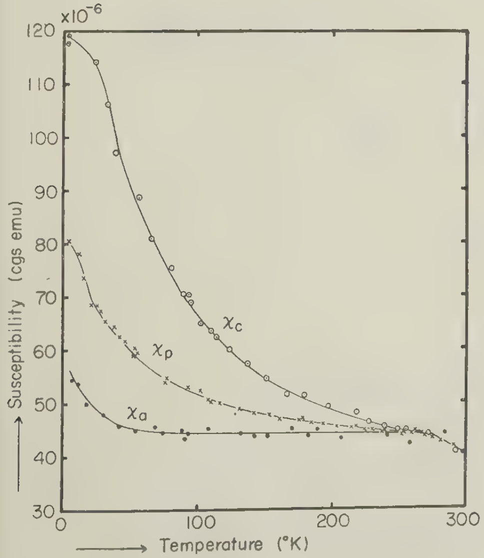

(b)

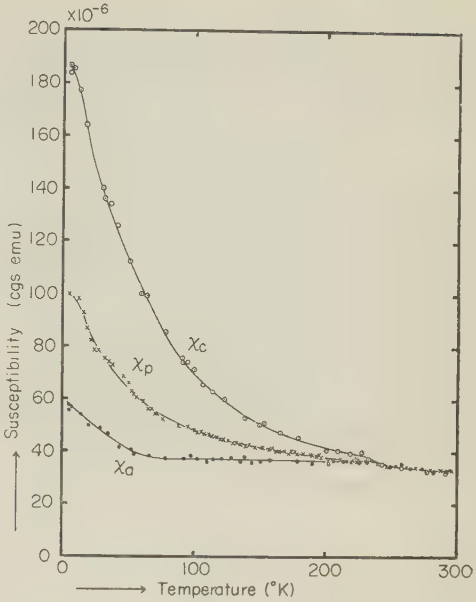

(c)

Fig. 3. χ_c, χ_a and powder susceptibility χ_p vs. temperature curves for $CrSe_{1.00}$ (a), $CrSe_{1.04}$ (b) and $CrSe_{1.07}$ (c).

Specific heats were measured for the compound $CrSe_{1.00}$ from 100°K to 400°K. The result is shown in Fig. 7. A peak in specific heat vs. temperature curve is seen at 320°K, which coincides nearly with the breaking point in the susceptibility curve mentioned above. *X*-ray powder photographs were taken at room temperature and −70°C and showed the diffraction lines due to the *NiAs* structure, and the change in the lattice parameters was found to be of the order of the thermal expansion, showing that no lattice change occurred during heating of the specimen up to 320°K.

§ 3. Discussions

Corliss and Hastings[3] confirmed the existence of antiferromagnetic ordering of ionic spin moments in powder specimens of chromium selenide below room temperature. The diffracted intensity of neutrons due to antiferromagnetic ordering was found to decrease with the rise of temperature but a faint long range order scattering remained yet up to room temperature. However, they have not yet succeeded in finding the Néel point of this compound. It was again pointed that the asymptotic Curie point is about 200°K. Although two critical temperatures 279°K (the breaking point of susceptibility-temperature curve) and 320°K (a peak point of specific heat) were obtained as the possible Néel point of this crystal, the latter may be the true Néel point, because specific heat is the more intrinsic properties than the susceptibility, and further, this assumption is more consistent with the result of neutron diffraction experiment than to take the former.

It is noted that the temperature dependence of the susceptibilities in the c-plane as well as along the c-axis for chromium selenide below the estimated Néel point are quite different from that of the ordinary antiferromagnetic crystals. In ordinary crystals the susceptibility parallel to spin axis decreases with lowering temperature and that perpendicular to spin

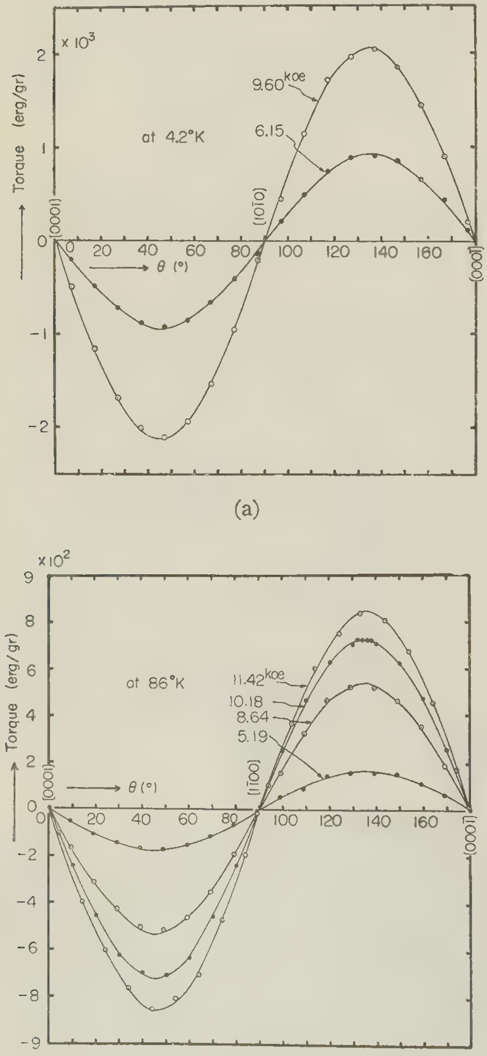

(a)

(b)

Fig. 4. (a), (b). Torque curves for $CrSe_{1.00}$ at 4.2°K and the ones at 86°K.

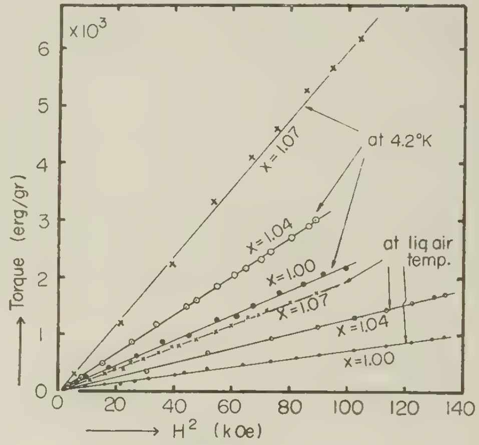

Fig. 5. H^2-plots of torque values.

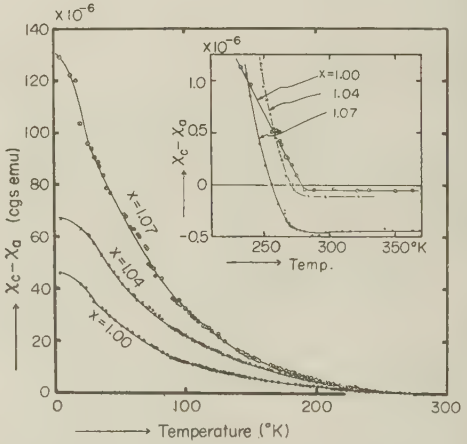

Fig. 6. $(\chi_c-\chi_a)$ vs. temperature curves for chromium selenides.

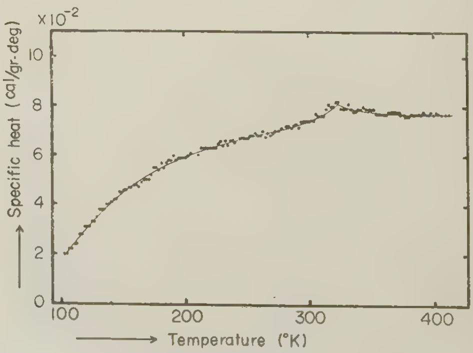

Fig. 7. Specific heat vs. temperature curve for $CrSe_{1.00}$.

axis is constant below Néel point, so that the values of χ_c and χ_a should not be greater than the one at Néel point. It is desirable to investigate the spin ordering of a single crystal of this compound with a neutron diffractometer just above and below room temperature.

Considering from the fact that χ_c and χ_a below 50°K rise rapidly with the lowering of temperature, it may be assumed that there are paramagnetic islands in the crystal as has been done in the case of cobaltous oxide.

Acknowledgements

The author wishes to express his cordial thanks to Professors T. Hirone and H. Watanabe for their encouragement and useful discussions. Also he wishes to express his hearty thanks to Dectors S. Maeda, N. Tsuya and K. Adachi for their valuable discussion.

References

1) H. Haraldsen and D. Kowalski: Z. Anorg. u. Allgem. Chem., **224** (1935) 329.
2) I. Tsubokawa: J. Phys. Soc. Japan, **11** (1956) 662.
3) L. M. Corliss and J. M. Hastings: Private communication.
4) T. Hirone and K. Adachi: J. Phys. Soc. Japan, **12** (1957) 156.
5) T. Hirone, S. Maeda and N. Tsuya: Rev. Sci. Instr., **25** (1954) 516.

JOURNAL OF THE PHYSICAL SOCIETY OF JAPAN, Vol. 15, No. 12, DECEMBER, 1960

The Change of the Curie Temperature of Iron-Nickel Alloys Due to Hydrostatic Pressure

By Takejiro KANEKO

The Research Institute for Iron, Steel and Other Metals, Tohoku University

(Received August 5, 1960)

The change of the Curie temperature due to hydrostatic pressure was measured for two iron-nickel alloys with a nickel concentration of 30 and 32 atomic percent respectively. Hydrostatic pressure was produced with an apparatus of Bridgman's type and the measurements of magnetization were performed by the ballistic method. The change of the Curie temperature due to pressure was estimated to be $-3\cdot 10^{-3}$ and $-2.7\cdot 10^{-3}$ deg. $kg^{-2}\,cm^2$ for specimens with a nickel concentration of 30 and 32% respectively. Based on Smoluchowski's fomula, the volume dependence of saturation magnetization at absolute zero $1/I_0\cdot\partial I_0/\partial\omega$ and that of the molecular field coefficient $1/N\cdot\partial N/\partial\omega$ for a 30% nickel alloy were found to be 27 and -16 from the experimental results. And then taking into consideration the volume dependence of the saturation magnetization at absolute zero, the relations among the volume dependence of the Curie temperature, molecular field coefficient and exchange integral are discussed.

§ 1. Introduction

According to several authors the magnetic properties of an iron-nickel alloy with a nickel concentration of about 30 atomic percent show a remarkable pressure dependence: Ebert and Kussmann[1)] measured its magnetization at various temperatures under the action of high hydrostatic pressure, and based on the fact that the ferromagnetic magnetization does not vanish even by the action of infinitely large pressure, they concluded that the Curie temperature of the alloy mentioned above did not change with hydrostatic pressure. On the other hand Patrick[2)] measured the change of the Curie temperature due to pressure by the A. C. transformer method and obtained a value $-5.8 \cdot 10^{-3}$ deg./atoms. Since the spontaneous magnetization should vanish at Curie temperature, however, the method of measurement used by Ebert and Kussmann may be more desirable than that used by Patrick for the purpose of finding out the change of the Curie temperature. So that the present author measured the change of the Curie temperature with nearly the same method as that used by Ebert and Kussmann for two iron-nickel alloys with a nickel concentration of 30 and 32 atomic percent respectively.

§ 2. Specimen and Experimental Procedure

Two iron-nickel alloys, containing 30 and 32 atomic percent of nickel, were melted in a vacuum induction furnace, cast in a metal mould, 20 mm in diameter, forged and then machined into rods, 70 mm in length and 3 in diameter. They were then annealed at 650°C for about 60 hours and, in order to maintain the γ phase (f.c.c. structure) which is stable at high temperature for these alloys, rapidly quenched in ice-water. It could be confirmed that the specimens consisted merely of f.c.c. structure since the alloy had the Curie temperature which coincided with that of γ-phase alloy.

Hydrostatic pressure was produced by means of an equipment of Bridgman's type[3] using paraffine oil as the pressure fluid. A part of the equipment is shown in Fig. 1. High pressure container *A* is made of non-magnetic copper-beryllium alloy, 14 mm in outside diameter and 3 mm in inside diameter. Specimen *B* was inserted in this container and sealed with a Bridgman's type of packing. The measurements of magnetization were performed by the ballistic method. A search coil *C* was wound around the pressure container. The liquid in the container *A* was compressed by means of primary and transmitting pistons under the action of primary pressure, which was measured by using the Bouldon's tube. The pressure in the container was calculated from the ratio of cross-sectional areas of primary and transmitting pistons. In this case, it has to be taken into account that there are errors of a few percent because of the indirect measurement of pressure. In order to investigate the temperature dependence of magnetization, all of these were immersed in heat bath *D*. Temperature in the heat bath was measured with a thermocouple *E* placed outside the pressure container and the specimen was kept at the same temperature in each case of measurement for more than 30 minutes. The magnetizing solenoid *F* can produce a sufficient uniform magnetic field within 0.1% for the specimens.

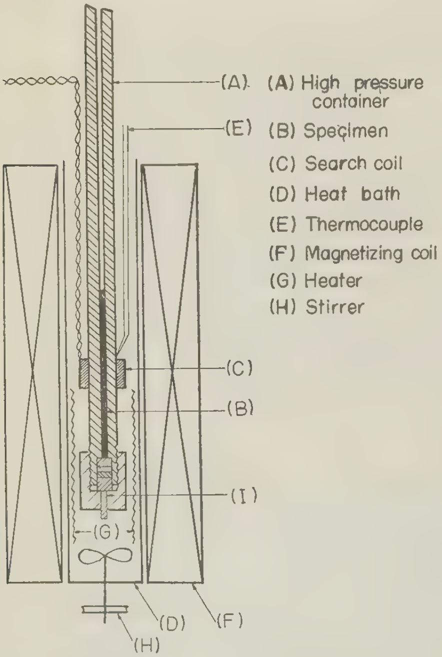

Fig. 1. Schematic diagram of a part of the measuring equipment.

§ 3. Results and Discussion

In Figs. 2 and 3 are shown the magnetization curves of a specimen with a nickel concentra-

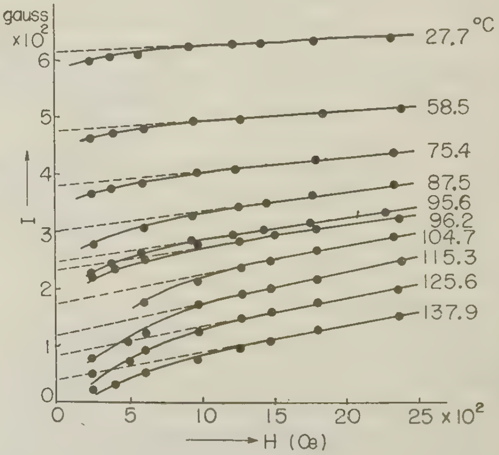

Fig. 2. The curves of magnetization versus magnetic field at various temperatures under normal pressure. (70Fe-30Ni alloy)

tion of 30% under a pressure of 1 as well as 3000 kg cm^{-2}, respectively, at various temperatures. Spontaneous magnetization was obtained by the extrapolation of the magnetization to $H=0$ after technical saturation. It was found that the magnetization was saturated nearly completely above the field strength of 1500 Oe for various temperatures. And the spontaneous magnetization versus temperature curves are shown in Fig. 4. The Curie temperature at each pressure was obtained by plotting the square of magnetization with the temperature as in Fig. 4. From these results the change of the Curie temperature with pressure for a specimen with a nickel concentration of 30% was found to be -3.10^{-3} deg. kg^{-1} cm^2. A specimen with a nickel concentration of 32% was measured by the same procedure as above. The results of measurement are shown in Fig. 5. From these results, the change of the Curie temperature with pressure was found to be $-2.7\cdot10^{-3}$ deg.kg^{-1} cm^2. The tendencies of the change of the Curie temperature due to pressure for the two alloys agreed with those of Patrick's results.

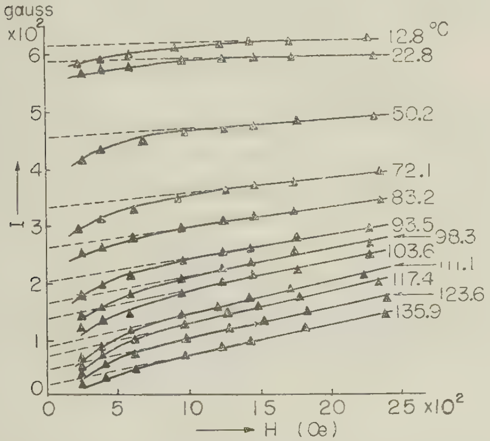

Fig. 3. The curves of magnetization versus magnetic field at various temperatures under 3000 kg cm^{-2}. (70Fe-30Ni alloy)

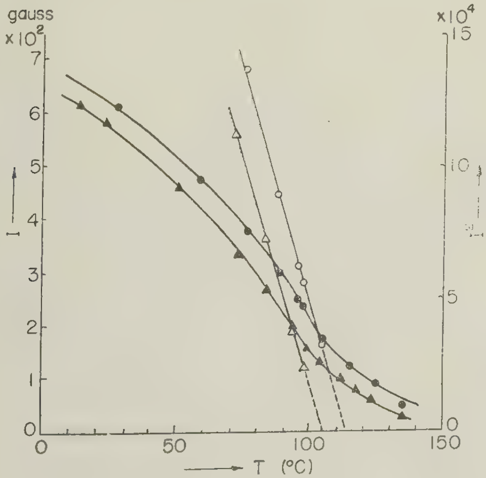

Fig. 4. The curves of magnetization and square of magnetization versus temperature for 70Fe-30Ni alloy.

magnetization ●: under 1 kg cm^{-2}
▲: under 3000 kg cm^{-2}
square of magnetization ○: under 1 kg cm^{-2}
△: under 3000 kg cm^{-2}

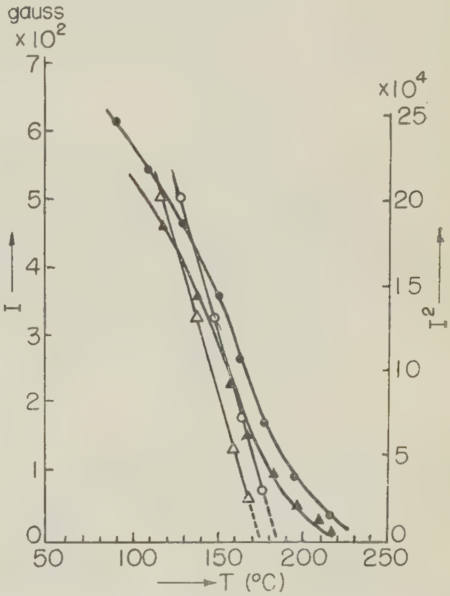

Fig. 5. The curves of magnetization and square of magnetization versus temperature for 68Fe-32Ni alloy.

magnetization ●: under 1 kg cm^{-2}
▲: under 3200 kg cm^{-2}
square of magnetization ○: under 1 kg cm^{-2}
△: under 3200 kg cm^{-2}

As to the origin of the pressure dependence of the Curie temperature mentioned here, the variation of the exchange interaction as well as that of saturation magnetization at absolute zero by the application of pressure should be considered, though the latter would not absolutely be independent of the former. However, the measurement of the pressure dependence of the saturation magnetization has scarcely been done, so that the effect of pressure[4] on the Curie temperature has hitherto been discussed merely by taking the variation of exchange interaction into account. Recently the pressure dependence of the specific magnetization $1/\sigma_0\cdot\partial\sigma_0/\partial P$ was estimated directly by Kondorskii[5] for iron-nickel alloys. For an alloy with a nickel concentration of 38% this author obtained a rather large value, $-54\cdot10^{-7}\,\mathrm{kg^{-1}\,cm^2}$. So that the change of the Curie temperature caused by the second factor mentioned above should be taken into account.

As for the pressure dependence of the saturation magnetization, the theoretical result by Smoluchowski[5] can be applied: Let the saturation magnetizations per unit volume at a finite temperature and at absolute zero be denoted here by I and I_0 respectively, and also I_0 be assumed to be given by

$$I_0=n\mu_B g\bar{s}\ , \tag{1}$$

where n is the number of magnetic atoms, μ_B the Bohr magneton, g Lande's facter and $\mu_B g\bar{s}$ the average magnetic moment. And if the temperature dependence of the saturation magnetization at constant volume is represented by a Brillouin function, then, by using a thermodynamical relation

$$\frac{\partial V}{\partial H}=-\frac{\partial(VI)}{\partial P}\ , \tag{2}$$

the following equations are obtained:

$$\frac{1}{I_0}\cdot\frac{\partial I_0}{\partial\omega}=-\left\{\frac{1}{\theta}\cdot\frac{\partial\theta}{\partial\omega}\cdot\frac{\partial I/\partial T)_v}{(\partial I/\partial T)_v-I/T}-\frac{I-(1/\kappa)\cdot(\partial\omega/\partial H)}{I-T(\partial I/\partial T)_v}\right\}\Big/\left\{1-\frac{(\partial I/\partial T)_v}{(\partial I/\partial T)_v-I/T}\right\}, \tag{3}$$

$$\left(\frac{\partial I}{\partial T}\right)_v=\left(\frac{\partial I}{\partial T}\right)_P-\frac{3\alpha}{\kappa}\cdot\left(\frac{\partial\omega}{\partial H}\right)_P-3\alpha I\ .$$

These equations give the relation between the volume dependence of the saturation magnetization at absolute zero and that of the Curie temperature. Here ω means the relative volume change $\Delta V/V$, κ the volume compressibility and α the linear thermal expansion coefficient. putting the observed values of the quantities on the right-hand side of equation (3), we obtained

$$\frac{1}{I_0}\cdot\frac{\partial I_0}{\partial\omega}=27\ . \tag{4}$$

Here the observed values at 30°C under 1 kg cm^{-2} were used; $\alpha^*=1.1\cdot10^{-5}\,\mathrm{deg^{-1}}$., $1/\kappa^*=1.5\cdot10^6\,\mathrm{kg\,cm^{-2}}$, $\partial\omega/\partial H^*=2.3\cdot10^{-8}\,\mathrm{Oe^{-1}}$[4], $I=605$ gauss, $(\partial I/\partial T)_P=-4.5$ gauss deg^{-1}.

As for the change of the Curie temperature due to pressure, the value from iso-volume I-T curves should be chosen, but taking into account the fact that the Curie temperature decreases lineally with pressure[2], the isobar curve can be used instead of iso-volume curves. Hence, in order to obtain equation (4), the value $1/\theta\cdot\partial\theta/\partial\omega=11$ from the isobar curve in Fig. 4 is used.

From equation (4) the pressure dependence of the specific magnetization at absolute zero, $1/\sigma_0\cdot\partial\sigma_0/\partial\ P$, was obtained as

$$\frac{1}{\sigma_0}\cdot\frac{\partial\sigma_0}{\partial P}=-180\cdot10^{-7}\,\mathrm{kg^{-1}\,cm^2}\ . \tag{5}$$

According to Kondorskii's result, $1/\sigma_0\cdot\partial\sigma_0/\partial P$ increases from $-11\cdot10^{-7}$ to $-54\cdot10^{-7}\,\mathrm{kg^{-1}\,cm^2}$ as the nickel concentration decreases from 45 to 38%, so that the present result shown in equation (5) may be reasonable.

As for the variation of the molecular field coefficient N with the volume change, the following relation was used by Smoluchowski:

$$\frac{1}{N}\cdot\frac{\partial N}{\partial\omega}=\frac{1}{\theta}\cdot\frac{\partial\theta}{\partial\omega}-\frac{1}{I_0}\cdot\frac{\partial I_0}{\partial\omega}\ . \tag{6}$$

Inserting the values obtained above for $1/\theta\cdot\partial\theta/\partial\omega$ and $1/I_0\cdot\partial I_0/\partial\omega$ into the equation (6), the result

$$\frac{1}{N}\cdot\frac{\partial N}{\partial\omega}=-16\ , \tag{7}$$

$$N=\frac{2zJ}{ng^2\mu_B{}^2}\ . \tag{8}$$

In this equation n would also be considered to be pressure dependent since for the proposed model due to Smoluchowski it is possible to assume that magnetic and non-magnetic atoms of nickel coexist. Such assumption was once proposed in the case of pure nickel, in which it was considered that different states of atoms e.g. atoms in singlet and triplet states coexist. By the application of pressure they would transform into each other, so that n may be changed. Therefore the result obtained above does not directly represent the dependence of exchange integral J on the interatomic distance.

Acknowledgements

The author wishes to express his sincere thanks to Professor T. Hirone for his kind guidance in the studies of the present project.

---

* Adopted from Kornetzki's paper. See P. 303 in reference 4).

Also he wishes to express his cordial thanks to Dr. S. Maeda for his encouragement and advice on the construction of the apparatus and to Drs. H. Watanabe and K. Adachi for their valuable discussions.

References

1) F. Ebert and A. Kussmann: Phys. Z. **39** (1938) 598.
2) L. Patrick: Phys. Rev. **93** (1955) 384.
3) P. W. Bridgman: *The Physics of High Pressure* (G. Bell and Sons, London, 1949).
4) M. Kornetzki: Z. Phys. **98** (1936) 289.
5) E. I. Kondorskii and V. L. Sedov: Sov. Phys. JETP **35**(8) (1959) 586.
6) R. Smoluchowski: Phys. Rev. **59** (1941) 309; **60** (1941) 249.

JOURNAL OF THE PHYSICAL SOCIETY OF JAPAN, Vol. 15, No. 12, DECEMBER, 1960

Magnetic Resonance in $MnCO_3$

Muneyuki DATE

Department of Physics, Faculty of Science, Osaka University, Osaka

(Received August 6, 1960)

Magnetic resonance of the single crystal of $MnCO_3$ was investigated using microwave frequencies 9 to 36 kMc/sec. Parasaitic ferromagnetic resonance was observed at 4.2°K which can be explained by the theory of magnetic resonance developed for α-Fe_2O_3 by Motizuki and Pincus. The effective field H_{DM} due to the Dzyaloshinsky-Moriya interaction was obtained to be 3.7 K Oe and the other resonanue constant $\sqrt{2H_E \mathrm{H}_A'}$ to be 1.4 K Oe, where H_E is the exchange field and H_A' the anisotropy field in the basal plane.

§ 1. Introductions

Dzyaloshinsky[1] has pointed out that the parasitic ferromagnetism of α-Fe_2O_3 and several other substances can be explained by assuming an anisotropic exchange interaction of the form $\vec{D}(\vec{S}_1 \times \vec{S}_2)$. Subsequently Moriya[2] has shown that such an exchange term can be derived by considering the spin-orbit coupling in the superexchange mechanism and that the constant vector $\vec{D}$ contains spin-orbit coupling constant in the first order.

Attempt to obtain the resonance formula containing such an anisotropy term has been made by Motizuki[3] and by Pincus[4]. They showed that the experimental results for α-Fe_2O_3 obtained by Anderson et al[5]. and Kumagai et al[6]. can be explained by introducing a new effective field H_{DM} due to the Dzyaloshinsky-Moriya interaction. Theoretical treatment of the magnetic resonance in α-Fe_2O_3 was first made by Shimizu[7], but he treated phenomenologically the weak ferromagnetism which appears in α-Fe_2O_3 without looking into the origin of the parasitic ferromagnetism. Pincus pointed out that, beside the energy of spin canting due to the Dzyaloshinsky-Moriya interaction, a very small anisotropy energy in the basal plane has an important effect on the frequency of the oscillation of the weak ferromagnetic moment in the basal plane and he showed that the frequency formula of this mode is given by

$$\left(\frac{\omega}{\gamma}\right)^2 = H_0(H_0 + H_{DM}) + 2H_E H_A' , \qquad (1)$$

where H_0, H_E, H_A' and H_{DN} represent the external field, the exchange field, the anisotropy field in the c-plane, and the effective exchange field due to the $\vec{D}(\vec{S}_1 \times \vec{S}_2)$ term, respectively. Eq. (1) is valid for magnetic fields applied in the c-plane. When the external field is not in the c-plane, the following equation is to be used:

$$\left(\frac{\omega}{\gamma}\right)^2 = H_0 \sin\theta(H_0 \sin\theta + H_{DM}) + 2H_E H_A' , \qquad (2)$$

where θ is the angle between the c-axis and the magnetic field. Using eqs. (1) and (2), the experimental results obtained by Anderson and Kumagai were satisfactorily explained by Pincus.

It must be noted, however, that the existing experimental results on α-Fe_2O_3 are not satisfactory to test the applicability of the theory developed by Motizuki and Pincus because of the following reason. The effective fields H_{DM} and $\sqrt{2H_EH_A'}$ of α-Fe_2O_3 were determined as 1.3×10^4 and 4.1×10^3 Oe, respectively, but these large values mean that only a limited portion of eq. (1) could be verified by experiments which made use of the usual microwave frequencies and magnetic fields. In fact, the experimental points fall on an approximately linear portion corresponding to intermediate frequencies and fields. Perhaps one or two mm-waves may be necessary to observe the asymptotic part of eq. (1) for high field, which is not an easy matter with the present microwave techniques.

Other than α-Fe_2O_3, however, there are several magnetic substances showing weak ferromagnetism. A few carbonate, such as $CoCO_3$ and $MnCO_3$ are known to be the typical examples. The magnetic properties of $MnCO_3$ indicate that eqs. (1) and (2) could be checked fully with the use of the usual microwaves.

The magnetic susceptibility of this crystal was measured by Borivik-Romanov and Orlova[8], who showed that below the Néel temperature T_N of 32°K the canted spins are in the basal c-plane. Recently neutron diffraction study of the powdered specimen was performed by Pickart[9]. The induced moment due to Dzyaloshinsky-Moriya interaction was obtained as $0.2\mu_B$ from which we can infer that the effective field H_{DM} may be small compared with that in α-Fe_2O_3. The purpose of this paper is to report the experimental result of the magnetic resonance observed in the natural single crystal of $MnCO_3$ at different temperatures and the analysis of the data obtained.

§ 2. Experimental Procedure

The single crystal of $MnCO_3$ used in our experiment is a natural rhodochrosite obtained from Osarizawa Mine, Akita Prefecture, Japan, in Aipril 1955. The crystal structure of $MnCO_3$ is the well known calcite type, having a rhomcohedral unit cell of $a=5.84$Å and $\alpha=47°46'$. The single crystal of $MnCO_3$ is very cleavable as calcite is

Microwave frequencies used for our experiment are 9 to 36 kMc/sec supplied from klystrons 2K25, 2K33, and 35V10. Usual transmission method was adopted. Low temperature cryostats are the same as those described in the preceding paper[10].

§ 3. Experimental Results

Paramagnetic resonance was observed at room temperature in the whole frequency range. Part of the results are shown in Fig. 1 and 2. It must be noted that there is a considerable angular dependence of the resonance line width which can not be explained by dipolar interaction and the usual exchange narrowing effect. Detailed calculation shows that the pure dipole width along the c-axis is larger than that found experimentally, which

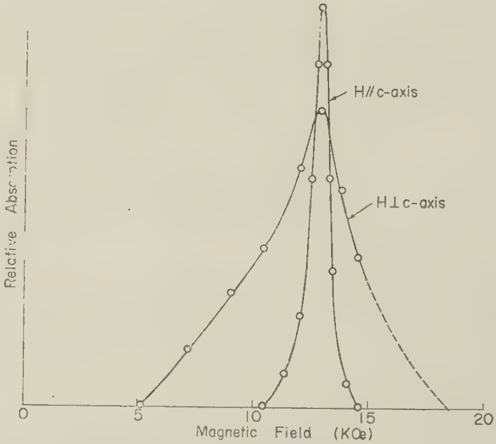

Fig. 1. Resonance line shapes in paramagnetic $MnCO_3$ single crystal at room temperature (36.43 kMc/sec).

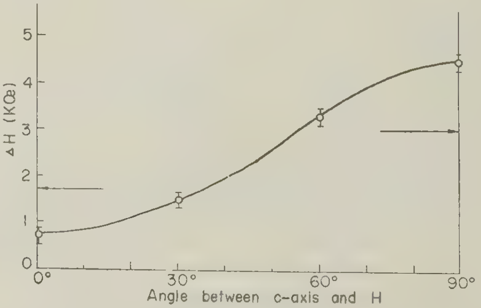

Fig. 2. Angular dependence of resonance line width in paramagnetic $MnCO_3$ at 36.43 kMc/sec. Arrows show the calculated dipolar widths.

means that the usual exchange narrowing occurs for this case. On the other hand, the calculated dipolar width in the c-plane is smaller than that found by experiment which can not be explained by the current theory of line width. Line broadening due to the anisotropic exchange interaction of the $\vec{D}(\vec{S}_1\times\vec{S}_2)$ form might be important for this case. The g-value is isotropic and is 2.00 ± 0.01.

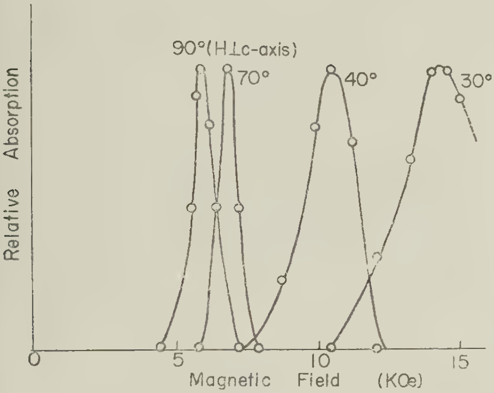

Fig. 3. Resonance line shapes in $MnCO_3$ single crystal at 4.2°K (22.34 kMc/4ec). Angles show the declination from the c-aqis.

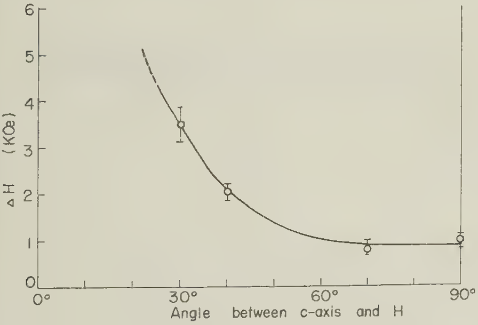

Fig. 4. Angular dependence of resonance line width in $MnCO_3$ at 4.2°K (22.34 kMc/sec).

The experimental results of the resonance curves at 4.2°K are shown in Fig. 3. Considerable angular dependence was observed, which may be due to the parasitic ferromagnetism appeared in $MnCO_3$ below 32°K. Observation of the angular dependence of the resonance line was also made and the results are shown in Fig. 4. The angular and the frequency dependences of the resonance points are shown in Fig. 5. In the c-plane no anisotropy was observed in accordance with the theoretical expectation of Motizuki and Pincus. The full lines drawn in Fig. 5 are the theoretical curve due to eq. (2). The coincidence between theory and experiment is satisfactory.

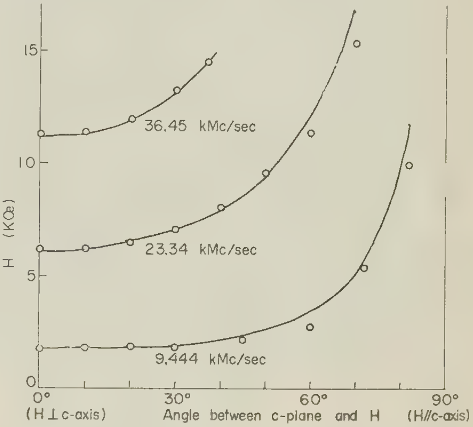

Fig. 5. Angular and frequency dependence of resonance points in $MnCO_3$ at 4.2°K (H // c-plane).

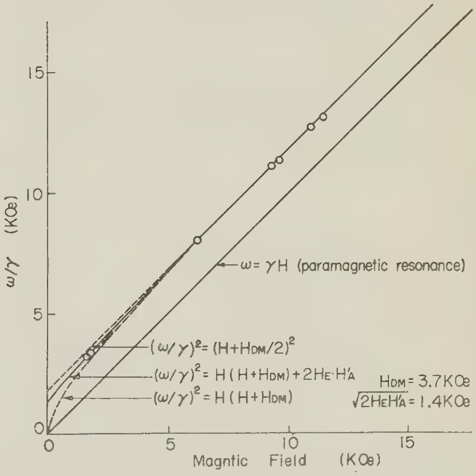

Fig. 6. Frequency field diagram of the resonance points in $MnCO_3$ at 4.2°K. (H // c-plane).

Now let us consider the resonance constants H_{DM} and $2H_EH_A'$. The frequency field diagram of the resonance points are shown in Fig. 6. The experimental points lie on the asymptotic line described by $\omega/\gamma=H+3.7/2$, except for two resonance points belonging to the 9 kMc/sec region. Thus we obtain the resonance constant H_{DM} to be 3.7°K Oe. So far the resonance in the asymptotic line has not been observed in α-Fe_2O_3. Then we obtain the constant $2H_EH_A'$ by satisfying two resonance points in the 9 kMc/sec region. Thus $2H_EH_A'=2.0$ K Oe^2 was decided as being the most favourable value. For comparison, the asymptotic line and the resonance curve of $H_A=0$ are shown in Fig. 6. The coincidence of the theory with the experiment is satisfactory at 4.2°K. Detailed measurement of the temperature dependence of the magnetic resonance have not been performed because of the experimental difficulties near 30°K. However our preliminary data show that eqs. (1) and (2) are valid for all temperatures below 30°K, while the short range order effect was found to survive even at considerably high temperatures, resulting in a broadening of the paramagnetic resonance.

The author wishes to express his cordial thanks to Profs. Itoh and Nagamiya and Dr. Motizuki for their valuable discussions and stimulations during the course of the experiment. He is also indepted to Profs. Kiriyama and Yoshimura for supplying a natural single crystal of $MnCO_3$. A part of the experiment was subsidized by a grant from the Ministry of Education.

References

1) I. Dzyaloshinsky: J. Phys. Chem. Solids **4** (1958) 241.
2) T. Moriya: Phys. Rev. Letters **4** (1960) 228.
3) K. Motizuki: Presented in the Annual Meeting of the Phys. Soc. Japan, April 1960.
4) P. Pincus: to be published in Phys. Rev. Letters.
5) P. W. Anderson, F. R. Merritt, J. P. Remeika and W. A. Yager: Phys. Rev. **93** (1954) 717.
6) H. Kumagai, H. Abe, K. Ono, I. Hayashi, J. Shimada and K. Iwanaga: Phys. Rev. **99** (1955).
7) M. Shimizu: J. Phys. Soc. Japan **11** (1956) 1078.
8) A. Borivic-Romanov and M. Orlova: Z. Eks. Teor. Piz. **31** (1956) 579.
9) S. J. Pickart: Bull. Am. Phys. Soc. **5** (1960) 59.
10) M. Date: J. Phys. Soc. Japan **14** (1959) 1244.

JOURNAL OF THE PHYSICAL SOCIETY OF JAPAN, Vol. 15, No. 12, DECEMBER, 1960

Direct Viewing of Imperfections in Germanium p-n Junction

Masami TOMONO

Central Research Laboratory, Hitachi, Ltd., Kokubunji, Tokyo

(Received Sept. 2, 1960)

A p-n junction was made by alloying indium on an n-type germanium pellet and it was put into an electrolyte solution of copper salt. When suitable reverse voltage was applied on the junction by a charged condenser, copper shaded pattern was deposited on the opposite side of the alloyed surface in accordance with the density of the reverse current flowing through every part of the p-n junction. By this method, the breakdown at the imperfections of p-n junction due to the defects in the germanium crystal, those at the periphery of p-type recrystallized layer, and those inside p-n junction grown in alloying process were observed. Then, the cross section was made referring to the pattern, and several kinds of the imperfections of p-n junction were observed under microscope.

§ 1. Introduction

Previously, the author observed imperfect germanium p-n junction under the microscope, and investigated the electrical characteristics of the alloyed p-n-p transistor with such imperfect emitter junction¹⁾. At the same time, he assumed various types of imperfection of the p-n junction, and supposed that an m-n junction nearly $1\,\mu$ in diameter and making imperfect rectifying contact with the germanium might be a kind of the imperfection and the large saturation current in the reverse direction flew through the part, or in some cases, the breakdown voltage of the junction became strikingly low. If such small imperfections exist, their finding will be extremely difficult even by the observation of cross section of the *p-n* junction with a microscope. So far relatively large imperfections of the *p-n* junction have been reported frequently but the relation-ship with the degradation of the electrical characteristics of the junction has not been clarified in most cases[2),3)]. Thus, for finding such defect, two-step procedure would become necessary: firstly to find its approximate location from external and secondly to examine that portion carefully. For the silicon *p-n* junction, it has been well known, from light emitting phenomenon at the part of the junction where breakdown occurs with reverse voltage applied, that breakdown easily occurs at the worked parts of the grown junction[4)], the indented part, the prominent lines of etch pits, the junction-periphery and the misfit boundary of the *p-n* junction made by impurity diffusion[5)], and that wide area of junction emits light by internal field emission[6)]. As for germanium, the light emitting phenomenon was also reported but the correlation with the imperfections of *p-n* junction has not been clear[7)]. It has been known that, when copper is deposited on a germanium surface electrolytically, shaded pattern of copper is developed according to the density of the current flowing through the part of the surface into the copper salt solution[8),9)]. The conventional method using copper sulphate solution for this purpose, however, fails to developed plated pattern sharp enough to permit detection of fine imperfections of *p-n* junction. The author used the method improved by Tokuyama[10)] to get a sharp deposited pattern on on the opposite germanium surface corresponding to the density of reverse current which flows through the imperfection of the *p–n* junction. The purpose of this paper is to present such improved method of plating as well as the results of investigation of some imperfections of *p-n* junction which were detected using this method.

§ 2. Method of Experiment

A p^+-*n* junction about 1 mm in diameter was made by alloying indium at about 500°C on an *n*-type germanium pellet 60 to 100 μ thick and 2.5Ω cm in resistivity. The germanium surface on that side alloyed with indium was covered with shellac, and its p^+ electrode was biased negative in adequated plating electrolyte. The germanium surface not alloyed with indium was so placed as to face a platinum electrode which was bised positive. Between the electrodes a current was then caused to flow for electroplating on the *n*-type germanium surface. In this situation, it is expected that if any local imperfections exist within *p-n* junction, the current flow should be concentrated to those areas of the germanium surface which correspond to the imperfections, resulting in the correspondingly shadded pattern of copper plating. The conventional method using copper sulphate solution for this purpose[8),9)], however, failed to get sharp plated pattern with high fidelity. The use of the plating solution of the following specification by Tokuyama[10)] made it possible to get comparatively good results.

20% solution of $CuSo_4$	5% (volume)
H_2O_2 (30%)	5% (volume)
HF (48%)	5% (volume)
Deionized water	85% (volume)

The plating in this solution by continuous current under constant voltage permitted to obtain some reproducible deposited pattern corresponding relatively large imperfections within *p-n* juntion. This plating method will be described "continuous current method" in report. However, this method was not satisfactory to reveal relatively small imperfections within *p-n* junction. The author could get sharp deposited pattern for this case with reproducibility and high fidelity by the following method[10)]. The circuit used is as shown in Fig. 1. First, a switch S_1 was operated to etch side, with another switch S_2 closed, to bias the sample positive and the platinum electrode negative, thus the surface of *n*-type germanium was cleaned by electrolytic etching. After this, the switch S_1 was operated to plating side, with the switch S_2 opened, to allow a condenser *C* to be charged at a voltage of V. Next, S_2 was closed, then at the initial instant a relatively large discharging current is caused by the condenser *C* but after discharging from *C* an only relatively small voltage is applied between the electrodes as the voltage V is lowered due to a series resistance *R*. This method[10)] is described "pulse method" in this paper. The values actually used by the author are; V: 3 to 100 volts, R: 500 kΩ and C: 2 μF.

The value of V should be selected properly according to the properties of the sample, and for detection of the breakdown characteristic of each prat of p-n junction, it should be increased from a small values gradually. In this case, for developing the copper plating pattern for one value of V firstly and thereafter examining it with respect to another value of voltage, it is imperative that the deposited copper of the first time should be completely dissolved by the electrolytic etching prior to repeating electroplating for another value of V, otherwise, being affected by the first plating, the deposited pattern in the second case may not perfectly develop. The time which was allowed for plating was adjusted properly in the range of 15 to 300 seconds as required for a completely developed deposited pattern to be seen with the eye. The sample to which copper locally deposited in this way observed on the surface alloyed with indium to examine the configuration of the portions around indium dots. Next, the alloyed indium dot was amalgamated with mercury. This amalgam was then dissolved away with nitric acid so that recrystallized p-type germanium layer was exposed, and as needed, this p-type layer was further applied with chemical etching to permit the examination of the imperfections within recrystallized layer and also the finding of the relationship between the pattern of deposited copper on the opposite surface of germanium and the imperfections in the recrystallized layer. Finally, cross sections of those portions to which much copper was deposited were observed with a microscope to clarify through what imperfection in p-n junction an excess reverse current flew.

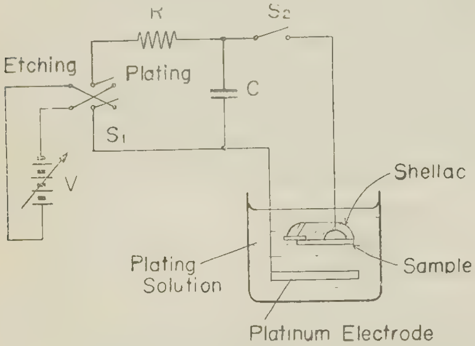

Fig. 1. Plating circuit under pulse method.

§ 3. Result of Experiment

3.1 Plating Pattern Under Constant Voltage and Continuous Current

For an ordinary p-n junction having relatively good reverse characteristics, it is frequently seen that a spot pattern develops relatively uniformly but at random on the surface of n-type germanium as shown in Fig. 2, if the sample is applied with plating by continuous current at a relatively low voltage without the condenser C in Fig. 1. On the other hand, for a sample having relatively poor reverse characteristics in which location of the imperfection within p-n junction is unknown, sometimes no specific pattern develops as shown in Fig. 3(a) with the plating at a low voltage (3V in this example), though specific pattern may develop as shown in Fig. 3(b) if the plating is carried out at a higher voltage (26V in this example). Another example is shown in Fig. 4 for the sample with considerably poor reverse characteristics. (a) gives the plating pattern at 2V on a sample which was made by alloying indium to the indented part on the germanium surface. A semicircular black pattern on the right-hand side of the sample is not caused by the copper deposition but represents a stepped part shaded by the illumination at the periphery of the backside of indium dot electrolytically etched more deeply than other parts. (b) shows the plating pattern at 6V on a sample of imperfect p-n junction which was made by alloying thin indium layer on germanium as reported by the author previously[1]. The patterns in both figures, though not sharp, indicate that considerably clear imperfection exists within p-n junticon. Fig. 5 shows the plating pattern for a sample which has poor reverse characteristics but in which location of the imperfection withoin p-n junction is not known. (b) gives a photograph of the sample subjected to the electrolytic etching of (a). At first, no specific evidence of abnormality could be observed on the surface of n-tpye germanium, but after the removal of surface layer by electrolytic etching, imperfection of germanium sigle crystal analogous in configuration to the semicircular deposited pattern has been revealed.

3.2 Plating Pattern under Pulse Method

A description that follows is of plating pattern developed under pulse method of Fig.

1. Fig. 6 shows the reproducibility of the plating pattern obtained under pulse method in Fig. 1. The sample used was made by alloying indium on an n-type germanium, but the periphery of the p-n junction was not removed by etching. Of course, this sample permitted comparatively large reverse current and was not so good in its characteristics. (a) shows the deposited pattern by this method where V in Fig. 1 is 100 V. In this case, very sharp pattern compared with Fig. 4 was developed at those areas of the opposite surface which correspond to the periphery of p-n junction. (b) shows. the sample after copper

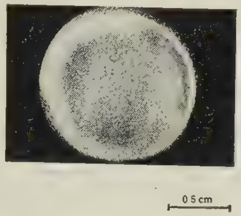

Fig. 2. Copper plating pattern under constant voltage and continuous current for p-n junction with relatively good reverse characteristics.

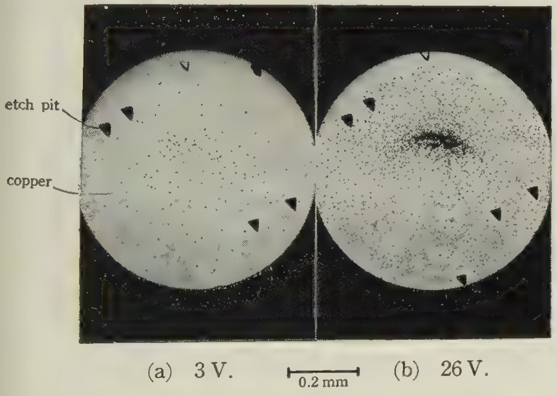

(a) 3 V. (b) 26 V.

Fig. 3. Voltage dependence of copper plating pattern for sample with poor reverse characteristics in which location of imperfection is unknown.

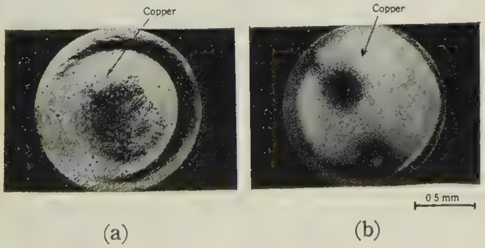

(a) (b)

Fig. 4. Plating pattern for sample with relatively large imperfection within p-n junction.

(a) Sample made by alloying indium on indented part of n-type germanium

(b) Sample made by alloying thin indium layer on n-type germanium.

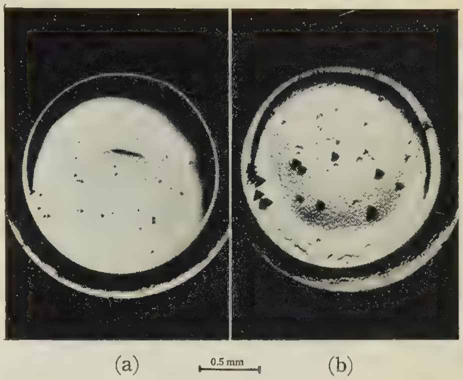

(a) (b)

Fig. 5. Correspondence between copper plating pattern and imperfection of germanium bulk for sample with poor reverse characteristics but in which location of imperfection is unknown.

(a) Sample applied with copper plating.

(b) Sample applied with electrolytic etching after removal of copper deposit.

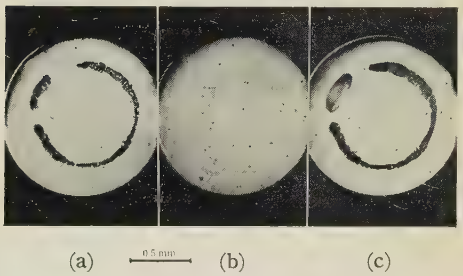

(a) (b) (c)

Fig. 6. Reproducibility of copper plating pattern under pulse method.

(a) First copper plating pattern.

(b) After removal of copper by forward current.

(c) Second copper plating pattern.

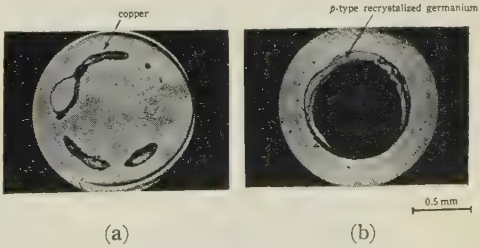

(a) (b)

Fig. 7. Relationship between shapes of copper plating pattern on backside and periphery of p-n junction.

(a) Plating pattern on backside surface.

(b) Alloyed indium on front surface,

deposit had been completely dissolved by forward current. (c) shows the pattern which was resubjected to the pulse method. It is found that the reproducibility of the plating pattern is considerably high. From those figures, it was perceived that along the periphery of the alloyed junction there was an area with low breakdown voltage and on the backside of this area copper deposited in a ring form. The similar plating pattern has been obtained on many samples. A ring-formed plating pattern developed on the backside of n-type germanium under pulpse method (V of Fig. 1:100V) is shown in Fig. 7 in comparison with the results of observation of the same sample from the alloyed side. This sample permits relatively large flow of reverse current because the periphery of its p-n junction has not been removed by etching. As the photograph in (b) was printed out with the negative film turned over, the photograph in (a) showing the backside and that in (b) showing the front surface have the same sense. The periphery of an exposed p-type recrystallized layer formd by indium overspreading[11] in (b) is quite analogous in shape to the copper plating pattern

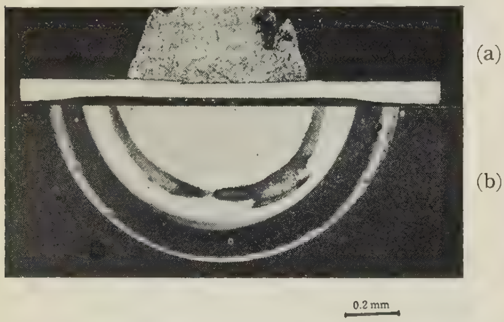

Fig. 8. Correspondence between copper plating pattern and cross-section of sample not applied with electrolytic etching to the periphery of p-n junction.
(a) Cross-section.
(b) Copper plating pattern on backside.

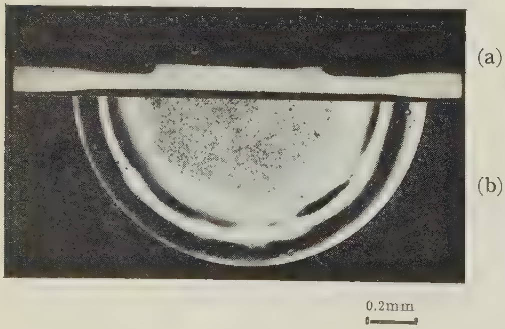

Fig. 9. Correspondence between coper plating pattern and cross-section of sample applied with electrolytic etching to the periphery of p-n junction.
(a) Cross-section.
(b) Copper plating pattern on backside.

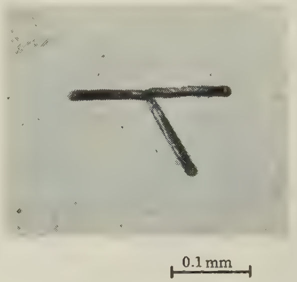

Fig. 10. Bar-shaped imperfection within germanium bulk.

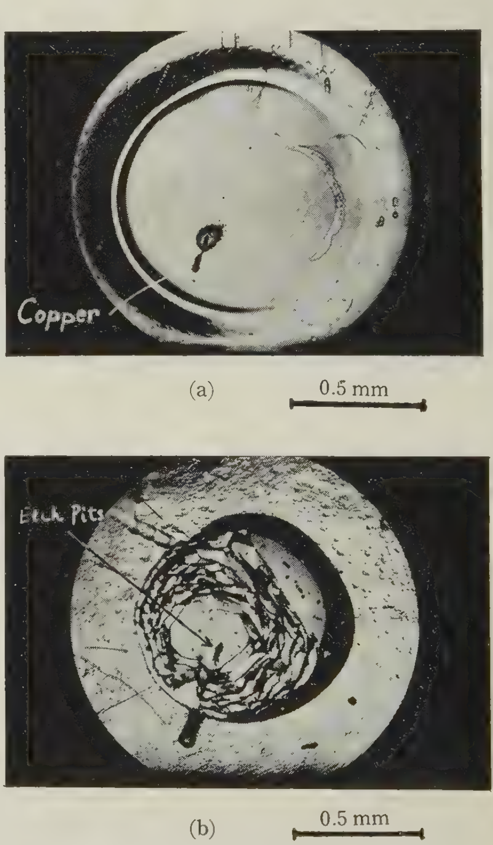

Fig. 11. Correspondence between copper plating pattern and bar-shaped imperfection of bulk germanium.
(a) Copper plating pattern on backside.
(b) Front surface applied with chemical etching.

in (a), but it is also seen that the marked copper deposition is limited only to a part of the backside region corresponding to the exposed p-type layer. In Fig. 8, the results of comparative observation between the plating pattern by pulse method (V:100V) and cross-section of junction are shown on the sample which permitted relatively large reverse current because of not being applied with electrolytic etching after alloying· (a) shows cross-section of the junction, and (b) shows plating pattern on the portion at which the

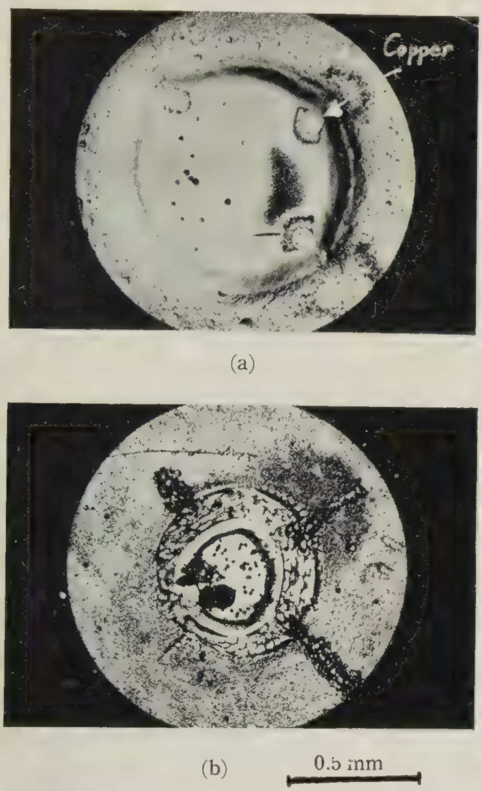

(a)

(b)

Fig. 12. Corresponkence between copper plating Pattern on backside and scratch on front surface of germanium.

(a) Copper plating plattern on backside.

(b) Front surface applied with chemical etching.

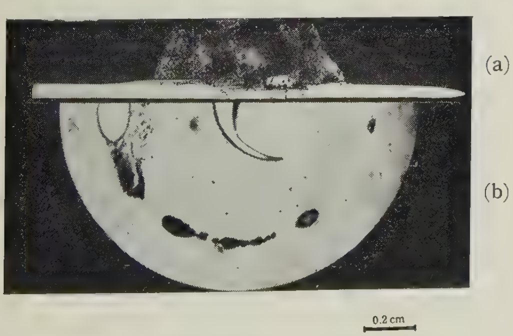

(a)

(b)

Fig. 13. Copper plating pattern caused by punch-through.

(a) Cross-section.

(b) Copper plating pattern on backside

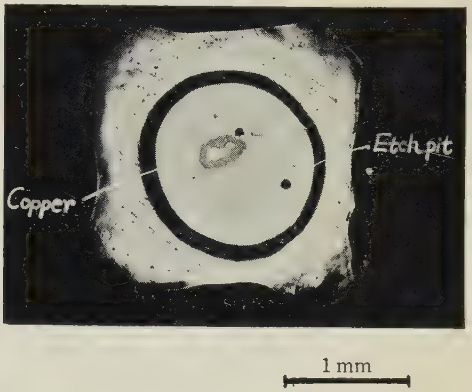

Fig. 14. Copper plating pattern for a sample with shot defect within p-n junction.

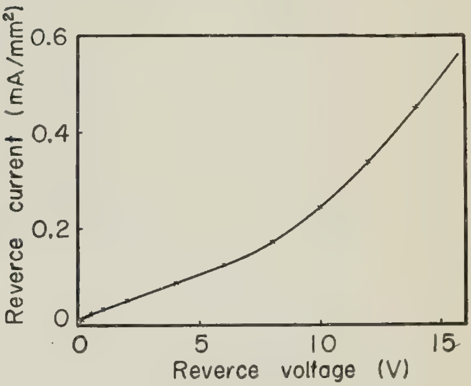

Fig. 15. Reverse voltage-current characteristics of p-n junction with badly poor properties.

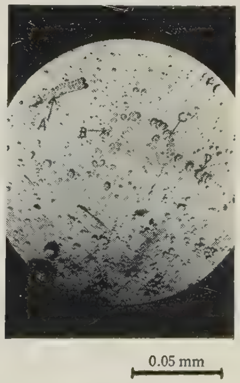

Fig. 16. Rod-shaped etching pattern on germanium pellet.

cross-section was taken. As seen from the cross-section of (a), copper deposited markedly on the backside corresponding to the exposed *p*-type recrystallized layer especially to such part that *p*-type germanium layer has overspread and grown where germanium bulk did scarcely melt. It is apparent that non-uniform contacting area exists between the overspread *p*-type germanium layer and the base *n*-type germanium at the right-hand end. Fig. 9 shows an example of plating by pulse method (V of Fig. 1:100V) on the sample which was applied with the electrolytic etching to remove the periphery of alloyed dot[2),12)]. The sample was improved in characteristics to have more than 100V breakdown voltage. (a) shows the cross-section of sample, indicating that the periphery of the junction has been scooped out enough not to leave imperfect part as seen in Fig. 8. (b) shows the plating pattern on the backside surface. With respect to the part at which the cross-section was taken, (b) is aligned with (a). A double concentric black pattern at the periphery in (b) is not caused by the copper deposition but represents a stepped part which was formed by electrolytic etching to clean the germanium surface on the backside and is shaded by the illumination. Copper is deposited in spots approximately uniformly over the opposite surface of *p-n* junction indicating that breakdown has not occurred with 100V at any part of the whole *p-n* junction. The periphery of *p-n* junction is completely free from imperfection. This represents a typical case where imperfection of the periphery of *p-n* junction has been completely removed by the electrolytic etching. Needless to say, however, sometimes the imperfection may remain partilly at the periphery after the electrolytic etching. Sometimes, a special etching pattern as shown in Fig. 10 is observed on the surface of a germanium. Such a pattern extends from the front to the backside surface of the germanium pellet in some cases but does not in the other. Selecting a germanium pellet on one surface of which such special bar-shaped etching pattern exists but on the backside none appears, the author applied the alloying of indium on that surface which has the pattern. This sample permitted a flow of extremely high reverse current. Fig. 11 shows photographs of a sample with the bar-shoped imperfection. The indium was alloyed on the imperfection. It has been verified experimentally that such sample in general has badly poor reverse characteristics as described later. (a) shows the deposited pattern by pulse method (V in Fig. 1:100V) on the oposite side of the surface alloyed with indium. Marked copper plating pattern has developed at such a location as is slightly to the inside of the periphery of alloyed part and had no anomaly before alloying. (b) shows a condition of the recrystallized surface which appeared after the indium dot on the surface of the sample was removed as amalgam with mercury and the exposed *p*-type germanium was etched chemically with dilute CP-4. Printing of the photograph for (b) was made with the negative film turned over. From (b), it is seen that etch pits are prominently developed and dislocations are concentrated especially to those parts where copper deposition is prominent in (a). Fig. 12 shows the the results of observation on sample was made by first giving a scratch in X shape with a diamond and then alloying indium thereto on a germanium pellet. This sample also is poor in characteristics because of its high reverse current. (a) shows pattern of copper plating (V:100V) to the oposite side of the surface alloyed with indium. Copper deposition is made on three of those places where the scratch intersects the periphery of the alloyed indium dot. but at the other place, no copper is deposited. Regarding to this place, it is seen from (b) that the scratch is very narrow compared with other three places. (b) shows the sample after the indium is removed with mercury and the exposed *p*-type layer was etched chemically with dilute CP-4. Printing of (b) was made with the negative film turned over. Immediately to the inside of two parts at which the scratches intersect the right-hand periphery, two groups of prominent etch pits are observed. Certainly, these positions may correspond to the positions on the backside at which copper was deposited. Fig. 13 shows a different kind of copper plating pattern. (b) in the same figure shows the plating pattern developed by the pulse method. It is featured particulary by a semicircular plating pattern located near the center, in addition to the ones along the periphery of the indium alloyed part. In (a), a cross-section photograph is given for the part corresponding to the cutaway part of (b). Prominent copper deposition pattern at the periphery of indium dot on the left-hand in (b) corresponds to the *p*-type germanium recrystallized layer which was grown by over-spreading on the surface of germanium remaining not fused into an indium melt and which made imperfect contact with the germanium bulk as mentioned earlier. Significance of the semicircular plating pattern in the center is that a slight deviation of the germanium pellet surface from (111) plane results in a small inclination of bottom of the *p*-type recrystallized layer in (a) to back surface of the germanium bulk, reducing the distance gradually to a minimum at the part where the semicircular plating pattern develops. In this case, the minium distance is about 13μ. It is belived that at the time of application of 100V pulse voltage the punch-through has occurred at this minimum-distance part and large current has flowed. Finally in Fig. 14 is shown an example of copper plating patterns by pulse method found frequently to the samples which are still badly poor in reverse characteristics after the removal of the periphery of alloyed part by electrolytic etching. It is seen that copper is markedly deposited to relatively small locallized area. Though copper deposition by pulse method in this figure is considerably sharp compared with the blurred one under constant voltage in Fig. 4(b), it seems that the cause of both cases is the same. In Fig. 14, it is remarkable that no copper deposition appears at the part of etch pits produced by electrolytic etching. This fact is perceived also in Fig. 3, Fig. 12 and Fig. 13.

3.3 Relations between Copper Plating Pattern and Reverse Characteristics of *p-n* Junction

A *p-n* junction, which is made by alloying indium on a germanium pellet with a bar-shaped imperferction or scratch on the surface as shown in Fig. 11 and Fig. 12, has an extremely low breakdown voltage. As an example of this, result on a sample which has a scratch on one surface nearly as in Fig. 12 is shown in Fig. 15. A breakdown occurs at a very low voltage, and reverse current increases approximately owing to the the Ohm's law nearly up to 8V. Beyond 8V, occurrence of a second breakdown is seen. (a) in Fig. 16 shows a germanium pellet on which many rod-shaped etching patterns are observed. A, B, C,····in the figure are the rod-shaped patterns. As seen from these examples, the rod-shaped patterns may be either imperfection involved previously in the germanium crystal or scratches incurred in working proceess.

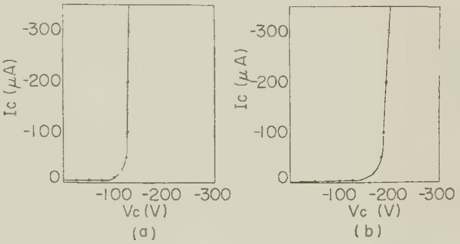

Fig. 17. Comparison of reverse characteristics between *p-n* junctions made from germanium with and without rod-shaped etch patterns.

(a) With rod-shaped pattern.

(b) Without rod-shaped pattern.

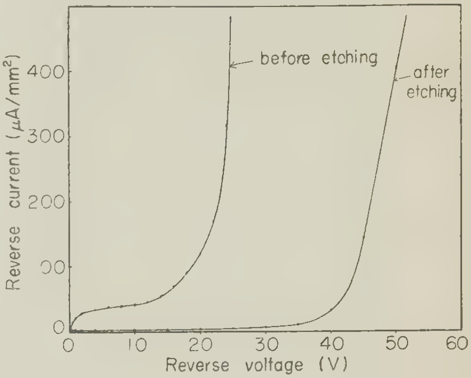

Fig. 18. Comparison of revers characteristics before and after removal of imperfections at periphery of *p-n* junction by electrolytic etching.

Samples with and without these kinds of imperfection were selected each by fives and alloyed with indium to make the respective *p-n* junctions. The average reverse characteristics of each group of *p-n* junctions are as shown in Fig. 17. (a) is for samples with imperfections on the surface, and (b) for samples without them. It is apparent that the former is lower in breakdown voltage, though not so low as in Fig. 15. Fig. 18 shows comparison of reverse characteristics between two cases: in one case, a sample was as in Fig. 6, 7 and 8, not applied with etching and in the other, the same sample was applied with electrolytic etching enough to remove imperfections at the periphery of *p-n* junction nearly campletely. From these figures it is known that the sample which is poor in reverse characteristics before electrolytic etching is remarkably improved after etching.

§ 4. Dicussion of Results

4.1 Copper Plating Method

As earlier mentioned, copper electrolyte in § 2 permits revelation of imperfections of *p-n* junction with a good contrast as well as a comparatively good reproducibility. With this electrolyte, well contrasted plating pattern can be obtained under pulse method as shown in Fig. 1. Alternatively, if a copper plating is applied at a relatively low voltage V by the method above, an observation of the resulted pattern is made and after reversal of the current for dissolving the deposited copper, a second copper plating is applied at a higher voltage and if this process is repeated with the successively increased plating voltages, it is expected possible to see how breakdown is caused by the imperfections of *p-n* junction at the respective breakdown voltages. The details of this method will be reported by Tokuyama[13]. Fig. 4 and Fig. 5 show the samples containing in *p-n* junction small localized imperfections which break down at a very low voltage without utilization of pulse method or make non-rectifying contact. In Fig. 3, breakdown does not occur with 3V but does locally with 26V. In Fig. 7, Fig. 8, etc., breakdown occurs at relatively high voltage, but Fig. 9 indicates that breakdown never occurs with 100V.

4.2 Relations Between Lattice Defect and Breakdown

The patterns shown in Fig. 3 is probably due to the same cause as in Fig. 5, and the breakdown voltage in these cases is again relatively low. As seen from (b) of Fig. 5, the cause may consist in a special defect present in a germanium single crystal. This defect is considered to be probably a dislocation array due to the misfit at fine domain boundary which is produced as the single crystal grows out of a melt. With respect to the possibility of such locallized boundary being produced in the growing process of germanium single crystal, the author has had an experimental evidence. Bar-shaped defect in (b) of Fig. 11 as seen from the side alloyed with indium is an example of such defect shown in Fig. 10 and is deemed not to be merely a small angle grain boundary. This defect extends very short in the publling-up direction of the single crystal (that is, in the direction perpendicular to the photograph). Based on the observation on a great number of germanium single crystals, it is believed that the defect mentioned above is formed by a germanium melt which is locally included in the grown crystal, as reported in a following paper to be published shortly[14]. When indium is alloyed on such defect as seen from (b) of Fig. 11 copper deposition does not occur along the whole length of the defect at the alloyed part but does only in that part corresponding to the bottom of the pan-shaped recrystallized layer. (b) makes it clear that many dislocations crowd together in bar shape in the recrystallized germanium layer corresponding to that part where copper deposition occurs. Fig. 3 and Fig. 5 described above seem to show the similar phenomenon. As for the sample which is given a scratch with diamond on the germanium surface, the same phenomenon is observed as shown in Fig. 12. The reason why the bottom part of the *p-n* junction of Fig. 12 has not been affected at all is merely that the depth of scratch is so small that at that part the scratch has completely fused into an indium melt. On a side wall of the pan-shaped recrystallized layer, this scratch causes a crowded dislocation array to appear in the recrystallized *p*-type layer as shown in (b) of Fig. 12. At the part where the dislocation array exists in the recrystallized layer, breakdown is liable to occur as clearly shown in (a) of Fig. 12. Though badly low in sharpness because of low voltage and continuous current, the plating pattern in (a) of Fig. 4 has the same cause as in Fig. 12. The fact that copper has not deposited by pulse method at the part where etch pits exist at random as described in 3.2 indicates that the breakdown voltage owing to these isolated dislocations is considerably high (refer to Fig. 3, Fig. 12, Fig. 13, Fig. 14, etc.). The details of this will also be reported by Tokuyama[13]. It is believed that the cause for the poor reverse characteristics of *p-n* junctions described above is such that when dislocations crowd together across the *p-n* junction very thin indium parts exist locally in the *p*-type recrystallized germanium layer and it comes into direct contact with the *n*-type germanium, thereby shorting the *p-n* junction. This supposition may be supposed from a known fact that arsenic and antimony are liable to diffuse along the medium angle grain boundary of the germanium single crystal[15]. Examples in Fig. 11 and Fig. 12 conespond to such case possibly and the reverse current owing to the Ohm's law as shown in Fig. 15 is convincing from this supposition. Moreover, this will apply for some cases where relatively large reverse current flows at a voltage of 1 to 2V, resulting in the application of copper plating on the backside as shown in (a) of Fig. 4 and Fig. 5. The details well be reported by Tokuyama[13]. As for the cases in Fig. 3 and Fig. 17 where defect within germanium bulk causes the breakdown voltage to be lowered but the reverse current at low voltage is not so high, number of dislocations across the *p-n* junction is not so large as in the above-mentioned case and invasion of indium to the part of dislocations may not be remarkable, therefore the lowering of the breakdown voltage may be due to any other cause. In this case, the dislocation will not so crowd as in Fig. 11 and Fig. 12 indeed, but dislocation array, namely, grain boundary surely exists. Conversion to *p*-type of such grain boundary is well known[16]. In this case *p*-type layer enters locally at *p-n* junction from *p*-type recrystallized layer into bulk germanium. Every part of the layer thus entered is not uniform but at some part a transition to the *n*-type through a weak *n*-type from an extremely weak *p*-type may be made. At such part, breakdown voltage may be lowered. As another cause for the lowered breakdown voltage, a deviation of the junction from a plane may also be considered[17].

4.3 Breakdown at Periphery of *p-n* Junction

For a sample which is, as shown in Fig. 6, not applied with etching after indium alloying, the periphery of *p-n* junction is liable to break down. This is a well-known fact[2),12),18]. In such part where the periphery of alloyed indium is out of true circle and takes an irregular shape, a larger number of weakpoints exists as clearly seen from the left-halves of photographs (a) and (b) of Fig. 7. Unlimited to these examples, such a tendency as mentioned above has been verified by the author on many samples. A comparison between (a) and (b) of Fig. 8 indicates that the structure with low breakdown voltage exists at the end of thin *p*-type recrystallized layer which was extruded by the so-called overspreading from the indium dot in (a). The process of this overspreading may be such that an indium melt nearly saturated with germanium in the heating process of alloying decreases in viscosity at the maximum temperature which takes place in the final stage of the heating process, and it spreads to some extent over the bulk germanium hitherto exposed. In the subsequent cooling process, recrystallization of *p*-type germanium takes place on the germanium part covered with indium by overspreading[11]. This recrystallized *p*-type germanium, however, is difficult to fit to the base germanium, because the germanium surface has not been wetted enough with indium melt obstructed by the oxide, etc. as a result of which there may be lattice defect due to misfit and other various defective structures between the base germanium and the recrystallized layer. As the surface tension of the indium melt increases in the cooling process of alloying, the part which spreads later recontracts partially and results in an exposed *p*-type recrystallized layer on the surface. Because of these defects at the periphery with overspreading structure, breakdown may be liable to occur as reported in a separate paper[13]. To some extent, the imperfection in the overspread end may be supposed from the right-hand end of Fig. 8(a). As seen from (a), of Fig. 9, breakdown at the periphery disappears if the imperfections of *p-n* junction periphery are compeletely removed.

4.4 Punch-Through

A semicircular plating pattern in the center of (b) of Fig. 13 is considered to be caused by a punch-through phenomenon as described in 3.2. For a *p-n* junction with highly doped *p*-type layer which was made by alloying indium on an *n*-type germanium pellet 2.5Ωcm in resistivity, the thickness of the space charge layer when the *p-n* junction is applied with a voltage of 100V in the reverse direction is about 17μ by the following equation[19]:

$$W_s=(2\kappa/q)^{1/2}(V/N_d)^{1/2},$$

where W_s, κ, V and N_d denote thickness of space charge layer, dielectric constant, voltage applied to the space charge layer and number of doner impurities in a unit volume of *n*-type germanium, respectively. The thickness of the *n*-type germanium measured at the position where copper is deposited in semicircular shape is 13 μ based on the photograph in (a) of Fig. 13. The possibility of punch-through occurring at this position is easily supposed.

4.5 Other Cases

For a sample which has badly poor reverse characteristics after complete removal of the imperfections at *p-n* junction periphery, it is sometimes seen that relatively small deposition of copper takes place at some places corresponding to the inside of the *p-n* junction. This may be cause with little doubt by an *m-n* junction, that is, a small indium part left in the *p*-type recrystallized layer and coming into direct contact with the *n*-type germanium, as published by the author previously[1)]. In (b) of Fig. 4 showing a sample which was prepared by alloying thin indium layer to the *n*-type germanium as published by the author previously, the existence of such *m-n* junction at two parts may be shown by the plating pattern though blurred since pulse method is not used. This will be published in detail by Tokuyama[13)].

Acknowledgment

The author wishes to acknowledge the cooperation of Mr. T. Tokuyama and Mr. K. Uehara who supplied many useful data.

References

1) M. Tomono: J. Phys. Soc. Japan **15** (1960) 1233.
2) J. S. Hanson: IBM Journal **1** (1957) 279.
3) A. S. Rose: RCA Rev. **29** (1958) 423.
4) R. Newman: Phys. Rev. **100** (1955) 700.
5) A. G. Chynoweth and G. L. Pearson: J. Appl. Phys. **29** (1958) 1103.
6) A. G. Chynoweth and K. G. Mckay: Phys. Rev. **106** (1957) 418.
7) J. T. Nelson and J. C. Irvin: J. Appl. Phys. **30** (1959) 1847; M. Kikuchi: J. Phys. Soc. Japan **14** (1959) 1830.
8) J. H. Forster and L. E. Miller: B.S.T.J. **4** (1956) 767.
9) P. R. Camp: J. Appl. Phys. **25** (1954) 459.
10) T. Tokuyama: To be published.
11) J. I. Pankove: J. Appl. Phys. **28** (1957) 1054.
12) H. P. Burcham *et al*: Transistor Technology **3** (1958) 175.
13) T. Tokuyama: To be published.
14) M. Tomono: To be published.
15) F. Karstensen: Z. f. Naturf. **14a** (1959) 1031.
16) G. L. Pearson: Phys. Rev. **76** (1949) 459; W. E. Taylor, N. H. Odell and H. Y. Fan: Phys. Rev. **88** (1952) 867; A. G. Tweet: Phys. Rev. **99** (1955) 1182; H. F. Mataré: J. Appl. Phys. **30** (1959) 581; B. Reed, O. A. Weinreich, and H. F. Matré: Phys. Rev. **113** (1959) 454.
17) J. Shields: J. Electr. Cont. **4** (1957) 58; M. Takabayashi: J. Appl. Phys. Japan (in Japanese) **27** (1958) 726.
18) M. Kikuchi: J. Phys. Soc. Japan **12** (1957) 133.
19) W. Shockley: B.S.T.J. **28** (1949) 435.

JOURNAL OF THE PHYSICAL SOCIETY OF JAPAN, Vol. 15, No. 12, DECEMBER, 1960

Microwave Spectrum of Formaldehyde
I. *K*-type Doubling Spectra

Takeshi OKA,* Hiromasa HIRAKAWA,† and Koichi SHIMODA
Department of Physics, Faculty of Science,
University of Tokyo, Tokyo, Japan

(Received, July 2, 1960)

Microwave spectral lines for the direct transitions between the *K*-type doublets were measured from 3 kMc to 40 kMc for H_2CO and for its isotopically substituted molecules HDCO, $H_2C^{13}O$ and H_2CO^{18}. The observed spectra and the previously reported data for H_2CO were analyzed by a digital computer by the use of Kivelson and Wilson's method for the centrifugal distortion correction.

The asymmetry parameter b and B-C were obtained for each isotopic species as follows:

	B-C (Mc/sec)	b
H_2CO	4832.13±0.01	−0.0098370±0.0000010
$H_2C^{13}O$	4595.47±0.02	−0.0093205±0.0000010
H_2CO^{18}	4391.08±0.02	....
HDCO	5347.77±0.04	−0.0161170±0.0000020
D_2CO	6097.35±0.02	−0.0271170±0.0000020

It was found that the observed frequencies fit well to those calculated from the centrifugal distortion constants which were derived by the vibration-rotation interaction theory.

§ 1. Introduction

Formaldehyde is a planar, slightly asymmetric top molecule with rather large electric dipole moment (μ=2.33 Debye). The direct transitions between the *K*-type doublets provide abundant and strong spectral lines all over the microwave region.

The *K*-type doubling lines of H_2CO were first measured and assigned in the *K*-band region by Sharbaugh and Bragg.[1] Lawrance and Strandberg extended the measurement from 7 to 72 kMc and analyzed the spectrum by a semi-classical treatment of centrifugal distortion.[2a)] Though the rotational constants obtained by them are quite reasonable, the centrifugal distortion constants used in the analysis can not be explained from the vibration-rotation theory.

An extensive study for this molecule as well as for the isotopically substituted molecules has been carried out in this laboratory.[3a)3b)3c)3d)4a)4b)4c)] Hirakawa, Miyahara and Shimoda measured the *K*-type doubling spectral lines of H_2CO, $H_2C^{13}O$ and H_2CO^{18} down to 2.8 kMc using an S band wave guide cell.[3a)] Hirakawa, Oka and Shimoda synthesized deuterated samples and measured the *K*-type doubling lines for HDCO and D_2CO from 2.8 kMc to 20 kMc.[3b)]

These *K*-type doubling lines are so strong that some of them were used for the maser experiments.[4a)4b)4c)5)]

At this stage it is quite necessary to obtain accurate rotational constants and molecular structure for the formaldehyde molecule. One of the difficulties in the analysis of the spectra is the rather large effects of the centrifugal distortion. The treatment of the centrifugal distortion has been reported by several authors.[2a)2b)2c)6a)6b)6c)6d)] Hillger and Strandberg[2b)] and Kivelson and Wilson[6a)] proposed independently a convenient approximate formula for the centrifugal distortion of *K*-type doubling lines. The more accurate Kivelson and Wilson's first order treatment which was applied in the analysis of the spectra of SO_2 and O_3 was adopted in this report. The same trial was done by Erlandsson for the *K*-type doubling lines of H_2CO from K=1 to K=3.[7)] But the centrifugal distortion constants obtained by him can not be explained by the vibration-rotation interaction theory either.

---

* Present address; Department of Chemistry, Faculty of Science, University of Tokyo, Tokyo, Japan.

† Present address; Japan Atomic Energy Research Institute, Ibaraki, Japan.

In this report the reasonable centrifugal distortion constants calculated from the vibration-rotation interaction theory have been used in the calculation. The discussions about the molecular structure and the calculation of the vibration-rotation interaction quantities will appear in the second and the third part of this series, which will hereafter be referred to as II and III, respectively.

§2. Experimental

a. Sample

Well dried paraformaldehyde powder was heated slowly to evolve formaldehyde monomer. The spectra of $H_2C^{13}O$ and H_2CO^{18} species were measured with their natural abundances. The deuterated formaldehyde monomer was evolved by heating deuterated calcium formate with a sand bath. The deuterated calcium formate was prepared by the following procedure:

$$(COOH)_2 \xrightarrow{\text{deuteration}} (COOD)_2 \xrightarrow{\text{distillation}} DCOOD \xrightarrow{CaO} Ca(DCOO)_2 .$$

As the yield of formaldehyde monomer from the decomposition of calcium formate is not

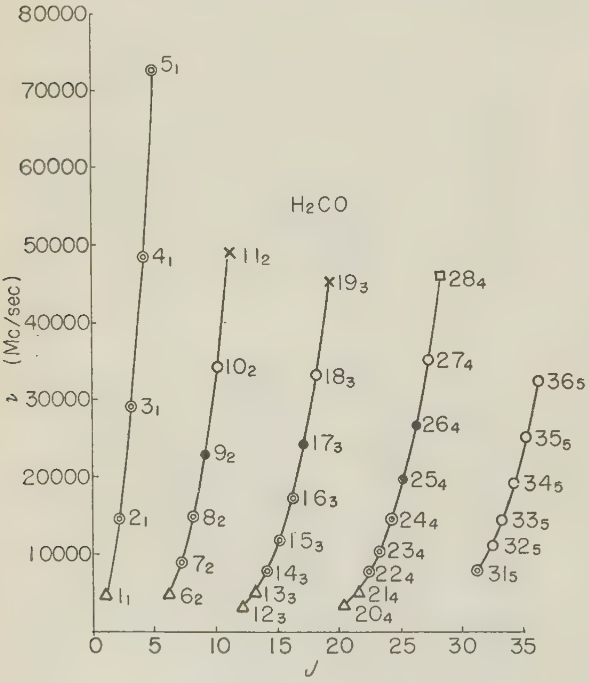

Fig. 1-5. Observed K-type doubling lines vs. J

The observers of the spectrum.

- ● Bragg and Sharbaugh (1).
- ⊙ Lawrance and Strandberg (2a).
- × Okaya: J. Phys. Soc. Japan **11**, 249 (1956).
- △ Hirakawa, Miyahara and Shimoda (3a).
- □ Miyahara, unpublished.
- ○ This work.

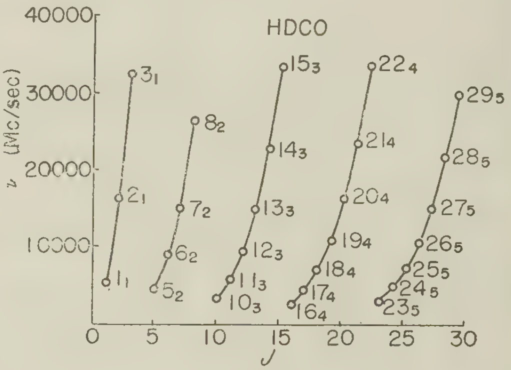

Fig. 2.

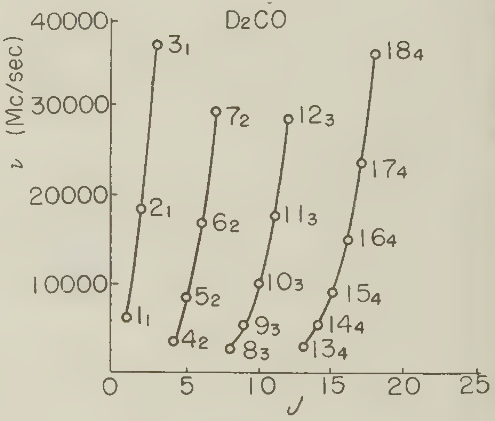

Fig. 3.

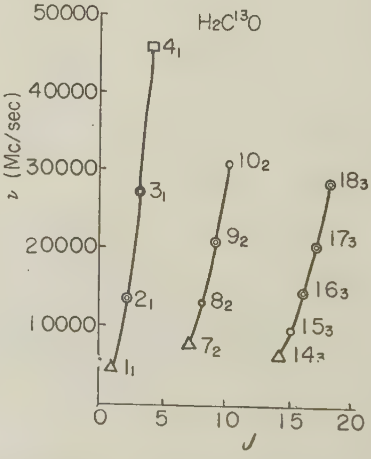

Fig. 4.

high,[8] the formaldehyde was trapped by dry ice and was led to the sample cell.

b. Spectrograph

The microwave spectrometer used was of the conventional type with 100 kc sinusoidal Stark modulation. The klystrons which were used to cover from 2.8 kMc to 40 kMc were 723A, 2K22, 2K26, 7V40, 2K25, X-13, X-12, and 35V10. S, X, and K band wave guides were used for the absorption cell. The ultimate sensitivities for the spectrograph using these cells were about $1\times10^{-8}\,\mathrm{cm}^{-1}$, $3\times10^{-8}\,\mathrm{cm}^{-1}$ and 2×10^{-7}, respectively. In searching for the high J, K lines which were very weak by the Boltzmann factor, the wave guide was heated to increase the intensities of the spectral lines.

c. Observed Spectra

The observed K-type doubling lines are shown in Figs. 1~5 and Tables II~VI with their calculated intensities. As the statistical weight due to the nuclear spin is three times larger for the K=odd states than for the K=even states for H_2CO, the spectral lines for K=odd states are stronger. The situation is reversed in the case of D_2CO.

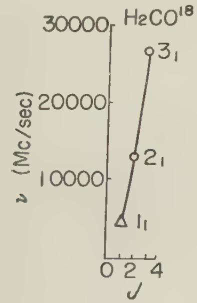

Fig. 5.

The calculation of the intensity was done by the use of the following formulas.

H_2CO

$$\begin{cases} K_{-1}\ \text{even} & \alpha=795\times10^{-14}\lambda\nu^2\exp(-E_{\mathrm{rot}}/kT) \\ K_{-1}\ \text{odd} & \alpha=2.39\times10^{-13}\lambda\nu^2\exp(-E_{\mathrm{rot}}/kT) \end{cases}$$

HDCO $\alpha=2.35\times10^{-13}\lambda\nu^2\exp(-E_{\mathrm{rot}}/kT)$

D_2CO

$$\begin{cases} K_{-1}\ \text{even} & \alpha=1.21\times10^{-13}\lambda\nu^2\exp(-E_{\mathrm{rot}}/kT) \\ K_{-1}\ \text{odd} & \alpha=6.05\times10^{-14}\lambda\nu^2\exp(-E_{\mathrm{rot}}/kT) \end{cases}$$

where λ is a line strength and ν is a frequency.

The intensities for the spectral lines of $H_2C^{13}O$ and H_2CO^{18} were derived by multiplying the corresponding lines of H_2CO with the natural abundance ratios of C^{13} and O^{18}, respectively.

§ 3. Centrifugal Distortion

One of the difficulties in the analysis of the spectrum of such a light molecule as formaldehyde is the effect of centrifugal distortion. The rotational Hamiltonian derived from the vibration-rotation interaction theory can be written to the second order of approximation as follows.[6a]

$$H=\frac{1}{2}\sum_{\alpha,\beta}\sigma_{\alpha\beta}P_\alpha P_\beta+\frac{1}{4}\sum_{\alpha,\beta,\gamma,\delta}\tau_{\alpha\beta\gamma\delta}P_\alpha P_\beta P_\gamma P_\delta \quad (1)$$

The first term is the rotational energy of the rotor averaged by the vibrational wave functions. The second term is the energy of the centrifugal distortion. The actual value for the coefficients $\tau_{\alpha\beta\gamma\delta}$ will be treated in III. It will be shown from symmetry consideration that many of these coefficients vanish. For a planar molecule with C_{2v} symmetry such as H_2CO and D_2CO, Eq. (1) can be reduced to the form

$$\begin{aligned} H=&\frac{1}{2}\sum_{\alpha}\sigma_{\alpha\alpha}P_\alpha^2+\frac{1}{4}\sum_{\alpha}\tau_{\alpha\alpha\alpha\alpha}P_\alpha{}^4 \\ &+\frac{1}{4}\sum_{\alpha\beta}\tau_{\alpha\alpha\beta\beta}(P_\alpha{}^2P_\beta{}^2+P_\beta{}^2P_\alpha{}^2) \\ &+\frac{1}{2}\tau_{xzxz}(P_x{}^2P_z{}^2+P_z{}^2P_x{}^2)\,. \end{aligned} \quad (2)$$

For a planar molecule with C_s symmetry such as HDCO, Eq. (1) becomes

$$\begin{aligned} H=&\frac{1}{2}\sum_{\alpha}\sigma_{\alpha\alpha}P_\alpha{}^2+\frac{1}{2}\sigma_{xz}(P_xP_z+P_zP_x) \\ &+\frac{1}{4}\sum_{\alpha}\tau_{\alpha\alpha\alpha\alpha}P_\alpha{}^4+\frac{1}{4}\sum_{\alpha,\beta}\tau_{\alpha\alpha\beta\beta}(P_\alpha{}^2P_\beta{}^2+P_\beta{}^2P_\alpha{}^2) \\ &+\frac{1}{2}\tau_{xzxz}(P_x{}^2P_z{}^2+P_z{}^2P_x{}^2) \\ &+\frac{1}{2}\sum_{\alpha,\beta,\gamma}\tau_{\alpha\alpha\beta\gamma}(P_\alpha{}^2P_\beta P_\gamma+P_\gamma P_\beta P_\alpha{}^2) \end{aligned} \quad (3)$$

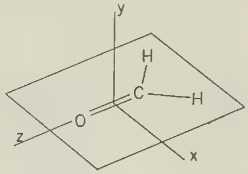

Fig. 6.

In these formulas the z axis is taken as the C_2 axis of symmetry and the y axis is taken perpendicular to the molecular plane as shown in Fig. 6.

Eq. (3) shows that the principal axes of inertia fixed to the equilibrium position of the particles are no longer the principal axes due to the vibration-rotation interaction. When the in-plane rotation of the molecule-fixed x, z axes by an angle $\theta=\sigma_{xz}/(\sigma_{xx}-\sigma_{zz})$ is carried out, the off-diagonal term quadratic in angular momentum operators is shown to be negligible to the second order of approximation. The last term in Eq. (3) has no diagonal elements for the equilibrium asymmetric rotor wave function and its effect is of the fourth order. Thus Eq. (3) takes the same form as Eq. (2) to the second order of approximation.

It is seen from the form of Eq. (2) that the rotational Hamiltonian accurate to the second order of approximation does not mix the Four group of the asymmetric rotor wave functions O$^{\pm}$, E$^{\pm}$. Thus for a low J, K levels Eq. (2) can be solved exactly. They are useful in discussing the low J, K transitions.

For high J, K levels the eigenvalues of the Eq. (2) can not easily be derived. Kivelson and Wilson devised a method to solve the problem by the first order perturbation theory,[6b)] that is, the last three terms in Eq. (2) are averaged by the asymmetric rotor wave functions which are derived from the first term of Eq. (2). This approximation is thought to be very good in the case of C_{2v} formaldehyde molecules because the second order perturbation which was neglected contains only the terms

$$\sum_{J,'K'}\frac{|\langle JK|H_{\mathrm{cent}},J'K'\rangle|^2}{W_{JK}-W_{J'K'}},$$

with $K'=K\pm 2$ and $K\pm 4$ for which the denominator will be very large.

The energy is written as follows[6a)]

$$W=W_0+A_1W_0^2+A_2W_0J(J+1)+A_3J^2(J+1)^2+A_4J(J+1)\langle P_z^2\rangle+A_5\langle P_z^4\rangle+A_6\langle P_z^2\rangle W_0 \quad (4)$$

where W_0 is the pure rotational energy and A_i's are related to the centrifugal distortion constants and rotational constants. $\langle P_z^2\rangle$ and $\langle P_z^4\rangle$ are the mean value of P_z^2 and P_z^4 respectively averaged by the asymmtric rotor wave functions. They are calculated by the method of continued fraction proposed by Kivelson and Wilson.[6b)] Among the seven centrifugal distortion constants appearing in Eq. (2), only four are independent in the case of a planar molecule because of the following relations

$$\begin{aligned}\tau_{yyyy}&=\frac{C^4}{B^4}\tau_{xxxx}+\frac{C^4}{A^4}\tau_{zzzz}+\frac{2C^4}{A^2B^2}\tau_{xxzz}\\ \tau_{xxyy}&=\frac{C^2}{B^2}\tau_{xxxx}+\frac{C^2}{A^2}\tau_{xxzz}\\ \tau_{yyzz}&=\frac{C^2}{A^2}\tau_{zzzz}+\frac{C^2}{B^2}\tau_{xxzz}\,.\end{aligned} \quad (5)$$

Thus the total energy can be expressed by ten quantities: three rotational constants, four centrifugal distortion constants and the three rotational quantum numbers. From Eq. (4) and Eq. (5), the frequencies for the K-type doubling spectral lines can be derived as

$$\nu=\nu_0+\tilde{\boldsymbol{\tau}}\boldsymbol{R}\boldsymbol{W} \quad (6)$$

with $\boldsymbol{\tau}=\begin{pmatrix}\tau_{xxxx}\\ \tau_{zzzz}\\ \tau_{zzxx}\\ \tau_{zxzx}\end{pmatrix}$ and $\boldsymbol{W}=\begin{pmatrix}J(J+1)\Delta W\\ (W_u+W_l)\Delta W\\ J(J+1)\Delta\langle P_z^2\rangle\\ \Delta\langle P_z^4\rangle\\ \Delta\{W\langle P_z^2\rangle\}\end{pmatrix}$

where Δ means the difference of the quantities in the upper state from that in the lower state and w denotes the eigenvalue $w(b)$ in the rotational energy expression

$$W_0=\frac{B+C}{2}J(J+1)+\left(A-\frac{B+C}{2}\right)w(b)\,. \quad (7)$$

$\boldsymbol{R}$ is a matrix of four rows and five columns whose elements are derived after tedious calculations, and are listed in Table I. In the derivation of the $\boldsymbol{R}$ matrix the relation

Table I. The **R** matrix

$-\frac{B^4-C^4}{8bB^4}$	$\frac{C^2(B+C)^2}{16A^2B^2b^2}$	$-\frac{AC(B^2+C^2)}{2B^4}$	$\frac{A^2C^2}{B^4}$	$\frac{C^2(B+C)}{2bB^3}$
$\frac{C^4}{8bA^4}$	$\frac{C^4}{16b^2A^4}$	$\frac{C^3}{2A^2B}$	$\frac{C^2}{B^2}$	$\frac{C^3}{2bA^2B}$
$\frac{C^4}{4bA^2B^2}$	$-\frac{C^3(B+C)}{8b^2A^3B}$	$\frac{C^2(B^2+2AC)}{2AB^3}$	$-\frac{2AC^2}{B^3}$	$-\frac{C^2(B+2C)}{2bAB^2}$
0	0	$\frac{1}{2}$	$-\frac{A^2}{B^2}$	$-\frac{1}{2b}$

$1/A+1/B=1/C$ was used. This relation is exact for the rotational constants appearing in Eq. (5) since they are equilibrium values, but only approximate for those in Eq. (4). The difference is of the second order and will be neglected in the present treatment. Less accurate formula for the K-type doubling lines proposed by Hillger and Strandberg and that by Kivelson and Wilson were useful in the first crude determination of the molecular constants and centrifugal distortion correction and is rewritten here.[2b)6b)]

$$\nu=\nu_0[1+T_1J(J+1)K+T_2(K-1)J(J+1)+T_3K(K^2+2)+T_4K(K-1)(2K-1)+T_5K(K^2-1)] . \qquad (8)$$

§ 4. Analysis of the Spectra

K-type doubling lines were analyzed by Eqs. (6) and (8). First, a rough determination of $A-(B+C)/2$ and the asymmetry parameter $b=(C-B)/(2A-B-C)$ was done by Eq. (8). Then the calculated values were refined by more precise calculation using Eq. (8). It was recognized that the dependences of the coefficients to be multiplied to τ_{xxxx}, τ_{xxzz}, and τ_{zzzz} on the rotational quantum numbers did not differ greatly from each other. By this fact it was given up to determine the centrifugal distortion constants from the observed spectra but rather it was tried to fit the calculated frequencies to the observed ones

Table II. Observed and calculated frequencies for the K-type doubling lines of H_2CO (Mc/sec)

Transition	Distortion correction	Calculated frequency	Observed frequency	Error	Calculated intensity (cm⁻¹)
1_1	−2.40	4829.73	4829.73	−0.00	6.0×10^{-6}
2_1	−7.71	14488.68	14488.65	−0.03	2.9×10^{-5}
3_1	−16.98	28975.14	28974.85	−0.29	8.0×10^{-5}
4_1	−32.10	48284.59	48284.60	−0.01	1.6×10^{-4}
5_1	−53.79	72409.78	72409.35	−0.43	2.8×10^{-4}
6_2	−13.15	4954.56	4954.76	0.20	1.2×10^{-6}
7_2	−25.07	8884.54	8884.87	0.33	3.0×10^{-6}
8_2	−44.46	14726.03	14726.74	0.71	6.5×10^{-6}
9_2	−74.40	22964.44	22965.71	1.27	1.3×10^{-5}
10_2	−118.65	34098.00	34100.32	2.32	2.3×10^{-5}
11_2	−181.96	48610.05	48612.70	2.65	3.7×10^{-5}
12_3	−26.86	3226.14	3225.58	−0.56	7.0×10^{-7}
13_3	−45.09	5137.38	5136.58	−0.80	1.4×10^{-6}
14_3	−72.87	7893.04	7892.03	−1.01	2.6×10^{-6}
15_3	−113.98	11754.41	11753.13	−1.28	4.4×10^{-6}
16_3	−173.62	17028.85	17027.60	−1.25	7.0×10^{-6}
17_3	−258.04	24069.48	24068.31	−1.17	1.1×10^{-5}
18_3	−374.91	33270.90	33270.80	−0.10	1.6×10^{-5}
19_3	−533.29	45061.67	45063.10	1.43	2.2×10^{-5}
20_4	−73.61	3520.79	3518.85	−1.94	4.3×10^{-8}
21_4	−111.83	5140.99	5138.57	−2.42	6.5×10^{-8}
22_4	−166.73	7365.59	7362.60	−2.99	1.0×10^{-7}
23_4	−244.20	10369.72	10366.51	−3.21	1.5×10^{-7}
24_4	−351.77	14364.05	14361.54	−2.51	2.0×10^{-7}
25_4	−498.86	19597.54	19595.23	−2.31	2.7×10^{-7}
26_4	−696.81	26359.60	26358.82	−0.78	3.5×10^{-7}
27_4	−959.56	34979.97	34982.80	2.83	4.3×10^{-7}
28_4	−1303.11	45827.55	45835.58	8.03	4.9×10^{-7}
31_5	−371.20	7833.80	7833.20	−0.60	1.3×10^{-8}
32_5	−518.86	10607.39	10608.74	1.35	1.6×10^{-8}
33_5	−717.14	14207.35	14211.68	4.33	1.9×10^{-8}
34_5	−981.56	18830.62	18841.20	10.58	2.2×10^{-8}
35_5	−1325.63	24713.35	24730.40	17.05	2.4×10^{-8}

with the smallest modification of the calculated centrifugal distortion constants.

The procedure employed in the analysis of the spectra was as follows:

i) Rotational energy tables were prepared by the use of the continued fraction method, around the probable values of the asymmetry parameters. The approximate value for the asymmetry parameter was obtained from the King, Hainer and Cross's table for low *J*, *K* transitions. Accurate calculations of eigenvalues were necessary because the trasitions between *K*-type doublets correspond to $\varDelta J=0$ and $\varDelta K=0$. The differences between the eigenvalues of the same *J*, *K* but the +and−matrices multiplied by a rather large quantity $A-(B+C)/2$ are observed directly. It was seen that a complete linearlity existed when the step of the asymmetry parameter was less than 0.00001 and $w(b)$ in Eq. (7) were calculated to ten figures. The digital parametron computer PC-1 was used throughout.

ii) B-C was calculated from the 1_1 and 2_1 lines by means of the exact formulas obtained by solving Eq. (2)

$$\nu_{1_1}=B-C+\frac{1}{4}(\tau_{xxxx}-\tau_{yyyy})+\frac{1}{2}(\tau_{xxzz}+2\tau_{xzxz}-\tau_{yyzz})$$

$$\nu_{2_1}=3(B-C)+\frac{15}{4}(\tau_{xxxx}-\tau_{yyyy})+\frac{3}{2}(\tau_{xxzz}+2\tau_{xzxz}-\tau_{yyzz})\,, \tag{9}$$

with the calculated centrifugal distortion constants and observed the frequencies.

iii) Probable value of the asymmetry parameter which could be obtained by the approximate formula Eq. (8) was assumed, and the rotational constants were determined either by the *R*-branch frequencies if available or by the calculated inertia defect.

iv) The elements of the **R** matrix and **W** vector in Eq. (6) were calculated by the digital computer PC-1 and the centrifugal distortion corrections were made by using the centrifugal distortion constants obtained from vibration-rotation theory.

v) The calculated centrifugal distortion correc-

Table III. Observed and calculated frequencies for the *K*-type doubling lines of HDCO (Mc/sec)

Transition	Distortion correction	Calculated frequency	Observed frequency	Error	Calculated intensity (cm⁻¹)
1_1	−1.50	5346.25	5346.64	0.39	9.7×10^{-6}
2_1	−5.08	16038.12	16038.06	−0.06	4.7×10^{-5}
3_1	−11.89	32072.57	32072.56	−0.01	1.3×10^{-4}
5_2	−7.16	4489.07	4489.08	0.01	5.3×10^{-6}
6_2	−15.29	8923.00	8922.59	−0.41	1.6×10^{-5}
7_2	−29.73	15908.43	15907.38	−1.05	4.2×10^{-5}
8_2	−58.52	26147.54	26150.16	2.62	9.2×10^{-5}
10_3	−16.95	3283.58	3283.09	−0.49	1.9×10^{-6}
11_3	−31.88	5703.39	5702.6	−0.79	4.6×10^{-6}
12_3	−56.96	9413.11	9412.51	−0.60	1.0×10^{-5}
13_3	−96.70	14873.61	14873.02	−0.59	2.0×10^{-5}
14_3	−156.74	22626.48	22624.65	−1.83	3.7×10^{-5}
15_3	−249.81	33271.61	33274.70	3.09	6.5×10^{-5}
16_4	−38.02	2947.81	2946.67	−1.14	5.8×10^{-7}
17_4	−64.57	4715.49	4713.90	−1.59	1.2×10^{-6}
18_4	−106.37	7324.13	7322.35	−1.78	2.2×10^{-6}
19_4	−169.66	11076.78	11074.30	−2.48	3.9×10^{-6}
20_4	−264.73	16345.96	16343.41	−2.55	6.5×10^{-6}
21_4	−404.97	23578.57	23578.92	0.25	1.0×10^{-5}
22_4	−602.28	33298.85	33303.12	4.27	1.5×10^{-5}
23_5	−91.69	3331.97	3330.66	−1.31	1.4×10^{-7}
24_5	−144.93	5019.76	5018.25	−1.51	2.3×10^{-7}
25_5	−224.49	7419.07	7418.3	−0.77	3.7×10^{-7}
26_5	−341.13	10769.98	10769.9	−0.08	5.8×10^{-7}
27_5	−508.94	15368.91	15374.56	5.65	8.5×10^{-7}
28_5	−745.92	21586.70	21597.0	10.30	1.2×10^{-6}

tions were added to the rigid rotor frequencies and the discrepancy between the calculated and the observed frequencies was minimized by adjusting the asymmetry parameter and centrifugal distortion constants. The minimization was done by putting larger weights on the low J, K transitions because the neglect of higher order quantities will affect high J, K levels more than low J, K levels.

Table IV. Observed and calculated frequencies for the K-type doubling lines of D_2CO (Mc/sec)

Transition	Distortion correction	Calculated frequency	Observed frequency	Error	Calculated intensity (cm⁻¹)
1_1	−1.23	6096.12	6096.10	−0.02	3.3×10^{-6}
2_1	−4.24	18287.80	18287.90	0.10	1.6×10^{-5}
3_1	−10.17	36567.60	36567.74	0.14	4.2×10^{-5}
4_2	−3.27	3687.18	3687.28	0.10	2.5×10^{-6}
5_2	−9.54	8518.46	8519.10	0.64	1.1×10^{-5}
6_2	−20.76	16759.17	16759.64	0.47	3.2×10^{-5}
7_2	−40.47	29435.76	29436.02	0.26	7.5×10^{-5}
8_3	−8.69	2850.49	2850.62	0.13	6.0×10^{-7}
9_3	−18.44	5638.02	5636.98	−0.04	2.0×10^{-6}
10_3	−36.19	10305.09	10304.64	−0.45	5.5×10^{-6}
11_3	−66.56	17651.80	17650.80	−1.00	1.2×10^{-5}
12_3	−115.61	28597.05	28596.74	−0.39	2.6×10^{-5}
13_4	−22.02	3080.35	3079.48	−1.13	8.5×10^{-7}
14_4	−41.24	5462.88	5461.54	−1.34	2.1×10^{-6}
15_4	−73.82	9261.71	9259.88	−1.84	4.9×10^{-6}
16_4	−126.78	15082.06	15080.34	−1.72	1.0×10^{-6}
17_4	−209.56	23674.65	23672.78	−1.77	1.9×10^{-6}
18_4	−333.95	35917.03	35916.94	−0.09	3.2×10^{-5}

Table V. Observed and calculated frequencies for the K-type doubling lines of $H_2C^{13}O$ (Mc/sec)

Transition	Distortion correction	Calculated frequency	Observed frequency	Error	Calculated intensity (cm⁻¹)
1_1	−2.35	4593.12	4593.26	0.14	6.5×10^{-8}
2_1	−7.54	13778.85	13778.86	0.01	3.3×10^{-7}
3_1	−16.57	27555.68	27555.73	0.05	9.0×10^{-7}
4_1	−31.30	45919.48	45920.08	0.60	1.8×10^{-6}
7_2	−22.78	8012.33	8012.56	0.23	3.4×10^{-8}
8_2	−40.39	13287.37	13287.13	−0.24	7.5×10^{-8}
9_2	−67.54	20736.00	20736.40	0.40	1.5×10^{-7}
10_2	−107.73	30818.37	30819.74	1.37	1.8×10^{-7}
15_3	−98.61	10064.18	10063.82	−0.36	5.0×10^{-8}
16_3	−151.13	14592.51	14592.44	−0.07	8.0×10^{-8}
17_3	−223.36	20649.78	20649.30	−0.48	1.3×10^{-7}
18_3	−324.77	28581.72	28582.40	0.68	1.8×10^{-7}

Table VI. Observed and calculated frequencies for the K-type doubling lines of H_2CO^{18} (Mc/sec)

Transition	Distortion correction	Calculated frequency	Observed frequency	Error	Calculated intensity (cm⁻¹)
1_1	−2.24	4388.85	4388.85	0.00	1.2×10^{-8}
2_1	−7.15	13165.85	13165.84	−0.01	9.5×10^{-8}
3_1	−15.79	26331.05	26330.64	0.59	1.6×10^{-7}

It was found that the observed frequencies could be made to fit well to the calculated ones by a small adjustment on τ_{xxxx}. The final results are shown in Table II∼VI. It is seen that the agreement is quite satisfactory in spite of the neglect of higher order quantities in the vibration-rotation interaction theory and the approximate equilibrium structure used in the calculation.

The rotational constants and the centrifugal distortion constants adopted for the analysis of the spectra are listed in Tables VII.

§ 5. Discussions

In Table VIII, $B-C$, $A-(B+C)/2$, and b obtained for H_2CO are compared with the previous values obtained by other workers. It will be seen that the difference between the Lawrance and Strandberg's or Erlandsson's data and the value obtained in the present work is beyond the experimental error. This is due to the difference in the estimation of the distortion corrections. For example, it is seen in Table II that the distortion correction in this paper for the 2_1 line of H_2CO is −7.71 Mc while theirs are −0.56 Mc and −0.57 Mc. As is seen from the Eq. (9) the centrifugal distortion correction for this frequency contains the term $3\tau_{zzzz}$ which can not be so small as was adopted by them. It can be said that the centrifugal distortions are made fairly well by less accurate centrifugal distortion constants. This is the reason why it was given up to determine the centrifugal distortion constants from the frequencies by the least-squares method. The situation is quite different from the cases of SO_2 and O_3. For these molecules the b-type transitions $\varDelta J=0$ or ± 1 and $\varDelta K=\pm 1$ are observed and τ_{zzzz} plays the most important role in determining

Table VII. Molecular constants used in the analysis of the observed spectral lines (Mc/sec)

H_2CO	$A-\frac{B+C}{2}-245610 \quad \pm 25$ $B-C=4832.13 \pm 0.01$ $B+C=72838.44 \pm 0.10$ $b=-0.0098370 \pm 0.0000010$	$\tau_{xxxx}=-0.39220$ $\tau_{zzzz}=-101.831$ $\tau_{xxzz}=1.4101$ $\tau_{xzxz}=-3.2920$ $(\tau_{xxxx})_{calc}=-0.40331$
$H_2C^{13}O$	$A-\frac{B+C}{2}=246525 \quad \pm 25$ $B-C=4595.47 \quad \pm 0.02$ $b=-0.0093205 \pm 0.0000010$	$\tau_{xxxx}=-0.37283$ $\tau_{zzzz}=-101.833$ $\tau_{xxzz}=1.3124$ $\tau_{xzxz}=-3.1622$ $(\tau_{xxxx})_{calc}=-0.38084$
H_2CO^{18}	$B-C=4391.08 \pm 0.02$	
D_2CO	$A-\frac{B+C}{2}=112427 \quad \pm 20$ $B-C=6097.35 \pm 0.02$ $b=-0.027117 \pm 0.000002$	$\tau_{xxxx}=-0.31942$ $\tau_{zzzz}=-25.4940$ $\tau_{xxzz}=0.92728$ $\tau_{xzxz}=-1.7808$ $(\tau_{xxxx})_{calc}=-0.31250$
HDCO	$A-\frac{B+C}{2}=165905 \pm 10$ $B-C=5347.77 \quad \pm 0.04$ $B+C=64472.50 \pm 0.50$ $b=-0.016117 \pm 0.000002$	$\tau_{xxxx}=-0.37016$ $\tau_{zzzz}=-57.1865$ $\tau_{xxzz}=1.45748$ $\tau_{xzxz}=-2.30378$ $(\tau_{xxxx})_{calc}=-0.36106$

Table VIII. Comparison with the previous data

	$B-C$(Mc/sec)	$A-\frac{B+C}{2}$(Mc/sec)	b
Lawrance and Strandberg(2a)	4829.7±0.3	245687	−0.009829
Erlandsson(7)	4829.7	245686	−0.009829
This work	4832.17±0.01	245610	−0.009837

the centrifugal distortion corrections.[6c)6d)] The centrifugal distortion formula for a symmetric top molecule can partly explain the correction for these molecules, while in the case of K-type doubling spectrum, the centrifugal distortion correction itself is the result of the K-type doubling of $\langle P_z^2\rangle$ and $\langle P_z^4\rangle$.

Many unassigned spectral lines have been observed. In the cases of HDCO and D_2CO, where the sample was evolved by heating the calcium formate, some of them are due to the impurities evolved in the decomposition. In the cases of H_2CO some of them were ascribed to the spectral lines of methanol which was produced in the decomposition of para-formaldehyde. Other numerous lines may be due to the vibrationally excited formaldehyde molecule. These lines will be measured hereafter by using a high temperature spectrograph.

§ 6. Acknowledgement

The authors are indebted to Mr. Akira Miyahara for his collaboration with us in the preliminary measurement of the spectra, and to Mr. Kunitaka Kondo for his help in some of the calculation.

They owe much to Prof. Yonezo Morino of the Department of Chemistry for his discussions and continued interest to this work.

They are also grateful to Prof. Hidetoshi Takahashi who allowed us to use the digital computer PC−1. Without the computer the tedious calculations of the rotational energy, $\langle P_z^2\rangle$, and $\langle P_z^4\rangle$ would have been impossible.

References

1) J. K. Bragg and A. H. Sharbaugh: Phys. Rev. **75** (1949) 1774 (L).
2a) R. B. Lawrance and M. W. P. Strandberg: Phys. Rev. **83** (1951) 363.
2b) R. F. Hillger and M. W. P. Strandberg: Phys. Rev. **83** (1951) 575.
2c) D. W. Posener and M. W. P. Strandberg: Phys. Rev. **95** (1954) 374.
3a) H. Hirakawa, A. Miyahara and K. Shimoda: J. Phys. Soc. Japan **11** (1956) 334 (s. n.)
3b) H. Hirakawa, T. Oka and K. Shimoda: J. Phys. Soc. Japan **11** (1956) 1207 (s.n.).
3c) K. Kondo, H. Hirakawa, A. Miyahara, T. Oka and K. Shimoda: J. Phys. Soc. Japan **15** (1960) 303.
3d) K. Kondo and T. Oka: J. Phys. Soc. Japan **15** (1960) 307.
4a) H. Takuma, T. Shimizu and K. Shimoda: J. Phys. Soc. Japan **14** (1959) 1595.
4b) K. Shimoda, H. Takuma and T. Shimizu: J. Phys. Soc. Japan **15** (1960) 2036.
4c) T. Yajima and K. Shimoda: J. Phys. Soc. Japan **15** (1960) 1668.
5) P. Thaddeus, J. Loubser, L. Krisher and H. Lecar: J. Chem. Phys. **31** (1959) 1677 (L).
6a) E. B. Wilson, Jr. and H. B. Howard: J. Chem. Phys. **4** (1936) 260.
6b) D. Kivelson and E. B. Wilson, Jr.: J. Chem. Phys. **20** (1952) 1575.
6c) D. Kivelson: J. Chem. Phys. **22** (1954) 904.
6d) L. Pierce: J. Chem. Phys. **24** (1956) 139.
7) E. G. Erlandsson: Arkiv för Fysik 16 (1959) 181.
8) K. A. Hofmann and H. Schibsted: Berichte **51** (1918) 1398.

JOURNAL OF THE PHYSICAL SOCIETY OF JAPAN, Vol. 15, No. 12, DECEMBER, 1960

Microwave Spectrum of Formaldehyde
II. Molecular Structure in the Ground State

By Takeshi OKA*

Department of Physics, Faculty of Science,
University of Tokyo, Tokyo, Japan

(Received, July 2, 1960)

Rotational constants for the isotopic formaldehyde molecules H_2CO, $H_2C^{13}O$, H_2CO^{18}, HDCO and D_2CO were determined from the parameters used in the analysis of K-type doubling spectra and the frequencies of $1_{01} \leftarrow 0_{00}$ transitions. In the cases of isotopic species for which the R-branch transitions were not measured, the calculated inertia defect was used in the determination of the rotational constants.

From the rotational constants, the zero-point structure of formaldehyde molecule, r_z, was determined by a new method taking into account the zero-point vibration-rotation interaction and electronic interaction. The following zero-point molecular structure was obtained;

$$r_{C-H} = 1.117_4 \pm 0.002\ \text{A}$$
$$\angle HCO = 122°5' \pm 20'$$
$$r_{C=O} = 1.206_3 \pm 0.002\ \text{A} \qquad \text{planar.}$$

All of the rotational constants calculated from these geometrical parameters fit to the observed values within the experimental error. In contrast to the previous researches, ∠HCO is much larger than 120°. It was also confirmed that the formaldehyde molecule is completely planar in the ground vibrational state.

§1. Introduction

Investigations on the structure of the formaldehyde molecule have been worked out by several workers.[1)2)3)4)5)] In 1934, Dieke and Kistiakowsky obtained two rotational constants from the analysis of the fine structure of ultraviolet spectrum.[1)] Their values were accurate and agreed very well with the Lawrance and Strandberg's values from microwave spectrum worked out 15 years later.[4)] Since three independent quantities are necessary to determine the molecular structure of formaldehyde on the assumption of C_{2v} planar structure, Dieke and Kistiakowsky assumed ∠HCH to be 110° and obtained C=O bond length to be 1.270 A. Herzberg assumed C−H bond length in formaldehyde to be equal to the value in ethylene, that is, 1.071 A and obtained $r_{C=O} = 1.225$A and $\angle HCH = 123°26'$.[3)] Lawrance and Strandberg analyzed the microwave spectrum of H_2CO and $H_2C^{13}O$ and obtained $r_{C=H} = 1.12 \pm 0.01$A, $r_{C-O} = 1.21 \pm 0.01$A and $\angle HCH = 118° \pm 1$.[4)] In 1954 Davidson, Stoicheff and Bernstein studied the fine structure of the vibration-rotation bands in infra-red and Raman spectra of HDCO and determined the structure of formaldehyde molecule with several assumptions.[5)] There is also an electron diffraction study by Stevenson, Luvalle and Schomaker which indicated the C=O distance to be 1.21±0.01 A.[2)]

By the use of the parameters from the extensive analysis of the H_2CO, $H_2C^{13}O$, H_2CO^{18}, HDCO and D_2CO in the first part of this series of reports on the microwave spectrum of formaldehyde, the accurate determination of molecular structure will be carried out in the present paper.

Usually the structure of a molecule is determined by fitting the calculated moments of inertia obtained by assumed structural constants to the observed ones. The structure thus obtained is the effective r_0 structure But the observed moments of inertia by no means give the exact inter-nuclear distances because they are affected by the zero-point vibration-rotation and electronic interaction The former effect is rather large in the case of light molecules such as formaldehyde and cannot be neglected in the accurate structural determination. If spectral lines of the molecu structuralle in the vibrationally excited states were observed sufficiently enough, this effect might be subtracted to give the equilibrium r_e structure. However this was impossible in the case of formaldehyde, and it was tried to obtain the zero point structure denoted by r_z, by subtracting from the observed moments of inertia the harmonic vibration-rotation interactions terms. These harmonic terms can be calculated when the normal vibration calculation is complete, and will be discussed in the third part of this series.

---

* Present address: Department of Chemistry, Faculty of Science, University of Tokyo, Tokyo, Japan.

The inertia defect is mainly due to these harmonic terms. Usually a molecule is said to be planar when the inertia defect $\Delta = I_{cc} - I_{bb} - I_{aa}$ is nearly equal to zero. But recently Costain and Dowling suggested the two N-H bonds in NH_2CHO to be 7° and 12° out of plane of the molecule though the inertia defect is nearly equal to zero.$^{6)}$ Strictly speaking, the planarity of a molecule can only be concluded after the calculation of the inertia defect. This was tested in the case of formaldehyde, and this molecule was actually shown to be planar.

The second interaction due to the bonding electrons must also be considered. Since the two π electrons protruding out of the plane of molecule and the two lone-pair electrons of oxygen atom are out of the C=O axis, the effect of these electrons was not negligible in determining the internuclear distances.

§ 2. Rotational Constants

The asymmetry parameter

$$b = \frac{C - B}{2A - B - C}$$

and $B - C$ have been obtained in I for H_2CO, $H_2C^{13}O$, HDCO and D_2CO. Another quantity is necessary to determine the rotational constants A, B, and C. The R-branch $1_{01} \leftarrow 0_{00}$ transitions which have the frequencies $B + C$ and appear in the millimeter wave region have been observed for $H_2CO^{4)}$ and $HDCO^{7)}$ as 72838.14 Mc and 64472.12 Mc, respectively, and the rotational constants of these isotopic species can be determined accurately. The centrifugal distortion correction adopted for these lines were −0.30 Mc and −0.38 Mc, respectively, which were calculated from the centrifugal distortion constants used in the analysis in I.

For $H_2C^{13}O$ and D_2CO, the R-branch transitions which would appear at 71027 Mc and 58473 Mc respectively, could not be measured. The calculated inertia defect was used to determine the rotational constants for these species. From the values of $A - C$, $B - C$ and calculated moments of inertia, the smallest rotational constant C can be determined as

$$C = \sqrt{(A - C)(B - C) - \frac{ABC\Delta \times 10^{-5}}{5.05531}}. \qquad (1)$$

The close agreement between the calculated and the observed inertia defect in the cases of H_2CO and HDCO indicates that the rotational constants determined in this way are fairly accurate. But the probable errors for B and C are larger in this case than those determined from the R-branch transition.

In the case of H_2CO^{18} for which only $B - C$ was obtained owing to the weakness of the spectrum, the largest rotational constant A was assumed to be equal to that of H_2CO. This assumption seems to be quite reasonable in view of the fact that A of H_2CO and $H_2C^{13}O$ are nearly equal. Thus the rotational constants and the effective moments of inertia for formaldehyde molecules were determined as listed in Table I. The observed inertia defects 0.0574 amu A² for H_2CO and 0.0679 amu A² for HDCO are seen to agree very well with the calculated values 0.0561 and

Table I. Rotational constants (in Mc/sec) and effective moments of inertia (in amu A^2) for formaldehyde molecules.

H_2CO	$A = 282029 \pm 25$	$I_{aa} = 1.79284 \pm 0.00020$
	$B = 38835.28 \pm 0.10$	$I_{bb} = 13.01731 \pm 0.00005$
	$C = 34003.16 \pm 0.10$	$I_{cc} = 14.86718 \pm 0.00005$
		$\Delta = 0.05739 \pm 0.00030$
$H_2C^{13}O$	$A = 282038 \pm 25$	$I_{aa} = 1.7924 \pm 0.0002$
	$B = 37810.83 \pm 2$	$I_{bb} = 13.3700 \pm 0.0007$
	$C = 33215.36 \pm 2$	$I_{cc} = 15.2198 \pm 0.0010$
		$\Delta^* = 0.0574 \pm 0.0010$
H_2CO^{18}	$A^* = 282029 \pm 35$	$I_{aa} = 1.7925 \pm 0.0003$
	$B = 36906.12 \pm 5$	$I_{bb} = 13.6978 \pm 0.0020$
	$C = 32515.04 \pm 5$	$I_{cc} = 15.5476 \pm 0.0025$
		$\Delta^* = 0.0573 \pm 0.0010$
D_2CO	$A = 141664 \pm 20$	$I_{aa} = 3.5685 \pm 0.0006$
	$B = 32285.4 \pm 10$	$I_{bb} = 15.6582 \pm 0.0060$
	$C = 26188.1 \pm 10$	$I_{cc} = 19.3038 \pm 0.0080$
		$\Delta^* = 0.07721 \pm 0.0010$
HDCO	$A = 198122 \pm 25$	$I_{aa} = 2.55161 \pm 0.0003$
	$B = 34910.13 \pm 1$	$I_{bb} = 14.48093 \pm 0.0004$
	$C = 29562.36 \pm 1$	$I_{cc} = 17.10050 \pm 0.0006$
		$\Delta = 0.06787 \pm 0.0013$

* Calculated or assumed values.

0.0674 amu A^2, respectively.

§ 3. Vibration-Rotation Interaction

Usually the structure of a molecule is determined directly from the effective moments of inertia obtained from the experiment. These structures are called zero point structure and are denoted by r_0. However this is not correct because of the vibration-rotation and electronic interaction. For this reason the r_0 structure may be called effective structure. Costain[8)] showed that the substituted bond length r_s devised by Kraitchman[9)] represent fairly well the equilibrium bond length. In the following treatment the molecular structure in the ground vibrational state will be searched for.

As was shown by Nielsen[10)], the rotational energy of a vibrating molecule is expressed as follows.

$$
\begin{aligned}
&\mathrm{H}=\mathrm{H}^{(0)}+\mathrm{H}^{(2)}\,,\\
&\mathrm{H}^{(0)}=\frac{1}{2}\sum_{\alpha}\frac{P^2{}_{\alpha}}{I^{(e)}_{\alpha\alpha}}\,,\\
&\mathrm{H}^{(2)}=\sum_{\alpha,\beta}\sum_{s}\Bigg[\frac{1}{4\pi}\sqrt{\frac{h}{c}}\left\{\frac{3k_{sss}}{\omega_s{}^{3/2}}a_s{}^{(\alpha\beta)}+\sum_{s'}{}'\frac{k_{sss'}}{\omega_{s'}{}^{3/2}}a_{s'}^{(\alpha\beta)}\right\}\\
&\qquad+\frac{h}{8\pi^2c}\left\{4\sum_{s'}{}'\frac{\omega_s}{\omega_s{}^2-\omega_{s'}{}^2}\zeta_{ss'}^{(\alpha)}\zeta_{ss'}^{(\beta)}-\frac{1}{\omega_s}\left(A_{ss}^{(\alpha\beta)}-\sum_{\xi}\frac{a_s{}^{(\alpha\xi)}a_s{}^{(\beta\xi)}}{I^{(e)}_{\xi\xi}}\right)\right\}\Bigg]\frac{P_\alpha P_\beta}{I^{(e)}_{\alpha\alpha}I^{(e)}_{\beta\beta}}\left(v_s+\frac{1}{2}\right)\\
&\qquad+\frac{1}{4}\sum_{\alpha,\beta,\gamma,\delta}\tau_{\alpha\beta\gamma\delta}P_\alpha P_\beta P_\gamma P_\delta\,. \qquad (2)
\end{aligned}
$$

Due to the perturbation Hamiltonian $\mathrm{H}^{(2)}$, the effective moments of inertia $(I_{\alpha\alpha})_{\mathrm{eff}}$ will differ from the equilibrium value $I^{(e)}_{\alpha\alpha}$. The terms in Eq. (2) can be interpreted as follows. The terms in $\mathrm{H}^{(0)}$ express the energy of the rotation of a molecule whose component atoms are at their equilibrium positions and are rotating with the molecule-fixed axes determined by the Eckart's condition. The five terms in the perturbation $\mathrm{H}^{(2)}$ are due to four kinds of effect. The first two which include the anharmonic potential constants k_{sss} and $k_{sss'}$ represent the variation in the rotational energy owing to the shift of the equilibrium position of the vibrating nuclei due to the anharmonicity of the potential. The third term represents the Coriolis interaction. When the nuclei are vibrating about their equilibrium positions, the molecule does not rotate smoothly due to the Coriolis interaction. Each nucleus vibrates back and forth about the molecule-fixed axes in a perpendicular direction to their intrinsic vibrational displacements. This situation can be understood if we consider a diatomic molecule vibrating in a stretching mode. Owing to the Coriolis interaction the nuclei vibrate in a perpendicular direction to the internuclear axis fixed by the Eckart's condition. This motion couples with other vibrations in the direction and when the vibrations are averaged out, the rotational energy differs slightly from the original value and gives the third term. The fourth term represents the mean square amplitude of vibration in the normal coordinate expansion of the moment of inertia. The fifth term comes from the shift of the equilibrium positions of nuclei due to the centrifugal distortion of the molecule. In the present analysis the fifth term has been considered separately as shown in I and the obtained moments of inertia includes the effect of the first four terms. *The first two terms represent the real shift of the equilibrium nuclear positions, while the latter two are only the result of averaging over the vibrations.* From the above physical interpretation all the harmonic vibration-rotation terms were subtracted from the effective moments of inertia to obtain the zero point molecular structure.

It was shown that the effective moments of inertia obtained from the rotational constants are expressed as[11)]

$$
\begin{aligned}
(I_{\alpha\alpha})_{\mathrm{eff}}=I^{(e)}_{\alpha\alpha}-\sum_{s}\left(v_s+\frac{1}{2}\right)\Bigg[&\frac{1}{2\pi}\sqrt{\frac{h}{c}}\left\{\frac{3k_{sss}}{\omega_s{}^{3/2}}a_s{}^{(\alpha\alpha)}+\sum_{s'}{}'\frac{k_{sss'}}{\omega_{s'}{}^{3/2}}a_{s'}{}^{(\alpha\alpha)}\right\}\\
&+\frac{h}{\pi^2c}\left\{\sum_{s'}{}'\frac{\omega_{s'}{}^2}{\omega_s(\omega_s{}^2-\omega_{s'}{}^2)}(\zeta_{ss'}^{(\alpha)})^2+\frac{3}{4}\frac{A_{ss}^{(\alpha\alpha)}}{\omega_s}\right\}\Bigg]-\frac{h^3}{8\pi^2}C_\alpha\tau_{zzzz}I^2_{\alpha\alpha} \qquad (3)
\end{aligned}
$$

with

$$C_x = C_z = -2\ , \quad C_y = 3\ .$$

In deriving the above expression from Eq. (2), the relation

$$\sum_{\xi} \frac{a_s{}^{(\alpha\xi)} a_s{}^{(\beta\xi)}}{I_{\xi\xi}^{(e)}} = -4 \sum_{s'} \varphi_{ss'}^{(\alpha)} \varphi_{ss'}^{(\beta)} + 4A_{ss}^{(\alpha\beta)}$$

was used.[11] The last term in Eq. (3) came from these centrifugal distortion terms which was reduced to quadratic form in angular momentum operators by the commutation relation. The harmonic terms in Eq. (3) was obtained by the calculation of the vibration-rotation interaction.

§ 4. Electronic Interaction

Usually it is assumed in the calculation of the moments of inertia that all electrons are fixed at the positions of nuclei. This is not actually the case and in such a light molecule as formaldehyde which has a double bond, this effect is by no means negligible.

The effect of electrons in a molecule on the value of the moments of inertia has been considered by Johnson and Strandberg[12] and by Rosenblum, Nethercot and Townes[13] in the cases of H_2CCO and CO, respectively. It was shown by Johnson and Strandberg that the rotational Hamiltonian, taking into account the motion of electrons, is written as

$$H = \frac{1}{2} \sum \sum [I^n + I^e]_{ij}^{-1} P_i P_j + \frac{mv}{e} \sum_i \sum_j G_{ij} \frac{P_i P_j}{I_i^n}\ . \tag{4}$$

where $[I^n]$ is the moments of inertia tensor of nuclear system and $[I^e]$ is the inertia tensor of the electrons about the nuclear axes. $[I^n + I^e]$ is the usual inertia tensor calculated on the assumption that the electrons are fixed at the nuclei. The error introduced by assuming the nuclear axes to be the atomic axes is negligibly small. G_{ij}'s in Eq. (4) are related to the g tensor of the rotational magnetic moments as

$$\frac{2v}{e} M_p G_{ij} = g_{ij}$$

where g_{ij} are components of the familiar g tensor of the rotational magnetic moments and are measured by microwave Zeeman effect. In the case of a molecule with C_{2v} symmetry, the off-diagonal elements of I^e tensor and g tensor vanish from the symmetry. Even for the case of HDCO where C_{2v} symmetry does not exist, the off-diagonal terms in these tensors can safely be neglected because they are of the second order quantity. Then from the Eq. (4) the variation of the moments of inertia ΔI_{ii} due to the electronic interaction can be written as

$$\Delta I_{ii} = \frac{m I_{ii}}{M_p} g_{ii}\ . \tag{5}$$

The same formula can be obtained by the extension of the formulation given by Rosenblum et al for the case of a diatomic molecule to the case of an asymmetric rotor. The neglect of $\sum_i m_i r_i^2$ they did is unnecessary.

The value of g tensor for H_2CO, HDCO, and D_2CO have been obtained by Kondo et al and is listed in Table II.[14]

Table II. g-values of formaldehyde molecule.[14]

Molecules	g_{aa}	g_{bb}	g_{cc}
H_2CO	-2.90 ± 0.05	-0.35 ± 0.10	-0.02 ± 0.10
HDCO	-2.00 ± 0.05	-0.32 ± 0.10	-0.02 ± 0.10
D_2CO	-1.46 ± 0.05	-0.29 ± 0.10	-0.02 ± 0.10

Johnson and Strandberg reported in their paper on H_2CCO, that the largest of this correction was ΔI_{aa} which still was negligible. Since the data of Zeeman effect was absent for the molecule, they estimated g_{aa} to be $+0.48$ by taking only the σ bonding electrons in the C-H bond into acount. However this seems to be smaller than the actual value. As is seen from Table II, g_{aa} of formaldehyde molecule is very large. The same situation exists in the case of CO molecule where g_{bb} is also very large in view of the relatively large moment of inertia perpendicular to the CO axis. Both of them are interpreted by taking into account of the two π electrons on the CO bond and in the case of H_2CO two lone-pair electrons on the oxygen atom.[14]

§ 5. Molecular Structure

The zero-point moments of inertia and the effect of zero-point vibration and electronic interaction are listed in Table III. Since the rotational constants are more accurate for H_2CO and HDCO than those for other isotopic species, it was not tried to make a least-squares-fit. The difference between the C—H bond and C—D bond was taken into account.

First, H···H and D···D distances were

determined from the smallest moments of inertia of H_2CO and D_2CO. The CO distance was determined from several sets.

H_2CO, $H_2C^{13}O$ ······ $1.206_3 \pm 0.002$ A
H_2CO, H_2CO^{18} ······ $1.201_1 \pm 0.005$ A
H_2CO, D_2CO ······ $1.204_9 \pm 0.001$ A
(C−H=C−D assumed)

Table III. Zero point moments of inertia (amu A^2).

		Zero-point vibration correction	Electronic correction	Zero-point moment of inertia obs.	calc.
H_2CO	I_{aa}	0.02550	−0.00283	1.81517	——
	I_{bb}	0.05892	−0.00248	13.07375	——
	I_{cc}	0.02320	−0.00016	14.89022	14.88892
$H_2C^{13}O$	I_{aa}	0.02529	−0.00283	1.81490	1.81517
	I_{bb}	0.05951	−0.00248	13.4270	——
	I_{cc}	0.02360	−0.00016	15.2432	15.2422
H_2CO^{18}	I_{aa}	0.02526	−0.00283	1.81493	1.81517
	I_{bb}	0.06000	−0.00248	13.7553	13.7576
	I_{cc}	0.02396	−0.00016	15.5714	15.5728
D_2CO	I_{aa}	0.03917	−0.00284	3.60483	——
	I_{bb}	0.06812	−0.00247	15.7239	——
	I_{cc}	0.02496	−0.00021	19.3286	19.3287
HDCO	I_{aa}	0.03299	−0.00278	2.58151	2.5822
	I_{bb}	0.06392	−0.00252	14.5410	14.5447
	I_{cc}	0.02439	−0.00019	17.1229	17.1269

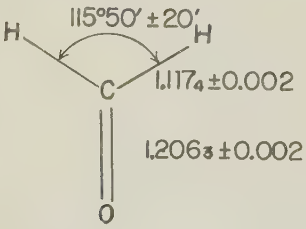

Fig. 1. Molecular structure of formaldehyde.

From these values the first set was adopted and C−H and C−D distances and HCO and DCO angles were taken as independent quantities. The final molecular structure thus determined is denoted by r_z and is shown in Fig. 1. The moments of inertia calculated from these values are listed in Table III. The satisfactory agreement of the calculated values with the observed ones for all the moments of inertia shows that this molecule is completely planar. For the purpose of comparison the effective molecular structure r_0 which was obtained from the effective moments of inertia with the neglect of the difference between C−H and C−D bonds, and the substituted molecular structure r_s obtained by the Costain's method are also listed in Table IV. It is seen that the values of bond distances decrease in the order $r_z > r_0 > r_s$. This is reasonable because the substituted bond length is nearer to the equilibrium value while the molecular structure obtained in this report is of the zero point value.

Table IV. Molecular structure of formaldehyde derived by different methods and different authors.

	$r_{C=O}$(A)	r_{C-H}(A)	∠HCO
This work (r_z)	1.2063	1.117_4	122°5′
〃 (r_0)	1.2051	1.110_9	121°56
〃 (r_s)	1.2042	1.101_9	121°40′
Dieke and Kistiakowsky[1)]	1.27	1.17	125°*
Herzberg[3)]	1.225	1.071*	118°17′
Stevenson et al[2)] (E.D.)	1.213		
Lawrance and Strandberg[4)] (M.W.)	1.21	1.12	121°
Davidson et al[5)] (I.R.)	1.213*	1.097	120°40′

* assumed.

Table V. Structure of CHO group in various compounds.

	$r_{C=O}$(A)	r_{C-H}(A)	∠HCO
H_2CO	1.2063	1.117	122°5′
CH_3CHO[a)]	1.216	1.114	118°36′
NH_2CHO[6)]	1.193	1.102	122°58′
HFCO[b)]	1.190	1.093	120°40′
HCOOH[c)]	1.202	1.097	124°8′
$HCOOCH_3$[d)]	1.200	1.101	124°50′
HCCCHO[e)]	1.2150	1.055	122°19′

a) R. B. Kilb, C. C. Lin and E. B. Wilson, Jr.: J. Chem. Phys. **26** (1957) 1695.
b) P. Favero, A. M. Mirri and J. G. Baker: J. Chem. Phys. **31** (1959) 566.
c) G. H. Kwei and R. F. Curl, Jr.: J. Chem. Phys. **32** (1960) 1592(L).
d) R. F. Curl, Jr.: J. Chem. Phys. **30** (1959) 1529.
e) C. C. Costain and J. R. Morton: J. Chem. Phys. **31** (1959) 389.

§6. Discussions

The structure of formaldehyde molecule has been discussed by several authors. The structures previously obtained are listed in Table IV with the present values. It will be pointed out that HCO angle is fairly larger than 120°.

HCO angles in other compounds possessing HCO group are listed in Table V. For most of them ∠HCO's are larger than 120°C.

Torkington explained the Herzberg's value where HCO angle is less than 120° considering the H^+CHO^- resonating structure.[15] This explanation is not compatible with the present result. The Urey-Bradly type potential constants used by Miyazawa in the normal vibration calculation of formaldehyde showed that the force between the two hydrogen atoms was negligible, and rather large van der Waals repulsive force exists between the non-bonded hydrogen and oxygen atoms.[16] This force will explain the fact that HCO angle in formaldehyde is larger than 120°. In ethylene molecule where also CCH angle is larger than 120°, the deviation from 120° is less than that of formaldehyde. (∠HCH=11.76±0.5°[17]). This agrees with the result of normal vibration calculation in which the repulsive force between the non-bonded carbon and hydrogen atoms was shown to be smaller because of the larger interatomic separation. Recently the structure of ethylene was determined by Bartell and Bonham by means of electron diffraction study in which they reported the angle HCH to be 115.5±0.6°[18]. The fact that ClCO angle in phosgene molecure is 124.3° can also be explained from this point of view.[19]

§ 7. Acknowledgement

The autor is indebted to Prof. Koichi Shimoda for his valuable guidance and counsels during the course of this study. He is also indebted to Prof. Yonezo Morino of the Department of Chemistry for his helpful discussions and encouragement.

References

1) G. H. Dieke and C. B. Kistiakowsky: Phys. Rev. **45** (1934) 4.
2) D. B. Stevenson, J. E. LuValle and V. Schomaker: J. Am. Chem. Soc. **61** (1939) 2508.
3) G. Herzberg: "Infrared and Raman Spectra" D. van Nostrand Co., Inc., New York (1949).
4) R. B. Lawrance and M. W. P. Strandberg: Phys. Rev. **83** (1951) 363.
5) D. W. Davidson, B. I. Stoicheff and H. J. Bernstein: J. Chem. Phys. **22** (1954) 289.
6) C. C. Costain and J. M. Dowling: J. Chem. Phys. **32** (1960) 158.
7) T. Yajima, T. Oka and K. Shimoda: J. Phys. Soc. Japan, to be published.
8) C. C. Costain: J. Chem. Phys. **29** (1958) 864.
9) J. Kraitchman: Am. J. Phys. **21** (1953) 17.
10) H. H. Nielsen: Revs. Mod. Phys. **23** (1951) 90.
11) T. Oka and Y. Morino: J. Mol. Spectroscopy to be published.
12) H. R. Johnson and M. W. P. Strandberg: J. Chem. Phys. **20** (1952) 687.
13) B. Rosenblum, A. H. Nethercot, Jr., and C. H. Townes: Phys. Rev. **101** (1958) 400.
14) K. Kondo, H. Hirakawa, A. Miyahara, T. Oka and K. Shimoda: J. Phys. Soc. Japan **15** (1960) 303.
15) P. Torkington: Nature **163** (1949) 446.
16) T. Miyazawa: J. Chem. Soc. Japan **76** (1955) 1132.
17) J. M. Dowling and B. P. Stoicheff: Bull. Am. Phys. Soc. Ser. II 3 (1958) 313.
18) L. S. Bartell and R. A. Bonham, J. Chem. Phys., **31** (1959) 400.
19) G. W. Robinson: J. Chem. Phys. **21** (1953) 1741.

JOURNAL OF THE PHYSICAL SOCIETY OF JAPAN, Vol. 15, No. 12, DECEMBER, 1960

Theory of Non-linear Responses

By Osamu NAKADA
Hitachi Central Research Laboratory
Kokubunji, Tokyo

(Received August, 23, 1960)

A phenomenological equation for a non-linear response to a time-dependent excitation is presented. The response function is expressed as a series of multiple integrals containing the excitation, where the first term corresponds to Boltzmann's linear superposition term. The non-linearity of an excitation-response system can be characterized, according to our formulation, by higher order after-effect functions. Associated equations including Fourier representations and the inversion formulae are derived. The generalized Kramers-Kronig relations between the real and imaginary parts of Fourier transforms of higher order after-effect functions are also derived. Applications of the theory to sinusoidal and step function-like excitations, especially with exponential after-effect functions, are discussed in detail.

§ 1. Introduction

The phenomena of retarded non-linear responses to time-dependent external excitations are commonly found in various fields of physics and engineering. Electric currents in some kinds of circuits manifest such non-linear characteristics. The other conspicuous examples are found in the viscoelasticity of high polymeric substance, especially in the deformation of filamentous or crystalline polymers.[1)]

The phenomenological theory of the stationary linear response is well established on the basis of Boltzmann's superposition principle.[2)] [11)] But the corresponding general treatment of the stationary non-linear response seems to be lacking, though Leaderman[3)], Burte and Halsey[4)], Sawaragi and Tokumaru[5)] and other investigator proposed several specialized models in order to explain non-linear viscoelasticity phenomena. Yamamoto[6)] and Segawa[7)] discussed the non-linearity of viscoelasticity on the basis of a three-dimensional Maxwell or Voigt models. Recently Saito[8)] suggested a possibility of generalization of Boltzmann's equation up to higher order terms of excitations.

On the other hand the non-linearity introduces also serious problems in the treatment of the automatic control where the linear response theory has usually been most effectively applied.[9)] The conventional describing function method fails in treating the non-linear transients.

In the following we derive a general expression for the non-linear responses to time-dependent excitations.

§ 2. Series Expansion of the Response Function

We denote the excitation by $\sigma(t)$, and the resulting response by $\varepsilon(t)$. We will express by $\phi_n(t)\,(n=1, 2, \cdots)$ a series of complete normalized orthogonal functions defined in $\{-\infty<t<+\infty\}$, and expand $\sigma(t)$ and $\varepsilon(t)$ by means of $\phi_n(t)$:

$$\sigma(t)=\sum_{i\ 1}^{\infty} a_i\phi_i(t)\ , \tag{1}$$

$$\varepsilon(t)=\sum_{i=1}^{\infty} b_i\phi_i(t)\ . \tag{2}$$

The expansion coefficients a_i and b_i are given, according to the definition of $\phi_n(t)$, by

$$a_i=\int_{-\infty}^{\infty} \sigma(t)\bar{\phi}_i(t)dt\ , \tag{3}$$

$$b_i=\int_{-\infty}^{\infty} \varepsilon(t)\bar{\phi}_i(t)dt\ , \tag{4}$$

where $\bar{\phi}_i(t)$ means the complex conjugate of $\phi_i(t)$. Now we will make following assumptions.

ASSUMPTION I. The excitation is not preceded by the response. (Causality)

ASSUMPTION II. Each of orthogonal expansion coefficients b_i's of the response function $\varepsilon(t)$, defined by Eq. (4), can be expanded in Taylor series of orthogonal expansion coefficient a_i's of the excitation function $\sigma(t)$, defined by Eq. (3). (Convergence)

THEOREM I. If Assumptions I and II are satisfied in the excitation and the response, the response function $\varepsilon(t)$ can be expressed as either

$$\varepsilon(t)=\int_{-\infty}^{\infty}\sigma(t_1)J_1(t,t_1)dt_1+\int_{-\infty}^{\infty}\int_{-\infty}^{\infty}\sigma(t_1)\sigma(t_2)J_2(t,t_1,t_2)dt_1dt_2$$
$$+\int_{-\infty}^{\infty}\int_{-\infty}^{\infty}\int_{-\infty}^{\infty}\sigma(t_1)\sigma(t_2)\sigma(t_3)J_3(t,t_1,t_2,t_3)dt_1dt_2dt_3+\cdots, \tag{5}$$

or

$$\varepsilon(t)=\int_{-\infty}^{\infty}\sigma(t-\tau_1)J_1(t,\tau_1)d\tau_1+\int_{-\infty}^{\infty}\int_{-\infty}^{\infty}\sigma(t-\tau_1)\sigma(t-\tau_2)J_2(t,\tau_1,\tau_2)d\tau_1d\tau_2$$
$$+\int_{-\infty}^{\infty}\int_{-\infty}^{\infty}\int_{-\infty}^{\infty}\sigma(t-\tau_1)\sigma(t-\tau_2)\sigma(t-\tau_3)J_3(t,\tau_1,\tau_2,\tau_3)d\tau_1d\tau_2d\tau_3+\cdots. \tag{5'}$$

Here $J_n(t,t_1,t_2,\cdots,t_n)$'s or $J_n(t,\tau_1,\tau_2,\cdots,\tau_n)$'s are characteristic after-effect function (or weighting functions) of the excitation-response system, and they are restricted by the condition:

$$J_n(t,t_1,t_2,\cdots,t_n)=0 \qquad \text{when any } t_i>t\,, \tag{6}$$
$$J_n(t,\tau_1,\tau_2,\cdots,\tau_n)=0 \qquad \text{when any } \tau_i<0\,. \tag{6'}$$

PROOF: As the response $\varepsilon(t)$ is completely determined once given the excitation $\sigma(t)$ in the range of $-\infty<t<\infty$, each b_i should be a unique function of the set of a_i's. Recalling here Assumption II, we will expand each b_i in Taylor series of a_i's:

$$b_i(a_1,a_2,\cdots)=b_i(0,0,\cdots)+\sum_{j=1}^{\infty}\gamma_j{}^i a_j+\sum_{j,k=1}^{\infty}\gamma^i_{j,k}a_ja_k+\sum_{j,k,l=1}^{\infty}\gamma^i_{j,k,l}a_ja_ka_l+\cdots, \tag{7}$$

where

$$\begin{aligned}\gamma_j{}^i&=[\partial b_i/\partial a_j]_{a_j=0}\,,\\ \gamma^i_{j,k}&=\tfrac{1}{2}[\partial^2 b_i/\partial a_j\partial a_k]_{a_j,a_k=0}\,,\\ \gamma^i_{j,k,l}&=\tfrac{1}{6}[\partial^3 b_i/\partial a_j\partial a_k\partial a_l]_{a_j,a_k,a_l=0}\,.\end{aligned} \tag{8}$$

Substitution of Eqs. (7) and (3) into Eq. (2) leads, after interchanging the operations of integral and summation, to Eq. (5) with

$$\begin{aligned}J_1(t,t_1)&=\sum_{i,j=1}^{\infty}\gamma_j{}^i\phi_i(t)\bar{\phi}_j(t_1)\,,\\ J_2(t,t_1,t_2)&=\sum_{i,j,k=1}^{\infty}\gamma^i_{j,k}\phi_i(t)\bar{\phi}_j(t_1)\bar{\phi}_k(t_2)\,,\\ J_3(t,t_1,t_2,t_3)&=\sum_{i,j,k,l=1}^{\infty}\gamma^i_{j,k,l}\phi_i(t)\bar{\phi}_j(t_1)\bar{\phi}_k(t_2)\bar{\phi}_l(t_3)\,,\end{aligned} \tag{9}$$

$J_n(t,t_1,t_2,\cdots,t_n)$ means the weight factor for the simultaneous contributions from excitations at $t_1,t_2,\cdots,t_n$ to the response at t. Hence, in order to obey the law of causality (i.e. Assumption I), it should satisfy the condition (6). Changing the variables to $\tau_n=t-t_n$ in Eqs. (5) and (6), we obtain Eqs. (5′) and (6′). (Q. E. D.)

If we take account of Eqs. (6) or (6′), we can put upper limits of integrals in Eq. (5) or lower limits of integrals in Eq. (5′) equal to zero.

Next we consider the stationary response system.

ASSUMPTION III. If the response $\varepsilon(t)\equiv\varepsilon_1(t)$ occurs against the excitation $\sigma(t)=\sigma_1(t)$, the response $\varepsilon(t)\equiv\varepsilon_1(t-s)$ should occur against the excitation $\sigma(t)\equiv\sigma_1(t-s)$ for an arbitrary s. (Stationariness)

THEOREM II. If Assumption III as well as Assumptions I and II are satisfied, the response $\varepsilon(t)$ can be expressed as

$$\varepsilon(t)=\int_{-\infty}^{\infty}\sigma(t-\tau_1)J_1(\tau_1)d\tau_1+\int_{-\infty}^{\infty}\int_{-\infty}^{\infty}\sigma(t-\tau_1)\sigma(t-\tau_2)J_2(\tau_1,\tau_2)d\tau_1 d\tau_2$$
$$+\int_{-\infty}^{\infty}\int_{-\infty}^{\infty}\int_{-\infty}^{\infty}\sigma(t-\tau_1)\sigma(t-\tau_2)\sigma(t-\tau_3)J_2(\tau_1,\tau_2,\tau_3)d\tau_1 d\tau_2 d\tau_3+\cdots\,, \tag{10}$$

where

$$J_n(\tau_1,\tau_2,\cdots,\tau_n)=0 \quad \text{when any} \quad \tau_i<0\,. \tag{11}$$

PROOF: The response $\varepsilon_1(t)$ to the excitation $\sigma_1(t)$ is, by Eq. (5′), written as

$$\varepsilon_1(t)=\int_{\infty}^{\infty}\sigma_1(t-\tau_1)\,J_1(t,\tau_1)dt_1+\int_{-\infty}^{\infty}\int_{-\infty}^{\infty}\sigma_1(t-\tau_1)\sigma_1(t-\tau_2)J_2(t,\tau_1,\tau_2)d\tau_1 d\tau_2$$
$$+\int_{-\infty}^{\infty}\int_{-\infty}^{\infty}\int_{-\infty}^{\infty}\sigma(t-\tau_1)\sigma(t-\tau_2)\sigma(t-\tau_3)J_3(t,\tau_1,\tau_2,\tau_3)d\tau_1 d\tau_2 d\tau_3+\cdots\,. \tag{12}$$

Similarly the response for the excitation $\sigma_1(t-s)$ is given by

$$\varepsilon(t)=\int_{-\infty}^{\infty}\sigma_1(t-s-\tau_1)J_1(t,\tau_1)d\tau_1+\int_{-\infty}^{\infty}\int_{\infty}^{\infty}\sigma_1(t-s-\tau_1)\sigma_1(t-s-\tau_2)J_2(t,\tau_1,\tau_2)d\tau_1 d\tau_2$$
$$+\int_{-\infty}^{\infty}\int_{-\infty}^{\infty}\int_{-\infty}^{\infty}\sigma_1(t-s-\tau_1)\sigma_1(t-s-\tau_2)\sigma_1(t-s-\tau_3)J_3(t,\tau_1,\tau_2,\tau_3)d\tau_1 d\tau_2 d\tau_3+\cdots\,. \tag{13}$$

According to Assumption III, the right-hand side of Eq. (13) should be equal to $\varepsilon_1(t-s)$, which is given from Eq. (12) by

$$\varepsilon_1(t-s)=\int_{-\infty}^{\infty}\sigma_1(t-s-\tau_1)\,J_1(t-s,\tau_1)d\tau_1+\int_{-\infty}^{\infty}\int_{-\infty}^{\infty}\sigma_1(t-s-\tau_1)\sigma(t-s-\tau_2)J_2(t-s,\tau_1,\tau_2)d\tau_1 d\tau_2$$
$$+\int_{-\infty}^{\infty}\int_{-\infty}^{\infty}\int_{-\infty}^{\infty}\sigma_1(t-s-\tau_1)\sigma_1(t-s-\tau_2)\sigma_1(t-s-\tau_3)J_3(t-s,\tau_1,\tau_2,\tau_3)d\tau_1 d\tau_2 d\tau_3+\cdots\,. \tag{14}$$

Comparing term by term in the right-hand sides of Eqs. (13) and (14), we get

$$\begin{aligned} &J_1(t,\tau_1)\equiv J_1(t-s,\tau_1)\,,\\ &J_2(t,\tau_1,\tau_2)\equiv J_2(t-s,\tau_1,\tau_2)\,,\\ &J_3(t.\,\tau_1,\tau_2,\tau_3)\equiv J_3(t-s,\tau_1,\tau_2,\tau_3)\,, \end{aligned} \tag{15}$$

for arbitrary value of s. This means that $J_1, J_2, J_3, \cdots$ should not depend on t:

$$\begin{aligned} &J_1(t,\tau_1)\equiv J_1(\tau_1)\,,\\ &J_2(t,\tau_1,\tau_2)\equiv J_2(\tau_1,\tau_2)\,,\\ &J_3(t,\tau_1,\tau_2,\tau_3)\equiv J_3(\tau_1,\tau_2,\tau_3)\,. \end{aligned} \tag{16}$$

Substituting Eq. (16) to Eqs. (5′) and (6′) we get Eqs. (10) and (11). (Q. E. D.)

Lower limits of integrals in Eq. (10) can be put equal to zero according to Eq. (11). Eq. (10) gives a general relation between the excitation and the response in a stationary response system. If we neglect all higher terms in Eq. (10) it reduces to the wellknown Boltzmann's equation in the linear viscoelasticity. The higher order terms mean the multi-dimensional superposition of the simultaneous effect of excitations at past many instant. So Eq. (10) can be regarded as a natural generalization of Boltzmann's superposition principle, and the functions J_n may be called the n th order after-effect function (or weighting function).

Further if we can assume the response to be odd with respect to the excitation, i.e., if the response $-\varepsilon(t)$ is to occur against the excitation $-\sigma(t)$, the even order terms in Eq. (10) vanish.

By integrating Eq. (10) by parts, assuming $\sigma(-\infty)=0$, we obtain

$$\varepsilon(t)=\int_{-\infty}^{\infty}\sigma'(t-\tau_1)K_1(\tau_1)d\tau_1+\int_{\infty}^{\infty}\int_{-\infty}^{\infty}\sigma'(t-\tau_1)\sigma'(t-\tau_2)K_2(\tau_1,\tau_2)d\tau_1 d\tau_2$$
$$+\int_{-\infty}^{\infty}\int_{-\infty}^{\infty}\int_{-\infty}^{\infty}\sigma'(t-\tau_1)\sigma'(t-\tau_2)\sigma'(t-\tau_3)K_3(\tau_1,\tau_2,\tau_3)d\tau_1 d\tau_2 d\tau_3+\cdots, \tag{17}$$

where

$$K_1(\tau_1)=\int_{-\infty}^{\tau_1}J_1(\tau_1')d\tau_1',$$
$$K_2(\tau_1,\tau_2)=\int_{-\infty}^{\tau_1}\int_{-\infty}^{\tau_2}J_2(\tau_1',\tau_2')d\tau_2'd\tau_1, \tag{18}$$
$$K_3(\tau_1,\tau_2,\tau_3)=\int_{-\infty}^{\tau_1}\int_{-\infty}^{\tau_2}\int_{-\infty}^{\tau_3}J_3(\tau_1',\tau_2',\tau_3')d\tau_3'd\tau_2'd\tau_1'.$$

§ 3. Fourier Representation

Hereafter we will deal only with the stationary response system.

We will define the Fourier transforms $\bar{\sigma}(\omega)$, $\bar{\varepsilon}(\omega)$, $\bar{J}_1(\omega_1)$, $\bar{J}_2(\omega_1, \omega_2)$, etc. by

$$\bar{\sigma}(\omega)=\frac{1}{\sqrt{2\pi}}\int_{-\infty}^{\infty}\sigma(t)e^{-i\omega t}dt,$$
$$\bar{\varepsilon}(\omega)=\frac{1}{\sqrt{2\pi}}\int_{-\infty}^{\infty}\varepsilon(t)e^{-i\omega t}dt,$$
$$\bar{J}_1(\omega_1)=\int_{-\infty}^{\infty}J_1(\tau_1)e^{-i\omega_1\tau_1}d\tau_1, \tag{19}$$
$$\bar{J}_2(\omega_1,\omega_2)=\frac{1}{\sqrt{2\pi}}\int_{-\infty}^{\infty}\int_{-\infty}^{\infty}J_2(\tau_1,\tau_2)e^{-(i\omega_1\tau_1+i\omega_2\tau_2)}d\tau_1 d\tau_2,$$
$$\bar{J}_3(\omega_1,\omega_2,\omega_3)=\frac{1}{2\pi}\int_{-\infty}^{\infty}\int_{-\infty}^{\infty}\int_{-\infty}^{\infty}J_3(\tau_1,\tau_2,\tau_3)e^{-(i\omega_1\tau_1+i\omega_2\tau_2+i\omega_3\tau_3)}d\tau_1 d\tau_2 d\tau_3.$$

Then, starting from Eq. (10) and making use of the relations

$$\int_{-\infty}^{\infty}\delta(t)e^{-i\omega t}dt=1, \tag{20}$$
$$\frac{1}{2\pi}\int_{-\infty}^{\infty}e^{-i\omega t}d\omega=\delta(t), \tag{20'}$$

we get

$$\bar{\varepsilon}(\omega)=\bar{\sigma}(\omega)\bar{J}_1(\omega)+\int_{-\infty}^{\infty}\int_{-\infty}^{\infty}\bar{\sigma}(\omega_1)\bar{\sigma}(\omega_2)\bar{J}_2(\omega_1,\omega_2)\delta(\omega_1+\omega_2-\omega)d\omega_1 d\omega_2$$
$$+\int_{-\infty}^{\infty}\int_{-\infty}^{\infty}\int_{-\infty}^{\infty}\bar{\sigma}(\omega_1)\bar{\sigma}(\omega_2)\bar{\sigma}(\omega_3)\bar{J}_3(\omega_1,\omega_2,\omega_3)\delta(\omega_1+\omega_2+\omega_3-\omega)d\omega_1 d\omega_2 d\omega_3+\cdots. \tag{21}$$

§ 4. Inversion Formulae

So far we regarded the quantity $\sigma(t)$ as the excitation and the quantity $\varepsilon(t)$ as the response. But depending on experimental condition we may as well observe $\sigma(t)$ as the response to the given excitation $\varepsilon(t)$. For this case we need only to interchange $\sigma(t)$ and $\varepsilon(t)$ in the above treatment. To avoid the confusion we will denote by $G_n(\tau_1, \tau_2, \cdots, \tau_n)$ the n th order after-effect function in the response $\sigma(t)$ to the excitation $\varepsilon(t)$. Fourier transform $\bar{G}_n$ is defined similarly as $\bar{J}_n$. The equations corresponding to Eqs. (10) and (21) are

$$\sigma(t)=\int_{-\infty}^{\infty}\varepsilon(t-\tau_1)G_1(\tau_1)d\tau_1+\int_{\infty}^{\infty}\int_{-\infty}^{\infty}\varepsilon(t-\tau_1)\varepsilon(t-\tau_2)G_2(\tau_1,\tau_2)d\tau_1 d\tau_2$$
$$+\int_{-\infty}^{\infty}\int_{-\infty}^{\infty}\int_{-\infty}^{\infty}\varepsilon(t-\tau_1)\varepsilon(t-\tau_1)\varepsilon(t-\tau_3)G_3(\tau_1,\tau_2,\tau_3)d\tau_1 d\tau_2 d\tau_3+\cdots, \tag{22}$$

$$\bar{\sigma}(\omega)=\bar{\varepsilon}(\omega)\bar{G}_1(\omega)+\int_{-\infty}^{\infty}\int_{-\infty}^{\infty}\bar{\varepsilon}(\omega_1)\bar{\varepsilon}(\omega_2)\bar{G}_2(\omega_1,\,\omega_2)\delta(\omega_1+\omega_2-\omega)d\omega_1d\omega_2$$
$$+\int_{-\infty}^{\infty}\int_{-\infty}^{\infty}\int_{-\infty}^{\infty}\bar{\varepsilon}(\omega_1)\bar{\varepsilon}(\omega_2)\bar{\varepsilon}(\omega_3)\bar{G}_3(\omega_1,\,\omega_2,\,\omega_3)\delta(\omega_1+\omega_2+\omega_3-\omega)d\omega_1d\omega_2d\omega_3+\cdots\,. \tag{23}$$

Substituting Eq. (23) into the right-hand side of Eq. (21), collecting the same order terms of $\bar{\varepsilon}(\omega)$, and comparing the both sides, we obtain the following inversion formulae.

$$\begin{aligned}
&\bar{G}_1(\omega)=1/\bar{J}_1(\omega)\,,\\
&\bar{G}_2(\omega_1,\,\omega_2)=-\bar{J}_2(\omega_1,\,\omega_2)/\bar{J}(\omega_1)\bar{J}(\omega_2)\bar{J}_1(\omega_1+\omega_2)\,,\\
&\bar{G}_3(\omega_1,\,\omega_2,\,\omega_3)=\left[\bar{J}_3(\omega_1,\,\omega_2,\,\omega_3)+\frac{2}{3}\sum_{\substack{(i,j,k)\\ \text{cyclic}}}\frac{J_2(\omega_i,\,\omega_j+\omega_k)\bar{J}_2(\omega_j+\omega_k)}{\bar{J}_1(\omega_j+\omega_k)}\right]\\
&\qquad\div\bar{J}_1(w_1)\bar{J}_1(\omega_2)\bar{J}_1(\omega_3)\bar{J}_1(\omega_1+\omega_2+\omega_3)\,.
\end{aligned} \tag{24}$$

§ 5. Kramers-Kroning relations

We will separate the real and imaginary parts of $\bar{J}_n(\omega_1,\,\omega_2,\,\cdots,\,\omega_n)$ defined by Eq. (19) as follows:

$$\bar{J}_n(\omega_1,\,\cdots,\,\omega_n)=\bar{J}_n'(\omega_1,\,\cdots,\,\omega_n)-i\bar{J}_n''(w_1,\,\cdots,\,\omega_n)\,. \tag{25}$$

Then, as is well-known, $\bar{J}_1'$ and $\bar{J}_1''$ are connected each other by the Kramers-Kronig relations[10 11]:

$$\bar{J}_1'(\omega)=\frac{2\omega}{\pi}\mathscr{P}\int_0^{\infty}\frac{J_1''(\omega')}{\omega'^2-\omega^2}d\omega'\,, \tag{26}$$

$$\bar{J}_1''(\omega)=-\frac{2}{\pi}\mathscr{P}\int_0^{\infty}\frac{\omega'\bar{J}_1(\omega)}{\omega'^2-\omega^2}d\omega'\,, \tag{27}$$

where $\mathscr{P}$ means to take Cauchy's principal value of integral. Taking account of the symmetry character of J_1' and $\bar{J}_1''$ we can either express the relations as

$$\bar{J}_1'(\omega)=\frac{1}{\pi}\mathscr{P}\int_{-\infty}^{\infty}\frac{\bar{J}_1''(\omega')}{\omega'-\omega}d\omega'\,, \tag{28}$$

$$\bar{J}_1''(\omega)=-\frac{1}{\pi}\mathscr{P}\int_{-\infty}^{\infty}\frac{\bar{J}_1'(\omega')}{\omega'-\omega}d\omega'\,. \tag{29}$$

These relations can be regarded as the consequences of the causality assumption, which postulates that the after-effect function $J_1(\tau)$ has non-vanishing values only in the range $0<\tau$. The situation is just similar for higher order functions $\bar{J}_2(\omega_1,\,\omega_2)$, $\bar{J}_3(\omega_1,\,\omega_2,\,\omega_3)$, $\cdots$ as for $\bar{J}_1(\omega)$, the causality being expressed by Eq. (11). Thus it will be possible to generalize the Kramers-Kronig relations to those higher order functions.

Now we begin with $\bar{J}_2(\omega_1,\,\omega_2)$. Referring to Eq. (19) and also to the causality relations (11) we can express $\bar{J}_2'$ and $\bar{J}_2''$ as

$$\bar{J}_2'(\omega_1,\,\omega_2)=\frac{1}{\sqrt{2\pi}}\int_0^{\infty}\int_0^{\infty}J_2(\tau_1,\,\tau_2)\cos(\omega_1\tau_1+\omega_2\tau_2)d\tau_1d\tau_2\,, \tag{30}$$

$$\bar{J}_2''(\omega_1,\,\omega_2)=\frac{1}{\sqrt{2\pi}}\int_0^{\infty}\int_0^{\infty}J_2(\tau_1,\,\tau_2)\sin(\omega_1\tau_1+\omega_2\tau_2)d\tau_1d\tau_2\,, \tag{31}$$

or

$$\bar{J}_2'(\omega_1,\,\omega_2)=\bar{J}_{cc}(\omega_1,\,\omega_2)-\bar{J}_{ss}(\omega_1,\,\omega_2)\,, \tag{32}$$

$$\bar{J}_2''(\omega_1,\,\omega_2)=\bar{J}_{sc}(\omega_1,\,\omega_2)+\bar{J}_{cs}(\omega_1,\,\omega_2)\,, \tag{33}$$

where

$$\bar{J}_{cc}(\omega_1, \omega_2)=\frac{1}{\sqrt{2\pi}}\int_0^\infty\int_0^\infty J_2(\tau_1, \tau_2)\cos\omega_1\tau_1\cos\omega_2\tau_2 d\tau_1 d\tau_2\ ,$$
$$\bar{J}_{sc}(\omega_1, \omega_2)=\frac{1}{\sqrt{2\pi}}\int_0^\infty\int_0^\infty J_2(\tau_1, \tau_2)\sin\omega_1\tau_1\cos\omega_1\tau_1 d\tau_1 d\tau_2\ , \quad \text{etc.}; \tag{34}$$

We apply the inverse Fourier transformation to $J_2(\tau_1,\tau_2)$ appearing in the integrand in the right-hand side of Eq. (32). Then

$$\bar{J}_2'=\frac{1}{\sqrt{2\pi}}\left(\frac{\pi}{2}\right)^2\int_0^\infty\cdots\int_0^\infty J_{sc}(\omega_1', \omega_2')\sin\omega_1'\tau_1'\cos\omega_2'\tau_2'\cos\omega_1\tau_1\cos\omega_2\tau_2 d\omega_1' d\omega_2' d\tau_1 d\tau_2$$
$$-\frac{1}{\sqrt{2\pi}}\left(\frac{2}{\pi}\right)^2\int_0^\infty\cdots\int_0^\infty J_{cs}(\omega_1', \omega_2')\cos\omega_1'\tau_1'\sin\omega_2'\tau_2'\sin\omega_1\tau_1\sin\omega_2\tau_2 d\omega_1' d\omega_2' d\tau_1 d\tau_2\ . \tag{35}$$

Integrating with respect to τ_1 and τ_2 we get

$$\bar{J}_2'(\omega_1, \omega_2)=\frac{1}{\sqrt{2\pi}}\cdot\frac{2}{\pi}\mathscr{P}\int_0^\infty J_{sc}(\omega_1', \omega_2)\frac{\omega_1'}{\omega_1'^2-\omega_1^2}d\omega_1'$$
$$+\frac{1}{\sqrt{2\pi}}\cdot\frac{2}{\pi}\mathscr{P}\int_0^\infty J_{cs}(\omega_1', \omega_2)\frac{\omega_1}{\omega_1'^2-\omega_1^2}d\omega_1'\ . \tag{36}$$

By the symmetry characters of $\bar{J}_{sc}$ and $\bar{J}_{cs}$

$$\bar{J}_2'(\omega_1, \omega_2)=\frac{1}{\sqrt{2\pi}}\cdot\frac{1}{\pi}\mathscr{P}\int_{-\infty}^\infty J_{sc}(\omega_1', \omega_2)\frac{\omega_1'}{\omega_1'^2-\omega_1^2}d\omega_1'$$
$$+\frac{1}{\sqrt{2\pi}}\cdot\frac{1}{\pi}\mathscr{P}\int_{-\infty}^\infty J_{cs}(\omega_1', \omega_2)\frac{\omega_1}{\omega_1'^2-\omega_1^2}d\omega_1'\ , \tag{36'}$$

and also by the symmetry we can easily verify

$$\frac{1}{\sqrt{2\pi}}\cdot\frac{1}{\pi}\mathscr{P}\int_{-\infty}^\infty J_{sc}(\omega_1', \omega_2)\frac{\omega_1}{\omega_1'^2-\omega_1^2}d\omega_1'=0\ ,$$
$$\frac{1}{\sqrt{2\pi}}\cdot\frac{1}{\pi}\mathscr{P}\int_{-\infty}^\infty J_{cs}(\omega_1', \omega_2)\frac{\omega_1'}{\omega_1'^2-\omega_1^2}d\omega_1'=0\ . \tag{37}$$

Adding Eqs. (36′) and (37) we get

$$\bar{J}_2'(\omega_1, \omega_2)=\frac{1}{\pi}\mathscr{P}\int_{-\infty}^\infty \bar{J}_2''(\omega_1, \omega_2)\frac{1}{\omega_1'-\omega_1}d\omega_1'\ . \tag{38}$$

Since $\bar{J}_2'(\omega_1, \omega_2)$ should be a symmetric function with respect to ω_1 and ω_2 we have also the relation

$$\bar{J}_2'(\omega_1, \omega_2)=\frac{1}{\pi}\mathscr{P}\int_{-\infty}^\infty \bar{J}_2''(\omega_1, \omega_2)\frac{1}{\omega_2'-\omega_2}d\omega_2'\ . \tag{38'}$$

In the similar manner we can derive the inverse relation

$$\bar{J}_2''(\omega_1, \omega_2)=-\frac{1}{\pi}\mathscr{P}\int_{-\infty}^\infty J_1'(\omega_1', \omega_2)\frac{1}{\omega_1'-\omega_1}d\omega_1'=-\frac{1}{\pi}\mathscr{P}\int_{-\infty}^\infty J_1'(\omega_1, \omega_2')\frac{1}{\omega_2'-\omega_2}d\omega_2'\ . \tag{39}$$

It is easy, though tedious, to extend the above treatment to higher order functions. Thus we get the generalized Kramers-Kronig relations

$$\bar{J}_n'(\omega_1, \cdots, \omega_n)=\frac{1}{\pi}\mathscr{P}\int_{-\infty}^\infty \bar{J}_n''(\omega_1, \cdots, \omega_i', \cdots, \omega_n)\frac{1}{\omega_i'-\omega_i}d\omega_i'\ , \tag{40}$$

$$\bar{J}_n''(\omega_1, \cdots, \omega_n)=-\frac{1}{\pi}\mathscr{P}\int_{-\infty}^\infty \bar{J}_1'(\omega_1, \cdots, \omega_i', \cdots, \omega_n)\frac{1}{\omega_i'-\omega_i}d\omega_i'\ . \tag{41}$$

It is seen that Eqs. (38)–(41) as well as Eqs. (27) and (28) have just the similar forms which are known as Hilbert transforms in the theory of complex variable.[12] Though we derived the generalized Kramers-Kronig relations according to an elementary method, we may either prove them directly from the regularity of the complex function $\bar{J}_n(z_1, \cdots, z_n)$ in the right half plane of each z_i.[11-13]

It should be noted that the relations corresponding to Eqs. (25) and (26) do not hold for $\bar{J}_n(\omega_1, \cdots, \omega_n)$ for $n>1$. In fact, Eqs. (25) and (26) are equivalent to Eqs. (27) and (28) only as the consequence of the fact that $\bar{J}_1'(\omega)$ and $\bar{J}_1''(\omega)$ are odd and even functions of ω respectively while J_n' or J_n'' for $n > 1$ are neither odd nor even functions with respect to each of ω_i's does not hold for higher order functions with respect to each independent ω_i.

§ 6. Applications

i) Sinusoidal excitation

When the excitation is given by

$$\sigma(t)=\sigma_0 \cos \omega t\ , \tag{42}$$

the resulting response $\varepsilon(t)$ is calculated by substitution of Eq. (25) to Eq. (10) as follows:

$$\begin{aligned}\varepsilon(t)=\sigma_0[A_1 \cos \omega t+A_2 \sin \omega t]+\sigma_0^2[B_1 \cos 2\omega t+B_2 \sin 2\omega t+B_3]\\ +\sigma_0^3[C_1 \cos 3\omega t+C_2 \sin 3\omega t+C_3 \cos \omega t+C_4 \sin \omega t]+\cdots\ ,\end{aligned} \tag{43}$$

where

$$\begin{aligned}A_1&=\bar{J}_1'(\omega)\ ,\\ A_2&=\bar{J}_1''(\omega)\ ,\\ B_1&=\sqrt{\frac{\pi}{2}}\,\bar{J}_2'(\omega, \omega)\ ,\\ B_2&=\sqrt{\frac{\pi}{2}}\,\bar{J}_2''(\omega, \omega)\ ,\\ B_3&=\sqrt{\frac{\pi}{2}}\,\bar{J}_2'(\omega, -\omega)\ ,\\ C_1&=\frac{\pi}{2}\bar{J}_3'(\omega, \omega, \omega)\ ,\\ C_2&=\frac{\pi}{2}\bar{J}_3''(\omega, \omega, \omega)\ ,\\ C_3&=\frac{3\pi}{2}\bar{J}_3'(\omega, \omega, -\omega)\ ,\\ C_4&=\frac{3\pi}{3}\bar{J}_3''(\omega, \omega, -\omega)\ .\end{aligned} \tag{44}$$

The energy dissipation per one cycle Q is calculated as

$$\begin{aligned}Q=\int_{\text{one cycle}} \sigma d\varepsilon=\int_{\text{one cycle}} \sigma\frac{d\varepsilon}{dt}\, dt=\int_{\text{one cycle}} \sigma_0 \cos \omega t[\omega\sigma_0(-A_1 \sin \omega t+A_2 \cos \omega t)\\ +2\omega\sigma_0^2(-B_1 \sin 2\omega t+B_2 \cos 2\omega t)+3\omega\sigma_0^3(-C_1 \sin 3\omega t+C_2 \cos 3\omega t\\ -C_3 \sin \omega t+C_4 \cos \omega t)]dt=\pi(\sigma_0^2 A_2+3\sigma_0^4 C_2)\ .\end{aligned} \tag{45}$$

ii) *Step function-like excitation*

a) One step excitation

When we substitute

$$\sigma=\begin{cases}0\ , & t<0\ ,\\ \sigma_0\ , & t\geq 0\ ,\end{cases} \tag{46}$$

into Eq. (10) we get

$$\varepsilon(t)=\sigma_0 K_1(t)+\sigma_0^2 K_2(t, t)+\sigma_0^3 K_3(t, t, t)+\cdots\ . \tag{47}$$

This case corresponds to the creep process in the viscoelasticity phenomena. Then K_i mean the ith order creep function.

b) Two steps excitation

For the two steps excitation

$$\sigma=\begin{cases}0\,, & t<0\,,\\ \sigma_1\,, & 0\leq t<t_1\\ \sigma_1+\sigma_2\,, & t_1\leq t\,,\end{cases} \tag{48}$$

we obtain

$$\begin{aligned}\varepsilon(t)=&\sigma_1K_1(t)+\sigma_2K_1(t-t_1)+\sigma_1{}^2K_2(t,t)\\ &+2\sigma_1\sigma_2K_2(t,t-t_1)+\sigma_2{}^2K_2(t-t_1,t-t_1)\\ &+\sigma_1{}^3K_3(t,t,t)+3\sigma_1{}^2\sigma_2K_3(t,t,t-t_1)\\ &+3\sigma_1\sigma_2{}^2K_3(t,t-t_1,t-t_1)\\ &+\sigma_2{}^3K_3(t-t_1,t-t_1,t-t_1)\,.\end{aligned} \tag{49}$$

If we put $\sigma_1=-\sigma_2\equiv\sigma_0$ in Eq. (49), we obtain a recovery process following a creep,

$$\begin{aligned}\varepsilon(t)=&\sigma_0K_1(t)-\sigma_0K_1(t-t_1)+\sigma_0{}^2K_2(t,t)\\ &-2\sigma_0{}^2K_2(t,t-t_1)+\sigma_0{}^2K_2(t-t_1,t-t_1)\\ &+\sigma_0{}^2K_3(t,t,t)-3\sigma_0{}^3K_3(t,t,t-t_1)\\ &+3\sigma_0{}^3K_3(t,t-t_1,t-t_1)\\ &-\sigma_0{}^3K_3(t-t_1,t-t_1,t-t_1)+\cdots\,.\end{aligned} \tag{50}$$

Subtracting Eq. (50) from Eq. (47) and putting $t-t_1=s$, we get the recovery function $\varepsilon_r(s)$:

$$\begin{aligned}\varepsilon_r(s)=&\sigma_0K_1(s)+2\sigma_0{}^2K_2(s+\Delta t,s)-\sigma_0{}^2K_2(s,s)\\ &+3\sigma_0{}^3K_3(s+\Delta t,s+\Delta t,s)\\ &-3\sigma_0{}^3K_3(s+\Delta t,s,s)+\sigma_0{}^3K_3(s,s,s)\cdots\,,\end{aligned} \tag{51}$$

where $\Delta t\equiv t_1$. In the case of an odd response Eq. (51) reduces to

$$\begin{aligned}\varepsilon_r(s)=&\sigma_0K_1(s)+\sigma_0{}^3K_3(s,s,s)\\ &+[3\sigma_0{}^3\{K_3(s+\Delta t,s+\Delta t,s)\\ &-K_3(s+\Delta t,s,s)\}]+\cdots\,.\end{aligned} \tag{52}$$

§ 7. After-effect Functions

According to the treatment hitherto made, the non-linearity of an excitation-response system is characterized by the higher order after-effect functions $J_2, J_3, \cdots$ just as much as the linear response is characterized by the first order after-effect function J_1. So the experimental determination of the higher order after-effect functions becomes an important problem in order to describe the non-linear character in a compact way. Though a number of methods, rigorous or approximate, for the determination of J_1 have been proposed, the rigorous determination of the higher order functions seems to be rather troublesome, unless some limitations for their functional forms are introduced.

As the most simple and convenient approximation for J_1 the exponential function is commonly used. Generalizing this approximation to the higher order function we will tentatively assume

$$\begin{aligned}&J_1(\tau_1)=k_1e^{-\tau_1/T_1}\,,\\ &J_2(\tau_1,\tau_2)=k_2e^{-\tau_1/T_2}e^{-\tau_2/T_2}\,,\\ &J_3(\tau_1,\tau_2,\tau_3)=k_3e^{-\tau_1/T_3}e^{-\tau_2/T_3}e^{-\tau_3/T_3}\,.\end{aligned} \tag{53}$$

Then the following responses result for the sinusoidal and step function-like excitation.

i) *Sinusoidal excitation*

When the excitation is given by Eq. (42), $\bar{J}_1{}'$, $\bar{J}_1{}''$, $\bar{J}_2{}'$, $\cdots$ etc. in Eq. (44) are calculated as

$$\begin{aligned}&A_1=k_1T_1/(1+\omega^2T_1{}^2)\,,\\ &A_2=k_1\omega T_1{}^2/(1+\omega^2T_1{}^2)\,,\\ &B_1=k_2T_2{}^2(1-\omega^2T_2{}^2)/2(1+\omega^2T_2{}^2)^2\,,\\ &B_2=k_2\omega T_2{}^3/(1+\omega^2T_2{}^2)^2\,,\\ &B_3=k_2T_2{}^2/(1+\omega^2T_2{}^2)^2\,,\\ &C_1=k_3T_3{}^3(1-3\omega^2T_3{}^2)/4(1+\omega^2T_3{}^2)^3\,,\\ &C_2=k_3T_3{}^3(3\omega T_3-\omega^3T_3{}^3)/4(1+\omega^2T_3{}^2)^3\,,\\ &C_3=3k_3T_3{}^3/4(1+\omega^2T_3{}^2)^3\,,\\ &C_4=3k_3\omega T_3{}^4/4(1+\omega^2T_2{}^2)^2\,.\end{aligned} \tag{54}$$

ii) *One step excitation*

For the one step excitation (Eq. (29)), the integrated after-effect functions $K_1, K_2, K_3\cdots$ are given by

$$\begin{aligned}&K_1(t)=k_1T_1(1-e^{-t/T_1})\,,\\ &K_2(t,t)=k_2T_2{}^2(1-e^{-t/T_2})^2\,,\\ &K_3(t,t,t)=k_3T_3{}^2(1-e^{-t/T_3})^3\,.\end{aligned} \tag{55}$$

§ 8. Discussion

We derived the formula (10) starting from three assumptions of causality, convergence and stationariness. Among them the assumption of causality is self-evident and will be needless to discuss about it. The assumption of stationariness is needed for the after-effect functions to be independent on the absolute time. The formula (5) without the assumption of stationariness is more general than Eq. (10), but will be less convenient in actual applications. The assumption of the convergence of the series (7) will be the most essential in our formulation. It takes place of the assumption of the superposition in the linear theory of Boltzmann. Though it is much less stringent than the superposition assumption, it will still restrict severely the applicability of the theory. The existence of the subharmonic mode in the non-linear vibration, for instance, can not be proved by our treatment it will possibly correspond to a certain singular point of the function $b_i(a_1, a_2, \cdots)$.

Finally we will mention a property of the recovery function. In the recovery function (35) in an antisymmetric response, the terms in [ ] mean the deviation of the recovery function from the creep function. The absolute value of K_3 will monotonically increase with the increase of parameters, so that if K_3 is positive definite the deviation will be also positive and if K_3 is negative the deviation will also be negative. This property is confirmed partly, at least, by Leaderman's experiments on non-linear creep and recovery of rubbers.[3)]

Our theory is also applicable to an analytical treatment of non-linear automatic feedback control system, on which we shall discuss in a later report.

Acknowledgment

The author would like to express his sincere thanks to Professor N. Saito of Waseda University and K. Okano of Institute of Physical and Chemical Research for their valuable suggestions and kind discussions on the present subject. He is also grateful heartily to Dr. H. Kitagawa, Dr. M. Fukumura, Dr. S. Kawamatsu and many colleagues in his laboratory for their kind interest and encouragement throughout this work.

References

1) H. A. Stuart: "Die Physik der Hochpolymeren" **4** (1956) 126.
2) L. Boltzmann: Pogg. Ann. Physik **7** (1876) 624. See also H. Leaderman: "Elastic and creep properties of filamentous materials" (1943) 20.
3) H. Leaderman: J. Polymer Sci. **16** (1955) 261.
4) H. Burte, G. Halsey: Text. Res. J. **18** (1948) 449.
5) Y. Sawaragi, H. Tokumaru: Mem. Fac. Eng., Kyoto University, **16** (1954) 100.
6) M. Yamamoto: J. Phys. Soc. Japan **14** (1959) 313.
7) W. Segawa: J. Phys. Soc. Japan **14** (1959) 1102.
8) N. Saito: Private communication.
9) J. G. Truxal: 'Control System Synthesis' (1955).
10) H. A. Kramers: Atti Congr. intern. fis. Como **2** (1926) 545. R. de L. Kronig: J. Opt. Soc. Amer. **12** (1926) 547.
11) J. R. MacDonald, M. K. Brachman: Rev. Mod. Phys. **28** (1956) 393.
12) P. M. Morse, H. Feshbach: 'Methods of Theoretical Physics' (1953) 367.
13) K. Okano: Private communication.

JOURNAL OF THE PHYSICAL SOCIETY OF JAPAN, Vol. 15, No. 12, DECEMBER, 1960

Theory of Electrochemical Diodes

By Isao OSHIDA

Kobayashi Institute of Physical Research,
Kokubunzi, Tokyo

(Received June 6, 1960)

The electric behaviour of electrochemical diodes, consisting of a pair of indifferent electrodes immersed in an electrolytic solution being capable of reversible oxidation-reduction, was investigated theoretically. The general current-voltage relation was obtained by solving the differential equation of diffusion of ions with the proper boundary conditions. The non-ohmic property, the shunting effect for rapidly changing voltage and the rectifying action were deduced.

§ Introduction.

Accompanied with the recent advance in the field of electronics, some attempts to use the element with electrolytic solution in electric circuits have appeared. Thus electrochemical diodes[1)2)], transistors[3)], switches[4)], and so on have been devised. In this paper, the electric behaviours of the electrochemical diodes were deduced theoretically on the ground of the equation of diffusion of ions. Similar treatment has appeared in the theory of polarography^5). However, in the case of polarography, the dimensions of the electrodes are extremely different, one being a small drop of mercury and the other a comparatively large unpolarizable electrode, and in the theoretical approach the latter is regarded as an infinitely large electrode at infinity. In the case of the electro-chemical diodes or triodes, such a treatment is not allowed. Mainly concerning a pair of similar electrodes, the equation of ionic diffusion could be solved. The general current-voltage behaviour was deduced, which shows the nonohmic saturation property and the shunting effect for rapidly changing voltage. The case of dissimilar electrodes was considered for those having cylindrical symmetry, which proved to show the rectifying character.

§ 2. Comparison of Ionic Diffusion and Translation.

An electrochemical diode with a pair of parallel-plate electrodes is the easiest for theoretical treatment, if the distance between the electrodes is so small that the convection of the solution is suppressed and that the end-effect can be neglected. Such a condition is realized, for example, by the clearance of a few tenths of a millimeter or less for the electrodes of ordinary dimension of a few centimeters. In such a narrow space, the diffusion of ion always surpasses the translational motion. On application of Einstein's formula for Brownian motion for the diffusion of ion,

$$\tau_1 = \frac{\lambda^2}{2D},$$

where D and λ are the coefficent of diffusion and the distance between the electrodes, respectively, the mean time interval τ_1 necessary for an ion to go across the gap λ can be estimated. On the other hand, if the electric field F exists between the electrodes, the time necessary for an ion to translate from an electrode to the other is

$$\tau_2 = \frac{\lambda}{BF},$$

where B is the mobility of the ion. If $\tau_2 \ll \tau_1$ the ion travels from one electrode to the other mainly by translation before the diffusion takes place in a sensible degree. On the other hand, when $\tau_1 \ll \tau_2$, an ion travels between the electrodes chiefly by diffusion. When

$$\lambda = \lambda_m = \frac{2D}{BF},$$

the both effects become to be of the same magnitude. If we put tentative values $D = 10^{-5}$ cm^2. sec^{-2}, $B = 5 \times 10^{-4}$ cm. volt^{-1}. sec^{-1} and $F = 1$ volt. cm^{-1}, λ_m becomes 0.4mm. Then it may be said that for a far smaller gap λ the diffusion predominates over the translation. This is the case which will be studied in the following.

§ 3. A Parallel-Plate Diode. The Fundamental Equation.

A pair of electrodes, parallel conductive plates, are immersed in an electrolytic solution executing oxidation and reduction completely reversibly. It is assumed that the exchange of electrons at the electrodes is very rapid and can be considered to be instantaneous. In practice, an aqueous solution of iodine and potassium iodide is used, in which the iodide ions I^- and triiodide ions I_3^- composed of I_2 and I^- are present. At the cathode, a reducing reaction

$$I_3 + 2e \rightarrow 3I^-$$

takes place, while at the anode an oxidizing reaction

$$3I^- - 2e \rightarrow I_3^-$$

occurs.

Here the more general cases are considered, in which the reduced species R and the oxidized species O can be transformed into one from the other by the exchange of n electrons:

$$O + ne \rightarrow R$$

$$R - ne \rightarrow O$$

Interesting properties are observed only when the concentration of one of the molecular species, the reduced or the oxidized, is very small compared to the other. So

$$C_O \ll C_R \qquad (1)$$

is assumed, where C_R and C_O are the concentrations of the reduced and the oxidized species respectively. The conclusions obtained are to be used also for the contrary case such as $C_R \ll C_O$ *mutatis mutandis.*

The diffusions of the both ionic species obey the equations

$$\frac{\partial C_R}{\partial t}=D_R\frac{\partial^2 C_R}{\partial x^2} \tag{2a}$$

$$\frac{\partial C_O}{\partial t}=D_O\frac{\partial^2 C_O}{\partial x^2} \tag{2b}$$

respectively. D_R and D_O are the coefficients of diffusion of both species and x is the coordinate. The cathode and the anode are located at $x=0$ and $x=L$, respectively, and accordingly L is the interval of the both electrodes.

There are two differential equations of second order, and accordingly there should be four boundary conditions. In the first place, there is no generation or cancellation of matter at the electrodes,

$$D_R\left(\frac{\partial C_R}{\partial x}\right)_{x=0}+D_O\left(\frac{\partial C_O}{\partial x}\right)_{x=0}=0, \tag{3a}$$

$$D_R\left(\frac{\partial C_R}{\partial x}\right)_{x=L}+D_O\left(\frac{\partial C_O}{\partial x}\right)_{x=L}=0. \tag{3b}$$

Secondly the anodic current,

$$i=nFAD_O\left(\frac{\partial C_O}{\partial x}\right)_{x=L}=-nFAD_R\left(\frac{\partial C_R}{\partial x}\right)_{x=L}, \tag{4a}$$

and the cathodic current,

$$i=nFAD_O\left(\frac{\partial C_O}{\partial x}\right)_{x=0}=-nFAD_R\left(\frac{\partial C_R}{\partial x}\right)_{x=0}, \tag{4b}$$

must be equal owing to the conservation of electric charge. Here F is Faraday's constant and A the area of the electrode. From (4a) and (4b), we have

$$\left(\frac{\partial C_O}{\partial x}\right)_{x=L}-\left(\frac{\partial C_O}{\partial x}\right)_{x=0}=0 \tag{5a}$$

$$\left(\frac{\partial C_R}{\partial x}\right)_{x=L}-\left(\frac{\partial C_R}{\partial x}\right)_{x=0}=0 \tag{5b}$$

(3a), (3b), (5a) and (5b) furnish only three boundary conditions, not four, because these equations are not independent of each other but one of them can be derived from the other three. The last condition is obtainable from Nernst's formula connecting the electrode potential E and the concentration C. Applying Nernst's equation to the both electrodes, we have

$$E_{x=0}=E^0+\frac{RT}{nF}\ln\frac{f_O C_O(0,t)}{f_R C_R(0,t)}, \tag{6a}$$

$$E_{x=L}=E^0+\frac{RT}{nF}\ln\frac{f_O C_O(L,t)}{f_R C_R(L,t)}, \tag{6b}$$

where E^0 means the standard electrode potential of the redox system, R the gas constant, T absolute temperature, and f_R and f_O the activity coefficients of the reduced and the oxidized forms in the solution respectively. Since the difference $E_{x=L}-E_{x=0}$ should be equal to the voltage V applied between the two electrodes, we get

$$\frac{RT}{nF}\left\{\ln\frac{f_O C_O(L,t)}{f_R C_R(L,t)}-\ln\frac{f_O C_O(0,t)}{f_R C_R(0,t)}\right\}=V,$$

or, assuming for the sake of simplicity $f_O=f_R=1$,

$$\frac{C_O(L,t)}{C_R(L,t)}\Big/\frac{C_O(0,t)}{C_R(0,t)}=\exp\left(\frac{nFV}{RT}\right). \tag{7}$$

Besides these boundary conditions, there are the initial conditions:

$$C_R=C_R^0 \tag{8a}$$

$$C_O=C_O^0 \tag{8b}$$

where C_R^0 and C_O^0 denote the initial stoichiometric concentration of the reduced and the oxidized ionic species respectively.

Introducing the assumption

$$D_R=D_O=D \tag{9}$$

to make the problem easy to handle, (3a) and (3b) become

$$\left(\frac{\partial C_R}{\partial x}\right)_{x=0}+\left(\frac{\partial C_O}{\partial x}\right)_{x=0}=0 \tag{10a}$$

$$\left(\frac{\partial C_R}{\partial x}\right)_{x=L}+\left(\frac{\partial C_O}{\partial x}\right)_{x=L}=0 \tag{10b}$$

respectively.

§ 4. The Steady State.

For steady state under a constant potential V, $\partial C/\partial t=0$ and, from (2a) and (2b), C_R and C_O should be linear function of x;

$$C_R=A_R x+B_R \tag{11a}$$

$$C_O=A_O x+B_O \tag{11b}$$

The initial conditions (8a) and (8b) are unnecessary in this case, but in place of them there should be the other conditions that the stoichiometric total amounts of the reduced and the oxidized species must be conserved as a whole after the steady state is build up. These conditions are

$$\int_0^L C_R dx=C_R^0 L \tag{12a}$$

and

$$\int_0^L C_O dx=C_O^0 L \tag{12b}$$

where C_R^0 and C_O^0 are the initial stoichometric concentrations of the both species respectively. The four constants A_R, B_R, A_O and B_O in (11a) and (11b) are determined by the four conditions (7), (10a), (12a) and (12b), thereby (5a), (5b) and (10b) are satisfied automatically.

The equation determining the coefficient A_O is

$$A_O^2-\frac{C_O^0+C_O^0}{L}\coth\frac{nFV}{2RT}\cdot A_O+\frac{C_O^0C_R^0}{L^2}=0 \quad (13)$$

which leads to

$$A_O=\frac{C_O^0+C_R^0}{2L}\coth\frac{nFV}{2RT}\cdot\left[1\pm\left\{1-\frac{4\,C_O^0C_R^0}{(C_O^0+C_R^0)^2}\tanh^2\frac{nFV}{2RT}\right\}^{\frac{1}{2}}\right]. \quad (14)$$

The lower sign should be chosen, because $V=0$ corresponds to the homogeneous concentration $A=0$.

Taking into consideration that

$$C_O^0\ll C_R^0 \quad (15)$$

and ignoring the small terms higher than the second power of C_O^0/C_R^0, we obtain

$$A_O=\frac{C_O^0}{L}\tanh\frac{nFV}{2RT}. \quad (16)$$

Then the concentration of the oxidized species is given by

$$C_O=\frac{C_O^0x}{L}\tanh\frac{nFV}{2RT}+C_O^0\left(1-\frac{1}{2}\tanh\frac{nFV}{2RT}\right). \quad (17)$$

The expression of the current i versus voltage V can be obtained from substitution of (17) in (4a) or (4b), that is

$$i=\frac{nFAD_OC_O^0}{L}\tanh\frac{nFV}{2RT}. \quad (18)$$

This is shown in Fig. 1, the dimensionless voltage V/V_0 being taken as the abscissa, where $V_0=2RT/nF$, and the dimensionless current i/i_0 as the ordinate, i_0 being $nFAD_O \times C_O^0/L$.

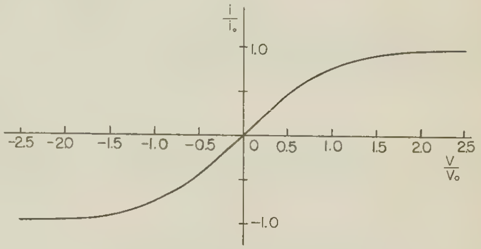

Fig. 1.

§ 5. The Indicial Admittance.

In this section, the case of suddenly applied constant voltage;

$$V=0 \text{ if } t<0,$$
$$V=V_0 \text{ (constant) if } t>0, \quad (19)$$

is studied. In this case, it is convenient to consider the deviation in the concentration from that of the steady state given by (17). Thus the quantity

$$\gamma=C_O-\bar{C}_O \quad (20)$$

is introduced, where $\bar{C}_O$ represents the steady-state C_O given by (17). For this γ, the boundary conditions are

$$(\gamma)_{x=0}=(\gamma)_{x=L}=0, \quad (21)$$

and the initial condition

$$(\gamma)_{t=0}=(C_O)_{t=0}-\bar{C}_O=C_O^0-\bar{C}_O=C_O^0\left(\frac{1}{2}-\frac{x}{L}\right)\tanh\frac{nFV}{2RT}. \quad (22)$$

γ satisfies also the equation of diffusion

$$\frac{\partial\gamma}{\partial t}=D\frac{\partial^2\gamma}{\partial x^2}. \quad (23)$$

To solve (23) under the conditions (21) and (22) is the typical problem occurring in the theory of heat conduction⁶⁾. The result is

$$\gamma=\frac{C_O^0}{\pi}\tanh\frac{nFV}{2RT}\cdot\sum_{s=1}^{\infty}\frac{1}{s}\exp\left(-\frac{4s^2\pi^2Dt}{L}\right)\cdot\sin\frac{2s\pi x}{L}, \quad (24)$$

and accordingly

$$C_O=C_O^0+C_O^0\tanh\frac{nFV}{2RT}\left[\frac{x}{L}-\frac{1}{2}+\frac{1}{\pi}\sum_{s=1}^{\infty}\frac{1}{s}\exp\left(-\frac{4s^2\pi^2Dt}{L^2}\right)\cdot\sin\frac{2s\pi x}{L}\right], \quad (25)$$

from which the current i is obtainable as a function of V and t, thus

$$i=\frac{nFAD_0C_0{}^0}{L}\tanh\frac{nFV}{2RT}\cdot\left[1+2\sum_{s=1}^{\infty}\exp\left(-\frac{4s^2\pi^2Dt}{L^2}\right)\right]. \tag{26}$$

Since the infinite series in the brackets is known as Jacobi's theta function, (26) can be written as

$$i=\frac{nFAD_0C_0{}^0}{L}\tanh\frac{nFV}{2RT}\cdot\vartheta_3\left(0\,\middle|\,\frac{4\pi iDt}{L^2}\right). \tag{27}$$

Introducing the quantities

$$\xi=\frac{4\pi Dt}{L^2}, \tag{28}$$

$$i_0=\frac{nFADC_0{}^0}{L}\tanh\frac{nFV}{2RT}, \tag{29}$$

the equation (27) can be written as

$$i=i_0\vartheta_3(0\mid i\xi)=i_0[1+2\sum_{s=1}^{\infty}\exp(-S^2\pi\xi)]. \tag{30}$$

Applying Jacobi's imaginary transformation

$$\vartheta_3(v\mid\tau)=\frac{\sqrt{i}}{\sqrt{\tau}}\exp\left(-\frac{v^2\pi i}{\tau}\right)\cdot\vartheta_3\left(\frac{v}{\tau}\,\middle|\,-\frac{1}{\tau}\right)$$

to (30); we obtain

$$i=\frac{i_0}{\sqrt{\xi}}\left[1+2\sum_{s=1}^{\infty}\exp(-s^2\pi/\xi)\right], \tag{31}$$

which is convenient for small t. The current-time relation calculated from (30) and (31) is shown in Fig. 2.

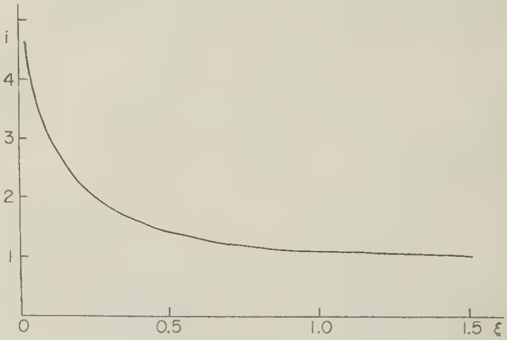

Fig. 2.

§6. The General Time-dependent Voltage.

Now the most general case in which the applied voltage V is any function $f(t)$ time,

$$V=0 \text{ if } t<0, \qquad V=f(t) \text{ if } t>0, \tag{32}$$

is considered. If V were a constant, the concentrations at the electrodes would be

$$(C)_{x=0}=C_0{}^0\left(1-\frac{1}{2}\tanh\frac{nFV}{2RT}\right), \qquad (C)_{x=L}=C_0{}^0\left(1+\frac{1}{2}\tanh\frac{nFV}{2RT}\right). \tag{33}$$

Since V is a function of time, we may put

$$\frac{C_0{}^0}{2}\tanh\frac{nFf(t)}{2RT}=g(t), \tag{34}$$

and

$$C-C_0{}^0=\varphi \tag{35}$$

and then the problem is reduced to finding the solution of

$$\frac{\partial \varphi}{\partial t} = D \frac{\partial^2 \varphi}{\partial x^2}\,, \tag{36}$$

which satisfies the time-dependent boundary conditions

$$\varphi = 0 \text{ all over, if } t<0,$$
$$(\varphi)_{x=0} = -g(t), \text{ if } t>0.$$
$$(\varphi)_{x=L} = g(t).$$

The solution is, after the case of heat conduction,

$$\begin{aligned}\varphi &= -\frac{8D\pi}{L^2}\sum_{s=1}^{\infty}\exp\left(-\frac{4s^2\pi^2 Dt}{L^2}\right)\sin\frac{2s\pi x}{L}\int_0^t g(\lambda)\exp\left(\frac{4s^2\pi^2 Dt}{L^2}\right)d\lambda \\ &= -\frac{4\pi D C_0{}^0}{L^2}\sum_{s=1}^{\infty} S\exp\left(-\frac{4s^2\pi^2 Dt}{L}\right)\sin\frac{2s\pi x}{L}\int_0^t \exp\left(\frac{4s^2\pi^2 D\lambda}{L^2}\right)\tan\mathrm{h}\,\frac{nFf(\lambda)}{2RT}d\lambda\,. \end{aligned}\tag{37}$$

The corresponding current is

$$i(t) = -\frac{8n\pi^2 FAD^2 C_0}{L^3}\sum_{s=1}^{\infty} s^2\exp\left(-\frac{4s^2\pi^2 Dt}{L^2}\right)\int_0^t \exp\left(\frac{4s^2\pi^2 D\lambda}{L^2}\right)\tan\mathrm{h}\,\frac{nFf(\lambda)}{2RT}d\lambda\,, \tag{38}$$

which gives the current for any change in voltage $f(t)$. For example, the linearly increasing voltage with a constant rate k

$$f(t) = kt\,, \tag{39}$$

leads to the current

$$i = i_0\left[\tan\mathrm{h}\,\beta kt + 2\beta k\sum_{S=1}^{\infty}\exp(-ps^2 t)\int_0^t \exp(ps^2\lambda)\sec\mathrm{h}^2\,\beta k\lambda d\lambda\right], \tag{40}$$

where

$$i_0 = \frac{nFAD_0C_0}{L}\,,$$

$$\beta = \frac{nF}{2RT}\,,$$

$$p = \frac{4\pi^2 D}{L^2}\,.$$

The current-time relation (40) is shown in Fig. 3, which is written for $i_0=1$, $\beta=1$, $k=1$ and $p=1$. The sudden rise of the current is observed; the transient phenomena means that the diode has the shunting effect for high frequency input signals.

§ 7. Co-axial Cylindrical Electrodes.

To study the case in which the sizes of the two electrodes are very different, the co-axial cylindrical electrodes, the cathode at $r=a$ and the anode at $r=b$, are considered. If it is assumed that

$$a \ll b\,, \tag{41}$$

the rectifying character appears as shown in the following.

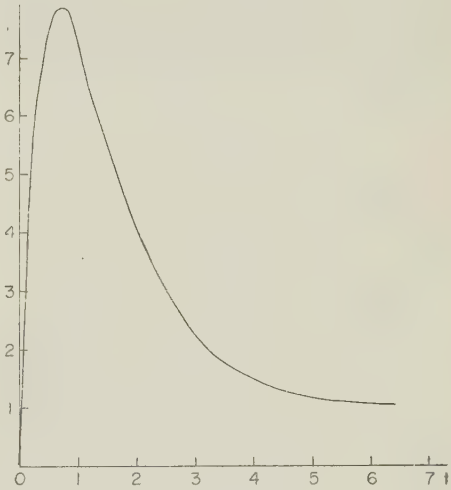

Fig. 3.

The equations of diffusion referred to the cylindrical coordinates, in which the concentrations are the functions of r only, are

$$\frac{\partial C_R}{\partial t} = \frac{D}{r}\frac{\partial}{\partial r}\left(r\frac{\partial C_R}{\partial r}\right), \tag{42a}$$

$$\frac{\partial C_O}{\partial t}=\frac{D}{r}\frac{\partial}{\partial r}\left(r\frac{\partial C_O}{\partial r}\right). \tag{42b}$$

The boundary conditions corresponding to (10a) and (10b) are

$$\left(\frac{\partial C_R}{\partial r}\right)_{r=a}+\left(\frac{\partial C_O}{\partial r}\right)_{r=a}=0\,, \tag{43a}$$

$$\left(\frac{\partial C_R}{\partial r}\right)_{r=b}+\left(\frac{\partial C_O}{\partial r}\right)_{r=b}=0\,, \tag{43b}$$

those corresponding to (5a) and (5b)

$$b\left(\frac{\partial C_O}{\partial r}\right)_{r=b}=a\left(\frac{\partial C_O}{\partial r}\right)_{r=a}=0\,, \tag{44a}$$

$$b\left(\frac{\partial C_R}{\partial r}\right)_{r=b}-a\left(\frac{\partial C_R}{\partial r}\right)_{r=a}=0\,, \tag{44b}$$

and that corresponding to (7)

$$\frac{C_O(b,\,t)}{C_R(b,\,t)}\Big/\frac{C_O(a,\,t)}{C_R(a,\,t)}=\exp\left(\frac{nFV}{RT}\right). \tag{45}$$

As only the steady state is considered here, C_O and C_R should satisfy

$$\frac{d}{dr}\left(r\frac{dc}{dr}\right)=0\,,$$

and so

$$C_O=\alpha_O \log \gamma+\beta_O \tag{46a}$$

$$C_R=\alpha_R \operatorname{lon} \gamma+\beta_R. \tag{46b}$$

With this type of solution, (44a) and (44b) satisfied automatically, so to determine the four constants α_O, β_O, α_R and β_R, the conditions corresponding to (12a) and (12b) should be adopted again. A procedure similar to §4 leads to, because of the conditions (1) and

$$a\ll b\,, \tag{47}$$

the expression of the steady current per unit length of the cylinder

$$i=2\pi nFD\alpha_O=2\pi nFDC_O^0\left\{\exp\left(\frac{nFV}{RT}\right)-1\right\}. \tag{48}$$

The result is shown in Fig. 4, for $2\pi nFDC_O^0=i_O=11.7$ and $\frac{RT}{nF}=V_O=0.0128$. A typical rectifying character can be observed. It is noted that the result does not contain C_R and a explicitly.

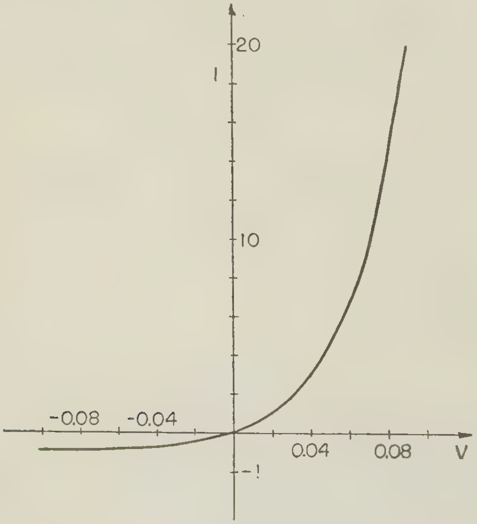

Fig. 4.

If the minority carrier is the reduced form, it is easy to see that the rectifying character is revered, that is the larger current flows when the outer electrode is in negative potential.

Acknowlegements.

The author expresses his hearty thanks to Dr. Yasundo Takahashi, Professor of California University, who kindly sent him the literature hardly available in Japan, to Professor Keiichi Eda of Gakushuin University for kind discussions, to Miss Mizuko Yoshida who helped him in numerical calculations and drawing the figures and Miss Mitsuko Hirose for her preparing the manuscript. This work was partly supported by a Scientific Research Expenditure of the Education Ministry.

References

1) H. B. Read, J. B. McQuitty, R. N. Lane and R. M. Hurd: Yale Sci. Mag. **32** (1958), No. 5, 13–21. The theoretical expressions for the electric current given in this reference, although only the final results are given, do not coincide with those derived here and do not seem to be correct ones.
2) R. N. Lane and D. B. Cameron: Electronics **32** (1959) 53–5.
3) H. Letaw and J. Bardeen: J. Appl. Phys. **25** (1954) 600–606.
4) J. D. Cooney: Control Engineering **6** (1959) 121–124.
5) *e.g.* P. Delahay: *New Instrumental Methods in Electrochemistry*, New York and London, 1954. Ch. 3, Ch. 6 and Appendix 2, Section 3.
6) *e.g.* H. S. Carslaw: *Introduction to the Mathematical Theory of the Conduction of Heat in Solids*, 2nd ed. London 1921.

JOURNAL OF THE PHYSICAL SOCIETY OF JAPAN, Vol. 15, No. 12, DECEMBER, 1960

Dielectric β-Relaxations in Some Linear High Polymers

By Kaoru YAMAFUJI

Department of Physics, Faculty of Science,
Kyusyu University, Hukuoka, Japan

(Received July 29, 1960)

The dielectric β-dispersions in the amorphous part of the linear high polymers may be roughly classified into two categories according to their mechanisms: the first is the dielectric dispersions in the polymers which have long flexible dipoles, and the second is those which have rather short dipoles rigidly attached to their main chains. While the β-dispersions in the polymers of the first group are inferred to be mainly due to the micro-Brownian motions of their long dipoles, no convincing theory referring to the mechanism of those of the second group has been proposed up to present.

In this paper, the dielectric β-dispersions of these second group polymers are investigated. The approximate magnitudes of some quantities appearing in our theory are evaluated by the observed values obtained from the mechanical dispersion. Taking account of the phenomenological nature of our theory, agreements between the theory and the observations may be satisfactory.

§1. Introduction

Since the existence of the mechanical β-dispersions for some linear high polymers was reported by several authors⁽¹⁾ in the early years of the nineteen fifties, a great number of investigations have been done up to now for the mechanical and dielectric dispersions in high polymers. As a result of these efforts, two or three kinds of mechanical and dielectric dispersions have been known for each of many linear high polymers. As there is no unified nomenclature for the specification of these dispersions, we shall call, them, in accordance with usual name, α-, β-, γ-dispersions and so on in their turns of appearance from high temperature and low frequency sides to low temperature and high frequency sides. However, this nomenclature makes the discussion of these dispersions much complicated, for the term α-, β-, or γ-dispersion means only the sequence of appearance from the high temperature and low frequency sides and there may be, therefore, various possible mechanisms for the β-, or γ-dispersions of the various kinds of polymers.

On the other hand, however, dielectric dispersions for the amorphous part seem to have a common nature.* Almost all of the dispersions are attributed to the deformations of the high polymer chains which are caused by the motions of the permanent dipoles under the effect of external electric field. Therefore, it may be somewhat useful to classify these dispersions from the side of the motions of the dipoles. There may be, roughly speaking, three kinds of such deformations of the chains due to the motions of the permanent dipoles. These are as follows:

(1) The deformations accompanied with rather large changes in the directions or locations of the dipoles and with large apparent activation energies.

(2) The deformations accompanied with rather large changes of the directions or locations of the dipoles but with comparatively small apparent activation energies.

(3) The deformations accompanied with rather small changes of the directions or locations of the dipoles and also with small apparent activation energies.

For a typical example of the deformations of the type (1), there would be the change of the dipole orientations due to the segmental rotations or translations of the main chains. Most of the α-dispersions are attributed to such deformations of the main chains. The mechanism and the properties of the α-dispersion have been discussed by many authors[2] and some convincing theories seem to have been established, although these theories seem to be not satisfactory in many points.[3]

---

* In this paper, we shall discuss only the dielectric disperions due to the amorphous part of the linear high polymers. The dieletric dispersions in the high polymers which have the hydrogen bonds are also excluded.

As is well known, the segmental rotations and translations of the main chains tend to be less and less active as the temperature becomes lower than the glass transition temperature, T_g. In other words, the relaxation times characteristic of such motions are apt to be longer and longer as the temperature becomes lower, and hence the α-dispersion becomes hardly observable at the temperatures far below T_g. Since the β-, and γ-dispersions are mainly observed at the temperatures below T_g, they seem to be attributed to the deformations of the types (2) and (3).

The first example for the deformations of the type (2) would be the rotational motions of the chain end dipoles in the amorphous part. Reddish[4] attributed the dielectric β-dispersion of the polyethylenetelephthalate to such rotational motions of the —OH groups in the chain ends. The magnitude of the β-dispersion due to the mechanism may have a remarkable dependence on the degree of polymerization and, further, it would be fairly small because the number of the chain end dipoles is quite small. The detailed experimental work with respect to these points[5] shows us, however, that the magnitude of β-dispersion seems to have rather weak dependence on the degree of polymerization, and hence the β-dispersion due to such a mechanism seems to have not yet been found out at the present stage.

The second instance of the type (2) would be the deformations due to the rotational motions of the long flexible side dipoles such as, for example, ester groups of PMMA. Since these motions do not need so large apparent activation energy, they would be also active at the temperatures below T_g. The β-dispersions of a series of linear high polymers such as polymethylmethacrylate (PMMA), polyethylmethacrylate (PEMA), poly-α-chloroacrylate, and so on, may be attributed to this mechanism.[6][16]

Besides the above polymers whose dipoles are long and flexible, there are another kind of polymers whose dipoles are short and rigidly attached to the main chains. Polyvinylchloride (PVC), polyvinylbromide (PVBr) and polymonochlorotrifluoroethylene (PCFE) are the examples of this kind of polymers. Since the β-dispersions are mainly observed in the temperatures far below T_g and the rotational and translational motions of the main chains are frozen in this temperature range, most of the β-dispersions for these linear high polymers would be due to the deformations of the type (3), that is, the deformations accompanied with rather small changes of the directions or locations of the dipoles. Here, the term "dipoles" means the composite dipoles of those of a monomer unit or of a structural unit like the monomer. One may consider several "models" describing such small motions of the dipoles. The first is as follows:

(a) Each dipole bound temporarily to one of the directions of the local equilibria is performing a small vibration in the vicinity of the local equilibrium. The β-dispersion is the superposition of the resonance absorptions by these oscillators.

The properties of the dispersion due to the above mechanism have already been investigated.[7] However, the limiting condition in which the dispersion due to the above mechanism can occur depends upon the fact that whether the oscillators could keep up their stationary characters during a period of the applied electric field or not. In the viscous media, such as we are now considering, the life times during which oscillators stay in one of the vibrational normal modes are expected to be much shorter than the period of the electric field, $10\sim10^{-7}$ sec. Thus, the possibility of the appearance of the dispersion due to the above mechanism seems to be little at least for the dispersion in the radio frequency range.

The second is the theoretical approach from the liquid-like model.** Because the rotational and translational motions of the main chains are frozen at the temperatures far below T_g, each dipole is bound in the vicinity of a local equilibrium direction during the time far longer than the period of the electric field, $10\sim10^{-7}$ sec. Thus, the

---

** A theory based on a view point of the liquid-like model has been developed by Okano[8] independently of us. His calculation is an application of Kirkwood's formulations to the β-dispersion.

small motions of the dipoles in the vicinity of the local equilibrium directions could be approximately described as those in the high visco-elastic liquid:

(b) Since the dipoles are bound high visco-elastically to one of the local equilibrium directions, they follow the change of the direction of the local electric field with a little delay on account of both the restoring and frictional forces. The β-dispersion is due to such a delaying phenomenon.

The third is the approach from the side of the crystalline solid:

(c) Each dipole performs the transition from one of the local equilibrium directions to another by the thermal agitations. If the transition probabilities for such transitions can be divided into two or three groups distinctly, the dispersions can also be divided into two or three groups accordingly.

Since the above mentioned model, (b), lies between the site model, (c), and the continuous rotating model in the viscous liquid, we may call it the "quasi-liquid" model. In this paper, the β-dispersions due to the deformations of the type (3) are investigated with the aid of the model (b). However, the site model is also useful in many points and will be discussed in the following paper.[13)]

In § 2, a phenomenological simple calculation is done in deriving an expression for the dielectric β-dispersion of the type (3), especially for PVC. The orders of the magnitudes of some quantities which appear in our theory are estimated from the observed values obtained from the mechanical β-dispersion. In § 3, the calculated results in § 2 are compared with the observations in the following three points: (A) the magnitude and the temperature dependence of the static dielectric constant, (B) the magnitude and the temperature dependence of the frequency of the maximum absorption, and (C) the shape of the absorption curve and its temperature dependence. Finally, the dielectric β-dispersions in other second group polymers such as PCFE are discussed in § 4.

§ 2. Phenomenological Theory

In this section we shall derive an expression for the dielectric β-dispersion curve due to the small deformations of the chains based on the model (b). First, we shall discuss the case of the linear chain polymers which have a single rigid dipole per monomer such as PVC. The extension of the theory to the case in which there are two or more dipoles per monomer such as PCFE will be discussed in § 4. Since, in the present case, we are not interested in the intra-monomer deformations of polymer molecules, the motions of dipoles can be approximately regarded as same as those of monomer units.

According to the molecular theoretical interpretation of the relaxation phenomenon, the dielectric dispersion is to be caused by an energy transfer from the rotational degree of freedom of dipoles to some other degrees of freedom, and the activation energy of dispersion is related, in some way or others, to the energy of coupling between the rotational degree of freedom and the remaining degrees of freedom of the molecular motion. Since the activation energy of the β-dispersion is fairly large, the interactions among monomers pertaining to the β-dispersion would be rather strong, though they are not so strong as in the case of α-dispersion. Then, it is to be expected that the small rotations around the quasi-stable positions affect those of many neighboring monomers and bring about the coupled motions of these monomers. For simplicity, however, we shall assume that all the dipoles in the system are divided into many groups each of which contains only the dipoles of several monomers rotating in the same way as a whole, and that each group of dipoles is moving independently of the other groups in a high elastic medium under the influence of both restoring and frictional forces. A slightly more extended consideration which takes into account the coupled motions among groups explicitly will be discussed in Appendix. In the following we shall call the j-th group of dipoles simply the j-th dipole but will represent a group of dipoles.

We shall put the "local" polar axis in the direction of the chain having its origine in the vicinity of the j-th dipole. Further, we shall treat the three dimensional motions of dipoles approximately by assuming that it is confined in the plane perpendicular to the local direction of the chain and denote the rotational angle of the j-th dipole by φ_j measured from its equilibrium directions in the absence of the external electric field. Then, the phenomenological equation of motion of the j-th dipole is expressed as follows.

$$I_j\frac{d^2\varphi_j}{dt^2}+\zeta_j\frac{d\varphi_j}{dt}+\gamma_j\varphi_j=\mu_j\sin\theta_i{}^0\sin(\varphi_j{}^0-\varphi_j)E_r\,, \tag{2.1}$$

where I_j, ζ_j, γ_j, and μ_j are the moment of inertia in the vicinity of the quasi-stable positions, the rotational friction constant, elastic restoring force constant of small rotation and the dipole moment of the j-th dipole, respectively, and E_r is Onsager's directing field which is in the direction ($\theta_j{}^0$, $\varphi_j{}^0$). Because the dipoles are rotating in a high elastic medium, we can easily prove that the first term in Eq. (2.1) is negligible. Then, the solution of Eq. (2.1) leads to a superposition of the dielectric dispersions of Debye type for the periodic external field of angular frequency ω:

$$\varepsilon(i\omega)-\varepsilon_\infty=\frac{4\pi}{3}\frac{E_r}{E}\sum_{j\ 1}^{N'}\frac{\mu_j{}^2}{\gamma_j}\frac{1}{1+i\omega\tau_j}\,, \tag{2.2}$$

where

$$\tau_j=\frac{\zeta_j}{\gamma_j}\,. \tag{2.3}$$

The static dielectric constant for β-dispersion is at once derived from Eq. (2.2), and is given by

$$\varepsilon_0-\varepsilon_\infty=\frac{4\pi}{3}\frac{E_r}{E}\sum_{j=1}^{N'}\frac{\mu_j{}^2}{\gamma_j}\,. \tag{2.4}$$

In Eqs. (2.2) and (2.4), N$'$ is the number of the groups of dipoles per unit volume. Since γ_j and ζ_j are, respectively, distributed in a certain range with some shape in general, the summations in Eqs. (2.2) and (2.4) are replaced by the integrals in which the summands are multiplied by the distribution functions. The shape of the distribution function of the relaxation times will be investigated in Appendix.

One of the important differences between our equation of dispersion and that of the phenomenological theory of α-dispersion or Debye's equation in liquid is in the definition of the relaxation time. While the relaxation time of Debye's is given by $\tau_D=\zeta_D/kT$, where k is the Boltzmann constant and T is the absolute temperature, ours is expressed as $\tau=\zeta/\gamma$. Although the similar mechanism to ours had been proposed with respect to the dielectric losses in the dipolar liquids, [9] the order of the magnitude of the relaxation time did not agree with observed values in liquids. In the glass state of the polymer, however, the medium is so high visco-elastic that our mechanism becomes meaningful as we shall discuss in § 3.

We shall now consider about γ_j and ζ_j. The detailed knowledge of these quantities is, of course, obtained by the molecular theoretical consideration. Our request in this paper is, however, not to find a detailed quantitative agreement between the theory and the observation, but only to know whether Eq. (2.2) based on our mechanism would give the correct order of the magnitudes and the correct qualitative tendencies of the observed data or not. It is, therefore, enough for our purpose to know only the approximate magnitudes and qualitative tendencies of γ_j and ζ_j. We shall, then, evaluate the approximate magnitudes of γ_j and ζ_j from the observed values for the β-dispersion of the dynamic rigidity.

The rotational friction constant of the dipole, ζ_j, is proportional to its shear viscosity, η_j', which is expressed by Stokes' law as

$$\zeta_j=8\pi a_j'^3\eta_j'\,, \tag{2.5}$$

where a_j' is the effective radius of the dipole when we replace it by a sphere. We shall assume that the average value of η_j' is approximately given from the observed value for the β-dispersion of the dynamic rigidity by

$$\eta'\cong G''(\omega_m)/\omega_m\,, \tag{2.6}$$

and similarly, for γ_j,

$$\gamma\cong G'(\omega_m)a'N'^{-2/3}\,. \qquad (2.7)^{***}$$

In Eqs. (2.6) and (2.7), ω_m is the maximum frequency of the absorption and G' and G'' are, respectively, the real and imaginary parts of the dynamic rigidity. In deriving Eq. (2.7), we used the facts that the shear elastic force may be most effective to the small rotations of composite dipoles and that only the nearest neighbors are remarkably dragged in such motions.

Although the condition under which the external force acts on the monomers is, of

---

*** Strictly speaking, $G'(\omega_0)$ should be used in place of $G'(\omega_m)$ in Eq. (2.7) where ω_0 is such an angular frequency that $\omega_{m,\beta}\gg\omega_0\gg\omega_{m,\alpha}$. However, the change of G' with angular frequencies is so small for the β-dispersions that it would be admissible to use $G'(\omega_m)$ instead of $G'(\omega_0)$.

course, different between the mechanical and the dielectric measurements, the replacements in Eqs. (2.6) and (2.7) are seen to be enough to evaluate the magnitudes and the temperature dependences of γ_j's and ζ_j's approximately. One may, however, have an objection that it is not reasonable to substitute the macroscopic quantities for the microscopic ones. Although this objection may be valid in principle, it happens to be unsuitable for our case. The detailed consideration in this respect will be given in § 3.

§ 3. Comparison with Observations

Since the equation of the dielectric β-dispersion due to small deformations of the chains, Eq. (2.2), is derived in a much simplified semi-phenomenological way, it is not reasonable to expect the detailed quantitative agreements between the theory and the observations. However, Eq. (2.2) should give not only the qualitative tendencies of the observations correctly but also the magnitudes of the observed quantities approximately so long as our mechanism is valid. In this section, we shall discuss this subject.

(3/1). The Static Dielectric Constant

The static dielectric constant for the β-dispersion in our case is given by Eq. (2.4). Evaluating the approximate magnitude of the static dielectric constant from this equation, we shall make further simplifications that we ignore the distributions of μ_j's and γ_j's and replace the quantities of composite dipoles by those of individual monomers. These replacements may bring about only the factors of the order of unity, which gives no serious effect to our purpose. Then, eq. (2.4) becomes

$$(\varepsilon_0-\varepsilon_\infty)_\beta \simeq \frac{4\pi}{3}\frac{E_r}{E}\frac{N\langle\mu^2\rangle}{G'aN^{-2/3}}, \qquad (3.1)$$

where N is the number of monomers per unit volume and a is the effective Stokes' radius for a monomer. The suffix β on the left hand side represents that the quantity is the static dielectric constant for β-dispersion. If we substitute the appropriate values on the right hand side of Eq. (3.1), for instance in the case of *PVC*, $N \sim 1.4\times10^{22}$ per cm³, $\langle\mu^2\rangle^{1/2} \sim 1.7\times10^{-18}$ esu, $a \sim 4\times10^{-8}$ cm, $G' \sim 1.5\times10^{10}$ dyne/cm² (−20°C)[1] and $E_r/E \sim 2.3$ the magnitude of the β-dispersion, $(\varepsilon_0-\varepsilon_\infty)_\beta$, in *PVC* becomes 4×10^{-1} (−20°C). Since Onsager's directing field may be replaced by $E_r=[3\varepsilon_s(\varepsilon_\infty+2)^2/9(2\varepsilon_s+\varepsilon_\infty)]E$, the value of the ratio E_r/E is calculated from the observed data. The order of magnitude of this value agrees fairly well with the observed data. (See Fig. 1.)

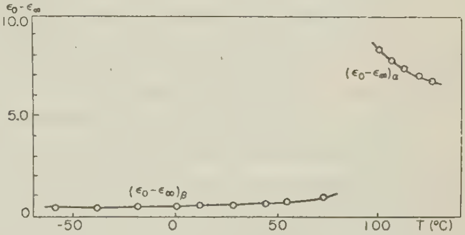

Fig. 1. The static dielectric constants for the α- and β- dispersions in PVC.[10]

As was mentioned above, there may be some objection to replace the microscopic quantities by the macroscopic ones. Although such a replacement leads to the correct results qualitatively in the usual case, it often yields wrong values in the order of the magnitude. However, such an objection would be unsuitable as far as the relaxation time, τ, is concerned because τ is given by the ratio ζ/γ and, further, we are interested in only the logarithm of τ. Then the possible errors for ζ and γ, if exist, would cancel each other. As for the elastic restoring force constant of small rotation γ, the value calculated from Eq. (2.7) is nearly the same as the value obtained from the more detailed molecular theoretical calculation in Appendix. In fact, the former is given by 5×10^{-13} while the latter is 8×10^{-13} in the case of *PVC*. Moreover, the value of γ estimated from the apparent activation energy for the β-dispersion in *PVC* (∼10 kcal/mol) is also 6×10^{-13}, showing the expected agreement for the order of magnitude. Thus we may conclude the objection that such a replacement would lead to a wrong order of magnitude for τ and γ seems to be unsuitable for our case.

For comparing the static dielectric constant corresponding to β-dispersion with the observations, it is more convenient to consider the ratio of the static dielectric constant for β-dispersion to that for α-one, because the uncertain factors, such as the mean square of the dipole moment, Onsager's directing field, etc., are eliminated by this procedure.

Since the static dielectric constant for α-dispersion at the temperatures far above T_g is given by

$$(\varepsilon_0-\varepsilon_\infty)_\alpha=\frac{4\pi}{3}\frac{E_r}{E}\frac{N\langle\mu^2\rangle}{kT}, \qquad (3.2)$$

its ratio to Eq. (3.1) yields

$$\frac{\varDelta\varepsilon_\beta}{\varDelta\varepsilon_\alpha}=\frac{(\varepsilon_0-\varepsilon_\infty)_\beta}{(\varepsilon_0-\varepsilon_\infty)_\alpha}=\frac{kT_\alpha}{G'(T_\beta)aN^{-2/3}}, \qquad (3.3)$$

where T_α and T_β are the temperatures at which α- and β-dispersions are observed, respectively. In Table I, the theoretical values of $\varDelta\varepsilon_\beta/\varDelta\varepsilon_\alpha$ are compared with the observed values of $\varDelta\varepsilon_\beta/\varDelta\varepsilon_\alpha$ for a few polymers appropriate for our theory. Though the values of a may be different for various kinds of polymers, we shall choose it as $a\sim4\times10^{-8}$ cm for convenience. The observed values in Table I are corrected for the degree of crystallization. The agreements between the theoretical and observed values are satisfactory.

Table I. Comparison of theoretical and observed values of the static dielectric constants for β-dispersions to α-ones in polyvinylchloride (PVC), polyvinylbromide (PVBr) and polyvinylacetate (PVAc).[10,13]

polymers	$\left(\frac{\varDelta\varepsilon_\beta}{\varDelta\varepsilon_\alpha}\right)_{\text{obs.}}$	$\left(\frac{\varDelta\varepsilon_\beta}{\varDelta\varepsilon_\alpha}\right)_{\text{theo.}}$	compared temperature
PVC	0.06	0.07	$\frac{0^\circ\mathrm{C}(\beta)}{100^\circ\mathrm{C}(\alpha)}$
PVBr	0.05	0.06	$\frac{10^\circ\mathrm{C}(\beta)}{85^\circ\mathrm{C}(\alpha)}$
PVAc	0.03	0.03	$\frac{-15^\circ\mathrm{C}(\beta)}{52^\circ\mathrm{C}(\alpha)}$

In our equation of the static dielectric constant for β-dispersion, only the real part of the rigidity, G', is the temperature dependent factor. Since G' decreases as the temperature becomes higher, the static dielectric constant for β-dispersion is expected to increase with temperature. Although the observed values of the latter quantity for *PVC* actually increased by some twice during the temperature range 0°C∼60°C (Cf. Fig. 1.), it can be explained from the temperature increase of G'. Besides, since the temperature change of G' is rather slow at lower temperatures, it is expected that the static dielectric constant will also change slowly with temperature. This agrees with the tendencies of the observed data, too. At higher temperatures, such as near T_g, the relaxation times characteristic of α- and β-dispersions become, however, comparable in the orders of magnitudes. Then the treatment such that of § 2 begins to lose its validity. Therefore, we cannot predict the behavior of $(\varepsilon_0-\varepsilon_\infty)_\beta$ near and at higher temperatures than T_g. However, since the number of dipoles pertaining to the β-dispersion due to the small deformations of the chains is, roughly speaking, the order of $N(1-\exp(-\tau_\alpha/\tau_\beta))$, it is inferred that the increment of $(\varepsilon_0-\varepsilon_\infty)_\beta$ becomes low at temperatures near T_g and, finally, it will begin to saturate and decrease.

(3/2). The Frequency of the Maximum Absorption

Now we shall consider the frequency of the maximum absorption. In the case of *PVC*, the value of τ evaluated from the data due to Schmieder and Wolf[1] and from the relations Eqs. (2.3), (2.5) and (2.6) gives $\tau\sim 9.4\times10^{-2}$. Then we obtain the logarithm of the frequency of the maximum absorption, $\log f_m$, as

$$\begin{aligned}\log_{10}(f_m)&=\log_{10}(\omega_m/2\pi)\\&=\log_{10}(1/2\pi\tau)\sim0.2 \text{ (at } -30^\circ\text{C)}.\end{aligned}$$

This is of nearly the same order of magnitude as the observed value. (Cf. Fig. 2.)

The similar situations are realized for other

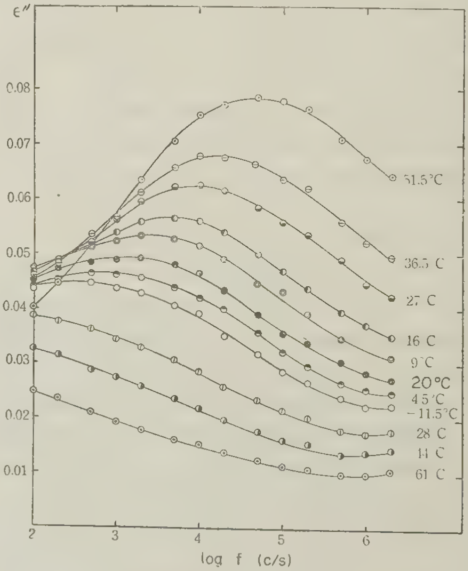

Fig. 2. The $\varepsilon''-\log f$ curve for the β-dispersion in PVC.[10]

polymers. In our theory, the temperature dependence of f_m is due to that of η' as well as that of G'. Since the activation energy of dynamic viscosity is nearly the same as that of the dielectric dispersion, the temperature dependence of f_m in our theory should bring about the coincidence with the observed values approximately. The correct temperature dependence should, of cource, be obtained from the more detailed molecular considerations based on our mechanism. As was mentioned above, G' is also a temperature dependent factor in f_m. It gives a little decrease of the transferring velocity of f_m to higher frequencies with increasing temperature.

(3/3). The Shape of the Absorption Curve

The marked broadness of the observed absorption curves are understood to be a consequence of the superposition of the many Debye absorption curves each of which has a single relaxation time τ. The relaxation time spectrum for the dielectric β-dispersion, $L_\varepsilon(\tau)$, seems to have following two characteristic features[3]: (1) the spectrum is rather symmetrical in $\log L_\varepsilon(\tau)-\log\tau$ curve compared with the mechanical retardation spectrum; (2) the Cole's parameter, $\bar{\beta}$, has the values nearly equal to 0.3 at the temperatures far below T_g both in the cases of the amorphous and the crystalline high polymers. This is in marked contrast to the α-dispersion for which the values of $\bar{\beta}$ lie between 0.3 for the crystalline polymers and 0.7~0.9 for the amorphous polymers.

The simple calculation in § 2 gives us no information about the detailed shape of the absorption curve and hence we must attempt some extension whose details are given in Appendix. However, the above characteristic features are not so satisfactorily explained by the calculations in Appendix. The theory of the relaxation time spectrum for the dielectric β-dispersion will be the next subject of investigation.

§ 4. Dielectric β-Dispersion in PCFE

In § 2 we discussed the case of the polymers which have only a single rigid dipole per monomer unit such as PVC. Here, we shall extend the discussion in § 2 to the case of two or more dipoles per monomer unit. Polymonochlorotrifluoroethylene (PCFE), polyethylenetelephthalate (PET), etc. are the examples of such polymers. Although the dielectric β-dispersions of these polymers are very similar to those of the linear vinylpolymers, the magnitudes of the α-dispersions for these polymers are much smaller than those of the linear vinyl-polymers. (Cf. Table II.)

Table II. The magnitudes of the dispersions for PCFE and PET.[12] (Data for PVC[10] is added for comparison.)

polymer	$(\varepsilon_0-\varepsilon_\infty)_{\alpha,\mathrm{obs.}}$	$(\varepsilon_0-\varepsilon_\infty)_{\beta,\mathrm{obs.}}$	$(\varepsilon_0-\varepsilon_\infty)_{\beta,\mathrm{theo.}}$
PCFE	0.24 (100°C)	1.2 (0°C)	1.9 (0°C)
PET	1.8 (82°C)	0.54 (30°C)	0.4 (30°C)
PVC	8.4 (100°C)	0.5 (30°C)	0.5 (30°C)

First, we shall consider the case of PCFE, which has three C-F dipoles and a C-Cl dipole per monomer unit. Suppose the angle between C-Cl and C-F dipoles is of the regular tetrahedron exactly, the dipole moment per monomer unit decreases to 0.2 Debye unit or so by the cancellation among the dipole moments of a C-Cl dipole and three C-F dipoles. Since PCFE has, however, the spiral structure including 14 monomers in a period[11] and, moreover, we are considering about the amorphous part, the cancellation among these dipole moments may be rather incomplete. Taking into account the fact that the root mean square of the dipole moment of $CClF_3$ is 0.46 Debye unit, the root mean square of the dipole moment per monomer unit would be expected to be approximately 0.4~0.5 Debye unit. Substituting the following appropriate values,

$$N_{\mathrm{PVC}}\sim 1.4\times 10^{22}\ \text{per cm}^3,$$
$$N_{\mathrm{PCFE}}\sim 1.0\times 10^{22}\ \text{per cm}^3,$$
$$(\langle\mu^2\rangle_{\mathrm{PVC}})^{1/2}\sim 2.0\times 10^{-18}\ \text{esu},$$
$$(\langle\mu^2\rangle_{\mathrm{PCFE}})^{1/2}\sim 0.5\times 10^{-18}\ \text{esu},$$
$$\text{and } (E_r/E)_{\mathrm{PVC}}\sim 3,\ (E_r/E)_{\mathrm{PCEF}}\sim 2,$$

into Eq. (3.2), the ratio the dielectric constant of the α-dispersion for PVC to that for PCFE becomes

$$\frac{(\varepsilon_0-\varepsilon_\infty)_{\alpha,\mathrm{PVC}}}{(\varepsilon_0-\varepsilon_\infty)_{\alpha,\mathrm{PCFE}}}\sim 34\ ,$$

which is approximately of the same value with the observed value 35 calculated from the Table II. This means that the monomer can be regarded as the nearly rigid motional unit in the case of α-dispersion.

On the other hand, the monomer cannot be regarded as a rigid motional unit in the case of the β-dispersion. For, in this case, the motion of the dipole is the small "diffusional" rotation near the minimum point of the potential, and hence the external electric field forces to attract the dipole pairs CCl-CF and CF-CF in the opposite directions to each other. Then, it may be possible to occur such a motion in which the pairs CCl-CF and CF-CF perform the small "diffusion" rotations partially independently under the effect of the periodic electric field. Therefore, we must substitute the root mean square of the dipole moment for CCl-CF or CF-CF pair into in Eq. (3.1). Substituting the appropriate values,

$$N \sim N_{\mathrm{CCl\text{-}CF}} + N_{\mathrm{CF\text{-}CF}} \sim 2 \times 10^{22} \text{ per cm}^3,$$
$$\langle \mu^2 \rangle^{1/2} \sim 1.7 \times 10^{-18} \text{ esu},$$
$$G' \sim 8 \times 10^9 \text{ dyne/cm}^2 \text{ (at 0°C)},^{1)}$$
$$a \sim 4 \times 10^{-8} \text{ cm and } E_r/E \sim 2 \text{ },$$

into the right hand side of Eq. (3.1), $(\varepsilon_0 - \varepsilon_\infty)_\beta$ for PCFE becomes 1.9 (at 0°C). If we take into account the fact that the small diffusion rotations of CF-CCl and CF-CF pairs are not "completely" but "partially" independent, the value of N should be decreased and hence the value 1.9 also should be decreased. At any rate, this is of the same order of magnitude with the observed data. (See Table II.)

The similar situation is also realized in the case of PET. (See also Table II.) However, it seems to be somewhat doubtful whether the cause of the small magnitude for the $(\varepsilon_0 - \varepsilon_\infty)_\alpha$ in such a high crystallized polymer as PET can be attributed only to the small resultant dipole moment per monomer caused by the spiral structure of the chain or not.

§ 5. Conclusion

Our theory based on the mechanism proposed in this paper with respect to the dielectric β-dispersions for the linear vinylpolymers such as polyvinylchloride agrees with observations qualitatively as well as semi-quantitatively. Our calculation is, however, based on the semi-phenomenological ground so that we cannot proceed more in details of the agreements with the observations. Furthermore, the discussion in § 2 was done under the assumption that the relaxation times characteristic of α-dispersion are far longer than those of β-one. Of course, this assumption begins to loose its validity in the temperatures such that the α- and β-dispersions appear at nearly the same frequencies. To improve these situations, it is necessary to build up a general theory which is based on the molecular theory and which involves both the cases of the α- and β-dispersions.

In this paper, the discussions are limited to the case of the β-dispersion due to the small deformations of the chains. As was mentioned in § 1, there are also the β-dispersions due to the micro-Brownian motions of the long flexible dipoles, which are hardly treated by our present model. In this case, and as for the possibility of simultaneous discussions about the α- and β-dispersions, the site model seems to be useful in some points. The discussions with the aid of the site model will be published in the near future.[13]

The author would like to express his sincere thanks to Professor Tamoyasu Tanaka for his stimulating suggestion of the problem and for helpful discussions. It is also his pleasure to thank Professor Yôichi Ishida (Department of Applied Chemistry) for his kind informations about the unpublished data and for valuable discussions.

Appendix

We shall try to extend the calculation in § 2 to a more detailed molecular theoretical way and obtain some information about the shape of the absorption curve for the β-dispersion.

At the temperatures far below T_g, the segmental rotations and translations of the main chains are not active and only the small deformations of the chains would be active. The segmental motions of the main chains are interpreted as the cooperative micro-Brownian motions of the segments each of which includes 10~50 monomers in it. Then the "small deformation of the chain" could be interpreted as the small deformations within each segment in which at least both ends of the segment are fixed. In other words, only the small rotational or translational motions of a few monomers could be active at the temperatures far below T_g and these motions could bring about the small deformations of the other monomers at most within the segment and not others. Therefore, it is enough for the β-dispersion to consider only the motions of the monomers within each segment and the interactions among the nearest neighbor chains.

Then, if we consider the case of the linear chain polymers which have a single rigid dipole per monomer such as PVC, the diffusion equation for the configurational distribution function f of these dipoles can be written as

$$\frac{\partial f}{\partial t}=\frac{kT}{\zeta}\sum_{l,m,n}\left[\frac{\partial^2 f}{\partial\varphi^2_{l,m,n}}-\frac{1}{kT}\frac{\partial}{\partial\varphi_{l,m,n}}\left\{f\left(\frac{\partial V}{\partial\varphi_{l,m,n}}\right)\right\}\right], \tag{A.1}$$

where ζ is the rotational frictional constant concerning the micro-Brownian motion of a monomer, k the Boltzmann constant, T the temperature. In Eq. (A.1), we assume that the dipoles are arranged nearly simple cubical way and l denotes a number of the concerning dipole along the chain from the fixed end and m, n denote a number of this dipole in the two perpendicular directions to the chain, respectively. We again, for simplicity, confines the three dimentional motions of the dipoles to the two dimensional rotational ones in the plane perpendicular to the local direction of the chain and denote the rotational angle of the l, m, n,-th dipole by $\varphi_{l,m,n}$ measured from its equilibrium direction in the absence of the external electric field.

The total potential energy V is given by

$$V=V_0+V_e\,, \tag{A.2}$$

where

$$\begin{aligned}V_0=&\frac{1}{2}\sum_{l,m,n}A_{l,m,n}(\varphi_{l,m,n}-\varphi_{l-1,m,n})^2+\frac{1}{2}\sum_{l,m,n}B_{l,m,n}(\varphi_{l,m,n}-\varphi_{l,m-1,n})^2\\&+\frac{1}{2}\sum_{l,m,n}B'_{l,m,n}(\varphi_{l,m,n}-\varphi_{l,m,n-1})^2+\frac{1}{2}\sum_{l,m,n}C_{l,m,n}\varphi^2_{l,m,n}\,,\end{aligned} \tag{A.3}$$

and

$$V_e=-\sum_{l,m,n}\mu_{l,m,n}\sin\theta^0_{l,m,n}\cos(\varphi^0_{l,m,n}-\varphi_{l,m,n})E_r\exp(i\omega t). \tag{A.4}$$

In Eq. (A.3), A's and B's, B''s are the elastic restoring force constants among the neighbor dipoles along and perpendicular to the chain, respectively. The last term of Eq. (A.3) may be necessary because each dipole tends to stay in its own equilibrium position. The E_r, θ^0's, and φ^0's in Eq. (A.4) are defined in § 2.

Instead of solving Eq. (A.1), we may derive the following average value equation:

$$\begin{aligned}\zeta\langle\dot\varphi\rangle_{l,m,n}&+A_{l,m,n}(2\langle\varphi\rangle_{l,m,n}-\langle\varphi\rangle_{l-1,m,n}-\langle\varphi\rangle_{l+1,m,n})\\&+B_{l,m,n}(2\langle\varphi\rangle_{l,m,n}-\langle\varphi\rangle_{l,m-1,n}-\langle\varphi\rangle_{l,m+1,n})\\&+B'_{l,m,n}(2\langle\varphi\rangle_{l,m,n}-\langle\varphi\rangle_{l,m,n-1}-\langle\varphi\rangle_{l,m,n+1})\\&+C_{l,m,n}\langle\varphi\rangle_{l,m,n}=F_{l,m,n}\exp(i\omega t)\,,\end{aligned} \tag{A.5}$$

where

$$F_{l,m,n}\equiv\mu_{l,m,n}\sin\theta^\circ_{l,m,n}\sin(\varphi^\circ_{l,m,n}-\varphi_{l,m,n})E_r\,. \tag{A.5$'$}$$

While the boundary conditions along the chains should be the rigid boundaries, it would bring about any serious effect if we choose any boundary conditions in the two perpendicular directions. Hence we may choose also the rigid boundaries in these two directions.

First, we shall consider the simple case in which each of all the $A_{l,m,n}$'s equals to A, $B_{l,m,n}$'s to B, $B'_{l,m,n}$'s to B', $C_{l,m,n}$'s to C and $\mu^2_{l,m,n}$'s to $\langle\mu^2\rangle$. Then with the aid of

$$u_{j_\rho k_\rho}\equiv\sqrt{\frac{2}{N_\rho}}\sin\left(\frac{j_\rho k_\rho}{N_\rho}\pi\right),\quad \sum_{k_\rho\ 1}^{N}u_{j_\rho k_\rho}u_{j'_\rho k_\rho}=\delta_{j_\rho j'_\rho}\,, \tag{A.6}$$

$\rho=1, 2, 3$, we obtain

$$\varepsilon(i\omega)-\varepsilon_\infty=\frac{4\pi N\langle\mu^2\rangle}{3\gamma}\cdot\frac{\Xi(i\omega)}{\Xi(0)}, \qquad N=N_1N_2N_3, \tag{A.7}$$

where

$$\frac{\Xi(i\omega)}{\Xi(0)}=\sum_{k_1k_2k_3}\frac{1}{N_1N_2N_3}\frac{\gamma}{i\omega\zeta+4A\sin^2(k_1/N_1)\pi+4B\sin^2(k_2/N_2)\pi+4B'\sin^2(k_3/N_3)\pi+C}, \tag{A.8}$$

and

$$\gamma^{-1}\equiv\Xi(0)=\sum_{k_1k_2k_3}\frac{1}{N_1N_2N_3}\frac{1}{4A\sin^2(k_1/N_1)\pi+4B\sin^2(k_2/N_2)\pi+4B'\sin^2(k_3/N_3)\pi+C}. \tag{A.9}$$

Comparing Eq. (A. 7) with Eq. (2.2), it is clear that γ in Eq. (A.9) acts just the same role as the phenomenological rotating elastic force constant defined by Eq. (2.1). Since the intra-chain interactions are much larger than the inter-chain ones in general, we may assume $A, C\gg B, B'$. Then, Eq. (A.9) may be estimated approximately as

$$\gamma^{-1}\cong\sum_{k_1}\frac{1}{N_1}\frac{1}{4A\sin^2(k^1/N_1)\pi+C}=\frac{1}{\sqrt{C(4A+C)}}, \tag{A.10}$$

Since, from its definition, A is the energy required to twist the chain and hence is the same order of magnitude as the energy of the chemical bond and C is the energy required per monomer in order to turn the untwisted chain by an angle $\pi/2$, we may take the values of A and C as[14)]

$$2A=5 \text{ e.v.} \qquad \text{and } C=1/30 \text{ e.v.}\ .$$

Then γ becomes approximately as

$$\gamma\cong[C(4A+C)]^{1/2}\cong(1/3)^{1/2} \text{ e.v.} \cong 8\times10^{-13}\text{ erg},$$

which is the same order of magnitude as the value of the phenomenological rotating elastic constant calculated by Eq. (2.7). (See § 3.) Since this value of γ leads to the correct order for the magnitude of the β-dispersion, we may conclude that the β-dispersion can be attributed to the small deformations of the monomers and dipoles within the segment.

The function $\Xi(i\omega)$ in Eq. (A.8) is a familiar function appearing in the cases of the lattice vibrations or the impurity bands, and the much complicated calculations are necessary for estimating it. However, the above condition among the force constants, $A, C\gg B, B'$, make the estimation of $\Xi(i\omega)$ a little easier. We may expand the summand of the right hand side in Eq. (A.8) by means of the powers of B/A or B'/A. Then Eq. (A.8) becomes as

$$\Xi(i\omega)=\sum_{s=0}^{\infty}\Xi^{(s)}(i\omega), \tag{A.11}$$

where

$$\Xi^{(s)}(i\omega)\equiv\sum_{k_1k_2k_3}\frac{(-1)^s}{N_1N_2N_3}\frac{(4B\sin^2(k_2/N_2)\pi+4B'\sin^2(k_3/N_3)\pi)^s}{(i\omega\zeta+C+4A\sin^2(k_1/N_1)\pi)^{s+1}}. \tag{A.12}$$

If we approximately replace the summation by integral, the first few terms of $\Xi^{(s)}(i\omega)$'s are estimated as

$$\begin{aligned}
\Xi^{(0)}(i\omega)&=\frac{1}{\sqrt{(i\omega\zeta+C)(i\omega\zeta+C+4A)}},\\
\Xi^{(1)}(i\omega)&=\frac{-2(B+B')(i\omega\zeta-C+2A)}{\sqrt{(i\omega\zeta+C)^3(i\omega\zeta+C+4A)^3}},\\
\Xi^{(2)}(i\omega)&=\frac{(3B^2+8BB'+3B'^2)[4A^2+5(i\omega\zeta+C+2A)^2]}{\sqrt{(i\omega\zeta+C)^5(i\omega\zeta+C+4A)^5}},\\
&\cdots\cdots\cdots\cdots\cdots\cdots
\end{aligned} \tag{A.13}$$

Since the dielectric relaxation time spectrum $L_\varepsilon(\tau)$ is defined by

$$\frac{\varepsilon(i\omega)-\varepsilon_\infty}{\varepsilon_0-\varepsilon_\infty}=\int_{-\infty}^{\infty}\frac{L_\varepsilon(\tau)}{1+i\omega\tau}d\log\tau\,, \tag{A.14}$$

it can be estimated by an inverse transformation of the above Stieltjes-Hilbert transformation as

$$L_\varepsilon(\tau)=\frac{1}{\pi}\text{ Imaginary part of }\left[\frac{\varepsilon(-1/\tau)-\varepsilon_\infty}{\varepsilon_0-\varepsilon_\infty}\right]. \tag{A.15}$$

With the aid of the following relation derived from Eq. (A.7),

$$\frac{\varepsilon(i\omega)-\varepsilon_\infty}{\varepsilon_0-\varepsilon_\infty}=\frac{\Xi(i\omega)}{\Xi(0)}$$

and

$$\Xi(0)\equiv\gamma^{-1}\simeq\sqrt{C(4A+C)}\,,$$

we obtain

$$L_\varepsilon(\tau)=\sum_{S=0}^{\infty}L_\varepsilon^{(S)}(\tau) \tag{A.16}$$

and

$$\begin{aligned}
L_\varepsilon^{(0)}(\tau)&=\frac{1}{\pi}\frac{\tau}{\sqrt{(\tau-\tau_1)(\tau_2-\tau)}}\,,\\
L_\varepsilon^{(1)}(\tau)&=\frac{1}{\pi}\frac{2(2A+C)(B+B')}{C(4A+C)}\frac{\tau^2(\tau-\tau_3)}{\sqrt{(\tau-\tau_1)^3(\tau_2-\tau)^3}}\,,\\
L_\varepsilon^{(2)}(\tau)&=\frac{1}{\pi}\frac{(2A+C)^2(3B^2+8BB'+3B'^2)}{C^2(4A+C)^2}\times\frac{5\tau^3(\tau-\tau_3)^2+4\tau^5A^2/(C+2A)^2}{\sqrt{(\tau-\tau_1)^5(\tau_2-\tau)^5}}\,.
\end{aligned} \tag{A.17}$$

if $\tau_1<\tau<\tau_2$ and 0 if $\tau<\tau_1$ and $\tau_2<\tau$, where

$$\tau_1\equiv\zeta/(C+4A)\,,\qquad \tau_2\equiv\zeta/C\,,\qquad \tau_3\equiv\zeta/(C+2A)\,. \tag{A.18}$$

The leading term in Eq. (A.17) is, of course, essentially the "wedge type" spectrum characteristic of the linear Rouse chain, which has the gradient 1/2 in log-log scale. Since $\tau_3\ll\sqrt{\tau_1\tau_2}$, the first correction term has the gradient 3/2 near $\log\tau=(\log\tau_1+\log\tau_2)/2$, the second correction term 5/2.

Our calculation in this Appendix is essentially the same as the three dimensional Rouse model. The relaxation time spectrum for the Rouse model is very similar to the lattice vibrational spectrum.[3] In fact, the retardation time spectrum for the linear Rouse model, $L(\tau)=\pi^{-1}\tau_\alpha^{-1/2}(\tau-\tau_\alpha)^{-1/2}$, is just the same as the lattice vibrational spectrum for the perfect linear lattice, $G_1(\omega^2)=\pi^{-1}\omega^{-1}(\omega_L^2-\omega^2)^{-1/2}$, in which ω^2 is replaced by $-1/\tau$. Therefore, our relaxation time spectrum is very similar to the three dimentional lattice vibrational spectrum, $G_3(\omega^2)$, in the case of $A\gg B, B'$ in which ω^2 is replaced by $-1/\tau$,

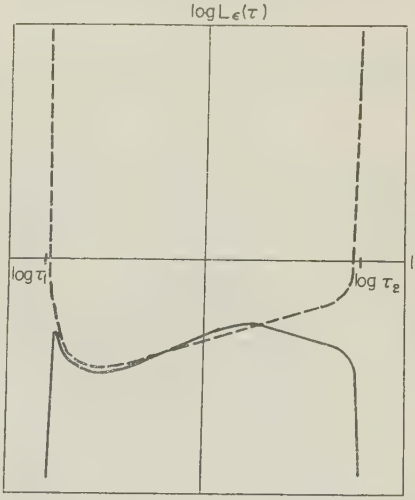

Fig. 3. The schematic graph for the relaxation time spectrum of the dielectric β-dispersion derived in Appendix. The dotted line is the leading term in Eq. (A.16).

which is schematically plotted in Fig. 3.

Although it can be easily shown that the gradient of the broader curve in Fig. 3 is possible to be smaller if we choose the ratios A to B and B' appropriately, the Rouse model seems to have a fault that it has unsymmetrical shape in log-log scale because $G(\omega^2)$ has symmetrical shape in ω^2-scale with respect to $\omega_L{}^2/2$ in general. The effect of the distributions of the force constants can be investigated by iteration method. However, these distributions also do not cause to the above characteristic features so seriously change so long as the width of the distribution is small. Then establishing the convincing theory of the relaxation time spectrum for the dielectric β-dispersion which has two characteristic features mentioned in § 3 will be the future subject of investigation.

References

1) K. Schmieder and K. Wolf: Kolloid-Z. **134** (1953) 149;
S. Iwayanagi and T. Hideshima: J. Phys. Soc. Japan **8** (1953) 368; etc.
2) J. G. Kirkwood and R. M. Fuoss: J. Chem. Phys. **9** (1941) 329;
R. E. Rouse, Jr.: J. Chem. Phys. **21** (1953) 1272; etc.
3) K. Yamafuji and Y. Ishida: to be published in Kolloid-Z.
4) W. Reddish: Trans. Faraday Soc. **46** (1950) 459.
5) Y. Ishida: Kolloid-Z. **171** (1960) 71.
6) J. G. Powles: J. Polymer Sci. **22** (1956) 79;
A. Odajima, J. Sohma and M. Koike: J. Phys. Soc. Japan **12** (1957) 272;
W. P. Slichter and E. R. Mandell: J. Appl. Phys. **30** (1959) 1473; etc.
7) T. Tanaka and Y. Ishida: Suppl. Progr. Theor. Phys. No. **10** (1959) 121; J. Phys. Soc. Japan **15** (1960) 261.
8) M. Okano: *Abstract Book of the Annual Meeting of Phys. Soc. of Japan* (Oct. 1959, Tokyo), No. 6, p. 35.
9) Debye and Ramm: Ann. Physik (V) **28** (1937) 28.
10) Y. Ishida: Kolloid-Z. **168** (1960) 29.
11) H. S. Kaufman: J. Chem. American Soc. **75** (1953) 1477.
12) S. Saito and T. Nakajima: J. Polymer Sci. **31** (1958) 423.
13) Y. Ishida and K. Yamafuji: to be published.
14) H. Frölich: Proc. Phys. Soc. **54** (1942) 422.

JOURNAL OF THE PHYSICAL SOCIETY OF JAPAN, Vol. 15, No. 12, DECEMBER, 1960

Hyperfine Structure of the Spectra of Pr I and Pr II

By Kiyoshi MURAKAWA

Aeronautical Research Institute, University of Tokyo,
Komaba-machi, Meguro-ku, Tokyo

(Received August 17, 1960)

In the spectrum of Pr I three lines were classified and the hfs was measured, from which the interval factor of the level $4f^36s^2\,{}^4I_{11/2}$ was determined. From this and the known interval factor of $4f^36s^2\,{}^4I_{9/2}$ it was concluded that the value of a_{4f} determined from the hfs of Pr II is also appropriate for Pr I. The configuration $4f^3({}^4I)6s$ of Pr II was treated as of intermediate coupling, and the hfs lead to a reasonable value of a_{4f} and $a(6s)$. From the value of $a(6s)$ the magnetic moment of Pr^{141} was calculated to be 4.0 ± 0.2 n.m.

§ 1. Introduction

Some years ago Suwa and the author[1] measured the hyperfine structure (hfs) of the spectrum of Pr II; from the hfs of the term $4f^3({}^4I)6s$ it was concluded that $a(6s)=0.426\,\mathrm{cm}^{-1}$ and $a_{4f}=0.0227\,\mathrm{cm}^{-1}$, in which the relativity correction of the $4f$ electron was neglected and it was put

$$a'=\frac{16}{21}a_f\,,\quad a''=\frac{48}{35}a_f\,,\ \text{and}\ a'''=-\frac{1}{14}a_f\,.$$

From the value of $a(6s)$ the magnetic moment of Pr^{141} was deduced to be $\mu=+4.0\pm0.1$ n.m.

At about the same time Lew[2] measured the hfs of the level $4f^3 6s^2\ {}^4I_{9/2}$ of Pr I, and obtained $a_{4f}=706.2$ Mc/sec$=0.02356$ cm^{-1}.

It is natural to expect that the value of a_{4f} deduced from Pr I is equal to or slightly smaller than that deduced from Pr II, but Lew's value is somewhat larger than our expectation. It is the purpose of the present paper to clarify this point.

For that purpose it would be desirable to measure the hfs of all the levels belonging to $4f^3 6s^2\ {}^4I$ (Pr I); but no classification of Pr I is available at present, so in the present work only the hfs of ${}^4I_{11/2}$ and ${}^4I_{9/2}$ could be studied.

§ 2. Experimental Arrangement

As a light source a liquid air cooled hollow cathode discharge tube was used. The hfs was resolved by means of a silvered or dielectric multilayer coated Fabry-Pérot etalon. In order to test which lines were self-reversed, a hot hollow cathode carrying strong discharge current was also used.

§ 3. Hyperfine Structure of the Spectrum of Pr I

It was found that the first line which shows self-reversal is λ4951.4; this is the strongest line in the visible region. From the hfs it was concluded that this line represents the transition $4f^3 6s^2\ {}^4I_{9/2}-20_{9/2}$, the hfs being shown schematically in Fig. 1. The hfs of the final level is known from the work of Lew[2]. The hfs intervals measured by Lew are indicated by stars; they were originally expressed in units of Mc/sec, but now they are converted in units of cm^{-1}.

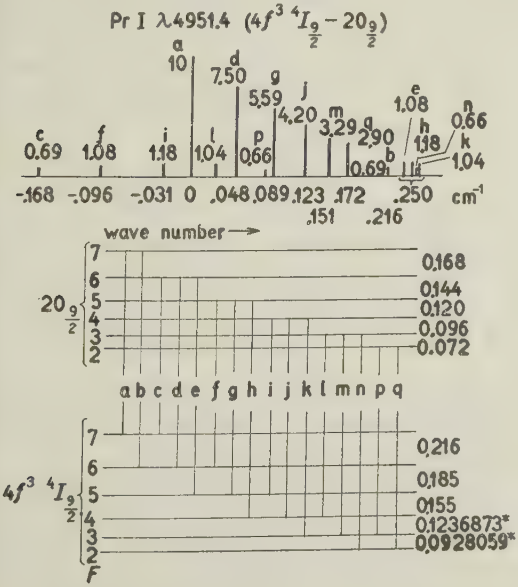

Fig. 1. Hfs of the line Pr I λ4951.4.

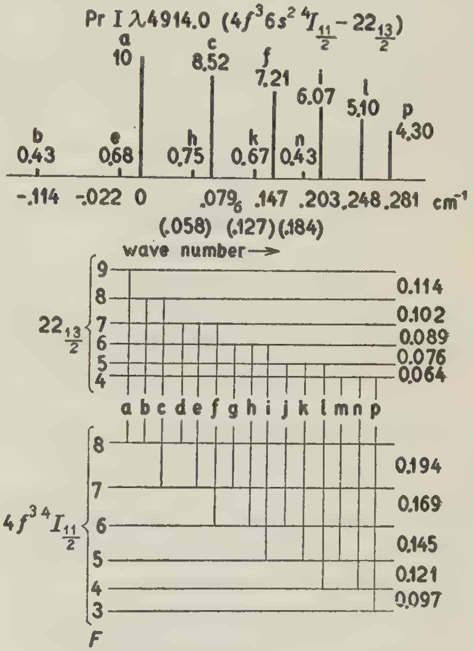

Fig. 2. Hfs of the line Pr I λ4914.0.

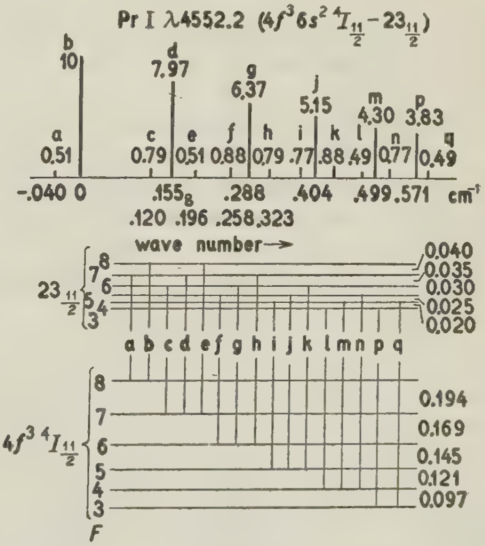

Fig. 3. Hfs of the line Pr I λ4552.2.

In addition to λ4951.4, two lines λλ4914.0 and 4552.2 could be classified, the hfs being shown in Figs. 2 and 3. Numbers in parentheses were calculated. From the hfs, we get the interval factor of the level $4f^36s^2\ {}^4I_{11/2}$: $A({}^4I_{11/2})=0.02425\ \mathrm{cm}^{-1}$. For the level $4f^36s^2\ {}^4I_{9/2}$, Lew obtained $A({}^5I_{9/2})=926.02\ \mathrm{Mc/sec}=0.0308891\ \mathrm{cm}^{-1}$.

Since the spin-orbit coupling parameter of the $4f$ electron ($\zeta=682.6$) of Pr I is small, we can assume that the configuration $4f^3$ is of LS-coupling.

If the $4f^36s^2$-configuration of Pr I were pure, we could calculate a_{4f} according to the usual formula

$$A(f^3\ {}^4I_{15/2})=\frac{176}{225}a_f\ ,$$

$$A(f^3\ {}^4I_{13/2})=\frac{2612}{2925}a_f\ ,$$

$$A(f^3\ {}^4I_{11/2})=\frac{14920}{14157}a_f\ ,$$

$$A(f^3\ {}^4I_{9/2})=\frac{476}{363}a_f\ .$$

Under this assumption, we get $a_{4f}=0.0230\ \mathrm{cm}^{-1}$ from ${}^4I_{11/2}$ and $a_{4f}=0.02356\ \mathrm{cm}^{-1}$ from ${}^4I_{9/2}$.

This discrepancy can be interpreted by assuming that the term $4f^36s^2\ {}^4I$ is mixed with $4f^36s7s\ {}^4I$, etc. We can put

$$\begin{aligned}4f^36s^2\ {}^4I'_{9/2}=K_1 4f^36s^2\ {}^4I_{9/2}&+K_2 4\overrightarrow{f}^3\overleftarrow{6}s\overrightarrow{7}s\ {}^4I_{9/2}\\ &+K_3 4\overrightarrow{f}^3\overrightarrow{6}s\overleftarrow{7}s\ {}^4I_{9/2}+\cdots\ ,\\ K_1\approx 1\ .&\end{aligned}$$

As a first approximation we may cut off the series at K_3 and assume

$$A({}^4I'_{9/2})=K_1^2\frac{476}{363}a_{4f}+\frac{3}{11}X(a(6s),\ a(7s),\ K_2,\ K_3)\ .$$

Putting $A=0.03089\ \mathrm{cm}^{-1}$, $a_{4f}=0.0227\ \mathrm{cm}^{-1}$ (this value was obtained from Pr II), $K_1=1$ in this expression, we get $X=0.0041$.

As a rough approximation we can assume

$$A({}^4I'_{11/2})=K_1^2\frac{14920}{14157}a_{4f}+\frac{5}{143}Y\ .$$

Putting $A=0.02425\ \mathrm{cm}^{-1}$, $a_{4f}=0.0227\ \mathrm{cm}^{-1}$, $K_1=1$ in this expression, we get $Y=0.009$.

X and Y have the same sign and are of the same order of magnitude. We may therefore consider $a_{4f}=0.0227\ \mathrm{cm}^{-1}$ to be appropriate for the hfs of Pr I.

§ 4. Hyperfine Structure of Pr II

In the previous work[1] hfs of some levels of the configuration $4f^36s$ was measured. In the present work no extension was made, except that the hfs of the line λ4189.5 ($4f^36s\ {}^5I_7-z^5I_7$)[3] was measured. The interval factor of the lower level was found to be $0.0441\ \mathrm{cm}^{-1}$. This is not so accurate, however, owing to the existence of close lying line.

As before, let us assume that the group of electrons $4f^3$ is of LS-coupling, to which the $6s$ electron is combined via intermediate coupling. Then the energy matrix is as given in Table I.

Table I. Energy matrix of $f^3s\ {}^{5,3}I$ in LS-coupling ($\zeta\equiv\zeta_f$).

$J=8$,	${}^5I$	$-3G+3\zeta$	
$J=7$,	${}^5I$	$-3G+\zeta$	$-\zeta$
	${}^3I$	$-\zeta$	$G+\frac{5}{2}\zeta$
$J=6$,	${}^5I$	$-3G-\frac{3}{4}\zeta$	$-\frac{1}{4}\sqrt{\frac{55}{3}}\zeta$
	${}^3I$	$-\frac{1}{4}\sqrt{\frac{55}{3}}\zeta$	$G-\frac{5}{12}\zeta$
$J=5$,	${}^5I$	$-3G-\frac{9}{4}\zeta$	$-\frac{1}{4}\sqrt{\frac{35}{3}}\zeta$
	${}^3I$	$-\frac{1}{4}\sqrt{\frac{35}{3}}\zeta$	$G-\frac{35}{12}\zeta$
$J=4$,	${}^5I$	$-3G-\frac{7}{2}\zeta$	

Fitting the observed levels to the energy matrix, the parameter values $\zeta=682.6$ and $G=243$ were obtained. Then the compositions of the levels were determined by the usual method; the result of the calculations follows.

$$\psi_J=K_1\ {}^5I_J+K_2\ {}^3I_J\ .$$

$$\left\{\begin{array}{lll}{}^5I_7': & K_1=0.955\ , & K_2=0.295\ ,\\ {}^3I_7': & K_1=-0.295\ , & K_2=0.955\ .\end{array}\right.$$

$$\left\{\begin{array}{lll}{}^5I_6': & K_1=0.903_5\ , & K_2=0.428_5\ ,\\ {}^3I_6': & K_1=-0.428_5\ , & K_2=0.903_5\ .\end{array}\right.$$

$$\left\{\begin{array}{lll}{}^5I_5': & K_1=0.839\ , & K_2=0.544_5\ ,\\ {}^3I_5': & K_1=-0.544_5, & K_2=0.839\ .\end{array}\right.$$

Let us first assume that there is no configuration mixing. Then the hfs interval factor for $J=7, 6, 5$ is given by

$$A_J=K_1^2A({}^5I_J)+2K_1K_2A({}^{3,5}I_J)+K_2^2A({}^3I_J)\ .$$

The expression for $A(I_J)$ follows.

$$A({}^5I_8)=\frac{11}{15}a_f+\frac{1}{16}a(s)\ ,$$

$$A({}^5I_7)=\frac{86}{105}a_f+\frac{5}{112}a(s)\ ,$$

$$A({}^{3,5}I_7)=\frac{1}{140}a_f+\frac{3}{56}a(s)\ ,$$

$$A({}^3I_7)=\frac{53}{63}a_f-\frac{1}{28}a(s)\ ,$$

$$A({}^5I_6)=\frac{4343}{4620}a_f+\frac{1}{56}a(s)\ ,$$

$$A({}^{3,5}I_6)=\frac{13}{126}\sqrt{\frac{1}{165}}a_f+\frac{\sqrt{165}}{168}a(s)\ ,$$

$$A({}^3I_6)=\frac{743}{756}a_f-\frac{1}{168}a(s)\ ,$$

$$A({}^5I_5)=\frac{743}{660}a_f-\frac{1}{40}a(s)\ ,$$

$$A({}^{3,5}I^5)=\frac{\sqrt{105}}{1485}a_f+\frac{\sqrt{105}}{120}a(s)\ ,$$

$$A({}^3I_5)=\frac{1421}{1188}a_f+\frac{1}{24}a(s)\ ,$$

$$A({}^5I_4)=\frac{476}{330}a_f-\frac{1}{10}a(s)\ .$$

Table II. Interval factor of $4f^36s\ {}^5I$ and ${}^3I$.

	obs.	calc.
$A({}^5I_8)$	0.0437	0.0433
$A({}^5I_7)$	~0.0441	0.0476
$A({}^3I_7)$	—	−0.0061
$A({}^5I_6)$	0.0536	0.0526
$A({}^3I_6)$	—	−0.0039
$A({}^5I_5)$	0.0622	0.0572
$A({}^3I_5)$	−0.0032	0.0026
$A({}^5I_4)$	−0.0100	(−0.0100)

Fitting the observed hfs to these formulas, we get, as before, the values $a_{4f}=0.0227\ \mathrm{cm}^{-1}$ and $a(6s)=0.426\ \mathrm{cm}^{-1}$, (Table II).

In reality the term $4f^36s^{5,3}I$ is mixed with $5s4f^36s^2\ {}^{5,3}I$, $5s4f^36s7s^{5,3}I$, etc.

If we cut off the series at $5s4f^36s^2\ {}^{5,3}I$, it can be seen that in the above-mentioned calculation for a_{4f}, the contribution from $5s$ and $6s$ almost vanishes, and the value $a_{4f}=0.0227\ \mathrm{cm}^{-1}$ seems to be accurate to about 1.5%. The expression for $a(6s)$, however, is now somewhat invalid and is slightly dependent on $a(5s)$. We may assume therefore that the value $a(6s)=0.426\ \mathrm{cm}^{-1}$ is in reality to be slightly modified, and the magnetic moment $\mu(\mathrm{Pr}^{141})=+4.0\pm0.1$ n.m. (that was given previously) suffers a slight change and is now

$$\mu(\mathrm{Pr}^{141})=+4.0\pm0.2\ \text{n.m.}\ .$$

This is in good agreement with $3.9_2\pm0.2$ n.m. obtained by Baker and Bleaney[4] by means of paramagnetic resonance experiment.

References

1) K. Murakawa and S. Suwa: J. Phys. Soc. Japan **9** (1954) 93.

2) H. Lew: Phys. Rev. **91** (1953) 619.

3) The classification of Pr II was taken from N. Rosen, G. R. Harrison and J. R. McNally: Phys. Rev. **60** (1941) 722.

4) J. M. Baker and B. Bleaney: Proc. Phys. Soc. London A **68** (1955) 936.

JOURNAL OF THE PHYSICAL SOCIETY OF JAPAN, Vol. 15, No. 12, DECEMBER, 1960

On the Viscosity of Irradiated Polymers. III. Effect of Branching

By Kanji KATSUURA*

Department of Applied Physics, Faculty of Engineering,
University of Tokyo, Tokyo, Japan

(Received August 24, 1960)

The intrinsic viscosity of an irradiated polymetric substance is calculated with inclusion of the effect of branching. The contribution of a branched polymer to the intrinsic viscosity is evaluated according to Debye-Bueche's theory with some modifications. The distribution of molecular size and crosslink unit is obtained through an extention of the Saito's theory. Our results agree with experiment fairly well. The essential reason for the large discrepancy between Saito's calculation and experiment is shown to be his neglect of branching.

§ 1. Introduction

In a polymeric substance under irradiation, crosslinking between a pair of polymers and scission of a polymer take place simultaneously. This leads to a polymer with long branches and changed molecular size and results in changes in the distribution of molecular size and crosslink unit in the polymeric system. Among many properties which depend on the distribution, we are interested in the intrinsic viscosity.

In general, a theoretical treatment of properties of a branched polymeric substance confronts with two problems. Firstly, we must know the property of a branched molecule, and secondary, the distribution of molecular size and crosslink unit.

In connection with the first problem, Kirkwook-Riseman1) and Debye-Bueche2) gave different approaches to the contribution to the intrinsic viscosity of a polymer molecule. Here we will follow the Debye-Bueche's approach because of its mathematical simplicity.

Concerning the second problem, a theory of the molecular size and crosslink unit distribution was presented by Stockmayer3), but unfortunately his method is inconvenient for the calculation of the intrinsic viscosity. From a quite different point of view, Saito4)5) developed a more general and convenient theory of molecular size distribution in terms of an integro-differential equation. He could calculate the intrinsic viscosity according to simple Staudinger's rule neglecting the effect of branching.6) We will obtain the molecular size and crosslink unit distribution of an irradiated polymeric system according to Saito's method and evaluate the intrinsic viscosity taking the effect of branching into account. The closest parallel to our development will be found in the work of Kilb,7) who evaluated the intrinsic viscosity using Kirkwood-Riseman's theory and Stockmayer's distribution function.

In Section 2, the distribution function will be obtained. The contribution to the intrinsic viscosity of a branched polymer molecule will be evaluated in Section 3. In Section 4, the intrinsic viscosity of an irradiated polymeric substance will be obtained when the initial molecular distribution is Poisson-like. For more general initial molecular size distributions, the intrinsic viscosity will be derived for small radiation doses in Section 5. In Section 6, our theoretical results will be compared with experimental data.

§ 2. The Molecular Size and Crosslink Unit Distribution

Through our calculation we make the following assumptions: (1) the number of crosslinks or scissions is proportional to radiation dose: (2) crosslinks and scissions occur at random: (3) the number of crosslinks is small compared with the total number of monomer units: (4) the cyclization, a crosslink within a molecule, can be neglected.

A polymer molecule will be specified by the degree of polymerization p and the number of crosslink units n_c. For convenience, we will use one half of the number of chain ends $q=n_c+1$ instead of crosslink units. We define the molecular size and chain end distribution $n(p,q,R)\,dpdq$ of a polymeric system as the number of polymers whose degree of polymerization lies between p and $p+dp$, one half of the number of chain ends between q and $q+dq$ when the system has been irradiated up to radiation dose R.

---

* On leave from the Kurashiki Rayon Co., Ltd., Osaka, Japan.

To calculate $n(p,q,R)$, we will follow closely Saito's formulation[4)], though we make some necessary generalization.

a) The case when only crosslinks occur. When the radiation dose increases from R to $R+dR$, $n(p,q,R)$ loses $pn(p,q,R)2cdR$ and gains

$$\frac{1}{2N}\int_0^q ds\int_0^p dl(p-l)n(l,S,R)n(p-l,q-s,R)2cdR$$

according to Saito. Here N is the total number of monomers, and $2c$ is the probability that a monomer crosslinks with another monomer by irradiation of unit dose. $2c$ corresponds to Charlesby's α[8)]. Putting

$$cR=t,$$

$$n(p,q,R)/N=n(p,q,R) \text{ or } m(p,q,t),$$

we get

$$\frac{\partial m(p,q,t)}{\partial t}=-2pm(p,q,t)$$
$$+\int_0^q ds\int_0^p dll(p-l)m(l,s,t)m(p-l,q-s,t). \quad (1)$$

Hereafter we will call the normalized molecular size and chain end distribution function $m(p,q,R)$ simply the distribution function. The Laplace transform of $m(p,q,t)$, i. e.

$$f(z,x,t)=\int_0^\infty dq\int_0^\infty dpm(p,q,t)e^{-zp}e^{-xq} \quad (2)$$

satisfies the following equation:

$$\frac{\partial f}{\partial t}=2\frac{\partial f}{\partial z}+\left(\frac{\partial f}{\partial z}\right)^2. \quad (3)$$

The equation can be solved to give

$$\left.\begin{aligned}&f(z,x,t)=G(z_0,x)-\{G'(z_0,x)\}^2t,\\&z=z_0-2\{1-G'(z_0,x)\}t,\end{aligned}\right\} \quad (4)$$

where

$$G(z_0,x)=f(z_0,x,0), \text{ and } G'(z_0,x)=\partial G(z_0,x)/z_0$$

It should be noted that Eq. (3) has just the same form as Eq. (7) in Saito's paper I,[4)] so that the solution is also given by (4) which is similar to Eq. (8) in that paper. But, in our case f depends on x parametrically and this parametric dependence on x is essential in our following treatment.

b) The case when only scissions occur. We first note that, when only scissions occur, the distribution function for a system of linear molecules has the form

$$m(p,q,R)=\delta(q-1)m^\dagger(p,R),$$

because a scission of a linear molecule never gives a branched molecule. Saito has obtained the molecular size distribution $m^\dagger(p,R)$:

$$m^\dagger(p,R)=e^{-prR}\Big\{m^\dagger(p,0)+2rR\int_p^\infty m^\dagger(p,0)dp$$
$$+(rR)^2\int_p^\infty dp\int_p^\infty m^\dagger(p,0)dp\Big\}, \quad (5)$$

where r stands for the probability of scission per unit monomer per unit radiation dose, which Charlesby called β[8)].

c) The case when crosslinks and scissions simultaneously. Suppose we break virtually all the crosslinks in an irradiated polymeric system, then the distribution function will be given as in the case **b**, if the polymeric system had initially no crosslink units. Then we restore all the crosslinks. By this procedure we obtain the real distribution function corresponding to the irradiated system in terms of the Laplace transform, namely Eq. (4) solved under the initial condition $\delta(q-1)$ $m^\dagger(p,R)$ given by (5).

§ 3. The Contribution of a Branched Molecule to the Intrinsic Viscosity.

Following Debye-Bueche's theory, the contribution $\eta(p,q)$ to the intrinsic viscosity of a branched molecule can be expressed as

$$\eta(p,q)\propto p^\alpha g(q,p)^{2-\alpha}, \quad (6)$$

$$g(q)=\frac{R_e(p,q)^2}{R_e(p,o)^2}, \quad (7)$$

on the assumption that the proportionality of $R_e^2(p,q)$ to the degree of polymerization p. Here $R_e(p,q)$ represents the effective radius of the polymer molecule with the degree of polymerization p and the number of end points q. The exponent α of p in (6) corresponds to that of the Standinger's empirical law. We will regard it as constant for the present, though it should depend on p and q from a more rigorous viewpoint.

Consequently the effect of branching on the intrinsic viscosity only appears through the effective radius. So we should like to know $R_e(p,q)$ as a function of p and q, but it is beyond the scope of this theory to get the exact functional form of $R_e(p, q)$. Now we are forced to adopt the conventional assumption that R_e^2 is proportional to the mean square radius R^2 averaged over all the possible configurations.

The mean square radii of branched molecules have been calculated by Stockmayer[9] and more generally by Kataoka[10], on the assumption that the chains constituting polymer molecules obey random flight statistics. Kataoka obtained the following equation for R^2, when a polymer molecule contains merely branch units of equal functionality and no rings:

$$R^2=\frac{a^2p}{n_b(n_b+1)(n_b+2)}(n_b^2+\sum_{(k,l)}\nu_{kl}), \tag{8}$$

where a indicates the effective bond length, and n_b represents the number of branches in the molecule. A branch means a chain lying between a branch unit and an adjacent branch unit or chain end. ν_{kl} is the number of branches constituting a chain which connects two branches named k and l. Summation should be carried out over all the pairs of branches. Eq. (8) was derived by taking an average over all the molecules having same values of p, n_b and $\sum_{(k,l)}\nu_{kl}$. By (8) Kataoka could obtain g for crosslinked molecules of the normal form, one of which is shown in Fig. 1a.

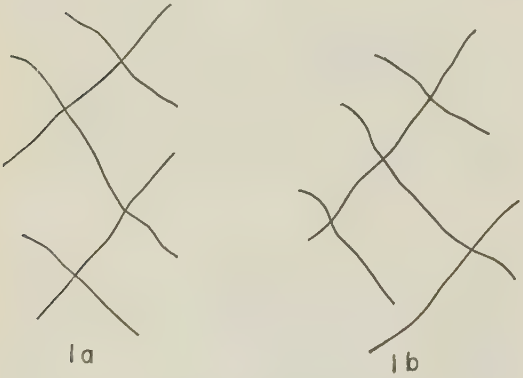

Fig. 1. Forms of crosslinked molecules.

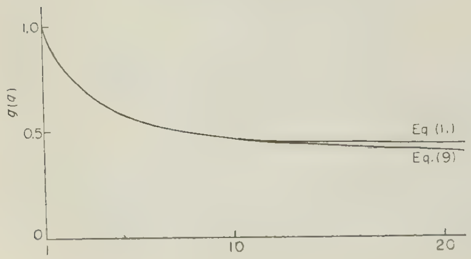

Fig. 2. Values of $g(q)$ plotted against q.

$$g(q)=\frac{3q^3+9q^2-18q+8}{q(3q-1)(3q-2)}. \tag{9}$$

We draw the curve of (9) in Fig. 2.

When the number of crosslink units is larger than four, polymer molecules of different forms, as shown in Fig. 1b, come into existence. These molecules have smaller R's than the molecule of the normal form with same p and n_b. We use, however, Eq. (9) because it may differ from the exact value only by ten percents at the largest. (See Appendix)

§ 4. The Intrinsic Viscosity. I. Poisson Distribution.

In this section we will evaluate effects of radiation on the intrinsic viscosity of a polymeric substance initially composed of linear molecules and having a Poisson-like molecular size distribution. With the aid of the result in the preceding Section, the intrinsic viscosity $[\eta]$ of the irradiated polymeric system can be expressed as

$$[\eta]=K\int_0^\infty dq\int_0^\infty dp p^\alpha g(q)^{2-\alpha} p m(p, q, R). \tag{10}$$

For mathematical simplicity, we approximate $g(q)^{2-\alpha}$ by a finite Dirichlet series.

$$g(q)^{2-\alpha}=Ae^{-aq}+Be^{-bq}+C. \tag{11}$$

The values of these coefficients are given in Table I, and the curve (11) is traced in Fig. 2 when $\alpha=1$.

Table I.

α	Ae^{-a}	Be^{-b}	C	e^{-a}	e^{-b}
1.0	0.466	0.102	0.431	0.737	0.243
0.9	0.484	0.119	0.397	0.735	0.250
0.8	0.498	0.137	0.365	0.733	0.256
0.7	0.509	0.155	0.336	0.731	0.261
0.6	0.518	0.173	0.309	0.278	0.264
0.5	0.524	0.192	0.284	0.726	0.266

First we suppose only crosslinks occur. Then

$$[\eta]=K\{AJ(a)+BJ(b)+CJ(0)\}, \tag{12}$$

where

$$J(a)=\int_0^\infty dq\int_0^\infty dp p^{\alpha+1}e^{-aq}m(p, q, t). \tag{13}$$

Making use of the equation obtained by Saito[6)],

$$\int_0^\infty p^{\alpha+1} m(p,q,t)dp=$$

$$\frac{e^{\alpha\pi i}\Gamma(\alpha+2)}{2\pi i}\int_c \frac{dz}{z^{\alpha+2}}\int_0^\infty m(p,q,t)e^{-zp}dp, \qquad (14)$$

we obtain

$$J(a)=\frac{e^{\alpha\pi i}\Gamma(\alpha+2)}{2\pi i}\int_c \frac{dz}{z^{\alpha+2}} f(Z,a,t). \qquad (15)$$

The integration should be performed along the contour C in Fig. 3. Substituting (4) into (15), we get

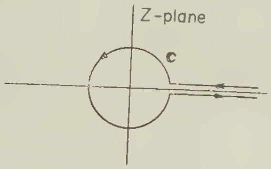

Fig. 3. Contour of integration.

$$J(a)=\frac{e^{\alpha\pi i}\Gamma(\alpha+2)}{2\pi i}\int_c \frac{dz}{z^{\alpha+2}}\{G(z_0,a)-G'(z_0,a)t\} \qquad (16)$$

$$=\frac{1}{\Gamma(1-\alpha)}\int_{\rho=0}^{\rho=\infty}\frac{G''(\rho_0,a)}{\rho^\alpha}d\rho_0, \qquad (17)$$

where

$$\rho=\rho_0-2\{1+G'(\rho_0,a)\}t. \qquad (18)$$

In the case $a=0$, Saito[6)] derived (17). This procedure could be easily extended to our case, $a \neq 0$.

The initial distribution function is now

$$m(p,q,0)=u^{-2}e^{-p/u}\delta(q-1), \qquad (19)$$

where u is the number average degree of polymerization.

$$G(\rho_0,a)=f(\rho_0,a,0)$$
$$=\int_0^\infty dp\int_0^\infty dq\, m(p,q,0)e^{-\rho_0 p}e^{-aq}$$
$$=u^{-1}(1+u\rho_0)^{-1}e^{-a}. \qquad (20)$$

Substitute (20) into (17) and put $(1+u\rho_0)^{-1}=y$. Then we get

$$J(a)=\frac{2u^\alpha e^{-a}}{\Gamma(1-\alpha)}\int_0^{y_0}\frac{y^{1+\alpha}}{\{1-y-2ut(1-e^{-\alpha}y^2)\}^\alpha}dy, \quad (21)$$

where y_0 is the root of the equation

$$1-y-2uty(1-e^{-a}y^2)=0 \qquad (22)$$

that tends to unity when a tends to zero.

When scissions occur in addition to cross-linking, we should use the following distribution function as the initial distribution.

$$m(p,q,R)=(u/1+ruR)^{-2}$$
$$\exp[-p(u/1+ruR)^{-1}]\delta(q-1). \qquad (23)$$

This leads to $J(a)$ having $(u/1+ruR)$ instead of u. Numerical calculations were carried out using a high speed electronic computor, TAC. For various values of α and r/c, we obtained the ratio $[\eta]/[\eta]_0$, where $[\eta]_0$ indicates the intrinsic viscosity before irradiation. These results are given in Table II. In Fig. 4, we draw $[\eta]/[\eta]_0$ against R/R_g, where R_g is the dose at incipient gelation, which occurs when $4c>r$.

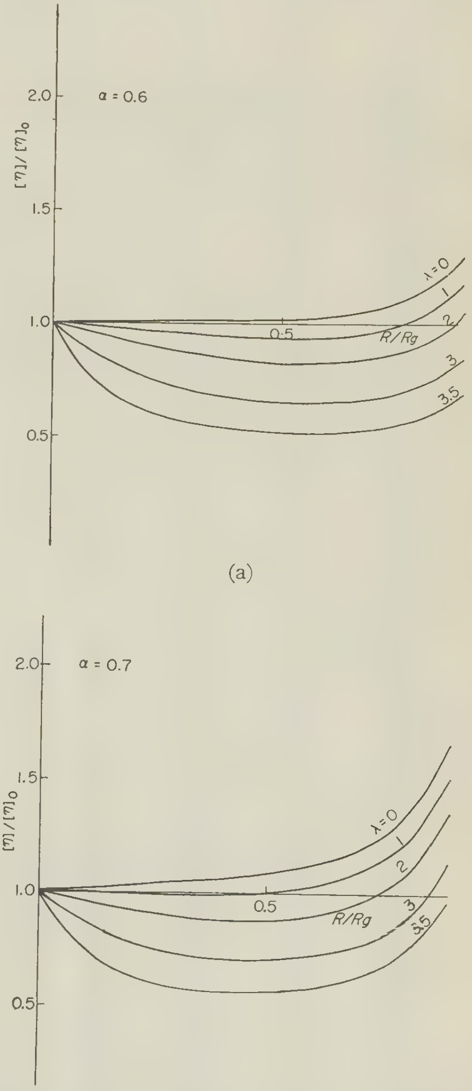

(a)

(b)

Fig. 4. The ration $[\eta]/[\eta]_0$ against R/R_g.

§ 5. The Intrinsic Viscosity. II. Small Radiation Doses.

In this Section, we will evaluate the effect of the initial molecular size distribution on the viscosity-dose curve at small radiation doses. To clarify the relationship between the initial molecular size distribution and the radiation-induced change of the intrinsic viscosity, Inokuti[11] has discussed the coefficient $A_1(\lambda, \alpha)$ in the following expansion:

$$[\eta]/[\eta]_0=1+A_1(\lambda, \alpha)R+A_2(\lambda, \alpha)R^2+\cdots. \quad (24)$$

Table II. The Values of $[\eta]/[\eta]_0$ when the initial molecular size distribution is Poisson-like.

	cuR	$\alpha=0.6$	$\alpha=0.7$	$\alpha=0.8$	$\alpha=0.9$
$\lambda=0$	0.0250	1.005	1.014	1.026	1.041
	0.0500	1.006	1.029	1.053	1.084
	0.0750	1.008	1.043	1.084	1.132
	0.1000	1.012	1.061	1.123	1.191
	0.1250	1.017	1.087	1.173	1.283
	0.1500	1.032	1.126	1.248	1.408
	0.1750	1.063	1.195	1.372	1.616
	0.2000	1.132	1.329	1.614	2.027
	0.2250	1.306	1.673	2.257	3.205
	0.2300	1.379	1.818	2.543	3.757
	0.2350	1.482	2.034	2.982	4.645
	0.2400	1.654	2.402	3.768	6.325
	0.2450	2.039	3.275	5.765	10.943
$\lambda=1.0$	0.0256	0.989	0.997	1.006	1.018
	0.0526	0.975	0.992	1.011	1.035
	0.0811	0.962	0.987	1.019	1.055
	0.1111	0.950	0.986	1.031	1.082
	0.1429	0.939	0.990	1.054	1.138
	0.1765	0.936	1.005	1.096	1.216
	0.2121	0.947	1.044	1.177	1.359
	0.2500	0.990	1.137	1.350	1.658
	0.2903	1.121	1.400	1.841	2.548
	0.2987	1.179	1.514	2.063	2.969
	0.3072	1.262	1.686	2.407	3.650
	0.3158	1.403	1.982	3.026	4.941
	0.3245	1.723	2.690	4.604	8.497
$\lambda=2.0$	0.0263	0.974	0.979	0.985	0.994
	0.0556	0.944	0.956	0.968	0.986
	0.0882	0.914	0.930	0.952	0.978
	0.1250	0.885	0.908	0.939	0.974
	0.1667	0.856	0.888	0.932	0.990
	0.2143	0.833	0.877	0.938	1.021
	0.2692	0.821	0.884	0.972	1.096
	0.3333	0.833	0.929	1.072	1.280
	0.4091	0.913	1.100	1.399	1.871
	0.4259	0.953	1.181	1.553	2.158
	0.4434	1.013	1.304	1.794	2.623
	0.4615	1.117	1.520	2.233	3.511
	0.4804	1.362	2.044	3.364	5.970
	cuR	$\alpha\alpha=0.6$	$\alpha=0.7$	$\alpha=0.8$	$\alpha=0.9$
$\lambda=3.0$	0.0270	0.959	0.961	0.964	0.971
	0.0588	0.912	0.918	0.925	0.937
	0.0968	0.865	0.872	0.884	0.900
	0.1429	0.817	0.827	0.844	0.864
	0.2000	0.767	0.782	0.806	0.841
	0.2727	0.721	0.741	0.774	0.822
	0.3684	0.680	0.709	0.756	0.827
	0.5000	0.653	0.700	0.775	0.889
	0.6923	0.666	0.762	0.916	1.166
	0.7419	0.683	0.801	0.996	1.309
	0.7966	0.713	0.865	1.123	1.548
	0.8571	0.771	0.985	1.361	2.011
	0.9245	0.919	1.293	1.992	3.312
$\lambda=4.0$	0.0278	0.943	0.942	0.943	0.947
	0.0625	0.880	0.880	0.881	0.887
	0.1071	0.814	0.812	0.815	0.821
	0.1667	0.745	0.742	0.746	0.752
	0.2500	0.671	0.669	0.674	0.688
	0.3750	0.596	0.593	0.600	0.617
	0.5833	0.516	0.514	0.524	0.547
	1.0000	0.431	0.431	0.445	0.476
	2.2500	0.328	0.334	0.358	0.404
	2.8750	0.303	0.310	0.337	0.387
	3.9167	0.274	0.284	0.314	0.369
	6.0000	0.240	0.253	0.287	0.349
	12.2500	0.195	0.212	0.252	0.324
$\lambda=5.0$	0.0286	0.927	0.924	0.922	0.923
	0.0667	0.846	0.841	0.837	0.836
	0.1200	0.760	0.750	0.745	0.741
	0.2000	0.667	0.653	0.645	0.638
	0.3333	0.565	0.547	0.535	0.531
	0.6000	0.449	0.427	0.412	0.404
	1.4000	0.305	0.279	0.260	0.249
$\lambda=6.0$	0.0294	0.911	0.905	0.901	0.900
	0.0714	0.812	0.801	0.791	0.786
	0.1364	0.704	0.686	0.672	0.661
	0.2500	0.584	0.559	0.539	0.522
	0.5000	0.443	0.412	0.387	0.368
	1.5000	0.259	0.225	0.198	0.177
$\lambda=7.0$	0.0303	0.895	0.887	0.880	0.876
	0.0769	0.777	0.761	0.746	0.736
	0.1579	0.645	0.619	0.598	0.579
	0.3333	0.491	0.457	0.429	0.403
	1.0000	0.292	0.254	0.222	0.197

He did not take the effect of branching into account, however. Considering the effect, we followed the method and could obtain A_1 for a system initially composed of linear molecules. By use of notations;

$$f_{\alpha+1}=\int_0^\infty p^{\alpha+1}m^\dagger(p, 0)dp, \quad (25)$$

$$I(\alpha)=\int_0^\infty dp\,p^{\alpha+1}\int_0^p dl\,l(p-l)m^\dagger(l,0)m^\dagger(p-l,0), \tag{26}$$

where $m^\dagger(p,0)$ indicates the initial molecular size distribution, A_1 can be expressed as follows:

$$A_1=-\frac{c\alpha}{\alpha+2}\cdot\frac{f_{\alpha+2}}{f_{\alpha+1}}(\lambda-\lambda_0), \tag{27}$$

where

$$\lambda_0=\frac{\alpha+2}{\alpha}\left\{g(2)^{2-\alpha}\frac{I(\alpha)}{f_{\alpha+2}}-2\right\}. \tag{28}$$

If we put $g(2)=1$, namely if we assume that a polymer molecules with one crosslink unit has the same R_e as the linear molecule with the same degree of polymerization, our result coincides with Inokuti's. The quantities $f_{\alpha+2}$ and $I(\alpha)$ have been calculated for several molecular size distributions by him[11)] and by him and the author.[12)]

For

$$m^\dagger(p,0)=\frac{b^{b+1}}{u^2\Gamma(b+1)}\left(\frac{p}{u}\right)^{b-1}e^{-bp/u}, \tag{29}^*$$

$f_{\alpha+1}$ and $I(\alpha)$ are given as follows:

$$f_{\alpha+2}=(u/b)^{\alpha+1}\Gamma(b+2+\alpha)/\Gamma(b+1), \tag{30}$$

$$I(\alpha)=(u/b)^{\alpha+1}\Gamma(2b+3+\alpha)/\Gamma(2b+2). \tag{31}$$

Then

$$A_1=-\frac{c\alpha u}{\alpha+2}\left(1+\frac{\alpha+1}{b}\right)(\lambda-\lambda_0), \tag{32}$$

where

$$\lambda_0=\frac{\alpha+2}{\alpha}\left\{g(2)^{2-\alpha}\frac{\Gamma(2b+3+\alpha)\Gamma(b+1)}{\Gamma(b+2+\alpha)\Gamma(2b+2)}-2\right\}. \tag{33}$$

If $\lambda<4$, namely $4c>r$, gelation occurs. The dose R_g at incipient gelation is

$$R_g=1/2cf_2=(2cu)^{-1}b/(b+1.) \tag{34}$$

We expand $[\eta]/[\eta]_0$ in powers of R/R_g.

$$[\eta]/[\eta]_0=1+a_1(R/R_g)+a_2(R/R_g)^2+\cdots. \tag{35}$$

$$a_1=A_1R_g=-\frac{\alpha}{2\alpha+4}\cdot\frac{b+1+\alpha}{b+1}(\lambda-\lambda_0). \tag{36}$$

We draw contours for constant a_1's on $\lambda-b$ plane for $\alpha=1$. (Fig. 5). Fig. 5 shows that a_1 increases with b and decreases with λ. The dependence of a_1 on b is strong when λ is near four.

§ 6. Comparison with Experiment.

Shultz et al[13)] measured the intrinsic viscosity of irradiated polystyrene in benzene. The experimental $[\eta]/[\eta]_0$ versus R/R_g are plotted in Fig. 6. The exponent α in the Staudinger's law is 0.74 for the benzene solution of polystyrene. The ratio $\lambda=r/c$ was obtained to be 0.74 by the measurement of the gel fraction according to Charlesby. Soito has shown, however, the Charlesby's method gave an overestimated value of λ because of the neglect of cyclization.[5)]

Kilb's measurement[7)] was made on dimethylsilicone oil. The data were plotted in

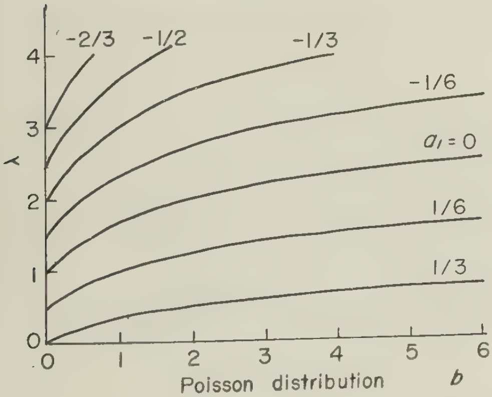

Fig. 5. Contours for constant a_1's on $\lambda-b$ plane.

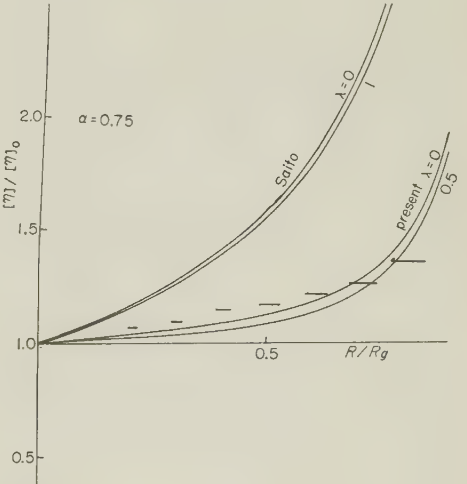

Fig. 6. The experimental $[\eta]/[\eta]_0$ of irradiated polystyrene in benzene, measured by Shultz, et al.

---

* We call (29) the generalized Poisson distribution. The parameter b is connected with the ratio of the weight average degree of polymerization P_w to the number average P_n in the following way:

$$P_w/P_n=1+1/b\,.$$

If $b=1$, (29) reduces to the Poisson distribution; and if $b=\infty$, to the uniform distribution.

Fig. 7. α is 0.79 for the toluene solution of the silicone polymer. The value of λ for this polymer is 0.1, which was obtatined by chemical techniques.

Our calculated $[\eta]/[\eta]_0$ coincides with these experiments fairly well as in Figs. 6 and 7. The effect of branching lowered Saito's curves* towards the observed values.

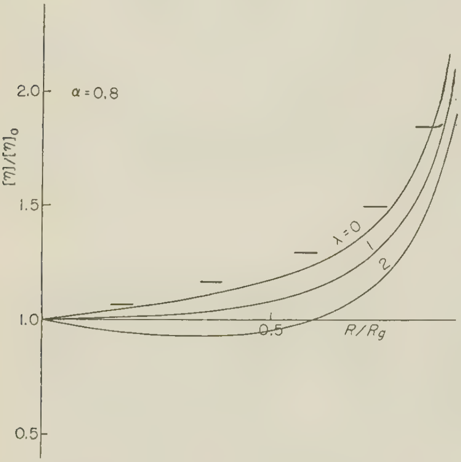

Fig. 7. The data of Kilb, of dimethylsilicone oil in toluene.

§ 7. Concluding Remarks.

We conclude that the large discrepancy between Saito's theory and experiment should be due to the neglect of the effect of branching. The present theory, however, is not yet satisfactory. It contains several ambiguous assumptions: (1) the proportionality of R_e^2 to R^2; (2) the neglect of cyclization; (3) the neglect of dependence of α on p and R_e.

Concerning (1) we note the recent work of Zimm and Kilb.[15] They proposed that the ratio of the intrinsic viscosity of branched molecule to that of a linear molecule of the same weight should be rather $\{R^2(q)/R^2(0)\}^{1/2}$ than $\{R^2(q)/R^2(0)\}^{2-\alpha}$, which we adopted. The other two assumptions (2) and (3) have never been examined quantitatively, but fortunately they should be valid at least for small radiation doses. This is one of the advantages of the theory at small radiation doses.

Besides, we can point out the following merits; firstly that the present theory at small radiation doses enables us to analyse experimental data of a polymeric substance whose initial distribution is not necessarily Poisson-like; secondly in the sense that it contains only $g(2)$, but not $g(q)(q \geqq 3)$, which is difficult to evaluate exactly.

In view of our conclusion, accurate measurements of the intrinsic viscosity at small doses are very desirable.

Acknowledgements

The author wishes to thank Professor A. Amemiya of the University of Tokyo and Professor O. Saito of the Chuo University for their helpful discussions and encouragements. Thanks are also due to Mr. M. Inokuti of the University of Tokyo for invaluable suggestions and advices during the work; to Dr. T. Watanabe of the Japan Atomic Energy Research Institute and Mr. Y. Hirano of the Kurashiki Rayon Co., Ltd. for their interest and valuable comments. Further, he is grateful to Dr. T. Murata and Dr. K. Nakazawa of the Electronic Computer Laboratory of the Faculty of Engineering, University of Tokyo for providing the author with opportunities for electronic computation.

Appendix: A Lower Limit of *g*

By (8) we get the following expression:

$$g=\frac{6}{n_b(n_b+1)(n_b+2)}\left(n_b^2+\sum_{(k,l)}\nu_{kl}\right). \qquad \text{(A1)}$$

We will estimate $\sum_{(k,l)}\nu_{kl}$ following a probability-theoretic argument. A molecule with n crosslink units has $2n+2$ chain ends, and each crosslink unit has four branches. So the probability P that one of the four branches attached to a crosslink unit does not reach a chain end but another crosslink unit is

$$\frac{4n-(2n+2)}{4n}=\frac{n-1}{2n}.$$

If the molecule has no ring structure, a crosslink unit C_i should be connected with another crosslink unit C_j through only one chain. We will obtain an average value of ν_{ij} the number of branches constituting the chain.

By use of P, we obtain the probability P_1 that one of the branches attached to C_i reaches directly C_j:

---

* In fact, Saito performed numerical evaluation of his expression (Eq. (10) in his paper III[6]) only for $\alpha=1/2$ and $\alpha=1$. For general values of α, numerical evaluation was made by the author.[14]

$$P_1=4{}_4C_4P^4\frac{1}{n-1}\cdot\frac{n-2}{n-1}\cdot\frac{n-3}{n-1}\cdot\frac{n-4}{n-1}$$
$$+3{}_4C_3P^3(1-P)\frac{1}{n-1}\cdot\frac{n-2}{n-1}\cdot\frac{n-3}{n-1}$$
$$+2{}_4C_2P^2(1-P)^2\frac{1}{n-1}\cdot\frac{n-2}{n-1}$$
$$+{}_4C_4P(1-P)^3\frac{1}{n-1}. \qquad \text{(A2)}$$

The first term represents the probability that one of the four branches reaches C_j and the other branches other crosslink units. The second stands for the probability that one reaches C_j, two other crosslink units, and the other a chain end. We should note that our approach leads to a finite probability that C_i does not connect with any other crosslink unit, namely that it is isolated. This is inconsistent with our starting point, since we have had a single molecular network in mind. But it is an inevitable failure of such a probability-theoretic approach as ours. It is clear, however, that our approach must give a lower limit to the exact value of $\sum_{(k,l)}\nu_{kl}$. Now we approximate $(n-2)/(n-1)$, $(n-3)/(n-1)$, and $(n-4)/(n-1)$ by unity in (A2) for simplicity. It will be easily seen that this approximation still assures the evaluation of a lower limit. With this approximation (A2) reduces to

$$P_1=4P\frac{1}{n-1}=\frac{2}{n}, \qquad \text{(A3)}$$

which permits a naive interpretation.

Similarly we can obtain P_2, the probability that $\nu_{ij}=2$.

$$P_2=4P\frac{n-2}{n-1}(4P-1)\frac{1}{n-1}=4P(4P-1)\frac{1}{n-1}. \qquad \text{(A4)}$$

Generally, the probability that $\nu_{ij}=k$ is given by

$$P_k=4P(4P-1)^{k\ \ 1}\frac{1}{n-1}. \qquad \text{(A5)}$$

Now the required quantity $\sum_{(k,l)}\nu_{kl}$ can be expressed as

$$\sum_{(k,l)}\nu_{kl}=9{}_nC_2\sum_{k=1}^{n\ \ 1}kP_k. \qquad \text{(A6)}$$

The factor 9 comes from the fact that a chain specified by crosslink units i, j should have weight 9 in the specification by means of branches k and l belonging to the crosslink units i and j, respectively. The summation yields

$$\sum_{(k,l)}\nu_{kl}=\frac{9n^2(n-1)}{4}\left\{1-\frac{3n-2}{n-2}\left(\frac{n-2}{n}\right)^n\right\}. \qquad \text{(A7)}$$

Substituting (A7) into (A1) and taking care of the relation $n_b=3n+1$, we obtain

$$\lim_{n\to\infty} g=\frac{1}{2}(1-3e^{-2})=0.297.$$

References

1) J. G. Kirkwood and J. Riseman: J. Chem. Phys. **16** (1948) 565.
2) P. Debye and A. M. Bueche: J. Chem. Phys. **16** (1948) 573.
3) W. H. Stockmayer: J. Chem. Phys. **11** (1943) 45; **12** (1944) 125.
4) O. Saito: J. Phys. Soc. Japan **13** (1958) 198.
5) O. Saito: J. Phys. Soc. Japan **13** (1958) 1451.
6) O. Saito: J. Phys. Soc. Japan **13** (1958) 1465.
7) R. W. Kilb: J. Chem. Phys. **63** (1959) 1838.
8) A. Charlesby: *Atomic Radiation and Polymers* (Pergamon Press, London, 1959).
9) B. H. Zimm and W. H. Stockmayer: J. Chem. Phys. **17** (1949) 1301.
10) S. Kataoka: Mimeographic circular on chemical physics in Japanese, Busseironkenkyu **66** (1953) 102.
11) M. Inokuti: J. Phys. Soc. Japan **14** (1959) 79.
12) M. Inokuti and K. Katsuura: J. Phys. Soc Japan **14** (1959) 1379.
13) A. R. Shultz, P. I. Roth, and G. B. Rathmann: J. Polym. Sci. **22** (1956) 495.
14) K. Katsuura, unpublished.
15) B. H. Zimm and R. W. Kilb: J. Polym. Sci. **37** (1959) 19.

JOURNAL OF THE PHYSICAL SOCIETY OF JAPAN, Vol. 15, No. 12, DECEMBER, 1960

Ultrasonic Studies in Chemically Active Liquid Media
(1) Aqueous Solution of N_2O_4

By M. KRISHNAMURTHI

Director's Research Laboratories,
Indian Institute of Science, Bangalore (India)

and M. SURYANARAYANA

Department of Physics, Nizam College,
Hyderabad (India)

Using a pulse method the ultrasonic absorption has been studied in the frequency range of 2 to 10 Mc/s in dilute aqueous solutions of nitrogen tetroxide gas at room temperature. The absorption peaks ($\alpha\lambda$ vs frequency) observed in this study are attributed to the ionic dissociation reaction of the nitrous acid into its constituent ions. The rate constants of the forward and backward reactions are calculated using the theory of Tabuchi. The variation of the logarithm of the rate constant of the bimolecular ionic reaction, namely, $\log_{10} k_b$, with the square root of ionic strength qualitatively follows Brönsted's theory for ionic reactions in solutions.

§ 1. Introduction

The factors that contribute to the absorption of an ultrasonic wave as it propagates through a medium are, according to the classical theories, shear viscosity, thermal conduction and heat radiation in that order of importance. The coefficient of absorption α, due to viscosity and heat conduction increases as the square of the acoustic frequency f. In other words $\alpha\lambda$, the absorption per wavelength, increases almost linearly with frequency. During the past few years many liquids and solutions have been encountered where $\alpha\lambda$ instead of increasing linearly with frequency goes through a maximum at some frequency. At frequencies far away from this and on either side of it, α/f^2 remains constant as required by the classical theory. This behaviour is traced to the relaxation of the molecules of the liquid at that frequency. Various types of relaxation such as thermal relaxation and structural relaxation are envisaged. Besides these, it is now realized that the presence of a reversible chemical reaction in a liquid medium can also give rise to peaks in ultrasonic absorption. Theoretical considerations reveal that the frequency at which such a peak occurs is related to the rate of the reaction. In media where reversible chemical reactions are taking place, disturbances in the equilibrium between the various participants and products of the reaction may not be in phase with the changes in pressure produced by the sound wave, with the result that the absorption per wavelength $\alpha\lambda$ passes through a maximum near a characteristic frequency f_c. This is the case of a relaxation due to chemical reaction.

Einstein$^{1)}$ is probably the earliest to have interpreted the excess sound absorption in terms of relaxation due to a chemical reaction. Liebermann$^{2)}$ used the concept to explain the excess absorption in the aqueous solutions of magnesium sulphate. But, Freedman$^{3)}$ and independently, Manes$^{4)}$, have considered the absorption of sound in liquid media in general chemical equilibrium. In the development of the theory they made some simplifying assumptions. For example, Freedman assumed that the volume change due to chemical reaction is zero. Recently, Tabuchi$^{5)}$ developed a more generalized theory which connects the kinetics of chemical reaction with the dispersion and absorption of sound in liquids. He showed that if the necessary simplifying assumptions are made in his theory, the equations approximate to those derived by Freedman and Manes. Another interesting feature of Tabuchi's theory over that of Freedman and Manes is that it is extended to include the electrolyte solutions also.

The present work deals with the study of ultrasonic absorption in aqueous solutions of nitrogen tetroxide. The peaks of absorption observed in this study are attributed to the ionic dissociation of the nitrous acid. Tabuchi's theory is used to calculate the rate constants of the ionic reaction mentioned above. The essential equations of Tabuchi's theory used in these calculations will now be given briefly.

§ 2. Tabuchi's Theory

Let the molecules of the type $A, B, \cdots Q, R, \cdots$ be contained in a liquid whose volume is v and assumed to be in the chemical equilibrium

$$a \cdot A + b \cdot B + \cdots \rightleftharpoons q \cdot Q + r \cdot R + \qquad (1)$$

An arbitrary molecule is denoted by i and n_i represents the number of moles of the molecule i. When a sound wave passes through the liquid the total number of moles of each species changes periodically with time depending on the frequency. This is usually accompanied by change in volume as well as the internal energy. Taking into account these two factors, Tabuchi derives equations for the curves showing the variation of the velocity and absorption with the acoustic frequency. He also connects the equations for these curves with the relaxation time τ, the rate constants k_f and k_b of the chemical reaction and arrives at the equation

$$\chi(1+i\omega\tau)\frac{\Delta nq}{q} + \xi\frac{\Delta v}{v} - \left(\frac{E}{RT^2}\right)\Delta T = 0 \qquad (2)$$

where ω is the acoustic circular frequency and E is the reaction heat at constant volume of the chemical reaction and χ and ξ are defined as follows:

$$\chi = \sum_A \frac{a^2}{n_A} + \sum_Q \frac{q^2}{n_Q}, \qquad (3)$$

and

$$\xi = \sum_A a - \sum_Q q, \qquad (4)$$

also

$$\frac{1}{\tau} = r_f \cdot v \cdot \chi$$

$$= r_f \cdot v \cdot \sum_A \frac{a^2}{n_A} + r_b \cdot v \cdot \sum_Q \frac{q^2}{n_Q}, \qquad (5)$$

in which r_f and r_b are the forward and backward reaction rates. The forward and backward reaction rates are related to the corresponding rate constants k_f and k_b by the equations

$$r_f = k_f\left(\frac{n_A}{v}\right)^a \left(\frac{n_B}{v}\right)^b, \qquad (6)$$

$$r_b = k_b\left(\frac{n_Q}{v}\right)^q \left(\frac{n_R}{v}\right)^r. \qquad (7)$$

In the application of this theory to electrolyte solutions, the activity coefficients of the molecular species have to be used in the rate equations. This involves necessary changes in the equations given above.

Fur a uni-univalent electrolyte dissociating into two ions such as

$$A \rightleftharpoons B^+ + C^-,$$

where $a=1$; $b=1$; $c=1$; the valencies $Z_A=0$; $Z_B=1$; $Z_C=-1$ the general equations are reduced to

$$\chi = \left(\frac{1}{n_A} + \frac{1}{n_{B^+}} + \frac{1}{n_{C^-}}\right) - \log_e \frac{(f\pm)^2}{n_{B^+}+n_{C^-}}, \qquad (8)$$

and

$$\frac{1}{\tau} = k_f \cdot n_A \cdot \chi \qquad (9)$$

In equation (8) $f_\pm$ represents the mean activity coefficient of the ions B^+ and C^-.

Tabuchi further derives an equation for the complex velocity of sound in terms of the static isothermal compressibility, the density and the heat capacities $C_P{}^0$ and $C_V{}^0$ of the solution at zero frequency and C_P and C_V at infinite frequency of sound. The heat capacities are related by the equations

$$C_P{}^0 = \frac{W}{\chi} + C_P, \qquad (10)$$

$$C_V{}^0 = \frac{E^2}{RT^2\chi} + C_V, \qquad (11)$$

where W is a complicated function involving the partial molar volumes of the components of the reaction. He ultimately connects the characteristic values of the ultrasonic absorption curves (i.e. $\alpha\lambda$ vs ω curve) with the parameters defined previously. Thus he gets

$$\omega_{\max} = (C_P{}^0 C_V{}^0 / C_P C_V)^{\frac{1}{2}} / \tau, \qquad (12)$$

and

$$(\alpha\lambda)_{\max} = \pi/2 \frac{C_V{}^0 C_P - C_P{}^0 C_V}{(C_P{}^0 C_V{}^0 C_P C_V)^{\frac{1}{2}}}. \qquad (13)$$

§ 3. Experimental Technique

In this work, the pulse method of Pellam and Galt[6] is used with some modifications. Instead of a reflector on the receiving side another identical x-cut quartz crystal is used as a receiver of the traversed ultrasonic beam. The experiment is performed at four frequencies, namely 2.12, 3.23, 6.36 and 10.61

Mc/s. As observations are confined to the Fresnel region of the ultrasonic beam, frequencies below 2 Mc/s could not be employed.

A schematic diagram of the experimental arrangement is given in Fig. 1.

Nitrogen tetroxide gas is produced from dilute hydrochloric acid and sodium nitrite. The gas thus obtained is passed through distilled water. The strength of the solution is determined by titration using a standard potassium permanganate solution. The titration carried out before and after an ultrasonic observation does not differ by more than 2 percent. Only dilute solutions have been used in this work to ensure constancy of concentration during the observations and also to avoid bubbles of gas forming within the liquid under ultrasonic excitation. It is estimated that the error in the measurement of absorption is smaller than ±5 percent.

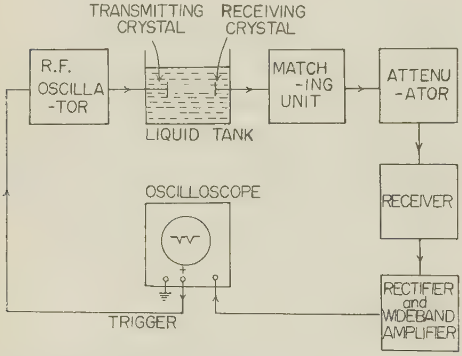

Fig. 1. Schematic diagram of the experimental arrangement.

§ 4. Results

The ultrasonic absorption α, is determined at various concentrations of the aqueous solutions of nitrogen tetroxide gas at 2.12, 3.23, 6.36 and 10.6 Mc/s and at a temperature close to 28°C. Curves connecting α/f^2 and concentration are drawn for each frequency. Values of α/f^2 are read out from these graphs for representative concentrations. For theoretical analysis of the results the excess absorption, (i.e., absorption over and above the classical contribution due to viscosity, heat conduction etc.) should be considered.

It is interesting to note that the ultrasonic velocity of the solution at any concentration is not significantly different from the velocity in the solvent even though the absorption is considerable. Fig. 2 shows the behaviour of $\alpha\lambda$ vs frequency at various concentrations. It is seen from this figure that the frequency of peak absorption increases with increasing concentration up to a limit after which it is independent of concentration. Preliminary results of this work have been reported earlier[7].

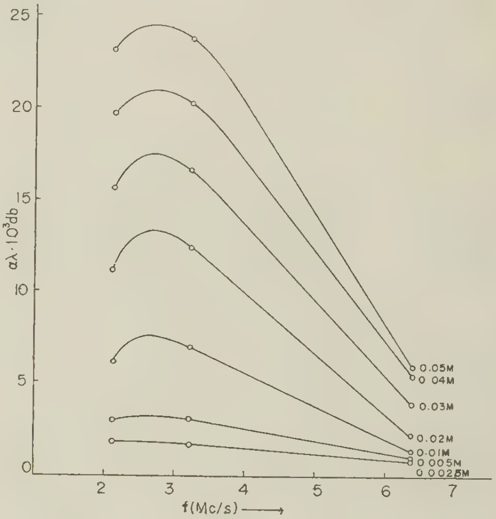

Fig. 2. Dependence of $\alpha\lambda$, the ultrasonic absorption per wavelength, on f, the frequency, in the aqueous solution of N_2O_4 at various concentrations (moles/litre).

§ 5. Discussion of the Results

Krishnamurthi[8] found a similar relaxation phenomenon in the case of aqueous solutions of sulphur dioxide near about 6 Mc/s. On the other hand, non-aqueous solutions of sulphur dioxide do not show such a relaxation thus excluding the possibility that the pure gas is causing the relaxation. The relaxation effect in the aqueous SO_2 solutions is, therefore, attributed to a dynamic chemical equilibrium between H_2SO_3 and H^+ and HSO_3^- ions.

Nitrogen tetroxide gas has been thoroughly studied by Richards and Reid[9),10)] and it is known to exhibit a frequency of peak absorption in the region of 400 Kc/s as compared to about 1 Mc/s for SO_2 gas. In aqueous solution, N_2O_4 undergoes a chemical change and a dynamic equilibrium[11] is set up as indicated by the equation II given below:

$$N_2O_4 + H_2O \rightarrow HNO_2 + HNO_3 \qquad \text{I}$$

$$HNO_2 \rightleftharpoons H^+ + NO_2^-. \qquad \text{II}$$

On an analogy with SO_2 solutions the aqueous solutions of N_2O_4 also must exhibit peaks of absorption. It is indeed the case (Fig. 2). Thus the relaxation effects observed in the case of the aqueous N_2O_4 solutions are attributed to the reversible chemical reaction II mentioned above.

As an additional check to show that the nitrite ion is causing the relaxation, the ultrasonic propagation in the aqueous solutions of sodium nitrite has been studied in the frequency range of 2 to 26 Mc/s. The results of this study are given in Table I. It is seen from this table that for any concentration of the aqueous solution of sodium nitrite, the absorption coefficient α/f^2 is not a constant for different frequencies in the range 2 to 10 Mc/s, thus indicating a relaxation effect in these solutions also in that frequency range.

Table I. Ultrasonic velocity and absorption in the aqueous solutions of sodium nitrite (29°C).

Concentration (c) Mole/Litre	Density (ρ) gm/c.c.	Velocity (V) m/sec	α/f^2 in 10^{-14} db metre^{-1} sec^2 at frequencies f (Mc/s) of			
			2.12	3.23	6.36	10.61, 15.50 and 25.8
1.0	1.060	1542	267	182	82	25
0.8	1.048	1533	223	138	67	20
0.6	1.035	1527	162	93	42	18
0.4	1.021	1521	111	48	25	17
0.2	1.008	1512	67	26	17	17
0.0	0.996	1503	16	16	16	16

§ 6. Ultrasonics and Fast Reactions

The chemical reactions which take place between ions generally proceed very rapidly and are commonly called instantaneous reactions. The conventional chemical and physical methods of following the reactions are unsuitable in such cases. In addition, the usual methods of initiating a reaction by mixing becomes inadequate. One has to resort to indirect methods for measuring such fast reaction rates. One possibility is the use of ultrasonics for such a study.

When a chemical equilibrium exists in a solution, it can be disturbed by a rapid variation of pressure or temperature of the medium. The speed of the chemical reaction determines the extent to which it can keep up with this variation and observations can be made either directly or indirectly on the subsequent shifting of the equilibrium which proceeds with a finite time lag. This type of method (called the relaxation method) seems to be one of the most promising for investigating extremely fast reactions. Ultrasonic data have been used in the calculation of reaction rates of ionic reactions in aqueous solutions by some of the previous workers. The work done on the aqueous solutions of magnesium sulphate by Bies[12)], manganous sulphate by Kor and Verma[13)] and ammonia by Eigen and Schoen[14)] may be mentioned in this connection.

It is stated earlier that Tabuchi worked out the theory for determining the speed of a reversible chemical reaction from a study of the ultrasonic absorption and velocity. His theory is used here for finding the rate constants of the reaction II mentioned earlier. The method of arriving at the various parameters required in the evaluation of the rate constants will be given briefly.

The heat of reaction E for the ionic dissociation reaction is given in the international critical tables (Vol. V; p. 178, 1929). The degree of dissociation, δ can be calculated from the equilibrium constant K given in the International critical tables (Vol. VII; p. 239, 1929) by means of the relation

$$K=\frac{\delta^2\cdot c\cdot f^2{\pm}}{(1-\delta)},$$

where $f_\pm$ is the mean ionic activity coefficient. The mean ionic activity coefficient follows from the well-known Debye-Hückel's theory and is given by

$$-\log_{10}f_\pm=\frac{0.5\sqrt{\mu}}{1+\sqrt{\mu}}-0.1\mu,$$

where μ is the ionic strength of the solution being equal to $c(\delta+1)$ for a concentration of c moles per litre. Since K and $f_\pm$ both involves the degree of dissociation, we can calculate δ by the method of successive approximations. Since $f_\pm$ is nearly unity, a rough value of δ is determined from K by putting $f_\pm=1$. This value of δ is used to calculate $f_\pm$. The process is repeated till $f_\pm$ and δ remain constant. The values of n_A, n_B and n_C are obtained from the expressions $n_A=(1-\delta)c$ and $n_B=n_C=c\delta$.

The heat capacities $C_P{}^0$ and $C_V{}^0$ of the solutions at zero frequency are taken to be the same as those for water as we are dealing with dilute solutions. In these calculations $C_P{}^0$ and $C_V{}^0$ are expressed in heat capacities per mole of HNO_2.

The value of χ is calculated from equation (8) and is used in equation (11) for the evaluation of C_V, the heat capacity at constant volume for infinite frequency of sound.

Since the formula for C_P in equation (10) involves some uncertain parameters like the molar volumes of the ions taking part in the reaction, an indirect method of calculating C_P is adopted by the use of equation (13) where all the quantities are known except C_P. This equation uses $(\alpha\lambda)_{\max}$ in nepers while the curves (Fig. 2) give $\alpha\lambda$ in decibels and are to be converted to nepers.

From (12) the relaxation time of the chemical reaction is evaluated and finally used in the equation (9) to calculate the rate constant k_f of the forward reaction. The rate constant k_b of the reverse reaction can be calculated from the equilibrium constant $K=\frac{k_f}{k_b}$.

The following values are used in the calculations:

Heat of reaction	−3345 cal/mol
Formula weight (HNO_2)	47.02 g
Equilibrium constant	0.0005 mol/litre
$C_P{}^0$, Heat capacity per mole of HNO_2	46.96 cal/mol-deg.
$C_V{}^0$, Heat capacity per mole of HNO_2	46.35 cal/mol-deg.
Temperature	301°K

The various parameters used in the calculations and the rate constants are given in Table II.

Table II. Aqueous solutions of N_2O_4 (28°C).

c Concentration of HNO_2 (Moles/Litre)	Degree of dissociation δ	Mean activity coefficient $f_\pm$	$(\alpha\lambda)_{\max}\times10^3$ in nepers	Relaxation Frequency (Mc/s)	C_P cal/mol-deg	C_V cal/mol-deg	χ	$\tau\times10^{+8}$ in sec.	$k_f\times10^{-5}$ sec^{-1}	$k_b\times10^{-9}$ (Litre/Mole) sec^{-1}	$\sqrt{\mu}$	$\log_{10}(k_b)$
0.05	0.117	0.802	2.82	2.70	46.89	46.20	402	5.91	9.55	1.91	0.236	9.281
0.04	0.127	0.823	2.42	2.70	46.90	46.22	461	5.91	10.5	2.11	0.212	9.324
0.03	0.143	0.839	2.02	2.70	46.91	46.24	548	5.91	12.0	2.40	0.185	9.380
0.02	0.168	0.860	1.50	2.70	46.92	46.27	701	5.90	14.5	2.90	0.153	9.462
0.01	0.221	0.892	0.86	2.55	46.93	46.30	1084	6.25	19.0	3.79	0.111	9.579
0.005	0.290	0.918	0.37	2.20	46.94	46.32	1719	7.24	22.1	4.43	0.080	9.646
0.0025	0.377	0.938	0.19	1.80	46.94	46.33	2836	8.84	25.6	5.02	0.059	9.701
0	—	—	—	—	—	—	—	—	—	(5.75)	—	(9.760)

The influence of the ionic strength μ on the velocity coefficient of a bimolecular reaction between charged particles in solutions is given by the equation (14) due to Brönsted[15)], namely,

$$\log_{10}\left(\frac{k_b}{k_0}\right)=q\cdot Z_A\cdot Z_B\cdot\sqrt{\mu}\,, \tag{14}$$

where k_0 is the velocity coefficient corresponding to zero ionic strength, Z_A and Z_B are the valencies of the reacting ions and q is a constant given explicitly by the theory of interionic attraction proposed by Debye and Hückel. For aqueous solutions at room temperature the value of q is nearly unity. In fact, at 29°C, q is equal to 1.025.

The theory thus implies that the logarithm

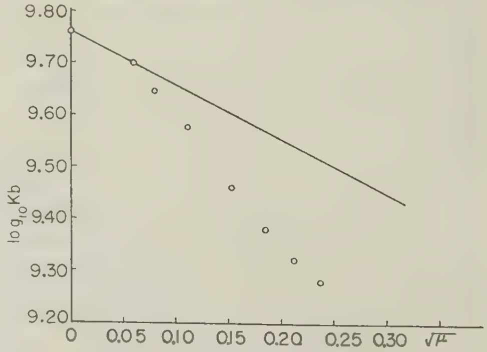

Fig. 3. Variation of $\log_{10} k_b$ with the square root of the ionic strength, μ, of the aqueous solutions of N_2O_4. The solid line is expected according to theory. The observed values are represented by (0).

of the velocity coefficient is a linear function of the square root of the ionic strength, the gradient being positive for reactions involving two ions of like sign and negative in the case of two ions of unlike sign. Further, the theory requires that the gradient should be nearly unity at room temperature when the reaction is between two univalent ions in aqueous solutions.

Fig. 3 represents the variation of $\log_{10} k_b$ with the square root of the ionic strength of the solutions studied in this work. It should be noted that in calculating the ionic strength of the solutions one should consider the valencies and concentrations of all the ionic species present in the solution. The chemical equation I given earlier shows that when N_2O_4 is dissolved in water both HNO_2 and HNO_3 are produced in equimolar quantities. While HNO_2 is weakly ionized, HNO_3 is completely ionized. These factors are taken into consideration in calculating the ionic strength of the solutions given in Table II.

The decrease of $\log_{10} k_b$ (Fig. 3) with the increase of the ionic strength indicates that the reaction involves two ions of opposite sign. The solid line represents the theoretically expected line according to equation (14). The value of k_0 of this equation is found by the extrapolation of the graph between k_b and the concentration of HNO_2. It can be seen from the graph that the experimental values show near agreement with the theory only at very low dilutions. In some cases of slow ionic reactions, it has been observed that the variation of $\log_{10} k_b$ with the ionic strength at low dilutions can be represented (reference 15 p. 110) to within ±20 per cent by Bronsted's equation (14). The study of fast ionic reactions is a subject of recent origin and until more experimental data accumulate it is not possible to compare the experimental results with the existing theory. However, it may be concluded that the variation of the reaction rate of fast ionic reactions qualitatively follows the predictions of the theory.

This work was carried out at the Physical Laboratories, Osmania University, Hyderabed. The authors thank Professor S. Bhagavantam for suggesting the problem and for his encouragement during the progress of this work.

References

1) A. Einstein: Sitzber. Berliner. Akad. Wiss. (1920) 380.
2) L. Liebermann: Phys. Rev. **76** (1949) 1520.
3) E. Freedman: J. Chem. Phys. **21** (1953) 1784.
4) M. Manes: J. Chem. Phys. **21** (1953) 1791.
5) D. Tabuchi: J. Chem. Phys. **26** (1957) 993.
6) J. R. Pellam and J. H. Galt: J. Chem. Phys. **14** (1946) 608.
7) M. Krishnamurthi and M. Suryanarayana: Curr. Sci. **24** (1955) 369.
8) M. Krishnamurthi: Proc. Indian Acad. Sci. **41A** (1955) 125.
9) W. T. Richards and J. A. Reid: J. Chem. Phys. **114** (1933) 1.
10) W. T. Richards and J. A. Reid: J. Amer. Chem. Soc. **54** (1932) 3014.
11) G. Charlot: Qualitative Inorganic Analisis (John Wiley) (1954) 296.
12) D. A. Bies: J. Chem. Phys. **23** (1955) 428.
13) S. K. Kor and G. S. Verma: J. Chem. Phys. **29** (1958) 9.
14) M. Eigen and J. Schoen: Z. Physik, Chem. (N.F.), Frankfurt **3** (1955) 126.
15) E. A. Moelwyn Hughes: The Kinetics of Reactions in Solutions (Oxford University Press, London), (1950) 93-96.

JOURNAL OF THE PHYSICAL SOCIETY OF JAPAN, Vol. 15, No. 12, DECEMBER, 1960

Volume Viscoelasticity of Polymers and Other Highly Dissipative Materials

By Yasaku WADA, Hidenori HIROSE, Hiromichi UMEBAYASHI
and Motoharu OTOMO

Department of Applied Physics, Faculty of Engineering,
University of Tokyo, Tokyo, Japan

(Received August 30, 1960)

A new method for determining the real and imaginary parts of bulk modulus of polymers and other solid materials is represented. The method, as is called "suspension method", consists of measurements of sound velocity and attenuation in a suspension of powders and is superior in experimental accuracy to the existing method which essentially consists of the comparison of longitudinal and shear wave measurements. The new method has also a merit in the applicability to the sample in powdery state.

The results are given for styrene-butadiene rubber, natural rubber, polyethylene, polypropylene, polytrifluoromonochloroethylene, paraffin and yeast cell, among which styrene-butadiene rubber is most fully investigated. From these results, the followings are concluded: In the primary dispersion of amorphous polymers, the relaxation strength is of the same order of magnitude for bulk and shear moduli, and moreover, relaxation times, their distribution and temperature dependence have no appreciable discrepancy between two moduli. In the case of crystalline polymers, the mechanical dispersions are quite different between the power samples which have undergone no treatment after polymerization and the ones moulded from the powder.

Nomenclature

K', K'':	Real and imaginary parts of complex bulk modulus of a solid, respectively.
G', G'':	Real and imaginary parts of complex shear modulus of a solid, respectively.
K_1:	Real part of bulk modulus of a liquid.
ρ, ρ_1:	Density of solid and liquid respectively.
η_1:	Shear viscosity of a liquid.
V, V_1:	Sound velocity in suspension and liquid, respectively.
α, α_1:	Attenuation coefficient of sound in suspension and liquid, respectively.
c:	Volume fraction of solid particles in a suspension.
a:	Average radius of particles.
f:	Frequency of sound. $\omega=2\pi f$.
λ:	Wave length of sound.
V_l, V_s:	Longitudinal and shear wave velocities in a solid, respectively.
α_l, α_s:	Longitudinal and shear wave attenuation coefficients in a solid, respectively.

§ 1. Introduction

The fact that there is a viscous energy-dissipating mechanism associated with pure volume deformation for many gases and liquids has been firmly established recently. In the case of polymers the information on this subject is not so extensive and rather contradictory. For the primary dispersion region of amorphous polymers, there exist three kinds of opinion about the relaxation of bulk modulus. Marvin et al.[1] have found the relaxation phenomena of bulk modulus to be of comparable order of magnitude with shear modulus in both relaxation strength and relaxation time, whereas Nolle and Sieck,[2] Cunningham and Ivey[3] have found that the relaxation strength of bulk modulus is much smaller than that of shear. Recently Kono[4] said that the relaxation strength is of the same order of magnitude for both moduli, but the relaxation time and its temperature dependence are quite different and accordingly different molecular mechanisms should be associated with volume and shear deformations. A recent theory by Nakada[5] supports the results by Marvin on the whole, though Nakada has pointed out a small difference in the relaxation mechanism between bulk and shear moduli.

There is a basic experimental problem involved in obtaining these data of complex bulk modulus. All the informations abovementioned come from a comparison of the velocity and attenuation of shear waves (governed by the shear modulus, G) and longitudinal waves (governed by both the shear and bulk moduli, $K+4G/3$). Since the attenuation of shear waves in polymers is generally very large, the observed values of velocity and attenuation are likely to include appreciable errors. When combined with longitudinal wave measurement, therefore, the calculated imaginary part of bulk modulus very probably has a large scatter.

For example, a set of values—$V_l=1945\ m/s$, $\alpha_e=0.94$ nepers/cm, $\rho=1.00$g/cc, $f=100$Mc/s—results in $K'=3.0\times10^{10}$, $G'=0.6\times10^{10}$, $K''=1.0\times10^{9}$, $G''=0.9\times10^{9}$ dyn/cm², when combined with $V_s=775$m/s and $\alpha_s=6.1$ nepers/cm. On the contrary, the same values give $K'=2.8\times10^{10}$, $G'=0.8\times10^{10}$, $K''=0$ and $G''=1.6\times10^{9}$ dyn/cm², when combined with $V_s=880$m/s and $\alpha_s=7.5$ nepers/cm. In fact, a scatter of this order of magnitude in the shear wave data is very probable to occur and yet the conclusions about K'' are quite contradictory: $K''\fallingdotseq G''$ from the former data and $K''\ll G''$ from the latter.

From this reason, in order to deduce any reliable conclusion, it is necessary to measure directly the real and imaginary parts of bulk modulus of a sample. A few attempts to this purpose have been made, using a transient technique[6] and a dynamic one.[7,8] But, up to this time at least, the published results are rather scanty. The present paper represents a new method (which we call the "suspension method") for the direct determination of complex bulk modulus of polymers and other solid materials, with some results for rubbers, crystalline polymers, paraffin and yeast cell in its living state.

§ 2. Suspension Method

The new method described here is based on the fact that, when sound waves propagate through a suspension, suspended particles undergo only volume deformation on account of the lack of shear elasticity in a liquid.

Urick[9] has shown a simple theory on the sound velocity in a suspension of finely divided solid particles whose density is similar to the suspending liquid. According to him, when the radius of particle is much smaller than the wave length, the velocity becomes

$$V=\left[\{\rho_1(1-c)+\rho c\}\left\{\frac{(1-c)}{K_1}+\frac{c}{K'}\right\}\right]^{-\frac{1}{2}} . \qquad (1)$$

When c is small, the above equation can be

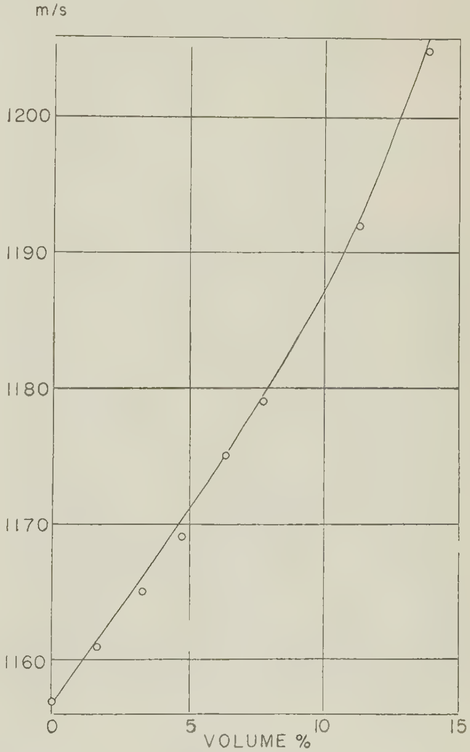

Fig. 1. Sound velocity at 1 Mc/s in polymethyl methacrylate suspension in methyl alcohol (10°C). Particles are perfectly spherical with average radius of 40μ. Solid line represents calculated values from Eq. (3), in which K' is estimated from longitudinal and shear wave velocity in a moulded plate of the polymer.

expanded as

$$V=V_1\left[1+\frac{1}{2}\left(\frac{K'-K_1}{K'}-\frac{\rho-\rho_1}{\rho_1}\right)c\right], \qquad (2)$$

where $V_1=(K_1/\rho_1)^{1/2}$.

Urick and Ament[10] have extended the theory to a more general case, where the particle and liquid are different in density and accordingly they oscillate in a sound field in different phase and amplitude. Assuming particles to be spherical, the velocity is given by

$$V=V_1\frac{1-\frac{1}{8}\left(\frac{vc}{1+uc}\right)^2}{\left[1-\frac{K'-K_1}{K'}c\right]^{\frac{1}{2}}[1+uc]^{\frac{1}{2}}}, \qquad (3)$$

where u and v are functions of ρ/ρ_1 and βa ($\beta=\sqrt{\omega\rho_1/2\eta_1}$) and graphically given in the original paper.

Eq. (3) is experimentally verified by the present authors as illustrated in Fig. 1.

For a dilute suspension, Eq. (3) can be approximated as

$$V=V_1\left[1+\frac{1}{2}\left(\frac{K'-K_1}{K'}-u\right)c\right]. \qquad (4)$$

Using Eq. (4) we can obtain the real part of bulk modulus of the particle from the measurement of sound velocity in a suspension.

Our primary concern, however, is with the imaginary part of bulk modulus. One of the present authors[11] has pointed out in an investigation of the attenuation of ultrasonic waves in a suspension of viscoelastic spheres that some parts of the attenuation should be attributed to the dynamic loss associated with volume deformation of particles, while the other parts are due to the well-known effects: the scattering of sound by particles and the viscous drag effect. The expression of attenuation coefficient due to the dynamic loss of particles, α_k, can easily be obtained as follows: When K' and V^{-1} in Eq. (2) are substituted by complex quantities, $K'+iK''$ and $V^{-1}-i\alpha_k/\omega$ respectively, it follows under the assumption $K''\ll K'$

$$\alpha_k=\left(\frac{\omega}{2V}\right)\frac{K_1K''}{K'^2}c\,. \qquad (5)$$

Eq. (5) is of course only valid under the same assumptions as for Eq. (2). A more general theory by Okano[12], however, has revealed that the same formula applies also to the case where ρ and ρ_1 are not similar.

Taking into consideration all the origins of attenuation, the total attenuation coefficient of a suspension can be written as

$$\alpha=\alpha_1+\alpha_s+\alpha_v+\alpha_k, \qquad (6)$$

where α_s and α_v are contributions from scattering and viscous drag effect respectively. Since α_s and α_v can be evaluated under some reasonable assumptions from the following equations respectively;[13 14]

$$\alpha_s=\left(\frac{\omega}{2V}\right)\left(\frac{\omega a}{V}\right)^3\left\{\frac{1}{3}\left(\frac{K'-K_1}{K'}\right)^2+\left(\frac{\rho-\rho_1}{2\rho+\rho_1}\right)^2\right\}c \quad (7)$$

and

$$\alpha_v=\left(\frac{\omega}{2V}\right)\frac{\frac{9}{4\beta a}\left(1+\frac{1}{\beta a}\right)\left(\frac{\rho-\rho_1}{\rho_1}\right)^2}{\left\{\frac{9}{4\beta a}\left(1+\frac{1}{\beta a}\right)\right\}^2+\left\{\frac{2\rho+\rho_1}{2\rho_1}+\frac{9}{4\beta a}\right\}^2}c, \quad (8)$$

we can obtain α_k, and hence K'', from observed value of α.

If the shear viscosity of the liquid medium is much smaller than the volume viscosity of the particle K''/ω, α_v becomes a negligible fraction of α. Furthermore, if the frequency of sound is so low that a/λ is small enough compared with unity, α_s also can be neglected. Under these conditions α_k becomes nearly equal to $(\alpha-\alpha_1)$. In fact this is the case with a suspension of polymer particles in water or alcohol measured by the sound whose wave length is more than twenty times the particle radius.

For Eqs. (4) and (5) to be a good approximation, the following conditions are required:

(1) The wave-length of sound waves must be large enough compared with the particle radius. Though a theoretical criterion is not attained here, experiments show the condition $a/\lambda\leqq 0.05$ to be satisfactory to the above requirement. For particles of radius 1μ, for example, the upper limit of frequency is about 50 Mc/s. The lower limit of frequency depends on the available quantity of the suspension. If only one litre of a suspension is available, the frequency perhaps cannot be extended to lower than several hundreds kilocycles per second. In the low frequency range, the standing wave tube technique may probably be useful.

(2) The shape of particle must be spherical or nearly spherical, so that the particle may undergo uniform dilatation and compression in a sound field. The irregularity of the surface of particle might prevent sound

pressure from applying in equal phase and intensity to the whole surface. This unfavorable effect of surface irregularity is depressed at low sound frequencies.

(3) The concentration of the suspension must be so small that the linear relation of both velocity and attenuation against concentration may hold. Within this restriction, however, concentration as large as possible is desirable for the precise determination of $(V-V_1)/c$ and $(\alpha-\alpha_1)/c$. One must make, therefore, a preliminary test as to the concentration dependence of velocity and attenuation and decide the most appropriate concentration.

(4) The liquid medium must have a good affinity to the particle. If not, microbubles of air on the particle-liquid interface and coagulation of particles might cause an appreciable error. Of course, dissolution or swelling of particles by the liquid is also undesirable.

The suspension method described here affords a new method for measuring dynamic mechanical properties of powder materials, whether polymeric substances or not. No technique for this purpose has been developed as yet, according to the authors, before this work.

§ 3. Experimental Technique

A pulsed compressional wave was generated and received in a suspension by a pair of X-cut quartz transducers. A schematic diagram of the apparatus is illustrated in Fig. 2. The receiving crystal was moved by a calibrated screw drive so that the change in distance between the transducers could be read within 1/100 mm. The crystals used were of sufficient cross section to insure a well collimated plane wave and no correction for the divergence of beam was necessary.

The wave velocity was determined from the amount of displacement of the receiving crystal which gave a shift of ten microseconds to the received signal on the oscilloscope. In purpose of obtaining an accuracy within 0.1%, the time axis of the oscilloscope was exactly synchronized by a 100kc/s quartz oscillator and the carrier wave of the received pulse, not the envelope of the pulse, was displayed on the oscilloscope screen. The change in relative distance between the crystals results in a change in the received pulse height. By compensating this change by use of a calibrated attenuator, the attenuation coefficient in a suspension was obtained.

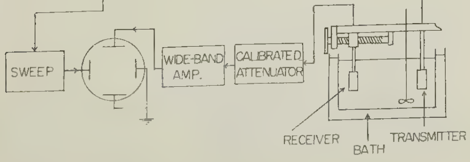

Fig. 2. Block diagram of apparatus.

Measurements were made at 1/3, 1 and 3 Mc/s, in the temperatures above 0°C for water suspensions and above −70°C for alcohol suspensions. The temperature of suspension was controlled by a liquid bath surrounding the sample vessel. As a bath liquid, water and alcohol-dry ice mixture were used above and below the room temperature, respectively. A continuous stirring of the suspension was necessary not only to insure a temperature uniformity throughout the suspension, but also to avoid settling under gravity.

In order to calculate K' and K'' from the sound velocity and attenuation in a suspension, the values of K_1, α_1, ρ and ρ_1 at each temperature are also required. K_1 and α_1 were determined from the sound velocity and attenuation in a suspending liquid, measured following the same procedures as a suspension. The density of particle and liquid was measured at 20°C by the pycnometer method, and the thermal expansion coefficient was determined by a dilatometer, the details of procedures having been described elsewhere.[15] The shape and average radius of particles were examined from microscopic observation.

In the case of styrene-butadiene rubber, polyethylene and polytrifluoromonochloroethylene, the measurement of sound propagation was also made for a plate-shaped sample moulded from particles. This experiment was performed using the same apparatus as the suspension method, by inserting the plate in the path of the sound beam. Details are seen in a literature.[4] From the velocity and attenuation in a plate, the modulus and loss factor were calculated by the well-known equations:

$$K'+\frac{4}{3}G'=\rho V_l^2\frac{1-\left(\dfrac{\alpha_l V_l}{\omega}\right)^2}{\left\{1+\left(\dfrac{\alpha_l V_l}{\omega}\right)^2\right\}^2}, \tag{9}$$

$$\frac{K''+\dfrac{4}{3}G''}{K'+\dfrac{4}{3}G'}=\frac{2\left(\dfrac{\alpha_l V_l}{\omega}\right)}{1-\left(\dfrac{\alpha_l V_l}{\omega}\right)^2}, \tag{10}$$

$$G'=\rho V_s^2\frac{1-\left(\dfrac{\alpha_s V_s}{\omega}\right)^2}{\left\{1+\left(\dfrac{\alpha_s V_s}{\omega}\right)^2\right\}^2}, \tag{11}$$

$$\frac{G''}{G'}=\frac{2\left(\dfrac{\alpha_s V_s}{\omega}\right)}{1-\left(\dfrac{\alpha_s V_s}{\omega}\right)^2}. \tag{12}$$

§ 4. Styrene-butadiene Rubber

The original form of styrene-butadiene rubber sample used in this study was a latex of 50% concentration. The concentration was determined by perfectly drying the latex at 80°C, 1 cm Hg. The radius of particles is less than 1 micron. Diluting the latex by distilled water, the concentration dependence of sound velocity and attenuation was measured. The result showed that both velocity and attenuation have a linear relation to concentration below 20%. A suspension of 11.1% volume fraction was therefore used as a sample.

The temperature dependence of velocity and attenuation of the suspension is illustrated in Figs. 3 and 4. From the smoothed curves in Figs. 3 and 4, K' and K'' are calculated using Eqs. (4) & (5) respectively, as shown in Fig. 5.

The broken lines in Fig. 5 show for comparison Cunningham and Ivey's data[3] of K', G' and G'' at 1 Mc/s for GR-S which is a

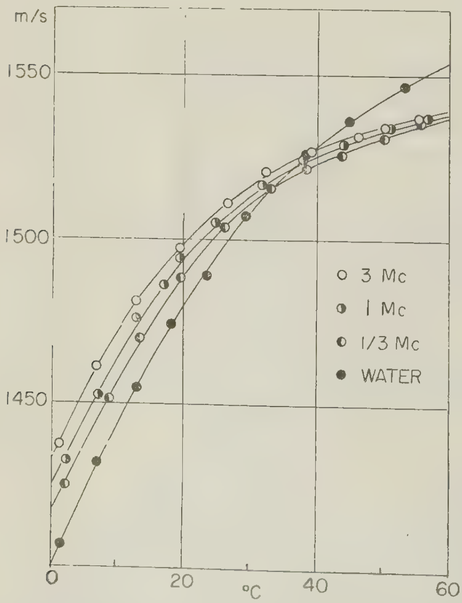

Fig. 3. Sound velocity *versus* temperature in aqueous suspension of styrene-butadiene rubber (c=11.1%).

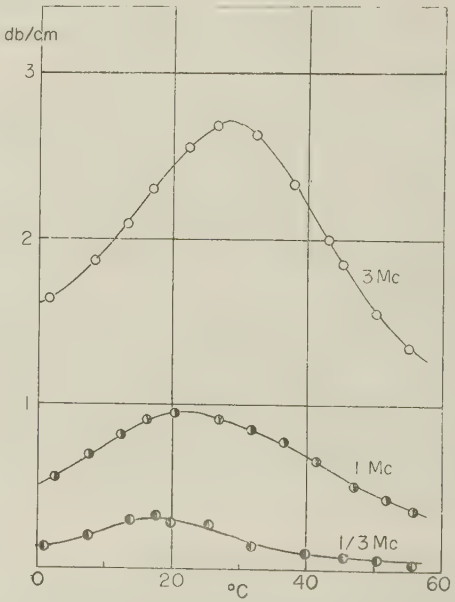

Fig. 4. Attenuation of sound in aqueous suspension of styrene-butadiene rubber (c=11.1%). Attenuation in water is negligibly small.

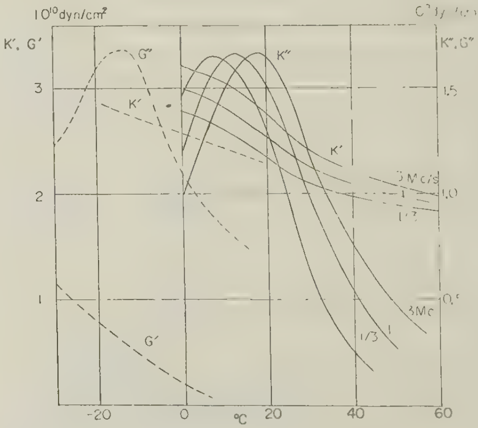

Fig. 5. Real and imaginary parts of bulk modulus of styrene-butadiene rubber. Broken lines show Cunningham-Ivey's data for GR-S at 1 Mc/s.

sort of styrene-butadiene rubber. Comparing K'' of the present study with G'', it is evidently seen that the relaxation strength is of the same order of magnitude for volume and shear deformation. On the other hand, the peak temperature seems at first sight to be quite different for K'' and G''; the peak of K'' at 1 Mc/s is higher than that of G'' by 27° at the same frequency. This discrepancy, however, should be attributed to the difference in styrene content between GR-S and the present sample. The glass transition temperature T_g is $-61°$ C for GR-S,[16] whereas T_g of the present sample determined from volume dilatometry is $-27°$C, being 34° higher. The higher peak temperature of K'' accordingly might be due to the higher styrene content of our sample.

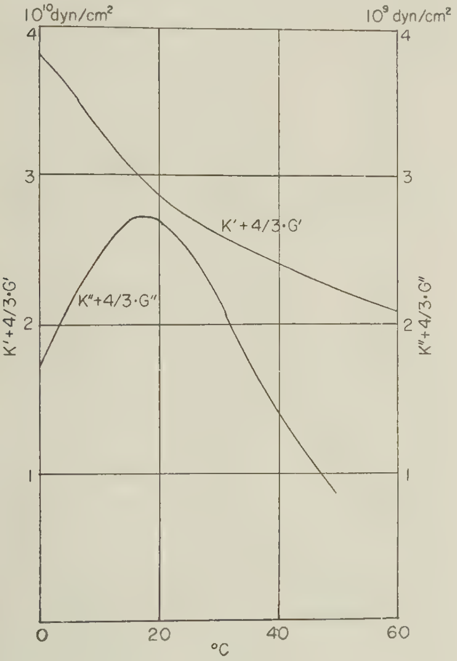

Fig. 6. Real and imaginary parts of $K+4G/3$ of styrene-butadiene rubber at 1 Mc/s.

The validity of this prediction can be verified from the following experiment. Fig. 6 shows the real and imaginary parts of $K+4G/3$ at 1 Mc/s obtained from the longitudinal wave propagation in the rubber plate made of the latex used in the present investigation. The peak temperature of $K''+4G''/3$ is 13°C in agreement with K'' in Fig. 5. The peak value of $K''+4G''/3$ is about twice larger than K'', hence K'' and G'' are of nearly the

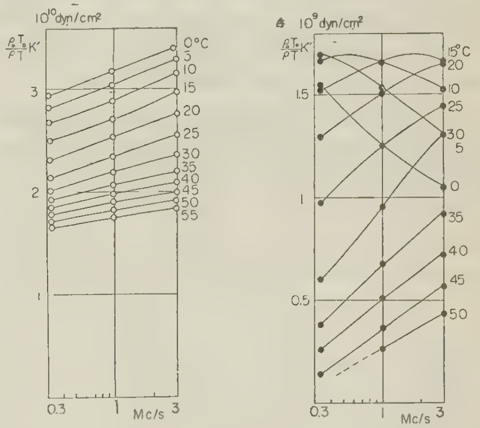

Fig. 7. Real and imaginary parts of bulk modulus of styrene-butadiene rubber multiplied by vertical shift factor plotted against frequency in logarithmic scale.

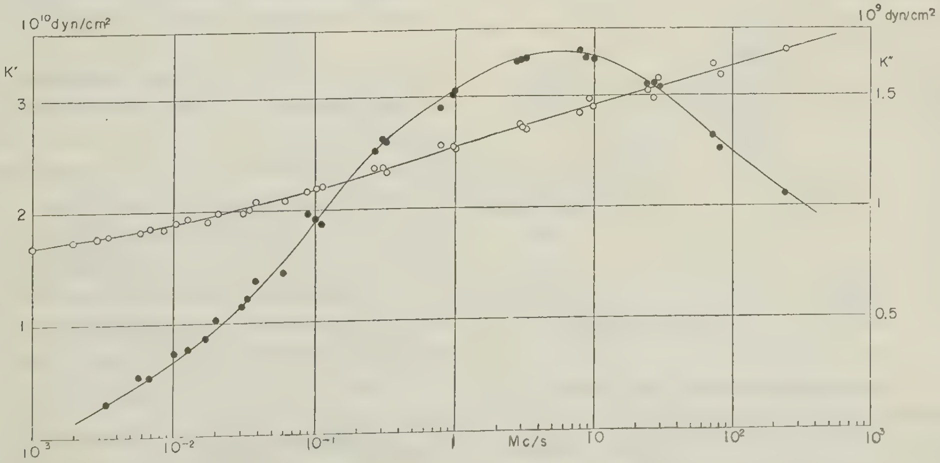

Fig. 8. Reduced curves of K' and K'' of styrenebutadiene rubber ($T_0=20°$C).

same magnitude at their maxima. It may now be quite safely concluded, therefore, that the transition region lies at the same temperatures for bulk and shear moduli.

Now we shall apply the well-known reduction scheme of Ferry17) to the present results. Fig. 7 shows K' and K'' multiplied by the vertical shift factor $\rho_0 T_0/\rho T$, plotted against frequency in logarithmic scale. The reduced curves at 20°C are obtained in Fig. 8 by the horizontal shift, in which the same reduction factor was employed for K' and K''.

The frequency range of the reduced curves is not broad enough to allow a precise conclusion as to the relaxation spectrum. But it may be noted here that, in the low frequency side of the K'' curve, K'' is proportional to square root of the frequency. This behavior should result in a wedge-type relaxation spectrum of slope 1/2, as is widely observed in shear deformation of rubber.18)

The reduction factor a_T is plotted against temperature in Fig. 9. The curve is best fitted by Williams-Landel-Ferry's equation:19)

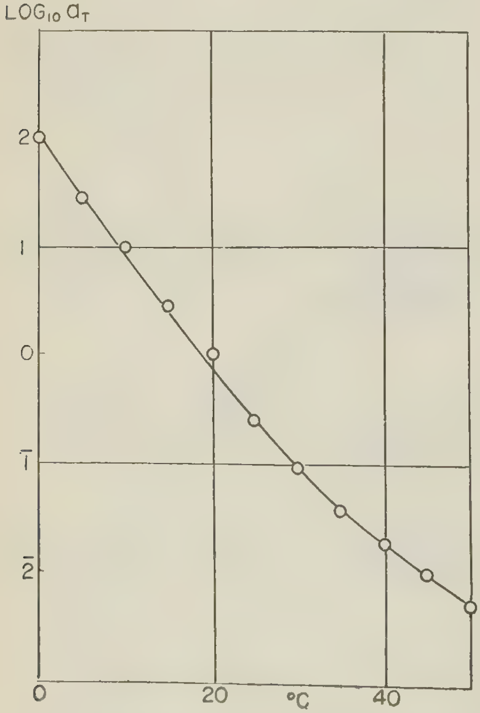

Fig. 9. Reduction factor a_T for bulk modulus of styrene-butadiene rubber plotted against temperature ($T_0=20$°C). Solid line represents Williams-Landel-Ferry's equation ($T_s=20$°C).

$$\log_{10} a_T = -\frac{8.86(T-T_S)}{101.6+(T-T_S)}, \qquad (13)$$

when T_S is chosen as 20°C. This T_S value is 47° higher than T_g. The factor a_T may be differentiated to give the apparent activation energy $H=Rd(\log a_T)/d(1/T)$. H is 34 kcal/mol in this case.

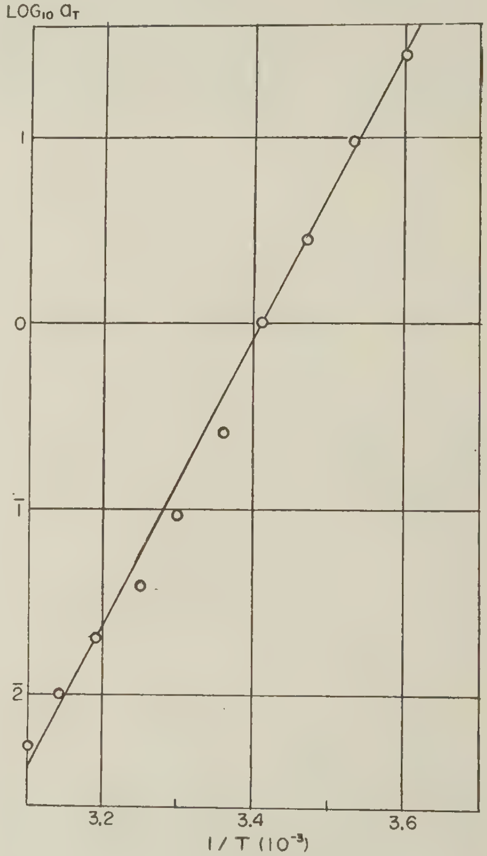

Fig. 10. Reduction factor for bulk modulus of styrene-butadiene rubber plotted against reciprocal of absolute temperature ($T_0=20$°C).

All the above-mentioned behaviors about the bulk modulus, i.e. the relaxation strength, relaxation times, their distribution and temperature dependence, are quite similar also in the case of the shear modulus. Within the precision and frequency range available in this work, there is no appreciable discrepancy between the relaxation mechanisms of volume and shear deformation, hence the molecular mechanisms involved also should be of nearly the same character.

§ 5. Natural Rubber

The original form of natural rubber suspension used in this study was a latex of 50% concentration, the particle radius being 1 micron or less. The latex was diluted by distilled water to 10% volume fraction. Since the transition region of natural rubber, when measured even at megacycles range, lies below 0°C, the result is rather incomplete as is illustrated in Fig. 11.

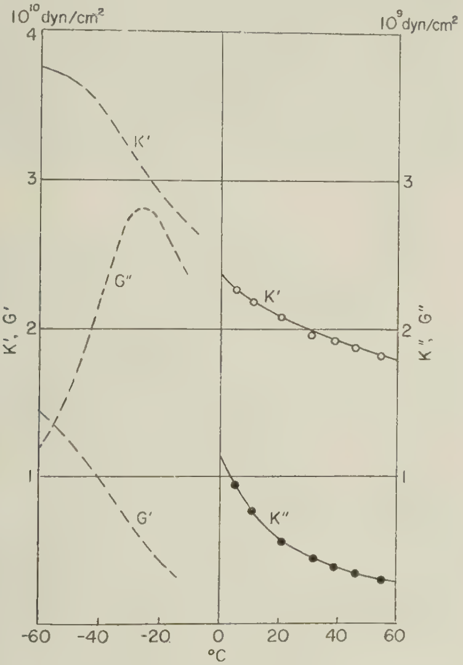

Fig. 11. Real and imaginary parts of bulk modulus of natural rubber at 1 Mc/s. Broken lines indicate Cunningham and Ivey's data[3)] of natural rubber at 1 Mc/s.

It may be safely said, however, that the prediction by Cunningham and Ivey,[3)] $K'' \ll G''$ at transition region, might not be the case. The present result rather suggests that K'' is of the same order of magnitude as G'', as is the case with styrene-butadiene rubber.

§ 6. Polyethylene

Many of the crystalline polymers, such as Ziegler polyethylene, polypropylene, fluorine-containing polymers etc., are originally polymerized into a shape of fine powders. The suspension method described in this paper can well be applied to the determination of viscoelastic properties of these materials.

Ziegler polyethylene powders, sifted from coarse grains by a 100 mesh sieve, were suspended in methyl alcohol, volume concentration being 6.5%. Particles are nearly spherical in shape and the average radius is about 30 microns. The values obtained are illustrated in Fig. 12. One sees that K''/K' has a remarkable maximum at -35°C.

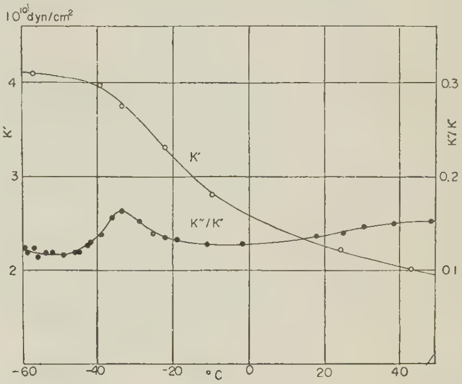

Fig. 12. Real part and loss factor of bulk modulus of Ziegler polyethylene powder at 1 Mc/s.

Many investigations have so far been performed on the dynamic mechanical properties of polyethylene.[20)] It is a well established fact that polyethylene exhibits three dispersion regions, labeled as α, β and γ descending from higher temperatures. When measured at 1 Mc/s, three peaks of the loss factor are expected to appear in the vicinity of 80°, 20° and -65°C, respectively. In case of Ziegler polyethylene, the β peak is very slight, often undetectable because of its high crystallinity. Of course these date have been obtained for moulded samples and mostly for shear deformation.

The dispersion phenomena of polyethylene powder in Fig. 12 is quite unexpected from these previous data. In the present case the β and γ peaks completely disappear and instead a new one reveals itself in the vicinity of -35°C. This variation cannot be considered to come from the peculiarity of the present sample, nor from the different mechanisms involved in volume and shear deformations. The reason is in what follows. When our powder was moulded into a plate and the longitudinal and shear wave propagations in the plate were measured, the γ peak clearly appeared both for $(K''+4G''/3)/(K'+4G'/3)$ and G''/G' at -65°C (see Fig. 13).

From these results, we may conclude that the virgin powders of polyethylene which have not undergone any treatment after polymerization is quite different from the moulded block in mechanical behaviors and accordingly in molecular arrangement. In this connection the studies of other types of behavior of the powder, such as dielectric, thermal, nuclear-magnetic and the like, is very desirable.

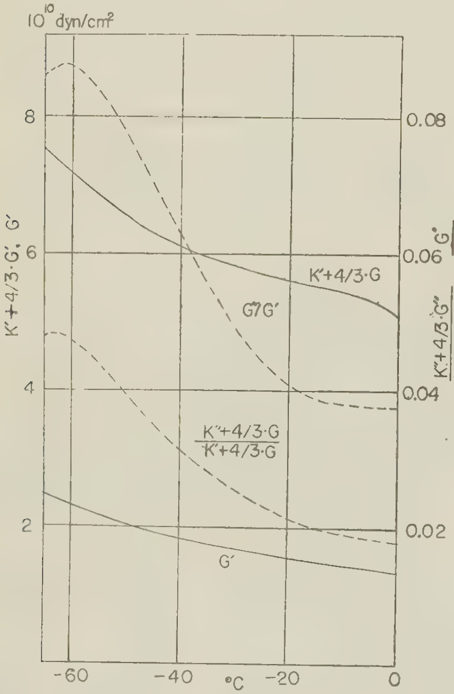

Fig. 13. Moduli and loss factors in moulded plate Ziegler polyethylene at 1 Mc/s.

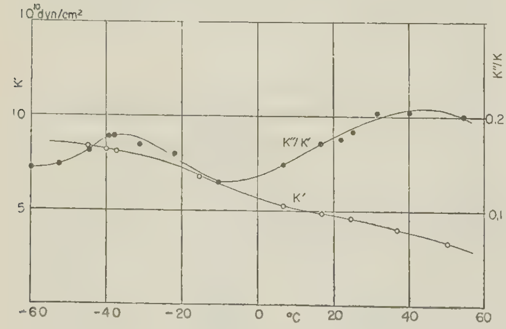

Fig. 14. Real part and loss factor of bulk modulus for polypropylene at 1 Mc/s.

§ 7. Polypropylene

Polypropylene powders (Moplen-2) used is about 10 microns in radius. The velocity and attenuation of sound at 1 Mc/s were measured for 8.7% suspension in methyl alcohol. The calculated values of K' and K''/K' are shown in Fig. 14.

The data available about the mechanical properties of this polymer is at this time so scanty, therefore no discussion will be given here.

§ 8. Polytrifluoromonochloroethylene

Polytrifluoromonochloroethylene powders used in our experiment is about 25 microns in average radius, being not spherical in shape. The powders, after separated from coarse grains by a 100 mesh sieve, was suspended in methyl alcohol at volume fraction of 3.0%. The results are given in Fig. 15.

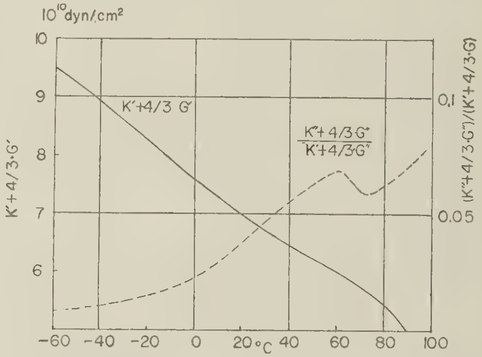

Fig. 15. Real part and loss factor of bulk modulus of polytrifluoromonochloroethylene powder at 1 Mc/s.

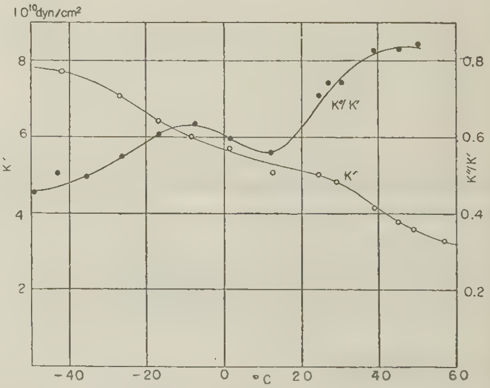

Fig. 16. Real part and loss factor of longitudinal wave modulus of moulded polytrifluoromonochloroethylene at 1 Mc/s.

For comparison, a longitudinal wave measurement at 1 Mc/s was performed for the plate moulded from these powders, the results being represented in Fig. 16. The dispersion region is quite different between the powder and plate as is the case with polyethylene.

§ 9. Paraffin

Fine spherical powders of engineering paraffin was prepared as follows: Paraffin is emulsified by violent stirring in hot water plus emulsifier and slowly cooled down below freezing point under continuous stirring. The powders thus yielded are filtered and dried. The average radius of powders depends on the velocity of stirring, being 15 microns in our case. A suspension of 6.1% in methyl alcohol was used. The observed values of K' and K''/K' are given in Fig. 17.

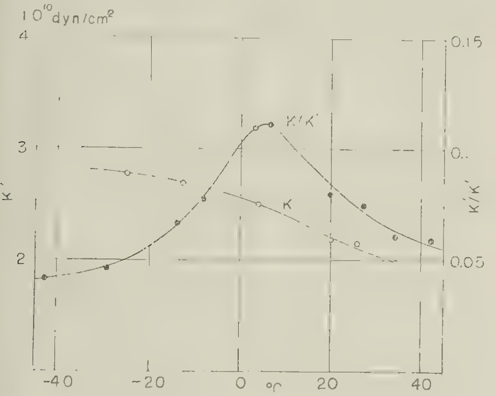

Fig. 17. Real part and loss factor of bulk modulus of engineering paraffin (M.P.=54°C) at 1 Mc/s.

There exists an evident peak of K''/K' at 6°C. This is very reasonable when compared with the data by Mikhailov and Soloview,[21] in which the loss factor at 100 kc/s associated with Young's modulus is found to become maximum at −12°C. The molecular mechanism of this dispersion may persumably be associated with the premelting phenomena in paraffin.

§ 10. Yeast Cell

Using the techniques described in this paper, we can obtain some informations about the mechanical properties of micro-organism in its living state from the velocity and attenuation of sound in an aqueous suspension of the organism.

As a preliminary study, yeast cells (Saccharomyces cerevisiae) which are nearly spherical with radius of 2.8 microns were suspended in water in a concentration of 10% and measured by ultrasonic waves at 1 Mc/s. The temperature range of observation was restricted in the upper side by the death of organism and, below 20°C, the organism falled into "sleep."

The obtained results are represented in Fig. 18. Since a yeast cell is not in a single phase, but surrounded with a thin cell wall, the physical meanings of K' and K''/K' shown in Fig. 18 are somewhat complicated. If the influence of the cell wall is neglected for simplicity, the values should be associated with protoplasm in the cell. K' in Fig. 18 is nearly independent of temperature. This type of behavior is known to be characteristic to some aqueous solutions of organic substance, because K' increases with temperature for water, but decreases for organic substance. The protoplasm in the cell is an aqueous solution of proteins and fits this case.

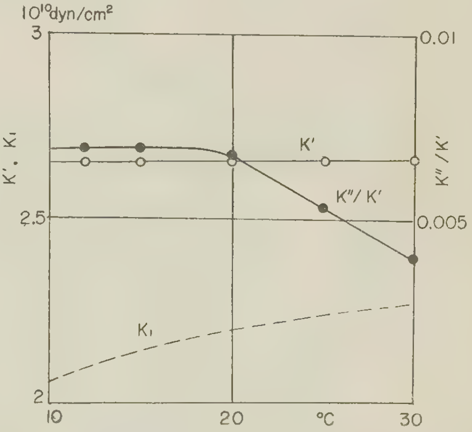

Fig. 18. Real part and loss factor of bulk modulus of yeast cell at 1 Mc/s. Broken line represents real part of bulk modulus of pure water for comparison.

§ 11. Acknowledgements

The authors are deeply indebted to Dr. S. Koga for his help in study of the yeast cell and to Assist. Prof. S. Fukutomi for his aid in obtaining part of the data presented in this report. They also wish to thank Mr. K. Okano for his helpful comments on the theoretical basis of this study.

References

1) R. S. Marvin, R. Aldrich and H. S. Sack: J. Appl. Phys. **25** (1954) 1213.
2) A. W. Nolle and P. W. Sieck: ibid. **23** (1952) 888.
3) J. R. Cunningham and D. G. Ivey: ibid. **27** (1956) 967.
4) R. Kono: J. Phys. Soc. Japan **15** (1960) 718.

5) O. Nakada: J. Polym. Sci. **43** (1960) 149.
6) R. O. Davies and G. O. Jones: Proc. Phys. Roy. Soc. (London) **A217** (1953) 26.
7) W. Philippoff and J. Brodnyan: J. Appl. Phys. **26** (1955) 846.
8) J. E. McKinney, S. Edelman and R. S. Marvin: ibid. **27** (1956) 425.
9) R. J. Urick: ibid. **18** (1947) 983.
10) R. J. Urick and W. S. Ament: J. Acoust. Soc. Am. **21** (1949) 116.
11) Y. Wada: J. Phys. Soc. Japan **13** (1958) 1390.
12) K. Okano: Private communication.
13) P. S. Epstein: Theodore von Karman Aniversary Volume (California Institute of Technology, Pasadena, California, 1941).
14) A. J. Urick: J. Acoust. Soc. Am. **20** (1948) 283.
15) Y. Wada, H. Hirose, T. Asano and S. Fukutomi: J. Phys. Soc. Japan **14** (1959) 1064.
16) R. H. Wiley and G. M. Brauer: J. Polym. Sci. **3** (1948) 455.
17) J. D. Ferry: J. Am. Chem. Soc. **72** (1950) 3746.
18) J. D. Ferry, L. D. Grandine, Jr. and E. R Fitzgerald: J. Appl. Phys. **24** (1953) 911.
19) M. L. Williams, R. F. Landel and J. D. Ferry: J. Am. Chem. Soc. **77** (1955) 3701.
20) Y. Wada: J. Phys. Soc. Japan **13** (1958) 1408.
21) I. G. Mikhailov and V. A. Soloview: Akust Zh. USSR. **3** (1957) 65.

JOURNAL OF THE PHYSICAL SOCIETY OF JAPAN, Vol. 15, No. 12, DECEMBER, 1960

Optical Properties of KCl : Tl in the Extreme Ultraviolet Region

By Kiyoshi AOYAGI and Goro KUWABARA

Department of Physics, Faculty of Science,
University of Tokyo

(Received August 4, 1960)

The optical properties of KCl : Tl in the vacuum ultraviolet range were studied between room and liquid nitrogen temperatures. A new band was observed in both the absorption and excitation spectra on the long wave length tail of the exciton band, i.e. 7.19 ev at −180°C. From the measurements of the temperature dependence and the emission spectrum the band is supposed to be associated with a transition in Cl ions in the neighborhood of a Tl ion.

Excitation and emission spectra of fluorescence by the light in the fundamental band region, as well as thermal glow and optical stimulation curves of phosphorescence were also measured. The process of this luminescence is discussed.

§1. Introduction

Alkali-halide phosphors activated with thallium have been extensively studied both experimentally and theoretically. Three prominent absorption bands, denoted as A, B, and C band, were found and assigned as transitions from the ground state $^1S_0$ to the excited levels of a thallium ion such as $^3P_1$ and $^1P_1$.

Recently, however, detailed experimental studies(1) revealed that these bands have more complex structures than expected from the simple assignment, and in order to explain complex behaviors the mixing of electron transfer states with those of thallium ions has been proposed,(2) but definite conclusions have not yet been attained.

Some of the bands corresponding to transfers of an electron from the neighboring chlorine ion to the thallium or the transitions to the perturbed exciton states may be expected to appear in the long wave length side of the exciton band of pure alkali-halides, and Yuster and Delbecq(3) have observed one band for KI : Tl.

In order to see the effects of the configuration mixing, it may be valuable to study also some other alkali-halides, especially of various anions, which have the spin-orbit interaction of different magnitude. Moreover, if the bands assigned to the perturbed or localized exciton states are clearly observed, it may be interesting to study the mechanism of excitation of thallium ions with lights in those bands.

On the other hand, it is well known that those phosphors luminesce by excitation with high energy particles, X-ray or with light in the fundamental absorption band. This phenomenon is common for most of practical phosphors, and in this case an activator excited not directly by incident particles or photons but indirectly by free carriers and excitons produced simultaneously by radiation. Alkali-halides phosphors activated with thallium are most suited for elucidating the detailed mechanism of energy transfer through the crystal, because in these phosphors the optical transitions corresponding to direct excitation and those producing free carriers and excitons are well separated with each other.

Several experiments, especially intended for the study of the behavior of excitons, have been reported on alkali-iodides.(4) In these crystals, however, the fundamental band has a complex structure probably because of the large spin-orbit interaction and moreover the *C* band lies so closely to the exciton band that it seems rather difficult to distinguish the effects of direct and indirect excitation of thallium ions.

In these respects potassium chloride, in which the spin-orbit interaction is small and both bands are separated as much as 1.3 ev, is suited also for this purpose.

§ 2. Experimental Procedures

Measurements of excitation and absorption spectra were performed with a vacuum monochromator constructed in our laboratory, which is equipped with a concave grating working at nearly normal incidence as shown in Fig. 1a. The grating is of Bausch & Lomb Optical Co. with 40 cm concave radius and 600 lines per mm. The light source is a hydrogen discharge lamp with a hot-cathode operated at several hundred watts. For the purpose of excitation and photoconductivity measurement this spectrometer is intended to give high intensity rather than resolution. The optical arrangements in the detector chamber were changed according to the purposes of measurements. The intensity of light below 250 mμ was measured by means of 1P28 photomultiplier tube with a fluorescent screen of sodium salicylate which is reported to have a constant efficiency below 300 mμ. The slit width was about 3 mμ in wave length for the measurements of excitation spectra and about 1 mμ for absorption spectra. For the measurements at low temperatures the crystal holder was attached to a double Dewar vessel shown in Fig. 1b. To prevent some vapors to adhere to the surface of the specimen at low temperatures, liquid nitrogen was poured into the outer shell of the double Dewar vessel at first. The crystal holder was warmed with a heater to about room temperature and then after half an hour the

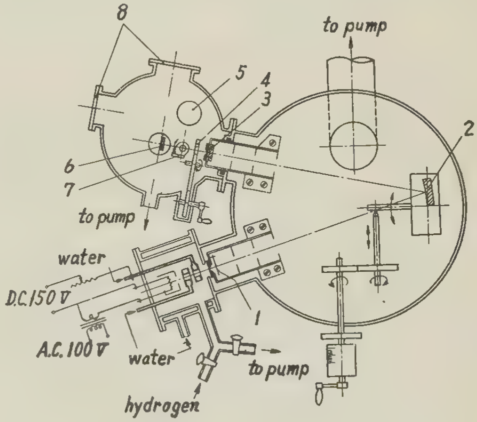

Fig. 1a. Vacuum monochromator. 1: shutter, 2: grating, 3: window of LiF, 4: filter holder, 5: photomultiplier tube, 6: specimen, 7: fluorescent screen of sodium salicylate, 8: quartz windows.

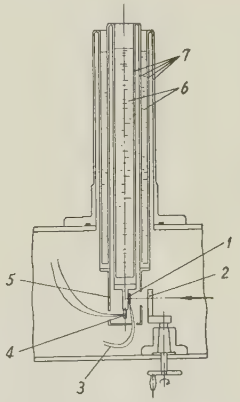

Fig. 1b. Double Dewar vessel. 1: specimen, 2: fluorescent screen of sodium salicylate, 3: thermo-junction, 4: heater, 5: radiation shield, 6: liquid nitrogen, 7: stainless steel.

specimen cooled down by filling the inner vessel with liquid nitrogen.

Single crystals of KCl : Tl were grown by the Kyropoulos method from the melts containing 0.001∼10 mole per cent of thallium and annealed for several hours. Concentrations of thallium in the crystals were estimated from the absorption intensity in the A band assuming the oscillator strength of this band to be 0.1 at room temperature, and were found to be of the order of 10^{-2} of those in the melts.

The emission spectra were photographed with a small quartz spectrograph from the same side of the crystal as the exciting light to prevent reabsorption of the emission, and Neopan-SSS photographic films of Fuji Photo Film Co. were used.

§ 3. Results and Discussions

(1) *D-band*

The excitation spectra of KCl : Tl single crystals at 12 and −180°C for equal number of incident photons are shown in Fig. 2. The well-known three bands, namely A, B and C band, are observed in these spectra. On the higher energy side of the C band another band was found, to which somewhat similar band had been reported by Eby and Teegarden[2]. However, it is probably different from ours, as will be seen in the following details. The peak of the new excitation band lies at about 7.01 ev at room temperature, and shifts towards higher energy side with decrease of temperature.

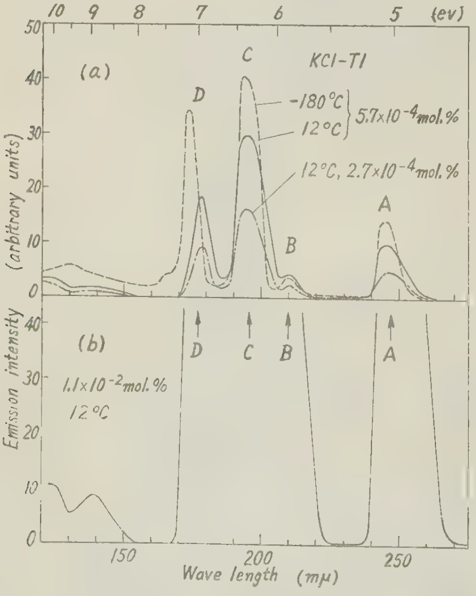

Fig. 2. Excitation spectra of KCl : Tl crystals with different thallium concentrations.

Curve (a) in Fig. 3 shows the absorption spectrum at liquid nitrogen temperature of one of the KCl : Tl crystals quoted in Fig. 2, and (b) shows that of an undoped crystal* grown from the same reagent grade KCl. When we plotted the differences of these two absorption curves, near the tail of the fundamental band there appeared one absorption band which precisely coincides with the band found in the excitation spectra. Curve (d) is the absorption spectrum of this band at room temperature obtained by the same way.

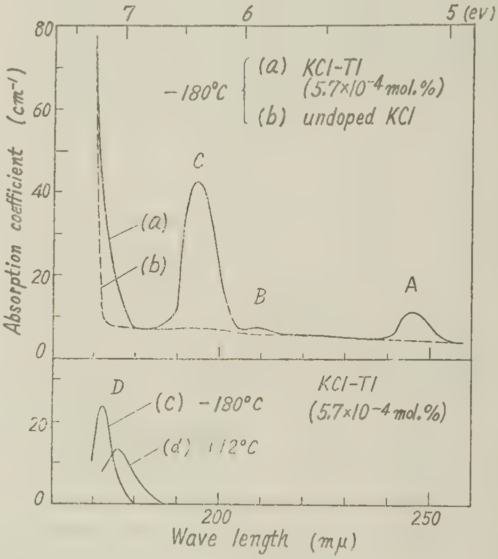

Fig. 3. Absorption spectra of a KCl crystal containing 5.7×10^{-4} mole per cent thallium (a) and of undoped KCl crystal (b) at liquid nitrogen temperature. Curve (c) is the absorption spectrum of the D band obtained by subatacting (b) from (a), and curve (d) is for room temperature.

The new band, which is found both in the absorption and excitation spectra is denoted as D band in this paper. As shown in Fig. 4 the absorption intensity of the D band increases almost linearly with the increase of thallium concentration within the range of the present experiment, i.e. from 2.7×10^{-4} to 1.1×10^{-2} mole per cent.

---

* The undoped KCl crystals prepared in our laboratory has an absorption coefficient ca. 65 cm^{-1} at 175 mμ at room temperature, which is somewhat larger than that reported by Kobayashi *et al.*[5] This may be due to a presence of bromine impurities as they suggested.

Fig. 5 shows the temperature dependence of the absorption hand. The peak lies at 7.01 ev (177 mμ) and 7.19 ev (172 mμ) at 12 and −180°C respectively, and the rate of the shift was -9.4×10^{-4} ev/deg between these temperatures, which is nearly equal to that of the exciton band.⁽⁶⁾

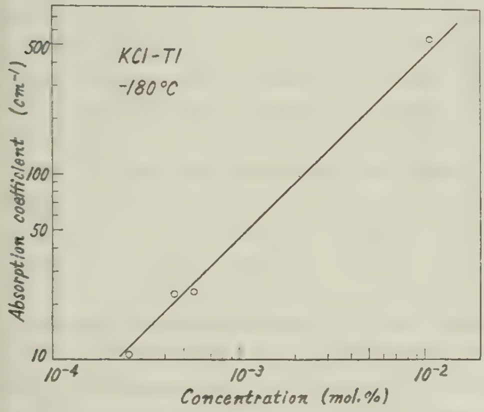

Fig. 4. Concentration dependence of the maximum absorption coefficient of the D band at liquid nitrogen temperature.

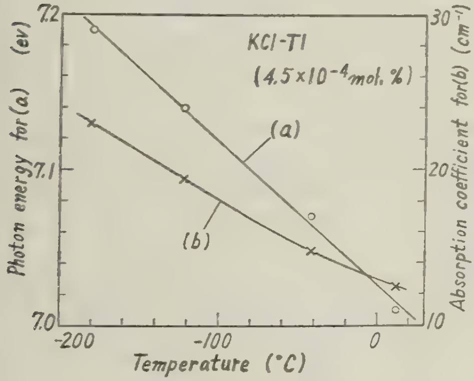

Fig. 5. Temperature dependences of the peak position and the absorption coefficient of the D band.

The shape of the absorption band could not be determined precisely because of the exciton band tail, but it appears to be simple and intermediate between the Gaussian and the Lorentzian. The width of half maximum of the D band was 0.29 ev at 12°C and 0.21 ev at −180°C. The absorption intensity, i.e. the product of the maximum height and the half width, is nearly five times as large as that of the A band, but it increases slightly with the decrease of temperature. Taking into consideration the difference of the refractive index, the oscillator strength of the D band was estimated to be 2.7 times of the A band at −180°C for a crystal containing 4.5×10^{-4} mole per cent of Tl.

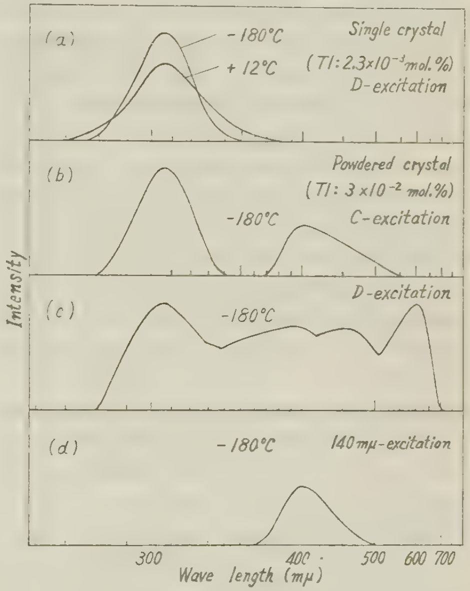

Fig. 6. Microphotometer curves of the emission spectra. (a) of KCl-1.3×10^{-3} more % Tl single crystal excited by the D light at 12 and −180°C; (b), (c) and (d) of KCl-3×10^{-2} mole % Tl powdered crystal at −180°C excited by the C, D and 140 mμ light, respectively. The corrections for the slit width and the sensitivity of films are not made.

Fig. 6a is the microphotometer curve of the emission of a KCl : Tl single crystal excited by the D band light. The ordinate is the absorbance of the photographic films. The emission spectrum was consisted of only the 305 mμ emission band characteristic of thallium ion. Taking into consideration the overlap of the D band with the tail of the fundamental absorption, i.e. subtracting the amount of light absorbed in the tail of the exciton band, the quantum efficiency of the emission by light absorbed in the D band was estimated to be about 1.5 times of that of the emission excited by light in the A band, and it remained nearly constant within the temperature range of the present experiment. According to Bünger,⁽⁷⁾ the quantum efficiency of the emission by the A light is ca. 0.5. Therefore it is concluded that the light in the D band causes luminescence due to thallium with a quantum efficiency of nearly unity. The details of the emission spectrum will be described at the end of this section.

From these results on the D band, it is supposed that the band may be due to an excitation of perturbed chlorine ions neighboring to a thallium ion, i.e. the D band corresponds to the β band of the F center. A similar absorption band has been reported for KI : Tl.(3)

If we take the above assignment for the D band, the oscillator strength may be reasonable but the fine structure due to a spin-orbit interaction is expected. According to Knox,(2) the spin-orbit splittings on the transfer spectra will be the combination of those for Cl and Tl atoms, which are about 0.1 ev and 0.97 ev respectively.

No structures, however, was observed in the D band, even though the pass band was 0.03 ev in this region and sufficient for resolving.

If we take the large value for the separations, the other members of the transfer spectra may lie in the A, B and C band regions or in the exciton band. At present, it can not be decided which of the above assumptions is correct. However, it is noted that no structure have yet been reported even for the β band of KCl or NaCl.(8)

The excitation of Tl ions by the D band light may be caused by an auto-excitation process. However, the high quantum efficiency of the D band, such as ca. 1.5 times of the A band, is difficult to understand from a simple picture, and for explanation we must assume that the light of the exciton band tail overlapping with the D band somewhat contributes to the excitation of Tl or that the A band is composed of two bands, one of which is not associated with the luminescence.

It has been reported that KCl : Tl has three emission bands. In our experiment, however, in the case of single crystals only the 305 mμ band was observed by excitation with light in the A, B, C or D band and neither 475 mμ

Table I. List of the emission bands of KCl : Tl crystals including an undoped KCl powdered crystal. R: room temperature, LN: liquid nitrogen temperature, S: strong, M: medium, and W: weak.

Excited band (mμ)	Crystal	Tl (mol. %)	Temp.	Emission band (mμ)				
				247	305	377, 400	475	580 ∼600
A(247)	Single	3×10^{-2}	R		S			
B(210)	Single	3.9×10^{-4}	R		S			
C(196)	Single	2.3×10^{-3}	R		S			
			LN		S			
	Powder	3×10^{-2}	R		S			
			LN		S	M	W	
D {177 at R. 172 at L.M.}	Single	2.3×10^{-3}	R		S			
			LN		S			
	Powder	3×10^{-2}, 5.7×10^{-4}	R		S			
			LN		S	M	M	S
140	Single	3×10^{-2}, 2.3×10^{-3}	R		S			
			LN			?		
	Powder	3×10^{-2}, 5.7×10^{-4}	R		S			
			LN			M	?	
		Undoped	LN			M	W	

nor 247 mμ band could be detected both at 12° and at −180°C. Taking the characteristics of the photographic films and the spectrograph into consideration, the intensities of these emission bands were estimated, if they existed, to be less than one twenteith of that of the 305 mμ band in all cases for crystals prepared in our laboratory. This result appears to somewhat contradict the generally accepted view that all the emission bands are due to the same single Tl center, but we will not touch these problems in this paper.

However, in order to see the effects of form of a specimen or mechanical treatment, the powder specimens were prepared by grinding the single crystals, and emission spectra under the excitation with lights in the various bands at room and liquid nitrogen temperature were examined. The results including those for single crystals are summarized in Table I.

In the case of single crystals all of the emission, or at least most part of the emission was the 305 mμ band irrespective of the exciting lights or the temperature, while in the case of powdered specimens other emission bands, except the 247 mμ band, appeared at low temperatures under the excitation with lights in the C, D or fundamental band. The microphotometer curves of these emission bands are shown in (b), (c) and (d) of Fig. 6. The band peaked at about 400 mμ was observed also for the powdered specimen of undoped KCl under the excitation with the fundamental band light at low temperatures. This fact will be discussed in the later section. The appearance of various emission bands in the case of powdered crystals may be explained that new centers or excitation bands due to the lattice defects were produced by grinding.

(2) *Fluorescence and Phosphorescence by Light in the Fundamental Band Region*

Let us first consider the luminescence at room temperature. On the higher energy side of the D band in the excitation spectra of Fig. 2, almost no luminescence is observed with the exciton band and as the photon energy is increased above the higher energy side of this band, the intensity of the luminescence rises gradually, which is the 305 mμ emission band at room temperature as shown in Table I.

The dip at 130 mμ coincides with the peak of the 2nd fundamental absorption band, and can be interpreted to be mainly caused by rise of reflection loss. The same reason, however, can not explain the deep minimum at the exciton band completely, rather it is supposed that the exciton causes little luminescence at least at room temperature.

Strictly speaking the luminescent intensity for light in the fundamental band range varied with the irradiation time, that is, under the excitation with the 2nd fundamental band light, the luminescence was hardly observed at first for a freshly prepared KCl : Tl crystal and gradually increases with irradiation, saturating at some intensity. The saturation value or the efficiency of the luminescence depends on the intensity of exciting light as well as on the concentration of Tl, but does not vary linearly with them and the luminescence efficiency of the crystal containing 1.1×10^{-2} mole % of Tl for the 140 mμ light was estimated to be about one fifth of that for the A band at light intensity of ca. 10^{13} photons/cm^2 sec.

The irradiation of light in the 2nd fundamental band makes the crystal phosphorescent as well as fluorescent. As the irradiation proceeds, the phosphorescent intensity also increases and attains the saturation value, which depends upon the intensity of exciting light and upon the Tl concentration as in the case of fluorescence. But the incident photon numbers necessary for saturation are different for fluorescence and phosphorescence.

The emisson band of the phosphorescence at room temperature was found to be composed of the 305 mμ band characteristic of Tl ions. The decay of the phosphorescence, the half life of which is ca. 110 sec at 20°C, can not be strictly expressed by a simple exponential curve.

The excitation spectrum of the phosphorescence of a crystal with 1.6×10^{-3} mole % Tl for exciting light of equal intensity (ca. 10^{13} photons/cm^2 sec) is given in Fig. 7. This curve was obtained by repeating the following procedures; the intensity of the phosphorescence saturated by excitation with a monochromatic light was measured and the crystal was restored to the initial state by heating to 100°C for about ten minutes and then excited again with another monochromatic light.

From this figure it is concluded that the phosphorescence of the 305 mμ band appears by irradiation with lights in the 2nd fundamental band as well as the B, C and D band due to Tl, but not by those in the A and the exciton band, and that the spectral distribution in the fundamental band region is similar to that of the fluorescence.

The luminescent behaviors of KCl : Tl crystals at low temperatures were rather different from those at room temperature. In the excitation spectrum shown as dashed curve in Fig. 2 a small hump is observed at the low energy tail of the exciton band. The efficiency, decreasing once at the peak of exciton band, increases again with the increase of photon energy and shows a peak at the 2nd fundamental band i.e. 130 mμ.

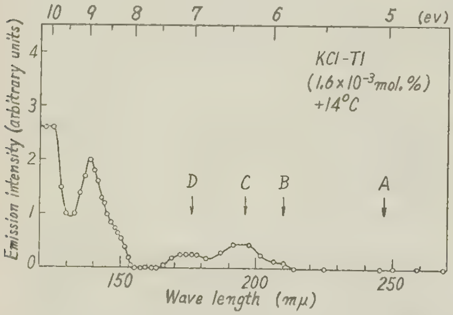

Fig. 7. Excitation spectrum of the phosphorescence at room temperature.

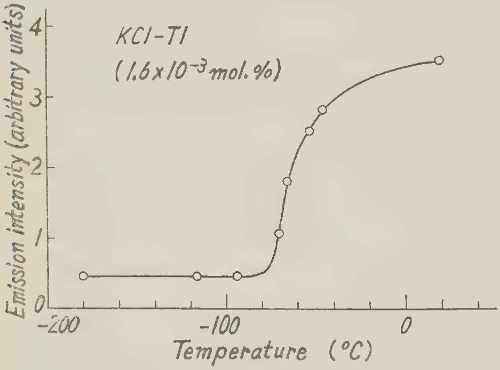

Fig. 8. Temperature dependence of the fluorescence excited with 140 mμ light.

The fluorescent spectrum of a single crystal at −180°C by the 140 mμ light is composed of almost only one band with a peak at ca. 400 mμ.

In Fig. 8 the luminescent intensity of a crystal with high Tl concentration under irradiation with the 140 mμ light is shown as a function of temperature. The intensity abruptly changes near −70°C, below which the fluorescence is mainly composed of the 400 mμ band. While a crystal containing small amount of Tl behaved differently, i.e. the fluorescent intensity rather increased at low temperatures.

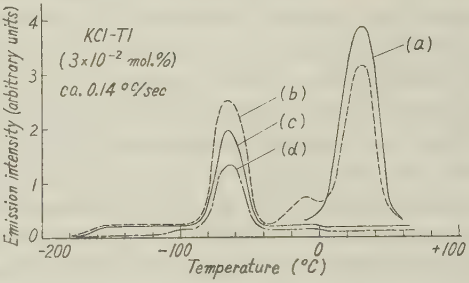

Fig. 9. Thermal glow curves of a KCl : Tl crystal excited with light of 140 mμ at −16 or −180°C. Curve (a) and (b) are total emission; (c) and (d) are visible emission measured with a filter transparent above ca. 380 or 430 mμ, respectively.

In order to study the mechanism of phosphorescence the thermal glow experiment was performed. Curves (a) and (b) in Fig. 9 are the results for a crystal excited with the 140 mμ light at −16° and −180°C, respectively. Three prominent peaks were observed at −65°, −10° and 32°C, conforming with the results obtained by previous authors. The spectral composition of the emission was examined by inserting a filter, which transmits the light longer than 380 or 430 mμ. The emission associated with the peak at 32°C was entirely cut off by either of two filters, and is supposed to be the 305 mμ band, while most or the greater part of the emission associated with the peak at −65°C transmits these filters, showing that the emission is composed of lights above 360 mμ, probably the 400 mμ band. This result is different from that reported by Johnson and Williams,(9) and will be discussed in the later section.

The KCl : Tl crystal, which became phosphorescent, shows a burst of luminescence by stimulation with selective visible light. The spectral distribution of the efficiency of stimulating light measured at room temperature has a peak near 570 mμ. A part of the stimulated emission transmits a filter transparent from 300 to 400 mμ and is supposed to be the 305 mμ band. The effects of various stimulating lights on the thermal glow curve were also studied. The crystals excited with the 140 mμ light at −180°C were irradiated at this temperature with the 546,435 or 365 mμ light from a mercury lamp. All of the thermal glow peaks entirely disappeared simultaneously by irradiation with the 546 mμ light of ca. 10^{18} photons/cm², and the lights 435 and 365 mμ affected slightly.

The effects of the fundamental band light on KCl : Tl single crystals are summarized as follows:

At room temperature (1) the exciton band light causes scarcely any fluorescence or phosphorescence, (2) the crystal shows long lasting phosphorescence as well as fluorescence by irradiation with light which has been supposed to create free electrons and holes in the crystal, (3) the excitation spectra for fluorescence and phosphorescence are similar with each other, (4) in all cases the emission is the 305 mμ band, which is characteristic of Tl ions, (5) the phosphorescence can be stimulated thermally as well as optically;

At low temperatures below about −60°C (6) the emission is mainly the 400 mμ band, (7) the fluorescence can be excited by light which can be absorbed strongly in the surface layer more effectively than at room temperature.

These characteristics may indicate that the fluorescence and the phosphorescence occur by a similar mechanism and that free charge carriers created by light play a dominant role in the transfer of energy absorbed by the host crystal to the emitting centers.

The 305 mμ emission at room temperature is supposed to occur by the following mechanism. Either of an electron or a hole is captured near a Tl ion and when another kind of carriers happens to approach, they recombine with each other giving the energy to the Tl ion by auto-excitation or by dipole transfer. We tentatively assume that a Tl ion itself acts as an electron-trap.

The difference between the fluorescence and the phosphorescence lies in that in the former the electrons trapped by Tl ions recombine with holes produced directly by photons, and in the latter with those holes which have been once captured by some hole-traps and then released again by lattice vibrations. The rises of the fluorescent and phosphorescent intensities with irradiation are interpreted as processes of filling up of carrier traps.

Delbecq *et al*(10) have observed the spin resonance signal due to holes for X-rayed KCl crystals doped with Tl, which disappears at −65°C simultaneously with an absorption band at 350 mμ, and ascribed it to the self-trapped holes.

The present experiment seems to be closely related to these phenomena, i.e. the glow peak of the 400 mμ band or the abrupt change of fluorescence intensity at −65°C corresponds to the temperature above which the self-trapped holes become unstable.

Accordingly, the luminescence at low temperatures is explained by assuming an emitting center other than TI. This center emits the 400 mμ band and may be a kind of lattice defects intrinsic to KCl crystals, which acts as a recombination center as well as an electron-trap much more effectively than Tl at low temperatures, since the faint 400 mμ band is observed also in the undoped crystals. It is supposed that these defects increase by doping as well as by mechanical treatment, and moreover that they are distributed near the surface of the crystal, because the 400 mμ band is effectively excited with light at the peak of the fundamental band, which is strongly absorbed in the surface layer.

At low temperatures most of the recombinations occur at or near the recombination centers and consequently the 400 mμ band is mainly observed.

When the crystal irradiated at liquid nitrogen temperature is gradually warmed up, the self-trapped hole begin to move at −65°C and some of them will recombine with electrons trapped by the recombination centers emitting the 400 mμ band, while the rest will be trapped by hole-traps near the Tl and as the temperature is raised they recombine with electrons which have been trapped by Tl emitting the 305 mμ band.

In the above explanation we have assumed two kinds of traps each for electrons and holes including self-trapping. Some of them may correspond to color centers already reported,(11) but could not be detected by optical absorption measurement, probably because they were too small in numbers. The optical stimulation of the phosphorescence is supposed to be associated with the ionization of electron-traps, probably Tl atoms, which corresponds to the thermal glow peak at 32°C.

Above speculations for the behaviors of free carriers may be checked by the photoconductivity measurement, which is now in progress.

As for excitons it is concluded that they are ineffective as an energy carrier to Tl ions at room temperature even in the highly doped crystal (3×10^{-2} mole % Tl). The difference between the exciton and the second band light for luminescence may be due to some kind of lattice defects densely populated in the surface layer, which annihilate excitons but are inactive for free carriers.

However, the small humps between the exciton and the D band peak observed in the excitation spectra at low temperatures may correspond to the exciton-induced luminescence.

§ 4. Conclusions

The optical properties of KCl : Tl crystals, especially below 200 mμ were studied with a vacuum spectrometer.

A new single band was found on the exciton band tail in the absorption and excitation spectra. The intensity of the band is ca. five times of the A band and increases linearly with the Tl concentration. The absorption peak is situated at 7.01 ev at room temperature and shifts to the higher energy side with the decrease of temperature similarly to the exciton band. This band causes the 305 mμ emission band characteristic of Tl ion, and is assigned as the excitation of Cl ions neighboring to Tl ions.

The lights in the fundamental band region, except the exciton band, also causes phosphorescence as well as fluorescence. The emissions are mainly the 305 mμ and the 400 mμ band at room and low temperatures, respectively.

It is supposed that a Tl ion is excited by the recombination of free carriers, when it occurs in the neighborhood of the Tl, and that the 400 mμ band predominant below ca. −70°C is associated with the defects other than Tl, which are distributed near the surface, enhanced by doping or by mechanical treatment and act as recombination centers.

References

1) D. A. Patterson and C. C. Klick: Phys. Rev. **105** (1957) 401.
D. A. Patterson: Phys. Rev. **112** (1958) 298.
2) R. S. Knox: Phys. Rev. **115** (1959) 1095.
3) P. H. Yuster and C. J. Delbecq: J. Chem. Phys. **21** (1953) 852.
4) M. Tomura and Y. Kaifu: J. Phys. Soc. Japan **15** (1960) 1295.
M. Ueta and T. Ishii: J. Phys. Soc. Japan **14** (1959) 857.
K. J. Teegarden: Phys. Rev. **105** (1957) 1222.
5) K. Kobayashi and T. Tomiki: J. Phys. Soc. Japan **15** (1960) 1350.
6) W. Martienssen: J. Phys. Chem. Solids **2** (1957) 257.
7) W. Bünger: Z. Phys. **66** (1930) 311.
8) R. Onaka: unpublished.
9) P. D. Johnson and F. E. Williams: J. Chem. Phys. **21** (1953) 125.
10) C. J. Delbecq, P. Smaller and P. H. Yuster: Phys. Rev. **111** (1958) 1235.
11) F. Seitz: Rev. Mod. Phys. **26** (1954) 7.
H. N. Hersh: J. Chem. Phys. **30** (1959) 790; **31** (1959) 909.

JOURNAL OF THE PHYSICAL SOCIETY OF JAPAN, Vol. 15, No. 12, DECEMBER, 1960

Effect of Oxygen upon Sintered Cadmium Sulphide Photoconducting Films

By Saburo KITAMURA

Central Research Laboratories, Matsushita Electric Industrial Co., Ltd., Osaka

(Received August 1, 1960)

The dark conductivity and decay time of sintered CdS films prepared by firing in nitrogen gas were higher than those of sintered CdS films prepared by firing in the mixture of nitrogen gas and hydrogen sulphide. Accordingly it was thought that the sintered CdS films prepared by firing in nitrogen gas have many sulphur vacancies acting as donors.

As a result of heat-treatment in oxygen of the sintered CdS films prepared by firing in nitrogen gas, the dark conductivity and decay time decreased. A new peak appeared at 680 mμ in spectral response of the photocurrent. The activation energy obtained by measuring the slope of the curve of logarithm of dark conductivity plotted against $1/T$(°K) increased, while the trap concentration obtained by measuring the thermally stimulated current decreased with the increase in temperature of heat-treatment in oxygen. The results of experiments supported the interpretation that sulphur vacancies acting as donors had been occupied by oxygen atoms, and then vanished. At the same time there were produced new exciting centers at about 1.8 eV below the bottom of the conduction band.

By electron-microscopic observations it was found that by heat treatment above 400°C in oxygen, CdO grains were produced on the surface or near the grain boundary of the sintered CdS film, and when the whole surface of the CdS film was coated by CdO layers, photoconductivity was not observed.

§ 1. Introduction

Sintered cadmium sulphide (CdS) photoconducting films have comparatively large photocurrent and are utilized in many electronic devices. However, the investigation of the properties of sintered CdS films is difficult, because there are many barriers interposed between different crystallites in the films and the properties of barriers are supposed to be different from those of the bulk of crystallites. The properties of CdS single crystals have been investigated by many workers, and it seems correct to claim that the properties of the bulk of crystallites in the films are similar to those of a single crystal.

The surface phenomena of CdS single crystals have also been investigated recently. The heat-treatment in vacuum, air, oxygen, hydrogen, hydrogen sulphide, cadmium vapour and sulphur vapour have been reported.[1,2,3,4] Especially, the phenomena in the case of heat-treatment in vacuum, hydrogen and cadmium vapour suggested that sulphur vacancies were produced near the surface of crystals by heat-treatment, and that the oxygen atoms perhaps occupied the sulphur vacancies.

By the investigations of CdS single crystals, it was ascertained that halogen or group III B metal impurities or sulphur vacancies act as donors, and group I B metal impurities or cadmium vacancies act as acceptors.[4,5] To obtain high photoconductivity the compensation of donors and acceptors may be necessary. If the sintered CdS films are prepared in inert gas, there seems to appear donor levels due to sulphur vacancies. In the present study, the author attempted to show how the effect of oxygen appears upon these sintered CdS films.

To prepare sintered CdS films, two different methods have been used. In one method cadmium halide was used as flux material,[6,7] while in the other activated CdS powder was sintered after having been spread or compressed.[8,9] The first method is rather easier to control the properties than the second. In the present paper some results obtained by heat-treatment in oxygen of sintered CdS films prepared by the first method are presented.

§ 2. Preparation of Sintered CdS Films

The sintered CdS photoconducting film was prepared by the flux method using $CdCl_2$ as flux material on a fused quartz plate. A formulation found to be particularly suitable for general application of sintered CdS film had the following composition[7]: 20g of high purity CdS powder, 2 g of $CdCl_2$, 100 cc of distilled water. The purity of CdS powder was found by chemical analysis to be 99.99% or more, and by spectroscopic analysis it was found that there were traces of Si and Zn. All components were blended and ground in a quartz mixer. To add Cu as the activator in sintered CdS film, 0.2 cc of 0.1 mol $CuCl_2$ solution (0.05 atom % of CdS) was added in the suspension. The suspension was then sprayed on the surface of 20×10 mm fused quartz plate by a spray gun made of quartz, and the sprayed layer was dried for 4 hours at 100°C in nitrogen gas. Next, the sprayed layer was fired for 15 minutes at 600°C in a furnace in which nitrogen gas purified by pyrogallol and liquid nitrogen was flowing, and was then cooled at a rate of about 10 deg per minute.

The process of firing was as follows: $CdCl_2$ was first melted by heating, CdS powder was dissolved in melted $CdCl_2$, and then dissolved CdS was recrystallized by the evaporation of melted $CdCl_2$. When all $CdCl_2$ had evaporated, sintered CdS film of thickness of about 10 μ was obtained on the fused quartz plate. As the result of electron-microscopic observation it was found that the sintered CdS film was consisted of many crystalline grains of about 1 μ. The electron-micrograph of the surface of sintered CdS film is presented in Fig. 12(a). The thickness of sintered CdS film can be varied by varying the quantity of the suspension to be sprayed.

In and Ga were usually used as the electrode material in order to make ohmic contact, but in the following experiments these metals could not be used, because the electrodes were to be heated above 600°C in oxygen together with sintered CdS films. The author used Au as the electrode material. Before spraying the suspension on the surface of fused quartz plate Au was evaporated on it. In this case the property of electrode contact was ohmic above 0.1 volts of applied voltage and nonohmic below 0.1 volts. In the following experiments all measurements were carried out above 0.1 volts of applied voltage. The interelectrode distance was 0.5 mm, and the length of electrodes was 10 mm. Fig. 1 shows a diagram of such a specimen.

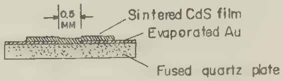

Fig. 1. Diagram of a specimen.

§ 3. Properties of Sintered CdS Films

The sintered CdS films prepared by firing in nitrogen gas using $CdCl_2$ as the flux material have some Cl impurities, and perhaps have many sulphur vacancies. The dark conductivity of sintered CdS films thus prepared was much larger than that of those prepared by firing in nitrogen gas plus hydrogen sulphide. The photoconducting properties of these CdS films are represented in Table I. The properties of sintered CdS films prepared by firing in nitrogen gas were extremely affected by oxygen, but there were little effects of oxygen upon those prepared by firing in nitrogen gas plus hydrogen sulphide. In the investigations of evaporated CdS films, Kuwabara[10] reported that the dark conductivity of CdS film evaporated in vacuum was varied by exposing to air. Also, in the investigations of CdS single crystal, it was reported that sulphur vacancies played as donors.[4] Hence, sintered CdS films prepared by firing in nitrogen gas should have some sulphur vacancies.

When Cu was added to sintered CdS films, the dark conductivity was decreased and the ratio of photocurrent to dark current was increased.

§ 4. Heat-treatment of Sintered CdS : Cl Films in Oxygen

Sintered CdS films added with Cl and having some sulphur vacancies were heated at fixed temperatures in the range of 100∼600°C for 10 minutes in a furnace through which oxygen is flowing. The properties of sintered CdS : Cl films heat-treated at various temperatures

Table I. Properties of sintered CdS films.

Specimen No.	Atmosphere	Activator	Photocurrent μA	Dark current μA	Dark conductivity (Ωcm^{-1})	Decay time m sec.
1	N_2	none added	160	940	2.4×10^{-2}	160
2	〃	〃	200	6500	1.5×10^{-1}	210
3	〃	〃	100	3500	7.5×10^{-2}	170
4	〃	Cu added	330	150	3.7×10^{-3}	65
5	〃	〃	400	500	1.2×10^{-2}	70
6	〃	〃	450	550	1.4×10^{-2}	60
7	N_2+H_2S	none added	70	130	3.3×10^{-3}	80
8	〃	〃	60	160	4.0×10^{-3}	90
9	〃	Cu added	540*	0.5*	1.3×10^{-6}	7
10	〃	〃	60*	0.02*	5.0×10^{-8}	5

Photocurrent: Values obtained by deducting the dark current from the current at the illumination of 200 Lx and at applied voltage of D.C. 2 volts.
Dark current: Current flowing with the applied voltage of D.C. 2 volts in darkness.
Decay time: Time interval until the photocurrent decays to one-half its value for continuous white light illumination of 200 Lx.
*: Values measured with applied voltage of D.C. 20 volts.

were measured by electrical and optical methods.

(a) *Variation of Photocurrent and Dark Current*

One example of variations of photocurrent* and dark current* of sintered CdS films heat-treated in oxygen is shown in Fig. 2. By heat-treatment both photocurrent and dark current were decreased, and the degree of decrease of the dark current is larger than that of the photocurrent. When the sintered CdS films were heated at 650°C, the photocurrent was negligible, while dark current was very large.

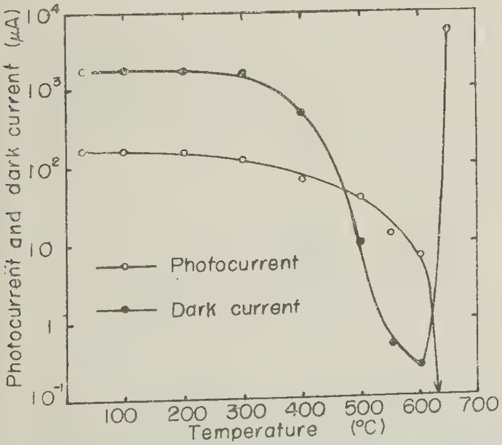

Fig. 2. Variations by heat-treatment in oxygen of photocurrent* and dark current* of sintered CdS:Cl film.

(b) *Spectral Response*

The spectral response of photocurrent of sintered CdS films heat-treated at various temperatures in oxygen was measured by a spectro-photometer of Beckmann type in the range of 400~900 mμ. Light source was an incandescent lamp of 30 watts. Spectral response curves are presented in Fig. 3. The

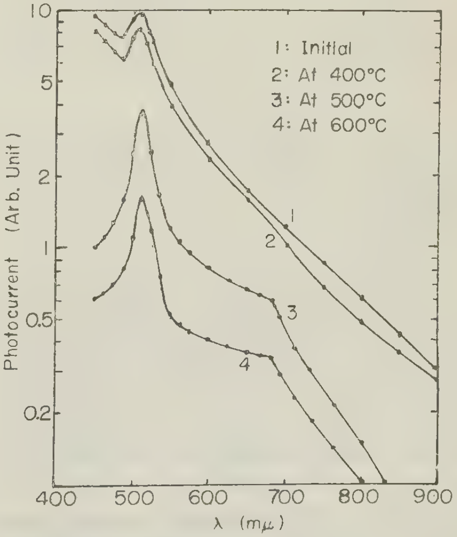

Fig. 3. Spectral response curves of sintered CdS:Cl films heat-treated in oxygen.

---

*: Values measured with applied voltage of D.C. 2 volts.

*: Values measured with applied voltage of D.C. 20 volts.

spectral response curves of sintered CdS : Cl films heat-treated in oxygen below 400°C were found to have only one broad peak at 520 mμ, and by treatment above 450°C a peak at 520 mμ became sharp and a new peak was produced at about 680 mμ.

(c) *Dark Conductivity as a Function of Temperature*

Variations of the dark conductivity as a function of temperature of three specimens, that is CdS : Cl films before heat-treatment, after treatments at 400°C, and at 500°C respectively are illustrated in Fig. 4. Below room temperature, the plot of logarithm of the conductivity against $1/T$(°K) gave a curve with linear portion below−100°C. The slopes of such linear portions for three films corresponded to energies of 0.01 eV, 0.015 eV and 0.02 eV respectively. Above−100°C, the slopes of curves increased with temperature rise.

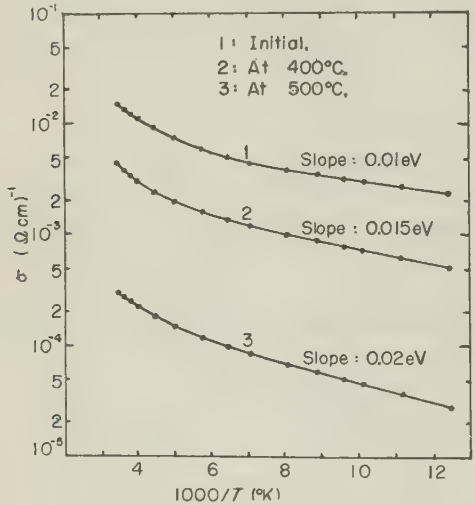

Fig. 4. Dark conductivity of sintered CdS:Cl films heat-treated in oxygen as a function of temperature.

(d) *Thermally Stimulated Current*

The thermally stimulated current is associated with the motion of electrons made free from traps by thermal energy. Measurements of thermally stimulated current were made in the following manner: The sintered CdS film was cooled to liquid nitrogen temperature, and exposed to illumination of white light for 30 sec. Then it was heated in the dark at a rate of about 1 deg per second with applied voltage of D. C. 1 volt. The difference between the current measured in this way and the normal dark current at the corresponding temperature is the thermally stimulated current.

Fig. 5 gives the curves of thermally stimlated current for the initial film and the film heat-treated at 500°C in oxygen. Both the initial film and the heat-treated film had a large broad rise of thermally stimulated current, with a peak at about −140°C. The initial film had fairly large current above 0°C, but the heat-treated film had a small current above 40°C and had an additional small peak at roomtemperature.

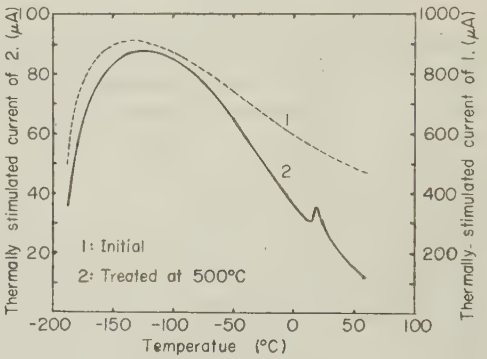

Fig. 5. Thermally stimulated current of sintered CdS : Cl films as a function of temperature: D.C. 1 volt applied, heating rate of about 1 deg/sec.

(e) *Decay Time of Photocurrent*

The decay time of the photocurrent relating to electron traps was as long as about 100∼200 m sec. It was found that the decay time of the photocurrent becomes short with heat-treatment in oxygen.

§ 5. Heat-treatment of Sintered CdS : Cl : Cu Films in Oxygen

The dark conductivity and decay time of sintered CdS : Cl film were very large, and the sintered CdS : Cl : Cu film in which Cu was added had fairly small dark conductivity and large ratio of the photocurrent to the dark current. It was seen that the concentrations of electron traps were decreased by added Cu. In the following experiments, the quantity of added Cu was 0.05 atom % of CdS. The effects of oxygen upon the sintered CdS : Cl : Cu films were remarkable. The method of heat-treatment in oxygen was the same as that in § 4.

(a) *Variation of Photocurrent and Dark Current*

The variations of photocurrent* and dark current* of sintered CdS : Cl : Cu films heat-treatment in oxygen are shown in Fig. 6. The dark conductivity was considerably decreased by heat-treatment in oxygen, so that the ratio of the photocurrent to the dark current became 10^4 or more by heat-treatment at 500∼600°C.

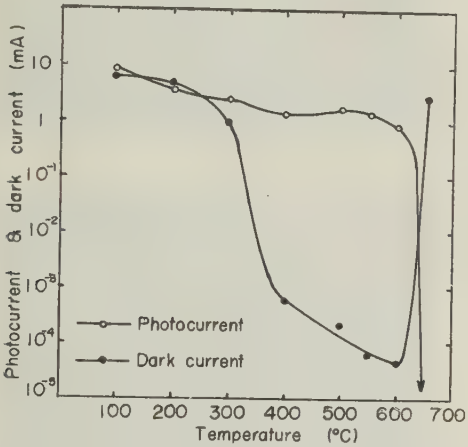

Fig. 6. Variation of photocurrent* and dark current* of sintered CdS:Cl:Cu films by heat-treatment in oxygen.

(b) *Spectral Response*

There were two peaks at about 520 mμ and 620 mμ in the spectral response curves of sintered CdS : Cl : Cu films as shown in Fig. 7. A peak at about 520 mμ corresponded to the absorption edge, and a broad peak at about 620 mμ was produced by added Cu. A broad peak at about 620 mμ became sharp and shifted to red region by the heat-treatment in oxygen. A peak at 520 mμ became sharp by the heat-treatment in oxygen and became low by heat-treatment at 600°C.

(c) *Dark Conductivity as a Function of Temperature*

The variations of dark conductivity of sintered CdS : Cl : Cu films heat-treated in oxygen are given in Fig. 8 as a function of temperature. The conductivity decreased with heat-treating temperature in oxygen, and the slope of the curve of logarithm of conductivity plotted against $1/T$(°K) was increased.

(d) *Rise and Decay Time of Photocurrent*

The rise and decay time were measured by an arrangement consisted of an electromagnetic oscillograph, an incandescent lamp and a shutter. The results are given in Fig. 9. Measurements of rise and decay time were made at applied voltage of D. C. 20 V, with illumination of 200 Lx, and at room temperature. The decay time of photocurrent was extremely decreased by heat-treatment at 200∼300°C in oxygen. The rise time of photocurrent varied very little by heat-treatment in oxygen.

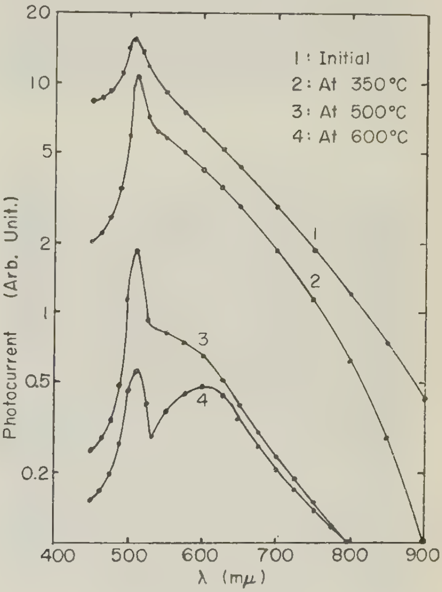

Fig. 7. Spectral response curves of sintered CdS : Cl : Cu films heat-treated in oxygen.

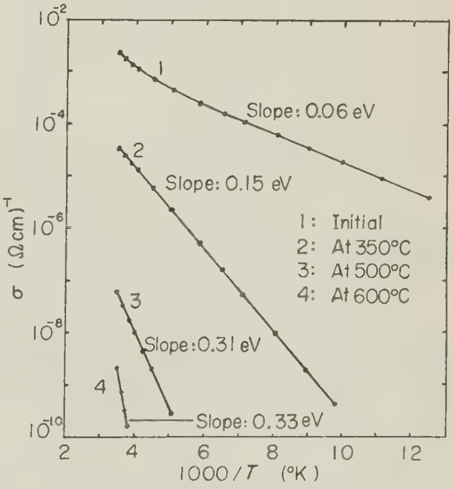

Fig. 8. Dark conductivity of sintered CdS:Cl:Cu films heat-treated in oxygen as a function of temperature.

(e) *Thermally Stimulated Current*

The thermally stimulated current of the sintered CdS : Cl : Cu films was measured by the same method as that in § 4. The results of measurements are shown in Fig. 10. The sintered CdS : Cl : Cu films at initial state had large number of traps, and by heat-treatment in oxygen the trap concentration was decreased, and a peak at about room temperature appeared by heat-treatment at 350∼500°C in oxygen. By heat-treatment at 600°C in oxygen the peak at about room temperature has almost vanished.

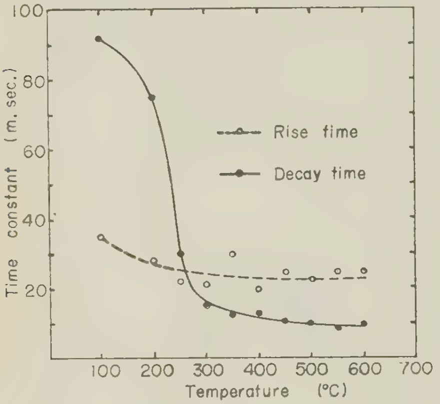

Fig. 9. Rise and decay time constants of sintered CdS : Cl : Cu film heat-treated in oxygen.

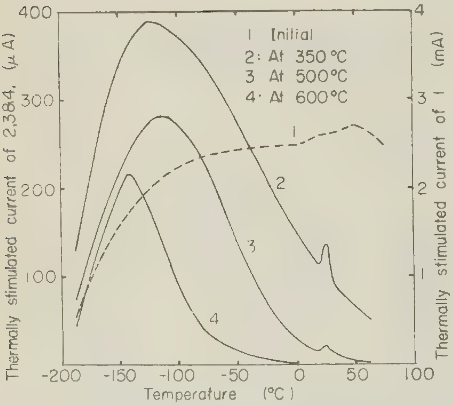

Fig. 10. Thermally stimulated current of the sintered CdS:Cl:Cu films heat-treated in oxygen as a function of temperature: D.C. 37 volts applied, heating rate of about 1 deg/sec.

§ 6. Observation of Produced CdO by an Electron-microscope

It was expected that CdO will be produced by heat-treatment of sintered CdS : Cl : Cu film in oxygen. The quantity of produced CdO in CdS : Cl : Cu films was measured by the method of X-ray diffraction. The results are illustrated in Fig. 11. It was found that CdO was produced by heat-treatment of sintered CdS : Cl : Cu films in oxygen above 400°C. By heat-treatment at 650°C, the quantity of produced CdO was found to be about 20% of CdS.

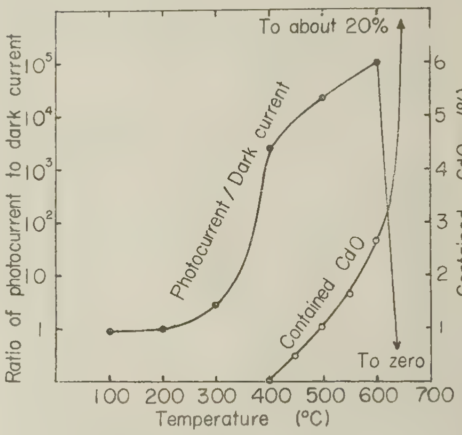

Fig. 11. The quantity of produced CdO in sintered CdS : Cl : Cu films and the ratio of the photocurrent to the dark current as a function of temperature in the case of heat-treatment in oxygen.

The variations of the surface of sintered CdS : Cl : Cu films by heating in oxygen were observed as shown in Fig. 12 by an electron-microscope with carbon replica method. At 300°C in oxygen, there were found some small particles on the surface, and at 500°C many particles, and at 600°C, these particles grew up and the whole surface of CdS : Cl : Cu films was covered by the grown particles. The shape of some of the grown particles on the surface of CdS : Cl : Cu film was cubic. By heating in oxygen at 650°C, it was seen that the produced CdO covered the whole surface of CdS : Cl : Cu film, so that the photoconductivity was negligible.

§ 7. Discussion

The sintered CdS films prepared by firing in nitrogen gas had large dark conductivity and long decay time, but the sintered CdS films prepared by firing in nitrogen gas plus hydrogen sulphide had small dark conductivity and short decay time. Both of the two sintered CdS films had many donors of Cl,

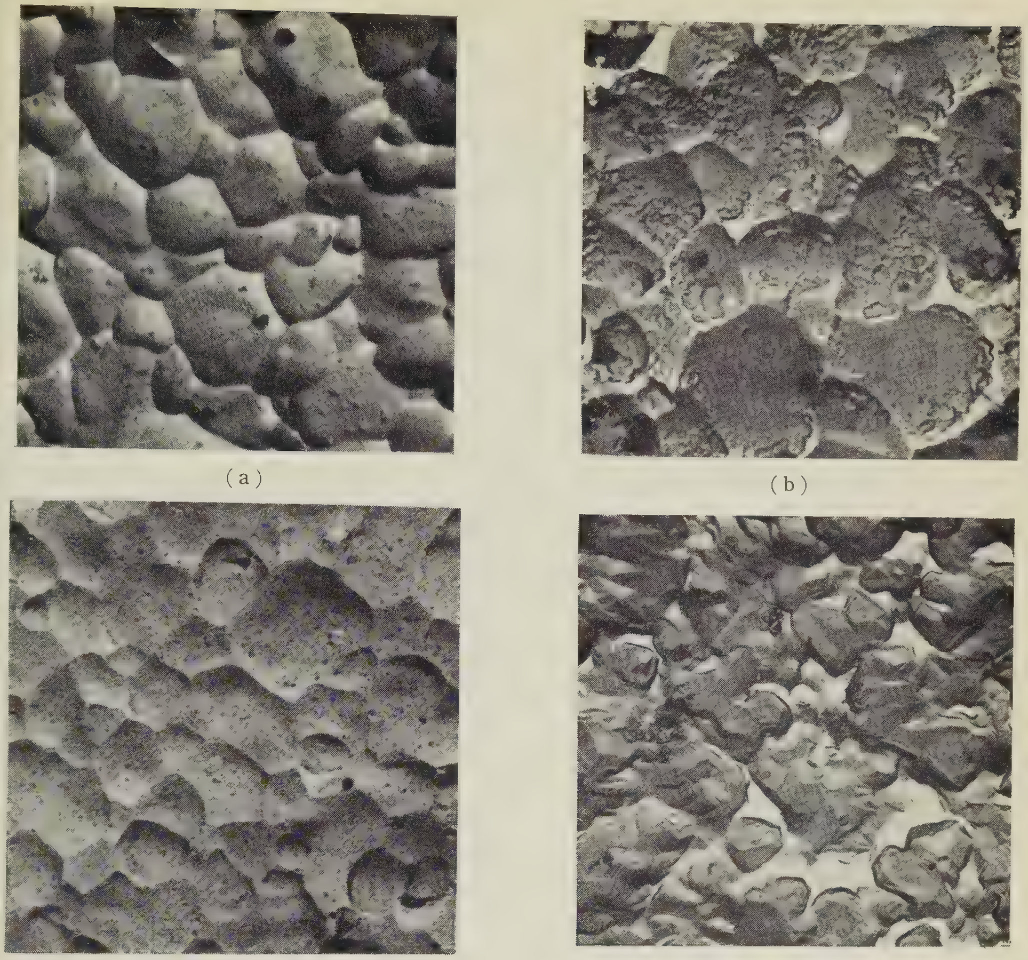

(a) (b)

(c) (d)

Fig. 12. Electron-micrographs of the surfaces of sintered CdS:Cl:Cu films heat-treated in oxygen. (×10000)

(a) Initial state; (b) Heat-treated at 300°C; (c) Heat-treated at 500°C; (d) Heat-treated at 650°C.

but the former should have many sulphur vacancies and by heat-treatment in oxygen these sulphur vacancies should have been occupied by oxygen atoms. By heat-treatment in oxygen at high temperature CdO has been produced on the surface and grain boundary of sintered CdS film.

(1) When sintered CdS films prepared by firing in nitrogen gas were heated in oxygen, the dark conductivity decreased. Below 300°C the degree of decrease was small, and above 300°C it was large. The dark conductivity was produced by thermally excited electrons from donors, so that it was thought that the concentration of donors was decreased by introducing oxygen. It seems that the sulphur vacancies were occupied by oxygen atoms so that the sulphur vacancies acting as donors had vanished.

(2) When sintered CdS : Cl films were heated in oxygen above 400°C, there was observed a new peak at 680 mμ in the spectral response curves. By this fact, it was found that an optical exciting centers were produced at 1.8 eV beneath the conduction band by introduced oxygen. In the case of CdS : Cl : Cu films, the peak at 620 mμ was slightly shifted to longer wavelength region, and the peak at 680 mμ did not appear.

(3) The activation energy corresponding to the slope of the curve of logarithm of conductivity plotted against the reciprocal of

Kelvin temperature increased with heat-treatment in oxygen. This fact shows that there was a new level below previous levels.

(4) By heat-treatment in oxygen, the decay time of photocurrent decreased, and it seems that the concentration of trap decreased. This fact supports the interpretation introduced in (1).

(5) The trap concentrations estimated by measuring thermally stimulated current are shown in Table II, where the trap concentration have decreased with heat-treatment in oxygen. When the CdS films were heated in oxygen, there resulted two peaks in thermally stimulated current curves at about −150°C and at room temperature, and by heat-treatment at 600°C a peak at room temperature in thermally stimulated current curves vanished. It was thought that there were many traps with the trap depth corresponding to energy of about room temperature of thermally stimulated current in the sintered CdS films at initial state, and these traps vanished by heating at 600°C in oxygen. But it is still unknown whether the peak at room temperature is produced by sulphur vacancies or by other defects.

Table II. Concentration of traps.

Specimen		Number of traps/cm³
CdS : Cl films	initial	about 5×10^{20}
〃	heat-treatment in oxygen at 500°C.	4×10^{19}
CdS : Cl : Cu films	initial	about 4×10^{19}
〃	heat-treatment in oxygen at 350°C.	4×10^{18}
〃	at 500°C.	2×10^{18}
〃	at 600°C.	1×10^{18}

(6) CdO was produced on the surface or grain boundaries of sintered CdS films by heat-treatment in oxygen, and finally the whole surfaces of CdS films were convered with CdO layers. Then the dark conductivity was very large and the photoconductivity was not observed as shown in Fig. 11. When there was little CdO in the sintered CdS films, the dark conductivity was fairly small, but it was unknown whether or not the photoconductivity of sintered CdS film was influenced by these CdO. While the dark conductivity of evaporated CdO film was higher than that of sintered CdS : Cl film, the photoconductivity of CdO film was very small. Therefore, the decreasing phenomena of dark conductivity would be due to the occupation of sulphur vacancies by oxygen atoms, but not directly due to CdO grains.

The mechanism that the introduced oxygen destroyed the sulphur vacancies as donor and produced a new exciting center at about 1.8 eV below conducting band, will be explained by detailed investigation on single crystals. And also, further experiments on grain boundaries will be necessary.

Acknowledgements

The author wishes to express his gratitude to Assistant Professor K. Fukuda of Kyoto University for his valuable suggestions rendered during the course of this work. The author is much indebted to Mr. T. Kubo, Mr. T. Yamashita and Mr. S. Matsuura in our laboratory for their interests and endeavors in measurements and preparations of specimens.

References

1) B. Seraphin: Ann. d. Phys. **13** (1953) 198.
2) W. Muscheid: Ann. d. Phys. **13** (1953) 322.
3) J. Woods: J. Electr. Contr. **5** (1958) 417.
4) F. A. Kröger, H. J. Vink and J. van den Boomgaard: ZS f. Phys. Chem. **203** (1954) 1.
5) R. H. Bube: J. Chem. Phys. **23** (1955) 15.
6) S. M. Thomsen and R. H. Bube: Rev. Sci. Instr. **26** (1955) 664.
7) S. Kitamura: J. Appl. Phys. Japan **29** (1960) 636.
8) N. A. de Gier, W. van Gool and J. G. van Santen: Philips Techn. Rev. **20** (1959) 277.
9) M. J. B. Thomas and E. J. Zdonuk: J. Electrochem. Soc. **106** (1959) 964.
10) G. Kuwabara: J. Phys. Soc. Japan **9** (1954) 97.

JOURNAL OF THE PHYSICAL SOCIETY OF JAPAN, Vol. 15, No. 12, DECEMBER, 1960

Possibility of Supervelocity of Glass Fracture

By Shin-ichi HYODO

Department of Applied Physics, Faculty of Engineering,
University of Tokyo

(Received August 1, 1960)

Extrapolating the Glathart-Preston equation for the variation of the glass strength with the loading time, it is assumed that, before a fracture is caused in soda-lime glass within the order of microseconds, the stress applied on it must have attained a value extraordinarily higher than the one for usual impacts—the difference in magnitude being nearly one order. From this assumption it is suggested that the local compression strain in soda-lime glass when subjected to impact by underwater sparks must surpass the ordinary linear elastic limit and accordingly that there may be a possibility of propagation of this fracture at a velocity higher than the normal limit.

Quite recently it has been reported by the writer[1)] that a glass fracture velocity remarkably higher than the usually accepted limiting one was observed when the fracture was initiated by underwater disruptive electric spark. In this paper are given some discussions concerning how a fracture in glass can propagates at such a supervelocity.

It has been known for some time that the rate of loading, as well as the duration of loading, has an effect on the breaking strength of glass. A statistical consideration by Hirata and Terao[2)] indicates that, when loading or the applied stress increases linearly with time, the mean stress at the moment of fracture, i.e. the breaking strength, may increase rapidly with the increasing rate of loading. With regard to the effect of the duration of loading, Glathart and Preston[3)] proposed the following empirical relation:

$$1/f = a + m \log t \qquad (1)$$

where f is the breaking strength, t is the duration of loading, and a and m are constants. These two results coincide in suggesting that a very large value of stress is required for producing a fracture within a very short time. Therefore, it would not be so extravagant to assume a relation as shown by the curve in Fig. 1 between the breaking strength of glass and the time required for starting the fracture. To draw this curve the values extrapolated from Eq. (1) were used as a measure. According to this equation the strength at the "threshold time" would become infinite, so an 'ideal strength' supposed as $10\,\mathrm{kg^3/mm^2}$ was adopted as a substitute for it.

It is worthy of noticing that in ordinary discharge circuits, where the damping condition is satisfied, the duration of impact by underwater sparks is comparable to the "threshold time" of all those glasses which were tested wet by Preston and his collaborator. It appears, therefore, not so unreasonable to assume a very high rate of loading in the case of underwater spark impact as shown by the line (A) in Fig. 1, so that fracture may be initiated within such a short time after the beginning of application of stress. On the other hand, the stress-time curves of glass under other mechanical impacts are supposed to be in the hatched area on the right side of the line (B). Positive

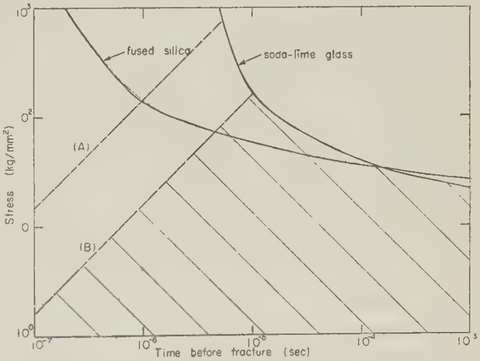

Fig. 1. Schematic representation of variation of the breaking strength of glass with the length of time before fracture, and of the increase of loading.

supports for this assumption, however, are difficult to find except in the difference of impact velocity: while the velocity of rifle bullets is usually not more than 800 m/sec, the propagation velocity of the pressure wave generated by underwater sparks is at least twice as large.*

From these presumptions it may be deduced that the breaking strength of soda-lime glass when subjected to impact by underwater sparks is greater than in the case of impact given by other methods by nearly one order in magnitude. If Young's modulus of soda-lime glass at room temperature is taken as 7.2×10^3 kg/mm^2, the percentage strain for such a high stress must attain 10% or more. On the basis of Anderegg's[4)] experiment, Taylor[5)] assumes that a fracture starts when the strongest bond in the atomic network of glass is suddenly stretched to 14.5%. So long as Hooke's law holds, it may be considered that, in the case of underwater spark impact, nearly all the bonds in the region of glass subjected to impact must have been compressed, or, in the peripheral region elongated, to such a limiting extent safely before fracturing. It seems unlikely that such a rubber-like process can take place in glass. As the stress-strain relation of solids generally tends to deviate from linearity for large strains, it is not so absurd to suppose that the effective Young's modulus of glass under the impact of underwater sparks would have become considerably larger than the one in an ordinary state. Although the stress-strain curve is apt to bend downward for large strain in the elongation test due to plastic deformation, for high-speed compression such as underwater spark impact, the curve is considered to bend upward because of the presence of a high atomic repulsion force. This is partly suggested by the results of the high pressure experiment made by Bridgman, which shows that the compressibility of matter generally decreases from the normal value under a very high hydrostatic pressure.

From the energy condition during the propagation of a Griffith-type crack (whose length is $2c$) Mott[6)] indicated that the fracture velocity $\dot{c}$ is determined by

$$\dot{c}=(2\pi/k)^{\frac{1}{2}}(E/\rho)^{\frac{1}{2}}(1-c_0/c)^{\frac{1}{2}}\ , \qquad (2)$$

where $2c_0$ is Griffith's critical crack size, E is Young's modulus, ρ is the density, and k is a constant. This shows that as c increases $\dot{c}$ tends toward a certain fraction of the sound wave velocity $(E/\rho)^{\frac{1}{2}}$. It is no wonder then that the limiting value may increase if the value of E increases. In addition, the coefficient $(2\pi/k)^{\frac{1}{2}}$ may change, probably increase a little, from the value 0.38 estimated by Robert and Wells,[7)] for, in order to determine k by solving an integral equation, they assumed a Westergaad condition, which would not be satisfied to a sufficient degree when the rate of loading grows to a very high value.

In other words, with the glass-fracture caused by underwater spark impact, the strain energy to be released by fracture would be more concentrated near the origin of the crack than in usual cases, so the higher production of kinetic energy following a higher fracture velocity is required to be balanced with the rapid decrease of the elastic strain energy.

Various objections against the foregoing opinion may be expected. The writer thinks it his duty to give answers beforehand to some conceivable objections. The first objection may be that, "as the water is able to lower the activation energy of glass-fracture, the difference of the breaking strength illustrated in Fig. 1 may be an over-estimation." It may be true to some extent, but except for the glass baked out in vacuum the effect of water on the strength of glass is not so remarkable as to influence the order of magnitude, according to Baker and Preston.[8)] The second one is that, "in the experiment of Kolsky[9)] who used stress waves from a small charge of explosives to study the fracture of soda-glass rods, their breaking strength was only about twice as great when specimens were loaded for a few microseconds as when loaded for a few seconds." This result was brought out from the observation of the circular cracks on the cylindrical surface of glass rods, but he remarked that no cracks were observed inside the rods, and so he predicted that there might be a very high internal strength of soda glass for loading time of the order of a microsecond. It should be this high internal strength that makes the region of glass around the origin of fracture capable of bearing such a high strain energy as fore-mentioned. The third one may be that, "if the rate of loading plays an important part in the supervelocity of fracture as the writer asserts, why has it not been found in the cracking caused by high explosives?" "Really Pugh and his co-workers[10] found by Kerr-cell photography that the glass fracture velocity went as high as 3500 m/sec, but they attributed it to the development of secondary fractures." This may be true, for the shock wave was so fast (6150 m/sec) and so intense that it maintained the ability to develop secondary fractures successively in front of the proceeding cracks all the way of propagation. However, if they had traced each of these secondary cracks individually, which, they said, was actually impossible with their photographs on account of the complete shattering by too violent shock waves, a supervelocity would have been observed.

---

* As there are some photographic evidences showing that cracks have started already just before a bullet reaches the surface of glass, the initial loading rate of a bullet impact may be somewhat lowered by the "cushion" of the Mach wave accompanying it.

It should be borne in mind that, when a comparison is made with the impact by explosives, the impact by underwater spark is characterized not only by high rate of loading but also by short duration of loading. In the longer duration of loading the excess strain energy to drive a crack would be continuously supplied to the specimen for a longer period after the initiation of fracture, so the local stress field around the tip of the proceeding crack would keep a "quasi-equilibrium" during such a short time as covered by the total frames in high-speed photography. This may be, in the writer's opinion, the reason why a gradual decrease of fracture velocity has not been found until quite recently. On the other hand, the duration of underwater spark impact is sufficiently short and the stress wave accompanying a large strain is attenuated much faster than the elastic wave of small amplitude.

In conclusion of this article it is to be remarked that as shown in Fig. 1, the "threshold time" for fused silica lies at about 0.2 μ sec, so the supervelocity of fracture of fused silica would not be observed so distinctly as in soda-lime glass, unless any adequate procedure to increase the rate of loading, such as decreasing the time constant of a discharge circuit, is taken.

The writer is greatly indebted to Prof. Moriso Hirata of the University of Tokyo for his helpful suggestions.

References

1) S. Hyodo and F. Okuda: J. Phys. Soc. Japan **15** (1960) 2093.
2) M. Hirata and N. Terao: Oyo-buturi (in Japanese) **20** (1951) 234.
3) J. L. Glathart and F. W. Preston: J. Appl. Phys. **17** (1946) 189.
4) F. O. Anderegg: Ind. Eng. Chem. **31** (1939) 290.
5) N. W. Taylor: J. Appl. Phys., **18** (1947) 943.
6) N. F. Mott: Engineering, **165** (1948) 16.
7) D. K. Roberts and A. A. Wells: Engineering, **178** (1954) 820.
8) T. C. Baker and F. W. Preston: J. Appl. Phys. **17** (1946) 170.
9) H. Kolsky and Y. Y. Shi: Proc. Phys. Soc. (London) **72** (1958) 447.
10) E. M. Pugh *et al*: J. Appl. Phys. **23** (1953) 48.

Short Notes

This section is intended to secure prompt publication of important discoveries in physics. The reports should not exceed 800 words in length. A figure of size 7 cm×7 cm will be counted as 150 words.

J. PHYS. SOC. JAPAN **15** (1960) 2354

Spontaneous Magnetization of Magnesium Ferrite-Manganite System

By Kiyoshi MURAMORI and Syohei MIYAHARA
Department of Physics, Faculty of Science, Hokkaido University, Sapporo, Japan

(Received September 1, 1960)

In the previous paper[1] it has been shown that magnetic behaviors of $MgMn_2O_4$ are consistent with the theory of triangular arrangements. In order to clarify the magnetic properties of solid solutions of $MgFe_2O_4$, which is confirmed to be typically ferrimagnetic, and $MgMn_2O_4$, we measured saturation magnetizations of those compounds.

Specimens measured are powders with the formula $MgFe_{2-a}Mn_aO_4$, where a are values from 0.0 to 2.0 at intervals of 0.2 and were prepared by the same way as $MgMn_2O_4$ reported previously[1]. X-ray patterns of those specimens at room temperature indicate a cubic spinel for a from 0.0 to 1.2, two phases of a cubic and a tetragonal spinel for $a=1.4$ and 1.6, and a tetragonal spinel for $a=1.8$ and 2.0. The details of the structures of those specimens will be published soon. Magnetizations were measured by Sucksmith's ring balance from Curie temperatures to liquid nitrogen temperature under a magnetic field up to about 13000 oersteds which is enough strong to saturate the magnetizations of all specimens.

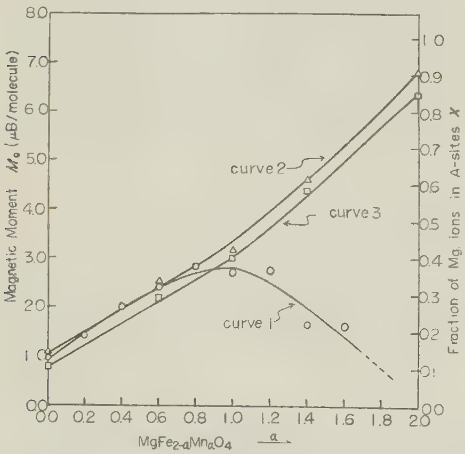

Fig. 1. Curves 1 and 2 show experimental and theoretical values of magnetic moments (M_0) and Curve 3 shows fraction of Mg ions located on A-sites (x).

It has been known that the cation distribution, and consequently, the saturation magnetic moment of $MgFe_2O_4$ depends sensitively on the thermal treatment of the specimen. Therefore the determination of the cation distributions of the series were all made for specimens which were cooled from 900°C to room temperature at the rate of 0.5° C/min. The distributions were determined from the intensity ratios of (220) and (422) X-ray diffraction lines to (400) line, where all manganese ions were assumed to be located on B-sites. The fractions of magnesium ions (x) located on A-sites are plotted in Fig. 1. In the same figure, the magnetic moments calculated by Néel's theory[3] from observed cation distributions are compared with the observed magnetic moments. Observed magnetic moment of $MgFe_2O_4$ agrees with the data by Kriessman et al.[2] for a specimen quenched from 500°C and is equal to the value expected from Néel's theory[3]. For specimens from $a=0.0$ to about 1.0, observed magnetic moments are in good agreement with the values expected from Néel's theory, where experimentally determined cation distributions are assummed. Magnetic moments of specimens $a>1.0$, however, are much smaller than those expecied from Néel's theory and decrease with increasing manganese compositions. This tendency of magnetic moments is the same feature as that of solid solutions of magnetic ferrites and zinc ferrite obtained by Guillaud et al. and Gorter[4]. Susceptibility measurements are now going on. Details will be published shortly.

References

1) K. Muramori and S. Miyahara: J. Phys. Soc. Japan **15** (1960) 1906.
2) C. J. Kriessman and S. F. Harrison: Phys. Rev. **103** (1956) 857.
3) L. Néel: Ann. de Phys. **3** (1948) 137.
4) E. W. Gorter: Philips Res. Rep. **9** (1954) 295.

J. PHYS. SOC. JAPAN **15** (1960) 2355

Anisotropy on Poly-Crystalline Sheets of V-permendur

By Chinji KURODA

Electrical Communication Laboratory Nippon Telegraph and Telephone Public Corporation
1551, Kichijoji, Musashino-shi
Tokyo, Japan

(Received June 20, 1960)

An unusual magnetic anisotrpy of the ferromagnetic poly-crystalline sheet material was found. The specimens containing Fe 49-5 wt. %, Co 48.9 wt. % and V 1.6 wt. % were prepared by rolling at room temperature the sheet of 2 mm thickness and punching out. Their dimensions were 21 mm in diameter and 0.35 mm in thickness. For the measurement of anisotropy, torque magnetometer method was used, the principle of which was alike that of Penoyer's[1], and torque curves were recorded automatically. After verifying that the magnetic qualities for technical magnetization were most favorable by annealing at 850°C in dry hydrogen atomosphere, the measurements of torque curves were performed for the specimens which had undergone the same heat-treatment.

Figs. 1 and 2 show the torque curves obtained at field strengths from 200 oe to 440 oe and from 500 oe to 9,500 oe respectively. Through that torque curves, it is seen that the directions of easy magnetization are at 45° and 135° to the rolling direc-(R.D.) and the types of the curves are mostly represented by 4θ term. It is an unusual behavior that the torque amplitude has a maximum value at about 500 oe as is shown in the Figs.

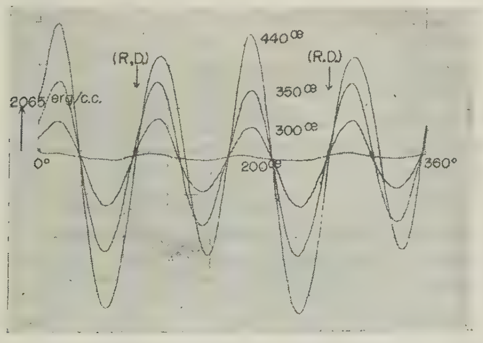

Fig. 1. Torque curves at room temperature obtained at low magnetic fields.

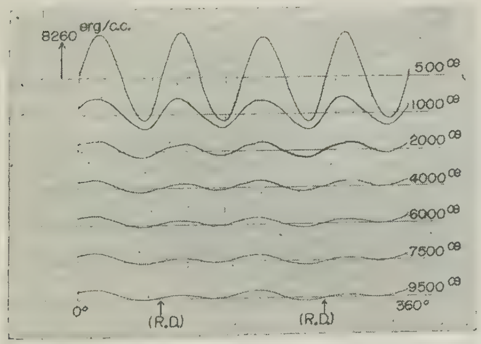

Fig. 2. Torque curves at room temperature obtained at high magnetic fields. They show the decrease of torque amplitude with field strength.

The torque curve measured at 9,500 oe could be thought to represent the recrystallization structure that was obtained by annealing at 850°C. However the decrease of torque amplitude with increase of field strength in rather low field can not be understood by taking in only the recrystallization structure, although the torque curves even in such low fields obviously has a connection with that structure.

Several authors have reported on torque reversal for some single crystals and interpreted it under the consideration of the precipitates or inhomogeneous structures distributed cubically.[2),3)] S. Chikazumi also mentioned[4)] that on the single crystals which exhibit magnetic annealing effect the torque reversal could occur.

Since our specimens were the poly-crystal, these effects should be smeared out at any field strength. Therefore, these interpretations can not be used in a straight manner to understand this torque decrease.

At first sight, it seems to be understood by considering the preferential distribution of grain orientation caused by recrystallization and above mentioned mechanisms. But, the directional order mechanism[4)] gives the too much low field strength for the maximum torque amplitude. Also, because of low V contents and low annealing temperature, no preciptitates are expected. And microscopical observations did not show any precipitates. Then, the precipitation mechanism can not interpret this torque decrease too.

However, if the lattice defects, which were not completely annihilated on the recrystallization at 850°C, formed some ordered structure directionaly arranged to the rolling stress direction and each crystallite orientations, it may be possible that their total shape anisotropy causes this torque decrease. The fact that the re-annealing at 850°C after the annealing at 1,100°C did not give the torque decrease seems to support this mechanism.

More detailed studied studies will be reported later.

References

1) R. F. Penoyer: Proc. A.I.E.E. Conference on magnetism (1956) 365.
2) E. A. Nesbitt, H. J. Williams and R. M. Bozorth: J. Appl. Phys. **25** (1954) 1014.
3) E. A. Nesbitt and R. D. Heidenreich: J. Appl. Phys. **30** (1959) 1000.
4) S. Chikazumi: J. Phys. Soc. Japan **11** (1956) 718.

J. PHYS. SOC. JAPAN **15** (1960) 2356

Anomalous photovoltaic Effect of CdS Single Crystals

By Sumiaki IBUKI, Hiroyoshi KOMIYA and
Hirosuke YAMASHITA

*Research Laboratory, Mitsubishi Electric Mfg. Co.
(80 Nakano, Minamishimizu, Amagasaki,
Hyogo, Japan)*

(Received September 2, 1960)

Some researches on the hole conduction[1], photovoltaic effect by electron diffusion[2] and efficiency as a solar converter[3] of CdS have recently been reported. We have also investigated the photovoltaic effect of CdS single crystals, then we report some results obtained by another electrode construction.

CdS single crystals were grown by sublimation recrystallization in N_2 atmosphere containing In vapor and their resistivities were about several KΩ cm in dark. As shown in Fig. 2., a half side of crystal is covered with evaporated layer of Cu and after heat-treatment of several minutes at 600°C, both ends of the crystal are soldered with in metal. Using these cells we obtained open circuit voltage of 0.5 V (positive for Cu side) and short circuit current of about 1 mA/cm² under direct sun light. It was found, however, that in a low light level polarity of photo-induced voltage was changed to negative sign for Cu side as shown in Fig. 1. It is supposed that this effect may be induced by the electron diffusion. In order to verify this hypothesis, the photovoltage was measured, scanning a light spot on the crystal surface. The measured results are shown in Fig. 2.

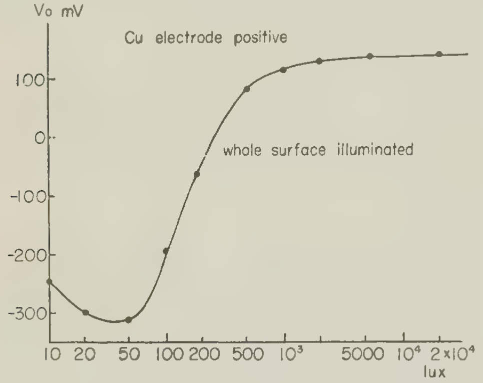

Fig. 1. Open circuit voltage-light intensity.

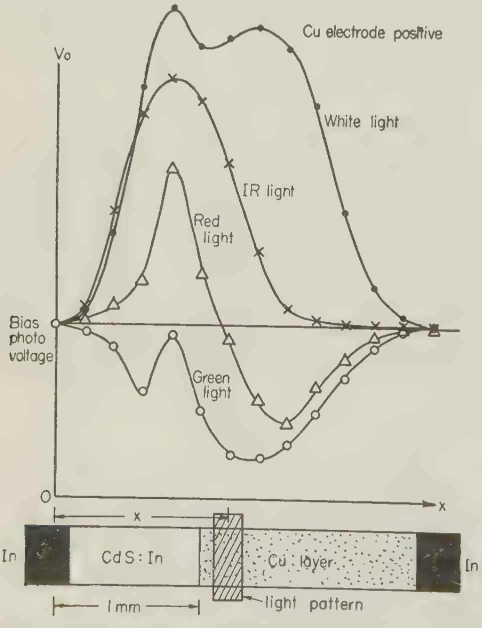

Fig. 2. Photo voltage caused by local illumination.

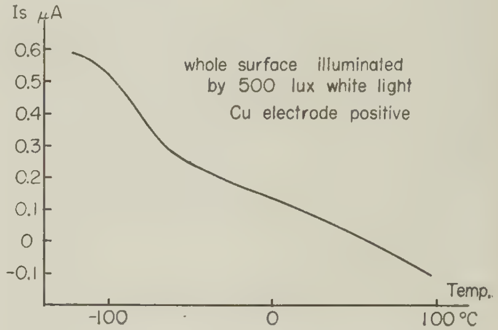

Fig. 3. Temperature dependency of short circuit current.

From above results, it is concluded that the photovoltage is caused by P-N junction grown near the boundary between CdS and Cu layer. But from the results observed by means of weak green and red-light spot, the electron diffusion current caused by large gradient of electron densities seems to produce the negative photovoltage[2]. While, the negative photovoltage was neither seen when the crystal whose electrodes are In only was illuminated partially nor when the other crystal whose half side was covered with evaporated Cu layer which was not heat-treated at all. It is considered, therefore, that heat-treated Cu layer plays also a main role upon the electron diffusion. Hence we might be able to conclude that the facts that temperature dependency of short circuit current is so remarkable and at high temperature its polarity is changed as given in Fig. 3, will be explained by the superposition of the above mentioned two phenomena, i.e. P-N junction and electron diffusion current.

Detailed results will be published in near future.

References

1) J. Woods & J. A. Champion: J. Elect. and Cont. **7** (1959) 243.
2) H. Kallmann et al: P. R. **117** (1960) 1482.
3) P. Rappaport: RCA Rev. **20** (1959) 373.

J. PHYS. SOC. JAPAN **15** (1960) 2357~2358

On the Mechanism of Reversible Appearance of Residual Magnetization at low Temperature Transition in αFe_2O_3

By Kiiti SIRATORI, Akira TASAKI and Shūichi IIDA

Department of Physics, Faculty of Science University of Tokyo, Tokyo

(Received September 17, 1960)

αFe_2O_3 is a parasitic ferromagnet above $T_c = -20°C$ where the axis of spin lies in the (111) plane of the rhombohedral crystal. The weak ferromagnetism disappears below T_c where the spin axis changes from in the (111) plane to along [111] axis¹⁾. It has been found experimentally that the weak residual magnetization of αFe_2O_3, which has once disappeared by passing through the transition point from high temperature, appears again in the same direction when the temperature is raised²⁾. The intensity, however, decreases in the first cycle to about 2/3~1/2, and remains constant for the following repetitions. (Fig. 1)

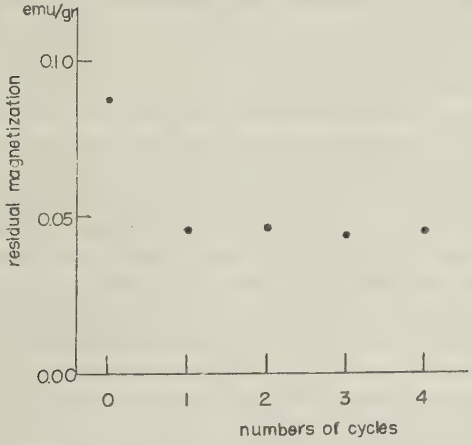

Fig. 1. Residual magnetization of polycrystalline αFe_2O_3 at room temperature after cooling-heating cycles.

Now there are three easy spin axes in a basal plane above T_c. We put an assumption that in each domain, one of the three axes is more preferable than the other two, probably due to the presence of internal irregularies. Then there exist two lowest energy states in each domain, corresponding to the two degenerate spin states of a usual antiferromagnet. This crystal being the canted antiferromagnet³⁾, the two states have weak magnetizations pointing in antiparallel with each other along U_2 axis perpendicular to the preferred axis. It is pointed out, in this paper, that the spin axis should rotate reversibly from within the basal plane to along [111] axis in the transition, which results in one to one correspondence of the two degenerate states before and after the transition or a complete recovery of the residual magnetization.

The assumed expression of the magnetic anisotropy is

$$E = K_u \cos^2\theta + K_1' \cos\theta \sin^3\theta \sin 3\phi - K_u' \sin^2\theta \sin^2\phi \quad (1)$$

where θ and ϕ are the polar angles of the spin axis from [111] and U_2 axis respectively, and $K_u > 0$ when $T > T_c$. The first two terms are those that are considered to be dominant in trigonal crystals and have been presented already by Dzyaloshinsky*. The third term is added to express the presence of the preferred axis. As is known already, Eq. (1) gives a deviation of spin axis from (111) plane even above T_c, where $\theta (\lesssim \pi/2)$ is given by

$$\cos\theta / \sin 3\theta = -|K_1'|/2K_u \quad \text{if} \quad K_u' \ll |K_1'| \quad (2)$$

On lowering the temperature, K_u and θ will be decreased continuously. If the condition that $-K_u > |K_1'|/2$ (or $\theta > \theta_1 = 45°$) is attained, the energy of a spin with $\theta = 0°$ becomes lower than that with θ of Eq. (2). Further, when $-K_u > 1.18|K_1'|/2$ or ($\theta > \theta_2 = 34° 16'$), the latter becoming unstable, the spins may flip to the [111] direction from this region ($\theta_1 > \theta > \theta_2$) through wall displacement or rotation. On reheating the spins are turned back reversibly to the original position, the process of which is accompanied with a small hysteresis as has been observed by Lin⁵⁾.

In actual crystals the direction and the value of K_u' will be distributed statistically. But, so long as the value of K_u' is large enough to restrict the spin axis in one σ_d plane, spins will "remember" their states and magnetization will appear again after a cooling-heating cycle.

It is very interesting to notice that if it is possible, by applying a strong field, to cool down the specimen aligning the spins of the entire crystal to a direction perpendicular to the magnetic field, the present mechanism (if the mutul interaction of the domains through strain, antiferromagnetic wall etc. is neglected) will results in a zero residual magnetization after reheating process. However, the first trial to check this point (with a field of 40 KOe) gives negative results. The details will be published shortly.

Note added in proof: This correspondence of states will be confirmed by the observation of piezomagnetism of αFe_2O_3 below the transition point. This experiment is now in preparation. The authors wish to thank Mr. T. Inoue for this suggestion.

References

1) L. Néel: Rev. Mod. Phys. **25** (1953) 58; C. G.

---

* K_1' has the same origin as the cubic K_1 term. It can be rougly estimated from the resonance data of Fe^{3+} in $\alpha Al_2O_3$⁴⁾ that $K_1' \lesssim 3 \times 10^{-2}$ cm⁻¹/ion.

Shull, W. A. Strauser and E. O. Wollan: Phys. Rev. **83** (1951) 333.
2) G. Haigh: Phil. Mag. **2** (1957) 505; S. T. Lin: J. Appl. Phys. **21** **Suppl.** (1960) 273s.
3) I. Dzyaloshinsky: J. Phys. Chem. Solid **4** (1958) 241; T. Moriya: Phys. Rev. Lett. **4** (1960) 228.
4) G. S. Bogle and H. F. Symmons: Proc. Phys. Soc. **73** (1959) 531.
5) S. T. Lin: Private ccmmunication.

J. PHYS. SOC. JAPAN **15** (1960) 2358

Antiferromagnetism of $FeSn_2$

By Kazuo KANEMATSU, KŌ YASUKŌCHI
Department of Physics, College of Science and Engineering, Nihon University, Tokyo
and Tetuo OHOYAMA
Department of Physics, Faculty of Science, Tokyo Metropolitan University

(Received September 21, 1960)

In the course of our study on magnetic properties of intermetallic compounds composed of iron group transition elements and those of IVb group in the periodic table, a variety of magnetic behaviors was found in various compounds[1)2)3)]. As to the iron—tin system, it was reported by Asanuma[4)] that γ-FeSn ($Fe_{1.3}Sn$) was a ferromagnetic with the Curie point of 676°K, and we also found a strong ferromagnetism in Fe_3Sn_2. In this note the antiferromagnetic behavior found in the compound $FeSn_2$ is reported.

As the compound is formed peritectically at 496°C[5)], the specimen was prepared by a sintering method as in the following: Pieces of electrolytic iron (99.9%) and tin (99.999%) were mixed in the stoichiometric proportion, sealed in an evacuated telex tube, and after prefired by an electric furnace at 460°C for 3 days, the product was crushed into powder. The powder thus obtained was heated again at 460°C and the above procedure was repeated for several times, until the finish of the peritectic reaction was ascertained by X-ray diffraction.

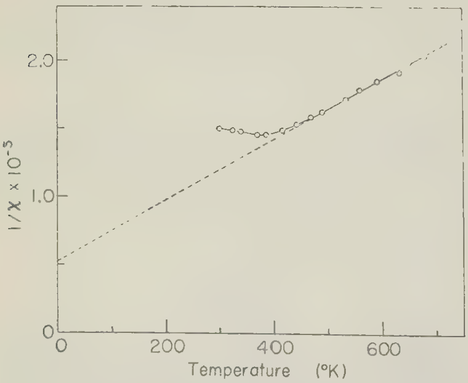

Fig. 1. Inverse susceptibility, $1/\chi_g$, versus temperature curve of $FeSn_2$.

In the X-ray diagram of the specimen used for the magnetic measurements, no diffraction lines were found which come from tin, iron, or any other compounds in the system than $FeSn_2$. The diffraction lines could be indexed as a tetragonal structure with lattice constants $a=6.50_2$Å, $c=5.31_5$Å, and $c/a=0.816$, and the relative intensities of these lines were in good agreement with those reported by Nowotny and Schubert[6)], who determined that the compound $FeSn_2$ has a body centered tetragonal, C16 type of structure.

The temperature dependence of the magnetic susceptibility was measured by a magnetic balance of torsion type from the room temperature up to 460°C with a field of 7.5 kilo-oersteds. The results are shown in Fig. 1. Here the reciprocals of the magnetic susceptibility are plotted against temperature. It is seen that the behavior is antiferromagnetic, and the temperature corresponding to the minimum of the curve, 380°K, may be considered as the antiferromagnetic Néel point. The Curie-Weiss law holds very well at temperatures above 500°K. The effective magnetic moment per iron is calculated from the Curie constant to be 3.36 μ_B and the asymptotic Curie temperature is estimated to be −230°K.

Among the intermetallic compounds between iron group transition elements and those of IVb group, $MnSn_2$, $FeGe_2$, and $CoSn_2$, as well as $FeSn_2$, are known to have the C16 type of structure. In recent magnetic measurements on the compounds of above series, we found that $MnSn_2$[2)], like as the present compound $FeSn_2$, was antiferromagnetic, and $FeGe_2$[3)] was parasitic ferromagnetic, while $CoSn_2$ was weakly paramagnetic. When the temperature was increased from the room temperature to 750°K, the magnetic susceptibility of $CoSn_2$ increased monotonically from 1.5×10^{-7} to 3.5×10^{-7}. Though the origin of this increase is uncertain at present, it would not be ascribed to antiferromagnetism.

References

1) K. Yasukōchi, T. Ohoyama, and K. Kanematsu: J. Phys. Soc. Japan **14** (1959) 1820, ($Mn_{3.25}Ge$). K. Yasukōchi, K. Kanematsu, and T. Ohoyama: J. Phys. Soc. Japan **15** (1960) 932, (Mn_5Ge_2).
2) K. Yasukōchi, K. Kanematsu, and T. Ohoyama: to be published, (Mn-Sn system).
3) K. Yasukōchi, K. Kanematsu, and T. Ohoyama: to be published, (Fe-Ge system).
4) M. Asanuma: J. Phys. Soc. Japan **15** (1960) 1343.
5) M. Hansen: *Constitution of Binary Alloys* (McGraw-Hill Book Co., 1958).
6) H. Nowotny and K. Schubert: Z. Metallkde **37** (1946) 17.

J. PHYS. SOC. JAPAN **15** (1960) 2359

Thermoelectric Power of Titanium- and Vanadium-Carbides

By Seiichiro NOGUCHI and Takao SATO
Department of Physics, Tokyo Metropolitan University, Tokyo

(Received September 24, 1960)

A number of investigations have been made for the metallic carbides and nitrides with the sodium chrolide structure and the nature of their bonding has been discussed[1),2)] in conjunction with their properties such as hardness and melting point, etc. The metallic carbides such as TiC and VC are of great interest since they have appreciably higher melting point and hardness than their constituent metals. These properties suggest that the compounds have stronger bonding and the nature of the principal bonding is the homopolar bond. Although the metal atoms and carbon atoms in these substances may be considered to bind each other in homopolar sense, they are present as considerably good electric conductors.

To reveal the nature of the conduction in these compounds, we must obtain further informations on the electrical properties of them. The Hall coefficients of TiC and VC have been measured by Tsuchida and Takagi[3)], who have shown that the numbers of the conduction electrons are 0.18 and 1.21 for TiC and VC, respectively, using the nearly free electron approximation. It is much interested that the difference between these numbers is almost unity. The number of outer electrons of titanium is four while that of vanadium is five. If all the outer electrons of the metal atoms contribute the bonding, the melting point of VC should be higher than that of TiC. In the fact, however, VC has rather lower melting point than TiC. This indicates that the numbers of the electrons contributing to the bonding may be slightly less in VC than in TiC. Assuming that the number of the electrons contributing to the bonding is nearly the same in both substances, we may expect that the number of conduction electrons of VC is more than that of TiC by almost unity per metal atom. The numbers of the conduction electrons supposed by their melting points are in good agreement with those obtained by the Hall measurements. To obtain further informations of the conduction electrons in these compounds, we made the measurement of the thermoelectric power of them at room temperature and at liquid nitrogen temperature. The data shown in Table I were analyzed with the assumption that the conduction electrons are nearly free. Then we may write the absolute thermoelectric power as

$$S=-(\pi^2k^2T/e\zeta)\,, \qquad (1)$$

where ζ is Fermi energy, the other symbols have their usual meanings.

Table I.

	S (μV/deg)		ζ (eV)
	R.T.	Liq. N_2	
TiC	-10.81	-7.2	2.02
VC	-4.12	$+0.34$	5.31

The Fermi energy can be derived from the absolute thermoelectric power at room temperature. Employing the values of these Fermi energies and the condition that VC has one more electron than TiC per metal atom, we can obtain the following relations in the nearly free assumption;

$$\left.\begin{aligned} \frac{2\pi(2m^*)^{3/2}}{h^3}\int_0^{2.02} E^{1/2}dE&=x,\\ \frac{2\pi(2m^*)^{3/2}}{h^3}\int_0^{5.31} E^{1/2}dE&=1+x\,. \end{aligned}\right\} \qquad (2)$$

The numbers of the conduction electrons are easily obtained from above relations and they are 0.31 per titanium atom for TiC and 1.31 per vanadium atom for VC. Although our assumption is very simple, the agreement between the numbers of the electrons reduced by the present experiment and those by the Hall measurements is wonderfully good. The results therefore will be considered that the assumption used here is rather good one for these systems, namely it will be said that the behavior of their conduction electrons is nealy free. The effective mass of the electron is obtained to be 0.78 m from the relation between the provisional state density and the energy, where m is the mass of free electron.

Recently, the band-model approximation of the metallic carbides with NaCl structure has been proposed by Bilz.[4)] In his model, the Fermi energies are shown as about 3 eV for TiC and 5.5 eV for VC. The values of the Fermi energy obtained from our measurements are in good agreement with the values estimated by Bilz.

The authors wish to express their sincere thanks to Prof. Takagi and Mr. Tsuchida for their kind offer of the specimens.

References

1) R. E. Rundle: Acta Cryst. **1** (1948) 180.
2) W. Hume-Rothery: Phil. Mag. **44** (1953) 1154.
3) H. Takagi, M. Mekata and A. Tsuchida: Talk at the Meating of the Physical Society of Japan, 1959 Nov.
4) H. Bilz: Z. f. Phys. **153** (1958) 338.

J. PHYS. SOC. JAPAN **15** (1960) 2360

Indirect Transition in Narrow Junction of Ge–Si Alloy

By Kei-ichi ANDO
Semiconductor Department, Research Section,
Sony Corporation, Shinagawa
Tokyo

(Received Sept. 28, 1960)

This concerns only Si rich Ge–Si alloys. The impurity that is doped is phosphorus ($\sim 10^{19}\,\mathrm{cm}^{-3}$). Al-b (B:2 3%) was used as p-type dot of alloying and made abrupt p–n junctions by alloying.

Contents of Ge in Ge–Si were determined by X-ray in measuring of lattice constant.

Voltage-current characteristic of the diode was measured in room temperature, in liquid nitrogen, and in liquid helium. Details of the characteristics in helium are shown in Fig. 1. The cusps were found only in liquid helium. These cusps represent the energies of phonons that help indirect transition in conserving momentum during the tunneling, but in low temperature, electron cannot absorb phonons as the lattice vibrations do not produce such phonons.

Results of the measurement on the various content of Ge–Si are given in Table.

Contents of Ge in Si % (atomic)	Energy of Phonons (Mc/sec)					
	TA	O		(O+TA)		(O+O)
0	3.87	13.35		20.10		28.80
3.35	4.10	13.3		19.3	24.2	27.8
4.13	4.83	13.3	16.6	19.0	24.6	
5.44	4.83	13.0		19.1	23.2	29.0
9.1	4.35	13.3		18.4	24.2	29.5

Mc/sec was used to facilitate a contrast with the spectrum of lattice vibration.¹⁾ The data of Si were measured by Esaki-Miyahara and Holonyak et al.²⁾ Optical researches of Si were also performed by Macfarlane et al and Hayne et al.³⁾

Energy of TA does not gradually decrease but makes maximum in 4–5% Ge. O is almost the same, (TA+O) decreases and (O+O) increases in the region of this measurement. According to the calculation of Braunstein et al,⁴⁾ Hamiltonian of lattice vibration of Ge–Si is

$$\boldsymbol{H} = -\frac{1}{2}\hbar^2\left[\sum_{\mathrm{Ge}} M_{\mathrm{Ge}}{}^{-1}\cdot\frac{\partial^2}{\partial X_{\mathrm{Ge}}{}^2} + \sum_{\mathrm{Si}} M_{\mathrm{Si}}{}^{-1}\cdot\frac{\partial^2}{\partial X_{\mathrm{Si}}{}^2}\right] + \frac{1}{2}\left[\sum_{\mathrm{Ge}}\sum_{\mathrm{Ge}} X_{\mathrm{Ge}}X_{\mathrm{Ge}}\frac{\partial^2\phi}{\partial X_{\mathrm{Ge}}\partial X_{\mathrm{Ge}}} + \sum_{\mathrm{Ge}}\sum_{\mathrm{Si}} X_{\mathrm{Ge}}X_{\mathrm{Si}}\frac{\partial^2\phi}{\partial X_{\mathrm{Ge}}\partial X_{\mathrm{Si}}} + \sum_{\mathrm{Si}}\sum_{\mathrm{Si}} X_{\mathrm{Si}}X_{\mathrm{Si}}\frac{\partial^2\phi}{\partial X_{\mathrm{Si}}\partial X_{\mathrm{Si}}}\right].$$

Energy of phonons decrease as Si goes to Ge. But in this measurement, the energy of phonons are not so.

As this measurement covers only a small region of Ge in Ge–Si, it is impossible to infer the mechanism and the structure of band. But in Si side of Ge–Si, it is necessary to consider that the conduction minimum of Si moves toward the minimum of Ge in the direction of [100], and where the minimum of Ge is.

Besides four cusps, more cusps have been found, which are not possibe to imply now.

The author would like to thank the members of Electrotechnical Lab. and Mr. Hoshi in Sony Corp.

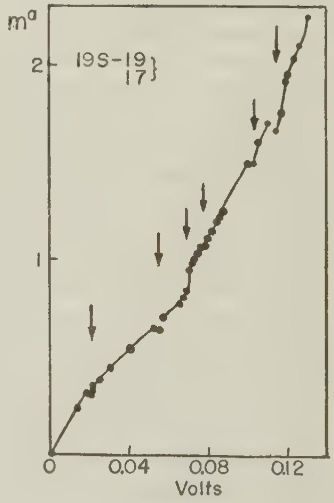

Fig. 1.

References

1) B. N. Brockhouse: Phys. Rev. Letter **2** (1959) 258.
2) L. Esaki and Miyahara: Solid State Electronics **1** (1960) 13. N. Holonyak, I. A. Lesk, R. N. Hall, J. J. Tiemann and H. Ehrenreich: Phys. Rev. Letter **3** (1959) 167.
3) G. G. Macfarlane, T. P. McLean, J. E. Quarrington and V. Roberts: Phys. Chem. Solids **8** (1959) 388. J. R. Haynes, M. Lax and W. F. Flood: Phys. Chem. Solids **8** (1959) 392.
4) R. Braunstein, A. R. Moore and F. Herman: Phys. Rev. **109** (1958) 695.

J. PHYS. SOC. JAPAN **15** (1960) 2361

Weak Ferromagnetism of $NaNiF_3$

By Shinji OGAWA

Research Institute of Applied Electricity,
Hokkaido University, Sapporo

(Received Sept. 28, 1960)

Rüdorff and Kändler[1)] have briefly mentioned that $NaNiF_3$ was ferromagnetic at liquid nitrogen temperature. In this note some characteristics of the so-called weak ferromagnetism found in $NaNiF_3$ will be reported.

The crystal structure of $NaNiF_3$ has been determined by X-ray to be orthorhombic. The lattice constants at 295°K are: $a=5.361$Å, $b=5.524$Å, and $c=7.688$Å. The most probable space group is D_{2h}^{16}-Pbnm. The magnetization of polycrystalline $NaNiF_3$ measured from 77°K to 300°K has a field-dependence expressed as $\sigma=\sigma_0+\chi H$ below about 150°K. The magnetic torques, L, of a $NaNiF_3$ single crystal in the planes containing the c-axis have an angular dependence of $L=\pm\sigma_0 H\sin\theta$, below 149°K. Near the direction perpendicular to the c-axis, the torque was extremely unstable and suddenly changed its sign. Typical torque curves in the b–c plane at 77°K are shown in Fig. 1. In the a–c plane torque curves deviated somewhat from the $\sin\theta$ curve. In the plane perpendicular to the c-axis a torque of two-fold symmetry, the amplitude of which is nearly proportional to H^2, was observed and is shown in Fig. 2. It is concluded from the torque measurement that the spontaneous magnetization, σ_0, appears in the c-direction and it is not rotated toward the b-direction but rotated in some degree toward the a-direction by an applied magnetic field of up to 10 kOe.. The σ_0 determined from the torque in the b–c plane is plotted against temperature in Fig. 3. It disappears above a cirtical temperature $T_c=149$°K. At 77°K σ_0 is 0.058 μ_B per molecule of $NaNiF_3$. It is only about 3% of the spin magnetic moment of a Ni^{2+} ion.

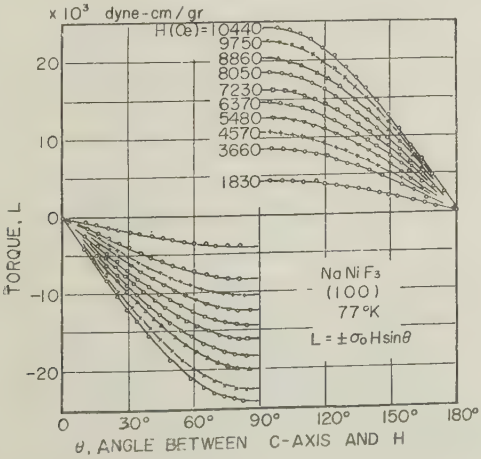

Fig. 1. Torque curves in (100) plane.

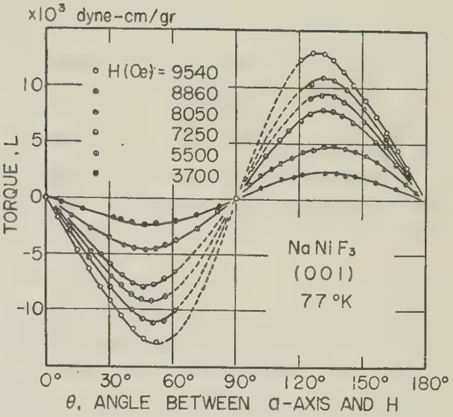

Fig. 2. Torque curves in (001) plane.

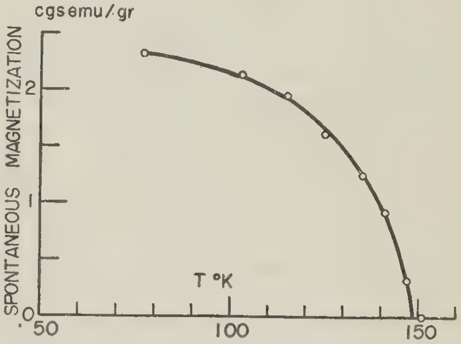

Fig. 3. Temperature dependence of σ_0.

Some rare earth orthoferrites show a similar torque behavior[2)], and Bozorth[3)] has discussed a relation among their spin structure, spin direction, and direction of spontaneous magnetization from the symmetry consideration which was first pointed out by Dzyaloshinsky[4)]. His argument can be applied to $NaNiF_3$ crystal which has the same crystal symmetry. $NaNiF_3$ has probably a G-type spin structure[5)] and is believed to be a canted antiferromagnet in which the spins of Ni^{2+} ions are approximately directed along the a-axis and slightly incline toward the c-axis.

A rapid increase of the anisotropy of paramagnetic susceptibility, which is characteristic of a weak ferromagnet[6)], has also been observed near T_c. Details will be published elsewhere.

References

1) W. Rüdorff and J. Kändler: Naturwiss. **44** (1957) 418.
2) R. C. Sherwood, J. P. Remeika and H. J. Williams: J. Appl. Phys. **30** (1959) 217.
3) R. M. Bozorth: Phys. Rev. Letters **10** (1958) 362.
4) I. Dzyaloshinsky: J. Phys. Chem. Solids **4** (1958) 241.
5) E. O. Wollan and W. C. Koehler: Phys. Rev. **100** (1955) 545.
6) T. Moriya: Phys. Rev. **117** (1960) 635.

J. Phys. Soc. Japan **15** (1960) 2362~2363

Anomalous Temperature Dependence of Lattice Constant of Cr O_2

By Kiiti Siratori and Shūichi Iida

Department of Physics, Faculty of Science University of Tokyo, Tokyo

(Received Oct. 11, 1960)

Previously, we studied the crystallographic and magnetic properties of $Mn_xCr_{1-x}O_2$ system, and reported that the Vegard's law is not satisfied in this system[1]. All the specimens crystallize in rutile type tetragonal structure, but c vs. x curve shows two anomalies. In order to study the reason of these anomalies, temperature dependence of the lattice constants were measured.

The specimens used were the same as had been in the previous study. Variation of the X-ray diffraction angles of (211) and (220) lines was observed at several temperatures with a counter type spectrometer and with Cu $K\alpha$ radiation. Relative accuracy of the measurement is about ± 0.002A for both a and c. The temperature dependence of a, c and $\sqrt[3]{a^2c}$ for CrO_2 and $Mn_{0.05}Cr_{0.95}O_2$ are shown in Fig. 1. As is shown, c has a maximum at about 0°C, which becomes broad when Mn is added, whereas the unit cell volume varies almost linearly with temperature. It seems that this phenomenon is independent of the magnetic transition, since there is no anomaly at the Curie temperature (124°C). It has been confirmed that all the specimens with $x<0.17$ have negative temperature coefficient of c in the temperature range of $0° < T < 200°$C.

It will be very probable that these anomalous variation of c will cease at a certain temperature, T_s, above 200°C, and will show a normal linear increase with temperature above this point. Therefore, it is concluded that there is a certain structural transition in the temperature range $0° < T < T_s$. The authors are now inclined to believe that this transition is a Jahn-Teller distortion of $(3d)^2$ orbitals of Cr^{4+}.

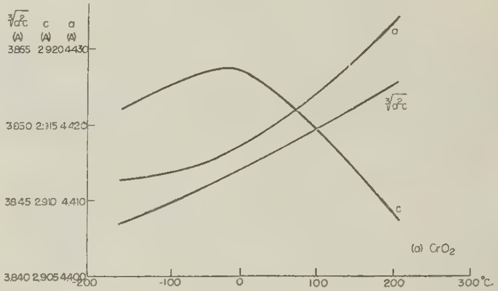

Fig. 1 (a).

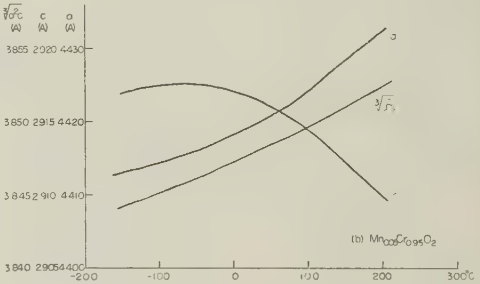

Fig. 1 (b).

Fig. 1. Temperature dependence of a, c and $\sqrt[3]{a^2c}$.

It is well known that many magnetic oxides have a crystal distortion that cannot be expected merely from the symmetry of the crystal and is accounted for well by the Jahn-Teller effect of the magnetic ions participated[2]. There are also some oxides as CuO, CrF_2 and $CrCl_2$, that have a crystal

Table I.

Parameters of oxygen octahedron around cation in CrO_2 and MnO_2

	CrO_2	MnO_2
O_1 O_2	2.57 A	2.51 A
O_1 O_3	2.68	2.66
O_1 O_5	2.92	2.87
M $O_{1,2}$	1.94	1.91
M O_3	1.84	1.85
$\angle O_1$ M O_2	83°	82.5°

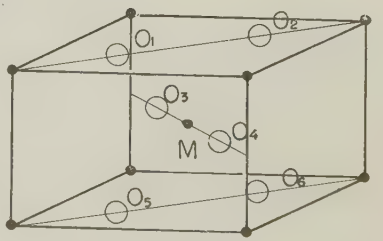

structure with no distortion apparently, but the legand anions construct a distorted octahedron and the distortion of which can be most reasonably explained by the Jahn-Teller effect of the cations at the center³⁾. However, few is known on the effect of the cations with degenerated $d\varepsilon$ orbitals (π orbitals) only. It is considered that the order of magnitude in this case will not be so small compared with those of the typical degenerated $d\gamma$ orbitals (σ orbitals).* But care should be taken in this case (1) to the presence of spin-orbit coupling interaction of the $d\varepsilon$ electrons (this term is not active in the case of $d\gamma$ orbitals) and (2) to the admixture of the state ($d\varepsilon^1\, d\gamma^1$) through interelectronic Coulomb interaction.

In relation to these argument, the shape of the oxygen octahedron around Cr^{4+} ion becomes important. From the intensity measurements of (111) and (210) reflection, parameter u is determined to be 0.294±0.005 for CrO_2 and 0.298±0.005 for MnO_2 at room temperature (temperature factor is neglected). Parameters of the oxygen octahedron calculated from these values are shown in Table I.

However, the study is in an initial stage at present and no decisive answer is given whether this crystal is strictly rutile type or not. Detailed report will be presented in the near future.

Thanks are due to Mr. T. Inoue for his helpful suggestion and discussions.

References

1) K. Siratori and S. Iida: J. Phys. Soc. Japan **15** (1960) 210.
2) J. D. Dunitz and L. E. Orgel: J. Phys. Chem. Solids **3** (1957) 20; J. Kanamori: J. Appl. Phys. Suppl. **31** (1960) 14s.
3) J. D. Dunitz and L. E. Orgel: op. cit.; J. W. Cable, M. K. Wilkinson and E. O. Wollan: Phys. Rev. **118** (1960) 950.

---

* Due to private discussion with Dr. J. Kanamori.

J. PHYS. SOC. JAPAN **15** (1960) 2363

A Note on Date's Paper "Magneto-plasma Resonance in Semiconductors (I)"

By Kazuo YAMAGATA

The Research Institute for Iron, Steel and Other Metals, Tohoku University, Sendai

(Received October 5, 1960)

A theory of magneto-plasma resonance in semiconductors was developed by Date in his paper entitled "Magneto-plasma Resonance in Semiconductors (I)" which appeared in this journal¹⁾. It may be said that the treatment can be justified under the assumptions that the specimen is spherical and that the energy surfaces of the semiconductors are spherical. In his paper the author stated that the theory can be applicable to the usual semiconductors such as silicon and germanium. It must, however, be noticed that the energy surfaces of the usual semiconductors are not spherical but highly anisotropic except a few ones such as indium antimonide.

From the physical point of view, there are three difference effective masses, conductivity or plasma, magneto-plasma and cyclotron mass. It seems apart from reality to assume that the three masses can be represented by one mass parameter even in the case that the parameter may depend on the directions of the static magnetic field and the oscillating electric field. For the purpose of clarifying these ambiguities, we performed calculations on the case of spherical specimen of semiconductors with one type of carriers with anisotropic effective mass.

All the reports preceding the above mentioned one are developed for the case of spherical energy surfaces²⁾. We must, therefore, start from the fundamental equation of the electron transport theory. The starting equation is

$$\frac{d}{dt}\{M\cdot\boldsymbol{v}(t)\}=q\{\boldsymbol{E}(t)-L\cdot\boldsymbol{P}(t)\}+\frac{q}{c}\{\boldsymbol{v}(t)\times\boldsymbol{H}\}-\nu\{M\cdot\boldsymbol{v}(t)\},$$

where M is the mass tensor with principal values m_1, m_2 and m_3, $\nu=1/\tau$ is the relaxation frequency. In the case that the oscillating electric field is parallel to the x-direction and the static external magnetic field to the z-direction, one of the diagonal elements of couductivity tensor is

$$\sigma_{xx}=\frac{Nq^2}{m_1}\cdot\frac{1}{(i\omega_1'+\nu)+\dfrac{\omega_c{}^2}{(i\omega_2'+\nu)}},$$

where $\omega_1'=\omega-(\omega_{1p}^2/\omega)$ with $\omega_{1p}=(L_lNq^2/m_1)^{1/2}$, $\omega_2'=\omega-(\omega_{2p}^2/\omega)$ with $\omega_{2p}=(L_lNq^2/m_2)^{1/2}$ and $\omega_c=(qH/c)(m_1 m_2)^{-1/2}$.

The above result shows that three types of effective mass must be introduced. That is to say m_1, $(m_1 m_2)^{1/2}$ and m_2. It is not much accidental to meet with the anisotropy with the factor of 20, and in such a case we have three effective masses with the ratio of 1 and 4.5 to 20. This is the consequence of the fact that the motion of carriers in the magneto-plasma resonance consists of longitudinal plasma motion, transeverse plasma motion and cyclotron motion. In the cases that the energy surfaces are many valley type, that the sample is not a sphere and that the magnetic field are not parallel to the principal axes, the calculation may be somewhat laborious. The principal features of the above result may not, however, be altered.

References

1) M. Date: J. Phys. Soc. Japan **15** (1960) 1488.
2) See, for example, G. Dresselhauss, A. F. Kip, and C. Kittel: Phys. Rev. **100** (1955) 618; P. A. Wolff: ibid. **112** (1958) 66.

J. PHYS. SOC. JAPAN **15** (1960) 2364

Optical Bleaching of Gamma-Irradiated KCl at Room Temperature

By Noriaki ITOH and Tokuo SUITA

Department of Nuclear Engineering, College of Engineering, Osaka University

(Received September 8, 1960)

It has been already shown[1] that a part of F centers formed by ionizing particles bleaches quickly by F light illumination, whereas the remaining part bleaches at a considerably slower rate. In order to clarify such two step bleaching, we investigated the effects of bleaching temperature and initial concentration of F centers on the bleaching phenomena in gamma-irradiated KCl.

The specimens were obtained from the ingot purchased from Harshaw Chemical Co. In order to obtain uniform coloration, the specimens were gamma-irradiated in the Co^{60} cave of JAERI (Japan Atomic Energy Research Institute). The optical absorption was measured with Cary Spectrophotometer, and F light illumination was done by the spectrometer with 3 mm slit width.

From the bleaching curves at 18°C and at −25’C for gamma-irradiated specimens at various dosage the concentration N_q of quickly bleaching F center was obtained. Fig. 1 shows the dependence of N_q on the gamma ray dose for the two bleaching temperatures. When the gamma-ray dose is lower than 3×10^6 r, there is no difference in N_q for the two bleaching temperatures. This difference, however, increases with increasing gamma ray dose, accompanied with the increasing rate of formation of complex centers such as M, R_1, and R_2 centers. The dependence of the ratio of N_q at −25°C to the initial concentration N_F of F centers on the gamma ray dose is also shown in Fig. 1.

Qualitatively, the difference between N_q at two bleaching temperatures may correspond to the formation of complex centers. This seems to be supported by the fact that this difference is nearly proportional to the initial rate of M center formation, which will be a measure of complex center formation by F light bleaching. (In the early stage of bleaching, the growth rate of R centers is much smaller than that of M centers). It is also interesting that the difference is proportional to the initial concentration of F centers.

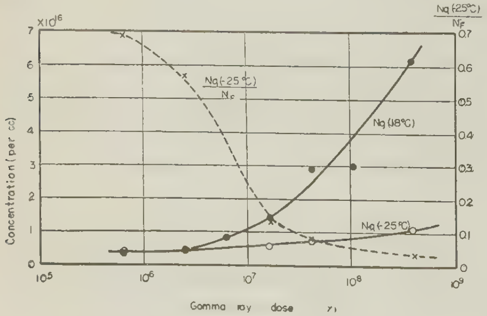

Fig. 1.

The above results seem to show that the quickly bleaching component of F centers at room temperature is composed of two parts; one which is related to the complex center formation, increases with the bleaching temperature;[3] the other is independent of the bleaching temperature. The latter may be due to recombination of electrons with positive holes at some hole trapping centers which have larger cross section for electron trapping than those which correspond to more stable F centers. It should be noted that the relation between the latter part and the gamma ray dose shows a saturation curve on a linear scale and its saturation value is nearly 10^{16}/cc.

The bleaching curve at −25°C which does not include the effect of complex center formation shows that F centers formed by gamma-irradiation have two different kinds of bleaching characteristic. As clearly seen from the (N_q/N_F)-dose curve in Fig. 1, in the early stage of irradiation only quickly bleaching F centers are formed, while with increasing irradiation dose the concentration of this type of F centers saturates and stable F centers increase.

It has been reported by several authors that F centers formed by ionizing radiation have two parts, by studying the formation curve of F centers[4] and that the first part which is dependent on impurities and increases with higher rate saturates nearly at the value of 10^{16}/cc, in Harshaw KCl. Combining with the present results it seems possible to conclude that F centers formed in the first stage bleach at much higher rate by F light illumination. The formation mechanism of F centers in the early stage seems to be different from that in the later stage, which may cause the differences in the trapping states of positive holes recombining with electrons from F centers. In order to clarify the formation mechanism in each stage further experiments should be done.

Most parts of the present work were done while the one of the authors was in the course of Nuclear Engineering School of JAERI. The authors would like to express their gratitude to Prof. Y. Takagi and Dr. K. Kubo for their valuable discussions.

References

1) F. Seitz: Rev. Mod. Phys. **26** (1954) 7.
2) H. Okura: J. Phys. Soc. Japan **12** (1957) 1313. See also T. Tomiki: J. Phys. Soc. Japan **14** (1959) 1114.
3) S. Petroff: Z. f. Physik **127** (1950) 443.
4) P. V. Mitchell, D. A. Wiegand and R. Smoluchowski: Phys. Rev. **117** (1960) 442.

J. PHYS. SOC. JAPAN **15** (1960) 2365～2366

The Energy Spectra of Secondary Electrons in Various Materials Irradiated by Gamma Rays from ^{60}Co and ^{137}Cs

By Nobuo ODA

Department of Physics, Rikkyo (St. Paul's) University, Tokyo

and Hirosi SUZUKI

Institute for Physics, College of General Education, Tokyo University, Tokyo

(Received September 16, 1960)

A knowledge of the energy distribution of the electrons traveling past a point in the medium under irradiation of X- or γ-rays is necessary for a complete understanding of the physical, chemical, and biological processes which occur during irradiation. It can be shown that the electron flux spectrum, $n(E)$, within a medium having a stopping power $S(E)$ is, under the equilibrium conditions and with the effect of δ-ray neglected,

$$n(E)=\frac{1}{S(E)}\int_{E}^{E_{\max}} N(E_i)dE_i \tag{1}$$

where $N(E_i)$ is the number of electrons set in motion with the initial energy E_i per energy interval per cubic centimeter of medium absorbing the quantum radiation and called the initial distribution.

Hayward[1] measured the initial distribution in water for non-collimated ^{60}Co γ-rays with a scintillation spectrometer. The same quantity was also measured for collimated ^{60}Co γ-rays with a similar apparatus by Bruce and Johns[2] and the electron flux spectrum was derived with use of the equation (1). Using a magnetic beta spectrometer, Aglintsev et al[3] measured directly the energy spectra of secondary electrons knocked out from plexiglas, copper, and lead irradiated by ^{60}Co and ^{137}Cs γ-rays.

We have tried to measure the secondary electron flux spectra for ^{60}Co and ^{137}Cs γ-rays with a scintillation spectrometer. The target materials used are plastic (polyethylene), aluminum, copper, and lead.

The experimental arrangements are as follows: an about 8 mc ^{60}Co or 10 mc ^{137}Cs source was held on a plastic support behind a 10 cm long, 3 mm diameter lead collimator. The gamma-ray beam leaving the collimator passed through three 2 mm thick aluminum diaphragms of adequate diameters which were provided to prevent the secondary electrons ejected from the inner surface of the collimator from reaching the detector, and then was incident normally on the target disk. The thicknesses of the target materials were 400 mg/cm^2 for ^{60}Co source and 200 mg/cm^2 for ^{137}Cs source respectively. These thicknesses are large enough to give the secondary electron equilibrium condition in these targets. The plastic scintillator of 5 mm thickness mounted on a lucite light pipe which was optically coupled to the face of a EMI 6097 photomultiplier tube was placed in contact with the back surface of the target disk. The scintillator was covered with an aluminum foil light reflector of about 1 mg/cm^2 thickness. The pulse-height distribution from the detector was measured with a linear amplifier and a single channel differential analyzer. The linearity and zero of the discrimination level of the analyzer were checked with a mercury-relay pulse generator. The resolution and the factor relating pulse-height to energy of the instrument were determined from the internal conversion line of ^{137m}Ba (625 Kev). The peak resulting from the internal conversion line was appeared as a Gaussian distribution with a half-width of about 100 Kev.

In this arrangement, however, it is inevitable that the detector system is exposed to primary γ-rays. Consequently, in order to obtain the spectrum of secondary electrons which enter into the scintillator from the target, it is necessary to subtract from the pulse-height spectrum directly obtained the part due to the Compton recoil electrons produced in the scintillator-light pipe system by the primary γ-rays.

The energy spectra of secondary electrons released from the various target materials were thus obtained by subtraction of the pulse-height spectra measured without target disks from those measured with target disks. In order to prevent the gain drifts to introduce a noticeable error in the subtractions, the pulse-height distribution measurements with and without target and the pulse-height calibration with the coversion line of ^{137m}Ba were performed in a cyclic fashion. Three to five times of these cycles were performed per each target.

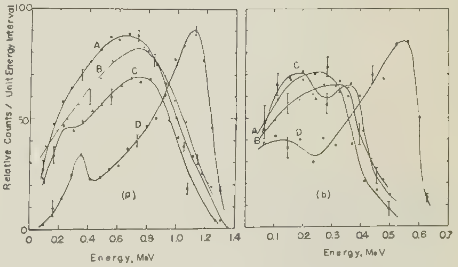

Fig. 1. Energy spectra of secondary electron flux for gamma rays of ^{60}Co (a) and ^{137}Cs (b) sources: (A) polyethylene; (B) aluminum; (C) copper; (D) lead.

The results for ^{60}Co and ^{137}Cs γ-rays are shown in Figs. 1 (a) and (b), respectively. These spectra are the ones for electrons traveling into the forward hemisphere past a point in the medium and do not contain the ones for the backward direction. The backward part may be appreciable for the medium with a higher atomic number such as lead.

References

1) E. Hayward: Phys. Rev., **136** (1952) 493.
2) W. R. Bruce and H. E. Johns: Brit. J. Radiol., **28** (1955) 443.
3) K. K. Aglintsev, V. V. Mitrofanov and V. V. Smirnov: Atomnaya Energy., **2**, **1** (1957) 66.

J. PHYS. SOC. JAPAN **15** (1960) 2366

Electroluminescence of CdS Single Crystal

By Hirosuke YAMASHITA, Sumiaki IBUKI, Michio YOSHIZAWA and Hiroyoshi KOMIYA

Research Laboratory, Mitsubishi Electric Mfg. Co, Ltd. Amagasaki, Japan

(Received August 15, 1960)

The electroluminescence of CdS Single Crystals, containing carrier injection type, have been reported by G. Diemer[1] and R. W. Smith[2]. Here we describe our new experimental results and some interpretations about the above phenomena.

Samples of crystals have flaky forms of about 7 mm in length, 2 mm in width and 0.4 mm in thickness. These crystals are thought to be very pure and show high resistances above $10^{10}\Omega$ under illumination of 1000 lx from a tungsten lamp. Electrodes are In which are soldered on both ends in length of the crystal and d.c. voltage is applied between these electrodes through a suitable series resistance at room temperature.

As increasing applied voltage on the sample and increasing current through the sample, yellow, green and orange spots appear on and near the anode electrode as the same manner of luminescence observed by Diemer[1] and Smith[2].

When the current intensity exceeds a few hundreds of μA, clear green curtains begin to appear (Fig. 1). They stretch towards the cathode from preceding green or yellow spots and their lengths are about 1 mm. Throughout the observation green curtain sways to right and left, spreading or contracting in parallel to the field. By more detailed inspections it becomes clear that the green curtain consists of many stripes perpendicular to the field and the stripes flow into the end of the curtain. Rates of the fluctuations of these green curtains are seemed to be as slow as about several cycles per sec., and consequently it is supposed that the fluctuation is caused by the change of internal space charge related to the hole injection.

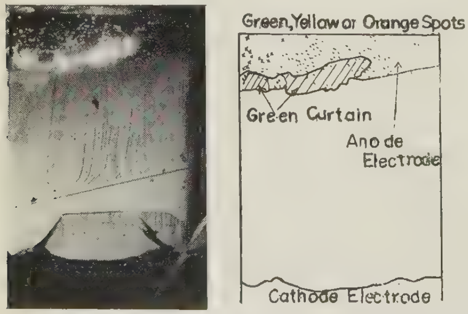

Fig. 1. Microscopic photograph of electroluminescence of CdS Single Crystal. Due to the long exposure time green curtains are overlapped together.

Increasing current up to about 1 mA, red luminescence appears and breakdown occurs in the crystal. After that the resistance of crystal is seen to be about a few hundreds of kilo-ohms. In this state wherefore it may be considered that the interior construction of the crystal has been changed by oxidation or thermal dissociation.

As the results of studying the spectral distribution of emitted light, it has become clear that the green emission has a very narrow band at about 5300 Å and the orange emission has a broad band whose maximum lying at about 6000 Å. It is considered that the yellow emission is composed of mixing green and orange emission. Measuring the brightness of luminescences through optical filters of 5300 Å or 6000 Å, we find out that they have not linear but rather sublinear characteristics against the value of current, therefore it is concluded that the recombination producing green and orange emission is not monomolecular such as exciton decay but rather bimolecular mechanism. The orange emission is caused perhaps by the recombination of electron with hole through an impurity center or a Cd vacancy but further detail can not be yet explained.

We are considering that the green luminescence is due to the recombination of shallow trapped electron with free hole, both of them are injected from electrodes of opposite signs respectively and that the depth of the electron trap related to the radiative recombination producing the green luminescence is about one tenth of eV from the bottom of conduction band.

References

1) G. Diemer: Philips Res. Rep. **9**, 109, (1954).
2) R. W. Smith: Phys. Rev. **105**, 900, (1957).

J. Phys. Soc. Japan **15** (1960) 2367~2368

X-ray Study of Lattice Defects in Si Single Crystals by Transmission Berg-Barrett Technique*

By Mitsuru Yoshimatsu
Rigaku Denki Co. Ltd., Haijima, Akijima, Tokyo
and Kazutaka Kohra
Institute of Physics, College of General Education, University of Tokyo, Komaba, Meguro, Tokyo

(Received Sept. 27, 1960)

The Berg-Barrett technique, which has been used for taking X-ray diffraction micrographs in reflection, is possible to be extended to take micrographs in transmission. With this technique, which might be called the transmission Berg-Barrett technique, lattice defects in thin specimens of Si single crystals were studied.** In comparison with the Lang technique,[3] no special apparatus is necessary, the exposure time is much shorter and, although resolution is poorer, individual dislocations can be resolved in favourable cases.

Experimental arrangement (Fig. 1) is the same in principle as those used by some other investigators,[4],[5],[6] but extinction effect instead of abnormal transmission is utilized to obtain the image contrast. Accordingly the specimen must be sufficiently thin. A Mo tube of ordinary focal size (Philips) was used. Instrumental resolution[7] due to apparent focal width and dispersion between $K\alpha_1$ and $K\alpha_2$ is roughly estimated to be of order of 10 microns in both directions perpendicular and parallel to the incident plane for low index reflection of the symmetrical Laue case.

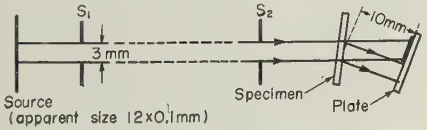

Fig. 1. Schematic diagram of the transmission Berg-Barrett technique.

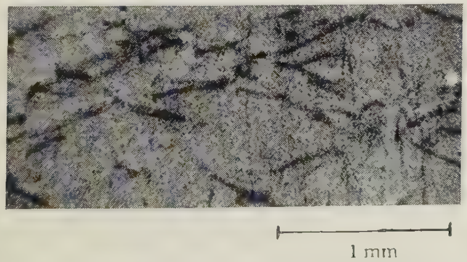

Fig. 2. Individual dislocations in a Si single crystal. (220) reflection.

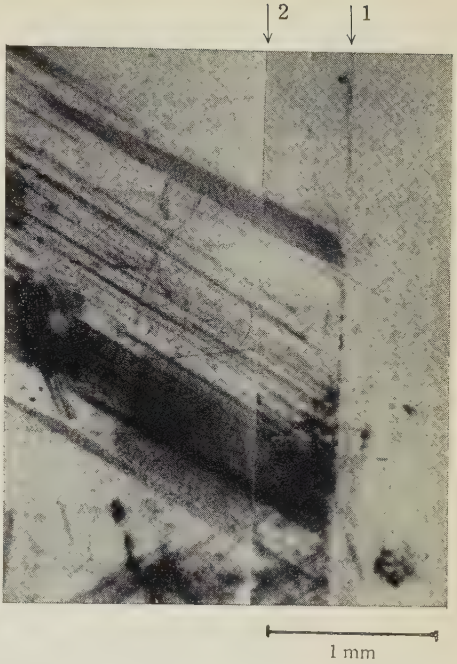

Fig. 3. Lattice defects in the neighbourhood of a twin boundary of a Si single crystal. (111) reflection. The twin boundary lies at the line 1. Two photographs are connected at the line 2.

Fig. 2 shows a (220) reflection photograph from a slice (0.28 mm thick) of Si single crystal, the surface of which is normal to the growth axis [111]. Individual dislocation lines are resolved. The width of each dislocation line image is about 20 microns, being about twice as large as the estimated value.

Fig. 3 shows a (111) reflection photograph from the neighbourhood of a twin boundary (111), which is normal to the growth axis. The specimen (0.5mm thick) was cut normal to the twin plane. To obtain a good contrast of the image, it is desirable to take the photograph from small area of the specimen, in order to suppress the background due to continuous X-rays. For this reason, two photographs were successively taken and connected to each other. It is to be noted that there are many streaks and a few bands besides dislocation lines at only one side of the twin boundary. These streaks and bands seem to be attributed to lattice defects such as stacking faults. A further study will be soon reported.

References

1) J. B. Newkirk: Trans. AIME. **215** (1959) 483,

---

* This was reported at the Annual Meeting of Physical Society of Japan (April, 1960).

** This possibility was suggested by Newkirk.[1] Independently of us, Webb[2] used also this technique to study dislocations in whiskers of NaCl.

2) W. W. Webb: J. Appl. Phys. **31** (1960) 194.
3) A. R. Lang: Acta Cryst. **12** (1959) 249.
4) H. Barth und W. Hosemann: Zs. f. Naturforsch. **13**a (1958) 680.
5) Z. Ishii and K. Kohara: J. Phys. Soc. Japan **14** (1959) 1250.
6) V. Gerold und F. Meier: Zs. f. Physik **155** (1959) 387.
7) M. Yoshimatsu and K. Kohra: J. Phys. Soc. Japan **15** (1960) 1760.

J. PHYS. SOC. JAPAN **15** (1960) 2368~2369

"Energy Analysis of Electron Diffraction Patterns"

By Hiroshi WATANABE
Hitachi Central Research Lab. Kokubunji, Tokyo, Japan

(Received Oct. 8, 1960)

The energy analysis of electron diffraction patterns was carried out by Leonhard[1] and the present author[2] using Möllenstedt type velocity analysers[3]. However, the diffraction patterns analysed by them were *selected area* diffraction patterns which are not so suitable for the intensity measurement as *ordinary* diffraction patterns. A selected area diffraction pattern does not exactly correspond to the area defined by the selector aperture, as pointed out by Agar[4]. Therefore, in order to study the exact intensity distribution of energy spectrum the analysis of ordinary diffraction pattern is required. The present note describes a new experimental arrangement which meets the above requirement and some preliminary results obtained by it.

The electron optical system is shown in Fig. 1. Both transmission and reflection patterns can be analysed. A focusing lens and a reducing lens (Fig. 1) project the reduced diffraction pattern on a plane with a fine slit, and then the part of the projected pattern passing through the fine slit is analysed by the analyser lens. The pattern on the plane of the fine slit and energy loss spectrum obtained in the analysis are shown schematically in (b) and (c) of Fig. 1. In this analyser the angular deviation due to the energy loss of 1 ev is about 10^{-4} radians, and the scattering angle in which we are interested is between 10^{-3} and 10^{-1} radians. By the reducing lens the scattering angle is reduced to the order of angular deviation due to energy loss.

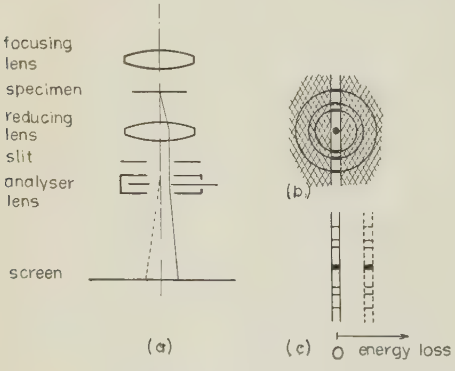

Fig. 1. (a) Schematic diagram of the electron optical system. (b) Diffraction pattern on the fine slit plane. (c) Energy loss spectrum on the final screen.

The energy analysis was carried out with the following specimens: (a) single crystals of molybdenite (tr), Ge, CdS and Si (re), (b) smoke particles of ZnO and MgO (tr), (c) evaporated metals of Al and Au (tr). Here (tr) and (re) mean transmission and reflection observation, respectively.

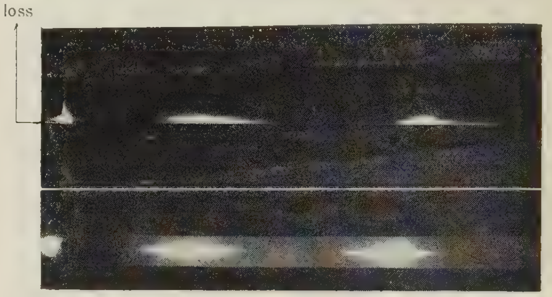

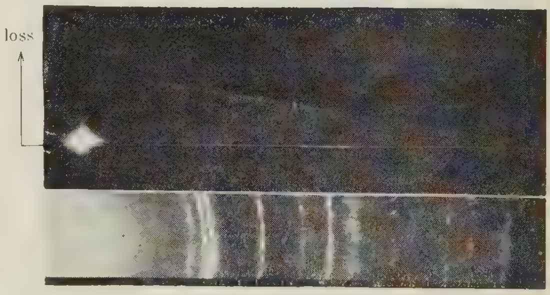

Fig. 2. Energy loss spectrum of reflection diffraction pattern from CdS single crystal.

Fig. 3. Energy loss spectrum of transmission diffraction pattern from ZnO smoke particles.

Some examples are shown in Figs. 2 and 3. The accerelating voltage is 30 kv, and the diameter of the electron beam on the specimen is about $0.1\,\mathrm{mm}\phi$. Summerizing the experimental result the following conclusions are drawn regarding electron scattering phenomena in crystals:

(a) In single crystals the inelastic scattering occurs mainly in the directions of diffracted beam as will as in the direction of the incident. The elastic diffuse scattering, i.e. the scattering with no detectable energy loss and in the directions satisfying no Bragg condition, does not occur strongly. These results are independent of transmission or reflection.

(b) In smoke particles, on the contrary, the most portion of the inelastic scattering occurs only in the direction of the incident. The elastic diffuse scattering occurs remarkably.*

(c) In evaporated metals, the inelastic scattering occurs in the same way as in case (a). The elastic diffuse scattering occurs remarkably, too.*

The author wishes to thank Professors R. Uyeda, S. Takagi, K. Kohra and Mr. F. Fujimoto for their helpful discussions on the experimental results.

References

1) F. Leonhard: Zeits. Naturforsh. **9a** (1954) 727.
2) H. Watanabe: J. Phys. Soc. Japan **10** (1955) 321.
3) G. Möllenstedt: Optik **5** (1946) 499.
4) A. W. Agar: Brit. J.A.P. **11** (1960) 185.

---

* Mr. F. Fujimoto suggested to the author that this may be attributed to the elastic secondary scattering by crystallites. (cf. J. M. Cowley and A. L. G. Ress: Proc. Phys. Soc. London **649** (1951) 609).

Errata

The Dipole Moment and End-to-end Length of the Isotactic Vinyl Polymer

By Tsugio Mori

I. Mutual Dependence between Dipole Moment and End-to-end Length

J. Phys. Soc. Japan **15** (1960) 1482

Page	Column	Line		Should be read
1483	right	14	is	in
1485	left	3	or ····=o	or ····=**o**
1486	left	10 from the bottom	ridid	rigid
1486	right	3	ridid	rigid
1487	right	17	ε	ζ

II. A Special Simplified Model and Numerical Calculations

J. Phys. Soc. Japan **15** (1960) 1638

1638	synopsis	2	are derived.	were derived.

X-ray observations on Cleavage Faces of LiF Single Crystals

By Mitsuru Yoshimatsu and Kazutake Kohra

J. Phys. Soc. Japan **15** (1960) 1760

Page	Column	Line		Should be read
1760	left	15	discriminated distorted	discriminate the distorted
1762	Fig. 4.		(d) (220)	(d) $(2\bar{2}0)$
1762	Fig. 4.	caption	snbgrain	subgrain
1765	Fig. 11.	caption	Charge	Change
1765	Fig. 12.	last line	Fig. 12	Fig. 11
1769	right	20	while	While

Lines 1 and 2 of the left column, page 1764, should be inserted between the last line of the left column and the first line of the right column, page 1763; ......of the incident beam (geometrical divergence, spectral distribution of the wave length), dimension of the X-ray source, and...... .

PROGRESS OF THEORETICAL PHYSICS

CONTENTS

Progress of Theoretical Physics Vol. 24, No. 1, July 1960

Abandonment of the Assumption of the Displacement Invariance and Replacement of the Assumption of Field by the Assumption of Particle .... Takao TATI .. 1
On the Test of Global Symmetry .... S. FURUI and T. SAKUMA .. 18
On Ratios of the Renormalized and the Bare Coupling Constants in the Beta Decay Interaction .... Ichiro KAWAKAMI .. 27
Electromagnetic Mass Difference of Elementary Particles .... Hiroshi KATSUMORI .. 35
A Possible Interpretation of High Energy Nuclear Events .... N. YAJIMA, S. TAKAGI and K. KOBAYAKAWA .. 59
On the Inelastically Scattered Proton and the Dipole γ-Absorption .... Yoshiyuki SAKAMOTO .. 81
Composite Model and the Nature of Vector Interactions in Strangeness-Violating Decays .... C. ISO, M. KAWAGUCHI and Y. MIYAMOTO .. 97
A Relativistic Model for a Shell of Flowing Radiation in a Homogeneous Universe .... P. C. VAIDYA and K. B. SHAH .. 111
A Study on the Low Energy n-p System .... Tetsuo HAMADA .. 126
The Proton-Neutron Mass Difference and the Inner Structure of the Nucleon .... T. KANKI and K. YAMAMOTO .. 135
Neutrino and Cosmology .... Asher PERES .. 149
Propagation of Shock Waves in Inhomogeneous Gases. II—*Hydromagnetic Shock*— .... Y. ŌNO, S. SAKASHITA and H. YAMAZAKI .. 155
Spin-Lattice Relaxation of Donor Electrons in Silicon .... Jun KONDO .. 161
Theory of Matter with Super Light Velocity .... Sho TANAKA .. 171
Ground States of Ca Isotopes .... Toshiya KOMODA .. 201
Letters to the Editor:
    High Energy Limit of Vertex Function in Quantum Field Theory .... S. ARAMAKI .. 210
    On the G_A/G_V Ratio in β-Decay .... C. IHARA .. 211
    Possible Corrections to Nuclear Magnetic Moments Due to Pairing Forces in Nuclei. I .... J. SAWICKI .. 213
    On the Interaction in Nucleon Core .... S. MINAMI .. 216
    Some Remarks on Fermi-Yang Model .... Y. ATAKA .. 218
    A Proton-Proton Potential .... T. HAMADA .. 220
    Non-Static Effect in the $T=0$ Two-Nucleon Interaction ...... T. HAMADA .. 222
    Note on the Radiative Corrections for the Electron-Electron Scattering .... K. HIIDA, T. MUROTA, M. GOTO and M. SASANUMA .. 223
    Note on the Radiative Correction to Electron-Electron Collision .... H. SUURA .. 225
Contents of Journ. Phys. Soc. of Japan, Vol. 15, No. 5 .... i–ii

---

Price $ 1.25 per copy
$ 15.00 per year (postage inclusive)
Annual dues for foreign members (individual subscribers)
$ 12.00 (postage inclusive)
〃 for foreign members of the Physical Society of Japan
$ 10.00 (postage inclusive)

Application for membership, subscriptions and orders for back numbers should be sent, directly or through book-dealers, to

The Publication Office
in
Yukawa Hall, Kyoto University, Kyoto, Japan

. . . .

Contents

(Vol. 15)

No. 1

Page

Radiations from Ba^{141} .... Kunio NAGATANI 1
Angular Correlation Measurements in the Decay of In^{114m} ...... Mitsuhiro KAWAMURA 3
Elastic Scattering of 14 MeV Protons by Deuterons and by Protons .... Seishi KIKUCHI, Junpei SANADA, Shigeki SUWA, Izuo HAYASHI, Keigo NISIMURA and Kiyoji FUKUNAGA 9
Investigation of the Reaction $Mg^{25}(p, \gamma)Al^{26}$ .... Jiro MUTO 17
Gamma-rays from the Reaction $Al^{27}(p, \gamma)Si^{28}$ .... Kotoyuki OKANO 28
A 160 cm Synchro- and Variable Energy Ordinary Cyclotron ...... Seishi KIKUCHI, Itaru NONAKA, Hiroshi IKEDA, Hiroo KUMAGAI, Yoshio SAJI, Junpei SANADA, Shigeki SUWA, Akira ISOYA, Izuo HAYASHI, Kazuhisa MATSUDA, Hisashi YAMAGUCHI, Takashi MIKUMO, Keigo NISHIMURA, Takashi KARASAWA, Shinsaku KOBAYASHI, Ken KIKUCHI, Satoru ITO, Arata SUZUKI, Seiichiro TAKEUCHI and Hiroshi OGAWA 41
On the Variation Principle in the Kinetic Theory of Dense Gases, I .... Terutosi MURAKAMI 60
Dislocation Model of Liquid Structure .... Sanchi MIZUSHIMA 70
Approach to Equilibrium of A Large Fermion System .... Kyoji NISHIKAWA 78
Annealing of γ-ray Damage in Germanium .... Tsunesaburo ASADA, Haruo SAITO, Kazumi OMURA, Taiji OKU and Masahiro OKA 93
A. C. and D. C. Field Effects on Cleaned Germanium Surfaces .... Shinji KAWAJI 95
Crystal Structure of Silicon Carbide of 174 Layers .... Takanori TOMITA 99
Electron Diffraction Study of Ice .... Kohji SHIMAOKA 106
Theory of Electron-Oscillations in Non-uniform Plasmas .... Masao SUMI 120
Electroluminescence in Zinc Sulfide Single Crystals .... Shin-ichiro NARITA 128
Electron Microscope Study of the Decomposition Process of Oxide Coated Cathods .... Shoichi HIROTA and Tetsuji IMAI 137
Thermoluminescence of Zinc Sulfide Phosphors .... Kikusaburo OSADA 145
A Refinement of the Linearized Transonic Flow Theory .... Iwao HOSOKAWA 149
General Theory of Electrically Conducting Perfect Gas Flow past a Three-Dimensional Thin Body .... Shigenori ANDO 157
Condenser Microphones with Plastic Diaphragms for Airborne Ultrasonics, II .... Kiichiro MATSUZAWA 167
A Linearized Theory of Magnetohydrodynamic Flow past a Fixed Body in a Parallel Magnetic Field .... Hirowo YOSINOBU 175
Magnetohydrodynamic Flow past a Sphere .... Kanefusa GOTOH 189

SHORT NOTES

Effect of Charged Dislocation on the Thermoelectric Power of Semiconductors .... Tokio OHTA 197
Influence of Foreign Magnetic Nuclei on NMR .... Akira MIYAKE and Riichirô CHÛJÔ 198
Thermal Conductivity of KNO_3 .... Ikushi YOSHIDA and Shozo SAWADA 199
On a Solution of the Paraxial Ray Equation in an Axially Symmetrical Electrostatic Field .... Noboru SHIBATA 200
NMR Second Moment of a Radical Oscillating in a Periodic Potential .... Riichirô CHÛJÔ 201
Temperature Dependecce of T_1 of Cl^{35} in Para-dichlorobenzene .... Akira HIRAI 201
Synthesis of AIN Crystals .... Tetsuo MATSUMURA and Yasaku TANABE 203
Crystal Growth of CdS in the Vertical Furnace .. Haruo FUJISAKI and Yasaku TANABE 204
Dislocations in Si Single Crystals .... Takashi FURUOYA and Yozo SASAKI 205
Observation of Layer Structure in Dislocation Free Silicon Crystals with the Use of X-ray Anomalous Transmission .... Zensho ISHII, Takashi FURUOYA, Yozo SASAKI and Kazutake KOHRA 206
Intervalley Scattering of Hot Electrons .... Motoichi SHIBUYA and Wataru SASAKI 207
On the Quasi-two-dimensional Laminar Boundary Layer .... Nisiki HAYASI 208

Magnetic Properties of $\mathrm{Mn}_x\mathrm{Cr}_{1-x}\mathrm{O}_2$ .... Kiiti SIRATORI and Shuichi IIDA 210
Formation Mechanism of F-Centers in KCl Single Crystals Heated in Potassium Vapor .... Hiroyuki MIZUNO and Morio INOUE 211

Errata

Relative Intensities of Zeemman Components in Nuclear Quadrupole Resonance Spectrum .... Masaharu TOYAMA 186

No. 2

Three New Isotopes, Co^{63}. Ca^{75} and As^{81} .... Haruhiko MORINAGA. Tokihiro KUROYANAGI, Hidehiko MITSUI and Katsufusa SHODA 213
On the Stability of an Electron Gas at Low Density .... Masao SHIMIZU 217
Detection and Determination of Equilibrium Vacancy Concentrations in Aluminum .... Soji NENNO and J. W. KAUFFMAN 220
Une Nouvelle Forme du Nitrure de Nickel: $\mathrm{Ni}_4\mathrm{N}$ .... Nobuzo TERAO 227
Crystal Texture of LiF Single Crystals by X-ray Technique .... Hiroshi NIMURA 231
The Theory of the Fine Structure of the X-ray Absorption Spectrum, II. .... Toshio SHIRAIWA 240
Studies on the Magnetic Anisotropy Induced by Cold-Rolling of Ferromagnetic Crystal II. Iron-Aluminum Alloys .... Sōshin CHIKAZUMI, Kenzō SUZUKI and Hiroko IWATA 250
Dielectric Relaxation in High Polymers, II. Vinylic High Polymers .... Tomoyasu TANAKA and Yōichi ISHIDA 261
Indirect Nuclear Spin-Spin Couplings in Saturated Hydrocarbon Molecules .... Eiko HIROIKE 270
Potential Barrier of Phenol from its Microwaue Spectrum .... Takeshi KOJIMA 284
Zeeman Effect of Nuclear Quadrupole Resonance Spectrum in 1, 3, 5-Trichlorobenzene .... Yonezo MORINO and Masaharu TOYAMA 288
Microwave Spectrum of Ethyl Iodide, I .... Takahiro KASUYA and Takeshi OKA 296
Microwave Zeeman Effect of Formaldehyde .... Kunitaka KONDO, Hiromasa HIRAKAWA, Akira MIYAHARA, Takeshi OKA and Koichi SHIMODA 303
Stark-Zeeman Effects on Asymmetric Top Molecules. Formaldehyde $\mathrm{H}_2\mathrm{CO}$ .... Kunitaka KONDO and Takeshi OKA 307
Luminescences from KBr/KI Single Crystals .... Masao TOMURA aud Yôzo KAIFU 314
Flow of a Viscous, Electrically Conducting Fluid along a Circular Cylinder or a Flat Plate with Uniform Section .... Michiru YASUHARA 321
Two-dimensional Flow of an Ideal Gas with Small Electric Conductivity past a Thin Profile .... Takeo SAKURAI 326
A New Type of Thermal Conductivity Gas Detector, I. .... Shinzan SÔMA and Yû TAKEUCHI 333
Non-ideality Effects upon the Sedimentation Equilibrium in a Density Gradient .... Hiroshi FUJITA 336
Maxwell's Formula for Three-Dimensional and Large Deformation .... Wataru SEGAWA 339
Ultrasonic Propagation through Aqueous Solutions of Acetates .... M. KRISHNAMURTHI and M. SURYANARAYANA 345
Ultrasonic Propagation through Binary Mixtures containing Acetic Acid .... M. KRISHNAMURTHI and M. SURYANARAYANA 349

SHORT NOTES

Photoconductivity in Nickel Doped Germanium.................. Yoshitaka FURUKAWA 353
Fluorine N.S.R. Spectroscopy, II. A "Distant" Carbon-13 Isotope Effect.......... .... George Van Dyke TIERS 354
Nuclear Quadrupole Resonance of Nitrogen in Cyanuryl Chloride................. .... Shoji KOJIMA and Midori MINEMATSU 355
On the X-ray Temperature Diffuse Scattering of Anthracene and Stearic Acid .... Shoichi ANNAKA and J. L. AMORÓS 356
Photoconductivity of Cd-ZnS Mixed Crystal........ Makoto KIKUCHI and Sigeru IIZIMA 357
Fine Structure in the $\mathrm{N}^{14}(\gamma\ n)\mathrm{N}^{13}$ Activation Curve, II. ....

.... Naoshi MUTSURO, Kazuo SATO and Masanori MISHINA 358

Thickness Dependence of Domain Orientation in Thin Nickel Films .... Kaizo KUWAHARA and Mitita GOTO 359

Magnetic and Electrical Anomalies of Iron Telluride Single Crystals .... Rokuroh NAYA, Miyuki MURAKAMI and Eiji HIRAHARA 360

Differential Cross Sections for the $N^{14}(d, p)N^{15}$ Ground State Reaction at the Deuteron Energy of 16 MeV .... Susumu MORITA, Nawoyuki KAWAI, Naoyuki TAKANO, Yorio GOTO, Reiko HANADA. Yutaka NAKAJIMA, Shigeo TAKEMOTO and Yûki YAEGASHI 361

A Curious Characteristic of P-N-P-N Junctions.................................. ....Takao KURATA and Kiichi KOMATSUBARA 362

Some Properties of X-ray damaged Rochelle Salt ....Kenkichi OKADA 363

Lower Exiled States in P^{29}......Tatsuo TABATA, Hisao FUKUDA and Kotoyuki OKANO 364

Errata

Angular Distributions of Protons from the Reaction $^{12}C(\alpha, p)^{15}N$ .... Itaru NONAKA, Hisashi YAMAGUCHI, Takashi MIKUMO, Iwao UMEDA, Tetsuo TABATA and Saburo HITAKA 365

No. 3

Energy Spectrum and Angular Distributions of Neutrons from the Reaction $Be^9(p, n)B^9$ at 8 to 14 MeV of Proton Energies ....Yoshio SAJI 367

Decay of Cl^{34m} ....Tsutomu TŌHEI 372

Ferromagnetism of an Electron Gas ....Masao SHIMIZU 376

Configurational Changes of Polypeptide Molecules in the Helix-Coil Transition Region, I. ....Kazuo NAGAI 407

Proton Magnetic Resonance and X-ray Diffraction Studies of Polypropylene........ .... Atsuo NISHIOKA, Yasuhiro KOIKE, Masakazu OWAKI, Tsunezo NARABA and Yoshinori KATO 416

On the Paramagnetic Inelastic Scattering of Neutrons due to Ions in the Anisotropic Crystalline Field ....Yasusada YAMADA 429

Paramagnetic Resonance of Manganese in Alkali-Chlorides......Hisamitsu YOSHIMURA 435

On the Proton Resonance of Several Hexammine Complex Salts ....Pil Hyon KIM 445

On the Magnetic Susceptibility of FeF_2 ....Akio HONMA 456

Volume Magnetostriction of Cobalt-Nickel Alloys ....Takejiro KANEKO 463

Magnetic Anisotropy Measurements of MnO Single Crystal...................... Enji UCHIDA, Hisamoto KONDOH, Yoshihide NAKAZUMI and Takeo NAGAMIYA 466

Effect of Solvent on the Extension of High Polymer Molecule ......Hiroshi MIZUTANI 475

Paramagnetic Susceptibility of $CoCl_2 \cdot 6H_2O$ and its Deuterated Salts..Taiichiro HASEDA 483

Photo- and Thermochemical Reactions in Potassium Chloride Crystals—A Quantitative Study of the M Centre ....Tetsuhiko TOMIKI 488

On the Acoustic Radiation from a Flanged Circular Pipe....................... .... Yûkichi NOMURA, Ichirô YAMAMURA and Sakari INAWASHIRO 510

Measures of Finite Strain and Stress-Strain Relations ....Wataru SEGAWA 518

On Similar Solutions of the Steady Quasi-two-dimensional Incompressible Laminar Boundary-layer Equations ....: ....Nisiki HAYASI 522

SHORT NOTES

Heat Capacity of a Single Crystal of $MnCl_2 \cdot 4H_2O$ .... H. FORSTAT, G. O. TAYLOR and B. S. KING 528

Purification of Alkali Halide Crystals through Fractional Distillation and Normal Freezing ....Hiroshi KANZAKI and Keishiro KIDO 529

Ferrimagnetic Resonance in Polycrystalline Europium-Iron Garnet $(En_3Fe_5O_{13})$ .... Yûzō SHICHIJō, Tomonao MIYADAI and Hisao TAKATA 530

Microwave Discharge Chamber ....Shūji FUKUI and Satio HAYAKAWA 531

Maser Oscillation on 6-6 Line of $N^{15}H_3$....Isao TAKAHASHI, Tsuneo HASHI, Masaru YAMANO, Motokazu YAMAMOTO, Shigeyoshi SUZUKI and Tsutomu MAKITA 532

Domain Patterns on Thin Films of Perminvar .... Yuzi GOMI, Yuzo ODANI and Makoto SUGIHARA 533

Jump Phenomenon in Resonance Curve of Ferroelectric Ceramics .... Katsuo NEGISHI 534

Chain Wall in Permalloy Thin Films .... Yuzi GOMI and Yuzo ODANI 535

Diffuse Scattering of X-rays by Gamma-ray Irradiated Rochelle Salt .... Koichi TOYODA, Akira SHIMADA and Tetsuro TANAKA 536

Influence of Preparation and Quenching on the Magnetic Properties of Precipitates in Cu-Co Alloy .... Masayoshi SATŌ and Tadayasu MITUI 537

Opitical Bleaching of R-bands in LiF Crystals .... Kuniya FUKUDA, Akizo OKUDA and Yoichi UCHIDA 538

Errata

A 160 cm Synchro- and Variable Energy Ordinary Cyclotron .... Seishi KIKUCHI et al. 527

Electron Microscope Study of the Decomposition Process of Oxide Coated Cathods .... Shoichi HIROTA and Tetsuji IMAI 539

No. 4

Excitation Functions for Alpha-Induced Reactions on Mangenese-55 .... Shigeo TANAKA, Michiaki FURUKAWA, Takashi MIKUMO, Shiro IWATA, Masuo YAGI and Hiroshi AMANO 545

Differential Cross Sections for the Reaction $C^{12}(d.\ p)C^{13}$ in the Energy Range of Deuterons from 15- to 20-MeV .... Susumu MORITA, Nawoyuki KAWAI, Naoyuki TAKANO, Yorio GOTÔ, Reiko HANADA, Yutaka NAKAJIMA, Shigeo TAKEMOTO ahd Yûki YAEGASHI 550

Elastic and Inelastic Scattering of 11.2 MeV Deuterons .... Minoru TAKEDA 557

On the Phase Transition of Tungsten Trioxide below Room Temperature .... Sigetosi TANISAKI 566

Crystal Structure of Monoclinic Tungsten Trioxide at Room Temperature .... Sigetosi TANISAKI 573

Magnetic Properties of Iron Phosphide Fe_2P .... Shū CHIBA 581

Internal Friction of Quartz .... Yosio HIKI 586

Interaction of Exciton with Electron Trapping Centers in Alkali Halide Crystals. 2. Quantum Yield for the $U \to F$ Conversion and its Dependence on U-Center Concentration .... Masayasu UETA, Masamitsu HIRAI and Hiroyuki WATANABE 593

Multiple-Anode Proportional Counter X-Ray Diffractometer .... Jun-ichi CHIKAWA 602

The Quantitative Interpretation of Luminescent Properties of Cu-Activated Calcium Orthophosphate .... Yasuo UEHARA 612

Germanium Crystal as a Neutron Monochrometer and the Determination of its Higher Order Contaminations .... John T. WAJIMA, Brice M. RUSTAD and Edward MELKONIAN 630

Readiative Collisions between Molecular and Electron Beams, V. Angular Momentum Distributions of CH Separating from Simple Organic Molecules .... Tadao HORIE, Takayuki NAGURA aud Masamoto OTSUKA 641

Microwave Spectrum of Cis-1, 2-Dichlorethylene .... Tadao SHIMIZU and Hiroshi TAKUMA 646

Theory of Solutions of Chin Molecules .... Hiroshi OKAMOTO 650

Theory of Electric Birefringence in Dilute Solutions of Tobacco Mosaic Virus .... Sekiko OGAWA and Syoten OKA 658

Notes on the Theory of Meissner Effect ..... Masayuki ASAMI and Fumihiko TAKANO 669

Breakdown of Argon at Low Pressure in a Longitudinal Magnetic Field .... Kenji MITANI and Hiroshi KUBO 678

Ion-Electron Relaxation of Plasmas in a Magnetic Field, II. .... Taro KIHARA, Yukio MIDZUNO, Kyoko SAKUMA and Toshio SHIZUME 684

Axially Symmetric Stagnation-point Flow of an Electrically Conducting Fluid under Transverse Magnetic Field .... Tsunehiko KAKUTANI 688

Stokes Flow of an Electrically Conducting Fluid in a Uniform Magnetic Field .... Kanefusa GOTOH 696

An Investigation of Psychrometer, II. .... Yoshirô ÔMORI 706
The Dynamic Bulk Viscosity of Polystyrene and Polymethyl Methacrylate .... Ryusuke KONO 718

SHORT NOTES

Measurement of Piezoelectric Constants of a CdS Crystal .... Toshio TANAKA and Shoji TANAKA 726
Electrical Conductivity of α-Fe$_2$O$_3$ .... Tanehiro NAKAU 727
On the Proton Chemical Shift in Deuterium Substituted p-Xylene and Toluene .... Hazime KUSUMOTO, Junkichi ITOH, Kozo HIROTA and Tomiko UEDA 728
Cold-emitting Cathode Materials .... Yoshihiko MIZUSHIMA, Yoshitaka IGARASHI and Tetsuji IMAI 729
Tunneling Probability in Germanium $p-n$ Junctions .... Yoshitaka FURUKAWA 730
180° Domain Wall Motions in BaTiO$_3$ Crystal .... Kazuo HUSIMI 731
The Dislocation Etch Pits of CdS Crystals .... Jiro NISHIMURA 732
Piezoresistivity in Semiconductive Barium Titanates .... Osamu SABURI 733
Magnetic Susceptibility of CoBr$_2\cdot$6H$_2$O .... M. GARBAR 734
Some Experiments on Plasma Alfvén Waves .... Shigeo NAGAO and Teruyuki SATO 735
A Gamma Ray in Ti^{45} Decay .... Chikai ISHII and Kasuke TAKAHASHI 736
Angular Dependencies of Efficiencies for Sodium-Iodide Crystals .. Tadayoshi DOKE, Atsushi NAKAMOTO, Yasukiyo TAKAMI, Manabu HATTORI and Shinji OKANO 737

Errata

Volume Magnetostriction of Cobalt-Nickel Alloys .... Takejiro KANEKO 738
Maxwell's Formula for Three-Dimensional and Large Deformation.... Wataru SEGAWA 738

No. 5

The Reaction Li$^7(p, n)$Be^7, B$^{11}(p, n)$C^{11} and Al$^{27}(p, n)$Si^{27} at 8 to 14 MeV .... Kazuo HISATAKE, Yoshihide ISHIZAKI, Akira ISOYA, Teruo NAKAMURA, Yoshihiro NAKANO, Bunsaburo SAHEKI, Yoshio SAJI and Kazunori YUASA 741
Protons from the $p+d$ Breakup Reaction at Proton Energies of 14 MeV and 10 MeV .... Seishi KIKUCHI, Junpei SANADA, Shigeki SUWA, Izuo HAYASHI, Keigo NISIMURA and Kiyoji FUKUNAGA 749
Measurements of the Polarization in Proton-Helium Elastic Scattering .... Keigo NISIMURA Shigeki SUWA, Izuo HAYASHI, Kiyoji FUKUNAGA, Norio RYU and Masao SEKI 754
Elastic and Inelastic Scattering of Protons from N, Ne, Mg, Si, S and A in the Energy Range from 7.6 MeV to 14.2 MeV .... Yukiyasu ODA, Minoru TAKEDA, Takashi YAMAZAKI, Chuin HU, Naoyuki TAKANO, Ken KIKUCHI, Shinsaku KOBAYASHI, Kazuhisa MATSUDA and Yukio NAGAHARA 760
Radial Distribution Function of Fluids, III .... Kazuo HIROIKE 771
Expansion Theorem of Density Matrix, Virial Expansion and New Formula of Multiple Scattering .... Toshio YOKOTA 779
Theoretical Study on the Properties of Coercive Field of BaTiO$_3$ Single Crystal .... Ryuji ABE 795
Heitler-London Approach to Electrical Conductivity and Application to d-Electron Conductions .... Jiro YAMASHITA and Tatumi KUROSAWA 802
Anomalous Growth of MoO$_3$ Crystals .... Eiji YODA 821
The Change in Electron Mobility in Indium Antimonide at Low Electric Field .... Yasuo KANAI 830
Visible Light Emission and Microplasma Phenomena in Silicon $p-n$ Junction, I. .... Makoto KIKUCHI and Kenkichi TACHIKAWA 835
A Possible Mode of Twin in the ε-phase of Cu-Sb Alloy .... Michiyasu DOI 849
Shape of Nucleus Domain Anchored to a Screw Dislocation in Ferroelectric Crystal .... Hidetosi TAKAHASI, Terutaro NAKAMURA and Yoshihiro ISHIBASHI 853
Dynamical Theory of Electron Diffraction in Laue-case, II. Numerical Calculation of Intensities .... Fuminori FUJIMOTO 859

The effects of Deuteron Irradiation on the Nuclear Magnetic Resonance in Teflon .... Hazime KUSUMOTO 867
On the Intramolecular Light Scattering of the Non-Gaussian Chain .... Akira MIYAKE 875
Influence of the Molecular Weight Distribution on the Polymer Properties .... Akira MIYAKE 883
Theory of the Nuclear Magnetic Resonance of Co^{59} in CoO .... Kazuo MOTIZUKI 888
Interaction between Rold-like Polyelectrolytes .... Tsuyoshi OHNISHI, Nobuhisa IMAI and Fumio OOSAWA 896
Formation of Plasma by Low Energy Ion Injection and Cyclotron Heating .... Tarô DODO 906
The Study of the Opitical Properties of Conducting Tin Oxide Films and their Interpretation in Terms of a Tentative Band Scheme .... Toshihiro ARAI 916

SHORT NOTES

Screened Impurity Potentials in Metals .... E. C. MCIRVINE 928
Magnetic Anisotropy Induced by Cold Rolling of Cu–Co Alloy .... Tadayasu MITUI 929
On the Alpha-particles from the N^{14}(d, α)C^{12} Ground State Reaction .. Nawoyuki KAWAI 930
Ferromagnetism of Mn–Zn Alloy .... Seiji TEZUKA, Sukeyoshi SAKAI and Yasuaki NAKAGAWA 931
Ferrimagnetism of Mn$_5$Ge$_2$ ... Kō YASUKŌCHI, Kazuo KANEMATSU and Tetuo OHOYAMA 932
Spin Order in the Doublet at the Second Excited Level in Even-even Medium Nuclei .... Mitsuo SAKAI 933
On the $F \to F'$ Conversion in the Presence of A-, M-, R-, and Z_1-Centers .... Hiroshi OHKURA, Katsunobu AWANE and Shigeko MIYAMOTO 934
Observation of Microplasma Pulses and Electroluminescence in Gallium Phosphide Single Crystal .... Makoto KIKUCHI and Takashi IIZUKA 935
Magnetic Annealing of Co and Co–Ni Alloys .... Minoru TAKAHASHI and Tatsuo KŌNO 936
Electrical Properties of Stannic Oxide Films .... Isamu IMAI 937
Post-Irradiation Effect in Visible Absorption Spectra of Polyvinyl Chloride Sheets .... Yoichi OKADA, Takao ITO and Ayao AMEMIYA 938
Interaction Effects in K$_3$Fe(CN)$_6$ .... Taiichiro OHTSUKA 939
Temperature Dependence of Infrared Absorption Bands of n-Higher Alcohols .... Mitugi HASIKUNI 941
Stress in Very Thin Vacuum-Evaporated Films of Silver .... Koreo KINOSITA, Hideki KONDO and Ichiro SAWAMURA 942
Electron Spin Resonance in Irradiated Polytetrafluoroethylene: Decomposition of the Complex Spectrum .... Maoyuki TAMURA 943

Errata

Theory of Viscoelasticity of Amorphous Polymers, II. A Note on the Time-Temperature Reducibility of the Relaxation and Retardation Spectra .... Osamu NAKADA 945
Measures of Finite Strain and Stress-Strain Relations .... Wataru SEGAWA 945

No. 6

Further Study of the Reaction ^{7}Li(γ, t)^{4}He ...... Mitsuo MIWA and Mikio YAMANOUCHI 947
Reactions of Argon-40 with Alpha-Particles .... Shigeo TANAKA, Michiaki FURUKAWA, Takashi MIKUMO, Shiro IWATA, Masuo YAGI ahd Hiroshi AMANO 952
On the First and the Second Excited States in Ge^{74} .... Toshimitsu YAMAZAKI, Hidetsugu IKEGAMI and Mitsuo SAKAI 957
Theory of Formation Energy of the External and the Internal Surface for Free Electron Metals .... Akira SUGIYAMA 965
Interaction of Conduction Electrons with Acoustic Waves in Simple Semiconductors .... Nobuo MIKOSHIBA 982
Electrical Properties of Germanium Selenide GeSe .... Sizuo ASANABE and Atuyosi OKAZAKI 989
Low Field Magnetoresistance Effect of Plastically Deformed n-type Silicon .... Koji KAMADA 998

Growth and Evaporation of Tungsten Oxide Crystals .... Hatsujiro HASHIMOTO, Kenzo TANAKa and Eiji YODA 1006
Dislocations in Pure Iron Foils Deformed by Bending .... Tadayoshi YAMASHITA and Youji TANEDA 1015
Dynamical Theory of Electron Diffraction in Laue-case, III. Forbidden Reflection .... Fuminori FUJIMOTO 1022
Study on the Ordered Alloys of Gold-Manganese System by Electron Diffraction, I. Au_3Mn .... Denjiro WATANABE 1030
Re-appreciation of the Second Order Transition Phenomena in Polyethylene .... Ryuichi NAKANE 1040
The Binding Energy of the σ Bond, I. General Theory .... Kiyosi O-OHATA 1048
Intramolecular NMR Second Moment of the Polymer Chain .... Akira MIYAKE 1057
Zeeman Quadrupole Spectra in p-dichlorobenzene and p-chlorobenzoic Acid .... Shizuko OGAWA and Kikuo OHI 1064
Statistical Mechanics of Antiferromagnetic Layer Crystal, $FeCl_2$ .... Sigeo YOMOSA 1068
Ionization in Argon Mixtures by Electrons in an Electric Field ...... Mikiya YAMANE 1076
Non-linear Effects on Electron-Plasma Oscillations .... Masao SUMI 1086
Oscillations in a Plasma in a Weak Magnetic Field .... Kiyoe KATO 1093
Transport Properties of Plasmas in a Strong Magnetic Field .... Taro KIHARA, Yukio MIZUNO and Shobu KANEKO 1101
Flow of a Condensing Vapour with Heat Exchange .... Keishiro NIU 1108
Selbstzündung des n-Hexan-Luft-Gemisches in Stoßwellen .... Kunio TERAO 1113

SHORT NOTES

Magnetic Anisotropy of Chalcopyrite .... Teruo TERANISHI 1123
Electron Emission Current from Oxide Coated Cathode Subject to High Electric Field .... Chokichiro SHIBATA 1124
Magnetic Hyperfine Structure of the 3,2 Line of Ammonia .... Koichi SHIMODA and Kunitaka KONDO 1125
Some Observations on the Domain Walls in Thin Films .... Yasuo GONDO and Zenya FUNATOGAWA 1126
On the Possibility of Ferromagnetism for an Electron Gas .... Masao SHIMIZU 1127
Structure of Giant Resonance in $Al^{27}(p,\gamma)$ Reaction .... Motoharu KIMURA, Katsufusa SHODA, Naoshi MUTSURO, Tsutomu TOHEI, Kazuo SATO, Kunishige KURODA, Katumi KURIYAMA and Tosimitu AKIBA 1128
The Behaviours of Free Radicals Trapped in γ-Irradiated Polyethylene .... Hisatsugu KASHIWABARA and Kenichi SHINOHARA 1129
Temperature Dependence of Tunnel Diode Characteristics ...... Yoshitaka FURUKAWA 1130
Paramagnetic Resonance of Mn^{++}–F^- Pair in Sodium Chloride .. Yasaburo YOKOZAWA 1131
Inverse Solution of the Thomas-Fermi Equation .... Louis GOLD 1132
A Simple Model of Aqueous Solution of Strong Electrolyte .... Takeshi SATOH 1134
Correction to the Paper "Two-dimensional Flow of an Ideal Gas with Small Electric Conductivity past a Thin Profile" .... Takeo SAKURAI 1135
The Magnetic Properties of Mn-Sn-C Alloys .... Mitsuru ASANUMA 1136
Conductivity Induced by Injected Electrons in Liquid Dielectrics .... Pyong-un CHONG, Tomihiko SUGIMOTO and Yoshio INUISHI 1137

Errata

Magnetic Hyperfine Spectrum of H_2CO by a Maser .... Hiroshi TAKUMA, Tadao SHIMIZU and Koichi SHIMODA 1139
Angular Dependencies of Efficiencies for Sodium-Iodide Crystals .. Tadayoshi DOKE, Atsushi NAKAMOTO, Yasukiyo TAKAMI, Manabu HATTORI and Shinji OKANO 1139
Theory of the Nuclear Magnetic Resonance of Co^{59} in CoO .... Kazuko MOTIZUKI 1140

No. 7

Gamma Rays from Several Elements Bombarded by 10 and 14 MeV Protons .... Tetsuo WAKATSUKI, Yasuo HIRAO, Eiji OKADA, Iwao MIURA, Kenzo SUGIMOTO and Akira MIZOBUCHI 1141

Elastic and Inelastic Scattering of Protons from Nickel Isotopes; Ni^{58} and Ni^{60}, in the Energy Range from 7.0 MeV to 15.3 MeV .... Shinsaku KOBAYASHI, Kazuhisa MATSUDA, Yukio NAGAHARA, Yukiyasu ODA and Nobuhiro YAMAMURO 1151
Elastic and Inelastic Scattering of Alpha Particles by Carbon .... Takashi MIKUMO, Hisashi YAMAGUCHI, Itaru NONAKA, Masatoshi ODERA, Yoshio HASHIMOTO, Motoo KONDO and Takashi MAKI 1158
Elastic and Inelastic Scattering of Protons by Oxygen in the Energy Region of 6.9 MeV and 15.6 MeV .... Shinsaku KOBAYASHI 1164
On the High Energy Soft Component Near Sea Level .... Tadashi KAMEDA 1175
Ferroelectricity in Potassium Ferrocyanide Trihydrate and its Isomorphous Substances .... Shigeru WAKU, Kunio MASUNO, Toshisuke TANAKA and Hiroshi IWASAKI 1185
Interaction of Conduction Electrons with Acoustic Waves in Many-Valley Semiconductors .... Nobuo NIKOSHIBA 1189
Filamentary Crystals grown from the Solid Metal .... George SINES 1199
Heitler-London Approach to Electrical Conductivity, II. A Proof of the Hopping Motion .... Tatsumi KUROSAWA 1211
Exchange Interaction and Cubic Crystal Field Splitting Parameter of Fe^{3+} in Spinel Structure .... Yoshikazu SUGIURA 1217
Characteristics of Germanium p-n Junction with Irregular Structure.. Masami TOMONO 1223
Note on the Field Dependence of the Mobility in Semiconductors .... Masumi HATTORI and Hisanao SATO 1237
Dynamic Behaviour of Twinning in Tin Crystals at Various Temperatures and Strain Rates .... Saiyu MARUYAMA 1243
Study on the Ordered Alloys of Gold-Manganese System by Electron Diffraction, II. Au$_4$Mn .... Denjiro WATANABE 1251
The Binding Energy of the σ Bond, II. Application to the Diamond Crystal .... Kiyosi O-OHATA 1258
Magnetic Properties of the Pd and Pt Group Transition Metal Complexes .... Hiroshi KAMIMURA, Shoichiro KOIDE, Hisao SEKIYAMA and Satoru SUGANO 1264
Microwave Spectrum of Ethyl Iodide, II. .... Takahiro KASUYA 1273
Proton Magnetic Resonance in Hydrogen Bonded Dimers in Solids .... Kiyoshi KUME and Yoshinobu KAKIUCHI 1277
Microwave Spectrum of Methyl Mercaptan .... Takeshi KOJIMA 1284
Heating of a Plasma by Acoustic Waves................................. Tarô DODO 1292
Exciton-Induced Luminescence in KI/Tl.............. Masao TOMURA and Yozo KAIFU 1295
Dichroism of Z Bands .... Masakazu ISHIGURO, Etsu SUGIOKA and Nozomu TAKEUCHI 1302
Thermal Bleaching of Color Centers in KCl Crystals Containing U Centers........ .... Masamitsu HIRAI 1308
Effect of Transverse Magnetic Field on the Flow due to an Oscillating Flat Plate, II. .... Tsunehiko KAKUTANI 1316
Steady Temperature Field in a Composite Doubly Infinite Strip ...... Václav VODIČKA 1332
Circulation Preserving Motions .... A. C. SRIVASTAVA 1337

SHORT NOTES

Thickness-Dependence of Stress in Vacuum Deposited Silver Films............... .... Koreo KINOSITA and Hideki KONDO 1339
Electron Spin Resonance of Mn^{++} in SrCl$_2$, CdCl$_2$ and CdBr$_2$ .... Hiroshi KOGA, Kazumi HORAI and On MATUMURA 1340
Ultrasonic Measurement of Magnetization in Mn-ferrite Single Crystal........... .... Kazuo HUSIMI, Katsumi NISHIGUCHI and Toshimasa SUZUKI 1341
The Temperature and Pressure Dependence of the Nuclear Resonance of Co^{59} in Face-Centered-Cubic Cobalt Metal .... Yoshitaka KŌI, Akira TSUJIMURA and Yoshinori YUKIMOTO 1342
The Ferromagnetism of the Compound γ-FeSn .... Mitsuru ASANUMA 1343
Optical Absorption of Localized Exciton in KCl:I and NaCl:I Single Crystals...... .... Kuniya FUKUDA, Riso KATO, Kaizo NAKAMURA and Yoichi UCHIDA 1344
Avalanche Breakdown in CdS Single Crystal ...... Sigeru IIZIMA and Makoto KIKUCHI 1345
Pulse Photoconduction and Carrier Lifetime in CdS Single Crystals .... Junji SHIRAFUJI and Yoshio INUISHI 1346

Some Observations on Plastic Deformation and Slip Lines of Sodium Chloride Whisker........................Kan-Ichi KAMIYOSHI and Tsutomu YAMAKAMI 1347
Dislocation Etch Pits on a- and b-Faces of GASH Crystal ....Terutaro NAKAMURA and Kikuo OHI 1348
On A-centers in Colored KCl Crystals........Hiroshi OHKURA and Katsunobu AWANE 1349
Absorption Band due to a Presence of Impurity Bromine in KCl Crystal ....Koichi KOBAYASHI and Tetsuhiko TOMIKI 1350
Induced Magnetic Anisotropy of Evaporated Ni-Fe Films.............................Minoru TAKAHASHI, Denjiro WATANABE, Tatsuo KŌNO and Shiro OGAWA 1351
Fixing of Magnetic Moment of Ferromagnetic Fine Precipitates in Cu-Co Alloy during Aging..Kazuo KOBAYASHI 1352
Ferrimagnetic Resonance in a Single Crystal of Europium-Iron Garnet ....Tomonao MIYADAI, Hisao TAKATA and Yūzō SHICHIJŌ 1354
Electrical Properties of Chromium Sulfides .... Takahiko KAMIGAICHI, Kan-ichi MASUMOTO and Tadamiki HIHARA 1355
Exciton-Induced Photoconductivity of U Centers in KCl Crystal ....Masayasu UETA and Masamitsu HIRAI 1356

Errata

Excitation Functions for Alpha-Induced Reactions on Manganese-55.. Shigeo TANAKA, Michiaki FURUKAWA, Takashi MIKUMO, Shiro IWATA, Masuo YAGI and Hiroshi AMANO 1357

No. 8

Angular Distribution of n-p Scattering at 14.1 MeV ....Teruo NAKAMURA 1359
On the High Energy Soft Components at 2770m Altitude..Tadashi KAMEDA and Toshio MAEDA 1367
Graphitization Stress in Polycrystalline Carbon as An Origin of Dislocations ....Takuro TSUZUKU 1373
Kinematic Theory of Ferroelectric Domain Growth ....Terutaro NAKAMURA 1379
Change in Modulus of Rigidity of Brass Wires by Cold-Working and Subsequent Annealing... Jun KUROYANAGI 1386
Study on Some Tl Base Alloys, with Reference to their Electronic Structure...Ryōji SUGANUMA 1395
Observations of Dislocation Networks in an Alloy of Body-Centered Cubic Lattice by Electron Microscopy .... Soji NENNO, Toshio SABURI, Masayoshi TAGAYA and Zenji NISHIYAMA 1409
An X-ray Study on the Structure of Cobalt Dichloride Hexahydrate ......Joji MIZUNO 1412
Study on the Twin Formation in Evaporated Silver Films .... Akira NAGASAWA and Shiro OGAWA 1421
X-ray Line Broadening from the Polished Surfaces of Silver and Gold..Masao KURIYAMA 1426
X-Ray Measurement of the Scattering Factor of Iron in Ordered Fe_3Al............................... Yukitomo KOMURA, Yujiro TOMIIE and Robert NATHANS 1434
The Photoionization of H_2 and the Spatial Correlation between Electrons.. Mikio SHIMIZU 1440
The Binding Energy of the σ Bond, III. Discussion on the Ionic Structures ....Kiyoshi O-OHATA 1449
On the Effect of Heat Treatment in a Magnetic Field on Magnetic Properties of Iron-Aluminium Alloys ....Makoto SUGIHARA 1456
Magnetic Anisotropy of Iron-Cobalt Ferrite Measured by Ferromagnetic Resonance .... Yoshikazu SUGIURA 1461
The Recovery of Initial Magnetic Susceptibility in Pure Nickel ....Mitsuru ASANUMA 1469
The Electron Paramagnetic Resonance of Mn^{2+} Ions Surrounded by an Octahedron of Fluorine Ions ....Shinji OGAWA 1475
The Dipole Moment and End-to-end Length of the Isotactic Vinyl Polymer, I. Mutual Dependence between Dipole Moment and End-to-end Length ....Tsugio MORI 1482
Magneto-plasma Resonance in Semiconductors ....Muneyuki DATE 1488

Proton Magnetic Resonance in Pure and Doped Ice ....Kiyoshi KUME 1493
Radiation Effects on Dimethyl-diphenyl Siloxane Copolymer. I. Protective Effect of Phenyl Radical on the Cross-linking......Mitsuru KOIKE and Akibumi DANNO 1501
Interpretation of Exciton Induced Luminescence in KI/Tl ....Masao TOMURA 1508
Jets of a Perfectly Conducting Inviscid Gas in the Presence of a Magnetic Field parallel to the Stream ....Shigeki MORIOKA 1516
Some Remarks on the Magnetogasdynamic Linearized Theory ....Shigenori ANDO 1523

SHORT NOTES

On the Ferromagnetism in Manganese-Aluminium-Iron System ....Ichiro TSUBOYA and Makoto SUGIHARA 1534
The Influence of Oxidation and Reduction on the Parasitic Ferromagnetism of αFe_2O_3 ....Akira TASAKI, Kiiti SIRATORI and Shūichi IIDA 1535
Emission Spectra from Glow Discharge through Vapors of Aromatic Hydrocarbons and n-Hexane...........Masato NISHI, Shiro HAMAMURA and Hiroshi ARAKI 1536
Observation of an Anomaly in Transistor Characteristics.........Osamu NAKAHARA 1537
Resonance Transfer of Ionization Energy in Semiconductors ....Shigeharu KOSHINO and Toshihiko ANDO 1538
Dislocations in Ferroelectric Glycine Sulfate Single Crystals ....Hiroo TOYODA 1539
A Diffuse Reflexion from a Silicon Carbide Crystal ....Takanori TOMITA 1540
On the Determination of Diffusion Coefficient of Boron in Silicon .... Jiro YAMAGUCHI, Shiro HORIUCHI, Koji MATSUMURA and Yasumasa OGINO 1541
On the Weak Interaction of Baryons............................Seitaro NAKAMURA 1543

Errata

Dynamical Theory of Electron Diffraction in Laue-case ....Fuminori FUJIMOTO 1545

No. 9

Reactions of Iron-54 with Alpha-Particles...............Shigeo TANAKA, Michiaki FURUKAWA, Shiro IWATA, Masuo YAGI, Hiroshi AMANO and Takashi MIKUMO 1547
Gamma-rays from the 7.56 MeV Level in O^{15} ...Tatsuo TABATA and Kotoyuki OKANO 1552
Lower Excited States in P^{29} from the $Si^{28}(p,\gamma)P^{29}$ Reaction ....Kotoyuki OKANO, Tatsuo TABATA, Kyue FUKUDA and Jiro MUTO 1556
On the Electronic Component of Extensive Air Showers near the Axis................................. Tadashi KAMEDA, Yoshio TOYODA and Toshio MAEDA 1565
Lattice Frequency of Ionic Crystals ....S. S. MITRA and S. K. JOSHI 1575
The Resonance Type Absorption of Very Thin Silver and Gold Films ....Shigeo YAMAGUCHI 1577
Electrical Properties of Pseudo-binary Systems of Ag_2VI's; $Ag_2Te_xSe_{1-x}$, $Ag_2Te_xS_{1-x}$, and $Ag_2Se_xS_{1-x}$..Shin-ya MIYATANI 1586
Temperature Dependence of the Optical Absorption Edge of Tungsten Trioxide Single Crystal...Tsuruji IWAI 1596
Association of Vacancies with Calcium Impurities in Potassium Chloride Crystals .... Tosiyuki NINOMIYA 1601
Measurement of the Intensity in Electron Diffraction by a CdS Single Crystal .... Satio TAKAGI and Fuminori FUJIMOTO 1607
Elektronische Wechselwirkung zwischen Wasserstoff und aufgedampften Nickelfilmen ....Yoshihiko MIZUSHIMA 1614
The Binding Energy of the σ Bond. IV. Discussion on the Higher Order Terms ....Kiyosi O-OHATA 1632
The Dipole Moment and End-to-end Length of the Isotactic Vinyl Polymer, II. A Special Simplified Model and Numerical Calculations ....Tsugio MORI 1638
The Superexchange Interaction between Cr^{+3} pair in Chromium Bi-nuclear Complex Ions..Hanako KOBAYASHI, Taiichiro HASEDA, Eizo KANDA and Masayasu MORI 1646
A Study of Sorbed Water on Cellulose by Pulsed NMR Technique......Masahumi SASAKI, Takao KAWAI, Akira HIRAI, Tsuneo HASHI and Akira ODAJIMA 1652
Study of Aqueous Solution of Strong Electrolyte—Reexamination of Molecular Refraction ....Takeshi SATOH and Koreaki HAYASHI 1658

On the Magnetic Properties of a $CrBr_3$ Single Crystal .... Ichiro TSUBOKAWA 1664
The Three-Level Gas Maser as a Microwave Spectrometer .... Tatsuo YAJIMA and Koichi SHIMODA 1668
Monte Carlo Calculations of Motion of Electrons in Helium .... Tomizo ITOH and Toshimitsu MUSHA 1675
Ion Optics in Long, Multistage Accelerator Tubes .... Masateru SONODA, Akira KATASE, Masao SEKI and Yoshihisa WAKUTA 1680
Transport Coefficients of Plasmas in a Magnetic Field .... Shobu KANEKO 1685

SHORT NOTES

Effect of Heat-Treatment upon Sintered Cadmium Sulphide Photoconductive Films .... Saburo KITAMURA 1697
Ferroelectricity in the Potassium Ferrocyanide Group Ferroelectrics Substituted by Deuterium for Hydrogen .... Shigeru WAKU, Kunio MASUNO and Toshisuke TANAKA 1698
Impurity Shift of Pure Quadrupole Resonance Frequency .... Yoshiro IMAEDA 1699
Measurement of Temperature Dependence of T_1 of Proton in Some High Polymers by Pulsed NMR Technique .... Takao KAWAI, Masahumi SASAKI, Akira HIRAI, Tsuneo HASHI and Akira ODAJIMA 1700
On the Mechanism of the Electrical Conduction in CdSe .... Hirosi TUBOTA, Hiromichi SUZUKI and Kazuyoshi HIRAKAWA 1701
Characteristics of Krypton Counters .... Tatsusaburo SUZUKI and Jiro YUHARA 1702
Magnetoresistance Effect in the Magnetization Reversal of Permalloy Films .... Eiji TATSUMOTO, Kaizo KUWAHARA and Mitita GOTO 1703
Magnetostriction of Yttrium Iron Garnet... Akira NAKAMURA and Yoshikazu SUGIURA 1704
The Influence of Aging Treatment on the Temperature Dependence of the Electric Resistance in Alnico 5 Magnet .... Tatsuo FUJIWARA and Tetsuo KATO 1705
Preparation of Ferromagnetic Chromium Dioxide .... Buichi KUBOTA 1706
A New Method to Determine Hydration Energy of Ion .... Yoshio ISHIDA 1707
On the Stripe Pattern during Rolling of Viscous Materials .... Toshimaro SONO, Masayoshi FUKUSHIMA and Eiichi FUKADA 1708
α-Trapping Centers in n-Type Silicon .... Jun'ichi OKADA and Tetsuro SUZUKI 1709
Die Schwankung der Zündstelle eines brennbaren Gemisches bei der Selbst-Zündung in Stosswellen .... Kunio TERAO 1710
Electron Spin Resonance of Manganese in Ammonium Chloride .... Hidetaro ABE and Hiroko SHIRAI 1711
A Note on the Magnetic Resonance in Metals .... Ko SUGIHARA 1712
$1/f$ Noise and Channel in Ge PN Junction .... Kiichi KOMATSUBARA, Yoshio INUISHI, Hiroshi EDAGAWA and Tsutomu SHIBAIKE 1713
Spin Wave Resonance in Ni Films .... Hiroshi NOSE 1714
Magnetic Property of Cr_2O_5 .... Eiichi HIROTA and Buichi KUBOTA 1715
Thermal Bleaching of F-Counters of Gamma-Irradiated KCl at Temperatures .... Noriaki ITOH and Tokuo SUITA 1716
Oscillatory Magnetoresistance in N-Type PbTe .... Yasuo KANAI, Riro NII and Naozo WATANABE 1717
Sign Reversal of Hall Coefficients at Low Temperatures in Heavily Compensated p-type Germanium... Hiroo YONEMITSU, Hajime MAEDA and Hisao MIYAZAWA 1717

Errata

Study on Some Tl Base Alloys, with Reference to their Electronic Structure .... Ryōji SUGANUMA 1696

No. 10

Energy Dependence of Angular Distribution of the Reaction $Al^{27}(p, \alpha)Mg^{24}$ in the Energy Region between 10.5 and 14.5 MeV .... Hiroshi OGATA, Hidehiko ITOH, Yoshiko MASUDA, Kunio TAKAMATSU, Maumi KAWASHIMA, Akira MASAIKE and Isao KUMABE 1719

Angular Distribution of the Reactions $Co^{59}(p, \alpha)Fe^{56}$ at 7.7∼14.1 MeV and $Mn^{55}(p, \alpha)Cr^{52}$ at 7.6∼12.9 MeV ....Hiroshi OGATA, Hidehiko ITOH, Yoshiko MASUDA, Kunio TAKAMATSU, Maumi KAWASHIMA, Akira MASAIKE and Isao KUMABE 1726

A Study of Pulse Height Distribution of Boron—Trifluoride Proportional Counters .... Mikiya YAMANE 1732

Mixing Ratio of the 440-keV Gamma Radiation in ^{23}Na ....Akira MIZOBUCHI, Toshio KATOH and Jian-zhi RUAN 1737

(d, α) Reactions on Some Light Nuclei ....Chuin HU 1741

Emission of ^{8}Li, ^{9}Li and ^{8}B Fragments from Stars Produced by 4.3 GeV π^--Mesons in Nuclear Emulsion..........Kuni IMAEDA, Mitsuko KAZUNO and Nobuo ITO 1753

X-ray Observations on Cleavage Faces of LiF Single Crystals .... Mitsuru YOSHIMATSU and Kazutake KOHRA 1760

Study on the Ordered Phases with Long Period in the Gold-Zinc Alloy System. I. Survey of Crystal Structures and Calorimetric Measurement ....Hiroshi IWASAKI, Makoto HIRABAYASHI, Kunio FUJIWARA, Denjiro WATANABE and Shiro OGAWA 1771

On the Superconducting Ground State ....Ziro MIKURA 1783

Impurity Trapped Interstitials and the Low Temperature Annealing Stages of Irradiated Copper ....Ryukiti R. HASIGUTI 1807

The Structure Analysis of $AuCu_3$ by Means of a Fourier Transformation of X-ray Diffuse Scatterings........Kenji DOI 1815

Visible Light Emission and Microplasma Phenomena in Silicon *p-n* Junction II. Classification of weak spots in diffused *p-n* junctions....Makoto KIKUCHI 1822

Optical and Structural Anomalies in Potassium Ferrocyanide Trihydrate Crystals .... Hiroo TOYODA, Nobukazu NIIZEKI and Shigeru WAKU 1831

Thomas-Fermi-Dirac Model of Compressed Ions ....Shigehiro KOBAYASHI 1842

On the Magnetic Properties of the Compound Mn_2As ....Motoyoshi YUZURI and Motohiko YAMADA 1845

Plasma Oscillations in a Magnetic Field ....Ikuo KAJI and Masafumi KITO 1851

Pulse Photoconductivity of Additively Colored KBr ....Masami ONUKI and Hiroshi OHKURA 1862

Dichroism of Z_4 and F Bands ....Masakazu ISHIGURO and Nozomu TAKEUCHI 1871

Wall-effect upon Two-dimensional Stokes Flow of an Electrically Conducting Liquid in a Uniform Magnetic Field ....Yorisaburo TAKAISI 1876

Glass Transition Phenomena and Rheological Properties of Petroleum Asphalt ....Yasaku WADA and Hidenori HIROSE 1885

On the Flow of an Electrically Conducting Fluid Near an Accelerated Plate in the Presence of a Magnetic Field ....A. S. GUPTA 1894

SHORT NOTES

Time Decrease of Permeability of Substitutional Ferromagnetic Alloys ....Chinji KURODA 1898

The Effect of Cation Vacancies on the Magnetic Annealing of $Co_xFe_{3-x}O_4$ .... Tohru INOUE, Hiroshi MIZUTA and Shūichi IIDA 1899

Colour Center and Gaseous Ions Produced in High Frequency Spark between the Electrodes of Semi-metals, Metal Elements, and Ionic-crystals ....Toshiyoshi YUASA 1900

Magnetic Transition in $TiCl_3$ ....Shinji OGAWA 1901

On "Screened Impurity Potentials in Metals"..Ralph J. HARRISON and Arthur PASKIN 1902

Electrical Properties of Heavily Doped N-type Germanium......Yoshitaka FURUKAWA 1903

Radiation of Plasma Oscillation ....Shoji KOJIMA and Shigeo HAGIWARA 1904

The Effect of θ′ Phase on the Plastic Deformation of an Age-Hardenable Al–Cu 4% Alloy ....Keisuke MATSUURA and Shigeyasu KODA 1905

Magnetic Properties of $MgMn_2O_4$ ....Kiyoshi MURAMORI and Syohei MIYAHARA 1906

Errata

Sign Reversal of Hall Coefficients at Low Temperatures in Heavily Compensated *p*-type Germanium...Hiroo YONEMITSU, Hajime MAEDA and Hisao MIYAZAWA 1907

No. 11

Decay of Potassium 44 .... Kazusuke SUGIYAMA, Tsutomu TŌHEI, Masumi SUGAWARA, Tsunekichi DAZAI and Yukinori KANDA 1909
Absolute Cross Section of the Reaction $Cu^{63}(\gamma, n)Cu^{62}$ for Lithium Gamma Rays.... .... Shinjiro YASUMI, Minoru YATA, Kunio TAKAMATSU, Akira MASAIKE and Yoshiko MASUDA 1913
Multipole Interaction Stabilizing Cubic Molecular Crystals.............Taro KIHARA 1920
Anisotropic Hall Coefficients in n-Type Germanium ....Hisao MIYAZAWA and Hajime MAEDA 1924
On the Electrical and Optical Properties of p-type Cadmium Telluride Crystals.... .... Shôji YAMADA 1940
Concentration Dependence of the Hall Coefficient in the Magnesium-Cadmium Alloys .... Sei-ichiro NOGUCHI and Takao SATO 1945
Theory of Thermoelectric Power of Ionic Crystals, IV..................Eijiro HAGA 1949
Measurement of Microwave Dielectric Constants of Ferroelectrics Part I. Dielectric Constants of $BaTiO_3$ Single Crystal at 3.3 KM c/s........................ .... Eiji NAKAMURA and Jiro FURUICHI 1955
Theory of Resistance Minimum in Dilute Paramagnetic Alloys ....Kensuke TANI 1960
Direct Observation of Lattice Defects in Cold-worked High Manganese Steels by Means of Electron Microscopy..........Zenji NISHIYAMA and Ken-ichi SIMIZU 1963
Antiferromagnetic Resonance in NiO in Far-infrared Region........Hisamoto KONDOH 1970
Magnetostriction and Crystal Anisotropy of Nickel-Chromium and Nickel-Vanadium Alloys............................Tokuo WAKIYAMA and Sōshin CHIKAZUMI 1975
Studies on the Preparation of Pure Alkali Chlorides........................... ....Koichi KOBAYASHI and Tetsuhiko TOMIKI 1982
On the Magnetic Anisotropy of Single Crystal of Chromium Telluride .... Tokutaro HIRONE and Shôko CHIBA 1991
Total Cross Sections of Carbon, Oxygen, Fluorin and Thorium for Fast Neutrons ....Kineo TSUKADA and Takayoshi FUSE 1994
Temperature Dependence of Surface Potential in Silver Chloride Single Crystals.. ....Hisawo WAKABAYASI 2000
On the Magnetic Properties of Cr_2As and Cu_2Sb ....Motoyoshi YUZURI 2007
X-ray Studies on the Ferrite-Haematite Solid Solutions ....Chisato OKAZAKI 2013
X-Ray Study on the Binding Properties of Cu_2O and Ag_2O Crystals....Tadasu SUZUKI 2018
Dislocation Networks and Moiré Patterns of Molybdenite .... Yoshihiro KAMIYA, Keiichi ANDO, Minoru NONOYAMA and Ryozi UYEDA 2025
Beam-Type Masers for Radiofrequency Spectroscopy......................... .... Koichi SHIMODA, Hiroshi TAKUMA and Tadao SHIMIZU 2036
On the Paramagnetic Susceptibility of Sm^{3+} ion ....Norikiyo URYU 2041
Electroluminescence of Insulated Particles, II ....Keiji MAEDA 2051
Pseudokinematical Approximation in Electron Diffraction by Crystal ....Mitsuhiko HAYASHI 2054
Magnetic Properties of Potassium Iron Group Fluorides KMF_3.................. ....Kinshiro HIRAKAWA, Kazuyoshi HIRAKAWA and Takasu HASHIMOTO 2063
The Perturbation Method due to the Small Change in the Shape of the Boundary .... Tomoyuki SAITO 2069
Transonic Flow past a Wavy Wall ....Iwao HOSOKAWA 2080
Selbstzündung von Kohlenwasserstoff Luftgemischen in Stosswellen......Kunio TERAO 2086
Glass Cracking Caused by Underwater Spark....Shin-ichi HYODO and Fumiko OKUDA 2093

SHORT NOTES

Fatigue Properties of Zinc Single Crystals and Polycrystals .... Mikio YAMAMOTO and Jirô WATANABE 2099
NMR of Co^{59} in Ferromagnetic Hexagonal Cobalt Metal .... Yoshitaka KÔI, Akira TSUJIMURA and Toshimoto KUSHIDA 2100
Dielectric Constants and Loss Tangents of $(Glycine)_3H_2SO_4$(TGS) at 3.3 KM c/s .... Eiji NAKAMURA and Jiro FURUICHI 2101
Some Properties of Titanium Sesquioxides Containing Vanadium Ions .... Tatsuyuki KAWAKUBO, Taketoshi YANAGI and Shoichiro NOMURA 2102

Photoconductivity of Cu-activated Cadmium Sulphide-Selenide........Sumitada ASANO 2103
On the Ferrimagnetic Resonance of Europium Iron Garnet ....W. P. WOLF 2104
Reflection and Absorption Spectra of LiF in the Extreme Ultraviolet Region..................Riso KATO, Kaizo NAKAMURA, Atsuo MATSUI and Yoichi UCHIDA 2105
The Effect of Plastic Deformation on the Cluster Formation in an Al-Cu 4 % Alloy .... Keisuke MATSUURA and Shigeyasu KODA 2106
Distribution Coefficient of Zinc in Gallium Arsenide ....Akikazu SHIBATA 2107
Interaction Types and Selection Rules in Baryon Processes........Seitaro NAKAMURA 2108
The Magnetic Properties of $NiBr_2$ ....Ichiro TSUBOKAWA 2109
Infrared Absorption of Electrons Through Piezoelectric Scattering....Toshio TANAKA 2110
Optical Properties of Irradiated LiF Crystals in the Extreme Ultraviolet Region ....Riso KATO, Shin-ichi NAKASHIMA, Kaizo NAKAMURA and Yoichi UCHIDA 2111
Study of Solid-Solution Single Crystals Containing $BaTiO_3$..........Tunetaro SAKUDO 2112
On the Reversible Optical Conversion Between A- and B-centers in Colored KCl Crystals..............................Hiroshi OHKURA and Takeshi UCHIDA 2114
Anomalous Paramagnetic Resonance in $Ni(NH_3)_6Cl_2$ ....Muneyuki DATE 2115
Absorption Spectra of Potassium Bromide-Thallium Phosphors......Tokumichi TAMAI 2116
N Bands in Alkali Halide Crystals..................................Sadao HATTORI 2117
A Correction to my Paper "The Dipole Moment and End-to-end Length of the Isotactic Vinyl Polymer, I." ....Tsugio MORI 2118
Analysis of the NMR Spectra of Acrylic Acid and Ethyl Acrylate...Yoji ARATA, Hiroshi SHIMIZU and Shizuo FUJIWARA 2119
On the Resistance Anomaly of Dilute Zinc Alloys at Low Temperatures....Yoshio MUTO 2119
Infrared Absorption of Free Carriers in Ionic Crystals ....Toshio TANAKA 2121
Strong Interaction of Baryons ....Seitaro NAKAMURA 2122

Errata

Emission of ^{8}Li, ^{9}Li and ^{8}B Fragments from Stars Produced by 4.3 GeV π^--Mesons in Nuclear Emulsion..........Kuni IMAEDA, Mitsuko KAZUNO and Nobuo ITO 2123

No. 12

Excitation Functions for Alpha-Particle Reactions on Fe^{56} and Fe^{57}..Shigeo TANAKA, Michiaki FURUKAWA, Shiro IWATA, Masuo YAGI, Hiroshi AMANO and Takashi MIKUMO 2125
Multipolarity of γ-ray Absorption in $U^{238}(\gamma, f)$ Reaction produced by $F(p, \alpha\gamma)\gamma$ rays ....Eiko TAKEKOSHI 2129
Search for Weak Gamma-Rays in the Positron Decay of Mn^{51} ....Masao NOZAWA, Hisashi YAMAMOTO, Yasukazu YOSHIZAWA and Yujiro KOH 2137
Beta- and Gamma-Ray Spectroscopy of Mn^{52} and $Mn^{53\,m}$ .... Toshio KATOH, Masao NOZAWA, Yasukazu YOSHIZAWA and Yujiro KOH 2140
Polarization of Protons Scattered from Complex Nuclei...................Shotaro YAMABE Michiya KONDO, Shohei KATO, Takashi YAMAZAKI and Jian-zhi RUAN 2154
Reactions of Nickel with Alpha-Particles ....Shigeo TANAKA 2159
Excitation Function for the Reaction $B^{21}(p, n)C^{11}$ up to $E_p=15$ MeV and energy Levels of C_{12}............................Michiaki FURUKAWA, Yoshihide ISHIZAKI, Yoshihiro NAKANO, Tadashi NOZAKI, Yoshio SAJI and Shigeo TANAKA 2167
The $N^{14}(d, n)O^{15}$ Reaction in the Energy Range from 1.5- to 2.9 MeV......Susumu MORITA, Nawoyuki KAWAI, Yorio GOTO, Takashi KAMI and Masahiro MUKAE 2170
Gamma Radiations Following the Decay of Dy^{165}...................................Akira HASHIZUME, Tan TAKAHASHI, Yoshihiko TENDO and Yohko ENOMOTO 2175
Decays of Photoreaction Products of Selenium.................Tokihiro KUROYANAGI 2179
^{8}Li Emission from Nuclear Disintegrations Produced by 4.3 GeV Negative π-Mesons .... Masaomi (Takahata) OHTA 2187
A Model Theory of Liquid ....Akiya OOKAWA 2191
Surface Free Energy of a Dilute Gas ....Takuji TSUZUKI 2197
Ferrimagnetic Resonance in Europium-Iron Garnet ....Tomonao MIYADAI 2205
Thermal Conduction in Ferroelectric Ceramics.......................Ikushi YOSHIDA 2211
Paramagnetic Susceptibility of an Electron Gas in Alkali Metals ......Masao SHIMIZU 2220
Magnetic Susceptibilities of Non-Ferromagnetic Transition Metals .... Masao SHIMIZU and Takeshi TAKAHASHI 2236

The Magnetic Properties of Single Crystals of Chromium Selenide .... Ichiro TSUBOKAWA 2243
The Change of the Curie Temperature of Iron-Nickel Alloys due to Hydrostantic Pressure .... Takejiro KANEKO 2247
Magnetic Resonance in $MnCO_3$ .... Muneyuki DATE 2251
Direct Viewing of Imperfections In Germanium *p-n* Junction .... Masami TOMONO 2254
Microwave Spectrum of Formaldehyde I. K-type Doubling Spectra .... Takeshi OKA, Hiromasa HIRAKAWA and Koichi HHIMODA 2265
Microwave Spectrum of Formaldehyde II. Molecular Structure in the Ground State .... Takeshi OKA 2274
Theory of Non-Linear Responses .... Osame NAKADA 2280
Theory of Electrochemical Diode .... Isao OSHIDA 2288
Dielectric β-Relaxations in some Linear High Polymers .... Kaoru YAMAFUJI 2295
Hyperfine Structure of the Spectra of Pr I and Pr II .... Kiyoshi MURAKAWA 2306
On the Viscosity of Irradiated Polymers. III. Effect of Branching.. Kanji KATSUURA 2310
Ultrasonic Studies in Chemically Active Liquid Media (1) Aqueous Solution of N_2O_4 .... M. KRISHNAMURTHI and M. SURYANARAYANA 2318
Volume Viscoelasticity of Polymers and Other Highly Dissipative Metals .... Yasaku WADA, Hidenori HIROSE, Hiromichi UMEBAYASHI and Motoharu OTOMO 2324
Optical Properties of KCl:Tl in the Extreme Ultraviolet Region .... Kiyoshi AOYAGI and Goro KUWABARA 2334
Effect of Oxygen upon Sintered Cadmium Sulphide Photoconducting Films .... Saburo KITAMURA 2343
Possibility of Supervelocity of Glass Fracture .... Shin-ichi HYODO 2351

SHORT NOTES

Spontaneous Magnetization of Magnesium Ferrite-Manganite System .... Kiyoshi MURAMORI and Shohei MIYAHARA 2354
Anisotropy on Poly-Crystalline Sheets of V-permendur .... Chinji KURODA 2355
Anomalous Photovoltaic Effect of CdS Single Crystals .... Sumiaki IBUKI, Hiroyoshi KOMIYA and Hirosuke YAMASHITA 2356
On the Mechanism of Reversible Appearance of Residual Magnetization at low Temperature Transition in αFe_2O_3 .... Kiiti SIRATORI, Akira TASAKI and Shūichi IIDA 2357
Antiferromagnetism of $FeSn_2$ .... Kazuo KANEMATSU, Kō YASUKŌCHI and Tetuo OHOYAMA 2358
Thermoelectric Power of Titanium- and Vanadium-Carbides .... Seiichiro NOGUCHI and Takao SATO 2359
Indirect Transition in Narrow Junction of Ge-Si Alloy .... Kei-ichi ANDO 2360
Weak Ferromagnetism of $NaNiF_3$ .... Shinji OGAWA 2361
Anomalous Temperature Dependence of Lattice Constant of $Cr\ O_2$ .... Kiiti SIRATORI and Shūichi IIDA 2362
A Note on Date's Paper "Magneto-plasma Resonance in Semiconductors..(I)" .... Kazuo YAMAGATA 2363
Optical Bleaching so of Gamma-Irradiatec KCl at room Temperature .... Noriaki ITOH and Tokuo SUITA 2364
The Energy Spectra of Secondary Electrons in Various Materials Irradiated by Gamma Rays from ^{60}Co and ^{137}Cs .... Nobuo ODA and Hirosi SUZUKI 2365
Electroluminescence of CdS Single Crystal .... Hirosuke YAMASHITA, Sumiaki IBUKI, Michio YOSHIZAWA and Hiroshi KOMIYA 2366
X-ray Study of Lattice Defects in Si Single Crystals by Transmission Berg-Barrett Technique .... Mitsuru YOSHIMATSU and Kazutaka HOHRA 2367
"Energy Analysis of Electron Diffraction Patterns" .... Hiroshi WATANABE 2368

Errata

X-ray Observations on Cleavage Faces of LiF Single Crystals.... Mitsuru YOSHIMATSU 2369
The Dipole Moment and End-to-end Length of the Isotactic Vinyl Polymer .... Tsugio MORI 2369

AUTHOR INDEX TO VOL. 15 NOS. 1~12

ABE Hidetaro;
  ——— and H. SHIRAI: Electron Spin Resonance of Manganese in Ammonium Chloride 1711
ABE Ryuji: Theoretical Study on the Properties of Coercive Field of $BaTiO_3$ Single Crystal 795
AKIBA Tosimitu: [cf. KIMURA Motoharu (1128)]
AMANO Hiroshi: [cf. TANAKA Shigeo (545, 952, 1547, 2125); TANAKA Shigeo (1357) (Errata)]
AMEMIYA Ayao: [cf. OKADA Yoichi (938)]
AMORÓS J. L.: [cf. ANNAKA Shoichi (356)]
ANDO Kei-ichi: [cf. KAMIYA Yoshihiro (2025)]
  ———: Indirect Transition in Narrow Junction of Ge-Si Alloy. (S.N.) 2360
ANDO Shigenori: General Theory of Electrically Conducting Perfect Gas Flow past a Three-Dimensional Thin Body 157
  ———: Some Remarks on the Magnetogasdynamic Linearized Theory........1523
ANDO Toshihiko: [cf. KOSHINO Shigeharu (1538)]
ANNAKA Shoichi;
  ——— and J. L. AMORÓS: On the X-Ray Temperature Diffuse Scattering of Anthracene and Stearic Acid. (S.N.).................... 356
AOYAGI Kiyoshi;
  ——— and G. KUWABARA: Optical Properties of KCl: Tl in the Extreme Ultraviolet Region 2334
ARAKI Hiroshi: [cf. NISHI Masato (1536)]
ARAI Toshihiro: The Study of the Optical Properties of Conducting Tin Oxide Films and their Interpretation in Terms of a Tentative Band Scheme 916
ARATA Yoji;
  —, H. SHIMIZU and S. FUJIWARA: Analysis of the NMR Spectra of Acrylic Acid and Ethyl Acrylate. (S.N.) 2119
ASADA Tsunesaburo;
  ———, H. SAITO, K. OMURA, T. OKU and M. OKA: Annealing of γ-Ray Damage in Germanium 93
ASAMI Masayuki;
  ——— and F. TAKANO: Notes on the Theory of Meissner Effect 669
ASANABE Sizuo;
  ——— and A. OKAZAKI; Electrical Properties of Germanium Selenide GeSe .. 989
ASANO Sumitada: Photoconductivity of Cu-activated Cadmium Sulphide-Selenide. (S.N.)..2103
ASANUMA Mitsuru: The Magnetic Properties of Mn-Sn-C Alloys. (S.N.).............1136
  ———: The Ferromagnetism of the Compound γ-FeSn. (S.N.) 1343
  ———: The Recovery of Initial Magnetic Susceptibility in Pure Nickel......1469
AWANE Katsunobu: [cf. OHKURA Hiroshi (934, 1349)] (S.N.)
CHIBA Shôko: [cf. HIRONE Tokutaro (1991)]
CHIBA Shû: Magnetic Properties of Iron Phosphide Fe_2P 581
CHIKAWA Jun-ichi: Multiple-Anode Proportional Counter X-Ray Diffractometer 602
CHIKAZUMI Sôshin: [cf. WAKIYAMA Tokuo (1975)]
  ———, K. SUZUKI and H. IWATA: Studies on the Magnetic Anisotropy Induced by Cold-Rolling of Ferromagnetic Crystal, II. Iron-Aluminum Alloys 250
CHONG Pyong-un;
  -, T. SUGIMOTO and Y. INUICHI: Conductivity Induced by Injected Electrons in Liquid Dielectrics. (S.N.) 1137
CHÛJÔ Riichiro: [cf. MIYAKE Akira (198)]
  -: NMR Second Moment of a Radical Oscillating in a Periodic Potential. (S.N.).................... 201
DANNO Akibumi: [cf. KOIKE Mitsuru (1501)]
DATE Muneyuki: Magneto-plasma Resonance in Semiconductors....................1488
  : Magnetic Reseonance in $MnCO_3$ 2251
  : Anomalous Paramagnetic Resonance in $Ni(NH_3)_6Cl_2$. (S.N.) 2115

DAZAI Tsunekichi: [cf. SUGIYAMA Kazusuke (1909)]

DODO Tarô: Formation of Plasma by Low Energy Iron Injection and Cyclotron Heating 906

: Heating of a Plasma by Acoustic Waves 1292

DOI Kenji: The Structure Analysis of AuCu$_3$ by Means of a Fourier Transformation of X-ray Diffuse Scatterings 1815

DOI Michiyasu: A Possible Mode of Twin in the ε-phase of Cu-Sb Alloy 849

DOKE Tadayoshi;

—, A NAKAMOTO, Y. TAKAMI, M. HATTORI and S. OKANO: Angular Dependencies of Efficiencies for Sodium-Iodide Crystals. (S.N.) 737

EDAGAWA Hiroshi;

, K. KOMATSUBARA, Y. INUISHI and T. SHIBAIKE: $1/f$ Noise and Channel in Ge PN Junction 1713

ENOMOTO Yohko: [cf. HASHIZUME Akira (2175)]

FORSTAT H.;

-, G. O. TAYLOR and B. R. KING: Heat Capacity of a Single Crystal of MnCl$_2$·4H$_2$O. (S.N.) 528

FUJIMOTO Fuminori: Dynamical Theory of Electron Diffraction in Laue-case, II. Numerical Calculation of Intensities 859

: Dynamical Theory of Electron Diffraction in Laue-case, III. Forbidden Reflection 1022

: Dynamical Theory of Electron Diffraction in Laue-case. (Errata) 1545

: [cf. TAKAGI Satio (1607)]

FUJISAKI Haruo;

and Y. TANABE: Crystal Growth of CdS in the Vertical Furnace. (S.N.) 204

FUJITA Hiroshi: Non-ideality Effects upon the Sedimentation Equilibrium in a Density Gradient 336

FUJIWARA Kunio: [cf. IWASAKI Hiroshi (1771)]

FUJIWARA Shizuo: [cf. ARATA Yoji (2119)] (S.N.)

FUJIWARA Tatsuo;

and T. KATO: The Influence of Aging Treatment on the Temperature Dependence of the Electric Resistance in Alnico 5 Magnet. (S.N.) 1705

FUKADA Eiichi: [cf. SONE Toshimaro (1708)]

FUKUDA Hisao: [cf. TABATA Tatsuo (364)]

FUKUDA Kuniya;

, A. OKUDA and Y. UCHIDA: Optical Bleaching of R-bands in LiF Crystals. (S.N.) 538

, R. KATO, K. NAKAMURA and Y. UCHIDA: Optical Absorption of Localized Exciton in KCl:I and NaCl:I Single Crystals. (S.N.) 1344

FUKUDA Kyue: [cf. OKANO Kotoyuki (1556)]

FUKUI Shûji;

and S. HAYAKAWA: Microwave Discharge Chamber. (S.N.) 531

FUKUNAGA Kiyoji: [cf. KIKUCHI Seishi (9); NISIMURA Keigo (754)]

FUKUSHIMA Masayoshi: [cf. SONE Toshimaro (1708)]

FUNATOGAWA Zenya: [cf. GONDO Yasuo (1126)]

FURUICHI Jiro: [cf. NAKAMURA Eiji (1955, 2101)] (S.N.)

FURUKAWA Michiaki: [cf. TANAKA Shigeo (545, 952, 1547, 2125) TANAKA Shigeo (1357) (Errata)]

, Y. ISHIZAKI, Y. NAKANO, T. NOZAKI, Y. SAJI and S. TANAKA: Excitation Function for the Reaction B$^{11}(p, n)$C^{11} up to $E_p=15$ MeV and Energy Levels of C^{12} 2167

FURUKAWA Yoshitaka: Photoconductivity in Nickel Doped Germanium. (S.N.) 353

———: Tunneling Probability in Germanium p-n Junctions. (S.N.) 730

: Temperature Dependence of Tunnel Diode Characteristics. (S.N.) 1130

———: Electrical Properties of Heavily Doped N-type Germanium 1903

FURUOYA Takashi: [cf. ISHII Zensho (206)]

——— and Y. SASAKI: Dislocations in Si Single Crystals. (S.N.) 205

FUSE Takayoshi: [cf. TSUKADA Kineo (1994)]
GARBER M.: Magnetic Susceptibility of $CoBr_2 \cdot 6H_2O$. (S.N.) 734
GOLD Louis: Inverse Solution of the Thomas-Fermi Equation. (S.N.) 1132
GOMI Yuzi;
 ———, Y. ODANI and M. SUGIHARA: Domain Patterns on Thin Films of Perminvar. (S.N.) 533
 ——— and Y. ODANI: Chain Wall in Permalloy Thin Films. (S.N.) 535
GONDO Yasuo;
 ——— and Z. FUNATOGAWA: Some Observations on the Domain Walls in Thin Films. (S.N.) 1126
GOTO Mitita: [cf. KUWAHARA Kaizo (359); TATSUMOTO Eiji (1703)]
GOTÔ Yorio: [cf. MORITA Susumu (361, 550, 2170)]
GOTOH Kanefusa: Magnetohydrodynamic Flow past a Sphere 189
 ———: Stokes Flow of an Electrically Conducting Fluid in a Uniform Magnetic Field 696
GUPTA A. S.: On the Flow of an Electrically Conducting Fluid Near an Accelerated Plate in the Presence of a Magnetic Field 1894
HAGA Eijiro: Theory of Thermoelectric Power of Ionic Crystals, IV. 1949
HAGIWARA Shigeo: [cf. KOJIMA Shoji (1904)]
HAMAMURA Shiro: [cf. NISHI Masato (1936)]
HANADA Reiko: [cf. MORITA Susumu (361, 550)]
HARRISON Ralph J.;
 ——— and A. PASKIN: On "Screened Impurity Potentials in Metals". (S.N.)..1902
HASEDA Taiichiro: Paramagnetic Susceptibility of $CoCl_2 \cdot 6H_2O$ and its Deuterated Salts.. 483
HASEDA Taiichiro: [cf. KOBAYASHI Hanako (1646)]
HASIGUTI Ryukiti R.: Impurity Trapped Interstitials and the Low Temperature Annealing Stages of Irradiated Copper 1807
HASHI Tsuneo;
 ———, I. TAKAHASHI, M. YAMANO, M. YAMAMOTO, S. SUZUKI and T. MAKITA: Maser Oscillation on 6-6 Line of $N^{15}H_3$. (S.N.)............................ 532
HASHI Tsuneo: [cf. SASAKI Masahumi (1652); KAWAI Takao (1700)]
HASHIKUNI Mitugi: Temperature Dependence of Infrared Absorption Bands of *n*-Higher Alcohols. (S.N.).. 941
HASHIMOTO Hatsujiro;
 ———, K. TANAKA and E. YODA: Growth and Evaporation of Tungusten Oxide Crystals 1006
HASHIMOTO Takasu: [cf. HIRAKAWA Kinshiro (2063)]
HASHIMOTO Yoshio: [cf. MIKUMO Takashi (1158)]
HASHIZUME Akira;
 ———, T. TAKAHASHI, Y. TENDO and Y. ENOMOTO: Gamma Radiations Following the Decay of Dy^{165}..2175
HATTORI Manabu: [cf. DOKE Tadayoshi (737)]
HATTORI Masumi;
 ——— and H. SATO: Note on the Field Dependence of the Mobility in Semiconductors 1237
HATTORI Sadao: N Bands in Alkali Halide Crystals. (S.N.) 2117
HAYAKAWA Satio: [cf. FUKUI Shûji (531)]
HAYASHI Koreaki: [cf. SATOH Takeshi (1658)]
HAYASHI Izuo: [cf. KIKUCHI Seishi (9, 41); NISHIMURA Keigo (754)]
HAYASHI Mitsuhiko: Pseudokinematical Approximation in Electron Diffraction by Crystal 2054
HAYASI Nisiki: On the Quasi-two-dimensional Laminar Boundary Layer. (S.N.) 208
 ———: On Similar Solutions of the Steady Quasi-two-dimensional Incompressible Laminar Boundary-layer Equations.. 522
HIHARA Tadamiki: [cf. KAMIGAICHI Takahiko (1355)] (S.N.)
HIKI Yosio: Internal Friction of Quartz.. 586
HIRABAYASHI Makoto: [cf. IWASAKI Hiroshi (1771)]
HIRAI Akira: Temperature Dependence of T_1 of Cl^{35} in Para-dichloro-benzene. (S.N.).. 201

———: [cf. SASAKI Masahumi (1652); Kawai Takao (1700)] (S.N.)
HIRAI Masamitsu: [cf. UETA Masayasu (593,1356)]
———: Thermal Bleaching of Color Centers in KCl Crystals Containing *U* Centers 1308
HIRAHARA Eiji: [cf. NAYA Rokuroh (360)]
HIRAKAWA Hiromasa: [cf. KONDO Kunitaka (303); OKA Takeshi (2265)]
HIRAKAWA Kazuyoshi: [cf. TUBOTA Hirosi (1701); HIRAKAWA Kinshiro (2063)]
HIRAKAWA Kinshiro;
———, K. HIRAKAWA and T. HASHIMOTO: Magnetic Properties of Potassium Iron Group Fluorides KMF_3 2063
HIRAO Yasuo: [cf. WAKATSUKI Tetsuo (1141)]
HIROIKE Eiko: Indirect Nuclear Spin-Spin Couplings in Saturated Hydrocarbon Molecules 270
HIROIKE Kazuo: Radial Distribution Function of Fluids, III.... 771
HIRONE Tokutaro;
——— and S. CHIBA: On the Magnetic Anisotropy of Single Crystal of Chromium Telluride 1991
HIROSE Hidenori: [cf. WADA Yasaku (1885, 2324)]
HIROTA Eiichi;
——— and B. KUBOTA: Magnetic Property of Cr_2O_5. (S.N.)....1715
HIROTA Kozo: [cf. KUSUMOTO Hajime (728)]
HIROTA Shoichi;
——— and T. IMAI: Electron Microscope Study of the Decomposition Process of Oxide Coated Cathods 137
——— and T. IMAI: Electron Microscope of the Decomposition Process of Oxide Coated Cathods. (Errata) 539
HISATAKE Kazuo;
———, Y. ISHIZAKI, A. ISOYA, T. NAKAMURA, Y. NAKANO, B. SAHEKI, Y. SAJI and K. YUASA: The Reaction $Li^7(p, n)Be^7$, $B^{11}(p, n)C^{11}$ and $Al^{27}(p, n)Si^{27}$ at 8 to 14 MeV 741
HITAKA Saburo: [cf. NONAKA Itaru (365)]
HONMA Akio: On the Magnetic Susceptibility of FeF_2.... 456
HORAI Kazumi: [cf. KOGA Hiroshi (1340)]
HORIE Tadao;
———, T. NAGURA and M. OTSUKA: Radiative Collisions between Molecular and Electron Beams, V. Angular Momentum Distributions of CH Separating from Simple Organic Molecules 641
HORIUCHI Shiro: [cf. YAMAGUCHI Jiro (1541)]
HOSOKAWA Iwao: A Refinement of the Linearized Transonic Flow Theory.... 149
———: Transonic Flow past a Wavy Wall 2080
HUSIMI Kazuo: 180° Domain Wall Motions in $BaTiO_3$ Crystal. (S.N.) 731
———, K. NISHIGUCHI and T. SUZUKI: Ultrasonic Measurement of Magnetization in Mn-ferrite Single Crystal 1341
HU Chuin: [cf. ODA Yukiyasu (760)]
———: (d, α) Reactions on Some Light Nuclei 1741
HYODO Shin-ichi;
——— and F. OKUDA: Glass Cracking Caused by Underwater Spark 2093
———: Possibility of Supervelocity of Glass Fracture....2351
IBUKI Sumiaki;
———, H. KOMIYA and H. YAMASHITA: Anomalous Photovoltaic Effect of CdS Single Crystals. (S.N.)....2356
———: [cf. YAMASHITA Hirosuke (2366)] (S.N.)
IGARASHI Yoshitaka: [cf. MIZUSHIMA Yoshihiko (729)]
IIDA Shūichi: [cf. SIRATORI Kiiti (210); TASAKI Akira (1535); INOUE Tohru (1899); SIRATORI Kiiti (2357, 2362)] (S.N.)
IIZIMA Sigeru: [cf. KIKUCHI Makoto (357)]
——— and M. KIKUCHI: Avalanche Breakdown in CdS Single Crystal. (S.N.)..1345
IIZUKA Takashi: [cf. KIKUCHI Makoto (935)]

IKEDA Hiroshi: [cf. KIKUCHI Seishi (41)]

IKEGAMI Hidetsugu: [cf. YAMAZAKI Toshimitsu (957)]

IMAEDA Kuni;

———, M. KAZUNO and N. ITO: Emission of ^{8}Li, ^{9}Li and ^{8}B Fragments from Stars Produced by 4.3 GeV π^--Mesons in Nuclear Emulsion 1753

———, M. KAZUNO and N. ITO: Emission of ^{8}Li, ^{9}Li and ^{8}B Fragments from Stars Produced by 4.3 GeV π^--Mesons in Nuclear Emulsion. (Errata)........2123

IMAEDA Yoshiro: Impurity Shift of Pure Quadrupole Resonance Frequency 1699

IMAI Isamu: Electrical Properties of Stannic Oxide Films. (S.N.) 937

IMAI Nobuhisa: [cf. OHNISHI Tsuyoshi (896)]

IMAI Tetsuji: [cf. HIROTA Shoichi (137, 539); MIZUSHIMA Yoshihiko (729)]

INAWASHIRO Sakari: [cf. NOMURA Yûkichi (510)]

INOUE Morio: [cf. MIZUNO Hiroyuki (211)]

INOUE Tohru;

———, H. MIZUTA and S. IIDA: The Effect of Cation Vacancies on the Magnetic Annealing of Co$_x$Fe$_{3-x}$O$_4$. (S.N.) 1899

INUISHI Yoshio: [cf. CHONG Pyong-un (1137); SHIRAFUJI Junji (1346); KOMATSUBARA Kiichi (1713)]

ISHIBASHI Yoshihiro: [cf. TAKAHASHI Hidetosi (853)]

ISHIDA Yōichi: [cf. TANAKA Tomoyasu (261)]

ISHIDA Yoshio: A New Method to Determine Hydration Energy of Ion. (S.N.)........1707

ISHII Chikai;

——— and K. TAKAHASHI: A Gamma Ray in Ti^{45} Decay. (S.N.).............. 736

ISHIGURO Masakazu;

———, E. SUGIOKA and N. TAKEUCHI: Dichroism of Z Bands................1302

——— and N. TAKEUCHI: Dichroism of Z_4 and F Bands......................1871

ISHII Zensho;

———, T. FURUOYA, Y. SASAKI and K. KOHRA: Observation of Layer Structure in Dislocation Free Silicon Crystals with the Use of X-ray Anomalous Transmission. (S.N.).. 206

ISHIZAKI Yoshihide: [cf. HISATAKE Kazuo (741); FURUKAWA Michiaki (2167)]

ISOYA Akira: [cf. KIKUCHI Seishi (41); HISATAKE Kazuo (741)]

ITO Nobuo: [cf. IMAEDA Kuni (1753, 2123)]

ITO Satoru: [cf. KIKUCHI Seishi (41)]

ITO Takao: [cf. OKADA Yôichi (938)]

ITOH Junkichi [cf. KUSUMOTO Hazime (728)]

ITOH Hidehiko: [cf. OGATA Hiroshi (1719)]

ITOH Noriaki;

——— and T. SUITA: Thermal Bleaching of F-Counters of Gamma-Irradiated KCl at Temperatures. (S.N.)..1716

——— and T. SUITA: Optical Bleaching of Gamma-Irradiated KCl at Room Temperature. (S.N.)..2364

ITOH Hidehiko: [cf. OGATA Hiroshi (1726)]

ITOH Tomizo;

——— and T. MUSHA: Monte Carlo Calculations of Motion of Electrons in Helium 1675

IWAI Tsuruji: Temperature Dependence of the Optical Absorption Edge of Tungsten Trioxide 1596

IWASAKI Hiroshi;

———, M. HIRABAYASHI, K. FUJIWARA, D. WATANABE and S. OGAWA: Study on the Ordered Phases with Long Period in the Gold-Zinc Alloy System. I. Survey of Crystal Structures and Calorimetric Measurement 1771

———: [cf. WAKU Shigeru (1185)]

IWATA Hiroko: [cf. CHIKAZUMI Sōshin (250)]

IWATA Shiro: [cf. TANAKA Shigeo (545, 952, 1357, 1547, 2125)]

JOSHI S. K.: [cf. MITRA S. S. (1575)]

KAIFU Yôzo: [cf. TOMURA Masao (314, 1925)]

KAJI Ikuo;

and M. KITO: Plasma Oscillations in a Magnetic Field....1851

KAKIUCHI Yoshinobu: [cf. KUME Kiyoshi (1277)]

KAKUTANI Tsunehiko: Axially Symmetric Stagnation-point Flow of an Electrically Conducting Fluid under Transverse Magnetic Field 688

———: Effect of Transverse Magnetic Field on the Flow due to an Oscillating Flat Plate, II....1316

KAMADA Koji: Low Field Magnetoresistance Effect of Plastically Deformed n-type Silicon 998

KAMEDA Tadashi: On the High Energy Soft Component Near Sea Level 1175

and T. MAEDA: On the High Energy Soft Components at 2770 m Altitude....1367

——, Y. TOYODA and T. MAEDA: On the Electronic Component of Extensive Air Showers near the Axis 1565

KAMIGAICHI Takahiko;

, K. MASUMOTO and T. HIHARA: Electrical Properties of Chromium Sulfides. (S.N.) 1355

KAMIMURA Hiroshi;

, S. KOIDE, H. SEKIYAMA and S. SUGANO: Magnetic Properties of the Pd and Pt Group Transition Metal Complexes....1264

KAMIYA Yoshihiro;

, K. ANDO, M. NONOYAMA and R. UYEDA: Dislocation Networks and Moiré Patterns of Molybdenite 2025

KAMIYOSHI Kan-Ichi;

——— and T. YAMAKAMI: Some Observations on Plastic Deformation and Slip Lines of Sodium Chloride Whisker. (S.N.)....1347

KANAI Yasuo: The Change in Electron Mobility in Indium Antimonide at Low Electric Field 830

, R. NII and N. WATANABE: Oscillatory Magnetoresistance in N-Type PbTe. (S.N.) 1717

KANDA Eizo: [cf. KOBAYASHI Hanako (1646)]

KANDA Yukinori [cf. SUGIYAMA Kazusuke (1909)]

KANEKO Shobu: Transport Coefficients of Plasmas in a Magnetic Field 1685

KANEKO Takejiro: Volume Magnetostriction of Cobalt-Nickel Alloys 463

———: Volume Magnetostriction of Cobalt-Nickel Alloys. (Errata) 738

———: The Change of the Curie Temperature of Iron-Nickel Alloys Due to Hydrostatic Pressure 2247

KANEMATSU Kazuo;

, K. YASUKOCHI and T. OHOYAMA: Antiferromagnetism of $FeSn_2$. (S.N.)..2358

KANZAKI Hiroshi;

——— and K. KIDO: Purification of Alkali Halide Crystals through Fractional Distillation and Normal Freezing. (S.N.).... 529

KARASAWA Takashi: [cf. KIKUCHI Seishi (41)]

KASHIWABARA Hisatsugu;

and K. SHINOHARA: The Behaviours of Free Radicals Trapped in γ-Irradiated Polyethylene. (S.N.) 1129

KASUYA Takahiro;

and T. OKA: Microwave Spectrum of Ethyl Iodide, I 296

———: Microwave Spectrum of Ethyl Iodide, II 1273

KATASE Akira: [cf. SONODA, Masateru (1680)]

KATO Kiyoe: Oscillations in a Plasma in a Weak Magnetic Field....1093

KATO Riso: [cf. FUKUDA Kuniya (1344)]

, K. NAKAMURA, A. MATSUI and Y. UCHIDA: Reflection and Absorption Spectra of LiF in the Extreme Ultraviolet Region. (S.N.) 2105

———, S. NAKASHIMA, K. NAKAMURA and Y. UCHIDA: Optical Properties of Irradiated LiF Crystals in the Extreme Ultraviolet Region. (S.N.) 2111

KATO Shohei: [cf. YAMABE Shotaro (2154)]

KATO Tetsuo: [cf. FUJIWARA Tatsuo (1705)] (S.N.)

KATO Yoshinori: [cf. NISHIOKA Atsuo (416)]

KATOH Toshio: [cf. MIZOBUCHI, Akira (1737)]
———, M. NOZAWA, Y. YOSHIZAWA and Y. KATO: Beta- and Gamma-Ray Spectroscopy of Mn^{52} and Mn^{52m} 2140
KATSUURA Kanji: On the Viscosity of Irradiated Polymers. III. Effect of Branching .. 2310
KAUFFMAN J. W.: [cf. NENNO Soji (220)]
KAWAI Nawoyuki: [cf. MORITA Susumu (361, 550, 2170)]
———: On the Alpha-particles from the N^{14}(d, α)C^{12} Ground State Reaction. (S.N.) 930
KAWAI Takao: [cf. SASAKI Masahumi (1652)]
———, M. SASAKI, A. HIRAI, T. HASHI and A. ODAJIMA: Measurement of Temperature Dependence of T_1 of Proton in Some High Polymers by Pulsed NMR Technique. (S.N.) 1700
KAWAJI Shinji: A.C. and D.C. Field Effects on Cleaned Germanium Surfaces 95
KAWAKUBO Tatsuyuki;
———, T. YANAGI and S. NOMURA: Some Properties of Titanium Sesquioxides Containing Vanadium Ions. (S.N.) 2102
KAWAMURA Mitsuhiro: Angular Correlation Measurements in the Decay of In^{114m} 3
KAWASHIMA Maumi: [cf. OGATA Hiroshi (1719, 1726)]
KAZUNO Mitsuko: [cf. IMAEDA Kuni (1753); IMEDA Kuni (2123) (Errata)]
KIDO Keishiro: [cf. KANZAKI Hiroshi (529)]
KIHARA Taro;
———, Y. MIDZUNO, K. SAKUMA and T. SHIZUME: Ion-Electron Relaxation of Plasmas in a Magnetic Field, II 684
———, Y. MIDZUNO and S. KANEKO: Transport Properties of Plasmas in a Strong Magnetic Field 1101
———: Multipole Interaction Stabilizing Cubic Molecular Crystals 1920
KIKUCHI Ken: [cf. KIKUCHI Seishi (41); ODA Yukiyasu (760)]
KIKUCHI Makoto: [cf. IIZIMA Sigeru (1345)]
——— and S. IIZIMA: Photoconductivity of Cd-ZnS Mixed Crystals. (S.N.) .. 357
——— and K. TACHIKAWA: Visible Light Emission and Microplasma Phenomena in Silicon p-n Junction, I 835
——— and T. IIZUKA: Observation of Microplasma Pulses and Electroluminescence in Gallium Phosphide Single Crystal. (S.N.) 935
———: Visible Light Emission and Microplasma Phenomena in Silicon p-n Junction. II. Classification of weak spots in diffused p-n junctions 1822
KIKUCHI Seishi;
———, J. SANADA, S. SUWA, I. HAYASHI, K. NISHIMURA and K. FUKUNAGA: Elastic Scattering of 14 Mev Protons by Deuterons and by Protons 9
———, I. NONAKA, H. IKEDA, H. KUMAGAI, Y. SAJI, J. SANADA, S. SUWA, A. ISOYA, I. HAYASHI, K. MATSUDA, H. YAMAGUCHI, T. MIKUMO, K. NISIMURA, T. KARASAWA, S. KOBAYASHI, K. KIKUCHI, S. ITO, A. SUZUKI, S. TAKEUCHI and H. OGAWA: A 160 cm Synchro- and Variable Energy Ordinary Cyclotron .. 41
———, et al.: A 160 cm Synchro- and Variable Energy Ordinary Cyclotron. (Errata) 527
———, J. SANADA, S. SUWA, I. HAYASHI, K. KISIMURA and K. FUKUNAGA: Protons from the $p+d$ Breakup Reaction at Proton Energies of 14 MeV and 10 MeV 749
KIM Pil Hyon: On the Proton Resonance of Several Hexammine Complex Salts 445
KIMURA Motoharu;
———, K. KURIYAMA, K. SHODA, N. MUTSURO, T. TOHEI, T. AKIBA, K. SATO and K. KURODA: Structure of Giant Resonance in Al^{27}(p, γ) Reaction. (S.N.) .. 1128
KING B. R.: [cf. FORSTAT, H. (528)]
KINOSITA Koreo;
———, H. KONDO and I. SAWAMURA: Stress in Very Thin Vacuum-Evaporated Films of Silver. (S.N.) 942
——— and H. KONDO: Thickness-Dependence of Stress in Vacuum Deposited Silver Films. (S.N.) 1339
KITAMURA Saburo: Effect of Heat-Treatment upon Sintered Cadmium Sulphide Photo-

conductive Films. (S.N.) 1697

——: Effect of Oxygen upon Sintered Cadmium Sulphide Photoconducting Films 2343

KITO Masafumi: [cf. KAJI Ikuo (1851)]

KOBAYASHI, Hanako;

, T. HASEDA, E. KANDA and M. MORI: The Superexchange Interaction between Cr^{+3} pair in Chromium Bi-nuclear Complex Ions 1646

KOBAYASHI Kazuo: Fixing of Magnetic Moment of Ferromagnetic Fine Precipitates in Cu-Co Alloy during Aging 1352

KOBAYASHI Koichi;

— and T. TOMIKI: Absorption Band due to a Presence of Impurity Bromine in KCl Crystal. (S.N.) 1350

- and T. TOMIKI: Studies on the Preparation of Pure Alkali Chlorides 1982

KOBAYASHI Shigehiro: Thomas-Fermi-Dirac Model of Compressed Ions 1842

KOBAYASHI Shinsaku: [cf. KIKUCHI Seishi (41); ODA Yukiyasu (760)]

, K. MATSUDA, Y. NAGAHARA, Y. ODA and N. YAMAMURO: Elastic and Inelastic Scattering of Protons from Nickel Isotopes; Ni^{58} and Ni^{60}, in the Energy Range from 7.0 MeV to 15.3 MeV 1151

: Elastic and Inelastic Scattering of Protons by Oxygen in the Energy Region of 6.9 MeV and 15.6 MeV 1164

KODA Shigeyasu: [cf. MATSUURA Keisuke (1905, 2106)] (S.N.)

KOGA, Hiroshi;

, K. HORAI and O. MATUMURA: Electron Spin Resonance of Mn^{++} in $SrCl_2$, $CdCl_2$ and $CdBr_2$. (S.N.) 1340

KOH Yujiro: [cf. NOZAWA Masao (2137); KATOH Toshio (2140)]

KOHRA Kazutake: [cf. ISHII Zensho (206) (S.N.); YOSHIMATSU Mitsuru (1760, 2367) (S.N.); YOSHIMATSU Mitsuru (2369) (Errata)]

KŌI Yoshitaka;

—, A. TSUJIMURA and Y. YUKIMOTO: The Temperature and Pressure Dependence of the Nuclear Resonance of Co^{59} in Face-Centered-Cubic Cobalt Metal. (S.N.) 1342

, A. TSUJIMURA and T. KUSHIDA: NMR of Co^{59} in Ferromagnetic Hexagonal Cobalt Metal. (S.N.) 2100

KOIDE Shoichiro: [cf. KAMIMURA Hiroshi (1264)]

KOIKE Mitsuru;

— and A. DANNO: Radiation Effects on Dimethyl-diphenyl Siloxane Copolymer. I. Protective Effect of Phenyl Radical on the Cross-linking 1501

KOIKE Yasuhiro: [cf. NISHIOKA Atsuo (416)]

KOJIMA Shoji;

—— and M. MINEMATSU: Nuclear Quadrupole Resonance of Nitrogen in Cyanuryl Chloide. (S.N.) 355

— and S. HAGIWARA: Radiation of Plasma Oscillation. (S.N.) 1904

KOJIMA Takeshi: Potential Barrier of Phenol from its Microwave Spectrum 284

——: Microwave Spectrum of Methyl Mercaptan 1284

KOMATSUBARA Kiichi: [cf. KURATA Takao (362)]

———, Y. INUISHI, H. EDAGAWA and T. SHIBAIKE: $1/f$ Noise and Channel in Ge PN Junction. (S.N.) 1713

KOMIYA Hiroyoshi: [cf. IBUKI Sumiaki (2356); YAMASHITA Hirosuke (2366)] (S.N.)

KOMURA Yukitomo;

———, Y. TOMIIE and R. NATHANS: X-Ray Measurement of the Scattering Factor of Iron in Ordered Fe_3Al 1434

KONDO Hideki: [cf. KINOSITA Koreo (942, 1339)]

KONDO Kunitaka: [cf. SHIMODA Koichi (1125)]

—, H. HIRAKAWA, A. MIYAHARA, T. OKA and K. SHIMODA: Microwave Zeeman Effect of Formaldehyde 303

—— and T. OKA: Stark-Zeeman Effects on Asymmetric Top Molecules. Formaldehyde H_2Co 307

KONDO Michiya: [cf. YAMABE Shotaro (2154)]

KONDO Motoo: [cf. MIKUMO Takashi (1158)]

KONDOH Hisamoto: [cf. UCHIDA Enji (466)]
——: Antiferromagnetic Resonance in NiO in Far-infrared Region 1970
KONO Ryusuke: The Dynamic Bulk Viscosity of Polystyrene and Polymethyl Methacrylate 718
KONO Tatsuo: [cf. TAKAHASHI Minoru (936, 1351)]
KOSHINO Shigeharu:
—— and T. ANDO: Resonance Transfer of Ionization Energy in Semiconductors 1538
KRISHNAMURTHI M.;
—— and M. SURYANARAYANA: Ultrasonic Propagation through Aqueous Solutions of Acetates 345
—— and M. SURYANARAYANA: Ultrasonic Propagation through Binary Mixtures containing Acetic Acid 349
—— and M. SURYANARAYANA: Ultrasonic Studies in Chemically Active Liquid Media, (1) Aqueous Solutions of N_2O_2 2318
KUBO Hiroshi: [cf. MITANI Kenji (678)]
KUBOTA Buichi: Preparation of Ferromagnetic Chromium Dioxide. (S.N.) 1706
——: [cf. HIROTA Eiichi (1715)] (S.N.)
KUMABE Isao: [cf. OGATA Hiroshi (1719, 1726)]
KUMAGAI Hiroo: [cf. KIKUCHI Seishi (41)]
KUME Kiyoshi;
—— and Y. KAKIUCHI: Proton Magnetic Resonance in Hydrogen Bonded Dimers in Solids 1277
——: Proton Magnetic Resonance in Pure and Doped Ice 1493
KURATA Takao;
—— and K. KOMATSUBARA: A Curious Characteristic of P-N-P-N Junctions. (S.N.) 362
KURIYAMA Katumi: [cf. KIMURA Motoharu (1128)]
KURIYAMA Masao: X-ray Line Broadening from the Polished Surfaces of Silver and Gold 1426
KURODA Chinji: Time Decrease of Permeability of Substitutional Ferromagnetic Alloys. (S.N.) 1898
——: Anisotropy on Poly-Crystalline Sheets of V-Permendur. (S.N.)........2355
KURODA Kunishige: [cf. KIMURA Motoharu (1128)]
KUROSAWA Tatsumi: [cf. YAMASHITA Jiro (802)]
——: Heitler-London Approach to Electrical Conductivity, II. A Proof of the Hopping Motion........1211
KUROYANAGI Jun: Change in Modulus of Rigidity of Brass Wires by Cold-Working and Subsequent Annealing........1386
KUROYANAGI Tokihiro: [cf. MORINAGA Haruhiko (213)]
——: Decays of Photoreaction Products of Selenium 2179
KUSHIDA Toshimoto: [cf. KÔI Yoshitaka (2100)] (S.N.)
KUSUMOTO Hazime;
——, J. ITOH, K. HIROTA and T. UEDA: On the Proton Chemical Shift in Deuterium Substituted *p*-Xylene and Toluene. (S.N.)........ 728
——: The Effects of Deuteron Irradiation on the Nuclear Magnetic Resonance in Teflon 867
KUWABARA Goro: [cf. AOYAGI Kiyoshi (2334)]
KUWAHARA Kaizo: [cf. TATSUMOTO Eiji (1703)] (S.N.)
—— and M. GOTO: Thickness Dependence of Domain Orientation in Thin Nickel Films. (S.N) 359
MAEDA Hajime: [cf. YONEMITSU Hiroo (1717) (S.N.); YONEMITSU Hiroo (1907) (Errata); MIYAZAWA Hisao (1924)]
MAEDA Keiji: Electroluminescence of Insulated Particles, II 2051
MAEDA Toshio: [cf. KAMEDA Tadashi (1367, 1565)]
MAKI Takashi: [cf. MIKUMO Takashi (1158); MORITA Susumu (2170)]
MAKITA Tsutomu: [cf. TAKAHASHI Isao (532)]

Maruyama Saiyu: Dynamic Behaviour of Twinning in Tin Crystals at Various Temperatures and Strain Rates 1243
Masaike Akira: [cf. Ogata Hiroshi (1719, 1726)]
Masuda Yoshiko: [cf. Ogata Hiroshi (1719, 1726); Yasumi Shinjiro (1913)]
Masumoto Kan-ichi: [cf. Kamigaichi Takahiko (1355)] (S.N.)
Masuno Kunio: [cf. Waku Shigeru (1185); Waku Shigeru (1698) (S.N.)]
Matsuda Kazuhisa: [cf. Kikuchi Seishi (41); Oda Yukiyasu (760); Kobayashi Shinsaku (1151)]
Matsui Atsuo: [cf. Kato Riso (2105)] (S.N.)
Matsumura Koji: [cf. Yamaguchi Jiro (1541)] (S.N.)
Matsumura On: [cf. Koga Hiroshi (1340)] (S.N.)
Matsumura Tetsuo;
——— and Y. Tanabe: Synthesis of AlN Crystals. (S.N.) 203
Matsuura Keisuke;
——— and S. Koda: The Effect of θ' Phase on the Plastic Deformation of an Age-Hardenable Al-Cu 4%. (S.N.) 1905
——— and S. Koda: The Effect of Plastic Deformation on the Cluster Formation in an Al-Cu 4% Alloy. (S.N.) 2106
Matsuzawa Kiichiro: Condenser Microphones with Plastic Diaphragms for Airborne Ultrasonics, II 167
McIrvine E. C.: Screened Impurity Potentials in Metals. (S.N.) 928
Melkonian Edward: [cf. Wajima John T. (630)]
Midzuno Yukio: [cf. Kihara Taro (684, 1101)]
Mikoshiba Nobuo: Interaction of Conduction Electrons with Acoustic Waves in Simple Semiconductors 982
Mikoshiba Nobuo: Interaction of Conduction Electrons with Acoustic Waves in Many-Valley Semiconductors 1189
Mikumo Takashi: [cf. Kikuchi Seishi (41); Nonaka Itaru (365); Tanaka Shigeo (545, 952); Tanaka Shigeo (1357) (Erata); Tanaka Shigeo (1547, 2125)]
———, H. Yamaguchi, I. Nonaka, M. Odera, Y. Hashimoto, M. Kondo and T. Maki: Elastic and Inelastic Scattering of Alpha Particles by Carbon 1158
Mikura Ziro: On the Superconducting Ground State 1783
Minematsu Midori: [cf. Kojima Shoji (355)]
Mishina Masanori: [cf. Mutsuro Naoshi (358)]
Mitani Kenji;
——— and H. Kubo: Breakdown of Argon at Low Pressure in a Longitudinal Magnetic Field 678
Mitra S. S.;
——— and S. K. Joshi: Lattice Frequency of Ionic Crystals 1575
Mitsui Hidehiko: [cf. Morinaga Haruhiko (213)]
Mitsui Tadayasu: [cf. Satō Masayoshi (537)]
———: Magnetic Anisotropy Induced by Cold Rolling of Cu-Co Alloy. (S.N.) .. 929
Miura Iwao: [cf. Wakatsuki Tetsuo (1141)]
Miwa Mitsuo;
——— and M. Yamanouchi: Further Study of the Reaction $^{7}\mathrm{Li}(\gamma, t)^{4}\mathrm{He}$ 947
Miyadai Tomonao: [cf. Shichijō Yūzō (530)]
———, H. Takata and Y. Shichijō: Ferrimagnetic Resonance in a Single Crystal of Europium-Iron Garnet. (S.N.) 1354
———: Ferrimagnetic Resonance in Europium-Iron Garnet 2205
Miyahara Akira: [cf. Kondo Kunitaka (303)]
Miyahara Syohei: [cf. Muramori Kiyoshi (2354)] (S.N.)
——— and M. Kiyoshi: Magnetic Properties of $MgMn_2O_4$. (S.N.) 1906
Miyake Akira;
——— and R. Chûjô: Influence of Foreign Magnetic Nuclei on NMR. (S.N.) .. 198
———: On the Intramolecular Light Scattering of the Non-Gaussian Chain .. 875
———: Influence of the Molecular Weight Distribution on the Polymer Properties 883

———: Intramolecular NMR Second Moment of the Polymer Chain..........1057

MIYAMOTO Shigeko: [cf. OHKURA Hiroshi (934)]

MIYATANI Shin-ya: Electrical Properties of Pseudo-binary Systems of Ag$_2$VI's; Ag$_2$Te$_x$Se$_{1-x}$, Ag$_2$Te$_x$S$_{1-x}$ and Ag$_2$Se$_x$S$_{1-x}$ 1586

MIYAZAWA Hisao: [cf. YONEMITSU Hiroo (1717) (S.N.); YONEMITSU Hiroo (1907) (Errata)]

——— and H. MAEDA: Anisotropic Hall Coefficients in n-Type Germanium ..1924

MIZOBUCHI Akira: [cf. WAKATSUKI Tetsuo (1141)]

———, T. KATOH and J. RUAN: Mixing Ratio of the 440-keV Gamma Radiation in ^{23}Na 1737

MIZUNO Hiroyuki;

——— and M. INOUE: Formation Mechanism of F-Centers in KCl Single Crystals Heated in Potassium Vapor 211

MIZUNO Joji: An X-ray Study on the Structure of Cobalt Dichloride Hexahydrate 1412

MIZUSHIMA Sanchi: Dislocation Model of Liquid Structure 70

MIZUSHIMA Yoshihiko;

———, Y. IGARASHI and T. IMAI: Cold-emitting Cathode Materials. (S.N.).... 729

———: Elektronische Wechselwirkung zwischen Wasserstoff und aufgedampften Nickelfilmen 1614

MIZUTA Hiroshi: [cf. INOUE, Tohru (1899)] (S.N.)

———: Effect of Solvent on the Extension of High Polymer Molecule 475

MORI Masayasu: [cf. KOBAYASHI Hanako (1646)]

MORI Tsugio: The Dipole Moment and End-to-end Length of the Isotactic Vinyl Polymer, I. Mutual Dependence between Dipole Moment and End-to-end Length 1482

———: The Dipole Moment and End-to-end Length of the Isotactic Vinyl Polymer, II. A Special Simplified Model and Numerical Calculations 1638

———: The Dipole Moment and End-to-end Length of the Isotactic Vinyl Polymer. (Errata)..2369

—: A Correction to my Paper " The Dipole Moment and End-to-end Length of the Isotactic Vinyl Polymer, I." (S.N.) 2118

MORINAGA Haruhiko;

———, T. KUROYANAGI, H. MITSUI and K. SHODA: Three New Isotopes, Co^{63}, Ga^{75} and As^{81} 213

MORINO Yonezo;

—— and M. TOYAMA: Zeeman Effect of Nuclear Quadrupole Resonance Spectrum in 1, 3, 5-Trichlorobenzene 288

MORIOKA Shigeki: Jets of a Perfectly Conducting Inviscid Gas in the Presence of a Magnetic Field parallel to the System 1516

MORITA Susumu;

——, N. KAWAI, N. TAKANO, Y. GOTO, R. HANADA, Y. NAKAJIMA, S. TAKEMOTO and Y. YAEGASHI: Differential Cross Sections for the N^{14}(d, p)N^{15} Ground State Reaction at the Deuteron Energy of 16 MeV 361

, N. KAWAI, N. TAKANO, Y. GOTO, R. HANADA, Y. NAKAJIMA, S. TAKEMOTO and Y. YAEGASHI: Differential Cross Sections for the Reaction C^{12}(d, p)C^{13} in the Energy Range of Deuterons from 15- to 20-MeV 550

–, N. KAWAI, Y. GOTO, T. MAKI and M. MUKAE: The N^{14}(d, n)O^{15} Reaction in the Energy Range from 1.5- to 2.9-MeV 2170

MOTIZUKI Kazuko: Theory of the Nuclear Magnetic Resonance of Co^{59} in CoO 888

———: Theory of the Nuclear Magnetic Resonance of Co^{59} in CoO. (Errata)..1140

MUKAE Masahiro: [cf. MORITA Susumu (2170)]

MURAKAMI Miyuki: [cf. NAYA Rokuroh (300)]

MURAKAMI Terutosi: On the Variation Principle in the Kinetic Theory of Dense Gases, I 60

MURAKAWA Kiyoshi: Hyperfine Structure of the Spectra of Pr I and Pr II 2306

MURAMORI Kiyoshi: [cf. MIYAHARA Syohei (1906)] (S.N.)

and S. MIYAHARA: Spontaneous Magnetization of Magnesium Ferrite-Manganite System. (S.N.) 2354

MUSHA Toshimitsu: [cf. ITOH Tomizo (1675)]

MUTO Jiro: Investigation of the Reaction Mg^{25}(p, γ)Al^{26}........................... 17

: [cf. OKANO Kotoyuki (1556)]
MUTO Yoshio: On the Resistance Anomaly of Dilute Zinc Alloys at Low Temperatures. (S.N.) 2119
NAGAHARA Yukio: [cf. ODA Yukiyasu (760)]
———: [cf. KOBAYASHI Shinsaku (1151)]
NAGAI Kazuo: Configurational Changes of Polypeptide Molecules in the Helix-Coil Transition Region, I 407
NAGAMIYA Takeo: [cf. UCHIDA Enji (466)]
NAGAO Shigeo;
——— and T. SATO: Some Experiments on Plasma Alfvén Waves. (S.N.) 375
NAGASAWA Akira;
and S. OGAWA: Study on the Twin Formation in Evaporated Silver Films 1421
NAGATANI Kunio: Radiations from Ba^{141} 1
NAGURA Takayuki: [cf. HORIE Tadao (641)]
NAKADA Osamu: Theory of Viscoelasticity of Amorphous Polymers, II. A Note on the Time-Temperature Reducibility of the Relaxation and Retardation Spectra (Errata) 945
: Theory of Non-Linear Response, I. 2280
: Observation of an Anomaly in Transistor Characteristics. (S.N.) 1537
NAKAGAWA Yasuaki: [cf. TEZUKA Seiji (931)]
NAKAJIMA Yutaka: [cf. MORITA Susumu (361, 550)]
NAKAMOTO Atsushi: [cf. DOKE Tadayoshi (737)]
NAKAMURA Akira;
and Y. SUGIURA: Magnetostriction of Yttrium Iron Garnet. (S.N.) 1704
NAKAMURA Eiji;
and J. FURUICHI: Measurement of Microwave Dielectric Constants of Ferroelectrics Part I. Dielectric Constants of $BaTiO_3$ Single Crystal at 3.3 KM c/s 1955
— and J. FURUICHI: Dielectric Constants and Loss Tangents of $(Glycine)_3$-H_2SO_4(TGS) at 3.3 KM c/s. (S.N.) 2101
NAKAMURA Kaizo: [cf. FUKUDA Kuniya (1345); KATO Riso (2105, 2111)] (S.N.)
NAKAMURA Teruo: [cf. HISATAKE Kazuo (741)]
———: Angular Distribution of *n-p* Scattering at 14.1 MeV 1359
NAKAMURA Terutaro: [cf. TAKAHASI Hidetosi (853)]
——— and K. OHI: Dislocation Etch Pits on *a*- and *b*-Faces of GASH Crystal. (S.N.) 1348
: Kinematic Theory of Ferroelectric Domain Growth 1379
NAKAMURA Seitaro: On the Weak Interaction of Baryons. (S.N.) 1543
———: Interaction Types and Selection Rules in Baryon Processes. (S.N.) 2108
———: Strong Interaction of Baryons 2122
NAKANE Ryuichi: Re-appreciation of the Second Order Transition Phenomena in Polyethylene 1040
NAKANO Yoshihiro: [cf. HISATAKE Kazuo (741)]
———: [cf. FURUKAWA Michiaki (2167)]
NAKAU Tanehiro: Electrical Conductivity of α-Fe_2O_3. (S.N.) 727
NAKAZUMI Yoshihide: [cf. UCHIDA Enji (466)]
NAKASHIMA Shin-ichi: [cf. KATO Riso (2111)] (S.N.)
NATHANS Robert: [cf. KOMURA Yukitomo (1434)]
NARABA Tsunezo: [cf. NISHIOKA Atsuo (416)]
NARITA Shin-ichiro: Electroluminescence in Zinc Sulfide Single Crystals 128
NAYA Rokuroh;
———, M. MURAKAMI and E. HIRAHARA: Magnetic and Electrical Anomalies of Iron Telluride Single Crystals 360
NEGISHI Katsuo: Jump Phenomenon in Resonance Curve of Ferroelectric Ceramics. (S.N.) 534
NENNO Soji;
——— and J. W. KAUFFMAN: Detection and Determination of Equilibrium

Vacancy Concentrations in Aluminum 220
———, T. SABURI, M. TAGAYA and Z. NISHIYAMA: Observations of Dislocation Networks in an Alloy of Body-Centered Cubic Lattice by Electron Microscopy..1409
NII Riro: [cf. KANAI Yasuo (1717)]
NIIZEKI Nobukazu: [cf. TOYODA Hiroo (1831)]
NIMURA Hiroshi: Crystal Texture of LiF Single Crystal by X-Ray Technique 231
NINOMIYA Tosiyuki: Association of Vacancies with Calcium Impurities in Potassium Chloride Crystals 1601
NISHI Masato;
—, S. HAMAMURA and H. ARAKI: Emission Spectra from Glow Discharge through Vapors of Aromatic Hydrocarbons and n-Hexane 1536
NISHIGUCHI Katsumi: [cf. HUSIMI Kazuo (1341)] (S.N.)
NISHIKAWA Kyoji: Approach to Equilibrium of A Large Fermion System 78
NISHIMURA Jiro: The Dislocation Etch Pits of CdS Crystals. (S.N.) 732
NISHIOKA Atsuo;
———, Y. KOIKE, M. OWAKI, T. NARABA and Y. KATO: Proton Magnetic Resonance and X-ray Diffraction Studies of Polypropylene 416
NISIMURA Keigo: [cf. KIKUCHI Seishi (9, 41)]
———, S. SUWA, I. HAYASHI, K. FUKUNAGA, N. RYU and M. SEKI: Measurements of the Polarization in Proton-Helium Elastic Scattering 754
NISHIYAMA Zenji: [cf. NENNO Soji (1409)]
——— and K. SIMIZU: Direct Observation of Lattice Defects in Cold-worked High Manganese Steels by Means of Electron Microscopy 1963
NIU Keishiro: Flow of a Condensing Vapor with Heat Exchange 1108
NOGUCHI Sei-ichro;
——— and T. SATO: Concentration Dependence of the Hall Coefficient in the Magnesium-Cadmium Alloys..1945
——— and T. SATO: Thermoelectric Power of Titanium- and Vanadium-Carbides 2359
NOMURA Shoichiro: [cf. KAWAKUBO Tatsuyuki (2102)] (S.N.)
NOMURA Yûkichi;
———, I. YAMAMURA and S. INAWASHIRO: On the Acoustic Radiation from a Flanged Circular Pipe.. 510
NONAKA Itaru: [cf. KIKUCHI Seishi (41); MIKUMO Takashi (1158)]
———, H. YAMAGUCHI, T. MIKUMO, I. UMEDA, T. TABATA and S. HITAKA: Angular Distributions of Protons from the Reactions $^{12}C(\alpha, p)^{15}N$. (Errata) .. 365
NONOYAMA Minoru: [cf. KAMIYA Yoshihiro (2025)]
NOSE Hiroshi: Spin Wave Resonance in Ni Films. (S.N.) 1714
NOZAKI Tadashi: [cf. FURUKAWA Michiaki (2167)]
NOZAWA Masao: [cf. KATOH Toshio (2140)]
———, H. YAMAMOTO and Y. YOSHIZAWA: Search for Weak Gamma-Rays in the Positron Decay of Mn^{51} 2137
ODA Nobuo;
——— and H. SUZUKI: The Energy Spectra of Secondary Electrons in Various Materials Irradiated by Gamma Rays from "^{60}Co and ^{137}Cs". (S.N.) 2365
ODA Yukiyasu: [cf. KOBAYASHI Shinsaku (1151)]
———, M. TAKEDA, T. YAMAZAKI, C. HU, N. TAKANO, K. KIKUCHI, S. KOBAYASHI, K. MATSUDA and Y. NAGAHARA: Elastic and Inelastic Scattering of Protons from N, Ne, Mg, Si, S and A in the Energy Range from 7.6 MeV to 14.2 MeV 760
ODERA Masatoshi: [cf. MIKUMO Takashi (1158)]
ODAJIMA Akira: [cf. SASAKI Masahumi (1652); KAWAI Takao (1700) (S.N.)]
ODANI Yuzo: [cf. GOMI Yuzi (533, 535)]
OGATA Hiroshi;
—, K. TAKAMATSU, M. KAWASHIMA, A. MASAIKE, I. KUMABE, H. ITOH and Y. MASUDA: Energy Dependence of Angular Distribution of the Reaction $Al^{27}(p, \alpha)Mg^{24}$ in the Energy Region between 10.5 and 14.5 MeV 1719

, H. ITOH, Y. MASUDA, K. TAKAMATSU, M. KAWASHIMA, A. MASAIKE and I. KUMABE: Angular Distribution of the Reaction $Co^{59}(p, \alpha)Fe^{56}$ at 7.7∼14.1 MeV and $Mn^{55}(p, \alpha)Cr^{52}$ at 7.6∼12.9 MeV 1726

OGAWA Hiroshi: [cf. KIKUCHI Seishi (41)]

OGAWA Sekiko;

— and S. OKA: Theory of Electric Birefringence in Dilute Solutions of Tobacco Mosaic Virus 658

OGAWA Shinji: Magnetic Transition in $TiCl_3$. (S.N.) 1901

———: The Electron Paramagnetic Resonance of Mn^{2+} Ions Surrondued by an Octahedron 1475

———: Weak Ferromagnetism of $NaNiF_3$. (S.N.) 2361

OGAWA Shiro: [cf. TAKAHASHI Minoru (1351) (S.N.); NAGASAWA Akira (1421); IWASAKI Hiroshi (1771)]

OGAWA Shizuko;

— and K. OHI: Zeeman Quadrupole Spectra in p-dichlorobenzene and p-chlorobenzoic Acide 1064

OGINO Yasumasa: [cf. YAMAGUCHI Jiro (1541)] (S.N.)

OHI Kikuo: [cf. NAKAMURA Terutaro (1348) (S.N.); OGAWA Sizuko (1064)]

OHKURA Hiroshi: [cf. ONUKI Masami (1862)]

, K. AWANE and S. MIYAMOTO: On the $F \rightarrow F'$ Conversion in the Presence of A-, M-, R- and Z_1-Centers. (S.N.) 934

——— and A. Katsunobu: On A-centers in Colored KCl Crystals. (S.N.) 1349

– and T. UCHIDA: On the Reversible Optical Conversion Between A- and B-centers in Colored KCl Crystals. (S.N.) 2114

OHNISHI Tsuyoshi;

——, N. IMAI and F. OOSAWA: Interaction between Rod-like Polyelectrolytes .. 896

OHOYAMA Tetuo: [cf. KANEMATSU Kazuo (2358)] (S.N.)

OHTA (TAKAHATA) Masaomi: ^8Li Emission from Nuclear Disintegrations Produced by 4.3 GeV Negative π-Mesons 2187

OHTA Tokio: Effect of Charged Dislocation on the Thermoelectric Power of Semiconductors. (S.N.) 197

OHTSUKA Taiichiro: Interaction Effects in $K_3Fe(CN)_6$. (S.N.) 939

OKA Masahiro: [cf. ASADA Tsunesaburo (93)]

OKA Syoten: [cf. OGAWA Sekiko (658)]

OKA Takeshi: [cf. KASUYA Takahiro (296); KONDO Kunitaka (303, 307)]

——, H. HIRAKAWA and K. SHIMODA: Microwave Spectrum of Formaldehyde, I. K-type Doubling Spectra 2265

: Microwave Spectrum of Formaldehyde, II. Molecular Structure in the Ground State 2274

OKADA Eiji: [cf. WAKATSUKI Tetsuo (1141)]

OKADA Junichi;

——— and T. SUZUKI: α-Trapping Centers in n-Type Silicon. (S.N.) 1703

OKADA Kenkichi: Some Properties of X-ray damaged Rochelle Salt. (S.N.) 369

OKADA Yôichi;

———, T. ITO and A. AMEMIYA: Post-Irradiation Effect in Visible Absorption Spectra of Polyvinyl Chloride Sheets. (S.N.) 938

OKAMOTO Hiroshi: Theory of Solutions of Chain Molecules 650

OKANO Kotoyuki: [cf. TABATA Tatsuo (364)]

——: Gamma-rays from the Reaction $Al^{27}(p, \gamma)Si^{28}$ 28

OKANO Kotoyuki: [cf. TABATA Tatsuo (1552)]

—, T. TABATA, K. FUKUDA and J. MUTO: Lower Excited States in P^{29} from the $Si^{28}(p, \gamma)P^{29}$ Reaction 1556

OKANO Masaharu: [cf. DOKE Tadayoshi (737)]

OKAZAKI Atuyosi: [cf. ASANABE Sizuo (989)]

OKAZAKI Chisato: X-ray Studies on the Ferrite-Haematite Solid Solutions 2013

OKU Taiji: [cf. ASADA Tsunesaburo (93)]

OKUDA Akizo: [cf. FUKUDA Kuniya (538)]

OKUDA Fumiko: [HYODO Shin-ichi (2093)]
OMORI Yoshirô: An Investigation of Psychrometer, II. 706
OMURA Kazumi: [cf. ASADA Tsunesaburo (93)]
ONUKI Masami;
———— and H. OHKURA: Pulse Photoconductivity of Additively Colored KBr..1862
O-OHATA Kiyosi: The Binding Energy of the σ Bond, I. General Theory 1048
——: The Binding Energy of the σ Bond, II. Application to the Diamond Crystal 1258
——: The Binding Energy of the σ Bond, III. Discussion on the Ionic Structures 1449
———: The Binding Energy of the σ Bond, IV. Discussion on the Higher Order Terms 1632
OOKAWA Akiya: A Model Theory of Liquid 2191
OOSAWA Fumio: [cf. OHNISHI Tsuyoshi (896)]
OSADA Kikusaburo: Thermoluminescence of Zinc Sulfide Phosphors 145
OSHIDA Isao: Theory of Electrochemical Diodes....................................2288
OTSUKA Masamoto: [cf. HORIE Tadao (641)]
OTOMO Motoharu: [cf. WADA Yasaku (2324)]
OWAKI Masakazu: [cf. NISHIOKA Atsuo (416)]
PASKIN Arthur: [cf. HARRISON Ralph J. (1902)]
RUAN Jian-zhi: [cf. MIZOBUCHI Akira (1737); YAMABE Shotaro (2154)]
RUSTAD Brice: [cf. WAJIMA John. T. (630)]
RYU Norio: [cf. NISIMURA Keigo (754)]
SABURI Osamu: Piezoresistivity in Semiconductive Barium Titanates. (S.N.) 733
SABURI Toshio: [cf. NENNO Soji (1409)]
SAHEKI Bunsaburo: [cf. HISATAKE Kazuo (741)]
SAITO Haruo: [cf. ASADA Tsunesaburo (93)]
SAITO Tomoyuki: The Perturbation Method due to the Small Change in the Shape of the Boundary 2069
SAJI Yoshio: [cf. KIKUCHI Seishi (41); HISATAKE Kazuo (741)]
——: Energy Spectrum and Angular Distributions of Neutrons from the Reaction $\mathrm{Be}^9(p, n)\mathrm{B}^9$ at 8 to 14 MeV of Proton Energies 367
——: [cf. FURUKAWA Michiaki (2167)]
SAKAI Mitsuo: [cf. YAMAZAKI Toshimitsu (957)]
———: Spin Order in the Doublet at the Second Excited Level in Even-even Medium Nuclei. (S.N.) 993
SAKAI Sukeyoshi: [cf. TEZUKA Seiji (931)]
SAKUDO Tunetaro: Study of Solid-Solution Single Crystals Containing $BaTiO_3$. (S.N.)..2112
SAKUMA Kyoko: [cf. KIHARA Taro (684)]
SAKURAI Takeo: Two-dimensional Flow of an Ideal Gas with Small Electric Conductivity past a Thin Profile 326
———: Correction to the Paper "Two-dimensional Flow of an Ideal Gas with Small Electric Conductivity past a Thin Profile". (S.N.) 1135
SANADA Junpei: [cf. KIKUCHI Seishi (9, 41)]
SASAKI Masahumi: [cf. KAWAI Takao (1700)] (S.N.)
———, T. KAWAI, A. HIRAI, T. HASHI and A. ODAJIMA: A Study of Sorbed Water on Cellulose by Pulsed NMR Technique 1652
SASAKI Wataru: [cf. SHIBUYA Motoichi (207)]
SASAKI Yozo: [cf. FURUOYA Takashi (205); ISHII Zensho (206)]
SATO Hisanao: [cf. HATTORI Masumi (1237)]
SATO Kazuo: [cf. KIMURA Motoharu (1128); MUTSURO Naoshi (358)]
SATŌ Masayoshi;
and T. MITUI: Influence of Preparation and Quenching on the Magnetic Properties of Precipitates in Cu-Co Alloy. (S.N.) 537
SATO Takao: [cf. NOGUCHI Sei-ichiro (1945); NOGUCHI Sei-ichiro (2359) (S.N.)]
SATO Teruyuki: [cf. NAGAO Shigeo (735)]
SATOH Takeshi: A Simple Model of Aqueous Solution of Strong Electrolyte. (S.N.) ..1134
and K. HAYASHI: Study of Aqueous Solution of Strong Electrolyte—

Reexamination of Molecular Refraction 1658
SAWADA Shozo: [cf. YOSHIDA Ikushi (199)]
SAWAMURA Ichiro: [cf. KINOSITA Koreo (942)]
SEGAWA Wataru: Maxwell's Formula for Three-Dimensional and Large Deformation.. 339
: Measures of Finite Strain and Strees-Strain Relations 518
: Maxwell's Formula for Three-Dimensional and Large Deformation (Errata) 738
: Measures of Finite Strain and Strees-Strain Relation. (Errata)........ 945
SEKI masao: [cf. NISIMURA Keigo (754)]
SEKIYAMA Hisao: [cf. KAMIMURA Hiroshi (1264)]
SHIBAIKE Tsutomu: [cf. KOMATSUBARA Kiichi (1713)] (S.N.)
SHIBATA Akikazu: Distribution Coefficient of Zinc in Gallium Arsenide. (S.N.)........ 2107
SHIBATA Chokichiro: Electron Emission Current from Oxide Coated Cathode Subject to High Electric Field. (S.N.) 1124
SHIBATA Noboru: On a Solution of the Paraxial Ray Equation in an Axially Symmetrical Electrostatic Field. (S.N.) 200
SHIBUYA Motoichi;
and W. SASAKI: Intervalley Scattering of Hot Electrons. (S.N.) 207
SHICHIJŌ Yūzō;
, T. MIYADAI and H. TAKATA: Ferrimagnetic Resonance in Polycrystalline Europium-Iron Garnet ($Eu_3Fe_5O_{12}$). (S.N.) 530
SHIMADA Akira: [cf. TOYODA Koichi (536)]
SHIMAOKA Kohji: Electron Diffraction Study of Ice 106
SHIMIZU Hiroshi: [cf. ARATA Yoji (2119)]
SHIMIZU Ken-ichi: [cf. NISHIYAMA Zenji (1963)]
SHIMIZU Masao: On the Stability of an Electron Gas at Low Density 217
: Ferromagnetism of an Electron Gas 376
: On the Possibility of Ferromagnetism for Electron Gas. (S.N.) 1127
—: Paramagnetic Susceptibility of an Electron Gas in Alkaki Metals 2220
and T. TAKAHASHI: Magnetic Susceptibilities of Non-Ferromagnetic Transition Metals 2236
SHIMIZU Mikio: The Photoionization of H_2 and the Spatial Correlation between Electrons.. 1440
SHIMIZU Tadao: [cf. SHIMODA Koichi (2036)]
and H. TAKUMA: Microwave Spectrum of Cis-1, 2-Dichloroethylene.... 646
SHIMODA Koichi: [cf. KONDO Kunitaka (303); OKA Takeshi (2265)]
and K. KONDO: Magnetic Hyperfine Structure of the 3, 2 Line of Ammonia. (S.N.) 1125
—, H. TAKUMA and T. SHIMIZU: Beam-Type Masers for Radiofrequency Spectroscopy 2036
SHINOHARA Kenichi: [cf. KASHIWABARA Hisatsugu (1129)]
SHIRAFUJI Junji;
— and Y. INUISHI: Pulse Photoconduction and Carrier Lifetime in CdS Single Crystals. (S.N.) 1346
SHIRAI Hiroko: [cf. ABE Hidetaro (1711)]
SHIRAIWA Toshio: The Theory of the Fine Structure of the X-ray Absorption Spectrum, II. 240
SHIZUME Toshio: [cf. KIHARA Taro (684)]
SHODA Katsufusa: [cf. MORINAGA Haruhiko (213); KIMURA Motoharu (1128)]
SINES George: Filamentary Crystals grown from the Solid Metal 1199
SIRATORI Kiiti: [cf. TASAKI Akira (1535)] (S.N.)
— and S. IIDA: Magnetic Properties of $Mn_xCr_{1-x}O_2$. (S.N.) 210
, A. TASAKI and S. IIDA: On the Mechanism of Reversible Appearance of Residual Magnetization at low Temperature Transition in α Fe_2O_3. (S.N.).. 2357
— and S. IIDA: Anomalous Temperature Dependence of Lattice Constant of CrO_2. (S.N.) 2362
SÔMA Shinzau;
——— and Y. TAKEUCHI: A New Type of Thermal Conductivity Gas Detector, I. 333

SONO Toshimaro;
——, M. FUKUSHIMA and E. FUKADA: On the Stripe Pattern during Rolling of Viscous Materials. (S.N.) 1708
SONODA Masateru;
———, A. KATASE, M. SEKI and Y. WAKUTA: Ion Optics in Long, Multistage Accelerator Tubes 1680
SUGANO Satoru: [cf. KAMIMURA Hiroshi (1264)]
SUGANUMA Ryōji: Study on Some Tl Base Alloys, with Reference to their Electronic Structure 1395
——: Study on Some Tl Base Alloys, with Reference to their Electronic Structure. (Errata) 1696
SUGAWARA Masumi: [cf. SUGIYAMA Kazusuke (1909)]
SUGIHARA Ko: A Note on the Magnetic Resonance in Metals. (S.N.) 1712
SUGIHARA Makoto: [cf. GOMI Yuzi (533); TSUBOYA Ichiro (1534) (S.N.)]
———: On the Effect of Heat Treatment in a Magnetic Field on Magnetic Properties of Iron-Aluminium Alloys 1456
SUGIMOTO Kenzo: [cf. WAKATSUKI Tetsuo (1141)]
SUGIMOTO Tomihiko: [cf. CHONG Pyong-un (1137)]
SUGIOKA Etsu: [cf. ISHIGURO Masakazu (1302)]
SUGIURA Yoshikazu: Exchange Interaction and Cubic Crystal Field Splitting Parameter of Fe^{3+} in Spinel Structure 1217
——: [cf. NAKAMURA Akira (1704)] (S.N.)
SUGIYAMA Akira: Theory of Formation Energy of the External and the Internal Surface for Free Electron Metals 965
———: Magnetic Anisotropy of Iron-Cobalt Ferrite Measured by Ferromagnetic Resonance 1461
SUGIYAMA Kazusuke;
———, T. TŌHEI, M. SUGAWARA, T. DAZAI and Y. KANDA: Decay of Potassium 44 1909
SUITA Tokuo: [cf. ITOH Noriaki (1716, 2364) (S.N.)]
SUMI Masao: Theory of Electron-Oscillations in Non-Uniform Plasma 120
———: Non-Linear Effects on Electron-Plasma Oscillations 1068
SURYANARAYANA M.: [cf. KRISHNAMURTHI M. (345, 349, 2318)]
SUWA Shigeki: [cf. KIKUCHI Seishi (9, 41); NISHIMURA Keigo (754)]
SUZUKI Arata: [cf. KIKUCHI Seishi (41)]
SUZUKI Hiroshi: [cf. ODA Nobuo (2365)] (S.N.)
SUZUKI Kenzō: [cf. CHIKAZUMI Sōshin (250)]
SUZUKI Shigeyoshi: [cf. TAKAHASHI Isao (532)]
SUZUKI Tadasu: X-Ray Study on the Binding Properties of Cu_2O and Ag_2O Crystals .. 2018
SUZUKI Tatsusaburo;
——— and Jiro YUHARA: Characteristics of Krypton Counters. (S.N.) 1702
SUZUKI Tetsuro: [cf. OKADA Junichi (1709)] (S.N.)
SUZUKI Toshimasa: [cf. HUSIMI Kazuo (1341)] (S.N.)
SRIVASTAVA A. C.: Circulation Preserving Motions 1337
TABATA Tatsuo: [cf. NONAKA Itaru (365); OKANO Kotoyuki (1556)]
———, H. FUKUDA and K. OKANO: Lower Excited States in P^{29}. (S.N.) 364
—— and K. OKANO: Gamma-rays from the 7.56 MeV Level in O^{15} 1552
TACHIKAWA Kenkichi: [cf. KIKUCHI Makoto (835)]
TAGAYA Masayoshi: [cf. NENNO Soji (1409)]
TAKAGI Satio;
and F. FUJIMOTO: Measurement of the Intensity in Electron Diffraction by a CdS Single Crystal 1607
TAKAHASHI Isao;
–, T. HASHI, M. YAMANO, M. YAMAMOTO, S. SUZUKI and T. MAKITA: Maser Oscillation on 6-6 Line of $N^{16}H_3$. (S.N.) 532
TAKAHASHI Kasuke: [cf. ISHII Chikai (736)]
TAKAHASHI Hidetosi;
, T. NAKAMURA and Y. ISHIBASHI: Shape of Nucleus Domain Anchored to a Screw Dislocation in Ferroelectric Crystal 853

Conduction in CdSe. (S.N.) 1701

UCHIDA Enji:

——, H. KONDOH, Y. NAKAZUMI and T. NAGAMIYA: Magnetic Anisotropy Measurements of MnO Single Crystal 466

UCHIDA Yoichi: [cf. FUKUDA Kuniya (538, 1344) (S.N.); KATO Riso (2105, 2111) (S.N.)]

UEDA Tomiko: [cf. KUSUMOTO Hazime (728)]

UEHARA Yasuo: The Quantitative Interpretation of Luminescent Properties of Cu-Activated Calcium Orthophosphate.. 612

UETA Masayasu;

——, M. HIRAI and H. WATANABE: Interaction of Exciton with Electron Trapping Centers in Alkali Halide Crystals, 2. Quantum Yield for the $U\rightarrow F$ Conversion and its Dependence on *U*-Center Concentration 593

— and M. HIRAI: Exciton-Induced Photoconductivity of *U* Centers in KCl Crystal. (S.N.) 1356

UMEBAYASHI Hiromichi: [cf. WADA Yasaku (2324)]

UMEDA Iwao: [cf. NONAKA Itaru (365)]

URYU Norikiyo: On the Paramagnetic Susceptibility of Sm^{3+} ion 2041

UYEDA Ryozi: [cf. KAMIYA Yoshihiro (2025)]

VODIČKA Václav: Steady Temperature Field in a Composite Doubly Infinite Strip 1332

WADA Yasaku;

– and H. HIROSE: Glass Transition Phenomena and Rheological Properties of Petroleum Asphalt 1885

, H. HIROSE, H. UMEBAYASHI and M. OTOMO: Volume Viscoelasticity of Polymers and Other Highly Dissipative Materials 2324

WAJIMA John T.;

, B. M. RUSTAD and E. MELKONIAN: Germanium Crystal as a Neutron Monochrometer and the Determination of its Higher Order Contaminations.. 630

WAKABAYASHI Hisawo: Temperature Dependence of Surface Potential in Silver Chloride Single Crystals 2000

WAKATSUKI Tetsuo;

—, Y. HIRAO, E. OKADA, I. MIURA, K. SUGIMOTO and A. MIZOBUCHI: Gamma Rays from Several Elements bombarded by 10 and 14 MeV Protons..1141

WAKIYAMA Tokuo;

- and Sōshin CHIKAZUMI: Magnetostriction and Crystal Anisotropy of Nickel-Chromium and Nickel-Vanadium 1975

WAKU Shigeru: [cf. TOYODA Hiroo (1831)]

—, K. MASUNO, T. TANAKA and H. IWASAKI: Ferroelectricity in Potassium Ferrocyanide Trihydrate and its Isomorphous Substances....................1185

—, K. MASUNO and T. TANAKA: Ferroelectricity in the Potassium Ferrocyanide Group Ferroelectrics Substituted by Deuterium for Hydrogen. (S.N.)..1698

WAKUTA Yoshihisa: [cf. SONODA Masateru (1680)]

WATANABE Denjiro: Study on the Ordered Alloys of Gold-Manganese System by Electron Diffraction, I. Au$_4$Mn 1030

: [cf. TAKAHASHI Minoru (1351) (S.N.); IWASAKI Hiroshi (1771)]

—: Study on the Ordered Alloys of Gold-Manganese System by Electron Diffraction, II. Au$_3$Mn 1251

WATANABE Hiroshi: "Energy Analysis of Electron Diffraction Patterns." (S.N.) 2368

WATANABE Hiroyuki: [cf. UETA Masayasu (593)]

WATANABE Jirô: [cf. YAMAMOTO Mikio (2099)] (S.N.)

WATANABE Naozo: [cf. KANAI YASUO (1717)] (S.N.)

WOLF W. P.: On the Ferrimagnetic Resonance of Europium Iron Garnet. (S.N.)......2104

YAEGASHI Yûki: [cf. MORITA Susumu (361) (S.N.); MORITA Susumu (550)]

YAGI Masuo: [cf. TANAKA Shigeo (545); TANAKA Shigeo (1357) (Errata); TANAKA Shigeo (1547, 2125)]

YAJIMA Tatsuo;

—— and K. SHIMODA: The Three-Level Gas Maser as a Microwave Spectrometer 1668

YAMADA Yasusada: On the Paramagnetic Inelastic Scattering of Neutrons due to Ions

in the Anisotropic Crystalline Field 429
YAMADA Motohiko: [YUZURI Motoyoshi (1845)]
YAMADA Shôji: On the Electrical and Optical Properties of p-type Cadmium Telluride Crystals 1940
YAMAFUJI Kaoru: Dielectric β-Relaxations in Some Linear High Polymers............2295
YAMAGATA Kazuo: A Note on the Paper " Magneto-Plasma Resonance in Semiconductors I. " (S.N.)....................................2363
YAMAGUCHI Hisashi: [cf. KIKUCHI Seishi (41)]
YAMAGUCHI Jiro;
———, S. HORIUCHI, K. MATSUMURA and Y. OGINO: On the Determination of Diffusion Coefficient of Boron in Silicon 1541
YAMABE Shotaro;
———, M. KONDO, S. KATO, T. YAMAZAKI, and J. RUAN: Polarization of Protons Scattered from Complex Nuclei....................................2154
YAMAGUCHI Hisashi: [cf. MIKUMO Takashi (1158)]
YAMAGUCHI Shigeo: The Resonance Type Absorption of Very Thin Silver and Gold Films 1577
YAMAKAMI Tsutomu: [cf. KAMIYOSHI Kan-Ichi (1347)] (S.N.)
YAMAMOTO Mikio;
——— and J. WATANABE: Fatigue Properties of Zinc Single Crystals and Polycrystals (S.N.)....................................2099
YAMAMOTO Hisashi: [cf. NOZAWA Masao (2137)]
YAMAMOTO Motokazu: [cf. TAKAHASHI Isao (532)]
YAMAMURO Nobuhiro: [cf. KOBAYASHI Shinsaku (1151)]
YAMAMURA Ichirô: [cf. NOMURA Yûkichi (510)]
YAMANE Mikiya: Ionization in Argon Mixtures by Electrons in an Electric Field 1076
———: A Study of Pulse Height Distribution of Boron—Trifluoride Proportional Counters 1732
YAMANO Masaru: [cf. TAKAHASHI Isao (532)]
YAMANOUCHI Mikio: [cf. MIWA Mitsuo (947)]
YAMASHITA Hirosuke: [cf. IBUKI Sumiaki (2356)] (S.N.)
——— and T. KUROSAWA: Heitler-London Approach to Electrical Conductivity and Application to d-Electron Conductions 802
———, S. IBUKI, T. YOSHIZAWA and H. KOMIYA: Electroluminescence of CdS Single Crystal. (S.N.) 2366
YAMASHITA Tadayoshi;
——— and Y. TANEDA: Dislocations in Pure Iron Foils Deformed by Bending..1015
YAMAZAKI Takashi: [cf. ODA Yukiyasu (760); YAMABE Shotaro (2154)]
YAMAZAKI Toshimitsu;
———, H. IKEGAMI and M. SAKAI: On the First and the Second Excited States in Ge^{74} 957
YANAGI Taketoshi: [cf. KAWAKUBO Tatsuyuki (2102)]
YASUHARA Michiru: Flow of a Viscous, Electrically Conducting Fluid along a Circular Cylinder or a Flat Plate with Uniform Suction.................................... 321
YASUKŌCHI Kō: [cf. KANEMATSU Kazuo (2358)] (S N.)
———, K. KANEMATSU and T. OHOYAMA: Ferrimagnetism of Mn$_5$Ge$_2$. (S.N.).. 932
YASUMI Shinjiro;
———, M. YATA, K. TAKAMATSU, A. MASAIKE and Y. MASUDA: Absolute Cross Section of the Reaction Cu$^{63}(\gamma, n)$Cu^{62} for Lithium Gamma Rays 1913
YATA Minoru: [cf. YASUMI Shinjiro (1913)]
YODA Eiji: [cf. HASHIMOTO Hatsujiro (1006)]
———: Anomalous Growth of MoO$_3$ Crystals 821
YOKOTA Toshio: Expansion Theorem of Density Matrix, Virial Expansion and New Formula of Multiple Scattering 779
YOKOZAWA Yasaburo: Paramagnetic Resonance of Mn^{++}-F$^-$ Pair in Sodium Chloride. (S.N.)....................................1131
YOMOSA Sigeo: Statistical Mechanics of Antiferromagnetic Layer Crystal, FeCl$_2$......1068

YONEMITSU Hiroo;

———, H. MAEDA and H. MIYAZAWA: Sign Reversal of Hall Coefficients at Low Temperatures in Heavily Compensated *p*-type Germanium. (S.N.) 1717

———. H, MAEDA and H. MIYAZAWA: Sign Reversal of Hall Coefficients at Low Temperatures in Heavily Compensated *p*-type Germanium. (Errata) 1907

YOSHIDA Ikushi;

——— and S. SAWADA: Thermal Conductivity of KNO_3. (S.N.) 199

———: Thermal Conduction in Ferroelectric Ceramics 2211

YOSHIMATSU Mitsuru;

——— and K. KOHRA: X-ray Observations on Cleavage Faces of LiF Single Crystals..1760

——— and K. KOHRA: X-ray Study of Lattice Defects in Si Single Crystals by Transmission Berg-Barrett Technique. (S.N.) 2367

——— and K. KOHRA: X-ray Observations on Cleavage Faces of LiF Single Crystals. (Errata) 2369

YOSHIMURA Hisamitsu: Paramagnetic Resonance of Manganese in Alkali-Chlorides.... 435

YOSHINOBU Hirowo: A Linearized Theory of Magnetohydrodynamic Flow past a Fixed Body in a Parallel Magnetic Field.. 175

YOSHINOBU Yasukazu: [cf. NOZAWA Masao (2137); KATOH Toshio (2140)]

YOSIZAWA Michio: [cf. YAMASHITA Hirosuke (2366)] (S.N.)

YUASA Kazunori: [cf. HISATAKE Kazuo (741)]

YUASA Toshiyoshi: Color Center and Gaseous Ions Produced in High Frequency Spark between the Electrodes of Semi-metals, Metal Elements, and Ionic-crystals. (S.N.)..1900

YUHARA Jiro: [cf. SUZUKI Tatsusaburo (1702)]

YUKIMOTO Yoshinori: [cf. KŌI Yoshitaka (1342)] (S.N.)

YUZURI Motoyoshi;

——— and M. YAMADA: On the Magnetic Properties of the Compound Mn_2As..1845

———: On the Magnetic Properties of Cr_2As and Cu_2Sb 2007